

World Clinical *Radiology*

2015 March 28 First Edition: 1-727

Edited by Edwin JR van Beek, MD, PhD, FRCR, FRCPE, Professor

Place of Publication: Pleasanton (CA)





PREFACE

- I Core progresses in clinical radiology in 2014
van Beek EJR

2014 ADVANCES IN CARDIOPULMONARY IMAGING

- 1 Lung cancer screening-don't forget the chest radiograph
Gossner J
- 4 Coronary plaque imaging by coronary computed tomography angiography
Sato A
- 16 Unusual fistulas and connections in the cardiovascular system: A pictorial review
Ghandour A, Rajiah P
- 24 Effectiveness of chest radiography, lung ultrasound and thoracic computed tomography in the diagnosis of congestive heart failure
Cardinale L, Priola AM, Moretti F, Volpicelli G
- 32 Multi-detector computed tomography in the diagnosis and management of acute aortic syndromes
Hallinan JTPD, Anil G
- 43 Coronary venous system in cardiac computer tomography: Visualization, classification and role
Mlynarski R, Mlynarska A, Sosnowski M
- 53 Nuclear imaging in detection and monitoring of cardiotoxicity
D'Amore C, Gargiulo P, Paolillo S, Pellegrino AM, Formisano T, Mariniello A, Della Ratta G, Iardino E, D'Amato M, La Mura L, Fabiani I, Fusco F, Perrone Filardi P
- 60 Role of cardiac CTA in estimating left ventricular volumes and ejection fraction
Singh RM, Singh BM, Mehta JL
- 68 Radiation pneumonitis after stereotactic radiation therapy for lung cancer
Yamashita H, Takahashi W, Haga A, Nakagawa K
- 76 Imaging of community-acquired pneumonia: Roles of imaging examinations, imaging diagnosis of specific pathogens and discrimination from noninfectious diseases
Nambu A, Ozawa K, Kobayashi N, Tago M

- 91 Spontaneous pneumomediastinum and Macklin effect: Overview and appearance on computed tomography
Murayama S, Gibo S
- 2014 ADVANCES IN GASTROINTESTINAL IMAGING**
- 96 Management of hepatocellular carcinoma: The role of contrast-enhanced ultrasound
Zheng SG, Xu HX, Liu LN
- 104 Treatment of metastatic liver tumors using stereotactic ablative radiotherapy
Nair VJ, Pantarotto JP
- 112 Imaging pitfalls of pancreatic serous cystic neoplasm and its potential mimickers
Ishigami K, Nishie A, Asayama Y, Ushijima Y, Takayama Y, Fujita N, Takahata S, Ohtsuka T, Ito T, Igarashi H, Ikari S, Metz CM, Honda H
- 124 Role of interventional radiology in the management of acute gastrointestinal bleeding
Ramaswamy RS, Choi HW, Mouser HC, Narsinh KH, McCammack KC, Treesit T, Kinney TB
- 135 Multi-detector CT features of acute intestinal ischemia and their prognostic correlations
Moschetta M, Telegrafo M, Rella L, Stabile Ianora AA, Angelelli G
- 144 Partial splenic artery embolization in cirrhotic patients
Haddock TA, McWilliams JP
- 153 Magnetic resonance cholangiography in the assessment and management of biliary complications after OLT
Girometti R, Cereser L, Bazzocchi M, Zuiani C
- 166 Gastrointestinal imaging-practical magnetic resonance imaging approach
Liu B, Ramalho M, AlObaidy M, Busireddy KK, Altun E, Kalubowila J, Semelka RC
- 189 Incorporating GSA-SPECT into CT-based dose-volume histograms for advanced hepatocellular carcinoma radiotherapy
Shirai S, Sato M, Noda Y, Kumayama Y, Shimizu N
- 198 Upper gastrointestinal barium evaluation of duodenal pathology: A pictorial review
Gupta P, Debi U, Sinha SK, Prasad KK
- 204 Expectations from imaging for pre-transplant evaluation of living donor liver transplantation
Hennedige T, Anil G, Madhavan K
- 219 Malrotation: Current strategies navigating the radiologic diagnosis of a surgical emergency
Tackett JJ, Muise ED, Cowles RA

2014 ADVANCES IN GENITOURINARY IMAGING

- 226 Diffusion-weighted magnetic resonance imaging in management of bladder cancer, particularly with multimodal bladder-sparing strategy
Yoshida S, Koga F, Kobayashi S, Tanaka H, Satoh S, Fujii Y, Kihara K

- 237 Multimodality imaging of renal inflammatory lesions
Das CJ, Ahmad Z, Sharma S, Gupta AK

2014 ADVANCES IN MUSCULOSKELETAL IMAGING

- 246 Imaging of skeletal muscle in vitamin D deficiency
Bignotti B, Cadoni A, Martinoli C, Tagliafico A

- 252 Rotator cuff disorders: How to write a surgically relevant magnetic resonance imaging report?
Tawfik AM, El-Morsy A, Badran MA

- 262 Comparative review of vertebroplasty and kyphoplasty
Ruiz Santiago F, Santiago Chinchilla A, Guzmán Álvarez L, Pérez Abela AL, Castellano García MM, Pajares López M

- 277 Bone mineral density in cone beam computed tomography: Only a few shades of gray
Campos MJS, de Souza TS, Mota Júnior SL, Fraga MR, Vitral RWF

- 283 From histology to micro-CT: Measuring and modeling resorption cavities and their relation to bone competence
Vanderoost J, van Lenthe GH

- 297 Skeletal dysplasias: A radiographic approach and review of common non-lethal skeletal dysplasias
Panda A, Gamanagatti S, Jana M, Gupta AK

- 315 A handy review of carpal tunnel syndrome: From anatomy to diagnosis and treatment
Ghasemi-rad M, Nosair E, Vegh A, Mohammadi A, Akkad A, Lesha E, Mohammadi MH, Sayed D, Davarian A, Maleki-Miyandoab T, Hasan A

2014 ADVANCES IN NEURORADIOLOGY/HEAD AND NECK IMAGING

- 332 Clinical decision support systems for brain tumor characterization using advanced magnetic resonance imaging techniques
Tsolaki E, Kousi E, Svolos P, Kapsalaki E, Theodorou K, Kappas C, Tsougos I

- 342 fMRI contributions to addressing autobiographical memory impairment in temporal lobe pathology
Denkova EJ, Manning L

- 355 Orbital inflammatory disease: Pictorial review and differential diagnosis
Pakdaman MN, Sepahdari AR, Elkhamary SM

- 365 Use of cone beam computed tomography in periodontology
Acar B, Kamburoğlu K

- 374 Role of ¹⁸F-FDG PET/CT in pre and post treatment evaluation in head and neck carcinoma
Tantiwongkosi B, Yu F, Kanard A, Miller FR
- 389 Application of fluorodeoxyglucose positron emission tomography in the management of head and neck cancers
Siddiqui F, Yao M
- 403 Sustained attention in psychosis: Neuroimaging findings
Sepede G, Spano MC, Lorusso M, De Berardis D, Salerno RM, Di Giannantonio M, Gambi F
- 416 Neuroimaging in Huntington's disease
Niccolini F, Politis M
- 428 Clinical significance of computed tomography assessment for third molar surgery
Nakamori K, Tomihara K, Noguchi M
- 435 Intraoperative perfusion magnetic resonance imaging: Cutting-edge improvement in neurosurgical procedures
Ulmer S
- 441 Imaging of the temporomandibular joint: An update
Bag AK, Gaddikeri S, Singhal A, Hardin S, Tran BD, Medina JA, Curé JK
- 457 Measuring consciousness in coma and related states
Di Perri C, Thibaut A, Heine L, Soddu A, Demertzi A, Laureys S
- 466 Echography in brain imaging in intensive care unit: State of the art
Caricato A, Pitoni S, Montini L, Bocci MG, Annetta P, Antonelli M
- 473 MRI in central nervous system infections: A simplified patterned approach
Rangarajan K, Das CJ, Kumar A, Gupta AK
- 483 Low dose four-dimensional computerized tomography with volume rendering reconstruction for primary hyperparathyroidism: How I do it?
Platz TA, Kukar M, Elmarzouky R, Cance W, Abdelhalim A
- 487 Role of functional imaging in the development and refinement of invasive neuromodulation for psychiatric disorders
Williams NR, Taylor JJ, Lamb K, Hanlon CA, Short EB, George MS
- 510 Recent advances in imaging technologies in dentistry
Shah N, Bansal N, Logani A
- 524 Application of magnetic resonance imaging in cervical spondylotic myelopathy
Zhang C, Das SK, Yang DJ, Yang HF

531 Partial volume effect modeling for segmentation and tissue classification of brain magnetic resonance images: A review
Tohka J

541 Functional topography of the corpus callosum investigated by DTI and fMRI
Fabri M, Pierpaoli C, Barbaresi P, Polonara G

2014 ADVANCES IN NUCLEAR MEDICINE AND MOLECULAR IMAGING

553 Recent developments in optimal experimental designs for functional magnetic resonance imaging
Kao MH, Temkit M, Wong WK

562 Neural mechanisms of mindfulness and meditation: Evidence from neuroimaging studies
Marchand WR

571 Impact of dose calculation algorithm on radiation therapy
Chen WZ, Xiao Y, Li J

578 Congenital hyperinsulinism: Role of fluorine-18L-3, 4 hydroxyphenylalanine positron emission tomography scanning
Gopal-Kothandapani JS, Hussain K

587 FDG-PET/CT response evaluation during EGFR-TKI treatment in patients with NSCLC
van Gool MH, Aukema TS, Hartemink KJ, Valdés Olmos RA, van Tinteren H, Klomp HM

594 Nuclear medicine and the failed joint replacement: Past, present, and future
Palestro CJ

607 Echographic imaging of tumoral cells through novel nanosystems for image diagnosis
Di Paola M, Chiriacò F, Soloperto G, Conversano F, Casciaro S

619 Clinical use of bone-targeting radiopharmaceuticals with focus on alpha-emitters
Wieder HA, Lassmann M, Allen-Auerbach M, Czernin J, Herrmann K

625 Radiogenomic imaging-linking diagnostic imaging and molecular diagnostics
Goyen M

629 Postoperative reactive lymphadenitis: A potential cause of false-positive FDG PET/CT
Liu Y

2014 ADVANCES IN PEDIATRIC IMAGING

634 Imaging of Gaucher disease
Simpson WL, Hermann G, Balwani M

646 2-deoxy-2-(¹⁸F)fluoro-D-glucose positron emission tomography/computed tomography imaging in paediatric oncology
Freebody J, Wegner EA, Rossleigh MA

661 Quantitative magnetic resonance imaging of the fetal brain in utero: Methods and applications
Biegon A, Hoffmann C

668 Paediatric computed tomography radiation dose: A review of the global dilemma
Almohiy H

674 Imaging of the small bowel: Crohn's disease in paediatric patients
Casciani E, De Vincentiis C, Poletti E, Masselli G, Di Nardo G, Civitelli F, Cucchiara S, Gualdi GF

690 Role of MRI in the diagnosis and treatment of osteomyelitis in pediatric patients
Pugmire BS, Shailam R, Gee MS

2014 ADVANCES IN VASCULAR AND INTERVENTIONAL RADIOLOGY

698 Pathophysiology, clinical features and radiological findings of differentiation syndrome/all-trans-retinoic acid syndrome
Cardinale L, Asteggiano F, Moretti F, Torre F, Ulisciani S, Fava C, Rege-Cambrin G

704 Vascular anomalies: A pictorial review of nomenclature, diagnosis and treatment
Nosher JL, Murillo PG, Liszewski M, Gendel V, Gribbin CE

2014 ADVANCES IN WOMEN'S IMAGING

720 Use of stereotactic radiosurgery in the treatment of gynecologic malignancies: A review
Long B, Eskander RN, Tewari KS

ABOUT COVER

Edwin JR van Beek, MD, PhD, FRCR, FRCPE, Professor; Ahmed AKA Razek, MD, Professor; Mirko D'Onofrio, MD, Assistant Professor; Masahito Kawabori, MD, PhD, Doctor, Postdoctoral Fellow; Bilal Battal, MD, Associate Professor; Georgios Plataniotis, MD, PhD, Doctor; Ritesh Agarwal, MD, Associate Professor; John L Nosher, MD, Professor; Mohamed R Nouh, MD, Senior Lecturer.

EDITORS FOR THIS BOOK

Responsible Electronic Editor: *Ya-Jing Lu*
Proofing Science Editor: *Xue-Mei Gong*

NAME OF BOOK

World Clinical Radiology

ISBN 978-0-9914430-9-3

PUBLICATION DATE

March 28, 2015

EDITOR

Edwin JR van Beek, MD, PhD, Professor, Clinical Research Imaging Centre and Department of Medical Radiology, University of Edinburgh, Edinburgh EH16 4TJ, United Kingdom

PUBLISHER

Baishideng Publishing Group Inc
8226 Regency Drive, Pleasanton, CA 94588-3144, United States
Telephone: +1-925-223-8242

Fax: +1-925-223-8243

E-mail: bpgoffice@wjgnet.com

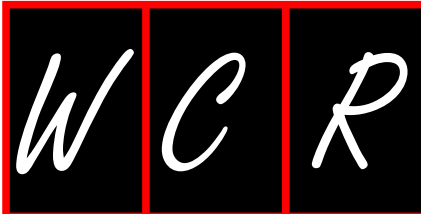
<http://www.wjgnet.com>

COPYRIGHT

© 2015 Baishideng Publishing Group Inc. Articles published by this book are distributed under the terms of the Creative Commons Attribution Non-commercial License, which permits use, distribution, and reproduction in any medium, provided the original work is properly cited, the use is non commercial and is otherwise in compliance with the license.

SPECIAL STATEMENT

All articles published in this book owned by the Baishideng Publishing Group (BPG) represent the views and opinions of their authors, and not the views, opinions or policies of the BPG, except where otherwise explicitly indicated.



Lung cancer screening-don't forget the chest radiograph

Johannes Gossner

Johannes Gossner, Department of Clinical Radiology, Evangelisches Krankenhaus Göttingen-Weende, 37074 Göttingen, Germany

Author contributions: Gossner J contributed solely to this work.
Correspondence to: Johannes Gossner, MD, Department of Clinical Radiology, Evangelisches Krankenhaus Göttingen-Weende, An der Lutter 24, 37074 Göttingen, Germany. johannesgossner@gmx.de
Telephone: +49-551-50341762 Fax: +49-551-50341127
Received: November 1, 2013 Revised: January 18, 2014
Accepted: April 11, 2014
Published online: March 28, 2015

Abstract

Lung cancer is a major health burden and early detection only bears the possibility of curative treatment. Screening with computed tomography (CT) recently demonstrated a mortality reduction in selected patients and has been incorporated in clinical guidelines. Problems of screening with CT are the excessive number of false positive findings, costs, radiation burden and from a global point of view shortage of CT capacity. In contrast, chest radiography could be an ideal screening tool in the early detection of lung cancer. It is widely available, easy to perform, cheap, the radiation burden is negligible and there is only a low rate of false positive findings. Large randomized controlled trials could not show a mortality reduction, but different large population-based cohort studies have shown a lung cancer mortality reduction. It has been argued that community-based cohort studies are more closely reflecting the "real world" of everyday medicine. Radiologists should be aware of the found mortality reduction and realize that early detection of lung cancer is possible when reading their daily chest radiographs. Offering a chest radiograph in selected scenarios for the early detection of lung cancer is therefore still justified.

© 2015 Baishideng Publishing Group Inc. All rights reserved.

Key words: Lung cancer; Screening; Mortality; Chest radiograph

Core tip: Screening with computed tomography (CT) recently demonstrated a mortality reduction in selected patients with lung cancer, but there are several shortcomings of screening with CT (false positive findings, high costs, radiation burden, shortage of capacity). In contrast, chest radiography could be an ideal screening tool in the early detection of lung cancer. It is widely available, its radiation burden is negligible and there is only a low rate of false positive findings. In contrast to randomized controlled trials different large population-based cohort studies have shown a lung cancer mortality reduction using chest radiography. In conclusion, early detection of lung cancer is also possible with chest radiography.

Original sources: Gossner J. Lung cancer screening-don't forget the chest radiograph. *World J Radiol* 2014; 6(4): 116-118 Available from: URL: <http://www.wjgnet.com/1949-8470/full/v6/i4/116.htm> DOI: <http://dx.doi.org/10.4329/wjr.v6.i4.116>

Lung cancer is a major health burden and early detection only bears the possibility of curative treatment. Therefore a screening test would be desirable. A number of older studies have tested chest radiography and sputum cytology and most of them showed no reduction in mortality compared to randomized control groups^[1]. The publication of the results of the National Lung Screening Trial (NLST), showing mortality reduction of 20% in patients undergoing screening with low-dose chest computed tomography (CT) in comparison to patients undergoing chest radiography, renewed the interest in screening for lung cancer^[2]. Based on these results screening with CT for selected patient groups has recently been incorporated in different clinical guidelines. For example the American Association of Thoracic Surgery advocates screening with annual low-dose chest CT for smokers or former

smokers with a 30-pack year history beginning at the age of 55^[3]. The main problem with CT screening is the excessive number of false positive findings. In the first two screening rounds of the NLST 27.3% and 27.8% of participants showed suspect findings (*i.e.*, a nodule measuring at least 4 mm). Of these nodules only 3.8% turned out to be lung cancers (230 out of 7731 positive results). This leads to high costs with further diagnostics and causes considerable anxiety in affected individuals with a suspect nodule. CT is also expensive *per se* and from a global point of view not readily available everywhere. Most health care systems will not be able to finance such a CT-based screening program. The radiation burden due to repeated CT scans should also be taken into account.

In contrast, chest radiography could be an ideal screening tool in the early detection of lung cancer. It is widely available, easy to perform, cheap, its radiation burden is negligible and there is only a low rate of false positive findings. As randomized controlled trials (RCT) have shown no reduction in lung cancer mortality compared to control groups it has been concluded by most investigators that screening with chest radiography is ineffective^[1]. This view has been repeatedly challenged: most RCT have shown a survival advantage for screened individuals because of a stage shift in diagnosed cancers^[4,5]. Because RCT are prone to selection bias (selection of highly motivated individuals and problem of generating two comparable groups) population based cohort studies may give a more realistic view of the situation in medical care^[5,6]. Recently, a group of Italian investigators presented their follow-up data of a large population based cohort study^[7]. Participation in this trial was offered to all patients at risk for lung cancer (smokers with more than 10 pack years between 45 and 75 years of age) by their general practitioner. The trial consisted of a baseline two view chest radiography and an annually repeated examination (single view) for the following four years. Five thousand eight hundred and fifteen subjects participated and follow up was 8 years. Compared to a statistical control population derived from the national health services data there was a lung cancer mortality reduction of 18% (172 deaths to lung cancer instead of 210 expected). Interestingly, there were only 3.4% false positive findings and only 0.16% unnecessary invasive procedures^[7]. There are also several case-control studies from Japan showing a reduction of lung cancer mortality between 40% and 60% using screening with chest radiography and sputum cytology^[8]. One population based case-control study from Japan used X-ray screening only and found a lung cancer mortality reduction of more than 20%^[9]. Newer technologies like digital radiography, bone suppression or computer-aided nodule detection may further enhance the sensitivity of chest radiography in the detection of early lung cancer, but have not been adopted in the studies mentioned above^[10]. Caro *et al*^[11] calculated cost-effectiveness of lung cancer screening with chest radiography. They concluded that even an achieved mortality reduction of 6% could be cost-effective.

In conclusion, radiologists should realize that screen-

ing with chest radiography leads to reduced lung cancer mortality in population-based cohort studies. Radiologists should be aware that early detection of lung cancer is possible when reading their daily chest radiographs. And in the clinically common scenario of a worried middle aged smoker asking for lung cancer “screening” a chest radiograph is still justified.

Despite the exiting results of the NLST there are many unresolved issues with CT-based screening for lung cancer (how to reduce false-positive findings, optimal patient selection, long term outcome of screened patients, transferability of the results of the NLST to other populations)^[12]. Until more data from ongoing trials is available, CT-based screening should therefore not be advocated and used cautiously only.

REFERENCES

- 1 **Humphrey LL**, Teutsch S, Johnson M. Lung cancer screening with sputum cytologic examination, chest radiography, and computed tomography: an update for the U.S. Preventive Services Task Force. *Ann Intern Med* 2004; **140**: 740-753 [PMID: 15126259 DOI: 10.7326/0003-4819-140-9-200405040-00015]
- 2 **Aberle DR**, Adams AM, Berg CD, Black WC, Clapp JD, Fagerstrom RM, Gareen IF, Gatsonis C, Marcus PM, Sicks JD. Reduced lung-cancer mortality with low-dose computed tomographic screening. *N Engl J Med* 2011; **365**: 395-409 [PMID: 21714641 DOI: 10.1056/NEJMoa1102873]
- 3 **Jaklitsch MT**, Jacobson FL, Austin JH, Field JK, Jett JR, Keshavjee S, MacMahon H, Mulshine JL, Munden RF, Salgia R, Strauss GM, Swanson SJ, Travis WD, Sugarbaker DJ. The American Association for Thoracic Surgery guidelines for lung cancer screening using low-dose computed tomography scans for lung cancer survivors and other high-risk groups. *J Thorac Cardiovasc Surg* 2012; **144**: 33-38 [PMID: 22710039 DOI: 10.1016/j.jtcvs.2012.05.060]
- 4 **Strauss GM**, Gleason RE, Sugarbaker DJ. Chest X-ray screening improves outcome in lung cancer. A reappraisal of randomized trials on lung cancer screening. *Chest* 1995; **107**: 270S-279S [PMID: 7781405 DOI: 10.1378/chest.107.6_Supplement.270S]
- 5 **Strauss GM**, Dominioni L. Chest X-ray screening for lung cancer: overdiagnosis, endpoints, and randomized population trials. *J Surg Oncol* 2013; **108**: 294-300 [PMID: 23982825]
- 6 **Dominioni L**, Rotolo N, Mantovani W, Poli A, Pisani S, Conti V, Paolucci M, Sessa F, Paddeu A, D'Ambrosio V, Imperatori A. A population-based cohort study of chest x-ray screening in smokers: lung cancer detection findings and follow-up. *BMC Cancer* 2012; **12**: 18 [PMID: 22251777 DOI: 10.1186/1471-2407-12-18]
- 7 **Dominioni L**, Poli A, Mantovani W, Pisani S, Rotolo N, Paolucci M, Sessa F, Conti V, D'Ambrosio V, Paddeu A, Imperatori A. Assessment of lung cancer mortality reduction after chest X-ray screening in smokers: a population-based cohort study in Varese, Italy. *Lung Cancer* 2013; **80**: 50-54 [PMID: 23294502 DOI: 10.1016/j.lungcan.2012.12.014]
- 8 **Sagawa M**, Nakayama T, Tsukada H, Nishii K, Baba T, Kurita Y, Saito Y, Kaneko M, Sakuma T, Suzuki T, Fujimura S. The efficacy of lung cancer screening conducted in 1990s: four case-control studies in Japan. *Lung Cancer* 2003; **41**: 29-36 [PMID: 12826309 DOI: 10.1016/S0169-5002(03)00197-1]
- 9 **Nakayama T**, Baba T, Suzuki T, Sagawa M, Kaneko M. An evaluation of chest X-ray screening for lung cancer in gunma prefecture, Japan: a population-based case-control study. *Eur J Cancer* 2002; **38**: 1380-1387 [PMID: 12091070]
- 10 **Freedman M**. State-of-the-art screening for lung cancer (part 1): the chest radiograph. *Thorac Surg Clin* 2004; **14**: 43-52

- [PMID: 15382307 DOI: 10.1016/S1547-4127(04)00036-2]
11 **Caro JJ**, Klittich WS, Strauss G. Could chest X-ray screening for lung cancer be cost-effective? *Cancer* 2000; **89**: 2502-2505 [PMID: 11147636 DOI: 10.1002/1097-0142(20001201)89:11]

- 12 **Zompatori M**, Mascalchi M, Ciccarese F, Sverzellati N, Pastorino U. Screening for lung cancer using low-dose spiral CT: 10 years later, state of the art. *Radiol Med* 2013; **118**: 51-61 [PMID: 22744348 DOI: 10.1007/s11547-012-0843-5]

P- Reviewers: Ng SH, Razek AAKA, Sijens PE
S- Editor: Qi Y **L- Editor:** A **E- Editor:** Liu SQ



Coronary plaque imaging by coronary computed tomography angiography

Akira Sato

Akira Sato, Cardiovascular Division, Faculty of Medicine, University of Tsukuba, Ibaraki 305-8577, Japan

Author contributions: Sato A analyzed the data and wrote the paper.

Correspondence to: Akira Sato, MD, Cardiovascular Division, Faculty of Medicine, University of Tsukuba, 1-1-1 Tennodai, Tsukuba, Ibaraki 305-8577, Japan. asato@md.tsukuba.ac.jp

Telephone: +81-29-8533143 Fax: +81-29-8533143

Received: December 27, 2013 Revised: February 9, 2014

Accepted: April 17, 2014

Published online: March 28, 2015

Abstract

Coronary computed tomography angiography (CTA) has become the useful noninvasive imaging modality alternative to the invasive coronary angiography for detecting coronary artery stenoses in patients with suspected coronary artery disease (CAD). With the development of technical aspects of coronary CTA, clinical practice and research are increasingly shifting toward defining the clinical implication of plaque morphology and patients outcomes by coronary CTA. In this review we discuss the coronary plaque morphology estimated by CTA beyond coronary angiography including the comparison to the currently available other imaging modalities used to examine morphological characteristics of the atherosclerotic plaque. Furthermore, this review underlies the value of a combined assessment of coronary anatomy and myocardial perfusion in patients with CAD, and adds to an increasing body of evidence suggesting an added diagnostic value when combining both modalities. We hope that an integrated, multi-modality imaging approach will become the gold standard for noninvasive evaluation of coronary plaque morphology and outcome data in clinical practice.

© 2015 Baishideng Publishing Group Inc. All rights reserved.

Key words: Coronary computed tomography angiog-

raphy; Coronary plaque; Vulnerable plaque; Clinical outcome

Core tip: With the development of technical aspects of coronary computed tomography angiography (CTA), clinical practice and research are increasingly shifting toward defining the clinical implication of plaque morphology and patients outcomes by coronary CTA. In this review we discuss the coronary plaque morphology estimated by CTA beyond coronary angiography including the comparison to the currently available other imaging modalities used to examine morphological characteristics of the atherosclerotic plaque. We hope that an integrated, multi-modality imaging approach will become the gold standard for noninvasive evaluation of coronary plaque morphology and outcome data in clinical practice.

Original sources: Sato A. Coronary plaque imaging by coronary computed tomography angiography. *World J Radiol* 2014; 6(5): 148-159 Available from: URL: <http://www.wjgnet.com/1949-8470/full/v6/i5/148.htm> DOI: <http://dx.doi.org/10.4329/wjr.v6.i5.148>

INTRODUCTION

For the past decade, invasive coronary angiography (ICA) has been used as the gold standard for the diagnosis of coronary narrowing and clinical decision making for coronary interventions. However, coronary angiography has several limitations, including the substantial interpretation variability of visual estimates and assessment of lesion severity for diffuse atherosclerotic lesions and intermediate-severity lesions^[1-3]. The recent advent of multidetector computed tomography (MDCT) has greatly improved the image quality, and may therefore allow more precise evaluation of coronary stenosis^[4-6]. Multicenter studies have confirmed the accuracy of 64-slice MDCT for directly

Table 1 Respective pros and cons of multi-detector computed tomography and coronary angiogram for analysis of coronary artery disease

	Pros	Cons
MDCT	It can be performed with short examination times, and is generally available and easily performed It is a noninvasive character, and contributes important information of plaque morphology and characterization in the arterial wall Calcium score	Study population was limited to selected patients chosen for good CTA image quality with absence of motion artifacts or severe calcification Quantitative measurement of plaque morphology is slightly limited
CAG	Serial MDCT plaque imaging Excellent image quality can be observed with absence of artifacts Degree of luminal stenosis can be measured by QCA Gold standard for the diagnosis of coronary narrowing and clinical decision making for coronary interventions	Radiation exposure, which is currently between 9 and 1 mSv for a retrospectively gated MDCT coronary angiogram Contrast medium is used It is an invasive character, and contributes no plaque morphologic information Substantial interpretation variability of visual estimates and assessment of lesion severity for diffuse atherosclerotic lesions and intermediate-severity lesions Catheterization costs are expensive. Contrast medium is used

MDCT: Multi-detector computed tomography; CTA: Computed tomography angiography; CAG: Coronary angiogram; QCA: Quantitative coronary angiography.

visualizing and detecting coronary artery stenoses in patients with suspected coronary artery disease (CAD)^[7-10]. Furthermore, the introduction of 256-slice, 320-detector scanner, and dual-source computed tomography (DSCT) developed to significantly improve faster scan times, wider volume coverage, and high spatial resolution^[11]. With the improvement of technical aspects of coronary computed tomography angiography (CTA), clinical practice and research are increasingly shifting toward defining the clinical implication of plaque morphology and patients outcomes by coronary CTA (Table 1). In this review, we discuss the coronary plaque morphology estimated by CTA beyond coronary angiography including the comparison to the currently available other imaging modalities used to examine morphological characteristics of the atherosclerotic plaque.

Coronary plaque imaging

With the development of MDCT, it is possible not only to detect coronary artery stenosis but also to evaluate coronary plaque quality and quantity such as can be done with intravascular ultrasound (IVUS) and optical coherence tomography (OCT)^[12,13]. Leber *et al*^[14] demonstrated that 64-slice CTA-derived measurements showed good correlations with IVUS for lumen and plaque area determinations using individually adapted window settings, although their ability to quantify the grade of a luminal obstruction was limited by the significant trends toward overestimation of the lumen area and underestimation of the plaque area. Our group published that the lumen cross-sectional area (CSA) and percent area stenosis of 32 de novo coronary lesions measured by CTA were closely correlated to those obtained by IVUS (Figure 1); however the lumen CSA measured by CTA was systematically overestimated and percent area stenosis was slightly underestimated^[15]. Voros *et al*^[16] conducted a meta-analysis to assess the accuracy of coronary CTA against IVUS regarding coronary vessel and plaque sizes, as well

as the accuracy of computed tomography (CT) to detect any plaque compared with IVUS. This meta-analysis confirmed that coronary CTA slightly overestimated luminal area, presumably because of partial volume effects that lead to overestimation of the size of very bright structures (such as the contrast-enhanced lumen), whereas plaque area volume, and area stenosis measurements are similar between CT and IVUS. For plaque characterization, it has been shown that CT-derived attenuation values are different in calcified and noncalcified plaques. They also demonstrated that low-density noncalcified plaques, the presumed lipid-rich plaques on CT, correlated best with the sum of necrotic core plus fibro-fatty tissue by IVUS/virtual histology^[17]. Kashiwagi *et al*^[13] revealed that plaque with vascular remodeling and low CT attenuation values had the MDCT morphological features of thin cap fibroatheroma (TCFA) observed by OCT, and a ring-like enhancement observed by MDCT was one important sign of TCFA. Motoyama *et al*^[18] showed that the CT characteristics of plaques associated with acute coronary syndrome (ACS) include positive vascular remodeling, low plaque density, and spotty calcification. Presence of all 3 [*i.e.*, positive remodeling (PR), non-calcified plaque measuring < 30 Hounsfield units (HU), and spotty calcification] showed a high positive predictive value, and absence of all 3 showed a high negative predictive value, for the culprit plaques associated with ACS. Coronary CTA is able to successfully characterize ruptured plaques as low-attenuation plaque with PR. However, Ozaki *et al*^[19] demonstrated that CTA fails to characterize lesions at risk of intact fibrous cap-ACS which are often referred to as plaque erosions and responsible for up to one-third of culprit lesions in ACS patients.

The introduction of DSCT marked another technological improvement of MDCT in cardiac imaging, as the temporal resolution was further increased from 165 ms to 83 ms, thus eliminating the need to control the heart rate during the scan by use of β -blockers. Studies comparing

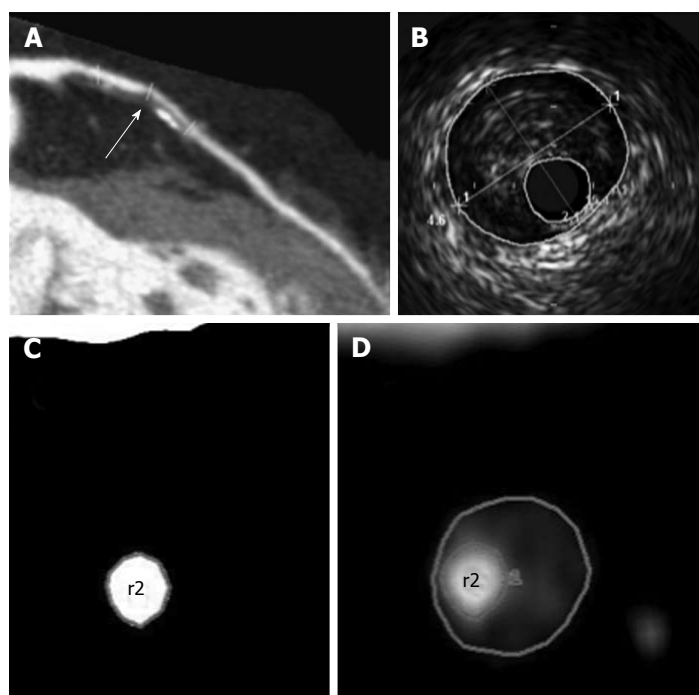


Figure 1 The window settings for the lumen and outer vessel boundary by computed tomography angiography are the same as those for intravascular ultrasound imaging^[19]. A: A curved multiplanar reconstructed CTA image reveals a significant stenosis in the left anterior descending artery (arrow); B: An IVUS cross-section reveals a lumen area of 2.1 mm² and a vessel area of 15.4 mm²; C: The cross-sectional CTA images show the luminal CSA of 2.1 mm²; D: Vessel CSA of 15.4 mm². CTA: Computed tomography angiography; IVUS: Intravascular ultrasound; CSA: Cross-sectional area.

DSCT with single-source CT demonstrated that DSCT maintains high diagnostic accuracy in the diagnostic examination of a wide range of patient subsets, *e.g.*, patients with higher and even irregular heart rates^[20]. Westwood *et al*^[21] showed the systematic review of the accuracy of dual-source cardiac CT for detection of arterial stenosis in some or all difficult to image patients. The pooled, per-patient estimates of sensitivity were 97.7% (95%CI: 88.0%, 99.9%) and 97.7% (95%CI: 93.2%, 99.3%) for patients with arrhythmias and high heart rates, respectively. The corresponding pooled estimates of specificity were 81.7% (95%CI: 71.6%, 89.4%) and 86.3% (95%CI: 80.2%, 90.7%), respectively. In patients with high coronary calcium scores, previous bypass grafts, or obesity, only per-segment or per-artery data were available. Sensitivity estimates remained high (> 90% in all but one study), and specificities ranged from 79.1% to 100%. We showed the table summarizing various studies reporting analysis of coronary plaque by MDCT (Table 2).

Non-culprit coronary plaques imaging

Approximately 6% of PCI patients will have clinical plaque progression requiring non-target lesion percutaneous coronary intervention (PCI) by 1 year, and greater CAD burden confers a significantly higher risk for clinical plaque progression^[22]. The prospect study showed that on multivariate analysis, nonculprit lesions associated with recurrent events were more likely than those not associated with recurrent events to be characterized by a plaque burden of 70% or greater (HR = 5.03; 95%CI: 2.51-10.11; $P < 0.001$) or a minimal luminal area of 4.0 mm² or less (HR = 3.21; 95%CI: 1.61-6.42; $P = 0.001$) or to be classified on the basis of radiofrequency intravascular ultrasonography as thin-cap fibroatheromas (HR = 3.35; 95%CI: 1.77-6.36; $P < 0.001$)^[23]. Our group showed

that the number of coronary plaques in non-culprit lesions on CTA images was more significantly observed in acute myocardial infarction (AMI) patients than in stable angina pectoris patients with normal myocardial perfusion imaging (MPI)^[24]. Specifically, non-calcified, mixed, and vulnerable plaques were more significantly observed in AMI patients than in SAP patients (Figure 2). Leber *et al*^[25] found that non-calcified plaques contribute to a higher degree to the total plaque burden in AMI than in SAP. In addition, 64-slice CTA enabled the visualization of lipid cores and spotty calcifications that are frequently associated with plaque ruptures^[14]. We suggested that all three major coronary arteries in patients with AMI were extensively diseased and have multiple vulnerable plaques that could potentially cause another occurrence of ACS, although the natural course of vulnerable plaque development and disruption has not yet been clearly established^[24]. Recent studies have demonstrated that metabolic syndrome was associated with an increasing risk of cardiovascular disease^[26]. Furthermore, IVUS study has shown that metabolic syndrome is associated with lipid-rich plaques that contribute to the increasing risk of plaque vulnerability^[27]. Within the AMI group, the number of PR and low attenuation plaque was significantly higher in patients with metabolic syndrome than in those without the syndrome. This finding might explain the mechanism of metabolic syndrome contributing to the increased risk of cardiovascular events^[24]. We showed the table comparing various imaging for analysis of coronary vulnerable plaque (Table 3).

Coronary plaque characteristics on MDCT and slow-flow phenomenon/cardiac troponin T elevation

Cardiac biomarker troponin T (cTnT) is sensitive and specific for detection of myocardial damage. Porto *et al*^[36]

Table 2 Various studies reporting analysis of coronary plaque by multi-detector computed tomography

Ref.	n	Imaging techniques	Major findings
Leber <i>et al</i> ^[12]	59	64-detector	The mean plaque areas and the percentage of vessel obstruction measured by IVUS and 64-slice CT were 8.1 mm ² vs 7.3 mm ² ($P < 0.03$, $r = 0.73$) and 50.4% vs 41.1% ($P < 0.001$, $r = 0.61$), respectively
Kashiwagi <i>et al</i> ^[13]	105	64-detector	Vascular remodeling and low CT attenuation values had the MDCT morphological features of TCFA observed by OCT, and a ring-like enhancement was one important sign of TCFA
Leber <i>et al</i> ^[14]	46	16-detector	The MDCT-derived density measurements within coronary lesions revealed significantly different values for hypochoic (49 HU \pm 22), hyperechoic (91 HU \pm 22), and calcified plaques (391 HU \pm 156, $P < 0.02$)
Sato <i>et al</i> ^[15]	102	64-detector	Lumen CSA and percent area stenosis of coronary lesions were closely correlated to those obtained by IVUS, however the lumen CSA measured by CTA was systematically overestimated and percent area stenosis was slightly underestimated
Voros <i>et al</i> ^[17]	60	64-detector	Low-density noncalcified plaques, the presumed lipid-rich plaques on CT, correlated best with the sum of necrotic core plus fibro-fatty tissue by IVUS/virtual histology
Motoyama <i>et al</i> ^[18]	71	16, 64-detector	Presence of positive remodeling, non-calcified plaque < 30 HU, and spotty calcification showed a high positive predictive value for with ACS
Ozaki <i>et al</i> ^[19]	66	16, 64-detector	CTA fails to characterize lesions at risk of intact fibrous cap-ACS which are often referred to as plaque erosions
Sato <i>et al</i> ^[24]	226	64-detector	Number of coronary plaques in non-culprit lesions was more significantly observed in AMI patients than in SAP patients with normal MPI. Non-calcified, mixed, and vulnerable plaques were more significantly observed in AMI patients than in SAP patients
Leber <i>et al</i> ^[25]	15	4-detector	Non-calcified plaques contribute to a higher degree to the total plaque burden in AMI than in SAP
Schroeder <i>et al</i> ^[41]		16-detector	Mean CT density of 14-47 HU was found in lipid-rich plaque
Pohle <i>et al</i> ^[43]		16-detector	The mean CT attenuation within plaque that corresponded to hyper-echogenic appearance in IVUS was 121 \pm 34 HU ($n = 76$). The mean CT attenuation within plaque that corresponded to hypo-echogenic appearance was 58 \pm 43 HU ($n = 176$, $P < 0.001$)
Pundziute <i>et al</i> ^[44]	100	64-detector	In multivariate analysis, significant predictors of events were the presence of CAD, obstructive CAD, obstructive CAD in LM/LAD, number of segments with plaques, number of segments with obstructive plaques, and number of segments with mixed plaques
Pundziute <i>et al</i> ^[45]	50	64-detector	TCFA on virtual histology IVUS were most prevalent in mixed plaques, suggesting a higher degree of vulnerability of these mixed plaques

IVUS: Intravascular ultrasound; CT: Computed tomography; MDCT: Multi-detector computed tomography; OCT: Optical coherence tomography; CTA: Computed tomography angiography; HU: Hounsfield units; CSA: Cross-sectional area; AMI: Acute myocardial infarction; SAP: Stable angina pectoris; MPI: Myocardial perfusion imaging; TCFA: Thin-cap fibroatheromas; CAD: Coronary artery disease; LAD: Left anterior descending artery.

Table 3 Characteristics of various imaging modalities for analysis of coronary vulnerable plaque

Modalities	Characteristics of vulnerable plaque
MDCT	Low-attenuation, positive remodeling, spotty calcification ^[18] Ring-like enhancement ^[13] , napkin-ring sign ^[28,29]
IVUS	Low echoic, positive remodeling, spotty calcification ^[30] Echo signal attenuation ^[31]
OCT	Lipid-rich plaque by a signal-poor region with a diffuse border ^[32] TCFA (large lipid core and a thin fibrous cap < 65 μ m) ^[33] Macrophages imaging ^[34]
Angioscopy	Intensive yellow plaque, presence of thrombus ^[35]

MDCT: Multi-detector computed tomography; IVUS: Intravascular ultrasound; OCT: Optical coherence tomography; TCFA: Thin-cap fibroatheroma.

found that the cause of periprocedural myocardial necrosis after PCI was the impairment of flow in coronary side branches and distal embolization of atheromatous or thrombotic materials. Therefore, pre-PCI plaque composition may have an impact on myocardial injury/infarction during PCI. However, there are few published data regarding the relation between pre-PCI plaque composition by MDCT and post-PCI cardiac biomarker levels (Table 4).

Table 4 Coronary plaque characteristics on multi-detector computed tomography and slow-flow phenomenon/cardiac troponin T elevation

Ref.	Minimum CT value (HU)	Positive remodeling index	Calcification	Ring-like appearance
Nakazawa <i>et al</i> ^[37]	67.0 \pm 10.1	N/A	N/A	55.60%
Uetani <i>et al</i> ^[38]	< 50	1.10 \pm 0.21	37.70%	N/A
Watabe <i>et al</i> ^[39]	43 (26.5-75.7)	1.20 \pm 0.18	Spotty (50%)	31.00%
Kodama <i>et al</i> ^[40]	23.5 (9.5-40)	1.5 (1.3-1.8)	CPC (63%)	10.00%

CT: Computed tomography; HU: Hounsfield units; CPC: Circumferential plaque calcification; N/A: Not available.

Nakazawa *et al*^[37] reported that patients who experienced transient no-reflow during PCI had lower plaque CT density values in culprit lesions. Uetani *et al*^[38] demonstrated that post-procedural myocardial injury was associated with the volume and fraction of low-attenuation plaques by MDCT. Our group showed that CT attenuation value of < 55 HU was associated with post-PCI cTnT elevation^[39]. While in earlier studies, a mean CT density of 14-47 HU was found in lipid-rich plaque^[41,42], Pohle *et al*^[43] showed a mean density of 58 HU (median 53) and Leber *et al*^[14] reported that a low CT density value (49 \pm 22 HU) is considered to correspond to soft plaque identified on

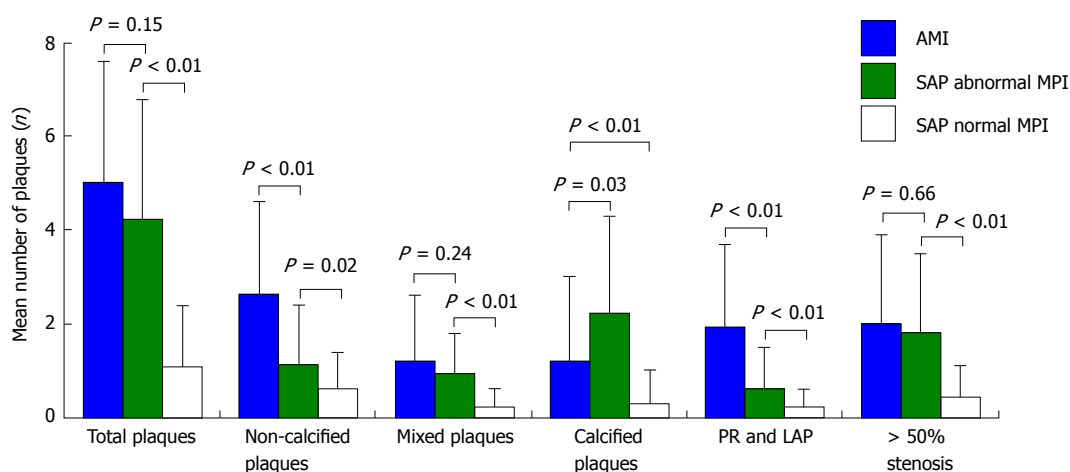


Figure 2 Mean number of the coronary plaques in the non-culprit segments of the acute myocardial infarction and stable angina pectoris patients^[24]. AMI: Acute myocardial infarction; SAP: Stable angina pectoris; MPI: Myocardial perfusion imaging; PR: Positive remodeling; LAP: Low-attenuation plaques.

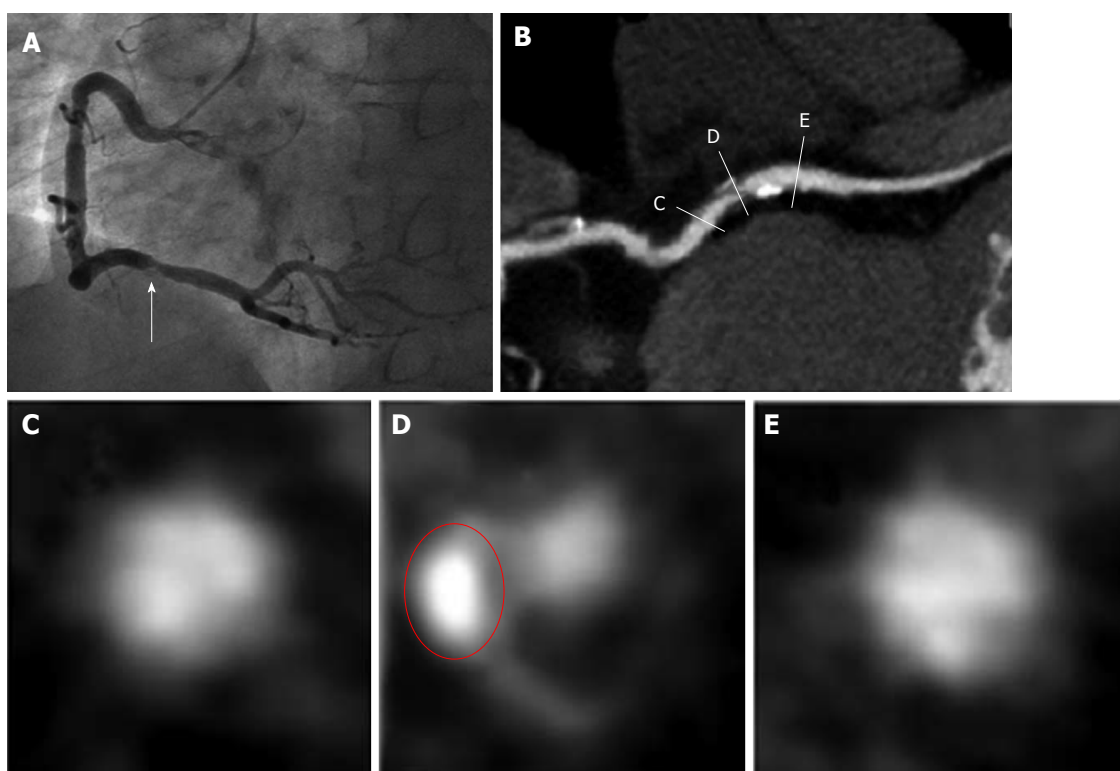


Figure 3 The computed tomography characteristics of a culprit lesion in the 52-year-old male patient with post-percutaneous coronary intervention troponin T elevation $\geq 3 \times$ the upper limit of normal^[31]. Coronary angiogram (A) and multiplanar reconstructed image (B) show severe stenosis in the mid right coronary artery. Cross-sectional images show the proximal reference (C), culprit lesion (D), and distal reference (E). The lesion has positive remodeling (remodeling index 1.28), spotty calcification, and low CT density (16 HU). Red circle indicates area of spotty calcification. CT: computed tomography; HU: Hounsfield units.

IVUS. This difference most likely results from the natural course of atherosclerotic plaque or slice thickness and contrast medium concentration that affect plaque density measurements. It will be possible to use our cutoff point of CT attenuation value < 55 HU for prediction of post-PCI cTnT elevation clinically. PR and spotty calcification were also significant predictors of post-PCI cTnT elevation. Furthermore, presence of all 3 CT characteristics (CT attenuation value < 55 HU, remodeling index > 1.05 , and spotty calcification) showed a high positive predictive

value (PPV) of 94%, and their absence showed a high negative predictive value (NPV) of 90% (Figure 3). Kodama *et al*^[40] demonstrated that CTA-verified circumferential plaque calcification (CPC) with low-attenuation plaque and PR were determinants of slow-flow phenomenon (SF) during PCI. The conditional logistic regression analysis revealed that CPC, plaque density, and dyslipidemia were the predictors of SF, with CPC being the strongest (OR = 79; 95%CI: 8-783, $P < 0.0001$). A previous study exploring potential prognostic predictors of cardiovascular events

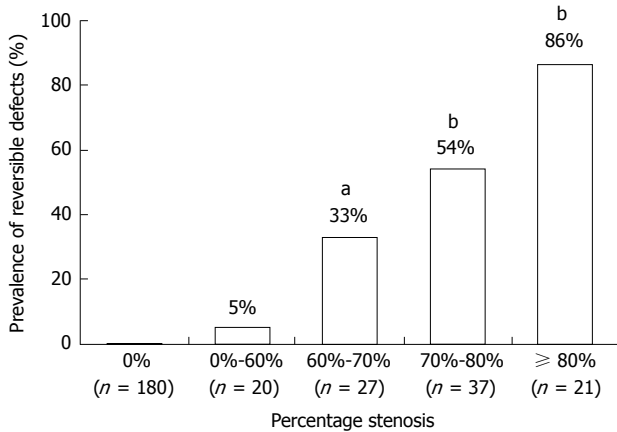


Figure 4 Prevalence of reversible defects evaluated by single-photon emission tomography in the study groups defined according to the percentage stenosis obtained by computed tomography angiography^[15]. Numbers under the bars represent the number of vessels. ^a*P* = 0.018, ^b*P* < 0.0001 vs percentage stenosis of 0%-60%.

on MDCT showed that mixed lesions were associated with adverse events on follow-up^[44]. Thin-cap fibroatheromas on virtual histology IVUS were most prevalent in mixed plaques, suggesting a higher degree of vulnerability of these mixed plaques on MDCT^[45]. These data suggest that it would be worthwhile to consider the identification of these vulnerable plaques by MDCT before PCI. If the plaque has the characteristics of low plaque density, PR, and spotty calcification, a plan for prevention of post-PCI cTnT elevation can be made before the PCI procedure.

Coronary CTA and nuclear MPI

Stress nuclear MPI using single-photon emission tomography (SPECT) is an established method for assessment of the functional significance of coronary stenosis and delivers valuable information for risk stratification^[46]. Disagreement between CTA $\geq 50\%$ stenosis and reversible MPI defects is common^[47]. CTA and MPI are measuring two different things, vessel patency and perfusion, respectively. Only 50% of obstructed vessels with $\geq 50\%$ luminal narrowing by CTA show abnormal MPI^[48]. We previously indicated that 64-slice CTA alone was not always sufficient to assess the functional significance of anatomic stenoses, especially stenoses of intermediate grade (Figure 4). When stenosis severity by CTA was < 60%, ischemia was seldom observed, and when stenosis severity was $\geq 80\%$, ischemia was common. For intermediate stenosis severity values of 60%-80%, the prevalence of reversible defects was difficult to determine, given CTA's current spatial resolution^[15]. We also demonstrated that combined CTA and stress nuclear MPI provide improved diagnostic accuracy for the noninvasive detection of CAD in comparison with that of 64-slice CTA alone. One hundred thirty symptomatic patients with suspected CAD underwent both 64-slice CTA and stress thallium-201 MPI before ICA. Of 390 arteries in 130 patients, 54 (14%) were nonevaluable by CTA due to severe calcifications, motion artifacts, and poor opacifica-

tion. All nonevaluable arteries were considered positive. The sensitivity, specificity, PPV and NPV were 95%, 80%, 69%, and 97%, respectively, for CTA alone and 94%, 92%, 85%, 97%, respectively, for CTA with stress nuclear MPI for all nonevaluable arteries on CTA. Per-patient analysis showed a significant increase in specificity and PPV^[49]. The results of hybrid SPECT/CTA imaging have provided a marked increase in specificity and PPV to detect hemodynamically significant coronary lesions compared to those of 16-slice CTA alone^[50]. Cardiac 3D SPECT/CT fusion imaging has been shown to provide additional information about hemodynamic relevance and facilitates lesion interpretation by allowing exact allocation of perfusion defects to the subtending coronary artery^[51]. Pazhenkottil *et al*^[52] demonstrated that the impact of hybrid SPECT/CT imaging in 318 consecutive patients. Referral to revascularization was higher in patients with matched abnormalities (41%), compared with those with unmatched abnormalities (11%) or those with normal studies (0%).

Available clinical experience points toward tailoring the initial diagnostic approach according to the pretest probability of the patient^[53]. In low-to-intermediate likelihood patients, CTA may well be the best initial test due to its high NPV; however, in intermediate-to-high probability patients, CTA's low PPV may result in unnecessary radiation exposure, and stress nuclear MPI might be a better first-line test. In fact, the high diagnostic accuracy of stress nuclear MPI may argue in favor of stress nuclear MPI as the initial test. From the present study, we cannot definitely conclude which is the better first-line test, and we acknowledge that further head-to-head comparisons between the two modalities are required.

Recently, the addition of physiologic measures of coronary flow by fractional flow reserve (FFR) to anatomic-based assessment of stenosis severity by ICA to guide decisions of coronary revascularization improves event-free survival in a manner that is long-lived and cost-effective^[54,55]. Ko *et al*^[56] demonstrated that FFR compared with combinations of coronary CTA and CT myocardial perfusion imaging findings in 86 myocardial perfusion territories. The FFR is lowest in patients who have both stenosis $\geq 50\%$ on coronary CTA and myocardial perfusion abnormalities and highest in patients with no significant stenosis and no myocardial perfusion defects. Among patients with discrepant results, FFR correlates better with myocardial perfusion abnormalities than with angiographic stenosis.

Min *et al*^[57] demonstrated that use of noninvasive FFR_{CT} plus CT among stable patients with suspected or known CAD was associated with improved diagnostic accuracy and discrimination *vs* CT alone for the diagnosis of hemodynamically significant CAD when FFR determined at the time of ICA was the reference standard (Figure 5). On a per-patient basis, diagnostic accuracy, sensitivity, specificity, PPV, and NPV of FFR_{CT} plus CT were 73% (95%CI: 67%-78%), 90% (95%CI: 84%-95%), 54% (95%CI: 46%-83%), 67% (95%CI: 60%-74%), and

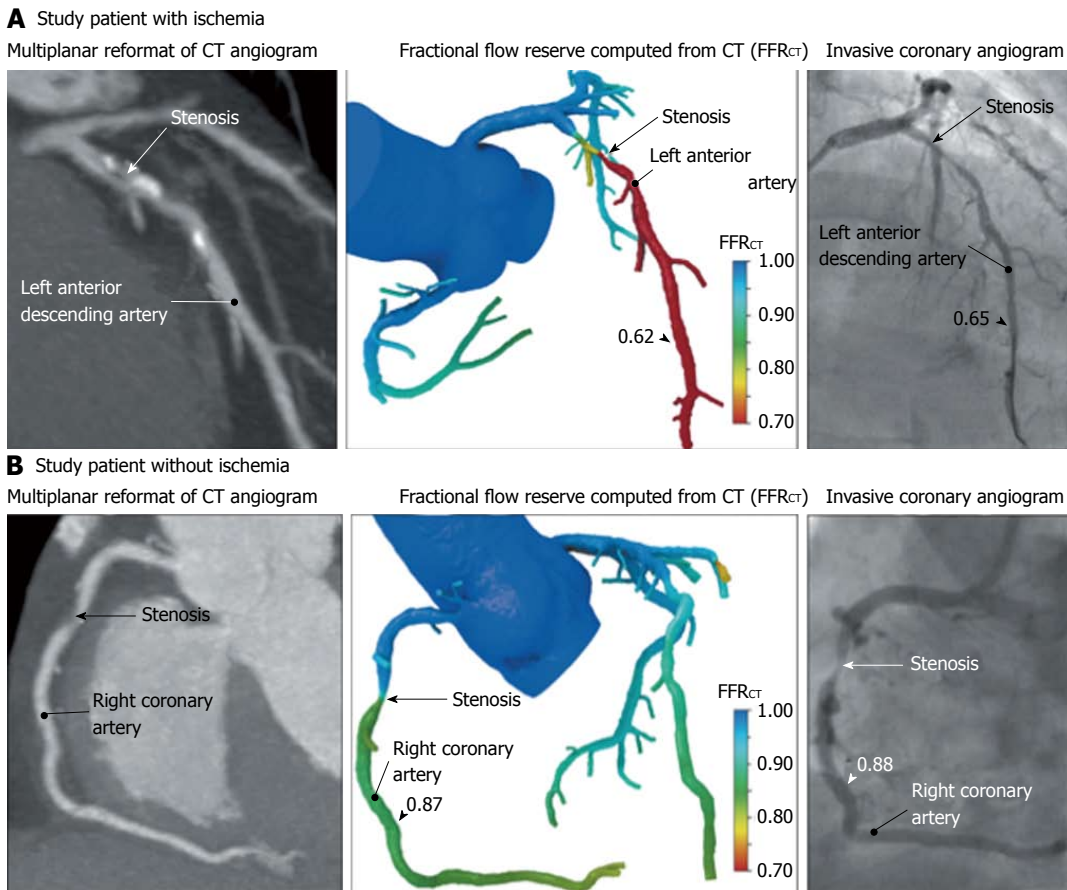


Figure 5 One patient (A) has ischemia and the other patient (B) does not have ischemia^[49]. A: Multiplanar reformat of a computed tomography (CT) angiogram demonstrating obstructive stenosis of the proximal portion of the left anterior descending artery (LAD) and a computed fractional flow reserve (FFR_{CT}) value of 0.62, indicating vessel ischemia. Invasive coronary angiogram demonstrates obstructive stenosis of the proximal portion of the LAD and measured fractional flow reserve (FFR) values of 0.65, indicating vessel ischemia; B: CT angiogram demonstrating obstructive stenosis of the mid portion of the right coronary artery (RCA) and an FFR_{CT} value of 0.87, indicating no vessel ischemia. Invasive coronary angiogram demonstrates obstructive stenosis of the mid portion of the RCA and a measured FFR value of 0.88, indicating no vessel ischemia.

84% (95%CI: 74%-90%), respectively. Compared with obstructive CAD diagnosed by CT alone [area under the receiver operating characteristic curve (AUC), 0.68; 95%CI: 0.62-0.74], FFR_{CT} was associated with improved discrimination (AUC, 0.81; 95%CI: 0.75-0.86; $P < 0.001$).

The CORE320 study compared the combination of CT perfusion (CTP) and coronary artery assessment with SPECT imaging and conventional coronary angiography^[58]. Sixteen centers enrolled 381 patients who underwent combined CTA-CTP and SPECT/MPI prior to conventional coronary angiography. The patient-based diagnostic accuracy defined by the AUC of integrated CTA-CTP for detecting or excluding flow-limiting CAD was 0.87 (95%CI: 0.84-0.91). In patients without prior myocardial infarction, the AUC was 0.90 (95%CI, 0.87-0.94) and in patients without prior CAD the AUC for combined CTA-CTP was 0.93 (95%CI: 0.89-0.97). For the combination of a CTA stenosis $\geq 50\%$ stenosis and a CTP perfusion deficit, the sensitivity, specificity, positive predictive, and negative predictive values (95%CI) were 80% (72%-86%), 74% (68%-80%), 65% (58%-72%), and 86% (80%-90%), respectively. For flow-limiting disease defined by ICA-SPECT/MPI, the accuracy of CTA was significantly increased by the addition

of CTP at both the patient and vessel levels (Figure 6).

Recent advances in the development of noninvasive imaging techniques have enabled quantification of vessel wall inflammation with ¹⁸F-fluorodeoxyglucose positron emission tomography/computed tomography (¹⁸F-FDG PET/CT). The post hoc analysis in the dal-PLAQUE study demonstrated the possible role of FDG-PET especially in relationship of serum inflammatory biomarkers with plaque inflammation assessed by FDG PET/CT. They showed a positive correlation between baseline serum myeloperoxidase (MPO) and baseline carotid arterial wall (target) to background (blood) of the most diseased segment (TBR_{mds}). This relation remained present at 3-mo follow-up and was independent of traditional risk factors. This study is the first to investigate the relationship between MPO and vessel wall ¹⁸F-FDG uptake^[59]. Longitudinal studies will be needed to investigate whether vessel wall inflammation measured by ¹⁸F-FDG PET/CT is predictive for future cardiovascular events.

Prognostic value of CTA in symptomatic and asymptomatic individuals

Currently, the main clinical advantage of CTA appears to be related to its high NPV. The ability to rule out sig-

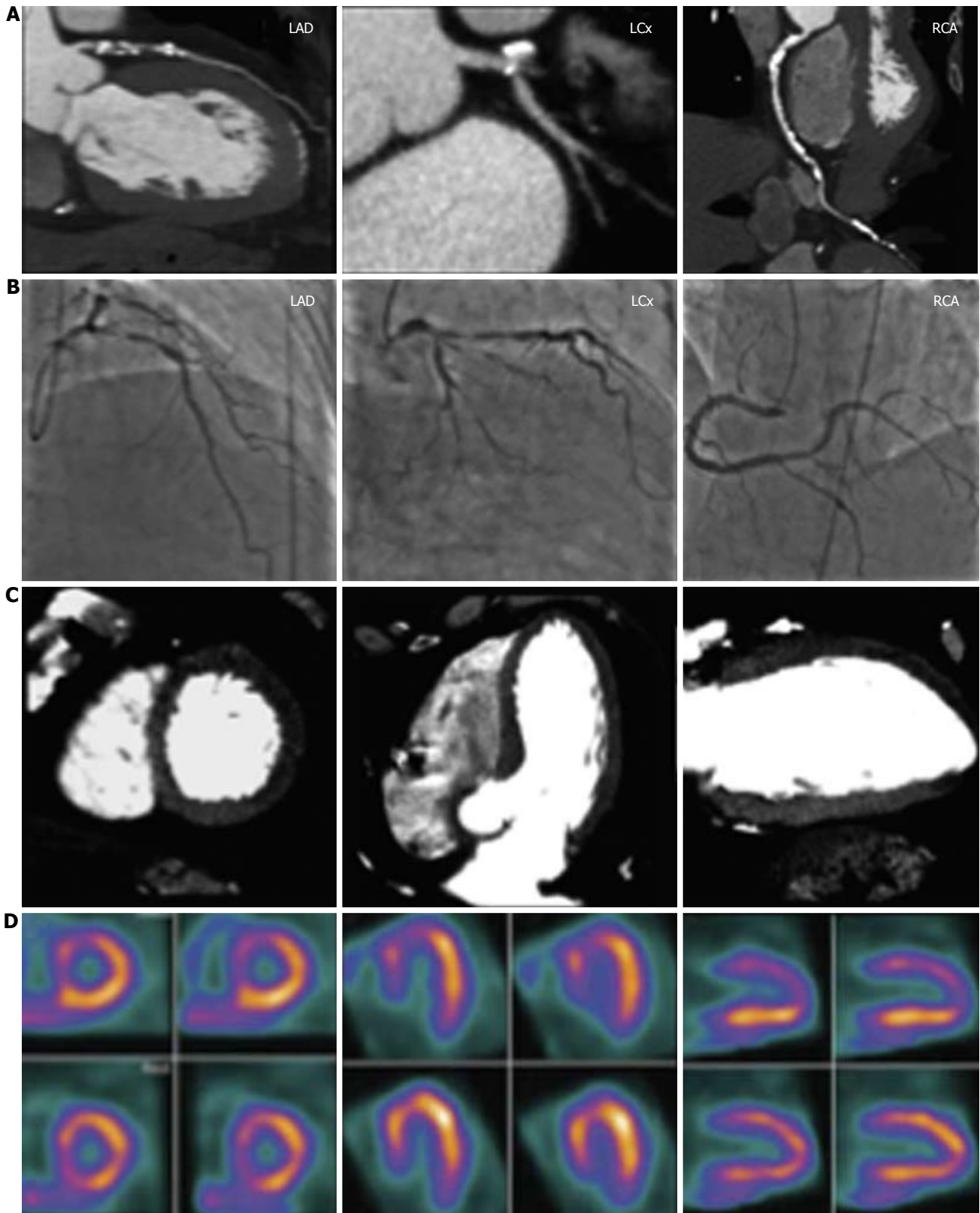


Figure 6 A complete CORE320 imaging data set for a 64-year-old male without prior history of coronary artery disease with chest pain symptoms^[50]. The left anterior descending coronary artery revealed a 96% diameter stenosis by computed tomography angiography (CTA) (row A) and an 85% diameter stenosis by invasive coronary angiography (ICA) (row B). The computed tomography myocardial perfusion (CTP) (row C) study revealed a mild defect in the distal anteroseptal wall, and moderate defects in the basal anteroseptal, the basal anterior, the distal anterior, and apical walls, while the single photon emission computed tomography (SPECT) (row D) study revealed moderate defects in the distal anterior, the distal anteroseptal, the basal anteroseptal and apical walls. The left circumflex artery revealed an 87% diameter stenosis by CTA, a 79% diameter stenosis by ICA, mild defects in the distal inferoseptal and distal inferolateral walls, and moderate defects in the distal anterolateral and distal anterior walls by CTP, and a moderate defect in the distal anterior wall by SPECT. The right coronary artery revealed a 60% diameter stenosis by CTA, a 77% diameter stenosis by ICA, a mild defect in the distal inferoseptal wall by CTP, and no myocardial perfusion defects by SPECT.

nificant CAD in symptomatic patients with a low pre-test likelihood of disease makes CT a useful tool to diagnose many patients with acute chest pain who are often at a low risk of actually ACS. Recently, several randomized large trials have evaluated clinical value of coronary CTA for chest pain triage in the emergency department. Litt *et al*⁶⁰ demonstrated that among the 908 of 1370 patients with acute chest pain to undergo coronary CT angiography, 640 could be immediately discharged after negative findings on a CT scan, and none died or had a myocardial infarction within 30 d. As compared with patients receiving traditional care, patients in the coronary CTA group had a higher rate of discharge from the emergency department (49.6% *vs* 22.7%), a shorter length of stay (median, 18.0 h *vs* 24.8 h; $P < 0.001$), and a higher rate of detection of coronary disease (9.0% *vs* 3.5%). Hoffmann *et al*⁶¹ demonstrated that among the randomized 1000 low-risk acute chest pain patients in a multicenter trial, 501 patients underwent coronary CTA as a first triage test. After early coronary CTA, as compared with standard evaluation, the mean length of stay in the hospital was reduced by 7.6 h ($P < 0.001$) and more patients were discharged directly from the emergency department (47% *vs* 12%, $P < 0.001$). No patient with negative findings on CT experienced AMI, and only 23 MI occurred in the entire patient cohort (plus 52 cases of unstable angina).

The use of coronary CTA has been advocated as a potentially valuable atherosclerotic imaging tool for risk stratification^{62,63}. Several studies have explored the prognostic value of coronary CTA, primarily limited to symptomatic populations^{64,65}. Recent article by Hadamitzky *et al*⁶⁶ add a new data on CCTA that predict both death and myocardial infarction as well as need for subsequent revascularizations out to 5 years. CCTA imaging may be a valuable tool in the assessment of long-term prognosis in patients with suspected CAD. Atherosclerosis imaging such as coronary artery calcium scoring (CACS) or carotid intimal-medial thickness for individuals without chest pain syndrome has been advocated recently for use by professional consensus guidelines⁶⁷. Furthermore, CACS has been demonstrated to improve risk re-stratification above and beyond global risk scores that combine traditional CAD risk factors^{68,69}. However, in a large international multicenter study of individuals without chest pain syndrome, the additional risk-predictive advantage by coronary CTA is not clinically meaningful compared with a risk model based on CACS. At present, the application of coronary CTA for risk assessment of individuals without chest pain syndrome should not be justified⁷⁰.

CONCLUSION

With further improvements in CT technology, coronary CTA become accurate detection of coronary plaques in clinical practice. Assessment of both coronary stenosis and perfusion has great potential application to further advance the evaluation of patients with CAD. In low-to-intermediate likelihood patients, CTA may well be

the best initial test due to its high NPV; however, in intermediate-to-high probability patients, CTA's low PPV may result in unnecessary radiation exposure, and stress nuclear MPI might be a better first-line test. The choice of the optimal first line-test remains a question that is not answered in this review. This review underlies the value of a combined assessment of coronary anatomy and myocardial perfusion in patients with CAD, and adds to an increasing body of evidence suggesting an added diagnostic value when combining both modalities. We hope that an integrated, multi-modality imaging approach will become the gold standard for noninvasive evaluation of coronary plaque morphology and outcome data in clinical practice.

REFERENCES

- 1 **White CW**, Wright CB, Doty DB, Hiratza LF, Eastham CL, Harrison DG, Marcus ML. Does visual interpretation of the coronary arteriogram predict the physiologic importance of a coronary stenosis? *N Engl J Med* 1984; **310**: 819-824 [PMID: 6700670 DOI: 10.1056/NEJM198403293101304]
- 2 **Marcus ML**, Harrison DG, White CW, McPherson DD, Wilson RF, Kerber RE. Assessing the physiologic significance of coronary obstructions in patients: importance of diffuse undetected atherosclerosis. *Prog Cardiovasc Dis* 1988; **31**: 39-56 [PMID: 3293119 DOI: 10.1016/0033-0620(88)90010-2]
- 3 **Vogel RA**. Assessing stenosis significance by coronary arteriography: are the best variables good enough? *J Am Coll Cardiol* 1988; **12**: 692-693 [PMID: 3403827 DOI: 10.1016/S0735-1097(88)80058-5]
- 4 **Ropers D**, Baum U, Pohle K, Anders K, Ulzheimer S, Ohnesorge B, Schlundt C, Bautz W, Daniel WG, Achenbach S. Detection of coronary artery stenoses with thin-slice multidetector row spiral computed tomography and multiplanar reconstruction. *Circulation* 2003; **107**: 664-666 [PMID: 12578863 DOI: 10.1161/01.CIR.0000055738.31551.A9]
- 5 **Achenbach S**, Ropers D, Hoffmann U, MacNeill B, Baum U, Pohle K, Brady TJ, Pomerantsev E, Ludwig J, Flackskampf FA, Wicky S, Jang IK, Daniel WG. Assessment of coronary remodeling in stenotic and nonstenotic coronary atherosclerotic lesions by multidetector spiral computed tomography. *J Am Coll Cardiol* 2004; **43**: 842-847 [DOI: 10.1016/j.jacc.2003.09.053]
- 6 **Raff GL**, Gallagher MJ, O'Neill WW, Goldstein JA. Diagnostic accuracy of noninvasive coronary angiography using 64-slice spiral computed tomography. *J Am Coll Cardiol* 2005; **46**: 552-557 [PMID: 16053973 DOI: 10.1016/j.jacc.2005.05.056]
- 7 **Hamon M**, Biondi-Zoccai GG, Malagutti P, Agostoni P, Morello R, Valgimigli M, Hamon M. Diagnostic performance of multislice spiral computed tomography of coronary arteries as compared with conventional invasive coronary angiography: a meta-analysis. *J Am Coll Cardiol* 2006; **48**: 1896-1910 [PMID: 17084268 DOI: 10.1016/j.jacc.2006.08.028]
- 8 **Vanhoenacker PK**, Heijenbroek-Kal MH, Van Heste R, Decramer I, Van Hoe LR, Wijns W, Hunink MG. Diagnostic performance of multidetector CT angiography for assessment of coronary artery disease: meta-analysis. *Radiology* 2007; **244**: 419-428 [PMID: 17641365 DOI: 10.1148/radiol.2442061218]
- 9 **Budoff MJ**, Dowe D, Jollis JG, Gitter M, Sutherland J, Halamert E, Scherer M, Bellinger R, Martin A, Benton R, Delago A, Min JK. Diagnostic performance of 64-multidetector row coronary computed tomographic angiography for evaluation of coronary artery stenosis in individuals without known coronary artery disease: results from the prospective multicenter ACCURACY (Assessment by Coronary Computed Tomographic Angiography of Individuals Undergoing Inva-

- sive Coronary Angiography) trial. *J Am Coll Cardiol* 2008; **52**: 1724-1732 [DOI: 10.1016/j.jacc.2008.07.031]
- 10 **Miller JM**, Rochitte CE, Dewey M, Arbab-Zadeh A, Niinuma H, Gottlieb I, Paul N, Clouse ME, Shapiro EP, Hoe J, Lardo AC, Bush DE, de Roos A, Cox C, Brinker J, Lima JA. Diagnostic performance of coronary angiography by 64-row CT. *N Engl J Med* 2008; **359**: 2324-2336 [PMID: 19038879 DOI: 10.1056/NEJMoa0806576]
 - 11 **Schuleri KH**, George RT, Lardo AC. Applications of cardiac multidetector CT beyond coronary angiography. *Nat Rev Cardiol* 2009; **6**: 699-710 [PMID: 19851349 DOI: 10.1038/nrcardio.2009.172]
 - 12 **Leber AW**, Knez A, von Ziegler F, Becker A, Nikolaou K, Paul S, Wintersperger B, Reiser M, Becker CR, Steinbeck G, Boekstegers P. Quantification of obstructive and nonobstructive coronary lesions by 64-slice computed tomography: a comparative study with quantitative coronary angiography and intravascular ultrasound. *J Am Coll Cardiol* 2005; **46**: 147-154 [PMID: 15992649 DOI: 10.1016/j.jacc.2005.03.071]
 - 13 **Kashiwagi M**, Tanaka A, Kitabata H, Tsujioka H, Kataiwa H, Komukai K, Tanimoto T, Takemoto K, Takarada S, Kubo T, Hirata K, Nakamura N, Mizukoshi M, Imanishi T, Akasaka T. Feasibility of noninvasive assessment of thin-cap fibroatheroma by multidetector computed tomography. *JACC Cardiovasc Imaging* 2009; **2**: 1412-1419 [PMID: 20083077 DOI: 10.1016/j.jcmg.2009.09.012]
 - 14 **Leber AW**, Knez A, Becker A, Becker C, von Ziegler F, Nikolaou K, Rist C, Reiser M, White C, Steinbeck G, Boekstegers P. Accuracy of multidetector spiral computed tomography in identifying and differentiation the composition of coronary atherosclerotic plaques: a comparative study with intracoronary ultrasound. *J Am Coll Cardiol* 2004; **43**: 1241-1247 [DOI: 10.1016/j.jacc.2003.10.059]
 - 15 **Sato A**, Hiroe M, Tamura M, Ohigashi H, Nozato T, Hikita H, Takahashi A, Aonuma K, Isobe M. Quantitative measures of coronary stenosis severity by 64-Slice CT angiography and relation to physiologic significance of perfusion in non-obese patients: comparison with stress myocardial perfusion imaging. *J Nucl Med* 2008; **49**: 564-572 [DOI: 10.2967/jnumed.107.042481]
 - 16 **Voros S**, Rinehart S, Qian Z, Joshi P, Vazquez G, Fischer C, Belur P, Hulthen E, Villines TC. Coronary atherosclerosis imaging by coronary CT angiography: current status, correlation with intravascular interrogation and meta-analysis. *JACC Cardiovasc Imaging* 2011; **4**: 537-548 [PMID: 21565743 DOI: 10.1016/j.jcmg.2011.03.006]
 - 17 **Voros S**, Rinehart S, Qian Z, Vazquez G, Anderson H, Murreria L, Wilmer C, Carlson H, Taylor K, Ballard W, Karpalotis D, Kalynych A, Brown C 3rd. Prospective validation of standardized, 3-dimensional, quantitative coronary computed tomographic plaque measurements using radiofrequency backscatter intravascular ultrasound as reference standard in intermediate coronary arterial lesions: results from the ATLANTA (assessment of tissue characteristics, lesion morphology, and hemodynamics by angiography with fractional flow reserve, intravascular ultrasound and virtual histology, and noninvasive computed tomography in atherosclerotic plaques) I study. *JACC Cardiovasc Interv* 2011; **4**: 198-208 [DOI: 10.1016/j.jcin.2010.10.008]
 - 18 **Motoyama S**, Kondo T, Sarai M, Sugiura A, Harigaya H, Sato T, Inoue K, Okumura M, Ishii J, Anno H, Virmani R, Ozaki Y, Hishida H, Narula J. Multislice computed tomographic characteristics of coronary lesions in acute coronary syndromes. *J Am Coll Cardiol* 2007; **50**: 319-326 [PMID: 17659199 DOI: 10.1016/j.jacc.2007.03.044]
 - 19 **Ozaki Y**, Okumura M, Ismail TF, Motoyama S, Naruse H, Hattori K, Kawai H, Sarai M, Takagi Y, Ishii J, Anno H, Virmani R, Serruys PW, Narula J. Coronary CT angiographic characteristics of culprit lesions in acute coronary syndromes not related to plaque rupture as defined by optical coherence tomography and angioscopy. *Eur Heart J* 2011; **32**: 2814-2823 [PMID: 21719455 DOI: 10.1093/eurheartj/ehr189]
 - 20 **Sun Z**, Ng KH. Coronary computed tomography angiography in coronary artery disease. *World J Cardiol* 2011; **3**: 303-310 [PMID: 21949572 DOI: 10.4330/wjc.v3.i9.303]
 - 21 **Westwood ME**, Raatz HD, Misso K, Burgers L, Redekop K, Lhachimi SK, Armstrong N, Kleijnen J. Systematic review of the accuracy of dual-source cardiac CT for detection of arterial stenosis in difficult to image patient groups. *Radiology* 2013; **267**: 387-395 [PMID: 23392425 DOI: 10.1148/radiol.13121136]
 - 22 **Glaser R**, Selzer F, Faxon DP, Laskey WK, Cohen HA, Slater J, Detre KM, Wilensky RL. Clinical progression of incidental, asymptomatic lesions discovered during culprit vessel coronary intervention. *Circulation* 2005; **111**: 143-149 [PMID: 15623544 DOI: 10.1161/01.CIR.0000150335.01285.12]
 - 23 **Stone GW**, Maehara A, Lansky AJ, de Bruyne B, Cristea E, Mintz GS, Mehran R, McPherson J, Farhat N, Marso SP, Parise H, Templin B, White R, Zhang Z, Serruys PW. A prospective natural-history study of coronary atherosclerosis. *N Engl J Med* 2011; **364**: 226-235 [PMID: 21247313 DOI: 10.1056/NEJMoa1002358]
 - 24 **Sato A**, Ohigashi H, Nozato T, Hikita H, Tamura M, Miyazaki S, Takahashi Y, Kuwahara T, Takahashi A, Hiroe M, Aonuma K. Coronary Artery Spatial Distribution, Morphology, and Composition of Non-culprit Coronary Plaques by 64-slice Computed Tomography Angiography in Patients With Acute Myocardial Infarction. *Am J Cardiol* 2010; **105**: 930-935 [DOI: 10.1016/j.amjcard.2009.11.028]
 - 25 **Leber AW**, Knez A, White CW, Becker A, von Ziegler F, Muehling O, Becker C, Reiser M, Steinbeck G, Boekstegers P. Composition of coronary atherosclerotic plaques in patients with acute myocardial infarction and stable angina pectoris determined by contrast-enhanced multislice computed tomography. *Am J Cardiol* 2003; **91**: 714-718 [PMID: 12633805]
 - 26 **Malik S**, Wong ND, Franklin SS, Kamath TV, L'Italien GJ, Pio JR, Williams GR. Impact of the metabolic syndrome on mortality from coronary heart disease, cardiovascular disease, and all causes in United States adults. *Circulation* 2004; **110**: 1245-1250 [PMID: 15326067 DOI: 10.1161/01.CIR.0000140677.20606.0E]
 - 27 **Amano T**, Matsubara T, Uetani T, Nanki M, Marui N, Kato M, Arai K, Yokoi K, Ando H, Ishii H, Izawa H, Murohara T. Impact of metabolic syndrome on tissue characteristics of angiographically mild to moderate coronary lesion integrated backscatter intravascular ultrasound study. *J Am Coll Cardiol* 2007; **49**: 1149-1156 [DOI: 10.1016/j.jacc.2006.12.028]
 - 28 **Maurovich-Horvat P**, Schlett CL, Alkadhi H, Nakano M, Otsuka F, Stolzmann P, Scheffel H, Ferencik M, Kriegl MF, Seifarth H, Virmani R, Hoffmann U. The napkin-ring sign indicates advanced atherosclerotic lesions in coronary CT angiography. *JACC Cardiovasc Imaging* 2012; **5**: 1243-1252 [PMID: 23236975 DOI: 10.1016/j.jcmg.2012.03.019]
 - 29 **Otsuka K**, Fukuda S, Tanaka A, Nakanishi K, Taguchi H, Yoshikawa J, Shimada K, Yoshiyama M. Napkin-ring sign on coronary CT angiography for the prediction of acute coronary syndrome. *JACC Cardiovasc Imaging* 2013; **6**: 448-457 [PMID: 23498679 DOI: 10.1016/j.jcmg.2012.09.016]
 - 30 **DeMaria AN**, Narula J, Mahmud E, Tsimikas S. Imaging vulnerable plaque by ultrasound. *J Am Coll Cardiol* 2006; **47**: C32-C39 [PMID: 16631508 DOI: 10.1016/j.jacc.2005.11.047]
 - 31 **Kimura S**, Kakuta T, Yonetsu T, Suzuki A, Iesaka Y, Fujiwara H, Isobe M. Clinical significance of echo signal attenuation on intravascular ultrasound in patients with coronary artery disease. *Circ Cardiovasc Interv* 2009; **2**: 444-454 [PMID: 20031755 DOI: 10.1161/CIRCINTERVENTIONS.108.821124]
 - 32 **Yabushita H**, Bouma BE, Houser SL, Aretz HT, Jang IK, Schlorndorf KH, Kauffman CR, Shishkov M, Kang DH, Halpern EF, Tearney GJ. Characterization of human atherosclerosis by optical coherence tomography. *Circulation*

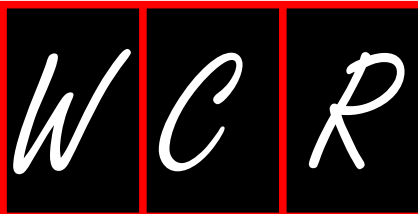
- 2002; **106**: 1640-1645 [PMID: 12270856 DOI: 10.1161/01.CIR.0000029927.92825.F6]
- 33 **Kume T**, Okura H, Yamada R, Kawamoto T, Watanabe N, Neishi Y. Frequency and spatial distribution of thin-cap fibroatheroma assessed by 3-vessel intravascular ultrasound and optical coherence tomography: An ex vivo validation and an initial in vivo feasibility study. *Circ J* 2009; **73**: 1086-1091 [DOI: 10.1253/circj.CJ-08-0733]
- 34 **Tearney GJ**, Yabushita H, Houser SL, Aretz HT, Jang IK, Schlendorf KH, Kauffman CR, Shishkov M, Halpern EF, Bouma BE. Quantification of macrophage content in atherosclerotic plaques by optical coherence tomography. *Circulation* 2003; **107**: 113-119 [PMID: 12515752 DOI: 10.1161/01.CIR.0000044384.41037.43]
- 35 **Ohtani T**, Ueda Y, Mizote I, Oyabu J, Okada K, Hirayama A, Kodama K. Number of yellow plaques detected in a coronary artery is associated with future risk of acute coronary syndrome: detection of vulnerable patients by angioscopy. *J Am Coll Cardiol* 2006; **47**: 2194-2200 [PMID: 16750684 DOI: 10.1016/j.jacc.2006.01.064]
- 36 **Porto I**, Selvanayagam JB, Van Gaal WJ, Prati F, Cheng A, Channon K, Neubauer S, Banning AP. Plaque volume and occurrence and location of periprocedural myocardial necrosis after percutaneous coronary intervention: insights from delayed-enhancement magnetic resonance imaging, thrombolysis in myocardial infarction myocardial perfusion grade analysis, and intravascular ultrasound. *Circulation* 2006; **114**: 662-669 [DOI: 10.1161/CIRCULATIONAHA.105.593210]
- 37 **Nakazawa G**, Tanabe K, Onuma Y, Yachi S, Aoki J, Yamamoto H, Higashikuni Y, Yagishita A, Nakajima H, Hara K. Efficacy of culprit plaque assessment by 64-slice multidetector computed tomography to predict transient no-reflow phenomenon during percutaneous coronary intervention. *Am Heart J* 2008; **155**: 1150-1157 [PMID: 18513532 DOI: 10.1016/j.ahj.2008.01.006]
- 38 **Uetani T**, Amano T, Kunimura A, Kumagai S, Ando H, Yokoi K, Yoshida T, Kato B, Kato M, Marui N, Nanki M, Matsubara T, Ishii H, Izawa H, Murohara T. The association between plaque characterization by CT angiography and post-procedural myocardial infarction in patients with elective stent implantation. *JACC Cardiovasc Imaging* 2010; **3**: 19-28 [DOI: 10.1016/j.jcmg.2009.09.016]
- 39 **Watabe H**, Sato A, Akiyama D, Kakefuda Y, Adachi T, Ojima E, Hoshi T, Murakoshi N, Ishizu T, Seo Y, Aonuma K. Impact of Coronary Plaque Composition on Cardiac Troponin Elevation After Percutaneous Coronary Intervention in Stable Angina Pectoris: A Computed Tomography Analysis Blood urea nitrogen and creatinine levels at admission for mortality risk assessment in patients with acute coronary syndromes. *J Am Coll Cardiol* 2012; **52**: 1881-1889 [DOI: 10.1016/j.jacc.2012.01.051]
- 40 **Kodama T**, Kondo T, Oida A, Fujimoto S, Narula J. Computed tomographic angiography-verified plaque characteristics and slow-flow phenomenon during percutaneous coronary intervention. *JACC Cardiovasc Interv* 2012; **5**: 636-643 [DOI: 10.1016/j.jcin.2012.02.016]
- 41 **Schroeder S**, Kopp AF, Baumbach A, Meisner C, Kuettner A, Georg C, Ohnesorge B, Herdeg C, Claussen CD, Karsch KR. Noninvasive detection and evaluation of atherosclerotic coronary plaques with multislice computed tomography. *J Am Coll Cardiol* 2001; **37**: 1430-1435 [PMID: 11300457 DOI: 10.1016/S0735-1097(01)01115-9]
- 42 **Becker CR**, Nikolaou K, Muders M, Babaryka G, Crispin A, Schoepf UJ, Loehrs U, Reiser MF. Ex vivo coronary atherosclerotic plaque characterization with multi-detector-row CT. *Eur Radiol* 2003; **13**: 2094-2098 [PMID: 12692681 DOI: 10.1007/s00330-003-1889-5]
- 43 **Pohle K**, Achenbach S, Macneill B, Ropers D, Ferencik M, Moselewski F, Hoffmann U, Brady TJ, Jang IK, Daniel WG. Characterization of non-calcified coronary atherosclerotic plaque by multi-detector row CT: comparison to IVUS. *Atherosclerosis* 2007; **190**: 174-180 [PMID: 16494883]
- 44 **Pundziute G**, Schuijf JD, Jukema JW, Boersma E, de Roos A, van der Wall EE, Bax JJ. Prognostic value of multislice computed tomography coronary angiography in patients with known or suspected coronary artery disease. *J Am Coll Cardiol* 2007; **49**: 62-70 [PMID: 17207724 DOI: 10.1016/j.jacc.2006.07.070]
- 45 **Pundziute G**, Schuijf JD, Jukema JW, Decramer I, Sarno G, Vanhoenacker PK, Reiber JH, Schalijs MJ, Wijns W, Bax JJ. Head-to-head comparison of coronary plaque evaluation between multislice computed tomography and intravascular ultrasound radiofrequency data analysis. *JACC Cardiovasc Interv* 2008; **1**: 176-182 [DOI: 10.1016/j.jcin.2008.01.007]
- 46 **Hachamovitch R**, Berman DS, Shaw LJ, Kiat H, Cohen I, Cabico JA, Friedman J, Diamond GA. Incremental prognostic value of myocardial perfusion SPECT for the prediction of cardiac death: differential stratification for risk of cardiac death and MI. *Circulation* 1998; **97**: 535-543 [DOI: 10.1161/01.CIR.97.6.535]
- 47 **Hacker M**, Jakobs T, Matthiesen F, Vollmar C, Nikolaou K, Becker C, Knez A, Pfluger T, Reiser M, Hahn K, Tiling R. Comparison of spiral multidetector CT angiography and myocardial perfusion imaging in the noninvasive detection of functionally relevant coronary artery lesions: first clinical experiences. *J Nucl Med* 2005; **46**: 1294-1300 [PMID: 16085585]
- 48 **Schuijf JD**, Wijns W, Jukema JW, Atsma DE, de Roos A, Lamb HJ, Stokkel MP, Dibbets-Schneider P, Decramer I, De Bondt P, van der Wall EE, Vanhoenacker PK, Bax JJ. Relationship between noninvasive coronary angiography with multi-slice computed tomography and myocardial perfusion imaging. *J Am Coll Cardiol* 2006; **48**: 2508-2514 [PMID: 17174190 DOI: 10.1016/j.jacc.2006.05.080]
- 49 **Sato A**, Nozato T, Hikita H, Miyazaki S, Takahashi Y, Kuwahara T, Takahashi A, Hiroe M, Aonuma K. Incremental value of combining 64-slice computed tomography angiography with stress nuclear myocardial perfusion imaging to improve noninvasive detection of coronary artery disease. *J Nucl Cardiol* 2010; **17**: 19-26 [DOI: 10.1007/s12350-009-9150-5]
- 50 **Rispler S**, Keidar Z, Ghersin E, Roguin A, Soil A, Dragu R, Litmanovich D, Frenkel A, Aronson D, Engel A, Beyar R, Israel O. Integrated single-photon emission computed tomography and computed tomography coronary angiography for the assessment of hemodynamically significant coronary artery lesions. *J Am Coll Cardiol* 2007; **49**: 1059-67 [DOI: 10.1016/j.jacc.2006.10.069]
- 51 **Gaemperli O**, Schepis T, Valenta I, Husmann L, Scheffel H, Duerst V, Eberli FR, Luscher TF, Alkadhi H, Kaufmann PA. Cardiac image fusion from stand-alone SPECT and CT: clinical experience. *J Nucl Med* 2007; **48**: 696-703 [PMID: 17475956 DOI: 10.2967/jnumed.106.037606]
- 52 **Pazhenkotti AP**, Nkoulou RN, Ghadri JR, Herzog BA, Küest SM, Husmann L, Wolfrum M, Goetti R, Buechel RR, Gaemperli O, Lüscher TF, Kaufmann PA. Impact of cardiac hybrid single-photon emission computed tomography/computed tomography imaging on choice of treatment strategy in coronary artery disease. *Eur Heart J* 2011; **32**: 2824-2829 [DOI: 10.1093/eurheartj/ehr232]
- 53 **Meijboom WB**, van Mieghem CA, Mollet NR, Pugliese F, Weustink AC, van Pelt N, Cademartiri F, Nieman K, Boersma E, de Jaegere P, Krestin GP, de Feyter PJ. 64-slice computed tomography coronary angiography in patients with high, intermediate, or low pretest probability of significant coronary artery disease. *J Am Coll Cardiol* 2007; **50**: 1469-1475 [PMID: 17919567]
- 54 **Tonino PA**, De Bruyne B, Pijls NH, Siebert U, Ikeno F, van't Veer M, Klauss V, Manoharan G, Engström T, Oldroyd KG, Ver Lee PN, MacCarthy PA, Fearon WF, FAME Study Investigators. Fractional flow reserve vs angiography for guiding percutaneous coronary intervention. *N Engl J Med* 2009; **360**: 213-224 [DOI: 10.1056/NEJMoa0807611]

- 55 **Fearon WF**, Bornschein B, Tonino PA, Gothe RM, Bruyne BD, Pijls NH, Siebert U. Economic evaluation of fractional flow reserve-guided percutaneous coronary intervention in patients with multivessel disease. *Circulation* 2010; **122**: 2545-2550 [PMID: 21126973 DOI: 10.1161/CIRCULATIONAHA.109.925396]
- 56 **Ko BS**, Cameron JD, Meredith IT, Leung M, Antonis PR, Nassis A, Crossett M, Hope SA, Lehman SJ, Troupis J, DeFrance T, Seneviratne SK. Computed tomography stress myocardial perfusion imaging in patients considered for revascularization: a comparison with fractional flow reserve. *Eur Heart J* 2012; **33**: 67-77 [DOI: 10.1093/eurheartj/ehr268]
- 57 **Min JK**, Leipsic J, Pencina MJ, Berman DS, Koo BK, van Mieghem C, Erglis A, Lin FY, Dunning AM, Apruzzese P, Budoff MJ, Cole JH, Jaffer FA, Leon MB, Malpeso J, Mancini GB, Park SJ, Schwartz RS, Shaw LJ, Mauri L. Diagnostic accuracy of fractional flow reserve from anatomic CT angiography. *JAMA* 2012; **308**: 1237-1245 [PMID: 22922562 DOI: 10.1001/2012.jama.11274]
- 58 **Rochitte CE**, George RT, Chen MY, Arbab-Zadeh A, Dewey M, Miller JM, Niinuma H, Yoshioka K, Kitagawa K, Nakamori S, Laham R, Vavere AL, Cerci RJ, Mehra VC, Nomura C, Kofeod KF, Jinzaki M, Kuribayashi S, de Roos A, Laule M, Tan SY, Hoe J, Paul N, Rybicki FJ, Brinker JA, Arai AE, Cox C, Clouse ME, Di Carli MF, Lima JA. Computed tomography angiography and perfusion to assess coronary artery stenosis causing perfusion defects by single photon emission computed tomography: the CORE320 study. *Eur Heart J* 2013 [DOI: 10.1093/eurheartj/eh488]
- 59 **Duivenvoorden R**, Mani V, Woodward M, Kallend D, Suchankova G, Fuster V, Rudd JH, Tawakol A, Farkouh ME, Fayad ZA. Relationship of serum inflammatory biomarkers with plaque inflammation assessed by FDG PET/CT: the dal-PLAQUE study. *JACC Cardiovasc Imaging* 2013; **6**: 1087-1094 [PMID: 24135322 DOI: 10.1016/j.jcmg.2013.03.009]
- 60 **Litt HI**, Gatsonis C, Snyder B, Singh H, Miller CD, Entrikin DW, Leaming JM, Gavin LJ, Pacella CB, Hollander JE. CT angiography for safe discharge of patients with possible acute coronary syndromes. *N Engl J Med* 2012; **366**: 1393-1403 [PMID: 22449295 DOI: 10.1056/NEJMoa1201163]
- 61 **Hoffmann U**, Truong QA, Schoenfeld DA, Chou ET, Wodard PK, Nagurney JT, Pope JH, Hauser TH, White CS, Weiner SG, Kalanjian S, Mullins ME, Mikati I, Peacock WF, Zakrofsky P, Hayden D, Goehler A, Lee H, Gazelle GS, Wiviott SD, Fleg JL, Udelson JE. Coronary CT angiography versus standard evaluation in acute chest pain. *N Engl J Med* 2012; **367**: 299-308 [PMID: 22830462 DOI: 10.1056/NEJMoa1201161]
- 62 **Min JK**, Shaw LJ, Berman DS. The present state of coronary computed tomography angiography a process in evolution. *J Am Coll Cardiol* 2010; **55**: 957-965 [PMID: 20202511 DOI: 10.1016/j.jacc.2009.08.087]
- 63 **Achenbach S**, Raggi P. Imaging of coronary atherosclerosis by computed tomography. *Eur Heart J* 2010; **31**: 1442-1448 [PMID: 20484566 DOI: 10.1093/eurheartj/ehq150]
- 64 **Min JK**, Shaw LJ, Devereux RB, Okin PM, Weinsaft JW, Russo DJ, Lippolis NJ, Berman DS, Callister TQ. Prognostic value of multidetector coronary computed tomographic angiography for prediction of all-cause mortality. *J Am Coll Cardiol* 2007; **50**: 1161-1170 [PMID: 17868808 DOI: 10.1016/j.jacc.2007.03.067]
- 65 **Ostrom MP**, Gopal A, Ahmadi N, Nasir K, Yang E, Kakadiaris I, Flores F, Mao SS, Budoff MJ. Mortality incidence and the severity of coronary atherosclerosis assessed by computed tomography angiography. *J Am Coll Cardiol* 2008; **52**: 1335-1343 [PMID: 18929245 DOI: 10.1016/j.jacc.2008.07.027]
- 66 **Hadamitzky M**, Täubert S, Deseive S, Byrne RA, Martinoff S, Schömig A, Hausleiter J. Prognostic value of coronary computed tomography angiography during 5 years of follow-up in patients with suspected coronary artery disease. *Eur Heart J* 2013; **34**: 3277-3285 [PMID: 24067508 DOI: 10.1093/eurheartj/eh293]
- 67 **Greenland P**, Alpert JS, Beller GA, Benjamin EJ, Budoff MJ, Fayad ZA, Foster E, Hlatky MA, Hodgson JM, Kushner FG, Lauer MS, Shaw LJ, Smith SC Jr, Taylor AJ, Weintraub WS, Wenger NK, Jacobs AK, Anderson JL, Albert N, Buller CE, Creager MA, Ettinger SM, Guyton RA, Halperin JL, Hochman JS, Nishimura R, Ohman EM, Page RL, Stevenson WG, Tarkington LG, Yancy CW. 2010 ACCF/AHA guideline for assessment of cardiovascular risk in asymptomatic adults: a report of the American College of Cardiology Foundation/American Heart Association Task Force on Practice Guidelines. *J Am Coll Cardiol* 2010; **56**: e50-e103 [DOI: 10.1016/j.jacc.2010.09.001]
- 68 **Detrano R**, Guerci AD, Carr JJ, Bild DE, Burke G, Folsom AR, Liu K, Shea S, Szklo M, Bluemke DA, O'Leary DH, Tracy R, Watson K, Wong ND, Kronmal RA. Coronary calcium as a predictor of coronary events in four racial or ethnic groups. *N Engl J Med* 2008; **358**: 1336-1345 [PMID: 18367736 DOI: 10.1056/NEJMoa072100]
- 69 **Polonsky TS**, McClelland RL, Jorgensen NW, Bild DE, Burke GL, Guerci AD, Greenland P. Coronary artery calcium score and risk classification for coronary heart disease prediction. *JAMA* 2010; **303**: 1610-1616 [PMID: 20424251]
- 70 **Cho I**, Chang HJ, Sung JM, Pencina MJ, Lin FY, Dunning AM, Achenbach S, Al-Mallah M, Berman DS, Budoff MJ, Callister TQ, Chow BJ, Delago A, Hadamitzky M, Hausleiter J, Maffei E, Cademartiri F, Kaufmann P, Shaw LJ, Raff GL, Chinnaiyan KM, Villines TC, Cheng V, Nasir K, Gomez M, Min JK. Coronary computed tomographic angiography and risk of all-cause mortality and nonfatal myocardial infarction in subjects without chest pain syndrome from the CONFIRM Registry (coronary CT angiography evaluation for clinical outcomes: an international multicenter registry). *Circulation* 2012; **126**: 304-313 [PMID: 22685117 DOI: 10.1161/CIRCULATIONAHA.111.081380]

P- Reviewers: Imbriaco M, Patanè S, Pocar M, Raja SG

S- Editor: Ji FF **L- Editor:** A **E- Editor:** Liu SQ





Unusual fistulas and connections in the cardiovascular system: A pictorial review

Abed Ghandour, Prabhakar Rajiah

Abed Ghandour, Prabhakar Rajiah, Cardiothoracic Imaging Section, Department of Radiology, University Hospitals of Cleveland, Case Medical Center, Case Western Reserve University School of Medicine, Cleveland, OH 44106, United States

Author contributions: Ghandour A and Rajiah P both contributed in writing and editing the manuscript.

Correspondence to: Prabhakar Rajiah, MD, Cardiothoracic Imaging Section, Department of Radiology, University Hospitals of Cleveland, Case Medical Center, Case Western Reserve University School of Medicine, 11100 Euclid Avenue, Cleveland, OH 44106, United States. radprabhakar@gmail.com

Telephone: +1-216-8443112 Fax: +1-216-8445205

Received: January 3, 2014 Revised: March 6, 2014

Accepted: March 13, 2014

Published online: March 28, 2015

Abstract

A fistula is an abnormal vascular connection leading to diversion of blood from a high resistance arterial circuit to low resistance venous circuit. Coronary artery fistulas are abnormal communications of the coronary artery with a chamber of the heart, or with any segment of systemic or pulmonary circulation, bypassing the myocardial capillaries. Other unusual fistulas include connection between aorta and the right atrium/superior vena cava, aorta and the inferior vena cava or between a coronary artery bypass graft and a cardiac vein. Abnormal connections also include origin of the coronary artery from the pulmonary artery. In this article, we review the imaging, particularly computed tomography and magnetic resonance imaging of unusual fistulas and connections involving the cardiovascular system, particularly the coronary arteries and the aorta.

© 2015 Baishideng Publishing Group Inc. All rights reserved.

Key words: Coronary; Artery; Fistula

Core tip: Computed tomography and magnetic resonance imaging are very useful imaging modalities in

determining the type and demonstrating the anatomy of these fistulas, which is essential for surgical/interventional planning. Careful analysis in multiple planes and three-dimensional reconstruction is required for comprehensive evaluation of fistulas. Treatment depends on the symptoms and the anatomy.

Original sources: Ghandour A, Rajiah P. Unusual fistulas and connections in the cardiovascular system: A pictorial review. *World J Radiol* 2014; 6(5): 169-176 Available from: URL: <http://www.wjgnet.com/1949-8470/full/v6/i5/169.htm> DOI: <http://dx.doi.org/10.4329/wjr.v6.i5.169>

INTRODUCTION

An arteriovenous (AV) fistula is an abnormal communication between an artery and vein, which results in the shunting of blood from the high-resistance arterial circuit to the low-resistance venous circuits. AV fistulas involving the coronary arteries and the aorta are rare. AV fistulas can be either congenital or acquired secondary to surgeries or interventions. In this article, we review the imaging, particularly computed tomography (CT) and magnetic resonance imaging (MRI) of unusual fistulas and connections involving the cardiovascular system, particularly the coronary arteries and the aorta.

PATHOPHYSIOLOGY

AV fistula leads to decreased peripheral resistance and increased venous resistance, venous pressure and volume. This results in higher heart rate, stroke volume, cardiac output and cardiac work in order to compensate for the lack of perfusion. If left untreated, this may be followed by myocardial hypertrophy, dilation, and then hyperdynamic cardiac failure. Also, the decreased arterial perfusion distal to fistula may raise the renal venous pressure and decrease the arterial perfusion pressure resulting in

activation of the renin-angiotensin system, increasing aldosterone and causing plasma expansion. This creates an abnormal low-resistance circuit that steals from the high-resistance normal capillary bed circuit which can cause tissue ischemia.

ROLE OF IMAGING

Imaging plays an important role in the diagnosis and management of these fistulas. Coronary angiography is the traditional technique used in the evaluation of coronary fistulas, although identification of the exact site of drainage is often difficult, since it is usually into a low pressure chambers, with significant dilution of radiographic contrast^[1]. Coronary angiography is an invasive procedure and does not provide three-dimensional (3D) information, particularly the exact anatomy and relationship to adjacent structures, which is vital in surgical planning. Echocardiography has a limited role in the evaluation of coronary fistulas, especially in demonstration of the anatomy and drainage. Transesophageal echocardiography has higher accuracy than transthoracic echocardiography. Color-flow Doppler demonstrates flow abnormalities within the fistula.

Cross sectional modalities such as CT and MRI are the most useful imaging modalities in diagnosis and accurate characterization of cardiovascular fistulas. Both these modalities have high spatial and temporal resolutions, multi-planar imaging/reconstruction capabilities and wide field of view. CT is more widely available in many centers and can be performed rapidly, often without the need for any sedation/anesthesia even in children. CT angiography has high spatial and temporal resolution and is performed with intravenous contrast and with ECG gating to avoid motion artifacts. Radiation dose can be minimized by using several techniques such as prospective ECG triggering, retrospective ECG gating with tube current modulation, automatic tube current modulation, low kilovoltage, and iterative reconstruction algorithms. Multi-planar reformats and 3D reconstruction techniques such as volume rendering and surface shading enable exquisite demonstration of the anatomy of the fistulas, which is essential for surgical/interventional planning. CT scan has been shown to have high sensitivity of up to 87% compared to coronary angiography in the detection of coronary artery fistulas, with a lower sensitivity of 58% for fistulas draining in cardiac chambers^[2]. Disadvantages of CT include the use of ionizing radiation and use of potentially nephrotoxic contrast media.

MRI does not involve the use of ionizing radiation or potentially nephrotoxic contrast medium. Anatomic information of the vasculature is obtained with MR angiography, which typically requires the use of Gadolinium-based contrast agent but equivalent information can be obtained without the use of contrast medium through navigator gated 3D whole-heart steady state free precession (SSFP) sequences. Anatomical information can be obtained using black blood (double inversion recovery) or

bright blood (cine SSFP) sequences. Flow can be quantified using phase contrast velocity encoded sequences, through the pulmonary artery and aorta, thus giving an estimate of the Qp:Qs ratio (pulmonary to systemic flow). Presence of myocardial ischemia can be identified using stress perfusion imaging and infarcts can be identified using delayed enhancement MRI sequences^[3].

CORONARY ARTERY FISTULA

Coronary artery fistula is an abnormal communication between the coronary artery with a chamber of the heart (coronary cameral) or with any segment of systemic or pulmonary circulation (coronary AV fistula) close to the heart, bypassing the myocardial capillaries. Coronary artery fistulas are typically congenital but may also be acquired following trauma or invasive cardiac procedures (pacemaker, endomyocardial biopsy, coronary angiography, septal myectomy). Congenital coronary artery fistulas are very rare, accounting for 0.2%-0.4% of congenital cardiac abnormalities^[4]. It has been reported in 0.05%-0.25% of patients undergoing coronary angiography, with an estimated prevalence of 0.002% in the general population^[5]. Pathologically, it is characterized by dilation of involved vessel, thinned fistulous wall, thrombosis, atherosclerotic changes, myocardial hypertrophy and fibrosis^[6].

As discussed above, the communication of the coronary artery could be with the lumen of a cardiac chamber (right ventricle -41%, right atrium -26%, left atrium -5%, left ventricle -3%), coronary sinus (7%), superior vena cava (SVC) (1%), pulmonary artery (17%) or the pulmonary vein. 90% of venous drainage is seen into the systemic venous side^[7]. The right coronary artery is the most common artery involved in fistulous formation (50% of cases) and is often symptomatic. Left coronary artery accounts for 42% of fistulas and is often asymptomatic. Both right coronary artery (RCA) and left coronary artery (LCA) are involved in 5% of cases^[5]. Majority of fistulas are single, but multiple and complex fistulas have been reported. Cardiovascular anomalies are associated in 5%-30% of cases^[6].

Left-to-right shunt is seen in 90% of cases^[7]; however, the shunt ratio is not large, as a result of which most patients are asymptomatic, especially in the adult population. Pediatric patients are usually symptomatic^[7]. Clinical presentations include-continuous heart murmur, dyspnea, orthopnea, right ventricular dysfunction/failure, fatigue, chest pain, endocarditis, stroke, arrhythmias, myocardial ischemia/infarction due to coronary steal, pericardial effusion or sudden death. Larger shunts are complicated by cardiac failure, pulmonary hypertension, thrombosis, rupture, or aneurysm.

Coronary artery fistulas are conservatively treated with imaging follow up in asymptomatic patients. Spontaneous thrombosis has been reported in few patients (1%-2%)^[5]. Medical treatment includes anti platelet therapy and antibiotic prophylaxis for infective endocarditis. Some

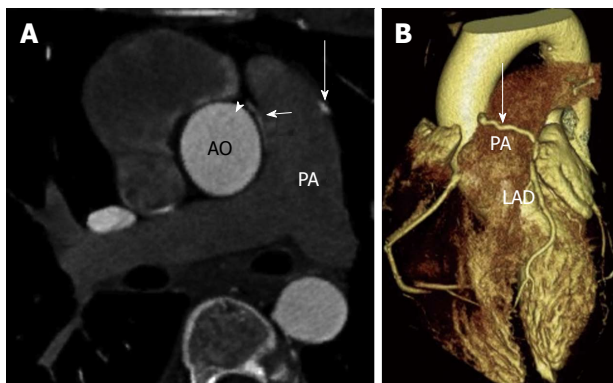


Figure 1 Coronary to pulmonary artery fistula. A: Axial contrast enhanced coronary computed tomography angiography shows left anterior descending (LAD) artery (long arrow) and right coronary artery (arrowhead) fistulas draining into the pulmonary artery. A jet of contrast (short arrow) is seen emptying into the pulmonary artery; B: Three-dimensional volume rendered computed tomography image shows the LAD coronary artery crossing anterior to the pulmonary artery (PA) to drain into it. AO: Aorta.

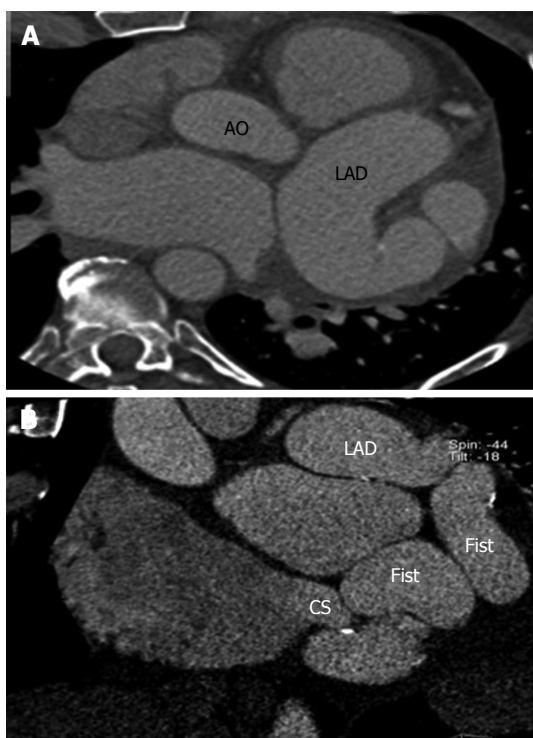


Figure 2 Left anterior descending to coronary sinus fistula. A: Axial coronary computed tomography angiography (CTA) shows dilated, tortuous left anterior descending coronary artery (LAD); B: Sagittal reconstructed coronary CTA shows a LAD fistula draining into the coronary sinus. Fist: Fistula; CS: Coronary sinus; AO: Aorta.

centers perform closure even in asymptomatic patients to avoid long term morbidity and mortality^[2]. Definitive repair can be performed using surgical ligation or percutaneous techniques such as transcatheter embolization of the fistulous connection using detachable platinum coils or polytetrafluoroethylene-covered coronary artery stent grafts, both of which have been shown to have similar outcomes^[8]. Surgery is performed in larger fistulas, larger flow, multiple fistulas, complex fistulas, aneurysm, or

large vascular branches. Embolization is performed in single drainage, proximal fistulous vessel, termination away from coronary arteries, absence of associated disorders requiring surgery, and older age. Imaging is used for follow up after surgery/intervention to ensure there is complete closure of fistula and no recanalization^[5].

Coronary artery-cameral fistula

This is the most common type of coronary artery fistula, resulting in communication between a coronary artery and a cardiac chamber. This is mostly congenital and believed to be persistent embryonic intratrabecular spaces and sinusoids^[8]. As discussed above, the most frequent chamber involved in this fistula is the right ventricle, followed by right atrium, then left atrium and finally the left ventricle.

Coronary artery to pulmonary artery fistula

A fistulous communication between the coronary artery and the pulmonary artery is the second most common type of coronary artery fistula, accounting for 17% of these cases. Some studies have shown this to be as high as 30% of all fistulas^[9]. The RCA is more often involved than the LCA as a site of origin. This fistula is often asymptomatic and is only incidentally discovered in imaging. CT and MRI show the coronary artery or its branches draining into the pulmonary artery (Figure 1). On CT, demonstration of this fistula requires good contrast opacification of the coronary arteries and non-contrast opacification of the pulmonary artery. Evaluation might be challenging due to low pressure circulation of these fistula causing low blood flow and small caliber of fistula^[10,11]. Asymptomatic fistulas are managed conservatively by follow up whereas symptomatic fistulas require surgery or transcatheter closure.

Coronary artery-coronary sinus fistula

Fistulous communication between the coronary artery and the coronary sinus is the third commonest type of coronary artery fistula, accounting for 7% of cases (Figures 2-4). On CT and MRI, the coronary artery or arteries are dilated and tortuous and a communication with the coronary sinus which is dilated can be demonstrated (Figure 5). When there is a severely dilated coronary sinus, coronary artery fistula should be in the differential diagnosis. Other causes of coronary sinus dilation include tricuspid regurgitation, tricuspid stenosis, pulmonary hypertension and right heart dysfunction. Coronary sinus is also dilated in the presence of a persistent left superior vena cava (LSVC) draining into the coronary sinus, interrupted inferior vena cava (IVC) with hemiazygos connection to LSVC or hepatic veins to coronary sinus (CS) connection, all of which are not associated with a left-to-right shunt or unroofed coronary sinus (partial or complete) or total anomalous pulmonary venous connection, both of which are associated with left-to-right shunt^[12]. In symptomatic patients, fistulas are repaired by surgery or percutaneous technique, since spontaneous closure is rare^[5].

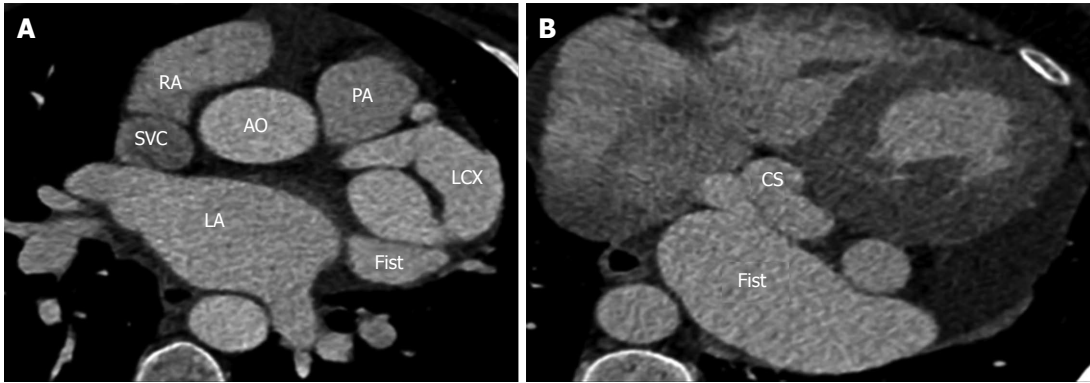


Figure 3 Left circumflex coronary artery to coronary sinus fistula. A: Axial coronary computed tomography angiography (CTA) shows dilated, tortuous left circumflex coronary artery (LCX) due to a LCX fistula (Fist); B: Axial coronary CTA shows the LCX Fist drains into the coronary sinus (CS). PA: Pulmonary artery; AO: Aorta; LA: Left atrium; RA: Right atrium; SVC: Superior vena cava.



Figure 4 Right coronary artery to coronary sinus fistula. Three-dimensional volume rendered computed tomography angiography image shows a coronary artery fistula between the right coronary artery (RCA) and the coronary sinus (CS).

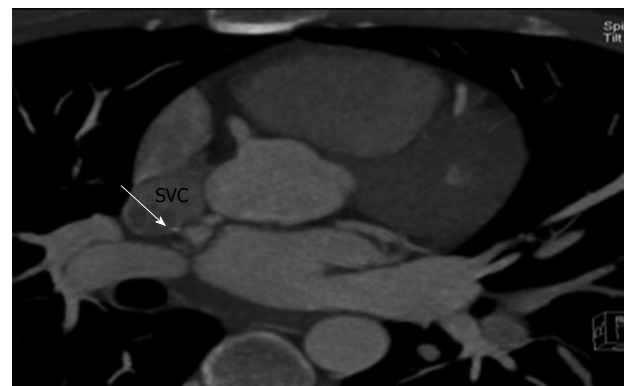


Figure 6 Right coronary artery to superior vena cava fistula. Axial maximum intensity projection reconstruction of coronary computed tomography angiography shows a fistula (arrow) between the right coronary artery and the superior vena cava (SVC).

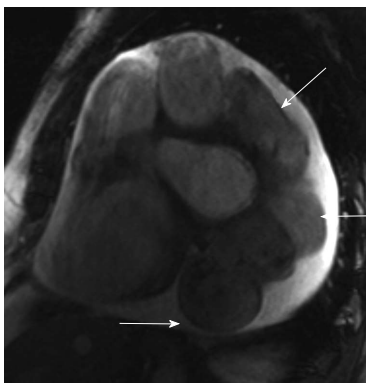


Figure 5 Magnetic resonance imaging appearances of coronary artery fistula. Short axis steady state free precession magnetic resonance imaging image shows dilated, tortuous left anterior descending artery draining into the coronary sinus. There is also a small circumferential pericardial effusion.

Coronary artery-SVC fistula

Fistulous communication between coronary artery and the SVC is rare, accounting for 1% of these fistulas^[13]. Majority of these fistulas drain into a normal right sided SVC (Figure 6), typically originating from the right coronary artery and less commonly the left circumflex artery.

Occasionally, these fistulas drain into a persistent left SVC (Figure 7). Majority of these fistulas originate from the left circumflex artery^[14]. CT and MRI are ideal imaging modalities in the demonstration of these rare fistulas.

Complex coronary fistula

Occasionally coronary artery fistulas can be complex, with multiple sites of origin and drainage, which may be challenging to diagnose. Multiple fistulas can be seen in 11%-16% of cases^[9]. One such case is shown in Figure 8, which is an arterial-arterial fistula originating from the proximal right coronary artery and 1st diagonal branch, which terminates in the pulmonary artery. CT and MRI with multi-planar and 3D reconstructions are vital in precise characterization of the fistula anatomy, which is essential for surgical planning.

ANOMALOUS ORIGIN OF THE CORONARY ARTERY FROM PULMONARY ARTERY

Anomalous origin of left coronary artery from pulmonary artery (ALCAPA) is a rare (0.25%-0.5%) congenital

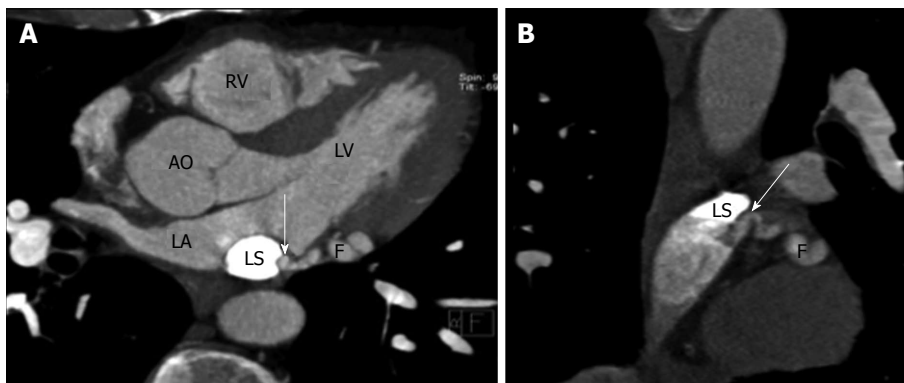


Figure 7 Left circumflex coronary artery to persistent left superior vena cava fistula. A: Axial coronary computed tomography angiography (CTA) image shows a fistulous connection (F) between left circumflex artery and a persistent left left circumflex coronary artery (LS) which eventually drained into the coronary sinus; B: Sagittal coronary CTA reconstructed images shows fistula (arrow) between the left circumflex artery and persistent left superior vena cava (LS). AO: Aorta; LA: Left atrium.

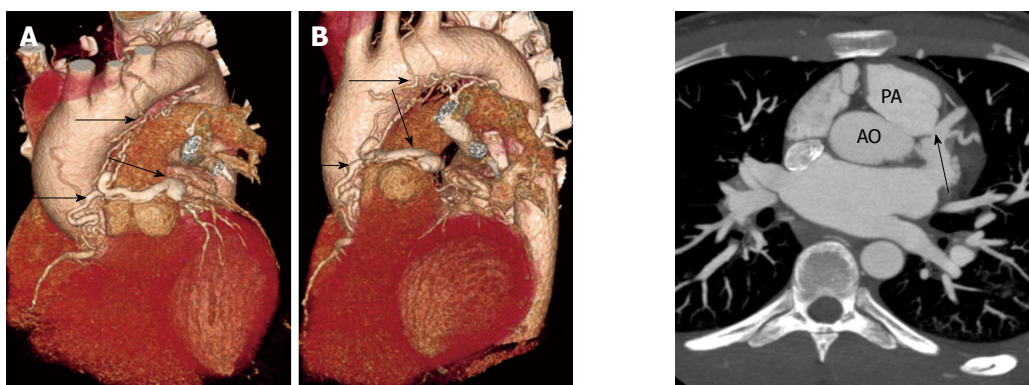


Figure 8 Complex coronary artery fistula. A and B: 3D volume rendered coronary computed tomography angiography shows an arterial-arterial fistula originating from the proximal right coronary artery and 1st diagonal branch, which terminates in the pulmonary artery. The plexus has an aneurysmal segment that wraps around the anterior aspect of the main pulmonary artery. There is direct communication between the aneurysmal segment and the leftward aspect of the proximal MPA. Also, there are multiple smaller branches around the aortic root, MPA, ascending aorta, and transverse arch. A branch originating from the aortic arch continuous with a small 1.8-cm contrast-filled cavity adjacent to the aortic arch, between the trachea and aortic arch.

Figure 9 Anomalous origin of the left coronary artery from the pulmonary artery. Axial MIP image shows origin of the left coronary artery (arrow) from the main pulmonary artery. PA: Pulmonary artery; AO: Aorta.

cardiac anomaly^[15], with the most common form being Bland White Garland syndrome (LCA from pulmonary artery) (Figure 9). There are two types of ALCAPA, the infant and adult types. Physiologically, ALCAPA is not a major problem during fetal and early neonatal life since during this period; the pulmonary artery pressure is similar to systemic arterial pressure, resulting in antegrade coronary flow. However, after birth, the pulmonary arterial pressure decreases resulting in retrograde flow from the LCA to the pulmonary artery. Presentation and hemodynamics depends on the artery involved, myocardial distribution, pulmonary resistance, and number and size of collaterals. In the more common infant type, there is no development of collaterals between the RCA and the LCA, as a result of which these vessels are of normal caliber. Retrograde flow from the LCA to the low pressure pulmonary artery is maintained, producing a left-to-right shunt. The myocardial hypoperfusion results in myocardial infarction and congestive cardiac failure, leading to

death in 90% within one year. Adult type is less common and is characterized by extensive collateral vessel formation between RCA and the LCA, resulting in dilation and tortuosity of these vessels. The anomalous vessel acts as a vein diverting flow from the normal coronary artery to the pulmonary artery, the so called “steal” phenomenon. This often results in chronic myocardial ischemia, LV dysfunction, mitral regurgitation and arrhythmias, which may cause sudden death, seen in 80%-90% of these cases^[16].

CT and MRI demonstrate the origin of the left coronary artery from the main pulmonary artery, usually from its left inferolateral aspect just beyond the valvular level. In addition, reverse flow from the left coronary artery to the pulmonary artery can be demonstrated using phase contrast velocity encoded MRI image or with SSFP sequence. In neonates, the coronary arteries are of normal size, but in adults the coronary arteries are dilated and tortuous due to shunting of blood from RCA to LCA and into pulmonary artery. Prominent intercoronary collateral vessels may also be seen. Myocardial damage can be evaluated using delayed enhancement sequences, which will estimate the extent of viable myocardium, especially in adult patients. Presence of scarring is also

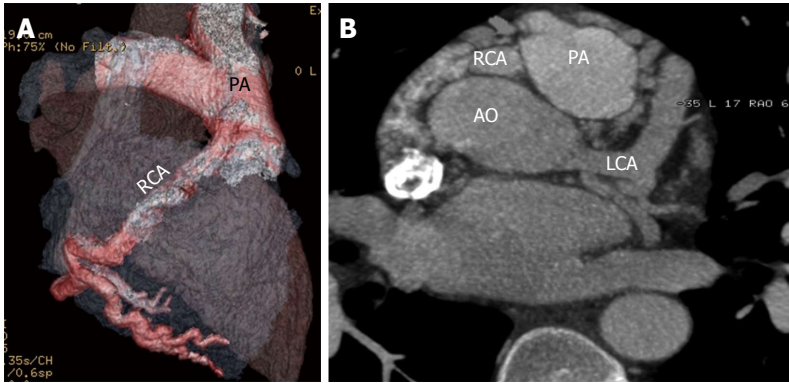


Figure 10 Anomalous origin of the right coronary artery from the pulmonary artery. A: reconstructed computed tomography angiography (CTA) image shows origin of the right coronary artery (RCA) from the main pulmonary artery (PA); B: Axial coronary CTA shows the origin of the RCA from the pulmonary artery. To compensate for this there is dilated left coronary artery (LCA), which provides collateral supply to the RCA circulation. AO: Aorta.

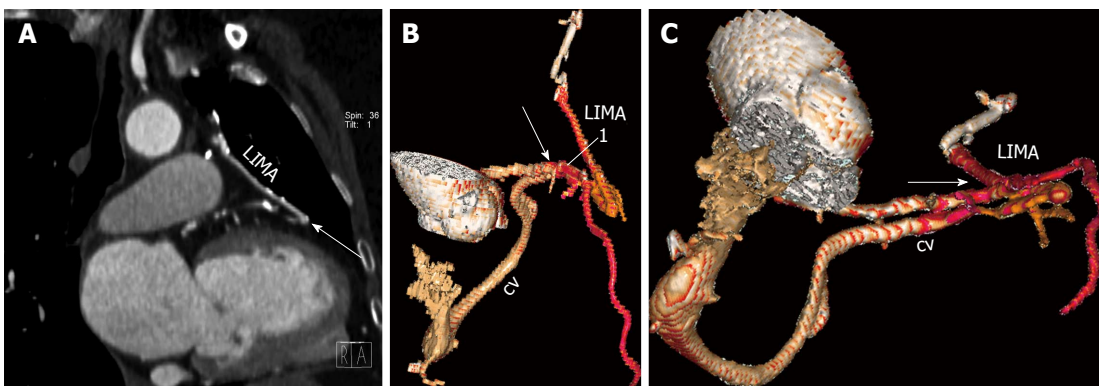


Figure 11 Coronary artery bypass graft to cardiac vein fistula. A: Coronal coronary computed tomography angiography image shows a fistulous communication (arrow) between the left internal mammary artery (LIMA) graft and the great cardiac vein (CV); B: 3D volume rendered computed tomography (CT) image shows fistulous communication (arrow) between the LIMA graft and the great CV; C: Axial oblique reconstructed 3D volume rendered CT image demonstrates the fistulous communication (arrow).

a substrate for arrhythmias. Other MRI findings include LV hypertrophy/dilation, wall motion abnormalities and mitral regurgitation. Dilated bronchial arteries may also be seen. Ideal treatment is reestablishment of a two coronary artery system, either using coronary button transfer (preferred in infants), Takeuchi procedure, or placement of coronary artery bypass graft (CABG) after ligation of LCA origin (preferred in adults). Single-coronary system repair such as ligation of LCA is not preferred due to higher complications. Percutaneous closure and cardiac transplantation are other options^[13].

In ARCAPA, there is anomalous origin of the right coronary artery from the pulmonary artery (Figure 10). This has an incidence of 0.002% in general population compared to 0.008% for ALCAPA^[17]. Occasionally, a left anterior descending or left circumflex coronary arterial branch may originate from the pulmonary artery. Very rarely, both coronary arteries may originate from the pulmonary artery.

BYPASS GRAFT TO CARDIAC VEIN FISTULA

A fistulous communication between a CABG and cardiac

vein is extremely rare, with less than 25 cases reported in the literature^[18]. It happens more frequently with aorto-coronary venous bypass grafts than with arterial grafts. The fistulous communication can occur either in the immediate post-operative period or may manifest after several months or even years^[18,19]. This may be asymptomatic or present with heart failure, angina, or continuous precordial murmur. CT or MRI demonstrates the communication between a coronary artery bypass graft and the cardiac vein (Figure 11). Careful analysis is required since the communication may be subtle and may be confused for a normal anastomosis with a coronary artery. Treatment for small shunts is medical management, whereas large shunts which are usually symptomatic require a repeat CABG or embolization of the fistula.

AORTA TO RIGHT ATRIUM FISTULA

A fistulous communication between the aorta and the right atrium is rare. This often results from an intimal tear near the aortic root, especially in patients with prior cardiac surgery (1/3 rd of all cases). Dense pericardial adhesions resulting from the previous surgery contain the free rupture and contribute to the formation of the aorto-

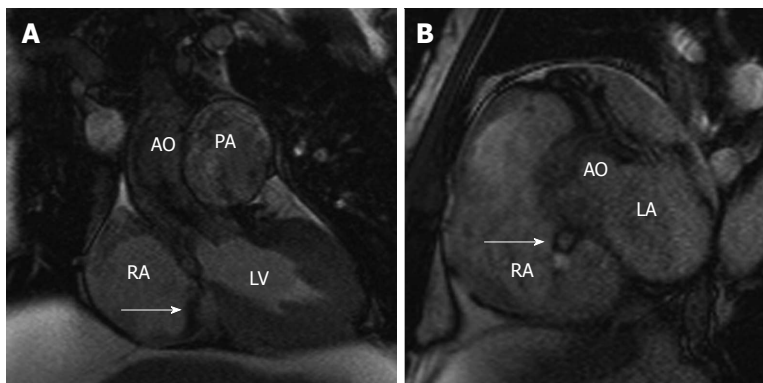


Figure 12 Aorta to right atrium fistula. A: Coronal state free precession (SSFP) magnetic resonance imaging (MRI) image in a patient with bicuspid aortic valve and infective endocarditis shows a fistulous communication between the aorta (AO) and the right atrium (RA), with a jet of abnormal flow (arrow) demonstrated between the aorta and the right atrium; B: Sagittal short axis SSFP MRI image in the same patient shows the fistulous connection (arrow) between the aorta and the right atrium. LA: Left atrium.

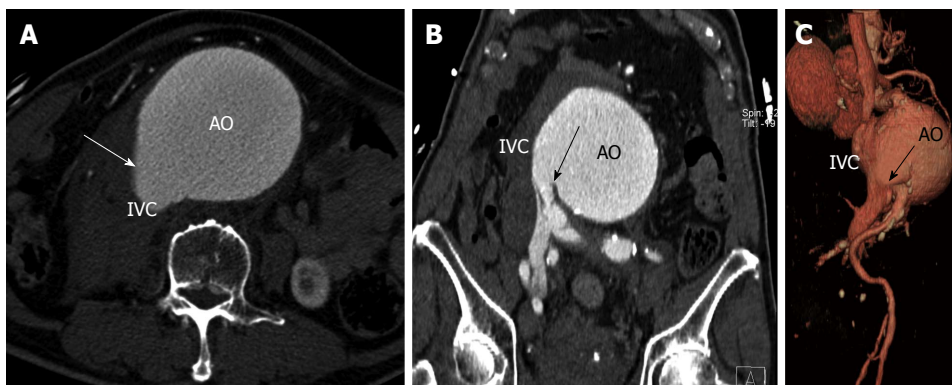


Figure 13 Aorta to inferior vena cava fistula. A: Axial contrast computed tomography (CT) of the abdomen in a patient with history of abdominal aortic aneurysm (AO) shows similar contrast opacification of the inferior vena cava (IVC). There is a communication demonstrated (arrow) between the aorta and IVC; B: Coronal contrast CT of the abdomen demonstrates the site of fistulous communication between the aorta and the distal IVC adjacent to the right common iliac vein; C: Volume rendered 3D computed tomography angiography shows fistulous communication (arrow) between the abdominal aorta and IVC.

right atrial fistula. Also, this may be associated with right coronary artery disruption. Rarely, it occurs in patients with infective endocarditis (native or prosthetic valve), causing rapid bacterial invasion with tissue destruction. High intra-aortic pressure promotes progression of the tear towards the outer side of aortic wall draining into the right atrium. This type of fistula may be seen in any of the sinuses, but less common in the non-coronary sinus^[20]. It has been reported after transcatheter closure of septal defect^[20] and aortic dissection repair^[21]. Sixty percent of patients develop heart failure and 40% eventually die. On CT, a defect can be demonstrated between the aorta and the right atrium. MRI is the ideal modality for demonstration of this fistula, with a dark jet of flow demonstrated on cine SSFP or GRE images (Figure 12). The fistula can be closed either by surgery or by transcatheter technique.

AORTA TO IVC FISTULA

A fistula between the aorta and the IVC is very rare. It can be due to trauma, post-surgery (laminectomy), ruptured abdominal aortic aneurysm, infection, connective

tissue disorders (Marfans, Ehler Danlos), or neoplasms. 80% of these fistulas are secondary to ruptured abdominal aortic aneurysm. This fistula is seen in 3%-6% of ruptured abdominal aortic aneurysms^[22] and may or may not be associated with retroperitoneal hemorrhage. Clinical features include tachycardia, congestive cardiac failure, leg swelling, abdominal thrill, machinery type bruit, renal failure, or peripheral ischemia. CT and MRI demonstrate early contrast opacification of a dilated IVC, at the same time and with similar attenuation to that of abdominal aorta. Loss of normal anatomic plane between the aorta and IVC is also shown (Figure 13). Occasionally, a direct communication can be demonstrated between the aorta and IVC^[23]. The most common site is the distal posterolateral aorta and adjacent IVC. Other sites are the aorta and iliac veins and aorta and renal vein. Identification of the exact site of the fistulous communication is essential for pre-surgical planning and to avoid massive blood loss. Surgery is performed immediately, with closure of fistula done from the aneurismal sac or ligation of infrarenal IVC/iliac veins. Complications include dislodgement of atheromatous debris or embolization across the fistula leading to pulmonary embolism^[24]. Endovascular treat-

ment of these fistulas has also been reported^[25].

CONCLUSION

In this review, we have discussed several unusual types of cardiovascular fistulas and abnormal connections involving the coronary arteries and the aorta. CT and MRI are very useful imaging modalities in determining the type and demonstrating the anatomy of these fistulas, which is essential for surgical/interventional planning. Careful analysis in multiple planes and 3D reconstruction is required for comprehensive evaluation of fistulas. Treatment depends on the symptoms and the anatomy.

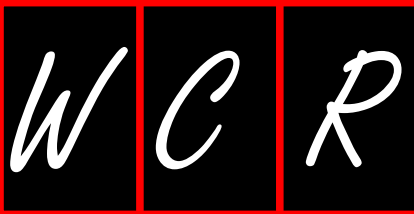
REFERENCES

- 1 **Schmitt R**, Froehner S, Brunn J, Wagner M, Brunner H, Chevaty O, Gietzen F, Christopoulos G, Kerber S, Fellner F. Congenital anomalies of the coronary arteries: imaging with contrast-enhanced, multidetector computed tomography. *Eur Radiol* 2005; **15**: 1110-1121 [PMID: 15756551]
- 2 **Kacmaz F**, Isiksalan Ozbulbul N, Alyan O, Maden O, Demir AD, Atak R, Senen K, Erbay AR, Balbay Y, Olcer T, Ilkay E. Imaging of coronary artery fistulas by multidetector computed tomography: is multidetector computed tomography sensitive? *Clin Cardiol* 2008; **31**: 41-47 [PMID: 18203118 DOI: 10.1002/clc.20286]
- 3 **Parga JR**, Ikari NM, Bustamante LN, Rochitte CE, de Avila LF, Oliveira SA. Case report: MRI evaluation of congenital coronary artery fistulae. *Br J Radiol* 2004; **77**: 508-511 [PMID: 15151973 DOI: 10.1259/bjr/24835123]
- 4 **Chen CC**, Hwang B, Hsiung MC, Chiang BN, Meng LC, Wang DJ, Wang SP. Recognition of coronary arterial fistula by Doppler 2-dimensional echocardiography. *Am J Cardiol* 1984; **53**: 392-394 [PMID: 6695760 DOI: 10.1016/0002-9149(84)90489-2]
- 5 **Zenooz NA**, Habibi R, Mammen L, Finn JP, Gilkeson RC. Coronary artery fistulas: CT findings. *Radiographics* 2009 **29**: 781-789 [PMID: 19448115 DOI: 10.1148/rg.293085120]
- 6 **Said SA**, Lam J, van der Werf T. Solitary coronary artery fistulas: a congenital anomaly in children and adults. A contemporary review. *Congenit Heart Dis* 2006; **1**: 63-76 [PMID: 18377549 DOI: 10.1111/j.1747-0803.2006.00012.x]
- 7 **Wilcox WD**, Neal MJ, Alpert BS, Taylor AB, Dooley KJ. Localized occurrence of congenital coronary artery fistula in the southeast United States. *Am J Cardiol* 1986; **57**: 361-363 [PMID: 3946236 DOI: 10.1016/0002-9149(86)90929-X]
- 8 **Gowda RM**, Vasavada BC, Khan IA. Coronary artery fistulas: clinical and therapeutic considerations. *Int J Cardiol* 2006; **107**: 7-10 [PMID: 16125261 DOI: 10.1016/j.ijcard.2005.01.067]
- 9 **Dodge-Khatami A**, Mavroudis C, Backer CL. Congenital Heart Surgery Nomenclature and Database Project: anomalies of the coronary arteries. *Ann Thorac Surg* 2000; **69**: S270-S297 [PMID: 10798435 DOI: 10.1016/S0003-4975(99)01248-5]
- 10 **Tomasian A**, Lell M, Currier J, Rahman J, Krishnam MS. Coronary artery to pulmonary artery fistulae with multiple aneurysms: radiological features on dual-source 64-slice CT angiography. *Br J Radiol* 2008; **81**: e218-e220 [PMID: 18769007 DOI: 10.1259/bjr/64015972]
- 11 **Zeina AR**, Blinder J, Rosenschein U, Barmer E. Coronary-pulmonary artery fistula diagnosed by multidetector computed tomography. *Postgrad Med J* 2006; **82**: e15 [PMID: 16822914]
- 12 **Shah SS**, Teague SD, Lu JC, Dorfman AL, Kazerooni EA, Agarwal PP. Imaging of the coronary sinus: normal anatomy and congenital abnormalities. *Radiographics* 2012; **32**: 991-1008 [PMID: 22786990]
- 13 **Galbraith AJ**, Werner D, Cutforth RH. Fistula between left coronary artery and superior vena cava. *Br Heart J* 1981; **46**: 99-100 [PMID: 7272120 DOI: 10.1136/hrt.46.1.99]
- 14 **Yanagihara K**, Ueno Y, Kobayashi T, Isobe J, Watanabe S, Itoh M. Coronary artery fistula into a persistent left superior vena cava: report of a case. *Surg Today* 1997; **27**: 966-968 [PMID: 10870586]
- 15 **Pfannschmidt J**, Ruskowski H, de Vivie ER. [Bland-White-Garland syndrome. Clinical aspects, diagnosis, therapy]. *Klin Padiatr* 1992; **204**: 328-334 [PMID: 1405418 DOI: 10.1055/s-2007-1025367]
- 16 **Peña E**, Nguyen ET, Merchant N, Dennie G. ALCAPA syndrome: not just a pediatric disease. *Radiographics* 2009; **29**: 553-565 [PMID: 19325065 DOI: 10.1148/rg.292085059]
- 17 **Gupta R**, Marwah A, Shrivastva S. Anomalous origin of right coronary artery from pulmonary artery. *Ann Pediatr Cardiol* 2012; **5**: 95-96 [PMID: 22529614]
- 18 **Farand P**, Brochu MC, Belzile F, Benko A, Dalery K. Fistula between a coronary artery bypass graft pseudoaneurysm and the coronary sinus. *Can J Cardiol* 2008; **24**: 920 [PMID: 19052674 DOI: 10.1016/S0828-282X(08)70705-0]
- 19 **Khunnawat C**, Mukerji S, Abela GS, Thakur RK. Unusual complications of coronary artery bypass graft surgery. *Am J Cardiol* 2006; **98**: 1665-1666 [PMID: 17145231]
- 20 **Chandra S**, Vijay S, Kaur D, Dwivedi S. Congenital aorta right atrial fistula: successful transcatheter closure with the Amplatzer occluder. *Pediatr Cardiol* 2011; **32**: 1057-1059 [PMID: 21681644 DOI: 10.1007/s00246-011-0026-5]
- 21 **Hsu RB**, Chien CY, Wang SS, Chu SH. Aorto-right atrial fistula: a rare complication of aortic dissection. *Tex Heart Inst J* 2000; **27**: 64-66 [PMID: 10830634]
- 22 **Schmidt R**, Bruns C, Walter M, Erasmi H. Aorto-caval fistula--an uncommon complication of infrarenal aortic aneurysms. *Thorac Cardiovasc Surg* 1994; **42**: 208-211 [PMID: 7825158]
- 23 **Cinara IS**, Davidovic LB, Kostic DM, Cvetkovic SD, Jakovljevic NS, Koncar IB. Aorto-caval fistulas: a review of eighteen years experience. *Acta Chir Belg* 2005; **105**: 616-620 [PMID: 16438071]
- 24 **Ravi R**, Peter SB, Swamination TS, Chandrasekar V. Spontaneous Aortocaval Fistula due to Aneurysm Rupture- A Case Report. *Ind J Radiol Imaging* 2006; **16**: 453-456
- 25 **Vethrus M**, McWilliams R, Tan CK, Brennan J, Gilling-Smith G, Harris PL. Endovascular repair of abdominal aortic aneurysms with aortocaval fistula. *Eur J Vasc Endovasc Surg* 2005; **30**: 640-643 [PMID: 16168683 DOI: 10.1016/j.ejvs.2005.07.017]

P- Reviewers: Hsu JL, Júnior EA, Nagamachi S

S- Editor: Wen LL L- Editor: A E- Editor: Liu SQ





Effectiveness of chest radiography, lung ultrasound and thoracic computed tomography in the diagnosis of congestive heart failure

Luciano Cardinale, Adriano Massimiliano Priola, Federica Moretti, Giovanni Volpicelli

Luciano Cardinale, Adriano Massimiliano Priola, Federica Moretti, Institute of Radiology, University of Turin, AOU San Luigi Gonzaga, 10043 Orbassano, Torino, Italy
Giovanni Volpicelli, Department of Emergency Medicine, University of Turin, AOU San Luigi Gonzaga, 10043 Orbassano, Torino, Italy

Author contributions: Cardinale L and Volpicelli G planned the research and collected the materials; Priola AM and Moretti F were involved in the collection of clinical data; Moretti F wrote the paper assisted by Priola AM and Volpicelli G; Volpicelli G and Cardinale L reviewed this commentary and supervised its publication; Volpicelli G was involved in the language translation.

Correspondence to: Luciano Cardinale, MD, PhD, Institute of Radiology, University of Turin, AOU San Luigi Gonzaga, Regione Gonzole 10, 10043 Orbassano, Torino, Italy. luciano.cardinale@gmail.com
Telephone: +39-1-1902601 Fax: +39-1-19026303
Received: December 28, 2013 Revised: April 22, 2014
Accepted: May 15, 2014
Published online: March 28, 2015

Abstract

Hydrostatic pulmonary edema is as an abnormal increase in extravascular water secondary to elevated pressure in the pulmonary circulation, due to congestive heart failure or intravascular volume overload. Diagnosis of hydrostatic pulmonary edema is usually based on clinical signs associated to conventional radiography findings. Interpretation of radiologic signs of cardiogenic pulmonary edema are often questionable and subject. For a bedside prompt evaluation, lung ultrasound (LUS) may assess pulmonary congestion through the evaluation of vertical reverberation artifacts, known as B-lines. These artifacts are related to multiple minimal acoustic interfaces between small water-rich structures and alveolar air, as it happens in case of thickened interlobular septa due to increase of

extravascular lung water. The number, diffusion and intensity of B lines correlates with both the radiologic and invasive estimate of extravascular lung water. The integration of conventional chest radiograph with LUS can be very helpful to obtain the correct diagnosis. Computed tomography (CT) is of limited use in the work up of cardiogenic pulmonary edema, due to its high cost, little use in the emergencies and radiation exposure. However, a deep knowledge of CT signs of pulmonary edema is crucial when other similar pulmonary conditions may occasionally be in the differential diagnosis.

© 2015 Baishideng Publishing Group Inc. All rights reserved.

Key words: Dyspnea; Ultrasonography; Emergency department; Lung diseases; Interstitial/ultrasonography; Pulmonary edema/radiography; Pulmonary edema/ultrasonography; Heart failure/complications; Heart Failure/ultrasonography

Core tip: Acute decompensated heart failure (ADHF) is a frequent emergency condition that represents a diagnostic challenge for the emergency physicians. Imaging has a fundamental role in the diagnosis of heart failure, but the efficacy of the diagnostic process is highly dependent from the ability to integrate information drawn from lung ultrasound (LUS), chest radiography and computed tomography (CT). Chest radiography and LUS are the most used diagnostic tools: the first one combining relative low cost with the panoramic view that allows exclusion of many pulmonary conditions that comes into the differential diagnosis; otherwise the second one has higher sensitivity in the diagnosis of the early signs of pulmonary congestion and permit to perform the examination at bedside during the first clinical approach. CT scan is the best method to have a panoramic thoracic view and CT scan is a powerful method but it has many limitations due to costs, availability in emergency situations and relatively high

radiation exposure. The modern clinician and radiologist should be aware of the potential and limitations of these diagnostic tools and be prepared to integrate information derived from a correct use of ultrasound, conventional radiology and CT.

Original sources: Cardinale L, Priola AM, Moretti F, Volpicelli G. Effectiveness of chest radiography, lung ultrasound and thoracic computed tomography in the diagnosis of congestive heart failure. *World J Radiol* 2014; 6(6): 230-237 Available from: URL: <http://www.wjgnet.com/1949-8470/full/v6/i6/230.htm> DOI: <http://dx.doi.org/10.4329/wjr.v6.i6.230>

INTRODUCTION

Acute decompensated heart failure (ADHF) is a frequent emergency condition that, often represents a diagnostic challenge for the emergency physicians. Accurate assessment of effectiveness of medical treatment on reducing pulmonary congestion, which is the consequence of elevated cardiac filling pressure, is a basic step for a correct management of patients with ADHF. Most patients hospitalized for ADHF are not submitted to invasive hemodynamic measurements, and clinical improvement relies on change in physical findings, radiologic imaging, and hormone levels. Physical findings of elevated filling pressure are often inadequate and rarely decisive to assess real clinical improvement when considered alone^[1-3].

Chest X-ray (CXR) is the traditional first line procedure to assess pulmonary congestion, but interpretation of radiologic signs, such as vascular opacity redistribution and interstitial edema, are often questionable and subjective, while different levels of expertise of the readers may cause high inter-observer variability.

In doubtful cases, lung ultrasound (LUS) has been shown to be of value in assessing pulmonary congestion by the evaluation of vertical comet tail artifacts, named B-lines. These artifacts represent easy-to-acquire and highly reproducible bedside signs of diffuse interstitial syndrome, but their limitation is the low specificity^[4,5].

B-lines are caused by a change of the normal balance between the air and fluid pulmonary content, when air is lost and fluid are increased. The multiple and small air-fluid interfaces due to small water-rich structures surrounded by air presenting in the lung periphery, create a reverberation phenomenon represented on the screen by multiple B-lines^[6]. However, this phenomenon is irrespective of the cardiogenic or pulmonary origin of the condition.

Concerning thoracic computed tomography (CT) scan, it is rarely used for diagnosing pulmonary congestion, unless highly selected cases where other pulmonary interstitial conditions come into the differential. Signs of hydrostatic pulmonary edema on high-resolution CT should always be recognized, even if edema may sometimes be misdiagnosed and the differential diagnosis not always is easily read by the radiologist. Indeed, sometimes signs of pulmonary congestion on CT imaging represent

an unexpected condition on patients investigated for other diseases^[7].

This review describes the specific signs of cardiogenic pulmonary edema of these three main imaging techniques and discuss their role in the diagnostic process.

CHEST X-RAY

In the acute phase of decompensated heart failure, the early pulmonary alteration is congestion of the vascular bed due to progressive increase of capillary hydrostatic pressure. When pressure increases further and the lymphatic vessels become congested, fluids begin to accumulate in the interstitium around arteries, veins, and airways, and particularly in the interlobular septa. In the early phase, this mechanism protects the lung against the final stage of congestion, that is leakage of fluids into the alveolar spaces, the alveolar edema. The radiologic findings at chest radiography reflect the anatomic-pathologic alterations.

As severity of congestion increases, the sequence of signs visible on chest radiographs are: (1) vascular opacity "redistribution" towards the upper lobes and distention of the upper pulmonary veins; (2) enlargement and loss of definition of hilar structures; (3) septal lines in the lower lung, indicated as Kerley A and B lines; (4) peribronchial and perivascular cuffing with widening and blurring of the margins; and (5) thickening of interlobar fissures with subpleural fluid accumulation (Figure 1)^[8,9].

Redistribution, known also as cephalization, occurs only in the setting of chronic pulmonary venous hypertension, very often encountered in mitral stenosis (Figure 2). Cardiomegaly and pleural effusions are adjunctive radiologic findings quite frequently detected in cardiogenic pulmonary congestion. When congestion increases and becomes alveolar edema, chest radiography shows bilateral and usually symmetric parenchymal opacities, with a central or basilar distribution, without air bronchogram^[10] (Figure 3).

The distribution of alveolar edema may be influenced by gravity. In this case performing the examination in supine or orthostatic position and right or left decubitus, may consistently change the radiologic pattern. Moreover, a coexistent condition of chronic obstructive lung disease may influence irregular distribution of edema as fluids tend to leak in the area of the lung where the structure of the organ is less subverted.

In the emphysematous lung, edema of the alveolar spaces will not be imaged because of alveolar destruction in over-inflated areas, while accentuation of interstitial signs of congestion may still being detected at CXR.

In case of large, acute myocardial infarction (MI) that involves the function of the mitral valve, a regional asymmetric distribution of pulmonary edema may produce atypical radiologic patterns that mimic non-cardiogenic edema or, in some cases, even pneumonia (Figure 4).

This pattern is caused by the flow vector due to mitral regurgitation, which may be massively directed toward the right superior pulmonary vein^[11]. However, opacities



Figure 1 Posterior-anterior chest X-ray in a patient with congestive heart failure and interstitial pulmonary edema. In the figure are shown radiographic signs that suggest interstitial pulmonary edema including enlarged and loss of definition of large pulmonary vessels, both Kerley's A and Kerley's B lines associated with cardiomegaly.



Figure 3 Supine radiogram in a patient with cardiogenic alveolar edema. Note that the vascular perihilar structures are not defined because of the presence of confluent peripheral and gravitational consolidations, with large pleural effusion. Cardiomegaly is also present.

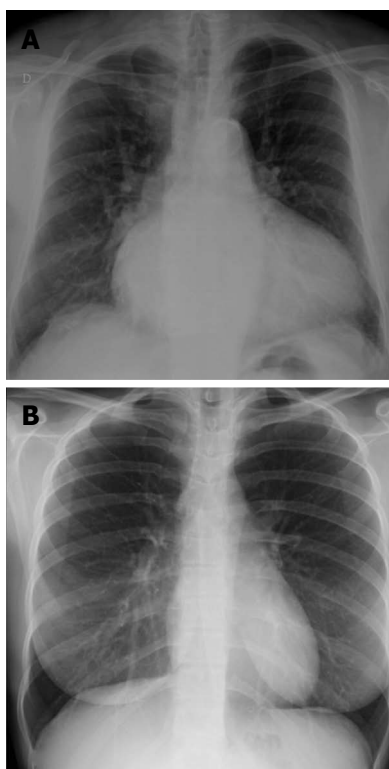


Figure 2 Posterior-anterior chest X-ray demonstrating enlargement of atrial and left ventricles, with redistribution of lung circulation from bases to apex suggestive to pulmonary congestion (A), note the blood vessels are more prominent in the upper lung fields compared to the lung bases, just the opposite of normal (B).



Figure 4 Antero-posterior chest radiograph with asymmetric pulmonary edema with grade 3 mitral insufficiency shows pulmonary edema predominantly within the right upper lobe.

due to alveolar edema may rapidly change their dimension and even dissolve on the effect of treatment. Thus, radiologic follow-up may sometimes contribute to resolve the diagnostic dilemma.

Signs of pulmonary congestion at chest radiography may even precede clinical symptoms. Conversely, pulmonary edema may be still visible radiographically for hours or even days after hemodynamic recovery^[12].

To date, CXR represents the first line imaging exam in patients presenting to the emergency department (ED)

complaining of acute dyspnea. The possibility of correct diagnosis at CXR is greater the more severe and prolonged will be pulmonary congestion, because the radiologic signs are more accurate and clearly visible. Relating the diagnosis of cardiogenic pulmonary congestion, CXR is moderately specific (specificity 76%, 83%), but not very sensitive (50%-68%)^[13].

Therefore, CXR does not have a direct role in the pathway for the diagnosis of heart failure, where the standard of care is cardiac and LUS. The main reason of this limitation is that CXR is not sensitive enough, because heart failure cannot be ruled out with certainty in the presence of a normal radiologic pattern. However, our opinion is that CXR is highly useful to diagnose alternative diagnoses when they are, together with decompensated heart failure in the differential.

LUNG ULTRASOUND

Quite recently, LUS opened new perspectives in the bedside evaluation of pulmonary congestion. Many authors produced a growing number of papers showing the power of LUS in diagnosing pulmonary diseases^[14-20].

Rather than from technologic progress, development



Figure 5 Lung ultrasound scan showing multiple B-lines from a case of cardiogenic pulmonary oedema. When a similar pattern is visualised on multiple locations in the anterior and lateral chest, it is diagnostic of the interstitial syndrome.

of modern LUS is mainly based on discovering the significance of sonographic artifacts^[21]. Particularly, some vertical echogenic linear artifacts, known as B-lines, are simple, noninvasive signs of pulmonary interstitial fluid that can be easily evaluated at bedside. B-lines originate from multiple small subpleural air/fluid acoustic interfaces, due to the fact that air and water are two elements with opposite values of acoustic impedance^[22]. This phenomenon is related to the contrast between air-filled and water-rich structures, which generate multiple reverberation of the ultrasound beam that is visualized on the screen as linear vertical artifacts, the B-lines (Figure 5).

In the normally aerated lung, only a very few B-lines can be detected by sonography^[23].

When the water content increases and air decreases due to disease, the thickened interlobular septa and fluid into the alveolar spaces cause the appearance of multiple and diffuse B-lines (Figure 6)^[4,5].

Any condition of the lung where alveolar air is partially lost and interstitial fluids or cellularity are diffusely increased, causes the appearance of B-lines at LUS. B-lines underlines the so called interstitial syndrome.

The fundamental technique for diagnosing interstitial syndrome consists of examining the anterior and lateral chest using four intercostal scans per side, corresponding to the upper and inferior areas anteriorly and the upper and basal areas laterally. A positive scan is characterized by a minimum of three B-lines, whereas a positive examination is defined by at least two positive areas per side^[5,17] (Figure 6).

Simple detection of B-lines does not allow differentiation of the disease involving the lung interstitium, but other organ ultrasound signs can be used to confirm the diagnosis of pulmonary congestion in decompensated heart failure. For convenience a focused cardiac sonography can be performed using the same probe used for lung examination, looking for global left ventricle function impairment, which will be detected in about 50% of cases with acute decompensated heart failure^[24].

Regarding LUS, other signs than B-lines may be evaluated for differentiating similar patterns of interstitial

syndrome from cardiogenic and non-cardiogenic causes. These includes evaluation of pleural sliding and irregularities, distribution of B-lines and sub-pleural consolidations. Some studies showed the reliability of these signs in differentiating signs of cardiogenic pulmonary edema from ARDS and pulmonary fibrosis^[25].

The primary diagnosis of pulmonary interstitial fluid in the emergency setting is crucial for the differential diagnosis between a cardiogenic and non-cardiogenic respiratory failure. Some studies showed the usefulness of B-lines as a primary diagnostic test in acute respiratory failure patients^[20,26]. Lung ultrasound appears to be particularly useful in differentiating between exacerbation of chronic obstructive pulmonary disease (COPD), a condition that does not show B-lines, and decompensated heart failure. In a study performed in dyspneic patients in the emergency department, diffuse B-lines were detected in 100% of patients with cardiogenic pulmonary oedema but was absent in 92% of cases with exacerbation of COPD and 98.75% of those with normal lungs^[26]. Conclusion of the study was that sonographic detection of B-lines might help distinguish pulmonary edema from exacerbation of COPD.

Other studies showed the correlation between B-lines and natriuretic peptides in the primary evaluation of acute decompensated heart failure in the Emergency department^[27]. Pulmonary interstitial fluid, sonographically demonstrated by B-lines, was strictly correlated with natriuretic hormones level. Conclusions of these studies was that LUS can be used alone or can provide additional predictive power to natriuretic peptides in the immediate evaluation of dyspneic patients to diagnose the cardiac origin of the symptom.

Another great potential of LUS is that B-lines are highly sensitive to the resolution of lung congestion in patients admitted to the hospital for acute decompensated heart failure. Clearance of B-lines represents a direct sign of effective treatment, but also may be useful to specify the diagnosis in cases where the origin of B-lines cannot be differentiated at a first examination^[28].

Finally, LUS may be also useful to diagnose unsuspected conditions when it is performed in combination with other tools, showing similar performances as compared to other more panoramic chest diagnostic imaging tools^[29-32].

COMPUTED TOMOGRAPHY

On high resolution computed tomography (HRCT), signs of hydrostatic edema generally results in a combination of septal thickening and ground-glass opacities. Incidence and predominance of these signs is individually variable^[33-39] (Figure 7).

Crazy paving and consolidation are also frequently imaged. In some patients, ill-defined perivascular and centrilobular opacities may also be detected, or ground-glass opacity may appear lobular and patchy with a tendency to have a parahilar and gravitational distribution (Figure 8)^[40].

There is some evidence that a parahilar or bat wing

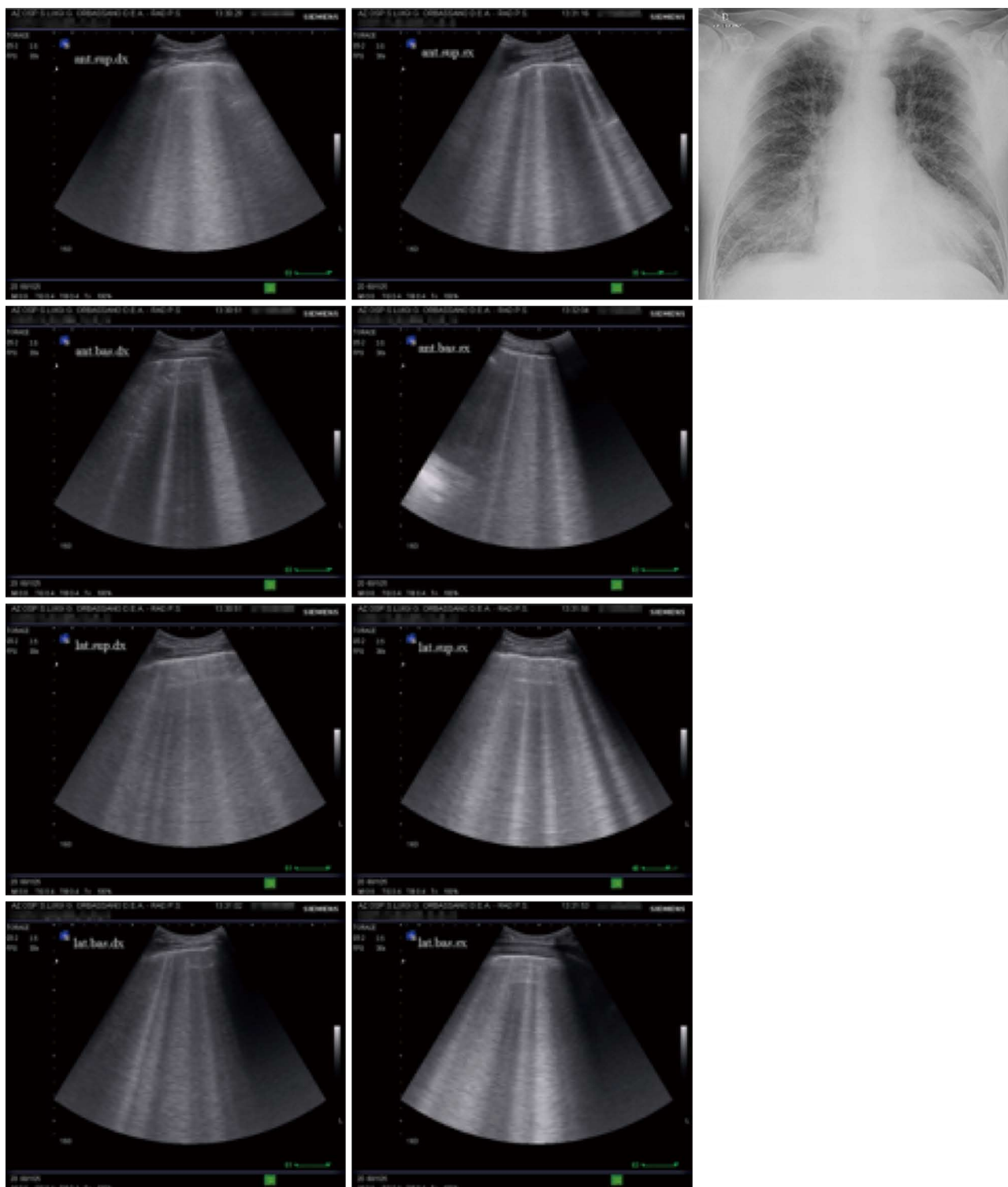


Figure 6 A typical sonographic pattern of diffuse alveolar-interstitial syndrome (left side) and corresponding chest radiograph (right side) in a case of acute cardiogenic pulmonary oedema. In the sonographic images on either side of the radiogram, the presence of multiple adjacent comet-tail artefacts (at least three per scan and in all chest areas examined) can be easily distinguished. The images illustrate the sonographic B+ pattern corresponding to the radiological finding of pulmonary oedema.

distribution of edema is typically found in patients who have a rapid accumulation of fluid^[40]. Occasionally edema may have unilateral distribution, as may happen in patients with a prolonged lateral decubitus, or asymmetric and even with bizarre distribution in patients with region-

al emphysema^[29]. In studies on hydrostatic edema in dog lungs, high resolution CT patterns showed predominantly central, peribronchovascular, and posterior distribution of edema, associated with an apparent increased thickness of bronchial walls^[30,31].

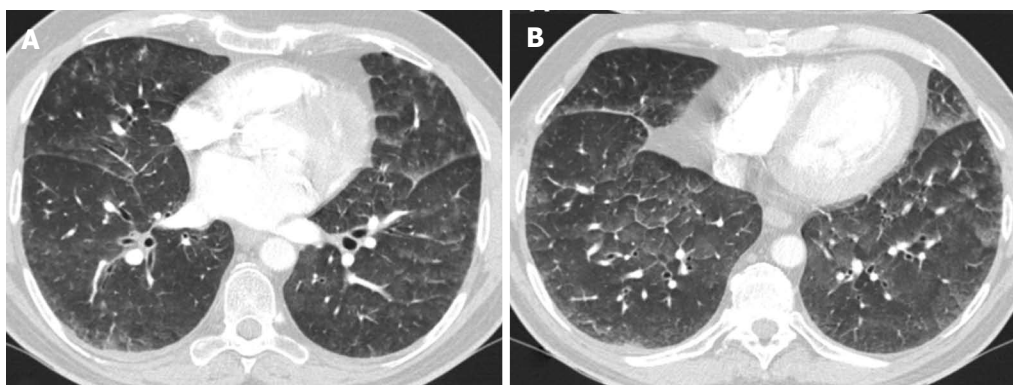


Figure 7 Computed tomography scan through lower lobes shows, limited areas of ground-glass opacity, with thickening of major fissures reflecting subpleural interstitial edema. Is also present interlobular septal and peribronchovascular interstitial thickening.

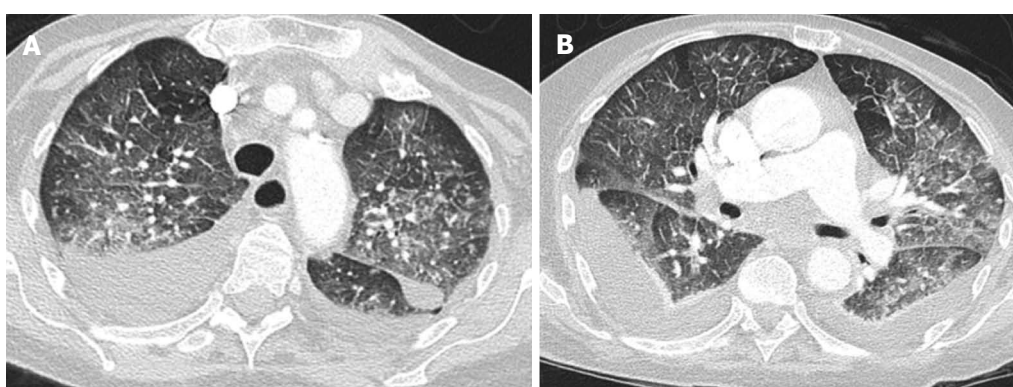


Figure 8 Computed tomography scan through aortic arch and pulmonary arteries planes shows ground-glass opacity with geographic distribution and partial sparing of the lung periphery. Thickening of interlobular septa and sub-pleural edema and bilateral pleural effusion with passive atelectasis of lower lobes is also present.

Table 1 A proposed diagnostic algorithm for the diagnosis of pulmonary edema

Lung ultrasound	Chest X-ray	Chest CT
First line in emergency and critically ill monitoring and to assess pulmonary congestion in typical clinical presentation	Second line to confirm doubtful cases in emergency or critically ill after haemodynamic recovery	Third step differential diagnosis of Pulmonary Embolism

CT: Computed tomography.

STRENGTHS AND WEAKNESSES OF INTEGRATED USE OF LUS, CHEST X-RAY AND CT FOR THE DIAGNOSIS OF CARIOGENIC PULMONARY EDEMA

Imaging has a fundamental role in the diagnosis of heart failure, but the efficacy of the diagnostic process is highly dependent from the ability to integrate information drawn from LUS, chest radiography and CT (Table 1).

Chest radiography has the great advantage of combining relative low cost with the panoramic view that allows exclusion of many pulmonary conditions that comes into the differential diagnosis. CT scan is the best method to

Table 2 Diagnostic accuracy of chest X-ray and ultrasound in patients with heart failure

	Sensitivity
X-ray	56%
US	100%

Difference of patients showing radiologic and ultrasound (US) signs of congestive heart failure (personal data not published).

have a panoramic thoracic view, and much more sensitive than chest radiography for the first diagnosis of many conditions, like pulmonary embolism and early phase of cardiogenic pulmonary edema. However, it has many limitations due to costs, availability in emergency situations and relatively high radiation exposure. However, in recent years technological advances have made it possible to improve the modulation of dose exposure to follow the principles of radiological protection. Besides radiation exposure, low availability and feasibility are other fundamental limitations. CT scan cannot be performed as routine technique in heart failure because of the high prevalence of this disease and high costs of use.

However, while LUS and chest radiography are the first choice imaging technique in most cases, in selected cases where multiple conditions are in the differential, CT

scan may become the method of reference. This is the case in acutely dyspneic patients when the differential diagnosis with pulmonary embolism is a challenge. In other cases, when the differential diagnosis includes diffuse parenchymal lung diseases, the high-resolution CT of the chest may be useful to rule-out or confirm pulmonary congestion.

Lung ultrasound has the limitation of being a surface imaging technique far less panoramic than chest radiography and CT scan. However, the great advantages of LUS are a higher sensitivity than chest radiography in the diagnosis of the early signs of interstitial thickening due to pulmonary congestion, and the possibility to perform the examination at bedside during the first clinical approach (Table 2).

CONCLUSION

In the diagnostic imaging of pulmonary congestion due to decompensated heart failure, LUS and CXR are the most used diagnostic tools. Lung ultrasound does not fully replace CXR but may be of great help in some specific situations, like in the emergency setting when a prompt diagnostic evaluation of dyspneic patients at bedside is needed and also for monitoring clinical evolution. Moreover, LUS outperforms conventional radiology for the diagnosis of early signs of pulmonary congestion and should always be considered when radiologic signs are not detected on CXR but heart failure is still considered a possibility. However, LUS standing alone has a limited specificity for cardiogenic pulmonary congestion. Indeed, the main ultrasound signs of the interstitial syndrome, the B lines, are also detected in other pulmonary conditions, even chronic, characterized by loss of aeration and increase in fluids. Moreover, CXR is superior to LUS as a panoramic imaging modality that allows an immediate and comprehensive evaluation of the thoracic structures. CT scan is a powerful method for the evaluation of the thorax and even more panoramic, but is of limited use in the first diagnosis of decompensated heart failure in comparison to CXR and LUS. However, in selected cases it may be of help in the differential diagnosis of interstitial lung diseases or other causes of respiratory failure. Very often, in cases when a CT study is performed to investigate other conditions, the diagnosis of pulmonary congestion is incidental.

Integration of information obtained by the correct use of these three thoracic imaging, may improve the accuracy of the diagnostic process for cardiogenic pulmonary edema. The modern clinician and radiologist should be aware of the potential and limitations of these diagnostic tools and be prepared to integrate information derived from a correct use of ultrasound, conventional radiology and CT.

ACKNOWLEDGMENTS

We thanks for his support Professor Andrea Veltri, Chief

of Radiology Unit, AOUS Luigi Gonzaga, Orbassano (TO)/IT.

REFERENCES

- 1 **Stevenson LW**, Perloff JK. The limited reliability of physical signs for estimating hemodynamics in chronic heart failure. *JAMA* 1989; **261**: 884-888 [PMID: 2913385 DOI: 10.1001/jama.261.6.884]
- 2 **Chakko S**, Woska D, Martinez H, de Marchena E, Futterman L, Kessler KM, Myerberg RJ. Clinical, radiographic, and hemodynamic correlations in chronic congestive heart failure: conflicting results may lead to inappropriate care. *Am J Med* 1991; **90**: 353-359 [PMID: 1825901 DOI: 10.1016/0002-9343(91)80016-F]
- 3 **Badgett RG**, Lucey CR, Mulrow CD. Can the clinical examination diagnose left-sided heart failure in adults? *JAMA* 1997; **277**: 1712-1719 [PMID: 9169900 DOI: 10.1001/jama.277.21.1712]
- 4 **Lichtenstein D**, Mézière G, Biderman P, Gepner A, Barré O. The comet-tail artifact. An ultrasound sign of alveolar-interstitial syndrome. *Am J Respir Crit Care Med* 1997; **156**: 1640-1646 [PMID: 9372688 DOI: 10.1164/ajrccm.156.5.96-07096]
- 5 **Volpicelli G**, Mussa A, Garofalo G, Cardinale L, Casoli G, Perotto F, Fava C, Frascisco M. Bedside lung ultrasound in the assessment of alveolar-interstitial syndrome. *Am J Emerg Med* 2006; **24**: 689-696 [PMID: 16984837 DOI: 10.1016/j.ajem.2006.02.013]
- 6 **Lichtenstein D**, Mezière G, Biderman P, Gepner A. The comet-tail artifact: an ultrasound sign ruling out pneumothorax. *Intensive Care Med* 1999; **25**: 383-388 [PMID: 10342512 DOI: 10.1007/s001340050862]
- 7 **Storto ML**, Kee ST, Golden JA, Webb WR. Hydrostatic pulmonary edema: high-resolution CT findings. *AJR Am J Roentgenol* 1995; **165**: 817-820 [PMID: 7676973 DOI: 10.2214/ajr.165.4.7676973]
- 8 **Heitzman ER**, Ziter FM. Acute interstitial pulmonary edema. *Am J Roentgenol Radium Ther Nucl Med* 1966; **98**: 291-299 [PMID: 5925099 DOI: 10.2214/ajr.98.2.291]
- 9 **Milne EN**, Pistolesi M, Miniati M, Giuntini C. The radiologic distinction of cardiogenic and noncardiogenic edema. *AJR Am J Roentgenol* 1985; **144**: 879-894 [PMID: 3872571 DOI: 10.2214/ajr.144.5.879]
- 10 **Maffessanti M**, Lucangelo U, Pellegrin A. Radiologia toracica in terapia intensiva. *Radiol Med* 2010; **115**: S34-S44
- 11 **Cardinale L**, Volpicelli G, Lamorte A, Martino J. Revisiting signs, strengths and weaknesses of Standard Chest Radiography in patients of Acute Dyspnea in the Emergency Department. *J Thorac Dis* 2012; **4**: 398-407 [PMID: 22934143]
- 12 **Pistolesi M**, Miniati M, Milne EN, Giuntini C. The chest roentgenogram in pulmonary edema. *Clin Chest Med* 1985; **6**: 315-344 [PMID: 3907943]
- 13 **Mant J**, Doust J, Roalfe A, Barton P, Cowie MR, Glasziou P, Mant D, McManus RJ, Holder R, Deeks J, Fletcher K, Qume M, Sohanpal S, Sanders S, Hobbs FD. Systematic review and individual patient data meta-analysis of diagnosis of heart failure, with modelling of implications of different diagnostic strategies in primary care. *Health Technol Assess* 2009; **13**: 1-207, iii [PMID: 19586584 DOI: 10.3310/hta13320]
- 14 **Lichtenstein DA**. Ultrasound in the management of thoracic disease. *Crit Care Med* 2007; **35**: S250-S261 [PMID: 17446785 DOI: 10.1097/01.CCM.0000260674.60761.85]
- 15 **Volpicelli G**, Silva F, Radeos M. Real-time lung ultrasound for the diagnosis of alveolar consolidation and interstitial syndrome in the emergency department. *Eur J Emerg Med* 2010; **17**: 63-72 [PMID: 20945542 DOI: 10.1097/MEJ.0b013e3283101685]
- 16 **Volpicelli G**. Lung sonography. *J Ultrasound Med* 2013; **32**: 165-171 [PMID: 23269722]

- 17 **Volpicelli G**, Elbarbary M, Blaivas M, Lichtenstein DA, Mathis G, Kirkpatrick AW, Melniker L, Gargani L, Noble VE, Via G, Dean A, Tsung JW, Soldati G, Copetti R, Bouhemad B, Reissig A, Agricola E, Rouby JJ, Arbelot C, Liteplo A, Sargsyan A, Silva F, Hoppmann R, Breitreutz R, Seibel A, Neri L, Storti E, Petrovic T. International evidence-based recommendations for point-of-care lung ultrasound. *Intensive Care Med* 2012; **38**: 577-591 [PMID: 22392031 DOI: 10.1007/s00134-012-2513-4]
- 18 **Bouhemad B**, Zhang M, Lu Q, Rouby JJ. Clinical review: Bedside lung ultrasound in critical care practice. *Crit Care* 2007; **11**: 205 [PMID: 17316468 DOI: 10.1186/cc5668]
- 19 **Picano E**, Frassi F, Agricola E, Gligorova S, Gargani L, Motola G. Ultrasound lung comets: a clinically useful sign of extravascular lung water. *J Am Soc Echocardiogr* 2006; **19**: 356-363 [PMID: 16500505 DOI: 10.1016/j.echo.2005.05.019]
- 20 **Volpicelli G**, Cardinale L, Garofalo G, Veltri A. Usefulness of lung ultrasound in the bedside distinction between pulmonary edema and exacerbation of COPD. *Emerg Radiol* 2008; **15**: 145-151 [PMID: 18236088 DOI: 10.1007/s10140-008-0701-x]
- 21 **Lichtenstein DA**, Mezière G, Lascols N, Biderman P, Courret JP, Gepner A, Goldstein I, Tenoudji-Cohen M. Ultrasound diagnosis of occult pneumothorax. *Crit Care Med* 2005; **33**: 1231-1238 [PMID: 15942336 DOI: 10.1097/01.CCM.0000164542.86954.B4]
- 22 **Soldati G**, Copetti R, Sher S. Sonographic interstitial syndrome: the sound of lung water. *J Ultrasound Med* 2009; **28**: 163-174 [PMID: 19168766]
- 23 **Volpicelli G**, Caramello V, Cardinale L, Mussa A, Bar F, Frascisco MF. Detection of sonographic B-lines in patients with normal lung or radiographic alveolar consolidation. *Med Sci Monit* 2008; **14**: CR122-CR128 [PMID: 18301355]
- 24 **Vasan RS**, Larson MG, Benjamin EJ, Evans JC, Reiss CK, Levy D. Congestive heart failure in subjects with normal versus reduced left ventricular ejection fraction: prevalence and mortality in a population-based cohort. *J Am Coll Cardiol* 1999; **33**: 1948-1955 [PMID: 10362198 DOI: 10.1016/S0735-1097(99)00118-7]
- 25 **Copetti R**, Soldati G, Copetti P. Chest sonography: a useful tool to differentiate acute cardiogenic pulmonary edema from acute respiratory distress syndrome. *Cardiovasc Ultrasound* 2008; **6**: 16 [PMID: 18442425 DOI: 10.1186/1476-7120-6-16]
- 26 **Lichtenstein D**, Mezière G. A lung ultrasound sign allowing bedside distinction between pulmonary edema and COPD: the comet-tail artifact. *Intensive Care Med* 1998; **24**: 1331-1334 [PMID: 9885889 DOI: 10.1007/s001340050771]
- 27 **Gargani L**, Frassi F, Soldati G, Tesorio P, Gheorghiane M, Picano E. Ultrasound lung comets for the differential diagnosis of acute cardiogenic dyspnoea: a comparison with natriuretic peptides. *Eur J Heart Fail* 2008; **10**: 70-77 [PMID: 18077210 DOI: 10.1016/j.ejheart.2007.10.009]
- 28 **Volpicelli G**, Caramello V, Cardinale L, Mussa A, Bar F, Frascisco MF. Bedside ultrasound of the lung for the monitoring of acute decompensated heart failure. *Am J Emerg Med* 2008; **26**: 585-591 [PMID: 18534289 DOI: 10.1016/j.ajem.2007.09.014]
- 29 **Maffessanti M**, Dalpiaz G. Pulmonary Edema in Diffuse Lung Disease: Clinical Features, Pathology, HRCT. Milan: Springer, 2004: 186-189
- 30 **Forster BB**, Müller NL, Mayo JR, Okazawa M, Wiggs BJ, Paré PD. High-resolution computed tomography of experimental hydrostatic pulmonary edema. *Chest* 1992; **101**: 1434-1437 [PMID: 1582313 DOI: 10.1378/chest.101.5.1434]
- 31 **Scillia P**, Delcroix M, Lejeune P, Mélot C, Struyven J, Naeije R, Gevenois PA. Hydrostatic pulmonary edema: evaluation with thin-section CT in dogs. *Radiology* 1999; **211**: 161-168 [PMID: 10189466 DOI: 10.1148/radiology.211.1.r99ap07161]
- 32 **Volpicelli G**, Melniker LA, Cardinale L, Lamorte A, Frascisco MF. Lung ultrasound in diagnosing and monitoring pulmonary interstitial fluid. *Radiol Med* 2013; **118**: 196-205 [PMID: 22744356 DOI: 10.1007/s11547-012-0852-4]
- 33 **Ketai LH**, Godwin JD. A new view of pulmonary edema and acute respiratory distress syndrome. *J Thorac Imaging* 1998; **13**: 147-171 [PMID: 9671417 DOI: 10.1097/00005382-199807000-00001]
- 34 **Gluecker T**, Capasso P, Schnyder P, Gudinchet F, Schaller MD, Revelly JP, Chiolero R, Vock P, Wicky S. Clinical and radiologic features of pulmonary edema. *Radiographics* 1999; **19**: 1507-1531; discussion 1507-1531 [PMID: 10555672 DOI: 10.1148/radiographics.19.6.g99no211507]
- 35 **Todo G**, Herman PG. High-resolution computed tomography of the pig lung. *Invest Radiol* 1986; **21**: 689-696 [PMID: 3580031 DOI: 10.1097/00004424-198609000-00003]
- 36 **Webb WR**, Stein MG, Finkbeiner WE, Im JG, Lynch D, Gamsu G. Normal and diseased isolated lungs: high-resolution CT. *Radiology* 1988; **166**: 81-87 [PMID: 3336706]
- 37 **Bessis L**, Callard P, Gotheil C, Biaggi A, Grenier P. High-resolution CT of parenchymal lung disease: precise correlation with histologic findings. *Radiographics* 1992; **12**: 45-58 [PMID: 1734481 DOI: 10.1148/radiographics.12.1.1734481]
- 38 **Malagari K**, Nikita A, Alexopoulou E, Brountzos E, Papatheanasiou M, Mitromaras J, Zakyntinos E, Papiris S, Kelekis DA. Cirrhosis-related intrathoracic disease. Imaging features in 1038 patients. *Hepatogastroenterology* 2005; **52**: 558-562 [PMID: 15816477]
- 39 **Tanaka N**, Matsumoto T, Miura G, Emoto T, Matsunaga N. HRCT findings of chest complications in patients with leukemia. *Eur Radiol* 2002; **12**: 1512-1522 [PMID: 12042962 DOI: 10.1007/s003300101112]
- 40 **Mukhopadhyay P**, Rezzoug F, Webb CL, Pisano MM, Greene RM. Suppression of chondrogenesis by Id helix-loop-helix proteins in murine embryonic orofacial tissue. *Differentiation* 2009; **77**: 462-472 [PMID: 19349107]

P- Reviewers: Tripoliti EE, Yew DT **S- Editor:** Ji FF
L- Editor: A **E- Editor:** Zhang DN



Multi-detector computed tomography in the diagnosis and management of acute aortic syndromes

James Thomas Patrick Decourcy Hallinan, Gopinathan Anil

James Thomas Patrick Decourcy Hallinan, Gopinathan Anil,
Department of Diagnostic Imaging, National University Health
System, Singapore 119074, Singapore

Author contributions: Hallinan JTPD and Anil G contributed
equally to this work.

Correspondence to: Gopinathan Anil, MD, FRCR, FAMS,
Department of Diagnostic Imaging, National University Hospital,
5 Lower Kent Ridge Road, Singapore 119074,
Singapore. ivyanil10@gmail.com

Telephone: +65-97-296614 Fax: +65-67-797101

Received: January 14, 2014 Revised: February 26, 2014

Accepted: April 17, 2014

Published online: March 28, 2015

Abstract

Acute aortic syndrome (AAS) is a spectrum of conditions, which may ultimately progress to potentially life-threatening aortic rupture. This syndrome encompasses aortic dissection (AD), intramural haematoma, penetrating atherosclerotic ulcer and unstable thoracic aortic aneurysms. Multi-detector CT (MDCT) is crucial for the diagnosis of AAS, especially in the emergency setting due to its speed, accuracy and ready availability. This review attends to the value of appropriate imaging protocols in obtaining good quality images that can permit a confident diagnosis of AAS. AD is the most commonly encountered AAS and also the one with maximum potential to cause catastrophic outcome if not diagnosed and managed promptly. Hence, this review briefly addresses certain relevant clinical perspectives on this condition. Differentiating the false from the true lumen in AD is often essential; a spectrum of CT findings, *e.g.*, "beak sign", aortic "cobwebs" that allows such differentiation have been described with explicit illustrations. The value of non enhanced CT scans, especially useful in the diagnosis of an intramural hematoma has also been illustrated. Overlap in the clinical and imaging features of the various conditions presenting as AAS is not unusual. However, on most instances MDCT enables the right

diagnosis. On select occasions MRI or trans-esophageal echocardiography may be required as a problem solving tool.

© 2015 Baishideng Publishing Group Inc. All rights reserved.

Key words: Acute aortic syndrome; Computed tomography scan; Aortic dissection; Intramural haematoma; Penetrating aortic ulcer; Aortic aneurysm

Core tip: Acute aortic syndrome (AAS) is a spectrum of conditions, which may ultimately progress to potentially life-threatening aortic rupture. This syndrome encompasses aortic dissection (AD), intramural haematoma, penetrating atherosclerotic ulcer and unstable thoracic aortic aneurysms. Multidetector computed tomography (MDCT) is crucial in the diagnosis of AAS in the emergency setting due to its speed, accuracy and ready availability. This review will focus on the use of MDCT in AAS including the imaging protocols, spectrum of radiological findings, implications for planning and follow-up of endovascular and surgical treatment, and potential diagnostic pitfalls.

Original sources: Hallinan JTPD, Anil G. Multi-detector computed tomography in the diagnosis and management of acute aortic syndromes. *World J Radiol* 2014; 6(6): 355-365 Available from: URL: <http://www.wjgnet.com/1949-8470/full/v6/i6/355.htm> DOI: <http://dx.doi.org/10.4329/wjr.v6.i6.355>

INTRODUCTION

Acute aortic syndrome (AAS) is a term used to describe a constellation of emergency aortic conditions requiring prompt diagnosis and treatment. These inter-related conditions include aortic dissection (AD), intramural haematoma (IMH) and penetrating atherosclerotic ulcer (PAU)^[1]. In addition, unstable thoracic aortic aneurysm

at high risk for rupture may also be considered an AAS. This syndrome has an estimated incidence of (2-3.5)/100000 per year^[2]. The most common risk factors are hypertension and genetic conditions of the connective tissue such as Marfan's syndrome. The clinical presentations of the various entities of AAS are essentially indistinguishable from each other with severe chest or abdominal pain being the most common symptom. Clinical suspicion of AAS should herald prompt diagnostic imaging as mortality from AAS increases by approximately 1%-2% per hour^[3]. MDCT typically with electrocardiographic gating (ECG-gated MDCT) is the technique of choice for diagnosis of AAS due to the rapid acquisition times and ready availability in the emergency department^[4]. Other diagnostic imaging modalities include conventional and transoesophageal echocardiography and magnetic resonance imaging (MRI), that are usually reserved for problem solving or if there is contraindication to the use of iodinated contrast^[1,2,5]. This review will focus on MDCT in the diagnosis of AAS. MDCT protocols will be discussed along with the discriminating and overlapping radiological diagnostic features of AAS.

MDCT PROTOCOL FOR AAS

MDCT angiography with electrocardiographic (ECG) gating enables the evaluation of AAS with reduced pulsation artefacts (Figure 1) in the ascending aorta compared to non-gated MDCT angiography^[6]. The ECG-gating can either be performed prospectively (scanning performed at a specified segment of the cardiac cycle), or retrospectively (scanning performed throughout the cardiac cycle but data gathered in a specified segment of the cardiac cycle is selected retrospectively for generating images). A retrospective acquisition allows increased scope for correction of artefacts from dysrhythmias or motion, but comes at the cost of increased radiation exposure^[1,6]. ECG-gating with motion-free images allows for improved assessment of the ascending aorta, aortic annulus, sinuses of Valsalva and coronary arteries^[6,7]. There is also improved depiction of the site of primary intimal tear, extent of the intimomedial flap and involvement of the aortic branches. Studies have also shown a reduction in radiation dose of as much as 45%-50% using ECG-gated high pitch CT compared to non-ECG-synchronised standard-pitch CT^[8,9]. Although ECG-gating is preferred, its absence rarely precludes the diagnosis of clinically significant acute aortic conditions if an experienced reader is interpreting the non-gated CT aortogram.

The details of the scan protocol vary according to the scanner system being used. As an illustration we have described here the protocol of ECG-gated CT angiography on a 64-section helical CT system (Somatom Sensation, Siemens, Erlangen, Germany) performed in our department. Z-axis coverage is determined on a planning topogram from the root of the neck to the common femoral artery bifurcation. A 100 mL bolus injection of intrave-

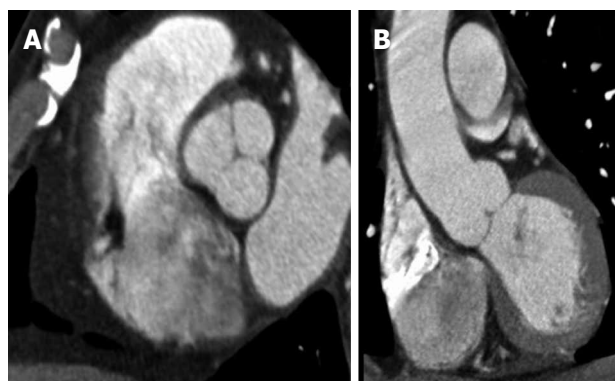


Figure 1 Cardiac-gated computed tomography aortogram in a 55-year-old with chest pain and suspected acute aortic syndrome. A: Axial oblique; B: Coronal reconstructions. No dissection or aneurysm was detected. Retrospective reconstruction at 78% of the cardiac cycle allowed for accurate evaluation of the aortic root and valve cusps in both axial oblique and coronal reconstructions with no pulsation artefacts.

nous contrast (Iohexol 300 mg/mL, Nycomed) is injected at a rate of 3-4 mL a second. Bolus tracking is used to trigger scanning when the attenuation of the descending aorta reaches 150 HU. Retrospective gating is typically used with images reconstructed at 78% of the R-R interval. The section thickness is 0.6 mm with 3 mm reconstructions in the axial, coronal and sagittal oblique planes sent to the PACS for reporting. Additional post processing is performed by the reporting radiologist when clinically indicated for three-dimensional reconstructions to obtain volume rendered images, maximum intensity projections and shaded surface display. Delayed phase images are useful in selected cases of suspected aortic rupture or in cases of dissection to determine the opacification of both the lumina. Although a contrast enhanced CT angiogram is the standard of care, a non-enhanced CT that precedes the angiogram is useful in AAS to evaluate for IMH, which can progress to frank dissection. NECT can also be useful to assess for secondary signs of aortic rupture such as hyperdense, haemorrhagic pericardial, pleural or mediastinal fluid collections. In patients with known allergy to iodinated contrast medium or at high risk of contrast induced nephropathy, the preliminary information obtained through a non-enhanced CT scan may sometimes suffice to make the further clinical decision.

AD

The most common pathology in AAS is AD that begins as a tear or ulcer in the aortic intima allowing blood to penetrate and disrupt the aortic media^[2]. Haemorrhage may also occur *de novo* within the media due to rupture of the vasa vasorum leading to dissection. Irrespective of the initiating cause AD involves separation of the aortic layers and formation of a false lumen^[10]. The false lumen is separated from the true lumen by an intimomedial flap (Figures 2-7). The dissection may then propagate in an antegrade and/or less likely retrograde fashion with a po-



Figure 2 A 47-year-old gentleman with Stanford type B aortic dissection. The dissection flap is flat in all the computed tomography angiographic images. The ascending aorta is not involved and the true lumen is smaller in calibre and shows early and more intense enhancement than the false lumen at the level of the right pulmonary artery (A). The small calibre true lumen gives rise to the coeliac axis (B) and is outlined by atherosclerotic calcifications (C).

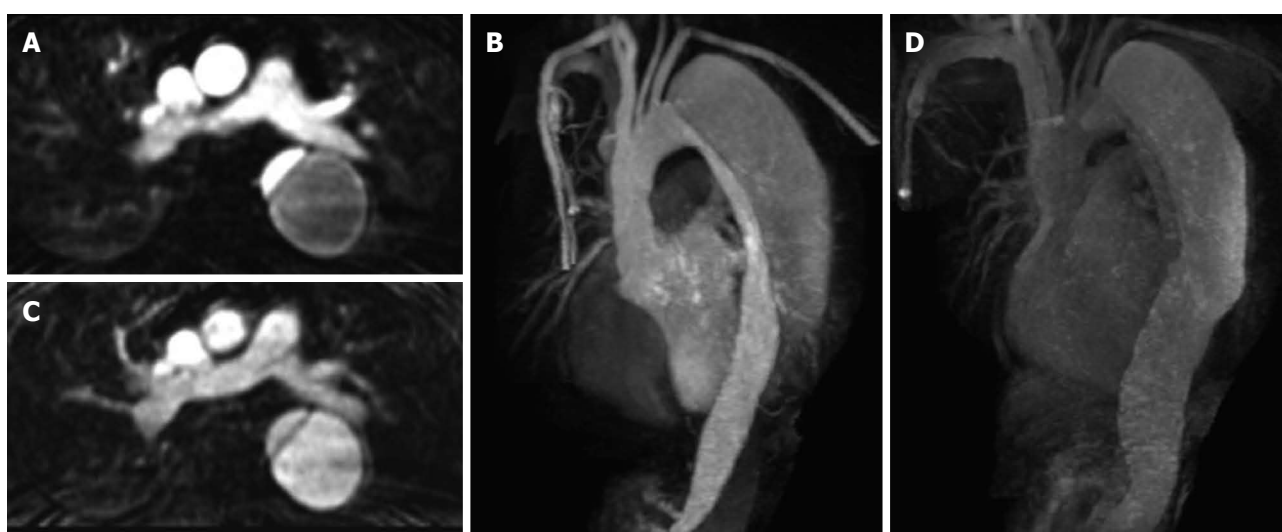


Figure 3 Axial contrast enhanced magnetic resonance aortogram of the same patient as in Figure 2 with type B aortic dissection. In the arterial phase image (A: Axial; B: Coronal 3D reconstruction; 30 s post injection) the true lumen is of small calibre and shows early intense contrast enhancement compared to the larger false lumen. In the second delayed phase (70 s post injection) the enhancement between the lumens becomes more similar (C: Axial; D: Coronal 3D reconstruction).



Figure 4 A 35-year-old gentleman with Marfan's syndrome and a type B aortic dissection. Axial images (A and B) from a computed tomography aortogram reveals an intimomedial flap (arrows) with strands of incompletely sheared aortic media or "cobwebs" seen in the descending thoracic aorta (dashed arrows).

tential to fenestrate back into the aortic lumen or rupture out through the adventitia with life threatening consequences^[11]. Dissection can extend into aortic branches and when it involves major visceral arteries, it can lead to cata-

strophic consequences such as a cerebrovascular event, bowel ischemia, acute renal failure, limb gangrene *etc.*

Risk factors for dissection include hypertension, smoking, trauma (typically road traffic accidents), vas-

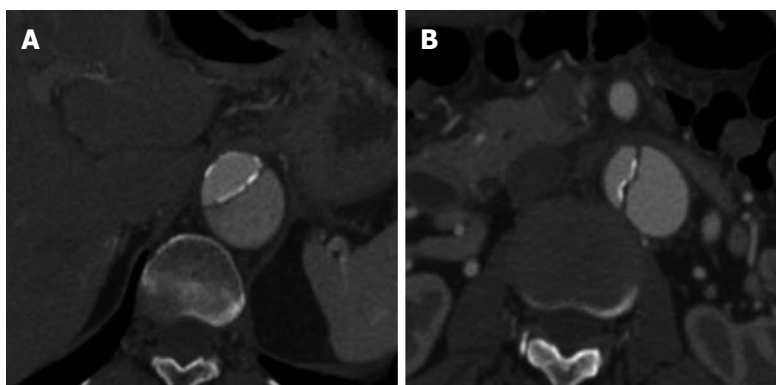


Figure 5 A 59-year-old lady with a type B aortic dissection. Axial images from a computed tomography aortogram show atherosclerotic calcifications outlining the true lumen at the lower thoracic aorta (A). The true lumen is of smaller calibre and shows early and more intense enhancement than the false lumen at this level. More inferiorly at the level of the left renal vein (B), eccentric intimal-medial flap calcification (note the calcification along the true luminal aspect of the flap) is exquisitely demonstrated.



Figure 6 A 45-year-old with a type B aortic dissection. An axial image from a computed tomography aortogram at the upper abdominal aorta shows the "beak" sign (arrow): note the acute angle between the dissection flap and the outer wall of the larger calibre false lumen. The "beak" or space formed by the acute angle is filled with high-attenuation contrast-enhanced blood in this case but it may stay unopacified when filled with clots.

cular inflammation (*e.g.*, Takayasu's arteritis) or infection (*e.g.*, syphilis) and genetic connective tissue disorders (*e.g.*, Marfan's and Ehlers-Danlos syndromes). Propagation of the blood within the media to form a dissection requires pre-existing medial degeneration or cystic medial necrosis, which leads to a weakened aortic wall and represents the end point of many of the risk factors listed above^[2,10].

Two anatomical classification systems exist for AD: De Bakey and Stanford. The Stanford classification is most commonly used as it has a direct bearing on the subsequent therapy. Stanford type A dissections involve the ascending aorta (proximal to the origin of the brachiocephalic artery origin) with or without aortic arch or descending aorta (distal to the left subclavian artery origin) involvement^[2]. Type A dissections are typically treated as a surgical emergency. Mortality is estimated at 20% in the first 24 h without immediate surgical management and approximately 40% in the first week^[12,13]. Complications of type A dissection include aortic regurgitation, aortic rupture, tamponade and compromise of the arch branches or coronary arteries leading to myo-

cardial infarction. Type B constitutes all those dissections that do not involve the ascending aorta. It more often involves the descending aorta and is typically treated medically with anti-hypertensive medications. Without adequate management, uncomplicated type B dissections have an estimated 10% mortality at 1 mo in comparison to 50% for type A dissections^[2,12]. Type B dissections can be complicated by branch disruption and end organ malperfusion, progression to type A dissection and rupture. The role of endovascular repair is well established in Stanford type B lesions while in select situations it may be performed even in type A lesions^[14]. The aim of endovascular intervention is to occlude the intimal tear allowing for false lumen thrombosis and regression, typically by placing an aortic endograft. End-organ ischaemia and malperfusion may also be improved by placement of branch stents and the use of aortic fenestrations to relieve compression of the true by a distended false lumen^[1,14,15].

MDCT angiography has a sensitivity and specificity of close to 100% for diagnosis of acute AD^[16,17]. Cardiac synchronisation should be performed to limit pulsation artefacts in the ascending aorta, which on non-gated MDCT are often the cause of false-positive findings of a thoracic dissection. In AD, the role of MDCT angiography can be summarized as to identify^[1,14,18]: (1) Sites of primary entry and re-entry; (2) Intimal-medial flap, false and true lumen morphology along with the presence of calcifications and thrombus; (3) Extent of the dissection and involvement of the ascending and descending aorta; (4) Evidence of rupture; (5) Involvement of the aortic valve, coronary and aortic arch branches; (6) Abdominal aortic branch patency and evidence of end-organ malperfusion; and (7) Morphology and diameter of the aorta along with the patency, size and tortuosity of the iliac and femoral arteries (useful for endovascular treatment planning).

The intimal-medial flap forms a double-barrelled aorta and separates the true from the false lumen^[4]. This is seen in approximately 70% of cases on MDCT angiography and with three dimensional reconstructs the complex,

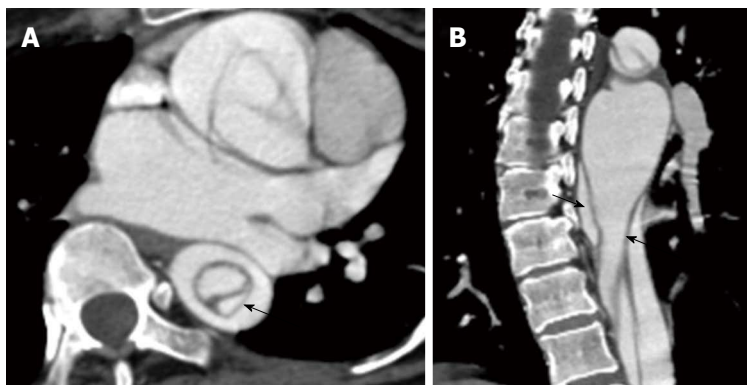


Figure 7 A 37-year-old gentleman with Marfan's syndrome and a type A aortic dissection. The axial image at the level of the left atrium shows an intimal intussusception type dissection in the descending thoracic aorta with the true lumen surrounded by the false lumen (A and B; intimal flap highlighted by the arrows).

often spiralling nature of the dissection can be seen in better detail^[19]. Other appearances include a circumferential intimal flap due to complete dissection of the intima. The true lumen takes on a cylindrical or filiform shape and this may result in an intimal intussusception producing a “windsock” appearance (Figure 7). Differentiation between the false and true lumen is useful for endovascular treatment planning as an endograft should be placed within the true lumen^[1,15].

The true lumen can usually be identified by tracing back or forth from an uninvolved portion of the aorta; this may be difficult if the aortic root is involved proximally or the dissection extends into the iliac vessels distally^[1,20]. In these cases the most useful imaging signs include a false lumen that is larger in calibre than the true lumen and the “beak” sign^[20]. In most cases of acute dissections the false lumen is larger in calibre than the true lumen. This is likely due to sustained systolic pressure in the false lumen exceeding that of the true lumen leading to compression. The “beak” sign (Figure 6) is only seen in the false lumen and is often present in most patients with dissection. It is usually noted both in acute and chronic dissection and is defined as the presence of an acute angle between the dissection flap and the outer wall of the false lumen; the space formed by the acute angle could be filled with high-attenuation material (contrast-enhanced blood) or low-attenuation material (hematoma)^[21,22]. Other less common and less reliable signs for differentiation between the true and false lumen have been documented in the literature. The false lumen may contain thrombus and fine ribbons of low attenuation (“cobwebs”), which likely represent strands of incompletely sheared aortic media (Figure 4)^[22]. Differential contrast enhancement between the true and false lumen is not unusual with the true lumen often showing early opacification with contrast in the arterial phase, while the false lumen starts opacifying later in the portovenous and delayed phase (Figure 3)^[23]. The surface of the dissection flap that is calcified generally involves the intimal surface of the true lumen; this is described as eccentric flap calcification. The side of the flap subtending the false lumen

will have soft tissue attenuation (Figure 5). In acute dissections the lumen with outer wall calcification tends to be the true lumen. Along with eccentric flap calcification this is due to the presence of atherosclerotic calcified plaque in the aortic intima of the true lumen (Figures 2 and 5). A less useful sign is the curvature of the intimal dissection flap. Researchers have found equal incidence of curvature of the flap towards or away from the false lumen. However, in chronic dissections the dissection flap is more likely to be flat. This is likely due to interval healing and development of fibrosis and thickening leading to reduced flap mobility^[19,24].

A thrombosed dissection and an aneurysm with mural thrombus may have a similar appearance. The following features will aid the differentiation: (1) Mural thrombus would not have a spiralling pattern like a dissection; (2) Mural thrombus tends to have an irregular surface rather than the smooth surface of the dissection flap; and (3) in an aneurysm with mural thrombus, the calcium will be along the outer wall while in the thrombosed false lumen it would be along the flap. A thrombosed dissection can be indistinguishable from intramural hematoma; however the differentiation is of only academic interest since management stays the same in both conditions.

AORTIC IMH

Aortic IMH is considered a variant of dissection and is characterised by bleeding of the vasa vasorum in the aortic media without intimal tear (Figure 8). It accounted for 5.7% of AAS in the International Registry of Acute Aortic Dissection (IRAD)^[12,25]. The vasa vasorum may spontaneously rupture or haemorrhage may occur due to an intimal defect/PAU^[1]. IMH may progress to aneurysmal dilatation and rupture (20%-45%), provoke a secondary intimal tear that can progress to dissection (28%-47%), or may regress (10%)^[26]. The most common site of IMH is in the descending aorta (approximately 2/3rds) and risk factors are similar to those for dissection with hypertension being the most prevalent one^[2,25]. The clinical presentation of IMH is also similar to aortic dissection;

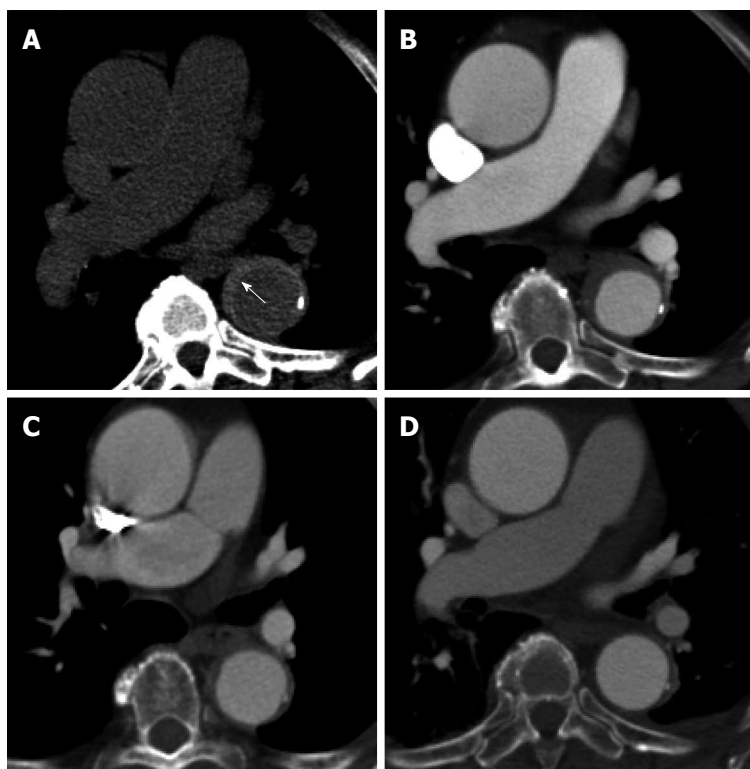


Figure 8 A 61-year-old lady with severe chest pain, breathlessness and a prior history of atrial flutter. Computed tomography aortogram in the emergency department shows hyperdense, eccentric wall thickening of the aortic wall consistent with an intramural haematoma (A, white arrow). A concurrent contrast enhanced axial image at the same level shows no leakage of contrast into this thickened aortic wall (B). The intramural haematoma shows partial resolution at 1 mo (C) and complete resolution at 6 mo (D).

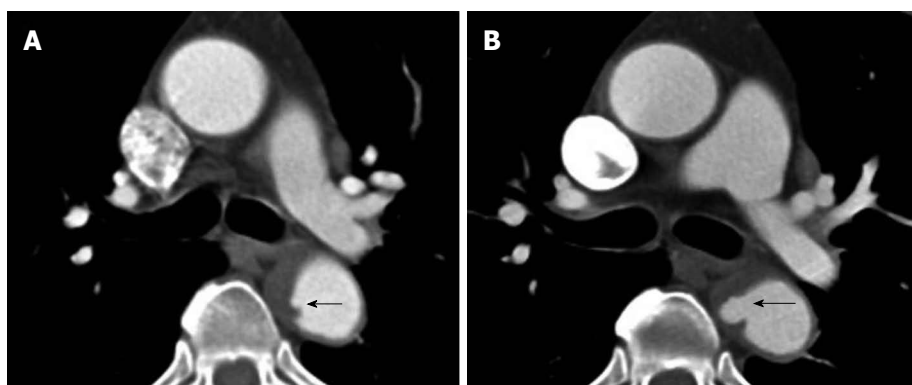


Figure 9 Computed tomography aortogram in a 75-year-old man shows an intramural hematoma (note the eccentric wall thickening in the descending aorta) with intimal surface defect (A: arrow). At one year follow up it has progressed into a frank penetrating ulcer (B: arrow).

chest pain is the usual symptom in ascending aortic IMH while back pain accompanies descending aortic IMH^[27]. IMH is classified along the lines of dissection into Stanford type A and B categories^[1]. Stanford type A IMH is typically treated surgically, with 30 d mortality of 14% *vs* 36% for those treated medically^[28]. In contrast, type B IMH is initially treated medically with antihypertensive medications with a 30-d mortality of 8%^[27]. However, close CT follow-up is recommended in these patients as aneurysmal dilatation or progression to frank dissection of the aorta will require emergency open surgical or endovascular repair^[1,27].

On MDCT, IMH is seen as a hyperdense, crescent shaped region within the aortic wall on non-enhanced CT^[1,4,29]. No enhancement is seen and by definition no intimomedial flap or tear should be visualized^[30]. Unlike a dissection that spirals down, IMH tends to have constant circumferential relationship with the aortic lumen. With the higher resolution of modern imaging technologies, small projections or ulcerations can sometimes be seen communicating between the aortic lumen and the IMH^[4,31]. Studies based on non-cardiac gated CT showed a sensitivity of greater than 96% for the detection of IMH using both unenhanced and contrast enhanced CT^[1,32].

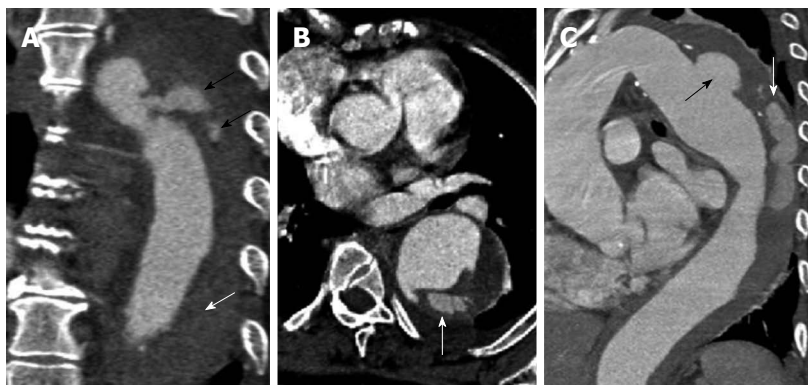


Figure 10 A 62-year-old with acute chest pain. A computed tomography aortogram (A-coronal) shows a penetrating atherosclerotic ulcer at the proximal descending aorta with contrast seen within the aortic media (black arrows) and non-opacifying hyperdensity throughout the rest of the descending thoracic aortic wall compatible with intramural haematoma (white arrow). The axial image (B) shows the contrast extending within the aortic wall and splitting the same. The sagittal oblique reconstruction (C) gives a better demonstration of the penetrating atherosclerotic ulcer at the distal aortic arch (black arrow) with intramural hematoma and progressing into an aortic dissection (white arrow).

PAU

This entity is a manifestation of advanced, severe atherosclerotic disease that leads to disruption of the aortic intima with extension of blood into the aortic media (Figure 9)^[1,2,4]. This is in contrast to the underlying pathological process in AD, which usually results from disease of the media without any underlying atherosclerotic intimal plaque^[33,34]. Disruption of the media by the deep ulceration may lead to vasa vasorum haemorrhage and IMH producing acute chest or back pain with risk of progression to aortic dissection^[25,35]. PAU can also penetrate beyond the aortic media leading to focal outpouching of the adventitia, producing a pseudoaneurysm with risk of frank rupture^[4,29]. Saccular aortic aneurysms may represent the end point of such PAU^[36].

PAU most commonly occurs in the descending thoracic aorta (90%) and is associated with type B IMH in the majority of cases. It is seen as a focal contrast-filled outpouching into the aortic wall on MDCT (Figure 10)^[37,38]. Other MDCT features include overhanging edges with a focal bulge of the external aortic contour. It can be differentiated from a benign atherosclerotic ulcer as the latter would not have contrast extending into the aortic media and would not be associated with an IMH^[39]. Given the relationship with IMH the use of unenhanced images can improve visualisation of crescentic high attenuation haemorrhage in the aortic wall along with displacement of intimal calcifications^[1,22].

The natural history and management of patients with PAU remains controversial. PAU tends to have a worse prognosis than dissection with increased incidence of rupture even if the ulcer is limited to the descending thoracic or abdominal aorta^[25]. Most patients are symptomatic although in approximately a quarter of cases PAU may present incidentally^[1,40]. The condition typically occurs in elderly patients with multiple co-morbidities and risk factors for atherosclerosis^[41]. These factors, especially underlying coronary and peripheral arterial atherosclerosis, may preclude open surgical repair in this group of

patients^[42]. Open surgical repair, typically with a synthetic graft is performed in patients with ascending aortic PAU (these are rare) and in patients with haemodynamic instability and high risk of rupture, *e.g.*, rapid enlargement of the lesion^[1,18]. Endovascular graft placement in patients with symptomatic PAU is an alternative with potentially lower morbidity and mortality^[43-45]. Sometimes, conservative management with antihypertensive therapy may be adequate or may be the best option in PAU especially in asymptomatic patients with involvement of the descending aorta and in those who are poor candidates for any form of invasive treatment. The medically treated patients need at least an annual follow-up to assess for disease progression, which has a strong likelihood in initially symptomatic patients^[19,44,46,47].

UNSTABLE THORACIC AORTIC ANEURYSM

Thoracic aortic aneurysms are relatively uncommon and defined as the permanent dilatation of the aorta to more than 150% of its usual diameter or greater than 5 cm. True aneurysms tend to be fusiform and involve all three layers of the aortic wall^[48]. False or pseudoaneurysms are typically saccular and often limited by the adventitia alone (Figure 11). The most common cause for both types is atherosclerosis (approximately 70%), although false saccular aneurysms often arise following surgery, trauma or due to an infective/inflammatory aetiology^[1,19,49].

Thoracic aortic aneurysms are often clinically asymptomatic but they are considered unstable when showing rapid increase in size or evidence of contained or impending rupture on MDCT. Unstable thoracic aortic aneurysms may be considered an AAS, especially when symptomatic as they are clinically indistinguishable from dissection, IMH or PAU^[4]. The risk of rupture is related to the diameter of the aneurysm sac, with a significantly higher risk for those in the ascending aorta measuring greater than 6 cm, and 7.2 cm in the descending aorta^[50].

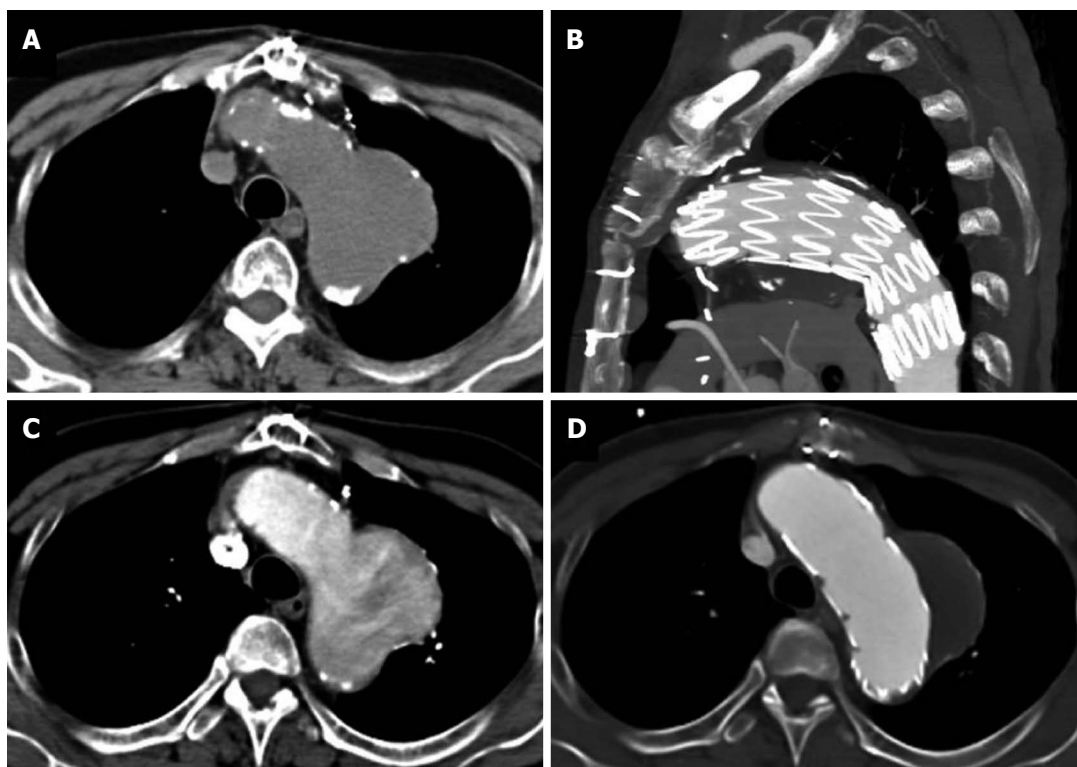


Figure 11 A 68-year-old with chest pain and long standing hypertension. A saccular aneurysm is seen arising from the lateral aortic arch just distal to the origin of the left subclavian artery on this computed tomography aortogram. Atherosclerotic calcifications are seen at the periphery of the aneurysm (A) and there is heterogeneous contrast opacification secondary to turbulent flow on the arterial phase (B). No evidence of rupture is apparent. The aneurysm was excluded using an aortic stent graft as seen in the sagittal plane (C). The excluded sac has completely thrombosed with no endoleak as seen on an axial image (D).

On serial CT scans an annual increase in diameter of the thoracic aortic aneurysm of at least 1 cm is also considered a sign of increased likelihood of rupture^[19,51]. Other morphological MDCT signs of impending rupture should also be taken into account for therapeutic decision making. These include associated IMH with a high attenuating crescent in the aortic wall, discontinuity of circumferential intimal atherosclerotic calcifications within a fusiform aneurysm, a “draped” aortic appearance conforming to the anterolateral contour of an adjacent vertebral body, eccentric or nipple like contour to the aorta, and poor visualisation of the posterior aortic wall^[1,19,52,53]. Frank rupture of a thoracic aortic aneurysm on MDCT is suggested by peri aneurysmal fat stranding, mediastinal haematoma, haemothorax most commonly on the left, hemopericardium or pericardial effusion and evidence of haemodynamic compromise, *e.g.*, collapsed IVC^[1,19].

Therapy should be considered for all symptomatic aneurysms regardless of size due to the high risk of rupture. Otherwise surgical or endovascular therapy should be considered for ascending thoracic aortic aneurysms measuring greater than 5.5 cm, and those in the descending thoracic aorta measuring greater than 6 cm. Similar to dissection open surgical or hybrid surgical and endovascular techniques are the mainstay of ascending thoracic aortic aneurysm therapy^[13]. Smaller aneurysms, typically less than 5.5 cm in diameter can be followed up with serial CT or MRI on an annual basis. However those with underlying genetic connective tissue predispositions to

aneurysm formation such as Marfan’s syndrome should be considered for therapy at smaller diameters. Overall decision on when to intervene should be tailored to the individual clinical scenario and involve an experienced multidisciplinary team^[1,19,54,55].

OTHER IMAGING MODALITIES AND TECHNIQUES

This article has focused on the use of MDCT in the diagnosis and management of AASs while other imaging modalities including conventional angiography, transoesophageal or transthoracic echocardiography and MRI have a complimentary/alternative role in dealing with this clinical problem. MDCT also has some disadvantages including radiation exposure and potential risk of contrast induced nephropathy, which can be overcome by using alternative methods. Conventional angiography is historically the gold standard for evaluation of AASs. However it is invasive, unable to assess for IMH, and can lead to false negative exclusion of dissection. Transthoracic echocardiography can be used in the initial evaluation of suspected AASs in the emergency department. The technique can sometimes visualise the proximal extent of an aortic dissection but can provide vital secondary evidence of aortic root/valve dysfunction and pericardial effusions or tamponade. Invasive transoesophageal echocardiography can then be considered for further detailed

evaluation, and is especially valuable in unstable patients as it can be performed at the bedside. In experienced hands the technique has high sensitivity and specificity for ascending aortic dissection. It has the ability to detect the entry and re-entry site of dissection and can evaluate for the direction of flow within the false lumen. Additional evaluation of the aortic valvular and left ventricular function is useful to exclude proximal extension of the dissection into the aortic root and left coronary artery respectively. Transoesophageal echocardiography is of limited use at the proximal aortic arch since artefacts from air in the adjacent right main bronchus interferes with echocardiographic imaging. Other limitations of the technique include inability to visualise surrounding structures in the mediastinum, and inadequate assessment of anatomical detail required for planning endovascular or hybrid therapy^[1-3].

MRI is a useful modality in the assessment of AASs but has limited scope in the emergency setting due to the longer acquisition times and potentially limited availability^[1,2]. In stable patients it has a role in confirming IMH, when CT is indeterminate. It can provide high resolution multiphase images of the aorta without the use of ionising radiation^[5,6]. Real time examination of the aortic root and valve function can also be performed with MRI. This modality is likely to play an increasing role in the follow-up of patients with AASs allowing for a comprehensive assessment. MRI is also the modality of choice for patients with contraindications to CT and iodinated contrast^[5,7].

CONCLUSION

MDCT is the modality of choice for the evaluation of suspected AAS in the emergency setting. High sensitivity, rapid acquisitions and easy access to the technique are its major advantages over transoesophageal echocardiography and MRI. There is a wide base of expertise available in interpreting MDCT with limited interpersonal variability in the inference. Most radiologists and vascular surgeons are comfortable and confident of using this modality in diagnosing and treating AAS. Detailed assessment of the morphology of the aorta using MDCT allows for the classification of the interlinked AASs and helps in determining the treatment. It permits assessment of life-threatening complications associated with acute aortic conditions. It is also useful in identifying some of the other conditions such as acute pulmonary embolism and pneumothorax that can mimic AAS.

REFERENCES

- 1 **Chiu KW**, Lakshminarayan R, Ettles DF. Acute aortic syndrome: CT findings. *Clin Radiol* 2013; **68**: 741-748 [PMID: 23582433 DOI: 10.1016/j.crad.2013.03.001]
- 2 **Nienaber CA**, Powell JT. Management of acute aortic syndromes. *Eur Heart J* 2012; **33**: 26-35b [PMID: 21810861 DOI: 10.1093/eurheartj/ehrl86]
- 3 **Jánosi RA**, Erbel R, Konorza TF. Recent advances in the diagnosis of acute aortic syndromes. *Expert Opin Med Diagn*

- 2012; **6**: 529-540 [PMID: 23480835 DOI: 10.1517/17530059.2012.704362]
- 4 **Ueda T**, Chin A, Petrovitch I, Fleischmann D. A pictorial review of acute aortic syndrome: discriminating and overlapping features as revealed by ECG-gated multidetector-row CT angiography. *Insights Imaging* 2012; **3**: 561-571 [PMID: 23129238 DOI: 10.1007/s13244-012-0195-7]
- 5 **Akin I**, Kische S, Ince H, Nienaber C. Penetrating aortic ulcer, intramural hematoma, acute aortic syndrome: when to do what. *J Cardiovasc Surg (Torino)* 2012; **53**: 83-90 [PMID: 22433727]
- 6 **Fleischmann D**, Mitchell RS, Miller DC. Acute aortic syndromes: new insights from electrocardiographically gated computed tomography. *Semin Thorac Cardiovasc Surg* 2008; **20**: 340-347 [PMID: 19251175 DOI: 10.1053/j.semtcvs.2008.11.011]
- 7 **Chin AS**, Fleischmann D. State-of-the-art computed tomography angiography of acute aortic syndrome. *Semin Ultrasound CT MR* 2012; **33**: 222-234 [PMID: 22624967 DOI: 10.1053/j.sult.2012.01.003]
- 8 **Apfaltrer P**, Hanna EL, Schoepf UJ, Spears JR, Schoenberg SO, Fink C, Vliegenthart R. Radiation dose and image quality at high-pitch CT angiography of the aorta: intraindividual and interindividual comparisons with conventional CT angiography. *AJR Am J Roentgenol* 2012; **199**: 1402-1409 [PMID: 23169737 DOI: 10.2214/AJR.12.8652]
- 9 **Bolen MA**, Popovic ZB, Tandon N, Flamm SD, Schoenhagen P, Halliburton SS. Image quality, contrast enhancement, and radiation dose of ECG-triggered high-pitch CT versus non-ECG-triggered standard-pitch CT of the thoracoabdominal aorta. *AJR Am J Roentgenol* 2012; **198**: 931-938 [PMID: 22451563 DOI: 10.2214/AJR.11.6921]
- 10 **Mészáros I**, Mórocz J, Szlávi J, Schmidt J, Tornóci L, Nagy L, Szép L. Epidemiology and clinicopathology of aortic dissection. *Chest* 2000; **117**: 1271-1278 [PMID: 10807810]
- 11 **Golledge J**, Eagle KA. Acute aortic dissection. *Lancet* 2008; **372**: 55-66 [PMID: 18603160 DOI: 10.1016/S0140-6736(08)60994-0]
- 12 **Hagan PG**, Nienaber CA, Isselbacher EM, Bruckman D, Karavite DJ, Russman PL, Evangelista A, Fattori R, Suzuki T, Oh JK, Moore AG, Malouf JF, Pape LA, Gaca C, Sechtem U, Lenferink S, Deutsch HJ, Diedrichs H, Marcos y Robles J, Llovet A, Gilon D, Das SK, Armstrong WF, Deeb GM, Eagle KA. The International Registry of Acute Aortic Dissection (IRAD): new insights into an old disease. *JAMA* 2000; **283**: 897-903 [PMID: 10685714]
- 13 **Loebe M**, Ren D, Rodriguez L, La Francesca S, Bismuth J, Lumsden A. Acute and chronic thoracic aortic disease: surgical considerations. *HSR Proc Intensive Care Cardiovasc Anesth* 2012; **4**: 243-250 [PMID: 23439669]
- 14 **Fanelli F**, Dake MD. Standard of practice for the endovascular treatment of thoracic aortic aneurysms and type B dissections. *Cardiovasc Intervent Radiol* 2009; **32**: 849-860 [PMID: 19688371 DOI: 10.1007/s00270-009-9668-6.Epub]
- 15 **Patel PJ**, Grande W, Hieb RA. Endovascular management of acute aortic syndromes. *Semin Intervent Radiol* 2011; **28**: 10-23 [PMID: 22379272 DOI: 10.1055/s-0031-1273936]
- 16 **Manghat NE**, Morgan-Hughes GJ, Roobottom CA. Multidetector row computed tomography: imaging in acute aortic syndrome. *Clin Radiol* 2005; **60**: 1256-1267 [PMID: 16291307 DOI: 10.1016/j.crad.2005.06.011]
- 17 **Shiga T**, Wajima Z, Apfel CC, Inoue T, Ohe Y. Diagnostic accuracy of transesophageal echocardiography, helical computed tomography, and magnetic resonance imaging for suspected thoracic aortic dissection: systematic review and meta-analysis. *Arch Intern Med* 2006; **166**: 1350-1356 [PMID: 16831999 DOI: 10.1001/archinte.166.13.1350]
- 18 **Berger FH**, van Lienden KP, Smithuis R, Nicolaou S, van Delden OM. Acute aortic syndrome and blunt traumatic aortic injury: pictorial review of MDCT imaging. *Eur J*

- Radiol* 2010; **74**: 24-39 [PMID: 19665857 DOI: 10.1016/j.ejrad.2009.06.023.Epub]
- 19 **Smith AD**, Schoenhagen P. CT imaging for acute aortic syndrome. *Cleve Clin J Med* 2008; **75**: 7-9, 12, 15-7 passim [PMID: 18236724 DOI: 10.3949/ccjm.75.1.7]
 - 20 **Batra P**, Bigoni B, Manning J, Aberle DR, Brown K, Hart E, Goldin J. Pitfalls in the diagnosis of thoracic aortic dissection at CT angiography. *Radiographics* 2000; **20**: 309-320 [PMID: 10715333 DOI: 10.1148/radiographics.20.2.g00mc04309]
 - 21 **McMahon MA**, Squirrell CA. Multidetector CT of Aortic Dissection: A Pictorial Review. *Radiographics* 2010; **30**: 445-460 [PMID: 20228328 DOI: 10.1148/rg.302095104]
 - 22 **Williams DM**, Joshi A, Dake MD, Deeb GM, Miller DC, Abrams GD. Aortic cobwebs: an anatomic marker identifying the false lumen in aortic dissection--imaging and pathologic correlation. *Radiology* 1994; **190**: 167-174 [PMID: 8259399]
 - 23 **Castañer E**, Andreu M, Gallardo X, Mata JM, Cabezuelo MA, Pallardó Y. CT in nontraumatic acute thoracic aortic disease: typical and atypical features and complications. *Radiographics* 2003; **23** Spec No: S93-110 [PMID: 14557505 DOI: 10.1148/rg.23si035507]
 - 24 **LePage MA**, Quint LE, Sonnad SS, Deeb GM, Williams DM. Aortic dissection: CT features that distinguish true lumen from false lumen. *AJR Am J Roentgenol* 2001; **177**: 207-211 [PMID: 11418429 DOI: 10.2214/ajr.177.1.1770207]
 - 25 **Evangelista A**, Mukherjee D, Mehta RH, O'Gara PT, Fattori R, Cooper JV, Smith DE, Oh JK, Hutchison S, Sechtem U, Isselbacher EM, Nienaber CA, Pape LA, Eagle KA. Acute intramural hematoma of the aorta: a mystery in evolution. *Circulation* 2005; **111**: 1063-1070 [PMID: 15710757 DOI: 10.1161/01.CIR.0000156444.26393.80]
 - 26 **Ganaha F**, Miller DC, Sugimoto K, Do YS, Minamiguchi H, Saito H, Mitchell RS, Dake MD. Prognosis of aortic intramural hematoma with and without penetrating atherosclerotic ulcer: a clinical and radiological analysis. *Circulation* 2002; **106**: 342-348 [PMID: 12119251 DOI: 10.1161/01.CIR.0000022164.26075.5A]
 - 27 **von Kodolitsch Y**, Csösz SK, Koschyk DH, Schalwat I, Loose R, Karck M, Dieckmann C, Fattori R, Haverich A, Berger J, Meinertz T, Nienaber CA. Intramural hematoma of the aorta: predictors of progression to dissection and rupture. *Circulation* 2003; **107**: 1158-1163 [PMID: 12615795 DOI: 10.1161/01.CIR.0000052628.77047.EA]
 - 28 **Attia R**, Young C, Fallouh HB, Scarci M. In patients with acute aortic intramural haematoma is open surgical repair superior to conservative management? *Interact Cardiovasc Thorac Surg* 2009; **9**: 868-871 [PMID: 19651636 DOI: 10.1510/icvts.2009.211854]
 - 29 **Nienaber CA**, Richartz BM, Rehders T, Ince H, Petzsch M. Aortic intramural haematoma: natural history and predictive factors for complications. *Heart* 2004; **90**: 372-374 [PMID: 15020504 DOI: 10.1136/hrt.2003.027615]
 - 30 **Litmanovich D**, Bankier AA, Cantin L, Raptopoulos V, Boiselle PM. CT and MRI in diseases of the aorta. *AJR Am J Roentgenol* 2009; **193**: 928-940 [PMID: 19770313 DOI: 10.2214/AJR.08.2166]
 - 31 **Sueyoshi E**, Matsuoka Y, Imada T, Okimoto T, Sakamoto I, Hayashi K. New development of an ulcerlike projection in aortic intramural hematoma: CT evaluation. *Radiology* 2002; **224**: 536-541 [PMID: 12147853 DOI: 10.1148/radiol.2242011009]
 - 32 **O'Gara PT**, DeSanctis RW. Acute aortic dissection and its variants. Toward a common diagnostic and therapeutic approach. *Circulation* 1995; **92**: 1376-1378 [PMID: 7664413 DOI: 10.1161/01.CIR.92.6.1376]
 - 33 **Stanson AW**, Kazmier FJ, Hollier LH, Edwards WD, Pailorero PC, Sheedy PF, Joyce JW, Johnson MC. Penetrating atherosclerotic ulcers of the thoracic aorta: natural history and clinicopathologic correlations. *Ann Vasc Surg* 1986; **1**: 15-23 [PMID: 3504683 DOI: 10.1016/S0890-5096(06)60697-3]
 - 34 **Timperley J**, Banning AP. Prognosis of aortic intramural hematoma with and without penetrating atherosclerotic ulcer: a clinical and radiological analysis. *Circulation* 2003; **107**: e63 [PMID: 12628960 DOI: 10.1161/01.CIR.0000057816.67442.15]
 - 35 **Braverman AC**. Penetrating atherosclerotic ulcers of the aorta. *Curr Opin Cardiol* 1994; **9**: 591-597 [PMID: 7987039 DOI: 10.1097/00001573-199409000-00014]
 - 36 **Quint LE**, Williams DM, Francis IR, Monaghan HM, Sonnad SS, Patel S, Deeb GM. Ulcerlike lesions of the aorta: imaging features and natural history. *Radiology* 2001; **218**: 719-723 [PMID: 11230645 DOI: 10.1148/radiology.218.3.r01mr24719]
 - 37 **Coady MA**, Rizzo JA, Elefteriades JA. Pathologic variants of thoracic aortic dissections. Penetrating atherosclerotic ulcers and intramural hematomas. *Cardiol Clin* 1999; **17**: 637-657 [PMID: 10589337 DOI: 10.1016/S0733-8651(05)70106-5]
 - 38 **Davies RR**, Goldstein LJ, Coady MA, Tittle SL, Rizzo JA, Kopf GS, Elefteriades JA. Yearly rupture or dissection rates for thoracic aortic aneurysms: simple prediction based on size. *Ann Thorac Surg* 2002; **73**: 17-27; discussion 27-8 [PMID: 11834007 DOI: 10.1016/S0003-4975(01)03236-2]
 - 39 **Birchard KR**. Acute aortic syndrome and acute traumatic aortic injury. *Semin Roentgenol* 2009; **44**: 16-28 [PMID: 19064069 DOI: 10.1053/j.ro.2008.10.002]
 - 40 **Cho KR**, Stanson AW, Potter DD, Cherry KJ, Schaff HV, Sundt TM. Penetrating atherosclerotic ulcer of the descending thoracic aorta and arch. *J Thorac Cardiovasc Surg* 2004; **127**: 1393-1399; discussion 1393-1399; [PMID: 15115998]
 - 41 **Harris JA**, Bis KG, Glover JL, Bendick PJ, Shetty A, Brown OW. Penetrating atherosclerotic ulcers of the aorta. *J Vasc Surg* 1994; **19**: 90-8; discussion 98-9 [PMID: 8301743 DOI: 10.1016/S0741-5214(94)70124-5]
 - 42 **Svensson LG**, Labib SB, Eisenhauer AC, Butterly JR. Intimal tear without hematoma: an important variant of aortic dissection that can elude current imaging techniques. *Circulation* 1999; **99**: 1331-1336 [PMID: 10077517]
 - 43 **Brinster DR**. Endovascular repair of the descending thoracic aorta for penetrating atherosclerotic ulcer disease. *J Card Surg* 2009; **24**: 203-208 [PMID: 19178611 DOI: 10.1111/j.1540-8191.2008.00660.x.]
 - 44 **Eggebrecht H**, Plicht B, Kahlert P, Erbel R. Intramural hematoma and penetrating ulcers: indications to endovascular treatment. *Eur J Vasc Endovasc Surg* 2009; **38**: 659-665 [PMID: 19800821 DOI: 10.1016/j.ejvs.2009.09.001]
 - 45 **Patatas K**, Shrivastava V, Ettles DF. Penetrating atherosclerotic ulcer of the aorta: a continuing debate. *Clin Radiol* 2013; **68**: 753-759 [PMID: 23541075 DOI: 10.1016/j.crad.2012.11.014.Epub]
 - 46 **Nathan DP**, Boonn W, Lai E, Wang GJ, Desai N, Woo EY, Fairman RM, Jackson BM. Presentation, complications, and natural history of penetrating atherosclerotic ulcer disease. *J Vasc Surg* 2012; **55**: 10-15 [PMID: 22047830 DOI: 10.1016/j.jvs.2011.08.005.Epub]
 - 47 **Botta L**, Buttazzi K, Russo V, Parlapiano M, Gostoli V, Di Bartolomeo R, Fattori R. Endovascular repair for penetrating atherosclerotic ulcers of the descending thoracic aorta: early and mid-term results. *Ann Thorac Surg* 2008; **85**: 987-992 [PMID: 18291184 DOI: 10.1016/j.athoracsur.2007.10.079]
 - 48 **Debakey ME**, Henly WS, Cooley DA, Morris GC, Crawford ES, Beall AC. Surgical management of dissecting aneurysms of the aorta. *J Thorac Cardiovasc Surg* 1965; **49**: 130-149 [PMID: 14261867]
 - 49 **Agarwal PP**, Chughtai A, Matzinger FR, Kazerooni EA. Multidetector CT of thoracic aortic aneurysms. *Radiographics* 2009; **29**: 537-552 [PMID: 19325064 DOI: 10.1148/rg.292075080]
 - 50 **Booher AM**, Eagle KA. Diagnosis and management issues in thoracic aortic aneurysm. *Am Heart J* 2011; **162**: 38-46.e1 [PMID: 21742088 DOI: 10.1016/j.ahj.2011.04.010]
 - 51 **Coady MA**, Rizzo JA, Elefteriades JA. Developing surgical

- intervention criteria for thoracic aortic aneurysms. *Cardiol Clin* 1999; **17**: 827-839 [PMID: 10589349 DOI: 10.1016/S0733-8651(05)70118-1]
- 52 **Bhalla S**, West OC. CT of nontraumatic thoracic aortic emergencies. *Semin Ultrasound CT MR* 2005; **26**: 281-304 [PMID: 16274000 DOI: 10.1053/j.sult.2005.07.002]
- 53 **Posniak HV**, Olson MC, Demos TC, Benjoya RA, Marsan RE. CT of thoracic aortic aneurysms. *Radiographics* 1990; **10**: 839-855 [PMID: 2217974 DOI: 10.1148/radiographics.10.5.2217974]
- 54 **Svensson LG**, Khitin L. Aortic cross-sectional area/height ratio timing of aortic surgery in asymptomatic patients with Marfan syndrome. *J Thorac Cardiovasc Surg* 2002; **123**: 360-361 [PMID: 11828302 DOI: 10.1067/mtc.2002.118497]
- 55 **Hiratzka LF**, Bakris GL, Beckman JA, Bersin RM, Carr VF, Casey DE, Eagle KA, Hermann LK, Isselbacher EM, Kazerooni EA, Kouchoukos NT, Lytle BW, Milewicz DM, Reich DL, Sen S, Shinn JA, Svensson LG, Williams DM. 2010 ACCF/AHA/AATS/ACR/ASA/SCA/SCAI/SIR/STS/SVM guidelines for the diagnosis and management of patients with Thoracic Aortic Disease: a report of the American College of Cardiology Foundation/American Heart Association Task Force on Practice Guidelines, American Association for Thoracic Surgery, American College of Radiology, American Stroke Association, Society of Cardiovascular Anesthesiologists, Society for Cardiovascular Angiography and Interventions, Society of Interventional Radiology, Society of Thoracic Surgeons, and Society for Vascular Medicine. *Circulation* 2010; **121**: e266-e369 [PMID: 20233780 DOI: 10.1161/CIR.0b013e3181d4739e]
- 56 **Evangelista A**, Carro A, Moral S, Teixido-Tura G, Rodríguez-Palomares JF, Cuéllar H, García-Dorado D. Imaging modalities for the early diagnosis of acute aortic syndrome. *Nat Rev Cardiol* 2013; **10**: 477-486 [PMID: 23797792 DOI: 10.1038/nrcardio.2013.92.Epub]
- 57 **Hunold P**, Bischoff P, Barkhausen J, Vogt FM. Acute chest pain: the role of MR imaging and MR angiography. *Eur J Radiol* 2012; **81**: 3680-3690 [PMID: 21543179 DOI: 10.1016/j.ejrad.2011.04.032.Epub]

P- Reviewers: Kato M, Kirali K Paraskevas KI **S- Editor:** Ji FF
L- Editor: A **E- Editor:** Zhang DN



Coronary venous system in cardiac computer tomography: Visualization, classification and role

Rafal Mlynarski, Agnieszka Mlynarska, Maciej Sosnowski

Rafal Mlynarski, Agnieszka Mlynarska, Maciej Sosnowski, Unit of Noninvasive Cardiovascular Diagnostics, Medical University of Silesia, Upper-Silesian Cardiology Center, Katowice 40-635, Poland

Rafal Mlynarski, Agnieszka Mlynarska, Department of Electrocardiology, Medical University of Silesia, Upper-Silesian Cardiology Center, Katowice 40-635, Poland

Maciej Sosnowski, 2nd Chair and Division of Cardiology, Medical University of Silesia, Upper-Silesian Cardiology Center, Katowice 40-635, Poland

Author contributions: All authors who wrote this paper had substantial contribution to conception and design and final approval of the version to be published.

Correspondence to: Rafal Mlynarski, MD, PhD, Department of Electrocardiology, Medical University of Silesia, Upper-Silesian Cardiology Center, ul. Ziolowa 45/47, Katowice 40-635, Poland. rafal_mlynarski@mp.pl

Telephone: +48-60-6484161 Fax: +48-32-2524098

Received: December 31, 2013 Revised: February 28, 2014

Accepted: May 16, 2014

Published online: March 28, 2015

Abstract

The role of the coronary venous system was underestimated for many years. In the last 20 years, a few percutaneous cardiology techniques in which the anatomy of the coronary venous system was significant were developed and are in use. The most important seems to be cardiac resynchronization therapy, which is an invasive method for the treatment of heart failure. Unfortunately, one of the major problems is the significant anatomical variability of the coronary venous system. The description of the selected anatomical structures is only useful in selected cases such as, for example, the obstruction of selected vessels, a huge Thebesian valve, *etc.* The 3D images can add significant value; however, their usefulness is limited due to the different points of view that are obtained during intra-operational fluoroscopy. After summarizing all of the articles and

guidelines, it can be recommended that the visualization of the coronary venous system be performed in certain patients before cardiac resynchronization. The best option is to use tomography with retrospective gating with the optimal reconstruction of cardiac veins that occurs during the diastolic phases.

© 2015 Baishideng Publishing Group Inc. All rights reserved.

Key words: Coronary venous system; Coronary sinus; Thebesian valve; Cardiac computed tomography; Cardiac resynchronization therapy; Percutaneous mitral annuloplasty

Core tip: In the article role of the analysis of coronary venous system in cardiac computed tomography (CT) was presented. In the last 20 years, a few percutaneous cardiology techniques in which the anatomy of the coronary venous system was significant were developed and are in use. The description of the selected anatomical structures in CT is useful in selected cases such as, for example, the obstruction of selected coronary veins, a huge Thebesian valve, *etc.*

Original sources: Mlynarski R, Mlynarska A, Sosnowski M. Coronary venous system in cardiac computer tomography: Visualization, classification and role. *World J Radiol* 2014; 6(7): 399-408 Available from: URL: <http://www.wjgnet.com/1949-8470/full/v6/i7/399.htm> DOI: <http://dx.doi.org/10.4329/wjr.v6.i7.399>

INTRODUCTION

The role of the coronary venous system was not appreciated for many years. In the last 20 years, the number of percutaneous cardiology techniques in which the anatomy of the coronary venous system was significant were developed and are in use. The most important seems to

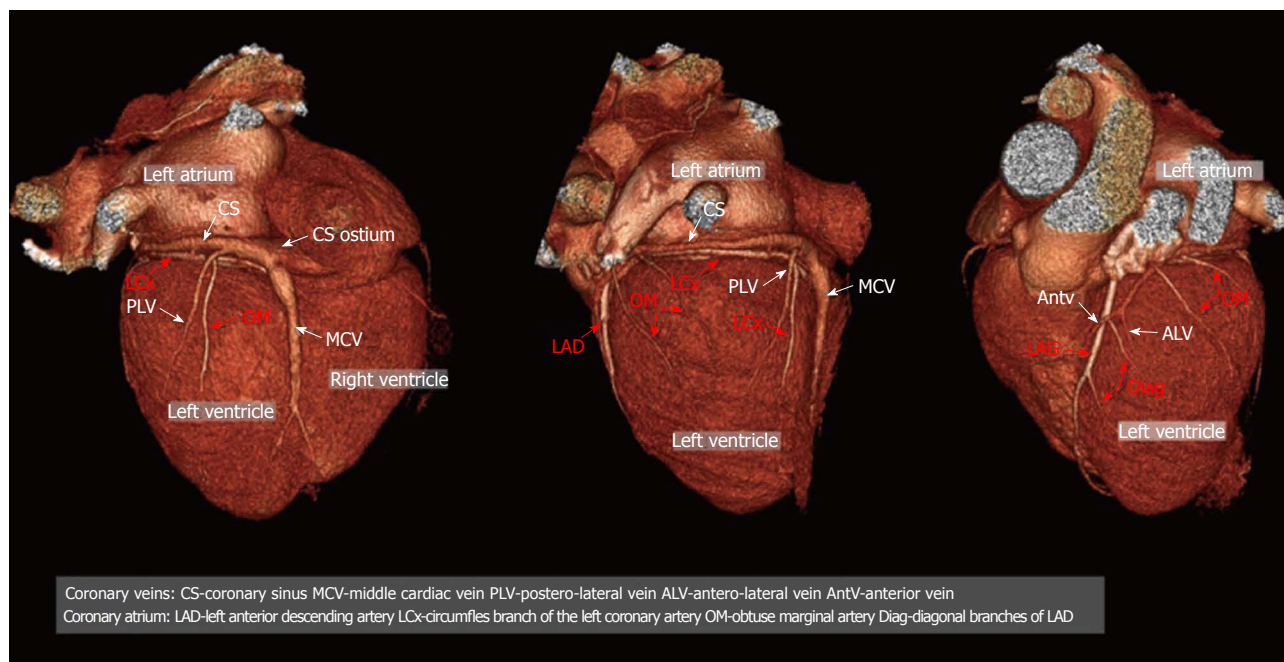


Figure 1 Example of the three-dimensional (3D) anatomy of coronary vessels (arteries and veins). Posterior, lateral antero-lateral view of the heart; 3D volume rendering projections. CS: Coronary sinus; MCV: Middle cardiac vein; PLV: Postero-lateral vein; ALV: Antero-lateral vein; AntV: Anterior vein; LAD: Left anterior descending artery; LCx: Circumflex branch of the left coronary artery; OM: Obtuse marginal artery; Diag: Diagonal branches of LAD.

be cardiac resynchronization therapy (CRT), which is an invasive method for the treatment of heart failure^[1-5]. The most recent European guidelines for this method were published in 2012 and 2013^[6,7]. In this method, an additional left ventricle (LV) lead is placed in the target coronary vein on the surface of the left ventricle. Proper implantation provides the possibility of pacing the left ventricle together with the classic pacing of the right ventricle and usually the right atrium. The most important challenge of left ventricle lead implantation is the precise placement in the area where the electrical parameters are assumed to be optimal^[8-10]. The lead is implanted *via* the right atrium by the cannulation of the coronary sinus (CS) ostium to the coronary sinus and the great cardiac vein to the lateral or posterolateral veins (typically), which are called the target veins^[11,12]. Unfortunately, one of the major problems is the significant anatomical variability of the coronary venous system^[13,14].

ANATOMY OF THE CORONARY VEIN SYSTEM

The coronary sinus ostium is located in the posteroseptal area of the right atrium and is the final part of the coronary venous system. The coronary sinus usually begins in the place where the vein of Marshall (which is sometimes called the oblique vein of the left atrium) is typically connected to the great cardiac vein^[9,15-18]. The vein of Marshall is a small vein that courses on the surface of the right atrium with the ligament of the left vena cava. Sometimes, the valve of Vieussens also occurs^[19,20]. The role of the coronary sinus is to collect veins and join

them together; it collects blood from the myocardium and delivers deoxygenated blood to the right atrium. The coronary sinus transversely in the right atrioventricular groove on the posterior side of the heart close to the distal part of circumflex branch of the left coronary artery^[21-24]. The first branch, which is the beginning of the great cardiac vein is the anterior vein, is sometimes called the anterior interventricular vein and runs parallel to the left descending artery^[25].

The area between the anterior vein and the middle cardiac vein is a place where more veins occur in different variants. Depending on the area of drainage, they are called the anterolateral, lateral, posterolateral and posterior veins. There are no strict borders on the left ventricle in the nomenclature of veins. Their number and locations depends on many factors (this will be the subject of a separate paragraph in this article due to its important function in many invasive cardiovascular procedures). Another border of the coronary venous system is the middle cardiac vein. The middle cardiac vein begins close to the apex of the heart and goes into the posterior interventricular groove and finally enters the coronary sinus close to the coronary sinus ostium^[15,26,27]. A three-dimensional (3D)/2D reconstructions of the coronary venous system in cardiac computed tomography (CT) are presented in Figures 1 and 2.

COMPUTED TOMOGRAPHY

Since the beginning of cardiac CT, different authors have tried to examine the coronary venous system. At the very beginning, the papers usually had only anatomical merit. One of the first was Christiaens *et al*^[25]. The authors

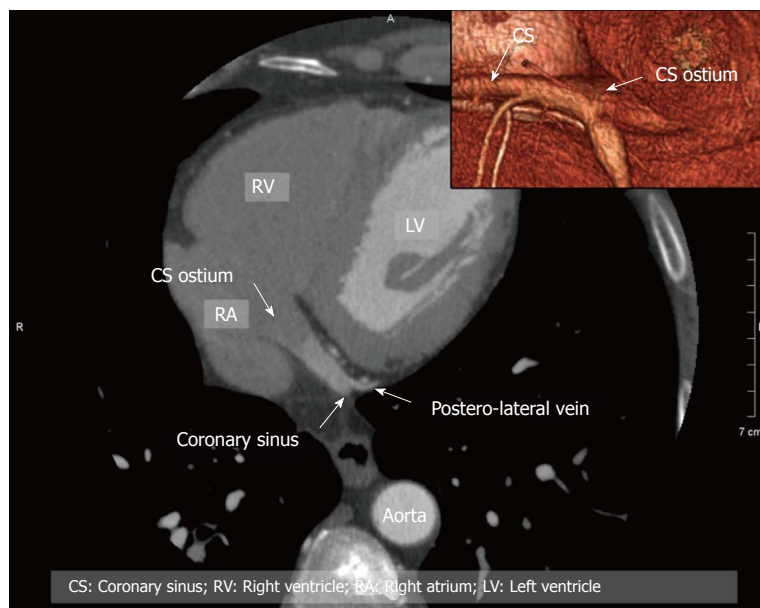


Figure 2 Example of anatomy of coronary vessels in two-dimensional (2D)/3D with reference to the coronary sinus. CS: Coronary sinus; RV: Right ventricle; RA: Right atrium; LV: Left ventricle.

examined 50 consecutive patients using 16-row MDCT (Siemens, Sensation 16). They were able to measure the coronary sinus in two directions, which were 12.2 ± 3.6 in the antero-posterior and 15.3 ± 3.7 in supero-inferior direction with a detailed analysis of the profile of the coronary sinus branches. The first paper that described the anatomical variants was the paper of Jongbloed *et al*^[28]. They examined 38 patients using 16-slice CT (Toshiba, Aquilion 16) in which the insertion and continuity of the main tributaries, the number of antero and posterolateral tributaries and the distances between the main tributaries were evaluated. Another study using a 16-slice scanner was the study of Abbara *et al*^[29]. The authors used a 16-slice scanner (Siemens, Sensation 16). The authors concluded the feasibility of CT coronary venous imaging especially in the planning of transvenous procedures where the cannulation of the coronary sinus is necessary. In this paper, the authors used an image-quality scale using both conspicuity and contrast-to-noise ratio (CNR), which is very precise; however, this was seldom used in papers that described the coronary venous system. The paper of Tada *et al*^[30] discussed the examination of 70 patients using an 8-slice detector. The authors stressed that the venous flow shows an aphasical pattern during the cardiac cycle. This can be a crucial element for the image quality of the coronary venous system. In the paper of Tada, the CVS was greater on the reconstructions that were performed during systole. It can be seen that the images reconstructed in the diastolic phases can cause an underestimate CVS and its tributaries that is similar to the coronary arteries. Another paper describing the coronary venous system in cardiac CT using the latest generation scanner is a paper by Genc *et al*^[31]. The authors prospectively examined 357 subjects who had undergone a cardiac CT due to coronary artery disease using a 128-slice Dual Source ECG-gated MDCT (Siemens). All of the veins were visualized in all of the included patients including at least one target vein for cardiac

resynchronization. The posterior cardiac vein and the left marginal vein were visualized in approximately 87%, and the small cardiac vein in 20%. The results obtained by Genc *et al*^[31] suggested more detailed images when compared to the older scanners (16-64 slices); however, for a pre-procedural clinical analysis/visualization any of the cardiac CT scanners should be acceptable; however, a more detailed post-processing and analysis of the images is recommended.

The above-mentioned papers influenced the evolution of the imaging the coronary veins and were a prelude to later papers.

The challenge is how to visualize the coronary venous system in cardiac CT. In our earlier research, we documented that the optimal phases for reconstruction should be performed during diastolic phases 30%-50% RR. It can be easily performed on scanners with retrospective gating despite the higher dose of radiation^[32]. In Figures 3 and 4 we present the influence of the phase of reconstruction on the visualization of heart vessels-veins and arteries.

IMAGES AND CARDIAC RESYNCHRONISATION

A description of the selected anatomical structures is only useful in selected cases such as, for example, the obstruction of selected vessels, a huge Thebesian valve, *etc.* The images do have added value; however, their usefulness is limited due to the different points of view that are obtained during intra-operational fluoroscopy in comparison with 3D visualizations that are performed using cardiac CT. We attempted to resolve this problem in 2009. The results of our research were published in the PACE journal^[33]. We determined that the key features that images must have are: (1) that they be similar in quality to intra-operative fluoroscopy; (2) that they give a

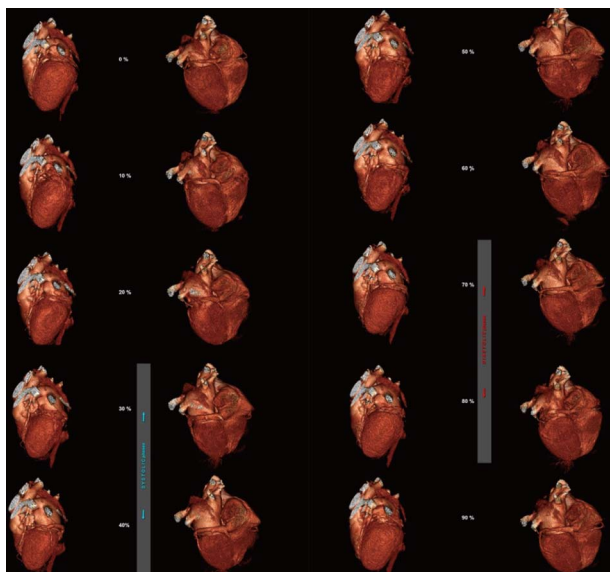


Figure 3 Influence of the phase of reconstruction on the quality of reconstructions of the coronary arteries and veins. Posterior and antero-lateral view of the heart; three-dimensional Volume rendering.

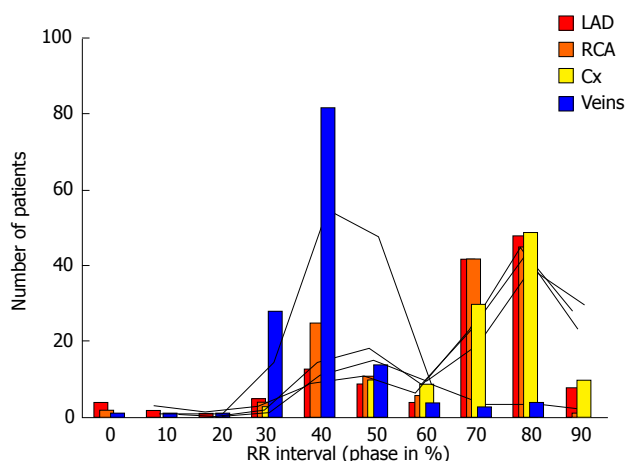


Figure 4 Influence of the phase of reconstruction on the quality of reconstructions of the coronary arteries and veins. LAD: Left anterior descending artery; Cx: Circumflex

semitransparent view of the heart; (3) that they show the semitransparent bones, sternum and vertebral column as a position reference for the implanting physician; (4) that they provide the anterior-posterior (AP), left anterior oblique (LAO) and right anterior oblique (RAO) views; and (5) that they show 3D views in order to evaluate all of the important anatomical aspects.

The cardiac veins are indicated using markers (3D arrows) that are added to the image during post-processing. Finally, the heart is corrected in order to fulfill AP, LAO and RAO-Figure 5^[33]. By using this solution in 83 patients (74%), it was possible to obtain very similar images to those that were obtained during the CRT implantation procedure within all three views. In 24% patients, it was not possible to obtain the AP view with the coronary sinus and its ostium due to the large amount of contrast

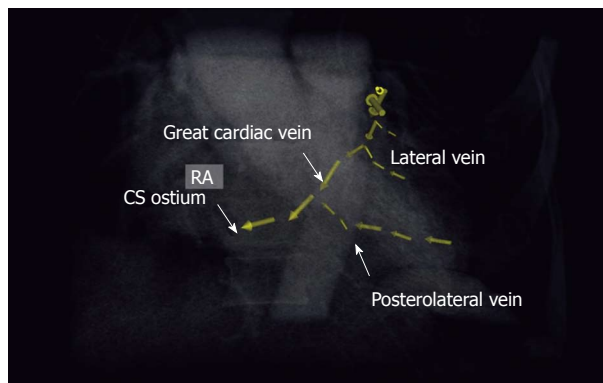


Figure 5 Proposed scheme of reconstruction necessary to fulfill cardiac resynchronization therapy requirements^[33]. RA: Right atrium; CS: Coronary sinus;

agent in the right heart. We were also able to visualize the coronary venous system with the vein of Marshall (23%) and the Thebesian valve in 41% of the patients. After seven years of experience with this method, in most cases we are able to obtain proper images. One prospective randomized trial in which Girsky *et al.*^[34] examined the usefulness of venous cardiac CT angiography for the facilitation of CRT implantation was also published. The authors included 26 patients who had full qualification for CRT-D implantation. The images of eight patients were analyzed using electron-beam CT and 18 patients using 64-slice CT. According to the methods described, the authors used prospective gating to reduce the radiation. They also used a two-second delay for imaging the coronary veins as a modification of routine coronary arteries visualization. According to their results, the CT images helped to decrease the time required for the cannulation of the coronary sinus and the total length of the procedures. A significant reduction in the utilization of a contrast agent, fluoroscopy and some of the equipment that was used was also observed.

There are a few technical-anatomical challenges during the implantation of a left ventricle lead. According to the Blendea and Singh^[35], these can include: (1) Lack of successful coronary sinus cannulation caused by the Thebesian valve or a strange (narrow) angle of entrance from the right atrium; (2) Valve of Vieussens on the border of the coronary sinus and the great cardiac vein; (3) Accidental placement of the LV lead into the vein of Marshall, which is unacceptable for LV pacing; (4) Coronary sinus spasm or stenosis; and (5) Lack of target veins-posterolateral, lateral or sometimes anterolateral.

Images generated by cardiac CT can facilitate placement preparation of the procedure, shorten the time of implantation or lower the exposure to X-ray.

THEBESIAN VALVE

The Thebesian valve is the part of the cardiac anatomy that can present problems during coronary sinus cannulation. It is a semicircular fold membrane of the right atrium at the orifice of the coronary sinus, and it is a cau-

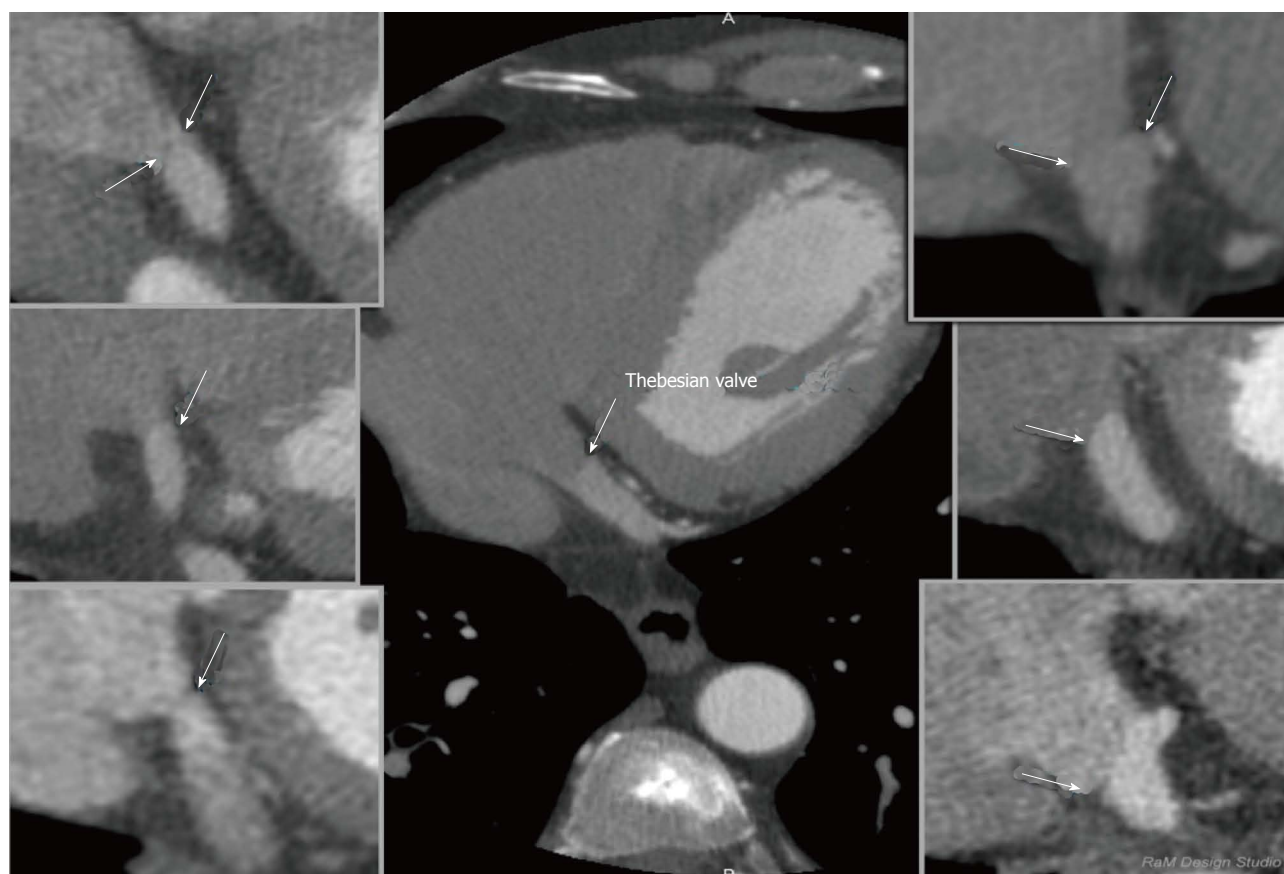


Figure 6 Examples of thebesian valves in cardiac computed tomography; two-dimensional multi-planar reformatting projections.

dal remnant of the embryonic sinoatrial valve. It is situated at the base of the superior vena cava and sometimes is called the coronary sinus guard dog^[36,37]. The valve may have a different size, shape or structure or it can be completely absent^[38-43]. One of the largest researches that evaluated the Thebesian valve in autopsied hearts was presented in the paper by Mak *et al*^[36]. A wide variety of Thebesian valve morphologies were observed in the 75 hearts that were examined, ranging from the absence of the valve to cases in which the valve completely occluded the CS ostium. A Thebesian valve was present in the majority of the hearts that were examined (55/75 hearts-73%). In a study of 50 human CSs of the heart, Silver and Rowley showed that the Thebesian valve covered the ostium in 41% of the cases, including 20% that were totally covered and in 26% of hearts that had an increased weight^[44]. In contrast, El-Maasarany *et al*^[45] obtained different results. In their study, the valve was present in 87.5% (35/40)-in those cases it was a thin semi-lunar fold. In four of the 40 patients (10%), the valve had the form of a narrow circular rim surrounding the ostium. The valve was absent in only one case. These differences between the researches indicate the huge anatomical variability of the coronary venous system. Based on our research we proposed a tomographic classification of the Thebesian valve^[46]. Our paper was the first in which a heart failure subgroup (EF < 40%) was examined. This might be of special significance since this group is a po-

tential target for cardiac resynchronization. In this group, the prevalence of the Thebesian valve appeared to be significantly lower as compared to groups with a preserved (41%-60%) or normal (approximately 60%) ejection fraction. However, there were no significant differences in the angle of entrance or in the CS diameter between the groups. The prevalence of the valve in heart failure patients is probably caused by atrial enlargement and the stretching of the CS as well as the Thebesian valve. In fact, the Thebesian valve can be relatively well described in MSCT. None of the authors have suggested that any special techniques are required for performing MSCT to visualize the Thebesian valve. A precise evaluation of a standard cardiac scan should be enough to describe this valve. An example of the visualization of Thebesian valve is presented in Figure 6.

INFLUENCE OF CARDIAC PATHOLOGIES ON THE CORONARY VENOUS SYSTEM

Most percutaneous cardiological procedures are performed in patients with different pathologies of the heart. The question of whether those pathologies significantly influence the coronary venous system is interesting. Computed tomography of the heart is an ideal tool to perform such research. In 2007 Chen *et al*^[47] examined 23 consecutive patients with chronic systolic heart failure and an ejection

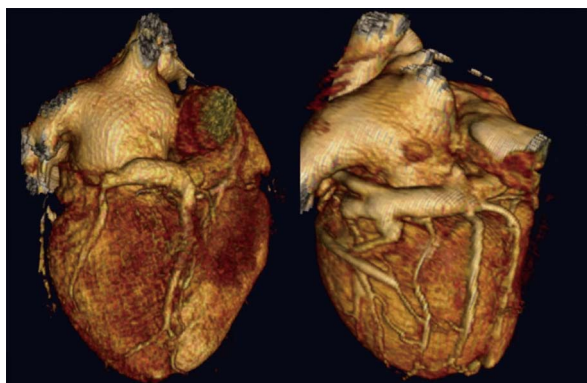


Figure 7 Example of coronary venous system in patients after CABG; three-dimensional Volume rendering.

tion fraction < 40%. The authors concluded that heart failure extends the total length between the PIV and AIV as compared to the control group. Similar results were also obtained by our team^[48]. During MSCT of patients with heart failure, the average number of visible veins per case was 3.44 in the HF group and 2.72 in patients with a normal ejection fraction ($P = 0.0246$). The statistical correlation between a reduction in ejection fraction and an increase in the number of veins was found ($r = -0.2446$, $P < 0.05$). We also examined the influence of heart failure on the variants of the coronary venous system and found that for two of the seven common variants of the coronary venous system at least two target veins (posterolateral and lateral) were presented for cardiac resynchronization. We concluded that an association possibly exists between a failing heart and cardiac venous retention.

Another important question is whether there are some problems with performing MSCT in heart failure patients. First of all, we have to look at the volume of contrast agent because renal impairment often coexists in HF patients, secondly because the use of beta blockers to stabilize the heart rhythm are often contraindicated in these patients and finally these patients often have a problem holding their breath, which is necessary in order to avoid any motion artifacts^[49]. Another important observation is the coronary venous system in patients after bypass grafts^[50]. We documented that the average number of visible coronary veins in the CABG group was significantly higher (5.3 ± 1.3), while in the control group, it was 3.1 ± 1.1 ($P = 0.001$). An example of such an image is presented in Figure 7.

PERCUTANEOUS MITRAL ANNULOPLASTY

Percutaneous mitral annuloplasty (PMA) is another method in which the visualization of the coronary venous system is important. In this technique devices are implanted into the coronary sinus and the great cardiac vein in order to reduce mitral ischemic regurgitation^[51-55]. Its safety and usefulness were evaluated in human stud-

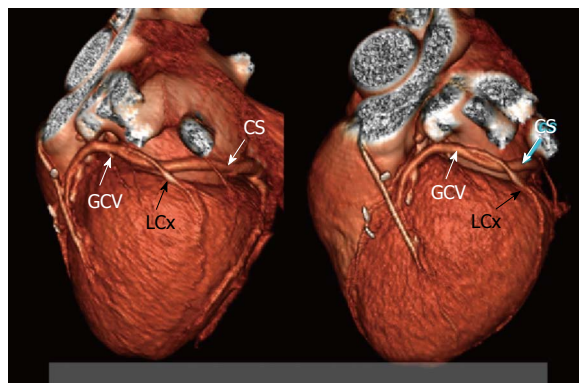


Figure 8 Mutual relations between coronary sinus/great cardiac vein and circumflex branch of left coronary artery-twisted variant which is very risky for LCx compression by PMA device; three-dimensional Volume rendering. CS: Coronary sinus; GCV: Great cardiac vein; LCx: Circumflex branch.

ies such as the AMADEUS trial^[56,57]. Why is knowledge about the anatomy so important? In selected patients, a close relationship between the left circumflex artery (LCx) and the coronary sinus can cause the LCx to be accidentally occluded during the placement of a device—an example is presented in Figure 8. Computed tomography allows the visualization of the relationships between the mitral valve (MV), the LCx and CS and therefore the risk of occluding the LCx can be minimized^[58-60]. Mutual relations between coronary sinus / great cardiac vein and the circumflex branch of left coronary artery—potential role before percutaneous mitral annuloplasty are presented in Figure 9. Several studies have confirmed the considerable anatomical variability in the relative positions of the LCx, the CS and the MV. For example, Maselli *et al*^[61] examined the hearts of 61 patients who had died of non-cardiological causes. In the era of non-invasive procedures, visualization using MSCT can play a vital role. One of the earliest studies was that of Maselli *et al*^[61] in 2007. The authors analyzed 105 consecutive patients who had been referred for MSCT coronary angiography. Patients were divided into three groups depending on the presence of CAD and heart failure. They concluded that the LCx, CS and mitral valve could be analyzed. Another study evaluating the relationship of the coronary sinus and great cardiac vein to the mitral annulus is a paper by del Valle-Fernandez *et al*^[62]. The authors reviewed 390 CT angiograms in order to evaluate patients with a coronary sinus that was more than 200 Hounsfield units in phases 40%, 75% and 0% RR, the absence of a mitral prosthesis and without any anomalies or diseases of the mitral valve. A 64-slice scanner was used in this research and 56 patients were chosen for the final analysis. The authors were able to precisely evaluate the anatomical relationship between the mitral annulus and the coronary sinus. They concluded that the distance between the CS and the mitral annulus varies along the cardiac cycle. The authors also found that the LCx lies between the CS and the mitral annulus in 86% of the subjects that were included.

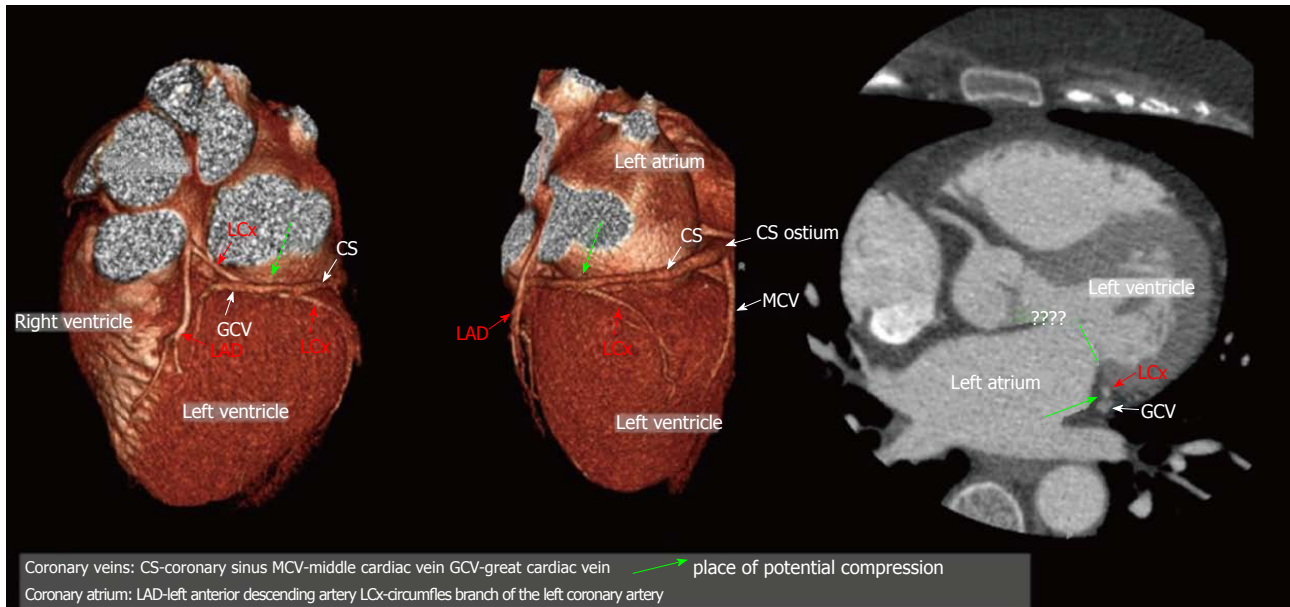


Figure 9 Mutual relations between coronary sinus/great cardiac vein and circumflex branch of left coronary artery - potential role before percutaneous mitral annuloplasty; three-dimensional Volume rendering. CS: Coronary sinus; MCV: Middle cardiac vein; PLV: Postero-lateral vein; ALV: Antero-lateral vein; AntV: Anterior vein; LAD: Left anterior descending artery; LCx: Circumflex branch of the left coronary artery.

PLACE ON INTERNATIONAL GUIDELINES

Most papers have had a huge influence on the creation of clinical guidelines-in the 2010 version of the appropriate use criteria for cardiac CT, noninvasive coronary vein mapping prior to the placement of a biventricular pacemaker received an A (8), which means that it is highly recommended^[63]. When the imaging technology was evaluated and the images started to have an acceptable quality and became more common, creating clinical-practical guidelines was only a matter of time. The most important seem to be the 2012 EHRA/HRS expert consensus statement on cardiac resynchronization therapy in heart failure: implant and follow-up recommendations and management^[64]. In this document some key elements of using CT before cardiac resynchronization were outlined including the statement that cardiac CT angiography provides a detailed assessment of the coronary arteries and can image and quantify the coronary venous system, including branch vein variability and potential obstacles to placement prior to a CRT procedure in individual patients. There are also limited data suggesting that pre-procedural knowledge about the 3D coronary venous anatomy can facilitate CRT by decreasing the length of the procedure, the time that the patient is receiving radiation and the utilization of guide catheters. The authors also stressed that the target population for cardiac resynchronization-the heart failure population-is not the overall population and can cause some difficulties such as the necessity of using a contrast agent during CT, the ability to do a breath-hold, proper renal function and sometimes the necessity of using intravenous B-Blockers to control the rhythm, which can be contraindicated in the heart failure population.

LIMITATIONS OF COMPUTED TOMOGRAPHY BEFORE ELECTROPHYSIOLOGY PROCEDURES

As was written previously, and underlined in the guidelines, CT is not an examination for the entire population. There are some limitations that apply mostly to patients with heart failure who are potentially qualified for CRT such as: (1) Necessity of a breath hold-elderly patient with advanced heart failure can have problems with this and this can cause motion artifacts; (2) Heart rhythm below 65/min-a higher value than 65/min sometimes requires the administration of Beta Blockers, which can be contraindicated in this population; and (3) During procedures like CRT a large amount of contrast agent, which is also used during CT, is used. This can cause significant problems in the population who suffer from renal failure-prophylaxis of contrast-induced nephropathy should be implemented.

Some physicians are also afraid of the dosage of radiation, which is substantial during CT. Fortunately, progress in the manufacture of CT scanners means that this dosage is continuously decreased by the new techniques that are used in the latest scanners. An example of this is the visualization of the pulmonary veins with a low dosage by using a dual source CT^[65]. To date there are no data to support a direct link between CT imaging and a future risk of developing cancer; however, health care practitioners should make every effort to minimize their patients' radiation exposure^[66].

CONCLUSION

After summarizing all of the articles and guidelines, it can

be recommended that the visualization of the coronary venous system be considered in certain patients before cardiac resynchronization. The best option is to use tomography with a retrospective ECG gating. Typically, the optimal reconstruction of cardiac veins is during the diastolic phases (30%-40% and 50%) and in our opinion this might complement the standard reconstruction for coronary arteries. If a candidate for CRT had an MSCT examination with retrospective gating performed earlier, it is possible to refer to this exam and reconstruct the coronary venous system without exposing the patient to additional radiation. However, it is necessary to remember that because some diseases or the progress of some diseases can significantly influence the coronary venous tree anatomy, the period between the MSCT exam and CRT should not be too long. In most cardiac resynchronization centers, CRT is almost a routine procedure-it is difficult to recommend MSCT visualization as a routine procedure because intra-operational fluoroscopy is usually enough for the proper implantation of a left ventricle lead. However, in certain cases where difficulties in cannulation are expected, a pre-procedural MSCT should be considered.

Considering and recommending MSCT before percutaneous mitral annuloplasty is too early because of the lack of experience with this method, even in cases in which some device had received a CE mark. However, in such a situation, parallel reconstruction during the systolic (70%-80%) and diastolic phases (30%-40%-50%) should be considered in order to define the anatomical relation between the mitral valve, the coronary sinus and the circumflex branch of the left coronary artery with the highest precision.

REFERENCES

- Sohaib SM**, Whinnett ZI, Ellenbogen KA, Stellbrink C, Quinn TA, Bogaard MD, Bordachar P, van Gelder BM, van Geldorp IE, Linde C, Meine M, Prinzen FW, Turcott RG, Spotnitz HM, Wichterle D, Francis DP. Cardiac resynchronization therapy optimisation strategies: systematic classification, detailed analysis, minimum standards and a roadmap for development and testing. *Int J Cardiol* 2013; **170**: 118-131 [PMID: 24239155 DOI: 10.1016/j.ijcard.2013.10.069]
- Guha K**, Konstantinou D, Mantziari L, Modi BN, Chandrasekaran B, Khalique Z, McDonagh T, Sharma R. The impact of age on clinical outcomes following cardiac resynchronization therapy. *J Interv Card Electrophysiol* 2014; **39**: 95-102 [PMID: 24293176]
- Nayar V**, Hiari N, Prasad R, Belham MR, Dutka DP, Pugh PJ. Eligibility for cardiac resynchronization therapy among patients with heart failure, according to UK NICE guideline criteria. *Int J Cardiol* 2013; **168**: 4401-4402 [PMID: 23706281 DOI: 10.1016/j.ijcard.2013.05.041]
- Witte KK**. Cardiac resynchronization therapy for chronic heart failure: predicting and measuring 'response'. *Heart* 2013; **99**: 293-294 [PMID: 23349344 DOI: 10.1136/heartjnl-2012-303359]
- Kloch B**, Klochek M, Czarnecka D, Wojciechowska W, Wiliński J, Kawecka Jaszcz K. Impact of cardiac resynchronization therapy on physical ability and quality of life in patients with chronic heart failure. *Kardiologia Pol* 2012; **70**: 581-588 [PMID: 22718376]
- McMurray JJ**, Adamopoulos S, Anker SD, Auricchio A, Böhm M, Dickstein K, Falk V, Filippatos G, Fonseca C, Gomez-Sanchez MA, Jaarsma T, Køber L, Lip GY, Maggioni AP, Parkhomenko A, Pieske BM, Popescu BA, Rønnevik PK, Rutten FH, Schwitzer J, Seferovic P, Stepinska J, Trindade PT, Voors AA, Zannad F, Zeiher A, Bax JJ, Baumgartner H, Ceconi C, Dean V, Deaton C, Fagard R, Funck-Brentano C, Hasdai D, Hoes A, Kirchhof P, Knuuti J, Kolh P, McDonagh T, Moulin C, Popescu BA, Reiner Z, Sechtem U, Sirnes PA, Tendera M, Torbicki A, Vahanian A, Windecker S, McDonagh T, Sechtem U, Bonnet LA, Avraamides P, Ben Lamin HA, Brignole M, Coca A, Cowburn P, Dargie H, Elliott P, Flachskampf FA, Guida GF, Hardman S, Jung B, Merkely B, Mueller C, Nanas JN, Nielsen OW, Orn S, Parissis JT, Ponikowski P. ESC guidelines for the diagnosis and treatment of acute and chronic heart failure 2012: The Task Force for the Diagnosis and Treatment of Acute and Chronic Heart Failure 2012 of the European Society of Cardiology. Developed in collaboration with the Heart Failure Association (HFA) of the ESC. *Eur J Heart Fail* 2012; **14**: 803-869 [PMID: 22828712 DOI: 10.1093/eurjhf/hfs105]
- Brignole M**, Auricchio A, Baron-Esquivias G, Bordachar P, Boriani G, Breithardt OA, Cleland J, Deharo JC, Delgado V, Elliott PM, Gorenek B, Israel CW, Leclercq C, Linde C, Mont L, Padeletti L, Sutton R, Vardas PE, Zamorano JL, Achenbach S, Baumgartner H, Bax JJ, Bueno H, Dean V, Deaton C, Erol C, Fagard R, Ferrari R, Hasdai D, Hoes AW, Kirchhof P, Knuuti J, Kolh P, Lancellotti P, Linhart A, Nihoyannopoulos P, Piepoli MF, Ponikowski P, Sirnes PA, Tamargo JL, Tendera M, Torbicki A, Wijns W, Windecker S, Kirchhof P, Blomstrom-Lundqvist C, Badano LP, Aliyev F, Bänsch D, Baumgartner H, Bsata W, Buser P, Charron P, Daubert JC, Dobreanu D, Faerestrang S, Hasdai D, Hoes AW, Le Heuzey JY, Mavrakis H, McDonagh T, Merino JL, Nawar MM, Nielsen JC, Pieske B, Poposka L, Ruschitzka F, Tendera M, Van Gelder IC, Wilson CM. 2013 ESC Guidelines on cardiac pacing and cardiac resynchronization therapy: the Task Force on cardiac pacing and resynchronization therapy of the European Society of Cardiology (ESC). Developed in collaboration with the European Heart Rhythm Association (EHRA). *Eur Heart J* 2013; **34**: 2281-2329 [PMID: 23801822 DOI: 10.1093/eurheartj/ehs150]
- Buss SJ**, Schulz F, Wolf D, Hosch W, Galuschky C, Schummers G, Giannitsis E, Kauczor HU, Zugck C, Becker R, Hardt SE, Katus HA, Korosoglou G. Quantitative analysis of left ventricular dyssynchrony using cardiac computed tomography versus three-dimensional echocardiography. *Eur Radiol* 2012; **22**: 1303-1309 [PMID: 22270144 DOI: 10.1007/s00330-011-2375-0]
- Giazitzoglou E**, Katritsis DG. Antegrade visualisation of the coronary sinus for left ventricular pacing. *Hellenic J Cardiol* 2008; **49**: 102-105 [PMID: 18459468]
- Cazeau S**, Alonso C, Jauvert G, Lazarus A, Ritter P. Cardiac resynchronization therapy. *Europace* 2004; **5** Suppl 1: S42-S48 [PMID: 15450279]
- Riedlbauchová L**, Cihák R, Bytesník J, Vancura V, Frídl P, Hosková L, Kautzner J. Optimization of right ventricular lead position in cardiac resynchronization therapy. *Eur J Heart Fail* 2006; **8**: 609-614 [PMID: 16504581]
- Randhawa A**, Saini A, Aggarwal A, Rohit MK, Sahni D. Variance in coronary venous anatomy: a critical determinant in optimal candidate selection for cardiac resynchronization therapy. *Pacing Clin Electrophysiol* 2013; **36**: 94-102 [PMID: 23106173 DOI: 10.1111/pace.12026]
- Blendea D**, Shah RV, Auricchio A, Nandigam V, Orencole M, Heist EK, Reddy VY, McPherson CA, Ruskin JN, Singh JP. Variability of coronary venous anatomy in patients undergoing cardiac resynchronization therapy: a high-speed rotational venography study. *Heart Rhythm* 2007; **4**: 1155-1162

- [PMID: 17765613]
- 14 **Mlynarski R**, Mlynarska A, Sosnowski M. Anatomical variants of coronary venous system on cardiac computed tomography. *Circ J* 2011; **75**: 613-618 [PMID: 21242643]
 - 15 **Noheria A**, DeSimone CV, Lachman N, Edwards WD, Gami AS, Maleszewski JJ, Friedman PA, Munger TM, Hammill SC, Hayes DL, Packer DL, Asirvatham SJ. Anatomy of the coronary sinus and epicardial coronary venous system in 620 hearts: an electrophysiology perspective. *J Cardiovasc Electrophysiol* 2013; **24**: 1-6 [PMID: 23066703 DOI: 10.1111/j.1540-8167.2012.02443.x]
 - 16 **Macedo PG**, Kapa S, Mears JA, Fratianni A, Asirvatham SJ. Correlative anatomy for the electrophysiologist: ablation for atrial fibrillation. Part I: pulmonary vein ostia, superior vena cava, vein of Marshall. *J Cardiovasc Electrophysiol* 2010; **21**: 721-730 [PMID: 20158562 DOI: 10.1111/j.1540-8167.2010.01728.x]
 - 17 **Kim SY**, Hong YJ, Lee HJ, Hur J, Choi BW, Kim YJ. Anomalous great cardiac vein draining into the right atrium combined with a single left coronary artery. *Int J Cardiovasc Imaging* 2013; **29** Suppl 1: 53-56 [PMID: 23443338 DOI: 10.1007/s10554-013-0195-9]
 - 18 **Goldberg SP**, Fonseca BM, Younoszai AK, Campbell DN. An unusual location of a persistent vein of Marshall. *Ann Thorac Surg* 2009; **88**: 305 [PMID: 19559259 DOI: 10.1016/j.athoracsur.2008.10.015]
 - 19 **Strohmer B**. Valve of Vieussens: an obstacle for left ventricular lead placement. *Can J Cardiol* 2008; **24**: e63 [PMID: 18787728]
 - 20 **Hasdemir C**, Alp A, Can LH. Successful balloon dilatation of the valve of Vieussens for left ventricular lead placement. *Pacing Clin Electrophysiol* 2009; **32**: 828-829 [PMID: 19545352 DOI: 10.1111/j.1540-8159.2009.02376.x]
 - 21 **Gokhroo RK**, Bisht DS, Padmanabhan D, Gupta S. Coronary sinus anatomy: ajmer working group classification. *J Invasive Cardiol* 2014; **26**: 71-74 [PMID: 24486664]
 - 22 **Kawata H**, Mulpuru S, Phan H, Patel J, Gadiyaram V, Chen L, Sawhney N, Feld G, Birgersdotter-Green U. Gender difference in coronary sinus anatomy and left ventricular lead pacing parameters in patients with cardiac resynchronization therapy. *Circ J* 2013; **77**: 1424-1429 [PMID: 23459446]
 - 23 **Alikhani Z**, Li J, Merchan JA, Nijhof N, Mendel J, Orlov MV. Coronary sinus anatomy by computerized tomography, overlaid on live fluoroscopy can be successfully used to guide left ventricular lead implantation: a feasibility study. *J Interv Card Electrophysiol* 2013; **36**: 217-222 [PMID: 23196855 DOI: 10.1007/s10840-012-9736-8]
 - 24 **Osman F**, Kundu S, Tuan J, Pathmanathan RK. Use of coronary venous angioplasty to facilitate optimal placement of left ventricular lead during CRT. *Pacing Clin Electrophysiol* 2009; **32**: 281-282 [PMID: 19170924 DOI: 10.1111/j.1540-8159.2008.02217.x]
 - 25 **Christiaens L**, Ardilouze P, Ragot S, Mergy J, Allal J. Prospective evaluation of the anatomy of the coronary venous system using multidetector row computed tomography. *Int J Cardiol* 2008; **126**: 204-208 [PMID: 17493696]
 - 26 **Bali HK**, Chattree KK, Bali SK, Chauhan HK, Shukla CP. Collateral approach for LV lead implantation in a case with abnormal venous anatomy. *Indian Heart J* 2013; **65**: 607-610 [PMID: 24206886 DOI: 10.1016/j.ihj.2013.08.022]
 - 27 **Gilard M**, Mansourati J, Etienne Y, Larlet JM, Truong B, Bosch J, Blanc JJ. Angiographic anatomy of the coronary sinus and its tributaries. *Pacing Clin Electrophysiol* 1998; **21**: 2280-2284 [PMID: 9825333]
 - 28 **Jongbloed MR**, Lamb HJ, Bax JJ, Schuijff JD, de Roos A, van der Wall EE, Schalij MJ. Noninvasive visualization of the cardiac venous system using multislice computed tomography. *J Am Coll Cardiol* 2005; **45**: 749-753 [PMID: 15734621]
 - 29 **Abbara S**, Cury RC, Nieman K, Reddy V, Moselewski F, Schmidt S, Ferencik M, Hoffmann U, Brady TJ, Achenbach S. Noninvasive evaluation of cardiac veins with 16-MDCT angiography. *AJR Am J Roentgenol* 2005; **185**: 1001-1006 [PMID: 16177423]
 - 30 **Tada H**, Naito S, Koyama K, Taniguchi K. Three-dimensional computed tomography of the coronary venous system. *J Cardiovasc Electrophysiol* 2003; **14**: 1385 [PMID: 14678120]
 - 31 **Genc B**, Solak A, Sahin N, Gur S, Kalaycioglu S, Ozturk V. Assessment of the coronary venous system by using cardiac CT. *Diagn Interv Radiol* 2013; **19**: 286-293 [PMID: 23337097 DOI: 10.5152/dir.2013.012]
 - 32 **Mlynarski R**, Sosnowski M, Wlodyka A, Chromik K, Kargul W, Tendera M. Optimal image reconstruction intervals for noninvasive visualization of the cardiac venous system with a 64-slice computed tomography. *Int J Cardiovasc Imaging* 2009; **25**: 635-641 [PMID: 19415522 DOI: 10.1007/s10554-009-9463-0]
 - 33 **Mlynarski R**, Sosnowski M, Wlodyka A, Kargul W, Tendera M. A user-friendly method of cardiac venous system visualization in 64-slice computed tomography. *Pacing Clin Electrophysiol* 2009; **32**: 323-329 [PMID: 19272061 DOI: 10.1111/j.1540-8159.2008.02239.x]
 - 34 **Girsky MJ**, Shinbane JS, Ahmadi N, Mao S, Flores F, Budoff MJ. Prospective randomized trial of venous cardiac computed tomographic angiography for facilitation of cardiac resynchronization therapy. *Pacing Clin Electrophysiol* 2010; **33**: 1182-1187 [PMID: 20579305 DOI: 10.1111/j.1540-8159.2010.02821.x]
 - 35 **Blendea D**, Singh JP. Lead positioning strategies to enhance response to cardiac resynchronization therapy. *Heart Fail Rev* 2011; **16**: 291-303 [PMID: 21184174 DOI: 10.1007/s10741-010-9212-4]
 - 36 **Mak GS**, Hill AJ, Moisiuc F, Krishnan SC. Variations in Thebesian valve anatomy and coronary sinus ostium: implications for invasive electrophysiology procedures. *Europace* 2009; **11**: 1188-1192 [PMID: 19587062 DOI: 10.1093/europace/eup179]
 - 37 **Kautzner J**. Thebesian valve: the guard dog of the coronary sinus? *Europace* 2009; **11**: 1136-1137 [PMID: 19706637 DOI: 10.1093/europace/eup227]
 - 38 **Ghosh SK**, Raheja S, Tuli A. Obstructive Thebesian valve: anatomical study and implications for invasive cardiologic procedures. *Anat Sci Int* 2014; **89**: 85-94 [PMID: 24043316]
 - 39 **Cao M**, Chang P, Garon B, Shinbane JS. Cardiac resynchronization therapy: double cannulation approach to coronary venous lead placement via a prominent thebesian valve. *Pacing Clin Electrophysiol* 2013; **36**: e70-e73 [PMID: 22432962 DOI: 10.1111/j.1540-8159.2012.03362.x]
 - 40 **Loukas M**, Clarke P, Tubbs RS, Kolbinger W. Adam Christian Thebesius, a historical perspective. *Int J Cardiol* 2008; **129**: 138-140 [PMID: 17692957]
 - 41 **Kuroda M**, Takahashi T, Mita N, Kagaya S, Miyoshi S, Saito S. Difficult cannulation of the coronary sinus due to a large Thebesian valve. *Anesth Analg* 2013; **116**: 563-566 [PMID: 23400976 DOI: 10.1213/ANE.0b013e31827bc77e]
 - 42 **Parikh MG**, Halleran SM, Bharati S, Trohman RG. Successful percutaneous cardiac resynchronization despite an occlusive Thebesian valve. *Pediatr Cardiol* 2011; **32**: 1223-1227 [PMID: 21805325 DOI: 10.1007/s00246-011-0066-x]
 - 43 **Anh DJ**, Eversull CS, Chen HA, Mofrad P, Mourlas NJ, Mead RH, Zei PC, Hsia HH, Wang PJ, Al-Ahmad A. Characterization of human coronary sinus valves by direct visualization during biventricular pacemaker implantation. *Pacing Clin Electrophysiol* 2008; **31**: 78-82 [PMID: 18181913 DOI: 10.1111/j.1540-8159.2007.00928.x]
 - 44 **Silver MA**, Rowley NE. The functional anatomy of the human coronary sinus. *Am Heart J* 1988; **115**: 1080-1084 [PMID: 2966548]
 - 45 **El-Maasarany S**, Ferrett CG, Firth A, Sheppard M, Heinlein MY. The coronary sinus conduit function: anatomical study (relationship to adjacent structures). *Europace* 2005; **7**:

- 475-481 [PMID: 16087113]
- 46 **Mlynarski R**, Mlynarska A, Tendera M, Sosnowski M. Coronary sinus ostium: the key structure in the heart's anatomy from the electrophysiologist's point of view. *Heart Vessels* 2011; **26**: 449-456 [PMID: 21240507 DOI: 10.1007/s00380-010-0075-3]
- 47 **Chen JJ**, Lee WJ, Wang YC, Tsai CT, Lai LP, Hwang JJ, Lin JL. Morphologic and topologic characteristics of coronary venous system delineated by noninvasive multidetector computed tomography in chronic systolic heart failure patients. *J Card Fail* 2007; **13**: 482-488 [PMID: 17675063]
- 48 **Mlynarska A**, Mlynarski R, Sosnowski M. Coronary venous retention—a feature in heart failure as evidenced by mean of cardiac computed tomography. *Pacing Clin Electrophysiol* 2012; **35**: 1472-1479 [PMID: 23035935 DOI: 10.1111/pace.12000]
- 49 **Mangalat D**, Kalogeropoulos A, Georgiopolou V, Stillman A, Butler J. Value of Cardiac CT in Patients With Heart Failure. *Curr Cardiovasc Imaging Rep* 2009; **2**: 410-417 [PMID: 20369033]
- 50 **Mlynarski R**, Mlynarska A, Sosnowski M. Association between changes in coronary artery circulation and cardiac venous retention: a lesson from cardiac computed tomography. *Int J Cardiovasc Imaging* 2013; **29**: 885-890 [PMID: 23076605 DOI: 10.1007/s10554-012-0139-9]
- 51 **Siminiak T**, Dankowski R, Baszko A, Lee C, Firek L, Kalnucki P, Szyszka A, Groothuis A. Percutaneous direct mitral annuloplasty using the Mitralign Bident system: description of the method and a case report. *Kardiol Pol* 2013; **71**: 1287-1292 [PMID: 24399585 DOI: 10.5603/KP.2013.0325]
- 52 **Sack S**. [Percutaneous mitral annuloplasty with the VIA-COR coronary sinus system for the treatment of functional mitral regurgitation in heart failure patients. Development and results]. *Herz* 2009; **34**: 468-476 [PMID: 19784565 DOI: 10.1007/s00059-009-3287-5]
- 53 **Masson JB**, Webb JG. Percutaneous mitral annuloplasty. *Coron Artery Dis* 2009; **20**: 183-188 [PMID: 19339881 DOI: 10.1097/MCA.0b013e328326c6e6]
- 54 **Lansac E**, Di Centa I, Al Attar N, Messika-Zeitoun D, Raf-foul R, Vahanian A, Nataf P. Percutaneous mitral annuloplasty through the coronary sinus: an anatomic point of view. *J Thorac Cardiovasc Surg* 2008; **135**: 376-381 [PMID: 18242272 DOI: 10.1016/j.jtcvs.2007.05.071]
- 55 **Feldman T**. Percutaneous mitral annuloplasty: not always a cinch. *Catheter Cardiovasc Interv* 2007; **69**: 1062-1063 [PMID: 17525966]
- 56 **Siminiak T**, Hoppe UC, Schofer J, Haude M, Herrman JP, Vainer J, Firek L, Reuter DG, Goldberg SL, Van Bibber R. Effectiveness and safety of percutaneous coronary sinus-based mitral valve repair in patients with dilated cardiomyopathy (from the AMADEUS trial). *Am J Cardiol* 2009; **104**: 565-570 [PMID: 19660613 DOI: 10.1016/j.amjcard.2009.04.021]
- 57 **Schofer J**, Siminiak T, Haude M, Herrman JP, Vainer J, Wu JC, Levy WC, Mauri L, Feldman T, Kwong RY, Kaye DM, Duffy SJ, Tübler T, Degen H, Brandt MC, Van Bibber R, Goldberg S, Reuter DG, Hoppe UC. Percutaneous mitral annuloplasty for functional mitral regurgitation: results of the CARILLON Mitral Annuloplasty Device European Union Study. *Circulation* 2009; **120**: 326-333 [PMID: 19597051 DOI: 10.1161/CIRCULATIONAHA.109.849885]
- 58 **Gopal A**, Shah A, Shareghi S, Bansal N, Nasir K, Gopal D, Budoff MJ, Shavelle DM. The role of cardiovascular computed tomographic angiography for coronary sinus mitral annuloplasty. *J Invasive Cardiol* 2010; **22**: 67-73 [PMID: 20124591]
- 59 **Tops LF**, Van de Veire NR, Schuijff JD, de Roos A, van der Wall EE, Schalij MJ, Bax JJ. Noninvasive evaluation of coronary sinus anatomy and its relation to the mitral valve annulus: implications for percutaneous mitral annuloplasty. *Circulation* 2007; **115**: 1426-1432 [PMID: 17353434]
- 60 **Mlynarski R**, Mlynarska A, Wilczek J, Sosnowski M. Optimal visualization of heart vessels before percutaneous mitral annuloplasty. *Cardiol J* 2012; **19**: 459-465 [PMID: 23042308]
- 61 **Maselli D**, Guarracino F, Chiamonti F, Mangia F, Borelli G, Minzioni G. Percutaneous mitral annuloplasty: an anatomic study of human coronary sinus and its relation with mitral valve annulus and coronary arteries. *Circulation* 2006; **114**: 377-380 [PMID: 16864726 DOI: 10.1161/CIRCINTERVENTIONS.109.873281]
- 62 **del Valle-Fernández R**, Jelnin V, Panagopoulos G, Ruiz CE. Insight into the dynamics of the coronary sinus/great cardiac vein and the mitral annulus: implications for percutaneous mitral annuloplasty techniques. *Circ Cardiovasc Interv* 2009; **2**: 557-564 [PMID: 20031774]
- 63 **Taylor AJ**, Cerqueira M, Hodgson JM, Mark D, Min J, O'Gara P, Rubin GD. ACCF/SCCT/ACR/AHA/ASE/ASNC/NASCI/SCAI/SCMR 2010 Appropriate Use Criteria for Cardiac Computed Tomography. A Report of the American College of Cardiology Foundation Appropriate Use Criteria Task Force, the Society of Cardiovascular Computed Tomography, the American College of Radiology, the American Heart Association, the American Society of Echocardiography, the American Society of Nuclear Cardiology, the North American Society for Cardiovascular Imaging, the Society for Cardiovascular Angiography and Interventions, and the Society for Cardiovascular Magnetic Resonance. *J Cardiovasc Comput Tomogr* 2010; **4**: 407.e1-407.33 [PMID: 21232696 DOI: 10.1016/j.jacc.2010.07.005]
- 64 **Daubert JC**, Saxon L, Adamson PB, Auricchio A, Berger RD, Beshai JF, Breithard O, Brignole M, Cleland J, DeLurgio DB, Dickstein K, Exner DV, Gold M, Grimm RA, Hayes DL, Israel C, Leclercq C, Linde C, Lindenfeld J, Merkely B, Mont L, Murgatroyd F, Prinzen F, Saba SF, Shinbane JS, Singh J, Tang AS, Vardas PE, Wilkoff BL, Zamorano JL, Anand I, Blomström-Lundqvist C, Boehmer JP, Calkins H, Cazeau S, Delgado V, Estes NA, Haines D, Kusumoto F, Leyva P, Ruschitzka F, Stevenson LW, Torp-Pedersen CT. 2012 EHRA/HRS expert consensus statement on cardiac resynchronization therapy in heart failure: implant and follow-up recommendations and management. *Europace* 2012; **14**: 1236-1286 [PMID: 22930717 DOI: 10.1093/europace/eus222]
- 65 **Thai WE**, Wai B, Lin K, Cheng T, Heist EK, Hoffmann U, Singh JP, Truong QA. Pulmonary venous anatomy imaging with low-dose, prospectively ECG-triggered, high-pitch 128-slice dual-source computed tomography. *Circ Arrhythm Electrophysiol* 2012; **5**: 521-530 [PMID: 22586259 DOI: 10.1161/CIRCEP.111.968313]
- 66 **Shapiro BP**, Young PM, Kantor B, Choe YH, McCollough CH, Gerber TC. Radiation dose reduction in CT coronary angiography. *Curr Cardiol Rep* 2010; **12**: 59-67 [PMID: 20425185 DOI: 10.1007/s11886-009-0074-0]

P-Reviewer: Gong QY, Mani V, Storto G, Vogl TJ
S-Editor: Wen LL L-Editor: A E-Editor: Lu YJ



Nuclear imaging in detection and monitoring of cardiotoxicity

Carmen D'Amore, Paola Gargiulo, Stefania Paolillo, Angela Maria Pellegrino, Tiziana Formisano, Antonio Mariniello, Giuseppe Della Ratta, Elisabetta Iardino, Marianna D'Amato, Lucia La Mura, Irma Fabiani, Flavia Fusco, Pasquale Perrone Filardi

Carmen D'Amore, Stefania Paolillo, Angela Maria Pellegrino, Tiziana Formisano, Antonio Mariniello, Giuseppe Della Ratta, Elisabetta Iardino, Marianna D'Amato, Lucia La Mura, Irma Fabiani, Flavia Fusco, Pasquale Perrone Filardi, Department of Advanced Biomedical Sciences, Federico II University, 80131 Naples, Italy

Paola Gargiulo, SDN Foundation, Institute of Diagnostic and Nuclear Development, 80129 Naples, Italy

Author contributions: D'Amore C and Gargiulo P contributed to this work, generated the tables and wrote the manuscript; Paolillo S, Pellegrino AM, Formisano T and Mariniello A contributed to the writing of the manuscript; Della Ratta G, Iardino E, D'Amato M, La Mura L, Fabiani I and Fusco F contributed to med-line; and Perrone Filardi P reviewed the manuscript.

Correspondence to: Pasquale Perrone Filardi, MD, PhD, Department of Advanced Biomedical Sciences, Federico II University, Via Pansini, 5, 80131 Naples, Italy. fpperron@unina.it
Telephone: +39-81-7462224 Fax: +39-81-7462224

Received: February 21, 2014 Revised: April 21, 2014

Accepted: May 29, 2014

Published online: March 28, 2015

Abstract

Cardiotoxicity as a result of cancer treatment is a novel and serious public health issue that has a significant impact on a cancer patient's management and outcome. The coexistence of cancer and cardiac disease in the same patient is more common because of aging population and improvements in the efficacy of anti-tumor agents. Left ventricular dysfunction is the most typical manifestation and can lead to heart failure. Left ventricular ejection fraction measurement by echocardiography and multigated radionuclide angiography is the most common diagnostic approach to detect cardiac damage, but it identifies a late manifestation of myocardial injury. Early non-invasive imaging techniques are needed for the diagnosis and monitoring

of cardiotoxic effects. Although echocardiography and cardiac magnetic resonance are the most commonly used imaging techniques for cardiotoxicity assessment, greater attention is focused on new nuclear cardiology techniques, which can identify high-risk patients in the early stage and visualize the pathophysiologic process at the tissue level before clinical manifestation. The aim of this review is to summarize the role of nuclear imaging techniques in the non-invasive detection of myocardial damage related to antineoplastic therapy at the reversible stage, focusing on the current role and future perspectives of nuclear imaging techniques and molecular radiotracers in detection and monitoring of cardiotoxicity.

© 2015 Baishideng Publishing Group Inc. All rights reserved.

Key words: Cardiotoxicity; Cardiac nuclear imaging; Early diagnosis; Scintigraphy; Positron emission tomography

Core tip: Cardiomyopathy is a potential complication of various anticancer drugs, such as anthracyclines and biological therapy. Left ventricular dysfunction is the most common manifestation of cardiotoxicity and is monitored with left ventricular ejection fraction measurement, but it is a late manifestation of myocardial injury. Thus, the cardiologist and oncologist should collaborate to identify new non-invasive techniques to detect cardiac dysfunction at an early and potentially reversible stage, before the onset of clinical manifestation. To achieve this aim, nuclear imaging techniques may offer good future perspectives for early detection of myocardial damage using novel molecular tracers.

Original sources: D'Amore C, Gargiulo P, Paolillo S, Pellegrino AM, Formisano T, Mariniello A, Della Ratta G, Iardino

E, D'Amato M, La Mura L, Fabiani I, Fusco F, Perrone Filardi P. Nuclear imaging in detection and monitoring of cardiotoxicity. *World J Radiol* 2014; 6(7): 486-492 Available from: URL: <http://www.wjgnet.com/1949-8470/full/v6/i7/486.htm> DOI: <http://dx.doi.org/10.4329/wjr.v6.i7.486>

INTRODUCTION

Over the last few decades, early diagnosis and development of new antitumor agents have significantly improved the survival of cancer patients. However, conventional and new oncologic drugs frequently have a wide range of cardiac adverse effects, in particular myocardial toxicity. Anthracyclines (doxorubicin, epirubicin), cyclophosphamide, monoclonal antibodies (trastuzumab) and other tyrosine kinase inhibitors (TKIs) are antineoplastic drugs more frequently associated with cardiotoxicity^[1]. These drugs may cause irreversible damage, such as that induced by anthracyclines, through free radical production, adrenergic function alteration and cardiac myocyte death due to calcium overload^[2,3], or potential completely reversible dysfunction, like that related to TKI administration^[4].

Left ventricular (LV) dysfunction is the most typical manifestation of cardiotoxicity and it contributes to increased mortality during chemotherapy^[5]. Cardiotoxicity has been defined by the Cardiac Review and Evaluation Committee supervising trastuzumab clinical trials^[6] as: (1) a decrease in cardiac LV ejection fraction (EF), either globally or more severe in the septum; (2) the onset of symptoms associated with congestive heart failure (HF); (3) the presence of signs associated with congestive HF; and (4) a reduction in LVEF from baseline of at least 5% to below 55% with signs and symptoms of congestive HF, or a decline in LVEF of at least 10% to below 55% without signs and symptoms of congestive HF. The serial assessment of LVEF is the most common modality for detection of cardiotoxicity and a reduction more than 10% from baseline or a decrease in LVEF below 50% are considered interruption criteria for anticancer drugs administration^[7-9]. Notwithstanding, guidelines do not specify the timing and the duration of follow-up and what technique is preferable to assess LV function during and after cancer treatment^[10].

Echocardiography (ECHO) plays an important role in evaluation and monitoring of cancer patients treated with cardiotoxic antineoplastic drugs due to its availability and repeatability. Conversely, inter- and intra-observer variability during serial measurement of LVEF and underestimation of myocardial contractile dysfunction should be considered. To overcome these limitations, novel echocardiographic techniques, such as tissue velocity imaging and strain imaging, could be used to detect the presence of myocardial contractile dysfunction before impairment of LVEF^[11].

In addition, cardiac magnetic resonance imaging (CMR) is a well recognized imaging technique to screen

chemotherapy-related cardiomyopathy^[12]. It provides reproducible and noninvasively assessment of LV volume, mass and function^[13,14]. Moreover, several studies^[13,15,16] emphasized its role in early detection of myocardial damage, however high cost and low availability limit clinical routine use.

Although ECHO and CMR are the two most commonly used imaging techniques for non-invasive chemotherapeutic myocardial toxicity assessment, nuclear imaging may still have a role in the evaluation and monitoring of cancer patients treated with cardiotoxic drugs. Besides providing sensitive and accurate estimation of LVEF, nuclear imaging techniques using specific radiotracer molecules represent an emerging tool for non-invasive detection of biological processes preceding anatomical involvement and physiological consequences of myocardial damage induced by antineoplastic drugs (Tables 1 and 2).

In this review we will summarize the role of nuclear cardiology in the non-invasive detection of myocardial damage related to antineoplastic therapy, focusing on the current role and future perspectives of nuclear imaging and molecular radiotracers in the assessment of cardiac toxicity.

^{99m}Tc-MUGA

Multigated radionuclide angiography (MUGA) is a non-invasive technique using ^{99m}Tc-erythrocytes to visualize the cardiac blood pool through a γ camera with gated acquisition^[17]. The series of heart planar images at each stage of the cardiac cycle permit accurate and highly reproducible quantification of LV volumes and LVEF during cancer therapy^[18]. However, its use may be hampered by soft tissue attenuation artifacts and may expose patients to ionizing radiation^[14,19]. In 28 patients treated with increasing cumulative doses of doxorubicin for non-Hodgkin lymphoma, Nousianen *et al*^[20] documented that a MUGA scan had 90% sensitivity and 72% specificity for predicting development of chronic HF. However, the results of this little prospective study were not confirmed by a large retrospective study^[21] conducted on 630 patients randomized to increasing dose of doxorubicin or placebo. In fact, Swain *et al*^[21] observed that 66% of patients experiencing doxorubicin-related chronic HF showed no clinically relevant decline in LVEF value assessed by MUGA scan from baseline levels (ranging from 0 to 30% of the absolute value), suggesting that it is not accurate in HF prediction.

^{99m}Tc GBPS

^{99m}Tc gated blood-pool SPECT (single photon emission computed tomography) is a nuclear technique enabling acquisition of 3-dimensional scanned images. ^{99m}Tc gated blood-pool SPECT provides information on LVEF, right ventricular EF and wall motion useful for monitoring and personalizing therapy in HF patients^[21]. A good cor-

Table 1 Radiotracer for cardiac nuclear imaging

Technique	Tracer	Action
SPECT	^{99m} Tc-erythrocyte	Contractile function
	¹¹¹ In-antimyosin	Imaging necrosis/cell death
	¹²³ I-MIBG	Neuronal imaging (presynaptic uptake and storage)
	¹¹¹ In-Tz	Therapeutic target imaging
	^{99m} Tc-annexin V	Imaging necrosis/cell death
	¹²³ I-BMIPP	Fatty acid use
PET	¹⁸ F-FDG	Glucose metabolism
	Presynaptic tracers	Visualize inhibition of neurotransmission
	true catecholamines	
	¹⁸ F-6-fluorodopamine	
	¹¹ C-epinephrine	
	catecholamine analogs	False neurotransmitters
	¹¹ C-HED	
	¹¹ C-phenylephrine	
	¹⁸ F-6-fluoro-metaraminol	
	Postsynaptic tracers	Visualize transmission of sympathetic signal to target tissue
	¹¹ C-CGP12177	
¹¹ C-CGP12388		
¹¹ C-GB67		

SPECT: Single photon emission computed tomography; PET: Positron emission tomography; HED: Hydroxyephedrine; FDG: Fluorodeoxyglucose; ¹²³I-BMIPP: ¹²³I-15-(p-iodophenyl)-3-(R,S)-methylpentadecanoic acid.

relation between gated blood-pool SPECT and MUGA in LVEF estimation was documented^[22]. However, gated blood-pool SPECT tends to underestimate LVEF values (33% ± 13%)^[23] compared with MUGA (41% ± 14%, $P = 0.001$), first-pass radionuclide ventriculography (45% ± 13%, $P < 0.0001$) and echocardiography (37% ± 15%, $P = 0.004$).

¹¹¹IN-ANTIMYOSIN SPECT

The immunoscintigraphic agent ¹¹¹In-antimyosin is a specific marker for myocardial cell injury and necrosis, binding to intracellular myosin when sarcolemma disruption occurs and the cell is irreversibly damaged. It has been studied in myocardial infarction, myocarditis, cardiac transplant rejection and anthracycline cardiotoxicity^[24].

¹¹¹In-antimyosin SPECT can play a role in subclinical assessment of LV dysfunction as documented in several studies^[24,25]. Estorch *et al.*^[25] showed an increased uptake of ¹¹¹In-antimyosin after anthracycline chemotherapy (doxorubicin or mitoxantrone) in breast cancer patients without cardiovascular risk factors or previous chemotherapy or mediastinal radiotherapy, and the degree of myocardial antimyosin uptake was associated with changes in LVEF. Moreover, the presence in some patients of radiotracer uptake not associated with a significant reduction in LVEF after chemotherapy suggested the potential use of this technique to detect cellular damage before the onset of LV functional impairment, allowing the identification of patients at risk of HF. Similar results have also been obtained by Carrió *et al.*^[24], who documented a significant reduction in LVEF after chemotherapy in patients treated with an anthracycline dose of 420-600 mg/m² ($P < 0.001$)

and no significant change in patients treated with a dose of 240-300 mg/m². Moreover, patients with heart-to-lung ratio (HLR) ≥ 1.90 at a cumulative anthracycline dose of 240-300 mg/m² developed a reduction in LVEF greater than 10% at a subsequent cumulative doxorubicin dose of 420-600 mg/m². These data encouraged the use of antimyosin scintigraphy to identify patients with a high risk of developing systolic LV dysfunction when treated with an increasing dose of chemotherapeutic drugs. In addition, Valdés Olmos *et al.*^[26] observed that patients with a persistent reduction in LVEF after chemotherapy had a significantly higher HLR value (1.83 ± 0.37) than patients with transient LVEF decrease (1.52 ± 0.21; $P < 0.01$), revealing that cardiac uptake of ¹¹¹In-antimyosin could also be useful in discriminating between patients with transient and persistent LV dysfunction and in guiding clinical decisions about discontinuation of anthracycline therapy.

¹²³I-METAIODOBENZYLGUANIDINE SPECT

¹²³I-metaiodobenzylguanidine (¹²³I-MIBG) SPECT is a promising technique for detection of early anthracycline injury and for identification of patients at high risk of developing cardiotoxicity.

Chemotherapy-induced cardiomyopathy activates a compensatory response that increases adrenergic sympathetic and renin-angiotensin system activity to preserve organ perfusion^[27]. In patients with chronic HF, increased norepinephrine (NE) release, depletion of NE deposits and downregulation of human NE transporter (hNET1)

Table 2 Techniques used for detection of anticancer therapy cardiomyopathy

Methods	Advantages	Limits
Echocardiography	Non-invasive Absence of adverse effects Analysis of systolic and diastolic function Tissue velocity imaging and strain imaging useful for early detection of subclinical alteration	Inter- and intra-observer variability Low sensitivity of EF assessment for early diagnosis
Magnetic resonance imaging	Accurate heart anatomic description Absence of radiation exposure Accurate and reproducible EF assessment Cardiac innervation assessment	Limited availability High costs Not applicable in patients with metallic device Low information about its role in the early detection
Multiple-gated acquisition scintigraphy	High sensitivity and specificity EF assessment No inter- and intra-observer variability	Low sensitivity of EF for early diagnosis Less information about diastolic function Radiation exposure
Positron emission tomography	Myocardial metabolic and perfusion evaluation	Limited availability

EF: Ejection fraction.

have been shown^[28]. ¹²³I-MIBG is a norepinephrine analogue, showing the same uptake, storage and release mechanisms of NE. Unlike NE, MIBG is not metabolized by catechol-o-methyl transferase and monoamine oxidase^[29]; so, labelled with ¹²³I, it can be used to generate scintigraphic images of cardiac efferent sympathetic innervation. After ¹²³I-MIBG administration, early (15 min) and late (4 h) post injection images are acquired to determine heart to mediastinal ratio (H/M) and washout rate (WR). Consequently, increased NE in the cardiac synaptic space and a reduction in the presynaptic space, induced by HF, reduced MIBG cardiac uptake and accelerated the washout rate.

Studies^[30,31] conducted in asymptomatic patients treated with anthracyclines revealed that ¹²³I-MIBG was useful for assessment of myocardial adrenergic derangement and identification of patients at risk of developing cardiotoxicity. In addition, in 36 patients undergoing MIBG scintigraphy who had a diagnosis of sarcoma and no history of cardiac disease or previous cancer treatment, Carrió *et al*^[30] found an insignificant decrease in LVEF and MIBG uptake at an intermediate cumulative dose of doxorubicin (240-300 mg/m²). However, when a high cumulative dose of doxorubicin 420-600 mg/m² was used, the experimenters documented a significant impairment of ¹²³I-MIBG uptake ($P < 0.001$) and a reduction in LVEF ($P < 0.05$), and proposed that the degree of H/M reduction was also correlated with the dose of anthracycline administrated.

¹¹¹IN-TRASTUZUMAB SPECT

In cancer patients, anthracyclines can increase the levels of human epidermal growth factor receptor 2 (HER2) expressed by myocytes. In patients pre-treated with anthracyclines, trastuzumab, a chemotherapeutic agent with a direct effect on HER2, often causes cardiotoxicity, likely as a result of the inhibition of cardiac HER2 that activates the apoptotic pathways and amplifies anthracycline oxidative stress. Thus, ¹¹¹In-trastuzumab (¹¹¹In-Tz) SPECT

can be used to evaluate the myocyte HER2 expression and the risk of development LV dysfunction in patients treated with this drug^[32].

In a small study, Behr *et al*^[33] investigated ¹¹¹In-Tz scintigraphy in 20 patients with metastatic breast cancer expressing the HER2/neu receptor, pre-treated with anthracyclines and scheduled for administration of Tz as second-line therapy. They documented myocardial ¹¹¹In-Tz uptake prior to Tz in 7 patients; of these, 6 developed clinical HF (II-IV NYHA class), whereas none of 13 patients without uptake had adverse cardiac events, suggesting that pre-treatment scanning with ¹¹¹In-Tz could predict cardiotoxicity. In contrast to these results, Perik *et al*^[34] documented increased ¹¹¹In-Tz uptake at the start of trastuzumab therapy only in 1 of 17 studied patients, who had received extensive anthracycline pre-treatment, and normal ¹¹¹In-Tz uptake at baseline scintigraphy in 3 patients who developed Tz-induced cardiomyopathy.

^{99m}Tc-ANNEXIN V SPECT

Apoptosis of myocardial cells plays a critical role in the onset of cardiomyopathy and has been observed in several conditions, such as hypoxia, ischemia, cardiac overload, acute myocardial infarction, anthracycline-induced cardiomyopathy and end-stage HF. In apoptotic cells, the early stage is characterized by activation of proteases and sphingomyelinases and consequent exposure of phosphatidylserine molecules on the outer surface of the cell membrane. ^{99m}Tc-annexin V has a high affinity for the exposed phosphatidylserine molecule and thus allows imaging of apoptotic cell death^[35].

In animals, annexin V scintigraphy has been used to assess acute and chronic doxorubicin-induced cardiomyopathy based on early apoptosis. Increased ^{99m}Tc-annexin V uptake was observed in the myocardium of doxorubicin-treated animals and cardiac oxidative stress was confirmed by histological analysis^[36,37].

Further studies are needed of the clinical use of this radiotracer, in particular early identification of myocardial

damage related to antineoplastic drugs.

¹²³I-15-(P-iodophenyl)-3-(R,S)-METHYLPENTADECANOIC ACID SPECT

Taxanes are used in the treatment of breast, lung and ovarian cancer, and they can cause ischemia, arrhythmias and HF. Taxanes can impair the microtubular transport system in cardiomyocytes, resulting in failure to store free fatty acids in the cytosol lipid pool and impairment of mitochondrial free fatty acid uptake for beta-oxidation. ¹²³I-15-(p-iodophenyl)-3-(R,S)-methylpentadecanoic acid (¹²³I-BMIPP) scintigraphy has been used to assess this biochemical perturbation in free fatty acid oxidation^[38]. Saito *et al*^[38] showed significantly lower BMIPP uptake scores after chemotherapy than those before treatment (23.4 ± 3.4 vs 26.6 ± 0.8 , $P < 0.001$). Moreover, 6 of 25 studied patients, who developed LV dysfunction, also had a significant decrease in total BMIPP uptake scores, suggesting the use of ¹²³I-BMIPP SPECT for detecting of taxane-induced cardiotoxicity. The value of ¹²³I-BMIPP in prediction of cardiotoxicity was also documented in 36 patients with various malignancies treated with doxorubicin^[39]. In this study, Saito *et al*^[39] showed a significant dose-related reduction in ¹²³I-BMIPP uptake (0.095 ± 0.25 vs 0.071 ± 0.019 ; $P < 0.001$) after doxorubicin chemotherapy and a higher rate of LV dysfunction development in patients with decreased uptake, but with normal LVEF at echocardiography.

POSITRON EMISSION TOMOGRAPHY

Positron emission tomography (PET) is the gold standard technique to assess myocardial metabolism and perfusion due to its high spatial and temporal resolution and high diagnostic sensibility and accuracy. Cardiac PET radiotracers are divided into two categories, those evaluating myocardial perfusion and those evaluating myocardial metabolism.

In the cardio-oncologic field, PET is useful for the diagnosis of metastatic lesion and assessment of the response to chemotherapy. However, fluorine-18-fluorodeoxyglucose (¹⁸F-FDG)-PET imaging is used to monitor the response to treatment of primary cardiac lymphoma^[40,41] and to evaluate metastatic pericardial involvement^[42]. The role of PET in the early detection of cardiotoxicity is still debated. Nony *et al*^[43] showed a significant decrease in LVEF ($P = 0.046$) assessed by radionuclide angiography after treatment with doxorubicin, but no significant effect was observed in myocardial blood flow evaluated with PET in 6 female cancer patients without heart disease. Recently, Borde *et al*^[44] analyzed changes in myocardial glucose metabolism using FDG-PET and suggested increased glucose utilization was evidence of cellular alteration preceding the cardiotoxicity cascade in patients treated with adriamycin.

Like SPECT, PET imaging can play a key role in the evaluation of cardiac autonomic dysfunction associ-

ated with HF^[45]. PET provides several advantages over SPECT, with higher spatial and temporal resolution and routinely available attenuation correction. In addition, PET radiotracers more closely resemble the endogenous neurotransmitters than ¹²³I-MIBG used for SPECT imaging, and the variety of available tracers may allow for more detailed analysis of neuronal signalling^[46]. There are two types of presynaptic positron-emitting tracers to assess the presynaptic sympathetic integrity in the heart, radiolabeled catecholamines and radiolabeled catecholamine analogs. The first type behaves identically to endogenous neurotransmitters, thus it is metabolically active and can complicate kinetic data analysis. Catecholamine analogs work as false neurotransmitters and are incapable of following the entire metabolic pathway of true catecholamines. Instead, postsynaptic tracers transmit the sympathetic signal to target tissue. Compared with the availability of presynaptic tracers, only a small number of tracers for postsynaptic neuronal imaging are clinically used. Experimental studies showed a significant reduction in the amount of LV β -adrenoceptors^[47] and ¹¹C-hydroxyephedrine in HF catecholamine uptake^[48,49] associated with LV dysfunction. Thus, studies are needed to validate this new radiotracer in the cardio-oncology field.

However, the complexity of most of the radiolabeling ligands, the requirement of laborious and specific knowledge, the high cost and the low availability limit clinical use of PET.

CONCLUSION

Cardiotoxicity is one of the principal adverse effects of anticancer therapy of clinical and prognostic importance. LVEF reduction is the most valid criterion to assess the presence of myocardial damage during or after chemotherapy. However, changes in LVEF occur when a critical amount of myocardial damage has taken place and compensatory mechanisms are exhausted^[50]. Thus, cardiologists and oncologists should work together to identify new non-invasive, sensitive and non-expensive diagnostic tools that can accurately recognize cardiotoxicity at the subclinical stage to reduce cardiac morbidity and mortality in cancer patients. Further interesting future perspectives in early detection of myocardial damage are offered by nuclear imaging using new molecular tracers which may be able to identify patients at high risk of developing LV dysfunction during and after cancer treatment. Several studies are needed to validate the clinical application of new molecular markers for the identification of early cellular damage.

REFERENCES

- 1 Yeh ET, Tong AT, Lenihan DJ, Yusuf SW, Swafford J, Champion C, Durand JB, Gibbs H, Zafarmand AA, Ewer MS. Cardiovascular complications of cancer therapy: diagnosis, pathogenesis, and management. *Circulation* 2004; **109**: 3122-3131 [PMID: 15226229 DOI: 10.1161/01.

- CIR.0000133187.74800.B9]
- 2 **Smith LA**, Cornelius VR, Plummer CJ, Levitt G, Verrill M, Canney P, Jones A. Cardiotoxicity of anthracycline agents for the treatment of cancer: systematic review and meta-analysis of randomised controlled trials. *BMC Cancer* 2010; **10**: 337 [PMID: 20587042 DOI: 10.1186/1471-2407-10-337]
 - 3 **Olivetti G**, Melissari M, Capasso JM, Anversa P. Cardiomyopathy of the aging human heart. Myocyte loss and reactive cellular hypertrophy. *Circ Res* 1991; **68**: 1560-1568 [PMID: 2036710 DOI: 10.1161/01.RES.68.6.1560]
 - 4 **Ewer MS**, Lippman SM. Type II chemotherapy-related cardiac dysfunction: time to recognize a new entity. *J Clin Oncol* 2005; **23**: 2900-2902 [PMID: 15860848 DOI: 10.1200/JCO.2005.05.827]
 - 5 **Kendal WS**. Dying with cancer: the influence of age, comorbidity, and cancer site. *Cancer* 2008; **112**: 1354-1362 [PMID: 18286532 DOI: 10.1002/cncr.23315]
 - 6 **Seidman A**, Hudis C, Pierri MK, Shak S, Paton V, Ashby M, Murphy M, Stewart SJ, Keefe D. Cardiac dysfunction in the trastuzumab clinical trials experience. *J Clin Oncol* 2002; **20**: 1215-1221 [PMID: 11870163 DOI: 10.1200/JCO.20.5.1215]
 - 7 **Schwartz RG**, McKenzie WB, Alexander J, Sager P, D'Souza A, Manatunga A, Schwartz PE, Berger HJ, Setaro J, Surkin L. Congestive heart failure and left ventricular dysfunction complicating doxorubicin therapy. Seven-year experience using serial radionuclide angiocardiology. *Am J Med* 1987; **82**: 1109-1118 [PMID: 3605130 DOI: 10.1016/0002-9343(87)90212-9]
 - 8 **van Royen N**, Jaffe CC, Krumholz HM, Johnson KM, Lynch PJ, Natale D, Atkinson P, Deman P, Wackers FJ. Comparison and reproducibility of visual echocardiographic and quantitative radionuclide left ventricular ejection fractions. *Am J Cardiol* 1996; **77**: 843-850 [PMID: 8623737 DOI: 10.1016/S0002-9149(97)89179-5]
 - 9 **Mitani I**, Jain D, Joska TM, Burtness B, Zaret BL. Doxorubicin cardiotoxicity: prevention of congestive heart failure with serial cardiac function monitoring with equilibrium radionuclide angiocardiology in the current era. *J Nucl Cardiol* 2003; **10**: 132-139 [PMID: 12673177 DOI: 10.1067/mnc.2003.7]
 - 10 **Eschenhagen T**, Force T, Ewer MS, de Keulenaer GW, Suter TM, Anker SD, Avkiran M, de Azambuja E, Balligand JL, Brutsaert DL, Condorelli G, Hansen A, Heymans S, Hill JA, Hirsch E, Hilfiker-Kleiner D, Janssens S, de Jong S, Neubauer G, Pieske B, Ponikowski P, Pirmohamed M, Rauchhaus M, Sawyer D, Sugden PH, Wojta J, Zannad F, Shah AM. Cardiovascular side effects of cancer therapies: a position statement from the Heart Failure Association of the European Society of Cardiology. *Eur J Heart Fail* 2011; **13**: 1-10 [PMID: 21169385 DOI: 10.1093/eurjhf/hfq213]
 - 11 **Yu CM**, Sanderson JE, Marwick TH, Oh JK. Tissue Doppler imaging a new prognosticator for cardiovascular diseases. *J Am Coll Cardiol* 2007; **49**: 1903-1914 [PMID: 17498573 DOI: 10.1016/j.jacc.2007.01.078]
 - 12 **Hendel RC**, Patel MR, Kramer CM, Poon M, Hendel RC, Carr JC, Gerstad NA, Gillam LD, Hodgson JM, Kim RJ, Kramer CM, Lesser JR, Martin ET, Messer JV, Redberg RF, Rubin GD, Rumsfeld JS, Taylor AJ, Weigold WG, Woodward PK, Brindis RG, Hendel RC, Douglas PS, Peterson ED, Wolk MJ, Allen JM, Patel MR. ACCF/ACR/SCCT/SCMR/ASNC/NASCI/SCAI/SIR 2006 appropriateness criteria for cardiac computed tomography and cardiac magnetic resonance imaging: a report of the American College of Cardiology Foundation Quality Strategic Directions Committee Appropriateness Criteria Working Group, American College of Radiology, Society of Cardiovascular Computed Tomography, Society for Cardiovascular Magnetic Resonance, American Society of Nuclear Cardiology, North American Society for Cardiac Imaging, Society for Cardiovascular Angiography and Interventions, and Society of Interventional Radiology. *J Am Coll Cardiol* 2006; **48**: 1475-1497 [PMID: 17010819 DOI: 10.1016/j.jacc.2006.07.003]
 - 13 **Fallah-Rad N**, Lytwyn M, Fang T, Kirkpatrick I, Jassal DS. Delayed contrast enhancement cardiac magnetic resonance imaging in trastuzumab induced cardiomyopathy. *J Cardiovasc Magn Reson* 2008; **10**: 5 [PMID: 18272009 DOI: 10.1186/1532-429X-10-5]
 - 14 **Walker J**, Bhullar N, Fallah-Rad N, Lytwyn M, Golian M, Fang T, Summers AR, Singal PK, Barac I, Kirkpatrick ID, Jassal DS. Role of three-dimensional echocardiography in breast cancer: comparison with two-dimensional echocardiography, multiple-gated acquisition scans, and cardiac magnetic resonance imaging. *J Clin Oncol* 2010; **28**: 3429-3436 [PMID: 20530277 DOI: 10.1200/JCO.2009.26.7294]
 - 15 **Fallah-Rad N**, Walker JR, Wassef A, Lytwyn M, Bohonis S, Fang T, Tian G, Kirkpatrick ID, Singal PK, Krahn M, Grenier D, Jassal DS. The utility of cardiac biomarkers, tissue velocity and strain imaging, and cardiac magnetic resonance imaging in predicting early left ventricular dysfunction in patients with human epidermal growth factor receptor II-positive breast cancer treated with adjuvant trastuzumab therapy. *J Am Coll Cardiol* 2011; **57**: 2263-2270 [PMID: 21616287 DOI: 10.1016/j.jacc.2010.11.063]
 - 16 **Wassmuth R**, Lentzsch S, Erdbruegger U, Schulz-Menger J, Doerken B, Dietz R, Friedrich MG. Subclinical cardiotoxic effects of anthracyclines as assessed by magnetic resonance imaging-a pilot study. *Am Heart J* 2001; **141**: 1007-1013 [PMID: 11376317 DOI: 10.1067/mhj.2001.115436]
 - 17 **Hesse B**, Lindhardt TB, Acampa W, Anagnostopoulos C, Ballinger J, Bax JJ, Edenbrandt L, Flotats A, Germano G, Stopar TG, Franken P, Kelion A, Kjaer A, Le Guludc D, Ljungberg M, Maenhout AF, Marcassa C, Marving J, McKiddie F, Schaefer WM, Stegger L, Underwood R. EANM/ESC guidelines for radionuclide imaging of cardiac function. *Eur J Nucl Med Mol Imaging* 2008; **35**: 851-885 [PMID: 18224320 DOI: 10.1007/s00259-007-0694-9]
 - 18 **Altena R**, Perik PJ, van Veldhuisen DJ, de Vries EG, Gieterma JA. Cardiovascular toxicity caused by cancer treatment: strategies for early detection. *Lancet Oncol* 2009; **10**: 391-399 [PMID: 19341970 DOI: 10.1016/S1470-2045(09)70042-7]
 - 19 **Corapçioğlu F**, Sarper N, Berk F, Sahin T, Zengin E, Demir H. Evaluation of anthracycline-induced early left ventricular dysfunction in children with cancer: a comparative study with echocardiography and multigated radionuclide angiography. *Pediatr Hematol Oncol* 2006; **23**: 71-80 [PMID: 16326416 DOI: 10.1080/08880010500313603]
 - 20 **Nousiainen T**, Jantunen E, Vanninen E, Hartikainen J. Early decline in left ventricular ejection fraction predicts doxorubicin cardiotoxicity in lymphoma patients. *Br J Cancer* 2002; **86**: 1697-1700 [PMID: 12087452 DOI: 10.1038/sj.bjc.6600346]
 - 21 **Swain SM**, Whaley FS, Ewer MS. Congestive heart failure in patients treated with doxorubicin: a retrospective analysis of three trials. *Cancer* 2003; **97**: 2869-2879 [PMID: 12767102 DOI: 10.1002/cncr.11407]
 - 22 **Groch MW**, DePuey EG, Belzberg AC, Erwin WD, Kamran M, Barnett CA, Hendel RC, Spies SM, Ali A, Marshall RC. Planar imaging versus gated blood-pool SPECT for the assessment of ventricular performance: a multicenter study. *J Nucl Med* 2001; **42**: 1773-1779 [PMID: 11752072]
 - 23 **Hacker M**, Hoyer X, Kupzyk S, La Fougere C, Kois J, Stempfle HU, Tiling R, Hahn K, Störk S. Clinical validation of the gated blood pool SPECT QBS processing software in congestive heart failure patients: correlation with MUGA, first-pass RNV and 2D-echocardiography. *Int J Cardiovasc Imaging* 2006; **22**: 407-416 [PMID: 16328851 DOI: 10.1007/s10554-005-9031-1]
 - 24 **Carrió I**, Lopez-Pousa A, Estorch M, Duncker D, Berná L, Torres G, de Andrés L. Detection of doxorubicin cardiotoxicity in patients with sarcomas by indium-111-antimyosin monoclonal antibody studies. *J Nucl Med* 1993; **34**: 1503-1507 [PMID: 8355070]

- 25 **Estorch M**, Carrió I, Martínez-Duncker D, Berná L, Torres G, Alonso C, Ojeda B. Myocyte cell damage after administration of doxorubicin or mitoxantrone in breast cancer patients assessed by indium 111 antimyosin monoclonal antibody studies. *J Clin Oncol* 1993; **11**: 1264-1268 [PMID: 8315423]
- 26 **Valdés Olmos RA**, ten Bokkel Huinink WW, ten Hoeve RF, van Tinteren H, Bruning PF, van Vlies B, Hoefnagel CA. Usefulness of indium-111 antimyosin scintigraphy in confirming myocardial injury in patients with anthracycline-associated left ventricular dysfunction. *Ann Oncol* 1994; **5**: 617-622 [PMID: 7993837]
- 27 **Francis GS**, Cohn JN. The autonomic nervous system in congestive heart failure. *Annu Rev Med* 1986; **37**: 235-247 [PMID: 2871803 DOI: 10.1146/annurev.me.37.020186.001315]
- 28 **Triploskiadis F**, Karayannis G, Giamouzis G, Skoularigis J, Louridas G, Butler J. The sympathetic nervous system in heart failure physiology, pathophysiology, and clinical implications. *J Am Coll Cardiol* 2009; **54**: 1747-1762 [PMID: 19874988 DOI: 10.1016/j.jacc.2009.05.015]
- 29 **Strashun A**. Adriamycin, congestive cardiomyopathy, and metaiodobenzylguanidine. *J Nucl Med* 1992; **33**: 215-222 [PMID: 1732443]
- 30 **Carrió I**, Estorch M, Berná L, López-Pousa J, Tabernero J, Torres G. Indium-111-antimyosin and iodine-123-MIBG studies in early assessment of doxorubicin cardiotoxicity. *J Nucl Med* 1995; **36**: 2044-2049 [PMID: 7472595]
- 31 **Valdés Olmos RA**, ten Bokkel Huinink WW, ten Hoeve RF, van Tinteren H, Bruning PF, van Vlies B, Hoefnagel CA. Assessment of anthracycline-related myocardial adrenergic derangement by [123I]metaiodobenzylguanidine scintigraphy. *Eur J Cancer* 1995; **31A**: 26-31 [PMID: 7695974 DOI: 10.1016/0959-8049(94)00357-B]
- 32 **de Korte MA**, de Vries EG, Lub-de Hooge MN, Jager PL, Gietema JA, van der Graaf WT, Sluiter WJ, van Veldhuisen DJ, Suter TM, Sleijfer DT, Perik PJ. 111Indium-trastuzumab visualises myocardial human epidermal growth factor receptor 2 expression shortly after anthracycline treatment but not during heart failure: a clue to uncover the mechanisms of trastuzumab-related cardiotoxicity. *Eur J Cancer* 2007; **43**: 2046-2051 [PMID: 17719768]
- 33 **Behr TM**, Béhé M, Wörmann B. Trastuzumab and breast cancer. *N Engl J Med* 2001; **345**: 995-996 [PMID: 11575295 DOI: 10.1056/NEJM200109273451312]
- 34 **Perik PJ**, Lub-De Hooge MN, Gietema JA, van der Graaf WT, de Korte MA, Jonkman S, Kosterink JG, van Veldhuisen DJ, Sleijfer DT, Jager PL, de Vries EG. Indium-111-labeled trastuzumab scintigraphy in patients with human epidermal growth factor receptor 2-positive metastatic breast cancer. *J Clin Oncol* 2006; **24**: 2276-2282 [PMID: 16710024 DOI: 10.1200/JCO.2005.03.8448]
- 35 **Bennink RJ**, van den Hoff MJ, van Hemert FJ, de Bruin KM, Spijkerboer AL, Vanderheyden JL, Steinmetz N, van Eck-Smit BL. Annexin V imaging of acute doxorubicin cardiotoxicity (apoptosis) in rats. *J Nucl Med* 2004; **45**: 842-848 [PMID: 15136635]
- 36 **Panjrath GS**, Jain D. Monitoring chemotherapy-induced cardiotoxicity: role of cardiac nuclear imaging. *J Nucl Cardiol* 2006; **13**: 415-426 [PMID: 16750786 DOI: 10.1016/j.nuclcard.2006.03.002]
- 37 **Panjrath GS**, Patel V, Valdiviezo CI, Narula N, Narula J, Jain D. Potentiation of Doxorubicin cardiotoxicity by iron loading in a rodent model. *J Am Coll Cardiol* 2007; **49**: 2457-2464 [PMID: 17599610 DOI: 10.1016/j.jacc.2007.02.060]
- 38 **Saito K**, Takeda K, Imanaka-Yoshida K, Imai H, Sekine T, Kamikura Y. Assessment of fatty acid metabolism in taxan-induced myocardial damage with iodine-123 BMIPP SPECT: comparative study with myocardial perfusion, left ventricular function, and histopathological findings. *Ann Nucl Med* 2003; **17**: 481-488 [PMID: 14575384 DOI: 10.1007/BF03006439]
- 39 **Saito K**, Takeda K, Okamoto S, Okamoto R, Makino K, Tameda Y, Nomura Y, Maeda H, Ichihara T, Nakano T. Detection of doxorubicin cardiotoxicity by using iodine-123 BMIPP early dynamic SPECT: quantitative evaluation of early abnormality of fatty acid metabolism with the Rutland method. *J Nucl Cardiol* 2000; **7**: 553-561 [PMID: 11144469 DOI: 10.1067/mnc.2000.108351]
- 40 **Lee JC**, Platts DG, Huang YT, Slaughter RE. Positron emission tomography combined with computed tomography as an integral component in evaluation of primary cardiac lymphoma. *Clin Cardiol* 2010; **33**: E106-E108 [PMID: 20552627 DOI: 10.1002/clc.20725]
- 41 **Kaderli AA**, Baran I, Aydin O, Bicer M, Akpınar T, Ozkalemkas F, Yesilbursa D, Gullulu S. Diffuse involvement of the heart and great vessels in primary cardiac lymphoma. *Eur J Echocardiogr* 2010; **11**: 74-76 [PMID: 19759028 DOI: 10.1093/ejehocard/jep111]
- 42 **Weijs LE**, Arsos G, Baarslag HJ, Wittebol S, de Klerk JM. Pericardial involvement in a non-Hodgkin lymphoma patient: coregistered FDG-PET and CT imaging. *Eur Heart J* 2007; **28**: 2698 [PMID: 17567624]
- 43 **Nony P**, Guastalla JP, Rebattu P, Landais P, Lievre M, Bontemps L, Itti R, Beaune J, Andre-Fouet X, Janier M. In vivo measurement of myocardial oxidative metabolism and blood flow does not show changes in cancer patients undergoing doxorubicin therapy. *Cancer Chemother Pharmacol* 2000; **45**: 375-380 [PMID: 10803920 DOI: 10.1007/s002800051005]
- 44 **Borde C**, Kand P, Basu S. Enhanced myocardial fluorodeoxyglucose uptake following Adriamycin-based therapy: Evidence of early chemotherapeutic cardiotoxicity? *World J Radiol* 2012; **4**: 220-223 [PMID: 22761982 DOI: 10.4329/wjr.v4.i5.220]
- 45 **Lautamäki R**, Tipre D, Bengel FM. Cardiac sympathetic neuronal imaging using PET. *Eur J Nucl Med Mol Imaging* 2007; **34** Suppl 1: S74-S85 [PMID: 17479262 DOI: 10.1007/s00259-007-0442-1]
- 46 **Langer O**, Halldin C. PET and SPET tracers for mapping the cardiac nervous system. *Eur J Nucl Med Mol Imaging* 2002; **29**: 416-434 [PMID: 12002720 DOI: 10.1007/s002590100640]
- 47 **Merlet P**, Delforge J, Syrota A, Angevin E, Mazière B, Crouzel C, Valette H, Loisançe D, Castaigne A, Randé JL. Positron emission tomography with 11C CGP-12177 to assess beta-adrenergic receptor concentration in idiopathic dilated cardiomyopathy. *Circulation* 1993; **87**: 1169-1178 [PMID: 8096441 DOI: 10.1161/01.CIR.87.4.1169]
- 48 **Vesalainen RK**, Pietilä M, Tahvanainen KU, Jartti T, Teräs M, Nägren K, Lehtikoinen P, Huupponen R, Ukkonen H, Saraste M, Knuuti J, Voipio-Pulkki LM. Cardiac positron emission tomography imaging with [11C]hydroxyephedrine, a specific tracer for sympathetic nerve endings, and its functional correlates in congestive heart failure. *Am J Cardiol* 1999; **84**: 568-574 [PMID: 10482157 DOI: 10.1016/S0002-9149(99)00379-3]
- 49 **Hartmann F**, Ziegler S, Nekolla S, Hadamitzky M, Seyfarth M, Richardt G, Schwaiger M. Regional patterns of myocardial sympathetic denervation in dilated cardiomyopathy: an analysis using carbon-11 hydroxyephedrine and positron emission tomography. *Heart* 1999; **81**: 262-270 [PMID: 10026349]
- 50 **Popat S**, Smith IE. Therapy Insight: anthracyclines and trastuzumab--the optimal management of cardiotoxic side effects. *Nat Clin Pract Oncol* 2008; **5**: 324-335 [PMID: 18364726 DOI: 10.1038/ncponc1090]

P- Reviewer: Vinh-Hung V S- Editor: Song XX
L- Editor: Cant MR E- Editor: Lu YJ



Role of cardiac CTA in estimating left ventricular volumes and ejection fraction

Robin Man Singh, Balkrishna Man Singh, Jawahar Lal Mehta

Robin Man Singh, Department of Medicine, University of Louisville, Louisville, KY 40202, United States

Balkrishna Man Singh, Baptist Health Heart Institute, 9501 Baptist Health Drive, Little Rock, AR 72205, United States

Jawahar Lal Mehta, Division of Cardiology, University of Arkansas for Medical Sciences, Little Rock, AR 72205, United States

Author contributions: Singh RM performed a thorough review of the subject with initial writing and review; Singh BM helped to review and edit the article; Mehta JL helped to guide the review and make constructive revision in the article.

Correspondence to: Balkrishna Man Singh, MD, FACC, Baptist Health Heart Institute, 9501 Baptist Health Drive, Suite 600, Little Rock, AR 72205, United States. bkmansingh@yahoo.com
Telephone: +1-501-3505242 Fax: +1-501-9781996

Received: January 20, 2014 Revised: July 7, 2014

Accepted: July 17, 2014

Published online: March 28, 2015

Abstract

Left ventricular ejection fraction (LVEF) is an important predictor of cardiac outcome and helps in making important diagnostic and therapeutic decisions such as the treatment of different types of congestive heart failure or implantation of devices like cardiac resynchronization therapy-defibrillator. LVEF can be measured by various techniques such as transthoracic echocardiography, contrast ventriculography, radionuclide techniques, cardiac magnetic resonance imaging and cardiac computed tomographic angiography (CTA). The development of cardiac CTA using multi-detector row CT (MDCT) has seen a very rapid improvement in the technology for identifying coronary artery stenosis and coronary artery disease in the last decade. During the acquisition, processing and analysis of data to study coronary anatomy, MDCT provides a unique opportunity to measure left ventricular volumes and LVEF simultaneously with the same data set without the need for additional contrast or radiation exposure. The develop-

ment of semi-automated and automated software to measure LVEF has now added uniformity, efficiency and reproducibility of practical value in clinical practice rather than just being a research tool. This article will address the feasibility, the accuracy and the limitations of MDCT in measuring LVEF.

© 2015 Baishideng Publishing Group Inc. All rights reserved.

Key words: Stroke volume; Ventricular ejection fraction; Computerized tomography; X ray

Core tip: Left ventricular ejection fraction (LVEF) is an important predictor of cardiac morbidity and mortality. Different noninvasive and invasive techniques are now available to measure LVEF. Multi-detector row CT (MDCT) has seen a very rapid improvement in the technology for identifying coronary artery stenosis. Using the same data set without additional contrast or radiation exposure, MDCT provides a unique opportunity to measure LV volumes and LVEF with great reliability and adds incremental value. This article will address the feasibility, the accuracy and the limitations of MDCT in measuring LVEF.

Original sources: Singh RM, Singh BM, Mehta JL. Role of cardiac CTA in estimating left ventricular volumes and ejection fraction. *World J Radiol* 2014; 6(9): 669-676 Available from: URL: <http://www.wjgnet.com/1949-8470/full/v6/i9/669.htm> DOI: <http://dx.doi.org/10.4329/wjr.v6.i9.669>

INTRODUCTION

Ischemic heart disease (IHD) is the leading cause of morbidity and mortality in developed countries^[1]. LVEF can provide valuable diagnostic, prognostic and therapeutic information^[2,3]. LVEF, LV volume and mass are inde-

pendent cardiac predictors of morbidity and mortality in patients with IHD^[2-4]. LVEF is an important parameter which is needed to make clinical decisions to guide medical or surgical therapy, and assess prognosis and outcome^[5]. Various noninvasive and invasive techniques have evolved over time to measure LVEF and cardiac volumes such as echocardiography^[6,7], radionuclide ventriculography^[8], cardiac MRI^[9,10], and contrast ventriculography (CVG) in patients undergoing invasive cardiac catheterization. Echocardiography is the most commonly used technique to measure ventricular dimensions and LVEF in clinical practice, due to its ease, cost, portability, reproducibility, noninvasive nature and lack of radiation or contrast exposure. In patients undergoing cardiac computed tomographic angiography (CTA) to study CAD, it is now feasible to measure LV volume and LVEF using the same data set without the need for additional contrast or radiation exposure. Single detector row helical computed tomography (CT)^[11] has been used to measure LVEF. However, this technique has limitations in studying coronary anatomy. Electron beam CT (EBCT)^[12,13], with high temporal resolution of 50 milliseconds seems to give good measurement of LVEF, but the superiority of MDCT over EBCT in the detection of coronary stenosis in clinical practice has resulted in MDCT being the preferred imaging modality amongst cardiac CTA to detect coronary artery stenosis due to its ability for retrospective gating and higher spatial resolution despite lower temporal resolution. MDCT has been used to measure LVEF^[14,15] and has been shown to be in good agreement with other techniques such as echocardiography, CVG, radionuclide techniques and MRI.

FEASIBILITY OF MDCT TO MEASURE LV VOLUMES AND LVEF

Rapid developments in both the hardware and software in MDCT technology have led to an increase in the use of this technology to detect CAD. The 16 slice CT scanner made it feasible to complete the cardiac scan with 1 breath hold time. However, it was the development of the 64 slice scanner that made it possible to obtain sub-millimeter slice thickness with a high level of spatial resolution in the X, Y and Z axis along with a significant improvement in temporal resolution. Three-dimensional isometric data sets (voxel) of nearly 0.5 mm each are now possible with the 64 slice or higher scanners due to its ability to post-process and reconstruct images in any plane without image distortion. Electrocardiographic gating during image acquisition and the ability to perform retrospective gating allows acquisition of three-dimensional volumetric data in relation to time reference and cardiac cycle, making it a truly four-dimensional data set. The development of 64 to 312 slice scanners have made it possible to complete the scan not only in one full breath, but also within 1-2 cardiac cycles, making it less prone to registration artifacts due to arrhythmias or breathing.

Developments in software technology have made it possible to post-process and create multi-planar reconstructions from these large numbers of original axial images in a very time efficient manner. This has made it possible to obtain reliable coronary anatomy imaging in most cases. Although limited by both spatial and temporal resolution compared to invasive coronary angiography, this technique of noninvasive coronary angiography by MDCT has come as close as possible to defining coronary anatomy and stenosis without the need for invasive cardiac catheterization in many cases. Hence, MDCT is being increasingly used in the evaluation of chest pain to detect CAD in appropriate subsets of patients.

Excellent visualization of bypass grafts and the 3-dimensional relationship between anomalous coronary artery origin and course have made this the test of choice for evaluation of bypass grafts and coronary anomalies. The study of pulmonary venous anatomy prior to pulmonary vein isolation ablation procedures and the integration of MDCT images in the electrophysiology laboratory help expedite the ablation procedure. Similarly, detailed analysis of the cardiac venous anatomy and identification of the lateral marginal vein are helpful in the implantation of CRT-D.

Noninvasive coronary angiography is the most common indication for cardiac CTA^[16-18]. The same data set is now available to measure LV volumes and LVEF using retrospective gating and identify the end-systolic and end-diastolic frames. Typically, 8 phases of cardiac cycles are analyzed for coronary angiography, and this is usually sufficient for LVEF measurement as well. Additional phase analysis can be performed if needed. Reconstruction of the images at 0%, 12.5%, 25%, 37.5%, 50%, 62.5%, 75% and 87.5% phases of the cardiac cycle are automatically post-processed. In the manual technique, the short axis images of the LV cavity (multi-planar reconstruction) are arranged from the 0% to 87.5% phases and usually the 0% phase correlates with the end diastolic phase and the 37.5% phase correlates with the end-systolic phase. Using these multiphase reconstructions, the software can be used to play a cine loop of the LV systolic function.

In the semi-manual method, LV cavity reconstruction is carried out by multi-planar reconstruction in the 4 chamber and 2 chamber views. Using the ellipsoid volumetric calculation by tracing the endocardial border, LV volumes are measured both in end-diastole (LVEDV) and end-systole (LVESV) in 4 chamber, 2 chamber and biplane views. LVEF is measured as $\text{LVEDV} - \text{LVESV} / \text{LVEDV}$ (Figure 1).

Contrast opacification of the LV is excellent during coronary CTA and this allows for good endocardial separation from the contrast filled LV cavity. The development of newer software which identifies the contrast density separation of the LV cavity from the myocardium has allowed semi-automated to fully automated measurements of LV volume and LVEF. One such technique allows an automated recognition and calculation of LVEDV and LVESV (Figure 2).

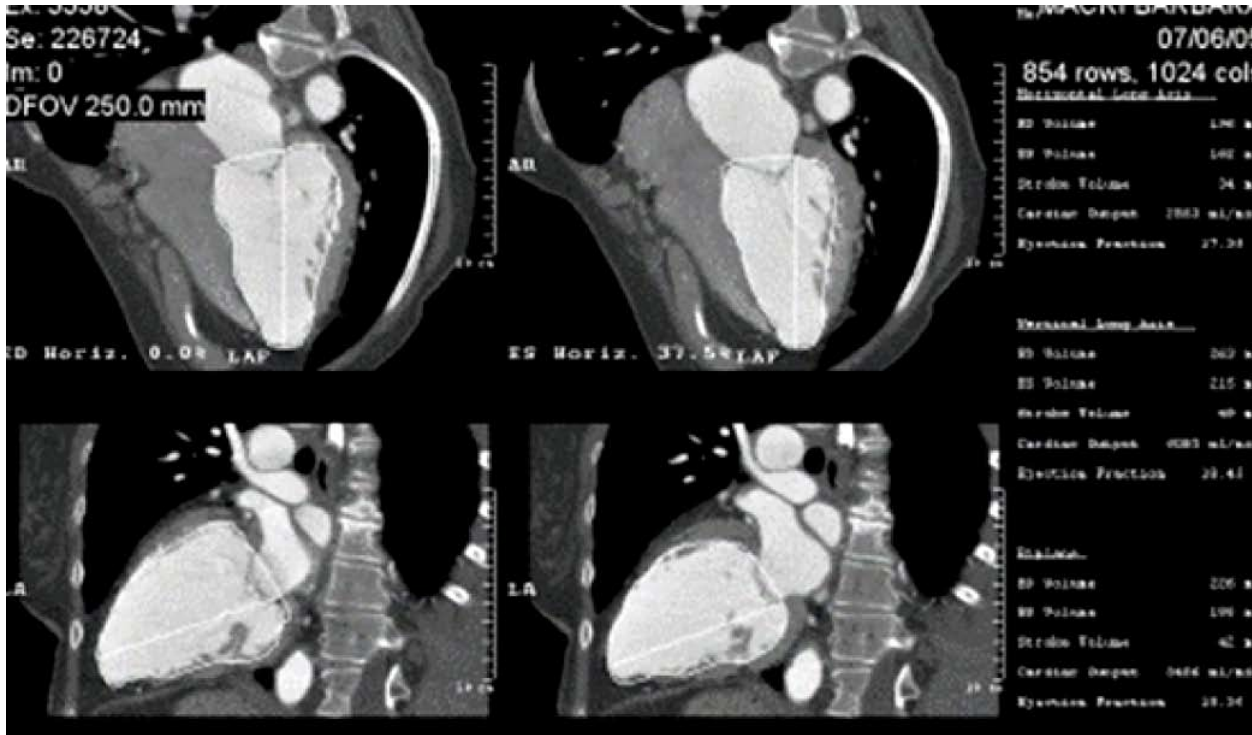


Figure 1 Multi-planar reconstruction of left ventricular cavity in 4 chamber and 2 chamber views and semi-automated calculation of left ventricular volume in both end-systole and end-diastole in biplane and 4 and 2 chamber views by the area length method. Patient with cardiomyopathy and a very low left ventricular ejection fraction of 0.20.

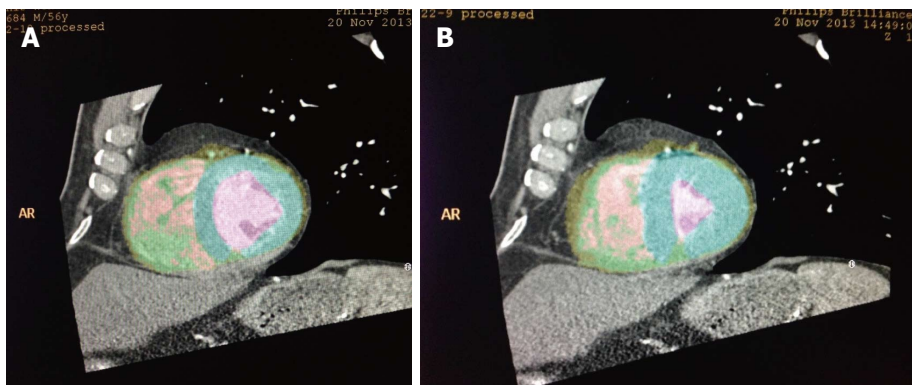


Figure 2 Automatic recognition of left ventricular cavity by automated software to calculate left ventricular volumes in end-diastole (A) and end-systole (B) to calculate left ventricular ejection fraction.

Different vendors have different software to calculate the LV volumes and LVEF. In the example shown in Figure 2, there is automatic endocardial edge detection and the software calculates the LVEDV, LVESV and LVEF as shown in Figure 3. The time-volume curve also shows the quality of the data obtained and good data are characterized by a smooth change in the LVEDV to LVESV and then back to the LVEDV as shown in Figure 3.

Figure 4 shows some compromise in the time volume data.

Radiation exposure is a major concern during cardiac computed tomographic angiography, but it can be substantially diminished by dose modulation. Dose modulation is a technique which minimizes radiation exposure

during cardiac computed tomographic angiography by prospective gating at phases which are usually not important for analysis of coronary anatomy. Since most of the coronary anatomy is analyzed around 75% phase (the phase where coronary arteries appear to have the least motion), radiation exposure can be substantially diminished by more than 50% by decreasing the current (milliAmperes) of radiation exposure at phases away from the 75% phase. Despite the use of dose modulation, left ventricular contrast opacification is adequate for endocardial definition even during systole and does not seem to compromise the capacity to measure ventricular volumes both in end-diastole and end-systole, and left ventricular ejection fraction.

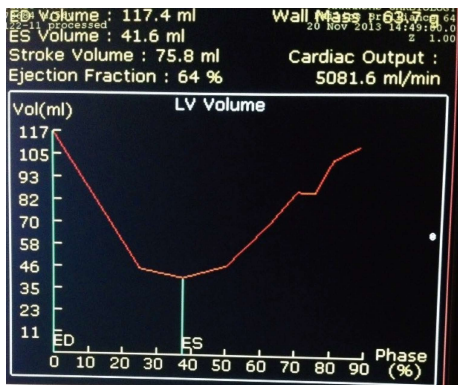


Figure 3 Time-volume curve display of left ventricular volume over different phases of the cardiac cycle (R-R interval) and calculation of left ventricular ejection fraction is displayed automatically. Please note the smooth normal curve without registration artifact.

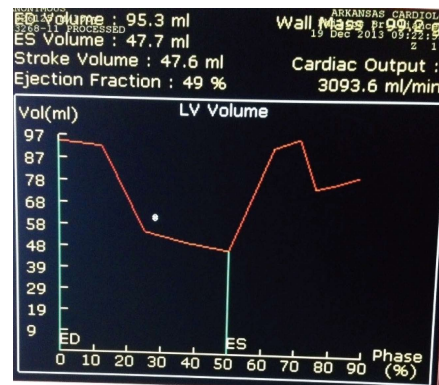


Figure 4 Shows some compromise in the time volume data as shown by the lack of smooth transition of the volume curve, and this likely represents some registration artifact towards the later part of diastole due to arrhythmias such as atrial fibrillation or frequent PVCs. This can lead to errors in the calculation of Left ventricular ejection fraction (LVEF). A quick look at the analysis of this time volume curve data is helpful to assess the quality of the data obtained for LVEF assessment and its limitations.

COMPARISON OF THE TECHNIQUES OF LV VOLUME MEASUREMENT AND LVEF BY VARIOUS METHODS

MDCT using retrospective gating allows for LV volume and LVEF measurements, which appear to have a good correlation with cardiac MRI, currently accepted as the gold standard^[14,15,19-22]. LVEF measurement is possible utilizing different noninvasive and invasive techniques such as echocardiography, radionuclide techniques, cardiac MRI, and CVG. Echocardiography is the most commonly used technique to measure LVEF. Echocardiography may have technical, acoustic and operator limitations^[23]. It is also subject to alteration in ventricular geometry^[6,7]. Nuclear imaging using a SPECT gating also has limitations due to restrictions in both the spatial resolution and the definition of endocardial borders within the myocardium^[8,24]. However, for the purpose of LVEF measurement, the estimation of LV endocardial contour is done by radioactive count, and anatomical resolution is not always so important. Prospective gating EBCT has advantages in measuring LVEF because of high temporal resolution, but has limited spatial resolution and is inferior in defining coronary anatomy compared to MDCT. Although cardiac MRI appears to be more accurate in measuring left ventricular volume and LVEF, the technique has limitations in defining coronary anatomy compared to MDCT. This modality also takes a much longer time, is more expensive, and is not feasible in some patients who have implanted devices, non-compatible with MRI. Invasive contrast ventriculography (CVG) has limitations due to the invasive nature of the test. In addition, calculation of the left ventricular volume is based on the assumption of the shape of the ventricle, and this may not be accurate in patients with an altered left ventricular geometry. MDCT is frequently used as a noninvasive coronary angiographic tool to evaluate suspected symptomatic CAD patients. Simultaneous measurement of LVEF using the same data provides a unique opportunity and can add incremental value to the test.

LV volume measurements are possible using various techniques. Current automated software allows LV volume measurement by MDCT based on short axis image reformations as in echocardiography and cardiac MRI. For calculation of LV volume measurement and LVEF, identification of the end-diastolic and end-systolic phases is needed. This is made possible by retrospective gating and post-processing of the images at various phases. In our experience, phase reconstructions at 12.5% phase apart seem to suffice, but reconstructions at every 5% phase of the R-R interval can also be done, but will be more time-consuming. Short axis images at the mid ventricular level are obtained in a semi-automated technique. In the current automated software, end-systolic and end-diastolic short axis images are identified automatically as noted in Figure 2. LV volumes and LVEF are then measured automatically as shown in Figure 3.

The LV volume and EF can be measured by different methods depending on the technique used. The area length method is a technique used primarily in invasive left ventriculography and in echocardiography, as an ellipsoid model is used to measure the LV volume. This technique can also be used in some semi-automated techniques in MDCT using volume measurements in four chamber, two chamber and biplane views. The Simpson method is also commonly used in cardiac MRI, EBCT, MDCT and echocardiography.

The automated technique in MDCT, as shown in Figure 2, employs a threshold-based region growing algorithm. This allows identification of the cardiac chambers and their volume based on the separation of myocardium from LV cavity based on the separation of contrast and tissue signal density. LV volume measurements based on this method do not depend on geometric assumptions and are more accurate than area length method. Since cardiac CTA by MDCT is carried out primarily for coronary angiography, the current technique, volume and timing of contrast injection along with saline bolus allows

for good opacification of the LV. The use of 64 slice or higher MDCT with rapid scan times provide superior results. The automated technique seems to work well even with dose modulation without any limitations of the detection of the contrast edge. Once the LVEDV and LVESV are measured, LVEF is calculated as discussed earlier. The time-volume curve allows the display of LV volume change over the different phases which provide additional qualitative information about the study. It can identify limitations due to arrhythmias, poor contrast opacification or obesity.

ACCURACY OF MDCT IN MEASURING LVEF

In our study of 52 patients, we compared the 16 row detector MDCT with TTE to measure LV volume and LVEF and found MDCT to be a useful tool for measuring LVEF^[25]. Biplane measurements by these two techniques correlated better for LV volumes and LVEF, but MDCT gave higher values compared to TTE and this has also been shown in other studies using 64 slice^[26,27]. Many other subsequent studies have found MDCT to be a useful tool for measuring LVEF when compared with TTE.

The feasibility of accurate assessment of LVEF and volume has been shown using a single heartbeat 320-row MDCT detector^[28]. Similarly in a comparison of 128 slice CT compared to echocardiography, MDCT provided comparable results to echocardiography for LVEF and LV volumes, although LV volume was overestimated by MDCT compared to echocardiography^[29]. A recent study using a head to head comparison of LVEF measurement with 64-slice MDCT, biplane LV CVG and both 2D and 3D TTE found 64-slice MDCT to be more accurate than LV CVG and TTE. This study used cardiac MRI as the reference standard for measuring LVEF^[30]. However, it should be noted that gadolinium-enhanced cardiac MRI carries a risk of nephrogenic systemic fibrosis in patients with renal failure, and is, thus a limiting factor in this patient population, just as contrast-induced nephropathy would be a concern with MDCT in some patients.

Semi-automatic software to measure LV volume by MDCT has been found to have good reproducibility for LVEF measurement, but it is important to understand the limitations of MDCT in semi-automatic and automatic measurement of LVEF^[31].

In a comparison of SPECT versus MDCT to measure LVEF in 292 patients, MDCT gave significantly higher LVEF compared to SPECT and the values may not be interchangeable between different methods of measurement^[32]. In another small study of 15 patients, MDCT compared well with biplane LV CVG for measuring LVEF^[33]. There appears to be a minor systematic overestimation of LVEDV and LVESV, and underestimation of EF of 2.1% by MDCT compared to cardiac MRI^[34]. LVEF measurement in a wide spectrum of LV dysfunction requires further validation compared to other techniques such as EBCT^[35]. Studies comparing LVEF

measurement by simultaneous multimodality images such as echocardiography, LV CVG and SPECT are limited^[36].

A recent systematic review and meta-analysis of 27 eligible studies concluded that MDCT can measure LVEF accurately compared to MRI and TTE^[37]. Twelve studies compared MDCT with MRI and 15 studies compared MDCT with TTE to measure LVEF in this meta-analysis, and MDCT appears to be a useful tool for measuring LVEF in patients undergoing coronary CTA. Simultaneous measurement of LVEF at the time of coronary CTA by MDCT seems to provide additional incremental prognostic value^[38].

LIMITATIONS OF MDCT IN LVEF MEASUREMENT AND TECHNIQUES TO IMPROVE THESE LIMITATIONS

It should be noted that the current limitations of MDCT do not favor the use of MDCT for the sole purpose of LVEF measurement. This is due to a myriad of reasons, including radiation and contrast exposure, cost, risks of iodine allergy and potential renal failure. The risk of contrast induced-nephropathy is increased in patients with preexisting renal dysfunction, diabetes, heart failure, increased age and other comorbid conditions. The high volume of contrast administered for cardiac CTA may also increase the risk of contrast-induced nephropathy in high risk patients. Pretest risk assessment and good hydration are important in all patients undergoing a contrast study such as cardiac CTA, and for that reason many patients may not be candidates for cardiac CTA for fear of contrast-induced nephropathy and its consequences. The technique has limitations in patients with obesity, renal failure, arrhythmias and difficult breath hold time. On the other hand, simultaneous measurements of LVEF in patients undergoing cardiac CTA for noninvasive coronary angiography are feasible, reproducible, and fairly accurate compared to other modalities.

High temporal and spatial resolution is needed for accurate measurement of LVEF^[39]. MDCT has good spatial resolution, but has a limited temporal resolution of 125-250 milliseconds compared to EBCT^[40] or MRI and can cause motion artifacts^[41]. Image quality in patients with higher heart rate may be of poor quality due to limited temporal resolution and may compromise the accuracy^[42,43].

MDCT with temporal resolution of 20 milliseconds would be desirable to avoid motion artifacts, but is not yet feasible with current technology^[44]. In the early studies using 4 row MDCT, LVEF measurement was underestimated due to poor temporal resolution, and overestimation of LVESV was found as compared to LV CVG and MRI^[45,46].

An increase in temporal resolution is a desirable goal to improve the quality of MDCT, and two strategies have been utilized so far. First, gantry rotation time is shortened with the new scanners^[16,47,48] and secondly, more

gantry rotations allowing more R-R intervals for image reconstruction are available using multi-segmental image reconstruction algorithms^[49,50]. Multiple cardiac cycles are used to create image reconstruction in this method, and thus may improve temporal resolution to less than 100 milliseconds. However, significant variations in the R-R cycle could be a limitation in the multi-segmental image reconstruction due to non-uniformity of ventricular contraction.

Rapid gantry rotations of up to 0.33 s per rotation attained with newer MDCTs can also improve the temporal resolution^[51]. Dual source CT can also increase the temporal resolution to 83 milliseconds in single segmental reconstructions^[52].

Lower heart rates are needed to obtain better images by MDCT to evaluate coronary anatomy, and consequently beta-blockers are frequently used to slow the heart rate during image acquisition. This introduces the effect of heart rate change and negative inotropic effects on LVEF measurement^[42]. Dual-source CT is less dependent on the heart rate and may improve LVEF measurement. The patients with arrhythmia such as atrial fibrillation and frequent premature ventricular complexes may produce significant registration artifacts and may introduce error in the calculation of LVEF. However, with the use of recent higher slice MDCT, this should be less of a concern as most of the data acquisition can be completed within one or two cardiac cycles.

Techniques to reduce radiation exposure are possible using higher detector rows and faster rotation times. Reduced tube current during unnecessary cardiac phase (dose modulation) helps reduce radiation^[53]. Since most of the coronary anatomy analysis is done in late diastole close to 75% phase, this normally does not compromise analysis of the coronary anatomy. The degree of contrast density separation of the LV cavity from the myocardium is adequate even with dose modulation in systole for the purpose of LVESV calculation and should not compromise LVEF measurement. Analysis of the quality of data and the LV time volume curve may be helpful in assessing the quality of the study.

LVEF measurement by MDCT is based on a volumetric data set. LVEF measurement should be less susceptible to error in patients with LV enlargement or deformity. LVEF measurement by MDCT correlates well with MRI in patients with LV dysfunction or LV dilation^[54].

Cardiac MRI is considered the gold standard for the measurement of LV volume, LVEF and regional wall motion assessment. Lack of radiation and contrast exposure, along with higher temporal resolution are advantageous. However, MDCT requires a short breath hold time, and can be performed even in patients with pacemakers and implanted defibrillators. In contrast to MDCT using single breath hold image acquisition, cardiac MRI needs multiple short breath holds for cine MRI. Both techniques are susceptible to arrhythmias with image degradation. In addition, MDCT is superior to

cardiac MRI for coronary imaging due to a higher spatial resolution, and it is in this group of patients that LVEF measurement can be performed to provide additional clinical information. Processing time may also be a limiting factor in some cases, but now with the use of automated software, the LVEF calculation is faster and likely to improve further.

CONCLUSION

LVEF measurement at the time of cardiac CTA for the study of coronary anatomy using MDCT seems reasonable given the feasibility, reproducibility, and accuracy of the data. This information can be obtained at the time of coronary imaging without the need for additional radiation or contrast exposure. Developments in hardware, software and work stations, along with the availability of automated techniques to measure LVESV and LVEDV have made this technique time efficient. The use of MDCT for the sole purpose of LVEF measurement is not reasonable at this time given the radiation exposure, contrast exposure and cost. Instead, this should be used as a complimentary technique to measure LVEF in patients undergoing cardiac CTA for noninvasive coronary angiography.

REFERENCES

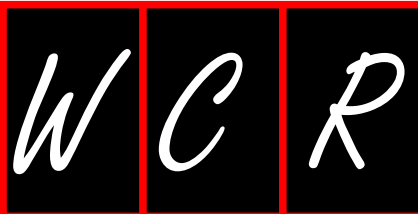
- 1 **Murray CJ**, Lopez AD. Alternative projections of mortality and disability by cause 1990-2020: Global Burden of Disease Study. *Lancet* 1997; **349**: 1498-1504 [PMID: 9167458 DOI: 10.1016/S0140-6736(96)07492-2]
- 2 **Sanz G**, Castañer A, Betriu A, Magriña J, Roig E, Coll S, Paré JC, Navarro-López F. Determinants of prognosis in survivors of myocardial infarction: a prospective clinical angiographic study. *N Engl J Med* 1982; **306**: 1065-1070 [PMID: 7070402 DOI: 10.1056/NEJM198205063061801]
- 3 **White HD**, Norris RM, Brown MA, Brandt PW, Whitlock RM, Wild CJ. Left ventricular end-systolic volume as the major determinant of survival after recovery from myocardial infarction. *Circulation* 1987; **76**: 44-51 [PMID: 3594774 DOI: 10.1161/01.CIR.76.1.44]
- 4 **Hammermeister KE**, DeRouen TA, Dodge HT. Variables predictive of survival in patients with coronary disease. Selection by univariate and multivariate analyses from the clinical, electrocardiographic, exercise, arteriographic, and quantitative angiographic evaluations. *Circulation* 1979; **59**: 421-430 [PMID: 761323]
- 5 Risk stratification and survival after myocardial infarction. *N Engl J Med* 1983; **309**: 331-336 [PMID: 6866068]
- 6 **Buck T**, Hunold P, Wentz KU, Tkalec W, Nesser HJ, Erbel R. Tomographic three-dimensional echocardiographic determination of chamber size and systolic function in patients with left ventricular aneurysm: comparison to magnetic resonance imaging, cineventriculography, and two-dimensional echocardiography. *Circulation* 1997; **96**: 4286-4297 [PMID: 9416895 DOI: 10.1161/01.CIR.96.12.4286]
- 7 **Qin JX**, Jones M, Shiota T, Greenberg NL, Tsujino H, Firstenberg MS, Gupta PC, Zetts AD, Xu Y, Ping Sun J, Cardon LA, Odabashian JA, Flamm SD, White RD, Panza JA, Thomas JD. Validation of real-time three-dimensional echocardiography for quantifying left ventricular volumes in the presence of a left ventricular aneurysm: in vitro and in vivo studies. *J Am Coll Cardiol* 2000; **36**: 900-907 [PMID: 10987618]

- DOI: 10.1016/S0735-1097(00)00793-2]
- 8 **Bavelaar-Croon CD**, Kayser HW, van der Wall EE, de Roos A, Dibbets-Schneider P, Pauwels EK, Germano G, Atsma DE. Left ventricular function: correlation of quantitative gated SPECT and MR imaging over a wide range of values. *Radiology* 2000; **217**: 572-575 [PMID: 11058662 DOI: 10.1148/radiology.217.2.r00nv15572]
 - 9 **Pattynama PM**, Lamb HJ, van der Velde EA, van der Wall EE, de Roos A. Left ventricular measurements with cine and spin-echo MR imaging: a study of reproducibility with variance component analysis. *Radiology* 1993; **187**: 261-268 [PMID: 8451425]
 - 10 **Bellenger NG**, Burgess MI, Ray SG, Lahiri A, Coats AJ, Cleland JG, Pennell DJ. Comparison of left ventricular ejection fraction and volumes in heart failure by echocardiography, radionuclide ventriculography and cardiovascular magnetic resonance; are they interchangeable? *Eur Heart J* 2000; **21**: 1387-1396 [PMID: 10952828 DOI: 10.1053/euhj.2000.2011]
 - 11 **Mochizuki T**, Murase K, Higashino H, Koyama Y, Doi M, Miyagawa M, Nakata S, Shimizu K, Ikezoe J. Two- and three-dimensional CT ventriculography: a new application of helical CT. *AJR Am J Roentgenol* 2000; **174**: 203-208 [PMID: 10628479]
 - 12 **Lipton MJ**, Higgins CB, Farmer D, Boyd DP. Cardiac imaging with a high-speed Cine-CT Scanner: preliminary results. *Radiology* 1984; **152**: 579-582 [PMID: 6540463]
 - 13 **Lipton MJ**, Farmer DW, Killebrew EJ, Bouchard A, Dean PB, Ringertz HG, Higgins CB. Regional myocardial dysfunction: evaluation of patients with prior myocardial infarction with fast CT. *Radiology* 1985; **157**: 735-740 [PMID: 4059561]
 - 14 **Juergens KU**, Grude M, Maintz D, Fallenberg EM, Wichter T, Heindel W, Fischbach R. Multi-detector row CT of left ventricular function with dedicated analysis software versus MR imaging: initial experience. *Radiology* 2004; **230**: 403-410 [PMID: 14668428 DOI: 10.1148/radiol.2302030042]
 - 15 **Grude M**, Juergens KU, Wichter T, Paul M, Fallenberg EM, Muller JG, Heindel W, Breithardt G, Fischbach R. Evaluation of global left ventricular myocardial function with electrocardiogram-gated multidetector computed tomography: comparison with magnetic resonance imaging. *Invest Radiol* 2003; **38**: 653-661 [PMID: 14501493 DOI: 10.1097/01.rli.0000077070.40713.76]
 - 16 **Raff GL**, Gallagher MJ, O'Neill WW, Goldstein JA. Diagnostic accuracy of noninvasive coronary angiography using 64-slice spiral computed tomography. *J Am Coll Cardiol* 2005; **46**: 552-557 [PMID: 16053973 DOI: 10.1016/j.jacc.2005.05.056]
 - 17 **Achenbach S**, Giesler T, Ropers D, Ulzheimer S, Derlien H, Schulte C, Wenkel E, Moshage W, Bautz W, Daniel WG, Kalender WA, Baum U. Detection of coronary artery stenoses by contrast-enhanced, retrospectively electrocardiographically-gated, multislice spiral computed tomography. *Circulation* 2001; **103**: 2535-2538 [PMID: 11382719 DOI: 10.1161/01.CIR.103.21.2535]
 - 18 **Ropers D**, Baum U, Pohle K, Anders K, Ulzheimer S, Ohnesorge B, Schlundt C, Bautz W, Daniel WG, Achenbach S. Detection of coronary artery stenoses with thin-slice multidetector row spiral computed tomography and multiplanar reconstruction. *Circulation* 2003; **107**: 664-666 [PMID: 12578863 DOI: 10.1161/01.CIR.0000055738.31551.A9]
 - 19 **Halliburton SS**, Petersilka M, Schwartzman PR, Obuchowski N, White RD. Evaluation of left ventricular dysfunction using multiphasic reconstructions of coronary multi-slice computed tomography data in patients with chronic ischemic heart disease: validation against cine magnetic resonance imaging. *Int J Cardiovasc Imaging* 2003; **19**: 73-83 [PMID: 12602485 DOI: 10.1023/A: 1021793420007]
 - 20 **Koch K**, Oellig F, Kunz P, Bender P, Oberholzer K, Mildenerberger P, Hake U, Kreitner KF, Thelen M. [Assessment of global and regional left ventricular function with a 16-slice spiral-CT using two different software tools for quantitative functional analysis and qualitative evaluation of wall motion changes in comparison with magnetic resonance imaging]. *Rofo* 2004; **176**: 1786-1793 [PMID: 15573290 DOI: 10.1055/s-2004-813730]
 - 21 **Mahnken AH**, Koos R, Katoh M, Spuentrup E, Busch P, Wildberger JE, Kühl HP, Günther RW. Sixteen-slice spiral CT versus MR imaging for the assessment of left ventricular function in acute myocardial infarction. *Eur Radiol* 2005; **15**: 714-720 [PMID: 15682266 DOI: 10.1007/s00330-004-2592-x]
 - 22 **Heuschmid M**, Rothfuss J, Schröder S, Küttner A, Fenchel M, Stauder N, Mahnken AH, Burgstahler C, Miller S, Claussen CD, Kopp AF. [Left ventricular functional parameters: comparison of 16-slice spiral CT with MRI]. *Rofo* 2005; **177**: 60-66 [PMID: 15657821 DOI: 10.1055/s-2004-813768]
 - 23 **Malm S**, Frigstad S, Sagberg E, Larsson H, Skjaerpe T. Accurate and reproducible measurement of left ventricular volume and ejection fraction by contrast echocardiography: a comparison with magnetic resonance imaging. *J Am Coll Cardiol* 2004; **44**: 1030-1035 [PMID: 15337215 DOI: 10.1016/j.jacc.2004.05.068]
 - 24 **Manrique A**, Faraggi M, Véra P, Vilain D, Lebtahi R, Cribier A, Le Guludec D. 201Tl and 99mTc-MIBI gated SPECT in patients with large perfusion defects and left ventricular dysfunction: comparison with equilibrium radionuclide angiography. *J Nucl Med* 1999; **40**: 805-809 [PMID: 10319754]
 - 25 **Bansal D**, Singh RM, Sarkar M, Sureddi R, Mcbreen KC, Griffis T, Sinha A, Mehta JL. Assessment of left ventricular function: comparison of cardiac multidetector-row computed tomography with two-dimension standard echocardiography for assessment of left ventricular function. *Int J Cardiovasc Imaging* 2008; **24**: 317-325 [PMID: 17701445 DOI: 10.1007/s10554-007-9252-6]
 - 26 **Lessick J**, Ghersin E, Abadi S, Yalonetsky S. Accuracy of the long-axis area-length method for the measurement of left ventricular volumes and ejection fraction using multidetector computed tomography. *Can J Cardiol* 2008; **24**: 685-689 [PMID: 18787718 DOI: 10.1016/S0828-282X(08)70666-4]
 - 27 **Ko SM**, Kim YJ, Park JH, Choi NM. Assessment of left ventricular ejection fraction and regional wall motion with 64-slice multidetector CT: a comparison with two-dimensional transthoracic echocardiography. *Br J Radiol* 2010; **83**: 28-34 [PMID: 19546180 DOI: 10.1259/bjr/38829806]
 - 28 **de Graaf FR**, Schuijff JD, van Velzen JE, Nacifora G, Kroft LJ, de Roos A, Schalij MJ, Jukema JW, van der Wall EE, Bax JJ. Assessment of global left ventricular function and volumes with 320-row multidetector computed tomography: A comparison with 2D-echocardiography. *J Nucl Cardiol* 2010; **17**: 225-231 [PMID: 19953354 DOI: 10.1007/s12350-009-9173-y]
 - 29 **Lim SJ**, Choo KS, Park YH, Kim JS, Kim JH, Chun KJ, Jeong DW. Assessment of left ventricular function and volume in patients undergoing 128-slice coronary CT angiography with ECG-based maximum tube current modulation: a comparison with echocardiography. *Korean J Radiol* 2011; **12**: 156-162 [PMID: 21430931 DOI: 10.3348/kjr.2011.12.2.156]
 - 30 **Greupner J**, Zimmermann E, Grohmann A, Dübel HP, Althoff TF, Borges AC, Rutsch W, Schlattmann P, Hamm B, Dewey M. Head-to-head comparison of left ventricular function assessment with 64-row computed tomography, biplane left cineventriculography, and both 2- and 3-dimensional transthoracic echocardiography: comparison with magnetic resonance imaging as the reference standard. *J Am Coll Cardiol* 2012; **59**: 1897-1907 [PMID: 22595410 DOI: 10.1016/j.jacc.2012.01.046]
 - 31 **van Ooijen PM**, de Jonge GJ, Oudkerk M. Informatics in radiology: postprocessing pitfalls in using CT for automatic and semiautomatic determination of global left ventricular function. *Radiographics* 2012; **32**: 589-599 [PMID: 22323618 DOI: 10.1148/rg.322115058]
 - 32 **Abadi S**, Brook OR, Rispler S, Frenkel A, Engel A, Keidar Z. Hybrid cardiac SPECT/64-slice CTA-derived LV function

- parameters: correlation and reproducibility assessment. *Eur J Radiol* 2010; **75**: 154-158 [PMID: 19443161 DOI: 10.1016/j.ejrad.2009.04.039]
- 33 **Chaosuwannakit N**, Rerkpattanapipat P, Wangsuphachart S, Srimahachota S. Reliability of the evaluation for left ventricular ejection fraction by ECG-gated multi-detector CT (MDCT): comparison with biplane cine left ventriculography. *J Med Assoc Thai* 2007; **90**: 532-538 [PMID: 17427532]
- 34 **Dewey M**, Müller M, Teige F, Hamm B. Evaluation of a semi-automatic software tool for left ventricular function analysis with 16-slice computed tomography. *Eur Radiol* 2006; **16**: 25-31 [PMID: 15965660 DOI: 10.1007/s00330-005-2817-7]
- 35 **Baik HK**, Budoff MJ, Lane KL, Bakhsheshi H, Brundage BH. Accurate measures of left ventricular ejection fraction using electron beam tomography: a comparison with radionuclide angiography, and cine angiography. *Int J Card Imaging* 2000; **16**: 391-398 [PMID: 11215924 DOI: 10.1023/A:1026536510821]
- 36 **Yamamuro M**, Tadamura E, Kubo S, Toyoda H, Nishina T, Ohba M, Hosokawa R, Kimura T, Tamaki N, Komeda M, Kita T, Konishi J. Cardiac functional analysis with multi-detector row CT and segmental reconstruction algorithm: comparison with echocardiography, SPECT, and MR imaging. *Radiology* 2005; **234**: 381-390 [PMID: 15670995 DOI: 10.1148/radiol.2342031271]
- 37 **Asferg C**, Usinger L, Kristensen TS, Abdulla J. Accuracy of multi-slice computed tomography for measurement of left ventricular ejection fraction compared with cardiac magnetic resonance imaging and two-dimensional transthoracic echocardiography: a systematic review and meta-analysis. *Eur J Radiol* 2012; **81**: e757-e762 [PMID: 22381439 DOI: 10.1016/j.ejrad.2012.02.002]
- 38 **de Graaf FR**, van Werkhoven JM, van Velzen JE, Antoni ML, Boogers MJ, Kroft LJ, de Roos A, Schaliq MJ, Jukema JW, van der Wall EE, Schuijff JD, Bax JJ. Incremental prognostic value of left ventricular function analysis over non-invasive coronary angiography with multidetector computed tomography. *J Nucl Cardiol* 2010; **17**: 1034-1040 [PMID: 20694585 DOI: 10.1007/s12350-010-9277-4]
- 39 **Setser RM**, Fischer SE, Lorenz CH. Quantification of left ventricular function with magnetic resonance images acquired in real time. *J Magn Reson Imaging* 2000; **12**: 430-438 [PMID: 10992310]
- 40 **Lipton MJ**. Quantitation of cardiac function by cine-CT. *Radiol Clin North Am* 1985; **23**: 613-626 [PMID: 3877947]
- 41 **Hong C**, Becker CR, Huber A, Schoepf UJ, Ohnesorge B, Knez A, Brüning R, Reiser MF. ECG-gated reconstructed multi-detector row CT coronary angiography: effect of varying trigger delay on image quality. *Radiology* 2001; **220**: 712-717 [PMID: 11526271]
- 42 **Schroeder S**, Kopp AF, Kuettner A, Burgstahler C, Herdeg C, Heuschmid M, Baumbach A, Claussen CD, Karsch KR, Seipel L. Influence of heart rate on vessel visibility in noninvasive coronary angiography using new multislice computed tomography: experience in 94 patients. *Clin Imaging* 2002; **26**: 106-111 [PMID: 11852217]
- 43 **Sechtem U**, Pflugfelder P, Higgins CB. Quantification of cardiac function by conventional and cine magnetic resonance imaging. *Cardiovasc Intervent Radiol* 1987; **10**: 365-373 [PMID: 3123062]
- 44 **Ritchie CJ**, Godwin JD, Crawford CR, Stanford W, Anno H, Kim Y. Minimum scan speeds for suppression of motion artifacts in CT. *Radiology* 1992; **185**: 37-42 [PMID: 1523332]
- 45 **Wintersperger BJ**, Hundt W, Knez A. Left ventricular systolic function assessed by ECG gated multirow-detector spiral computed tomography (multi-detector row CT): comparison to ventriculography. *Eur Radiol* 2002; **12**: S192
- 46 **Lüders F**, Fischbach R, Seifarth H, Wessling J, Heindel W, Juergens KU. [Dual-source computed tomography: effect on regional and global left ventricular function assessment compared to magnetic resonance imaging]. *Rofo* 2009; **181**: 962-969 [PMID: 19517343]
- 47 **Leber AW**, Knez A, von Ziegler F, Becker A, Nikolaou K, Paul S, Wintersperger B, Reiser M, Becker CR, Steinbeck G, Boekstegers P. Quantification of obstructive and nonobstructive coronary lesions by 64-slice computed tomography: a comparative study with quantitative coronary angiography and intravascular ultrasound. *J Am Coll Cardiol* 2005; **46**: 147-154 [PMID: 15992649 DOI: 10.1016/j.jacc.2005.03.071]
- 48 **Heuschmid M**, Küttner A, Flohr T, Wildberger JE, Lell M, Kopp AF, Schröder S, Baum U, Schaller S, Hartung A, Ohnesorge B, Claussen CD. [Visualization of coronary arteries in CT as assessed by a new 16 slice technology and reduced gantry rotation time: first experiences]. *Rofo* 2002; **174**: 721-724 [PMID: 12063601 DOI: 10.1055/s-2002-32227]
- 49 **Kachelriess M**, Kalender WA. Electrocardiogram-correlated image reconstruction from subsecond spiral computed tomography scans of the heart. *Med Phys* 1998; **25**: 2417-2431 [PMID: 9874836 DOI: 10.1118/1.598453]
- 50 **Boese JM**, Bahner ML, Albers J, van Kaick G. [Optimizing temporal resolution in CT with retrospective ECG gating]. *Radiologe* 2000; **40**: 123-129 [PMID: 10758625 DOI: 10.1007/s001170050020]
- 51 **Nieman K**, Cademartiri F, Lemos PA, Raaijmakers R, Pattynama PM, de Feyter PJ. Reliable noninvasive coronary angiography with fast submillimeter multislice spiral computed tomography. *Circulation* 2002; **106**: 2051-2054 [PMID: 12379572 DOI: 10.1161/01.CIR.0000037222.58317.3D]
- 52 **Achenbach S**, Ropers D, Kuettner A, Flohr T, Ohnesorge B, Bruder H, Theessen H, Karakaya M, Daniel WG, Bautz W, Kalender WA, Anders K. Contrast-enhanced coronary artery visualization by dual-source computed tomography-initial experience. *Eur J Radiol* 2006; **57**: 331-335 [PMID: 16426789 DOI: 10.1016/j.ejrad.2005.12.017]
- 53 **Jakobs TF**, Becker CR, Ohnesorge B, Flohr T, Suess C, Schoepf UJ, Reiser MF. Multislice helical CT of the heart with retrospective ECG gating: reduction of radiation exposure by ECG-controlled tube current modulation. *Eur Radiol* 2002; **12**: 1081-1086 [PMID: 11976849 DOI: 10.1007/s00330-001-1278-x]
- 54 **Barkhausen J**, Ruehm SG, Goyen M, Buck T, Laub G, Debatin JF. MR evaluation of ventricular function: true fast imaging with steady-state precession versus fast low-angle shot cine MR imaging: feasibility study. *Radiology* 2001; **219**: 264-269 [PMID: 11274568 DOI: 10.1148/radiology.219.1.r01a p12264]

P- Reviewer: Lai S, Nagamachi S S- Editor: Wen LL
L- Editor: Webster JR E- Editor: Lu YJ





Radiation pneumonitis after stereotactic radiation therapy for lung cancer

Hideomi Yamashita, Wataru Takahashi, Akihiro Haga, Keiichi Nakagawa

Hideomi Yamashita, Wataru Takahashi, Akihiro Haga, Keiichi Nakagawa, Department of Radiology, University of Tokyo Hospital, Tokyo 113-8655, Japan

Author contributions: Yamashita H designed the study and performed the majority of work, including literature review and writing the first draft of the manuscript; Takahashi W, Haga A and Nakagawa K provided advice regarding important intellectual content of the topical discussion.

Correspondence to: Hideomi Yamashita, MD, PhD, Department of Radiology, University of Tokyo Hospital, 7-3-1 Hongo, Bunkyo-ku, Tokyo 113-8655,

Japan. yamachan07291973@yahoo.co.jp

Telephone: +81-3-58008667 Fax: +81-3-58008935

Received: December 7, 2013 Revised: July 1, 2014

Accepted: July 15, 2014

Published online: March 28, 2015

Abstract

Stereotactic body radiation therapy (SBRT) has a local control rate of 95% at 2 years for non-small cell lung cancer (NSCLC) and should improve the prognosis of inoperable patients, elderly patients, and patients with significant comorbidities who have early-stage NSCLC. The safety of SBRT is being confirmed in international, multi-institutional Phase II trials for peripheral lung cancer in both inoperable and operable patients, but reports so far have found that SBRT is a safe and effective treatment for early-stage NSCLC and early metastatic lung cancer. Radiation pneumonitis (RP) is one of the most common toxicities of SBRT. Although most post-treatment RP is Grade 1 or 2 and either asymptomatic or manageable, a few cases are severe, symptomatic, and there is a risk for mortality. The reported rates of symptomatic RP after SBRT range from 9% to 28%. Being able to predict the risk of RP after SBRT is extremely useful in treatment planning. A dose-effect relationship has been demonstrated, but suggested dose-volume factors like mean lung dose, lung V20, and/or lung V2.5 differed among the reports. We found

that patients who present with an interstitial pneumonitis shadow on computed tomography scan and high levels of serum Krebs von den Lungen-6 and surfactant protein D have a high rate of severe radiation pneumonitis after SBRT. At our institution, lung cancer patients with these risk factors have not received SBRT since 2006, and our rate of severe RP after SBRT has decreased significantly since then.

© 2015 Baishideng Publishing Group Inc. All rights reserved.

Key words: Radiation pneumonitis; Stereotactic radiation therapy; Dose-volume factors; Krebs von den Lungen-6; Surfactant protein D; Computed tomography changes

Core tip: Radiation pneumonitis (RP) is one of the most common toxicities after stereotactic body radiation therapy (SBRT). Although most RP is Grade 1 or 2 and either asymptomatic or manageable, a few cases are severe and there is a risk for mortality. A dose-effect relationship has been demonstrated that can be used for treatment planning. Other prognostic indicators of severe radiation pneumonitis after SBRT are an interstitial pneumonitis shadow on computed tomography scan and high levels of serum Krebs von den Lungen-6 and surfactant protein D before treatment.

Original sources: Yamashita H, Takahashi W, Haga A, Nakagawa K. Radiation pneumonitis after stereotactic radiation therapy for lung cancer. *World J Radiol* 2014; 6(9): 708-715 Available from: URL: <http://www.wjgnet.com/1949-8470/full/v6/i9/708.htm> DOI: <http://dx.doi.org/10.4329/wjr.v6.i9.708>

INTRODUCTION

Stereotactic body radiotherapy (SBRT) is becoming standard of care therapy for patients with inoperable

early-stage non-small cell peripheral lung cancer or lung cancer with limited demarcated metastases. The delivery of higher doses to smaller lung planning target volumes (PTVs) limits toxicity in the normal lung tissue surrounding the tumor to very limited areas. Local control of up to 95% at 2 years has been reported^[1-4].

Given the improved local control and toxicity results reported by recent lung SBRT studies^[1-4], future directions for this technique include the treatment of larger lesions. Palma *et al*^[5] and Diot *et al*^[6] suggest that toxicity might increase with lesion size, and this possibility should be anticipated and closely monitored.

Symptomatic lung toxicity with SBRT is typically less than 10%^[7]; however, occurrences up to 25% have been reported^[8], highlighting the necessity of developing SBRT treatment parameters that ensure consistently low toxicity levels.

Radiation-induced pneumonitis is the most frequent acute pulmonary toxicity. The majority of patients develop asymptomatic Grade 1 pneumonitis. Clinically symptomatic pneumonitis develops in less than 10% of patients, but most patients develop late pulmonary toxicity characterized by localized pulmonary fibrosis in the high-dose region^[9]. Because this fibrosis is usually asymptomatic, we considered post-SBRT pulmonary function changes the clinically relevant endpoint of our review.

A dose-effect relationship has been demonstrated for SBRT that is similar to that observed in conventionally fractionated radiation therapy^[10,11]; but a study by Guckenberger *et al*^[12] failed to demonstrate this relationship in early-stage non-small cell lung cancer. Gluckenberg's results were based on a large number of patients^[12] and confirmed the findings in other studies that post-SBRT pulmonary function was either stable^[13-17] or almost asymptomatic^[18,19]. These data were encouraging and further supported the safety of SBRT.

SBRT has been widely used as a safe and effective treatment for primary or metastatic lung tumors for a number of years^[20]. According to the protocol of the Japan Clinical Oncology Group (JCOG) 0403 study^[21,22], the only absolute contraindication to SBRT is pregnancy.

In Japan, medical service fees officially cover SBRT treatment for primary and metastatic lung cancers only if the tumor is under 5 cm in size, there are no more than three tumors, and there is no metastatic disease in other organs. In Japan, surgery is generally the first-line treatment for early primary lung cancer, so primary lung cancer patients who undergo SBRT are in poor condition and either have multiple primary cancers or co-morbidities such as serious cardiovascular disease. Most Japanese patients with primary lung tumors who received SBRT had low pulmonary function from chronic obstructive pulmonary disease due to long smoking histories.

Contraindications to SBRT were (1) a history of irradiation to the concerned site; (2) severe interstitial pneumonitis or pulmonary fibrosis; (3) severe diabetes or connective tissue disease; and (4) common use of steroids.

LOCAL CONTROL RATE OF SBRT

SBRT with 3D conformal or intensity-modulation techniques is an effective treatment for localized early-stage lung cancer, with local control rates of 85.5% to 100% 2 to 3 years following treatment^[1-4]. SBRT is also being employed to treat metastatic lung cancer, although the survival rates are not comparable to those for early-stage (T1 - T2, N0) disease^[2].

The excellent local control rates for early-stage lung cancer treated with SBRT are leading to extensive use of this technique in clinical practice and to randomized trials comparing surgery to SBRT for Stage I non-small cell lung cancers in operable patients. Two randomized trials to compare SBRT to surgery for operable patients with Stage I lung cancer were launched in 2008: one in the Netherlands [the Randomized Clinical Trial of Either Surgery or Stereotactic Radiotherapy for Early Stage (IA) Lung Cancer trial] and one in the United States (testing the Cyberknife by Accuray Inc., Sunnyvale, CA, United States).

PREVIOUS REPORTS OF TOXICITIES AFTER SBRT

The safety of SBRT is being confirmed in multi-institutional Phase II trials for peripheral lung cancer in both inoperable^[16,23] and operable patients^[22]. In the Radiation Therapy Oncology Group (RTOG) trial 0236^[23], protocol-specific, treatment-related Grade 3 and 4 adverse events occurred in 12.7% (7/59) and 3.6% (2/59) of cases, respectively. No Grade 5 adverse events were reported. In the Nordic Phase II study of SBRT^[16], Grade 3 toxicities were seen in 21% (12/57) of cases, but no Grade 4 or 5 toxicities were reported. Nishio *et al*^[22] reported Grade 3 toxicities in 6.2% of operable patients in the JCOG 0403 trial.

Severe clinical toxicities after SBRT are fairly uncommon and occur more frequently in cases of centrally located tumors, such as those near the trachea, primary bronchus, major blood vessels and pericardium^[5]. Rates of serious toxicities are low in most studies. Previous reports have described skin, chest wall, and brachial plexus toxicities with their associated risk factors^[24-27].

This review documents clinically significant radiation pneumonitis (RP) rates for medically inoperable non-small cell lung cancer (NSCLC) patients treated with SBRT, adding to the sparse literature on pulmonary toxicity resulting from hypo-fractionated radiotherapy.

RP AFTER SBRT

RP is one of the most common toxicities after SBRT, as well as after conventional radiotherapy to the lung. Scoring systems should be considered when interpreting RP results. The reported rates of symptomatic RP after SBRT range from 9% to 28%^[8,10,11,28-31]. Although most of the RP was Grade 1 or 2 and either asymptomatic or

manageable, a few cases were severe and there was a risk for mortality^[8]. It is very important to develop a method to predict the risk of RP after SBRT for lung cancer.

Grade 3 RP was observed in 3.6% of the overall patients in RTOG 0236^[23] and in 3.1% of the operable patients in JCOG 0403^[22]. Baumann *et al.*^[16] reported that no one developed Grade 3 pneumonitis in their Phase II trial of SBRT.

McGarry *et al.*^[31] reported that 2% (1/47) of patients developed circulating tumor cells and 6.4% (3/47) of patients developed Grade 2 and 3 RP in the updated Indiana University Phase I trial that included tumors up to 7 cm in size plus central lesions. G2 toxicity occurred at a dose of 48 Gy, and G3 toxicities developed after 54 Gy and 72 Gy in 3 fractions prescribed to the 80% iso-dose line^[32]. Using similar criteria, Onishi reported 4.1% G2 (10/245), 1.2% G3 (3/245), and 1.2% G4 (3/245) RP in a multi-institutional trial of SBRT in Japan^[33]. Nagata and colleagues reported no G3 or G4 RP using a slightly less potent dose of 48 Gy in 4 fractions delivered to the isocenter^[1].

In the RTOG, Ricardi *et al.*^[32] treated 62 patients to 45 Gy in 3 fractions to the 80% iso-dose line and reported a 3.2% incidence of Grade 3 RP that required steroids or intermittent oxygen. When Stephans *et al.*^[34] treated ($n = 56$) patients to 50 Gy in 5 fractions and ($n = 38$) patients to 60 Gy in 3 fractions, there was a 2.3% incidence of RP that required steroids (for all 94 patients).

Grills *et al.*^[35] recently published a case-control study comparing SBRT to wedge resection. In that report, there was 11% G2 - 3 RP using a CTC *vs* a grading system based on the Common Terminology of Criteria of Adverse Events. Only 2% of these patients required temporary steroids for management. Finally, G3 RP occurred at a rate of 3.6% (2/55) in RTOG 0236^[23].

Although the reported toxicities of lung SBRT have, for the most part, been minor, the dose constraints to use during treatment planning are based on extremely limited clinical data, most of which has not been validated^[36]. Even the recent QUANTEC lung article devoted only one paragraph to the risk of pneumonitis in lung SBRT patients^[7]. Baker *et al.*^[37] reported in QUANTEC that the greatest incidence of pneumonitis was Grade 1 (64.2%) (169/263), and there were 26 cases (9.9%) of Grade 2 pneumonitis and 3 cases (1.1%) of Grade 3 pneumonitis.

DOSE-VOLUME FACTORS FOR RP AFTER SBRT

Table 1 summarizes published reports that focused on the dose volumetrics associated with Grade 2 RP or worse after SBRT. The RP rates varied from 9.4% to 28.0%, and the suggested dose-volume factors for RP differed among the reports. This variation might be caused by differences in the PTV volume, dose fractionation schedule, or RP scoring system.

Since most patients with pulmonary metastases had residual or recurrent disease after first-line treatment with

chemotherapy, it appeared appropriate to consider a V20 of 30% as the dose restriction in SBRT for metastatic lung cancer.

Borst *et al.*^[10] evaluated the relationship between the mean lung dose (MLD) and the incidence of RP after SBRT. They calculated the MLD in the normalized total dose form, using the linear-quadratic model with a α/β ratio of 3. A significant dose-response relationship was found between RP and MLD.

According to Baker *et al.*^[10], the data from their center and the Japanese group demonstrate that a V20 of less than 10% is readily achievable, and at those levels pneumonitis is not statistically predictable. Analogously, an MLD of approximately 5 - 6 Gy is achievable, and at this dosage pneumonitis should not develop. Therefore, dosimetric guidelines of a V20 of less than 10% and an MLD of less than 6 Gy are a reasonable way to reduce the occurrence of Grades 2 - 4 RP. A German article suggested that a higher MLD or higher V2.5 - V50 (V2.5 in particular) was associated with symptomatic RP^[9].

The Mayo Clinic recently reported on a series of patients treated at their institution with consecutive daily fractions of SBRT^[32]. There was a 12.5% overall incidence of Grade 2 pneumonitis, but a 14.3% incidence in patients treated either with 54 Gy in three fractions for peripheral lesions or 48 Gy in four fractions for central lesions. In a univariate analysis, a PTV maximum dose greater than 60 Gy was predictive of RP ($P = 0.016$), although the overall number of events was small ($n = 4$). No other factors were statistically significant^[32]. The decline in pulmonary function seemed to be transient, similar to the initial experience at Indiana University^[38].

It is unclear exactly how RP correlates with changes in pulmonary function testing. This is an area that requires further research. It is interesting to note, however, that a dose of radiation higher than V10 was predictive of RP in the Indiana University patients, at least on univariate analysis. The same findings were reported by the Cleveland Clinic^[34]. The conformity index was not predictive under univariate or multivariate modeling.

At our institution, we suppress the patient's respiration during SBRT using abdominal compression in order to reduce lung V20 and MLD^[8,39]. We had used irradiation dose of 48 Gy in 4 fractions (Figure 1). We also used 4D cone beam computed tomography (CT) to evaluate internal target volume and tumor motion just before SBRT, with the result that the margin between the internal target volume and the PTV became narrower^[40,41].

EXPRESSION OF KREBS VON DEN LUNGEN-6 IS A PREDICTOR OF RP AFTER SBRT

High levels of the glycoprotein Krebs von den Lungen-6 (KL-6) indicate interstitial pneumonitis (IP), and the levels rise significantly with physical activity in IP cases. In the human body, KL-6 only develops in type II alveolus

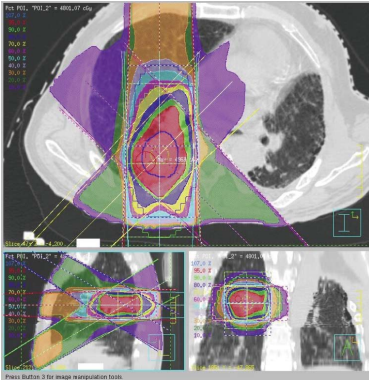


Figure 1 Dose distribution of stereotactic body radiation therapy of 48 Gy in 4 fractions.

epithelial cells, bronchial epithelial cells, and bronchus gland cells. A small quantity of KL-6 is present in the liquid coating the alveoli in normal lungs, but it occurs in higher levels in hyperplastic type II alveolus epithelial cells when IP is present. Inflammation also occurs in IP, which increases the permeability of the blood vessels and allows KL-6 to move into the blood where it can be measured. Blood levels of KL-6, surfactant protein D (SP-D), surfactant protein A (SP-A), and monocyte chemoattractant protein-1 are evaluated whenever there is an injury to the lung stroma, and KL-6 is the most sensitive (93.9%) and specific (96.3%) of these measures where the detection of RP is concerned^[42]. SP-D levels at 50 to 60 Gy (midway through radiation therapy) showed greater sensitivity and positive predictive values for RP detection (74% and 68%, respectively) than SP-A (26% and 21%, respectively)^[43].

Factors other than dose volumetrics also affect the incidence of pneumonitis after SBRT. Hara *et al.*^[44] evaluated 16 patients who received single-fraction SBRT from 20 to 35 Gy. Serum KL-6 levels rose significantly between pretreatment presentation and two months after SBRT was administered, and it was significantly correlated with Grade 3 RP by the RTOG criteria.

Iwata *et al.*^[45] reported that pretreatment serum KL-6 levels, gender, and PTV volume were associated with symptomatic RP in a univariate analysis, and pretreatment KL-6 levels remained significant in a multivariate analysis. They concluded that patients with pretreatment KL-6 levels $\geq 300 \mu\text{mL}$ should be followed carefully for RP. CT or X-ray imaging of the lung before and after SBRT should also help to predict severe RP.

To limit the risk of severe RP, we recommended to everyone prescreening for interstitial pneumonitis with CT scans and checking serum KL-6 and SP-D levels. After introducing these measures, we reported that the incidence of Grade 4 and 5 RP decreased from 18.8% to 3.5%^[45].

Takeda *et al.*^[46] reported that the sooner RP appeared on chest X-ray after SBRT was administered, the more severe it was. The radiographic appearance of RP during the initial 2 mo after SBRT indicated a 40% risk for Grade 3 RP. The risk was only 1.2% when radiologic changes appeared 3 mo after SBRT.

Evaluating KL-6 and SP-D levels, radiologic imaging before and after treatment, and adjusting dose-volume factors during treatment planning helps lower the risk of severe pneumonitis after SBRT. While the biomarkers are both sensitive and specific for RP, the pathophysiological mechanisms underlying their predictive value are unclear, which makes some clinicians hesitate to use them.

At our institution, Grades 4 and 5 RP occurred in 6 out of 32 patients (18.8%) who received SBRT treatment for lung cancer before 2005 and only 3 out of 85 patients (3.5%) between 2006 and 2013^[8,39]. We believe that the significant reduction in the occurrence of Grades 4 - 5 RP is due to our use of prognostic biomarkers and radiography to select appropriate patients for SBRT treatment. After 2006, patients were excluded from SBRT if they had an obvious IP shadow on their CT scan (slice thickness 3.0 mm), and/or if serum KL-6 and SP-D levels were high^[39].

RP AFTER SBRT FOR METASTATIC LUNG CANCER

SBRT is also used to treat pulmonary metastases in selected patients and treatment results seem comparable to those obtained by surgical metastasectomy^[47]. In this setting, the literature reports that Grade 3 RP occurred in 3% to 5% of cases^[2,47,48]. According to Inoue^[48], the incidence of G3/4 adverse respiratory events after SBRT for pulmonary metastases was 10%.

GENE EXPRESSION CLASSIFIER

It was reported that radiation pneumonitis after SBRT treatment for lung cancer was associated with pro-inflammatory genes such as TGFB1 or CD44. Accumulating the number of cases appropriate for statistically significant gene analysis might be difficult, and there is no information about predisposing genetic risk factors for lung cancer.

Yuan *et al.*^[49] reported in 2009 that he and his colleagues at the M.D. Anderson Cancer Center in Houston, Texas, United States, performed an association analysis between pneumonitis onset risk in both Black and White patients who received radiotherapy and/or chemotherapy for NSCLC (94% in both cases). The polymorphism marker on the THFB1 and T869C genes was associated with a low risk of developing RP or IP.

In recent years, many studies have found that SBRT for early stage lung cancer is both effective and safe^[1,50], but there are only a few reports about the development of dangerous and lethal radiation pneumonitis that can result from SBRT^[8], or the pulmonary fibrosis that may also appear^[50].

TIMELINE AND PATTERN OF CT CHANGES

There have been few studies on CT findings in radiation-

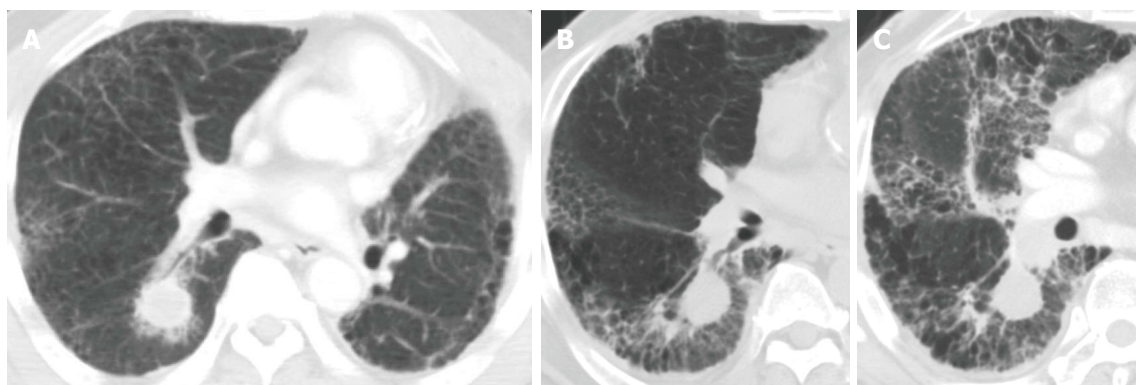


Figure 2 Computed tomography image. A: Before stereotactic body radiation therapy (SBRT) but after surgery for a left lung cancer. The nodule in the lower lobe of the right lung (S6) increased to 23 mm; B: Taken at post-SBRT month 5; C: Taken at post-SBRT month 7. Acute exacerbation of interstitial pneumonitis was found.

Table 1 Summary of reports on Grade 2 radiation pneumonitis after stereotactic body radiation therapy

First author	Ref.	Year	Gy	Pt No.	Median PTV, cc	Median follow-up in months	G2- RP	G3 RP	G4 RP	G5 RP	RP factor 1	RP factor 2
Onishi	[32]	2004	18-75Gy/1-25Fr	245	NA	24	6.50%	1.20%	1.20%	0%		
McGarry	[31]	2005	24Gy/3Fr	47	NA	NA	8.40%	4.30%	2.10%	0%		
Takahashi	[40]	2006	15-30Gy	32	NA	18	12.50%		0%	6%		
Yamashita	[8]	2007	48Gy/4-6Fr	25	43.9	17	28.00%	4%	4%	12%	CI	
Baumann	[16]	2008	45Gy/3Fr	60	NA	23	NA	21%	0%	0%		
Ricardi	[27]	2009	45Gy/3Fr or 26Gy/1Fr	60	NA	30.9	14.30%	3.20%	0%	0%	MLD	
Borst	[10]	2009	35-60Gy/4-8Fr	128	9.6	16.1	10.90%	0.80%	0%	0%	MLD	
Stephans	[13]	2009	60Gy/3Fr or 50Gy/5Fr	86	39.9/30.4	15.3	2.30%	0%	0%	0%		
Rusthoven	[2]	2009	48-60Gy/3Fr	7	NA	15.4	2.60%					
Yamashita	[39]	2010	48Gy/4Fr	117	NA	14.7	NA	1.70%	1.70%	6.00%	KL-6 and SP-D	IP-shadow
Timmerman	[23]	2010	60Gy/3Fr or 54Gy/3Fr	55	NA	34.4	NA	12.70%	3.60%	0%		
Nagata	[20]	2010	48Gy/4Fr	104	NA	46.8	NA	6.20%	0%	0%		
Guckenberger	[9]	2010	26Gy/1Fr or 37.5Gy/3Fr	59	33	13	18.60%	0%	0%	0%	MLD	V2.5-50
Ong	[28]	2010	55Gy/5Fr or 60Gy/8Fr	18	137	12.8	27.80%	11.10%	0%	0%	V5	
Grills	[35]	2010	48Gy/4Fr or 60Gy/5Fr	58	NA	30	11%	2%	0%	0%		
Stauder	[30]	2011	32-60Gy/3-5Fr	74	42.9	15.8	12.50%	2.30%	0%	1.10%	Max dose	
Matsuo	[53]	2012	48Gy/4Fr	74	32.5	31.4	20.30%	1.40%	0%	0%	V25	PTV volume
Barriger	[29]	2012	24-66Gy/3-5Fr	84	48.3	17	9.40%	2%	0.40%	0%	MLD (4Gy)	V20 (4%)
Baker	[37]	2013	Multiple	240	37.6	15.6	11%	1.10%	0%	0%	MLD (6Gy)	V20 (10%)

MLD: Mean lung dose; NA: Not available.

induced lung disease after SBRT for lung cancer^[50]. Due to the differences in dose delivery and distribution, biologic effects, and overall treatment time, it is reasonable to expect that any CT changes that occur after SBRT will not have the same appearance, geographic extent, and progression timeline as those following CRT for lung cancers^[51].

Like CRT-induced CT changes, CT findings after SBRT have two stages: early acute radiation pneumonitis that occurs within 6 mo of treatment and radiation fibrosis that occurs 6 mo or more after treatment^[51,52]. In most cases, radiologic changes in normal lung tissue do not occur until at least 3 mo after SBRT. Clinical symptoms of acute radiation-induced lung injury develop approximately 3 to 6 mo after treatment. All of the severe RP cases in our institution consisted of the acute exacerbation of IP that was spread out over the radiation field (Figure 2)^[39].

The analysis of SBRT-induced normal lung density changes by Diot *et al*^[6] indicates that self-limiting acute

effects in normal lung tissue are more pronounced than late effects, and acute CT changes in patients treated with 3 fractions were considerably less than those in patients treated with 4 or 5 fractions. The changes seemed to be explained by either increased low-dose exposure in normal lung tissue or differences in tumor volume.

CONCLUSION

On the basis of this review, radiation-induced pneumonitis is the most frequent acute pulmonary toxicity following SBRT for lung cancer. The majority of patients develop asymptomatic Grade 1 or asymptomatic and/or manageable Grade 2 pneumonitis, and clinically symptomatic pneumonitis is observed in less than 10%. A dose-effect relationship has been demonstrated that is useful in treatment planning. Since patients with an IP shadow on CT scan and high levels of serum KL-6 and SP-D before SBRT treatment develop severe radiation

pneumonitis at a high rate after treatment, they should not receive SBRT.

REFERENCES

- Nagata Y**, Takayama K, Matsuo Y, Norihisa Y, Mizowaki T, Sakamoto T, Sakamoto M, Mitsumori M, Shibuya K, Araki N, Yano S, Hiraoka M. Clinical outcomes of a phase I/II study of 48 Gy of stereotactic body radiotherapy in 4 fractions for primary lung cancer using a stereotactic body frame. *Int J Radiat Oncol Biol Phys* 2005; **63**: 1427-1431 [PMID: 16169670]
- Rusthoven KE**, Kavanagh BD, Burri SH, Chen C, Cardenes H, Chidel MA, Pugh TJ, Kane M, Gaspar LE, Schefter TE. Multi-institutional phase I/II trial of stereotactic body radiation therapy for lung metastases. *J Clin Oncol* 2009; **27**: 1579-1584 [PMID: 19255320 DOI: 10.1200/JCO.2008.19.6386]
- Timmerman R**, McGarry R, Yiannoutsos C, Papiez L, Tudor K, DeLuca J, Ewing M, Abdulrahman R, DesRosiers C, Williams M, Fletcher J. Excessive toxicity when treating central tumors in a phase II study of stereotactic body radiation therapy for medically inoperable early-stage lung cancer. *J Clin Oncol* 2006; **24**: 4833-4839 [PMID: 17050868]
- Xia T**, Li H, Sun Q, Wang Y, Fan N, Yu Y, Li P, Chang JY. Promising clinical outcome of stereotactic body radiation therapy for patients with inoperable Stage I/II non-small-cell lung cancer. *Int J Radiat Oncol Biol Phys* 2006; **66**: 117-125 [PMID: 16765528]
- Palma DA**, van Sörnsen de Koste J, Verbakel WF, Vincent A, Senan S. Lung density changes after stereotactic radiotherapy: a quantitative analysis in 50 patients. *Int J Radiat Oncol Biol Phys* 2011; **81**: 974-978 [PMID: 20932655 DOI: 10.1016/j.ijrobp.2010.07.025]
- Diot Q**, Kavanagh B, Schefter T, Gaspar L, Stuhr K, Miften M. Regional normal lung tissue density changes in patients treated with stereotactic body radiation therapy for lung tumors. *Int J Radiat Oncol Biol Phys* 2012; **84**: 1024-1030 [PMID: 22583607 DOI: 10.1016/j.ijrobp.2011.11.080]
- Marks LB**, Bentzen SM, Deasy JO, Kong FM, Bradley JD, Vogelius IS, El Naqa I, Hubbs JL, Lebesque JV, Timmerman RD, Martel MK, Jackson A. Radiation dose-volume effects in the lung. *Int J Radiat Oncol Biol Phys* 2010; **76**: S70-S76 [PMID: 20171521 DOI: 10.1016/j.ijrobp.2009.06.091]
- Yamashita H**, Nakagawa K, Nakamura N, Koyanagi H, Tago M, Igaki H, Shiraishi K, Sasano N, Ohtomo K. Exceptionally high incidence of symptomatic grade 2-5 radiation pneumonitis after stereotactic radiation therapy for lung tumors. *Radiat Oncol* 2007; **2**: 21 [PMID: 17553175]
- Huang K**, Dahele M, Senan S, Guckenberger M, Rodrigues GB, Ward A, Boldt RG, Palma DA. Radiographic changes after lung stereotactic ablative radiotherapy (SABR)--can we distinguish recurrence from fibrosis? A systematic review of the literature. *Radiother Oncol* 2012; **102**: 335-342 [PMID: 22305958 DOI: 10.1016/j.radonc.2011.12.018]
- Guckenberger M**, Baier K, Polat B, Richter A, Krieger T, Wilbert J, Mueller G, Flentje M. Dose-response relationship for radiation-induced pneumonitis after pulmonary stereotactic body radiotherapy. *Radiother Oncol* 2010; **97**: 65-70 [PMID: 20605245 DOI: 10.1016/j.radonc.2010.04.027]
- Borst GR**, Ishikawa M, Nijkamp J, Hauptmann M, Shirato H, Onimaru R, van den Heuvel MM, Belderbos J, Lebesque JV, Sonke JJ. Radiation pneumonitis in patients treated for malignant pulmonary lesions with hypofractionated radiation therapy. *Radiother Oncol* 2009; **91**: 307-313 [PMID: 19321217 DOI: 10.1016/j.radonc.2009.02.003]
- Guckenberger M**, Klement RJ, Kestin LL, Hope AJ, Belderbos J, Werner-Wasik M, Yan D, Sonke JJ, Bissonnette JP, Xiao Y, Grills IS. Lack of a dose-effect relationship for pulmonary function changes after stereotactic body radiation therapy for early-stage non-small cell lung cancer. *Int J Radiat Oncol Biol Phys* 2013; **85**: 1074-1081 [PMID: 23154077 DOI: 10.1016/j.ijrobp.2012.09.016]
- Stephans KL**, Djemil T, Reddy CA, Gajdos SM, Kolar M, Machuzak M, Mazzone P, Videtic GM. Comprehensive analysis of pulmonary function Test (PFT) changes after stereotactic body radiotherapy (SBRT) for stage I lung cancer in medically inoperable patients. *J Thorac Oncol* 2009; **4**: 838-844 [PMID: 19487961 DOI: 10.1097/JTO.0b013e3181a99ff6]
- Bral S**, Gevaert T, Linthout N, Versmissen H, Collen C, Engels B, Verdries D, Everaert H, Christian N, De Ridder M, Storme G. Prospective, risk-adapted strategy of stereotactic body radiotherapy for early-stage non-small-cell lung cancer: results of a Phase II trial. *Int J Radiat Oncol Biol Phys* 2011; **80**: 1343-1349 [PMID: 20708849 DOI: 10.1016/j.ijrobp.2010.04.056]
- Fritz P**, Kraus HJ, Blaschke T, Mühlnickel W, Strauch K, Engel-Riedel W, Chemaissani A, Stoelben E. Stereotactic, high single-dose irradiation of stage I non-small cell lung cancer (NSCLC) using four-dimensional CT scans for treatment planning. *Lung Cancer* 2008; **60**: 193-199 [PMID: 18045732]
- Baumann P**, Nyman J, Hoyer M, Gagliardi G, Lax I, Wennerberg B, Drugge N, Ekberg L, Friesland S, Johansson KA, Lund JS, Morhed E, Nilsson K, Levin N, Paludan M, Sederholm C, Traberg A, Wittgren L, Lewensohn R. Stereotactic body radiotherapy for medically inoperable patients with stage I non-small cell lung cancer - a first report of toxicity related to COPD/CVD in a non-randomized prospective phase II study. *Radiother Oncol* 2008; **88**: 359-367 [PMID: 18768228 DOI: 10.1016/j.radonc.2008.07.019]
- Ohashi T**, Takeda A, Shigematsu N, Kunieda E, Ishizaka A, Fukuda J, Deloar HM, Kawaguchi O, Takeda T, Takemasa K, Isoke K, Kubo A. Differences in pulmonary function before vs. 1 year after hypofractionated stereotactic radiotherapy for small peripheral lung tumors. *Int J Radiat Oncol Biol Phys* 2005; **62**: 1003-1008 [PMID: 15990001]
- Henderson M**, McGarry R, Yiannoutsos C, Fakiris A, Hoopes D, Williams M, Timmerman R. Baseline pulmonary function as a predictor for survival and decline in pulmonary function over time in patients undergoing stereotactic body radiotherapy for the treatment of stage I non-small-cell lung cancer. *Int J Radiat Oncol Biol Phys* 2008; **72**: 404-409 [PMID: 18394819 DOI: 10.1016/j.ijrobp.2007.12.051]
- Miyamoto T**, Baba M, Yamamoto N, Koto M, Sugawara T, Yashiro T, Kadono K, Ezawa H, Tsujii H, Mizoe JE, Yoshikawa K, Kandatsu S, Fujisawa T. Curative treatment of Stage I non-small-cell lung cancer with carbon ion beams using a hypofractionated regimen. *Int J Radiat Oncol Biol Phys* 2007; **67**: 750-758 [PMID: 17293232]
- Nagata Y**, Negoro Y, Aoki T, Mizowaki T, Takayama K, Kokubo M, Araki N, Mitsumori M, Sasai K, Shibamoto Y, Koga S, Yano S, Hiraoka M. Clinical outcomes of 3D conformal hypofractionated single high-dose radiotherapy for one or two lung tumors using a stereotactic body frame. *Int J Radiat Oncol Biol Phys* 2002; **52**: 1041-1046 [PMID: 11958900]
- Matsuo Y**, Takayama K, Nagata Y, Kunieda E, Tateoka K, Ishizuka N, Mizowaki T, Norihisa Y, Sakamoto M, Narita Y, Ishikura S, Hiraoka M. Interinstitutional variations in planning for stereotactic body radiation therapy for lung cancer. *Int J Radiat Oncol Biol Phys* 2007; **68**: 416-425 [PMID: 17363190]
- Nishio T**, Kunieda E, Shirato H, Ishikura S, Onishi H, Tateoka K, Hiraoka M, Narita Y, Ikeda M, Goka T. Dosimetric verification in participating institutions in a stereotactic body radiotherapy trial for stage I non-small cell lung cancer: Japan clinical oncology group trial (JCOG0403). *Phys Med Biol* 2006; **51**: 5409-5417 [PMID: 17047260]
- Timmerman R**, Paulus R, Galvin J, Michalski J, Straube W, Bradley J, Fakiris A, Bezjak A, Videtic G, Johnstone D, Fowler J, Gore E, Choy H. Stereotactic body radiation therapy for inoperable early stage lung cancer. *JAMA* 2010; **303**:

- 1070-1076 [PMID: 20233825 DOI: 10.1001/jama.2010.261]
- 24 **Andolino DL**, Forquer JA, Henderson MA, Barriger RB, Shapiro RH, Brabham JG, Johnstone PA, Cardenes HR, Fakiris AJ. Chest wall toxicity after stereotactic body radiotherapy for malignant lesions of the lung and liver. *Int J Radiat Oncol Biol Phys* 2011; **80**: 692-697 [PMID: 21288656 DOI: 10.1016/j.ijrobp.2010.03.020]
 - 25 **Dunlap NE**, Cai J, Biedermann GB, Yang W, Benedict SH, Sheng K, Schefter TE, Kavanagh BD, Larner JM. Chest wall volume receiving & gt; 30 Gy predicts risk of severe pain and/or rib fracture after lung stereotactic body radiotherapy. *Int J Radiat Oncol Biol Phys* 2010; **76**: 796-801 [PMID: 19427740 DOI: 10.1016/j.ijrobp.2009.02.027]
 - 26 **Hoppe BS**, Laser B, Kowalski AV, Fontenla SC, Pena-Greenberg E, Yorke ED, Lovelock DM, Hunt MA, Rosenzweig KE. Acute skin toxicity following stereotactic body radiation therapy for stage I non-small-cell lung cancer: who's at risk? *Int J Radiat Oncol Biol Phys* 2008; **72**: 1283-1286 [PMID: 19028267 DOI: 10.1016/j.ijrobp.2008.08.036]
 - 27 **Ricardi U**, Filippi AR, Guarneri A, Giglioli FR, Mantovani C, Fiandra C, Anglesio S, Ragona R. Dosimetric predictors of radiation-induced lung injury in stereotactic body radiation therapy. *Acta Oncol* 2009; **48**: 571-577 [PMID: 19031164 DOI: 10.1080/02841860802520821]
 - 28 **Ong CL**, Palma D, Verbakel WF, Slotman BJ, Senan S. Treatment of large stage I-II lung tumors using stereotactic body radiotherapy (SBRT): planning considerations and early toxicity. *Radiother Oncol* 2010; **97**: 431-436 [PMID: 20971523 DOI: 10.1016/j.radonc.2010.10.003]
 - 29 **Barriger RB**, Forquer JA, Brabham JG, Andolino DL, Shapiro RH, Henderson MA, Johnstone PA, Fakiris AJ. A dose-volume analysis of radiation pneumonitis in non-small cell lung cancer patients treated with stereotactic body radiation therapy. *Int J Radiat Oncol Biol Phys* 2012; **82**: 457-462 [PMID: 21035956 DOI: 10.1016/j.ijrobp.2010.08.056]
 - 30 **Stauder MC**, Macdonald OK, Olivier KR, Call JA, Lafata K, Mayo CS, Miller RC, Brown PD, Bauer HJ, Garces YI. Early pulmonary toxicity following lung stereotactic body radiation therapy delivered in consecutive daily fractions. *Radiother Oncol* 2011; **99**: 166-171 [PMID: 21571384 DOI: 10.1016/j.radonc.2011.04.002]
 - 31 **McGarry RC**, Papiez L, Williams M, Whitford T, Timmerman RD. Stereotactic body radiation therapy of early-stage non-small-cell lung carcinoma: phase I study. *Int J Radiat Oncol Biol Phys* 2005; **63**: 1010-1015 [PMID: 16115740]
 - 32 **Ricardi U**, Filippi AR, Guarneri A, Giglioli FR, Ciammella P, Franco P, Mantovani C, Borasio P, Scagliotti GV, Ragona R. Stereotactic body radiation therapy for early stage non-small cell lung cancer: results of a prospective trial. *Lung Cancer* 2010; **68**: 72-77 [PMID: 19556022 DOI: 10.1016/j.lungcan.2009.05.007]
 - 33 **Onishi H**, Araki T, Shirato H, Nagata Y, Hiraoka M, Gomi K, Yamashita T, Niibe Y, Karasawa K, Hayakawa K, Takai Y, Kimura T, Hirokawa Y, Takeda A, Ouchi A, Hareyama M, Kokubo M, Hara R, Itami J, Yamada K. Stereotactic hypofractionated high-dose irradiation for stage I non-small cell lung carcinoma: clinical outcomes in 245 subjects in a Japanese multiinstitutional study. *Cancer* 2004; **101**: 1623-1631 [PMID: 15378503]
 - 34 **Stephans KL**, Djemil T, Reddy CA, Gajdos SM, Kolar M, Mason D, Murthy S, Rice TW, Mazzone P, Machuzak M, Mekhail T, Videtic GM. A comparison of two stereotactic body radiation fractionation schedules for medically inoperable stage I non-small cell lung cancer: the Cleveland Clinic experience. *J Thorac Oncol* 2009; **4**: 976-982 [PMID: 19633473 DOI: 10.1097/JTO.0b013e3181ad5f509]
 - 35 **Grills IS**, Mangona VS, Welsh R, Chmielewski G, McInerney E, Martin S, Wloch J, Ye H, Kestin LL. Outcomes after stereotactic lung radiotherapy or wedge resection for stage I non-small-cell lung cancer. *J Clin Oncol* 2010; **28**: 928-935 [PMID: 20065181 DOI: 10.1200/JCO.2009.25.0928]
 - 36 **Timmerman RD**. An overview of hypofractionation and introduction to this issue of seminars in radiation oncology. *Semin Radiat Oncol* 2008; **18**: 215-222 [PMID: 18725106 DOI: 10.1016/j.semradonc.2008.04.001]
 - 37 **Baker R**, Han G, Sarangkasiri S, DeMarco M, Turke C, Stevens CW, Dilling TJ. Clinical and dosimetric predictors of radiation pneumonitis in a large series of patients treated with stereotactic body radiation therapy to the lung. *Int J Radiat Oncol Biol Phys* 2013; **85**: 190-195 [PMID: 22929858 DOI: 10.1016/j.ijrobp.2012.03.041]
 - 38 **Timmerman R**, Papiez L, McGarry R, Likes L, DesRosiers C, Frost S, Williams M. Extracranial stereotactic radioablation: results of a phase I study in medically inoperable stage I non-small cell lung cancer. *Chest* 2003; **124**: 1946-1955 [PMID: 14605072]
 - 39 **Yamashita H**, Kobayashi-Shibata S, Terahara A, Okuma K, Haga A, Wakui R, Ohtomo K, Nakagawa K. Prescreening based on the presence of CT-scan abnormalities and biomarkers (KL-6 and SP-D) may reduce severe radiation pneumonitis after stereotactic radiotherapy. *Radiat Oncol* 2010; **5**: 32 [PMID: 20459699 DOI: 10.1186/1748-717X-5-32]
 - 40 **Takahashi W**, Yamashita H, Kida S, Masutani Y, Sakumi A, Ohtomo K, Nakagawa K, Haga A. Verification of planning target volume settings in volumetric modulated arc therapy for stereotactic body radiation therapy by using in-treatment 4-dimensional cone beam computed tomography. *Int J Radiat Oncol Biol Phys* 2013; **86**: 426-431 [PMID: 23562767 DOI: 10.1016/j.ijrobp.2013.02.019]
 - 41 **Nakagawa K**, Haga A, Kida S, Masutani Y, Yamashita H, Takahashi W, Sakumi A, Saotome N, Shiraki T, Ohtomo K, Iwai Y, Yoda K. 4D registration and 4D verification of lung tumor position for stereotactic volumetric modulated arc therapy using respiratory-correlated cone-beam CT. *J Radiat Res* 2013; **54**: 152-156 [PMID: 22843380 DOI: 10.1093/jrr/rrh058]
 - 42 **Onishi H**, Yokoyama A, Kondo K, Hamada H, Abe M, Nishimura K, Hiwada K, Kohno N. Comparative study of KL-6, surfactant protein-A, surfactant protein-D, and monocyte chemoattractant protein-1 as serum markers for interstitial lung diseases. *Am J Respir Crit Care Med* 2002; **165**: 378-381 [PMID: 11818324]
 - 43 **Kong FM**, Ao X, Wang L, Lawrence TS. The use of blood biomarkers to predict radiation lung toxicity: a potential strategy to individualize thoracic radiation therapy. *Cancer Control* 2008; **15**: 140-150 [PMID: 18376381]
 - 44 **Hara R**, Itami J, Komiyama T, Katoh D, Kondo T. Serum levels of KL-6 for predicting the occurrence of radiation pneumonitis after stereotactic radiotherapy for lung tumors. *Chest* 2004; **125**: 340-344 [PMID: 14718465]
 - 45 **Iwata H**, Shibamoto Y, Baba F, Sugie C, Ogino H, Murata R, Yanagi T, Otsuka S, Kosaki K, Murai T, Miyakawa A. Correlation between the serum KL-6 level and the grade of radiation pneumonitis after stereotactic body radiotherapy for stage I lung cancer or small lung metastasis. *Radiother Oncol* 2011; **101**: 267-270 [PMID: 21640420 DOI: 10.1016/j.radonc.2011.05.031]
 - 46 **Takeda A**, Ohashi T, Kunieda E, Enomoto T, Sanuki N, Takeda T, Shigematsu N. Early graphical appearance of radiation pneumonitis correlates with the severity of radiation pneumonitis after stereotactic body radiotherapy (SBRT) in patients with lung tumors. *Int J Radiat Oncol Biol Phys* 2010; **77**: 685-690 [PMID: 20510193 DOI: 10.1016/j.ijrobp.2009.06.001]
 - 47 **Hof H**, Hoess A, Oetzel D, Debus J, Herfarth K. Stereotactic single-dose radiotherapy of lung metastases. *Strahlenther Onkol* 2007; **183**: 673-678 [PMID: 18040611]
 - 48 **Norihisa Y**, Nagata Y, Takayama K, Matsuo Y, Sakamoto T, Sakamoto M, Mizowaki T, Yano S, Hiraoka M. Stereotactic body radiotherapy for oligometastatic lung tumors. *Int J Ra-*

- diat Oncol Biol Phys* 2008; **72**: 398-403 [PMID: 18374506 DOI: 10.1016/j.ijrobp.2008.01.002]
- 49 **Yuan X**, Liao Z, Liu Z, Wang LE, Tucker SL, Mao L, Wang XS, Martel M, Komaki R, Cox JD, Milas L, Wei Q. Single nucleotide polymorphism at rs1982073: T869C of the TGFbeta 1 gene is associated with the risk of radiation pneumonitis in patients with non-small-cell lung cancer treated with definitive radiotherapy. *J Clin Oncol* 2009; **27**: 3370-3378 [PMID: 19380441 DOI: 10.1200/JCO.2008.20.6763]
- 50 **Takeda A**, Enomoto T, Sanuki N, Nakajima T, Takeda T, Sayama K, Kunieda E. Acute exacerbation of subclinical idiopathic pulmonary fibrosis triggered by hypofractionated stereotactic body radiotherapy in a patient with primary lung cancer and slightly focal honeycombing. *Radiat Med* 2008; **26**: 504-507 [PMID: 18975053 DOI: 10.1007/s11604-008-0261-8]
- 51 **Guckenberger M**, Heilman K, Wulf J, Mueller G, Beckmann G, Flentje M. Pulmonary injury and tumor response after stereotactic body radiotherapy (SBRT): results of a serial follow-up CT study. *Radiother Oncol* 2007; **85**: 435-442 [PMID: 18053602]
- 52 **Kimura T**, Matsuura K, Murakami Y, Hashimoto Y, Kenjo M, Kaneyasu Y, Wadasaki K, Hirokawa Y, Ito K, Okawa M. CT appearance of radiation injury of the lung and clinical symptoms after stereotactic body radiation therapy (SBRT) for lung cancers: are patients with pulmonary emphysema also candidates for SBRT for lung cancers? *Int J Radiat Oncol Biol Phys* 2006; **66**: 483-491 [PMID: 16904838]
- 53 **Matsuo Y**, Shibuya K, Nakamura M, Narabayashi M, Sakanaka K, Ueki N, Miyagi K, Norihisa Y, Mizowaki T, Nagata Y, Hiraoka M. Dose--volume metrics associated with radiation pneumonitis after stereotactic body radiation therapy for lung cancer. *Int J Radiat Oncol Biol Phys* 2012; **83**: e545-e549 [PMID: 22436782 DOI: 10.1016/j.ijrobp.2012.01.018]

P- Reviewer: Can MM, Storto G, Sun Z **S- Editor:** Wen LL
L- Editor: A **E- Editor:** Lu YJ



Imaging of community-acquired pneumonia: Roles of imaging examinations, imaging diagnosis of specific pathogens and discrimination from noninfectious diseases

Atsushi Nambu, Katsura Ozawa, Noriko Kobayashi, Masao Tago

Atsushi Nambu, Noriko Kobayashi, Masao Tago, Department of Radiology, Teikyo University Mizonokuchi Hospital, Kawasaki City, Kanagawa 213-8507, Japan

Katsura Ozawa, Department of Internal Medicine, Kofu Municipal Hospital, Kofu City, Yamanashi Prefecture 400-0832, Japan

Author contributions: All the authors contributed to this paper. Correspondence to: Atsushi Nambu, MD, PhD, Department of Radiology, Teikyo University Mizonokuchi Hospital, 3-8-3 Mizonokuchi Takatsu-ku, Kawasaki City, Kanagawa 213-8507, Japan. nambu-a@gray.plala.or.jp

Telephone: +81-44-8443333 Fax: +81-44-8443340

Received: December 29, 2013 Revised: July 14, 2014

Accepted: September 04, 2014

Published online: March 28, 2015

Abstract

This article reviews roles of imaging examinations in the management of community-acquired pneumonia (CAP), imaging diagnosis of specific CAP and discrimination between CAP and noninfectious diseases. Chest radiography is usually enough to confirm the diagnosis of CAP, whereas computed tomography is required to suggest specific pathogens and to discriminate from noninfectious diseases. *Mycoplasma pneumoniae* pneumonia, tuberculosis, *Pneumocystis jirovecii* pneumonia and some cases of viral pneumonia sometimes show specific imaging findings. Peribronchial nodules, especially tree-in-bud appearance, are fairly specific for infection. Evidences of organization, such as concavity of the opacities, traction bronchiectasis, visualization of air bronchograms over the entire length of the bronchi, or mild parenchymal distortion are suggestive of organizing pneumonia. We will introduce tips to effectively make use of imaging examinations in the management of CAP.

© 2015 Baishideng Publishing Group Inc. All rights reserved.

Key words: Community-acquired pneumonia; Computed tomography; Infection; Pneumonia; Lung disease

Core tip: This review article discusses imaging diagnosis of community-acquired pneumonia (CAP). As imaging findings of CAP are considered nonspecific, this topic is rarely focused on in radiology journals. However, we believe that imaging examinations contribute much more than generally considered if detailed evaluation of the imaging findings is made. In this article, we will introduce tips to effectively make use of imaging examinations in the management of CAP.

Original sources: Nambu A, Ozawa K, Kobayashi N, Tago M. Imaging of community-acquired pneumonia: Roles of imaging examinations, imaging diagnosis of specific pathogens and discrimination from noninfectious diseases. *World J Radiol* 2014; 6(10): 779-793 Available from: URL: <http://www.wjg-net.com/1949-8470/full/v6/i10/779.htm> DOI: <http://dx.doi.org/10.4329/wjrt.v6.i10.779>

INTRODUCTION

Community-acquired pneumonia (CAP) is defined as infectious pneumonia that is acquired in the social community^[1]. This term is opposed to hospital-acquired pneumonia (synonym for nosocomial pneumonia), which is infected in the hospital (24 h later after the hospitalization)^[2]. The third term, nursing home acquired pneumonia that is acquired in the nursing home, has recently been proposed, which has intermediate characteristics between community-acquired and hospital-acquired pneumonia^[3]. The pathogens of CAP include a wide variety of microbes, including not only ordinary bacteria but also mycobacteria, viruses, or fungi^[4]. They manifest as pneumonia in various

forms, and their imaging findings are often nonspecific^[4]. However, characteristic imaging findings of several pathogens are sometimes suggestive of the diagnosis of specific pneumonia. In addition, imaging examinations sometimes offer clues for the differentiation between infectious pneumonia and noninfectious diseases. In this article, we discuss the roles of imaging examinations, and illustrate characteristic imaging findings of several pathogens (Table 1), some particular clinical conditions related to CAP (Table 2), and differences between infectious pneumonia and non-infectious diseases (Table 3).

CLINICAL ASPECTS OF CAP

Appropriate clinical assessment is the first step for the diagnosis of CAP^[1]. Patients with CAP usually complain of fever, cough, sputum, difficulty breathing or chest pain^[1]. Chest pain is indicative of associated pleuritis. Heckerling *et al*^[5] proposed 5 criteria that suggest infectious pneumonia: temperature > 37.8 °C, pulse > 100 beats/min, crackles, decreased breath sounds and the absence of asthma. According to their nomogram for determining the probability of having pneumonia, when assuming a 10% prevalence of pneumonia in the patient population, if these five criteria are met, the probability of pneumonia reaches 70%^[5]. Heckerling also suggested in another report that patients with an acute asthma attack or the absence of abnormal auscultatory findings should not undergo chest radiography because the probability of pneumonia is low in these settings^[6].

When clinical findings are suggestive of CAP, blood test, various tests for determining the causative pathogen and chest radiography are performed^[7]. Laboratory data usually show an elevation of white blood cell count, C reactive protein and erythrocyte sedimentation rate.

Tests for pathogens include sputum culture, blood culture (in case of suspected sepsis), various antigen tests including pharyngeal swab test for influenza viruses or urine antigen tests for *Legionella pneumophila* and *Streptococcus pneumoniae*, antibody tests, gram stain, paired serum tests and cold agglutination test^[7].

Pneumonia with relatively mild clinical symptoms, atypical clinical symptoms such as arthralgia, skin rash or headache, or lack of leukocytosis is referred to as atypical pneumonia^[8]. The causative pathogens of atypical pneumonia include *Mycoplasma pneumoniae*, *Chlamydia pneumoniae*, various viruses and *Legionella pneumophila*.

ROLES OF IMAGING EXAMINATIONS

Imaging examinations are indispensable for the management of CAP. The primary role of imaging examinations is to confirm the diagnosis of pneumonia^[4]. If a patient has clinical symptoms suggestive of infection pneumonia, such as fever, cough or sputum, and the imaging findings are consistent with pneumonia, a definitive diagnosis of infectious pneumonia can be made. Imaging examinations also play a complementary role for the evaluation of treatment effects of antibiotics although treatment effects

may be determined based solely on clinical findings^[9]. It is generally difficult to determine specific pathogens of infectious pneumonia based only on the imaging findings. However, as characteristic imaging findings of several pathogens have been reported, they may help choose subsequent examinations or first antibiotics. This is especially true for the exclusion of tuberculosis, which requires quite different treatment strategies from those of ordinary bacterial pneumonia. As tests for tuberculosis are not routine in most institutions, imaging examinations can be the first opportunity to suggest the possibility of tuberculosis. Also, as many tests for pathogens take some time, they are not in time for the determination of the initial treatment for CAP which is critical for controlling the disease. Suggesting possible diagnoses of specific pneumonia on imaging examinations helps determine the initial treatment. Imaging examinations may also be usable for differentiating noninfectious diseases from infectious pneumonia. As the imaging findings of noninfectious diseases have extensively been investigated, they may provide enough information to suspect a certain disease although direct comparative studies between infectious pneumonia and noninfectious diseases are limited. Imaging examinations may also reveal underlying diseases that result in pneumonia or complications. Chest radiography is usually enough to confirm the diagnosis of pneumonia and to evaluate treatment effects, whereas computed tomography (CT) is required to suggest causative pathogens, to exclude noninfectious pneumonia and to reveal underlying diseases.

INDICATIONS FOR CT IN THE MANAGEMENT OF CAP

There has been little evidence for the validity of CT in the management of CAP so far^[9]. Japanese guideline of imaging diagnosis for CAP has given a grade C recommendation (lacking direct evidence) for the use of CT only in the situation where chest radiograph is negative for the presence of pneumonia despite a strong clinical suspicion^[9]. General indications of CT for CAP include severe or complex pneumonia, pneumonia in immunocompromised patients, pneumonia intractable to antibiotics, recurrent or non-resolving pneumonia, patients with clinical suspicion of pneumonia but normal or questionable chest radiographic findings, and pneumonia with a suspicion of underlying diseases^[4]. However, in clinical practice indications of CT are evaluated for each individual case depending on the severity of pneumonia, or the probability of tuberculosis or noninfectious diseases. It should also be noted that the prevalence of non-infectious diseases or tuberculosis in patients with respiratory symptoms is relatively high in referral hospitals as patients with atypical clinical presentations are more likely referred to these hospitals.

IMAGING FINDINGS OF CAP

Patterns of imaging findings

CAP has classically been divided into three distinctive

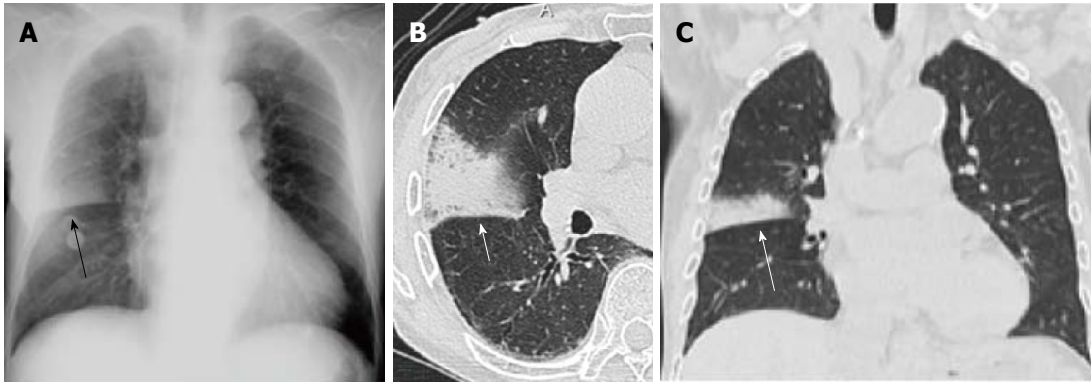


Figure 1 *Streptococcus pneumoniae* pneumonia showing alveolar pneumonia in a man in his 80s. A: Chest radiograph shows a nonsegmental consolidation in the right middle lung field, which is demarcated by the minor fissure suggestive of upper lobe pneumonia (arrow); B, C: Thin-section computed tomography (B) and a coronal reformatted image (C) demonstrate a nonsegmental consolidation with air bronchograms suggestive of alveolar pneumonia (arrows).

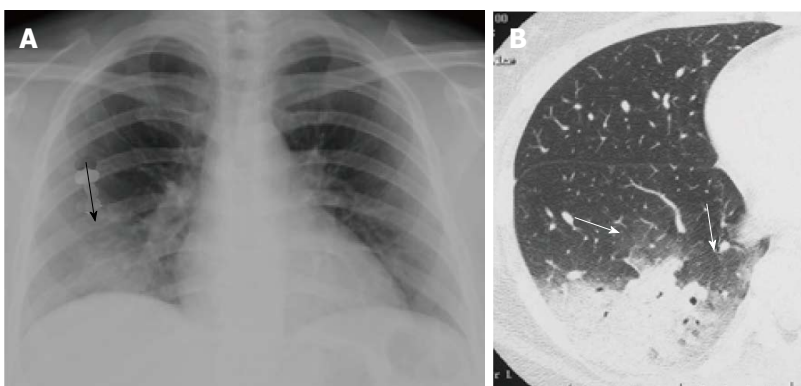


Figure 2 *Mycoplasma pneumoniae* pneumonia showing alveolar pneumonia in a woman in her 30s. A: Chest radiograph demonstrates ill-defined consolidation in the right lower lung field (arrow); B: Thin-section CT reveals a non-segmental consolidation with air bronchograms at the dorsal aspect of the right lower lobe. Areas of ground-glass opacity are also noted around the consolidation (arrows). CT: Computed tomography.

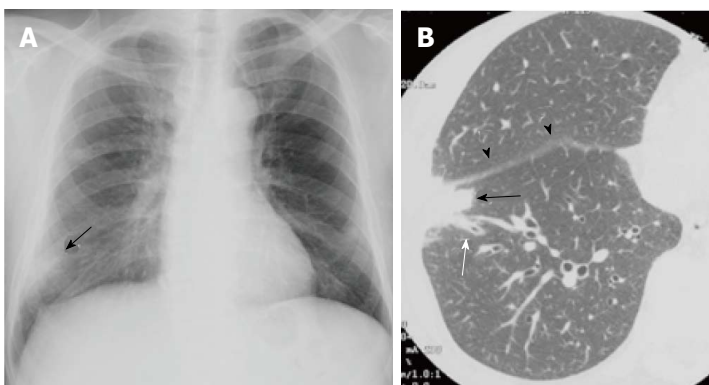


Figure 3 *Chlamydomphila pneumoniae* pneumonia showing alveolar pneumonia in a man in his 60s. A: Chest radiograph shows an ill-defined consolidation at the right lower lung field (arrow); B: On thin-section CT, a subpleural focal consolidation is seen at the right S8 of the right lower lobe, partially extending into the middle lobe (black arrow). The interlobular fissure is mildly thickened (arrow heads). Mild bronchial wall thickening is also noted (white arrow). CT: Computed tomography.

patterns on imaging examinations, namely consolidation (alveolar/lobar pneumonia), peribronchial nodules (bronchopneumonia) and ground-glass opacity (GGO)^[4,10]. The fourth, a unique uncommon pattern of CAP is random nodules, suggestive of hematogenous pulmonary infection or granulomatous infection.

In fact, many pathogens can cause pneumonia with more than one pattern. In addition, consolidation, peribronchial nodules and GGO can often coexist in a case of pneumonia although one of these findings usually predominates. Virulence, amount or size of pathogens, affinity to certain cells, and immune response of hosts may relate to the different manifestations of CAP on imaging examinations. However, the reason why CAP has

different patterns of imaging findings is unknown.

Consolidation predominant pattern (alveolar/ lobar pneumonia)

Consolidation predominant pneumonia is referred to as alveolar pneumonia (Figures 1-4). When it affects almost an entire lung lobe, it is called “lobar pneumonia”. This consolidation is believed to be formed by the spread of inflammation through pores of Kohn or canals of Lambert at the periphery of the lung. Thus, it usually appears in a nonsegmental consolidation in the early stage of disease^[10]. Most bacterial pneumonias exemplified by *Streptococcus* and *Klebsiella* pneumonia appear in consolidation predominant pattern^[4].

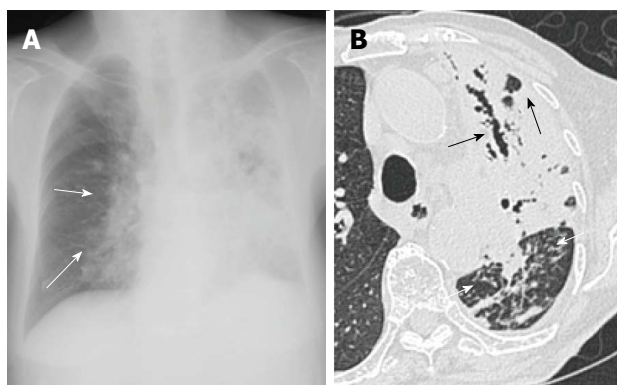


Figure 4 Tuberculous pneumonia in a woman in her 80s. A: Chest radiograph shows extensive consolidations with poor aeration of the left lung and peribronchovascular consolidations of the right lung (arrows); B: Thin-section computed tomography reveals extensive consolidation with air bronchograms and cavities in the left upper lobe (black arrows). Note that the bronchi in the consolidation are dilated. Dense centrilobular nodules are seen in the left lower lobe (white arrows).

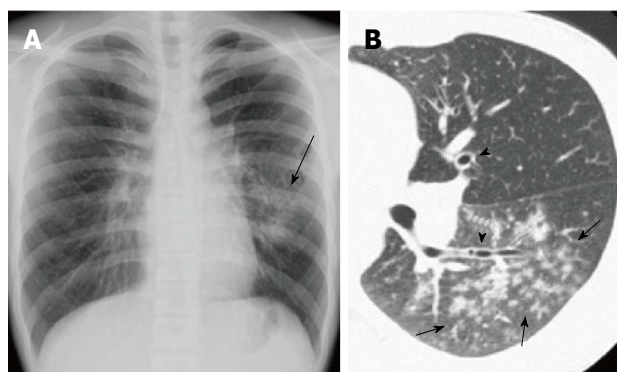


Figure 5 *Mycoplasma pneumoniae* pneumonia showing bronchopneumonia in a man in his 10s. A: Chest radiograph shows reticulonodular opacities and focal consolidation in the left middle to lower lung field (arrow). The left pulmonary hilum appears enlarged; B: Thin-section computed tomography demonstrates fluffy centrilobular nodules with surrounding ground-glass opacity in the left lower lobe (arrows). Note that central bronchial wall is thickened (arrow heads).

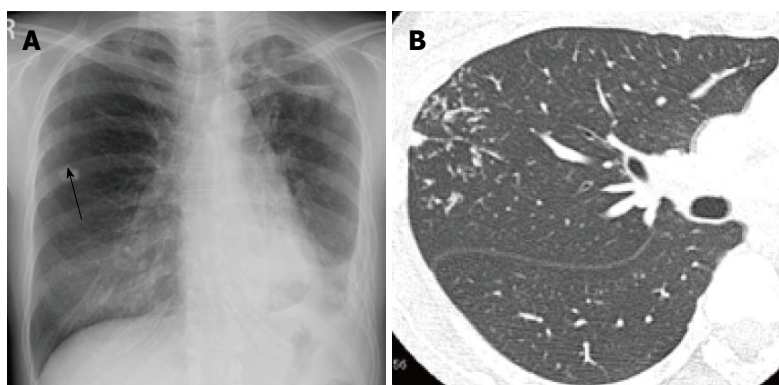


Figure 6 Postprimary tuberculosis in a woman in her 40s. A: Chest radiograph shows faint nodular opacities in the right middle lung field (arrow). There is also volume loss of the left lung with patchy consolidations and thickening of the pleura and possible left pleural effusion, indicative of old tuberculosis; B: Thin-section computed tomography demonstrates centrilobular branching opacities (tree-in-bud appearance) in the right upper lobe (arrows). The branching opacities are denser, more distributed and more peripherally located than those of ordinary bronchopneumonia (compare with Figure 3).

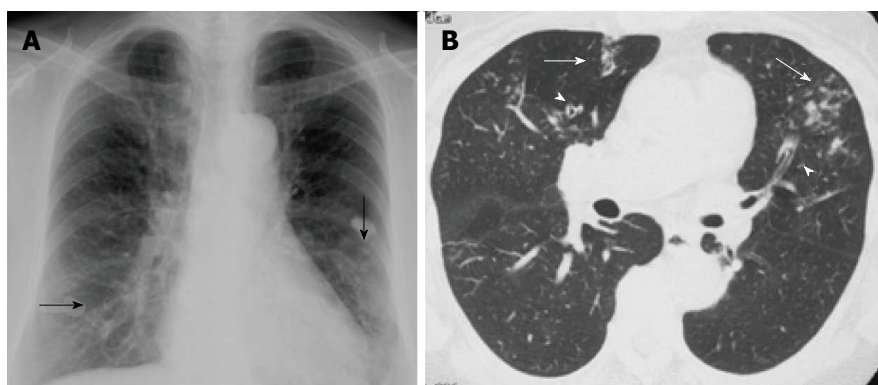


Figure 7 *Chlamydomphila pneumoniae* pneumonia showing infectious bronchiolitis in a woman in her 60s. A: Chest radiograph shows faint reticulonodular opacities in both lower lung fields (arrows); B: Thin-section computed tomography reveals centrilobular nodules (arrows) with bronchiectasis (arrow heads) in the middle lobe and lingula.

Peribronchial nodules predominant pattern (bronchopneumonia)

This pattern is characterized by the predominance of peribronchial nodules including centrilobular nodules with or without peribronchial consolidations (Figure 5)^[4,10]. In contrast to consolidation predominant pattern, these consolidations are probably formed by enlargement and coalescence of the peribronchial nodules. Bronchial wall thickening is often associated. Pneumonia with this

pattern is called bronchopneumonia. However, bronchopneumonia is sometimes indistinguishable from alveolar pneumonia. When centrilobular nodules predominate, namely when bronchioles and peribronchiolar areas are mainly affected, it may be referred to as infectious bronchiolitis (Figures 6-9)^[4]. *Hemophilus influenzae*, *Mycoplasma pneumoniae*, *Chlamydomphila pneumoniae*, and viruses are the representative pathogens of this disease entity^[4]. Tuberculosis and atypical mycobacterial infection also fall in

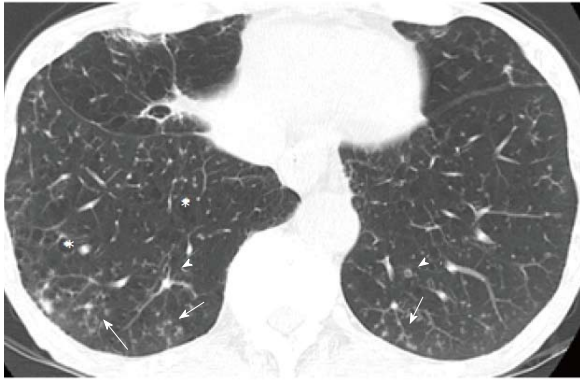


Figure 8 Chronic transbronchial infection (diffuse aspiration bronchiolitis) in a man in his 70s. This patient had a history of esophageal carcinoma and associated repeated aspiration. Thin-section computed tomography at the level of lung base shows centrilobular nodules (arrows) with bronchiectasis (arrow heads). Low attenuation areas suggestive of pulmonary emphysema are also present (*).

this category. However, in fact, most pathogens can take this pattern of pneumonia^[4].

Bronchopneumonia may follow a chronic clinical course. In such a case, bronchiectasis, prominent reticular opacities or architectural distortion, indicative of chronic process of the disease, are usually present (Figures 7-9).

GROUND-GLASS OPACITY PREDOMINANT PATTERN

Infectious pneumonia sometimes appears as predominantly GGO (Figures 10-14). Pathologically these GGO may correspond to incomplete alveolar filling by inflammatory cells or exudate, pulmonary edema secondary to infection leaving air in the alveoli, or interstitial infiltrates of inflammatory cells (interstitial pneumonia). This pattern of infectious pneumonia is sometimes referred to as interstitial pneumonia^[4,10].

Viruses, *Mycoplasma pneumoniae* and *Pneumocystis jirovecii* are the representative pathogens of pneumonia with this pattern^[4].

It should also be noted that resolving alveolar pneumonia can also appear in GGO predominant pattern because alveolar aeration gets restored as pneumonia diminishes.

RANDOM NODULES PREDOMINANT

The fourth pattern distinctive from common pneumonias is random nodules. Random nodules are probably produced by hematogenous spread of the disease^[1] or granulomatous infection. Some viral pneumonia epitomized by *varicella-zoster* pneumonia can assume this pattern (Figure 15)^[11]. Hematogenous dissemination of pathogens such as military tuberculosis (Figure 16)^[12] or septic emboli (Figure 17)^[13] also falls in this category.

Granulomatous infection, such as tuberculosis, non-tuberculous mycobacterial infection or fungal infection (Figure 18), sometimes take a form of nodules that are

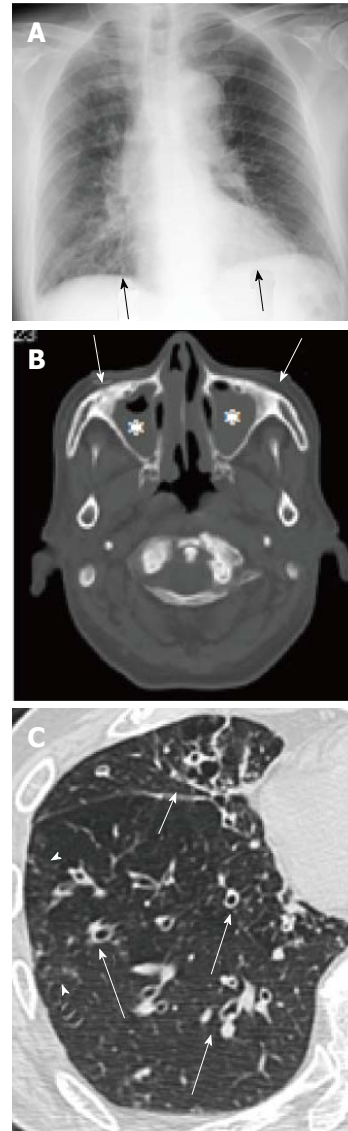


Figure 9 Sinobronchial syndrome in a man in his 70s. A: Chest radiograph shows bilateral reticulonodular opacities in both lower lung fields (arrows); B: computed tomography (CT) at the level of maxillary sinus demonstrates opacification of the maxillary sinuses (*) and bone sclerosis of the sinus walls (arrows), suggestive of chronic paranasal sinusitis; C: Thin-section CT reveals bronchial wall thickening with bronchiectasis (arrows) and minimal centrilobular opacities (arrow heads).

unrelated to bronchovascular bundles on imaging examinations. The nodules are usually larger and sparser than those of pneumonia caused by hematogenous spread.

IMAGING FINDINGS OF REPRESENTATIVE CAP CAUSED BY SPECIFIC PATHOGENS

Streptococcus pneumoniae pneumonia

Streptococcus pneumoniae pneumonia is the most common CAP, accounting for 40% of CAP^[4]. It usually appears in alveolar/lobar pneumonia on chest radiograph and CT (Figure 1)^[4,14-16]. Lower lobe is preferentially involved but multi-lobe involvement is also common^[14]. Bilateral lung disease is seen in about half of cases^[14].

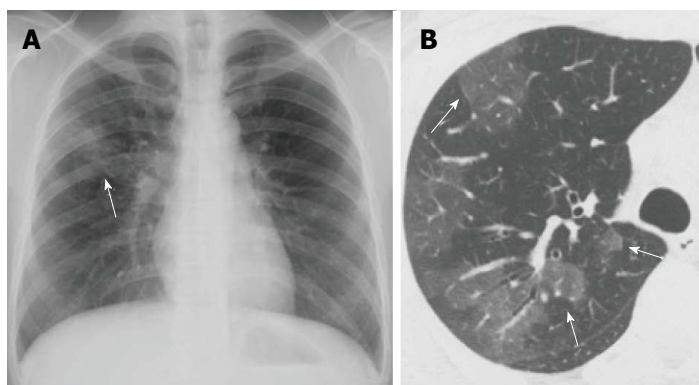


Figure 10 *Mycoplasma pneumoniae* pneumonia showing ground-glass opacity predominant pneumonia in a woman in her 30s. A: Chest radiograph shows patchy ground-glass opacity (GGO) with peribronchial nodules in the right middle lung field (arrow); B: Thin-section computed tomography reveals areas of GGO in the right upper lobe. Note that the GGO are partly demarcated by interlobular septa (arrows).

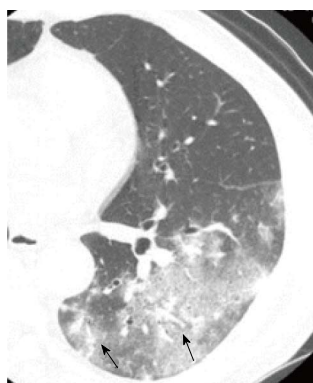


Figure 11 *Chlamydomphila pneumoniae* pneumonia showing ground-glass opacity predominant pneumonia in a man in her 60s. Thin-section computed tomography shows patchy ground-glass opacity in the left lower lobe, in which thickened bronchovascular bundles are present (arrows).

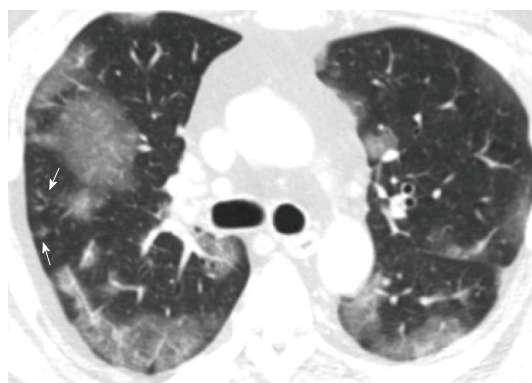


Figure 13 *H1N1 influenza pneumonia* in a man in his 40s. Thin-section computed tomography shows patchy ground-glass opacity that are sharply demarcated from the surrounding lung parenchyma by interlobular septa (geographic distribution) in both lungs. Faint centrilobular nodules are also seen (arrow).

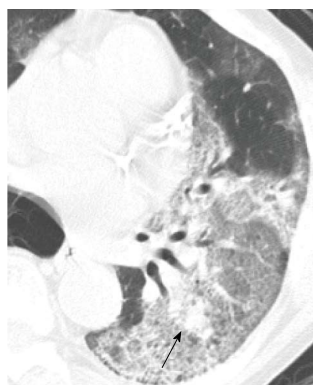


Figure 12 *Legionella pneumophila* pneumonia in a man in his 50s. Thin-section computed tomography shows extensive ground-glass opacity (GGO) in the left lower lobe intermingled with focal consolidations that are sharply demarcated from the surrounding GGO (arrow).

***Mycoplasma pneumoniae* pneumonia**

Mycoplasma pneumoniae pneumonia commonly affects young people^[4,16]. It is clinically characterized by dry cough, fever, and general fatigue^[8]. Chest radiograph shows reticulonodular opacities or patchy consolidations^[17]. On CT, centrilobular nodules and lobular to acinar areas of consolidation or GGO with bronchial wall thickening are the most common findings (Figure 5)^[4,14,16,17]. These findings are consistent with bronchopneumonia. The bronchial wall thickening is often seen

in central bronchi. This finding may be related to the fact that *Mycoplasma pneumoniae* targets bronchial epithelium^[14]. Bronchopneumonia with central bronchial wall thickening in children and young adults are fairly specific findings for *Mycoplasma pneumoniae*. However, extensive GGO (Figure 10) or consolidation (Figure 2) is also not uncommon^[16]. GGO predominance in *Mycoplasma pneumoniae* pneumonia may represent permeability edema rather than cellular infiltrates with edema. Acute respiratory distress syndrome may ensue^[18].

***Chlamydomphila pneumoniae* pneumonia**

It has been well known that *Chlamydomphila pneumoniae* pneumonia often appears as part of co-infection. Therefore, strict diagnostic criteria should be used to diagnose this pneumonia. We have been using the diagnostic criteria for acute infection of *Chlamydomphila pneumoniae* using ELISA kit established by Kishimoto *et al.*^[19,20]; *Chlamydomphila pneumoniae* pneumonia is considered to be present when IgA or IgG index exceeds over 3.0, or there is interval increase more than 1.0 in IgA or 1.35 in IgG in paired serum specimens. These criteria were proved to be accurate for acute *Chlamydomphila pneumoniae* infection, yielding a specificity of 93.4% (*i.e.*, 7.6% of healthy population shows more than this cut-off value) and sensitivity of 64.9%^[19].

Chest radiograph shows patchy consolidations or reticular opacities (Figure 3, Figure 7)^[21]. At the time of

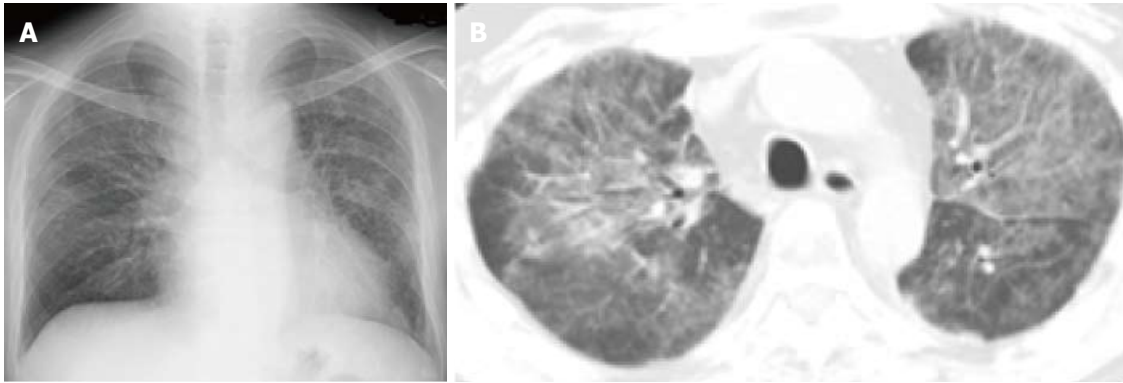


Figure 14 *Pneumocystis jirovecii* pneumonia in a man in his 20s. A: Chest radiograph shows bilateral reticulonodular opacities; B: Chest computed tomography with a 5 mm slice thickness demonstrates bilateral ground-glass opacity with reticulations.

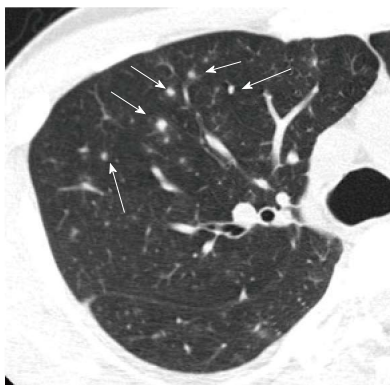


Figure 15 Random nodules predominant pneumonia (*varicella-zoster* pneumonia) in a man in his 30s. Thin-section computed tomography demonstrates scattered small solid or ground-glass opacity nodules which are unrelated to centrilobular structures (arrows).

reinfection, reticular opacities predominate^[21]. On CT, various patterns are seen, including alveolar pneumonia (Figure 3), bronchopneumonia (Figure 7) and GGO predominant pneumonia (Figure 11)^[16,22]. Consequently, imaging findings of *Chlamydomphila pneumoniae* pneumonia is virtually non-specific. However, bronchopneumonia or infectious bronchiolitis in elderly patients with pulmonary emphysema or other chronic debilitating lung disease may be one of the characteristic manifestations of *Chlamydomphila pneumoniae* pneumonia^[16].

Legionella pneumophila pneumonia

Legionella pneumophila pneumonia is a fatal pneumonia, and therefore, early diagnosis and treatment is crucial^[23]. Chest radiographic findings include unilateral nonsegmental poorly defined airspace consolidation^[24]. CT findings consist mainly of consolidation and GGO^[25]. Bilateral lung disease is seen in two thirds of cases^[25]. It has been reported that sharply marginated peribronchial consolidations within GGO are characteristic of *Legionella* pneumonia seen in about one third of the cases (Figure 12)^[25].

Viral pneumonia

There are innumerable causative viruses for pneumonia. Therefore, the imaging findings of virus pneumonia

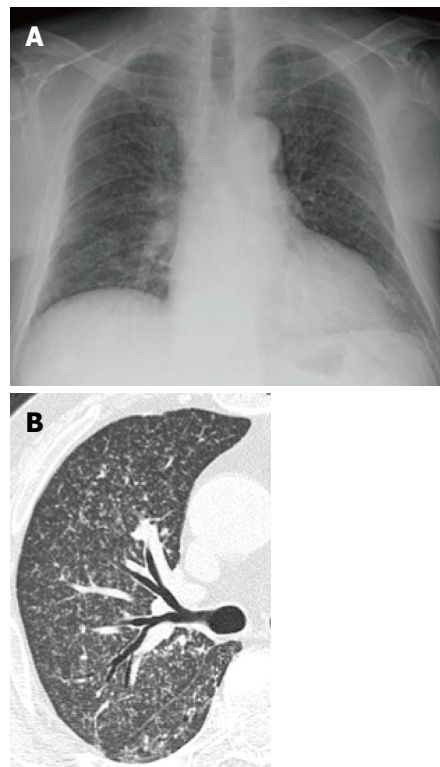


Figure 16 Miliary tuberculosis in a man in his 60s. A: Chest radiograph diffuse reticulonodular opacities in both lungs; B: Thin-section computed tomography demonstrates diffuse miliary nodules with a random distribution.

are diverse. Viral pneumonia can virtually take any form of the above mentioned patterns. Among them, bronchopneumonia and GGO predominance are the most common presentations of viral pneumonia (Figure 13)^[4]. Random nodule pattern is characteristic of *varicella-zoster* (VZ) pneumonia (Figure 15)^[11] although miliary tuberculosis or mycosis, or bacterial emboli shares this finding. It is conceivable that random nodules seen in VZ pneumonia are due to the fact that VZ hematogenously infects the lung^[26]. Scattered small nodules with calcification are also sometimes seen in patients with a past history of VZ pneumonia^[11,26].

Mixed infection, namely accompanying bacterial pneumonia, is also common in viral pneumonia. In such

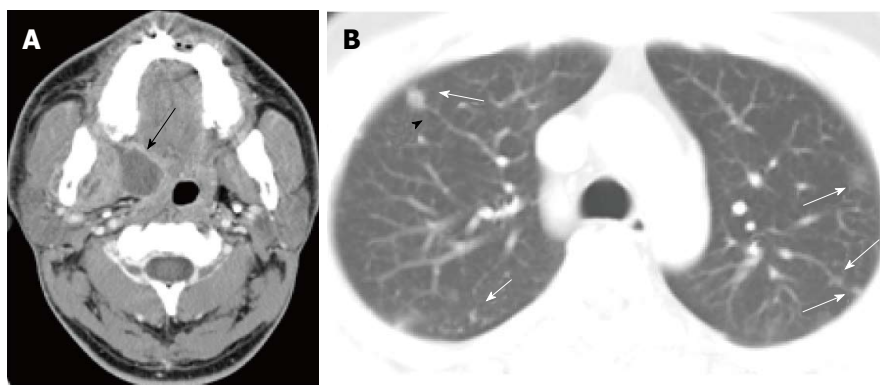


Figure 17 Pulmonary septic emboli from paratonsillar abscess in a man in his 20s. A: Enhanced computed tomography (CT) at the level of oropharynx shows an abscess at the right paratonsillar region (arrow); B: Chest CT with a 5 mm slice thickness reveals small nodules in both lungs (arrows), some of which are in contact with the periphery of pulmonary vessels (arrow head).

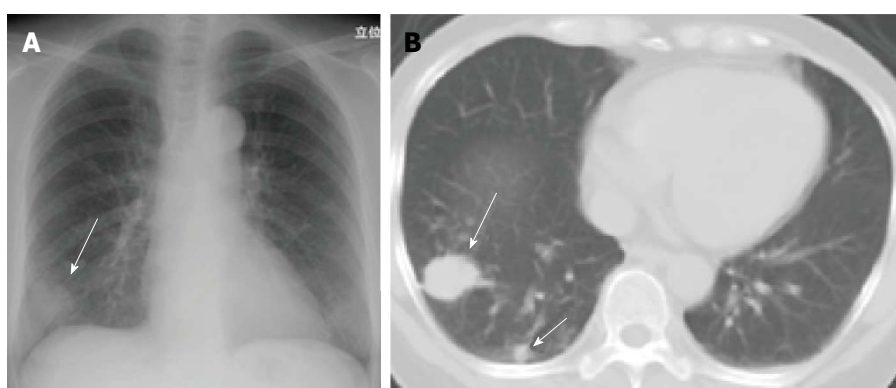


Figure 18 *Cryptococcus neoformans* pneumonia in a woman in her 50s. A: Chest radiograph shows a mass in the right lung base (arrow); B: Chest computed tomography with a 5 mm slice thickness shows a mass and nodule in the right lower lobe (arrows). Multiple nodules/masses in the same pulmonary lobe are considered characteristic findings of *Cryptococcus* pneumonia.

a case, consolidation often predominates. However, pure viral pneumonia may also demonstrate consolidations. Therefore, it is difficult to make a diagnosis of mixed infection with imaging examinations alone.

TUBERCULOSIS

Although tuberculosis is distinct from common bacterial pneumonia in terms of clinical presentation and treatment, it can manifest as CAP^[4]. Tuberculosis is classified into two forms in terms of clinical manifestation, namely primary and postprimary tuberculosis. On CT, primary tuberculosis shows hilar and mediastinal lymphadenopathy, pleural effusion and pulmonary nodules or consolidations^[27], while postprimary tuberculosis demonstrates centrilobular nodules with tree-in-bud appearance, and relatively large nodules suggestive of granulomas with or without cavities^[28-30]. Tuberculosis shows finer and denser branching opacities than bronchopneumonia of common bacteria, which pathologically correspond to filling of bronchioles with caseous material (Figure 6)^[29]. This appearance is named “tree-in-bud appearance”^[29]. Tuberculosis sometimes appears in alveolar pneumonia (tuberculous pneumonia or caseous pneumonia)^[31]. In

this case, tuberculosis mimics alveolar pneumonia caused by common bacteria. Tuberculous pneumonia, however, shows mildly dilated air bronchograms within the consolidation (Figure 4). Tuberculosis may assume nodules that are larger than centrilobular nodules and has no particular relation with the structures of secondary lobule with or without cavitation. These nodules are referred to as tuberculoma, representing granuloma on pathology^[32]. Tuberculosis may also appear as random miliary nodules (miliary tuberculosis)^[12] (Figure 16).

FUNGUS INFECTION

Fungal pneumonia is usually seen in patients with immune suppression. Therefore, it is relatively uncommon to manifest as CAP. However, cryptococcosis can occur in nearly immunocompetent patients^[4]. Fungal pneumonia may appear in alveolar pneumonia, bronchopneumonia, or more commonly nodular lesions with or without cavities, suggestive of granulomas (Figure 18)^[33].

Pneumocystis that infects human was reclassified as fungus and was renamed *Pneumocystis jirovecii* from *Pneumocystis carinii*^[4]. It is a common pathogen of opportunistic infection. However, it should be noted that *Pneumocystis*

Table 1 Specific imaging findings¹ of representative pathogens for community-acquired pneumonia

Pathogens	Specific imaging appearances
<i>Streptococcus pneumoniae</i>	Alveolar/lobar pneumonia
<i>Mycoplasma pneumoniae</i>	Bronchopneumonia with bronchial wall thickening affecting central bronchi
<i>Chlamydia pneumoniae</i>	Infectious bronchiolitis with bronchial dilatation
<i>Legionella pneumophila</i>	Sharply marginated peribronchial consolidations within ground-glass opacities
<i>varicella-zoster</i>	Scattered nodules with a random distribution
<i>Tubercle bacillus</i>	Tree-in-bud appearance with finer and denser branching opacities than bronchopneumonia of common bacteria (postprimary tuberculosis)
<i>Cryptococcus neoformans</i>	Multiple nodules/masses with or without cavities in the same pulmonary lobe
<i>Pneumocystis jirovecii</i>	Bilateral patchy ground-glass opacities with a geographic distribution

¹Note that these imaging findings may be fairly specific but are not sensitive (*i.e.*, other imaging findings are also not uncommon.) for these pathogens.

Table 2 Particular clinical conditions related to community-acquired pneumonia

Pathophysiological conditions	Imaging findings
Aspiration pneumonia	Bronchopneumonia or patchy ground-glass opacities at dorsal parts of the lung (S2, S1+2, S6 and S10) intrabronchial materials
Sinobronchial syndrome	Centrilobular or peribronchial nodules with bronchial wall thickening with bronchiectasis and mucus in the bronchi findings of paranasal sinusitis
Pneumonia on a background of pulmonary emphysema	Consolidation with pseudocavities or pseudohoneycombing, delayed resolution

jirovecii pneumonia can occur in mildly immunocompromised patients, such as those with diabetes or with steroid medication. Therefore, it may be encountered in the clinical settings of CAP. *Pneumocystis jirovecii* pneumonia is radiologically characterized by bilateral patchy GGO with or without a parahilar distribution (Figure 14)^[34]. Unless the patient is treated, the GGO may progress to consolidations^[34]. On CT, bilateral symmetric GGO are the most common finding (Figure 14)^[35,36]. Small nodules, foci of consolidation, and linear opacities may be seen^[35,36]. Cysts may also be seen^[35,36].

PARTICULAR CLINICAL CONDITIONS RELATED TO COMMUNITY-ACQUIRED PNEUMONIA

Aspiration pneumonia

Aspiration pneumonia is caused by inhalation of bacteria, food, gastric acid or other materials that provoke pulmonary inflammation or edema (*e.g.*, paraffin liquid)^[37]. Therefore, aspiration pneumonia has several different pathophysiological aspects, namely bacterial pneumonia caused by oral flora (usually anaerobic bacteria), chemical pneumonitis caused by gastric acid or exogenous lipid, and granulomatous reaction to foreign bodies^[37]. Aspiration pneumonia commonly occurs in patients with deteriorated consciousness, chronic debilitating disease, and tracheal or gastric tubes^[37-40]. Therefore, it more commonly appears in hospital-acquired pneumonia^[37-40]. However, postoperative status for esophageal or gastric cancer and reflux esophagitis are also known risk factors of aspiration pneumonia and thus aspiration pneumonia may manifest as CAP^[37-40].

It commonly affects dorsal parts of the lung (S2, S1+2,

S6 and S10) and demonstrates findings of bronchopneumonia or infectious bronchiolitis (Figure 19)^[37-40]. Aspirated materials are sometimes seen in the bronchial lumens (Figure 19)^[40]. Patchy GGO with peribronchial distribution are also common manifestation (Figure 20). This finding is considered to be related to permeability edema due to endothelial injury by aspirated gastric acid. Acute respiratory distress syndrome (ARDS) may result from aspiration and is referred to as Mendelson's syndrome^[41].

Chronic infectious bronchiolitis radiologically mimicking diffuse panbronchiolitis is named diffuse aspiration bronchiolitis (Figure 8)^[42].

Sinobronchial syndrome

Sinobronchial syndrome is defined as chronic and repeated infection of the lower respiratory tract and paranasal sinuses, which includes diffuse panbronchiolitis^[43]. It was once believed to be caused by aspiration of purulent discharge in the paranasal sinuses. However, altered immune status is now considered to lead to both paranasal sinusitis and infectious bronchiolitis^[43]. Chest radiograph shows reticulonodular opacities with lower lung field predominance (Figure 9). On CT, centrilobular or peribronchial nodules with bronchial wall thickening and mucus in the bronchi are seen (Figure 9). There are usually evidences of chronic and repeated infection, such as bronchiectasis, parenchymal distortion or reticular opacities. Comparison with previous imaging examinations is essential to make a diagnosis of acute exacerbation of infection.

Pneumonia on a background of pulmonary emphysema

When pneumonia develops on a background of pulmonary emphysema, parenchymal consolidations caused by pneumonia appear to have multiple cavities due to underlying low attenuation areas (Figure 21)^[7,10]. This appearance is referred

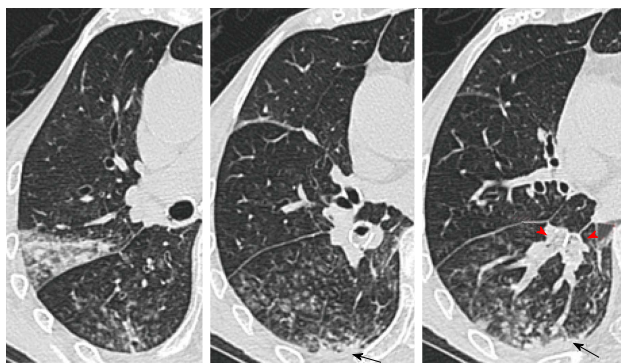


Figure 19 Aspiration pneumonia in a woman in her 70s (causative pathogen unknown). Thin-section computed tomography images show centrilobular nodules with surrounding ground-glass opacities and subpleural non-segmental consolidations (arrows) at the dorsal portions of the right lung. Note that the lumens of segmental bronchi are filled with aspirated materials (arrow heads).

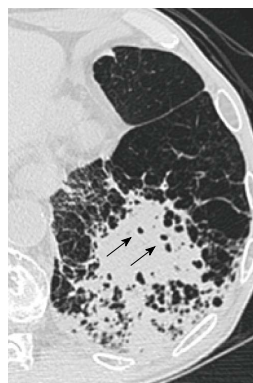


Figure 21 Pneumonia on a background of pulmonary emphysema in a man in his 70s (causative pathogen unknown). Thin-section computed tomography shows patchy consolidations with small air-containing spaces consistent with preexistent low attenuation areas in the left lower lobe.

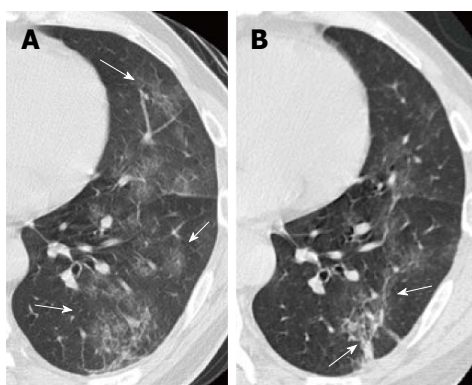


Figure 20 Pneumonia caused by aspiration of gastric fluid in a man in his 50s. A: Initial thin-section computed tomography (CT) shows patchy ground-glass opacity in the left lung with reticulations; B: Thin-section CT 2 d later demonstrates partly increased attenuation with concave margin of the opacities as well as a general resolution of pneumonia.

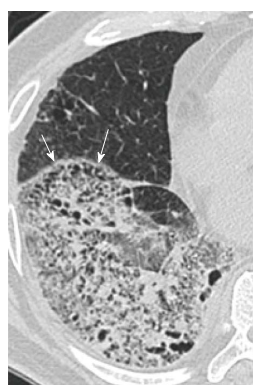


Figure 22 Pneumonia on a background of pulmonary emphysema mimicking honeycombing in a man in his 60s (causative pathogen unknown). Thin-section computed tomography shows an extensive area of ground-glass opacity intermingled with consolidation in the right lower lobe. Pseudohoneycombing is seen along the interlobar fissure (arrows).

to as “Swiss cheese appearance”^[10]. If low attenuation areas predominate, it may mimics honeycombing (Figure 22). These pseudocavitations and pseudohoneycombing must be distinguished from true cavities and honeycombing. Also, resolution is delayed in pneumonia associated with pulmonary emphysema. It should also be noted that infection is the most common cause of acute exacerbation of chronic obstructive pulmonary disease^[44].

REPRESENTATIVE DIFFERENTIAL DIAGNOSES OF COMMUNITY-ACQUIRED PNEUMONIA

General consideration

There is no imaging finding that is 100% specific for infectious pneumonia. Consolidation and GGO are virtually non-specific. However, peribronchial nodules, especially tree-in-bud appearance are fairly specific for infection^[4]. When viewed with CT, consolidation, GGO and peribronchial nodules are coexistent in most cases of infectious pneumonia. Therefore, peribronchial nodules

can often be a diagnostic clue for infectious pneumonia.

Cryptogenic organizing pneumonia

Cryptogenic organizing pneumonia (COP) (formerly bronchiolitis obliterans organizing pneumonia) is clinically characterized by dry cough and dyspnea that continue for a couple of months^[45]. A typical clinical scenario is that the respiratory symptoms do not improve despite medication with antibiotics^[45]. On imaging examinations, it typically shows patchy consolidations which sometimes predispose peribronchial areas with or without extensive areas of GGO^[44-47]. Nodules are not uncommon^[45-48]. There are often evidences of organization, such as concavity of the opacities, traction bronchiectasis, visualization of air bronchograms over the entire length of the bronchi, or mild parenchymal distortion (Figure 23). Reversed halo sign or atoll sign is also suggestive of COP (Figure 24)^[48]. This sign indicates a central GGO surrounded by a ring of consolidation with a thickness of 2 mm or more (just like the reverse of halo sign or atoll in the sea)^[48]. It is seen in 20% of patients with COP^[48]. Although this sign was first considered specific for COP,

Table 3 Representative differential diagnoses of community-acquired pneumonia

Discriminators from community-acquired pneumonia	
Non-infectious pneumonia	
Cryptogenic organizing pneumonia	Relatively chronic clinical course (often for more than one month), evidences of organization (concavity of the opacities, traction bronchiectasis, clear visualization of peripheral air bronchograms, or mild parenchymal distortion), reversed halo sign
Chronic eosinophilic pneumonia	Bilateral nonsegmental consolidations with peripheral predominance
Lipoid pneumonia	Presence of fat within the consolidation on both visual assessment and computed tomography value measurement
Neoplasm	Lack of inflammatory response on laboratory data, chronic clinical course
Mucinous invasive adenocarcinoma	bulging contour, stretching or thinning of bronchi, cavities
Malignant lymphoma	Infiltrative spread around the consolidation (halo sign, galaxy sign, or thickening of surrounding vessels, <i>etc.</i>)

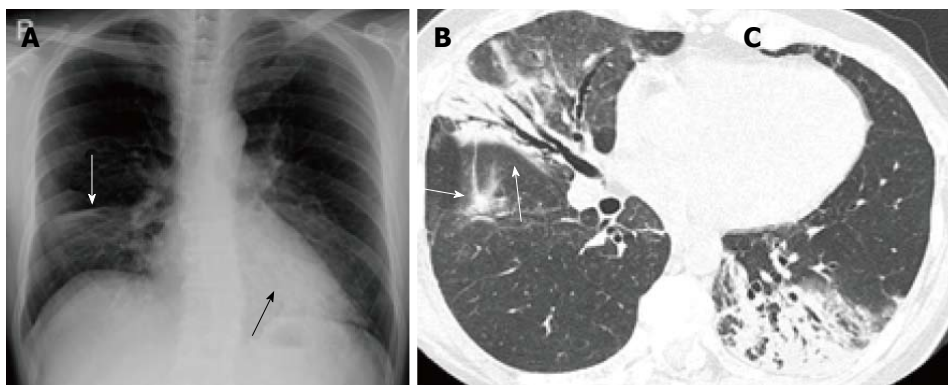


Figure 23 Cryptogenic organizing pneumonia in a woman in her 50s. A: Chest radiograph shows a consolidation in the right lower lung field with depression of the right minor fissure suggestive of volume loss of the middle lobe (white arrow). Retrocardiac consolidation is marginally seen (black arrow); B, C: Thin-section computed tomography of the right lung (B) and left lung (C) demonstrate consolidations with air bronchograms in both lungs. Note that the bronchi within the consolidations are mildly dilated and that the consolidations have concaved margins (arrows), suggesting organization of the disease.

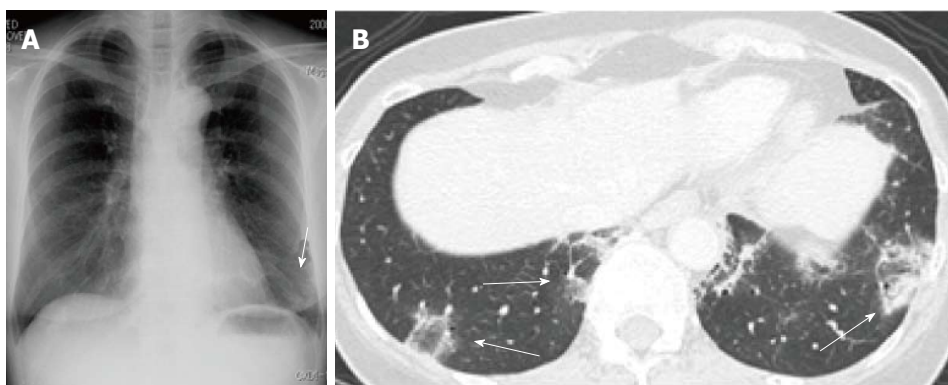


Figure 24 Cryptogenic organizing pneumonia with reversed halo sign in a woman in her 50s: courtesy of Dr. Takahiro Haruyama and Dr. Asako Yamamoto, attending radiologists at the department of Radiology, Teikyo University School of Medicine. A: Chest radiograph shows an ill-defined consolidation in the left lower lung field (arrow); B: Thin-section computed tomography reveals bibasilar ground-glass opacity with a ring of consolidation (reversed halo sign) (arrows).

it has been shown that other diseases may demonstrate reversed halo sign since then. These diseases include invasive pulmonary fungal infections, paracoccidioidomycosis, *Pneumocystis jirovecii* pneumonia, tuberculosis, lymphomatoid granulomatosis, Wegener granulomatosis, lipoid pneumonia and sarcoidosis. It is also seen in pulmonary neoplasms and infarction, and following radiation therapy and radiofrequency ablation of pulmonary malignancies^[49,50]. However, as it has not been reported that reversed halo was seen in CAP so far, it is considered useful to differentiate COP from CAP^[50].

Organizing pneumonia that is histologically identical

to COP may develop secondary to infectious pneumonia, organ transplantation, drug use or in association with collagen vascular disease^[45]. The imaging findings are the essentially the same as COP. However, associated findings related to the primary diseases may be seen, such as findings of bronchopneumonia or honeycombing.

Chronic eosinophilic pneumonia

Chronic eosinophilic pneumonia (CEP) is defined as eosinophilic pneumonia for more than 2 wk and is the most common subtype in eosinophilic lung diseases^[51,52]. It is clinically characterized by eosinophilia, and coexistence



Figure 25 Chronic eosinophilic pneumonia in a woman in her 30s. Chest radiograph shows bilateral subpleural consolidations with upper to middle lung field predominance, consistent with the appearance, “the photographic negative of pulmonary edema”.

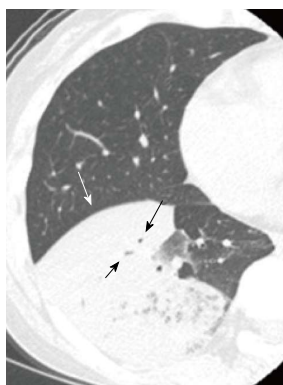


Figure 26 Invasive mucinous adenocarcinoma (formerly mucinous bronchioloalveolar carcinoma) in a woman in her 60s. Thin-section computed tomography shows a nonsegmental consolidation with a bulging fissure (white arrow) and narrowed air bronchograms (black arrows).



Figure 27 Pulmonary malignant lymphoma (mucosa associated lymphoid tissue lymphoma) in a woman in her 30s. Thin-section computed tomography shows a focal consolidation with dilated air bronchograms in the lingula of the left upper lobe. Note mild thickening of the vessels penetrating the consolidation (arrows), suggestive of infiltrative growth of malignant lymphoma along the vessels.

of atopic medial otitis and asthma^[51,52].

Chest radiograph typically shows bilateral nonsegmental consolidations with peripheral predominance^[51,52]. This appearance is referred to as “the photographic negative

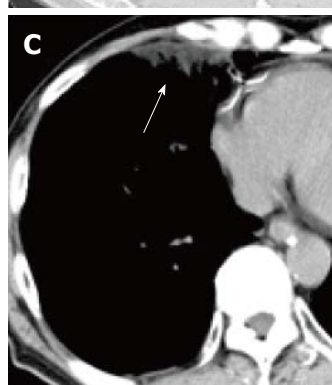
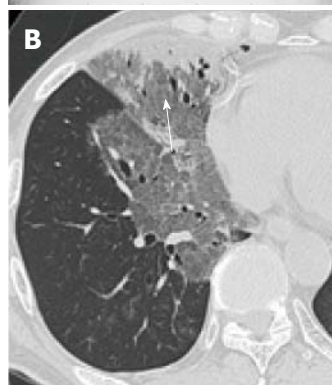
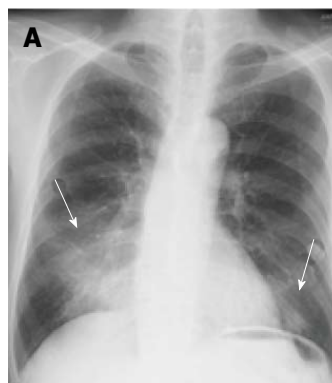


Figure 28 Exogenous lipid pneumonia in a woman in her 30s: Courtesy of Dr. Kazuhiro Suzuki, an attending radiologist, at the department of Radiology, Juntendo University School of Medicine. This patient had been taking petrolatum (paraffin) for intractable constipation. The presence of lipid was confirmed by transbronchial lung biopsy. A: Chest radiograph shows bilateral consolidations in the lower lung fields (arrows); B: Thin-section CT demonstrates an area of clearly demarcated ground-glass opacity with a subpleural consolidation (arrow); C: Chest computed tomography (CT) with a mediastinal window setting reveals the subpleural consolidation to be of fat attenuation (arrow, mean CT value -45HU).

of pulmonary edema” (Figure 25)^[51,52]. On CT, bilateral or unilateral peripheral consolidations and GGO are seen^[47,53]. Linear or band-like opacities parallel to the pleura may be seen at the later stage of the disease^[47,53]. CEP may mimic COP. Thickening of interlobular septa is more commonly seen in CEP, whereas nodules and peribronchial distribution of the opacities are more common in COP^[47].

Neoplasm

Invasive mucinous adenocarcinoma (formerly mucinous bronchioloalveolar carcinoma) and malignant lymphoma may appear in alveolar consolidations, and thus may

mimic alveolar pneumonia (Figures 26, 27)^[54-56]. These neoplasms lack evidence of inflammation on the laboratory data, or if any, the values of inflammatory markers are milder than expected from the extent of disease on imaging examinations. On CT, bronchi in the consolidation are stretched or narrowed, and the consolidation may have a bulging contour at the interlobar fissures in invasive mucinous adenocarcinoma (Figure 26)^[55]. It has also been reported that focal areas of the parenchymal opacification on CT may suggest infectious pneumonia rather than invasive mucinous adenocarcinoma when they show bronchial wall thickening proximal to the lesion and pleural thickening associated with the lesion, whereas invasive mucinous adenocarcinoma is characterized as the presence of a bubble-like low attenuation area within the tumor^[56].

Malignant lymphoma often assumes an infiltrative growth, which may appear as halo sign (ground-glass opacities around the nodule or consolidation)^[57] or as surrounding miliary nodules or thickening of surrounding vessels (Figure 27).

Lipoid pneumonia

Lipoid pneumonia is divided into endogenous and exogenous type. Exogenous lipoid pneumonia results from the chronic aspiration or inhalation of animal, vegetable or petroleum-based oils or fats^[58]. Exogenous lipoid pneumonia is considered as a subtype of aspiration pneumonia. CT shows consolidations and GGO with reticular opacities (crazy-paving appearance). The consolidations may have CT values indicative of fat (-150-300HU) (Figure 28)^[57]. Visual assessment for the presence of fat is also essential as consolidation even without fat may apparently have areas of low CT value comparable to that of fat due to volume averaging between air and inflammatory infiltrates or exudate.

CONCLUSION

Imaging findings of CAP are varied and often nonspecific. However, some characteristic findings are sometimes suggestive of specific pathogens. In addition, imaging examinations, especially CT, can offer clues to the differentiation between infectious pneumonia and noninfectious diseases. To accomplish this differentiation, familiarity with imaging characteristics of CAP as well as those of noninfectious diseases is indispensable.

REFERENCES

- 1 **Niederman MS**, Bass JB, Campbell GD, Fein AM, Grossman RF, Mandell LA, Marrie TJ, Sarosi GA, Torres A, Yu VL. Guidelines for the initial management of adults with community-acquired pneumonia: diagnosis, assessment of severity, and initial antimicrobial therapy. American Thoracic Society. Medical Section of the American Lung Association. *Am Rev Respir Dis* 1993; **148**: 1418-1426 [PMID: 8239186]
- 2 Hospital-acquired pneumonia in adults: diagnosis, assessment of severity, initial antimicrobial therapy, and preven-

- tive strategies. A consensus statement, American Thoracic Society, November 1995. *Am J Respir Crit Care Med* 1996; **153**: 1711-1725 [PMID: 8630626]
- 3 **Guay DR**. Guidelines for the management of adults with health care-associated pneumonia: implications for nursing facility residents. *Consult Pharm* 2006; **21**: 719-725 [PMID: 17069468]
- 4 **Müller NL**, Franquet T, Lee KS. In: McAllister L, editor. Imaging of pulmonary infections. Philadelphia, Pa: Wolters Kluwer/Lipponcott Williams & Wilkins, 2007
- 5 **Heckerling PS**, Tape TG, Wigton RS, Hissong KK, Leikin JB, Ornato JP, Cameron JL, Racht EM. Clinical prediction rule for pulmonary infiltrates. *Ann Intern Med* 1990; **113**: 664-670 [PMID: 2221647]
- 6 **Heckerling PS**. The need for chest roentgenograms in adults with acute respiratory illness. Clinical predictors. *Arch Intern Med* 1986; **146**: 1321-1324 [PMID: 3718128]
- 7 **Freifeld AG**, Bow EJ, Sepkowitz KA, Boeckh MJ, Ito JI, Mullen CA, Raad II, Rolston KV, Young JA, Wingard JR. Infectious Diseases Society of America. Clinical practice guideline for the use of antimicrobial agents in neutropenic patients with cancer: 2010 Update by the Infectious Diseases Society of America. *Clin Infect Dis* 2011; **52**: 427-431 [DOI: 10.1093/cid/cir073]
- 8 **Bragg F**. Primary Atypical Pneumonia. *AJPH* 1944; **34**: 347-357
- 9 **Ashizawa K**, Arakawa H, Takahashi M, Tanaka N, Fujimoto K. Japanese guideline for imaging diagnosis of adult community-acquired pneumonia. Japanese Radiological Society and Japanese College of Radiology, 2007
- 10 **Fraser RS**, Pare JAP, Fraser RG, Pare PD. Infectious disease of the lungs. Synopsis of diseases of the chest. 2nd ed. W.B. Saunders company; 1994: 287-391
- 11 **Kim JS**, Ryu CW, Lee SI, Sung DW, Park CK. High-resolution CT findings of varicella-zoster pneumonia. *AJR Am J Roentgenol* 1999; **172**: 113-116 [PMID: 9888749]
- 12 **Oh YW**, Kim YH, Lee NJ, Kim JH, Chung KB, Suh WH, Yoo SW. High-resolution CT appearance of miliary tuberculosis. *J Comput Assist Tomogr* 1994; **18**: 862-866 [PMID: 7962790]
- 13 **Kuhlman JE**, Fishman EK, Teigen C. Pulmonary septic emboli: diagnosis with CT. *Radiology* 1990; **174**: 211-213 [PMID: 2294550]
- 14 **Tanaka N**, Matsumoto T, Kuramitsu T, Nakaki H, Ito K, Uchisako H, Miura G, Matsunaga N, Yamakawa K. High resolution CT findings in community-acquired pneumonia. *J Comput Assist Tomogr* 1996; **20**: 600-608 [PMID: 8708064]
- 15 **Reittner P**, Ward S, Heyneman L, Johkoh T, Müller NL. Pneumonia: high-resolution CT findings in 114 patients. *Eur Radiol* 2003; **13**: 515-521 [PMID: 12594553]
- 16 **Nambu A**, Saito A, Araki T, Ozawa K, Hiejima Y, Akao M, Ohki Z, Yamaguchi H. Chlamydia pneumoniae: comparison with findings of Mycoplasma pneumoniae and Streptococcus pneumoniae at thin-section CT. *Radiology* 2006; **238**: 330-338 [PMID: 16304082]
- 17 **Reittner P**, Müller NL, Heyneman L, Johkoh T, Park JS, Lee KS, Honda O, Tomiyama N. Mycoplasma pneumoniae pneumonia: radiographic and high-resolution CT features in 28 patients. *AJR Am J Roentgenol* 2000; **174**: 37-41 [PMID: 10628450]
- 18 **Radisic M**, Torn A, Gutierrez P, Defranchi HA, Pardo P. Severe acute lung injury caused by Mycoplasma pneumoniae: potential role for steroid pulses in treatment. *Clin Infect Dis* 2000; **31**: 1507-1511 [PMID: 11096025]
- 19 **Kishimoto T**, Kubota Y, Matsushima T, Izutsu H, Matsumoto A, Soejima R, Morikawa T, Kawagoe K. [Assay of specific anti-Chlamydia pneumoniae antibodies by ELISA method. 1. Evaluation of ELISA kit using outer membrane complex]. *Kansenshogaku Zasshi* 1996; **70**: 821-829 [PMID: 8890550]

- 20 **Kishimoto T**, Matsushima T, Morikawa T, Kawagoe K. [Assay of specific anti-Chlamydia pneumoniae antibodies by ELISA method. 3. Setting of serological criteria]. *Kansenshogaku Zasshi* 1999; **73**: 457-466 [PMID: 10386026]
- 21 **McConnell CT**, Plouffe JF, File TM, Mueller CF, Wong KH, Skelton SK, Marston BJ, Breiman RF. Radiographic appearance of Chlamydia pneumoniae (TWAR strain) respiratory infections. CBPIS Study Group. Community-based Pneumonia Incidence Study. *Radiology* 1994; **192**: 819-824 [PMID: 8058954]
- 22 **Okada F**, Ando Y, Wakisaka M, Matsumoto S, Mori H. Chlamydia pneumoniae pneumonia and Mycoplasma pneumoniae pneumonia: comparison of clinical findings and CT findings. *J Comput Assist Tomogr* 2005; **29**: 626-632 [PMID: 16163032]
- 23 **Burdet C**, Lepeule R, Duval X, Caseris M, Rioux C, Lucet JC, Yazdanpanah Y. Quinolones versus macrolides in the treatment of legionellosis: a systematic review and meta-analysis. *J Antimicrob Chemother* 2014; **69**: 2354-2360 [PMID: 24827889]
- 24 **Kirby BD**, Peck H, Meyer RD. Radiographic features of Legionnaires' disease. *Chest* 1979; **76**: 562-565 [PMID: 498829]
- 25 **Sakai F**, Tokuda H, Goto H, Tateda K, Johkoh T, Nakamura H, Matsuoka T, Fujita A, Nakamori Y, Aoki S, Ohdama S. Computed tomographic features of Legionella pneumophila pneumonia in 38 cases. *J Comput Assist Tomogr* 2007; **31**: 125-131 [PMID: 17259844]
- 26 **Mohsen AH**, McKendrick M. Varicella pneumonia in adults. *Eur Respir J* 2003; **21**: 886-891 [PMID: 12765439]
- 27 **Leung AN**, Müller NL, Pineda PR, FitzGerald JM. Primary tuberculosis in childhood: radiographic manifestations. *Radiology* 1992; **182**: 87-91 [PMID: 1727316]
- 28 **Lee KS**, Song KS, Lim TH, Kim PN, Kim IY, Lee BH. Adult-onset pulmonary tuberculosis: findings on chest radiographs and CT scans. *AJR Am J Roentgenol* 1993; **160**: 753-758 [PMID: 8456658]
- 29 **Im JG**, Itoh H, Shim YS, Lee JH, Ahn J, Han MC, Noma S. Pulmonary tuberculosis: CT findings--early active disease and sequential change with antituberculous therapy. *Radiology* 1993; **186**: 653-660 [PMID: 8430169]
- 30 **Im JG**, Itoh H, Lee KS, Han MC. CT-pathology correlation of pulmonary tuberculosis. *Crit Rev Diagn Imaging* 1995; **36**: 227-285 [PMID: 7546270]
- 31 **Lee KS**, Kim YH, Kim WS, Hwang SH, Kim PN, Lee BH. Endobronchial tuberculosis: CT features. *J Comput Assist Tomogr* 1991; **15**: 424-428 [PMID: 2026803]
- 32 **Murayama S**, Murakami J, Hashimoto S, Torii Y, Masuda K. Noncalcified pulmonary tuberculomas: CT enhancement patterns with histological correlation. *J Thorac Imaging* 1995; **10**: 91-95 [PMID: 7769636]
- 33 **Fox DL**, Müller NL. Pulmonary cryptococcosis in immunocompetent patients: CT findings in 12 patients. *AJR Am J Roentgenol* 2005; **185**: 622-626 [PMID: 16120909]
- 34 **Lyon R**, Haque AK, Asmuth DM, Woods GL. Changing patterns of infections in patients with AIDS: a study of 279 autopsies of prison inmates and nonincarcerated patients at a university hospital in eastern Texas, 1984-1993. *Clin Infect Dis* 1996; **23**: 241-247 [PMID: 8842257]
- 35 **Feurestein IM**, Archer A, Pluda JM, Francis PS, Falloon J, Masur H, Pass HI, Travis WD. Thin-walled cavities, cysts, and pneumothorax in Pneumocystis carinii pneumonia: further observations with histopathologic correlation. *Radiology* 1990; **174**: 697-702 [PMID: 2305052]
- 36 **Kuhlman JE**, Kavuru M, Fishman EK, Siegelman SS. Pneumocystis carinii pneumonia: spectrum of parenchymal CT findings. *Radiology* 1990; **175**: 711-714 [PMID: 2343118]
- 37 **Marik PE**. Aspiration pneumonia and aspiration pneumonia. *N Engl J Med* 2001; **344**: 665-671 [PMID: 11228282]
- 38 **DePaso WJ**. Aspiration pneumonia. *Clin Chest Med* 1991; **12**: 269-284 [PMID: 1855371]
- 39 **Marom EM**, McAdams HP, Erasmus JJ, Goodman PC. The many faces of pulmonary aspiration. *AJR Am J Roentgenol* 1999; **172**: 121-128 [PMID: 9888751]
- 40 **Franquet T**, Giménez A, Rosón N, Torrubia S, Sabaté JM, Pérez C. Aspiration diseases: findings, pitfalls, and differential diagnosis. *Radiographics* 2000; **20**: 673-685 [PMID: 10835120]
- 41 **Berris B**, Kasler D. Pulmonary aspiration of gastric acid--mendelson's syndrome. *Can Med Assoc J* 1965; **92**: 905-907 [PMID: 14289137]
- 42 **Okada F**, Ando Y, Yoshitake S, Ono A, Tanoue S, Matsumoto S, Wakisaka M, Maeda T, Mori H. Clinical/pathologic correlations in 553 patients with primary centrilobular findings on high-resolution CT scan of the thorax. *Chest* 2007; **132**: 1939-1948 [PMID: 18079227]
- 43 **Kadowaki T**, Yano S, Kobayashi K, Araki K, Tokushima T, Yamadori I. Pulmonary capillary hemangiomas-like foci detected by high resolution computed tomography. *Intern Med* 2010; **49**: 175-178 [PMID: 20075585]
- 44 **Huerta A**, Crisafulli E, Menéndez R, Martínez R, Soler N, Guerrero M, Montull B, Torres A. Pneumonic and nonpneumonic exacerbations of COPD: inflammatory response and clinical characteristics. *Chest* 2013; **144**: 1134-1142 [PMID: 23828375 DOI: 10.1378/chest.13-0488]
- 45 **Cordier JF**. Cryptogenic organizing pneumonia. *Eur Respir J* 2006; **28**: 422-446 [PMID: 16880372]
- 46 **Lee KS**, Kullnig P, Hartman TE, Müller NL. Cryptogenic organizing pneumonia: CT findings in 43 patients. *AJR Am J Roentgenol* 1994; **162**: 543-546 [PMID: 8109493]
- 47 **Arakawa H**, Kurihara Y, Niimi H, Nakajima Y, Johkoh T, Nakamura H. Bronchiolitis obliterans with organizing pneumonia versus chronic eosinophilic pneumonia: high-resolution CT findings in 81 patients. *AJR Am J Roentgenol* 2001; **176**: 1053-1058 [PMID: 11264110]
- 48 **Kim SJ**, Lee KS, Ryu YH, Yoon YC, Choe KO, Kim TS, Sung KJ. Reversed halo sign on high-resolution CT of cryptogenic organizing pneumonia: diagnostic implications. *AJR Am J Roentgenol* 2003; **180**: 1251-1254 [PMID: 12704033]
- 49 **Godoy MC**, Viswanathan C, Marchiori E, Truong MT, Benveniste MF, Rossi S, Marom EM. The reversed halo sign: update and differential diagnosis. *Br J Radiol* 2012; **85**: 1226-1235 [PMID: 22553298]
- 50 **Maturu VN**, Agarwal R. Reversed Halo Sign: A Systematic Review. *Respir Care* 2014; **59**: 1440-1449 [PMID: 24782557]
- 51 **Akuthota P**, Weller PF. Eosinophilic pneumonias. *Clin Microbiol Rev* 2012; **25**: 649-660 [PMID: 23034324]
- 52 **Cottin V**, Cordier JF. Eosinophilic lung diseases. *Immunol Allergy Clin North Am* 2012; **32**: 557-586 [PMID: 23102066]
- 53 **Mayo JR**, Müller NL, Road J, Sisler J, Lillington G. Chronic eosinophilic pneumonia: CT findings in six cases. *AJR Am J Roentgenol* 1989; **153**: 727-730 [PMID: 2773727]
- 54 **Lewis ER**, Caskey CI, Fishman EK. Lymphoma of the lung: CT findings in 31 patients. *AJR Am J Roentgenol* 1991; **156**: 711-714 [PMID: 2003430]
- 55 **Jung JI**, Kim H, Park SH, Kim HH, Ahn MI, Kim HS, Kim KJ, Chung MH, Choi BG. CT differentiation of pneumonic-type bronchioloalveolar cell carcinoma and infectious pneumonia. *Br J Radiol* 2001; **74**: 490-494 [PMID: 11459727]
- 56 **Kim TH**, Kim SJ, Ryu YH, Chung SY, Seo JS, Kim YJ, Choi BW, Lee SH, Cho SH. Differential CT features of infectious pneumonia versus bronchioloalveolar carcinoma (BAC) mimicking pneumonia. *Eur Radiol* 2006; **16**: 1763-1768 [PMID: 16418864]
- 57 **Kim Y**, Lee KS, Jung KJ, Han J, Kim JS, Suh JS. Halo sign on high resolution CT: findings in spectrum of pulmonary diseases with pathologic correlation. *J Comput Assist Tomogr* 1999; **23**: 622-626 [PMID: 10433297]

58 **Gondouin A**, Manzoni P, Ranfaing E, Brun J, Cadranet J, Sadoun D, Cordier JF, Depierre A, Dalphin JC. Exogenous lip-

id pneumonia: a retrospective multicentre study of 44 cases in France. *Eur Respir J* 1996; **9**: 1463-1469 [PMID: 8836660]

P- Reviewer: Boots RJ, Fujita J, Kelesidis T **S- Editor:** Song XX
L- Editor: A **E- Editor:** Lu YJ



Spontaneous pneumomediastinum and Macklin effect: Overview and appearance on computed tomography

Sadayuki Murayama, Shinji Gibo

Sadayuki Murayama, Department of Radiology, Graduate School of Medical Science, University of the Ryukyus, Okinawa 903-0215, Japan

Shinji Gibo, Department of Radiology, Urasoe General Hospital, Okinawa 901-2132, Japan

Author contributions: Murayama S designed and wrote the paper; Gibo S provided case examples for this article.

Correspondence to: Sadayuki Murayama, MD, PhD, Department of Radiology, Graduate School of Medical Science, University of the Ryukyus, 207 Uehara, Nishihara-cho, Okinawa 903-0215, Japan. sadayuki@med.u-ryukyu.ac.jp

Telephone: +81-98-8951160 Fax: +81-98-8951420

Received: April 23, 2014 Revised: June 16, 2014

Accepted: September 23, 2014

Published online: March 28, 2015

Abstract

Spontaneous pneumomediastinum (SPM) is described as free air or gas located within the mediastinum that is not associated with any noticeable cause such as chest trauma. SPM has been associated with many conditions and triggers, including bronchial asthma, diabetic ketoacidosis, forceful straining during exercise, inhalation of drugs, as well as other activities associated with the Valsalva maneuver. The Macklin effect appears on thoracic computed tomography (CT) as linear collections of air contiguous to the bronchovascular sheaths. With the recent availability of multidetector-row CT, the Macklin effect has been seen in the clinical setting more frequently than expected. The aim of this review article is to describe the CT imaging spectrum of the Macklin effect in patients with SPM, focusing on the common appearance of the Macklin effect, pneumorrhachis, and persistent SPM with pneumatocele.

© 2015 Baishideng Publishing Group Inc. All rights reserved.

Key words: Pneumomediastinum; Spontaneous pneumomediastinum; Computed tomography; Macklin effect; Interstitial emphysema

Core tip: The Macklin effect can be frequently seen on imaging by multidetector-row computed tomography (CT) of patients who are found to have spontaneous pneumomediastinum from respiratory causes other than chest trauma. The collections of air dissect along the bronchovascular sheaths to the hilum and into the mediastinum. The Macklin effect as seen on CT may help differentiate respiratory from other etiologies of pneumomediastinum.

Original sources: Murayama S, Gibo S. Spontaneous pneumomediastinum and Macklin effect: Overview and appearance on computed tomography. *World J Radiol* 2014; 6(11): 850-854 Available from: URL: <http://www.wjgnet.com/1949-8470/full/v6/i11/850.htm> DOI: <http://dx.doi.org/10.4329/wjr.v6.i11.850>

INTRODUCTION

Pneumomediastinum is described as free air or gas located within the mediastinum. It can be precipitated by various triggers that are either intrathoracic, such as stenosis or blockage of an airway, Valsalva maneuver, blunt trauma to the chest, or ruptured alveoli; or extrathoracic, such as fractured sinus, iatrogenic manipulation during tooth extraction, or ruptured intestine^[1].

Spontaneous pneumomediastinum (SPM) is described as free air or gas located within the mediastinum that is not associated with any noticeable cause such as chest trauma. The first case series of SPM was reported by Hamman^[2] in 1939; therefore, the condition is called Hamman syndrome^[3]. Respiratory pneumomediastinum is a result of rupture along the alveolar tree, which leads to an abrupt increase in the intra-alveolar pressure. Released alveolar air centripetally dissects through the pulmonary interstitium along the bronchovascular sheaths



Figure 1 Chest computed tomography scan of an 82-year-old woman shows an injury to the posterior wall of the trachea, massive pneumomediastinum, and subcutaneous emphysema due to ruptured pars membrana (arrow).

toward the pulmonary hila, into the mediastinum^[3]. This pathophysiological mechanism was described by Macklin *et al*^[4] in 1944, and is known as the Macklin effect.

SPM is usually a benign, self-limiting illness affecting young males. However, it is a condition that is not widely recognized by clinicians. There have been several reports describing the appearance of the Macklin effect on computed tomography (CT) images of patients with SPM^[5-12]. This review article will describe the CT imaging spectrum of the Macklin effect as observed in patients with SPM.

THE MAIN CAUSES OF SPM

SPM occurs predominantly in young males^[13,14], and is an uncommon entity. The prevalence of SPM reportedly ranges from 1 of 8005 to 1 of 42000 hospital accidents and emergency admissions^[13,15]. Three different mechanisms can produce pneumomediastinum: (1) disruption of a cutaneous or mucosal barrier (usually the tracheo-bronchial tree or the esophagus), which allows the entry of gas into the mediastinum; (2) gas produced by organisms in the mediastinum or adjacent chest; or (3) rupture of an alveolus. Alveolar rupture is known as SPM^[14,16]. SPM has been associated with many conditions and triggers, such as bronchial asthma^[17], diabetic ketoacidosis^[18], forceful straining during exercise^[19], inhalation of drugs^[20], childbirth^[21], severe cough or vomiting^[22], and other activities associated with the Valsalva maneuver^[23]. Recent case reports have shown that SPM has also occurred in patients with gastroesophageal reflux disease^[24], anorexia nervosa^[25], in individuals swallowing a foreign body such as a peach seed or pork rib^[26], and in a patient who practiced yoga^[27].

Although pneumomediastinum can be spontaneous, without known precipitating events and without injury to mediastinal organs, pneumomediastinum can be an ominous sign of injury to mediastinal structures, including ruptured esophagus (Boerhaave syndrome) or ruptured trachea (Figure 1). Whenever pneumomediastinum is identified on imaging studies, the problem is differentiating those patients with mediastinal organ injuries from

patients without organ injuries. The former require admission, diagnostic studies, and surgical treatment, while the latter can simply be observed, thereby avoiding unnecessary admissions and diagnostic tests^[28].

SPM is uncommon in children. However, because of the increasing concern regarding the risks to children exposed to radiation, Chapdelaine *et al*^[29] studied whether the extensive radiologic workup of SPM affects its management and outcome. Of 53 cases of SPM, 26 (49%) were related to bronchospasm, 11 (21%) were associated with respiratory infections, and 8 (15%) were of unknown etiology. Inhaled foreign bodies were associated with 4 cases. No esophageal perforations were identified. Posteroanterior chest x-ray (CXR) diagnosed every case except 1, and the mean number of CXRs performed during hospitalization was 3. Only 3 patients developed subsequent pneumothorax, and no patient needed pleural drainage. Of the 8 patients with SPM of unknown etiology, 5 underwent barium swallow and 2 underwent chest CT, and all findings were within normal limits. The authors concluded that SPM is usually self limited, and the prognosis depends on the underlying disorder. Therefore, for patients with clinical improvement, an aggressive work up and follow-up chest imaging are rarely justified.

CT DEMONSTRATION OF THE MACKLIN EFFECTS IN SPM

Macklin and Macklin first observed that released alveolar air from alveolar rupture centripetally dissects through the pulmonary interstitium along the bronchovascular sheaths toward the pulmonary hila and into the mediastinum^[4]. Wintermark and Schnyder recently reported that the rate of Macklin effect seen on chest CTs of patients with blunt trauma to the chest was 39%. They concluded that CT-associated Macklin effect was a sign of severe blunt trauma to the chest^[30]. However, there have been several reports of the Macklin effect on the CT scans of patients with SPM^[5-12].

As demonstrated in Figures 2-5, the Macklin effect appears on thoracic computed tomography (CT) as linear collections of air contiguous to the bronchovascular sheaths^[5-12]. The air dissects into the pulmonary hila and from there enters the mediastinum. We previously reported that using multidetector-row (MD)CT, we detected the Macklin effect in 8 of 9 patients with nontraumatic pneumomediastinum, which was a higher rate of detection than had been previously reported^[5]. Sakai *et al*^[6] also reported a high detection rate of the Macklin effect using 64-detector-row CT. They found interstitial gas in the perihilar region of all 20 of their patients. We speculated that the increased detection rate of the Macklin effect was a result of using MDCT with application of thin collimation, a one-breath-hold technique, and visualization of magnified images on a monitor with cathode ray tubes. These factors might facilitate the identification of subtle Macklin effects. Therefore, we may conclude that

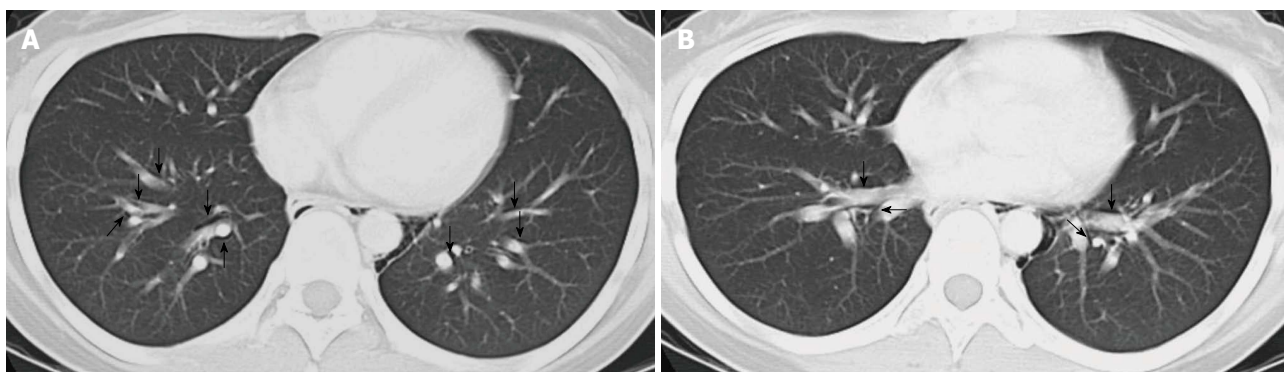


Figure 2 A 21-year-old woman with hypothyroidism and symptoms of cervical discomfort and tenderness. Multidetector-row computed tomography scan demonstrates air collection along the perivascular connective tissue, the Macklin effect (arrows), in the peripheral area (A) and in the perihilar area (B), and pneumomediastinum. Reprinted from ref. [5].



Figure 3 A 15-year-old girl with acute myeloid leukemia. Multidetector-row computed tomography scan demonstrates air collection along the perivascular connective tissue and the Macklin effect (arrow) in the perihilar area. A small pneumomediastinum is also noted.

alveolar rupture described as the Macklin effect is even frequently seen in patients with SPM.

CXRs are generally useful for diagnosing pneumomediastinum, although there have been false-negative results. For false-negative cases, Okada *et al*^[7] concluded that because of thin slices obtained on CT, CT is more effective than CXR alone for diagnosing pneumomediastinum. Sixty-four-detector-row CT reveals minute changes in organs and peripheral tissues. However, the Macklin effect was not detected in the peripheral lung of 4 of our reported 12 cases^[5] and in 11 of 20 cases in Sakai's report^[6]. We believe that since the Macklin effect develops as linear collections of air in the pulmonary interstitium that extend along the bronchi and contiguous blood vessels to gradually reach the perihilar bronchovascular sheath, the longer that time passes after its onset, the less often it is seen in the periphery of CT scans (Figure 3).

Complications of SPM

SPM is occasionally associated with pneumorrhachis, the presence of air within the spinal epidural space (Figure 4). A literature review of 48 patients with pneumorrhachis revealed that only 1 case had neurologic symptoms and signs; the other cases were successfully managed con-

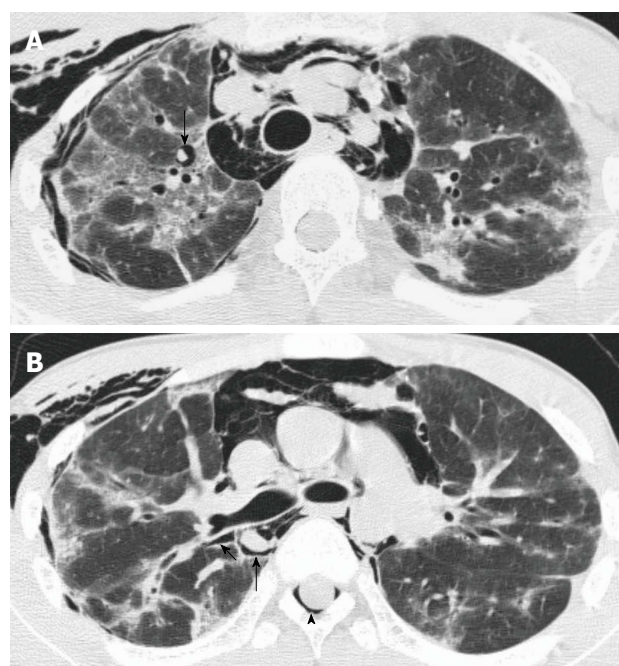


Figure 4 A 15-year-old girl with cryptogenic organizing pneumonia associated with graft-vs-host disease. Multidetector-row computed tomography scan demonstrates air collection along the perivascular connective tissue, the Macklin effect (arrows) in the peripheral area (A) and in the perihilar area (B), and massive pneumomediastinum. This patient also has spinal pneumorrhachis (arrowhead). Reprinted from ref. [5].

servatively^[31]. This literature review described a 72-year-old man with progressive motor weakness and sensory deficits in the lower extremities, who had a large accumulation of intraspinal air. He recovered completely after a C7 laminectomy. Kono *et al*^[32] reported pneumorrhachis in 4 of 42 children with SPM, and the patients with pneumorrhachis did not have neurological symptoms. Therefore, in SPM, a collection of air within the spinal canal is mostly self limiting and benign. Pneumomediastinum concomitant with pneumoperitoneum is very rare in SPM, with only a few cases reported. It also appears to resolve with conservative treatment, without intervention^[33,34].



Figure 5 A 16-year-old girl with persistent spontaneous pneumomediastinum and pneumatocele. Computed tomography shows massive pneumomediastinum and perihilar and peripheral Macklin effects (arrows). In the left lower lobe, a pneumatocele (arrowhead) is observed.

Although the Macklin effect appears on thoracic CT as linear collections of air contiguous to the bronchovascular sheaths, the onset, which is alveolar rupture, is rarely observed on CT. The released alveolar air rapidly dissects into the pulmonary hila and from there enters the mediastinum. We did have an SPM patient with a pneumatocele (Figure 5). This young female patient had interstitial pneumonia with prolonged SPM and cervical subcutaneous air. Patients found to have a Macklin effect involving peribronchovascular air and pneumatocele^[35] will have a prolonged SPM, and clinical intervention is required.

CONCLUSION

The Macklin effect can be frequently observed on the MDCT images of patients with SPM not associated with trauma. A Macklin effect seen on CT may help differentiate respiratory from other etiologies of pneumomediastinum. However, especially in pediatric patients with SPM who improve clinically, aggressive investigation and follow-up CXRs are rarely warranted, and the efficacy of CT is limited.

REFERENCES

- Zylak CM, Standen JR, Barnes GR, Zylak CJ. Pneumomediastinum revisited. *Radiographics* 2000; **20**: 1043-1057 [PMID: 10903694 DOI: 10.1148/radiographics.20.4.g00j131043]
- Hamman L. Spontaneous mediastinal emphysema. *Bull Johns Hopkins Hosp* 1939; **64**: 1-21
- Wintermark M, Wicky S, Schnyder P, Capasso P. Blunt traumatic pneumomediastinum: using CT to reveal the Macklin effect. *AJR Am J Roentgenol* 1999; **172**: 129-130 [PMID: 9888752 DOI: 10.2214/ajr.172.1.9888752]
- Macklin MT, Macklin CC. Malignant interstitial emphysema of the lungs and mediastinum as an important occult complication in many respiratory diseases and other conditions: interpretation of the clinical literature in the light of laboratory experiment. *Medicine* 1944; **23**: 281-358 [DOI: 10.1097/00005792-194412000-00001]
- Rosenberg JC, Bowles AL. Nonneoplastic disorders of the mediastinum. In: Fishman AP (ed) *Pulmonary diseases and disorders*, 2nd ed. New York: McGraw-Hill, 1988: 2079-2083
- Sakai M, Murayama S, Gibo M, Akamine T, Nagata O. Frequent cause of the Macklin effect in spontaneous pneumomediastinum: demonstration by multidetector-row computed tomography. *J Comput Assist Tomogr* 2006; **30**: 92-94 [PMID: 16365580 DOI: 10.1097/01.rct.0000187416.07698.8d]
- Okada M, Adachi H, Shibuya Y, Ishikawa S, Hamabe Y. Diagnosis and treatment of patients with spontaneous pneumomediastinum. *Respir Investig* 2014; **52**: 36-40 [PMID: 24388369 DOI: 10.1016/j.resinv.2013.06.001]
- Kaneki T, Kubo K, Kawashima A, Koizumi T, Sekiguchi M, Sone S. Spontaneous pneumomediastinum in 33 patients: yield of chest computed tomography for the diagnosis of the mild type. *Respiration* 2000; **67**: 408-411 [PMID: 10940795 DOI: 10.1159/000029539]
- Gunluoglu MZ, Cansever L, Demir A, Kocaturk C, Melek H, Dincer SI, Bedirhan MA. Diagnosis and treatment of spontaneous pneumomediastinum. *Thorac Cardiovasc Surg* 2009; **57**: 229-231 [PMID: 19670118 DOI: 10.1055/s-2008-1039059]
- Franquet T, Rodríguez S, Hernández JM, Martino R, Giménez A, Hidalgo A, Domingo P. Air-leak syndromes in hematopoietic stem cell transplant recipients with chronic GVHD: high-resolution CT findings. *J Thorac Imaging* 2007; **22**: 335-340 [PMID: 18043388 DOI: 10.1097/RTI.0b013e3180cab6cf]
- Satoh K, Kobayashi T, Kawase Y, Mitani M, Nakano S, Takahashi K, Takashima H, Ohkawa M, Tanabe M, Kojima K. CT appearance of interstitial pulmonary emphysema. *J Thorac Imaging* 1996; **11**: 153-154 [PMID: 8820025 DOI: 10.1097/00005382-199621000-00006]
- Franquet T, Giménez A, Torrubia S, Sabaté JM, Rodríguez-Arias JM. Spontaneous pneumothorax and pneumomediastinum in IPF. *Eur Radiol* 2000; **10**: 108-113 [PMID: 10663725 DOI: 10.1007/s003300050014]
- Mondello B, Pavia R, Ruggeri P, Barone M, Barresi P, Monaco M. Spontaneous pneumomediastinum: experience in 18 adult patients. *Lung* 2007; **185**: 9-14 [PMID: 17310299 DOI: 10.1007/s00408-006-0002-7]
- Kelly S, Hughes S, Nixon S, Paterson-Brown S. Spontaneous pneumomediastinum (Hamman's syndrome). *Surgeon* 2010; **8**: 63-66 [PMID: 20303884 DOI: 10.1016/j.surge.2009.10.007]
- McMahon DJ. Spontaneous pneumomediastinum. *Am J Surg* 1976; **131**: 550-551 [PMID: 1275141 DOI: 10.1016/0002-9610(76)90008-8]
- Koullias GJ, Korkolis DP, Wang XJ, Hammond GL. Current assessment and management of spontaneous pneumomediastinum: experience in 24 adult patients. *Eur J Cardiothorac Surg* 2004; **25**: 852-855 [PMID: 15082293 DOI: 10.1016/j.ejcts.2004.01.042]
- Newcomb AE, Clarke CP. Spontaneous pneumomediastinum: a benign curiosity or a significant problem? *Chest* 2005; **128**: 3298-3302 [PMID: 16304275 DOI: 10.1378/chest.128.5.3298]
- Weathers LS, Brooks WG, DeClue TJ. Spontaneous pneumomediastinum in a patient with diabetic ketoacidosis: a potentially hidden complication. *South Med J* 1995; **88**: 483-484 [PMID: 7716607 DOI: 10.1097/00007611-199504000-00022]
- Partridge RA, Coley A, Bowie R, Woolard RH. Sports-related pneumothorax. *Ann Emerg Med* 1997; **30**: 539-541 [PMID: 9326870 DOI: 10.1016/S0196-0644(97)70018-0]
- Beauchamps G. Spontaneous pneumothorax and pneumomediastinum. In: Pearson FG, Deslauriers J, Ginsberg RJ, Hiebert CA, McKneally MF, Urschel HC, editors. *Thoracic surgery*. New York: Churchill Livingstone, 1995: 1037-1054
- Sutherland FW, Ho SY, Campanella C. Pneumomediastinum during spontaneous vaginal delivery. *Ann Thorac Surg* 2002; **73**: 314-315 [PMID: 11837245 DOI: 10.1016/S0003-4975(01)02729-1]
- Jougon JB, Ballester M, Delcambre F, Mac Bride T, Dromer CE, Velly JF. Assessment of spontaneous pneumomediastinum: experience with 12 patients. *Ann Thorac Surg* 2003; **75**: 1711-1714 [PMID: 12822604 DOI: 10.1016/S0003-4975(03)00027-4]

- 23 **Panacek EA**, Singer AJ, Sherman BW, Prescott A, Rutherford WF. Spontaneous pneumomediastinum: clinical and natural history. *Ann Emerg Med* 1992; **21**: 1222-1227 [PMID: 1416301 DOI: 10.1016/S0196-0644(05)81750-0]
- 24 **Huang HR**, Wong KS, Lien R, Chiu CY. Spontaneous pneumomediastinum due to gastroesophageal reflux disease in an adolescent boy. *Respirology* 2008; **13**: 744-745 [PMID: 18513250 DOI: 10.1111/j.1440-1843.2008.01298.x]
- 25 **Hochlehnert A**, Löwe B, Bludau HB, Borst M, Zipfel S, Herzog W. Spontaneous pneumomediastinum in anorexia nervosa: a case report and review of the literature on pneumomediastinum and pneumothorax. *Eur Eat Disord Rev* 2010; **18**: 107-115 [PMID: 20148397 DOI: 10.1002/erv.1002]
- 26 **Cho TJ**, Kim H. Unusual presentation of spontaneous pneumomediastinum. *Lung India* 2010; **27**: 239-241 [PMID: 21139723 DOI: 10.4103/0970-2113.71961]
- 27 **Hafberg E**, Gudmundsson G, Gudbjartsson T. [Spontaneous pneumomediastinum after yoga practice - a case report]. *Laeknabladid* 2009; **95**: 279-281 [PMID: 19420409]
- 28 **Banki F**, Estrera AL, Harrison RG, Miller CC, Leake SS, Mitchell KG, Khalil K, Safi HJ, Kaiser LR. Pneumomediastinum: etiology and a guide to diagnosis and treatment. *Am J Surg* 2013; **206**: 1001-1006; discussion 1006 [PMID: 24296102 DOI: 10.1016/j.amjsurg.2013.08.009]
- 29 **Chapdelaine J**, Beaunoyer M, Daigneault P, Bérubé D, Bütter A, Ouimet A, St-Vil D. Spontaneous pneumomediastinum: are we overinvestigating? *J Pediatr Surg* 2004; **39**: 681-684 [PMID: 15136999 DOI: 10.1016/j.jpedsurg.2004.01.045]
- 30 **Wintermark M**, Schnyder P. The Macklin effect: a frequent etiology for pneumomediastinum in severe blunt chest trauma. *Chest* 2001; **120**: 543-547 [PMID: 11502656 DOI: 10.1378/chest.120.2.543]
- 31 **Belotti EA**, Rizzi M, Rodoni-Cassis P, Ragazzi M, Zanolari-Caledrerari M, Bianchetti MG. Air within the spinal canal in spontaneous pneumomediastinum. *Chest* 2010; **137**: 1197-1200 [PMID: 20442120 DOI: 10.1378/chest.09-0514]
- 32 **Kono T**, Kuwashima S, Fujioka M, Kobayashi C, Koike K, Tsuchida M, Seki I. Epidural air associated with spontaneous pneumomediastinum in children: uncommon complication? *Pediatr Int* 2007; **49**: 923-927 [PMID: 18045298 DOI: 10.1111/j.1442-200X.2007.02480.x]
- 33 **Lantsberg L**, Rosenzweig V. Pneumomediastinum causing pneumoperitoneum. *Chest* 1992; **101**: 1176 [PMID: 1555448 DOI: 10.1378/chest.101.4.1176]
- 34 **Uva JL**. Spontaneous pneumothoraces, pneumomediastinum, and pneumoperitoneum: consequences of smoking crack cocaine. *Pediatr Emerg Care* 1997; **13**: 24-26 [PMID: 9061731 DOI: 10.1097/00006565-199702000-00008]
- 35 **Hussain N**, Noce T, Sharma P, Jagjivan B, Hegde P, Pappagallo M, Bhandari A. Pneumatocèles in preterm infants: incidence and outcome in the post-surfactant era. *J Perinatol* 2010; **30**: 330-336 [PMID: 19812584 DOI: 10.1038/jp.2009.162]

P- Reviewer: Lassandro F, Li YZ, Shen J **S- Editor:** Ji FF
L- Editor: A **E- Editor:** Lu YJ



Management of hepatocellular carcinoma: The role of contrast-enhanced ultrasound

Shu-Guang Zheng, Hui-Xiong Xu, Lin-Na Liu

Shu-Guang Zheng, Hui-Xiong Xu, Lin-Na Liu, Department of Medical Ultrasound, Tenth People's Hospital of Tongji University, Shanghai 200072, China

Author contributions: Zheng SG, Xu HX and Liu LN conducted literature research; Zheng SG wrote the paper; Liu LN prepared the figure; Xu HX edited and revised the paper.

Supported by National Natural Science Foundation of China, Nos. 81371570, 81301229 and 81301299; Key Project from Shanghai Health Bureau, No. 20114003; Shanghai Talent Development Project from Shanghai Human Resource and Social Security Bureau, No. 2012045

Correspondence to: Hui-Xiong Xu, MD, PhD, Department of Medical Ultrasound, Shanghai Tenth People's Hospital, Tenth People's Hospital of Tongji University, No. 301 Yanchangzhong Road, Shanghai 200072, China. xuhuixiong@hotmail.com

Telephone: +86-21-66301031 Fax: +86-21-66301031

Received: June 23, 2013 Revised: October 31, 2013

Accepted: November 15, 2013

Published online: March 28, 2015

Abstract

Hepatocellular carcinoma (HCC) is the sixth most common neoplasm and the third cause of cancer death worldwide. Contrast enhanced ultrasound (CEUS) has been applied for more than ten years and plays increasingly important roles in the management of HCC. On the basis of the Guideline and Good Clinical Practice Recommendations for CEUS in the liver-update 2012 and related literature about the management of HCC, we summarize the main roles and applications of CEUS in the management of HCC, including HCC surveillance, diagnosis, CEUS-guided treatment, treatment response evaluation and follow-up. The diagnostic algorithm for HCC is also suggested. Meanwhile, the comparisons between CEUS and contrast enhanced computed tomography/magnetic resonance imaging (CECT/CEMRI) in these areas are made. Although CEUS is subject to the same limitation as ordinary US and is inferior to CECT/CEMRI in some aspects, CEUS has proved to be of great value in the management of HCC with inher-

ent advantages, such as sufficient high safety profile making it suitable for patients with renal failure or allergic to iodine, absence of radiation, easy reproducibility and high temporal resolution. The tremendous application of CEUS to the diagnosis and treatment of HCC provides more opportunities for patients with HCC diagnosed at different stages.

© 2015 Baishideng Publishing Group Inc. All rights reserved.

Key words: Hepatocellular carcinoma; Contrast enhanced ultrasound; Ultrasound contrast agent; Imaging; Sonography

Core tip: Whether contrast enhanced ultrasound (CEUS) is comparable to contrast enhanced computed tomography/magnetic resonance imaging (CECT/CEMRI) in the management of hepatocellular carcinoma (HCC) is a controversial topic recently. Regarding to this issue, we list almost all the updated applications of CEUS in this paper and discuss the main role of CEUS in the management of HCC by comparison with CECT/CEMRI.

Original sources: Zheng SG, Xu HX, Liu LN. Management of hepatocellular carcinoma: The role of contrast-enhanced ultrasound. *World J Radiol* 2014; 6(1): 7-14 Available from: URL: <http://www.wjgnet.com/1949-8470/full/v6/i1/7.htm> DOI: <http://dx.doi.org/10.4329/wjrv6.i1.7>

INTRODUCTION

Hepatocellular carcinoma (HCC) is the sixth most common neoplasm and the third cause of cancer death worldwide^[1,2]. In most cases, HCC develops within an established background of chronic liver disease (70%-90% of all patients) and most of the patients have a background of liver cirrhosis^[3]. The development of HCC is

thought to occur through a multistep process in about 90% of cases in the following sequence: large regenerative nodule (RN), low- or high-grade dysplastic nodule (DN), DN with a focus of HCC, well differentiated HCC, and moderately to poorly differentiated HCC^[4]. On a histopathologic basis, portal tracts, including the portal vein and normal hepatic artery, are decreased with increasing grade of malignancy and are almost absent in HCC. On the other hand, abnormal arteries due to tumour angiogenesis progressively increase in the course of hepatocarcinogenesis. This progressive neo-angiogenesis provides the clue for clinical diagnosis of HCC using imaging techniques.

With the progress in HCC research and the application of new techniques, the management of HCC is updated frequently and patients with HCC at various stages have more optional therapeutic strategies. The patients can benefit from more effective treatments that will dramatically improve their survival. Among these new techniques, contrast enhanced ultrasound (CEUS) plays increasingly important roles in the management of HCC^[2,5-8]. Since the advent of the second generation microbubble contrast agents (such as SonoVue, Definity and Luminity) and nonlinear harmonic contrast imaging technique, CEUS has been applied to HCC management for more than ten years, including HCC surveillance, diagnosis, CEUS-guided treatment, treatment response evaluation and follow-up^[9]. A series of CEUS application modes, such as 2D or 3D transabdominal CEUS and intraoperative CEUS (IO-CEUS), are developed and applied clinically for management of HCC^[8]. Beside the above-mentioned vascular change, HCC tends to lack Kupffer cells (reticuloendothelial cells), particularly in case of progressive dedifferentiation from well to moderately and poorly differentiated HCC. This has become of particular importance with the introduction of Sonazoid, a new contrast agent which can be engulfed by Kupffer cells. This contrast agent has a postvascular phase, which begins 10 min after contrast administration and lasts for 60 min. HCC always shows an enhancement defect in the postvascular phase due to the lack of Kupffer cells whereas benign lesions always show sustained enhancement. The advent of Sonazoid brings CEUS into the era of cell functional imaging or molecular US imaging^[7,10-12].

Here, on the basis of the Guideline and Good Clinical Practice Recommendations for CEUS in the liver -update 2012^[7] and other literature about the management of HCC, we summarize the main roles and applications of CEUS in the management of HCC.

SURVEILLANCE FOR HCC

In cirrhotic livers, the risk of HCC increases with the increase in nodule size. Nodules < 1 cm are rarely malignant. Attention should be paid to nodules > 1 cm. The rate of HCC is 66% in nodules 1-2 cm in diameter, about 80% in nodules 2-3 cm and 92%-95% in nodules > 3 cm. The most challenging situation for imaging techniques

is the diagnosis of nodules 1-3 cm in diameter^[7]. It has been proven that surveillance for HCC can decrease the disease-related mortality. For screening HCC in high-risk patients with viral-related cirrhosis or chronic alcoholic liver disease, US follow-up (at 3-6 mo intervals) is recommended, according to the AASLD guidelines^[2,6], due to its simple, non-invasive, cost-effective and real-time features, although the tumor detectability by US is not high enough^[8,13]. CEUS has not yet been recommended as the sole imaging tool for screening HCC, which is largely ascribed to that examining the entire liver during the arterial phase to find hyperenhancing nodules is difficult or impossible by CEUS because of the short duration of the arterial phase. Washout in the portal or late phase is helpful for detection, whereas it is only observable in about 50% of cases. Sonazoid, unlike SonoVue, is different from pure blood-pool UCA, and its postvascular phase lasts up to 60 min, which may improve the detection rate of HCC by CEUS. CEUS with Sonazoid detects liver malignancies as defects in the postvascular phase with a sensitivity of 95%, specificity of 93%, positive predictive value (PPV) of 99%, and negative predictive value (NPV) of 97%^[4,7,14-16].

CHARACTERIZATION OF HCC BY CEUS

HCC has generally been regarded as a hypervascular tumor. Conventional color Doppler US and power Doppler US have limited ability to depict intralesional vascularity, because both of them are insensitive to slow-flowing, deeply located blood vessels and are usually associated with many artifacts. Thus, their diagnostic capability for HCC is limited. On CEUS, HCC in cirrhotic livers typically exhibits arterial hyper-enhancement in comparison with the surrounding liver tissue, which is encountered in 93.5%-97% of cases^[17-20]. Hyper-enhancement in the arterial phase is usually homogeneous and intense in HCC, but may be inhomogeneous in larger nodules (> 5 cm), because of the regions of necrosis. A thin, perilesional, rim-like hyperenhancement is seen in about 5%-34.6% of HCC cases, which may represent the tumor capsule or blood vessels around the lesion^[17-20]. In most of the cases, HCC always shows earlier enhancement than the surrounding liver tissue. The detection rates of hyper-enhancement in lesions ≤ 1.0 cm, 1.1-2.0 cm, and 2.1-3.0 cm are 67%, 83%-88%, and 92%-100%, respectively^[19,23]. Apparently, CEUS has a relatively low ability to determine the characteristics of smaller lesions.

Washout in the late phase is observed overall in about half of the cases of HCC but more rarely in small nodules (20%-30% in those 1-2 cm)^[7]. This is more frequent in patients in Eastern countries, because washout is found in 80.4% of HCC cases in the portal phase and in 95.3% of HCC cases in the late phase^[17,18]. However, in those 1-2 cm, only 53.5% exhibited washout in the portal phase and 69%-90.7% in the late phase^[19,24]. Washout is observed more frequently and quickly in HCC with poorer grades of differentiation than in well-differentiated HCC, which tend

to be iso-enhanced in the late phase^[25-27]. In comparison with other liver malignancies such as intrahepatic cholangiocarcinoma (ICC) and metastatic liver cancer, washout in the late phase is usually less marked in HCC^[7,28-32]. In addition, washout tends to start later in HCC, usually not before 60 s after UCA injection, and in about 25% of cases, appearing only after 180 s; therefore, it is important to observe nodules in cirrhosis until very late (> 4 min) to increase the sensitivity for the diagnosis of HCC^[7].

The tumor thrombus in the portal or hepatic vein is an important sign of HCC progression and determines HCC stage and therapeutic strategy. Thus, it is crucial to differentiate the malignant thrombus from benign thrombosis. CEUS is also valuable in evaluating the presence and extension of the portal or hepatic vein thrombosis caused by tumor invasion. Hyper-enhancement of the thrombus in the arterial phase indicates malignant thrombosis whereas non-enhancement indicates benign thrombosis. CEUS seems to be superior to CT in detection (100% *vs* 68%) and characterization (98% *vs* 68%) of the portal thrombosis complicating HCC^[33]. The tumor source of the malignant portal vein thrombus may be invisible on US, especially in the case of diffuse HCC in which portal vein thrombus may be the only visible clue. Moving the transducer from the thrombus to the adjacent liver tissue is recommended to find if there is any washout region and the washout regions should undergo reinjection to observe the arterial hyper-enhancement^[7].

In cirrhotic livers, arterial hyperenhancement with subsequent washout facilitates the diagnosis of HCC when other lesions such as hemangioma, ICC, abscess, and hypervascular liver metastasis are excluded. On the other hand, arterial hyperenhancement without subsequent washout is also highly suspicious for HCC, mainly well-differentiated HCC, but is not conclusive^[7,34-36]. An inconclusive CEUS pattern should prompt other contrast imaging (CECT or CEMRI), and if these are still inconclusive, biopsy is recommended. In general, the sensitivity, specificity, and PPV of CEUS in diagnosing HCC are 88.8%, 89.2% and 91.3%, respectively^[18]. The diagnostic ability is highly associated with the nodular size; the sensitivities in nodules 1.0-2.0, 2.1-3.0 and 3.1-5.0 cm are 69%-80%, 97% and 100%, respectively, and the accuracies are 82%-87%, 97% and 100%, respectively^[17,19,24].

The 2005 American Association for the Study of Liver Diseases (AASLD) guidelines has accepted CEUS as a reference imaging for the diagnosis of HCC just like contrast-enhanced CT or MRI^[6]. CEUS is still a part of the Japanese guideline on HCC and the Asian Pacific Association for the Study of the Liver consensus recommendations on HCC but has been removed from the latest American guidelines^[6]. This is partly justified by the fact that no UCA is licensed for the liver in the United States and additionally because of perceived possibility of false-positive HCC diagnosis in patients with ICC when CEUS is used alone. The role of CEUS in differential diagnosis between HCC and ICC is still controversial. ICC always enhances later and more slightly and washes out more quickly than HCC on CEUS. In fact, in experienced

hands, CEUS has the same accuracy as contrast-enhanced CT in diagnosing ICC and the likelihood of misdiagnosis is minimal^[29-32].

The other major concern in cirrhotic livers is to make a distinction between HCC and other nodules such as large RN, low-grade and high-grade DN. Pathologically, large RN and low-grade DN generally show arterial and capillary supply similar to that detected in the adjacent cirrhotic nodules, whereas high-grade DN and HCC may show abnormally increased arterial supply. About 33.3%-60% of high grade DN cases show arterial hyper-enhancement whereas 40%-66.7% show hypo-enhancement^[21,24]. Washout is seldom found in the late phase for high grade DN, in contrast to typical HCC. Occasionally, cancerous foci of very well differentiated HCC is encountered within DN, which is called nodule-in-nodule lesion or DN with a focus of HCC. Differentiation between HCC and these nodules is always a major concern in cirrhotic livers, as the appearance in BUS may be similar but their prognosis is substantially different from each other. CEUS facilitates the detection of HCC portion in DN, because HCC portion generally shows arterial hyper-enhancement.

HCC in cirrhotic livers usually does not harbor reticuloendothelial (Kupffer) cells, different from normal and cirrhotic liver parenchyma and from most solid benign liver lesions. The absence of Kupffer cells causes a defect in Sonazoid uptake in the postvascular phase. The diagnostic capability of CEUS with Sonazoid in the postvascular phase is similar to that of MRI with superparamagnetic iron oxide (SPIO) and has been endorsed in the Japanese guidelines for the management of HCC^[10-12,37,38].

Furthermore, CEUS has an inherent advantage over CECT or CEMRI: its real-time imaging can not only dynamically display the vascular perfusion of HCC, but also carry on quantitative analysis for FLL on the basis of time intense curve, which indeed helps radiologists to read CEUS images accurately and to avoid misdiagnose due to some subjective biases^[2,5,7,8,19].

Little information is available for the role of CEUS in the diagnosis of HCC in non-cirrhotic livers. On CEUS, the enhancement pattern has no difference in comparison with that in cirrhotic livers. However, the lesions that should be differentiated may be different, especially for those appearing arterial hyper-enhancement and subsequent sustained enhancement. Under such circumstance, the lesions need to be differentiated from those including focal nodular hyperplasia, liver adenoma, and some small hemangioma. For the lesions that show arterial hyper-enhancement and subsequent washout, attention also should be paid to exclude liver metastasis and ICC, because the latter two lesions are often encountered in non-cirrhotic livers^[29-32,39,40].

DIAGNOSTIC WORK-UP FOR HCC BASED ON US AND CEUS

The diagnosis of HCC should be based not only on the

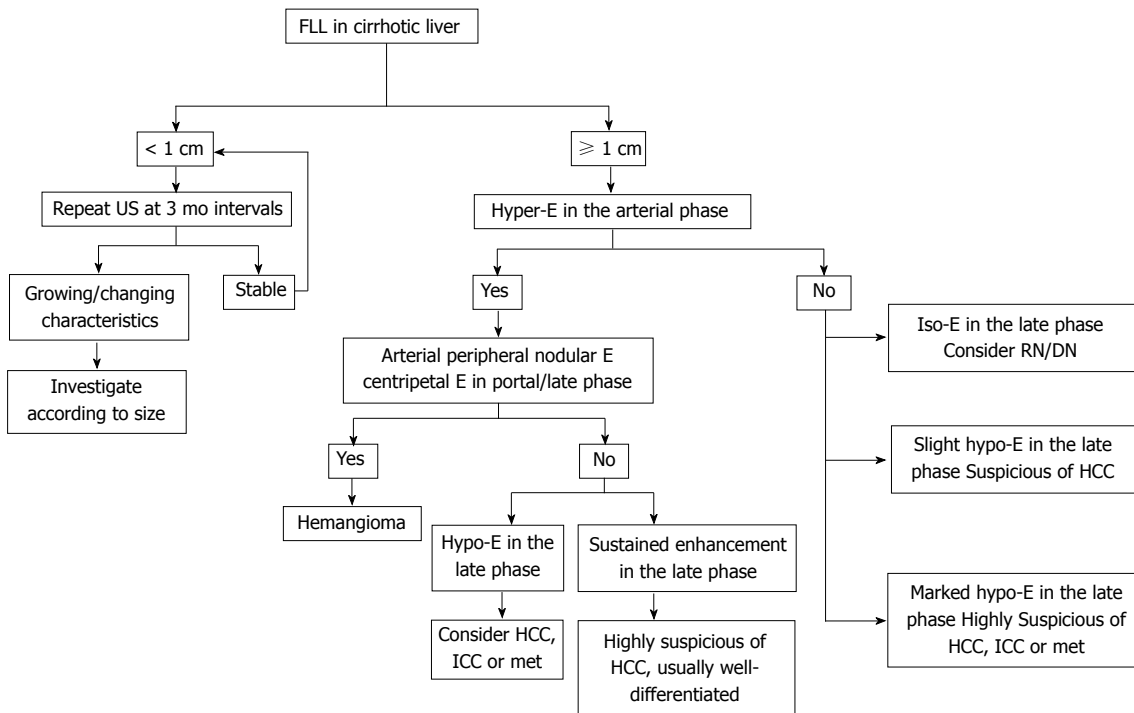


Figure 1 The diagnostic algorithm for hepatocellular carcinoma. FLL: Focal liver lesion; US: Ultrasound; RN: Regenerative nodule; DN: Dysplastic nodule; HCC: Hepatocellular carcinoma; ICC: Intrahepatic cholangiocarcinoma; met: Metastasis; E: Enhancement.

imaging findings but also on clinical background, such as liver cirrhosis or hepatitis. Recent studies show that alpha-fetoprotein determination lacks adequate sensitivity and specificity for effective surveillance and diagnosis^[41,42]. Thus, diagnosis of HCC should be based on imaging techniques and/or biopsy. The application of dynamic imaging criteria should be applied only to patients with cirrhosis of any etiology and to patients with chronic hepatitis B who may not have fully developed cirrhosis or have regressed cirrhosis^[6]. In view of the updated AASLD guideline and the 2012 liver CEUS guideline, the diagnosis algorithm for HCC is suggested as following (Figure 1).

CEUS-GUIDED PERCUTANEOUS BIOPSY AND THERAPY

Clinically, percutaneous biopsy and therapy are commonly operated under the guidance of US or CT, whereas a part of HCC in patients with cirrhotic livers or repeated treatment history usually cannot be figured out on unenhanced US^[7,13,43]. Although CT-guided percutaneous treatment is a well-established technique and a useful method for HCC lesions undetected by US, its inconvenience and radiation exposure have to be taken into account^[13].

In order to get the definite pathologic diagnosis before therapy, US-guided percutaneous biopsy has already been regarded as the preferred choice for the cases that cannot show typical manifestations on imaging. CEUS prior to biopsy procedures can increase the diagnostic yield by 10% and decrease the false negative rate, especially in large tumors with areas of necrosis. CEUS can

localize the site for biopsy more accurately by demonstrating regions of the vascularized viable tumor, which should be targeted, and regions of necrosis, which should be avoided^[7,44].

Besides surgical resection and liver transplantation, local percutaneous therapy, such as ethanol ablation (EA), radiofrequency ablation (RFA), microwave ablation (MWA) and cryotherapy, is always the primary choice in the management of HCC as a minimally invasive method, especially for small, recurrent, and residual HCC lesions after local ablation or transcatheter arterial chemoembolization (TACE)^[5]. Survival after ablation in Child-Pugh A patients is 50%-70% at 5 years, paralleling the outcome after surgical resection^[2,45,46]. As a new guidance tool, CEUS represents a significant improvement in all steps of HCC percutaneous therapy. Prior to the percutaneous therapy, CEUS can be used to assess the HCC lesion size, number, margins and its relationship with the surrounding structures, which is helpful to devise the best therapeutic strategy, to reduce the risk of complications, and to compare the patterns before and after treatment^[7]. CEUS can not only accurately tell the location of HCC but also guide real-time puncture during the arterial phase, or its sufficient long portal-venous and late phases. Moreover, UCA can be administrated repeatedly to guide percutaneous therapy at multiple sites or for multi-lesions^[7,8,47].

TREATMENT RESPONSE EVALUATION AND FOLLOW-UP

With respect to the evaluation of HCC treatment re-

sponse, currently, the use of contrast enhanced imaging to detect the viable tumor or recurrent HCC is widely accepted^[8,47-49]. Previously, CECT or CEMRI has been regarded as the reference standard for treatment response evaluation after local therapies. Recently, several studies have proven that CEUS has the same ability to evaluate treatment response as CECT or CEMRI, thus CEUS can be performed as an alternative method to spare CECT or CEMRI for this purpose^[8,50-53]. CEUS, similar to CECT or CEMRI, also follows the guideline of the modified Response Evaluation Criteria in Solid Tumor (mRECIST)^[54]. In this guideline, viable HCC is defined as uptake of contrast agent in the arterial phase of CEUS; while complete response is defined as disappearance of any intratumoral arterial enhancement in HCC lesions^[54]. In past decades, the assessment of HCC treatment response is mainly on the basis of change in tumor size, but it disregards the extent of necrosis and seems unsuitable for TACE and some targeted therapies, such as Sorafenib or monoclonal antibodies, in which anti-tumor effect mainly results from destroying the tumor blood vessel or suppressing angiogenesis. The change of microvascularization is also confirmed as the criterion for treatment response evaluation in mRECIST. Thus, on CEUS, the disappearance of intratumor arterial enhancement indicates internal necrosis after the treatment of HCC^[54,55].

It should be noted that the time point of treatment response evaluation by CEUS is not limited except for percutaneous therapy. Because on CEUS the reactive hyperemia generated in the procedure of percutaneous therapy, such as RFA, EA and MWA, will cover the ablated HCC lesions in several days, the residual viable tumor may be missed. Within 2 wk after percutaneous therapy, the reactive hyperemia around the ablated lesion is apt to be misdiagnosed as false positive residual HCC. Given the above-mentioned phenomena, some experts have recommended that CEUS should be performed in a month after percutaneous therapy. However, there is still controversy over the role of CEUS *vs* CECT in the treatment response evaluation of HCC after ablation, which is probably influenced by the individual opinion and familiarity with the techniques^[16]. Frieser *et al*^[56] has concluded that CEUS is equal to CECT in evaluating treatment response; Gallotti *et al*^[57] found that CEUS was excellent in evaluating treatment response after RFA, whereas it was inadequate for evaluating treatment response after EA.

After the treatment of HCC, contrast enhanced imaging in a month may fail to detect the tiny viable tumor tissue, especially when neoangiogenesis is not obvious. Therefore, the follow-up should aim to detect the progression of incomplete necrotic HCC and find the intrahepatic recurrence as early as possible, so that the patients can benefit timely from additional and effective therapy that will improve their survival, save the costs and reduce the side effects^[15,58,59].

According to the previous studies, compared with CECT after HCC ablation, the sensitivity, specificity, PPV, NPV and overall accuracy of follow-up CEUS in

detecting local tumor progression were 67.5%, 97.4%, 81.8%, 94.4% and 92.3%, respectively, and for detection of new intrahepatic recurrence were 77.7%, 92.0%, 92.4%, 76.7% and 84.0%, respectively^[15,16]. Thus, CEUS is not comparable to CECT, because, similar to surveillance, it is difficult to provide an overview of the liver to detect all possible HCC progressions and intrahepatic recurrences on CEUS even if reinjection of UCA is carried out^[5,7,15,16]. But when follow-up CECT or CEMRI is contraindicated or not inclusive, CEUS as a substitute or complementary method can be applied to assess the HCC progression and intrahepatic recurrence^[7,15].

Thus, for the treatment response assessment of HCC, CEUS can be equal to CECT/CEMRI. And as a complement to CECT/CEMRI, CEUS may be used in follow-up protocols.

IO-CEUS

IO-CEUS is commonly used for intraoperatively detecting and locating HCC before resection and has attracted more attention of surgeons. Generally, CECT or CEMRI are considered as standard and basic imaging tools for preoperative staging and detection of metastasis or primary liver tumors. However, intraoperative ultrasound (IOUS) is increasingly used by most centers as several studies showed that up to 40% of malignant lesions are missed by the preoperative cross-sectional imaging^[60,61]. Even though the cross-sectional imaging techniques have continuously improved, IOUS was still able to detect additional liver lesions in 10% of patients^[60]. The use and value of IO-CEUS during surgery was reported firstly by Leen *et al*^[62] in 2006, and IO-CEUS also showed even significantly better sensitivity in detecting liver metastasis compared to CECT, CEMRI and IOUS with an alteration of surgical management in almost 30% of cases^[60,62]. Recently, Loss *et al*^[60] reported that more than 50% additional liver lesions were found on IO-CEUS compared to preoperative imaging and IOUS, and that with IO-CEUS equipped with a high frequency linear transducer, some liver lesions even smaller than 10 mm in diameter can be detected and characterized^[60]. The improved sensitivity of IO-CEUS was also confirmed by other studies^[63-65]. Though most of the above-mentioned studies were not focused on HCC, IO-CEUS remains to be of potential value. It is now recognized that the more aggressive the surgical approach adopted, the higher the impact of IO-CEUS becomes^[7,62].

In conclusion, although CEUS is subject to the same limitation as baseline US and is inferior to CECT/CEMRI in some aspects, CEUS is proved to be of great value in management of HCC with inherent advantages, such as sufficient high safety profile suitable for patients with renal failure or allergic to iodine, absence of radiation, easy repeatability and high temporal resolution. The tremendous application of CEUS to the diagnosis and treatment of HCC provides more opportunities for patients with HCC at different stages.

REFERENCES

- 1 **Ferlay J**, Shin HR, Bray F, Forman D, Mathers C, Parkin DM. Estimates of worldwide burden of cancer in 2008: GLOBOCAN 2008. *Int J Cancer* 2010; **127**: 2893-2917 [PMID: 21351269 DOI: 10.1002/ijc.25516]
- 2 **Forner A**, Llovet JM, Bruix J. Hepatocellular carcinoma. *Lancet* 2012; **379**: 1245-1255 [PMID: 22353262 DOI: 10.1016/S0140-6736(11)61347-0]
- 3 **Sherman M**. Hepatocellular carcinoma: epidemiology, surveillance, and diagnosis. *Semin Liver Dis* 2010; **30**: 3-16 [PMID: 20175029 DOI: 10.1055/s-0030-1247128]
- 4 **International Consensus Group for Hepatocellular Neoplasia**. Pathologic diagnosis of early hepatocellular carcinoma: a report of the international consensus group for hepatocellular neoplasia. *Hepatology* 2009; **49**: 658-664 [PMID: 19177576 DOI: 10.1002/hep.22709]
- 5 **Claudon M**, Cosgrove D, Albrecht T, Bolondi L, Bosio M, Calliada F, Correas JM, Darge K, Dietrich C, D'Onofrio M, Evans DH, Filice C, Greiner L, Jäger K, Jong Nd, Leen E, Lencioni R, Lindsell D, Martegani A, Meairs S, Nolsøe C, Piscaglia F, Ricci P, Seidel G, Skjoldbye B, Solbiati L, Thorelius L, Tranquart F, Weskott HP, Whittingham T. Guidelines and good clinical practice recommendations for contrast enhanced ultrasound (CEUS) - update 2008. *Ultraschall Med* 2008; **29**: 28-44 [PMID: 18270887 DOI: 10.1055/s-2007-963785]
- 6 **Bruix J**, Sherman M. Management of hepatocellular carcinoma: an update. *Hepatology* 2011; **53**: 1020-1022 [PMID: 21374666 DOI: 10.1002/hep.24199]
- 7 **Claudon M**, Dietrich CF, Choi BI, Cosgrove DO, Kudo M, Nolsøe CP, Piscaglia F, Wilson SR, Barr RG, Chammas MC, Chaubal NG, Chen MH, Clevert DA, Correas JM, Ding H, Forsberg F, Fowlkes JB, Gibson RN, Goldberg BB, Lassau N, Leen EL, Mattrey RF, Moriyasu F, Solbiati L, Weskott HP, Xu HX. Guidelines and good clinical practice recommendations for Contrast Enhanced Ultrasound (CEUS) in the liver - update 2012: A WFUMB-EFSUMB initiative in cooperation with representatives of AFSUMB, AIUM, ASUM, FLAUS and ICUS. *Ultrasound Med Biol* 2013; **39**: 187-210 [PMID: 23137926 DOI: 10.1016/j.ultrasmedbio]
- 8 **Xu HX**. Contrast-enhanced ultrasound: The evolving applications. *World J Radiol* 2009; **1**: 15-24 [PMID: 21160717 DOI: 10.4329/wjr.v1.i1.15]
- 9 **Bauer A**, Hauff P, Lazenby J, von Behren P, Zomack M, Reinhardt M, Schlieff R. Wideband harmonic imaging: a novel contrast ultrasound imaging technique. *Eur Radiol* 1999; **9** Suppl 3: S364-S367 [PMID: 10602930]
- 10 **Hatanaka K**, Kudo M, Minami Y, Ueda T, Tatsumi C, Kitai S, Takahashi S, Inoue T, Hagiwara S, Chung H, Ueshima K, Maekawa K. Differential diagnosis of hepatic tumors: value of contrast-enhanced harmonic sonography using the newly developed contrast agent, Sonazoid. *Intervirol* 2008; **51** Suppl 1: 61-69 [PMID: 18544950 DOI: 10.1159/000122600]
- 11 **Hatanaka K**, Kudo M, Minami Y, Maekawa K. Sonazoid-enhanced ultrasonography for diagnosis of hepatic malignancies: comparison with contrast-enhanced CT. *Oncology* 2008; **75** Suppl 1: 42-47 [PMID: 19092271 DOI: 10.1159/000173423]
- 12 **Inoue T**, Kudo M, Hatanaka K, Takahashi S, Kitai S, Ueda T, Ishikawa E, Hagiwara S, Minami Y, Chung H, Ueshima K, Maekawa K. Imaging of hepatocellular carcinoma: qualitative and quantitative analysis of postvascular phase contrast-enhanced ultrasonography with sonazoid. Comparison with superparamagnetic iron oxide magnetic resonance images. *Oncology* 2008; **75** Suppl 1: 48-54 [PMID: 19092272 DOI: 10.1159/000173424]
- 13 **Maruyama H**, Yoshikawa M, Yokosuka O. Current role of ultrasound for the management of hepatocellular carcinoma. *World J Gastroenterol* 2008; **14**: 1710-1719 [PMID: 18350602]
- 14 **Maruyama H**, Takahashi M, Ishibashi H, Yoshikawa M, Yokosuka O. Contrast-enhanced ultrasound for characterization of hepatic lesions appearing non-hypervascular on CT in chronic liver diseases. *Br J Radiol* 2012; **85**: 351-357 [PMID: 21224305 DOI: 10.1259/bjr/20440141]
- 15 **Zheng SG**, Xu HX, Lu MD, Xie XY, Xu ZF, Liu GJ, Liu LN. Role of contrast-enhanced ultrasound in follow-up assessment after ablation for hepatocellular carcinoma. *World J Gastroenterol* 2013; **19**: 855-865 [PMID: 23430451 DOI: 10.3748/wjg.v19.i6.855]
- 16 **Liu LN**, Xu HX, Zhang YF, Xu JM. Hepatocellular carcinoma after ablation: the imaging follow-up scheme. *World J Gastroenterol* 2013; **19**: 797-801 [PMID: 23429970 DOI: 10.3748/wjg.v19.i6.797]
- 17 **Xu HX**, Liu GJ, Lu MD, Xie XY, Xu ZF, Zheng YL, Liang JY. Characterization of small focal liver lesions using real-time contrast-enhanced sonography: diagnostic performance analysis in 200 patients. *J Ultrasound Med* 2006; **25**: 349-361 [PMID: 16495496]
- 18 **Xu HX**, Liu GJ, Lu MD, Xie XY, Xu ZF, Zheng YL, Liang JY. Characterization of focal liver lesions using contrast-enhanced sonography with a low mechanical index mode and a sulfur hexafluoride-filled microbubble contrast agent. *J Clin Ultrasound* 2006; **34**: 261-272 [PMID: 16788957]
- 19 **Xu HX**, Xie XY, Lu MD, Liu GJ, Xu ZF, Zheng YL, Liang JY, Chen LD. Contrast-enhanced sonography in the diagnosis of small hepatocellular carcinoma & lt; or =2 cm. *J Clin Ultrasound* 2008; **36**: 257-266 [PMID: 18088056]
- 20 **Quaia E**, Calliada F, Bertolotto M, Rossi S, Garioni L, Rosa L, Pozzi-Mucelli R. Characterization of focal liver lesions with contrast-specific US modes and a sulfur hexafluoride-filled microbubble contrast agent: diagnostic performance and confidence. *Radiology* 2004; **232**: 420-430 [PMID: 15286314]
- 21 **Bolondi L**, Gaiani S, Celli N, Golfieri R, Grigioni WF, Leoni S, Venturi AM, Piscaglia F. Characterization of small nodules in cirrhosis by assessment of vascularity: the problem of hypovascular hepatocellular carcinoma. *Hepatology* 2005; **42**: 27-34 [PMID: 15954118]
- 22 **Gaiani S**, Celli N, Piscaglia F, Cecilioni L, Losinno F, Giangregorio F, Mancini M, Pini P, Fornari F, Bolondi L. Usefulness of contrast-enhanced perfusional sonography in the assessment of hepatocellular carcinoma hypervascular at spiral computed tomography. *J Hepatol* 2004; **41**: 421-426 [PMID: 15336445]
- 23 **Chen MH**, Dai Y, Yan K, Fan ZH, Yin SS, Yang W, Wu W, Wang YB, Li JY. The role of contrast-enhanced ultrasound on the diagnosis of small hepatocellular carcinoma (& lt; / =3cm) in patients with cirrhosis. *Hepatol Res* 2006; **35**: 281-288 [PMID: 16784887]
- 24 **Xu HX**, Lu MD, Liu LN, Zhang YF, Guo LH, Xu JM, Liu C. Discrimination between neoplastic and non-neoplastic lesions in cirrhotic liver using contrast-enhanced ultrasound. *Br J Radiol* 2012; **85**: 1376-1384 [PMID: 22553290 DOI: 10.1259/bjr/19932596]
- 25 **Fan ZH**, Chen MH, Dai Y, Wang YB, Yan K, Wu W, Yang W, Yin SS. Evaluation of primary malignancies of the liver using contrast-enhanced sonography: correlation with pathology. *AJR Am J Roentgenol* 2006; **186**: 1512-1519 [PMID: 16714638]
- 26 **Iavarone M**, Sangiovanni A, Forzenigo LV, Massironi S, Fraquelli M, Aghemo A, Ronchi G, Biondetti P, Roncalli M, Colombo M. Diagnosis of hepatocellular carcinoma in cirrhosis by dynamic contrast imaging: the importance of tumor cell differentiation. *Hepatology* 2010; **52**: 1723-1730 [PMID: 20842697 DOI: 10.1002/hep.23903]
- 27 **Xu H**, Lu M. The current status of contrast-enhanced ultrasound in China. *J Med Ultrason* 2010; **37**: 97-106
- 28 **Barreiros AP**, Piscaglia F, Dietrich CF. Contrast enhanced ultrasound for the diagnosis of hepatocellular carcinoma (HCC): comments on AASLD guidelines. *J Hepatol* 2012; **57**: 930-932 [PMID: 22739095 DOI: 10.1016/j.jhep.2012.04.018]
- 29 **Chen LD**, Xu HX, Xie XY, Xie XH, Xu ZF, Liu GJ, Wang Z, Lin MX, Lu MD. Intrahepatic cholangiocarcinoma and he-

- patocellular carcinoma: differential diagnosis with contrast-enhanced ultrasound. *Eur Radiol* 2010; **20**: 743-753 [PMID: 19760416 DOI: 10.1007/s00330-009-1599-8]
- 30 **Chen LD**, Xu HX, Xie XY, Lu MD, Xu ZF, Liu GJ, Liang JY, Lin MX. Enhancement patterns of intrahepatic cholangiocarcinoma: comparison between contrast-enhanced ultrasound and contrast-enhanced CT. *Br J Radiol* 2008; **81**: 881-889 [PMID: 18941048 DOI: 10.1259/bjr/22318475]
- 31 **Xu HX**, Chen LD, Liu LN, Zhang YF, Guo LH, Liu C. Contrast-enhanced ultrasound of intrahepatic cholangiocarcinoma: correlation with pathological examination. *Br J Radiol* 2012; **85**: 1029-1037 [PMID: 22374276 DOI: 10.1259/bjr/21653786]
- 32 **Xu HX**, Lu MD, Liu GJ, Xie XY, Xu ZF, Zheng YL, Liang JY. Imaging of peripheral cholangiocarcinoma with low-mechanical index contrast-enhanced sonography and SonoVue: initial experience. *J Ultrasound Med* 2006; **25**: 23-33 [PMID: 16371552]
- 33 **Rossi S**, Ghittoni G, Ravetta V, Torello Viera F, Rosa L, Serassi M, Scabini M, Vercelli A, Tinelli C, Dal Bello B, Burns PN, Calliada F. Contrast-enhanced ultrasonography and spiral computed tomography in the detection and characterization of portal vein thrombosis complicating hepatocellular carcinoma. *Eur Radiol* 2008; **18**: 1749-1756 [PMID: 18369630 DOI: 10.1007/s00330-008-0931-z]
- 34 **Forner A**, Vilana R, Ayuso C, Bianchi L, Solé M, Ayuso JR, Boix L, Sala M, Varela M, Llovet JM, Brú C, Bruix J. Diagnosis of hepatic nodules 20 mm or smaller in cirrhosis: Prospective validation of the noninvasive diagnostic criteria for hepatocellular carcinoma. *Hepatology* 2008; **47**: 97-104 [PMID: 18069697]
- 35 **Jang HJ**, Kim TK, Burns PN, Wilson SR. Enhancement patterns of hepatocellular carcinoma at contrast-enhanced US: comparison with histologic differentiation. *Radiology* 2007; **244**: 898-906 [PMID: 17709836]
- 36 **Leoni S**, Piscaglia F, Golfieri R, Camaggi V, Vidili G, Pini P, Bolondi L. The impact of vascular and nonvascular findings on the noninvasive diagnosis of small hepatocellular carcinoma based on the EASL and AASLD criteria. *Am J Gastroenterol* 2010; **105**: 599-609 [PMID: 19935786 DOI: 10.1038/ajg.2009.654]
- 37 **Kudo M**, Hatanaka K, Kumada T, Toyoda H, Tada T. Double-contrast ultrasound: a novel surveillance tool for hepatocellular carcinoma. *Am J Gastroenterol* 2011; **106**: 368-370 [PMID: 21301463 DOI: 10.1038/ajg.2010.432]
- 38 **Moriyasu F**, Itoh K. Efficacy of perflubutane microbubble-enhanced ultrasound in the characterization and detection of focal liver lesions: phase 3 multicenter clinical trial. *AJR Am J Roentgenol* 2009; **193**: 86-95 [PMID: 19542399 DOI: 10.2214/AJR.08.1618]
- 39 **Zheng SG**, Xu HX, Liu LN, Wang Y, Zhang YF, Guo LH, Liu C, Xu JM, Sun LP, Wu J. Parametric imaging with contrast-enhanced ultrasound: Usefulness for characterization of dynamic effects of microvascularization for hepatocellular carcinoma and focal nodular hyperplasia. *Clin Hemorheol Microcirc* 2013; **55**: 375-389 [PMID: 23271200]
- 40 **Lin MX**, Xu HX, Lu MD, Xie XY, Chen LD, Xu ZF, Liu GJ, Xie XH, Liang JY, Wang Z. Diagnostic performance of contrast-enhanced ultrasound for complex cystic focal liver lesions: blinded reader study. *Eur Radiol* 2009; **19**: 358-369 [PMID: 18795298 DOI: 10.1007/s00330-008-1166-8]
- 41 **Singal A**, Volk ML, Waljee A, Salgia R, Higgins P, Rogers MA, Marrero JA. Meta-analysis: surveillance with ultrasound for early-stage hepatocellular carcinoma in patients with cirrhosis. *Aliment Pharmacol Ther* 2009; **30**: 37-47 [PMID: 19392863 DOI: 10.1111/j.1365-2036.2009.04014.x]
- 42 **Lok AS**, Sterling RK, Everhart JE, Wright EC, Hoefs JC, Di Bisceglie AM, Morgan TR, Kim HY, Lee WM, Bonkovsky HL, Dienstag JL. Des-gamma-carboxy prothrombin and alpha-fetoprotein as biomarkers for the early detection of hepatocellular carcinoma. *Gastroenterology* 2010; **138**: 493-502 [PMID: 19852963 DOI: 10.1053/j.gastro.2009.10.031]
- 43 **Miyamoto N**, Hiramatsu K, Tsuchiya K, Sato Y. Contrast-enhanced sonography-guided radiofrequency ablation for the local recurrence of previously treated hepatocellular carcinoma undetected by B-mode sonography. *J Clin Ultrasound* 2010; **38**: 339-345 [PMID: 20572066 DOI: 10.1002/jcu.20720]
- 44 **Wu W**, Chen MH, Yin SS, Yan K, Fan ZH, Yang W, Dai Y, Huo L, Li JY. The role of contrast-enhanced sonography of focal liver lesions before percutaneous biopsy. *AJR Am J Roentgenol* 2006; **187**: 752-761 [PMID: 16928941]
- 45 **Lencioni R**. Loco-regional treatment of hepatocellular carcinoma. *Hepatology* 2010; **52**: 762-773 [PMID: 20564355 DOI: 10.1002/hep.23725]
- 46 **Cho YK**, Kim JK, Kim MY, Rhim H, Han JK. Systematic review of randomized trials for hepatocellular carcinoma treated with percutaneous ablation therapies. *Hepatology* 2009; **49**: 453-459 [PMID: 19065676 DOI: 10.1002/hep.22648]
- 47 **Xu HX**. Era of diagnostic and interventional ultrasound. *World J Radiol* 2011; **3**: 141-146 [PMID: 21666820 DOI: 10.4329/wjr.v3.i5.141]
- 48 **Xu HX**, Lu MD, Xie XH, Xie XY, Kuang M, Xu ZF, Liu GJ, Wang Z, Chen LD, Lin MX. Treatment response evaluation with three-dimensional contrast-enhanced ultrasound for liver cancer after local therapies. *Eur J Radiol* 2010; **76**: 81-88 [PMID: 19500929 DOI: 10.1016/j.ejrad.2009.05.006]
- 49 **Xu HX**, Lu MD, Xie XH, Xie XY, Xu ZF, Chen LD, Liu GJ, Liang JY, Lin MX, Wang Z, Huang B. Three-dimensional contrast-enhanced ultrasound of the liver: experience of 92 cases. *Ultrasonics* 2009; **49**: 377-385 [PMID: 19041996 DOI: 10.1016/j.ultras.2008.10.009]
- 50 **Salvaggio G**, Campisi A, Lo Greco V, Cannella I, Meloni MF, Caruso G. Evaluation of posttreatment response of hepatocellular carcinoma: comparison of ultrasonography with second-generation ultrasound contrast agent and multidetector CT. *Abdom Imaging* 2010; **35**: 447-453 [PMID: 19562414 DOI: 10.1007/s00261-009-9551-6]
- 51 **Lu MD**, Yu XL, Li AH, Jiang TA, Chen MH, Zhao BZ, Zhou XD, Wang JR. Comparison of contrast enhanced ultrasound and contrast enhanced CT or MRI in monitoring percutaneous thermal ablation procedure in patients with hepatocellular carcinoma: a multi-center study in China. *Ultrason Med Biol* 2007; **33**: 1736-1749 [PMID: 17629608]
- 52 **Andreana L**, Kudo M, Hatanaka K, Chung H, Minami Y, Maekawa K, Ruggiero G. Contrast-enhanced ultrasound techniques for guiding and assessing response to locoregional treatments for hepatocellular carcinoma. *Oncology* 2010; **78** Suppl 1: 68-77 [PMID: 20616587]
- 53 **Inoue T**, Kudo M, Hatanaka K, Arizumi T, Takita M, Kitai S, Yada N, Hagiwara S, Minami Y, Sakurai T, Ueshima K, Nishida N. Usefulness of contrast-enhanced ultrasonography to evaluate the post-treatment responses of radiofrequency ablation for hepatocellular carcinoma: comparison with dynamic CT. *Oncology* 2013; **84** Suppl 1: 51-57 [PMID: 23428859 DOI: 10.1159/000345890]
- 54 **Lencioni R**, Llovet JM. Modified RECIST (mRECIST) assessment for hepatocellular carcinoma. *Semin Liver Dis* 2010; **30**: 52-60 [PMID: 20175033 DOI: 10.1055/s-0030-1247132]
- 55 **Forner A**, Ayuso C, Varela M, Rimola J, Hessheimer AJ, de Lope CR, Reig M, Bianchi L, Llovet JM, Bruix J. Evaluation of tumor response after locoregional therapies in hepatocellular carcinoma: are response evaluation criteria in solid tumors reliable? *Cancer* 2009; **115**: 616-623 [PMID: 19117042 DOI: 10.1002/cncr.24050]
- 56 **Frieser M**, Kiesel J, Lindner A, Bernatik T, Haensler JM, Janika R, Hahn EG, Strobel D. Efficacy of contrast-enhanced US versus CT or MRI for the therapeutic control of percutaneous radiofrequency ablation in the case of hepatic malignancies. *Ultraschall Med* 2011; **32**: 148-153 [PMID: 21225567 DOI: 10.1055/s-0029-1245934]

- 57 **Gallotti A**, D'Onofrio M, Ruzzenente A, Martone E, De Robertis R, Guglielmi A, Pozzi Mucelli R. Contrast-enhanced ultrasonography (CEUS) immediately after percutaneous ablation of hepatocellular carcinoma. *Radiol Med* 2009; **114**: 1094-1105 [PMID: 19756947 DOI: 10.1007/s11547-009-0436-0]
- 58 **Liu LN**, Xu HX, Lu MD, Xie XY. Percutaneous ultrasound-guided thermal ablation for liver tumor with artificial pleural effusion or ascites. *Chin J Cancer* 2010; **29**: 830-835 [PMID: 20800026]
- 59 **Frapas E**, Lassau N, Zappa M, Vullierme MP, Koscielny S, Vilgrain V. Advanced Hepatocellular Carcinoma: early evaluation of response to targeted therapy and prognostic value of Perfusion CT and Dynamic Contrast Enhanced-Ultrasonography. Preliminary results. *Eur J Radiol* 2013; **82**: e205-e211 [PMID: 23273822 DOI: 10.1016/j.ejrad.2012.12.004]
- 60 **Loss M**, Schneider J, Uller W, Wiggermann P, Scherer MN, Jung W, Schlitt HJ, Stroszczyński C, Jung EM. Intraoperative high resolution linear contrast enhanced ultrasound (IOUS) for detection of microvascularization of malignant liver lesions before surgery or radiofrequency ablation. *Clin Hemorheol Microcirc* 2012; **50**: 65-77 [PMID: 22538536 DOI: 10.3233/CH-2011-1444]
- 61 **Sietses C**, Meijerink MR, Meijer S, van den Tol MP. The impact of intraoperative ultrasonography on the surgical treatment of patients with colorectal liver metastases. *Surg Endosc* 2010; **24**: 1917-1922 [PMID: 20112115 DOI: 10.1007/s00464-009-0874-8]
- 62 **Leen E**, Ceccotti P, Moug SJ, Glen P, MacQuarrie J, Angerson WJ, Albrecht T, Hohmann J, Oldenburg A, Ritz JP, Horgan PG. Potential value of contrast-enhanced intraoperative ultrasonography during partial hepatectomy for metastases: an essential investigation before resection? *Ann Surg* 2006; **243**: 236-240 [PMID: 16432357 DOI: 10.1097/01.sla.0000197708.77063.07]
- 63 **Fioole B**, de Haas RJ, Wicherts DA, Elias SG, Scheffers JM, van Hillegersberg R, van Leeuwen MS, Borel Rinkes IH. Additional value of contrast enhanced intraoperative ultrasound for colorectal liver metastases. *Eur J Radiol* 2008; **67**: 169-176 [PMID: 17467944 DOI: 10.1016/j.ejrad.2007.03.017]
- 64 **Jung EM**, Ross CJ, Rennert J, Scherer MN, Farkas S, von Breitenbuch P, Schnitzbauer AA, Piso P, Lamby P, Menzel C, Schreyer AG, Feuerbach S, Schlitt HJ, Loss M. Characterization of microvascularization of liver tumor lesions with high resolution linear ultrasound and contrast enhanced ultrasound (CEUS) during surgery: First results. *Clin Hemorheol Microcirc* 2010; **46**: 89-99 [PMID: 21135485 DOI: 10.3233/CH-2010-1336]
- 65 **Larsen LP**, Rosenkilde M, Christensen H, Bang N, Bolvig L, Christiansen T, Laurberg S. The value of contrast enhanced ultrasonography in detection of liver metastases from colorectal cancer: a prospective double-blinded study. *Eur J Radiol* 2007; **62**: 302-307 [PMID: 17194561 DOI: 10.1016/j.ejrad.2006.11.033]

P- Reviewer: Yoshida S **S- Editor:** Wen LL
L- Editor: Wang TQ **E- Editor:** Wang CH



Treatment of metastatic liver tumors using stereotactic ablative radiotherapy

Vimoj J Nair, Jason R Pantarotto

Vimoj J Nair, Jason R Pantarotto, Division of Radiation Oncology, Ottawa Hospital Research Institute, University of Ottawa, Ottawa K1H 8L6, Ontario, Canada

Author contributions: Nair VJ and Pantarotto JR contributed equally to this work.

Supported by The Ottawa Hospital Foundation; the Ethel Ward Cushing Legacy Endowment Fund for a stereotactic ablative radiotherapy fellowship

Correspondence to: Jason R Pantarotto, MD, FRCPC, Chair, Division of Radiation Oncology, Ottawa Hospital Research Institute, University of Ottawa, 501 Smyth Road, Ottawa K1H 8L6, Ontario, Canada. jpantarotto@toh.on.ca

Telephone: +1-613-7377700 **Fax:** +1-613-2473511

Received: August 26, 2013 **Revised:** December 16, 2013

Accepted: January 6, 2014

Published online: March 28, 2015

Key words: Liver; Metastasis; Stereotactic; Radiotherapy; Ablative

Core tip: The body of evidence related to the use of stereotactic ablative radiotherapy (SABR) in metastatic liver disease has substantially grown and evolved over the past decade. This review summarizes the current evidence supporting liver SABR with particular attention given to patient selection, target delineation, organ at risk dose volume constraints, response evaluation imaging and the various SABR techniques for delivering ablative radiotherapy to the liver.

Original sources: Nair VJ, Pantarotto JP. Treatment of metastatic liver tumors using stereotactic ablative radiotherapy. *World J Radiol* 2014; 6(2): 18-25 Available from: URL: <http://www.wjgnet.com/1949-8470/full/v6/i2/18.htm> DOI: <http://dx.doi.org/10.4329/wjrr.v6.i2.18>

Abstract

The prognosis of patients with metastatic liver disease remains dismal with a median survival of only 6-12 mo. As 80%-90% of patients are not candidates for surgical therapy, there is a need for effective non-surgical therapies that would improve outcomes in these patients. The body of evidence related to the use of stereotactic ablative radiotherapy (SABR) in metastatic liver disease has substantially grown and evolved over the past decade. This review summarizes the current evidence supporting liver SABR with particular attention given to patient selection, target delineation, organ at risk dose volume constraints, response evaluation imaging and the various SABR techniques for delivering ablative radiotherapy to the liver. Even though it is unclear what dose-fractionation scheme, delivery system, concomitant therapy or patient selection strategy yields the optimum liver SABR outcomes, clear and growing evidence is available that SABR is a safe and effective therapy for the treatment of oligometastatic liver disease.

INTRODUCTION

Metastatic disease to the liver constitutes the most common malignant hepatic tumor, accounting for 45% of all liver tumors followed by hepatocellular carcinoma at 28%^[1]. Any clinical or radiological evidence of cancer cells in the liver would deem the patient as stage IV no matter what the primary source of the malignancy is and the intent of treatment traditionally has been palliative. With advances in systemic and local therapies a steady decline in the nihilistic approach to patients with liver metastasis has evolved. The definition of the term "oligometastases" as an intermediate state in the multi-step nature of cancer spread between stages of purely localised and widely spread metastases has made its way into the common vernacular of the clinic. The implication is that patients with oligometastatic disease can be cured with metastasis directed therapy before it disseminates further. This ap-

© 2015 Baishideng Publishing Group Inc. All rights reserved.

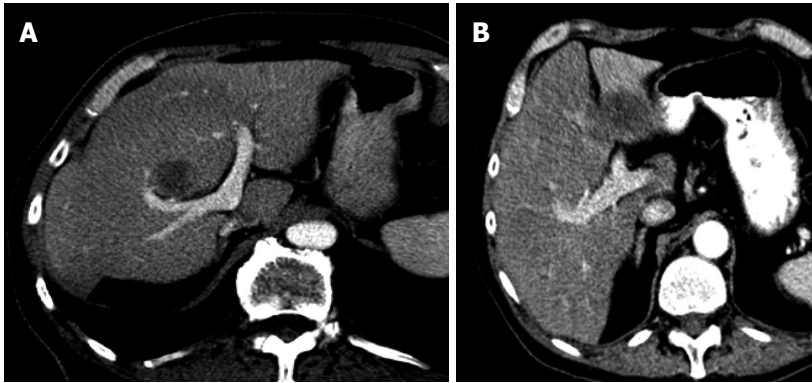


Figure 1 Images demonstrating tumors close to the critical structures. In these cases stereotactic ablative radiotherapy could prove useful than radiofrequency ablation or other alternative non-surgical therapies. A more fractionated regimen would be useful to minimise toxicity when abutting luminal structures. A: tumor abutting vascular trunk; B: Tumor close to luminal gastrointestinal structures (stomach in this case).

appears to be true for liver metastasis arising from cancers of the colon or rectum where the natural history of cancer can be relatively indolent and spread can be paradoxically limited to just one organ (the liver) for a long time before ever metastasizing elsewhere. The majority of the experience with liver metastasis-directed therapies is with colorectal cancer (CRC) liver metastases (CRCLM). Approximately 50% of colon cancer patients will be diagnosed with hepatic metastases, either at the time of initial presentation or as a result of disease recurrence^[2]. With improved outcomes with systemic agents in non-colorectal malignancies an increased demand for liver metastasis-directed therapies in other histopathologies that presents with oligometastases is on the rise.

Among the liver metastasis-directed therapies currently available, surgery forms the standard of care. Modern series analyzing post liver resection survival for patients with CRCLM report 5-year survival of 37%-58% and 10-year survival of 22%-28%^[3]. This improved survival confirms the hypothesis that there could be a subset of patients with liver metastasis who could benefit from liver metastasis-directed therapy; especially when one considers the fact that the 5 years survival for patients with CRCLM without treatment is less than 10% (median survival 6-12 mo)^[4]. In patients with non-CRC, non-neuroendocrine metastasis, a 5- and 10-year survival of 36% and 23% respectively has been reported with resection, with liver metastases originating from breast cancer having the best survival and melanoma and squamous cell cancers or any origin having the worst survival^[5]. Despite the benefits of liver metastasis resection, 80%-90% of patients of such patients are not resectable at diagnosis and hence cannot avail this benefit^[6]. The quandary in patients with inoperable oligometastatic disease lies in deciding what treatment options would provide the best outcomes. Traditionally chemotherapy would be the next option. Numerous histopathology and biology specific chemotherapy agents and targeted therapies have been developed to improve outcomes. However with neoadjuvant chemotherapy, only 10%-30% of these tumors are converted into a resectable status^[7,8]. Also the high systemic toxicity from most of the therapies precludes many patients from completing their course and generally would seek alternative liver directed therapies especially when they have only 1-5 metastasis confined to liver.

Traditionally, radiation therapy for liver metastases was considered to be a palliative therapy due to the low tolerance of the whole liver (20-30 Gy in 2-3 Gy per fraction) and the potential for radiation induced liver disease (RILD). Also the associated survival was very poor. Though less used, radiotherapy to the whole or partial liver still continues to be used for symptom palliation^[9]. Other options for liver metastases are radiofrequency ablation (RFA), cryotherapy, laser-induced thermotherapy, and high-intensity focal ultrasound^[10]. However these liver metastasis-directed ablative therapies have some limitations such as maximum diameter of the metastasis, number of metastases and location within the liver, susceptibility to trauma for adjacent intestine or biliary vessels or for RFA specifically loss of effectiveness with large vessels in proximity which may act as a heat sink (Figure 1)^[11]. Hence there is demand for a non-surgical therapeutic option which can globally treat tumors in most locations and sizes and produce a good response. Liver stereotactic ablative radiotherapy (SABR) is one such technique that may be able to overcome some of these limitations.

SABR FOR LIVER METASTASIS

The Canadian Association of Radiation Oncology has defined stereotactic body radiotherapy (SBRT) as the precise delivery of highly conformal and image-guided hypofractionated external beam radiotherapy, delivered in a single or few fraction(s), to an extracranial body target with doses at least biologically equivalent to a radical course when given over a protracted conventionally (1.8-3.0 Gy/fraction) fractionated schedule^[12]. SABR, stereotactic radiotherapy or radiosurgery are other terms used to describe this technique. Advanced radiation planning and delivery techniques have helped in conforming the ablative radiation doses tightly to the target with a surrounding sharp dose gradient, and have enabled greater confidence of intra-fraction tumour position with improved image guidance.

The initial experience with SABR for liver tumors was based on the principles of intracranial radiosurgery with a fixed body frame for rigid immobilisation. The earliest report was in 1995 in Stockholm, Sweden where investigators reported the results of 42 extracranially (solitary

Table 1 Prospective clinical trials in the literature studying stereotactic ablative radiotherapy in liver metastases and their results

Ref.	Design	No of patients	Tumor size	SABR dose	Toxicity	Outcomes
Scorsetti <i>et al</i> ^[15]	Phase II (preliminary report)	61 (76 tumors)	1.8-134.3 cm ³ (mean 18.6 cm ³)	75 Gy in 3 fractions	No case of RILD. Twenty-six percent had grade 2 transaminase increase (normalised in 3 mo). Grade 2 fatigue in 65% patients, one grade 3 chest wall pain which regressed within 1 year.	1-yr LC94, 22-mo LC 90.6%
Goodman <i>et al</i> ^[16]	Phase I (HCC and liver mets)	26 (19 liver mets)	0.8-146.6 mL (median, 32.6 mL)	Dose escalation, 18-30 Gy (1 fr)	No dose-limiting toxicity 4 cases of Grade 2 late toxicity (2 GI, 2 soft tissue/rib)	1-yr local failure, 3% 2-yr OS, 49% (mets only)
Ambrosino <i>et al</i> ^[17]	Prospective cohort	27	20-165 mL (median, 69 mL)	25-60 Gy (3 fr)	No serious toxicity	Crude LC rate 74%
Lee <i>et al</i> ^[18]	Phase I - II	68	1.2-3090 mL (median, 75.9 mL)	Individualized dose, 27.7-60 Gy (6 fr)	No RILD, 10% Grade 3/4 acute toxicity No Grade 3/4 late toxicity	1-yr LC, 71% Median survival, 17.6 mo
Rusthoven <i>et al</i> ^[19]	Phase I - II	47	0.75-97.98 mL (median, 14.93 mL)	Dose escalation, 36-60 Gy (3 fr)	No RILD, Late Grade 3/4 < 2%	1-yr LC, 95% 2-yr LC, 92% Median survival, 20.5 mo
Høyer <i>et al</i> ^[10]	Phase II (CRC oligometas)	64 (44 liver mets)	1-8.8 cm (median, 3.5 cm)	45 Gy (3 fr)	One liver failure, two severe late GI Toxicities	2-yr LC, 79% (by tumor) and 64% (by patient)
Méndez Romero <i>et al</i> ^[20]	Phase I - II (HCC and mets)	25 (17 liver mets)	1.1-322 mL (median, 22.2 mL)	30-37.5 Gy (3 fr)	Two Grade 3 liver toxicities	2-yr LC, 86% 2-yr OS, 62%
Herfarth <i>et al</i> ^[21]	Phase I - II	35	1-132 mL (median, 10 mL)	Dose escalation, 14-26 Gy (1 fr)	No significant toxicity reported	1-yr LC, 71% 18-mo LC, 67% 1-yr OS, 72%

SABR: Stereotactic ablative radiotherapy; RILD: Radiation induced liver disease; CRC: Colorectal cancer; HCC: Hepatocellular carcinoma; GI: Gastrointestinal; LC: Local control.

tumors in lung, liver or retroperitoneal space) treated tumors in 31 patients. They reported a response rate of 43% for 14 liver metastases treated with 20-45 Gy in 1-4 fractions, with a prolonged time to maximum response (approximately 16 mo for a 13-cm liver metastasis). No liver toxicity was observed but 1 patient developed grade 4 hemorrhagic gastritis^[13]. In a 1998 update, the local control rate was 95% with a mean survival of 17.8 mo after SABR for 21 patients with liver metastases^[14]. However due to the highly mobile nature of liver tumors with respiration and also their capacity to deform with this motion relative to the external frame, improved image guidance techniques were required to ensure accurate delivery of the high radiation doses. Soon various groups embarked on liver SABR programs and presented their institutional data. Table 1 shows the various prospective clinical trials in the literature studying SABR in liver metastases^[10,15-21].

From various prospective and retrospective trials, SABR for liver metastases shows a local control rates ranging from 70%-100% at 1 year and 60%-90% at 2 years. Median overall survival after SABR ranges from 10 to 34 mo, with 2-year overall survival rates ranging from 30% to 83%, with occasional long-term survivors^[10].

PATIENT SELECTION

There is no consensus regarding the selection criteria for patients for liver SABR. Even though tumors of most histopathologies are selected, the most common are CRCLM. Table 2 demonstrates the most commonly accepted criteria for selecting patients for SABR for liver

metastasis. In general, patients with 1-3 liver metastasis with maximum tumor diameter < 6 cm, liver confined disease, good performance status with pre-treatment Child-Pugh status A are the best candidates for SABR. Patients with underlying hepatic conditions (*e.g.*, chronic hepatitis or cirrhosis) may not be good candidates but this is mainly an issue in SABR for hepatocellular cancers and not with metastases.

In our centre, generally select patients with 1-3 oligo-metastatic liver metastases with pre-treatment Child-Pugh status A/B and tumor size ≤ 6 cm are selected for SABR treatment. In addition tumors unsuitable for RFA treatment due to their size criteria or location close to vessels or gastrointestinal structures are also selected for treatment.

SABR PLATFORMS AND TECHNICAL CONSIDERATIONS

There are various platforms for delivering SABR therapy for patients with liver tumors. The most common is using a modern linear accelerator equipped with some form of image guidance system to deliver SABR. SABR specific units such as the Vero[®] (Mitsubishi Heavy Industries Ltd., Tokyo, Japan and BrainLAB AG, Feldkirchen, Germany) and CyberKnife[®] (Accuray Inc., Sunnyvale, CA, United States) are also on the market. All these modalities report comparable outcomes with their techniques. The CyberKnife[®] is a robotic SABR platform where a miniaturised linear accelerator is mounted on a robotic arm possessing 6 axis of freedom and aligns accurately to the

Table 2 Organ at risk constraints in various prospective trials depending on their fractionation schemes^[10,15,19,21,28-29,31]

Normal Liver (Liver-CTV-RFA cavities)	D30% = 6-12 Gy, D50% = 4-7 Gy	V _{15 Gy} < 700 mL	30% < 21 Gy, 50% < 15 Gy	V _{15 Gy} < 700 mL	V _{15 Gy} < 700 mL	V _{5 Gy} ≤ 700 mL, Dmean < 15 Gy	V _{15 Gy} < 700 mL	V _{21 Gy} < 700 mL
Stomach	Dmax ≤ 12 Gy	NA	D _{5 mL} < 21 Gy	Dmax ≤ 30 Gy	D _{1 mL} < 21 Gy	Dmax < 30 Gy; D _{5 mL} < 22.5 Gy	V _{21 Gy} < 1%	Dmax ≤ 32 Gy, D _{10 mL} < 28 Gy
Bowel	Small bowel Dmax ≤ 35 Gy	D < 5% volume < 20 Gy	D _{5 mL} < 21 Gy	Dmax ≤ 30 Gy	D _{1 mL} < 21 Gy	Dmax < 30 Gy	Duodenum, small bowel V _{21 Gy} < 1%	Duodenum: Dmax ≤ 32 Gy; D _{5 mL} < 18 Gy Jejunum/ileum: Dmax ≤ 35 Gy, D _{5 mL} ≤ 19.5 Gy Colon: ≤ 38 Gy, D _{20 mL} ≤ 25 Gy Dmax ≤ 35 Gy, D _{5 mL} < 27.5 Gy
Esophagus	Dmax ≤ 14 Gy	NA	D _{5 mL} < 21 Gy	NA	D _{1 mL} < 21 Gy	NA	V _{21 Gy} < 1%	
Kidney	NA	75% volume of each kidney < 5 Gy	NA	Total kidney D35% < 15 Gy	Total kidney D35% < 15 Gy	NA	V _{15 Gy} < 35% for both kidneys	Renal hilum/vascular trunk < 2/3 ≤ 23 Gy Renal cortex (right and left): 200 mL < 17.5 Gy (3.5 Gy/fraction)
Spinal cord	NA	Dmax < 12 Gy	NA	Dmax ≤ 18 Gy	Dmax < 18 Gy	Dmax ≤ 20 Gy	D _{0.1 cm³} < 18 Gy	Dmax ≤ 30 Gy, D _{0.25 mL} < 22.5 Gy
Heart/pericardium	NA	NA	D _{5 mL} < 21 Gy	NA	D _{1 mL} < 30 Gy	NA	V _{30 Gy} < 1%	Dmax ≤ 38 Gy, D _{15 mL} < 32 Gy
Skin	NA	NA	NA	NA	NA	NA	NA	Dmax ≤ 32 Gy, D _{10 mL} < 30 Gy
Great vessels	NA	NA	NA	NA	NA	NA	NA	Dmax ≤ 53 Gy, D _{10 mL} < 47 Gy
Chest wall	NA	NA	NA	NA	NA	NA	D _{30 cm³} < 30 Gy	NA

CTV: Clinical target volume; Dx%: Dose to x%; Dx mL/cm³: Dose to x mL/cm³; RFA: Radiofrequency ablation; NA: Not available.

tumor and delivers the radiation in forms of hundreds of beamlets which allows optimisation of tumor dose and spares nearby normal tissues. The CyberKnife Synchrony[®] Respiratory Tracking System utilizes real time imaging of chest position and correlates that with tumor position *via* two orthogonally mounted X-ray units. Implanted fiducials are tracked in real time and used as a surrogate for tumour position. During treatment the system adjusts the position of the delivered beam during respiration so that the dose is delivered consistently to the moving tumor. The different SABR platforms perform image guidance using various imaging modalities such as megavoltage (MV) orthogonal imaging, fluoroscopy, ultrasound, or MV/kV cone beam CT for checking the tumor location prior to treatment.

The various SABR systems rely on imaging of some form of surrogate for the tumor(s) such as the liver itself, implanted fiducials, air-diaphragm interface or air-rib interfaces to help ensure that dose is delivered accurately^[10]. Modern linac-based radiation delivery techniques such as volume modulated arc therapy have made the radiation delivery much faster and hence lessen the amount of uncertainties during treatment.

FIDUCIAL IMPLANTATION, TREATMENT SIMULATION AND PLANNING

For those centres that use fiducials to help identify tumour position within the liver, implantation is usually performed at least one week prior to simulation. For the purpose of image guidance, gold based fiducials are commonly used. There is some evidence that platinum fiducials are better as they are better visualized on the same

treatment planning magnetic resonance imaging (MRI) sequences that gives the best tumor definition and hence a fiducial to fiducial based image registration while treatment planning is possible^[22]. The location of implanted fiducials is also important. Seppenwoolde *et al.*^[23] showed that for liver treatment a close arrangement of fiducials to the tumour is recommended. An ideal implantation would surround the tumor (Figure 2), where the tumor centre is closer to the fiducial centroid^[10]. The fiducials are usually implanted transcutaneously or through endoscopic ultrasound guidance depending on where they are located in the liver. For robotic SABR using the CyberKnife system, identifying fiducials as distinct entities on orthogonal X-rays acquired on the unit is required. Optimal conditions for this include a minimum of 2 cm distance between any two fiducials and a minimum of 15° degree angle within any three fiducials. Fiducials should not be placed in the same plane in such a way that they form about a 45-degree angle with the horizon. No fiducial should be greater than 5 to 6 cm away from the lesion. To track rotational movement, a minimum of three fiducials placed in three different orthogonal planes is necessary.

The treatment planning simulation is usually done after a week of fiducial implantation to allow for development of fibroblastic reaction around the fiducials, making it more fixed to the implanted tissue^[24]. Depending on the SABR platform used, the patient is simulated in the treatment planning position. Use of a body frame with reference fiducial markers or equivalent customized external vacuum-type or synthetic body mould is used in most linac based system to reduce both the patient and respiratory liver motion. Respiratory control is usually achieved by

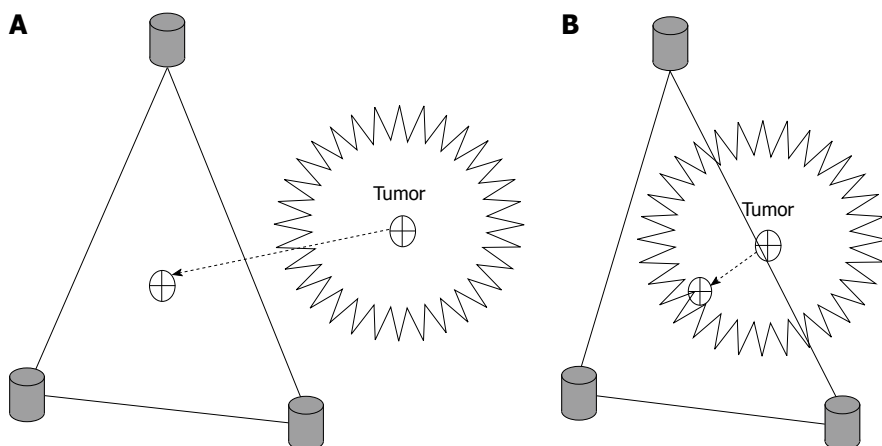


Figure 2 Diagram showing ideal post implantation distribution of the fiducials around the tumor (Adapted from Seppenwoolde *et al*^[23]). Ideally the fiducial arrangement should be centred around the tumor, bracketing the lesion (B) and not lateralized to one side (A). At least 3 fiducials should be implanted.

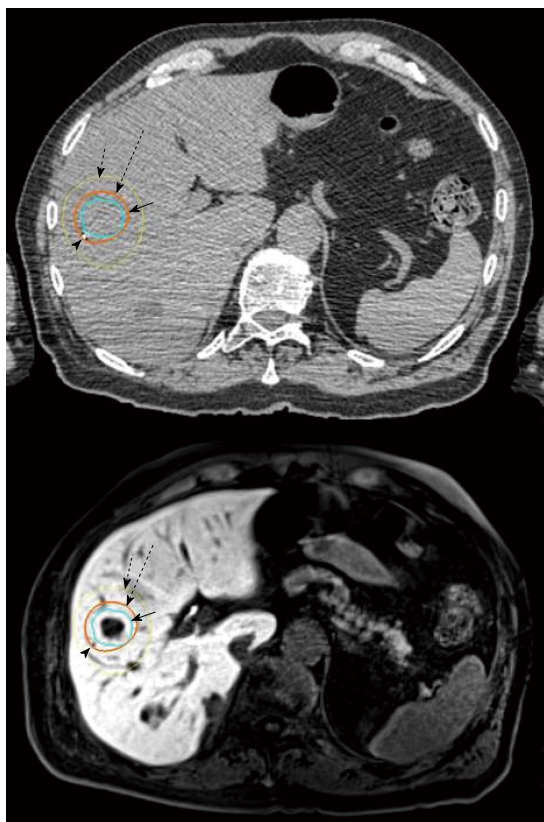


Figure 3 Demonstrating the tight prescription isodose (long broken arrow) around the planning target volume (solid arrow). The steep dose fall gradient is demonstrated by the 50% isodose curve (short broken arrow) around the prescription isodose. Platinum fiducials showed as arrow head as seen in both computed tomography and magnetic resonance imaging.

gating, active breath control or simply using an abdominal compression plate^[25]. Robotic SABR system that perform real time tracking do not require patients to be in any rigid or semi-rigid immobilisation as the system will track the fiducials with breathing. A non-contrast CT scan, contrast enhanced CT scan and ideally a contrast enhanced MRI is used for treatment planning purposes, usually acquired in the same phase of respiration to facilitate easy fusion.

A 4D-CT scan is also of benefit for assessing liver tumor motion and creating larger margins to account for tumor motion. The planning CT and MRI images are registered in the treatment planning system. Some centres use planning PET-CT scans for target delineation^[26].

A gross tumour volume (GTV) is defined as all tumor appreciated on clinical and radiological studies. The clinical target volume (CTV) is generally the same as the GTV for SABR treatments. Centres using 4D-CT to account for respiratory motion may use the minimum intensity projection or maximum intensity projection or a combination to contour the internal target volume (ITV), alternatively they may fuse the 4D-CT images at end-inspiration and end-expiration and contour the tumor in each image and sum of the two would generate the ITV^[27]. The CTV to planning target volume (PTV) margin varies depending on the SABR technique and platform. Most centres use a 5 mm radial margin and a 10 mm cranio-caudal margin to create a PTV. Centres that use fiducial based guidance may use a symmetrical 5 mm margin or less.

The goal of SABR treatment planning for liver metastasis is to produce highly conformal dose distributions with multiple beams using either coplanar or non-coplanar geometries (Figure 3). The prescription dose is generally prescribed to the planning isodose covering the PTV (generally the 80%-90% isodose line). Intensity modulation radiotherapy can be more beneficial around concave targets compared to spherical targets in liver SABR^[28]. In contrast to conventionally fractionated radiotherapy; dose heterogeneities with the target are generally acceptable in the form of a higher dose within the primary tumor, as long as there is no overlap with an organ at risk. Radiobiologically this distribution may also be desirable because as the tumor centre is considered to be relatively hypoxic and hence relatively radioresistant^[29].

TUMOR AND ORGAN AT RISK DOSE VOLUME CONSTRAINTS

Due to lack of clear evidence, various dose fractionation

schemes are used by various centres depending on the technique available and also based on the clinical scenario such as size or location of the tumor. In a phase I trial led by the group at the University of Colorado, it was shown that it is safe to treat up to 3 liver metastases to 60 Gy in 3 fractions as long as a minimum of 700 mL of normal liver receives < 15 Gy total dose in 3 fractions^[19]. Another phase I dose escalation trial from UTSW did not reach maximal tolerated dose but reached the pre-defined maximal dose of 60 Gy in 5 fractions. In this trial at least 700 mL of normal liver had to receive < 21 Gy^[30]. Goodman *et al*^[16] reported a phase I trial of single session SABR to the liver where doses were safely escalated from 18 Gy to 30 Gy in 1 fraction for liver tumors (both metastases and hepatocellular carcinomas). There was no dose limiting toxicity. Lee *et al*^[18] reported the results of a phase I trial which gave individualised tumor prescriptions in 6 fractions guided by NTCP calculations using the Lyman model of normal tissue complication probability. Using this model, the calculated risk of hepatic toxicity was escalated from 5% to 20%. However due to the lack of any RILD noted in none of the 68 patients in the study, there is criticisms that even though this model may be a useful tool for guiding dose selection, it may not predict the actual risk of liver toxicity^[9]. As fractionations beyond the above mentioned are considered to be less ablative and higher total doses may increase liver toxicity, that has been attempted less.

It may be logical to say that for tumor abutting luminal GI structures, a more protracted dose fractionation may be reasonable. Also due to the lesser experience with SABR for larger tumors (> 6 cm in maximal diameter), a more individualised approach similar to the University of Toronto approach or use of a less ablative dose per fraction may be reasonable^[9].

The existence of a dose-response ratio with liver SABR has also been studied. A pooled analysis of 47 CRCLM patients demonstrated that total dose, dose per fraction and biological effective dose (BED) were significant for local control on multivariate analysis. The estimated dose of 46-54 Gy in 3 fractions or a BED of 117 Gy₁₀ (EQD2 = 98 Gy) would be required for a 1-year local control rate of > 90%^[31]. Vautravers-Dewas *et al*^[32] in their series of 42 patients could not demonstrate a clear dose response, however their dose prescription was limited to 40 Gy in 4 fractions and 45 Gy in 3 fractions (BED 80-113 Gy₁₀, EQD2 = 66-94 Gy). The similarity in the BED between the regimens may have contributed to the results. Lanciano *et al*^[11] in a retrospective series treating a cohort of patients mixed histopathologies with higher SABR doses with time also demonstrated that a dose response relationship is possible. An increase local control was noticed for a BED > 100 Gy₁₀ (EQD2 = 90 Gy). All three studies mentioned above did not show tumor size to be a predictor of outcome, counter to traditional beliefs.

Severe (grade 3 or above) toxicity due to SABR to the liver is uncommonly reported. Currently there is no con-

sensus regarding the organ at risk (OAR) dose volume constraints due to the different fractionation schemes and techniques that each centre uses. The Quantitative Analyses of Normal Tissue Effects in the Clinic recommends a mean liver dose of < 15 Gy in three fractions and < 20 Gy in 6 fractions and ≥ 700 mL of normal liver receives ≤ 15 Gy in three to five fractions for a < 5% risk of RILD^[34]. Pre-existing liver dysfunction, as measured by the Child-Pugh score, should be recorded, as well as any change in status of Child-Pugh score after treatment^[9].

Gastrointestinal toxicity is also less commonly reported even though it depends on the location of the tumor. Intestinal ulceration and perforations were reported in 3 patients with bowel doses greater than 30 Gy in 3 fractions^[10]. Grade 3 subcutaneous toxicity has been reported in a single patient with skin doses of 48 Gy in 3 fractions^[30]. Rib fractures has been reported in patients receiving maximum doses to 51.8 Gy and 66.2 Gy in 6 fractions to 0.5 cm³ of rib^[18]. The various prospective trials for liver metastases with their OAR dose volume constraints depending on their fractionation schemes are given in Table 2^[10,15-16,19,21,30,33-34]. Many centres also follow the Rule *et al*^[30] publication of dose volume constraints which even though unvalidated, provides some basic planning constraints for the planners to achieve. But in general, SABR treatments which spare at least 700 cc of liver is associated with almost no toxicity.

In our centre, we would treat with a risk adapted strategy based on the tumor size and capacity for liver sparing. For smaller tumors, we adopt an aggressive strategy with lesser number of fractions such as 54 Gy in 3 fractions and for larger tumors which are close to the intestine, we use protracted fractionation upto 5 fractions (48 Gy in 5 fractions). As fractions more than 5 are not generally classified as SBRT in the United States, the experience with higher doses with protracted fractions is limited.

POST TREATMENT RESPONSE EVALUATION

Post treatment response imaging is usually done by contrast enhanced CT scan or MRI scan at frequent intervals, generally starting 3 mo following treatment and then at least every 3 mo for a year. After a year, the follow-up protocol varies between centres^[15-16,19,21,30,33-34]. Some centres also use PET-CT scan for the post SABR follow-up^[15].

Herfarth *et al*^[35] studied the CT changes of patients treated in a prospective phase I - II post SABR (single fraction) using non-enhanced and contrast enhanced scans acquired at different times after contrast injection. He described three different types of reaction based on time after imaging post SABR corresponding to the histological changes seen in veno-occlusive disease (VOD). Type I occurred up to 3 mo, type II occurred at 3 to 6 mo, and type III occurred more than 6 mo after SABR. The post treatment change is usually a hypodense area (liver metastasis are also typically hypodense) which reduces in size with time. This hypodense area may be

larger than the primary tumor size as the prescription isodose conforms around the PTV which is larger than actual tumor. However there may be a surrounding radiation reaction which may be initially enhancing (pseudo progression) and may undergo change with time.

There are concerns regarding the use of RECIST criteria for post SABR liver imaging. A recent retrospective study by Jarraya *et al*^[36] also reports the use of changes in enhancement in addition to size criteria for response evaluation following SABR. They report that the post SABR VOD that was seen in early imaging as a hypodense area would become fibrotic, becoming smaller and denser on successive follow-ups. The “thin” rim enhancement radiation reaction seen early during the post SABR imaging is likely due to the presence of granulation tissue related to inflammatory response to the treatment. Usually there is a clear border between the target and normal parenchyma at the treatment margin especially with robotic SABR. The authors also described a thick lobular enhancement pattern which could be suggestive of local recurrence, which could present earlier than a size progression. In order to objectively identify necrosis, a objective definition of a difference of ≤ 10 Hounsfield units between the non-contrast and contrast-CT scans in the hypodense areas was used, even if there was an increase in size^[36]. It is important for the treating physician and the radiologist to be aware of these treatment induced changes post SABR, and in case of any suspicion serial imaging may be required to assess these tumors closely and to distinguish between tumor recurrence and pseudo progression due to radiation reaction.

FUTURE CONSIDERATIONS

As with any other treatment, the role of liver SABR for metastatic disease needs to be evaluated by conducting randomised clinical trials comparing the various competing therapies. As out of field recurrences develop in a significant number of patients post SABR, there is a rationale in combining SABR with various systemic and targeted agents. So an optimum combination of various modalities needs to be studied further. Due to the difference in radiobiology, there is also a need to study the various histopathology-specific dose fractionation schemes in order to maximise tumor control and minimise toxicity by delivering lower doses for relatively radio responsive tumors. The role of functional imaging for both radiation planning and for post treatment response evaluation to rule out radiation induced change *vs* recurrence also needs to be elucidated.

CONCLUSION

Stereotactic ablative body radiotherapy is a well-tolerated and effective therapy for patients with liver metastasis who are not suitable candidates for resection. More prospective trial data is required to find the optimum fractionation schedules and to compare its efficacy and toxic-

ity with other competing ablative therapies.

REFERENCES

- 1 **Kasper HU**, Drebber U, Dries V, Dienes HP. Liver metastases: incidence and histogenesis. *Z Gastroenterol* 2005; **43**: 1149-1157 [PMID: 16220456 DOI: 10.1055/s-2005-858576]
- 2 **Mohammad WM**, Balaa FK. Surgical management of colorectal liver metastases. *Clin Colon Rectal Surg* 2009; **22**: 225-232 [PMID: 21037813 DOI: 10.1055/s-0029-1242462]
- 3 **Haddad AJ**, Bani Hani M, Pawlik TM, Cunningham SC. Colorectal liver metastases. *Int J Surg Oncol* 2011; **2011**: 285840 [PMID: 22312501 DOI: 10.1155/2011/285840]
- 4 **Bengmark S**, Hafström L. The natural history of primary and secondary malignant tumors of the liver. I. The prognosis for patients with hepatic metastases from colonic and rectal carcinoma by laparotomy. *Cancer* 1969; **23**: 198-202 [PMID: 5763253]
- 5 **Adam R**, Chiche L, Aloia T, Elias D, Salmon R, Rivoire M, Jaeck D, Saric J, Le Treut YP, Belghiti J, Mantion G, Mentha G. Hepatic resection for noncolorectal nonendocrine liver metastases: analysis of 1,452 patients and development of a prognostic model. *Ann Surg* 2006; **244**: 524-535 [PMID: 16998361]
- 6 **Dawood O**, Mahadevan A, Goodman KA. Stereotactic body radiation therapy for liver metastases. *Eur J Cancer* 2009; **45**: 2947-2959 [PMID: 19773153 DOI: 10.1016/j.ejca.2009.08.011]
- 7 **Kemeny N**. Management of liver metastases from colorectal cancer. *Oncology (Williston Park)* 2006; **20**: 1161-1176, 1179; discussion 1179-1180, 1185-1186 [PMID: 17024869]
- 8 **Adam R**, Delvart V, Pascal G, Valeanu A, Castaing D, Azoulay D, Giacchetti S, Paule B, Kunstlinger F, Ghémard O, Levi F, Bismuth H. Rescue surgery for unresectable colorectal liver metastases downstaged by chemotherapy: a model to predict long-term survival. *Ann Surg* 2004; **240**: 644-657; discussion 657-658 [PMID: 15383792]
- 9 **Schefter TE**, Kavanagh BD. Radiation therapy for liver metastases. *Semin Radiat Oncol* 2011; **21**: 264-270 [PMID: 21939855 DOI: 10.1016/j.semradonc.2011.05.006]
- 10 **Høyer M**, Swaminath A, Bydder S, Lock M, Méndez Romero A, Kavanagh B, Goodman KA, Okunieff P, Dawson LA. Radiotherapy for liver metastases: a review of evidence. *Int J Radiat Oncol Biol Phys* 2012; **82**: 1047-1057 [PMID: 22284028 DOI: 10.1016/j.ijrobp.2011.07.020]
- 11 **Lanciano R**, Lamond J, Yang J, Feng J, Arrigo S, Good M, Brady L. Stereotactic body radiation therapy for patients with heavily pretreated liver metastases and liver tumors. *Front Oncol* 2012; **2**: 23 [PMID: 22645716 DOI: 10.3389/fonc.2012.00023]
- 12 **Sahgal A**, Roberge D, Schellenberg D, Purdie TG, Swaminath A, Pantarotto J, Filion E, Gabos Z, Butler J, Letourneau D, Masucci GL, Mulroy L, Bezjak A, Dawson LA, Parliament M. The Canadian Association of Radiation Oncology scope of practice guidelines for lung, liver and spine stereotactic body radiotherapy. *Clin Oncol (R Coll Radiol)* 2012; **24**: 629-639 [PMID: 22633542 DOI: 10.1016/j.clon.2012.04.006]
- 13 **Blomgren H**, Lax I, Näslund I, Svanström R. Stereotactic high dose fraction radiation therapy of extracranial tumors using an accelerator. Clinical experience of the first thirty-one patients. *Acta Oncol* 1995; **34**: 861-870 [PMID: 7576756 DOI: 10.3109/02841869509127197]
- 14 **Blomgren H**, Lax I, Göranson H, Kræpelien T, Nilsson B, Näslund I, R Svanström, Tilikidis A. Radiosurgery for tumors in the body: clinical experience using a new method. *J Radio-surg* 1998; **1**: 63-74 [DOI: 10.1023/B:JORA.0000010880.40483.c4]
- 15 **Scorsetti M**, Arcangeli S, Tozzi A, Comito T, Alongi F, Navarra P, Mancosu P, Reggiori G, Fogliata A, Torzilli G, Tomatis S, Cozzi L. Is stereotactic body radiation therapy

- an attractive option for unresectable liver metastases? A preliminary report from a phase 2 trial. *Int J Radiat Oncol Biol Phys* 2013; **86**: 336-342 [PMID: 23433800 DOI: 10.1016/j.ijrobp.2012.12.021]
- 16 **Goodman KA**, Wiegner EA, Maturen KE, Zhang Z, Mo Q, Yang G, Gibbs IC, Fisher GA, Koong AC. Dose-escalation study of single-fraction stereotactic body radiotherapy for liver malignancies. *Int J Radiat Oncol Biol Phys* 2010; **78**: 486-493 [PMID: 20350791 DOI: 10.1016/j.ijrobp.2009.08.020]
 - 17 **Ambrosino G**, Polistina F, Costantin G, Francescon P, Guglielmi R, Zanco P, Casamassima F, Febbraro A, Gerunda G, Lumachi F. Image-guided robotic stereotactic radiosurgery for unresectable liver metastases: preliminary results. *Anticancer Res* 2009; **29**: 3381-3384 [PMID: 19661360]
 - 18 **Lee MT**, Kim JJ, Dinniwell R, Brierley J, Lockwood G, Wong R, Cummings B, Ringash J, Tse RV, Knox JJ, Dawson LA. Phase I study of individualized stereotactic body radiotherapy of liver metastases. *J Clin Oncol* 2009; **27**: 1585-1591 [PMID: 19255313 DOI: 10.1200/JCO.2008.20.0600]
 - 19 **Rusthoven KE**, Kavanagh BD, Cardenes H, Stieber VW, Burri SH, Feigenberg SJ, Chidel MA, Pugh TJ, Franklin W, Kane M, Gaspar LE, Scheffter TE. Multi-institutional phase I/II trial of stereotactic body radiation therapy for liver metastases. *J Clin Oncol* 2009; **27**: 1572-1578 [PMID: 19255321]
 - 20 **Méndez Romero A**, Wunderink W, Hussain SM, De Pooter JA, Heijmen BJ, Nowak PC, Nuytens JJ, Brandwijk RP, Verhoef C, Ijzermans JN, Levendag PC. Stereotactic body radiation therapy for primary and metastatic liver tumors: A single institution phase i-ii study. *Acta Oncol* 2006; **45**: 831-837 [PMID: 16982547]
 - 21 **Herfarth KK**, Debus J, Lohr F, Bahner ML, Rhein B, Fritz P, Höss A, Schlegel W, Wannemacher MF. Stereotactic single-dose radiation therapy of liver tumors: results of a phase I/II trial. *J Clin Oncol* 2001; **19**: 164-170 [PMID: 11134209]
 - 22 **Nair VJ**, Szanto J, Vandervoort E, Henderson E, Avruch L, Malone S, Pantarotto J. Feasibility, Detectability and Experience with Platinum Seed Internal Fiducial Markers for CT-MRI Fusion and Real-time Tumor Tracking During Stereotactic Ablative Radiation Therapy. Presented at ASTRO 54th Annual Meeting; 2012 Oct 28-31; Boston, USA. United States: Elsevier Science Inc, 2012: 821
 - 23 **Seppenwoolde Y**, Wunderink W, Wunderink-van Veen SR, Storchi P, Méndez Romero A, Heijmen BJ. Treatment precision of image-guided liver SBRT using implanted fiducial markers depends on marker-tumour distance. *Phys Med Biol* 2011; **56**: 5445-5468 [PMID: 21813963 DOI: 10.1088/0031-9155/56/17/001]
 - 24 **Imura M**, Yamazaki K, Kubota KC, Itoh T, Onimaru R, Cho Y, Hida Y, Kaga K, Onodera Y, Ogura S, Dosaka-Akita H, Shirato H, Nishimura M. Histopathologic consideration of fiducial gold markers inserted for real-time tumor-tracking radiotherapy against lung cancer. *Int J Radiat Oncol Biol Phys* 2008; **70**: 382-384 [PMID: 17881147 DOI: 10.1016/j.ijrobp.2007.06.064]
 - 25 **Scheffter TE**, Kavanagh BD, Timmerman RD, Cardenes HR, Baron A, Gaspar LE. A phase I trial of stereotactic body radiation therapy (SBRT) for liver metastases. *Int J Radiat Oncol Biol Phys* 2005; **62**: 1371-1378 [PMID: 16029795 DOI: 10.1016/j.ijrobp.2005.01.002]
 - 26 **Kavanagh BD**, Scheffter TE, Cardenes HR, Stieber VW, Raben D, Timmerman RD, McCarter MD, Burri S, Nedzi LA, Sawyer TE, Gaspar LE. Interim analysis of a prospective phase I/II trial of SBRT for liver metastases. *Acta Oncol* 2006; **45**: 848-855 [PMID: 16982549 DOI: 10.1080/02841860600904870]
 - 27 **Liu J**, Wang JZ, Zhao JD, Xu ZY, Jiang GL. Use of combined maximum and minimum intensity projections to determine internal target volume in 4-dimensional CT scans for hepatic malignancies. *Radiat Oncol* 2012; **7**: 11 [PMID: 22284745 DOI: 10.1186/1748-717X-7-11]
 - 28 **Liu R**, Buatti JM, Howes TL, Dill J, Modrick JM, Meeks SL. Optimal number of beams for stereotactic body radiotherapy of lung and liver lesions. *Int J Radiat Oncol Biol Phys* 2006; **66**: 906-912 [PMID: 16904842 DOI: 10.1016/j.ijrobp.2006.05.014]
 - 29 **Benedict SH**, Yenice KM, Followill D, Galvin JM, Hinson W, Kavanagh B, Keall P, Lovelock M, Meeks S, Papiez L, Purdie T, Sadagopan R, Schell MC, Salter B, Schlesinger DJ, Shiu AS, Solberg T, Song DY, Stieber V, Timmerman R, Tomé WA, Verellen D, Wang L, Yin FF. Stereotactic body radiation therapy: the report of AAPM Task Group 101. *Med Phys* 2010; **37**: 4078-4101 [PMID: 20879569 DOI: 10.1118/1.3438081]
 - 30 **Rule W**, Timmerman R, Tong L, Abdulrahman R, Meyer J, Boike T, Schwarz RE, Weatherall P, Chinsoo Cho L. Phase I dose-escalation study of stereotactic body radiotherapy in patients with hepatic metastases. *Ann Surg Oncol* 2011; **18**: 1081-1087 [PMID: 21046264 DOI: 10.1245/s10434-010-1405-5]
 - 31 **Chang DT**, Swaminath A, Kozak M, Weintraub J, Koong AC, Kim J, Dinniwell R, Brierley J, Kavanagh BD, Dawson LA, Scheffter TE. Stereotactic body radiotherapy for colorectal liver metastases: a pooled analysis. *Cancer* 2011; **117**: 4060-4069 [PMID: 21432842 DOI: 10.1002/cncr.25997]
 - 32 **Vautravers-Dewas C**, Dewas S, Bonodeau F, Adenis A, Lacornerie T, Penel N, Lartigau E, Mirabel X. Image-guided robotic stereotactic body radiation therapy for liver metastases: is there a dose response relationship? *Int J Radiat Oncol Biol Phys* 2011; **81**: e39-e47 [PMID: 21377292 DOI: 10.1016/j.ijrobp.2010.12.047]
 - 33 **Pan CC**, Kavanagh BD, Dawson LA, Li XA, Das SK, Miften M, Ten Haken RK. Radiation-associated liver injury. *Int J Radiat Oncol Biol Phys* 2010; **76**: S94-100 [PMID: 20171524 DOI: 10.1016/j.ijrobp.2009.06.092]
 - 34 **Wulf J**, Guckenberger M, Haedinger U, Oppitz U, Mueller G, Baier K, Flentje M. Stereotactic radiotherapy of primary liver cancer and hepatic metastases. *Acta Oncol* 2006; **45**: 838-847 [PMID: 16982548]
 - 35 **Herfarth KK**, Hof H, Bahner ML, Lohr F, Höss A, van Kaick G, Wannemacher M, Debus J. Assessment of focal liver reaction by multiphasic CT after stereotactic single-dose radiotherapy of liver tumors. *Int J Radiat Oncol Biol Phys* 2003; **57**: 444-451 [PMID: 12957256 DOI: 10.1016/S0360-3016(03)00586-8]
 - 36 **Jarraya H**, Mirabel X, Taieb S, Dewas S, Tresch E, Bonodeau F, Adenis A, Kramar A, Lartigau E, Ceugnart L. Image-based response assessment of liver metastases following stereotactic body radiotherapy with respiratory tracking. *Radiat Oncol* 2013; **8**: 24 [PMID: 23363610 DOI: 10.1186/1748-717X-8-24]

P- Reviewers: Gao C, Vinh-Hung V, Yokoyama Y
S- Editor: Cui XM **L- Editor:** A **E- Editor:** Wang CH



Imaging pitfalls of pancreatic serous cystic neoplasm and its potential mimickers

Kousei Ishigami, Akihiro Nishie, Yoshiki Asayama, Yasuhiro Ushijima, Yukihisa Takayama, Nobuhiro Fujita, Shunichi Takahata, Takao Ohtsuka, Tetsuhide Ito, Hisato Igarashi, Shuji Ikari, Catherine M Metz, Hiroshi Honda

Kousei Ishigami, Catherine M Metz, Department of Radiology, University of Iowa Hospitals and Clinics, Iowa City, IA 52242, United States

Akihiro Nishie, Yoshiki Asayama, Yasuhiro Ushijima, Yukihisa Takayama, Nobuhiro Fujita, Hiroshi Honda, Department of Clinical Radiology, Kyushu University, 3-1-1 Maidashi, Higashi-ku, Fukuoka City, Japan

Shunichi Takahata, Takao Ohtsuka, Department of Surgery and Oncology, Kyushu University, 3-1-1 Maidashi, Higashi-ku, Fukuoka 812-8582, Japan.

Tetsuhide Ito, Hisato Igarashi, Department of Medicine and Bioregulatory Science, Kyushu University, 3-1-1 Maidashi, Higashi-ku, Fukuoka 812-8582, Japan

Shuji Ikari, Department of Internal Medicine, Hokkaido Gastroenterology Hospital, Sapporo 065-0041, Japan

Author contributions: All authors substantially contributed to the clinical study, acquisition of the data, interpretation of the data, and providing of cases; Ishigami K wrote the manuscript and played a major role in image selection; Honda H and Nishie A critically revised the article for important intellectual content.

Correspondence to: Kousei Ishigami, MD, PhD, Visiting Associate Professor, Department of Radiology, University of Iowa Hospitals and Clinics, 3885 JPP, 200 Hawkins Drive, Iowa City, IA 52242, United States. Ishigamikousei@aol.com

Telephone: +1-319-3561071 Fax: +1-319-3562220

Received: November 12, 2013 Revised: February 11, 2014

Accepted: March 3, 2014

Published online: March 28, 2015

Abstract

The aim of this article is to clarify diagnostic pitfalls of pancreatic serous cystic neoplasm (SCN) that may result in erroneous characterization. Usual and unusual imaging findings of SCN as well as potential SCN mimickers are presented. The diagnostic key of SCN is to look for a cluster of microcysts (honeycomb pattern), which may not be always found in the center. Fibrosis in SCN may be mistaken for a mural nodule of intraductal papillary mucinous neoplasm (IPMN). The

absence of cyst wall enhancement may be helpful to distinguish SCN from mucinous cystic neoplasm. However, oligocystic SCN and branch duct type IPMN may morphologically overlap. In addition, solid serous adenoma, an extremely rare variant of SCN, is difficult to distinguish from neuroendocrine tumor.

© 2015 Baishideng Publishing Group Inc. All rights reserved.

Key words: Serous cystic neoplasm; Intraductal papillary mucinous neoplasm; Mucinous cystic neoplasm; Computed tomography; Magnetic resonance imaging

Core tip: Most serous cystic neoplasm (SCN) consist of a combination of microcystic, macrocystic, and solid-appearing components. The imaging appearance of each component simply reflects the different sizes of cysts that comprise the SCN. The diagnostic key of SCN is to look for a cluster of microcysts (honeycomb pattern). However, differentiation between oligocystic SCN and branch duct type intraductal papillary mucinous neoplasm, and between neuroendocrine tumor and extremely rare solid serous adenoma, may be difficult.

Original sources: Ishigami K, Nishie A, Asayama Y, Ushijima Y, Takayama Y, Fujita N, Takahata S, Ohtsuka T, Ito T, Igarashi H, Ikari S, Metz CM, Honda H. Imaging pitfalls of pancreatic serous cystic neoplasm and its potential mimickers. *World J Radiol* 2014; 6(3): 36-47 Available from: URL: <http://www.wjgnet.com/1949-8470/full/v6/i3/36.htm> DOI: <http://dx.doi.org/10.4329/wjr.v6.i3.36>

INTRODUCTION

Pancreatic serous cystic neoplasm (SCN) is almost always benign^[1-3]. Surgical resection may be indicated when it is large or symptomatic (e.g., recurring pancreatitis), or

when it is difficult to distinguish from potentially malignant mucin-producing pancreatic cystic neoplasms, such as intraductal papillary mucinous neoplasm (IPMN) and mucinous cystic neoplasm (MCN)^[4-8]. However, unusual imaging findings of SCN may result in mischaracterization and lead to unnecessary surgical resection. Therefore, it is important to be aware of unusual imaging findings of SCN and possible causes of mischaracterization. The aim of this manuscript is to clarify unusual imaging findings and diagnostic pitfalls of SCN that may result in erroneous characterization. Surgically resected SCN cases were reviewed and compared to the imaging findings of MCN and IPMN. Additionally, imaging findings of SCN mimickers are presented.

SCN

Between 2001 and 2011, 16 cases of pancreatic SCN were surgically resected. On preoperative imaging, seven of 16 (43.8%) were correctly characterized as SCN (no other differential diagnoses or most likely diagnosis). However, nine of 16 (56.2%) were not correctly diagnosed as SCN. Two were diagnosed as less likely for SCN (SCN was included in the differential diagnoses, but it was not the most likely diagnosis), and seven were mischaracterized as unlikely for SCN (SCN was not included in the differential diagnoses). Of these nine mischaracterized cases, the most likely imaging diagnoses were IPMN ($n = 5$), MCN ($n = 3$), and neuroendocrine tumor (NET) ($n = 1$).

There were 6 male and 10 female patients. The ages ranged from 27 to 75 years old (mean 57 years old). Six of the SCNs were found in the pancreatic head and 10 were in the pancreatic body/tail. The sizes ranged from 2.1 to 7.4 cm (mean 4.5 cm).

Because SCN is not usually surgically resected, there were a substantial number of mischaracterized SCN cases in this patient population. We retrospectively reviewed these 16 cases and clarified the potential causes for mischaracterization.

CONTROL GROUPS

MCN

Between 2001 and 2011, there were 23 surgically resected pancreatic MCN cases. There was one male patient and 22 female patients. The ages ranged from 17 to 76 years old (mean 42 years old). All but one case were found in the body/tail. The sizes ranged from 2.5 to 13.7 cm (mean 5.7 cm).

IPMN

Between 2007 and 2011, there were 72 IPMN cases that were further evaluated by multidetector-row CT (MDCT) and magnetic resonance imaging (MRI)/MR cholangiopancreatography (MRCP) for preoperative planning. In the clinical setting, many IPMNs are easily diagnosed if the communication with the main pancreatic duct (MPD) and prominent downstream MPD are evident. To focus on diagnostically problematic cases, we selected IPMN

cases based on the following inclusion criteria: (1) branch duct type IPMN; (2) no communication with the pancreatic duct on MRCP; (3) no downstream MPD dilatation; and (4) no large solid component occupying the cystic space.

There were seven branch duct type IPMN cases that fit the inclusion criteria. All seven cases were surgically proven. There was one male patient and six female patients. The ages ranged from 45 to 72 years old (mean 62 years old). All were found in the pancreatic body/tail. The sizes ranged from 3.4 to 4.6 cm (mean 3.8 cm).

IMAGING REVIEW

Imaging classification of SCN

MRCP and contrast-enhanced dynamic MDCT or MRI studies of SCN were reviewed, and components of the SCN were classified into three types: microcystic, macrocystic, and solid-appearing. A microcystic component referred to a cluster of microcysts that displayed a honeycomb pattern (high signal on MRCP, Figure 1)^[9-14]. A macrocystic component was defined as a cyst larger than 2 cm (Figure 2)^[15-17]. A solid-appearing component was defined as having no high signal on MRCP with iso to high attenuation/signal intensity on the pancreatic parenchymal phase (radiologically solid regardless of whether it was histologically solid or microcystic, Figure 3).

Based on the SCN components, SCN were classified as: (1) microcystic type; (2) oligocystic type (consisting of a macrocyst and a few small cysts without a honeycomb pattern)^[15-17]; (3) solid-appearing type; and (4) mixed type (combination of at least two different components, Figure 2).

Based on the imaging classification of SCN, nine mischaracterized cases were reviewed and potential causes of mischaracterization were clarified.

Wall enhancement and wall thickness

Presence or absence of cyst wall enhancement and wall thickness were compared between macrocysts in SCN and control groups (branch duct type IPMN and MCN). Cyst wall enhancement was evaluated on the axial images of the equilibrium phase of contrast-enhanced CT (4 min after initiation of the intravenous contrast). For this evaluation, the portions where lesions abutted the pancreatic parenchyma or adjacent organs were avoided.

If wall enhancement was appreciated, wall thickness was measured. Cyst wall thickness was classified as follows: (1) wall thickness was 2 mm or more; (2) wall enhancement was perceptible but wall thickness was less than 2 mm; and (3) no wall enhancement. Cyst wall thickness was compared between macrocysts in SCN and control groups (IPMN and MCN).

ADDITIONAL CASE PRESENTATION

To better illustrate imaging findings of SCN, additional cases of usual and unusual SCN and SCN mimickers are presented.

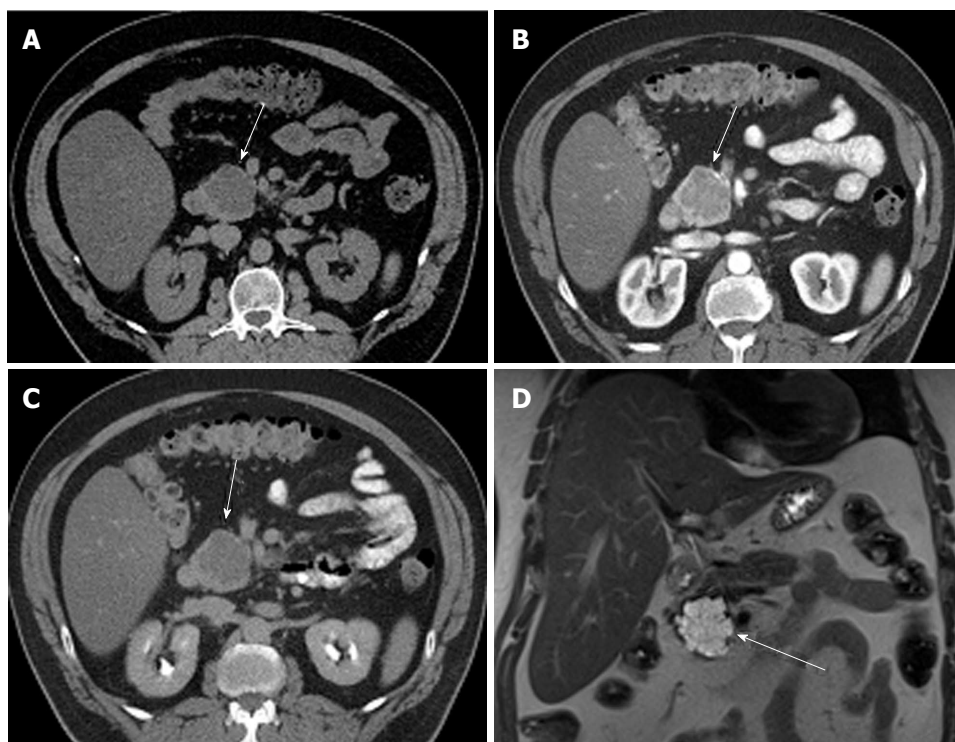


Figure 1 A 65-year-old male with clinically diagnosed typical microcystic serous cystic neoplasm. A: Unenhanced axial computed tomography (CT) shows a low density mass (arrow) relative to the pancreatic head; B: The pancreatic parenchymal phase of a contrast-enhanced CT shows mild patchy tumor enhancement (arrow); C: The equilibrium phase shows the mass to be low density (arrow); D: Coronal T2-weighted single-shot fat saturation-echo magnetic resonance image clearly demonstrate the mass (arrow) consisting of a cluster of microcysts (honeycomb pattern).

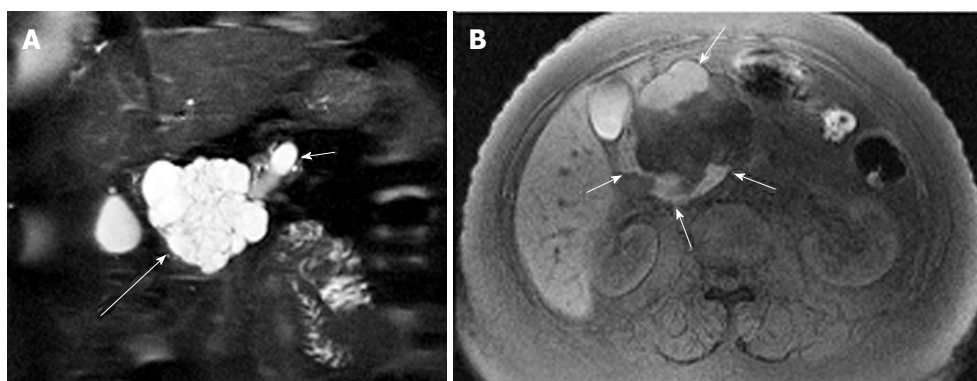


Figure 2 A 57-year-old female with mixed microcystic and macrocystic serous cystic neoplasm. A: Coronal T2-weighted single-shot fast spin-echo magnetic resonance (MR) image with fat saturation shows a cystic mass (large arrow) in the pancreatic head consisting of central microcysts and peripheral macrocysts. The small arrow indicates dilatation of the upstream main pancreatic duct. B: Axial T1-weighted gradient-echo MR image with fat saturation shows high intensity fluid in the macrocysts (arrows), representing hemorrhage. Hemorrhage may be seen in macrocysts, although it is uncommon.

OUTCOME

Of the surgically resected pancreatic SCN, there were six microcystic, five oligocystic, four mixed, and one solid-appearing type (Figure 3). Of the four mixed types, three were mixed microcystic and macrocystic, and one was mixed microcystic and solid (Figure 4). Therefore, ten of 16 (62.5%) had microcystic and eight of 16 (50%) had macrocystic components. Eight cases were further evaluated for the presence or absence of cyst wall enhancement and wall thickness.

Of the nine mischaracterized SCN cases, there were

five oligocystic (Figures 5 and 6), two microcystic, one mixed micro and macrocystic, and one solid-appearing type. All five oligocystic SCN were mischaracterized as either IPMN (Figure 7) or MCN. In two microcystic SCNs, fibrosis in the cystic lesion was erroneously characterized as a mural nodule of IPMN (Figures 8 and 9). In two of three mixed micro and macrocystic SCN, a cluster of microcysts was noted at the peripheral portion (not centrally located) (Figure 10), and one was mischaracterized as a branch duct type IPMN. One solid-appearing SCN was mischaracterized as a neuroendocrine tumor (Figure 3).

The presence or absence of cyst wall enhancement

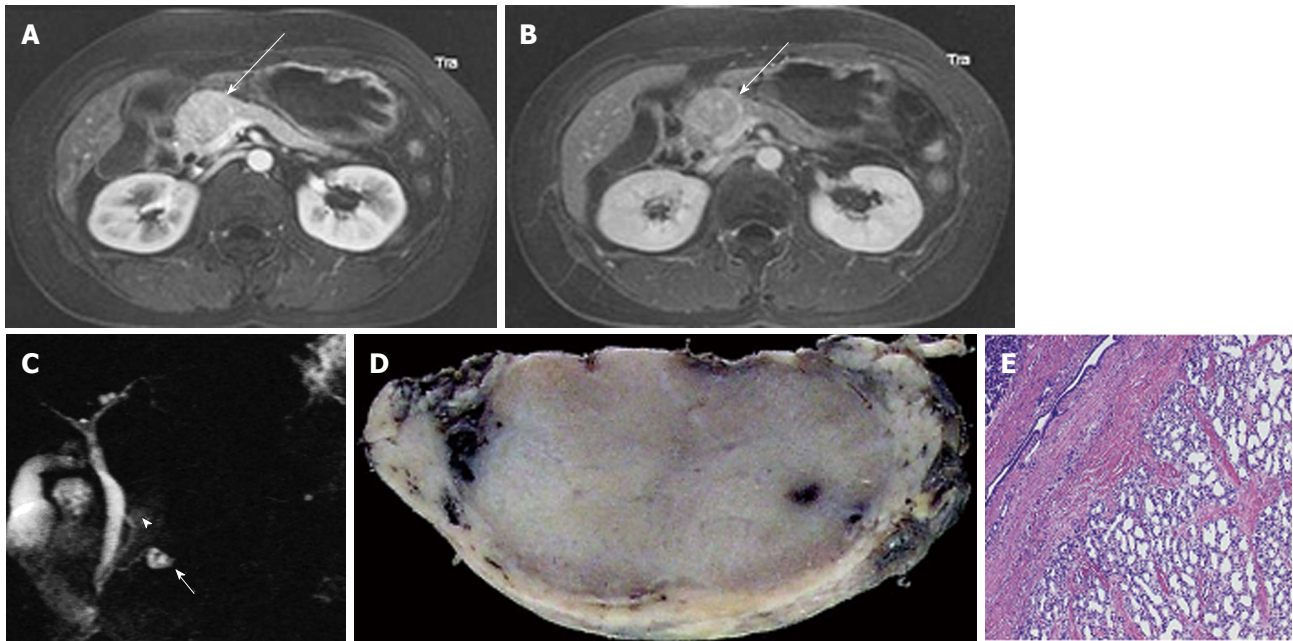


Figure 3 A 43-year-old female with solid-appearing serous cystic neoplasm in the pancreatic head. A: The arterial phase of an axial contrast enhanced (CE) T1-weighted gradient-echo (GRE) magnetic resonance (MR) image with fat saturation shows an enhancing mass in the pancreatic head (arrow); B: The equilibrium phase of an axial CE T1-weighted GRE MR imaging shows the tumor (arrow) to be low intensity (wash-out); C: The pancreatic head mass (arrowhead) is not clearly demonstrated on MR cholangiopancreatography. The pancreatic head mass appears radiologically solid (solid-appearing). An arrow shows a concomitant small intraductal papillary mucinous neoplasm; D: Macroscopic view of the resected specimen shows the mass appears solid; E: Microscopic view shows the tumor consisting of small cystic structures with intervening fibrous stroma.

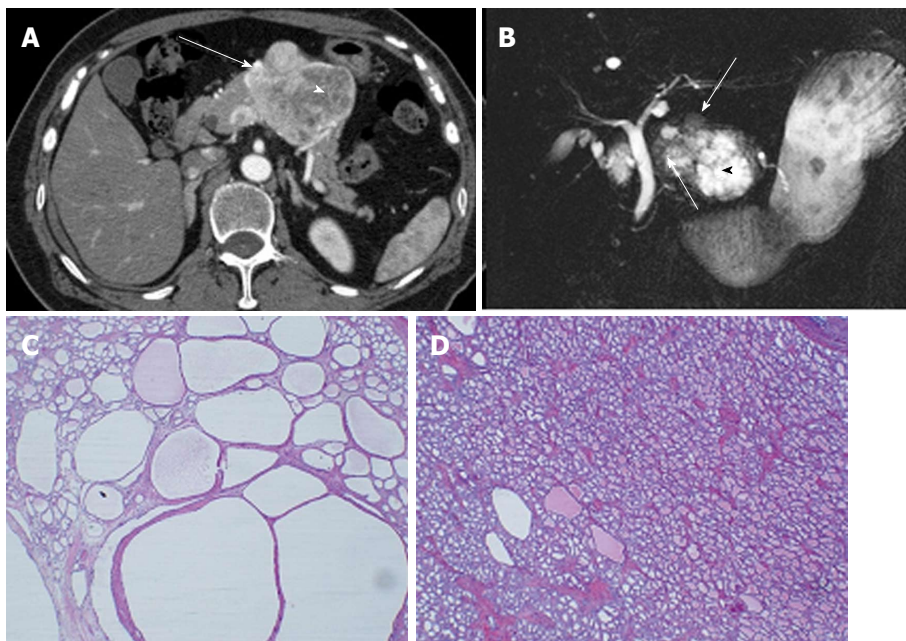


Figure 4 A 64-year-old female with mixed microcystic and solid-appearing serous cystic neoplasm. A: The pancreatic parenchymal phase of an axial contrast enhanced-computed tomography (CT) shows a large enhancing mass in the pancreatic body. The right side of the tumor shows avid arterial enhancement (arrow), and the left side is low density (arrowheads); B: Magnetic resonance cholangiopancreatography shows a microcystic component at the left side of the tumor (arrowhead) that corresponds to the low density area on CT. In contrast, the right side of the tumor is radiologically solid-appearing (arrow); C: Microscopic view of the left side of the tumor [microcystic component (arrowheads in A and B)] consists of various sizes of small cystic spaces; D: Microscopic view of the right side of the tumor [solid-appearing component (arrows in A and B)] consists of smaller sized microcysts. It is radiologically solid-appearing but histologically microcystic.

and wall thickness is shown in Table 1. In SCN, seven of eight showed no wall enhancement (Figures 5 and 10). In contrast, all of the MCN cases ($n = 23$) showed wall enhancement and 15 (65.2%) showed 2 mm or more wall

thickness. Of the branch duct type IPMN cases ($n = 7$), four showed wall enhancement but three did not. There was a significant difference with respect to wall enhancement and wall thickening between SCN and MCN (P

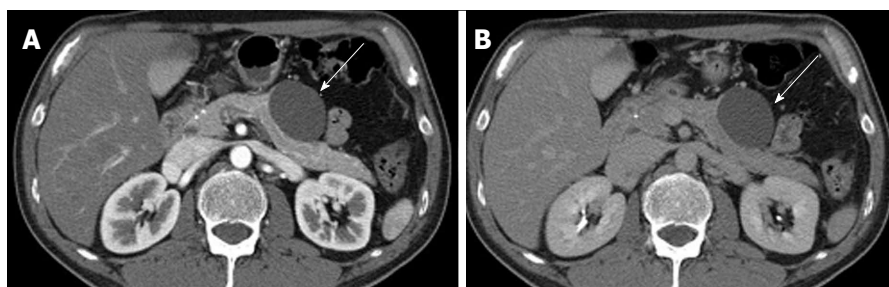


Figure 5 A 40-year-old female with oligocystic serous cystic neoplasm (unilocular). A: The pancreatic parenchymal phase of an axial contrast enhanced-computed tomography shows a unilocular cystic mass arising from the pancreatic body (arrow); B: The equilibrium phase shows no cyst wall enhancement (arrow).

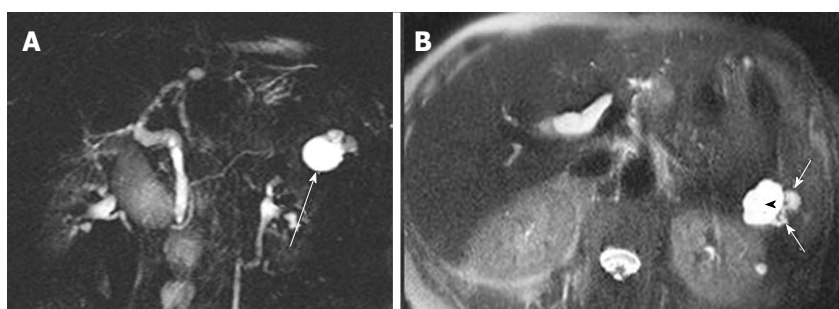


Figure 6 A 61-year-old female with oligocystic serous cystic neoplasm showing a cyst-by-cyst pattern. A: Magnetic resonance cholangiopancreatography demonstrates a cystic mass (arrow) in the pancreatic tail consisting of a macrocyst and two adjacent smaller cysts; B: Axial T2-weighted single-shot fast spin-echo magnetic resonance image shows a lobulated macrocyst (arrowhead) with adjacent smaller cysts (small arrows) in the pancreatic tail (cyst-by-cyst pattern).

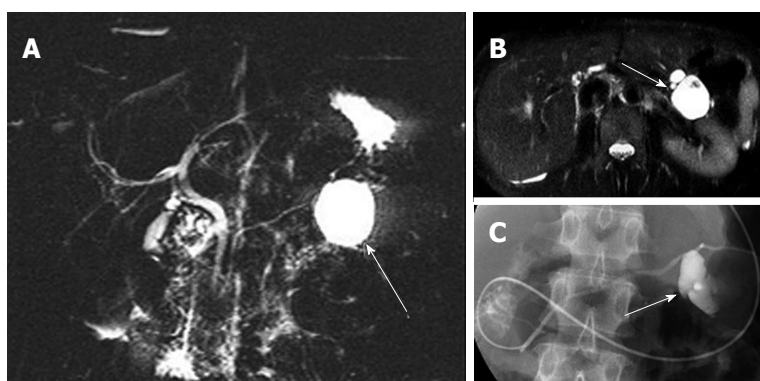


Figure 7 A 45-year-old female with branch duct type intraductal papillary mucinous neoplasm mimicking oligocystic serous cystic neoplasm (also see Figure 6). A: Magnetic resonance cholangiopancreatography shows a cystic mass (arrow) in the body of the pancreas. The communication with the main pancreatic duct (MPD) is not apparent even with the source images (not shown). There is no downstream MPD dilatation; B: Axial T2-weighted single-shot fast spin-echo magnetic resonance image with fat saturation demonstrates a mass showing a cyst-by-cyst pattern (arrow); C: Endoscopic retrograde pancreatography shows the cystic lesion to be opacified (arrow), representing communication with the pancreatic duct.

Table 1 Cyst wall enhancement and wall thickness *n* (%)

	No wall enhancement	Wall thickness < 2 mm	Wall thickness ≥ 2 mm
SCN ^a	7 (87.5)	1 (12.5)	0
MCN ^b	0	8 (34.8)	15 (65.2)
IPMN	3 (42.9)	3 (42.9)	1 (14.3)

SCN: Serous cystic neoplasm; MCN: Mucinous cystic neoplasm; IPMN: Intraductal papillary mucinous neoplasm. Typically, macrocysts in SCN show no wall enhancement and MCNs show wall enhancement. IPMN may or may not show wall enhancement. There is a significant difference between SCN and MCN (^a*P* < 0.01, Kruskal-Wallis test), although no significant difference is shown between SCN and IPMN. The presence or absence of wall enhancement is helpful for differentiating SCN *vs* MCN, but it is not for SCN *vs* IPMN. In addition, MCN may present as a relatively thin-walled cyst (< 2 mm).

< 0.01, Kruskal-Wallis test), although there was no sig-

nificant difference between SCN and branch duct type IPMN.

DISCUSSION

Pancreatic SCN is almost always benign (> 98%)^[1,2]. The American College of Radiology^[18] recommends consideration of surgical resection for SCN larger than 4 cm. However, most previously reported malignant SCNs with evidence of metastatic disease were larger than 10 cm^[1,2] (Figure 11). Therefore, a threshold of 4 cm potentially includes many benign SCNs. As long as it is not symptomatic, this size criterion alone may not warrant surgical resection. Moreover, to avoid unnecessary surgical resection, it is important, not only to be familiar with typical imaging findings of SCN, but to also understand unusual imaging findings and diagnostic pitfalls.

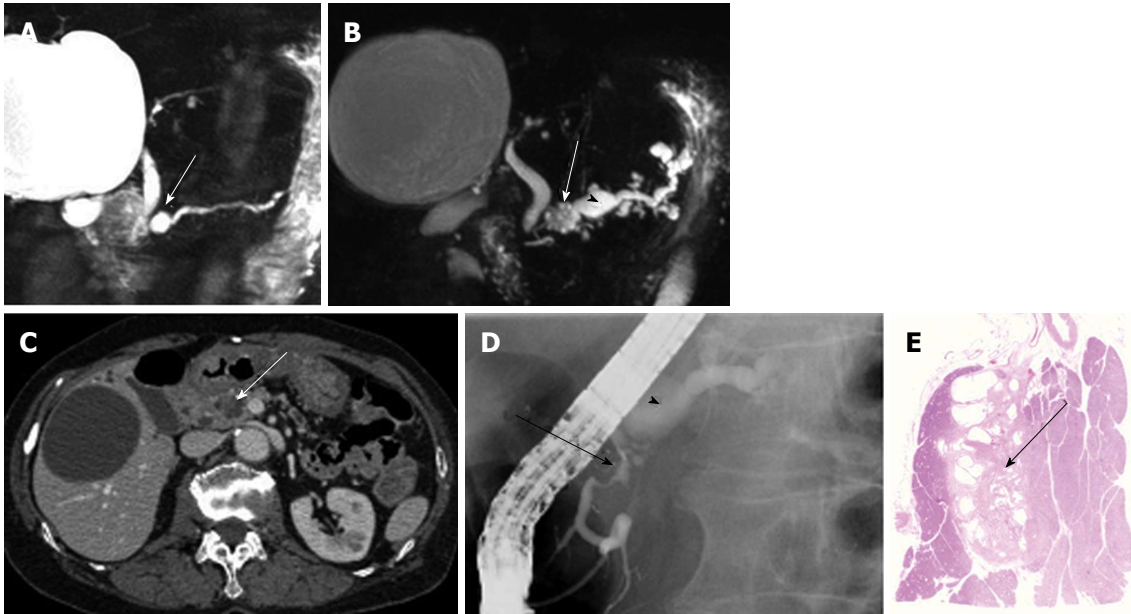


Figure 8 A 74-year-old female with microcystic serous cystic neoplasm and intraductal papillary mucinous neoplasm. A: Magnetic resonance cholangiopancreatography (MRCP) shows a cystic mass (arrow) in the pancreatic head with mild upstream main pancreatic duct (MPD) dilatation; B: Follow-up MRCP 5 years after Figure 8A shows interval increase in size of the cystic lesion (arrow) with fusiform dilatation of the upstream MPD (arrowhead) and cystic dilatation of multiple branch ducts. In retrospect, the cystic lesion in the pancreatic head appears microcystic without downstream MPD dilatation; C: The portal venous phase of an axial contrast enhanced-computed tomography shows an enhancing component (arrow) within the cystic lesion. Intraductal papillary mucinous neoplasm (IPMN) with solid component was suspected; D: Endoscopic retrograde pancreatography shows extrinsic compression of the MPD due to the cystic lesion in the pancreatic head (arrow) without cyst opacification, although fusiform dilatation of the upstream MPD (arrowhead) is demonstrated; E: Resected specimen shows the cystic mass in the pancreatic head consisting of microcysts. The enhancing component eventually represented fibrosis (arrow) within microcystic serous cystic neoplasm. In addition, the fusiform dilatation of the MPD turned out to be IPMN.

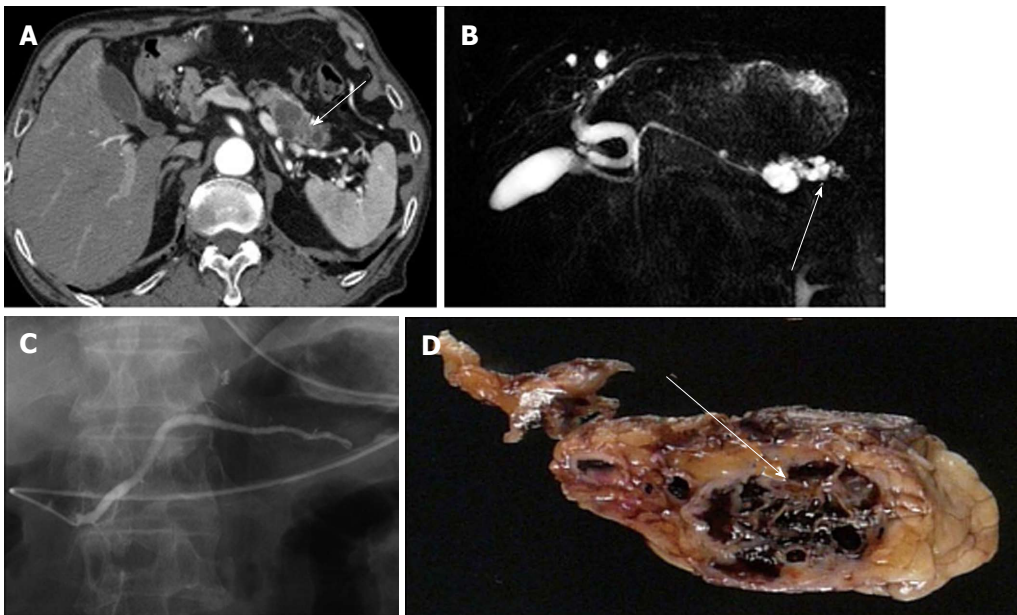


Figure 9 A 74-year-old male with microcystic serous cystic neoplasm mischaracterized as intraductal papillary mucinous neoplasm with a solid component. A: The pancreatic parenchymal phase of an axial contrast enhanced-computed tomography shows a cystic lesion with an enhancing component (arrow) in the pancreatic tail; B: Magnetic resonance cholangiopancreatography (MRCP) shows the cystic lesion to be elongated, and the upstream main pancreatic duct (MPD) appears to be dilated (arrow). There is no dilatation of the downstream MPD. The extrahepatic bile duct is tortuous, likely due to distal gastrectomy (Billroth I reconstruction); C: Endoscopic retrograde pancreatography shows the cystic lesion to be unopacified. There is no communication with the pancreatic duct or upstream MPD dilatation. MRCP findings eventually represented a part of the cystic lesion along the course of the pancreas rather than MPD dilatation (arrow, B); D: Macroscopic view of the resected specimen (short axis cut section) shows the cystic lesion consisting of microcysts and fibrosis (arrow).

Typical imaging findings of SCN are well known. Microcystic SCN consists of a cluster of microcysts; the so-

called “honeycomb pattern”^[10-14] (Figure 1). Microcystic SCN can be hypervascular and may appear solid on con-

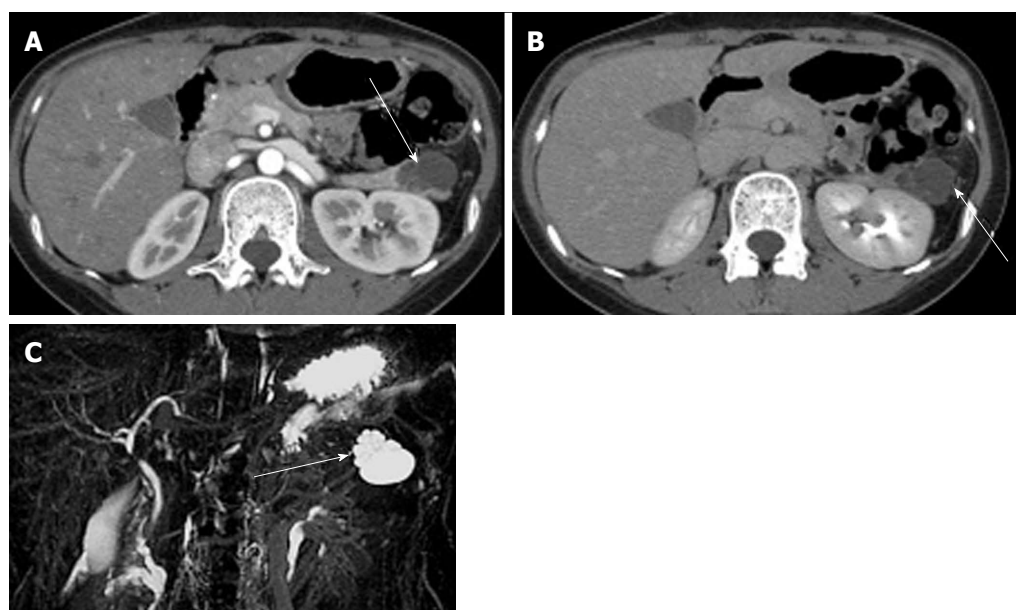


Figure 10 A 27-year-old female with mixed microcystic and macrocystic serous cystic neoplasm. A: The pancreatic parenchymal phase of an axial contrast enhanced- computed tomography shows a lobulated cystic mass (arrow) in the pancreatic tail; B: The equilibrium phase shows no cyst wall enhancement (arrow); C: Magnetic resonance cholangiopancreatography clearly shows a cluster of microcysts (honeycomb pattern) in the peripheral portion of this cystic lesion (arrow).

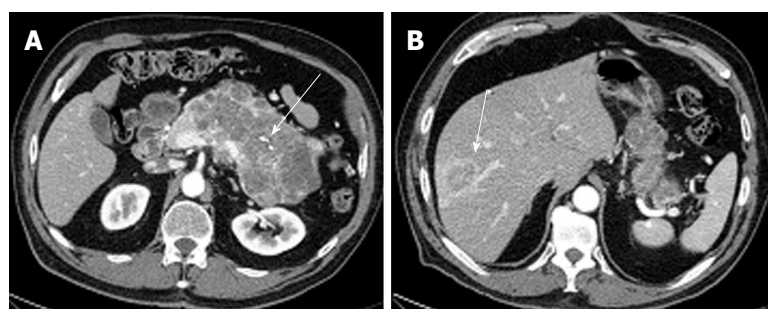


Figure 11 A 78-year-old female with a large serous cystic neoplasm with liver metastasis. A: The pancreatic parenchymal phase of an axial contrast enhanced- computed tomography (CT) demonstrates a large low density mass with patchy enhancement in the body and tail of the pancreas. Central calcification is noted (arrow); B: Axial CT cranial to Figure 11A shows a low density liver mass with peripheral and patchy enhancement in segment VIII (arrow). The appearance is similar to the pancreatic mass.

trast-enhanced computed tomography. MRI and MRCP can clearly demonstrate the microcystic nature of the lesion^[9]. A macrocyst is defined as a cyst measuring more than 2 cm (or 1 cm) in diameter^[11,15-17]. The mixed type most commonly consists of microcystic and macrocystic components^[10,11,19]. Typically, microcysts are noted in the center and macrocysts are located peripherally^[10,11,19]. In addition, fibrosis with or without calcification may be seen in the center^[10,11,19].

In our series, two microcystic SCNs were mischaracterized as IPMN with mural nodule because fibrosis in the SCN mimicked a mural nodule. One case showed interval growth (Figure 8) with dilatation of the MPD. Dilatation of the MPD turned out to be a concomitant IPMN. In spite of benignancy, it has been reported that SCN may show interval growth on imaging follow-up^[19-21]. Another case demonstrated an elongated shape along the course of the pancreatic tail (Figure 9), and part of the cystic lesion was erroneously considered MPD dilatation. In retrospect, neither case demonstrated downstream MPD dilatation, nor did endoscopic retrograde cholangiopancreatography (ERCP) demonstrate communication between the cystic lesions and the MPD.

When diagnosing mixed micro and macrocystic SCN,

the diagnostic key is to look for a honeycomb pattern. It should be emphasized that the honeycomb pattern may not always be in the central portion. The honeycomb pattern may be seen peripherally (Figure 10), and MRI/MRCP can better characterize and demonstrate a cluster of microcysts than CT. In addition, it may be helpful to understand the imaging spectrum of SCN by explaining that most SCNs consist of the combination of microcystic, macrocystic, and solid-appearing components. The imaging appearance of each component simply reflects the different sizes of cysts that comprise the SCN.

Solid variant SCN (solid serous adenoma) is extremely rare^[22-24]. Even though imaging findings often appear solid (not very bright on MRCP with hypervascularity), it may be histologically microcystic (Figure 3). That is why we call such imaging findings “solid-appearing”. Solid-appearing components may be seen in mixed type SCNs (Figure 4). The differential diagnosis of solid serous adenoma (histologically solid) and solid-appearing SCN is neuroendocrine tumor (NET). Hayashi *et al*^[25] reported that the Hounsfield units of SCN on unenhanced CT were lower than those of NET, and the relative wash-out ratio was higher in SCN than in NET. According to Hayashi *et al*^[25], unenhanced CT showed all three SCNs to

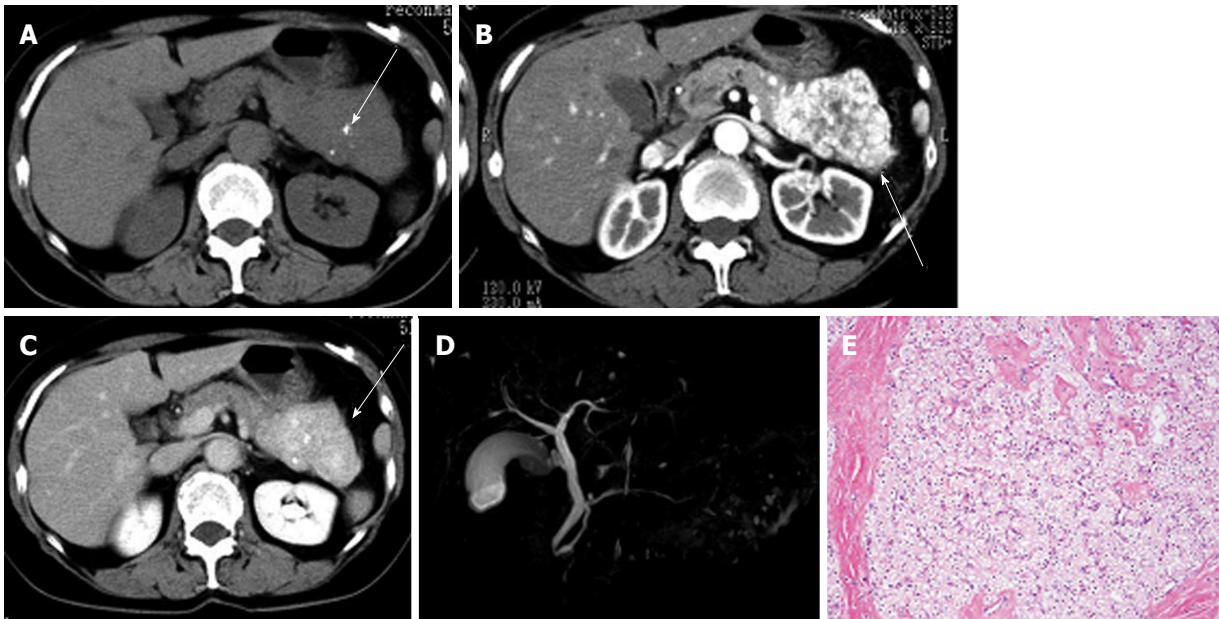


Figure 12 A 65-year-old female with solid serous adenoma. A: Unenhanced axial computed tomography shows a large mass with central calcification (arrow) in the tail and body of the pancreas. The lesion is isodense to the normal pancreatic parenchyma; B: The pancreatic parenchymal phase shows avid tumor enhancement (arrow); C: The equilibrium phase shows the mass to be high density (arrow) relative to the normal pancreatic parenchyma, representing persistent enhancement (no wash-out); D: Magnetic resonance cholangiopancreatography does not show the mass or cystic spaces; E: Microscopic view of the resected specimen shows a solid nest of tumor cells with abundant fibrous stroma.

be low density and only one of 14 NETs to be low density. The delayed phase showed two of three SCNs to be low density (wash-out) but NET did not show wash-out. These criteria may be useful for the differential diagnosis between solid-appearing (histologically microcystic) SCN and NET because no contrast stasis is expected in the microcystic spaces of SCN. However, for solid serous adenoma (histologically solid), it is uncertain if this criteria is helpful for the differential diagnosis because fibrosis in solid serous adenoma may cause delayed enhancement of the lesion (Figure 12). Additionally, the enhancement pattern of NET is variable, and NET can be low density in the delayed phase (Figure 13). If imaging findings do not suggest a microcystic nature, endoscopic ultrasound-guided biopsy should be considered to exclude NET.

Von Hippel-Lindau (VHL) associated SCN is another variant of SCN (Figure 14)^[26]. VHL-associated SCN is usually multifocal, and it may present as diffuse pancreatic involvement^[26]. In patients with VHL disease, concomitant NET may be encountered^[26,27]. In addition, cases of SCN concomitant NET and mixed SCN and NET have been reported in patients with and without VHL disease^[28-30]. Similar to solid serous adenoma, prospective imaging diagnosis of mixed SCN and NET is difficult.

Oligocystic SCN consists of a macrocyst and a few small cysts showing a “cyst-by-cyst” pattern^[15-17]. In our series, the cyst wall of the macrocyst was thin, and wall enhancement was not typically seen. Owing to a common capsule, wall enhancement is seen in MCN^[31,32]. We evaluated cyst wall enhancement in the equilibrium phase CT because we hypothesized that the contrast enhancement

of fibrosis in the capsule would be more conspicuous in equilibrium than in the arterial or portal venous phases. The presence or absence of cyst wall enhancement may be helpful for the differential diagnosis between oligocystic SCN and MCN (Figure 5), although the cyst wall of MCN may be thin (< 2 mm) in some cases. On the other hand, distinguishing oligocystic SCN from branch duct type IPMN may be difficult^[33,34], especially when MDCT or MRI/MRCP fails to demonstrate the communication with the pancreatic duct (Figure 7). Because the presence or absence of cyst wall enhancement is not helpful, and oligocystic SCN lacks a honeycomb pattern, imaging findings of oligocystic SCN and IPMN may overlap (Figures 6 and 7). Even though it is morphologically suspicious for an oligocystic SCN, branch duct type IPMN cannot be excluded because branch duct type IPMN is more common than oligocystic SCN. In such cases, ERCP (to evaluate the communication with the MPD) or EUS-guided cyst aspiration may be necessary to differentiate the two^[35-40].

Other than IPMN and MCN, non-neoplastic pancreatic cysts such as lymphoepithelial cyst (LEC)^[41,42] (Figure 15) and extensively necrotic/hemorrhagic pancreatic tumors such as solid pseudopapillary neoplasm (SPN) (Figure 16) may mimic SCN^[43-46]. Both LEC and SPN may present as high intensity masses on T2-weighted images and MRCP. Diffusion-weighted imaging (DWI) is helpful for the differential diagnosis because LEC and SPN may show high intensity on DWI owing to high proteinaceous fluid and hemorrhage/solid components, respectively. In contrast, it is unusual for SCN to contain proteinaceous or hemorrhagic fluid although SCN can be partially hem-



Figure 13 A 65-year-old male with neuroendocrine tumor (well-differentiated neuroendocrine carcinoma). A: Unenhanced axial computed tomography shows a large mass with central calcification (arrow) in the pancreatic body; B: The venous phase shows moderate and relatively homogeneous tumor enhancement (arrow). (The arterial phase was not available for this case); C: The delayed phase shows the tumor to be low density (arrow). Wash-out may not always be suggestive of serous cystic neoplasm (also see Figure 12).

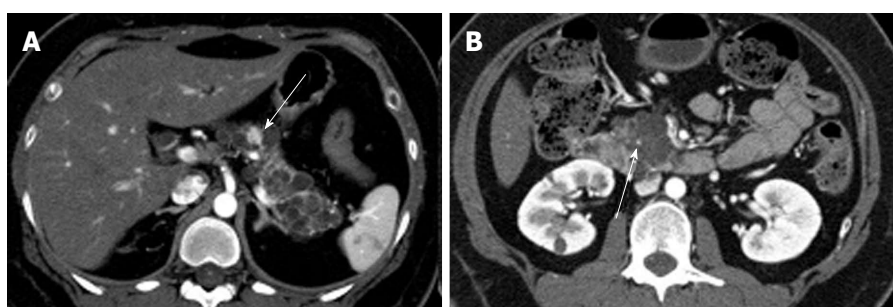


Figure 14 A 43-year-old female with von Hippel-Lindau disease. A: The arterial phase of an axial contrast enhanced-computed tomography demonstrates numerous cystic lesions in the body and tail of the pancreas. There is a solid hypervascular lesion in the pancreatic body (arrow), representing neuroendocrine tumor; B: A multilocular cystic lesion in the pancreatic head consists of a punctate central calcification (arrow) with microcystic (right side) and macrocystic (left side) components, representing serous cystic neoplasm.

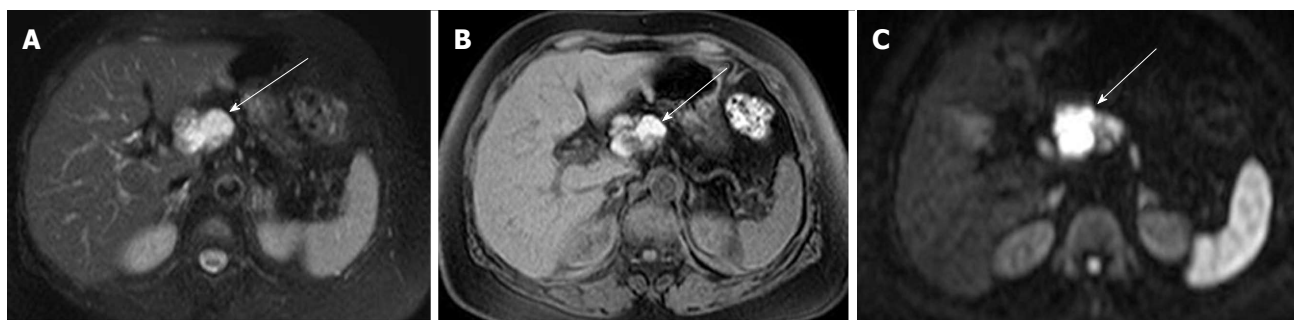


Figure 15 A 72-year-old female with pancreatic lymphoepithelial cyst. A: Axial T2-weighted fast spin-echo magnetic resonance (MR) image with fat saturation shows a high intensity mass (arrow), which is exophytic from the neck of the pancreas (not shown); B: Axial T1-weighted gradient-echo (GRE) MR image with fat saturation shows the mass to be high intensity (arrow). Findings on T2-weighted image (Figure 14A) may mimic microcystic serous cystic neoplasm (SCN). However, the widespread distribution of high signal is somewhat unlikely for hemorrhage within microcysts of SCN because each locule should be separated by multiple septations; C: Axial diffusion-weighted MR image (b-factor = 1000) shows the mass to be high intensity (arrow), unlikely for SCN.

orrhagic (Figure 2)^[19]. In addition, care should be taken to exclude extrapancreatic masses such as peripancreatic lymphadenopathy. Necrotic lymph nodes or metastasis from mucinous adenocarcinoma may mimic pancreatic cystic neoplasms (Figure 17).

Pancreatic pseudocyst is a common non-neoplastic cystic lesion occurring after pancreatitis or trauma^[47-49]. Pancreatic pseudocyst typically presents as a unilocular cyst. The thickness of cyst wall varies depending on the ages of pseudocysts. Cyst wall enhancement may not be

seen or may be barely seen at an earlier age. However, differentiating acute pseudocysts from SCN may not be problematic because recent episodes of pancreatitis or trauma should be documented. In chronic pseudocyst, a thickened enhancing cyst wall can be seen (Figure 18). For chronic pseudocyst without documented history of pancreatitis, the distinction from MCN may be more difficult. Additionally, cases of SCN with subtotal cystic degeneration have been reported^[50], which may be difficult to distinguish from pseudocyst.

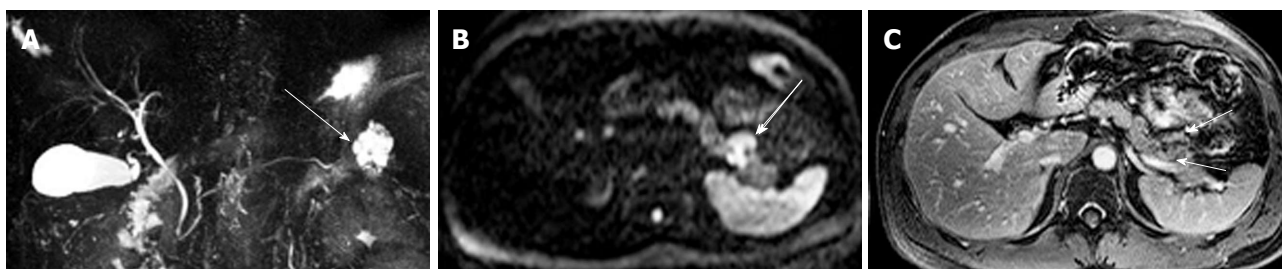


Figure 16 A 39-year-old male with solid pseudopapillary neoplasm. A: Magnetic resonance cholangiopancreatography shows a high intensity pancreatic tail mass (arrow) that appears as a cluster of microcysts, mimicking microcystic serous cystic neoplasm (SCN); B: Axial diffusion-weighted magnetic resonance (MR) image (b-factor = 1000) shows the mass to be high intensity (arrow), unlikely for microcystic SCN; C: The equilibrium phase of an axial contrast enhanced T1-weighted gradient-echo MR image shows peripheral solid enhancing component within the tumor (arrows).

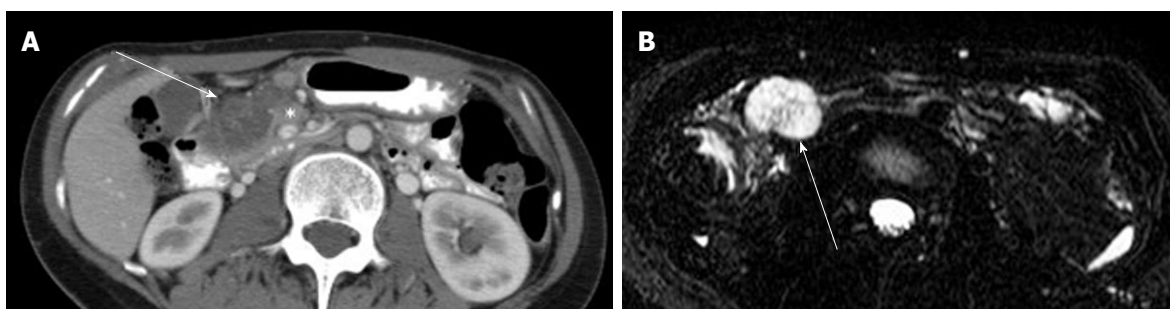


Figure 17 A 32-year-old female with lymph node metastasis from mucinous adenocarcinoma of the transverse colon (not shown). A: The portal venous phase of an axial computed tomography shows a low density mass (arrow) adjacent to the pancreatic head (asterisk); B: Axial magnetic resonance cholangiopancreatography shows the mass to be high intensity, mimicking microcystic serous cystic neoplasm (SCN). However, the presence of primary tumor and the lesion location (transverse mesocolon) are suggestive of lymph node metastasis rather than microcystic SCN.

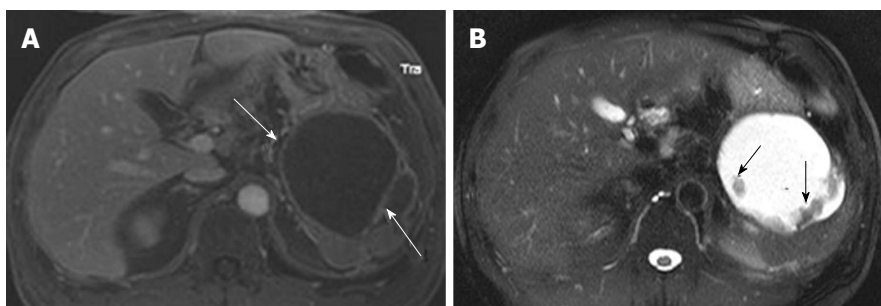


Figure 18 A 56-year-old male with chronic pancreatic pseudocyst. A: The venous phase of an axial contrast enhanced T1-weighted gradient-echo magnetic resonance image demonstrates a cystic lesion with thick cyst wall and septation (arrows) arising from the pancreatic tail. Although this is a male patient, making mucinous cystic neoplasm unlikely, imaging findings of chronic pseudocyst may still mimic mucinous cystic neoplasm; B: The axial fast spin-echo T2-weighted magnetic resonance image with fat saturation shows non-enhancing debris (A) attached to the cyst wall and the septum (arrows).

CONCLUSION

The diagnostic key of microcystic or mixed micro and macrocystic SCN is to look for a honeycomb pattern, which may not always be located in the center. Care should be taken not to erroneously characterize fibrosis in SCN as a mural nodule of IPMN. Although the presence or absence of cyst wall enhancement in the equilibrium phase may be helpful for the differential diagnosis between SCN with macrocysts and MCN, it is not helpful for SCN versus branch duct type IPMN. Differentiation between oligocystic SCN and branch duct type IPMN, and between NET and extremely rare solid serous adenoma, may be difficult.

ACKNOWLEDGEMENTS

The author would like to thank Nichole Jenkins, MA, Department of Radiology University of Iowa Hospitals and Clinics for her assistance in editing this manuscript.

REFERENCES

- 1 **Kimura W**, Moriya T, Hirai I, Hanada K, Abe H, Yanagisawa A, Fukushima N, Ohike N, Shimizu M, Hatori T, Fujita N, Maguchi H, Shimizu Y, Yamao K, Sasaki T, Naito Y, Tanno S, Tobita K, Tanaka M. Multicenter study of serous cystic neoplasm of the Japan pancreas society. *Pancreas* 2012; **41**: 380-387 [PMID: 22415666 DOI: 10.1097/MPA.0b013e31822a27db]

- 2 **Khashab MA**, Shin EJ, Amateau S, Canto MI, Hruban RH, Fishman EK, Cameron JL, Edil BH, Wolfgang CL, Schulick RD, Giday S. Tumor size and location correlate with behavior of pancreatic serous cystic neoplasms. *Am J Gastroenterol* 2011; **106**: 1521-1526 [PMID: 21468008 DOI: 10.1038/ajg.2011.117]
- 3 **Galanis C**, Zamani A, Cameron JL, Campbell KA, Lillemoeg KD, Caparrelli D, Chang D, Hruban RH, Yeo CJ. Resected serous cystic neoplasms of the pancreas: a review of 158 patients with recommendations for treatment. *J Gastrointest Surg* 2007; **11**: 820-826 [PMID: 17440789]
- 4 **Tanaka M**, Fernández-del Castillo C, Adsay V, Chari S, Falconi M, Jang JY, Kimura W, Levy P, Pitman MB, Schmidt CM, Shimizu M, Wolfgang CL, Yamaguchi K, Yamao K. International consensus guidelines 2012 for the management of IPMN and MCN of the pancreas. *Pancreatol* 2012; **12**: 183-197 [PMID: 22687371 DOI: 10.1016/j.pan.2012.04.004]
- 5 **Talukdar R**, Nageshwar Reddy D. Treatment of pancreatic cystic neoplasm: surgery or conservative? *Clin Gastroenterol Hepatol* 2014; **12**: 145-151 [PMID: 23978346 DOI: 10.1016/j.cgh.2013.08.031]
- 6 **Farrell JJ**, Fernández-del Castillo C. Pancreatic cystic neoplasms: management and unanswered questions. *Gastroenterology* 2013; **144**: 1303-1315 [PMID: 23622140 DOI: 10.1053/j.gastro.2013.01.073]
- 7 **Malleo G**, Bassi C, Salvia R. Appraisal of the surgical management for pancreatic serous cystic neoplasms. *Surg Endosc* 2013; **27**: 2646-2647 [PMID: 23355171 DOI: 10.1007/s00464-012-2783-5]
- 8 **Zanini N**, Fantini L, Casadei R, Pezzilli R, Santini D, Calculli L, Minni F. Serous cystic tumors of the pancreas: when to observe and when to operate: a single-center experience. *Dig Surg* 2008; **25**: 233-239; discussion 240 [PMID: 18607110 DOI: 10.1159/000142947]
- 9 **Gabata T**, Terayama N, Yamashiro M, Takamatsu S, Yoshida K, Matsui O, Usukura M, Takeshita M, Minato H. Solid serous cystadenoma of the pancreas: MR imaging with pathologic correlation. *Abdom Imaging* 2005; **30**: 605-609 [PMID: 15723180]
- 10 **Kalb B**, Sarmiento JM, Kooby DA, Adsay NV, Martin DR. MR imaging of cystic lesions of the pancreas. *Radiographics* 2009; **29**: 1749-1765 [PMID: 19959519 DOI: 10.1148/rg.296095506]
- 11 **Sun HY**, Kim SH, Kim MA, Lee JY, Han JK, Choi BI. CT imaging spectrum of pancreatic serous tumors: based on new pathologic classification. *Eur J Radiol* 2010; **75**: e45-e55 [PMID: 20056368 DOI: 10.1016/j.ejrad.2009.11.017]
- 12 **Lee SE**, Kwon Y, Jang JY, Kim YH, Hwang DW, Kim MA, Kim SH, Kim SW. The morphological classification of a serous cystic tumor (SCT) of the pancreas and evaluation of the preoperative diagnostic accuracy of computed tomography. *Ann Surg Oncol* 2008; **15**: 2089-2095 [PMID: 18478300 DOI: 10.1245/s10434-008-9959-1]
- 13 **Kucera JN**, Kucera S, Perrin SD, Caracciolo JT, Schmulewitz N, Kedar RP. Cystic lesions of the pancreas: radiologic-endosonographic correlation. *Radiographics* 2012; **32**: E283-E301 [PMID: 23150863 DOI: 10.1148/rg.327125019]
- 14 **Sahani DV**, Kambadakone A, Macari M, Takahashi N, Chari S, Fernandez-del Castillo C. Diagnosis and management of cystic pancreatic lesions. *AJR Am J Roentgenol* 2013; **200**: 343-354 [PMID: 23345356 DOI: 10.2214/AJR.12.8862]
- 15 **Goh BK**, Tan YM, Yap WM, Chew PC, Chow PK, Chung YF, Wong WK, Ooi LL. Pancreatic serous oligocystic adenomas: clinicopathologic features and a comparison with serous microcystic adenomas and mucinous cystic neoplasms. *World J Surg* 2006; **30**: 1553-1559 [PMID: 16773248]
- 16 **Santos LD**, Chow C, Henderson CJ, Blomberg DN, Merrett ND, Kennerson AR, Killingsworth MC. Serous oligocystic adenoma of the pancreas: a clinicopathological and immunohistochemical study of three cases with ultrastructural findings. *Pathology* 2002; **34**: 148-156 [PMID: 12009097]
- 17 **Lee JH**, Kim JK, Kim TH, Park MS, Yu JS, Choi JY, Kim JH, Kim YB, Kim KW. MRI features of serous oligocystic adenoma of the pancreas: differentiation from mucinous cystic neoplasm of the pancreas. *Br J Radiol* 2012; **85**: 571-576 [PMID: 21304008 DOI: 10.1259/bjr/42007785]
- 18 **Berland LL**, Silverman SG, Gore RM, Mayo-Smith WW, Megibow AJ, Yee J, Brink JA, Baker ME, Federle MP, Foley WD, Francis IR, Herts BR, Israel GM, Krinsky G, Platt JF, Shuman WP, Taylor AJ. Managing incidental findings on abdominal CT: white paper of the ACR incidental findings committee. *J Am Coll Radiol* 2010; **7**: 754-773 [PMID: 20889105 DOI: 10.1016/j.jacr.2010.06.013]
- 19 **Choi JY**, Kim MJ, Lee JY, Lim JS, Chung JJ, Kim KW, Yoo HS. Typical and atypical manifestations of serous cystadenoma of the pancreas: imaging findings with pathologic correlation. *AJR Am J Roentgenol* 2009; **193**: 136-142 [PMID: 19542405 DOI: 10.2214/AJR.08.1309]
- 20 **El-Hayek KM**, Brown N, O'Rourke C, Falk G, Morris-Stiff G, Walsh RM. Rate of growth of pancreatic serous cystadenoma as an indication for resection. *Surgery* 2013; **154**: 794-800; discussion 800-802 [PMID: 24074417 DOI: 10.1016/j.surg.2013.07.005]
- 21 **Fukasawa M**, Maguchi H, Takahashi K, Katanuma A, Osanai M, Kurita A, Ichiya T, Tsuchiya T, Kin T. Clinical features and natural history of serous cystic neoplasm of the pancreas. *Pancreatol* 2010; **10**: 695-701 [PMID: 21242709 DOI: 10.1159/000320694]
- 22 **Machado MC**, Machado MA. Solid serous adenoma of the pancreas: an uncommon but important entity. *Eur J Surg Oncol* 2008; **34**: 730-733 [PMID: 18440191 DOI: 10.1016/j.ejso.2008.03.009]
- 23 **Stern JR**, Frankel WL, Ellison EC, Bloomston M. Solid serous microcystic adenoma of the pancreas. *World J Surg Oncol* 2007; **5**: 26 [PMID: 17338818]
- 24 **Reese SA**, Traverso LW, Jacobs TW, Longnecker DS. Solid serous adenoma of the pancreas: a rare variant within the family of pancreatic serous cystic neoplasms. *Pancreas* 2006; **33**: 96-99 [PMID: 16804417]
- 25 **Hayashi K**, Fujimitsu R, Ida M, Sakamoto K, Higashihara H, Hamada Y, Yoshimitsu K. CT differentiation of solid serous cystadenoma vs endocrine tumor of the pancreas. *Eur J Radiol* 2012; **81**: e203-e208 [PMID: 21330085 DOI: 10.1016/j.ejrad.2011.01.111]
- 26 **Pajak J**, Liszka Ł, Mrowiec S, Zielińska-Pajak E, Gołka D, Lampe P. Serous neoplasms of the pancreas constitute a continuous spectrum of morphological patterns rather than distinct clinico-pathological variants. A study of 40 cases. *Pol J Pathol* 2011; **62**: 206-217 [PMID: 22246906]
- 27 **Matsubayashi H**, Uesaka K, Kanemoto H, Sugiura T, Mizuno T, Sasaki K, Ono H, Hruban R. Multiple endocrine neoplasms and serous cysts of the pancreas in a patient with von Hippel-Lindau disease. *J Gastrointest Cancer* 2010; **41**: 197-202 [PMID: 20140653 DOI: 10.1007/s12029-010-9134-3]
- 28 **Blandamura S**, Parenti A, Famengo B, Canesso A, Moschino P, Pasquali C, Pizzi S, Guzzardo V, Ninfo V. Three cases of pancreatic serous cystadenoma and endocrine tumour. *J Clin Pathol* 2007; **60**: 278-282 [PMID: 16644876]
- 29 **Agarwal N**, Kumar S, Dass J, Arora VK, Rathi V. Diffuse pancreatic serous cystadenoma associated with neuroendocrine carcinoma: a case report and review of literature. *JOP* 2009; **10**: 55-58 [PMID: 19129617]
- 30 **Mohan H**, Garg S, Punia RP, Dalal A. Combined serous cystadenoma and pancreatic endocrine neoplasm. A case report with a brief review of the literature. *JOP* 2007; **8**: 453-457 [PMID: 17625299]
- 31 **Yamaguchi H**, Ishigami K, Inoue T, Eguchi T, Nagata S, Kuroda Y, Nishihara Y, Yamaguchi K, Tanaka M, Tsuneyoshi M. Three cases of serous oligocystic adenomas of the pancreas; evaluation of cyst wall thickness for preoperative differentia-

- tion from mucinous cystic neoplasms. *J Gastrointest Cancer* 2007; **38**: 52-58 [PMID: 19065725]
- 32 **Kim SH**, Lim JH, Lee WJ, Lim HK. Macrocytic pancreatic lesions: differentiation of benign from premalignant and malignant cysts by CT. *Eur J Radiol* 2009; **71**: 122-128 [PMID: 18448299 DOI: 10.1016/j.ejrad.2008.03.012]
- 33 **Berman L**, Mitchell KA, Israel G, Salem RR. Serous cystadenoma in communication with the pancreatic duct: an unusual radiologic and pathologic entity. *J Clin Gastroenterol* 2010; **44**: e133-e135 [PMID: 20216080 DOI: 10.1097/MCG.0b013e3181d3458d]
- 34 **Kobayashi T**, Shimura T, Araki K, Mochida Y, Suzuki H, Suehiro T, Kuwano H. Macrocytic serous cystadenoma mimicking branch duct intraductal papillary mucinous neoplasm. *Int Surg* 2009; **94**: 176-181 [PMID: 20108623]
- 35 **Khashab MA**, Kim K, Lennon AM, Shin EJ, Tignor AS, Amateau SK, Singh VK, Wolfgang CL, Hruban RH, Canto MI. Should we do EUS/FNA on patients with pancreatic cysts? The incremental diagnostic yield of EUS over CT/MRI for prediction of cystic neoplasms. *Pancreas* 2013; **42**: 717-721 [PMID: 23558241 DOI: 10.1097/MPA.0b013e3182883a91]
- 36 **Del Chiaro M**, Verbeke C, Salvia R, Klöppel G, Werner J, McKay C, Friess H, Manfredi R, Van Cutsem E, Löhner M, Segersvärd R. European experts consensus statement on cystic tumours of the pancreas. *Dig Liver Dis* 2013; **45**: 703-711 [PMID: 23415799 DOI: 10.1016/j.dld.2013.01.010]
- 37 **Thornton GD**, McPhail MJ, Nayagam S, Hewitt MJ, Vlavianos P, Monahan KJ. Endoscopic ultrasound guided fine needle aspiration for the diagnosis of pancreatic cystic neoplasms: a meta-analysis. *Pancreatol* 2013; **13**: 48-57 [PMID: 23395570 DOI: 10.1016/j.pan.2012.11.313]
- 38 **Cizginer S**, Turner BG, Bilge AR, Karaca C, Pitman MB, Brugge WR. Cyst fluid carcinoembryonic antigen is an accurate diagnostic marker of pancreatic mucinous cysts. *Pancreas* 2011; **40**: 1024-1028 [PMID: 21775920 DOI: 10.1097/MPA.0b013e31821bd62f]
- 39 **Bhutani MS**, Gupta V, Guha S, Gheonea DI, Saftoiu A. Pancreatic cyst fluid analysis--a review. *J Gastrointest Liver Dis* 2011; **20**: 175-180 [PMID: 21725515]
- 40 **Sakorafas GH**, Smyrniotis V, Reid-Lombardo KM, Sarr MG. Primary pancreatic cystic neoplasms revisited. Part I: serous cystic neoplasms. *Surg Oncol* 2011; **20**: e84-e92 [PMID: 21237638 DOI: 10.1016/j.suronc.2010.12.002]
- 41 **Adsay NV**, Hasteh F, Cheng JD, Bejarano PA, Lauwers GY, Batts KP, Klöppel G, Klimstra DS. Lymphoepithelial cysts of the pancreas: a report of 12 cases and a review of the literature. *Mod Pathol* 2002; **15**: 492-501 [PMID: 12011254]
- 42 **Adsay NV**, Hasteh F, Cheng JD, Klimstra DS. Squamous-lined cysts of the pancreas: lymphoepithelial cysts, dermoid cysts (teratomas), and accessory-splenic epidermoid cysts. *Semin Diagn Pathol* 2000; **17**: 56-65 [PMID: 10721807]
- 43 **Yao X**, Ji Y, Zeng M, Rao S, Yang B. Solid pseudopapillary tumor of the pancreas: cross-sectional imaging and pathologic correlation. *Pancreas* 2010; **39**: 486-491 [PMID: 19940797 DOI: 10.1097/MPA.0b013e3181bd6839]
- 44 **Sakorafas GH**, Smyrniotis V, Reid-Lombardo KM, Sarr MG. Primary pancreatic cystic neoplasms of the pancreas revisited. Part IV: rare cystic neoplasms. *Surg Oncol* 2012; **21**: 153-163 [PMID: 21816607 DOI: 10.1016/j.suronc.2011.06.007]
- 45 **Kim SY**, Park SH, Hong N, Kim JH, Hong SM. Primary solid pancreatic tumors: recent imaging findings updates with pathology correlation. *Abdom Imaging* 2013; **38**: 1091-1105 [PMID: 23640523 DOI: 10.1007/s00261-013-0004-x]
- 46 **Hammond NA**, Miller FH, Day K, Nikolaidis P. Imaging features of the less common pancreatic masses. *Abdom Imaging* 2013; **38**: 561-572 [PMID: 22711184 DOI: 10.1007/s00261-012-9922-2]
- 47 **Buerke B**, Domagk D, Heindel W, Wessling J. Diagnostic and radiological management of cystic pancreatic lesions: important features for radiologists. *Clin Radiol* 2012; **67**: 727-737 [PMID: 22520033 DOI: 10.1016/j.crad.2012.02.008]
- 48 **Ellis CT**, Barbour JR, Shary TM, Adams DB. Pancreatic cyst: pseudocyst or neoplasm? Pitfalls in endoscopic retrograde cholangiopancreatography diagnosis. *Am Surg* 2010; **76**: 725-730 [PMID: 20698379]
- 49 **Takahashi N**, Papachristou GI, Schmit GD, Chahal P, LeRoy AJ, Sarr MG, Vege SS, Mandrekar JN, Baron TH. CT findings of walled-off pancreatic necrosis (WOPN): differentiation from pseudocyst and prediction of outcome after endoscopic therapy. *Eur Radiol* 2008; **18**: 2522-2529 [PMID: 18563416 DOI: 10.1007/s00330-008-1039-1]
- 50 **Panarelli NC**, Park KJ, Hruban RH, Klimstra DS. Microcystic serous cystadenoma of the pancreas with subtotal cystic degeneration: another neoplastic mimic of pancreatic pseudocyst. *Am J Surg Pathol* 2012; **36**: 726-731 [PMID: 22498822 DOI: 10.1097/PAS.0b013e31824cf879]

P- Reviewers: Ding MX, Karatag O **S- Editor:** Gou SX
L- Editor: A **E- Editor:** Wu HL



Role of interventional radiology in the management of acute gastrointestinal bleeding

Raja S Ramaswamy, Hyung Won Choi, Hans C Mouser, Kazim H Narsinh, Kevin C McCammack, Tharintorn Treesit, Thomas B Kinney

Raja S Ramaswamy, Hyung Won Choi, Kazim H Narsinh, Kevin C McCammack, Tharintorn Treesit, Thomas B Kinney, Department of Vascular and Interventional Radiology, University of California San Diego Medical Center, San Diego, CA 92103, United States

Hans C Mouser, Department of Radiology, Indiana University Medical Center, Indianapolis, IN 46202, United States

Author contributions: All authors contributed equally to this paper.

Correspondence to: Raja S Ramaswamy, MD, Department of Vascular and Interventional Radiology, University of California San Diego Medical Center, 200 West Arbor Drive, #8756, San Diego, CA 92103, United States. rramaswamy@ucsd.edu

Telephone: +1-619-5436222 Fax: +1-619-5431234

Received: December 15, 2013 Revised: February 20, 2014

Accepted: March 11, 2014

Published online: March 28, 2015

© 2015 Baishideng Publishing Group Inc. All rights reserved.

Key words: Interventional radiology; Angiography; Therapeutic management; Upper gastrointestinal bleeding; Lower gastrointestinal bleeding; Embolization

Core tip: Acute gastrointestinal bleeding can lead to significant morbidity and mortality without appropriate treatment. The role of interventional radiology is crucial in patients that have persistent bleeding despite medical and endoscopic treatment. Computed tomography angiography and nuclear scintigraphy can localize lesions and provide information helpful for the Interventional Radiologist. The source of bleeding can be then be stabilized with endovascular angiography/transcatheter arterial embolization which is safe and effective with minimal complications due to the advances in catheter technology.

Abstract

Acute gastrointestinal bleeding (GIB) can lead to significant morbidity and mortality without appropriate treatment. There are numerous causes of acute GIB including but not limited to infection, vascular anomalies, inflammatory diseases, trauma, and malignancy. The diagnostic and therapeutic approach of GIB depends on its location, severity, and etiology. The role of interventional radiology becomes vital in patients whose GIB remains resistant to medical and endoscopic treatment. Radiology offers diagnostic imaging studies and endovascular therapeutic interventions that can be performed promptly and effectively with successful outcomes. Computed tomography angiography and nuclear scintigraphy can localize the source of bleeding and provide essential information for the interventional radiologist to guide therapeutic management with endovascular angiography and transcatheter embolization. This review article provides insight into the essential role of Interventional Radiology in the management of acute GIB.

Original sources: Ramaswamy RS, Choi HW, Mouser HC, Narsinh KH, McCammack KC, Treesit T, Kinney TB. Role of interventional radiology in the management of acute gastrointestinal bleeding. *World J Radiol* 2014; 6(4): 82-92 Available from: URL: <http://www.wjgnet.com/1949-8470/full/v6/i4/82.htm> DOI: <http://dx.doi.org/10.4329/wjr.v6.i4.82>

INTRODUCTION

Acute gastrointestinal bleeding (GIB) is a common clinical presentation that can lead to significant morbidity and mortality without appropriate treatment. The estimated annual incidence is approximately 40-150 cases per 10000 persons for upper GIB and 20-27 cases per 100000 persons for lower GIB^[1,2]. Mortality rate for both upper and lower GIB is estimated to be around 4%-10%^[1,2]. GIB can be a sequelae of many different etiologies, such as infec-

tion, vascular anomaly, inflammatory diseases, trauma, and malignancy^[2-9]. GIB is conventionally categorized by the anatomical location of the bleeding source. A GIB source proximal to the ligament of Treitz, which occurs more frequently, is classified as part of upper gastrointestinal (GI), and a source distal to the ligament of Treitz is considered to be part of lower GI. Diagnostic and treatment approach of GIB depends on its location, severity, and etiology. The role of radiology becomes especially important in patients whose GIB remains resistant to medical and endoscopic treatment. Radiology offers diagnostic imaging studies and endovascular therapeutic interventions that can be performed promptly and effectively.

CLINICAL EVALUATION AND MANAGEMENT OF THE PATIENT

Initial evaluation of patients with GIB begins with a history and physical examination^[10,11]. GIB can manifest with various signs, such as tachycardia, orthostatic hypotension, and chronic anemia^[11,12]. In patients who are hemodynamically unstable, resuscitation with fluid replacement and blood product administration should occur promptly to maintain intravascular volume and stabilize vital signs^[10]. Correction of coagulopathy may also be needed in certain cases^[10]. Diagnostic workup should immediately follow assessment and resuscitation, if not occurring simultaneously, to minimize adverse patient outcomes^[10,13,14].

Patient history and physical examination can help to determine whether GIB is of upper or lower GI source and guide subsequent workup^[11,15]. GIB that manifests as hematemesis or melena are commonly due to an upper GI source^[11,15]. Patients with active brisk upper GIB can also present with hematochezia and without any associated hematemesis or melena^[11,13,15]. Nasogastric tube lavage is sometimes performed to confirm an upper GI source of bleeding, but a negative result does not necessarily rule it out^[11,13,15]. Because of the intermittent nature of GIB and the possibility of a bleeding source distal to the pylorus, gastric lavage test is expected to yield negative results in certain cases. Approximately one quarter of upper GI hemorrhage is due to peptic ulcer disease and often associated with non-steroidal anti-inflammatory drug use and *Helicobacter pylori* infection^[15,16]. Other causes of acute upper GIB include varices, vascular abnormalities, angiodysplasia, gastritis, esophagitis, post Endoscopic Retrograde Cholangiopancreatography-papillotomy, and neoplasms^[2,4,10].

Patients with lower GIB commonly presents with hematochezia as most lower GIB sources are located in the colon. Less commonly, patients may present with melena if the source of bleeding is located in the small bowel or right colon. Of note, 10% to 15% of patients with hematochezia are reported to have an upper GI bleeding site^[17]. Diverticulosis is the most common cause of hematochezia, with the incidence increasing with ages older than 65. Other causes include inflammatory bowel disease, ischemic colitis, neoplasia, polyps, vascular mal-

formations, post-polypectomy, and angiodysplasia^[12,18]. Although most lower GIB resolves spontaneously with conservative management, 10%-15% of cases eventually require endovascular intervention^[19].

Endoscopy is the first diagnostic and therapeutic intervention of choice for both upper and lower GIB and thus a consultation with a gastroenterologist should not be delayed when a patient presents with GIB. For patients suspected of having an upper GI source of bleeding, esophagoduodenoscopy (EGD) is performed. Factors that may predict endoscopic treatment failure include patients that present with shock, hemoglobin less than 10, greater than six units of blood transfused, and significant comorbidities.

With regards to upper GI bleeding, larger ulcer size and location of an ulcer on the posterior wall of the duodenal bulb are also associated with increased rates of technical failure^[20,21].

Patients that present with hematochezia and suspected of having a lower GI source, colonoscopy is the initial diagnostic test of choice. For active lower GIB that is rapid and heavy, endoscopic view may be limited and yield inconclusive results. If a colonoscopy fails to identify the source of bleeding, then EGD may be performed in addition. Some studies have shown that endoscopy has a 92% sensitivity and near 100% specificity of identifying upper GI lesions and sensitivity of 90% and positive predictive value of 87% for identifying lower GI lesions^[22,23]. An unprepared colon limits the colonoscopy study and while blood may be seen within the colon lumen the exact site of bleeding is difficult to identify^[23].

If a lesion is identified endoscopically, therapeutic intervention can be done to effectively stabilize bleeding. Endoscopic therapies include epinephrine injection, sclerotherapy, and metal clip placement. Metal clips are especially useful in patients who require transcatheter or surgical intervention later on as clips can be visualized by imaging studies and facilitate lesion localization during angiography or surgery^[9,17].

INDICATIONS FOR ANGIOGRAPHY

When a patient has non-diagnostic endoscopic results or remains refractory to medical and endoscopic treatment, radiologic imaging and endovascular intervention are the next intervention of choice. Non-invasive radiologic imaging options include computed tomography angiography (CTA) and nuclear scintigraphy. However, these imaging modalities are only diagnostic and require subsequent endovascular or surgical intervention to stabilize bleeding^[24,25].

COMPUTED TOMOGRAPHY

CTA can detect flow rates as low as 0.3 mL/min and has a sensitivity of 50%-86% and specificity of 92%-95% for identifying lesions responsible for GIB^[24,26,27]. In addition to identifying the site of bleeding; CTA can often identify the etiology of GIB which may be useful for further

management.

At our institution, we use the following protocol for CTA: noncontrast (unenhanced), arterial phase, and portal venous phase with intravenous contrast at 4-5 mL/s. We also recommend the following acquisition parameters: section thickness of 1 mm with reconstruction interval of 0.8 mm, pitch of 0.900, rotation time of 0.5 s, tube voltage of 120 kV, and automatic tube current modulation in the x/y/z axis directions. We do not administer oral contrast as this may mask the bleeding source.

On nonenhanced CT, focal hyperattenuation within the bowel is indicative of recent hemorrhage and may represent a "sentinel clot". Extravasation of contrast is the hallmark finding used to determine the source of bleeding. Further, a changing appearance of the focus of extravasated contrast with time between phases confirms the presence of active bleeding^[25]. Although CTA can only serve as a diagnostic tool; it provides important information about vascular anatomy variance that becomes useful for endovascular intervention or surgical planning.

NUCLEAR SCINTIGRAPHY

The role of nuclear medicine for the detection of acute GI bleeding varies on an institutional basis. Nuclear scintigraphy plays a very important role in the detection of lower GI bleeding and when positive, has the ability to stratify patients that would benefit from intervention versus medical management. Although there is significant variability in reported detection of bleeding site by scintigraphy, the Society of Nuclear Medicine procedure guidelines states that bleeding rates as low as 0.1-0.35 mL/min can be detected^[28]. Tc-99m labeled red blood cell studies have an overall sensitivity of 95% and specificity of 93%^[29]. Patients with immediate blush on red blood cell scintigraphy are more likely to require urgent angiography and those with delayed blush have low angiographic yield^[30]. GI bleeding often is intermittent and nuclear scintigraphy has the advantage of continuous monitoring to localize sites of intermittent bleeding for potential angiography and intervention^[31].

ANGIOGRAPHIC EVALUATION OF ACUTE GI HEMORRHAGE

In emergent cases or in hospitals where CTA or nuclear scintigraphy is not available, patients with active GIB who fail medical and endoscopic intervention should undergo endovascular angiographic evaluation. Angiography is able to identify an active bleeding rate of at least 0.5 to 1 mL/min^[32,33]. For lower GIB, angiography performed with digital subtraction has a sensitivity of 60%, specificity of 100%, positive and negative predictive values of 100% and 24%, respectively^[34].

Access for endovascular angiography is gained *via* the common femoral artery^[35,36]. The aim of endovascular angiography is to identify bleeding vessel(s) and use selective catheterization to prepare for embolization^[36,37]. At

our institution, based on clinical scenario (patient history, CTA, endoscopic findings) the most suspected bleeding vessel is first studied. For suspected upper GIB, the celiac artery is commonly interrogated first as a majority of upper GIB is caused by gastroduodenal ulcers which are supplied by branches of the celiac artery^[35-38] (Figure 1). If angiographically negative, selective left gastric and the gastroduodenal artery evaluation is done. If the source of bleeding is thought to be in the small bowel or if no evidence of bleeding is seen upon interrogation of the celiac artery or its branches, the superior mesenteric artery (SMA) is evaluated next^[36,37]. If these angiographic studies are all negative, then evaluation of the inferior mesenteric artery (IMA) is considered. Selective injections are used to confirm any findings that are suspicious on nonselective angiograms^[36,37].

For suspected lower GIB, the SMA and IMA are examined^[36]. If bleeding appears to originate the proximal colon, the SMA is initially evaluated. If bleeding appears to originate in the distal colon, the IMA is selected^[36,39]. The two most common causes of lower GIB are colonic diverticular disease and angiodysplasia^[2,32] (Figures 2 and 3). However, when congenital variant vascular anatomy is suspected, such as in cases where a lower GI bleed simulates an upper GI bleed, all three major arterial supplies should be evaluated^[36]. If negative, the internal iliac arteries should be evaluated as the middle and inferior rectal arteries can be a source of hemorrhage^[36,39].

At our institution, under fluoroscopy we use non-ionic contrast is injected at a flow rate of 5-7 mL/s for celiac and super mesenteric arteriography, and 2-3 mL/s for inferior mesenteric arteriography. Digital subtraction angiogram is used to better visualize the vasculature by subtracting pre-contrast image from later images and effectively removing soft tissue and bones from the images. This is limited by peristalsis (consider giving glucagon) or patient breathing (which can be dealt with by studying unsubtracted images). Extravasation of contrast agent is indicative of active bleeding^[36]. Positive findings include mucosal blushes with abnormal vessels suggestive of tumor, prolonged contrast spots suggestive of inflammation, and visualization of arteries and veins on the same phase of the study suggestive of an arteriovenous malformation. Other lesions to consider include pseudoaneurysms and arteriovenous fistulas^[36,39].

There are several artifacts that mimic extravasation including bowel subtraction artifact, hypervascular mucosa, parts of the renal collecting system, and adrenal gland opacification^[39]. With respect to angiography, contrast extravasation may not been seen; however, a pathologic finding may indicate the source of bleeding. For example, visualization of varices at unsuspected sites may indicate the site of pathology. Further, angiodysplasia is often diagnosed by early and persistent filling of a draining vein and by abnormal clusters of vessels within the bowel wall. Possible pitfalls for failing to identify the bleeding focus include bleeding from a venous origin and technically related issues such as failure to inject the correct

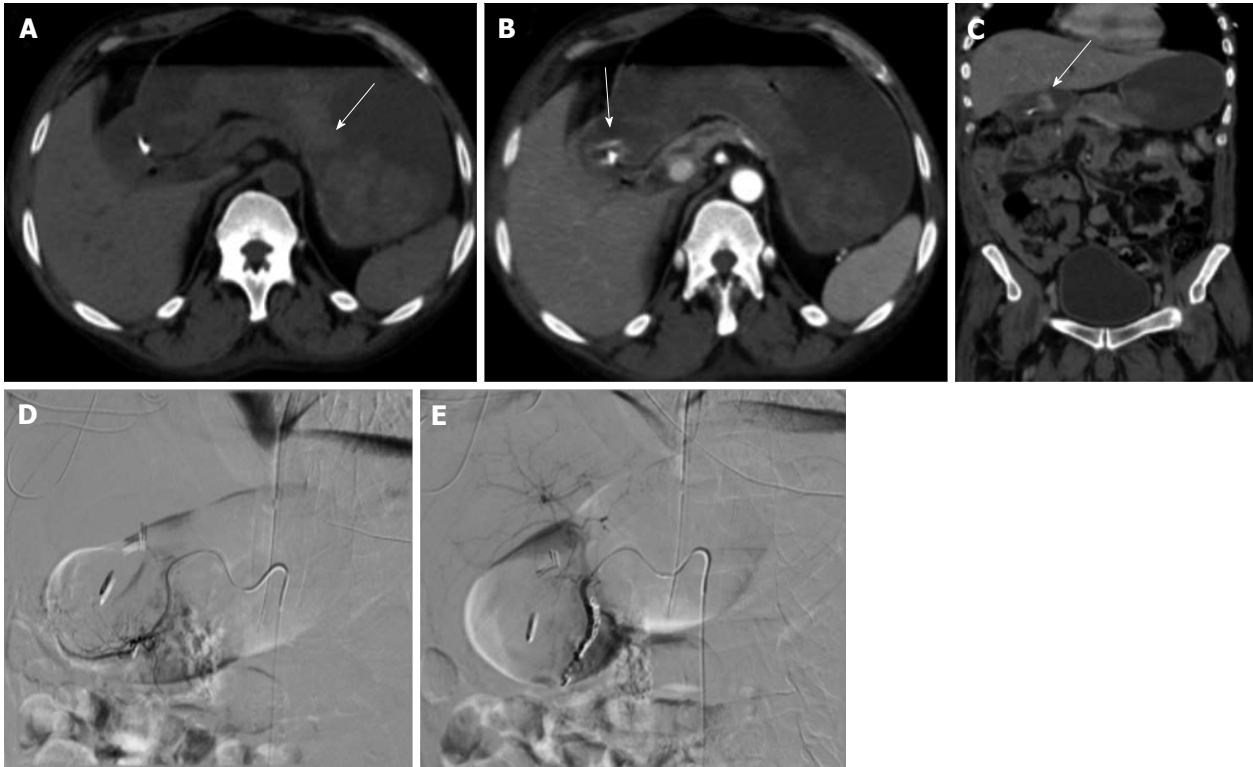


Figure 1 Upper gastrointestinal bleed secondary to gastric/duodenal ulcers. Fifty-four-year-old male with history of gastric ulcers which were treated by clipping through endoscopy. Despite endoscopic intervention, the patient presented with dropping hematocrit requiring transfusion. A: Noncontrast; B and C: contrast enhanced computed tomography imaging demonstrates active extravasation at the level of the gastric antrum with blood product filling the stomach; D and E: Active extravasation was found at the gastroduodenal artery (not shown) which was embolized with coils and gelfoam.

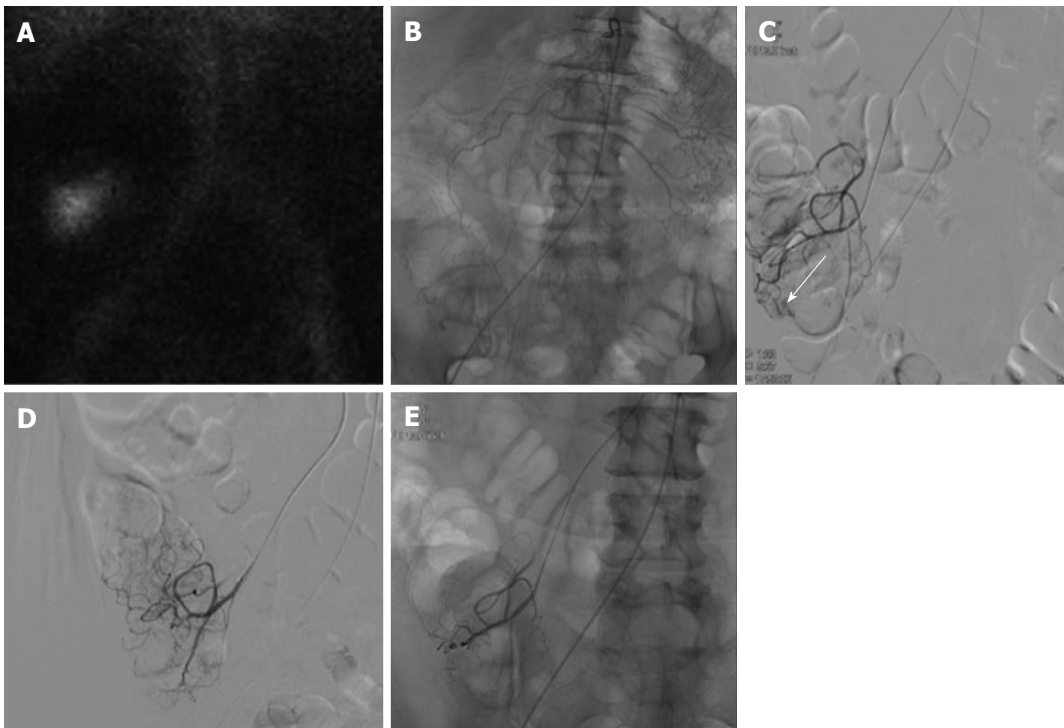


Figure 2 Lower gastrointestinal bleeding secondary to angiodysplasia. Sixty-one-year-old female with multiple bloody stools prior to admission and negative colonoscopy. A: Tc-99m red blood cell study demonstrates active bleeding in the region of the cecum; B and C: Selective catheterization of the distal ileocolic artery demonstrates a small focus of hemorrhage consistent with an area of angiodysplasia; D and E: Coil embolization was performed with two 3 mm coils. Post embolization images demonstrates resolved bleeding.



Figure 3 Lower gastrointestinal bleed secondary to diverticulitis. Sixty-eight-year-old male with history of esophageal carcinoma with acute diverticulitis with drifting hematocrit. A: Tc-99m labeled red blood cell study demonstrates bleeding at the hepatic flexure of the colon; B: Selective catheter angiography at the middle colic artery demonstrates active extravasation into a diverticulum present at the hepatic flexure the colon; C: Coil embolization of the right lateral aspect of the middle colic artery, across a small perforating vessel associated with a diverticular hemorrhage.

artery and bleeding outside the field of imaging^[39,40].

If patient is not actively bleeding or contrast extravasation is not visualized under fluoroscopy, the interventional radiologist may choose to restudy the same vessels or sub-selectively catheterize vessels likely supplying the suspected site of bleeding identified by prior endoscopic clipping or imaging studies to help increase the diagnostic yield and reduce false negative studies^[39,40].

ANGIOGRAPHIC MANAGEMENT OF ACUTE GI HEMORRHAGE

One of the advantages of endovascular angiography is that it can be both a diagnostic and therapeutic tool. Also, endovascular angiography can be performed emergently without any bowel preparation. However, if the patient had prior oral contrast this may limit the diagnostic ability of a mesenteric angiogram thus oral contrast should be avoided in patients who undergo CT imaging prior to angiographic intervention^[40-42].

Endovascular angiography serves as an effective and safe alternative to surgical intervention for patients whose GIB is refractory to medical and endoscopic treatment. Hemostasis is achieved by reducing blood flow to the bleeding vessel and thus decreasing perfusion pressure and facilitating clot formation at the site of bleeding^[40-43].

TRANSCATHETER ARTERIAL EMBOLIZATION

Transcatheter arterial embolization (TAE) is effective for controlling acute GIB^[41]. Some studies have shown that TAE is safer than surgical intervention in the high risk patient population and has a lower 30-d mortality rate^[38,44]. TAE is a viable option and temporizing measure in circumstances where endoscopic and/or surgical approach is not ideal.

The goal of TAE is super-selective embolization of bleeding vessels to reduce arterial perfusion pressure while maintaining adequate collateral blood flow to

minimize the risk of bowel infarction^[43]. A 5 French angiographic catheter is used to access the celiac, superior mesenteric, or inferior mesenteric arteries depending on the suspected location of bleeding and its supplying vasculature. In some cases this catheter can be guided to the site of bleeding; however, if it does not reach the bleeding site, then a smaller coaxial 3 French microcatheter can be advanced through the 4 or 5 Fr catheter.

Smaller guidewires, such as 0.018 in or smaller are used to guide the microcatheters as close as possible to the bleeding site. Caution must be taken to move the guide wire and microcatheter as carefully and steadily as possible to avoid vessel perforation, dissection, and vasospasm while reaching as close as possible to the site of bleeding. When no contrast extravasation is visualized under fluoroscopy, blind embolization of suspected bleeding vessel may be done at the discretion of the interventional radiologist^[38,45].

For upper GI bleeding, bleeding visualized in the stomach fundus is treated by left gastric artery embolization and bleeding in the gastric antrum/proximal duodenum by gastroduodenal embolization. When embolizing the gastroduodenal artery, if only the proximal portion is occluded, then bleeding may be by the pancreaticoduodenal arcade, also known as bleeding *via* the “back door”. Empiric embolization has also shown to be effective^[40,42] (Figures 4 and 5).

For lower GI bleeding the catheter should be positioned as close to the bleeding site as possible. If the source is in the SMA, the catheter advanced to the vasa rectum and if in the IMA the catheter should be placed in the marginal or terminal artery if possible. Embolization should only be performed when the catheter has been advanced to the mesenteric border of the colon. The bowel distal to the ligament of Treitz does not have a dual supply; therefore, the risk of bowel infarction is higher^[39,40,42] (Figures 6 and 7).

The type of embolic agent used is conventionally dependent on the interventional radiologist’s experience and preference, etiology of bleeding, and availability of the agent. Embolic agents include coils, glue, onyx, Gelfoam,

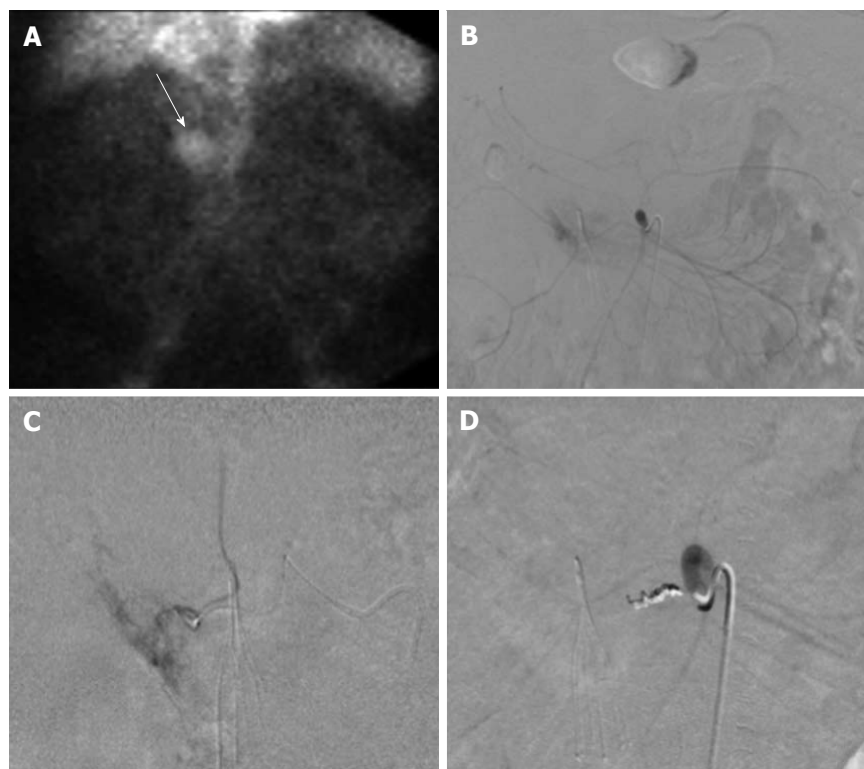


Figure 4 Sixty-six-year-old male with ongoing gastrointestinal hemorrhage requiring multiple transfusions over the last 72 h. EGD performed revealed ulcers in the first and second portion of the duodenum. A: Technetium-99m tagged RBC scan demonstrates brisk hemorrhage arising from the proximal small bowel/duodenum; B and C: Digitally subtracted images reveal active extravasation in the second portion of the duodenum from the inferior pancreaticoduodenal artery corresponding to area of hemorrhage on tagged RBC scan; D: Successful and uncomplicated coil embolization of the inferior pancreaticoduodenal artery with cessation of active hemorrhage. EGD: Esophagoduodenoscopy; RBC: Red blood cell.

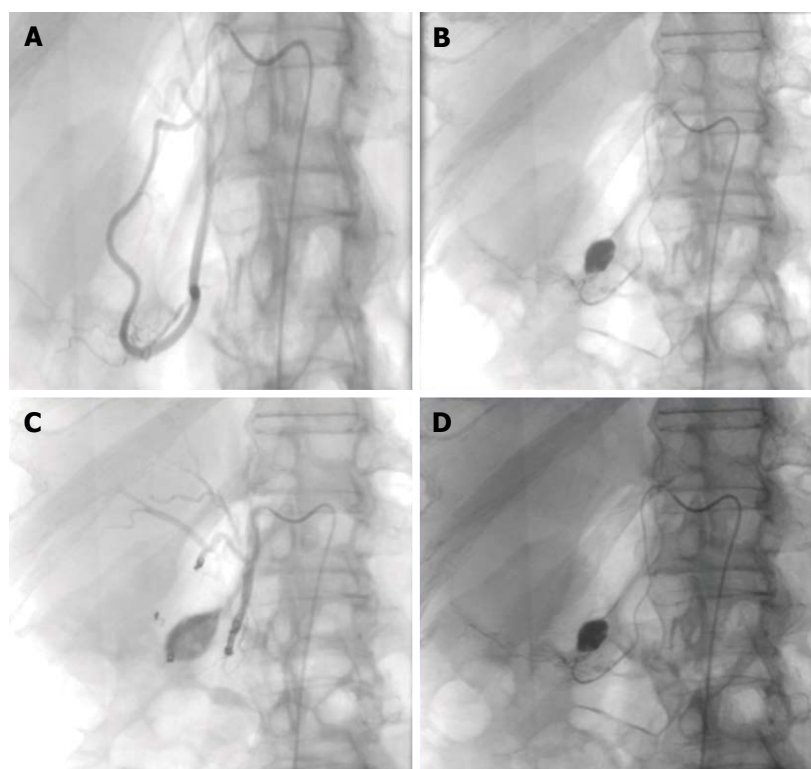


Figure 5 Seventy-two-year-old female with worsening abdominal pain and acute gastrointestinal hemorrhage. Upper gastrointestinal endoscopy reveals multiple large bleeding ulcers in the duodenum. A and B: Selective catheter angiography of the gastroduodenal and pancreaticoduodenal arteries demonstrates active extravasation; C: A combination of gelfoam slurry and coils were used to embolize branches of the pancreaticoduodenal and gastroduodenal artery; D: Representative post embolization image demonstrates no further evidence of active extravasation or bleeding.

polyvinyl alcohol particles (PVA), and Amplatzer vascular plugs. The most commonly used embolic agents are coils and PVA^[46-49].

Coils come in a variety of sizes and shapes, ranging from sub-millimeter to centimeters. Coils are composed of a metal component that acts as a physical occlusion and a fiber component that stimulates the thrombogenic process. Coils can be visualized under fluoroscopy after

placement which is an important advantage when compared to Gelfoam or PVA. Newer types of embolization coils have the ability to be removed after deployment if the initial placement is felt to be unsatisfactory^[46,50].

Gelfoam (absorbable compressed sponge) is a temporary agent made of subcutaneous porcine adipose tissue that remains effective for weeks to months before recanalization occurs. For this reason, Gelfoam is not rec-

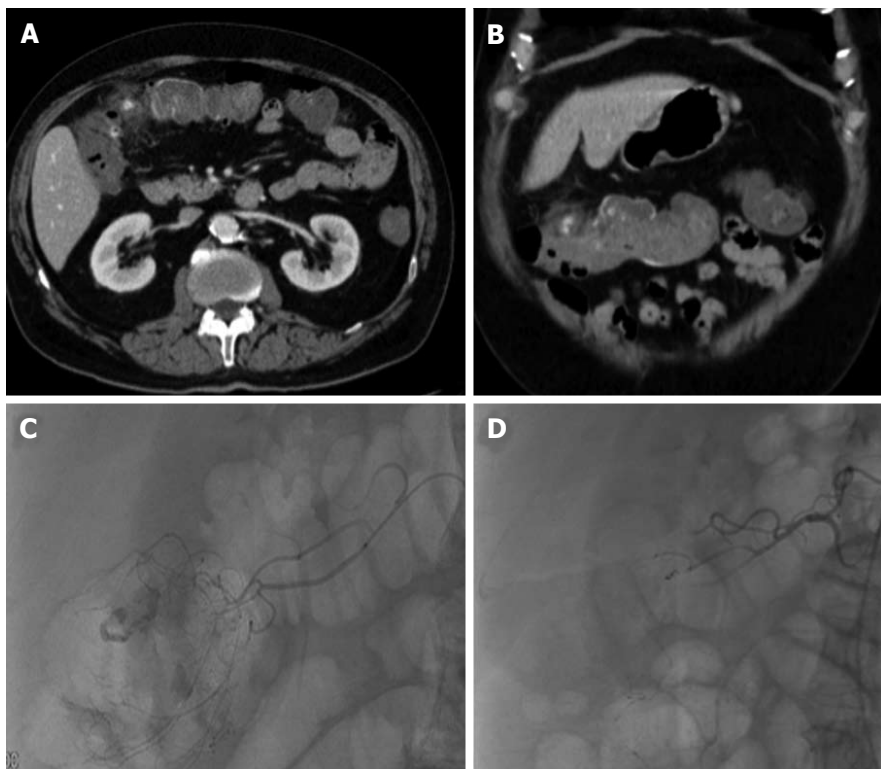


Figure 6 Lower gastrointestinal bleed from acute diverticulitis. Seventy-three-year-old male patient with bloody diarrhea, severely hypotensive (blood pressure 70/40) requiring 10 units of packed red blood cells. A and B: Contrast enhanced computed tomography abdomen demonstrates acute diverticulitis at the hepatic flexure, with active hemorrhage; C: Visceral angiography demonstrates the region of active bleeding in the ascending colon at the hepatic flexure; D: Successful distal Gelfoam and coil embolization of the supplying right colic artery branches.

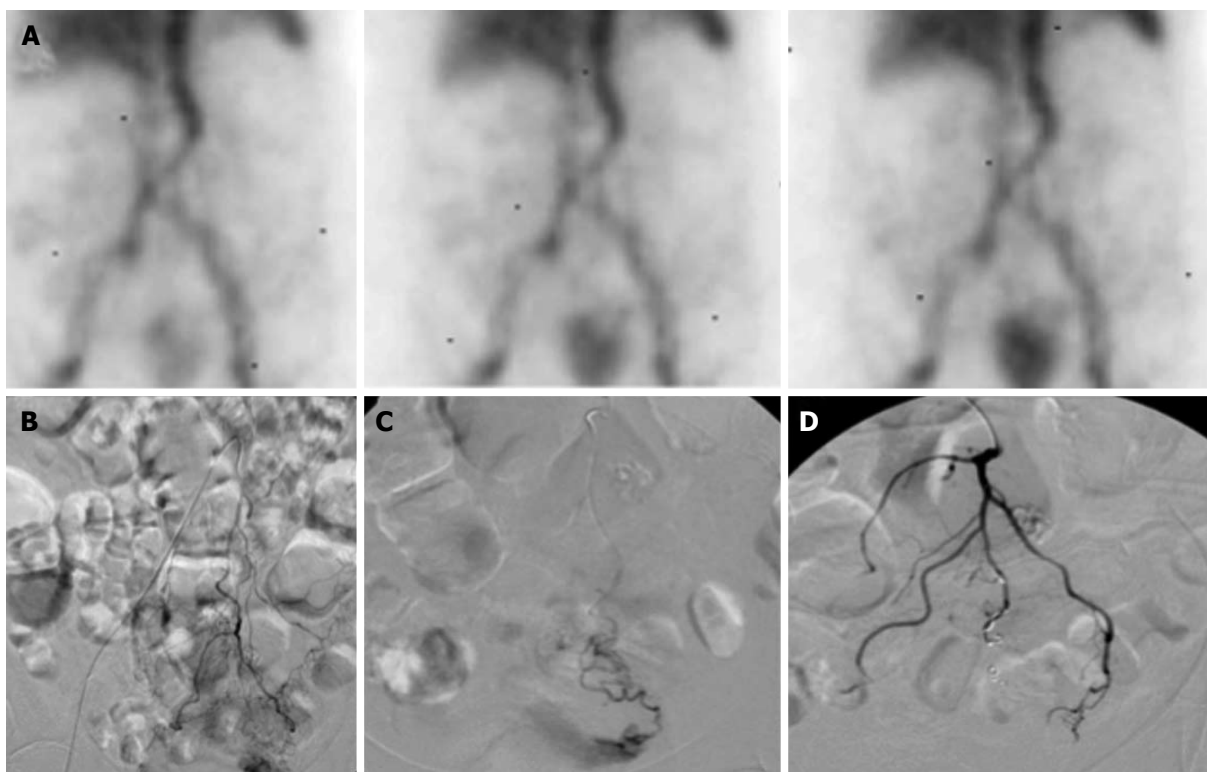


Figure 7 Lower gastrointestinal bleed secondary to supratherapeutic international normalized ratio. Seventy-six-year-old female with supratherapeutic INR (3.5) with painless hematochezia. A: Tc-99m labeled RBC study demonstrates brisk gastrointestinal bleeding localized to the sigmoid colon; B and C: Catheter angiography demonstrates active extravasation from a tertiary branch of the inferior mesenteric artery supplying the distal sigmoid colon which was subsequently embolized; D: With coils and no evidence of continued bleeding. RBC: Red blood cell.

ommended as a single agent. Gelfoam can also be mixed with saline to form a slurry, which helps with delivery. Advantages of gelfoam include: widespread availability, cost-effectiveness, and allows future access to emboli-

zed vessels after resorption. Disadvantages include that the preparation of particles can be time consuming and recanalization of vessels is unpredictable^[51]. In addition, because Gelfoam is made of small particulates, it is dif-

difficult to control its placement and can be deployed more distally than intended, which can result in higher risk of bowel ischemia from embolization of nearby collateral vessels^[36,50,51].

Several studies have shown that recurrent bleeding is more likely to occur when PVA particles, Gelfoam, or coils are used alone^[46,48,52]. Using coils with Gelfoam or PVA particles on both sides of the bleeding vessel is recommended to avoid “backdoor” bleeding and decrease the risk of recurrent bleeding^[48,53]. Some studies have shown that for upper GIB, which is commonly due to gastroduodenal ulcers, successful hemostasis can be achieved by embolizing the gastroduodenal artery or pancreaticoduodenal artery using coils alone^[54,56], or using coils and Gelfoam together to embolize distally and proximally in the gastroduodenal arterial trunk^[46,48,52]. Clinical success rate of embolization for upper GIB have been cited to be around 44%-100%^[41,44,46,57].

For lower GIB, some studies recommend against using Gelfoam, and instead advocate using coils and larger PVA particles^[43,58,59]. Small PVA particles, less than 250 μm , and Gelfoam particles may travel distally and occlude vessels at the arteriolar level. This results in occlusion of intramural circulation or submucosal plexus beyond the level of collateralization and increases the risk of bowel infarction^[59,60]. More peripheral embolization just proximal to the vasa recta is recommended to minimize the length of bowel at risk for ischemia. In most of the reported series in the literature, the target artery of embolization was the vasa recta and in technically difficult cases the marginal artery or more proximally^[57,61,62].

Anecdotally, coil embolization at the marginal artery may result in a higher rebleeding rate. Further, if a secondary intervention is required, this may close the door for future access to the bleeding vessel. Advantages to using microcoils include the ability to visualize under direct fluoroscopy and permitting decreasing perfusion pressure while collateral flow prevents infarction. Early rebleeding (less than 30 d) is reported to range from 10%-30%. Rebleeding may be secondary to a new site of bleed or recanalization of the previously embolized artery. Success rate for embolization of lower GIB has ranged from 88%-93%^[43,57,60].

N-butyl 2-cyanoacrylate (NBCA) glue or ethylene-vinyl alcohol copolymer (Onyx[®], Micro Therapeutics, Inc., Irvine, CA, United States of America) is a promising newer embolic agent to control GI bleeding. There is a growing body of evidence that supports the use of cyanoacrylates in embolization for lower GI hemorrhage. Advantages of using NBCA include the ability to occlude vessel beyond the most distal site of microcatheter advancement, permanent vessel closure, the option for using ultra-microcatheters not suitable for microcoil delivery, and more efficient obliteration of bleeding pseudoaneurysms with complex anatomy. Further, the rebleeding rate after use of cyanoacrylate is 4%-15%, which appears lower than the rate reported from employing coils or particles 0%-26%^[59,63-66].

However, NBCA is considerably more expensive and

requires a steeper learning curve. It has been reported in the literature that the time for TAE using NBCA was significantly lower than when using other liquid agents^[49,55]. There is a significant risk of glue reflux, bowel infarction, and future bowel stenosis^[67]. Also, the glue may polymerize with the catheter tip, which may subsequently get stripped off as the catheter is retracted. This poses the risk of non-target embolization or the catheter becoming adherent to the artery. Prompt catheter removal and aspiration of the guide catheter after microcatheter removal can significantly reduce this risk^[52,68].

Another potential agent, Onyx, is a liquid embolic agent composed of ethylene-vinyl alcohol copolymer dissolved in dimethyl sulphoxide (DMSO). In 2010, Lenhart *et al*^[69] reported their experience with the use of Onyx in the setting of acute upper GIB, becoming the first study published on arterial embolotherapy with Onyx as an embolic agent in the gastrointestinal tract. Their reported success rate was 81% and the complication rate minimal. The main advantages of Onyx[®] are its nonadhesive properties, high radiopacity and long solidification periods which make the embolization procedure more predictable. The DMSO solvent has disadvantages including severe vasospasm, excretion *via* respiration/perspiration which can cause an odor for days. The most prohibitive and restrictive factor however is its high cost and requirement for DMSO compatible catheters^[52,69].

VASOPRESSIN INFUSION

Vasopressin infusion is a less frequently used treatment for acute GIB^[58]. It was more commonly used before the advancement and improvement of transcatheter technique. Vasopressin acts by constricting arteries and reducing blood flow to the target site, but can also cause systemic side effects such as cardiac arrhythmia and bowel ischemia. In addition, vasopressin infusion has a high rebleeding rate after infusion is stopped. It requires much longer procedure time including catheter placement for 24-48 h and intensive monitoring during vasopressin infusion. However, when GIB is caused by diffuse lesions or super-selective catheterization is not possible, vasopressin infusion may be the remaining therapeutic option before surgical intervention. Vasopressin infusion is used more often for lower GIB than upper GIB as vessels responsible for lower GIB tend to be smaller in diameter and thus more responsive to the constricting effect of vasopressin^[58,70]. Some studies have shown that the cardiac side effects of vasopressin can be alleviated by using intravenous nitroglycerin infusion to increase coronary blood flow and cardiac output^[70]. Vasopressin infusion has a success rate of 59%-90% and a high rate of rebleeding rate of up to 36%-43%^[70].

COMPLICATIONS

Endovascular embolization and vasopressin infusion can increase the risk of bowel ischemia by reducing blood flow to the segment of bowel supplied by the target ves-

- 26 **García-Blázquez V**, Vicente-Bártulos A, Olavarria-Delgado A, Plana MN, van der Winden D, Zamora J, EBM-Connect Collaboration. Accuracy of CT angiography in the diagnosis of acute gastrointestinal bleeding: systematic review and meta-analysis. *Eur Radiol* 2013; **23**: 1181-1190 [PMID: 23192375 DOI: 10.1007/s00330-012-2721-x]
- 27 **Rondonotti E**, Marmo R, Petracchini M, de Franchis R, Penazio M. The American Society for Gastrointestinal Endoscopy (ASGE) diagnostic algorithm for obscure gastrointestinal bleeding: eight burning questions from everyday clinical practice. *Dig Liver Dis* 2013; **45**: 179-185 [PMID: 22921043 DOI: 10.1016/j.dld.2012.07.012]
- 28 **Ford PV**, Bartold SP, Fink-Bennett DM, Jolles PR, Lull RJ, Maurer AH, Seabold JE. Procedure guideline for gastrointestinal bleeding and Meckel's diverticulum scintigraphy. Society of Nuclear Medicine. *J Nucl Med* 1999; **40**: 1226-1232 [PMID: 10405149]
- 29 **Bunker SR**, Lull RJ, Tanasescu DE, Redwine MD, Rigby J, Brown JM, Brachman MB, McAuley RJ, Ramanna L, Landry A. Scintigraphy of gastrointestinal hemorrhage: superiority of 99mTc red blood cells over 99mTc sulfur colloid. *AJR Am J Roentgenol* 1984; **143**: 543-548 [PMID: 6331732 DOI: 10.2214/ajr.143.3.543]
- 30 **Ng DA**, Opelka FG, Beck DE, Milburn JM, Witherspoon LR, Hicks TC, Timmcke AE, Gathright JB. Predictive value of technetium Tc 99m-labeled red blood cell scintigraphy for positive angiogram in massive lower gastrointestinal hemorrhage. *Dis Colon Rectum* 1997; **40**: 471-477 [PMID: 9106699]
- 31 **Allen TW**, Tulchinsky M. Nuclear medicine tests for acute gastrointestinal conditions. *Semin Nucl Med* 2013; **43**: 88-101 [PMID: 23414825 DOI: 10.1053/j.semnuclmed.2012.11.001]
- 32 **Zuckerman GR**, Prakash C. Acute lower intestinal bleeding. Part II: etiology, therapy, and outcomes. *Gastrointest Endosc* 1999; **49**: 228-238 [PMID: 9925703]
- 33 **Winzelberg GG**, Froelich JW, McKusick KA, Waltman AC, Greenfield AJ, Athanasoulis CA, Strauss HW. Radionuclide localization of lower gastrointestinal hemorrhage. *Radiology* 1981; **139**: 465-469 [PMID: 6971455 DOI: 10.1148/radiology.139.2.6971455]
- 34 **Defreyne L**, Uder M, Vanlangenhove P, Van Maele G, Kunnen M, Kramann B. Angiography for acute lower gastrointestinal hemorrhage: efficacy of cut film compared with digital subtraction techniques. *J Vasc Interv Radiol* 2003; **14**: 313-322 [PMID: 12631635]
- 35 **Navuluri R**, Patel J, Kang L. Role of interventional radiology in the emergent management of acute upper gastrointestinal bleeding. *Semin Intervent Radiol* 2012; **29**: 169-177 [PMID: 23997408 DOI: 10.1055/s-0032-1326925]
- 36 **Walker TG**, Salazar GM, Waltman AC. Angiographic evaluation and management of acute gastrointestinal hemorrhage. *World J Gastroenterol* 2012; **18**: 1191-1201 [PMID: 22468082 DOI: 10.3748/wjg.v18.i11.1191]
- 37 **Walker TG**. Acute gastrointestinal hemorrhage. *Tech Vasc Interv Radiol* 2009; **12**: 80-91 [PMID: 19853226 DOI: 10.1053/j.tvir.2009.08.002]
- 38 **Eriksson LG**, Ljungdahl M, Sundbom M, Nyman R. Transcatheter arterial embolization versus surgery in the treatment of upper gastrointestinal bleeding after therapeutic endoscopy failure. *J Vasc Interv Radiol* 2008; **19**: 1413-1418 [PMID: 18755604 DOI: 10.1016/j.jvir.2008.06.019]
- 39 **Valji K**. The practice of interventional radiology with online cases and videos. Philadelphia, PA: Elsevier/Saunders, 2012
- 40 **Funaki B**. On-call treatment of acute gastrointestinal hemorrhage. *Semin Intervent Radiol* 2006; **23**: 215-222 [PMID: 21326767 DOI: 10.1055/s-2006-948758]
- 41 **Yap FY**, Omene BO, Patel MN, Yohannan T, Minocha J, Knuttinen MG, Owens CA, Bui JT, Gaba RC. Transcatheter embolotherapy for gastrointestinal bleeding: a single center review of safety, efficacy, and clinical outcomes. *Dig Dis Sci* 2013; **58**: 1976-1984 [PMID: 23361570 DOI: 10.1007/s10620-012-2547-z]
- 42 **Funaki B**, Kostelic JK, Lorenz J, Ha TV, Yip DL, Rosenblum JD, Leef JA, Straus C, Zaleski GX. Superselective microcoil embolization of colonic hemorrhage. *AJR Am J Roentgenol* 2001; **177**: 829-836 [PMID: 11566683 DOI: 10.2214/ajr.177.4.1770829]
- 43 **Evangelista PT**, Hallisey MJ. Transcatheter embolization for acute lower gastrointestinal hemorrhage. *J Vasc Interv Radiol* 2000; **11**: 601-606 [PMID: 10834491]
- 44 **Mirsadraee S**, Tirukonda P, Nicholson A, Everett SM, McPherson SJ. Embolization for non-variceal upper gastrointestinal tract haemorrhage: a systematic review. *Clin Radiol* 2011; **66**: 500-509 [PMID: 21371695 DOI: 10.1016/j.crad.2010.11.016]
- 45 **Eriksson LG**, Sundbom M, Gustavsson S, Nyman R. Endoscopic marking with a metallic clip facilitates transcatheter arterial embolization in upper peptic ulcer bleeding. *J Vasc Interv Radiol* 2006; **17**: 959-964 [PMID: 16778228 DOI: 10.1097/01.RVI.0000223719.79371.46]
- 46 **Aina R**, Oliva VL, Therasse E, Perreault P, Bui BT, Dufresne MP, Soulez G. Arterial embolotherapy for upper gastrointestinal hemorrhage: outcome assessment. *J Vasc Interv Radiol* 2001; **12**: 195-200 [PMID: 11265883]
- 47 **Loffroy R**, Guiu B, D'Athis P, Mezzetta L, Gagnaire A, Jouve JL, Ortega-Deballon P, Cheynel N, Cercueil JP, Krausé D. Arterial embolotherapy for endoscopically unmanageable acute gastroduodenal hemorrhage: predictors of early rebleeding. *Clin Gastroenterol Hepatol* 2009; **7**: 515-523 [PMID: 19418601 DOI: 10.1016/j.cgh.2009.02.003]
- 48 **Loffroy R**, Guiu B, Mezzetta L, Minello A, Michiels C, Jouve JL, Cheynel N, Rat P, Cercueil JP, Krausé D. Short- and long-term results of transcatheter embolization for massive arterial hemorrhage from gastroduodenal ulcers not controlled by endoscopic hemostasis. *Can J Gastroenterol* 2009; **23**: 115-120 [PMID: 19214287]
- 49 **Toyoda H**, Nakano S, Kumada T, Takeda I, Sugiyama K, Osada T, Kiriyaama S. Estimation of usefulness of N-butyl-2-cyanoacrylate-lipiodol mixture in transcatheter arterial embolization for urgent control of life-threatening massive bleeding from gastric or duodenal ulcer. *J Gastroenterol Hepatol* 1996; **11**: 252-258 [PMID: 8742922]
- 50 **Frisoli JK**, Sze DY, Kee S. Transcatheter embolization for the treatment of upper gastrointestinal bleeding. *Tech Vasc Interv Radiol* 2004; **7**: 136-142 [PMID: 16015558]
- 51 **Abdel-Aal AK**, Bag AK, Saddekni S, Hamed MF, Ahmed FY. Endovascular management of nonvariceal upper gastrointestinal hemorrhage. *Eur J Gastroenterol Hepatol* 2013; **25**: 755-763 [PMID: 23492985 DOI: 10.1097/MEG.0b013e32835fb9a9]
- 52 **Loffroy RF**, Abualsaud BA, Lin MD, Rao PP. Recent advances in endovascular techniques for management of acute non-variceal upper gastrointestinal bleeding. *World J Gastrointest Surg* 2011; **3**: 89-100 [PMID: 21860697 DOI: 10.4240/wjgs.v3.i7.89]
- 53 **Lubarsky M**, Ray CE, Funaki B. Embolization agents-which one should be used when? Part 1: large-vessel embolization. *Semin Intervent Radiol* 2009; **26**: 352-357 [PMID: 21326545 DOI: 10.1055/s-0029-1242206]
- 54 **Ledermann HP**, Schoch E, Jost R, Decurtins M, Zollikofer CL. Superselective coil embolization in acute gastrointestinal hemorrhage: personal experience in 10 patients and review of the literature. *J Vasc Interv Radiol* 1998; **9**: 753-760 [PMID: 9756062]
- 55 **Toyoda H**, Nakano S, Takeda I, Kumada T, Sugiyama K, Osada T, Kiriyaama S, Suga T. Transcatheter arterial embolization for massive bleeding from duodenal ulcers not controlled by endoscopic hemostasis. *Endoscopy* 1995; **27**: 304-307 [PMID: 7555935 DOI: 10.1055/s-2007-1005697]
- 56 **van Vugt R**, Bosscha K, van Munster IP, de Jager CP, Rutten MJ. Embolization as treatment of choice for bleeding peptic ulcers in high-risk patients. *Dig Surg* 2009; **26**: 37-42 [PMID: 19155626 DOI: 10.1159/000193476]

- 57 **Defreyne L**, Vanlangenhove P, De Vos M, Pattyn P, Van Maele G, Decruyenaere J, Troisi R, Kunnen M. Embolization as a first approach with endoscopically unmanageable acute nonvariceal gastrointestinal hemorrhage. *Radiology* 2001; **218**: 739-748 [PMID: 11230648 DOI: 10.1148/radiology.218.3.r01m r05739]
- 58 **Darcy M**. Treatment of lower gastrointestinal bleeding: vasopressin infusion versus embolization. *J Vasc Interv Radiol* 2003; **14**: 535-543 [PMID: 12761306]
- 59 **Kusano S**, Murata K, Ohuchi H, Motohashi O, Atari H. Low-dose particulate polyvinylalcohol embolization in massive small artery intestinal hemorrhage. Experimental and clinical results. *Invest Radiol* 1987; **22**: 388-392 [PMID: 3496319]
- 60 **Gordon RL**, Ahl KL, Kerlan RK, Wilson MW, LaBerge JM, Sandhu JS, Ring EJ, Welton ML. Selective arterial embolization for the control of lower gastrointestinal bleeding. *Am J Surg* 1997; **174**: 24-28 [PMID: 9240947 DOI: 10.1016/S0002-9610(97)00044-5]
- 61 **Nicholson AA**, Ettles DF, Hartley JE, Curzon I, Lee PW, Duthie GS, Monson JR. Transcatheter coil embolotherapy: a safe and effective option for major colonic haemorrhage. *Gut* 1998; **43**: 79-84 [PMID: 9771409]
- 62 **Peck DJ**, McLoughlin RF, Hughson MN, Rankin RN. Percutaneous embolotherapy of lower gastrointestinal hemorrhage. *J Vasc Interv Radiol* 1998; **9**: 747-751 [PMID: 9756061]
- 63 **Hur S**, Jae HJ, Lee M, Kim HC, Chung JW. Safety and efficacy of transcatheter arterial embolization for lower gastrointestinal bleeding: a single-center experience with 112 patients. *J Vasc Interv Radiol* 2014; **25**: 10-19 [PMID: 24286939 DOI: 10.1016/j.jvir.2013.09.012]
- 64 **Yata S**, Ihaya T, Kaminou T, Hashimoto M, Ohuchi Y, Umekita Y, Ogawa T. Transcatheter arterial embolization of acute arterial bleeding in the upper and lower gastrointestinal tract with N-butyl-2-cyanoacrylate. *J Vasc Interv Radiol* 2013; **24**: 422-431 [PMID: 23380738 DOI: 10.1016/j.jvir.2012.11.024]
- 65 **Huang CC**, Lee CW, Hsiao JK, Leung PC, Liu KL, Tsang YM, Liu HM. N-butyl cyanoacrylate embolization as the primary treatment of acute hemodynamically unstable lower gastrointestinal hemorrhage. *J Vasc Interv Radiol* 2011; **22**: 1594-1599 [PMID: 21875815 DOI: 10.1016/j.jvir.2011.07.018]
- 66 **Frodsham A**, Berkmen T, Ananian C, Fung A. Initial experience using N-butyl cyanoacrylate for embolization of lower gastrointestinal hemorrhage. *J Vasc Interv Radiol* 2009; **20**: 1312-1319 [PMID: 19800541 DOI: 10.1016/j.jvir.2009.06.031]
- 67 **Lang EK**. Transcatheter embolization in management of hemorrhage from duodenal ulcer: long-term results and complications. *Radiology* 1992; **182**: 703-707 [PMID: 1535883 DOI: 10.1148/radiology.182.3.1535883]
- 68 **Lee CW**, Liu KL, Wang HP, Chen SJ, Tsang YM, Liu HM. Transcatheter arterial embolization of acute upper gastrointestinal tract bleeding with N-butyl-2-cyanoacrylate. *J Vasc Interv Radiol* 2007; **18**: 209-216 [PMID: 17327553 DOI: 10.1016/j.jvir.2006.12.003]
- 69 **Lenhart M**, Paetzel C, Sackmann M, Schneider H, Jung EM, Schreyer AG, Feuerbach S, Zorger N. Superselective arterial embolisation with a liquid polyvinyl alcohol copolymer in patients with acute gastrointestinal haemorrhage. *Eur Radiol* 2010; **20**: 1994-1999 [PMID: 20379821 DOI: 10.1007/s00330-010-1762-2]
- 70 **Bush HL**, Nabseth DC. Intravenous nitroglycerin to improve coronary blood flow and left ventricular performance during vasopressin therapy. *Surg Forum* 1979; **30**: 226-228 [PMID: 120016]
- 71 **Gomes AS**, Lois JF, McCoy RD. Angiographic treatment of gastrointestinal hemorrhage: comparison of vasopressin infusion and embolization. *AJR Am J Roentgenol* 1986; **146**: 1031-1037 [PMID: 3485897 DOI: 10.2214/ajr.146.5.1031]
- 72 **Leitman IM**, Paull DE, Shires GT. Evaluation and management of massive lower gastrointestinal hemorrhage. *Ann Surg* 1989; **209**: 175-180 [PMID: 2783842]
- 73 **Bandi R**, Shetty PC, Sharma RP, Burke TH, Burke MW, Kastan D. Superselective arterial embolization for the treatment of lower gastrointestinal hemorrhage. *J Vasc Interv Radiol* 2001; **12**: 1399-1405 [PMID: 11742013]
- 74 **Mallory A**, Schaefer JW, Cohen JR, Holt SA, Norton LW. Selective intra-arterial vasopressin infusion for upper gastrointestinal tract hemorrhage: a controlled trial. *Arch Surg* 1980; **115**: 30-32 [PMID: 6985789]
- 75 **Formanek G**, Frech RS, Amplatz K. Arterial thrombus formation during clinical percutaneous catheterization. *Circulation* 1970; **41**: 833-839 [PMID: 5444526]
- 76 **Barrett BJ**, Parfrey PS. Clinical practice. Preventing nephropathy induced by contrast medium. *N Engl J Med* 2006; **354**: 379-386 [PMID: 16436769 DOI: 10.1056/NEJMc050801]
- 77 **Murphy SW**, Barrett BJ, Parfrey PS. Contrast nephropathy. *J Am Soc Nephrol* 2000; **11**: 177-182 [PMID: 10616853]

P- Reviewers: Chan WP, Murata S, Metwalli ZA
S- Editor: Song XX **L- Editor:** A **E- Editor:** Liu SQ



Multi-detector CT features of acute intestinal ischemia and their prognostic correlations

Marco Moschetta, Michele Telegrafo, Leonarda Rella, Amato Antonio Stabile Ianora, Giuseppe Angelelli

Marco Moschetta, Michele Telegrafo, Leonarda Rella, Amato Antonio Stabile Ianora, Giuseppe Angelelli, DIM, Interdisciplinary Department of Medicine, Section of Diagnostic Imaging, University of Bari Medical School, 70124 Bari, Italy
Author contributions: All the authors contributed to this paper in all its parts.

Correspondence to: Marco Moschetta, MD, Professor, DIM, Interdisciplinary Department of Medicine, Section of Diagnostic Imaging, University of Bari Medical School, Piazza Giulio Cesare 11, 70124 Bari, Italy. marco.moschetta@gmail.com
Telephone: +39-80-5478840 Fax: +39-80-5592911
Received: December 20, 2013 Revised: February 8, 2014
Accepted: March 13, 2014
Published online: March 28, 2015

Abstract

Acute intestinal ischemia is an abdominal emergency occurring in nearly 1% of patients presenting with acute abdomen. The causes can be occlusive or non occlusive. Early diagnosis is important to improve survival rates. In most cases of late or missed diagnosis, the mortality rate from intestinal infarction is very high, with a reported value ranging from 60% to 90%. Multi-detector computed tomography (MDCT) is a fundamental imaging technique that must be promptly performed in all patients with suspected bowel ischemia. Thanks to the new dedicated reconstruction program, its diagnostic potential is much improved compared to the past and currently it is superior to that of any other noninvasive technique. The increased spatial and temporal resolution, high-quality multi-planar reconstructions, maximum intensity projections, vessel probe, surface-shaded volume rendering and tissue transition projections make MDCT the gold standard for the diagnosis of intestinal ischemia, with reported sensitivity, specificity, positive and negative predictive values of 64%-93%, 92%-100%, 90%-100% and 94%-98%, respectively. MDCT contributes to appropriate treatment planning and provides important prognostic information

thanks to its ability to define the nature and extent of the disease. The purpose of this review is to examine the diagnostic and prognostic role of MDCT in bowel ischemia with special regard to the state of art new reconstruction software.

© 2015 Baishideng Publishing Group Inc. All rights reserved.

Key words: Multi-detector computed tomography; Bowel ischemia; Mesenteric infarction

Core tip: Multi-detector computed tomography is the most accurate imaging technique that must be promptly performed in all patients with bowel ischemia. Thanks to the new dedicated reconstruction program, its diagnostic potential is much improved compared to the past and currently it is superior to that of any other noninvasive technique. In the field of bowel ischemia, MDCT allows for correct diagnosis, is useful for appropriate treatment planning and provides important prognostic information as it is able to define the nature and extent of the disease.

Original sources: Moschetta M, Telegrafo M, Rella L, Stabile Ianora AA, Angelelli G. Multi-detector CT features of acute intestinal ischemia and their prognostic correlations. *World J Radiol* 2014; 6(5): 130-138 Available from: URL: <http://www.wjgnet.com/1949-8470/full/v6/i5/130.htm> DOI: <http://dx.doi.org/10.4329/wjr.v6.i5.130>

INTRODUCTION

Acute intestinal ischemia is an abdominal emergency occurring when blood flow to the bowel loops decreases because of mesenteric arterial hypoperfusion, impaired venous drainage or occlusion^[1-3]. It is estimated that nearly 1% of patients presenting with acute abdomen have

ischemic intestinal disease involving the small bowel or colon^[3-5].

Bowel ischemia is considered a potentially transient and reversible event; however, it may lead to intestinal infarction that requires surgical or interventional management. For this reason, early diagnosis is important to improve survival rates^[6]. In most cases of late or missed diagnosis, the mortality rate from intestinal infarction is very high, with a reported value ranging from 60% to 90%^[6-8].

Multi-detector computed tomography (MDCT) is a fundamental imaging technique that must be promptly performed in all patients with acute abdomen and suspected bowel ischemia. In fact, MDCT allows for correct diagnosis, contributes to appropriate treatment planning and provides important prognostic information thanks to its ability to define the nature of the disease and the extent of the anatomical damage^[9].

ETIOLOGY AND PATHOPHYSIOLOGY

The causes of intestinal ischemia can be occlusive or non occlusive. Occlusive causes are due to the embolic or thrombotic occlusion of arterial or venous vessels and account for about 80% of all cases of intestinal ischemia^[10]. Between 36% to 50% of intestinal infarctions are caused by embolic obstruction of the superior mesenteric artery in patients with cardiac pathology, while in 50%-60% of cases intestinal ischemia is caused by arterial thrombosis^[10,11]. Venous thrombosis accounts for about 10%-15% of all cases of intestinal ischemia^[10-12]. The most frequent cause of venous infarction is secondary to bowel closed-loop obstruction. This event does not lead to vascular thrombosis but to the twisting of the loops on their vascular pedicle which produces severe venous stasis. Another cause of venous intestinal ischemia is bowel obstruction, which causes an overdistension of the bowel wall, preventing the outflow of the venous blood^[13-18]. More rarely, intestinal infarction of the occlusive type can be due to generalized vasculitis or hypercoagulable states^[10,16].

Non occlusive causes account for about 20%-30% of all intestinal ischemia^[17]. In these forms, there is a significant reduction in blood flow within the arteries and veins. Hypovolemic shock, severe heart failure, abnormal blood concentration, episodes of neurogenic vasodilation and vasoconstriction secondary to drugs determine non occlusive bowel infarction in most cases^[7].

In cases of arterial and non occlusive ischemia, the first bowel reaction is in the spasm of the involved loops. In a more advanced phase, the microvascular wall damage causes hemorrhagic foci on the thinned bowel wall and the microflora proliferation leads to the hypotonic bowel dilatation. If the bowel ischemia persists for long enough, the entire bowel wall becomes necrotic and intramural air spreads through the mesenteric veins and into the portal venous system. If the underlying pathological process is removed, blood plasma or red blood cells may migrate from the disrupted mucosa into the lumen^[1,2,9].

In cases of venous ischemia, the initial phase is characterized by spastic reflex ileus and is followed by hypotonic reflex ileus masked by progressive intestinal intramural and mesenteric edema. Prolonged stasis reduces the arterial flow and the progression to intestinal infarction causes an extensive submucosal hemorrhage and edema. The consequent loss of bowel wall integrity and the intestinal bacteria proliferation cause intestinal necrosis and peritonitis^[9,10].

DIAGNOSIS AND COMPUTED TOMOGRAPHY

In the 1950s, the diagnosis of bowel ischemia was generally performed only during surgical exploration or at autopsy, but since the 1970s, the constant progress in imaging technology has gradually changed the diagnostic possibilities. Traditional radiography detects advanced stage findings such as bowel overdistension with the presence of air-fluid levels, pneumatosis and gas in the portal venous system. Ultrasonography is generally difficult to perform in patients with mesenteric infarction due to the presence of abundant intestinal meteorism and the poor compliance of these patients. However, its use is justified in order to rule out other diseases that could cause acute abdominal symptoms^[19,20]. The gold standard investigation for detecting intestinal ischemia is angiography with its diagnostic and therapeutic applications^[21]. However, this investigation is invasive, has a high cost and is often not available^[10,22,23].

Since its introduction into clinical practice, computed tomography (CT) has been used more and more often for recognizing early signs of intestinal ischemia and infarction. While the first results reported in the literature did not to be appear very encouraging^[24,25], the spread of spiral CT equipment has certainly increased the potential of this investigation^[26].

MDCT, thanks to the increased spatial and temporal resolution, high-quality multi-planar reconstructions (MPR), maximum intensity projections (MIP) and three-dimensional rendering, is considered the gold standard for the diagnosis of intestinal ischemia, with reported sensitivity, specificity, positive and negative predictive values of 64%-93%, 92%-100%, 90%-100% and 94%-98%, respectively. It allows the visualization of the early signs of bowel ischemia and infarction and the etiological diagnosis of the disease, which is crucial for treatment planning in acute patients^[9,10].

Recent experiences reported that dual-energy CT (DE-CT) provides a variety of post-processing options in the assessment of abdominal vascular diseases. In fact, DE-CT has also been reported to improve diagnostic accuracy and reduce radiation exposure and contrast material dose in the field of mesenteric vascular diseases. Besides, it seems to improve image quality in the study of abdominal and lower extremity arteries by virtual manipulation of keV-settings^[27-30].

CT TECHNIQUE

The use of CT devices with volumetric image acquisition and high temporal resolution is crucial because of the critical clinical conditions and consequent poor compliance of patients suspected of having bowel infarction and referred for CT examination. The study protocol consists of unenhanced and contrast enhanced scans from the diaphragm dome to the pubic symphysis with the patient in the supine position.

After the intravenous injection of contrast medium (120-140 mL at a flow rate of 3-3.5 mL/s), scans are performed with a biphasic technique in the arterial (40 s mean delay) and venous (65 s mean delay) phases, with different technical parameters according to the CT device being used. Contrast medium injection may not be necessary if the unenhanced images clearly demonstrate the presence of the typical alterations of advanced stage bowel infarction. With single detector row spiral CT, the following parameters are used: slice thickness, 5 mm; reconstruction index, 2.5-5; pitch, 1.5; tube rotation time, 1 s. With multi-detector row CT, the parameters are: slice thickness, 0.5 mm; reconstruction index, 1-2.5 mm; pitch, 1.25-1.75; tube rotation time, 0.5-0.75 s. The administration of oral contrast medium to distend the bowel loops is not recommended because of the severe clinical condition and in order to keep the investigation time to a minimum. It is always recommended to visualize the obtained images with different window and level settings. In fact, a window set on the soft tissue values (width-W: 300-350; level-L: 40-50) can demonstrate alterations of the bowel wall, abdominal organs, mesentery and vascular structures; the window setting used to visualize the lung parenchyma (W: 450-1000; L: -100-0) will aid the recognition of extraluminal gas^[10].

Unenhanced CT is reportedly required for the diagnosis of intestinal ischemia^[31,32] in order to evaluate submucosal hemorrhage, hyperdense/calcified thrombi and atherosclerotic plaque and to obtain a baseline attenuation measurement of the bowel wall for the assessment of the enhancement. The arterial phase is performed for evaluating arterial stenoses, thrombi/emboli and occlusion^[32,33], while the venous phase is for evaluating venous patency and abdominal organs which may be affected by ischemia.

On the other hand, a recent study which aims to reduce the radiation dose demonstrates that unenhanced CT is not necessary for the diagnosis of acute mesenteric ischemia because bowel enhancement can be assessed by using normal enhancing bowel as an internal reference and because of the low sensitivity of submucosal hemorrhage for the diagnosis. Major abdominal lesions can be readily diagnosed by using standard venous phase imaging, although important errors occur when relying only on the portal phase to assess the arterial system. The arterial phase is an integral component in the diagnosis of intestinal ischemia and should not be excluded to achieve dose reduction^[32-34].

CT POST-PROCESSING

The widespread introduction of MDCT has revolutionized the field of computed tomography thanks to the high spatial and temporal resolution and the ability to create isotropic voxel data and, consequently, reliable MPR and three-dimensional (3D) reconstructions. Specialized 3D reconstruction techniques allow the visualization of the anatomical details which are difficult to evaluate by using axial images alone. Such details may require the use of oblique or curved reconstructions, or more complex methods such as MIP, minimum intensity projection (MinIP), surface-shaded volume rendering (SS-VRT) and virtual endoscopy^[35-37].

3D reconstructions are obtained by means of dedicated computer software that can handle the volumetric data of CT. Even if the use of 3D reconstructions increases the total exam evaluation time, it has been demonstrated how using 3D reconstruction techniques for examining volumetric data improves the interpretation, recognition and description of specific clinical conditions^[37-39].

In cases of intestinal ischemia, MPR and 3D reconstructions allow easy detection and understanding of CT findings. In fact, reconstructions such as curved MPR, MIP, vessel probe (VP), SS-VRT and tissue transition projections (TTP) are particularly useful for the assessment of the vascular and bowel signs of intestinal ischemia.

Curved MPR are a subcategory of MPR reconstructions; they display all voxels contained in a selectable curved surface as a single bi-dimensional image which allows following winding structures along their natural path of development in a single image. This technique is particularly useful for the study of the vascular system. The vessel is displayed as a straight line resulting in vascular defects, stenoses and dilatations being easily detected.

MIP is a data visualization method that enables the detection of highly dense structures, distinguishing them from the surrounding tissues in order to better understand the extension of some structures, such as vessels, nodules, calcifications, surgical clips and foreign bodies. MIP is used in CT angiography because it can follow the complete course of vessels even if they are tortuous, allowing the evaluation of eventual enlargements and defects^[35].

VP is a program that allows vessels to be simultaneously examined in 3D, curved reformat and cross-sectional reformat views. It can study and measure arteries from between 0.5 and 18 mm in diameter and calculate the degree of stenosis. It can display images in a variety of formats, including automatic and simultaneous orthogonal cross-sections, orthogonal MPR, oblique and curved MPR, 3D and curved reformat views. This fast and simple software has also been used in the field of the preoperative T staging of esophageal and gastric cancer for examining the visceral wall^[40,41].

In cases of intestinal ischemia, curved MPR, MIP and VP are useful for evaluating the course of mesenteric vessels, searching for any filling defect (Figure 1A).



Figure 1 Arterial mesenteric ischemia. A: Vessel probe in multiplanar (MPR) mode reconstructions showing bowel ischemia caused by the occlusion of the superior mesenteric artery (arrows). Bowel loop dilatation is associated (arrowheads); B and C: Computed tomography transverse scans show bowel wall dilatation (arrowheads) with loss of wall enhancement (arrows) in a case of arterial bowel ischemia diagnosed in the early stage; D: Coronal maximum intensity projection reconstruction; E: Coronal MPR reconstruction. Bowel ischemia caused by the occlusion of the superior mesenteric artery. Bowel loop dilatation (arrowheads) and parietal pneumatosis of the right colon (short arrows) are associated.

SS-VRT is a technique that creates a 3D visual illustration of CT volumetric data from any desired perspective. SS-VRT images provide a three-dimensional view that is significantly superior to other volume rendering techniques^[35,37]. These techniques typically select voxels to be included in a surface rendering based on a selected range of Hounsfield values. By properly choosing the Hounsfield range, different types of tissues can be selected: parenchyma, bone, airways and vessels. By analyzing a combination of Hounsfield ranges, a volume of CT data can be segmented into several tissue types. The main diagnostic utility of SS-VRT techniques is its ability to reproduce structures of a specific density with great detail. With successive interactive steps of exclusion/inclusion of different tissue types and resizing/trimming of the regions of interest, surfaces that would otherwise be very difficult to visualize can be detected. In patients with intestinal ischemia due to vascular occlusion, SS-VRT images allow a 3D assessment of the course of mesenteric vessels.

Moreover, the application of a range of densitometric values corresponding to the transition zone between the bowel content (air or contrast medium) and the surrounding tissue makes the bowel wall transparent. These reconstructions, called tissue transition projections, allow the evaluation and extent of loop dilatation which are prognostic indicators in patients affected by intestinal ischemia^[35,37].

CT FINDINGS

There is a significant correlation between the CT findings of bowel ischemia and the pathological damage. Unenhanced scans can show atherosclerotic calcification and the hyperdense aspect of the vascular structure involved in cases of recent thrombosis, parietal pneumatosis, air in the mesenteric vessels or portal branches, and pneumoperitoneum or retroperitoneum. In all other cases, intravenous injection of contrast medium is essential in order to detect the causes and signs of the ischemia. In occlusive, embolic or thrombotic forms, CT allows visualization of the site of the vascular obstruction, appearing as a defective opacification of the vascular lumen. It is most easily recognized when the occlusion is at the level of the main trunks^[10,26]. Most changes occurring during the initial phase of ischemia affect the cells and cannot therefore be visualized. The earliest recognizable alteration in the course of ischemia is vasodilation; in this phase, CT examination after contrast medium injection will show diffuse parietal hyperdensity at the level of the involved loops^[3,10,26,42]. This hyperdensity is already evident in the arterial phase and persists during the venous phase; it can most easily be recognized by comparing the density of the normal and pathological segments of the bowel^[3,10]. This sign occurs in about 51% of patients and indicates that the ischemia has not yet caused irreversible damage of the bowel and can be treated conserva-

tively^[10,43]. Without treatment, the mentioned alterations will evolve parallel with the anatomical damage. The hyperemic phase is followed by intense vasoconstriction that is aggravated by the compression of the intramural capillaries due to the overdistension of the bowel wall. The characteristic CT findings in this phase are the reduced or absent enhancement of the ischemic bowel after intravenous injection of the contrast medium. The persistence of the vasospasm causes an increase in capillary permeability with submucosal edema leading to the wall thickening and the interruption of the peristaltic activity, followed by bowel dilation^[26] (Figure 1B and C). In venous infarction, venous stasis and hemorrhagic bulging of the mucosal and sub-mucosal layers lead to a higher degree of wall thickening than in the arterial type, associated with the typical target appearance of the loop (Figure 2)^[26,44]. In 30%-70% of cases, vascular stasis causes edema and vascular bulging at the level of the mesentery which can be detected as an irregular hyperdensity of the mesenteric adipose tissue. These density changes indicate the onset of cellular necrosis that starts at the level of the mucosal epithelium and then extends to the other wall layers. In fact, the damage to the mucosal epithelium removes an important mechanical barrier between the bowel lumen and the bowel wall, causing the migration of intestinal gas, enzymes and anaerobic bacteria from the lumen into the wall thickness, as well as the passage of fluid from the wall into the bowel lumen. In this phase, CT shows the presence of air within the wall thickness, a sign known as parietal pneumatosis (Figure 1D and E). This is certainly one of the most important lesions in cases of suspected bowel ischemia; it has an incidence ranging between 22% and 72% in the literature and indicates advanced stage disease. The air within the wall may be arranged in a linear or curved shape; the bubbles are sometimes located in the central part of the wall and take on the ray-like appearance described as the “kiwi sign”. In order to determine whether any gas is present within the intestinal wall, other diseases or factors that could induce pneumatosis must first be excluded, such as lung disease, peptic ulcer, collagen disturbances and steroid treatments. However, the clinical data need to be considered for a differential diagnosis^[10,26,44,45]. Reactive endoabdominal fluid collections may be observed in this phase, generally located close to the ischemic loops. With the progression of the anatomical damage, air may migrate from the bowel wall into the branches of the portomesenteric veins. If air can be seen at the level of the main branch of the portal vein or the intrahepatic portal branches, this is a sure sign of a very advanced phase of mesenteric infarction (present in 9%-36% of cases), although it does not necessarily indicate transmural bowel necrosis. The only pathognomonic sign of transmural necrosis is bowel perforation, which is seen as pneumoperitoneum or retroperitoneum (described in 6%-20% of cases) and diffuse ascites (20%-22% of cases)^[10,26,44].

CT PROGNOSTIC CORRELATIONS

The prognostic value of CT findings of intestinal isch-

emia has been already reported in the literature and can be explained by the correlation between the progression of intestinal ischemic damage and the corresponding alterations detected on imaging.

Usually, outcome is closely correlated with the kind of vascular obstruction, with a reported mortality rate of 89% in the arterial and 11% in the venous forms^[9].

Parietal hyperdensity, the absence of wall enhancement and bowel wall thickening all indicate a good outcome, whereas loop dilatation, parietal and portomesenteric pneumatosis and pneumoperitoneum/pneumoretroperitoneum are all indicators of unfavorable outcome^[1-3,9,10,46].

Bowel wall hyperdensity reflects vasodilation, which is the first consequence of hypoxic damage. The absence of wall enhancement corresponds to the ensuing vasoconstriction; bowel-loop thickening and dilatation are related to the increased capillary permeability, pneumatosis and the presence of air within the mesenteric-portal system reflect the necrosis of the intestinal mucosa, whereas pneumoperitoneum/pneumoretroperitoneum corresponds to a transmural extension of the necrosis^[3,9,10,47]. Therefore, wall hyperdensity, the absence of enhancement and wall thickening are an early stage of the disease, in contrast to loop dilation, parietal and portomesenteric pneumatosis and pneumoperitoneum/pneumoretroperitoneum which reflect an advanced stage of disease and are characterized by high mortality rates. Furthermore, hyperdensity and bowel wall thickening significantly correlate to venous forms, whereas loop dilatation, parietal pneumatosis, the presence of gas within the mesenteric venules and portal branches, as well as pneumoperitoneum/pneumoretroperitoneum are typical of arterial forms of ischemia. On the other hand, the absence of wall enhancement and the presence of ascites are not specific CT findings with respect to the nature of ischemia as their incidence is almost the same in both arterial and venous obstructions.

These findings may have a temporal justification; in fact, it has been demonstrated that in arterial obstructions, the pathophysiological events leading to wall necrosis occur in rapid succession, whereas a longer time interval is required for the initial vascular damage of venous occlusions to develop into the anatomical damage. Thus, the possibility of detecting wall abnormalities typical of the early phase of the disease is greater in venous infarctions than in the arterial forms. Wall thickening and the target appearance of the intestinal loops indicate a good prognosis, more frequently associated with venous infarction owing to a larger intramural hemorrhagic component and superinfection. Portomesenteric pneumatosis is considered to be a negative sign with an associated mortality rate of 75%-90%^[10,48]; it indicates advanced bowel necrosis and correlates with unfavorable outcome, especially when associated with other ischemic wall abnormalities.

DIFFERENTIAL DIAGNOSIS

CT signs of bowel ischemia have different levels of spec-

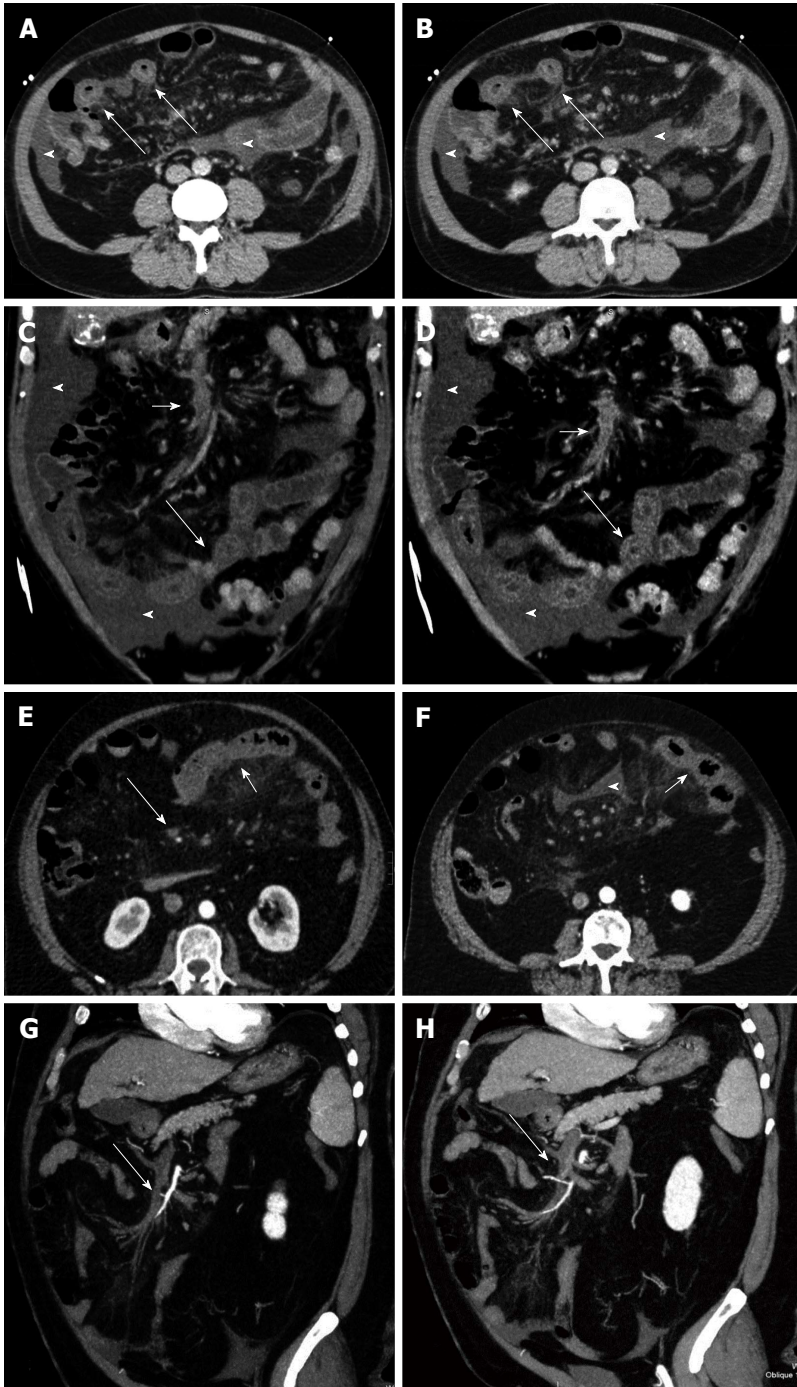


Figure 2 Venous mesenteric ischemia. A and B: Transverse computed tomography (CT) scans; C and D: Coronal MPR reconstructions. Bowel ischemia caused by the occlusion of the superior mesenteric vein (short arrows). The target sign with concentric bowel wall thickening is well evident (long arrows). Ascites is associated (arrowheads); E and F: Transverse CT scans; G and H: Coronal curved multiplanar reconstructions. Bowel ischemia caused by the occlusion of the superior mesenteric vein (long arrows). The target sign with concentric bowel wall thickening is well evident (short arrows). Ascites is associated (arrowheads).

ificity. For this reason, differential diagnosis with other abdominal disease is crucial.

Thickening of the bowel wall is the most common but least specific CT finding. Most bowel tumors present as focal thickenings, while benign conditions present as segmental and diffuse bowel thickenings extending for 6-40 cm or greater than 40 cm, respectively. Segmental or diffuse bowel wall involvement usually does not exceed 1 cm in thickness and may have a stratified white or grey attenuation pattern in contrast-enhanced scans^[48,49].

The stratified pattern of attenuation, including the “target sign”, indicates bowel inflammation or ischemia. In cases of bowel ischemia, this finding should be evaluated in the clinical context and in association with other

imaging findings, such as occlusion of the mesenteric vessels, intestinal pneumatosis, air in the mesenteric or portal veins, bowel dilatation and ascites. Bowel wall thickening with a stratified pattern may also be seen in the active phase of Crohn’s disease (CD). However, CD, which predominantly affects the ileum and right colon, is characterized by CT signs such as discontinuous involvement of the bowel wall, prominent vasa recta, fistulas and abscesses, and proliferation of the fat tissue along the mesenteric border of the bowel^[44-46].

The white pattern of attenuation is caused by intense enhancement of the bowel wall and may occur in both ischemic and inflammatory bowel disease (Figure 3). Hyperenhancement of the ischemic bowel may be due to

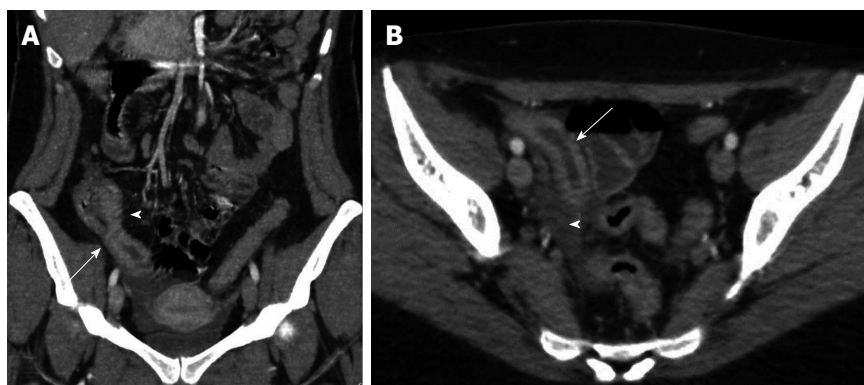


Figure 3 Crohn's disease. A: Computed tomography (CT) coronal reconstruction shows terminal ileal loop thickening with white attenuation pattern (arrow) and perivisceral vasa recta (arrowhead); B: Transverse CT scan shows thickening of the terminal ileal loop (arrow) associated with perivisceral endoperitoneal fluid (arrowhead).

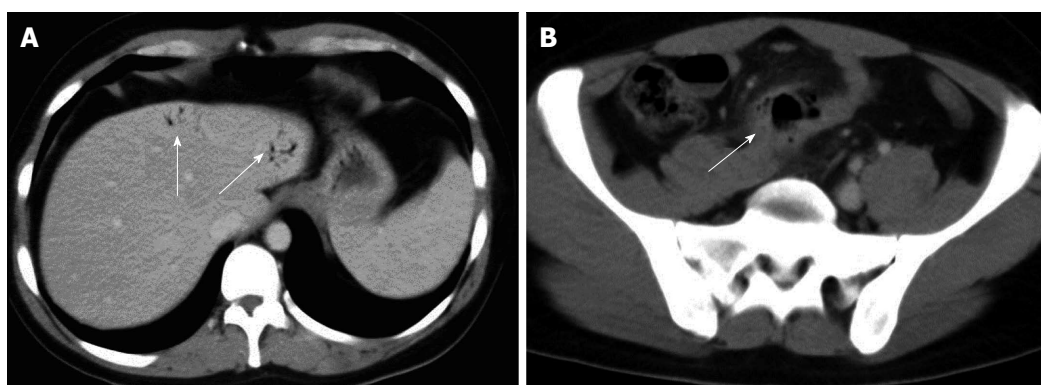


Figure 4 Intrahepatic portal air from diverticulitis. A: Computed tomography transverse scan shows the presence of intrahepatic portal air (arrows); B: Pelvic sigmoid diverticulitis complicated by peridiverticular abscess (arrow).

the early vasodilation at the level of the involved loops, the mesenteric venous occlusion or to the reperfusion after occlusive or non-occlusive ischemia. Associated imaging findings of bowel ischemia have to be considered for the correct diagnosis.

The grey pattern of attenuation indicates decreased enhancement of the bowel wall. Its acute onset reflects a decreased blood supply and is pathognomonic of intestinal ischemia. The hypoattenuating bowel wall is caused by intense vasoconstriction and by wall edema in cases of mesenteric venous occlusion and bowel obstruction^[49-51]. The delayed onset of grey pattern reflects transmural fibrosis and occurs in patients with chronic CD or chronic radiation enteritis.

The combination of parietal pneumatosis and portomesenteric venous gas is a highly specific finding because it is associated with the presence of bowel ischemia in approximately 70% of cases. On the other hand, the sole finding of portomesenteric vein gas is associated with several causes besides mesenteric ischemia. In fact, it can be caused by some conditions such as wall alterations, bowel distension and abdominal sepsis. Wall alterations include several gastrointestinal ulcerative diseases, such as gastric ulcer, perforated gastric carcinoma and inflammatory bowel disease. Portomesenteric vein gas secondary to bowel distension can be due to iatrogenic visceral dilatation, paralytic or mechanical ileus, blunt trauma and barotrauma. Besides, some infectious abdominal processes, including diverticulitis, abdominal abscess and

appendicitis, have been associated with portomesenteric vein gas (Figure 4)^[49-51].

Parietal pneumatosis has to be distinguished from pneumatosis cystoides intestinalis, an uncommon disease characterized by the presence of multiple gas-filled cysts in the submucosa and subserosa of the intestinal wall. The parietal cysts cause bowel obstruction in 16.3% of cases and the diagnosis of the disease is based on endoscopy. Plain radiography of the abdomen and CT easily detect the typical grape-like gas clusters into the bowel wall, allowing a differential diagnosis of intestinal pneumatosis with its typical linear shape^[51,52].

CONCLUSION

Bowel infarction is an uncommon but often underestimated cause of non traumatic acute abdomen and early diagnosis is crucial in order to avoid irreversible damage to the bowel wall. MDCT is a fundamental imaging technique that must be promptly performed in all patients with acute abdomen and suspected bowel ischemia. Thanks to the dedicated reconstruction program, its diagnostic potential is much improved compared to the past and currently is superior to that of any other noninvasive technique. In the field of bowel ischemia, MDCT allows for correct diagnosis, is useful for appropriate treatment planning and provides important prognostic information as it is able to define the nature of the disease and the extent of the anatomical damage.

REFERENCES

- 1 **Romano S**, Romano L, Grassi R. Multidetector row computed tomography findings from ischemia to infarction of the large bowel. *Eur J Radiol* 2007; **61**: 433-441 [PMID: 17157468 DOI: 10.1016/j.ejrad.2006.11.002]
- 2 **Romano S**, Lassandro F, Scaglione M, Romano L, Rotondo A, Grassi R. Ischemia and infarction of the small bowel and colon: spectrum of imaging findings. *Abdom Imaging* 2006; **31**: 277-292 [PMID: 16283583 DOI: 10.1007/s00261-005-0376-7]
- 3 **Horton KM**, Fishman EK. Multi-detector row CT of mesenteric ischemia: can it be done? *Radiographics* 2001; **21**: 1463-1473 [PMID: 11706217 DOI: 10.1148/radiographics.21.6.g01nv091463]
- 4 **Kaleya RN**, Sammartano RJ, Boley SJ. Aggressive approach to acute mesenteric ischemia. *Surg Clin North Am* 1992; **72**: 157-182 [PMID: 1731382]
- 5 **Moore WM**, Hollier LH. Mesenteric artery occlusive disease. *Cardiol Clin* 1991; **9**: 535-541 [PMID: 1913732]
- 6 **Goldberg MA**, Mueller PR, Saini S, Lee MJ, Girard MJ, Dawson SL, Hallisey MJ, Cortell ED, Hahn PF, Brink JA. Importance of daily rounds by the radiologist after interventional procedures of the abdomen and chest. *Radiology* 1991; **180**: 767-770 [PMID: 1871292]
- 7 **Scholz FJ**. Ischemic bowel disease. *Radiol Clin North Am* 1993; **31**: 1197-1218 [PMID: 8210346]
- 8 **Sánchez-Fernández P**, Mier y Díaz J, Blanco-Benavides R. [Acute mesenteric ischemia. Profile of an aggressive disease]. *Rev Gastroenterol Mex* 2000; **65**: 134-140 [PMID: 11464607]
- 9 **Moschetta M**, Stabile Ianora AA, Pedote P, Scardapane A, Angelelli G. Prognostic value of multidetector computed tomography in bowel infarction. *Radiol Med* 2009; **114**: 780-791 [PMID: 19551344 DOI: 10.1007/s11547-009-0422-6]
- 10 **Angelelli G**, Scardapane A, Memeo M, Stabile Ianora AA, Rotondo A. Acute bowel ischemia: CT findings. *Eur J Radiol* 2004; **50**: 37-47 [PMID: 15093234 DOI: 10.1016/j.ejrad.2003.11.01]
- 11 **Rha SE**, Ha HK, Lee SH, Kim JH, Kim JK, Kim JH, Kim PN, Lee MG, Auh YH. CT and MR imaging findings of bowel ischemia from various primary causes. *Radiographics* 2000; **20**: 29-42 [PMID: 10682769 DOI: 10.1148/radiographics.20.1.g00ja0629]
- 12 **Rhee RY**, Gloviczki P. Mesenteric venous thrombosis. *Surg Clin North Am* 1997; **77**: 327-338 [PMID: 9146716 DOI: 10.1016/S0039-6109(05)70552-1]
- 13 **Balthazar EJ**, Liebeskind ME, Macari M. Intestinal ischemia in patients in whom small bowel obstruction is suspected: evaluation of accuracy, limitations, and clinical implications of CT in diagnosis. *Radiology* 1997; **205**: 519-522 [PMID: 9356638]
- 14 **Balthazar EJ**, Birnbaum BA, Megibow AJ, Gordon RB, Whelan CA, Hulnick DH. Closed-loop and strangulating intestinal obstruction: CT signs. *Radiology* 1992; **185**: 769-775 [PMID: 1438761]
- 15 **Megibow AJ**, Balthazar EJ, Cho KC, Medwid SW, Birnbaum BA, Noz ME. Bowel obstruction: evaluation with CT. *Radiology* 1991; **180**: 313-318 [PMID: 2068291]
- 16 **Kim JK**, Ha HK, Byun JY, Yang SK, Jung HY, Min YI, Kim PN, Lee MG, Auh YH. CT differentiation of mesenteric ischemia due to vasculitis and thromboembolic disease. *J Comput Assist Tomogr* 2008; **25**: 604-611 [PMID: 11473193 DOI: 10.1097/00004728-200107000-00016]
- 17 **Chabert S**, Porcheron J, Balique JG. [Management of acute intestinal arterial ischemia]. *J Chir (Paris)* 1999; **136**: 130-135 [PMID: 10549009]
- 18 **Vinci R**, Angelelli G, Stabile Ianora AA, Gaballo A, Rotondo A. [Vascular complications in intestinal obstructions. The role of computed tomography]. *Radiol Med* 1999; **98**: 157-161 [PMID: 10575445]
- 19 **Danse EM**, Van Beers BE, Goffette P, Dardenne AN, Laterre PF, Pringot J. Acute intestinal ischemia due to occlusion of the superior mesenteric artery: detection with Doppler sonography. *J Ultrasound Med* 1996; **15**: 323-326 [PMID: 8683669]
- 20 **Nicoloff AD**, Williamson WK, Moneta GL, Taylor LM, Porter JM. Duplex ultrasonography in evaluation of splanchnic artery stenosis. *Surg Clin North Am* 1997; **77**: 339-355 [PMID: 9146717 DOI: 10.1016/S0039-6109(05)70553-3]
- 21 **Sardo P**, Cepich MS, Giulini SM. [Diagnostic and therapeutic role of angiography in acute vascular insufficiency of the superior mesenteric artery]. *Radiol Med* 1988; **75**: 319-325 [PMID: 3375475]
- 22 **Wolf EL**, Sprayregen S, Bakal CW. Radiology in intestinal ischemia. Plain film, contrast, and other imaging studies. *Surg Clin North Am* 1992; **72**: 107-124 [PMID: 1731379]
- 23 **Bakal CW**, Sprayregen S, Wolf EL. Radiology in intestinal ischemia. Angiographic diagnosis and management. *Surg Clin North Am* 1992; **72**: 125-141 [PMID: 1731380]
- 24 **Alpern MB**, Glazer GM, Francis IR. Ischemic or infarcted bowel: CT findings. *Radiology* 1988; **166**: 149-152 [PMID: 3336673]
- 25 **Smerud MJ**, Johnson CD, Stephens DH. Diagnosis of bowel infarction: a comparison of plain films and CT scans in 23 cases. *AJR Am J Roentgenol* 1990; **154**: 99-103 [PMID: 2104734 DOI: 10.2214/ajr.154.1.2104734]
- 26 **Taourel PG**, Deneuille M, Pradel JA, Régent D, Bruel JM. Acute mesenteric ischemia: diagnosis with contrast-enhanced CT. *Radiology* 1996; **199**: 632-636 [PMID: 8637978]
- 27 **Vlahos I**, Chung R, Nair A, Morgan R. Dual-energy CT: vascular applications. *AJR Am J Roentgenol* 2012; **199**: S87-S97 [PMID: 23097172 DOI: 10.2214/AJR.12.9114]
- 28 **Huang SY**, Nelson RC, Miller MJ, Kim CY, Lawson JH, Husarik DB, Boll DT. Assessment of vascular contrast and depiction of stenoses in abdominopelvic and lower extremity vasculature: comparison of dual-energy MDCT with digital subtraction angiography. *Acad Radiol* 2012; **19**: 1149-1157 [PMID: 22743115 DOI: 10.1016/j.acra.2012.04.014]
- 29 **Sudarski S**, Apfaltrer P, W Nance J, Schneider D, Meyer M, Schoenberg SO, Fink C, Henzler T. Optimization of keV-settings in abdominal and lower extremity dual-source dual-energy CT angiography determined with virtual monoenergetic imaging. *Eur J Radiol* 2013; **82**: e574-e581 [PMID: 23763858 DOI: 10.1016/j.ejrad.2013.04.040]
- 30 **He J**, Ma X, Wang Q, Fan J, Sun Z. Spectral CT demonstration of the superior mesenteric artery: comparison of monochromatic and polychromatic imaging. *Acad Radiol* 2014; **21**: 364-368 [PMID: 24360636 DOI: 10.1016/j.acra.2013.11.004]
- 31 **Gore RM**, Yaghamai V, Thakrar KH, Berlin JW, Mehta UK, Newmark GM, Miller FH. Imaging in intestinal ischemic disorders. *Radiol Clin North Am* 2008; **46**: 845-875, v [PMID: 19103136 DOI: 10.1016/j.rcl.2008.05.004]
- 32 **Wiesner W**, Khurana B, Ji H, Ros PR. CT of acute bowel ischemia. *Radiology* 2003; **226**: 635-650 [PMID: 12601205 DOI: 10.1148/radiol.2263011540]
- 33 **Kirkpatrick ID**, Kroeker MA, Greenberg HM. Biphasic CT with mesenteric CT angiography in the evaluation of acute mesenteric ischemia: initial experience. *Radiology* 2003; **229**: 91-98 [PMID: 12944600 DOI: 10.1148/radiol.2291020991]
- 34 **Schieda N**, Fasih N, Shabana W. Triphasic CT in the diagnosis of acute mesenteric ischaemia. *Eur Radiol* 2013; **23**: 1891-1900 [PMID: 23471431]
- 35 **Perandini S**, Faccioli N, Zaccarella A, Re T, Mucelli RP. The diagnostic contribution of CT volumetric rendering techniques in routine practice. *Indian J Radiol Imaging* 2010; **20**: 92-97 [PMID: 20607017 DOI: 10.4103/0971-3026.63043]
- 36 **Moschetta M**, Scardapane A, Telegrafo M, Lorusso V, Angelelli G, Stabile Ianora AA. Differential diagnosis between benign and malignant ulcers: 320-row CT virtual gastroscopy. *Abdom Imaging* 2012; **37**: 1066-1073 [PMID: 22289996 DOI: 10.1007/s00261-012-9849-7]
- 37 **Li AE**, Fishman E. Cervical spine trauma: evaluation by

- multidetector CT and three-dimensional volume rendering. *Emerg Radiol* 2003; **10**: 34-39 [PMID: 15290528]
- 38 **Salvolini L**, Bichi Secchi E, Costarelli L, De Nicola M. Clinical applications of 2D and 3D CT imaging of the airways-a review. *Eur J Radiol* 2000; **34**: 9-25 [PMID: 10802203 DOI: 10.1016/S0720-048X(00)00155-8]
- 39 **Fox LA**, Vannier MW, West OC, Wilson AJ, Baran GA, Pilgram TK. Diagnostic performance of CT, MPR and 3DCT imaging in maxillofacial trauma. *Comput Med Imaging Graph* 1995; **19**: 385-395 [PMID: 8734776 DOI: 10.1016/0895-6111(95)00022-4]
- 40 **Moschetta M**, Ianora AA, Marzullo A, Scardapane A, Angelelli G. Vessel probe CT protocol in the study of esophageal carcinoma: can it improve preoperative T staging? *Eur J Surg Oncol* 2010; **36**: 663-669 [PMID: 20627648 DOI: 10.1016/j.ejso.2010.05.011]
- 41 **Moschetta M**, Stabile Ianora AA, Anglani A, Marzullo A, Scardapane A, Angelelli G. Preoperative T staging of gastric carcinoma obtained by MDCT vessel probe reconstructions and correlations with histological findings. *Eur Radiol* 2010; **20**: 138-145 [PMID: 19504100 DOI: 10.1007/s00330-009-1482-7]
- 42 **Bartnicke BJ**, Balfe DM. CT appearance of intestinal ischemia and intramural hemorrhage. *Radiol Clin North Am* 1994; **32**: 845-860 [PMID: 8084999]
- 43 **Klein HM**, Lensing R, Klosterhalfen B, Töns C, Günther RW. Diagnostic imaging of mesenteric infarction. *Radiology* 1995; **197**: 79-82 [PMID: 7568858]
- 44 **Catalano O**. [Computed tomography in the diagnostic approach to acute mesenteric ischemia]. *Radiol Med* 1995; **89**: 440-446 [PMID: 7597225]
- 45 **Lorusso V**, Stabile Ianora AA, Rubini G, Losco M, Niccoli Asabella A, Fonio P, Moschetta M. [Atypical appearance of pneumatosis intestinalis at multidetector CT]. *Recenti Prog Med* 2012; **103**: 542-545 [PMID: 23096749 DOI: 10.1701/1166.12906]
- 46 **Saba L**, Mallarini G. Computed tomographic imaging findings of bowel ischemia. *J Comput Assist Tomogr* 2008; **32**: 329-340 [PMID: 18520533 DOI: 10.1097/RCT.0b013e3180dc8cb1]
- 47 **Gellett LR**, Harries SR, Roobottom CA. Urgent contrast enhanced computed tomography in the diagnosis of acute bowel infarction. *Emerg Med J* 2002; **19**: 480-481 [PMID: 12205021 DOI: 10.1136/emj.19.5.480]
- 48 **Yikilmaz A**, Karahan OI, Senol S, Tuna IS, Akyildiz HY. Value of multislice computed tomography in the diagnosis of acute mesenteric ischemia. *Eur J Radiol* 2011; **80**: 297-302 [PMID: 20719444 DOI: 10.1016/j.ejrad.2010.07.016]
- 49 **Peloponissios N**, Halkic N, Pugnale M, Jornod P, Nordback P, Meyer A, Gillet M. Hepatic portal gas in adults: review of the literature and presentation of a consecutive series of 11 cases. *Arch Surg* 2003; **138**: 1367-1370 [PMID: 14662541 DOI: 10.1001/archsurg.138.12.1367]
- 50 **Fernandes T**, Oliveira ML, Castro R, Araújo B, Viamonte B, Cunha R. Bowel wall thickening at CT: simplifying the diagnosis. *Insights Imaging* 2014; **5**: 195-208 [PMID: 24407923 DOI: 10.1007/s13244-013-0308-y]
- 51 **Sebastià C**, Quiroga S, Espin E, Boyé R, Alvarez-Castells A, Armengol M. Portomesenteric vein gas: pathologic mechanisms, CT findings, and prognosis. *Radiographics* 2000; **20**: 1213-1214; discussion 1214-1216 [PMID: 10992012]
- 52 **Milone M**, Di Minno MN, Musella M, Maietta P, Iaccarino V, Barone G, Milone F. Computed tomography findings of pneumatosis and portomesenteric venous gas in acute bowel ischemia. *World J Gastroenterol* 2013; **19**: 6579-6584 [PMID: 24151384 DOI: 10.3748/wjg.v19.i39.6579]

P- Reviewers: Algin O, Kumar J, Zhu YQ **S- Editor:** Zhai HH
L- Editor: Roemmele A **E- Editor:** Liu SQ



Partial splenic artery embolization in cirrhotic patients

Tyson A Hadduck, Justin P McWilliams

Tyson A Hadduck, Justin P McWilliams, Department of Interventional Radiology, David Geffen School of Medicine, UCLA, Los Angeles, CA 90095, United States

Author contributions: Hadduck TA and McWilliams JP equally contributed to this paper.

Correspondence to: Justin McWilliams, MD, Assistant Professor, Department of Interventional Radiology, David Geffen School of Medicine, UCLA, 757 Westwood Plaza, Suite 2125C, Los Angeles, CA 90095,

United States. jumcwilliams@mednet.ucla.edu

Telephone: +1-310-2678773 Fax: +1-310-2673631

Received: December 9, 2013 Revised: February 9, 2014

Accepted: May 8, 2014

Published online: March 28, 2015

Abstract

Splenomegaly is a common sequela of cirrhosis, and is frequently associated with decreased hematologic indices including thrombocytopenia and leukopenia. Partial splenic artery embolization (PSE) has been demonstrated to effectively increase hematologic indices in cirrhotic patients with splenomegaly. This is particularly valuable amongst those cirrhotic patients who are not viable candidates for splenectomy. Although PSE was originally developed decades ago, it has recently received increased attention. Presently, PSE is being utilized to address a number of clinical concerns in the setting of cirrhosis, including: decreased hematologic indices, portal hypertension and its associated sequela, and splenic artery steal syndrome. Following PSE patients demonstrate significant increases in platelets and leukocytes. Though progressive decline of hematologic indices occur following PSE, they remain improved as compared to pre-procedural values over long-term follow-up. PSE, however, is not without risk and complications of the procedure may occur. The most common complication of PSE is post-embolization syndrome, which involves a constellation of symptoms including fever, pain, and nausea/vomiting. The rate of complications has been shown to increase as the percent of total splenic volume embolized increases. The purpose of this review is to explore the current literature in re-

gards to PSE in cirrhotic patients and to highlight their techniques, and statistically summarize their results and associated complications.

© 2015 Baishideng Publishing Group Inc. All rights reserved.

Key words: Partial splenic embolization; Cirrhosis; Liver disease; Thrombocytopenia; Leukopenia

Core tip: Splenomegaly is a common sequela of cirrhosis, and is frequently associated with decreased hematologic indices including thrombocytopenia and leukopenia. Partial splenic artery embolization (PSE) has been demonstrated to effectively increase hematologic indices in cirrhotic patients with splenomegaly. This is particularly valuable amongst cirrhotic patients that are not viable candidates for splenectomy. Although PSE was originally developed decades ago, it has recently received increased attention. Presently, PSE is being utilized to address a number of clinical concerns in the setting of cirrhosis, including: decreased hematologic indices, portal hypertension and its associated sequela, and splenic artery steal syndrome.

Original sources: Hadduck TA, McWilliams JP. Partial splenic artery embolization in cirrhotic patients. *World J Radiol* 2014; 6(5): 160-168 Available from: URL: <http://www.wjgnet.com/1949-8470/full/v6/i5/160.htm> DOI: <http://dx.doi.org/10.4329/wjr.v6.i5.160>

INTRODUCTION

Portal hypertension in the setting of cirrhosis commonly leads to splenomegaly^[1]. Additionally, cirrhosis is frequently associated with decreased hematologic indices, including thrombocytopenia and anemia. The prevalence of leukopenia amongst cirrhotic patients is more common than in the general population, and varies from 5% to 61%^[2]. The pathogenesis of each hematologic deficiency in cirrhotic patients is multi-factorial in nature. Splenic sequestration, however, serves as a common

link; and is a contributing factor in the development of thrombocytopenia, anemia, and leukopenia in cirrhotic patients^[3].

Decreased hematologic indices can have significant clinical ramifications. Thrombocytopenia increases a patient's risk of spontaneous bleeding, and may preclude surgical or endovascular interventions. Leukopenia decreases the patient's ability to overcome infection, and may serve as a contraindication to the use of chemotherapies in hepatocellular carcinoma. Anemia places a patient at increased risk should bleeding occur, may prevent surgical or endovascular interventions and can leave a patient dependent on transfusions^[2].

Operative splenectomy can be used to treat splenomegaly in cirrhotic patients. While splenectomy is an effective treatment of splenomegaly in the setting of cirrhosis, it is not without risk^[4]. Major complications include portal vein thrombosis and sepsis^[4,5]. Additionally, some cirrhotic patients may be poor surgical candidates, thus necessitating alternative approaches to splenomegaly amongst some cirrhotic patients. In 1973, Maddison performed the first splenic artery embolization. A farmer with non-alcoholic cirrhosis presented with intractable esophageal variceal bleeding which was resistant to treatment with intra-splenic arterial infusion of vasopressin. In the setting of significant prior bleeding surgical intervention was contraindicated, and Maddison^[6] performed an intra-arterial embolization of the splenic artery utilizing autologous clot as the embolic agent. The patient responded well and no complications were reported at 5 mo follow-up.

Despite Maddison's^[6] early success, numerous complications of total splenic artery embolization were soon discovered^[7]. Complications included splenic abscess, splenic rupture, pneumonia, septicemia, and death. In response to these complications, Spigos *et al.*^[8] transitioned to partial splenic embolization (PSE) paired with antibiotic prophylaxis and demonstrated significantly better outcomes. Soon partial splenic embolization gained popularity and served as a therapeutic option for cirrhotic patients with hypersplenism who were poor surgical candidates.

Amin published a 2009 prospective randomized trial of 40 cirrhotic patients who presented with hypersplenism, treating half with PSE and half with splenectomy. Over the six-month follow-up period cohorts receiving splenectomy and PSE both demonstrated a significant increase in their leukocyte and platelet counts. Patients treated with PSE had slowly decreasing leukocyte and platelet levels during the follow-up period, though they remained significantly above pre-PSE levels. Of the 20 patients treated with PSE one died of myocardial infarction within one day postop, one developed splenic abscess, and one developed a portal vein thrombus. Of the 20 patients treated with splenectomy, three patients developed portal vein thrombosis. The surgical cohort had longer procedure times, longer hospitalizations, required transfusions more frequently, and reported more post-procedural pain^[9].

CLINICAL APPLICATIONS AND OUTCOMES OF PSE

In 2007 Koconis *et al.*^[10] published a review of partial splenic artery embolization in patients with portal hypertension, thoroughly summarizing the English language literature and addressing numerous utilizations of PSE. Benefits included increased hepatic protein synthesis, increased circulating platelet and leukocyte levels, and improvements in hepatic encephalopathy. The most contemporary study noted in the Koconis *et al.*^[10] review was published in 2005. We performed a review of the English language literature for PSE and focused on papers from 2005 through the present. Ultimately, eight studies were identified, and have been included in our review (Table 1)^[9,11-17]. In 2012, Smith *et al.*^[18] also published an excellent review of splenic artery embolization, which followed a similar structure.

Hematologic indices

One of the primary goals of PSE is to increase circulating platelets and leukocytes. Resultantly, serum platelet and leukocyte counts are a natural choice for measuring procedural effectiveness. Prior to exploration of the data it should be noted that Zhu *et al.*^[14] reported trends in laboratory values following PSE *via* a line graph without citing specific values. Consequently, reported values from Zhu *et al.*^[14] represent approximations. Assessment of leukocyte and platelet values following PSE demonstrates a few trends (Table 1). First, within two weeks of PSE both platelet and white blood cell values significantly increase. This was found to be consistent in all included studies. Pre-PSE platelet values ranged from 37.4-56 K/ μ L, and at two weeks following PSE platelet values ranged from 80-240.7 K/ μ L. Leukocytes also increased, with pre-PSE values ranging 2.3-4.2 K/ μ L and then jumping to 4.0-12.6 K/ μ L at two weeks. A second trend, which was uniform across every study and cohort, is the consistent decline in both leukocyte and platelet values in the months and years following PSE. Though the rate of decline varied from study to study, the presence of a decline is consistent. Finally, there is a direct relationship between the percent of spleen which is targeted *via* PSE and the magnitude of the response of circulating platelets and leukocytes. By dividing their study into cohorts based upon the percent of spleen targeted, the 2009 Zhu *et al.*^[14] study further demonstrated this point. Simply put, the larger the volume of targeted spleen, the greater the resultant increase in circulating leukocytes and platelets.

PSE's ability to increase platelet and leukocyte counts has produced other clinical applications. Pegylated interferon and ribavirin induces sustained virological response in 42%-82% of patients with hepatitis C, however, thrombocytopenia is an absolute contraindication to the administration of therapy^[19]. Over the past decade the use of PSE to increase platelet counts has facilitated antiviral treatment in patients who would have otherwise been too thrombocytopenic. Tahara completed a retro-

Table 1 Study demographics and outcomes of partial splenic embolization

Ref.	Year	Country	Study type	Number of Pts	Length of follow-up	Mean \pm SD, platelet count prior to PSE in K/ μ L	Mean \pm SD, WBC count prior to PSE in K/ μ L	Indication for PSE	Extent of spleen targeted	Mean \pm SD, platelet count at 2 wk in K/ μ L	Mean \pm SD, platelet count at 1 mo in K/ μ L	Mean \pm SD, WBC count at 2 wk in K/ μ L	Mean \pm SD, WBC count at 1 mo in K/ μ L	Mean \pm SD, WBC count at 1 yr in K/ μ L
Kim <i>et al</i> ^[11]	2012	South Korea	Case series report	11	6-28 mo	Not provided	Not provided	All patients S/P OLT; 6/11 w/ thrombocytopenia, 5/11 w/refractory ascites	70%-80%	Not provided	Not provided	Not provided	Not provided	Not provided
Elmonem <i>et al</i> ^[12]	2010	Egypt	Case series report	23	2 yr	41.3 \pm 13.0	2.3 \pm 0.47	Hypersplenism in Cirrhosis w/leukopenia and thrombocytopenia, no HCC, and no SBP	50%-70%	124.3 \pm 23.9	115.8 \pm 18.4	8.26 \pm 1.54	6.53 \pm 1.74	4.62 \pm 1.13
Zhu <i>et al</i> ^[14]	2009	China	Nonrandomized prospective trial	Total 62 Group A: 12 Group B: 34 Group C: 16	5 yr	Group A: 40.2 \pm 13.0 Group B: 37.4 \pm 12.3 Group C: 43.6 \pm 11.7	Group A: 2.42 \pm 0.44 Group B: 2.54 \pm 0.57 Group C: 2.64 \pm 0.4	Hypersplenism in Cirrhosis, w/ thrombocytopenia or neutropenia. No SBP, no Severe jaundice	50%-70%	Group A: 170 ¹ Group B: 130 ¹ Group C: 80 ¹	Group A: 130 ¹ Group B: 110 ¹ Group C: 70 ¹	Group A: 7.5 ¹ Group B: 6.5 ¹ Group C: 4.0 ¹	Group A: 6.0 ¹ Group B: 5.5 ¹ Group C: 3.7 ¹	Group A: 4.5 ¹ Group B: 4.0 ¹ Group C: 3.0 ¹
Amin <i>et al</i> ^[9]	2009	Egypt	Randomized control trial	Total 40 PSE: 20 SPL: 20	6 mo	PSE: 39.7 \pm 9.7 SPL: 47.2 \pm 10.3	PSE: 3.3 \pm 0.7 SPL: 2.8 \pm 1.1	Cirrhosis w/o bone marrow disease, ischemic heart disease, renal failure, malignancy, or medical instability	50%	PSE: 211.5 \pm 36.2 SPL: 240.7 \pm 52.0	Not provided	2.6	Not provided	Not provided
Zhu <i>et al</i> ^[16]	2008	China	Randomized control trial	Total 60 GF: 32 PVA: 28	3 yr	GF: 47.06 \pm 14.85 PVA: 44.36 \pm 16.67	GF: 2.62 \pm 0.67 PVA: 2.57 \pm 0.63	Hypersplenism in cirrhosis w/ thrombocytopenia or neutropenia. No SBP, no HCC, no hyperbilirubinemia	50%-70%	GF: 135.4 \pm 28.1 PVA: 153.4 \pm 37.1	GF: 113.2 \pm 17.6 PVA: 125.4 \pm 23.3	GF: 6.6 \pm 1.5 PVA: 7.5 \pm 1.7	GF: 5.1 \pm 0.9 PVA: 5.7 \pm 1.2	GF: 4.2 \pm 0.6 PVA: 4.7 \pm 1.0
Hayashi <i>et al</i> ^[17]	2007	Japan	Nonrandomized prospective trial	42	1 yr	45 \pm 11.7	2.9 \pm 1.0	Thrombocytopenia caused by hypersplenism due to cirrhosis	70%-80%	Not provided	116 \pm 51	Not provided	103 \pm 34	Not provided
Lee <i>et al</i> ^[15]	2007	China	Nonrandomized prospective trial	10	1 yr	56 \pm 8.0	Not provided	Thrombocytopenia in setting of cirrhosis	20%-40%	192	Not provided	Not provided	145	Not provided
N'Kontchou <i>et al</i> ^[13]	2005	France	Retrospective review	32	1-87 mo	48 \pm 14	4.2 \pm 1.6	Cirrhosis w/severe cytopenia/leukopenia preventing treatment or severe purpur, or painful splenomegaly	50%	Not provided	137.5 \pm 77.4	Not provided	Not provided	Not provided

¹Data From Zhu *et al*^[14,16] was extracted from a graph without exact values, values used are the authors closest approximations. PSE: Partial splenic artery embolization; SPL: Splenectomy; GF: Gel foam; PVA: Polyvinyl alcohol.

spective cohort study of 30 hepatitis C patients who were unable receive antiviral therapy secondary to thrombocytopenia and consequently were treated with PSE^[20]. All 30 patients were able to receive therapy with pegylated interferon and ribavirin following a PSE-related increase in their platelet counts. A handful of other studies have demonstrated similar findings over the past decade^[21-23].

Similar to the use of PSE to improve platelet counts prior to antiviral therapy in patients with hepatitis C, PSE has been used to increase hematologic indices to facilitate treatment of hepatocellular carcinoma. Hidaka *et al.*^[24] reported a 20 subject trial in which patients with multiple hepatocellular carcinoma lesions measuring less than 3 cm and platelet counts less than 80 received PSE to facilitate further treatment with radiofrequency ablation. Of the 20 patients, 18 demonstrated significant increases in prothrombin function as well as platelet counts, and ultimately were treated with radiofrequency ablation. A smaller study demonstrated PSE to be an effective preoperative therapy to increase platelet counts prior to hepatectomy^[25]. Five patients received PSE prior to hepatectomy, while 23 patients received concomitant splenectomy with hepatectomy. The patients in the PSE arm received fewer blood transfusions and experienced fewer postoperative complications. Survival rates between the two arms were not significantly different.

Portal hypertension and associated sequelae

PSE has been demonstrated to improve portal hemodynamics in cirrhotic patients. PSE decreases splenic blood flow, splenic venous pressure, and portal venous pressure^[26-28]. Additionally, in a trial of 7 patients with cirrhosis and hepatocellular carcinoma treated with a combination of transcatheter hepatic arterial embolization and PSE, Han *et al.*^[29] demonstrated a significant decrease in portal venous pressures following therapy. Interestingly, however, most studies which explored the hemodynamic effects of PSE did not demonstrate improvements in portal blood volume^[26-28].

Portal venous hypertension is associated with numerous clinical manifestations. By improving portal hemodynamics, associated improvements in the sequelae of portal hypertension can be seen. Portal venous hypertension can lead to refractory ascites, and PSE has been found to decrease the incidence and magnitude of ascites^[11]. Esophageal varices are also a common complication in patients with cirrhosis. Increased splenic arterial flow, splenic congestion, and portal venous pressures are all associated with an increased rupture risk of esophageal varices amongst cirrhotic patients^[30,31]. By improving portal hemodynamics, PSE is associated with a decreased risk of variceal bleeding. Citing 4 studies, which included a total of 50 patients, Koconis *et al.*^[10] asserted that PSE decreased the annual incidence of variceal hemorrhage by 80%. Pålsson *et al.*^[32] performed PSE in 26 patients with history of bleeding esophageal varices and thrombocytopenia, 19 of whom had cirrhosis. The cohort demonstrated a decrease in the number of variceal bleed-

ing episodes from 4.3 prior to treatment to 1.1 after PSE. Ohmoto conducted a study of 84 cirrhotic patients with large esophageal varices and thrombocytopenia^[33]. 42 patients were treated with endoscopic variceal ligation (EVL) and 42 were treated with EVL and PSE. The combination therapy cohort demonstrated a reduced development of new varices from 88% to 67% ($P = 0.038$), decreased episodes of variceal bleeding from 34% to 17% ($P = 0.024$), and improved overall survival from 31% to 50% ($P = 0.042$). The literature also contains a case report of PSE being utilized to effectively address a 45-d decrease in hemoglobin secondary to diffuse gastric bleeding in portal hypertensive gastropathy^[34].

PSE-related alterations in portal blood flow have also been shown to improve hepatic function^[35]. Increased thrombopoietin, albumin, and cholinesterase levels as well as decreased alanine aminotransferase levels and total bilirubin levels have been demonstrated in cirrhotic patients following PSE^[35,36]. These changes, however, are not uniform amongst all cirrhotic patients. Improved liver function following PSE is most pronounced in patients with initial splenic volumes greater than 600 cc^[36]. In patients with hepatocellular carcinoma, PSE has been combined with transcatheter arterial chemoembolization (TACE) for promising results. In a comparison of patients treated with TACE and concomitant PSE *vs* TACE alone, those in the combined treatment cohort demonstrated improvements in platelet counts and hepatic reserve^[37].

Splenic artery steal syndrome

Following liver transplant, approximately 5% of patients experience splenic artery steal syndrome (SASS). SASS is siphoning of arterial flow away from a transplanted liver due to a dominant splenic artery. While the hemodynamics of SASS are not completely understood, it is thought that increased resistance of the hepatic arterial bed and decreased resistance of the splenic arterial bed contribute to SASS^[38]. High resistance of the hepatic arteries following liver transplant may be attributed to many causes, including a poorly compliant graft, post-operative edema, and subcapsular hematoma. Increased hepatic arterial resistance, when combined with low splenic arterial resistance due to splenomegaly, significantly increases splenic arterial flow while reflexively decreasing hepatic flow. Management of SASS may be surgical or endovascular. Surgical approaches include formation of an aortohepatic conduit or splenic arterial banding or ligation^[38]. Proximal splenic artery embolization, *via* deployment of coils or an Amplatzer plug in the splenic artery immediately distal to the pancreatic and short gastric arteries, has been established as a safe and effective option in the non-surgical management of SASS^[39-42].

COMPLICATIONS OF PSE

In exploring the morbidity and mortality associated with PSE, Koconis *et al.*^[10] reviewed 33 studies published be-

tween 1990 and 2005, and collectively representing 401 patients. In total, 15 major complications and 4 deaths were reported, for a major complication rate of 3.7% and a mortality rate of 1%. The rate of PSE-related complications consistently increased with volumes of splenic embolization near or greater than 70%^[10].

PSE is not without risk, and the studies included in our review re-demonstrated many of the complications associated with the procedure (Table 2). Collectively, the studies we included demonstrate a direct relationship between the volume of spleen targeted for embolization and the severity of post-procedural complications. The 2009 Zhu *et al*^[14] study further illustrated this point by subdividing patients in their study by percent of spleen targeted. The cohort receiving the greatest embolization (> 70%) also demonstrated the largest burden of complications. On the other hand, the patients with the least extensive embolization (< 50%) had the shortest hospital stays, lowest rate of embolization syndrome, and experienced no serious complications. Though not explicitly subdivided into cohorts based upon percent of spleen targeted during embolization, the 2008 Zhu *et al*^[16] study also demonstrated an increased rate of complications among patients with embolization of > 70% of splenic volume. This correlates with the literature which has identified Child-Pugh class C and large splenic infarct volume as independent risk factors for complications with PSE^[43]. Of the papers we included, Kim *et al*^[11] had the smallest sample size, 11, and was an outlier in regards to their reported complications. Kim *et al*^[11] reported 100% of their patients experienced post-embolization syndrome, but also reported zero serious complications. This was particularly surprising in that Kim *et al*^[11] targeted 70%-80% of the spleen for embolization, more than any other study.

WORK-UP

Workup of a patient prior to PSE includes a thorough history and physical, routine laboratory studies, imaging, and prophylactic antibiotics and vaccinations. A basic laboratory panel including a CBC, PT/PTT, liver function tests, renal function tests, and a hepatitis panel is commonly noted^[12,44,45]. While less frequently mentioned, anti-platelet antibody studies and bone marrow biopsies have also been described^[8,37]. Abdominal computed tomography (CT) and ultrasound are useful to establish a splenic volume baseline and to screen for portal or splenic vein thrombosis^[9,12-14,44-46]. Additionally, many authors endorse an upper gastrointestinal endoscopy in the workup prior to PSE to screen and/or treat esophageal varices^[9,44,45]. Some authors, though not all, endorse the administration of pre-procedural broad spectrum antibiotics and/or vaccines. While Pneumovax 23 is the most commonly cited vaccination, the literature also makes note of H. influenza B and meningococcal vaccinations^[18,46]. At our institution, broad-spectrum antibiotics are initiated just prior to PSE, and are continued for one to two weeks;

additional vaccinations are not used.

TECHNIQUE

Numerous articles have described the technique of PSE, and generally concur in their description^[9,12,46]. Vascular access is gained with a 5 French sheath in the femoral artery *via* the Seldinger technique. A 4 or 5 French cobra-type catheter is then utilized to isolate the celiac axis and splenic artery. Celiac and splenic angiography is performed to identify the distribution of splenic arteries, as well as document the presence of any collateral flow.

After mapping the anatomy of the celiac axis and the splenic artery, the catheter is secured at the site of embolization. Either a proximal or distal embolization may be performed. In the proximal, nonselective, approach the catheter is placed immediately distal to the origins of the pancreatic and short gastric arteries, and an embolic agent is released. Embolic agents are dispersed throughout the spleen and small, diffuse, randomized infarcts occur. In the distal, selective, approach, the catheter is advanced into a distal segmental branch of the splenic artery. The entire distal splenic segment is then embolized. Some authors believe sub-selection of the superior spleen is more likely to be associated with post procedural pneumonia and atelectasis, and therefore favor embolizing the inferior spleen; however, comparative studies have not been performed^[18]. A microcatheter is preferred to secure access in the distal splenic segmental arteries. Of the contemporary studies reviewed for this paper, seven noted whether a distal or proximal approach was utilized. Six of the seven studies utilized a distal approach^[12-15,44,47]. Though no randomized studies comparing distal and proximal PSE in cirrhotic patients have been completed, the majority of interventionalists report employing the distal approach. It should be noted, however, that the selection of a distal *vs* proximal approach may depend on the specific clinical scenario. Proximal embolization requires less time to accomplish and can be performed without use of microcatheter techniques. On the other hand sub-selecting distal splenic branches for embolization requires more time, but allows for greater precision in the percentage of splenic parenchyma that is targeted for embolization.

After identifying and securing the targeted vascular supply, embolization is performed. A variety of substances have been employed as embolic agents. Early descriptions of PSE mention the use of autologous clot. More contemporary approaches include gelatin sponge, polyvinyl alcohol particles (PVA), and tris-acryl gelatin microspheres. All of the above agents are typically delivered *via* a suspension containing contrast and, frequently, antibiotics. Of the studies reviewed, 14 noted the material used in embolization^[9,12-18,33,44-48]. 8 of 14 used gel foam, 2 used tris-acryl gelatin microspheres, 2 used PVA particles, 1 used gel foam and PVA particles in separate cohorts, and 1 used a combination of tris-acryl gelatin microspheres and PVA. Of the studies which reported

Table 2 Complications in partial splenic artery embolization

Ref.	Year	Country	Study type	Complication: Frequency of post embolization	Complication: Mean length of post embolization syndrome-days	Major complications: Total number	Persistent thrombocytopenia	Splenomegaly	Pleural effusion/ascites	Variceal bleeding	Portal vein thrombosis	Bacterial peritonitis	Splenic abscess	PSE-related death	Repeat embolization required
Kim <i>et al</i> ^[11]	2012	South Korea	Case series report	100.00%	Not provided	0.00%	0.00%	0.00%	0.00%	0.00%	0.00%	0.00%	0.00%	0.00%	0.00%
Elmonem <i>et al</i> ^[12]	2010	Egypt	Case series report	91.30%	Not provided	34.80%	4.30%	4.30%	8.70%	0.00%	4.30%	4.30%	4.30%	4.30%	4.30%
Zhu <i>et al</i> ^[14]	2009	China	Nonrandomized prospective trial	Total 85.5% Group A: 100% Group B: 91.2% Group C: 62.5%	Group A: 13 Group B: 7 Group C: 3	Total 14.5% Group A: 50% Group B: 8.8% Group C: 0%	Total 0% Group A: 0% Group B: 0% Group C: 0%	Total 4.8% Group A: 0% Group B: 16.6% Group C: 2.9%	Total 1.6% Group A: 1.6% Group B: 8.3% Group C: 0%	Total 1.6% Group A: 1.6% Group B: 8.3% Group C: 0%	Total 1.6% Group A: 1.6% Group B: 8.3% Group C: 0%	Total 1.6% Group A: 1.6% Group B: 8.3% Group C: 0%	Total 1.6% Group A: 1.6% Group B: 8.3% Group C: 0%	Total 1.6% Group A: 1.6% Group B: 8.3% Group C: 0%	Total 0% Group A: 0% Group B: 0% Group C: 0%
Amin <i>et al</i> ^[9]	2009	Egypt	Randomized control trial	Not provided	PSE: 2.1 (0.4) SPL: 4.3 (1.1) GF: 6.4 (3.6) PVA: 7.6 (2.8)	PSE: 25% SPL: 25% GF: 25.0% PVA: 21.4%	PSE: 0% SPL: 0% GF: 0% PVA: 0%	PSE: 10% SPL: 0% GF: 9.4% PVA: 0%	PSE: 0% SPL: 0% GF: 3.1% PVA: 0%	PSE: 0% SPL: 15% GF: 3.1% PVA: 7.1% 3.6%	PSE: 5% SPL: 0% GF: 6.3% PVA: 0%	PSE: 0% SPL: 0% GF: 6.3% PVA: 0%	PSE: 5% SPL: 0% GF: 3.1% PVA: 0%	PSE: 5% SPL: 0% GF: 3.1% PVA: 0%	PSE: 0% SPL: 0% GF: 0% PVA: 0%
Hayashi <i>et al</i> ^[17]	2007	Japan	Nonrandomized prospective trial	100.00%	Not provided	11.90%	0.00%	0.00%	9.50%	0.00%	0.00%	0.00%	0.00%	0.00%	0.00%
Lee <i>et al</i> ^[15]	2007	China	Nonrandomized prospective trial	100.00%	Not provided	10.00%	0.00%	0.00%	10.00%	0.00%	0.00%	0.00%	0.00%	0.00%	0.00%
N'Kontchou <i>et al</i> ^[13]	2005	France	Retrospective review	78.10%	14	28.10%	3.10%	0.00%	6.30%	0.00%	6.30%	0.00%	6.30%	6.3% ¹	3.10%

¹Both deaths in the trial were in patients with > 70% splenic embolization. PSE: Partial splenic artery embolization; SPL: Splenectomy; GF: Gel foam; PVA: Polyvinyl alcohol.

use of tris-acryl gelatin microspheres, one study reported using 500-700 µm microspheres, another reported using 300-500 µm microspheres, and the final study noted using microspheres ranging 200-1000 µm^[3,14,47]. In 2008 Zhu *et al*^[6] published a study comparing the results of gelfoam embolization with PVA. Ultimately, the study demonstrated a slightly greater increase in platelet and leukocyte counts with PVA as compared to gelfoam. The study, however, also demonstrated greater frequency and magnitude of post-embolization syndrome amongst patients embolized with PVA as compared to gelfoam. At this time, no specific agent has clearly been established as a superior embolic agent in PSE.

Although coils and Amplatzer plugs are more commonly used to perform proximal splenic artery embolization (SAE) in the setting of trauma, recently, a small number of studies have highlighted the effectiveness of proximal SAE among patients with portal hypertension. Though only reporting use in six patients, Quintini *et al*^[49] demonstrated coil-induced proximal SAE to be a safe and effective treatment for refractory ascites in patients with previous orthotopic liver transplants. Additionally, Zhu *et al*^[50] performed a retrospective review of Amplatzer plugs vs coiling in SAE. While the majority of the patients included in the study received SAE secondary to splenic artery steal syndrome, one eighth of the subjects were included secondary to portal hypertension.

Some authors set their initial target at embolization of 50%-70% of the splenic blood volume. Others, however, embrace a more conservative approach and will target 30%-40% of the spleen with the expectations of repeating the embolization with a higher target area (up to 70%) if clinical symptoms do not respond to initial treatment. In an attempt to avoid embolization of a greater portion of the spleen many authors report an iterative process of delivering small aliquots of embolic material, and following each aliquot with an angiogram to determine the extent of embolization. The increased number of iterations allows providers to more precisely target a specific percent of splenic

tissue, without excessively embolizing the spleen.

POST PSE CARE

The vast majority of patients experience some degree of pain, fever, and nausea/vomiting following PSE. These symptoms are collectively described as post-embolization syndrome^[44]. Our review of the recent literature found that post-embolization syndrome is reported in 78.1%-100% of patients undergoing PSE (Tables 1 and 2). Patients are frequently hospitalized to receive supportive care for 24-48 h or until the post-embolization syndrome has resolved. Care is centered on antibiotic prophylaxis and pain management. Many antibiotics including amoxicillin/clavulanate, ofloxacin, phenoxymethylpenicillin, cotrimoxazole, cefoperazone, and erythromycin have been described in the literature. Post-procedural analgesia typically involves a combination of NSAIDs, scheduled morphine, and patient controlled analgesia.

Occasionally, patients experience more serious complications (Table 2). Severe complications are reported in 0%-34.8% of patients following PSE. The most common severe complication is pleural effusion and/or ascites, and can be treated with thoracentesis or paracentesis respectively. Other common morbidities include portal vein thrombosis and splenic abscess. Most practitioners advocate the use of anticoagulation in the treatment of post-PSE portal vein thrombosis, though Zhu *et al.*^[50] reported resolution of thrombus with watchful waiting. Presentation of splenic abscess has been reported between 10 d to 3 mo following PSE. Additionally, the majority of PSE-related deaths involve the development of a splenic abscess. Consequently, if post-procedural fever or other signs of infection develop, the threshold for ordering follow up imaging, usually with CT, should be low. Furthermore, due to the risks of splenic abscess, and the extended window in which it may develop, all PSE patients should be educated on the signs and symptoms of splenic abscess prior to the procedure and again upon discharge. Treatment of post-PSE splenic abscess includes percutaneous drainage and antibiotics, or occasionally, splenectomy. Mortality rates range from 0%-6.3% of patients undergoing PSE.

Follow up abdominal CT scan is frequently utilized in the first several weeks after PSE to confirm the percentage of infarcted splenic tissue. In the months following PSE, the spleen gradually decreases in size, but patients are usually followed clinically rather than monitoring with imaging, unless a complication is suspected.

CONCLUSION

PSE is an effective procedure in cirrhotic patients. It decreases rates of ascites and esophageal variceal bleeding while increasing hematologic indices. PSE can be an effective option for patients who are not surgical candidates and for whom splenectomy is contraindicated. In such patients, PSE may provide the necessary increase in

hematologic indices to facilitate other treatments.

Still, PSE is not without its shortcomings. There are numerous morbidities associated with PSE. At the very least, almost all patients will experience post-embolization syndrome and will require post-procedural hospitalization. Several studies demonstrate major complication rates up to 15%-30% following PSE. The studies included in our review represented 260 patients, and collectively experienced a serious complication rate of 20.0% following PSE. In our study we included pleural effusions and ascites as major complications, and these accounted for 19 of the 52 complications. If we were to not include pleural effusions and ascites as major complications the average complication rate would have been 12.7%. Additionally, PSE-related mortality is consistently reported in 0%-6% of patients. The 260 patients included in our review collectively averaged a 2.3% mortality rate. In efforts to minimize PSE-related complications, targeted splenic volume for PSE ought to be below 70%. While an improvement of leukocyte and platelet counts has proven persistent, the magnitude of the increase consistently declines in the months and years following PSE.

Although PSE may not be appropriate in all cirrhotic patients, in the appropriate clinical context it is an efficacious tool which may provide clinical benefit for patients who otherwise may not be candidates for other medical and surgical interventions.

REFERENCES

- 1 **Orlando R**, Lirussi F, Basso SM, Lumachi F. Splenomegaly as risk factor of liver cirrhosis. A retrospective cohort study of 2,525 patients who underwent laparoscopy. *In Vivo* 2011; **25**: 1009-1012 [PMID: 22021698]
- 2 **Bashour FN**, Teran JC, Mullen KD. Prevalence of peripheral blood cytopenias (hypersplenism) in patients with nonalcoholic chronic liver disease. *Am J Gastroenterol* 2000; **95**: 2936-2939 [PMID: 11051371 DOI: 10.1111/j.1572-0241.2000.02325.x]
- 3 **Qamar AA**, Grace ND. Abnormal hematological indices in cirrhosis. *Can J Gastroenterol* 2009; **23**: 441-445 [PMID: 19543577]
- 4 **Ogata T**, Okuda K, Sato T, Hirakawa Y, Yasunaga M, Horiuchi H, Nomura Y, Kage M, Ide T, Kuromatsu R, Kinoshita H, Tanaka H. Long-term outcome of splenectomy in advanced cirrhotic patients with hepatocellular carcinoma and thrombocytopenia. *Kurume Med J* 2013; **60**: 37-45 [PMID: 24064764 DOI: 10.2739/kurumemedj.MS62010]
- 5 **McCormick PA**, Murphy KM. Splenomegaly, hypersplenism and coagulation abnormalities in liver disease. *Baillieres Best Pract Res Clin Gastroenterol* 2000; **14**: 1009-1031 [PMID: 11139352 DOI: 10.1053/bega.2000.0144]
- 6 **Maddison FE**. Embolic therapy of hypersplenism. *Invest Radiol* 1973; **8**: 280-281 [DOI: 10.1097/00004424-197307000-00054]
- 7 **Castaneda-Zuniga WR**, Hammerschmidt DE, Sanchez R, Amplatz K. Nonsurgical splenectomy. *AJR Am J Roentgenol* 1977; **129**: 805-811 [PMID: 410243 DOI: 10.2214/ajr.129.5.805]
- 8 **Spigos DG**, Jonasson O, Mozes M, Capek V. Partial splenic embolization in the treatment of hypersplenism. *AJR Am J Roentgenol* 1979; **132**: 777-782 [PMID: 107745 DOI: 10.2214/ajr.132.5.777]
- 9 **Amin MA**, el-Gendy MM, Dawoud IE, Shoma A, Negm AM, Amer TA. Partial splenic embolization versus splenectomy

- for the management of hypersplenism in cirrhotic patients. *World J Surg* 2009; **33**: 1702-1710 [PMID: 19513783 DOI: 10.1007/s00268-009-0095-2]
- 10 **Koconis KG**, Singh H, Soares G. Partial splenic embolization in the treatment of patients with portal hypertension: a review of the english language literature. *J Vasc Interv Radiol* 2007; **18**: 463-481 [PMID: 17446537 DOI: 10.1016/j.jvir.2006.12.734]
 - 11 **Kim H**, Suh KS, Jeon YM, Park MS, Choi Y, Mori S, Hong G, Lee HW, Yi NJ, Lee KW. Partial splenic artery embolization for thrombocytopenia and uncontrolled massive ascites after liver transplantation. *Transplant Proc* 2012; **44**: 755-756 [PMID: 22483487 DOI: 10.1016/j.transproceed.2012.01.066]
 - 12 **Elmonem SA**, Tantawy HI, Ragheb AS, Matar NEH, Tantawi I. The outcome of partial splenic embolization for hypersplenism in cirrhotic patients. *Egypt J Radiol Nuc Med* 2011; **42**: 35-42 [DOI: 10.1016/j.ejrm.2011.01.002]
 - 13 **N'Kontchou G**, Seror O, Bourcier V, Mohand D, Ajavon Y, Castera L, Grando-Lemaire V, Ganne-Carrie N, Sellier N, Trinchet JC, Beaugrand M. Partial splenic embolization in patients with cirrhosis: efficacy, tolerance and long-term outcome in 32 patients. *Eur J Gastroenterol Hepatol* 2005; **17**: 179-184 [PMID: 15674095 DOI: 10.1097/00042737-200502000-00008]
 - 14 **Zhu K**, Meng X, Qian J, Huang M, Li Z, Guan S, Jiang Z, Shan H. Partial splenic embolization for hypersplenism in cirrhosis: a long-term outcome in 62 patients. *Dig Liver Dis* 2009; **41**: 411-416 [PMID: 19070555 DOI: 10.1016/j.dld.2008.10.005]
 - 15 **Lee CM**, Leung TK, Wang HJ, Lee WH, Shen LK, Liu JD, Chang CC, Chen YY. Evaluation of the effect of partial splenic embolization on platelet values for liver cirrhosis patients with thrombocytopenia. *World J Gastroenterol* 2007; **13**: 619-622 [PMID: 17278231]
 - 16 **Zhu K**, Meng X, Li Z, Huang M, Guan S, Jiang Z, Shan H. Partial splenic embolization using polyvinyl alcohol particles for hypersplenism in cirrhosis: a prospective randomized study. *Eur J Radiol* 2008; **66**: 100-106 [PMID: 17532166 DOI: 10.1016/j.ejrad.2007.04.010]
 - 17 **Hayashi H**, Beppu T, Masuda T, Mizumoto T, Takahashi M, Ishiko T, Takamori H, Kanemitsu K, Hirota M, Baba H. Predictive factors for platelet increase after partial splenic embolization in liver cirrhosis patients. *J Gastroenterol Hepatol* 2007; **22**: 1638-1642 [PMID: 17683504 DOI: 10.1111/j.1440-1746.2007.05090.x]
 - 18 **Smith M**, Ray CE. Splenic artery embolization as an adjunctive procedure for portal hypertension. *Semin Intervent Radiol* 2012; **29**: 135-139 [PMID: 23729984 DOI: 10.1055/s-0032-1312575]
 - 19 **Sato K**, Takagi H, Ichikawa T, Kakizaki S, Mori M. Emerging therapeutic strategies for hepatitis C virus infection. *Curr Mol Pharmacol* 2008; **1**: 130-150 [PMID: 20021428 DOI: 10.2174/1874467210801020130]
 - 20 **Tahara H**, Takagi H, Sato K, Shimada Y, Tojima H, Hirokawa T, Ohyama T, Horiuchi K, Naganuma A, Arai H, Kakizaki S, Mori M. A retrospective cohort study of partial splenic embolization for antiviral therapy in chronic hepatitis C with thrombocytopenia. *J Gastroenterol* 2011; **46**: 1010-1019 [PMID: 21594564 DOI: 10.1007/s00535-011-0407-9]
 - 21 **Takahara M**, Miyake Y, Miyatake H, Imagawa A, Nakatsu M, Ando M, Hirohata M, Yamamoto K. Partial splenic embolization facilitates the adherence to peginterferon in chronic hepatitis C with thrombocytopenia. *Intern Med* 2011; **50**: 2731-2736 [PMID: 22082883 DOI: 10.2169/internalmedicine.50.6143]
 - 22 **Miyake Y**, Ando M, Kaji E, Toyokawa T, Nakatsu M, Hirohata M. Partial splenic embolization prior to combination therapy of interferon and ribavirin in chronic hepatitis C patients with thrombocytopenia. *Hepatol Res* 2008; **38**: 980-986 [PMID: 18657124 DOI: 10.1111/j.1872-034X.2008.00357.x]
 - 23 **Foruny JR**, Blázquez J, Moreno A, Bárcena R, Gil-Grande L, Quereda C, Pérez-Eliás MJ, Moreno J, Sánchez J, Muriel A, Rodríguez-Sagrado MA, Moreno S. Safe use of pegylated interferon/ribavirin in hepatitis C virus cirrhotic patients with hypersplenism after partial splenic embolization. *Eur J Gastroenterol Hepatol* 2005; **17**: 1157-1164 [PMID: 16215426 DOI: 10.1097/00042737-200511000-00002]
 - 24 **Hidaka H**, Kokubu S, Nakazawa T, Minamino T, Takada J, Tanaka Y, Okuwaki Y, Watanabe M, Shibuya A, Saigenji K. Therapeutic benefits of partial splenic embolization for thrombocytopenia in hepatocellular carcinoma patients treated with radiofrequency ablation. *Hepatol Res* 2009; **39**: 772-778 [PMID: 19473438 DOI: 10.1111/j.1872-034X.2009.00508.x]
 - 25 **Yoshidome H**, Kimura F, Shimizu T, Minamino T, Kato A, Yoshitomi H, Furukawa K, Takeuchi D, Takayashiki T, Suda K, Takano S, Miyazaki M. Usefulness of preoperative partial splenic embolization in hepatocellular carcinoma and hypersplenic thrombocytopenia. *Hepatogastroenterology* 2011; **58**: 2062-2066 [PMID: 22234078]
 - 26 **Chikamori F**, Kuniyoshi N, Kawashima T, Takase Y. Short-term portal hemodynamic effects of partial splenic embolization for hypersplenism. *Hepatogastroenterology* 2007; **54**: 1847-1849 [PMID: 18019732]
 - 27 **Yamashiro K**, Mukaiya M, Kumura H, Katsuramaki T, Sasaki K, Denno R, Hirata K. Partial splenic embolization in patients with liver cirrhosis and hepatocellular carcinoma: Effects on portal hemodynamics. *J Hep Bil Pancr Surg* 1994; **2**: 172-175 [DOI: 10.1007/BF01222244]
 - 28 **Mukaiya M**, Hirata K, Yamashiro K, Katsuramaki T, Kimura H, Denno R. Changes in portal hemodynamics and hepatic function after partial splenic embolization (PSE) and percutaneous transhepatic obliteration (PTO). *Cancer Chemother Pharmacol* 1994; **33** Suppl: S37-S41 [PMID: 8137483 DOI: 10.1007/BF00686666]
 - 29 **Han MJ**, Zhao HG, Ren K, Zhao DC, Xu K, Zhang XT. Partial splenic embolization for hypersplenism concomitant with or after arterial embolization of hepatocellular carcinoma in 30 patients. *Cardiovasc Intervent Radiol* 1997; **20**: 125-127 [PMID: 9030503 DOI: 10.1007/s002709900119]
 - 30 **Kayacetin E**, Efe D, Doğan C. Portal and splenic hemodynamics in cirrhotic patients: relationship between esophageal variceal bleeding and the severity of hepatic failure. *J Gastroenterol* 2004; **39**: 661-667 [PMID: 15293137 DOI: 10.1007/s00535-003-1362-x]
 - 31 **Garcia-Tsao G**, Groszmann RJ, Fisher RL, Conn HO, Atterbury CE, Glickman M. Portal pressure, presence of gastroesophageal varices and variceal bleeding. *Hepatology* 1985; **5**: 419-424 [PMID: 3873388 DOI: 10.1002/hep.1840050313]
 - 32 **Pålsson B**, Hallén M, Forsberg AM, Alwmark A. Partial splenic embolization: long-term outcome. *Langenbecks Arch Surg* 2003; **387**: 421-426 [PMID: 12607123]
 - 33 **Ohmoto K**, Yoshioka N, Tomiyama Y, Shibata N, Takesue M, Yoshida K, Kuboki M, Yamamoto S. Improved prognosis of cirrhosis patients with esophageal varices and thrombocytopenia treated by endoscopic variceal ligation plus partial splenic embolization. *Dig Dis Sci* 2006; **51**: 352-358 [PMID: 16534680 DOI: 10.1007/s10620-006-3137-8]
 - 34 **Shimizu T**, Onda M, Tajiri T, Yoshida H, Mamada Y, Taniai N, Aramaki T, Kumazaki T. Bleeding portal-hypertensive gastropathy managed successfully by partial splenic embolization. *Hepatogastroenterology* 2002; **49**: 947-949 [PMID: 12143250]
 - 35 **Hidaka H**, Kokubu S, Saigenji K, Isobe Y, Maeda T. Restoration of thrombopoietin production after partial splenic embolization leads to resolution of thrombocytopenia in liver cirrhosis. *Hepatol Res* 2002; **23**: 265 [PMID: 12191674 DOI: 10.1016/S1386-6346(02)00002-5]
 - 36 **Hayashi H**, Beppu T, Masuda T, Okabe H, Imai K, Hashimoto D, Ikuta Y, Chikamoto A, Watanabe M, Baba H. Large splenic volume may be a useful predictor for partial splenic

- embolization-induced liver functional improvement in cirrhotic patients. *J Hepatobiliary Pancreat Sci* 2014; **21**: 51-57 [PMID: 23798315 DOI: 10.1002/jhbp.1]
- 37 **Ishikawa T**, Kubota T, Horigome R, Kimura N, Honda H, Iwanaga A, Seki K, Honma T, Yoshida T. Concurrent partial splenic embolization with transcatheter arterial chemoembolization for hepatocellular carcinoma can maintain hepatic functional reserve. *Hepatol Res* 2013; Epub ahead of print [PMID: 23941627 DOI: 10.1111/hepr.12222]
- 38 **Saad WE**. Nonocclusive hepatic artery hypoperfusion syndrome (splenic steal syndrome) in liver transplant recipients. *Semin Intervent Radiol* 2012; **29**: 140-146 [PMID: 23729985 DOI: 10.1055/s-0032-1312576]
- 39 **Chao CP**, Nguyen JH, Paz-Fumagalli R, Dougherty MK, Stockland AH. Splenic embolization in liver transplant recipients: early outcomes. *Transplant Proc* 2007; **39**: 3194-3198 [PMID: 18089351 DOI: 10.1016/j.transproceed.2007.07.089]
- 40 **Sevmis S**, Boyvat F, Aytakin C, Gorur SK, Karakayali H, Moray G, Haberal M. Arterial steal syndrome after orthotopic liver transplantation. *Transplant Proc* 2006; **38**: 3651-3655 [PMID: 17175358 DOI: 10.1016/j.transproceed.2006.10.145]
- 41 **Mogl MT**, Nüssler NC, Presser SJ, Podrabsky P, Denecke T, Grieser C, Neuhaus P, Guckelberger O. Evolving experience with prevention and treatment of splenic artery syndrome after orthotopic liver transplantation. *Transpl Int* 2010; **23**: 831-841 [PMID: 20180930 DOI: 10.1111/j.1432-2277.2010.01062.x]
- 42 **Maurer MH**, Mogl MT, Podrabsky P, Denecke T, Grieser C, Fröling V, Scheurig-Münkler C, Guckelberger O, Kroencke TJ. Splenic artery syndrome after orthotopic liver transplantation: treatment with the Amplatzer vascular plug. *Cardiovasc Intervent Radiol* 2011; **34**: 1208-1213 [PMID: 21184225 DOI: 10.1007/s00270-010-0083-9]
- 43 **Hayashi H**, Beppu T, Okabe K, Masuda T, Okabe H, Baba H. Risk factors for complications after partial splenic embolization for liver cirrhosis. *Br J Surg* 2008; **95**: 744-750 [PMID: 18412294 DOI: 10.1002/bjs.6081]
- 44 **Sakai T**, Shiraki K, Inoue H, Sugimoto K, Ohmori S, Murata K, Takase K, Nakano T. Complications of partial splenic embolization in cirrhotic patients. *Dig Dis Sci* 2002; **47**: 388-391 [PMID: 11855556 DOI: 10.1023/A:1013786509418]
- 45 **Pandey R**, Garg R, Darlong V, Punj J, Kumar A. Role of splenic artery partial embolization in a patient with portal hypertension and pancytopenia undergoing hysterectomy under anesthesia. *AANA J* 2012; **80**: 96-98 [PMID: 22586877]
- 46 **Gowda NK**, D'Souza D, Golzarian J. Partial splenic artery embolization. *Endovascular Today* 2012; **11**: 74-76
- 47 **Noguchi H**, Hirai K, Aoki Y, Sakata K, Tanikawa K. Changes in platelet kinetics after a partial splenic arterial embolization in cirrhotic patients with hypersplenism. *Hepatology* 1995; **22**: 1682-1688 [PMID: 7489974 DOI: 10.1002/hep.184022061]
- 48 **Sockrider CS**, Boykin KN, Green J, Marsala A, Mladenka M, McMillan R, Zibari GB. Partial splenic embolization for hypersplenism before and after liver transplantation. *Clin Transplant* 2002; **16** Suppl 7: 59-61 [PMID: 12372046 DOI: 10.1034/j.1399-0012.16.s7.9.x]
- 49 **Quintini C**, D'Amico G, Brown C, Aucejo F, Hashimoto K, Kelly DM, Eghtesad B, Sands M, Fung JJ, Miller CM. Splenic artery embolization for the treatment of refractory ascites after liver transplantation. *Liver Transpl* 2011; **17**: 668-673 [PMID: 21618687 DOI: 10.1002/lt.22280]
- 50 **Zhu X**, Tam MD, Pierce G, McLennan G, Sands MJ, Lieber MS, Wang W. Utility of the Amplatzer Vascular Plug in splenic artery embolization: a comparison study with conventional coil technique. *Cardiovasc Intervent Radiol* 2011; **34**: 522-531 [PMID: 20700592 DOI: 10.1007/s00270-010-9957-0]

P- Reviewers: Ferraioli G, Kiyosue H, Vogl TJ, Yuan Z

S- Editor: Ma YJ **L- Editor:** A **E- Editor:** Liu SQ



Magnetic resonance cholangiography in the assessment and management of biliary complications after OLT

Rossano Girometti, Lorenzo Cereser, Massimo Bazzocchi, Chiara Zuiani

Rossano Girometti, Lorenzo Cereser, Massimo Bazzocchi, Chiara Zuiani, Institute of Diagnostic Radiology, Department of Medical and Biological Sciences, University of Udine, 33100 Udine, Italy

Author contributions: Girometti R and Cereser L wrote the paper; Girometti R, Cereser L, Bazzocchi M and Zuiani C designed the paper; Cereser L, Bazzocchi M and Zuiani C performed literature research; all the authors selected and supervised the editing of study images and tables

Correspondence to: Rossano Girometti, MD, Research Assistant Professor of Radiology, Institute of Diagnostic Radiology, Department of Medical and Biological Sciences, University of Udine, via Colugna n. 50, 33100 Udine, Italy. rgirometti@sirm.org

Telephone: +39-04-32559266 Fax: +39-04-32559867

Received: January 17, 2014 Revised: March 5, 2014

Accepted: May 28, 2014

Published online: March 28, 2015

Abstract

Despite advances in patient and graft management, biliary complications (BC) still represent a challenge both in the early and delayed period after orthotopic liver transplantation (OLT). Because of unspecific clinical presentation, imaging is often mandatory in order to diagnose BC. Among imaging modalities, magnetic resonance cholangiography (MRC) has gained widespread acceptance as a tool to represent the reconstructed biliary tree noninvasively, using both the conventional technique (based on heavily T2-weighted sequences) and contrast-enhanced MRC (based on the acquisition of T1-weighted sequences after the administration of hepatobiliary contrast agents). On this basis, MRC is generally indicated to: (1) avoid unnecessary procedures of direct cholangiography in patients with a negative examination and/or identify alternative complications; and (2) provide a road map for interventional procedures or surgery. As illustrated in the review, MRC is accurate in the diagnosis of different types of biliary

complications, including anastomotic strictures, non-anastomotic strictures, leakage and stones.

© 2015 Baishideng Publishing Group Inc. All rights reserved.

Key words: Orthotopic liver transplantation; Orthotopic liver transplantation complications; Magnetic resonance imaging cholangiopancreatography; Endoscopic retrograde cholangiography; Bile ducts obstruction

Core tip: The review is focused on three main topics, in order to emphasize why magnetic resonance cholangiography (MRC) is the preferred imaging modality to noninvasively assess the biliary system after orthotopic liver transplantation. First, the authors describe the different techniques that can be used, namely conventional MRC and contrast-enhanced MRC. Second, exemplificative imaging findings are illustrated in order to show the diagnostic reliability of the technique. Third, the Authors discuss the state-of-the-art role for MRC in assessing biliary complications as emerging from updated literature review.

Original sources: Girometti R, Cereser L, Bazzocchi M, Zuiani C. Magnetic resonance cholangiography in the assessment and management of biliary complications after OLT. *World J Radiol* 2014; 6(7): 424-436 Available from: URL: <http://www.wjgnet.com/1949-8470/full/v6/i7/424.htm> DOI: <http://dx.doi.org/10.4329/wjr.v6.i7.424>

INTRODUCTION

Despite improvements in organ preservation, surgical technique, immunosuppression and postoperative management, biliary complications (BC) still represent the “Achille’s heel” of orthotopic liver transplantation (OLT), occurring in 10%-34% of graft recipients^[1,2]. BC are as-

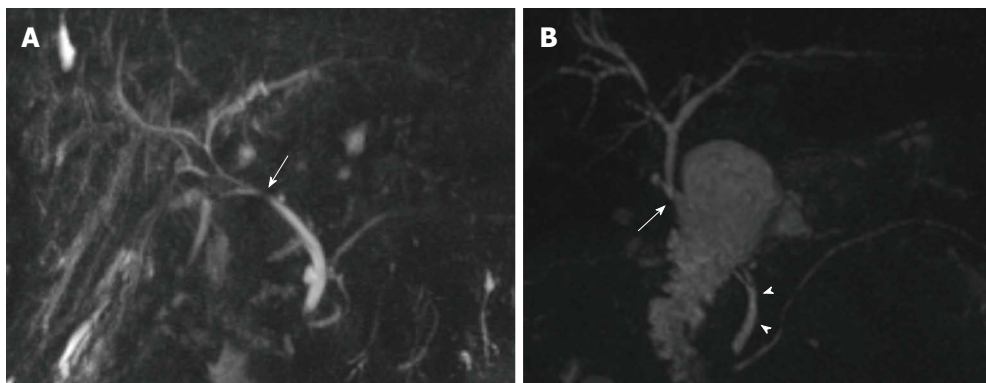


Figure 1 Biliary reconstructions variants after orthotopic liver transplantation illustrated by coronal maximum intensity projection reconstruction from 3D magnetic resonance cholangiography. A: Choledocho-choledochostomy with mild donor-to-recipient discrepancy in ductal calibers giving prominence to the anastomotic site (arrow); B: Bilioenteric anastomosis (arrow) between donor's common bile duct and a jejunal loop. Note the recipient common bile duct remnant (arrowheads).

sociated with a significant morbidity and mortality rate (2%-7%)^[3,4], representing the second leading cause of graft dysfunction and loss after rejection^[1]. Prompt recognition or exclusion of BC is crucial in order to address patient to proper treatment. However, differentiating BC from other post-OLT complications can be difficult based solely on clinical presentation and biochemical findings, thus making imaging essential in the diagnostic process^[5].

Among different imaging modalities, magnetic resonance cholangiography (MRC) plays a key role in evaluating BC after OLT. Due to the technical advances occurred over the last decades, MRC can be performed on magnetic resonance (MR) systems equipped with highly performing gradients, multichannel phased-array coils and dedicated sequences in order to produce panoramic and detailed representation of the biliary tree without significant motion-related artefacts^[2]. Although it is questionable whether MRC can be viewed as the new standard of reference in biliary imaging^[6], this technique has gained acceptance as the most reliable alternative to direct cholangiography in depicting the biliary system. In the setting of liver transplant, MRC is useful both in the pre- and post-operative period, e.g. in assessing the biliary anatomy of living donors^[7,8]. Moreover, MRC is safe, repeatable and reproducible^[7].

In this review, we: (1) describe different technical approaches to MRC; (2) discuss the evidence-based role of MRC in assessing BC after adult OLT; and (3) illustrate imaging findings of main BC. Although split-liver transplantation and LDLT are not directly discussed in this work, the paper statements on the use of MRC can be extended to these variants of transplantation.

CLINICAL OVERVIEW

Classification of biliary complications

BC can be classified according to the clinical phenotype, localization, timing of occurrence and etiology^[5]. A useful classification for radiologists is based on the temporary

onset from OLT, which is of help in identifying the most probable complication occurring at the time of image interpretation. Complications occurring within 3 mo after OLT are defined as “early”, and are typically represented by bile leakage and nonanastomotic strictures (NAS) related to hepatic artery thrombosis (HAT)^[5]. “Late” complications occur a few months to several years later, and mainly consist in strictures. Anastomotic strictures (AS) show a tendency to develop earlier (within 4-5 mo) compared to non-HAT related NAS^[5,9]. Overall, the large majority of BC (up to 80%) present within 6 mo from OLT^[9], with annual incidence less than 4% after the first post-transplant year^[10].

The characteristics of main BC are shown in Table 1, including the time of onset and main risk factors. Notably, split-liver transplant and LDLT have been associated with a moderate increase in BC, e.g., because of cut-surface leakage originating both in donors and recipients^[11].

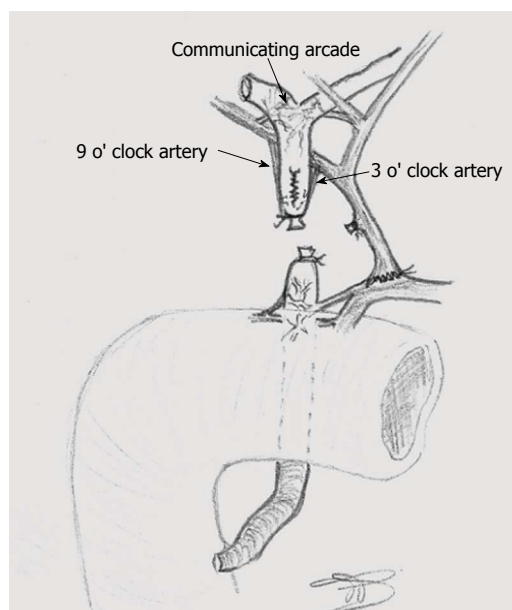
Biliary reconstruction

Prior to the examination, type of transplant (e.g., left/right split-liver transplant or living donor liver transplantation) and surgical technique should be evaluated in order to correctly interpret patient anatomy and MRC findings. Nowadays, biliary reconstruction during OLT is performed according to two main options^[5] (Figure 1): (1) choledocho-choledochostomy, consisting in an end-to-end anastomosis between donor and recipient choledochal ducts (duct-to-duct technique); and (2) bilioenteric anastomosis, consisting in an end-to-side anastomosis between the donor hepatic duct and a recipient jejunal loop (Roux-en-Y hepaticojejunostomy). Compared to bilioenteric anastomosis, duct-to-duct anastomosis is technically simpler and preserves the sphincter of Oddi as a barrier against bacterial colonization of the biliary tract^[12]. This is why choledocho-choledochostomy is the preferred technique of biliary reconstruction. Bilioenteric anastomosis is usually reserved for cases of primary sclerosing cholangitis (PSC) as the indication to OLT, surgical salvage after BC or re-transplantation^[12].

Table 1 Overview of main biliary complications occurring after liver transplantation

Type of complication	Prevalence in adult OLT patients	Risk factors	Time of onset from OLT	Clinical features	Treatment
Bile leak	7.8% OLT 9.5% LDLT	T-tube displacement or removal (T-tube leak) technical failure during surgery (anastomotic leak) HAT (nonanastomotic leak) Ischemic-related injury, immunologically-related injury, cytotoxic injury induced by bile salts (nonanastomotic leak in pts. without HAT)	1-3 mo	Fever, abdominal complaint, signs of cholestasis and or cholangitis	Leaving the T-tube open (T-Tube leaks) ERC with Sphincterotomy and stent placement Percutaneous drainage
Anastomotic stricture	13% OLT 19% LDLT	Older donor age Roux-en-Y choledochojejunostomy Technical factors (earlier manifestation) Ischemia of the donor bile duct (earlier manifestation) Previous anastomotic leakage (late manifestation)	within 6 mo-1 yr, occasionally later	Biliary obstruction	Surgical revision (repair or conversion to bilio-enteric anastomosis) ERC with balloon dilatation and stent placement (usually repeated procedures) Surgical revision (conversion to bilio-enteric anastomosis)
NAS	5%-25%	HAT Microangiopathic injury (prolonged warm or cold ischemia times of the graft) (ITBL) Immunogenic injury (ABO incompatibility between donor and recipient, chronic ductopenic rejection, primitive sclerosing cholangitis) (ITBL) Cytotoxic injury by bile salts (ITBL)	Within 6 mo (HAT-associated) After 6 mo (ITBL)	Cholestasis with recurrent cholangitis	Biliary toilette, dilatation ± stent placement <i>via</i> ERC/PTC Medical therapy (ursodeoxycholic acid and antibiotics if recurrent cholangitis)
Stones, casts and sludge	5.70%	Anastomotic and nonanastomotic biliary strictures Presence of T-tube or stent Hepaticojejunostomy Ischemia Infectious alteration in bile composition	Within 1 yr (casts and sludge) After 1 yr (stones)	Biliary obstruction	Conversion to hepaticojejunostomy (rarely) Retransplantation Bile ducts toilette using ERC/PTC Medical therapy with ursodeoxycholic acid Retransplantation
Sphincter of Oddi dysfunction and papillary stenosis	2%-7%	Denervation of the recipient common bile duct leading to sphincter of Oddi spasm Inflammation and/or scarring of the sphincter of Oddi	6 mo to 1 yr	Increased cholestatic enzymes	Endoscopic sphincterotomy

Data from^[5,11]. OLT: Orthotopic liver transplantation; NAS: Nonanastomotic strictures; ITBL: Ischemic-type biliary lesions; HAT: Hepatic artery thrombosis.

**Figure 2** Arterial supply to the biliary tree in liver-transplanted patients.

The vascular supply of the biliary tract

Contrary to liver parenchyma, the biliary tree is nourished by arterial vessels only, which can be divided in two interconnected systems (Figure 2). The first one supplies the common bile duct and consist of the ascending axial branches originating from the gastroduodenal artery, which run on medial (“3 o’clock”) and lateral (“9 o’clock”) aspects of the common bile duct and communicate (usually) with the right hepatic artery. The second system is the peribiliary vascular plexus, which supplies the hepatic confluence and intrahepatic bile ducts. It consists of a complex arterial network originating from terminal arterial branches, being supported mainly through a “communicating arcade” running between hilar branches of the hepatic artery, with substantial anatomic variability^[5,13].

Although surgical technique is aimed to preserve as much as possible biliary vascularization both in the donor and recipient, surgical sacrifice of arterial branches during the transplant make the bile ducts sensitive to “disconnection” from the hepatic artery and/or recipient gastro-

duodenal artery, as occurs during organ preservation or HAT. Hypoperfusion from HAT translates into ischemic cholangitis (“macroangiopathic” injury), with extensive bile epithelium necrosis, intraductal casts formation, bile leakage and evolution to scarring and multiple strictures, typically involving the hepatic confluence and intra-hepatic bile ducts^[9]. Surgical preservation of adequate perfusion at biliary ends and periductal tissue is also essential in reducing the risk of anastomotic stenosis^[5]. Furthermore, hypoperfusion may result from a variety of transplant-related or immunologically-mediated causes (Table 1), causing “microangiopathic” ischemic damage of the peribiliary plexus. Such a damage translates into a macroscopic MRC pattern similar to that of macroangiopathic injury^[5], as illustrated below.

Diagnostic approach to biliary complications

Clinical and laboratory diagnosis of BC is challenging, since manifestations such as fever, increase in bilirubin and altered liver function tests significantly overlap with other post-OLT entities, including rejection^[9]. Of note, BC may co-exist with different types of complications or being a consequence of HAT, thus making differential diagnosis even more difficult. However, prompt recognition of primary or secondary biliary involvement is mandatory to allow proper treatment.

Ultrasound with color Doppler examination and/or contrast-enhanced ultrasound (CEUS) represent the first-line tool in excluding HAT as the primary source of BC and in assessing fluid collections suspicious for bilomas^[14]. Despite the high negative predictive value (NPV) reported by some authors^[15], US shows well known limitations in clinical practice, especially in the case of biliary obstruction. US lacks panoramicity and is often impaired by reduced patients’ compliance and presence of bowel gas and surgical dressing material. Additionally, the presence of epithelial casts filling the bile ducts in the post-operative period may further limit sonographic visibility^[16]. As a consequence, it is difficult to establish the type and the site of the obstructive cause with US. Although biliary dilatation is a reliable indirect sign of biliary obstruction, biliary dilatation develops slowly and disproportionately with regard to the severity of the stricture^[17], being undetectable in more than 60% with anastomotic stenosis^[18]. In summary, normal US examination should not preclude further investigations in case of clinical suspicion.

According to Zoepf *et al.*^[16], Computed Tomography (CT) is able to show biliary dilatation in up to 40% and 83% of anastomotic and nonanastomotic strictures, respectively. However, because of limited contrast resolution and relative inability to show the anastomotic site, CT correctly identifies the site of biliary obstruction in 10% of patients only^[2,16]. The main role for CT is then to assess HAT^[19] and/or detect intra- and extra-hepatic hypoattenuating collections when a suspicious biloma has been raised by US.

The use of T-tube after OLT is still a matter for de-

bate^[5]. When available, T-tube cholangiography under fluoroscopic or CT guidance is a rapid and accurate tool to demonstrate the presence of bile leak during the limited period of time in which direct access to bile ducts is present (1-3 mo). According to Singh *et al.*^[20], T-tube cholangiography should be preferred over MRC because the distension of the bile ducts with contrast medium permits better stricture analysis and functional assessment. Therefore, once the T-tube is removed, alternative imaging methods must be used.

Because of the above limitations of US, CT and T-tube cholangiography, ERC and PTC are still considered the standard of reference in imaging patients with duct-to-duct anastomosis and bilioenteric anastomosis, respectively. The advantage of ERC and PTC is to allow interventional procedures such as sphincterotomy, ballooning or stenting, which are the first-line treatment of biliary obstruction. On the other hand, morbidity and mortality rates associated with direct cholangiography procedures have encouraged the use of MRC as the preferred, panoramic tool to assess BC, limiting ERC and PTC to interventional rather than diagnostic purpose^[5,21]. We further discuss the role for ERC/PTC and MRC in the dedicated paragraph below, together with the advantages and disadvantages of these techniques.

Further investigations such as hepatobiliary scintigraphy provided controversial results, gaining no routine use^[5]. On the contrary, liver biopsy is frequently necessary to establish final diagnosis underlying graft dysfunction^[22], especially if microangiopathic biliary injury is suspected.

MRC TECHNIQUE

The goal of MRC is to provide a panoramic representation of hyperintense biliary tree against a low signal intensity background. Currently, two techniques are used to obtain images with such an elevated contrast, namely conventional MRC (C-MRC) and contrast-enhanced MRC (CE-MRC) (Figure 3). The difference between these techniques relies on the type of sequence, use of *iv* contrast agent, timing of acquisition and clinical indication.

Regardless of the technique, MRC is rarely used as a standing-alone examination. MRI scanning protocols in post-OLT patients should always include non cholangiographic sequences in order to evaluate liver parenchyma and/or extrabiliary manifestations of BC such as bilomas and perihepatic free fluid^[2].

Conventional MRC

In C-MRC, image contrast is the result of heavily T2-weighted sequences with a long TE. This emphasizes differences in transverse relaxation times between “slow motion” fluids such as the bile (long T2) and background tissues with intermediate to short T2^[21]. In our Institution, we administer oral 1:10 mL water solution of a gadolinium chelate contrast agent just before the acquisition of MRC in order to suppress overlapping fluid signal

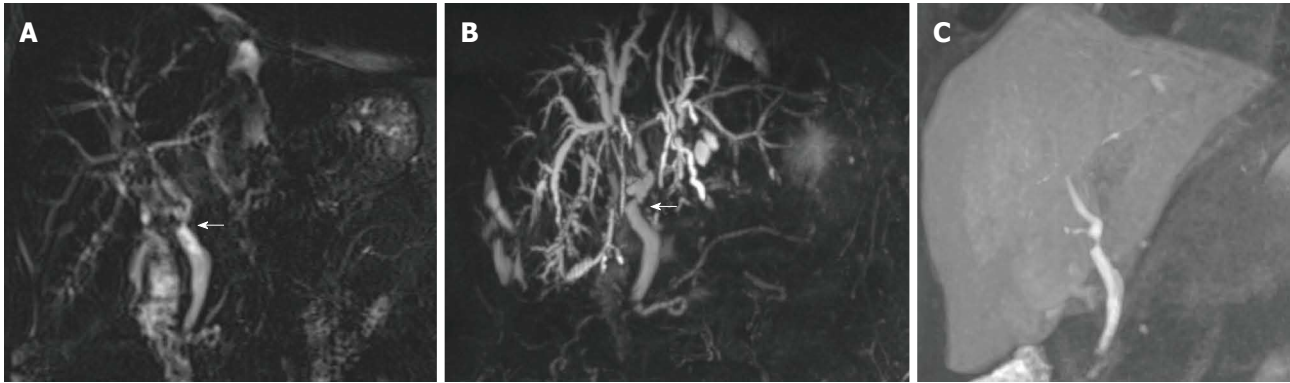


Figure 3 Technical variants of magnetic resonance cholangiography, as shown in coronal images of a 66-year-old male patient transplanted for alcoholic cirrhosis. A: Conventional, T2-weighted 2D MRC; B: MIP reconstruction from conventional, T2-weighted 3D MRC; C: Thick MIP reconstruction from T1-weighted, contrast-enhanced MRC. Both the degree and functional significance of the mild anastomotic stricture indicated by arrows are better showed by contrast passage in (C). MRC: Magnetic resonance cholangiography; MIP: Maximum intensity projection.

from the stomach and/or duodenum with paramagnetic effects on the T2 relaxation time^[23]. However, because of the risk to mask the Vaterian region of the common bile duct as a possible site of BC, the use of oral negative contrast agent is a matter of expertise and institutional preferences. Based on the inherent high contrast of C-MRC, no *in* administration of gadolinium-based contrast agents is needed, which is of relevance in patients with renal function impairment at risk of developing Nephrogenic Systemic Fibrosis (NSF)^[24].

C-MRC can be performed with the 3D and/or 2D approach choosing among a variety of well-established MRC sequences (Figure 3). The 3D technique is usually based on respiratory-triggered or navigator-gated volumetric Turbo/Fast Spin Echo sequences acquired during normal patient respiration, and provides numerous thin slices with higher signal-to-noise ratio and spatial resolution as a base for multiplanar reformations ad maximum intensity projection (MIP) reconstructions^[25]. Compared to the 2D variant, 3D C-MRC has the advantage of higher longitudinal spatial resolution, with the capability of achieving isotropic imaging and assessing more subtle anatomic and pathological details, such as small calculi^[25]. On the other hand, 3D C-MRC can be significantly affected by motion artifacts in non-collaborating patients. The 2D technique is acquired more rapidly, during few and short breath-holds using thick slices, thus reducing the effects of respiratory artefacts on image quality^[26]. Different sequences are currently available to perform 2D C-MRC, including RARE (rapid acquisition with relaxation enhancement), HASTE (half-Fourier acquisition single-shot turbo spin echo) and SS-F/TSE (single-shot fast/turbo spin echo)^[26].

To our knowledge, only a few studies by Kinner *et al*^[26,27] compared the 2D and 3D techniques in assessing BC after OLT. According to these Authors, overall image quality and accuracy are comparable in patients with biliary obstruction, regardless of the C-MRC sequence. However, the 3D technique shows slight better diagnostic performance in assessing BC, especially in the case of

patients with choledocho-choledochostomy and biliary strictures^[27]. Although the use of the 2D or 3D technique depends on institutional preferences, both approaches should be used in the standard examination, in order to exploit the advantages and counterbalance the drawbacks of each technique.

Contrast-enhanced MRC

Over the last years, there has been an increasing interest in the use of CE-MRC in the post-surgical assessment of the biliary tree^[28]. This technique is based on *in* administration of hepatospecific contrast agents such as gadoxetic acid (Gd-EOB-DTPA), gadobenate dimeglumine (Gd-BOPTA)^[29] or mangafodipir trisodium^[30], that are excreted into the bile after hepatocellular uptake, thus complementing morphological C-MRC with information on the bile flow. In our experience, the most suitable contrast agent in this setting is gadoxetic acid, because of larger hepatocellular uptake (50% of the administered dose) and the relatively short time to achieve the hepatobiliary phase, *i.e.*, 10 to 20 min after contrast administration in patients with preserved liver function^[31]. As T2-shortening effects might mask the biliary tree on T2-weighted images, it is mandatory to perform CE-MRC after C-MRC, using a volumetric, high-resolution T1-weighted 3D fat-saturated sequence^[31]. The use of larger flip angles (*e.g.*, 35°) is recommended in order to increase the conspicuity of the biliary tree over the background^[32].

Despite the increasing use of CE-MRC, there is a paucity of literature-based evidence in the setting of OLT, mainly focused on the preoperative evaluation of liver donors^[33,34]. However, studies on patients with BC after hepatobiliary surgery, including OLT subjects, suggest that CE-MRC improves the accuracy of C-MRC in evaluating bile leakage showing the site of the leak and direct contrast extravasation into perihepatic/peribiliary fluid collections^[35]. Moreover, CE-MRC is indicated to “functionally” assess the degree of biliary obstruction according to the presence or absence of the contrast medium downstream in the bile duct (Figure 3). This is

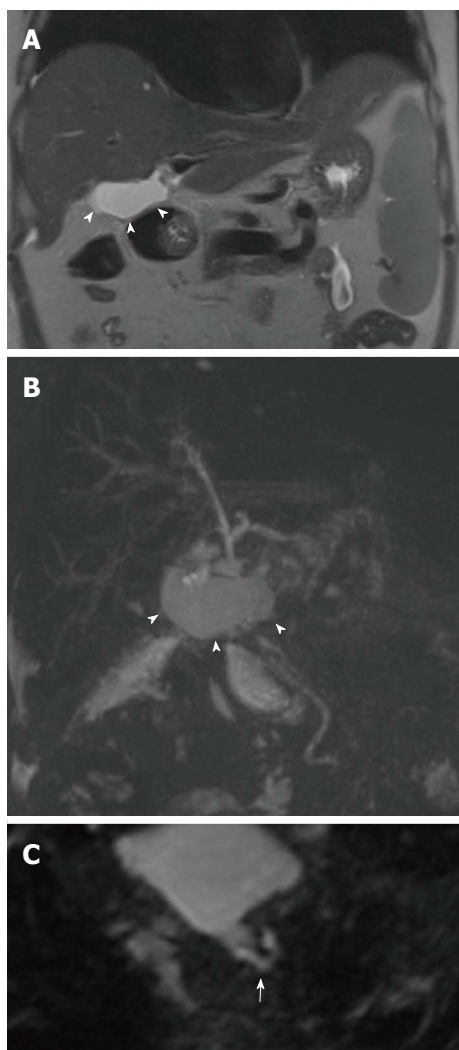


Figure 4 Bile leakage in a 54-year-old male subject transplanted for hepatitis C virus-related cirrhosis. Perihilar biloma shown by arrowheads on coronal T2-weighted HASTE image (A) and paracoronar MIP reconstruction from 3D MRC (B). Thin communication between the anastomotic site and fluid collection is visible on the axially-reformatted 3D source image (arrow in C). MRC: Magnetic resonance cholangiography; MIP: Maximum intensity projection.

of importance in patients with bilioenteric anastomosis, since the diagnosis of anastomotic stricture can be difficult even in the presence of biliary dilatation^[31]. In our experience, the degree of contrast flow is helpful (1) in the distinction between “normal” scarring of the anastomotic site and obstructive anastomotic stenosis in patients with choledocho-choledochostomy; or (2) in the assessment of diffuse bile ducts damage in the case of bile casts syndrome.

Hepatocellular uptake of gadoxetic acid is mediated by the same anionic transporter of bilirubin. As a consequence, biliary excretion of gadoxetic acid is limited or delayed by impaired liver function^[35]. Although impaired biliary excretion can be used as an indirect sign of biliary obstruction^[31,35], this translates into reduced visualization of the bile ducts or the need to perform delayed image acquisitions up to 90-180 min after contrast administration^[31]. In our opinion, the costs inherent to contrast

agents imply that CE-MRC should be used to complement C-MRC when “functional” information is needed, after careful evaluation of patients liver function. In our Institution, we avoid CE-MRC when bilirubin level is higher than 5 mg/dL.

MRC FINDINGS

Normal findings after OLT

Normal post-OLT Imaging findings mirror some “physiologic” effects of the surgical procedure. Not surprisingly, then, it is frequent to observe small amounts of free fluid or small fluid collections in the perihepatic region, intersegmental fissure and subhepatic space, as well as along the resection margin after split liver-OLT and LDLT^[36]. Clinical and biochemical correlation is helpful in order not to misinterpret these findings as bilomas. Collections tend to resolve spontaneously after few weeks from the intervention^[20].

Mild anastomotic narrowing with minimal concentric wall thickening of the common bile duct is a frequent MRC finding^[2] that should be interpreted as normal, unless biliary dilatation upstream and symptoms of biliary origin are present^[37]. In most cases, anastomotic narrowing is the effect of surrounding edema, resolving during the first weeks after OLT^[11]. In our experience, narrowing or kinking of the common bile duct at the anastomotic site are common findings, especially in the case of redundancy or disproportion between the donor and recipient common bile ducts^[3]. These conditions are useful in identifying the site of anastomosis in the case of choledocho-choledochostomy, and should not be assessed as a complication unless biliary obstruction is associated (Figure 1).

Bile leakage

Leakage represents the most common early biliary complication. In up to 80% of patients with leakage^[9], leaks manifest at the insertion of the T-tube, usually as a consequence of dislocation or after the removal of the device^[38]. Other sites include: (1) the biliary anastomosis or cystic duct remnant, as an effect of technical failure^[11]; (2) the cut-surface after split-liver OLT or LDLT, possibly in relation to patent or aberrant bile ducts and necrosis of liver tissue^[5]; and (3) wherever along the biliary tree (intrahepatic and/or extrahepatic bile leakage) because of bile ducts ischemia after HAT (see above).

On T2-weighted C-MRC, biliary leakage manifests indirectly as bilomas, *i.e.*, a well-delineated fluid collections lying in the perihilar or subhepatic space, as well as along the resection margin in LDLT or split-liver OLT. A variable amount of free bile can be associated around the perihepatic space or intersegmental fissure. These findings can be indistinguishable from normal postoperative free fluid or collections. Bilomas can be suspected when a thin, hyperintense direct communication between a fluid collection and the T-tube entry site and/or biliary anastomosis is shown^[11] (Figure 4). When leakage is suspected, CE-MRC is an effective complement to C-MRC

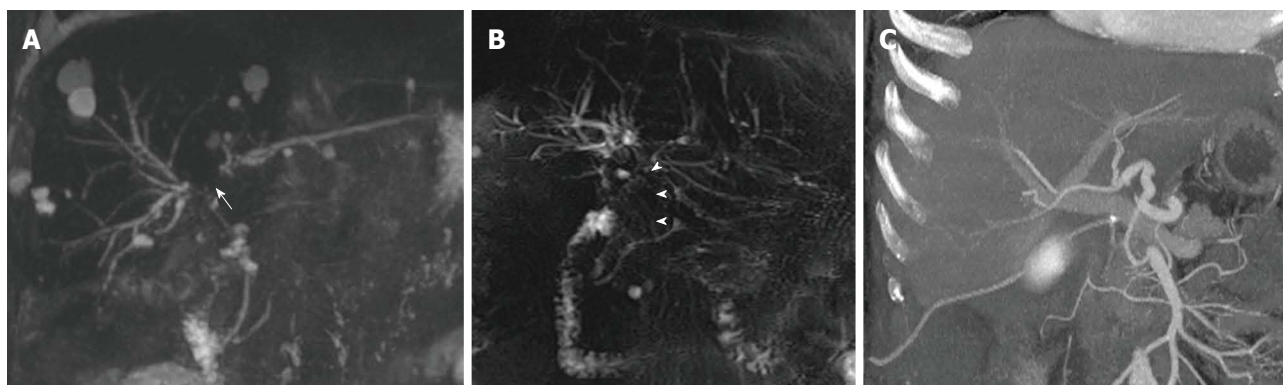


Figure 5 Nonanastomotic strictures in two different transplanted patients. A: MIP reconstruction shows early effects of HAT in a 58-year-old subject with hepatitis B virus infection, consisting in a stricture of the hepatic confluence (arrow) and multiple intrahepatic bilomas; B: ITBL in a 68 male patient transplanted for alcoholic cirrhosis. 2D MRC image shows a stricture of the hepatic confluence extended to the donor common hepatic duct (arrowheads); C: CT angiography found patent hepatic artery in this patient. MRC: Magnetic resonance cholangiography; MIP: Maximum intensity projection; ITBL: Ischemic-type biliary lesions.

in order to demonstrate both the site of contrast extravasation and contrast transit into the biloma or free fluid, with sensitivity for combined C-MRC and CE-MRC of 84%^[35]. Confirmation of diagnosis is usually obtained during therapeutic ERC.

Strictures

Strictures can be classified into anastomotic strictures (AS) or nonanastomotic strictures (NAS) according to the site of manifestation, which reflects different pathological mechanisms of origin (Table 1). NAS are further differentiated into forms associated with HAT (macroangiopathic damage) and forms occurring during later from OLT, in the presence of patent hepatic artery (microangiopathic damage). Non-HAT associated NAS are overall categorized as Ischemic-type biliary lesions (ITBL)^[5,9,11].

Anastomotic strictures

In patients with choledocho-choledochostomy, luminal narrowing manifests as a focal tract of decreased or absent bile signal intensity of the reconstructed common bile duct, lying between donor and recipient remnants of the cystic duct. A variable degree of common bile duct angulation can be associated^[11]. AS can be classified as mild, moderate or severe. Of note, MIP reconstructions from 3D C-MRC tend to overestimate the degree of luminal narrowing compared to ERC^[39,40]. Consequently, 3D source data and/or 2D MRC should always be evaluated when assessing strictures, although functional effects on the bile flow are easily inferred by the degree (1) of the associated suprastenotic biliary dilatation; and (2) contrast passage downward when using CE-MRC.

In the case of bilioenteric AS, luminal narrowing appears as a focal absence of biliary signal in the segment immediately above the jejunal loop, corresponding to low-signal thickening of the common bile duct on axial or axially-reformatted 3D images^[2,41]. However, the accuracy of C-MRC in evaluating AS is lower in patients with bilioenteric anastomoses compared to those with choledocho-choledochostomy, regardless of the use of 2D

or 3D technique^[27]. This difference has been explained by the difficulty in correctly identifying the anastomotic site, which is partially masked by the hyperintense fluid content of the anastomotic bowel tract. Furthermore, mild duct dilatation is frequently present in patients with patent bilioenteric anastomosis due to physiological changes in caliber as the bile duct enters the bowel wall^[26] or temporary folding of the anastomotic site caused by the anastomotic loop motility^[41]. CE-MRC with delayed imaging has the potential to clearly define the presence of biliary obstruction, thus avoiding false-positive results. Based on the degree of contrast transit at 30 min from contrast injection, the degree of bile duct obstruction can be classified as^[51]: (1) complete (absence of contrast filling in the proximal part of the stricture); (2) near-complete (significantly delayed contrast agent filling only in the proximal part of the stricture); and (3) partial (passage of contrast agent beyond the stricture).

Nonanastomotic strictures

Regardless of the timing of onset and different pathogenic mechanism (Table 1), NAS related to HAT and ITBL manifest with a similar pattern of extensive biliary injury, consisting in irregularly marginated bile ducts with multiple focal stenoses typically involving the hepatic confluence (with the hepatic duct) and/or intrahepatic bile ducts (Figure 5). Bile ducts segments above or between strictures show a variable degree of biliary dilatation upstream^[11]. The involvement of intrahepatic ducts equal or larger than the second-order should be clearly identified, because this findings is associated with worst response to therapy^[42]. The involvement of small peripheral ducts (third-order or larger) is typical of microangiopathic forms of NAS, frequently evolving to ducts rarefaction over time^[5]. Potential disadvantages of MRC are the difficulty in establishing the degree and length of dominant strictures^[43], as well as the identification of subtle alterations of peripheral bile ducts^[27]. Additionally findings of NAS include (Figure 6): (1) intrahepatic or extrahepatic bilomas in HAT-related forms, as a conse-

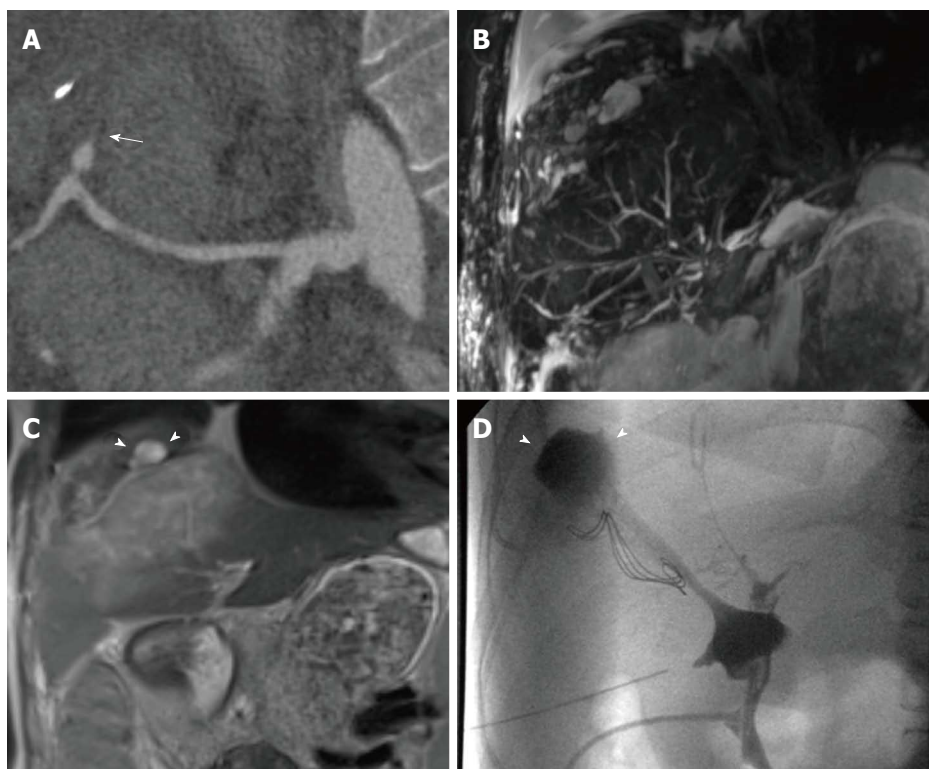


Figure 6 Multiple findings in a 28-year-old female patient transplanted for primary sclerosing cholangitis. Because of the hepatic artery thrombosis shown on curved-reformatted CT image (arrow in A), the biliary tree appears as fragmented and anatomically ill-defined on a panoramic maximum intensity projection view (B). Coronal T2-weighted HASTE image (C) shows extensive, hyperintense ischemic damage of liver parenchyma, together with intrahepatic fluid collections (arrowheads) confirmed to be the effect of bile leakage on T-tube cholangiography (arrowheads in D).

quence of the necrosis of bile duct walls^[11]; (2) ischemic damage of liver parenchyma; and (3) casts and sludge filling bile ducts, originated by the aggregation between bile products and desquamated epithelial cells^[5].

Recurrent PSC and biliary involvement secondary to chronic rejection may mimic NAS. In particular, chronic rejection has been associated with diffuse “vanishing bile duct” appearance involving more peripheral intrahepatic branches, thus showing some aspects in common with late NAS^[11]. Timing of presentation, clinical history and results of liver biopsy are helpful in performing differential diagnosis.

Other complications

Sludge, casts and stones: Sludge, casts and stones are usually a concomitant manifestation of AS and NAS, showing a common appearance of an intense filling defects surrounded by a thin rim of bile signal. Typical locations include larger intrahepatic ducts^[2] or the common bile duct immediately above a stricture. Usually, stones form later than sludge and casts, showing more rounded shape and smooth margins (Figure 7)^[11]. Casts can be extensively distributed along biliary branches, obscuring the visibility of the hyperintense bile on C-MRC images. The only indirect sign of casts can be intermediate signal on T1- and T2-weighted noncholangiographic images with portal distribution, with periportal enhancement on postcontrast images due inflammation of the peribili-

ary space^[44]. Notably, cast can accumulate extensively in the so-called “biliary-cast syndrome” (BCS), in which hardened, lithogenic material occupies the biliary ductal system shaping on the bile ducts, regardless of ischemic injury^[45]. Since diagnosis of BCS and smaller filling defects is challenging on C-MRC, the use of CE-MRC has been advocated as a useful tool to improve diagnostic accuracy^[46].

Differential diagnosis with stones, sludge and casts mainly includes aerobilia. Aerobilia is frequent after ERC or in patients with bilioenteric anastomosis. Air bubbles usually form an air-fluid level on axial images^[11] (Figure 8) and can be associated with characteristic magnetic susceptibility artefact on noncholangiographic images obtained with GRE T1-weighted or Diffusion-weighted sequences (Figure 9).

Sphincter of Oddi dysfunction and papillary stricture:

Distal obstruction of the common bile ducts usually translates into significant biliary dilatation of the recipient portion of the extrahepatic bile duct, although dilatation can rarely extend to intrahepatic bile ducts. In our experience, serial acquisition of “cinematic” 2D MRC images are useful in establishing the diagnosis, showing persistent lack of visualization of the Vaterian sphincter tract of the common bile duct, suggesting spasm or stenosis (Figure 10). Final diagnosis is usually obtained with ERC or manometry of the sphincter of Oddi^[11].

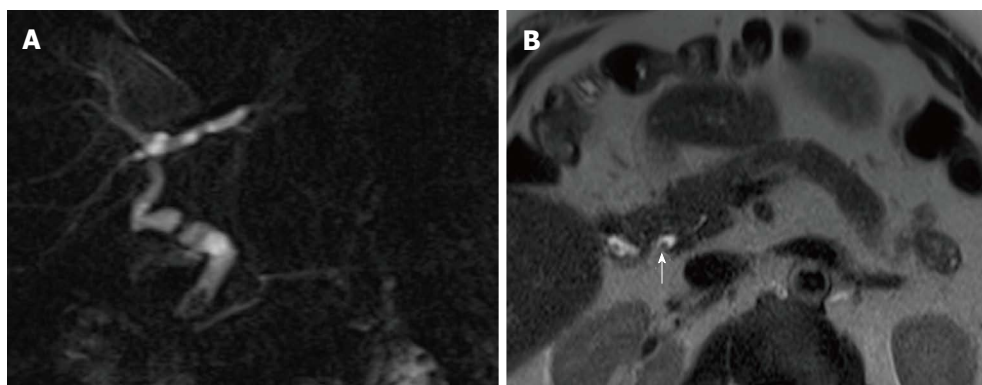


Figure 7 Calculi in a 62-year-old male subject who underwent orthotopic liver transplantation for hepatitis C virus-infection and hepatocellular carcinoma. A: The patient shows chronic kinking and moderate anastomotic stricture without biliary obstruction; B: Filling defect visible in the distal common bile duct were confirmed on axial HASTE image (arrow) and proven to be small calculi on ERC.

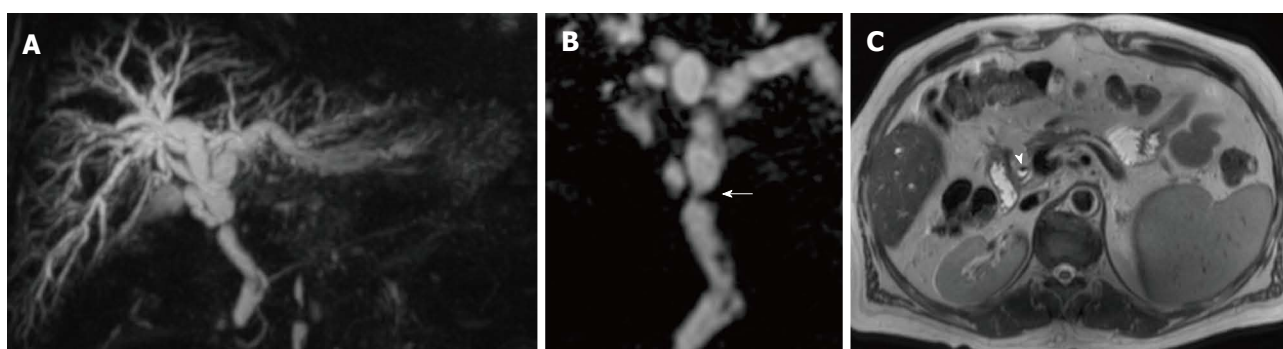


Figure 8 Anastomotic stricture in a 54-year-old male patient who underwent orthotopic liver transplantation for alcoholic cirrhosis. A: Coronal MIP reconstruction shows the stricture at the middle third of the extrahepatic bile duct, with biliary dilatation upstream; B: The degree of the stricture is better delineated on the paracoronally-reformatted thin 3D image (arrow); C: Filling defects visible on MRC images correspond to pneumobilia, appearing as air-fluid levels (arrowhead) on the axial T2-weighted HASTE sequence. MRC: Magnetic resonance cholangiography; MIP: Maximum intensity projection.

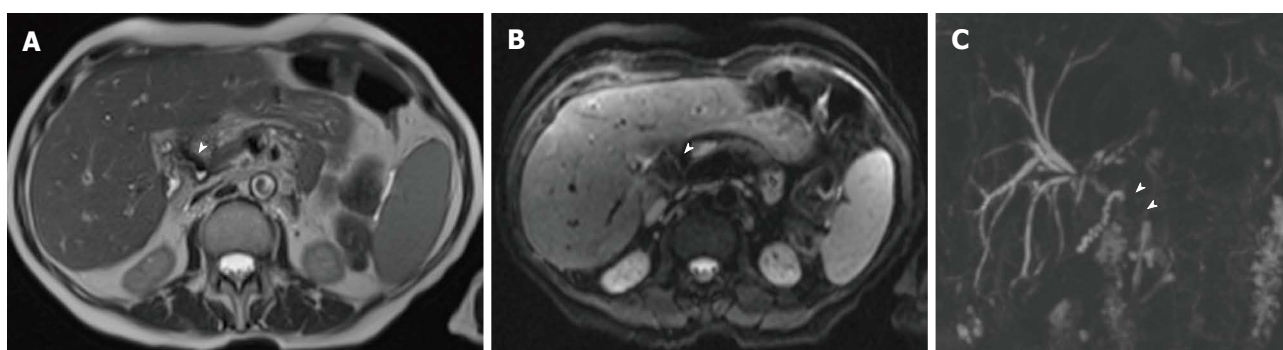


Figure 9 Aerobilia in a 62-year-old female patient transplanted for alcoholic cirrhosis. Anintense filling defect in the common bile duct on T2-weighted axial HASTE image (arrowhead in A) is associated to distortion artifact on axial Diffusion-weighted sequence (arrowhead in B). The effect of pneumobilia was to extensively mask the common bile duct on 3D magnetic resonance cholangiography (arrowheads in C).

ROLE FOR MRC IN PATIENT'S MANAGEMENT

ERC still represents the standard of reference for biliary obstruction complicating OLT^[1]. One might conclude that patients with suspicious BC should undergo ERC after preliminary US and/or CT evaluation. On the other hand, ERC is associated with a significant risk of pancreatitis, bleeding, infection, perforation and sedation-related

complications, with morbidity and mortality rates of 10% and 0.5%, respectively^[1]. The risk of complications is even higher when using PTC. Thus, the risk profile for diagnostic procedures of direct cholangiography seems not justifiable given the high diagnostic accuracy of MRC, which shows 97% sensitivity and 98% specificity for biliary obstruction according to a recent metanalysis^[47]. Unfortunately, there is a relative paucity of studies^[3,21,43,48-53] investigating the role for MRC in the specific setting of

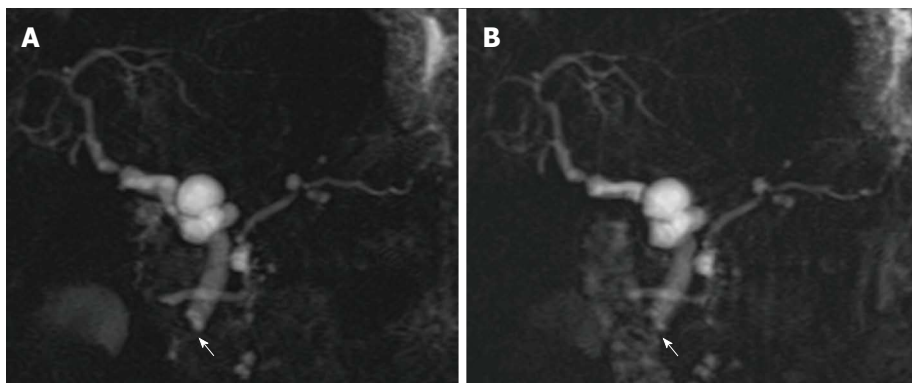


Figure 10 Sphincter of Oddi dysfunction in a liver-transplanted female patient with cholestasis and abdominal complaint years after orthotopic liver transplantation. Serial 2D cinematic magnetic resonance cholangiography images (A) and (B) acquired after few seconds show redundancy of the reconstructed common bile duct, which appear slightly dilated in the recipient tract, and persistent lack of visualization of the Vaterian sphincter complex, with typical “meniscus sign” (arrow) suggesting spasm.

Table 2 Results of previous systematic reviews on the role for magnetic resonance cholangiography in assessing biliary complications after orthotopic liver transplantation

Goal	Jorgensen <i>et al</i> ^[11]	Xu <i>et al</i> ^[55]	
	Biliary obstruction	All biliary complications	Subset of strictures
Pooled	96.0%	0.95%	0.94%
sensitivity	(0.92%-0.98%)	(0.92%-0.97%)	(0.88%-0.98%)
Pooled	0.94%	0.92%	0.95%
specificity	(0.90%-0.97%)	(0.89%-0.94%)	(0.88%-0.99%)
AUC	0.99	0.97	0.97
Pooled PLR	17.00 (9.4-29.6)	10.23 (6.21-16.84)	9.96 (2.52-39.36)
Pooled NLR	0.04 (0.02-0.08)	0.08 (0.06-0.12)	0.09 (0.04-0.17)

Number between parentheses represent the 95%CI. Analysis by Xu *et al* is stratified for the whole of complications and the subset of strictures. AUC: Area under the curve at Summary Receiving Operating Characteristic (SROC) curve; PLR: Positive likelihood ratio; NLR: Negative likelihood ratio.

post-OLT BC, leading to difficulties in generalizing results from general population to transplant recipients^[1]. For instance, some authors^[47] have hypothesized that reduced biliary dilatation following post-OLT strictures might limit the accuracy of MRC. Detractors of MRC also argue that, although MRC correlates well with direct cholangiography procedures ($P = 0.01$)^[54], the examination delays the diagnosis when interventional ERC or PTC are finally needed. This is why the use of MRC still depends on local preferences based on availability, expertise and costs.

Based on the above premises, one might ask which evidence-based task can be reasonably attributed to MRC in patients management. Table 2 shows the results of the two systematic reviews^[1,55] focusing on this topic. Interestingly, Jorgensen *et al*^[11] provide indirect information on the role for MRC by hypothesizing clinical scenarios with pre-test probability of BC of 25% and 50%, respectively. In the case of positive MRC, the post-test probability of BC reaches 80% and 94%, respectively, whereas in the case of negative MRC, the post-test probability reduces to 1% and 4%, respectively. These estimates emphasize

the results of previous direct comparison between MRC, ERC and PTC^[54], suggesting that the strength of MRC is represented by the large negative predictive value (94.4%), which is of help in excluding BC and avoiding unnecessary invasive procedures in patients with clinical low-to-moderate risk of BC^[54]. Unfortunately, several methodological flaws affect the studies included in the above systematic reviews, including small sample size, uncertainty in clinical criteria defining the suspicion for BC, verification bias given the heterogeneity in the standard of reference tools and absence of a standardized MRC technique^[1,55]. This is why the increasing (and reasonable) practice of using MRC as a screening tool for BC should be more adequately supported by: (1) prospective, large studies performed on patients initially assessed as having low-to-moderate risk for BC; (2) studies of cost-effectiveness on the systematic use of MRC in this category of patients.

On the other hand, it should be emphasized that a positive MRC examination cannot be simply considered as a cause of diagnostic delay. Differently from ERC and PTC, C-MRC depicts the bile ducts: (1) in their normal state, rather than artificially dilated by contrast injection pressure; and (2) below and above obstruction sites^[54], thus making visible the whole biliary tract, regardless of impaired contrast passage. CE-MRC can complement this panoramic information as illustrated above. As a consequence, a positive MRC examination provides a road-map useful to plan better interventional or surgical approach, thus potentially contributing to reduce morbidity related to invasive procedures.

CONCLUSION

MRC has gained widespread acceptance as a tool to panoramically and reliably represent the biliary tree in post-OLT patients with suspected BC. Conventional technique, based on 2D or 3D heavily T2-weighted sequences, can be now complemented by CE-MRC using hepatospecific contrast agents, thus adding functional information to the morphological depiction of bile ducts.

Although a consensus on the best study protocol is still lacking, a combination of the available technique is reasonably the best choice to enhance the diagnostic capabilities of MRC.

Because of the inherent high contrast of bile ducts, MRC has the capability to reliably identify most relevant BC, including bile leakage, AS, NAS and a variety of further disorders including calculi or sphincter of Oddi dysfunction. However, concerns still exist regarding the cost-effectiveness of this imaging modality in the everyday clinical practice, since positive MRC examinations often lead to ERC and PTC, which are still considered as the standard of reference for final diagnosis. A review of the literature suggests that, despite the absence of large multicentric trials on proper target populations, the high negative predictive of MRC is of value in excluding BC in patients with low-to-moderate risk, thus avoiding unnecessary invasive procedures. On the other hand, positive MRC provides a detailed road-map for interventional procedures or surgery, thus further contributing to reduce morbidity.

In summary, MRC is gaining an increasing role in the diagnosis and management of BC after OLT, and should be performed confidently in patients with low-to-intermediate risk of disease.

ACKNOWLEDGMENTS

The authors thank: (1) Dr. Paolo Divis for having edited the images and drawn Figure 2; (2) Dr. Iliana and Sandra Bednarova' for having revised English language.

REFERENCES

- Jorgensen JE, Waljee AK, Volk ML, Sonnenday CJ, Elta GH, Al-Hawary MM, Singal AG, Taylor JR, Elmunzer BJ. Is MRCP equivalent to ERCP for diagnosing biliary obstruction in orthotopic liver transplant recipients? A meta-analysis. *Gastrointest Endosc* 2011; **73**: 955-962 [PMID: 21316670 DOI: 10.1016/j.gie.2010.12.014]
- Pecchi A, De Santis M, Di Benedetto F, Gibertini M, Gerunda G, Torricelli P. Role of magnetic resonance cholangiography in biliary complications of orthotopic liver transplantation. *Radiol Med* 2010; **115**: 1065-1079 [PMID: 20680501 DOI: 10.1007/s11547-010-0563-7]
- Valls C, Alba E, Cruz M, Figueras J, Andía E, Sanchez A, Lladó L, Serrano T. Biliary complications after liver transplantation: diagnosis with MR cholangiopancreatography. *AJR Am J Roentgenol* 2005; **184**: 812-820 [PMID: 15728602 DOI: 10.2214/ajr.184.3.01840812]
- Boraschi P, Donati F. Complications of orthotopic liver transplantation: imaging findings. *Abdom Imaging* 2004; **29**: 189-202 [PMID: 15290945]
- Seehofer D, Eurich D, Veltzke-Schlieker W, Neuhaus P. Biliary complications after liver transplantation: old problems and new challenges. *Am J Transplant* 2013; **13**: 253-265 [PMID: 23331505 DOI: 10.1111/ajt.12034]
- Shanmugam V, Beattie GC, Yule SR, Reid W, Loudon MA. Is magnetic resonance cholangiopancreatography the new gold standard in biliary imaging? *Br J Radiol* 2005; **78**: 888-893 [PMID: 16177010 DOI: 10.1259/bjr/51075444]
- Sirvanci M, Duran C, Ozturk E, Balci D, Dayangaç M, Onat L, Yüzer Y, Tokat Y, Killi R. The value of magnetic resonance cholangiography in the preoperative assessment of living liver donors. *Clin Imaging* 2007; **31**: 401-405 [PMID: 17996603 DOI: 10.1016/j.clinimag.2007.05.003]
- An SK, Lee JM, Suh KS, Lee NJ, Kim SH, Kim YJ, Han JK, Choi BI. Gadobenate dimeglumine-enhanced liver MRI as the sole preoperative imaging technique: a prospective study of living liver donors. *AJR Am J Roentgenol* 2006; **187**: 1223-1233 [PMID: 17056909 DOI: 10.2214/AJR.05.0584]
- Verdonk RC, Buis CI, Porte RJ, Haagsma EB. Biliary complications after liver transplantation: a review. *Scand J Gastroenterol Suppl* 2006; **(243)**: 89-101 [PMID: 16782628]
- Brown RS, Russo MW, Lai M, Shiffman ML, Richardson MC, Everhart JE, Hoofnagle JH. A survey of liver transplantation from living adult donors in the United States. *N Engl J Med* 2003; **348**: 818-825 [PMID: 12606737 DOI: 10.1056/NEJMsa021345]
- Girometti R, Cereser L, Como G, Zuiani C, Bazzocchi M. Biliary complications after orthotopic liver transplantation: MRCP findings. *Abdom Imaging* 2008; **33**: 542-554 [PMID: 17851711 DOI: 10.1007/s00261-007-9316-z]
- García-Criado A, Gilabert R, Bargalló X, Brú C. Radiology in liver transplantation. *Semin Ultrasound CT MR* 2002; **23**: 114-129 [PMID: 11866218]
- Gunji H, Cho A, Tohma T, Okazumi S, Makino H, Shuto K, Mochizuki R, Matsubara K, Hayano K, Mori C, Murakami G, Ochiai T. The blood supply of the hilar bile duct and its relationship to the communicating arcade located between the right and left hepatic arteries. *Am J Surg* 2006; **192**: 276-280 [PMID: 16920417 DOI: 10.1016/j.amjsurg.2006.01.046]
- Claudon M, Dietrich CF, Choi BI, Cosgrove DO, Kudo M, Nolsøe CP, Piscaglia F, Wilson SR, Barr RG, Chammas MC, Chaubal NG, Chen MH, Clevert DA, Correas JM, Ding H, Forsberg F, Fowlkes JB, Gibson RN, Goldberg BB, Lassau N, Leen EL, Mattrey RF, Moriyasu F, Solbiati L, Weskott HP, Xu HX. Guidelines and good clinical practice recommendations for Contrast Enhanced Ultrasound (CEUS) in the liver - update 2012: A WFUMB-EFSUMB initiative in cooperation with representatives of AFSUMB, AIUM, ASUM, FLAUS and ICUS. *Ultrasound Med Biol* 2013; **39**: 187-210 [PMID: 23137926]
- Hussaini SH, Sheridan MB, Davies M. The predictive value of transabdominal ultrasonography in the diagnosis of biliary tract complications after orthotopic liver transplantation. *Gut* 1999; **45**: 900-903 [PMID: 10562590 DOI: 10.1136/gut.45.6.900]
- Zoepf T, Maldonado-Lopez EJ, Hilgard P, Dechêne A, Malago M, Broelsch CE, Schlaak J, Gerken G. Diagnosis of biliary strictures after liver transplantation: which is the best tool? *World J Gastroenterol* 2005; **11**: 2945-2948 [PMID: 15902733]
- Girometti R, Molinari C, Del Pin M, Toniutto P, Bitetto D, Como G, Zuiani C, Bazzocchi M. Degree of bile-duct dilatation in liver-transplanted patients with biliary stricture: a magnetic resonance cholangiography-based study. *Radiol Med* 2012; **117**: 1097-1111 [PMID: 22438111 DOI: 10.1007/s11547-012-0805-1]
- Zemel G, Zajko AB, Skolnick ML, Bron KM, Campbell WL. The role of sonography and transhepatic cholangiography in the diagnosis of biliary complications after liver transplantation. *AJR Am J Roentgenol* 1988; **151**: 943-946 [PMID: 3051961 DOI: 10.2214/ajr.151.5.943]
- Katyal S, Oliver JH, Buck DG, Federle MP. Detection of vascular complications after liver transplantation: early experience in multislice CT angiography with volume rendering. *AJR Am J Roentgenol* 2000; **175**: 1735-1739 [PMID: 11090412 DOI: 10.2214/ajr.175.6.1751735]
- Singh AK, Nachiappan AC, Verma HA, Uppot RN, Blake MA, Saini S, Boland GW. Postoperative imaging in liver transplantation: what radiologists should know. *Radiographics* 2010; **30**: 339-351 [PMID: 20228321 DOI: 10.1148/rg.302095124]

- 21 **Fulcher AS**, Turner MA. Orthotopic liver transplantation: evaluation with MR cholangiography. *Radiology* 1999; **211**: 715-722 [PMID: 10352596]
- 22 **Desai M**, Neuberger J. Chronic liver allograft dysfunction. *Transplant Proc* 2009; **41**: 773-776 [PMID: 19328977 DOI: 10.1016/j.transproceed.2009.01.038]
- 23 **Chan JH**, Tsui EY, Yuen MK, Szeto ML, Luk SH, Wong KP, Wong NO. Gadopentetate dimeglumine as an oral negative gastrointestinal contrast agent for MRCP. *Abdom Imaging* 2000; **25**: 405-408 [PMID: 10926195]
- 24 **Chow DS**, Bahrami S, Raman SS, Rotchel S, Sayre JW, Bussittil RW, Lu DS. Risk of nephrogenic systemic fibrosis in liver transplantation patients. *AJR Am J Roentgenol* 2011; **197**: 658-662 [PMID: 21862808 DOI: 10.2214/AJR.10.5976]
- 25 **Nandalur KR**, Hussain HK, Weadock WJ, Wamsteker EJ, Johnson TD, Khan AS, D'Amico AR, Ford MK, Nandalur SR, Chenevert TL. Possible biliary disease: diagnostic performance of high-spatial-resolution isotropic 3D T2-weighted MRCP. *Radiology* 2008; **249**: 883-890 [PMID: 18941164 DOI: 10.1148/radiol.2493080389]
- 26 **Kinner S**, Dechène A, Ladd SC, Zöpf T, de Dechène EM, Gerken G, Lauenstein TC. Comparison of different MRCP techniques for the depiction of biliary complications after liver transplantation. *Eur Radiol* 2010; **20**: 1749-1756 [PMID: 20157816 DOI: 10.1007/s00330-010-1714-x]
- 27 **Kinner S**, Dechène A, Paul A, Umutlu L, Ladd SC, de Dechène EM, Zöpf T, Gerken G, Lauenstein TC. Detection of biliary stenoses in patients after liver transplantation: is there a different diagnostic accuracy of MRCP depending on the type of biliary anastomosis? *Eur J Radiol* 2011; **80**: e20-e28 [PMID: 20580506 DOI: 10.1016/j.ejrad.2010.06.003]
- 28 **Salvolini L**, Urbinati C, Valeri G, Ferrara C, Giovagnoni A. Contrast-enhanced MR cholangiography (MRCP) with Gd-EOB-DTPA in evaluating biliary complications after surgery. *Radiol Med* 2012; **117**: 354-368 [PMID: 22020424 DOI: 10.1007/s11547-011-0731-4]
- 29 **Ergen FB**, Akata D, Sarikaya B, Kerimoglu U, Hayran M, Akhan O, Hussain HK. Visualization of the biliary tract using gadobenate dimeglumine: preliminary findings. *J Comput Assist Tomogr* 2008; **32**: 54-60 [PMID: 18303288 DOI: 10.1097/RCT.0b013e3180616b87]
- 30 **Fayad LM**, Holland GA, Bergin D, Iqbal N, Parker L, Curcillo PG, Kowalski TE, Park P, Intenzo C, Mitchell DG. Functional magnetic resonance cholangiography (fMRC) of the gallbladder and biliary tree with contrast-enhanced magnetic resonance cholangiography. *J Magn Reson Imaging* 2003; **18**: 449-460 [PMID: 14508782 DOI: 10.1002/jmri.10369]
- 31 **Boraschi P**, Donati F. Biliary-enteric anastomoses: spectrum of findings on Gd-EOB-DTPA-enhanced MR cholangiography. *Abdom Imaging* 2013; **38**: 1351-1359 [PMID: 23820693 DOI: 10.1007/s00261-013-0007-7]
- 32 **Stelter L**, Grieser C, Fernández CM, Rothe JH, Streitparth F, Seehofer D, Hamm B, Denecke T. Flip angle modulations in late phase Gd-EOB-DTPA MRI improve the identification of the biliary system. *Eur J Radiol* 2012; **81**: e991-e995 [PMID: 22884706 DOI: 10.1016/j.ejrad.2012.07.015]
- 33 **Mangold S**, Bretschneider C, Fenchel M, Seeger A, Kramer U, Klumpp B, Nadalin S, Königsrainer A, Claussen CD, Miller S. MRI for evaluation of potential living liver donors: a new approach including contrast-enhanced magnetic resonance cholangiography. *Abdom Imaging* 2012; **37**: 244-251 [PMID: 21479607 DOI: 10.1007/s00261-011-9736-7]
- 34 **Lee MS**, Lee JY, Kim SH, Park HS, Kim SH, Lee JM, Han JK, Choi BI. Gadoteric acid disodium-enhanced magnetic resonance imaging for biliary and vascular evaluations in preoperative living liver donors: comparison with gadobenate dimeglumine-enhanced MRI. *J Magn Reson Imaging* 2011; **33**: 149-159 [PMID: 21182133 DOI: 10.1002/jmri.22429]
- 35 **Kantarci M**, Pirimoglu B, Karabulut N, Bayraktutan U, Ogul H, Ozturk G, Aydinli B, Kizrak Y, Eren S, Yilmaz S. Non-invasive detection of biliary leaks using Gd-EOB-DTPA-enhanced MR cholangiography: comparison with T2-weighted MR cholangiography. *Eur Radiol* 2013; **23**: 2713-2722 [PMID: 23695221 DOI: 10.1007/s00330-013-2880-4]
- 36 **Ito K**, Siegelman ES, Stolpen AH, Mitchell DG. MR imaging of complications after liver transplantation. *AJR Am J Roentgenol* 2000; **175**: 1145-1149 [PMID: 11000180 DOI: 10.2214/ajr.175.4.1751145]
- 37 **Campbell WL**, Foster RG, Miller WJ, Lecky JW, Zajko AB, Lee KY. Changes in extrahepatic bile duct caliber in liver transplant recipients without evidence of biliary obstruction. *AJR Am J Roentgenol* 1992; **158**: 997-1000 [PMID: 1566706 DOI: 10.2214/ajr.158.5.1566706]
- 38 **Holt AP**, Thorburn D, Mirza D, Gunson B, Wong T, Haydon G. A prospective study of standardized nonsurgical therapy in the management of biliary anastomotic strictures complicating liver transplantation. *Transplantation* 2007; **84**: 857-863 [PMID: 17984838]
- 39 **Pavone P**, Laghi A, Catalano C, Broglia L, Panebianco V, Messina A, Salvatori FM, Passariello R. MR cholangiography in the examination of patients with biliary-enteric anastomoses. *AJR Am J Roentgenol* 1997; **169**: 807-811 [PMID: 9275901 DOI: 10.2214/ajr.169.3.9275901]
- 40 **Tang Y**, Yamashita Y, Arakawa A, Namimoto T, Mitsuzaki K, Abe Y, Katahira K, Takahashi M. Pancreaticobiliary ductal system: value of half-Fourier rapid acquisition with relaxation enhancement MR cholangiopancreatography for postoperative evaluation. *Radiology* 2000; **215**: 81-88 [PMID: 10751471 DOI: 10.1148/radiology.215.1.r00ap0281]
- 41 **Pecchi A**, De Santis M, Gibertini MC, Tarantino G, Gerunda GE, Torricelli P, Di Benedetto F. Role of magnetic resonance imaging in the detection of anastomotic biliary strictures after liver transplantation. *Transplant Proc* 2011; **43**: 1132-1135 [PMID: 21620070 DOI: 10.1016/j.transproceed.2011.03.016]
- 42 **Buis CI**, Verdonk RC, Van der Jagt EJ, van der Hilst CS, Slooff MJ, Haagsma EB, Porte RJ. Nonanastomotic biliary strictures after liver transplantation, part 1: Radiological features and risk factors for early vs. late presentation. *Liver Transpl* 2007; **13**: 708-718 [PMID: 17457932 DOI: 10.1002/lt.21166]
- 43 **Boraschi P**, Braccini G, Gigoni R, Sartoni G, Neri E, Filipponi F, Mosca F, Bartolozzi C. Detection of biliary complications after orthotopic liver transplantation with MR cholangiography. *Magn Reson Imaging* 2001; **19**: 1097-1105 [PMID: 11711234]
- 44 **Shaikh F**, Elazzazi M, Ryan A, Semelka RC. Debris-filled biliary system: a difficult diagnosis on MRI and MRCP. *Clin Imaging* 2012; **36**: 153-155 [PMID: 22370138 DOI: 10.1016/j.clinimag.2011.08.009]
- 45 **Gor NV**, Levy RM, Ahn J, Kogan D, Dodson SF, Cohen SM. Biliary cast syndrome following liver transplantation: Predictive factors and clinical outcomes. *Liver Transpl* 2008; **14**: 1466-1472 [PMID: 18825683 DOI: 10.1002/lt.21492]
- 46 **Kim YK**, Kim CS, Lee JM, Ko SW, Chung GH, Lee SO, Han YM, Lee SY. Value of adding T1-weighted image to MR cholangiopancreatography for detecting intrahepatic biliary stones. *AJR Am J Roentgenol* 2006; **187**: W267-W274 [PMID: 16928904 DOI: 10.2214/AJR.05.0266]
- 47 **Romagnuolo J**, Bardou M, Rahme E, Joseph L, Reinhold C, Barkun AN. Magnetic resonance cholangiopancreatography: a meta-analysis of test performance in suspected biliary disease. *Ann Intern Med* 2003; **139**: 547-557 [PMID: 14530225]
- 48 **Boraschi P**, Donati F, Gigoni R, Salemi S, Urbani L, Filipponi F, Falaschi F, Bartolozzi C. Complications after liver transplantation: evaluation with magnetic resonance imaging, magnetic resonance cholangiography, and 3-dimensional contrast-enhanced magnetic resonance angiography in a single session. *Can Assoc Radiol J* 2008; **59**: 259-263 [PMID: 19385153]
- 49 **Laghi A**, Pavone P, Catalano C, Rossi M, Panebianco V, Alfani D, Passariello R. MR cholangiography of late biliary

- complications after liver transplantation. *AJR Am J Roentgenol* 1999; **172**: 1541-1546 [PMID: 10350286 DOI: 10.2214/ajr.172.6.10350286]
- 50 **Cereser L**, Girometti R, Como G, Molinari C, Toniutto P, Bitetto D, Zuiani C, Bazzocchi M. Impact of magnetic resonance cholangiography in managing liver-transplanted patients: preliminary results of a clinical decision-making study. *Radiol Med* 2011; **116**: 1250-1266 [PMID: 21744253 DOI: 10.1007/s11547-011-0707-4]
- 51 **Kitazono MT**, Qayyum A, Yeh BM, Chard PS, Ostroff JW, Coakley FV. Magnetic resonance cholangiography of biliary strictures after liver transplantation: a prospective double-blind study. *J Magn Reson Imaging* 2007; **25**: 1168-1173 [PMID: 17520726 DOI: 10.1002/jmri.20927]
- 52 **Meersschaut V**, Mortelé KJ, Troisi R, Van Vlierberghe H, De Vos M, Defreyne L, de Hemptinne B, Kunnen M. Value of MR cholangiography in the evaluation of postoperative biliary complications following orthotopic liver transplantation. *Eur Radiol* 2000; **10**: 1576-1581 [PMID: 11044927]
- 53 **Beltrán MM**, Marugán RB, Oton E, Blesa C, Nuño J. Accuracy of magnetic resonance cholangiography in the evaluation of late biliary complications after orthotopic liver transplantation. *Transplant Proc* 2005; **37**: 3924-3925 [PMID: 16386586 DOI: 10.1016/j.transproceed.2005.10.044]
- 54 **Katz LH**, Benjaminov O, Belinki A, Geler A, Braun M, Knizhnik M, Aizner S, Shaharabani E, Sulkes J, Shabtai E, Pappo O, Atar E, Tur-Kaspa R, Mor E, Ben-Ari Z. Magnetic resonance cholangiopancreatography for the accurate diagnosis of biliary complications after liver transplantation: comparison with endoscopic retrograde cholangiography and percutaneous transhepatic cholangiography - long-term follow-up. *Clin Transplant* 2010; **24**: E163-E169 [PMID: 21039885 DOI: 10.1111/j.1399-0012.2010.01300.x]
- 55 **Xu YB**, Min ZG, Jiang HX, Qin SY, Hu BL. Diagnostic value of magnetic resonance cholangiopancreatography for biliary complications in orthotopic liver transplantation: a meta-analysis. *Transplant Proc* 2013; **45**: 2341-2346 [PMID: 23953547 DOI: 10.1016/j.transproceed.2013.03.031]

P- Reviewer: Dirchwolf M, Maurea S, Radmard AR
S- Editor: Song XX **L- Editor:** A **E- Editor:** Lu YJ



Gastrointestinal imaging-practical magnetic resonance imaging approach

Baodong Liu, Miguel Ramalho, Mamdoh AIObaidy, Kiran K Busireddy, Ersan Altun, Janaka Kalubowila, Richard C Semelka

Baodong Liu, Miguel Ramalho, Mamdoh AIObaidy, Kiran K Busireddy, Ersan Altun, Janaka Kalubowila, Richard C Semelka, Department of Radiology, University of North Carolina at Chapel Hill, North Carolina, NC 27599-7510, United States
Author contributions: Liu B, Ramalho M, AIObaidy M, Busireddy KK, Altun E, Kalubowila J and Semelka RC equally contributed to this work; including literature review, manuscript writing, manuscript editing, figures collection and writing figures captions.

Correspondence to: Richard C Semelka, MD, Department of Radiology, University of North Carolina at Chapel Hill, 2001 Old Clinic Bldg., CB 7510, Chapel Hill, North Carolina, NC 27599-7510, United States. richsem@med.unc.edu

Telephone: +1-919-9669676 Fax: +1-919-8437147

Received: February 11, 2014 Revised: April 15, 2014

Accepted: May 31, 2014

Published online: March 28, 2015

Abstract

Over the past two decades, advances in cross-sectional imaging such as computed tomography and magnetic resonance imaging (MRI) have dramatically changed the concept of gastrointestinal imaging. MR is playing an increasing role in the evaluation of gastrointestinal disorders. MRI combines the advantages of excellent soft-tissue contrast, noninvasiveness, functional information and lack of ionizing radiation. Furthermore, recent developments of MRI have led to improved spatial and temporal resolution as well as decreased motion artifacts. In this article we describe the technical aspects of gastrointestinal MRI and present a practical approach for a well-known spectrum of gastrointestinal disease processes.

© 2015 Baishideng Publishing Group Inc. All rights reserved.

Key words: Magnetic resonance imaging; Crohn's disease; Celiac disease; Appendicitis; Diverticulitis; Rectal cancer; Gastric tumors; Small bowel tumors

Core tip: The implementation of fast and ultra-fast sequences and dedicated advanced imaging protocols render magnetic resonance imaging (MRI) an excellent tool for gastrointestinal (GI) imaging. State of the art MRI/magnetic resonance enterography has rapidly emerged as successful gastrointestinal imaging modality, offering detailed anatomic and morphologic information and also permitting evaluation of extra-luminal manifestation and extension of disease. The lack of ionizing radiation makes MRI the preferred modality in many GI disease processes. In this article we describe the technical aspects of gastrointestinal MRI and present a practical approach for a well-known spectrum of gastrointestinal disease processes.

Original sources: Liu B, Ramalho M, AIObaidy M, Busireddy KK, Altun E, Kalubowila J, Semelka RC. Gastrointestinal imaging-practical magnetic resonance imaging approach. *World J Radiol* 2014; 6(8): 544-566 Available from: URL: <http://www.wjgnet.com/1949-8470/full/v6/i8/544.htm> DOI: <http://dx.doi.org/10.4329/wjr.v6.i8.544>

INTRODUCTION

Medical imaging of the gastrointestinal (GI) tract is crucial for the diagnosis of GI diseases. Historically, barium techniques have been the only available method. Although many diagnoses have been made on the basis of these exams, the diagnostic performance of these exams for certain abnormalities has been disappointing^[1].

Over the past two decades, advances in cross-sectional imaging such as computed tomography (CT) and magnetic resonance imaging (MRI) have dramatically changed the concept of GI imaging. Recently, developments in endoscopic techniques, especially the advent of capsule

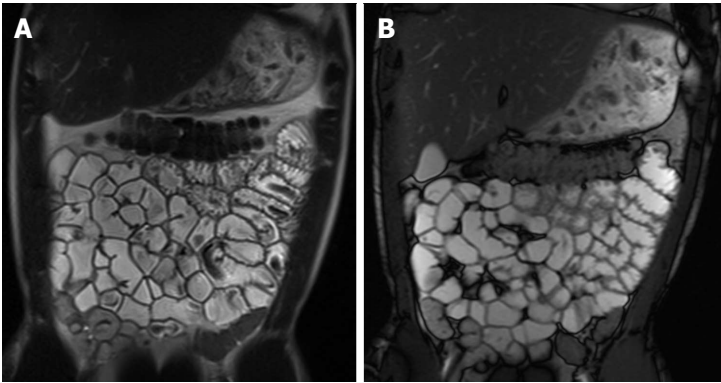


Figure 1 Coronal T2-weighted single shot fast spin echo and coronal balanced steady state free precession images. Good bowel distension is achieved with the administration of peroral fluid (A and B). Balanced steady state free precession sequence (B) is robust to flow voids; in addition to its ability to demonstrate fine anatomical details including bowel thickness, mesenteric vessels and lymph nodes; even without the use of spasmolytic agents.

endoscopy (CE) have made it possible to provide direct mucosal visualization of the GI tract. However, CE also has such limitations in disease localization, and is contraindicated in patients with suspected of bowel stricture or obstruction^[1,2].

MR and CT techniques optimized for small bowel imaging are playing an increasing role in the evaluation of gastrointestinal disorders. Several studies have shown the advantage of these techniques over traditional barium fluoroscopic examinations. Cross-sectional techniques have several advantages, including their ability to display the entire thickness of the gastric and bowel wall, visualize the deep pelvis ileal loops without superimposition, and evaluate the mesentery and perienteric fat. Another intrinsic advantage is the possibility to assess solid organs and provide a global overview of the abdominopelvic cavity.

The preference of MR over CT is mainly based on available resources and public policies. However, similar to fluoroscopic procedures, CT is associated with patients' radiation exposure. With the increasing awareness of radiation exposure, there has been a more global interest in implementing techniques that either reduce or eliminate radiation exposure^[3]. This may be of particular importance in radiosensitive patient population with chronic inflammatory bowel disease; who may require multiple studies over a lifetime^[4]. As a result, MRI has become increasingly important as a method of evaluating various gastrointestinal disease processes^[5].

MRI combines the advantages of excellent soft-tissue contrast, noninvasiveness, functional information and lack of ionizing radiation. Furthermore, recent developments of MRI have led to improved spatial and temporal resolution as well as decreased motion artifacts^[6]. In this article we describe technical aspects of gastrointestinal MRI and present a practical approach for a well-known spectrum of gastrointestinal disease processes.

PRACTICAL ASPECTS OF GASTROINTESTINAL MRI TECHNIQUE

Similar to other imaging techniques, adequate luminal

distension is desirable since poorly distended loops can simulate^[7] or hide pathologic processes; especially in less experienced hands. Two different techniques to provide sufficient luminal distension of the small bowel have been proposed: MR enteroclysis and MR enterography. MR enteroclysis is associated with excellent image quality because of superb bowel distension achieved by fluid administration after nasojejunal intubation. However, the placement of the catheter is unpleasant and stressful for the patient. The improved distention achieved with enteroclysis does not necessarily translate into an improvement in diagnostic effectiveness^[8,9] and peroral fluid administration results in effective and most often satisfactory means of achieving small bowel distention. One advantage of MR enteroclysis may reside in the detection of mesenteric small bowel tumors^[10,11].

Three groups of contrast agents can be utilized to achieve distension and are classified as positive (bright lumen), negative (dark lumen), or biphasic contrast agents. Biphasic contrast agents (water-based) are usually preferred because they are easy to implement and provide excellent signal characteristics, resulting in bright lumen on T2-weighted and dark lumen on T1-weighted sequences. Tap water is frequently used as a biphasic contrast agent, especially when imaging the upper gastrointestinal segment (stomach, duodenum and proximal jejunum); however, it is rapidly reabsorbed in the small intestine, leading to a poor distension of the distal jejunum and ileum. In order to slow intestinal absorption of water, higher-osmolality and viscosity agents are routinely added^[12-14]. After a 4 to 6-h fast, patients are asked to drink between 1000 mL and 1500 mL of intraluminal contrast (Figure 1); 45 to 55 min prior to examination. Metoclopramide (20 mg) may be added directly to the oral contrast to promote gastric emptying. Adverse effects are rare, usually mild and transitory, and experienced mainly after the termination of the MR examination^[15].

Some patients cannot tolerate the ingestion of high volumes of oral contrast; in our experience, we found that luminal distension is not as critical as on CT and the MR examination can still be performed even if only a

small volume has been ingested.

Patients undergoing magnetic resonance enterography (MRE) should be examined in prone position. This position may facilitate separation of small bowel loops while decreasing the volume of peritoneal cavity to be imaged, and, as a result, the number of coronal sections to be acquired^[16]. Hence, acquisition times and consequently the time span for breath holding can be decreased. However, many patients may not tolerate lying prone in the MR scanner, and therefore supine position is almost always adequate.

Gastrointestinal MR evaluation is based on the ultra-fast imaging generally applied for body MRI. Body MRI is still based on T1-weighted and T2-weighted sequences plus or minus fat-suppression and postgadolinium T1-weighted sequences. A combination of single-shot fast/turbo spin-echo T2-weighted and gradient recalled echo (GRE) T1-weighted sequences with intravenous gadolinium enhancement and fat-suppression result in consistent image quality of the gastrointestinal tract. Two- or three-dimensional balanced steady-state free precession (bSSFP) sequences are additionally collected as part of the MRE protocol.

Single-Shot turbo spin echo (TSE)/FSE T2-weighted sequences are very robust to motion and usually acquired with and without fat-saturation. These sequences have high sensitivity for fluid and are crucial to depict edema in or adjacent to the bowel wall. This is especially important in Crohn's disease (CD), which can be regarded as a marker for active inflammation. Single-shot sequences are susceptible to flow artifacts, and thus intraluminal flow voids can be seen (Figure 1).

Because bSSFP sequences are relatively robust with regard to motion artifacts and intraluminal flow voids, these sequences are performed in the beginning of the study prior to glucagon or intravenous contrast administration. These sequences can be performed quickly and are complementary to single-shot TSE/FSE sequences and the preferred pulse sequence to evaluate the mesentery. The ratio of T1/T2 contrast provides images that appear primarily T2-weighted, with very high signal for all types of fluid. This feature allows good evaluation of the bowel wall, particularly in the definition of edema and of bowel wall layering appearance. Cine-analysis can also be performed with this technique allowing supplementary functional information. We generally acquire 15-25 frames per section location during free breathing. These images may then be displayed as a cine loop to assess bowel motility to exclude or confirm fixed stenoses, segmental dilatation, and detect adhesions.

T1-weighted GRE MRI represents the core of the body MR protocol. Since these sequences are quite prone to bowel motion artifacts, spasmolytic agents (*e.g.*, Glucagon[®] or Buscopan[®]) should be administered intravenously immediately before image acquisition. Buscopan[®] is less expensive; however, it is not Food and Drug Administration approved and therefore not available in the United States. These sequences are performed as either 2D or 3D techniques, and on newer MR sys-

tems, the most commonly used is the 3D-GRE with fat-suppression. Post-contrast coronal and axial images are also acquired. Our protocol includes an arterial and interstitial phase in the coronal plane and an enteric (early hepatic-venous) phase (circa 50 s) in the axial plane. Gadolinium-enhanced T1-weighted images are helpful to detect both intestinal tumors and inflammatory bowel diseases with high sensitivity^[17].

Diffusion-weighted imaging (DWI) has been increasingly used for body MRI. Initial studies underline a possible value of DWI also for small bowel imaging, aiding in the assessment of disease activity^[18,19]. A set of coronal diffusion-weighted images ($b = 0-50 \text{ s/mm}^2$; $b = 600-800 \text{ s/mm}^2$) may be added to the protocol, depending on the indication of the examination and preference of the radiologist. This is especially important in pregnant patients those with contraindications to gadolinium administration (Figure 2).

PRACTICAL APPROACH TO INFLAMMATORY CONDITIONS-SMALL BOWEL

CD

CD is a chronic relapsing inflammatory disease of the gastrointestinal tract involving all layers of the bowel wall and may be classified as active inflammatory (without fistulas or strictures), penetrating, or fibrostenotic disease^[20]. Although any segment of the gastrointestinal tract may be involved with CD, it most commonly involves the terminal ileum, and frequently in association with disease in the right colon.

Endoscopy and histologic examination have served as the standard approach for the diagnosis of CD; however, diagnosing lesions in the small bowel between the distal duodenum and mid ileum has been a challenge. Furthermore, the major disadvantage of endoscopic methods endoscopic tests and biopsies will evaluate the mucosa but do not evaluate inflammation or fibrosis within the submucosa or deeper tissues. Currently, CT enterography and MRE are the only two imaging modalities that enable the visualization of submucosal tissues throughout the entire small bowel; however, as stated above, MRE does not expose patients to ionizing radiation and it provides additional technical and diagnostic advantages^[21].

The following important questions can be addressed on MRE: (1) extent of small and large bowel involvement; (2) distinction between active inflammatory and fibrotic stricturing disease; (3) recognition of penetrating disease \pm extramural complications; (4) evaluation of response to medical therapy; and (5) detection of recurrent disease following surgery.

A relatively simple and accurate approach for evaluation of CD activity is based on the association of T2-weighted and post-gadolinium T1-weighted sequences. This combination allows comprehensive evaluation and discrimination between quiescent disease and active inflammation and for evaluation of complications includ-

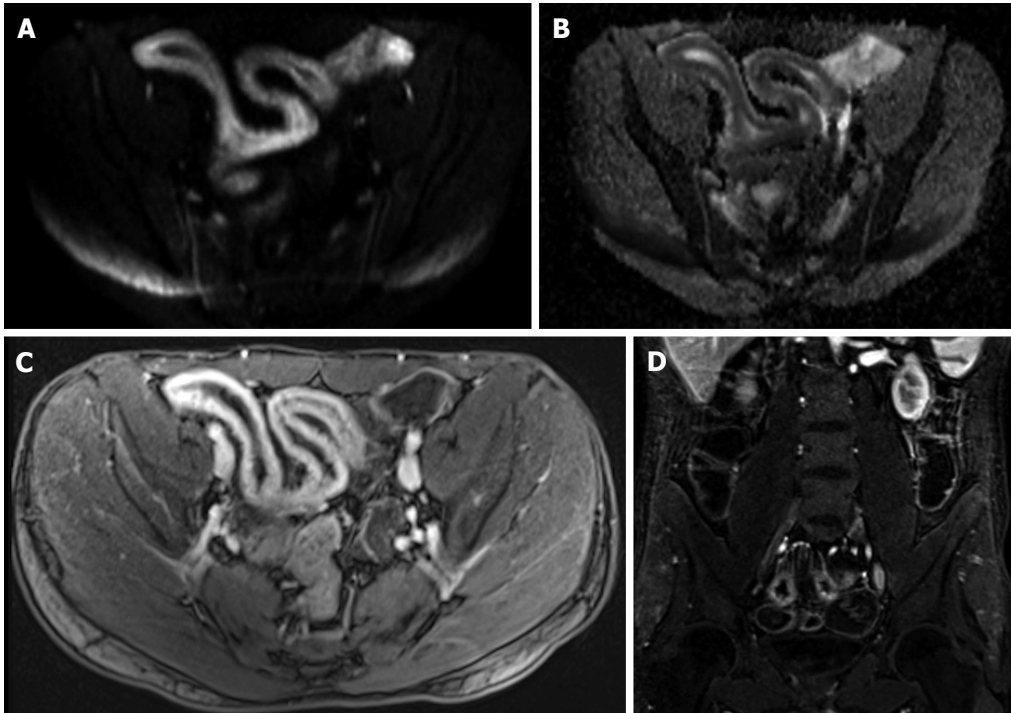


Figure 2 Active distal ileal Crohn's disease. Axial diffusion weighted imaging (A) ($b = 150$) and (B) apparent diffusion coefficient map as well as (C) axial and (D) coronal fat-suppressed post-gadolinium 3D-GRE T1-weighted images. There is a long segment of distal ileal diffuse thickening associated with diffusion restriction (A and B) as well as significant contrast enhancement (C) and vasa recta engorgement (comb sign) (D) in keeping with active Crohn's disease. GRE: Gradient recalled echo.

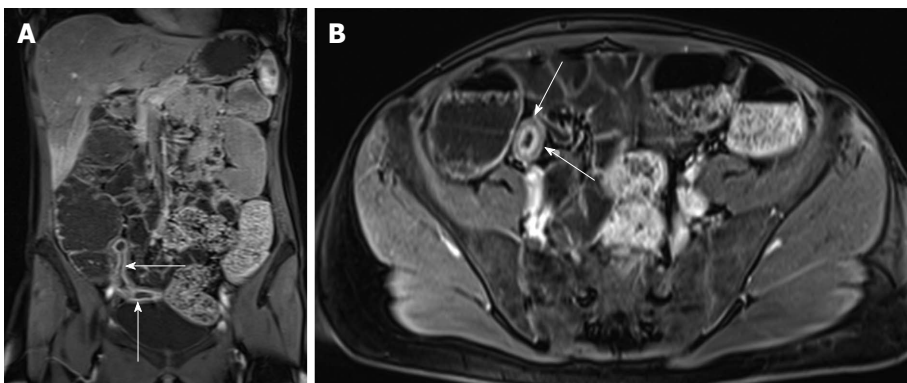


Figure 3 Enhancement of bowel wall layers in active Crohn's disease. Coronal (A) and (B) axial fat-suppressed post-gadolinium 3D-GRE T1-weighted images during the (A) arterial and (B) enteric phase in a patient with active Crohn's disease. There is extensive mucosal enhancement involving the affected terminal ileum (arrows, A), reflecting active disease. Enteric phase images (B) shows serosal enhancement providing the tri-laminar appearance of active disease (arrows, B). GRE: Gradient recalled echo.

ing abscesses or fistulas^[21,22].

Findings perceived on post-gadolinium T1-weighted images

Increased mucosal enhancement has long been one of the most important findings and is the most sensitive finding of disease activity, which may approach 100% sensitivity^[23-27]. Imaging findings of mucosal enhancement; bowel wall edematous thickening (> 3 mm); and enhancement of different bowel layers, termed “mural stratification”, are classic features of active small bowel disease^[28,29] (Figure 3). Quantitative bowel enhancement parameters were found to correlate highly with histologic and endoscopic disease severity^[30].

Other findings include stranding extending into the mesenteric border fat and engorgement of the hyperemic vasa recta surrounding the inflamed bowel segment (comb sign) and reactively enlarged and hyper-enhancing mesenteric lymph nodes.

Perceived on T2-weighted images

Bowel wall thickening with increased T2-signal within or adjacent to the abnormal bowel on fat-suppressed images indicates active inflammation^[31]. Other signs include fluid accumulation in adjacent intraperitoneal and mesenteric spaces (Figure 4).

Fibrofatty proliferation or creeping of the mesenteric fat along the mesentery and onto the involved bowel seg-

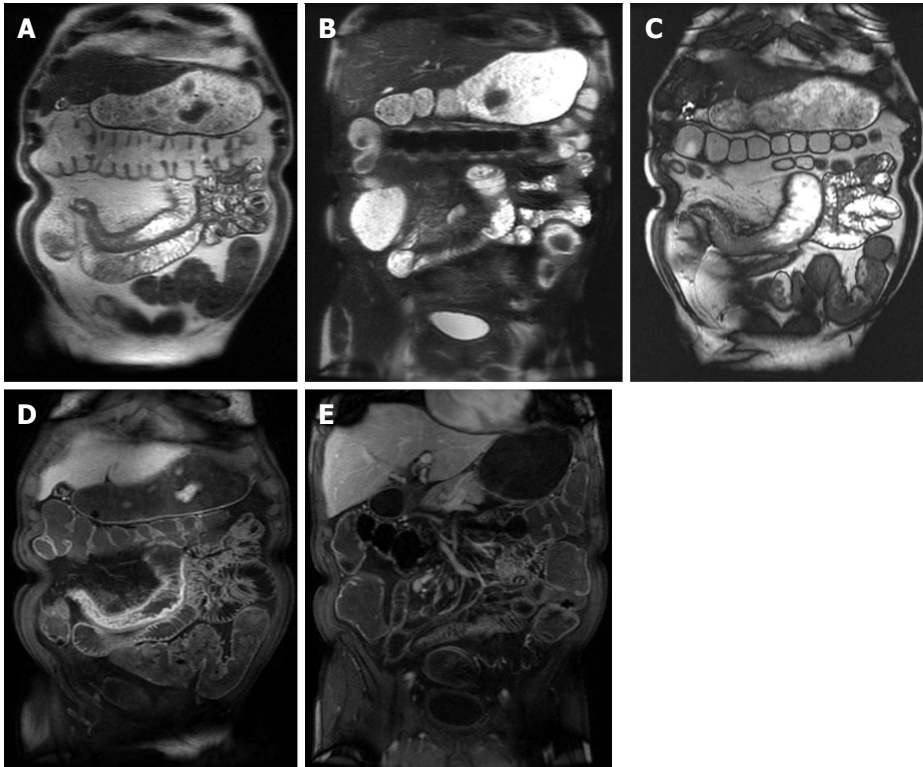


Figure 4 Active Crohn's disease. A and B: Coronal T2-weighted single shot fast spin echo without and with fat suppression and © coronal balanced steady state free precession image as well as coronal fat-suppressed post-gadolinium 3D-GRE T1-weighted images during the (D) arterial and E: interstitial phases. There is abnormal bowel wall thickening and edema involving distal ileal segments, associated with small fluid collection in the adjacent mesentery (A and B), engorgement of the mesenteric vessels (comb sign) (C-E), and extensive mucosal enhancement (D and E), in addition to the presence of enhancing mesenteric lymph nodes, in keeping with active Crohn's disease.

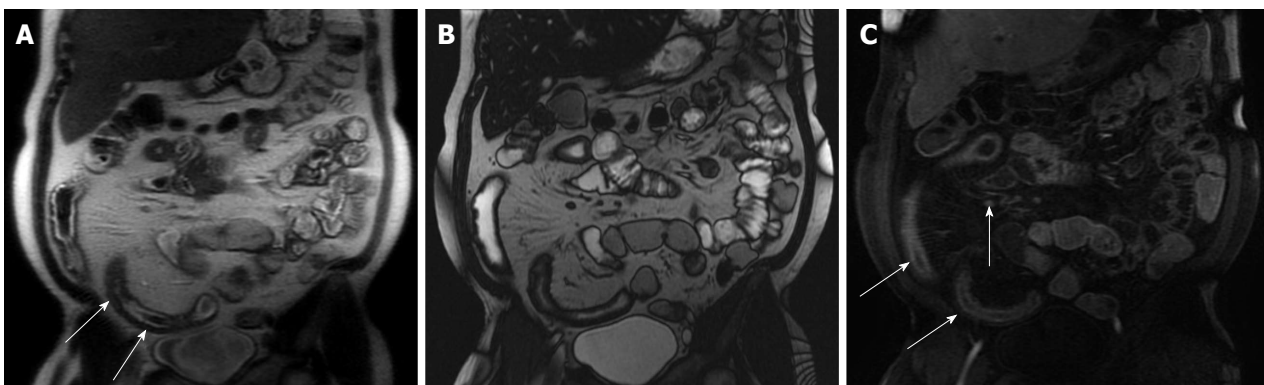


Figure 5 Active Crohn's disease. A: Coronal T2-weighted single shot fast spin echo and (B) coronal balanced steady state free precession (bSSFP) images as well as (C) coronal fat-suppressed post-gadolinium 3D-GRE T1-weighted images during the interstitial phase. There is an abnormal segment of distal ileal thickening with diffuse submucosal increased T2 signal intensity (arrows, A) displaying high signal intensity, consistent with edema. The bSSFP image (B) doesn't demonstrate submucosal edema, but clearly depicts mesenteric lymph nodes and comb sign, associated with extensive mucosal enhancement (arrows, C), reflecting disease activity. Fibrofatty proliferation around the affected ileal segments is also seen. GRE: Gradient recalled echo.

ment (Figure 5) suggests a chronically inflamed bowel loop, a sign mostly seen in chronic disease. However, when it is associated with engorged perpendicular distal mesenteric vessels (comb sign), it is considered surgically pathognomonic for the disease and highly specific for active CD^[32]. Comb sign is usually well depicted on bSSFP sequences (Figure 5).

Practical interpretive approach to a thickened bowel wall segment

Active inflammation: Bowel wall thickening and en-

hancement on post-gadolinium T1-weighted images, plus high signal intensity on T2-weighted fat-suppressed images^[21] (Figures 4 and 5).

Chronic disease without active inflammation: Bowel wall thickening and reduced and homogeneous enhancement on post-gadolinium T1-weighted images without a layering enhancement; plus low T2-signal intensity on fat-suppressed images with possible stenosis with obstruction and occasionally sacculations or dilated amorphous bowel loops. In the fibrostenotic disease subtype, MRE

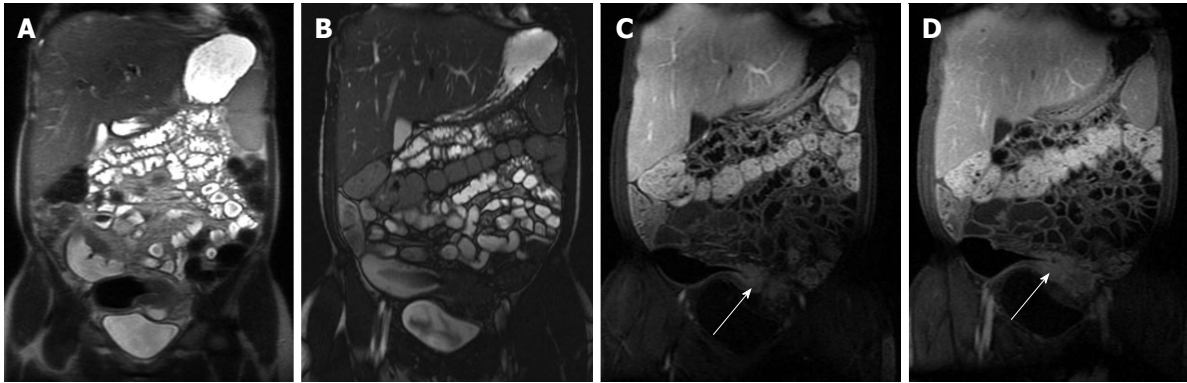


Figure 6 Chronic Crohn's disease. A: Coronal T2-weighted single shot fast spin echo and (B) coronal balanced steady state free precession (bSSFP), images as well as coronal fat-suppressed post-gadolinium 3D-GRE T1-weighted images during the (C) arterial and (D) interstitial phases. There is an intermediately low T2 signal intensity bowel wall thickening involving the distal ileum (A), also well-appreciated on bSSFP image (B), showing negligible enhancement on post-gadolinium images (arrows, C and D), consistent with chronic fibrotic segment without superimposed inflammation. A pre-stenotic dilatation is observed. GRE: Gradient recalled echo.

demonstrates a fixed narrowing of the involved bowel with associated wall thickening and marked pre-stenotic dilatation^[21]. On MRE cine imaging, fibrotic strictures appear as aperistaltic bowel segment that often demonstrate fixed mural thickening and luminal narrowing; these sequences help to differentiate a fibrotic stricture from small bowel obstruction secondary to spasm associated with active inflammatory disease^[33] (Figure 6).

Chronic disease with active inflammation: These features can overlap with active inflammation and sometimes only distinguished upon further short-term follow-up post-trial medical treatment. Acute on chronic involvement is suggested by marked enhancement of the mucosa with substantial low T2 signal intensity and minimal enhancement of the outer layer; therefore, appreciation of these findings may have a role in the evaluation of acute exacerbations of CD. The presence of sub-mucosal intramural fat deposition, which is also related to prior or ongoing chronic inflammation, can be accurately identified when combining features from steady state free precession as well as T2-weighted images with and without fat-suppression (Figure 7).

Complications of CD

Complications of CD are also well shown in MRE and include: fistulas, phlegmons, abscesses and bowel obstruction. Fistulas and sinus tracts are demonstrated by the high signal intensity of their fluid content on steady-state free-precession and single-shot fast/turbo spin echo T2-weighted images, and enhancement of the linear tract on the post gadolinium T1-weighted sequences. Enter-enteric (Figure 8) and entero-colic fistulas are not uncommon. Fistulous communication with adjacent pelvic organs can also be seen. They should be suspected when crowded retracted and angulated small bowel loops are appreciated; known as star sign. Deep fissuring ulcers are occasionally appreciated, and better see on bSSFP images. Extra-enteric collections and abscesses (Figures 9 and 10) can be recognized by their fluid content and increased wall enhancement on post-gadolinium images. The ir-

regular morphology of an abscess cavity and appreciation of its rounded configuration on multiple planes allows distinction from tubular-shaped bowel.

Identifying active inflammation is rarely an interpretive problem in MRE. However, active inflammation can mask underlying fibrosis related to chronic disease of the bowel wall. In the setting of active inflammation, short-term MRE follow-up may be implemented to confirm improvements of active inflammation and to then evaluate the presence of unmasked chronic fibrotic disease^[21]. It is important to identify fibrotic strictures because these are unresponsive to medical therapy and oftentimes require surgical intervention.

Assessment of inflammatory activity of CD is important to identify patients with active inflammation so that appropriate medical therapy may be prescribed. Given the advent of new medications some with serious side effects such as tumor necrosis factors alpha inhibitors, objective measures of activity are needed to justify their use and judge their effectiveness. Currently, there is no gold standard for determination of CD activity. Various authors have proposed MRE-based scoring systems for the assessment of inflammatory activity that includes features such as bowel wall thickening, lumen narrowing and the number of peri-intestinal lymph nodes^[34-37]. However, these evaluation algorithms are relatively demanding, which may ultimately limit clinical utilization. Quantitative bowel enhancement parameters were found to correlate highly with histologic and endoscopic disease severity^[30,38]. Although the perfusion analysis seems to be an accurate tool and correlates well with clinical parameters, it is relatively time consuming and requires special software and image post-processing. A recent study by Taylor *et al*^[30] outlines another difficulty regarding perfusion analyses of the bowel wall. The use of DWI may also help in assessing disease severity and is thought to be a promising tool, especially if the use of a contrast agent is contraindicated^[39].

For clinical follow-up of patients with CD, MRE is the preferred examination of choice due to lack of ionizing radiation and allowance of more frequent monitoring, which is important given the costs and side effects asso-

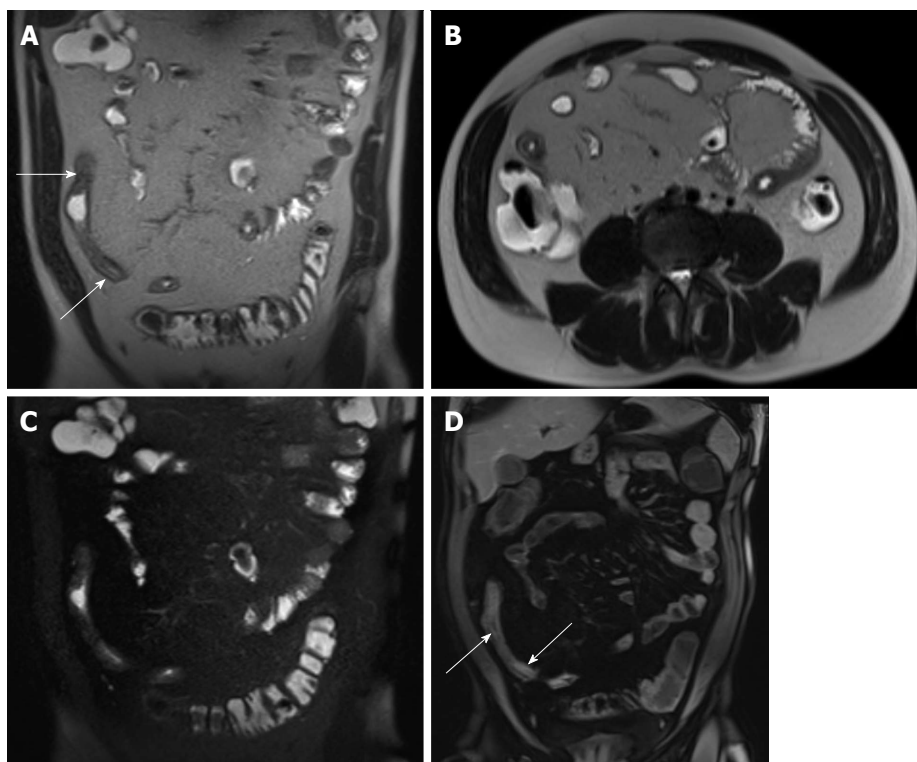


Figure 7 Acute on chronic Crohn's disease. A: Coronal and (B) axial T2-weighted single shot fast spin echo (SSFSE) as well as (C) coronal fat-suppressed T2-weighted SSFSE and (D) coronal fat-suppressed interstitial post-gadolinium 3D-GRE T1-weighted images during the interstitial phase. There is distal small bowel segment which demonstrates diffuse thickening and luminal narrowing (arrows, A), associated with submucosal high signal intensity on T2-weighted images (A and B) and with low-signal intensity on the fat-suppressed T2-weighted images (C), related to submucosal fat deposition, in keeping with chronic Crohn's disease. There is also a superimposed increased mucosal enhancement in affected bowel segments (arrows, D) and comb sign post-gadolinium images (D), reflecting disease activity, in keeping with acute on top of chronic disease. GRE: Gradient recalled echo.

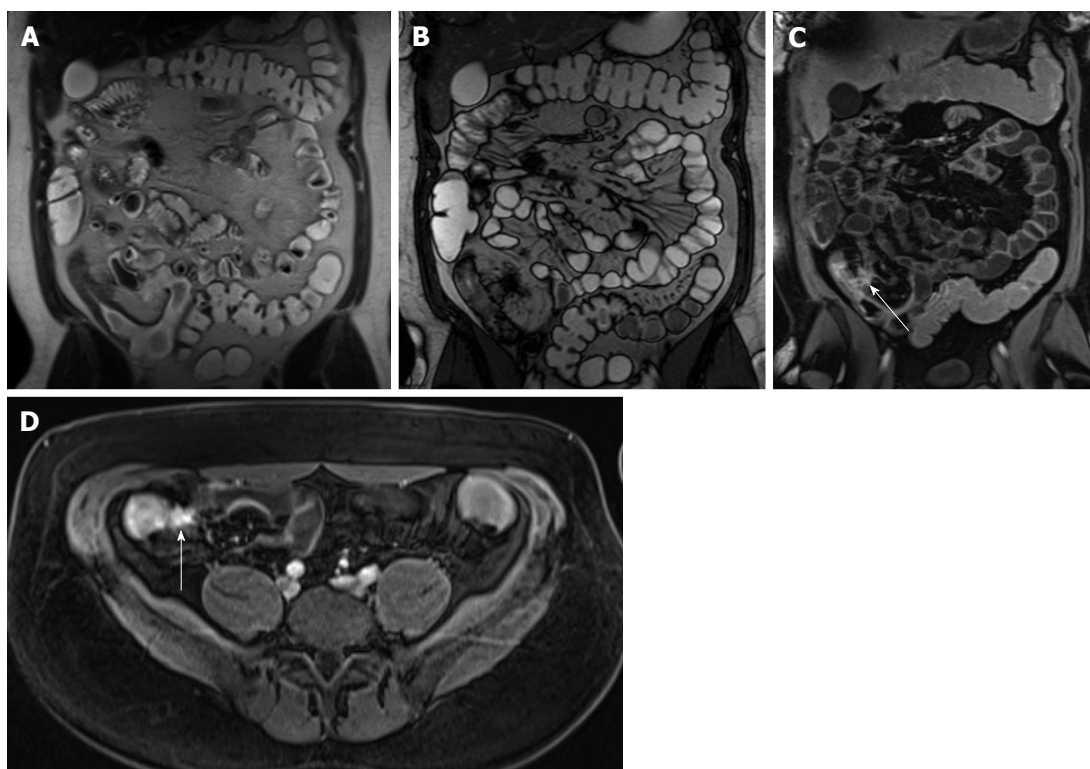


Figure 8 Enteroenteric fistula in active Crohn's disease. A: Coronal T2-weighted single shot fast spin echo and (B) coronal balanced steady state free precession images as well as (C) axial and (D) coronal fat-suppressed post-gadolinium 3D-GRE T1-weighted images during the (C) enteric and (D) interstitial phases. There is short-segment terminal ileal wall thickening (A and B), which shows extensive mucosal enhancement (C and D). There is also a linear tract extending from the involved segment to an adjacent ileal loop, showing increased enhancement, consistent with enteroenteric fistula (arrows, C and D). GRE: Gradient recalled echo.

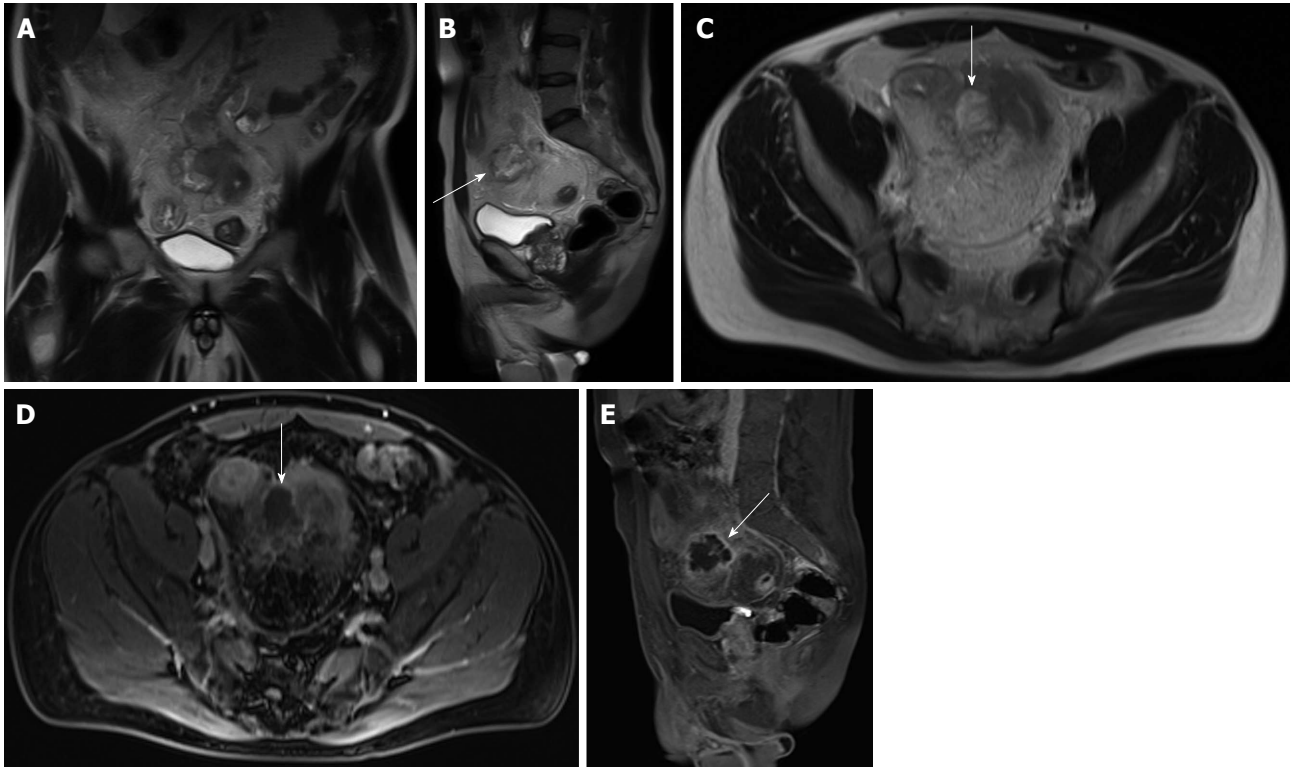


Figure 9 Abscess formation complicating active Crohn's disease. A: Coronal; B: Sagittal; C: Axial T2-weighted TSE images; D: Axial; E: Sagittal fat-suppressed post-gadolinium 3D-GRE T1-weighted images during the interstitial phase. Here is evidence of thickened small bowel loop segment and interloop mesenteric high T2 signal fluid collection (A, arrows, B and C) is noted, associated with rim enhancement (arrows, D and E) in keeping with mesenteric abscess formation complicating active Crohn's disease. GRE: Gradient recalled echo.

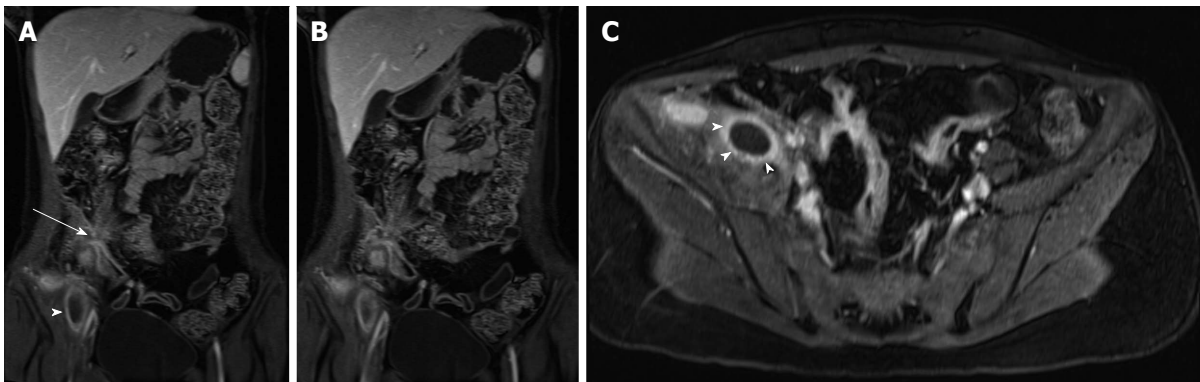


Figure 10 Active distal ileal Crohn's disease with complex fistulization and iliopsoas abscess formation. A and B: Coronal; C: Axial fat-suppressed post-gadolinium 3D-GRE T1-weighted images. There is evidence of terminal ileal thickening and enhancement in keeping with active Crohn's disease, associated with complex ileoileal and ileosigmoidal fistula formation (star sign, arrow, A and B) as well as iliopsoas inflammation and abscess formation (arrowheads, A, B and C). GRE: Gradient recalled echo.

ciated with medical treatment (Figure 11). Furthermore, MRE is also adequate for detection of recurrent disease following surgery (Figure 12).

CELIAC DISEASE

Celiac disease is a permanent gluten-sensitive enteropathy of the gastrointestinal tract that affects the small intestine in genetically susceptible individuals. It is a systemic disease that may entail a variety of autoimmune disorders; the most important finding is an inflamed and flattened

small intestinal mucosa with impaired function^[40]. The disease may present at any age and may show a wide range of clinical presentations of variable severity. The diagnosis of celiac disease can be challenging due to a wide range of clinical manifestations and the lack of specificity. Although the diagnosis is confirmed by small-intestine biopsy, patients who are referred for MRE with nonspecific gastro-intestinal complaints might have celiac disease as the underlying pathology.

MRE allow the visualization of the entire small bowel, and can demonstrate findings useful to suggest the

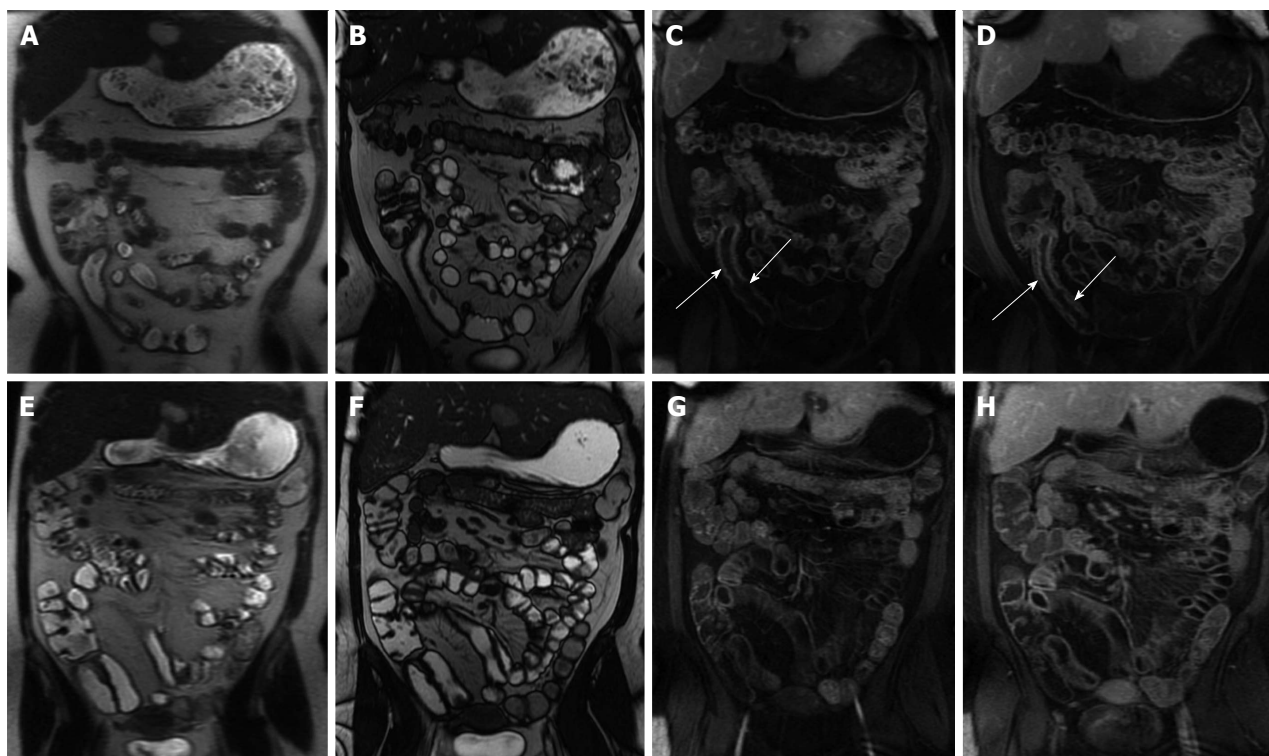


Figure 11 Imaging followup in a patient with Crohn's disease. A and E: Coronal T2-weighted single shot fast spin echo; B and F: Coronal balanced steady state free precession images; C and G: Coronal; D and H: Axial fat-suppressed post-gadolinium 3D-GRE T1-weighted images. There is evidence of active Crohn's disease involving a long segment of the terminal ileum (A, B, C and D) in form of diffuse wall thickening and submucosal mucosal enhancement (arrows, C and D). Four-month re-evaluation shows interval decreased wall thickening and significant decreased mucosal/serosal enhancement, consistent with favourable response to medical therapy. GRE: Gradient recalled echo.

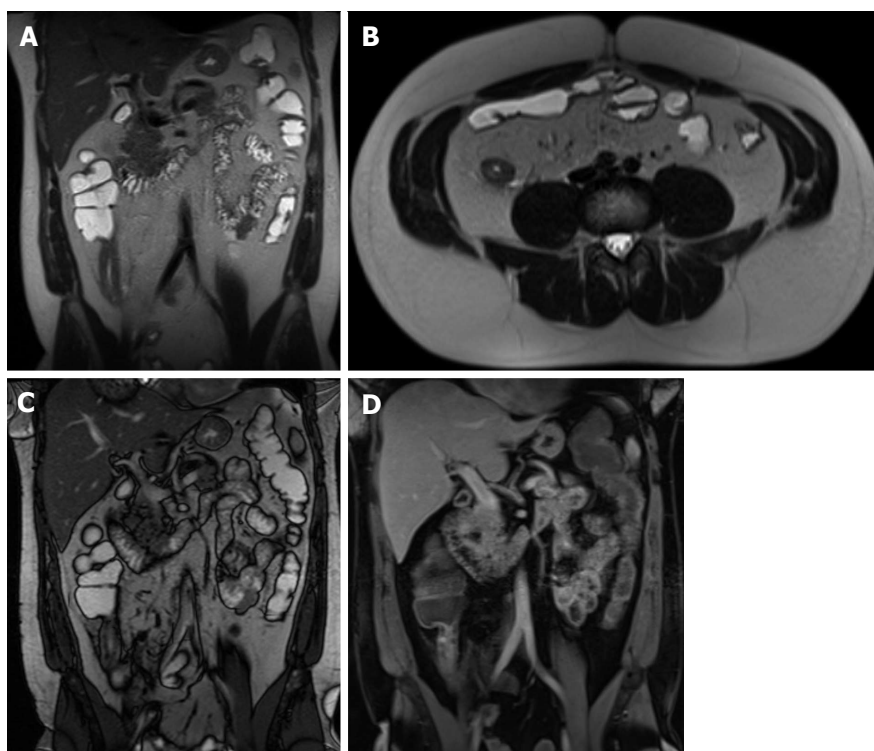


Figure 12 Recurrent Crohn's disease post-surgery. A: Coronal; B: Axial T2-weighted single shot fast spin echo images; C: Coronal balanced steady state free precession; D: Coronal fat suppressed post-gadolinium 3D-GRE T1-weighted images. The patient is post distal ileal resection with a low-lying ileocolic anastomosis. The remaining distal ileum displays signs of active inflammation, namely bowel wall thickening and submucosal edema (A and B) associated with mucosal and serosal increased enhancement post-gadolinium (D) in keeping with recurrent Crohn's disease post-surgery. GRE: Gradient recalled echo.

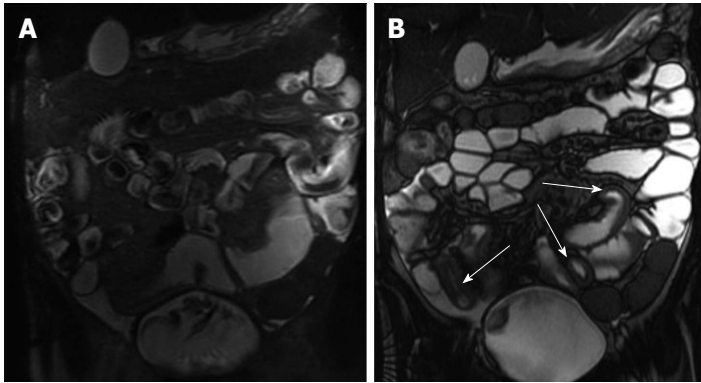


Figure 13 Type 2 Gluten-sensitive enteropathy (Celiac disease). A: Coronal T2-weighted single shot fast spin echo; B: Coronal balanced steady state free precession images show an abnormal ileal fold pattern with substantial decrease in the number of jejunal folds suggesting the diagnosis of celiac disease. Concomitantly, jejunal and ileal segments with increased mural thickening and stratification are seen (arrows, B), consistent with superimposed active inflammation.

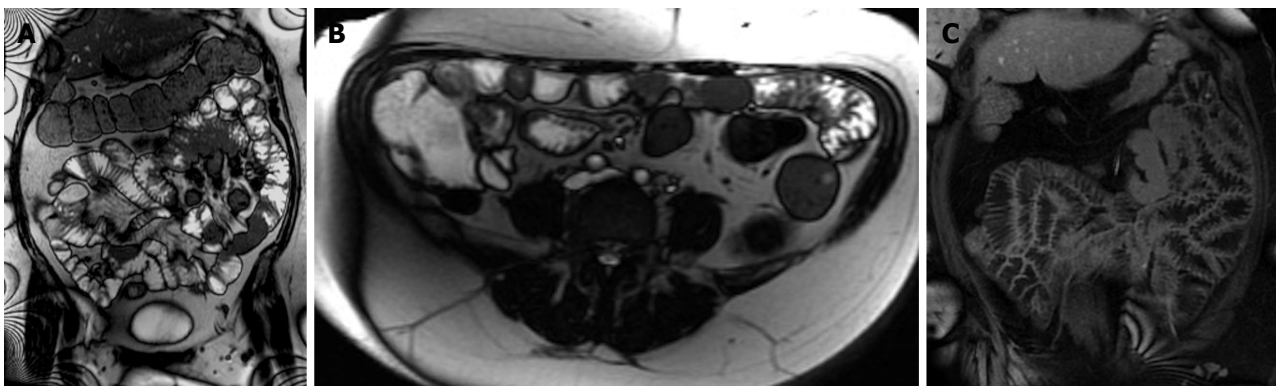


Figure 14 Gluten-sensitive enteropathy (celiac disease). A: Coronal T2-weighted single shot fast spin echo; B: Coronal balanced steady state free precession; C: Coronal fat-suppressed post-gadolinium 3D-GRE T1-weighted images during the interstitial phase. There is abnormal ileal fold pattern with increased number of folds mimicking the appearance of the jejunum (ileal jejunitization) in keeping with the diagnosis of celiac disease. GRE: Gradient recalled echo.

diagnosis of celiac disease in symptomatic adult patients. Among these findings, fold-pattern abnormality is the most distinctive^[41,42]. Furthermore, because there are diseases that can resemble celiac disease histologically, MRE can help in excluding other disease entities^[43], such as lymphoma. Due to greater contrast resolution, MRE may be the preferred method of evaluation.

Fold-pattern abnormalities can best be assessed on bSSFP and single-shot fast/turbo spin-echo T2-weighted pulse sequences. A decreased number of jejunal folds (less than three folds per inch) or complete flattening of the folds can be seen in celiac disease (Figure 13). Also, the ileal folds can be increased (more than 5 folds per inch), a sign called “ileal jejunitization” (Figure 14). Jejunoileal fold pattern reversal is present when both ileal jejunitization and a decreased number of jejunal folds are present in the same patient. This fold-pattern reversal is very specific for celiac disease^[41]. However, less specific imaging findings can be seen including strictures, lymphadenopathy, and perienteric stranding. Also, intussusception, visible as the “double halo sign” of bowel-within-bowel, and enlarged lymph nodes (> 1 cm)^[41,42] are frequently encountered.

Small bowel lymphomas are associated with the concomitant presence of celiac disease^[44] and should be suspected in cases in which considerable enlargement of

lymph nodes (> 2 cm) are identified.

MISCELLANEOUS

Infectious diseases of the small bowel are the most prevalent disease processes in the small bowel after CD. *Yersinia enterocolitica* and *Campylobacter jejuni* represent the most common pathogens. Because of the increasing number of immunocompromised patients, the spectrum of pathogens has become wider during the past decades, including *Mycobacterium avium-intracellulare*, *Cryptosporidium* species, and cytomegalovirus. Infectious diseases may mimic CD; because they often manifest as terminal ileitis. Hence, clinical features always need to be considered in order to establish the correct diagnosis^[45].

The small bowel is highly sensitive to radiation exposure, with the ileum showing the lowest radiation tolerance. Radiation enteritis typically affects the distal ileum and is often associated with rectosigmoid involvement^[46] (Figure 15). The rectum is affected more frequently than the small bowel in pelvic radiotherapy, where proctitis is estimated to occur in 19% of cases^[47]. Typical imaging findings include luminal narrowing with small bowel obstruction and pre-stenotic dilatation as well as symmetric wall thickening and edema. Gadolinium-enhanced T1-



Figure 15 Radiation proctocolitis. A: Coronal; B: Axial; C: Sagittal T2-weighted TSE. The rectum and distal sigmoid colon demonstrates increased wall thickness with intermediate signal intensity on T2-weighted images (arrows, A, B and C). This patient underwent hysterectomy and radiation therapy. These findings are compatible with radiation proctocolitis. TSE: Turbo spin echo.

weighted images reveal increased enhancement in the affected bowel wall. Furthermore, submucosal edema can be depicted in early-stage radiation enteritis on T2-weighted images. Care is required to exclude malignancy, especially lymphoma, suggested by mass-like thickening, infiltration of adjacent tissues, and nodal enlargement^[45].

PRACTICAL APPROACH TO INFLAMMATORY CONDITIONS-LARGE BOWEL

Inflammatory bowel disease

CD and Ulcerative Colitis (UC) are the two main forms of chronic inflammatory bowel disease (IBD)^[48] with 20%-25% of diagnoses being made during childhood^[49]. Ileocolonoscopy with biopsy is the primary tool to make the diagnosis of colonic IBD. However, as mentioned above, intramural changes and extra-luminal abnormalities cannot be appreciated. Furthermore, concomitant small bowel involvement must be excluded.

Given the present role of MRE in small bowel CD, we believe that MRE \pm colonic enema (MR colonography) might have a similar role in colonic IBD. Often, the degree of distension of the large bowel achieved with oral contrast agents is suboptimal; however, previous reports have shown high sensitivity for differentiating type and severity of colonic IBD with comparable diagnostic accuracy to endoscopy^[50]. Furthermore, a recent meta-analysis^[51] suggested that MRI is a potentially effective method even without the administration of colonic enema. Recently, Rimola *et al.*^[50] demonstrated that MRE in combination with a water-based enema is adequately able to assess disease activity in patients with established CD (Figure 16). Current evidence suggests adequate accuracy in evaluating disease activity in established IBD patients. Initial diagnosis and additional differentiation between UC and CD has not been defined yet. MRI findings of UC are similar to those of CD. UC is chronic inflammatory bowel disease restricted to the mucosa and distinctively limited to the colon (Figures 17 and 18) with a pre-

dictable distribution, *i.e.*, the disease begins in the rectum and extends proximally in a continuous fashion to involve part or the entire colon (pancolitis). In case of pancolitis, a backwash ileitis may also be present.

Diverticulitis

MRI can effectively diagnose acute diverticulitis, with reported sensitivity of 86% to 94% and specificity of 88% to 92%^[52]. It is likely that continually improving MRI techniques may result in higher sensitivity and specificity in the future. Buckley *et al.*^[53] described MRI findings in patients with acute colonic diverticulitis, identifying findings similar to CT: bowel wall thickening, pericolic stranding, presence of diverticula (Figure 19), and presence of complications such as perforation and abscess formation^[53]. MRI is also comparable to CT in its ability to identify alternative diagnoses^[54].

Appendicitis

Traditionally, acute appendicitis has been diagnosed on the basis of clinical findings. Despite having high sensitivity (up to 100%), clinical evaluation has relatively low specificity (73%)^[55]. The exact role of imaging in the setting of suspected appendicitis is still a matter of debate. CT is the preferred imaging technique for the diagnosis and assessment of appendicitis in the United States^[56] and has been shown to reduce the negative-finding appendectomy rate from 24% to 3%^[57]. There are several individual CT findings that suggest a diagnosis of appendicitis like appendiceal enlargement (> 6 mm in diameter) that has a high positive predictive value^[58]. Likewise, the sensitivity of adjacent fat infiltration is high for the diagnosis of appendicitis^[59]. However, the visualization of an appendicolith has been shown to have a low positive predictive value for the diagnosis of appendicitis^[58]. Complications, such as perforated appendicitis, extraluminal gas or abscess can be diagnosed with high specificity^[60]. If appendicitis can be ruled out, the most common alternative imaging-based diagnoses are gynecologic diseases, diverticulitis, colitis, or epiploic appendagitis^[61].

MRI has demonstrated promising accuracy for the

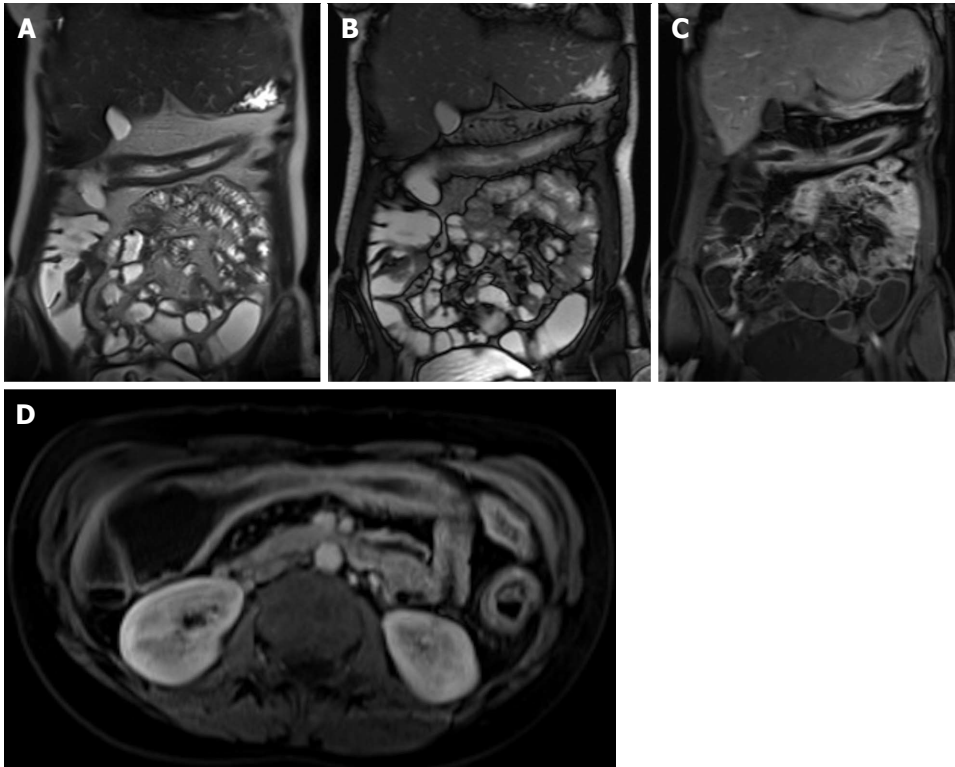


Figure 16 Crohn's colitis. A: Coronal T2-weighted single shot fast spin echo; B: Coronal balanced steady state free precession images; C: Coronal; D: Axial fat-suppressed post-gadolinium 3D-GRE T1-weighted images. There is a segmental uniform thickening of the transverse colon associated with submucosal edema (A and B), mucosal hyper-enhancement, and engorgement of the supplying mesenteric vessels (C and D) in keeping with active Crohn's colitis. Also of note is the focal hyper-enhancement of the terminal ileum (C). GRE: Gradient recalled echo.

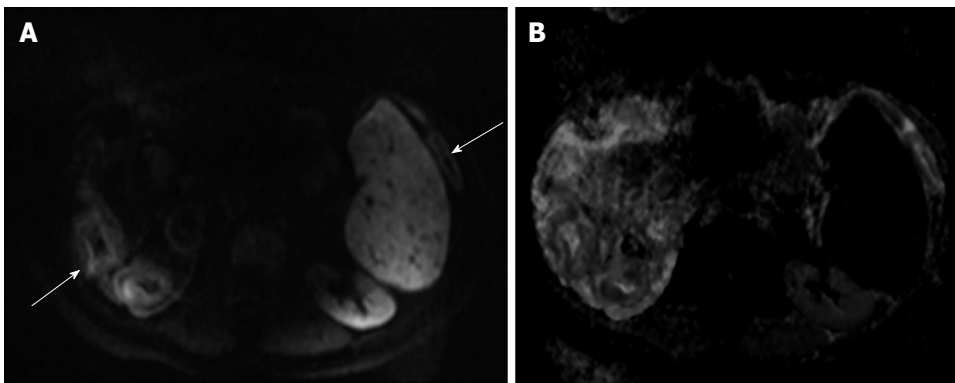


Figure 17 Active colonic ulcerative colitis. A: Axial diffusion-weighted imaging ($b = 650 \text{ s/mm}^2$); B: ADC map images. There is diffuse thickening involving the colon associated with diffuse mucosal diffusion restriction (arrows A) in keeping with active ulcerative colitis. ADC: Analog-digital conversion.

assessment and diagnosis of appendicitis, albeit in a relatively small series of patients, who often were pregnant (Figure 20)^[62]. A recent study showed that the accuracy of conditional or immediate MRI was similar to that of conditional CT in patients suspected of having appendicitis^[63]. However, due to the non-wide availability of MRI systems, relative lack of required expertise and extensive cost-effectiveness studies; the role of MRI is somewhat limited. At this time, MRI is used in only select cases at many institutions, primarily after ultrasound yields nondiagnostic findings in pregnant women.

As in CT, the inflamed appendix and surrounding tissues show marked enhancement on gadolinium-enhanced

T1-weighted fat-suppressed images. Recently, Leeuwenburgh *et al.*^[64] suggested that the most significant MRI features of acute appendicitis include appendix enlargement (diameter > 7 mm), peri-appendiceal fat stranding, and restricted diffusion of appendiceal wall; the presence of all these three features on MRI leads to a correct diagnosis of 96%, whereas their absence practically rules out appendicitis.

GASTRIC AND SMALL BOWEL TUMORS

Gastric tumors

Adenocarcinoma: Gastric carcinoma is one of the most

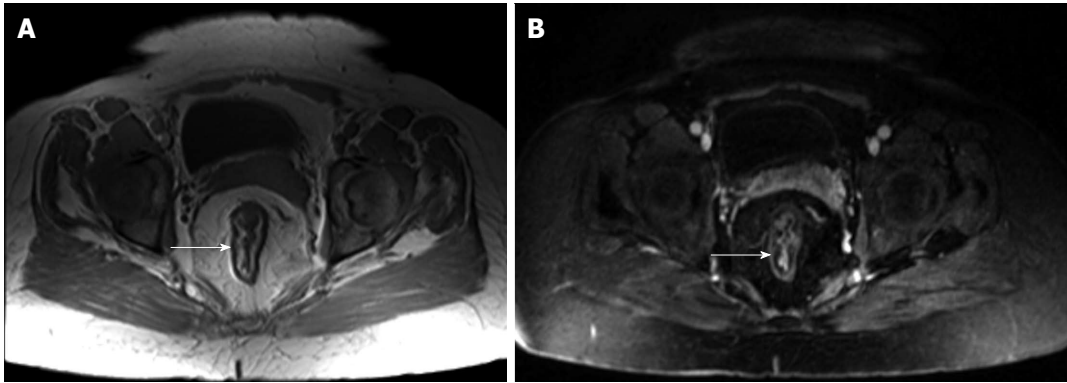


Figure 18 Chronic ulcerative colitis. A: Axial in-phase T1-weighted; B: Axial fat-suppressed post-gadolinium 3D-GRE T1-weighted images. There is diffuse rectal submucosal increased T1 signal (arrow, A), which demonstrates low signal on fat-suppression (arrow, B), but no significant arterial enhancement (B), in keeping with chronic ulcerative colitis. GRE: Gradient recalled echo.

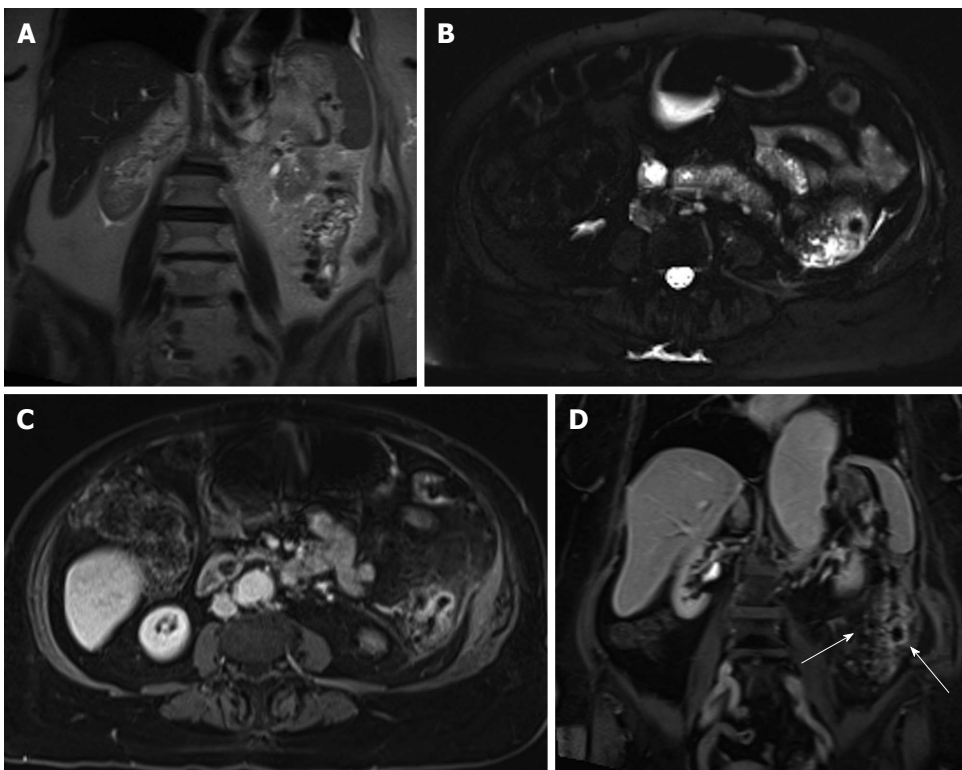


Figure 19 Left colonic diverticulitis. A: Coronal T2-weighted single shot fast spin echo (SSFSE); B: Axial fat-suppressed T2-weighted SSFSE; C: Axial and D: Coronal fat-suppressed post-gadolinium 3D-GRE T1-weighted images during the interstitial phase. There is wall thickening of the descending colon (A), with pericolic free fluid, better depicted on axial T2-weighted SSFSE image (B). Post-gadolinium images (C and D) show marked enhancement of the left colon, with pericolic enhancement including the pre-renal fascia. Coronal postgadolinium image (D) shows left colonic diverticula and associated bowel wall and vasa recti engorgement (arrows), consistent with inflammation. GRE: Gradient recalled echo.

common causes of cancer-related death worldwide. Borrmann proposed the original classification of advanced gastric cancer in 1926 based on macroscopic evaluation of the tumor. Advanced gastric cancer was classified by Borrmann as fungating (type 1), excavated (type 2), ulcerated infiltrating (type 3), and diffusely infiltrating (type 4) based on shape and infiltration margin. The prognosis of this disease depends on a variety of factors including Borrmann classification^[65].

It is generally accepted that the goals of MRI is to demonstrate the primary tumor, but also assess the

depth of invasion and detect extra gastric disease^[66,67]. On gadolinium-enhanced fat-suppressed T1-weighted images, the tumor shows heterogeneous enhancement compared to normal gastric wall. Infiltrative tumors (linitis plastica) enhances modestly (Figure 21). In contradistinction, other morphologic types enhance more intensely; however, these tend yet to be better demonstrated in the arterial phase, as normal gastric mucosa tends to enhance substantially. Previous studies have shown that MRI has similar diagnostic accuracy in the diagnosis and preoperative staging of gastric cancer compared to

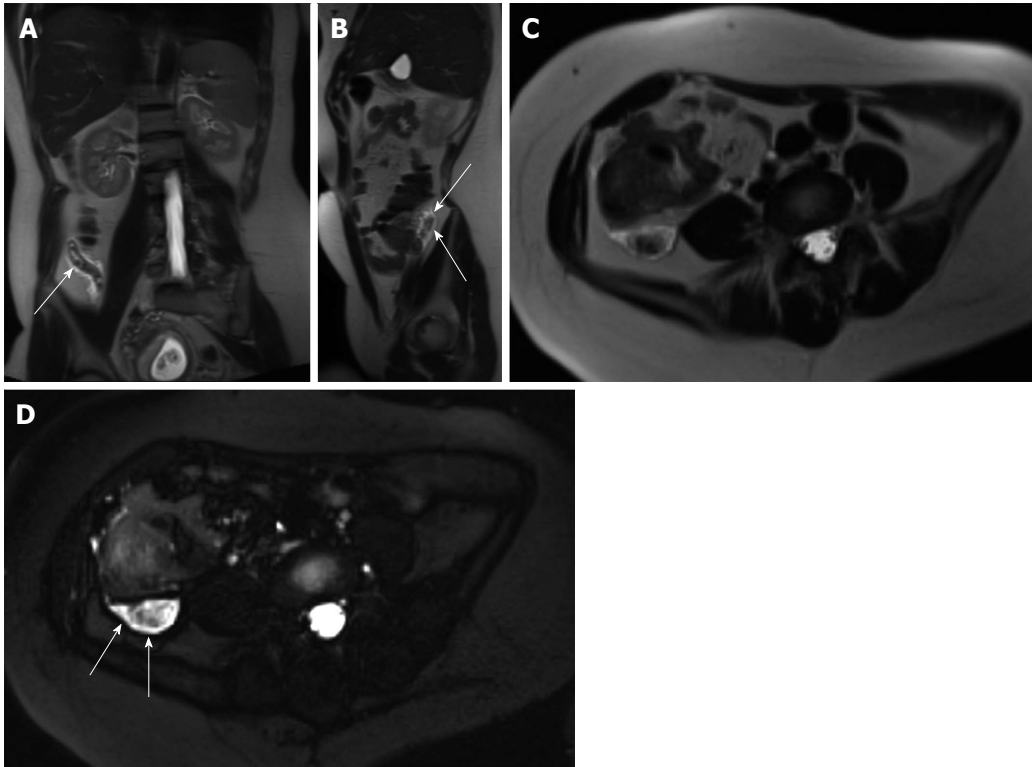


Figure 20 Acute appendicitis in a pregnant patient. A: Coronal; B: Sagittal; and C: Axial single shot fast spin echo (SSFSE) T2 as well as D: fat-suppressed SSFSE T2 images. There is a blind-ended tubular structure at the retrocecal region (arrows, A, B) associated with uniform, diffuse wall thickening and dilatation, reaching up to 13 mm in diameter (C and D) as well as periappendiceal edema and small periappendiceal fluid (A-D) collection, in keeping with acute appendicitis. Edema and fluid appear significantly more conspicuous on fat-suppressed images (arrows, D). Noted is a gravid uterus (A).

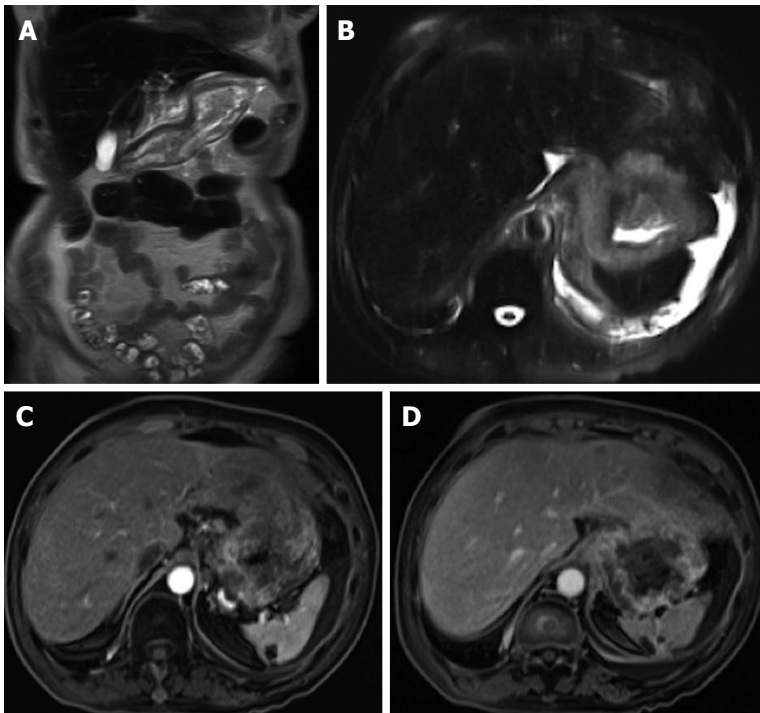


Figure 21 Gastric adenocarcinoma. A: Coronal T2-weighted single shot fast spin echo (SSFSE); B: Axial fat suppressed T2-weighted SSFSE; C: Axial arterial; D: Interstitial post-gadolinium 3D-GRE T1-weighted images. There is diffuse heterogeneous wall thickening of the stomach (A and B) with heterogeneous enhancement (C and D) consistent with linitis plastica. GRE: Gradient recalled echo.

multidetector CT^[67]. Maccioni *et al*^[67] have shown similar detection rate of gastric lesions; however, the T staging

accuracy for gastric cancer was superior for MRI (60% *vs* 48%). This aspect has been previously described by Sohn

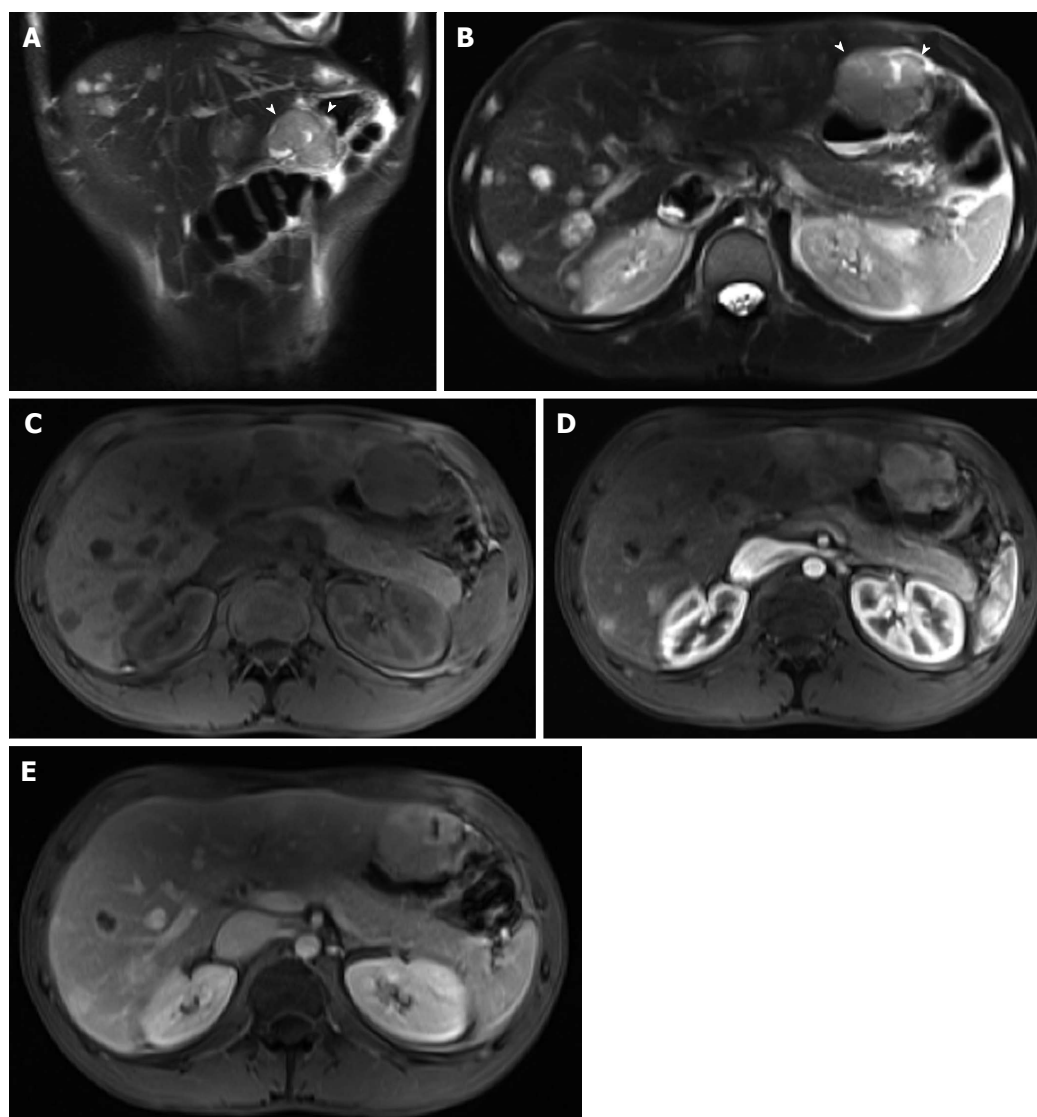


Figure 22 Metastatic malignant gastric gastrointestinal stromal tumors. A: Coronal T2-weighted single shot fast spin echo (SSFSE); B: Axial fat suppressed T2-weighted SSFSE; C: Pre- and post-gadolinium 3D-GRE T1-weighted images during the (D) arterial and (E) interstitial phases. There is a hyperintense mass within the wall of the gastric antrum, which abuts the edge of the left lobe of the liver; Central necrosis is seen (arrowheads, A and B). Multiple liver lesions show heterogeneously increased T2 signal and hypervascular characteristics, fading to isointensity on late phase of enhancement, consistent with metastases. GRE: Gradient recalled echo.

et al^[68] showing a slightly improved accuracy with MRI (73.3% *vs* 66.7%). The presence of involved lymph nodes is acknowledged to be an independent factor of poor prognosis. The overall accuracy for nodal staging with MRI is similar to that attained with CT^[67,68].

Gastrointestinal stromal tumors: Gastrointestinal stromal tumors (GISTs) are the most common mesenchymal neoplasms, which can occur anywhere in the GI tract. Approximately 60%-70% of GISTs occur in the stomach, followed by the small intestine at 25%-35%^[69]. GISTs can either grow into the mucosa causing ulceration or protrude towards the serosal side^[70]. These are solid tumors that can undergo liquefactive necrosis and intratumoral hemorrhage. On MRI, the tumor's large size coupled with intense enhancement and regions of necrosis are typical features of GISTs. Moreover, MRI may be helpful in determining the organ of origin in large tumors, as

well as detecting metastases of GISTs involving the liver and peritoneum (Figure 22). Also, MRI can provide additional information on the tumor response to medical treatment^[71].

Lymphoma: The stomach is the most commonly involved site in GI tract, followed by the small bowel (ileo-cecal region) and rectum^[72]. Diffuse gastric wall thickening is almost always present in gastric lymphoma (Figure 23). Lymphoma also has other characteristics including homogeneous T2 signal intensity, substantial lymph nodes enlargement, and splenomegaly^[73].

Small bowel tumors

The incidence of primary tumors is low, accounting for approximately 1% to 3% of all gastrointestinal tumors. Although small bowel tumors are rare, they are commonly considered in the differential diagnosis of small

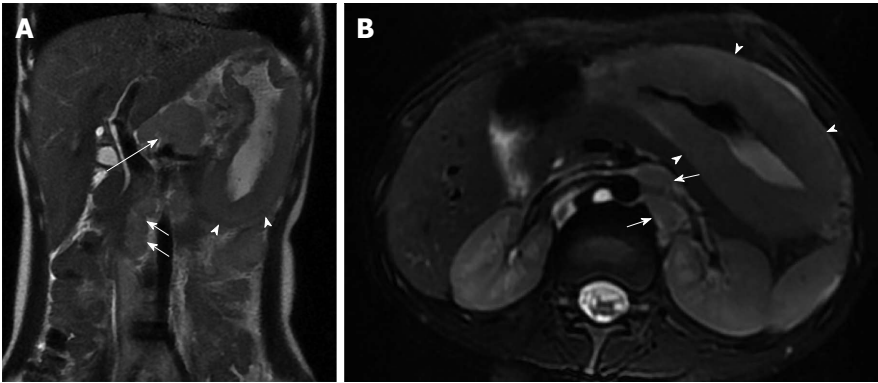


Figure 23 Non-Hodgkin lymphoma of the stomach. A: Coronal T2-weighted single shot fast spin echo (SSFSE) and (B) axial fat-suppressed T2-weighted SSFSE images. There is marked, diffuse, asymmetric gastric wall thickening with smooth outlines, predominantly involving the gastric body and antrum, associated with mildly increased heterogeneous T2 signal intensity (arrowheads, A and B), large conglomerate nodal mass at the gastrohepatic ligament (long arrow, A), and multiple enlarged retroperitoneal lymph nodes (short arrows A and B). Constellation of findings is diagnostic of non-Hodgkin gastric lymphoma with diffuse abdominal lymphadenopathy.

bowel disease because of their nonspecific presenting symptoms such as pain, obstruction, bleeding, and weight loss.

Secondary intestinal tumors, which originate from other parts of the body and metastasize to the small intestine, are clinically common and may cause symptoms similar to primary intestinal neoplasms^[74]. MRE has been shown to be a useful technique for the study of suspected bowel masses^[75]. Factors that affect the diagnostic performance of a specific modality include the size and characteristics of the tumor, extra-enteric extension, and eventual small bowel obstruction. The degree of distention and motion artifacts also influences the quality of the study. Although there is paucity of data regarding the sensitivity of MRE for the detection of small-bowel masses, one study showed no significant difference between MRI and wireless capsule endoscopy for the detection of large, clinically significant polyps in patients with polyposis syndromes with additional advantage of improved localization with MRE^[11].

On MRE, hyper-enhancing masses are usually well depicted when biphasic enteric contrast material is administered. Although any tumor may appear as focal intraluminal mass, location along the GI tract (duodenal, jejunal, or ileal), as well as focal areas of bowel wall thickening or areas of increased mural enhancement, suggest the presence of a tumoral mass. For example, a pedunculated or predominantly exophytic mass suggests a gastrointestinal stromal tumor^[76] (Figure 24), while an exophytic mass combined with adjacent lymphadenopathy with or without significant dilatation of the small bowel suggests small bowel lymphoma^[76] (Figure 25). Carcinoid tumors arise from neuroendocrine precursors or small bowel wall and may manifest as hypervascular masses, often in the ileum or as enhancing carpet lesions, mimicking the wall thickening of CD. Mesenteric carcinoid metastases demonstrate a desmoplastic reaction that may contain eccentric calcifications (not depicted on MRE) or may be clustered near the mesenteric root^[77] (Figure 26). Carcinoid metastases to the liver can appear hypervascular and usually show washout on the delayed imaging mimicking

hepatocellular carcinomas (Figure 26). Adenocarcinomas assume a variety of shapes but are generally located in the proximal small bowel (Figure 27) and typically result in proximal dilatation greater than that observed with other neoplasms.

COLORECTAL TUMORS

Colorectal adenocarcinoma

Ninety-six percent of colorectal cancers are adenocarcinomas^[78]. A combination of thin-section 3D-GRE fat-suppressed gadolinium-enhanced T1-weighted and high-resolution T2-weighted fast-spin echo (FSE) provides excellent information about tumor size, bowel wall involvement, peri-tumoral extension, and lymph node detection; especially for tumors located proximally to rectal ampulla^[79,80].

MRI has established itself as the primary method for local staging as well as preoperative planning and post-neoadjuvant assessment of the rectal cancers. Rectal cancer MRI evaluation requires a dedicated protocol. The only sequence that is required is a high-resolution T2-weighted fast spin echo. Sagittal plane images are initially acquired, followed by axial and coronal images perpendicular to the rectal wall at the level of the tumor, termed short- and long-axis images, respectively. With high-resolution T2-weighted imaging as a gold standard sequence, it proved to be superior in T staging, especially when the patient's comfort and acceptance are taken into consideration^[81-83]. The ability of MR to delineate the mesorectal fascia and related structures makes it effective to accurately predict curative resection of the rectal cancer^[81,84].

Practical aspects of rectal cancer MR staging include tumor size evaluation, longitudinal and axial localization, tumor extent through the rectal wall layers, extramural invasion of the mesorectal fat and/or mesorectal fascia as well as deep pelvic organs invasion or anal canal extension in case of low lying rectal tumors. Short-axis T2 high-resolution imaging is critical for more accurate tumor (T) staging and yields higher accuracy for deeper tumoral extension (T3-4) (Figure 28); however, transrec-

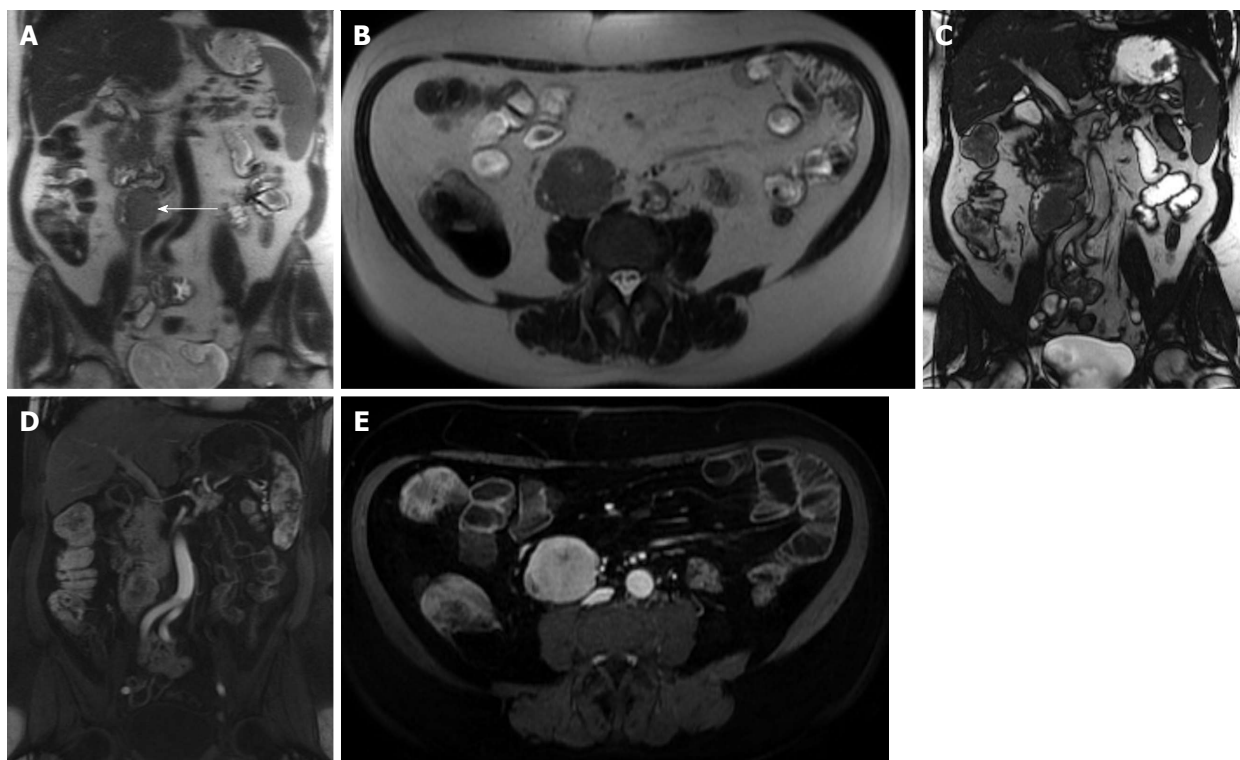


Figure 24 Jejunal gastrointestinal stromal tumor. A: Coronal and (B) axial T2-weighted single shot fast spin echo, and (C) coronal balanced steady state free precession images as well as (D) coronal and (E) axial fat-suppressed post-gadolinium 3D-GRE T1-weighted images. There is a well-defined intramural, exophytic mass lesion arising from the proximal jejunum, in a patient with malrotation, which demonstrates intermediately increased T2 signal (arrow, A, B), early moderate hypervascularity (D) and progressive enhancement (E) post-gadolinium associated with a tiny central area of necrosis in keeping with jejunal gastrointestinal stromal tumor. Lack of proximal bowel obstruction is consistent with its eccentric origin. GRE: Gradient recalled echo.

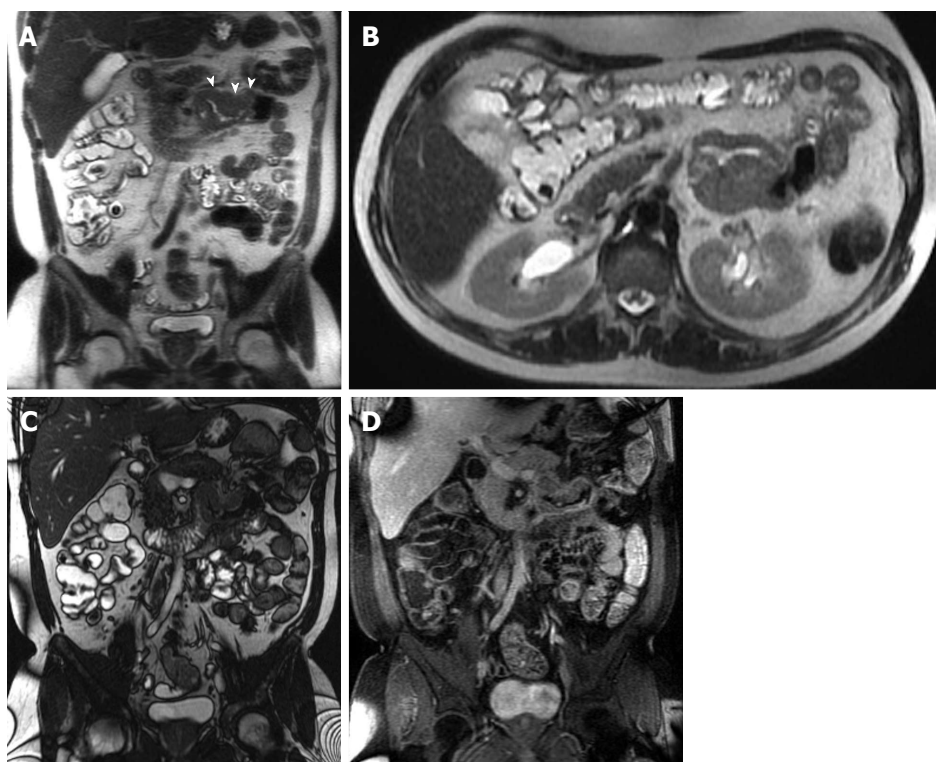


Figure 25 Jejunal lymphoma. A: Coronal and (B) axial T2-weighted single shot fast spin echo, (C) coronal balanced steady state free precession, and (D) coronal fat-suppressed post-gadolinium 3D-GRE T1-weighted images. There is a short segment of proximal jejunal circumferential, irregular, asymmetric wall thickening resulting in luminal narrowing (arrowheads, A) and demonstrates and intermediate T2 signal (A and B) and mild enhancement post-gadolinium (D) in keeping with a pathologically proven jejunal lymphoma. GRE: Gradient recalled echo.

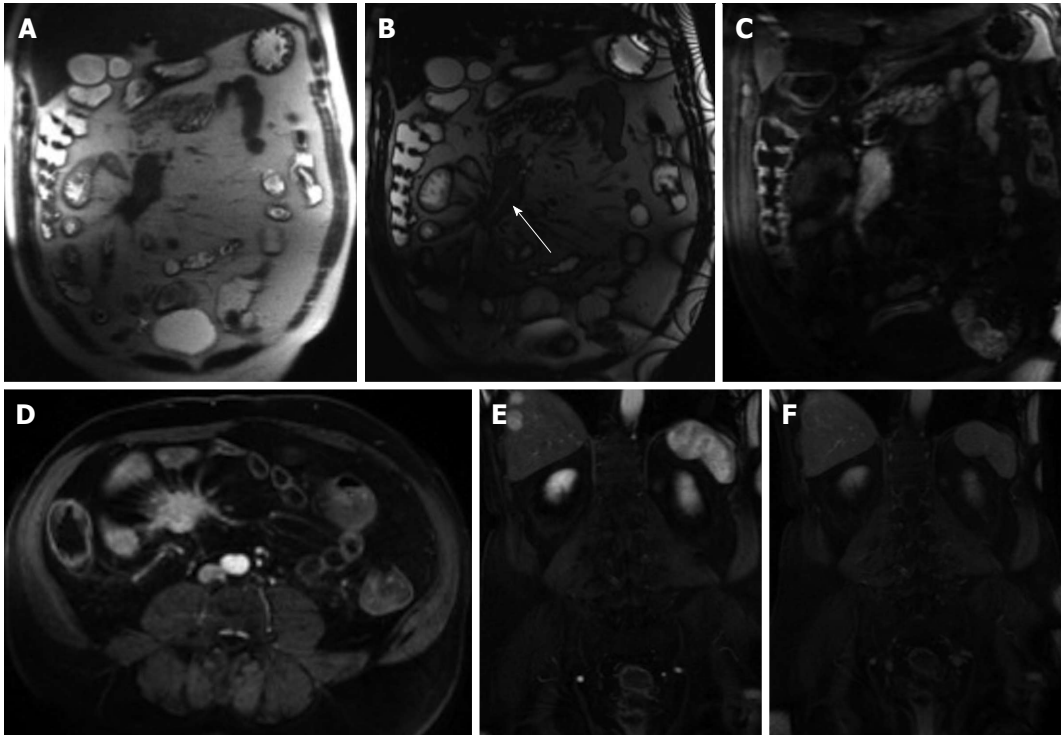


Figure 26 Mesenteric carcinoid. A: Coronal T2-weighted single shot fast spin echo; B: Coronal balanced steady state free precession; C and D: Coronal arterial; E: Axial enteric; F: Coronal interstitial fat-suppressed post-gadolinium 3D-GRE T1-weighted images. There is a large mesenteric mass encasing the superior mesenteric artery and its branches (arrow, B) associated with desmoplastic reaction and small bowel retraction noted on pre-contrast images (A, B), which demonstrates hypervascular (C) and typical sunburst margins (D). Liver metastases are seen with the typical wash-in (D) and washout (F) appearance mimicking the appearance of hepatocellular carcinoma. GRE: Gradient recalled echo.

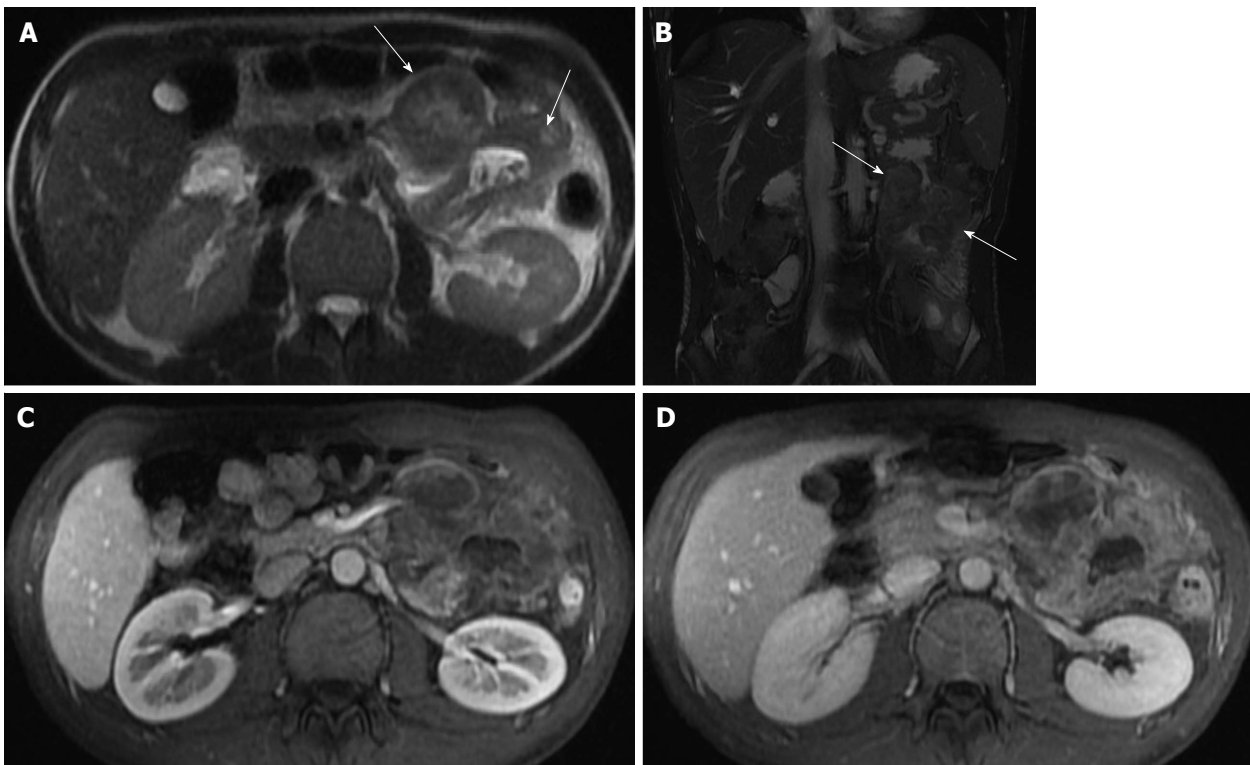


Figure 27 Jejunal adenocarcinoma. A: Axial T2-weighted single shot fast spin echo and (B) coronal balanced steady state free precession images as well as axial fat-suppressed post-gadolinium 3D-GRE T1-weighted images during the (C) hepatic arterial dominant and (D) hepatic venous phases. There is significant circumferential, irregular, asymmetric wall thickening of the proximal jejunum with exophytic extension (arrows, A and B) and hypovascular enhancement pattern (C and D) in keeping with a pathologically proven jejunal adenocarcinoma. GRE: Gradient recalled echo.

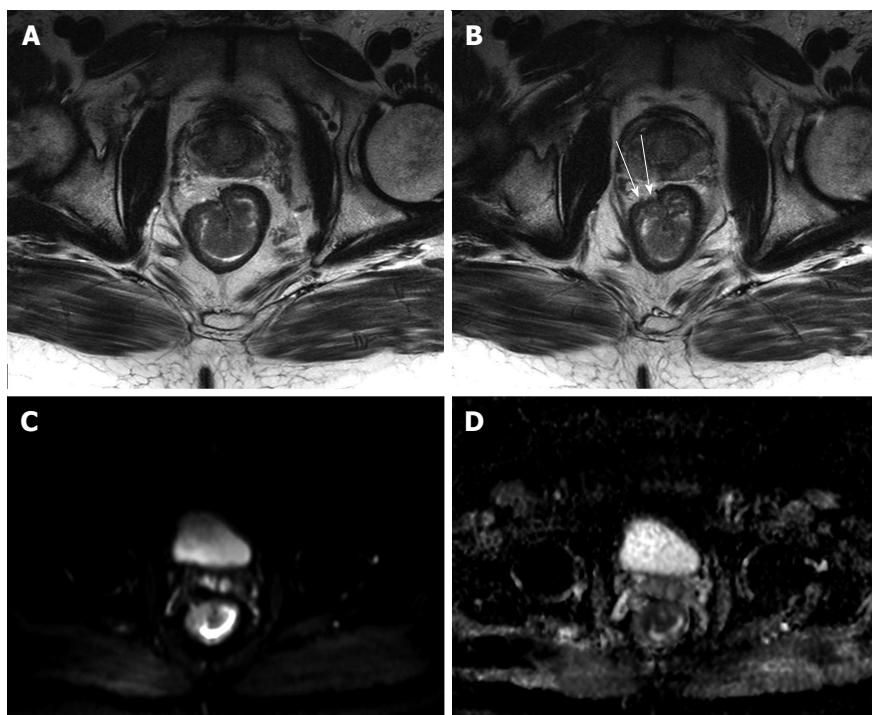


Figure 28 Stage T3 rectal cancer. A and B: Axial high-resolution T2-weighted images as well as axial (C) diffusion-weighted imaging ($b = 650 \text{ s/mm}^2$) and (D) ADC map images. There is a large polypoidal mass lesion arising from the right anterolateral lower rectal wall (A and B) with two foci of tumoral extension beyond the low-signal serosal layer (arrows, B) that show diffusion restriction (C and D) in keeping with stage T3 rectal tumor. ADC: Analog-digital conversion.

tal ultrasound has higher reported accuracy in superficial tumors (T1-T2)^[85]. A limitation of MR is its inability to easily differentiate T2 from early T3 tumors and certainly cannot differentiate between T1 and T2 cancers^[85]. With the advent of endorectal coils, the T staging accuracy has been reported to be between 70%-90%^[84,86,87]; however, patient's compliance, limited availability and cost contribute to its less wide application^[85]. MRI has 92% accuracy in predicting circumferential resection margin when a cutoff point of 1 mm is used^[88]. Nodal involvement can be evaluated using MRI, which rely on short-axis nodal measurement, signal heterogeneity of the cortex, marginal irregularity, or surrounding fat infiltration. The use of superparamagnetic iron oxide particles appears to be promising^[89]. Studies also showed that diffusion weighted imaging and perfusion imaging are useful in following-up tumor treatment response including assessing the response to neoadjuvant therapy and determining residual disease or local tumor recurrence^[90-93]. The main difficulty in assessing the response to chemoradiation is the distinction between fibrosis with and without residual tumor^[94]. Studies evaluating the ability of MRI after chemoradiation to predict tumor clearance from the mesorectal fascia have shown a high negative predictive value of 100%, at the expense of many false-positives leading to a low positive predictive value (PPV) of 50%-60%^[95]. Two studies reported a PPV of 83% and 91% and the PPV increased to 94% when > 70% volume downsizing was combined with MR morphological changes^[96,97]. The detection of very small volumes of disease remains a problem with techniques that only give information on

morphological data. Although 18-Fludeoxyglucose positron emission tomography provides additional functional information, it cannot solve the problem of detection of residual tumor in fibrosis, as shown by a study on the assessment of clearance from the mesorectal fascia^[98].

Benign lesions of the small and large bowel

Some lesions have typical features on MR imaging, which is crucial for a correct diagnosis. For instance, hemangiomas are typically strongly hyperintense on T2-weighted MR images; lipomas or tumors with a marked fat content will show high T1 signal intensity that suppresses on fat-suppressed T1-weighted images (Figure 29). However, many other benign neoplasms such as leiomyomas, fibromas and neurogenic tumors may be indistinguishable from other hypervascular lesions on MRE/MRI.

CONCLUSION

The implementation of fast and ultra-fast sequences and dedicated advanced imaging protocols render MRI an excellent tool for GI imaging. State of the art MRI/MRE has rapidly emerged as successful gastrointestinal imaging modality; offering detailed anatomic and morphologic information and also permitting evaluation of extraluminal manifestation and extension of disease. These features have now been shown to alter physician level of confidence and management procedures including medical or surgical approaches.

The lack of ionizing radiation makes MRI the preferred modality in many GI disease processes, especially

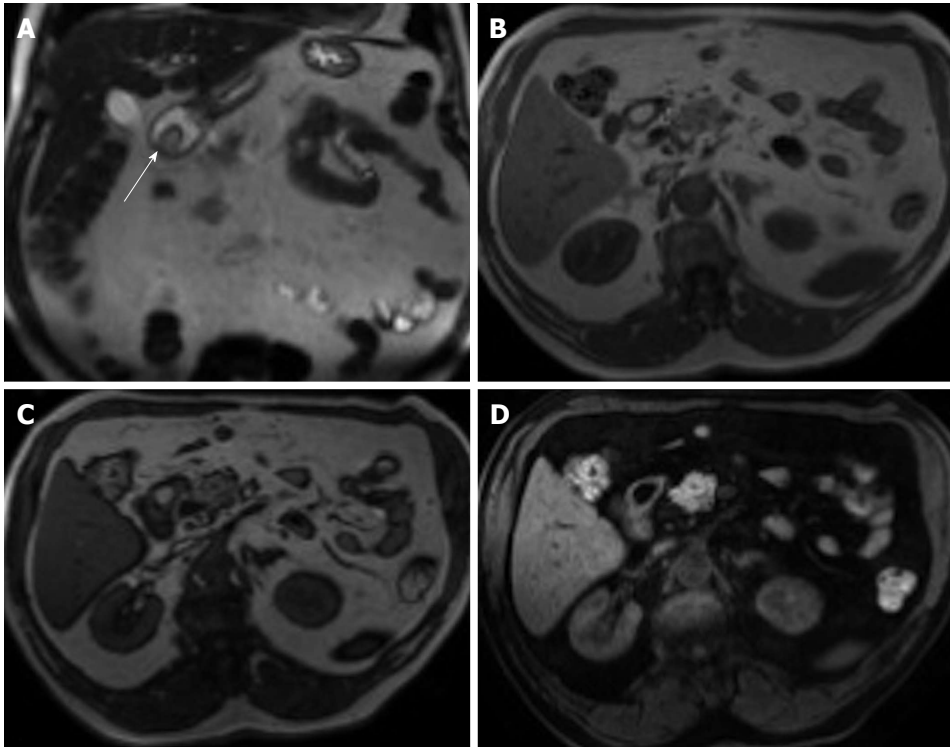


Figure 29 Duodenal lipoma. A: Coronal T2-weighted single shot fast spin echo (SSFSE); B: Axial GRE in-phase; C: Opposed-phase T1-weighted; D: Axial fat-suppressed 3D-GRE T1-weighted images. Small, well-defined, intra-luminal, duodenal mass lesion; which demonstrates intermediately high signal on SSFSE (arrow, A), high signal intensity on the in-phase T1 weighted image (B), no drop of signal on the opposed-phase images (C), and homogenously low signal intensity on the fat-suppressed image (D) in keeping with duodenal lipoma. GRE: Gradient recalled echo.

in young patients in the setting of CD, considering that the majority will undergo frequent imaging evaluation. Pregnant patients and those with iodinated contrast agents allergy or decreased renal function may also benefit from MRI. The main drawbacks may be related to relative non-wide availability at present time, economic constrains, and need for highly subspecialized radiologists.

Whenever cross-sectional imaging is requested, especially MRI or CT, the current trend is to weigh the strengths and weaknesses of both techniques considering a risk-benefit analysis. The choice of a diagnostic technique should be determined taking in account patient's age, clinical status and estimated follow-up exams.

REFERENCES

- 1 **Umschaden HW**, Szolar D, Gasser J, Umschaden M, Haselbach H. Small-bowel disease: comparison of MR enteroclysis images with conventional enteroclysis and surgical findings. *Radiology* 2000; **215**: 717-725 [PMID: 10831690 DOI: 10.1148/radiology.215.3.r00jn12717]
- 2 **Rondonotti E**, Herreras JM, Pennazio M, Caunedo A, Mascarenhas-Saraiva M, de Franchis R. Complications, limitations, and failures of capsule endoscopy: a review of 733 cases. *Gastrointest Endosc* 2005; **62**: 712-716; quiz 752, 754 [PMID: 16246685 DOI: 10.1016/j.gie.2005.05.002]
- 3 **Brenner DJ**, Hall EJ. Computed tomography--an increasing source of radiation exposure. *N Engl J Med* 2007; **357**: 2277-2284 [PMID: 18046031 DOI: 10.1056/NEJMra072149]
- 4 **Froehlich JM**, Patak MA, von Weymarn C, Juli CF, Zollkofer CL, Wentz KU. Small bowel motility assessment with magnetic resonance imaging. *J Magn Reson Imaging* 2005; **21**: 370-375 [PMID: 15779029 DOI: 10.1002/jmri.20284]
- 5 **Cronin CG**, Lohan DG, Browne AM, Roche C, Murphy JM. Does MRI with oral contrast medium allow single-study depiction of inflammatory bowel disease enteritis and colitis? *Eur Radiol* 2010; **20**: 1667-1674 [PMID: 20069426 DOI: 10.1007/s00330-009-1701-2]
- 6 **Ramalho M**, Herédia V, Cardoso C, Matos AP, Palas J, De Freitas J, Semelka RC. Magnetic resonance imaging of small bowel Crohn's disease. *Acta Med Port* 2012; **25**: 231-240 [PMID: 23079251]
- 7 **Lee SS**, Kim AY, Yang SK, Chung JW, Kim SY, Park SH, Ha HK. Crohn disease of the small bowel: comparison of CT enterography, MR enterography, and small-bowel follow-through as diagnostic techniques. *Radiology* 2009; **251**: 751-761 [PMID: 19276325 DOI: 10.1148/radiol.2513081184]
- 8 **Negaard A**, Paulsen V, Sandvik L, Berstad AE, Borthne A, Try K, Lygren I, Storaas T, Klow NE. A prospective randomized comparison between two MRI studies of the small bowel in Crohn's disease, the oral contrast method and MR enteroclysis. *Eur Radiol* 2007; **17**: 2294-2301 [PMID: 17483955 DOI: 10.1007/s00330-007-0648-4]
- 9 **Schreyer AG**, Geissler A, Albrich H, Schölmerich J, Feuerbach S, Rogler G, Völk M, Herfarth H. Abdominal MRI after enteroclysis or with oral contrast in patients with suspected or proven Crohn's disease. *Clin Gastroenterol Hepatol* 2004; **2**: 491-497 [PMID: 15181618]
- 10 **Gupta A**, Postgate AJ, Burling D, Ilangovan R, Marshall M, Phillips RK, Clark SK, Fraser CH. A prospective study of MR enterography versus capsule endoscopy for the surveillance of adult patients with Peutz-Jeghers syndrome. *AJR Am J Roentgenol* 2010; **195**: 108-116 [PMID: 20566803 DOI: 10.2214/AJR.09.3174]
- 11 **Caspari R**, von Falkenhausen M, Krautmacher C, Schild H, Heller J, Sauerbruch T. Comparison of capsule endoscopy and magnetic resonance imaging for the detection of polyps of the small intestine in patients with familial adenomatous polyposis or with Peutz-Jeghers' syndrome. *Endoscopy* 2004;

- 36: 1054-1059 [PMID: 15578294 DOI: 10.1055/s-2004-826041]
- 12 **Kinner S**, Kuehle CA, Herbig S, Haag S, Ladd SC, Barkhausen J, Lauenstein TC. MRI of the small bowel: can sufficient bowel distension be achieved with small volumes of oral contrast? *Eur Radiol* 2008; **18**: 2542-2548 [PMID: 18500525 DOI: 10.1007/s00330-008-1041-7]
 - 13 **Kuehle CA**, Ajaj W, Ladd SC, Massing S, Barkhausen J, Lauenstein TC. Hydro-MRI of the small bowel: effect of contrast volume, timing of contrast administration, and data acquisition on bowel distention. *AJR Am J Roentgenol* 2006; **187**: W375-W385 [PMID: 16985108 DOI: 10.2214/AJR.05.1079]
 - 14 **Laghi A**, Paolantonio P, Iafra F, Borrelli O, Dito L, Tomei E, Cucchiara S, Passariello R. MR of the small bowel with a biphasic oral contrast agent (polyethylene glycol): technical aspects and findings in patients affected by Crohn's disease. *Radiol Med* 2003; **106**: 18-27 [PMID: 12951547]
 - 15 **Ajaj W**, Goehde SC, Schneemann H, Ruehm SG, Debatin JF, Lauenstein TC. Oral contrast agents for small bowel MRI: comparison of different additives to optimize bowel distension. *Eur Radiol* 2004; **14**: 458-464 [PMID: 14634782 DOI: 10.1007/s00330-003-2177-0]
 - 16 **Prassopoulos P**, Papanikolaou N, Grammatikakis J, Rousomoustakaki M, Maris T, Gourtsoyiannis N. MR enteroclysis imaging of Crohn disease. *Radiographics* 2001; **21** Spec No: S161-S172 [PMID: 11598255 DOI: 10.1148/radiographics.21.suppl_1.g01oc02s161]
 - 17 **Martin DR**, Danrad R, Herrmann K, Semelka RC, Hussain SM. Magnetic resonance imaging of the gastrointestinal tract. *Top Magn Reson Imaging* 2005; **16**: 77-98 [PMID: 16314698]
 - 18 **Kiryu S**, Dodanuki K, Takao H, Watanabe M, Inoue Y, Takazoe M, Sahara R, Unuma K, Ohtomo K. Free-breathing diffusion-weighted imaging for the assessment of inflammatory activity in Crohn's disease. *J Magn Reson Imaging* 2009; **29**: 880-886 [PMID: 19306416 DOI: 10.1002/jmri.21725]
 - 19 **Oto A**, Kayhan A, Williams JT, Fan X, Yun L, Arkani S, Rubin DT. Active Crohn's disease in the small bowel: evaluation by diffusion weighted imaging and quantitative dynamic contrast enhanced MR imaging. *J Magn Reson Imaging* 2011; **33**: 615-624 [PMID: 21563245 DOI: 10.1002/jmri.22435]
 - 20 **Maglente DD**, Gourtsoyiannis N, Rex D, Howard TJ, Kelvin FM. Classification of small bowel Crohn's subtypes based on multimodality imaging. *Radiol Clin North Am* 2003; **41**: 285-303 [PMID: 12659339]
 - 21 **Martin DR**, Kalb B, Sauer CG, Alazraki A, Goldschmid S. Magnetic resonance enterography in Crohn's disease: techniques, interpretation, and utilization for clinical management. *Diagn Interv Radiol* 2012; **18**: 374-386 [PMID: 22517074 DOI: 10.4261/1305-3825.DIR.4893-11.2]
 - 22 **Martin DR**, Lauenstein T, Sitaraman SV. Utility of magnetic resonance imaging in small bowel Crohn's disease. *Gastroenterology* 2007; **133**: 385-390 [PMID: 17681157 DOI: 10.1053/j.gastro.2007.06.036]
 - 23 **Marcos HB**, Semelka RC. Evaluation of Crohn's disease using half-fourier RARE and gadolinium-enhanced SGE sequences: initial results. *Magn Reson Imaging* 2000; **18**: 263-268 [PMID: 10745134]
 - 24 **Albert JG**, Martiny F, Krummenerl A, Stock K, Lesske J, Göbel CM, Lotterer E, Nietsch HH, Behrmann C, Fleig WE. Diagnosis of small bowel Crohn's disease: a prospective comparison of capsule endoscopy with magnetic resonance imaging and fluoroscopic enteroclysis. *Gut* 2005; **54**: 1721-1727 [PMID: 16020490 DOI: 10.1136/gut.2005.069427]
 - 25 **Low RN**, Sebrechts CP, Politoske DA, Bennett MT, Flores S, Snyder RJ, Pressman JH. Crohn disease with endoscopic correlation: single-shot fast spin-echo and gadolinium-enhanced fat-suppressed spoiled gradient-echo MR imaging. *Radiology* 2002; **222**: 652-660 [PMID: 11867781 DOI: 10.1148/radiol.2223010811]
 - 26 **Semelka RC**, Shoenut JP, Silverman R, Kroeker MA, Yaffe CS, Micflikier AB. Bowel disease: prospective comparison of CT and 1.5-T pre- and postcontrast MR imaging with T1-weighted fat-suppressed and breath-hold FLASH sequences. *J Magn Reson Imaging* 1991; **1**: 625-632 [PMID: 1823167]
 - 27 **Low RN**, Francis IR, Politoske D, Bennett M. Crohn's disease evaluation: comparison of contrast-enhanced MR imaging and single-phase helical CT scanning. *J Magn Reson Imaging* 2000; **11**: 127-135 [PMID: 10713944 DOI: 10.1002/(SICI)1522-2586(200002)11:2<127::AID-JMRI8>3.0.CO;2-G]
 - 28 **Masselli G**, Gualdi G. MR imaging of the small bowel. *Radiology* 2012; **264**: 333-348 [PMID: 22821694 DOI: 10.1148/radiol.12111658]
 - 29 **Choi D**, Jin Lee S, Ah Cho Y, Lim HK, Hoon Kim S, Jae Lee W, Hoon Lim J, Park H, Rae Lee Y. Bowel wall thickening in patients with Crohn's disease: CT patterns and correlation with inflammatory activity. *Clin Radiol* 2003; **58**: 68-74 [PMID: 12565208]
 - 30 **Taylor SA**, Punwani S, Rodriguez-Justo M, Bainbridge A, Greenhalgh R, De Vita E, Forbes A, Cohen R, Windsor A, Obichere A, Hansmann A, Rajan J, Novelli M, Halligan S. Mural Crohn disease: correlation of dynamic contrast-enhanced MR imaging findings with angiogenesis and inflammation at histologic examination--pilot study. *Radiology* 2009; **251**: 369-379 [PMID: 19276323 DOI: 10.1148/radiol.2512081292]
 - 31 **Schunk K**, Kern A, Oberholzer K, Kalden P, Mayer I, Orth T, Wanitschke R. Hydro-MRI in Crohn's disease: appraisal of disease activity. *Invest Radiol* 2000; **35**: 431-437 [PMID: 10901105]
 - 32 **Masselli G**, Gualdi G. CT and MR enterography in evaluating small bowel diseases: when to use which modality? *Abdom Imaging* 2013; **38**: 249-259 [PMID: 23011551 DOI: 10.1007/s00261-012-9961-8]
 - 33 **Froehlich JM**, Waldherr C, Stoupis C, Erturk SM, Patak MA. MR motility imaging in Crohn's disease improves lesion detection compared with standard MR imaging. *Eur Radiol* 2010; **20**: 1945-1951 [PMID: 20379822 DOI: 10.1007/s00330-010-1759-x]
 - 34 **Rimola J**, Ordás I, Rodríguez S, Panés J. Colonic Crohn's disease: value of magnetic resonance colonography for detection and quantification of disease activity. *Abdom Imaging* 2010; **35**: 422-427 [PMID: 19536590 DOI: 10.1007/s00261-009-9545-4]
 - 35 **Rimola J**, Ordás I, Rodríguez S, García-Bosch O, Aceituno M, Llach J, Ayuso C, Ricart E, Panés J. Magnetic resonance imaging for evaluation of Crohn's disease: validation of parameters of severity and quantitative index of activity. *Inflamm Bowel Dis* 2011; **17**: 1759-1768 [PMID: 21744431 DOI: 10.1002/ibd.21551]
 - 36 **Rimola J**, Rodríguez S, García-Bosch O, Ordás I, Ayala E, Aceituno M, Pellisé M, Ayuso C, Ricart E, Donoso L, Panés J. Magnetic resonance for assessment of disease activity and severity in ileocolonic Crohn's disease. *Gut* 2009; **58**: 1113-1120 [PMID: 19136510 DOI: 10.1136/gut.2008.167957]
 - 37 **Rimola J**, Ordás I, Rodríguez S, Ricart E, Panés J. Imaging indexes of activity and severity for Crohn's disease: current status and future trends. *Abdom Imaging* 2012; **37**: 958-966 [PMID: 22072290 DOI: 10.1007/s00261-011-9820-z]
 - 38 **Giusti S**, Faggioni L, Neri E, Fruzzetti E, Nardini L, Marchi S, Bartolozzi C. Dynamic MRI of the small bowel: usefulness of quantitative contrast-enhancement parameters and time-signal intensity curves for differentiating between active and inactive Crohn's disease. *Abdom Imaging* 2010; **35**: 646-653 [DOI: 10.1007/s00261-010-9624-6]
 - 39 **Oto A**, Zhu F, Kulkarni K, Karczmar GS, Turner JR, Rubin D. Evaluation of diffusion-weighted MR imaging for detection of bowel inflammation in patients with Crohn's disease. *Acad Radiol* 2009; **16**: 597-603 [PMID: 19282206 DOI: 10.1016/j.acra.2008.11.009]
 - 40 **Ciclitira PJ**, King AL, Fraser JS. AGA technical review on Celiac Sprue. American Gastroenterological Association.

- Gastroenterology* 2001; **120**: 1526-1540 [PMID: 11313324]
- 41 **Paolantonio P**, Tomei E, Rengo M, Ferrari R, Lucchesi P, Laghi A. Adult celiac disease: MRI findings. *Abdom Imaging* 2007; **32**: 433-440 [PMID: 16967239 DOI: 10.1007/s00261-006-9089-9]
 - 42 **Tomei E**, Semelka RC, Braga L, Laghi A, Paolantonio P, Marini M, Passariello R, Di Tola M, Sabbatella L, Picarelli A. Adult celiac disease: what is the role of MRI? *J Magn Reson Imaging* 2006; **24**: 625-629 [PMID: 16888777 DOI: 10.1002/jmri.20664]
 - 43 **AGA Institute**. AGA Institute Medical Position Statement on the Diagnosis and Management of Celiac Disease. *Gastroenterology* 2006; **131**: 1977-1980 [PMID: 17087935 DOI: 10.1053/j.gastro.2006.10.003]
 - 44 **Chott A**, Vesely M, Simonitsch I, Mosberger I, Hanak H. Classification of intestinal T-cell neoplasms and their differential diagnosis. *Am J Clin Pathol* 1999; **111**: S68-S74 [PMID: 9894471]
 - 45 **Lauenstein TC**, Umutlu L, Kloeters C, Aschoff AJ, Ladd ME, Kinner S. Small bowel imaging with MRI. *Acad Radiol* 2012; **19**: 1424-1433 [PMID: 22841341 DOI: 10.1016/j.acra.2012.05.019]
 - 46 **Palmer JA**, Bush RS. Radiation injuries to the bowel associated with the treatment of carcinoma of the cervix. *Surgery* 1976; **80**: 458-464 [PMID: 968730]
 - 47 **Miller DG**, Ivey M, Young J. Home parenteral nutrition in treatment of severe radiation enteritis. *Ann Intern Med* 1979; **91**: 858-860 [PMID: 42336]
 - 48 **Beattie RM**, Croft NM, Fell JM, Afzal NA, Heuschkel RB. Inflammatory bowel disease. *Arch Dis Child* 2006; **91**: 426-432 [PMID: 16632672 DOI: 10.1136/adc.2005.080481]
 - 49 **Loftus EV**. Clinical epidemiology of inflammatory bowel disease: Incidence, prevalence, and environmental influences. *Gastroenterology* 2004; **126**: 1504-1517 [PMID: 15168363]
 - 50 **Gandolfi L**. Comparison of magnetic resonance imaging and endoscopy in distinguishing the type and severity of inflammatory bowel disease. *Gastrointest Endosc* 1996; **43**: 86-87 [PMID: 9026433]
 - 51 **Horsthuis K**, Bipat S, Stokkers PC, Stoker J. Magnetic resonance imaging for evaluation of disease activity in Crohn's disease: a systematic review. *Eur Radiol* 2009; **19**: 1450-1460 [PMID: 19189109 DOI: 10.1007/s00330-008-1287-0]
 - 52 **Heverhagen JT**, Sitter H, Zielke A, Klose KJ. Prospective evaluation of the value of magnetic resonance imaging in suspected acute sigmoid diverticulitis. *Dis Colon Rectum* 2008; **51**: 1810-1815 [PMID: 18443876 DOI: 10.1007/s10350-008-9330-4]
 - 53 **Buckley O**, Geoghegan T, McAuley G, Persaud T, Khosa F, Torreggiani WC. Pictorial review: magnetic resonance imaging of colonic diverticulitis. *Eur Radiol* 2007; **17**: 221-227 [PMID: 16625348 DOI: 10.1007/s00330-006-0236-z]
 - 54 **Destigter KK**, Keating DP. Imaging update: acute colonic diverticulitis. *Clin Colon Rectal Surg* 2009; **22**: 147-155 [PMID: 20676257 DOI: 10.1055/s-0029-1236158]
 - 55 **Hong JJ**, Cohn SM, Ekeh AP, Newman M, Salama M, Leblang SD. A prospective randomized study of clinical assessment versus computed tomography for the diagnosis of acute appendicitis. *Surg Infect (Larchmt)* 2003; **4**: 231-239 [PMID: 14588157 DOI: 10.1089/109629603322419562]
 - 56 **Ralls PW**, Balfe DM, Bree RL, DiSantis DJ, Glick SN, Levine MS, Megibow AJ, Saini S, Shuman WP, Greene FL, Laine LA, Lillemoe K. Evaluation of acute right lower quadrant pain. American College of Radiology. ACR Appropriateness Criteria. *Radiology* 2000; **215** Suppl: 159-166 [PMID: 11037421]
 - 57 **Raman SS**, Osuagwu FC, Kadell B, Cryer H, Sayre J, Lu DS. Effect of CT on false positive diagnosis of appendicitis and perforation. *N Engl J Med* 2008; **358**: 972-973 [PMID: 18305278 DOI: 10.1056/NEJMc0707000]
 - 58 **Daly CP**, Cohan RH, Francis IR, Caoili EM, Ellis JH, Nan B. Incidence of acute appendicitis in patients with equivocal CT findings. *AJR Am J Roentgenol* 2005; **184**: 1813-1820 [PMID: 15908536 DOI: 10.2214/ajr.184.6.01841813]
 - 59 **Pereira JM**, Sirlin CB, Pinto PS, Jeffrey RB, Stella DL, Casola G. Disproportionate fat stranding: a helpful CT sign in patients with acute abdominal pain. *Radiographics* 2004; **24**: 703-715 [PMID: 15143223]
 - 60 **Bixby SD**, Lucey BC, Soto JA, Theysohn JM, Ozonoff A, Varghese JC. Perforated versus nonperforated acute appendicitis: accuracy of multidetector CT detection. *Radiology* 2006; **241**: 780-786 [PMID: 17114626 DOI: 10.1148/radiol.2413051896]
 - 61 **Stoker J**, van Randen A, Laméris W, Boermeester MA. Imaging patients with acute abdominal pain. *Radiology* 2009; **253**: 31-46 [PMID: 19789254 DOI: 10.1148/radiol.2531090302]
 - 62 **Wallace GW**, Davis MA, Semelka RC, Fielding JR. Imaging the pregnant patient with abdominal pain. *Abdom Imaging* 2012; **37**: 849-860 [PMID: 22160283 DOI: 10.1007/s00261-011-9827-5]
 - 63 **Leeuwenburgh MM**, Wiarda BM, Wiezer MJ, Vrouwenraets BC, Gratama JW, Spilt A, Richir MC, Bossuyt PM, Stoker J, Boermeester MA. Comparison of imaging strategies with conditional contrast-enhanced CT and unenhanced MR imaging in patients suspected of having appendicitis: a multicenter diagnostic performance study. *Radiology* 2013; **268**: 135-143 [PMID: 23481162 DOI: 10.1148/radiol.13121753]
 - 64 **Leeuwenburgh MM**, Jensch S, Gratama JW, Spilt A, Wiarda BM, Van Es HW, Cobben LP, Bossuyt PM, Boermeester MA, Stoker J. MRI features associated with acute appendicitis. *Eur Radiol* 2014; **24**: 214-222 [PMID: 24013847 DOI: 10.1007/s00330-013-3001-0]
 - 65 **Borrmann R**. Geschwulste des Magens und des Duodenum. In: Henke F, Lubarsch O. Handbuch der speziellen pathologischen Anatomie und Histologie. Berlin: Verlag von J Springer, 1926: 812-1054
 - 66 **Marcos HB**, Semelka RC. Stomach diseases: MR evaluation using combined t2-weighted single-shot echo train spin-echo and gadolinium-enhanced spoiled gradient-echo sequences. *J Magn Reson Imaging* 1999; **10**: 950-960 [PMID: 10581508 DOI: 10.1002/(SICI)1522-2586(199912)10:6<950::AID-JMRI7>3.0.CO;2-H]
 - 67 **Maccioni F**, Marcelli G, Al Ansari N, Zippi M, De Marco V, Kagarmanova A, Vestri A, Marcheggiano-Clarke L, Marini M. Preoperative T and N staging of gastric cancer: magnetic resonance imaging (MRI) versus multi detector computed tomography (MDCT). *Clin Ter* 2010; **161**: e57-e62 [PMID: 20499021]
 - 68 **Sohn KM**, Lee JM, Lee SY, Ahn BY, Park SM, Kim KM. Comparing MR imaging and CT in the staging of gastric carcinoma. *AJR Am J Roentgenol* 2000; **174**: 1551-1557 [PMID: 10845479 DOI: 10.2214/ajr.174.6.1741551]
 - 69 **Miettinen M**, Lasota J. Gastrointestinal stromal tumors--definition, clinical, histological, immunohistochemical, and molecular genetic features and differential diagnosis. *Virchows Arch* 2001; **438**: 1-12 [PMID: 11213830]
 - 70 **Chourmouzi D**, Sinakos E, Papalavrentios L, Akriviadis E, Drevelegas A. Gastrointestinal stromal tumors: a pictorial review. *J Gastrointest Liver Dis* 2009; **18**: 379-383 [PMID: 19795038]
 - 71 **Stroszczyński C**, Jost D, Reichardt P, Chmelik P, Gaffke G, Kretzschmar A, Schneider U, Felix R, Hohenberger P. Follow-up of gastro-intestinal stromal tumours (GIST) during treatment with imatinib mesylate by abdominal MRI. *Eur Radiol* 2005; **15**: 2448-2456 [PMID: 16132930 DOI: 10.1007/s00330-005-2867-x]
 - 72 **Ghimire P**, Wu GY, Zhu L. Primary gastrointestinal lymphoma. *World J Gastroenterol* 2011; **17**: 697-707 [PMID: 21390139 DOI: 10.3748/wjg.v17.i6.697]
 - 73 **Masselli G**, Colaiacomo MC, Marcelli G, Bertini L, Casciani E, Laghi F, D'Amico P, Caprasecca S, Poletti E, Gualdi G. MRI of the small-bowel: how to differentiate primary neo-

- plasms and mimickers. *Br J Radiol* 2012; **85**: 824-837 [PMID: 22422388 DOI: 10.1259/bjr/14517468]
- 74 **Masselli G**, Gualdi G. Evaluation of small bowel tumors: MR enteroclysis. *Abdom Imaging* 2010; **35**: 23-30 [PMID: 19096749 DOI: 10.1007/s00261-008-9490-7]
- 75 **Minardi AJ**, Zibari GB, Aultman DF, McMillan RW, McDonald JC. Small-bowel tumors. *J Am Coll Surg* 1998; **186**: 664-668 [PMID: 9632155]
- 76 **Amzallag-Bellenger E**, Oudjit A, Ruiz A, Cadot G, Soyer PA, Hoeffel CC. Effectiveness of MR enterography for the assessment of small-bowel diseases beyond Crohn disease. *Radiographics* 2012; **32**: 1423-1444 [PMID: 22977028 DOI: 10.1148/rg.325115088]
- 77 **Hoeffel C**, Crema MD, Belkacem A, Azizi L, Lewin M, Arrivé L, Tubiana JM. Multi-detector row CT: spectrum of diseases involving the ileocecal area. *Radiographics* 2006; **26**: 1373-1390 [PMID: 16973770 DOI: 10.1148/rg.265045191]
- 78 **Beaumont C**, Pandey T, Gaines Fricke R, Laryea J, Jambhekar K. MR evaluation of rectal cancer: current concepts. *Curr Probl Diagn Radiol* 2013; **42**: 99-112 [PMID: 23683851 DOI: 10.1067/j.cpradiol.2012.08.002]
- 79 **Shoenut JP**, Semelka RC, Silverman R, Yaffe CS, Micflikier AB. Magnetic resonance imaging evaluation of the local extent of colorectal mass lesions. *J Clin Gastroenterol* 1993; **17**: 248-253 [PMID: 8228088]
- 80 **Zijta FM**, Bipat S, Stoker J. Magnetic resonance (MR) colonography in the detection of colorectal lesions: a systematic review of prospective studies. *Eur Radiol* 2010; **20**: 1031-1046 [PMID: 19936754 DOI: 10.1007/s00330-009-1663-4]
- 81 **Taylor FG**, Swift RI, Blomqvist L, Brown G. A systematic approach to the interpretation of preoperative staging MRI for rectal cancer. *AJR Am J Roentgenol* 2008; **191**: 1827-1835 [PMID: 19020255 DOI: 10.2214/AJR.08.1004]
- 82 **Karatağ O**, Karatağ GY, Özkurt H, Değirmenci HK, Avlanmış Ö, Başak M, Baykan A. The ability of phased-array MRI in preoperative staging of primary rectal cancer: correlation with histopathological results. *Diagn Interv Radiol* 2012; **18**: 20-26 [PMID: 21671218 DOI: 10.4261/1305-3825.DIR.3394-10.2]
- 83 **Halefoglu AM**, Yildirim S, Avlanmis O, Sakiz D, Baykan A. Endorectal ultrasonography versus phased-array magnetic resonance imaging for preoperative staging of rectal cancer. *World J Gastroenterol* 2008; **14**: 3504-3510 [PMID: 18567078]
- 84 **MERCURY Study Group**. Diagnostic accuracy of preoperative magnetic resonance imaging in predicting curative resection of rectal cancer: prospective observational study. *BMJ* 2006; **333**: 779 [PMID: 16984925 DOI: 10.1136/bmj.38937.646400.55]
- 85 **Samee A**, Selvasekar CR. Current trends in staging rectal cancer. *World J Gastroenterol* 2011; **17**: 828-834 [PMID: 21412492 DOI: 10.3748/wjg.v17.i7.828]
- 86 **Beets-Tan RG**, Beets GL, Vliegen RF, Kessels AG, Van Boven H, De Bruine A, von Meyenfeldt MF, Baeten CG, van Engelshoven JM. Accuracy of magnetic resonance imaging in prediction of tumour-free resection margin in rectal cancer surgery. *Lancet* 2001; **357**: 497-504 [PMID: 11229667]
- 87 **Hünerbein M**, Pegios W, Rau B, Vogl TJ, Felix R, Schlag PM. Prospective comparison of endorectal ultrasound, three-dimensional endorectal ultrasound, and endorectal MRI in the preoperative evaluation of rectal tumors. Preliminary results. *Surg Endosc* 2000; **14**: 1005-1009 [PMID: 11116406 DOI: 10.1007/s004640000345]
- 88 **Brown G**, Radcliffe AG, Newcombe RG, Dallimore NS, Bourne MW, Williams GT. Preoperative assessment of prognostic factors in rectal cancer using high-resolution magnetic resonance imaging. *Br J Surg* 2003; **90**: 355-364 [PMID: 12594673 DOI: 10.1002/bjs.4034]
- 89 **Koh DM**, Brown G, Temple L, Raja A, Toomey P, Bett N, Norman AR, Husband JE. Rectal cancer: mesorectal lymph nodes at MR imaging with USPIO versus histopathologic findings--initial observations. *Radiology* 2004; **231**: 91-99 [PMID: 14976266]
- 90 **Park MJ**, Kim SH, Lee SJ, Jang KM, Rhim H. Locally advanced rectal cancer: added value of diffusion-weighted MR imaging for predicting tumor clearance of the mesorectal fascia after neoadjuvant chemotherapy and radiation therapy. *Radiology* 2011; **260**: 771-780 [PMID: 21846762 DOI: 10.1148/radiol.111102135]
- 91 **Gollub MJ**, Gultekin DH, Akin O, Do RK, Fuqua JL, Gonen M, Kuk D, Weiser M, Saltz L, Schrag D, Goodman K, Paty P, Guillem J, Nash GM, Temple L, Shia J, Schwartz LH. Dynamic contrast enhanced-MRI for the detection of pathological complete response to neoadjuvant chemotherapy for locally advanced rectal cancer. *Eur Radiol* 2012; **22**: 821-831 [PMID: 22101743 DOI: 10.1007/s00330-011-2321-1]
- 92 **Lambregts DM**, Cappendijk VC, Maas M, Beets GL, Beets-Tan RG. Value of MRI and diffusion-weighted MRI for the diagnosis of locally recurrent rectal cancer. *Eur Radiol* 2011; **21**: 1250-1258 [PMID: 21240647 DOI: 10.1007/s00330-010-2052-8]
- 93 **Sassen S**, de Booi M, Sosef M, Berendsen R, Lammering G, Clarijs R, Bakker M, Beets-Tan R, Warmerdam F, Vliegen R. Locally advanced rectal cancer: is diffusion weighted MRI helpful for the identification of complete responders (ypT0N0) after neoadjuvant chemoradiation therapy? *Eur Radiol* 2013; **23**: 3440-3449 [PMID: 23832319 DOI: 10.1007/s00330-013-2956-1]
- 94 **Beets-Tan RG**, Beets GL. Local staging of rectal cancer: a review of imaging. *J Magn Reson Imaging* 2011; **33**: 1012-1019 [PMID: 21509856 DOI: 10.1002/jmri.22475]
- 95 **Chen CC**, Lee RC, Lin JK, Wang LW, Yang SH. How accurate is magnetic resonance imaging in restaging rectal cancer in patients receiving preoperative combined chemoradiotherapy? *Dis Colon Rectum* 2005; **48**: 722-728 [PMID: 15747073 DOI: 10.1007/s10350-004-0851-1]
- 96 **Dresen RC**, Beets GL, Rutten HJ, Engelen SM, Lahaye MJ, Vliegen RF, de Bruine AP, Kessels AG, Lammering G, Beets-Tan RG. Locally advanced rectal cancer: MR imaging for restaging after neoadjuvant radiation therapy with concomitant chemotherapy. Part I. Are we able to predict tumor confined to the rectal wall? *Radiology* 2009; **252**: 71-80 [PMID: 19403847 DOI: 10.1148/radiol.2521081200]
- 97 **Barbaro B**, Fiorucci C, Tebala C, Valentini V, Gambacorta MA, Vecchio FM, Rizzo G, Coco C, Crucitti A, Ratto C, Bonomo L. Locally advanced rectal cancer: MR imaging in prediction of response after preoperative chemotherapy and radiation therapy. *Radiology* 2009; **250**: 730-739 [PMID: 19244043 DOI: 10.1148/radiol.2503080310]
- 98 **Vliegen RF**, Beets GL, Lammering G, Dresen RC, Rutten HJ, Kessels AG, Oei TK, de Bruine AP, van Engelshoven JM, Beets-Tan RG. Mesorectal fascia invasion after neoadjuvant chemotherapy and radiation therapy for locally advanced rectal cancer: accuracy of MR imaging for prediction. *Radiology* 2008; **246**: 454-462 [PMID: 18227541 DOI: 10.1148/radiol.2462070042]

P- Reviewer: Chen F, Imbriaco M, Lichtor T **S- Editor:** Ji FF
L- Editor: A **E- Editor:** Liu SQ



Incorporating GSA-SPECT into CT-based dose-volume histograms for advanced hepatocellular carcinoma radiotherapy

Shintaro Shirai, Morio Sato, Yasutaka Noda, Yoshitaka Kumayama, Noritaka Shimizu

Shintaro Shirai, Morio Sato, Yasutaka Noda, Yoshitaka Kumayama, Noritaka Shimizu, Department of Radiology, Wakayama Medical University, Wakayama Shi, Wakayama 641-8510, Japan

Author contributions: Shirai S, Sato M, Noda Y, Kumayama Y and Shimizu N contributed to this paper.

Correspondence to: Morio Sato, MD, Professor, Department of Radiology, Wakayama Medical University, 811-1 Kimiidera, Wakayama Shi, Wakayama 641-8510,

Japan. morisato@mail.wakayama-med.ac.jp

Telephone: +81-73-4410604 Fax: +81-73-4443110

Received: December 26, 2013 Revised: April 15, 2014

Accepted: May 28, 2014

Published online: March 28, 2015

Abstract

In single photon emission computed tomography-based three-dimensional radiotherapy (SPECT-B-3DCRT), images of Tc-99m galactosyl human serum albumin (GSA), which bind to receptors on functional liver cells, are merged with the computed tomography simulation images. Functional liver is defined as the area of normal liver where GSA accumulation exceeds that of hepatocellular carcinoma (HCC). In cirrhotic patients with a gigantic, proton-beam-untreatable HCC of ≥ 14 cm in diameter, the use of SPECT-B-3DCRT in combination with transcatheter arterial chemoembolization achieved a 2-year local tumor control rate of 78.6% and a 2-year survival rate of 33.3%. SPECT-B-3DCRT was applied to HCC to preserve as much functional liver as possible. Sixty-four patients with HCC, including 30 with Child B liver cirrhosis, received SPECT-B-3DCRT and none experienced fatal radiation-induced liver disease (RILD). The Child-Pugh score deteriorated by 1 or 2 in $> 20\%$ of functional liver volume that was irradiated with ≥ 20 Gy. The deterioration in the Child-Pugh score decreased when the radiation plan was designed to irradiate $\leq 20\%$ of the functional liver volume in patients given

doses of ≥ 20 Gy ($_{FLV20Gy}$). Therefore, $_{FLV20Gy} \leq 20\%$ may represent a safety index to prevent RILD during 3DCRT for HCC. To supplement $_{FLV20Gy}$ as a qualitative index, we propose a quantitative indicator, F_{20Gy} , which was calculated as $F_{20Gy} = 100\% \times (\text{the GSA count in the area irradiated with } \geq 20 \text{ Gy}) / (\text{the GSA count in the whole liver})$.

© 2015 Baishideng Publishing Group Inc. All rights reserved.

Key words: Functional image-guided radiotherapy; Galactosyl human serum albumin; Dose-volume histogram; Three-dimensional radiotherapy; Hepatocellular carcinoma

Core tip: Three-dimensional conformal radiotherapy, which is designed to preserve functional liver, can be visualized by single photon emission computed tomography with Tc-99m-galactosyl human serum albumin (GSA). This treatment modality has promising therapeutic effects for hepatocellular carcinomas (HCCs) of > 14 cm in diameter that are unmanageable by proton beam therapy. A treatment plan designed to irradiate $\leq 20\%$ of the functional liver volume ($_{FLV20Gy} \leq 20\%$) did not cause radiation-induced liver disease. Therefore, $_{FLV20Gy} \leq 20\%$ may be a useful safety marker for three-dimensional radiotherapy of HCC of various sizes. It is also possible to estimate the effects of radiotherapy on the liver by dividing the GSA count in the region of the liver irradiated with ≥ 20 Gy by the GSA count of the entire liver.

Original sources: Shirai S, Sato M, Noda Y, Kumayama Y, Shimizu N. Incorporating GSA-SPECT into CT-based dose-volume histograms for advanced hepatocellular carcinoma radiotherapy. *World J Radiol* 2014; 6(8): 598-606 Available from: URL: <http://www.wjgnet.com/1949-8470/full/v6/i8/598.htm> DOI: <http://dx.doi.org/10.4329/wjr.v6.i8.598>

INTRODUCTION

The development of computed tomography (CT) has contributed to radiation treatment (RT) planning by its ability to reveal the precise location of target tissue and at-risk organs in three dimensions, thus enabling dose-volume histograms (DVHs) to be created^[1]. The introduction of DVHs has had significant benefits in terms of better target control and reduced adverse effects. However, even in cases where a DVH was used, RT may cause radiation-induced liver disease (RILD), which is sometimes fatal, in patients with advanced hepatocellular carcinoma (HCC)^[2,3]. In the normal tissue complication probability model, which is used to predict disorders based on the DVH, the volume-adverse effect coefficient is relatively large (0.32-0.40)^[4,5]. Therefore, attempts to reduce the irradiation volume do not always prevent RILD^[2,3]. Furthermore, the proportion of irradiated normal liver relative to the entire normal liver (NL/V_{Gy}) often fails to predict RILD^[2,3,6].

The onset of RILD was commonly attributed to the presence of liver cirrhosis in patients with HCC^[2,3]. For example, Ikai *et al.*^[7] reported marked variability in the function of normal liver in patients with liver cirrhosis and in patients with portal vein tumor thrombus (PVTT), which led to the adoption of a surgical therapeutic strategy. Radiation oncologists generally use and rely upon CT-based DVH. Many radiation oncologists may not acknowledge or cope with the possible variations in liver function in normal liver.

Because single photon emission computed tomography (SPECT) with liver scintigraphy reflects the function of normal liver^[7-9], we anticipated that SPECT could be used to evaluate localized liver function. Nanashima *et al.*^[8] reported that SPECT images obtained using Tc-99m-galactosyl human serum albumin (GSA) provided a better assessment of local liver function than conventional CT images. Furthermore, Shuke *et al.*^[9] reported that GSA was the best radioisotope for evaluating liver function by scintigraphy. Therefore, we merged SPECT images obtained using GSA (GSA-SPECT) with CT simulation images to prepare isodose curves. We then used the merged images for treatment planning for HCC, including cases with PVTT, hepatic vein tumor thrombus (HVTT) and/or bile tract tumor thrombus (BT TT)^[10,11]. We refer to this approach as SPECT-based three-dimensional conformal radiotherapy (SPECT-B-3DCRT).

The aim of this article is to describe the technical details, safety and efficacy of SPECT-B-3DCRT. We also describe its potential limitations and possible strategies to overcome its limitations.

COMBINING RT WITH TRANSCATHETER ARTERIAL CHEMOEMBOLIZATION

Transcatheter arterial chemoembolization (TACE) is perhaps the most widely performed multidisciplinary therapy for unresectable HCC^[12]. However, because

TACE is commonly ineffective in patients with HCC \geq 5 cm in diameter or HCC with blood vessel invasion^[12,13], we combined SPECT-B-3DCRT together with TACE in such patients, with the aim of improving treatment outcomes^[10,11]. Namely, TACE was applied for intrahepatic metastasis out of the radiation field. RT is also applied to metastases in bone, liver and brain. Accordingly, TACE plus RT is an effective multidisciplinary therapy for patients with otherwise limited treatment options^[10,11,14-16].

DEFINITION OF FUNCTIONAL LIVER

There is increasing research into the use of GSA in internal medicine and surgery in the context of hepatology^[17,18], but it has been overlooked in relation to RT. When we first considered applying GSA-SPECT to RT, we found no reliable studies describing the potential relationship between GSA and RT. However, we found some studies describing the use of Tc-99m-macroaggregated albumin in RT of lung cancer. Although different radioisotopes are used for different cancers, these earlier reports highlighted the need to select an appropriate radioisotope and evaluate organ function before commencing RT^[19,20,21]. The first step for evaluating liver function involved fusing the SPECT image to the CT simulation image. The state of the liver varies considerably in HCC patients, ranging from normal liver function to Child C cirrhotic liver^[17]. Therefore, the next step was to establish a definition of functional liver. Unfortunately, a universal definition of functional liver cannot be used because the extent of cirrhotic liver varies considerably among patients. Christian *et al.*^[19] proposed a threshold for organ function in individual organs. Based on a study by Sawamura *et al.*^[22], we defined functional liver as the region of the liver in which radioisotope accumulation exceeded that of the HCC, while dysfunctional liver was defined as the region of the liver in which radioisotope accumulation was similar to that of the HCC^[10,11] (Figures 1 and 2). This definition of functional liver was therefore qualitative but not quantitative.

SPECT-B-3DCRT TECHNIQUE

The current Japanese guidelines for RT of HCC recommend that small HCCs are irradiated with 80-90 Gy in 40-45 fractions^[23]. However, surgical hepatectomy and radiofrequency ablation (RFA) are also used to treat small HCCs. At our institute, RT is generally requested for HCCs that cannot be managed surgically or by RFA, especially in patients with giant HCCs with intrahepatic metastasis and liver cirrhosis. All the patients in this series were asked by the surgeon and/or hepatologists to undergo radiotherapy because of the presence of PVTT. The administration of sorafenib was limited to liver function of Child-Pugh A classification and the cost of sorafenib, approximately 6000 dollars per month, was a financial burden on the patients. Surgical hepatic lobectomy was not scheduled because of the presence of

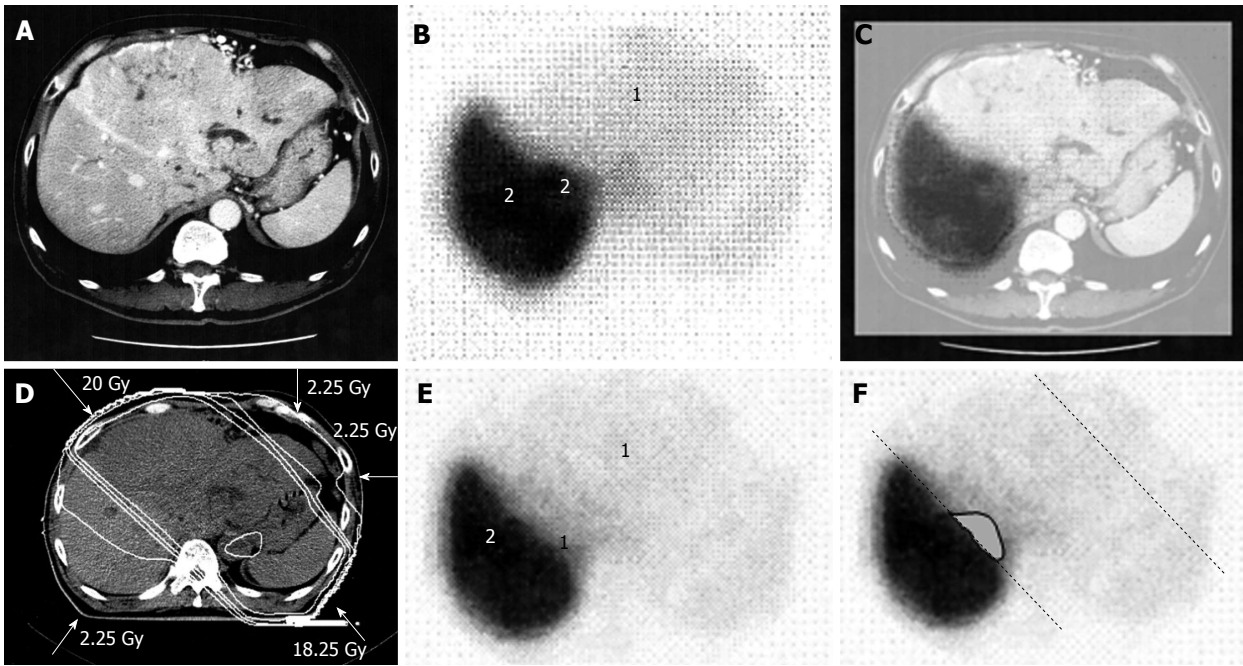


Figure 1 A 58-year-old man with hepatocellular carcinoma with a maximum diameter of 18.0 cm. A: Contrast-enhanced computed tomography; B: Single photon emission computed tomography with Tc-99m-galactosyl human serum albumin before radiotherapy; C: The merged image of A and B. The regions (1) without GSA accumulation in B correspond to main tumor located in the left lobe. The regions (2) of high accumulation in B correspond to functional liver. These regions were identified using the merged image (C); D: Dose distribution based on the CT simulation; E: GSA-SPECT image obtained 2 mo after RT shows regions without GSA accumulation (1) along the two high-dose beams, with preservation of functional liver (2); F: The extent of radiation-induced dysfunctional liver is shown as the gray area with a black border and was determined by comparing B and E. GSA: Galactosyl human serum albumin; SPECT: Single photon emission computed tomography; CT: Computed tomography; RT: Radiotherapy.

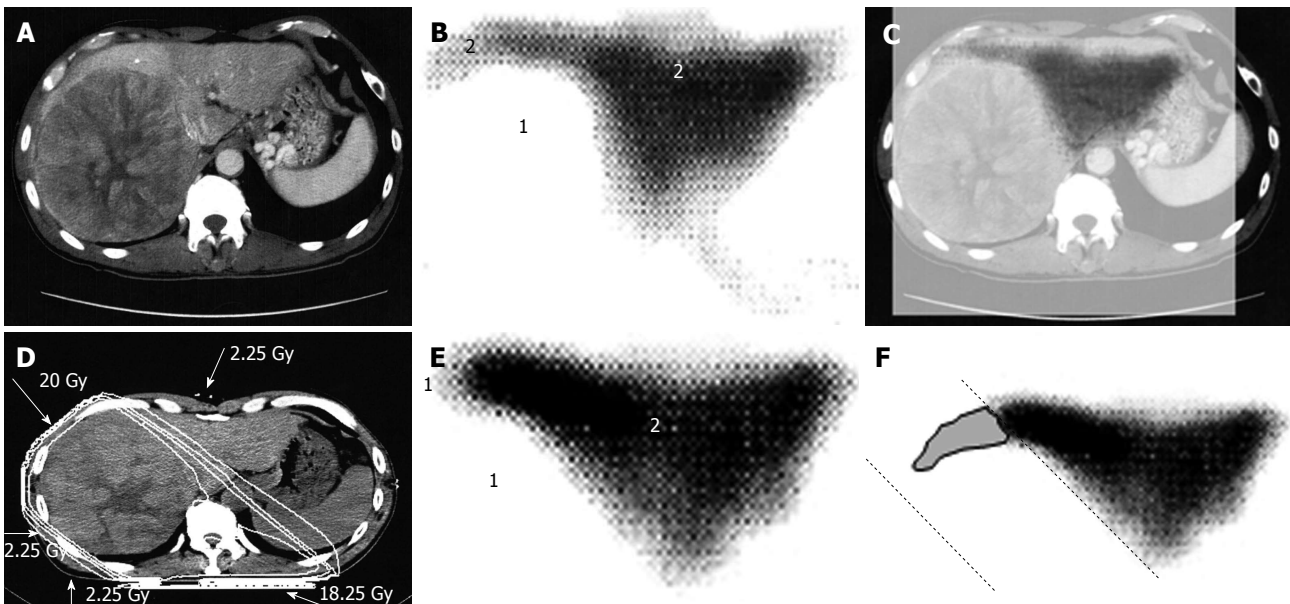


Figure 2 A 53-year-old man with hepatocellular carcinoma with a maximum diameter of 16.5 cm. A: Contrast-enhanced computed tomography; B: Single photon emission computed tomography with Tc-99m-galactosyl human serum albumin before radiotherapy; C: The merged image of A and B; The regions (1) without GSA accumulation in B correspond to main tumor located in the right lobe. The regions (2) of high accumulation in B correspond to functional liver. These regions were identified using the merged image (C); D: Dose distribution based on the CT simulation; E: GSA-SPECT image obtained 2 mo after RT shows regions without GSA accumulation (1) along the two high-dose beams, with preservation of functional liver (2); F: The extent of radiation-induced dysfunctional liver is shown as the gray area with a black border and was determined by comparing B and E. GSA: Galactosyl human serum albumin; SPECT: Single photon emission computed tomography; CT: Computed tomography; RT: Radiotherapy.

intrahepatic metastases in the other lobe. Namely, treatment of surgery and internal medicine were not indicated

for medical and social reasons. Therefore, we prescribed 45 Gy (18 fractions, 2.5 Gy/fraction) for the main tumor

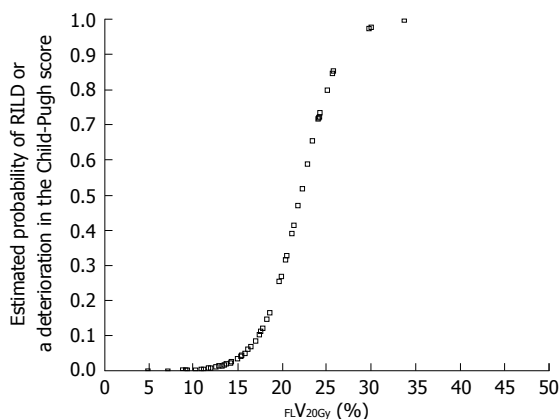


Figure 3 Estimated probability of radiation-induced liver disease or a deterioration in the Child-Pugh score by ≥ 1 point according to percentage of functional liver irradiated with ≥ 20 Gy (FLV_{20Gy}). Probability values were estimated by logistic regression analysis. RILD: Radiation-induced liver disease.

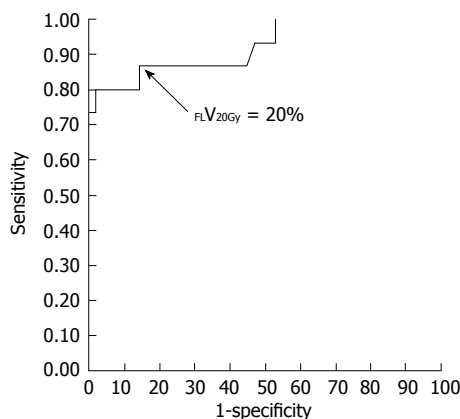


Figure 4 Receiver-operating characteristic curve for the percentage of functional liver volume irradiated with ≥ 20 Gy (FLV_{20Gy}). The optimal cutoff value for FLV_{20Gy} was 20% for predicting radiation-induced liver disease or a deterioration in the Child-Pugh score of ≥ 1 point. At this cutoff value, sensitivity and specificity were 0.867 and 0.857, respectively. The area under the receiver-operating characteristic curve was 0.923 ($P < 0.001$). *Journal of Gastroenterology and Hepatology Research* gave assurance that the copyright for this figure is retained by the authors.

and the vessel tumor thrombus to prevent RILD^[11,15] (Figures 1 and 2). If the tumor size and/or type necessitated applying a greater dose to functional liver than was initially planned, we decided to omit some of the tumor from the irradiation field, providing that the omitted volume was $< 5\%$ of the whole tumor and was treated by TACE^[13]. Our objective was to avoid RILD in such cases. Furthermore, to account for respiratory mobilization^[2,3], the clinical target volume margin was routinely set 2-3 cm greater than the gross tumor volume margin. We also reduced the margin for respiration mobilization from 2-3 cm to 1 cm by asking the patients to hold their breath at the end of expiration^[10,11]. To minimize the effects of respiration, the patient practiced breath holding for 10-15 s at the end of expiration until the position could be maintained with a maximum variance of 5 mm under X-ray fluoroscopic monitoring. Treatment planning was also designed to reduce the radiation exposure to the liver^[10,11]. In short, the beam angle and dose preserved the functional volume visualized using the merged SPECT-CT image. We conducted SPECT-B-3DCRT in 64 patients with HCC, including 30 patients with Child B liver cirrhosis. We confirmed that a deterioration in the Child-Pugh score of 1 or 2 only occurred in patients when $> 20\%$ of the entire functional liver volume was irradiated with ≥ 20 Gy (Figures 3 and 4)^[16]. Figure 3 depicted the abrupt rise of FLV_{20Gy} from approximately 20% and Figure 4 depicted FLV_{20Gy} of 20% corresponded to the cutoff value in receiver operating characteristic analysis. Therefore, our treatment plan specified that $\leq 20\%$ of the functional liver volume would be irradiated with ≥ 20 Gy to minimize the deterioration in the Child-Pugh score.

The stomach, intestine, spinal cord and kidneys are at-risk organs during liver RT^[24,25]. The use of supplementary beams and/or setting a couch angle of $\leq 90^\circ$ helped to reduce irradiation of the stomach, intestine and spinal cord to ≤ 38.25 Gy, while $\leq 30\%$ of the total volume

of both kidneys was exposed to ≥ 20 Gy^[10,11].

The merged SPECT-CT images provided us with an unexpected but promising finding. The growth of gigantic HCCs is coupled with significant destruction of functional liver, especially of the tissue surrounding the tumor. Consequently, the target tissue becomes greater and it becomes easier to preserve functional liver with appropriate treatment planning^[14].

TREATMENT OF HCC ≥ 14 CM IN DIAMETER

Japanese RT guidelines suggest proton beam irradiation to treat HCC of ≥ 5 cm^[23]. Sugahara *et al.*^[26] reported that proton beam therapy brought about 2-year local tumor control rate of 87% and 2-year survival rate of 36%. These results seem to surpass our results below. However, median tumor size of their study was 11 cm (range, 10-14 cm) and proton beam therapy is not indicated for HCC of ≥ 14 cm^[26]. That is the reason why we introduced treating HCC of ≥ 14 cm using SPECT-B-3DCRT. We assessed the merged SPECT-CT images for HCC of ≥ 14 cm in diameter and found that the majority of functional liver was localized to the non-main HCC-bearing lobe rather than the main HCC-bearing lobe^[15] (Figures 1 and 2). Our clinical research indicated that SPECT-B-3DCRT did not affect liver function when $\geq 80\%$ of functional liver was located in the non-main HCC-bearing lobe^[15]. In 12 patients who received SPECT-B-3DCRT, the local tumor control rate was 78.6% and the 2-year survival rate was 33.3%, without serious adverse effects (Figure 5). Based on these findings, we recommend the use of SPECT-B-3DCRT for patients with gigantic (≥ 14 cm) HCC that cannot be managed by resection or proton beam therapy.

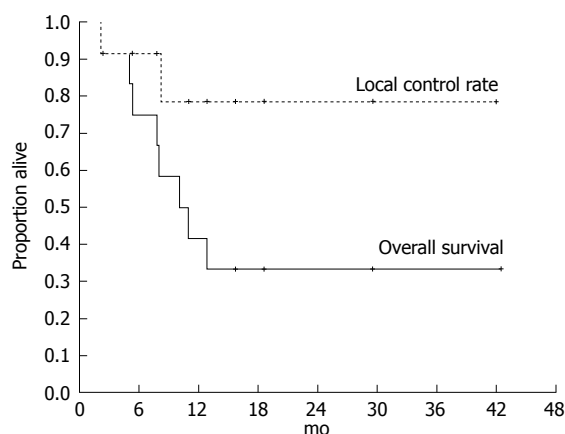


Figure 5 Kaplan-Meier analysis of the local control rate of the irradiated tumor and the survival in 12 cases of hepatocellular carcinoma exceeding 14 cm following single photon emission computed tomography-based three-dimensional radiotherapy. Cancer and Clinical oncology gave assurance that the copyright for this figure is retained by the authors.

TREATMENT OF HCC 5-14 CM IN DIAMETER

If functional liver is predominantly located in the non-main HCC-bearing lobe, SPECT-B-3DCRT can be performed without significant concerns, as described above. However, in some patients, the majority of functional liver is located in the main HCC-bearing lobe. If the main HCC-bearing lobe is the right lobe and $> 50\%$ of functional liver volume is in the main HCC-bearing lobe, the treatment strategy should be developed very carefully.

We treated 26 patients with HCCs of 5-14 cm with PVTT, leading to the control rate of 92.2% of the PVTT and 1-year and 2-year survival rate of 44.4% and 30%, respectively^[10]. Figure 6 shows a typical patient with an HCC of 5-14 cm in diameter. This patient had a right PVTT. SPECT revealed that 85% of functional liver was in the right lobe adjacent to the PVTT. If the RT plan was prepared for normal liver using CT images alone, we would expect that short-axis beams (hypothetical main beams, Figure 6F) would result in less irradiation of normal liver than that with long-axis beams (actual main beams, Figure 6C). $NL.V_{20Gy}$ would be 30.8% for the long-axis beam plan and 23.1% for the short-axis beam plan. However, $FL.V_{20Gy}$ based on SPECT images was 23.8% for the long-axis beam plan and 43.7% for the short-axis beam plan (Figure 7). Therefore, in this patient, RT using short-axis beams would likely cause RILD.

Cheng *et al*^[2] reported that 17/89 (19.1%) and 7/89 (7.9%) patients who received 3DCRT with treatment planning without SPECT experienced RILD and fatal RILD, respectively. In the study by Liang *et al*^[3], 17/109 (15.6%) and 13/109 (11.9%) patients developed RILD and fatal RILD, respectively. In our series, 3/64 (4.7%) and 0 patients (0%) who received SPECT-B-3DCRT experienced RILD and fatal RILD, respectively^[16]. Therefore, we believe that GSA-SPECT helps to predict and may ultimately reduce the risk of non-fatal and fatal RILD.

TREATMENT OF HCC < 5 CM IN DIAMETER

SPECT-B-3DCRT can be applied to HCC of ≤ 5 cm with PVTT, HVTT and/or BTTT. In this situation, functional liver surrounds the main tumor and is therefore likely to be damaged by RT. Regrettably, as we encountered no patient with HCC < 5 cm with PVTT^[10,11], we described the content of radiotherapy for HCC < 5 cm by referring to other manuscripts. Mornex *et al*^[27] reported that 3DCRT caused Grade 4 toxicity in 2/11 (22%) Child B patients and Grade 3 toxicity in 3/16 (19%) Child A patients with a HCC ≤ 5 cm in diameter. Therefore, smaller HCCs require more careful treatment planning than larger HCCs. In this context, we consider that treatment planning with $FL.V_{20Gy} \leq 20\%$ is an important approach for preserving functional liver (Figures 3 and 4). If $FL.V_{20Gy}$ is $> 20\%$ of the planned volume of the main tumor to be irradiated, we suggest that the treatment plan is revised to omit part of the main tumor. This residual part of the tumor can be treated by TACE instead^[16].

LIMITATIONS OF FUNCTIONAL LIVER

If merged SPECT-CT images are available, the concept of functional liver is particularly useful for treatment planning in individual patients. However, functional liver is a qualitative rather than quantitative concept, making it difficult to compare data on functional liver among institutes. Therefore, an objective definition of functional liver should be established and standardized.

DOSE-FUNCTION HISTOGRAM AND FUNCTIONAL COUNT RATE (F_{Gy})

Sugahara *et al*^[17] used GSA SPECT to evaluate the function of the right and left lobes before surgical hepatectomy in a quantitative manner by determining the liver uptake of GSA relative to the total dose of GSA injections. Christian *et al*^[19] and Seppenwoolde *et al*^[21] used lung perfusion SPECT for treatment planning and evaluated the extent of functional lung. Therefore, software has been developed to determine the dose-function histograms (DFH) from perfusion SPECT images for use in treatment planning for lung cancer^[20].

Based on these previous reports, we propose functional count rate (F_{Gy}) as a quantitative index of functional liver. F_{Gy} is defined as the percentage of the functional liver rate in the DFH and is based on V_{Gy} , the percentage of liver volume in the DVH. F_{Gy} is calculated using the following formula: $F_{Gy} = 100 \times (\text{GSA count in the area of the liver indicated by the isodose curve}) / (\text{GSA count for the entire liver})$. Because we use $FL.V_{20Gy} \leq 20\%$ as a qualitative safety marker, F_{20Gy} was calculated for the patient presented in Figure 8. For this patient, F_{20Gy} , $NL.V_{20Gy}$ and $FL.V_{20Gy}$ were 22.2, 20.6 and 18.1, respectively. We consider that, because DFH and F_{Gy} link the area of the isodose curve to liver

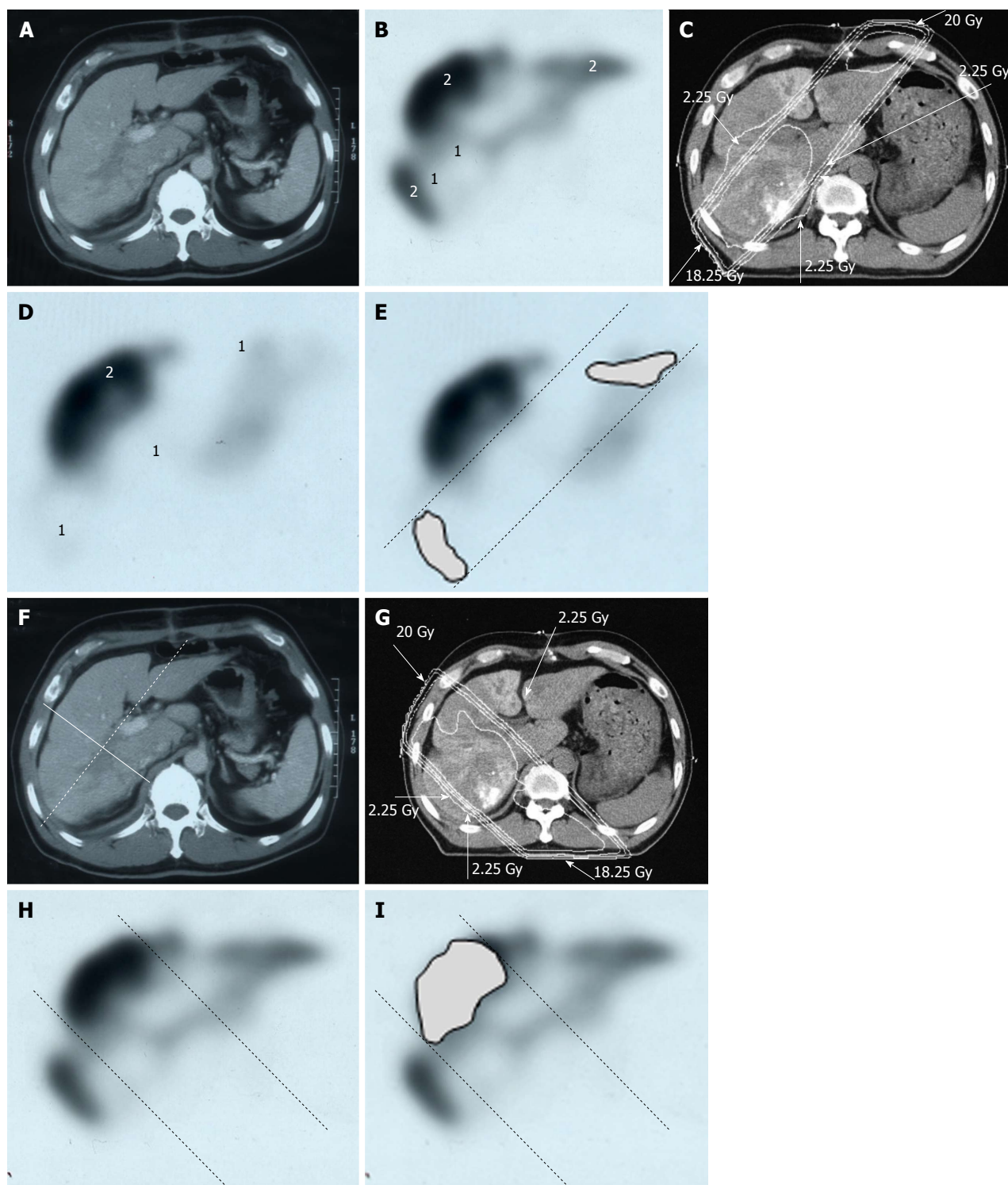


Figure 6 Distribution of functional liver and treatment planning for a 60-year-old male with hepatocellular carcinoma and liver cirrhosis of Child-Pugh grade A. A: Contrast-enhanced computed tomography shows a PVTT in the right first portal vein originating from the right posterior sub-segment branch of the portal vein; B: GSA-SPECT taken before RT at the same level as A confirms that functional liver (2) is unevenly distributed between the anterior and lateral sides of the right PVTT. 1 = dysfunctional liver; C: The two main radiation beams were angled in the left-anterior to right-posterior direction (20 Gy) and in the right-posterior to left-anterior direction (18.25 Gy beam); D: GSA-SPECT image obtained 2 mo after RT shows functional liver (2) and preservation of the right anterior sub-segment. This image also shows that the extent of dysfunctional liver has increased in the right posterior and left medial sub-segments; E: The extent of radiation-induced dysfunctional liver is shown as the dark gray area; F-I: Hypothetical treatment planning; F: The hypothetical main beams are angled in the right-anterior to left-posterior direction (solid lines), unlike the actual beams (dotted lines); G: The hypothetical radiation beams are angled in the right-anterior to left-posterior direction (20 Gy) and in the left-posterior to right-anterior direction (18.25 Gy). Although the radiation-induced destruction of normal liver can be estimated, it is difficult to predict the extent of radiation-induced destruction of functional liver from CT simulation alone; H: GSA-SPECT image together with the hypothetical main beams; I: The gray area indicates the extent of radiation-induced dysfunctional liver likely to be induced by the hypothetical main beams. The relative difference in the destruction of functional liver between the real and the hypothetical treatment plans can be estimated by comparing E and I. PVTT: Portal vein tumor thrombus; GSA-SPECT: Galactosyl human serum albumin-single photon emission computed tomography with Tc-99m-galactosyl human serum albumin image; RT: Radiotherapy; CT: Computed tomography.

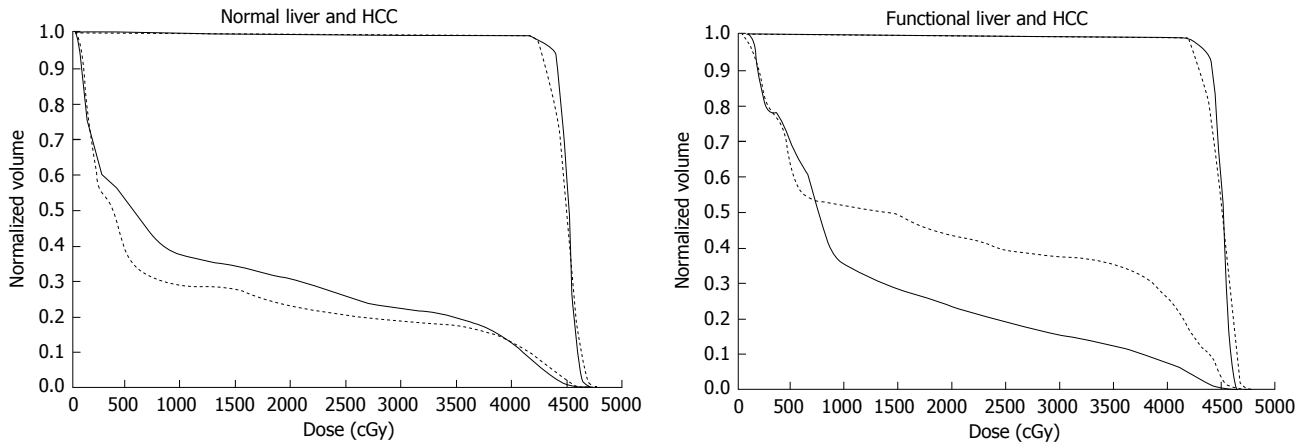


Figure 7 Comparison of dose-volume histograms between actual treatment plans (solid lines) and hypothetical treatment plans (dotted lines). A: Comparison of the DVH for normal liver. In this case, the percentage of the normal liver irradiated with ≥ 20 Gy ($nL_{V_{20Gy}}$) was 23.1% for the hypothetical treatment plan vs 30.8% for the actual treatment plan. Therefore, irradiation of normal liver is lower for the hypothetical treatment plan than for the actual treatment plan; B: Comparison of the DVH for functional liver. In this case, the percentage of functional liver irradiated with ≥ 20 Gy ($fL_{V_{20Gy}}$) was 43.7% for the hypothetical treatment plan vs 23.8% for the actual treatment plan. Therefore, irradiation of functional liver is lower for the actual treatment plan than for the hypothetical treatment plan. The difference between $nL_{V_{20Gy}}$ and $fL_{V_{20Gy}}$ in these two settings is due to the uneven distribution of functional liver. DVH: Dose-volume histograms; HCC: Hepatocellular carcinoma.

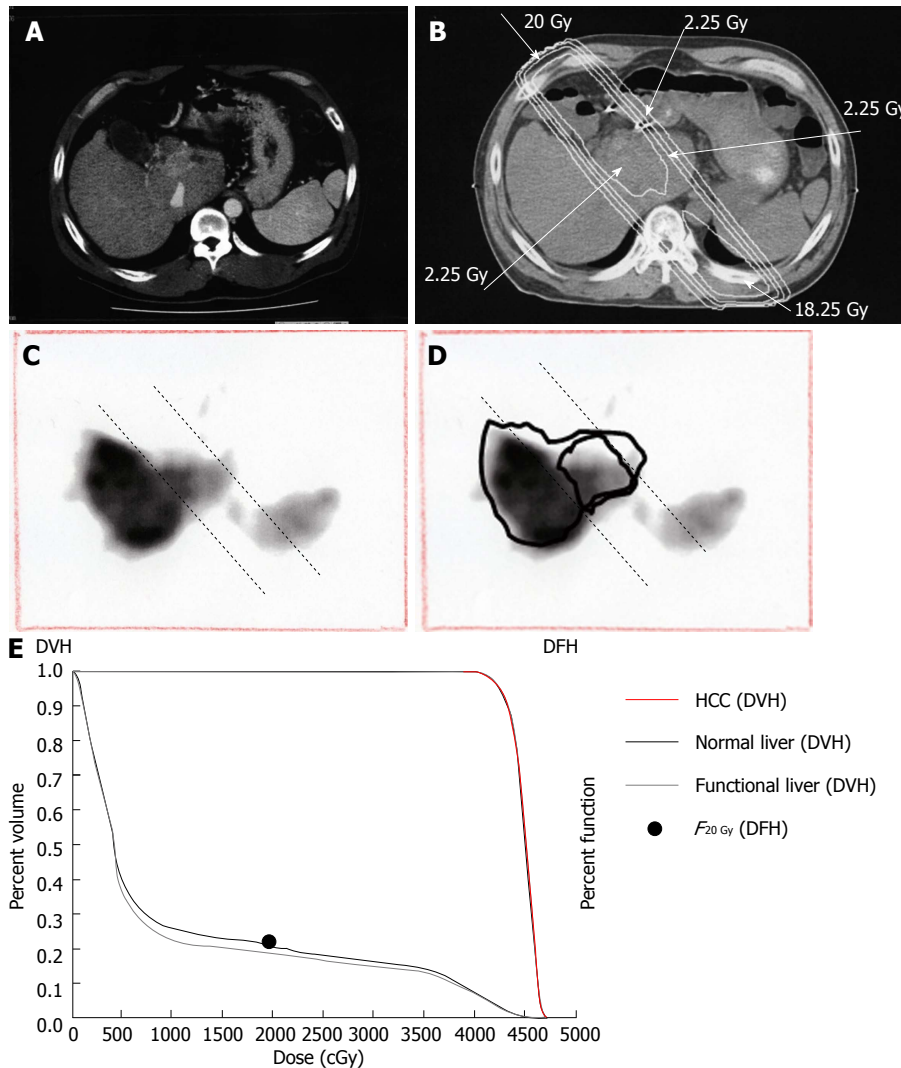


Figure 8 Quantitative analysis of radiation-induced dysfunctional liver. A: Computed tomographic image of a 52-year-old man with a recurrent tumor thrombus in the main portal vein after undergoing left hepatectomy for hepatocellular carcinoma; B: Isodose curves used for treatment planning; C: F_{20Gy} was calculated from the GSA count of the entire liver and the area within the 20 Gy isodose curve; D: F_{20Gy} was calculated from a single photon emission computed tomography with Tc-99m-galactosyl human serum albumin image using the formula: $F_{20Gy} = 100 \times (\text{GSA count in the area of the liver within the 20 Gy isodose curve}) / (\text{GSA count for the entire liver})$; E: In this patient, F_{20Gy} was 22.2%. GSA: Galactosyl human serum albumin; DVH: Dose volume histogram; DFH: Dose function histogram; HCC: Hepatocellular carcinoma.

function in a quantitative manner, they could replace DVH and V_{Gy} as gold-standard methods for evaluating the effects of RT on liver function. However, further studies are needed to confirm the clinical utility of DFH and F_{Gy} in treatment planning for patients with HCC and liver dysfunction.

CONCLUSION

SPECT-B-3DCRT combined with TACE can be performed in patients with HCC of any size, together with a PVTT, HVTT and/or BTTT, offering improved safety and therapeutic outcomes compared with existing modalities. Although $FLV_{20Gy} \leq 20\%$ is a qualitative assessment, it is a useful safety marker for predicting the risk of RILD. We also consider that DFH and F_{Gy} are promising quantitative markers for predicting the effects of SPECT-B-3DCRT in patients with HCC.

ACKNOWLEDGMENTS

Journal of Gastroenterology and Hepatology Research gave assurance that the copyright for this figure is retained by the authors.

REFERENCES

- Mohan R, Brewster LJ, Barest GD. A technique for computing dose volume histograms for structure combinations. *Med Phys* 1987; **14**: 1048-1052 [PMID: 3696069 DOI: 10.1118/1.595984]
- Cheng JC, Wu JK, Lee PC, Liu HS, Jian JJ, Lin YM, Sung JL, Jan GJ. Biologic susceptibility of hepatocellular carcinoma patients treated with radiotherapy to radiation-induced liver disease. *Int J Radiat Oncol Biol Phys* 2004; **60**: 1502-1509 [PMID: 15590181 DOI: 10.1016/j.ijrobp.2004.05.048]
- Liang SX, Zhu XD, Xu ZY, Zhu J, Zhao JD, Lu HJ, Yang YL, Chen L, Wang AY, Fu XL, Jiang GL. Radiation-induced liver disease in three-dimensional conformal radiation therapy for primary liver carcinoma: the risk factors and hepatic radiation tolerance. *Int J Radiat Oncol Biol Phys* 2006; **65**: 426-434 [PMID: 16690430 DOI: 10.1016/j.ijrobp.2005.12.031]
- Burman C, Kutcher GJ, Emami B, Goitein M. Fitting of normal tissue tolerance data to an analytic function. *Int J Radiat Oncol Biol Phys* 1991; **21**: 123-135 [PMID: 2032883 DOI: 10.1016/0360-3016(91)90172-Z]
- Lyman JT. Complication probability as assessed from dose-volume histograms. *Radiat Res Suppl* 1985; **8**: S13-S19 [PMID: 3867079 DOI: 10.2307/3583506]
- Kim TH, Kim DY, Park JW, Kim SH, Choi JI, Kim HB, Lee WJ, Park SJ, Hong EK, Kim CM. Dose-volumetric parameters predicting radiation-induced hepatic toxicity in unresectable hepatocellular carcinoma patients treated with three-dimensional conformal radiotherapy. *Int J Radiat Oncol Biol Phys* 2007; **67**: 225-231 [PMID: 17056199]
- Ikai I, Yamaoka Y, Yamamoto Y, Ozaki N, Sakai Y, Satoh S, Shinkura N, Yamamoto M. Surgical intervention for patients with stage IV-A hepatocellular carcinoma without lymph node metastasis: proposal as a standard therapy. *Ann Surg* 1998; **227**: 433-439 [PMID: 9527067]
- Nanashima A, Yamaguchi H, Shibasaki S, Morino S, Ide N, Takeshita H, Tsuji T, Sawai T, Nakagoe T, Nagayasu T, Oga- wa Y. Relationship between CT volumetry and functional liver volume using technetium-99m galactosyl serum albumin scintigraphy in patients undergoing preoperative portal vein embolization before major hepatectomy: a preliminary study. *Dig Dis Sci* 2006; **51**: 1190-1195 [PMID: 16944008 DOI: 10.1007/s10620-006-8031-x]
- Shuke N, Aburano T, Nakajima K, Yokoyama K, Sun BF, Matsuda H, Muramori A, Michigishi T, Tonami N, Hisada K. [The utility of quantitative ^{99m}Tc -GSA liver scintigraphy in the evaluation of hepatic functional reserve: comparison with ^{99m}Tc -PMT and ^{99m}Tc -Sn colloid]. *Kaku Igaku* 1992; **29**: 573-584 [PMID: 1434071]
- Shirai S, Sato M, Suwa K, Kishi K, Shimono C, Kawai N, Tanihata H, Minamiguchi H, Nakai M. Single photon emission computed tomography-based three-dimensional conformal radiotherapy for hepatocellular carcinoma with portal vein tumor thrombus. *Int J Radiat Oncol Biol Phys* 2009; **73**: 824-831 [PMID: 18755560 DOI: 10.1016/j.ijrobp.2008.04.055]
- Shirai S, Sato M, Suwa K, Kishi K, Shimono C, Sonomura T, Kawai N, Tanihata H, Minamiguchi H, Nakai M. Feasibility and efficacy of single photon emission computed tomography-based three-dimensional conformal radiotherapy for hepatocellular carcinoma 8 cm or more with portal vein tumor thrombus in combination with transcatheter arterial chemoembolization. *Int J Radiat Oncol Biol Phys* 2010; **76**: 1037-1044 [PMID: 19540053 DOI: 10.1016/j.ijrobp.2009.03.023]
- Yamada R, Sato M, Kawabata M, Nakatsuka H, Nakamura K, Takashima S. Hepatic artery embolization in 120 patients with unresectable hepatoma. *Radiology* 1983; **148**: 397-401 [PMID: 6306721]
- Arata S, Tanaka K, Okazaki H, Kondo M, Morimoto M, Saito S, Numata K, Nakamura S, Sekihara H. Risk factors for recurrence of large HCC in patients treated by combined TAE and PEI. *Hepatogastroenterology* 2001; **48**: 480-485 [PMID: 11379338]
- Shirai S, Sato M, Noda Y, Kishi K, Kawai N, Minamiguchi H, Nakai M, Sanda H, Sahara S, Ikoma A, Sonomura T. Distribution of functional liver volume in hepatocellular carcinoma patients with portal vein tumor thrombus in the 1st branch and main trunk using single photon emission computed tomography-application to radiation therapy. *Cancers (Basel)* 2011; **3**: 4114-4126 [DOI: 10.3390/cancers3044114]
- Shirai S, Sato M, Noda Y, Kishi K, Ikoma A, Sanda H, Sonomura T, Minamiguchi H, Nakai M, Kawai N. SPECT-based radiation therapy and transcatheter arterial chemoembolization for unresectable hepatocellular carcinoma sized 14 cm or greater. *Cancer Clin Oncol* 2012; **1**: 65-76 [DOI: 10.5539/cco.v1n1p65]
- Shirai S, Sato M, Noda Y, Kumayama Y, Sonomura T, Kawai N, Minamiguchi H, Nakai M, Sanda H, Tanaka F. The safety indicator of radiotherapy for advanced hepatoma with liver cirrhosis. *J Gastroenterol Hepatol Res* 2013; **2**: 730-736
- Sugahara K, Togashi H, Takahashi K, Onodera Y, Sanjo M, Misawa K, Suzuki A, Adachi T, Ito J, Okumoto K, Hattori E, Takeda T, Watanabe H, Saito K, Saito T, Sugai Y, Kawata S. Separate analysis of asialoglycoprotein receptors in the right and left hepatic lobes using Tc-GSA SPECT. *Hepatology* 2003; **38**: 1401-1409 [PMID: 14647051 DOI: 10.1053/jhep.2003.09031]
- Kaibori M, Ha-Kawa SK, Maehara M, Ishizaki M, Matsui K, Sawada S, Kwon AH. Usefulness of Tc- 99m -GSA scintigraphy for liver surgery. *Ann Nucl Med* 2011; **25**: 593-602 [PMID: 21800021 DOI: 10.1007/s12149-011-0520-0]
- Christian JA, Partridge M, Nioutsikou E, Cook G, McNair HA, Cronin B, Courbon F, Bedford JL, Brada M. The incorporation of SPECT functional lung imaging into inverse radiotherapy planning for non-small cell lung cancer. *Radiother Oncol* 2005; **77**: 271-277 [PMID: 16274762 DOI: 10.1016/j.radonc.2005.08.008]
- Marks LB, Sherouse GW, Munley MT, Bentel GC, Spencer DP. Incorporation of functional status into dose-volume analysis. *Med Phys* 1999; **26**: 196-199 [PMID: 10076973 DOI: 10.1118/1.598503]

- 21 **Seppenwoolde Y**, Muller SH, Theuws JC, Baas P, Belderbos JS, Boersma LJ, Lebesque JV. Radiation dose-effect relations and local recovery in perfusion for patients with non-small-cell lung cancer. *Int J Radiat Oncol Biol Phys* 2000; **47**: 681-690 [PMID: 10837952 DOI: 10.1016/S0360-3016(00)00454-5]
- 22 **Sawamura T**, Nakada H, Hazama H, Shiozaki Y, Sameshima Y, Tashiro Y. Hyperasialoglycoproteinemia in patients with chronic liver diseases and/or liver cell carcinoma. Asialoglycoprotein receptor in cirrhosis and liver cell carcinoma. *Gastroenterology* 1984; **87**: 1217-1221 [PMID: 6092193]
- 23 **Japanese Society for Therapeutic Radiology and Oncology.** Hepatocellular carcinoma. In: Radiotherapy planning guideline 2012 (in Japanese). Tokyo: Kinbara Pub, 2012: 161-164
- 24 **Emami B**, Lyman J, Brown A, Coia L, Goitein M, Munzner JE, Shank B, Solin LJ, Wesson M. Tolerance of normal tissue to therapeutic irradiation. *Int J Radiat Oncol Biol Phys* 1991; **21**: 109-122 [PMID: 2032882 DOI: 10.1016/0360-3016(91)90171-Y]
- 25 **Park W**, Lim DH, Paik SW, Koh KC, Choi MS, Park CK, Yoo BC, Lee JE, Kang MK, Park YJ, Nam HR, Ahn YC, Huh SJ. Local radiotherapy for patients with unresectable hepatocellular carcinoma. *Int J Radiat Oncol Biol Phys* 2005; **61**: 1143-1150 [PMID: 15752895 DOI: 10.1016/j.ijrobp.2004.08.028]
- 26 **Sugahara S**, Oshiro Y, Nakayama H, Fukuda K, Mizumoto M, Abei M, Shoda J, Matsuzaki Y, Thono E, Tokita M, Tsuboi K, Tokuyue K. Proton beam therapy for large hepatocellular carcinoma. *Int J Radiat Oncol Biol Phys* 2010; **76**: 460-466 [PMID: 19427743 DOI: 10.1016/j.ijrobp.2009.02.030]
- 27 **Mornex F**, Girard N, Beziat C, Kubas A, Khodri M, Trepo C, Merle P. Feasibility and efficacy of high-dose three-dimensional-conformal radiotherapy in cirrhotic patients with small-size hepatocellular carcinoma non-eligible for curative therapies--mature results of the French Phase II RTF-1 trial. *Int J Radiat Oncol Biol Phys* 2006; **66**: 1152-1158 [PMID: 17145534 DOI: 10.1016/j.ijrobp.2006.06.015]

P- Reviewer: Francica G, Kumar P, Picardi A **S- Editor:** Ji FF
L- Editor: Roemmele A **E- Editor:** Liu SQ



Upper gastrointestinal barium evaluation of duodenal pathology: A pictorial review

Pankaj Gupta, Uma Debi, Saroj Kant Sinha, Kaushal Kishor Prasad

Pankaj Gupta, Department of Radiodiagnosis, Postgraduate Institute of Medical Education and Research, Chandigarh 160012, India

Uma Debi, Division of GE Radiology, Department of Superspeciality of Gastroenterology, Postgraduate Institute of Medical Education and Research, Chandigarh 160012, India

Saroj Kant Sinha, Department of Superspeciality of Gastroenterology, Postgraduate Institute of Medical Education and Research, Chandigarh 160012, India

Kaushal Kishor Prasad, Division of GE Histopathology, Department of Superspeciality of Gastroenterology, Postgraduate Institute of Medical Education and Research, Chandigarh 160012, India

Author contributions: Gupta P and Debi U contributed in generating the figures and writing the article; Sinha SK contributed in writing the article; and Prasad KK contributed in writing the article, revising the article critically and gave final approval of the version to be published.

Correspondence to: Kaushal Kishor Prasad, MD, PDC, CFN, MAMS, FICPath, Additional Professor, Chief, Division of GE Histopathology, Department of Superspeciality of Gastroenterology, Postgraduate Institute of Medical Education and Research, Sector-12, Chandigarh 160012, India. kaushalkp10@hotmail.com
Telephone: +91-172-2756604 Fax: +91-172-2744401

Received: February 11, 2014 Revised: April 15, 2014

Accepted: July 18, 2014

Published online: March 28, 2015

Abstract

Like other parts of the gastrointestinal tract (GIT), duodenum is subject to a variety of lesions both congenital and acquired. However, unlike other parts of the GIT *viz.* esophagus, rest of the small intestine and large intestine, barium evaluation of duodenal lesions is technically more challenging and hence not frequently reported. With significant advances in computed tomography technology, a thorough evaluation including intraluminal, mural and extramural is feasible in a single non-invasive examination. Notwithstanding, barium evaluation still remains the initial and sometimes the only imaging study in several parts of the world. Hence,

a thorough acquaintance with the morphology of various duodenal lesions on upper gastrointestinal barium examination is essential in guiding further evaluation. We reviewed our experience with various common and uncommon barium findings in duodenal abnormalities.

© 2015 Baishideng Publishing Group Inc. All rights reserved.

Key words: Barium study; Duodenum; Upper gastrointestinal tract; Small bowel; Pathology

Core tip: Barium evaluation of duodenal pathologies is technically more challenging than rest of gastrointestinal tract. Barium study still forms an initial and integral part of evaluation as it provide useful clues to the diagnosis and guide further evaluation. This article should alert the radiologist to consider various common and uncommon duodenal pathologies in the correct clinical setting to guide the clinician for further investigations to ensure correct diagnosis and enable appropriate treatment.

Original sources: Gupta P, Debi U, Sinha SK, Prasad KK. Upper gastrointestinal barium evaluation of duodenal pathology: A pictorial review. *World J Radiol* 2014; 6(8): 613-618 Available from: URL: <http://www.wjgnet.com/1949-8470/full/v6/i8/613.htm> DOI: <http://dx.doi.org/10.4329/wjr.v6.i8.613>

INTRODUCTION

Duodenum is often an overlooked segment of the gastrointestinal tract (GIT) as much of the GIT Radiology literature has focused on the esophagus, stomach, distal small bowel and colon. Duodenum like other parts of the GIT is affected by a variety of pathologic conditions including congenital, inflammatory and neoplastic diseases. While some of the congenital abnormalities like duplications and diverticulae are usually asymptomatic, others

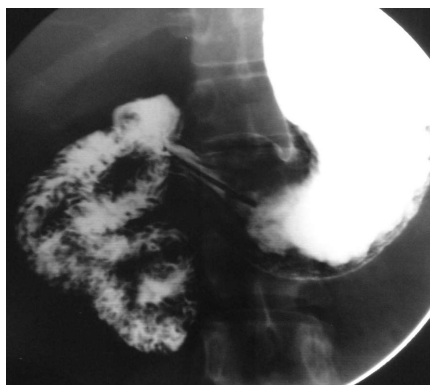


Figure 1 Upper gastrointestinal barium study reveals that the duodenojejunal flexure does not cross the left of the midline suggestive of malrotation.



Figure 2 Widening of the duodenal C-loop is noted. Ultrasonography (not shown) showed a well-defined cystic lesion suggestive of duplication. This is a non-specific barium finding.

like annular pancreas and malrotation may manifest in the first decade of life. Inflammatory involvement of the duodenum results from peptic ulcer disease, Crohn's disease (CD) and adjacent inflammatory conditions. Duodenal neoplasms are rare and malignant tumors are much more common than benign tumors. Although, there are no specific signs of the various duodenal pathologies on upper GIT barium series, barium evaluation still forms an integral part of evaluation of patients in several parts of the world due to easy availability and relatively less cost. However, computed tomography (CT) and endoscopy have a greater sensitivity and specificity in detecting duodenal pathologies. CT, in particular provides information about both intramural and extramural disease processes. When used as an initial imaging tool, barium examination does provide useful clues to the underlying pathophysiological processes and as such guide the choice of further tests. Barium examination of duodenum may be contraindicated in suspected leak, history of recent surgery or acute trauma. In these situations, water soluble contrast study replaces barium study. Correct diagnosis requires a thorough knowledge of the appearance of disease processes of duodenum on barium studies. We present a brief barium pictorial review of common and uncommon duodenal lesions.

ANATOMY

Except for the bulb, duodenum is a retroperitoneal structure. It lies within the anterior pararenal space. Forming a C-loop segment around the pancreatic head, this 30 cm tube extends from pylorus to the ligament of Treitz. It is arbitrarily divided into four parts based on their anatomic orientation. The relationship of the proximal and distal end to the spine is important. The pyloric end of the duodenum lies to the right of the spine and the duodenojejunal (DJ) flexure to the left of the pedicle of the spine.

CONGENITAL ANOMALIES

Midgut malrotation

The embryological basis is inadequate rotation of the intestinal loop around the axis of the superior mesenteric artery (SMA) during fetal life, around 10th week of development. Malrotation may occur as an isolated congenital anomaly or as a part of visceral situs anomalies^[1]. In practical terms, malrotation can be classified into three types: non-rotation, malrotation and reverse rotation^[2]. Former, the most common type is usually asymptomatic and incidentally detected and is imprecisely labeled as non-rotation. Reverse rotation is rare.

Upper gastrointestinal (UGI) barium study is accurate for detection of malrotation. The DJ junction does not cross the midline and is below the duodenal bulb (Figure 1). Delayed evaluation usually shows abnormal location of the right colon. Though abnormal position of caecum is suggestive, normal position does not exclude the diagnosis as it can be normally location in 20% cases^[3].

Duplication

Most common site for duplication in the GIT is ileocecal region. Duodenal duplication is relatively uncommon congenital anomaly, accounting for less than 10% of all GIT duplications^[4]. It is typically located along the mesenteric aspect of the first and second parts of the duodenum. On barium evaluation, extrinsic mass effect is noted on the duodenum and greater curvature of the stomach (Figure 2). Though rare, communication with the duodenum can be found. The barium findings are non-specific. Differential diagnosis include choledochal cyst, pancreatic lesions including pancreatic masses, pseudocyst, *etc.* and large duodenal diverticulum. A specific diagnosis can be made on high resolution ultrasonography if classical multi-layered appearance (gut signature) is seen^[5].

Diverticulum

Duodenal diverticulum can be congenital or acquired. It is a frequent incidental finding detected in about 5% of upper GIT barium studies^[6]. The most common site is along mesenteric border of second part of duodenum near the ampulla of Vater. It is seen as barium filled out pouching along the medial aspect of the second part of duodenum, although other locations are not uncommon (Figure 3).



Figure 3 Barium filled out pouching is noted along the medial aspect of the second part of the duodenum (arrow) suggestive of a duodenal diverticulum.

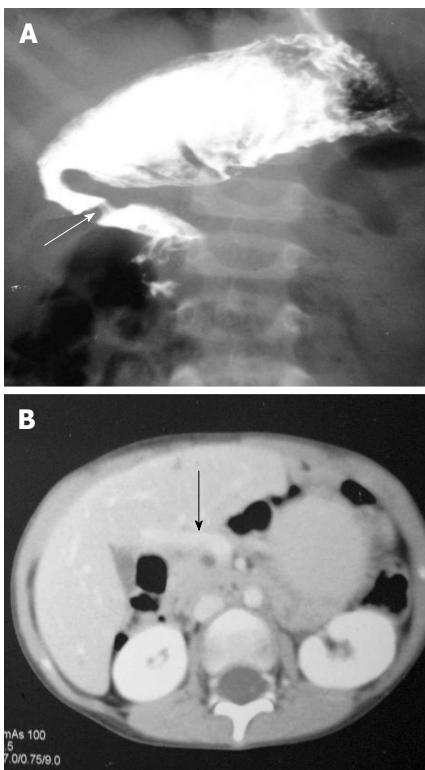


Figure 4 Upper gastrointestinal barium study (A) shows a band like extrinsic narrowing of the first part of the duodenum (arrow), axial computed tomography image (B) reveals the anomalous position of the portal vein anterior to the duodenum (arrow) suggestive of preduodenal portal vein.

Preduodenal portal vein

It usually occurs in association with other congenital malformation, most commonly malrotation, pancreatic, splenic and cardiac anomalies. The portal vein passes anterior to the duodenum and pancreatic head^[7]. On barium study, it appears as an extrinsic linear impression on the proximal duodenum or obstruction of the proximal duodenum (Figure 4A). The correct diagnosis is made by contrast enhanced CT that shows the abnormal location of portal vein (Figure 4B).

Annular pancreas

The embryologic basis of the annular pancreas is a defect

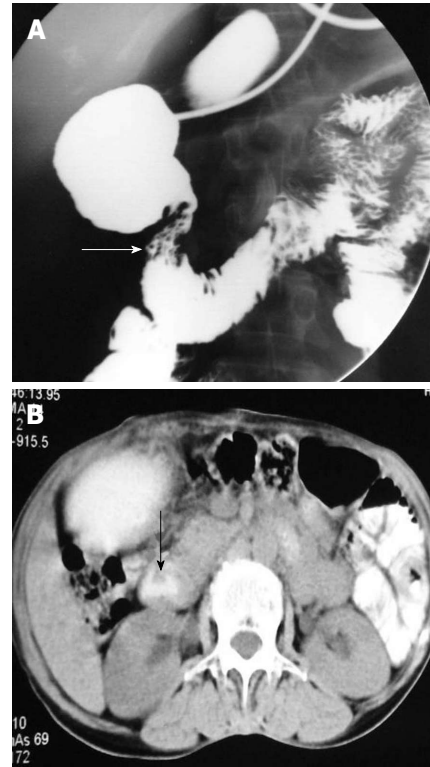


Figure 5 Upper gastrointestinal barium study (A) demonstrates smooth circumferential extrinsic narrowing of the second part of the duodenum (arrow), axial computed tomography image (B) shows pancreatic parenchyma incompletely surrounding the duodenum (arrow), features suggestive of partial annular pancreas.

in the normal rotation of the ventral pancreatic anlage. The result of this aberration is encircling of the second part of duodenum by pancreatic tissue. The annulus encircles the duodenum partially or completely^[8]. Pathologically, it is usually loosely applied to the serosa of the duodenum. In extreme cases, the pancreatic tissue is interdigitated with the wall of the duodenum. On barium study, it produces a smooth or tapered narrowing of the second part of the duodenum (Figure 5A). The diagnosis is confirmed by cross-sectional imaging, usually a CT scan (Figure 5B).

Duodenal web

There are several varieties of webs: complete duodenal atresias (imperforate webs), wind sock webs and webs with central or eccentric apertures. The most common sites of web are in vicinity of the ampulla either preampullary or postampullary location^[8] (Figure 6). Upper GIT barium study shows the abnormality as a short segment transverse filling defect in the descending duodenum.

Brunner gland hyperplasia

Brunner's gland hyperplasia is a frequent asymptomatic finding on upper GIT barium evaluation. It is seen as solitary or multiple nodular filling defects that are typically less than 5 mm in diameter in the proximal duodenum^[9]. When extensive, the nodules lead to a cobblestone or Swiss-cheese pattern (Figure 7). The differential diagnoses for such filling defects in the duodenum include heterotopia,



Figure 6 A short segment narrowing (arrow) suggestive of a web is noted at the junction of first and second part of duodenum. In addition, multiple diverticula are seen at the medial aspect of the second part of the duodenum (arrowheads).

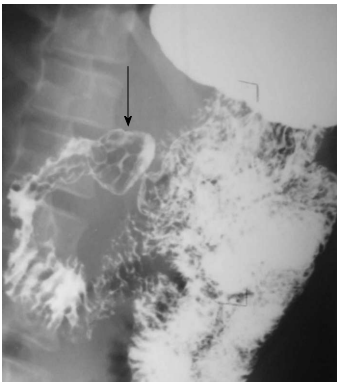


Figure 7 Multiple nodular filling defects are noted in the duodenal cap (arrow) along with fold thickening in the second part of the duodenum. These findings suggest a diagnosis of Brunner gland hyperplasia.

nodular lymphoid hyperplasia, multiple adenomas in familial adenomatous polyposis, hamartomas in Peutz-Jeghers syndrome, carcinoid tumors and metastatic deposits.

ACQUIRED DISEASES

Inflammatory diseases

Peptic ulcer disease: Duodenal ulcers (DUs) are common and affect nearly one-tenth of the adult population. DUs are almost always benign. This is unlike gastric ulcers where 5% of the ulcers can be malignant. Though endoscopy is the most sensitive and specific method for diagnosis of suspected DUs, it is invasive and costly. Double-contrast UGI barium study still remains a useful alternative to endoscopy^[10]. More than 90% of DUs occur in the duodenal bulb and nearly 50% of these occur on the anterior wall. Ulcer craters are seen as well-defined round or ovoid pools of barium, surrounded by a symmetrical mound of edematous mucosa. Adjacent radiating mucosal folds converge to the edge of the crater. Healed ulcer leads to deformity of the bulb (Figure 8A). The uncommon variety of DUs, postbulbar ulcers are usually located along the medial aspect of the second part of duodenum above the ampulla of Vater (Figure

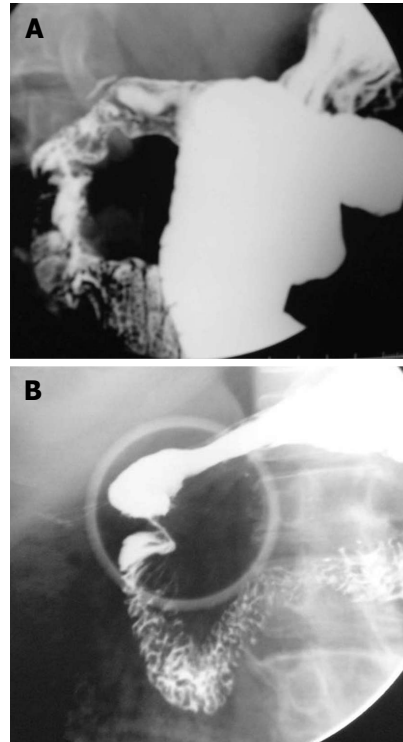


Figure 8 Upper gastrointestinal barium study shows deformity of the duodenal cap (A), stricture is noted at the junction of first and second part of the duodenum (B). These findings are secondary to healed bulbar (A) and post bulbar duodenal ulcers (B).

8B). Diagnosis on barium study is hampered by location; however indentation of the lateral wall of the duodenum opposite the ulcer due to spasm offers a clue^[10].

Tuberculosis: Duodenal tuberculosis (TB) comprises 2% of gastrointestinal TB. Clinically, the patients are divided into two groups: those having dyspeptic symptoms and those with obstructive symptoms. In the former group, barium findings include: luminal narrowing, ulcerations and extrinsic compression. These changes typically spare the proximal duodenum. Less frequently, scarring of duodenal cap, widening of the C-loop are noted. In the group with obstructive symptoms, findings include luminal narrowing of varying degrees (Figure 9) or cut off at junction of second and third part of duodenum resembling the SMA syndrome.

Concomitant tuberculous involvement of rest of the GIT is fairly common. Associated involvement of biliary tract can be noted (Figure 9). This takes the form of air in the common bile duct or reflux of barium into the biliary tree.

CD: CD affects the upper GIT mucosa in 20%-40% of patients. Early disease leads to irregular thickening, edema and cobblestone appearance. With disease progression, there is fibrosis and stenosis of the involved segment. Finally a string sign may develop. There are three patterns of involvement in advanced disease. The first and the most common pattern is the contiguous involvement of stomach and duodenum^[11]. Other two patterns are isolat-



Figure 9 There is narrowing of the distal second part of the duodenum with reflux of barium into the common bile ducts. This patient had concomitant involvement of the ileocecal junction (not shown). Histopathology revealed a diagnosis of gastrointestinal tuberculosis.



Figure 10 A long segment narrowing with irregular outline and proximal dilatation is noted in the fourth part of duodenum. In addition few strictures are also noted in proximal jejunum. Detailed evaluation in this patient revealed a diagnosis of Crohn's disease.

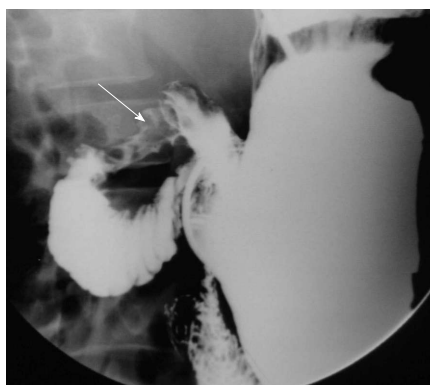


Figure 11 Mild luminal narrowing with ulceration is noted in the proximal duodenum. Computed tomography of this patient (not shown) revealed mural thickening of the duodenum with cystic changes suggestive of cystic dystrophy.

ed involvement of proximal and distal duodenum (Figure 10). Less common findings are development of fissures, pseudodiverticulae and reflux of contrast into the biliary tree. Advanced gastroduodenal involvement may lead to pseudo-Billroth I appearance.



Figure 12 Upper gastrointestinal barium study shows cut off of the duodenum at the junction of second and third part with collapsed distal duodenum suggestive of superior mesenteric artery syndrome.

Extrinsic inflammatory or neoplastic diseases affecting the duodenum: Nonspecific duodenal wall thickening may occur in inflammatory conditions of pancreas or gall bladder. In addition, adjacent neoplastic processes can involve duodenum, *e.g.*, pancreatic adenocarcinoma.

Duodenal dystrophy: This entity is associated with groove pancreatitis, a variant of chronic pancreatitis. It is characterised by the presence of multiple cystic lesions in the duodenal wall that is thickened because of chronic inflammation^[12]. Barium findings are non-specific and demonstrate only stenosis of the involvement segment with or without irregularity of outline (Figure 11). Endoscopic ultrasound is the modality of choice. CT shows thickened duodenal wall between the duodenal lumen and pancreas. Cystic lesions are noted within the thickened wall.

SMA syndrome

SMA syndrome is a rare condition characterised by acute angulation of SMA leading to compression of the third part of the duodenum between the SMA and the aorta^[13]. The basic etiological factor is loss of abdominal fat due to a variety of debilitating conditions. Upper GIT barium study shows extrinsic compression of the third part, dilatation of the proximal duodenum and a collapsed small bowel distal to the impression of SMA (Figure 12).

Neoplasms

Duodenal tumors account for about one-third of small bowel neoplasm. Overall small bowel tumors comprise only 5% of the gastrointestinal tumors. Benign tumors are rare. These include adenomatous polyp, lipoma and leiomyoma. Primary adenocarcinoma is the most common malignant lesion of the duodenum and is usually found in the periampullary region^[14] (Figure 13). It presents as either a polypoidal mass causing filling defect or an irregular, annular constricting lesion with deformity of the lumen and mucosal irregularity. Rare malignant lesions include lymphoma (Figure 14) and malignant gastrointestinal stromal tumors.

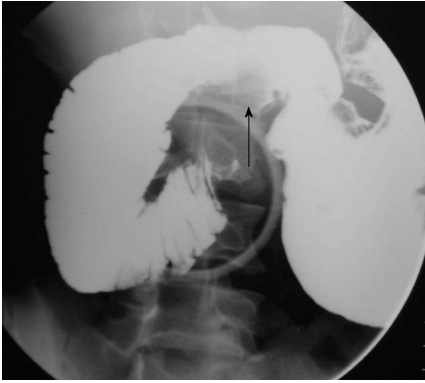


Figure 13 A mass is noted in relation to the medial aspect of the first and second part of the duodenum with ulceration (arrow). In addition stricture with mucosal irregularity is seen in distal third part of duodenum. Endoscopic biopsy revealed adenocarcinoma.

CONCLUSION

Duodenal pathologies are distinct from those in rest of the GIT. Upper gastrointestinal barium study comprises one of the initial methods of evaluation of duodenal pathologies. Though, not entirely specific for a particular pathological entity, barium studies do provide a fairly good idea about the underlying disease pattern and guide further management.

REFERENCES

- 1 **Snyder WH**, Chaffin L. Embryology and pathology of the intestinal tract: presentation of 40 cases of malrotation. *Ann Surg* 1954; **140**: 368-379 [PMID: 13198074 DOI: 10.1097/00000658-195409000-00013]
- 2 **Maxson RT**, Franklin PA, Wagner CW. Malrotation in the older child: surgical management, treatment, and outcome. *Am Surg* 1995; **61**: 135-138 [PMID: 7856973]
- 3 **Berdon WE**. The diagnosis of malrotation and volvulus in the older child and adult: a trap for radiologists. *Pediatr Radiol* 1995; **25**: 101-103 [PMID: 7596651]
- 4 **Macpherson RI**. Gastrointestinal tract duplications: clinical, pathologic, etiologic, and radiologic considerations. *Radiographics* 1993; **13**: 1063-1080 [PMID: 8210590 DOI: 10.1148/radiographics.13.5.8210590]
- 5 **Fidler JL**, Saigh JA, Thompson JS, Habbe TG. Demonstration of intraluminal duodenal diverticulum by computed tomography. *Abdom Imaging* 1998; **23**: 38-39 [PMID: 9437060 DOI: 10.1007/s002619900281]
- 6 **Stone EE**, Brant WE, Smith GB. Computed tomography of duodenal diverticula. *J Comput Assist Tomogr* 1989; **13**: 61-63 [PMID: 2492039 DOI: 10.1097/00004728-198901000-00012]
- 7 **Talus H**, Roohipur R, Depaz H, Adu AK. Preduodenal portal vein causing duodenal obstruction in an adult. *J Am Coll Surg* 2006; **202**: 552-553 [PMID: 16500261 DOI: 10.1016/j.jamcollsurg.2005.08.022]
- 8 **Hwang JI**, Chiang JH, Yu C, Cheng HC, Chang CY, Muel-

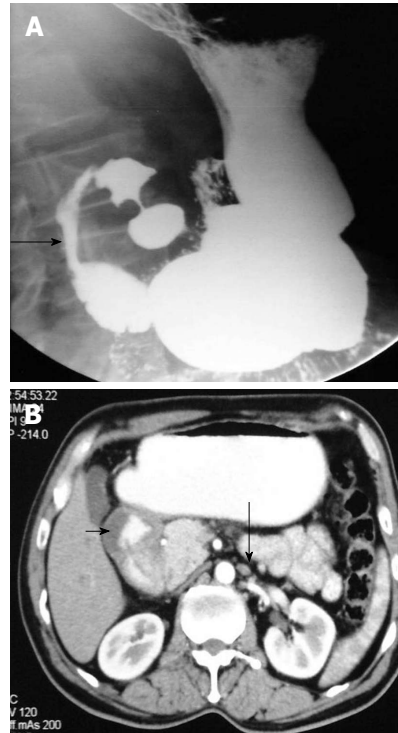


Figure 14 A long segment narrowing of the second part (arrow) of the duodenum is noted (A), axial computed tomography image (B) shows circumferential mural thickening of the duodenum (short arrow) with few para-aortic lymph nodes (long arrow). Endoscopic biopsy revealed a diagnosis of non-Hodgkin lymphoma.

- ler PR. Pictorial review: Radiological diagnosis of duodenal abnormalities. *Clin Radiol* 1998; **53**: 323-332 [PMID: 9630268 DOI: 10.1016/S0009-9260(98)80002-0]
- 9 **Gore RM**, Levine MS. Textbook of gastrointestinal radiology. 2nd ed. Philadelphia, PA: Saunders. 2000: 593-595
- 10 **Levine MS**, Creteur V, Kressel HY, Laufer I, Herlinger H. Benign gastric ulcers: diagnosis and follow-up with double-contrast radiography. *Radiology* 1987; **164**: 9-13 [PMID: 3588932 DOI: 10.1148/radiology.164.1.3588932]
- 11 **Nugent FW**, Richmond M, Park SK. Crohn's disease of the duodenum. *Gut* 1977; **18**: 115-120 [PMID: 856671 DOI: 10.1136/gut.18.2.115]
- 12 **Procacci C**, Graziani R, Zamboni G, Cavallini G, Pederzoli P, Guarise A, Bogina G, Biasiutti C, Carbognin G, Bergamo-Andreis IA, Pistolesi GF. Cystic dystrophy of the duodenal wall: radiologic findings. *Radiology* 1997; **205**: 741-747 [PMID: 9393530 DOI: 10.1148/radiology.205.3.9393530]
- 13 **Lippl F**, Hannig C, Weiss W, Allescher HD, Classen M, Kurjak M. Superior mesenteric artery syndrome: diagnosis and treatment from the gastroenterologist's view. *J Gastroenterol* 2002; **37**: 640-643 [PMID: 12203080 DOI: 10.1007/s005350200101]
- 14 **Kazerooni EA**, Quint LE, Francis IR. Duodenal neoplasms: predictive value of CT for determining malignancy and tumor resectability. *AJR Am J Roentgenol* 1992; **159**: 303-309 [PMID: 1632344 DOI: 10.2214/ajr.159.2.1632344]

P- Reviewer: El-Sayed M, Li YY, Maglinte DDT, Perju-Dumbrava D, Slomiany BL

S- Editor: Wen LL **L- Editor:** A **E- Editor:** Liu SQ



Expectations from imaging for pre-transplant evaluation of living donor liver transplantation

Tiffany Henedige, Gopinathan Anil, Krishnakumar Madhavan

Tiffany Henedige, Gopinathan Anil, Department of Diagnostic Imaging, National University Health and Yong Loo Lin School of Medicine, Singapore 119074, Singapore

Krishnakumar Madhavan, Department of Department of General Surgery, National University Hospital Singapore, Singapore 119074, Singapore

Author contributions: All the three authors have contributed equally to this work.

Correspondence to: Gopinathan Anil, MD, DNB, FRCR (Lon), FAMS, Department of Diagnostic Imaging, National University Health and Yong Loo Lin School of Medicine, 5 Lower Kent Ridge Road, Singapore 119288, Singapore. ivyanil10@gmail.com
Telephone: +65-97296614 Fax: +65-67797101

Received: February 8, 2014 Revised: March 25, 2014

Accepted: July 15, 2014

Published online: March 28, 2015

Abstract

Living donor liver transplant (LDLT) is a major surgical undertaking. Detailed pre-operative assessment of the vascular and biliary anatomy is crucial for safe and successful harvesting of the graft and transplantation. Computed tomography (CT) and magnetic resonance imaging (MRI) are currently the imaging modalities of choice in pre-operative evaluation. These cross-sectional imaging techniques can reveal the vascular and biliary anatomy, assess the hepatic parenchyma and perform volumetric analysis. Knowledge of the broad indications and contraindications to qualify as a recipient for LDLT is essential for the radiologist reporting scans in a pre-transplant patient. Similarly, awareness of the various anatomical variations and pathological states in the donor is essential for the radiologist to generate a meaningful report of his/her observations. CT and MRI have largely replaced invasive techniques such as catheter angiography, percutaneous cholangiography and endoscopic retrograde cholangiopancreatography. In order to generate a meaningful report based on these pre-operative imaging scans, it is also mandatory for the radiologist to be aware of the sur-

geon's perspective. We intend to provide a brief overview of the common surgical concepts of LDLT and give a detailed description of the minimum that a radiologist is expected to seek and report in CT and MR scans performed for LDLT related evaluation.

© 2015 Baishideng Publishing Group Inc. All rights reserved.

Key words: Liver transplantation; Pre-living donor liver transplant imaging; Vascular anatomy and variants; Biliary anatomy and variants; Computed tomography; Magnetic resonance imaging

Core tip: Living donor liver transplantation (LDLT) has evolved to a widely accepted therapeutic option. As a radiologist, knowledge of the various anatomical variations and pathological states in both the donor and recipient are imperative to generating a meaningful report in pre-operative evaluation. This paper provides a brief overview of the common surgical concepts of LDLT and gives a detailed description of the minimum that a radiologist is expected to seek and report in computed tomography and magnetic resonance scans performed for LDLT related evaluation.

Original sources: Henedige T, Anil G, Madhavan K. Expectations from imaging for pre-transplant evaluation of living donor liver transplantation. *World J Radiol* 2014; 6(9): 693-707 Available from: URL: <http://www.wjgnet.com/1949-8470/full/v6/i9/693.htm> DOI: <http://dx.doi.org/10.4329/wjr.v6.i9.693>

INTRODUCTION

Living donor liver transplantation (LDLT) has evolved into a widely accepted therapeutic option to ease the persistent shortage of cadaveric livers for deceased donor liver transplantation (DDLTL)^[1]. Together with improved surgical techniques and advances in immunology, the

outcome in terms of LDLT recipient survival is as good as those attained after DDLT with full-sized deceased donor organs^[2]. LDLT enables healthy volunteers to donate a portion of their liver to compatible recipients. Resection of a portion of the liver from a donor is an immense personal and surgical undertaking; hence a detailed knowledge of the vascular and biliary anatomy and the presence of variants are imperative to ensure safe and successful harvesting of the graft and transplantation^[3]. The risk to the donor from LDLT is estimated to be 0.5% mortality and up to 21% post-operative morbidity^[4].

In the past, semi-invasive techniques such as catheter angiography and endoscopic retrograde cholangiopancreatography were used to delineate vascular and biliary anatomy respectively. Liver biopsies were commonly performed for ruling out diffuse parenchymal changes such as steatosis. With the exponential progress in computed tomography (CT) and MR techniques, today it is possible to obtain the same information non-invasively. Some of the major limitations of conventional invasive techniques such as morbidity and mortality, high cost, higher radiation exposure as well as sub-optimal demonstration of venous anatomy have been overcome by shifting to pre-operative evaluation with CT and MRI^[5].

INDICATIONS FOR TRANSPLANT

The major indications for liver transplantation (LT) are irreversible hepatic failure and hepatocellular carcinoma (HCC)^[6]. Advanced cirrhosis secondary to chronic viral hepatitis or alcohol abuse is the most frequent cause of hepatic failure that leads to transplantation^[1]. Cholestatic and metabolic diseases are the other pathologies that often result in end-stage liver disease. The usual cholestatic diseases that end up in LT are primary biliary cirrhosis, primary sclerosing cholangitis and biliary atresia^[1]. Several metabolic diseases like non-alcoholic steatohepatitis, Wilson's disease, haemochromatosis, cystic fibrosis and glycogen storage disease may eventually need a LT for patient survival^[1,7].

RECIPIENT CRITERIA

Various criteria have been described to assess the eligibility of a recipient to obtain a liver transplant. The rationale of these criteria is to ensure that LT is done for those patients who need it the most and in those who are most likely to benefit from it. The guidelines on ensuring fair allocation of the cadaveric graft, a scarce resource, among transplant candidates, have gone through various stages of evolution. Features of decompensated cirrhosis such as ascites, encephalopathy, refractory variceal hemorrhage and hepatorenal syndrome are accounted for while triaging a patient for transplantation^[6]. Before 2002, Child-Turcotte-Pugh (CTP) Score was the primary basis for prioritization of candidates for LT. Currently, priority is assigned to a patient on the transplantation list on the basis of his/her highest estimated short-term

mortality risk determined using the Model for End-Stage Liver Disease (MELD) score^[6]. The MELD is a multi-parameteric mathematical score that utilizes the patient's serum bilirubin, serum creatinine and the international normalized ratio to predict survival with higher scores indicating a sicker patient; hence in more urgent need of LT. The MELD was initially developed to predict death within three months of the procedure in patients who had undergone a transjugular intrahepatic portosystemic shunt. As it was found to be a reliable measure in estimation of short-term mortality risk, it was adopted over CTP for determining and prioritizing recipients of LT^[8]. Compared to CTP, MELD is a more objective scoring system that avoids potential inter-observer bias and also takes into account renal dysfunction, a common problem among cirrhotics. Adjustments to MELD scores are made for patients with HCC depending on the stage of the disease.

Although HCC is an indication for LT in the appropriate setting, extensive disease can be a contraindication. In 1998 Mazzaferro *et al*^[9] reported excellent outcomes after LT in patients with a solitary HCC less than 5 cm in diameter or with up to 3 HCC nodules that were each less than 3 cm in diameter; these tumor characteristics and an absence of involvement of the main and primary branches of the portal vein by tumour formed the Milan criteria. Patients outside these criteria are generally believed to have poor tumor biology with high chances of recurrence and hence less likely to benefit from a liver transplant. Strict adherence to Milan Criteria may however preclude patients with a slightly more advanced HCC who may have acceptable, if not excellent long term outcomes from undergoing a transplant. This was the rationale behind the development of the University of California San Francisco (UCSF) criteria. According to UCSF criteria, patients with a single hepatoma < 6.5 cm in diameter or less than 4 hepatomas, with the largest < 4.5 cm in diameter and the sum of the diameters of all the tumors < 8 cm have a recurrence-free survival rate after LT close to that achieved with the Milan criteria^[10]. The Milan and UCSF criteria provide broad guidelines to cadaveric liver allocation in many countries. However, every case still merits individual evaluation in a multidisciplinary meeting before being subjected to surgery.

Some of the absolute contraindications to transplantation include active extra-hepatic malignancy, non-hepatic active or uncontrolled infection, thrombosis of the entire portal and superior mesenteric venous system, active substance abuse, advanced cardiopulmonary disease or other co-morbidities that would compromise post-surgical recovery^[6].

DONOR CRITERIA

The initial steps in the assessment of a potential liver donor include blood type compatibility, biochemical tests, viral markers and relevant co-morbidities. If these are satisfactory, radiological evaluation follows. If indicated,

a liver biopsy may have to be performed^[11]. Variation in anatomy of potential donors can alter surgical approach or even preclude surgery^[12,13]. Adequate liver volume with respect to both the graft for the recipient and remnant liver for the donor also needs to be assessed.

SURGICAL CONSIDERATIONS

For the reporting radiologist, understanding the surgeon's perspective on LDLT is imperative so that the necessary information can be conveyed pre-operatively. The three most often harvested grafts for LDLT are the right lobe, left lobe and left lateral segment grafts. The type of hepatectomy is based on the vascular and biliary anatomy as well as the estimated graft and remnant liver volume^[14].

Traditionally, liver surgery relies on Couinaud's liver segment classification that divides the liver into eight functionally independent segments^[15]. The right hepatic vein (RHV) divides the right lobe into anterior (V and VIII) and posterior (VI and VII) sectors, the middle hepatic vein (MHV) divides the liver into right (V-VIII) and left lobes (II to IV) and the left hepatic vein (LHV) divides the left lobe into a medial (IVa and IVb) and lateral part (II and III). The portal vein divides the liver into superior (VII, VIII, IVa and II) and inferior (VI, V, IVb and III) segments.

Left lateral hepatectomy that harvests segment II and III is the most common LDLT technique and usually used for paediatric recipients or recipients of small size. Most of the adult recipients need a left or right liver graft; this decision depends on the residual volume of donor liver and size of the recipient. The techniques of right or left hepatectomy are fairly standardized worldwide^[16-18]. Some controversy exists regarding the inclusion of the middle hepatic vein (MHV) with right or left sided grafts. When the donor's left lobe volume is more than 30% of total hepatic volume, a right hepatectomy (segments V-VIII) can be done^[19]. Left lobe is usually small; hence left hepatectomy generally includes the middle hepatic vein so as to obtain a reasonably large graft volume and to maintain good tissue viability for transplantation. However, if the middle hepatic vein is the dominant vein with a small right hepatic vein, this may not be advisable. Right hepatic grafts are often harvested without the MHV trunk. Such grafts are at risk for congestion of right paramedian sector with subsequent graft dysfunction and septic complications. To avoid such outcomes, MHV drainage to recipient IVC may be reconstructed with vascular grafts for segment V and VIII veins^[19]. The caudate lobe is generally left behind because of its direct venous drainage in to the IVC. However, for smaller left sided grafts the caudate lobe may need to be harvested together with rest of the left lobe and separate venous drainage reconstruction for the caudate lobe may be required.

IMAGING OVERVIEW

In the past, B mode ultrasound (US) in conjunction with

Doppler and color flow imaging formed a routine part of preoperative evaluation of LDLT. However, it is highly operator dependent and subject to factors which are difficult to control and affect image quality such as a large body habitus, a high-riding liver and overlying bowel gas. A key limitation lies in the fact that US has limited ability to estimate liver volume^[20]. In current practice, CT and MRI have largely displaced ultrasound from preoperative assessment for LDLT candidates.

In general, the spatial resolution of CT is superior to that of MR. CT is also relatively less expensive, requires a shorter scan time and is more easily assessable. However, CT involves exposure to ionizing radiation. MR on the other hand requires a longer scan time and high degree of patient compliance (*e.g.*, during breath hold sequences). Often normal patients (as these donors always are) do not comply well with these requirements leading to image degradation. Similarly, patients with pacemakers, metallic hardware or claustrophobia may not be able to undergo MR imaging. There is no ionizing radiation involved in MR imaging and it has better contrast resolution than CT scan. In addition, the Gadolinium-based contrast agents used for MR imaging are generally safer compared to the iodinated CT contrast agents with no nephrotoxicity and extremely rare anaphylactic reactions^[21].

Source images from both modalities can be post processed for multi-planar reformation and three-dimensional (3D) reconstruction with maximum intensity projection (MIP) and volume rendering (VR) at commercially available workstations. This enables the branching points of the vessels and biliary ducts in relation to their intended site of incision to be viewed with little or no interruption between consecutive sections or on 3D images. 3D imaging with VR gives a stereoscopic view of the anatomy while MIP images may accentuate the visualization of smaller segmental vessels or ducts^[22].

In the following sections of this article we will describe the role of CT and MR imaging in the evaluation of the vascular and biliary anatomy along with their variants as well as assessment of the hepatic parenchyma and volumetric analysis. We shall then address the impact of these factors in the selection of potential donors and the surgical decision-making. In our practice, multi-detector CT and MRI are used as a compliment to each other in pre-LDLT donor evaluation. Initially the donor undergoes a CT scan that primarily evaluates the vascular anatomy and looks for any gross parenchymal abnormalities; if there is no contra-indication for donor selection on CT scan, further evaluation with MRI is performed for assessing the biliary anatomy and hepatic fat content.

HEPATIC ARTERIAL SYSTEM

According to Couinaud^[23], the liver develops in 3 sectors with each one having its own embryological artery; the left gastric artery irrigates the left lateral segment, the common hepatic artery supplies the paramedian segments, and the superior mesenteric artery feeds the right

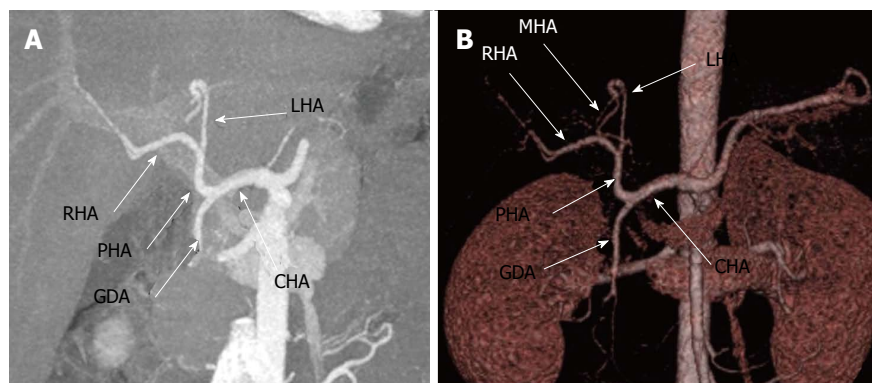


Figure 1 Conventional hepatic arterial anatomy depicted in (A) maximum intensity projection and (B) 3D volume-rendered images generated from a computed tomography angiogram. The CHA comes off the celiac axis, gives off the GDA to become the PHA which then bifurcates into the RHA and LHA. Note the MHA (the slender branch arising from left hepatic artery as seen in 1B) arising from LHA. CHA: Common hepatic artery; GDA: Gastroduodenal artery; PHA: Proper hepatic artery; RHA: Right hepatic artery; LHA: Left hepatic artery; MHA: Middle hepatic artery.

Table 1 Michel's classification of hepatic arterial variants

Type	Frequency of occurrence (%)	Description
I	55	RHA and LHA from the CHA
II	10	Replaced LHA from LGA
III	11	Replaced RHA from SMA
IV	1	Replaced RHA and LHA
V	8	Accessory LHA from LGA
VI	7	Accessory RHA from SMA
VII	1	Accessory RHA and LHA
VIII	4	Accessory RHA and LHA and replaced LHA or RHA
IX	4.5	CHA from SMA
X	0.5	CHA from LGA

RHA: Right hepatic artery; LHA: Left hepatic artery; CHA: Common hepatic artery; LGA: Left gastric artery; SMA: Superior mesenteric artery.

lateral segment. In early fetal life, the liver is large and gut is small; but as the fetus grows, the liver stays relatively small while the gut grows rapidly. The three hepatic arteries fuse at the hilum of the liver, and some of them regress while the enteric branches expand. Thus emerges the conventional hepatic arterial anatomy where the liver is supplied by right and left hepatic arteries after bifurcation of a proper hepatic artery, a branch of the common hepatic artery (CHA) beyond the origin of gastro duodenal artery (Figure 1). This pattern is seen in slightly more than 50% of individuals with many other possible variations^[5]. If some of the embryonic hepatic arteries do not regress or fail to detach from their embryonic source, it may result in “aberrant” (variant) hepatic arteries. An aberrant hepatic artery is an artery supplying the liver but arising from a source outside the conventional anatomy (*i.e.*, proper hepatic artery located in the celiac circulation). An aberrant hepatic artery may be “replacing” or “accessory”. An aberrant replacing hepatic artery substitutes the normal (usual) hepatic artery that is absent. An aberrant accessory hepatic artery is present in addition to one that is normally (usually) present. Some sort of aberrant (variable) hepatic artery, either replacing or accessory, occurs in approximately 42% of individuals. The Michel classification of hepatic arterial anatomy describes ten subtypes with the variants II, III, V and IX being the most significant ones with respect to LDLT. Table 1

describes the different subtypes and their frequency of occurrence^[24].

Both arterial-phase CT and MRI have a diagnostic accuracy comparable to that of catheter angiography and intra-operative finding^[13,25,26]. However, Schroeder *et al*^[4] found CT to be more accurate in detecting variations in vascular anatomy. This is probably related to the inherently superior spatial resolution of CT compared to MR. Hepatic artery thrombosis (HAT) is one of the most dreaded complications of LT and can be drastically decreased by excluding grafts with unfavorable anatomy^[27]. In the past, a potential graft with a narrow hepatic artery of less than 2 mm in diameter was regarded as a contraindication for LDLT due to the high risk of HAT. However, with developments in microvascular surgical techniques, this rarely disqualifies a potential donor from providing the graft^[28]. Grafts with multiple arteries and several arterial variants are often not preferred by the surgeon. Grafts with multiple arterial feeders are often found to perfuse poorly in the recipient and may need an alternative inflow source such as an aorto-hepatic interposition graft^[29]. A short right hepatic artery is another variant that may often make the anastomosis technically difficult and need extensive reconstructive surgery.

In right lobe grafts, it is important to determine the origin of the segment IV artery^[30]. There is some inconsistency in the nomenclature and origin of this artery; it has been variably described as middle hepatic artery (MHA), medial segment artery, left medial artery, and segment IV artery. Anatomical studies suggest that MHA most often arise from the left hepatic artery (LHA) (approximately 60%) while CT based studies show 62.5% of the arterial supply to segment 4 originating from the right hepatic artery (RHA)^[31]. While harvesting a right-sided graft, it is mandatory to preserve MHA to ensure adequate regeneration and function of the residual liver in the donor. Prior knowledge of MHA variation is especially important since its origin is very difficult to identify intra-operatively unless extensive dissection is done around the porta hepatis. During right lobectomy, the surgeon transects the right hepatic artery, distal to the branches to segment IV and hence it is also prudent to seek the length of the RHA beyond the origin of the segment IV artery so as to ensure there is adequate length of graft hepatic artery to anastomose with the recipient

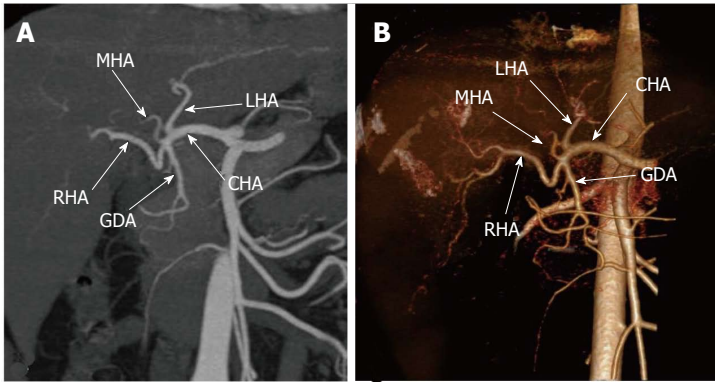


Figure 2 Maximum intensity projection (A) and volume rendered (B) images generated from a computed tomography angiogram shows a variant arterial anatomy. The CHA arises from the celiac trunk, it gives off the LHA followed by the GDA and MHA; thereafter it continues as the RHA in (A) MIP and (B) volume rendered images generated from a CT angiogram. CHA: Common hepatic artery; LHA: Left hepatic artery; GDA: Gastroduodenal artery; RHA: Right hepatic artery; MHA: Middle hepatic artery.

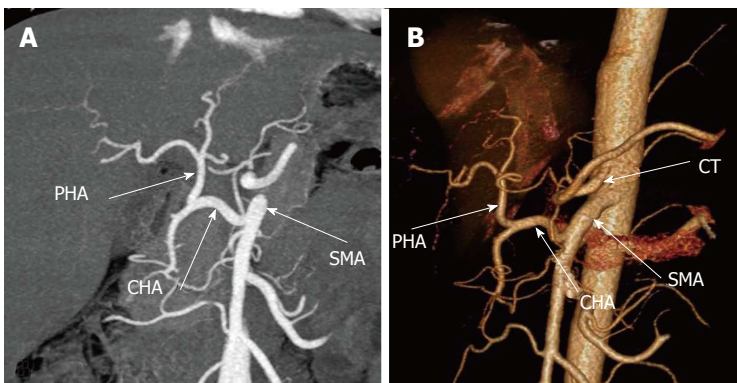


Figure 3 Michel type IX variant is shown in the (A) maximum intensity projection and (B) volume rendered images generated from a computed tomography angiogram. There is a replaced CHA that comes off the SMA. CHA: Common hepatic artery; SMA: Superior mesenteric artery; PHA: Proper hepatic artery; CT: celiac trunk).



Figure 4 Coronal maximum intensity projection generated from a computed tomography angiogram shows Michel type II variant with a replaced left hepatic artery coming off the left gastric artery. LHA: Left hepatic artery; LGA: Left gastric artery; CHA: Common hepatic artery.

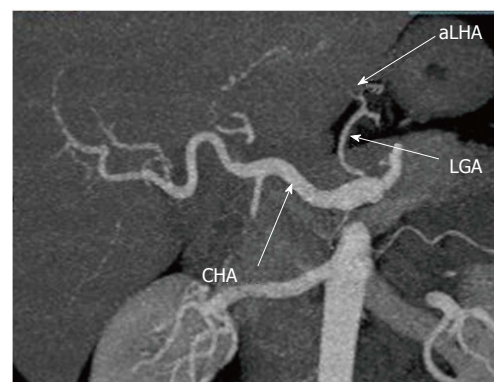


Figure 5 Coronal maximum intensity projection generated from a computed tomography angiogram shows Michel type V variant where an accessory left hepatic artery arises from the left gastric artery. LHA: Left hepatic artery; LGA: Left gastric artery; aLHA: Accessory left hepatic artery.

hepatic artery. In left lobe resection, MHA arising from RHA will necessitate two anastomoses: one for the LHA and another one for the MHA.

When the RHA or LHA take off before the origin of the gastroduodenal artery (Figure 2) or if there is a trifurcation of the CHA into the gastroduodenal, RHA and LHA, clamping of the CHA can compromise perfusion to the stomach and duodenum. Such an anomaly can even preclude the subject from being a donor^[5]. The main hepatic artery may take an aberrant course deep to the portal vein if it arises from the superior mesenteric artery instead of the celiac trunk (Michel type IX, Figure 3). This variation, when present in the recipient often mandates a change in the usual sequence of vascular

anastomoses, such that the portal venous anastomosis will have to follow (rather than precede) the arterial anastomosis^[29]. A similar significant variation to be sought in the recipient is a replaced or accessory LHA arising from the left gastric artery (Michel type II and V, Figure 4 and 5 respectively); this artery would require to be ligated at its origin while removing the native liver to avoid major bleeding. A replaced right hepatic artery arising from the SMA (Michel type III, Figure 6) is a significant variation when present in the donor or the recipient as it means additional steps are required for both harvesting and re-implanting the graft^[5].

Left lateral segment and left lobe grafts are associated with a higher incidence of arterial complications^[32].

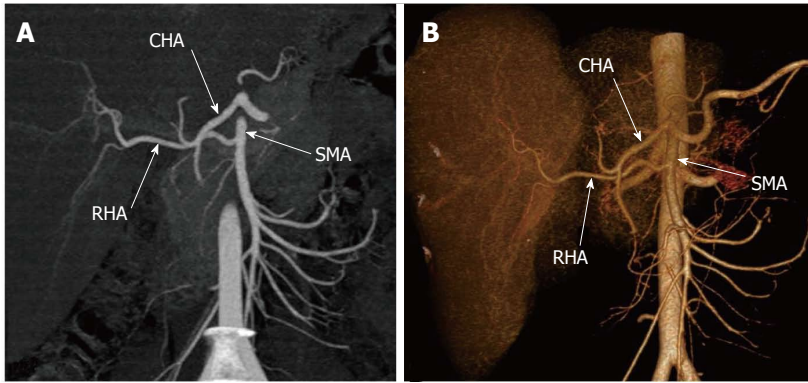


Figure 6 Maximum intensity projection (A) and volume rendered (B) images generated from a computed tomography angiogram shows Michel type III variant with a replaced right hepatic artery arising from the superior mesenteric artery. RHA: Right hepatic artery; SMA: Superior mesenteric artery; CHA: Common hepatic artery.

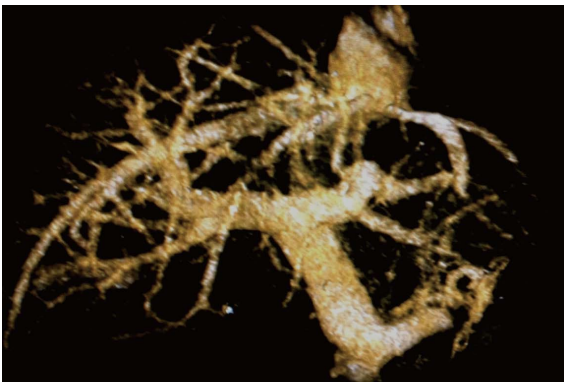


Figure 7 Normal portal and hepatic venous anatomy is demonstrated in this 3D volume rendered image. The MPV divides into RPV and LPV. The RPV then divides into the RAPV and RPPV. The three hepatic veins open into the IVC. MPV: Main portal vein; LPV: Left portal vein; RPV: Right portal vein; RAPV: Right anterior portal vein; RPPV: Right posterior portal vein.

Complications such as HAT that results in hepatic infarction and bile duct ischemia are more frequent with such grafts^[32]. Anastomotic bleeding, stenosis and pseudoaneurysm formation are some of the other common arterial complications. Significant difference in caliber between donor and recipient arteries, small caliber of the anastomosed vessels, clamp injury and presence of an interpositional conduit are among the usual causes for anastomotic stenosis and HAT^[33].

PORTAL VENOUS SYSTEM

The normal portal venous anatomy (Figure 7) consists of the main portal vein and its two branching vessels, the right and left portal veins^[34]. The right portal vein is a short trunk that further divides into anterior and posterior branches. The left portal vein has a horizontal segment that turns at right angles at the base of the umbilical fissure to form the umbilical segment. The umbilical segment then gives branches to segments II to IV while the caudate lobe receives direct supply from the transverse segment.

The portal venous anatomy is best appreciated in the coronal images^[5]. Portal venous variants account for approximately 20% of all significant vascular variants^[34]. Up to 20% of potential donors may get excluded from

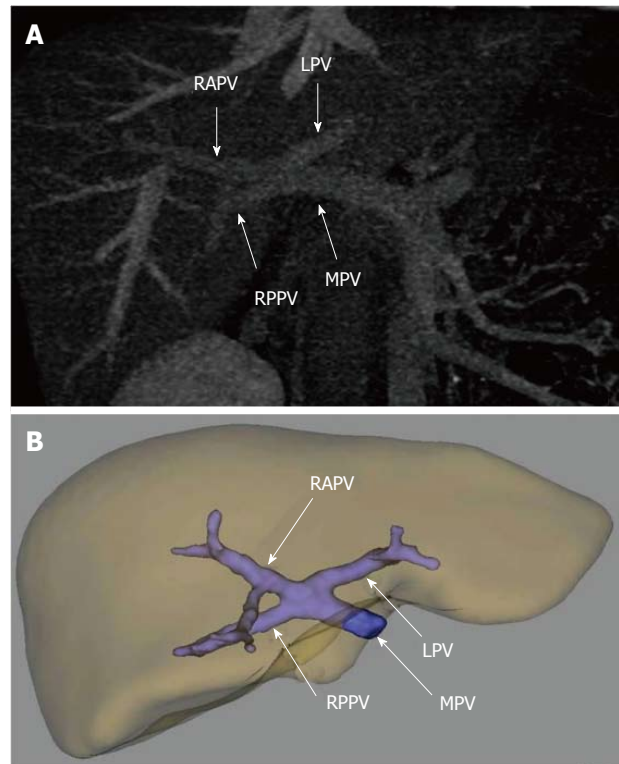


Figure 8 (A) Maximum intensity projection and (B) 3D volume rendered image generated using dedicated software demonstrates trifurcation of the main portal vein into the right anterior portal vein, right posterior portal vein and left portal vein. MPV: Main portal vein; RAPV: Right anterior portal vein; RPPV: Right posterior portal vein; LPV: Left portal vein.

surgery due to variations in portal vein anatomy^[35]. The angle of portal vein branching is significant to the recipient. If the angle is too acute, the graft may surround and consume the vein during the regeneration process leading to ischemia and infarction^[5]. In such cases, vascular reconstruction may have to be performed. Adequate length of the portal vein is also important for satisfactory anastomosis. A significant portal venous variant to note in a right lobe graft is the presence of portal venules to segment IV as they are important collateral pathways. This knowledge is important for anastomosis and to avoid bleeding and ischemia.

A vital variation is the absence of the right portal vein that is seen in 16.5% of right anterior, right poste-

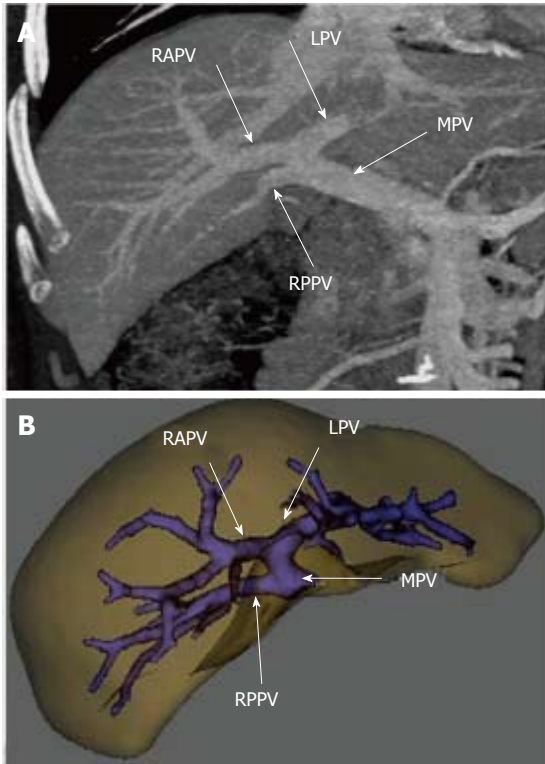


Figure 9 (A) maximum intensity projection and (B) 3 D volume rendered image generated using dedicated software shows an early origin of right posterior portal vein from the main portal vein that later bifurcates in to the right anterior portal vein and left portal vein. RPPV: Right posterior portal vein; MPV: Main portal vein; RAPV: Right anterior portal vein; LPV: Left portal vein.

rior and left portal venous branches (Figure 8) or direct origin of the right posterior portal vein (RPPV) from the main portal vein (Figure 9) or a right anterior portal vein (RAPV) arising from the left portal vein^[36]. Trifurcation of the portal vein is important to note pre-operatively as it can often be a contra-indication for surgery or may need alternate surgical planning. For instance, in a right lobe graft, this variant as well as a direct origin of RPPV would necessitate anastomosis of two portal veins, which increases the risk of post-operative portal vein thrombosis^[35]. If the RAPV is arising from the left portal vein, the distance of its origin from the bifurcation should be noted. Such donors need the portal vein to be transected distal to the RAPV. Hence there is a possibility that this plane of transection may be intraparenchymal leading to an extra-parenchymal length insufficient for anastomosis to the recipient's portal vein. A left portal vein arising from the RAPV may cause a technical problem during right lobe transplant due to the short length of the graft portal vein.

Diameter of the portal vein is also important and should be measured at the level of the expected anastomosis. The presence or absence of portal vein thrombosis in the recipient can also impact the suitability for a transplant^[37]. Acute thrombus may be recanalized by intra-operative thrombectomy. However in case of chronic thrombosis or cavernoma formation, careful scrutiny is

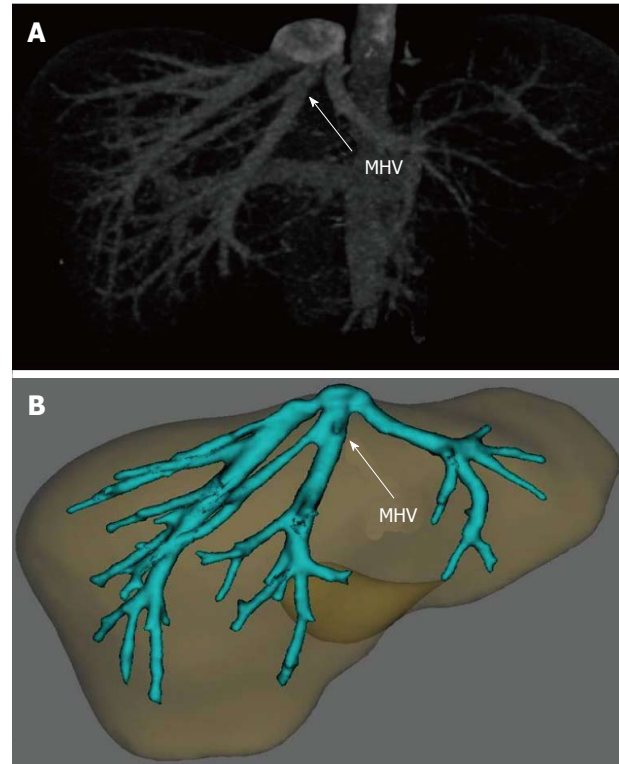


Figure 10 (A) maximum intensity projection and (B) 3 D volume rendered image generated using dedicated software demonstrates early bifurcation of the middle hepatic vein with large veins draining into it from the right hepatic lobe. MHV: Middle hepatic vein.

required to identify a suitable vein for anastomosis.

Both CT and MR are equally good in providing anatomical information on the portal venous system^[4]. Complications that may occur with respect to the portal veins in the recipient are stenosis and thrombosis. Portal vein stenosis tends to develop at the anastomosis while thrombosis is seen with vessel malalignment, differences in caliber of the anastomosed vessels causing turbulent flow or prior thrombosis in the recipient^[33].

HEPATIC VENOUS SYSTEM

The plane of transection is determined by the anatomy of the hepatic veins. Hence a detailed hepatic venous mapping that includes the number, size and drainage pattern of the hepatic veins is imperative in CT/MR evaluation of the donor. The normal hepatic venous system comprises of three main venous tributaries that drain into the inferior vena cava (IVC) (Figure 7). Usually, the right hepatic vein (RHV) drains liver segments V-VII, the MHV drains segments IV, V and VIII and the LHV drains segments II and III^[38]. Variations in hepatic venous anatomy have been reported in up to 30% of patients^[35]. The site of drainage of the middle hepatic vein is particularly relevant. In 60% of cases, the MHV and LHV form a common trunk that drains into the IVC^[38].

In right lobe dissection, the surgical plane typically courses 1 cm to the right of the MHV^[12]. Early bifurca-

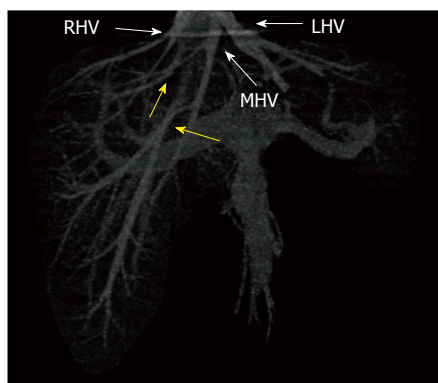


Figure 11 Three-dimensional volume rendered image generated from venous phase computed tomography scan show a relatively small right hepatic vein draining only the dome of the right lobe and two accessory right hepatic veins (yellow arrows). In this case, the caudal accessory right hepatic vein drains the bulk of the right lobe. RHV: Right hepatic vein; MHV: Middle hepatic vein; LHV: Left hepatic vein.

tion of the MHV and large branching veins draining into it from the right lobe (Figure 10) will necessitate alteration of the transection plane as well as separate anastomosis of segment V and VIII branches to the IVC using conduits. Early confluence of the hepatic veins may also result in a small graft that may not be adequate to maintain the metabolic function in the recipient^[5,35]. In case of left lobe grafts, the anatomy of segment IV venous drainage is particularly important. If the segment IV vein is not patent, the graft would get congested with hepatofugal portal venous flow and eventual graft atrophy. The draining veins of segment IV can be highly variable, multiple in number and small in caliber often draining into the middle hepatic vein.

In LDLT, special attention must be paid to the presence of accessory hepatic veins draining directly into the IVC that have to be dissected separately and can be a source of excessive haemorrhage if not identified preoperatively^[5]. An accessory RHV occurs in 52.5% of patients, two accessory veins in 12% (Figure 11) and an accessory vein draining the caudate lobe in 12% with the most common being the accessory inferior RHV^[39,40]. The size of the accessory hepatic vein and its distance from the confluence of the hepatic veins into the IVC should be reported. If this distance is more than 4 cm, it may be difficult to surgically implant both veins in the recipient with a single partially occluded clamp on the IVC^[5]. Small accessory veins, usually less than 3 mm in size may be suitable for ligation while a similar treatment of the larger ones can lead to congestion of the graft.

The hepatic veins are best evaluated in the axial plane with the MHV as the landmark. In case of multiple hepatic veins, the vein that extends from hepatic venous confluence with the IVC towards the gall bladder fossa is considered the MHV. CT and MRI are equally good in venous mapping^[4]. However, the authors feel most confident about this interpretation when reading non-contrast T1W images. Complications that may occur with respect to the hepatic veins are stenosis and thrombosis,

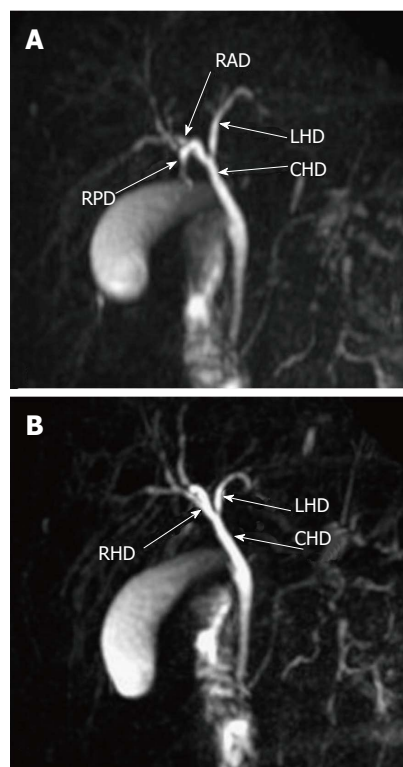


Figure 12 Thick slab magnetic resonance cholangiopancreatography images in different coronal planes demonstrates the normal biliary anatomy where right hepatic duct is formed by fusion of the right anterior duct and right posterior duct. The RHD then joins the LHD to form the CHD. RHD: Right hepatic duct; RAD: Right anterior duct; RPD: Right posterior duct; LHD: Left hepatic duct; CHD: Common hepatic duct.

usually at the site of anastomosis. Again, size discrepancy between the anastomosed vessels is a predisposing factor. Post transplant regeneration of the graft can compresses short and narrow venous anastomoses leading to graft congestion and dysfunction^[41]. Various graft materials have been used to create hepatic venous reconstructions allowing for wide ostium anastomoses that can then withstand compression during regeneration^[42].

BILIARY SYSTEM

Conventional biliary tract anatomy (Figure 12) is as follows: The right anterior duct drains segments V and VIII, and the right posterior duct drains segments VI and VII. The right hepatic duct is formed by fusion of the anterior duct and the posterior duct. The left hepatic duct drains segments II, III and IV. The duct draining the caudate lobe usually joins the origin of the right or left hepatic ducts^[43]. The right and left hepatic bile ducts merge to form the common hepatic duct (CHD). The cystic duct drains into the CHD below the confluence of right and left hepatic ducts to form the common bile duct. This normal biliary anatomy is seen in only 58% of individuals^[44]. The frequency of variations is very high in biliary anatomy^[45]. The more frequently encountered and clinically significant variations of biliary anatomy are (1) right posterior duct draining into the left hepatic

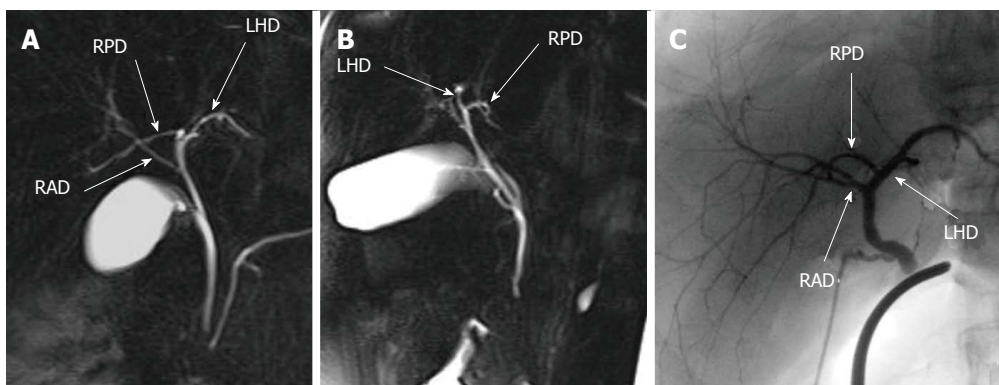


Figure 13 Thick slab coronal magnetic resonance cholangiopancreatography images at 15 degrees left anterior oblique (A) and 80 degrees right anterior oblique (B) projections demonstrate a variant biliary anatomy- the magnetic resonance cholangiopancreatography drains into the magnetic resonance cholangiopancreatography, note the intra-operative cholangiographic appearance of the same variant (C). RHD: Right hepatic duct; RAD: Right anterior duct; RPD: Right posterior duct; LHD: Left hepatic duct; CHD: Common hepatic duct.

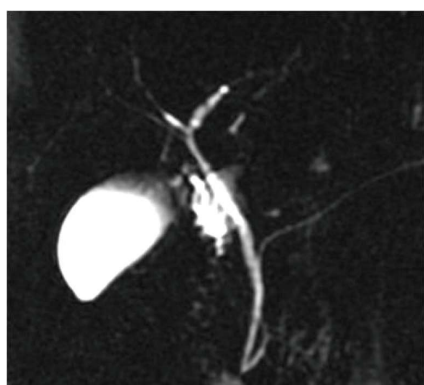


Figure 14 Thick slab magnetic resonance cholangiopancreatography shows a variant biliary anatomy- trifurcation pattern with a common confluence of the right posterior duct right anterior duct and left hepatic duct. RPD: Right posterior duct; RAD: Right anterior duct; LHD: Left hepatic duct.

duct (Figure 13) seen in 13%-19% of individuals^[43]; (2) trifurcation pattern where there is confluence of the right posterior, right anterior, and left hepatic ducts (Figure 14) that is seen in 11 % of the population^[44]; and (3) the right posterior duct draining directly into the common hepatic duct (Figure 15) or common bile duct. Several other biliary variations involving aberrant and accessory ducts have been described in the literature. An aberrant duct is the only duct draining a particular hepatic segment while an accessory duct is an additional duct draining the same area of liver. Failure to recognize even minor variations can cause post-operative complications like bilomas or biliary leaks that can be extremely difficult to manage.

CT and MR imaging assessment of the biliary tract in potential liver donors include magnetic resonance cholangiopancreatography (MRCP), intravenous administration of liver-specific contrast agents in excretory MR (eMRCP) and CT cholangiogram (CTCh). As the contrast agent used in CTCh is limited to a few countries and not yet available at our institution, MR remains the imaging modality of choice in assessing the biliary tree. The main stay of MRCP in the donor evaluation is a high quality respiratory-triggered thin slice coronal 3D MRCP

sequence. In patients with irregular breathing, thin slice 2D MRCP acquisitions in dead coronal as well as right anterior oblique and left anterior oblique projections may be obtained with breath hold. Each of these breath-hold sequences typically takes 15-20 s. Thick slab MRCP in multiple radial planes is optional. We perform eMRCP with gadoxetate disodium (a hepatocyte-specific MR contrast agent) administration followed by three dimensional image acquisitions, 20 min from injection, in all the three orthogonal planes using a 3D fast spoiled gradient echo sequence.

CTCh involves the use of ionizing radiation and the slow infusion of a dilute biliary contrast agent (cholograffin). Although acquisition of images is quicker compared to MR, it needs a longer preparation time and there is higher potential for adverse drug reactions with CTCh. The advantages of CTCh include higher spatial resolution (Figure 16) and a lower cost^[46]. CTCh allows for depiction to at least the second order intrahepatic biliary ducts. Schroeder *et al*^[47] found that MRCP revealed only about one third of the biliary variants found on CTCh. Yeh *et al*^[46] also found eMRCP inferior to CTCh in visualization of second order bile ducts. Some studies have shown complete agreement between CTCh and endoscopic retrograde cholangiopancreatography^[47,48]. MR imaging of the biliary ducts in general is better suited in the evaluation of pathological states wherein biliary ductal dilatation occurs secondary to obstructing calculi or masses^[49] while normal caliber bile ducts of potential donors are better demonstrated with CTCh. The limitations of MR-specific artifacts (*e.g.*, pseudo-obstruction of the common hepatic duct caused by pulsatile vascular compression by the right hepatic artery) do not exist for CTCh^[50].

Variations in biliary anatomy have a statistically significant association with variations in portal venous anatomy^[51]. Biliary tract complications after liver transplantation have been reported in 10%-25% of cases, proving fatal in up to 10% of complicated cases^[52,53]. Biliary complications essentially occur in the form of biliary leaks and anastomotic strictures with the presence of more

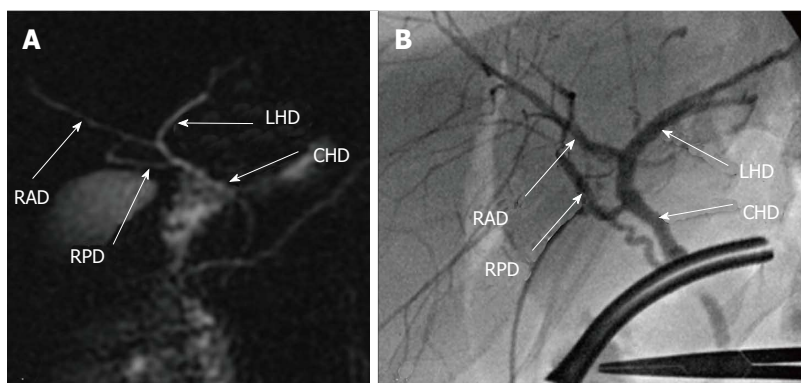


Figure 15 (A) Magnetic resonance cholangiopancreatography and (B) intra-operative cholangiogram in the same patient demonstrates a variant biliary anatomy—the right posterior duct drains directly into the common hepatic duct. RPD: Right posterior duct; RAD: Right anterior duct; LHD: Left hepatic duct; CHD: Common hepatic duct.

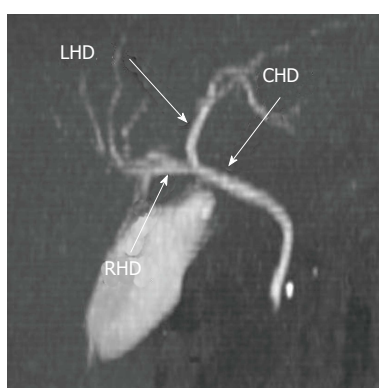


Figure 16 Maximum intensity projection image generated from a computed tomography cholangiogram. Normal biliary anatomy is demonstrated here. LHD: Left hepatic duct; RHD: Right hepatic duct; CHD: Common hepatic duct.

than one graft bile duct and more than one anastomosis increasing the frequency of biliary complications^[54]. A bile leak from the cut surface of a graft is typically self-limiting. Biliary strictures may develop at the anastomosis or may occur at non-anastomotic sites secondary to ischaemia caused by hepatic artery compromise^[55].

HEPATIC PARENCHYMA

Evaluation of the hepatic parenchyma is mainly to identify and characterize focal liver lesions and exclude diffuse liver disease. Focal lesions have been identified in up to 18% of donor liver evaluations^[25]; however most of them are benign cysts or haemangiomas. MR is superior in characterization of focal liver lesions^[56,57]. Fatty liver is the most common diffuse liver disease that may preclude an outwardly healthy patient from being a donor. Grafts with more than 30% fatty change carries high risk of graft non-function in the recipient and liver dysfunction in the donor^[58]. Hence pre-operative detection and quantification of fatty liver is vital. Uniform fatty change of the liver is easier to quantify; however hepatic steatosis can often be heterogeneous. Generally, fatty changes are more pronounced in the right lobe than in the left as for-

mer receives greater amount of portal venous blood flow.

Hepatic steatosis is identified on CT scan as reduced attenuation relative to the spleen (Figure 17). This is best evaluated on a non-contrast study as relative densities of the liver and spleen can vary on post contrast scans depending on the phase of image acquisition^[27]. The attenuation value of normal liver on unenhanced CT ranges between 55 and 65 Hounsfield units (HU) and is generally at least 8 HU higher relative to the spleen; the liver is regarded as fatty when the liver attenuation is at least 10 HU less than the spleen^[59]. This method has high sensitivity (88%-95%) and specificity (90%-99%)^[60]. Liver attenuation values also reflect the severity of fatty change. Hepatic CT attenuation value below 48 HU may be considered as fatty liver and a value of 40 HU represents approximately 30% fatty change^[61]. With more than 30% macrovesicular steatosis the hepatic parenchyma appears hypoattenuating compared to the hepatic vessels on non-enhanced CT scan^[62]. Similarly, a hepatic to splenic attenuation ratio of 0.8 is almost 100% specific for moderate to severe (> 30%) macrovesicular steatosis^[63]. According to Limanond *et al*^[64], a hepatic-splenic attenuation difference of more than 5 HU was consistent with absence of significant macrovesicular steatosis (0%-5%), a difference of -10 to 5 HU was suggestive of mild to moderate steatosis (6%-30%). The same authors reported a specificity of 100% for the detection of moderate to severe (> 30%) macrovesicular steatosis when the hepatic-splenic attenuation difference was less than -10 HU. Dual energy CT can also be used in detecting and quantifying hepatic steatosis but there is limited literature to validate its utility in this context.

MR is an extremely sensitive modality in detection and characterization of hepatic steatosis. Fatty liver is seen as increased signal intensity on conventional T1W spin echo sequence. However, these sequences are seldom used for hepatic fat evaluation due to their poor sensitivity. Detection and quantification of fatty liver is much better performed with chemical shift imaging or MR proton spectroscopy^[27]. Chemical shift imaging utilizes the differences of resonance frequencies between water and fat

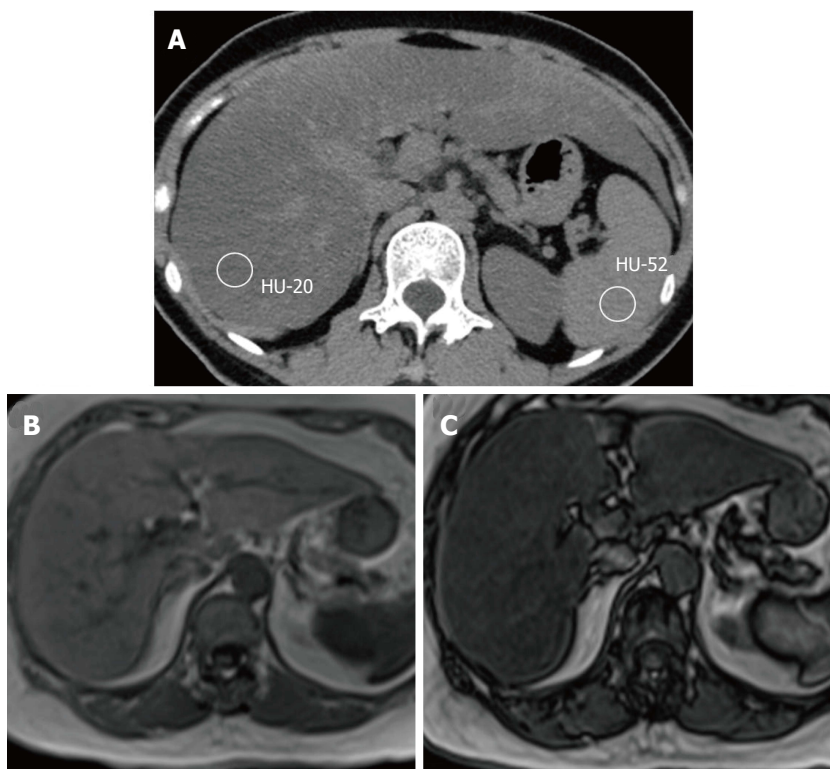


Figure 17 Diffuse hepatic steatosis is demonstrated here. In the non-enhanced computed tomography scan (A) the hepatic parenchyma has significantly lower attenuation than spleen. The out phase magnetic resonance imaging image (C) shows a drop in the hepatic signal intensity compared to that in the in-phase image (B).

proton signals to quantify fat accumulation. By acquiring images at echo times when water and fat signals are in-phase and out-of-phase, the extent of hepatic steatosis can be quantified based on signal change^[65]. Loss of signal on out-of-phase images suggests fatty liver (Figure 17). Nowadays, the in-phase and out-of-phase images are obtained near simultaneously (*i.e.*, less than a few milliseconds apart) using breath-hold gradient-echo sequences. The spleen or skeletal muscle can be used as an internal standard for calculating the percentage of relative signal loss of the liver^[66]. This technique provides a relatively simple way of estimating the degree of steatosis. Three circular regions of interest (ROI) can be placed in the liver; two in the right lobe and one in the left with three ROI placed within the spleen at anatomically matched levels. The mean signal intensity can then be calculated using the formula: $[(SI_{\text{in-phase}} - SI_{\text{out-of-phase}}) / SI_{\text{in-phase}}] \times 100$ where $SI = \text{average liver signal intensity} / \text{average spleen intensity}$ ^[67]. Fischer *et al.*^[68] found that this dual echo MR imaging technique for liver fat quantification was actually superior to histopathological analysis. This method is accurate in detection of hepatic fat fraction when it is in the 15%-50% range. Although this method is technically simple and highly sensitive, absolute quantification of hepatic fat is not possible with this technique. Fast spin echo T2 weighted sequences with and without fat saturation may be used in a similar fashion to estimate fat fraction of the liver.

MR spectroscopy is the most accurate non-invasive method of evaluating fatty liver. It can quantify the absolute fat concentration in the liver and is highly sensitive to small changes in hepatic triglyceride levels.

LIVER VOLUME

The size of the graft is one of the most crucial factors that have to be taken into account when considering LDLT^[69]. The normal liver weighs between 2%-2.7% of the total body weight; for LDLT, a graft that is at least 0.8% of the recipient's body weight ratio is considered adequate. Liver remnant volume of 30%-40% of the total liver volume is adequate for donor survival, this is provided the liver parenchyma is normal^[70]. The minimum graft volume required to provide sufficient functional hepatocytes to the recipient is about 40% of the standard liver mass^[71], which can be calculated using the body surface area^[72].

If the graft is too large, haemostasis, vascular anastomosis and abdominal closure may prove problematic^[20]. A graft that is too small has increased likelihood of dysfunction secondary to inadequate functional hepatic mass and possible excessive portal perfusion^[73]. A small for size graft is also prone to torsion and may necessitate additional surgical maneuvers like fixation of falciform ligament to anterior aspect of the peritoneal cavity^[27].

For volumetric analysis, any cross-sectional imaging that provides sufficient contrast between the liver parenchyma and the surrounding tissues can be used. This is achievable both with portal venous phase CT and T1-weighted MR, with CT being marginally superior due to inherently sharper images obtained with it^[4]. Hepatic volumes can be determined by manually tracing the contours of the entire liver and the intended graft excluding the large vessels, major fissures and the gallbladder fossa using contiguous CT or MR images^[70]. The cross-sectional area within the region of interest is determined on

each slice and the sum of all the slices estimates the liver volume. 3D software reconstruction of the liver can be performed which allows the surgeon to better determine the size and shape of the intended graft by performing virtual hepatectomies. Dedicated software programs also allow calculation of the potential residual volume in the donor and the potential volume in the recipient by clicking a few buttons^[74]. Studies have shown that automated volumetric results are comparable to manual volumetric results with the former being more efficient^[75,76]. Usually the calculated liver volume over-estimates the weight of the graft^[70], this is most likely due to lack of perfusion of the graft when it is weighed intra-operatively.

CONCLUSION

As discussed above, CT and MR are complementary modalities that allow for a comprehensive non-invasive assessment of a potential liver donor while either of these modalities is adequate for pre-transplant radiological assessment of a potential recipient. Knowledge of the broad indications and contraindications to qualify as a recipient for LDLT is essential for the radiologist reporting scans in a pre-transplant patient. Similarly, awareness of the various anatomical variations and pathological states in the donor is essential for the radiologist to generate a meaningful report of his/her observations. A radiologist oblivious to these facts would not be able to effectively harness the immense potential of non invasive imaging modalities in contributing towards a LT program.

Both CT and MR are comparable in terms of illustration of vascular anatomy. MRCP and in particular eMRCP are extensively used for evaluating the biliary anatomy of the potential donor. Few studies have shown CTCh to be superior to MRI for this purpose, but limited availability of the CT cholangiographic contrast agent limits the application of this technique. MR outperforms CT in evaluation of focal liver lesions and diffuse parenchymal disease. Volumetric analysis is marginally better with CT compared to MRI.

In most successful LDLT programs the radiologist is an integral part of the transplant team and is present during transplant planning discussions. Only a cross-fertilization of knowledge in their respective areas can lead to a high level of predictability of transplant results and an ongoing increase in success of the program.

ACKNOWLEDGMENTS

Dr. Anand Kumar Singh, Department of Radiology, Massachusetts General Hospital, Boston, United States; and Ajith AV, CT applications specialist, Philips Healthcare, Singapore.

REFERENCES

- 1 Adam R, McMaster P, O'Grady JG, Castaing D, Klempnauer JL, Jamieson N, Neuhaus P, Lerut J, Salizzoni M, Pollard S, Muhlbacher F, Rogiers X, Garcia Valdecasas JC, Berenguer

- J, Jaeck D, Moreno Gonzalez E. Evolution of liver transplantation in Europe: report of the European Liver Transplant Registry. *Liver Transpl* 2003; **9**: 1231-1243 [PMID: 14625822 DOI: 10.1016/j.lts.2003.09.018]
- 2 Settmacher U, Neuhaus P. [Innovations in liver surgery through transplantation from living donors]. *Chirurg* 2003; **74**: 536-546 [PMID: 12883803 DOI: 10.1007/s00104-003-0675-x]
- 3 Zhuang ZG, Qian LJ, Gong HX, Zhou Y, Chai WM, Li QG, Xu JR. Multidetector computed tomography angiography in the evaluation of potential living donors for liver transplantation: single-center experience in China. *Transplant Proc* 2008; **40**: 2466-2477 [PMID: 18929770 DOI: 10.1016/j.transproceed.2008.08.031]
- 4 Schroeder T, Malagó M, Debatin JF, Goyen M, Nadalin S, Ruehm SG. "All-in-one" imaging protocols for the evaluation of potential living liver donors: comparison of magnetic resonance imaging and multidetector computed tomography. *Liver Transpl* 2005; **11**: 776-787 [PMID: 15973711 DOI: 10.1002/lt.20429]
- 5 Sahani D, Mehta A, Blake M, Prasad S, Harris G, Saini S. Preoperative hepatic vascular evaluation with CT and MR angiography: implications for surgery. *Radiographics* 2004; **24**: 1367-1380 [PMID: 15371614 DOI: 10.1148/rg.245035224]
- 6 O'Leary JG, Lepe R, Davis GL. Indications for liver transplantation. *Gastroenterology* 2008; **134**: 1764-1776 [PMID: 18471553 DOI: 10.1053/j.gastro.2008.02.028]
- 7 Farrell GC. Non-alcoholic steatohepatitis: what is it, and why is it important in the Asia-Pacific region? *J Gastroenterol Hepatol* 2003; **18**: 124-138 [PMID: 12542595 DOI: 10.1046/j.1440-1746.2003.02989.x]
- 8 Kamath PS, Wiesner RH, Malinchoc M, Kremers W, Therneau TM, Kosberg CL, D'Amico G, Dickson ER, Kim WR. A model to predict survival in patients with end-stage liver disease. *Hepatology* 2001; **33**: 464-470 [PMID: 11172350 DOI: 10.1053/jhep.2001.22172]
- 9 Mazzaferro V, Regalia E, Doci R, Andreola S, Pulvirenti A, Bozzetti F, Montalto F, Ammatuna M, Morabito A, Gennari L. Liver transplantation for the treatment of small hepatocellular carcinomas in patients with cirrhosis. *N Engl J Med* 1996; **334**: 693-699 [PMID: 8594428 DOI: 10.1056/NEJM199603143341104]
- 10 Yao FY, Ferrell L, Bass NM, Watson JJ, Bacchetti P, Venook A, Ascher NL, Roberts JP. Liver transplantation for hepatocellular carcinoma: expansion of the tumor size limits does not adversely impact survival. *Hepatology* 2001; **33**: 1394-1403 [PMID: 11391528 DOI: 10.1053/jhep.2001.24563]
- 11 Valentín-Gamazo C, Malagó M, Karliova M, Lutz JT, Frilling A, Nadalin S, Testa G, Ruehm SG, Erim Y, Paul A, Lang H, Gerken G, Broelsch CE. Experience after the evaluation of 700 potential donors for living donor liver transplantation in a single center. *Liver Transpl* 2004; **10**: 1087-1096 [PMID: 15349997 DOI: 10.1002/lt.20223]
- 12 Marcos A, Ham JM, Fisher RA, Olzinski AT, Posner MP. Surgical management of anatomical variations of the right lobe in living donor liver transplantation. *Ann Surg* 2000; **231**: 824-831 [PMID: 10816625 DOI: 10.1097/0000658-200006000-00006]
- 13 Lee VS, Morgan GR, Teperman LW, John D, Diflo T, Pandharipande PV, Berman PM, Lavelle MT, Krinsky GA, Rofsky NM, Schlossberg P, Weinreb JC. MR imaging as the sole preoperative imaging modality for right hepatectomy: a prospective study of living adult-to-adult liver donor candidates. *AJR Am J Roentgenol* 2001; **176**: 1475-1482 [PMID: 11373217 DOI: 10.2214/ajr.176.6.1761475]
- 14 Tanaka K, Uemoto S, Tokunaga Y, Fujita S, Sano K, Nishizawa T, Sawada H, Shirahase I, Kim HJ, Yamaoka Y. Surgical techniques and innovations in living related liver transplantation. *Ann Surg* 1993; **217**: 82-91 [PMID: 8424706 DOI: 10.1097/0000658-199301000-00014]

- 15 **Couinaud C.** Surgical anatomy of the liver revisited. Paris, France: Couinaud, 1989: 130-132
- 16 **Nadalin S,** Bockhorn M, Malagó M, Valentin-Gamazo C, Frilling A, Broelsch CE. Living donor liver transplantation. *HPB (Oxford)* 2006; **8**: 10-21 [PMID: 18333233 DOI: 10.1080/13651820500465626]
- 17 **Tüzüner A,** Ersöz S, Hazinedaroğlu S, Karayalçın K, Yerdel MA, Anadol E. Technical implications of living donor liver transplantation: a single-center experience. *Transplant Proc* 2004; **36**: 212-213 [PMID: 15013349 DOI: 10.1016/j.transproc.2003.11.068]
- 18 **Chen WH,** Xin W, Wang J, Huang QJ, Sun YF, Xu Q, Yu SN. Multi-slice spiral CT angiography in evaluating donors of living-related liver transplantation. *Hepatobiliary Pancreat Dis Int* 2007; **6**: 364-369 [PMID: 17690030]
- 19 **Makuuchi M,** Sugawara Y. Technical progress in living donor liver transplantation for adults. *HPB (Oxford)* 2004; **6**: 95-98 [PMID: 18333057 DOI: 10.1080/13651820410032914]
- 20 **Redvanly RD,** Nelson RC, Stieber AC, Dodd GD. Imaging in the preoperative evaluation of adult liver-transplant candidates: goals, merits of various procedures, and recommendations. *AJR Am J Roentgenol* 1995; **164**: 611-617 [PMID: 7863881 DOI: 10.2214/ajr.164.3.7863881]
- 21 **Shellock FG,** Kanal E. Safety of magnetic resonance imaging contrast agents. *J Magn Reson Imaging* 1999; **10**: 477-484 [PMID: 10508312 DOI: 10.1002/(SICI)1522-2586(199909)10:3<477::AID-JMRI33>3.3.CO;2-5]
- 22 **Hyodo T,** Kumano S, Kushihata F, Okada M, Hirata M, Tsuda T, Takada Y, Mochizuki T, Murakami T. CT and MR cholangiography: advantages and pitfalls in perioperative evaluation of biliary tree. *Br J Radiol* 2012; **85**: 887-896 [PMID: 22422383 DOI: 10.1259/bjr/21209407]
- 23 **Couinaud C.** Surgical anatomy of the liver revisited: Embryology. Paris: Couinaud, 1989: 11-24
- 24 **Michel NA.** Blood supply and anatomy of the upper abdominal organs with a descriptive atlas. Philadelphia, Pa: Lippincott, 1955: 64-69
- 25 **Fulcher AS,** Szucs RA, Bassignani MJ, Marcos A. Right lobe living donor liver transplantation: preoperative evaluation of the donor with MR imaging. *AJR Am J Roentgenol* 2001; **176**: 1483-1491 [PMID: 11373218 DOI: 10.2214/ajr.176.6.1761483]
- 26 **Schroeder T,** Nadalin S, Stattaus J, Debatin JF, Malagó M, Ruehm SG. Potential living liver donors: evaluation with an all-in-one protocol with multi-detector row CT. *Radiology* 2002; **224**: 586-591 [PMID: 12147860 DOI: 10.1148/radiol.2242011340]
- 27 **Mortelé KJ,** Cantisani V, Troisi R, de Hemptinne B, Silverman SG. Preoperative liver donor evaluation: Imaging and pitfalls. *Liver Transpl* 2003; **9**: S6-14 [PMID: 12942472 DOI: 10.1053/jlts.2003.50199]
- 28 **Mori K,** Nagata I, Yamagata S, Sasaki H, Nishizawa F, Takada Y, Moriyasu F, Tanaka K, Yamaoka Y, Kumada K. The introduction of microvascular surgery to hepatic artery reconstruction in living-donor liver transplantation--its surgical advantages compared with conventional procedures. *Transplantation* 1992; **54**: 263-268 [PMID: 1496539 DOI: 10.1097/00007890-199208000-00014]
- 29 **Nghiem HV.** Imaging of hepatic transplantation. *Radiol Clin North Am* 1998; **36**: 429-443 [PMID: 9520993 DOI: 10.1016/S0033-8389(05)70033-6]
- 30 **Kamel IR,** Kruskal JB, Raptopoulos V. Imaging for right lobe living donor liver transplantation. *Semin Liver Dis* 2001; **21**: 271-282 [PMID: 11436577 DOI: 10.1055/s-2001-15399]
- 31 **Mizumoto R,** Suzuki H. Surgical anatomy of the hepatic hilum with special reference to the caudate lobe. *World J Surg* 1988; **12**: 2-10 [PMID: 3344582 DOI: 10.1007/BF01658479]
- 32 **Haberal M,** Sevmis S, Karakayali H, Moray G, Yilmaz U, Ozcay F, Torgay A, Aydogan C, Arslan G. A novel technique for hepatic arterial reconstruction in living-donor liver transplant. *Exp Clin Transplant* 2007; **5**: 585-589 [PMID: 17617047]
- 33 **Caiado AH,** Blasbalg R, Marcelino AS, da Cunha Pinho M, Chammas MC, da Costa Leite C, Cerri GG, de Oliveira AC, Bacchella T, Machado MC. Complications of liver transplantation: multimodality imaging approach. *Radiographics* 2007; **27**: 1401-1417 [PMID: 17848699 DOI: 10.1148/rg.275065129]
- 34 **Cheng YF,** Huang TL, Lee TY, Chen TY, Chen CL. Variation of the intrahepatic portal vein; angiographic demonstration and application in living-related hepatic transplantation. *Transplant Proc* 1996; **28**: 1667-1668 [PMID: 8658830]
- 35 **Kamel IR,** Kruskal JB, Pomfret EA, Keogan MT, Warmbrand G, Raptopoulos V. Impact of multidetector CT on donor selection and surgical planning before living adult right lobe liver transplantation. *AJR Am J Roentgenol* 2001; **176**: 193-200 [PMID: 11133565 DOI: 10.2214/ajr.176.1.1760193]
- 36 **Soyer P,** Bluemke DA, Choti MA, Fishman EK. Variations in the intrahepatic portions of the hepatic and portal veins: findings on helical CT scans during arterial portography. *AJR Am J Roentgenol* 1995; **164**: 103-108 [PMID: 7998521 DOI: 10.2214/ajr.164.1.7998521]
- 37 **Matsuura T,** Yanagi Y, Saeki I, Hayashida M, Taguchi T. Outcome of modified portal vein anastomosis for recipients with portal vein thrombosis or stenosis before living donor liver transplantation. *J Pediatr Surg* 2011; **46**: 2291-2295 [PMID: 22152867 DOI: 10.1016/j.jpedsurg.2011.09.015]
- 38 **Soyer P,** Heath D, Bluemke DA, Choti MA, Kuhlman JE, Reichle R, Fishman EK. Three-dimensional helical CT of intrahepatic venous structures: comparison of three rendering techniques. *J Comput Assist Tomogr* 1996; **20**: 122-127 [PMID: 8576462 DOI: 10.1097/00004728-199601000-00023]
- 39 **Pomfret EA,** Pomposelli JJ, Lewis WD, Gordon FD, Burns DL, Lally A, Raptopoulos V, Jenkins RL. Live donor adult liver transplantation using right lobe grafts: donor evaluation and surgical outcome. *Arch Surg* 2001; **136**: 425-433 [PMID: 11296114 DOI: 10.1001/archsurg.136.4.425]
- 40 **Fan ST,** Lo CM, Liu CL. Technical refinement in adult-to-adult living donor liver transplantation using right lobe graft. *Ann Surg* 2000; **231**: 126-131 [PMID: 10636112 DOI: 10.1097/00000658-200001000-00018]
- 41 **Akbulut S,** Yilmaz M, Eris C, Kutlu R, Yilmaz S. Living-donor liver transplant using the right hepatic lobe without the right hepatic vein: solving the drainage problem. *Exp Clin Transplant* 2013; **11**: 278-282 [PMID: 23767945 DOI: 10.6002/ect.2012.0060]
- 42 **Lee SG.** Techniques of reconstruction of hepatic veins in living-donor liver transplantation, especially for right hepatic vein and major short hepatic veins of right-lobe graft. *J Hepatobiliary Pancreat Surg* 2006; **13**: 131-138 [PMID: 16547674 DOI: 10.1007/s00534-005-1019-7]
- 43 **Puente SG,** Bannura GC. Radiological anatomy of the biliary tract: variations and congenital abnormalities. *World J Surg* 1983; **7**: 271-276 [PMID: 6868640 DOI: 10.1007/BF01656159]
- 44 **Mortelé KJ,** Ros PR. Anatomic variants of the biliary tree: MR cholangiographic findings and clinical applications. *AJR Am J Roentgenol* 2001; **177**: 389-394 [PMID: 11461869 DOI: 10.2214/ajr.177.2.1770389]
- 45 **Testa G,** Malagó M, Broelsch CE. Complications of biliary tract in liver transplantation. *World J Surg* 2001; **25**: 1296-1299 [PMID: 11596893 DOI: 10.1007/s00268-001-0113-5]
- 46 **Yeh BM,** Breiman RS, Taouli B, Qayyum A, Roberts JP, Coakley FV. Biliary tract depiction in living potential liver donors: comparison of conventional MR, mangafodipir trisodium-enhanced excretory MR, and multi-detector row CT cholangiography--initial experience. *Radiology* 2004; **230**: 645-651 [PMID: 14990830 DOI: 10.1148/radiol.2303021775]
- 47 **Cheng YF,** Lee TY, Chen CL, Huang TL, Chen YS, Lui CC. Three-dimensional helical computed tomographic cholangiography: application to living related hepatic transplanta-

- tion. *Clin Transplant* 1997; **11**: 209-213 [PMID: 9193844]
- 48 **Fleischmann D**, Ringl H, Schöfl R, Pötzi R, Kontrus M, Henk C, Bankier AA, Kettenbach J, Mostbeck GH. Three-dimensional spiral CT cholangiography in patients with suspected obstructive biliary disease: comparison with endoscopic retrograde cholangiography. *Radiology* 1996; **198**: 861-868 [PMID: 8628884]
- 49 **Romagnuolo J**, Bardou M, Rahme E, Joseph L, Reinhold C, Barkun AN. Magnetic resonance cholangiopancreatography: a meta-analysis of test performance in suspected biliary disease. *Ann Intern Med* 2003; **139**: 547-557 [PMID: 14530225 DOI: 10.7326/0003-4819-139-7-200310070-00006]
- 50 **Watanabe Y**, Dohke M, Ishimori T, Amoh Y, Okumura A, Oda K, Hayashi T, Hiyama A, Dodo Y. Pseudo-obstruction of the extrahepatic bile duct due to artifact from arterial pulsatile compression: a diagnostic pitfall of MR cholangiopancreatography. *Radiology* 2000; **214**: 856-860 [PMID: 10715058 DOI: 10.1148/radiology.214.3.r00mr09856]
- 51 **Lee VS**, Morgan GR, Lin JC, Nazzaro CA, Chang JS, Teperman LW, Krinsky GA. Liver transplant donor candidates: associations between vascular and biliary anatomic variants. *Liver Transpl* 2004; **10**: 1049-1054 [PMID: 15390332 DOI: 10.1002/lt.20181]
- 52 **Kapoor V**, Baron RL, Peterson MS. Bile leaks after surgery. *AJR Am J Roentgenol* 2004; **182**: 451-458 [PMID: 14736680 DOI: 10.2214/ajr.182.2.1820451]
- 53 **Suhocki PV**, Meyers WC. Injury to aberrant bile ducts during cholecystectomy: a common cause of diagnostic error and treatment delay. *AJR Am J Roentgenol* 1999; **172**: 955-959 [PMID: 10587128 DOI: 10.2214/ajr.172.4.10587128]
- 54 **Alawi K**, Khalaf H, Medhat Y, Allam N, Al-Saghir M, Al-Sofayan M, Al-Bahili H, Al-Hamoudi W, Abdo A, Sebayel M. Risk factors for biliary complications after living-donor liver transplant: a single-center experience. *Exp Clin Transplant* 2008; **6**: 101-104 [PMID: 18816235]
- 55 **Bhargava P**, Vaidya S, Dick AA, Dighe M. Imaging of orthotopic liver transplantation: review. *AJR Am J Roentgenol* 2011; **196**: WS15-WS25, Quiz WS15-WS25 [PMID: 21343537]
- 56 **Petersein J**, Spinazzi A, Giovagnoni A, Soyer P, Terrier F, Lencioni R, Bartolozzi C, Grazioli L, Chiesa A, Manfredi R, Marano P, Van Persijn Van Meerten EL, Bloem JL, Petre C, Marchal G, Greco A, McNamara MT, Heuck A, Reiser M, Laniado M, Claussen C, Daldrup HE, Rummeny E, Kirchin MA, Pirovano G, Hamm B. Focal liver lesions: evaluation of the efficacy of gadobenate dimeglumine in MR imaging—a multicenter phase III clinical study. *Radiology* 2000; **215**: 727-736 [PMID: 10831691 DOI: 10.1148/radiology.215.3.r00jn14727]
- 57 **Hawthornt H**, Schoenberg SO, Knopp MV, Essig M, Miltner P, van Kaick G. Hepatic lesions: morphologic and functional characterization with multiphase breath-hold 3D gadolinium-enhanced MR angiography—initial results. *Radiology* 1999; **210**: 89-96 [PMID: 9885592 DOI: 10.1148/radiology.210.1.r99ja1489]
- 58 **Marsman WA**, Wiesner RH, Rodriguez L, Batts KP, Porayko MK, Hay JE, Gores GJ, Krom RA. Use of fatty donor liver is associated with diminished early patient and graft survival. *Transplantation* 1996; **62**: 1246-1251 [PMID: 8932265 DOI: 10.1097/00007890-199611150-00011]
- 59 **Piekarski J**, Goldberg HI, Royal SA, Axel L, Moss AA. Difference between liver and spleen CT numbers in the normal adult: its usefulness in predicting the presence of diffuse liver disease. *Radiology* 1980; **137**: 727-729 [PMID: 6934563]
- 60 **Boll DT**, Merkle EM. Diffuse liver disease: strategies for hepatic CT and MR imaging. *Radiographics* 2009; **29**: 1591-1614 [PMID: 19959510 DOI: 10.1148/rg.296095513]
- 61 **Kodama Y**, Ng CS, Wu TT, Ayers GD, Curley SA, Abdalla EK, Vauthey JN, Charnsangavej C. Comparison of CT methods for determining the fat content of the liver. *AJR Am J Roentgenol* 2007; **188**: 1307-1312 [PMID: 17449775 DOI: 10.2214/AJR.06.0992]
- 62 **Lee SW**, Park SH, Kim KW, Choi EK, Shin YM, Kim PN, Lee KH, Yu ES, Hwang S, Lee SG. Unenhanced CT for assessment of macrovesicular hepatic steatosis in living liver donors: comparison of visual grading with liver attenuation index. *Radiology* 2007; **244**: 479-485 [PMID: 17641368 DOI: 10.1148/radiol.2442061177]
- 63 **Park SH**, Kim PN, Kim KW, Lee SW, Yoon SE, Park SW, Ha HK, Lee MG, Hwang S, Lee SG, Yu ES, Cho EY. Macrovesicular hepatic steatosis in living liver donors: use of CT for quantitative and qualitative assessment. *Radiology* 2006; **239**: 105-112 [PMID: 16484355 DOI: 10.1148/radiol.2391050361]
- 64 **Limanond P**, Raman SS, Lassman C, Sayre J, Ghobrial RM, Busuttill RW, Saab S, Lu DS. Macrovesicular hepatic steatosis in living related liver donors: correlation between CT and histologic findings. *Radiology* 2004; **230**: 276-280 [PMID: 14695401 DOI: 10.1148/radiol.2301021176]
- 65 **Reeder SB**, Sirlin CB. Quantification of liver fat with magnetic resonance imaging. *Magn Reson Imaging Clin N Am* 2010; **18**: 337-357, ix [PMID: 21094444 DOI: 10.1016/j.mric.2010.08.013]
- 66 **Qayyum A**, Goh JS, Kakar S, Yeh BM, Merriman RB, Coakley FV. Accuracy of liver fat quantification at MR imaging: comparison of out-of-phase gradient-echo and fat-saturated fast spin-echo techniques—initial experience. *Radiology* 2005; **237**: 507-511 [PMID: 16244259 DOI: 10.1148/radiol.2372040539]
- 67 **Qayyum A**, Chen DM, Breiman RS, Westphalen AC, Yeh BM, Jones KD, Lu Y, Coakley FV, Callen PW. Evaluation of diffuse liver steatosis by ultrasound, computed tomography, and magnetic resonance imaging: which modality is best? *Clin Imaging* 2009; **33**: 110-115 [PMID: 19237053 DOI: 10.1016/j.clinimag.2008.06.036]
- 68 **Fischer MA**, Raptis DA, Montani M, Graf R, Clavien PA, Nanz D, Alkadhi H, Scheffel H. Liver fat quantification by dual-echo MR imaging outperforms traditional histopathological analysis. *Acad Radiol* 2012; **19**: 1208-1214 [PMID: 22841289 DOI: 10.1016/j.acra.2012.05.009]
- 69 **Ishiko T**, Inomata Y, Beppu T, Asonuma K, Okajima H, Takeitchi T, Baba H. Age and donor safety in living-donor liver transplant in 110 consecutive cases at 1 institute. *Exp Clin Transplant* 2008; **6**: 190-193 [PMID: 18954295]
- 70 **Kamel IR**, Kruskal JB, Warmbrunn G, Goldberg SN, Pomfret EA, Raptopoulos V. Accuracy of volumetric measurements after virtual right hepatectomy in potential donors undergoing living adult liver transplantation. *AJR Am J Roentgenol* 2001; **176**: 483-487 [PMID: 11159100 DOI: 10.2214/ajr.176.2.1760483]
- 71 **Lo CM**, Fan ST, Liu CL, Wei WI, Lo RJ, Lai CL, Chan JK, Ng IO, Fung A, Wong J. Adult-to-adult living donor liver transplantation using extended right lobe grafts. *Ann Surg* 1997; **226**: 261-269; discussion 261-269 [PMID: 9339932 DOI: 10.1097/00000658-199709000-00005]
- 72 **Urata K**, Kawasaki S, Matsunami H, Hashikura Y, Ikegami T, Ishizone S, Momose Y, Komiyama A, Makuuchi M. Calculation of child and adult standard liver volume for liver transplantation. *Hepatology* 1995; **21**: 1317-1321 [PMID: 7737637 DOI: 10.1002/hep.1840210515]
- 73 **Emond JC**, Renz JF, Ferrell LD, Rosenthal P, Lim RC, Roberts JP, Lake JR, Ascher NL. Functional analysis of grafts from living donors. Implications for the treatment of older recipients. *Ann Surg* 1996; **224**: 544-552; discussion 552-554 [PMID: 8857858 DOI: 10.1097/00000658-199610000-00012]
- 74 **Singh AK**, Cronin CG, Verma HA, Boland GW, Saini S, Mueller PR, Sahani DV. Imaging of preoperative liver transplantation in adults: what radiologists should know. *Radiographics* 2011; **31**: 1017-1030 [PMID: 21768236 DOI: 10.1148/rg.314105197]
- 75 **Nakayama Y**, Li Q, Katsuragawa S, Ikeda R, Hiai Y, Awai K, Kusunoki S, Yamashita Y, Okajima H, Inomata Y, Doi K.

Hennedige T *et al.* Imaging in pre-LDLT work-up

Automated hepatic volumetry for living related liver transplantation at multisection CT. *Radiology* 2006; **240**: 743-748 [PMID: 16857979 DOI: 10.1148/radiol.2403050850]

76 **Suzuki K**, Epstein ML, Kohlbrenner R, Garg S, Hori M, Oto

A, Baron RL. Quantitative radiology: automated CT liver volumetry compared with interactive volumetry and manual volumetry. *AJR Am J Roentgenol* 2011; **197**: W706-W712 [PMID: 21940543 DOI: 10.2214/AJR.10.5958]

P- Reviewer: Chen F, Kilickesmez O, Verma S, Yuan Z

S- Editor: Wen LL **L- Editor:** A **E- Editor:** Lu YJ



Malrotation: Current strategies navigating the radiologic diagnosis of a surgical emergency

John J Tackett, Eleanor D Muise, Robert A Cowles

John J Tackett, Eleanor D Muise, Robert A Cowles, Section of Pediatric Surgery, Department of Surgery, Yale University School of Medicine, New Haven, CT 06520, United States
Author contributions: Tackett JJ, Muise ED and Cowles RA contributed to this work and wrote the paper.

Correspondence to: Robert A Cowles, MD, Associate Professor of Surgery, Section of Pediatric Surgery, Department of Surgery, Yale University School of Medicine, Box 208062, New Haven, CT 06520, United States. robert.cowles@yale.edu
Telephone: +1-203-7852701 Fax: +1-203-7853820

Received: December 31, 2013 Revised: June 20, 2014

Accepted: July 17, 2014

Published online: March 28, 2015

ily on clinical acumen and suspicion, radiologic imaging is critical in determining which patients need surgery. Surgeons and radiologists must cooperate and communicate effectively during the radiographic evaluation of a child with malrotation. Additionally, the algorithm for imaging malrotation must be adapted based upon the tools and staff available at any given institution.

Original sources: Tackett JJ, Muise ED, Cowles RA. Malrotation: Current strategies navigating the radiologic diagnosis of a surgical emergency. *World J Radiol* 2014; 6(9): 730-736 Available from: URL: <http://www.wjgnet.com/1949-8470/full/v6/i9/730.htm> DOI: <http://dx.doi.org/10.4329/wjr.v6.i9.730>

Abstract

The most accurate and practical imaging algorithm for the diagnosis of intestinal malrotation can be a complex and sometimes controversial topic. Since 1900, significant advances have been made in the radiographic assessment of infants and children suspected to have anomalies of intestinal rotation. We describe the current methods of abdominal imaging of malrotation along with their pros and cons. When associated with volvulus, malrotation is a true surgical emergency requiring rapid diagnosis and treatment. We emphasize the importance of close cooperation and communication between radiology and surgery to perform an effective and efficient diagnostic evaluation allowing prompt surgical decision making.

© 2015 Baishideng Publishing Group Inc. All rights reserved.

Key words: Malrotation; Midgut volvulus; Treitz; Ladd; Heterotaxy; Infant

Core tip: Malrotation, especially when associated with midgut volvulus, is a surgical emergency that must be astutely recognized, quickly diagnosed, and emergently treated operatively. While the diagnosis depends heav-

INTRODUCTION

Surgeons are often consulted for evaluation of pediatric abdominal problems presenting to the emergency department. It is common for these patients to be evaluated by radiographic imaging in addition to a focused history and physical examination. The surgeon and radiologist must always have a particularly high-level of suspicion in cases of possible malrotation that may require emergency surgery after evaluation.

CASE PRESENTATION

A 5-day-old full term male infant presents to the emergency department with continuous bilious non-bloody vomiting and irritability after his last three feeds. He was born by normal spontaneous vaginal delivery without complications and was noted to be breast-feeding well prior to discharge on day-of-life 2; he continued breast-feeding and passing stools at home for the past 4 d until this evening. On exam, his abdomen is minimally distended and he is crying constantly. The clinical picture suggests an obstruction distal to the ampulla of Vater,

and the surgeon has a heightened concern for malrotation with midgut volvulus. Before subjecting this infant to the morbidity of surgery, the surgeon calls a colleague in the Radiology Department to discuss appropriate imaging workup for malrotation.

Embryology

Anomalies of intestinal rotation, commonly referred to as malrotation, are a result of errors during embryologic development. In malrotation, the midgut does not complete its normal lengthening and rotation, and thus is incorrectly positioned within the peritoneal cavity. Normally the process of lengthening and rotation begins between the 4th and 5th wk of gestation. From this time until about week 10, the midgut is outgrowing the abdominal cavity and is forced to herniate through the umbilicus to continue unhindered growth^[1]. During weeks 10 and 11, the intestine returns to the peritoneal cavity. From the 11th wk forward, the small bowel undergoes fixation.

The small intestine is a straight tube early in development that derives its blood primarily from the superior mesenteric artery (SMA). This vessel divides the midgut into two parts: the cephalad or prearterial portion, and the caudad or postarterial portion^[2]. The prearterial portion is made up of duodenojejunal loops, while the postarterial portion are cecocolic loops^[3]. The SMA is important not only because it supplies the majority of blood flow to the small intestine, but also because it serves as the axis for the normal embryologic rotation of the bowel during development.

When the bowel herniates through the umbilicus, the prearterial portion rotates 180° counterclockwise around the axis of the SMA, while the postarterial portion rotates 90° counterclockwise. During the 10th and 11th wk, the prearterial portion of the gut reenters first followed by the postarterial portion. While the bowel returns into the abdominal cavity, both segments complete a total turn of 270°. This configuration places the normal anatomy of the C-loop of the duodenum posterior to the SMA and the transverse colon anterior to the SMA.

The blood from the SMA is distributed throughout smaller vessels running within the mesentery of the bowel. In normal development, the mesenteric root passes along the retroperitoneum from the ligament of Treitz to the proximal cecum^[4]. When normal rotation of the small bowel is not completed in embryologic development, the mesenteric root is foreshortened^[5]. The small bowel is then supported only by this foreshortened pedicle containing the SMA. The small bowel may then twist (volvulus), about this narrow axis^[6]. There are two major types of rotational abnormalities that have been described as malrotation and result in this foreshortening: incomplete rotation and non-rotation^[7]. During *incomplete rotation*, neither the cranial nor the caudal portion rotates more than 180°. The proximal midgut becomes fixed to the right of the SMA and the cecum becomes fixed directly anterior to the SMA. This pattern has the classic features of Ladd's bands covering and impinging upon the anterior portion

of the duodenum and the close proximity of the fixation points for the cranial and caudal midgut along with the SMA. In *non-rotation*, neither portion rotates more than 90°. Under-rotation leaves the proximal midgut fixed anterior to the right of the SMA and the cecum anterior to the left of the SMA, and the mesentery is still narrowed and foreshortened.

History

Two individuals recognized for their descriptions of small bowel anatomy and malrotation are Václav Treitz and William Ladd. Treitz (1819-1872), a professor of anatomy in Prague, described the area of tissue which we now recognize as the Ligament of Treitz^[3]. This area that bears his name gives physicians a common point to localize where the duodenum becomes the jejunum after exiting the retroperitoneum. Some have described the ligament as a "weak thin membranous structure" that is seldom demonstrated on CT^[8].

William Ladd (1880-1967) is considered the father of pediatric surgery in North America. During World War 1, Ladd dedicated his career to the surgical care of children and became surgeon-in-chief at Boston Children's Hospital^[3]. First in 1932 and then again in 1936, he published articles describing his approach to duodenal obstruction and malrotation with midgut volvulus. In these articles, he described a procedure involving detorsion of the volvulized bowel in a counterclockwise fashion, dividing the bands of tissue extending from the cecum across the duodenum and into the lateral peritoneal gutter, and finally spreading the mesentery from the cecum in the left upper quadrant to the small bowel in the right hemi-abdomen. This procedure later became known as Ladd's procedure^[9]. Rather than attempting to restore normal intestinal rotation, Ladd's operation aimed to convert malrotation to an arrangement of broadened nonrotation with the goal of minimizing the chance of recurrent volvulus^[7]. While historically Ladd had the availability of flat plate radiography to guide his work-up of children with malrotation, many different imaging modalities have become available to help guide diagnosis and treatment of this surgical emergency.

Imaging modalities

Plain X-ray: Radiographs are often the first step in the imaging evaluation of pediatric patients with suspected malrotation. This relatively inexpensive and widely available test allows the radiologist and surgeon to quickly exclude other potential diagnoses. Unfortunately, the most common finding on plain film of a patient with malrotation is "normal bowel gas pattern"^[2]. While abdominal radiographs in a newborn cannot rule-out malrotation, they can occasionally demonstrate findings that are concerning enough to prompt the surgeon to consider operative exploration: "double bubble" sign of duodenal obstruction, lack of bowel gas distal to the duodenum, bowel malposition (small intestine on the right and large intestine on the left, found in *non-rotation*, Figure 1), or pneumatosis intes-



Figure 1 This plain film illustrates an infant with malposition of the small bowel on the right and large bowel on the left suggesting malrotation.

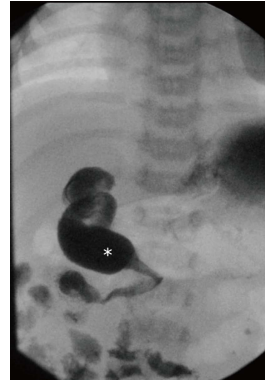


Figure 2 This Upper gastrointestinal demonstrates abnormal position of the duodenal-jejunal junction (white star) to the right of the spine. Normally the duodenum should sweep across from right to left across the spine.

tinalis with or without portal venous gas.

Ultrasound: Ultrasonography can be used as an adjunct to plain film radiography by determining the position of the superior mesenteric vessels and the relationship to the third portion of the duodenum. In normal anatomy, the SMA lies left of the superior mesenteric vein (SMV); reversal of this relationship may suggest malrotation^[10]. Orzech *et al*^[10] state that ultrasound can serve as an excellent screening tool for malrotation especially when complete inversion of the mesenteric vessels along with a “whirlpool” appearance of the mesentery around the SMA is found, prompting urgent exploration. They further suggest that “normal” positioning of the vessels may exist on a spectrum, and thus deviation from the classic position does not always imply malrotation, therefore clinical correlation and pretest probability should direct further studies including possible confirmative upper gastrointestinal studies.

Acknowledging the variation in normal SMA/SMV anatomy, some have supported the use of graded compression ultrasonography as a tool to assess the retroperitoneal position of the third portion of the duodenum (D3). Menten *et al*^[11] state that “based on anatomical and embryological arguments, a retromesenteric D3 excludes intestinal malrotation”. They proposed that the utilization of gradual compression to obtain transverse and sagittal images of the aortomesenteric angle could demonstrate truly normal rotation if D3 was visualized between the aorta and the SMA. Senior pediatric radiologists with over 26 years of combined experience performed the study that affirmed the use of ultrasound over upper gastrointestinal series recommended by Yousefzadeh *et al*^[12] two years earlier based on his own series of pediatric cases.

Upper gastrointestinal imaging: Thought of as the “gold standard” test to detect malrotation by most of the pediatric community, upper gastrointestinal imaging series (UGI) utilizes enteral contrast to obtain imaging of the prearterial gastrointestinal tract. An UGI involves administration of contrast orally or into the stomach and capturing images

as the contrast traverses the esophagus, stomach, duodenal c-loop, and eventually the duodenal-jejunal junction (DJJ). UGI findings suggestive of malrotation or volvulus include low DJJ position, absence of the DJJ from its typical anatomical position to the left of the vertebral body pedicle, jejunum located on the right (Figure 2), duodenal redundancy, and DJJ corkscrew appearance^[13].

Imaging quality depends on the position of the patient during the study, a not insignificant challenge in the pediatric population. In 2013, a group in South Africa published their technique to optimize UGI results^[14]. They used external metal markers along the child’s midline to aid in orienting the anatomical position of the patient during the study; they further invested in a three-person team to control the child’s positioning during the entirety of the study. They describe their techniques as follows: “study commences with the child swallowing contrast on their left side (to prevent duodenal filling) to evaluate the esophagus...the child is then placed on its right side to allow duodenal filling and to observe the course of the duodenum...once a sufficient contrast bolus is visualized in the duodenum, the child must be turned rapidly to an unrotated supine position...to capture the c-loop^[14]”.

Barium enema: The cecum may be malpositioned in malrotation as is the case with the DJJ; thus, a barium enema can be used to visualize the position of the cecum. Abnormal position of the cecum on preoperative imaging can be found in 80% and 87% of surgically proven cases of malrotation^[15]. The normally rotated cecum is found in the right lower quadrant of the abdomen and up to 20% of patients with malrotation will have a normally positioned cecum^[2]. No radiographic findings related to the cecum can unequivocally rule-out risk of malrotation^[16]. As such, the barium enema is rarely used alone, but may prompt surgical exploration if a patient presents acutely and cecal malpositioning clinically correlates with the patient’s exam.

Computed tomography: Like ultrasound, computed to-

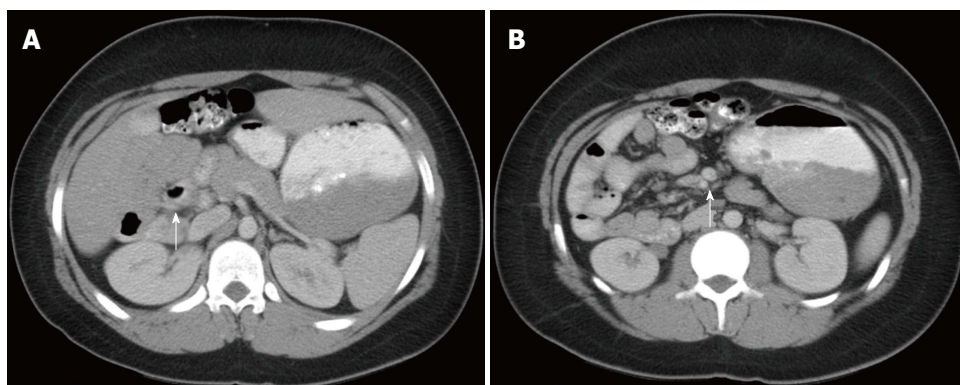


Figure 3 This axial view of an abdominal computed tomography. A: Illustrates the duodenal-jejunal junction (white arrow) in the right hemi-abdomen suggesting malrotation; B: Illustrates superior mesenteric artery Superior Mesenteric Artery (SMA)/Superior Mesenteric Vein (SMV) inversion (white arrow) with the SMA to the right of the SMV. This inversion suggests malrotation.



Figure 4 This coronal view of an abdominal computed tomography illustrates the terminal ileum and cecum (white arrows). Positioning of the cecum in the left hemi-abdomen is suggestive of malrotation.

mography (CT) imaging can be used to evaluate the position of D3, the DJJ (Figure 3A), and the anatomical relationship between the SMA and SMV (Figure 3B). Based on a study by Taylor, CT imaging of abnormal D3 position had a sensitivity and specificity of diagnosing malrotation of 97.3% and 99% respectively^[17]. Due to the variation in normal SMA/SMV anatomy as previously discussed, the accuracy of identifying “abnormal” SMA/SMV relation in making the diagnosis of malrotation was 76.8%^[17]. One unique aspect of a CT is that when used with contrast enhancement it can recognize perfusion abnormalities that may be missed on laboratory studies^[18]. CT can be performed quickly on a child with extremely minimal invasiveness, but does subject the child to a significant dose of radiation when compared to an UGI (Figure 4).

MRI: Magnetic resonance imaging (MRI) can be used, much like CT, as a cross-sectional imaging modality to identify findings of malrotation including: dilation of the proximal duodenum, non-retroperitoneal positioning of the duodenum, bowel malpositioning, and inversion of the SMA/SMV relationship^[2]. The MRI avoids radiation but relies on the patient holding still for the duration of the lengthier exam. Additionally, the MRI is the most

expensive imaging modality available to aid in diagnosing malrotation.

Current controversies

Some believe that localizing the DJJ with UGI cannot give reliable data to rule-out malrotation. One author touts that ultrasonographic imaging in the hands of an experienced technician may demonstrate a retromesenteric D3, which alone can prove that a patient “will not have malrotation and will not develop midgut volvulus^[12]”. Menten *et al*^[11] support this assertion, describing a graded compression-technique to demonstrate positioning between the SMA and aorta. These techniques rely on availability of experienced radiology staff, and some hospitals may not have this capability or around-the-clock availability to allow for this focused ultrasound exam. Furthermore, at least one case of normal D3 retroperitoneal positioning on cross-sectional CT imaging in a child with malrotation has been reported, thus calling to question the conclusion that normal positioning always rules out malrotation^[17].

One group of infants in particular has added controversy to the approach of workup for malrotation: infants with heterotaxy (Figure 5). Anomalies of intestinal rotation are common in these infants; unfortunately, these children can also suffer from life-threatening cardiac anomalies. There is debate whether these children should undergo elective surgery to broaden the mesentery and prevent volvulus even if an anomaly of rotation is identified^[19]. Some have suggested that watchful waiting may be appropriate as volvulus appears to be rare in this population^[20]. Importantly, Tashjian *et al*^[21] stated that if a surgeon decides to perform a Ladd’s procedure on a patient with heterotaxia it should occur only when the congenital heart disease is well controlled. Additionally, during operative planning when imaging children with heterotaxia, it is difficult to determine the width of the mesenteric root since there is often insufficient data on the location of the cecum relative to the DJJ^[3]. This debate still has yet to be studied in detail with long-term follow-up analysis.

Table 1 Positive and negative attributes of commonly used imaging modalities when applied to cases of suspected malrotation

Imaging modality	Pros	Cons
Plain film	Inexpensive, quick, may demonstrate classic appearance of duodenal obstruction, may give earlier indication for operative exploration	May masquerade as other abnormalities, may delay treatment (especially when read as “normal”), cannot exclude malrotation
Ultrasound	Avoids radiation exposure, may demonstrate “whirlpool sign” indicative of volvulus, duplex to determine relationship of D3 and superior mesenteric vessels, Possibility to evaluate normal abdominal anatomy	Normal sonogram may not exclude malrotation, quality related to technician experience
Upper GI	Currently considered the “gold standard”, relatively non-invasive, available at pediatric centers, easily demonstrates duodenal obstruction, allows for visualization of the duodenojejunal junction, delayed imaging may show position of the cecum	Small amount of radiation, challenge to position patient for optimal imaging, may be distorted by bowel distention or indwelling tubes, duodenojejunal junction may have normal variation in position
Barium Enema	Easily demonstrates position of entire large bowel (especially cecum) quickly	Small amount of radiation, normal cecum position does not rule out proximal malrotation
CT	Quick, allows for viewing position of SMA/SMV, may demonstrate “whirlpool sign” indicative of volvulus, visualization of all abdominal anatomy	High radiation exposure, requires patient to remain still for short period of time, normal relationship between SMA/SMV does not exclude malrotation
MRI	No radiation exposure, allows for viewing position of SMA/SMV, may demonstrate “whirlpool sign”, visualization of all abdominal anatomy	Requires patient to remain still for a longer period of time, expensive, not accessible

CT: Computed tomography; MRI: Magnetic resonance imaging; GI: Gastrointestinal imaging; SMA: Superior mesenteric artery; SMV: Superior mesenteric vein.

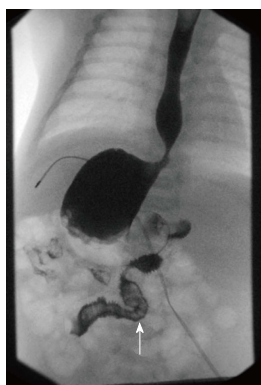


Figure 5 This Upper gastrointestinal in an infant with heterotaxia demonstrates abnormal positioning of the stomach to the right, the liver near the midline, and the duodenum running left to right. The duodenal-jejunal junction (white arrow) is seen inferior to the duodenum demonstrating malrotation.

DISCUSSION

Cooperation

The most important factor in the evaluation of a child with bilious emesis and abdominal tenderness is cooperation between the surgery and radiology teams. Malrotation with volvulus is a surgical emergency in which immediate operative intervention to untwist the volvulus and prevent bowel loss is imperative. Even given prompt diagnosis and preoperative optimization, surgery still carries morbidity and mortality risks associated with anesthesia and the operation itself.

Close communication between the examining surgeon and the radiologist is critical to determine the imaging study best suited to evaluate the given clinical presentation of the child, and to discuss possible limitations of certain studies at specific institutions. Whether initially utilizing radiography/fluoroscopy or cross sectional imaging, lapses in communication should not introduce delay

from the time of initial evaluation to the time a decision to operate is made. As discussed, not all imaging results will be straightforward or immediately diagnostic in the evaluation of malrotation, so the coordination of multiple studies should be anticipated and discussed to optimize imaging for the patient.

Proposed decision algorithm

Knowing the importance of cooperation between the surgeon and the radiologist, we propose below a decision algorithm for an infant or child with possible malrotation. It has been discussed that “negative” radiographic results for most imaging modalities are not 100% reliable in ruling out malrotation. Whenever imaging results are positive for malrotation, we recommend considering operative exploration. It is important to keep in mind that even “positive” radiographic results suggesting malrotation must always be correlated with the clinical picture before committing to an operation.

We suggest beginning with the history and physical along with laboratory results; if there is strong evidence of an emergent ischemic process, the patient may need urgent operative exploration without the delay of imaging. If this is not the case, we recommend starting with easily accessible and inexpensive plain radiography. If the radiograph is negative for evidence of malrotation, the surgeon-radiologist team should discuss whether the hospital is equipped to perform experienced gradual-compression ultrasonography. If there is an experienced radiologist available, the non-irradiating imaging can be performed. If this imaging modality is negative or not available to the team, then an UGI should be performed. Negative UGI results should pause the imaging decision pathway.

Based on the discussed sensitivity and accuracy of the ultrasound and UGI, negative results may strongly suggest that the patient does not have malrotation either

my demonstrating normal anatomy or by elucidating evidence of a different diagnosis. At this point, we recommend reassessing the clinical concern for possible malrotation. If the concern is lower, then watchful waiting may be acceptable. If there is still high clinical suspicion, then the imaging should proceed with a barium enema. This pause for decision-making should be short and cooperatively communicated between the surgeon and radiologist, as it would be ideal to obtain a barium enema while the patient is still on the X-ray table from the UGI. A negative barium enema in a patient with high clinical suspicion should prompt a discussion about CT imaging. At this point, do the risks of irradiation with CT imaging outweigh the risks of negative operative exploration or delaying surgery for close observation? If the perceived benefits of the CT outweigh the risks, then CT should be obtained. In the setting of CT results negative for evidence of malrotation, we recommend close observation with low threshold to repeat UGI or consider operation if the exam or labs worsen.

Due to its cost, both in time and dollars, we do not feel that an MRI can give additional information over the previous imaging studies without significantly delaying the diagnosis. Additionally, due to the length of time the patient must remain still, the patient would almost certainly need to be sedated and intubated in order to obtain imaging. We feel the risk of anesthesia for this imaging modality is not acceptable for the benefit of the imaging results gathered.

We recognize that the above algorithm is based on the expectation that plain film radiography, ultrasound, fluoroscopy, and advanced radiography are easily and readily available. Many centers around the world may not have access to these imaging modalities, and the algorithm should be adjusted as such. Additionally, it should be considered that a patient may have intermittent volvulus that, depending on the time of the imaging, may cause false negative results. These cases rely on the clinical evaluation to determine if imaging studies should be repeated.

In conclusion, malrotation presenting in the newborn or older child can become a surgical emergency. Delay in diagnosis, specifically in the setting of a midgut volvulus, can lead to intestinal necrosis, increased mortality, and intestinal failure with dependence on parenteral nutrition. When malrotation is being considered, it is important that pediatric surgeons and pediatric radiologists work closely to discuss available imaging options and communicate a clear workflow of studies while making the decision of whether or not an operation is needed. In the heterotaxy population, even positive imaging can be difficult to interpret clinically and little consensus exists regarding the treatment of this subset of patients.

We have proposed an imaging algorithm based on the current literature and an evaluation of the pros and cons of the different imaging modalities (Table 1). Our algorithm begins with a plain film radiograph followed by either ultrasound or UGI series depending on resources available. However, it is important to stress that any algo-

rithm is useless without the communication and cooperation of the surgery and radiology teams. Teamwork in diagnosis is the key to optimal outcomes in children with malrotation.

ACKNOWLEDGEMENTS

We would like to acknowledge Dr. Lauren Ehrlich (Department of Radiology, Yale University School of Medicine) for providing us with de-identified radiographic images.

REFERENCES

- 1 **Frazer JE**, Robbins RH. On the Factors concerned in causing Rotation of the Intestine in Man. *J Anat Physiol* 1915; **50**: 75-110 [PMID: 17233053 DOI: 10.1053/j.sempedsurg.2003.08.009]
- 2 **Strouse PJ**. Malrotation. *Semin Roentgenol* 2008; **43**: 7-14 [PMID: 18053823 DOI: 10.1053/j.ro.2007.08.002]
- 3 **Lamp B**, Levin TL, Berdon WE, Cowles RA. Malrotation and midgut volvulus: a historical review and current controversies in diagnosis and management. *Pediatr Radiol* 2009; **39**: 359-366 [PMID: 19241073 DOI: 10.1007/s00247-009-1168-y]
- 4 **McVay MR**, Kokoska ER, Jackson RJ, Smith SD, Jack Barney Award. The changing spectrum of intestinal malrotation: diagnosis and management. *Am J Surg* 2007; **194**: 712-717; discussion 712-717 [PMID: 18005759 DOI: 10.1016/j.amjsurg.2007.08.035]
- 5 **Daneman A**. Malrotation: the balance of evidence. *Pediatr Radiol* 2009; **39** Suppl 2: S164-S166 [PMID: 19308379 DOI: 10.1007/s00247-009-1152-6]
- 6 **Irish MS**, Pearl RH, Caty MG, Glick PL. The approach to common abdominal diagnosis in infants and children. *Pediatr Clin North Am* 1998; **45**: 729-772 [PMID: 9728184 DOI: 10.1016/S0031-3955(05)70043-2]
- 7 **Shew SB**. Surgical concerns in malrotation and midgut volvulus. *Pediatr Radiol* 2009; **39** Suppl 2: S167-S171 [PMID: 19308380 DOI: 10.1007/s00247-008-1129-x]
- 8 **Kim SK**, Cho CD, Wojtowycz AR. The ligament of Treitz (the suspensory ligament of the duodenum): anatomic and radiographic correlation. *Abdom Imaging* 2008; **33**: 395-397 [PMID: 17653583 DOI: 10.1007/s00261-007-9284-3]
- 9 **Ladd WE**. Surgical disease of the alimentary tract in infants. *New Eng J Med* 1936; **215**: 705-708 [DOI: 10.1056/NEJM193610152151604]
- 10 **Orzech N**, Navarro OM, Langer JC. Is ultrasonography a good screening test for intestinal malrotation? *J Pediatr Surg* 2006; **41**: 1005-1009 [PMID: 16677901 DOI: 10.1016/j.jpedsurg.2005.12.070]
- 11 **Menten R**, Reding R, Godding V, Dumitriu D, Clapuyt P. Sonographic assessment of the retroperitoneal position of the third portion of the duodenum: an indicator of normal intestinal rotation. *Pediatr Radiol* 2012; **42**: 941-945 [PMID: 22684229 DOI: 10.1007/s00247-012-2403-5]
- 12 **Yousefzadeh DK**. The position of the duodenojejunal junction: the wrong horse to bet on in diagnosing or excluding malrotation. *Pediatr Radiol* 2009; **39** Suppl 2: S172-S177 [PMID: 19308381 DOI: 10.1007/s00247-008-1116-2]
- 13 **Sizemore AW**, Rabbani KZ, Ladd A, Applegate KE. Diagnostic performance of the upper gastrointestinal series in the evaluation of children with clinically suspected malrotation. *Pediatr Radiol* 2008; **38**: 518-528 [PMID: 18265969 DOI: 10.1007/s00247-008-0762-8]
- 14 **Dekker G**, Andronikou S, Greyling J, Louw B, Brandt A. Contrast meals and malrotation in children-metal mark-

- ers for improved accuracy. *Pediatr Radiol* 2013; **43**: 115-118 [PMID: 23160646 DOI: 10.1007/s00247-012-2503-2]
- 15 **Applegate KE**. Evidence-based diagnosis of malrotation and volvulus. *Pediatr Radiol* 2009; **39** Suppl 2: S161-S163 [PMID: 19308378 DOI: 10.1007/s00247-009-1177-x]
- 16 **Slovic TL**, Strouse PJ. Malrotation: some answers but more questions. *Pediatr Radiol* 2009; **39**: 315-316 [PMID: 19241072 DOI: 10.1007/s00247-009-1169-x]
- 17 **Taylor GA**. CT appearance of the duodenum and mesenteric vessels in children with normal and abnormal bowel rotation. *Pediatr Radiol* 2011; **41**: 1378-1383 [PMID: 21594544 DOI: 10.1007/s00247-011-2118-z]
- 18 **Aidlen J**, Anupindi SA, Jaramillo D, Doody DP. Malrotation with midgut volvulus: CT findings of bowel infarction. *Pediatr Radiol* 2005; **35**: 529-531 [PMID: 15536561 DOI: 10.1007/s00247-004-1355-9]
- 19 **Chang J**, Brueckner M, Touloukian RJ. Intestinal rotation and fixation abnormalities in heterotaxia: early detection and management. *J Pediatr Surg* 1993; **28**: 1281-1284; discussion 1285 [PMID: 8263687 DOI: 10.1016/S0022-3468(05)80313-6]
- 20 **Choi M**, Borenstein SH, Hornberger L, Langer JC. Heterotaxia syndrome: the role of screening for intestinal rotation abnormalities. *Arch Dis Child* 2005; **90**: 813-815 [PMID: 15890694 DOI: 10.1136/adc.2004.067504]
- 21 **Tashjian DB**, Weeks B, Brueckner M, Touloukian RJ. Outcomes after a Ladd procedure for intestinal malrotation with heterotaxia. *J Pediatr Surg* 2007; **42**: 528-531 [PMID: 17336193 DOI: 10.1016/j.jpedsurg.2006.10.060]

P- Reviewer: Shen L **S- Editor:** Wen LL **L- Editor:** A
E- Editor: Lu YJ



Diffusion-weighted magnetic resonance imaging in management of bladder cancer, particularly with multimodal bladder-sparing strategy

Soichiro Yoshida, Fumitaka Koga, Shuichiro Kobayashi, Hiroshi Tanaka, Shiro Satoh, Yasuhisa Fujii, Kazunori Kihara

Soichiro Yoshida, Fumitaka Koga, Shuichiro Kobayashi, Yasuhisa Fujii, Kazunori Kihara, Department of Urology, Tokyo Medical and Dental University Graduate School, Tokyo 113-8677, Japan

Fumitaka Koga, Department of Urology, Tokyo Metropolitan Cancer and Infectious Diseases Center Komagome Hospital, Tokyo 113-0021, Japan

Hiroshi Tanaka, Shiro Satoh, Department of Radiology, Ochanomizu Surugadai Clinic, Tokyo 101-0062, Japan

Author contributions: Yoshida S, Kobayashi S, Tanaka H, Satoh S, Fujii Y and Kihara K contributed to conception; Yoshida S and Koga F wrote the paper.

Correspondence to: Fumitaka Koga, MD, PhD, Department of Urology, Tokyo Metropolitan Cancer and Infectious diseases Center Komagome Hospital, 3-18-22 Honkomagome, Bunkyo-ku, Tokyo 113-8677, Japan. f-koga@cick.jp

Telephone: +81-3-38232101 Fax: +81-3-38241552

Received: December 29, 2013 Revised: April 10, 2014

Accepted: May 14, 2014

Published online: March 28, 2015

differences in the motion of water molecules among tissues and this information is useful in assessing the biological behavior of cancers. Promising results in predicting and monitoring the response to CRT have been reported in several types of cancers. Recently, growing evidence has emerged showing that DW-MRI can serve as an imaging biomarker in the management of bladder cancer. The qualitative analysis of DW-MRI can be applied to detecting cancerous lesion and monitoring the response to CRT. Furthermore, the potential role of quantitative analysis by evaluating apparent diffusion coefficient values has been shown in characterizing bladder cancer for biological aggressiveness and sensitivity to CRT. DW-MRI is a potentially useful tool for the management of bladder cancer, particularly in multimodal bladder-sparing approaches for MIBC.

© 2015 Baishideng Publishing Group Inc. All rights reserved.

Key words: Diffusion magnetic resonance imaging; Bladder cancer; Urothelial carcinoma; Chemotherapy; Radiotherapy

Abstract

Bladder-sparing strategy for muscle-invasive bladder cancer (MIBC) is increasingly demanded instead of radical cystectomy plus urinary diversion. Multimodal therapeutic approaches consisting of transurethral resection, chemotherapy, radiotherapy and/or partial cystectomy improve patients' quality of life by preserving their native bladder and sexual function without compromising oncological outcomes. Because a favorable response to chemoradiotherapy (CRT) is a prerequisite for successful bladder preservation, predicting and monitoring therapeutic response is an essential part of this approach. Diffusion-weighted magnetic resonance imaging (DW-MRI) is a functional imaging technique increasingly applied to various types of cancers. Contrast in this imaging technique derives from

Core tip: Diffusion-weighted magnetic resonance imaging (DW-MRI) is a functional imaging increasingly applied in the management of bladder cancer. This imaging offers unique information reflecting physiological character of the tissues by quantifying the diffusion of water molecules. DW-MRI provides accurate information for the diagnosis of bladder cancer in a noninvasive manner. Furthermore, growing evidence has emerged showing that DW-MRI can serve as an imaging biomarker of bladder cancer for assessing biologic aggressiveness and therapeutic sensitivity and for monitoring the therapeutic response. This review focuses on the potential role of DW-MRI in multimodal organ-preservation strategies for bladder cancer.

Original sources: Yoshida S, Koga F, Kobayashi S, Tanaka H, Satoh S, Fujii Y, Kihara K. Diffusion-weighted magnetic resonance imaging in management of bladder cancer, particularly with multimodal bladder-sparing strategy. *World J Radiol* 2014; 6(6): 344-354 Available from: URL: <http://www.wjgnet.com/1949-8470/full/v6/i6/344.htm> DOI: <http://dx.doi.org/10.4329/wjr.v6.i6.344>

INTRODUCTION

Bladder cancer is the second most common genitourinary cancer in the United States and some 55600 new cases and 15100 deaths from bladder cancer are estimated to have occurred in 2012^[1]. At the initial diagnosis, a third of all cases are diagnosed as muscle-invasive bladder cancer (MIBC)^[2], and radical cystectomy has long been the treatment of choice for the treatment of localized MIBC. However, concern for patients' quality of life has strengthened the trend toward bladder-sparing approaches with various treatment modalities^[3]. In this treatment approach, meticulous evaluation of the bladder cancer is essential. Diffusion-weighted magnetic resonance imaging (DW-MRI) is a functional imaging technique increasingly applied to various types of cancer. Recently, growing evidence has emerged showing that DW-MRI can serve as an imaging technique that is useful for characterizing the pathophysiology of cancer. The biological behavior assessed with this imaging technique will play an important role in multimodal organ-preserving strategies for MIBC. Thus, this review focuses on the potential role of DW-MRI in multimodal organ-preservation strategies for MIBC.

Trimodality bladder-sparing strategy for MIBC

Favorable oncological and functional outcomes using bladder-sparing trimodality therapy combined with transurethral resection of bladder tumor (TURBT), chemotherapy and radiotherapy have been reported by several groups including Harvard University, the University of Paris and the University of Erlangen in Germany^[4-6]. In most trimodality bladder-sparing approaches, patients who achieve complete response (CR) after the trimodal treatment are selectively subjected to consolidative therapies for bladder preservation, whereas those who do not achieve CR are advised to undergo early radical cystectomy. The 5-year survival rates after trimodality bladder-preserving trials were reported to be 50%-60%, which is comparable to those of radical cystectomy series^[7, 8].

In the trimodality bladder preservation strategies, clinically tumor-free status after TURBT followed by chemoradiotherapy (CRT), as well as lower T stage and completeness of the TURBT, are important prognostic factors^[6, 9-11]. However, even the patients who clinically achieved CR after TURBT followed by CRT still may develop local tumor recurrence and lymph node metastases. Zietman *et al*^[12] reported that two-thirds of non-MIBC (NMIBC) recurrences developed in the original MIBC sites. Tunio *et al*^[13] also showed that 21% of the MIBC

patients who achieved CR after trimodality therapy developed MIBC recurrence, and 69% of the recurrences arose from the original MIBC site. This problem could be due, in part, to subclinical viable bladder cancer cells remaining in the original MIBC site, which were missed by conventional imaging studies and biopsy-based evaluation^[14].

Limitations of conventional radiological evaluations in bladder-sparing strategy for MIBC

Contrast-enhanced CT and conventional MRI are the standard techniques that have been used for the radiological evaluation of urinary system tumors. While CT is generally used to screen for metastasis, MRI plays a pivotal role in the staging of bladder cancer because of its superior soft tissue delineation, especially in the context of muscle-invasion. The diagnostic accuracy of MRI in differentiating MIBC from NMIBC is reported to be 75%-92%^[15, 16]. However, these anatomical imaging techniques are not ideal for tissue characterization and assessing tumor aggressiveness. Furthermore, these anatomical imaging techniques often overestimate the extent of tumor after TURBT and CRT due to the post-treatment changes. In multimodal organ-preserving strategies, generally, prior to CRT, TURBT is performed for debulking of the tumor. Both TURBT and CRT can induce local fibrotic and inflammatory changes, both of which manifest as bladder wall thickening^[17]. Additionally, after the combined therapy, bladder cancer may regress and present as a flat lesion. Therefore, anatomical assessment of therapeutic response based on the response evaluation criteria in solid tumors on T2WI is not appropriate for discriminating small remnants of cancerous tissue from these secondary changes. Dobson *et al*^[18] showed the utility of dynamic contrast-enhanced (DCE) MRI for discriminating cancerous tissue from radiation-induced fibrosis in thickened bladder walls. However, inflammatory changes secondary to treatments may persist for many years^[19]. These false-positive results on DCE are often problematic, and they lower its specificity for detecting residual bladder cancer^[19]. Thus, the utility of T2WI and DCE is still limited in monitoring the therapeutic response after TURBT and CRT^[20].

DIFFUSION-WEIGHTED MRI IN CANCER

Biophysical basis and clinical application

The DW-MRI technique was initially devised by Stejskal and Tanner in 1965. Since 1985, DW-MRI has been mainly used for neuroimaging, especially for diagnosis of acute cerebral infarction and intracranial tumors^[21]. With the recent advent of echo planar imaging, high gradient amplitudes, multichannel coils, and parallel imaging, DW-MRI of the abdomen and pelvis has become possible, and a growing number of studies have demonstrated the usefulness of this imaging technique in the diagnosis of malignant tumors of the abdomen^[22, 23]. Because the signal of DW-MRI is derived from the inherent tissue contrast,

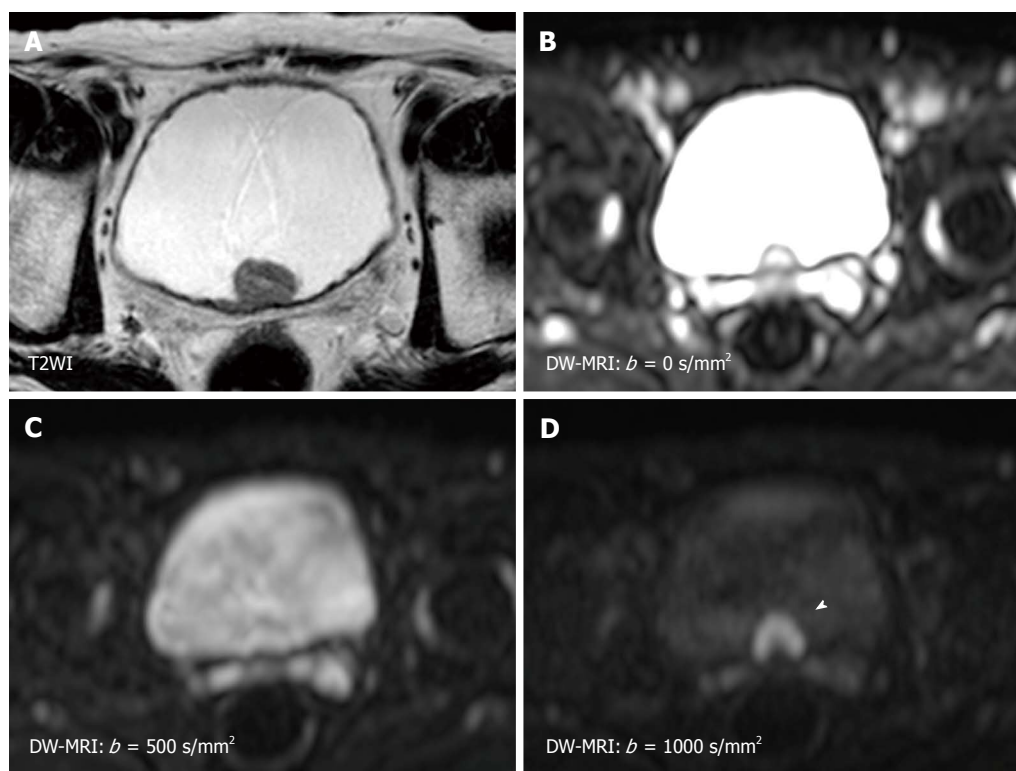


Figure 1 Magnetic resonance images of a 79-year-old man with non-muscle invasive bladder cancer (urothelial cancer, stage pTa, grade 2 > 3). A: T2WI shows a hypointense tumor at the trigone; B: The signal intensity of diffusion-weighted magnetic resonance imaging depends on both water diffusion and the T2 relaxation time; C: Due to the very long T2 relaxation time of urine, the signal of the urine in the bladder remains high on the diffusion-weighted magnetic resonance imaging with a b -value of 500 s/mm². This is known as the “T2 shine-through effect”; D: Using a b -value of 1000 s/mm² decreases the signal of the urine, as well as those of the seminal vesicles, while the bladder cancer (arrow head) shows little signal attenuation with the increased b -value.

this imaging technique requires no contrast agent and is applicable to patients with allergies to contrast agents or those with renal insufficiency. Furthermore, the addition of DW-MRI to a routine MRI examination requires only a few additional minutes and can be adopted for most current clinical MRI scanners.

DW-MRI is a functional imaging technique, the contrast of which results from quantifying the microscopic mobility of water molecules in tissue^[22,23]. In biological tissues, the diffusion of water molecule is inversely correlated to the tissue cellularity and the integrity of cell membranes. In the area of tumor tissues, which have a high cellular density with intact cell membranes, water molecule diffusion is restricted, while the diffusion of water molecule is less restricted in areas of low cellular density. Areas where the diffusion is restricted generally show high signal intensity on DW-MRI, and malignant lesions typically show high signal intensity because of their higher cellularity, tissue disorganization, and decreased extracellular space, all of which restrict water diffusion. In recent years, an increasing number of studies have shown the usefulness of visual assessment of DW-MRI for detecting malignant tumors, and DW-MRI has quickly become a useful adjunct for assessing various types of tumors including bladder cancer^[24-27].

Quantifying the degree of diffusion

The sensitivity of the diffusion is varied by changing the

“ b -value” which is proportional to the gradient amplitude, the duration of the applied gradient, and the time interval between the paired gradients^[22,23]. Small b -values attenuate the signals of water molecules with a large degree of motion or a great diffusion distance. By using higher b -values, the perfusion in the intra-vascular space is restricted and slow-moving water molecules or small diffusion distances can be distinguished (Figure 1). Therefore, DW-MRI should be performed using three or more b -values including $b = 0$ s/mm², $b \geq 100$ s/mm², and $b \geq 500$ s/mm². Comparing the images obtained at different b -values is useful for characterizing the lesion. The apparent diffusion coefficient (ADC) value is assessed for quantitative evaluation of DW-MRI by evaluating the signal attenuation of tissue on DW-MRI with increasing b -values. Generally, the software automatically calculates the ADC values, and the calculated ADC values for each pixel of the image are displayed as a parametric map. By drawing regions of interests (ROI) on this ADC map, the ADC value of the delineated region can be easily obtained. However, because of their poor anatomical details, DW-MRI and ADC maps should be evaluated in combination with T1WI and T2WI, and the correlation with anatomical images is important to accurately set the ROI for the target lesion. Quantitative evaluation of DW-MRI by assessing the ADC value is potentially useful for tissue characterization based on the differences in water diffusion. The correlation of tumor ADC values with their

biological aggressiveness has been reported for various types of malignancies^[28-30]. However, the reproducibility of the ADC value is an intrinsic limitation in ADC measurement because the ADC value depends on the MRI system and imaging protocol used. To standardize the ADC assessment, some trials using ADC ratio, calculated with respect to surrounding normal tissues, have been performed recently.

Predicting treatment sensitivity

The important clinical implication of DW-MRI in multimodal organ preservation strategies for MIBC is the ability to predict therapeutic response prior to treatment. In a number of prospective studies in various types of cancers including brain tumors and cervical and rectal cancers^[31-35], the potential of DW-MRI to predict the sensitivity to radiotherapy has been shown. The tumors with higher ADC values are less likely to respond to the treatment. The hypothesized mechanism underlying this relationship is the presence of necrosis reflected in a higher ADC value, which predicts a poor outcome related to hypoxia-mediated radioresistance. Meanwhile, soon after the initiation of chemotherapy and/or radiotherapy, immediate cell death can be observed after the commencement of the treatment, which is reflected as an early increase in the ADC value. In cervical cancer and rectal cancer, this early increase in ADC value is observed in patients who show good response to CRT, and can be a potential early biomarker for treatment outcomes^[35-38]. Following this early ADC increase, edema and fibrosis cause a subsequent ADC decrease^[35-37].

Monitoring treatment response

Importantly, the DW-MRI can be an imaging biomarker in monitoring treatment effect. In response to successful treatment, cell necrosis and loss of cell membrane integrity are induced, leading to increased water diffusion. Furthermore, tumor apoptosis induced by treatment results in cell shrinkage. These changes are reflected by increases in ADC value^[22]. Clinical studies in many types of malignancies, including liver cancer, cerebral gliomas, and soft-tissue sarcoma, have demonstrated the correlation between therapeutic effect and changes in water diffusion in tumors^[39-41].

CLINICAL APPLICATION OF DW-MRI IN BLADDER CANCER

Detecting bladder cancer

Since the first report by Matsuki *et al.*^[26] showing the utility of DW-MRI for detecting bladder cancer, a number of studies have shown the usefulness of DW-MRI for the diagnosis of bladder cancer^[24-27]. On DW-MRI with a high *b*-value, bladder cancers generally show a hyperintense signal, while the signals of the surrounding tissues, including urine, are much less intense^[26,42] (Figure 1). This good signal contrast is obtained between bladder cancer

and the surrounding tissue. The sensitivity, specificity and accuracy for detecting bladder cancer were reported to be 90%-98%, 92%-93% and 91%-97%, respectively^[24,25,27]. In several studies, quantitative analysis consistently showed restricted diffusion and lower ADC values in bladder cancer compared with the surrounding structures^[26,42].

Detecting lymph node metastasis

MIBC has the potential to metastasize to lymph nodes and distant organs, and detecting metastatic lesion is another problem in managing MIBC. At the time of surgery, 25% of the patients who undergo radical cystectomy have a lymph node metastasis. Lymph node staging has been generally performed by CT or conventional MRI based on size criteria and morphological appearance, and the accuracy for staging nodal disease ranges from 73% to 90%^[43]. On DW-MRI, benign lymph nodes show high signal intensity due to their highly cellular structures composed of lymphoid elements (Figure 2). The utility of DW-MRI has been shown in lymph node staging in various cancers^[44-48]. Papalia *et al.*^[49] showed that malignant lymph nodes have a significantly lower ADC value than benign lymph nodes with sensitivity of 76.4% and specificity of 89.4% in a study that included 36 patients with bladder cancer undergoing radical cystectomy. However, there is a substantial overlap in ADC values between malignant and benign lymph nodes, and discriminating malignant nodes from benign nodes on DW-MRI is still challenging^[50]. Recently, Thoeny *et al.*^[51] reported an excellent diagnostic accuracy of 90% in detecting pelvic lymph nodal involvement by the combined use of ultra-small super paramagnetic iron oxide (USPIO) and DW-MRI. This agent is taken up by macrophages resulting signal loss in normal lymph nodes, while the signal of metastatic lymph nodes is not influenced^[51-55]. Further studies are needed to confirm this encouraging result.

Detecting bone metastasis

DW-MRI for evaluating primary bladder cancer occasionally shows abnormal signals of pelvic bones or femur heads. Bone metastasis typically shows clear high signal intensity on DW-MRI^[56,57]. However, as well as benign bone tumors, hematopoietic bone marrow also appears as a hyperintense lesion on DW-MRI because of rich hematopoietic cells^[58,59]. These false-positive findings in detecting metastasis should be kept in mind for staging bladder cancer^[60]. Furthermore, identifying microscopic metastases or developing metastases remains a challenge, and a third of MIBC patients have undetected metastases at the initial diagnosis^[61].

Characterizing histopathological features

Because the contrast of DW-MRI is based on difference in the degree of water diffusion between tissues, the spatial resolution of DW-MRI is generally low. However, using the clear contrast between bladder cancer and the surrounding tissues, the utility of DW-MRI for staging of

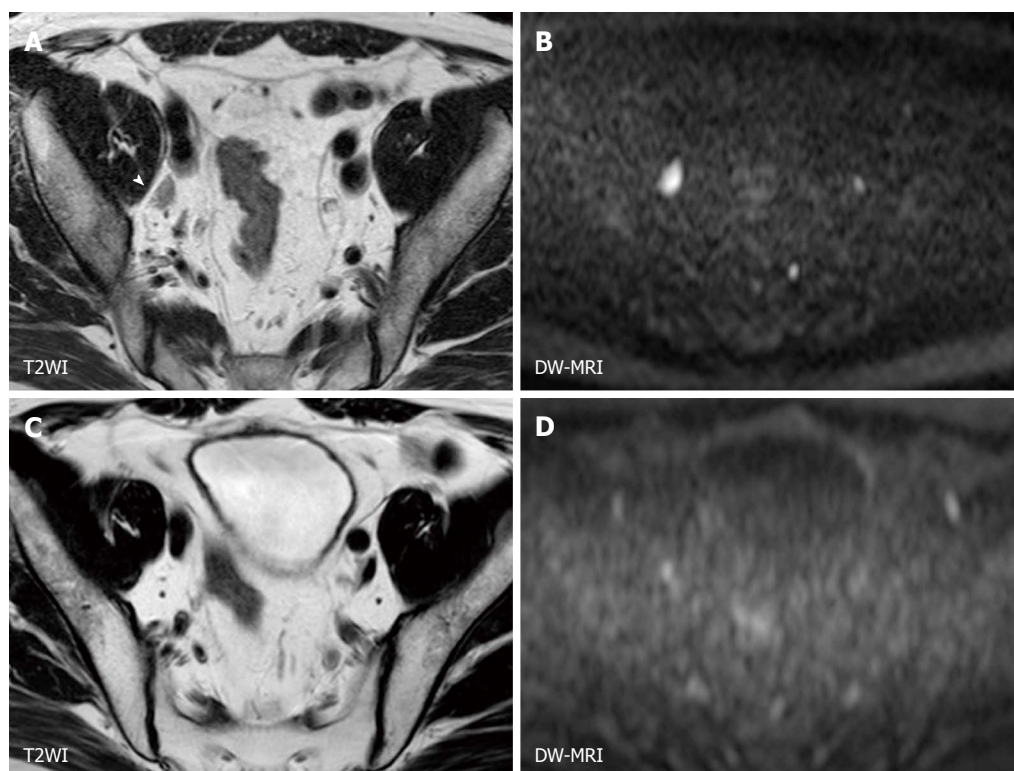


Figure 2 Magnetic resonance images of a 45-year-old man with muscle-invasive bladder cancer (urothelial cancer, stage cT3N1) before and after chemoradiotherapy. A: Before CRT, an enlarged right external iliac lymph node (arrow head) is visible on T2WI; B: The lymph node on the corresponding DW-MRI shows a hyperintense signal; C and D: After CRT, size reduction on T2WI (C) and signal attenuation on DW-MRI (D) in lymph node is evident, consistent with the expected treatment response. CRT: Chemoradiotherapy; DW-MRI: Diffusion-weighted magnetic resonance imaging.

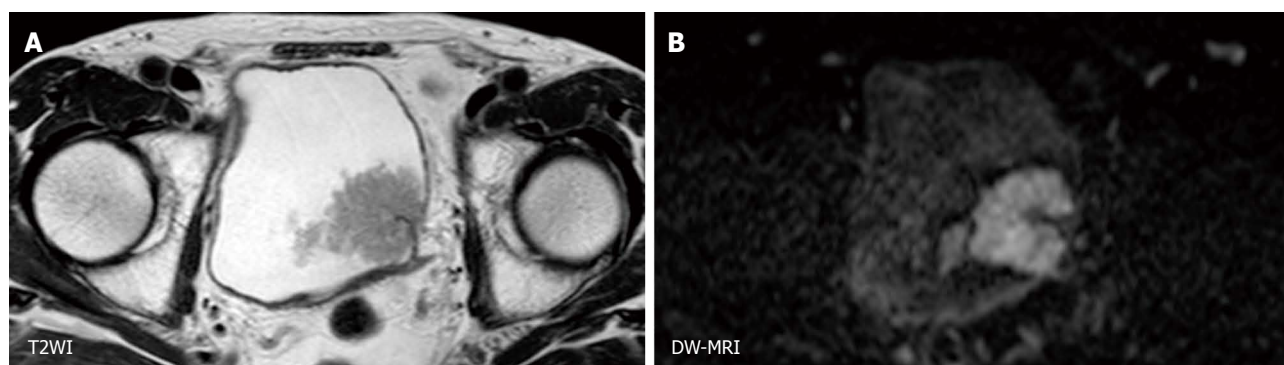


Figure 3 Magnetic resonance images of a 63-year-old man with non-muscle-invasive bladder cancer (urothelial cancer, stage pT1, grade 2 > 3). A: T2WI shows a large papillary tumor on the left bladder wall; B: DW-MRI displays a C-shaped high-signal tumor with a low-signal-intensity stalk connecting to the bladder wall. This C-shaped high signal is known as an "inchworm sign", which is a criterion for T staging in non-muscle-invasive bladder cancer (stage cT1 or less). DW-MRI: Diffusion-weighted magnetic resonance imaging.

bladder cancer based on the signal shape and contrast has been shown (Figure 3). On DW-MRI, bladder cancers generally show a hyperintense signal in distinct contrast to the hypointense signal of the submucosal layer and the intermediate signal of the intact bladder wall. On the basis of these findings, El-Assmy *et al*^[62] reported the ability to discriminate MIBC from NMIBC with an accuracy of 63.6% in a study that included 106 patients. Takeuchi *et al*^[63] reported that bladder cancer staging accuracy improved from 67 to 88% when DW-MRI was added to T2WI.

Furthermore, the utility of DW-MRI in characterizing bladder cancer has been consistently shown in multiple studies using quantitative analysis (Figures 4 and 5). Takeuchi *et al*^[63] reported that the ADC value of grade 3 tumors was significantly lower than that of grade 1 and 2 tumors in a prospective study that included 40 patients. Avcu *et al*^[64] also reported similar results showing an inverse correlation between the ADC value and the histological grade. The existence of a substantial overlap between the histological grades or stages poses a limit to qualitative analysis and the clinical application

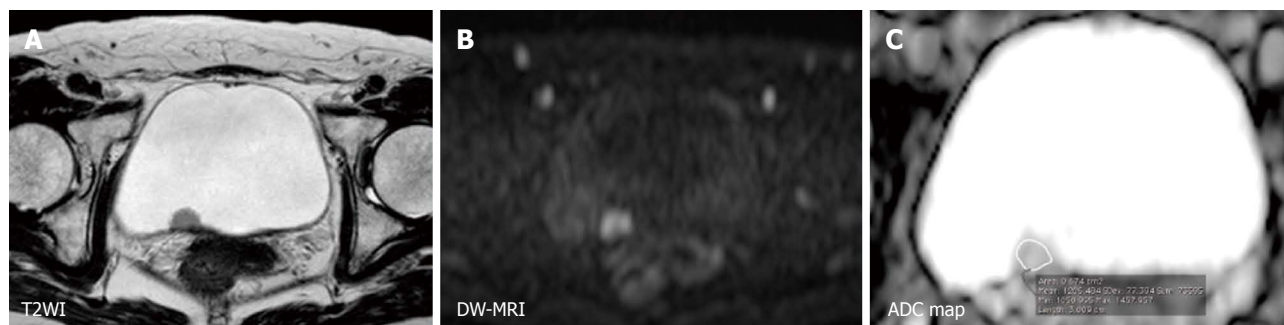


Figure 4 Magnetic resonance images of a 52-year-old woman with non-muscle-invasive bladder cancer (urothelial cancer, pTa, grade 2). A: T2WI shows a hypointense tumor at the posterior wall; B: DW-MRI displays the tumor as a high-signal mass; C: The corresponding ADC map demonstrates a lesser degree of restricted diffusion. The mean ADC value with the ROI positioned not extending over the tumor is 1.21×10^{-3} s/mm². DW-MRI: Diffusion-weighted magnetic resonance imaging; ADC: Apparent diffusion coefficient.

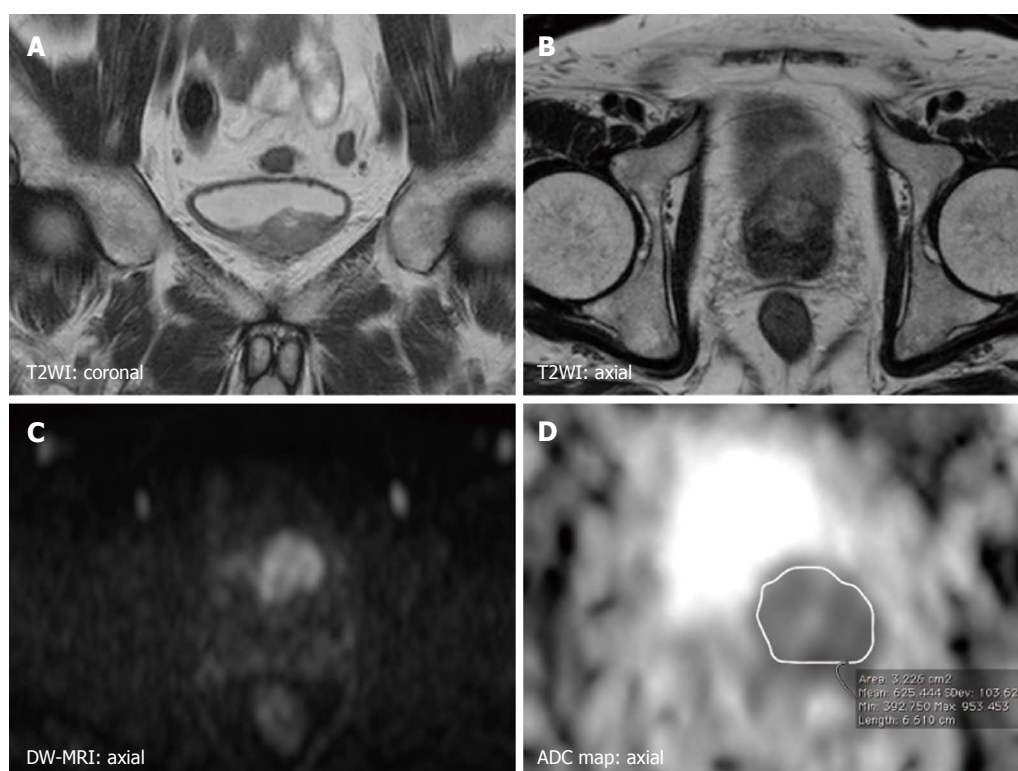


Figure 5 Magnetic resonance images of a 75-year-old man with muscle-invasive bladder cancer (urothelial cancer, stage cT4, grade 3). A and B: T2WI shows a large hypointense tumor at the bladder neck, invading the prostate; C: DW-MRI displays the tumor as a high-signal mass; D: The corresponding ADC map demonstrates restricted diffusion. The mean ADC value of the tumor is 0.63×10^{-3} mm²/s. DW-MRI: Diffusion-weighted magnetic resonance imaging; ADC: Apparent diffusion coefficient.

of this technique. However, these studies indicated that advanced and aggressive bladder cancers tend to have a low ADC values. Actually, Kobayashi *et al.*^[27] found that clinically aggressive tumors, including MIBC and high-grade T1 tumors, had a significantly lower ADC value than the other less aggressive tumors. A threshold ADC value differentiated these two entities with 87% accuracy in a series of 121 patients. The underlying mechanisms whereby the ADC value reflects these tumor characters are thought to be the tumor cell morphological characters such as dense cellularity and large cellular size^[22,23]. Recent studies have shown an inverse correlation between ADC value and the Ki-67 labeling index, a marker of cell

proliferation, in bladder cancer^[65-67]. These data suggest the potential of ADC value to serve as a quantitative biomarker characterizing the biological features of bladder cancer.

Predicting metastatic potential

The potential role of ADC values in predicting the metastatic potential of localized high-grade bladder cancers was shown in a small study that included 17 patients. This study showed that invasive high-grade bladder cancers with metastasis had lower ADC values than those without metastasis^[68]. ADC value can be a supplemental parameter for predicting the presence of metastasis, which

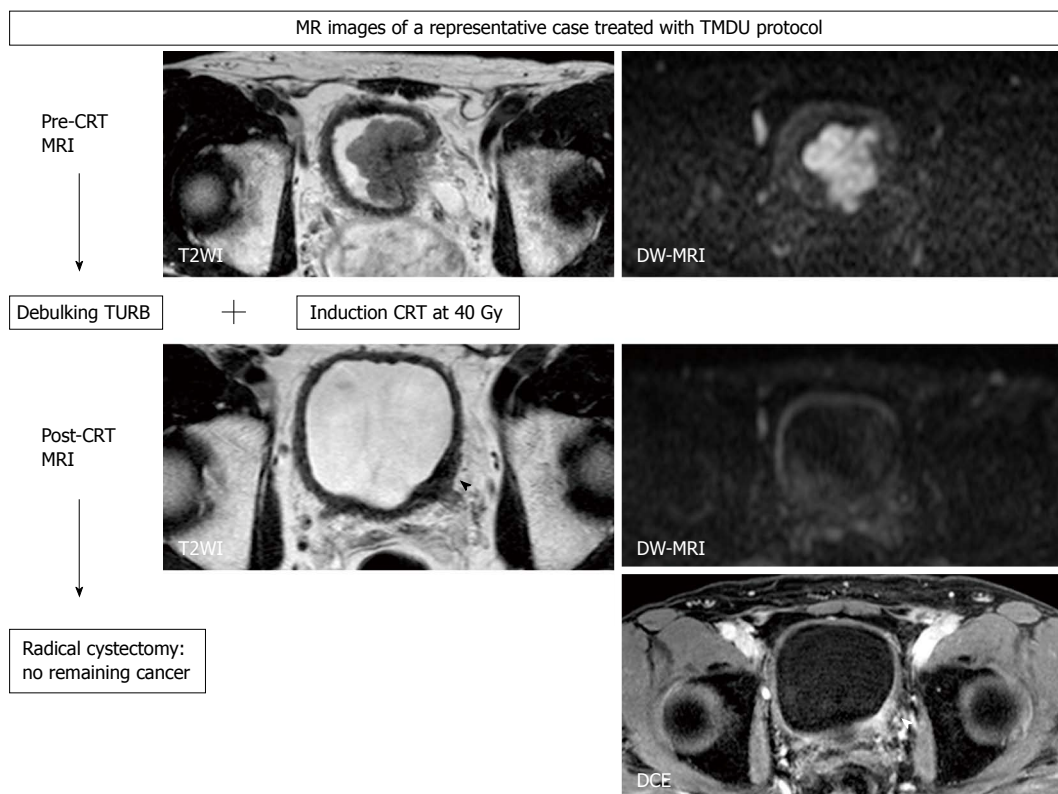


Figure 6 Magnetic resonance images of a 61-year-old man with muscle-invasive bladder cancer (urothelial cancer, stage cT3, grade 3) treated with the Tokyo Medical and Dental University protocol consisting of transurethral resection of bladder tumor and induction chemoradiotherapy (CRT) followed by radical or partial cystectomy. T2WI shows a large hypointense tumor at the bladder neck, invading the prostate. At the diagnosis, DW-MRI with a b -value of 1000 s/mm^2 displays a hyperintense lobulated mass. After TURBT and CRT, this lesion shows wall thickening (arrow head) on T2WI and enhancement on DCE, while the abnormal signal on DW-MRI is diminished to normal signal intensity. Histopathologic examination of the cystectomized sample reveals no remaining bladder cancer, revealing the findings of post-CRT T2WI and DCE to be false-positive findings reflecting post-treatment changes in bladder tissues. TURBT: Transurethral resection of bladder tumor; CRT: Chemoradiotherapy; DW-MRI: Diffusion-weighted magnetic resonance imaging; DCE: Dynamic contrast-enhanced.

has a great impact on treatment decisions.

POTENTIAL ROLES OF DW-MRI IN MULTIMODALITY BLADDER-SPARING STRATEGIES

Novel bladder-sparing approach incorporating consolidative partial cystectomy with pelvic lymph node dissection

We started a pilot study of a selective bladder-sparing protocol incorporating consolidative partial cystectomy with pelvic lymph node dissection after induction low-dose chemoradiotherapy (LCRT) in 1997 at Tokyo Medical and Dental University (TMDU)^[10,11,14,69-71]. Consolidative partial cystectomy with pelvic lymph node dissection is intended to eradicate possible remaining subclinical residual tumor tissue in the original MIBC sites and micrometastases in the pelvic lymph nodes. Candidates for bladder preservation are selected based on the extent, location, and post-LCRT status of the tumor. More than one-third of MIBC patients without any metastasis meet our criteria for partial cystectomy. Partial cystectomy with pelvic lymph node dissection was performed in 70 patients following LCRT. A functional native bladder was

preserved in 91% of patients, and none has developed MIBC or lymph node recurrence^[10,14].

Predicting sensitivity to CRT

In the majority of CRT-based bladder-sparing protocols for localized MIBC, patients who achieve a clinical CR are subjected to consolidative treatment with CRT for bladder preservation. In these protocols, treatment effect cannot be histologically evaluated. In the above-mentioned bladder-sparing protocol incorporating partial cystectomy, histopathological therapeutic effects of LCRT can be assessed, which is one of advantages of the TMDU protocol. By comparing DW-MRIs taken before and after LCRT with this therapeutic effect, the utility of DW-MRI for predicting treatment sensitivity and in monitoring therapeutic response can be evaluated^[20,67].

We found a significant inverse correlation between LCRT sensitivity and ADC value of the tumor^[67]. LCRT-sensitive MIBCs had significantly lower ADC values than LCRT-resistant MIBCs. With a defined cut-off ADC value, the sensitivity, specificity and accuracy in predicting LCRT sensitivity were 92%, 90%, and 91%, respectively. These findings are consistent with previous reports on other tumors including brain, cervix and rectum^[31-35]. However, the presence of necrosis is not common in

MIBC, which is understood to be the background of the correlation between lower ADC values and favorable CRT response. One possible explanation of this correlation found in MIBC is that the relationship between the proliferative activity and the ADC value of MIBC; highly proliferating MIBCs show low ADC values^[65,67]. Because favorable CRT response in highly proliferating MIBC has been reported^[72,73], a low ADC value would be predictive of a better CRT sensitivity of MIBC.

Monitoring response to CRT

We also showed the utility of DW-MRI in monitoring the therapeutic response of MIBC treated with LCRT, as has been reported for other cancers. The sensitivity/specificity/accuracy of T2WI, DCE, and DW-MRI in predicting pathologic CR were 43%/45%/44%, 57%/18%/33%, and 57%/92%/80%, respectively^[20]. DW-MRI improved the accuracy for detecting the remaining cancer after LCRT, primarily due to its increased specificity (Figure 6). However, the low sensitivity in detecting small lesions is a notable limitation, which makes it difficult to detect microscopic residual cancers, as is the case with the other imaging techniques. Further studies are necessary to evaluate the potential of DW-MRI as an imaging technique in the context of bladder-sparing approaches. Multiple approaches, including DW-MRI and biopsies to monitor the therapeutic response, may improve the accuracy of these techniques. However, the limits discussed here in detecting remaining cancers justify partial cystectomies to eliminate the possibly of remaining microscopic tumors in the original invasive cancer site, even in the patients who achieve clinical CR after CRT.

CONCLUSION

Recent studies have shown that the DW-MRI is a unique imaging technique that provides qualitative and quantitative information on biological features of bladder cancer, and is potentially useful as an imaging technique in the management of bladder cancer, particularly in multimodal bladder-sparing strategies for MIBC. Further large prospective studies are needed to clarify the practical roles of DW-MRI in the management of bladder cancer.

REFERENCES

- 1 Siegel R, Naishadham D, Jemal A. Cancer statistics, 2012. *CA Cancer J Clin* 2012; **62**: 10-29 [PMID: 22237781 DOI: 10.3322/caac.20138]
- 2 Tsukamoto T, Kitamura H, Takahashi A, Masumori N. Treatment of invasive bladder cancer: lessons from the past and perspective for the future. *Jpn J Clin Oncol* 2004; **34**: 295-306 [PMID: 15333680 DOI: 10.1093/jco/hyh048]
- 3 Gilbert SM, Wood DP, Dunn RL, Weizer AZ, Lee CT, Montie JE, Wei JT. Measuring health-related quality of life outcomes in bladder cancer patients using the Bladder Cancer Index (BCI). *Cancer* 2007; **109**: 1756-1762 [PMID: 17366596 DOI: 10.1002/cncr.22556]
- 4 Housset M, Maulard C, Chretien Y, Dufour B, Delanian S, Huart J, Colardelle F, Brunel P, Baillet F. Combined radiation and chemotherapy for invasive transitional-cell carcinoma of the bladder: a prospective study. *J Clin Oncol* 1993; **11**: 2150-2157 [PMID: 8229129]
- 5 Kachnic LA, Kaufman DS, Heney NM, Althausen AF, Griffin PP, Zietman AL, Shipley WU. Bladder preservation by combined modality therapy for invasive bladder cancer. *J Clin Oncol* 1997; **15**: 1022-1029 [PMID: 9060542]
- 6 Rödel C, Grabenbauer GG, Kühn R, Papadopoulos T, Dunst J, Meyer M, Schrott KM, Sauer R. Combined-modality treatment and selective organ preservation in invasive bladder cancer: long-term results. *J Clin Oncol* 2002; **20**: 3061-3071 [PMID: 12118019 DOI: 10.1200/JCO.2002.11.027]
- 7 Eisenberg MS, Dorin RP, Bartsch G, Cai J, Miranda G, Skinner EC. Early complications of cystectomy after high dose pelvic radiation. *J Urol* 2010; **184**: 2264-2269 [PMID: 20952024 DOI: 10.1016/j.juro.2010.08.007]
- 8 Stein JP, Lieskovsky G, Cote R, Groshen S, Feng AC, Boyd S, Skinner E, Bochner B, Thangathurai D, Mikhail M, Raghavan D, Skinner DG. Radical cystectomy in the treatment of invasive bladder cancer: long-term results in 1,054 patients. *J Clin Oncol* 2001; **19**: 666-675 [PMID: 11157016]
- 9 Perdonà S, Autorino R, Damiano R, De Sio M, Morrica B, Gallo L, Silvestro G, Farella A, De Placido S, Di Lorenzo G. Bladder-sparing, combined-modality approach for muscle-invasive bladder cancer: a multi-institutional, long-term experience. *Cancer* 2008; **112**: 75-83 [PMID: 18008364 DOI: 10.1002/cncr.23137]
- 10 Koga F, Kihara K, Yoshida S, Yokoyama M, Saito K, Masuda H, Fujii Y, Kawakami S. Selective bladder-sparing protocol consisting of induction low-dose chemoradiotherapy plus partial cystectomy with pelvic lymph node dissection against muscle-invasive bladder cancer: oncological outcomes of the initial 46 patients. *BJU Int* 2012; **109**: 860-866 [PMID: 21854531 DOI: 10.1111/j.1464-410X.2011.10425.x]
- 11 Koga F, Yoshida S, Kawakami S, Kageyama Y, Yokoyama M, Saito K, Fujii Y, Kobayashi T, Kihara K. Low-dose chemoradiotherapy followed by partial or radical cystectomy against muscle-invasive bladder cancer: an intent-to-treat survival analysis. *Urology* 2008; **72**: 384-388 [PMID: 18455771 DOI: 10.1016/j.urology.2008.03.017]
- 12 Zietman AL, Grocela J, Zehr E, Kaufman DS, Young RH, Althausen AF, Heney NM, Shipley WU. Selective bladder conservation using transurethral resection, chemotherapy, and radiation: management and consequences of Ta, T1, and Tis recurrence within the retained bladder. *Urology* 2001; **58**: 380-385 [PMID: 11549485 DOI: 10.1016/S0090-4295(01)01219-5]
- 13 Tunio MA, Hashmi A, Qayyum A, Mohsin R, Zaeem A. Whole-pelvis or bladder-only chemoradiation for lymph node-negative invasive bladder cancer: single-institution experience. *Int J Radiat Oncol Biol Phys* 2012; **82**: e457-e462 [PMID: 21945107 DOI: 10.1016/j.ijrobp.2011.05.051]
- 14 Koga F, Kihara K. Selective bladder preservation with curative intent for muscle-invasive bladder cancer: a contemporary review. *Int J Urol* 2012; **19**: 388-401 [PMID: 22409269 DOI: 10.1111/j.1442-2042.2012.02974.x]
- 15 Tekes A, Kamel I, Imam K, Szarf G, Schoenberg M, Nasir K, Thompson R, Bluemke D. Dynamic MRI of bladder cancer: evaluation of staging accuracy. *AJR Am J Roentgenol* 2005; **184**: 121-127 [PMID: 15615961 DOI: 10.2214/ajr.184.1.01840121]
- 16 Hayashi N, Tochigi H, Shiraishi T, Takeda K, Kawamura J. A new staging criterion for bladder carcinoma using gadolinium-enhanced magnetic resonance imaging with an endorectal surface coil: a comparison with ultrasonography. *BJU Int* 2000; **85**: 32-36 [PMID: 10619941 DOI: 10.1046/j.1464-410x.2000.00358.x]
- 17 Raza SA, Jhaveri KS. MR imaging of urinary bladder carcinoma and beyond. *Radiol Clin North Am* 2012; **50**: 1085-1110 [PMID: 23122040 DOI: 10.1016/j.rcl.2012.08.011]
- 18 Dobson MJ, Carrington BM, Collins CD, Ryder WD, Read G,

- Hutchinson CE, Hawnaur JM. The assessment of irradiated bladder carcinoma using dynamic contrast-enhanced MR imaging. *Clin Radiol* 2001; **56**: 94-98 [PMID: 11222064 DOI: 10.1053/crad.2000.0560]
- 19 **Johnson RJ**, Carrington BM, Jenkins JP, Barnard RJ, Read G, Isherwood I. Accuracy in staging carcinoma of the bladder by magnetic resonance imaging. *Clin Radiol* 1990; **41**: 258-263 [PMID: 2340697 DOI: 10.1016/S0009-9260(05)81661-7]
- 20 **Yoshida S**, Koga F, Kawakami S, Ishii C, Tanaka H, Numao N, Sakai Y, Saito K, Masuda H, Fujii Y, Kihara K. Initial experience of diffusion-weighted magnetic resonance imaging to assess therapeutic response to induction chemoradiotherapy against muscle-invasive bladder cancer. *Urology* 2010; **75**: 387-391 [PMID: 19914691 DOI: 10.1016/j.urology.2009.06.111]
- 21 **Le Bihan D**, Breton E, Lallemand D, Grenier P, Cabanis E, Laval-Jeantet M. MR imaging of intravoxel incoherent motions: application to diffusion and perfusion in neurologic disorders. *Radiology* 1986; **161**: 401-407 [PMID: 3763909 DOI: 10.1148/radiology.161.2.3763909]
- 22 **Koh DM**, Collins DJ. Diffusion-weighted MRI in the body: applications and challenges in oncology. *AJR Am J Roentgenol* 2007; **188**: 1622-1635 [PMID: 17515386 DOI: 10.2214/AJR.06.1403]
- 23 **Padhani AR**, Liu G, Koh DM, Chenevert TL, Thoeny HC, Takahara T, Dzik-Jurasz A, Ross BD, Van Cauteren M, Collins D, Hammoud DA, Rustin GJ, Taouli B, Choyke PL. Diffusion-weighted magnetic resonance imaging as a cancer biomarker: consensus and recommendations. *Neoplasia* 2009; **11**: 102-125 [PMID: 19186405]
- 24 **Abou-El-Ghar ME**, El-Assmy A, Refaie HF, El-Diasty T. Bladder cancer: diagnosis with diffusion-weighted MR imaging in patients with gross hematuria. *Radiology* 2009; **251**: 415-421 [PMID: 19304915 DOI: 10.1148/radiol.2503080723]
- 25 **Ceylan K**, Taken K, Gecit I, Pirincci N, Gunes M, Tanik S, Karaman I. Comparison of cystoscopy with diffusion-weighted magnetic resonance images used in the diagnosis and follow-up of patients with bladder tumors. *Asian Pac J Cancer Prev* 2010; **11**: 1001-1004 [PMID: 21133614]
- 26 **Matsuki M**, Inada Y, Tatsugami F, Tanikake M, Narabayashi I, Katsuoka Y. Diffusion-weighted MR imaging for urinary bladder carcinoma: initial results. *Eur Radiol* 2007; **17**: 201-204 [PMID: 16865369 DOI: 10.1007/s00330-006-0281-7]
- 27 **Kobayashi S**, Koga F, Yoshida S, Masuda H, Ishii C, Tanaka H, Komai Y, Yokoyama M, Saito K, Fujii Y, Kawakami S, Kihara K. Diagnostic performance of diffusion-weighted magnetic resonance imaging in bladder cancer: potential utility of apparent diffusion coefficient values as a biomarker to predict clinical aggressiveness. *Eur Radiol* 2011; **21**: 2178-2186 [PMID: 21688007 DOI: 10.1007/s00330-011-2174-7]
- 28 **Costantini M**, Belli P, Rinaldi P, Bufi E, Giardina G, Franceschini G, Petrone G, Bonomo L. Diffusion-weighted imaging in breast cancer: relationship between apparent diffusion coefficient and tumour aggressiveness. *Clin Radiol* 2010; **65**: 1005-1012 [PMID: 21070905 DOI: 10.1016/j.crad.2010.07.008]
- 29 **Yoshida S**, Masuda H, Ishii C, Tanaka H, Fujii Y, Kawakami S, Kihara K. Usefulness of diffusion-weighted MRI in diagnosis of upper urinary tract cancer. *AJR Am J Roentgenol* 2011; **196**: 110-116 [PMID: 21178054 DOI: 10.2214/AJR.10.4632]
- 30 **Kitajima K**, Takahashi S, Ueno Y, Miyake H, Fujisawa M, Kawakami F, Sugimura K. Do apparent diffusion coefficient (ADC) values obtained using high b-values with a 3-T MRI correlate better than a transrectal ultrasound (TRUS)-guided biopsy with true Gleason scores obtained from radical prostatectomy specimens for patients with prostate cancer? *Eur J Radiol* 2013; **82**: 1219-1226 [PMID: 23518144 DOI: 10.1016/j.ejrad.2013.02.021]
- 31 **DeVries AF**, Kremser C, Hein PA, Griebel J, Kreczy A, Ofner D, Pfeiffer KP, Lukas P, Judmaier W. Tumor microcirculation and diffusion predict therapy outcome for primary rectal carcinoma. *Int J Radiat Oncol Biol Phys* 2003; **56**: 958-965 [PMID: 12829130 DOI: 10.1016/S0360-3016(03)00208-6]
- 32 **Liu Y**, Bai R, Sun H, Liu H, Zhao X, Li Y. Diffusion-weighted imaging in predicting and monitoring the response of uterine cervical cancer to combined chemoradiation. *Clin Radiol* 2009; **64**: 1067-1074 [PMID: 19822239 DOI: 10.1016/j.crad.2009.07.010]
- 33 **Mardor Y**, Roth Y, Ochershvilli A, Spiegelmann R, Tichler T, Daniels D, Maier SE, Nissim O, Ram Z, Baram J, Orenstein A, Pfeffer R. Pretreatment prediction of brain tumors' response to radiation therapy using high b-value diffusion-weighted MRI. *Neoplasia* 2004; **6**: 136-142 [PMID: 15140402 DOI: 10.1593/neo.03349]
- 34 **Dzik-Jurasz A**, Domenig C, George M, Wolber J, Padhani A, Brown G, Doran S. Diffusion MRI for prediction of response of rectal cancer to chemoradiation. *Lancet* 2002; **360**: 307-308 [PMID: 12147376 DOI: 10.1016/S0140-6736(02)09520-X]
- 35 **Sun YS**, Zhang XP, Tang L, Ji JF, Gu J, Cai Y, Zhang XY. Locally advanced rectal carcinoma treated with preoperative chemotherapy and radiation therapy: preliminary analysis of diffusion-weighted MR imaging for early detection of tumor histopathologic downstaging. *Radiology* 2010; **254**: 170-178 [PMID: 20019139 DOI: 10.1148/radiol.2541082230]
- 36 **Hein PA**, Kremser C, Judmaier W, Griebel J, Pfeiffer KP, Kreczy A, Hug EB, Lukas P, DeVries AF. Diffusion-weighted magnetic resonance imaging for monitoring diffusion changes in rectal carcinoma during combined, preoperative chemoradiation: preliminary results of a prospective study. *Eur J Radiol* 2003; **45**: 214-222 [PMID: 12595106 DOI: 10.1016/S0720-048X(02)00231-0]
- 37 **Kremser C**, Judmaier W, Hein P, Griebel J, Lukas P, de Vries A. Preliminary results on the influence of chemoradiation on apparent diffusion coefficients of primary rectal carcinoma measured by magnetic resonance imaging. *Strahlenther Onkol* 2003; **179**: 641-649 [PMID: 14628131 DOI: 10.1007/s00066-003-1045-9]
- 38 **Harry VN**, Semple SI, Gilbert FJ, Parkin DE. Diffusion-weighted magnetic resonance imaging in the early detection of response to chemoradiation in cervical cancer. *Gynecol Oncol* 2008; **111**: 213-220 [PMID: 18774597 DOI: 10.1016/j.ygyno.2008.07.048]
- 39 **Chen CY**, Li CW, Kuo YT, Jaw TS, Wu DK, Jao JC, Hsu JS, Liu GC. Early response of hepatocellular carcinoma to transcatheter arterial chemoembolization: choline levels and MR diffusion constants--initial experience. *Radiology* 2006; **239**: 448-456 [PMID: 16569781 DOI: 10.1148/radiol.2392042202]
- 40 **Chenevert TL**, McKeever PE, Ross BD. Monitoring early response of experimental brain tumors to therapy using diffusion magnetic resonance imaging. *Clin Cancer Res* 1997; **3**: 1457-1466 [PMID: 9815831]
- 41 **Einarsdóttir H**, Karlsson M, Wejde J, Bauer HC. Diffusion-weighted MRI of soft tissue tumours. *Eur Radiol* 2004; **14**: 959-963 [PMID: 14767604 DOI: 10.1007/s00330-004-2237-0]
- 42 **El-Assmy A**, Abou-El-Ghar ME, Refaie HF, El-Diasty T. Diffusion-weighted MR imaging in diagnosis of superficial and invasive urinary bladder carcinoma: a preliminary prospective study. *ScientificWorldJournal* 2008; **8**: 364-370 [PMID: 18454244 DOI: 10.1100/tsw.2008.55]
- 43 **Barentsz JO**, Jager GJ, van Vierzen PB, Witjes JA, Strijk SP, Peters H, Karssemeijer N, Ruijs SH. Staging urinary bladder cancer after transurethral biopsy: value of fast dynamic contrast-enhanced MR imaging. *Radiology* 1996; **201**: 185-193 [PMID: 8816542 DOI: 10.1148/radiology.201.1.8816542]
- 44 **Beer AJ**, Eiber M, Souvatzoglou M, Holzapfel K, Ganter C, Weirich G, Maurer T, Kübler H, Wester HJ, Gaa J, Krause BJ. Restricted water diffusibility as measured by diffusion-weighted MR imaging and choline uptake in (11)C-choline PET/CT are correlated in pelvic lymph nodes in patients with prostate cancer. *Mol Imaging Biol* 2011; **13**: 352-361 [PMID: 20490932 DOI: 10.1007/s11307-010-0337-6]

- 45 **Budiharto T**, Joniau S, Lerut E, Van den Bergh L, Mottaghy F, Deroose CM, Oyen R, Ameye F, Bogaerts K, Hausermans K, Van Poppel H. Prospective evaluation of 11C-choline positron emission tomography/computed tomography and diffusion-weighted magnetic resonance imaging for the nodal staging of prostate cancer with a high risk of lymph node metastases. *Eur Urol* 2011; **60**: 125-130 [PMID: 21292388 DOI: 10.1016/j.eururo.2011.01.015]
- 46 **Eiber M**, Beer AJ, Holzapfel K, Tauber R, Ganter C, Weirich G, Krause BJ, Rummeny EJ, Gaa J. Preliminary results for characterization of pelvic lymph nodes in patients with prostate cancer by diffusion-weighted MR-imaging. *Invest Radiol* 2010; **45**: 15-23 [PMID: 19996762 DOI: 10.1097/RLI.0b013e3181bbdc2f]
- 47 **Nakamatsu S**, Matsusue E, Miyoshi H, Kakite S, Kaminou T, Ogawa T. Correlation of apparent diffusion coefficients measured by diffusion-weighted MR imaging and standardized uptake values from FDG PET/CT in metastatic neck lymph nodes of head and neck squamous cell carcinomas. *Clin Imaging* 2012; **36**: 90-97 [PMID: 22370129 DOI: 10.1016/j.clinimag.2011.05.002]
- 48 **Rechichi G**, Galimberti S, Oriani M, Perego P, Valsecchi MG, Sironi S. ADC maps in the prediction of pelvic lymph nodal metastatic regions in endometrial cancer. *Eur Radiol* 2013; **23**: 65-74 [PMID: 22821394 DOI: 10.1007/s00330-012-2575-2]
- 49 **Papalia R**, Simone G, Grasso R, Augelli R, Faiella E, Gualianone S, Cazzato R, Del Vescovo R, Ferriero M, Zobel B, Gallucci M. Diffusion-weighted magnetic resonance imaging in patients selected for radical cystectomy: detection rate of pelvic lymph node metastases. *BJU Int* 2012; **109**: 1031-1036 [PMID: 21883835 DOI: 10.1111/j.1464-410X.2011.10446.x]
- 50 **Mir N**, Sohaib SA, Collins D, Koh DM. Fusion of high b-value diffusion-weighted and T2-weighted MR images improves identification of lymph nodes in the pelvis. *J Med Imaging Radiat Oncol* 2010; **54**: 358-364 [PMID: 20718916 DOI: 10.1111/j.1754-9485.2010.02182.x]
- 51 **Thoeny HC**, Triantafyllou M, Birkhaeuser FD, Froehlich JM, Tshering DW, Binsler T, Fleischmann A, Vermathen P, Studer UE. Combined ultrasmall superparamagnetic particles of iron oxide-enhanced and diffusion-weighted magnetic resonance imaging reliably detect pelvic lymph node metastases in normal-sized nodes of bladder and prostate cancer patients. *Eur Urol* 2009; **55**: 761-769 [PMID: 19144456 DOI: 10.1016/j.eururo.2008.12.034]
- 52 **Birkhäuser FD**, Studer UE, Froehlich JM, Triantafyllou M, Bains LJ, Petralia G, Vermathen P, Fleischmann A, Thoeny HC. Combined ultrasmall superparamagnetic particles of iron oxide-enhanced and diffusion-weighted magnetic resonance imaging facilitates detection of metastases in normal-sized pelvic lymph nodes of patients with bladder and prostate cancer. *Eur Urol* 2013; **64**: 953-960 [PMID: 23916692 DOI: 10.1016/j.eururo.2013.07.032]
- 53 **Fortuin AS**, Meijer H, Thompson LC, Witjes JA, Barentsz JO. Ferumoxtran-10 ultrasmall superparamagnetic iron oxide-enhanced diffusion-weighted imaging magnetic resonance imaging for detection of metastases in normal-sized lymph nodes in patients with bladder and prostate cancer: do we enter the era after extended pelvic lymph node dissection? *Eur Urol* 2013; **64**: 961-93; discussion 963 [PMID: 23972400 DOI: 10.1016/j.eururo.2013.08.017]
- 54 **Froehlich JM**, Triantafyllou M, Fleischmann A, Vermathen P, Thalmann GN, Thoeny HC. Does quantification of USPIO uptake-related signal loss allow differentiation of benign and malignant normal-sized pelvic lymph nodes? *Contrast Media Mol Imaging* 2012; **7**: 346-355 [PMID: 22539405 DOI: 10.1002/cmmi.503]
- 55 **Triantafyllou M**, Studer UE, Birkhäuser FD, Fleischmann A, Bains LJ, Petralia G, Christe A, Froehlich JM, Thoeny HC. Ultrasmall superparamagnetic particles of iron oxide allow for the detection of metastases in normal sized pelvic lymph nodes of patients with bladder and/or prostate cancer. *Eur J Cancer* 2013; **49**: 616-624 [PMID: 23084842 DOI: 10.1016/j.ejca.2012.09.034]
- 56 **Lecouvet FE**, El Mouedden J, Collette L, Coche E, Danse E, Jamar F, Machiels JP, Vande Berg B, Omoumi P, Tombal B. Can whole-body magnetic resonance imaging with diffusion-weighted imaging replace Tc 99m bone scanning and computed tomography for single-step detection of metastases in patients with high-risk prostate cancer? *Eur Urol* 2012; **62**: 68-75 [PMID: 22366187 DOI: 10.1016/j.eururo.2012.02.020]
- 57 **Mosavi F**, Johansson S, Sandberg DT, Turesson I, Sörensen J, Ahlström H. Whole-body diffusion-weighted MRI compared with (18)F-NaF PET/CT for detection of bone metastases in patients with high-risk prostate carcinoma. *AJR Am J Roentgenol* 2012; **199**: 1114-1120 [PMID: 23096187 DOI: 10.2214/ajr.11.8351]
- 58 **Ording Müller LS**, Avenarius D, Olsen OE. High signal in bone marrow at diffusion-weighted imaging with body background suppression (DWIBS) in healthy children. *Pediatr Radiol* 2011; **41**: 221-226 [PMID: 20652234 DOI: 10.1007/s00247-010-1774-8]
- 59 **Steiner RM**, Mitchell DG, Rao VM, Schweitzer ME. Magnetic resonance imaging of diffuse bone marrow disease. *Radiol Clin North Am* 1993; **31**: 383-409 [PMID: 8446756]
- 60 **Takeuchi M**, Suzuki T, Sasaki S, Ito M, Hamamoto S, Kawai N, Kohri K, Hara M, Shibamoto Y. Clinicopathologic significance of high signal intensity on diffusion-weighted MR imaging in the ureter, urethra, prostate and bone of patients with bladder cancer. *Acad Radiol* 2012; **19**: 827-833 [PMID: 22341371 DOI: 10.1016/j.acra.2012.01.013]
- 61 **Prout GR**, Griffin PP, Shipley WU. Bladder carcinoma as a systemic disease. *Cancer* 1979; **43**: 2532-2539 [PMID: 455239]
- 62 **El-Assmy A**, Abou-El-Ghar ME, Mosbah A, El-Nahas AR, Refaie HF, Hekal IA, El-Diasty T, Ibrahim el H. Bladder tumour staging: comparison of diffusion- and T2-weighted MR imaging. *Eur Radiol* 2009; **19**: 1575-1581 [PMID: 19247665 DOI: 10.1007/s00330-009-1340-7]
- 63 **Takeuchi M**, Sasaki S, Ito M, Okada S, Takahashi S, Kawai T, Suzuki K, Oshima H, Hara M, Shibamoto Y. Urinary bladder cancer: diffusion-weighted MR imaging--accuracy for diagnosing T stage and estimating histologic grade. *Radiology* 2009; **251**: 112-121 [PMID: 19332849 DOI: 10.1148/radiol.2511080873]
- 64 **Avcu S**, Koseoglu MN, Ceylan K, Bulut MD, Unal O. The value of diffusion-weighted MRI in the diagnosis of malignant and benign urinary bladder lesions. *Br J Radiol* 2011; **84**: 875-882 [PMID: 21224296 DOI: 10.1259/bjr/30591350]
- 65 **Kobayashi S**, Koga F, Kajino K, Yoshita S, Ishii C, Tanaka H, Saito K, Masuda H, Fujii Y, Yamada T, Kihara K. Apparent diffusion coefficient value reflects invasive and proliferative potential of bladder cancer. *J Magn Reson Imaging* 2014; **39**: 172-178 [PMID: 23589321 DOI: 10.1002/jmri.24148]
- 66 **Yoshida S**, Kobayashi S, Koga F, Ishioka J, Ishii C, Tanaka H, Nakanishi Y, Matsuoka Y, Numao N, Saito K, Masuda H, Fujii Y, Kihara K. Apparent diffusion coefficient as a prognostic biomarker of upper urinary tract cancer: a preliminary report. *Eur Radiol* 2013; **23**: 2206-2214 [PMID: 23494496 DOI: 10.1007/s00330-013-2805-2]
- 67 **Yoshida S**, Koga F, Kobayashi S, Ishii C, Tanaka H, Tanaka H, Komai Y, Saito K, Masuda H, Fujii Y, Kawakami S, Kihara K. Role of diffusion-weighted magnetic resonance imaging in predicting sensitivity to chemoradiotherapy in muscle-invasive bladder cancer. *Int J Radiat Oncol Biol Phys* 2012; **83**: e21-e27 [PMID: 22414281 DOI: 10.1016/j.ijrobp.2011.11.065]
- 68 **Rosenkrantz AB**, Mussi TC, Spieler B, Melamed J, Taneja SS, Huang WC. High-grade bladder cancer: association of the apparent diffusion coefficient with metastatic disease: preliminary results. *J Magn Reson Imaging* 2012; **35**: 1478-1483 [PMID: 22282396 DOI: 10.1002/jmri.23590]
- 69 **Yoshida S**, Saito K, Koga F, Yokoyama M, Kageyama Y,

- Masuda H, Kobayashi T, Kawakami S, Kihara K. C-reactive protein level predicts prognosis in patients with muscle-invasive bladder cancer treated with chemoradiotherapy. *BJU Int* 2008; **101**: 978-981 [PMID: 18190628 DOI: 10.1111/j.1464-410X.2007.07408.x]
- 70 **Kageyama Y**, Okada Y, Arai G, Hyochi N, Suzuki M, Masuda H, Hayashi T, Kawakami S, Okuno T, Ishizaka K, Kihara K. Preoperative concurrent chemoradiotherapy against muscle-invasive bladder cancer: results of partial cystectomy in elderly or high-risk patients. *Jpn J Clin Oncol* 2000; **30**: 553-556 [PMID: 11210165]
- 71 **Kageyama Y**, Yokoyama M, Sakai Y, Saito K, Koga F, Yano M, Arai G, Hyochi N, Masuda H, Fujii Y, Kawakami S, Kobayashi T, Kihara K. Favorable outcome of preoperative low dose chemoradiotherapy against muscle-invasive bladder cancer. *Am J Clin Oncol* 2003; **26**: 504-507 [PMID: 14528080 DOI: 10.1097/01.coc.0000037665.11701.22]
- 72 **Matsumoto H**, Wada T, Fukunaga K, Yoshihiro S, Matsuyama H, Naito K. Bax to Bcl-2 ratio and Ki-67 index are useful predictors of neoadjuvant chemoradiation therapy in bladder cancer. *Jpn J Clin Oncol* 2004; **34**: 124-130 [PMID: 15078907]
- 73 **Rödel C**, Grabenbauer GG, Rödel F, Birkenhake S, Kühn R, Martus P, Zörcher T, Fürsich D, Papadopoulos T, Dunst J, Schrott KM, Sauer R. Apoptosis, p53, bcl-2, and Ki-67 in invasive bladder carcinoma: possible predictors for response to radiochemotherapy and successful bladder preservation. *Int J Radiat Oncol Biol Phys* 2000; **46**: 1213-1221 [PMID: 10725634]

P- Reviewers: Msaouel P, Plataniotis G **S- Editor:** Ji FF
L- Editor: A **E- Editor:** Zhang DN



Multimodality imaging of renal inflammatory lesions

Chandan J Das, Zohra Ahmad, Sanjay Sharma, Arun K Gupta

Chandan J Das, Zohra Ahmad, Sanjay Sharma, Arun K Gupta, Department of Radiodiagnosis, All India Institute of Medical Sciences, New Delhi, Delhi 110029, India
Author contributions: All the authors solely contributed to this paper.

Correspondence to: Sanjay Sharma, MD, Department of Radiodiagnosis, All India Institute of Medical Sciences, Ansari Nagar East, Gautam Nagar, New Delhi, Delhi 110029, India. drssharma@hotmail.com

Telephone: +91-98-11687277 Fax: +91-98-11687277

Received: April 3, 2014 Revised: August 19, 2014

Accepted: September 6, 2014

Published online: March 28, 2015

Abstract

Spectrum of acute renal infections includes acute pyelonephritis, renal and perirenal abscesses, pyonephrosis, emphysematous pyelonephritis and emphysematous cystitis. The chronic renal infections that we routinely encounter encompass chronic pyelonephritis, xantho-granulomatous pyelonephritis, and eosinophilic cystitis. Patients with diabetes, malignancy and leukaemia are frequently immunocompromised and more prone to fungal infections *viz.* angioinvasive aspergillus, candida and mucor. Tuberculosis and parasitic infestation of the kidney is common in tropical countries. Imaging is not routinely indicated in uncomplicated renal infections as clinical findings and laboratory data are generally sufficient for making a diagnosis. However, imaging plays a crucial role under specific situations like immunocompromised patients, treatment non-responders, equivocal clinical diagnosis, congenital anomaly evaluation, transplant imaging and for evaluating extent of disease. We aim to review in this article the varied imaging spectrum of renal inflammatory lesions.

© 2015 Baishideng Publishing Group Inc. All rights reserved.

Key words: Imaging modalities; Renal infection; Cystitis; Pyelonephritis; Pyonephrosis; Xanthogranulomatous; Magnetic resonance imaging

Core tip: Imaging in renal infections is challenging, given the relatively non-specific nature of findings in majority of the cases. A careful assessment of clinical situation in question is essential to accurately choose the imaging modality which would provide most information. In this review we discuss the appropriateness of specific imaging modalities, to allow the radiologist to choose the best modality for a given clinical situation. In addition, some entities such as acute pyelonephritis, Xanthogranulomatous pyelonephritis and emphysematous pyelonephritis have some specific imaging features. In this review we describe and illustrate such specific features, to facilitate their recognition when present.

Original sources: Das CJ, Ahmad Z, Sharma S, Gupta AK. Multimodality imaging of renal inflammatory lesions. *World J Radiol* 2014; 6(11): 865-873 Available from: URL: <http://www.wjgnet.com/1949-8470/full/v6/i11/865.htm> DOI: <http://dx.doi.org/10.4329/wjrr.v6.i11.865>

INTRODUCTION

Renal infections range from mild to severe, acute to chronic (Table 1) and may be associated with predisposing risk factors like diabetes mellitus, human immunodeficiency virus (HIV), leukemia, vesico-ureteric reflux and staghorn calculi.

Acute infections include acute pyelonephritis which may be focal or diffuse, may resolve with time or worsen to abscess formation depending on the treatment rendered and immune status of the patient. Immunocompromised state might predispose an individual to more severe and life threatening conditions like emphysematous pyelonephritis which may warrant a nephrectomy. An obstructing pathology with a superimposed infection may lead to pyonephrosis for which drainage is the treatment of choice. Renal infections may take a turn for the worse in a chronic irreversibly damaging form like

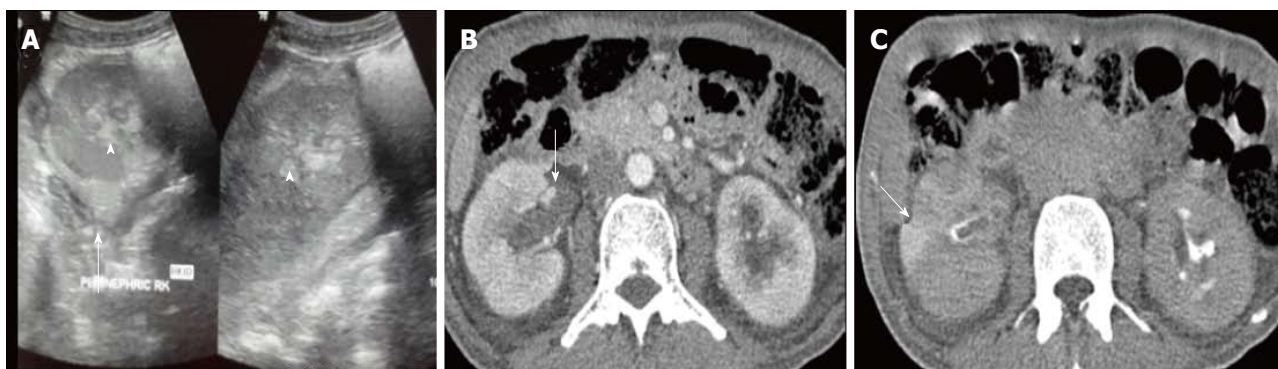


Figure 1 Acute pyelonephritis in a 40 years old male. A: US shows soft tissue in bilateral PCS (arrowhead) with increased echogenicity of perinephric fat (arrow); B: CECT nephrographic phase shows bilateral enlarged kidneys with heterogeneous enhancement. There is soft tissue thickening and abnormal enhancement of bilateral PCS and ureter (arrow); C: CECT delayed phase shows striated nephrogram (arrow) seen as linear bands of contrast extending from cortex to medulla. US: Ultrasonography; PCS: Pelvicalyceal system; CECT: Contrast-enhanced computed tomography.

Table 1 Spectrum of renal infections		
Acute	Chronic	Others
Acute pyelonephritis	Chronic pyelonephritis	Tuberculosis
Focal nephritis	Xanthogranulomatous pyelonephritis	Fungal
Abscess	Malakoplakia	
Emphsematous pyelonephritis	Eosinophilic cystitis	
Papillary necrosis		
Pyonephrosis		

chronic pyelonephritis and xanthogranulomatous pyelonephritis. Tuberculosis involves the kidney with calyceal irregularity being the earliest manifestation, later leading to scarring, fibrosis and infundibular and ureteric stricture formation. Immunocompromised individuals are particularly predisposed to fungal infections, the most common organisms being *Candida*, *Aspergillus* and *Mucor*. Some rare inflammatory conditions encountered are malakoplakia and eosinophilic cystitis.

Acute infection is usually diagnosed based on clinical symptoms and laboratory data without imaging examinations. Hence, imaging is not routinely indicated in uncomplicated renal infections. However, imaging plays a pivotal role in evaluating infections in situations like immunocompromised state, treatment non-responders, congenital anomaly evaluation, and post transplant for evaluating extent of the disease. We wish to review in this article the varied imaging spectrum of renal inflammatory lesions.

IMAGING MODALITIES

Imaging is not routinely indicated in urinary tract infections, however with severe symptoms, high risk immunocompromised state, diabetic patients and antibiotic non-responders, it becomes necessary^[1]. Plain radiography may provide evidence of gas in the renal area in emphysematous pyelonephritis or abscess and the typical mass like calcification in end stage renal tuberculosis (Putty kidney). Ultrasound (US) is the initial screening modality

and is used for guiding interventions as well. The role of intravenous urography (IVU) has diminished lately, however it still remains the best modality to diagnose calyceal irregularity of early tuberculosis, papillary necrosis and to evaluate congenital anomalies. Computed tomography (CT) is the gold standard for diagnosis and assessment of severity of acute pyelonephritis and its complications. Magnetic resonance imaging (MRI) is indicated in pregnancy and patients with contraindication to iodinated contrast such as transplant recipients. Diffusion weighted MRI (DW-MRI) has been applied to differentiate hydronephrosis from pyonephrosis as well as to detect infected cysts and tumors.

ACUTE PYELONEPHRITIS

Acute pyelonephritis is usually diagnosed based on clinical symptoms and laboratory data without imaging examinations. In many cases of mild acute pyelonephritis, enhanced CT or ultrasonography may show no abnormal findings. The recommended phases of CT scan for evaluating renal infections are a non-contrast scan, nephrographic phase at 50-90 s and excretory phase at 2 min if there is obstruction^[2]. Striated nephrogram which is an appearance described for acute pyelonephritis shows discrete rays of alternating hypoattenuation and hyperattenuation radiating from the papilla to the cortex along the direction of the excretory tubules (Figures 1 and 2). This appearance is ascribed to the decreased flow of contrast due to stasis and eventual hyperconcentration in the infected tubules^[3]. Striated nephrogram is not specific and is also seen in some other conditions like renal vein thrombosis, ureteric obstruction and contusion^[4]. Pyelonephritis may manifest as wedge shaped zones of decreased attenuation or a hypodense mass in its focal form (Figure 3). The diffuse form of acute pyelonephritis may cause global enlargement, poor enhancement of renal parenchyma, absent excretion of contrast and streakiness of fat. Hemorrhagic bacterial nephritis which is relatively uncommon shows hyperattenuating areas representing parenchymal bleeding on non-contrast scan^[5].

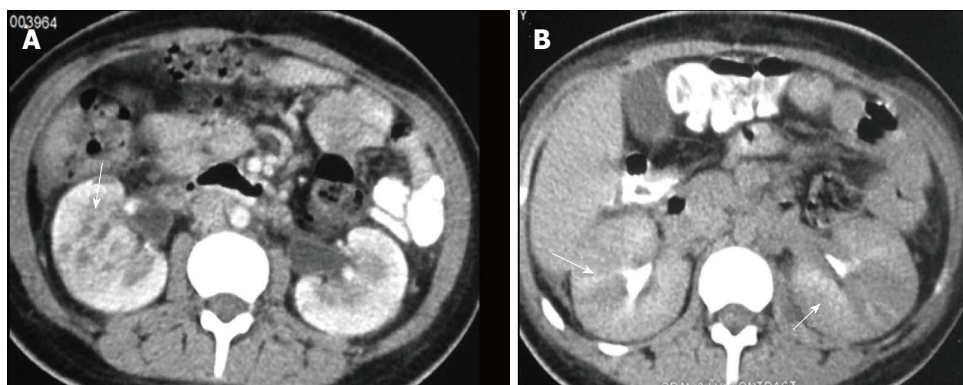


Figure 2 Acute pyelonephritis. A: CECT venous phase shows heterogeneous parenchymal enhancement with pelvic wall thickening (arrow); B: CECT delayed phase shows alternating discrete rays of hyper and hypoattenuation (arrows) giving the appearance of a striated nephrogram. CECT: Contrast-enhanced computed tomography.



Figure 3 Contrast-enhanced computed tomography shows acute pyelonephritis manifesting as a focal wedge shaped hypodensity with surrounding fat stranding as seen in right kidney (arrow).

RENAL ABSCESS

Renal and perinephric abscesses develop as a complication of focal pyelonephritis or hematogenous infection. Early abscess appears as a poorly marginated non-enhancing area of decreased attenuation. A mature abscess shows a sharply marginated, complex cystic mass with necrosis and a peripheral enhancing rim^[6]. US may show internal echoes, septations and loculations (Figure 4). DW-MRI can readily pick up abscesses showing restriction of diffusion (Figure 5). In a transplant patient DW-MRI has an important role to play as contrast may be contraindicated due to deranged renal parameters (Figure 6).

PYONEPHROSIS

Pyonephrosis is pus collection in an obstructed collecting system, the cause of obstruction being calculus, stricture, tumour or congenital anomaly. US shows dilated pelvicalyceal system (PCS) with debris and fluid-fluid levels within (Figure 7)^[1]. On CT, high density of urine in dilated PCS with contrast layering, parenchymal or perinephric inflammatory changes and thickening of pelvic wall suggests infection (Figure 8). DW-MRI may have an additional role in distinguishing hydronephrosis from

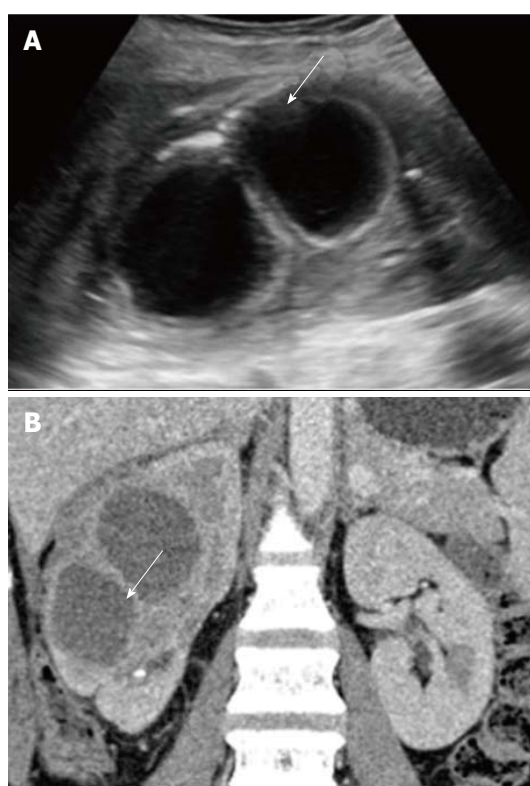


Figure 4 Mature abscess. A: US shows a complex cystic lesion with thick walls in right kidney; B: CECT shows a sharply marginated area of low attenuation due to parenchymal necrosis with peripheral enhancing rim that suggest a mature abscess. US: Ultrasonography; CECT: Contrast-enhanced computed tomography.

pyonephrosis as pyonephrosis tends to show restricted diffusion (Figure 9)^[7]. Contrast enhanced MRI may show enhancement and wall thickening of the renal pelvis (Figure 10).

XANTHOGRANULOMATOUS PYELONEPHRITIS

Xanthogranulomatous pyelonephritis is a chronic granulomatous process commonly associated with recurrent

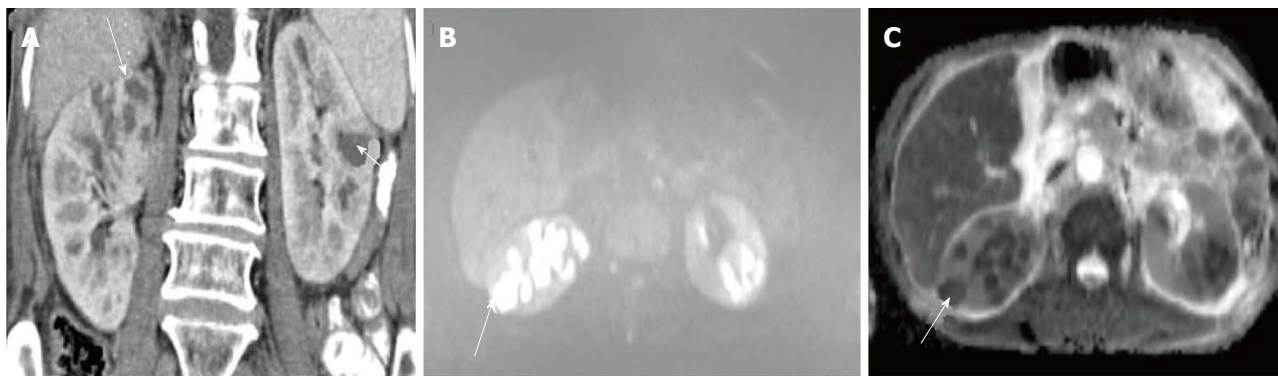


Figure 5 Diffusion weighted magnetic resonance imaging. A: CECT of a diabetic middle aged male shows multiple peripherally enhancing lesions in bilateral kidneys (arrows). B, C: DW-MRI (b = 1000) (B) and corresponding ADC maps (C) show that the lesions have restricted diffusion. Aspiration revealed the pyogenic nature of the abscess. There was excellent response to antibiotics. CECT: Contrast-enhanced computed tomography; DW-MRI: Diffusion weighted magnetic resonance imaging.

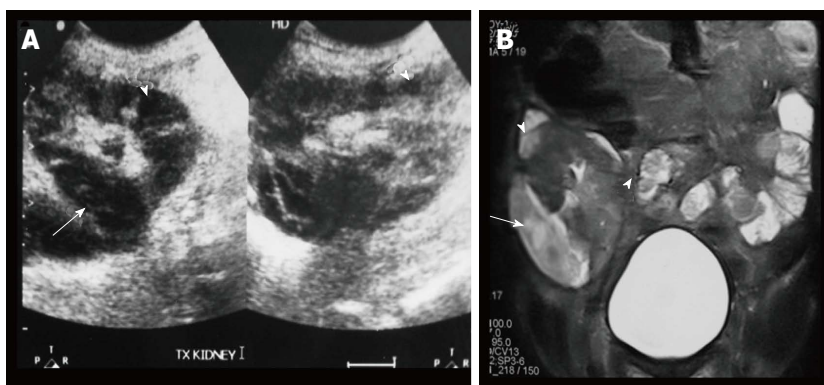


Figure 6 Acute pyelonephritis in transplant kidney. A: USG of transplanted kidney in a 25 years old patient shows multiple hypoechoic lesions (arrowheads) within the cortex and one large hypoechoic lesion laterally (arrow); B: Coronal T2W MR shows multiple hyperintensities (arrowheads) in the renal cortex and a large well defined abscess (arrow) laterally suggestive of acute pyelonephritis with abscess formation.

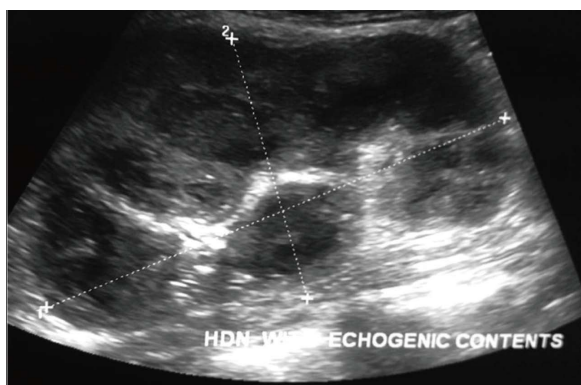


Figure 7 Ultrasonography shows hydronephrosis with echogenic debris within suggestive of pyonephrosis.

E. coli and *Proteus mirabilis* infection affecting middle aged females and children. Most (90%) of the affected individuals have a staghorn calculus. Pathologically there is replacement of renal parenchyma with foamy macrophages which appear as multiple hypoechoic masses on sonography and as low attenuation rounded masses on CT which represent dilated calyces and abscess cavities (Figure 11) filled with pus and debris^[8]. It can manifest as either diffuse (80%) or focal (15%) forms which are treated by nephrectomy and partial nephrectomy respectively^[9]. Typical features of xanthogranulomatous pyelo-

nephritis are presence of a central calculus, expansion of the calyces with hypodense material in a non-functioning enlarged kidney and inflammatory changes in the perinephric fat. Atypical features include absence of calculi (10%), focal instead of diffuse involvement (10%) and renal atrophy instead of enlargement.

EMPHYSEMATOUS PYELONEPHRITIS

Emphysematous pyelonephritis is a life threatening, necrotising infection with gas formation and is associated with diabetes mellitus or immunocompromised state. The presence of gas is attributed to fermentation by bacteria in the presence of high glucose levels^[10]. USG shows non-dependent echoes within the parenchyma and collecting system with dirty shadowing. However, USG is not sensitive to small amounts of gas (Figure 12). CT is performed for evaluating severity, extent of disease, parenchymal destruction, fluid collections and abscess formation. It is divided into two forms depending on severity and prognosis. Type 1 is the more severe type with a mortality rate of 80%. It is characterised by severe parenchymal destruction, intraparenchymal gas and paucity of pus collection (Figure 13). Type 2 is less common and has a lower mortality rate of 20%. It has less parenchymal destruction and renal or perirenal fluid collections (Figure 14). A comparison of the types of emphysema-

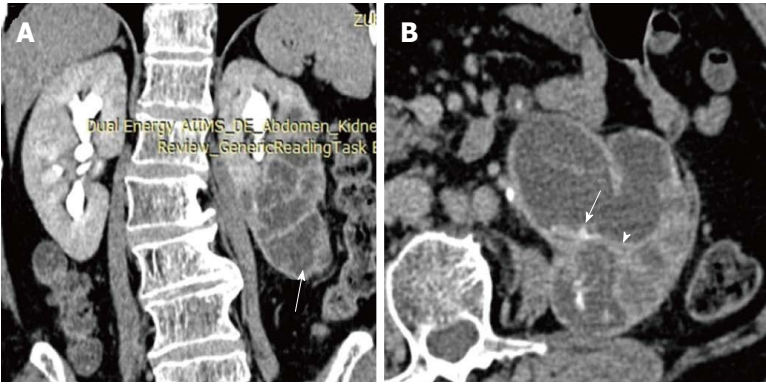


Figure 8 Pyonephrosis in duplex left kidney. Coronal (A) and axial (B) sections of delayed phase CECT shows left duplex kidney with obstruction and hydronephrosis of lower moiety (arrow, A). Walls of the PCS shows thickening and crescentic enhancement (arrowhead, B) suggesting pyonephrosis. PCS: Pelvicalyceal system; CECT: Contrast-enhanced computed tomography.

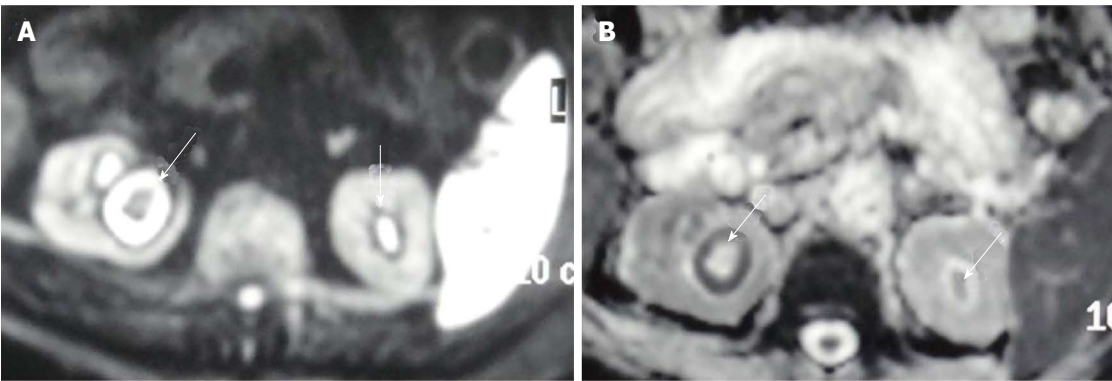


Figure 9 Diffusion weighted magnetic resonance imaging at b = 1000 (A) and corresponding ADC map (B) show hydronephrosis with diffusion restriction suggestive of pyonephrosis (arrows).

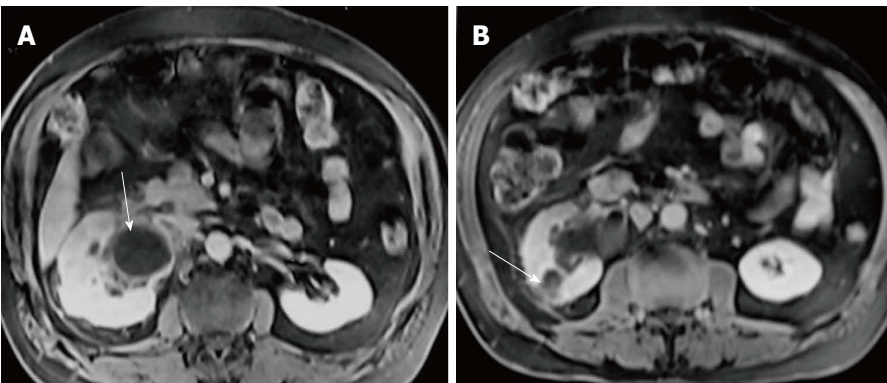


Figure 10 Axial sections of post gadolinium magnetic resonance imaging. A 42 years old male with right hydronephrosis, peripheral enhancement of dilated pelvis (arrow, A) representing pyonephrosis along with a heterogeneously enhancing focal lesion in right kidney (arrow, B) suggestive of focal pyelonephritis.

Table 2 Emphysematous pyelonephritis

	TYPE 1 -33%	TYPE 2 -66%
Parenchymal destruction	Severe – streaky gas radiating from medulla to cortex with crescent of subcapsular gas	Less
Fluid collection	None as the reduced immune response limits pus collection	Renal or perirenal fluid collection is characteristic
Mortality	80%	20%
Treatment	Nephrectomy	Aggressive medical treatment with percutaneous drainage

tous pyelonephritis is presented in Table 2.

Emphysematous pyelitis is usually accompanied by obstruction due to calculus, neoplasm or stricture and

50% of the affected patients are diabetics^[10-12]. CT shows gas within the dilated PCS and urinary bladder (Figure 15 A). Emphysematous cystitis shows an air fluid level in the

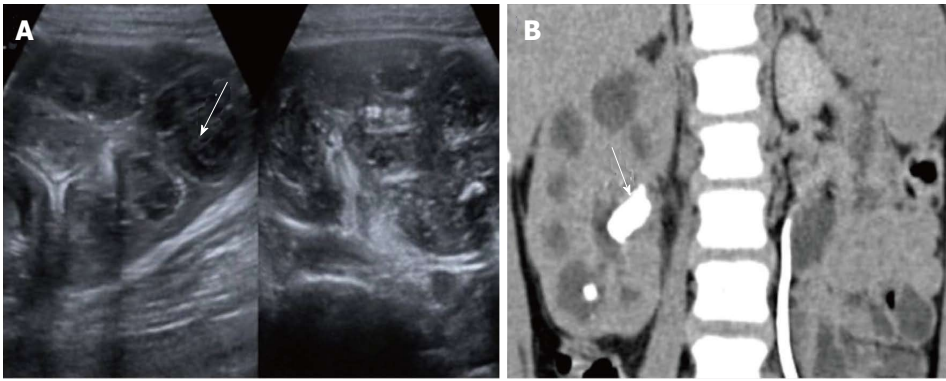


Figure 11 Xanthogranulomatous pyelonephritis. A: USG shows enlarged kidney with parenchyma replaced with multiple hypoechoic masses (arrow, A) comprising inflammatory exudate; B: Computed tomography shows multiple low-attenuation rounded masses, corresponding to either dilated calyces or focal areas of parenchymal destruction with a central staghorn calculus (arrow, B).



Figure 12 Emphysematous pyelonephritis. Ultrasonography shows dilated calyces with echoes within pelvis and renal parenchyma with dirty shadowing.



Figure 13 Type 1 emphysematous pyelonephritis. A: Plain abdominal radiograph shows large amount of gas outlining the right kidney (arrow); B, C: Contrast-enhanced computed tomography axial (B) and coronal (C) images show gas pockets and parenchymal destruction destroying and replacing almost the entire right kidney. No perirenal collections are noted.

bladder lumen or linear streaks of air in the bladder wall (Figure 15B). Before making a diagnosis of emphysematous cystitis, history of instrumentation must be ruled out.

It is important to make the distinction between emphysematous pyelitis and pyelonephritis as the former is a less aggressive infection and does not require nephrectomy. In pyelitis, air is limited to PCS while in pyelonephritis it enters the parenchyma.

CHRONIC PYELONEPHRITIS

Chronic pyelonephritis may be caused by reflux of infected urine in childhood, recurrent infections or as a result of a remote single infection^[13]. Imaging shows focal polar scars with underlying calyceal distortion with global atrophy and hypertrophy of residual tissue (Figure 16)^[14]. Lobar infarcts can be differentiated by their lack of calyceal involvement. Fetal lobulations are differentiated by depressions lying between calyces rather than overlying calyces

TUBERCULOSIS

Renal tuberculosis (TB) may occur due to hematogenous

dissemination. In half of the affected patients of genitourinary TB, there may be no lung involvement^[15]. The earliest finding in TB which can be picked up on Intravenous Urography (IVU) is caliectasis with a feathery contour, later appearing as a phantom calyx or a cavity communicating with a deformed calyx (Figure 17A). These findings can also be picked up on CT. Over the course of the disease, the granulomas coalesce forming mass like lesions (tuberculoma) which may rupture into the PCS^[16]. Eventually as the disease evolves, fibrosis ensues leading to infundibular stenosis. In the late stage, the kid-



Figure 14 Type 2 Emphysematous pyelonephritis. Contrast-enhanced computed tomography shows extensive inflammatory changes in right kidney and perinephric space with presence of gas within along with perirenal collection. The patient responded to antibiotics and percutaneous drainage.



Figure 15 Emphysematous pyelitis and cystitis. A: Para-sagittal reformed CECT of a 42 years old diabetic lady showing air within dilated PCS with surrounding inflammatory changes; B: Axial CECT shows bladder wall thickening and air within the bladder lumen. PCS: Pelvicalyceal system; CECT: Contrast-enhanced computed tomography.



Figure 16 Coronal contrast-enhanced computed tomography shows atrophic right kidney with multiple cortical scars overlying the dilated calyces. This appearance is typical of chronic pyelonephritis.

ney either becomes calcified or shrunken (putty kidney) (Figure 17B) or an enlarged sac with caseous material (case cavernous type autonephrectomy). Ureteric involvement may manifest as wall thickening causing strictures and shortening leading to a beaded appearance. Bladder involvement results in a contracted thimble shape with

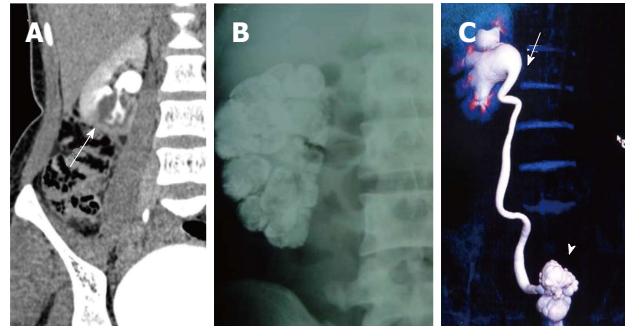


Figure 17 Renal tuberculosis. A: Delayed CECT shows a cavitation at the lower pole of right kidney communicating with the PCS. This finding is fairly typical of GU TB. This adolescent male was a known case of pulmonary tuberculosis; B: Plain abdominal radiograph in a different patient shows diffuse parenchymal calcification of right kidney suggestive endstage autonephrectomy or putty kidney; C: Volume rendered technique image of delayed phase CECT shows a contracted thimble bladder (arrowhead), hiked up right pelvis (arrow) and hydronephrosis. This patient had acid fast bacilli cultured from urine. PCS: Pelvicalyceal system; CECT: Contrast-enhanced computed tomography; TB: Tuberculosis.

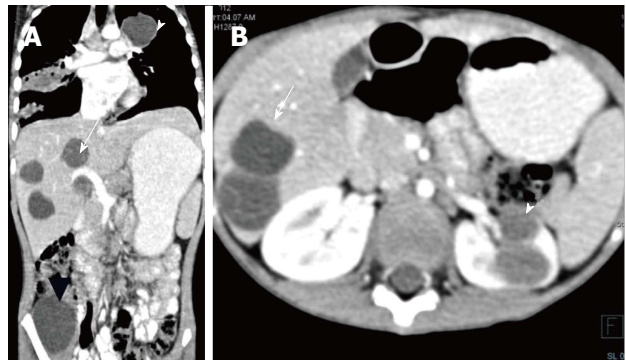


Figure 18 Disseminated hydatidosis. A: Coronal reformed CECT of a 7 years old boy shows multiple hydatid cysts in lung (white arrowhead), liver (arrow) and right iliacus (black arrowhead); B: Axial CECT shows multiple liver (arrow) and renal hydatid cysts (arrowhead). CECT: Contrast-enhanced computed tomography.

multiple diverticulae (Figure 17C).

PARASITIC INFECTION

Schistosomiasis can appear in the acute phase as nodular bladder wall thickening, later causing it to become contracted, fibrotic and thick walled with curvilinear calcifications. This chronic phase of schistosomiasis is considered to be premalignant. Liver is the most common organ involved by hydatid disease while renal involvement comprises only 5% of patients. Hydatid disease affecting the kidney may appear as a unilocular or multilocular cystic lesion(s) with or without peripheral calcification^[17] (Figure 18). Occasionally on communication with the pelvicalyceal system (PCS) it may lead to hydatiduria.

FUNGAL INFECTION

Fungal infection of the urinary tract is a severe life threatening infection particularly affecting patients with dia-

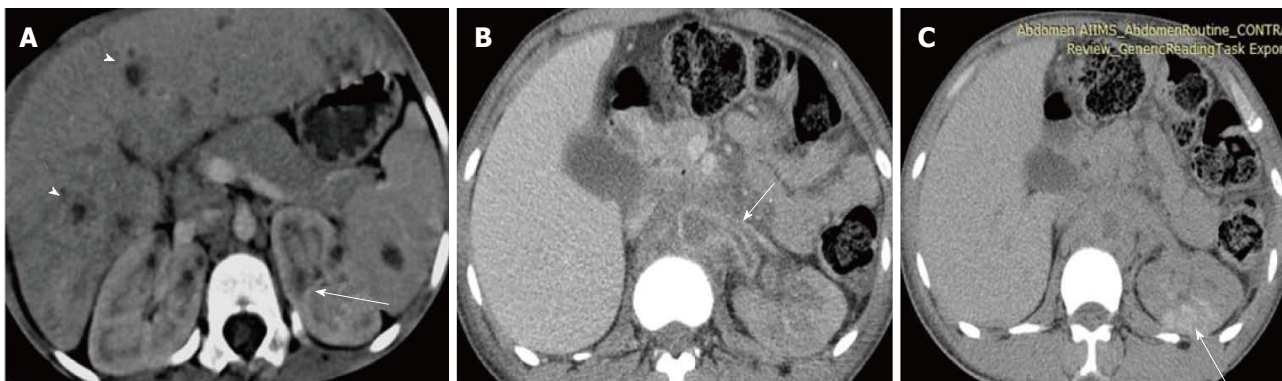


Figure 19 Fungal infection. A: CECT shows liver, spleen and bilateral kidneys studded with small hypodense lesions in a 10 years old leukemia patient who was proven to have *Aspergillus* infection on aspiration cytology. The patient also had lung involvement with contiguous cardiac thrombus (not shown); B, C: Nephrographic (B) and delayed (C) phase CECT in a 26 years old aplastic anemia patient reveal a poorly enhancing, non-excreting left kidney with perinephric inflammation. Aorta and left renal artery are almost completely occluded by a non-enhancing thrombus (arrow B). On delayed image (Figure C), patchy areas of enhancement (arrow) noted in left kidney are characteristic of acute pyelonephritis. FNAC from the perirenal soft tissue revealed fungal hyphae and diagnosis of angioinvasive fungal infection (*Mucor*) was made and Amphotericin B was started. However patient expired two days later. CECT: Contrast-enhanced computed tomography.

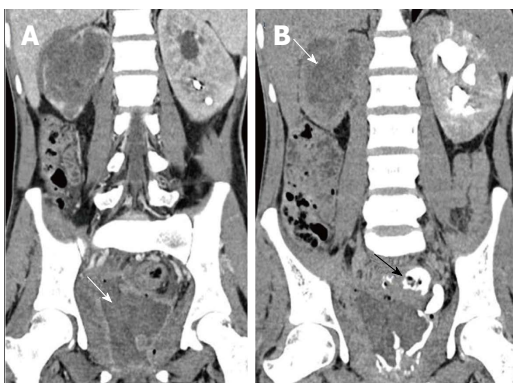


Figure 20 Eosinophilic cystitis. A 25 years old man who presented with hematuria and worsening irritative symptoms over past one year. Clinical suspicion was that of a bladder malignancy. A: Coronal reformatted CECT in nephrographic phase shows diffuse mass like bladder wall thickening and irregularity with air specks in the wall. Mass like soft tissue is replacing entire right kidney with perinephric spread; B: Delayed coronal CECT shows opacification of rectum through a fistulous communication (arrow). Note made of striated nephrogram in left kidney suggesting ongoing acute inflammatory process. Biopsy revealed eosinophilic infiltration and fibrosis within the bladder wall with no evidence of malignancy. CECT: Contrast-enhanced computed tomography.

betes mellitus, haematological malignancy, HIV or other immunocompromised status. The common fungal organisms are *Candida* and *Aspergillus* which may be acquired by hematogenous or ascending urinary tract infection. There is formation of multiple renal abscesses appearing as hypoattenuating lesions with a striated nephrogram signifying acute pyelonephritis (Figure 19A). There can also be conglomeration of fungal hyphae and inflammatory cells into a fungal ball which appears as an irregular filling defect in the collecting system^[1]. Diagnosis requires demonstration of fungi in tissues. *Mucor* is a rare organism which has a tendency to invade vessels and cause infarction with high mortality requiring combined surgical and aggressive medical management to improve outcome (Figure 19B, C)^[18]. *Pneumocystis carini* infection in HIV patients presents as diffuse punctate calcifications in kid-

neys and organs of the reticuloendothelial system^[19].

EOSINOPHILIC CYSTITIS

Eosinophilic cystitis is a rare chronic inflammatory disease of urinary bladder due to eosinophil infiltration into the bladder wall leading to fibrosis and muscle necrosis^[20]. It clinically presents with hematuria, frequency and irritative symptoms. The mean age at diagnosis is 41.6 years with an equal sex distribution^[21].

On imaging, there is diffuse bladder wall thickening which is often more than 10 mm with characteristic preservation of the mucosal line and enhancement on delayed images (Figure 20)^[22,23]. This entity is often confused with a neoplastic etiology, therefore biopsy is essential. There may be associated diffuse or segmental bowel wall thickening and hepatic nodules^[22].

CONCLUSION

Over the years imaging modalities used for renal infections have evolved from USG and IVU to CT and MRI. CT remains the mainstay in evaluation of inflammatory disease of kidney and urinary bladder. Ultrasonography forms an excellent screening tool for evaluation in the emergency setting. An IVU continues to be invaluable in some indications like tuberculosis. Upcoming role of DW-MRI deserves mention in identifying abscesses and differentiating pyonephrosis from hydronephrosis.

REFERENCES

- 1 **Kawashima A**, Sandler CM, Goldman SM, Raval BK, Fishman EK. CT of renal inflammatory disease. *Radiographics* 1997; **17**: 851-866; discussion 867-868 [PMID: 9225387 DOI: 10.1148/radiographics.17.4.9225387]
- 2 **Stunell H**, Buckley O, Feeney J, Geoghegan T, Browne RF, Torreggiani WC. Imaging of acute pyelonephritis in the adult. *Eur Radiol* 2007; **17**: 1820-1828 [PMID: 16937102]
- 3 **Gold RP**, Mcclennan BL, Kenney PJ, Breatnach ES, Stanley

- RJ, Lebowitz RI. Acute infections of the renal parenchyma. In: Pollack HM, editor. *Clinical urography*. Philadelphia, Pa: Saunders, 1990: 799-821
- 4 **Saunders HS**, Dyer RB, Shifrin RY, Scharling ES, Bechtold RE, Zagoria RJ. The CT nephrogram: implications for evaluation of urinary tract disease. *Radiographics* 1995; **15**: 1069-185; discussion 1069-1085 [PMID: 7501851]
 - 5 **Rigsby CM**, Rosenfield AT, Glickman MG, Hodson J. Hemorrhagic focal bacterial nephritis: findings on gray-scale sonography and CT. *AJR Am J Roentgenol* 1986; **146**: 1173-1177 [PMID: 3518368 DOI: 10.2214/ajr.146.6.1173]
 - 6 **Browne RF**, Zwirowich C, Torreggiani WC. Imaging of urinary tract infection in the adult. *Eur Radiol* 2004; **14** Suppl 3: E168-E183 [PMID: 14749952 DOI: 10.1007/s00330-003-2050-1]
 - 7 **Cova M**, Squillaci E, Stacul F, Manenti G, Gava S, Simonetti G, Pozzi-Mucelli R. Diffusion-weighted MRI in the evaluation of renal lesions: preliminary results. *Br J Radiol* 2004; **77**: 851-857 [PMID: 15482997]
 - 8 **Loffroy R**, Guiu B, Watfa J, Michel F, Cercueil JP, Krausé D. Xanthogranulomatous pyelonephritis in adults: clinical and radiological findings in diffuse and focal forms. *Clin Radiol* 2007; **62**: 884-890 [PMID: 17662737 DOI: 10.1016/j.crad.2007.04.008]
 - 9 **Kim JC**. US and CT findings of xanthogranulomatous pyelonephritis. *Clin Imaging* 2001; **25**: 118-121 [PMID: 11483422]
 - 10 **Grayson DE**, Abbott RM, Levy AD, Sherman PM. Emphysematous infections of the abdomen and pelvis: a pictorial review. *Radiographics* 2002; **22**: 543-561 [PMID: 12006686]
 - 11 **Kiris A**, Ozdemir H, Bozgeyik Z, Kocakoc E. Ultrasonographic target appearance due to renal calculi containing gas in emphysematous pyelitis. *Eur J Radiol Extra* 2004; **52**: 119-21 [DOI: 10.1016/j.ejrex.2004.09.011]
 - 12 **Joseph RC**, Amendola MA, Artze ME, Casillas J, Jafri SZ, Dickson PR, Morillo G. Genitourinary tract gas: imaging evaluation. *Radiographics* 1996; **16**: 295-308 [PMID: 8966288]
 - 13 **Craig WD**, Wagner BJ, Travis MD. Pyelonephritis: Radiologic-Pathologic review in adults. *Radiographics* 2008; **28**: 255-276 [PMID: 18203942 DOI: 10.1148/rg.281075171]
 - 14 **Goldman SM**. Acute and chronic urinary infection: present concepts and controversies. *Urol Radiol* 1988; **10**: 17-24 [PMID: 3043871 DOI: 10.1007/bf02926529]
 - 15 **Becker JA**. Renal tuberculosis. *Urol Radiol* 1988; **10**: 25-30 [PMID: 3043873 DOI: 10.1007/bf02926530]
 - 16 **Hammond NA**, Nikolaidis P, Miller FH. Infectious and inflammatory diseases of the kidney. *Radiol Clin North Am* 2012; **50**: 259-270, vi [PMID: 22498442 DOI: 10.1016/j.rcl.2012.02.002]
 - 17 **Pedrosa I**, Saíz A, Arrazola J, Ferreirós J, Pedrosa CS. Hydatid disease: radiologic and pathologic features and complications. *Radiographics* 2000; **20**: 795-817 [PMID: 10835129]
 - 18 **Sharma R**, Shivanand G, Kumar R, Prem S, Kandpal H, Das CJ, Sharma MC. Isolated renal mucormycosis: an unusual cause of acute renal infarction in a boy with aplastic anaemia. *Br J Radiol* 2006; **79**: e19-e21 [PMID: 16823048 DOI: 10.1259/bjr/17821080]
 - 19 **Radin DR**, Baker EL, Klatt EC, Balthazar EJ, Jeffrey RB, Megibow AJ, Ralls PW. Visceral and nodal calcification in patients with AIDS-related Pneumocystis carinii infection. *AJR Am J Roentgenol* 1990; **154**: 27-31 [PMID: 2104720 DOI: 10.2214/ajr.154.1.2104720]
 - 20 **Teegavarapu PS**, Sahai A, Chandra A, Dasgupta P, Khan MS. Eosinophilic cystitis and its management. *Int J Clin Pract* 2005; **59**: 356-360 [PMID: 15857336]
 - 21 **Pomeranz A**, Eliakim A, Uziel Y, Gottesman G, Rathaus V, Zehavi T, Wolach B. Eosinophilic cystitis in a 4-year-old boy: successful long-term treatment with cyclosporin A. *Pediatrics* 2001; **108**: E113 [PMID: 11731640 DOI: 10.1542/peds.108.6.e113]
 - 22 **Kim MS**, Park H, Park CS, Lee EJ, Rho MH, Park NH, Joh J. Eosinophilic cystitis associated with eosinophilic enterocolitis: case reports and review of the literature. *Br J Radiol* 2010; **83**: e122-e125 [PMID: 20505026 DOI: 10.1259/bjr/36109223]
 - 23 **Leibovitch I**, Heyman Z, Ben Chaim J, Goldwasser B. Ultrasonographic detection and control of eosinophilic cystitis. *Abdom Imaging* 1994; **19**: 270-271 [PMID: 8019361 DOI: 10.1007/bf00203525]

P- Reviewer: Gao BL, Tsushima Y S- Editor: Song XX
L- Editor: A E- Editor: Lu YJ



Imaging of skeletal muscle in vitamin D deficiency

Bianca Bignotti, Angela Cadoni, Carlo Martinoli, Alberto Tagliafico

Bianca Bignotti, Carlo Martinoli, Radiology Department, University of Genoa, 16138 Genoa, Italy

Angela Cadoni, Alberto Tagliafico, Institute of Anatomy, Department of Experimental Medicine, University of Genoa, 16138 Genoa, Italy

Author contributions: Bignotti B, Cadoni A, Martinoli C and Tagliafico A entirely contributed to this paper.

Supported by Partially founded by the European Society of Musculoskeletal Radiology, Young Investigator Grant to Alberto Tagliafico; UNIGE, No. PRA 2012

Correspondence to: Alberto Tagliafico, MD, Institute of Anatomy, Department of Experimental Medicine, University of Genoa, Via de Toni 14, 16138 Genoa, Italy. albertotagliafico@gmail.com

Telephone: +39-347-9745122 Fax: +39-347-9745122

Received: December 27, 2013 Revised: February 28, 2014

Accepted: April 9, 2014

Published online: March 28, 2015

Key words: Muscle; Vitamin D; Vitamin D deficiency; Ultrasound; Computed tomography; Magnetic resonance imaging

Core tip: Elderly people are prone to accidental falls and many fractures sometimes due to vitamin D deficiency. In this narrative review we will discuss the role of skeletal muscle imaging in vitamin D-deficient individuals. The aim of this paper is to improve and encourage the role of radiologists in this field.

Original sources: Bignotti B, Cadoni A, Martinoli C, Tagliafico A. Imaging of skeletal muscle in vitamin D deficiency. *World J Radiol* 2014; 6(4): 119-124 Available from: URL: <http://www.wjgnet.com/1949-8470/full/v6/i4/119.htm> DOI: <http://dx.doi.org/10.4329/wjr.v6.i4.119>

Abstract

Elderly people are prone to accidental falls and one of the main risk factor is considered muscle weakness. Several studies focused on muscle weakness and muscle morphology changes in the elderly that may be associated with vitamin D deficiency. The prevalence of vitamin D deficiency is higher than previously though representing an important issue for public health and prevention. There is an increased interest in vitamin D effects in skeletal muscle and imaging modalities are particularly involved in this field. In patients with vitamin D deficiency, ultrasound, computed tomography, densitometry and magnetic resonance imaging (MRI) can efficiently describe changes in muscle morphology and size. Moreover, new imaging modalities, such as MRI spectroscopy, may improve knowledge about the metabolic effects of vitamin D in skeletal muscle. In this narrative review we will discuss the role of skeletal muscle imaging in vitamin D-deficient individuals. The aim of this paper is to improve and encourage the role of radiologists in this field.

INTRODUCTION

Elderly people are prone to accidental falls. Many factors are involved in falls risks such as visual impairment, neurological disorders, orthopaedic disabilities, and drug effects. More than 33% of people aged over 65 fall each year and this issue is closely related to muscle weakness^[1]. It has been suggested that reduced muscle strength and weakness may be associated with vitamin D deficiency, which is common among elderly people^[2]. Vitamin D deficiency in adults primarily affects bone, up to osteomalacia in severe cases, due to the combination of bone mineralization defects and resorption, the latter of which is a result of secondary hyperparathyroidism^[3]. Vitamin D deficiency has also been associated with a decline in physical performance and loss of muscle strength and decreased muscle mass. Symptomatic myopathy can occur in osteomalacia, and a more subtle muscular impairment is often present in patients with moderate or mild vitamin D deficiency^[4].

Beside the vitamin D skeletal and extraskelatal effects^[5], there is an increased interest on vitamin D effects

in skeletal muscle. Imaging modalities are particularly involved in this issue. Ultrasound (US), computed tomography (CT), densitometry and magnetic resonance imaging (MRI) can assess, with different physical principles the effects of vitamin D deficiency measuring changes in muscle morphology and size. Moreover, new imaging modalities, such as MRI spectroscopy, may improve knowledge about metabolic effects of vitamin D in skeletal muscle at a microscopical level. In this narrative review we will discuss recent developments in skeletal muscle imaging among elderly people with vitamin D deficiency.

VITAMIN D AND SKELETAL MUSCLE

The role of vitamin D in bone health and mineral homeostasis has been well established. There is growing evidence that vitamin D exerts several effects in skeletal muscle, including enhanced muscle strength, function and performance in general. Cell culture models suggested muscle vitamin D role in calcium handling, proliferation and differentiation, protection against insulin-resistance and arachidonic acid mobilization^[6]. Vitamin D probably exerts its effects both indirectly, through calcium and phosphate pathways, and directly *via* binding of 1,25-dihydroxyvitamin D (1,25D) to the vitamin D receptor, that seems to be expressed in skeletal muscle cells, even if this topic is still under research^[5,6].

It has been supposed that the vitamin D relationship with muscle strength may influence the increasing risk of accidental falls in the elderly^[6]. Vitamin D deficiency is associated with proximal muscle weakness and reduction in performance speed, probably related to selective muscle atrophy of type II muscle fibers^[5,6]. Moreover, proximal muscle weakness in severe vitamin D deficiency may be caused by secondary hyperparathyroidism and consequent hypophosphatemia^[5]. It has been reported that proximal myopathy and muscle pain in subjects with severe vitamin D deficiency resolve in most cases with vitamin D supplementation^[7]. In addition, a recent systematic review focused on healthy adults reported that higher 25-hydroxyvitamin D levels may have a positive effect for increasing muscle strength and reducing the incidence of injuries, but further researches are needed to strengthen these hypotheses^[8]. It has also been suggested an association between low levels of vitamin D and fibromyalgia, in particular among women, but more researches in this field are still needed^[7].

Therefore, vitamin D role in skeletal muscle and its association with muscle weakness and falls are an active area of research supported by clinical, biochemical and imaging parameters.

SKELETAL MUSCLE IMAGING

Muscle imaging is complex and presents unique anatomical and morphological challenges, which require a continuous integration of dynamic, physiologic, and functional capabilities of modern imaging techniques. The optimal use of US and MRI in various muscle disorders,

including muscle strains and tears, delayed onset muscle soreness, myositis ossificans, muscle hernia, acute and chronic exertion compartment syndromes, inflammatory and infectious diseases, tumours and non-neoplastic masses is crucial to obtain the best information clinically useful. The value of CT, US, MRI in each muscle disorder has to be weighted up to take advantage of strengths and weaknesses of the each technique and to understand the appropriate place of modern imaging in the clinical management of patients with muscle disease^[9,10].

It is known that US, MRI, and CT are widely used with different purposes to visualize the normal anatomy of the musculo-skeletal system. However, in recent years, new and technologically advanced imaging techniques have been introduced for both clinical and research purposes to study the muscular anatomy from a physiological and microscopical point of view. For example, elastography has been introduced to assess the elastic properties of tendons and muscles. Using MRI, diffusion tensor imaging (DTI) has been introduced to study the architecture of the skeletal muscle. The DTI technique is based on the measurement of the apparent diffusion of water in a (biological) tissue. It is concluded that DTI fiber directions resemble fascicle directions visible in high-resolution images very well. Indeed, on DTI images it is possible to observe and study specific features of the skeletal muscle such as the pennate insertion on the aponeuroses and the pennation angle^[9,10]. DTI has the potential to be introduced in biomechanical research on skeletal muscle function. The imaging evaluation of skeletal muscle is often performed on US. The use of small-sized probes working in general at high frequencies (frequency band 7-15 MHz) is suitable for very superficial muscles. On the other hand, if a large and deep muscle should be evaluated, for example, at the level of the lower limb it should be better to use low-frequency probes with high penetration of the US-beam (frequency band 3.5-10 MHz). It is important to remember that to depict the normal anatomy of a large wide muscle, such as the biceps femoris and the sartorius, it is possible to use an extended field-of-view which is an option frequently available on the majority of US machines currently available. The advantage of US over MRI is that the muscle may be studied “*in vivo*” in a relaxed status and during contraction.

STUDYING THE RELATIONSHIP BETWEEN VITAMIN D AND MUSCLES WITH CLINICAL IMAGING

Changes in muscle morphology in patients with severe vitamin D deficiency have been reported in literature. In the elderly, muscular atrophy with fatty infiltration is associated with vitamin D deficiency. Muscle trophism can be evaluated with clinical imaging modalities. In particular, to study the skeletal muscle with diagnostic imaging several modalities may be used: US, CT, dual-energy X-ray absorptiometry (DEXA) and MRI. The cross-sectional area (CSA) of a muscle is normally used to evaluate mus-

Table 1 Percentage of selective atrophy of thigh muscle in patients with vitamin D deficiency: Our clinical records

Rectus femoris	Adductors	Semitendinosus	Semimembranosus	Biceps femoris	Gracilis	Sartorius
30%	23%	8%	30%	8%		

Note that the Gracilis muscle and the Sartorius muscle are spared.

cle size and volume. Moreover, CSA is directly related to muscle strength^[11]. MRI and CT can both assess CSA and muscle composition with different physical principles. US has a limited field-of-view: this limitation hampers direct measurement of CSA of large muscles due to insufficient visualization of the whole muscle bulk^[11]. US, MRI and CT can assess the presence of higher skeletal fat content than in normal muscles. Fatty replacement may present as a focal process or as a diffuse change involving one group of muscle of the entire skeletal muscle, as largely demonstrated for dystrophic muscle diseases^[12]. Table 1 shows the prevalence of selective complete fatty degeneration and atrophy of the thigh muscles as recorded in our clinical practice and as demonstrated in literature^[4]. This review has been focused on vitamin D deficiency and skeletal muscle, and it will not discuss the huge literature about skeletal muscle diseases.

We will discuss the role of each modality in assessing skeletal muscle in vitamin D-deficient patient. Research studies in literature frequently refers to skeletal muscle and sarcopenia, a syndrome with loss of skeletal muscle mass and strength that occurs in the elderly^[13]. In severe vitamin D deficient patients imaging of skeletal muscle may overlap with that of sarcopenia.

US

Using US it has been shown that quantitative muscle US is a potential alternative for assessment of disease severity and progression in several muscular diseases. The main findings in muscular diseases are increased echo intensity, reflecting increased infiltration of fat or fibrous tissue in muscles, and decreased muscle thickness, indicative of atrophy. Additional advantages of US are high discriminating ability, low cost, fast execution, and non-X-ray dependent nature. Structural abnormalities quantified with US may reflect muscle function or strength^[14-16]. Moreover, US has been proposed as a reliable method for monitoring the extent of sarcopenia measuring muscle thickness, especially of musculus vastus medialis and musculus intermedius^[11].

However, muscular US has been shown to have several disadvantages regarding the reliability of the results in terms of intra- and inter-observer agreement (Tagliafico *et al*^[9], personal communication).

US elastography assesses tissue stiffness before and after compression^[17]. Until now, there are limited data about the use of elastography to assess normal and pathologic skeletal muscle. However, it is likely that fatty infiltration of a muscle determines global reduce stiffness, as suggested in studies on inflammatory myositis^[17].

There are no significant radiological studies about US assessment of skeletal muscle in individuals with vitamin

D deficiency. We encourage research studies using US because this modality has the advantage of being available even at bedside, cheap and easily repeatable.

CT and densitometry (DEXA)

Regarding CT it has been shown that radiological measures of bone health measured with quantitative CT were not affected by persisting low vitamin D levels^[18]. Non-enhanced CT scan of the pelvis demonstrated that the fat content varied among the hip muscles, with an antero-posterior gradient from the hip flexors to the hip extensors. This gradient increased after fifty years of age. Higher fat content was associated with poorer performance on physical tests, even after adjustment for the CSA of the muscle. Figure 1 shows cross-sectional CT of thigh muscles in a patient with vitamin D deficiency. Higher fat content was also associated with greater age, higher body-mass index, and lower physical activity^[19]. This data has been supported by the data on muscle of the thigh and vitamin D deficiency^[4]. Using very sophisticated and new techniques it has been found that the characteristic increase in osteoid-covered surfaces in vitamin D-deficient bone hampers remodelling of the remaining mineralized bone tissue. Using spatially resolved synchrotron bone mineral density distribution analyses and spectroscopic techniques, the bone tissue within the osteoid frame has a higher mineral content with mature collagen and mineral constituents, which are characteristic of aged tissue^[20]. A recent cross-sectional study demonstrated a positive correlation between 1,25D levels and total skeletal muscle mass as measured on DEXA among subjects younger than 65 years^[21]. This was supported by greater isometric knee extension moment in women with higher 1,25D levels. However, no association was found between 25D levels and muscle mass or strength or in those over 65 years of age. Among 26 subjects with chronic kidney disease, thigh muscle CSA on MRI correlated significantly with a model including 1,25D levels, calcium levels, and daily physical activity. Functional parameters assessing gait and proximal musculature also independently correlated with 1,25D^[7,21].

MRI

By our group it has been shown that fatty degeneration of thigh muscles detected on MRI was associated with vitamin D deficiency and impaired balance and gait. Selective complete fatty degeneration of single muscles was observed^[4]. These data are also supported by previous studies on muscle biopsy specimens^[4].

Fatty replacement and atrophy can be evaluated with MRI using a scoring system from 0 to 3 (grade 0 = normal appearance; grade 3 = severe changes)^[4]. For illustra-

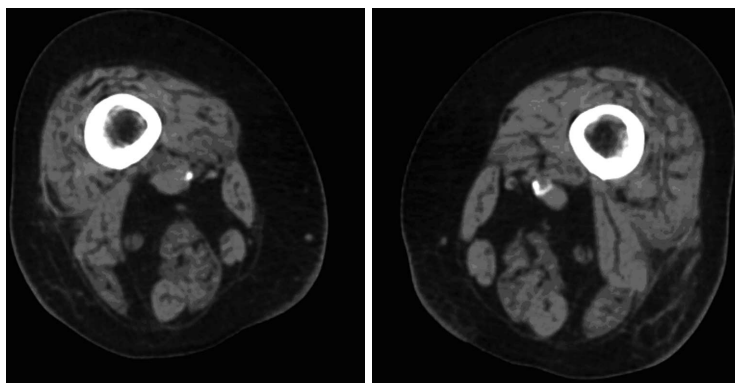


Figure 1 Cross-sectional computed tomography at the level of the middle thigh showing fatty degeneration and atrophy of skeletal muscles in a vitamin D-deficient patient.

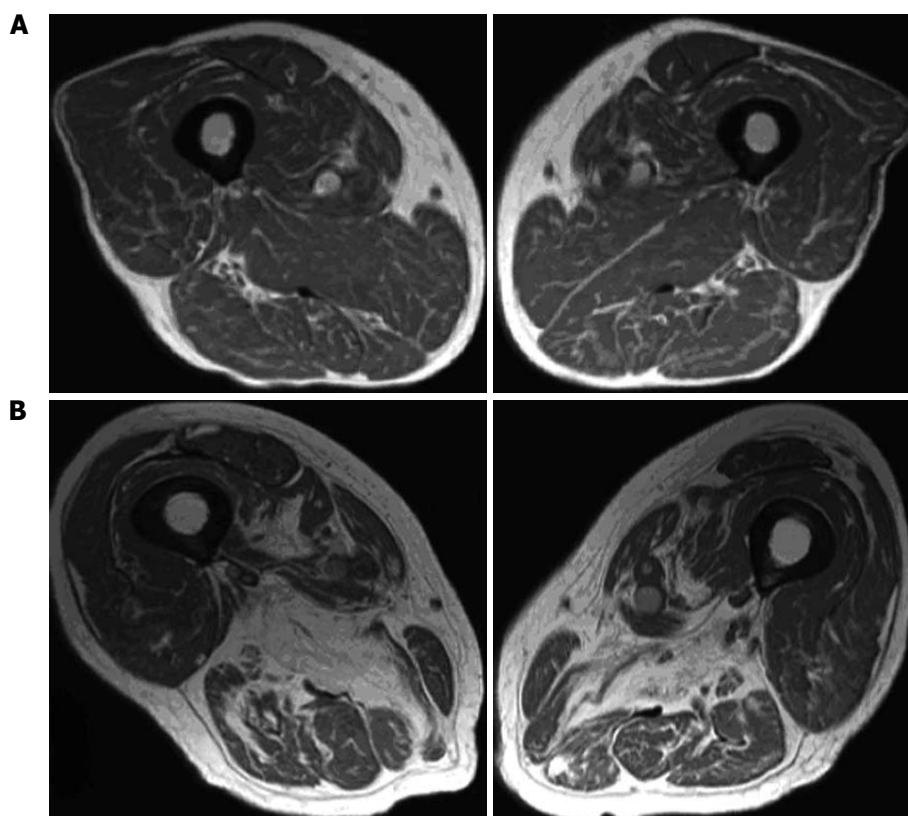


Figure 2 Magnetic resonance imaging of two different grades of fatty degeneration and atrophy involving thigh muscle in patients with vitamin D deficiency. A: Grade 1 (less than 30% of the volume of muscles involved); B: Grade 2 (30%-60% of the volume of muscles compromised).

tion, Figure 2 shows MRI of two different grade of fatty atrophy involving thigh muscle in patients with vitamin D deficiency. The hypothesis that arose was that atrophy of skeletal muscle fibers and their replacement by fat tissue are the anatomic basis for the impairment in muscular performance described in older vitamin D-deficient people^[4]. It may supposed that fatty substitution related to vitamin D deficiency may be the result of the lack of the known trophic effects of vitamin D on skeletal muscle cells^[4]. If the thigh muscles are affected, the lack of enough muscular bulk may hamper balance and gait. Clinical scores were concordant with this observation. Concerning technical MRI protocols we suppose that a standard, patient-friendly protocol, including T1 and T2 weighted sequences may be sufficient for the follow-up of elderly people with potential vitamin D deficiency. In another study of 366 older patients receiving MRI of one shoulder for the investigation of potential rotator cuff injury, a correlation between higher fatty infiltration

of rotator cuff muscles and lower serum levels of 25D was reported^[22]. After multivariate linear regression analysis, this association remained statistically significant in two muscle groups (*i.e.*, supraspinatus and infraspinatus muscles) but only among those whose MRI also demonstrated a full-thickness rotator cuff tear (228 patients).

Conventional MRI shows distribution pattern of fatty degeneration and it can be used for disease monitoring after treatment. Moreover, MRI allows standardize image protocols that can be useful to engage diagnostic or monitoring multi-centric trials.

New MRI sequences such as diffusion, perfusion and spectroscopy may improve the role of MRI in muscular evaluation of vitamin D role. In particular, spectroscopy magnetic resonance spectroscopy (MRS) may provide metabolic information on the musculoskeletal system. Phosphorus-31 MRS (31P-MRS) is a noninvasive technique that allows observation of mitochondrial function and oxidative phosphorylation *in vivo*. Based on the hy-

pothesis that a suboptimal mitochondrial function may lead to myopathy in vitamin D-deficient subjects, a recent study used ³¹P-MRS to observe that cholecalciferol therapy in vitamin D-deficient subjects improved both mitochondrial oxidative function and symptoms of myopathy and fatigue^[23]; this result represented a direct sign of a link between vitamin D and mitochondria in skeletal muscle. Therefore, MRS lead to improve knowledge about vitamin D effects on skeletal muscle.

CONCLUSION

Many studies examined the specific effects of vitamin D on muscle function and physical performance. However, a very important review stated that comparing these studies is made very difficult by the variety of outcome measures used to assess muscle function^[7]. We believe that including the role of diagnostic imaging to study the anatomy of skeletal muscle and not only its function may add new insights into vitamin D and muscle relationships. It has been suggested an association between vitamin D deficiency and structural muscle changes such as atrophy and fatty infiltration, both of which can be detected with cross-sectional imaging^[12]. However, there are several confounders as, for example, disuse, drug use and denervation. Moreover, skeletal muscle is a highly metabolic tissue that respond not only to vitamin D effects, but to a variety of hormones and factors including, but not limited to, IL-6, brain-derived neurotrophic factor, insulin, glucocorticoids, thyroid hormones^[7]. Each factor and hormone contributes and influences muscle differentiation, metabolism and function, through well known and emerging mechanisms^[7]. In addition, one of the main topic is that imaging modalities can't yet differ between extracellular fat and intracellular fat, of important pathophysiological significance^[7].

On the other hand, imaging modalities permit to monitor muscle changes in size and tissue architecture. Moreover, new imaging modalities such as MRS may improve the knowledge about the direct effects of vitamin D on skeletal muscle.

In conclusion, we believe that the use of diagnostic imaging should be strongly encouraged to have radiological outcomes added to clinical and biochemical outcomes. Additional studies are needed to determine the exact role of imaging in the care of patients with vitamin D deficiency.

REFERENCES

- 1 **Venning G.** Recent developments in vitamin D deficiency and muscle weakness among elderly people. *BMJ* 2005; **330**: 524-526 [PMID: 15746134]
- 2 **Semba RD,** Garrett E, Johnson BA, Guralnik JM, Fried LP. Vitamin D deficiency among older women with and without disability. *Am J Clin Nutr* 2000; **72**: 1529-1534 [PMID: 11101482]
- 3 **Lips P.** Vitamin D deficiency and secondary hyperparathyroidism in the elderly: consequences for bone loss and fractures and therapeutic implications. *Endocr Rev* 2001; **22**: 477-501 [PMID: 11493580]
- 4 **Tagliafico AS,** Ameri P, Bovio M, Puntoni M, Capaccio E, Murialdo G, Martinoli C. Relationship between fatty degeneration of thigh muscles and vitamin D status in the elderly: a preliminary MRI study. *AJR Am J Roentgenol* 2010; **194**: 728-734 [PMID: 20173152 DOI: 10.2214/AJR.09.3130]
- 5 **Wacker M,** Holick MF. Vitamin D - effects on skeletal and extraskeletal health and the need for supplementation. *Nutrients* 2013; **5**: 111-148 [PMID: 23306192 DOI: 10.3390/nu5010111]
- 6 **Dirks-Naylor AJ,** Lennon-Edwards S. The effects of vitamin D on skeletal muscle function and cellular signaling. *J Steroid Biochem Mol Biol* 2011; **125**: 159-168 [PMID: 21397021 DOI: 10.1016/j.jsbmb.2011.03.003]
- 7 **Girgis CM,** Clifton-Bligh RJ, Hamrick MW, Holick MF, Gunton JE. The roles of vitamin D in skeletal muscle: form, function, and metabolism. *Endocr Rev* 2013; **34**: 33-83 [PMID: 23169676 DOI: 10.1210/er.2012-1012]
- 8 **Redzic M,** Lewis RM, Thomas DT. Relationship between 25-hydroxyvitamin D, muscle strength, and incidence of injury in healthy adults: a systematic review. *Nutr Res* 2013; **33**: 251-258 [PMID: 23602241 DOI: 10.1016/j.nutres.2013.02.007]
- 9 **Tagliafico A,** Bignotti B, Airaldi S, Martinoli C. Correlation of Skeletal Muscle Anatomy to MRI and US Findings. In: Weber MA. *Magnetic Resonance Imaging of the Skeletal Musculature.* Berlin Heidelberg: Springer, 2014: 27-39
- 10 **Martinoli C,** Airaldi A, Bignotti B, Tagliafico A. Imaging the Skeletal Muscle: When to Use MR imaging and When to Use Ultrasound. In: Weber MA. *Magnetic Resonance Imaging of the Skeletal Musculature.* Berlin Heidelberg: Springer, 2014: 41-52
- 11 **Strasser EM,** Draskovits T, Praschak M, Quittan M, Graf A. Association between ultrasound measurements of muscle thickness, pennation angle, echogenicity and skeletal muscle strength in the elderly. *Age (Dordr)* 2013; **35**: 2377-2388 [PMID: 23456136 DOI: 10.1007/s11357-013-9517-z]
- 12 **Fischer D,** Wattjes MP. MRI in Muscle Dystrophies and Primary Myopathies. In: Weber MA. *Magnetic Resonance Imaging of the Skeletal Musculature.* Berlin Heidelberg: Springer, 2014: 241-254
- 13 **Cruz-Jentoft AJ,** Baeyens JP, Bauer JM, Boirie Y, Cederholm T, Landi F, Martin FC, Michel JP, Rolland Y, Schneider SM, Topinková E, Vandewoude M, Zamboni M. Sarcopenia: European consensus on definition and diagnosis: Report of the European Working Group on Sarcopenia in Older People. *Age Ageing* 2010; **39**: 412-423 [PMID: 20392703 DOI: 10.1093/ageing/afq034]
- 14 **Heckmatt JZ,** Leeman S, Dubowitz V. Ultrasound imaging in the diagnosis of muscle disease. *J Pediatr* 1982; **101**: 656-660 [PMID: 7131136]
- 15 **Mayans D,** Cartwright MS, Walker FO. Neuromuscular ultrasonography: quantifying muscle and nerve measurements. *Phys Med Rehabil Clin N Am* 2012; **23**: 133-48, xii [PMID: 22239880 DOI: 10.1016/j.pmr.2011.11.009]
- 16 **Pillen S,** Tak RO, Zwarts MJ, Lammens MM, Verrijp KN, Arts IM, van der Laak JA, Hoogerbrugge PM, van Engelen BG, Verrips A. Skeletal muscle ultrasound: correlation between fibrous tissue and echo intensity. *Ultrasound Med Biol* 2009; **35**: 443-446 [PMID: 19081667 DOI: 10.1016/j.ultrasmed-bio.2008.09.016]
- 17 **Drakonaki EE,** Allen GM, Wilson DJ. Ultrasound elastography for musculoskeletal applications. *Br J Radiol* 2012; **85**: 1435-1445 [PMID: 23091287 DOI: 10.1259/bjr/93042867]
- 18 **Dahlman I,** Gerdhem P, Bergström I. Vitamin D status and bone health in immigrant versus Swedish women during pregnancy and the post-partum period. *J Musculoskelet Neurol Interact* 2013; **13**: 464-469 [PMID: 24292616]
- 19 **Daguet E,** Jolivet E, Bousson V, Boutron C, Dahmen N, Bergot C, Vicaut E, Laredo JD. Fat content of hip muscles: an anteroposterior gradient. *J Bone Joint Surg Am* 2011; **93**: 1897-1905 [PMID: 22012527 DOI: 10.2106/JBJS.J.00509]
- 20 **Busse B,** Bale HA, Zimmermann EA, Panganiban B, Barth

- HD, Carriero A, Vettorazzi E, Zustin J, Hahn M, Ager JW, Püschel K, Amling M, Ritchie RO. Vitamin D deficiency induces early signs of aging in human bone, increasing the risk of fracture. *Sci Transl Med* 2013; **5**: 193ra88 [PMID: 23843449 DOI: 10.1126/scitranslmed.3006286]
- 21 **Marantes I**, Achenbach SJ, Atkinson EJ, Khosla S, Melton LJ, Amin S. Is vitamin D a determinant of muscle mass and strength? *J Bone Miner Res* 2011; **26**: 2860-2871 [PMID: 21915904 DOI: 10.1002/jbmr.510]
- 22 **Oh JH**, Kim SH, Kim JH, Shin YH, Yoon JP, Oh CH. The level of vitamin D in the serum correlates with fatty degeneration of the muscles of the rotator cuff. *J Bone Joint Surg Br* 2009; **91**: 1587-1593 [PMID: 19949122]
- 23 **Sinha A**, Hollingsworth KG, Ball S, Cheetham T. Improving the vitamin D status of vitamin D deficient adults is associated with improved mitochondrial oxidative function in skeletal muscle. *J Clin Endocrinol Metab* 2013; **98**: E509-E513 [PMID: 23393184 DOI: 10.1210/jc.2012-3592]

P- Reviewers: Arcangeli S, Shen J **S- Editor:** Gou SX
L- Editor: A **E- Editor:** Liu SQ



Rotator cuff disorders: How to write a surgically relevant magnetic resonance imaging report?

Ahmed M Tawfik, Ahmad El-Morsy, Mohamed Aboelnour Badran

Ahmed M Tawfik, Ahmad El-Morsy, Diagnostic and Interventional Radiology Department, Faculty of Medicine, Mansoura University, Mansoura 35112, Egypt

Mohamed Aboelnour Badran, Orthopaedic Surgery Department, Faculty of Medicine, Mansoura University, Mansoura 35112, Egypt

Author contributions: Tawfik AM, El-Morsy A and Badran MA designed the article; Tawfik AM and El-Morsy A acquired the data; Tawfik AM, El-Morsy A and Badran MA wrote the draft; Tawfik AM, El-Morsy A and Badran MA approved the final version.

Correspondence to: Ahmed M Tawfik, MD, PhD, Lecturer of Radiology and Consultant Radiologist, Diagnostic and Interventional Radiology Department, Faculty of Medicine, Mansoura University, El-Gomhoreya Street, Mansoura 35112, Egypt. ahm_m_tawfik@hotmail.com

Telephone: +20-50-2262239 Fax: +20-50-2259147

Received: December 28, 2013 Revised: April 7, 2014

Accepted: May 14, 2014

Published online: March 28, 2015

© 2015 Baishideng Publishing Group Inc. All rights reserved.

Key words: Magnetic resonance imaging; Rotator cuff tendons; Tendon tear; Review; Shoulder

Core tip: This review discusses the relevant anatomy of rotator cuff, mechanisms of rotator cuff injury, techniques of magnetic resonance imaging (MRI) used as well as all relevant MRI findings in an easy and ordered manner with illustrative figures and examples.

Original sources: Tawfik AM, El-Morsy A, Badran MA. Rotator cuff disorders: How to write a surgically relevant magnetic resonance imaging report? *World J Radiol* 2014; 6(6): 274-283 Available from: URL: <http://www.wjgnet.com/1949-8470/full/v6/i6/274.htm> DOI: <http://dx.doi.org/10.4329/wjr.v6.i6.274>

Abstract

Evaluation of rotator cuff is a common indication for magnetic resonance imaging (MRI) scanning of the shoulder. Conventional MRI is the most commonly used technique, while magnetic resonance (MR) arthrography is reserved for certain cases. Rotator cuff disorders are thought to be caused by a combination of internal and external mechanisms. A well-structured MRI report should comment on the relevant anatomic structures including the acromial type and orientation, the presence of os acromiale, acromio-clavicular degenerative spurs and fluid in the subacromial subdeltoid bursa. In addition, specific injuries of the rotator cuff tendons and the condition of the long head of biceps should be accurately reported. The size and extent of tendon tears, tendon retraction and fatty degeneration or atrophy of the muscles are all essential components of a surgically relevant MRI report.

INTRODUCTION

Rotator cuff disorders are common in the middle and old age population. They are a major cause of chronic shoulder pain. In addition, rotator cuff disorders result in loss of strength and stability of the shoulder^[1,2].

The balanced combination between accurate clinical examination, clear view of the patient's needs and disabilities and precise radiological diagnostic modalities is invaluable in the correct formulation of the treatment plan of the patient whether surgically or conservatively. Magnetic resonance imaging (MRI), which is considered by many authors the modality of choice for diagnosing rotator cuff disorders^[3,4], has a very important role in achieving this balance.

In this article, we discuss the techniques of MRI of the shoulder; the relevant rotator cuff anatomy, mechanisms of injury, and the specific imaging findings of rotator cuff disorders that are important for formulating a well-structured and complete MRI report.

MRI TECHNIQUE

MR imaging of the shoulder for evaluation of rotator cuff disorders may be carried out either conventionally (non-arthrographic), or with direct contrast distension of the joint (MR arthrography). Magnetic resonance arthrography was reported to be the most accurate imaging technique for diagnosis of both partial and full-thickness rotator cuff tears^[5,6], but is limited by invasiveness and necessity of fluoroscopic guidance for injection, and therefore not routinely used for rotator cuff disorders^[7,8]. An alternative technique, indirect MR arthrography, is a non-invasive technique using intravenous rather than intra-articular contrast to provide the arthrographic effect^[9,10]. Continuous advances in MRI field strength, gradients, and coil technology have allowed even more accuracy for conventional MRI than that reported in the early literature, and conventional MRI is still the most commonly used technique for diagnosis of rotator cuff tears^[3,11,12].

MR imaging is typically performed in the supine position with the arm by the side of the patient, in the neutral position. Images must be obtained in axial, coronal oblique and sagittal oblique planes^[13]. The sequences used may vary but typically include T1-, proton density- and T2-weighted sequences and it is recommended to have both fat-suppressed and non-fat-suppressed sequences. Additional imaging in the abduction external rotation (ABER) position of the shoulder was reported to improve sensitivity and increase diagnostic confidence for partial-thickness tears of the supraspinatus tendon^[10,14]. However, this technique is not widely spread due to difficult positioning and prolonged scan time.

ROTATOR CUFF ANATOMY

The rotator cuff consists of four muscles; the supraspinatus, infraspinatus, subscapularis and teres minor muscles. The supraspinatus muscle originates from the supraspinous fossa of the scapula and passes on the superior aspect of the humeral head to be inserted in the greater tuberosity. The infraspinatus muscle originates from the infraspinous fossa and shares a common tendinous insertion with the supraspinatus tendon on the greater tuberosity; together with the tendon of teres minor muscle^[15]. On the other hand, the subscapularis muscle originates from the subscapular fossa of the scapula and its wide tendon inserts in the lesser tuberosity, separated from the insertion of the other rotator muscles by the rotator interval.

The long head of biceps tendon is anatomically and functionally related to the rotator cuff. The tendon arises from the supraglenoid tubercle and its proximal segment (2-3 cm) is intra-articular. It exits the gleno-humeral joint and passes through the rotator interval between the subscapularis and supraspinatus tendons into the bicipital (intertubercular) groove of the proximal humerus^[16].

MECHANISMS OF ROTATOR CUFF INJURY

The exact pathophysiology of rotator cuff injury, after exclusion of acute trauma, is still not fully understood. The current understanding is that rotator cuff degeneration is caused by a multifactorial pathogenesis, including both internal and external mechanisms^[17,18].

Internal mechanisms

Those are mechanisms that originate from within the tendons in the form of degenerative processes, possibly age-related, that result in alterations in the tendon biology, morphology, vascularity and mechanical properties^[18,19].

External mechanisms

External mechanisms include the well-known impingement syndromes, of which the subacromial impingement is the commonest. Subacromial impingement is defined as entrapment of the subacromial subdeltoid bursa and the supraspinatus tendon between the coraco-acromial arch and the greater tuberosity of the humerus. The main causes of this type of impingement include abnormal acromion configuration^[20], osteoarthritis of the acromioclavicular (AC) joint and narrowed subacromial space^[21].

Another type of impingement syndromes is subcoracoid impingement; defined as entrapment of the subscapularis tendon in the coracohumeral interval (the space between the coracoid process and the anterior humerus). It is usually caused by abnormal coracoid configuration that may be congenital, traumatic or iatrogenic^[17,21].

Less common types of impingement include secondary external impingement due to glenohumeral instability in the absence of outlet stenosis of the rotator cuff tendons^[22], as well as internal impingement (intra-articular) due to compression of the articular surface of the tendons between the humeral head and glenoid^[23].

MRI FINDINGS

Acromion type

The acromion was classified according to its shape into three types (Figure 1). Type I has a flat under surface, type II a concave under surface and type three a concave under surface with anterior hook. Some authors added a further type IV to the original classification describing a convex under surface^[24,25]. The shape of acromion is best depicted on sagittal oblique MR images lateral to the AC joint plane. The most common type is type II, while type III is the one most commonly associated with rotator cuff tears where its anterior hook causes injury of the anterior fibres of the supraspinatus tendon^[26].

Acromion orientation

Normally, the acromion has no slope either anteriorly,

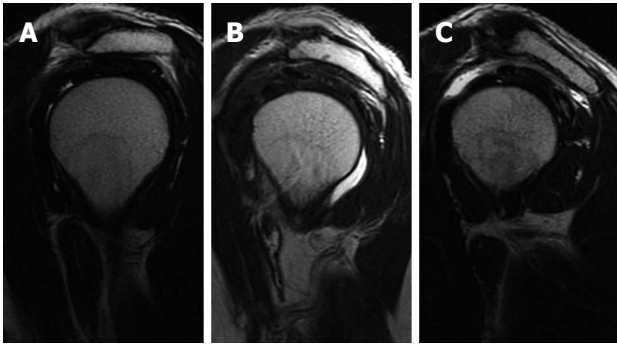


Figure 1 Acromion types. Sagittal oblique T2-weighted images of different patients showing type I flat acromion (A), type II concave under surface (B) and type III concave under surface with anterior hook (C).

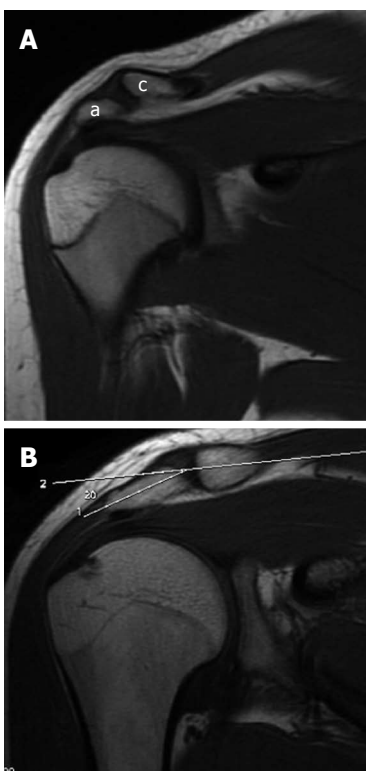


Figure 2 Acromion orientation. A: Coronal oblique T1-weighted image shows low lying acromion (a) in relation to the clavicle (c) at the Acromio-clavicular joint level; B: Coronal oblique T1-weighted image in another patient shows infero-lateral slope of the acromion. The angle between the acromion and the clavicle is tilted by 20 degrees.

laterally or inferiorly. A lateral or anterior down-sloping acromion and a low-lying acromion are thought to play a role in the development of subacromial impingement^[21].

A low-lying acromion is diagnosed when the lower acromial surface is below the lower surface of the clavicle at the AC joint level on the anterior coronal oblique MR image (Figure 2A). On the same image showing the AC joint, an infero-lateral slope is detected by measuring the angle between the acromion axis and the clavicle (Figure 2B); an angle more than 10 degrees is abnormal^[27]. An anterior slope is diagnosed on sagittal oblique images when the anterior part of the acromion is closer to the

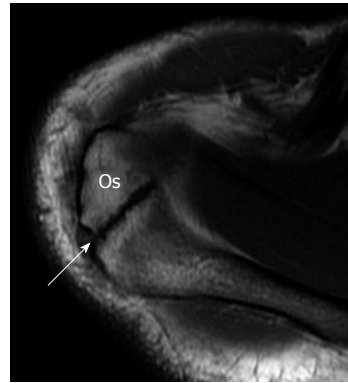


Figure 3 Os acromiale. Axial T1-weighted image showing the os acromiale.

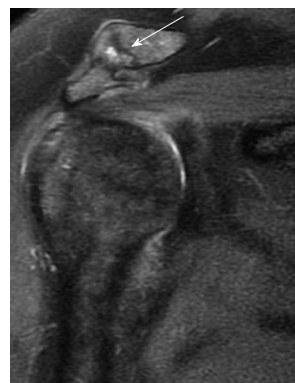


Figure 4 Acromio-clavicular joint osteoarthritis. Coronal oblique fat-sat proton-density-weighted image shows degenerative changes of the acromio-clavicular joint (arrow) in a patient with rotator cuff tear.

related part of the humeral convexity than its posterior part.

Os acromiale

The acromion is formed from multiple ossification centres with complete fusion between the ages of 22 and 25 years. If one of the ossification centres fails to fuse, an accessory ossicle is formed; the os acromiale^[28]. The os acromiale is mobile and is thought to contribute to impingement, but the reported incidence in normal population is between 1% and 15%^[28]. It is best assessed in the upper axial images (Figure 3) where a low signal space is detected between the high signal marrow of the distal acromion and the non-fused ossicle^[25]. On coronal oblique images it can be suspected by the presence of the so called “double AC joint”; the normal AC joint appears on the anterior image and the pseudo-articulation of the os acromiale appears on the posterior one^[27].

AC joint

Osteoarthritis of the AC joint (Figure 4) is a common finding in patients with rotator cuff disorders. However, its role in impingement remains unclear and could either be a risk factor for impingement or a result of rotator cuff injury and disturbed shoulder biomechanics. A large osteophyte arising from the inferior surface of

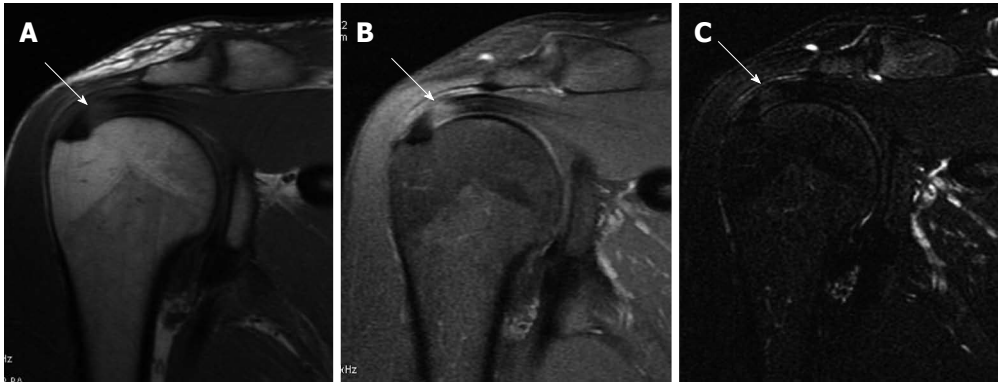


Figure 5 Supraspinatus tendinosis. A: Coronal oblique T1-weighted image. B: Coronal oblique fat-sat proton-density image. Images (A) and (B) show focal high signal intensity within the distal supraspinatus tendon (arrow); C: Coronal oblique fat-sat T2-weighted image shows focal high signal at the same site within supraspinatus tendon (arrow). Final diagnosis was tendinosis.



Figure 6 Partial interstitial supraspinatus tendon tear. Coronal oblique fat-sat proton-density-weighted image showing focal high signal within the supraspinatus tendon fibres (arrow). Also note the associated high signal intensity fluid in the subacromial subdeltoid bursa.

the joint is thought to be a cause of tendon tear^[29]. MRI is more sensitive than radiography for detection of AC joint degenerative disease. MRI can differentiate joint enlargement due to capsular hypertrophy (intermediate signal intensity) from joint effusion (bright signal on T2-weighted images). Osteophytes appear in late stages of the disease^[30].

Subacromial subdeltoid bursa

The subacromial subdeltoid bursa is a synovial lined structure between the acromion and deltoid muscle externally and the rotator cuff tendons internally. The subacromial and subdeltoid components are connected in 95% of individuals. Normally it is not connected with the joint space but communication occurs in association with full thickness supraspinatus tears^[31,32].

The normal bursa usually does not exceed 2 mm in thickness and is usually located posteriorly. On coronal MRI, features suggesting abnormal amount of fluid include thickness of fluid signal more than 3 mm, fluid signal medial to the level of the AC joint, and fluid in the anterior part of the bursa^[33].

Rotator cuff tendons and specific injuries

Tendinitis and tendinosis: Tendinitis and tendinosis typically appear as focal areas of increased signal intensity on proton density weighted images, that is less than that of fluid on T2-weighted images (Figure 5). Chronic forms are associated with thickening (tendinosis)^[34].

Partial thickness tear: A partial thickness tear appears on fat-suppressed T2-weighted MR images as fluid signal intensity with thinning, or an incomplete gap, in the tendon^[3]. The supraspinatus tendon is usually about 12 mm in average cranio-caudal thickness. Partial thickness tears are classified according to their depth into either grade I, in which less than one fourth of the fibres is torn; grade II, when more than one fourth and less than half of the tendon thickness is torn and grade III, when more than half of the tendon thickness is torn^[24,35].

According to the tear site, partial thickness tears of the supraspinatus tendon are classified into bursal; articular surface or intra-tendinous tears (Figure 6). Articular surface tears are more common^[35].

Full thickness tear: A full-thickness tendon tear appears as a focal, well-defined area of increased signal intensity on both T1- and T2-weighted images (Figure 7), that traverses the whole thickness of the tendon from the bursal to the articular surface^[7,36].

Full-thickness tendon tears are classified according to the tear dimensions as small (less than 1 cm), medium (between 1 and 3 cm), large (between 3 and 5 cm) or massive (exceeding 5 cm)^[24]. The dimensions are measured on coronal and sagittal T2 fat-suppressed images^[37].

The degree of retraction of the torn supraspinatus tendon is typically assessed on coronal oblique images. When the tendon stump is still close to the insertion site, it is classified as stage 1. A stump retracted to the level of the humeral head is classified as stage 2, while stage 3 denotes retraction of the stump to the level of the glenoid^[38,39].

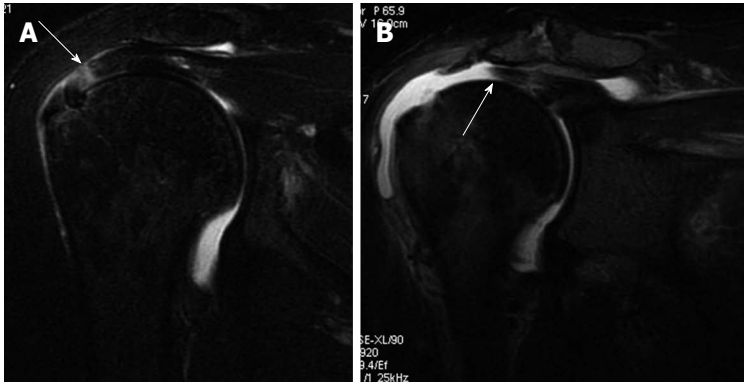


Figure 7 Full-thickness supraspinatus tendon tears in two different patients. A: Coronal oblique fat-sat T2-weighted image shows full-thickness supraspinatus tendon tear without significant tendinous retraction (arrow); B: Coronal oblique fat-sat T2-weighted image in another patient shows torn retracted supraspinatus tendon (arrow).

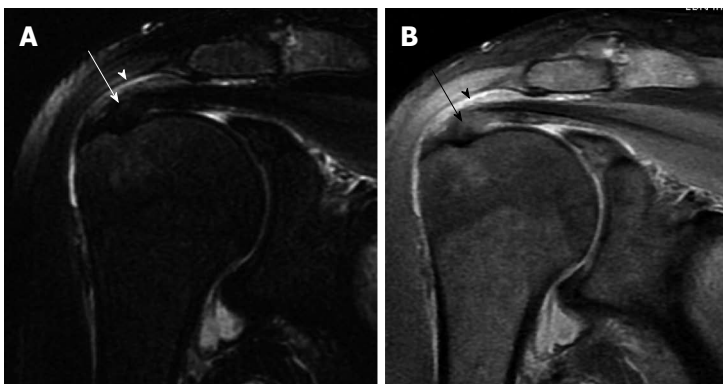


Figure 8 Subacromial impingement. A: Coronal oblique fat-sat T2-weighted image; B: Coronal oblique fat-sat proton-density-weighted image. Both images show findings associated with subacromial impingement in the form of osteoarthritis of the acromio-clavicular joint, distended subacromial subdeltoid bursa by fluid signal (arrowhead) and focal thickening of the distal supraspinatus tendon with partial irregularity of the bursal surface reported as partial tear (arrow).



Figure 9 Magic angle artifact. A: Coronal oblique T1-weighted image. B: Coronal oblique fat-sat proton-density image. Images (A) and (B) show focal high signal intensity within the distal supraspinatus tendon (arrow); C: Coronal oblique fat-sat T2-weighted image shows normal signal of the supraspinatus tendon (arrow). Final diagnosis was magic angle artifact with normal tendon.

Supraspinatus tendon: The most common site for rotator cuff tears is the supraspinatus tendon, especially at its distal part 1 to 2 cm from its insertion, the so called “critical zone”, where the vascularity is low and the effect of subacromial space narrowing or subacromial impingement is maximized (Figure 8)^[26].

The supraspinatus tendon is best evaluated on the

coronal oblique images. A potential pitfall is the magic angle artefact (Figure 9); that may occur whenever parallel collagen fibres are oriented at 55 degrees relative to the magnetic field. This effect is common at the distal end of the supraspinatus tendon and appears as high signal mimicking tendinitis or partial tear on short time of echo (TE) MR sequences. However, the high signal intensity

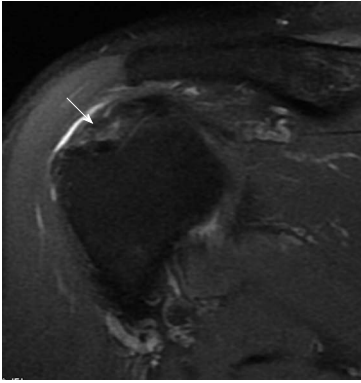


Figure 10 Infraspinatus tendinosis. Posterior coronal oblique fat-sat proton-density-weighted image showing focal thickening of the infraspinatus tendon fibres with abnormal high signal diagnosed as tendinosis (arrow). Also note fluid signal within the subacromial subdeltoid bursa.

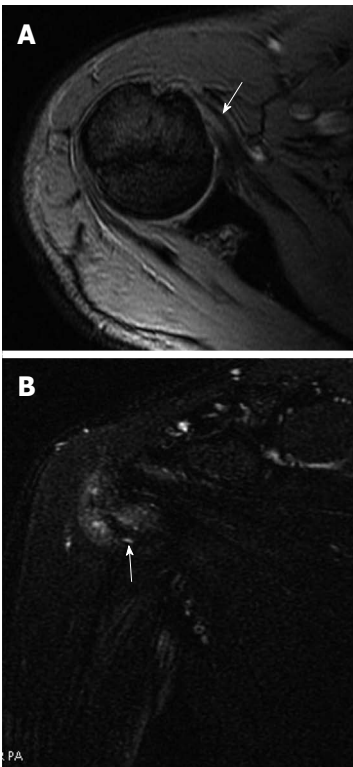


Figure 11 Subscapularis tendinosis. A: Axial gradient-recalled echo image showing focal high signal within the subscapularis tendon with fibres thickening (arrow); B: Anterior coronal oblique fat-sat T2-weighted image of the same patient showing high signal within the lower fibres of the subscapularis tendon (arrow).

disappears on using long TE sequences; for example T2 fat-suppressed sequence^[25].

Infraspinatus tendon: The infraspinatus tendon is most commonly torn as an extension from supraspinatus tear (postero-superior cuff tear)^[39]. The infraspinatus tendon is best evaluated on posterior coronal oblique fat-suppressed T2-weighted or STIR images (Figure 10). A second look may also be carried out on the upper axial images as well as on sagittal images^[13].

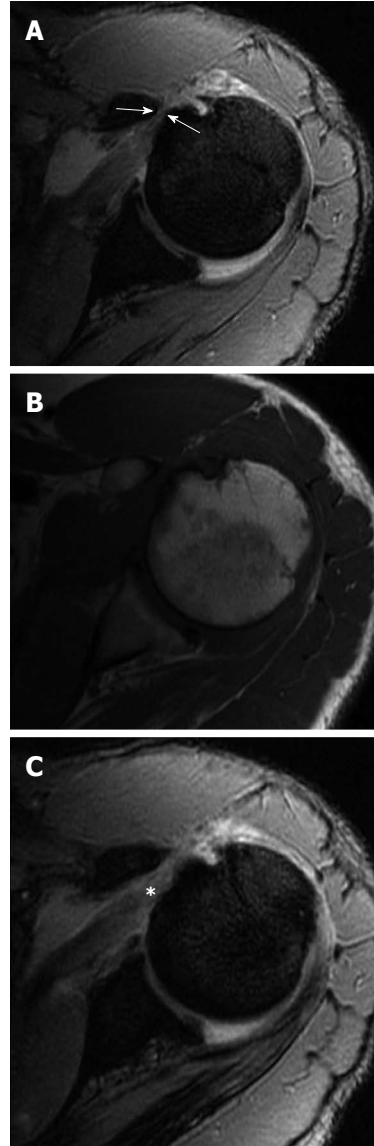


Figure 12 Sub-coracoid impingement. A and C: Axial gradient-recalled echo images; B: Axial T1-weighted image showing narrowed coraco-humeral distance (arrows in A) with tapered coracoid process, thickening and abnormal high signal of the subscapularis tendon (asterisk in C).

Subscapularis tendon: Subscapularis tendon tears may occur as a component of massive rotator cuff tears^[40,41]. The tendinous part of the subscapularis tendon is the broadest tendon among the rotator cuff and therefore commonly affected by tears and tendinitis (Figure 11).

The subscapularis tendon may be affected in isolation in traumatic injury^[41]. Subcoracoid impingement, which is a cause of subscapularis degenerative tears (Figure 12), is suspected when the distance between the coracoid process and the lesser tuberosity of the humerus is less than 6 mm on axial MR images^[21,42]. Other reported associated MRI signs include subcortical bone marrow edema of the coracoid process and lesser tuberosity of the humerus.

Teres minor tendon: The teres minor tendon is the least injured among rotator cuff tendons^[43]. The teres minor

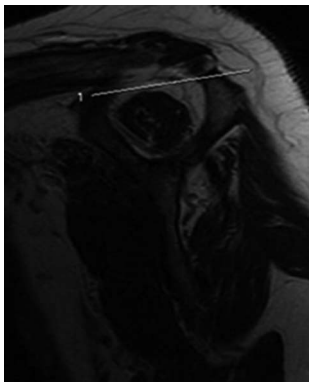


Figure 13 Supraspinatus muscle atrophy, tangent sign. Sagittal oblique T1-weighted image showing the upper border of supraspinatus muscle below the line extending between the scapular plate and spine.

tendon is best evaluated on posterior coronal oblique and axial MR images and to less extent on sagittal images.

Muscle atrophy and fatty degeneration

Atrophy of the supraspinatus muscle could be assessed by calculating the occupation ratio of the supraspinatus fossa. On the most lateral oblique sagittal image, atrophy of the supraspinatus muscle is diagnosed if the supraspinatus muscle occupies less than half the area of the fossa^[44,45].

The tangent sign (Figure 13) describes an additional straight line drawn from the top of the coracoid process to the top of the spine of the scapula on the same oblique sagittal image as above. Atrophy is diagnosed when the superior border of the muscle lies below the tangent line^[24,45,46].

Fatty degeneration of the supraspinatus muscles could be assessed on the T1-weighted oblique sagittal image in which the spine and body of the scapula appear. Fatty degeneration could be classified as either low (grade 0; no fat or grade 1; some fatty streaks) or moderate (grade 2; muscle > fat) or advanced (grade 3; muscle = fat and grade 4; muscle < fat)^[47-49].

Long head biceps tendon

MR evaluation of the intra-articular segment of the long head biceps tendon (LHBT) is best carried out on both oblique sagittal and oblique coronal images, while the extra-articular segment is best evaluated on axial images. The LHBT tendon is covered with a synovial sheath connected with the joint space along its course within the bicipital groove^[30,50]. Therefore, fluid signal around the tendon may be seen in cases of joint effusion, nevertheless in proportionate amount, and should not be mistaken for tenosynovitis. Tenosynovitis of the LHBT is diagnosed if fluid is detected around the tendon only or if the amount of fluid around the tendon is clearly out of proportion to that in the glenohumeral joint^[51]. Tendinosis of the LHBT is suspected when focal thickening and high signal (but less than that of fluid) of the tendon

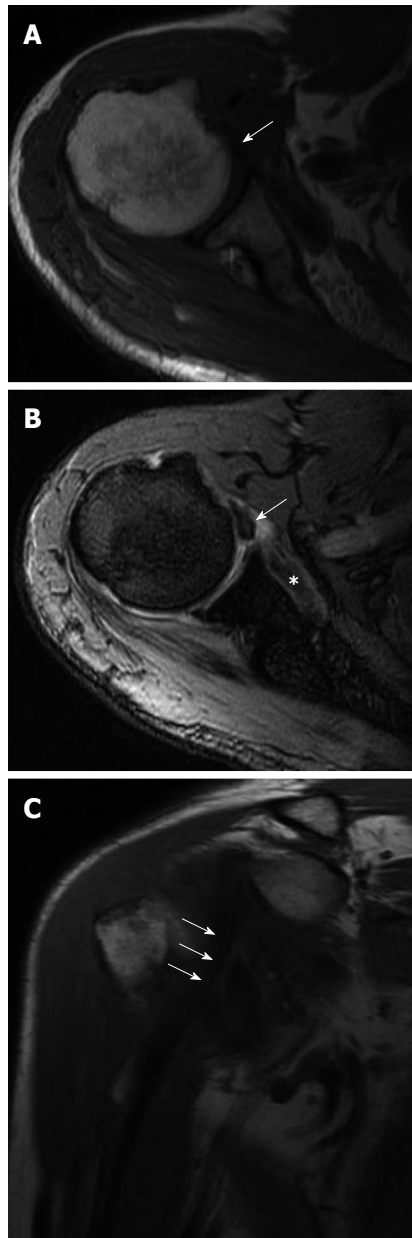


Figure 14 Subscapularis tendon avulsion with long head of biceps tendon dislocation. A: Axial T1-weighted image; B: Axial gradient-recalled echo image; C: Coronal oblique T1-weighted images showing avulsion of the subscapularis tendon (asterisk in B) with muscular atrophy and long head biceps tendon dislocation (arrows) with diffuse tendinous thickening and high signal.

or part of it is noted, usually associated with fluid signal within the synovial covering^[52]. The most commonly affected part is the supra-humeral portion or the horizontal part and it may be a result of impingement. Tears of the LHBT vary from partial to complete tear to tendon avulsion. Tears appear as focal areas of high signal intensity, similar to that of fluid on T2-weighted images. Avulsion is diagnosed by noting the absence of the intra-articular segment of the tendon with no signs of dislocation. A dislocated LHBT (Figure 14) is often medially displaced, and is commonly associated with subscapularis tendon tear^[50-52].

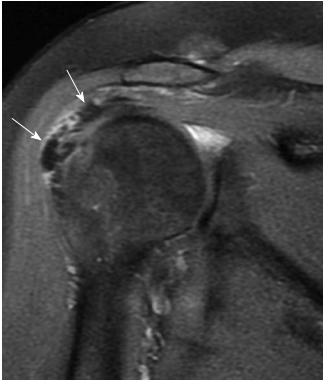


Figure 15 Calcific tendinopathy. Coronal oblique fat-sat proton-density-weighted image showing focal areas of signal void (calcifications) within the distal supraspinatus tendon fibres (arrows). Diagnosis was confirmed by ultrasonography.

Other findings

Bony changes: Erosions and degenerative changes of the lateral aspect of the greater tuberosity of the humerus (Figure 15) are common associated findings in rotator cuff disorders^[30]. This finding is important for surgical planning as it significantly decreases the hold of anchors used during repair of torn rotator cuff tendons.

Calcific tendinopathy: Calcific tendinopathy most commonly affects the supraspinatus tendon, less commonly the infraspinatus and other tendons. On MRI, calcifications typically appear as focal areas of signal void on all spin echo sequences (Figure 16), and is usually difficult to detect within the natively low signal tendon^[7,53]. The area of signal void increases on gradient-recalled echo sequence due to susceptibility effects^[30].

CONCLUSION

Evaluation of rotator cuff disorders is one of the commonest indications for magnetic resonance (MR) imaging of the shoulder. Complete and accurate interpretation of MR images is essential to provide the treating clinician with adequate information for choosing the best therapy and avoiding unnecessary interventions. Radiologists should be familiar with the technique of MRI of the shoulder, the anatomy of the rotator cuff and the mechanisms of rotator cuff injury. A well-structured MRI report should include full comment on the rotator cuff tendons and all other relevant structures.

REFERENCES

- 1 Meislin RJ, Sperling JW, Stitik TP. Persistent shoulder pain: epidemiology, pathophysiology, and diagnosis. *Am J Orthop (Belle Mead NJ)* 2005; **34**: 5-9 [PMID: 16450690]
- 2 Burbank KM, Stevenson JH, Czarnecki GR, Dorfman J. Chronic shoulder pain: part I. Evaluation and diagnosis. *Am Fam Physician* 2008; **77**: 453-460 [PMID: 18326164]
- 3 Magee T, Williams D. 3.0-T MRI of the supraspinatus tendon. *AJR Am J Roentgenol* 2006; **187**: 881-886 [PMID: 16985129

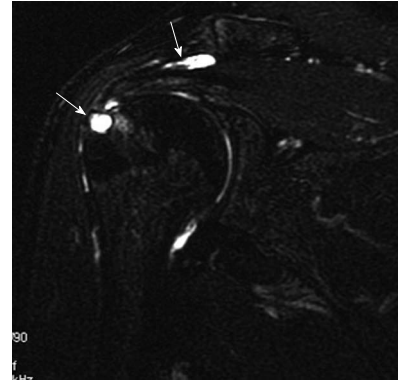


Figure 16 Bony degenerative changes. Coronal oblique fat-sat T2-weighted image showing focal fluid-like high signal within the distal supraspinatus tendon fibres reported as partial capsular surface tear with subcortical cystic erosion of the greater tuberosity at the rotator cuff insertion (thin arrow). Also note fluid signal within the subacromial subdeltoid bursa reported as bursitis (thick arrow).

- DOI: 10.2214/AJR.05.1047]
- 4 Tuite MJ. Magnetic resonance imaging of rotator cuff disease and external impingement. *Magn Reson Imaging Clin N Am* 2012; **20**: 187-200, ix [PMID: 22469399 DOI: 10.1016/j.mric.2012.01.011]
 - 5 Waldt S, Bruegel M, Mueller D, Holzapfel K, Imhoff AB, Rummeny EJ, Woertler K. Rotator cuff tears: assessment with MR arthrography in 275 patients with arthroscopic correlation. *Eur Radiol* 2007; **17**: 491-498 [PMID: 16969638 DOI: 10.1007/s00330-006-0370-7]
 - 6 de Jesus JO, Parker L, Frangos AJ, Nazarian LN. Accuracy of MRI, MR arthrography, and ultrasound in the diagnosis of rotator cuff tears: a meta-analysis. *AJR Am J Roentgenol* 2009; **192**: 1701-1707 [PMID: 19457838 DOI: 10.2214/AJR.08.1241]
 - 7 Teh J. Imaging of shoulder pathology. *Orthopaedics and Trauma* 2011; **25**: 19-29 [DOI: 10.1016/j.morth.2010.03.008]
 - 8 Jana M, Gamanagatti S. Magnetic resonance imaging in glenohumeral instability. *World J Radiol* 2011; **3**: 224-232 [PMID: 22007285 DOI: 10.4329/wjr.v3.i9.224]
 - 9 Yagci B, Manisali M, Yilmaz E, Ozkan M, Ekin A, Ozaksoy D, Kovanlikaya I. Indirect MR arthrography of the shoulder in detection of rotator cuff ruptures. *Eur Radiol* 2001; **11**: 258-262 [PMID: 11218024 DOI: 10.1007/s003300000546]
 - 10 Herold T, Bachthaler M, Hamer OW, Hente R, Feuerbach S, Fellner C, Strotzer M, Lenhart M, Paetzel C. Indirect MR arthrography of the shoulder: use of abduction and external rotation to detect full- and partial-thickness tears of the supraspinatus tendon. *Radiology* 2006; **240**: 152-160 [PMID: 16709790 DOI: 10.1148/radiol.2393050453]
 - 11 Dinnes J, Loveman E, McIntyre L, Waugh N. The effectiveness of diagnostic tests for the assessment of shoulder pain due to soft tissue disorders: a systematic review. *Health Technol Assess* 2003; **7**: iii, 1-166 [PMID: 14567906]
 - 12 Foad A, Wijdicks CA. The accuracy of magnetic resonance imaging and magnetic resonance arthrogram versus arthroscopy in the diagnosis of subscapularis tendon injury. *Arthroscopy* 2012; **28**: 636-641 [PMID: 22281195 DOI: 10.1016/j.arthro.2011]
 - 13 Farshad-Amacker NA, Jain Palrecha S, Farshad M. The primer for sports medicine professionals on imaging: the shoulder. *Sports Health* 2013; **5**: 50-77 [PMID: 24381700 DOI: 10.1177/1941738112468265]
 - 14 Schreinemachers SA, van der Hulst VP, Willems WJ, Bipat S, van der Woude HJ. Detection of partial-thickness supraspinatus tendon tears: is a single direct MR arthrography series in ABER position as accurate as conventional MR arthrography? *Skeletal Radiol* 2009; **38**: 967-975 [PMID: 19294377 DOI:

- 10.1007/s00256-009-0680-3]
- 15 **Mochizuki T**, Sugaya H, Uomizu M, Maeda K, Matsuki K, Sekiya I, Muneta T, Akita K. Humeral insertion of the supraspinatus and infraspinatus. New anatomical findings regarding the footprint of the rotator cuff. *J Bone Joint Surg Am* 2008; **90**: 962-969 [PMID: 18451386 DOI: 10.2106/JBJS.G.00427]
 - 16 **Denard PJ**, Dai X, Hanypsiak BT, Burkhart SS. Anatomy of the biceps tendon: implications for restoring physiological length-tension relation during biceps tenodesis with interference screw fixation. *Arthroscopy* 2012; **28**: 1352-1358 [PMID: 22925883 DOI: 10.1016/j.arthro.2012.04.143]
 - 17 **Seagger RM**, Wallace AL. Degenerative rotator cuff disease and impingement. *Orthopaedics and Trauma* 2011; **25**: 1-10 [DOI: 10.1016/j.mporth.2010.08.005]
 - 18 **Seitz AL**, McClure PW, Finucane S, Boardman ND, Michener LA. Mechanisms of rotator cuff tendinopathy: intrinsic, extrinsic, or both? *Clin Biomech (Bristol, Avon)* 2011; **26**: 1-12 [PMID: 20846766 DOI: 10.1016/j.clinbiomech.2010.08.001]
 - 19 **Via AG**, De Cupis M, Spoliti M, Oliva F. Clinical and biological aspects of rotator cuff tears. *Muscles Ligaments Tendons J* 2013; **3**: 70-79 [PMID: 23888289 DOI: 10.11138/mltj/2013.3.2.070]
 - 20 **Balke M**, Schmidt C, Dedy N, Banerjee M, Bouillon B, Liem D. Correlation of acromial morphology with impingement syndrome and rotator cuff tears. *Acta Orthop* 2013; **84**: 178-183 [PMID: 23409811 DOI: 10.3109/17453674.2013.773413]
 - 21 **Mulyadi E**, Harish S, O'Neill J, Rebello R. MRI of impingement syndromes of the shoulder. *Clin Radiol* 2009; **64**: 307-318 [PMID: 19185661 DOI: 10.1016/j.crad.2008.08.013]
 - 22 **Cowderoy GA**, Lisle DA, O'Connell PT. Overuse and impingement syndromes of the shoulder in the athlete. *Magn Reson Imaging Clin N Am* 2009; **17**: 577-93, v [PMID: 19887291 DOI: 10.1016/j.mric.2009.06.003]
 - 23 **Giaroli EL**, Major NM, Higgins LD. MRI of internal impingement of the shoulder. *AJR Am J Roentgenol* 2005; **185**: 925-929 [PMID: 16177410]
 - 24 **Morag Y**, Jacobson JA, Miller B, De Maeseneer M, Girish G, Jamadar D. MR imaging of rotator cuff injury: what the clinician needs to know. *Radiographics* 2006; **26**: 1045-1065 [PMID: 16844931 DOI: 10.1148/rg.264055087]
 - 25 **Fitzpatrick D**, Walz DM. Shoulder MR imaging normal variants and imaging artifacts. *Magn Reson Imaging Clin N Am* 2010; **18**: 615-632 [PMID: 21111969 DOI: 10.1016/j.mric.2010.07.006]
 - 26 **Khan Y**, Nagy MT, Malal J, Waseem M. The painful shoulder: shoulder impingement syndrome. *Open Orthop J* 2013; **7**: 347-351 [PMID: 24082973 DOI: 10.2174/1874325001307010347]
 - 27 **Stabler A**. Impingement and Rotator Cuff Disease. In: Davies AM, Hodler J, editors. *Imaging of the Shoulder: Techniques and Applications*. 1st ed. Berlin Heidelberg: Springer-Verlag, 2004: 121-159
 - 28 **Boehm TD**, Rolf O, Martetschlaeger F, Kenn W, Gohlke F. Rotator cuff tears associated with os acromiale. *Acta Orthop* 2005; **76**: 241-244 [PMID: 16097551 DOI: 10.1080/00016470510030643]
 - 29 **Roidis NT**, Motamed S, Vaishnav S, Ebramzadeh E, Karachalios TS, Itamura JM. The influence of the acromioclavicular joint degeneration on supraspinatus outlet impingement and the acromion shape. *J Orthop Surg (Hong Kong)* 2009; **17**: 331-334 [PMID: 20065375]
 - 30 **Vahlensieck M**. MRI of the shoulder. *Eur Radiol* 2000; **10**: 242-249 [PMID: 10663753 DOI: 10.1007/s003300050040]
 - 31 **van Holsbeeck M**, Strouse PJ. Sonography of the shoulder: evaluation of the subacromial-subdeltoid bursa. *AJR Am J Roentgenol* 1993; **160**: 561-564 [PMID: 8430553 DOI: 10.2214/ajr.160.3.8430553]
 - 32 **Prececutti M**, Garioni E, Madonia L, Draghi F. US anatomy of the shoulder: Pictorial essay. *J Ultrasound* 2010; **13**: 179-187 [PMID: 23396832 DOI: 10.1016/j.jus.2010.10.005]
 - 33 **White EA**, Schweitzer ME, Haims AH. Range of normal and abnormal subacromial/subdeltoid bursa fluid. *J Comput Assist Tomogr* 2006; **30**: 316-320 [PMID: 16628056 DOI: 10.1097/00004728-200603000-00030]
 - 34 **Sein ML**, Walton J, Linklater J, Harris C, Dugal T, Appleyard R, Kirkbride B, Kuah D, Murrell GA. Reliability of MRI assessment of supraspinatus tendinopathy. *Br J Sports Med* 2007; **41**: e9 [PMID: 17289860 DOI: 10.1136/bjsm.2006.034421]
 - 35 **Finnan RP**, Crosby LA. Partial-thickness rotator cuff tears. *J Shoulder Elbow Surg* 2010; **19**: 609-616 [PMID: 20171904 DOI: 10.1016/j.jse.2009.10.017]
 - 36 **Reinus WR**, Shady KL, Mirowitz SA, Totty WG. MR diagnosis of rotator cuff tears of the shoulder: value of using T2-weighted fat-saturated images. *AJR Am J Roentgenol* 1995; **164**: 1451-1455 [PMID: 7754891 DOI: 10.2214/ajr.164.6.7754891]
 - 37 **Dwyer T**, Razmjou H, Henry P, Gosselin-Fournier S, Holtby R. Association between pre-operative magnetic resonance imaging and reparability of large and massive rotator cuff tears. *Knee Surg Sports Traumatol Arthrosc* 2013; Epub ahead of print [PMID: 24170190 DOI: 10.1007/s00167-013-2745-z]
 - 38 **Patte D**. Classification of rotator cuff lesions. *Clin Orthop Relat Res* 1990; **(254)**: 81-86 [PMID: 2323151]
 - 39 **Cooper A**, Ali A. Rotator cuff tears. *Surgery* 2013; **31**: 168-171 [DOI: 10.1016/j.mpsur.2013.01.017]
 - 40 **Bergin D**, Parker L, Zoga A, Morrison W. Abnormalities on MRI of the subscapularis tendon in the presence of a full-thickness supraspinatus tendon tear. *AJR Am J Roentgenol* 2006; **186**: 454-459 [PMID: 16423952]
 - 41 **Lyons RP**, Green A. Subscapularis tendon tears. *J Am Acad Orthop Surg* 2005; **13**: 353-363 [PMID: 16148361]
 - 42 **Richards DP**, Burkhart SS, Campbell SE. Relation between narrowed coracohumeral distance and subscapularis tears. *Arthroscopy* 2005; **21**: 1223-1228 [PMID: 16226651 DOI: 10.1016/j.arthro.2005.06.015]
 - 43 **Melis B**, DeFranco MJ, Lädermann A, Barthelemy R, Walch G. The teres minor muscle in rotator cuff tendon tears. *Skeletal Radiol* 2011; **40**: 1335-1344 [PMID: 21604212 DOI: 10.1007/s00256-011-1178-3]
 - 44 **Thomazeau H**, Rolland Y, Lucas C, Duval JM, Langlais F. Atrophy of the supraspinatus belly. Assessment by MRI in 55 patients with rotator cuff pathology. *Acta Orthop Scand* 1996; **67**: 264-268 [PMID: 8686465 DOI: 10.3109/17453679608994685]
 - 45 **Moosmayer S**, Tariq R, Stiris MG, Smith HJ. MRI of symptomatic and asymptomatic full-thickness rotator cuff tears. A comparison of findings in 100 subjects. *Acta Orthop* 2010; **81**: 361-366 [PMID: 20450423 DOI: 10.3109/17453674.2010.483993]
 - 46 **Zanetti M**, Gerber C, Hodler J. Quantitative assessment of the muscles of the rotator cuff with magnetic resonance imaging. *Invest Radiol* 1998; **33**: 163-170 [PMID: 9525755 DOI: 10.1097/00004424-199803000-00006]
 - 47 **Goutallier D**, Postel JM, Bernageau J, Lavau L, Voisin MC. Fatty muscle degeneration in cuff ruptures. Pre- and post-operative evaluation by CT scan. *Clin Orthop Relat Res* 1994; **(304)**: 78-83 [PMID: 8020238]
 - 48 **Fuchs B**, Weishaupt D, Zanetti M, Hodler J, Gerber C. Fatty degeneration of the muscles of the rotator cuff: assessment by computed tomography versus magnetic resonance imaging. *J Shoulder Elbow Surg* 1999; **8**: 599-605 [PMID: 10633896 DOI: 10.1016/S1058-2746(99)90097-6]
 - 49 **Oh JH**, Kim SH, Choi JA, Kim Y, Oh CH. Reliability of the grading system for fatty degeneration of rotator cuff muscles. *Clin Orthop Relat Res* 2010; **468**: 1558-1564 [PMID: 19347412 DOI: 10.1007/s11999-009-0818-6]
 - 50 **Nakata W**, Katou S, Fujita A, Nakata M, Lefor AT, Sugimoto H. Biceps pulley: normal anatomy and associated lesions at MR arthrography. *Radiographics* 2011; **31**: 791-810 [PMID: 21571657 DOI: 10.1148/rg.313105507]

- 51 **Beall DP**, Williamson EE, Ly JQ, Adkins MC, Emery RL, Jones TP, Rowland CM. Association of biceps tendon tears with rotator cuff abnormalities: degree of correlation with tears of the anterior and superior portions of the rotator cuff. *AJR Am J Roentgenol* 2003; **180**: 633-639 [PMID: 12591665 DOI: 10.2214/ajr.180.3.1800633]
- 52 **Vinson EN**, Wittstein J, Garrigues GE, Taylor DC. MRI of selected abnormalities at the anterior superior aspect of the shoulder: potential pitfalls and subtle diagnoses. *AJR Am J Roentgenol* 2012; **199**: 534-545 [PMID: 22915393 DOI: 10.2214/AJR.12.8789]
- 53 **Zubler C**, Mengiardi B, Schmid MR, Hodler J, Jost B, Pfirrmann CW. MR arthrography in calcific tendinitis of the shoulder: diagnostic performance and pitfalls. *Eur Radiol* 2007; **17**: 1603-1610 [PMID: 17036154 DOI: 10.1007/s00330-006-0428-6]

P- Reviewer: Iagulli ND **S- Editor:** Ji FF **L- Editor:** A
E- Editor: Zhang DN



Comparative review of vertebroplasty and kyphoplasty

Fernando Ruiz Santiago, Alicia Santiago Chinchilla, Luis Guzmán Álvarez, Antonio Luis Pérez Abela, Maria del Mar Castellano García, Miguel Pajares López

Fernando Ruiz Santiago, Luis Guzmán Álvarez, Maria del Mar Castellano García, Radiology Department, Hospital of Traumatology, 18014 Granada, Spain

Alicia Santiago Chinchilla, Radiology Department, Ciudad Sanitaria Virgen de las Nieves, 18014 Granada, Spain

Antonio Luis Pérez Abela, Traumatology Department, Hospital of Traumatology, 18014 Granada, Spain

Miguel Pajares López, Traumatology Department, Hospital Clínico San Cecilio, 18012 Granada, Spain

Author contributions: Ruiz Santiago F, Santiago Chinchilla A and Guzmán Álvarez L contributed to study concepts; Ruiz Santiago F, Santiago Chinchilla A, Guzmán Álvarez L and Pérez Abela AL contributed to study design; all authors contributed to data acquisition, manuscript preparation and manuscript review.

Correspondence to: Fernando Ruiz Santiago, Philosophical Doctor, Chairman of Musculoskeletal Radiology, Radiology Department, Hospital of Traumatology, Carretera de Jaen SN, 18014 Granada, Spain. ferusan12@gmail.com

Telephone: +34-627-633829

Received: December 23, 2013 Revised: February 18, 2014

Accepted: May 8, 2014

Published online: March 28, 2015

Key words: Vertebroplasty; Kyphoplasty; Osteoporosis; Vertebral fracture; spine metastasis

Core tip: This extended review of current literature on vertebral augmentation is supported by our wide experience in the treatment of vertebral fractures. The most innovative topics are the possibility of treating multilevel vertebral fractures in the same session and the failure of vertebral augmentation due to mechanical disruption of the cement. This is intended to present a thorough review to physicians interested in osteoporosis and vertebral fractures.

Original sources: Ruiz Santiago F, Santiago Chinchilla A, Guzmán Álvarez L, Pérez Abela AL, Castellano García MM, Pajares López M. Comparative review of vertebroplasty and kyphoplasty. *World J Radiol* 2014; 6(6): 329-343 Available from: URL: <http://www.wjgnet.com/1949-8470/full/v6/i6/329.htm> DOI: <http://dx.doi.org/10.4329/wjr.v6.i6.329>

Abstract

The aim of this review is to compare the effectiveness of percutaneous vertebroplasty and kyphoplasty to treat pain and improve functional outcome from vertebral fractures secondary to osteoporosis and tumor conditions. In 2009, two open randomized controlled trials published in the *New England Journal of Medicine* questioned the value of vertebroplasty in treating vertebral compression fractures. Nevertheless, the practice of physicians treating these conditions has barely changed. The objective of this review is to try to clarify the most important issues, based on our own experience and the reported evidence about both techniques, and to guide towards the most appropriate choice of treatment of vertebral fractures, although many questions still remain unanswered.

© 2015 Baishideng Publishing Group Inc. All rights reserved.

INTRODUCTION

The treatment of pain related to vertebral body fractures by vertebroplasty or kyphoplasty has become a widespread practice. The main reported advantages of Kyphoplasty *vs* vertebroplasty are restoration of vertebral body height and a lower rate of cement extravasation. Although both techniques would appear effective in achieving pain relief, the impact on functional outcome is not sufficiently proved.

The choice of vertebroplasty or kyphoplasty and the selection of patients for one or other procedure remain unresolved questions. These issues are complicated by the considerable competition between the procedures and the conflicting claims made for each^[1]. The degree of pain relief and functional improvement obtained must play an important role in the choice between these techniques. Previous studies reported good outcomes that remained stable during long follow-up periods for both vertebro-

plasty and kyphoplasty^[2,3]. However, comparative studies are scarce. At present, different devices claiming advantages over more traditional methods are being developed.

Due to the existing controversies regarding the treatment of vertebral fractures, the objective of this review is to analyze the evidence of current literature supported by our own experience.

EPIDEMIOLOGY AND TYPES OF VERTEBRAL FRACTURES

Vertebral fractures can be secondary to high or low energy trauma. With population ageing most of the fractures (85%) are due to low energy trauma. These are more frequent in women and its prevalence increase with age in both sexes. High energy fractures are more frequent in men and are not related with older age. The incidence of clinically diagnosed vertebral fractures was assessed in a population-based study in Rochester, Minnesota, 1985-1989. The overall age- and sex-adjusted incidence rate was 117 per 100000 person-years (95%CI: 105 to 130). The age-adjusted rate in women (145 per 100000 person-years) was almost twice that in men (73 per 100000 person-years). Of all fractures, 47 (14%) followed severe trauma, 282 (83%) followed moderate or no trauma, and 12 (3%) were pathologic^[4].

Vertebral compression fractures (VCF) are the most common fracture in osteoporotic patients, followed by hip, wrist or ankle fractures. These are known as low energy fractures or insufficiency fractures because the main cause is the fragility of bone that make it prone to injury with minimal or not trauma. After suffering the first vertebral fracture, the risk of developing new vertebral fractures increases 5-10 times^[5].

Pathologic vertebral fractures are secondary to osseous involvement by a localized debilitating condition, mainly tumors. Most are due to malignancies such as metastases, myeloma and primary bone tumors, although benign tumors like haemangioma can also lead to a vertebral fracture. The spine is the musculoskeletal target most affected by metastases, mainly secondary to breast, lung, prostate, kidney and thyroid tumors^[6]. Nevertheless, even in oncologic patients, a third of the vertebral fractures are due to coexisting osteoporosis^[7]. Imaging techniques and biopsy help to differentiate the underlying cause.

Vertebral fractures happen in 50%-70% of patients with multiple myeloma. It may lead to spinal cord compression until 15% of the patients. On imaging its appearance may be misleading, simulating an osteoporotic vertebral compression fracture^[8].

IMAGING OF VERTEBRAL FRACTURES

Conventional Radiographs are usually the first technique used to study patients with suspected vertebral fracture. While its ability to diagnose high energy posttraumatic fractures is high, its findings may be misleading diagnos-

ing pathologic or insufficiency fractures.

When a high energy fracture is detected radiographically, many authors suggest the addition of computed tomography (CT) to the study, as it allows for better definition of fracture anatomy. When the clinical presentation suggests a fracture and conventional radiography is not diagnostic, a multi-slice CT or magnetic resonance imaging (MRI) help to clear out traumatism of spine. A prospective study found a CT sensitivity of 99% in detecting fractures compared to 87% with plain-film radiography^[9].

Osteoporotic vertebral fractures deformity usually is presented in two ways, wedge and biconcave (fish vertebra or diabolo-shaped vertebra) types, while pathological fractures often demonstrate predominately osteolytic changes. The presence of air collections within a vertebral body is considered a sign of vertebral cleft that may be due to fracture instability and/or necrosis (Kummel's disease) and is more frequently associated to benign osteoporotic fractures^[10]. Nevertheless cases associated to metastasis and myeloma has been described^[11] (Figure 1).

A 15% vertebral body height loss constitutes a vertebral compression fracture. The leading cause of vertebral compression fractures is osteoporosis. Morphologic changes that allow for the diagnosis of an osteoporotic fracture may require time for their development. Therefore, the absence of a fracture on plain-film radiography in an osteoporotic patient does not rule it out, and when symptoms persist, a MRI should be performed. MRI can detect fractures without vertebral deformities and can better discriminate between benign and malignant fractures^[12]. Additionally, MRI provides valuable information on factors such as the degree of edema, vertebral deformities, and invasion of the spinal canal, all of which are useful data for planning medical, percutaneous (kyphoplasty, vertebroplasty) or surgical treatment^[13].

Plain-film radiography is somewhat insensitive when it comes to the visualization of the bone destruction or marrow replacement, requiring, depending on the size of the lesion, between 30%-50% of bone density loss before the lesions become visible^[14]. The detection of blastic lesions may also be delayed with conventional radiography. One study reported that in the case of breast cancer, plain film detection of blastic lesion may be delayed by 3-6 mo^[15].

Based on vertebral morphology and bone marrow signal, MRI can differentiate between osteoporotic and pathologic fractures with high confidence. Pathologic fractures may show complete substitution of normal bone marrow or, when incomplete, tend to show and nodular or patchy pattern. Morphologic signs are a convex vertebral border, due to expansion by growing tumor, and the presence of asymmetric paravertebral mass. Acute osteoporotic vertebral fractures tend to show a band-like pattern of subchondral edema and, quite often, the lineal pattern of the vertebral fracture can be depicted inside the edema^[13]. A retropulsed bone fragment and the presence of intra vertebral cleft are characteristic

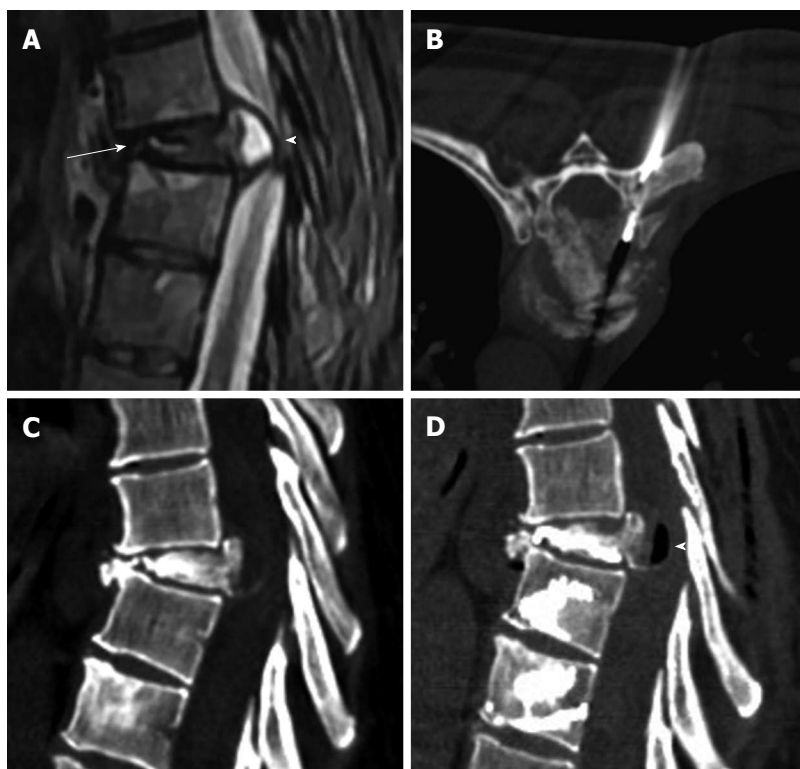


Figure 1 Sagittal T2 weighted (A) image shows metastatic compression fracture with intravertebral cleft (arrow) and epidural cyst (arrowhead), computed tomography guided biopsy (B), Sagittal computed tomography before (C) and after (D) vertebroplasty showing air filling of the cyst (arrowhead).

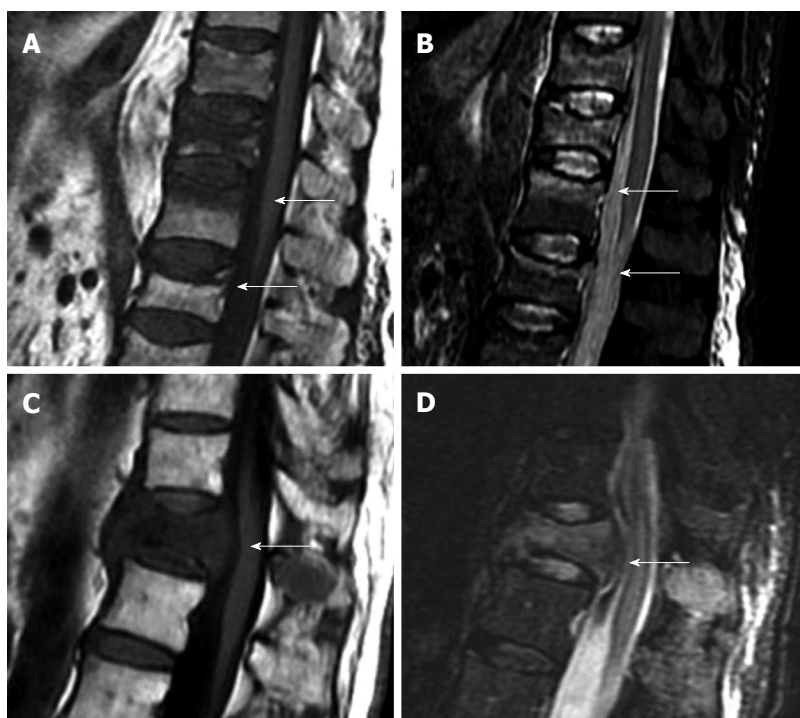


Figure 2 Sagittal T1 weighted (A) and STIR (B) images of osteoporotic fractures with typical band-like subchondral edema (arrows), sagittal T1 weighted (C) and STIR images (D) of a pathologic fracture, due to vertebral metastases, with typical convex border (arrows).

of benign compression fractures^[11]. Chronic vertebral compression fractures are characterized by morphologic changes with recovery of normal signal of the bone marrow (Figure 2).

MEDICAL TREATMENT OF VERTEBRAL FRACTURES

Non-operative treatment of traumatic vertebral com-

pression fractures is usually appropriate for patients with normal neurological status without suspected radiological instability, with an anterior vertebral body height > 50% of the posterior height and a Kyphotic angulation < 25°; or incomplete injury of the posterior column of the vertebral body^[16,17]. Although in some cases early closed reduction and casting can be performed, bracing alone and physiotherapy in younger patients (< 65 years) is usually the best treatment option. A short period of bed rest (less

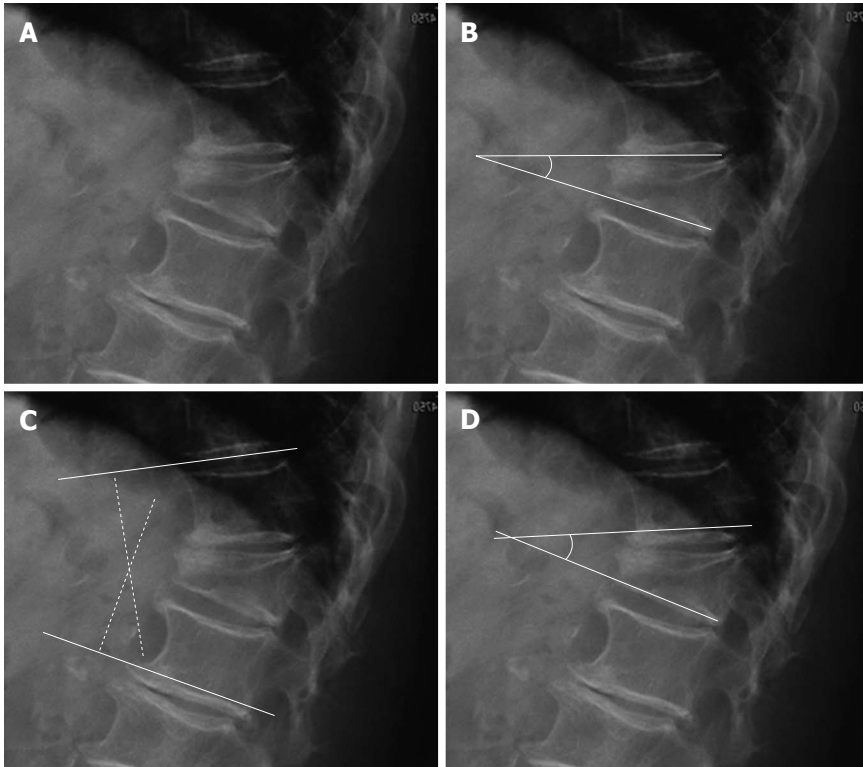


Figure 3 Segmental kyphotic deformity. A: Wedge fracture of T12; B: Local vertebral kyphosis angle; C: Regional kyphosis; D: Segmental kyphosis (SK). One vertebra, one disc=one segment. Sagittal index (SI): $SI = SK - X$ ($X = +5$ in the thoracic spine, $X = -10$ in the lumbar spine, $X = 0$ in T12-L1).

than 1 wk) avoids complications caused by immobilization. In older patients, percutaneous vertebral augmentation may promote early mobilization and reduce analgesic intake^[17].

Traditional treatment for osteoporotic fractures has been medical, including lifestyle changes (diet, smoking and exercise), pain management with rest, analgesic and anti-inflammatory drugs and external brace. Medical treatment for osteoporosis includes calcium supplements, vitamin D, hormone replacement and bisphosphonates. These treatments have strong effects on pain, but minimal effect on vertebral stability, vertebral height restoration or reduction of kyphotic deformity. Side effects of chronic medication and rest are increased demineralization of bone and greater risk of developing new fractures. Surgery is left for fractures with vertebral instability or neurological compression.

Traditional treatment for painful vertebral metastases is based on rest, braces, analgesic drugs, radiotherapy and chemotherapy. External beam radiation therapy is the current gold standard treatment for cancer patients with localized bone pain. Nevertheless, 20%-30% of patients do not experience pain relief with this approach. Radiation treatment can also result in additional early bone loss due to inflammation, and limited weight-bearing should be recommended during radiation to prevent pathological fractures. Radiotherapy control of pain is achieved in approximately 70%-80% of the cases, but its maximum effects usually takes place 1 mo after the beginning of treatment and osseous reinforcement up to 2 to 4 mo after, increasing the risk of vertebral collapse with its biomechanical consequences^[18].

PERCUTANEOUS AND SURGICAL TREATMENT OF VERTEBRAL FRACTURES

Criteria for surgical indication of high-energy fractures are variable^[19]. In our center, surgery is mainly indicated when the body fracture is associated to injury of the posterior column or in cases with neurologic deficit (deterioration of the initial neurologic status constitutes an emergency. It can also be indicated in cases without neurological deficit when there are other radiological signs of instability: central canal narrowing $> 50\%$, vertebral height loss $> 50\%$, fracture-dislocation, local vertebral kyphosis $> 25^\circ$ - 30° , regional traumatic angle of kyphosis $> 20^\circ$ and sagittal index (SI) $> 15^\circ$.

Local vertebral kyphosis angle is measured between the tangent to the upper endplate and the lower endplate of the injured vertebra. Regional kyphosis is the angle defined by the tangent to the upper endplate of the vertebra overlying the fracture and the tangent to the lower endplate of the vertebra underlying the injured vertebra. The SI is defined as segmental kyphotic deformity minus baseline sagittal contour in the segment with the fractured vertebral body. The segmental kyphotic deformity is the angle between the inferior endplate of the injured vertebra and the inferior endplate of the overlying vertebra. The baseline sagittal contour in each vertebral segment arbitrarily amounts to $+5^\circ$ for the thoracic region, 0° T12-L1 and -10° for the lumbar spine segments (Figure 3). The normal index is 0 ^[20].

Accepted methods for surgical decompression and stabilization include anterior or posterior approaches and

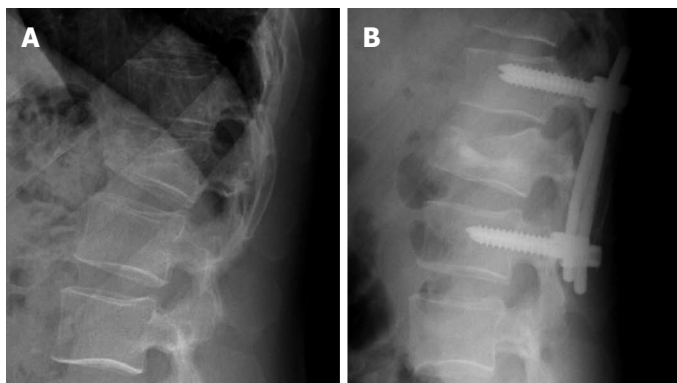


Figure 4 Forty-five years old man with acute Wedge impaction fracture of L1 (A) treated by posterior instrumentation and vertebral body kyphoplasty using biological cement (B).

a combination of both procedures. Instrumented fusion is better than laminectomy alone because it does not restore neurological function and it's associated with significant complications, such as persistent spinal instability and progressive kyphosis, mechanical pain and worsening of neurological injury^[19].

Sometimes, instrumentation is complemented with VT or KP. Transpedicular vertebral augmentation for the direct restoration of burst fractures in combination with posterior instrumentation may avoid the surgical anterior reconstruction. The aim is to reinforce the anterior column and prevent anterior vertebral body height loss^[21] (Figure 4).

The role of vertebroplasty and kyphoplasty in the treatment of high energy vertebral fractures is not still well defined, although good results with regard pain relief and quality of life have been reported using both procedures^[22,23]. In young patients it has been suggested the use of biological cement, instead of PMMA, due to its capacity of integrating with bone^[24]. Nevertheless, it has been reported that low resistance against flexural, tractive, and shear forces compared to PMMA, may lead to a higher risk of cement failure and subsequent loss of correction, mainly when fracture of the posterior wall of the vertebra is present^[25]. The aim of treating percutaneously these fractures is to recovery vertebral height and to obtain early relieving of pain in order to reducing recovery time in young active population.

The principal surgical options for treatment of osteoporotic VCFs are decompression and fusion. The success of surgical instrumentation is compromised by poor bone quality^[26]. As a result, interest in new and quick methods for pain relief and early functional restoration has increased. Percutaneous treatment of osteoporotic fractures is mainly indicated after failure of medical treatment, when the patient has a disabling pain or when there are severe side effects due to analgesic medication. In order to minimize these effects in patients with VCFs and reduce prolonged hospital resource utilization, VP and KP have been increasingly used with the expectation of a more rapid pain relief and earlier mobilization than that achieved with medical pain management^[27]. Recently a randomized non-blinded trial appeared, strongly indicating that vertebroplasty is dramatically superior to conservative therapy^[28].

Surgery in vertebral metastases is left for lesions affecting a unique vertebra or for treating neurological deficit secondary to compression or instability. Inconveniences of surgery are long recovery times and high morbidity and mortality^[29].

Although external beam radiation therapy is the current gold standard treatment for cancer patients with localized bone pain we have to take into consideration that the life expectancy of most patients with bone metastases is limited, and that around 12-20 wk are usually required before maximum benefits are obtained from post-radiation therapy. In these cases vertebral augmentation techniques in isolation or combined with thermal ablation provide the earliest possible pain relief^[30].

HISTORICAL NOTES

Deramon and Galibert performed the first vertebroplasty in France in 1984. It was performed in a patient with an aggressive haemangioma at the C2 level with resolution of pain. The results were so gratifying that cement injections were soon used in more patients with symptomatic hemangiomas and fractures due to tumors. The application of vertebroplasty in osteoporotic VCF was first published in 1989^[31]. The hopeful analgesic effect led to the widespread use of augmentation for treating osteoporotic VCF^[32]. Over the last years, osteoporotic fractures have become the main indication for vertebroplasty^[33].

Kyphoplasty is the most widely used modification of vertebroplasty and was developed specifically for use in the osteoporotic vertebra. The basic idea behind this procedure was to raise the end plate of fractured vertebral body with an orthopedic balloon to achieve a more favorable angle of kyphosis before the cement augmentation. Therefore, a cavity is first created within the vertebral body before injecting the cement. The first kyphoplasty was performed by the orthopedic specialist Mark Reiley in California in 1998 with good results^[34].

TECHNICAL ISSUES

Vertebroplasty involves the injection of polymethyl-metacrilate (PMMA) cement into an injured vertebral body *via* a needle that is placed percutaneously either using a transpedicular or extrapedicular approach. The



Figure 5 Sagittal STIR image (A) in a patient with multiple thoracolumbar compression fractures, eight vertebrae were treated in the same procedure (B and C).

injection has to be forced to surpass the local pressure of the trabecular bone of treated vertebra increasing the risk of leakage through the cracks of the fractured vertebra. It may be performed under general anesthesia, although more commonly the patient is given a local anesthetic at the injection site and conscious sedation^[35].

Kyphoplasty, a modification of vertebroplasty, involves the percutaneous insertion of an inflatable high-pressure bone tamp into the fractured vertebral body with the aim of elevate the end-plates by creating a cavity inside the vertebral body that filled with cement help to restore and stabilize the vertebral height. The cavity allows low pressure injection of more viscous cement, lowering the risk of extravasation^[33].

PMMA is the most frequent cement used in these procedures. It is the result of the polymerization of methyl methacrylate monomers to PMMA polymers. It is cheap, easy to manipulate, allows combination with radiopaque materials and gives the appropriate stiffness and strength to the vertebral body. However, it does not have osteoinductive or osteoconductive properties and, therefore, it will not integrate itself to host bone over time. Its stiffness may promote mechanical overload to adjacent vertebral bodies^[25].

New biological materials have been introduced as alternatives to PMMA, such as calcium phosphate and hydroxyapatite. These are not exothermic, allowing the deposition of new bone that, eventually, could replace the cement. These cements would in time become incorporated into the patient's bone, therefore functioning in a more physiological and biomechanically compatible fashion. This requires the presence of trabecular bone and the haversian canal system, thus cavity creation with a balloon will probably never be a part of the future of biological cements and prophylactic vertebroplasty^[33]. Nevertheless, biological cements are expensive; their manipulation is not easy due to their high viscosity that makes difficult the interstitial diffusion inside the vertebral body^[36]. These materials have been recommended in high-energy fractures of young patients^[37], although other

authors find a high rate of mechanical failure with these materials, due to its lower resistance to shear, flexion and distraction forces^[25].

The number of vertebrae augmentable per session also remains unclear, although extensive augmentation to more than three vertebral levels per session has been shown as feasible^[38]. However, it may lead to an increase of the amount of bone marrow floating to the pulmonary capillary system, increasing the risk of pulmonary fat embolism. Also, with PMMA there is some risk of incomplete polymerization, leading to increased residual toxic monomers that may result in adverse systemic effects, such as hypotension, bradycardia, asystole and bronchospasm. If the amount of cement injected in each vertebral body due to these reasons is reduced, it might result in incomplete stabilization of some vertebral body fractures leading to residual instability and pain. Notwithstanding, we have treated some cases of multilevel fractures in one single operative session with quite good results^[35] (Figure 5). We recommend carefully planning the positioning of the needles and the amount of cement to be injected; taking into account the anatomical characteristics of each vertebral fracture, such as location of the fracture lines, integrity of vertebral walls and the presence of vertebral clefts.

CLINICAL SUCCESS OF

VERTEBROPLASTY AND KYPHOPLASTY

Analgesic effect effects of these techniques can rely in many factors, such as ablation of C-nociceptive fibers by the thermal effect of the cement, mechanical stabilization of the fracture, height restoration of the vertebral body. The thermal effect also leads to tumor necrosis in patients with metastases^[39].

Mechanical stabilization of the vertebral body relies on basal bone density, volume and localization of the injected cement. The filling of 14% to 30% of the volume is able to recover vertebral stiffness, although partial recovery of the stiffness, below the pre-fracture state, would be enough to obtain clinical healing^[40].

Cadaveric studies have shown greater recovery of vertebral height with kyphoplasty (5.1 mm) than with vertebroplasty (2.3 mm)^[41]. Yet, clinical studies are contradictory. While some authors found greater height restoration with kyphoplasty^[42], others didn't find differences between both techniques^[43]. In comparison with cadaver studies, the disk and paravertebral soft tissues may hinder augmentation with more aggressive techniques in living patients.

Vertebroplasty can mainly restore vertebral height when there is fragment instability with intravertebral clefts, indicating non-union of the fracture fragments. The cleft may be filled with greater amount of cement, mainly when there is integrity of the walls of the vertebral body, without extravasations leading loss of intravertebral pressure^[41,44] (Figure 6).

Relationship between vertebral height restoration and

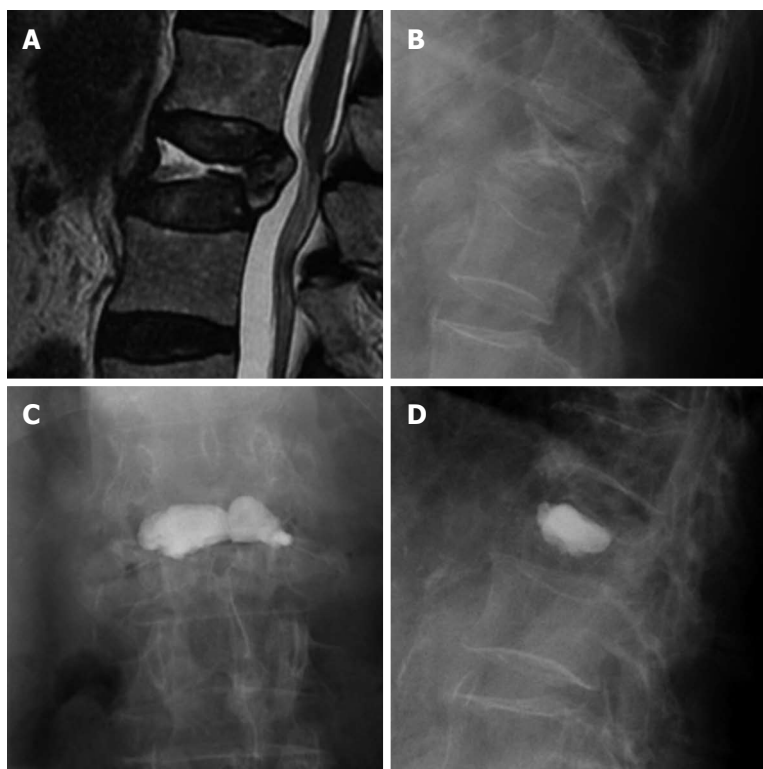


Figure 6 Sagittal T2 weighted image (A) and lateral X-ray film (B) of a vertebral fracture with intravertebral cleft, AP (C) and lateral (D) view after vertebroplasty.

clinical evolution is not well established. Some studies found no better pain resolution with height restoration and don't consider this factor mandatory in order to achieve pain control^[45].

Another issue to consider is the stability over time of the height restoration. A follow up of height loss after performing these techniques shows the loss to be greater in kyphoplasty, due to less homogeneous distribution of cement, than in vertebroplasty, where the cement intermingles with host bone. Therefore, height recovery differences tend to vanish with time^[46].

Short-term pain relief has been demonstrated in osteoporotic and tumor fractures treated with vertebroplasty and kyphoplasty^[47,48]. Long-term outcomes have not been so well established, although some reports state that the beneficial effects of vertebroplasty remain after a follow-up period of several years^[49,50].

Compared with medical treatments, pain relief after VP seems on the whole significantly superior. The follow-up point at which the difference becomes insignificant varies between studies at 3 mo^[51], 6 mo^[52] or 1 year^[53]. Regarding Kyphoplasty, two prospective controlled studies evaluated and compared the efficacy and safety of this technique *vs* medical management and found better long-term pain relief and superior functional outcome with kyphoplasty, up to 3 years^[54,55].

CLINICAL EVIDENCE OF AUGMENTATION EFFECTIVENESS

Two recent randomized works^[56,57] stated that there is not better results between vertebroplasty and a sham treatment that only inject local anesthetic in the fractured area.

Nevertheless, bias in both studies may invalidate their conclusions^[58]. First of all, the small sample size avoid that a better evolution in the vertebroplastic group reaches statistical significance. Second at all, the percentage of control patients that chose to pass to the vertebroplasty group was high enough to invalidate the randomization of the studies. With regard selection of the patients, those with high pain scores were not included. These patients tend to show better results after vertebroplasty^[59]. Another important factor was the inclusion of a high percentage of non-acute fractures; therefore, it is unclear if the origin of the back pain was the osteoporotic VCF or other common reasons for back pain in the elderly, such as arthritis of facet joint or disc pain. By nature of the patient population studied, "sham" facet injections may have led to decreased facet pain. Local anesthetic infiltration of the posterior longitudinal ligament is an established treatment for osteoarthritis back pain. Perhaps a sham procedure in which a dry needle was inserted might have been a more appropriate control. Other differences with previous studies are lower amount of injected PMMA, non-confirmation by imaging of vertebral fractures previous to procedure in patients with known fractures of less than 1 year and a lack of standardization of the medical treatment. The interpretation of the data is even more difficult due to the absence of a medical treatment group^[60].

It has been stated that a percentage of patients with pain following VCF do not have pain arising from the fracture itself, but due to instability or overload on the facet joints produced by adjacent vertebral body deformity^[61]. Since both causes of pain, VCF and osteoarthritis, may concur at the same time, we often combine

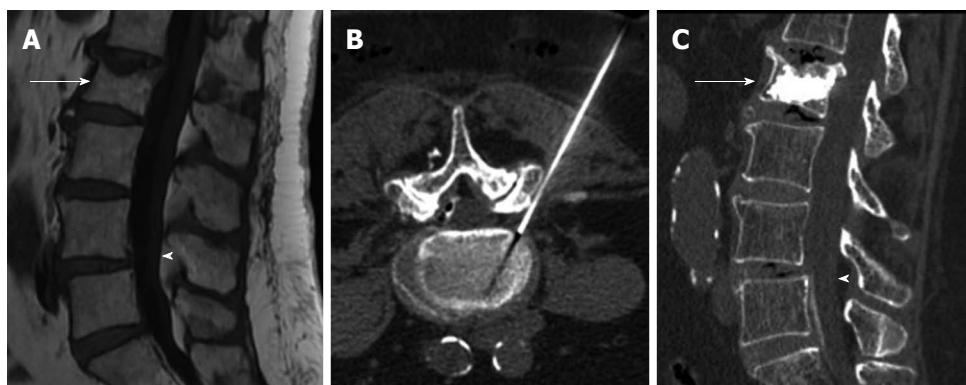


Figure 7 Sagittal T1 weighted image (A) showing vertebral compression fracture of L2 (arrow) and degenerative spondylolisthesis of L4 (arrowhead), computed tomography guided transforaminal epidural injection (B), Sagittal computed tomography after vertebroplasty (arrow) and epidural injection (arrowhead) (C).

vertebroplasty and spinal injection in the same session, mainly in older patients, relying on edema detected at the facet joints or on degenerative vertebral endplates changes, at the same or at a different level of the fractured vertebrae (Figure 7). This is supported by previous studies that found overall facet joint signal-change scores significantly higher at vertebral body levels affected by an acute/subacute compression fracture than in control levels with either normal bodies or chronic compression fractures^[62]. This practice does not add too much time to vertebroplasty procedures, avoiding multiple scheduling of patients.

It is highly recommended to perform a spine MRI close before any of these percutaneous procedures^[63]. The presence of a pattern of bone marrow edema is associated with a good clinical short term success relieving pain^[54]. Nevertheless, improvement has been also demonstrated in patients with vertebral fractures without bone marrow edema^[64].

Grades of recommendation of these techniques are based on the clinical evidence of published papers as follow^[65]: Good evidence [level I studies with consistent findings; *e.g.*, high quality randomized controlled trials (RCT)], Fair evidence (level II or III studies with consistent findings; *e.g.*, low quality RCT, case/control and cohorts studies), Poor quality evidence (level IV or V studies with consistent findings; *e.g.*, case series and expert opinions), or Insufficient evidence (inconsistent findings or lack of investigation for or against recommending intervention).

Meta-Analysis of published papers show fair to good evidence that in patients with osteoporotic VCF outcomes on physical disability, general health and pain relief are better with VP and KP than with medical management within the first 3 to 6 mo after intervention. Nevertheless, there is fair evidence that by the first or second year after intervention, VP provides a similar degree of pain control and physical function as that attained with optimal medical management. There is insufficient evidence whether KP results in greater pain relief one and 2 years after intervention^[27].

Although not assessed in comparative studies, the reported degree of acute pain improvement in tumor-associated vertebral compression fractures is far better than that typically reported with radiation and medical management. Nevertheless, studies yield poor-quality evidence^[27].

COMPLICATION OF TREATMENT OF VERTEBRAL FRACTURES

The aggregate rates of complications of vertebroplasty and kyphoplasty are small; ranging from 2%, when treating osteoporotic compression fractures, to 10% in cases related to malignant tumors^[46].

The main risk of these percutaneous procedures is the extravasation of PMMA. Investigations on cement leakage in vertebroplasty report a rate of 11%-76%. In investigations on kyphoplasty, cement leakage data ranges from 4.8% to 39%. Cement leakage is reported at a higher rate if CT scans are used^[45]. There are many routes by which cement may leak from a vertebra: paravertebral leakage, venous leakage or leakage into the spinal canal and intervertebral foramen (Figure 8). Injury of the surrounding soft tissues is mainly due to the high temperature of polymerization of PMMA. The most sensitive structures are neural tissues, spinal cord and nerve roots. Fortunately, most of the extravasations are to the disk or paravertebral tissues, hence asymptomatic. Transient radicular symptoms have been described in up to 3%-4% of the patients^[66] and only isolated cases of paraplegia after these procedures have been reported, most of them due to failure of technical issues^[48].

The monomers that don't contribute to the polymerization have systemic cardio-pulmonary effects. Pulmonary embolism can be due not only to the cement but also to the fat from the bone marrow extruded into the venous system by the high pressure injected cement or by inflating the balloons^[67].

The relationship between percutaneous vertebral augmentation and the development of new fractures it is not well stated. Previous studies have found a greater rate of

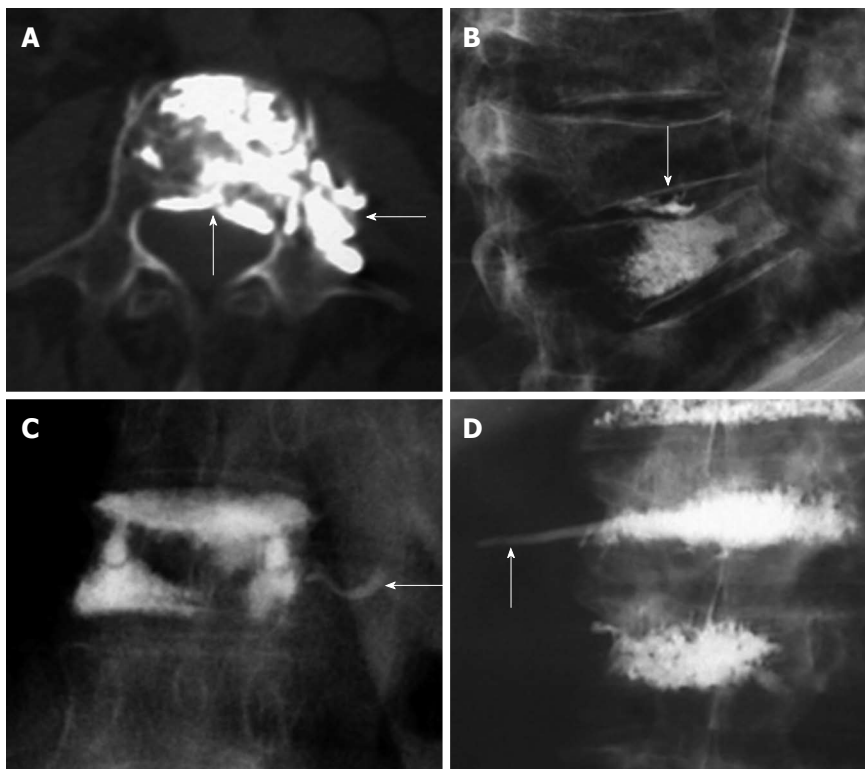


Figure 8 Axial computed tomography shows extravasations to epidural space and paravertebral area (arrows) (A), leakage to the intervertebral disc (arrow) (B), venous leakage (arrow) (C), tail of cement in the path of the needle (arrow) (D).

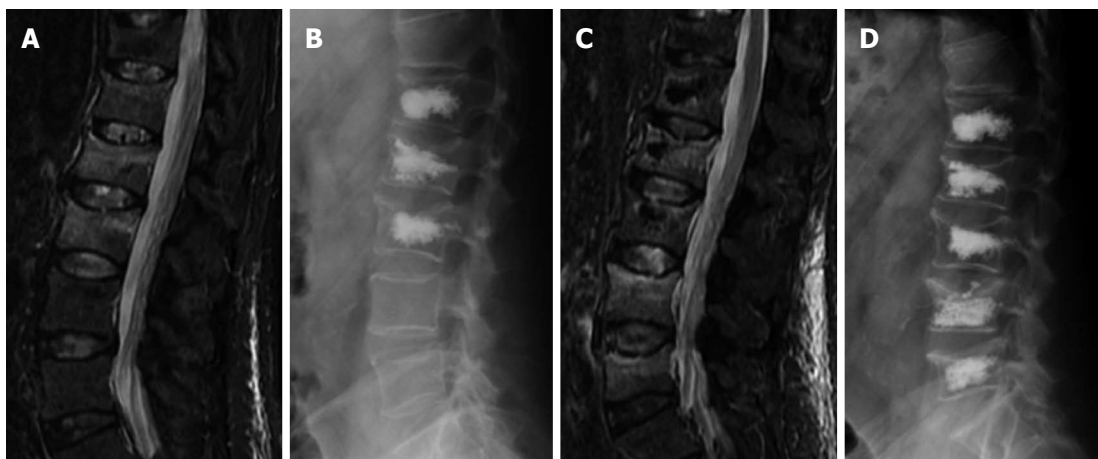


Figure 9 Sagittal STIR magnetic resonance image (A) shows fractures with edema of L1 to L3. Kyphoplasty was performed in these vertebrae (B), 3 wk later back pain returned and magnetic resonance imaging showed development of new fractures in L4 and L5 (C), vertebroplasty was performed at these levels (D).

new fractures in these patients than in the osteoporotic population, but the same as in those osteoporotic patients that have already developed a fracture^[68]. Another article found fewer incidences of new fractures in patients treated with kyphoplasty than in patients managed with medical therapy. This was attributed to improvement of mechanical conditions due to vertebral height restoration and kyphotic correction^[36]. The higher incidence of fractures in the early postoperative period could potentially be explained by increased patient activity and higher stress secondary to a diminished level of pain (Figure 9).

The possibility of treating adjacent vertebrae to the fractured vertebra is not supported by evidence studies^[69], but we think that it is highly recommended treating a

non-fractured vertebra when both, the upper and lower adjacent vertebrae, have been cemented.

Another complication is incomplete stabilization or residual instability of treated vertebral bodies. Due to the lack of data in spine literature regarding this issue as a cause of procedural failure, there are no figures. Relapse of vertebral instability may be due to mechanical failure of the cement, mainly when biological substitutes are used in fractures with loss of integrity of the posterior vertebral wall^[25]. Incomplete filling of vertebral fracture lines may be followed by persistent instability with residual edema. When a vertebral cleft or cyst exists, kyphoplasty might be more prone to cause instability than vertebroplasty because the cement ball does not intermingle

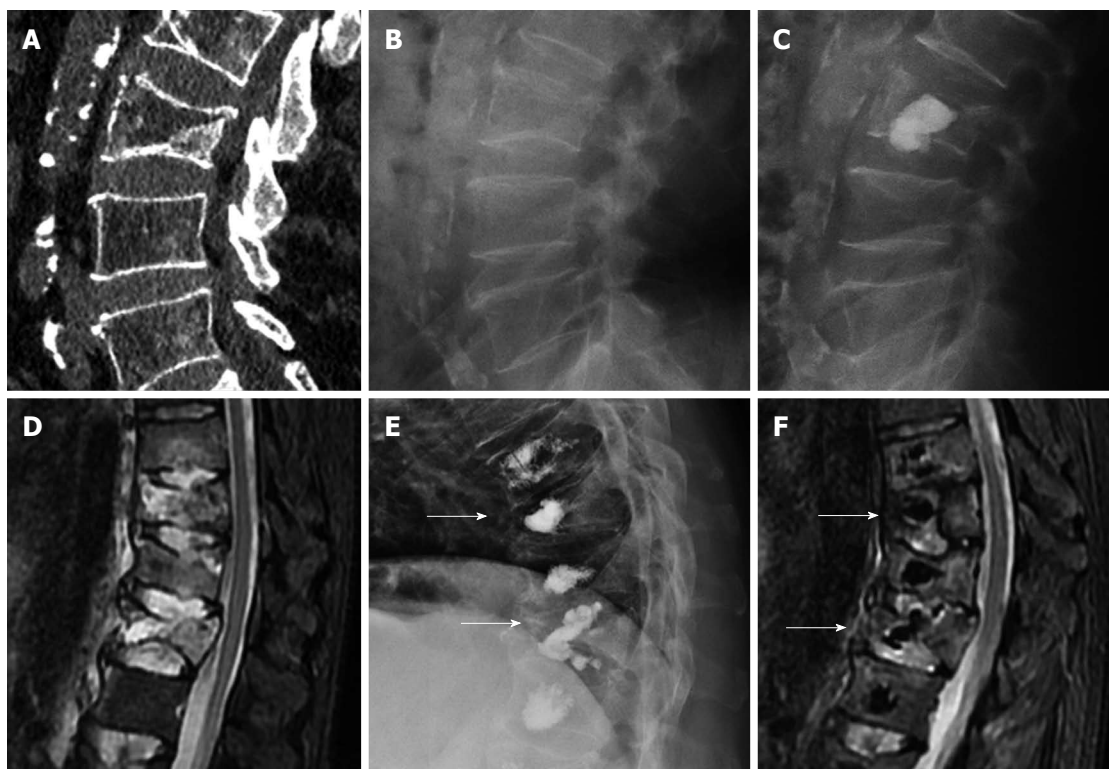


Figure 10 Sagittal computed tomography (A) a lateral radiography (B) showing fracture of L3 with intravertebral cyst (arrow), after Kyphoplasty (C) the ball of cement is not incorporated to the instable vertebral fracture, sagittal STIR image showing multiple thoracolumbar fractures with edema (D), treated with vertebroplasty, the cement do not stabilized the fracture of T10 and T12 (arrows) with persistent edema 6 mo after the procedure (E, F).

with vertebral trabeculae (Figure 10).

WHAT TREATMENT DO I CHOOSE?

Percutaneous vertebral augmentation has been shown to be more effective than prolonged non-operative medical treatment in patients with painful VCFs when adequate analgesia and improved functional status has not been achieved by nonoperative therapy^[70]. The choice of vertebroplasty or kyphoplasty and the selection of patients for one or other procedure remain unresolved questions. These issues are complicated by the considerable competition between the procedures and the conflicting claims made for each^[1]. Choice may well be influenced by degree of pain relief, functional improvement and anatomic and technical factors; including operator's experience or preference. Previous studies reported good outcomes that remained stable during long follow-up periods for both vertebroplasty^[71,72] and kyphoplasty^[73,74]. However, comparative studies are scarce and acknowledge the need of more high quality randomized controlled trials^[75]. A recent meta-analysis found significant differences regarding anatomical restoration by kyphoplasty versus vertebroplasty, such as a mean long term kyphotic correction of 2.64°, mean anterior vertebral height recovery of 3.67 mm and lower risk of cement extravasation (risk ratio of 0.7)^[76]. Nevertheless, these anatomic differences were not clinically relevant because most of the studies comparing both techniques found no differences in clinical outcome

in osteoporotic patients^[77-79]. Although a systematic review found greater quality of life and disability improvement in kyphoplasty over vertebroplasty, the need to define confounding variables was pointed out, because the selection of patients may depend on different indications for KP or VP in non-randomized studies, thus leading to misleading conclusions^[80]. An example could be a recent prospective study, included in this systematic review, that found better results in kyphoplasty patients but that was clearly biased because two of the oldest patients were arbitrarily reallocated in the vertebroplasty group^[81].

Based on these data, we recommend vertebroplasty as the primary treatment for osteoporotic VCF that do not respond to medical treatment. Kyphoplasty, which is a much more costly procedure, should only be used as an alternative approach in selected patients, such as those with a recent fracture affecting one or two vertebrae.

FUTURE DEVELOPMENTS

A variety of modifications of these techniques with variable success is being used. The commercial success of Kyphoplasty led to the development of several similar devices, but none have shown any benefit over vertebroplasty in an independent head-to-head trial^[53].

Now that the Kyphon device is off patent, there are legions of copycat devices available from most manufacturers. A modified procedure employs reusable hinged-tip curet to manually create a cavity in fractured vertebral

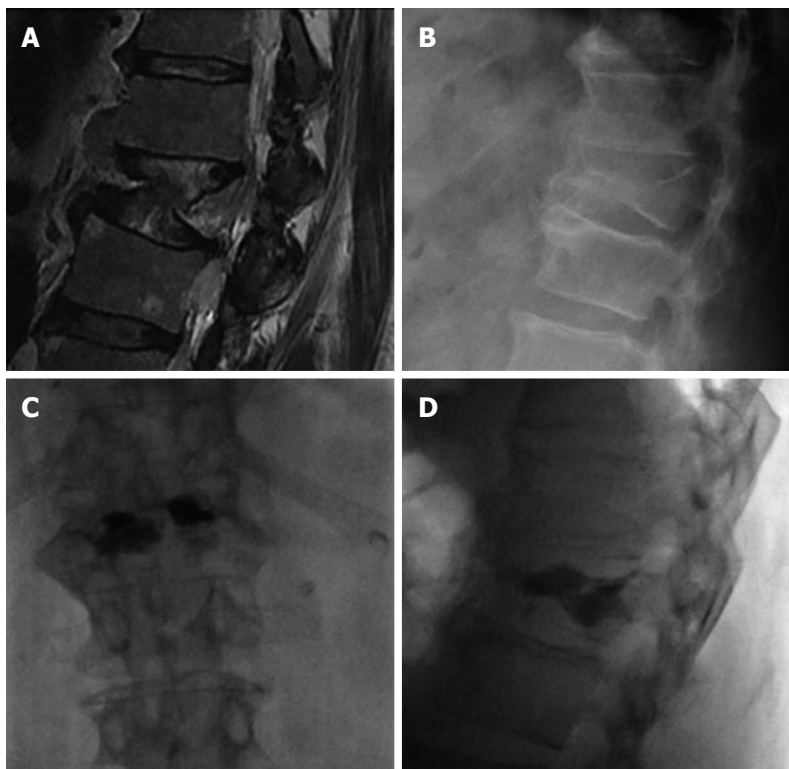


Figure 11 Sagittal T2 magnetic resonance weighted image (A) and lateral X-ray film (B) showing a severe collapse of L1, AP (C) and lateral (D) view after vessel-plasty.

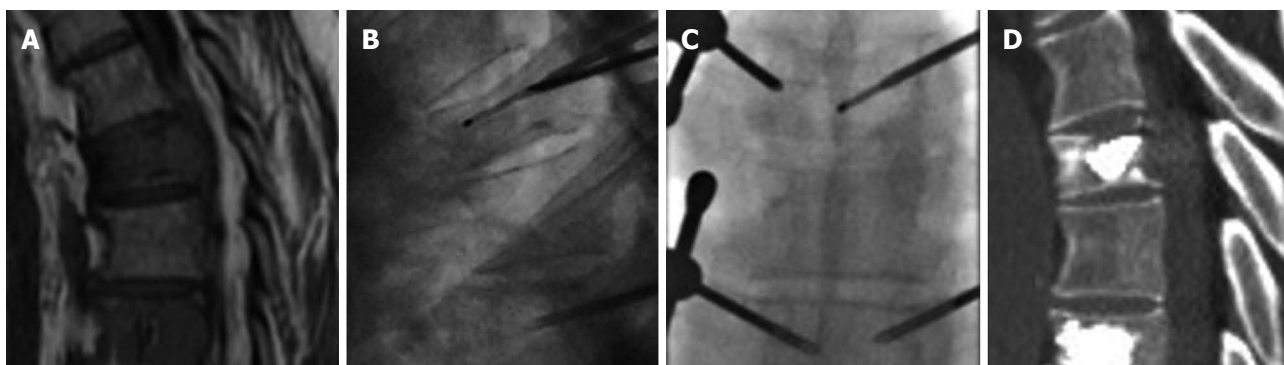


Figure 12 Sagittal magnetic resonance imaging T1 weighted image of a patient with vertebral metastases (A), radiofrequency thermal ablation was performed before cementation (B, C), post procedure computed tomography (D).

bodies under fluoroscopy guidance, allowing low resistance injection of more viscous cement^[82]. We have often used a similar curet to create space for the balloon when the hardness of the vertebral body prevented the balloon from creating a cavity of the appropriate size.

Vesselplasty has been introduced as a new alternative to vertebroplasty and kyphoplasty. It has been devised to obtain control of the volume of injected cement and restoration of the vertebral body height. It was first performed in 2004 by Darwono. Instead of using a balloon to create a cavity, vesselplasty uses a polyethylene terephthalate balloon container (vessel) that serves as both, a vertebral body expander and a bone cement container. Introduced into the collapsed vertebral body, it is expanded by the injection of PMMA. Due to the porous structure of the vessel, a small amount of bone cement interdigitates with the trabecular bone around the ves-

sel increasing its stability^[83]. We are now introducing this technique in our hospital and we have found it very useful in cases of severe vertebral collapse, where the vessel acts as a prosthetic material that minimally restores the crushed vertebral body (Figure 11).

Another issue is the combination of percutaneous cementoplasty using polymethyl methacrylate with other techniques, such as radiofrequency thermal ablation (RFTA). It is sometimes indicated to reinforce bone structures and stabilize bones with high risk of pathologic fractures resulting from metastatic disease, and it is especially indicated for weight bearing bones. The combined use of RF ablation and cementoplasty appears to be useful in order to achieve tumor necrosis and stabilize the fractured vertebrae. The coagulation necrosis produced by RFTA may promote the homogenous distribution of the bone cement within the ablated lesion. The

clinical use of this combined therapy has been reported in several studies, but experience with this approach in vertebral fractures is still limited. Bone cement heats up to 80 °C, which may help to strengthen the anticancer effects of RFTA^[84] (Figure 12). Radiofrequency assistance and heating the needle tip constantly can also be used to increase cement viscosity, lowering the extravasation.

CONCLUSION

This extended review try to update the knowledge about vertebral augmentation based in current literature and our own experience. However, operator's experience or preference is also important clues in deciding appropriate treatment of vertebral fracture. Nevertheless, we hope this review will be helpful to clinician dealing with spinal diseases.

REFERENCES

- 1 **Mathis JM.** Percutaneous vertebroplasty or kyphoplasty: which one do I choose? *Skeletal Radiol* 2006; **35**: 629-631 [PMID: 16703391 DOI: 10.1007/s00256-006-0145-x]
- 2 **Boonen S,** Van Meirhaeghe J, Bastian L, Cummings SR, Ranstam J, Tillman JB, Eastell R, Talmadge K, Wardlaw D. Balloon kyphoplasty for the treatment of acute vertebral compression fractures: 2-year results from a randomized trial. *J Bone Miner Res* 2011; **26**: 1627-1637 [PMID: 21337428 DOI: 10.1002/jbmr.364]
- 3 **Farrokhi MR,** Alibai E, Maghami Z. Randomized controlled trial of percutaneous vertebroplasty versus optimal medical management for the relief of pain and disability in acute osteoporotic vertebral compression fractures. *J Neurosurg Spine* 2011; **14**: 561-569 [PMID: 21375382 DOI: 10.3171/2010.12.SPINE10286]
- 4 **Cooper C,** Atkinson EJ, O'Fallon WM, Melton LJ. Incidence of clinically diagnosed vertebral fractures: a population-based study in Rochester, Minnesota, 1985-1989. *J Bone Miner Res* 1992; **7**: 221-227 [PMID: 1570766 DOI: 10.1002/jbmr.5650070214]
- 5 **Lindsay R,** Silverman SL, Cooper C, Hanley DA, Barton I, Broy SB, Licata A, Benhamou L, Geusens P, Flowers K, Stracke H, Seeman E. Risk of new vertebral fracture in the year following a fracture. *JAMA* 2001; **285**: 320-323 [PMID: 11176842 DOI: 10.1001/jama.285.3.320]
- 6 **Galasko CS.** Skeletal metastases. *Clin Orthop Relat Res* 1986; **(210)**: 18-30 [PMID: 3757360]
- 7 **Tan SB,** Kozak JA, Mawad ME. The limitations of magnetic resonance imaging in the diagnosis of pathologic vertebral fractures. *Spine (Phila Pa 1976)* 1991; **16**: 919-923 [PMID: 1948377 DOI: 10.1097/00007632-199108000-00009]
- 8 **Baur A,** Stabler A, Huber A, Reiser M. Diffusion-weighted magnetic resonance imaging of spinal bone marrow. *Semin Musculoskelet Radiol* 2001; **5**: 35-42 [PMID: 11371334 DOI: 10.1055/s-2001-12921]
- 9 **Hauser CJ,** Visvikis G, Hinrichs C, Eber CD, Cho K, Lavery RF, Livingston DH. Prospective validation of computed tomographic screening of the thoracolumbar spine in trauma. *J Trauma* 2003; **55**: 228-34; discussion 234-5 [PMID: 12913630 DOI: 10.1097/01.TA.0000076622.19246.CF]
- 10 **Freedman BA,** Heller JG. Kummel disease: a not-so-rare complication of osteoporotic vertebral compression fractures. *J Am Board Fam Med* 2009; **22**: 75-78 [PMID: 19124637 DOI: 10.3122/jabfm.2009.01.080100]
- 11 **Baur A,** Stähler A, Arbogast S, Duerr HR, Bartl R, Reiser M. Acute osteoporotic and neoplastic vertebral compression fractures: fluid sign at MR imaging. *Radiology* 2002; **225**: 730-735 [PMID: 12461253 DOI: 10.1148/radiol.2253011413]
- 12 **McKiernan FE.** The broadening spectrum of osteoporotic vertebral fracture. *Skeletal Radiol* 2009; **38**: 303-308 [PMID: 19183993 DOI: 10.1007/s00256-008-0632-3]
- 13 **Cuénod CA,** Laredo JD, Chevret S, Hamze B, Naouri JF, Chapaux X, Bondeville JM, Tubiana JM. Acute vertebral collapse due to osteoporosis or malignancy: appearance on unenhanced and gadolinium-enhanced MR images. *Radiology* 1996; **199**: 541-549 [PMID: 8668809]
- 14 **Kamholtz R,** Sze G. Current imaging in spinal metastatic disease. *Semin Oncol* 1991; **18**: 158-169 [PMID: 2014400]
- 15 **Kunkler IH,** Merrick MV, Rodger A. Bone scintigraphy in breast cancer: a nine-year follow-up. *Clin Radiol* 1985; **36**: 279-282 [PMID: 4064511 DOI: 10.1016/S0009-9260(85)80060-X]
- 16 **Tezer M,** Erturur RE, Ozturk C, Ozturk I, Kuzgun U. Conservative treatment of fractures of the thoracolumbar spine. *Int Orthop* 2005; **29**: 78-82 [PMID: 15714305 DOI: 10.1007/s00264-004-0619-1]
- 17 **Weninger P,** Schultz A, Hertz H. Conservative management of thoracolumbar and lumbar spine compression and burst fractures: functional and radiographic outcomes in 136 cases treated by closed reduction and casting. *Arch Orthop Trauma Surg* 2009; **129**: 207-219 [PMID: 19009303 DOI: 10.1007/s00402-008-0780-x]
- 18 **Gerszten PC,** Mendel E, Yamada Y. Radiotherapy and radiosurgery for metastatic spine disease: what are the options, indications, and outcomes? *Spine (Phila Pa 1976)* 2009; **34**: S78-S92 [PMID: 19829280 DOI: 10.1097/BRS.0b013e3181b8b6f5]
- 19 **Alpantaki K,** Bano A, Pasku D, Mavrogenis AF, Papagelopoulos PJ, Sapkas GS, Korres DS, Katonis P. Thoracolumbar burst fractures: a systematic review of management. *Orthopedics* 2010; **33**: 422-429 [PMID: 20806752 DOI: 10.3928/01477447-7-20100429-24]
- 20 **Farcy JP,** Weidenbaum M, Glassman SD. Sagittal index in management of thoracolumbar burst fractures. *Spine (Phila Pa 1976)* 1990; **15**: 958-965 [PMID: 2259988 DOI: 10.1097/00007632-199009000-00022]
- 21 **Verlaan JJ,** Dhert WJ, Verbout AJ, Oner FC. Balloon vertebroplasty in combination with pedicle screw instrumentation: a novel technique to treat thoracic and lumbar burst fractures. *Spine (Phila Pa 1976)* 2005; **30**: E73-E79 [PMID: 15682000 DOI: 10.1097/01.brs.0000152162.64015.fb]
- 22 **Schmelzer-Schmied N,** Cartens C, Meeder PJ, Dafonseca K. Comparison of kyphoplasty with use of a calcium phosphate cement and non-operative therapy in patients with traumatic non-osteoporotic vertebral fractures. *Eur Spine J* 2009; **18**: 624-629 [PMID: 19165509 DOI: 10.1007/s00586-008-0880-x]
- 23 **Knavel EM,** Thielen KR, Kallmes DF. Vertebroplasty for the treatment of traumatic nonosteoporotic compression fractures. *AJNR Am J Neuroradiol* 2009; **30**: 323-327 [PMID: 19039045 DOI: 10.3174/ajnr.A1356]
- 24 **Korovessis P,** Hadjipavlou A, Repantis T. Minimal invasive short posterior instrumentation plus balloon kyphoplasty with calcium phosphate for burst and severe compression lumbar fractures. *Spine (Phila Pa 1976)* 2008; **33**: 658-667 [PMID: 18344860 DOI: 10.1097/BRS.0b013e318166e0bb]
- 25 **Blatter TR,** Jestaedt L, Weckbach A. Suitability of a calcium phosphate cement in osteoporotic vertebral body fracture augmentation: a controlled, randomized, clinical trial of balloon kyphoplasty comparing calcium phosphate versus polymethylmethacrylate. *Spine (Phila Pa 1976)* 2009; **34**: 108-114 [PMID: 19139662 DOI: 10.1097/BRS.0b013e31818f8bc1]
- 26 **Lieberman IH,** Dudeney S, Reinhardt MK, Bell G. Initial outcome and efficacy of "kyphoplasty" in the treatment of painful osteoporotic vertebral compression fractures. *Spine (Phila Pa 1976)* 2001; **26**: 1631-1638 [PMID: 11464159 DOI: 10.1097/00007632-200107150-00026]

- 27 **McGirt MJ**, Parker SL, Wolinsky JP, Witham TF, Bydon A, Gokaslan ZL. Vertebroplasty and kyphoplasty for the treatment of vertebral compression fractures: an evidenced-based review of the literature. *Spine J* 2009; **9**: 501-508 [PMID: 19251485 DOI: 10.1016/j.spinee.2009.01.003]
- 28 **Klazen CA**, Lohle PN, de Vries J, Jansen FH, Tielbeek AV, Blonk MC, Venmans A, van Rooij WJ, Schoemaker MC, Juttman JR, Lo TH, Verhaar HJ, van der Graaf Y, van Everdingen KJ, Muller AF, Elgersma OE, Halkema DR, Fransen H, Janssens X, Buskens E, Mali WP. Vertebroplasty versus conservative treatment in acute osteoporotic vertebral compression fractures (Vertos II): an open-label randomised trial. *Lancet* 2010; **376**: 1085-1092 [PMID: 20701962 DOI: 10.1016/S0140-6736(10)60954-3]
- 29 **Jacofsky DJ**, Papagelopoulos PJ, Sim FH. Advances and challenges in the surgical treatment of metastatic bone disease. *Clin Orthop Relat Res* 2003; (415 Suppl): S14-S18 [PMID: 14600588 DOI: 10.1097/01.blo0000093046.96273.07]
- 30 **Callstrom MR**, Charboneau JW, Goetz MP, Rubin J, Atwell TD, Farrell MA, Welch TJ, Maus TP. Image-guided ablation of painful metastatic bone tumors: a new and effective approach to a difficult problem. *Skeletal Radiol* 2006; **35**: 1-15 [PMID: 16205922 DOI: 10.1007/s00256-005-0003-2]
- 31 **Lapras C**, Mottolese C, Deruty R, Lapras C, Remond J, Duquesnel J. [Percutaneous injection of methyl-metacrylate in osteoporosis and severe vertebral osteolysis (Galibert's technic)]. *Ann Chir* 1989; **43**: 371-376 [PMID: 2757346]
- 32 **Gangi A**, Kastler BA, Dietemann JL. Percutaneous vertebroplasty guided by a combination of CT and fluoroscopy. *AJNR Am J Neuroradiol* 1994; **15**: 83-86 [PMID: 8141070]
- 33 **Hargunani R**, Le Corroller T, Khashoggi K, Murphy KJ, Munk PL. Percutaneous vertebral augmentation: the status of vertebroplasty and current controversies. *Semin Musculoskelet Radiol* 2011; **15**: 117-124 [PMID: 21500131 DOI: 10.1055/s-0031-1275594]
- 34 **Garfin SR**, Yuan HA, Reiley MA. New technologies in spine: kyphoplasty and vertebroplasty for the treatment of painful osteoporotic compression fractures. *Spine (Phila Pa 1976)* 2001; **26**: 1511-1515 [PMID: 11462078 DOI: 10.1097/00007632-200107150-00002]
- 35 **Ruiz Santiago F**, Pérez Abela AL, Almagro Ratia MM. [The end of vertebroplasties]. *Radiologia* 2012; **54**: 532-538 [PMID: 22578911 DOI: 10.1016/j.rx.2012.02.002]
- 36 **Grafe IA**, Baier M, Nöldge G, Weiss C, Da Fonseca K, Hillmeier J, Libicher M, Rudofsky G, Metzner C, Nawroth P, Meeder PJ, Kasperk C. Calcium-phosphate and polymethylmethacrylate cement in long-term outcome after kyphoplasty of painful osteoporotic vertebral fractures. *Spine (Phila Pa 1976)* 2008; **33**: 1284-1290 [PMID: 18469705 DOI: 10.1097/BRS.0b013e3181714a84]
- 37 **Nakano M**, Hirano N, Ishihara H, Kawaguchi Y, Watanabe H, Matsuura K. Calcium phosphate cement-based vertebroplasty compared with conservative treatment for osteoporotic compression fractures: a matched case-control study. *J Neurosurg Spine* 2006; **4**: 110-117 [PMID: 16506477 DOI: 10.3171/spi.2006.4.2.110]
- 38 **Mailli L**, Filippidis DK, Broutzos EN, Alexopoulou E, Kelekis N, Kelekis A. Clinical outcome and safety of multi-level vertebroplasty: clinical experience and results. *Cardiovasc Intervent Radiol* 2013; **36**: 183-191 [PMID: 22735889 DOI: 10.1007/s00270-012-0379-z]
- 39 **Srikumaran U**, Wong W, Belkoff SM, McCarthy EF. Histopathologic analysis of human vertebral bodies after vertebral augmentation with polymethylmethacrylate with use of an inflatable bone tamp. A case report. *J Bone Joint Surg Am* 2005; **87**: 1838-1843 [PMID: 16085628 DOI: 10.2106/JBJS.D.02848]
- 40 **Molloy S**, Mathis JM, Belkoff SM. The effect of vertebral body percentage fill on mechanical behavior during percutaneous vertebroplasty. *Spine (Phila Pa 1976)* 2003; **28**: 1549-1554 [PMID: 12865843 DOI: 10.1097/01.BRS.0000076831.38265.8D]
- 41 **Hiwatashi A**, Yoshiura T, Yamashita K, Kamano H, Dashjants T, Honda H. Morphologic change in vertebral body after percutaneous vertebroplasty: follow-up with MDCT. *AJR Am J Roentgenol* 2010; **195**: W207-W212 [PMID: 20729417 DOI: 10.2214/AJR.10.4195]
- 42 **Grohs JG**, Matzner M, Trieb K, Krepler P. Minimal invasive stabilization of osteoporotic vertebral fractures: a prospective nonrandomized comparison of vertebroplasty and balloon kyphoplasty. *J Spinal Disord Tech* 2005; **18**: 238-242 [PMID: 15905767]
- 43 **Hiwatashi A**, Westesson PL, Yoshiura T, Noguchi T, Togao O, Yamashita K, Kamano H, Honda H. Kyphoplasty and vertebroplasty produce the same degree of height restoration. *AJNR Am J Neuroradiol* 2009; **30**: 669-673 [PMID: 19131409 DOI: 10.3174/ajnr.A1442]
- 44 **Carlier RY**, Gordji H, Mompont DM, Vernhet N, Feydy A, Vallée C. Osteoporotic vertebral collapse: percutaneous vertebroplasty and local kyphosis correction. *Radiology* 2004; **233**: 891-898 [PMID: 15486209 DOI: 10.1148/radiol.2333030400]
- 45 **Feltes C**, Fountas KN, Machinis T, Nikolakakos LG, Dimopoulos V, Davydov R, Kassam M, Johnston KW, Robinson JS. Immediate and early postoperative pain relief after kyphoplasty without significant restoration of vertebral body height in acute osteoporotic vertebral fractures. *Neurosurg Focus* 2005; **18**: e5 [PMID: 15771395 DOI: 10.3171/foc.2005.18.3.6]
- 46 **McCall T**, Cole C, Dailey A. Vertebroplasty and kyphoplasty: a comparative review of efficacy and adverse events. *Curr Rev Musculoskelet Med* 2008; **1**: 17-23 [PMID: 19468894 DOI: 10.1007/s12178-007-9013-0]
- 47 **Chi JH**, Gokaslan ZL. Vertebroplasty and kyphoplasty for spinal metastases. *Curr Opin Support Palliat Care* 2008; **2**: 9-13 [PMID: 18685387 DOI: 10.1097/SPC.0b013e3282f5d907]
- 48 **Garfin SR**, Buckley RA, Ledlie J. Balloon kyphoplasty for symptomatic vertebral body compression fractures results in rapid, significant, and sustained improvements in back pain, function, and quality of life for elderly patients. *Spine (Phila Pa 1976)* 2006; **31**: 2213-2220 [PMID: 16946656 DOI: 10.1097/01.brs.0000232803.71640.ba]
- 49 **Grados F**, Depriester C, Cayrolle G, Hardy N, Deramond H, Fardellone P. Long-term observations of vertebral osteoporotic fractures treated by percutaneous vertebroplasty. *Rheumatology (Oxford)* 2000; **39**: 1410-1414 [PMID: 11136886 DOI: 10.1093/rheumatology/39.12.1410]
- 50 **Pérez-Higueras A**, Alvarez L, Rossi RE, Quiñones D, Al-Assir I. Percutaneous vertebroplasty: long-term clinical and radiological outcome. *Neuroradiology* 2002; **44**: 950-954 [PMID: 12428134 DOI: 10.1007/s00234-002-0856-1]
- 51 **Rousing R**, Hansen KL, Andersen MO, Jespersen SM, Thomsen K, Lauritsen JM. Twelve-months follow-up in forty-nine patients with acute/semiacute osteoporotic vertebral fractures treated conservatively or with percutaneous vertebroplasty: a clinical randomized study. *Spine (Phila Pa 1976)* 2010; **35**: 478-482 [PMID: 20190623 DOI: 10.1097/BRS.0b013e3181b71bd1]
- 52 **Alvarez L**, Alcaraz M, Pérez-Higueras A, Granizo JJ, de Miguel I, Rossi RE, Quiñones D. Percutaneous vertebroplasty: functional improvement in patients with osteoporotic compression fractures. *Spine (Phila Pa 1976)* 2006; **31**: 1113-1118 [PMID: 16648745 DOI: 10.1097/01.brs.0000216487.97965.38]
- 53 **Nakano M**, Hirano N, Ishihara H, Kawaguchi Y, Matsuura K. Calcium phosphate cement leakage after percutaneous vertebroplasty for osteoporotic vertebral fractures: risk factor analysis for cement leakage. *J Neurosurg Spine* 2005; **2**: 27-33 [PMID: 15658123 DOI: 10.3171/spi.2005.2.1.0027]
- 54 **Wardlaw D**, Cummings SR, Van Meirhaeghe J, Bastian

- L, Tillman JB, Ranstam J, Eastell R, Shabe P, Talmadge K, Boonen S. Efficacy and safety of balloon kyphoplasty compared with non-surgical care for vertebral compression fracture (FREE): a randomised controlled trial. *Lancet* 2009; **373**: 1016-1024 [PMID: 19246088 DOI: 10.1016/S0140-6736(09)60010-6]
- 55 **Kasperk C**, Grafe IA, Schmitt S, Nöldge G, Weiss C, Da Fonseca K, Hillmeier J, Libicher M, Sommer U, Rudofsky G, Meeder PJ, Nawroth P. Three-year outcomes after kyphoplasty in patients with osteoporosis with painful vertebral fractures. *J Vasc Interv Radiol* 2010; **21**: 701-709 [PMID: 20304677 DOI: 10.1016/j.jvir.2010.01.003]
- 56 **Buchbinder R**, Osborne RH, Ebeling PR, Wark JD, Mitchell P, Wriedt C, Graves S, Staples MP, Murphy B. A randomized trial of vertebroplasty for painful osteoporotic vertebral fractures. *N Engl J Med* 2009; **361**: 557-568 [PMID: 19657121 DOI: 10.1056/NEJMoa0900429]
- 57 **Kallmes DF**, Comstock BA, Heagerty PJ, Turner JA, Wilson DJ, Diamond TH, Edwards R, Gray LA, Stout L, Owen S, Hollingworth W, Ghdoke B, Annesley-Williams DJ, Ralston SH, Jarvik JG. A randomized trial of vertebroplasty for osteoporotic spinal fractures. *N Engl J Med* 2009; **361**: 569-579 [PMID: 19657122 DOI: 10.1056/NEJMoa0900563]
- 58 **Baerlocher MO**, Munk PL, Liu DM, Tomlinson G, Badii M, Kee ST, Loh CT, Hardy BW, Murphy KJ. Clinical utility of vertebroplasty: need for better evidence. *Radiology* 2010; **255**: 669-674 [PMID: 20501705 DOI: 10.1148/radiol.10092107]
- 59 **Ryu KS**, Park CK. The prognostic factors influencing on the therapeutic effect of percutaneous vertebroplasty in treating osteoporotic vertebral compression fractures. *J Korean Neurosurg Soc* 2009; **45**: 16-23 [PMID: 19242566 DOI: 10.3340/jkns.2009.45.1.16]
- 60 **Orr RD**. Vertebroplasty, cognitive dissonance, and evidence-based medicine: what do we do when the 'evidence' says we are wrong? *Cleve Clin J Med* 2010; **77**: 8-11 [PMID: 20048024 DOI: 10.3949/ccjm.77a.09146]
- 61 **Wilson DJ**, Owen S, Corkill RA. Facet joint injections as a means of reducing the need for vertebroplasty in insufficiency fractures of the spine. *Eur Radiol* 2011; **21**: 1772-1778 [PMID: 21487701 DOI: 10.1007/s00330-011-2115-5]
- 62 **Lehman VT**, Wood CP, Hunt CH, Carter RE, Allred JB, Diehn FE, Morris JM, Wald JT, Thielen KR. Facet joint signal change on MRI at levels of acute/subacute lumbar compression fractures. *AJNR Am J Neuroradiol* 2013; **34**: 1468-1473 [PMID: 23449650 DOI: 10.3174/ajnr.A3449]
- 63 **Benz BK**, Gemery JM, McIntyre JJ, Eskey CJ. Value of immediate preprocedure magnetic resonance imaging in patients scheduled to undergo vertebroplasty or kyphoplasty. *Spine (Phila Pa 1976)* 2009; **34**: 609-612 [PMID: 19282740 DOI: 10.1097/BRS.0b013e31819740bb]
- 64 **Brown DB**, Glaiberman CB, Gilula LA, Shimony JS. Correlation between preprocedural MRI findings and clinical outcomes in the treatment of chronic symptomatic vertebral compression fractures with percutaneous vertebroplasty. *AJR Am J Roentgenol* 2005; **184**: 1951-1955 [PMID: 15908560 DOI: 10.2214/ajr.184.6.01841951]
- 65 **Watters WC**, Baisden J, Gilbert TJ, Kreiner S, Resnick DK, Bono CM, Ghiselli G, Heggeness MH, Mazanec DJ, O'Neill C, Reitman CA, Shaffer WO, Summers JT, Toton JF. Degenerative lumbar spinal stenosis: an evidence-based clinical guideline for the diagnosis and treatment of degenerative lumbar spinal stenosis. *Spine J* 2008; **8**: 305-310 [PMID: 18082461 DOI: 10.1016/j.spinee.2007.10.033]
- 66 **Chiras J**, Barragán-Campos HM, Cormier E, Jean B, Rose M, LeJean L. [Vertebroplasty: state of the art]. *J Radiol* 2007; **88**: 1255-1260 [PMID: 17878871 DOI: 10.1016/S0221-0363(07)91335-9]
- 67 **Choe DH**, Marom EM, Ahrar K, Truong MT, Madewell JE. Pulmonary embolism of polymethyl methacrylate during percutaneous vertebroplasty and kyphoplasty. *AJR Am J Roentgenol* 2004; **183**: 1097-1102 [PMID: 15385313 DOI: 10.2214/ajr.183.4.1831097]
- 68 **Hulme PA**, Krebs J, Ferguson SJ, Berlemann U. Vertebroplasty and kyphoplasty: a systematic review of 69 clinical studies. *Spine (Phila Pa 1976)* 2006; **31**: 1983-2001 [PMID: 16924218 DOI: 10.1097/01.brs.0000229254.89952.6b]
- 69 **Becker S**, Garoscio M, Meissner J, Tuschel A, Ogon M. Is there an indication for prophylactic balloon kyphoplasty? A pilot study. *Clin Orthop Relat Res* 2007; **458**: 83-89 [PMID: 17310933]
- 70 **Barr JD**, Jensen ME, Hirsch JA, McGraw JK, Barr RM, Brook AL, Meyers PM, Munk PL, Murphy KJ, O'Toole JE, Rasmussen PA, Ryken TC, Sanelli PC, Schwartzberg MS, Seidenwurm D, Tutton SM, Zoarski GH, Kuo MD, Rose SC, Cardella JF. Position statement on percutaneous vertebral augmentation: a consensus statement developed by the Society of Interventional Radiology (SIR), American Association of Neurological Surgeons (AANS) and the Congress of Neurological Surgeons (CNS), American College of Radiology (ACR), American Society of Neuroradiology (ASNR), American Society of Spine Radiology (ASSR), Canadian Interventional Radiology Association (CIRA), and the Society of NeuroInterventional Surgery (SNIS). *J Vasc Interv Radiol* 2014; **25**: 171-81 [PMID: 24325929 DOI: 10.1016/j.jvir.2013.10.001]
- 71 **Legroux-Gérot I**, Lormeau C, Boutry N, Cotten A, Duquesnoy B, Cortet B. Long-term follow-up of vertebral osteoporotic fractures treated by percutaneous vertebroplasty. *Clin Rheumatol* 2004; **23**: 310-317 [PMID: 15293091 DOI: 10.1007/s10067-004-0914-7]
- 72 **Masala S**, Mastrangeli R, Petrella MC, Massari F, Ursone A, Simonetti G. Percutaneous vertebroplasty in 1,253 levels: results and long-term effectiveness in a single centre. *Eur Radiol* 2009; **19**: 165-171 [PMID: 18704433 DOI: 10.1007/s00330-008-1133-4]
- 73 **Berlemann U**, Franz T, Orlor R, Heini PF. Kyphoplasty for treatment of osteoporotic vertebral fractures: a prospective non-randomized study. *Eur Spine J* 2004; **13**: 496-501 [PMID: 15083353 DOI: 10.1007/s00586-004-0691-7]
- 74 **Khanna AJ**, Reinhardt MK, Togawa D, Lieberman IH. Functional outcomes of kyphoplasty for the treatment of osteoporotic and osteolytic vertebral compression fractures. *Osteoporos Int* 2006; **17**: 817-826 [PMID: 16518574 DOI: 10.1007/s00198-006-0068-3]
- 75 **Ma XL**, Xing D, Ma JX, Xu WG, Wang J, Chen Y. Balloon kyphoplasty versus percutaneous vertebroplasty in treating osteoporotic vertebral compression fracture: grading the evidence through a systematic review and meta-analysis. *Eur Spine J* 2012; **21**: 1844-1859 [PMID: 22832872 DOI: 10.1007/s00586-012-2441-6]
- 76 **Xing D**, Ma JX, Ma XL, Wang J, Xu WG, Chen Y, Song DH. A meta-analysis of balloon kyphoplasty compared to percutaneous vertebroplasty for treating osteoporotic vertebral compression fractures. *J Clin Neurosci* 2013; **20**: 795-803 [PMID: 23428914 DOI: 10.1016/j.jocn.2012.05.038]
- 77 **Eck JC**, Nachtigall D, Humphreys SC, Hodges SD. Comparison of vertebroplasty and balloon kyphoplasty for treatment of vertebral compression fractures: a meta-analysis of the literature. *Spine J* 2008; **8**: 488-497 [PMID: 17588820 DOI: 10.1016/j.spinee.2007.04.004]
- 78 **Liu JT**, Liao WJ, Tan WC, Lee JK, Liu CH, Chen YH, Lin TB. Balloon kyphoplasty versus vertebroplasty for treatment of osteoporotic vertebral compression fracture: a prospective, comparative, and randomized clinical study. *Osteoporos Int* 2010; **21**: 359-364 [PMID: 19513578 DOI: 10.1007/s00198-009-0952-8]
- 79 **Santiago FR**, Abela AP, Alvarez LG, Osuna RM, García Mdel M. Pain and functional outcome after vertebroplasty and kyphoplasty. A comparative study. *Eur J Radiol* 2010; **75**: e108-e113 [PMID: 20138724 DOI: 10.1016/j.ejrad.2010.01.010]
- 80 **Papanastassiou ID**, Phillips FM, Van Meirhaeghe J, Beren-

- son JR, Andersson GB, Chung G, Small BJ, Aghayev K, Vri-
onis FD. Comparing effects of kyphoplasty, vertebroplasty,
and non-surgical management in a systematic review of ran-
domized and non-randomized controlled studies. *Eur Spine*
J 2012; **21**: 1826-1843 [PMID: 22543412 DOI: 10.1007/s00586-
012-2314-z]
- 81 **Kumar K**, Nguyen R, Bishop S. A comparative analysis of
the results of vertebroplasty and kyphoplasty in osteopo-
rotic vertebral compression fractures. *Neurosurgery* 2010;
67: ons171-ons88; discussion ons188 [PMID: 20679931 DOI:
10.1227/01.NEU.0000380936.00143.11]
- 82 **Vallejo R**, Benyamin R, Floyd B, Casto JM, Joseph NJ,
Mekhail N. Percutaneous cement injection into a created
cavity for the treatment of vertebral body fracture: pre-
liminary results of a new vertebroplasty technique. *Clin J*
Pain 2006; **22**: 182-189 [PMID: 16428953 DOI: 10.1097/01.
ajp.0000169675.41815.49]
- 83 **Flors L**, Lonjedo E, Leiva-Salinas C, Martí-Bonmatí L,
Martínez-Rodrigo JJ, López-Pérez E, Figueres G, Raoli I.
Vesselplasty: a new technical approach to treat symptomatic
vertebral compression fractures. *AJR Am J Roentgenol* 2009;
193: 218-226 [PMID: 19542417 DOI: 10.2214/AJR.08.1503]
- 84 **Georgy BA**, Wong W. Plasma-mediated radiofrequency
ablation assisted percutaneous cement injection for treating
advanced malignant vertebral compression fractures. *AJNR*
Am J Neuroradiol 2007; **28**: 700-705 [PMID: 17416824]

P- Reviewers: Sebestyén A, Tajali SB, Teli MGA
S- Editor: Song XX **L- Editor:** A **E- Editor:** Zhang DN



Bone mineral density in cone beam computed tomography: Only a few shades of gray

Marcio José da Silva Campos, Thainara Salgueiro de Souza, Sergio Luiz Mota Júnior, Marcelo Reis Fraga, Robert Willer Farinazzo Vitral

Marcio José da Silva Campos, Thainara Salgueiro de Souza, Sergio Luiz Mota Júnior, Marcelo Reis Fraga, Robert Willer Farinazzo Vitral, Department of Orthodontics, Juiz de Fora Federal University, 36036-900, Minas Gerais, Brasil

Author contributions: Campos MJS and de Souza TS contributed equally to this work, drafted and wrote the manuscript; Mota Júnior SL and Fraga MR revised the manuscript; Campos MJS and Vitral RWF were responsible for final approval of the version to be published.

Correspondence to: Robert Willer Farinazzo Vitral, DDS, MD, PhD, Professor and Chair of Orthodontics, Department of Orthodontics, Juiz de Fora Federal University, Juiz de Fora, 36036-900, Minas Gerais, Brasil. robertvitral@gmail.com

Telephone: +55-32-21023879 Fax: +55-32-21023879

Received: December 27, 2013 Revised: March 11, 2014

Accepted: April 25, 2014

Published online: March 28, 2015

Abstract

Cone beam computed tomography (CBCT) has often been used to determine the quality of craniofacial bone structures through the determination of mineral density, which is based on gray scales of the images obtained. However, there is no consensus regarding the accuracy of the determination of the gray scales in these exams. This study aims to provide a literature review concerning the reliability of CBCT to determine bone mineral density. The gray values obtained with CBCT show a linear relationship with the attenuation coefficients of the materials, Hounsfield Units values obtained with medical computed tomography, and density values from dual energy X-ray absorciometry. However, errors are expected when CBCT images are used to define the quality of the scanned structures because these images show inconsistencies and arbitrariness in the gray values, particularly when related to abrupt change in the density of the object, X-ray beam hardening effect, scattered radiation, projection data discontinuity-related effect, differences between CBCT

devices, changes in the volume of the field of view (FOV), and changes in the relationships of size and position between the FOV and the object evaluated. A few methods of mathematical correction of the gray scales in CBCT have been proposed; however, they do not generate consistent values that are independent of the devices and their configurations or of the scanned objects. Thus, CBCT should not be considered the examination of choice for the determination of bone and soft tissue mineral density at the current stage, particularly when values obtained are to be compared to predetermined standard values. Comparisons between symmetrically positioned structures inside the FOV and in relation to the exomass of the object, as it occurs with the right and left sides of the skull, seem to be viable because the effects on the gray scale in the regions of interest are the same.

© 2015 Baishideng Publishing Group Inc. All rights reserved.

Key words: Tomography; Cone-Beam computed tomography; Bone mineral density; Reproducibility of results

Core tip: The development of cone beam computed tomography (CBCT) has allowed for more frequent use of these images in dentistry for the evaluation of dentomaxillofacial structures. Yet, there is no consensus regarding the accuracy of CBCT to determine mineral density of craniofacial bone structures, although this technique has been used for this purpose in several types of analyses. According to the studies available to date, it may be concluded that CBCT should not be considered the examination of choice for the determination of mineral density of osseous and soft tissues, especially when values obtained are compared with predetermined standard values.

Original sources: Campos MJS, de Souza TS, Mota Júnior SL,

Fraga MR, Vitral RWF. Bone mineral density in cone beam computed tomography: Only a few shades of gray. *World J Radiol* 2014; 6(8): 607-612 Available from: URL: <http://www.wjgnet.com/1949-8470/full/v6/i8/607.htm> DOI: <http://dx.doi.org/10.4329/wjr.v6.i8.607>

INTRODUCTION

Bidimensional radiographic methods (periapical, occlusal, panoramic and cephalometric radiographs) are widely used in dentistry; however, they do not provide visualization of the regions of interest without the superimposition of structures and consequent camouflage of anatomical details. The advent of images acquired from computed tomography (CT) has made more precise quantitative and qualitative evaluation of the adjacent structures possible^[1,2].

Although the use of CT is routine in medical practice, this examination has not been extensively widespread in dentistry, due to the presence of image artifacts, high cost, complexity of the examination and high dose radiation^[3].

The development of cone beam computed tomography (CBCT), used for the evaluation of dentomaxillofacial structures, has allowed for more frequent use of these images in dentistry because it is a less complex device that produces images with satisfactory resolution, with little artifact incidence and lower dose of radiation^[4].

Multislice and cone beam CT images are frequently used to determine mineral density of craniofacial bone structures^[5-10]. Yet, there is no consensus regarding the accuracy of CBCT for this type of analysis. While some studies advocate its use^[10-15], others advocate that CBCT is not an adequate tool for this type of evaluation because the intensity values of CBCT are influenced by the characteristics of the system^[4,13,16] and by the scanned object^[16-18]. This study aims to provide a literature review concerning the reliability of CBCT for the determination of bone mineral density of craniofacial structures.

BONE MINERAL DENSITY

Mineral density is determined by the amount of mineral mass contained in a certain volume of a structure, described in units of mass per area (in bidimensional images) or per volume (in tridimensional images), where only mineral content is considered^[19]. Several methods may be used to determine bone mineral density, including digital image analysis of microradiographs, single photon absorciometry, dual photon absorciometry, dual energy X-ray absorciometry (DEXA) and quantitative ultrasound^[20-22]. However, these procedures present with limitations inherent to the techniques used because density is determined through images of superimposed structures, not producing tridimensional information^[23,24].

Nowadays, multislice computed tomography (MSCT) is one of the most useful medical imaging techniques for the acquisition of data regarding not only bone density,

but the density of all the tissues of the body. In these examinations, density is described in hounsfield units (HU) and represents the relative density of a body tissue according to a calibrated gray-level scale based on HU values of the air (-1000 HU), water (0 HU) and dense bone (+1000 HU)^[25]. HU values are directly related to the mass absorption coefficient of different tissues^[26] and, despite some variation^[27], these values may be used for the determination of density of the tissues with a high degree of accuracy^[10] and sensitivity, detecting density differences of 1% or less^[28]. However, the gray scale can vary between different scanners and with different energies on the same MSCT scanner^[25]. The factor with the highest influence on the determination of the gray scale is the energy of the X-ray beam (kVp), which is directly related to the capacity of penetration of the primary beam. The bigger the energy of the X-ray beam, the bigger and more uniform its penetration will be, resulting in smaller variation of attenuation, smaller contrast of images, and smaller density of the structures evaluated. The adequate setting of the energy applied allows for the determination of a correct density^[29].

CONE BEAM CT

After the development of CBCT, a less complex device with low operational cost and reduced radiation emission^[30-32] used for the acquisition of tridimensional images of dentomaxillofacial structures by Mozzo *et al.*^[33], the indication of medical CT for the evaluation of these structures decreased considerably, especially due to the higher radiation dose applied to the patient during image acquisition^[10,32]. Thus, CBCT has been proposed as a diagnostic method for the determination of bone mineral density^[10,11,18,34-36]. Gray values obtained with CBCT are used in an analog way as the HU values for the determination of mineral density^[16] and show a linear relationship with the attenuation coefficients of the materials^[13,15], HU values obtained with medical CT^[11,12,37,38], and density values from DEXA^[14].

Despite the correlation between gray values obtained with MSCT and CBCT, errors are expected when CBCT images are used to define the density of scanned structures^[39] because these images present with inconsistencies and arbitrariness of gray values^[16,40], especially when related to abrupt changes of density in the object^[41,42], X-ray beam hardening effect^[39,43], scattered radiation^[43] and projection data discontinuity-related effect^[16], making the validity of the measurements obtained questionable (Table 1).

In CBCT, the abrupt and discrepant variation of the attenuation coefficient of the X-rays in the scanned structures, as occurs in the presence of metallic structures, creates artifacts in the images, which are characterized by dark and bright streaks in the vicinity of the metal object. Once these artifacts exhibit a different color from that of the structure to be analyzed, they are responsible for the inconsistencies in the gray values in the areas where they are present^[15,41,42].

Another source of artifacts in CBCT images is the

Table 1 Factors that might lead to inconsistencies and arbitrariness of grey values on cone beam computed tomography images

Ref.	Factors
Nackaerts <i>et al.</i> ^[4]	Variation in the devices Image-acquisition settings
Mah <i>et al.</i> ^[13]	Relationship between the object evaluated and FOV
	The position held by the region of interest
Reeves <i>et al.</i> ^[15]	Variation in the devices
Katsumata <i>et al.</i> ^[16]	Abrupt changes of density in the object
	Projection data discontinuity-related effect
Bryant <i>et al.</i> ^[17]	Variation in the CBCT devices
	Image-acquisition settings
	Relationship between the object evaluated and FOV
	Projection data discontinuity-related effect
Katsumata <i>et al.</i> ^[18]	Relationship between the object evaluated and FOV
	The amount of exomass
	The dimensions of the FOV
Pauwels <i>et al.</i> ^[39]	The amount of exomass
	X-ray beam hardening effect
Schulze <i>et al.</i> ^[41]	Projection data discontinuity-related effect
	Variation in the devices
	Abrupt changes of density in the object
Pauwels <i>et al.</i> ^[42]	X-ray beam hardening effect
	Scattered radiation
Goodsitt <i>et al.</i> ^[43]	Abrupt changes of density in the object
	X-ray beam hardening effect
Liu <i>et al.</i> ^[50]	Scattered radiation
	The position held by the region of interest

CBCT: Cone beam computed tomography; FOV: Field of view.

phenomenon of X-ray beam hardening. In CBCT, when the beam of X-rays made up of broad spectrum photons reaches a certain material, the low energy photons are easily absorbed, altering the spectrum of the beam. Once the X-ray beam reaches a specific point or area of the object by different angles, varied alterations in the intensity of its energy spectrum occur before it strikes the detector, generating different readings of the attenuation coefficient of this point, and may produce dark streaks in the images obtained^[41]. Besides causing artifacts in the images, when the low energy photons are absorbed, the X-ray beam gains energy, passing through the tissues more easily, causing an underestimation of the attenuation coefficient and producing dark areas in the images^[42].

An underestimation of the attenuation coefficient due to the occurrence of darker gray values also occurs as a consequence of scattered radiation. When the X-ray beam interacts with the object being evaluated, some photons are diffracted from their original position and strike the detector in a random way. This scattered radiation is added to the primary radiation of the X-ray beam, overestimating the intensity measured by the system and underestimating the attenuation coefficient of the object, affecting the obtained values of density^[41]. CBCT devices have bigger detectors than the MSCT because the X-ray beam of the former is conical and of the latter is in the shape of a fan, favoring the occurrence of scattered radiation^[44].

Another type of artifact related to CBCT images is known as projection data discontinuity-related artifact,

which occurs when FOV is smaller than the scanned object. First, during the system rotation for the image acquisition, the X-ray beam strikes the parts of the object located outside the FOV, creating peripheral bright-band near the boundary of the FOV^[16,39], this effect being directly related to the mass and spatial distribution of materials or tissues outside the FOV^[17].

Besides the presence of artifacts and the inconsistency of the gray values attributed to the characteristics of CBCT, variation in the devices^[4,13,16], image-acquisition settings^[4,16], and the relationship between the object evaluated and FOV^[4,16-18] may also influence in the images obtained because alterations of these variables are associated with low reproducibility of gray values. Due mainly to the integration between some of these characteristics, in most instances, variables are not adequately controlled in the studies of reliability of values of density in CBCT.

At present, there are several models of CBCT devices in the market and significant fluctuations in gray values were demonstrated when different equipment was compared^[4,13]. Each CBCT scanner has its own factors of exposition and image reconstruction (FOV, kVp, mA, voxel size, exposure time). Some are fixed, others are variable^[13,39], making it difficult or even impossible for studies on determination of density in CBCT to draw conclusions for all the systems used^[39].

According to Pauwels *et al.*^[39], some CBCT devices with specific protocols of exposition generate stable gray values which may be related to HU and density. However, as with medical CT, the determination of gray values is specific to the scanner, depending on the calibration of the devices.

The determination of the dimensions of the FOV in CBCT is very variable due to its different applicability in dentistry. This adaptation of the size of the FOV according to the demand of the examination is a great advantage of the system because it exposes the patient to a minimum amount of radiation in order to evaluate the region of interest. However, it may have significant implications in the gray values of the structures, with small volume FOVs associated with reduced values of density^[18].

The decrease of gray values in the smallest FOV may be explained by the reduction of the diameter of the X-ray beam so as to irradiate only the region of interest^[45-48]. This X-ray beam limitation may lead to the decrease of the amount of low-energy photons and to the increase in the capacity of penetration of X-rays^[49], resulting in a relative reduction of the value of attenuation of X-rays and gray values^[43].

The manipulation of the dimensions of the FOV may also alter the amount of exomass, mass present outside the FOV during image acquisition, which is associated with the variability of the gray values in CBCT examinations^[17,18]. Katsumata *et al.*^[18] reported a significant variation of the gray values when objects of different mass were evaluated with different FOV volumes, where the greater volume FOV provided the elimination of the exomass, resulting in less variability of the gray values.

The variability of the gray values associated with the exomass may be explained by the projection data discontinuity caused by the variation of the superimpositions of the non-homogeneous and non-symmetrical tissues outside the FOV along the rotation of the X-ray beam during image acquisition^[16,39].

Another factor that may be related to the variability of the gray values in CBCT is the position held by the region of interest (specific area of measurement of density) inside the FOV. This variability occurred when density was determined in various places of a homogeneous structure^[4,50] and with more intensity when the same object was scanned repeatedly in different positions inside the FOV under the same exposure conditions^[4].

Despite the many variables that may affect image quality and the determination of gray values in CBCT examinations, great effort has been made in obtaining valid gray values in these images. Studies have described methods for mathematical correction of gray levels in CBCT examination using as reference X-ray attenuation coefficients of standardized materials^[13,15], gray values obtained in conventional CT examination^[50,51], and even correction algorithms during or after image acquisition^[51,52]. Yet, owing to different configurations of image acquisition, which may be specific for each CBCT device or altered for several applications of these examinations in dentistry, the correction methods of gray values obtained in CBCT still do not generate consistent values which are independent of the devices and their configurations or of the scanned objects^[15,50].

CONCLUSION

According to the studies available to date, it may be concluded that CBCT should not be considered the examination of choice for the determination of mineral density of osseous and soft tissues, especially when values obtained are compared with predetermined standard values. Comparisons between symmetrically positioned structures inside the FOV and in relation to the exomass of the object, as with the right and left sides of the skull, seem to be viable because the effects on the gray values in the regions of interest are the same.

REFERENCES

- 1 Schwarz MS, Rothman SL, Rhodes ML, Chafetz N. Computed tomography: Part I. Preoperative assessment of the mandible for endosseous implant surgery. *Int J Oral Maxillofac Implants* 1987; **2**: 137-141 [PMID: 3481354]
- 2 Velvart P, Hecker H, Tillinger G. Detection of the apical lesion and the mandibular canal in conventional radiography and computed tomography. *Oral Surg Oral Med Oral Pathol Oral Radiol Endod* 2001; **92**: 682-688 [PMID: 11740486 DOI: 10.1067/moe.2001.118904]
- 3 Marques AP, Perrella A, Arita ES, Pereira MF, Cavalcanti Mde G. Assessment of simulated mandibular condyle bone lesions by cone beam computed tomography. *Braz Oral Res* 2010; **24**: 467-474 [PMID: 21180970 DOI: 10.1590/S1806-83242010000400016]
- 4 Nackaerts O, Maes F, Yan H, Couto Souza P, Pauwels R, Jacobs R. Analysis of intensity variability in multislice and cone beam computed tomography. *Clin Oral Implants Res* 2011; **22**: 873-879 [PMID: 21244502 DOI: 10.1111/j.1600-0501.2010.02076.x]
- 5 Lindh C, Obrant K, Petersson A. Maxillary bone mineral density and its relationship to the bone mineral density of the lumbar spine and hip. *Oral Surg Oral Med Oral Pathol Oral Radiol Endod* 2004; **98**: 102-109 [PMID: 15243479 DOI: 10.1016/S1079-2104(03)00460-8]
- 6 Turkyilmaz I, Tözüm TF, Tümer C. Bone density assessments of oral implant sites using computerized tomography. *J Oral Rehabil* 2007; **34**: 267-272 [PMID: 17371564 DOI: 10.1111/j.1365-2842.2006.01689.x]
- 7 de Oliveira RC, Leles CR, Normanha LM, Lindh C, Ribeiro-Rotta RF. Assessments of trabecular bone density at implant sites on CT images. *Oral Surg Oral Med Oral Pathol Oral Radiol Endod* 2008; **105**: 231-238 [PMID: 18230392 DOI: 10.1016/j.tripleo.2007.08.007]
- 8 Park HS, Lee YJ, Jeong SH, Kwon TG. Density of the alveolar and basal bones of the maxilla and the mandible. *Am J Orthod Dentofacial Orthop* 2008; **133**: 30-37 [PMID: 18174068 DOI: 10.1016/j.ajodo.2006.01.044]
- 9 Choi JH, Park CH, Yi SW, Lim HJ, Hwang HS. Bone density measurement in interdental areas with simulated placement of orthodontic miniscrew implants. *Am J Orthod Dentofacial Orthop* 2009; **136**: 766.e1-766.e12; discussion 766-767 [PMID: 19962594 DOI: 10.1016/j.ajodo.2009.04.019]
- 10 Hsu JT, Chang HW, Huang HL, Yu JH, Li YF, Tu MG. Bone density changes around teeth during orthodontic treatment. *Clin Oral Investig* 2011; **15**: 511-519 [PMID: 20393863 DOI: 10.1007/s00784-010-0410-1]
- 11 Aranyarachkul P, Caruso J, Gantes B, Schulz E, Riggs M, Dus I, Yamada JM, Crigger M. Bone density assessments of dental implant sites: 2. Quantitative cone-beam computerized tomography. *Int J Oral Maxillofac Implants* 2005; **20**: 416-424 [PMID: 15973953]
- 12 Lagravère MO, Carey J, Ben-Zvi M, Packota GV, Major PW. Effect of object location on the density measurement and Hounsfield conversion in a NewTom 3G cone beam computed tomography unit. *Dentomaxillofac Radiol* 2008; **37**: 305-308 [PMID: 18757714 DOI: 10.1259/dmfr/65993482]
- 13 Mah P, Reeves TE, McDavid WD. Deriving Hounsfield units using grey levels in cone beam computed tomography. *Dentomaxillofac Radiol* 2010; **39**: 323-335 [PMID: 20729181 DOI: 10.1259/dmfr/19603304]
- 14 Marquezan M, Lau TC, Mattos CT, Cunha AC, Nojima LI, Sant'Anna EF, Souza MM, Araújo MT. Bone mineral density. *Angle Orthod* 2012; **82**: 62-66 [PMID: 21774580 DOI: 10.2319/031811-192.1]
- 15 Reeves TE, Mah P, McDavid WD. Deriving Hounsfield units using grey levels in cone beam CT: a clinical application. *Dentomaxillofac Radiol* 2012; **41**: 500-508 [PMID: 22752324 DOI: 10.1259/dmfr/31640433]
- 16 Katsumata A, Hirukawa A, Okumura S, Naitoh M, Fujishita M, Arijii E, Langlais RP. Effects of image artifacts on gray-value density in limited-volume cone-beam computerized tomography. *Oral Surg Oral Med Oral Pathol Oral Radiol Endod* 2007; **104**: 829-836 [PMID: 17448704]
- 17 Bryant JA, Drage NA, Richmond S. Study of the scan uniformity from an i-CAT cone beam computed tomography dental imaging system. *Dentomaxillofac Radiol* 2008; **37**: 365-374 [PMID: 18812597 DOI: 10.1259/dmfr/13227258]
- 18 Katsumata A, Hirukawa A, Okumura S, Naitoh M, Fujishita M, Arijii E, Langlais RP. Relationship between density variability and imaging volume size in cone-beam computerized tomographic scanning of the maxillofacial region: an in vitro study. *Oral Surg Oral Med Oral Pathol Oral Radiol Endod* 2009; **107**: 420-425 [PMID: 18715805 DOI: 10.1016/j.tripleo.2008.05.049]

- 19 **NIH Consensus Development Panel on Osteoporosis Prevention, Diagnosis, and Therapy.** Osteoporosis prevention, diagnosis, and therapy. *JAMA* 2001; **285**: 785-795 [PMID: 11176917 DOI: 10.1001/jama.285.6.785]
- 20 **Genant HK, Engelke K, Fuerst T, Glüer CC, Grampp S, Harris ST, Jergas M, Lang T, Lu Y, Majumdar S, Mathur A, Takada M.** Noninvasive assessment of bone mineral and structure: state of the art. *J Bone Miner Res* 1996; **11**: 707-730 [PMID: 8725168 DOI: 10.1002/jbmr.5650110602]
- 21 **Jäger A, Radlanski RJ, Taufall D, Klein C, Steinhöfel N, Döler W.** Quantitative determination of alveolar bone density using digital image analysis of microradiographs. *Anat Anz* 1990; **170**: 171-179 [PMID: 2375496]
- 22 **Hans D, Fuerst T, Uffmann M.** Bone density and quality measurement using ultrasound. *Curr Opin Rheumatol* 1996; **8**: 370-375 [PMID: 8864591 DOI: 10.1097/00002281-199607000-00016]
- 23 **Choël L, Duboeuf F, Bourgeois D, Briguet A, Lissac M.** Trabecular alveolar bone in the human mandible: a dual-energy x-ray absorptiometry study. *Oral Surg Oral Med Oral Pathol Oral Radiol Endod* 2003; **95**: 364-370 [PMID: 12627111 DOI: 10.1067/moe.2003.119]
- 24 **Chang HW, Huang HL, Yu JH, Hsu JT, Li YF, Wu YF.** Effects of orthodontic tooth movement on alveolar bone density. *Clin Oral Investig* 2012; **16**: 679-688 [PMID: 21519883 DOI: 10.1007/s00784-011-0552-9]
- 25 **White SC, Pharoah MJ.** Oral radiology: principles and interpretation. 5th ed. Philadelphia: Mosby, 2004
- 26 **Homolka P, Beer A, Birkfellner W, Nowotny R, Gahleitner A, Tschabitscher M, Bergmann H.** Bone mineral density measurement with dental quantitative CT prior to dental implant placement in cadaver mandibles: pilot study. *Radiology* 2002; **224**: 247-252 [PMID: 12091691 DOI: 10.1148/radiol.2241010948]
- 27 **Lecomber AR, Yoneyama Y, Lovelock DJ, Hosoi T, Adams AM.** Comparison of patient dose from imaging protocols for dental implant planning using conventional radiography and computed tomography. *Dentomaxillofac Radiol* 2001; **30**: 255-259 [PMID: 11571544 DOI: 10.1038/sj.dmfr.4600627]
- 28 **Kravitz ND, Kusnoto B.** Risks and complications of orthodontic miniscrews. *Am J Orthod Dentofacial Orthop* 2007; **131**: S43-S51 [PMID: 17448385 DOI: 10.1016/j.ajodo.2006.04.027]
- 29 **Wolbarst AB, Biwer BM, Cady R, Chen SY, Domotor S, Egidi P, LePoire DJ, Mo T, Peterson J, Walker S.** ISCORS Catalog of References to Parameter Values and Distributions Used in Environmental Pathway Modeling for Cleanup of Sites Contaminated with Radioactivity. *Health Phys* 2005; **89**: S91-S99 [PMID: 16224267 DOI: 10.1097/01.HP.0000177683.93443.f4]
- 30 **Mah J, Hatcher D.** Three-dimensional craniofacial imaging. *Am J Orthod Dentofacial Orthop* 2004; **126**: 308-309 [PMID: 15356493 DOI: 10.1016/j.ajodo.2004.06.024]
- 31 **Scarfe WC, Farman AG, Sukovic P.** Clinical applications of cone-beam computed tomography in dental practice. *J Can Dent Assoc* 2006; **72**: 75-80 [PMID: 16480609]
- 32 **Ludlow JB, Ivanovic M.** Comparative dosimetry of dental CBCT devices and 64-slice CT for oral and maxillofacial radiology. *Oral Surg Oral Med Oral Pathol Oral Radiol Endod* 2008; **106**: 106-114 [PMID: 18504152 DOI: 10.1016/j.tripleo.2008.03.018]
- 33 **Mozzo P, Procacci C, Tacconi A, Martini PT, Andreis IA.** A new volumetric CT machine for dental imaging based on the cone-beam technique: preliminary results. *Eur Radiol* 1998; **8**: 1558-1564 [PMID: 9866761 DOI: 10.1007/s003300050586]
- 34 **Lee S, Gantes B, Riggs M, Crigger M.** Bone density assessments of dental implant sites: 3. Bone quality evaluation during osteotomy and implant placement. *Int J Oral Maxillofac Implants* 2007; **22**: 208-212 [PMID: 17465345]
- 35 **Campos MJ, de Albuquerque EG, Pinto BC, Húngaro HM, Gravina MA, Fraga MR, Vitral RW.** The role of orthodontic tooth movement in bone and root mineral density: a study of patients submitted and not submitted to orthodontic treatment. *Med Sci Monit* 2012; **18**: CR752-CR757 [PMID: 23197239 DOI: 10.12659/MSM.883604]
- 36 **Salimov F, Tatli U, Kürkcü M, Akoğlan M, Oztunç H, Kurtoğlu C.** Evaluation of relationship between preoperative bone density values derived from cone beam computed tomography and implant stability parameters: a clinical study. *Clin Oral Implants Res* 2013; Epub ahead of print [PMID: 23772811 DOI: 10.1111/clar.12219]
- 37 **Naitoh M, Hirukawa A, Katsumata A, Ariji E.** Evaluation of voxel values in mandibular cancellous bone: relationship between cone-beam computed tomography and multislice helical computed tomography. *Clin Oral Implants Res* 2009; **20**: 503-506 [PMID: 19250241 DOI: 10.1111/j.1600-0501.2008.01672.x]
- 38 **Nomura Y, Watanabe H, Honda E, Kurabayashi T.** Reliability of voxel values from cone-beam computed tomography for dental use in evaluating bone mineral density. *Clin Oral Implants Res* 2010; **21**: 558-562 [PMID: 20443807 DOI: 10.1111/j.1600-0501.2009.01896.x]
- 39 **Pauwels R, Nackaerts O, Bellaiche N, Stamatakis H, Tsiklakis K, Walker A, Bosmans H, Bogaerts R, Jacobs R, Horner K.** Variability of dental cone beam CT grey values for density estimations. *Br J Radiol* 2013; **86**: 20120135 [PMID: 23255537 DOI: 10.1259/bjr.20120135]
- 40 **Hassan B, Metska ME, Ozok AR, van der Stelt P, Wesselink PR.** Comparison of five cone beam computed tomography systems for the detection of vertical root fractures. *J Endod* 2010; **36**: 126-129 [PMID: 20003950 DOI: 10.1016/j.joen.2009.09.013]
- 41 **Schulze R, Heil U, Gross D, Bruellmann DD, Dranischnikow E, Schwanecke U, Schoemer E.** Artefacts in CBCT: a review. *Dentomaxillofac Radiol* 2011; **40**: 265-273 [PMID: 21697151 DOI: 10.1259/dmfr/30642039]
- 42 **Pauwels R, Stamatakis H, Bosmans H, Bogaerts R, Jacobs R, Horner K, Tsiklakis K.** Quantification of metal artifacts on cone beam computed tomography images. *Clin Oral Implants Res* 2013; **24** Suppl A100: 94-99 [PMID: 22168574 DOI: 10.1111/j.1600-0501.2011.02382.x]
- 43 **Goodsitt MM, Chan HP, Way TW, Larson SC, Christodoulou EG, Kim J.** Accuracy of the CT numbers of simulated lung nodules imaged with multi-detector CT scanners. *Med Phys* 2006; **33**: 3006-3017 [PMID: 16964879 DOI: 10.1118/1.2219332]
- 44 **Kalender WA, Kyriakou Y.** Flat-detector computed tomography (FD-CT). *Eur Radiol* 2007; **17**: 2767-2779 [PMID: 17587058 DOI: 10.1007/s00330-007-0651-9]
- 45 **Palomo JM, Rao PS, Hans MG.** Influence of CBCT exposure conditions on radiation dose. *Oral Surg Oral Med Oral Pathol Oral Radiol Endod* 2008; **105**: 773-782 [PMID: 18424119 DOI: 10.1016/j.tripleo.2007.12.019]
- 46 **Pauwels R, Beinsberger J, Collaert B, Theodorakou C, Rogers J, Walker A, Cockmartin L, Bosmans H, Jacobs R, Bogaerts R, Horner K.** Effective dose range for dental cone beam computed tomography scanners. *Eur J Radiol* 2012; **81**: 267-271 [PMID: 21196094 DOI: 10.1016/j.ejrad.2010.11.028]
- 47 **Siewerdsen JH, Jaffray DA.** Cone-beam computed tomography with a flat-panel imager: magnitude and effects of x-ray scatter. *Med Phys* 2001; **28**: 220-231 [PMID: 11243347 DOI: 10.1118/1.1339879]
- 48 **Spies L, Evans PM, Partridge M, Hansen VN, Bortfeld T.** Direct measurement and analytical modeling of scatter in portal imaging. *Med Phys* 2000; **27**: 462-471 [PMID: 10757598 DOI: 10.1118/1.598914]
- 49 **Kheruka S, Naithani U, Maurya A, Painuly N, Aggarwal L, Gambhir S.** A study to improve the image quality in low-dose computed tomography (SPECT) using filtration. *Indian J Nucl Med* 2011; **26**: 14-21 [PMID: 21969774 DOI: 10.4103/0972-3919.84595]
- 50 **Liu Y, Bäuerle T, Pan L, Dimitrakopoulou-Strauss A, Strauss LG, Heiss C, Schnettler R, Semmler W, Cao L.** Calibration of

- cone beam CT using relative attenuation ratio for quantitative assessment of bone density: a small animal study. *Int J Comput Assist Radiol Surg* 2013; **8**: 733-739 [PMID: 23225074 DOI: 10.1007/s11548-012-0803-5]
- 51 **Naitoh M**, Aimiya H, Hirukawa A, Arijji E. Morphometric analysis of mandibular trabecular bone using cone beam computed tomography: an in vitro study. *Int J Oral Maxillofac Implants* 2010; **25**: 1093-1098 [PMID: 21197484]
- 52 **Kachelriess M**, Sourbelle K, Kalender WA. Empirical cupping correction: a first-order raw data pre-correction for cone-beam computed tomography. *Med Phys* 2006; **33**: 1269-1274 [PMID: 16752561 DOI: 10.1118/1.2188076]

P- Reviewer: Chang Z, Kamishima T,
Kwok YM, Neves FS, Peremans K

S- Editor: Ji FF **L- Editor:** Roemmele A **E- Editor:** Wu HL



From histology to micro-CT: Measuring and modeling resorption cavities and their relation to bone competence

Jef Vanderoost, G Harry van Lenthe

Jef Vanderoost, G Harry van Lenthe, Biomechanics Section, Department of Mechanical Engineering, KU Leuven, 3001 Leuven, Belgium

Author contributions: Vanderoost J and van Lenthe GH solely contributed to this paper.

Correspondence to: G Harry van Lenthe, PhD, Biomechanics Section, Department of Mechanical Engineering, KU Leuven, Celestijnenlaan 300c b2419, 3001 Leuven, Belgium. vanlenthe@kuleuven.be

Telephone: +32-16-322595 Fax: +32-16-322595

Received: December 22, 2013 Revised: April 22, 2014

Accepted: July 25, 2014

Published online: March 28, 2015

Abstract

The process of bone remodelling plays an essential role in the emergence and maintenance of bone geometry and its internal structure. Osteoclasts are one of the three main bone cell types that play a crucial role in the bone remodelling cycle. At the microstructural level, osteoclasts create bone deficits by eroding resorption cavities. Understanding how these cavities impair the mechanical quality of the bone is not only relevant in quantifying the impact of resorption cavities in healthy bone and normal aging, but maybe even more so in quantifying their role in metabolic bone diseases. Metabolic bone diseases and their treatment are both known to affect the bone remodelling cycle; hence, the bone mechanical competence can and will be affected. However, the current knowledge of the precise dimensions of these cavities and their effect on bone competence is rather limited. This is not surprising considering the difficulties in deriving three-dimensional (3D) properties from two-dimensional (2D) histological sections. The measurement difficulties are reflected in the evaluation of how resorption cavities affect bone competence. Although detailed 3D models are generally being used to quantify the mechanical impact of the cavities, the representation of the cavities themselves has basically

been limited to simplified shapes and averaged cavity properties. Qualitatively, these models indicate that cavity size and location are important, and that the effect of cavities is larger than can be expected from simple bone loss. In summary, the dimensions of osteoclast resorption cavities were until recently estimated from 2D measures; hence, a careful interpretation of resorption cavity dimensions is necessary. More effort needs to go into correctly quantifying resorption cavities using modern 3D imaging techniques like micro-computed tomography (micro-CT) and synchrotron radiation CT. Osteoclast resorption cavities affect bone competence. The structure-function relationships have been analysed using computational models that, on one hand, provide rather detailed information on trabecular bone structure, but on the other incorporate rather crude assumptions on cavity dimensions. The use of high-resolution representations and parametric descriptions could be potential routes to improve the quantitative fidelity of these models.

© 2015 Baishideng Publishing Group Inc. All rights reserved.

Key words: Resorption cavities; Histology; Micro-computed tomography

Core tip: Osteoclasts create bone deficits by eroding resorption cavities. Understanding how these cavities impair the mechanical quality of the bone is relevant in both in healthy bone and in metabolic bone diseases. However, the current knowledge of their dimensions and effect on bone competence remains limited. Until recently cavity dimensions were estimated from two-dimensional measures (histology), hence, careful interpretation was necessary. With new imaging techniques quantifying resorption cavities in three-dimensional becomes feasible. Computational models have shown that resorption cavities affect bone competence. The use of high-resolution representations and parametric descriptions could improve the quantitative fidelity of these models.

Original sources: Vanderoost J, van Lenthe GH. From histology to micro-CT: Measuring and modeling resorption cavities and their relation to bone competence. *World J Radiol* 2014; 6(9): 643-656 Available from: URL: <http://www.wjgnet.com/1949-8470/full/v6/i9/643.htm> DOI: <http://dx.doi.org/10.4329/wjr.v6.i9.643>

INTRODUCTION

The process of bone remodelling plays an essential role in emergence and maintenance of bone geometry and its internal structure. This system has been extensively investigated from different angles, including its biology, chemistry and (bio) mechanical consequences. From a structural and mechanical point of view the most essential part of the process is the resorption and formation of bone performed by the basic multicellular units (BMU). This group of cells is responsible for bone loss and bone gain and determines the mechanical properties of the bone both in structure and material properties. In case of metabolic bone diseases, the functioning of these cells is altered. Structurally, and consequently mechanically, resorption cavities formed during resorption, determine the bone deficit. These cavities are an essential element in modelling and predicting the effect of bone disease and treatment. Despite this fact, the effort going into specifically quantifying these cavities and their effect on bone strength is relatively limited. Besides that, measuring methods are numerous and their results require careful interpretation when used for modelling purposes. This review aims at bundling the knowledge on these cavities and their biomechanical role. More specifically, its goal is: (1) to provide an overview of methods that can quantify the geometric properties of resorption; and (2) to apply this information to critically review biomechanical models that incorporate these geometric properties. Our premise is a mechanical point of view; hence, for the purpose of this review we will focus on direct impact of the presence of cavities on bone competence rather than investigating the dynamic parameters of the remodelling process. Our focus lies on bone remodelling in trabecular bone. Since trabecular bone has a much higher specific bone surface than cortical bone, it is more vulnerable to these surface-based processes^[1,2].

METHODOLOGY

PubMed was searched in the first half of 2012 to identify relevant literature. The search terms used were “resorption cavities”, “Howship’s lacunae”, “resorption”, “erosion”, “remodelling” separately and in combination with “bone”, “trabecular bone” or “cancellous bone”. For the modelling section combinations with “remodelling”, “model” and “finite elements” were also used. Subsequently numerous cross-references were followed through. This review does not claim to cover all publications related to the subject. Specifically in section 5 (Characteristics of resorption cavities) only a selection of

publications was included, given the vast amount of studies analysing transiliac bone biopsies.

RESORPTION CAVITIES AND THE BONE REMODELLING CYCLE

Frost first introduced the concept of the BMU^[3]. These units are a group of cells which, in a coordinated way, control the bone remodelling process. A team of osteoclasts perform the bone resorption. These irregularly shaped cells remove old bone and form the resorption cavities or Howship’s lacunae, which are later refilled by the osteoblasts. The osteoblasts perform the bone formation by excreting the building blocks of the bone matrix (unmineralised bone or osteoid) and have a role in the mineralisation of this soft bone^[4,5]. Some osteoblasts get entombed in the bone matrix and differentiate to osteocytes. The cytoplasmic processes of these osteocytes extend through a network of canaliculi. It is assumed that this network monitors the local strain environment and thus has a role in the signalling process of bone remodelling^[2,5,6]. Other osteoblasts die or become bone lining cells. These cells digest unmineralised osteoid and might be involved in the localization and initiation of remodelling^[5]. The result of BMU action, the packet of new bone, is called a bone structural unit (BSU)^[7]. Bone structural units are the Haversian systems or osteons in cortical bone, and semi lunar structures separated by cement lines in trabecular bone^[8]. The BMU exists and moves in three dimensions, excavating and refilling a tunnel through cortical bone or a trench across the surface of cancellous bone^[9].

After resorption, an intermediary phase, called “reversal phase” as introduced by Baron^[10], exists in which mononuclear cells occupy the lacunae and no resorption takes place^[11]. It is in this phase that the cement line is formed.

Formation and resorption are coupled, both in space and in time. It has been observed that osteoclasts occupy the more superior parts of resorption lacunae, while mononuclear cells and preosteoblast-like cells are situated in the deeper parts. This supports the hypothesis that these cell types precede each other in the remodelling process^[11]. It is likely that formation is preceded by resorption and they may even occur simultaneously in the same remodelling unit^[4,6,12-15], yet interruptions in the process, both in formation and resorption, have been hypothesized^[14]. It has been suggested that mononuclear cells are also active in the resorption process, by digesting the organic matrix constituents^[11].

QUANTIFICATION OF RESORPTION CAVITIES

Almost all knowledge concerning resorption cavities is derived from transiliac bone biopsies. The main focus in this review is therefore on the measurement and in-

terpretation of resorption cavity properties obtained from biopsies following the nomenclature conventions proposed by Parfitt *et al.*^[6]. Biomarker data is increasingly used to analyse bone remodelling. However despite the problems cited below, the transiliac bone biopsies remain the golden standard for measuring bone turnover^[17].

Transiliac bone biopsies

The three-dimensional (3D) characteristics of resorption cavities are generally extrapolated from two-dimensional (2D) features measured on histological sections using stereological formulas. However this extrapolation is not without flaws since it assumes unbiased and random sampling and isotropy, which are not fulfilled in bone^[18]. 2D widths are transformed to 3D thicknesses by using the parallel plate model^[19] and the distribution is corrected for missing measurements^[20]. There are also intraobserver, interobserver, intermethod and sample variations that have to be taken into account^[11,13,18,21].

During histomorphometric analysis different staining methods can be used which highlight certain features. Toluidine blue is used to identify cavities under polarized light by looking at the presence of cut off collagen fibers (disruption of the lamellar system) at the edge of the cavity^[13,18,22]. The polarized light allows visualisation of the orientation of collagen lamellae along the mineralized bone surface. The identification of scalloped surfaces can however be subjective^[23]. Tartrate-resistand acid phosphatase can be used to mark active osteoclasts and thus “active” cavities^[24]. Von Kossa/van Gieson staining allows to discriminate osteoid from mineralized bone^[18].

Besides the general problems with histomorphometry, cavity related measurements are also influenced by choosing which cavities to include. Measurement of cavities always presents a snap shot, where not only active sites are visible but also aborted sites, where resorption “prematurely” stopped, interrupted sites, where resorption is temporarily halted, and reversals sites^[25]. Distinguishing between these sites is not straightforward and assuming cavities are first completely eroded before osteoblasts start refilling is also an oversimplification^[25]. Some authors^[11] perform the technically difficult task of identifying specific cell types (osteoclasts, mononuclear cells, pre-osteoblast-like cells) in the cavities to distinguish between different stages in resorption and thus identify “completed” cavities with the largest depth obtained in the cycle^[22,18]. But the presence of these cells might be heterogeneous and might be dependent on the specific histological section^[13]. Therefore, most cavities might not represent effective “active” resorption and cautious interpretation of resorption related parameters is necessary. Moreover, small erosions may be difficult to distinguish from minor surface irregularities and whether these erosions are seen depends on the magnification^[25]. Specifically, cavities with depth below 3 μm are often omitted^[14,26]. When all cavities are included, the resulting average size is smaller than the size of the completed ones, but including all cavities leads to valuable information concern-

ing the distribution of cavities and the eroded surface at a certain time point. It has to be realized that the deep cavities that cause perforation cannot be identified or included in the measurements^[13,18,23,27]. When investigating treatment effects it is useful to label surfaces using calcein in order to be sure that they were actively forming during the period of treatment^[28].

The administration of two time-spaced doses of tetracycline prior to bone biopsy enables assessment of dynamic indices of bone formation^[18]. However, resorption can't be assessed dynamically (with the exception of biological markers), since removed bone is invisible; hence only indirect measurements are available. As a consequence it is not possible to tell from these static measures how much resorption is actually going on^[4,13].

Quantification of erosion depth in transiliac bone biopsies

The depth of a cavity is generally indicated by erosion depth (E.De). Indirect measurements are more common, in which the depth is calculated from other parameters or assumed to be similar to formation parameters. Wall thickness (W.Th) is the most widely used (Figure 1). It is the distance between cement lines of “resting” cancellous surfaces without osteoid or lacunae, reflecting the amount of bone created during a remodelling event^[4,5,11,13]. Eriksen^[11] did not find a significant difference between the distribution of completed wall thickness and pre-osteoblast-like cell, or deepest, resorption depths in healthy subjects. Another measure is osteoid thickness^[13]. A third measure is mean interstitial bone thickness, calculated from measurement of W.Th on both sides of a trabecula and the mean trabecular plate thickness, but this is not as reliable^[13,29]. However, when the bone balance, calculated as the difference between W.Th and E.De^[8], is not zero, these parameters do not correctly represent the resorption depth.

Two direct methods have been developed to quantify the depth of a cavity (E.De) (Figure 1). Eriksen *et al.*^[11] introduced the method of lamellar counting. The average lamellar width is measured and the number of lamellae cut at the cavity edges is counted (Figure 1). The method relies heavily on accurate identification of cells to classify cavities: when this identification is not possible, cavities are excluded (about 24%)^[13]. A disadvantage of this method is that it is impossible to count the lamellae correctly when different BSU with different orientations overlap. Besides that, the lamellar thickness inside an osteon can vary and not all lamellae are parallel to the surface which is an assumption in this method^[30].

In the other direct method, the pre-resorption surface is reconstructed and used to measure cavity dimensions^[31]. This method is generally computerized and applies an interactive curve fitting method to the cavity edge. All identifiable cavities are included regardless of their stage of completion^[27]. Large differences between the results of both methods have been observed^[13,32]. They are partly explained by the number of cavities in-

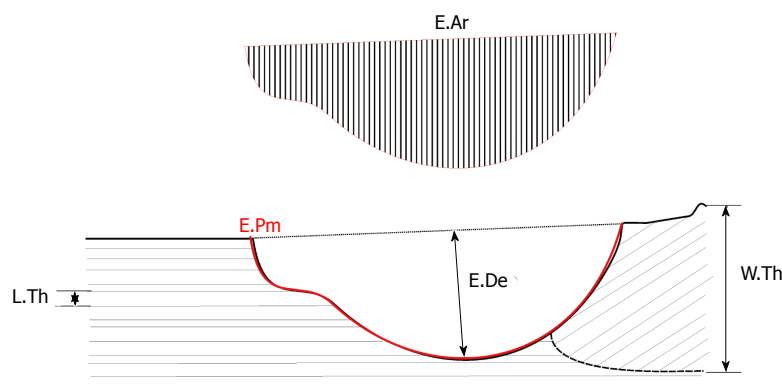


Figure 1 Schematic representation of different resorption cavity related measurements on 2D histological sections: Eroded area, erosion perimeter, wall thickness and lamellar thickness. E.Ar: Eroded area; E.Pm: Erosion perimeter; W.Th: Wall thickness; L.Th: Lamellar thickness.

cluded and the choice of maximum or mean depth: Eriksen method measures are systematically larger because the cavities are “completed” (with pre-osteoblast like cells), unidentified cavities were omitted and a constant lamellar width is assumed^[27,32]. Cohen-Solal *et al.*^[32] used the Garrahan method on completed cavities only (covered with osteoid), but still found values significantly lower than Eriksen. Roux *et al.*^[30] developed a method similar to Garrahan’s, and performed a direct comparison with the lamellar counting method. A rather high correlation was found ($R^2 = 0.76$, $P = 0.0001$) but with significantly lower values for the computerized method. Due to line reconstruction problems, cavities at the end of a trabecula could not be measured, while a higher number of lacunae were omitted during lamellar counting due to poor visibility of eroded lamellae. Again, the lacunae included seemed to determine the E.De outcome.

The measurement difficulties including the large variability and lack of consensus on the measurement technique have led to the publication of a recommendation not to directly evaluate resorption cavity depth in transiliac biopsies^[33]. However, E.De has a large mechanical impact (see below) and thus remains an important parameter in the assessment of the impact of resorption cavities on bone competence.

Quantification of erosion surface and volume in transiliac bone biopsies

The shape of a cavity can vary; hence cavity width and area can differ even for constant E.De^[28]. Consequently, taking parameters into account that go beyond erosion depth can be important when investigating the effect of disease and treatment on bone resorption. On histological sections, the total eroded perimeter (E.Pm) is the basic measure for the extend of cavities (Figure 1). The widely used erosion surface/bone surface (ES/BS) is calculated using this E.Pm. Just like all cavity measurement on biopsies, ES/BS is a snapshot of resorption and not a dynamic parameter^[33]. ES/BS is also a relative measure: adding a resorption cavity to the surface not only increases the eroded surface (ES) but also increases the total bone surface (BS) in the histological section, since the crenate surface of a cavity is larger than undamaged surface before resorption (Figure 1). Similar to E.De, some authors^[11] further specify this surface de-

pending on the cells and activity present in the lacunae. Osteoclast surface, Oc.S/BS, is often interpreted as “active” erosion surface in contrast to reversal surface. The relative amount of both types is case-dependent and interpretation of ES/BS can therefore be misleading, *i.e.*, an increased ES/BS can be caused by an increased reversal phase and not necessarily by increased osteoclast activity^[33]. Other formation parameters like osteoid surface (OS/BS) and osteoblast surface (Ob.S/BS) might be good indicators for related resorption parameters in healthy subjects with a stable bone balance. In general OS/BS seems to be larger than ES/BS. Several possible explanations exist: formation is slower, formation is initiated before the completion of resorption and/or the presence of arrested resorption cavities^[34].

The erosion volume or remodelling space, calculated from eroded area (Figure 1), is rarely determined on biopsies although it is highly correlated to bone resorption rate as indicated by urinary excretion of total deoxypyridioline^[30]. Some authors measure the E.Pm for each individual cavity (cavity length or eroded length) as an indication for shape changes of individual cavities^[31,35].

Quantification of number of cavities in transiliac bone biopsies

The number of cavities per bone surface (Nc/BS) is rarely measured, although it is a simple measure. Activation frequency (Ac.f) is more widely used. In theory, Ac.f is the number of new remodelling units activated anywhere on the surface in a given time and thus a good measure for the number of cavities present at a certain time. In practice the Ac.f is calculated as the inverse of the total period (remodelling period + quiescent period). This doesn’t correspond exactly with the conceptual definition^[13] and doesn’t take into account the 3D organisation of a BMU and the distance it travels^[9]. Being a highly derived variable the issues in calculation, assumptions and interpretation are numerous^[33] and interpretation is often complicated. Ac.f is thus especially interesting in a qualitative sense as to compare whether, in a certain situation, new cavities are introduced. Since cavities exist in different stages of resorption and cavities with interrupted resorption exist, the quantitative values cannot be readily used to assess the total numbers of cavities present at a certain time point.

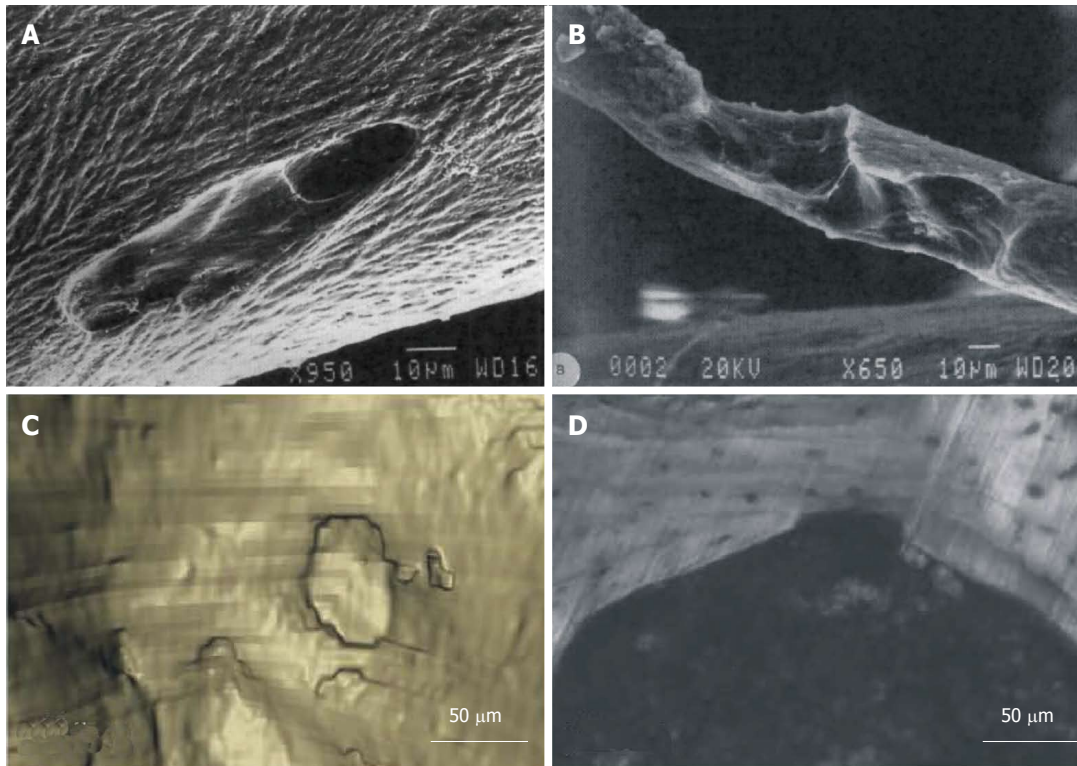


Figure 2 Three-dimensional visualizations of resorption cavities. Using scanning electron microscope (A, B) reprinted from^[37] and serial milling (C: Three-dimensional reconstruction; D: Corresponding cross section image) reprinted from^[38].

New imaging techniques

The use of 2D histomorphometry has limitations. Neither can it discriminate an increase in the number of remodelling events from an increase in the size of each individual event^[9] nor can the full volumetric extend of a cavity be measured^[36]. The development of 3D methods to assess BMU's are essential to advance our ability to study how alterations in its morphology occur with disease and treatment^[28]. Scanning Electron Microscope (SEM) images give a good indication of the 3D nature of resorption cavities as can be seen in Figure 2A and B^[37]. But currently, no clinical imaging devices are able to detect resorption cavities because of their small size compared to image resolution. It has been shown that high-resolution images (at least 1.4 µm or better) are required to consistently identify and measure individual resorption cavities^[38].

Recent developments in imaging techniques show great potential to quantify cavities in 3D and detect them automatically. Specifically, individual resorption cavities were measured in 3D on animal vertebrae using serial milling^[38] (Figure 2C and D). This technique was able to reveal that cavity size and location are related to the local trabecular microarchitecture. Goff *et al.*^[39] found that, on the human vertebral trabecular bone samples they investigated, half of the cavities were located on the intersections of trabeculae and most others were on plate like-trabeculae oriented in the main loading direction (cranial-caudal). Next to that confocal laser microscopy and vertical scanning profilometry have recently been

used to measure bone resorbing activity, extending *in vitro* measurements from ES/BS under microscope to full 3D measurements of volume and depth^[40,41].

Synchrotron-radiation based computer tomography (SR-CT) and high-resolution micro computer tomography (µCT) are technically able to obtain the necessary detail, but might not be able to capture enough cavities per specimen to characterize a population. The most promising development probably lies in high-resolution *in-vivo* µCT. Schulte *et al.*^[42] recently presented a new time-lapsed imaging method which allows quantification of dynamic resorption parameters at a resolution of 10.5 µm. They were able to effectively measure 3D ES and BS by comparing subsequent 3D reconstructions of the same bone separated by 4 wk. The non-invasive nature of this technology allows longer periods of investigation and might enable researchers to reveal time-dependent evolutions in resorption; yet improvements in image resolution are needed to be able to dynamically track individual resorption cavities.

CHARACTERISTICS OF RESORPTION CAVITIES

The following section will provide a limited overview of measured cavity properties in health and specific disease. It does not cover the full range of studies analysing transiliac bone biopsies, but aims at providing a general indication of resorption cavity properties found in literature and showing the wide range of values that have been reported.

This is relevant in relation to biomechanical modelling since, as discussed in section 6, several biomechanical models neither incorporate the most relevant nor most accurate properties. Based on measurement issues described before, we will focus on E.De and W.Th as measures for cavity depth. For the extend of cavities we will provide data on ES/BS and when available on EV/BV. All reported data in this section are related to transiliac bone biopsies, except when indicated differently.

Healthy bone

Cavities are often elongated, have varying depths and can lie close together. Sizes varied from $50\ \mu\text{m} \times 20\ \mu\text{m}$ to $1000\ \mu\text{m} \times 1000\ \mu\text{m}$, most were $200\ \mu\text{m} \times 500\ \mu\text{m}$ in size^[37]. In a single cavity about $0.05\ \text{mm}^3$ of bone tissue is removed^[5]. The frequency distribution of cavity sizes in a trabecular bone sample is skewed: there are few very deep cavities and a large amount of shallow ones^[13]. This is the case for all measurement methods, although, as explained above, the method and choice of included cavities does make a difference^[8,11,14,43].

It seems reasonable to accept that there is no difference in the biology of the bone remodelling process at different skeletal sites. Hence, if there would be a link between microdamage and resorption activity, this would impact local erosion measurements, since some bones are more heavily and frequently strained leading to more microdamage^[2]. Since the local loading environment is site-dependent and leading to differences in local trabecular microstructure, it is expected that different erosion patterns occur as well. Indeed, bone structure and turnover appeared different between the distal radius and the iliac crest. Specifically, W.Th, ES/BS and Ac.f were significantly lower in the distal radius^[44]. Given the fact that most cavity-related studies are based on bone biopsies from the iliac crest, these results should be critically reviewed before extrapolating the results to other skeletal sites.

There is little information regarding the location of the cavities on the trabecular surface itself. Analysis of trabecular thinning and connectedness of trabecular bone revealed that the site of activation of new BMU's may be preferentially located where trabeculae are either thinner or thicker, such as trabecular intersections^[27,45,46]. This would be consistent with the microdamage-theory since these locations are highly strained. Most remodelling is likely targeted at replacing fatigue-microdamaged bone or at removing hyper mineralized bone^[9].

Age-related changes in resorption cavity properties have been observed (Table 1). For children, growth to peak bone mass is realised by high formation, with Ac.f and W.Th decreasing with age, while bone resorption parameters (ES/BS) don't vary significantly^[23]. In adults, there is continued reduction in bone formation taking place with age as shown by a reduced W.Th^[8,29,47,48], while resorption continues with an unchanged or even increased amount of resorbed surface^[24,27,43,49]. No or only a small decrease in E.De has been reported^[22,24,27]. A

small decrease in (average) E.De would be a logical consequence of reduced W.Th because more shallow cavities, which were incompletely refilled, remain on the bone surface. But it also possible that resorption has increased and has caused deep perforation cavities, which are not measured: their absence in the cavity depth distribution would also shift the average depth to lower values.

Neither sex nor ethnic differences seem to exist when it comes to resorption parameters like E.De, W.Th and ES/BS, at least before menopause^[14,24,27,43,48,50,51]. But with menopause, there are significant differences between the sexes. In menopause, the age-related reduction in W.Th is accelerated and more BMU's are born (increased Ac.f), while resorption itself is hardly affected. As a consequence bone turnover is accelerated and females are subjected to an accelerated trabecular bone loss^[5,6,15,51-53]. Three to five years after menopause, the W.Th seems to recover to the premenopausal values and a more or less steady state emerges, in which the remodelling rate is still higher than premenopausal due to a higher Ac.f, but lower than during menopause^[6,53]. In men, this "temporarily" acceleration does not happen and the "normal" decrease in W.Th with age accompanied by with unchanged resorption, continues^[51,54,55].

Effect of osteoporosis

Metabolic bone diseases alter the bone remodelling cycle and can thus change the resorption cavity properties (Table 2). As we demonstrate below for osteoporosis, the limitations of the measurement methods hinder clear interpretation of the results.

As indicated earlier, the menopause causes, even in normal subjects, an increase in Ac.f and a negative bone balance. In post-menopausal osteoporosis (PmOP) these effects on Ac.f and W.Th are even stronger, with extreme loss in bone mass as a consequence^[17,32,56,57]. Again, given the likely increased presence of underfilled cavities associated with a reduced W.Th, one would expect a reduced average E.De, but an increased ES/BS. In contrast to normal post-menopausal women, a small but not significant increase in resorption depth has been observed^[15,17,32,56,57]. Furthermore, ES/BS is reduced or unchanged^[56,57]. Given this difference from normal age-related changes, we hypothesize that individual cavity depth might actually have increased in PmOP, but that this increase is not detected with the averaged values for E.De reported in literature. The presence of underfilled cavities and absence of perforating cavities in the measurement, shift this average to lower values, masking the real increase. The increased cavity depth might cause more perforations on already thinner trabeculae and, again, because these perforating cavities are not included in the ES/BS measurement, the real ES is underestimated. Idiopathic (primary) male osteoporosis leads to similar effects but while some studies find similar results as for PmOP^[54,58], others found unchanged W.Th and increased resorption parameters (ES/BS)^[47].

Prolonged corticoid treatment leads to secondary OP.

Table 1 Normal values for specific eroded surface, erosion depth and wall thickness as reported in literature for healthy patients

Sex	Parameter	Change with age	Mean age	Values	
F	ES/BS (%)	↓ ² ↑	10-30	2.15 (0.36) ^[43] 3.23 (2.6-4.02) ^[22]	
			30-60	3.43 (2.68-4.4) ^[22] 1.85 (0.82-4.21) ^[27] 1.78 ^u ^[43]	
			60-90 (post-meno)	4.59 (3.72-5.66) ^[22] 4.2 (1.7) ^[24] 7.1 ¹ (2.9-16.9) ^[56] 4.0 (2.0) ^[57] 1.66 (0.66) ^[43]	
			All ages	6.2 (2.9) ^[21]	
	E.De (μm)	↓	10-30	56.8 (50.2-63.4) ^[22]	
			30-60	63.4 (57.5-69.3) ^[22] 33.7 (24.4-46.6) ^[27]	
			60-90 (post-meno)	50.8 (46.9-54.7) ^[22] 27.21 (2.27) ^[24] 49.1 ¹ (38.3-61.7) ^[56] 49.4 (12.1) ^[32]	
	W.Th (μm)	↓	10-30	62.0 (8) ^[29]	
			30-60	49.0 (9.1) ^[48] 37.2 (3.8) ^[51] 38.1 (28.6-68.8) ^[53] 56.2 (7.1) ^[50] 50.4 (7.4) ^[29]	
			60-90 (post-meno)	48.8 ¹ [37.8-62.2] ^[56] 33.9 (4.7) ^[51] 32.2 (23.2-39.3) ^[53] 39.5 (2.0) ^[32] 32.1 (4.13) ^[57] 44.3 (4.9) ^[50] 40.2 (4.6) ^[29]	
			All ages	31-43.9 ^[13] 49.0 (2.5) ^[21]	
M and F	ES/BS (%)	↓ ²	10-30	16.3 (11.6-18.1) ^[102] 16.6 (5.6) ^[23]	
			30-60	4.03 (1.42) ^[11]	
			All ages	1.35 (0.39) ^[31] 1.94 (0.76-4.93) ^[103]	
	E.De (μm)	↓	30-60	62.6 ^[11]	
			All ages	28.9 (23.4-39.3) ^[31] 34.2 (22.8-51.3) ^[103]	
	W.Th (μm)	↓	10-30	44.2 (5.7) ^[102] 41.4 (5.7) ^[23]	
			30-60	61.9 (6.8) ^[11]	
			60-90	59.4 ^[13]	
	All ages			51.6 (35.8-74.4) ^[103]	
		ES/BS (%)	↓ ² ↑	10-30	3.32 (2.34-4.7) ^[22] 6.3 (0.6) ^[49] 2.84 (1.27) ^[43]
				30-60	3.55 (2.55-4.95) ^[22] 3.7 (0.9) ^[24] 1.81 (0.72-4.56) ^[27] 6.6 ² ^[51] 1.72 ² ^[43]
	60-90			3.99 (3.11-5.13) ^[22] 3.7 (0.6) ^[24] 6.4 ⁺ ^[49] 1.91 (0.42) ^[43]	
All ages					
E.De (μm)	↓	10-30	66.1 (57.1-75.1) ^[22]		
		30-60	64.1 (48.0-60.2) ^[22] 33.0 (3.16) ^[24] 35.6 (23.2-54.7) ^[27]		
		60-90	46.3 (44.3-48.3) ^[22] 28.94 (1.78) ^[24]		
W.Th (μm)	↓	10-30	62.0 (8.1) ^[29] 32.8 (2.6) ^[49]		
		30-60	50.2 (8.7) ^[48] 53 (8.6) ^[50] 49.2 (4.6) ^[29] 35.0 ² ^[49]		
		60-90	48.5 (8.6) ^[50] 43.8 (2.8) ^[29] 32.8 ² ^[49]		
		All ages	40.6 ^[13]		

¹Median; ²Indicates recalculation to age groups. Data ordered by sex [Female (F), Female and male (FM), Male (M)] and age groups (10-30 year, 30-60 year, 60-90 year or all ages mixed). Values presented as mean ± SD, mean [95% confidence interval (CI)], mean [10th-90th percentile], mean [Q1st-3rd quartile]. Also indicated is whether the parameters increase (↑), decrease (↓) with age or stay constant (b). ES/BS: Erosion surface/bone surface; E.De: Erosion depth; W.Th: Wall thickness.

The main effect is osteoblastic dysfunction, with significantly reduced W.Th as a consequence. Next to that, the lifespan of osteoclasts seems to be increased and changes in cavity surface shape have been observed^[59]. The change in cavity surface shape might have a different mechanical impact, especially in combination with an increased E.De and ES/BS, as indicated in most studies^[5,60-63].

Effect of anti-osteoporotic medication

Treatment for OP interferes with the bone remodelling cycle, hence, may affect osteoclast resorption cavities. This section presents an overview of the effect of some of the major anti-osteoporotic medication for which resorption cavity properties were reported and compared to untreated PmOP patients (Table 3).

Bisphosphonates (BP) reduce bone resorption by reducing the Ac.f: the number of new BMU's that initiate and thus the remodelling space decreases^[28,52,60,64-66]. The W.Th is reduced as well but no evidence of changes in ES/BS was found^[52,60,64,66,67]. It is debated whether osteoclasts are only prevented from starting new BMU's or that the amount of bone resorbed by a BMU is reduced as well; also the number and size of the resorption cavi-

ties might be reduced^[28,68,69]. The impact on resorption cavity properties would be similar: either only underfilled and thus shallow cavities remain or only new shallow cavities are resorbed. Indeed, superficial cavities have been observed next to giant hypernucleated osteoclasts^[70]. BPs thus prevent a significant increase in erosion depth and prevent further progression of the resorption pits^[67].

The trends observed for resorption parameters in other treatments are less clear and few studies found conflicting results. In contrast to BPs, both parathyroid hormone (PTH 1-84) and the cyclic hPTH(1-34) (Teriparatide), caused an increase in ES/BS, next to an increased Ac.f and W.Th, although it was not always significant^[71-73]. A larger surface is thus occupied by cavities, but the increased W.Th may keep them superficial. For patients treated with strontium Ranelate, a dual action bone agent, some studies found no significant differences in Ac.f or ES/BS while others found a significantly reduced ES/BS^[52,74].

In a recent three-dimensional dynamic bone histomorphometric study, Matheny *et al.*^[75] showed reductions in resorption cavity size (depth, width and volume) with antiresorptive agents (Raloxifene and Risondrenate) while the ES/BS was unchanged.

Table 2 Change of eroded surface, erosion depth and wall thickness in common bone diseases (postmenopausal osteoporosis, male idiopathic osteoporosis, glucocorticoid induced osteoporosis) as reported in literature

Disease	Parameter	Change	Values ¹	¹ Significantly lower than control	² Significantly higher than control
PmOP	W.Th (µm)	↓	40.74 ^a (31.6-54.3) ^[56] 36.2 (6.4) ^[121] 28.3 (20.1-34.8) ^[53] 35.3 (2.0) ^[32] 28.0 (4.44) ^[57] 29.3 (1.4) ^[73] 31.2 (0.4)-32.1 (0.5) ^[64] 41.8 (4.25)-49.0 (8.93) ^[67]		
	ES/BS (%)	b ↓	5.3 ^a (1.7-18.1) ^[56] 6.0 (3.0) ^[21] 4.8 (2.7) ^[57] 1.67 (0.48) ^[73] 4.9 (2.9) ^[71] 1.89 (0.12)-3.41 (0.5) ^[64] 4.49 (1.6) - 6.55 (1.62) ^[65] 2.18 (1.24) ^[61]		
	E.De (µm)	b	55 ^a (37.3-82) ^[56] 48.5 (43.8-53.2) ^[8] 50.0 (13.4) ^[32] 22 (5) ^[71] 13.5 (0.43)-15.8 (0.91) ^[64]		
MIOP	EV/BV (%)		0.46 (0.04)-1.21 (0.29) ^[64]		
	ES/BS (%)	↑	9.7 (1.7) ^[55] 7.5 (1.3-17.7) ^[58]		
	E.De (µm)	b	44.7 (9.3) ^[58]		
GC induced	W.Th (µm)	b ↓	35.3 (7.5) ^[58]		
	EV/BV (%)		0.44 (0.1) ^[60]		
OP	ES/BS (%)	b ↑	2.3 (0.4) ^[60] 4.06 (2.45) ^[61]		
	E.De (µm)	↑	15.0 (1.3) ^[60]		
	W.Th (µm)	↓	30.6 (0.8) ^[60]		

Significant difference *vs* control indicated (¹Significantly lower than control; ²Significantly higher than control); ^aMedian; Values presented as mean ± SD, mean (95%CI), mean [10th-90th percentile], mean [Q 1st-3rd quartile]; ^bAlso indicated in table is whether the parameters increase (↑), decrease (↓) due to the disease or stay constant. When more than one value is reported for the same reference, it concerns measurements at different time points. ES/BS: Erosion surface/bone surface; E.De: Erosion depth; W.Th: Wall thickness; PmOP: Postmenopausal osteoporosis.

Table 3 Change of eroded surface, erosion depth and wall thickness with treatment for postmenopausal osteoporosis as reported in literature

Treatment for PmOP	Parameter	Change	Values ¹
			¹ Significantly lower then no treatment
			² Significantly higher then no treatment
Bisphosphonates (oral/IV ibandronate, alendronate, risendronate)	EV/BV (%)	b	0.40 (0.1)-0.50 (0.1) ^[60]
	ES/BS (%)	b	2.2 (0.4)-2.6 (0.5) ^[60]
			5.3 (2.75) ^[67]
	E.De (µm)	b	1.29 (90%CI: 1.04-1.95)-1.62 (90%CI: 1.32-1.88) ^[66]
Strontium ranelate	ES/BS (%)	b	13.4 (1.0)-16.2 (1.0) ^[60]
			45.6 (9.45) ^[67]
	W.Th (µm)	b	30.0 (1.0)-31.4 (1.0) ^[60]
			41.6 (4.86) ^[67]
Strontium ranelate 6 m	ES/BS (%)	↓	2.92 (1.48-3.89) ^[52]
	ES/BS (%)	↓	1.21 (0.21) ^[74]
	ES/BS (%)	↑	0.78 (0.11) ^[74]
hPTH (1-34) (teriparatide)			10.1 (4.9) ² -11.8 (7.1) ^[71]
	W.Th (µm)	b	3.51 (Q 2.67-5.64)-4.0 (Q 2.8-6.0) ^[72]
PTH (1-84)	ES/BS (%)	↑ ^b	22 (5)-28 (7) ^[71]
			1.75 (0.35) ^[73]
	W.Th (µm)	b	33.1 (1.4) ^[73]

Significant difference *vs* control (no treatment) indicated (¹Significantly lower than control; ²Significantly higher than control). Values as mean ± SD, mean (95%CI), mean [10th-90th percentile], mean [Q 1st-3rd quartile]; ^bAlso indicated in table is whether the parameters increase (↑), decrease (↓) due to the treatment or stay constant. When more than one value is reported for the same reference, it concerns measurements at different time points or different doses. ES/BS: Erosion surface/bone surface; E.De: Erosion depth; W.Th: Wall thickness; PmOP: Postmenopausal osteoporosis.

BIOMECHANICAL CONSEQUENCES OF RESORPTION CAVITIES

Resorption by osteoclasts, as part of the bone remodeling cycle, causes cavities on the bone surface, since the cells reach their location through the bone marrow. During resorption and the following reversal phase, these cavities form structural defects, that weaken the bone^[6]. With a normal bone balance, this mechanical effect is quasi-constant, since an equal amount of cavities is re-filled simultaneously. If this balance is disrupted, the changes cause a structural and thus mechanical effect^[4,12].

Three main possible mechanisms have been identified by which bone turnover in general can influence bone biomechanics^[36]. These mechanisms are related to bone mass, yet they have effects that go beyond their direct impact on the bone volume and thus go beyond “standard” density-strength power relationships^[76,77]. First, there is the effect of modifications in tissue degree of mineralisation, which is not directly related to resorption. Second, the fenestration or disconnection of individual trabeculae that modify the trabecular architecture is a direct result of resorption^[76,78-80]. And third, the resorption cavities also act as stress risers. Experimental evaluation of these effects is difficult, forcing researchers to rely on modelling.

In the next paragraph we focus on different modelling approaches and their findings.

Modelling resorption cavities in finite element analyses

Numerous authors have tried to model the bone remodelling sequence, but few have directly incorporated the 3D microstructural properties of resorption. There have mainly been attempts using analytical models to predict local changes of bone properties like the bone density, based on BMU properties like birth-rate, formation, resorption and mineralisation rates^[81,82]. These models don't incorporate the real resorption cavity properties and are thus not further described in this review.

Simplified structural models can give insight in some of the basic mechanism of the effect of cavities on bone mechanical properties. Mechanical analyses of the effect of a cavity on a straight beam shows that the number and size of remodelling cavities may influence the mechanical behaviour of a trabecula independent of bone volume or total amount of bone turnover^[36].

Using a mechano-regulation algorithm to model and refill cavities of different depths on a 2D and 3D simplified finite element model of a bone trabeculum, it was shown that beyond a certain cavity depth the remodelling was not able to refill the cavity and a notching effect caused perforation^[83,84].

An extension of simple beam models is 2D and 3D lattice structures. Langton proposed a 2D stochastic model of resorption on a lattice structure where resorption was guided by a probability that a surface pixel is activated and a probability for the duration of resorption^[85]. Small bone volume losses caused high stiffness losses which are related to 2D nature of that model. Lattice 3D models are more robust, A model presented by Tayyar *et al*^[86] used planar structural units to test the effect of increased activation frequency during menopause on bone volume. He used rectangular shaped cavities with a maximum depth of 50 μm and 2% of the cavity volume was not refilled during formation^[86]. The volume loss was larger in case of menopause, with almost 40% of the bone loss caused by perforation (disconnection from the network).

Lattice models are unable to capture the complex and heterogeneous nature of trabecular bone. In a trabecular network, the mechanical effect of perforations or ruptures depends on the cavity location and specific trabecular properties. μCT -scans have enabled researchers to take the intricate trabecular structure into account when modelling resorption effects.

The stress-concentrating effect of resorption cavities on real isolated trabeculae was first investigated by McNamara *et al*^[87]. Cavities were identified on μCT -scans and the authors found from finite element analysis that micro-damage was inevitable around these lacunae, which might lead to more resorption than 'initially' intended to restore damaged bone^[87].

Different cavity-based erosion and formation algorithms have been applied to complete trabecular samples

as well, and FE analyses were performed to investigate the mechanical impact^[88-93]. These algorithms have been applied iteratively to simulate the effect of a sequence of remodelling cycles, with both formation and resorption, sometimes spanning several decades in the virtual life of the sample. The algorithms used had different grounds. One approach was to remove voxels on the entire bone surface based on a gaussian filter constrained to a certain cavity volume^[90,94], which not necessarily erodes individual cavities. Using this method they showed that a negative bone balance and increased activation frequency can cause extreme bone loss^[90]. Others considered the local mechanical environment of voxels and removed them based on the nonuniformity of local stress on the surface or a strain signal^[91,93]. Both models caused an evolution towards a typical anisotropic bone structure after several cycles, with a higher stiffness in the loading direction.

The approach of Van der Linden *et al*^[92] was the first to specifically take the cavity shape into account. They developed a computer simulation of bone remodelling on a 3D- μCT -based structure where voxels of bone matrix were removed as hemispherical cavities located at random locations on the bone surface. In a sequence of bone remodelling cycles, a formation deficit was modelled hence the cavities were not refilled completely. The model was used to simulate several bone loss scenarios^[95] as well as the effect of treatment with anti-resorptive agents by gradually changing cavity properties^[96]. They clearly showed the complex relationship between bone loss and stiffness loss and that bone loss alone cannot explain the mechanical changes. While Van der Linden *et al* based their amount of remodelling on the remodelling volume, Liu *et al*^[89] added hemispherical cavities at random locations according to the activation frequency. They observed a shift to less plate-like trabeculae and more, but thinner, rod-like trabeculae after the simulated menopause.

Hernandez *et al*^[88] used a similar 3D model to test the effect of resorption cavities on the trabecular bone strength. They digitally added cavities at regions of high strain or at random locations. For the first time, the cavities were modelled with an ellipsoidal shape. Adding resorption cavities caused a significant reduction in stiffness and yield strength, with even higher reduction for cavities at regions of high strain. The total removed bone volume was however the same, showing that cavities may influence bone mechanics independent of their effect on bone volume. The same research group continued to model the biomechanical effect of (uniform size) resorption cavities on voxel-based models and have shown a larger impact of cavities located in highly strained areas on the trabecular bone structure^[97].

Using a new approach that overcomes some of the modelling limitations described above and below, we recently simulated the effect of resorption cavities on the stiffness of a wide variety of trabecular bone structures using a parametric beam-shell finite element model^[98]. The reduction in bone stiffness due to cavities was signif-

icantly larger than for homogeneous erosion of the same bone volume and depended on the nature of the bone structure (rod-like *vs* plate-like trabeculae). A more specific study using the same modelling technique showed that glucocorticoid changes in the geometry of osteoclast resorption cavities affect trabecular bone stiffness^[99].

Slyfield *et al*^[100] were recently able to take the ultimate step in the 3D analysis of the mechanical effect of resorption cavities. They were able to demonstrate the role of resorption cavity size and location on mechanical failure (damage) of bone using 3D imaging of the failure process.

Modelling limitations

As described above, the different modelling approaches have revealed interesting effects of resorption on bone mechanical properties. There are however several disadvantages in the methods and potential flaws in the presented studies.

First, simplified (lattice) models are unable to capture the complex and heterogeneous nature of trabecular bone and are therefore less suited to model the combined mechanical effect of all the interacting structural properties.

Second, detailed μ CT-based models of trabecular bone have been used, but so far applied only to a limited number of trabecular bone samples. Given the enormous heterogeneity of trabecular bone structures, related to the anatomical site, the influence of the initial structure should be taken into account. It is as yet unclear whether resorption cavities have a similar impact on plate-like samples then on rod-like bone samples.

Third, state-of-the-art μ CT-based models add or remove bone by adding or removing voxels. Cavity shapes and sizes are thus limited to the voxel resolution. As our review of resorption cavity properties shows, a large variation in sizes exists and changes often occur on a sub-voxel-resolution level. High resolution imaging has shown that resorption cavities have very irregular shapes of which the mechanical impact can possibly not be modelled correctly on a voxel-basis^[37]. Potential solutions to this problem lie in the use of tetrahedral-based FE models, where surface nodes can be moved inwards to model cavities or by using parameter-based models of trabecular bone, like beam-shell finite element models^[101].

Fourth, state-of-the-art μ CT-based models assume, partly due to their voxel-based nature, cavities of a fixed size. However, cavity shapes and sizes are far from constant. *In vivo*, they exist in a skewed distribution of surface area and cavity depth. Moreover, at a certain snapshot in time, not all cavities are in the same remodelling stage: some may have just started while others are already being refilled. Furthermore all simulation studies have shown that the highest mechanical impact occurs when trabeculae are perforated or ruptures, especially when occurring in highly strained locations. The presence of just a few deep perforating cavities can thus change the mechanics decisively, while an averaged cavity depth might not cause

perforation. It is thus advisable to use a realistic spread of resorption cavity properties when modelling their mechanical impact.

Fifth, the choice of modelling parameters remains problematic. As we explained above, different measuring methods exist and all have specific disadvantages, requiring careful interpretation of the values before using them as a model basis. Resorption cavity depths used in simulation studies seem to be large compared to literature values, again due to the voxel-based nature of the models. Using dynamic parameters like the total remodelling space or Ac.f as a basis for a static study, might lead to an overestimation of the impact of resorption cavities^[88,89]. There is no single timepoint where the entire remodelling space has been removed by osteoclasts. Given the fact that ES/BS is commonly measured and there is less discussion concerning the measurement technique, it is likely the best parameter to quantify the extend of erosion.

CONCLUSION

Osteocyte resorption cavities affect bone competence. Hence, a proper quantification of the cavity dimensions will be beneficial in estimating the effect of metabolic bone diseases on bone mechanical quality. Until recently, the dimensions of osteoclast resorption cavities have been estimated from 2D measures. Their role in affecting bone quality has been analyzed using computational models that, on one hand, provide rather detailed information on trabecular bone structure, but on the other incorporate rather crude assumptions on cavity dimensions. Considering the 3D nature of the cavities this approach has clear limitations, requiring a careful interpretation. The introduction of 3D imaging techniques like μ CT and SR-CT has opened the door to quantifying these dimensions in an unbiased manner in 3D space. These data can be included in high-resolution computational models and in parametric descriptions of bone, thereby improving our understanding of their effect on bone competence. Further exploration of this area of research will disclose relevant information on the mechanical consequences of metabolic bone diseases and can aid in the development of (bio)mechanically relevant pharmacological and physical treatments.

REFERENCES

- 1 **Heaney RP**, Yates AJ, Santora AC. Bisphosphonate effects and the bone remodeling transient. *J Bone Miner Res* 1997; **12**: 1143-1151 [PMID: 9258743 DOI: 10.1359/jbmr.1997.12.8.1143]
- 2 **Seeman E**, Delmas PD. Bone quality--the material and structural basis of bone strength and fragility. *N Engl J Med* 2006; **354**: 2250-2261 [PMID: 16723616 DOI: 10.1056/NEJMra053077]
- 3 **Frost HM**. Tetracycline-based histological analysis of bone remodeling. *Calcif Tissue Res* 1969; **3**: 211-237 [PMID: 4894738 DOI: 10.1007/BF02058664]
- 4 **Rauch F**. Watching bone cells at work: what we can see

- from bone biopsies. *Pediatr Nephrol* 2006; **21**: 457-462 [PMID: 16520951 DOI: 10.1007/s00467-006-0025-6]
- 5 **Recker RR.** Bone biopsy and histomorphometry in clinical practice. *Rheum Dis Clin North Am* 1994; **20**: 609-627 [PMID: 7984781 DOI: 10.1359/prim.2008.0735]
 - 6 **Seeman E.** Structural basis of growth-related gain and age-related loss of bone strength. *Rheumatology (Oxford)* 2008; **47** Suppl 4: iv2-iv8 [PMID: 18556646]
 - 7 **Frost HM.** The skeletal intermediary organization. *Metab Bone Dis Relat Res* 1983; **4**: 281-290 [PMID: 6353132]
 - 8 **Eriksen EF.** Normal and pathological remodeling of human trabecular bone: three dimensional reconstruction of the remodeling sequence in normals and in metabolic bone disease. *Endocr Rev* 1986; **7**: 379-408 [PMID: 3536460 DOI: 10.1210/edrv-7-4-379]
 - 9 **Parfitt AM.** Targeted and nontargeted bone remodeling: relationship to basic multicellular unit origination and progression. *Bone* 2002; **30**: 5-7 [PMID: 11792557 DOI: 10.1016/S8756-3282(01)00642-1]
 - 10 **Baron R.** Importance of the intermediate phases between resorption and formation in the measurement and understanding of the bone remodeling sequence. *Bone Histomorphometry* 1977: 1977
 - 11 **Eriksen EF, Melsen F, Mosekilde L.** Reconstruction of the resorptive site in iliac trabecular bone: a kinetic model for bone resorption in 20 normal individuals. *Metab Bone Dis Relat Res* 1984; **5**: 235-242 [PMID: 6493035 DOI: 10.1016/0221-8747(84)90066-3]
 - 12 **Chavassieux P, Seeman E, Delmas PD.** Insights into material and structural basis of bone fragility from diseases associated with fractures: how determinants of the biomechanical properties of bone are compromised by disease. *Endocr Rev* 2007; **28**: 151-164 [PMID: 17200084 DOI: 10.1210/er.2006-0029]
 - 13 **Compston JE, Croucher PI.** Histomorphometric assessment of trabecular bone remodelling in osteoporosis. *Bone Miner* 1991; **14**: 91-102 [PMID: 1912765 DOI: 10.1016/0169-6009(91)90086-F]
 - 14 **Croucher PI, Gilks WR, Compston JE.** Evidence for interrupted bone resorption in human iliac cancellous bone. *J Bone Miner Res* 1995; **10**: 1537-1543 [PMID: 8686510 DOI: 10.1002/jbmr.5650101015]
 - 15 **Eriksen EF, Mosekilde L, Melsen F.** Trabecular bone remodeling and balance in primary hyperparathyroidism. *Bone* 1986; **7**: 213-221 [PMID: 3768200 DOI: 10.1016/8756-3282(86)90020-7]
 - 16 **Parfitt AM, Drezner MK, Glorieux FH, Kanis JA, Malluche H, Meunier PJ, Ott SM, Recker RR.** Bone histomorphometry: standardization of nomenclature, symbols, and units. Report of the ASBMR Histomorphometry Nomenclature Committee. *J Bone Miner Res* 1987; **2**: 595-610 [PMID: 3455637 DOI: 10.1002/jbmr.5650020617]
 - 17 **Recker RR, Lappe JM, Davies KM, Heaney RP.** Bone remodeling: Biochemical markers or bone biopsy? *J BONE MINER RES* 2006; **21**: 180-180
 - 18 **Vedi S, Compston J.** Bone histomorphometry. *Methods Mol Med* 2003; **80**: 283-298 [PMID: 12728725]
 - 19 **Gundersen HJ.** Stereology--or how figures for spatial shape and content are obtained by observation of structures in sections. *Microsc Acta* 1980; **83**: 409-426 [PMID: 7442556]
 - 20 **Kragstrup J, Gundersen HJG, Melsen F, Mosekilde L.** Estimation of the 3-Dimensional Wall Thickness of Completed Remodeling Sites in Iliac Trabecular Bone. *Metab Bone Dis Relat Res* 1982; **4**: 113-119
 - 21 **Arlot ME, Delmas PD, Chappard D, Meunier PJ.** Trabecular and endocortical bone remodeling in postmenopausal osteoporosis: comparison with normal postmenopausal women. *Osteoporos Int* 1990; **1**: 41-49 [PMID: 2133640]
 - 22 **Eriksen EF, Mosekilde L, Melsen F.** Trabecular bone resorption depth decreases with age: differences between normal males and females. *Bone* 1985; **6**: 141-146 [PMID: 4027092 DOI: 10.1016/8756-3282(85)90362-X]
 - 23 **Glorieux FH, Travers R, Taylor A, Bowen JR, Rauch F, Norman M, Parfitt AM.** Normative data for iliac bone histomorphometry in growing children. *Bone* 2000; **26**: 103-109 [PMID: 10678403 DOI: 10.1016/S8756-3282(99)00257-4]
 - 24 **Palle S, Chappard D, Vico L, Riffat G, Alexandre C.** Evaluation of the osteoclastic population in iliac crest biopsies from 36 normal subjects: a histoenzymologic and histomorphometric study. *J Bone Miner Res* 1989; **4**: 501-506 [PMID: 2816499 DOI: 10.1002/jbmr.5650040408]
 - 25 **Parfitt AM.** Morphometry of bone resorption: introduction and overview. *Bone* 1993; **14**: 435-441 [PMID: 8363889 DOI: 10.1016/8756-3282(93)90176-B]
 - 26 **Vedi S, Tighe JR, Compston JE.** Measurement of total resorption surface in iliac crest trabecular bone in man. *Metab Bone Dis Relat Res* 1984; **5**: 275-280 [PMID: 6493040 DOI: 10.1016/0221-8747(84)90014-6]
 - 27 **Croucher PI, Garrahan NJ, Mellish RW, Compston JE.** Age-related changes in resorption cavity characteristics in human trabecular bone. *Osteoporos Int* 1991; **1**: 257-261 [PMID: 1790413]
 - 28 **Allen MR, Erickson AM, Wang X, Burr DB, Martin RB, Hazelwood SJ.** Morphological assessment of basic multicellular unit resorption parameters in dogs shows additional mechanisms of bisphosphonate effects on bone. *Calcif Tissue Int* 2010; **86**: 67-71 [PMID: 19953232 DOI: 10.1007/s00223-009-9315-x]
 - 29 **Croucher PI, Mellish RW, Vedi S, Garrahan NJ, Compston JE.** The relationship between resorption depth and mean interstitial bone thickness: age-related changes in man. *Calcif Tissue Int* 1989; **45**: 15-19 [PMID: 2504458 DOI: 10.1007/BF02556655]
 - 30 **Roux JP, Arlot ME, Gineyts E, Meunier PJ, Delmas PD.** Automatic-interactive measurement of resorption cavities in transiliac bone biopsies and correlation with deoxyypyridinoline. *Bone* 1995; **17**: 153-156 [PMID: 8554923 DOI: 10.1016/S8756-3282(95)00174-3]
 - 31 **Garrahan NJ, Croucher PI, Compston JE.** A computerised technique for the quantitative assessment of resorption cavities in trabecular bone. *Bone* 1990; **11**: 241-245 [PMID: 2242290 DOI: 10.1016/8756-3282(90)90076-B]
 - 32 **Cohen-Solal ME, Shih MS, Lundy MW, Parfitt AM.** A new method for measuring cancellous bone erosion depth: application to the cellular mechanisms of bone loss in postmenopausal osteoporosis. *J Bone Miner Res* 1991; **6**: 1331-1338 [PMID: 1792944 DOI: 10.1002/jbmr.5650061210]
 - 33 **Recker RR, Kimmel DB, Dempster D, Weinstein RS, Wronski TJ, Burr DB.** Issues in modern bone histomorphometry. *Bone* 2011; **49**: 955-964 [PMID: 21810491 DOI: 10.1016/j.bone.2011.07.017]
 - 34 **Yamaguchi K, Croucher PI, Compston JE.** Comparison between the lengths of individual osteoid seams and resorption cavities in human iliac crest cancellous bone. *Bone Miner* 1993; **23**: 27-33 [PMID: 8274877 DOI: 10.1016/S0169-6009(08)80088-8]
 - 35 **Croucher PI, Wright CD, Garrahan NJ, Kudlac H, Williams AJ, Compston JE.** Characteristics of trabecular bone resorption cavities in patients with chronic renal failure. *Bone Miner* 1992; **16**: 139-137 [PMID: 1576489 DOI: 10.1016/0169-6009(92)90884-G]
 - 36 **Hernandez CJ.** How can bone turnover modify bone strength independent of bone mass? *Bone* 2008; **42**: 1014-1020 [PMID: 18373970 DOI: 10.1016/j.bone.2008.02.001]
 - 37 **Mosekilde L.** Consequences of the remodelling process for vertebral trabecular bone structure: a scanning electron microscopy study (uncoupling of unloaded structures). *Bone Miner* 1990; **10**: 13-35 [PMID: 2397325 DOI: 10.1016/0169-6009(90)90046-I]
 - 38 **Tkachenko EV, Slyfield CR, Tomlinson RE, Daggett JR,**

- Wilson DL, Hernandez CJ. Voxel size and measures of individual resorption cavities in three-dimensional images of cancellous bone. *Bone* 2009; **45**: 487-492 [PMID: 19482097 DOI: 10.1016/j.bone.2009.05.019]
- 39 **Goff MG**, Slyfield CR, Kummari SR, Tkachenko EV, Fischer SE, Yi YH, Jekir MG, Keaveny TM, Hernandez CJ. Three-dimensional characterization of resorption cavity size and location in human vertebral trabecular bone. *Bone* 2012; **51**: 28-37 [PMID: 22507299 DOI: 10.1016/j.bone.2012.03.028]
- 40 **Soysa NS**, Alles N, Aoki K, Ohya K. Three-dimensional characterization of osteoclast bone-resorbing activity in the resorption lacunae. *J Med Dent Sci* 2009; **56**: 107-112 [PMID: 20099473]
- 41 **Pascaretti-Grizon F**, Mabilieu G, Basle MF, Chappard D. Measurement by vertical scanning profilometry of resorption volume and lacunae depth caused by osteoclasts on dentine slices. *J Microsc* 2011; **241**: 147-152 [PMID: 21118208]
- 42 **Schulte FA**, Lambers FM, Kuhn G, Müller R. In vivo micro-computed tomography allows direct three-dimensional quantification of both bone formation and bone resorption parameters using time-lapsed imaging. *Bone* 2011; **48**: 433-442 [PMID: 20950723 DOI: 10.1016/j.bone.2010.10.007]
- 43 **Vedi S**, Compston JE, Webb A, Tighe JR. Histomorphometric analysis of bone biopsies from the iliac crest of normal British subjects. *Metab Bone Dis Relat Res* 1982; **4**: 231-236 [PMID: 7182722 DOI: 10.1016/0221-8747(82)90032-7]
- 44 **Schnitzler CM**, Biddulph SL, Mesquita JM, Gear KA. Bone structure and turnover in the distal radius and iliac crest: a histomorphometric study. *J Bone Miner Res* 1996; **11**: 1761-1768 [PMID: 8915784 DOI: 10.1002/jbmr.565011120]
- 45 **Compston JE**, Mellish RW, Croucher P, Newcombe R, Garrahan NJ. Structural mechanisms of trabecular bone loss in man. *Bone Miner* 1989; **6**: 339-350 [PMID: 2758162 DOI: 10.1016/0169-6009(89)90039-1]
- 46 **Wakamatsu E**, Sissons HA. The cancellous bone of the iliac crest. *Calcif Tissue Res* 1969; **4**: 147-161 [PMID: 5363270 DOI: 10.1007/BF02279116]
- 47 **Kelepouris N**, Harper KD, Gannon F, Kaplan FS, Haddad JG. Severe osteoporosis in men. *Ann Intern Med* 1995; **123**: 452-460 [PMID: 7639446 DOI: 10.7326/0003-4819-123-6-1995-09150-00010]
- 48 **Lips P**, Courpron P, Meunier PJ. Mean wall thickness of trabecular bone packets in the human iliac crest: changes with age. *Calcif Tissue Res* 1978; **26**: 13-17 [PMID: 737547 DOI: 10.1007/BF02013227]
- 49 **Clarke BL**, Ebeling PR, Jones JD, Wahner HW, O'Fallon WM, Riggs BL, Fitzpatrick LA. Changes in quantitative bone histomorphometry in aging healthy men. *J Clin Endocrinol Metab* 1996; **81**: 2264-2270 [PMID: 8964862 DOI: 10.1210/jc.81.6.2264]
- 50 **Charhon SA**, Edouard CM, Arlot ME, Meunier PJ. Effects of parathyroid hormone on remodeling of iliac trabecular bone packets in patients with primary hyperparathyroidism. *Clin Orthop Relat Res* 1985; 255-263 [PMID: 7067220]
- 51 **Parfitt AM**, Han ZH, Palnitkar S, Rao DS, Shih MS, Nelson D. Effects of ethnicity and age or menopause on osteoblast function, bone mineralization, and osteoid accumulation in iliac bone. *J Bone Miner Res* 1997; **12**: 1864-1873 [PMID: 9383691 DOI: 10.1359/jbmr.1997.12.11.1864]
- 52 **Arlot ME**, Jiang Y, Genant HK, Zhao J, Burt-Pichat B, Roux JP, Delmas PD, Meunier PJ. Histomorphometric and microCT analysis of bone biopsies from postmenopausal osteoporotic women treated with strontium ranelate. *J Bone Miner Res* 2008; **23**: 215-222 [PMID: 17922612 DOI: 10.1359/jbmr.071012]
- 53 **Recker R**, Lappe J, Davies KM, Heaney R. Bone remodeling increases substantially in the years after menopause and remains increased in older osteoporosis patients. *J Bone Miner Res* 2004; **19**: 1628-1633 [PMID: 15355557 DOI: 10.1359/JBMR.040710]
- 54 **Chavassieux P**, Meunier PJ. Histomorphometric approach of bone loss in men. *Calcif Tissue Int* 2001; **69**: 209-213 [PMID: 11730252]
- 55 **Delichatsios HK**, Lane JM, Rivlin RS. Bone histomorphometry in men with spinal osteoporosis. *Calcif Tissue Int* 1995; **56**: 359-363 [PMID: 7621341]
- 56 **Eriksen EF**, Hodgson SF, Eastell R, Cedel SL, O'Fallon WM, Riggs BL. Cancellous bone remodeling in type I (postmenopausal) osteoporosis: quantitative assessment of rates of formation, resorption, and bone loss at tissue and cellular levels. *J Bone Miner Res* 1990; **5**: 311-319 [PMID: 2343771 DOI: 10.1002/jbmr.5650050402]
- 57 **Kimmel DB**, Recker RR, Gallagher JC, Vaswani AS, Aloia JF. A comparison of iliac bone histomorphometric data in post-menopausal osteoporotic and normal subjects. *Bone Miner* 1990; **11**: 217-235 [PMID: 2268749 DOI: 10.1016/0169-6009(90)90061-J]
- 58 **Pernow Y**, Hauge EM, Linder K, Dahl E, Sääf M. Bone histomorphometry in male idiopathic osteoporosis. *Calcif Tissue Int* 2009; **84**: 430-438 [PMID: 19308628 DOI: 10.1007/s00223-009-9239-5]
- 59 **Søe K**, Delaissé JM. Glucocorticoids maintain human osteoclasts in the active mode of their resorption cycle. *J Bone Miner Res* 2010; **25**: 2184-2192 [PMID: 20499345 DOI: 10.1002/jbmr.1113]
- 60 **Chavassieux PM**, Arlot ME, Roux JP, Portero N, Daifotis A, Yates AJ, Hamdy NA, Malice MP, Freedholm D, Meunier PJ. Effects of alendronate on bone quality and remodeling in glucocorticoid-induced osteoporosis: a histomorphometric analysis of transiliac biopsies. *J Bone Miner Res* 2000; **15**: 754-762 [PMID: 10780867 DOI: 10.1359/jbmr.2000.15.4.754]
- 61 **Dalle Carbonare L**, Arlot ME, Chavassieux PM, Roux JP, Portero NR, Meunier PJ. Comparison of trabecular bone microarchitecture and remodeling in glucocorticoid-induced and postmenopausal osteoporosis. *J Bone Miner Res* 2001; **16**: 97-103 [PMID: 11149495 DOI: 10.1359/jbmr.2001.16.1.97]
- 62 **Dalle Carbonare L**, Bertoldo F, Valenti MT, Zenari S, Zanatta M, Sella S, Giannini S, Cascio VL. Histomorphometric analysis of glucocorticoid-induced osteoporosis. *Micron* 2005; **36**: 645-652 [PMID: 16243531 DOI: 10.1016/j.micron.2005.07.009]
- 63 **Weinstein RS**, Chen JR, Powers CC, Stewart SA, Landes RD, Bellido T, Jilka RL, Parfitt AM, Manolagas SC. Promotion of osteoclast survival and antagonism of bisphosphonate-induced osteoclast apoptosis by glucocorticoids. *J Clin Invest* 2002; **109**: 1041-1048 [PMID: 11956241 DOI: 10.1172/JCI14538]
- 64 **Chavassieux PM**, Arlot ME, Reda C, Wei L, Yates AJ, Meunier PJ. Histomorphometric assessment of the long-term effects of alendronate on bone quality and remodeling in patients with osteoporosis. *J Clin Invest* 1997; **100**: 1475-1480 [PMID: 9294113 DOI: 10.1172/JCI19668]
- 65 **Qiu S**, Phipps RJ, Ebetino FH, Palnitkar S, Sudhaker Rao D. Effect of risedronate on osteocyte viability and bone turnover in paired iliac bone biopsies from early postmenopausal women. *Calcif Tissue Int* 2010; **87**: 392-397 [PMID: 20809096 DOI: 10.1007/s00223-010-9411-y]
- 66 **Recker RR**, Ste-Marie LG, Langdahl B, Czerwinski E, Bonvoisin B, Masanaukaite D, Rowell L, Felsenberg D. Effects of intermittent intravenous ibandronate injections on bone quality and micro-architecture in women with postmenopausal osteoporosis: the DIVA study. *Bone* 2010; **46**: 660-665 [PMID: 19909829 DOI: 10.1016/j.bone.2009.11.004]
- 67 **Eriksen EF**, Melsen F, Sod E, Barton I, Chines A. Effects of long-term risedronate on bone quality and bone turnover in women with postmenopausal osteoporosis. *Bone* 2002; **31**: 620-625 [PMID: 12477578 DOI: 10.1016/S8756-3282(02)00869-4]
- 68 **Allen MR**, Burr DB. Bisphosphonate effects on bone turnover, microdamage, and mechanical properties: what we

- think we know and what we know that we don't know. *Bone* 2011; **49**: 56-65 [PMID: 20955825 DOI: 10.1016/j.bone.2010.10.159]
- 69 **Ott SM**. Bisphosphonates and BMU birth rate. *Osteoporos Int* 2010; **21**: 887; author reply 889-890 [PMID: 19649676]
- 70 **Weinstein RS**, Roberson PK, Manolagas SC. Giant osteoclast formation and long-term oral bisphosphonate therapy. *N Engl J Med* 2009; **360**: 53-62 [PMID: 19118304 DOI: 10.1056/NEJMoa0802633]
- 71 **Hodsman AB**, Kisiel M, Adachi JD, Fraher LJ, Watson PH. Histomorphometric evidence for increased bone turnover without change in cortical thickness or porosity after 2 years of cyclical hPTH(1-34) therapy in women with severe osteoporosis. *Bone* 2000; **27**: 311-318 [PMID: 10913928 DOI: 10.1016/S8756-3282(00)00316-1]
- 72 **Stepan JJ**, Burr DB, Li J, Ma YL, Petto H, Sipos A, Dobnig H, Fahrleitner-Pammer A, Michalská D, Pavo I. Histomorphometric changes by teriparatide in alendronate-pretreated women with osteoporosis. *Osteoporos Int* 2010; **21**: 2027-2036 [PMID: 20135094]
- 73 **Recker RR**, Bare SP, Smith SY, Varela A, Miller MA, Morris SA, Fox J. Cancellous and cortical bone architecture and turnover at the iliac crest of postmenopausal osteoporotic women treated with parathyroid hormone 1-84. *Bone* 2009; **44**: 113-119 [PMID: 18983947 DOI: 10.1016/j.bone.2008.09.019]
- 74 **Recker RR**, Marin F, Ish-Shalom S, Möricke R, Hawkins F, Kapetanios G, de la Peña MP, Kekow J, Farrerons J, Sanz B, Oertel H, Stepan J. Comparative effects of teriparatide and strontium ranelate on bone biopsies and biochemical markers of bone turnover in postmenopausal women with osteoporosis. *J Bone Miner Res* 2009; **24**: 1358-1368 [PMID: 19338452 DOI: 10.1359/jbmr.090904]
- 75 **Matheny JB**, Slyfield CR, Tkachenko EV, Lin I, Ehlert KM, Tomlinson RE, Wilson DL, Hernandez CJ. Antiresorptive agents reduce the size of resorption cavities: a three-dimensional dynamic bone histomorphometry study. *Bone* 2013; **57**: 277-283 [PMID: 23988275 DOI: 10.1016/j.bone.2013.08.018]
- 76 **Heaney RP**. Is the paradigm shifting? *Bone* 2003; **33**: 457-465 [PMID: 14555248 DOI: 10.1016/S8756-3282(03)00236-9]
- 77 **Garnero P**, Hausherr E, Chapuy MC, Marcelli C, Grandjean H, Muller C, Cormier C, Bréart G, Meunier PJ, Delmas PD. Markers of bone resorption predict hip fracture in elderly women: the EPIDOS Prospective Study. *J Bone Miner Res* 1996; **11**: 1531-1538 [PMID: 8889854 DOI: 10.1002/jbmr.5650111021]
- 78 **Parfitt AM**. What is the normal rate of bone remodeling? *Bone* 2004; **35**: 1-3 [PMID: 15207734 DOI: 10.1016/j.bone.2004.03.022]
- 79 **Gibson LJ**. Biomechanics of cellular solids. *J Biomech* 2005; **38**: 377-399 [PMID: 15652536 DOI: 10.1016/j.jbiomech.2004.09.027]
- 80 **Liu XS**, Sajda P, Saha PK, Wehrli FW, Bevil G, Keaveny TM, Guo XE. Complete volumetric decomposition of individual trabecular plates and rods and its morphological correlations with anisotropic elastic moduli in human trabecular bone. *J Bone Miner Res* 2008; **23**: 223-235 [PMID: 17907921 DOI: 10.1359/jbmr.071009]
- 81 **Hernandez CJ**, Beaupré GS, Carter DR. A theoretical analysis of the relative influences of peak BMD, age-related bone loss and menopause on the development of osteoporosis. *Osteoporos Int* 2003; **14**: 843-847 [PMID: 12904837]
- 82 **Hernandez CJ**, Beaupré GS, Carter DR. A theoretical analysis of the changes in basic multicellular unit activity at menopause. *Bone* 2003; **32**: 357-363 [PMID: 12689678 DOI: 10.1016/S8756-3282(03)00037-1]
- 83 **McNamara LM**, Prendergast PJ. Perforation of cancellous bone trabeculae by damage-stimulated remodelling at resorption pits: a computational analysis. *Eur J Morphol* 2005; **42**: 99-109 [PMID: 16123029 DOI: 10.1080/ejom.42.1-2.0099]
- 84 **Mulvihill BM**, McNamara LM, Prendergast PJ. Loss of trabeculae by mechano-biological means may explain rapid bone loss in osteoporosis. *J R Soc Interface* 2008; **5**: 1243-1253 [PMID: 18348960 DOI: 10.1098/rsif.2007.1341]
- 85 **Langton CM**, Haire TJ, Ganney PS, Dobson CA, Fagan MJ. Dynamic stochastic simulation of cancellous bone resorption. *Bone* 1998; **22**: 375-380 [PMID: 9556138 DOI: 10.1016/S8756-3282(97)00290-1]
- 86 **Tayyar S**, Weinhold PS, Butler RA, Woodard JC, Zardiackas LD, St John KR, Bledsoe JM, Gilbert JA. Computer simulation of trabecular remodeling using a simplified structural model. *Bone* 1999; **25**: 733-739 [PMID: 10593419 DOI: 10.1016/S8756-3282(99)00218-5]
- 87 **McNamara LM**, Van der Linden JC, Weinans H, Prendergast PJ. Stress-concentrating effect of resorption lacunae in trabecular bone. *J Biomech* 2006; **39**: 734-741 [PMID: 16439243 DOI: 10.1016/j.jbiomech.2004.12.027]
- 88 **Hernandez CJ**, Gupta A, Keaveny TM. A biomechanical analysis of the effects of resorption cavities on cancellous bone strength. *J Bone Miner Res* 2006; **21**: 1248-1255 [PMID: 16869723 DOI: 10.1359/jbmr.060514]
- 89 **Liu XS**, Huang AH, Zhang XH, Sajda P, Ji B, Guo XE. Dynamic simulation of three dimensional architectural and mechanical alterations in human trabecular bone during menopause. *Bone* 2008; **43**: 292-301 [PMID: 18550463 DOI: 10.1016/j.bone.2008.04.008]
- 90 **Müller R**. Long-term prediction of three-dimensional bone architecture in simulations of pre-, peri- and postmenopausal microstructural bone remodeling. *Osteoporos Int* 2005; **16** Suppl 2: S25-S35 [PMID: 15340800]
- 91 **Tsubota K**, Suzuki Y, Yamada T, Hojo M, Makinouchi A, Adachi T. Computer simulation of trabecular remodeling in human proximal femur using large-scale voxel FE models: Approach to understanding Wolff's law. *J Biomech* 2009; **42**: 1088-1094 [PMID: 19403138 DOI: 10.1016/j.jbiomech.2009.02.030]
- 92 **Van Der Linden JC**, Verhaar JA, Weinans H. A three-dimensional simulation of age-related remodeling in trabecular bone. *J Bone Miner Res* 2001; **16**: 688-696 [PMID: 11315996 DOI: 10.1359/jbmr.2001.16.4.688]
- 93 **van der Linden JC**, Day JS, Verhaar JA, Weinans H. Altered tissue properties induce changes in cancellous bone architecture in aging and diseases. *J Biomech* 2004; **37**: 367-374 [PMID: 14757456 DOI: 10.1016/S0021-9290(03)00266-5]
- 94 **Müller R**, Rüeegsegger P. Analysis of mechanical properties of cancellous bone under conditions of simulated bone atrophy. *J Biomech* 1996; **29**: 1053-1060 [PMID: 8817372 DOI: 10.1016/0021-9290(96)00006-1]
- 95 **van der Linden JC**, Homminga J, Verhaar JA, Weinans H. Mechanical consequences of bone loss in cancellous bone. *J Bone Miner Res* 2001; **16**: 457-465 [PMID: 11277263 DOI: 10.1359/jbmr.2001.16.3.457]
- 96 **van der Linden JC**, Verhaar JA, Pols HA, Weinans H. A simulation model at trabecular level to predict effects of antiresorptive treatment after menopause. *Calcif Tissue Int* 2003; **73**: 537-544 [PMID: 14508627 DOI: 10.1007/s00223-002-2151-x]
- 97 **Easley SK**, Chang MT, Shindich D, Hernandez CJ, Keaveny TM. Biomechanical effects of simulated resorption cavities in cancellous bone across a wide range of bone volume fractions. *J Bone Miner Res* 2012; **27**: 1927-1935 [PMID: 22576976 DOI: 10.1002/jbmr.1657]
- 98 **Vanderoost J**, van Lenthe GH. The effect of resorption cavities on bone stiffness is site dependent. *Comput Methods Biomech Biomed Engin* 2014; **17**: 1483-1491 [PMID: 23282095]
- 99 **Vanderoost J**, Søb K, Merrild DM, Delaissé JM, van Lenthe GH. Glucocorticoid-induced changes in the geometry of osteoclast resorption cavities affect trabecular bone stiffness. *Calcif Tissue Int* 2013; **92**: 240-250 [PMID: 23187898 DOI: 10.1007/s00223-012-9674-6]
- 100 **Slyfield CR**, Tkachenko EV, Fischer SE, Ehlert KM, Yi IH, Jekir

- MG, O'Brien RG, Keaveny TM, Hernandez CJ. Mechanical failure begins preferentially near resorption cavities in human vertebral cancellous bone under compression. *Bone* 2012; **50**: 1281-1287 [PMID: 22426306 DOI: 10.1016/j.bone.2012.02.636]
- 101 **Vanderoost J**, Jaecques SV, Van der Perre G, Boonen S, D'hooge J, Lauriks W, van Lenthe GH. Fast and accurate specimen-specific simulation of trabecular bone elastic modulus using novel beam-shell finite element models. *J Biomech* 2011; **44**: 1566-1572 [PMID: 21414627 DOI: 10.1016/j.jbiomech.2011.02.082]
- 102 **Rauch F**, Travers R, Parfitt AM, Glorieux FH. Static and dynamic bone histomorphometry in children with osteogenesis imperfecta. *Bone* 2000; **26**: 581-589 [PMID: 10831929 DOI: 10.1016/S8756-3282(00)00269-6]
- 103 **Croucher PI**, Garrahan NJ, Compston JE. Assessment of resorption cavity characteristics in trabecular bone: changes in primary and secondary osteoporosis. *Bone* 1993; **14**: 449-454 [PMID: 8363891 DOI: 10.1016/8756-3282(93)90178-D]

P- Reviewer: Kamishima T, Naraghi M, Quattrocchi CC

S- Editor: Ji FF **L- Editor:** A **E- Editor:** Lu YJ



Skeletal dysplasias: A radiographic approach and review of common non-lethal skeletal dysplasias

Ananya Panda, Shivanand Gamanagatti, Manisha Jana, Arun Kumar Gupta

Ananya Panda, Shivanand Gamanagatti, Manisha Jana, Arun Kumar Gupta, Department of Radiodiagnosis, All India Institute of Medical Sciences, Ansari Nagar, New Delhi 110029, India

Author contributions: Panda A and Gamanagatti S contributed equally to conception, article design, literature search, article drafting, critical revision and image preparation; Jana M helped with the article concept, revision literature search and image preparation; Gupta AK helped in images procurement, preparation and final approval of version of article to be published.

Correspondence to: Shivanand Gamanagatti, Additional Professor, Department of Radiodiagnosis, All India Institute of Medical Sciences, Room no 81-B, Ansari Nagar, New Delhi 110029, India. shiv223@rediffmail.com

Telephone: +91-986-8658057 Fax: +91-986-8398508

Received: May 16, 2014 Revised: July 2, 2014

Accepted: August 27, 2014

Published online: March 28, 2015

lolepiphyseal dysplasia; Multiple epiphyseal dysplasia; Achondroplasia; Algorithm; Approach

Core tip: This article describes the radiographic approach to skeletal dysplasias, reviews the essential radiographic features of various non-lethal epiphyseal, metaphyseal, diaphyseal, osteopenic and sclerosing dysplasias and also describes features to differentiate these entities from other similar dysplasias. In summary, working algorithms for diagnosis of common skeletal dysplasias have also been provided.

Original sources: Panda A, Gamanagatti S, Jana M, Gupta AK. Skeletal dysplasias: A radiographic approach and review of common non-lethal skeletal dysplasias. *World J Radiol* 2014; 6(10): 808-825 Available from: URL: <http://www.wjgnet.com/1949-8470/full/v6/i10/808.htm> DOI: <http://dx.doi.org/10.4329/wjr.v6.i10.808>

Abstract

Skeletal dysplasias are not uncommon entities and a radiologist is likely to encounter a suspected case of dysplasia in his practice. The correct and early diagnosis of dysplasia is important for management of complications and for future genetic counselling. While there is an exhaustive classification system on dysplasias, it is important to be familiar with the radiological features of common dysplasias. In this article, we enumerate a radiographic approach to skeletal dysplasias, describe the essential as well as differentiating features of common non-lethal skeletal dysplasias and conclude by presenting working algorithms to either definitively diagnose a particular dysplasia or suggest the most likely differential diagnoses to the referring clinician and thus direct further workup of the patient.

© 2015 Baishideng Publishing Group Inc. All rights reserved.

Key words: Skeletal dysplasia; Short limb dwarfism; Rhizomelia; Radiograph; Skeletal survey; Review; Spondy-

INTRODUCTION

Skeletal dysplasias also termed as *osteochondrodysplasias* are a large heterogeneous group of disorders comprising of abnormalities of bone or cartilage growth or texture. They occur due to genetic mutations and their phenotype continues to evolve throughout life. Skeletal dysplasias thus differ from *dysostoses* which are malformations of single or multiple bones in combination, are due to abnormal blastogenesis in-utero and phenotypically remain static throughout life^[1]. Currently more than 450 different entities have been described based on radiologic, molecular and biochemical criteria^[2]. While certain dysplasias individually are quite rare, their overall prevalence as a group has been reported to be 2.3-7.6 per 10000 births in various epidemiologic studies^[3-6]. However the actual prevalence may even be higher as concluded by these studies.

Some dysplasias are lethal in perinatal period and are

Table 1 Set of radiographs obtained in a skeletal survey^[1]

Skull (AP and lateral)
Thoracolumbar spine (AP and lateral)
Chest (AP)
Pelvis (AP)
One upper limb (AP)
One lower limb (AP)
Left hand (AP) (for bone age)

AP: Anteroposterior.

detected on antenatal ultrasound scans while the non-lethal dysplasia present early in infancy or childhood with disproportionate short stature, failure of linear growth or with other physical deformities.

The appropriate diagnosis of a dysplasia is dependent upon the integration of clinical and family history, physical examination, radiologic examination and molecular and biochemical tests. Among these, a radiologic evaluation is an integral part of the diagnostic workup of a dysplasia. A general radiologist will often encounter a set of radiographs of a patient with a suspected skeletal dysplasia. While some dysplasias can be easy to diagnose based on certain characteristic or so-called “text-book” findings, it is also important to have an appropriate approach to diagnosis. Thus in this article, we review the radiologic approach to the diagnosis of a non-lethal dysplasia and thereafter describe the radiologic features of a few important and more common non-lethal dysplasias.

RADIOLOGIC EVALAUTION

The radiologic evaluation begins with a complete skeletal survey ideally comprising of a set of radiographs outlined in Table 1.

In cases with epiphyseal irregularity or stippling, it is recommended to obtain radiographs of both sides upper and lower limbs. Also, because dysplasias continue to phenotypically evolve throughout life, serial radiographs are recommended and comparison should always be made with previous radiographs to assess evolution of disease and complications^[1]. It is also recommended to obtain radiographs early in childhood since the optimal age for recognition of most dysplasias is before the obliteration of growth cartilage. Later when there is epiphyseal fusion and growth ceases, the recognition of many dysplasias becomes difficult and even impossible^[7].

Offiah and Hall^[1], in their excellent article have enumerated the ABCs of evaluation, comprising of anatomical localisation, analysis of bones and assessment of complications. Anatomically, the abnormalities can be located in the axial skeleton (Table 2) or in the appendicular skeleton.

In axial skeleton skull and spine are most commonly involved. The skull can either be large (achondroplasia) or can have multiple wormian bones (cleidocranial dysplasia). Involvement of spine is commonly in the form of flattening and decreased vertebral body height termed as *platyspondyly* or there can be irregularity of end-

Table 2 Dysplasias with involvement of axial skeleton

Location	Examples
Skull	Achondroplasia, Cleidocranial dysplasia
Mandible	Pyknodysostosis
Clavicle	Cleidocranial dysplasia
Ribs	Asphyxiating thoracic dysplasia, Thanatophoric dysplasia
Spine	Spondyloepiphyseal dysplasia congenita, Mucopolysaccharidoses
Pelvis	Achondroplasia

plates. There may also be abnormal vertebral hooking or beaking which are characteristic for certain dysplasias (central beaking in Morquio’s syndrome, posterior hump-shaped vertebrae in spondyloepiphyseal dysplasia tarda).

The appendicular skeleton has to be assessed for (1) type of bone shortening and (2) location of abnormality, *i.e.*, epiphyseal, metaphyseal or diaphyseal. Shortening of the limbs can be (1) *rhizomelic* (involving proximal parts of limb, *i.e.*, humerus and femur); (2) *mesomelic* (involving middle parts of limb, *i.e.*, radius/ulna; tibia/fibula); (3) *acromelic* (involving hands and feet); or (4) *micromelic* (generalised shortening of entire limb).

Location of abnormality can be purely epiphyseal involving only the epiphyses, metaphyseal involving the metaphyses or *diaphyseal* involving only the diaphyses or there can be concomitant involvement of more than one location in appendicular skeleton. The involvement of appendicular skeleton has been summarised in Table 3.

In addition, look at the bone density (decreased in osteopenic and increased in sclerosing dysplasias respectively) and for an abnormal shape of bone (*e.g.*, champagne glass pelvis in achondroplasia).

Thirdly, complications are invariable sequelae of dysplasias because of altered bone shapes. An analysis of complications can also give a clue to the underlying diagnosis. Epiphyseal dysplasias lead to premature osteoarthritis and deformities like coxa vara and genu valgum. Spondylo-dysplasias lead to early kyphoscoliosis while fractures are typically noted in dysplasias with altered bone density like osteogenesis imperfecta and osteopetrosis.

COMMON RADIOLOGICAL GROUPINGS

After analysis of the skeletal survey, the radiologic findings can be further grouped into common radiographic groups. These radiographic groups have been created based on common X-ray findings. Within these radiological groups are dysplasias groups conforming to that X-ray appearance and within the dysplasia groups we have enumerated a few common entities. We have basically derived and modified these groups from the 2010 revision of the Nosology and Classification of Genetic Skeletal Disorders framed by the International Skeletal Dysplasia Society^[2,8] and from atlases of bone dysplasias^[9,10]. By using these groups, we generate radiological differential diagnoses when encountering a common constellation of

Table 3 Dysplasias with involvement of appendicular skeleton

Type of shortening	Examples	Location of abnormality	Examples
Rhizomelic	Achondroplasia Spondyloepiphyseal dysplasia congenita	Epiphyseal	Chondrodysplasia punctata Spondyloepiphyseal dysplasia
Mesomelic	Mesomelic dysplasia	Metaphyseal	Achondroplasia Chondroectodermal dysplasia
Acromelic	Acrodysostosis	Diaphyseal	Progressive diaphyseal dysplasia
Micromelic	Achondrogenesis	Combination	Spondylo-epimetaphyseal dysplasia Metatropic dysplasia Mucopolysaccharidoses

findings on skeletal surveys.

The groups include: (1) GROUP I: Epiphyseal dysplasias with/without spine involvement (Platyspondyly +/-); (2) GROUP II: Metaphyseal dysplasias with limb shortening/abnormal limb length; (3) GROUP III: Dysplasias with altered bone density; and (4) and GROUP IV: Miscellaneous dysplasias, *i.e.*, those which do not typically have limb shortening or be clearly bracketed anatomically into spondylo-epi/metaphyseal dysplasias.

RADIOGRAPHIC FEATURES OF COMMON DYSPLASIAS

After the radiological grouping of dysplasias, both essential diagnostic and differentiating radiographic features of various common non-lethal skeletal dysplasias in each group have been enumerated below. While we chiefly describe the radiographic appearances of dysplasias, we have also provided the Online Mendelian Inheritance in Man (OMIM) numbers for these dysplasias for reference. OMIM is a comprehensive compilation of all human genes and genetic phenotypes and OMIM numbers are assigned to genetic phenotypes. This is a free resource available on <http://www.ncbi.nlm.nih.gov/omim>^[11]. The OMIM numbers of dysplasias enumerated in this review have been provided for further information about clinical, genetic and phenotypic features of skeletal dysplasias. Since varying underlying genetic mutations can produce a common phenotype, *i.e.*, a common radiographic appearance, more than one OMIM number may also be found within a single dysplasia entity.

Group I-epiphyseal dysplasias

All dysplasias in this group have common radiological findings of abnormal epiphyses and epiphyseal irregularity leading to early osteoarthritis and deformities like coxa vara and genu valgum. In addition, there is secondary metaphyseal flaring and irregularity due to epiphyseal abnormality.

Within this broad group, there can be (1) isolated epiphyseal abnormality without platyspondyly as seen in chondrodysplasia punctata group; (2) concomitant involvement of spine (platyspondyly) as seen in Type II collagenopathies such as spondyloepiphyseal dysplasia congenita and tarda, Kniest dysplasia and achondrogenesis

type 2; and (3) concomitant metaphyseal involvement as seen in spondyl(epi)metaphyseal dysplasias, multiple epiphyseal dysplasia, pseudoachondroplasia, mucopolysaccharidoses, diastrophic dysplasia and achondrogenesis type 1.

Spondyloepiphyseal dysplasia congenita^[9,12-14]: OMIM: 183900^[15]. The mode of inheritance is autosomal dominant and is due to a mutation in *COL2A1* gene on chromosome locus 12q13.1 affecting Type II collagen protein.

Age of manifestation: At birth with delayed ossification of epiphyses as its hallmark. Essential radiographic features: (1) Bulbous and pear-shaped vertebrae at birth which later flatten leading to severe platyspondyly with thin intervertebral disc spaces (Figure 1A, B). The ensuing complications include kyphoscoliosis, lumbar lordosis and atlanto-axial instability. Atlanto-axial instability is secondary to odontoid hypoplasia and it subsequently endows a greatly increased risk of cervical myelopathy^[16,17]; (2) Absent pubic bones at birth with horizontal roofs of acetabula and short and broad iliac wings; (3) Absent epiphyses of calcaneum and knee at birth. Later, there's delay in the ossification of the heads of femur (Figure 1C). While delayed ossification of carpals and tarsal bones are noted, the hands and feet are typically not involved; and (4) Other features include large and dolicocephalic skull (Figure 1D) and rhizomelic shortening of extremities, more in lower than upper limbs and metaphyseal widening secondary to abnormal epiphyses (Figure 1E and F).

Differential diagnoses of SEDC include (1) Spondyloepiphyseal dysplasia tarda, (2) Morquio's syndrome, (3) Kniest dysplasia and (4) Metatropic dysplasia. The features favouring Morquio's syndrome include keratosulfuria clinically and central beaking of spine with increased or maintained intervertebral disc spaces on radiographs. Also hands and feet are always abnormal in Morquio's syndrome unlike SEDC.

Kniest dysplasia, (OMIM 156550)^[18] is also an autosomal dominantly inherited Type II collagenopathy like SEDC and affects the same gene locus. Similar to SEDC, it presents as a short trunk-short limb dwarfism with delayed ossification at birth and in infancy. But in addition to these features, dumbbell shaped femurs and coronal clefting of spine are also noted at birth. Later on, the epiphyses become enlarged giving rise to megaepiphyses with cloud-like calcifications at the growth plate. In

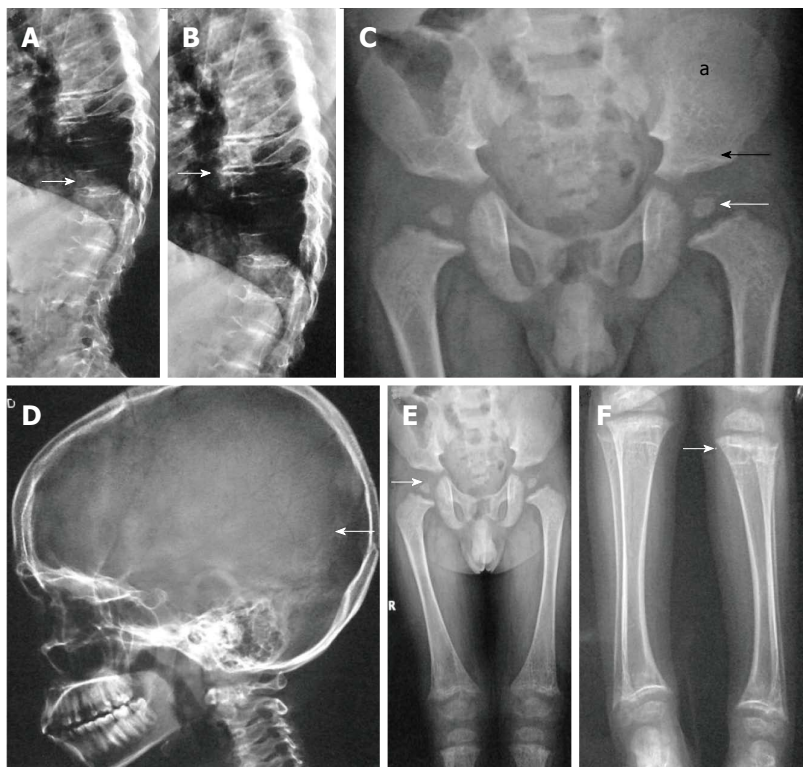


Figure 1 Spondyloepiphyseal dysplasia congenita. Lateral radiographs of dorsolumbar spine show platyspondyly (arrow, A) with severely reduced intervertebral disc spaces (arrow, B). Radiograph of pelvis (C) shows small femoral epiphyses (white arrow), horizontal acetabuli (black arrow) and short iliac wings (a). Radiograph of skull (D) shows relatively enlarged calvarium (arrow). Radiographs of lower limbs (E, F) show relatively short femurs and small epiphyses with secondary metaphyseal irregularity (arrow, F).

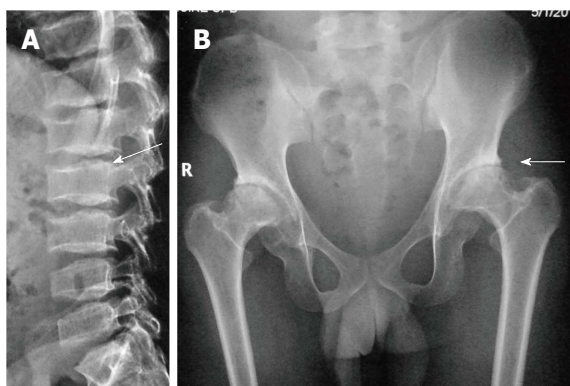


Figure 2 Spondyloepiphyseal dysplasia tarda. Lateral radiograph of lumbar spine (A) shows characteristic posterior hump (arrow). Radiograph of pelvis (B) shows bilateral flattened femoral heads, short necks and premature degenerative changes (arrow).

hands, there's characteristic flattening of epiphyses of metacarpals and enlargement at ends of metacarpals and proximal phalanges giving rise to bulbous metacarpophalangeal and proximal interphalangeal joints^[19,20].

Metatropic dysplasia (OMIM: 156530)^[21] is also an autosomal dominantly inherited dysplasia due to mutation on gene locus 12q24.1 affecting TRPV4 protein (transient receptor protein channel cation, subfamily V, member 4). It also manifests at birth with severe short limb rhizomelic dysplasia similar to achondroplasia and later evolves into a short trunk dysplasia similar to SEDC. Since metatropic dysplasia also presents with severe platyspondyly and progressive kyphoscoliosis in childhood, it can be mistaken for SEDC radiologically. However unlike SEDC, in metatropic dysplasia the metaphyses are also

enlarged and the coccyx is long and resembles a tail. Thus metatropic dysplasia is a differential diagnosis for both achondroplasia because of metaphyseal and rhizomelic involvement and SEDC because of severe platyspondyly^[22].

Spondyloepiphyseal dysplasia tarda^[9,12-14,23]: OMIM: 313400^[24]. The classical spondyloepiphyseal dysplasia tarda (SEDT) has a X-linked recessive inheritance and is noted only in males^[25]. This is caused due to a mutation of gene locus X.p22.2 affecting TRAPPC2 gene^[24]. However, more recently at least four types of SEDT with autosomal recessive inheritance (OMIM: 271600^[26], 271620^[27], 609223^[28], 600093^[29]) and autosomal dominant inheritance (OMIM: 184100)^[30] have also been described.

Age of manifestation: The classic age of presentation is between 5-10 years of age, though it can be variable, even first manifesting in the second decade of life. However, unlike SEDC, the appearance at birth is normal. **Essential radiographic features:** (1) Platyspondyly with heaping up and hyperostosis on the posterior two-thirds of endplates giving rise to a heaped-up or hump-shaped appearance (Figure 2A); (2) Small pelvis with mild-to-moderate epiphyseal irregularity leading to early osteoarthritis at hips (Figure 2B), knees and ankles. However hands, feet and skull are typically not involved; and (3) Other features: In addition to these findings, progressive narrowing of interpedicular distance in lumbar spine have also been described, similar to achondroplasia, in the autosomal recessive forms of SEDT^[31,32].

Differential diagnoses of SEDT include (1) SEDC and (2) Multiple epiphyseal dysplasia/Pseudochondroplasia. In SEDT, the disorder manifests predominantly

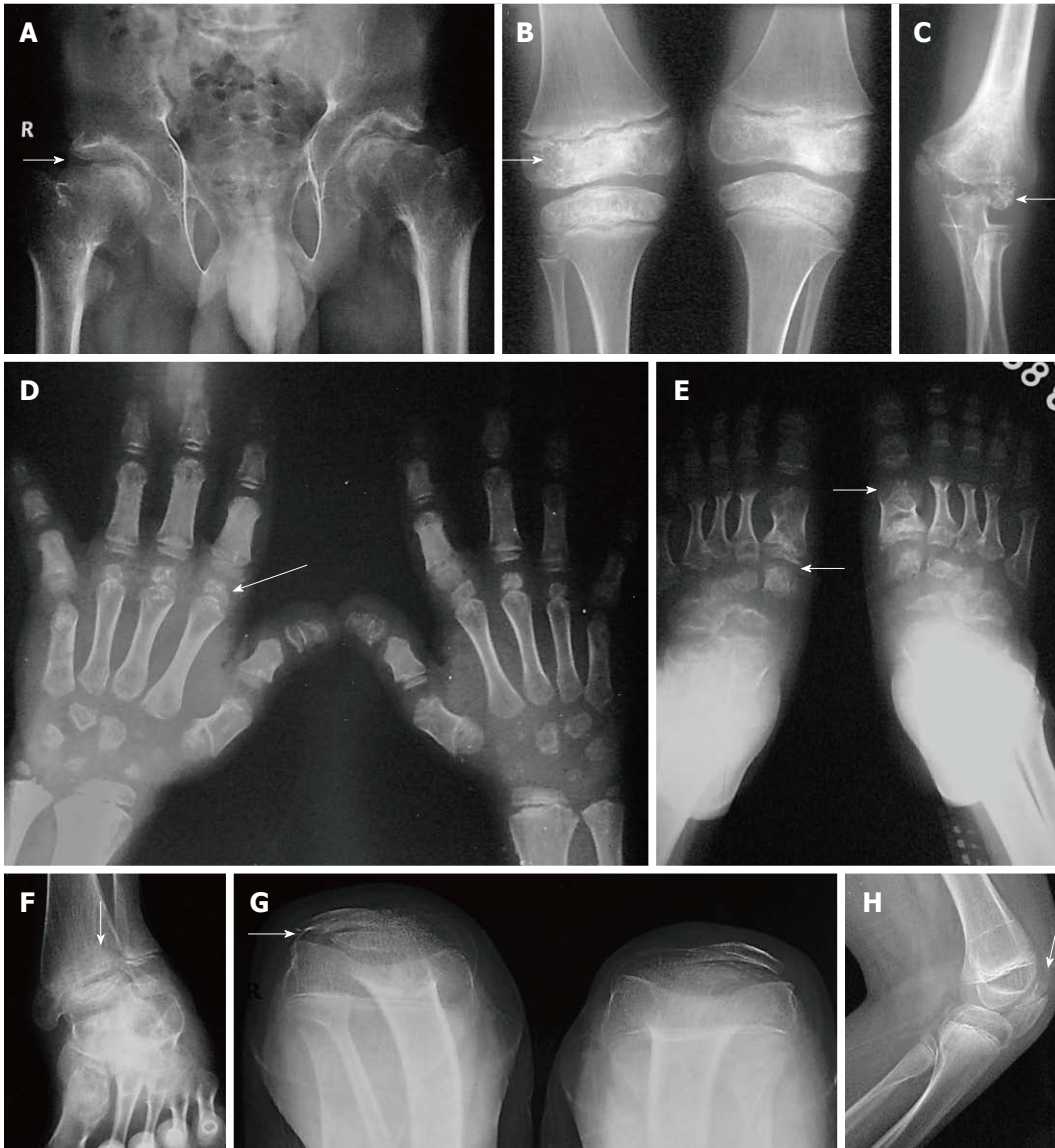


Figure 3 Multiple epiphyseal dysplasia. Radiographs of pelvis, knee and elbow (A-E) show epiphyseal irregularity in proximal femurs (arrow, A), around knee joints (arrow, B), elbow (arrow, C) with involvement of epiphyses of hands and feet (arrows in D, E) suggestive of multiple epiphyseal dysplasia. Radiograph of ankle (F) shows lateral tibio-talar slant. Radiograph of bilateral knees skyline view (G) and lateral view of left knee (H) show double-layered patellae (arrows).

in young boys and the spine, hips and joint changes are less severe whereas in SEDC, the short-trunk-short-limb dwarfism is apparent at birth itself with more severe and progressive deformities.

In multiple epiphyseal dysplasia/pseudoachondroplasia group, epiphyses of hands and feet are also involved and platyspondyly is typically absent EDM or moderate (pseudoachondroplasia).

Multiple epiphyseal dysplasia^[9,12,15] [No single OMIM number]: Multiple epiphyseal dysplasia (EDM) is a genetically heterogeneous entity caused by mutations in multiple genes^[33,34]. First described in EDM type 1 due to a mutation in cartilage oligomeric matrix protein (COMP) on gene locus 19p13 [OMIM: 132400], currently at least 6 types of MED are described termed as EDM2 [OMIM: 600204], EDM3 [OMIM: 600969], EDM4 [OMIM: 226900], EDM5 [OMIM: 607078] and EDM6[OMIM: 614135]^[33]. Most

cases of EDM are inherited in autosomal dominant manner while EDM4 has autosomal recessive inheritance.

Age of manifestation: Despite the genetic heterogeneity, MED usually presents after the age of 2-4 years when the child begins to walk. Essential radiographic features: (1) Bilateral and symmetric involvement of epiphyses of hips, knees, ankles, shoulders, elbows, wrists and hands and feet (Figure 3A-E); (2) Lateral tibio-talar slant wherein the lateral part of distal tibial epiphyses is thinner than the medial and the trochlea of the talus is shaped to conform to the abnormal ankle joint mortice (Figure 3F); (3) Double-layered patella as seen on a lateral X-ray of knee is considered highly pathognomic of EDM(Figure 3G, H). Double-layered patella is an important diagnostic clue for EDM^[36,37]. Initially considered diagnostic only for recessive EDM4, it has now also been found in other dominant forms of EDM^[38]. However, more recently, the uncommon occurrence of a double-layered patella in a patient with pseudoachondropla-

Table 4 Differences between pseudoachondroplasia and achondroplasia

Pseudoachondroplasia	Achondroplasia
Skull: Normal: "Achondroplasia with normal face"	Skull : Abnormal
Spine: Platyspondyly +	Spine: Platyspondyly -
Interpedicular distance normal	Interpedicular distance decreased in lumbar spine
Epiphyses and metaphyses abnormal	Only metaphyses abnormal
Trident hand and champagne-glass pelvis absent	Trident hand and champagne-glass pelvis present

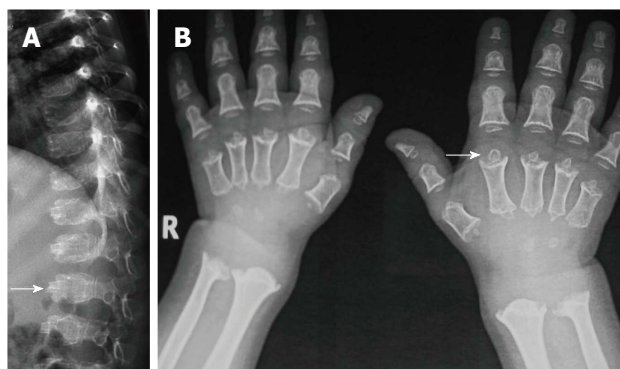


Figure 4 Pseudoachondroplasia. Lateral radiograph of spine shows typical central anterior tongue (arrow, A) in lumbar vertebrae. Radiograph of both hands (B) also show multiple abnormalities of epiphyses of metacarpals and phalanges with secondary metaphyseal widening (arrow).

sia was also described^[39]. This was attributed to the overlap between both EDM and milder forms of pseudoachondroplasia as both EDM1 and pseudoachondroplasia are caused due to mutations affecting the same *COMP* gene; and (4) Mild involvement of spine with anterior wedging, mild end plate irregularity and multiple Schmorl’s nodes mimicking Scheuermann’s disease and typical absence of platyspondyly.

Pseudoachondroplasia^[9,11,40]: OMIM: 177170^[41]. Pseudoachondroplasia is an autosomal dominantly inherited dysplasia caused due to mutation affecting the *COMP* gene similar to EDM on gene locus 19p13.11. Since both pseudoachondroplasia and EDM are genotypic alleles, there is considerable overlap in age of presentation and radiographic appearance in both entities. However, pseudoachondroplasia overall has more severe clinical and radiographic involvement as compared to EDM^[36].

Essential radiographic features: Vertebrae have a persistent oval shape in childhood with a tongue-like protrusion from the anterior aspect of vertebral bodies giving rise to central anterior tongue appearance (Figure 4). The central anterior tongue appearance is pathognomic of this entity. However, this disappears at older age and is replaced by platyspondyly giving rise to the short limb-short trunk dwarfism. Hence it is important to obtain early radiographs of spine to substantiate the diagnosis of pseudoachondroplasia.

Differential diagnoses of pseudoachondroplasia include (1) EDM and (2) achondroplasia. EDM and pseudoa-

chondroplasia may be differentiated on basis of presence of central anterior tongue and platyspondyly in former and double layered patella in EDM. Clinically too, in pseudoachondroplasia, there is joint and ligamentous laxity while in EDM, joints show restricted and painful movements^[9]. Secondly, in pseudoachondroplasia, the dwarfism and shortening of the extremities is quite dramatic as compared to EDM as pseudoachondroplasia is considered a more severe manifestation of mutation on same gene.

The radiographic differences between pseudoachondroplasia and achondroplasia^[13] have been enumerated in Table 4.

Chondrodysplasia punctata^[9,12,13]: Chondrodysplasia punctata (CDP) is another genetically heterogeneous dysplasia. The most common type is the X-linked dominant type also termed as Conradi-Hunermann type [OMIM: 302960] due to mutation on Xp11^[42]. Another type is the rhizomelic type chondrodysplasia punctata (RCDP) associated with peroxisomal enzyme disorder and has an autosomal recessive inheritance. RCDP is further divided into 3 sub-types, namely RCDP1 [OMIM: 215100], RCDP2 [OMIM: 222765] and RCDP3 [OMIM:600121] caused mutations affecting various genes encoding for peroxisomal enzymes^[43-45]. A third very uncommon type of CDP is the brachytelephalangi type which has X-linked recessive inheritance [OMIM:302950]^[46]. In addition to genetically inherited forms of CDP, CDP can also be seen in warfarin embryotoxicity with features similar to Conradi-Hunermann type of CDP and in babies born to mothers with auto-immune diseases like systemic lupus erythematosus^[47] who present with features similar to RCDP. Unlike the genetically inherited rhizomelic type which is usually lethal in the first year of life, babies born to mothers with auto-immune disorders survive longer and do not have any underlying peroxisomal disorder. Stippling can also be seen in Zellweger’s syndrome which is a separate peroxisomal enzyme biogenesis disorder^[43].

Essentially, the hallmark of CDP is stippling of epiphyses at birth. Later on, the stippling disappears and epiphyses become irregular with limb asymmetry (Figure 5 A-F). It is important to identify the radiologic type of chondrodysplasia punctata, namely rhizomelic/lethal or X-linked dominant type to prognosticate the patient. The differences between these two types have been summarised in Table 5.

Table 5 Differences between Rhizomelic and Conradi-Hunermann type Chondrodysplasia punctata

Rhizomelic/lethal type	Conradi-Hunermann type
Inheritance: Autosomal recessive	Inheritance: X-linked dominant
Symmetric rhizomelic limb shortening	Asymmetric and occasional limb shortening
Stippling in spine absent/coronal clefts present	Spine: stippling present at endplates and bodies, later leads to kyphoscoliosis
Stippling noted in large joints, sparing hands and feet	Hands and feet also involved in addition to large joints. No extracartilaginous stippling
Laryngeal and tracheal cartilage stippling also present	
Mental retardation present and death in infancy	Compatible with normal intelligence and normal life span

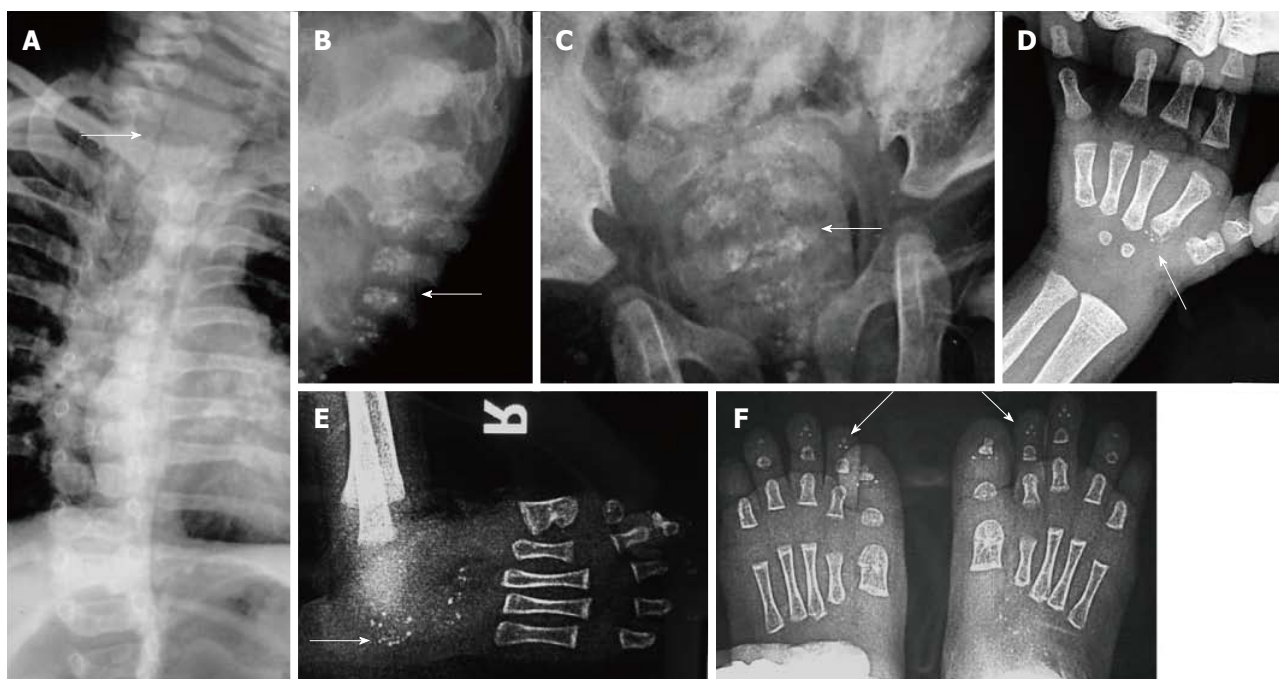


Figure 5 Chondrodysplasia punctata. Oblique view radiograph of dorsal spine (A) shows coronal clefting (arrow). Radiographs of another patient with chondrodysplasia punctata show stippling of vertebral bodies (arrows B, C), in toes (D), tarsal bones (E) and in carpals (F).

Mucopolysaccharidoses (Lysosomal disorders with skeletal involvement): Mucopolysaccharidoses (MPS) or lysosomal storage disorders are associated with absence of lysosomal enzymes required for degradation of glycosaminoglycans (GAGs) or mucopolysaccharides. There is secondary deposition of GAGs in various tissues causing coarse facies, mental retardation and hepatosplenomegaly. These disorders are also called dysostoses multiplex as they have multiple common skeletal abnormalities. The common skeletal features in this group include epiphyseal abnormalities, proximal pointed metacarpals and beaking in spine. The skeletal features of the two representative entities in this group namely Hurler's and Morquio's syndrome are enumerated as follows.

Hurler's syndrome (MPS I)^[9,12,13]: OMIM: 607014. Hurler's syndrome is an autosomal recessive disorder due to mutation on 4p16.3 causing deficiency of alpha-L-iduronidase enzyme^[48].

Age of manifestation: Babies with MPS 1 appear normal at birth with both clinical and radiographic features

manifesting over first two years of life. Specific non-skeletal features of MPS 1 include corneal clouding, coronary artery narrowing, endocardial fibroelastosis and cardiac valvular disease^[49,50].

Essential radiographic features: (1) Macrocephalic skull with frontal bossing and J-shaped sella (Figure 6A). The sinuses and facial bones are small and angle of mandible is increased. The J-shaped sella is secondary to pituitary gland enlargement due to deposition of GAGs in the gland; (2) Paddle or oar-shaped ribs in which the ribs are thin posteriorly and broad anteriorly (Figure 6B); (3) The lateral ends of clavicles are hypoplastic with small scapulae are small and there's associated cardiomegaly (Figure 6B and E); (4) While overall length of limbs is maintained, there is diaphyseal widening, more in upper than lower limbs. In older children distal radius and ulna may slope towards each other (Figure 6C). In hands, the tubular bones are typically short and wide and metacarpals appear broad distally and tapered proximally. In addition, osteoporosis and flexion deformities are noted (Figure 6D); (5) In spine, typically, the L2 or L1 vertebra

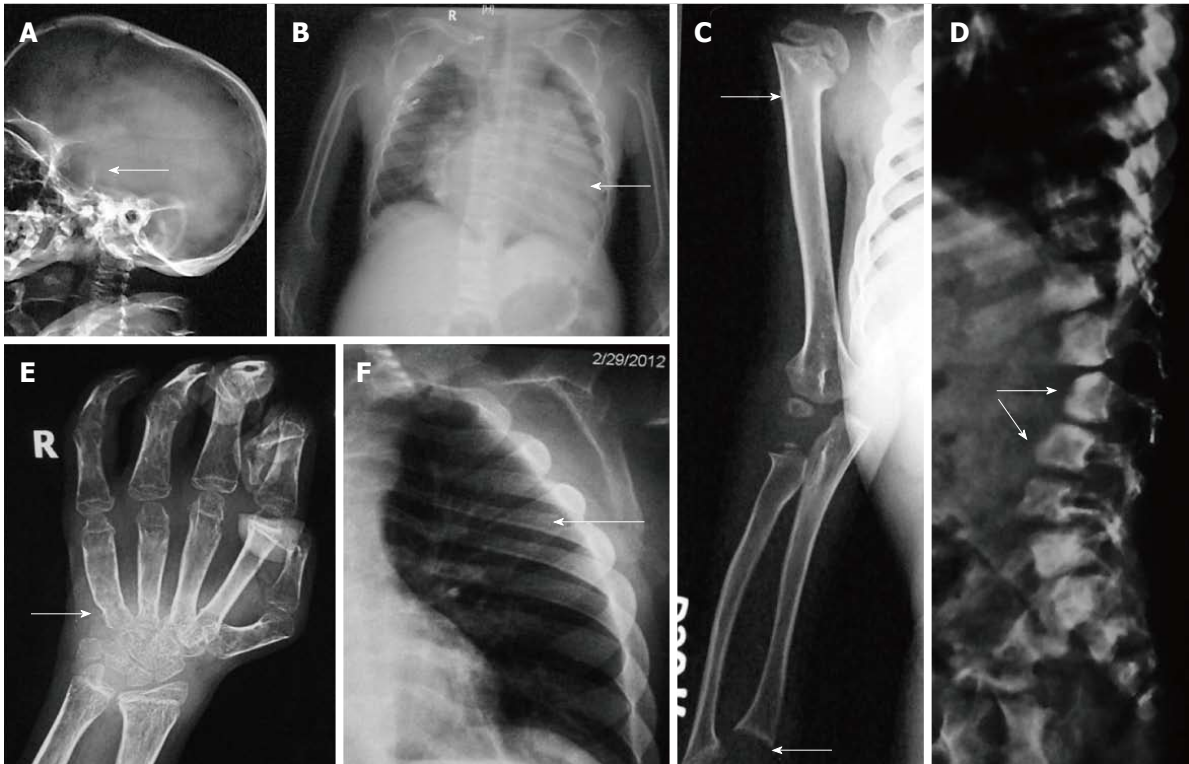


Figure 6 Hurler's syndrome. Radiographs of patient with Hurler's syndrome show macrocephaly with enlarged J-shaped sella (arrow, A), cardiomegaly (arrow, B) and paddle-shaped ribs (arrow, E). Also note relative diaphyseal widening in humerus (upper arrow, C) and sloping lower ends of radius and ulna (lower arrow, C). Radiograph of hands (D) shows proximal pointing (arrow), osteopenia and flexion deformities in distal interphalangeal joints, Radiograph of spine (F) shows hypoplastic L1 and antero-inferior beaking (arrows).

is hypoplastic and set slightly posteriorly giving rise to dorsolumbar kyphosis at that level with antero-inferior beaking of vertebrae (Figure 6E). Atlanto-axial instability is present while platyspondyly is absent; and (6) Other features include flared out iliac wings with sloping, shallow acetabular roofs and delayed ossification of femoral heads.

Morquio's syndrome (MPS IV)^[9,13]: Morquio's syndrome of MPS IV is caused by mutations in two genes, Type IVA [OMIM: 253000]; mutation on 16q24.3; enzyme galactosamine-6-sulfate sulfatase^[51] and type IVB [OMIM: 253010]; mutation on 3p21.33; enzyme beta-galactosidase^[52].

MPS IV shows similarities to MPS I such as enlarged skull, dorsolumbar kyphosis in spine and atlanto-axial instability. Features specific to MPS IV include normal sized sella (unlike MPS I) and platyspondyly with maintained/increased intervertebral disc spaces with central beaking (Figure 7A, B).

The hands typically show pointing of the base of second to fifth metacarpals and distal ends of phalanges. There is additional delayed and irregular ossification of carpals and tarsals (Figure 7C).

In limbs, along with epiphyseal irregularity, metaphyses are widened to accommodate the enlarged epiphyses. There is also delayed ossification of femoral heads with poorly developed acetabula leading to premature arthropathy mimicking SEDC (Figure 7D).

Recently, attenuated or non-classical skeletal phenotypes of MPS IV and VI have been described and contrasted with the classical phenotype mentioned^[53,54]. In attenuated form, involvement is usually limited to femoral epiphyses without the complete spectrum of skeletal involvement.

Initial diagnosis of MPS is made by qualitative and quantitative urine analysis for elevated GAGs and confirmed by decreased enzyme activity in leucocytes or cultured skin fibroblasts. Definitive diagnosis can be made by identifying the underlying genetic mutation^[55].

Group II-metaphyseal dysplasias

In this group, there is (1) predominant metaphyseal irregularity/widening and (2) abnormal limb length. Thus limb shortening can either be (1) rhizomelic as seen in achondroplasia group comprising of achondroplasia, hypochondroplasia and thanatophoric dysplasia (lethal) and metaphyseal chondrodysplasias or (2) mesomelic or acromelic as seen in chondroectodermal dysplasia (Ellis-Van-Creveld syndrome), Jeune's/Asphyxiating Thoracic Dysplasia (ATD) (lethal) and short rib polydactyly dysplasias.

Achondroplasia^[9,12,13,56]: OMIM: 100800; achondroplasia is the most common non-lethal dysplasia and is the prototype of rhizomelic dwarfism. It is inherited in an autosomal dominant fashion, with 80% occurring sporadically, attributable to spontaneous mutation on locus

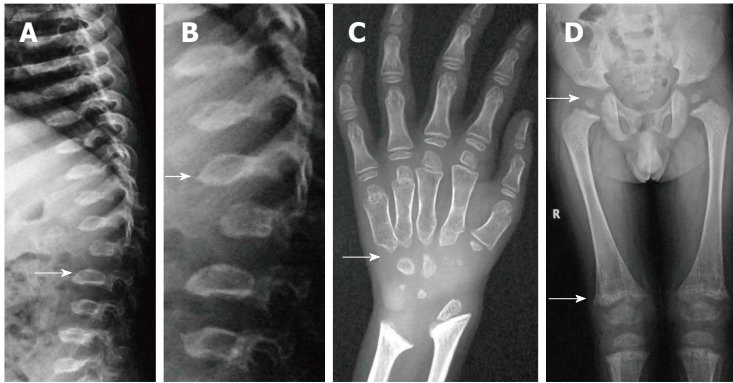


Figure 7 Morquio's syndrome. Radiographs of spine (A, B) show platyspondyly with maintained intervertebral disc height (arrow, A) and central beaking (arrow, B). Radiograph of hand (C) shows proximal pointing of metacarpals. Radiograph of pelvis and lower limbs (D) show delayed ossification of femoral heads, irregular epiphyses and secondary metaphyseal widening in proximal femur and around knee joint (arrows).

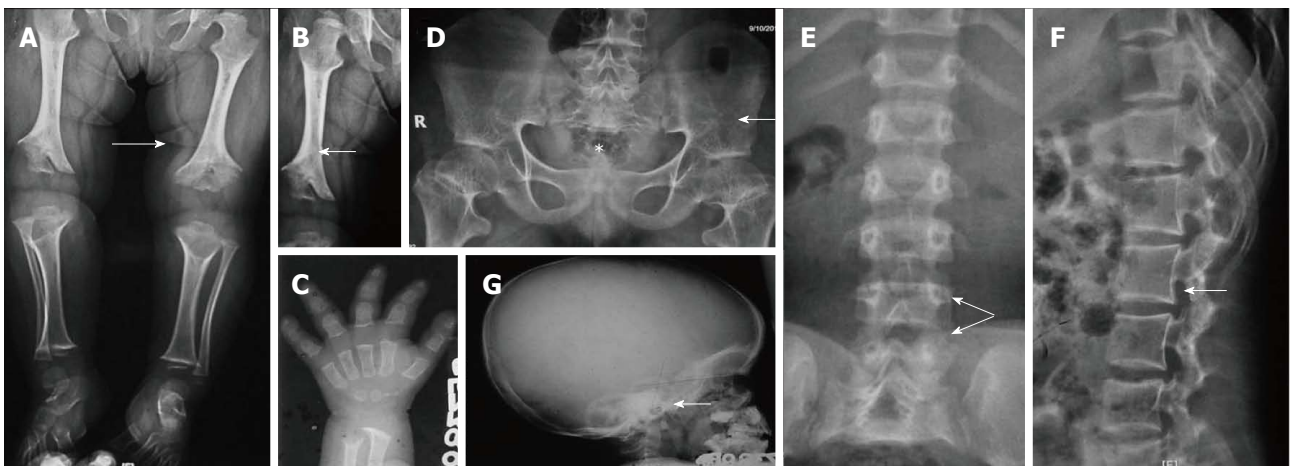


Figure 8 Achondroplasia. Radiograph of lower limbs (A, B) shows bilateral rhizomelic shortening with metaphyseal flaring (arrow, A) and chevron deformity in femur (arrow, B). Note trident hand appearance in (C). Radiograph of pelvis (D) shows short and broad pelvis (*), horizontal acetabuli (arrow) and round iliac wings. Radiographs of spine (E, F) show narrow interpedicular distance in lumbar spine (arrow, E) and posterior scalloping and thick, short pedicles (arrow, F). Radiograph of skull (G) shows enlarged cranial vault with narrowed foramen magnum (arrow).

4p16.3 affecting Fibroblast Growth Factor Receptor 3 (*FGFR3*) gene^[57]. Increased incidence of sporadic mutations have also been associated with increasing paternal age^[58].

Age of manifestation: The typical features of achondroplasia are obvious at birth. The most characteristic changes are found in the spine, especially in the lumbar region, pelvis, limbs and skull.

Essential radiological features: (1) Symmetric shortening of all long bones, with proximal portions being more affected and lower limb involvement being more than the upper limb (rhizomelia). There's relative flaring and splaying of metaphyses with normal epiphyses (Figure 8A); (2) In children, the epiphysis is located closer to metaphyses leading to an apparent increase in the depth of the articular cartilage space. The two limbs of the V of metaphysis appear to embrace the epiphysis giving rise to a ball and socket relationship/chevron deformity (Figure 8B). This appearance is more common at lower end of femur and tends to normalise with increasing age; (3) The hand bones appear thick and tubular with widely separated 2nd and 3rd digits of the hands and inability to approximate them in extension, leading to appearance of trident hand (Figure 8C); (4) The pelvic cavity is short and broad, also

called as champagne-glass appearance. There's squaring of iliac wings with some rounding of corners on a frontal projection (elephant ear shaped iliac wings). The inferior margins of iliac wings and the roofs of acetabulum are flat and horizontal (Figure 8D). The sacrosciatic notches are small with an exaggerated sacral tilt and large, anteriorly protruding sacral promontory; (5) In spine, there is progressive decrease in the interpedicular distance cranio-caudally in the lumbar spine, the decrease becoming more conspicuous with age (Figure 8E and F). Posterior scalloping of vertebral bodies is also common while anteriorly they may appear rounded giving rise to a bullet-shaped configuration. But the overall length of vertebral column and the vertebral heights are normal. There's associated dorso-lumbar kyphoscoliosis in sitting position with exaggerated lumbar lordosis on standing up. Achondroplasts are prone for premature and severe spinal canal stenosis; and (6) The skull shows narrowed skull base with narrowing of foramen magnum. There is compensatory over-expansion of the skull vault and frontal regions to accommodate the expanding brain (Figure 8G). There's relative mid-face hypoplasia and depressed nasal bones.

In general there's little difficulty in diagnosing achon-

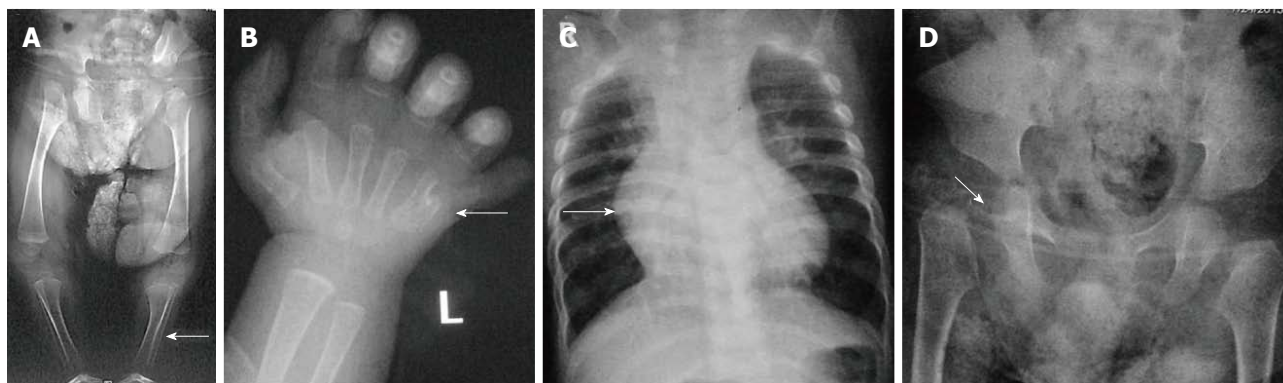


Figure 9 Chondroectodermal Dysplasia (Ellis Van-Creveld Syndrome). Multiple radiographs of patient with chondroectodermal dysplasia show mesomelia (arrow, A), polydactyly on ulnar aspect with fused metacarpals (arrow, B), cardiomegaly with right side enlargement due to atrial septal defect (arrow, C) and acetabular hook (arrow, D). Also note flared iliac wings in pelvis.

droplasia. At birth, it must be distinguished from thanatophoric dysplasia and in adulthood from hypochondroplasia.

Hypochondroplasia^[9,12]: OMIM: 146000; Hypochondroplasia, a milder form of achondroplasia, is caused due to a mutation of the same FGF receptor gene on locus on 4p16.3^[59]. Recently, non-FGFR3 mutations such as those affecting short stature homeobox gene (*SHOX*), also located on chromosome 4 have been identified and the molecular criteria for diagnosis of hypochondroplasia have been expanded^[60].

Age of presentation: It usually manifests after 2-4 years of age as short stature and limb shortening. Hence the clinician should be wary of diagnosing this condition in newborns.

Radiographic features: Spine and limb changes are similar to achondroplasia with decreased interpedicular distance in lumbar spine. But other vertebral changes are mild and spinal stenosis is less common. Limbs also show shortening but in addition to rhizomelia, mesomelia can also be seen^[61].

In contrast to achondroplasia, the skull, pelvis and hands are essentially normal. There may be slight enlargement of skull in frontal region (macrocephaly). There's mild symmetric brachydactyly involving all metacarpals and phalanges whereas in achondroplasia, the 2nd to 5th metacarpals and proximal phalanges are more affected. Thus the trident hand of achondroplasia is not seen in hypochondroplasia^[62].

Chondroectodermal dysplasia^[9,12]: OMIM: 225500, Chondrodysplasia punctata or Ellis-Van Creveld syndrome (EVC) is an autosomal recessively inherited dysplasia caused due to mutation affecting *EVC* gene on locus 4p16^[63].

Age of presentation: The condition can be noted at birth with dysplastic nails, teeth, polydactyly and congenital cardiac defects, most common being common atrium and atrioventricular cushion defects^[64].

Essential radiographic features: There is progressive

distal shortening of limbs leading to mesomelia and acromelia (Figure 9A) with postaxial hexadactyly in hands and feet, carpal fusion (syncarpalism) involving capitate and hamate (Figure 9B), premature ossification of femoral heads and narrow thorax with short ribs (Figure 9C). The pelvis is short with flared iliac wings, narrow base and hook like projection from acetabulum forming trident acetabula (Figure 9D). The pelvic changes normalise later while spine remains normal throughout.

Other features described recently in two patients with chondroectodermal dysplasia (CED) include genu valgum deformity, acroosteolysis (resorption of tips of phalanges), synmetacarpalism and synphalangism presenting at later age due to progressive skeletal involvement^[65].

Differential diagnoses: Other dysplasias with similar radiological features include Jeune's dysplasia and short rib dysplasia with/without polydactyly. But the combination of non-skeletal involvement of hair, nail, teeth and cardiac abnormalities with these radiologic findings are diagnostic of CED^[66].

Group III-dysplasias with altered bone density: osteopenic or osteosclerotic:

Osteopenic dysplasias are dysplasias with decreased bone density; of which osteogenesis imperfecta is the prototype. Likewise sclerosing or osteosclerotic dysplasias are dysplasias with increased bone density; of which osteopetrosis is the prototype. Both OI and osteopetrosis are genetically heterogeneous diseases, caused by multiple genetic mutations that phenotypically have a common appearance of decreased or increased bone density respectively. Simultaneously both these entities are also phenotypic alleles, namely single genetic mutation causes variable phenotypic manifestations. Due to the underlying genetic complexity for both these conditions, the clinical classification system is more commonly used to describe and prognosticate these patients. Therefore, all the OMIM numbers for these entities have been not been enumerated and we have mentioned only the OMIM number of common subtypes.

Osteogenesis imperfecta: Osteogenesis imperfecta (OI)

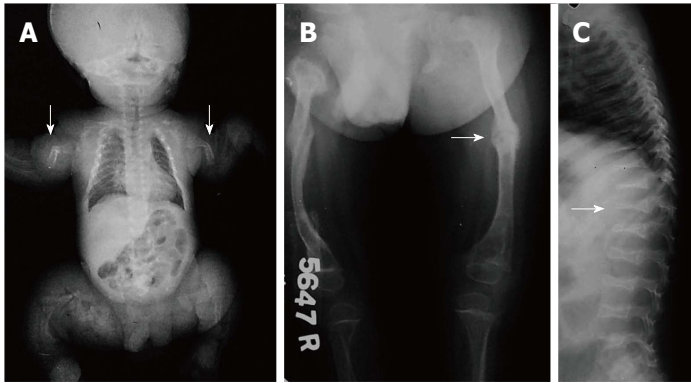


Figure 10 Osteogenesis Imperfecta. Infantogram of 1-mo baby shows diffuse osteopenia with multiple fractures in extremities (arrow). Radiograph of another patient shows fractures in bilateral femurs with callus formation (arrow). Radiograph of spine (C) shows osteopenia with codfish vertebrae.

is an autosomal dominantly or recessively inherited genetic disorder due to mutations in type 1 procollagen genes, characterised by decreased bone mass and increased bone fragility. Severity varies widely from perinatal lethality (type II) to milder forms with minimal fractures. Extraskelatal manifestations like blue sclerae, dentinogenesis imperfecta and deafness are also seen. Initially, Sillence *et al*^[67] divided OI into four subtypes based on clinical features and disease severity: OI type I, with blue sclerae (OMIM: 166200); OI type II, perinatal lethal or congenital type (OMIM: 166210); OI type III, a progressively deforming form with normal sclerae (OMIM: 259420); and OI type IV, with normal sclerae (OMIM: 166220) which has been further expanded to eight types(46-48)^[68-70]. The bone fragility increases in severity from type I < type IV < V < VI < VII < Type III < Type VIII < Type II^[68].

Essential radiological features: (1) Radiologically, OI is characterised by a triad of diffuse osteopenia, pencil-thin cortices, and multiple bony fractures. The fractures are usually multiple and heal with exuberant callus formation giving rise to “pseudotumour” formation. Associated findings include deformities and pseudoarthrosis; (2) The vertebrae are also osteopenic, have a biconcave “codfish vertebrae” appearance with areas of collapse (Figure 10 A-C); (3) The skull shows multiple wormian bones, lucent calvarium, enlarged sinuses and platybasia; and (4) The pelvis is also abnormal in shape with deformities like protusio acetabuli and “shepherd crook” femurs.

Differential diagnoses include battered baby syndrome, hypophosphatasia, juvenile idiopathic osteoporosis, all of which can be excluded by careful analysis of X-rays, clinical and biochemical evaluation^[68]. In addition, multiple new syndromes with congenital brittle bones have been elucidated which are similar to OI but have additional clinical features and are due to mutations in other than type 1 procollagen genes. These are referred to Syndromes Resembling Osteogenesis Imperfecta and should not be mistakenly labelled as OI without a complete evaluation^[71].

Osteosclerotic or sclerosing dysplasias: Based on a target site approach, these anomalies are classified into three groups, namely (1) dysplasias of endochondral bone formation: osteopetrosis, pyknodysostosis, bone islands, osteopoikilosis and osteopathia striata; (2) dys-

plasias of intramembranous bone formation: progressive diaphyseal dysplasia; and (3) mixed sclerosing dysplasias: melorheostosis and overlap syndromes^[72,73].

Osteopetrosis^[9,13]: Considered to be the prototype of sclerosing dysplasia, it is characterised by wide clinical and genetic heterogeneity with a common end-pathway of failure of normal osteoclastic resorption of bone and increased density in medullary portions of bones with sparing of cortices^[74]. The most severe form, termed as autosomal recessive type [OMIM:259700] is characterised by early onset of symptoms, obliteration of medullary canals with bone marrow failure leading to anemia, thrombocytopenia, hepatosplenomegaly and early death. On other hand, in dominant form, the onset occurs in adulthood with variable penetrance. These patients have mild anemia and present more with fractures and deformities [OMIM: 607364]^[2,75].

Essential radiological features: (1) There is diffuse sclerosis involving both the skull vault and base (Figure 11A) with progressive narrowing of foramina causing cranial nerve impingement, more so in the recessive type. In addition, there is prognathism with predisposition to mandibular osteomyelitis; (2) In limbs, despite increased density, there are multiple fractures. Fracture healing rate is normal but callus formation is defective comprising of osteoporotic bone. In addition, there is metaphyseal flaring leading to Erlenmeyer flask deformity^[76] (Figure 11B); (3) “Bone-within-bone” appearance typically noted in spine, pelvis and short tubular bones. In spine, this is termed as a sandwich vertebrae appearance due to end-plate sclerosis and relative lucency of centre of body. In pelvis, they appear as multiple dense white lines parallel to the iliac crest (Figure 11C-E).

Differential diagnoses include pycnodysostosis and craniotubular dysplasias. Craniotubular dysplasias comprising of disorders with concomitant involvement of long bones and skull further comprise of craniodiaphyseal dysplasias, craniometaphyseal dysplasias and craniometadiaphyseal dysplasias. These can mimic osteoporosis radiologically with sclerosis of skull, foraminal narrowing, cranial nerve impingement and tubulation defects in long bones leading to Erlenmeyer flask appearance^[76,77]. However in craniotubular dysplasia, there is an apparent increase in bone density that normalizes later, the verte-

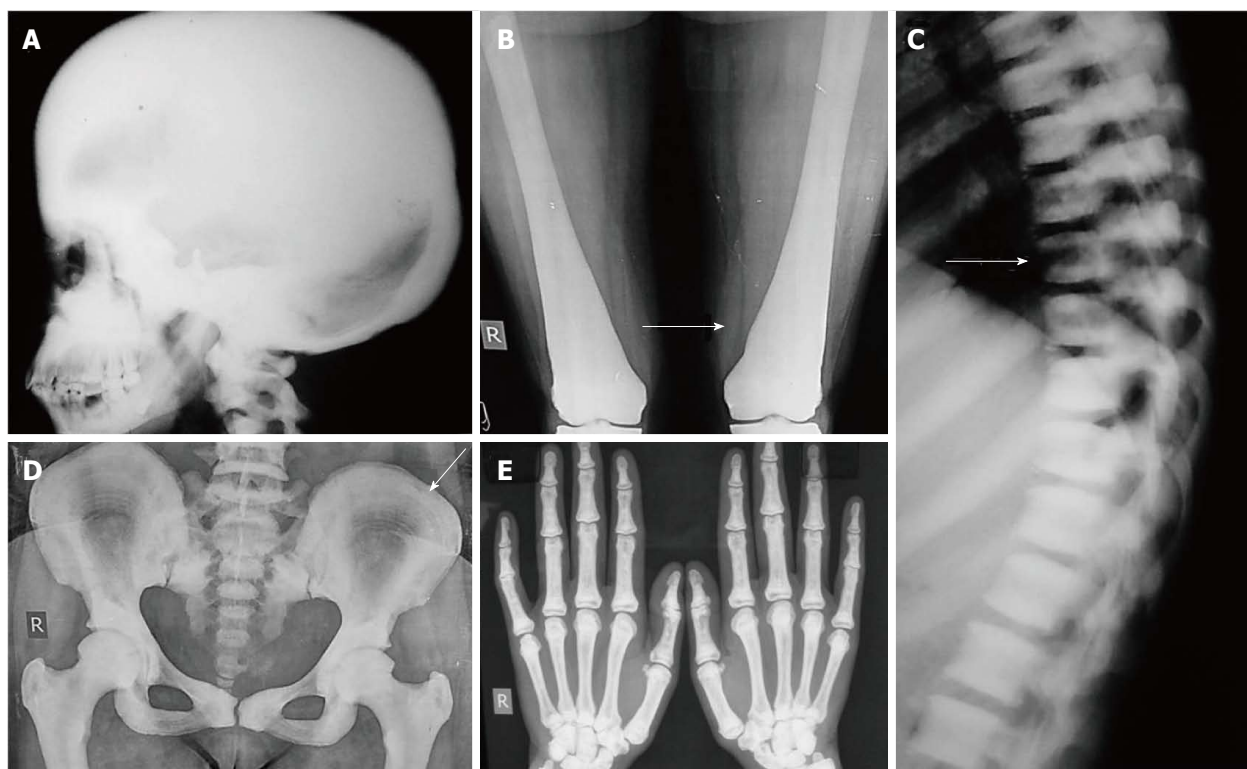


Figure 11 Osteopetrosis. Radiograph of skull shows diffusely increased density (A). Radiograph of bilateral femurs show obliteration of medullary cavity and Erlenmeyer flask deformity (arrow, B). Also note sandwich vertebrae (arrow, C) bone-within-bone appearance in pelvis (arrow, D) and increased density in hand bones (E).

brae are normal, hematopoiesis is maintained and pattern of tubular bone sclerosis and long bone involvement is different^[13].

Pknyodysostosis^[9,13]: OMIM: 265800. First described in 1965 by Maroteaux and Lamy^[36], Pknyodysostosis (PKND) is an autosomal recessive disorder due to mutation involving cathepsin K gene on locus 1q21^[78].

Age of presentation: They present early in childhood with a triad of increased bone density, short limb dwarfism and increased propensity for fractures.

Essential radiological features: (1) Skull shows widely open sutures and fontanelles with multiple wormian bones, mandibular hypoplasia with obtuse angle and increased sclerosis of vault, base and orbital rims (Figure 12A, C); (2) There is increased bone density involving both limb bones and pelvis (Figure 12B). The limb length is decreased and pelvis is also small with shallow acetabulae (Figure 12B); (3) In hands, there is typically acro-osteolysis, *i.e.*, resorption and tufting of terminal phalanges^[79] (Figure 12D); and (4) In limbs, medullary cavity is maintained while bowing of radius and Madelung's deformity can be occasionally seen.

Other radiological features include hypoplasia of lateral ends of clavicles similar to cleidocranial dysplasia, and occasional spool-shaped vertebrae^[13] (Figure 12A-D).

Pyknyodysostosis can be differentiated from osteopetrosis by its typical appearance of skull, mandible and hands^[72,80].

Osteopoikilosis [OMIM: 166700]^[81]: It is a benign

condition with autosomal dominant inheritance, more common in males characterised by multiple small (1-10 mm), symmetric, uniform radiopaque densities located at ends of long bones, carpals, tarsals and periacetabular and subglenoid areas^[72,74] (Figure 13A, B). An important differential can be osteoblastic metastases which can be differentiated by the variable size of lesions and by radionuclide scintigraphy^[82].

Osteopathia striata [OMIM: 300373]^[83]: Another benign condition with a X-linked dominant inheritance, it is more commonly seen in females and is characterised by bilateral symmetric involvement of long bones, pelvis and scapulae in the form of multiple vertical radio opaque lines in the metaphysis extending into the diaphysis^[72]. In the pelvis, this gives a sunburst effect^[13]. Other findings include osteosclerosis of long bones and skull leading to foraminal narrowing and cranial nerve compression^[83].

Melorheostosis: Melorheostosis can be both a sporadic, non-inherited disorder or an inherited disorder presenting with melorheostosis and osteopoikilosis and assigned an OMIM: 155950^[84]. Melorheostosis is a benign condition characterised clinically by pain and soft-tissue contractures. The distribution is asymmetric, can be monostotic (involving single bone) or polyostotic (involving multiple bones) or monomelic (involving one limb), most typically the lower limb. Other bones like skull, ribs, spine and short tubular bones can be affected at times. There is typically cortical thickening in a streaky or wavy pattern extending

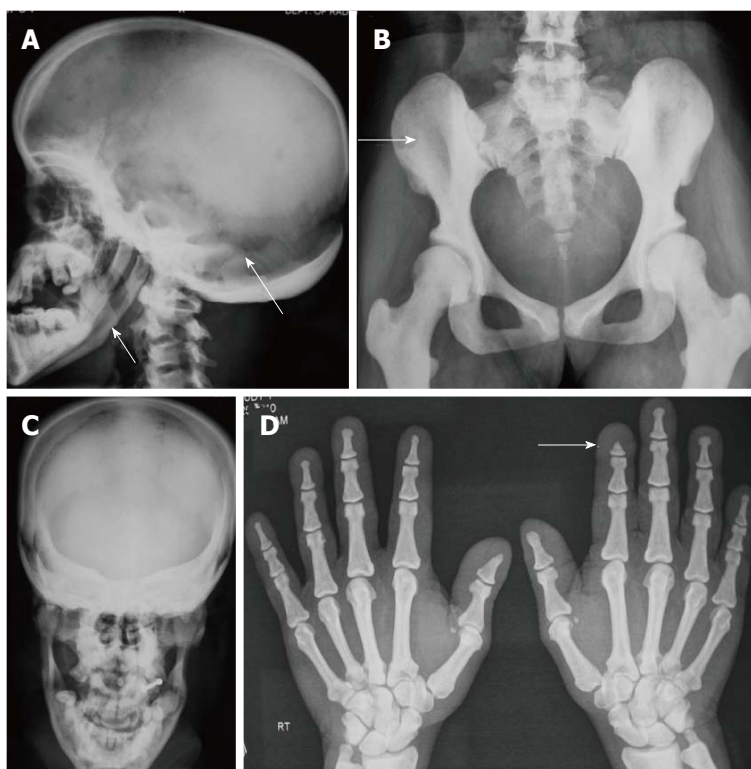


Figure 12 Pyknodysostosis. Radiographs of skull (A, C) show hypoplastic mandible, open sutures and increased bone density (arrows, A). Increased bone density also noted in pelvis (B) and hands (D). Also note acroosteolysis (arrow, D).



Figure 13 Osteopoikilosis (A,B) and Melorheostosis (C). Radiographs of pelvis (A) and hand (B) of a patient with osteopoikilosis show multiple bilateral symmetrical sclerotic lesions in periarticular location (arrows, A and B). Similar changes were also noted in knees, elbows and vertebral bodies (not shown). Radiograph of lower limb (C) of a young patient with melorheostosis shows "flowing wax appearance" (arrow, C).



Figure 14 Progressive diaphyseal dysplasia. Radiograph of patient with progressive diaphyseal dysplasia shows symmetrical thickening along bilateral femoral diaphysis (arrows) with sparing of epi- and metaphyses. The pelvis also shows increased bone density.

from the proximal to distal part of bone giving a "flowing wax candle appearance" (Figure 13C). The distribution

in children is usually endosteal (which can mimic bone islands and osteopoikilosis) but this evolves to a periosteal pattern in adults^[13,72,74].

Other osteosclerotic conditions include progressive diaphyseal dysplasia (Camurati-Engelmann's disease) and infantile cortical hyperostosis (Caffey's disease).

Progressive diaphyseal dysplasia: Progressive diaphyseal dysplasia, also called Camurati-Engelmann's disease [OMIM: 131300] is an autosomal dominant disorder (locus 19q13). There is bilateral symmetric, fusiform enlargement with increased density of diaphysis of long bones beginning mid-shaft and progressing towards both ends^[85]. In severe cases metaphyses may also be involved but typically, epiphyses are spared^[74] (Figure 14).

Caffey's disease: Caffey's disease [OMIM: 114000] is an inherited disorder with both autosomal dominant and recessive inheritance characterized by a clinical triad of (1) narrow age group of presentation (before 5th month

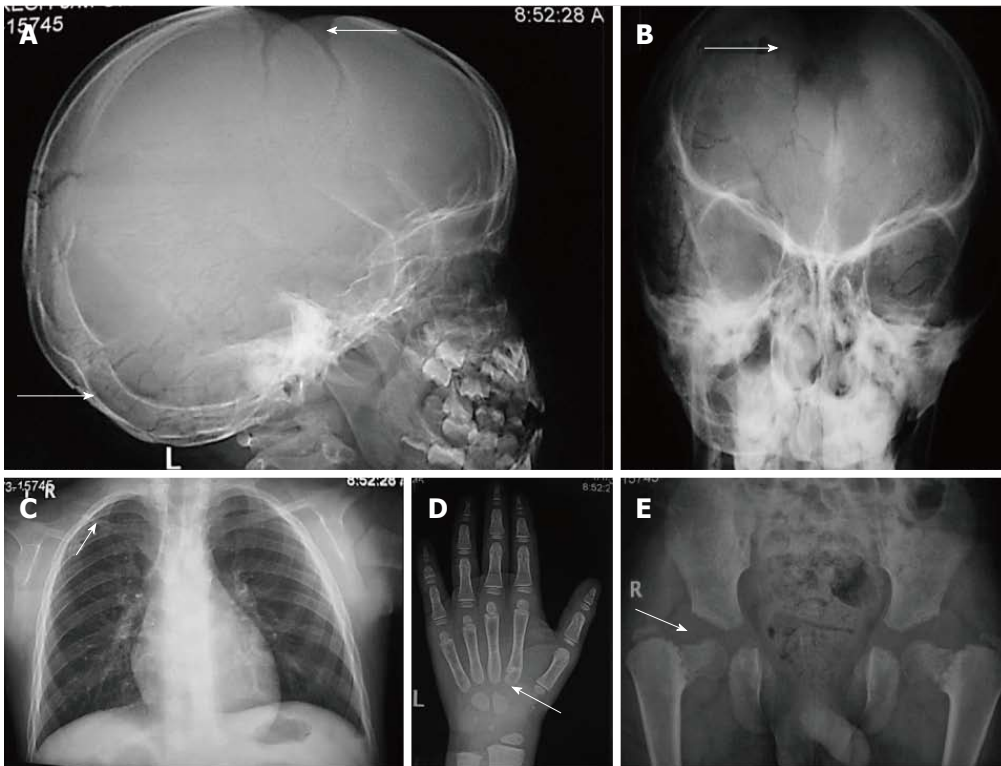


Figure 15 Cleidocranial dysplasia. Radiographs of skull (A, B) show open fontanelles and wormian bones (arrows, A) and hot cross bone appearance (arrow, B). Radiograph of chest(C) shows hypoplastic right clavicle (arrow). Radiograph of hand (D) shows elongated second digit with an accessory epiphyseal centre (arrow) Radiograph of pelvis (E) shows “chef-hat” shaped femoral heads (arrow) and widened pubis symphysis.

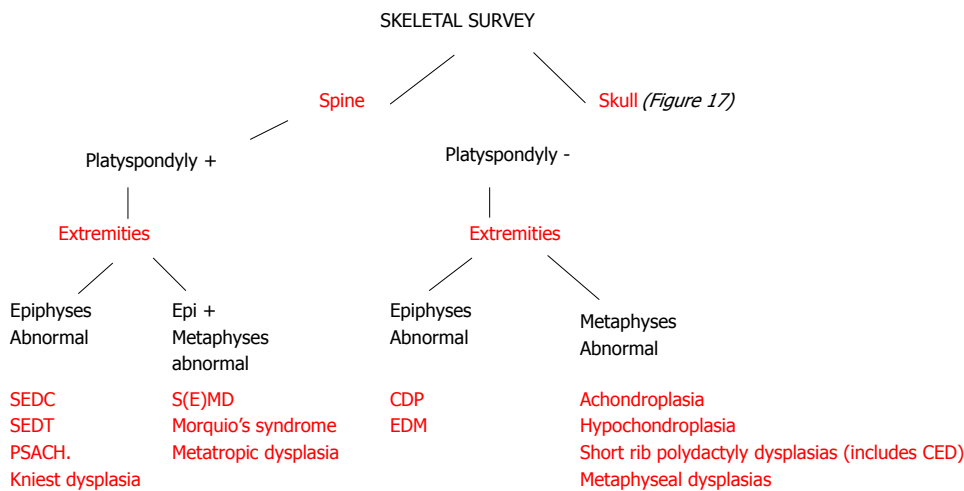


Figure 16 An algorithmic approach to skeletal dysplasias with spine and limb involvement. SEDT: Spondyloepiphyseal dysplasia tarda; CDP: Chondrodysplasia punctata; PSACH: Pseudoachondroplasia; EDM: Multiple epiphyseal dysplasia; CED: Chondroectodermal dysplasia.

of age); (2) hyperirritability, soft tissue swelling, bone lesions; and (3) mandible involvement^[86]. There is diffuse cortical thickening of mandible due to subperiosteal new bone formation. Other bones such as ulna, tibia, clavicle, scapulae and ribs can also be involved and radiographs show periosteal new bone formation in diaphysis sparing epiphyses and metaphyses^[13].

Group IV-miscellaneous entities

Cleidocranial dysplasia: OMIM:119600 is an autosomal dominant dysplasia with predominant membranous

bone involvement^[87]. Due to its dominant mode of inheritance it can be seen in multiple members of the same family and can present in childhood to as late as 30 years of life^[87].

Essential radiological features: (1) The skull shows delayed ossification of calvarium, multiple wormian bones, persistently open sutures and fontanelles giving a hot cross bun appearance. However the mandible is normal with maintained angle (Figure 15A, B); (2) The clavicles are either absent (10%) or hypoplastic (90%), hypoplasia affecting the lateral ends more than middle or medial ends (Figure

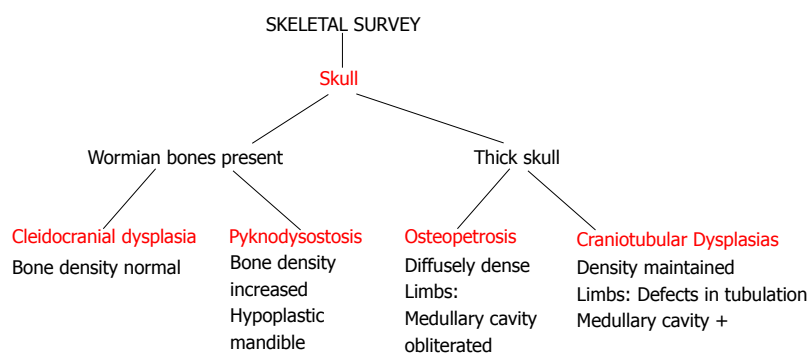


Figure 17 An algorithmic approach to skeletal dysplasias with skull involvement.

15C). Also the scapulae may be small and thoracic cage cone-shaped; (3) In hands and feet, the 2nd digit is elongated due to presence of accessory epiphyses for the second metacarpal while the distal phalanges are small and pointed (Figure 15D); and (4) The pelvis is small with widened symphysis pubis and abnormal shape of femoral heads called “chef-hat” appearance (Figure 15E).

Differential diagnosis: The appearance of skull and hypoplasia of clavicle may be confused with pyknodysostosis; however the bone density and mandibular angle is maintained in cleidocranial dysplasia and short stature is absent. Another differential diagnosis can be manibuloacral dysplasia^[88].

WORKING ALGORITHMIC APPROACH TO COMMON DYSPLASIAS

We present a working algorithm for radiological diagnosis of the commonly encountered dysplasias. This algorithm can help in initial diagnosis and lead the clinician to further work-up. Firstly, analyse the skeletal survey for spine and skull involvement. In spine, look for platyspondyly. And then look at the limbs for involvement of epiphyses and metaphyses. The involvement of these two regions can lead to diagnoses of many dysplasias as enumerated in Figure 16. After looking at the spine, look at the skull for either wormian bones or increased density of skull bones. The dysplasias with skull involvement have been in Figure 17.

CONCLUSION

To conclude, dysplasias are not as uncommon as once thought. A general radiologist is very likely to encounter a set of radiographs of a patient with suspected dysplasia. In such a case, the radiologist should have an algorithmic, step-wise approach to either definitely diagnose a certain dysplasia or to lead the clinician to an appropriate diagnosis and direct further workup. The correct label is essential for prognostication, clinical and orthopaedic management of the present child and also to counsel parents about future pregnancies and their outcome. Undoubtedly, the diagnosis and management of a dysplasia

needs teamwork between paediatrician, geneticist, radiologist and orthopaedist. But at the same time, a complete skeletal survey is an essential component of workup and hence it is important for radiologists to carefully analyse the bones, appearance and distribution of abnormalities on the survey and be familiar with the descriptions of common skeletal dysplasias.

REFERENCES

- Offiah AC, Hall CM.** Radiological diagnosis of the constitutional disorders of bone. As easy as A, B, C? *Pediatr Radiol* 2003; **33**: 153-161 [PMID: 12612812 DOI: 10.1007/s00247-002-0855-8]
- Warman ML, Cormier-Daire V, Hall C, Krakow D, Lachman R, LeMerrer M, Mortier G, Mundlos S, Nishimura G, Rimoin DL, Robertson S, Savarirayan R, Silencio D, Spranger J, Unger S, Zabel B, Superti-Furga A.** Nosology and classification of genetic skeletal disorders: 2010 revision. *Am J Med Genet A* 2011; **155A**: 943-968 [PMID: 21438135 DOI: 10.1002/ajmg.a.33909]
- Barbosa-Buck CO, Orioli IM, da Graça Dutra M, Lopez-Camelo J, Castilla EE, Cavalcanti DP.** Clinical epidemiology of skeletal dysplasias in South America. *Am J Med Genet A* 2012; **158A**: 1038-1045 [PMID: 22407836 DOI: 10.1002/ajmg.a.35246]
- Orioli IM, Castilla EE, Barbosa-Neto JG.** The birth prevalence rates for the skeletal dysplasias. *J Med Genet* 1986; **23**: 328-332 [PMID: 3746832 DOI: 10.1136/jmg.23.4.328]
- Andersen PE, Hauge M.** Congenital generalised bone dysplasias: a clinical, radiological, and epidemiological survey. *J Med Genet* 1989; **26**: 37-44 [PMID: 2783977 DOI: 10.1136/jmg.26.1.37]
- Rasmussen SA, Bieber FR, Benacerraf BR, Lachman RS, Rimoin DL, Holmes LB.** Epidemiology of osteochondrodysplasias: changing trends due to advances in prenatal diagnosis. *Am J Med Genet* 1996; **61**: 49-58 [PMID: 8741918 DOI: 10.1002/(SICI)1096-8628(19960102)61:1<49::AID-AJMG10>3.0.CO;2-W]
- Kozlowski K.** The radiographic clues in the diagnosis of bone dysplasias. *Pediatr Radiol* 1985; **15**: 1-3 [PMID: 3969291 DOI: 10.1007/BF02387842]
- Alanay Y, Lachman RS.** A review of the principles of radiological assessment of skeletal dysplasias. *J Clin Res Pediatr Endocrinol* 2011; **3**: 163-178 [PMID: 22155458 DOI: 10.4274/jcrpe.463]
- Spranger JW, Langer LO, Wiedemann HR.** Bone Dysplasias: An Atlas of Constitutional disorders of Skeletal Development. Philadelphia (PA): WB Saunders Co, 1974
- Taybi H, Lachman RS.** Radiology of Syndromes, Metabolic disorders and Skeletal Dysplasias. 4th ed. Philadelphia:

- Mosby Elsevier; 1996
- 11 OMIM [Internet]. Cited: 2014-06-24. Available from: URL: <http://www.ncbi.nlm.nih.gov/omim>
 - 12 **Lachman RS.** Skeletal Dysplasias. Caffey's Pediatric Diagnostic Imaging. 11th ed. In: Slovis TL, editor. Philadelphia: Mosby Elsevier, 2008: 2613-2671
 - 13 **Tachdjian MO.** Pediatric Orthopedics. 2nd ed. Philadelphia: W B Saunders Co, 1990: 690-843
 - 14 **Amirfeyz R,** Clark C, Gargan M. Spondyloepiphyseal dysplasia. *Current Orthopaedics* 2005; **19**: 309-313 [DOI: 10.1016/j.cuor.2005.06.007]
 - 15 OMIM Entry # 183900 Spondyloepiphyseal dysplasia congenital (SEDC) [Internet]. Cited: 2014-06-24. Available from: URL: <http://omim.org/entry/1839004>
 - 16 **McKay SD,** Al-Omari A, Tomlinson LA, Dormans JP. Review of cervical spine anomalies in genetic syndromes. *Spine (Phila Pa 1976)* 2012; **37**: E269-E277 [PMID: 22045003 DOI: 10.1097/BRS.0b013e31823b3ded]
 - 17 **Veeravagu A,** Lad SP, Camara-Quintana JQ, Jiang B, Shuer L. Neurosurgical interventions for spondyloepiphyseal dysplasia congenita: clinical presentation and assessment of the literature. *World Neurosurg* 2013; **80**: 437.e1-8 [DOI: 10.1016/j.wneu.2012.01.030]
 - 18 OMIM Entry # 156550 Kniest dysplasia [Internet]. Cited: 2014-06-24. Available from: URL: <http://omim.org/entry/156550>
 - 19 **Lachman RS,** Rimoin DL, Hollister DW, Dorst JP, Siggers DC, McAlister W, Kaufman RL, Langer LO. The Kniest syndrome. *Am J Roentgenol Radium Ther Nucl Med* 1975; **123**: 805-814 [PMID: 1147148 DOI: 10.2214/ajr.123.4.805]
 - 20 **Subramanian S,** Gamanagatti S, Sinha A, Sampangi R. Kniest syndrome. *Indian Pediatr* 2007; **44**: 931-933 [PMID: 18175850]
 - 21 OMIM Entry # 156530 Metatropic Dysplasia [Internet]. Cited: 2014-06-24. Available from: URL: <http://omim.org/entry/156530>
 - 22 **Kannu P,** Aftimos S, Mayne V, Donnan L, Savarirayan R. Metatropic dysplasia: clinical and radiographic findings in 11 patients demonstrating long-term natural history. *Am J Med Genet A* 2007; **143A**: 2512-2522 [PMID: 17879966 DOI: 10.1002/ajmg.a.31941]
 - 23 **MacKenzie JJ,** Fitzpatrick J, Babyn P, Ferrero GB, Ballabio A, Billingsley G, Bulman DE, Strasberg P, Ray PN, Costa T. X linked spondyloepiphyseal dysplasia: a clinical, radiological, and molecular study of a large kindred. *J Med Genet* 1996; **33**: 823-828 [PMID: 8933334 DOI: 10.1136/jmg.33.10.823]
 - 24 OMIM Entry # 313400 Spondyloepiphyseal dysplasia tarda, X-Linked (SEDT) [Internet]. Cited: 2014-06-24. Available from: URL: <http://omim.org/entry/313400>
 - 25 **Langer LO.** Spondyloepiphysial dysplasia tarda. Hereditary chondrodysplasia with characteristic vertebral configuration in the adult. *Radiology* 1964; **82**: 833-839 [PMID: 14153674 DOI: 10.1148/82.5.833]
 - 26 OMIM Entry # 271600 Spondyloepiphyseal dysplasia tarda, autosomal recessive. [Internet]. Cited: 2014-06-24. Available from: URL: <http://omim.org/entry/271600>
 - 27 OMIM Entry # 271620 Spondyloepiphyseal dysplasia tarda with mental retardation [Internet]. Cited: 2014-06-24. Available from: URL: <http://omim.org/entry/271620>
 - 28 OMIM Entry # 609223 Spondyloepiphyseal dysplasia tarda, autosomal recessive, Leroy-Spranger type [Internet]. Cited: 2014-06-24. Available from: URL: <http://omim.org/entry/609223>
 - 29 OMIM Entry # 600093 Spondyloepiphyseal dysplasia tarda with characteristic facies [Internet]. Cited: 2014-06-24. Available from: URL: <http://omim.org/entry/600093>
 - 30 OMIM Entry # 184100 Spondyloepiphyseal dysplasia tarda, autosomal dominant [Internet]. Cited: 2014-06-24. Available from: URL: <http://omim.org/entry/184100>
 - 31 **Huson SM,** Crowley S, Hall CM, Supramaniam G, Winter RM. Previously unrecognized form of familial spondyloepiphyseal dysplasia tarda with characteristic facies. *Clin Dysmorphol* 1993; **2**: 20-27 [PMID: 8298734]
 - 32 **Leroy JG,** Leroy BP, Emmerly LV, Messiaen L, Spranger JW. A new type of autosomal recessive spondyloepiphyseal dysplasia tarda. *Am J Med Genet A* 2004; **125A**: 49-56
 - 33 **Unger S,** Hecht JT. Pseudoachondroplasia and multiple epiphyseal dysplasia: New etiologic developments. *Am J Med Genet* 2001; **106**: 244-250 [PMID: 11891674 DOI: 10.1002/ajmg.10234]
 - 34 **Lachman RS,** Krakow D, Cohn DH, Rimoin DL. MED, COMP, multilayered and NEIN: an overview of multiple epiphyseal dysplasia. *Pediatr Radiol* 2005; **35**: 116-123 [PMID: 15503005 DOI: 10.1007/s00247-004-1323-4]
 - 35 OMIM Entry # 132400 Epiphyseal dysplasia, multiple, 1 (EDM1) [Internet]. Cited: 2014-06-24. Available from: URL: <http://omim.org/entry/132400>
 - 36 **Ramachandran G,** Mason D. Double-layered patella: marker for multiple epiphyseal dysplasia. *Am J Orthop (Belle Mead NJ)* 2004; **33**: 35-36 [PMID: 14763596]
 - 37 **Sheffield EG.** Double-layered patella in multiple epiphyseal dysplasia: a valuable clue in the diagnosis. *J Pediatr Orthop* 1998; **18**: 123-128 [PMID: 9449113]
 - 38 **Nakashima E,** Ikegawa S, Ohashi H, Kimizuka M, Nishimura G. Double-layered patella in multiple epiphyseal dysplasia is not exclusive to DTDST mutation. *Am J Med Genet A* 2005; **133A**: 106-107 [PMID: 15633184 DOI: 10.1002/ajmg.a.30481]
 - 39 **Vatanavicharn N,** Lachman RS, Rimoin DL. Multilayered patella: similar radiographic findings in pseudoachondroplasia and recessive multiple epiphyseal dysplasia. *Am J Med Genet A* 2008; **146A**: 1682-1686 [PMID: 18546327 DOI: 10.1002/ajmg.a.32313]
 - 40 **Heselson NG,** Cremin BJ, Beighton P. Pseudoachondroplasia, a report of 13 cases. *Br J Radiol* 1977; **50**: 473-482 [PMID: 871597 DOI: 10.1259/0007-1285-50-595-473]
 - 41 OMIM Entry # 177170 Pseudoachondroplasia (PSACH). [Internet]. Cited: 2014-06-24. Available from: URL: <http://omim.org/entry/177170>
 - 42 OMIM Entry # 302960 Chondrodysplasia punctata 2, X-linked dominant [Internet]. Cited: 2014-06-24. Available from: URL: <http://omim.org/entry/302960>
 - 43 OMIM Entry # 215100 Rhizomelic chondrodysplasia punctata, Type 1 (RCDP1) [Internet]. Cited: 2014-06-24. Available from: URL: <http://omim.org/entry/215100>
 - 44 OMIM Entry # 222765 Rhizomelic chondrodysplasia punctata, type 2 (RCDP2) [Internet]. Cited: 2014-06-24. Available from: URL: <http://omim.org/entry/222765>
 - 45 OMIM Entry # 600121 Rhizomelic chondrodysplasia punctata, Type 3 (RCDP3) [Internet]. Cited: 2014-06-24. Available from: URL: <http://omim.org/entry/600121>
 - 46 OMIM Entry # 302950 Chondrodysplasia punctata 1, X-linked recessive (CDPX1) [Internet]. Cited: 2014-06-24. Available from: URL: <http://omim.org/entry/302950>
 - 47 **Shanske AL,** Bernstein L, Herzog R. Chondrodysplasia punctata and maternal autoimmune disease: a new case and review of the literature. *Pediatrics* 2007; **120**: e436-e441 [PMID: 17671048 DOI: 10.1542/peds.2006-2997]
 - 48 OMIM Entry # 607014 Hurler syndrome [Internet]. Cited: 2014-06-24. Available from: URL: <http://omim.org/entry/607014>
 - 49 **Braunlin E,** Orchard PJ, Whitley CB, Schroeder L, Reed RC, Manivel JC. Unexpected coronary artery findings in mucopolysaccharidosis. Report of four cases and literature review. *Cardiovasc Pathol* 2014; **23**: 145-151 [PMID: 24508139 DOI: 10.1016/j.carpath.2014.01.001]

- 50 **Schroeder L**, Orchard P, Whitley CB, Berry JM, Tolar J, Miller W, Braunlin EA. Cardiac Ultrasound Findings in Infants with Severe (Hurler Phenotype) Untreated Mucopolysaccharidosis (MPS) Type I. *JIMD Rep* 2013; **10**: 87-94 [PMID: 23430808 DOI: 10.1007/8904_2012_208]
- 51 OMIM Entry # 253000 Mucopolysaccharidosis, Type IVA (MPS4A) [Internet]. Cited: 2014-06-24. Available from: URL: <http://omim.org/entry/253000>
- 52 OMIM Entry # 253010 Mucopolysaccharidosis Type IV [Internet]. Cited: 2014-06-24. Available from: URL: <http://omim.org/entry/253010>
- 53 **Lachman RS**, Burton BK, Clarke LA, Hoffinger S, Ikegawa S, Jin DK, Kano H, Kim OH, Lampe C, Mendelsohn NJ, Shediach R, Tanpaiboon P, White KK. Mucopolysaccharidosis IVA (Morquio A syndrome) and VI (Maroteaux-Lamy syndrome): under-recognized and challenging to diagnose. *Skeletal Radiol* 2014; **43**: 359-369 [PMID: 24389823 DOI: 10.1007/s00256-013-1797-y]
- 54 **Hendriksz CJ**, Harmatz P, Beck M, Jones S, Wood T, Lachman R, Gravance CG, Orii T, Tomatsu S. Review of clinical presentation and diagnosis of mucopolysaccharidosis IVA. *Mol Genet Metab* 2013; **110**: 54-64 [PMID: 23665161 DOI: 10.1016/j.ymgme.2013.04.002]
- 55 **Mendelsohn NJ**, Wood T, Olson RA, Temme R, Hale S, Zhang H, Read L, White KK. Spondyloepiphyseal dysplasias and bilateral legg-calvé-perthes disease: diagnostic considerations for mucopolysaccharidoses. *JIMD Rep* 2013; **11**: 125-132 [PMID: 23657977 DOI: 10.1007/8904_2013_231]
- 56 **Langer LO**, Baumann PA, Gorlin RJ. Achondroplasia. *Am J Roentgenol Radium Ther Nucl Med* 1967; **100**: 12-26 [PMID: 6023888 DOI: 10.2214/ajr.100.1.12]
- 57 OMIM Entry # 100800 Achondroplasia (ACH) [Internet]. Cited: 2014-06-24. Available from: URL: <http://omim.org/entry/100800>
- 58 **Orioli IM**, Castilla EE, Scarano G, Mastroiacovo P. Effect of paternal age in achondroplasia, thanatophoric dysplasia, and osteogenesis imperfecta. *Am J Med Genet* 1995; **59**: 209-217 [PMID: 8588588 DOI: 10.1002/ajmg.1320590218]
- 59 OMIM Entry # 146000 Hypochondroplasia (HCH) [Internet]. Cited: 2014-06-24. Available from: URL: <http://omim.org/entry/146000>
- 60 **Song SH**, Balce GC, Agashe MV, Lee H, Hong SJ, Park YE, Kim SG, Song HR. New proposed clinico-radiologic and molecular criteria in hypochondroplasia: FGFR 3 gene mutations are not the only cause of hypochondroplasia. *Am J Med Genet A* 2012; **158A**: 2456-2462 [PMID: 22903874 DOI: 10.1002/ajmg.a.35564]
- 61 **Bober MB**, Bellus GA, Nikkel SM, Tiller GE. Hypochondroplasia. In: Pagon RA, Adam MP, Ardinger HH, Bird TD, Dolan CR, Fong CT, Smith RJH, Stephens K, editors. GeneReviews® [Internet]. Seattle (WA): University of Washington, Seattle, 1993-2014 [PMID: 20301650]
- 62 **Hall BD**, Spranger J. Hypochondroplasia: clinical and radiological aspects in 39 cases. *Radiology* 1979; **133**: 95-100 [PMID: 472320]
- 63 OMIM Entry # 225500 Ellis-Van Creveld syndrome (EVC) [Internet]. Cited: 2014-06-24. Available from: URL: <http://omim.org/entry/225500>
- 64 **Hills CB**, Kochilas L, Schimmenti LA, Moller JH. Ellis-van Creveld syndrome and congenital heart defects: presentation of an additional 32 cases. *Pediatr Cardiol* 2011; **32**: 977-982 [PMID: 21533779 DOI: 10.1007/s00246-011-0006-9]
- 65 **Rudnik-Schöneborn S**, Zerres K, Graul-Neumann L, Wiegand S, Mellerowicz H, Hehr U. Two Adult Patients with Ellis-van Creveld Syndrome Extending the Clinical Spectrum. *Mol Syndromol* 2011; **1**: 301-306 [PMID: 22190900 DOI: 10.1159/000331338]
- 66 **Baujat G**, Le Merrer M. Ellis-van Creveld syndrome. *Orphanet J Rare Dis* 2007; **2**: 27 [PMID: 17547743 DOI: 10.1186/1750-1172-2-27]
- 67 **Sillence DO**, Senn A, Danks DM. Genetic heterogeneity in osteogenesis imperfecta. *J Med Genet* 1979; **16**: 101-116 [PMID: 458828 DOI: 10.1136/jmg.16.2.101]
- 68 **Rauch F**, Glorieux FH. Osteogenesis imperfecta. *Lancet* 2004; **363**: 1377-1385 [PMID: 15110498 DOI: 10.1016/S0140-6736(04)16051-0]
- 69 **Cabral WA**, Chang W, Barnes AM, Weis M, Scott MA, Leikin S, Makareeva E, Kuznetsova NV, Rosenbaum KN, Tiffit CJ, Bulas DI, Kozma C, Smith PA, Eyre DR, Marini JC. Prolyl 3-hydroxylase 1 deficiency causes a recessive metabolic bone disorder resembling lethal/severe osteogenesis imperfecta. *Nat Genet* 2007; **39**: 359-365 [PMID: 17277775 DOI: 10.1038/ng1968]
- 70 OMIM Entry # 610915 Osteogenesis imperfecta, Type VIII (OI8) [Internet]. Cited: 2014-06-24. Available from: URL: <http://omim.org/entry/610915>
- 71 **Plotkin H**. Syndromes with congenital brittle bones. *BMC Pediatr* 2004; **4**: 16 [PMID: 15339338 DOI: 10.1186/1471-2431-4-16]
- 72 **Vanhoenacker FM**, De Beuckeleer LH, Van Hul W, Balemans W, Tan GJ, Hill SC, De Schepper AM. Sclerosing bone dysplasias: genetic and radioclinical features. *Eur Radiol* 2000; **10**: 1423-1433 [PMID: 10997431 DOI: 10.1007/s003300000495]
- 73 **Greenspan A**. Sclerosing bone dysplasias--a target-site approach. *Skeletal Radiol* 1991; **20**: 561-583 [PMID: 1776023 DOI: 10.1007/BF01106087]
- 74 **Ihde LL**, Forrester DM, Gottsegen CJ, Masih S, Patel DB, Vachon LA, White EA, Matcuk GR. Sclerosing bone dysplasias: review and differentiation from other causes of osteosclerosis. *Radiographics* 2011; **31**: 1865-1882 [PMID: 22084176 DOI: 10.1148/rg.317115093]
- 75 **Stark Z**, Savarirayan R. Osteopetrosis. *Orphanet J Rare Dis* 2009; **4**: 5 [PMID: 19232111 DOI: 10.1186/1750-1172-4-5]
- 76 **Faden MA**, Krakow D, Ezgu F, Rimoin DL, Lachman RS. The Erlenmeyer flask bone deformity in the skeletal dysplasias. *Am J Med Genet A* 2009; **149A**: 1334-1345 [PMID: 19444897 DOI: 10.1002/ajmg.a.32253]
- 77 **Beighton P**. Craniometaphyseal dysplasia (CMD), autosomal dominant form. *J Med Genet* 1995; **32**: 370-374 [PMID: 7616544 DOI: 10.1136/jmg.32.5.370]
- 78 OMIM Entry # 265800 Pycnodysostosis [Internet]. Cited: 2014-06-24. Available from: URL: <http://omim.org/entry/265800>
- 79 **Lamy M**, Maroteaux P. [Pycnodysostosis]. *Rev Esp Pediatr* 1965; **21**: 433-437 [PMID: 5851549]
- 80 **Balthazar E**, Smith EH, Moskowitz H. Pycnodysostosis: an unusual case. *Br J Radiol* 1972; **45**: 304-307 [PMID: 5017720 DOI: 10.1259/0007-1285-45-532-304]
- 81 OMIM Entry # 166700 Buschke-ollendorff syndrome (BOS) [Internet]. Cited: 2014-06-24. Available from: URL: <http://omim.org/entry/166700>
- 82 **McArdle A**, O'Riordan C, Connolly EM. Osteopoikilosis masquerading as osseous metastases in breast cancer [Internet]. Cited: 2014-06-13. Available from: URL: <http://www.ncbi.nlm.nih.gov/pubmed/21990037>
- 83 OMIM Entry # 300373 Osteopathia striata with cranial sclerosis (OSCS) [Internet]. Cited: 2014-06-28. Available from: URL: <http://omim.org/entry/300373>
- 84 OMIM Entry # 155950 Melorheostosis, Isolated [Internet]. Cited: 2014-06-28. Available from: URL: <http://omim.org/entry/155950>
- 85 OMIM Entry # 131300 Camurati-Engelmann disease (CAEND) [Internet]. Cited: 2014-06-28. Available from: URL: <http://omim.org/entry/131300>
- 86 OMIM Entry # 114000 Caffey disease [Internet]. Cited: 2014-06-28. Available from: URL: <http://omim.org/entry/114000>
- 87 OMIM Entry # 119600 Cleidocranial dysplasia (CCD) [Internet]. Cited: 2014-06-28. Available from: URL: <http://omim.org/entry/119600>

org/entry/119600
88 OMIM Entry # 248370 Mandibuloacral dysplasia with Type

A lipodystrophy (MADA) [Internet]. Cited: 2014-06-28. Available from: URL: <http://omim.org/entry/248370>

P- Reviewer: Imashuku S, Kan L, Sawai H **S- Editor:** Song XX
L- Editor: A **E- Editor:** Lu YJ



A handy review of carpal tunnel syndrome: From anatomy to diagnosis and treatment

Mohammad Ghasemi-rad, Emad Nosair, Andrea Vegh, Afshin Mohammadi, Adam Akkad, Emal Lesha, Mohammad Hossein Mohammadi, Doaa Sayed, Ali Davarian, Tooraj Maleki-Miyandoab, Anwarul Hasan

Mohammad Ghasemi-rad, Andrea Vegh, Adam Akkad, Emal Lesha, Mohammad Hossein Mohammadi, Anwarul Hasan, Center for Biomedical Engineering, Department of Medicine, Brigham and Women's Hospital, Harvard Medical School, Cambridge, MA 02139, United States

Mohammad Ghasemi-rad, Adam Akkad, Anwarul Hasan, Harvard-MIT Division of Health Sciences and Technology, Massachusetts Institute of Technology, Cambridge, MA 02139, United States

Emad Nosair, Anatomical Sciences, Basic Medical Sciences Department, College of Medicine, Sharjah University, Sharjah 27272, The United Arab Emirates

Andrea Vegh, Department of Materials Science and Engineering, University of Toronto, Toronto, Ontario M5S1A4, Canada

Afshin Mohammadi, Tooraj Maleki-Miyandoab, Department of Radiology, Imam Khomaine Hospital, Urmia University of Medical Sciences, Urmia 5716763111, Iran

Emal Lesha, College of Science and Mathematics, University of Massachusetts Boston, Boston, MA 02138, United States

Mohammad Hossein Mohammadi, Department of Chemical Engineering, Sharif University of Technology, Tehran 1136511155, Iran

Doaa Sayed, Department of Clinical Dentistry, College of Dentistry, Ajman University of Science and Technology, Ajman 2441, The United Arab Emirates

Ali Davarian, Department of Biochemistry and Molecular Biophysics, Washington University School of Medicine, St. Louis, MO 63110, United States

Anwarul Hasan, Biomedical Engineering, and Department of Mechanical Engineering, American University of Beirut, Beirut 1107 2020, Lebanon

Author contributions: All authors contributed to this paper.

Correspondence to: Dr. Anwarul Hasan, Biomedical Engineering, Department of Mechanical Engineering, American University of Beirut, Beirut 1107 2020, Lebanon. mh211@aub.edu.lb

Telephone: +961-7-6597214 Fax: +961-1-744462

Received: December 18, 2013 Revised: March 28, 2014

Accepted: May 8, 2014

Published online: March 28, 2015

diagnosed disabling condition of the upper extremities. It is the most commonly known and prevalent type of peripheral entrapment neuropathy that accounts for about 90% of all entrapment neuropathies. This review aims to provide an outline of CTS by considering anatomy, pathophysiology, clinical manifestation, diagnostic modalities and management of this common condition, with an emphasis on the diagnostic imaging evaluation.

© 2015 Baishideng Publishing Group Inc. All rights reserved.

Key words: Carpal tunnel syndrome; Anatomy; Ultrasonography; Magnetic resonance imaging; Computed tomography; Ultrasonography; Diagnosis; Nerve conduction study; Treatment

Core tip: A review of the carpal tunnel syndrome (CTS) highlighting anatomy, diagnosis and eventual treatment. This paper synthesizes all the aspects necessary to properly and successfully treat CTS, unlike past reviews which have focused on simply just one or a few factors. This review contains all the necessary material to fully understand CTS.

Original sources: Ghasemi-rad M, Nosair E, Vegh A, Mohammadi A, Akkad A, Lesha E, Mohammadi MH, Sayed D, Davarian A, Maleki-Miyandoab T, Hasan A. A handy review of carpal tunnel syndrome: From anatomy to diagnosis and treatment. *World J Radiol* 2014; 6(6): 284-300 Available from: URL: <http://www.wjgnet.com/1949-8470/full/v6/i6/284.htm> DOI: <http://dx.doi.org/10.4329/wjrt.v6.i6.284>

INTRODUCTION

In the United States, about 2.7 million doctors' office visits/year are related to patients complaining about finger, hand or wrist symptoms^[1]. The diagnosis of these symp-

Abstract

Carpal tunnel syndrome (CTS) is the most commonly

toms can include various types of nerve entrapments, tendon disorders, overuse of muscles or nonspecific pain syndromes^[1]. The most common type among them is carpal tunnel syndrome (CTS), which accounts for 90% of all entrapment neuropathies^[2,3] and is one of the most commonly diagnosed disorders of the upper extremities^[3,4]. It is expected that 1 in 5 patients who complain of symptoms of pain, numbness and a tingling sensation in the hands will be diagnosed with CTS based on clinical examination and electrophysiological testing^[3]. CTS is estimated to occur in 3.8% of the general population^[3,5], with an incidence rate of 276:100000 per year^[6], and happens more frequently in women than in men, with a prevalence rate of 9.2% in women and 6% in men^[3,7]. It is most often seen bilaterally at a peak age range of 40 to 60 years old; however, it has been seen in patients as young as twenty and as old as eighty-seven years old^[3,8].

The carpal tunnel (CT) is found at the base of the palm. It is bounded partly by the eight carpal bones and partly by a tough fibrous roof called the transverse carpal ligament (TCL). The tunnel gives passage to: (1) eight digital flexor tendons (two for each of the medial four fingers); (2) flexor pollicis longus (FPL) tendon for the thumb; (3) their flexor synovial sheaths; and (4) the median nerve (MN)^[1]. CT is therefore quite tightly packed and any condition that might increase the volume of the structures inside it can cause compression of the MN. This in turn might lead to ischemia of the nerve which presents as pain and paresthesia^[1,8].

The American Academy of Orthopedic Surgeons (AAOS) defines CTS as “a symptomatic compression neuropathy of the median nerve at the level of the wrist”^[3,9]. MN gives sensory branches to the lateral three fingers and the lateral half of the ring finger so that when it is compressed, symptoms of CTS are manifested in those fingers^[3]. The palm of the hand, however, remains unaffected by CTS as it is supplied by the sensory cutaneous branch of median nerve (PCBMN). This branch arises about 6 cm proximally to the TCL, then passes superficially to the ligament so it is not affected by the pressure changes within the CT^[3].

Furthermore, the most common diagnosis in patients with symptoms of pain and numbness is idiopathic CTS with a tingling sensation along the MN distribution in the hands^[10]. Although this syndrome is widely recognized, its etiology remains largely unclear. Recent biomechanical, MRI and histological studies have strongly suggested the close relationship of the dysfunction of neuronal vasculature, synovial tissue and flexor tendons within the CT and the development of idiopathic CTS^[11,12].

CT is the fibro-osseous pathway on the palmar aspect of the wrist which connects the anterior compartment of the distal forearm with the mid-palmar space of the hand. On its bottom, the CT is made up of the carpal bones articulating together to form a backward convex bony arch, resulting in formation on the dorsal side and concave on the palmar side, forming a tunnel-like groove called the *sulcus carpi*. This osseous groove is topped volar by the tough flexor retinaculum (FR), which arches over

the carpus, thus converting the sulcus carpi into the CT.

FR can be differentiated into three continuous segments: (1) a proximal thin segment called the volar carpal ligament. It is the thickened deep antebrachial fascia of the forearm; (2) the middle tough segment is the TCL; and (3) the distal segment is formed from an aponeurosis which extends distally between the thenar and hypothenar muscles. Therefore, it is recommended to have a more extensive surgical release instead of only resection of the middle segment of the FR^[3].

The width of the CT is about 20 mm at the level of the hook of hamate, which is narrower compared to its proximal (24 mm) or distal (25 mm) end^[13,14] counterparts. Moreover, the narrowest sectional area of the tunnel is located 1 cm beyond the midline of the distal row of the carpal bones where its sectional area is about 1.6 cm²^[15].

In healthy individuals, the intra-CT pressure is about 3-5 mmHg when the wrist is in a neutral position^[16,17]. MN blood flow was found to be impaired when the CT pressure approached or exceeded 20-30 mmHg. Common functional positions of the wrist, *e.g.*, flexion, extension or even using a computer mouse, might result in an increase of tunnel compression pressures to levels high enough to impair MN blood flow^[18]. For example, placing the hand on a computer mouse increase the CT pressure to 16-21 mmHg, while using the mouse to point and click increased the CT pressure up to 28 to 33 mmHg^[19]. Interestingly, CT pressure was shown to increase to 63 mmHg with 40 degrees of wrist extension and 0 degrees of metacarpophalangeal flexion^[20].

The position of adjacent muscular structures is thought to play a significant role in these positional increases in CT pressure^[20]. In a study of the MN in fresh human cadavers, a significant distal bulk of the flexor digitorum superficialis (FDS) muscle was found to enter the proximal aspect of the tunnel during wrist extension^[21]. Similarly, the lumbrical muscles were shown to enter the distal aspect of the tunnel during metacarpophalangeal flexion. Computer modeling suggests that when the metacarpophalangeal joints are flexed to 90 degrees, the lumbrical muscles remain in the CT, even if the wrist is kept extended^[22].

A thorough knowledge of the complex anatomy of the CT and its surrounding structures in addition to an emphasis on its clinical applications is essential for a better understanding of the pathophysiology of CTS, along with its symptoms and signs. Such knowledge will enable surgeons to take the most appropriate and safest approach during open or endoscopic carpal tunnel release (ECTR) surgeries by accurately identifying structures at or near the CT in order to avoid or reduce its surgical complications and ensure optimal patient outcome. It is also important to be aware of the likely possible anatomical variations that might be the cause of MN compression or may be anticipated and more readily recognized by hand surgeons. This review aims to provide an overview of CTS by considering anatomy, pathophysiology, clinical manifestation, diagnostic modalities and manage-

ment of this common condition, with an emphasis on its diagnostic imaging evaluation.

CLINICAL AND SURGICAL ANATOMY OF CT

Movements of the wrist joint have an effect on the shape and width of the CT. The width of the tunnel decreases considerably during the normal range of wrist motion and since the bony walls of the tunnel are not rigid, the carpal bones move relative to each other with every wrist movement. Both flexion and extension increase the CT pressure. The cross section of the proximal opening of the CT was found to be significantly decreased with a flexing wrist joint. This is likely due to the radial shifting of the TCL and the movement of the distal end of the capitate bone. In extreme extension, the lunate bone compresses the passage as it is pushed towards the interior of the tunnel^[15].

TCL is the thick (2-4 mm) central segment of the FR. It is a strong fibrous band formed from interwoven bundles of fibrous connective tissues^[13] and is short and broad (average width is 25 mm and length is 31 mm)^[23,24]. It extends from the distal part of the radius to the distal segment of the base of the third metacarpal. The mean proximal limit of its central portion is 11 mm distal to the capitate-lunate joint and the mean distal limit of its distal portion is 10 mm distal to the carpometacarpal joint of the third metacarpal^[15].

Regarding laminar configuration of the TCL, four basic laminae were identified: (1) strong distal transverse; (2) proximal transverse; (3) ulnar oblique; and (4) radial oblique. The most common pattern showed predominance of the distal transverse and the ulnar oblique laminae in every layer of the FCL. In half of the dissected hand samples, the distal transverse and ulnar oblique laminae dominated in the superficial layer, while the proximal transverse and the radial oblique laminae dominated in the deep layer. So, the strong distal transverse lamina is likely to be excised during the final step of ECTR because of its superficial localization. This could be a major cause for the frequent occurrence of incomplete release. Moreover, the almost universal superficial ulnar oblique lamina predisposes to scarring, which may cause radial shifting of the ulnar neurovascular bundle and may affect the PCBMN. It is concluded that the minor complications of ECTR depend partly on the variations in the laminar arrangement of the TCL^[25]. In another study performed on eight dissected TCLs, the transverse fibers were the most prominent (> 60%), followed by the oblique fibers in the pisiform-trapezium direction (18%), the oblique fibers in the scaphoid-hamate direction (13%) and finally the longitudinal fibers (8%)^[26].

Borders of the TCL

The TCL is attached medially to the pisiform bone and hook of the hamate, while laterally it splits into superficial and deep laminae. The superficial lamina is attached

to the tubercle of the scaphoid and trapezium and the deep lamina is attached to the medial lip of the groove on the trapezium. Together with this groove, the two laminae form a tunnel, lined by a synovial sheath containing the tendon of flexor carpi radialis (FCR)^[24].

Proximal border of the TCL

Proximally, the TCL is attached to the volar carpal ligament which extends from the radius to the ulna over the flexor tendons as they enter the wrist^[24]. This border corresponds to the distal flexion wrist crease, which also crosses the proximal end of scaphoid and pisiform bones.

Distal border of the TCL

This border is attached to the central portion of the palmar aponeurosis (PA). As measured along the axis of the radial border of the ring finger, the average distance between this border and the superficial palmar arch ranges from 5.5-19 mm^[27-31]. The mean distance from this distal border to the nearest aspect of the motor branch of MN is about 2.7-6.5 mm^[23,32].

Immediately proximal to the distal end of the TCL and in line with the axis of ring finger, a palmar fat pad (fat drop sign) is visualized overlapping this border. It is a reliable anatomic landmark during CT release which must be retracted in order to visualize the distal end of the TCL^[14]. Its proximal aspect lies at about 2 mm proximally to the distal edge of the TCL. The distance between the distal end of the TCL and the palmar fat pad decreases by flexing the fingers, but the distance between the TCL and the palmar arch or the PCBMN is not markedly affected. When dividing the TCL from proximal to distal, visualization of the proximal part of the fat pad is a useful indication that the distal edge of the TCL is within approximately 2 mm and indicates that distal dissection beyond this level is unnecessary in order to avoid injury of the superficial palmar arch or the PCBMN^[32].

Surfaces of the TCL

Palmar (volar) surface: This surface gives partial origin to all the thenar and hypothenar muscles except the abductor digiti minimi muscle and it also receives partial insertion from the flexor carpi ulnaris (FCU) and palmaris longus (PL).

This surface is entirely hidden by the muscular attachments, which makes it appear much deeper than surgeons think. This might urge surgeons to make a longer incision for good exposure of the TCL and to complete its division^[33]. The middle part of this surface is crossed by the PL tendon (if present), with a nerve on each of its sides; palmar cutaneous branch of ulnar nerve (medially) and PCBMN (laterally). The ulnar nerve and vessels cross the medial part of this surface through a special fascial tunnel called the Guyon tunnel^[33].

The superficial branch of the radial artery arises from the radial artery just before the latter curves round the carpus. It passes through and occasionally over the the-

nar muscles, which it supplies. It sometimes anastomoses with the end of ulnar artery to complete the superficial palmar arch^[24].

When present, it is a slender and flattened tendon, which passes superficially to the TCL and lies medially to the tendon of FCR. It is partially inserted into its central part of the TCL and extends distally to attach to the proximal part of PA. Frequently, it sends a tendinous slip to the thenar muscles. The MN lies deep to this tendon but when absent, the nerve becomes separated from the skin only by a thin subcutaneous fat and deep fascia^[24].

PCBMN arises from the MN proximal to the TCL. It pierces the deep fascia and runs superficially to the TCL, just laterally to the PL tendon. It then divides into lateral branches supplying the thenar skin, communicating with the lateral cutaneous nerve of forearm. The medial branches supply the central palmar skin and communicate with the palmar cutaneous branch of ulnar nerve^[24].

Injury to the PCBMN is the most common complication of CT surgery^[34] and it has been suggested that the mini incision done between the superficial palmar arch and the most distal part of the PCBMN in the palmar region is the safe zone for CT surgery^[34]. Decreased levels of discomfort in patients undergoing endoscopic and subcutaneous types of CT release may be in part due to the preservation of the crossing cutaneous nerves during these procedures^[35].

Communicating sensory branches may be multiple and often arise in the proximal forearm and sometimes from the anterior interosseous branch. They pass medially between FDS and FDP and behind the ulnar artery to join the ulnar nerve. This communication is a factor in explaining anomalous muscular innervations in the hand^[24]. In relation to an incision for CT release, PCBMB was found to cross the incision only in one specimen (of 25 fresh frozen cadaveric hands), while its terminal branches were identified at the margin of the incision in another two specimens^[35].

It arises from the ulnar nerve near the middle of the forearm at about 4.9 cm proximally to the pisiform bone. It then runs distally just medially and parallel to the PL tendon. It enters the palm of hand superficially to the TCL. In 24 specimens, at least one, usually multiple, transverse palmar cutaneous branch was identified originating at about 3 mm distally to the pisiform within Guyon's canal. In another 10 specimens (of 25 hands), a nerve of Henle arose at about 14.0 cm proximally to the pisiform, travelling with the ulnar neurovascular bundle to the wrist flexion crease^[35].

They pass superficially to the FR and enter the hand by passing through a groove between the pisiform (medially) and the hook of hamate (laterally and more distally). The ulnar artery is radial to the nerve and can be easily felt on the ulnar side of the front of the wrist. They usually pass just over the ulnar to the superior portion of the hook of the hamate. Over the FR, they are kept in place by a fascial extension from the volar carpal ligament, forming the ulnar canal (Guyon's canal). This

extension is attached medially to the pisiform bone and blends laterally with the TCL^[33]. They lie in the shelter of the lateral edge of the tendon of FCU^[24]. Pisiform bone is palpated at the base of the hypothenar eminence and serves to mark the entry on its lateral side of the ulnar nerve and artery into the hand. The mean distance from the radial aspect of the pisiform to the radial border of Guyon's canal and the ulnar edge of the PL tendon is about 10.3 mm and 16.1 mm respectively^[23]. As the ulnar nerve passes between the pisiform and hook of hamate, it terminates by dividing into superficial and deep branches.

With the wrist in neutral position, a looped ulnar artery runs from 2-7 mm medially^[27] to 1-4 mm laterally to the hook of the hamate^[36]. It then continues to form the superficial palmar arch. With the wrist in radial deviation, the looped ulnar artery migrates to the ulnar side of Guyon's canal (-2-2 mm radially to the hook of the hamate). During ulnar deviation of the wrist, the ulnar artery shifts more laterally beyond the hook of the hamate (2-7 mm). So, in order to minimize postoperative bleeding and avoid iatrogenic ulnar vascular and neural injury, it is recommended to: (1) transect the TCL over 4-5 mm apart from the lateral margin of the hook of the hamate without placing the edge of the scalpel toward the ulnar side; (2) not to transect the TCL in the ulnar deviation wrist position^[27]; and (3) make the proximal portal just medial to the PL tendon in order to spare the ulnar neurovascular structures^[36]. However, injury to the ulnar artery within Guyon's canal has not been a problem during ECTR surgery^[14].

Variations: (1) An anomaly of the ulnar nerve with an aberrant branch was observed to cross the CT incision^[37]; and (2) A small arterial branch (average diameter, 0.7 mm) arising from the ulnar artery ran transversely just over the TCL in 6 (of the 24 specimens). This branch was consistently located within 15 mm proximally to the TCL distal margin^[27].

The deep surface of the TCL: With the carpal bones, this surface forms the CT which is traversed by nine flexor tendons of the fingers, their flexor synovial sheaths and the median nerve.

The median nerve is the softest and most volar structure in the CT. Its average cross-sectional area is 6.19 mm²^[38]. It lies directly beneath the TCL and is superficial to the nine digital flexor tendons (Figure 1). Proximally to the TCL, the MN lies just laterally to the tendons of FDS and between the tendons of FCR and PL (Figure 2). Its location extends an average of 11 mm radially to the hook of hamate^[27]. Distally to the TCL, it enlarges and flattens and usually divides into five or six branches: (1) the recurrent motor branch; (2) three proper digital nerves (two to the thumb and one to the radial side of index finger); and (3) two common digital nerves (one to index/ middle and one to middle/ ring)^[24]. Trapped or pinched nerves have a useful electrical property for the diagnosis in that the speed of its conduction slows at the



Figure 1 Sketch of the palm, showing specific details of the inner structures of the carpal tunnel (inside the wrist). The median nerve and its branches after the wrist are marked in yellow.



Figure 2 Sketch of the cross-section of the carpal tunnel on a hand. Median nerve is shown in yellow and the nine flexor tendons are marked in blue.

site of trouble due to demyelination.

Anomalies of the median nerve: Variations of the MN at the wrist were reported in about 11% of the examined specimens. Neural variations arising from the medial aspect of the MN were common and could be a cause of iatrogenic injury during endoscopic or open release^[39].

In a study performed on 246 carpal tunnels at operation, four groups of variations were described: (1) variations in the course of MN were found in 12%; (2) accessory branches at the distal portion of the CT in 7%; (3) high divisions of the MN in 3%; and (4) accessory branches proximal to the carpal canal in 1.5%. These findings emphasize the importance of approaching the MN from the ulnar side when opening the CT^[40].

High bifurcation of the MN

Persistent median artery: the median artery is a transitory vessel that represents the embryological axial artery of the forearm. It normally regresses in the second fetal month^[41,42]. Its persistence in the human adult has been documented as two different types: as a large, long vessel which reaches the hand (palmar type); or as a small and short vessel which ends before reaching the wrist joint (antebrachial type)^[43,44]. It occurred in about 3.4%-20% of a 646 population sample of hands^[37,45]. It is more frequent in females than in males, occurring unilaterally more often than bilaterally and slightly more frequently on the right than on the left. Most frequently, it arises from the caudal angle between the ulnar artery and its common interosseous trunk (59%). Other origins may be from the ulnar artery or from the common interosseous trunk. It ends as the 1st, 2nd or 1st and 2nd common digital arteries (65%) or joins the superficial palmar arch (35%). It pierces the MN in the upper third of the forearm in 41% of cases with the palmar type^[45]. The median artery in its palmar type passes under the FR, running in the CT together with the MN and flexor tendons. This relationship has been considered an etiological factor in CTS^[46].

An aberrant sensory branch arising from the ulnar side of the MN and piercing the ulnar margin of the

TCL was found in 3% of hands (of 110 in operations)^[39].

Martin-Gruber anastomosis is a motor communicating nerve, which may cross over from the median to ulnar nerve in the forearm (motor not sensory connections). It occurs in two patterns: either from the MN in the proximal forearm to the ulnar nerve in the middle to distal third of the forearm; or from the anterior interosseous nerve to the ulnar nerve^[47].

Other motor anastomoses between the MN and ulnar nerve include: (1) motor branch of the MN to superficial head of flexor pollicis brevis (FPB) and ulnar nerve to the deep head of the FPB; (2) anastomosis, of the MN and ulnar motor branches through first lumbrical or through innervation of the adductor pollicis muscle; (3) branch of the MN to third lumbrical joining neural branch to this muscle from deep branch of ulnar nerve; (4) the MN may also form anastomoses with branch of radial nerve close to abductor pollicis brevis which has the radial nerve innervating this muscle; and (5) first dorsal interosseous, adductor pollicis or even abductor digiti minimi may be innervated by the MN^[47].

Motor branch (recurrent or thenar branch)

It is a short and thick branch commonly arising from the radial side of the MN. It may however, arise from the volar or the ulnar side of the MN^[14]. It may be the first palmar branch or a terminal branch which arises level with the digital branches of MN. It runs laterally, just distal to the TCL, with a slight recurrent curve beneath the part of the PA covering the thenar muscles. It runs around the distal border of the TCL to lie superficially to the FPB, which it usually supplies, and continues either superficially to the muscle or through it. It gives a branch to the abductor pollicis brevis, which enters the medial edge of the muscle and then passes deep to it to supply the opponens pollicis, piercing its medial edge. Its terminal part occasionally gives a branch to the 1st dorsal interosseous, which may be its sole or partial innervation. It may arise in the CT and pierces the TCL, a point of surgical importance^[24]. The position of the motor branch (in 30 hands) was extraligamentous in 46%-60%, subligamentous in 31%-34% and transligamentous in 6%-23% of

116 fresh frozen cadaveric hands^[34,40]. So, the most common pattern of the motor branch is extraligamentous and recurrent. The mean distance between the distal edge of the TCL and this branch is about 2.7-6.5 mm^[23,32].

The flexor tendons

The flexor tendons are the four tendons of the FDS, four tendons of the FDP and the tendon of the FPL. The superficial tendons are all separate and the tendons for the middle and ring fingers lie superficially to those for the index and little fingers. The MN lies superficially to the tendons of FDS. The profundus tendons are still deeper to the FDS tendons. Only the slip to the index finger is separate; the other three are still fused and lie medially to the index slip^[33]. The FPL tendon passes radially through a special canal between the two laminae of the TCL and the groove of trapezium. It is surrounded by a separate synovial sheath called the "radial bursa" which extends along the thumb as far as the insertion of the tendon at the base of the distal phalanx. Proximally, the radial bursa extends to a point 2.5 cm above the wrist joint/TC. It is sometimes connected to the base of the second metacarpal or may be absent^[24].

MECHANICS OF FLEXOR TENDONS AND THE MN WITH FINGER AND WRIST MOVEMENTS

Along their course, the long flexor tendons pass through a flexor pulley system which includes the TCL, PA and the digital pulleys, where the lubricant effect of synovial fluid maintains low friction between these tendon and the pulleys. *In vivo* and during active flexion and extension of the wrist and fingers, measurements revealed that longitudinal tendon excursion is about 24-50 mm^[48,49], while MN excursion was found to range from 11-28 mm during wrist and elbow movement^[50,51].

It is highly suggested that non-inflammatory fibrosis and thickening of the synovium is a leading cause for MN compression^[52]. These synovial changes also alter the gliding characteristic of the subsynovial connective tissue (SSCT), where it moves en bloc with the tendons and MN, which may play a role in the etiology of CTS^[53,54]. About 90% of the synovial specimens resected from patients with idiopathic CTS did not exhibit inflammatory changes, but mostly edema or fibrosis^[55,56]. Other findings of chronic synovial degeneration were reported as indicated by the increase in fibroblast density, collagen fiber size and vascular proliferation^[57].

Additionally, the flexor tendons move upwards (volar displacement) from the floor of the CT during active finger movement^[58-60]. This movement causes a force of compression/ reaction between the tendons and the TCL. Almost the same amount of force of the flexor tendon could be applied to the TCL during finger movement^[61].

Because the SSCT and tendon are physically connect-

ed, a decrease in SSCT motion (due to fibrosis) relative to the tendon would increase the shear strain on the SSCT with tendon motion. Thus, this result suggests that the SSCT may be predisposed to maximum shear injury from activity done in 60 degrees of wrist flexion more than the motion in all other wrist positions^[62]. During hand and finger motions, friction between the FDS tendon and the MN is thought to play a role in the development of cumulative trauma disorders^[62]. Also, the ratio of MN excursion to tendon excursion was much lower in finger-only motions compared to wrist motions with or without finger motion^[63]. High velocity tendon motion was reported to predispose to SSCT shear injury^[64].

A step forward damage in the SSCT in the CT was observed to follow repeated stretch tests within the physiological range of tendon excursion^[12,62]. Similarly, repetitive hand activities caused thickening of the synovial lining of the tendons that share the CT with the MN^[20,65].

Furthermore, shear tension and injury of the SSCT in CTS patients is significantly higher than that in normal subjects^[66] and the excursion of the MN is markedly reduced^[50,51]. This finding may be consistent with the fact that fibrosis of the synovial tissue within the CT is often observed in CTS patients.

PALMAR APPONEUROSIS (STRUCTURE AND FUNCTION)

The deep fascia of the palm of hand (palmar fascia) is thin over the thenar and hypothenar eminences, but its central portion, the PA, is triangular in shape. It has great strength and thickness. Its apex is continuous proximally with the distal border of TCL and receives the expanded tendon of the PL. Its base divides below into four slips, one for each finger^[33].

The PA covers the central compartment of the hand which contains the long flexor tendons and their synovial sheaths, the lumbricals, the superficial palmar arch and branches of the median and ulnar nerves with their digital nerves and vessels. Between the flexor tendons and the fascia covering the deep palmar muscles lies the medial central palmar (mid-palmar) space which is continuous with the space of at distal forearm in front of pronator quadratus (Space of Parona) via the CT^[24].

The deeper part of each slip subdivides into two processes, which are inserted into the fibrous sheaths of the flexor tendons. At the points of division into the slips, numerous strong transverse fascicular fibers of the PA are positioned at the proximal margin of the flexor tendon sheath. They bind the separate processes together and are attached by vertical septa to the underlying transverse metacarpal ligament, thus forming a tunnel around the flexor tendon and a PA pulley for the flexor tendons in conjunction with the first and second annular pulleys of the digital flexor mechanism^[67,68].

The PA pulley might be considered as important as the annular and cruciate flexor tendon pulleys. The PA decreases the tendency to bowstring around the metacar-

pophalangeal joint with a combination of proximal annular pulleys^[69].

The PA forms a fibrotendinous complex that functions as the tendinous extension of the PL when present and as a strong stabilizing structure for the palmar skin of the hand. It has a deeper transverse portion that crosses the palm at the proximal end of the metacarpal bones.

Aponeurosis provides firm attachment to overlying skin, helps to form the ridges in the palm, which in turn help to increase friction so that we can grasp objects firmly, protects underlying structures and provides attachment to muscles. The transverse fascicular fibers of the PA at the proximal margin of the flexor tendon sheath appear to function as a pulley^[67].

CLINICAL DIAGNOSIS OF CTS

The stages of CTS symptoms and signs can be categorized into three stages. In the first stage, the patient will awaken from sleep with a feeling of a numb or swollen hand, with no actual swelling visible. They may feel severe pain coming from their wrist emanating to their shoulder, with a tingling in their hand and fingers known as brachialgia paresthetica nocturna. Patients will note that shaking or flicking of their hand will stop the pain and that their hand may feel stiff in the morning. The second stage involves the symptoms being felt during the day. These may be felt especially when the patient performs repeated hand or wrist movements or if they remain in the same position for a long time. Patients may also notice clumsiness when using their hands to grip objects, resulting in the objects falling. The third and final stage occurs when there is hypotrophy or atrophy of the thenar eminence. When this stage is reached, sensory symptoms may no longer be felt at all^[70].

When diagnosing a patient with CTS, it is important to create a case history relevant to the characteristic signs of CTS. The patient must be questioned about whether their symptoms occur mainly at night or during the day, whether certain positions or repeated movements provoke their symptoms, if they use any vibratory instruments for work, whether their symptoms are felt in the hand, wrist or shoulder (and where in the areas symptoms are felt), what patients may do to alleviate symptoms (shaking, flicking, *etc.*), or if the patient may have a predisposing factor^[70]. Many factors may in fact be connected to CTS. They can include inflammatory arthritis, diabetes mellitus, pregnancy, hypothyroidism, Colles' fracture, acromegaly, amyloidosis, adiposity, myxedema, chronic polyarthritis or the use of corticosteroids and estrogens^[1,70].

A proper physical examination of the patient's hand and wrist is an important first step towards the diagnosis of CTS as certain physical findings may suggest the presence of other conditions. Abrasions or ecchymosis on the wrist and hands may indicate that there has been injury to the tissue, which could also include injury to the

median nerve. If bony abnormalities like the boutonniere deformity, the swan neck deformity or the ulnar deviation of the wrist are found, it could be concluded that the patient suffers from rheumatoid arthritis. If bossing on the carpal or distal phalanx is observed, osteoarthritis may be the cause. Other neuropathy syndromes or carpo-metacarpal arthritis may be suspected if thenar atrophy is seen as this condition usually happens only with severe and chronic CTS, which is not as common^[71].

Since patient history and physical examination have only limited diagnostic value and do not reveal the specific areas of symptom occurrence, patients can additionally be asked to fill out a self-diagnosis questionnaire known as the Katz Hand Diagram. A Katz Hand Diagram allows the patient to specify where they are experiencing symptoms and to classify the symptoms as numbness, pain, tingling or hypoesthesia. The completed symptom diagram can then be classified into one of three patterns of CTS.

Classical pattern: symptoms experienced by at least two of either the first, second or third fingers. Symptoms may also involve the fourth and fifth fingers, as well as wrist pain and radiation of pain proximally to the wrist however should not involve the palm or dorsum of the hand is not allowed. Probable/possible pattern: includes the same symptoms as in the classical pattern, however the palmar symptoms should only be limited to the median side. Possible pattern: symptoms involving only one of the first, second or third finger. Unlikely pattern: no symptoms are present at all in the first, second or third finger^[70].

A classical or probable diagram indicates the presence of CTS (sensitivity = 64%; specificity = 73%)^[70-73]. An additional subjective test is referred to as the flick sign (sensitivity = 93%; specificity = 96%)^[71,73] where the patient is simply asked whether or not they relieve the symptoms which awaken them at night with flicking or shaking of their hands. If the patient reports that this does happen to them, this may be indicative of CTS^[74].

Additionally, traditional tests known as provocative tests can be easily conducted by the physician on the patient to determine the possibility of CTS. One such test is a wrist flexion test known as Phalen's test (sensitivity = 57%-91%; specificity = 33%-86%)^[71,73,74] that involves the patient placing their elbows on a flat surface, maintaining their forearms vertically and allowing their wrists to fall into flexion up to one minute.

The "reverse Phalen's test" (sensitivity = 57%; specificity = 78%)^[74], also known as the wrist extension test or "Wormser's test"^[75], is also possible and involves the patient actively extending their fingers and wrist for two minutes. Another well known test is Tinel's sign (sensitivity = 23%-60%; specificity = 64%-87%)^[71,73,74], where the physician taps along the patient's median nerve near the carpal tunnel. Durkan's test (sensitivity = 64%; specificity = 83%)^[74], or carpal compression, is a test where the physician presses on the proximal edge of the carpal ligament with their thumb, compressing the median nerve.

The hand elevation test (sensitivity = 75.5%; specificity = 98.5%)^[76] is done by asking the patient to raise both of their arms, along with their elbows and shoulders, and holding the position for up to two minutes. The tourniquet test (sensitivity = 21%-59%; specificity = 36%-87%)^[73,74], or Gillet test, is performed by having the physician raise a blood pressure cuff placed on the patient's arm to the level of their systolic blood pressure. For all of the above noted tests, if paresthesia develops or increases in the median nerve distribution within one minute or less, then the test is deemed to have a positive result and CTS in the patient may be suspected^[1,74].

It is important to note that, although provocative tests and physical examination are simple and low cost methods to test for reproduction of the patient's symptoms and to determine if CTS should be suspected, provocative tests have scarce or no diagnostic value^[1,70,71] and physical examination has inadequate predictive value if the likelihood of CTS is low^[77]. There have been no trends identified between testing positive for various provocative tests and the severity of CTS^[78] and therefore proper diagnostic conclusions based on these tests cannot be made.

Nerve conduction studies

Due to this lack of diagnostic value in the mentioned tests, if CTS is suspected in a patient, adjunctive electrodiagnostic tests can be performed for a better diagnosis as they quantify and stratify the severity of CTS^[71]. These tests include nerve conduction studies and electromyography which may help with the future decision of treatment options and they have a sensitivity of 56% to 85% and a specificity of at least 94%^[71]. Because of their high specificity and sensitivity percentages, nerve conduction studies are considered to be the gold standard for CTS diagnosis^[3,72]. Nerve conduction studies provide insight on the median nerve's true physiological health on a quantitative basis by comparing the latency and the amplitude of the nerve across the carpal tunnel to another nerve segment not passing through the carpal tunnel (*e.g.*, the radial or ulnar nerve)^[3]. This is done by transcutaneously stimulating the nerve to create an action potential through an electrical pulse and having the depolarization wave detected by a recording electrode, that has been placed proximally or distally, and defining the response time of the median nerve as the "sensory conduction velocity" (SCV)^[3,70,79].

It is necessary to compare the response of the median nerve to another nerve not within the carpal tunnel due to the fact that there are different factors like gender, age, obesity, temperature, finger diameter or concurrent systemic disease that can influence the latency or amplitude of the median nerve^[3,80,81]. Using these controls increases the accuracy and sensitivity of diagnosis, with a sensitivity of 80%-92% and a specificity of 80%-99%^[3,79]. Additional data may also be obtained by studying the distal motor latency (DML) in the median and ulnar nerves in the same hand^[3].

Diagnostic criteria for CTS in nerve conduction studies include the median nerve showing extended amounts of sensory and motor latencies as well as delayed or diminished sensory and motor conduction velocities^[3]. Nerve conduction studies focus on defining whether there has been damage to the median nerve inside the carpal tunnel to quantify the severity of this nerve damage using a scale and to define the physiology of this injury as a conduction block, demyelination or axonal degeneration^[3,9,70]. The electrophysiological classification of the severity of CTS has been defined by the American Association of Electrodiagnostic Medicine (AAEM) and is as follows: (1) Negative CTS: normal findings on all tests (including comparative and segmental studies); (2) Minimal CTS: abnormal findings only on comparative or segmental tests; (3) Mild CTS: SCV is slowed in the finger-wrist tract with normal DML; (4) Moderate CTS: SCV is slowed in the finger-wrist tract with increased DML; (5) Severe CTS: absence of sensory response is seen in the finger-wrist tract with increased DML; and (6) Extreme CTS: complete absence of a thenar motor response^[3,70,82].

Nerve conduction studies can be paired with electromyography in order to tell the difference between muscle weakness that has been created by neurological disorders and primary muscle conditions^[71]. Adjunctive tests are, however, best used for patients who present with untypical symptoms and examination or if they possess an intermediate probability of having CTS. Although nerve conduction studies are a more accurate way of diagnosing CTS, they cannot be used for every patient showing symptoms of CTS as this would be expensive and inefficient^[3,72]. Although nerve conduction studies are the most sensitive and accurate way to diagnose CTS, false positives and false negatives are still possible and account for 16%-34% of "clinically defined CTS" going undiagnosed^[3,83].

When diagnosing CTS, it is important to remember that many other conditions can produce similar symptoms to CTS^[71]. A thorough physical examination along with an accurate patient history is an important first step for a correct diagnosis and the following list include some of the conditions that CTS must be differentiated from, along with the physical findings they are associated with: Wrist arthritis: seen in patients experiencing limited motion at the wrist or if there are radiological findings of arthritis; Carpometacarpal arthritis of thumb: characterized by joint line pain, pain experienced during motion or arthritis in radiological findings; Cervical radiculopathy (C6-C7): symptoms can include neck pain and numbness in the thumb and index finger only; Flexor carpi radialis tenosynovitis: can be suspected if there is tenderness near the base of the thumb; Ulnar or cubital tunnel syndrome: signs can include first dorsal interosseous weakness or tingling in the fourth and fifth digit; Median nerve compression at elbow: if there is tenderness at the proximal forearm; Raynaud's phenomenon: if the patient has a history of symptoms related to cold exposure; Vibration

white finger: seen in patients who use vibrating hand tools at work; Volar radial ganglion: if a mass near the base of thumb is found above the wrist flexion crease; Brachial plexopathy (in particular of the upper trunk); Thoracic outlet syndrome and CNS disorders (multiple sclerosis, small cerebral infarction)^[3,70,71].

Electrodiagnostic testing can be helpful with a differential diagnosis by being able to identify other hand dysesthesia conditions like cervical radiculopathy, polyneuropathy or median nerve entrapment syndromes^[73,84]. Additionally, needle electromyography specifically may be helpful with disorders that are proximal to the median nerve as well as to rule out a radiculopathy^[70].

Quantitative sensory testing is also used for sensory or motor tests to give quantitative results when diagnosing CTS. These tests include testing for touch threshold using Semmes-Weinstein Monofilaments (SWMF) (sensitivity = 59%-72%; specificity = 59%-62%)^[73,74], also referred to as Weinstein Enhances Sensory Test (WEST), where a five piece SWMF/WEST set is used and the filaments are applied onto digit pulps. Positive results of this test are deemed as a threshold greater than 2.83 in digits D1-D3 (an abnormal result); usually D2 or D3 are also assessed and comparison with D5 can improve the specificity as it eliminates thresholds that are larger than 2.83 due to aged or calloused skin. Another quantitative test is the two-point discrimination test (sensitivity = 6%-32%; specificity = 64%-99%)^[73,74] where the patient is asked to differentiate between the touch of prongs as they are applied until the skin blanches. Positive results (an abnormal finding) of this test are > 5 mm on pulps. Testing for the vibration threshold, measuring with either a tuning fork (sensitivity = 55%; specificity = 81%)^[74] or vibrometer (sensitivity = 50%; specificity = 73%)^[74], is also possible. These tests include applying a tuning fork (at 256 cps) tangentially to the fingertip pulp D1-D3 after hitting it to the affected side and comparative site or by applying a vibration stimulus to the digital pulp with a vibrometer and observing if the patient's feeling is different compared with the normal site (D5) or alternate site or, in the case of the vibrometer, if the thresholds are greater than norms for positive results. Current perception threshold (sensitivity = 80%; specificity = 61%)^[74] is tested for by delivering different frequencies of current and touching the patient with the equipment delivering this current. This stimulates the sensory nerves and positive results can be identified by comparing the patient's thresholds and frequency ratios with established norms in a computer software analysis. Thenar weakness or thenar atrophy (sensitivity = 4%-28%; specificity = 82%-99%)^[71,73] can also be tested for by visually inspecting the abductor pollicis brevis to look for loss of muscle bulk (positive result for thenar atrophy) or to use Oxford grading for the abductor pollicis brevis and observing a grade less than 5 (for thenar weakness). Thenar muscles are innervated by the median nerve, so the impairment of these muscles is indicative of the compromise of the motor fibers^[74].

All in all, debate and disagreement still exist on the

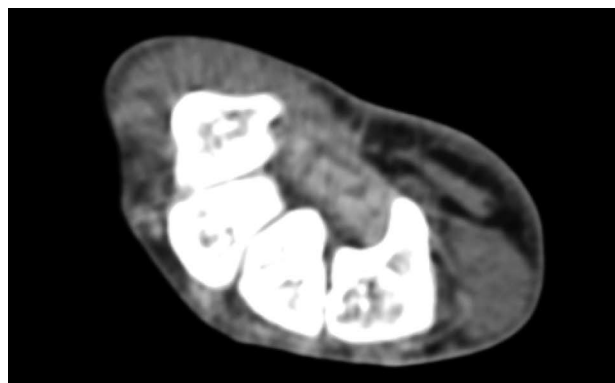


Figure 3 Axial computed tomography scan shows bony part of carpal tunnel at the level of outlet. Bony structures from left to right are HAMATE, CAPITATE, TRAPEZOID, TRAPEZIUM. FR (arrow) b and flexor tendons can be detected by computed tomography scan.

proper and accurate diagnosis of CTS. However, most experts can agree that the combination of nerve conduction studies (currently deemed the gold standard for diagnosis) and subjective symptoms allow for the most accurate way of diagnosing CTS^[78].

Computed tomography and conventional X-ray

Plain radiography has a limited role in diagnosing primary CTS as it cannot reveal the soft tissue part of the carpal tunnel. However, it might be useful in cases associated with bony stenosis, fracture and soft tissue calcification^[85]. Therefore, it should not be indicated unless there is a history of trauma to the hand or limitation in the range of wrist movement. CT scanning might provide a better alternative than plain radiography to clearly visualize the bony part of the carpal tunnel (Figure 3).

It can easily reveal the unusual bony structures and the structure occupying the space within the carpal tunnel that are not discovered by external examination^[86]. However, compression of the nerve cannot be clearly visualized unless it is due to the bony condition. In addition, several other reports have demonstrated the minor contribution of this approach in cases of primary CTS^[87,88]. In summary, plain radiograph and CT scan play minor roles in CTS diagnosis and they are difficult to standardize due to their inherent limitations in evaluating soft tissue changes^[85]. Therefore, CT scans and plain radiography should not be used as routine CTS diagnostic tools unless hard tissue related changes such as bone fracture, osseous carpal stenosis and calcifying of soft tissue are suspected^[85].

Ultrasonography

Due to recent advances at increasing resolution of sonographic pictures, it is possible to acquire a high quality image of peripheral nerves and fascia. Ultrasonography (US) is also able to identify changes in the flexor retinaculum, perineural and intraneural vascularization of the median nerve in idiopathic carpal tunnel syndrome (Figures 4-7). It can also identify the causes for secondary CTS. A study



Figure 4 Axial ultrasound image shows flexor retinaculum bowing as an echogenic line (arrow) in carpal tunnel and cross sectional area of median nerve (stellate) in a patient with carpal tunnel syndrome.

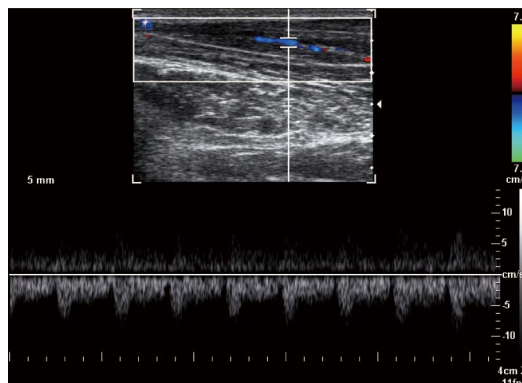


Figure 6 Spectral Doppler waveform of the median nerve shows low resistance hypervascularity of affected median nerve in a 40-year-old woman with severe carpal tunnel syndrome.

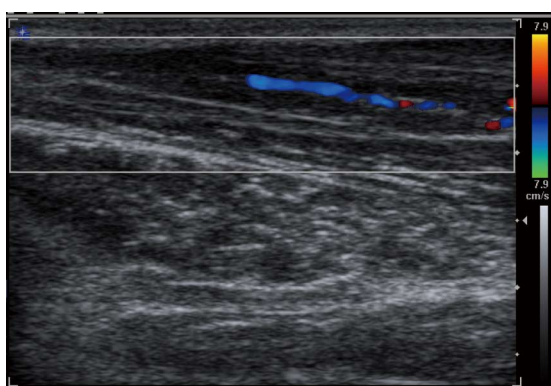


Figure 5 Longitudinal color Doppler sonogram in a 40-year-old woman with severe carpal tunnel syndrome shows intraneural hypervascularity in the median nerve.



Figure 7 Axial ultrasound image shows hypoechoic cable like neural fascicle (arrows) separated by substratum hyperechoic fat in a patient with secondary carpal tunnel syndrome due to lipofibromatous hamartoma of the median nerve.

by Nakamichi and Tachibana included 414 symptomatic wrists and 408 control wrists^[89]. Both sonography and nerve conduction studies were performed and the results were compared. The cross-sectional area of the median nerve was measured at the distal edge of the flexor retinaculum, the hook of hamate and the pisiform. Clear differences between the symptomatic patients and control patients were observed at all three levels. Nakamichi and Tachibana proposed cut off values of the CSA for each level ranging from an average of 12 mm² to 13, 11 and 14 mm² at all three levels. Specificity was found to be greater than 95% with sensitivity ranging from 43%-57%^[89].

Along the same lines, in a study carried out by El Miedany *et al*^[90], sensitivity and specificity were determined by measuring the CSA at the carpal tunnel inlet. Sensitivity and specificity measurements were found to be much higher than those presented by Nakamichi and Tachibana^[89]. The study included 96 symptomatic wrists and 156 control wrists, all of which were analyzed using both ultrasound and nerve conduction studies. Cut off for mild disease was 10 mm², moderate at 13 mm² and severe at 15 mm². Sensitivities and specifics for mild, moderate and severe disease were measured to be 98% and 100%, 98% and 97%, and 97% and 99%.

Theoretically, nerve enlargement results from a series of factors including inflammation, fibrosis, new axonal growth, endoneurial edema, demyelination, remyelination, *etc.* These indicators of increased CSA are all visible on US. Recent studies have shown that US is effective in confirming the diagnosis of CTS. One advantage that US has over NCS is that other lesions which display symptoms similar to CTS can be excluded from examination; these include tenosynovitis, mass lesions and anatomic defects. Moreover, US is low cost, readily available, noninvasive and total examination time is short. It can be recommended to use US as a replacement for clinical findings and first-line therapy in the diagnosis of CTS. However, in more complicated cases where diagnosis of CTS may require some confirmation, US would be a great tool as it is more sensitive and less invasive than nerve conduction studies.

It remains the case that there is not yet a reliable diagnostic standard for CTS. However, many of the studies in this review were able to rule out CTS if the CSA of the median nerve-in the carpal tunnel inlet was below 10 mm². Flexor retinaculum bowing, flattening of the median nerve and decreased longitudinal excursion on

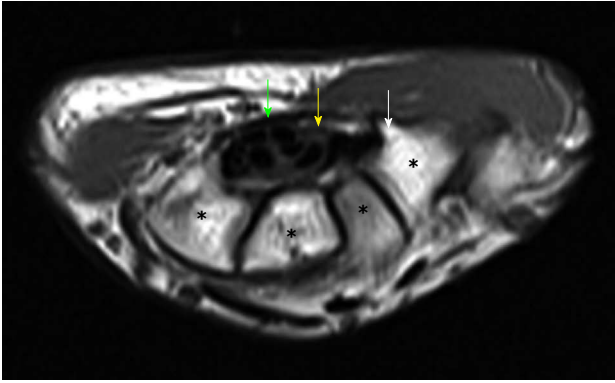


Figure 8 Axial T1W image of carpal tunnel at the level of tunnel outlet shows bony part of carpal tunnel as intermediate signal intensity composed from left to right hamate, capitate, trapezoid, trapezium. White arrow shows hook of hamate, yellow arrow shows median nerve, green arrow shows flexor retinaculum. Asterisks indicate carpal bones.

dynamic assessment are other measurements offered in addition to the CSA of the median nerve in the US assessment of CTS but are not as reliable. Limitations of US include axial and lateral resolution of the transducer that restrict the sonographic measurements as well as the challenge in differentiating the MN from the surrounding structures, especially in the distal CT. Ultrasonography can be implemented universally when a standardized protocol is used because the measurements are found to be reproducible.

Magnetic resonance imaging

Magnetic resonance (MR) imaging allows for good imaging of soft tissue. This makes MR imaging the optimal choice when studying CT in detail (Figure 8).

The drawbacks to MR imaging are that it is very costly, time consuming and not readily available. For these reasons, it is not advisable for MR imaging to be used in the diagnosis of CTS. The use of MR imaging is advisable in cases where the patient is resistant to therapy and/or for research. MR imaging does not add enough information of value to justify its use in the routine diagnosis of CTS in place of clinical and electrophysiological evaluation. Use of MR imaging can be justified in various circumstances, such as acute severe CTS following blunt trauma, arthritis, lack of evidence of nerve compression, surgical failure, long lasting CTS, detection of fibrous tissue and scars surrounding the MN and other anomalies of CT^[91]. MRI can be used to determine the exact point of nerve entrapment, for diagnosis in the case of ambiguous symptoms and to identify space-occupying lesions^[92].

MR imaging is useful for revealing the cause of nerve compression or elongation. Studies of MRI on CTS have shed tremendous light on the pathophysiology of idiopathic CTS. Typical indicators of idiopathic CTS are proximal enlargement of the cross-sectional area (CSA) of the median nerve of the carpal tunnel, greater signal intensity over the MN and palmar bowing of the TCL^[93].

The degree to which these findings are evident depends on the stage of the disease as enlargement of the CSA and increased signal intensity become more pronounced as the disease progresses. On T2-weighted MRI scans, high-signal intensity over the median nerve can indicate any of the following: accumulation of the axonal transportation, myelin sheath degeneration or edema^[94]. Enlargement of the structures within the carpal tunnel may be indicated by palmar bowing of the TCL. The severity of nerve compression can be determined accurately by sagittal images^[95]. It must be noted that no parameter has been developed that is able to be used to define CTS clearly. However, MRI provides the greatest diagnostic sensitivity for idiopathic CTS^[96]. MRI can be used to predict surgical outcomes in patients with CTS irrespective of NCSs. Moreover, patients prefer MRI to NCSs^[96]. MRI studies have indicated that increased T2-signal intensity in the median nerve and bowing of the flexor retinaculum seem to be the most sensitive MR signs of CTS. Increases in CSA area, flattening of the MN and peritendon pathology are other potential indicators of CTS on MRI^[97].

Previous reviews on MRI have pointed to the complications also encountered in this review. Original studies provide unsatisfactory descriptions of the reference diagnosis and only recruit asymptomatic referents^[93]. Consensus criteria of CTS include symptoms, clinical findings and electrophysiological criteria^[16,98]. The lack of consistency in diagnostic criteria provides for variations in patient spectra which takes a toll on the test accuracy^[99]. A possible remedy for this in the future would be to include more detailed descriptions of the symptoms of the referents before the original studies.

Bak *et al*^[100] studied twenty patients with CTS to determine if various MRI parameters correlated with nerve conduction test results. Results of the nerve conduction tests did not affect inclusion in the study. While no correlation was found, it should be noted that the patients did not show enlargement of the cross sectional area of the MN. The nerves seemed round rather than flat. Such a finding begs the question of diverse pathophysiological mechanisms behind CTS and how the diverse stages of chronicity of the disease affect the imaging outcome.

Unsatisfactory documentation of clinical characteristics has been shown to lead to overestimation of test accuracy. On the other hand, unsatisfactory documentation of reference diagnosis leads to underestimating test accuracy^[99]. Additionally, insufficient blinding and a poor description of results may also lead to the overestimation of test accuracy.

Two studies that used referents with contralateral symptom-free hands did not find the cross sectional area of the median nerve to be enlarged^[100,101], which is an observation made in other studies in which healthy volunteers were the referents. This finding can be attributed to other factors besides CTS. So long as there is a gold standard for the diagnosis of CTS, any other disease that causes similar symptoms may prove to hinder future studies.

TREATMENT OF CARPAL TUNNEL SYNDROME

Treatment of CTS can be classified as surgical and non-surgical. Surgical treatments include standard open carpal tunnel release, endoscopic carpal tunnel release, open carpal tunnel release combined with procedures and open carpal tunnel release using various incision techniques^[102]. Non-surgical treatments, also referred to as conservative treatments, include a wider range of options such as splinting, cortical steroid injections, non-steroidal anti-inflammatory drugs, B6 vitamin, diuretics, ultrasound therapy, ergonomic positioning, manual therapy intervention, lidocaine patches and acupuncture^[103-105]. Treatment decisions on carpal tunnel syndrome are based on the severity of the symptoms. Non-surgical treatments are recommended for patients with mild symptoms of CTS. Patients with moderate to severe symptoms are recommended for surgical evaluation.

Non-surgical treatment

Non-surgical treatment of CTS is recommended for patients that show mild to moderate symptoms of CTS. There is a variety of treatments that do not involve surgical procedures; however, splinting and steroids are most commonly used and supported by evidence^[102]. The most common splinting method is the neutral splint, which involves the immobilization of the wrist in a neutral position. This neutralizes flexion and extension of the wrist, thus increasing carpal tunnel pressure^[106] (Gerritsen, 2001 #73). Neutral splinting is generally recommended for use for a period of 6 wk during night time, however studies have shown better improvement in the full time use of the splints^[107]. Long term studies have shown considerable results of treatment success of night wrist splints at 3 mo of treatment^[108] and after 12 mo of additional treatment after 6 wk treatment with night splints^[109]. Other splinting methods include soft hand splints^[106,110], volar wrist cock-up and modified ulnar gutter splints^[111]. Soft hand splinting and neutral wrist splinting have been seen to show no significant differences within 3 mo of treatment^[112]; however, soft hand splinting can be considered an alternative to neutral wrist splinting^[113]. Treatment using steroids is done by local injection of corticosteroids directly into the patient's carpal tunnel. There is a risk associated with the injections and the possible decompression of the median nerve^[114], thus different approaches have been used regarding the injection site of the steroid. Injection through the wrist crease has been done using a distal or proximal approach to the wrist crease, with the distal approach resulting in a more comfortable and alternative approach^[115]. Other methods include intercarpal injections of steroids, shown to be a safe approach. Several studies have been conducted using an ulnar approach to the palmaris longus tendon^[114,116] and have shown the treatment to be effective and risk free. Overall, treatments involving local steroid injections are effective in relieving symptoms associated with CTS for a short time, thus they are considered an effective short-term treat-

ment^[110,117,118]. Local anesthetic injections such as procaine hydrochloride have been shown to be effective additions to steroid injections; however, studies have shown that procaine hydrochloride injections are as effective as steroid injections in short term treatment of CTS^[119,120].

A different approach to steroidal treatments is oral steroids such as prednisolone, proven effective for short-term treatment^[121]. Studies involving several types of nonsteroidal anti-inflammatory drugs have concluded that NSAIDs have no effect in pain relief and treatment of CTS and their effect has been compared to that of a placebo^[71,122]. However, other studies have shown effectiveness of NSAIDs drugs such as Naproxen in short term pain relief for CTS^[123]. Several studies have concluded that pyridoxine and diuretics, such as trichlor-methiazide, have no more effect than a placebo in the treatment of CTS^[71,122]. Ergonomic positioning has been tested for possible effects on CTS and, despite the presence of pain relief after a period of 12 wk under treatment, the evidence was not enough to prove the effect of ergonomic positioning on CTS^[124]. Heated lidocaine patches have also been identified as possible alternative short-term treatments for CTS, showing significant pain reduction following a two week study^[105]. Acupuncture is another treatment approach for CTS. Studies have shown significant pain reduction in patients with CTS using proximal and distal acupoints, as well as improvement of overall subjective symptoms using sham acupoints^[125,126]. Acupuncture has been shown to be as effective as night splints in the treatment of CTS^[105]. Ultrasound therapy is another alternative conservative treatment that has been shown to have positive effects in short term treatments of CTS in patients showing mild to moderate symptoms^[127,128]. Manual therapy intervention studies have concluded improved signs and symptoms for CTS^[104]. It is important to note the role of sonography in assessing the possible effects on different types of treatments for CTS, including corticosteroid injection and splinting treatments^[106].

Surgical treatment

Surgical treatment of CTS consists of the division of the transverse carpal ligament which reduces the pressure on the median nerve by increasing the space in the carpal tunnel^[2]. Surgery is recommended for most patients with moderate to severe CTS. There are two different categories of methods used for surgical treatment of CTS: open release and endoscopic release. Open carpal tunnel release consists of the standard method of open release, as well as several modified methods. Modifications to the standard open carpal tunnel release (OCTR) include new incision techniques, such as the mini-open release, and addition of other procedures such as epineurotomy^[102,129]. The standard open carpal tunnel release consists of a longitudinal incision at the base of the hand and in line with this incision, the incision of the subcutaneous tissue, the superficial palmar fascia and the muscle of the palmaris brevis^[129]. The mini-open carpal tunnel release is a relatively new technique that consists of a longitudinal

incision that varies from 1.5-3.0 cm, placed in line with the radial border of the ring finger^[129]. Different tools have been used for the mini-open carpal tunnel release, such as the Indiana Tome, the Knifelight, the Safeguard System and PSU retractor^[129]. Epineurotomy has been used as an additional procedure to the OCTR, with the prospective of minimizing median nerve compression occurring after standard OCTR^[72]. Endoscopic carpal tunnel release (ECTR) is another new technique that was developed by Okutsu and colleagues since 1986^[131]. The two most commonly used methods of endoscopic carpal tunnel release are the single-portal and dual-portal technique; techniques that differ based on the number of ports used to access the carpal tunnel^[130]. The single portal technique consists of the release of the transverse carpal ligament by using a single incision at the wrist. The double-portal technique consists of two incisions, one at the wrist and one at the palm of the hand. Several studies have tried to compare the efficiency and outcomes of the techniques involving carpal tunnel release procedures. Open carpal tunnel release and endoscopic carpal tunnel release have been shown to have no significant differences in outcomes within 12 wk of surgery^[132] and within 1 and up to 5 years of surgery^[129]. Mini-open carpal tunnel release and standard open carpal tunnel release have shown no significant differences within 4 mo of surgery^[133] and within 6 mo of surgery^[134]; however, mini-open carpal tunnel release has been shown to have better outcomes in earlier stages after surgery^[134]. ECTR release is sometimes favored over OCTR as dividing the skin from below preserves the muscle and overlying skin, thus facilitating return to work; however, it has an increased risk of nerve or artery injury because of limitations in visualization^[129]. ECTR has been shown to have better outcomes in muscle strength within 12 wk of surgery^[132] and better outcomes compared to both standard open and mini-open release within 4 wk of surgery^[133]. Additional epineurotomy procedures have been shown to have no significant difference in electrophysiological effects or nerve volume compared to the standard OCTR within 180 d after surgery^[135].

CONCLUSION

This review has explored and emphasized one of the most common entrapment neuropathies. There are several imaging modalities for assessing this condition but after analyzing the various options, it seems as if ultrasound examination with high-frequency probes and improved power Doppler technology should be used as the primary imaging investigation in the initial evaluation of CTS as it is the most beneficial and accurate. ECTR has been shown to have better outcomes than both standard open and mini-open release.

REFERENCES

- 1 **Katz JN**, Simmons BP. Clinical practice. Carpal tunnel syndrome. *N Engl J Med* 2002; **346**: 1807-1812 [PMID: 12050342 DOI: 10.1056/NEJMcp013018]
- 2 **Aroori S**, Spence RA. Carpal tunnel syndrome. *Ulster Med J* 2008; **77**: 6-17 [PMID: 18269111]
- 3 **Ibrahim I**, Khan WS, Goddard N, Smitham P. Carpal tunnel syndrome: a review of the recent literature. *Open Orthop J* 2012; **6**: 69-76 [PMID: 22470412 DOI: 10.2174/1874325001206010069]
- 4 **Mashoof AA**, Levy HJ, Soifer TB, Miller-Soifer F, Bryk E, Vigorita V. Neural anatomy of the transverse carpal ligament. *Clin Orthop Relat Res* 2001; **(386)**: 218-221 [PMID: 11347839]
- 5 **Uchiyama S**, Itsubo T, Nakamura K, Kato H, Yasutomi T, Momose T. Current concepts of carpal tunnel syndrome: pathophysiology, treatment, and evaluation. *J Orthop Sci* 2010; **15**: 1-13 [PMID: 20151245 DOI: 10.1007/s00776-009-1416-x]
- 6 **Mondelli M**, Giannini F, Giacchi M. Carpal tunnel syndrome incidence in a general population. *Neurology* 2002; **58**: 289-294 [PMID: 11805259]
- 7 **Rask MR**. Anterior interosseous nerve entrapment: (Kiloh-Nevin syndrome) report of seven cases. *Clin Orthop Relat Res* 1979; **(142)**: 176-181 [PMID: 498633]
- 8 **Phalen GS**. The carpal-tunnel syndrome. Seventeen years' experience in diagnosis and treatment of six hundred fifty-four hands. *J Bone Joint Surg Am* 1966; **48**: 211-228 [PMID: 5934271]
- 9 **American Academy of Orthopedic Surgeons**. Clinical practice guidelines on diagnosis of carpal tunnel syndrome. 1st ed. Rosemont: American Academy of Orthopedic Surgeons, 2007: 5
- 10 **Boscheinen-Morrin J**, Conolly W. *The Hand: Fundamentals of Therapy*. 3rd ed. Oxford: Butterworth Heinemann, 2001: 249
- 11 **Sud V**, Tucci MA, Freeland AE, Smith WT, Grinspun K. Absorptive properties of synovium harvested from the carpal tunnel. *Microsurgery* 2002; **22**: 316-319 [PMID: 12404351 DOI: 10.1002/micr.10051]
- 12 **Vanhees M**, Morizaki Y, Thoreson AR, Larson D, Zhao C, An KN, Amadio PC. The effect of displacement on the mechanical properties of human cadaver subsynovial connective tissue. *J Orthop Res* 2012; **30**: 1732-1737 [PMID: 22573580 DOI: 10.1002/jor.22143]
- 13 **Cobb TK**, Dalley BK, Posteraro RH, Lewis RC. Anatomy of the flexor retinaculum. *J Hand Surg Am* 1993; **18**: 91-99 [PMID: 8423326 DOI: 10.1016/0363-5023(93)90251-W]
- 14 **Rotman MB**, Donovan JP. Practical anatomy of the carpal tunnel. *Hand Clin* 2002; **18**: 219-230 [PMID: 12371025]
- 15 **Schmidt H**, Lanz U. *Surgical Anatomy of the Hand*. 1 ed. New York: Thieme Stuttgart, 2003: 29
- 16 **Gelberman RH**, Hergenroeder PT, Hargens AR, Lundborg GN, Akeson WH. The carpal tunnel syndrome. A study of carpal canal pressures. *J Bone Joint Surg Am* 1981; **63**: 380-383 [PMID: 7204435]
- 17 **Rojviroj S**, Sirichativapee W, Kowsuwon W, Wongwiwat-tananon J, Tamnanthong N, Jeeravipoolvarn P. Pressures in the carpal tunnel. A comparison between patients with carpal tunnel syndrome and normal subjects. *J Bone Joint Surg Br* 1990; **72**: 516-518 [PMID: 2187880]
- 18 **Rydevik B**, Lundborg G, Bagge U. Effects of graded compression on intraneural blood flow. An in vivo study on rabbit tibial nerve. *J Hand Surg Am* 1981; **6**: 3-12 [PMID: 7204915]
- 19 **Keir PJ**, Bach JM, Rempel D. Effects of computer mouse design and task on carpal tunnel pressure. *Ergonomics* 1999; **42**: 1350-1360 [PMID: 10582504 DOI: 10.1080/001401399184992]
- 20 **Werner R**, Armstrong T. Carpal tunnel syndrome: ergonomic risk factors and intra carpal canal pressure, carpal tunnel syndrome. *Phys Med Rehabil Clin N Am* 1997; **8**: 555-569
- 21 **Byl C**, Puttitz C, Byl N, Lotz J, Topp K. Strain in the median and ulnar nerves during upper-extremity positioning. *J Hand*

- Surg Am* 2002; **27**: 1032-1040 [PMID: 12457354 DOI: 10.1053/jhsu.2002.35886]
- 22 **Keir PJ**, Bach JM, Rempel DM. Effects of finger posture on carpal tunnel pressure during wrist motion. *J Hand Surg Am* 1998; **23**: 1004-1009 [PMID: 9848550 DOI: 10.1016/S0363-5023(98)80007-5]
 - 23 **Vasiliadis HS**, Tokis AV, Andrikoula SI, Kordalis NV, Beris AE, Xenakis T, Georgoulis AD. Microsurgical dissection of the carpal tunnel with respect to neurovascular structures at risk during endoscopic carpal tunnel release. *Arthroscopy* 2006; **22**: 807-812 [PMID: 16904575 DOI: 10.1016/j.arthro.2006.03.021]
 - 24 **Standing S**. Gray's Anatomy: The Anatomical Basis of Clinical Practice. 39 ed. New York: Elsevier/Churchill Livingstone, 2005: 913
 - 25 **Isogai S**, Murakami G, Wada T, Akita K, Yamashita T, Ishii S. Laminar configuration of the transverse carpal ligament. *J Orthop Sci* 2002; **7**: 79-83 [PMID: 11819137 DOI: 10.1007/s007760200013]
 - 26 **Prantil RK**, Xiu K, Kim KE, Gaitan DM, Sacks MS, Woo SL, Li ZM. Fiber orientation of the transverse carpal ligament. *Clin Anat* 2012; **25**: 478-482 [PMID: 22488997 DOI: 10.1002/ca.21257]
 - 27 **Omokawa S**, Tanaka Y, Ryu J, Suzuki J, Kish VL. Anatomy of the ulnar artery as it relates to the transverse carpal ligament. *J Hand Surg Am* 2002; **27**: 101-104 [PMID: 11810622]
 - 28 **Serra JM**, Benito JR, Monner J. Carpal tunnel release with short incision. *Plast Reconstr Surg* 1997; **99**: 129-135 [PMID: 8982196]
 - 29 **Rotman MB**, Manske PR. Anatomic relationships of an endoscopic carpal tunnel device to surrounding structures. *J Hand Surg Am* 1993; **18**: 442-450 [PMID: 8515013 DOI: 10.1016/0363-5023(93)90089-L]
 - 30 **Olave E**, Del Sol M, Gabriellp C, Mandiola E, Rodrigues CF. Biometric study of the relationships between palmar neurovascular structures, the flexor retinaculum and the distal wrist crease. *J Anat* 2001; **198**: 737-741 [PMID: 11465865]
 - 31 **Sacks JM**, Kuo YR, Mclean K, Wollstein R, Lee WP. Anatomical relationships among the median nerve thenar branch, superficial palmar arch, and transverse carpal ligament. *Plast Reconstr Surg* 2007; **120**: 713-718 [PMID: 17700123 DOI: 10.1097/01.prs.0000270305.37677.e7]
 - 32 **Madhav TJ**, To P, Stern PJ. The palmar fat pad is a reliable intraoperative landmark during carpal tunnel release. *J Hand Surg Am* 2009; **34**: 1204-1209 [PMID: 19540078 DOI: 10.1016/j.jhssa.2009.04.005]
 - 33 **Decker GAG**, Du Plessis DJ. Lee McGregor's Synopsis of Surgical Anatomy. The Bath Press, Lower Bristol Road, Bath BA2 3 BL. 12 ed. Bristol: John Wright & Sons Ltd., 1986: 483
 - 34 **Ozcanli H**, Coskun NK, Cengiz M, Oguz N, Sindel M. Definition of a safe-zone in open carpal tunnel surgery: a cadaver study. *Surg Radiol Anat* 2010; **32**: 203-206 [PMID: 19337677 DOI: 10.1007/s00276-009-0498-7]
 - 35 **Martin CH**, Seiler JG, Lesesne JS. The cutaneous innervation of the palm: an anatomic study of the ulnar and median nerves. *J Hand Surg Am* 1996; **21**: 634-638 [PMID: 8842957 DOI: 10.1016/S0363-5023(96)80017-7]
 - 36 **Hong JT**, Lee SW, Han SH, Son BC, Sung JH, Park CK, Park CK, Kang JK, Kim MC. Anatomy of neurovascular structures around the carpal tunnel during dynamic wrist motion for endoscopic carpal tunnel release. *Neurosurgery* 2006; **58**: ONS127-ONS33; discussion ONS127-ONS33; [PMID: 16543870 DOI: 10.1227/01.NEU.0000193883.02372.3E]
 - 37 **Lindley SG**, Kleinert JM. Prevalence of anatomic variations encountered in elective carpal tunnel release. *J Hand Surg Am* 2003; **28**: 849-855 [PMID: 14507518]
 - 38 **Mohammadi A**, Ghasemi-Rad M, Mladkova-Suchy N, Ansari S. Correlation between the severity of carpal tunnel syndrome and color Doppler sonography findings. *AJR Am J Roentgenol* 2012; **198**: W181-W184 [PMID: 22268209 DOI: 10.2214/AJR.11.7012]
 - 39 **Beris AE**, Lykissas MG, Kontogeorgakos VA, Vekris MD, Korompilias AV. Anatomic variations of the median nerve in carpal tunnel release. *Clin Anat* 2008; **21**: 514-518 [PMID: 18567020 DOI: 10.1002/ca.20650]
 - 40 **Lanz U**. Anatomical variations of the median nerve in the carpal tunnel. *J Hand Surg Am* 1977; **2**: 44-53 [PMID: 839054]
 - 41 **De Vriese B**. Recherches sur l'évolution des vaisseaux sanguins des membres chez l'homme. *Archives de Biologie* 1902; **18**: 665-730
 - 42 **Müller E**. Beiträge zur Morphologie des Gefässsystems. I. Die Armarterien des Menschen. *Anatomische Hefte* 1903; **22**: 377-575
 - 43 **Salmon M**, Dor J. Les Arte res des Muscles des Membres et du Tronc. Paris: Masson, 1933: 53-55
 - 44 **Huelin JG**, Barreiro FJ, Barcia EC. [Radio-anatomic study of the median artery]. *Acta Anat (Basel)* 1979; **105**: 250-255 [PMID: 539363]
 - 45 **Rodríguez-Niedenführ M**, Sañudo JR, Vázquez T, Nearn L, Logan B, Parkin I. Median artery revisited. *J Anat* 1999; **195** (Pt 1): 57-63 [PMID: 10473293]
 - 46 **Chalmers J**. Unusual causes of peripheral nerve compression. *Hand* 1978; **10**: 168-175 [PMID: 710998]
 - 47 **Wheless RC**. Textbook of Orthopaedics. Duke University Medical Center's Division of Orthopedic Surgery. Available from: URL: http://www.whelessonline.com/ortho/anatomy_of_carpal_tunnel
 - 48 **Wehbé MA**, Hunter JM. Flexor tendon gliding in the hand. Part I. In vivo excursions. *J Hand Surg Am* 1985; **10**: 570-574 [PMID: 4020072]
 - 49 **Korstanje JW**, Schreuders TR, van der Sijde J, Hovius SE, Bosch JG, Selles RW. Ultrasonographic assessment of long finger tendon excursion in zone v during passive and active tendon gliding exercises. *J Hand Surg Am* 2010; **35**: 559-565 [PMID: 20223603 DOI: 10.1016/j.jhssa.2010.01.010]
 - 50 **Hough AD**, Moore AP, Jones MP. Reduced longitudinal excursion of the median nerve in carpal tunnel syndrome. *Arch Phys Med Rehabil* 2007; **88**: 569-576 [PMID: 17466724 DOI: 10.1016/j.apmr.2007.02.015]
 - 51 **Tüzüner S**, Inceoğlu S, Bilen FE. Median nerve excursion in response to wrist movement after endoscopic and open carpal tunnel release. *J Hand Surg Am* 2008; **33**: 1063-1068 [PMID: 18762098 DOI: 10.1016/j.jhssa.2008.03.007]
 - 52 **Sternbach G**. The carpal tunnel syndrome. *J Emerg Med* 1999; **17**: 519-523 [PMID: 10338251]
 - 53 **Ettema AM**, Zhao C, Amadio PC, O'Byrne MM, An KN. Gliding characteristics of flexor tendon and tenosynovium in carpal tunnel syndrome: a pilot study. *Clin Anat* 2007; **20**: 292-299 [PMID: 16944527 DOI: 10.1002/ca.20379]
 - 54 **Netscher D**, Lee M, Thornby J, Polsen C. The effect of division of the transverse carpal ligament on flexor tendon excursion. *J Hand Surg Am* 1997; **22**: 1016-1024 [PMID: 9471069 DOI: 10.1016/S0363-5023(97)80041-X]
 - 55 **Nakamichi K**, Tachibana S. Histology of the transverse carpal ligament and flexor tenosynovium in idiopathic carpal tunnel syndrome. *J Hand Surg Am* 1998; **23**: 1015-1024 [PMID: 9848552]
 - 56 **Fuchs PC**, Nathan PA, Myers LD. Synovial histology in carpal tunnel syndrome. *J Hand Surg Am* 1991; **16**: 753-758 [PMID: 1880380]
 - 57 **Jinrok O**, Zhao C, Amadio PC, An KN, Zobitz ME, Wold LE. Vascular pathologic changes in the flexor tenosynovium (subsynovial connective tissue) in idiopathic carpal tunnel syndrome. *J Orthop Res* 2004; **22**: 1310-1315 [PMID: 15475214 DOI: 10.1016/j.orthres.2004.03.005]
 - 58 **Kiritzis PG**, Kline SC. Biomechanical changes after carpal tunnel release: a cadaveric model for comparing open, endoscopic, and step-cut lengthening techniques. *J Hand Surg Am* 1995; **20**: 173-180 [PMID: 7775747 DOI: 10.1016/S0363-5023(05)80003-6]

- 59 **Brown RK**, Peimer CA. Changes in digital flexor tendon mechanics after endoscopic and open carpal tunnel releases in cadaver wrists. *J Hand Surg Am* 2000; **25**: 112-119 [PMID: 10642480 DOI: 10.1053/jhsu.2000.jhsu025a0112]
- 60 **Richman JA**, Gelberman RH, Rydevik BL, Hajek PC, Braun RM, Gyllys-Morin VM, Berthoty D. Carpal tunnel syndrome: morphologic changes after release of the transverse carpal ligament. *J Hand Surg Am* 1989; **14**: 852-857 [PMID: 2794405]
- 61 **Uchiyama S**, Amadio PC, Berglund LJ, An KN. Analysis of the gliding pattern of the canine flexor digitorum profundus tendon through the A2 pulley. *J Biomech* 2008; **41**: 1281-1288 [PMID: 18328488 DOI: 10.1016/j.jbiomech.2008.01.011]
- 62 **Yoshii Y**, Zhao C, Zhao KD, Zobitz ME, An KN, Amadio PC. The effect of wrist position on the relative motion of tendon, nerve, and subsynovial connective tissue within the carpal tunnel in a human cadaver model. *J Orthop Res* 2008; **26**: 1153-1158 [PMID: 18383182 DOI: 10.1002/jor.20640]
- 63 **Lopes MM**, Lawson W, Scott T, Keir PJ. Tendon and nerve excursion in the carpal tunnel in healthy and CTD wrists. *Clin Biomech (Bristol, Avon)* 2011; **26**: 930-936 [PMID: 21550703 DOI: 10.1016/j.clinbiomech.2011.03.014]
- 64 **Yoshii Y**, Zhao C, Henderson J, Zhao KD, An KN, Amadio PC. Velocity-dependent changes in the relative motion of the subsynovial connective tissue in the human carpal tunnel. *J Orthop Res* 2011; **29**: 62-66 [PMID: 20607819 DOI: 10.1002/jor.21181]
- 65 **Armstrong TJ**, Castelli WA, Evans FG, Diaz-Perez R. Some histological changes in carpal tunnel contents and their biomechanical implications. *J Occup Med* 1984; **26**: 197-201 [PMID: 6716187]
- 66 **Osamura N**, Zhao C, Zobitz ME, An KN, Amadio PC. Evaluation of the material properties of the subsynovial connective tissue in carpal tunnel syndrome. *Clin Biomech (Bristol, Avon)* 2007; **22**: 999-1003 [PMID: 17822815 DOI: 10.1016/j.clinbiomech.2007.07.009]
- 67 **Manske PR**, Lesker PA. Palmar aponeurosis pulley. *J Hand Surg Am* 1983; **8**: 259-263 [PMID: 6875224]
- 68 **Doyle JR**. Anatomy and function of the palmar aponeurosis pulley. *J Hand Surg Am* 1990; **15**: 78-82 [PMID: 2299172]
- 69 **Phillips C**, Mass D. Mechanical analysis of the palmar aponeurosis pulley in human cadavers. *J Hand Surg Am* 1996; **21**: 240-244 [PMID: 8683053 DOI: 10.1016/S0363-5023(96)80107-9]
- 70 **Alfonso C**, Jann S, Massa R, Torreggiani A. Diagnosis, treatment and follow-up of the carpal tunnel syndrome: a review. *Neurol Sci* 2010; **31**: 243-252 [PMID: 20145967 DOI: 10.1007/s10072-009-0213-9]
- 71 **LeBlanc KE**, Cestia W. Carpal tunnel syndrome. *Am Fam Physician* 2011; **83**: 952-958 [PMID: 21524035]
- 72 **Katz JN**, Stirrat CR, Larson MG, Fossel AH, Eaton HM, Liang MH. A self-administered hand symptom diagram for the diagnosis and epidemiologic study of carpal tunnel syndrome. *J Rheumatol* 1990; **17**: 1495-1498 [PMID: 2273490]
- 73 **D'Arcy CA**, McGee S. The rational clinical examination. Does this patient have carpal tunnel syndrome? *JAMA* 2000; **283**: 3110-3117 [PMID: 10865306]
- 74 **MacDermid JC**, Wessel J. Clinical diagnosis of carpal tunnel syndrome: a systematic review. *J Hand Ther* 2004; **17**: 309-319 [PMID: 15162113 DOI: 10.1197/j.jht.2004.02.015]
- 75 **Wormser P**. [Hallucinations and suppressor zones]. *Monatsschr Psychiatr Neurol* 1950; **119**: 340-346 [PMID: 15423368]
- 76 **Ahn DS**. Hand elevation: a new test for carpal tunnel syndrome. *Ann Plast Surg* 2001; **46**: 120-124 [PMID: 11216604]
- 77 **Katz JN**, Larson MG, Sabra A, Krarup C, Stirrat CR, Sethi R, Eaton HM, Fossel AH, Liang MH. The carpal tunnel syndrome: diagnostic utility of the history and physical examination findings. *Ann Intern Med* 1990; **112**: 321-327 [PMID: 2306060]
- 78 **Priganc VW**, Henry SM. The relationship among five common carpal tunnel syndrome tests and the severity of carpal tunnel syndrome. *J Hand Ther* 2003; **16**: 225-236 [PMID: 12943125]
- 79 **Werner RA**, Andary M. Carpal tunnel syndrome: pathophysiology and clinical neurophysiology. *Clin Neurophysiol* 2002; **113**: 1373-1381 [PMID: 12169318]
- 80 **Sunderland S**. The nerve lesion in the carpal tunnel syndrome. *J Neurol Neurosurg Psychiatry* 1976; **39**: 615-626 [PMID: 993794]
- 81 **Salerno DF**, Franzblau A, Werner RA, Bromberg MB, Armstrong TJ, Albers JW. Median and ulnar nerve conduction studies among workers: normative values. *Muscle Nerve* 1998; **21**: 999-1005 [PMID: 9655117]
- 82 **Padua L**, Lo Monaco M, Padua R, Gregori B, Tonali P. Neurophysiological classification of carpal tunnel syndrome: assessment of 600 symptomatic hands. *Ital J Neurol Sci* 1997; **18**: 145-150 [PMID: 9241561]
- 83 **Witt JC**, Hentz JG, Stevens JC. Carpal tunnel syndrome with normal nerve conduction studies. *Muscle Nerve* 2004; **29**: 515-522 [PMID: 15052616 DOI: 10.1002/mus.20019]
- 84 **Spinner RJ**, Bachman JW, Amadio PC. The many faces of carpal tunnel syndrome. *Mayo Clin Proc* 1989; **64**: 829-836 [PMID: 2671521]
- 85 **Buchberger W**. Radiologic imaging of the carpal tunnel. *Eur J Radiol* 1997; **25**: 112-117 [PMID: 9283839]
- 86 **Bleeker ML**, Agnew J. New techniques for the diagnosis of carpal tunnel syndrome. *Scand J Work Environ Health* 1987; **13**: 385-388 [PMID: 3324318]
- 87 **Merhar GL**, Clark RA, Schneider HJ, Stern PJ. High-resolution computed tomography of the wrist in patients with carpal tunnel syndrome. *Skeletal Radiol* 1986; **15**: 549-552 [PMID: 3775421]
- 88 **Schmitt R**, Lucas D, Buhmann S, Lanz U, Schindler G. [Computed tomographic findings in carpal tunnel syndrome]. *Rofo* 1988; **149**: 280-285 [PMID: 2843958 DOI: 10.1055/s-2008-1048342]
- 89 **Nakamichi K**, Tachibana S. The use of ultrasonography in detection of synovitis in carpal tunnel syndrome. *J Hand Surg Br* 1993; **18**: 176-179 [PMID: 8501366]
- 90 **El Miedany YM**, Aty SA, Ashour S. Ultrasonography versus nerve conduction study in patients with carpal tunnel syndrome: substantive or complementary tests? *Rheumatology (Oxford)* 2004; **43**: 887-895 [PMID: 15100417]
- 91 **Britz GW**, Haynor DR, Kuntz C, Goodkin R, Gitter A, Kliot M. Carpal tunnel syndrome: correlation of magnetic resonance imaging, clinical, electrodiagnostic, and intraoperative findings. *Neurosurgery* 1995; **37**: 1097-1103 [PMID: 8584150]
- 92 **Khalil C**, Hancart C, Le Thuc V, Chantelot C, Chechin D, Cotten A. Diffusion tensor imaging and tractography of the median nerve in carpal tunnel syndrome: preliminary results. *Eur Radiol* 2008; **18**: 2283-2291 [PMID: 18418602 DOI: 10.1007/s00330-008-0971-4]
- 93 **Mesgarzadeh M**, Schneck CD, Bonakdarpour A, Mitra A, Conaway D. Carpal tunnel: MR imaging. Part II. Carpal tunnel syndrome. *Radiology* 1989; **171**: 749-754 [PMID: 2541464 DOI: 10.1148/radiology.171.3.2541464]
- 94 **Does MD**, Snyder RE. Multiexponential T2 relaxation in degenerating peripheral nerve. *Magn Reson Med* 1996; **35**: 207-213 [PMID: 8622585]
- 95 **Cudlip SA**, Howe FA, Clifton A, Schwartz MS, Bell BA. Magnetic resonance neurography studies of the median nerve before and after carpal tunnel decompression. *J Neurosurg* 2002; **96**: 1046-1051 [PMID: 12066905 DOI: 10.3171/jns.2002.96.6.1046]
- 96 **Jarvik JG**, Yuen E, Haynor DR, Bradley CM, Fulton-Kehoe D, Smith-Weller T, Wu R, Kliot M, Kraft G, Wang L, Erlich V, Heagerty PJ, Franklin GM. MR nerve imaging in a prospective cohort of patients with suspected carpal tunnel syndrome. *Neurology* 2002; **58**: 1597-1602 [PMID: 12058085]
- 97 **Pasternack II**, Malmivaara A, Tervahartiala P, Forsberg H,

- Vehmas T. Magnetic resonance imaging findings in respect to carpal tunnel syndrome. *Scand J Work Environ Health* 2003; **29**: 189-196 [PMID: 12828388]
- 98 **Stevens JC.** AAEM minimonograph #26: the electrodiagnosis of carpal tunnel syndrome. American Association of Electrodiagnostic Medicine. *Muscle Nerve* 1997; **20**: 1477-1486 [PMID: 9390659]
- 99 **Lijmer JG,** Mol BW, Heisterkamp S, Bossel GJ, Prins MH, van der Meulen JH, Bossuyt PM. Empirical evidence of design-related bias in studies of diagnostic tests. *JAMA* 1999; **282**: 1061-1066 [PMID: 10493205]
- 100 **Bak L,** Bak S, Gaster P, Mathiesen F, Ellemann K, Bertheussen K, Zeeberg I. MR imaging of the wrist in carpal tunnel syndrome. *Acta Radiol* 1997; **38**: 1050-1052 [PMID: 9394668]
- 101 **Socchetti A,** Raffaelli P, Giovagnoni A, Ercolani P, Mercante O, Pelliccioni G. MR imaging in the diagnosis of carpal tunnel syndrome. *Ital J Orthop Traumatol* 1992; **18**: 123-127 [PMID: 1399527]
- 102 **Shi Q,** MacDermid JC. Is surgical intervention more effective than non-surgical treatment for carpal tunnel syndrome? A systematic review. *J Orthop Surg Res* 2011; **6**: 17 [PMID: 21477381 DOI: 10.1186/1749-799X-6-17]
- 103 **Kummerddee W,** Kaewtong A. Efficacy of acupuncture versus night splinting for carpal tunnel syndrome: a randomized clinical trial. *J Med Assoc Thai* 2010; **93**: 1463-1469 [PMID: 21344811]
- 104 **Maddali Bonghi S,** Signorini M, Bassetti M, Del Rosso A, Orlandi M, De Scisciolo G. A manual therapy intervention improves symptoms in patients with carpal tunnel syndrome: a pilot study. *Rheumatol Int* 2013; **33**: 1233-1241 [PMID: 23064542 DOI: 10.1007/s00296-012-2507-0]
- 105 **Nalamachu S,** Nalamasu R, Jenkins J, Marriott T. An Open-Label Pilot Study Evaluating the Effectiveness of the Heated Lidocaine/Tetracaine Patch for the Treatment of Pain Associated with Carpal Tunnel Syndrome. *Pain Pract* 2013; Epub ahead of print [PMID: 23906384 DOI: 10.1111/papr.12105]
- 106 **Gerritsen AA,** Scholten RJ, Assendelft WJ, Kuiper H, de Vet HC, Bouter LM. Splinting or surgery for carpal tunnel syndrome? Design of a randomized controlled trial [ISRCTN18853827]. *BMC Neurol* 2001; **1**: 8 [PMID: 11801195]
- 107 **Walker WC,** Metzler M, Cifu DX, Swartz Z. Neutral wrist splinting in carpal tunnel syndrome: a comparison of night-only versus full-time wear instructions. *Arch Phys Med Rehabil* 2000; **81**: 424-429 [PMID: 10768530 DOI: 10.1053/mr.2000.3856]
- 108 **Povlsen B,** Bashir M, Wong F. Long-term result and patient reported outcome of wrist splint treatment for Carpal Tunnel Syndrome. *J Plast Surg Hand Surg* 2014; **48**: 175-178 [PMID: 24032598 DOI: 10.1010/2000656X.2013.837392]
- 109 **Gerritsen AA,** Korthals-de Bos IB, Laboyrie PM, de Vet HC, Scholten RJ, Bouter LM. Splinting for carpal tunnel syndrome: prognostic indicators of success. *J Neurol Neurosurg Psychiatry* 2003; **74**: 1342-1344 [PMID: 12933954]
- 110 **Ono S,** Clapham PJ, Chung KC. Optimal management of carpal tunnel syndrome. *Int J Gen Med* 2010; **3**: 255-261 [PMID: 20830201]
- 111 **Daniel ES,** Paul S. A comparison study of the volar wrist cock-up splint and ulnar gutter splint in carpal tunnel syndrome. *Occup Ther Health Care* 2000; **12**: 79-93 [PMID: 23931649 DOI: 10.1080/J003v12n04_06]
- 112 **De Angelis MV,** Pierfelice F, Di Giovanni P, Staniscia T, Uncini A. Efficacy of a soft hand brace and a wrist splint for carpal tunnel syndrome: a randomized controlled study. *Acta Neurol Scand* 2009; **119**: 68-74 [PMID: 18638040 DOI: 10.1111/j.1600-0404.2008.01072.x]
- 113 **Manente G,** Melchionda D, Staniscia T, D'Archivio C, Mazzone V, Macarini L. Changes in the carpal tunnel while wearing the Manu® soft hand brace: a sonographic study. *J Hand Surg Eur Vol* 2013; **38**: 57-60 [PMID: 22640934 DOI: 10.1177/1753193412446112]
- 114 **Jenkins PJ,** Duckworth AD, Watts AC, McEachan JE. Corticosteroid injection for carpal tunnel syndrome: a 5-year survivorship analysis. *Hand (N Y)* 2012; **7**: 151-156 [PMID: 23730233 DOI: 10.1007/s11552-012-9390-8]
- 115 **Kamanli A,** Bezginca M, Kaya A. Comparison of local steroid injection into carpal tunnel via proximal and distal approach in patients with carpal tunnel syndrome. *Bratisl Lek Listy* 2011; **112**: 337-341 [PMID: 21692409]
- 116 **Smith J,** Wisniewski SJ, Finnoff JT, Payne JM. Sonographically guided carpal tunnel injections: the ulnar approach. *J Ultrasound Med* 2008; **27**: 1485-1490 [PMID: 18809959]
- 117 **Martin BI,** Levenson LM, Hollingworth W, Kliot M, Heagerty PJ, Turner JA, Jarvik JG. Randomized clinical trial of surgery versus conservative therapy for carpal tunnel syndrome [ISRCTN84286481]. *BMC Musculoskelet Disord* 2005; **6**: 2 [PMID: 15656907 DOI: 10.1186/1471-2474-6-2]
- 118 **Carlson H,** Colbert A, Frydl J, Arnall E, Elliot M, Carlson N. Current options for nonsurgical management of carpal tunnel syndrome. *Int J Clin Rheumatol* 2010; **5**: 129-142 [PMID: 20490348 DOI: 10.2217/IJR.09.63]
- 119 **Karadaş O,** Omaç OK, Tok F, Ozgöl A, Odabaşı Z. Effects of steroid with repetitive procaine HCl injection in the management of carpal tunnel syndrome: an ultrasonographic study. *J Neurol Sci* 2012; **316**: 76-78 [PMID: 22336701 DOI: 10.1016/j.jns.2012.01.023]
- 120 **Karadaş Ö,** Tok F, Akarsu S, Tekin L, Balaban B. Triamcinolone acetone vs procaine hydrochloride injection in the management of carpal tunnel syndrome: randomized placebo-controlled study. *J Rehabil Med* 2012; **44**: 601-604 [PMID: 22674243 DOI: 10.2340/16501977-0990]
- 121 **Chang MH,** Ger LP, Hsieh PF, Huang SY. A randomised clinical trial of oral steroids in the treatment of carpal tunnel syndrome: a long term follow up. *J Neurol Neurosurg Psychiatry* 2002; **73**: 710-714 [PMID: 12438475]
- 122 **Chang MH,** Chiang HT, Lee SS, Ger LP, Lo YK. Oral drug of choice in carpal tunnel syndrome. *Neurology* 1998; **51**: 390-393 [PMID: 9710008]
- 123 **Nalamachu S,** Crockett RS, Gammaitoni AR, Gould EM. A comparison of the lidocaine patch 5% vs naproxen 500 mg twice daily for the relief of pain associated with carpal tunnel syndrome: a 6-week, randomized, parallel-group study. *MedGenMed* 2006; **8**: 33 [PMID: 17406167]
- 124 **Buchan S,** Amirfeyz R. Cochrane corner: ergonomic positioning or equipment for treating carpal tunnel syndrome. *J Hand Surg Eur Vol* 2013; **38**: 580-581 [PMID: 23704309 DOI: 10.1177/1753193413478507]
- 125 **Maeda Y,** Kettner N, Lee J, Kim J, Cina S, Malatesta C, Gerber J, McManus C, Im J, Libby A, Mezzacappa P, Morse LR, Park K, Audette J, Napadow V. Acupuncture-evoked response in somatosensory and prefrontal cortices predicts immediate pain reduction in carpal tunnel syndrome. *Evid Based Complement Alternat Med* 2013; **2013**: 795906 [PMID: 23843881 DOI: 10.1155/2013/795906]
- 126 **Khosrawi S,** Moghtaderi A, Haghighat S. Acupuncture in treatment of carpal tunnel syndrome: A randomized controlled trial study. *J Res Med Sci* 2012; **17**: 1-7 [PMID: 23248650]
- 127 **Piravej K,** Boonhong J. Effect of ultrasound thermotherapy in mild to moderate carpal tunnel syndrome. *J Med Assoc Thai* 2004; **87** Suppl 2: S100-S106 [PMID: 16083171]
- 128 **Ebenbichler GR,** Resch KL, Nicolakis P, Wiesinger GF, Uhl F, Ghanem AH, Fialka V. Ultrasound treatment for treating the carpal tunnel syndrome: randomised "sham" controlled trial. *BMJ* 1998; **316**: 731-735 [PMID: 9529407]
- 129 **Mintalucci DJ,** Leinberry CF. Open versus endoscopic carpal tunnel release. *Orthop Clin North Am* 2012; **43**: 431-437 [PMID: 23026458]
- 130 **Wongsiri S,** Suwanno P, Tangtrakulwanich B, Yuenyongviwat V, Wongsiri E. A new tool for mini-open carpal tunnel release

- the PSU retractor. *BMC Musculoskelet Disord* 2008; **9**: 126 [PMID: 18808664 DOI: 10.1186/1471-2474-9-126]
- 131 **Okutsu I**, Ninomiya S, Takatori Y, Ugawa Y. Endoscopic management of carpal tunnel syndrome. *Arthroscopy* 1989; **5**: 11-18 [PMID: 2706046]
- 132 **Ejiri S**, Kikuchi S, Maruya M, Sekiguchi Y, Kawakami R, Konno S. Short-term results of endoscopic (Okutsu method) versus palmar incision open carpal tunnel release: a prospective randomized controlled trial. *Fukushima J Med Sci* 2012; **58**: 49-59 [PMID: 22790892]
- 133 **Aslani HR**, Alizadeh K, Eajazi A, Karimi A, Karimi MH, Zaferani Z, Hosseini Khameneh SM. Comparison of carpal tunnel release with three different techniques. *Clin Neurol Neurosurg* 2012; **114**: 965-968 [PMID: 22421246 DOI: 10.1016/j.clineuro.2012.02.017]
- 134 **Yüçetaş SC**, Yildirim A. Comparative results of standard open and mini open, KnifeLight instrument-assisted carpal tunnel release. *J Neurol Surg A Cent Eur Neurosurg* 2013; **74**: 393-399 [PMID: 23929411 DOI: 10.1055/s-0033-1342932]
- 135 **Crnković T**, Bilić R, Trkulja V, Cesarik M, Gotovac N, Kolundžić R. The effect of epineurotomy on the median nerve volume after the carpal tunnel release: a prospective randomised double-blind controlled trial. *Int Orthop* 2012; **36**: 1885-1892 [PMID: 22588692 DOI: 10.1007/s00264-012-1565-y]

P- Reviewers: Cerimagic D, Karadas O **S- Editor:** Song XX
L- Editor: Roemmele A **E- Editor:** Zhang DN



Clinical decision support systems for brain tumor characterization using advanced magnetic resonance imaging techniques

Evangelia Tsolaki, Evanthia Kousi, Patricia Svolos, Efthychia Kapsalaki, Kyriaki Theodorou, Constastine Kappas, Ioannis Tsougos

Evangelia Tsolaki, Evanthia Kousi, Patricia Svolos, Kyriaki Theodorou, Constastine Kappas, Ioannis Tsougos, Medical Physics Department, University of Thessaly, Biopolis, 41110 Larissa, Greece

Efthychia Kapsalaki, Department of Radiology, University Hospital of Larissa, Biopolis, 41110 Larissa, Greece

Author contributions: Tsolaki E and Tsougos I designed the research; Tsolaki E, Kousi E and Svolos P performed the research; Tsolaki E, Kousi E and Tsougos I wrote the paper; Kapsalaki E, Theodorou K and Kappas C performed a critical review and data analysis.

Correspondence to: Ioannis Tsougos, MSc, PhD, Assistant Professor in Medical Physics Department, University of Thessaly, Panepistimiou 2, Biopolis, 41110 Larissa, Greece. tsougos@med.uth.gr

Telephone: +30-241-3501863 Fax: +30-241-3501863

Received: November 12, 2013 Revised: January 23, 2014

Accepted: March 17, 2014

Published online: March 28, 2015

Abstract

In recent years, advanced magnetic resonance imaging (MRI) techniques, such as magnetic resonance spectroscopy, diffusion weighted imaging, diffusion tensor imaging and perfusion weighted imaging have been used in order to resolve demanding diagnostic problems such as brain tumor characterization and grading, as these techniques offer a more detailed and non-invasive evaluation of the area under study. In the last decade a great effort has been made to import and utilize intelligent systems in the so-called clinical decision support systems (CDSS) for automatic processing, classification, evaluation and representation of MRI data in order for advanced MRI techniques to become a part of the clinical routine, since the amount of data from the aforementioned techniques has gradually in-

creased. Hence, the purpose of the current review article is two-fold. The first is to review and evaluate the progress that has been made towards the utilization of CDSS based on data from advanced MRI techniques. The second is to analyze and propose the future work that has to be done, based on the existing problems and challenges, especially taking into account the new imaging techniques and parameters that can be introduced into intelligent systems to significantly improve their diagnostic specificity and clinical application.

© 2015 Baishideng Publishing Group Inc. All rights reserved.

Key words: Decision support systems; Magnetic resonance imaging; Magnetic resonance spectroscopy; Diffusion weighted imaging; Diffusion tensor imaging; Perfusion weighted imaging; Pattern recognition

Core tip: The quantification of the imaging profile of brain neoplasms by combining conventional magnetic resonance imaging and advanced imaging techniques introduces critical underlying pathophysiological information which seems to be the key to success. Thus, it is evident that the pursuit of this goal should be oriented towards the development of decision support software that will utilize large amounts of clinical data with extremely significant diagnostic value which often remain unexploited, hence resulting in a more valid and precise method of differential diagnosis and the selection of the most successful treatment scheme.

Original sources: Tsolaki E, Kousi E, Svolos P, Kapsalaki E, Theodorou K, Kappas C, Tsougos I. Clinical decision support systems for brain tumor characterization using advanced magnetic resonance imaging techniques. *World J Radiol* 2014; 6(4):

INTRODUCTION

The introduction of magnetic resonance imaging (MRI) systems has induced revolutionary changes in the medical imaging field and has contributed much on a diagnostic and therapeutic level. In recent years, there has been a shift towards advanced MRI techniques, such as magnetic resonance spectroscopy ($^1\text{H-MRS}$), diffusion weighted imaging (DWI), diffusion tensor imaging (DTI) and perfusion weighted imaging (PWI), in order to resolve demanding diagnostic problems. These techniques offer a more detailed and non-invasive evaluation of brain tumors^[1-3] and have added incremental diagnostic information regarding brain tumor characterization over conventional MRI alone^[4,5].

$^1\text{H-MRS}$ has been studied for more than a decade as a promising diagnostic tool for a variety of pathologies. If coupled with the morphological features provided by MRI techniques, it can provide accurate identification and quantification of biologically important chemical compounds in soft tissue, thus increasing the understanding of the underlying pathologies. There have been numerous studies that indicate the significant contribution of $^1\text{H-MRS}$ for the characterization of brain tumors^[6-8], and fewer studies have concentrated on pediatric tumors^[9,10]. Even if $^1\text{H-MRS}$ does not change the final diagnosis, it may significantly rule out a differential diagnosis and thereby reduce the need for biopsy. However, challenges still remain in brain lesion classification regarding the use of $^1\text{H-MRS}$. The most important one is the limited number of available spectra per lesion type which may induce difficulties in reaching specific conclusions. Moreover, the simultaneous analysis and evaluation of multiple spectroscopic parameters is a time-consuming process, required specific expertise and may not be practical in a clinical environment.

In addition to $^1\text{H-MRS}$, the other advanced MRI techniques, DWI^[11], DTI^[12] and PWI have already found increasing use in the evaluation of cerebral tumors and still remain a subject of intense research^[1,13,14]. DWI probes local tissue microstructure reflected by the freedom of microscopic motion of water molecules and provides a sensitive means to detect alterations in the integrity of white matter structures, while PWI facilitates the prediction of brain lesion progression in conjunction with histopathology^[15].

It is evident that the continuously developing magnetic resonance systems have transformed from pure imaging systems to extremely precise metric systems that produce a considerable amount of numerical data that originate from the application of the aforementioned advanced MRI techniques. Taking into account the complex structure of the clinical data and the difficulty of

brain tumor discrimination due to their intrinsic heterogeneity, the research community has shifted towards the application of machine learning algorithms, in order to assign different tissue types to specific patterns. Several studies have previously investigated the differentiation of brain tumors in adults based on machine learning techniques^[16-20], as well as the discrimination of pediatric brain tumors^[21,22].

By importing and utilizing these intelligent techniques in a clinical decision support system (CDSS), several advanced MRI techniques may become a part of the clinical routine in order to resolve demanding diagnostic problems. CDSSs based on pattern recognition have been widely accepted in medical applications, due to their capability for optimization, flexibility, accuracy for predictive inference and interpretability^[23].

A CDSS according to van Bommel *et al.*^[24] is defined as any piece of software that takes, as input data, the information about a clinical situation and produces, as output, the inferences regarding the clinical situation that can assist practitioners with their decision-making, and that would be judged as “intelligent” by the program’s users.

Regarding brain tumor diagnosis, great efforts have been made in the implementation of intelligent systems for brain tumor differentiation, automatic processing, classification, evaluation and representation of clinical data. This effort is facilitated further by the evolvement of computer power that is available for the processing needs of these systems.

The purpose of the present study is to provide a literature review that focuses in the development of the CDSS, based on advanced MRI techniques for brain tumor characterization: (1) the first part provides an overview and an extensive description of the already developed CDSSs; and (2) in the second part, the study concludes to future objectives concerning the development of CDSSs for brain lesion characterization.

LITERATURE REVIEW

A thorough literature review was executed during the period 2000-2013. Initially, the research was limited to CDSS for brain tumor discrimination and the inclusion criterion was the kind of biomedical data that was utilized for their development. Specifically, the literature review was focused on the use of $^1\text{H-MRS}$, DWI, DTI and PWI data in CDSS development. To the best of our knowledge, up to this point none of the CDSS was developed using features extracted from DWI, DTI or PWI techniques. However, the interest of the scientific community focused on the use of spectroscopic data in order to develop these systems. Thus, the research identified articles that corresponded to clinical systems that were implemented using chemical shift imaging (CSI) or single voxel MRS^[25,26]. Furthermore, a number of articles and congress proceedings regarding the usability and effectiveness of these CDSS were collected.

Table 1 Validation results of the clinical decision support systems based on chemical shift imaging data

Ref.	Voxel assignment	Accuracy
De Edelenyi <i>et al.</i> ^[27]	Low-grade gliomas	92.9%
	High-grade gliomas	79.16%
	Metastasis	60%
	Meningiomas	100%
	Necrosis	100%
	Healthy tissue	100%
	Cerebrospinal fluid	100%
Simonetti <i>et al.</i> ^[29]	Healthy tissue	100%
	Cerebrospinal fluid	97%
	Glioma grade II	83%
	Glioma grade III	88%
	Glioma grade IV	100%
Luts <i>et al.</i> ^[32]	Glioma II	66.6%
	Glioma II / III	100%
	Glioma IV	100%
	Meningioma	100%
	Low grade gliomas vs grade III	89%
McKnight <i>et al.</i> ^[28]	Glioblastoma multiforme	100%
	Glioma II	100%

BRAIN TUMOR CDSS

CSI MRS data

The research revealed eight studies focused on the development of DSS based on proton MRSI, in order to gain information about the size, shape and the heterogeneity of the tumor. All of these studies used statistical or classification techniques in order to assign each voxel of the spectra to a specific tumor type and grade.

De Edelenyi *et al.*^[27] presented the first CDSS for brain tumor diagnosis focusing on CSI data. The authors proposed a method to create a “nosologic image” in order to extract information about the brain tumor type and the grade based on long TE ¹H-MRSI data, since biopsy does not always reveal the real grade of the tumor, due to tumor heterogeneity. Regarding this heterogeneity, each voxel of the spectroscopic image was colored according to the assigned histopathologic class (low or high grade glioma, metastasis and meningioma). However, McKnight *et al.*^[28] followed a different approach to extract image maps of long TE MV spectral data. Regarding the N-acetylaspartate and Cho levels of the spectrum, they investigated a score that was used to differentiate areas that present normal metabolite levels from regions that correspond to gliomas. Then, they utilized this score as a degree of abnormality throughout the lesion area. Afterwards, Simonetti *et al.*^[29] extracted nosologic images based not only to metabolic information but also exploiting the image variables of each voxel. They investigated the overlap between different classes (healthy, cerebrospinal fluid, grade II, grade III, grade IV) in the featured space, and constructed a probability map that corresponded to the probabilities of classification based on MRI and MRS data. Similarly to De Edelenyi *et al.*^[27], Simonetti *et al.*^[29] focused only on the metabolite and image characteristics of each voxel, ignoring the spatial information of the area under study. De Vos *et al.*^[30] used Short TE spectra to cre-

ate nosologic images. They applied canonical correlation analysis in order to investigate the tumor type and the heterogeneity of the region of interest. Similarly, Laudadio *et al.*^[31] applied canonical correlation analysis to 2-dimensional turbo MRSI data in order to combine spectra and spatial MRS information. The resulting correlation maps were used to construct nosologic images where all the detected tissue types were visualized. From the same research group, Luts *et al.*^[32] proposed a new method to generate nosologic images of the brain comparing to previous approaches. They used digital brain atlases presented by Prastawa *et al.*^[33] in order to investigate the incremental value of MRI over MRSI data. They added subject-specific abnormal tissue for image segmentation purposes, and the resulting framework was more flexible and able to exploit spatial information more efficiently, leading to improved nosologic images. Contrary to previous studies, Li *et al.*^[34] used unsupervised classification methods to construct nosologic images, in order to overcome the need of large datasets to train classifiers. Another difference was that they provided an error map along with the nosologic image in order to underline spectra variations due to tumor inhomogeneity.

The validation results of the majority of the clinical systems described previously are presented in Table 1.

Single voxel MRS data

Regarding the use of single voxel MRS data for CDSS development, during the last 10 years, four projects, the International Network for Pattern Recognition of Tumors Using Magnetic Resonance (INTERPRET) (2000-2002), eTUMOUR (2004-2009), HealthAgents (2005-2008) and CURIAM BT (2004-2010), were developed.

INTERPRET

INTERPRET was the outcome of a multicenter European collaboration^[35,36] that was funded under the 5th EU Framework Programme IST-1999-10310. A computer-based CDSS was developed in order to enable clinicians who have minimum knowledge of the MR spectrum to evaluate MR spectra and to discriminate between different brain tumors. During the INTERPRET development, one significant achievement was the creation of an important repository of brain tumors that contained 304 histopathological validated Short TE cases low grade gliomas [astrocytomas, oligodendrogliomas, oligoastrocytomas World Health Organization (WHO) grade II], meningiomas (WHO grade I and II) and high grade malignant tumors (glioblastomas, metastases). Another important achievement was the definition of a data acquisition protocol to ensure the compatibility between the MRS data coming from different clinical collaborative centers as well as the quality control protocol development, in order to define the quality requirements that MR spectra should fulfill.

Furthermore, a single voxel INTERPRET graphical user interface (GUI) was developed, providing easy access to the spectra database, to images and clinical informa-

Table 2 Validation results of the clinical decision support systems based on single voxel data

Ref.	CDSS	Differentiation problem	Accuracy			Supportive raw files	
			Short TE	Long TE	Short + Long TE		
Pérez-Ruiz <i>et al.</i> ^[38]	INTERRET	Low grade meningiomas <i>vs</i> low grade glial tumors	94 ^a	89 ^b 89 ^c 83 ^b	84 ^c	89 ^c	
		Pseudotumoural disease ^d <i>vs</i> tumors ^e <i>vs</i> normal brain	86 ^c	81 ^c	92 ^c		
García-Gómez <i>et al.</i> ^[41]	eTUMOUR	Low grade glioma <i>vs</i> high grade tumor	92	84	92		1.5 Tesla MRS data of Philips (sdat/spar) GE up to 9X (SAGE Pxxxx with an shf or sdf/shf) siemens scanners (numaris 4) jMRUI ^[58] text file
		Meningioma <i>vs</i> glioma/Met	92	78	94		
		Low men <i>vs</i> glioma/Met <i>vs</i> low grade glioma	87	75	90		
Sáez <i>et al.</i> ^[44]	HealthAgents	Aggressive tumor <i>vs</i> meningioma <i>vs</i> low grade glial	94	-			
		Meningioma <i>vs</i> metastasis	91	-			
		High grade tumor <i>vs</i> low grade tumor	87	68 (ch)			
		Affected tissue <i>vs</i> non affected tissue	99	-			
		Tumor <i>vs</i> non tumor	97	-			
		Aggressive tumor <i>vs</i> non aggressive tumor	81	72 (ch)			
		Glioma <i>vs</i> embryonal tumor	-	72 (ch)			
		Glioblastoma <i>vs</i> low grade glioma	84	-			
		Glioblastoma <i>vs</i> meningioma	91	-			
		Meningioma <i>vs</i> low grade glioma	92	-			
Vicente <i>et al.</i> ^[46]	CURIAM BT	Metastasis <i>vs</i> low grade glioma	85	-			
		Aggressive tumor <i>vs</i> non aggressive tumor	85	87 (ch)			1.5 or 3 Tesla MRS data of different manufactures (Siemens, GE, Philips) by means of jMRUI ^[58] and jDMS ^[56]
		Pilocytic astrocytoma/ependymoma grade II <i>vs</i> medulloblastoma	88 (ch)	85 (ch)	89 (ch)		
		Pilocytic astrocytoma <i>vs</i> medulloblastoma	92 (ch)	94 (ch)	95 (ch)		
		Pilocytic astrocytoma <i>vs</i> ependymoma grade II <i>vs</i> medulloblastoma	76 (ch)	69 (ch)	92 (ch)		

It is indicated where the classification accuracy corresponds to classifier trained on pediatric tumor data (ch). ^aInternational Network for Pattern Recognition of Tumors Using Magnetic Resonance (INTERPRET) version 1.1; ^bINTERPRET version 2.0; ^cINTERPRET version 3.0; ^dPseudotumoural disease: Acute infarct, multiple sclerosis, acute disseminated encephalomyelitis, and no specific pseudotumoural disease; ^eTumors: Astrocytoma World Health Organization (WHO) grade II, oligodendroglioma WHO grade II, oligoastrocytoma WHO grade II, astrocytoma WHO grade III, oligoastrocytoma WHO grade III. CDSS: Clinical decision support systems; MRS: Magnetic resonance spectroscopy; MRUI: Magnetic Resonance User Interface.

tion from all the validated cases of human brain tumors. It was designed to provide the display of classification plots, which is useful for the automatic classification of tumor spectra^[37]. The differentiation between different tumor groups was achieved by plotting the boundaries that were defined by the bisectors between the centroids of each class^[38]. The users could enter their own spectrum, position it automatically among the tumor groups of the system and compare it with other spectra.

Until 2010 many improvements have been gradually released in successive versions and can be categorized in three different aspects: GUI enhancements, increased analysis capabilities, and data quality and assessment checks^[38]. Specifically in the last version, an embedded database was developed for the permanent storage of the data into the system, more MRS data were supported compared to the previous versions (Short TE, Long TE and concatenated Short TE and Long TE Spectra) and six more classifiers were embedded to the system. Hence, the final version of INTERPRET not only offers the ability to differentiate common tumor types as in its first release, but also to differentiate among tumoral and pseudotumoural diseases (acute infarct, multiple sclerosis, acute disseminated encephalomyelitis). To address the latter classification problem, the metabolite ratios of the spectra were also used. The evaluation results of the different

versions of INTERPRET CDSS are shown to Table 2.

eTUMOUR

Another European project eTUMOUR took up the research on the development of CDSS^[39]. A more complex CDSS was developed that combined single voxel and CSI MRS data. The eTUMOUR CDSS upgraded and facilitated the clinical application of MRS in adult and pediatric brain tumor diagnosis, prognosis and treatment selection by using a combination of histology results, high resolution metabolic profiles (HR-MAS) and transcriptomic (DNA micro-arrays) *ex vivo* data to define the classification outcome^[40]. Regarding the acquisition and quality control procedure, the experience obtained from the INTERPRET project was used, whereas suitable protocols for the techniques of tissue analysis (HR-MAS, DNA microarrays and micro-RNA) were defined.

A web-based database (eTDB) was created, which was able to manage a wide range of data types such as clinical information, histological images, MRI, single voxel, MRSI, HR-MAS and DNA microarray data. This database comprised a complete and detailed GUI and also a structure for online uploading and downloading data *via* the web.

A user friendly computer aided decision system (CADS) DSS was developed and tested in eTUMOUR project.

The embedded classifiers were trained to solve three different discrimination problems (meningioma *vs* non-meningioma, aggressive tumor *vs* low grade glial and meningioma *vs* aggressive tumor *vs* low grade glial) using short time echo spectrum, long time echo spectrum and combination of both spectra (Table 2). Furthermore, the design of the DSS provided a comparative analysis with the average spectra of 12 standard brain tumor types of an unknown brain tumor. During the classification procedure the assigned class as well as the posterior probabilities of each class were displayed to the system^[39,41].

HealthAgents

HealthAgents^[42] was a distributed DSS (d-DSS) built upon INTERPRET and eTUMOUR projects. The great difference of this project was its architectural structure since it was based on agent-based architecture in order to decentralize the process of brain tumor differentiation in a distributed decision support framework that supports data partitioning and sharing^[43]. Since the accumulation of a sufficient number of cases for each tumor type or less common adult or childhood tumors was a very difficult and time consuming procedure, a collaborative network of different medical centers was constructed that contributed to the development of a repository of brain tumors, used for the training of robust classifiers for brain tumor differentiation.

The user, utilizes a local web-based GUI to enter the clinical data of a patient into the system and to request the appropriate classifiers from the network. These classifiers could be located anywhere on the collaborative HealthAgents network that consisted of different medical centers with their local existing databases of cases and their classifiers. Finally, the system would suggest the appropriate classifiers and indicate their specific location. Furthermore, a ranking tool was provided to the user, since many different classifiers coexisted in the system, in order to identify the classifiers that are more suitable for the diagnosis of particular case, to rank the obtained results from a set of classifiers and to solve possible conflicts between classifiers, by giving contradictory answers, which could occur when a test case was close to a decision boundary in one or more classifiers^[44].

Regarding the classification framework of the HealthAgents DSS its primary functionality was based on the INTERPRET DSS system. Until 2011, 25 classifiers were embedded and shared the system for the differentiation of aggressive tumors, like glioblastomas and metastases, benign meningiomas and low-glial mixture, such as astrocytomas grade II, oligodendrogliomas and oligoastrocytomas. The classification procedure was based on short time echo MRS data, long time echo MRS data and on the combination of them. The optimum classification results are presented to Table 2.

Curiam BT

Curiam BT^[45,46] was developed in parallel to eTUMOUR and HealthAgents projects. CURIAM BT supported

any kind of metabolic data either on short or long TE or both of different manufactures. Regarding the classification framework of this clinical system, it was able to determine the aggressiveness of a brain tumor in adults (non aggressive: grades I and II *vs* aggressive: grade III and IV) and to discriminate among the three most common pediatric brain tumors such as ependymoma grade II, pilocytic astrocytoma and medulloblastoma. Furthermore, compared with previous systems an additional opportunity was included, according to which the user could embed new classifiers to the system. Similar to the ranking tool in HealthAgents DSS, the audit and similarity methods were incorporated to the system to address the generalization ability of the coexisting classifiers. These methods proved to be significant as they provided the clinicians with the appropriate classifiers set regarding each differentiation problem and a specificity score of each classifier that determines its discrimination accuracy over time.

USABILITY AND EVALUATION OF CDSS

Regarding the evaluation of the single voxel CDSSs, there are several studies that reported their effectiveness and usability in the classification of different brain tumors during the clinical routine. These studies demonstrate the accuracy values that CDSSs present in various diagnostic problems, evaluate their contribution in combination with other diagnostic outcomes and survey CDSS usability regarding their user friendly module and acceptance by the clinical community. Considering the CDSSs that were based on CSI data, more research is needed since there is not a sufficient number of articles to demonstrate the overall contribution of these clinical systems to the clinical routine.

Fellows *et al*^[47] investigated the discrimination ability of INTERPRET version 2.0 in order to differentiate high and low grade tumors. The classification outcome of the system was compared with the neuroradiological tissue diagnosis and the conclusion of the spectroscopists. The results did not reveal significant differentiations between the accuracy levels of each participating modality.

INTERPRET version 3.0 proved to be superior for the characterization of grade III astrocytomas when compared to the spectroscopic and the radiologists' evaluation^[48].

Regarding the clinical evaluation of eTUMOUR, an agreement of 79.1% was obtained between the DSS outcome and the radiologic diagnosis. This rate increased up to 88.4% when the averaged spectra from DSS were used for brain tumor classification. When the CDSS, averaged spectra and radiologic findings were compared with the histopathological diagnosis, agreement scores of 76.7%, 79.1% and 81.4% were respectively achieved^[49].

When the CDSS results were compared with MRI, the overall percentage of correct predictions were 82.2% and 78.48%, respectively. Furthermore, the CDSS classification outcome was also compared with the corresponding outcome of MRI for the differentiation of

low grade gliomas, high grade gliomas and meningiomas. Specifically, the sensitivity and specificity values in low *vs* high grade gliomas classification problem, CDSS proved superior to the MRI corresponding values. Finally, the usefulness and applicability of the CADSS was rated 86% and 71%, respectively^[50].

Regarding the HealthAgents CDSS, an evaluation about its incremental diagnostic value was executed, and consequently 26 expert physicians were interviewed. As an overall response, they believed that the use of the CDSS would be beneficial for improving the quality of their brain tumor diagnoses. In addition, they considered the system easy to use, which is an important point in a DSS, especially in a clinical environment^[44].

When the evaluation of CURIAM BT was carried out, it reached 71% and 85% regarding the user's perspective on its usefulness and convenience, respectively^[51]. A comparing test was also executed in order to evaluate the contribution of CURIAM BT in the clinical routine. In that case, no significant differences were observed between the established diagnosis when conventional MRI, DWI and PWI were used, and the diagnosis derived from the above techniques combined with CDSS. Only in the case of high grade and low grade gliomas, did the observed differences reach 70%. Hence, a further evaluation should be implemented in order to investigate the CURIAM BT contribution in different diagnostic problems.

FUTURE PERSPECTIVES

One should consider CDSS as a supportive tool by providing additional information about the patient's state of health from which the clinician may establish a more educated and informed decision. As described in the "Usability and evaluation of CDSS" section, most of the studies proved the efficacy of the additional information that CDSS provide regarding improvements in clinical outcome. However, it is also evident that further evaluation should be implemented in order to investigate the CDSS contribution in different diagnostic problems. In addition, CDSS development involves much more than just the implementation of a software application. It requires adaptation by clinicians to use and engage in the refinement of CDSS both as a process and as a tool, as we move toward the goal of healthcare delivery that is consistent, effective, and of high quality^[52]. In order to accomplish the above objectives and to reinforce the application of CDSS in clinical routine, there are a number of future perspectives that should be implemented.

Regarding the classification framework of the clinical systems, there are two significant issues which arise. First, the improvement of the classification performance and second, the inclusion of more difficult differential diagnostic problems such as glioblastomas *vs* solitary metastasis. Hence, the retraining of the existing classifiers and the development of new ones, are necessary in order to optimize the classification performance and to extend the discrimination ability of the CDSS.

Until now all the CDSSs developed for brain tumor

differentiation are based on static classification methods. The use of static classifiers results in an implicit assumption that the learning procedure stops when the training set has been processed. The performance of a classifier strongly depends on the size of the training set for each class. Nevertheless, the accumulation of biomedical data is often a time-consuming and expensive procedure, and hence it may be not practical, especially in cases of uncommon cerebral pathologies like abscesses and lymphomas or pediatric brain tumors. In such cases, the implementation of incremental learning algorithms is a promising solution for clinical environments. Tortajada *et al.*^[53] evaluated the performance of an incremental classifier based on single voxel Short TE spectra in comparison to static classifiers. The results revealed that the classification performance was improved when the incremental classifiers were used comparing to performance of the static classifiers.

Another future objective is to incorporate metabolic data from both ¹H-MRS techniques (single voxel-CSI) into the classification framework of a DSS. The two techniques can be utilized simultaneously in order to investigate tumor heterogeneity whereas; the advantages of each spectroscopic technique can be exploited. Therefore, the metabolic characteristics of different tumor regions could be summarized into one image and the corresponding biochemical compounds can be studied. Hence, the spatial and the quantitative data of the spectrum will be used for an overall evaluation of the tumor. The complementary use of the spectroscopic techniques may contribute to the optimization and the accuracy of the preoperative diagnosis, and it may increase the understanding of the underlying pathologies.

An important future aspect is to enrich the DSS datasets with metabolic data from the peritumoral and contralateral regions regarding the brain tumor under study. With this perspective, the pattern recognition methods will be extended towards a more accurate differentiation scheme of brain tumors.

Growing intracranial neoplasms exhibit various effects in their peritumoral area. According to Chernov *et al.*^[54] lactate-producing neoplasms are associated with more prominent reduction of the relative NAA content in the surrounding cerebral tissue, independently on the presence or absence of any other factor. According to Fan *et al.*^[55] both a high Cho peak and elevated Cho/Cr ratio were found in the peritumoral regions of high-grade gliomas, but not in metastases. This suggests that the infiltration of adjacent brain tissue by tumor is a unique feature of high-grade glioma.

Another plan is to incorporate quantitative data from other MR-based methodologies. Di-Costanzo *et al.*^[56] showed that in the case of brain tumor classification, when ¹H-MRS parameters were considered as features, 83.3% of brain tumors were correctly classified. Whereas, when ¹H-MRS variables were combined with relative cerebral blood volume (rCBV) values from perfusion MRI, a 100% classification accuracy between high- and low-grade gliomas was achieved. They also showed that in a

peri-enhancing tumor region 73.7% of the cases were correctly classified when considering only ^1H -MRSI variables, 84.2% when considering ^1H -MRSI variables and apparent diffusion coefficient (ADC), and 89.5% when considering ^1H -MRSI variables, ADC and rCBV. Zonari *et al.*⁵⁷ achieved 80% sensitivity and 78.6% specificity when using rCBV parameter alone in grading cerebral neoplasms, and when combined with ^1H -MRS the sensitivity increased to 87.7% and specificity dropped to 76.2%.

Hence, it is evident that the continuous progress of imaging systems has induced revolutionary changes in the medical imaging field and has contributed utmost on a diagnostic and therapeutic level. The most important aspect however is that the continuous development of imaging techniques have transformed these modalities from conventional imaging to high-level metric systems, which may provide a quite large amount of quantitative information.

These large amounts of numeric data with an extremely significant diagnostic value may often remain unexploited during the clinical routine. The main reason for this is that the simultaneous analysis and evaluation of multiple parameters, is a time consuming process, requires specific expertise and may not be feasible during the clinical routine. It is prudent to mention that the available clinical time per patient may be estimated at about 30 min, while the process and evaluation of data from MRS and DTI usually takes more than 1 h. Especially when a specialized medical physicist for data manipulation is unavailable, these techniques are often handled by radiologists under a qualitative perspective rather than quantitative, which may lead to a biased differential diagnosis.

Therefore, an automatic evaluation of these data and a rapid display of the results are the minimum requirement during the clinical interpretation of an examination that will lead to a better clinical management of the patients, since the evaluation of the data will be done in an easier, and more effective way, which would ultimately lead to cost effectiveness by avoiding misdiagnosed cases. Towards this direction, the objective and future perspective would be to design and develop a CDSS, using incremental machine learning methods, based on all numeric data from the aforementioned advanced imaging techniques. The system should integrate and combine all the available metabolic, diffusion and perfusion data. The hypothesis is that the combination of multiple data from the aforementioned imaging modalities is expected to optimize the differential diagnosis of brain pathologies, which will be eventually beneficiary for tailored patient treatment.

Hence, these kind of systems should be specifically designed in such a way that the user (that is: radiologist, medical physicist and in general neuroscientists), with minimum knowledge of pattern recognition analysis, will be able to: (1) categorize and illustrate the clinical data on a single template in order to ensure that the data will

not be dispersed; (2) perform a fully automated pattern recognition analysis towards the optimum differential diagnosis; (3) quantify the degree of uncertainty in the prediction of ambiguous diagnostic problems by offering a diagnostic orientation; and (4) use the system as a supportive tool for the selection of the most appropriate treatment strategy and the most successful treatment scheme.

From our personal experience, it should be stressed that a CDSS by no means substitutes for the expert's diagnostic decision, but rather supports the clinician by evaluating simultaneously a large amount of complicated MR data. Thorough analysis and evaluation of these data requires additional time, which exceeds by far the available clinical time per patient, hence this information may remain unexploited.

Furthermore, despite the good discrimination ability of the embedded classification schemes, it should be emphasized that the decision-making process with the use of a clinical decision system should be a procedure of two individual parts. The first part should include the classification result or a good orientation towards a clinical outcome, based on the evaluation of quantitative MRI data and the second part should involve the co-evaluation of the aforementioned result with all the available diagnostic and imaging information. Under these perspectives, a well designed CDSS may be used as an assistant diagnostic tool which can be implemented into the clinical routine and substantially aid the interpretation of an exam and optimize decision making.

CONCLUSION

Diagnosis and consequently treatment of brain neoplasms may greatly benefit from the introduction and utilization of intelligent systems in the form of CDSS for automatic processing, classification, evaluation and representation of the spectroscopic data as part of the clinical routine. Major progress has been made in the last few years towards this direction, as several systems exist and are continuously developing. Nevertheless, the quantification of the imaging profile of neoplasms by combining conventional MRI and advanced imaging techniques (MRS, DWI, DTI and PWI) introduces critical underlying pathophysiological information which seems to be the key to success.

Thus, it is evident that the future directions should be oriented towards the development of software that will be implemented in the clinical routine, by utilizing large amounts of clinical data with extremely significant diagnostic value which often remain unexploited, resulting in a more valid and precise method for differential diagnosis of brain pathologies and the selection of the most successful treatment scheme.

REFERENCES

- 1 Chiang IC, Kuo YT, Lu CY, Yeung KW, Lin WC, Sheu FO,

- Liu GC. Distinction between high-grade gliomas and solitary metastases using peritumoral 3-T magnetic resonance spectroscopy, diffusion, and perfusion imagings. *Neuroradiology* 2004; **46**: 619-627 [PMID: 15243726 DOI: 10.1007/s00234-004-1246-7]
- 2 Liu X, Tian W, Kolar B, Yeane GA, Qiu X, Johnson MD, Ekholm S. MR diffusion tensor and perfusion-weighted imaging in preoperative grading of supratentorial nonenhancing gliomas. *Neuro Oncol* 2011; **13**: 447-455 [PMID: 21297125 DOI: 10.1093/neuonc/noq197]
 - 3 Tsougos I, Svolos P, Kousi E, Fountas K, Theodorou K, Fezoulidis I, Kapsalaki E. Differentiation of glioblastoma multiforme from metastatic brain tumor using proton magnetic resonance spectroscopy, diffusion and perfusion metrics at 3 T. *Cancer Imaging* 2012; **12**: 423-436 [PMID: 23108208 DOI: 10.1102/1470-7330.2012.0038]
 - 4 Chang SC, Lai PH, Chen WL, Weng HH, Ho JT, Wang JS, Chang CY, Pan HB, Yang CF. Diffusion-weighted MRI features of brain abscess and cystic or necrotic brain tumors: comparison with conventional MRI. *Clin Imaging* 2002; **26**: 227-236 [PMID: 12140151]
 - 5 Reiche W, Schuchardt V, Hagen T, Il'yasov KA, Billmann P, Weber J. Differential diagnosis of intracranial ring enhancing cystic mass lesions--role of diffusion-weighted imaging (DWI) and diffusion-tensor imaging (DTI). *Clin Neurol Neurosurg* 2010; **112**: 218-225 [PMID: 20053496 DOI: 10.1016/j.clineuro.2009.11.016]
 - 6 Möller-Hartmann W, Herminghaus S, Krings T, Marquardt G, Lanfermann H, Pilatus U, Zanella FE. Clinical application of proton magnetic resonance spectroscopy in the diagnosis of intracranial mass lesions. *Neuroradiology* 2002; **44**: 371-381 [PMID: 12012120 DOI: 10.1007/s00234-001-0760-0]
 - 7 Hollingworth W, Medina LS, Lenkinski RE, Shibata DK, Bernal B, Zurakowski D, Comstock B, Jarvik JG. A systematic literature review of magnetic resonance spectroscopy for the characterization of brain tumors. *AJNR Am J Neuroradiol* 2006; **27**: 1404-1411 [PMID: 16908548]
 - 8 Kousi E, Tsougos I, Tsolaki E, Fountas KN, Theodorou K, Fezoulidis I, Kapsalaki E, Kappas C. Spectroscopic evaluation of glioma grading at 3T: the combined role of short and long TE. *ScientificWorldJournal* 2012; **2012**: 546171 [PMID: 22919334 DOI: 10.1100/2012/546171]
 - 9 Astrakas LG, Zurakowski D, Tzika AA, Zarifi MK, Anthony DC, De Girolami U, Tarbell NJ, Black PM. Noninvasive magnetic resonance spectroscopic imaging biomarkers to predict the clinical grade of pediatric brain tumors. *Clin Cancer Res* 2004; **10**: 8220-8228 [PMID: 15623597 DOI: 10.1158/1078-0432.CCR.04-0603]
 - 10 Panigrahy A, Krieger MD, Gonzalez-Gomez I, Liu X, McComb JG, Finlay JL, Nelson MD, Gilles FH, Blüml S. Quantitative short echo time 1H-MR spectroscopy of untreated pediatric brain tumors: preoperative diagnosis and characterization. *AJNR Am J Neuroradiol* 2006; **27**: 560-572 [PMID: 16551993]
 - 11 Schaefer PW, Grant PE, Gonzalez RG. Diffusion-weighted MR imaging of the brain. *Radiology* 2000; **217**: 331-345 [PMID: 11058626]
 - 12 Tang CY, Friedman J, Shungu D, Chang L, Ernst T, Stewart D, Hajianpour A, Carpenter D, Ng J, Mao X, Hof PR, Buchsbaum MS, Davis K, Gorman JM. Correlations between Diffusion Tensor Imaging (DTI) and Magnetic Resonance Spectroscopy (1H MRS) in schizophrenic patients and normal controls. *BMC Psychiatry* 2007; **7**: 25 [PMID: 17578565 DOI: 10.1186/1471-244X-7-25]
 - 13 Zhang H, Rödiger LA, Shen T, Miao J, Oudkerk M. Perfusion MR imaging for differentiation of benign and malignant meningiomas. *Neuroradiology* 2008; **50**: 525-530 [PMID: 18379768 DOI: 10.1007/s00234-008-0373-y]
 - 14 Sentürk S, Oğuz KK, Cila A. Dynamic contrast-enhanced susceptibility-weighted perfusion imaging of intracranial tumors: a study using a 3T MR scanner. *Diagn Interv Radiol* 2009; **15**: 3-12 [PMID: 19263367]
 - 15 Järnum H, Steffensen EG, Knutsson L, Fründ ET, Simonsen CW, Lundbye-Christensen S, Shankaranarayanan A, Alsop DC, Jensen FT, Larsson EM. Perfusion MRI of brain tumours: a comparative study of pseudo-continuous arterial spin labelling and dynamic susceptibility contrast imaging. *Neuroradiology* 2010; **52**: 307-317 [PMID: 19841916 DOI: 10.1007/s00234-009-0616-6]
 - 16 Lukas L, Devos A, Suykens JA, Vanhamme L, Howe FA, Majós C, Moreno-Torres A, Van der Graaf M, Tate AR, Arús C, Van Huffel S. Brain tumor classification based on long echo proton MRS signals. *Artif Intell Med* 2004; **31**: 73-89 [PMID: 15182848 DOI: 10.1016/j.artmed.2004.01.001]
 - 17 Devos A, Lukas L, Suykens JA, Vanhamme L, Tate AR, Howe FA, Majós C, Moreno-Torres A, van der Graaf M, Arús C, Van Huffel S. Classification of brain tumours using short echo time 1H MR spectra. *J Magn Reson* 2004; **170**: 164-175 [PMID: 15324770 DOI: 10.1016/j.jmr.2004.06.010]
 - 18 Dimou I, Tsougos I, Tsolaki E, Kousi E, Kapsalaki E, Theodorou K, Kounelakis M, Zervakis M. Brain lesion classification using 3T MRS spectra and paired SVM kernels. *Biomed Signal Process Control* 2011; **6**: 314-320 [DOI: 10.1016/j.bspc.2011.01.001]
 - 19 Tsolaki E, Svolos P, Kousi E, Kapsalaki E, Fountas K, Theodorou K, Tsougos I. Automated differentiation of glioblastomas from intracranial metastases using 3T MR spectroscopic and perfusion data. *Int J Comput Assist Radiol Surg* 2013; **8**: 751-761 [PMID: 23334798 DOI: 10.1007/s11548-012-0808-0]
 - 20 Svolos P, Tsolaki E, Kapsalaki E, Theodorou K, Fountas K, Fezoulidis I, Tsougos I. Investigating brain tumor differentiation with diffusion and perfusion metrics at 3T MRI using pattern recognition techniques. *Magn Reson Imaging* 2013; **31**: 1567-1577 [PMID: 23906533 DOI: 10.1016/j.mri.2013.06.010]
 - 21 Davies NP, Wilson M, Harris LM, Natarajan K, Lateef S, Macpherson L, Sgouros S, Grundy RG, Arvanitis TN, Peet AC. Identification and characterisation of childhood cerebellar tumours by in vivo proton MRS. *NMR Biomed* 2008; **21**: 908-918 [PMID: 18613254 DOI: 10.1002/nbm.1283]
 - 22 Raschke F, Davies NP, Wilson M, Peet AC, Howe FA. Classification of single-voxel 1H spectra of childhood cerebellar tumors using LCModel and whole tissue representations. *Magn Reson Med* 2013; **70**: 1-6 [PMID: 22886824 DOI: 10.1002/mrm.24461]
 - 23 Lisboa PJ, Wong H, Harris P, Swindell R. A Bayesian neural network approach for modelling censored data with an application to prognosis after surgery for breast cancer. *Artif Intell Med* 2003; **28**: 1-25 [PMID: 12850311 DOI: 10.1016/S0933-3657(03)00033-2]
 - 24 van Bommel JH, Musen MA. Modeling for Decision Support. In: Handbook of Medical Informatics. Springer-Verlag, 1997
 - 25 Law M, Cha S, Knopp EA, Johnson G, Arnett J, Litt AW. High-grade gliomas and solitary metastases: differentiation by using perfusion and proton spectroscopic MR imaging. *Radiology* 2002; **222**: 715-721 [PMID: 11867790 DOI: 10.1148/radiol.2223010558]
 - 26 Kousi E, Tsougos I, Kapsalaki E. Proton Magnetic Resonance Spectroscopy of the Central Nervous System. In: Novel Frontiers of Advanced Neuroimaging. InTech, 2013: 19-50 [DOI: 10.5772/53892]
 - 27 De Edelenyi FS, Rubin C, Estève F, Grand S, Décorps M, Leffournier V, Le Bas JF, Rémy C. A new approach for analyzing proton magnetic resonance spectroscopic images of brain tumors: nosologic images. *Nat Med* 2000; **6**: 1287-1289 [PMID: 11062544 DOI: 10.1038/81401]
 - 28 McKnight TR, Noworolski SM, Vigneron DB, Nelson SJ. An automated technique for the quantitative assessment of 3D-MRSI data from patients with glioma. *J Magn Reson Imaging*

- 2001; **13**: 167-177 [PMID: 11169821 DOI: 10.1002/1522-2586(200102)13:2<167::AID-JMRI1026>3.0.CO;2-K]
- 29 **Simonetti AW**, Melssen WJ, van der Graaf M, Postma GJ, Heerschap A, Buydens LM. A chemometric approach for brain tumor classification using magnetic resonance imaging and spectroscopy. *Anal Chem* 2003; **75**: 5352-5361 [PMID: 14710812]
- 30 **De Vos M**, Laudadio T, Simonetti AW, Heerschap A, Van Huffel S. Fast nosologic imaging of the brain. *J Magn Reson* 2007; **184**: 292-301 [PMID: 17118683 DOI: 10.1016/j.jmr.2006.10.017]
- 31 **Laudadio T**, Martínez-Bisbal MC, Celda B, Van Huffel S. Fast nosological imaging using canonical correlation analysis of brain data obtained by two-dimensional turbo spectroscopic imaging. *NMR Biomed* 2008; **21**: 311-321 [PMID: 17907275 DOI: 10.1002/nbm.1190]
- 32 **Luts J**, Laudadio T, Idema AJ, Simonetti AW, Heerschap A, Vandermeulen D, Suykens JA, Van Huffel S. Nosologic imaging of the brain: segmentation and classification using MRI and MRSI. *NMR Biomed* 2009; **22**: 374-390 [PMID: 19105242 DOI: 10.1002/nbm.1347]
- 33 **Prastawa M**, Bullitt E, Ho S, Gerig G. A brain tumor segmentation framework based on outlier detection. *Med Image Anal* 2004; **8**: 275-283 [PMID: 15450222 DOI: 10.1016/j.media.2004.06.007]
- 34 **Li Y**, Sima DM, Van Cauter S, Himmelreich U, Croitor Sava AR, Pi Y, Liu Y, Van Huffel S. Unsupervised nosologic imaging for glioma diagnosis. *IEEE Trans Biomed Eng* 2013; **60**: 1760-1763 [PMID: 23192480 DOI: 10.1109/TBME.2012.2228651]
- 35 INTERPRET Consortium. Available from: URL: <http://azi-zu.uab.es/INTERPRET/>
- 36 **Tate AR**, Underwood J, Acosta DM, Julià-Sapé M, Majós C, Moreno-Torres A, Howe FA, van der Graaf M, Lefournier V, Murphy MM, Loosemore A, Ladroue C, Wesseling P, Luc Bosson J, Cabañas ME, Simonetti AW, Gajewicz W, Calvar J, Capdevila A, Wilkins PR, Bell BA, Rémy C, Heerschap A, Watson D, Griffiths JR, Arús C. Development of a decision support system for diagnosis and grading of brain tumours using in vivo magnetic resonance single voxel spectra. *NMR Biomed* 2006; **19**: 411-434 [PMID: 16763971 DOI: 10.1002/nbm.1016]
- 37 Single voxel DSS tutorial. Available from: URL: http://azi-zu.uab.es/INTERPRET/sv_tutorial/index.php#description
- 38 **Pérez-Ruiz A**, Julià-Sapé M, Mercadal G, Olier I, Majós C, Arús C. The INTERPRET Decision-Support System version 3.0 for evaluation of Magnetic Resonance Spectroscopy data from human brain tumours and other abnormal brain masses. *BMC Bioinformatics* 2010; **11**: 581 [PMID: 21114820 DOI: 10.1186/1471-2105-11-581]
- 39 Web accessible MR Decision Support System for Brain Tumour Diagnosis and Prognosis, Incorporating in vivo and ex vivo genomic and metabolic data. Available from: URL: <http://cordis.europa.eu/documents/documentlibrary/127824941EN19.doc>
- 40 **Arus C**, Celda B, Dasmahapatra S, Dupplaw D, Gonzalez-Velez H, Van Huffel S, Lewis P, Lluch i Ariet M, Mier M, Peet A, Robles M. On the Design of a Web-Based Decision Support System for Brain Tumour Diagnosis Using Distributed Agents. Hong Kong, 2006: 208-211 [DOI: 10.1109/WI-IATW.2006.97]
- 41 **García-Gómez JM**. Pattern Recognition Approaches for Biomedical Data in Computer-Assisted Cancer Research, PhD thesis, Universidad Politécnica de Valencia, Departamento de Sistemas Informáticos y Computación Inteligencia Artificial, Reconocimiento de Formas e Imagen Digital. 2009
- 42 **Gonzalez-Velez H**, Mier M, Julià-Sapé M, Garcia-Gomez TN, Robles JM, Peet A, Arus C, Celda B, Van Huffel S, Lewis P, Dupplaw D, Dasmahapatra S. HealthAgents: Distributed Multi-Agent Brain Tumor Diagnosis and Prognosis. *J Appl Intel* 2009; **30**: 191-202 [DOI: 10.1007/s10489-007-0085-8]
- 43 **Hu B**, Croitoru M, Roset R, Dupplaw D, Lurgi M, Dasmahapatra S, Lewis P, Martínez-Miranda J, Sáez C. The HealthAgents ontology: how to represent the knowledge behind a brain tumour distributed decision system. *Knowl Eng Rev* 2011; **26**: 303-328
- 44 **Sáez C**, García-Gómez JM, Vicente J, Tortajada S, Luts J, Dupplaw D, Van Huffel S, Robles M. A generic and extensible automatic classification framework applied to brain tumour diagnosis in HealthAgents. *Knowl Eng Rev* 2011; **26**: 283-301 [DOI: 10.1017/S0269888911000129]
- 45 **Sáez C**, García-Gómez JM, Vicente J, Tortajada S, Fuster E, Esparza M, Navarro A, Robles M. Curiam BT 1.0, Decision Support System for Brain Tumour Diagnosis. In ESMRMB Congress. Antalya, Turkey: EPOS Posters/Paper Posters/Info-RESO, 2009: 538
- 46 **Vicente J**. Clinical Decision Support Systems for Brain Tumour Diagnosis: Classification and Evaluation Approaches. Departamento de Física Aplicada - Departament de Física Aplicada, 2012
- 47 **Fellows GA**, Wright AJ, Sibtain NA, Rich P, Opstad KS, McIntyre DJ, Bell BA, Griffiths JR, Howe FA. Combined use of neuroradiology and 1H-MR spectroscopy may provide an intervention limiting diagnosis of glioblastoma multiforme. *J Magn Reson Imaging* 2010; **32**: 1038-1044 [PMID: 21031506 DOI: 10.1002/jmri.22350]
- 48 **Julià-Sapé M**, Coronel I, Majós C, Candiota AP, Serrallonga M, Cos M, Aguilera C, Acebes JJ, Griffiths JR, Arús C. Prospective diagnostic performance evaluation of single-voxel 1H MRS for typing and grading of brain tumours. *NMR Biomed* 2012; **25**: 661-673 [PMID: 21954036 DOI: 10.1002/nbm.1782]
- 49 **Celda B**, Cano JG, Martínez-Bisbal MC, Martínez-Granados B. Clinical evaluation of a fully automated Computer Aid Decision System (CADS) for brain tumour supported diagnosis. eTUMOUR project FP6-2002-LSH-503094. In Joint Annual Meeting ISMRM-ESMRMB; May 1-7, Stockholm, Sweden, 2010
- 50 **Celda B**, Monleon D, Pla P, Gil-Cano J, Martínez-Granados B, Molla E, Revert A, Mart-Bonmati L, Leon J. Computer Aid Decision System (CADS) of eTUMOUR. Initial results of clinical evaluation for brain tumour classification In ESMRMB Congress, October 1-3, Antalya, Turkey, 2009
- 51 **Sáez C**, García-Gómez JM, Alberich-Bayarri Á, Edo MÁ., Vanyó M, Català-Gregori A, Barber C, Poyatos C, Mollà E, Martí-Bonmatí L, Robles M. Clinical Validation of the Added Value of a Clinical Decision Support System for Brain Tumour Diagnosis-Based on SV 1H MRS: Randomized Controlled Trial of Effectiveness and Qualitative Evaluation. Proceedings of 24th European Medical Informatics (MIE) Conference; 2012, August 26-29; Pisa-Italy: Quality of Life through Quality of Information
- 52 **Bryan C**, Boren SA. The use and effectiveness of electronic clinical decision support tools in the ambulatory/primary care setting: a systematic review of the literature. *Inform Prim Care* 2008; **16**: 79-91 [PMID: 18713524]
- 53 **Tortajada S**, Fuster-Garcia E, Vicente J, Wesseling P, Howe FA, Julià-Sapé M, Candiota AP, Monleón D, Moreno-Torres A, Pujol J, Griffiths JR, Wright A, Peet AC, Martínez-Bisbal MC, Celda B, Arús C, Robles M, García-Gómez JM. Incremental Gaussian Discriminant Analysis based on Graybill and Deal weighted combination of estimators for brain tumour diagnosis. *J Biomed Inform* 2011; **44**: 677-687 [PMID: 21377545 DOI: 10.1016/j.jbi.2011.02.009]
- 54 **Chernov MF**, Kubo O, Hayashi M, Izawa M, Maruyama T, Usukura M, Ono Y, Hori T, Takakura K. Proton MRS of the peritumoral brain. *J Neurol Sci* 2005; **228**: 137-142 [PMID: 15694194 DOI: 10.1016/j.jns.2004.11.039]
- 55 **Fan G**, Sun B, Wu Z, Guo Q, Guo Y. In vivo single-voxel proton MR spectroscopy in the differentiation of high-grade gliomas and solitary metastases. *Clin Radiol* 2004; **59**: 77-85

- [PMID: 14697379 DOI: 10.1016/j.crad.2003.08.006]
- 56 **Di Costanzo A**, Scarabino T, Trojsi F, Popolizio T, Catapano D, Giannatempo GM, Bonavita S, Portaluri M, Tosetti M, d' Angelo VA, Salvolini U, Tedeschi G. Proton MR spectroscopy of cerebral gliomas at 3 T: spatial heterogeneity, and tumour grade and extent. *Eur Radiol* 2008; **18**: 1727-1735 [PMID: 18389246 DOI: 10.1007/s00330-008-0938-5]
- 57 **Zonari P**, Baraldi P, Crisi G. Multimodal MRI in the characterization of glial neoplasms: the combined role of single-voxel MR spectroscopy, diffusion imaging and echo-planar perfusion imaging. *Neuroradiology* 2007; **49**: 795-803 [PMID: 17619871 DOI: 10.1007/s00234-007-0253-x]
- 58 Magnetic Resonance User Interface (MRUI). Available from: URL: <http://sermn02.uab.es/mrui/>

P- Reviewers: Lichtor T, Schoenhagen P, Triantopoulou C
S- Editor: Gou SX **L- Editor:** Cant MR **E- Editor:** Liu SQ



FMRI contributions to addressing autobiographical memory impairment in temporal lobe pathology

Ekaterina J Denkova, Liliann Manning

Ekaterina J Denkova, Liliann Manning, Department of Psychology, University of Strasbourg, 67000 Strasbourg, France
Liliann Manning, Cognitive Neuropsychology and Physiopathology of Schizophrenia, INSERM U1114, 67000 Strasbourg, France

Author contributions: Denkova EJ and Manning L contributed to this review equally.

Correspondence to: Dr. Ekaterina J Denkova, Department of Psychology, University of Strasbourg, 12 rue Goethe, 67000 Strasbourg, France. ekaterina.denkova@yahoo.ca

Telephone: +33-3-68851927 Fax: +33-3-68851947

Received: December 17, 2013 Revised: February 20, 2014

Accepted: March 13, 2014

Published online: March 28, 2015

Abstract

Episodic autobiographical memory (AM) allows one, through the recollection of sensory-perceptual details, thoughts and feelings, to become aware of an event as belonging to one's own past as well as being able to project into one's future. Because AM provides a sense of self-continuity, contributes to the integrity of the self, and helps predicting future experiences, any deficit of AM may have debilitating consequences for everyday life functioning. Understanding AM failure and the underlying neural mechanisms has the potential to shed light on brain reorganization mechanisms and engagement of compensatory processes. Functional magnetic resonance imaging (fMRI) provides the most promising imaging method to tackle these issues. We reviewed evidence from the few studies that used fMRI to investigate the functionality of the residual tissue, the neural reorganization and compensatory mechanisms in patients with neurological conditions due to impaired medial temporal lobe. Overall, these studies highlight the importance of the left hippocampus, which when atrophied and not functional leads to AM deficits but its residual functionality may support relatively normal AM recollection. When damaged hippocampal tissue is not

functional, other brain regions (*e.g.*, the medial prefrontal cortex) may be involved to compensate impairment, but they appear generally ineffective to support detailed episodic recollection.

© 2015 Baishideng Publishing Group Inc. All rights reserved.

Key words: Functional magnetic resonance imaging; Autobiographical memory; Amnesia; Medial temporal lobe; Memory deficit; Reorganization

Core tip: Functional magnetic resonance imaging investigations of patients with impaired autobiographical memory (AM) can greatly contribute to further our understanding of brain reorganization mechanisms and engagement of compensatory processes after damage to the medial temporal lobe. These investigations are reviewed here. Overall, they highlight the importance of the left hippocampus, which when atrophied and not functional leads to deficits in AM but its residual functionality may support relatively normal AM recollection. When damaged hippocampal tissue is not functional, other brain regions (*e.g.*, the medial prefrontal cortex) may be involved to compensate impairment, but they appear generally ineffective to support detailed recollection.

Original sources: Denkova EJ, Manning L. FMRI contributions to addressing autobiographical memory impairment in temporal lobe pathology. *World J Radiol* 2014; 6(4): 93-105 Available from: URL: <http://www.wjgnet.com/1949-8470/full/v6/i4/93.htm> DOI: <http://dx.doi.org/10.4329/wjr.v6.i4.93>

INTRODUCTION

Remembering autobiographical memories (AM) involves recollection of contextual information (time and place)

and sensory-perceptual and affective details of personal experiences with a sense of self-awareness^[1-3]. AM, not surprisingly, contributes to both one's sense of personal identity (who we are) and sense of self-continuity. Over the last two decades, there has been a growing interest in understanding the neural correlates of normal AM and, more recently, impaired AM. The reasons of the remarkable increase in the number of studies in this topic is, very likely, the mentioned AM contribution to the construction of the sense of self across time, but also the important social role AM plays in the development of new relationships and the nurturing of existing ones, and most particularly, its role as a directive function, where the past serves as a basis for guiding present and future behaviors^[4,5]. In the context of the broader issue under consideration in this special topic [with focus on functional magnetic resonance imaging (fMRI)], the present review aims to discuss emerging research that highlights the usefulness of fMRI in the examination of AM in patients with damage to the core memory structures in the medial temporal lobe (MTL). The emphasis of this review is, therefore, on fMRI investigations of AM impairment due to neurological conditions affecting the MTL. The decision to focus on the MTL is driven by evidence that MTL plays a pivotal role in normal AM functioning and its damage typically leads to amnesia for past events^[6-9] (but see also^[10]) and that fMRI examinations of AM in neurological patients, which to date are limited in number, have been more often reported in the case of patients with damage to the MTL. The underlying question we would like to tackle is to what extent these investigations shed light on the functionality of the residual tissue, the neural reorganization and compensatory mechanisms (either efficient or not) in the case of damage to the MTL. Before discussing the fMRI studies of AM in patients with MTL damage, we introduce AM and summarize the highlights of neuroimaging evidence in healthy participants to provide the context to discuss functional neuroimaging findings in pathology.

THEORETICAL CONSIDERATIONS OF AM

Episodic AM allows one to become aware of an event as belonging to one's own past as well as being able to project into one's future. This sense of self-continuity across time^[2,3,11] is grounded in the recollection of sensory-perceptual details, thoughts and feelings. Typically, episodic memory has been distinguished from semantic memory, which refers to general knowledge, knowledge about public facts and people, as well as personal knowledge (*e.g.*, date of birth, the name of our parents and friends). However, these systems are highly interdependent^[12] in relation to the self. Turning back to episodic AM, some authors consider that it is a uniquely human system^[13] (but see^[14] for a different standpoint). Moreover, Tulving's Serial Parallel Independent model places this memory system at the apex of a pyramid, which implies the highest memory achievement in evolution^[15]. Tulving *et al.*^[2] defined AM as consisting of three major constructs:

sense of self, auto-noetic consciousness and subjectively sensed time. But even more closely related to the self, is Conway's Self Memory System^[11,12]. Very briefly, Conway views episodic memories and conceptual autobiographical knowledge as discrete systems that both operate with the "working self" in a bidirectional manner. The working self is conceived as a mechanism that controls access to memories according to the individual's present goals. Importantly, the working self is constrained by the memories and knowledge within the autobiographical knowledge base.

Recently, some studies show that the contribution of AM to the sense of self is not crucial. Klein^[16,17] and Klein *et al.*^[18] presented a series of patients both studied by him and reported in the literature, who have lost the entire fund of episodic memory and who are unable to simulate future personal events, but retain the sense of self. However, a distinction is made between the sense of self, which is preserved in amnesic patients^[19] and the sense of self-continuity across time, which depends on AM (Klein SB, personal communication to LM, December, 2013).

Importantly, recollection of past personal experience is considered to be a reconstructive process with memories recreated from their constituent elements. Particularly, autobiographical memories are not static records of the past; rather they are considered as mental reconstructions, which are constrained by two simultaneous, even contradictory, demands: correspondence with the real event and coherence, as time goes by, with the individual's self-image. More precisely, memory reconstruction must reflect reality by providing sensory-perceptive and eventually affective details that represent, as closely as possible, the experience and also be in accordance with the rememberer's current self-image and goals^[12]. By making available memories that match current self-beliefs and goals, the main function of AM would be to maintain the integrity of the self^[12].

Bearing in mind that AM provides a sense of self-continuity, contributes to the integrity of the self, and helps predicting future experiences, it is not surprising that AM impairment may have debilitating consequences for everyday life functioning. Consequently, understanding AM failure and the underlying neural mechanisms has the potential not only to strengthen the progress of memory research, but importantly, to shed light on brain reorganization mechanisms and eventually to help in planning treatment and in monitoring the effects of therapeutical interventions with the final aim to achieve better management of patients with AM deficits.

FMRI EXAMINATION OF NORMAL AM FUNCTIONING

The advent of fMRI made the examination *in vivo* of different human abilities, in general, possible. More particularly, fMRI (in contrast to earlier neuroimaging techniques, such as positron emission tomography) provides

the most promising new imaging method and offers a number of important advantages in the study of neural correlates of human memory. Among the main fMRI strengths are the improved spatial resolution, the fast speed of data acquisition which allows more flexible experimental designs and the unrestricted number of observations due to the absence of radiation exposure. Moreover, in the last decade, fMRI has undergone a rapid development and provided new ways to design experiments (*e.g.*, event-related, self-paced designs) and to analyze data (*e.g.*, independent component analysis, spatiotemporal partial least squares analysis, psychophysiological interactions analysis, dynamic causal modelling, multi-voxel pattern analysis) allowing segregation of the time-course of memory retrieval processes, examination of the connectivity among brain regions and investigation of memory representation in specific brain regions. This continuous progress has led to improved and refined testing of hypotheses about the neural correlates of both normal and impaired AM.

Evidence from fMRI studies in healthy participants allowed the establishing of a brain network of AM retrieval comprising the MTL, prefrontal cortex (PFC) and posterior cortices^[20,22]. Despite the proliferation of functional neuroimaging studies of AM over the last 10-15 years, many of the critical issues (*e.g.*, MTL involvement according to the remoteness of memories, lateralization of the AM networks) continue to be debated, leading nevertheless to greater refinement of the theories derived from the lesion research. For instance, there is a debate regarding the involvement of MTL, especially the hippocampus, in retrieval of personal events according to the age of memories. This debate originated from the lesion studies and is reflected in fMRI studies in healthy subjects. On the one hand, the Standard Consolidation Theory states that memories (without making a distinction between episodic and semantic memories) are initially dependant on the MTL but over time, they undergo consolidation in the neocortical structures and eventually become independent of the MTL^[23]. On the other hand, the Multiple Trace Theory postulates a life-long involvement of the MTL for retrieval of episodic and context-specific memories^[6,24]. Recently, the latter has been updated to explicitly include a transformation account of memory, which considers the dynamic nature of memories and suggests that episodic memories may transform to semantic or gist-like versions represented in neocortical areas outside of the hippocampus, but those that continue to contain rich episodic/contextual details remain dependant on the hippocampus^[25,26].

MTL

Neuroimaging evidence suggests that the MTL is a crucial node in the AM retrieval network^[21,27] involved in binding together the multimodal representations of an episode. Specifically, studies directly comparing autobiographical to semantic memory retrieval revealed greater engagement of the MTL, particularly on the left side^[28-30].

Of note, MTL activation observed by some semantic memory studies involving famous people recognition^[31,32] could be explained by the association of this semantic information with autobiographical memories^[33], as suggested by lesion research^[34,35]. As for the MTL's involvement according to age of memories, an increasing number of fMRI studies provided evidence that, when phenomenological qualities and especially vividness are considered, MTL activations are observed for retrieval of rich and vivid and both recent and remote autobiographical memories^[36-41], which resonates with the Multiple Trace Theory positing long-life involvement of MTL for vivid context-specific recollections.

Prefrontal cortex

Available evidence also highlights the role of different PFC sub-regions in AM retrieval^[22,27]. Specifically, among the PFC sub-regions, the ventrolateral PFC and the medial PFC appear to be systematically linked to retrieval of personal events^[27,38].

Lateral PFC: Systematic activation of the ventrolateral PFC during recollection of autobiographical memories is associated with successful memory retrieval, involving initial strategic search and selection of appropriate information^[27,42,43]. Specifically, activity in the lateral PFC has been observed early during retrieval^[28,29,44], supporting therefore its role in strategic search operations and initial recovery processes consistent with current models of AM^[1] that emphasize the reconstructive retrieval of memories. Additionally, the more ventral (orbital) portion of the lateral PFC, part of the frontotemporal junction interconnected through the ventral branch of the uncinate fascicle, has been attributed a crucial role in ephory (triggering) of memory retrieval^[45,46] and synchronisation of emotional and factual components of the personal memories during conscious self re-experiencing^[47-49]. The latter is also supported by recent evidence suggesting the involvement of parts of the ventrolateral PFC in enhanced re-experiencing of emotional autobiographical memories^[50].

Medial PFC: Activation of the medial PFC is also systematically reported during recollection of autobiographical memories^[27] and linked to the role of medial PFC in self-referential processes^[51], of which AM is an essential part. Indeed, there is evidence that increased activity in medial PFC distinguished real life AM from laboratory-based episodic memory imaging studies^[38,52,53] and its more ventral portions are associated with real self-relevant events^[54] and self-perspective^[55]. Recently, ventromedial PFC has been found to contain more information about remote memories (although both recent and remote memories are represented there^[37]). It should be noted that overall in the neuroimaging research, the medial PFC is linked to a variety of functions^[56], such as self-referential^[51] and emotional^[57] processing, mentalizing^[58,59], intuitive assessment of "felt rightness"^[60] as well as in some regulatory

mechanisms^[61]. Therefore, it can be suggested that medial PFC might in general be supporting processes related to self-awareness and self-regulation.

Posterior cortices

Retrieval of autobiographical memories in healthy participants also leads to activations in the posterior cortices (*e.g.*, precuneus, visual cortices), which are considered to support the multimodal and visual representations associated with the event and visual imagery (and visualized re-experiencing)^[20,62]. Specifically, fMRI studies provided evidence that posterior cortices are later involved during (re)construction of autobiographical memories^[28,29] to support the retrieval of specific details. For instance, precuneus because of its role in egocentric (view-dependant, relative to the observer) representation of a place, has been thought critical for autothetic awareness in remembering events from a first person perspective^[63]. This is by comparison to MTL, which is involved in allocentric (view-independent) representations^[64], but only those that are rich instead of schematic^[7].

In summary, fMRI investigations of AM in normal conditions have been very informative in establishing what is called the typical AM brain network, which can be used as a framework for investigation and better understanding of neural correlates of AM impairment.

FMRI INVESTIGATION OF AM IMPAIRMENT IN PATHOLOGIES AFFECTING MTL

Over the past decade, the rapid development of functional neuroimaging techniques and experimental designs (more flexible event-related, self-paced designs, shortened repetition times, new analyzing tools) has made the use of functional neuroimaging protocols in patients possible, which, besides clinical issues, advances our understanding of the neural networks of memory^[65,66] and its reorganization in case of damage. The use of functional neuroimaging techniques in brain damaged patients can help to better understand not only how damage alters the neural network supporting AM retrieval, but also potential reorganization of this network through compensatory mechanisms (efficient or not) solicited to cope with memory impairment. It is important to note, however, that the combined use of neuropsychological and neuroimaging methods has advantages over the use of either approach alone^[65,66]. The purpose of the review is not to provide an exhaustive literature review of memory impairment due to brain damage and its assessment with neuroimaging in general (for more general reviews on human memory disorders and the application of neuroimaging, we refer the readers to^[65,67,68]). Rather the aim is to present and discuss examples of studies that have used fMRI in particular (as the most advanced neuroimaging method and targeted by the scope of the present special topic) to investigate AM impairment in patients with

damage to the MTL regions, because of their critical importance for retrieval of specific autobiographical events as highlighted by functional neuroimaging research in normal subjects and lesion research (although the latter still continues to debate the long-life involvement of the hippocampus). Therefore, we will discuss studies that use fMRI protocols to investigate AM in patients with different neurological conditions affecting the MTL and hence, shed light on the functionality of damaged MTL and the potential reorganization of the AM network. We selected the studies based on that they examine AM through fMRI in pathologies with overt damage to the MTL (Table 1). The neurological conditions presented below differ in terms of the age at which they occur, their focal or diffuse nature, and progression.

Developmental amnesia

Developmental amnesia is a memory disorder associated with selective hippocampal damage resulting from hypoxic/ischemic episodes that occur perinatally or early in childhood^[69]. Typically, developmental amnesia is characterized by severely impaired episodic AM and relatively preserved semantic memory^[70,71], which makes it possible to investigate developmental deficits selectively and to shed light on the neural reorganisation of the AM network due to early life damage. In fact, among the first neuroimaging studies of AM in amnesic patients is the study carried out by Maguire *et al.*^[72], who used fMRI in the case of a developmental amnesic patient, Jon (initially reported by Vargha-Khadem *et al.*^[71]). Jon presented with impaired AM (but he was able to recall some personal memories) and had a relatively preserved semantic memory^[72]. Jon showed a similar pattern of brain activations to control subjects during memory retrieval but the activations and the interactions among them were different from those observed in controls. Of particular interest, Jon's retrieval of autobiographical events was associated with increased bilateral activity of the hippocampus, in spite of the 50% volume loss bilaterally. Moreover, hippocampus and medial PFC were significantly more activated during retrieval of events for which Jon had clear and conscious recollection (autothetic consciousness) compared to those he knew but could not remember experiencing. Overall, the findings suggest that the residual hippocampal tissue was functional and contributed to retrieval of the few preserved autobiographical "islands". Moreover, they point out the crucial role of autothetic awareness during AM retrieval mediated, very likely, by the medial PFC. Therefore, these findings provide insights to mechanisms of brain plasticity^[73].

Hypoxia (in adulthood)

Deprivation of oxygen supply (hypoxia) in adulthood also leads to damage to the MTL, specifically the hippocampus, and severe deficit in memory of past events^[74-76]. By comparison to patients with developmental amnesia, patients with hypoxic MTL damage in adulthood showed a much more severe pattern of memory impairment. In

Table 1 Summaries of functional magnetic resonance imaging studies investigating autobiographical memory in patients with medial temporal lobe damage

Ref.	Pathology	Patients	Lesion side	Remote memory profile	Compensatory Activations
Addis <i>et al</i> ^[97]	Temporal lobe epilepsy	11 patients	Left	Mild impairment episodic AM Relative preservation semantic AM	mPFC, posterior medial structures mPFC-PHG connectivity
Berry <i>et al</i> ^[124]	Limbic encephalitis	Single-case, Mrs B	Bilateral	Impaired AM (recent events)	Left vLPFC, posterior cortices
Maguire <i>et al</i> ^[72]	Developmental amnesia	Single-case, patient Jon	Bilateral	Impaired AM (few preserved events) relatively normal semantic memory	Functional residual hippocampi mPFC
Maguire <i>et al</i> ^[77]	Hypoxia in late age	Single-case, patient VC	Bilateral	Severe impairment AM	Lateral temporal areas (for personal facts)
Maguire <i>et al</i> ^[110]	Semantic dementia	Single-case, patient AM	Initially left later bilateral	Initially relatively intact AM followed by gradual deterioration	Year 1: Initially functional right and residual left hippocampi, Year2: mPFC, vLPFC, precuneus, Year 3: few occipito-temporal areas
Manning <i>et al</i> ^[98]	Temporal lobe epilepsy	Single-case, patient JR	Left	Preserved AM, impaired public memory	Contro-lesional right MTL, mPFC, posterior cortices
Meulenbroek <i>et al</i> ^[113]	Alzheimer's disease	21 patients	Bilateral	Episodic-to-semantic shift	mPFC, left vLPFC, posterior cortices
Viard <i>et al</i> ^[111]	Semantic dementia	Patients JPL and EP	JPL: bilateral EP: bilateral but sparing hippocampi	JPL: impaired AM EP: initially relatively preserved AM	JPL: right hippocampus, vLPFC, occipital areas EP: both hippocampi

AM: Autobiographical memory; mPFC: Medial prefrontal cortex; vLPFC: Vento-lateral prefrontal cortex; MTL: Medial temporal lobe; PHG: Parahippocampal gyrus.

an fMRI examination, Maguire *et al*^[77] investigated memory in a patient, VC (initially reported by Cipolotti *et al*^[75]), who had MTL damage due to hypoxia in late adulthood. Given that VC did not have reliable memory of personal past events to be investigated in a functional neuroimaging procedure^[78,79], only his memory for personal facts and general knowledge were examined. In the context of broadly comparable to control subjects' memory network, VC exhibited increased activity in lateral temporal regions compared to controls and did not show any activity in the residual hippocampi, while hippocampal activations were revealed in controls as well as in developmental amnesic patient Jon for personal facts. These findings suggest that in the case of hypoxic MTL damage in adulthood, deficits of AM are much more severe and could be due to the absence of residual functionality in lesioned hippocampi. Overall, combined together findings from developmental and adult-acquired amnesia due to hypoxia point to the importance of age at which damage occurs, which is of great importance for reorganization and compensatory brain mechanisms. This issue clearly needs further investigation by systematic fMRI examination of patients with damage occurring at different periods of life.

Temporal lobe epilepsy

Temporal lobe epilepsy (TLE) is a chronic neurological condition characterized by partial epileptic seizures originating in the temporal lobe, accompanied usually by hippocampus sclerosis^[80] and associated with memory deficit^[81]. Overall, memory for the past has been much less investigated than anterograde memory (*i.e.*, acquisition of

new information) in patients with TLE. However, in the last decade an increasing number of studies also explored remote memory in TLE patients^[82-88]. They revealed that TLE affects remote memory, particularly AM, with left TLE leading to severe AM deficit. Similarly to clinical neuropsychological studies, the majority of the functional neuroimaging studies focused on testing anterograde memory^[89,90] and on pre-surgical evaluation to predict post-surgical memory changes^[91-96], while only a handful of functional neuroimaging studies examined the neural correlates of AM in patients with TLE^[97,98] (see also^[99] for patients with transient epileptic amnesia). The studies by Manning *et al*^[98] and Addis *et al*^[97] presented left TLE patients with different AM profiles, which illustrates the fact that the same disease can lead to different patterns of memory performance and brain reorganization.

In a single-case report, Manning *et al*^[98] investigated the interaction between AM and semantic memory in a patient, JR (initially reported by Manning *et al*^[100]), who underwent surgical resection of the left MTL for treatment of long-standing TLE with teenage onset of seizures. JR presented a very rare pattern of remote memory dissociation, such as preserved AM and selectively impaired semantic memory for public events and famous people. During retrieval of autobiographical episodes associated with famous people, JR showed increased activations in the intact right MTL (parahippocampal gyrus), several posterior cortices (posterior cingulate cortex, precuneus, temporo-occipital junction) and medial PFC. These findings suggest that contralesional right MTL may be sufficient to adaptively take charge of AM in case of left MTL damage according to the age at which epilepsy

occurred and the developmental course of AM ability, which typically emerges gradually across the preschool years.

Addis *et al.*^[97] investigated the AM cerebral network in a group of patients with left TLE with significant left hippocampal atrophy and mild AM impairment (reflected in reduction of the episodic details of memories). The authors found that in the absence of significant activation and connections of the residual left hippocampal tissue, retrieval of personal memories in left TLE patients was associated with increased activations in the posterior cortices, including posterior cingulate/retrosplenial and precuneus, right hippocampus (albeit sub-threshold) as well as strong direct connections between the left medial posterior cortices (posterior cingulate/retrosplenial) and left medial PFC, and between left parahippocampal gyrus and left medial PFC. These findings suggest that the AM impairment in left TLE could be due to reduced engagement and connections of the lesioned left hippocampus, compensated to some degree by pathways involving medial PFC and medial posterior cortices, which were insufficient to support detailed episodic-specific recollections.

Overall, the above-mentioned studies provided complementary evidence that depending on the onset of the epilepsy, damage to the left hippocampus can differently affect AM and a different pattern of reorganization of the AM network can be observed, despite several apparent differences between the two studies (single case *vs* group study, after *vs* before surgical treatment). Specifically, in a case of late childhood/teenage occurring epilepsy, right MTL could be sufficient to successfully mediate AM. Otherwise, regions outside MTL could be solicited to compensate left MTL damage, such as medial PFC and medial posterior cortices, which support residual AM (less detailed memories) but appear inefficient to maintain an overall normal level of detailed, episodic-specific AM recollections.

Neurodegenerative diseases

Neurodegenerative diseases are neurological conditions characterized by progressive degeneration and/or death of neuronal cells. Of particular interest in the study of memory are semantic dementia, a form of fronto-temporal dementia, and Alzheimer's disease since both involve neurodegenerative processes in the temporal lobes^[101,102]. Usually in the memory literature, semantic dementia and Alzheimer's disease present a dissociable neuropsychological memory profile at an initial stage of the disease^[103,104]. While semantic dementia is characterized by a profound and amodal loss of semantic memory in the context of relatively preserved episodic AM^[105-107], Alzheimer's disease is typically characterized by severe impairment of episodic AM in the context of relative sparing of semantic memory^[108,109]. Despite the interesting dissociation within remote memory observed in these two neurodegenerative diseases, there are only a handful of fMRI studies examining AM in patients with semantic dementia and Alzheimer's disease.

Semantic dementia: Only two studies, to our knowledge to date, have investigated the neural correlates of AM in semantic dementia using fMRI^[110,111], one of them presenting a longitudinal fMRI follow-up of a semantic dementia patient^[110]. The fMRI studies provided evidence of efficient and inefficient compensatory mechanisms, which led to relative initial maintenance of normal level of AM performance and to impaired, namely lacking episodic-specificity AM, performance, respectively.

In a single-case report, Maguire *et al.*^[110] used fMRI to investigate neural correlates of AM in a semantic dementia patient, AM, as a function of the progression of the dementia at three separate occasions (years 1, 2 and 3). Initially, the patient showed relatively normal AM scores, but with the progression of the disease his AM gradually deteriorated. To begin with, the patient had volume loss in the left hippocampus and left anterior lateral temporal cortex. However, at year 3, the atrophy encompassed the temporal lobes bilaterally, including both hippocampi. As for changes through time of the AM retrieval network, initially at year 1, the patient exhibited increased activations in regions of the consensual AM network, including the intact right hippocampus, and importantly increased activation of the remnant left hippocampus, which was not further observed during the following fMRI examinations (years 2 and 3). Moreover, at year 2, the patient showed increased activations of ventromedial PFC and precuneus, among other brain regions, to finally end up at year 3 with disengagement of the AM network, except for the occipitotemporal cortices. These findings reveal how the progression of dementia and MTL atrophy could affect AM retrieval and the associated neural correlates. Initially, despite the volume loss in the left hippocampus, the residual hippocampal tissue was still functional and therefore could support relatively preserved recollection of personal events. Over the course of the dementia process, the hippocampus became inactive and it seemed to be compensated by increased activity in the medial PFC and precuneus, which, with the progression of the dementia, appeared in turn to become non-operational.

Viard *et al.*^[111] used fMRI to investigate AM according to the remoteness of memories in two semantic dementia patients, JPL and EP, with different patterns of hippocampal atrophy and AM profiles. While JPL presented with impaired AM recollections (reflected in reduction of specific episodic details) and severe atrophy of both hippocampi, EP presented with initially preserved AM recollections with greater reliance on visual imagery than healthy controls and relative preservation of both hippocampi, despite atrophy in adjacent temporal cortices. In terms of brain activations and interactions, while JPL exhibited less activity in the left anterior hippocampus (remote memories) and increased activity in the right posterior hippocampus, functionally connected with the posterior occipital cortices, EP exhibited increased activity in both left and right anterior hippocampi (for both recent and remote memories), which were functionally connected to each other. These findings suggest that

atrophy together with absence of functionality in the residual hippocampal tissue might explain impaired AM, suggesting that activation in right posterior hippocampus and interactions with occipital cortices may have been recruited to compensate left hippocampal deficit, but that this compensatory mechanism was insufficient to support a normal level of rich episodic-specific recollections.

Overall, evidence from fMRI studies of AM in semantic dementia patients highlights the importance of the left hippocampus in retrieval of vivid and specific autobiographical memories, which when atrophied and not functional leads to impaired AM. In the case of late age and progressive damage of MTL, initial functionality of the remnant left hippocampus, rather than the right hippocampus, could support a relatively normal level of AM performance at an early stage of the disease. Subsequent increased engagement of medial PFC and precuneus could be seen as a compensatory mechanism reflecting attempts to maintain AM, although it had gradually declined. It could be also speculated that precuneus involvement could reflect retrieval processes that are based on a more egocentric representation and greater reliance on a self-referential perspective during recollection.

Alzheimer's disease: Episodic to semantic shift is usually reported in patients with Alzheimer's disease and deficit in episodic AM recollection is the hallmark of the disease, even being detected at the very preliminary stage of the disease, known as amnesic mild cognitive impairment^[112]. The pattern of "semantization" of episodic AM has been observed in a group of 21 patients diagnosed with early stage, probable Alzheimer's disease who were examined using fMRI^[113]. Specifically, these patients presented with a decline in episodic recollection of personal experiences, which contained more semantic and repetitive information and also atrophy in both hippocampi. At the level of brain activations, patients with Alzheimer's disease showed increased activity in ventromedial PFC, left ventrolateral PFC and posterior cortices (lingual gyrus and precuneus). Moreover, increased activity in ventromedial and ventrolateral PFC was linked to decreased volume in the hippocampus. These findings suggest that increased engagement of ventromedial and ventrolateral PFC could reflect a compensatory mechanism supporting retrieval of less detailed and more "semantized" autobiographical memories (*i.e.*, episodic-to-semantic shift in the quality of recollection), very likely relying on some kind of self-involvement.

Encephalitis

Encephalitis is a neurological condition characterized by an acute inflammation of the brain, generally caused by a virus or autoimmunity (*e.g.*, herpes encephalitis, limbic encephalitis). There is usually extensive damage to the temporal lobes, including the medial temporal regions^[114-116] and extending to the PFC^[117,118], although not necessarily^[119], and a severe memory impairment^[114]. More specifically, neuropsychological research provides evidence

of retrograde amnesia, particularly for autobiographical events^[116,120-123]. Despite evidence that encephalitis severely affects retrograde memory, especially AM, and may lead to interesting dissociations in relation to the side of damage^[120], fMRI investigations of AM in encephalitic patients are very rare^[124]. In a single-case fMRI study, Berry *et al.*^[124] examined the neural correlates underlying "rehearsed" (reviewed) personal episodes in a woman, Mrs B, diagnosed with limbic encephalitis five years before the neuroimaging investigation and presenting with impaired memory for autobiographical events. The patient used a wearable camera, SenseCam (Microsoft Research, Cambridge) to recode images during personal events, and then reviewed the images approximately every two days during three weeks. During scanning, Mrs B viewed rehearsed SenseCam images, together with never reviewed and new images as well as events recorded in a written diary and also rehearsed every two days during three weeks. At the behavioral level, the patient showed better performance for "rehearsed" SenseCam images, which at the neural level was associated with increased activity in the left ventrolateral PFC, lateral temporal, parietal and occipital regions in the absence of MTL activations. This study suggests a potentially effective way of alleviating AM deficit with a rehearsal-based training using visual material and supported by frontal and posterior activations, which very likely reflects a more general recognition of the event rather than detailed specific recollection, especially given that during scanning, events were not remembered in detail but just recognized (as known or familiar). Further investigation involving detailed recollection of personal events would help better understand the effects of training procedures on AM brain network.

Summary

Altogether, the above-presented fMRI studies in patients with MTL damage highlight the importance of the left hippocampus, which when atrophied and not functional leads to deficits in AM. Available fMRI evidence suggests that atrophy in the left hippocampus does not necessarily lead to alteration in its activation pattern and to severe AM impairment; namely, residual functionality in the damaged hippocampus may underpin relatively normal AM recollection. When residual hippocampal tissue is not functional, other brain mechanisms come into play to compensate its silence. In some cases, engagement of contralesional MTL structures could be sufficient to support AM, but very likely only in some circumstances, dependent on the age at which damage occurred. In other cases, PFC, more often medial PFC, and posterior cortices could support compensatory processes engaged to deal with the AM deficit, but not necessarily always efficient to support rich and detailed recollections (Table 1). Given the evidence that medial PFC has been associated with processes related to the self^[51] and contains more information for remote memories^[37] in healthy subjects, it could be speculated that involvement of medial PFC in case of damage could reflect retrieval of more stable

gist-like aspects containing less episodic details of the memories (rather than true detailed episodic-specific recollection supported by hippocampus) accompanied by the overall sense of self-involvement.

CONCLUSION

Overall, the present review of fMRI studies in patients with AM impairment due to damage in MTL core memory structures summarizes the importance of fMRI data in providing insights on how brain damage affects the neural network supporting retrieval of autobiographical memories and how the brain appears to cope with damage by engaging compensatory mechanisms, which can either be efficient or not, so to mediate AM recollection. fMRI may supply additional information over that provided by neuropsychological assessment and structural MRI and combining them together during examination of brain damaged patients would lead to a better and more reliable understanding of memory disorders and the underlying brain activations pattern and, ultimately, better management of the patients. The studies discussed in the present review, presenting different pathological entities affecting MTL and associated with different patterns of AM loss, provide relevant theoretical and clinical information that can guide future functional neuroimaging research of memory impairment. Although the present review focused on the use of fMRI in patients with MTL damage, for completeness, it should be noted that fMRI has started to be used in other pathologies characterized by AM impairment, some of which we briefly enumerate below.

Traumatic brain injury

Traumatic brain injury (TBI) has usually been associated with impaired AM^[125-127] together with diffuse axonal injury mainly affecting the connection between frontal and temporal regions^[126,128]. Given the diffuse nature of damage, TBI presents a challenge in understanding impairment of AM, which might be linked to a more general deficit in executive functions and alteration of the sense of self. A recent single-case fMRI investigation^[129] of a TBI patient, ML (initially reported by Levine *et al.*^[125]), revealed decreased involvement of the medial prefrontal and posterior cortices for recently encoded personal events, of which retrieval is lacking specificity and auto-noetic awareness^[125]. This finding underscores the link between auto-noetic awareness and medial PFC, which could be involved as a compensatory mechanism only when auto-noetic awareness is relatively preserved.

Psychogenic amnesia

While all the above-presented findings underscore the importance of considering fMRI examination in patients with AM impairment due to overt brain damage, it should be also mentioned that fMRI can be used in patients without overt brain damage but who present with a specific deficit in AM, such as psychogenic amnesia (known also as dissociative amnesia)^[130,131], which af-

fects the ventrolateral PFC^[132] associated with retrieval of emotional memories (see above) and is linked to reduced MTL engagement^[133].

Affective disorders

Dysfunctions of AM are also widely reported in affective disorders, such as depression and post-traumatic stress disorder (PTSD)^[134-137], which are characterized by intrusions of memory of the traumatic event, bias toward negative memories and an overgeneralization (lacking specificity) of retrieval^[138,139]. Recently, there are some studies examining the neural correlates of AM in depression^[140,141] and PTSD^[142,143], which highlight the abnormal involvement of the PFC and/or emotion-related MTL region, *i.e.*, amygdala. Overall, the fMRI investigations in psychogenic amnesia and affective disorders could also be very informative regarding the interplay between memory and emotion, which has long been neglected, while there is no doubt of emotional and motivational influences on AM.

Psychiatric disorders: The case of schizophrenia

Schizophrenia has been also associated with impaired AM^[144-146] in the context of deficits in several cognitive operations (perception, memory) and emotional processing, caused very likely by a more general cognition – emotion disintegration^[147]. fMRI examination of AM in schizophrenia revealed an abnormal pattern of activation and correlations with memory performance in the PFC and striatum, respectively^[148]. Further fMRI investigations are needed to clearly understand AM deficits in schizophrenia and its link to a more general disturbance at the level of emotion-cognition interaction.

Finally, we would like to mention that it would also be of great use for investigating the effects of cognitive based training programs. Specifically, fMRI can be used before and after training programs to establish beneficial changes in neural activations leading to improved AM^[149]. Investigations of this sort are remarkably scarce in the AM research, but hopefully they will emerge in the near future and provide new opportunities to understand reorganization of brain network activation and brain plasticity.

REFERENCES

- 1 **Conway MA**, Pleydell-Pearce CW. The construction of autobiographical memories in the self-memory system. *Psychol Rev* 2000; **107**: 261-288 [PMID: 10789197 DOI: 10.1037/0033-295X.107.2.261]
- 2 **Tulving E**. Episodic memory and common sense: how far apart? *Philos Trans R Soc Lond B Biol Sci* 2001; **356**: 1505-1515 [PMID: 11571040 DOI: 10.1098/rstb.2001.0937]
- 3 **Tulving E**. Episodic memory: from mind to brain. *Annu Rev Psychol* 2002; **53**: 1-25 [PMID: 11752477 DOI: 10.1146/annurev.psych.53.100901.135114]
- 4 **Bluck S**. Autobiographical memory: exploring its functions in everyday life. *Memory* 2003; **11**: 113-123 [PMID: 12820825 DOI: 10.1080/741938206]
- 5 **Rasmussen AS**, Habermas T. Factor structure of overall autobiographical memory usage: the directive, self and social functions revisited. *Memory* 2011; **19**: 597-605 [PMID:

- 21919587 DOI: 10.1080/09658211.2011.592499]
- 6 **Moscovitch M**, Nadel L, Winocur G, Gilboa A, Rosenbaum RS. The cognitive neuroscience of remote episodic, semantic and spatial memory. *Curr Opin Neurobiol* 2006; **16**: 179-190 [PMID: 16564688 DOI: 10.1016/j.conb.2006.03.013]
 - 7 **Moscovitch M**, Rosenbaum RS, Gilboa A, Addis DR, Westmacott R, Grady C, McAndrews MP, Levine B, Black S, Winocur G, Nadel L. Functional neuroanatomy of remote episodic, semantic and spatial memory: a unified account based on multiple trace theory. *J Anat* 2005; **207**: 35-66 [PMID: 16011544 DOI: 10.1111/j.1469-7580.2005.00421.x]
 - 8 **Preston AR**, Wagner AD. The medial temporal lobe and memory. In: Kesner RP, Martinez JL. *Neurobiology of Learning and Memory*. Amsterdam: Elsevier, 2007: 305-337
 - 9 **Spiers HJ**, Maguire EA, Burgess N. Hippocampal amnesia. *Neurocase* 2001; **7**: 357-382 [PMID: 11744778 DOI: 10.1076/neur.7.5.357.16245]
 - 10 **Bright P**, Buckman J, Fradera A, Yoshimasu H, Colchester AC, Kopelman MD. Retrograde amnesia in patients with hippocampal, medial temporal, temporal lobe, or frontal pathology. *Learn Mem* 2006; **13**: 545-557 [PMID: 17015852 DOI: 10.1101/lm.265906]
 - 11 **Tulving E**. Episodic memory and autoevidence: Uniquely human? In: Terrace HS, Metcalfe J. *The Missing Link in Cognition: Origins of Self-Reflective Consciousness*. Oxford University Press, 2005: 3-56
 - 12 **Conway MA**. Memory and the self. *J Mem Lang* 2005; **53**: 594-628 [DOI: 10.1016/j.jml.2005.08.005]
 - 13 **Suddendorf T**, Addis DR, Corballis MC. Mental time travel and the shaping of the human mind. *Philos Trans R Soc Lond B Biol Sci* 2009; **364**: 1317-1324 [PMID: 19528013 DOI: 10.1098/rstb.2008.0301]
 - 14 **Suddendorf T**, Corballis MC. Behavioural evidence for mental time travel in nonhuman animals. *Behav Brain Res* 2010; **215**: 292-298 [PMID: 19962409 DOI: 10.1016/j.bbr.2009.11.044]
 - 15 **Tulving E**. Are there 256 kinds of memory? In: Nairne JS. *The Foundations of Remembering: Essays in Honor of Henry L. Roediger*: Psychology Press, 2007: 39-52
 - 16 **Klein SB**. *The Two Selves: Their Metaphysical Commitments and Functional Independence*. New York: Oxford University Press, 2014
 - 17 **Klein SB**. Self, memory, and the self-reference effect: an examination of conceptual and methodological issues. *Pers Soc Psychol Rev* 2012; **16**: 283-300 [PMID: 22291045 DOI: 10.1177/1088868311434214]
 - 18 **Klein SB**, Nichols S. Memory and the Sense of Personal Identity. *Mind* 2012; **121**: 677-702 [DOI: 10.1093/mind/fzs080]
 - 19 **Tulving E**. *Elements of episodic memory*. New York: Oxford University Press, 1983
 - 20 **Cabeza R**, St Jacques P. Functional neuroimaging of autobiographical memory. *Trends Cogn Sci* 2007; **11**: 219-227 [PMID: 17382578 DOI: 10.1016/j.tics.2007.02.005]
 - 21 **Maguire EA**. Neuroimaging studies of autobiographical event memory. *Philos Trans R Soc Lond B Biol Sci* 2001; **356**: 1441-1451 [PMID: 11571035 DOI: 10.1098/rstb.2001.0944]
 - 22 **St Jacques PL**, Cabeza R. Neural correlates of autobiographical memory. In: Ghetti S, Bauer PJ. *Origins and development of recollection*. New York: Oxford University Press, 2012: 188-218
 - 23 **Squire LR**, Alvarez P. Retrograde amnesia and memory consolidation: a neurobiological perspective. *Curr Opin Neurobiol* 1995; **5**: 169-177 [PMID: 7620304 DOI: 10.1016/0959-4388(95)80023-9]
 - 24 **Nadel L**, Moscovitch M. Memory consolidation, retrograde amnesia and the hippocampal complex. *Curr Opin Neurobiol* 1997; **7**: 217-227 [PMID: 9142752 DOI: 10.1016/S0959-4388(97)80010-4]
 - 25 **Winocur G**, Moscovitch M. Memory transformation and systems consolidation. *J Int Neuropsychol Soc* 2011; **17**: 766-780 [PMID: 21729403 DOI: 10.1017/S1355617711000683]
 - 26 **Winocur G**, Moscovitch M, Bontempi B. Memory formation and long-term retention in humans and animals: convergence towards a transformation account of hippocampal-neocortical interactions. *Neuropsychologia* 2010; **48**: 2339-2356 [PMID: 20430044 DOI: 10.1016/j.neuropsychologia.2010.04.016]
 - 27 **Svoboda E**, McKinnon MC, Levine B. The functional neuroanatomy of autobiographical memory: a meta-analysis. *Neuropsychologia* 2006; **44**: 2189-2208 [PMID: 16806314 DOI: 10.1016/j.neuropsychologia.2006.05.023]
 - 28 **Botzung A**, Denkova E, Ciuciu P, Scheiber C, Manning L. The neural bases of the constructive nature of autobiographical memories studied with a self-paced fMRI design. *Memory* 2008; **16**: 351-363 [PMID: 18432480 DOI: 10.1080/09658210801931222]
 - 29 **Daselaar SM**, Rice HJ, Greenberg DL, Cabeza R, LaBar KS, Rubin DC. The spatiotemporal dynamics of autobiographical memory: neural correlates of recall, emotional intensity, and reliving. *Cereb Cortex* 2008; **18**: 217-229 [PMID: 17548799 DOI: 10.1093/cercor/bhm048]
 - 30 **Greenberg DL**, Rice HJ, Cooper JJ, Cabeza R, Rubin DC, LaBar KS. Co-activation of the amygdala, hippocampus and inferior frontal gyrus during autobiographical memory retrieval. *Neuropsychologia* 2005; **43**: 659-674 [PMID: 15721179 DOI: 10.1016/j.neuropsychologia.2004.09.002]
 - 31 **Douville K**, Woodard JL, Seidenberg M, Miller SK, Leveroni CL, Nielson KA, Franczak M, Antuono P, Rao SM. Medial temporal lobe activity for recognition of recent and remote famous names: an event-related fMRI study. *Neuropsychologia* 2005; **43**: 693-703 [PMID: 15721182 DOI: 10.1016/j.neuropsychologia.2004.09.005]
 - 32 **Leveroni CL**, Seidenberg M, Mayer AR, Mead LA, Binder JR, Rao SM. Neural systems underlying the recognition of familiar and newly learned faces. *J Neurosci* 2000; **20**: 878-886 [PMID: 10632617]
 - 33 **Denkova E**, Botzung A, Manning L. Neural correlates of remembering/knowing famous people: an event-related fMRI study. *Neuropsychologia* 2006; **44**: 2783-2791 [PMID: 16879842 DOI: 10.1016/j.neuropsychologia.2006.05.029]
 - 34 **Snowden JS**, Griffiths HL, Neary D. Autobiographical experience and word meaning. *Memory* 1995; **3**: 225-246 [PMID: 8574865 DOI: 10.1080/09658219508253152]
 - 35 **Westmacott R**, Black SE, Freedman M, Moscovitch M. The contribution of autobiographical significance to semantic memory: evidence from Alzheimer's disease, semantic dementia, and amnesia. *Neuropsychologia* 2004; **42**: 25-48 [PMID: 14615074 DOI: 10.1016/S0028-3932(03)00147-7]
 - 36 **Addis DR**, Moscovitch M, Crawley AP, McAndrews MP. Recollective qualities modulate hippocampal activation during autobiographical memory retrieval. *Hippocampus* 2004; **14**: 752-762 [PMID: 15318333 DOI: 10.1002/hipo.10215]
 - 37 **Bonnici HM**, Chadwick MJ, Lutti A, Hassabis D, Weiskopf N, Maguire EA. Detecting representations of recent and remote autobiographical memories in vmPFC and hippocampus. *J Neurosci* 2012; **32**: 16982-16991 [PMID: 23175849 DOI: 10.1523/JNEUROSCI.2475-12.2012]
 - 38 **Gilboa A**. Autobiographical and episodic memory--one and the same? Evidence from prefrontal activation in neuroimaging studies. *Neuropsychologia* 2004; **42**: 1336-1349 [PMID: 15193941 DOI: 10.1016/j.neuropsychologia.2004.02.014]
 - 39 **Sheldon S**, Levine B. Same as it ever was: vividness modulates the similarities and differences between the neural networks that support retrieving remote and recent autobiographical memories. *Neuroimage* 2013; **83**: 880-891 [PMID: 23845428 DOI: 10.1016/j.neuroimage.2013.06.082]
 - 40 **Söderlund H**, Moscovitch M, Kumar N, Mandic M, Levine B. As time goes by: hippocampal connectivity changes with remoteness of autobiographical memory retrieval. *Hippocampus* 2012; **22**: 670-679 [PMID: 21404363 DOI: 10.1002/hipo.20927]

- 41 **Gilboa A**, Winocur G, Grady CL, Hevenor SJ, Moscovitch M. Remembering our past: functional neuroanatomy of recollection of recent and very remote personal events. *Cereb Cortex* 2004; **14**: 1214-1225 [PMID: 15166099 DOI: 10.1093/cercor/bhh082]
- 42 **Badre D**. Cognitive control, hierarchy, and the rostro-caudal organization of the frontal lobes. *Trends Cogn Sci* 2008; **12**: 193-200 [PMID: 18403252 DOI: 10.1016/j.tics.2008.02.004]
- 43 **Moscovitch M**, Winocur G. The frontal cortex and working with memory. In: Stuss DT, Knight R. Principles of frontal lobe function. New York: Oxford University Press, 2002: 188-209.
- 44 **Addis DR**, Knapp K, Roberts RP, Schacter DL. Routes to the past: neural substrates of direct and generative autobiographical memory retrieval. *Neuroimage* 2012; **59**: 2908-2922 [PMID: 22001264 DOI: 10.1016/j.neuroimage.2011.09.066]
- 45 **Markowitsch HJ**. Which brain regions are critically involved in the retrieval of old episodic memory? *Brain Res Brain Res Rev* 1995; **21**: 117-127 [PMID: 8866670 DOI: 10.1016/0165-0173(95)00007-0]
- 46 **Markowitsch HJ**. The functional neuroanatomy of episodic memory retrieval. *Trends Neurosci* 1997; **20**: 557-558 [PMID: 9416665]
- 47 **Brand M**, Markowitsch HJ. Memory processes and the orbitofrontal cortex. In: Zald DH, Rauch SL. The orbitofrontal cortex. Oxford: Oxford University Press, 2006: 285-230 [DOI: 10.1093/acprof:oso/9780198565741.003.0011]
- 48 **Brand M**, Markowitsch HJ. The role of the prefrontal cortex in episodic memory. In: Dere E, Huston JP, Easton A. Handbook of episodic memory. Amsterdam: Elsevier, 2008: 317-341
- 49 **Markowitsch HJ**, Thiel A, Reinkemeier M, Kessler J, Koyuncu A, Heiss WD. Right amygdalar and temporofrontal activation during autobiographic, but not during fictitious memory retrieval. *Behav Neurol* 2000; **12**: 181-190 [PMID: 11568430 DOI: 10.1155/2000/303651]
- 50 **Denkova E**, Dolcos S, Dolcos F. The Effect of Retrieval Focus and Emotional Valence on the Inferior Frontal Cortex Activity during Autobiographical Recollection. *Front Behav Neurosci* 2013; **7**: 192 [PMID: 24379766 DOI: 10.3389/fnbeh.2013.00192]
- 51 **Northoff G**, Heinzl A, de Greck M, Bermpohl F, Dobrowolny H, Panksepp J. Self-referential processing in our brain—a meta-analysis of imaging studies on the self. *Neuroimage* 2006; **31**: 440-457 [PMID: 16466680 DOI: 10.1016/j.neuroimage.2005.12.002]
- 52 **Cabeza R**, Prince SE, Daselaar SM, Greenberg DL, Budde M, Dolcos F, LaBar KS, Rubin DC. Brain activity during episodic retrieval of autobiographical and laboratory events: an fMRI study using a novel photo paradigm. *J Cogn Neurosci* 2004; **16**: 1583-1594 [PMID: 15622612 DOI: 10.1162/0898929042568578]
- 53 **McDermott KB**, Szpunar KK, Christ SE. Laboratory-based and autobiographical retrieval tasks differ substantially in their neural substrates. *Neuropsychologia* 2009; **47**: 2290-2298 [PMID: 19159634 DOI: 10.1016/j.neuropsychologia.2008.12.025]
- 54 **Summerfield JJ**, Hassabis D, Maguire EA. Cortical midline involvement in autobiographical memory. *Neuroimage* 2009; **44**: 1188-1200 [PMID: 18973817 DOI: 10.1016/j.neuroimage.2008.09.033]
- 55 **St Jacques PL**, Conway MA, Lowder MW, Cabeza R. Watching my mind unfold versus yours: an fMRI study using a novel camera technology to examine neural differences in self-projection of self versus other perspectives. *J Cogn Neurosci* 2011; **23**: 1275-1284 [PMID: 20521858 DOI: 10.1162/jocn.2010.21518]
- 56 **Amodio DM**, Frith CD. Meeting of minds: the medial frontal cortex and social cognition. *Nat Rev Neurosci* 2006; **7**: 268-277 [PMID: 16552413 DOI: 10.1038/nrn1884]
- 57 **Kober H**, Barrett LF, Joseph J, Bliss-Moreau E, Lindquist K, Wager TD. Functional grouping and cortical-subcortical interactions in emotion: a meta-analysis of neuroimaging studies. *Neuroimage* 2008; **42**: 998-1031 [PMID: 18579414 DOI: 10.1016/j.neuroimage.2008.03.059]
- 58 **Denny BT**, Kober H, Wager TD, Ochsner KN. A meta-analysis of functional neuroimaging studies of self- and other judgments reveals a spatial gradient for mentalizing in medial prefrontal cortex. *J Cogn Neurosci* 2012; **24**: 1742-1752 [PMID: 22452556 DOI: 10.1162/jocn_a_00233]
- 59 **Frith U**, Frith CD. Development and neurophysiology of mentalizing. *Philos Trans R Soc Lond B Biol Sci* 2003; **358**: 459-473 [PMID: 12689373 DOI: 10.1098/rstb.2002.1218]
- 60 **Moscovitch M**, Winocur G. The frontal cortex and working with memory. In: Stuss DT, Knight R. The Frontal Lobes. Oxford: Oxford University Press, 2002: 188-209
- 61 **Ochsner KN**, Silvers JA, Huhle JT. Functional imaging studies of emotion regulation: a synthetic review and evolving model of the cognitive control of emotion. *Ann N Y Acad Sci* 2012; **1251**: E1-E24 [PMID: 23025352 DOI: 10.1111/j.1749-6632.2012.06751.x]
- 62 **Hassabis D**, Maguire EA. Deconstructing episodic memory with construction. *Trends Cogn Sci* 2007; **11**: 299-306 [PMID: 17548229 DOI: 10.1016/j.tics.2007.05.001]
- 63 **Freton M**, Lemogne C, Bergouignan L, Delaveau P, Lehericy S, Fossati P. The eye of the self: precuneus volume and visual perspective during autobiographical memory retrieval. *Brain Struct Funct* 2013; Epub ahead of print [PMID: 23553546]
- 64 **Burgess N**, Becker S, King JA, O'Keefe J. Memory for events and their spatial context: models and experiments. *Philos Trans R Soc Lond B Biol Sci* 2001; **356**: 1493-1503 [PMID: 11571039 DOI: 10.1098/rstb.2001.0948]
- 65 **Kapur N**, Kopelman MD. Advanced brain imaging procedures and human memory disorder. *Br Med Bull* 2003; **65**: 61-81 [PMID: 12697617 DOI: 10.1093/bmb/65.1.61]
- 66 **Mayes AR**, Montaldi D. Exploring the neural bases of episodic and semantic memory: the role of structural and functional neuroimaging. *Neurosci Biobehav Rev* 2001; **25**: 555-573 [PMID: 11595275 DOI: 10.1016/S0149-7634(01)00034-3]
- 67 **Kopelman MD**. Disorders of memory. *Brain* 2002; **125**: 2152-2190 [PMID: 12244076 DOI: 10.1093/brain/awf229]
- 68 **Kopelman MD**, Kapur N. The loss of episodic memories in retrograde amnesia: single-case and group studies. *Philos Trans R Soc Lond B Biol Sci* 2001; **356**: 1409-1421 [PMID: 11571032 DOI: 10.1098/rstb.2001.0942]
- 69 **Gadian DG**, Aicardi J, Watkins KE, Porter DA, Mishkin M, Vargha-Khadem F. Developmental amnesia associated with early hypoxic-ischaemic injury. *Brain* 2000; **123** Pt 3: 499-507 [PMID: 10686173 DOI: 10.1093/brain/123.3.499]
- 70 **Vargha-Khadem F**, Gadian DG, Mishkin M. Dissociations in cognitive memory: the syndrome of developmental amnesia. *Philos Trans R Soc Lond B Biol Sci* 2001; **356**: 1435-1440 [PMID: 11571034 DOI: 10.1098/rstb.2001.0951]
- 71 **Vargha-Khadem F**, Gadian DG, Watkins KE, Connelly A, Van Paesschen W, Mishkin M. Differential effects of early hippocampal pathology on episodic and semantic memory. *Science* 1997; **277**: 376-380 [PMID: 9219696 DOI: 10.1126/science.277.5324.376]
- 72 **Maguire EA**, Vargha-Khadem F, Mishkin M. The effects of bilateral hippocampal damage on fMRI regional activations and interactions during memory retrieval. *Brain* 2001; **124**: 1156-1170 [PMID: 11353732 DOI: 10.1093/brain/124.6.1156]
- 73 **Manning L**. Do some neurological conditions induce brain plasticity processes? *Behav Brain Res* 2008; **192**: 143-148 [PMID: 18479763 DOI: 10.1016/j.bbr.2008.04.001]
- 74 **Andelman F**, Hoofien D, Goldberg I, Aizenstein O, Neufeld MY. Bilateral hippocampal lesion and a selective impairment of the ability for mental time travel. *Neurocase* 2010; **16**: 426-435 [PMID: 20401802 DOI: 10.1080/13554791003623318]
- 75 **Cipolotti L**, Shallice T, Chan D, Fox N, Scahill R, Harrison G,

- Stevens J, Rudge P. Long-term retrograde amnesia...the crucial role of the hippocampus. *Neuropsychologia* 2001; **39**: 151-172 [PMID: 11163373 DOI: 10.1016/S0028-3932(00)00103-2]
- 76 Klein SB, Loftus J, Kihlstrom JF. Memory and temporal experience: The effects of episodic memory loss on an amnesic patient's ability to remember the past and imagine the future. *Social Cognition* 2002; **20**: 353-379 [DOI: 10.1521/soco.20.5.353.21125]
- 77 Maguire EA, Frith CD, Rudge P, Cipolotti L. The effect of adult-acquired hippocampal damage on memory retrieval: an fMRI study. *Neuroimage* 2005; **27**: 146-152 [PMID: 15886022 DOI: 10.1016/j.neuroimage.2005.04.006]
- 78 Price CJ, Friston KJ. Scanning patients with tasks they can perform. *Hum Brain Mapp* 1999; **8**: 102-108 [PMID: 10524600]
- 79 Price CJ, Crinion J, Friston KJ. Design and analysis of fMRI studies with neurologically impaired patients. *J Magn Reson Imaging* 2006; **23**: 816-826 [PMID: 16649208 DOI: 10.1002/jmri.20580]
- 80 Engel J Jr. Introduction to temporal lobe epilepsy. *Epilepsy Res* 1996; **26**: 141-150 [PMID: 8985696 DOI: 10.1016/S0920-1211(96)00043-5]
- 81 Snyder PJ. Epilepsy as a "natural laboratory" for the study of human memory. *Brain Cogn* 1997; **35**: 1-4 [PMID: 9339298 DOI: 10.1006/brcg.1997.0924]
- 82 Després O, Voltzenlogel V, Hirsch E, Vignal JP, Manning L. [Memory improvement in patients with temporal lobe epilepsy at one-year postoperative]. *Rev Neurol (Paris)* 2011; **167**: 231-244 [PMID: 21159357 DOI: 10.1016/j.neurol.2010.08.008]
- 83 Herfurth K, Kasper B, Schwarz M, Stefan H, Pauli E. Autobiographical memory in temporal lobe epilepsy: role of hippocampal and temporal lateral structures. *Epilepsy Behav* 2010; **19**: 365-371 [PMID: 20875774 DOI: 10.1016/j.yebeh.2010.07.012]
- 84 St-Laurent M, Moscovitch M, Levine B, McAndrews MP. Determinants of autobiographical memory in patients with unilateral temporal lobe epilepsy or excisions. *Neuropsychologia* 2009; **47**: 2211-2221 [PMID: 19524089 DOI: 10.1016/j.neuropsychologia.2009.01.032]
- 85 Viskontas IV, McAndrews MP, Moscovitch M. Remote episodic memory deficits in patients with unilateral temporal lobe epilepsy and excisions. *J Neurosci* 2000; **20**: 5853-5857 [PMID: 10908628]
- 86 Voltzenlogel V, Despres O, Vignal JP, Kehrli P, Manning L. One-year postoperative autobiographical memory following unilateral temporal lobectomy for control of intractable epilepsy. *Epilepsia* 2007; **48**: 605-608 [PMID: 17326789 DOI: 10.1111/j.1528-1167.2006.00970.x]
- 87 Voltzenlogel V, Després O, Vignal JP, Steinhoff BJ, Kehrli P, Manning L. Remote memory in temporal lobe epilepsy. *Epilepsia* 2006; **47**: 1329-1336 [PMID: 16922877 DOI: 10.1111/j.1528-1167.2006.00555.x]
- 88 St-Laurent M, Moscovitch M, Tau M, McAndrews MP. The temporal unraveling of autobiographical memory narratives in patients with temporal lobe epilepsy or excisions. *Hippocampus* 2011; **21**: 409-421 [PMID: 20082294 DOI: 10.1002/hipo.20757]
- 89 Dupont S, Van de Moortele PF, Samson S, Hasboun D, Poline JB, Adam C, Lehericy S, Le Bihan D, Samson Y, Baulac M. Episodic memory in left temporal lobe epilepsy: a functional MRI study. *Brain* 2000; **123** (Pt 8): 1722-1732 [PMID: 10908201 DOI: 10.1093/brain/123.8.1722]
- 90 Sidhu MK, Stretton J, Winston GP, Bonelli S, Centeno M, Vollmar C, Symms M, Thompson PJ, Koepp MJ, Duncan JS. A functional magnetic resonance imaging study mapping the episodic memory encoding network in temporal lobe epilepsy. *Brain* 2013; **136**: 1868-1888 [PMID: 23674488 DOI: 10.1093/brain/awt099]
- 91 Bonelli SB, Powell RH, Yogarajah M, Samson RS, Symms MR, Thompson PJ, Koepp MJ, Duncan JS. Imaging memory in temporal lobe epilepsy: predicting the effects of temporal lobe resection. *Brain* 2010; **133**: 1186-1199 [PMID: 20157009 DOI: 10.1093/brain/awq006]
- 92 Bonelli SB, Thompson PJ, Yogarajah M, Powell RH, Samson RS, McEvoy AW, Symms MR, Koepp MJ, Duncan JS. Memory reorganization following anterior temporal lobe resection: a longitudinal functional MRI study. *Brain* 2013; **136**: 1889-1900 [PMID: 23715092 DOI: 10.1093/brain/awt105]
- 93 Cheung MC, Chan AS, Lam JM, Chan YL. Pre- and post-operative fMRI and clinical memory performance in temporal lobe epilepsy. *J Neurol Neurosurg Psychiatry* 2009; **80**: 1099-1106 [PMID: 19389718 DOI: 10.1136/jnnp.2009.173161]
- 94 Powell HW, Koepp MJ, Richardson MP, Symms MR, Thompson PJ, Duncan JS. The application of functional MRI of memory in temporal lobe epilepsy: a clinical review. *Epilepsia* 2004; **45**: 855-863 [PMID: 15230713 DOI: 10.1111/j.0013-9580.2004.41603.x]
- 95 Powell HW, Richardson MP, Symms MR, Boulby PA, Thompson PJ, Duncan JS, Koepp MJ. Preoperative fMRI predicts memory decline following anterior temporal lobe resection. *J Neurol Neurosurg Psychiatry* 2008; **79**: 686-693 [PMID: 17898035 DOI: 10.1136/jnnp.2007.115139]
- 96 Richardson MP, Strange BA, Thompson PJ, Baxendale SA, Duncan JS, Dolan RJ. Pre-operative verbal memory fMRI predicts post-operative memory decline after left temporal lobe resection. *Brain* 2004; **127**: 2419-2426 [PMID: 15459025 DOI: 10.1093/brain/awh293]
- 97 Addis DR, Moscovitch M, McAndrews MP. Consequences of hippocampal damage across the autobiographical memory network in left temporal lobe epilepsy. *Brain* 2007; **130**: 2327-2342 [PMID: 17681983 DOI: 10.1093/brain/awm166]
- 98 Manning L, Denkova E, Unterberger L. Autobiographical significance in past and future public semantic memory: a case-study. *Cortex* 2013; **49**: 2007-2020 [PMID: 23266012 DOI: 10.1016/j.cortex.2012.11.007]
- 99 Milton F, Butler CR, Benattayallah A, Zeman AZ. The neural basis of autobiographical memory deficits in transient epileptic amnesia. *Neuropsychologia* 2012; **50**: 3528-3541 [PMID: 23036282 DOI: 10.1016/j.neuropsychologia.2012.09.027]
- 100 Manning L, Chassagnon S, Hirsch E, Kehrli P, Maitrot D. Selective memory impairment for public events in a patient with left temporal lobe epilepsy. *Epilepsy Res* 2005; **64**: 45-47 [PMID: 15820669 DOI: 10.1016/j.eplepsyres.2005.02.003]
- 101 Chan D, Fox NC, Sahill RI, Crum WR, Whitwell JL, Leschziner G, Rossor AM, Stevens JM, Cipolotti L, Rossor MN. Patterns of temporal lobe atrophy in semantic dementia and Alzheimer's disease. *Ann Neurol* 2001; **49**: 433-442 [PMID: 11310620 DOI: 10.1002/ana.92]
- 102 Galton CJ, Gomez-Anson B, Antoun N, Scheltens P, Patterson K, Graves M, Sahakian BJ, Hodges JR. Temporal lobe rating scale: application to Alzheimer's disease and frontotemporal dementia. *J Neurol Neurosurg Psychiatry* 2001; **70**: 165-173 [PMID: 11160463 DOI: 10.1136/jnnp.70.2.165]
- 103 Hodges JR. Alzheimer's disease and the frontotemporal dementias: contributions to clinico-pathological studies, diagnosis, and cognitive neuroscience. *J Alzheimers Dis* 2013; **33** Suppl 1: S211-S217 [PMID: 22766737]
- 104 Irish M, Piguet O, Hodges JR, Hornberger M. Common and unique gray matter correlates of episodic memory dysfunction in frontotemporal dementia and alzheimer's disease. *Hum Brain Mapp* 2014; **35**: 1422-1435 [PMID: 23670951 DOI: 10.1002/hbm.22263]
- 105 Graham KS, Hodges JR. Differentiating the roles of the hippocampal complex and the neocortex in long-term memory storage: evidence from the study of semantic dementia and Alzheimer's disease. *Neuropsychology* 1997; **11**: 77-89 [PMID: 9055272 DOI: 10.1037/0894-4105.11.1.77]
- 106 Moss HE, Kopelman MD, Cappelletti M, Davies Pde M, Jaldow E. Lost for words or loss of memories? Autobiographical memory in semantic dementia. *Cogn Neuropsychol* 2003; **20**: 703-732 [PMID: 20957590 DOI: 10.1080/026432902420009

- 16]
- 107 **Piolino P**, Desgranges B, Belliard S, Matuszewski V, Lalevée C, De la Sayette V, Eustache F. Autobiographical memory and auto-noetic consciousness: triple dissociation in neurodegenerative diseases. *Brain* 2003; **126**: 2203-2219 [PMID: 12821510 DOI: 10.1093/brain/awg222]
- 108 **Addis DR**, Tippett LJ. Memory of myself: autobiographical memory and identity in Alzheimer's disease. *Memory* 2004; **12**: 56-74 [PMID: 15098621 DOI: 10.1080/09658210244000423]
- 109 **Greene JD**, Hodges JR, Baddeley AD. Autobiographical memory and executive function in early dementia of Alzheimer type. *Neuropsychologia* 1995; **33**: 1647-1670 [PMID: 8745122 DOI: 10.1016/0028-3932(95)00046-1]
- 110 **Maguire EA**, Kumaran D, Hassabis D, Kopelman MD. Autobiographical memory in semantic dementia: a longitudinal fMRI study. *Neuropsychologia* 2010; **48**: 123-136 [PMID: 19720072 DOI: 10.1016/j.neuropsychologia.2009.08.020]
- 111 **Viard A**, Desgranges B, Matuszewski V, Lebreton K, Belliard S, de La Sayette V, Eustache F, Piolino P. Autobiographical memory in semantic dementia: new insights from two patients using fMRI. *Neuropsychologia* 2013; **51**: 2620-2632 [PMID: 23954715 DOI: 10.1016/j.neuropsychologia.2013.08.07]
- 112 **Irish M**, Lawlor BA, O'Mara SM, Coen RF. Exploring the recollective experience during autobiographical memory retrieval in amnesic mild cognitive impairment. *J Int Neuropsychol Soc* 2010; **16**: 546-555 [PMID: 20298640 DOI: 10.1017/S1355617710000172]
- 113 **Meulenbroek O**, Rijpkema M, Kessels RP, Rikkert MG, Fernández G. Autobiographical memory retrieval in patients with Alzheimer's disease. *Neuroimage* 2010; **53**: 331-340 [PMID: 20570740 DOI: 10.1016/j.neuroimage.2010.05.082]
- 114 **Kapur N**, Barker S, Burrows EH, Ellison D, Brice J, Illis LS, Scholey K, Colbourn C, Wilson B, Loates M. Herpes simplex encephalitis: long term magnetic resonance imaging and neuropsychological profile. *J Neurol Neurosurg Psychiatry* 1994; **57**: 1334-1342 [PMID: 7964808 DOI: 10.1136/jnnp.57.11.1334]
- 115 **Kopelman MD**, Stanhope N, Kingsley D. Retrograde amnesia in patients with diencephalic, temporal lobe or frontal lesions. *Neuropsychologia* 1999; **37**: 939-958 [PMID: 10426519 DOI: 10.1016/S0028-3932(98)00143-2]
- 116 **Rosenbaum RS**, Moscovitch M, Foster JK, Schnyer DM, Gao F, Kovacevic N, Verfaellie M, Black SE, Levine B. Patterns of autobiographical memory loss in medial-temporal lobe amnesic patients. *J Cogn Neurosci* 2008; **20**: 1490-1506 [PMID: 18303977 DOI: 10.1162/jocn.2008.20105]
- 117 **Calabrese P**, Markowitsch HJ, Durwen HF, Widlitzek H, Haupts M, Holinka B, Gehlen W. Right temporofrontal cortex as critical locus for the ephory of old episodic memories. *J Neurol Neurosurg Psychiatry* 1996; **61**: 304-310 [PMID: 8795604 DOI: 10.1136/jnnp.61.3.304]
- 118 **Kataoka H**, Furiya Y, Ueno S. Limbic encephalitis with involvement of prefrontal cortices and persistent amnesia. *Neurologist* 2008; **14**: 255-257 [PMID: 18617853 DOI: 10.1097/NRL.0b013e31816b73fe]
- 119 **Tanaka Y**, Miyazawa Y, Hashimoto R, Nakano I, Obayashi T. Postencephalitic focal retrograde amnesia after bilateral anterior temporal lobe damage. *Neurology* 1999; **53**: 344-350 [PMID: 10430424 DOI: 10.1212/WNL.53.2.344]
- 120 **Buccione I**, Fadda L, Serra L, Caltagirone C, Carlesimo GA. Retrograde episodic and semantic memory impairment correlates with side of temporal lobe damage. *J Int Neuropsychol Soc* 2008; **14**: 1083-1094 [PMID: 18954490 DOI: 10.1017/S1355617708080922]
- 121 **Cermak LS**, O'Connor M. The anterograde and retrograde retrieval ability of a patient with amnesia due to encephalitis. *Neuropsychologia* 1983; **21**: 213-234 [PMID: 6877576 DOI: 10.1016/0028-3932(83)90039-8]
- 122 **O'Connor M**, Butters N, Miliotis P, Eslinger P, Cermak LS. The dissociation of anterograde and retrograde amnesia in a patient with herpes encephalitis. *J Clin Exp Neuropsychol* 1992; **14**: 159-178 [PMID: 1572943 DOI: 10.1080/01688639208402821]
- 123 **Tsukiura T**, Ohtake H, Fujii T, Miura R, Ogawa T, Yamadori A. Preserved ability to recognize keywords related to remote events in the absence of retrieval of relevant knowledge: a case of postencephalitic amnesia. *Brain Cogn* 2003; **51**: 1-11 [PMID: 12633586 DOI: 10.1016/S0278-2626(02)00529-8]
- 124 **Berry E**, Hampshire A, Rowe J, Hodges S, Kapur N, Watson P, Browne G, Smyth G, Wood K, Owen AM. The neural basis of effective memory therapy in a patient with limbic encephalitis. *J Neurol Neurosurg Psychiatry* 2009; **80**: 1202-1205 [PMID: 19286742 DOI: 10.1136/jnnp.2008.164251]
- 125 **Levine B**, Black SE, Cabeza R, Sinden M, McIntosh AR, Toth JP, Tulving E, Stuss DT. Episodic memory and the self in a case of isolated retrograde amnesia. *Brain* 1998; **121** (Pt 10): 1951-1973 [PMID: 9798749]
- 126 **Markowitsch HJ**, Calabrese P, Liess J, Haupts M, Durwen HF, Gehlen W. Retrograde amnesia after traumatic injury of the fronto-temporal cortex. *J Neurol Neurosurg Psychiatry* 1993; **56**: 988-992 [PMID: 8410040 DOI: 10.1136/jnnp.56.9.988]
- 127 **Piolino P**, Desgranges B, Manning L, North P, Jokic C, Eustache F. Autobiographical memory, the sense of recollection and executive functions after severe traumatic brain injury. *Cortex* 2007; **43**: 176-195 [PMID: 17405665 DOI: 10.1016/S0010-9452(08)70474-X]
- 128 **Kroll NE**, Markowitsch HJ, Knight RT, von Cramon DY. Retrieval of old memories: the temporofrontal hypothesis. *Brain* 1997; **120** (Pt 8): 1377-1399 [PMID: 9278629]
- 129 **Levine B**, Svoboda E, Turner GR, Mandic M, Mackey A. Behavioral and functional neuroanatomical correlates of anterograde autobiographical memory in isolated retrograde amnesic patient M.L. *Neuropsychologia* 2009; **47**: 2188-2196 [PMID: 19154750 DOI: 10.1016/j.neuropsychologia.2008.12.026]
- 130 **Kopelman MD**. Focal retrograde amnesia and the attribution of causality: An exceptionally critical view. *Cogn Neuropsychol* 2000; **17**: 585-621 [PMID: 20945196 DOI: 10.1080/026432900750002172]
- 131 **Markowitsch HJ**. Psychogenic amnesia. *Neuroimage* 2003; **20** Suppl 1: S132-S138 [PMID: 14597306 DOI: 10.1016/j.neuroimage.2003.09.010]
- 132 **Brand M**, Eggers C, Reinhold N, Fujiwara E, Kessler J, Heiss WD, Markowitsch HJ. Functional brain imaging in 14 patients with dissociative amnesia reveals right inferolateral prefrontal hypometabolism. *Psychiatry Res* 2009; **174**: 32-39 [PMID: 19783409 DOI: 10.1016/j.psychres.2009.03.008]
- 133 **Botzung A**, Denkova E, Manning L. Psychogenic memory deficits associated with functional cerebral changes: an FMRI study. *Neurocase* 2007; **13**: 378-384 [PMID: 18781436 DOI: 10.1080/13554790701851528]
- 134 **Brewin CR**, Hunter E, Carroll F, Tata P. Intrusive memories in depression: an index of schema activation? *Psychol Med* 1996; **26**: 1271-1276 [PMID: 8931173 DOI: 10.1017/S0033291700035996]
- 135 **Brewin CR**, Reynolds M, Tata P. Autobiographical memory processes and the course of depression. *J Abnorm Psychol* 1999; **108**: 511-517 [PMID: 10466275 DOI: 10.1037/0021-843X.108.3.511]
- 136 **Rubin DC**, Berntsen D, Bohni MK. A memory-based model of posttraumatic stress disorder: evaluating basic assumptions underlying the PTSD diagnosis. *Psychol Rev* 2008; **115**: 985-1011 [PMID: 18954211 DOI: 10.1037/a0013397]
- 137 **Rubin DC**, Dennis MF, Beckham JC. Autobiographical memory for stressful events: the role of autobiographical memory in posttraumatic stress disorder. *Conscious Cogn* 2011; **20**: 840-856 [PMID: 21489820 DOI: 10.1016/j.concog.2011.03.015]
- 138 **Watson LA**, Berntsen D, Kuyken W, Watkins ER. The characteristics of involuntary and voluntary autobiographical

- memories in depressed and never depressed individuals. *Conscious Cogn* 2012; **21**: 1382-1392 [PMID: 22850328 DOI: 10.1016/j.concog.2012.06.016]
- 139 **Brown AD**, Root JC, Romano TA, Chang LJ, Bryant RA, Hirst W. Overgeneralized autobiographical memory and future thinking in combat veterans with posttraumatic stress disorder. *J Behav Ther Exp Psychiatry* 2013; **44**: 129-134 [PMID: 22200095 DOI: 10.1016/j.jbtep.2011.11.004]
- 140 **Whalley MG**, Rugg MD, Brewin CR. Autobiographical memory in depression: an fMRI study. *Psychiatry Res* 2012; **201**: 98-106 [PMID: 22386970 DOI: 10.1016/j.psychres.2011.08.008]
- 141 **Young KD**, Bellgowan PS, Bodurka J, Drevets WC. Behavioral and neurophysiological correlates of autobiographical memory deficits in patients with depression and individuals at high risk for depression. *JAMA Psychiatry* 2013; **70**: 698-708 [PMID: 23677007 DOI: 10.1001/jamapsychiatry.2013.1189]
- 142 **St Jacques PL**, Botzung A, Miles A, Rubin DC. Functional neuroimaging of emotionally intense autobiographical memories in post-traumatic stress disorder. *J Psychiatr Res* 2011; **45**: 630-637 [PMID: 21109253 DOI: 10.1016/j.jpsychires.2010.10.011]
- 143 **St Jacques PL**, Kragel PA, Rubin DC. Neural networks supporting autobiographical memory retrieval in posttraumatic stress disorder. *Cogn Affect Behav Neurosci* 2013; **13**: 554-566 [PMID: 23483523 DOI: 10.3758/s13415-013-0157-7]
- 144 **Danion JM**, Cuervo C, Piolino P, Huron C, Riutort M, Peretti CS, Eustache F. Conscious recollection in autobiographical memory: an investigation in schizophrenia. *Conscious Cogn* 2005; **14**: 535-547 [PMID: 16091269 DOI: 10.1016/j.concog.2005.01.005]
- 145 **D'Argembeau A**, Raffard S, Van der Linden M. Remembering the past and imagining the future in schizophrenia. *J Abnorm Psychol* 2008; **117**: 247-251 [PMID: 18266503 DOI: 10.1037/0021-843X.117.1.247]
- 146 **Riutort M**, Cuervo C, Danion JM, Peretti CS, Salamé P. Reduced levels of specific autobiographical memories in schizophrenia. *Psychiatry Res* 2003; **117**: 35-45 [PMID: 12581819 DOI: 10.1016/S0165-1781(02)00317-7]
- 147 **Anticevic A**, Corlett PR. Cognition-emotion dysinteraction in schizophrenia. *Front Psychol* 2012; **3**: 392 [PMID: 23091464 DOI: 10.3389/fpsyg.2012.00392]
- 148 **Cuervo-Lombard C**, Lemogne C, Gierski F, Béra-Potelle C, Tran E, Portefaix C, Kaladjian A, Pierot L, Limosin F. Neural basis of autobiographical memory retrieval in schizophrenia. *Br J Psychiatry* 2012; **201**: 473-480 [PMID: 22539776 DOI: 10.1192/bjp.bp.111.099820]
- 149 **Ernst A**, Botzung A, Gounot D, Sellal F, Blanc F, de Seze J, Manning L. Induced brain plasticity after a facilitation programme for autobiographical memory in multiple sclerosis: a preliminary study. *Mult Scler Int* 2012; **2012**: 820240 [PMID: 23125932 DOI: 10.1155/2012/820240]

P- Reviewers: Kawabori M, Quattrocchi CC **S- Editor:** Zhai HH
L- Editor: Roemmele A **E- Editor:** Liu SQ



Orbital inflammatory disease: Pictorial review and differential diagnosis

Michael N Pakdaman, Ali R Sepahdari, Sahar M Elkhamary

Michael N Pakdaman, Ali R Sepahdari, Department of Radiological Sciences, David Geffen School of Medicine, University of California Los Angeles, Los Angeles, CA 90095, United States Sahar M Elkhamary, Radiology Department, King Khaled Eye Specialist Hospital, Saudi Arabia and Diagnostic Radiology Department, Mansoura Faculty of Medicine, Riyadh 12329, Egypt
Author contributions: Pakdaman MN, Sepahdari AR and Elkhamary SM contributed equally to this work; Sepahdari AR designed the review article structure; Pakdaman MN and Sepahdari AR performed literature review and write-up of this review manuscript; Elkhamary SM analyzed the clinical relevance and relevance of supporting articles, and contributed to drafting and revision of the manuscript; Sepahdari AR provided final approval of the version to be published.

Correspondence to: Ali R Sepahdari, MD, Assistant Professor, Department of Radiological Sciences, David Geffen School of Medicine, University of California Los Angeles, 757 Westwood Plaza, Suite 1621D, Los Angeles, CA 90095, United States. asephdari@mednet.ucla.edu

Telephone: +1-310-2676708 Fax: +1-310-2673635

Received: December 16, 2013 Revised: January 21, 2014

Accepted: April 11, 2014

Published online: March 28, 2015

by OID and discuss differential diagnosis by site and key imaging findings for each condition.

© 2015 Baishideng Publishing Group Inc. All rights reserved.

Key words: Orbit; Inflammation; Pseudotumor; Orbital inflammatory disease; Nonspecific orbital inflammation; Dacryoadenitis; Myositis; Orbital cellulitis; Optic perineuritis; Orbital apicitis

Core tip: This review provides a pictorial summary of orbital inflammatory disease (OID). It outlines many key aspects of OID on imaging that can be used to distinguish from other pathologic conditions. The review also provides an up-to-date overview of the best approaches to imaging workup when suspecting OID.

Original sources: Pakdaman MN, Sepahdari AR, Elkhamary SM. Orbital inflammatory disease: Pictorial review and differential diagnosis. *World J Radiol* 2014; 6(4): 106-115 Available from: URL: <http://www.wjgnet.com/1949-8470/full/v6/i4/106.htm> DOI: <http://dx.doi.org/10.4329/wjr.v6.i4.106>

Abstract

Orbital inflammatory disease (OID) represents a collection of inflammatory conditions affecting the orbit. OID is a diagnosis of exclusion, with the differential diagnosis including infection, systemic inflammatory conditions, and neoplasms, among other conditions. Inflammatory conditions in OID include dacryoadenitis, myositis, cellulitis, optic perineuritis, periscleritis, orbital apicitis, and a focal mass. Sclerosing orbital inflammation is a rare condition with a chronic, indolent course involving dense fibrosis and lymphocytic infiltrate. Previously thought to be along the spectrum of OID, it is now considered a distinct pathologic entity. Imaging plays an important role in elucidating any underlying etiology behind orbital inflammation and is critical for ruling out other conditions prior to a definitive diagnosis of OID. In this review, we will explore the common sites of involvement

INTRODUCTION

Orbital inflammatory disease (OID, aka orbital inflammatory pseudotumor, idiopathic orbital inflammatory syndrome, nonspecific orbital inflammation)^[1-3] was first described by Gleason in 1903^[4] and accounts for 6% of diseases involving the orbit. It is the third most common orbital disease after Grave's orbitopathy and lymphoproliferative diseases^[5]. OID is most commonly unilateral with symptoms and clinical findings depending on the site involved as well as the degree of inflammation, fibrosis, and any mass effect. Generally, acute OID presents with proptosis, extraocular motility disturbance, pain, erythema, and chemosis^[2]. As OID is a diagnosis

Table 1 Differential diagnosis of orbital inflammatory disease by site

Structure involved	Clinical condition	Common imaging findings	Differential diagnosis
Lacrimal gland	Dacryoadenitis	Diffuse lacrimal gland enlargement	Epithelial neoplasm, lymphoma
Extraocular muscles	Myositis	Unilateral EOM inflammation, usually involving surrounding fat and myotendinous junction	Dysthyroid orbitopathy
Optic nerve sheath	Perineuritis	Peripheral enhancement about the optic nerve, with varying infiltration of surrounding fat. Variable enhancement of the nerve substance	Optic nerve sheath meningioma, demyelinating optic neuritis
Orbital/periorbital fat	Cellulitis	Enhancing periorbital soft tissue with possible intraconal extension	Infectious orbital cellulitis, carotid cavernous fistula, cavernous sinus thrombosis
Orbital apex	Orbital apicitis, Tolosa-Hunt syndrome	Ill-defined, T2 hypointense enhancing tissue at orbital apex, variably involving middle cranial fossa and cavernous sinus	Meningioma, other dural infiltrative process
Periscleral	Periscleritis	Scleral thickening with periscleral edema and fluid in Tenon's capsule	Endophthalmitis

EOM: Extraocular muscles.

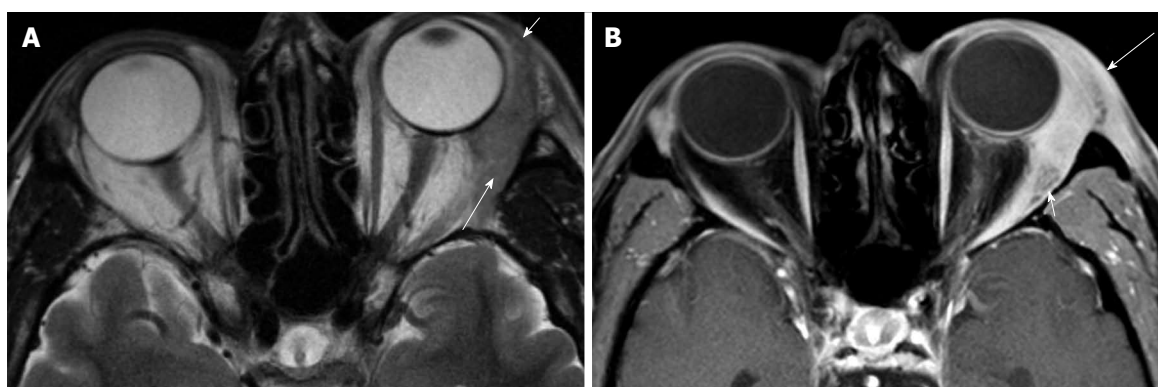


Figure 1 **Dacryoadenitis.** A: Axial T2 shows diffuse enlargement of the left lacrimal gland. Note the tapered posterior margin (long arrow), as well as the involvement of the orbital lobe (short arrow). These findings suggest a lymphoid or inflammatory process rather than an epithelial neoplasm; B: Axial fat-suppressed contrast-enhanced T1 shows infiltration of the preseptal (long arrow) and post-septal (short arrow) fat. These features suggest orbital inflammatory disease rather than orbital lymphoma.

of exclusion, patients must be evaluated to rule out any malignancy, infection, systemic inflammatory process, or other concomitant medical conditions^[6]. The differential diagnosis includes local and systemic inflammatory conditions caused by neoplasm, infection, vascular malformation, and trauma^[5].

Inflammation occurs as a non-specific response to potentially harmful stimuli and is marked by increased blood flow and vascular permeability, vasodilatation, release of soluble mediators, extravasation of fluids, and cellular influx^[7]. Imaging findings in inflammatory disease are most often related to increased blood-tissue permeability resulting in contrast enhancement, which is often best seen with the use of fat suppression. Other common imaging findings in inflammation include fibrosis and edema^[8].

The site of involvement by OID dictates the radiological differential diagnosis, which can be especially important given that the symptoms may be nonspecific. We will review the common sites of involvement by OID and discuss differential diagnosis by site, as outlined in Table 1. However, it is important to note that OID commonly involves multiple sites, and that this feature is often important in suggesting OID ahead of other lesions.

Dacryoadenitis

Inflammation of the lacrimal gland, termed “dacryoadenitis”, is commonly seen in OID. Clinically, dacryoadenitis presents as a painful, firm, erythematous mass with edema in the lateral upper lid, and possible ptosis^[9,10]. Because the abnormality diffusely involves the lymphoid structures of the lacrimal gland, the classic appearance is of diffuse enlargement of the gland, including the orbital and palpebral lobes (Figure 1)^[10,11]. This is an important feature in distinguishing inflammatory disease from an epithelial neoplasm, which will typically only involve a portion of the lacrimal gland, usually the orbital lobe (Figure 2). Additional features that suggest an inflammatory process are a compressed, “almond-shaped” appearance of the gland as well as a tapered posterior margin of the gland. In contrast, an epithelial neoplasm will typically be seen as well-circumscribed and round to oval in shape^[10,12]. The axial T2 magnetic resonance imaging (MRI) in Figure 1A shows diffuse enlargement of the left lacrimal gland. Note the tapered posterior margin, as well as the involvement of the orbital lobe. These findings suggest a lymphoid or inflammatory process rather than an epithelial neoplasm.

Although it is usually relatively straightforward to dis-

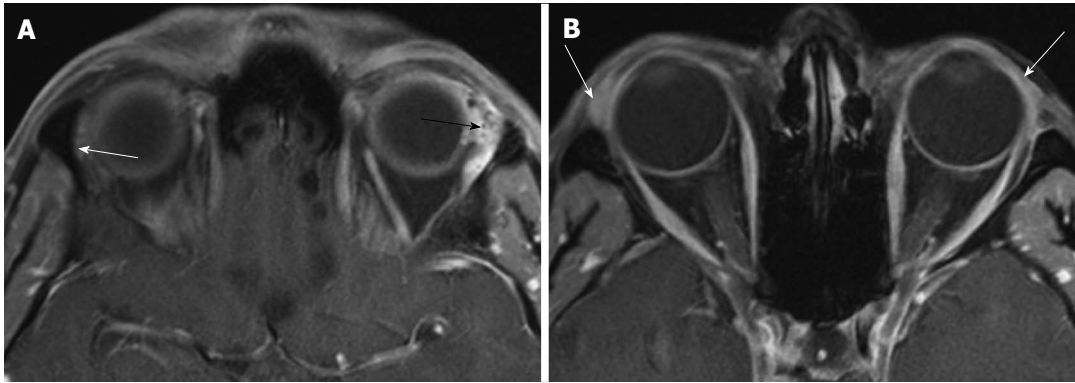


Figure 2 Adenoid cystic carcinoma of the lacrimal gland. A: Axial T1 non-enhanced MRI showing an enlarged, heterogeneous left lacrimal gland (black arrow). Compare this to the contralateral normal gland (white arrow); B: Axial T1 non-enhanced MRI showing sparing of the palpebral lobe (arrows). MRI: Magnetic resonance imaging.

tinguish an epithelial lacrimal gland neoplasm from a process involving the glandular lymphoid tissue, it is not always easy to distinguish lymphoma of the lacrimal gland from inflammatory disease. There are a few features that can aid in this distinction. First, inflammatory disease is more commonly bilateral (30% of chronic and 20% of acute inflammatory disease *vs* 12%-18% of lymphoma cases)^[13-15]. Second, inflammatory disease is more commonly associated with inflammation of the surrounding soft tissues. Figure 1B is an axial fat-suppressed contrast-enhanced T1 that shows infiltration of the preseptal and post septal fat. These features suggest OID rather than orbital lymphoma. There are exceptions to these rules, however. Sarcoid commonly produces diffuse lacrimal gland enlargement without infiltration of surrounding fat, a pattern that is more suggestive of lymphoma. Lymphoma may also have a surrounding inflammatory component in some cases^[12].

Diffusion-weighted imaging (DWI) is perhaps the most reliable technique to distinguish lymphoma from inflammatory disease. The densely packed cells in lymphoma inhibit the non-random motion of water, causing lymphoma to appear bright on DWI, with associated reduction in apparent diffusion coefficient (ADC) (Figure 3). An ADC of less than $0.92 \times 10^{-3} \text{ mm}^2/\text{s}$ was shown to be 100% sensitive and specific in distinguishing lymphoma from inflammatory disease^[3], though we have seen a handful of exceptions to this rule. Politi *et al.*^[13] found an ADC threshold of $0.775 \times 10^{-3} \text{ mm}^2/\text{s}$ was 96% sensitive and 93% specific for diagnosing ocular adnexal lymphoma.

Myositis

Orbital myositis is a non-infectious inflammatory condition primarily affecting the extraocular muscles (EOM)^[16]. Clinically, it presents with unilateral orbital or periorbital pain (17%-69%), painful and restricted eye movement (46%-54%), proptosis (32%-82%), periorbital edema (42%-75%), and hyperemia of the conjunctiva (33%-48%)^[17]. The classic appearance of EOM myositis includes a unilateral thickening of one or two EOMs, often also involving the surrounding fat, tendon, and myo-

tendinous junction (Figure 4). These are important features in distinguishing myositis from thyroid orbitopathy, which typically produces bilateral inflammation of EOM and spares the myotendinous junction. Of note, sparing of the myotendinous junction alone does not exclude OID. The lateral rectus and superior oblique muscles are also relatively spared early in the disease course in thyroid orbitopathy, and the condition often presents clinically with proptosis, chemosis, and diplopia. These findings may also suggest IgG4-related disease (IgG4-RD), which may present with similar clinical symptoms. The lymphocytic infiltration characteristic of IgG4-RD is often seen as inflammation of bilateral lacrimal glands and EOMs^[18]. The most frequently affected muscle is the inferior rectus. In patients with normal thyroid stimulating hormone and thyroid, these findings may suggest IgG4-RD and a serum IgG4 level may be considered.

The differential diagnosis for myositis also includes orbital cellulitis, which is commonly accompanied by fever, leukocytosis, and a clinical history of head and neck infection. Contrast-enhanced computed tomography (CT) imaging may identify the source of spread to the orbit and may also help identify any abscess that requires surgical intervention^[17]. Figure 5 demonstrates a case of infectious orbital cellulitis where corresponding sinus disease can be appreciated. Metastases and lymphoma may also mimic myositis and are often seen as a focal mass with increased signal intensity in the EOMs^[17]. Patients with low-flow carotid cavernous fistula (CCF) may also share features with myositis, as the venous congestion may appear on CT and MRI as inflamed EOM^[19] (Figure 6). Enlarged superior ophthalmic veins (SOVs) are typically seen in CCF. Transcranial doppler ultrasonography allows visualization of retrograde flow through the SOV, suggestive of CCF^[20] and angiography can be used to best characterize the fistulous communication (Figure 6C).

Contrast-enhanced T1 MRI with fat suppression best visualizes inflammation of the muscles, tendons, and surrounding fat, which is seen as swelling of the tendon and belly of the EOM. While not diagnostic, involvement of the perimuscular tendon is a distinguishing finding of non-thyroid inflammatory disease^[17]. In Figure 4C, a

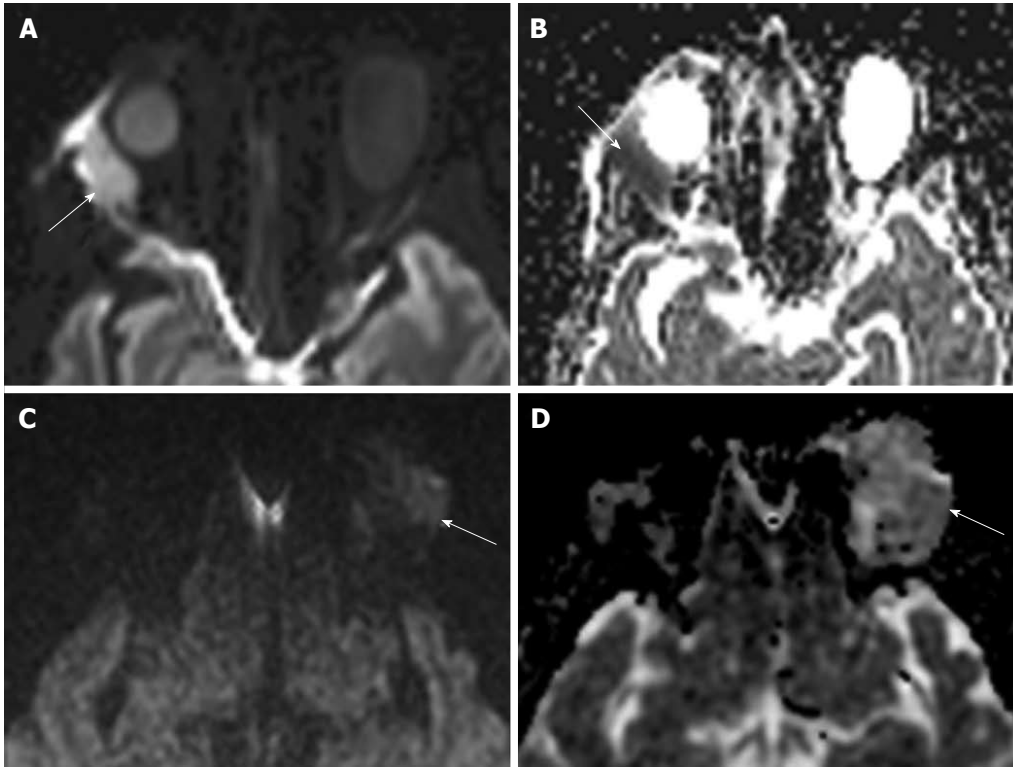


Figure 3 Lacrimal gland lymphoma (A and B) compared to inflammatory dacryoadenitis (C and D). A: DWI image in a patient with lacrimal gland lymphoma. Note the bright signal intensity (arrow) secondary to inhibition of water movement by the densely packed lymphoma cells; B: The corresponding ADC map of this patient shows an associated reduction in ADC, represented by the dark signal just lateral to the orbit (arrow); C: DWI image in a patient with inflammatory dacryocystadenitis. Note the dark signal compared to the patient with lymphoma (arrow); D: ADC map shows bright signal in the involved lacrimal gland (arrow) as compared to normal brain parenchyma. DWI: Diffusion-weighted imaging; ADC: Apparent diffusion coefficient.

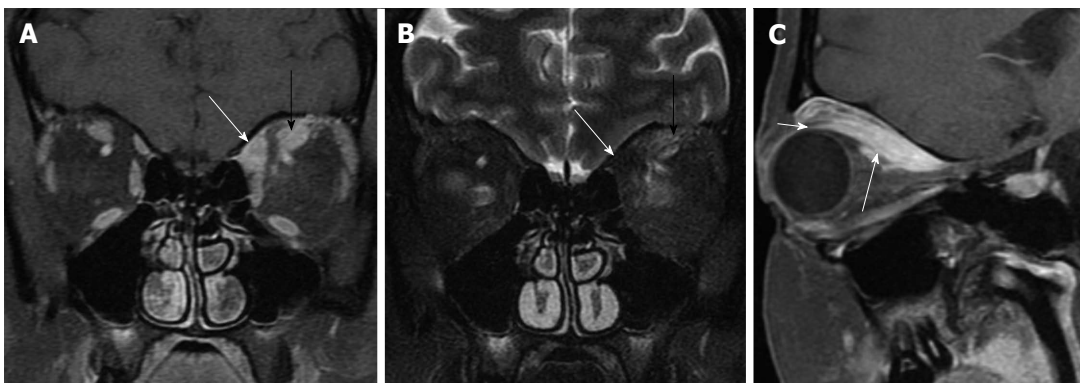


Figure 4 Myositic pseudotumor. A: Coronal fat-suppressed contrast-enhanced T1 shows enlarged left superior oblique (white arrow) and superior rectus (black arrow) muscles, and mild infiltration of the surrounding fat; B: Coronal fat-suppressed T2 shows low signal in the superior oblique muscle (white arrow), suggesting a more chronic, burned out process, whereas the superior rectus muscle (black arrow) shows brighter signal, indicative of a more acute process; C: Parasagittal oblique fat-suppressed contrast-enhanced T1 shows an enlarged superior rectus muscle belly (long arrow). The tendinous insertion (short arrow) is uncharacteristically spared by this process. Nevertheless, unilateral disease, infiltration of the surrounding fat, and early involvement of the superior oblique muscle indicate pseudotumor ahead of thyroid eye disease.

parasagittal oblique fat-suppressed contrast-enhanced T1 shows an enlarged superior rectus muscle belly with uncharacteristic sparing of the tendinous insertion. Nevertheless, unilateral disease, infiltration of the surrounding fat, and early involvement of the superior oblique muscle indicate pseudotumor ahead of thyroid eye disease. In cases where it is difficult to distinguish inflammation versus lymphoma, DWI can be used, as described above.

Cellulitis

Inflammatory orbital cellulitis describes inflammation of preseptal (peri-orbital) or postseptal (orbital) fat^[21]. Patients typically present with proptosis, chemosis, and painful diplopia^[21]. Cellulitis of preseptal and orbital soft tissue is best evaluated on contrast-enhanced T1 MRI with fat suppression, where the most common finding is poorly-defined periorbital enhancement enveloping

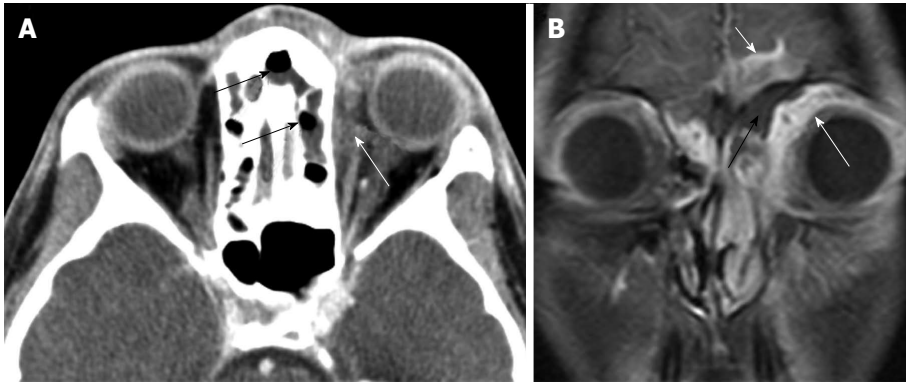


Figure 5 Infectious orbital cellulitis. A: Axial CT showing layering fluid in the ethmoid sinus and frontal recess on the left (black arrows), and infiltration of the orbital fat (white arrow); B: Coronal T1 fat saturated post-gadolinium MRI demonstrates orbital fat infiltration (long white arrow). Fluid in the adjacent ethmoid sinus (black arrow) and intracranial extension of the process (short white arrow) are also features that indicate infection rather than orbital inflammatory disease. CT: Computed tomography; MRI: Magnetic resonance imaging.

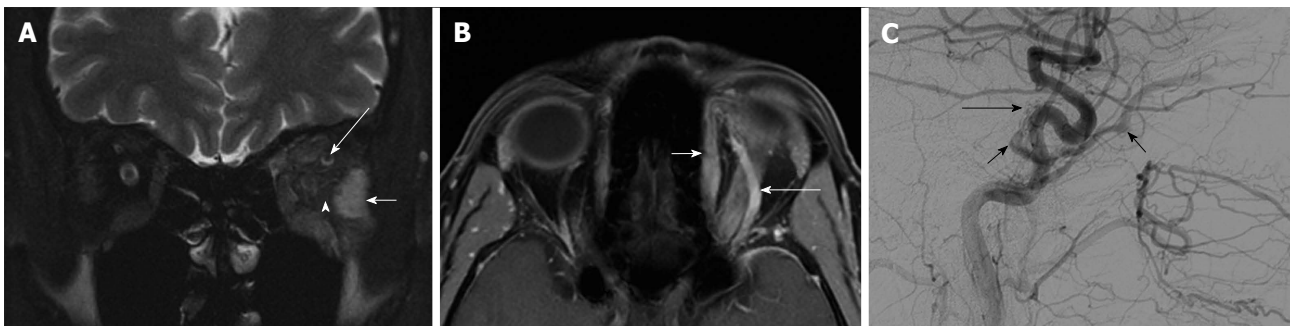


Figure 6 Indirect carotid-cavernous fistula. A: Coronal T2 MRI with fat saturation demonstrating mild infiltration of orbital fat (arrowhead) and thickening with high signal intensity in the EOMs. In this image, the lateral rectus muscle appears brightest (short white arrow). Note the enlarged SOV (long white arrow), suggesting CCF over myositis; B: Axial post-gadolinium T1 MRI with fat saturation. The SOV (long white arrow) is engorged secondary to retrograde flow from the cavernous sinus. The superior oblique muscle (short white arrow) is also enlarged; C: Angiogram with lateral projection common carotid artery injection (patient facing to the right) showing abnormal early filling in the cavernous sinus and SOV (short black arrows), as well as an abnormal tangle of vessels along dorsal surface of cavernous sinus (long black arrow), representing abnormally dilated intracavernous ICA branches. MRI: Magnetic resonance imaging; EOM: Extraocular muscles; SOV: Superior ophthalmic vein; CCF: Carotid cavernous fistula; ICA: Internal carotid artery.

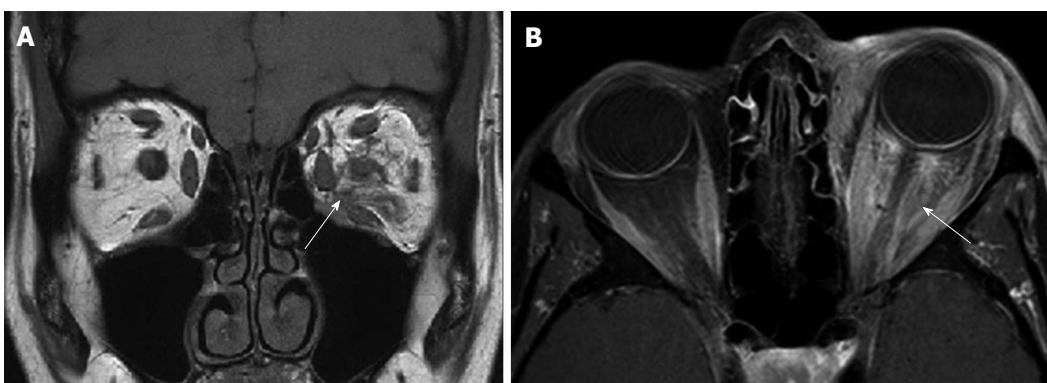


Figure 7 Diffuse cellulitic orbital inflammatory disease. A: Coronal T1-weighted image shows diffuse infiltration of the intraconal fat on the left (arrow); B: Axial fat-suppressed contrast-enhanced T1 shows diffuse enhancement throughout the intraconal fat. No well-defined focal mass or focal fluid collection is seen.

the globe and extending into post-septal fat¹⁴. Figure 7 is a T1-weighted MRI image showing diffuse infiltration of the intraconal fat. Infectious cellulitis shares similar imaging features, and it is important to obtain any clinical history of fever, sinusitis, or meningitis, as well as any evidence of leukocytosis^{2,11}. Presence of an abscess is a clear indicator of an infectious process. On T2 MRI,

infectious cellulitis typically presents as a hyperintense lesion, whereas OID lesions range from hypo- to hyperintense². Additional features suggesting inflammation of orbital and pre-septal fat include increased density and enhancement of periorbital soft tissues, eyelids, and orbital septum. Intraconal extension is a sign of advanced disease.

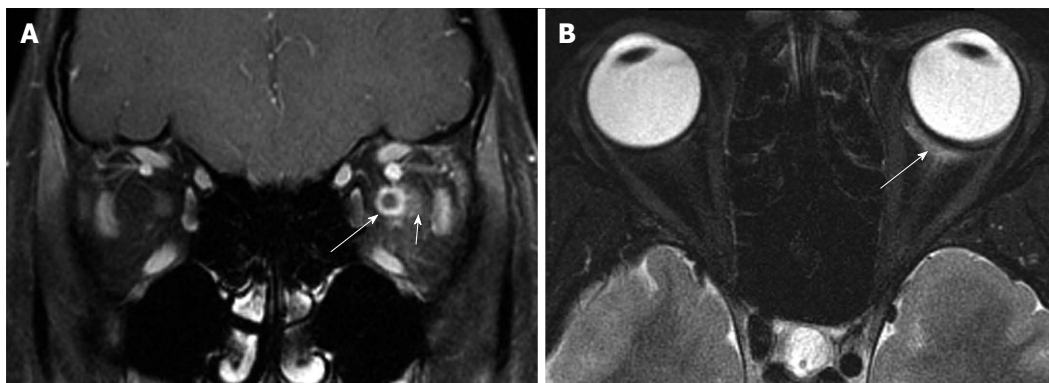


Figure 8 Perineuritic orbital inflammatory disease. A: Coronal fat-suppressed contrast-enhanced T1 shows circumferential enhancement about the left optic nerve (long arrow), with sparing of the nerve substance. There is also mild infiltration of the surrounding soft tissues (short arrow); B: Axial fat-suppressed T2 shows a small amount of edema about Tenon's capsule (arrow). This finding, along with clinical history of acute, painful presentation, help distinguish perineuritic pseudotumor from en plaque optic nerve sheath meningioma.

The differential diagnosis for inflammatory orbital cellulitis includes infection, CCF, cavernous sinus thrombosis, and Wegener's granulomatosis. Careful evaluation for any evidence of sinus disease is critical as infectious orbital cellulitis is a potentially life-threatening disease. Clinically, patients with infectious orbital cellulitis may have a history of diabetes or immunocompromise and a clinical history of sinus disease, recent dental procedures, or trauma. Due to the serious nature of infectious orbital cellulitis, a definitive diagnosis of OID may not be made until after a lack of response to empirical broad-spectrum antibiotic therapy^[5]. A CCF may be distinguished from OID by presence of an enlarged SOV, abnormal fullness of the cavernous sinus, or, in larger fistulas, flow voids on T2 MRI. Similar to CCF, cavernous sinus thrombosis presents with an enlarged SOV. A non-enhancing filling defect in the cavernous sinus on CT venography or contrast-enhanced MRI differentiates cavernous sinus thrombosis from CCF or OID. Wegener's granulomatosis (*i.e.*, granulomatosis with polyangiitis) may also mimic OID but is often accompanied by surrounding sinonasal wall destruction, which is best appreciated on CT.

Optic perineuritis

When intraorbital inflammation extends along the optic nerve and nerve sheath, it is termed "perineuritis"^[9]. Because inflammation affects the nerve sheath rather than the nerve itself, the primary presenting clinical feature is pain, while visual acuity, visual fields, and color vision are typically unaffected^[22]. Because the abnormality involves a loosely organized inflammatory infiltrate around the optic nerve, the classic appearance is of increased signal intensity surrounding the optic nerve, and extending into adjacent fat on post-gadolinium T1 MRI with fat-suppression (Figure 8A)^[9,22]. Enhancement of the optic nerve sheath is often poorly-defined^[23], which, in addition to a history of pain, may serve as an important feature in distinguishing perineuritis from meningioma (Figure 8B). This finding, along with clinical history of acute, painful presentation, help distinguish perineuritic pseudotumor from en plaque optic nerve sheath meningioma. Features

supporting a diagnosis of meningioma include a localized mass and calcifications on CT imaging^[9].

The differential diagnosis also includes demyelinating optic neuritis, though demyelinating disease almost always spares the soft tissues around the nerve while involving the nerve substance diffusely^[23]. It is important to distinguish perineuritis from optic neuritis, as the differential diagnosis and clinical course are quite different. Patients with optic neuritis (ON) are at high risk of developing multiple sclerosis and should be evaluated to rule out this disease. Diagnosis of optic perineuritis (OPN) is also critical, as prompt corticosteroid treatment may help prevent vision loss. Clinically, both OPN and ON typically present with eye pain and a swollen optic disc. While less commonly compared to ON, patients with OPN may also complain of vision impairment, though the vision impairment in OPN is often paracentral or arcuate^[23]. MRI of perineuritis often shows a "tram-track" pattern of enhancement around the nerve, rather than involving the nerve itself. Additionally, syphilitic infection, sarcoidosis, and viral encephalitides should be considered in patients with perineuritis^[24].

Periscleritis

Periscleritis may refer to inflammation of the sclera, uvea (iris, ciliary body, choroid), or tenon's capsule^[9]. This condition may present as a uveitis or a scleritis/episcleritis. Clinically, features of this inflammatory condition may mimic infection or tumor and are characterized by orbital pain, exophthalmos, and eyelid edema. Periscleritis can be clearly seen on MR or CT as a heterogeneous thickening along the outer rim of the eye^[25] (Figure 9), representing thickening of the sclera and/or uvea. Features of periscleritis can be best appreciated on axial T1 post-contrast MRI with fat saturation, which allows visualization of the enhancing vascular choroid as well as any extension into retrobulbar fat. A subchoroidal fluid collection displacing the retina may also be seen. Figure 9A shows an axial contrast-enhanced CT in an 87-year-old immunocompromised man with left eye pain and and ordering indication of "cellulitis". Note the mild infiltration of the

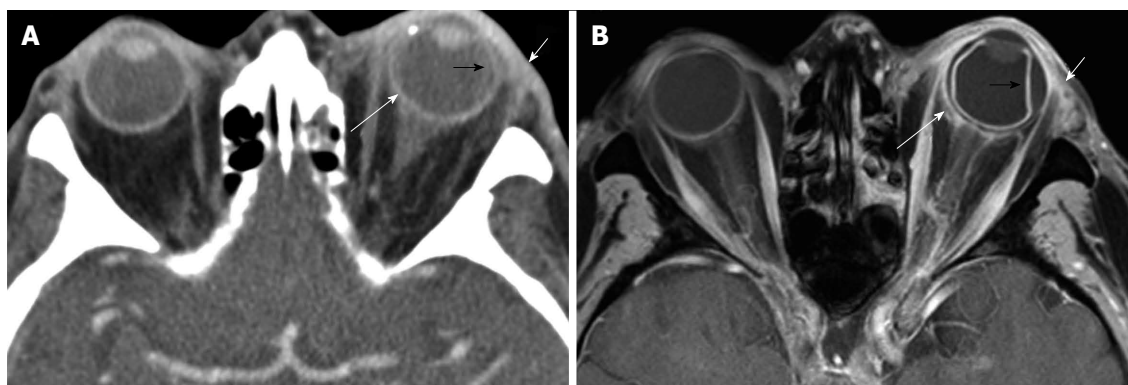


Figure 9 Periscleritic orbital inflammatory disease. Eighty-seven-year-old immunocompromised man with left eye pain and ordering indication of "cellulitis". A: Axial contrast-enhanced CT shows mild infiltration of the left periorbital fat (short white arrow). There is also periscleral edema (long white arrow), and subtle high density along the temporal surface of the globe that is suggestive of a subchoroidal fluid collection (black arrow); B: Axial fat-suppressed contrast-enhanced T1 shows these findings more conspicuously. Note that the elevated choroid layer (black arrow) extends anteriorly to the region of the ciliary body. Periscleral edema (long white arrow) extending to Tenon's capsule is better seen. CT: Computed tomography.

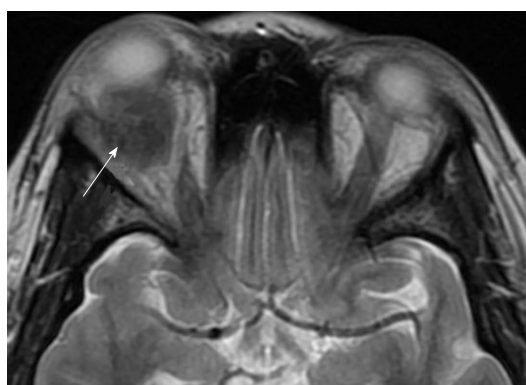


Figure 10 Orbital inflammatory disease producing a focal mass. Axial T2 shows a well-defined, T2 hypointense mass in the right orbit, discrete from adjacent extraocular muscles and from the lacrimal gland.

left periorbital fat, periscleral edema, and subtle high density along the temporal surface of the globe suggestive of a subchoroidal fluid collection. An axial fat-suppressed contrast-enhanced T1 MRI in this patient shows these findings more conspicuously (Figure 9B). Tenon's capsule (aka fascia bulbi or bulbar sheath) is a thin membrane that lies between the sclera and orbital fat^[26]. Thickening is often seen in this area and may be accompanied by a periscleral fluid collection.

The differential diagnosis includes any systemic inflammatory disease that causes posterior scleritis, such as lupus or rheumatoid arthritis. Endophthalmitis may also have a similar imaging appearance, but clinical vitritis should be readily apparent in these cases. Infectious periscleritis often arises secondary to sinus infection and it is important to evaluate the paranasal sinuses, particularly the ethmoid sinus, in patients with uveoscleral thickening^[4].

Focal mass

OID may also present as a focal inflammatory mass, which represents up to 9% of all orbital mass lesions and is the most common cause of painful orbital mass in adults^[6,9]. Clinical presentation is highly variable as an inflammatory

mass can be present anywhere in the orbit, with resulting symptoms related to mass effect and inflammation. A mass lesion in OID is best seen on axial T2 MRI, where it appears as a well-defined, T2 hypointense mass, discrete from adjacent EOM and from the lacrimal gland (Figure 10). The hypointensity appreciated in this image is secondary to fibrosis. On T1 MRI they appear slightly brighter, isointense to muscle, and show prominent post-gadolinium enhancement^[27]. As lesions progress, fibrosis develops, resulting in retraction of adjacent structures. Infiltration of inflammation and fibrosis into the sclera and periorbital soft tissue may lead to globe deformity. In fact, the degree of fibrosis and traction on other tissues often suggests a greater chronicity of disease.

Inflammatory pseudotumors are often difficult to distinguish from a true neoplasm^[28]. Lymphoma accounts for 20% of orbital mass lesions and is particularly difficult to distinguish from OID^[27,28]. Clinically, lymphomatous lesions present more commonly with palpable mass, while OID may present with eyelid edema, optic nerve atrophy, and conjunctival congestion^[27]. Imaging features of inflammatory pseudotumor that help distinguish it from lymphoma include marked T2 hypointensity and evidence of fibrosis. Lymphoma typically appears more lobular and, as described earlier, has greater diffusion restriction than OID on DWI. Metastases are usually brighter on T2 imaging. One exception to this is scirrhous breast cancer metastasis, which commonly produces a T2-hypointense, fibrotic mass with variable amount of traction on adjacent structures. Certain benign tumors, such as solitary fibrous tumor, can also show marked T2 hypointensity and overlap with OID in appearance^[29].

Diffuse OID

Diffuse orbital inflammation is found in approximately 4%-11% of patients with OID^[30]. Similar to focal mass, clinical presentation is highly variable as many sites of the orbit can be affected. Patients must be evaluated for systemic disease, including vasculitis and autoimmune conditions such as Churg-Strauss disease or Wegener's

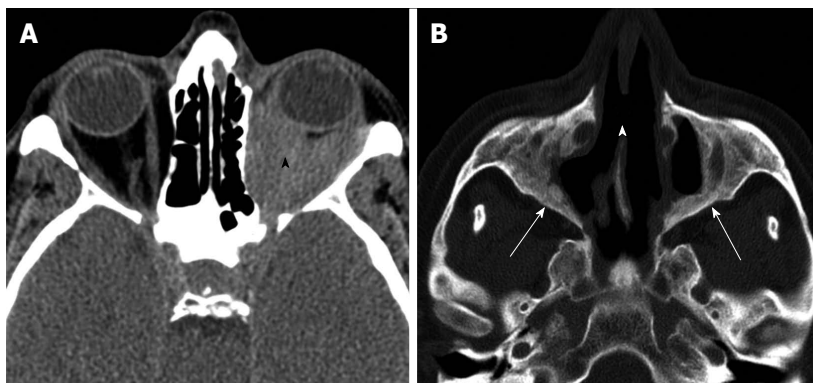


Figure 11 Wegener's granulomatosis. A: Non-enhanced axial CT through orbit demonstrating diffuse infiltration of orbital fat (black arrowhead); B: Axial CT in through sinuses in bone window shows destruction of medial maxillary sinus walls, perforation of nasal septum (white arrowhead), and chronic neo osteogenesis along sinus walls (white arrows). CT: Computed tomography.

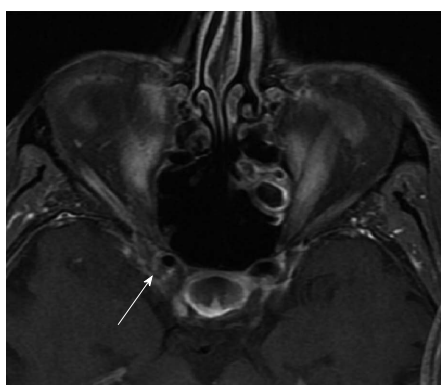


Figure 12 Orbital apicitis (Tolosa-Hunt). Axial fat-suppressed contrast-enhanced T1 shows ill-defined enhancement involving the right orbital apex, and extending into the middle cranial fossa along the margin of the cavernous sinus (arrow).

granulomatosis^[31,32]. Common characteristics of orbital involvement in Wegener's include diffuse infiltration of orbital fat and sinonasal destructive changes (Figure 11). Chest imaging and an immunologic workup are suggested prior to biopsy of diffuse OID. Lymphoma may also mimic diffuse OID and, as described earlier, appears more lobular and may be best distinguished from OID using DWI MRI^[3]. Chronic inflammation often contains regions with varying degrees of fibrosis, resulting in a heterogeneous appearance on MRI.

Orbital apicitis

Involvement of the orbital apex, while less common, is associated with the poorest outcome^[4,9,33]. Inflammatory lesions of the orbital apex are at risk of invading the optic nerve or extending into the cavernous sinus. Tolosa-Hunt syndrome is a rare clinical condition caused by cavernous sinus inflammation presenting with relapsing/remitting acute orbital pain and paralysis of cranial nerves III, IV, V₁, and VI^[34]. Extension of OID into the cavernous sinus is a common cause of this clinical condition and, similar to other OID lesions, intravenous steroid treatment is the mainstay of care^[11,34]. On T1 MRI, inflammation appears as an intermediate intensity lesion, as inflammatory tissue replaces the normal high-intensity fat at the orbital apex. Similar to other inflammatory pseudotumors, OID of the orbital apex appears hypointense

on T2, with a darker signal indicating higher degrees of fibrosis^[9,33]. In addition to the cavernous sinus, lesions of the orbital apex may also extend into the middle cranial fossa through the superior orbital fissure or optic canal, as well as the infratemporal fossa and pterygopalatine fossa through the inferior orbital fissure. Figure 12 shows an axial, fat-suppressed, contrast-enhanced T1 MRI in a patient with Tolosa-Hunt syndrome. Note the ill-defined enhancement involving the right orbital apex and extending into the middle cranial fossa along the margin of the cavernous sinus (arrow). Figure 13 shows bilateral cavernous sinus infiltration in a different patient, which resolved completely after treatment.

The differential diagnosis of orbital apex lesions includes meningioma, granulomatous disease, and local spread of central nervous system (CNS) pathology. Evidence of cystic foci likely represents necrotic lesions, which leads the diagnosis away from OID. Enhancement or fullness of the cavernous sinus can be appreciated on dynamic imaging and angiography may demonstrate narrowing of the cavernous sinus. Careful examination for disruption of the dural barrier and intracranial extension is critical. Common features of CNS involvement include abnormal soft tissue extending into the middle cranial fossa, expansion of the ipsilateral cavernous sinus walls, and post-gadolinium enhancement of the meninges or dura^[9].

Sclerosing orbital inflammation

Sclerosing orbital inflammation is a rare condition representing 6%-8% of all inflammatory lesions of the orbit^[35]. Previously thought to be along the spectrum of OID, it is now considered a distinct pathologic entity. Clinically, it is characterized by proptosis, mild external inflammatory signs, restricted motility, diplopia, and dull, chronic pain^[5]. The natural history of the condition often involves a chronic, indolent, progressive process involving dense fibrosis and lymphocytic infiltrate. On CT or MRI, it is most commonly described as a homogenous, diffuse, ill-defined mass most frequently in the anterior orbit and mid-orbit.

Definitive diagnosis is by biopsy, revealing dense scarring and fibrosis. While no definitive treatment has been identified, early and aggressive steroid therapy is recommended as vision loss may occur in up to 30% of

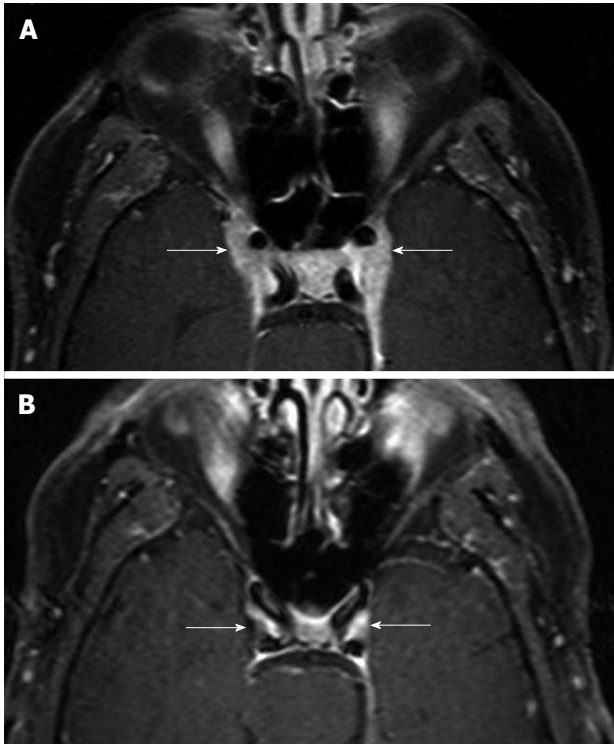


Figure 13 Tolosa-Hunt syndrome, before and after treatment. A: Axial fat-suppressed contrast-enhanced T1 showing bilateral cavernous sinus infiltration and enhancing tissue along the lateral margins of the cavernous sinus; B: Complete resolution after treatment.

affected patients^[5].

CONCLUSION

OID or orbital pseudotumor, represents a group of heterogeneous inflammatory diseases, the exact etiology of which is unknown. The condition may involve a number of structures in the orbit, the clinical presentations and imaging findings of which are variable and overlapping. As OID is a diagnosis of exclusion, other pathologic conditions affecting the orbit must be ruled out. Imaging plays an important role in evaluation of OID, with proper identification of involved structures being a critical first step toward diagnosis. CT, MRI with fat suppression, and DWI all play a role in distinguishing OID from other pathologies affecting the orbit. Treatment for OID consists of pulsed corticosteroid therapy and the degree of response may often provide clues as to the diagnosis.

REFERENCES

- Swamy BN, McCluskey P, Nemet A, Crouch R, Martin P, Bengler R, Ghabriel R, Wakefield D. Idiopathic orbital inflammatory syndrome: clinical features and treatment outcomes. *Br J Ophthalmol* 2007; **91**: 1667-1670 [PMID: 17620331 DOI: 10.1136/bjo.2007.124156]
- Kapur R, Sepahdari AR, Mafee MF, Putterman AM, Aakalu V, Wendel LJ, Setabutr P. MR imaging of orbital inflammatory syndrome, orbital cellulitis, and orbital lymphoid lesions: the role of diffusion-weighted imaging. *AJNR Am J Neuroradiol* 2009; **30**: 64-70 [PMID: 18842758 DOI: 10.3174/ajnr.A1315]
- Sepahdari AR, Aakalu VK, Setabutr P, Shiehorteza M, Naheedy JH, Mafee MF. Indeterminate orbital masses: restricted diffusion at MR imaging with echo-planar diffusion-weighted imaging predicts malignancy. *Radiology* 2010; **256**: 554-564 [PMID: 20656840 DOI: 10.1148/radiol.10091956]
- Yuen SJ, Rubin PA. Idiopathic orbital inflammation: distribution, clinical features, and treatment outcome. *Arch Ophthalmol* 2003; **121**: 491-499 [PMID: 12695246 DOI: 10.1001/archophth.121.4.491]
- Gordon LK. Orbital inflammatory disease: a diagnostic and therapeutic challenge. *Eye (Lond)* 2006; **20**: 1196-1206 [PMID: 17019419 DOI: 10.1038/sj.eye.6702383]
- Lee EJ, Jung SL, Kim BS, Ahn KJ, Kim YJ, Jung AK, Park CS, Song SY, Park NH, Kim MS. MR imaging of orbital inflammatory pseudotumors with extraorbital extension. *Korean J Radiol* 2005; **6**: 82-88 [PMID: 15968146]
- Ferrero-Miliani L, Nielsen OH, Andersen PS, Girardin SE. Chronic inflammation: importance of NOD2 and NALP3 in interleukin-1beta generation. *Clin Exp Immunol* 2007; **147**: 227-235 [PMID: 17223962 DOI: 10.1111/j.1365-2249.2006.03261.x]
- Narla LD, Newman B, Spottswood SS, Narla S, Kolli R. Inflammatory pseudotumor. *Radiographics* 2003; **23**: 719-729 [PMID: 12740472 DOI: 10.1148/rg.233025073]
- Ding ZX, Lip G, Chong V. Idiopathic orbital pseudotumour. *Clin Radiol* 2011; **66**: 886-892 [PMID: 21546008 DOI: 10.1016/j.crad.2011.03.018]
- Mafee MF, Edward DP, Koeller KK, Dorodi S. Lacrimal gland tumors and simulating lesions. Clinicopathologic and MR imaging features. *Radiol Clin North Am* 1999; **37**: 219-39, xii [PMID: 10026740]
- Lutt JR, Lim LL, Phal PM, Rosenbaum JT. Orbital inflammatory disease. *Semin Arthritis Rheum* 2008; **37**: 207-222 [PMID: 17765951 DOI: 10.1016/j.semarthrit.2007.06.003]
- Gündüz K, Shields CL, Günel I, Shields JA. Magnetic resonance imaging of unilateral lacrimal gland lesions. *Graefes Arch Clin Exp Ophthalmol* 2003; **241**: 907-913 [PMID: 14579116 DOI: 10.1007/s00417-003-0748-z]
- Politi LS, Forghani R, Godi C, Resti AG, Ponzoni M, Bianchi S, Iadanza A, Ambrosi A, Falini A, Ferreri AJ, Curtin HD, Scotti G. Ocular adnexal lymphoma: diffusion-weighted mr imaging for differential diagnosis and therapeutic monitoring. *Radiology* 2010; **256**: 565-574 [PMID: 20656841 DOI: 10.1148/radiol.10100086]
- Lacrimal Gland Tumor Study Group. An epidemiological survey of lacrimal fossa lesions in Japan: number of patients and their sex ratio by pathological diagnosis. *Jpn J Ophthalmol* 2005; **49**: 343-348 [PMID: 16187032 DOI: 10.1007/s10384-005-0224-x]
- Derr C, Shah A. Bilateral dacryoadenitis. *J Emerg Trauma Shock* 2012; **5**: 92-94 [PMID: 22416166 DOI: 10.4103/0974-2700.93096]
- Kralik SF, Kersten R, Glastonbury CM. Evaluation of orbital disorders and cranial nerve innervation of the extraocular muscles. *Magn Reson Imaging Clin N Am* 2012; **20**: 413-434 [PMID: 22877949 DOI: 10.1016/j.mric.2012.05.005]
- Costa RM, Dumitrascu OM, Gordon LK. Orbital myositis: diagnosis and management. *Curr Allergy Asthma Rep* 2009; **9**: 316-323 [PMID: 19656480]
- Inaba H, Hayakawa T, Miyamoto W, Takeshima K, Yamaoka H, Furukawa Y, Kawashima H, Ariyasu H, Wakasaki H, Furuta H, Nishi M, Nakao T, Sasaki H, Okada Y, Matsunaga K, Nakamura Y, Akamizu T. IgG4-related ocular adnexal disease mimicking thyroid-associated orbitopathy. *Intern Med* 2013; **52**: 2545-2551 [PMID: 24240795]
- Chapman PR, Gaddamanugu S, Bag AK, Roth NT, Vattoth S. Vascular lesions of the central skull base region. *Semin Ultrasound CT MR* 2013; **34**: 459-475 [PMID: 24216454 DOI: 10.1053/j.sult.2013.09.003]
- Kiliç T, Elmaci I, Bayri Y, Pamir MN, Erzen C. Value of

- transcranial Doppler ultrasonography in the diagnosis and follow-up of carotid-cavernous fistulae. *Acta Neurochir (Wien)* 2001; **143**: 1257-1264, discussion 1264-1265 [PMID: 11810390 DOI: 10.1007/s007010100022]
- 21 **Danesh-Meyer HV**, Rosser PM. Orbital inflammatory disease. *Int Ophthalmol Clin* 2007; **47**: 79-92, ix [PMID: 18049282 DOI: 10.1097/IIO.0b013e3181571eee]
 - 22 **Szatmáry G**. Imaging of the orbit. *Neurol Clin* 2009; **27**: 251-84, x [PMID: 19055983 DOI: 10.1016/j.ncl.2008.09.008]
 - 23 **Purvin V**, Kawasaki A, Jacobson DM. Optic perineuritis: clinical and radiographic features. *Arch Ophthalmol* 2001; **119**: 1299-1306 [PMID: 11545635]
 - 24 **Nakamura M**, Hara R, Kimura R, Ohgiya N, Yamamoto N, Morino I, Yamamoto M. Optic perineuritis not associated with syphilitic infection. *Neuro-Ophthalmology* 1999; **21**: 135-145 [DOI: 10.1076/noph.21.3.135.3900]
 - 25 **Atlas SW**, Grossman RI, Savino PJ, Sergott RC, Schatz NJ, Bosley TM, Hackney DB, Goldberg HI, Bilaniuk LT, Zimmerman RA. Surface-coil MR of orbital pseudotumor. *AJR Am J Roentgenol* 1987; **148**: 803-808 [PMID: 3493667 DOI: 10.2214/ajr.148.4.803]
 - 26 **Tenon JR**, Naus J, Blanken R. Anatomical observations on some parts of the eye and eyelids. 1805. *Strabismus* 2003; **11**: 63-68 [PMID: 12789585]
 - 27 **Yan J**, Wu Z, Li Y. The differentiation of idiopathic inflammatory pseudotumor from lymphoid tumors of orbit: analysis of 319 cases. *Orbit* 2004; **23**: 245-254 [PMID: 15590527 DOI: 10.1080/01676830490487980]
 - 28 **Kawakami K**, Ito R, Tono Y, Yazaki A, Murata T, Baba Y, Uchiyama T, Ito M. Orbital inflammatory lesion as an initial manifestation of systemic nasal type NK/T-cell lymphoma. *J Clin Exp Hematop* 2012; **52**: 137-139 [PMID: 23037631]
 - 29 **Yang BT**, Wang YZ, Dong JY, Wang XY, Wang ZC. MRI study of solitary fibrous tumor in the orbit. *AJR Am J Roentgenol* 2012; **199**: W506-W511 [PMID: 22997401 DOI: 10.2214/AJR.11.8477]
 - 30 **Yan J**, Qiu H, Wu Z, Li Y. Idiopathic orbital inflammatory pseudotumor in Chinese children. *Orbit* 2006; **25**: 1-4 [PMID: 16527767 DOI: 10.1080/01676830500505608]
 - 31 **Takanashi T**, Uchida S, Arita M, Okada M, Kashii S. Orbital inflammatory pseudotumor and ischemic vasculitis in Churg-Strauss syndrome: report of two cases and review of the literature. *Ophthalmology* 2001; **108**: 1129-1133 [PMID: 11382641]
 - 32 **Jordan N**, Verma H, Ekbote A, Sangle S, D'Cruz D. Dacryoadenitis and diffuse orbital inflammation: unusual first presentations of Churg-Strauss syndrome. *Orbit* 2011; **30**: 160-161 [PMID: 21574807 DOI: 10.3109/01676830.2011.569628]
 - 33 **Kline LB**, Hoyt WF. The Tolosa-Hunt syndrome. *J Neurol Neurosurg Psychiatry* 2001; **71**: 577-582 [PMID: 11606665]
 - 34 **Zurawski J**, Akhondi H. Tolosa-Hunt syndrome-a rare cause of headache and ophthalmoplegia. *Lancet* 2013; **382**: 912 [PMID: 24012271 DOI: 10.1016/S0140-6736(13)61442-7]
 - 35 **Pemberton JD**, Fay A. Idiopathic sclerosing orbital inflammation: a review of demographics, clinical presentation, imaging, pathology, treatment, and outcome. *Ophthal Plast Reconstr Surg* 2012; **28**: 79-83 [PMID: 22262301 DOI: 10.1097/IOP.0b013e318238ecf7]

P- Reviewers: Rajabi MT, Sharma S S- Editor: Song XX
L- Editor: A E- Editor: Liu SQ



Use of cone beam computed tomography in periodontology

Buket Acar, Kivanç Kamburoğlu

Buket Acar, Kivanç Kamburoğlu, Department of Dentomaxillofacial Radiology, Faculty of Dentistry, Ankara University, Ankara 06560, Turkey

Buket Acar, Department of Periodontology, Faculty of Dentistry, Hacettepe University, Ankara 06230, Turkey

Author contributions: Acar B and Kamburoğlu K contributed equally to this paper.

Correspondence to: Kivanç Kamburoğlu, DDS, MSc, PhD, Department of Dentomaxillofacial Radiology, Faculty of Dentistry, Ankara University, Emniyet District, İnci Taş Street, Yenimahalle, Ankara 06560, Turkey. dtkivo@yahoo.com

Telephone: +90-31-22965632 Fax: +90-31-22123954

Received: December 25, 2013 Revised: March 1, 2014

Accepted: April 25, 2014

Published online: March 28, 2015

Abstract

Diagnosis of periodontal disease mainly depends on clinical signs and symptoms. However, in the case of bone destruction, radiographs are valuable diagnostic tools as an adjunct to the clinical examination. Two dimensional periapical and panoramic radiographs are routinely used for diagnosing periodontal bone levels. In two dimensional imaging, evaluation of bone craters, lamina dura and periodontal bone level is limited by projection geometry and superpositions of adjacent anatomical structures. Those limitations of 2D radiographs can be eliminated by three-dimensional imaging techniques such as computed tomography. Cone beam computed tomography (CBCT) generates 3D volumetric images and is also commonly used in dentistry. All CBCT units provide axial, coronal and sagittal multi-planar reconstructed images without magnification. Also, panoramic images without distortion and magnification can be generated with curved planar reformation. CBCT displays 3D images that are necessary for the diagnosis of intra bony defects, furcation involvements and buccal/lingual bone destructions. CBCT applications provide obvious benefits in periodontics, however; it should be used only in correct

indications considering the necessity and the potential hazards of the examination.

© 2015 Baishideng Publishing Group Inc. All rights reserved.

Key words: Cone beam computed tomography; Periodontology; Radiology; Dentistry; Oral diagnosis

Core tip: Dentomaxillofacial cone beam computed tomography (CBCT) is now commonly used for a variety of diagnostic tasks in dentistry. Its applications in periodontal disease has not been very well reviewed and documented previously. This review paper will shed light into this innovative technology and its use in periodontology. Diagnosis of periodontal disease depends on clinical signs and symptoms. However, in the case of bone destruction, radiographs are valuable diagnostic tools as an adjunct to the clinical examination. Two dimensional periapical and panoramic radiographs are routinely used for diagnosing periodontal bone levels. In two dimensional imaging, evaluation of bone craters, lamina dura and periodontal bone level is limited by projection geometry and superposition of adjacent anatomical structures. Those limitations of 2D radiographs can be eliminated by three-dimensional imaging techniques such as computed tomography. CBCT generates 3D volumetric images and is also commonly used in dentistry. All CBCT units provide axial, coronal and sagittal multi-planar reconstructed images without magnification. Also, panoramic images without distortion and magnification can be generated with curved planar reformation. CBCT displays 3D images that are necessary for the diagnosis of intra bony defects, furcation involvements and buccal/lingual bone destructions. CBCT applications provide obvious benefits in periodontics, however; it should be used only in correct indications considering the necessity and the potential hazards of the examination.

Original sources: Acar B, Kamburoğlu K. Use of cone beam

computed tomography in periodontology. *World J Radiol* 2014; 6(5): 139-147 Available from: URL: <http://www.wjgnet.com/1949-8470/full/v6/i5/139.htm> DOI: <http://dx.doi.org/10.4329/wjr.v6.i5.139>

INTRODUCTION

Periodontal diseases consist of a variety of conditions affecting the periodontal tissues such as: gingiva, periodontal ligament, root cementum and alveolar bone. Some of these tissues are soft (gingiva, periodontal ligament) whereas some are hard tissues (root cementum and alveolar bone)^[1]. Inflammation of periodontal tissues is a common disease which results in attachment loss and destruction of alveolar bone. Diagnosis of periodontal diseases mainly depends on clinical signs and symptoms^[2]. However, in the case of bone destruction, radiographs are valuable diagnostic tools as an adjunct to the clinical examination. Although periapical and panoramic radiographs are routinely used for diagnosing periodontal bone levels, the projection geometry of the X-ray beam may cause magnification and distortion which makes it impossible to obtain accurate diagnosis^[3]. In panoramic and periapical radiographs, bone craters, lamina dura and periodontal bone level evaluation is limited by the superposition of adjacent anatomic structures and projection geometry. Conventional two-dimensional radiographs generate 2D images in which teeth roots are superimposed on the alveolar bone and as a result bone changes such as; furcation involvement, buccal and lingual alveolar bone defects are obscured^[4-6]. Limitations of 2D radiographs can be eliminated by using three-dimensional imaging techniques such as computed tomography (CT)^[7]. CT can be categorized into two groups according to the geometry of X-ray beam: 1-fan beam and 2-cone beam (Figure 1). Cone beam computed tomography (CBCT) generates 3D volumetric images and is commonly used in dentistry^[8]. CBCT technology has developed rapidly since it was first used in 1982 at Mayo Clinic Biodynamic Research Laboratory for angiography, radiotherapy and mammography applications. In CBCT technique, a cone-shaped X-ray beam rotates around the patient's head and collects base images used to construct 3D volumetric data from which multi-planar (axial, sagittal, coronal and cross-sectional) reconstructions can be generated^[7,8] (Figure 2). Voxel sizes affect CBCT image quality and alveolar defects can be evaluated with highest accuracy when smaller voxel sizes are utilized^[9]. Similarly, accuracy of alveolar bone height measurements are inversely proportional to voxel sizes of CBCT images evaluated^[10].

ADVANTAGES OF CBCT

A single rotation is sufficient during irradiation of the patient for acquisition of base projection images and CBCT scanners use two-dimensional flat-panel detectors

which provide a scan of the entire region of interest^[11,12]. The collimation of the X-ray beam to the area of interest minimizes the radiation dose. Most CBCT units offer different field of view (FOV) options with various sizes (Figure 3). The use of small FOV lowers the effective radiation dose^[8-13]. The voxels in CBCT units are isotropic that enables sub-millimeter geometric resolution, thereby; a high degree of measurement accuracy can be obtained (Figure 4). This feature contributes to the high diagnostic capacity of CBCT images obtained from high-density dento-maxillofacial structures such as teeth and bone^[8]. Whereas medical CT requires multiple rotations entailing high effective radiation doses, with CBCT, a single rotation is sufficient for the acquisition of base images^[8,14,15]. All CBCT units provide axial, coronal and sagittal multiplanar reconstructed images without magnification. Panoramic images can also be generated with curved planar reformation. Multiplanar image can be thickened by increasing the number of adjacent voxels and it is also possible to apply 3D volume rendering and modeling by use of appropriate software package^[8,11]. In comparison to medical CT, CBCT offers lower radiation dose and cost along with smaller space requirement^[14]. CBCT has better spatial resolution when compared with medical CT^[16,17] (Table 1).

LIMITATIONS OF CBCT

CBCT is not able to offer high contrast resolution and it can not utilized soft tissues, therefore; CBCT is mainly indicated for the evaluation of hard tissues in the dento-maxillofacial complex^[11,12]. When compared to 2D imaging, CBCT has higher cost and effective radiation dose but it has lower resolution and lack of availability^[13,16,17] (Table 2). Because of the shape of X-ray beam, the scatter radiation is higher in CBCT than with fan-beam tomography. Moreover, the beam-hardening artifacts that comprise radiolucent areas and radiopaque lines can occur more often in CBCT images (Figure 5). A significant limitation of CBCT imaging is the presence of metal artifacts, *i.e.*, image flaws that are unrelated to the scanned object, which are caused by metal and amalgam restorations and, to a lesser extent, root-canal filling material and implants. Such artifacts include streaks around materials as well as dark zones that affect the overall quality of the image. Streak artifacts appear as linear hyperdensities that radiate from a metallic object and may extend to the width of the field, affecting visualization of areas even on the opposite side of an image (Figure 6). Beam-hardening artifacts, which appear as dark bands adjacent to high-density structures, may mimic disease^[8,9,18].

RADIOLOGICAL EVALUATION OF PERIODONTAL TISSUES

Radiographs provide information about quantity, localization and pattern of bone resorption, changes in bone

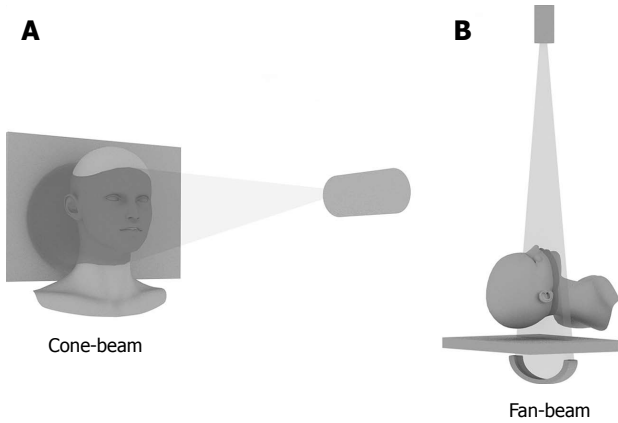


Figure 1 The diagram displays cone-beam and fan-beam shapes in cone beam computed tomography (A) and medical computed tomography (B).

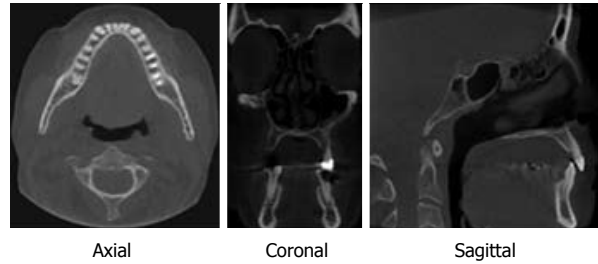
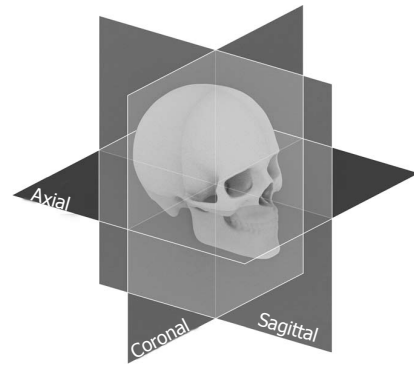


Figure 2 Multi-planar reconstructed images can be generated by cone beam computed tomography volumetric data.

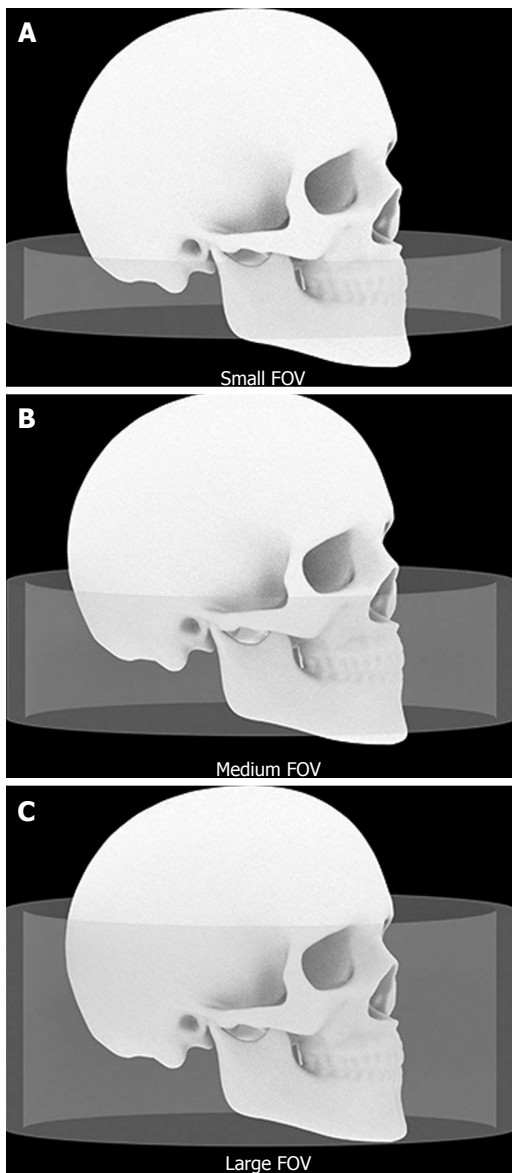


Figure 3 The dimensions of the irradiated regions with different field of view sizes are shown schematically. A: Small FOV; B: Medium FOV; C: Large FOV. FOV: Field of view.

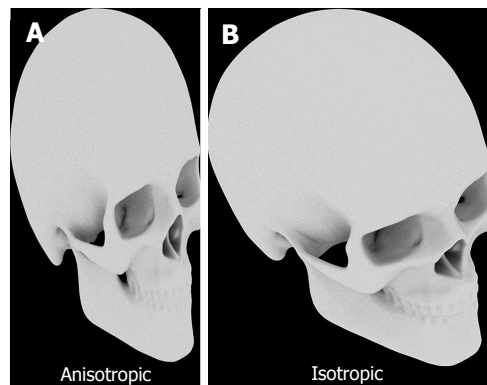


Figure 4 Anisotropic (A) and isotropic (B) 3D images.

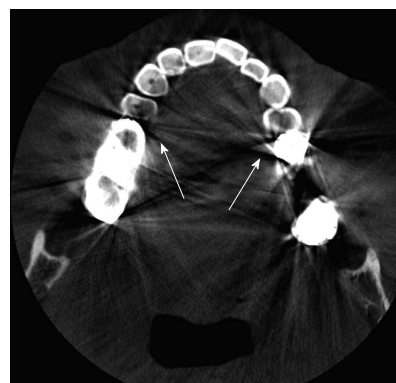


Figure 5 Beam-hardening artifacts caused by metal restorations (arrows).

trabeculations, conditions of lamina dura and periodontal space, length and shape of teeth roots, ratio of clinical crown length to root length. Some etiological factors of

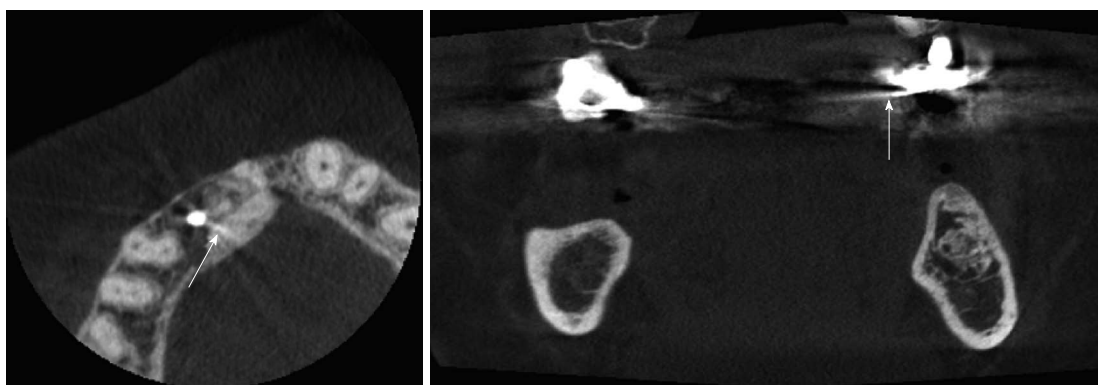


Figure 6 Streak artifacts are observed as radiopacity in a radial manner (arrows).

Table 1 Comparison of cone beam computerized tomography and medical computed tomography are listed in the table

CBCT	Medical CT
Single rotation	Multiple rotations
Lower radiation dose	Higher radiation dose
Isotropic voxels	Anisotropic voxels
Lower cost	Higher cost
Smaller space requirement	Larger devices
Better spatial resolution	Better contrast resolution
Deficiency to display soft tissues	Clear evaluation of soft tissues
Higher scatter radiation	Lower scatter radiation

Table 2 The table shows the features of cone beam computed tomography and conventional radiographs

CBCT	Conventional radiography
3D imaging	2D imaging
Cross-sectional and volumetric images	Superpositions
Elimination of image deformity	Distortion and magnification
Higher radiation dose	Lower radiation dose
Higher cost	Lower cost
Larger devices	Smaller space requirement

CT: computed tomography; CBCT: Cone beam computerized tomography.

CBCT: Cone beam computed tomography.

periodontal disease, such as calculus, incompatible restorations may be also seen in radiographs. Inter-proximal areas of maxillary and mandibular teeth can be clearly evaluated in bitewing radiographs because the projection geometry which is applied in this technique does not cause distortion and superposition of the teeth on each other in the image^[19,20].

Digital radiographs have not a proven superiority to conventional radiographs in diagnosis, although digital imaging has some distinct practical advantages including the elimination of processing procedure, less radiation dose, shorter exposure and image acquisition times, some benefits that software is allowed such as adjustment of image contrast, density and size^[18,21].

CBCT displays two dimensional and three dimensional images that are necessary for the diagnosis and treatment planning of intra bony defects, furcation involvements and buccal/lingual bone destructions^[4,7,22] but periapical radiographs have better image quality than CBCT including contrast resolution, clarity and detail^[17,23]. Mol *et al*^[19] observed that the CBCT images provided more accurate information on periodontal bone levels in three dimensions than the images of photostimulated phosphor plates. In a similar study, it was found that CBCT was better in morphological description of periodontal bone defects, while the images obtained by charged coupled device sensor provided more bone details^[24]. Moreover, it was reported that CBCT and conventional periapical radiographs differed in instead of

about measuring the height of the alveolar bone crest but there was not a significant difference between the two methods in detecting the depth and width of bone defects^[20]. Mengel *et al*^[25] demonstrated that CBCT images were better in detection of periodontal defects compared with periapical radiographs and medical CT. Likewise, Noujeim *et al*^[26] concluded that CBCT technique has better diagnostic accuracy than periapical films in the detection of interradicular periodontal bone defects.

Furcation involvement

An accurate diagnosis of inter radicular bone loss is an important issue prior to the decision of appropriate treatment options including apically repositioned flaps with or without tunnel preparation, root amputation, hemi-/trisection or root separation. Conventional two dimensional radiographs can be deceptive in evaluating periodontal tissue support and inter radicular bone due to superposition of anatomical structures. However, 3D images provide detailed information about areas of multi rooted teeth (Figure 7). CBCT images of maxillary molars provided detailed information of furcation involvement and a reliable basis for treatment decision^[23] (Figure 8). Intra-surgical furcation involvement measurements were compared by using CBCT images and it was reported that CBCT images demonstrated a high accuracy in assessing the loss of periodontal tissue and classifying the degree of furcation involvement in maxillary molars^[27]. Authors evaluated CBCT images of artificially created furcation involvement of the second molars in pig mandibles and

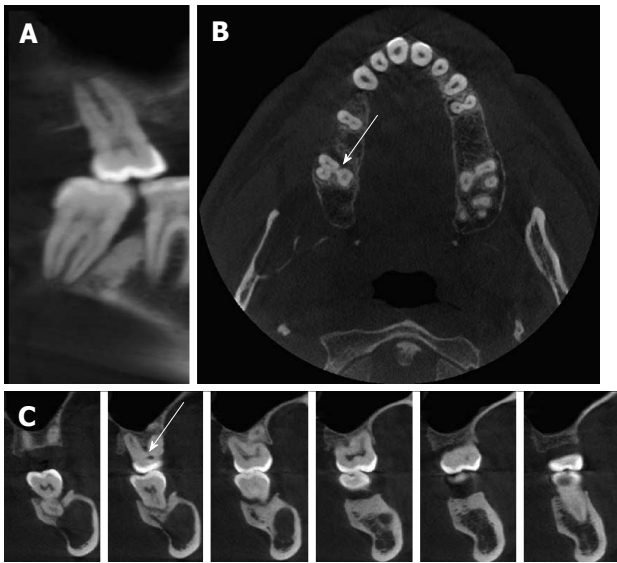


Figure 7 Furcation involvement can not be observed in the panoramic-like section (A) whereas it can be evaluated in the axial (B) and cross-sectional (C) cone beam computed tomography image (arrows).

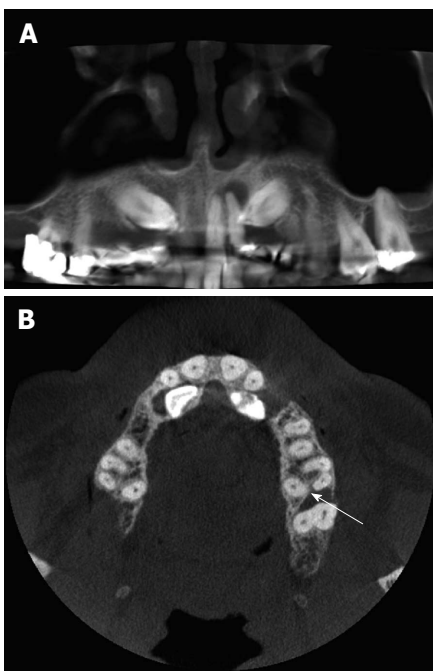


Figure 8 The amount and shape of bone resorption in the furcation area of maxillary molar tooth can not be assessed in the panoramic-like section (A), however, this involvement is seen in the axial section (B) (arrow).

accuracy for furcation lesion detection ranged between 78% and 88%^[5]. A study compared dental radiographs and high resolution CT (HR-CT) in detecting and grading of artificial furcation involvements in jaw specimens from cadavers. The diagnostic rate of dental radiographs was 21% whereas HR-CT was 100%^[28].

Soft tissue assessment

CBCT is a more appropriate tool for evaluating mineralized tissues than soft tissues^[12]. However, a practical

method named soft tissue CBCT (ST-CBCT), was reported^[29], and it was utilized to determine the dimensions and relationships of the structures of the dentogingival unit. The tongues were retracted toward the floor of patients' mouths and a plastic lip retractor was used to retract the soft tissues away from the teeth and gingiva during CBCT scans and the images that were obtained provided clear information for the analysis of various dentogingival unit measurements^[29]. Mentioned method was used in another study in which the average thickness of the palatal mucosa according to ages and specific localizations were determined on thirty one patients^[30]. The thickness of palatal mucosa has a major importance for the treatment planning of soft tissue grafts. However, this technique provides only quantitative assessment, thus the differences between the epithelial, fat and connective tissues can not be distinguished on ST-CBCT images^[29,30].

Periodontal ligament space

The earliest sign of periodontitis that can be detected on radiographs is a wedge-shaped radiolucent area in the inter-proximal region. At this stage, the continuity of lamina dura is lost and some changes in periodontal ligament space can be observed^[6,7,16]. Authors compared CBCT with conventional radiography in terms of their ability to produce images of periodontal ligament space on a phantom model with artificially created periodontal ligament of various thicknesses. Periapical radiographs were found to be superior to CBCT for the measurement of periodontal ligament space^[6]. However, authors of another study^[16] concluded that CBCT images had higher accuracy than intraoral radiographs in the determination of periodontal space in a similar research^[16]. Conflicting findings may be attributed to the differences between radiographic systems and settings used in various studies. Visibility of periodontal ligament space using different radiographic techniques should be assessed in further studies.

Alveolar bone defects

Radiographs are frequently utilized to diagnose the amount and shape of alveolar bone destruction that affects treatment planning in periodontal therapy^[25]. 2D radiographs can be insufficient for the detection of intra-bony alveolar defects due to obstruction of spongy bone changes by cortical plate. Thus, three-dimensional imaging is required for mapping of alveolar defects^[22] (Figure 9). Periodontal defects in pigs and human mandibles were displayed using intraoral radiography, panoramic radiography, CT and CBCT which were compared with histological specimens. The results of the mentioned study showed that 3D imaging had high accuracy in the detection of alveolar defects. Whereas, intraoral and panoramic radiographs could not determine the dehiscence unequivocally, tomographic images displayed all dehiscences and provided accurate measurements of the defects. Authors also reported that CBCT displayed the best



Figure 9 The vertical alveolar bone defects are viewed in cone beam computed tomography images (A, B) (white arrows) and the expansion of periodontal ligament space is also seen in the right maxillary first premolar tooth (B) (black arrow).

imaging quality^[25]. Authors evaluated periodontal defects in human dry cadaver skulls using CBCT and traditional methods. Consequently, they found that there was no difference between intraoral radiography and CBCT in linear measurements for all defects^[22]. In another study^[31], authors evaluated accuracy and reliability of CBCT for measuring alveolar bone height and detecting bony dehiscence and fenestration. CBCT measurements were found to be equivalent to direct measurements and dehiscences were diagnosed with higher accuracy than fenestrations^[31]. CBCT and multi-slice CT (MSCT) images were used for alveolar bone width measurements^[18]. There was no significance difference between the measurements obtained by CBCT and MSCT or direct measurements and radiographic methods^[18].

Regenerative periodontal therapy and bone grafts

Bone grafting is commonly used for maxillary sinus lifting and treatment of intra bony defects but evaluation of osseous defect regeneration with conventional radiography can be insufficient due to superimpositions^[25,32]. Furthermore, histological evaluation of a sample of the graft is not a preferred method due to its quite invasive procedure. CBCT was found to be significantly more accurate than digital intraoral radiographs when direct surgical measurements served as the gold standard for the evaluation of intra-bony defects' regenerative treatment outcomes. CBCT can replace surgical re-entry by providing 3D images and measurements that are almost

equivalent to direct surgical measurements^[32].

Dimensions of alveolar process should be examined in detail prior to dental implant placement to avoid various complications and evaluation of CBCT images has a major importance in preoperative planning and post-operative localization of dental implants^[8,33] (Figure 10). Moreover, the evaluation of CBCT images are preferred method to observe bone graft healing prior to dental implant placement^[17] (Figure 11). In a previous study^[33], which was based on measurement accuracy and reliability of CBCT and MSCT with the specific implant planning software package and the stereolithographic drill guide, authors applied implant surgeries in a one-stage flapless procedure. The deviations were acceptable and no complications were observed^[33]. In contrary, authors of another study concluded that CBCT may be deceptive compared to direct caliper measurements and they found that ridge mapping method gave more accurate results than CBCT^[34]. However, ridge mapping technique is an invasive technique whereas CBCT is not.

CBCT evaluation can be used for determining the width, height and distance to the anatomical structures of alveolar process in pre-surgical dental implant planning. Likewise, the surgical guide stents were used while dental implant surgery was produced by aid of CBCT images and software packages^[17]. Immediate implant placement enables one-stage surgery and eliminates bone recovery time. In this technique, dimensions of alveolar process which is selected for dental implant placement and relationships with adjacent anatomical structures of this region should be carefully assessed^[8,35]. Jin *et al.*^[35] studied bone thickness evaluation on the buccal and palatal aspects of the maxillary canine and premolars using CBCT and it was concluded that CBCT images might be advantageous in preoperative planning of dental implants^[35].

As a summary, in cases, where two-dimensional imaging is an inadequate method for accurate diagnosis of periodontal defect configuration and guiding for appropriate treatment planning, three-dimensional radiographic examinations may be required. Periodontal intra-bony defects and furcation involvements keep a challenge for the examiner. Misdiagnosed or misclassification of these pathologies can lead to progress of bone destruction and teeth loss as a result of improper treatment^[5,16]. CBCT evaluation can be used for determining the width, height and distance to the anatomical structures of alveolar process in pre-surgical dental implant planning. Likewise, the surgical guide stents used during dental implant surgery is produced by aid of CBCT images and software packages^[17]. There are numerous studies that 3D imaging had high accuracy in the detection of alveolar defects and furcation involvements^[18,25,27,28,31]. CBCT is well complied for imaging the highly mineralized structures such as bone or teeth but it cannot provide clear images of soft tissues. However, a novel, CBCT-based method to display and measure the dimensions of the palatal mucosa was reported in a recent study^[29,30]. There are contradictory results on whether CBCT or conventional radiographs

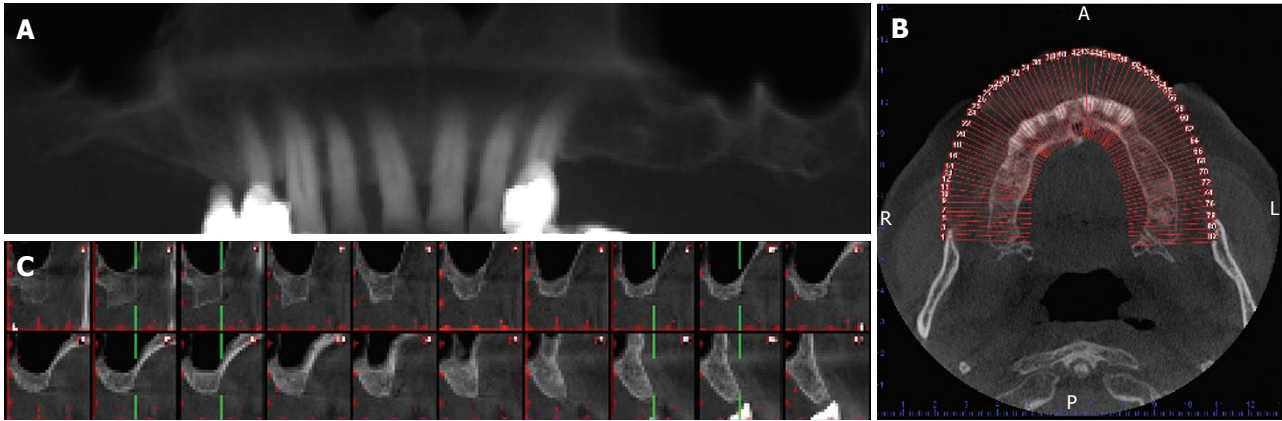


Figure 10 The images acquired for preoperative implant planning are displayed the distances between the alveolar process of maxillary molar areas and the bases of the maxillary sinuses (A), a curve is projected on the axial section (B) and the cross-sectional images are obtained (C).

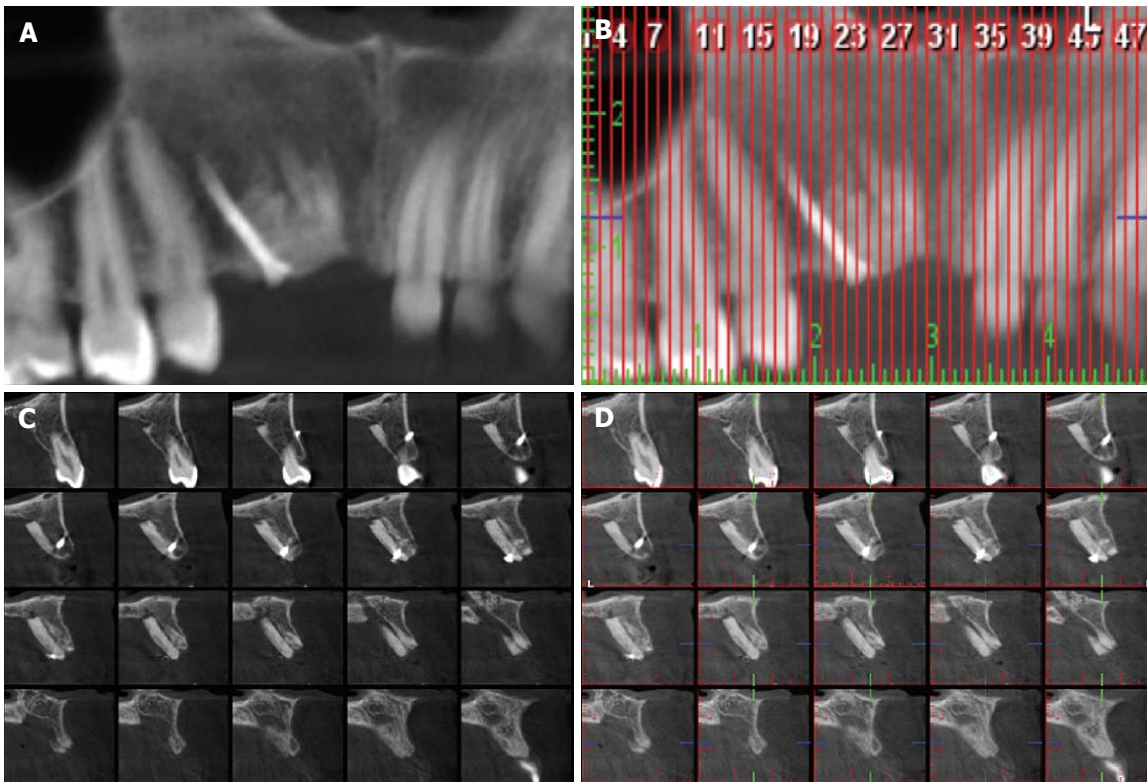


Figure 11 The block graft and mini screw providing graft stabilization are placed in the maxillary anterior region (A and B), the amount of bone augmentation can be evaluated in the cross-sectional images (C and D).

are more efficient in evaluation of periodontal ligament space^[6,16].

Assessment of regenerative periodontal therapy and bone grafts' outcomes can be performed accurately and reliably with CBCT imaging^[17,32]. In conclusion, CBCT applications provide obvious benefits in periodontology, although it should be used when two-dimensional radiographs are insufficient considering the necessity and the potential radiation hazards of the examination^[36].

REFERENCES

1 Lindhe J, Lang NP, Karring T. Clinical periodontology and

implant dentistry. In: Lindhe J, Karring T, Araújo M. The anatomy of periodontal tissues. Singapore: Blackwell Publishing Ltd, 2008: 3-8

2 Highfield J. Diagnosis and classification of periodontal disease. *Aust Dent J* 2009; **54** Suppl 1: S11-S26 [PMID: 19737262 DOI: 10.1111/j.1834-7819.2009.01140.x]

3 Newman M, Takei HH, Carranza FA. Clinical Periodontology. In: Carranza FA, Takei HH. Radiographic Aids in the Diagnosis of Periodontal Disease. Philadelphia: W.B. Saunders Company, 2002: 454-468

4 du Bois AH, Kardachi B, Bartold PM. Is there a role for the use of volumetric cone beam computed tomography in periodontics? *Aust Dent J* 2012; **57** Suppl 1: 103-108 [PMID: 22376102 DOI: 10.1111/j.1834-7819.2011.01659.x]

5 Umetsubo OS, Gaia BF, Costa FF, Cavalcanti MG. Detection

- of simulated incipient furcation involvement by CBCT: an in vitro study using pig mandibles. *Braz Oral Res* 2012; **26**: 341-347 [PMID: 22790499 DOI: 10.1590/S1806-83242012000400010]
- 6 **Ozmeric N**, Kostiuoutchenko I, Högler G, Frentzen M, Jervøe-Storm PM. Cone-beam computed tomography in assessment of periodontal ligament space: in vitro study on artificial tooth model. *Clin Oral Investig* 2008; **12**: 233-239 [PMID: 18247066 DOI: 10.1007/s00784-008-0186-8]
 - 7 **Mohan R**, Singh A, Gundappa M. Three-dimensional imaging in periodontal diagnosis - Utilization of cone beam computed tomography. *J Indian Soc Periodontol* 2011; **15**: 11-17 [PMID: 21772715 DOI: 10.4103/0972-124X.82256]
 - 8 **Scarfe WC**, Farman AG, Sukovic P. Clinical applications of cone-beam computed tomography in dental practice. *J Can Dent Assoc* 2006; **72**: 75-80 [PMID: 16480609]
 - 9 **de-Azevedo-Vaz SL**, Vasconcelos Kde F, Neves FS, Melo SL, Campos PS, Haiteir-Neto F. Detection of periimplant fenestration and dehiscence with the use of two scan modes and the smallest voxel sizes of a cone-beam computed tomography device. *Oral Surg Oral Med Oral Pathol Oral Radiol* 2013; **115**: 121-127 [PMID: 23217543 DOI: 10.1016/j.oooo.2012.10.003]
 - 10 **Sun Z**, Smith T, Kortam S, Kim DG, Tee BC, Fields H. Effect of bone thickness on alveolar bone-height measurements from cone-beam computed tomography images. *Am J Orthod Dentofacial Orthop* 2011; **139**: e117-e127 [PMID: 21300222 DOI: 10.1016/j.ajodo.2010.08.016]
 - 11 **Shah MA**, Shah SS, Dave DH. CBCT-A Positive Amelioration In Periodontics. *NJIRM* 2013; **4**: 144-148
 - 12 **Agrawal P**, Sanikop S, Patil S. New developments in tools for periodontal diagnosis. *Int Dent J* 2012; **62**: 57-64 [PMID: 22420472 DOI: 10.1111/j.1875-595X.2011.00099.x]
 - 13 **Tyndall DA**, Rathore S. Cone-beam CT diagnostic applications: caries, periodontal bone assessment, and endodontic applications. *Dent Clin North Am* 2008; **52**: 825-41, vii [PMID: 18805231 DOI: 10.1016/j.cden.2008.05.002]
 - 14 **Mischkowski RA**, Pulsfort R, Ritter L, Neugebauer J, Brochhagen HG, Keeve E, Zöllner JE. Geometric accuracy of a newly developed cone-beam device for maxillofacial imaging. *Oral Surg Oral Med Oral Pathol Oral Radiol Endod* 2007; **104**: 551-559 [PMID: 17613260 DOI: 10.1016/j.tripleo.2007.02.021]
 - 15 **Veyre-Goulet S**, Fortin T, Thierry A. Accuracy of linear measurement provided by cone beam computed tomography to assess bone quantity in the posterior maxilla: a human cadaver study. *Clin Implant Dent Relat Res* 2008; **10**: 226-230 [PMID: 18384410]
 - 16 **Jervøe-Storm PM**, Hagner M, Neugebauer J, Ritter L, Zöllner JE, Jepsen S, Frentzen M. Comparison of cone-beam computerized tomography and intraoral radiographs for determination of the periodontal ligament in a variable phantom. *Oral Surg Oral Med Oral Pathol Oral Radiol Endod* 2010; **109**: e95-e101 [PMID: 20123402 DOI: 10.1016/j.tripleo.2009.10.023]
 - 17 **Eshraghi T**, McAllister N, McAllister B. Clinical applications of digital 2-D and 3-D radiography for the periodontist. *J Evid Based Dent Pract* 2012; **12**: 36-45 [PMID: 23040338 DOI: 10.1016/S1532-3382(12)70010-6]
 - 18 **Loubele M**, Van Assche N, Carpentier K, Maes F, Jacobs R, van Steenberghe D, Suetens P. Comparative localized linear accuracy of small-field cone-beam CT and multislice CT for alveolar bone measurements. *Oral Surg Oral Med Oral Pathol Oral Radiol Endod* 2008; **105**: 512-518 [PMID: 17900939 DOI: 10.1016/j.tripleo.2007.05.004]
 - 19 **Mol A**, Balasundaram A. In vitro cone beam computed tomography imaging of periodontal bone. *Dentomaxillofac Radiol* 2008; **37**: 319-324 [PMID: 18757716 DOI: 10.1259/dmfr/26475758]
 - 20 **de Faria Vasconcelos K**, Evangelista KM, Rodrigues CD, Estrela C, de Sousa TO, Silva MA. Detection of periodontal bone loss using cone beam CT and intraoral radiography. *Dentomaxillofac Radiol* 2012; **41**: 64-69 [PMID: 22184627 DOI: 10.1259/dmfr/13676777]
 - 21 **Gomes-Filho IS**, Sarmiento VA, de Castro MS, da Costa NP, da Cruz SS, Trindade SC, de Freitas CO, de Santana Passos J. Radiographic features of periodontal bone defects: evaluation of digitized images. *Dentomaxillofac Radiol* 2007; **36**: 256-262 [PMID: 17586851 DOI: 10.1259/dmfr/25386411]
 - 22 **Misch KA**, Yi ES, Sarment DP. Accuracy of cone beam computed tomography for periodontal defect measurements. *J Periodontol* 2006; **77**: 1261-1266 [PMID: 16805691 DOI: 10.1902/jop.2006.050367]
 - 23 **Walter C**, Kaner D, Berndt DC, Weiger R, Zitzmann NU. Three-dimensional imaging as a pre-operative tool in decision making for furcation surgery. *J Clin Periodontol* 2009; **36**: 250-257 [PMID: 19236537 DOI: 10.1111/j.1600-051X.2008.01367.x]
 - 24 **Vandenbergh B**, Jacobs R, Yang J. Diagnostic validity (or acuity) of 2D CCD versus 3D CBCT-images for assessing periodontal breakdown. *Oral Surg Oral Med Oral Pathol Oral Radiol Endod* 2007; **104**: 395-401 [PMID: 17613257 DOI: 10.1016/j.tripleo.2007.03.012]
 - 25 **Mengel R**, Candir M, Shiratori K, Flores-de-Jacoby L. Digital volume tomography in the diagnosis of periodontal defects: an in vitro study on native pig and human mandibles. *J Periodontol* 2005; **76**: 665-673 [PMID: 15898924 DOI: 10.1902/jop.2005.76.5.665]
 - 26 **Noujeim M**, Prihoda T, Langlais R, Nummikoski P. Evaluation of high-resolution cone beam computed tomography in the detection of simulated interradicular bone lesions. *Dentomaxillofac Radiol* 2009; **38**: 156-162 [PMID: 19225086 DOI: 10.1259/dmfr/61676894]
 - 27 **Walter C**, Weiger R, Zitzmann NU. Accuracy of three-dimensional imaging in assessing maxillary molar furcation involvement. *J Clin Periodontol* 2010; **37**: 436-441 [PMID: 20374414 DOI: 10.1111/j.1600-051X.2010.01556.x]
 - 28 **Fuhrmann RA**, Bucker A, Diedrich PR. Furcation involvement: comparison of dental radiographs and HR-CT-slices in human specimens. *J Periodontol Res* 1997; **32**: 409-418 [PMID: 9266492 DOI: 10.1111/j.1600-0765.1997.tb00553.x]
 - 29 **Januário AL**, Barriviera M, Duarte WR. Soft tissue cone-beam computed tomography: a novel method for the measurement of gingival tissue and the dimensions of the dentogingival unit. *J Esthet Restor Dent* 2008; **20**: 366-373; discussion 374 [PMID: 19120781 DOI: 10.1111/j.1708-8240.2008.00210.x]
 - 30 **Barriviera M**, Duarte WR, Januário AL, Faber J, Bezerra AC. A new method to assess and measure palatal masticatory mucosa by cone-beam computerized tomography. *J Clin Periodontol* 2009; **36**: 564-568 [PMID: 19538329 DOI: 10.1111/j.1600-051X.2009.01422.x]
 - 31 **Leung CC**, Palomo L, Griffith R, Hans MG. Accuracy and reliability of cone-beam computed tomography for measuring alveolar bone height and detecting bony dehiscences and fenestrations. *Am J Orthod Dentofacial Orthop* 2010; **137**: S109-S119 [PMID: 20381751 DOI: 10.1016/j.ajodo.2009.07.013]
 - 32 **Grimard BA**, Hoidal MJ, Mills MP, Mellonig JT, Nummikoski PV, Mealey BL. Comparison of clinical, periapical radiograph, and cone-beam volume tomography measurement techniques for assessing bone level changes following regenerative periodontal therapy. *J Periodontol* 2009; **80**: 48-55 [DOI: 10.1902/jop.2009.080289]
 - 33 **Van Assche N**, van Steenberghe D, Quirynen M, Jacobs R. Accuracy assessment of computer-assisted flapless implant placement in partial edentulism. *J Clin Periodontol* 2010; **37**: 398-403 [PMID: 20447264 DOI: 10.1111/j.1600-051X.2010.01535.x]
 - 34 **Chen LC**, Lundgren T, Hallström H, Chelof F. Comparison of different methods of assessing alveolar ridge dimensions prior to dental implant placement. *J Periodontol* 2008; **79**: 401-405 [PMID: 18315421 DOI: 10.1902/jop.2008.070021]
 - 35 **Jin SH**, Park JB, Kim N, Park S, Kim KJ, Kim Y, Kook YA, Ko Y. The thickness of alveolar bone at the maxillary canine and

premolar teeth in normal occlusion. *J Periodontal Implant Sci* 2012; **42**: 173-178 [PMID: 23185698 DOI: 10.5051/jpis.2012.42.5.173]

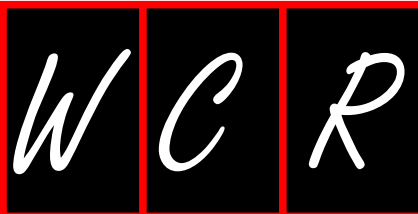
36 **Kamburođlu K**, Acar B, Yakar EN, Paksoy CS. Dento-maxillo-

facial Cone Beam Computed Tomography Part 1: Basic Principles (Dentomaksillofasiyal Konik Iřın Demetli Bilgisayarlı Tomografi Bölüm 1: Temel Prensipler). *J Clin Sc* 2012; **6**: 1125-1136

P- Reviewers: Ma YL, Oliveira L, Santos FA **S- Editor:** Ji FF

L- Editor: A **E- Editor:** Liu SQ





Role of ^{18}F -FDG PET/CT in pre and post treatment evaluation in head and neck carcinoma

Bundhit Tantiwongkosi, Fang Yu, Anand Kanard, Frank R Miller

Bundhit Tantiwongkosi, Division of Neuroradiology, Department of Radiology and Otolaryngology Head Neck Surgery, University of Texas Health Science Center at San Antonio, San Antonio, TX 78229, United States

Bundhit Tantiwongkosi, Imaging Service, South Texas Veterans Health Care System, San Antonio, TX 78229, United States

Fang Yu, Department of Radiology, University of Texas Health Science Center at San Antonio, San Antonio, TX 78229, United States

Anand Kanard, Department of Medical Oncology, University of Texas Health Science Center at San Antonio, San Antonio, TX 78229, United States

Frank R Miller, Department of Otolaryngology Head Neck Surgery, University of Texas Health Science Center at San Antonio, San Antonio, TX 78229, United States

Author contributions: All four authors actively and equally contributed to the writing and editing of the article as well as gathering the necessary illustrations.

Correspondence to: Bundhit Tantiwongkosi, MD, Division of Neuroradiology, Department of Radiology and Otolaryngology Head Neck Surgery, University of Texas Health Science Center at San Antonio, 7703 Floyd Curl Drive, Mail Code 7800, San Antonio, TX 78229, United States. tantiwongkos@uthscsa.edu
Telephone: +1-210-5673448 Fax: +1-210-5670008

Received: December 26, 2013 Revised: January 21, 2014

Accepted: April 9, 2014

Published online: March 28, 2015

patients present with cervical lymph node metastasis without obvious primary tumors on clinical examination or conventional cross sectional imaging. Treatment planning includes surgery, radiation, chemotherapy or combinations that could significantly alter the anatomy and physiology of this complex head and neck region, making assessment of treatment response and detection of residual/ recurrent tumor very difficult by clinical evaluation and computed tomography (CT) or magnetic resonance imaging (MRI). ^{18}F -2-fluoro-2-deoxy-D-glucose positron emission tomography/CT (^{18}F -FDG PET/CT) has been widely used to assess HNC for more than a decade with high diagnostic accuracy especially in detection of initial distant metastasis and evaluation of treatment response. There are some limitations that are unique to PET/CT including artifacts, lower soft tissue contrast and resolution as compared to MRI, false positivity in post-treatment phase due to inflammation and granulation tissues, *etc*. The aim of this article is to review the roles of PET/CT in both pre and post treatment management of HNSCC including its limitations that radiologists must know. Accurate PET/CT interpretation is the crucial initial step that leads to appropriate tumor staging and treatment planning.

© 2015 Baishideng Publishing Group Inc. All rights reserved.

Key words: Head and neck cancer; Positron emission tomography; Computed tomography; Staging; Post treatment; Recurrence

Abstract

Head and neck cancer (HNC) ranks as the 6th most common cancer worldwide, with the vast majority being head and neck squamous cell carcinoma (HNSCC). The majority of patients present with complicated locally advanced disease (typically stage III and IV) requiring multidisciplinary treatment plans with combinations of surgery, radiation therapy and chemotherapy. Tumor staging is critical to decide therapeutic planning. Multiple challenges include accurate tumor localization with precise delineation of tumor volume, cervical lymph node staging, detection of distant metastasis as well as ruling out synchronous second primary tumors. Some

Core tip: Positron emission tomography/computed tomography (PET/CT) has proven to be useful in evaluation of carcinoma of unknown primary origin before panendoscopy and biopsy, regional lymph node metastasis and distant metastasis. PET/CT could be the only study that reveals residual or recurrent tumors when the neck anatomy is markedly distorted after treatment. Limitations of PET/CT in evaluation of primary tumor extent are also discussed to alert the radiologists so they may suggest and correlate with appropriate im-

aging modalities. The article utilizes diagrams and multi planar reconstructed PET/CT from several histopathologically-proven cases with emphasis on imaging and clinical correlation.

Original sources: Tantiwongkosi B, Yu F, Kanard A, Miller FR. Role of ¹⁸F-FDG PET/CT in pre and post treatment evaluation in head and neck carcinoma. *World J Radiol* 2014; 6(5): 177-191 Available from: URL: <http://www.wjgnet.com/1949-8470/full/v6/i5/177.htm> DOI: <http://dx.doi.org/10.4329/wjr.v6.i5.177>

INTRODUCTION

Head neck cancers (HNC) are the sixth most common cancer worldwide. It is estimated that there are an annual total of 53640 new head neck (oral cavity, pharynx and larynx) cancer cases and 11520 deaths in the United States in 2013^[1]. There are many challenges in diagnosis, pretreatment staging and post treatment evaluation in these patients. The clinical signs and symptoms may be nonspecific and can vary depending on the tumor site in the head and neck (oral cavities, pharynx, larynx, nasal cavity, paranasal sinuses, salivary glands, thyroid and skin). Some cancers are so occult that escape detection by detailed physical examination, endoscopy and conventional cross sectional imaging. Contrast-enhanced computed tomography (CT), magnetic resonance imaging (MRI) and positron emission tomography/CT (PET/CT) are widely used to determine the presence and extent of the tumors both before and after treatment. However, PET/CT is superior to both CT and MRI in detection of carcinoma of unknown primary (CUP), cervical lymph node metastasis, distant metastasis, residual tumor, recurrent disease and second primary tumors resulting alteration in treatment planning^[2-5]. This article aims to review current roles of PET/CT in head neck cancer in both pre treatment staging and post treatment assessment.

PET/CT is useful and approved by the Centers for Medicare and Medicaid Services in patients with HNC for both pre treatment and post treatment phases. Before treatment, PET/CT can be used for delineation of extent of primary tumor (T), detection of an unknown primary tumor origin (I) or synchronous second primary tumor (I), detection of regional lymph node metastasis (N) and detection of distant metastasis (M). After therapeutic treatment, it is proven to be helpful in the assessment of therapy response, detection of residual primary tumor, long-term surveillance for recurrence in both the primary site and metastatic lymph nodes as well as the detection of distant metastases.

PRE-TREATMENT EVALUATION

Standard staging of head and neck squamous cell carcinoma (HNSCC) follows the systematic TNM classification per American Joint Committee on Cancer seventh

edition^[6]. The primary tumor extension (T stage) varies from site to site given differences in specific anatomic detail of each site, while regional lymph node involvement (N0 to N3 stage) shares similar classification with the exception of thyroid and nasopharyngeal cancers. Metastasis outside head neck regions (*e.g.*, mediastinal and axillary lymph nodes) represents distant metastasis (M stage)^[6]. Precise tumor staging is critical for treatment planning and prognosis. Prior to initiation of treatment, HNSCC is clinically staged by using clinical examination, imaging, and endoscopy with tissue biopsy or fine needle aspiration. Multiple studies suggest that PET/CT is superior to conventional imaging (CT or MRI) in initial staging and may alter management and treatment especially when unexpected cervical lymph node and/or distant metastasis is discovered^[2,5]. National Comprehensive Center Network issued an update in clinical practice guidelines in head neck cancer and PET/CT imaging in 2013 and suggested using PET/CT for initial staging of the oral cavity, oropharyngeal, hypopharyngeal, glottic, and supraglottic cancers for stage III-IV disease as well as mucosal melanoma and nasopharyngeal carcinoma (World Health Organization class 2-3 and N2-3 diseases)^[7].

Primary tumor staging (T)

The T stage of each site is determined by the size of the primary tumor and invasion into the deep structures^[6]. Contrast enhanced CT and MRI have been the primary imaging modalities for evaluating T stage of HNSCC due to their superior anatomic resolution and tissue contrast as compare to PET/CT performed without intravenous (IV) contrast. PET/CT performed with IV contrast provides both anatomic and metabolic details at the same time. However, there is no clear recommendation for routine use of PET/CT in initial T staging. Ha *et al*^[2] found that PET/CT upstaged T staging in 2 of 36 patients (5.5%) with subsequent changes in treatment planning. A prospective study by Scott and colleagues showed that PET changed T staging in 6 of 71 patients (8.5%)^[5]. MRI remains the preferred imaging method in the assessment of nasopharynx, oral cavity, perineural spread and bone marrow invasion^[8,9] while CT is the modality of choice for the larynx and bony cortex invasion^[10].

Oral cavity and oropharynx

Dental amalgam artifact is a unique problem for CT imaging in the oral cavity and oropharynx. When severe, it can obscure the entire tumor particularly in the oral cavity. PET and MRI are less affected by this type of artifact (Figure 1). MRI, however, is prone to motion artifact given it requires more imaging time. PET/CT also has a high false positivity due to normal lymphoid tissue uptake in the Waldeyer's ring. Seitz and colleagues did not find additional value of PET/CT to MRI in T staging of oral cavity and oropharyngeal cancers using histopathology as the gold standard. This is thought to be due to limited resolution of PET/CT in detection of small, superficial lesions and lesions obscured by dental artifact^[11]. PET/

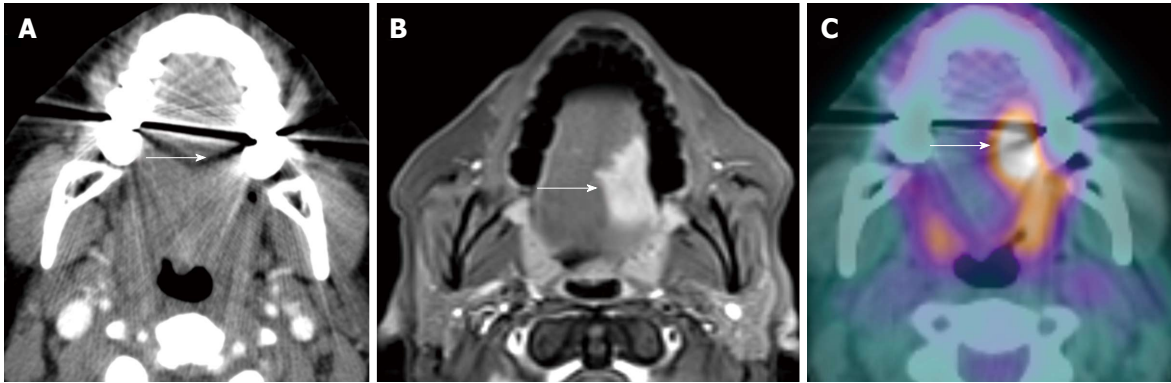


Figure 1 Dental amalgam artifact obscuring an oral cavity tumor. A: The T2 left lateral oral tongue squamous cell carcinoma (arrow) was obscured by the dental amalgam artifact on contrast-enhanced computed tomography (CT); B: The lesion is better evaluated on the contrast-enhanced T1W; C: Positron emission tomography/CT (PET/CT) images. Information from the PET portion is clearly less affected by streak artifact. However, PET/CT does not add additional information to magnetic resonance imaging in terms of primary oral cavity lesion extent for the majority of cases.

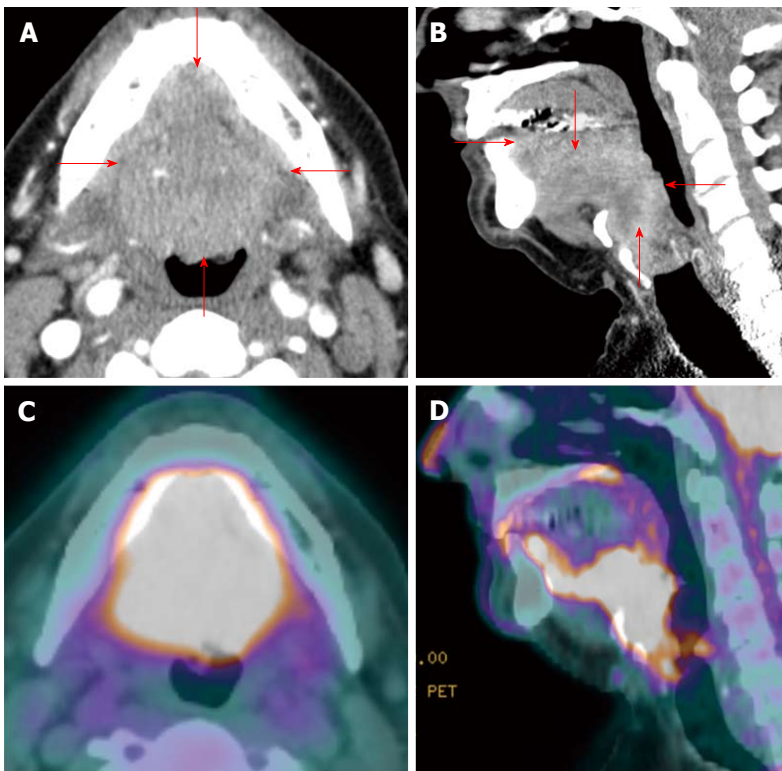


Figure 2 Positron emission tomography/computed tomography for delineation of oral cavity tumor extent. A T4a oral and base of tongue squamous cell carcinoma (red arrows) diffusely and symmetrically infiltrates the ventral aspect of the tongue, whose margins are difficult to appreciate on contrast enhanced computed tomography (CT) (A and B). On the other hand, positron emission tomography/CT (PET/CT) (C and D) clearly demarcates the tumor extent.

CT has unique benefits in that it can reveal the full tumor extent when the tumor is ill-defined with submucosal extension and diffuse infiltration. This can help the clinician in differentiating tumor border versus normal tissue planes (Figure 2).

A particular concern in the oral cavity is assessing mandibular/bone involvement. Superficial mandibular involvement by a resectable oral cavity cancer is often treated by marginal mandibulectomy while gross mandibular invasion typically requires segmental mandibulectomy with composite free flap reconstruction^[12] (Figure 3). Metabolic activity seen in the mandible tends to overestimate the presence of the tumor due to partial volume averaging and misregistration artifact (Figure 4). The CT portion of the PET/CT and ceCT has more sensitivity

and specificity than PET alone in assessment of mandibular invasion^[13]. MRI is useful in detection of bone marrow changes as compared to CT. CT is generally superior to MRI in the detection of cortical bone erosion. Overall MRI has similar accuracy as compared to CT and PET/CT. Accuracy is increased when the information of multiple imaging modalities are analyzed if available^[14].

Routinely CT is performed with the patient's mouth close and in neutral position. Apposition of oral cavity and oropharyngeal structures can obscure the tumors. CeCT with dynamic maneuvers (puffed cheek technique, open mouth position or modified Valsava maneuver) can delineate the presence and extent of the lesions^[15]. The puffed cheek technique performed during PET/CT scanning has been proven to be practical and improved lesion

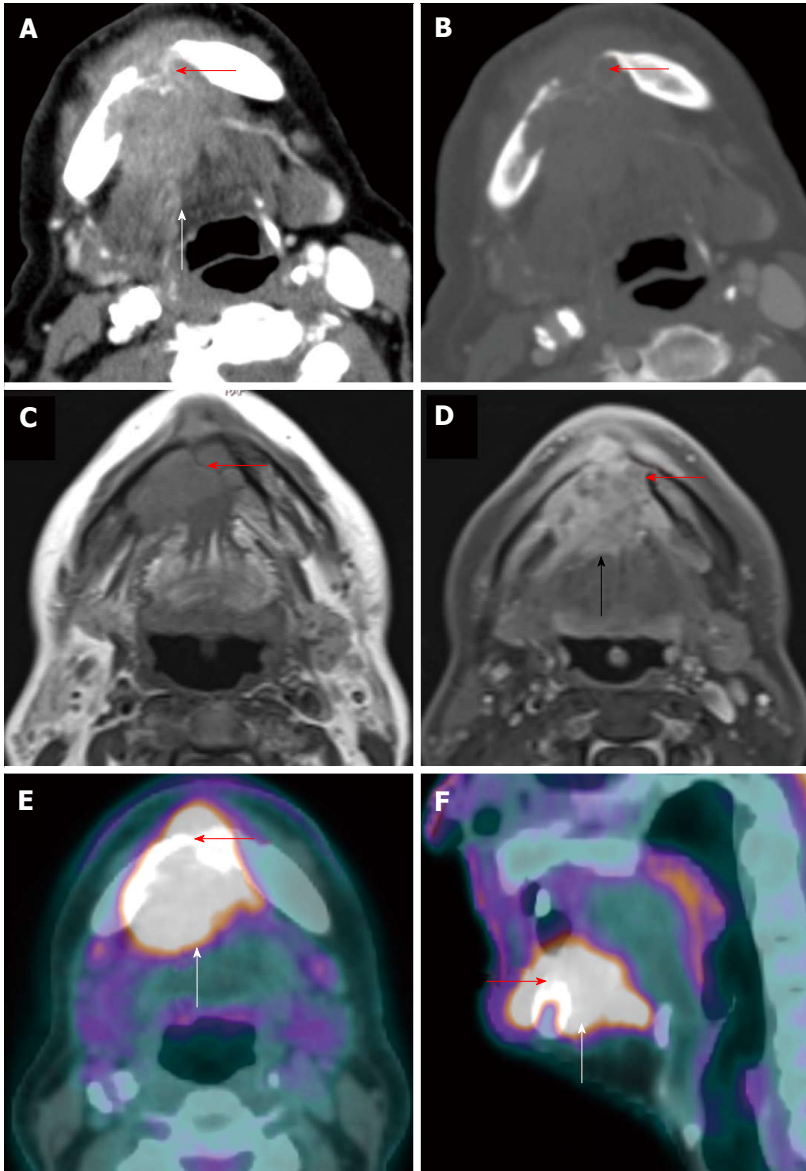


Figure 3 Positron emission tomography/computed tomography for detection of mandibular invasion. A T4a floor of mouth squamous cell carcinoma (white arrow) with through-and-through involvement (red arrow) of the anterior mandible is demonstrated on axial contrast-enhanced computed tomography (CT) (A: Soft tissue window; B: Bone window), axial contrast-enhanced magnetic resonance imaging (C: T1WI; D: Post contrast enhanced T1WI with fat saturation), and positron emission tomography/CT (E: Axial; F: Sagittal).

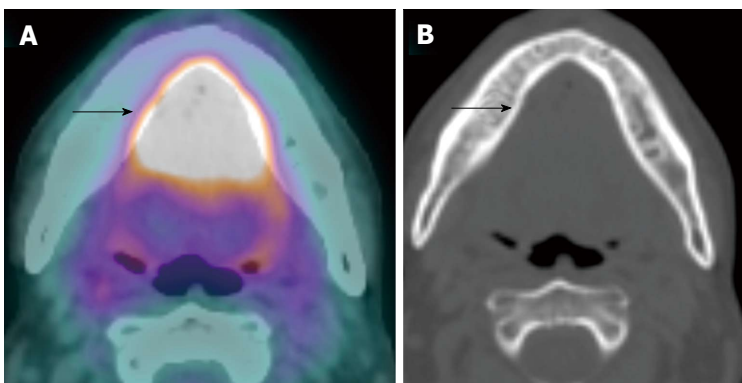


Figure 4 Shine-through artifact on positron emission tomography/computed tomography. A T4a floor of mouth squamous cell carcinoma (arrow) appeared to extend to involve the lingual cortex of the mandible seen on positron emission tomography/computed tomography (CT) (A), which is in fact artifactual. The corresponding CT (B) bone window and intraoperative findings confirmed an intact mandibular cortex.

detection^[16].

Nasopharynx

MRI is known to be superior to PET/CT for the assessment of locoregional invasion (parapharyngeal space, skull base, intracranium, sphenoid sinus) and retropharyngeal nodal metastasis by nasopharyngeal carcinoma^[9].

PET/CT tends to underestimate the extent and volume of tumor in the nasopharynx, skull base, brain and orbits as compare to MRI (Figure 5) which could have significant impact on staging or treatment planning especially when the discordance is outside the nasopharynx^[17]. Similar limitations of PET/CT are also noted in pediatric nasopharyngeal carcinoma patients^[18]. However PET/CT

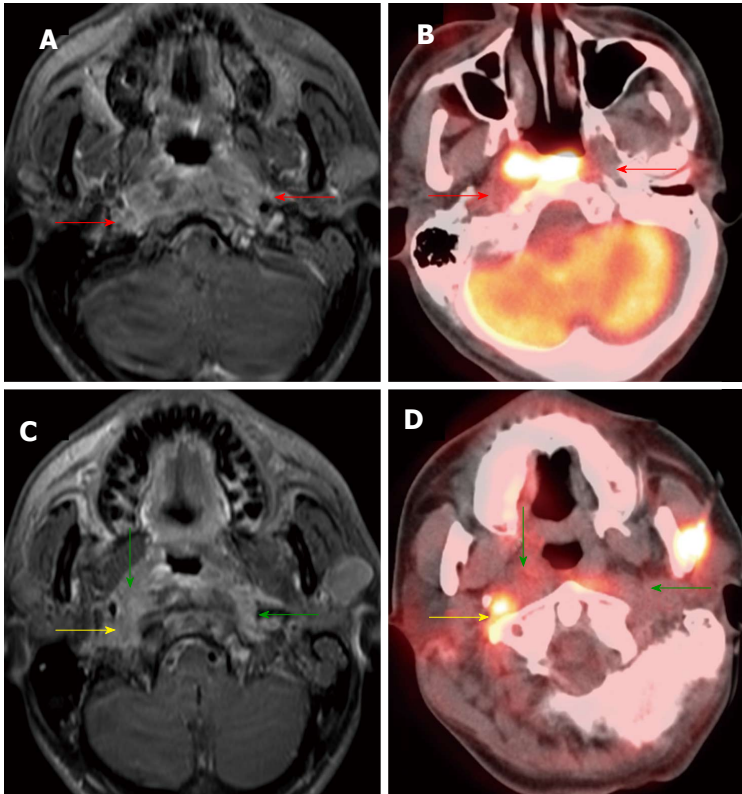


Figure 5 Positron emission tomography/computed tomography underestimates size and extension of the nasopharyngeal carcinoma and retropharyngeal lymph nodes compared to magnetic resonance imaging. The approximate lateral extension (red arrows) of the nasopharyngeal carcinoma is well demarcated on magnetic resonance imaging (MRI) (A). The tumor appears to be smaller on positron emission tomography/computed tomography (CT) (B) as compared to MRI because the lateral portion of the tumor is hypometabolic. Inferior to the primary tumor site, there is metastatic bilateral retropharyngeal lymphadenopathy (yellow and green arrows). The full extent of retropharyngeal lymph node involvement is better assessed by MRI (C) than CT (D). Only the right lateral retropharyngeal node is FDG avid.

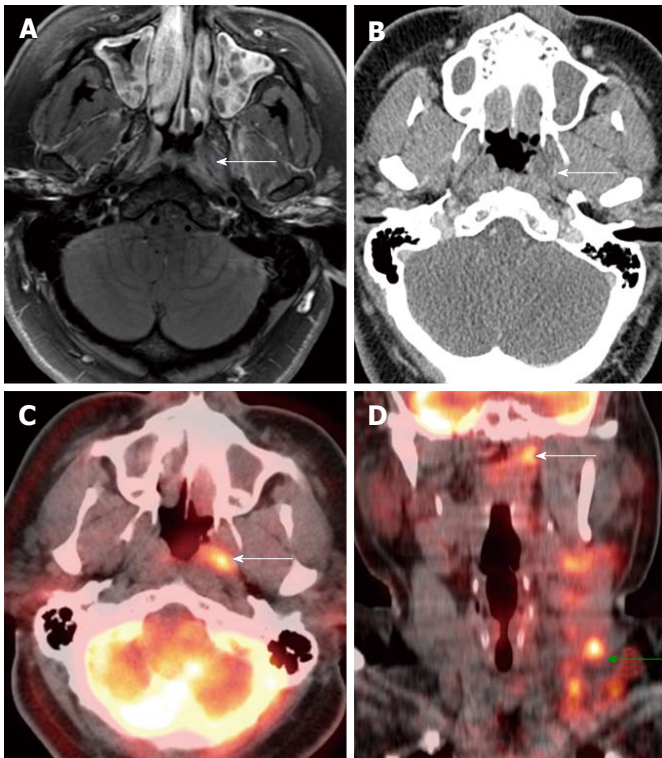


Figure 6 Positron emission tomography/computed tomography for detection of small submucosal nasopharyngeal carcinoma when computed tomography and magnetic resonance imaging are unrevealing in a patient presenting with metastatic cervical lymphadenopathy. Endoscopy was unremarkable. There was slight enhancement in the left side of the nasopharynx (white arrows) seen on magnetic resonance imaging (A) without abnormality on computed tomography (CT) (B). Positron emission tomography/CT (PET/CT) (C and D) revealed a focal hypermetabolic region in the left side of the nasopharynx (white arrows), suspicious for a submucosal tumor. Hypermetabolic left-sided cervical lymphadenopathy was also noted (green arrow). Biopsy revealed squamous cell carcinoma at the site of hypermetabolic activity in the left nasopharynx directed by PET/CT.

can be very helpful in identification of a subtle but focally hypermetabolic nasopharyngeal carcinoma when CT and MRI findings are not obvious (Figure 6). In addition PET/CT has the advantage of screening for distant metastatic disease.

Larynx

In primary laryngeal tumors the invasion of the preepi-

glottic fat and the paraglottic fat by laryngeal carcinoma (T3) increases the risk of regional lymph node metastasis. These tumors tend to have a higher recurrence rate and worse outcome when they invade the thyroid or cricoid cartilages, particularly when full thickness cartilage invasion (T4a) occurs^[19]. CT is more specific while MRI is more sensitive in detection of cartilage invasion^[10]. PET/CT without contrast adds no additional informa-

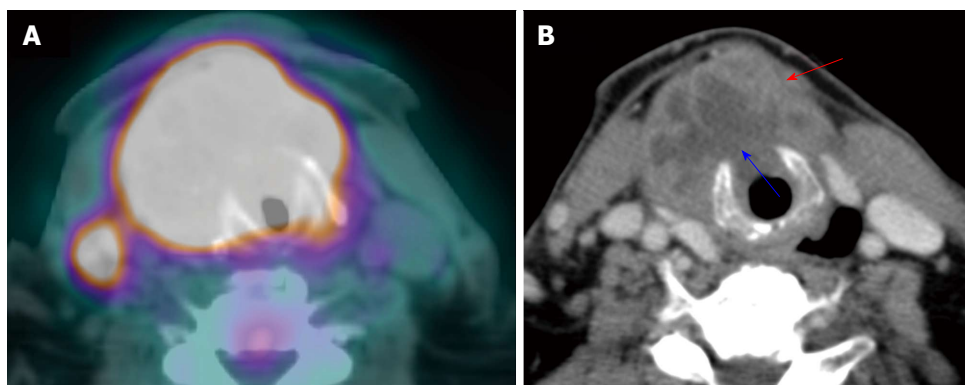


Figure 7 Laryngeal cartilage invasion. A large T4a squamous cell carcinoma of the larynx with through-and-through cricoid cartilage invasion (blue arrow) and extralaryngeal invasion (red arrow) demonstrated on both positron emission tomography/computed tomography (CT) (A) and contrast-enhanced CT (B).

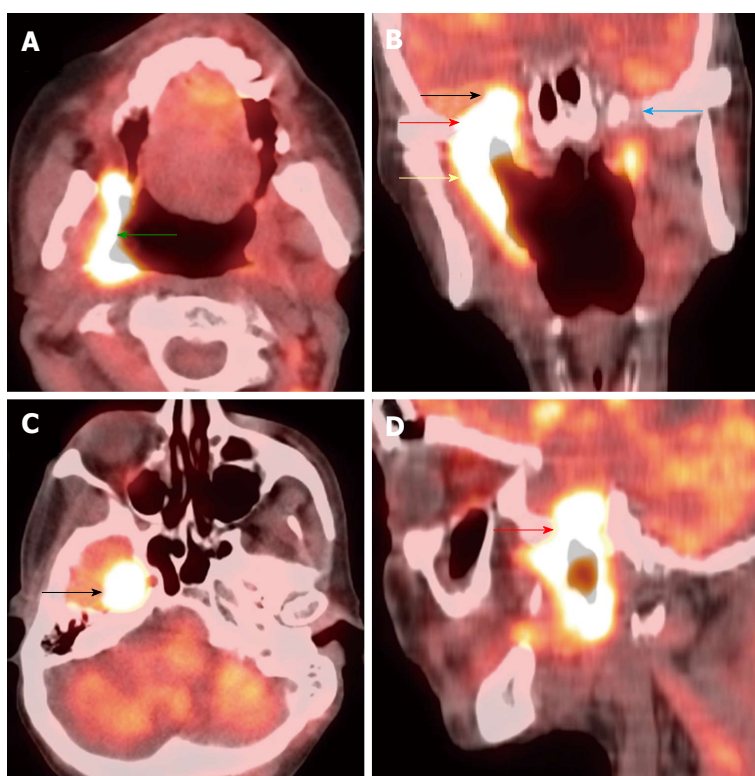


Figure 8 Perineural spread. Positron emission tomography/computed tomography (A: Axial; B: Coronal; C: Axial; D: Sagittal) demonstrates a T4b right oropharyngeal squamous cell carcinoma (green arrow) spreading along the mandibular branch of the trigeminal nerve (yellow arrow) through the right foramen ovale (red arrows) to involve the right cavernous sinus (black arrows). The left mandibular nerve in the foramen ovale is normal (blue arrow).

tion to CT or MRI with IV contrast (Figure 7). However, pretreatment PET/CT with IV contrast is valuable as a baseline study to compare to the post treatment study^[20].

Perineural spreading

Perineural spreading occurs when the tumor spreads along the peripheral nerve away from the primary tumor site, and is associated with poor outcomes. The patient may be asymptomatic and it may not be detected during surgery^[21]. MRI is the study of choice in detection of perineural spread due to its high tissue contrast. It is important for radiologists to be familiar with PET/CT findings of perineural spreading as some patients may not have MRI as the initial or post treatment evaluation. On PET/CT, perineural spread can present with abnormal linear or curvilinear hypermetabolic activity along the trigeminal or facial nerves^[18] (Figure 8).

Detection of CUP origin

Two to 7% of HNSCC patients present with metastatic cervical lymphadenopathy without definite primary sites^[22,23] detected by a complete history (nonspecific symptoms or no symptoms), thorough physical examination/office flexible fiberoptic endoscopy (small submucosal lesion), or conventional contrast enhanced CT/MRI (small lesion obscured by normal lymphoid tissue). The work up algorithm to search for the primary tumor is shown in Figure 9.

The choice of treatment depends on staging and histology^[24]. Failure to identify the primary tumor leads to nontargeted treatment (bilateral tonsillectomies, bilateral neck dissection, radiation to cover the whole pharyngeal mucosa and neck)^[25] resulting in increased complications, morbidity and mortality.

Various studies show that PET/CT is able to iden-

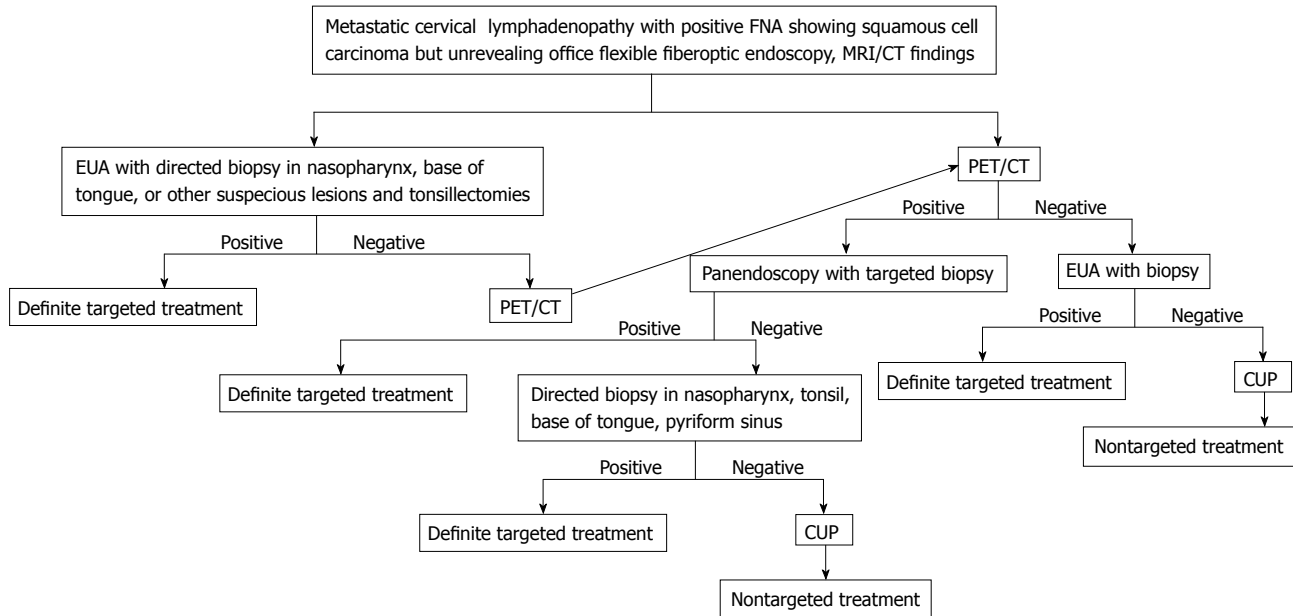


Figure 9 Algorithm in diagnosis and management of carcinoma of unknown primary. MRI: Magnetic resonance imaging; PET/CT: Positron emission tomography/computed tomography; CUP: Carcinoma of unknown primary.

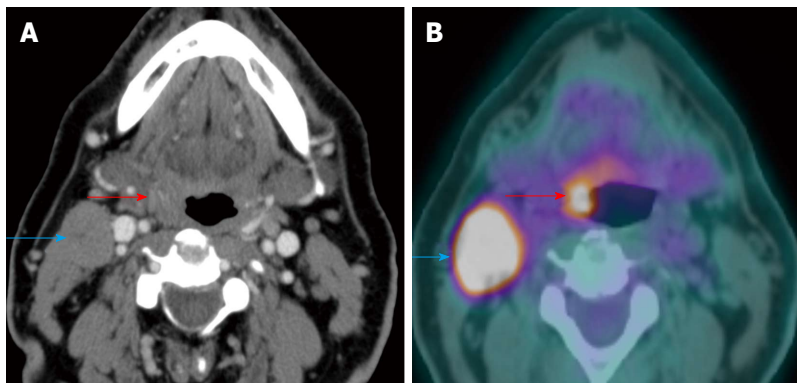


Figure 10 Carcinoma of unknown primary. The patient presented with palpable right level II a lymphadenopathy (blue arrows). Fine needle aspiration of the lymph node was positive for squamous cell carcinoma. Panendoscopy without biopsy and contrast-enhanced computed tomography (CT) (A) were unremarkable. Positron emission tomography/CT (B) showed a small hypermetabolic area in the right palatine tonsil (red arrows) proven to be squamous cell carcinoma by biopsy.

tify the primary cancer 29% to 54% of cases with 62% to 93% sensitivity, 33% to 93% specificity, 56% to 89% positive predictive value (PPV) and 25% to 96% negative predictive value (NPV)^[3,26-31]. The majority of the primary cancers are found in the palatine tonsils or base of tongue^[32] (Figure 10). A high detection rate of up to 54% can be achieved when the combination of CT, MRI, endoscopy under anesthesia and PET/CT are used. Due to variable negative predictive value of PET/CT, otolaryngologists should still strongly consider panendoscopy with directed biopsy and bilateral tonsillectomies when PET/CT yields negative result^[3]. Radiologists should be aware of recent panendoscopy with biopsy before PET/CT. Recent biopsy can cause false-positive result as high as 50%^[30]. It is still uncertain when PET/CT should be performed after biopsy to avoid false positivity, therefore if carcinoma of unknown primary is suspected it is best to obtain PET/CT prior to endoscopy and biopsy/tonsillectomy^[26,33]. Obtaining PET/CT prior to biopsy may alert the clinician to suspected primary tumor sites and avoid the false positive imaging result if PET/CT is obtained after biopsy.

Identification of second primary malignancy

Synchronous second primary malignancy (SPM) occurs within 6 mo when the index primary cancer is detected. Approximately 1.4% to 18%^[34] of head neck cancer patients have SPM, especially when the index cancers are laryngeal carcinomas. Most synchronous SPM are found in the lung (Figure 11), head and neck region itself (Figure 12) or esophagus^[35] with the majority of the tumors being squamous cell carcinoma^[36]. A recent study found that human papillomavirus (HPV)-seropositive patients, especially those who never smoked, have less risk of developing SPM as compared to HPV-seronegative group^[37]. Since SPM is one of the main causes of death in early-stage HNSCC, early detection and treatment of SPM increases survival^[34]. Detection of SPM also changes treatment planning^[33]. A meta-analysis revealed 87.5% sensitivity and 95% specificity of PET/CT in detection of SPM or distant metastasis^[38]. Negative PET/CT does not completely exclude the presence of SPM^[38].

Lymph node involvement (N)

The likelihood of cervical lymph node metastasis in

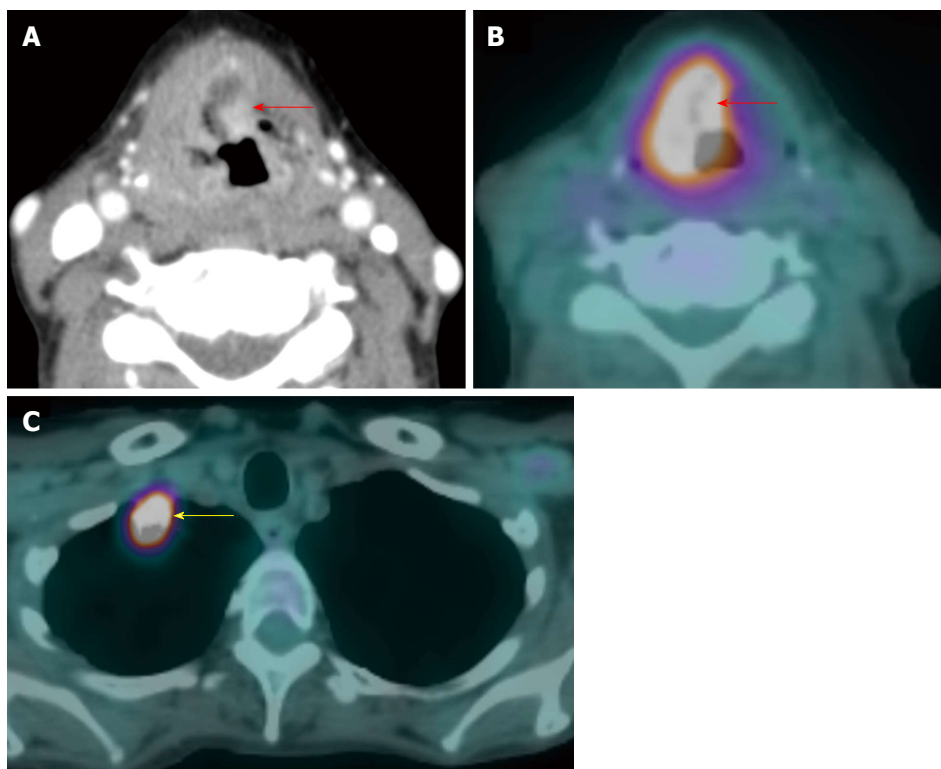


Figure 11 Synchronous second primary malignancy in the lung. A T4a supraglottic squamous cell carcinoma (red arrows) with extralaryngeal invasion is well demonstrated on computed tomography (CT) (A) and positron emission tomography/CT (B). There is a 3-cm hypermetabolic second primary squamous cell carcinoma (yellow arrow) in the right lung apex, discovered at the same time in this patient who had an extensive smoking and drinking history. The rest of the exam is unremarkable.

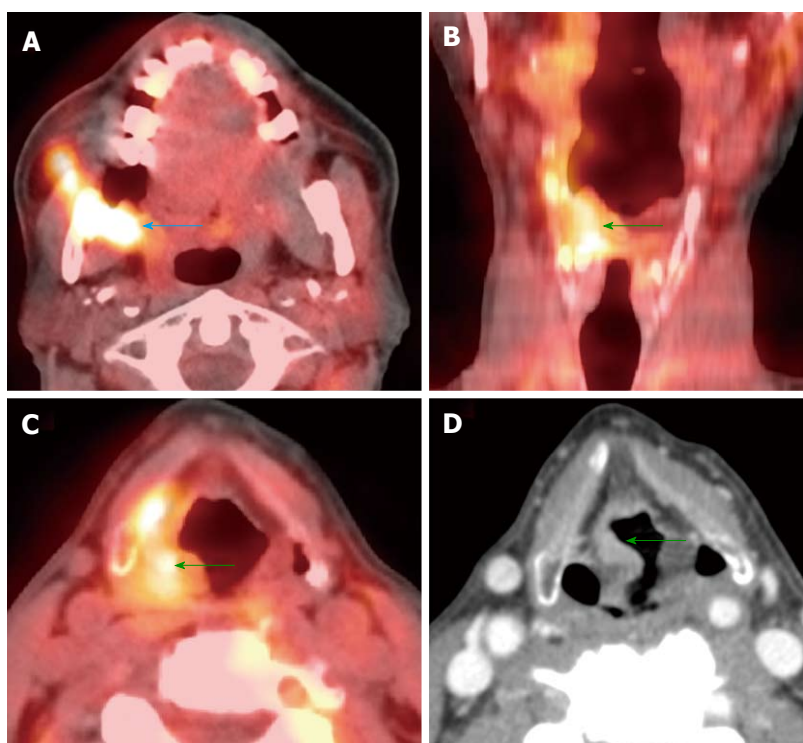


Figure 12 Synchronous second primary malignancy in the head and neck region. A T4b right retromolar trigone squamous cell carcinoma involving the masticator space (blue arrow) was seen on positron emission tomography/computed tomography (PET/CT) (A). There was another second primary tumor in the right aryepiglottic fold (green arrows) causing no symptoms, demonstrated by both PET/CT (B and C) and contrast-enhanced CT (D).

HNSCC depends on location, histology and staging of the primary tumor^[39]. The presence of metastatic nodes carries poor prognosis, decreases 5-year survival and necessitates treatment in the neck^[40,41]. Differentiation between metastatic lymph nodes and reactive nodes by

CT/MR size and morphologic criteria can be difficult^[42]. A meta-analysis by Kyzas *et al*^[39] showed higher sensitivity/specificity (80%/86%) of PET/CT as compared to other conventional diagnostic modalities (75%/79%). The higher sensitivity is due to the fact that PET can

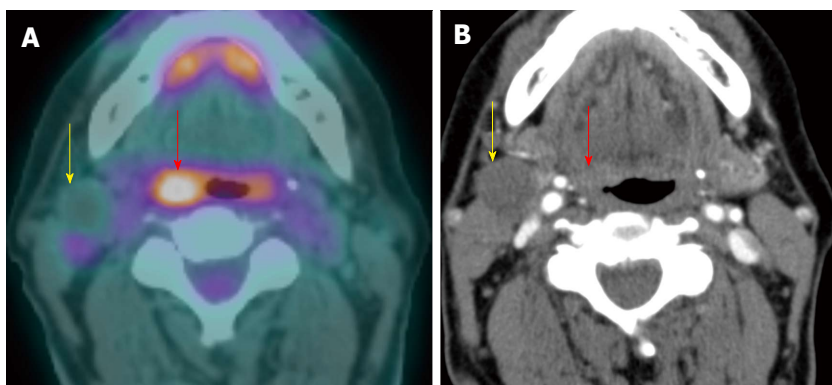


Figure 13 Hypometabolic necrotic lymph node. A T1N1M0 right glossopharyngeal sulcus squamous cell carcinoma (red arrow) is FDG avid on positron emission tomography/computed tomography (PET/CT) (A). There is a 1.7-cm necrotic right level II a lymph node seen on contrast-enhanced CT (B). The necrotic lymph node is hypometabolic and may potentially cause a false negative result if the CT portion of the PET/CT or corresponding contrast-enhanced CT were not correlated.

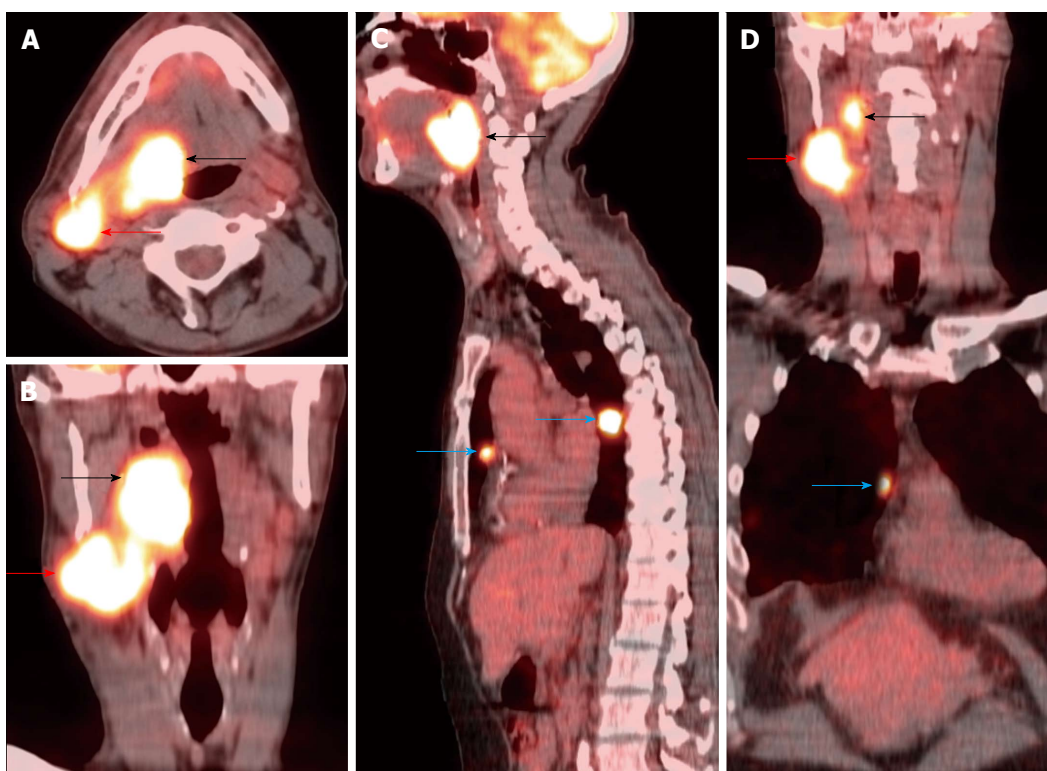


Figure 14 Lung metastasis at initial staging. A T3N2bM1 right base of tongue squamous cell carcinoma (black arrows) was FDG avid on positron emission tomography/computed tomography (A-D) with metastasis to the right level II a (red arrows) and lung (blue arrows).

show hypermetabolism in normal-sized metastatic lymph nodes. However PET is not 100% specific because inflammatory reactive nodes and adjacent granulation tissue can increase uptake^[43] yielding a false positive result. Radiologists should be aware that small necrotic lymph nodes may appear hypometabolic on PET especially in hyperglycemic patients^[44]. Therefore it is important to analyze both morphologic and metabolic information derived from PET/CT (Figure 13).

HNSCC patients whose metastatic lymph nodes are not palpable on physical examination or visualized on imaging are determined to be clinically N0 (cN0) stage^[6]. PET/CT failed to detect half of the cN0 which were confirmed to have metastasis by histopathology. This is thought to be due to small size of occult metastasis beyond resolution of PET (typically micrometastases < 5 mm), obscuration by physiologic glucose uptake in adja-

cent organs or hyperglycemia. Therefore it is not recommended to routinely use PET/CT to assess possible cervical lymph node metastasis in cN0 setting^[39]. However, pretreatment PET/CT may still be useful as an optional imaging to compare with the post treatment scan to discriminate malignant tissue from physiologic uptake^[45].

Distant metastasis (M)

Approximately 7% to 25% of patients with advanced stage HNSCC have distant metastases at initial presentation^[46]. The most common sites of metastasis include lung (Figure 14), bone and abdomen. Mediastinal lymph node involvement is considered distant metastasis^[6]. Contrast enhanced chest CT is commonly used to assess intrathoracic spread with 73% sensitivity and 80% specificity^[47]. Overall PET/CT is more accurate than conventional imaging in detecting metastatic foci^[48]. A meta-

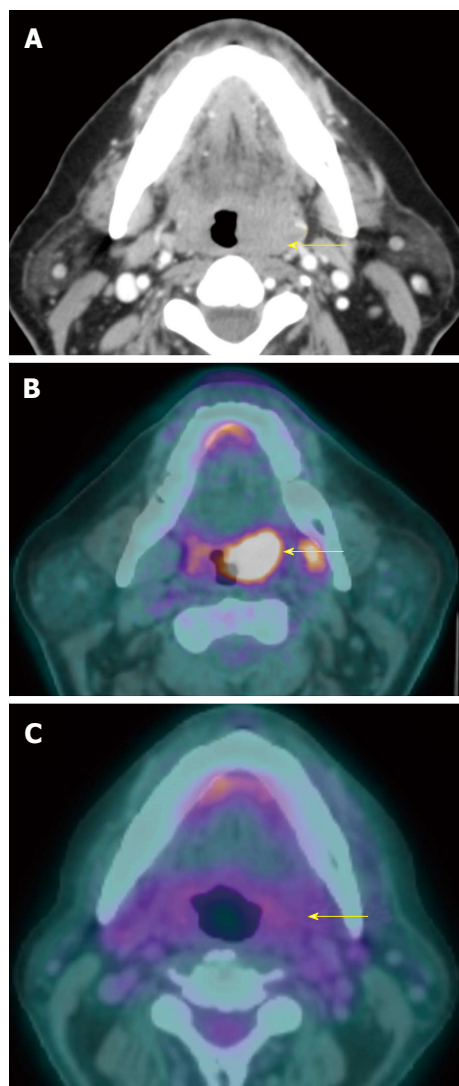


Figure 15 Complete treatment response at the primary tumor site. A T2N0M0 oral tongue squamous cell carcinoma (yellow arrow) seen on contrast-enhanced computed tomography (CT) (A) and positron emission tomography/CT (PET/CT) (B) showed complete response after 3 mo of chemoradiation demonstrated on PET/CT (C). The tumor is no longer hypermetabolic. The patients remained disease free for 3 years, proving true negative result of PET/CT.

analysis by Xu *et al.*^[49] revealed sensitivity and specificity of PET/CT around 87.5 % and 95% respectively. It is very important to detect distant metastases early in the workup as it changes prognosis and management. Extensive surgery with curative intent may cause significant morbidity and mortality and may be avoided in the event of documented distant metastases. PET/CT is recommended when distant spread is suspected in HNSCC patients with locoregionally advanced stage. However, negative PET/CT does not completely exclude absence of metastasis^[49].

Change in initial staging and management

Lonneux *et al.*^[50] performed a multicenter prospective study to evaluate the impact of PET/CT on the initial staging and management of patients with HNSCC. The group found that PET/CT improved the TNM classifica-

tion of the disease and altered the management of 13.7% of the patients mainly due to the ability of PET/CT to detect metastatic or additional disease.

POST TREATMENT EVALUATION

Therapy response assessment and residual tumor detection

A small early-stage HNSCC (*e.g.*, a T1N0 true vocal cord carcinoma) can be treated with a single modality^[51]. Advanced-staged disease (Stage III and IV) typically needs multimodality treatments including surgery, radiation and chemotherapy^[52]. Radical concurrent chemoradiation can be used as a definite therapy in preference to surgery to achieve similar cure rates with less morbidity and to preserve organ function^[53]. Surgery and radiation can cause significant inflammation, fibrosis and distortion of the anatomy preventing accurate differentiation between residual tumor and complete tumor response by conventional imaging^[54,55]. Inaccurate post treatment assessment may cause delayed or unnecessary treatment resulting in increased mortality and morbidity^[45]. Multiple studies have shown that PET/CT is superior to conventional anatomic imaging in assessment of tumor response and detection of residual tumor. This is helpful to the surgeon in selecting the appropriate patients for salvage surgery after chemoradiation^[4,56-58].

The sensitivity, specificity, PPV and NPV of PET/CT for detection of residual primary tumor were 94%, 82%, 75% and 95% respectively^[4]. It is noted that PET/CT has very high NPV, therefore negative result highly suggests absence of viable residual disease in both primary site and neck (Figures 15 and 16). The low PPV is due to treatment-related FDG-avid inflammation or infection (Figure 17). A positive PET/CT result in the post treatment phase needs careful correlation with clinical information and corresponding CT/MRI findings^[45]. It is suggested that PET/CT should be performed no sooner than 2 mo after completion of treatment to avoid false positive results; however it may be performed sooner if there is clinically suspected recurrent disease^[59]. We generally recommend performing PET/CT around 3 mo after completion of treatment at our institution.

Long-term surveillance

The purpose of obtaining PET/CT as a surveillance tool is to allow for the early detection of recurrent disease (both in the primary site and the neck) (Figure 18), assess for a metachronous second primary tumor (Figure 19) and to rule out distant metastases (Figure 20). PET/CT has 93% to 100% sensitivity and 63% to 94% specificity in detection of recurrent tumor in both primary site and the neck respectively^[45,60,61]. The NPV of a single PET/CT and double PET/CT (obtained within 6 mo period) are 91% and 98% respectively. Negative results of two consecutive PET/CT studies could potentially eliminate the need for routine post treatment imaging if there is no clinical suspicion of tumor recurrence^[62].

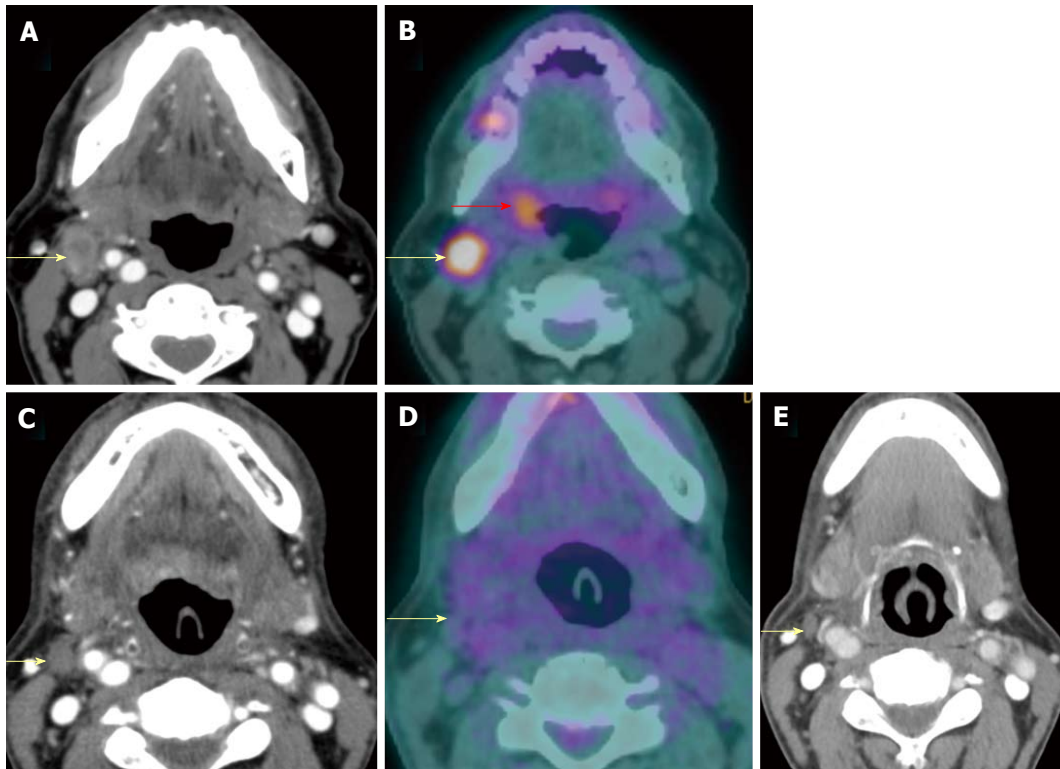


Figure 16 Complete response of a metastatic lymph node. A T2N2bM0 right palatine tonsil squamous cell carcinoma (red arrow) and right level II a metastatic lymph node (yellow arrows) were seen on both contrast-enhanced computed tomography (CT) (A) and positron emission tomography/CT (PET/CT) (B). After chemoradiation, the node was smaller on contrast-enhanced CT at 6 wk (C) and hypometabolic on PET/CT at 4 mo (D), representing complete response to treatment. Negative physical examination and PET/CT at 1 year (E) confirmed true negative result of the PET/CT performed at 4 mo.

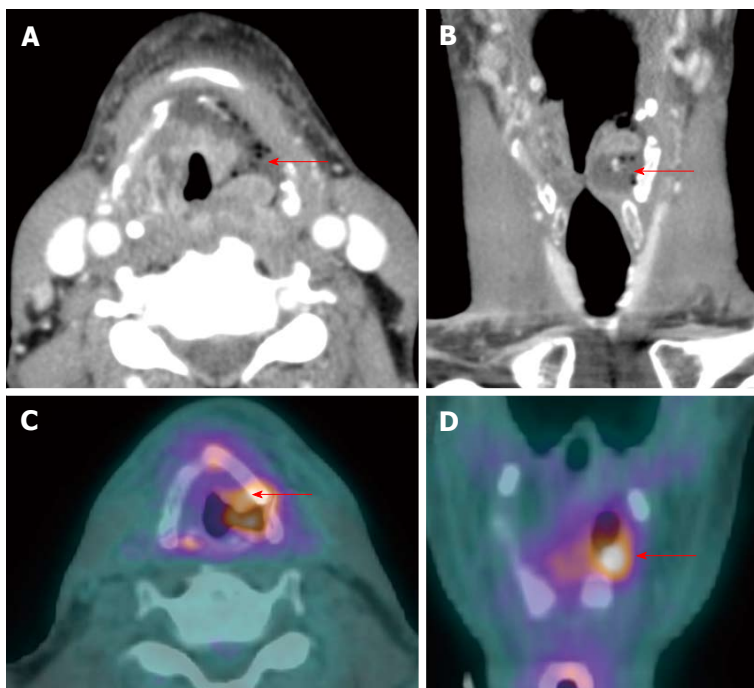


Figure 17 False positive positron emission tomography/computed tomography result due to post treatment infection. A T3N0M0 left supraglottic squamous cell carcinoma showed edema and necrosis at the tumor site (red arrows) on contrast-enhanced computed tomography (CT) (A and B) at 5 wk after chemoradiation and increased uptake on positron emission tomography/CT (PET/CT) (C and D) at 10 wk. The patient had severe throat pain and fever. A residual tumor can not be excluded, therefore endoscopy with biopsy was performed showing radiation-induced inflammation, tumor necrosis and superimposed actinomycosis causing a false positive result on PET/CT. Due to lack of viable tumor, no salvage surgery was performed. The patient was disease free at two-year follow up.

In addition there are no differences in survival between PET/CT detected and clinically detected recurrences^[63]. Although there is an appreciable radiation dose and lifetime cancer risk associated with PET/CT, the use of this examination is warranted when utilized in the appropriate clinical setting^[64].

Metachronous second primary tumor may occur after 6 mo of the index primary tumor with 2.8% annual rate^[65] (Figure 21). The incidence of distant metastasis following definitive treatment is 9% with the risk increased in patients with locally advanced stages^[65,66]. Overall 17.9% of HNSCC patients develop second primary cancers and/or

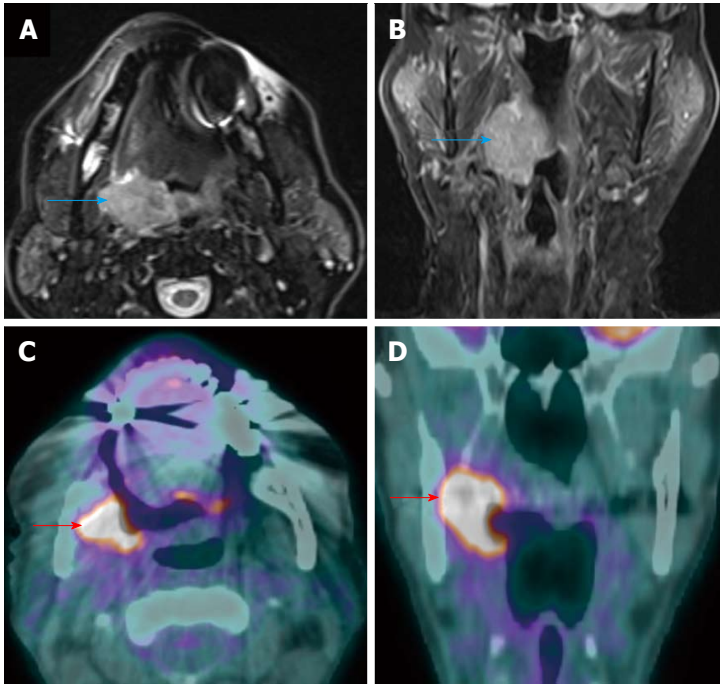


Figure 18 Recurrent primary tumor detected by positron emission tomography/computed tomography. A T3N0M0 right palatine tonsil squamous cell carcinoma was demonstrated on axial T2W magnetic resonance imaging (MRI) (blue arrow) (A) and coronal contrast-enhanced T1W MRI (B). MRI and positron emission tomography/computed tomography (PET/CT) performed 2 and 3 mo after completion of chemoradiation demonstrated complete treatment response (not shown). Surveillance PET/CT (C and D) revealed intense increase metabolism in the right palatine tonsil and medial pterygoid muscle (red arrows) representing a recurrent squamous cell carcinoma.

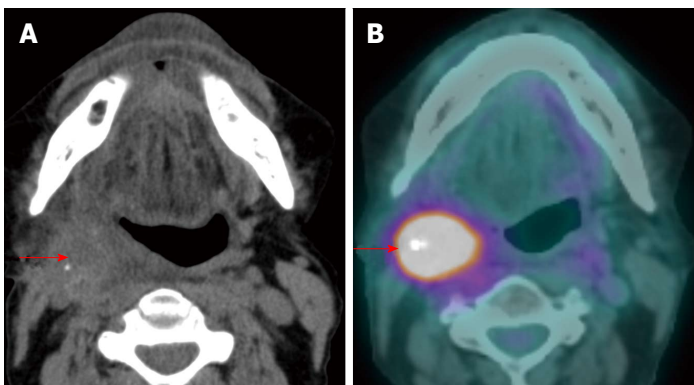


Figure 19 Recurrent nodal disease. A T2N1M0 right hypopharyngeal squamous cell carcinoma status post completed chemoradiation 2.5 years ago with complete response (not shown). The patient presented with right sided level II lymphadenopathy. Computed tomography (CT) without contrast (A) showed an ill-defined mass in the right level II. Positron emission tomography/CT (PET/CT) (red arrow) (B) demonstrated very intense metabolism in the mass. Biopsy confirmed a recurrent squamous cell carcinoma in the right level II a node.

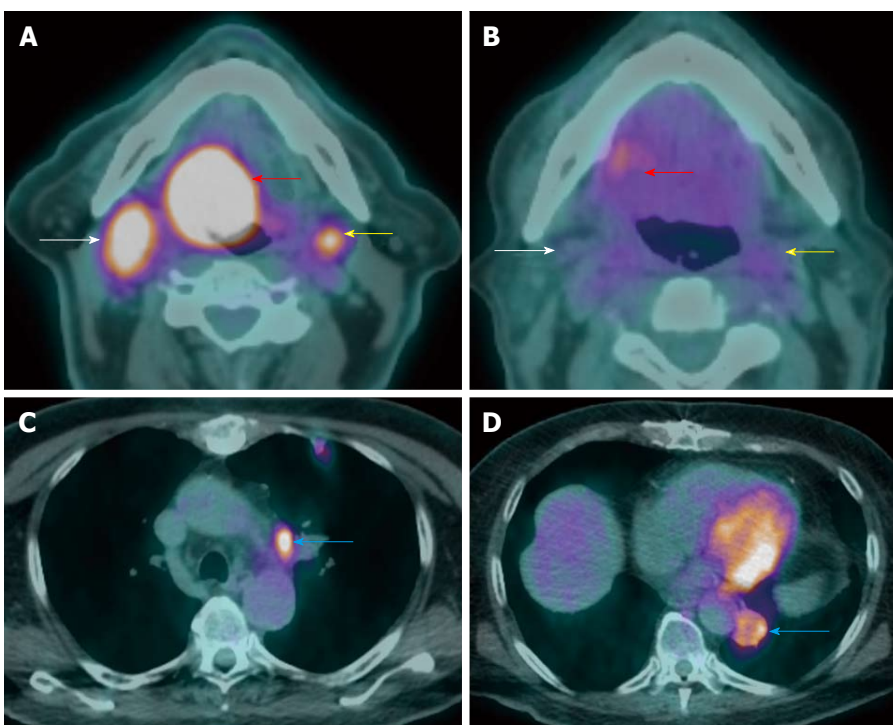


Figure 20 Failure of treatment due to distant metastasis. A T4aN2cM0 right base of tongue squamous cell carcinoma (red arrow) with bilateral level II a metastatic lymphadenopathy (white and yellow arrows) seen on positron emission tomography/computed tomography (PET/CT) at initial staging (A and B). The patient received chemoradiation. PET/CT (C and D) performed at 3 mo after treatment showed new lung metastases (blue arrow).



Figure 21 Metachronous second primary tumor. A T1N0M0 left floor of mouth squamous cell carcinoma (SCC) (not shown) s/p wide local excision with primary closure and selective neck dissection 3 yr ago. Surveillance positron emission tomography/computed tomography (A-C) showed a recurrent SCC at left floor of mouth (yellow arrow) and two metachronous second primaries at the left hypopharynx (black arrow) and left base of tongue (red arrow).

distant metastasis, especially in patients with recurrent diseases^[38,66]. The identification of distant metastatic lesions at the time of restaging recurrent tumors may allow the clinician to avoid aggressive surgery and focus on palliative chemoradiation options^[66]. PET/CT has strong utility in detecting second primary tumors or distant metastases with a sensitivity and specificity of 88.8% and 95.1% respectively^[38].

CONCLUSION

In the pre-treatment phase, PET/CT is useful in the evaluation of patients with carcinoma of unknown primary origin before panendoscopy and biopsy, detection of synchronous second primary tumor, staging of cervical lymph node metastasis and assessing for distant metastases. In the post-treatment phase, it is clear that PET/CT is recommended to assess treatment response, detect residual/recurrent tumor and rule out distant metastases. Radiologists should carefully analyze both CT and PET information and correlate it with other imaging modalities, previous studies and clinical information.

REFERENCES

- 1 **Siegel R**, Naishadham D, Jemal A. Cancer statistics, 2013. *CA Cancer J Clin* 2013; **63**: 11-30 [PMID: 23335087 DOI: 10.3322/caac.21166]
- 2 **Ha PK**, Hdeib A, Goldenberg D, Jacene H, Patel P, Koch W, Califano J, Cummings CW, Flint PW, Wahl R, Tufano RP. The role of positron emission tomography and computed tomography fusion in the management of early-stage and advanced-stage primary head and neck squamous cell carcinoma. *Arch Otolaryngol Head Neck Surg* 2006; **132**: 12-16 [PMID: 16415423]
- 3 **Miller FR**, Hussey D, Beeram M, Eng T, McGuff HS, Otto RA. Positron emission tomography in the management of unknown primary head and neck carcinoma. *Arch Otolaryngol Head Neck Surg* 2005; **131**: 626-629 [PMID: 16027287]
- 4 **Gupta T**, Master Z, Kannan S, Agarwal JP, Ghosh-Laskar S, Rangarajan V, Murthy V, Budrukkar A. Diagnostic performance of post-treatment FDG PET or FDG PET/CT imaging in head and neck cancer: a systematic review and meta-analysis. *Eur J Nucl Med Mol Imaging* 2011; **38**: 2083-2095 [PMID: 21853309 DOI: 10.1007/s00259-011-1893-y]
- 5 **Scott AM**, Gunawardana DH, Bartholomeusz D, Ramshaw JE, Lin P. PET changes management and improves prognostic stratification in patients with head and neck cancer: results of a multicenter prospective study. *J Nucl Med* 2008; **49**: 1593-1600 [PMID: 18794254 DOI: 10.2967/jnumed.108.053660]
- 6 **Edge SB**, Byrd DR, Compton CC, Fritz AG, Greene FL, Trotti A. *Cancer Staging Handbook From AJCC Cancer Staging Manual*. 7th ed. New York: Springer, 2010: 39-126
- 7 **National Comprehensive Cancer Network**. NCCN Clinical Practice Guidelines in Oncology™ 2013. Head and Neck Cancers v. 2. 2013. Available from: URL: http://www.nccn.org/professionals/physician_gls/f_guidelines.asp#head-and-neck
- 8 **Paes FM**, Singer AD, Checkver AN, Palmquist RA, De La Vega G, Sidani C. Perineural spread in head and neck malignancies: clinical significance and evaluation with 18F-FDG PET/CT. *Radiographics* 2013; **33**: 1717-1736 [PMID: 24108559 DOI: 10.1148/rg.336135501]
- 9 **Ng SH**, Chan SC, Yen TC, Chang JT, Liao CT, Ko SF, Liu FY, Chin SC, Fan KH, Hsu CL. Staging of untreated nasopharyngeal carcinoma with PET/CT: comparison with conventional imaging work-up. *Eur J Nucl Med Mol Imaging* 2009; **36**: 12-22 [PMID: 18704401 DOI: 10.1007/s00259-008-0918-7]
- 10 **Zbären P**, Becker M, Läng H. Pretherapeutic staging of hypopharyngeal carcinoma. Clinical findings, computed tomography, and magnetic resonance imaging compared with histopathologic evaluation. *Arch Otolaryngol Head Neck Surg* 1997; **123**: 908-913 [PMID: 9305239]
- 11 **Seitz O**, Chambron-Pinho N, Middendorp M, Sader R, Mack M, Vogl TJ, Bisdas S. 18F-Fluorodeoxyglucose-PET/CT to evaluate tumor, nodal disease, and gross tumor volume of oropharyngeal and oral cavity cancer: comparison with MR imaging and validation with surgical specimen. *Neuroradiology* 2009; **51**: 677-686 [PMID: 19727695 DOI: 10.1007/s00234-009-0586-8]
- 12 **Politi M**, Costa F, Robiony M, Rinaldo A, Ferlito A. Review of segmental and marginal resection of the mandible in patients with oral cancer. *Acta Otolaryngol* 2000; **120**: 569-579 [PMID: 11039866]
- 13 **Goerres GW**, Schmid DT, Schuknecht B, Eyrich GK. Bone invasion in patients with oral cavity cancer: comparison of conventional CT with PET/CT and SPECT/CT. *Radiology* 2005; **237**: 281-287 [PMID: 16118155]
- 14 **Gu DH**, Yoon DY, Park CH, Chang SK, Lim KJ, Seo YL, Yun EJ, Choi CS, Bae SH. CT, MR, (18)F-FDG PET/CT, and their combined use for the assessment of mandibular invasion by squamous cell carcinomas of the oral cavity. *Acta Radiol* 2010; **51**: 1111-1119 [PMID: 20929295 DOI: 10.3109/02841851.2010.520027]
- 15 **Henrot P**, Blum A, Toussaint B, Troufleau P, Stines J, Roland

- J. Dynamic maneuvers in local staging of head and neck malignancies with current imaging techniques: principles and clinical applications. *Radiographics* 2003; **23**: 1201-1213 [PMID: 12975510]
- 16 **Chang CY**, Yang BH, Lin KH, Liu RS, Wang SJ, Shih WJ. Feasibility and incremental benefit of puffed-cheek 18F-FDG PET/CT on oral cancer patients. *Clin Nucl Med* 2013; **38**: e374-e378 [PMID: 23989442 DOI: 10.1097/RLU.0b013e31826390cf]
 - 17 **King AD**, Ma BB, Yau YY, Zee B, Leung SF, Wong JK, Kam MK, Ahuja AT, Chan AT. The impact of 18F-FDG PET/CT on assessment of nasopharyngeal carcinoma at diagnosis. *Br J Radiol* 2008; **81**: 291-298 [PMID: 18344274 DOI: 10.1259/bjr/73751469]
 - 18 **Cheuk DK**, Sabin ND, Hossain M, Wozniak A, Naik M, Rodriguez-Galindo C, Krasin MJ, Shulkin BL. PET/CT for staging and follow-up of pediatric nasopharyngeal carcinoma. *Eur J Nucl Med Mol Imaging* 2012; **39**: 1097-1106 [PMID: 22532252 DOI: 10.1007/s00259-012-2091-2]
 - 19 Induction chemotherapy plus radiation compared with surgery plus radiation in patients with advanced laryngeal cancer. The Department of Veterans Affairs Laryngeal Cancer Study Group. *N Engl J Med* 1991; **324**: 1685-1690 [PMID: 2034244]
 - 20 **Chu MM**, Kositwattanarerk A, Lee DJ, Makkar JS, Genden EM, Kao J, Packer SH, Som PM, Kostakoglu L. FDG PET with contrast-enhanced CT: a critical imaging tool for laryngeal carcinoma. *Radiographics* 2010; **30**: 1353-1372 [PMID: 20833855 DOI: 10.1148/rg.305095764]
 - 21 **Liebig C**, Ayala G, Wilks JA, Berger DH, Albo D. Perineural invasion in cancer: a review of the literature. *Cancer* 2009; **115**: 3379-3391 [PMID: 19484787 DOI: 10.1002/cncr.24396]
 - 22 **Jereczek-Fossa BA**, Jassem J, Orecchia R. Cervical lymph node metastases of squamous cell carcinoma from an unknown primary. *Cancer Treat Rev* 2004; **30**: 153-164 [PMID: 15023433]
 - 23 **Miller FR**, Karnad AB, Eng T, Hussey DH, Stan McGuff H, Otto RA. Management of the unknown primary carcinoma: long-term follow-up on a negative PET scan and negative panendoscopy. *Head Neck* 2008; **30**: 28-34 [PMID: 17657782]
 - 24 **Calabrese L**, Jereczek-Fossa BA, Jassem J, Rocca A, Bruschini R, Orecchia R, Chiesa F. Diagnosis and management of neck metastases from an unknown primary. *Acta Otorhinolaryngol Ital* 2005; **25**: 2-12 [PMID: 16080309]
 - 25 **Issing WJ**, Taleban B, Tauber S. Diagnosis and management of carcinoma of unknown primary in the head and neck. *Eur Arch Otorhinolaryngol* 2003; **260**: 436-443 [PMID: 12684829]
 - 26 **Rudmik L**, Lau HY, Matthews TW, Bosch JD, Kloiber R, Molnar CP, Dort JC. Clinical utility of PET/CT in the evaluation of head and neck squamous cell carcinoma with an unknown primary: a prospective clinical trial. *Head Neck* 2011; **33**: 935-940 [PMID: 21674668 DOI: 10.1002/hed.21566]
 - 27 **Yabuki K**, Tsukuda M, Horiuchi C, Taguchi T, Nishimura G. Role of 18F-FDG PET in detecting primary site in the patient with primary unknown carcinoma. *Eur Arch Otorhinolaryngol* 2010; **267**: 1785-1792 [PMID: 20814690 DOI: 10.1007/s00405-010-1371-3]
 - 28 **Dandekar MR**, Kannan S, Rangarajan V, Purandare NC, Chaukar DA, Deshmukh A, D'cruz AK. Utility of PET in unknown primary with cervical metastasis: a retrospective study. *Indian J Cancer* 2011; **48**: 181-186 [PMID: 21768663 DOI: 10.4103/0019-509X.82882]
 - 29 **Padovani D**, Aimoni C, Zucchetta P, Paluzzi A, Pastore A. 18-FDG PET in the diagnosis of laterocervical metastases from occult carcinoma. *Eur Arch Otorhinolaryngol* 2009; **266**: 267-271 [PMID: 18587594 DOI: 10.1007/s00405-008-0733-6]
 - 30 **Johansen J**, Buus S, Loft A, Keiding S, Overgaard M, Hansen HS, Grau C, Bundgaard T, Kirkegaard J, Overgaard J. Prospective study of 18FDG-PET in the detection and management of patients with lymph node metastases to the neck from an unknown primary tumor. Results from the DAHANCA-13 study. *Head Neck* 2008; **30**: 471-478 [PMID: 18023031]
 - 31 **Wong WL**, Sonoda LI, Gharpurhy A, Gollub F, Wellsted D, Goodchild K, Lemon C, Farrell R, Saunders M. 18F-fluorodeoxyglucose positron emission tomography/computed tomography in the assessment of occult primary head and neck cancers--an audit and review of published studies. *Clin Oncol (R Coll Radiol)* 2012; **24**: 190-195 [PMID: 22183080 DOI: 10.1016/j.clon.2011.11.001]
 - 32 **Cianchetti M**, Mancuso AA, Amdur RJ, Werning JW, Kirwan J, Morris CG, Mendenhall WM. Diagnostic evaluation of squamous cell carcinoma metastatic to cervical lymph nodes from an unknown head and neck primary site. *Laryngoscope* 2009; **119**: 2348-2354 [PMID: 19718744 DOI: 10.1002/lary.20638]
 - 33 **Strobel K**, Haerle SK, Stoeckli SJ, Schrank M, Soyka JD, Veit-Haibach P, Hany TF. Head and neck squamous cell carcinoma (HNSCC)--detection of synchronous primaries with (18)F-FDG-PET/CT. *Eur J Nucl Med Mol Imaging* 2009; **36**: 919-927 [PMID: 19205699 DOI: 10.1007/s00259-009-1064-6]
 - 34 **Kim SY**, Roh JL, Yeo NK, Kim JS, Lee JH, Choi SH, Nam SY. Combined 18F-fluorodeoxyglucose-positron emission tomography and computed tomography as a primary screening method for detecting second primary cancers and distant metastases in patients with head and neck cancer. *Ann Oncol* 2007; **18**: 1698-1703 [PMID: 17716985]
 - 35 **Morris LG**, Sikora AG, Hayes RB, Patel SG, Ganly I. Anatomic sites at elevated risk of second primary cancer after an index head and neck cancer. *Cancer Causes Control* 2011; **22**: 671-679 [PMID: 21327458 DOI: 10.1007/s10552-011-9739-2]
 - 36 **Jones AS**, Morar P, Phillips DE, Field JK, Husband D, Helliwell TR. Second primary tumors in patients with head and neck squamous cell carcinoma. *Cancer* 1995; **75**: 1343-1353 [PMID: 7882285]
 - 37 **Peck BW**, Dahlstrom KR, Gan SJ, Caywood W, Li G, Wei Q, Zafereo ME, Sturgis EM. Low risk of second primary malignancies among never smokers with human papillomavirus-associated index oropharyngeal cancers. *Head Neck* 2013; **35**: 794-799 [PMID: 22711172 DOI: 10.1002/hed.23033]
 - 38 **Xu GZ**, Guan DJ, He ZY. (18)FDG-PET/CT for detecting distant metastases and second primary cancers in patients with head and neck cancer. A meta-analysis. *Oral Oncol* 2011; **47**: 560-565 [PMID: 21621450 DOI: 10.1016/j.oraloncology.2011.04.021]
 - 39 **Kyzas PA**, Evangelou E, Denaxa-Kyza D, Ioannidis JP. 18F-fluorodeoxyglucose positron emission tomography to evaluate cervical node metastases in patients with head and neck squamous cell carcinoma: a meta-analysis. *J Natl Cancer Inst* 2008; **100**: 712-720 [PMID: 18477804 DOI: 10.1093/jnci/djn125]
 - 40 **Snow GB**, Annyas AA, van Slooten EA, Bartelink H, Hart AA. Prognostic factors of neck node metastasis. *Clin Otolaryngol Allied Sci* 1982; **7**: 185-192 [PMID: 7105450]
 - 41 **Whitehurst JO**, Droulias CA. Surgical treatment of squamous cell carcinoma of the oral tongue: factors influencing survival. *Arch Otolaryngol* 1977; **103**: 212-215 [PMID: 849198]
 - 42 **van den Brekel MW**, Stel HV, Castelijns JA, Nauta JJ, van der Waal I, Valk J, Meyer CJ, Snow GB. Cervical lymph node metastasis: assessment of radiologic criteria. *Radiology* 1990; **177**: 379-384 [PMID: 2217772]
 - 43 **Kubota R**, Yamada S, Kubota K, Ishiwata K, Tamahashi N, Ido T. Intratumoral distribution of fluorine-18-fluorodeoxyglucose in vivo: high accumulation in macrophages and granulation tissues studied by microautoradiography. *J Nucl Med* 1992; **33**: 1972-1980 [PMID: 1432158]
 - 44 **Murakami R**, Uozumi H, Hirai T, Nishimura R, Katsuragawa S, Shiraishi S, Toya R, Tashiro K, Kawanaka K, Oya N, Tomiguchi S, Yamashita Y. Impact of FDG-PET/CT fused imaging on tumor volume assessment of head-and-neck

- squamous cell carcinoma: intermethod and interobserver variations. *Acta Radiol* 2008; **49**: 693-699 [PMID: 18568563 DOI: 10.1080/02841850802027034]
- 45 **Mosci C**, DG, Quan A. FDG-PET/CT Initial and Subsequent Therapy Evaluation: Progressing to PET/MR Imaging. *PET Clin* 2012; **7**: 369-380
- 46 **Gourin CG**, Watts TL, Williams HT, Patel VS, Bilodeau PA, Coleman TA. Identification of distant metastases with positron-emission tomography-computed tomography in patients with previously untreated head and neck cancer. *Laryngoscope* 2008; **118**: 671-675 [PMID: 18197136 DOI: 10.1097/MLG.0b013e3181625737]
- 47 **Brouwer J**, de Bree R, Hoekstra OS, Golding RP, Langendijk JA, Castelijns JA, Leemans CR. Screening for distant metastases in patients with head and neck cancer: is chest computed tomography sufficient? *Laryngoscope* 2005; **115**: 1813-1817 [PMID: 16222201]
- 48 **Yoo J**, Henderson S, Walker-Dilks C. Evidence-based guideline recommendations on the use of positron emission tomography imaging in head and neck cancer. *Clin Oncol (R Coll Radiol)* 2013; **25**: e33-e66 [PMID: 23021712 DOI: 10.1016/j.clon.2012.08.007]
- 49 **Xu GZ**, Zhu XD, Li MY. Accuracy of whole-body PET and PET-CT in initial N staging of head and neck cancer: a meta-analysis. *Head Neck* 2011; **33**: 87-94 [PMID: 20848421 DOI: 10.1002/hed.21400]
- 50 **Lonneux M**, Hamoir M, Reyckler H, Maingon P, Duvillard C, Calais G, Bridji B, Digue L, Toubreau M, Grégoire V. Positron emission tomography with [18F]fluorodeoxyglucose improves staging and patient management in patients with head and neck squamous cell carcinoma: a multicenter prospective study. *J Clin Oncol* 2010; **28**: 1190-1195 [PMID: 20124179 DOI: 10.1200/JCO.2009.24.6298]
- 51 **Spector JG**, Sessions DG, Chao KS, Haughey BH, Hanson JM, Simpson JR, Perez CA. Stage I (T1 N0 M0) squamous cell carcinoma of the laryngeal glottis: therapeutic results and voice preservation. *Head Neck* 1999; **21**: 707-717 [PMID: 10562683]
- 52 **Price KA**, Cohen EE. Current treatment options for metastatic head and neck cancer. *Curr Treat Options Oncol* 2012; **13**: 35-46 [PMID: 22252884 DOI: 10.1007/s11864-011-0176-y]
- 53 **Sherriff JM**, Ogunremi B, Colley S, Sanghera P, Hartley A. The role of positron emission tomography/CT imaging in head and neck cancer patients after radical chemoradiotherapy. *Br J Radiol* 2012; **85**: e1120-e1126 [PMID: 22744325 DOI: 10.1259/bjr/20976707]
- 54 **Bronstein AD**, Nyberg DA, Schwartz AN, Shuman WP, Griffin BR. Soft-tissue changes after head and neck radiation: CT findings. *AJNR Am J Neuroradiol* 1989; **10**: 171-175 [PMID: 2492719]
- 55 **Laubenbacher C**, Saumweber D, Wagner-Manslau C, Kau RJ, Herz M, Avril N, Ziegler S, Kruschke C, Arnold W, Schwaiger M. Comparison of fluorine-18-fluorodeoxyglucose PET, MRI and endoscopy for staging head and neck squamous-cell carcinomas. *J Nucl Med* 1995; **36**: 1747-1757 [PMID: 7562038]
- 56 **Andrade RS**, Heron DE, Degirmenci B, Filho PA, Branstetter BF, Seethala RR, Ferris RL, Avril N. Posttreatment assessment of response using FDG-PET/CT for patients treated with definitive radiation therapy for head and neck cancers. *Int J Radiat Oncol Biol Phys* 2006; **65**: 1315-1322 [PMID: 16750327]
- 57 **Kitagawa Y**, Nishizawa S, Sano K, Ogasawara T, Nakamura M, Sadato N, Yoshida M, Yonekura Y. Prospective comparison of 18F-FDG PET with conventional imaging modalities (MRI, CT, and 67Ga scintigraphy) in assessment of combined intraarterial chemotherapy and radiotherapy for head and neck carcinoma. *J Nucl Med* 2003; **44**: 198-206 [PMID: 12571209]
- 58 **Lell M**, Baum U, Greess H, Nömayr A, Nkenke E, Koester M, Lenz M, Bautz W. Head and neck tumors: imaging recurrent tumor and post-therapeutic changes with CT and MRI. *Eur J Radiol* 2000; **33**: 239-247 [PMID: 10699740]
- 59 **Nakamura S**, Toriihara A, Okochi K, Watanabe H, Shibuya H, Kurabayashi T. Optimal timing of post-treatment [18F]fluorodeoxyglucose-PET/CT for patients with head and neck malignancy. *Nucl Med Commun* 2013; **34**: 162-167 [PMID: 23196675 DOI: 10.1097/MNM.0b013e32835bdf3]
- 60 **Li P**, Zhuang H, Mozley PD, Denittis A, Yeh D, Machtay M, Smith R, Alavi A. Evaluation of recurrent squamous cell carcinoma of the head and neck with FDG positron emission tomography. *Clin Nucl Med* 2001; **26**: 131-135 [PMID: 11201470]
- 61 **Fischbein NJ**, AAssar OS, Caputo GR, Kaplan MJ, Singer MI, Price DC, Dillon WP, Hawkins RA. Clinical utility of positron emission tomography with 18F-fluorodeoxyglucose in detecting residual/recurrent squamous cell carcinoma of the head and neck. *AJNR Am J Neuroradiol* 1998; **19**: 1189-1196 [PMID: 9726451]
- 62 **McDermott M**, Hughes M, Rath T, Johnson JT, Heron DE, Kubicek GJ, Kim SW, Ferris RL, Duvvuri U, Ohr JP, Branstetter BF. Negative predictive value of surveillance PET/CT in head and neck squamous cell cancer. *AJNR Am J Neuroradiol* 2013; **34**: 1632-1636 [PMID: 23639557 DOI: 10.3174/ajnr.A3494]
- 63 **Ho AS**, Tsao GJ, Chen FW, Shen T, Kaplan MJ, Colevas AD, Fischbein NJ, Quon A, Le QT, Pinto HA, Fee WE, Sunwoo JB, Sirjani D, Hara W, Yao M. Impact of positron emission tomography/computed tomography surveillance at 12 and 24 months for detecting head and neck cancer recurrence. *Cancer* 2013; **119**: 1349-1356 [PMID: 23225544 DOI: 10.1002/cncr.27892]
- 64 **Huang B**, Law MW, Khong PL. Whole-body PET/CT scanning: estimation of radiation dose and cancer risk. *Radiology* 2009; **251**: 166-174 [PMID: 19251940 DOI: 10.1148/radiol.2511081300]
- 65 **Jovanovic A**, van der Tol IG, Kostense PJ, Schulten EA, de Vries N, Snow GB, van der Waal I. Second respiratory and upper digestive tract cancer following oral squamous cell carcinoma. *Eur J Cancer B Oral Oncol* 1994; **30B**: 225-229 [PMID: 7950835]
- 66 **Gourin CG**, Watts T, Williams HT, Patel VS, Bilodeau PA, Coleman TA. Identification of distant metastases with PET-CT in patients with suspected recurrent head and neck cancer. *Laryngoscope* 2009; **119**: 703-706 [PMID: 19205017]

P- Reviewers: Boffano P, Leonardi M, Liu YY, Schoenhagen P
S- Editor: Gou SX **L- Editor:** A **E- Editor:** Liu SQ



Application of fluorodeoxyglucose positron emission tomography in the management of head and neck cancers

Farzan Siddiqui, Min Yao

Farzan Siddiqui, Department of Radiation Oncology, Henry Ford Health System, Detroit, MI 48202, United States

Min Yao, Department of Radiation Oncology, University Hospitals Case Medical Center, Cleveland, OH 44106, United States

Author contributions: Both authors contributed to review of literature and manuscript preparation.

Correspondence to: Min Yao, MD, PhD, Department of Radiation Oncology, University Hospitals Case Medical Center, 11100 Euclid Avenue, Cleveland, OH 44106, United States. min.yao@uhhospitals.org

Telephone: +1-216-8443103 **Fax:** +1-216-8442005

Received: January 3, 2014 **Revised:** February 16, 2014

Accepted: March 7, 2014

Published online: March 28, 2015

Abstract

The use of fluorodeoxyglucose positron emission tomography (FDG PET) scan technology in the management of head and neck cancers continues to increase. We discuss the biology of FDG uptake in malignant lesions and also discuss the physics of PET imaging. The various parameters described to quantify FDG uptake in cancers including standardized uptake value, metabolic tumor volume and total lesion glycolysis are presented. PET scans have found a significant role in the diagnosis and staging of head and neck cancers. They are also being increasingly used in radiation therapy treatment planning. Many groups have also used PET derived values to serve as prognostic indicators of outcomes including loco-regional control and overall survival. FDG PET scans are also proving very useful in assessing the efficacy of treatment and management and follow-up of head and neck cancer patients. This review article focuses on the role of FDG-PET computed tomography scans in these areas for squamous cell carcinoma of the head and neck. We present the current state of the art and speculate on the future applications of this technology including protocol development, newer imaging methods such as combined

magnetic resonance and PET imaging and novel radiopharmaceuticals that can be used to further study tumor biology.

© 2015 Baishideng Publishing Group Inc. All rights reserved.

Key words: Fluorodeoxyglucose; Positron emission tomography; Squamous cell carcinoma; Head and neck cancer; Radiation therapy planning

Core tip: Fluorodeoxyglucose positron emission tomography (FDG PET) computed tomography (CT) scans should be obtained for patients for squamous cell carcinoma of the head and neck whenever clinically indicated and feasible. Pre-treatment scans are helpful in detecting the sites of primary cancer, staging the tumor and ruling out the presence of distant metastases. For patients undergoing radiation therapy, PET/CT scans provide anatomic as well as functional information to aid in treatment planning. After completion of radiotherapy, PET scans should be obtained approximately 12 wk after treatment to assess treatment response and to determine if any salvage therapy is required for persistent, recurrent or metastatic disease.

Original sources: Siddiqui F, Yao M. Application of fluorodeoxyglucose positron emission tomography in the management of head and neck cancers. *World J Radiol* 2014; 6(6): 238-251 Available from: URL: <http://www.wjgnet.com/1949-8470/full/v6/i6/238.htm> DOI: <http://dx.doi.org/10.4329/wjr.v6.i6.238>

INTRODUCTION

Head and neck cancers (HNC) account for approximately 650000 new cancers each year across the world and result in about 350000 deaths, representing 6% of all cancer cases^[1,2]. In the United States, approximately 52000 new

cases of oral cavity, pharyngeal and laryngeal cancers are diagnosed every year with approximately 11000 deaths^[3]. Approximately 95% of these are squamous cell carcinomas (HNSCC) and they often present in locally advanced stages. The treatment of head and neck cancers involves a multi-disciplinary approach and includes surgery, radiation therapy and chemotherapy. Traditional staging approaches for head and neck cancers include clinical examination and surgical pathologic staging. The advent of concurrent radiation and chemotherapy for organ preservation in head and neck cancers has reduced the incidence of surgical resection especially in locally advanced larynx cancers and oropharynx cancers^[4,5]. However, this has also brought forth the need to have detailed non-invasive imaging techniques to accurately identify tumor size and location, cervical lymph node involvement and presence or absence of distant metastases. The use of computed tomography (CT) scans and magnetic resonance imaging (MRI) scans allowed structural and anatomical information to be obtained and vastly improved the ability of oncologists to clinically stage these patients appropriately. However, the use of fluorine-18-fluorodeoxyglucose positron-emission tomography (FDG-PET) has added a new biologic and functional end-point to these imaging techniques and opened a whole new arena for research and development in management of head and neck cancers. Additionally, PET/CT and PET/MRI combinations are now able to provide both anatomic and functional information in co-registered images.

The review will focus on the current applications of FDG PET/CT scans in management of squamous cell cancers of the head and neck. The use of PET/MRI and FDG PET/CT for other head and neck cancers (*e.g.*, salivary gland, thyroid cancers *etc.*) is beyond the scope of this review.

BIOLOGY OF FDG-UPTAKE

Rapidly proliferating cancers cells utilize glucose as a source of energy and metabolism. Glucose undergoes glycolysis after intracellular transportation. This transportation is mediated by a family of glucose transporter proteins (GLUTs)^[6-8]. These trans-membrane proteins allow energy independent transport of glucose across the hydrophobic cell membrane. Thirteen GLUTs have been identified of which GLUT1, GLUT3, and GLUT4 have high affinity for glucose. The expression of GLUTs is induced by hypoxia-inducible factor, growth factors and various oncogenes^[9]. Increased expression of GLUT1 has been found in many cancers, including head and neck cancer^[9]. The degree of expression of GLUT1 has also been shown to be associated with aggressiveness of the cancer. Elevated glycolytic activity and increased expression of GLUT1 are found in advanced cancer stages and predict significantly poorer treatment outcomes^[10-13].

Fluorine¹⁸-FDG (¹⁸F-FDG) is an analog of glucose with ¹⁸F occupying the position of oxygen on carbon-2. Similar to glucose, GLUTs facilitate the transport of ¹⁸F-

FDG into the cell. In the next step, both glucose and FDG are phosphorylated by the hexokinase enzyme. Glucose, upon phosphorylation, enters the glycolytic pathway for energy production. FDG, on the other hand, cannot undergo glycolysis and is trapped as FDG-6-phosphate in the intracellular environment. This trapped FDG can then be imaged to spatially locate the metabolically active cancer cells. FDG uptake in cancer cells of HNSCC was shown to be significantly correlated with cell proliferation by flow cytometry^[14,15].

PHYSICS OF PET IMAGING

A detailed description of the physics of FDG-PET scanning is beyond the scope of this review. However, in brief, at the heart of this imaging technique is the radioisotope ¹⁸F. It is produced using a cyclotron and has a half-life of 110 min allowing it to be transported for use in PET scanner facilities.

¹⁸F decays by positron (β^+) emission 97% of the time and is converted to oxygen-18. The emitted positron travels a short distance in soft tissue, decelerates rapidly and interacts with an electron near the end of its track. This interaction is called the annihilation reaction and mass is converted to energy with the release of two 0.511MeV photons which travel outwards at 180° to each other. These annihilation photons are detected by scintillators and a simultaneous or coincident detection of these photons makes it possible to spatially localize the point of origin. The information is collected on a multitude of such coincident events and processed to generate a PET image.

Nowadays, most PET scans are co-registered with simultaneously obtained CT scans to produce PET/CT images which give functional information along with anatomic co-localization. For areas like the head and neck a smaller area can be scanned with intravenous contrast administration to obtain further normal tissue anatomy and tumor extent.

QUANTITATIVE IMAGE INTERPRETATION

In order to be used as a valid imaging biomarker, accurate and reproducible quantification of FDG uptake is necessary. A simplified measurement using standardized uptake value (SUV), given by the following formula, is now the most widely used method for the quantification of FDG uptake.

$$SUV = \frac{\text{Tissue activity } (\mu Ci / ml)}{\text{Injected Dose } (mCi) / \text{Body weight } (kg)}$$

In this formula, tissue activity is the radioactivity measured by the PET scanner within a region of interest (ROI) or the maximal value; injected dose is the dose of ¹⁸F-FDG administered, corrected for physical decay. The SUV in this formula represents the activity of ¹⁸F-FDG within the tumor measured over a certain interval after ¹⁸F-FDG

injection and normalized to the dose of ^{18}F -FDG administered and to the body weight^[16].

There are many different factors that can affect ^{18}F -FDG uptake and its subsequent quantification. The biologic factors include blood glucose level, interval between injection and start of PET study, patient motion and breathing, patient comfort, and inflammatory process near or at the tumor. There are also many technical and physical factors such as attenuation correction, calibration, image reconstruction, data analysis, *etc.*, which are beyond the scope of this review and have been discussed by others^[17-20]. Despite these, it has been shown that there is a good correlation between SUV and glucose utilization rate in various cancers including HNSCC^[21].

Various forms of SUV-based parameters have been described in literature. These include: (1) SUVmax- This measures the highest (maximal) SUV in a region of interest. This has been the most common used parameter in clinical practice as it is thought to be the most reproducible and independent of how the ROI is defined. However, it represents only a single point within the tumor/lesion and may not be representative of the entire tumor volume; (2) SUVmean or SUVaverage- This value may provide a more global picture of the tumor activity as it averages the intensity of uptake in a region of interest (ROI). This, however, suffers from the subjectivity and variability of the definition of this ROI which may differ between individuals and institutions; (3) Metabolic tumor volume (MTV)- This is measured in cubic centimeters and represents the tumor volume with active FDG uptake. There is no standard way for tumor segmentation from PET images (For further discussion, refer to Chapter 4 on PET in radiotherapy treatment planning). Threshold-based method is often used. Some authors used a threshold of SUV > 2.5. Others used 40% or 50% SUVmax as a threshold. The MTV is measured as the tumor volume with SUV above the threshold selected. However, the volumes vary significantly depending on the threshold selected; and (4) Total lesion glycolysis (TLG) - This is a product of the tumor volume, determined by CT - scan or MRI, and SUVmean.

USE OF PET/CT IN THE DIAGNOSIS AND STAGING OF HEAD AND NECK CANCERS

Primary cancers of the head and neck are mainly diagnosed by clinical examination in the office and supplemented by imaging studies such as CT scans and MRI. Staging of the primary tumor, *i.e.*, T-stage in the American Joint Committee on Cancer (AJCC) staging system, mainly depends on the tumor size and invasion of the primary tumor, which is better assessed by CT and MRI imaging.

Occasionally, in about 2%-9% of cases, patients may present with a lymph node in the neck with no obvious primary site visible on clinical or routine diagnostic imag-

ing tests^[22]. Such cases are labeled as unknown or occult primary head and neck cancers. Pathologic evaluation of the nodes, usually by fine needle aspiration, may reveal a diagnosis of squamous cell carcinoma or adenocarcinoma. Squamous cell histology indicates that the primary site is likely in the head and neck while adenocarcinomas mainly arise below the clavicle (*e.g.*, lung cancer, gastric cancer). The traditional method for detection of the primary site in cases of squamous cell histology involves examination under anesthesia and random biopsies from the nasopharynx, oropharynx, hypopharynx, larynx and any mucosal areas which appear abnormal. Tonsillectomy is often performed. These maneuvers are able to detect the primary site in about half of the cases initially labeled as unknown primary head and neck cancers^[23].

FDG-PET scans have been proven to be an invaluable tool in these cases. Rusthoven *et al.*^[24] summarized the results of 16 published studies with a combined total of 302 patients to evaluate the role FDG-PET in unknown primary head and neck cancers. They reported that FDG-PET was able to detect primary tumors in 24.5% (range, 5% to 73% in various studies) cases where conventional methods were unsuccessful. The primary site was found at the base of tongue in 27 patients (24.3%), tonsils in 20 patients (18.0%) and below the clavicle in 27 patients (24.3%). The sensitivity, specificity, and accuracy of FDG-PET in the detection of primary tumors were 88.3%, 74.9%, and 78.8%, respectively. Interestingly, PET scans were able to identify an additional 16% regional nodal metastases and 11% distant metastases previously undiscovered. Several prospective studies have confirmed these findings^[22,25]. Rudmik *et al.*^[25] recently reported results of 30 patients who underwent PET/CT. PET/CT was performed after conventional workup and prior to operative panendoscopy. The surgeons were blinded to the results. Patients had routine examination under anesthesia and directed biopsies, and the PET/CT results were then revealed to the surgeon intraoperatively. Additional biopsies were taken if the PET/CT was positive. The traditional work-up identified tumors in 25% of patients, whereas PET/CT-directed biopsies revealed the primary lesion in 55% of patients. The sensitivity, specificity, positive predictive value, and negative predictive value of PET/CT in detection of primary tumor were 92%, 63%, 79%, and 83%, respectively.

Detection of the site of primary cancer allows directed therapy to the tumor (surgery or radiation therapy) while sparing or minimizing the toxicity to uninvolved mucosal areas or tissues. The current paradigm for diagnosis and staging work-up for unknown primary cancers involves obtaining a PET/CT and then obtaining directed biopsies from the suspicious areas. Figure 1 illustrates a patient who presented with multiple left neck nodes. Conventional workup failed to identify the primary tumor but PET showed the primary tumor in left base of tongue.

As noted above, PET scans have also helped in identification of previously unidentified involved cervical

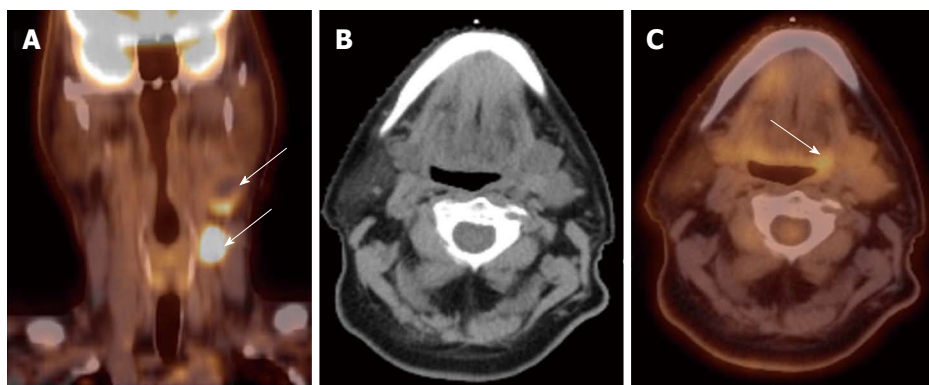


Figure 1 Computed tomography. A: A patient presented with multiple left neck nodes (arrows); B: The conventional methods as well as the computed tomography (CT) imaging could not identify the primary tumor; C: A positron emission tomography/CT scan showed increased fluorodeoxyglucose uptake in the left base of tongue (arrow) and a directed biopsy of this area confirmed the primary site.

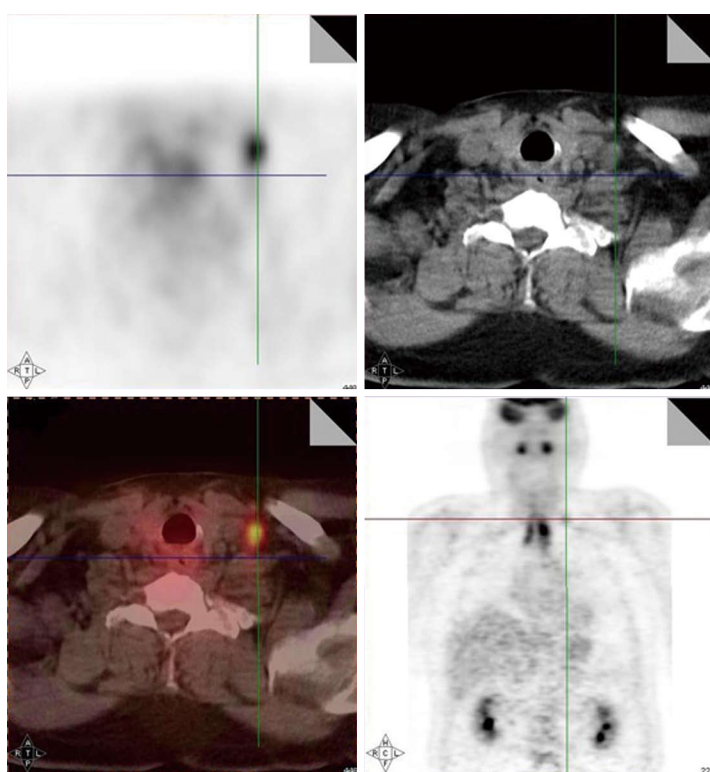


Figure 2 Increased fluorodeoxyglucose positron-uptake in the low neck revealed a metastatic lymph node which would otherwise be difficult to detect because of the presence of muscular and vascular structures in this region of the neck.

lymph nodes. Various CT and MRI based criteria have been developed to label lymph nodes are being involved by cancer or not^[26]. However, this may still result in 20%-30% rate of false-positive and false-negative results. Various reports comparing FDG-PET with other imaging modalities including ultrasound, CT and MRI have consistently reported a much higher sensitivity and specificity for PET scans when compared with the gold-standard, surgical lymph node dissection^[27,28]. This has specially been helpful in detecting lymph nodes which are at a distance from the primary or in the contralateral neck, especially when the lymph node has not reached size criteria by CT/MRI. PET is also very helpful in detecting involved lymph nodes in the lower neck where there are complex muscular and vascular structures (Figure 2). The average sensitivity and specificity for PET scan to detect

involved nodes are reported to be 90% or higher^[27].

Local-regionally advanced head and neck cancers metastasize to mediastinal lymph nodes, lungs, bone and liver. PET scans are also helpful in ruling out presence of distant metastases as PET images in head and neck cancer are often obtained from skull base to hips and PET are more sensitive in small metastasis than CT. Various reports have documented the incidence of distant metastases as detected by PET scans ranging from 6% to 25% for stage III/IV head and neck cancers^[29-34]. The sensitivity and specificity of PET scans for the detection of metastases are 77% and 94%, respectively. Hearle *et al*^[35] noted distant metastases in 10% of 299 patients evaluated with 97% sensitivity and 96% specificity. These PET findings resulted in a change in the management plan in 8% to 15% of cases^[30,36]. Figure 3 shows a head and neck

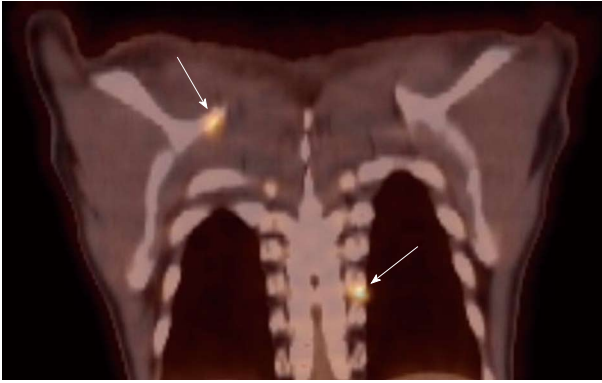


Figure 3 Small bone metastases detected in a patient with head and neck squamous cell carcinoma (arrow). These lesions were not visible on the computed tomography scan.

cancer patient with small bone metastases detected by PET scan but these lesions were missed in the CT scan.

The use of tobacco products (chewing and smoking) and alcohol have been associated with the development of head and neck cancers. This risk extends to other sites of the aero-digestive tract including lung and esophageal cancers. Synchronous primary cancers have been noted in approximately 10% of head and neck cancer patients. Strobel *et al.*^[37] reported 69 synchronous primary cancers in 62 patients among 589 consecutive patients imaged with PET scans. Most (80%) of these were in the upper aero-digestive tract. A recent report from Japan noted a higher rate (18%) of second primary cancers among 230 head and neck cancer patients^[38]. Evaluation of the diagnostic sensitivity showed that PET scans were most likely to detect second primaries in other head and neck sites and lungs while the sensitivity for finding gastric and esophageal cancers was much lower at 25% and 7.6%, respectively. Needless to say, the discovery of these second primary cancers resulted in a change in the management plan for these patients. Figure 4 shows a patient who presented with right oral tongue cancer and PET was obtained as part of the workup that revealed he also had a cancer in the soft palate as well in the upper esophagus. Figure 5 is an example of a patient with a synchronous laryngeal and lung squamous cell carcinomas.

RADIATION THERAPY PLANNING

Radiation treatment plays an important role in the management of head and neck cancer. Radiotherapy is given as a definitive treatment when the tumor is not resectable or when organ preservation is preferable^[5,39]. Radiotherapy is also given to patients who have high risk pathology features after surgery^[40,41]. Chemotherapy is often administered concurrently with radiotherapy in locally advanced disease.

In the past decade, intensity-modulated radiotherapy (IMRT) has become a standard radiation technique in head and neck cancer^[42,43]. IMRT is a highly conformal radiation technique which allows delivery of different

radiation dose to different adjacent structures, also called dose painting, thus enabling delivery of high dose to the tumor targets while sparing the normal tissues. The use of IMRT has led to a reduction in xerostomia and improvements in quality of life following treatment^[44-46]. However, highly conformal treatments can lead to disease not being included in the high-dose radiation treatment volume, resulting in locoregional failures. On the other hand, over-drawing the target volumes can result in high-dose radiation being unnecessarily delivered to normal tissues that may lead to increased toxicities. Therefore, accurate delineation of the tumor volume and regions at risk are critical in order to achieve the best treatment outcomes.

Since FDG PET scan has a high sensitivity in detecting tumor, it plays an important role in radiation treatment planning especially in IMRT planning. FDG PET scan is routinely obtained and co-registered with treatment planning CT images for treatment planning. Currently there are following several practical applications of PET in radiation treatment planning: (1) Detecting small lymph nodes that are not size criteria in CT and including these nodes in high dose target. In general, lymph nodes less than 1.0 cm in CT or MRI are usually called benign. However, PET scan has higher resolution and can detect malignant node as small as 0.5 to 0.6 cm. As mentioned above, PET has a high sensitivity for malignant lymph node, reported being up to 90%. Therefore, PET avid nodes are included in the high dose radiation targets especially when biopsy confirmed to be malignant. Figure 6 shows a patient with nasopharyngeal cancer, initially staged as T1N0 after conventional workup. However, FDG PET revealed hypermetabolic foci in the primary tumor in the nasopharynx and in bilateral level II lymph nodes which were small and were not called as lymphadenopathy in the CT and MRI (Figure 6B). Fine needle biopsies of the right level II lymph node was obtained and confirmed to contain metastatic disease. Therefore, these lymph nodes were included in the high dose area in the IMRT plan (Figure 6C); (2) Detecting the primary tumor in patients who present with “unknown primary” and including the primary tumor in the high dose target. As mentioned above, in head and neck cancer with unknown primary, FDG PET can detect primary tumor in 25% of patients where conventional work up were unsuccessful. Most of these primary tumors are in the oropharynx, such as tonsil and the base of the tongue. When the primary tumor is detected, the patient is treated with radiation field tailored to the primary tumor, thus avoiding radiating the whole pharyngeal axis which is the standard radiation technique in patients with unknown primary. Figure 7 illustrates the IMRT plan for the patient with the primary tumor detected in PET. The left base of tongue tumor detected by PET was included in the high dose field while the larynx and nasopharynx were spared; (3) Accurate delineation of the edge of the primary tumor. Accurate delineation of the edge of tumor to generate gross tumor volume (GTV) is the first step in target de-

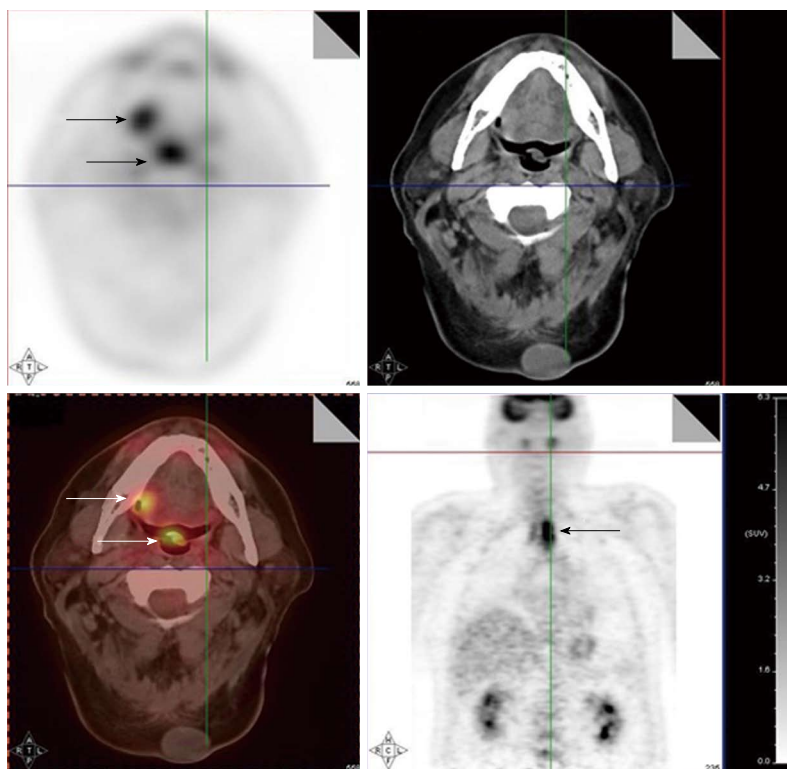


Figure 4 A positron emission tomography scan was obtained in a patient with a diagnosis of right oral tongue cancer (anterior arrow in axial views). The positron emission tomography/computed tomography revealed two additional primary cancers, one in the soft palate and the other in the upper esophagus.

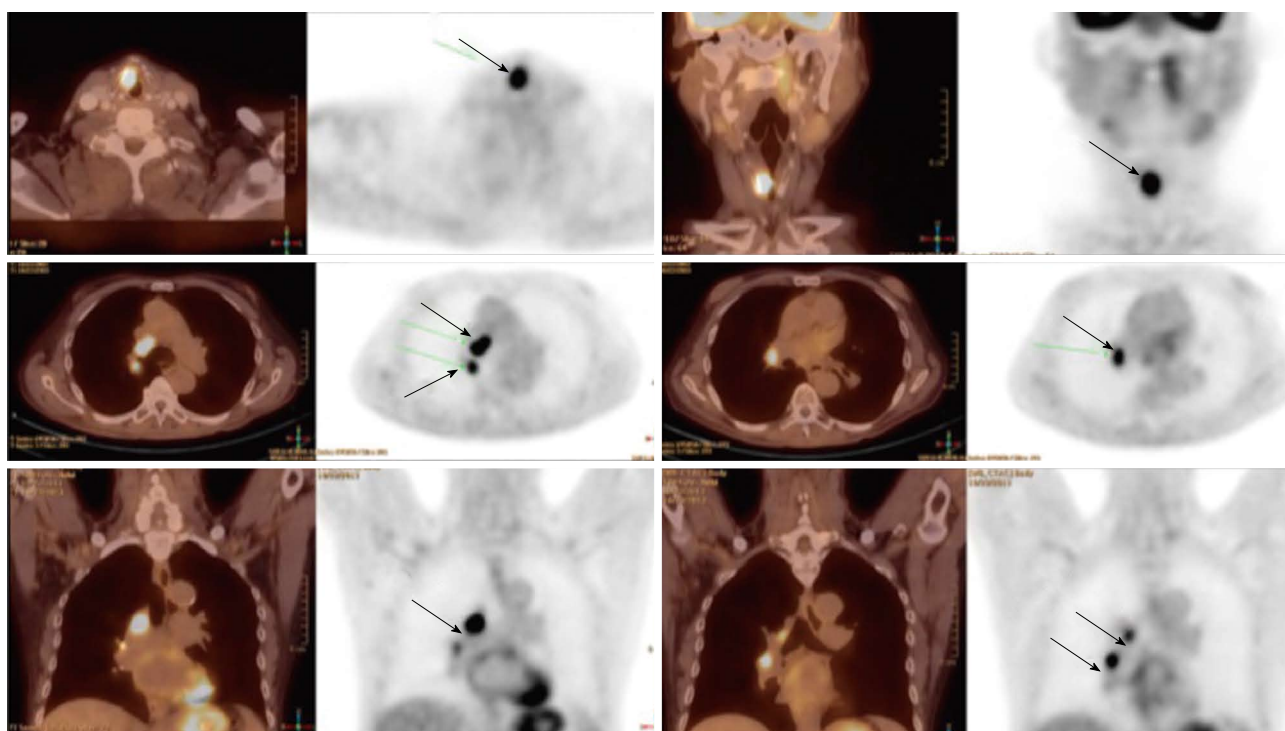


Figure 5 A patient with a synchronous laryngeal and lung squamous cell carcinomas. A 70-year-old male with diagnosis of squamous cell carcinoma of the glottic larynx T3N0M0 (A and B; arrow). He underwent a positron emission tomography/computed tomography scan which revealed additional lesions in the right lung which were biopsied endobronchial and shown to be a second primary lung cancer with mediastinal lymphadenopathy (C and D; arrows).

lineation for IMRT planning. It is often difficult to separate the tumor from surrounding soft tissue and muscle in CT imaging which is the primary imaging modality in radiation treatment planning, especially for tumor in the

oral tongue and oropharynx. Figure 8 shows a patient with oral tongue cancer, comparing CT (Figure 8A) *vs* PET (Figure 8B). The border of the tumor in the CT was not very clear, difficult to separate from the tongue

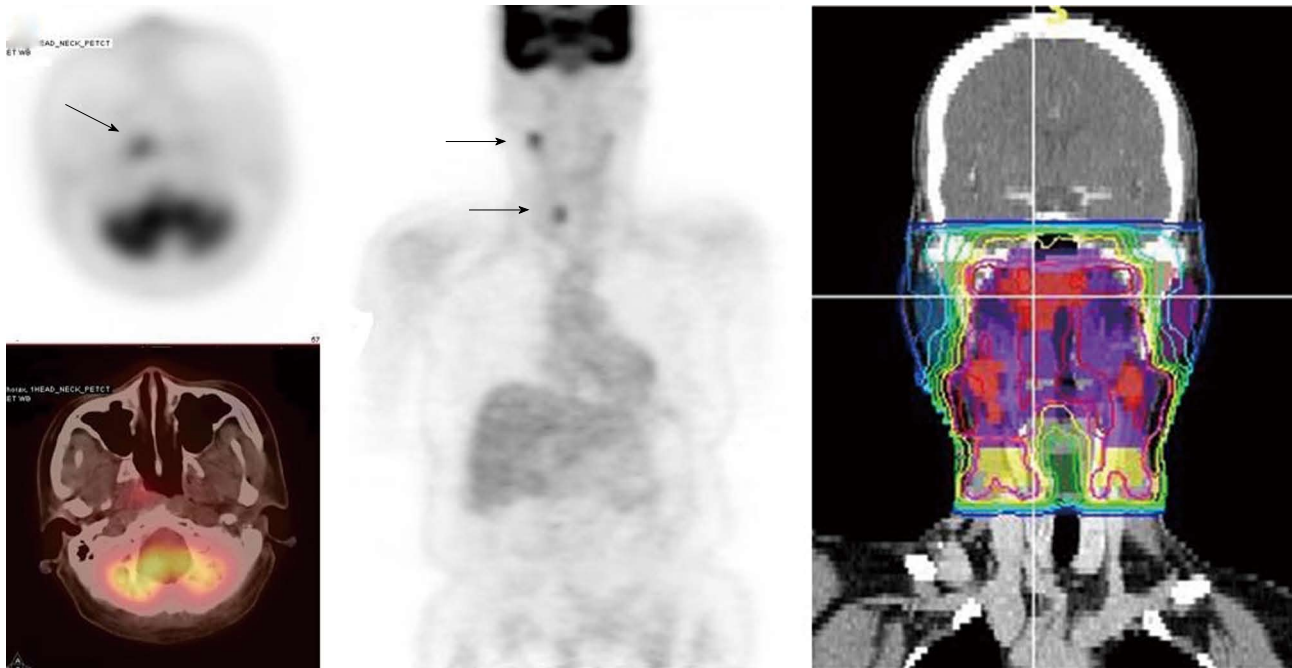


Figure 6 A patient with nasopharyngeal cancer. A: Initial stage was T1N0 when the patient was referred to our institution after conventional workup (arrow in axial image); B: Fluorodeoxyglucose positron emission tomography revealed hypermetabolic foci in the primary tumor in the nasopharynx and in bilateral level II lymph nodes which were small and were not called as lymphadenopathy in her computed tomography and magnetic resonance imaging. Fine needle biopsies of these lymph nodes were obtained. The right level II node (arrows) was confirmed to contain metastatic disease, while the left level II lymph node was not diagnostic; C: Intensity modulated radiotherapy plan for this patient. The right level II node was treated to a high dose of radiation. The lower neck was treated with an anterior-posterior field (From Woods C, Sohn J, Machtay M, Yao M. Radiation treatment planning for head and neck cancer with PET. *PET Clinics* 2012; 7: 396; with permission).

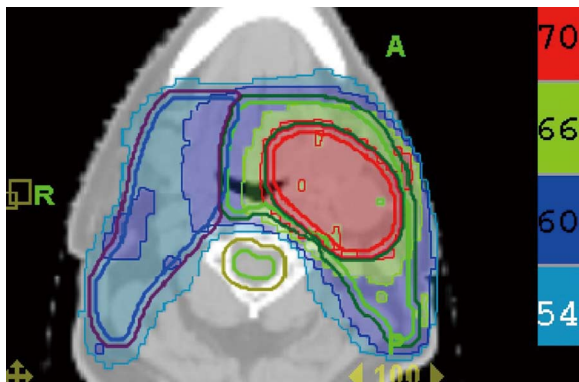


Figure 7 Treatment plan for the patient described in Figure 1. The base of tongue was found to be the primary cancer site and this area was included in the high dose intensity-modulated radiotherapy plan while sparing uninvolved mucosal areas.

muscle. Yet, the PET showed sharp contrast between the tumor and surrounding tissue. The GTV based on CT (Figure 8C) is much larger than that based on PET (Figure 8D). Several studies have published comparing GTV generated by CT *vs* those when PET was incorporated, and noted a trend for decreasing GTVs when PET was used^[47-52]. Some studies also showed that the interobserver variability decreased when PET was used for target delineation^[47]; and (4) In postoperative radiation, detecting recurrent tumor even before radiation and including the recurrent tumor in high dose target. Patients with high risk pathology features are treated with adjuvant chemo-

radiation for better local regional control and survival. Postoperative radiotherapy is often given 4 to 6 wk after surgery when the surgical wound is fully healed. However, some patients may have local regional recurrences even before radiation. Because of the anatomical distortion and fibrotic changes after surgery, and flap reconstruction, these recurrences are difficult to be detected by physical examination and CT imaging. FDG PET is ideal imaging modality at this setting. Shintani *et al*^[53] reported 91 consecutive patients referred to postoperative adjuvant radiation after complete surgical resection. These patients had FDG PET obtained at a median time of 28 d after surgery. They reported 27 patients with suspicious PET findings. Further biopsies led to changes in adjuvant treatment in 14 patients (15.4%), including increasing the radiation therapy dose in 6 patients, and extending the radiation therapy treatment volume and increasing the dose in 1 patient. Liao *et al*^[54] also reported 29 patients who had a PET scan obtained before postoperative radiation. They found 7 patients with positive PET studies, 3 with distant metastases and 4 with local regional recurrences. For those who had local regional disease detected by the PET, the radiation volumes and radiation dose have to be changed, with higher dose delivered to the recurrent tumor. Thus, for patients with high risk features, especially for those who have a prolonged interval from surgery to radiation, a post-surgery and pre-radiation FDG PET will be valuable in treatment decision and radiation treatment planning.

Following are some active investigations in further ex-

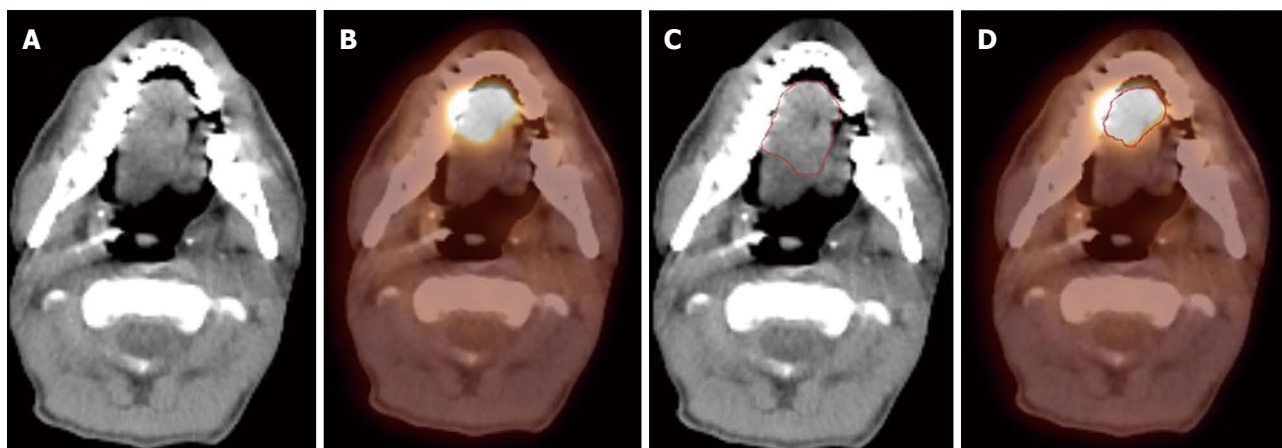


Figure 8 A patient with oral tongue cancer. The edge of the tumor was not very clear in the computed tomography (CT) image (A), but more obvious in the PET image (B). Gross tumor volume was outlined based on CT scan (C) vs with fluorodeoxyglucose positron emission tomography/CT (D). The volume included is larger with CT alone.

ploration how to use PET in radiation treatment in head and neck cancer: (1) Subvolume delineation and dose escalation. Tumors are not homogeneous. Since FDG uptake is correlated with tumor aggressiveness, the region of the tumor with higher FDG uptake may harbor more aggressive cancer cells and may require higher radiation dose to eradicate. Indeed, FDG-avid regions in the tumor have been shown to be correlated with hypoxia that is associated with tumor radioresistance^[55,56]. With the dose painting capability of IMRT, a higher radiation dose can be delivered to these tumor subvolumes to achieve potentially better tumor control. Schwartz *et al*^[57] studied theoretical IMRT models using PET derived volumes in 20 patients with head and neck cancer. They found that a mean dose of 74.9 Gy (range, 71.53-80.98 Gy) could be delivered to the PET-avid volume without overdosing the adjacent critical structures. Madani *et al*^[58] conducted a Phase I study of dose escalation to FDG-avid subvolumes. They reported it was feasible to deliver a radiation boost of 30 Gy in 10 fractions to the PET tumor volume before standard IMRT treatment, and they are planning a randomized phase II trial comparing this treatment regimen with standard IMRT; and (2) Adaptive radiation therapy. During the course of radiation treatment, the patient can have significant physical/anatomical changes due to tumor response. A second CT simulation and re-planning are required in order to ensure the tumor is being dosed appropriately. Changes also occur in the FDG uptake of the tumor during the course of radiotherapy and some investigators have explored adaptive radiotherapy and planning techniques to alter the plan based on the changes in PET imaging^[59,60].

ASSESSMENT OF TREATMENT EFFICACY, FURTHER MANAGEMENT AND FOLLOW-UP

FDG PET/CT scans have been proven to be a useful technology in assessing treatment response in patients

treated with definitive radiation and chemotherapy and for detecting residual and recurrent disease. PET/CT scans are usually performed 2 to 3 mo after treatment completion. The optimal timing of obtaining the scan has been debated in literature and based on many reports it has been determined that the 12-wk time point after completion of therapy may be the most appropriate^[61,62]. Scans obtained at earlier time-points (< 8 wk) have a high rate of false-positive FDG uptake in the radiation treatment field due to inflammatory changes. Scans done too late (> 16 wk) may allow residual loco-regional disease to grow and metastasize. If increased FDG uptake is noted at the primary site, patients should undergo a biopsy followed by a surgical resection for residual disease. Figure 9 shows a serial PET/CT scans in a patient treated for oropharyngeal squamous cell carcinoma.

The role of FDG PET/CT in decision making for neck dissection after chemoradiation has also been extensively investigated. Yao *et al*^[63] reported a 100% negative predictive value (NPV) and 43% positive predictive value (PPV) for PET scans done 12 wk after radiation in 53 patients who were noted to have a complete response at the primary site. A prospective study in 112 consecutive patients reported by Porceddu *et al*^[64] also noted the utility of the 12-wk post radiochemotherapy PET scan in decision making for neck dissection. Patients who had equivocal PET results underwent another scan 4 to 6 wk later. Patients who had CT abnormalities but were PET-negative were observed and no subsequent neck node failures were noted in these patients. Nine patients continued to have PET-positive disease in the neck of which 8 underwent surgery. Residual disease was noted pathologically in 6 of these 8. Another prospective study from MD Anderson Cancer Center reported on 98 patients^[65]. They stratified patients into low-risk and high-risk groups based on tumor stage, nodal stage, overall stage, tumor site, smoking history and HPV status. The most significant benefit of FDG PET/CT over CT scans was noted in detecting residual disease among high-risk patients. The NPV of PET/CT was 75% as compared to 37.5%

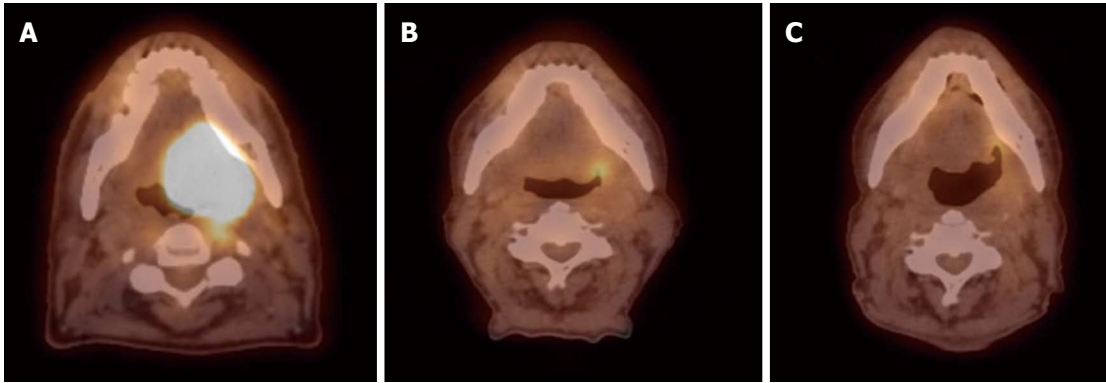


Figure 9 Sixty-six year old male was diagnosed with squamous cell carcinoma of the left base of tongue T4aN1M0. He received external beam radiation therapy (70 Gy in 35 fractions) with concurrent cisplatin 100 mg/m² (3 cycles). Positron emission tomography/computed tomography scans were done pre-treatment (A) and at 3-mo (B) and 8 mo (C) post-radiation therapy. Follow-up images show good response to treatment with sustained response at least 8 mo from treatment.

for CT alone.

The role of FDG-PET scans for long term follow-up surveillance for detection of loco-regional and distant metastatic recurrence has also been extensively investigated. Gupta *et al*^[66] conducted a meta-analysis of 51 studies involving 2,335 patients. They reported a NPV of approximately 95% for both primary and neck disease for response assessment and surveillance. A recent report analyzed the role of long-term surveillance PET/CT scans in 214 patients with negative scans after completion of therapy^[67]. Nine percent of these patients recurred on follow-up. This suggested a NPV for surveillance PET/CT of 91%. Based on these data the authors recommended that radiologic surveillance can be stopped early in those patients who are noted to have two consecutive negative PET/CT scans within 6 mo of each other.

PROGNOSIS

Many attempts have been made to establish PET/CT scan derived parameters as prognostic indicators. These studies have looked at pre-treatment, post-treatment and during treatment scans to obtain SUV and metabolic tumor volume (MTV) to serve as prognostic indices. Most of these studies have been retrospective. However, some prospective trials have also been reported. A recent review article summarizes these studies^[68].

Allal *et al*^[69] conducted a prospective study in 120 patients with HNSCC to evaluate the role of pre-treatment SUV in predicting for local control and disease-free survival. Seventy-three patients underwent radiation therapy with or without concurrent chemotherapy and 47 had surgery with or without adjuvant radiation therapy. At a median follow-up of 48 mo, 46 patients had recurrent and/or distant metastatic disease. In these patients the SUV was noted to be 5.8 *vs* 3.6 for those with disease controlled ($P = 0.002$). On the other hand, Vernon *et al*^[70] reviewed 42 patients receiving PET/CT guided definitive radiotherapy and found that neither SUV of the primary tumor nor SUV of the lymph node was predictive of tumor recurrence.

In another prospective study, FDG PET was obtained 4 wk prior to chemoradiotherapy and 8 wk after completion of treatment in 98 patients^[71]. Primary tumor and nodal SUVmax was calculated for both time points. The only prognostic factor for disease-specific survival was found to be the post-treatment primary tumor SUVmax. The mean SUVmax for those who failed was 7.2, compared to 4.2 for those who did not fail ($P < 0.01$). Pre-treatment SUVmax of primary tumor and lymph node were not found to be significantly associated with treatment outcomes. The conclusions from these studies are not consistent, partly due to the inherent problems with SUV measurement as it represents only a single point within the tumor but not represent the entire tumor. Additionally, there is heterogeneity in the patient population, heterogeneity in treatment modalities, small patient samples and the use of different endpoints.

In recent years, PET-based tumor volumes, *i.e.*, metabolic tumor volume (MTV), are being explored. La *et al*^[72] from Stanford University evaluated the prognostic value of MTV in 85 patients. A threshold of 50% maximal intensity was used to define the metabolic tumor volumes. They found that MTV had a significant relationship with disease-free survival ($P < 0.001$) and with overall survival ($P < 0.001$) on univariate analysis. An increase in MTV of 17.4 mL was significantly associated with an increased hazard of first event (recurrence or death). SUVmax did not show a significant relationship with either of these endpoints. Another report from the same group of investigators validated these findings in an additional 83 patients^[73]. Recently the results of a sub-group of patients enrolled on the RTOG 0522 trial were presented^[74]. Seventy-four patients underwent baseline and 8-wk post treatment PET scans. Baseline SUVmax or SUVpeak of the primary or nodal disease were not predictive for outcomes. However, patients having a primary tumor MTV above the cohort median had a significantly worse loco-regional control and progression free survival.

Some groups have also evaluated the utility of PET scans done during therapy. PET scans were done after neoadjuvant chemotherapy in 16 patients. These patients

then underwent surgical resection and histopathologic responses were correlated with SUVmax. Comparisons between pathologic responders and non-responders revealed that there was significant difference in post-chemotherapy SUVmax and percent decrease in SUVmax^[75].

The applicability of PET scans during the course of radiation therapy is harder to evaluate because of difficulty in image interpretation with inflammatory changes due to radiation and the cost of additional imaging. Such a study has, however, been done and reported on by Hentschel *et al*^[76]. This prospective study evaluated the role of serial PET scans during early phase of radiation therapy and the ability of these scans to predict treatment outcomes. Patients were divided into two groups and all of them underwent 4 PET scans. In one group, PET scans were obtained before treatment, at 10 Gy, 30 Gy and 50 Gy. In the other group, PET scans were obtained before treatment, at 20 Gy, 40 Gy, and 60 Gy. Patients who had a rapid early response with > 50% decline in SUVmax at 10 Gy or 20 Gy as compared to the pre-treatment SUVmax had a significantly higher overall survival, loco-regional control and disease-free survival at 2 years. The 2-year overall survival was 88% for those who had more than 50% decline in SUVmax compared to 38% for those with less than 50% decline ($P = 0.02$). The 2-year disease-free survival was 75% and 31%, respectively for those with > 50% decline as compared to < 50% decline in SUVmax. And the 2-year local-regional control rate was 88% *vs* 40% for those with > 50% decline *vs* those < 50% decline in SUVmax ($P = 0.06$).

There is currently no consensus on what time points to use for PET scan based prognostication and what parameters are the most useful. There may be value in combining traditional prognostic factors with PET based parameters. Yao *et al*^[77] showed that T-stage, N-stage and pretreatment SUV of the lymph node were significantly associated with distant metastasis. However, the combination of these factors can better predict distant metastasis-free survival. The 3-year distant metastasis-free survival was 98.1% for no factors, 88.6% for one factor, 68.3% for two factors, and 41.7% for three factors. Similarly, Moeller *et al*^[65] incorporated HPV status in their mortality risk assessment in addition to post-treatment tumor SUVmax. They noted FDG PET/CT was predictive for outcomes in HPV-negative and non-oropharyngeal primaries.

FUTURE DIRECTIONS

FDG PET/CT scan has been proven to be a useful technology on many fronts in head and neck cancer and has significant impact on the management as discussed above. Currently, there are many exciting new areas of research and development that are being actively investigated and will continue to expand the role of this imaging modality in the future. These efforts can be broadly categorized as follows: (1) Protocol development and standardization: a: Head and neck cancer staging - There may be a possibil-

ity of combining anatomical information, which forms the basis of the current AJCC system, with functional information obtained from PET scans; b: Standardized uptake value (SUV) - Even though SUV is a widely used and reported parameter it suffers from some drawbacks that make it difficult to compare values between different institutions^[19,78,79]. Further standardization in the way SUV is determined would allow inter-institutional collaboration and co-operative group clinical trials. Additional objectively measurable parameters which allow cross-platform and cross-hardware comparisons also need to be developed; c: PET/CT simulators - PET/CT scans are often co-registered with CT scans obtained for radiation therapy planning. PET/CT simulators are also available at some institutions which facilitate this. Consensus guidelines need to be developed for tumor and target volume delineation when using PET information for radiation treatment planning; d: PET as a prognostic indicator - The use of PET/CT scans as prognostic indicators in head and neck cancers and for follow-up and surveillance requires further research and investigation; and e: Economic analyses - Cost-benefit analyses suggest that PET/CT scans are cost-effective for diagnosis, staging and therapeutic decision making in head and neck cancers^[80,81]. Common availability and decreasing costs of this technology will allow greater use and acceptance; (2) Newer imaging technology - Magnetic resonance imaging (MRI) offers superior imaging for soft-tissue delineation but offers little functional information unless MR spectroscopy is performed. MR spectroscopy can be performed in a limited volume. Recently MR/PET hybrid technologies have been developed for used in the clinic. This offers the advantages of high-quality soft tissue imaging from MR with whole-body and functional imaging from the PET component^[82-84]. A recent review article highlights the potential for this new hybrid technology, the technical challenges and its use in clinical situations^[85]; and (3) Newer radiopharmaceuticals - Many new radioisotopes and radiotracers are being developed to image further functional characteristics of tumors including hypoxia, tumor proliferation, amino acid metabolism and presence of EGFR on tumor cells. An excellent review on this topic has been provided by Wang *et al*^[86]. As outlined in this review, a large number of efforts are being focused on hypoxia imaging. Hypoxia poses a major radiobiological disadvantage and confers radioresistance to the tumor. Hypoxic cells are not killed in response to radiation therapy and may be responsible for treatment failure, either locally or as distant metastasis. Some of the newer radiopharmaceuticals being used to image the hypoxic portion of the tumor include [¹⁸F]fluoromisonidazole (FMISO), copper-diacetyl-bis (N4-methylthiosamincarbazone) (Cu-ATSM) and [¹⁸F]fluoroazomycin arabinoside (FAZA). Once identified using PET scans, these hypoxic areas of the tumor can be preferentially targeted to receive a higher dose of radiation using IMRT technique.

The applications of FDG PET/CT scanning mentioned in this article highlight the extensive work done

by groups across the world to the study the usefulness and application of this technology in various scenarios. Future work will continue to highlight the importance of this imaging modality in head and neck cancers.

REFERENCES

- Jemal A, Bray F, Center MM, Ferlay J, Ward E, Forman D. Global cancer statistics. *CA Cancer J Clin* 2011; **61**: 69-90 [PMID: 21296855 DOI: 10.3322/caac.20107]
- Parkin DM, Bray F, Ferlay J, Pisani P. Global cancer statistics, 2002. *CA Cancer J Clin* 2005; **55**: 74-108 [PMID: 15761078 DOI: 10.3322/canjclin.55.2.74]
- Siegel R, Naishadham D, Jemal A. Cancer statistics, 2013. *CA Cancer J Clin* 2013; **63**: 11-30 [PMID: 23335087 DOI: 10.3322/caac.21166]
- Induction chemotherapy plus radiation compared with surgery plus radiation in patients with advanced laryngeal cancer. The Department of Veterans Affairs Laryngeal Cancer Study Group. *N Engl J Med* 1991; **324**: 1685-1690 [PMID: 2034244 DOI: 10.1056/NEJM199106133242402]
- Forastiere AA, Goepfert H, Maor M, Pajak TF, Weber R, Morrison W, Glisson B, Trotti A, Ridge JA, Chao C, Peters G, Lee DJ, Leaf A, Ensley J, Cooper J. Concurrent chemotherapy and radiotherapy for organ preservation in advanced laryngeal cancer. *N Engl J Med* 2003; **349**: 2091-2098 [PMID: 14645636 DOI: 10.1056/NEJMoa031317]
- Vander Heiden MG, Cantley LC, Thompson CB. Understanding the Warburg effect: the metabolic requirements of cell proliferation. *Science* 2009; **324**: 1029-1033 [PMID: 19460998 DOI: 10.1126/science.1160809]
- Vander Heiden MG, Locasale JW, Swanson KD, Sharfi H, Heffron GJ, Amador-Noguez D, Christofk HR, Wagner G, Rabinowitz JD, Asara JM, Cantley LC. Evidence for an alternative glycolytic pathway in rapidly proliferating cells. *Science* 2010; **329**: 1492-1499 [PMID: 20847263 DOI: 10.1126/science.1188015]
- Garber K. Energy deregulation: licensing tumors to grow. *Science* 2006; **312**: 1158-1159 [PMID: 16728625 DOI: 10.1126/science.312.5777.1158]
- Macheda ML, Rogers S, Best JD. Molecular and cellular regulation of glucose transporter (GLUT) proteins in cancer. *J Cell Physiol* 2005; **202**: 654-662 [PMID: 15389572 DOI: 10.1002/jcp.20166]
- Kunkel M, Reichert TE, Benz P, Lehr HA, Jeong JH, Wieand S, Bartenstein P, Wagner W, Whiteside TL. Overexpression of Glut-1 and increased glucose metabolism in tumors are associated with a poor prognosis in patients with oral squamous cell carcinoma. *Cancer* 2003; **97**: 1015-1024 [PMID: 12569601 DOI: 10.1002/cncr.11159]
- Zhou S, Wang S, Wu Q, Fan J, Wang Q. Expression of glucose transporter-1 and -3 in the head and neck carcinoma-the correlation of the expression with the biological behaviors. *ORL J Otorhinolaryngol Relat Spec* 2008; **70**: 189-194 [PMID: 18401196 DOI: 10.1159/000124293]
- Roh JL, Cho KJ, Kwon GY, Ryu CH, Chang HW, Choi SH, Nam SY, Kim SY. The prognostic value of hypoxia markers in T2-staged oral tongue cancer. *Oral Oncol* 2009; **45**: 63-68 [PMID: 18620902 DOI: 10.1016/j.oraloncology.2008.03.017]
- De Schutter H, Landuyt W, Verbeken E, Goethals L, Hermans R, Nuyts S. The prognostic value of the hypoxia markers CA IX and GLUT 1 and the cytokines VEGF and IL 6 in head and neck squamous cell carcinoma treated by radiotherapy +/- chemotherapy. *BMC Cancer* 2005; **5**: 42 [PMID: 15847702 DOI: 10.1186/1471-2407-5-42]
- Minn H, Joensuu H, Ahonen A, Klemi P. Fluorodeoxyglucose imaging: a method to assess the proliferative activity of human cancer in vivo. Comparison with DNA flow cytometry in head and neck tumors. *Cancer* 1988; **61**: 1776-1781 [PMID: 3355975 DOI: 3.0.CO;]
- Haberhorn U, Strauss LG, Reisser C, Haag D, Dimitrakopoulou A, Ziegler S, Oberdorfer F, Rudat V, van Kaick G. Glucose uptake, perfusion, and cell proliferation in head and neck tumors: relation of positron emission tomography to flow cytometry. *J Nucl Med* 1991; **32**: 1548-1555 [PMID: 1869977]
- Tomasi G, Turkheimer F, Aboagye E. Importance of quantification for the analysis of PET data in oncology: review of current methods and trends for the future. *Mol Imaging Biol* 2012; **14**: 131-146 [PMID: 21842339 DOI: 10.1007/s11307-011-0514-2]
- Boellaard R. Standards for PET image acquisition and quantitative data analysis. *J Nucl Med* 2009; **50** Suppl 1: 11S-20S [PMID: 19380405 DOI: 10.2967/jnumed.108.057182]
- Kinahan PE, Fletcher JW. Positron emission tomography-computed tomography standardized uptake values in clinical practice and assessing response to therapy. *Semin Ultrasound CT MR* 2010; **31**: 496-505 [PMID: 21147377 DOI: 10.1053/j.sult.2010.10.001]
- Huang SC. Anatomy of SUV. Standardized uptake value. *Nucl Med Biol* 2000; **27**: 643-646 [PMID: 11091106 DOI: 10.1016/S0969-8051(00)00155-4]
- Thie JA. Understanding the standardized uptake value, its methods, and implications for usage. *J Nucl Med* 2004; **45**: 1431-1434 [PMID: 15347707]
- Lindholm P, Minn H, Leskinen-Kallio S, Bergman J, Ruotsalainen U, Joensuu H. Influence of the blood glucose concentration on FDG uptake in cancer—a PET study. *J Nucl Med* 1993; **34**: 1-6 [PMID: 8418248]
- Jereczek-Fossa BA, Jassem J, Orecchia R. Cervical lymph node metastases of squamous cell carcinoma from an unknown primary. *Cancer Treat Rev* 2004; **30**: 153-164 [PMID: 15023433 DOI: 10.1016/j.ctrv.2003.10.001]
- Lee DJ, Rostock RA, Harris A, Kashima H, Johns M. Clinical evaluation of patients with metastatic squamous carcinoma of the neck with occult primary tumor. *South Med J* 1986; **79**: 979-983 [PMID: 3738594 DOI: 10.1097/00007611-198608000-00015]
- Rusthoven KE, Koshy M, Paulino AC. The role of fluorodeoxyglucose positron emission tomography in cervical lymph node metastases from an unknown primary tumor. *Cancer* 2004; **101**: 2641-2649 [PMID: 15517576 DOI: 10.1002/cncr.20687]
- Rudmik L, Lau HY, Matthews TW, Bosch JD, Kloiber R, Molnar CP, Dort JC. Clinical utility of PET/CT in the evaluation of head and neck squamous cell carcinoma with an unknown primary: a prospective clinical trial. *Head Neck* 2011; **33**: 935-940 [PMID: 21674668 DOI: 10.1002/hed.21566]
- Som PM. Detection of metastasis in cervical lymph nodes: CT and MR criteria and differential diagnosis. *AJR Am J Roentgenol* 1992; **158**: 961-969 [PMID: 1566697 DOI: 10.2214/ajr.158.5.1566697]
- Adams S, Baum RP, Stuckensen T, Bitter K, Hör G. Prospective comparison of 18F-FDG PET with conventional imaging modalities (CT, MRI, US) in lymph node staging of head and neck cancer. *Eur J Nucl Med* 1998; **25**: 1255-1260 [PMID: 9724374 DOI: 10.1007/s002590050293]
- Di Martino E, Nowak B, Hassan HA, Hausmann R, Adam G, Buell U, Westhofen M. Diagnosis and staging of head and neck cancer: a comparison of modern imaging modalities (positron emission tomography, computed tomography, color-coded duplex sonography) with panendoscopic and histopathologic findings. *Arch Otolaryngol Head Neck Surg* 2000; **126**: 1457-1461 [PMID: 11115282 DOI: 10.1001/archotol.126.12.1457]
- Brouwer J, Senft A, de Bree R, Comans EF, Golding RP, Castelijns JA, Hoekstra OS, Leemans CR. Screening for distant metastases in patients with head and neck cancer: is there a role for (18)FDG-PET? *Oral Oncol* 2006; **42**: 275-280

- [PMID: 16266820 DOI: 10.1016/j.oraloncology.2005.07.009]
- 30 **Goerres GW**, Schmid DT, Grätz KW, von Schulthess GK, Ey- rich GK. Impact of whole body positron emission tomogra- phy on initial staging and therapy in patients with squamous cell carcinoma of the oral cavity. *Oral Oncol* 2003; **39**: 547-551 [PMID: 12798396 DOI: 10.1016/S1368-8375(03)00016-2]
- 31 **Lonneux M**, Lawson G, Ide C, Bausart R, Remacle M, Pau- wels S. Positron emission tomography with fluorodeoxy- glucose for suspected head and neck tumor recurrence in the symptomatic patient. *Laryngoscope* 2000; **110**: 1493-1497 [PMID: 10983949 DOI: 10.1097/00005537-200009000-00016]
- 32 **Ng SH**, Chan SC, Liao CT, Chang JT, Ko SF, Wang HM, Chin SC, Lin CY, Huang SF, Yen TC. Distant metastases and synchronous second primary tumors in patients with newly diagnosed oropharyngeal and hypopharyngeal carcinomas: evaluation of (18)F-FDG PET and extended-field multi- detector row CT. *Neuroradiology* 2008; **50**: 969-979 [PMID: 18600319 DOI: 10.1007/s00234-008-0426-2]
- 33 **Teknos TN**, Rosenthal EL, Lee D, Taylor R, Marn CS. Posi- tron emission tomography in the evaluation of stage III and IV head and neck cancer. *Head Neck* 2001; **23**: 1056-1060 [PMID: 11774391 DOI: 10.1002/hed.10006]
- 34 **Schwartz DL**, Rajendran J, Yueh B, Coltrera M, Anzai Y, Krohn K, Eary J. Staging of head and neck squamous cell cancer with extended-field FDG-PET. *Arch Otolaryngol Head Neck Surg* 2003; **129**: 1173-1178 [PMID: 14623746 DOI: 10.1001/archotol.129.11.1173]
- 35 **Haerle SK**, Schmid DT, Ahmad N, Hany TF, Stoeckli SJ. The value of (18)F-FDG PET/CT for the detection of distant me- tastases in high-risk patients with head and neck squamous cell carcinoma. *Oral Oncol* 2011; **47**: 653-659 [PMID: 21658990 DOI: 10.1016/j.oraloncology.2011.05.011]
- 36 **Schmid DT**, Stoeckli SJ, Bandhauer F, Huguenin P, Schmid S, von Schulthess GK, Goerres GW. Impact of positron emis- sion tomography on the initial staging and therapy in locoreg- ional advanced squamous cell carcinoma of the head and neck. *Laryngoscope* 2003; **113**: 888-891 [PMID: 12792328 DOI: 10.1097/00005537-200305000-00021]
- 37 **Strobel K**, Haerle SK, Stoeckli SJ, Schrank M, Soyka JD, Veit- Haibach P, Hany TF. Head and neck squamous cell carci- noma (HNSCC)--detection of synchronous primaries with (18)F-FDG-PET/CT. *Eur J Nucl Med Mol Imaging* 2009; **36**: 919-927 [PMID: 19205699 DOI: 10.1007/s00259-009-1064-6]
- 38 **Kondo N**, Tsukuda M, Nishimura G. Diagnostic sensitivity of ¹⁸F-fluorodeoxyglucose positron emission tomography for detecting synchronous multiple primary cancers in head and neck cancer patients. *Eur Arch Otorhinolaryngol* 2012; **269**: 1503-1507 [PMID: 21984059 DOI: 10.1007/s00405-011-1784-7]
- 39 **Adelstein DJ**, Li Y, Adams GL, Wagner H, Kish JA, Ensley JF, Schuller DE, Forastiere AA. An intergroup phase III com- parison of standard radiation therapy and two schedules of concurrent chemoradiotherapy in patients with unresectable squamous cell head and neck cancer. *J Clin Oncol* 2003; **21**: 92-98 [PMID: 12506176 DOI: 10.1200/JCO.2003.01.008]
- 40 **Bernier J**, Domette C, Ozsahin M, Matuszewska K, Lefèb- vre JL, Greiner RH, Giralt J, Maingon P, Rolland F, Bolla M, Cognetti F, Bourhis J, Kirkpatrick A, van Glabbeke M. Post- operative irradiation with or without concomitant chemo- therapy for locally advanced head and neck cancer. *N Engl J Med* 2004; **350**: 1945-1952 [PMID: 15128894 DOI: 10.1056/NEJMoa032641]
- 41 **Cooper JS**, Pajak TF, Forastiere AA, Jacobs J, Campbell BH, Saxman SB, Kish JA, Kim HE, Cmelak AJ, Rotman M, Machtay M, Ensley JF, Chao KS, Schultz CJ, Lee N, Fu KK. Postoperative concurrent radiotherapy and chemotherapy for high-risk squamous-cell carcinoma of the head and neck. *N Engl J Med* 2004; **350**: 1937-1944 [PMID: 15128893 DOI: 10.1056/NEJMoa032646]
- 42 **Grégoire V**, De Neve W, Eisbruch A, Lee N, Van den Weyn- gaert D, Van Gestel D. Intensity-modulated radiation thera- py for head and neck carcinoma. *Oncologist* 2007; **12**: 555-564 [PMID: 17522243 DOI: 10.1634/theoncologist.12-5-555]
- 43 **Lee N**, Puri DR, Blanco AI, Chao KS. Intensity-modulated radiation therapy in head and neck cancers: an update. *Head Neck* 2007; **29**: 387-400 [PMID: 16358297 DOI: 10.1002/hed.20332]
- 44 **Chao KS**, Deasy JO, Markman J, Haynie J, Perez CA, Purdy JA, Low DA. A prospective study of salivary function spar- ing in patients with head-and-neck cancers receiving intensi- ty-modulated or three-dimensional radiation therapy: initial results. *Int J Radiat Oncol Biol Phys* 2001; **49**: 907-916 [PMID: 11240231 DOI: 10.1016/S0360-3016(00)01441-3]
- 45 **Lin A**, Kim HM, Terrell JE, Dawson LA, Ship JA, Eisbruch A. Quality of life after parotid-sparing IMRT for head-and-neck cancer: a prospective longitudinal study. *Int J Radiat Oncol Biol Phys* 2003; **57**: 61-70 [PMID: 12909216 DOI: 10.1016/S0360-3016(03)00361-4]
- 46 **Yao M**, Karnell LH, Funk GF, Lu H, Dornfeld K, Buatti JM. Health-related quality-of-life outcomes following IMRT ver- sus conventional radiotherapy for oropharyngeal squamous cell carcinoma. *Int J Radiat Oncol Biol Phys* 2007; **69**: 1354-1360 [PMID: 17689885 DOI: 10.1016/j.ijrobp.2007.05.003]
- 47 **Ciernik IF**, Dizendorf E, Baumert BG, Reiner B, Burger C, Davis JB, Lütolf UM, Steinert HC, Von Schulthess GK. Radiation treatment planning with an integrated positron emission and computer tomography (PET/CT): a feasibility study. *Int J Radiat Oncol Biol Phys* 2003; **57**: 853-863 [PMID: 14529793 DOI: 10.1016/S0360-3016(03)00346-8]
- 48 **Deantonio L**, Beldi D, Gambaro G, Loi G, Brambilla M, Inglese E, Krengli M. FDG-PET/CT imaging for staging and radiotherapy treatment planning of head and neck carcinoma. *Radiat Oncol* 2008; **3**: 29 [PMID: 18801181 DOI: 10.1186/1748-717X-3-29]
- 49 **Paulino AC**, Koshy M, Howell R, Schuster D, Davis LW. Comparison of CT- and FDG-PET-defined gross tumor vol- ume in intensity-modulated radiotherapy for head-and-neck cancer. *Int J Radiat Oncol Biol Phys* 2005; **61**: 1385-1392 [PMID: 15817341 DOI: 10.1016/j.ijrobp.2004.08.037]
- 50 **El-Bassiouni M**, Ciernik IF, Davis JB, El-Attar I, Reiner B, Burger C, Goerres GW, Studer GM. [18FDG] PET-CT-based intensity-modulated radiotherapy treatment planning of head and neck cancer. *Int J Radiat Oncol Biol Phys* 2007; **69**: 286-293 [PMID: 17707283 DOI: 10.1016/j.ijrobp.2007.04.053]
- 51 **Guido A**, Fuccio L, Rombi B, Castellucci P, Ceconi A, Bunkheila F, Fuccio C, Spezi E, Angelini AL, Barbieri E. Combined 18F-FDG-PET/CT imaging in radiotherapy tar- get delineation for head-and-neck cancer. *Int J Radiat Oncol Biol Phys* 2009; **73**: 759-763 [PMID: 18834671 DOI: 10.1016/j.ijrobp.2008.04.059]
- 52 **Wang D**, Schultz CJ, Jursinic PA, Bialkowski M, Zhu XR, Brown WD, Rand SD, Michel MA, Campbell BH, Wong S, Li XA, Wilson JF. Initial experience of FDG-PET/CT guided IMRT of head-and-neck carcinoma. *Int J Radiat Oncol Biol Phys* 2006; **65**: 143-151 [PMID: 16618577 DOI: 10.1016/j.ijrobp.2005.11.048]
- 53 **Shintani SA**, Foote RL, Lowe VJ, Brown PD, Garces YI, Kasperbauer JL. Utility of PET/CT imaging performed early after surgical resection in the adjuvant treatment planning for head and neck cancer. *Int J Radiat Oncol Biol Phys* 2008; **70**: 322-329 [PMID: 17889447 DOI: 10.1016/j.ijrobp.2007.06.038]
- 54 **Liao CT**, Fan KH, Lin CY, Wang HM, Huang SF, Chen IH, Kang CJ, Ng SH, Hsueh C, Lee LY, Lin CH, Yen TC. Impact of a second FDG PET scan before adjuvant therapy for the early detection of residual/relapsing tumours in high-risk patients with oral cavity cancer and pathological extracaps- ular spread. *Eur J Nucl Med Mol Imaging* 2012; **39**: 944-955 [PMID: 22434050 DOI: 10.1007/s00259-012-2103-2]
- 55 **Mees G**, Dierckx R, Vangestel C, Van de Wiele C. Molecular imaging of hypoxia with radiolabelled agents. *Eur J Nucl Med Mol Imaging* 2009; **36**: 1674-1686 [PMID: 19565239 DOI:

- 10.1007/s00259-009-1195-9]
- 56 **Pugachev A**, Ruan S, Carlin S, Larson SM, Campa J, Ling CC, Humm JL. Dependence of FDG uptake on tumor micro-environment. *Int J Radiat Oncol Biol Phys* 2005; **62**: 545-553 [PMID: 15890599 DOI: 10.1016/j.ijrobp.2005.02.009]
- 57 **Schwartz DL**, Ford EC, Rajendran J, Yueh B, Coltrera MD, Virgin J, Anzai Y, Haynor D, Lewellen B, Mattes D, Kinahan P, Meyer J, Phillips M, Leblanc M, Krohn K, Eary J, Laramore GE. FDG-PET/CT-guided intensity modulated head and neck radiotherapy: a pilot investigation. *Head Neck* 2005; **27**: 478-487 [PMID: 15772953 DOI: 10.1002/hed.20177]
- 58 **Madani I**, Duthoy W, Derie C, De Gerssem W, Boterberg T, Saerens M, Jacobs F, Grégoire V, Lonneux M, Vakaet L, Vanderstraeten B, Bauters W, Bonte K, Thierens H, De Neve W. Positron emission tomography-guided, focal-dose escalation using intensity-modulated radiotherapy for head and neck cancer. *Int J Radiat Oncol Biol Phys* 2007; **68**: 126-135 [PMID: 17448871 DOI: 10.1016/j.ijrobp.2006.12.070]
- 59 **Duprez F**, De Neve W, De Gerssem W, Coghe M, Madani I. Adaptive dose painting by numbers for head-and-neck cancer. *Int J Radiat Oncol Biol Phys* 2011; **80**: 1045-1055 [PMID: 20643512 DOI: 10.1016/j.ijrobp.2010.03.028]
- 60 **Hentschel M**, Appold S, Schreiber A, Abramyuk A, Abolmaali N, Kotzerke J, Baumann M, Zöphel K. Serial FDG-PET on patients with head and neck cancer: implications for radiation therapy. *Int J Radiat Oncol Biol Phys* 2009; **85**: 796-804 [PMID: 19728194 DOI: 10.1080/09553000903039180]
- 61 **Andrade RS**, Heron DE, Degirmenci B, Filho PA, Branstetter BF, Seethala RR, Ferris RL, Avril N. Posttreatment assessment of response using FDG-PET/CT for patients treated with definitive radiation therapy for head and neck cancers. *Int J Radiat Oncol Biol Phys* 2006; **65**: 1315-1322 [PMID: 16750327 DOI: 10.1016/j.ijrobp.2006.03.015]
- 62 **Porceddu SV**, Jarmolowski E, Hicks RJ, Ware R, Weih L, Rischin D, Corry J, Peters LJ. Utility of positron emission tomography for the detection of disease in residual neck nodes after (chemo)radiotherapy in head and neck cancer. *Head Neck* 2005; **27**: 175-181 [PMID: 15627258 DOI: 10.1002/hed.20130]
- 63 **Yao M**, Smith RB, Graham MM, Hoffman HT, Tan H, Funk GF, Graham SM, Chang K, Dornfeld KJ, Menda Y, Buatti JM. The role of FDG PET in management of neck metastasis from head-and-neck cancer after definitive radiation treatment. *Int J Radiat Oncol Biol Phys* 2005; **63**: 991-999 [PMID: 16099601 DOI: 10.1016/j.ijrobp.2005.03.066]
- 64 **Porceddu SV**, Pryor DI, Burmeister E, Burmeister BH, Poulsen MG, Foote MC, Panizza B, Coman S, McFarlane D, Coman W. Results of a prospective study of positron emission tomography-directed management of residual nodal abnormalities in node-positive head and neck cancer after definitive radiotherapy with or without systemic therapy. *Head Neck* 2011; **33**: 1675-1682 [PMID: 22076976 DOI: 10.1002/hed.21655]
- 65 **Moeller BJ**, Rana V, Cannon BA, Williams MD, Sturgis EM, Ginsberg LE, Macapinlac HA, Lee JJ, Ang KK, Chao KS, Chronowski GM, Frank SJ, Morrison WH, Rosenthal DI, Weber RS, Garden AS, Lippman SM, Schwartz DL. Prospective risk-adjusted [18F]Fluorodeoxyglucose positron emission tomography and computed tomography assessment of radiation response in head and neck cancer. *J Clin Oncol* 2009; **27**: 2509-2515 [PMID: 19332725 DOI: 10.1200/JCO.2008.19.3300]
- 66 **Gupta T**, Master Z, Kannan S, Agarwal JP, Ghosh-Laskar S, Rangarajan V, Murthy V, Budrukkar A. Diagnostic performance of post-treatment FDG PET or FDG PET/CT imaging in head and neck cancer: a systematic review and meta-analysis. *Eur J Nucl Med Mol Imaging* 2011; **38**: 2083-2095 [PMID: 21853309 DOI: 10.1007/s00259-011-1893-y]
- 67 **McDermott M**, Hughes M, Rath T, Johnson JT, Heron DE, Kubicek GJ, Kim SW, Ferris RL, Duvvuri U, Ohr JP, Branstetter BF. Negative predictive value of surveillance PET/CT in head and neck squamous cell cancer. *AJNR Am J Neuroradiol* 2013; **34**: 1632-1636 [PMID: 23639557 DOI: 10.3174/ajnr.A3494]
- 68 **Siddiqui F**, Faulhaber PF, Yao M, Le QT. The application of fdg-pet as prognostic indicators in head and neck squamous cell carcinoma. *PET Clin* 2012; **7**: 381
- 69 **Allal AS**, Slosman DO, Kebdani T, Allaoua M, Lehmann W, Dulguerov P. Prediction of outcome in head-and-neck cancer patients using the standardized uptake value of 2-[18F]fluoro-2-deoxy-D-glucose. *Int J Radiat Oncol Biol Phys* 2004; **59**: 1295-1300 [PMID: 15275712 DOI: 10.1016/j.ijrobp.2003.12.039]
- 70 **Vernon MR**, Maheshwari M, Schultz CJ, Michel MA, Wong SJ, Campbell BH, Massey BL, Wilson JF, Wang D. Clinical outcomes of patients receiving integrated PET/CT-guided radiotherapy for head and neck carcinoma. *Int J Radiat Oncol Biol Phys* 2008; **70**: 678-684 [PMID: 18262086 DOI: 10.1016/j.ijrobp.2007.10.044]
- 71 **Moeller BJ**, Rana V, Cannon BA, Williams MD, Sturgis EM, Ginsberg LE, Macapinlac HA, Lee JJ, Ang KK, Chao KS, Chronowski GM, Frank SJ, Morrison WH, Rosenthal DI, Weber RS, Garden AS, Lippman SM, Schwartz DL. Prospective imaging assessment of mortality risk after head-and-neck radiotherapy. *Int J Radiat Oncol Biol Phys* 2010; **78**: 667-674 [PMID: 20171802 DOI: 10.1016/j.ijrobp.2009.08.063]
- 72 **La TH**, Filion EJ, Turnbull BB, Chu JN, Lee P, Nguyen K, Maxim P, Quon A, Graves EE, Loo BW, Le QT. Metabolic tumor volume predicts for recurrence and death in head-and-neck cancer. *Int J Radiat Oncol Biol Phys* 2009; **74**: 1335-1341 [PMID: 19289263 DOI: 10.1016/j.ijrobp.2008.10.060]
- 73 **Tang C**, Murphy JD, Khong B, La TH, Kong C, Fischbein NJ, Colevas AD, Iagaru AH, Graves EE, Loo BW, Le QT. Validation that metabolic tumor volume predicts outcome in head-and-neck cancer. *Int J Radiat Oncol Biol Phys* 2012; **83**: 1514-1520 [PMID: 22270174]
- 74 **Schwartz D**, Harris J, Yao M, Trotti A, Garden A, Jones C, Harari PM, Foote R, Holland J, Ang K. Metabolic tumor volume as a predictive imaging biomarker in head and neck cancer: Pilot results from rtog 0522. *Int J Radiat Oncol Biol Phys* 2013; **87**: S192 [DOI: 10.1016/j.ijrobp.2013.06.496]
- 75 **Kikuchi M**, Shinohara S, Nakamoto Y, Usami Y, Fujiwara K, Adachi T, Hori SY, Tona Y, Yamazaki H, Imai Y, Naito Y. Sequential FDG-PET/CT after neoadjuvant chemotherapy is a predictor of histopathologic response in patients with head and neck squamous cell carcinoma. *Mol Imaging Biol* 2011; **13**: 368-377 [PMID: 20552285 DOI: 10.1007/s11307-010-0364-3]
- 76 **Hentschel M**, Appold S, Schreiber A, Abolmaali N, Abramyuk A, Dörr W, Kotzerke J, Baumann M, Zöphel K. Early FDG PET at 10 or 20 Gy under chemoradiotherapy is prognostic for locoregional control and overall survival in patients with head and neck cancer. *Eur J Nucl Med Mol Imaging* 2011; **38**: 1203-1211 [PMID: 21350962 DOI: 10.1007/s00259-011-1759-3]
- 77 **Yao M**, Lu M, Savvides PS, Rezaee R, Zender CA, Lavertu P, Buatti JM, Machtay M. Distant metastases in head-and-neck squamous cell carcinoma treated with intensity-modulated radiotherapy. *Int J Radiat Oncol Biol Phys* 2012; **83**: 684-689 [PMID: 22169673 DOI: 10.1016/j.ijrobp.2011.07.014]
- 78 **Hamberg LM**, Hunter GJ, Alpert NM, Choi NC, Babich JW, Fischman AJ. The dose uptake ratio as an index of glucose metabolism: useful parameter or oversimplification? *J Nucl Med* 1994; **35**: 1308-1312 [PMID: 8046485]
- 79 **Keyes JW**. SUV: standard uptake or silly useless value? *J Nucl Med* 1995; **36**: 1836-1839 [PMID: 7562051]
- 80 **Kurien G**, Hu J, Harris J, Seikaly H. Cost-effectiveness of positron emission tomography/computed tomography in the management of advanced head and neck cancer. *J Otolaryngol Head Neck Surg* 2011; **40**: 468-472 [PMID: 22420434]
- 81 **Sher DJ**, Tishler RB, Annino D, Punglia RS. Cost-effectiveness of CT and PET-CT for determining the need for

- adjuvant neck dissection in locally advanced head and neck cancer. *Ann Oncol* 2010; **21**: 1072-1077 [PMID: 19833820 DOI: 10.1093/annonc/mdp405]
- 82 **Berker Y**, Franke J, Salomon A, Palmowski M, Donker HC, Temur Y, Mottaghy FM, Kuhl C, Izquierdo-Garcia D, Fayad ZA, Kiessling F, Schulz V. MRI-based attenuation correction for hybrid PET/MRI systems: a 4-class tissue segmentation technique using a combined ultrashort-echo-time/Dixon MRI sequence. *J Nucl Med* 2012; **53**: 796-804 [PMID: 22505568 DOI: 10.2967/jnumed.111.092577]
- 83 **Drzezga A**, Souvatzoglou M, Eiber M, Beer AJ, Fürst S, Martinez-Möller A, Nekolla SG, Ziegler S, Ganter C, Rummeny EJ, Schwaiger M. First clinical experience with integrated whole-body PET/MR: comparison to PET/CT in patients with oncologic diagnoses. *J Nucl Med* 2012; **53**: 845-855 [PMID: 22534830 DOI: 10.2967/jnumed.111.098608]
- 84 **Keereman V**, Fierens Y, Broux T, De Deene Y, Lonneux M, Vandenberghe S. MRI-based attenuation correction for PET/MRI using ultrashort echo time sequences. *J Nucl Med* 2010; **51**: 812-818 [PMID: 20439508 DOI: 10.2967/jnumed.109.065425]
- 85 **Torigian DA**, Zaidi H, Kwee TC, Saboury B, Udupa JK, Cho ZH, Alavi A. PET/MR imaging: technical aspects and potential clinical applications. *Radiology* 2013; **267**: 26-44 [PMID: 23525716 DOI: 10.1148/radiol.13121038]
- 86 **Wang TJC**, Menda Y, Cheng SK, Wu CC, Lee NY. New tracers pet in head and neck squamous cell carcinoma. *PET Clin* 2012; **7**: 431-441 [DOI: 10.1016/j.cpet.2012.06.009]

P- Reviewers: Ciorba A, Raz E **S- Editor:** Wen LL **L- Editor:** A
E- Editor: Zhang DN



Sustained attention in psychosis: Neuroimaging findings

Gianna Sepede, Maria Chiara Spano, Marco Lorusso, Domenico De Berardis, Rosa Maria Salerno, Massimo Di Giannantonio, Francesco Gambi

Gianna Sepede, Maria Chiara Spano, Marco Lorusso, Rosa Maria Salerno, Massimo Di Giannantonio, Francesco Gambi, Department of Neuroscience and Imaging, Institute for Advanced Biomedical Technologies, University "G. D'Annunzio" of Chieti, "G. d'Annunzio" University of Chieti, 66013 Chieti Scalo (CH), Italy

Domenico De Berardis, Department of Mental Health, National Health Trust, 64100 Teramo, Italy

Author contributions: Sepede G, Gambi F, Salerno RM and Di Giannantonio M designed the research; Sepede G, Spano MC, Lorusso M and De Berardis D performed the PubMed research, selected the papers included in the qualitative review and summarized the results; Sepede G, Gambi F, Salerno RM and Di Giannantonio M wrote the paper; Spano MC and Lorusso M edited the language and contributed equally to this work.

Correspondence to: Gianna Sepede, MD, PhD, Department of Neuroscience and Imaging, Institute for Advanced Biomedical Technologies, University "G. D'Annunzio" of Chieti, Via dei Vestini 33, 66013 Chieti Scalo (CH), Italy. gsepede@libero.it
Telephone: +39-871-3556901 Fax: +39-871-3556930

Received: December 23, 2013 Revised: February 7, 2014

Accepted: May 16, 2014

Published online: March 28, 2015

Abstract

To provide a systematic review of scientific literature on functional magnetic resonance imaging (fMRI) studies on sustained attention in psychosis. We searched PubMed to identify fMRI studies pertaining sustained attention in both affective and non-affective psychosis. Only studies conducted on adult patients using a sustained attention task during fMRI scanning were included in the final review. The search was conducted on September 10th, 2013. 15 fMRI studies met our inclusion criteria: 12 studies were focused on Schizophrenia and 3 on Bipolar Disorder Type I (BDI). Only half of the Schizophrenia studies and two of the BDI studies reported behavioral abnormalities, but all of them evidenced significant functional differences in brain regions related to the sustained attention system. Altered functioning of the insula was found in both Schizophrenia and BDI,

and therefore proposed as a candidate trait marker for psychosis in general. On the other hand, other brain regions were differently impaired in affective and non-affective psychosis: alterations of cingulate cortex and thalamus seemed to be more common in Schizophrenia and amygdala dysfunctions in BDI. Neural correlates of sustained attention seem to be of great interest in the study of psychosis, highlighting differences and similarities between Schizophrenia and BDI.

© 2015 Baishideng Publishing Group Inc. All rights reserved.

Key words: Sustained attention; Affective psychosis; Non-affective psychosis; Schizophrenia; Bipolar disorder; Functional magnetic resonance imaging; Insula

Core tip: In the present paper, we systematically reviewed functional magnetic resonance imaging studies investigating sustained attention in affective and non-affective psychosis. We found that differences between cases (patients, unaffected relatives of psychotic probands) and controls in terms of functional activation of sustained attention system structures were detectable even when the groups performed comparably. In particular, the insular cortex seems to be a trait marker for psychosis in general, whereas other regions (thalamus, cingulate cortex, amygdala) seem to be differently impaired in affective and non-affective psychosis.

Original sources: Sepede G, Spano MC, Lorusso M, De Berardis D, Salerno RM, Di Giannantonio M, Gambi F. Sustained attention in psychosis: Neuroimaging findings. *World J Radiol* 2014; 6(6): 261-273 Available from: URL: <http://www.wjgnet.com/1949-8470/full/v6/i6/261.htm> DOI: <http://dx.doi.org/10.4329/wjcr.v6.i6.261>

INTRODUCTION

Sustained attention can be defined as the ability to main-

tain a high vigilance level for prolonged periods of time, allowing the subjects to respond in an appropriate way to infrequent and unpredictable stimuli^[1].

Abnormalities in sustained attention have been reported in both schizophrenic^[2-4] and Bipolar Disorder (BD) patients^[5-8] and several studies suggested a correlation with a worse prognosis and a poorer quality of life^[9-12]. Sustained attention deficits seem to be independent from medications^[13,14] and illness states^[15]. Studies comparing directly schizophrenic and BD patients found that the two groups were qualitatively similar in sustained attention deficits^[16], even though schizophrenic patients were usually quantitatively more impaired^[17-20]. A reduced attentional performance has also been highlighted in non-affected relatives of schizophrenic^[21,22] and bipolar patients^[23]: it has been therefore proposed as a candidate endophenotype for both affective^[24-26] and non-affective psychosis^[27-30]. Candidate endophenotypes must be associated with illness, state independent, heritable, and found in unaffected relatives of probands at a higher rate than in general population^[31]. By contrast, some behavioral studies failed to find any significant performance deficit in schizophrenic patients^[32], in bipolar patients^[33] or in unaffected relatives of bipolar probands^[34,35], so the role of sustained attention as a trait-marker of psychosis is still controversial. The discordant results reported in scientific literature may be due to the differences in experimental paradigms and inclusion/exclusion criteria.

The most commonly used tasks to assess sustained attention are the “oddball paradigms”, where subjects are required to identify rare and unpredictable target stimuli presented among a stream of frequent non-target stimuli^[36,37] or among both frequent and rare non-target stimuli, usually called “standards” and “novels” respectively^[38,39]. A particular kind of oddball paradigm is the Continuous Performance Test (CPT), initially developed by Beck *et al.*^[40] and nowadays considered a well validated instrument to measure sustained attention in both research and clinical settings^[41]. There are numerous versions of CPT, differing from one another for the sensorial modalities (visual or auditory)^[42,43] the perceptual complexity of the stimuli (CPT with degraded stimuli: DS-CPT)^[44] and the response required: only on targets, on both targets and non-targets and only on non-targets (Conners’ CPT II)^[45]. Other CPT versions increase the number of stimuli presented per minute to intensify the attentional load (*e.g.*, the Rapid Visual Information Processing task, RVIP)^[46]. Some CPTs are designed to assess both sustained attention and working memory resources, *e.g.*, the CPT-AX (a character or number preceded by another character or number as a target)^[47] or the CPI-IP (identical pairs of stimuli as a target)^[48]. Several scores are used to measure the behavioral performance in oddball paradigms: the rate of correct targets (“hits”, “H”) and incorrect targets (“omission errors”); the rate of correct non-target (“correct rejections”) and incorrect non-target (“false alarms”, “FA”) “commission”) and the mean reaction times (RT) to the stimuli. Subjects who respond accurately and rap-

idly to both target and non-target are considered good performers, whereas a high number of omissions indicate a reduced attention and a high number of commissions indicate augmented impulsivity. Using the signal detection theory^[49] other measures of accuracy may be calculated, such as the sensitivity index (d' , d' -prime), its nonparametric analog (A' , A' -prime) and the response criterion (B'' , beta, $\ln b$). d' is the standardized difference between hit rate and false alarm rate [$d' = z(\text{Hits}) - z(\text{False alarms})$] and it is considered a good measure of discriminability. B'' instead represents an index of response bias, the subject's tendency to under respond or over respond [$B'' = (1-H) - FA(1-FA)/H(1-H)+FA(1-FA)$].

Functional neuroimaging studies increase the possibility to detect subtle differences in brain functioning even in behaviorally intact subjects. In healthy individuals, sustained attention tasks usually elicit a widespread cortical and subcortical network, including dorsal and medial prefrontal cortex, parietal, temporal and occipital areas, cingulate gyrus, insula, cerebellum, and basal ganglia^[50-53]. Different components of sustained attention have their anatomical and functional correlates in different brain regions: subcortical structures have been associated with arousal control, dorsal frontal and temporoparietal cortex with attention maintenance over time, and anterior ventromedial regions, such as anterior cingulate cortex (ACC) and anterior insula, with conflict monitoring, target detection and error signaling^[54]. Moreover, ACC and insula are reported to play a crucial role in emotional regulation, linking emotion to cognition^[55,56].

The aim of the present paper is to review fMRI correlates of sustained attention in affective and non-affective psychosis, discussing the literature findings and the role of sustained attention as a candidate endophenotype for psychotic disorders.

SEARCH

We searched PubMed to identify functional magnetic resonance (fMRI) studies investigating sustained attention in affective and non-affective psychosis. The following search words were used, both alone and in combination: sustained attention, fMRI, affective psychosis, non-affective psychosis, Schizophrenia, Bipolar Disorder. The search was conducted on September 10th, 2013 and yielded 42 records. Moreover, we manually checked the reference lists of the identified articles and we found 9 further potential studies, for a total number of 51 records. Inclusion criteria were the following: articles written in English, patients' age ≥ 18 years, psychotic patients and/or subjects at augmented risk for psychosis, studies providing both behavioral and fMRI results during a sustained attention task. Structural MRI studies and fMRI studies reporting data acquired during paradigms other than sustained attention tasks or during resting state were excluded.

By reading titles and abstracts, we excluded 18 records. By reading the full texts of the 33 remaining arti-

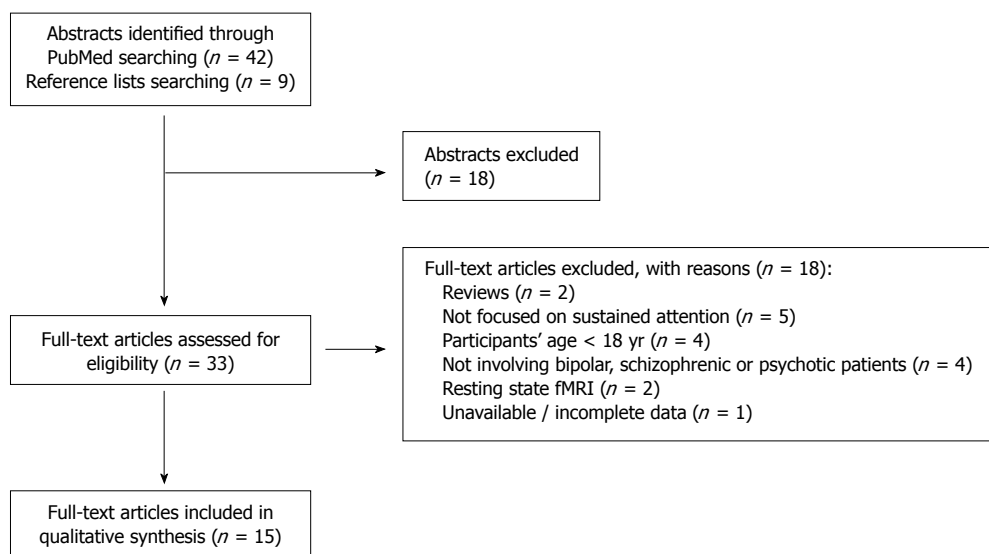


Figure 1 Flow chart of the systematic review. fMRI: Functional magnetic resonance imaging.

cles, we identified 15 papers meeting our inclusion criteria and therefore included in the qualitative synthesis (Figure 1).

RESEARCH

A total number of 578 subjects was tested by the 15 studies included in the qualitative synthesis: 272 normal comparisons (NC), 173 schizophrenic patients (SCZ), 17 unaffected relatives of schizophrenics (REL-SCZ), 10 subjects at ultra high risk for Schizophrenia (UHR-SCZ), 84 Bipolar Disorder type I patients (BDI) and 22 unaffected relatives of BDI patients (REL-BDI). The majority of SCZ were male (68.8%), conversely to what observed in BDI, where males represented only 30.9% of the total.

Sustained attention in schizophrenia

A total number of 12 studies was selected^[57-68]. The characteristic of the groups and the results of the studies are depicted in Table 1.

Right handedness was an inclusion criteria in 6 studies^[57,59,60,63,66,68]. Nine studies enrolled only SCZ, one had both a SCZ group and an additional group of UHR-SCZ^[61] and two had only REL-SCZ^[66,68]. In the study by Morey *et al.*^[61], patients were divided into early SCZ (mean illness duration 1.7 years) and chronic SCZ (mean illness duration 15.3 years). In the study by Honey *et al.*^[60], patients were divided into SCZ with both negative and positive symptoms ($n = 11$) and SCZ with predominantly positive symptoms ($n = 11$). The SCZ ($n = 173$) enrolled in the studies were clinically stable and in the majority of cases were medicated (range: 87.5%-100%). Only 2 of the 10 UHR-SCZ received medications at the moment of the scanning, whereas all the REL-SCZ ($n = 17$) and the NC ($n = 204$) were drug naïve. In seven of the 10 studies including a SCZ group, the mean illness duration was also reported^[58-63,65] and it ranged from 1.7 to 33 years. The

UHR-SCZ group in the study by Morey *et al.*^[61] met at least one of the following criteria: (1) reporting brief intermittent psychotic states; (2) reporting attenuated positive symptom states; and (3) being first-degree relatives of schizophrenic/schizotypal probands plus reporting a significant recent loss of social/work functioning. The 11 REL-SCZ enrolled by Sepede *et al.*^[68] were all unaffected siblings of schizophrenic patients, whereas the 6 REL-SCZ enrolled by Filbey *et al.*^[66] were presumed obligate carriers of schizophrenia (POCs): unaffected subjects having a first-degree relative (sibling or parent) plus a child affected by schizophrenia. Ten of the 12 studies used visual stimuli, whereas the other two^[62,65] used auditory stimuli. The tasks administered were: oddball tasks ($n = 4$), CPT-X ($n = 1$), DS-CPT-X ($n = 2$), CPT-IP ($n = 2$), RVIP ($n = 1$), and other attention tasks ($n = 2$), with a total duration of the experiment ranging from 6 to 49 min.

fMRI images were acquired using a 1.5 T scanner in seven studies, a 3 T scanner in 2 studies and a 4 T scanner in three studies. A block design was used to present the tasks in six studies, whereas an event-related design was used in other five studies. Only one study^[67] used a block/event-related mixed design. A whole brain approach was used in eight studies to analyze the BOLD fMRI signal whereas three studies^[60,61,67] used a region of interest (ROI) approach and/or a masked brain analysis, limiting the analysis to areas known to be involved in sustained attention processing and/or to areas showing significant between-group or within-condition differences. Only one study^[64] used the ROI analysis after the whole brain analysis. In the study by Honey *et al.*^[60], connectivity analyses were also performed.

Behavioral results

In four of the ten studies involving SCZ ($n = 57$), no significant behavioral differences were found with respect to NC^[57,58,63,64]. In the other six studies, SCZ ($n = 116$) performed worse than NC: a reduced accuracy was evi-

Table 1 Functional magnetic resonance imaging studies of sustained attention in Schizophrenia

Ref.	Participants	Task and behavioral results	fMRI methods and results
Volz <i>et al</i> ^[57] , 1999	SCZ (<i>n</i> = 14), age 34.1 ± 12.3, males 78.6%, medicated 100% NC (<i>n</i> = 20), age 28.2 ± 5.7, males 60%	CPT-IP. Type of stimuli: letters TNS = 720, Target = 25%, SET = 600 ms, ISI = 1200 ms, TET = 30 min Required response: on targets. Behavioral measures: hit rate, mean RT, <i>d'</i> , ln b Results: no between group differences	1.5 T, block design (4 blocks). baseline: finger tapping Whole brain analysis. Imaging package: SPM96 Results: NC > SCZ in the R mesial PFC, ACC and L TH
Eyler <i>et al</i> ^[58] , 2004	SCZ (<i>n</i> = 8)/SCA (<i>n</i> = 1) age 58.9 ± 9.9, males 55.6%, illness duration: 33 yr, medicated 100% NC (<i>n</i> = 10), age 59.8 ± 5.7, 12 males 60%	CPT-X. Type of stimuli: letters. TNS = 72 Target = 33.3% ISI = 500 ms, TET = 6 min 3 s Required response: on targets Behavioral measures: mean RT, <i>d'</i> Results: no between group differences	1.5 T, block design. baseline: digit fixation 8 task blocks and 9 baseline blocks Whole brain analysis. Imaging package: AFNI Results: NC > SCZ in R IFG/insula (BA 47/45) SCZ > NC in R postcentral gyrus (BA 3) and L cerebellum
Salgado-Pineda <i>et al</i> ^[59] , 2004	SCZ (<i>n</i> = 14), age 25.5 ± 4.1, males 50%, medicated 100%, illness duration: 1.9 yr NC (<i>n</i> = 14), age 25.1 ± 3.3, males 50%	CPT-IP. Type of stimuli: numbers. TNS = 900 Target = 15% ISI = 1100 ms, TET = 14min Required response: on targets Behavioral measures: omission errors, commission errors, mean RT, <i>d'</i> , ln b Results: Between group differences -omissions, commission and <i>d'</i> : NC > SCZ -mean RT: SCZ > NC	1.5 T, block design. baseline: digit response 2 task blocks and 2 baseline blocks. Whole brain analysis. Imaging package: SPM2 Results: NC > SCZ in R IFG (BA 44), R angular gyrus (BA 39), R STG (BA 37), R MTG (BA 21), R TH
Honey <i>et al</i> ^[60] , 2005	N-SCZ: SCZ with both negative and positive symptoms: (<i>n</i> = 11), age 42.6 ± 9.2, males 90.9%, age of onset: 22.2 yr, medicated 100% P-SCZ: SCZ with predominant positive symptoms: (<i>n</i> = 11) age 41.1 ± 9.2, males 81.8%, age of onset: 24.7 yr, medicated 100% NC (<i>n</i> = 12), age 33.3 ± 11.8, 12 males 83.3%	CPT-X with 2 levels of difficulty: undegraded and degraded stimuli (0% and 40% pixel inverted). Type of stimuli: digits TNS = 280 Target = 25% SET = 42 ms, ISI = 958 ms TET = 6 min Required response: on targets Behavioral measures: mean RT, <i>d'</i> Results: N-SCZ were less accurate than NC in target discrimination (<i>d'</i>)	3T, block design, baseline: screen fixation 10 task blocks and 10 baseline blocks. Imaging package: SPM2 Masked brain analysis (ROIs involved in attention processing, differentiating the groups and showing a task related activity associated to attentional load). Connectivity analysis (seed ROIs: ACC and cerebellar vermis) Results Task vs baseline: NC > (P-SCZ = N-SCZ) in R and L angular gyrus, MFG, L putamen (P-SCZ = N-SCZ) > NC in R and L SFG, R and L IPL, R SPL, R post central gyrus, L precentral gyrus, R and L TH, ACC, PCC, R MiFG, R IFG, cerebellum; P-SCZ > N-SCZ in R STG, R MiFG and L SPL Connectivity with ACC: NC > (P-SCZ = N-SCZ) in R and L MSFG, R and L IFG; (P-SCZ = N-SCZ) > NC in R and L precentral gyrus, R postcentral gyrus, cerebellum; P-SCZ > N-SCZ in ACC; N-SCZ > P-SCZ in SMA Connectivity with cerebellum: NC > (P-SCZ = N-SCZ) in R and L MSFG, L MFG; (P-SCZ = N-SCZ) > NC in L MiFG; P-SCZ > N-SCZ in R and L IFG, ACC, L SPL, R precentral gyrus, L postcentral gyrus
Morey <i>et al</i> ^[61] , 2005	UHR (<i>n</i> = 10), age 22.6 ± 4.4, male 50%, medicated 20%, Early SCZ (<i>n</i> = 15) age 24.1 ± 6.5, male 67%, age of onset 22.3 yr, illness duration 1.7 yr, medicated 86.7%	Visual oddball task Type of stimuli: circles ("targets"), squares (frequent non targets-"standards"), objects (rare non targets-"novels") TNS = 1400 Target = 3% SET = 500 ms, ISI = 1500 ms, TET = 36 min 24 s Required response: on both targets and non-targets	1.5T, 7 runs. Event-related design. Imaging package: SPM99 ROI analysis: ACC, MiFG, IFG, BG, and TH. Conditions: -Targets -Novels -Standards (baseline) Results Targets vs novels activations -in ACC, MiFG and IFC: NC > UHR, Early SCZ and Chronic SCZ -in IFG: (1) NC > Early SCZ and Chronic SCZ; (2) only NC and UHR showed R > L activations, whereas Early SCZ and Chronic SCZ showed a reduced laterality

Liddle <i>et al</i> ^[62] , 2006	Chronic SCZ (<i>n</i> = 11) age 38.1 ± 7.7, male 82%, age of onset 22.9 yr, illness duration 15.3 yr, medicated 100%	Behavioral measures: hit rate, <i>d'</i> , <i>B''</i>	Target <i>vs</i> baseline activations: -in ACC, MiFG and IFC: NC > Early SCZ and Chronic SCZ -in BG and TH: NC > Early SCZ and Chronic SCZ (results confirmed comparing Chronic SCZ with Older NC)
	NC (<i>n</i> = 16) age 28.0 ± 11.6, male 59%	Results: Between group differences: -Hit rate: NC > Early SCZ and chronic SCZ - <i>d'</i> : NC > UHR, Early SCZ and Chronic SCZ	
Gur <i>et al</i> ^[63] , 2007	Older NC (<i>n</i> = 10) age 34.0 ± 12.1, male 67%	Auditory oddball task Type of stimuli: 1500 Hz tones ("targets"), 1000 Hz tones (frequent non targets-"standards"), noises (rare non targets-"novels")	1.5 T, event related design, whole brain analysis Imaging package: SPM99. Conditions: -correct targets -correct novels -correct standards (baseline) -missed targets -standard false alarms
	SCZ (<i>n</i> = 24)/SCA (<i>n</i> = 4) age 31.6 ± 10.1, males 67.9%, illness duration 7 yr, medicated 96.4%	TNS = 488 Target = 10% SET = 200 ms, ISI = 2000 ms, TET = 16 min Required response: on targets Behavioral measures: RT, omissions, commissions Results: SCZ were significantly slower and less accurate than NC	Results Targets <i>vs</i> baseline activations: NC > SCZ: in L and R amygdala, R hippocampus, R and L STS, L and R insula, R and L orbitofrontal cortex (BA 47), ACC, PCC, L and R SPL, R and L IPL, L and R middle IFG, L and R superior MFG, L and R TH, L and R striatum, L and R cerebellum
Harrison <i>et al</i> ^[64] , 2007	NC (<i>n</i> = 28), age 28.2 ± 8.9, males 75 %	Visual oddball task. Stimuli: colored shapes Type of stimuli: red circles ("targets"), green circles (frequent non targets-"standards"), fractal images (rare non targets-"novels")	Results Targets <i>vs</i> novels activations: NC > SCZ in: L amygdala, L orbitofrontal cortex (BA 47), L anterior insula, rostral ACC and L striatum
	SCZ (<i>n</i> = 22), age 30.5 ± 9.1, males 59.1%, age of onset 22.5 yr, illness duration 12.4 yr, medicated 95.5%	TNS = 200 Target = 15% SET = 1000 ms, ISI = 2000 ms, TET = 7 min Required response: on targets Behavioral measures: hit rate, RT Results: no between group differences	4T, event related design, whole brain analysis. Imaging package: FEAT/FMRIB. Conditions: -targets -novels -standards (baseline)
Wolf <i>et al</i> ^[65] , 2008	NC (<i>n</i> = 28), age 31.6 ± 8.5, males 57.1 %	Multi-Source Interference Task (MSIT). Type of stimuli: digits SET = 2000 ms, ISI = 500 ms TNS = 160, TET = 11 min Required response: on all stimuli Behavioral measures: correct responses, RT	Results Targets <i>vs</i> baseline activations: NC > SCZ in R and L STG, L insula, R and L putamen, ACC, PCC, L SFG, L TH SCZ > NC in R insula, R MiFG, L IPL Novels <i>vs</i> baseline activations: NC > SCZ in L IOG and L IPL SCZ > NC in L MOG, L fusiform, L precuneus, L IFG, R angular gyrus, SOG, SPL, MiFG
	SCZ (<i>n</i> = 12), age 32.2 ± 8.0, males 100%, medicated 100%	Results: no between group differences	3T, block design. Imaging package: SPM5 Conditions: -low difficulty Task ("baseline") -high difficulty Task ("Task") -fixation ("Rest") Whole brain analysis and ROI analysis of deactivation ("Rest"- "Task") in medial PCC/rostral ACC and PCC/Precuneus
Filbey <i>et al</i> ^[66] , 2008	NC (<i>n</i> = 14), age 31.7 ± 8.0, males 100%	Auditory oddball task Type of stimuli: 2000 Hz tones ("targets"), 1000 Hz tones (frequent non targets-"standards"), sounds (rare non targets-"novels")	Results SCZ > NC in deactivation of medial PCC/rostral ACC and PCC/Precuneus. In SCZ the magnitude of deactivation correlates with response speed and level of emotional awareness
	POC-SCZ (<i>n</i> = 6) age 53, males 33.3% medicated 0% (drug naïve)	TNS = 200 Target = 15% SET = 150 ms, ISI = 1850 ms, TET = 6 min and 40 s Required response: on targets Behavioral measures: hit rate, RT Results: SCZ were significantly slower than NC	4T, event-related whole brain analysis. Imaging package: FEAT/FSL. Conditions: -targets -novels -standards (baseline)
		Sustained attention task Type of stimuli: colored circles Required response: on targets Behavioral measures: RT	Results Targets <i>vs</i> baseline activations: SCZ > NC in: L precentral gyrus, ACC/SMA, L and R insula, L hippocampus, L and R STG/MTG, L superior MOG Novels <i>vs</i> baseline activations: SCZ > NC in: L IFG
			1.5T. Block design. Imaging package: FSL Whole brain analysis baseline condition: circles fixation

	NC (<i>n</i> = 8) age 41, males 62.5%	Results: no between group differences	Results NC > POC-SCZ in: R IPL (BA 7), R SPL (BA 7), R MTG (BA 21), R MOG (BA 18), R PCC (BA 31), R SFG (BA 10), R lingual gyrus (BA 18/19), R precentral gyrus (BA 9/43), R parahippocampal gyrus (BA 28), L cuneus (BA 18), L striatum; POC-SCZ > NC in: L STG (BA 21), L SFG (BA9) and R MTG (BA 19)
Carter <i>et al</i> ^[67] , 2010	SCZ (<i>n</i> = 9), age 29.8 ± 12.0, males 100%	Visual selective attention task Type of stimuli: colored circles	4T. Block/event-related mixed design. 10 runs. Imaging package: SPM. Conditions: -target events (3 s before-13.5 s after the event) -transient activation (3 s before-7.5 s after the onset of task block) -sustained activation (15 s before-70.5 s after the onset of task block) Masked brain analysis and ROI analysis in ACC, IFG, MIFG, IPS, BG, caudate and TH
	NC (<i>n</i> = 12), age 25.5 ± 4.6, males 100%	TNS = 1960 Target = 5 % SET = 500 ms, ISI = 1000 ms TET = 49 min Required response: on both targets and non-targets Behavioral measures: correct targets, RT Results -correct target percentage: NC > SCZ -RT: SCZ > NC	Results -During transient activation NC > SCZ in: MiFG, IPS, caudate and TH -During target events NC > SCZ in TH In NC: positive correlation between accuracy and TH activation during sustained activation condition; In SCZ: negative correlation between RT and BG activation during target events
Sepede <i>et al</i> ^[68] , 2010	REL-SCZ (<i>n</i> = 11), age 34.4 ± 8.8, males 45.5% medicated 0% (drug naïve), smokers 36.4% NC (<i>n</i> = 11), age 32.0 ± 5.2, males 45.5%, smokers 36.4%	CPT-X with 3 levels of difficulty: undegraded and degraded stimuli (0%, 25% and 40% pixel inverted). Type of stimuli: digits TNT = 210, Target = 16% SET = 200 ms, ISI = 2000 ms, TET = 42 min Required response: on targets and non-targets Behavioral measures: correct targets, correct non-targets, RT Results: no between group differences	1.5T, event-related design, 3 runs (0%, 25% and 40% degraded) Whole brain analysis. Imaging package: BrainVoyager QX 1.9 Task conditions: -correct responses on target -incorrect responses on target -correct responses on non-targets (baseline) Results Correct targets <i>vs</i> baseline: NC > REL-SCZ in R precentral gyrus (BA 6/9), R and L insula (BA 13), MFG/dorsal ACC (BA 9/32) REL-SCZ > NC in deactivating PCC/retrosplenial cortex (BA 23/31) Incorrect target <i>vs</i> baseline: REL-SCZ > NC in L insula/IFG (BA 13/47) and R TH

SCZ: Schizophrenic patients; NC: Normal comparisons; SCA: Schizoaffective patients; REL-SCZ: Unaffected first degree relatives of schizophrenic patients; POC-SCZ: Presumed Obligate carriers of schizophrenic patients; UHR: Ultra high risk subjects; SET: Stimulus exposure time; ISI: Interstimulus interval; TNS: Total number of stimuli; TNT: Total number of targets; TET: Total experiment time; RT: Response time; R: Right; L: Left; PFC: Prefrontal cortex; ACC: Anterior cingulate cortex; PCC: Posterior cingulate cortex; MFG: Medial frontal gyrus; MSFG: Medial superior frontal gyrus; IFG: Inferior frontal gyrus; SFG: Superior frontal gyrus; SMA: Supplementary motor area; IPL: Inferior parietal lobule; SPL: Superior parietal lobule; IPS: Intraparietal sulcus; MTG: Middle temporal gyrus; STG: Superior temporal gyrus; STS: Superior temporal sulcus; MOG: Middle occipital gyrus; IOG: Inferior occipital gyrus; TH: Thalamus; BG: Basal ganglia.

denced by Honey *et al*^[60] and Morey *et al*^[61], whereas Wolf *et al*^[65] reported an increased mean reaction time and Salgado *et al*^[59], Liddle *et al*^[62] and Carter *et al*^[67] reported both reduced accuracy and increased mean reaction times with respect to NC. In their 10 UHR subjects, Morey *et al*^[61] reported a reduced accuracy. On the contrary, the 17 REL-SCZ enrolled by Filbey *et al*^[66] and Sepede *et al*^[68] performed similarly to controls.

FMRI results

Significant between-group differences in several brain regions were found in all the selected studies, even when the groups performed comparably. The most reported

differences were observed in cingulate gyrus, thalamus (TH), inferior parietal lobule (IPL), inferior frontal gyrus (IFG) and insula. The anterior part of the cingulate cortex (ACC) significantly differentiated the groups in seven studies: SCZ showed a reduced activation with respect to NC in 4 SCZ groups^[57,61-63], and the same pattern was observed in the UHR subjects enrolled by Morey *et al*^[61] and in the REL-SCZ enrolled by Sepede *et al*^[68]. By contrast, two studies^[60,65] reported an augmented activation in SCZ with respect to NC. Also the posterior part of the cingulate cortex (PCC) significantly differentiated the groups in six studies. Honey *et al*^[60] reported an increased activation in the SCZ with respect to NC, whereas a decreased

activation was found by Gur *et al.*^[63] and Liddle *et al.*^[62] Interestingly, in three studies, the PCC was reported to be deactivated during attention task, with respect to the baseline/control task, and the amount of the deactivation was larger in SCZ^[64] and REL-SCZ^[66,68] with respect to NC. A significant hypoactivation of the IFG was found in five studies^[58-62]. The medial regions of the prefrontal cortex, located dorso-rostrally with respect to the cingulate cortex, appeared to be hyperactivated in SCZ^[57,60] or REL-SCZ^[68].

The insular cortex significantly differentiated the groups in five studies. A reduced activation in SCZ was reported bilaterally by Liddle *et al.*^[62] and limited to the right hemisphere by Eylar *et al.*^[58] By contrast, Gur *et al.*^[63] found a reduced activation in the R insula, counterbalanced by an augmented activation in the L insula, and Wolf *et al.*^[65] reported a bilateral augmented activation. In the event-related study by Sepede *et al.*^[68], REL-SCZ hyperactivated the bilateral insula during correct target responses and hyperactivated the L insula during wrong target responses. An altered functioning of the inferior parietal lobule (IPL) was detected in 4 studies, three showing a reduced activation in SCZ with respect to NC^[60,62,66], one an increased activation^[63]. Other parietal regions were also reported to differentiate the groups. In the angular gyrus Salgado *et al.*^[59] and Honey *et al.*^[60] reported a reduced activation, Gur *et al.*^[63] an increased activation; in the superior parietal lobule (SPL) Liddle *et al.*^[62] and Filbey *et al.*^[66] found a reduced activation, Honey *et al.*^[60] an increased activation in SCZ with respect to NC.

When considering the subcortical regions, SCZ significantly hyperactivated the TH in six studies^[57,59,61,62,63,67], whereas Sepede *et al.*^[68] found an increased activation during wrong target responses in REL-SCZ. Other subcortical structures, such as the basal ganglia, appeared to be less activated in SCZ with respect to NC in 4 studies^[60,61,63].

SUSTAINED ATTENTION IN BIPOLAR DISORDER

Three studies enrolled BDI patients^[69-71] and one of these studies had also a group of unaffected, drug-naïve, BDI-REL^[71]. The characteristic of the groups and the results of the studies are depicted in Table 2. Right handedness was an inclusion criteria in two studies^[69,71]. The BDI ($n = 84$) enrolled in the three studies were euthymic ($n = 34$) or affected by a manic/mixed episode ($n = 50$). About 80% of the 74 patients in the studies by Fleck *et al.*^[70] and Sepede *et al.*^[71] were under medication at the moment of the fMRI scanning, whereas the 10 BDI in the study by Strakowski *et al.*^[69] were drug free. All the NC ($n = 68$) and the BDI-REL ($n = 22$) were drug naïve. In two of the studies^[69,71], the mean illness duration was also reported and it was 2.2 and 4.7 years respectively. The presence of psychotic features during the acute phases of the illness (95.8%) was reported only by Sepede *et al.*^[71] All the three selected studies used a visual CPT to assess sustained at-

tention (CPT-IP: $n = 2$; DS-CPT-X: $n = 1$), with a total duration of the experiment ranging from 6 to 15 min.

fMRI images were acquired using a 1.5 T ($n = 1$), a 3 T ($n = 1$) or a 4 T ($n = 1$) scanner, presenting the tasks with an event-related design ($n = 2$) or a block design ($n = 1$). A whole brain approach was used in two studies to analyze the BOLD fMRI, whereas Fleck *et al.*^[70] performed a whole brain analysis followed by a ROI analysis.

Behavioral results

In their group of 10 euthymic and unmedicated BDI, Strakowski *et al.*^[69] did not find any behavioral deficit with respect to NC. On the contrary, both Fleck *et al.*^[70] and Sepede *et al.*^[71] reported a reduced target accuracy in their manic/mixed ($n = 50$) or euthymic ($n = 24$) BDI patients. An impaired performance was also found in the group of 22 unaffected and unmedicated BDI-REL enrolled by Sepede *et al.*^[71].

fMRI results

Significant between-group differences in several brain regions were found in all the three selected studies, even when the groups performed comparably. The regions more reported to differentiate the groups were: IFG, insula, amygdala and IPL.

The IFG/insula showed an altered pattern of activation in all the three selected studies: an augmented activation in BDI with respect to NC was found by Strakowski *et al.*^[69], whereas Fleck *et al.*^[70] reported a reduced activation. In the study by Sepede *et al.*^[71], BDI showed a reduced activation during correct target responses and an augmented activation during wrong target responses, with REL-BDI showing an intermediate pattern of functioning between BDI and NC. The amygdala was found to be more activated with respect to NC in two studies, involving euthymic^[69] or manic^[70] BDI. The IPL seemed to be hyperactivated in the euthymic BDI enrolled by Strakowski *et al.*^[69] and in the REL-BDI by Sepede *et al.*^[71].

DISCUSSION

In this paper we systematically reviewed fMRI studies on sustained attention in affective and non-affective psychosis.

We found several studies on Schizophrenia that met our inclusion criteria, whereas the publications on BDI were very few. This result is quite surprising, considering the large amount of behavioral data that reported sustained attention deficits in both acute and euthymic phases of BDI.

Summarizing the literature findings on affective and non-affective psychosis, we highlighted that patients and at-risk subjects significantly differed from healthy comparisons in the functioning of several brain regions belonging to the sustained attention system, even when they were behaviorally intact. There were regions that seemed more impaired in Schizophrenia, other more impaired in Bipolar Disorder and other that appeared altered in both

Table 2 Functional magnetic resonance imaging studies of sustained attention in bipolar disorder

Ref.	Participants	Task and behavioral results	FMRI methods and results
Strakowski <i>et al</i> ^[69] , 2004	BDI (<i>n</i> = 10), age 25.5 ± 8.1, males 40%, euthymic, age of onset 23 yr, illness duration 2.2 yr, medicated 0% (drug free) NC (<i>n</i> = 10), age 25.3 ± 7.3, males 40%	CPT-IP. Type of stimuli: digits TNS = 400 SET = 700 ms, ISI = 750, TET = 6 min Required response: on targets. Behavioral measures: <i>d'</i> , percent correct, percent false positive Results: no between-group differences	3T, block design, 5 task blocks and 5 baseline blocks Baseline: digits fixation Whole brain analysis. Imaging package: CHIPS Results: BDI > NC in: R IFG/insula (BA 13/47), R and L ventral PFC (BA 10/47), parahippocampus/amygdala (BA 34), MCG/MTG (BA 18/19/39), R IPL (BA 40), R SPL (BA 7/40), L postcentral gyrus (BA 43), hypothalamus; NC > BDI in: L fusiform gyrus (BA 20) and L MFG (BA 11)
Fleck <i>et al</i> ^[70] , 2012	BDI (<i>n</i> = 50), age 30 ± 10, males 30%, manic, medicated 80% NC (<i>n</i> = 34), age 31 ± 9, males 41%	CPT-IP. Type of stimuli: digits TNS = 900, Target = 15%, SET = 750 ms, ISI = 1000 ms, TET = 15 min Required response: on targets Behavioral measures: <i>A'</i> , <i>B'</i> , RT, correct rejection Results: patients performed worse in terms of correct rejections and showed a trend <i>vs</i> a reduced <i>A'</i>	4T, Event-related design, 3 runs (periods) Whole brain analysis. Imaging package: AFNI ROi based analysis: anterior-limbic network (IFG, BG, TH, amygdala, cerebellar vermis) + SFG Baseline: visual count down condition Task conditions: -hits, misses and false alarms -correct rejections on non-targets Results: In period 1: NC > BD in cerebellum; BD > NC in TH; NC > BD in deactivation of L PCC and R angular gyrus In period 2: NC > BD in bilateral IFG and L TH In period 3: NC > BD in activation of R IFG Over time: BD activated and NC deactivated L striatum and bilateral amygdala Unmedicated BD > medicated BD in activation of R IFG and cerebellum
Sepede <i>et al</i> ^[71] , 2012	BDI (<i>n</i> = 24), age 34.8 ± 8.0, males 41.7%, euthymic, age of onset 29.9, illness duration 4.7 yr, psychotic features during acute phases 95.8%, medicated 83.3% REL-BDI (<i>n</i> = 22), age 31.5 ± 7.3, males 31.8% medicated 0% (drug naïve) NC (<i>n</i> = 24), age 32.5 ± 6.2, males 33.3%	CPT-X with 2 levels of difficulty: undegraded and degraded stimuli (0% and 40% pixel inverted) Type of stimuli: digits TNT = 80, Target = 20%, TNS = 408 ± 30 SET = 200 ms, ISI = 2000 ms, TET = 14 min Required response: on targets and non-targets Behavioral measures: correct target, correct non-targets, incorrect target, incorrect non-target, mean RT Results: both BDI and REL-BDI were less accurate than NC in target recognition (percent correct target)	1.5T, event-related design, 2 runs (0%, and 40% degraded). Whole brain analysis. Imaging package: BrainVoyager QX 1.9. Task conditions: -correct responses on target -incorrect responses on target -correct responses on non-targets (baseline) Results Correct target <i>vs</i> baseline: (NC = REL-BDI) > BDI in R insula (BA13) REL-BDI > (NC = BDI) in deactivating PCC/ retrosplenial cortex (BA 23/29) During the 40% degraded run, correct target condition: REL-BDI > (NC = BDI) in R and L IPL (BA 40), L insula/IFG (BA 13/45) Incorrect target <i>vs</i> baseline: (BDI = REL-BDI) > NC in middle PCC (BA 31) and R insula/IFG (BA 13/45) BDI > REL-BDI > NC in L insula (BA 13)

BDI: Bipolar disorder type 1 patients; REL-BDI: Unaffected relatives of bipolar disorder type 1 patients; NC: Normal comparisons; PFC: Prefrontal cortex; ACC: Anterior cingulate cortex; PCC: Posterior cingulate cortex; MFG: Medial frontal gyrus; SFG: Superior frontal gyrus; IFG: Inferior frontal gyrus; IPL: Inferior parietal lobule; SPL: Superior parietal lobule; MTG: Middle temporal gyrus; MOG: Middle occipital gyrus; TH: Thalamus; BG: Basal ganglia; R: Right; L: Left.

conditions.

In the studies on schizophrenic patients and subjects at augmented risk for schizophrenia, the most frequent dysfunctions were located in the cingulate gyrus and in the thalamus. The anterior part of the cingulate gyrus is a key region in sustained attention, cognitive control and

error processing^[72-74]. An altered function of ACC has been consistently reported in both schizophrenic patients and unaffected relatives^[75,76] during attentional control^[77] conflict/error monitoring^[78-81], working memory^[82-84] and semantic^[85] tasks.

The posterior part of the cingulate gyrus is usu-

ally deactivated during active tasks with respect to rest conditions, and it is therefore considered a part of the Default Mode Network (DMN) of the brain^[86]. It has a crucial role not only in internally focused tasks, but also in active regulation of the arousal state and in balancing between internally and externally oriented attention^[87]. A lower volume of PCC/retrosplenial cortex has been associated to a poorer outcome in Schizophrenia^[88], and an altered function of this region has been evidenced during semantic^[89], self-evaluation^[90,91] and fear-conditioning^[92] tasks.

The thalamus is a subcortical structure whose integrity is needed to the correct functioning of cognitive processes. It is not a simple passive relay station, but a nodal link actively connecting top-down to bottom-up components of the attention/arousal system^[1,93] and different cortical regions via cortico-thalamo-cortical pathways^[94]. Both structural and functional MRI studies on Schizophrenia frequently reported significant abnormalities in schizophrenic patients, so a disruption of thalamocortical connections was suggested as one of the possible neural basis of cognitive and sensorial symptoms of Schizophrenia^[95-98].

With regard to Bipolar Disorder, amygdala was found to be altered in two of the three reviewed. In humans, the amygdala plays a key role in detecting dangers and other emotionally salient stimuli in the environment, in order to make the subject ready to react in an appropriate way^[99]. During emotional tasks, an altered functioning of the amygdala in BD has been extensively reported, especially in manic patients^[100-103], but also during depressive^[104] and euthymic states^[105,106] of the illness. An important finding highlighted by the current review is that an augmented activation of the amygdala was observed also during attention tasks without any emotional components, this results suggesting that emotional limbic areas may interfere with cognition in BD^[107].

In our systematic review we reported that an altered functioning of the insula during sustained attention task was frequently found in both Schizophrenia and Bipolar Disorder.

The insular cortex, due to its location at the interface of frontal, parietal and temporal lobes, is involved in cognitive, emotional and somato-sensorial processes^[56,108], providing a hub that integrates salient stimuli with autonomic and sensorial data^[109]. Many studies reported an insular dysfunction in Schizophrenia, Bipolar Disorder, and “at-risk subjects”, during both tasks^[110-115] and resting state^[116-119], thus suggesting a key role of this region in vulnerability for psychosis, regardless of the affective or non-affective diagnostic distinction.

CONCLUSION

In the present paper, we systematically reviewed fMRI studies pertaining sustained attention in affective and non-affective psychosis.

We found that differences between cases (patients,

unaffected relatives of psychotic probands) and controls in terms of functional activation in brain regions belonging to the sustained attention system were detectable even when the groups performed comparably. In particular, the insular cortex seems to be a trait marker for psychosis in general, whereas other regions seem to be differently impaired in affective and non-affective psychosis: alterations of the cingulate cortex and thalamus appear to be more common in Schizophrenia whereas amygdalar dysfunctions may be more frequently observed in Bipolar Disorder. Therefore, investigating neural correlates of sustained attention seem to be of great interest in the study of affective and non-affective psychosis as it may clarify differences and similarities between these two disabling psychiatric conditions.

Limits of the study

An important limitation of the present paper is that we included in the qualitative synthesis only those studies conducted on selected versions of CPTs that were focused on sustained attention, excluding papers with CPT versions designed to measure other cognitive functions, such as working memory or emotional processing. Moreover, it's possible that our search strategy did not succeed in finding all the available literature on the topic and that adding other search words (*i.e.*, Continuous performance Test, oddball task) or other data bases would have improved the results. Due to the small number of published studies on Bipolar Disorder, our results should be interpreted with caution and further research are needed to clarify the role of sustained attention in affective psychosis.

REFERENCES

- 1 **Sarter M**, Givens B, Bruno JP. The cognitive neuroscience of sustained attention: where top-down meets bottom-up. *Brain Res Brain Res Rev* 2001; **35**: 146-160 [PMID: 11336780 DOI: 10.1016/S0165-0173(01)00044-3]
- 2 **Suwa H**, Matsushima E, Ohta K, Mori K. Attention disorders in schizophrenia. *Psychiatry Clin Neurosci* 2004; **58**: 249-256 [PMID: 15149289 DOI: 10.1111/j.1440-1819.2004.01227.x]
- 3 **Hahn B**, Robinson BM, Kaiser ST, Matveeva TM, Harvey AN, Luck SJ, Gold JM. Kraepelin and Bleuler had it right: people with schizophrenia have deficits sustaining attention over time. *J Abnorm Psychol* 2012; **121**: 641-648 [PMID: 22686867 DOI: 10.1037/a0028492]
- 4 **Üçök A**, Direk N, Koyuncu A, Keskin-Ergen Y, Yüksel Ç, Güler J, Karadayı G, Akturan E, Devrim-Üçök M. Cognitive deficits in clinical and familial high risk groups for psychosis are common as in first episode schizophrenia. *Schizophr Res* 2013; **151**: 265-269 [PMID: 24262680 DOI: 10.1016/j.schres.2013.10.030]
- 5 **Harmer CJ**, Clark L, Grayson L, Goodwin GM. Sustained attention deficit in bipolar disorder is not a working memory impairment in disguise. *Neuropsychologia* 2002; **40**: 1586-1590 [PMID: 11985840 DOI: 10.1016/S0028-3932(02)00019-2]
- 6 **Bora E**, Yuçel M, Pantelis C. Cognitive endophenotypes of bipolar disorder: a meta-analysis of neuropsychological deficits in euthymic patients and their first-degree relatives. *J Affect Disord* 2009; **113**: 1-20 [PMID: 18684514 DOI: 10.1016/j.jad.2008.06.009]
- 7 **Clark L**, Iversen SD, Goodwin GM. Sustained attention

- deficit in bipolar disorder. *Br J Psychiatry* 2002; **180**: 313-319 [PMID: 11925353 DOI: 10.1192/bjp.180.4.313]
- 8 **Robinson LJ**, Thompson JM, Gallagher P, Gray JM, Young AH, Ferrier IN. Performance monitoring and executive control of attention in euthymic bipolar disorder: employing the CPT-AX paradigm. *Psychiatry Res* 2013; **210**: 457-464 [PMID: 23880481 DOI: 10.1016/j.psychres.2013.06.039]
 - 9 **Hofer A**, Baumgartner S, Bodner T, Edlinger M, Hummer M, Kemmler G, Rettenbacher MA, Fleischhacker WW. Patient outcomes in schizophrenia II: the impact of cognition. *Eur Psychiatry* 2005; **20**: 395-402 [PMID: 16171654 DOI: 10.1016/j.eurpsy.2005.02.006]
 - 10 **González-Blanch C**, Perez-Iglesias R, Pardo-García G, Rodríguez-Sánchez JM, Martínez-García O, Vázquez-Barquero JL, Crespo-Facorro B. Prognostic value of cognitive functioning for global functional recovery in first-episode schizophrenia. *Psychol Med* 2010; **40**: 935-944 [PMID: 19751542 DOI: 10.1017/S0033291709991267]
 - 11 **Martino DJ**, Marengo E, Igoa A, Scápola M, Ais ED, Perinot L, Strejilevich SA. Neurocognitive and symptomatic predictors of functional outcome in bipolar disorders: a prospective 1 year follow-up study. *J Affect Disord* 2009; **116**: 37-42 [PMID: 19033081 DOI: 10.1016/j.jad.2008.10.023]
 - 12 **Pattanayak RD**, Sagar R, Mehta M. Neuropsychological performance in euthymic Indian patients with bipolar disorder type I: correlation between quality of life and global functioning. *Psychiatry Clin Neurosci* 2012; **66**: 553-563 [PMID: 23252921 DOI: 10.1111/j.1440-1819.2012.02400.x]
 - 13 **Liu SK**, Chen WJ, Chang CJ, Lin HN. Effects of atypical neuroleptics on sustained attention deficits in schizophrenia: a trial of risperidone versus haloperidol. *Neuropsychopharmacology* 2000; **22**: 311-319 [PMID: 10693159 DOI: 10.1016/S0893-133X(99)00137-2]
 - 14 **Goswami U**, Sharma A, Varma A, Gulrajani C, Ferrier IN, Young AH, Gallagher P, Thompson JM, Moore PB. The neurocognitive performance of drug-free and medicated euthymic bipolar patients do not differ. *Acta Psychiatr Scand* 2009; **120**: 456-463 [PMID: 19416126 DOI: 10.1111/j.1600-0447.2009.01390.x]
 - 15 **Martínez-Arán A**, Vieta E, Reinares M, Colom F, Torrent C, Sánchez-Moreno J, Benabarre A, Goikolea JM, Comes M, Salamero M. Cognitive function across manic or hypomanic, depressed, and euthymic states in bipolar disorder. *Am J Psychiatry* 2004; **161**: 262-270 [PMID: 14754775 DOI: 10.1176/appi.ajp.161.2.262]
 - 16 **Sánchez-Morla EM**, Barabash A, Martínez-Vizcaíno V, Tabarés-Seisdedos R, Balanzá-Martínez V, Cabranes-Díaz JA, Baca-Baldomero E, Gómez JL. Comparative study of neurocognitive function in euthymic bipolar patients and stabilized schizophrenic patients. *Psychiatry Res* 2009; **169**: 220-228 [PMID: 19758705 DOI: 10.1016/j.psychres.2008.06.032]
 - 17 **Liu SK**, Chiu CH, Chang CJ, Hwang TJ, Hwu HG, Chen WJ. Deficits in sustained attention in schizophrenia and affective disorders: stable versus state-dependent markers. *Am J Psychiatry* 2002; **159**: 975-982 [PMID: 12042186 DOI: 10.1176/appi.ajp.159.6.975]
 - 18 **Dickerson F**, Boronow JJ, Stallings C, Origoni AE, Cole SK, Yolken RH. Cognitive functioning in schizophrenia and bipolar disorder: comparison of performance on the Repeatable Battery for the Assessment of Neuropsychological Status. *Psychiatry Res* 2004; **129**: 45-53 [PMID: 15572184 DOI: 10.1016/j.psychres.2004.07.002]
 - 19 **Altshuler LL**, Ventura J, van Gorp WG, Green MF, Theberge DC, Mintz J. Neurocognitive function in clinically stable men with bipolar I disorder or schizophrenia and normal control subjects. *Biol Psychiatry* 2004; **56**: 560-569 [PMID: 15476685 DOI: 10.1016/j.biopsych.2004.08.002]
 - 20 **Schretlen DJ**, Cascella NG, Meyer SM, Kingery LR, Testa SM, Munro CA, Pulver AE, Rivkin P, Rao VA, Diaz-Asper CM, Dickerson FB, Yolken RH, Pearlson GD. Neuropsychological functioning in bipolar disorder and schizophrenia. *Biol Psychiatry* 2007; **62**: 179-186 [PMID: 17161829 DOI: 10.1016/j.biopsych.2006.09.025]
 - 21 **Birkett P**, Sigmundsson T, Sharma T, Touloupoulou T, Griffiths TD, Reveley A, Murray R. Reaction time and sustained attention in schizophrenia and its genetic predisposition. *Schizophr Res* 2007; **95**: 76-85 [PMID: 17630256 DOI: 10.1016/j.schres.2007.05.030]
 - 22 **Hilti CC**, Hilti LM, Heinemann D, Robbins T, Seifritz E, Cattapan-Ludewig K. Impaired performance on the Rapid Visual Information Processing task (RVIP) could be an endophenotype of schizophrenia. *Psychiatry Res* 2010; **177**: 60-64 [PMID: 20110130 DOI: 10.1016/j.psychres.2009.12.012]
 - 23 **Trivedi JK**, Goel D, Dhyani M, Sharma S, Singh AP, Sinha PK, Tandon R. Neurocognition in first-degree healthy relatives (siblings) of bipolar affective disorder patients. *Psychiatry Clin Neurosci* 2008; **62**: 190-196 [PMID: 18412842 DOI: 10.1111/j.1440-1819.2008.01754.x]
 - 24 **Fridberg DJ**, Hetrick WP, Brenner CA, Shekhar A, Steffen AN, Malloy FW, O'Donnell BF. Relationships between auditory event-related potentials and mood state, medication, and comorbid psychiatric illness in patients with bipolar disorder. *Bipolar Disord* 2009; **11**: 857-866 [PMID: 19922554 DOI: 10.1111/j.1399-5618.2009.00758.x]
 - 25 **Arts B**, Jabben N, Krabbendam L, van Os J. A 2-year naturalistic study on cognitive functioning in bipolar disorder. *Acta Psychiatr Scand* 2011; **123**: 190-205 [PMID: 20846251 DOI: 10.1111/j.1600-0447.2010.01601.x]
 - 26 **Ancín I**, Santos JL, Teixeira C, Sánchez-Morla EM, Bescós MJ, Argudo I, Torrijos S, Vázquez-Alvarez B, De La Vega I, López-Ibor JJ, Barabash A, Cabranes-Díaz JA. Sustained attention as a potential endophenotype for bipolar disorder. *Acta Psychiatr Scand* 2010; **122**: 235-245 [PMID: 20105148 DOI: 10.1111/j.1600-0447.2009.01532.x]
 - 27 **Chen WJ**, Faraone SV. Sustained attention deficits as markers of genetic susceptibility to schizophrenia. *Am J Med Genet* 2000; **97**: 52-57 [PMID: 10813804]
 - 28 **Cornblatt BA**, Malhotra AK. Impaired attention as an endophenotype for molecular genetic studies of schizophrenia. *Am J Med Genet* 2001; **105**: 11-15 [PMID: 11424979]
 - 29 **Giakoumaki SG**, Roussos P, Pallis EG, Bitsios P. Sustained attention and working memory deficits follow a familial pattern in schizophrenia. *Arch Clin Neuropsychol* 2011; **26**: 687-695 [PMID: 21813556 DOI: 10.1093/arclin/acr060]
 - 30 **Gottesman II**, Gould TD. The endophenotype concept in psychiatry: etymology and strategic intentions. *Am J Psychiatry* 2003; **160**: 636-645 [PMID: 12668349 DOI: 10.1176/appi.ajp.160.4.636]
 - 31 **Wang Q**, Chan R, Sun J, Yao J, Deng W, Sun X, Liu X, Sham PC, Ma X, Meng H, Murray RM, Collier DA, Li T. Reaction time of the Continuous Performance Test is an endophenotypic marker for schizophrenia: a study of first-episode neuroleptic-naïve schizophrenia, their non-psychotic first-degree relatives and healthy population controls. *Schizophr Res* 2007; **89**: 293-298 [PMID: 17055704 DOI: 10.1016/j.schres.2006.08.030]
 - 32 **Jones LA**, Cardno AG, Sanders RD, Owen MJ, Williams J. Sustained and selective attention as measures of genetic liability to schizophrenia. *Schizophr Res* 2001; **48**: 263-272 [PMID: 11295379 DOI: 10.1016/S0920-9964(00)00136-5]
 - 33 **Addington J**, Addington D. Attentional vulnerability indicators in schizophrenia and bipolar disorder. *Schizophr Res* 1997; **23**: 197-204 [PMID: 9075297 DOI: 10.1016/S0920-9964(96)00105-3]
 - 34 **Clark L**, Kempton MJ, Scarnà A, Grasby PM, Goodwin GM. Sustained attention-deficit confirmed in euthymic bipolar disorder but not in first-degree relatives of bipolar patients or euthymic unipolar depression. *Biol Psychiatry* 2005; **57**: 183-187 [PMID: 15652878 DOI: 10.1016/j.biopsych.2004.11.007]

- 35 **Walshe M**, Schulze KK, Stahl D, Hall MH, Chaddock C, Morris R, Marshall N, McDonald C, Murray RM, Bramon E, Kravariti E. Sustained attention in bipolar I disorder patients with familial psychosis and their first-degree relatives. *Psychiatry Res* 2012; **199**: 70-73 [PMID: 22513042 DOI: 10.1016/j.psychres.2012.03.018]
- 36 **Huettel SA**, McCarthy G. What is odd in the oddball task? Prefrontal cortex is activated by dynamic changes in response strategy. *Neuropsychologia* 2004; **42**: 379-386 [PMID: 14670576 DOI: 10.1016/j.neuropsychologia.2003.07.009]
- 37 **Kim H**. Involvement of the dorsal and ventral attention networks in oddball stimulus processing: a meta-analysis. *Hum Brain Mapp* 2014; **35**: 2265-2284 [PMID: 23900833 DOI: 10.1002/hbm.22326]
- 38 **Huang S**, Belliveau JW, Tengshe C, Ahveninen J. Brain networks of novelty-driven involuntary and cued voluntary auditory attention shifting. *PLoS One* 2012; **7**: e44062 [PMID: 22937153 DOI: 10.1371/journal.pone.0044062]
- 39 **Zaehle T**, Bauch EM, Hinrichs H, Schmitt FC, Voges J, Heinze HJ, Bunzeck N. Nucleus accumbens activity dissociates different forms of salience: evidence from human intracranial recordings. *J Neurosci* 2013; **33**: 8764-8771 [PMID: 23678119 DOI: 10.1523/JNEUROSCI.5276-12.2013]
- 40 **Beck LH**, Bransome ED, Mirsky AF, Rosvold HE, Sarason I. A continuous performance test of brain damage. *J Consult Psychol* 1956; **20**: 343-350 [PMID: 13367264 DOI: 10.1037/h0043220]
- 41 **Riccio CA**, Reynolds CR, Lowe P, Moore JJ. The continuous performance test: a window on the neural substrates for attention? *Arch Clin Neuropsychol* 2002; **17**: 235-272 [PMID: 14589726 DOI: 10.1016/S0887-6177(01)00111-1]
- 42 **Baker DB**, Taylor CJ, Leyva C. Continuous performance tests: a comparison of modalities. *J Clin Psychol* 1995; **51**: 548-551 [PMID: 7593677]
- 43 **Kasai K**, Nakagome K, Hiramatsu K, Fukuda M, Honda M, Iwanami A. Psychophysiological index during auditory selective attention correlates with visual continuous performance test sensitivity in normal adults. *Int J Psychophysiol* 2002; **45**: 211-225 [PMID: 12208528 DOI: 10.1016/S0167-8760(02)00013-2]
- 44 **Nuechterlein KH**, Parasuraman R, Jiang Q. Visual sustained attention: image degradation produces rapid sensitivity decrement over time. *Science* 1983; **220**: 327-329 [PMID: 6836276 DOI: 10.1126/science.6836276]
- 45 **Conners CK**, MHS Staff. Conners' Continuous Performance Test (CPT II) computer programs for Windows technical guide and software manual. North Tonawanda, NY: Multi-Health Systems: 2000
- 46 **Chen WJ**, Hsiao CK, Hsiao LL, Hwu HG. Performance of the Continuous Performance Test among community samples. *Schizophr Bull* 1998; **24**: 163-174 [PMID: 9502554 DOI: 10.1093/oxfordjournals.schbul.a033308]
- 47 **Cornblatt BA**, Lenzenweger MF, Erlenmeyer-Kimling L. The continuous performance test, identical pairs version: II. Contrasting attentional profiles in schizophrenic and depressed patients. *Psychiatry Res* 1989; **29**: 65-85 [PMID: 2772099 DOI: 10.1016/0165-1781(89)90188-1]
- 48 **Coull JT**, Frith CD, Frackowiak RS, Grasby PM. A frontoparietal network for rapid visual information processing: a PET study of sustained attention and working memory. *Neuropsychologia* 1996; **34**: 1085-1095 [PMID: 8904746 DOI: 10.1016/0028-3932(96)00029-2]
- 49 **Green DM**, Swets JA. Signal detection theory and psychophysics. New York: Wiley: 1966
- 50 **Adler CM**, Sax KW, Holland SK, Schmithorst V, Rosenberg L, Strakowski SM. Changes in neuronal activation with increasing attention demand in healthy volunteers: an fMRI study. *Synapse* 2001; **42**: 266-272 [PMID: 11746725 DOI: 10.1002/syn.1112]
- 51 **Ogg RJ**, Zou P, Allen DN, Hutchins SB, Dutkiewicz RM, Mulhern RK. Neural correlates of a clinical continuous performance test. *Magn Reson Imaging* 2008; **26**: 504-512 [PMID: 18068933 DOI: 10.1016/j.mri.2007.09.004]
- 52 **Mantini D**, Corbetta M, Perrucci MG, Romani GL, Del Gratta C. Large-scale brain networks account for sustained and transient activity during target detection. *Neuroimage* 2009; **44**: 265-274 [PMID: 18793734 DOI: 10.1016/j.neuroimage.2008.08.019]
- 53 **Grahn JA**, Manly T. Common neural recruitment across diverse sustained attention tasks. *PLoS One* 2012; **7**: e49556 [PMID: 23185360 DOI: 10.1371/journal.pone.0049556]
- 54 **Lawrence NS**, Ross TJ, Hoffmann R, Garavan H, Stein EA. Multiple neuronal networks mediate sustained attention. *J Cogn Neurosci* 2003; **15**: 1028-1038 [PMID: 14614813 DOI: 10.1162/089892903770007416]
- 55 **Bush G**, Luu P, Posner MI. Cognitive and emotional influences in anterior cingulate cortex. *Trends Cogn Sci* 2000; **4**: 215-222 [PMID: 10827444 DOI: 10.1016/S1364-6613(00)01483-2]
- 56 **Kurth F**, Zilles K, Fox PT, Laird AR, Eickhoff SB. A link between the systems: functional differentiation and integration within the human insula revealed by meta-analysis. *Brain Struct Funct* 2010; **214**: 519-534 [PMID: 20512376 DOI: 10.1007/s00429-010-0255-z]
- 57 **Volz H**, Gaser C, Häger F, Rzanny R, Pönisch J, Mentzel H, Kaiser WA, Sauer H. Decreased frontal activation in schizophrenics during stimulation with the continuous performance test—a functional magnetic resonance imaging study. *Eur Psychiatry* 1999; **14**: 17-24 [PMID: 10572321 DOI: 10.1016/S0924-9338(99)80711-1]
- 58 **Eyler LT**, Olsen RK, Jeste DV, Brown GG. Abnormal brain response of chronic schizophrenia patients despite normal performance during a visual vigilance task. *Psychiatry Res* 2004; **130**: 245-257 [PMID: 15135158 DOI: 10.1016/j.psychres.2004.01.003]
- 59 **Salgado-Pineda P**, Junqué C, Vendrell P, Baeza I, Bargalló N, Falcón C, Bernardo M. Decreased cerebral activation during CPT performance: structural and functional deficits in schizophrenic patients. *Neuroimage* 2004; **21**: 840-847 [PMID: 15006650 DOI: 10.1016/j.neuroimage.2003.10.027]
- 60 **Honey GD**, Pomarol-Clotet E, Corlett PR, Honey RA, McKenna PJ, Bullmore ET, Fletcher PC. Functional dysconnectivity in schizophrenia associated with attentional modulation of motor function. *Brain* 2005; **128**: 2597-2611 [PMID: 16183659 DOI: 10.1093/brain/awh632]
- 61 **Morey RA**, Inan S, Mitchell TV, Perkins DO, Lieberman JA, Belger A. Imaging frontostriatal function in ultra-high-risk, early, and chronic schizophrenia during executive processing. *Arch Gen Psychiatry* 2005; **62**: 254-262 [PMID: 15753238 DOI: 10.1001/archpsyc.62.3.254]
- 62 **Liddle PF**, Laurens KR, Kiehl KA, Ngan ET. Abnormal function of the brain system supporting motivated attention in medicated patients with schizophrenia: an fMRI study. *Psychol Med* 2006; **36**: 1097-1108 [PMID: 16650349 DOI: 10.1017/S0033291706007677]
- 63 **Gur RE**, Turetsky BI, Loughead J, Snyder W, Kohler C, Elliott M, Pratiwadi R, Ragland JD, Bilker WB, Siegel SJ, Kanes SJ, Arnold SE, Gur RC. Visual attention circuitry in schizophrenia investigated with oddball event-related functional magnetic resonance imaging. *Am J Psychiatry* 2007; **164**: 442-449 [PMID: 17329469 DOI: 10.1176/appi.ajp.164.3.442]
- 64 **Harrison BJ**, Yücel M, Pujol J, Pantelis C. Task-induced deactivation of midline cortical regions in schizophrenia assessed with fMRI. *Schizophr Res* 2007; **91**: 82-86 [PMID: 17307337 DOI: 10.1016/j.schres.2006.12.027]
- 65 **Wolf DH**, Turetsky BI, Loughead J, Elliott MA, Pratiwadi R, Gur RE, Gur RC. Auditory Oddball fMRI in Schizophrenia: Association of Negative Symptoms with Regional Hypoactivation to Novel Distractors. *Brain Imaging Behav* 2008; **2**: 132-145 [PMID: 19756228 DOI: 10.1007/s11682-008-9022-7]
- 66 **Filbey FM**, Russell T, Morris RG, Murray RM, McDonald C.

- Functional magnetic resonance imaging (fMRI) of attention processes in presumed obligate carriers of schizophrenia: preliminary findings. *Ann Gen Psychiatry* 2008; **7**: 18 [PMID: 18834530 DOI: 10.1186/1744-859X-7-18]
- 67 **Carter JD**, Bizzell J, Kim C, Bellion C, Carpenter KL, Dichter G, Belger A. Attention deficits in schizophrenia—preliminary evidence of dissociable transient and sustained deficits. *Schizophr Res* 2010; **122**: 104-112 [PMID: 20554160 DOI: 10.1016/j.schres.2010.03.019]
- 68 **Sepede G**, Ferretti A, Perrucci MG, Gambi F, Di Donato F, Nuccetelli F, Del Gratta C, Tartaro A, Salerno RM, Ferro FM, Romani GL. Altered brain response without behavioral attention deficits in healthy siblings of schizophrenic patients: an event-related fMRI study. *Neuroimage* 2010; **49**: 1080-1090 [PMID: 19646537 DOI: 10.1016/j.neuroimage.2009.07.053]
- 69 **Strakowski SM**, Adler CM, Holland SK, Mills N, DelBello MP. A preliminary FMRI study of sustained attention in euthymic, unmedicated bipolar disorder. *Neuropsychopharmacology* 2004; **29**: 1734-1740 [PMID: 15173843]
- 70 **Fleck DE**, Eliassen JC, Durling M, Lamy M, Adler CM, DelBello MP, Shear PK, Cerullo MA, Lee JH, Strakowski SM. Functional MRI of sustained attention in bipolar mania. *Mol Psychiatry* 2012; **17**: 325-336 [PMID: 20975662 DOI: 10.1038/mp.2010.108]
- 71 **Sepede G**, De Berardis D, Campanella D, Perrucci MG, Ferretti A, Serroni N, Moschetta FS, Del Gratta C, Salerno RM, Ferro FM, Di Giannantonio M, Onofri M, Romani GL, Gambi F. Impaired sustained attention in euthymic bipolar disorder patients and non-affected relatives: an fMRI study. *Bipolar Disord* 2012; **14**: 764-779 [PMID: 23036083 DOI: 10.1111/BDI.12007]
- 72 **Badgaiyan RD**, Posner MI. Mapping the cingulate cortex in response selection and monitoring. *Neuroimage* 1998; **7**: 255-260 [PMID: 9597666 DOI: 10.1006/nimg.1998.0326]
- 73 **Hester R**, Fassbender C, Garavan H. Individual differences in error processing: a review and reanalysis of three event-related fMRI studies using the GO/NOGO task. *Cereb Cortex* 2004; **14**: 986-994 [PMID: 15115734 DOI: 10.1093/cercor/bhh059]
- 74 **Kerns JG**, Cohen JD, MacDonald AW, Cho RY, Stenger VA, Carter CS. Anterior cingulate conflict monitoring and adjustments in control. *Science* 2004; **303**: 1023-1026 [PMID: 14963333 DOI: 10.1126/science.1089910]
- 75 **Eisenberg DP**, Berman KF. Executive function, neural circuitry, and genetic mechanisms in schizophrenia. *Neuropsychopharmacology* 2010; **35**: 258-277 [PMID: 19693005 DOI: 10.1038/npp.2009.111]
- 76 **Rasetti R**, Weinberger DR. Intermediate phenotypes in psychiatric disorders. *Curr Opin Genet Dev* 2011; **21**: 340-348 [PMID: 21376566 DOI: 10.1016/j.gde.2011.02.003]
- 77 **Blasi G**, Taurisano P, Papazacharias A, Caforio G, Romano R, Lobianco L, Fazio L, Di Giorgio A, Latorre V, Sambataro F, Papolizio T, Nardini M, Mattay VS, Weinberger DR, Bertolino A. Nonlinear response of the anterior cingulate and prefrontal cortex in schizophrenia as a function of variable attentional control. *Cereb Cortex* 2010; **20**: 837-845 [PMID: 19633177 DOI: 10.1093/cercor/bhp146]
- 78 **Laurens KR**, Ngan ET, Bates AT, Kiehl KA, Liddle PF. Rostral anterior cingulate cortex dysfunction during error processing in schizophrenia. *Brain* 2003; **126**: 610-622 [PMID: 12566282 DOI: 10.1093/brain/awg056]
- 79 **Kerns JG**, Cohen JD, MacDonald AW, Johnson MK, Stenger VA, Aizenstein H, Carter CS. Decreased conflict- and error-related activity in the anterior cingulate cortex in subjects with schizophrenia. *Am J Psychiatry* 2005; **162**: 1833-1839 [PMID: 16199829 DOI: 10.1176/appi.ajp.162.10.1833]
- 80 **Polli FE**, Barton JJ, Thakkar KN, Greve DN, Goff DC, Rauch SL, Manoach DS. Reduced error-related activation in two anterior cingulate circuits is related to impaired performance in schizophrenia. *Brain* 2008; **131**: 971-986 [PMID: 18158315 DOI: 10.1093/brain/awm307]
- 81 **Sambataro F**, Mattay VS, Thurin K, Safrin M, Rasetti R, Blasi G, Callicott JH, Weinberger DR. Altered cerebral response during cognitive control: a potential indicator of genetic liability for schizophrenia. *Neuropsychopharmacology* 2013; **38**: 846-853 [PMID: 23299932 DOI: 10.1038/npp.2012.250]
- 82 **Barch DM**, Carter CS, Braver TS, Sabb FW, MacDonald A, Noll DC, Cohen JD. Selective deficits in prefrontal cortex function in medication-naive patients with schizophrenia. *Arch Gen Psychiatry* 2001; **58**: 280-288 [PMID: 11231835 DOI: 10.1001/archpsyc.58.3.280]
- 83 **Henseler I**, Falkai P, Gruber O. A systematic fMRI investigation of the brain systems subserving different working memory components in schizophrenia. *Eur J Neurosci* 2009; **30**: 693-702 [PMID: 19686473 DOI: 10.1111/j.1460-9568.2009.06850.x]
- 84 **Karch S**, Leicht G, Giegling I, Lutz J, Kunz J, Buselmeier M, Hey P, Spörl A, Jäger L, Meindl T, Pogarell O, Möller HJ, Hegerl U, Rujescu D, Mülert C. Inefficient neural activity in patients with schizophrenia and nonpsychotic relatives of schizophrenic patients: evidence from a working memory task. *J Psychiatr Res* 2009; **43**: 1185-1194 [PMID: 19426993 DOI: 10.1016/j.jpsychires.2009.04.004]
- 85 **Sass K**, Heim S, Sachs O, Straube B, Schneider F, Habel U, Kircher T. Neural correlates of semantic associations in patients with schizophrenia. *Eur Arch Psychiatry Clin Neurosci* 2014; **264**: 143-154 [PMID: 23880958]
- 86 **Buckner RL**, Andrews-Hanna JR, Schacter DL. The brain's default network: anatomy, function, and relevance to disease. *Ann N Y Acad Sci* 2008; **1124**: 1-38 [PMID: 18400922 DOI: 10.1196/annals.1440.011]
- 87 **Leech R**, Sharp DJ. The role of the posterior cingulate cortex in cognition and disease. *Brain* 2014; **137**: 12-32 [PMID: 23869106]
- 88 **Mitelman SA**, Shihabuddin L, Brickman AM, Hazlett EA, Buchsbaum MS. Volume of the cingulate and outcome in schizophrenia. *Schizophr Res* 2005; **72**: 91-108 [PMID: 15560955 DOI: 10.1016/j.schres.2004.02.011]
- 89 **Tendolkar I**, Weis S, Guddat O, Fernández G, Brockhaus-Dumke A, Specht K, Klosterkötter J, Reul J, Ruhrmann S. Evidence for a dysfunctional retrosplenial cortex in patients with schizophrenia: a functional magnetic resonance imaging study with a semantic-perceptual contrast. *Neurosci Lett* 2004; **369**: 4-8 [PMID: 15380297 DOI: 10.1016/j.neulet.2004.07.024]
- 90 **Bedford NJ**, Surguladze S, Giampietro V, Brammer MJ, David AS. Self-evaluation in schizophrenia: an fMRI study with implications for the understanding of insight. *BMC Psychiatry* 2012; **12**: 106 [PMID: 22876974 DOI: 10.1186/1471-244X-12-106]
- 91 **van der Meer L**, de Vos AE, Stiekema AP, Pijnenborg GH, van Tol MJ, Nolen WA, David AS, Aleman A. Insight in schizophrenia: involvement of self-reflection networks? *Schizophr Bull* 2013; **39**: 1288-1295 [PMID: 23104865 DOI: 10.1093/schbul/sbs122]
- 92 **Holt DJ**, Coombs G, Zeidan MA, Goff DC, Milad MR. Failure of neural responses to safety cues in schizophrenia. *Arch Gen Psychiatry* 2012; **69**: 893-903 [PMID: 22945619 DOI: 10.1001/archgenpsychiatry.2011.2310]
- 93 **Coull JT**. Neural correlates of attention and arousal: insights from electrophysiology, functional neuroimaging and psychopharmacology. *Prog Neurobiol* 1998; **55**: 343-361 [PMID: 9654384 DOI: 10.1016/S0301-0082(98)00011-2]
- 94 **Sherman SM**, Guillery RW. Exploring the role of the thalamus and its role in cortical function. Cambridge: MIT Press, 2006
- 95 **Sim K**, Cullen T, Ongur D, Heckers S. Testing models of thalamic dysfunction in schizophrenia using neuroimaging. *J Neural Transm* 2006; **113**: 907-928 [PMID: 16252070 DOI: 10.1007/s00702-005-0363-8]

- 96 **Cronenwett WJ**, Csernansky J. Thalamic pathology in schizophrenia. *Curr Top Behav Neurosci* 2010; **4**: 509-528 [PMID: 21312411 DOI: 10.1007/7854_2010_55]
- 97 **Byne W**, Hazlett EA, Buchsbaum MS, Kemether E. The thalamus and schizophrenia: current status of research. *Acta Neuropathol* 2009; **117**: 347-368 [PMID: 18604544 DOI: 10.1007/s00401-008-0404-0]
- 98 **Shepherd AM**, Laurens KR, Matheson SL, Carr VJ, Green MJ. Systematic meta-review and quality assessment of the structural brain alterations in schizophrenia. *Neurosci Biobehav Rev* 2012; **36**: 1342-1356 [PMID: 22244985 DOI: 10.1016/j.neubiorev.2011.12.015]
- 99 **LeDoux JE**. Emotion circuits in the brain. *Annu Rev Neurosci* 2000; **23**: 155-184 [PMID: 10845062 DOI: 10.1146/annurev.neuro.23.1.155]
- 100 **Altshuler L**, Bookheimer S, Proenza MA, Townsend J, Sabb F, Firestone A, Bartzokis G, Mintz J, Mazziotta J, Cohen MS. Increased amygdala activation during mania: a functional magnetic resonance imaging study. *Am J Psychiatry* 2005; **162**: 1211-1213 [PMID: 15930074 DOI: 10.1176/appi.ajp.162.6.1211]
- 101 **Foland LC**, Altshuler LL, Bookheimer SY, Eisenberger N, Townsend J, Thompson PM. Evidence for deficient modulation of amygdala response by prefrontal cortex in bipolar mania. *Psychiatry Res* 2008; **162**: 27-37 [PMID: 18063349 DOI: 10.1016/j.psychres.2007.04.007]
- 102 **Bermopohl F**, Dalanay U, Kahnt T, Sajonz B, Heimann H, Ricken R, Stoy M, Hägele C, Schlagenhaut F, Adli M, Wrase J, Ströhle A, Heinz A, Bauer M. A preliminary study of increased amygdala activation to positive affective stimuli in mania. *Bipolar Disord* 2009; **11**: 70-75 [PMID: 19133968 DOI: 10.1111/j.1399-5618.2008.00648.x]
- 103 **Strakowski SM**, Eliassen JC, Lamy M, Cerullo MA, Allendorfer JB, Madore M, Lee JH, Welge JA, DelBello MP, Fleck DE, Adler CM. Functional magnetic resonance imaging brain activation in bipolar mania: evidence for disruption of the ventrolateral prefrontal-amygdala emotional pathway. *Biol Psychiatry* 2011; **69**: 381-388 [PMID: 21051038 DOI: 10.1016/j.biopsych.2010.09.019]
- 104 **Malhi GS**, Lagopoulos J, Ward PB, Kumari V, Mitchell PB, Parker GB, Ivanovski B, Sachdev P. Cognitive generation of affect in bipolar depression: an fMRI study. *Eur J Neurosci* 2004; **19**: 741-754 [PMID: 14984424 DOI: 10.1111/j.0953-816X.2003.03159.x]
- 105 **Lagopoulos J**, Malhi GS. A functional magnetic resonance imaging study of emotional Stroop in euthymic bipolar disorder. *Neuroreport* 2007; **18**: 1583-1587 [PMID: 17885606 DOI: 10.1097/WNR.0b013e3282efa07a]
- 106 **Surguladze SA**, Marshall N, Schulze K, Hall MH, Walshe M, Bramon E, Phillips ML, Murray RM, McDonald C. Exaggerated neural response to emotional faces in patients with bipolar disorder and their first-degree relatives. *Neuroimage* 2010; **53**: 58-64 [PMID: 20595014 DOI: 10.1016/j.neuroimage.2010.05.069]
- 107 **Gruber O**, Tost H, Sessler I, Schmael C, Scherk H, Ende G, Ruf M, Falkai P, Rietschel M. Pathological amygdala activation during working memory performance: Evidence for a pathophysiological trait marker in bipolar affective disorder. *Hum Brain Mapp* 2010; **31**: 115-125 [PMID: 19603410 DOI: 10.1002/hbm.20849]
- 108 **Mutschler I**, Wieckhorst B, Kowalewski S, Derix J, Wentlandt J, Schulze-Bonhage A, Ball T. Functional organization of the human anterior insular cortex. *Neurosci Lett* 2009; **457**: 66-70 [PMID: 19429164 DOI: 10.1016/j.neulet.2009.03.101]
- 109 **Menon V**, Uddin LQ. Saliency, switching, attention and control: a network model of insula function. *Brain Struct Funct* 2010; **214**: 655-667 [PMID: 20512370 DOI: 10.1007/s00429-010-0262-0]
- 110 **Pujol N**, Penadés R, Rametti G, Catalán R, Vidal-Piñero D, Palacios E, Bargallo N, Bernardo M, Junqué C. Inferior frontal and insular cortical thinning is related to dysfunctional brain activation/deactivation during working memory task in schizophrenic patients. *Psychiatry Res* 2013; **214**: 94-101 [PMID: 23993992 DOI: 10.1016/j.psychres.2013.06.008]
- 111 **Vu MA**, Thermenos HW, Terry DP, Wolfe DJ, Voglmaier MM, Niznikiewicz MA, McCarley RW, Seidman LJ, Dickey CC. Working memory in schizotypal personality disorder: fMRI activation and deactivation differences. *Schizophr Res* 2013; **151**: 113-123 [PMID: 24161536 DOI: 10.1016/j.schres.2013.09.013]
- 112 **Linnman C**, Coombs G, Goff DC, Holt DJ. Lack of insula reactivity to aversive stimuli in schizophrenia. *Schizophr Res* 2013; **143**: 150-157 [PMID: 23201307 DOI: 10.1016/j.schres.2012.10.038]
- 113 **Hummer TA**, Hulvershorn LA, Karne HS, Gunn AD, Wang Y, Anand A. Emotional response inhibition in bipolar disorder: a functional magnetic resonance imaging study of trait- and state-related abnormalities. *Biol Psychiatry* 2013; **73**: 136-143 [PMID: 22871393 DOI: 10.1016/j.biopsych.2012.06.036]
- 114 **Cooper D**, Barker V, Radua J, Fusar-Poli P, Lawrie SM. Multimodal voxel-based meta-analysis of structural and functional magnetic resonance imaging studies in those at elevated genetic risk of developing schizophrenia. *Psychiatry Res* 2014; **221**: 69-77 [PMID: 24239093 DOI: 10.1016/j.psychres.2013.07.008]
- 115 **Palaniyappan L**, Simmonite M, White TP, Liddle EB, Liddle PF. Neural primacy of the salience processing system in schizophrenia. *Neuron* 2013; **79**: 814-828 [PMID: 23972602 DOI: 10.1016/j.neuron.2013.06.027]
- 116 **Moran LV**, Tagamets MA, Sampath H, O'Donnell A, Stein EA, Kochunov P, Hong LE. Disruption of anterior insula modulation of large-scale brain networks in schizophrenia. *Biol Psychiatry* 2013; **74**: 467-474 [PMID: 23623456 DOI: 10.1016/j.biopsych.2013.02.029]
- 117 **He Z**, Deng W, Li M, Chen Z, Jiang L, Wang Q, Huang C, Collier DA, Gong Q, Ma X, Zhang N, Li T. Aberrant intrinsic brain activity and cognitive deficit in first-episode treatment-naïve patients with schizophrenia. *Psychol Med* 2013; **43**: 769-780 [PMID: 22883428 DOI: 10.1017/S0033291712001638]
- 118 **Vargas C**, López-Jaramillo C, Vieta E. A systematic literature review of resting state network--functional MRI in bipolar disorder. *J Affect Disord* 2013; **150**: 727-735 [PMID: 23830141 DOI: 10.1016/j.jad.2013.05.083]
- 119 **Whalley HC**, Sussmann JE, Romaniuk L, Stewart T, Papmeyer M, Sprooten E, Hackett S, Hall J, Lawrie SM, McIntosh AM. Prediction of depression in individuals at high familial risk of mood disorders using functional magnetic resonance imaging. *PLoS One* 2013; **8**: e57357 [PMID: 23483904 DOI: 10.1371/journal.pone.0057357]

P- Reviewer: Serafini G S- Editor: Wen LL

L- Editor: A E- Editor: Zhang DN



Neuroimaging in Huntington's disease

Flavia Niccolini, Marios Politis

Flavia Niccolini, Marios Politis, Neurodegeneration Imaging Group, Department of Clinical Neuroscience, King's College London, London SE5 8AF, United Kingdom

Flavia Niccolini, Marios Politis, Division of Brain Sciences, Department of Medicine, Hammersmith Hospital, Imperial College London, London W12 0NN, United Kingdom

Author contributions: Niccolini F collected the materials for the literature review and wrote the first draft of the manuscript; Politis M reviewed and edited this article.

Correspondence to: Marios Politis, MD, MSc, PhD, Senior Clinical Lecturer, Head of the Neurodegeneration Imaging Group, Department of Clinical Neuroscience, King's College London, 16 De Crespigny Park, London SE5 8AF, United Kingdom. marios.politis@kcl.ac.uk

Telephone: +44-207-8485682 Fax: +44-207-8480988

Received: December 11, 2013 Revised: February 28, 2014

Accepted: May 8, 2014

Published online: March 28, 2015

Abstract

Huntington's disease (HD) is a progressive and fatal neurodegenerative disorder caused by an expanded trinucleotide CAG sequence in huntingtin gene (HTT) on chromosome 4. HD manifests with chorea, cognitive and psychiatric symptoms. Although advances in genetics allow identification of individuals carrying the HD gene, much is still unknown about the mechanisms underlying the development of overt clinical symptoms and the transitional period between premanifestation and manifestation of the disease. HD has no cure and patients rely only in symptomatic treatment. There is an urgent need to identify biomarkers that are able to monitor disease progression and assess the development and efficacy of novel disease modifying drugs. Over the past years, neuroimaging techniques such as magnetic resonance imaging (MRI) and positron emission tomography (PET) have provided important advances in our understanding of HD. MRI provides information about structural and functional organization of the brain, while PET can detect molecular changes in the brain. MRI and PET are able to detect changes in the brains of HD gene carriers years ahead of the manifestation of the dis-

ease and have also proved to be powerful in assessing disease progression. However, no single technique has been validated as an optimal biomarker. An integrative multimodal imaging approach, which combines different MRI and PET techniques, could be recommended for monitoring potential neuroprotective and preventive therapies in HD. In this article we review the current neuroimaging literature in HD.

© 2015 Baishideng Publishing Group Inc. All rights reserved.

Key words: Huntington's disease; Premanifest Huntington's disease gene carriers; Functional magnetic resonance imaging; Magnetic resonance imaging; Positron emission tomography

Core tip: Huntington's disease (HD) is a hereditary and fatal neurodegenerative disorder. Although advances in genetics allow identification of individuals carrying the HD gene, much is still unknown about the mechanisms underlying the development of overt clinical symptoms and the transitional period between premanifestation and manifestation of the disease. Neuroimaging techniques such as magnetic resonance imaging and positron emission tomography may be a suitable biomarker for monitoring disease progression in HD and for assessing the efficacy of future disease modifying therapies. In this article, we provide an overview of the findings from neuroimaging techniques in HD.

Original sources: Niccolini F, Politis M. Neuroimaging in Huntington's disease. *World J Radiol* 2014; 6(6): 301-312 Available from: URL: <http://www.wjgnet.com/1949-8470/full/v6/i6/301.htm> DOI: <http://dx.doi.org/10.4329/wjr.v6.i6.301>

INTRODUCTION

Huntington's disease (HD) is an inherited neurodegenerative disorder characterised by chorea, cognitive dysfunction and psychiatric symptoms caused by an expanded

trinucleotide CAG sequence in huntingtin gene (HTT), which is on chromosome 4^[1]. HD prevalence varies by ethnic origin and different genetic profiles, in Caucasian populations of North America and Western Europe is 5.70 per 100000 whereas in Asian population is lower (0.40 per 100000)^[2]. Although juvenile onset and late onset of HD are not uncommon, the disease usually appears at mid-40s, and there is an inverse correlation between age of onset and the size of the CAG repeat expansion^[3]. However, subclinical changes and pathological processes are thought to precede the initiation of symptoms by several years^[4,5].

HD pathology is characterised by the formation of intranuclear inclusions of mutated huntingtin in the brain. These aggregates have been shown to interact and impair the function of a number of transcription factors leading to the loss of GABAergic medium spiny neurons (MSNs) in the striatum but also in cortical areas^[6,7]. Currently there is no proven biomarker for HD, no effective treatment, and the disease will eventually lead to death, typically 15-20 years following symptomatic onset^[8]. Much is still unknown about the mechanisms that underlie the clinical symptoms and the rate of progression from pre-clinical signs to development of overt symptoms.

Neuroimaging techniques such as magnetic resonance imaging (MRI) and functional MRI (fMRI) have played a critical role in characterizing structural and functional changes in the brain during the asymptomatic and symptomatic stage of the disease. PET imaging, by measuring the distribution of a radionuclide (radioligand) that is introduced into the body on a biologically active molecule, is a powerful technique for investigating *in vivo* abnormalities in brain metabolism and receptor distributions^[9]. This analytical imaging method has the potential to give both structural and kinetic information and in comparison with other imaging techniques, provides high sensitivity, and high spatial and temporal resolution^[10]. PET with the application of different radioligands has been used to measure metabolic changes in the brain of HD several years before disease onset (Table 1). In this article, we provide an overview of the findings from neuroimaging techniques in HD.

LITERATURE RESEARCH

PubMed was searched for papers that were published before December 2013. The following key words were used in the search: "Huntington's disease", "positron emission tomography", "magnetic resonance imaging", "functional magnetic imaging". Additional papers were identified from citations in the articles found in PubMed. Only articles published in English were considered. A total number of 37 MRI and 49 PET studies were reviewed.

MRI

Structural MRI studies

The most consistent change in the HD brain is a significant progressive volumetric loss of the striatum^[4,11-20]. A

reduction of 50%-54% in mean putamen volume and 28%-29% in mean caudate volume has been reported in patients with mild to moderate HD^[11,12]. Striatal atrophy has been also documented in early HD patients with Total Functional Capacity (TFC) scores between I-II^[14,15] and in premanifest HD gene carriers who were even 15-20 years before predicted disease onset^[4,13,16-20]. The amount of volume loss in the striatum correlates with the age of onset, the disease duration and the CAG repeat length^[14,15,21]. While motor impairment correlates with increased putamen atrophy, Mini-Mental Status Examination scores (MMSE) and cognitive assessments are inversely correlated with the amount of caudate volume loss^[11,12].

Cortical volume loss has been also reported in HD patients^[17-20,22,23]. Cortical thinning occurs early during the course of the disease and seems to be topographically selective proceeding from posterior to anterior cortical regions as the disease progresses^[22,23]. Individual variability in regional cortical thinning may also have a role in explaining phenotypic variability. For example, HD patients with more prominent bradykinesia showed significant cortical volume loss in frontal regions including the pre-motor and supplementary motor areas compared to HD patients with chorea^[23]. Additionally, regional cortical atrophy correlates with clinical measures such as TFC, Unified HD rating scale (UHDRS) and cognitive tests enhancing the role of this measurement as potential biomarker for assessing neuroprotective therapies^[23]. Widespread white matter (WM) atrophy has been identified in HD patients and has been associated with longer CAG length and decline in cognitive and motor performance^[24]. Changes in WM volume are detectable up to 12-15 years before the predicted onset and correlate with cognitive functions underlining the role of structural connectivity degeneration in the pathogenesis of HD^[25]. Diffusion tensor imaging (DTI) studies have also reported WM tract abnormalities in premanifest HD gene carriers and alterations in diffusion indices were correlated with cognitive performance^[26-28]. Dumas and coworkers^[28] have found abnormal WM connections of the sensori-motor cortex, which correlated with the 5-year probability for symptomatic conversion.

TRACK-HD is a multicentre longitudinal study, which focused in identifying sensitive and reliable biomarkers in premanifest HD gene carriers and early HD patients^[17-20]. Four groups were enrolled in TRACK-HD: 120 premanifest HD gene carriers which were subdivided in pre-HD A and pre-HD B according to the proximity to predicted disease onset (pre-HD A > 10.8 years; pre-HD B < 10.8 years), and 123 early HD patients subdivided in two groups according to the TFC scores (HD stage I, HD stage II). At 12 months follow-up significantly increased total brain volume atrophy rates were reported in both premanifest HD gene carriers and early HD patients. Caudate and putamen volume was reported reduced by 1.4% to 4.5% compared with baseline in premanifest and early HD group. Atrophy of WM was also increased in all groups^[18]. Over 24 mo, greater increases

Table 1 Key positron emission tomography imaging studies in Huntington's disease

Ref.	Subjects	PET radiopharmaceutical	Main findings
Dopaminergic system			
Ginovart <i>et al</i> ^[56] , 1997	5 HD patients 5 HCs	¹¹ C-b-CIT ¹¹ C-SCH23390 ¹¹ C-raclopride	50% decrease in striatal dopamine transporter (DAT) binding. 40% decrease in striatal D1 and D2 receptors binding. D1 and D2 binding in the striatum was significantly associated with the duration of symptoms Reduced D1 receptors binding in the temporal cortex
Bohnen <i>et al</i> ^[57] , 2000	19 HD patients 64 HCs	¹¹ C-DTBZ	Reduced nigrostriatal density of VMAT2 (caudate: 33%, putamen: 56%-75%)
Sedvall <i>et al</i> ^[58] , 1994	5 HD patients 1 premanifest <i>HD</i> gene carrier 5 HCs	¹¹ C-SCH 23390	75% reduction in striatal D1 receptor density in HD patients D1 binding in the premanifest <i>HD</i> gene carrier was in the lower range of the HCs
Turjanski <i>et al</i> ^[55] , 1995	10 HD patients 9 HCs for ¹¹ C-raclopride and 6 HCs for ¹¹ C-SCH 23390	¹¹ C-SCH 23390 ¹¹ C-raclopride	Parallel reduction of striatal D1 and D2 receptor binding (31%-39%) with greater loss of mean striatal D1 and D2 binding in the akinetic-rigid patients than those choreic patients without rigidity
Lawrence <i>et al</i> ^[60] , 1998	17 premanifest <i>HD</i> gene carriers	¹¹ C-SCH 23390 ¹¹ C-raclopride	Correlation between striatal D1 and D2 receptors binding and cognitive performance
Pavese <i>et al</i> ^[61] , 2003	12 HD patients HCs from previous studies	¹¹ C-raclopride	4.8% annual reduction in striatal D2 receptor binding D2 reduction receptor density in extrastriatal regions including amygdala, temporal and frontal cortex
Andrews <i>et al</i> ^[64] , 1999	9 premanifest <i>HD</i> gene carriers 4 HD patients 7 HCs 3 subjects at risk for HD	¹¹ C-SCH 23390 ¹¹ C-raclopride	Mean annual loss of D1 and D2 binding of 2% and 4% respectively in the group of asymptomatic <i>HD</i> gene carriers Mean annual loss of D1 binding of 5% and D2 binding of 3% in symptomatic HD patients UHDRS motor scores and TFC correlated with PET measures of striatal dopamine receptor in both groups Premanifest <i>HD</i> gene carriers with active progression had an increased mean annual loss of D1 and D2 receptor binding (5% and 6.5% respectively)
Pavese <i>et al</i> ^[62] , 2010	16 HD patients 11 premanifest <i>HD</i> gene carriers HCs from previous studies	¹¹ C-raclopride	62.5% of symptomatic HD patients and 54.5% of premanifest carriers showed cortical reductions in D2 binding HD patients with decreased cortical D2 binding had worse scores on neuropsychological tests assessing attention and executive functions than subjects without cortical dopamine dysfunction
Antonini <i>et al</i> ^[66] , 1998	10 premanifest gene carriers 8 HD patients	¹¹ C-raclopride	Correlation between CAG repeat length and the estimated percentage loss of striatal D2 binding after age correction in premanifest <i>HD</i> gene carriers and HD patients Rate of disease progression is faster during the earlier asymptomatic stages of the disease
Brain activation and metabolism			
Antonini <i>et al</i> ^[65] , 1996	10 premanifest <i>HD</i> gene carriers 8 HD patients HCs from previous studies	¹⁸ F-FDG ¹¹ C-raclopride	Annual loss of 2.3% in striatal glucose metabolism and 6.3% annual decline in D2 receptor binding
Kuwert <i>et al</i> ^[75] , 1990	23 HD patients 21 HCs	¹⁸ F-FDG	Decreases of caudate and regional cortical metabolism correlated with cognitive decline
Ciarmiello <i>et al</i> ^[79] , 2006	24 premanifest <i>HD</i> gene carriers 47 HD patients 30 HCs	¹⁸ F-FDG	Significant decrease in glucose uptake in the cortex (frontal and temporal lobes) and striatum in both premanifest <i>HD</i> gene carriers and HD patients Striatal and cortical hypometabolism in premanifest <i>HD</i> gene carriers precedes neuronal loss
Ciarmiello <i>et al</i> ^[80] , 2012	43 premanifest <i>HD</i> gene carriers	¹⁸ F-FDG	Premanifest <i>HD</i> gene carriers who phenoconverted after five years from the PET scan had a mean glucose uptake in the caudate significantly lower than the those who remained symptom-free after five years
Weeks <i>et al</i> ^[83] , 1997	7 HD patients 7 HCs	H ₂ ¹⁵ O	Impaired activation of the striatum and its frontal motor projection areas during motor tasks such as paced joystick movements
Tang <i>et al</i> ^[87] , 2013	12 premanifest <i>HD</i> gene carriers 12 HCs	¹⁸ F-FDG ¹¹ C-raclopride	Network analysis showed a significant spatial covariance pattern characterized by progressive changes in striato-thalamic and cortical metabolic activity network activity increased linearly over 7 yr and was not influenced by intercurrent phenoconversion
Neuroinflammation and activated microglia			
Pavese <i>et al</i> ^[99] , 2006	11 HD patients 10 HCs	¹¹ C-PK11195 ¹¹ C-raclopride	Significant microglial activation in the striatum and cortical regions of HD patients Striatal ¹¹ C-PK11195 binding correlates with loss of striatal dopamine D2 binding

Tai <i>et al.</i> ^[100] , 2007	11 premanifest <i>HD</i> gene carriers 10 HCs	¹¹ C-PK11195 ¹¹ C-raclopride	Striatal ¹¹ C-PK11195 binding correlated with UHDRS scores Increased striatal and cortical microglial activation in premanifest <i>HD</i> gene carriers Higher striatal ¹¹ C-PK11195 binding correlated with lower striatal D2 binding
Politis <i>et al.</i> ^[101] , 2011	8 premanifest <i>HD</i> gene carriers 8 HCs (¹¹ C-raclopride) 8 HCs (¹¹ C-PK11195)	¹¹ C-PK11195 ¹¹ C-raclopride	Increased levels of activated microglia in areas of the striatum associated with cognition and other areas related to cognitive function Levels of microglial activation correlated with clinical scales of disease severity and motor dysfunction and with a higher probability of HD onset over the next 5 yr
Cannabinoid system Van Laere <i>et al.</i> ^[111] , 2010	20 HD patients 14 HCs	¹⁸ FMK-9470	Decrease of CB1 availability throughout the gray matter of the cerebrum, cerebellum, and brain stem in HD patients.

PET: Positron emission tomography; HD: Huntington’s disease.

in caudate and putamen atrophy were observed in all four subgroups. Higher rates of whole brain and grey matter (GM) loss were reported in pre-HD B, HD-I and HD-II; whereas in the pre-HD A GM atrophy was confined to the striatum. Interestingly, WM atrophy around the striatum and within the corpus callosum and posterior WM tract was observed even in the earliest premanifest stage^[19]. At 36 mo, early HD patients showed further significant increases in whole brain, caudate, putamen and GM atrophy and these measures were strongly associated to TFC decline. Although in pre-HD A group increased rates of whole brain, striatal and WM atrophy were observed, these were not accompanied by progressive worsening of motor and cognitive performance. On the contrary, pre-HD B showed higher rates of brain structural loss compared to pre-HD A group and these were associated with significant decline in several motor and cognitive tests. Furthermore, striatal and GM volume measures were sensitive predictors of subsequent clinical diagnosis of HD in the pre-HD B group^[20]. Taken together, these findings suggest that MRI measures are able to track pathology in premanifest and manifest *HD* gene carriers and could be useful for the designing of future clinical trials.

Functional MRI studies

There is growing evidence that the severity of clinical manifestations in HD does not depend only on neuronal loss but also on neuronal dysfunction and circuitry reorganization, and these processes may occur at an early stage of the disease, possibly prior to neurodegeneration. Functional neuroimaging approaches such as functional MRI (fMRI) provide a dynamic images of the brain aiding to elucidate neural activity by measuring haemodynamic response (blood flow) of neural activation. Data from manifest HD patients have shown reduced task-activation in several subcortical and cortical regions as well as increased activation in different cortical areas, which were interpreted as a compensatory mechanism for task performances^[29-34]. Interestingly, in premanifest *HD* gene carriers further from disease onset increased activation in several brain regions was observed, whereas premanifest *HD* gene carriers closer to disease onset showed reduced activation in the striatum^[35-38]. Using fMRI and

a group independent component analysis, Unschuld and colleagues^[39] investigated networks of functional connectivity while performing a Stroop colour-naming task in both healthy controls and premanifest *HD* gene carriers and correlated with depressive symptoms. Stroop related activity of the ventromedial prefrontal cortex was more significantly correlated with depressive symptoms in premanifest *HD* gene carriers than healthy controls. This correlation was stronger in the premanifest HD subgroup with CAG repeat length greater than 42^[39]. Using a Tower of London fMRI task, the same group found significantly reduced functional coupling between the medial prefrontal cortex area and the left premotor cortex in a group of premanifest HD gene carriers and early manifest HD subjects^[40]. These findings suggest that impaired brain network connectivity reflects cognitive and mood dysfunction in HD subject even at the earlier stage of the disease. Recently, studies have been focused in investigating functional brain connectivity patterns at rest with fMRI (resting state fMRI). This approach has the potential to give insight into functional changes without the interference of cognitive ability to perform a given task^[41,42]. Resting state fMRI data have shown intrinsic reductions in functional connectivity in both premanifest and manifest *HD* gene carriers^[43-45]. In premanifest HD gene carriers reduced blood-oxygen-level-dependent (BOLD) synchrony was observed between the caudate and premotor cortex^[46]. Using a method that measures changes in synchrony in BOLD signal amplitude and across space, Poudel and coworkers^[44] have found several abnormal networks in both premanifest and manifest HD subjects. For example, they have reported a decreased resting state synchronization in the sensori-motor network of premanifest *HD* gene carriers, and interestingly, the level of synchrony was associated with motor performance as measured by speeded self-paced tapping^[44]. Overall these findings show abnormal functional network connectivity in both premanifest and manifest HD, suggesting that resting state fMRI may be useful in measuring early neuronal dysfunction and for monitoring progression of the disease.

Neurovascular alterations have been also found in premanifest *HD* gene carriers. Cortical arteriolar cerebral blood volume (CBV_a) was significantly elevated in pre-

manifest *HD* gene carriers compared to normal controls and correlated with genetic measures such as the CAG-age product score and the estimated years to onset^[47]. Metabolic brain changes may also occur in premanifest *HD* gene carriers and they may precede structural brain changes^[48]. N-acetylaspartate (NAA) and glutamate levels were decreased in the posterior cingulate cortex of 12 premanifest *HD* gene carriers and they correlated with cognitive decline as measured with the Montreal Cognitive Assessment^[47]. Neurovascular alterations and metabolic brain changes occurs before substantial brain atrophy suggesting that they may be used as potential biomarker for clinical and therapeutic future studies.

PET

Dopaminergic system

Altered dopamine signalling may play a key role in the pathogenesis of *HD*^[49,50]. In particular, striatal MSNs expressing dopamine receptors are primarily affected in *HD*, whereas presynaptic dopaminergic nerve terminals are relatively spared^[51]. PET studies in premanifest and manifest *HD* gene carriers have shown severe involvement of the postsynaptic dopaminergic system, whereas the dopaminergic nerve terminals seem to be less affected^[52-55]. An ¹⁸F-fluorodopa case-study did not demonstrate diminished striatal dopamine synthesis capacity suggesting an intact nigrostriatal pathway^[52]. However, Ginovart and coworker^[56], using PET with ¹¹C-b-CIT, have found a 50% decrease in striatal dopamine transporter (DAT) binding. In line with this finding, nigrostriatal density of the type-2 vesicular monoamine transporter (VMAT2) was found reduced in *HD* patients^[57]. It still remains unclear whether degeneration of nigrostriatal dopaminergic neurons or presynaptic terminal dysfunction takes place in *HD*.

Investigations of postsynaptic dopaminergic systems, specifically the role of D1 and D2 receptors, which are highly expressed in MSNs, have shown reduced receptor densities and activity in the striatum of *HD* patients even at the early stage of the disease. The radioligand ¹¹C-SCH23390 is a selective antagonist of D1 receptors while ¹¹C-raclopride is a selective reversible antagonist of D2 receptors. Striatal D1-dopamine receptor density was found reduced by 75% in five *HD* patients with mild to moderate disease compared to a group of healthy controls^[58]. Additionally, one premanifest *HD* gene carrier showed D1 binding in the lower range of the control subjects^[58]. Turjanski and colleagues^[55] have studied 10 non-neuroleptic treated patients with *HD* with either the choreic or the akinetic-rigid predominant phenotypes of the disease. They found severe parallel reduction of striatal D1 and D2 receptor binding with greater loss of mean striatal D1 and D2 binding in the akinetic-rigid patients than those choreic patients without rigidity^[55]. However, there were no significant correlations between D1 and D2 striatal receptor binding and the duration of symptoms. Mean ¹¹C-SCH23390 and ¹¹C-raclopride bind-

ing was found to be reduced by 40% in the striatum of five patients with *HD*^[56]. The degree of the decrease in D1 and D2 binding in the striatum was significantly associated with the duration of symptoms indicating that these two receptors may be reliable quantitative markers for monitoring disease progression^[56]. Moreover, a reduction in D1 receptor binding was found also in the temporal cortex suggesting that dopaminergic abnormalities occur in cortical areas and may play a role in the development of cognitive dysfunction observed in *HD*^[56]. Specifically, striatal D1 and D2 receptor density showed strong relationships with performance in several tasks assessing executive function, visuospatial ability, episodic memory, verbal fluency, perceptual speed and reasoning in a group of five *HD* patients^[59]. Thus, cortico-striatal and/or thalamo-cortical circuitry may be associated with cognitive impairment in *HD*^[59]. A correlation between striatal D1 and D2 receptors binding, but mainly D2, and cognitive performance was found also in 17 premanifest *HD* gene carriers, in whom both striatal dopamine receptor levels and cognitive performance were lower in the subjects closer to the predicted disease onset^[60]. Using ¹¹C-raclopride PET and statistical parametric mapping, Pavese and coworkers^[61] have found a reduction in D2 receptor density in cortical regions of symptomatic *HD* patients, which were also evident in frontal and/or temporal regions in 55% of premanifest *HD* gene carriers^[62], suggesting that changes in cortical D2 receptor availability might be an early event in *HD* pathophysiology. Van Oostrom and colleagues^[63] have also reported a reduction in striatal D2 receptor availability in 50% of premanifest *HD* gene carriers and these reductions correlated with increases in cumulative disease load as measured by disease burden (CAG index).

Clinically manifested *HD* patients have been shown to have constant loss of D2 receptor availability at around 5% per year in striatal and extrastriatal regions including frontal and temporal cortex, though no correlation between changes in UHDRS motor scores and reductions in striatal binding were observed^[61]. Longitudinal ¹¹C-raclopride PET studies in premanifest *HD* gene carriers have reported rates of decline from 4%^[64] up to 6.3%^[65]. Andrews and coworkers^[64] investigated striatal dopamine D1 and D2 receptor binding over a follow-up period of 40 mo in nine premanifest *HD* gene carriers and four symptomatic *HD* patients. They reported a mean annual loss of D1 and D2 binding of 2% and 4% respectively in the group of premanifest *HD* gene carriers and a mean annual loss of D1 binding of 5% and D2 binding of 3% in symptomatic *HD* patients^[64]. Additionally, UHDRS motor scores and TFC correlated with PET measures of striatal dopamine receptor in both groups. Interestingly, premanifest *HD* gene carriers who demonstrated active progression had an increased mean annual loss of D1 and D2 receptor binding (5% and 6.5% respectively). Thus, the authors conclude that PET measures of striatal D1 and D2 dopamine binding may be used to identify asymptomatic *HD* gene carriers who are actively

progressive^[64]. A reduction in the striatal dopamine D2 binding, in particular in the putamen, correlates weakly with the increasing probability of symptomatic conversion within 5 years, as calculated by an age and CAG repeat based model^[51]. Although, putaminal D2 binding correlated with predicted time to disease onset, the rate of change of D2 receptor changes were not increased around the onset of HD symptoms^[51]. A cross-sectional study by Antonini and colleagues^[66] indicated that striatal degeneration in HD patients might proceed in a non-linear fashion. They found a correlation between CAG repeat length and the estimated percentage loss of striatal D2 binding after age correction in premanifest *HD* gene carriers and symptomatic HD patients. While CAG repeat length influenced the rate of disease progression, the slopes of the correlation for asymptomatic mutation carriers and patients were significantly different, implying that the rate of disease progression is faster during the earlier asymptomatic stages of the disease^[66]. These data suggest that striatal D2 measures are more sensitive in premanifest HD than later in the disease.

While the loss of striatal dopamine D2 receptors is well known, few studies have addressed the extrastriatal D2 receptor distribution in patients with HD. Statistical parametric mapping of ¹¹C-raclopride binding in patients with HD suggest a loss of cortical dopamine D2 receptors in symptomatic HD patients^[61,62]. A significant reduction in postsynaptic dopamine D2 receptor binding was also found in the hypothalamus of nine premanifest HD patients and in 10 asymptomatic *HD* gene carriers^[67]. These findings suggest that hypothalamic dysfunction occurs early during the course of the disease and may be responsible for the development of commonly reported nonmotor symptoms in HD including progressive weight loss, alterations in sexual behaviour and disturbances in the wake-sleep cycle^[67].

Using PET with ¹¹C-FLB457, a radioligand with high affinity for dopamine D2 receptor, Esmacilzadeh and coworkers^[68] have investigated density of dopamine D2 receptors in extrastriatal brain regions in patients with mild to moderate HD. They found that unlike from striatum, D2 receptors seem to be relatively spared in the brain extrastriatal regions in HD patients suggesting that D2 receptor binding in brain regions outside the striatum may not be a reliable biomarker in HD^[68].

Moreover, PET with D1 and D2 receptor radioligands has been used to assess the efficacy of restorative therapy. In 1998, a multicentre open label pilot study was designed to evaluate the safety and efficacy of bilateral fetal striatal transplantation in HD^[69]. Five HD patients were transplanted and followed up clinically and with PET over a 3-10 year postoperative period^[70,71]. No significant differences were found over time between patients, grafted and non-grafted on the UHDRS and striatal D1 and D2 binding suggesting that there was no obvious surviving striatal graft tissue^[70,71].

Brain activation and metabolism

Measurements of cerebral blood flow and glucose me-

tabolism could serve as an index of neuronal integrity and functional state of the synapse^[72,73]. Striatal glucose hypometabolism and regional reductions in cortical glucose have been identified in HD patients and have been found to correlate with motor and cognitive symptoms^[65,74,75]. Specifically, decreases of caudate and regional cortical metabolism correlated with cognitive decline^[75,76], whereas striatal hypometabolism was associated with motor deficits and reduced TFC^[77]. Striatal and cortical hypometabolism has been also found in premanifest *HD* gene carriers to precede neuronal loss^[78-80]. A recent ¹⁸F-FDG PET study has shown that premanifest *HD* gene carriers who became symptomatic after five years from the PET scan had a mean glucose uptake in the caudate significantly lower than those who did not convert, and this difference was independent of mutation size^[80]. These findings suggest that reduced glucose levels may be contribute to the time of HD onset. In a combined ¹⁸F-FDG and ¹¹C-raclopride longitudinal study, premanifest *HD* gene carriers showed an annual loss of 2.3% in striatal glucose metabolism and 6.3% annual decline in D2 receptor binding^[65]. These findings suggest that glucose metabolism is a less sensitive marker of disease progression compared to ¹¹C-raclopride^[65]. On the other hand, decreased cortical metabolism in the early stage of HD is indicative of rapid progression^[81]. Indeed, cortical metabolism in the frontotemporal and parietal cortices was significantly lower in early HD subjects with faster progression of the disease as measured with the UHDRS and Independence Scale^[81].

PET with H₂¹⁵O has been used to investigate changes of motor-associated cortical activation in HD^[82,83]. During motor tasks such as paced joystick movements or sequential finger-to thumb opposition, HD patients showed impaired activation of the striatum and its frontal motor projection areas^[82,83] along with enhanced activity of the parietal areas^[82] and insular areas^[83]. These findings suggest that the loss of MSNs in the striatum leads to impairment of the basal ganglia-thalamo-cortical motor output and may induce a compensatory recruitment of additional accessory motor pathways^[82,83]. Moreover, different patterns of brain activation have been showed in HD patients during word generation task^[84]. HD patients showed decreased cerebral blood flows in the anterior cingulate and the inferior frontal gyri, which are important in lexical selection and a compensatory activation of the left supramarginal gyrus and the right inferior frontal gyrus, suggesting that compensatory language strategies are present in HD^[84].

¹⁸F-FDG PET imaging and network approaches have been used to identify spatial covariance patterns in premanifest HD^[85-87]. A cross-sectional analysis of metabolic changes from premanifest *HD* gene carriers and healthy controls, has reported a reproducible disease related pattern, characterized by relative bilateral increases in thalamic, occipital, and cerebellar glucose metabolism associated with bilateral decreases in striatal metabolism, which discriminated between the HD and healthy control groups^[86]. However, this pattern in *HD* gene carriers

did not show consistent changes over time, thus limiting its utility as a network biomarker of preclinical disease progression^[86]. Recently, Tang and coworkers^[87] demonstrated the feasibility of network-based approach by using longitudinal metabolic imaging data from premanifest HD carriers to identify a distinct spatial covariance pattern associated with disease progression. Changes in pattern expression over a seven years period were used to quantify the rate of progression in the preclinical period^[87]. They found a significant spatial covariance pattern characterized by progressive changes in striato-thalamic and cortical metabolic activity which increased linearly over 7 years and was not influenced by symptomatic conversion^[87]. Additionally, premanifest HD gene carriers which showed further increases in metabolic network activity at baseline (> 2 SD above the normal mean) had a greater risk of symptomatic conversion in the following 5-year period^[87]. These findings suggest that metabolic network measurements may provide a sensitive tool for evaluating disease progression prior to clinical diagnosis.

Measures of glucose brain metabolism have been used to assess the restoration of striato-cortical function in five HD patients who underwent bilateral striatal transplantation^[88,89]. In 2-year follow-up of these five patients, Gaura and colleagues^[89] reported that the three patients, who showed clinical improvement or stabilization, had increased in striatal/cortical glucose metabolic rate, which is suggestive of restoration of function of striatal-cortical connections. Conversely, findings from NEST-UK multicentre study failed to show significant change in ¹⁸F-FDG uptake over 2 years of follow-up^[70]. Thus, the ability of bilateral striatal transplantation to restore striato-cortical pathways remains to be elucidated.

Neuroinflammation and activated microglia

Recent evidence suggests that microglial activation plays a role in the pathogenesis of HD^[90,91]. Microglia constitute about 10% of the total brain cell population, and represent the main immunocompetent phagocytic cells in the central nervous system^[92]. Although microglial activation is unlikely to initiate neuronal death, it could contribute to the neurodegenerative processes^[93,94]. Indeed, upon exposure to neuronal insults such the presence of abnormal huntingtin protein aggregations, microglia become activated and release pro-inflammatory cytokines (*e.g.*, TNF- α and IL-1 β). These cytokines in turn cause further activation of microglia, resulting in a self-propagating inflammatory cascade, which may lead to neuronal death. Microglial activation upregulates the expression of the 18 kDa translocator protein (TSPO) which is involved in the release of proinflammatory cytokines during inflammation and is present at very low levels in the normal healthy CNS^[95,96]. The upregulation of TSPO expression can be detected *in vivo* with PET and selective radioligands such as ¹¹C-PK11195^[97,98]. Using PET with ¹¹C-PK11195, Pavese and coworkers^[99] have found significant microglial activation in the striatum and cortical regions of symptomatic HD patients, and reported that striatal PK binding correlates with loss of striatal dopa-

mine D2 binding as measured with ¹¹C-raclopride PET. Additionally, striatal ¹¹C-PK11195 binding correlated with clinical severity as measured with the UHDRS^[99]. In premanifest HD gene carriers ¹¹C-PK11195 binding was found to be also increased in striatum and cortical regions compared to a group of normal controls, and higher striatal ¹¹C-PK11195 binding correlated with lower striatal D2 binding^[100]. These findings suggest that early and widespread microglial activation occurs in premanifest HD gene carriers and it is associated with subclinical striatal neuronal loss of dopamine D2 receptor binding, indicating a potential role of activated microglia in HD pathogenesis.

A more recent multimodal imaging study using MRI, ¹¹C-PK11195 and ¹¹C-raclopride PET, has showed increased levels of activated microglia in several brain areas across HD gene carriers who were either premanifest or manifested patients^[101]. Of particular interest, high levels of activated microglia were observed in the associative part of the striatum, which is involved in cognitive function. High levels of microglial activation in the associative striatum and in the brain regions related to cognitive function correlated with a higher probability of symptomatic HD onset over the next 5 years in the group of premanifest HD gene carriers^[101]. These findings highlighted the role of immune response in the pathophysiology and clinical expression of HD.

Cannabinoid system

Dysregulation of the endocannabinoid system may play a critical role in the pathogenesis of HD. The type 1 cannabinoid receptors (CB1R) are expressed in the basal ganglia, mainly in the GABA-ergic striatal MSNs expressing D1 and D2 receptors and are a key modulator of synaptic transmission in the brain^[102-104]. Evidences from animal models of HD and postmortem tissue of HD brain have shown that decreased levels of CB1R and CB1 messenger RNA^[105-107]. Recently, *in vivo* imaging of CB1R has become feasible using PET with ¹⁸FMK-9470^[108] and ¹¹C-MePPEP^[109,110]. Using PET with ¹⁸FMK-9470, Van Laere and coworkers^[111] have investigated the levels of CB1R in the brain of 20 symptomatic HD patients. They found decreased CB1R availability throughout the grey matter of the cerebrum, cerebellum, and brain stem in HD patients. Further studies of CB1R system in premanifest HD gene carriers are expected in order to further understand the role of this system in the pathophysiology of HD.

CONCLUSION

Currently, there are no therapies able to slow down progression in HD and symptomatic treatments such as acetylcholinesterase inhibitors have provided limited evidence of their efficacy in HD^[112]. Identification of reliable biomarkers of HD progression will be important for the development and evaluation of disease-modifying treatments. Neuroimaging techniques may be a suitable biomarker for monitoring disease progression in HD

and for assessing the efficacy of future disease modifying therapies. Although MRI techniques have shown to be useful for monitoring disease progression, PET imaging is able to detect changes and specific targets early in pre-manifest HD stages. However, at this stage an integrative multimodal imaging approach, which combines different MRI and PET techniques, could be recommended.

REFERENCES

- 1 A novel gene containing a trinucleotide repeat that is expanded and unstable on Huntington's disease chromosomes. The Huntington's Disease Collaborative Research Group. *Cell* 1993; **72**: 971-983 [PMID: 8458085 DOI: 10.1016/0092-8674(93)90585-E]
- 2 Pringsheim T, Wiltshire K, Day L, Dykeman J, Steeves T, Jette N. The incidence and prevalence of Huntington's disease: a systematic review and meta-analysis. *Mov Disord* 2012; **27**: 1083-1091 [PMID: 22692795 DOI: 10.1002/mds.25075]
- 3 Djoussé L, Knowlton B, Hayden M, Almqvist EW, Brinkman R, Ross C, Margolis R, Rosenblatt A, Durr A, Dode C, Morrison PJ, Novelletto A, Frontali M, Trent RJ, McCusker E, Gómez-Tortosa E, Mayo D, Jones R, Zanko A, Nance M, Abramson R, Suchowersky O, Paulsen J, Harrison M, Yang Q, Cupples LA, Gusella JF, MacDonald ME, Myers RH. Interaction of normal and expanded CAG repeat sizes influences age at onset of Huntington disease. *Am J Med Genet A* 2003; **119A**: 279-282 [PMID: 12784292 DOI: 10.1002/ajmg.a.20190]
- 4 Paulsen JS, Langbehn DR, Stout JC, Aylward E, Ross CA, Nance M, Guttman M, Johnson S, MacDonald M, Beglinger LJ, Duff K, Kayson E, Biglan K, Shoulson I, Oakes D, Hayden M. Detection of Huntington's disease decades before diagnosis: the Predict-HD study. *J Neurol Neurosurg Psychiatry* 2008; **79**: 874-880 [PMID: 18096682 DOI: 10.1136/jnnp.2007.128728]
- 5 Duff K, Paulsen J, Mills J, Beglinger LJ, Moser DJ, Smith MM, Langbehn D, Stout J, Queller S, Harrington DL. Mild cognitive impairment in prediagnosed Huntington disease. *Neurology* 2010; **75**: 500-507 [PMID: 20610833 DOI: 10.1212/WNL.0b013e31818eccfa2]
- 6 Davies SW, Turmaine M, Cozens BA, DiFiglia M, Sharp AH, Ross CA, Scherzinger E, Wanker EE, Mangiarini L, Bates GP. Formation of neuronal intranuclear inclusions underlies the neurological dysfunction in mice transgenic for the HD mutation. *Cell* 1997; **90**: 537-548 [PMID: 9267033 DOI: 10.1016/S0092-8674(00)80513-9]
- 7 Li SH, Cheng AL, Zhou H, Lam S, Rao M, Li H, Li XJ. Interaction of Huntington disease protein with transcriptional activator Sp1. *Mol Cell Biol* 2002; **22**: 1277-1287 [PMID: 11839795 DOI: 10.1128/MCB.22.5.1277-1287.2002]
- 8 Browne SE, Beal MF. Oxidative damage in Huntington's disease pathogenesis. *Antioxid Redox Signal* 2006; **8**: 2061-2073 [PMID: 17034350 DOI: 10.1089/ars.2006.8.2061]
- 9 Politis M, Piccini P. Positron emission tomography imaging in neurological disorders. *J Neurol* 2012; **259**: 1769-1780 [PMID: 22297461 DOI: 10.1007/s00415-012-6428-3]
- 10 Phelps ME. Positron emission tomography provides molecular imaging of biological processes. *Proc Natl Acad Sci USA* 2000; **97**: 9226-9233 [PMID: 10922074 DOI: 10.1073/pnas.97.16.9226]
- 11 Harris GJ, Pearlson GD, Peyser CE, Aylward EH, Roberts J, Barta PE, Chase GA, Folstein SE. Putamen volume reduction on magnetic resonance imaging exceeds caudate changes in mild Huntington's disease. *Ann Neurol* 1992; **31**: 69-75 [PMID: 1531910 DOI: 10.1002/ana.410310113]
- 12 Harris GJ, Aylward EH, Peyser CE, Pearlson GD, Brandt J, Roberts-Twillie JV, Barta PE, Folstein SE. Single photon emission computed tomographic blood flow and magnetic resonance volume imaging of basal ganglia in Huntington's disease. *Arch Neurol* 1996; **53**: 316-324 [PMID: 8929153 DOI: 10.1001/archneur.1996.00550040044013]
- 13 Aylward EH, Codori AM, Barta PE, Pearlson GD, Harris GJ, Brandt J. Basal ganglia volume and proximity to onset in presymptomatic Huntington disease. *Arch Neurol* 1996; **53**: 1293-1296 [PMID: 8970459 DOI: 10.1001/archneur.1996.00550120105023]
- 14 Rosas HD, Goodman J, Chen YI, Jenkins BG, Kennedy DN, Makris N, Patti M, Seidman LJ, Beal MF, Koroshetz WJ. Striatal volume loss in HD as measured by MRI and the influence of CAG repeat. *Neurology* 2001; **57**: 1025-1028 [PMID: 11571328 DOI: 10.1212/WNL.57.6.1025]
- 15 Rosas HD, Koroshetz WJ, Chen YI, Skeuse C, Vangel M, Cudkovicz ME, Caplan K, Marek K, Seidman LJ, Makris N, Jenkins BG, Goldstein JM. Evidence for more widespread cerebral pathology in early HD: an MRI-based morphometric analysis. *Neurology* 2003; **60**: 1615-1620 [PMID: 12771251 DOI: 10.1212/01.WNL.0000065888.88988.6E]
- 16 Paulsen JS, Hayden M, Stout JC, Langbehn DR, Aylward E, Ross CA, Guttman M, Nance M, Kiebertz K, Oakes D, Shoulson I, Kayson E, Johnson S, Penziner E. Preparing for preventive clinical trials: the Predict-HD study. *Arch Neurol* 2006; **63**: 883-890 [PMID: 16769871 DOI: 10.1001/archneur.63.6.883]
- 17 Tabrizi SJ, Langbehn DR, Leavitt BR, Roos RA, Durr A, Craufurd D, Kennard C, Hicks SL, Fox NC, Scahill RI, Borowsky B, Tobin AJ, Rosas HD, Johnson H, Reilmann R, Landwehrmeyer B, Stout JC. Biological and clinical manifestations of Huntington's disease in the longitudinal TRACK-HD study: cross-sectional analysis of baseline data. *Lancet Neurol* 2009; **8**: 791-801 [PMID: 19646924 DOI: 10.1016/S1474-4422(09)70170-X]
- 18 Tabrizi SJ, Scahill RI, Durr A, Roos RA, Leavitt BR, Jones R, Landwehrmeyer GB, Fox NC, Johnson H, Hicks SL, Kennard C, Craufurd D, Frost C, Langbehn DR, Reilmann R, Stout JC. Biological and clinical changes in premanifest and early stage Huntington's disease in the TRACK-HD study: the 12-month longitudinal analysis. *Lancet Neurol* 2011; **10**: 31-42 [PMID: 21130037 DOI: 10.1016/S1474-4422(10)70276-3]
- 19 Tabrizi SJ, Reilmann R, Roos RA, Durr A, Leavitt B, Owen G, Jones R, Johnson H, Craufurd D, Hicks SL, Kennard C, Landwehrmeyer B, Stout JC, Borowsky B, Scahill RI, Frost C, Langbehn DR. Potential endpoints for clinical trials in premanifest and early Huntington's disease in the TRACK-HD study: analysis of 24 month observational data. *Lancet Neurol* 2012; **11**: 42-53 [PMID: 22137354 DOI: 10.1016/S1474-4422(11)70263-0]
- 20 Tabrizi SJ, Scahill RI, Owen G, Durr A, Leavitt BR, Roos RA, Borowsky B, Landwehrmeyer B, Frost C, Johnson H, Craufurd D, Reilmann R, Stout JC, Langbehn DR. Predictors of phenotypic progression and disease onset in premanifest and early-stage Huntington's disease in the TRACK-HD study: analysis of 36-month observational data. *Lancet Neurol* 2013; **12**: 637-649 [PMID: 23664844]
- 21 Aylward EH, Li Q, Stine OC, Ranen N, Sherr M, Barta PE, Bylsma FW, Pearlson GD, Ross CA. Longitudinal change in basal ganglia volume in patients with Huntington's disease. *Neurology* 1997; **48**: 394-399 [PMID: 9040728 DOI: 10.1212/WNL.48.2.394]
- 22 Rosas HD, Liu AK, Hersch S, Glessner M, Ferrante RJ, Salat DH, van der Kouwe A, Jenkins BG, Dale AM, Fischl B. Regional and progressive thinning of the cortical ribbon in Huntington's disease. *Neurology* 2002; **58**: 695-701 [PMID: 11889230 DOI: 10.1212/WNL.58.5.695]
- 23 Rosas HD, Salat DH, Lee SY, Zaleta AK, Pappu V, Fischl B, Greve D, Hevelone N, Hersch SM. Cerebral cortex and the clinical expression of Huntington's disease: complexity and heterogeneity. *Brain* 2008; **131**: 1057-1068 [PMID: 18337273 DOI: 10.1093/brain/awn025]
- 24 Hobbs NZ, Henley SM, Ridgway GR, Wild EJ, Barker RA,

- Scahill RI, Barnes J, Fox NC, Tabrizi SJ. The progression of regional atrophy in premanifest and early Huntington's disease: a longitudinal voxel-based morphometry study. *J Neurol Neurosurg Psychiatry* 2010; **81**: 756-763 [PMID: 19955112 DOI: 10.1136/jnnp.2009.190702]
- 25 **Paulsen JS**, Nopoulos PC, Aylward E, Ross CA, Johnson H, Magnotta VA, Juhl A, Pierson RK, Mills J, Langbehn D, Nance M. Striatal and white matter predictors of estimated diagnosis for Huntington disease. *Brain Res Bull* 2010; **82**: 201-207 [PMID: 20385209 DOI: 10.1016/j.brainresbull.2010.04.003]
- 26 **Reading SA**, Yassa MA, Bakker A, Dziorny AC, Gourley LM, Yallapragada V, Rosenblatt A, Margolis RL, Aylward EH, Brandt J, Mori S, van Zijl P, Bassett SS, Ross CA. Regional white matter change in pre-symptomatic Huntington's disease: a diffusion tensor imaging study. *Psychiatry Res* 2005; **140**: 55-62 [PMID: 16199141 DOI: 10.1016/j.psychres.2005.05.011]
- 27 **Rosas HD**, Tuch DS, Hevelone ND, Zaleta AK, Vangel M, Hersch SM, Salat DH. Diffusion tensor imaging in presymptomatic and early Huntington's disease: Selective white matter pathology and its relationship to clinical measures. *Mov Disord* 2006; **21**: 1317-1325 [PMID: 16755582 DOI: 10.1002/mds.20979]
- 28 **Dumas EM**, van den Bogaard SJ, Ruber ME, Reilman RR, Stout JC, Craufurd D, Hicks SL, Kennard C, Tabrizi SJ, van Buchem MA, van der Grond J, Roos RA. Early changes in white matter pathways of the sensorimotor cortex in premanifest Huntington's disease. *Hum Brain Mapp* 2012; **33**: 203-212 [PMID: 21264990 DOI: 10.1002/hbm.21205]
- 29 **Dierks T**, Linden DE, Hertel A, Günther T, Lanfermann H, Niesen A, Frölich L, Zanella FE, Hör G, Goebel R, Maurer K. Multimodal imaging of residual function and compensatory resource allocation in cortical atrophy: a case study of parietal lobe function in a patient with Huntington's disease. *Psychiatry Res* 1998; **84**: 27-35 [PMID: 9870415 DOI: 10.1016/S0925-4927(98)00040-7]
- 30 **Clark VP**, Lai S, Deckel AW. Altered functional MRI responses in Huntington's disease. *Neuroreport* 2002; **13**: 703-706 [PMID: 11973474 DOI: 10.1097/00001756-200204160-00033]
- 31 **Kim JS**, Reading SA, Brashers-Krug T, Calhoun VD, Ross CA, Pearlson GD. Functional MRI study of a serial reaction time task in Huntington's disease. *Psychiatry Res* 2004; **131**: 23-30 [PMID: 15246452 DOI: 10.1016/j.psychres.2004.03.02]
- 32 **Georgiou-Karistianis N**, Sritharan A, Farrow M, Cunnington R, Stout J, Bradshaw J, Churchyard A, Brawn TL, Chua P, Chiu E, Thiruvady D, Egan G. Increased cortical recruitment in Huntington's disease using a Simon task. *Neuropsychologia* 2007; **45**: 1791-1800 [PMID: 17321554 DOI: 10.1016/j.neuropsychologia.2006.12.023]
- 33 **Georgiou-Karistianis N**, Stout JC, Domínguez D JF, Carron SP, Ando A, Churchyard A, Chua P, Bohanna I, Dymowski AR, Poudel G, Egan GF. Functional magnetic resonance imaging of working memory in Huntington's disease: cross-sectional data from the IMAGE-HD study. *Hum Brain Mapp* 2014; **35**: 1847-1864 [PMID: 23913754 DOI: 10.1002/hbm.22296]
- 34 **Thiruvady DR**, Georgiou-Karistianis N, Egan GF, Ray S, Sritharan A, Farrow M, Churchyard A, Chua P, Bradshaw JL, Brawn TL, Cunnington R. Functional connectivity of the prefrontal cortex in Huntington's disease. *J Neurol Neurosurg Psychiatry* 2007; **78**: 127-133 [PMID: 17028117 DOI: 10.1136/jnnp.2006.098368]
- 35 **Paulsen JS**, Zimbelman JL, Hinton SC, Langbehn DR, Leveroni CL, Benjamin ML, Reynolds NC, Rao SM. fMRI biomarker of early neuronal dysfunction in presymptomatic Huntington's Disease. *AJNR Am J Neuroradiol* 2004; **25**: 1715-1721 [PMID: 15569736]
- 36 **Reading SA**, Dziorny AC, Peroutka LA, Schreiber M, Gourley LM, Yallapragada V, Rosenblatt A, Margolis RL, Pekar JJ, Pearlson GD, Aylward E, Brandt J, Bassett SS, Ross CA. Functional brain changes in presymptomatic Huntington's disease. *Ann Neurol* 2004; **55**: 879-883 [PMID: 15174024 DOI: 10.1002/ana.20121]
- 37 **Wolf RC**, Vasic N, Schönfeldt-Lecuona C, Landwehrmeyer GB, Ecker D. Dorsolateral prefrontal cortex dysfunction in presymptomatic Huntington's disease: evidence from event-related fMRI. *Brain* 2007; **130**: 2845-2857 [PMID: 17855375 DOI: 10.1093/brain/awm210]
- 38 **Wolf RC**, Sambataro F, Vasic N, Schönfeldt-Lecuona C, Ecker D, Landwehrmeyer B. Aberrant connectivity of lateral prefrontal networks in presymptomatic Huntington's disease. *Exp Neurol* 2008; **213**: 137-144 [PMID: 18588876 DOI: 10.1016/j.expneurol.2008.05.017]
- 39 **Unschuld PG**, Joel SE, Pekar JJ, Reading SA, Oishi K, McEntee J, Shanahan M, Bakker A, Margolis RL, Bassett SS, Rosenblatt A, Mori S, van Zijl PC, Ross CA, Redgrave GW. Depressive symptoms in prodromal Huntington's Disease correlate with Stroop-interference related functional connectivity in the ventromedial prefrontal cortex. *Psychiatry Res* 2012; **203**: 166-174 [PMID: 22974690 DOI: 10.1016/j.psychres.2012.01.002]
- 40 **Unschuld PG**, Liu X, Shanahan M, Margolis RL, Bassett SS, Brandt J, Schretlen DJ, Redgrave GW, Hua J, Hock C, Reading SA, van Zijl PC, Pekar JJ, Ross CA. Prefrontal executive function associated coupling relates to Huntington's disease stage. *Cortex* 2013; **49**: 2661-2673 [PMID: 23906595 DOI: 10.1016/j.cortex.2013.05.015]
- 41 **Fox MD**, Raichle ME. Spontaneous fluctuations in brain activity observed with functional magnetic resonance imaging. *Nat Rev Neurosci* 2007; **8**: 700-711 [PMID: 17704812 DOI: 10.1038/nrn2201]
- 42 **Greicius M**. Resting-state functional connectivity in neuropsychiatric disorders. *Curr Opin Neurol* 2008; **21**: 424-430 [PMID: 18607202 DOI: 10.1097/WCO.0b013e328306f2c5]
- 43 **Dumas EM**, van den Bogaard SJ, Hart EP, Soeter RP, van Buchem MA, van der Grond J, Rombouts SA, Roos RA. Reduced functional brain connectivity prior to and after disease onset in Huntington's disease. *Neuroimage Clin* 2013; **2**: 377-384 [PMID: 24179791 DOI: 10.1016/j.nicl.2013.03.001]
- 44 **Poudel GR**, Egan GF, Churchyard A, Chua P, Stout JC, Georgiou-Karistianis N. Abnormal synchrony of resting state networks in premanifest and symptomatic Huntington disease: the IMAGE-HD study. *J Psychiatry Neurosci* 2014; **39**: 87-96 [PMID: 24083458 DOI: 10.1503/jpn.120226]
- 45 **Werner CJ**, Dogan I, Saß C, Mirzazade S, Schiefer J, Shah NJ, Schulz JB, Reetz K. Altered resting-state connectivity in Huntington's disease. *Hum Brain Mapp* 2014; **35**: 2582-2593 [PMID: 23982979 DOI: 10.1002/hbm.22351]
- 46 **Unschuld PG**, Joel SE, Liu X, Shanahan M, Margolis RL, Biglan KM, Bassett SS, Schretlen DJ, Redgrave GW, van Zijl PC, Pekar JJ, Ross CA. Impaired cortico-striatal functional connectivity in prodromal Huntington's Disease. *Neurosci Lett* 2012; **514**: 204-209 [PMID: 22425717 DOI: 10.1016/j.neulet.2012.02.095]
- 47 **Hua J**, Unschuld PG, Margolis RL, van Zijl PC, Ross CA. Elevated arteriolar cerebral blood volume in prodromal Huntington's disease. *Mov Disord* 2014; **29**: 396-401 [PMID: 23847161 DOI: 10.1002/mds.25591]
- 48 **Unschuld PG**, Edden RA, Carass A, Liu X, Shanahan M, Wang X, Oishi K, Brandt J, Bassett SS, Redgrave GW, Margolis RL, van Zijl PC, Barker PB, Ross CA. Brain metabolite alterations and cognitive dysfunction in early Huntington's disease. *Mov Disord* 2012; **27**: 895-902 [PMID: 22649062 DOI: 10.1002/mds.25010]
- 49 **Tang TS**, Chen X, Liu J, Bezprozvanny I. Dopaminergic signaling and striatal neurodegeneration in Huntington's disease. *J Neurosci* 2007; **27**: 7899-7910 [PMID: 17652581 DOI:

- 10.1523/JNEUROSCI.1396-07.2007]
- 50 **van Oostrom JC**, Dekker M, Willemssen AT, de Jong BM, Roos RA, Leenders KL. Changes in striatal dopamine D2 receptor binding in pre-clinical Huntington's disease. *Eur J Neurol* 2009; **16**: 226-231 [PMID: 19138335 DOI: 10.1111/j.1468-1331.2008.02390.x]
- 51 **Reiner A**, Albin RL, Anderson KD, D'Amato CJ, Penney JB, Young AB. Differential loss of striatal projection neurons in Huntington disease. *Proc Natl Acad Sci USA* 1988; **85**: 5733-5737 [PMID: 2456581 DOI: 10.1073/pnas.85.15.5733]
- 52 **Leenders KL**, Frackowiak RS, Quinn N, Marsden CD. Brain energy metabolism and dopaminergic function in Huntington's disease measured in vivo using positron emission tomography. *Mov Disord* 1986; **1**: 69-77 [PMID: 2973559 DOI: 10.1002/mds.870010110]
- 53 **Häggglund J**, Aquilonius SM, Eckernäs SA, Hartvig P, Lundquist H, Gullberg P, Långström B. Dopamine receptor properties in Parkinson's disease and Huntington's chorea evaluated by positron emission tomography using 11C-N-methyl-spiperone. *Acta Neurol Scand* 1987; **75**: 87-94 [PMID: 2953165 DOI: 10.1111/j.1600-0404.1987.tb07900.x]
- 54 **Brandt J**, Folstein SE, Wong DF, Links J, Dannals RF, McDonnell-Sill A, Starkstein S, Anders P, Strauss ME, Tune LE. D2 receptors in Huntington's disease: positron emission tomography findings and clinical correlates. *J Neuropsychiatry Clin Neurosci* 1990; **2**: 20-27 [PMID: 1983772]
- 55 **Turjanski N**, Weeks R, Dolan R, Harding AE, Brooks DJ. Striatal D1 and D2 receptor binding in patients with Huntington's disease and other choreas. A PET study. *Brain* 1995; **118** (Pt 3): 689-696 [PMID: 7600086 DOI: 10.1093/brain/118.3.689]
- 56 **Ginovart N**, Lundin A, Farde L, Halldin C, Bäckman L, Swahn CG, Pauli S, Sedvall G. PET study of the pre- and post-synaptic dopaminergic markers for the neurodegenerative process in Huntington's disease. *Brain* 1997; **120** (Pt 3): 503-514 [PMID: 9126061 DOI: 10.1093/brain/120.3.503]
- 57 **Bohnen NI**, Koeppe RA, Meyer P, Ficarò E, Wernette K, Kilbourn MR, Kuhl DE, Frey KA, Albin RL. Decreased striatal monoaminergic terminals in Huntington disease. *Neurology* 2000; **54**: 1753-1759 [PMID: 10802780 DOI: 10.1212/WNL.54.9.1753]
- 58 **Sedvall G**, Karlsson P, Lundin A, Anvret M, Suhara T, Halldin C, Farde L. Dopamine D1 receptor number--a sensitive PET marker for early brain degeneration in Huntington's disease. *Eur Arch Psychiatry Clin Neurosci* 1994; **243**: 249-255 [PMID: 8172940 DOI: 10.1007/BF02191583]
- 59 **Bäckman L**, Robins-Wahlin TB, Lundin A, Ginovart N, Farde L. Cognitive deficits in Huntington's disease are predicted by dopaminergic PET markers and brain volumes. *Brain* 1997; **120** (Pt 12): 2207-2217 [PMID: 9448576 DOI: 10.1093/brain/120.12.2207]
- 60 **Lawrence AD**, Weeks RA, Brooks DJ, Andrews TC, Watkins LH, Harding AE, Robbins TW, Sahakian BJ. The relationship between striatal dopamine receptor binding and cognitive performance in Huntington's disease. *Brain* 1998; **121** (Pt 7): 1343-1355 [PMID: 9679785 DOI: 10.1093/brain/121.7.1343]
- 61 **Pavese N**, Andrews TC, Brooks DJ, Ho AK, Rosser AE, Barker RA, Robbins TW, Sahakian BJ, Dunnett SB, Piccini P. Progressive striatal and cortical dopamine receptor dysfunction in Huntington's disease: a PET study. *Brain* 2003; **126**: 1127-1135 [PMID: 12690052 DOI: 10.1093/brain/awg119]
- 62 **Pavese N**, Politis M, Tai YF, Barker RA, Tabrizi SJ, Mason SL, Brooks DJ, Piccini P. Cortical dopamine dysfunction in symptomatic and premanifest Huntington's disease gene carriers. *Neurobiol Dis* 2010; **37**: 356-361 [PMID: 19853661 DOI: 10.1016/j.nbd.2009.10.015]
- 63 **van Oostrom JC**, Maguire RP, Verschuuren-Bemelmans CC, Veenma-van der Duin L, Pruijm J, Roos RA, Leenders KL. Striatal dopamine D2 receptors, metabolism, and volume in preclinical Huntington disease. *Neurology* 2005; **65**: 941-943 [PMID: 16186542 DOI: 10.1212/01.wnl.0000176071.08694.cc]
- 64 **Andrews TC**, Weeks RA, Turjanski N, Gunn RN, Watkins LH, Sahakian B, Hodges JR, Rosser AE, Wood NW, Brooks DJ. Huntington's disease progression. PET and clinical observations. *Brain* 1999; **122** (Pt 12): 2353-2363 [PMID: 10581228 DOI: 10.1093/brain/122.12.2353]
- 65 **Antonini A**, Leenders KL, Spiegel R, Meier D, Vontobel P, Weigell-Weber M, Sanchez-Pernaute R, de Yébenes JG, Boesiger P, Weindl A, Maguire RP. Striatal glucose metabolism and dopamine D2 receptor binding in asymptomatic gene carriers and patients with Huntington's disease. *Brain* 1996; **119** (Pt 6): 2085-2095 [PMID: 9010012 DOI: 10.1093/brain/119.6.2085]
- 66 **Antonini A**, Leenders KL, Eidelberg D. [11C]raclopride-PET studies of the Huntington's disease rate of progression: relevance of the trinucleotide repeat length. *Ann Neurol* 1998; **43**: 253-255 [PMID: 9485067 DOI: 10.1002/ana.410430216]
- 67 **Politis M**, Pavese N, Tai YF, Tabrizi SJ, Barker RA, Piccini P. Hypothalamic involvement in Huntington's disease: an in vivo PET study. *Brain* 2008; **131**: 2860-2869 [PMID: 18829696 DOI: 10.1093/brain/awn244]
- 68 **Esmaeilzadeh M**, Farde L, Karlsson P, Varrone A, Halldin C, Waters S, Tedroff J. Extrastriatal dopamine D(2) receptor binding in Huntington's disease. *Hum Brain Mapp* 2011; **32**: 1626-1636 [PMID: 20886576 DOI: 10.1002/hbm.21134]
- 69 **Rosser AE**, Barker RA, Harrower T, Watts C, Farrington M, Ho AK, Burnstein RM, Menon DK, Gillard JH, Pickard J, Dunnett SB. Unilateral transplantation of human primary fetal tissue in four patients with Huntington's disease: NEST-UK safety report ISRCTN no 36485475. *J Neurol Neurosurg Psychiatry* 2002; **73**: 678-685 [PMID: 12438470 DOI: 10.1136/jnnp.73.6.678]
- 70 **Furtado S**, Sossi V, Hauser RA, Samii A, Schulzer M, Murphy CB, Freeman TB, Stoessl AJ. Positron emission tomography after fetal transplantation in Huntington's disease. *Ann Neurol* 2005; **58**: 331-337 [PMID: 16049929 DOI: 10.1002/ana.20564]
- 71 **Barker RA**, Mason SL, Harrower TP, Swain RA, Ho AK, Sahakian BJ, Mathur R, Elneil S, Thornton S, Hurrellbrink C, Armstrong RJ, Tyers P, Smith E, Carpenter A, Piccini P, Tai YF, Brooks DJ, Pavese N, Watts C, Pickard JD, Rosser AE, Dunnett SB. The long-term safety and efficacy of bilateral transplantation of human fetal striatal tissue in patients with mild to moderate Huntington's disease. *J Neurol Neurosurg Psychiatry* 2013; **84**: 657-665 [PMID: 23345280 DOI: 10.1136/jnnp-2012-302441]
- 72 **Sokoloff L**. Localization of functional activity in the central nervous system by measurement of glucose utilization with radioactive deoxyglucose. *J Cereb Blood Flow Metab* 1981; **1**: 7-36 [PMID: 7035471 DOI: 10.1038/jcbfm.1981.4]
- 73 **Sokoloff L**. Energetics of functional activation in neural tissues. *Neurochem Res* 1999; **24**: 321-329 [PMID: 9972882 DOI: 10.1023/A:1022534709672]
- 74 **Mazziotta JC**, Phelps ME, Pahl JJ, Huang SC, Baxter LR, Riege WH, Hoffman JM, Kuhl DE, Lanto AB, Wapenski JA. Reduced cerebral glucose metabolism in asymptomatic subjects at risk for Huntington's disease. *N Engl J Med* 1987; **316**: 357-362 [PMID: 2949152 DOI: 10.1056/NEJM198702123160701]
- 75 **Kuwert T**, Lange HW, Langen KJ, Herzog H, Aulich A, Feinendegen LE. Cortical and subcortical glucose consumption measured by PET in patients with Huntington's disease. *Brain* 1990; **113** (Pt 5): 1405-1423 [PMID: 2147116 DOI: 10.1093/brain/113.5.1405]
- 76 **Berent S**, Giordani B, Lehtinen S, Markel D, Penney JB, Buchtel HA, Starosta-Rubinstein S, Hichwa R, Young AB. Positron emission tomographic scan investigations of Huntington's disease: cerebral metabolic correlates of cognitive function. *Ann Neurol* 1988; **23**: 541-546 [PMID: 2970247 DOI: 10.1002/ana.410230603]

- 77 **Young AB**, Penney JB, Starosta-Rubinstein S, Markel DS, Berent S, Giordani B, Ehrenkaufer R, Jewett D, Hichwa R. PET scan investigations of Huntington's disease: cerebral metabolic correlates of neurological features and functional decline. *Ann Neurol* 1986; **20**: 296-303 [PMID: 2945510 DOI: 10.1002/ana.410200305]
- 78 **Hayden MR**, Martin WR, Stoessl AJ, Clark C, Hollenberg S, Adam MJ, Ammann W, Harrop R, Rogers J, Ruth T. Positron emission tomography in the early diagnosis of Huntington's disease. *Neurology* 1986; **36**: 888-894 [PMID: 2940474 DOI: 10.1212/WNL.36.7.888]
- 79 **Ciarmiello A**, Cannella M, Lastoria S, Simonelli M, Frati L, Rubinsztein DC, Squitieri F. Brain white-matter volume loss and glucose hypometabolism precede the clinical symptoms of Huntington's disease. *J Nucl Med* 2006; **47**: 215-222 [PMID: 16455626]
- 80 **Ciarmiello A**, Giovacchini G, Orobello S, Bruselli L, Elifani F, Squitieri F. 18F-FDG PET uptake in the pre-Huntington disease caudate affects the time-to-onset independently of CAG expansion size. *Eur J Nucl Med Mol Imaging* 2012; **39**: 1030-1036 [PMID: 22526956 DOI: 10.1007/s00259-012-2114-z]
- 81 **Shin H**, Kim MH, Lee SJ, Lee KH, Kim MJ, Kim JS, Cho JW. Decreased Metabolism in the Cerebral Cortex in Early-Stage Huntington's Disease: A Possible Biomarker of Disease Progression? *J Clin Neurol* 2013; **9**: 21-25 [PMID: 23346156 DOI: 10.3988/jcn.2013.9.1.21]
- 82 **Bartenstein P**, Weindl A, Spiegel S, Boecker H, Wenzel R, Ceballos-Baumann AO, Minoshima S, Conrad B. Central motor processing in Huntington's disease. A PET study. *Brain* 1997; **120** (Pt 9): 1553-1567 [PMID: 9313639 DOI: 10.1093/brain/120.9.1553]
- 83 **Weeks RA**, Ceballos-Baumann A, Piccini P, Boecker H, Harding AE, Brooks DJ. Cortical control of movement in Huntington's disease. A PET activation study. *Brain* 1997; **120** (Pt 9): 1569-1578 [PMID: 9313640 DOI: 10.1093/brain/120.9.1569]
- 84 **Lepron E**, Péran P, Cardebat D, Démonet JF. A PET study of word generation in Huntington's disease: effects of lexical competition and verb/noun category. *Brain Lang* 2009; **110**: 49-60 [PMID: 19615733 DOI: 10.1016/j.bandl.2009.05.004]
- 85 **Feigin A**, Leenders KL, Moeller JR, Missimer J, Kuenig G, Spetsieris P, Antonini A, Eidelberg D. Metabolic network abnormalities in early Huntington's disease: an [(18)F]FDG PET study. *J Nucl Med* 2001; **42**: 1591-1595 [PMID: 11696626]
- 86 **Feigin A**, Tang C, Ma Y, Mattis P, Zgaljardic D, Guttman M, Paulsen JS, Dhawan V, Eidelberg D. Thalamic metabolism and symptom onset in preclinical Huntington's disease. *Brain* 2007; **130**: 2858-2867 [PMID: 17893097 DOI: 10.1093/brain/awm217]
- 87 **Tang CC**, Feigin A, Ma Y, Habeck C, Paulsen JS, Leenders KL, Teune LK, van Oostrom JC, Guttman M, Dhawan V, Eidelberg D. Metabolic network as a progression biomarker of premanifest Huntington's disease. *J Clin Invest* 2013; **123**: 4076-4088 [PMID: 23985564 DOI: 10.1172/JCI69411]
- 88 **Bachoud-Lévi AC**, Rémy P, Nguyen JP, Brugières P, Le-faucher JP, Bourdet C, Baudic S, Gaura V, Maison P, Haddad B, Boissé MF, Grandmougin T, Jény R, Bartolomeo P, Dalla Barba G, Degos JD, Lisovoski F, Ergis AM, Pailhous E, Cesaro P, Hantraye P, Peschanski M. Motor and cognitive improvements in patients with Huntington's disease after neural transplantation. *Lancet* 2000; **356**: 1975-1979 [PMID: 11130527 DOI: 10.1016/S0140-6736(00)03310-9]
- 89 **Gaura V**, Bachoud-Lévi AC, Ribeiro MJ, Nguyen JP, Frouin V, Baudic S, Brugières P, Mangin JF, Boissé MF, Palfi S, Cesaro P, Samson Y, Hantraye P, Peschanski M, Remy P. Striatal neural grafting improves cortical metabolism in Huntington's disease patients. *Brain* 2004; **127**: 65-72 [PMID: 14607797 DOI: 10.1093/brain/awh003]
- 90 **Messmer K**, Reynolds GP. Increased peripheral benzodiazepine binding sites in the brain of patients with Huntington's disease. *Neurosci Lett* 1998; **241**: 53-56 [PMID: 9502214 DOI: 10.1016/S0304-3940(97)00967-1]
- 91 **Sapp E**, Kegel KB, Aronin N, Hashikawa T, Uchiyama Y, Tohyama K, Bhide PG, Vonsattel JP, DiFiglia M. Early and progressive accumulation of reactive microglia in the Huntington disease brain. *J Neuropathol Exp Neurol* 2001; **60**: 161-172 [PMID: 11273004]
- 92 **Kreutzberg GW**. Microglia: a sensor for pathological events in the CNS. *Trends Neurosci* 1996; **19**: 312-318 [PMID: 8843599 DOI: 10.1016/0166-2236(96)10049-7]
- 93 **Melton LM**, Keith AB, Davis S, Oakley AE, Edwardson JA, Morris CM. Chronic glial activation, neurodegeneration, and APP immunoreactive deposits following acute administration of double-stranded RNA. *Glia* 2003; **44**: 1-12 [PMID: 12951652 DOI: 10.1002/glia.10276]
- 94 **Nakanishi H**. Microglial functions and proteases. *Mol Neurobiol* 2003; **27**: 163-176 [PMID: 12777686]
- 95 **Banati RB**. Visualising microglial activation in vivo. *Glia* 2002; **40**: 206-217 [PMID: 12379908 DOI: 10.1002/glia.10144]
- 96 **Wilms H**, Claassen J, Röhl C, Sievers J, Deuschl G, Lucius R. Involvement of benzodiazepine receptors in neuroinflammatory and neurodegenerative diseases: evidence from activated microglial cells in vitro. *Neurobiol Dis* 2003; **14**: 417-424 [PMID: 14678758 DOI: 10.1016/j.nbd.2003.07.002]
- 97 **Banati RB**, Goerres GW, Myers R, Gunn RN, Turkheimer FE, Kreutzberg GW, Brooks DJ, Jones T, Duncan JS. [11C](R)-PK11195 positron emission tomography imaging of activated microglia in vivo in Rasmussen's encephalitis. *Neurology* 1999; **53**: 2199-2203 [PMID: 10599809 DOI: 10.1212/WNL.53.9.2199]
- 98 **Banati RB**, Newcombe J, Gunn RN, Cagnin A, Turkheimer F, Heppner F, Price G, Wegner F, Giovannoni G, Miller DH, Perkin GD, Smith T, Hewson AK, Bydder G, Kreutzberg GW, Jones T, Cuzner ML, Myers R. The peripheral benzodiazepine binding site in the brain in multiple sclerosis: quantitative in vivo imaging of microglia as a measure of disease activity. *Brain* 2000; **123** (Pt 11): 2321-2337 [PMID: 11050032 DOI: 10.1093/brain/123.11.2321]
- 99 **Pavese N**, Gerhard A, Tai YF, Ho AK, Turkheimer F, Barker RA, Brooks DJ, Piccini P. Microglial activation correlates with severity in Huntington disease: a clinical and PET study. *Neurology* 2006; **66**: 1638-1643 [PMID: 16769933 DOI: 10.1212/01.wnl.0000222734.56412.17]
- 100 **Tai YF**, Pavese N, Gerhard A, Tabrizi SJ, Barker RA, Brooks DJ, Piccini P. Microglial activation in presymptomatic Huntington's disease gene carriers. *Brain* 2007; **130**: 1759-1766 [PMID: 17400599 DOI: 10.1093/brain/awm044]
- 101 **Politis M**, Pavese N, Tai YF, Kiferle L, Mason SL, Brooks DJ, Tabrizi SJ, Barker RA, Piccini P. Microglial activation in regions related to cognitive function predicts disease onset in Huntington's disease: a multimodal imaging study. *Hum Brain Mapp* 2011; **32**: 258-270 [PMID: 21229614 DOI: 10.1002/hbm.21008]
- 102 **Herkenham M**, Lynn AB, de Costa BR, Richfield EK. Neuronal localization of cannabinoid receptors in the basal ganglia of the rat. *Brain Res* 1991; **547**: 267-274 [PMID: 1909204 DOI: 10.1016/0006-8993(91)90970-7]
- 103 **Mailleux P**, Vanderhaeghen JJ. Localization of cannabinoid receptor in the human developing and adult basal ganglia. Higher levels in the striatonigral neurons. *Neurosci Lett* 1992; **148**: 173-176 [PMID: 1300492 DOI: 10.1016/0304-3940(92)90832-R]
- 104 **Glass M**, Brotchie JM, Maneuf YP. Modulation of neurotransmission by cannabinoids in the basal ganglia. *Eur J Neurosci* 1997; **9**: 199-203 [PMID: 9058040 DOI: 10.1111/j.1460-9568.1997.tb01390.x]
- 105 **Glass M**, Dragunow M, Faull RL. The pattern of neurodegeneration in Huntington's disease: a comparative study of cannabinoid, dopamine, adenosine and GABA(A) receptor alterations in the human basal ganglia in Huntington's dis-

- ease. *Neuroscience* 2000; **97**: 505-519 [PMID: 10828533 DOI: 10.1016/S0306-4522(00)00008-7]
- 106 **Casteels C**, Martinez E, Bormans G, Camon L, de Vera N, Baekelandt V, Planas AM, Van Laere K. Type 1 cannabinoid receptor mapping with [18F]MK-9470 PET in the rat brain after quinolinic acid lesion: a comparison to dopamine receptors and glucose metabolism. *Eur J Nucl Med Mol Imaging* 2010; **37**: 2354-2363 [PMID: 20680268 DOI: 10.1007/s00259-010-1574-2]
- 107 **Casteels C**, Vandeputte C, Rangarajan JR, Dresselaers T, Riess O, Bormans G, Maes F, Himmelreich U, Nguyen H, Van Laere K. Metabolic and type 1 cannabinoid receptor imaging of a transgenic rat model in the early phase of Huntington disease. *Exp Neurol* 2011; **229**: 440-449 [PMID: 21459091 DOI: 10.1016/j.expneurol.2011.03.014]
- 108 **Burns HD**, Van Laere K, Sanabria-Bohórquez S, Hamill TG, Bormans G, Eng WS, Gibson R, Ryan C, Connolly B, Patel S, Krause S, Vanko A, Van Hecken A, Dupont P, De Lepeleire I, Rothenberg P, Stoch SA, Cote J, Hagemann WK, Jewell JP, Lin LS, Liu P, Goulet MT, Gottesdiener K, Wagner JA, de Hoon J, Mortelmans L, Fong TM, Hargreaves RJ. [18F]MK-9470, a positron emission tomography (PET) tracer for in vivo human PET brain imaging of the cannabinoid-1 receptor. *Proc Natl Acad Sci USA* 2007; **104**: 9800-9805 [PMID: 17535893 DOI: 10.1073/pnas.0703472104]
- 109 **Yasuno F**, Brown AK, Zoghbi SS, Krushinski JH, Chernet E, Tauscher J, Schaus JM, Phebus LA, Chesterfield AK, Felder CC, Gladding RL, Hong J, Halldin C, Pike VW, Innis RB. The PET radioligand [11C]MePPEP binds reversibly and with high specific signal to cannabinoid CB1 receptors in nonhuman primate brain. *Neuropsychopharmacology* 2008; **33**: 259-269 [PMID: 17392732 DOI: 10.1038/sj.npp.1301402]
- 110 **Terry GE**, Liow JS, Zoghbi SS, Hirvonen J, Farris AG, Lerner A, Tauscher JT, Schaus JM, Phebus L, Felder CC, Morse CL, Hong JS, Pike VW, Halldin C, Innis RB. Quantitation of cannabinoid CB1 receptors in healthy human brain using positron emission tomography and an inverse agonist radioligand. *Neuroimage* 2009; **48**: 362-370 [PMID: 19573609 DOI: 10.1016/j.neuroimage.2009.06.059]
- 111 **Van Laere K**, Casteels C, Dhollander I, Goffin K, Grachev I, Bormans G, Vandenberghe W. Widespread decrease of type 1 cannabinoid receptor availability in Huntington disease in vivo. *J Nucl Med* 2010; **51**: 1413-1417 [PMID: 20720046 DOI: 10.2967/jnumed.110.077156]
- 112 **Vattakatuchery JJ**, Kurien R. Acetylcholinesterase inhibitors in cognitive impairment in Huntington's disease: A brief review. *World J Psychiatry* 2013; **3**: 62-64 [PMID: 24255877 DOI: 10.5498/wjp.v3.i3.62]

P- Reviewers: Arsalidou M, Jeong Y, Orlacchio A, Walter M
S- Editor: Ma YJ **L- Editor:** A **E- Editor:** Zhang DN



Clinical significance of computed tomography assessment for third molar surgery

Kenji Nakamori, Kei Tomihara, Makoto Noguchi

Kenji Nakamori, Kei Tomihara, Makoto Noguchi, Department of Oral and Maxillofacial Surgery, Graduate School of Medicine and Pharmaceutical Sciences for Research, University of Toyama, Toyama 930-0194, Japan

Author contributions: Nakamori K reviewed the relevant literature and wrote the manuscript; Tomihara K and Noguchi M organized the research and edited and revised the manuscript.

Correspondence to: Kenji Nakamori, DDS, PhD, Department of Oral and Maxillofacial Surgery, Graduate School of Medicine and Pharmaceutical Sciences for Research, University of Toyama, 2630 Sugitani, Toyama 930-0194,

Japan. nakamori@med.u-toyama.ac.jp

Telephone: +81-76-434-5041 Fax: +81-76-434-5041

Received: December 24, 2013 Revised: March 27, 2014

Accepted: May 28, 2014

Published online: March 28, 2015

Abstract

Surgical extraction of the third molar is the most commonly performed surgical procedure in the clinical practice of oral surgery. Third molar surgery is warranted when there is inadequate space for eruption, malpositioning, or risk for cyst or odontogenic tumor formation. Preoperative assessment should include a detailed morphologic analysis of the third molar and its relationship to adjacent structures and surrounding tissues. Due to developments in medical engineering technology, computed tomography (CT) now plays a critical role in providing the clear images required for adequate assessment prior to third molar surgery. Removal of the maxillary third molar is associated with a risk for maxillary sinus perforation, whereas removal of the mandibular third molar can put patients at risk for a neurosensory deficit from damage to the lingual nerve or inferior alveolar nerve. Multiple factors, including demographic, anatomic, and treatment-related factors, influence the incidence of nerve injury during or following removal of the third molar. CT assessment of the third molar prior to surgery can identify some of these risk factors, such as the absence of cortication between the

mandibular third molar and the inferior alveolar canal, prior to surgery to reduce the risk for nerve damage. This topic highlight presents an overview of the clinical significance of CT assessment in third molar surgery.

© 2015 Baishideng Publishing Group Inc. All rights reserved.

Key words: Computed tomography; Third molar; Extraction; Oral surgery; Assessment

Core tip: Surgical extraction of the third molar is the most commonly performed procedure in oral surgery. Careful preoperative examinations, including the use of computed tomography (CT) assessment, assist in the planning of in predicting the risks related to surgical interventions. The clinical significance of CT assessment in relation to third molar surgery is therefore reviewed and discussed.

Original sources: Nakamori K, Tomihara K, Noguchi M. Clinical significance of computed tomography assessment for third molar surgery. *World J Radiol* 2014; 6(7): 417-423 Available from: URL: <http://www.wjgnet.com/1949-8470/full/v6/i7/417.htm> DOI: <http://dx.doi.org/10.4329/wjr.v6.i7.417>

INTRODUCTION

Surgical extraction of the third molar is the most common procedure performed by oral surgeons. Appropriate surgical procedures should be determined based on findings from the preoperative examinations that critically assess the morphology of the third molar, and its relationships with adjacent structures [particularly the inferior alveolar canal (IAC)] and surrounding tissues.

Preoperative imaging assessments have typically included conventional intraoral radiography or orthopantomography (OPG). Following more recent developments in medical engineering technology, computed tomography (CT)

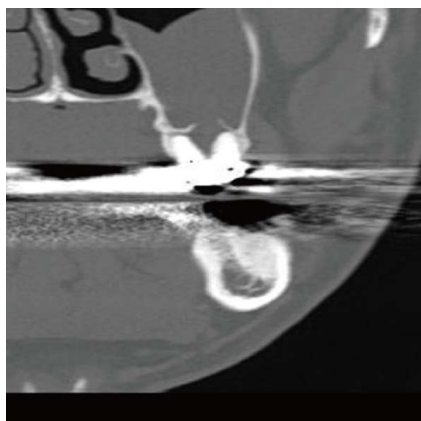


Figure 1 Coronal view of the maxillary molar with multi-detector computed tomography. The absence of cortication between the root apex and maxillary sinus can be observed.

now serves as an integral method to provide clear images for use in clinical practice. Multi-detector CT (MDCT) and cone-beam CT (CBCT) imaging of oral and maxillofacial regions serve as essential methods for diagnosis and treatment planning. Recently, the clinical importance of preoperative CT assessments in third molar surgery has been reported^[1-3]. In this article, the general problems related to third molar surgery are reviewed. In addition, current topics associated with the clinical significance of CT assessment for third molar surgery are discussed.

WHY SHOULD THE THIRD MOLAR BE EXTRACTED?

Third molars should be extracted when there is inadequate space for eruption in the retromolar region, between the second molar and the mandibular ramus. This can lead to a disturbed eruption of the third molar, which may create a flap of gingival tissue around the partially erupted tooth, or a pericoronal pocket, which can potentially develop into pericoronitis. In addition, Rahman *et al*^[4] recently reported that asymptomatic pericoronal tissue associated with impacted teeth showed a high rate of squamous metaplasia and proliferative activity. Although impacted teeth with pericoronal tissue can lead to cyst formation or odontogenic tumors, the prophylactic removal of disease-free third molars is still controversial^[5,6]. Extraction is also warranted when there is mesioangular or “horizontal” malpositioning of the third molar. Such malpositioning can lead to difficulties in plaque control between the second and third molars and may occasionally lead to second molar dental caries. Furthermore, this form of malpositioning may also affect the dental arch shape and result in tooth crowding.

COMPLICATIONS OF THIRD MOLAR SURGERY

Careful preoperative evaluation of the relationship be-

tween the maxillary third molar (UM3) and the maxillary sinus is critical in order to prevent perforation of this sinus. For example, a patient is at risk for perforation in the absence of cortication between the UM3 and the maxillary sinus. It is important to note that excessive curettage at the base of the root apex region should be avoided (Figure 1). Removal of the mandibular third molar (LM3) can put patients at risk for serious neurosensory deficits, particularly due to injury of the lingual nerve (LN) and the inferior alveolar nerve (IAN). Lastly, if the third molar is fully or partially impacted in the alveolar bone, bone removal and tooth sectioning are required. Such surgically invasive procedures may cause postoperative pain, edema, and limited opening or mobility of the mouth due to muscle spasms.

RISK FACTORS ASSOCIATED WITH NERVE INJURIES

LN and IAN nerve injuries are thought to be due to mechanical irritations from surgical intervention and are influenced by several demographic, anatomic, and treatment-related factors^[7,8]. Risk for injury is increased with the age of the patient because of technical difficulties during surgery, decreased bone elasticity, or increased incidence of tooth hypercementosis. In addition, age may contribute to a reduced capacity for damaged nerve fiber recovery. Furthermore, elderly patients with evidence of sclerotic change are at a considerably higher risk for pathologic osteomyelitis around the impacted tooth^[9]. Nakagawa *et al*^[10] reported that female patients are at a higher risk for IAN injuries due to decreased buccolingual thickness of the mandible. The risk for damage is increased with a thinner mandible as there is less space between the IAC and LM3. Additional anatomic risk factors for injury from surgery include tooth angulation, the presence of a distal overhang, and the degree of impaction, which are integrally related to the need for surgical intervention. Treatment-related risk factors include injection of local anesthesia, mucoperiosteal incision and elevation of the mucoperiosteal flap, bur usage during alveolar bone removal and tooth sectioning, stretching of the nerve during surgery, and accidental fractures of the lingual cortical bone of the mandible^[11]. These treatment-related risk factors are associated with the surgeon's level of experience^[12,13].

The lingual split technique for third molar extraction is highly associated with a risk for LN deficit, though the associated risk for LN morbidity remains controversial^[11,12]. Therefore, the most widely used technique in clinical practice to decrease the risk of LN injury is the buccal approach. Preoperative imaging assessments can also be employed to limit nerve injury occurrence. Ultrasonography should be used to detect the LN, since the location of the nerve in the mandible prohibits detection by CT imaging^[14]. As the IAN is located within the IAC, it can be indirectly evaluated through radiographic assessment of the IAC. Importantly, preoperative radiographic

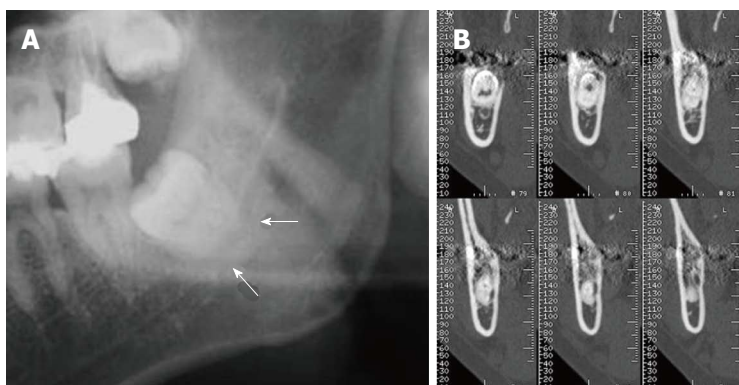


Figure 2 Root darkening and inferior alveolar canal shape. A: Darkening of the root is observed in this orthopantomography image. A black band is visible (white arrows) at the root apex site; B: A cross-sectional multi-detector computed tomography image indicates alterations (dumbbell shape) to the inferior alveolar canal shape and a loss of the lingual cortex of the mandibular bone.

Table 1 Specificity and sensitivity for predicting inferior alveolar nerve injury with third molar surgery

Imaging procedure	Sensitivity	Specificity
Orthopantomography ^[22-26]		
Darkening of the root	32%-71%	73%-96%
Interruption of the canal	22%-80%	47%-97%
Diversion of the canal	3%-50%	82%-100%
CT/Cone-beam CT ^[1,38,41,42]		
Cortication	66%-100%	46%-86%

CT: Electronic computer X-ray tomography technique.

assessment provides increased information on the relationship between the LM3 and the IAC and can be used to identify whether risk factors for IAN injury are present prior to LM3 extraction. In cases where preoperative examination has identified a high-risk factor, surgeons may consider the use of special surgical approaches, including coronectomy^[15,16], multistep extraction^[17,18], or orthodontic extraction techniques^[19-21] to decrease the risk for IAN injuries.

RADIOLOGICAL IMAGING

There are several different radiology procedures that can be used prior to third molar surgery. Conventional intraoral radiography provides surgeons with detailed information regarding structures at the exposed site. If two structures are superimposed, a parallax technique can be applied to determine the buccolingual relationship. However, it is sometimes difficult to position films or an imaging plate at an ideal position, as the LM3 is predominantly located posterior to the mandible.

OPG

OPG is widely used during treatment planning for third molar surgery because it enables assessment of the two-dimensional relationship between the tooth and the IAC. Rood and Shebab have outlined seven important findings that can be obtained from OPG images: darkening of the root, deflected roots, narrowing of the root, dark and bifid roots, interruption of the white line(s), and diversion and narrowing of the IAC^[22]. These authors concluded

that the diversion of IAC, darkening of the root and interruption of the white line were significantly related to IAN injuries. There have been several OPG assessment studies which support the usefulness of these seven findings^[3,23-25]. According to a meta-analysis study, three signs—darkening of the root or increased radiolucency, interruption of radiopaque borders of the mandibular canal, and diversion of the mandibular canal—have been implicated as the most significant predictive factors of a close relationship between the IAN and the LM3^[26]. It should be noted, though, that the statistical results from these analyses had various levels of specificity and sensitivity (Table 1).

Recent research indicated that high-risk signs identified by OPG are significantly associated with absence of the cortication between LM3 and IAC^[27,28]. In particular, darkening of the root is closely related to cortical bone loss and/or grooving of the root^[27,29-31] (Figure 2). Furthermore, interruption of radiopaque borders has been attributed to loss of cortical structure of the canal. A sign for diversion of the mandibular canal is classified by a nerve running between the roots or the interposition between the root and the mandibular cortical bone.

CT

CT and/or CBCT examinations enable easy assessment of three-dimensional anatomic relationships between the third molar and adjacent structures and surrounding tissues, as well as for detection of the mental foramen and bifid mandibular canal^[32-34]. Furthermore, if the third molar becomes dislocated during surgery, the CT image is a useful tool for detecting the dislocated tooth (Figure 3).

The accuracy of measurement by CT was evaluated by a comparative study of the skull, showing that medical CT (single-detector CT or MDCT) or CBCT is sufficient if preoperative CTs have been taken^[35,36]. Accurate assessment of the IAC position is important in the field of oral surgery, and several studies have reported the clinical significance of the position of the IAC with respect to LM3^[10,32,37]. When the IAN is positioned at the lingual site of the LM3, and sandwiched between the LM3 and the lingual cortex, it may become compressed during LM3 extraction. Several studies have reported that the predictive value of CT assessment for IAN injuries was

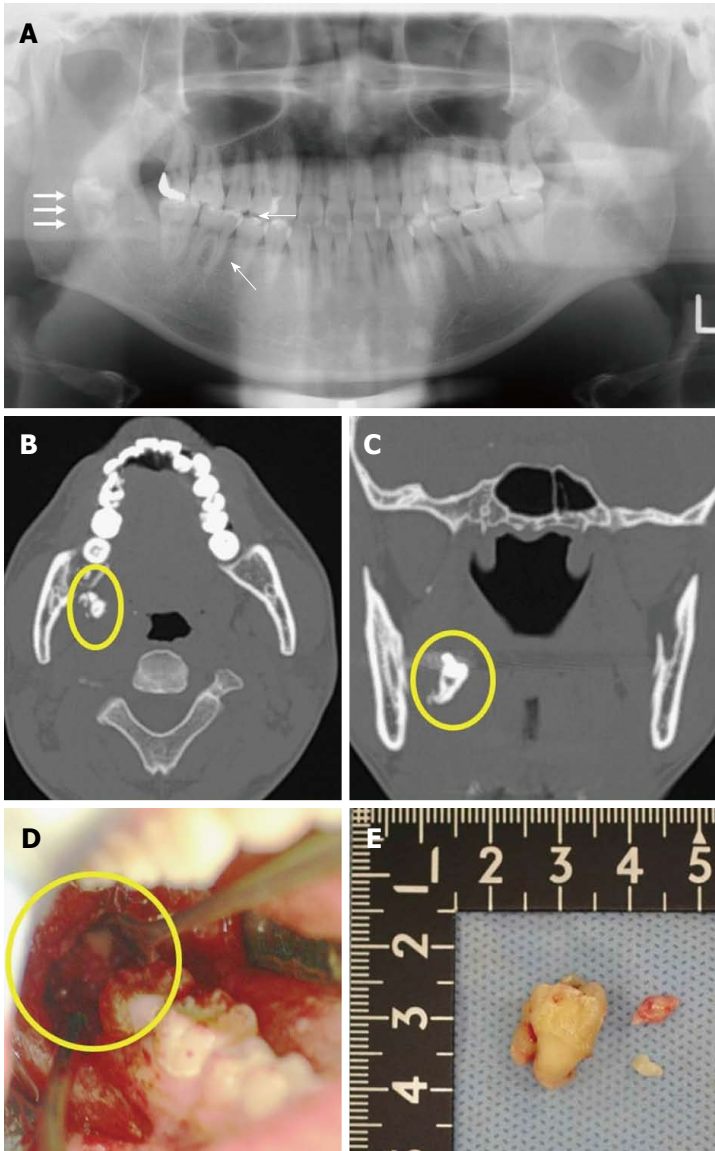


Figure 3 Imaging and surgical removal of a dislocated third mandibular molar (LM3). A: Orthopantomography showing a dislocated LM3 during surgical removal. The dislocated LM3 is superimposed over the middle part of the mandibular ramus (white arrows); B: Axial multi-detector computed tomography (MDCT) image and C: coronal MDCT image of the dislocated LM3 deviating into the pterygomandibular space (yellow circle); D: Surgical extraction; E: Extracted LM3.

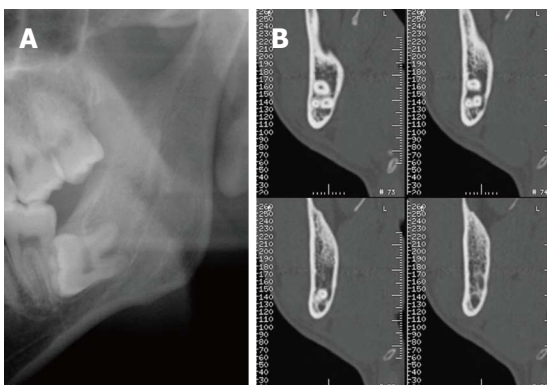


Figure 4 Radiolucency is not observed with orthopantomography. A: No significant radiolucency is observed in the roots of the third mandibular molar with orthopantomography; B: A cross-sectional multi-detector computed tomography image shows the dumbbell shape of the inferior alveolar canal and loss of the lingual cortex of the mandibular bone.

approximately 20%-30%^[1,37-39], and 30% when the nerve-vascular bundle was observed^[40].

CT images of reconstructed cross-sectional (or coronal) views have been used for assessment of the cortical status around the IAC. Two studies have suggested a predictive value for cortication status in IAN injuries^[2,41], which currently appears to be the gold standard finding for predicting signs of IAN injuries. In our own retrospective and prospective studies, the absence of cortication between LM3 and the IAC was a requirement for IAN injuries^[38,42,43]. In addition, Susarla *et al.*^[39] reported that the estimated cortical defect size, computed by counting the number of consecutive slice images with interruptions in the white line around the IAC, was closely related to IAN injury. If reconstruction software is unavailable, a reformatted coronal view can be obtained through reconstruction of the perpendicular image of the IAC, which is based on the axial and sagittal vertical planes^[38].

The shape of the IAC has become a significant new finding for estimating the proximity between the IAC and LM3^[38,42,44]. Although high-risk signs from OPG findings

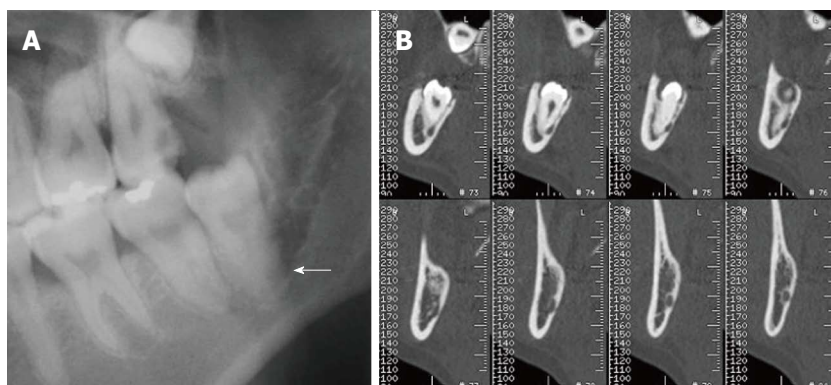


Figure 5 Root darkening and altered third mandibular molar (LM3) root. A: Darkening of the root observed by orthopantomography. A black band is visible (white arrow) at the root apex site; B: Alteration of the LM3 root (grooved) and loss of the lingual cortex of mandibular bone can be observed on cross-sectional multi-detector computed tomography images.

indicated a relationship with lost cortication, some alterations have been recognized in the IAC without the OPG finding (Figure 4). All IAC shapes are initially round/oval near the mandibular foramen, although some canals change shape toward the anterior aspect of the mandible^[42]. Alteration of canals is observed most often at the section closest to LM3 (Figure 4B). The altered canal shapes are described as “teardrop-shaped”, “dumbbell-shaped”^[42], or as an invagination^[44]. Collectively, the alteration indicates the degree of proximity between the IAC and LM3.

The number and shape of the LM3 roots can also be assessed by CT examination and should be recommended to surgeons seeking important clinical information. For instance, if the LM3 has three roots, a root-sectioning technique may be needed. However, the number of LM3 roots does not correlate with the incidence of IAN injury. A grooved root shape is intimated due to the close relationship between the root and IAC (Figure 5).

CONCLUSION

Preoperative CT examination is now considered an important assessment tool for third molar surgery. Despite this, standard eligibility criteria have not yet been established to necessitate the use of CT examination^[45,46]. Furthermore, standardized significant findings have not been put in place for third molar surgery. This may be due to the low incidence of complications during third molar surgery. To resolve these issues, multi-institutional studies and development of a uniform protocol are needed.

REFERENCES

- 1 **Susarla SM**, Dodson TB. Preoperative computed tomography imaging in the management of impacted mandibular third molars. *J Oral Maxillofac Surg* 2007; **65**: 83-88 [PMID: 17174769 DOI: 10.1016/j.joms.2005.10.052]
- 2 **Palma-Carrió C**, García-Mira B, Larrazabal-Morón C, Peñarocha-Diago M. Radiographic signs associated with inferior alveolar nerve damage following lower third molar extraction. *Med Oral Patol Oral Cir Bucal* 2010; **15**: e886-e890 [PMID: 20526245 DOI: 10.4317/medoral.15.e886]
- 3 **Monaco G**, Montecvecchi M, Bonetti GA, Gatto MR, Checchi L. Reliability of panoramic radiography in evaluating the topographic relationship between the mandibular canal and impacted third molars. *J Am Dent Assoc* 2004; **135**: 312-318 [PMID: 15058618 DOI: 10.14219/jada.archive.2004.0179]
- 4 **Rahman F**, Bhargava A, Tippu SR, Kalra M, Bhargava N, Kaur I, Srivastava S. Analysis of the immunorexpression of Ki-67 and Bcl-2 in the pericoronal tissues of impacted teeth, dentigerous cysts and gingiva using software image analysis. *Dent Res J (Isfahan)* 2013; **10**: 31-37 [PMID: 23878561 DOI: 10.4103/1735-3327.111764]
- 5 **Leone SA**, Edenfield MJ, Cohen ME. Correlation of acute pericoronitis and the position of the mandibular third molar. *Oral Surg Oral Med Oral Pathol* 1986; **62**: 245-250 [PMID: 3462627 DOI: 10.1016/0030-4220(86)90001-0]
- 6 **Weir S**, Lopes V, Malden N. Influence of SIGN guidelines on removal of third molars in The Lothians, Scotland, a clinical audit. *Oral Surg* 2010; **3**: 57-60 [DOI: 10.1111/j.1752-248X.2010.01081.x]
- 7 **Leung YY**, Cheung LK. Risk factors of neurosensory deficits in lower third molar surgery: an literature review of prospective studies. *Int J Oral Maxillofac Surg* 2011; **40**: 1-10 [PMID: 21035310 DOI: 10.1016/j.ijom.2010.09.005]
- 8 **Renton T**, Yilmaz Z, Gaballah K. Evaluation of trigeminal nerve injuries in relation to third molar surgery in a prospective patient cohort. Recommendations for prevention. *Int J Oral Maxillofac Surg* 2012; **41**: 1509-1518 [PMID: 23017786 DOI: 10.1016/j.ijom.2012.06.025]
- 9 **Miyamoto I**, Ishikawa A, Morimoto Y, Takahashi T. Potential risk of asymptomatic osteomyelitis around mandibular third molar tooth for aged people: a computed tomography and histopathologic study. *PLoS One* 2013; **8**: e73897 [PMID: 24040109 DOI: 10.1371/journal.pone.0073897]
- 10 **Nakagawa Y**, Ishii H, Nomura Y, Watanabe NY, Hoshiba D, Kobayashi K, Ishibashi K. Third molar position: reliability of panoramic radiography. *J Oral Maxillofac Surg* 2007; **65**: 1303-1308 [PMID: 17577493 DOI: 10.1016/j.joms.2006.10.028]
- 11 **Boffano P**, Rocca F, Gallesio C. Lingual nerve deficit following mandibular third molar removal: review of the literature and medicolegal considerations. *Oral Surg Oral Med Oral Pathol Oral Radiol* 2012; **113**: e10-e18 [PMID: 22669152 DOI: 10.1016/j.tripleo.2011.06.034]
- 12 **Cheung LK**, Leung YY, Chow LK, Wong MC, Chan EK, Fok YH. Incidence of neurosensory deficits and recovery after lower third molar surgery: a prospective clinical study of 4338 cases. *Int J Oral Maxillofac Surg* 2010; **39**: 320-326 [PMID: 20061121 DOI: 10.1016/j.ijom.2009.11.010]
- 13 **Jerjes W**, Upile T, Shah P, Nhembe F, Gudka D, Kafas P, McCarthy E, Abbas S, Patel S, Hamdoon Z, Abiola J, Vourvachis M, Kalkani M, Al-Khawalde M, Leeson R, Banu B, Rob J, El-Maaytah M, Hopper C. Risk factors associated with injury to the inferior alveolar and lingual nerves following third molar surgery-revisited. *Oral Surg Oral Med Oral Pathol Oral Radiol Endod* 2010; **109**: 335-345 [PMID: 20097103 DOI: 10.1016/j.tripleo.2009.10.010]
- 14 **Benninger B**, Kloenne J, Horn JL. Clinical anatomy of the

- lingual nerve and identification with ultrasonography. *Br J Oral Maxillofac Surg* 2013; **51**: 541-544 [PMID: 23182453 DOI: 10.1016/j.bjoms.2012.10.014]
- 15 **Fraffjord R**, Renton T. A review of coronectomy. *Oral Surg* 2010; **3**: 1-7
 - 16 **Renton T**. Update on coronectomy. A safer way to remove high risk mandibular third molars. *Dent Update* 2013; **40**: 362-364, 362-364 [PMID: 23909229]
 - 17 **Landi L**, Manicone PF, Piccinelli S, Raia A, Raia R. Staged removal of horizontally impacted third molars to reduce risk of inferior alveolar nerve injury. *J Oral Maxillofac Surg* 2010; **68**: 442-446 [PMID: 20116720 DOI: 10.1016/j.joms.2009.07.038]
 - 18 **Landi L**, Manicone PF, Piccinelli S, Raia A, Raia R. A novel surgical approach to impacted mandibular third molars to reduce the risk of paresthesia: a case series. *J Oral Maxillofac Surg* 2010; **68**: 969-974 [PMID: 20156664 DOI: 10.1016/j.joms.2009.09.097]
 - 19 **Park W**, Park JS, Kim YM, Yu HS, Kim KD. Orthodontic extrusion of the lower third molar with an orthodontic mini implant. *Oral Surg Oral Med Oral Pathol Oral Radiol Endod* 2010; **110**: e1-e6 [PMID: 20674416 DOI: 10.1016/j.tripleo.2010.04.031]
 - 20 **Wang Y**, He D, Yang C, Wang B, Qian W. An easy way to apply orthodontic extraction for impacted lower third molar compressing to the inferior alveolar nerve. *J Craniomaxillofac Surg* 2012; **40**: 234-237 [PMID: 21641229 DOI: 10.1016/j.jcms.2011.05.001]
 - 21 **Ma ZG**, Xie QY, Yang C, Xu GZ, Cai XY, Li JY. An orthodontic technique for minimally invasive extraction of impacted lower third molar. *J Oral Maxillofac Surg* 2013; **71**: 1309-1317 [PMID: 23763903 DOI: 10.1016/j.joms.2013.03.025]
 - 22 **Rood JP**, Shehab BA. The radiological prediction of inferior alveolar nerve injury during third molar surgery. *Br J Oral Maxillofac Surg* 1990; **28**: 20-25 [PMID: 2322523]
 - 23 **Blaeser BF**, August MA, Donoff RB, Kaban LB, Dodson TB. Panoramic radiographic risk factors for inferior alveolar nerve injury after third molar extraction. *J Oral Maxillofac Surg* 2003; **61**: 417-421 [PMID: 12684956 DOI: 10.1053/joms.2003.50088]
 - 24 **Kim JW**, Cha IH, Kim SJ, Kim MR. Which risk factors are associated with neurosensory deficits of inferior alveolar nerve after mandibular third molar extraction? *J Oral Maxillofac Surg* 2012; **70**: 2508-2514 [PMID: 22901857 DOI: 10.1016/j.joms.2012.06.004]
 - 25 **Szalma J**, Lempel E, Jeges S, Szabó G, Olasz L. The prognostic value of panoramic radiography of inferior alveolar nerve damage after mandibular third molar removal: retrospective study of 400 cases. *Oral Surg Oral Med Oral Pathol Oral Radiol Endod* 2010; **109**: 294-302 [PMID: 19846324 DOI: 10.1016/j.tripleo.2009.09.023]
 - 26 **Atieh MA**. Diagnostic accuracy of panoramic radiography in determining relationship between inferior alveolar nerve and mandibular third molar. *J Oral Maxillofac Surg* 2010; **68**: 74-82 [PMID: 20006158 DOI: 10.1016/j.joms.2009.04.074]
 - 27 **Umar G**, Bryant C, Obisesan O, Rood JP. Correlation of the radiological predictive factors of inferior alveolar nerve injury with cone beam computed tomography findings. *Oral Surg* 2010; **3**: 72-82 [DOI: 10.1111/j.1752-248X.2010.01088.x]
 - 28 **Shahidi S**, Zamiri B, Bronoosh P. Comparison of panoramic radiography with cone beam CT in predicting the relationship of the mandibular third molar roots to the alveolar canal. *Imaging Sci Dent* 2013; **43**: 105-109 [PMID: 23807934 DOI: 10.5624/isd.2013.43.2.105]
 - 29 **Tantanapornkul W**, Okochi K, Bhakdinaronk A, Ohbayashi N, Kurabayashi T. Correlation of darkening of impacted mandibular third molar root on digital panoramic images with cone beam computed tomography findings. *Dentomaxillofac Radiol* 2009; **38**: 11-16 [PMID: 19114418 DOI: 10.1259/dmfr/83819416]
 - 30 **Szalma J**, Vajta L, Lempel E, Jeges S, Olasz L. Darkening of third molar roots on panoramic radiographs: is it really predominantly thinning of the lingual cortex? *Int J Oral Maxillofac Surg* 2013; **42**: 483-488 [PMID: 22835682 DOI: 10.1016/j.jjom.2012.06.018]
 - 31 **Harada N**, Vasudeva SB, Joshi R, Seki K, Araki K, Matsuda Y, Okano T. Correlation between panoramic radiographic signs and high risk anatomical factors for impacted mandibular third molars. *Oral Surg* 2013; **6**: 129-136 [DOI: 10.1111/ors.12025]
 - 32 **Yamada T**, Ishihama K, Yasuda K, Hasumi-Nakayama Y, Ito K, Yamaoka M, Furusawa K. Inferior alveolar nerve canal and branches detected with dental cone beam computed tomography in lower third molar region. *J Oral Maxillofac Surg* 2011; **69**: 1278-1282 [PMID: 21256640 DOI: 10.1016/j.joms.2010.07.010]
 - 33 **Naitoh M**, Hiraiwa Y, Aimiya H, Gotoh K, Arijii E. Accessory mental foramen assessment using cone-beam computed tomography. *Oral Surg Oral Med Oral Pathol Oral Radiol Endod* 2009; **107**: 289-294 [PMID: 19071039 DOI: 10.1016/j.tripleo.2008.09.010]
 - 34 **Neves FS**, Nascimento MC, Oliveira ML, Almeida SM, Bóscolo FN. Comparative analysis of mandibular anatomical variations between panoramic radiography and cone beam computed tomography. *Oral Maxillofac Surg* 2013 Aug 24; Epub ahead of print [PMID: 23975215]
 - 35 **Williams FL**, Richtsmeier JT. Comparison of mandibular landmarks from computed tomography and 3D digitizer data. *Clin Anat* 2003; **16**: 494-500 [PMID: 14566895 DOI: 10.1002/ca.10095]
 - 36 **Ludlow JB**, Laster WS, See M, Bailey LJ, Hershey HG. Accuracy of measurements of mandibular anatomy in cone beam computed tomography images. *Oral Surg Oral Med Oral Pathol Oral Radiol Endod* 2007; **103**: 534-542 [PMID: 17395068 DOI: 10.1016/j.tripleo.2006.04.008]
 - 37 **Xu GZ**, Yang C, Fan XD, Yu CQ, Cai XY, Wang Y, He D. Anatomic relationship between impacted third mandibular molar and the mandibular canal as the risk factor of inferior alveolar nerve injury. *Br J Oral Maxillofac Surg* 2013; **51**: e215-e219 [PMID: 23411471 DOI: 10.1016/j.bjoms.2013.01.011]
 - 38 **Shiratori K**, Nakamori K, Ueda M, Sonoda T, Dehari H. Assessment of the shape of the inferior alveolar canal as a marker for increased risk of injury to the inferior alveolar nerve at third molar surgery: a prospective study. *J Oral Maxillofac Surg* 2013; **71**: 2012-2019 [PMID: 24045186 DOI: 10.1016/j.joms.2013.07.030]
 - 39 **Susarla SM**, Sidhu HK, Avery LL, Dodson TB. Does computed tomographic assessment of inferior alveolar canal cortical integrity predict nerve exposure during third molar surgery? *J Oral Maxillofac Surg* 2010; **68**: 1296-1303 [PMID: 20356665 DOI: 10.1016/j.joms.2010.01.021]
 - 40 **Tay AB**, Go WS. Effect of exposed inferior alveolar neurovascular bundle during surgical removal of impacted lower third molars. *J Oral Maxillofac Surg* 2004; **62**: 592-600 [PMID: 15122566 DOI: 10.1016/j.joms.2003.08.033]
 - 41 **Nakayama K**, Nonoyama M, Takaki Y, Kagawa T, Yuasa K, Izumi K, Ozeki S, Ikebe T. Assessment of the relationship between impacted mandibular third molars and inferior alveolar nerve with dental 3-dimensional computed tomography. *J Oral Maxillofac Surg* 2009; **67**: 2587-2591 [PMID: 19925976 DOI: 10.1016/j.joms.2009.07.017]
 - 42 **Ueda M**, Nakamori K, Shiratori K, Igarashi T, Sasaki T, Anbo N, Kaneko T, Suzuki N, Dehari H, Sonoda T, Hiratsuka H. Clinical significance of computed tomographic assessment and anatomic features of the inferior alveolar canal as risk factors for injury of the inferior alveolar nerve at third molar surgery. *J Oral Maxillofac Surg* 2012; **70**: 514-520 [PMID: 22079065 DOI: 10.1016/j.joms.2011.08.021]
 - 43 **Nakamori K**, Fujiwara K, Miyazaki A, Tomihara K, Tsuji M, Nakai M, Michifuri Y, Suzuki R, Komai K, Shimanishi M, Hiratsuka H. Clinical assessment of the relationship

between the third molar and the inferior alveolar canal using panoramic images and computed tomography. *J Oral Maxillofac Surg* 2008; **66**: 2308-2313 [PMID: 18940497 DOI: 10.1016/j.joms.2008.06.042]

- 44 **Selvi F**, Dodson TB, Nattestad A, Robertson K, Tolstunov L. Factors that are associated with injury to the inferior alveolar nerve in high-risk patients after removal of third molars. *Br J Oral Maxillofac Surg* 2013; **51**: 868-873 [PMID: 24012054 DOI: 10.1016/j.bjoms.2013.08.007]
- 45 **Lübbbers HT**, Matthews F, Damerau G, Kruse AL, Obwege-

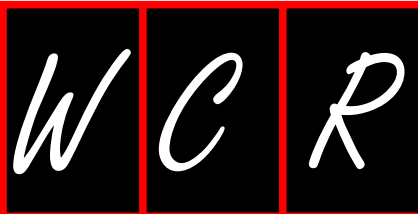
ser JA, Grätz KW, Eylich GK. Anatomy of impacted lower third molars evaluated by computerized tomography: is there an indication for 3-dimensional imaging? *Oral Surg Oral Med Oral Pathol Oral Radiol Endod* 2011; **111**: 547-550 [PMID: 20952229 DOI: 10.1016/j.tripleo.2010.06.010]

- 46 **Roeder F**, Wachtlin D, Schulze R. Necessity of 3D visualization for the removal of lower wisdom teeth: required sample size to prove non-inferiority of panoramic radiography compared to CBCT. *Clin Oral Investig* 2012; **16**: 699-706 [PMID: 21519882 DOI: 10.1007/s00784-011-0553-8]

P- Reviewer: Bernardin L, Bishnuhari P, Jain S, Mesquita RA, Morimoto Y, Sepahdari AR

S- Editor: Song XX **L- Editor:** A **E- Editor:** Lu YJ





Intraoperative perfusion magnetic resonance imaging: Cutting-edge improvement in neurosurgical procedures

Stephan Ulmer

Stephan Ulmer, Neuroradiology, Medical Radiological Institute, 8001 Zurich, Switzerland

Stephan Ulmer, Institute of Neuroradiology, Department of Radiology and Neuroradiology, University Hospital of Schleswig-Holstein, 24105 Kiel, Germany

Author contributions: Ulmer S reviewed the literature, analyzed own data, created all figures, wrote the paper and performed all corrections in the revision.

Correspondence to: Stephan Ulmer, MD, Neuroradiology, Medical Radiological Institute, Bahnhofplatz 3, 8001 Zurich, Switzerland. ulmer@email.com

Telephone: +41-44-2252090 Fax: +41-44-2118754

Received: January 16, 2014 Revised: April 17, 2014

Accepted: June 18, 2014

Published online: March 28, 2015

© 2015 Baishideng Publishing Group Inc. All rights reserved.

Key words: Intraoperative magnetic resonance imaging; Dynamic susceptibility contrast magnetic resonance imaging; Dynamic contrast enhanced magnetic resonance imaging; Surgically induced contrast enhancement; Neurosurgery

Core tip: The amount of brain tumor resection is one of the prognostic factors for time to tumor progression and median survival. To achieve maximum brain tumor removal, while preventing damage to “eloquent” brain regions, a variety of technical advances have been introduced, including intraoperative magnetic resonance imaging. Brain shift can thus be compensated; however, surgically induced contrast enhancement along the rim of the resection cavity hampers interpretation of these intraoperatively acquired images. Recently, perfusion techniques (dynamic contrast enhanced magnetic resonance imaging, dynamic susceptibility contrast magnetic resonance imaging) have been introduced that can differentiate residual tumor from surgically induced changes and thus overcome this remaining uncertainty in high grade brain tumor resection.

Original sources: Ulmer S. Intraoperative perfusion magnetic resonance imaging: Cutting-edge improvement in neurosurgical procedures. *World J Radiol* 2014; 6(8): 538-543 Available from: URL: <http://www.wjgnet.com/1949-8470/full/v6/i8/538.htm> DOI: <http://dx.doi.org/10.4329/wjr.v6.i8.538>

Abstract

The goal in brain tumor surgery is to remove the maximum achievable amount of the tumor, preventing damage to “eloquent” brain regions as the amount of brain tumor resection is one of the prognostic factors for time to tumor progression and median survival. To achieve this goal, a variety of technical advances have been introduced, including an operating microscope in the late 1950s, computer-assisted devices for surgical navigation and more recently, intraoperative imaging to incorporate and correct for brain shift during the resection of the lesion. However, surgically induced contrast enhancement along the rim of the resection cavity hampers interpretation of these intraoperatively acquired magnetic resonance images. To overcome this uncertainty, perfusion techniques [dynamic contrast enhanced magnetic resonance imaging (DCE-MRI), dynamic susceptibility contrast magnetic resonance imaging (DSC-MRI)] have been introduced that can differentiate residual tumor from surgically induced changes at the rim of the resection cavity and thus overcome this remaining uncertainty of intraoperative MRI in high grade brain tumor resection.

INTRODUCTION

The goal in brain tumor surgery is to remove the maximum achievable amount of the tumor, preventing damage to “eloquent” brain regions, as the amount of brain tumor resection is one of the prognostic factors for time to tumor progression and median survival^[1,2]. Preop-

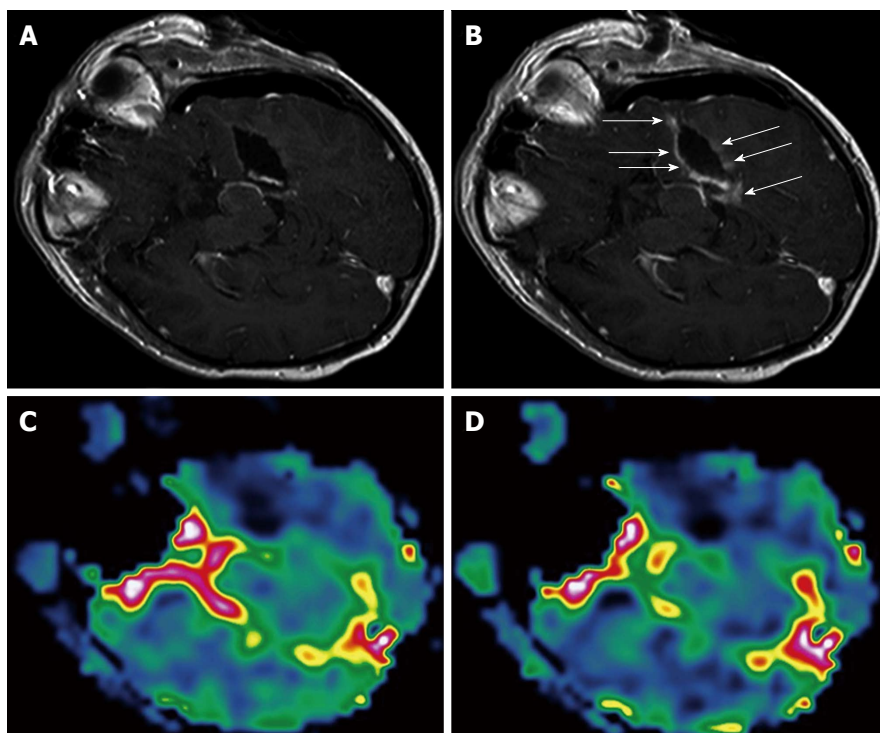


Figure 1 Surgically induced intraoperative contrast leakage. Reprinted from *NeuroImage* with permission^[9]. A: T1-weighted magnetic resonance (MR) image of the initial resection control. Residual tumor was depicted (not shown), neuronavigation was updated and the residual tumor was removed; B: T1-weighted MR image in identical orientation as in (A) of the second intraoperative resection control. At the border of the resection cavity there is contrast enhancement of previously non-enhancing tissue (arrows), which is caused by the neurosurgical resection leading to a leakage phenomenon. Perfusion maps of rCBV (C) and rCBF (D) at the second resection control demonstrate no elevated values in areas of contrast enhancement but complete resection of the tumor. rCBV: Regional cerebral blood volume; rCBF: Regional cerebral blood flow.

eratively acquired magnetic resonance (MR) images can nicely delineate the tumor extent and adjacent anatomical structures. The application of an operating microscope in the late 1950s^[3,4] revolutionized neurosurgery. Further advances included computer-assisted devices for surgical navigation^[4,5] and, more recently, intraoperative imaging^[6] to incorporate and correct for brain shift during the resection of the lesion. However, surgically induced contrast enhancement along the rim of the resection cavity^[7] hampers interpretation of these intraoperatively acquired MR images (Figure 1). To overcome this uncertainty, perfusion techniques have been introduced. Dynamic susceptibility contrast magnetic resonance imaging (DSC-MRI) is a T2*-weighted technique that enables calculation of regional cerebral blood flow (rCBF) and regional cerebral blood volume (rCBV) maps. The measurement takes only 1 min, 20 s and does not extend the overall scanning procedure. It can be applied various times as it is independent of T1-effects after saturation, has proven to be as reliable as preoperatively performed DSC-MRI^[8,9] and can distinguish residual tumor from surgically induced artefacts. Dynamic contrast-enhanced T1-weighted perfusion (DCE-MRI) has alternatively been used intraoperatively^[10]. The beauty of this approach that requires more time than DSC-MRI (also at 3T) is that there is a by-product with the acquired T1-weighted images as the slope of contrast enhancement can easily be analyzed without the need for additional software.

A quickly climbing slope depicts residual tumor tissue. However, the following still needs to be proven: can the DCE-MRI be repeatedly applied, is analysis unaffected by the commonly used absorbable hemostats (such as surgical[®], Ethicon 360), and can it reliably differentiate other sources of contrast enhancement over time, such as bleedings. Both techniques, however, can differentiate residual tumor from surgically induced changes at the rim of the resection cavity and thus overcome the remaining uncertainty of intraoperative MRI in high grade brain tumor resection.

The extent of tumor resection is one of the prognostic factors for time to tumor progression and median survival for patients with both high and low grade gliomas^[1,2]. Various attempts have been undertaken to achieve the maximum resection of a lesion. Most of them are imaging-based. Beginning in 1980, intraoperative ultrasound was the first imaging modality guiding neurosurgical procedures^[3]. Preoperatively acquired images were integrated in computer-assisted devices for surgical navigation beginning in 1986^[4,5]. Prior to resection of a lesion, an “image-to-patient” registration is necessary to align the MRI coordinates with the patient’s head position in the OR. However, due to brain shift during the resection of the lesion, or leakage of CSF, these preoperatively acquired images were progressively imprecise over time. The double-donut was the first intraoperative MRI system at the Brigham and Women’s hospital in

Boston in 1997^[6]. This enabled an update of the underlying anatomy at any time during the resection of a lesion, including an update of the navigation system. One major drawback, besides the costs of such a system, is that there is a surgically induced contrast enhancement along the resection cavity margin in intraoperatively acquired T1-weighted images after contrast administration^[7] that can hamper judgment concerning the differentiation between residual solid tumor or just surgically induced artefact, especially taken together with the well known brain shift that may also preclude the comparison with preoperatively acquired images. Another approach that found wide acceptance was the use of intravenous administration of 5-aminolevulinic acid^[11], leading to tumor fluorescence intraoperatively that also resulted in more complete tumor removal. However, lack of visible fluorescence in the adjacent tissue is not as highly predictive of normal tissue as biopsy proven^[12]. Thus, some centers (where available) use both complementary methods. However, the contrast enhancement in these intraoperative images remains a challenge with conventional imaging only.

INTRAOPERATIVE SETUP

Instead of using the double-donut setup, which requires that the surgeon is within the magnetic field thus requiring non-magnetic tools^[6], “twin operating theatres” have been proposed for both low^[13,14] and more recently high field systems, with the need to transfer the patient between the imaging and surgical site. This has become the setup of choice in most institutions^[8,15,16], although some move the magnet towards the surgical site^[17]. Lower field systems with permanent magnets are also in use^[18], which is a compromise but does not allow advanced imaging (see below). To use the conventional neurosurgical setup, including neuronavigation, microscope and conventional ferromagnetic instruments, the patient has to be outside the 0.5 mT or 5-Gauss line of the magnet during the surgical procedures to avoid a pull of ferromagnetic objects into the bore of the scanner, especially when the patient is positioned for scanning. Also, these objects interfere with imaging and can hamper image quality, causing artefacts. Dynamic sequences like DSC-MRI require a high field scanner (1.5 T or more), which come in “closed-bore” designs. Head fixation devices need to be MR-compatible. Whenever the surgeon wants an update, MRI can be performed after removing all ferromagnetic objects and sterile coverage of the craniotomy.

ADVANCED INTRAOPERATIVE MRI

To define residual tumor, various approaches have been performed using advanced imaging techniques. It has been demonstrated that parts of brain tumors do not enhance as biopsy proven^[19] which can be depicted by MR spectroscopy (MRS), a technique that is very susceptible to artefacts and also time consuming. However, it helps to

delineate typical changes associated with brain tumors and to define the real extent of a lesion more precisely than the use of conventional MR imaging only. Recently, this had been used intraoperatively to identify residual tumor with a sensitivity of 85.7% and specificity of 100%^[20]. However, air filled (resection) cavities might preclude MRS, or small residual tumor areas might be missed, and it is impossible to map the complete rim of a resection cavity intraoperatively due to time restraints, thus the area to be monitored has to be defined.

Perfusion imaging in clinical routine is most commonly performed as DSC-MRI-weighted perfusion, which is T2*-weighted or as DCE-MRI. Both techniques are most commonly used for stroke imaging but also in neuro-oncology and intraoperatively.

DSC-MRI

DSC-MRI enables calculation of regional maps for relative blood volume and flow by administering conventional MR contrast agents while T2*-weighted images (*i.e.*, 40 images/slice) are being acquired. In areas of blood-brain barrier breakdown (such as brain tumors), distinct zones with increased cerebral blood flow and volume can be depicted, which correspond to neovascularization and active metabolism within the tumor^[21-28]. Prior to the DSC measurement, 2 cc of contrast agent are injected for reduction of the T1 effect (saturation). For perfusion imaging, the contrast agent is administered as a bolus, followed by a saline flush with a flow rate of 5 cc/s during a dynamic susceptibility-dependent T2*-weighted GE EPI sequence (*i.e.*, TR/TE = 17/8 ms; FOV 240 mm; matrix 128 × 128; EPI factor = 17, number of slices 30 with slice thickness of 3.5 mm, duration: 1 min 20 s^[8,9]). These data are then transferred to a workstation to create maps of the rCBF and rCBV and to measure the mean transit time of the contrast agent passing through the brain^[29] based on the tissue dilution theorem. As absolute quantification is not yet possible, ratios to the unaffected hemisphere or adjacent tissue are created to judge the perfusion data. As T2*-weighted images are susceptible to artefacts caused by air fluid levels (such as resection cavities) or air filled spaces (like sinus), its intraoperative application required a multistage approach. Initially, a phantom study was performed using a model with a rigorous air water level that showed only moderate artefacts. In a second step, a model with continuous laminar flow was used that showed susceptibility artefacts close to the tubes (overestimation of perfusion adjacent to vessels^[8]). In patients, residual tumor was depicted intraoperatively by DSC-MRI^[8], which is independent of brain shift and surgically induced disruption of the blood brain barrier and was proven by histology. In a third step, the reliability of intraoperatively acquired data was demonstrated in a series of patients with high grade gliomas who had undergone pre- and intraoperative DSC-MRI with some residual tumor in the early intraoperative resection control^[8,9]. Ratios of identical areas within the tumor tissue

did not differ significantly between pre- and intraoperatively acquired data. Furthermore, there was a high correlation of the analyzed rCBV and rCBF ratios between pre- and intraoperative MRI exams. Intraoperatively, flexible two-channel surface coils were used, whereby one part was placed below the patient's head at the beginning of the operation and the second part adjusted prior to intraoperative scanning on the craniotomy defect, both draped in a sterile fashion. DSC-MRI was performed in 1 min 20 s, which did not extend overall intraoperative MR imaging. Intraoperative sedation (such as propofol anesthesia) reduces the absolute values of CBF and CBV; however, the ratios between tumor and unaffected contralateral tissue remain constant^[30]. DSC-MRI can be repeated various times as previously used contrast agent leads to a desired saturation of T1 effects but does not influence T2*-weighted images.

DCE-MRI

Dynamic contrast-enhanced T1-weighted perfusion MR imaging (DCE-MRI)^[31-33] is the other commonly used perfusion technique. In DCE-MRI, k-trans is analyzed, which is the transfer coefficient (endothelial permeability surface product). DCE-MRI requires various sampling points over time and usually takes much longer than DSC-MRI. T1 is reduced by clinically used contrast agents, leading to a signal intensity increase in T1-weighted images. Thus, DCE-MRI measures contrast agent concentration as a function of time. Very recently, DCE-MRI was used intraoperatively at a 3 T MR scanner^[10]. The used setup took 3 min and 45 s for the perfusion sequence. In addition to a pharmacokinetic modelling, the authors analyzed the slope of the signal intensity increase in these T1-weighted images. Residual solid tumor could be distinguished from surgically induced contrast enhancement at the rim of the resection border by a quickly climbing slope in tumors, compared to a low-amplitude undulating curve in brain tissue as proven by histology. This may have great potential as it is obviously much easier to apply and analysis of the slope of contrast enhancement does not require any additional software as such programs come with the scanner software. However, it still has to be proven whether or not DCE-MRI can be repeatedly applied in the unlikely event of multiple resection controls, whether analysis is affected by commonly used absorbable hemostats (such as surgical[®], Ethicon 360), and also if it can reliably differentiate other sources of contrast enhancement over time, such as bleedings.

CONCLUSION

The goal in brain tumor surgery is to remove the maximum achievable amount of the tumor, preventing damage to “eloquent” brain regions, as the amount of brain tumor resection is one of the prognostic factors for time to tumor progression and median survival^[1,2]. Preoperatively acquired MR images can nicely delineate the

tumor extent and adjacent anatomical structures. The application of an operating microscope in the late 1950s^[34] revolutionized neurosurgery. Further advances included computer-assisted devices for surgical navigation^[4,5] and, more recently, intraoperative imaging^[6] to incorporate and correct for brain shift during the resection of the lesion. However, surgically induced contrast enhancement along the rim of the resection cavity^[7] hampers interpretation of these intraoperatively acquired MR images. To overcome this uncertainty, perfusion techniques have been introduced. DSC-MRI is a T2*-weighted technique that enables calculation of rCBF and rCBV maps. The measurement takes only 1 min 20 s and therefore does not extend the overall scanning procedure. It can be applied various times as it is independent of T1-effects after saturation, has proven to be as reliable as preoperatively performed DSC-MRI^[8,9], and can distinguish residual tumor from surgically induced artefacts. DCE-MRI has also been used intraoperatively as an alternative^[10]. The beauty of this approach that requires more time than DSC-MRI (also at 3 T) is that there is a by-product with the acquired T1-weighted images as the slope of contrast enhancement can easily be analyzed without the need for additional software. A quickly climbing slope depicts residual tumor tissue. However, it still has to be proven that DCE-MRI can be repeatedly applied, that analysis is unaffected by commonly used absorbable hemostats (such as surgical[®], Ethicon 360), and that it can also reliably differentiate other sources of contrast enhancement over time, such as bleedings. Both techniques can differentiate residual tumor from surgically induced changes at the rim of the resection cavity and thus overcome the remaining uncertainty of intraoperative MRI in high grade brain tumor resection.

REFERENCES

- 1 **Keles GE**, Anderson B, Berger MS. The effect of extent of resection on time to tumor progression and survival in patients with glioblastoma multiforme of the cerebral hemisphere. *Surg Neurol* 1999; **52**: 371-379 [PMID: 10555843 DOI: 10.1016/S0090-3019(99)00103-2]
- 2 **Sanai N**, Berger MS. Operative techniques for gliomas and the value of extent of resection. *Neurotherapeutics* 2009; **6**: 478-486 [PMID: 19560738 DOI: 10.1016/j.nurt.2009.04.005]
- 3 **Rubin JM**, Mirfakhraee M, Duda EE, Dohrmann GJ, Brown F. Intraoperative ultrasound examination of the brain. *Radiology* 1980; **137**: 831-832 [PMID: 6255514]
- 4 **Roberts DW**, Strohbehn JW, Hatch JF, Murray W, Kettenberger H. A frameless stereotaxic integration of computerized tomographic imaging and the operating microscope. *J Neurosurg* 1986; **65**: 545-549 [PMID: 3531430 DOI: 10.3171/jns.1986.65.4.0545]
- 5 **Watanabe E**, Watanabe T, Manaka S, Mayanagi Y, Takakura K. Three-dimensional digitizer (neuronavigator): new equipment for computed tomography-guided stereotaxic surgery. *Surg Neurol* 1987; **27**: 543-547 [PMID: 3554569 DOI: 10.1016/090-3019(87)90152-2]
- 6 **Black PM**, Moriarty T, Alexander E, Stieg P, Woodard EJ, Gleason PL, Martin CH, Kikinis R, Schwartz RB, Jolesz FA. Development and implementation of intraoperative magnetic resonance imaging and its neurosurgical applications.

- Neurosurgery* 1997; **41**: 831-842; discussion 842-845 [PMID: 9316044 DOI: 10.1097/00006123-199710000-00013]
- 7 **Knauth M**, Aras N, Wirtz CR, Dörfler A, Engelhorn T, Sartor K. Surgically induced intracranial contrast enhancement: potential source of diagnostic error in intraoperative MR imaging. *AJNR Am J Neuroradiol* 1999; **20**: 1547-1553 [PMID: 10512244]
 - 8 **Ulmer S**, Helle M, Jansen O, Mehdorn HM, Nabavi A. Intraoperative dynamic susceptibility contrast weighted magnetic resonance imaging (iDSC-MRI)-Technical considerations and feasibility. *Neuroimage* 2009; **45**: 38-43 [PMID: 19100843 DOI: 10.1016/j.neuroimage.2008.11.021]
 - 9 **Ulmer S**, Hartwigsen G, Riedel C, Jansen O, Mehdorn HM, Nabavi A. Intraoperative dynamic susceptibility contrast MRI (iDSC-MRI) is as reliable as preoperatively acquired perfusion mapping. *Neuroimage* 2010; **49**: 2158-2162 [PMID: 19900562 DOI: 10.1016/j.neuroimage.2009.10.084]
 - 10 **Özduman K**, Yıldız E, Dinçer A, Sav A, Pamir MN. Using intraoperative dynamic contrast-enhanced T1-weighted MRI to identify residual tumor in glioblastoma surgery. *J Neurosurg* 2014; **120**: 60-66 [PMID: 24138206 DOI: 10.3171/2013.9.JNS121924]
 - 11 **Stummer W**, Pichlmeier U, Meinel T, Wiestler OD, Zanella F, Reulen HJ. Fluorescence-guided surgery with 5-aminolevulinic acid for resection of malignant glioma: a randomised controlled multicentre phase III trial. *Lancet Oncol* 2006; **7**: 392-401 [PMID: 16648043 DOI: 10.1016/S1470-2045(06)70665-9]
 - 12 **Roberts DW**, Valdés PA, Harris BT, Fontaine KM, Hartov A, Fan X, Ji S, Lollis SS, Pogue BW, Leblond F, Tosteson TD, Wilson BC, Paulsen KD. Coregistered fluorescence-enhanced tumor resection of malignant glioma: relationships between δ -aminolevulinic acid-induced protoporphyrin IX fluorescence, magnetic resonance imaging enhancement, and neuropathological parameters. Clinical article. *J Neurosurg* 2011; **114**: 595-603 [PMID: 20380535 DOI: 10.3171/2010.2.JNS091322]
 - 13 **Steinmeier R**, Fahlbusch R, Ganslandt O, Nimsky C, Buchfelder M, Kaus M, Heigl T, Lenz G, Kuth R, Huk W. Intraoperative magnetic resonance imaging with the magnetom open scanner: concepts, neurosurgical indications, and procedures: a preliminary report. *Neurosurgery* 1998; **43**: 739-747; discussion 747-748 [PMID: 9766299 DOI: 10.1097/00006123-199810000-00005]
 - 14 **Tronnier VM**, Wirtz CR, Knauth M, Lenz G, Pastyr O, Bonsanto MM, Albert FK, Kuth R, Staubert A, Schlegel W, Sartor K, Kunze S. Intraoperative diagnostic and interventional magnetic resonance imaging in neurosurgery. *Neurosurgery* 1997; **40**: 891-900; discussion 900-902 [PMID: 9149246 DOI: 10.1097/00006123-199705000-00001]
 - 15 **Hall WA**, Martin AJ, Liu H, Pozza CH, Casey SO, Michel E, Nussbaum ES, Maxwell RE, Truwit CL. High-field strength interventional magnetic resonance imaging for pediatric neurosurgery. *Pediatr Neurosurg* 1998; **29**: 253-259 [PMID: 9917543 DOI: 10.1159/000028732]
 - 16 **Nimsky C**, Ganslandt O, Von Keller B, Romstöck J, Fahlbusch R. Intraoperative high-field-strength MR imaging: implementation and experience in 200 patients. *Radiology* 2004; **233**: 67-78 [PMID: 15317949 DOI: 10.1148/radiol.2331031352]
 - 17 **Sutherland GR**, Kaibara T, Louw D, Hoult DI, Tomanek B, Saunders J. A mobile high-field magnetic resonance system for neurosurgery. *J Neurosurg* 1999; **91**: 804-813 [PMID: 10541238 DOI: 10.3171/jns.1999.91.5.0804]
 - 18 **Hadani M**, Spiegelman R, Feldman Z, Berkenstadt H, Ram Z. Novel, compact, intraoperative magnetic resonance imaging-guided system for conventional neurosurgical operating rooms. *Neurosurgery* 2001; **48**: 799-807; discussion 807-809 [PMID: 11322440]
 - 19 **Stadlbauer A**, Buchfelder M, Doelken MT, Hammen T, Ganslandt O. Magnetic resonance spectroscopic imaging for visualization of the infiltration zone of glioma. *Cent Eur Neurosurg* 2011; **72**: 63-69 [PMID: 20635312 DOI: 10.1055/s-0030-1253410]
 - 20 **Pamir MN**, Özduman K, Yıldız E, Sav A, Dinçer A. Intraoperative magnetic resonance spectroscopy for identification of residual tumor during low-grade glioma surgery: clinical article. *J Neurosurg* 2013; **118**: 1191-1198 [PMID: 23432196 DOI: 10.3171/2013.1.JNS111561]
 - 21 **Belliveau JW**, Rosen BR, Kantor HL, Rzedzian RR, Kennedy DN, McKinstry RC, Vevea JM, Cohen MS, Pykett IL, Brady TJ. Functional cerebral imaging by susceptibility-contrast NMR. *Magn Reson Med* 1990; **14**: 538-546 [PMID: 2355835 DOI: 10.1002/mrm.1910140311]
 - 22 **Rosen BR**, Belliveau JW, Vevea JM, Brady TJ. Perfusion imaging with NMR contrast agents. *Magn Reson Med* 1990; **14**: 249-265 [PMID: 2345506 DOI: 10.1002/mrm.1910140211]
 - 23 **Edelman RR**, Mattle HP, Atkinson DJ, Hill T, Finn JP, Mayman C, Ronthal M, Hoogewoud HM, Kleefield J. Cerebral blood flow: assessment with dynamic contrast-enhanced T2*-weighted MR imaging at 1.5 T. *Radiology* 1990; **176**: 211-220 [PMID: 2353094]
 - 24 **Conturo TE**, Akbudak E, Kotys MS, Chen ML, Chun SJ, Hsu RM, Sweeney CC, Markham J. Arterial input functions for dynamic susceptibility contrast MRI: requirements and signal options. *J Magn Reson Imaging* 2005; **22**: 697-703 [PMID: 16261571 DOI: 10.1002/jmri.20457]
 - 25 **Østergaard L**. Principles of cerebral perfusion imaging by bolus tracking. *J Magn Reson Imaging* 2005; **22**: 710-717 [PMID: 16261573 DOI: 10.1002/jmri.20460]
 - 26 **Provenzale JM**, Wang GR, Brenner T, Petrella JR, Sorensen AG. Comparison of permeability in high-grade and low-grade brain tumors using dynamic susceptibility contrast MR imaging. *AJR Am J Roentgenol* 2002; **178**: 711-716 [PMID: 11856703 DOI: 10.2214/ajr.178.3.1780711]
 - 27 **Sorensen AG**, Copen WA, Ostergaard L, Buonanno FS, Gonzalez RG, Rordorf G, Rosen BR, Schwamm LH, Weisskoff RM, Koroshetz WJ. Hyperacute stroke: simultaneous measurement of relative cerebral blood volume, relative cerebral blood flow, and mean tissue transit time. *Radiology* 1999; **210**: 519-527 [PMID: 10207439 DOI: 10.1148/radiology.210.2.r99fe06519]
 - 28 **Sugahara T**, Korogi Y, Kochi M, Ikushima I, Hirai T, Okuda T, Shigematsu Y, Liang L, Ge Y, Ushio Y, Takahashi M. Correlation of MR imaging-determined cerebral blood volume maps with histologic and angiographic determination of vascularity of gliomas. *AJR Am J Roentgenol* 1998; **171**: 1479-1486 [PMID: 9843274 DOI: 10.2214/ajr.171.6.9843274]
 - 29 **Emblem KE**, Nedregaard B, Nome T, Due-Tonnessen P, Hald JK, Scheie D, Borota OC, Cvcancarova M, Bjornerud A. Glioma grading by using histogram analysis of blood volume heterogeneity from MR-derived cerebral blood volume maps. *Radiology* 2008; **247**: 808-817 [PMID: 18487536 DOI: 10.1148/radiol.2473070571]
 - 30 **Rasmussen M**, Juul N, Christensen SM, Jónsdóttir KY, Gyldensted C, Vestergaard-Poulsen P, Cold GE, Østergaard L. Cerebral blood flow, blood volume, and mean transit time responses to propofol and indomethacin in peritumor and contralateral brain regions: perioperative perfusion-weighted magnetic resonance imaging in patients with brain tumors. *Anesthesiology* 2010; **112**: 50-56 [PMID: 19952725 DOI: 10.1097/ALN.0b013e3181c38bd3]
 - 31 **Brix G**, Semmler W, Port R, Schad LR, Layer G, Lorenz WJ. Pharmacokinetic parameters in CNS Gd-DTPA enhanced MR imaging. *J Comput Assist Tomogr* 1991; **15**: 621-628 [PMID: 2061479 DOI: 10.1097/00004728-199107000-00018]
 - 32 **Bullock PR**, Mansfield P, Gowland P, Worthington BS, Firth JL. Dynamic imaging of contrast enhancement in brain tumors. *Magn Reson Med* 1991; **19**: 293-298 [PMID: 1881318 DOI: 10.1002/mrm.1910190217]
 - 33 **Donahue KM**, Weisskoff RM, Parmelee DJ, Callahan RJ,

Ulmer S. Intraoperative MR perfusion imaging

Wilkinson RA, Mandeville JB, Rosen BR. Dynamic Gd-DTPA enhanced MRI measurement of tissue cell volume fraction. *Magn Reson Med* 1995; **34**: 423-432 [PMID: 7500882 DOI: 10.1002/mrm.1910340320]

34 **Kriss TC**, Kriss VM. History of the operating microscope: from magnifying glass to microneurosurgery. *Neurosurgery* 1998; **42**: 899-907; discussion 907-908 [PMID: 9574655 DOI: 10.1097/00006123-199804000-00116]

P- Reviewer: Sivak S **S- Editor:** Ji FF
L- Editor: Roemmele A **E- Editor:** Liu SQ



Imaging of the temporomandibular joint: An update

Asim K Bag, Santhosh Gaddikeri, Aparna Singhal, Simms Hardin, Benson D Tran, Josue A Medina, Joel K Curé

Asim K Bag, Aparna Singhal, Simms Hardin, Benson D Tran, Josue A Medina, Joel K Curé, Section of Neuroradiology, The Department of Radiology, School of Medicine, The University of Alabama at Birmingham, Birmingham, AL 35249-6830, United States

Santhosh Gaddikeri, Department of Radiology, University of Washington, SS-202 Seattle, WA 98195-7117, United States

Author contributions: Bag AK contributed to the arthritis, images and overall integrity, manuscript revision and final approval the manuscript; Gaddikeri S contributed to the internal derangement and manuscript revision; Singhal A contributed to the normal joint anatomy, anatomic variation and manuscript revision; Hardin S contributed to the anatomic variation and manuscript revision; Tran BD contributed to the deposition diseases and tumors, manuscript revision; Medina JA contributed to the imaging techniques, manuscript revision; Curé JK contributed to the images, overall integrity, manuscript revision and final approval.

Correspondence to: Asim K Bag, Assistant Professor, Section of Neuroradiology, The Department of Radiology, School of Medicine, The University of Alabama at Birmingham, JT N432, 619 19th Street South, Birmingham, AL 35249-6830, United States. abag@uabmc.edu

Telephone: +1-205-9349952 Fax: +1-205-9759262

Received: December 28, 2013 Revised: February 27, 2014

Accepted: June 20, 2014

Published online: March 28, 2015

tumors are also discussed in this article.

© 2015 Baishideng Publishing Group Inc. All rights reserved.

Key words: Temporomandibular joint; Magnetic resonance imaging; Imaging; Computed tomography; Anatomy; Pathologies

Core tip: "Imaging of the temporomandibular joint: An update" is a thorough review of the imaging techniques and imaging appearances of normal anatomy, anatomic variation and pathologies of the temporomandibular joint (TMJ). Numerous images are appropriately used for illustration of the key concepts of TMJ imaging. Nice blend of exquisite details and beautiful illustrative images is the main feature of this article. The purpose of this article is easy understanding of many difficult aspects of imaging of the TMJ.

Original sources: Bag AK, Gaddikeri S, Singhal A, Hardin S, Tran BD, Medina JA, Curé JK. Imaging of the temporomandibular joint: An update. *World J Radiol* 2014; 6(8): 567-582 Available from: URL: <http://www.wjgnet.com/1949-8470/full/v6/i8/567.htm> DOI: <http://dx.doi.org/10.4329/wjr.v6.i8.567>

Abstract

Imaging of the temporomandibular joint (TMJ) is continuously evolving with advancement of imaging technologies. Many different imaging modalities are currently used to evaluate the TMJ. Magnetic resonance imaging is commonly used for evaluation of the TMJ due to its superior contrast resolution and its ability to acquire dynamic imaging for demonstration of the functionality of the joint. Computed tomography and ultrasound imaging have specific indication in imaging of the TMJ. This article focuses on state of the art imaging of the temporomandibular joint. Relevant normal anatomy and biomechanics of movement of the TMJ are discussed for better understanding of many TMJ pathologies. Imaging of internal derangements is discussed in detail. Different arthropathies and common

INTRODUCTION

Pain related to the temporomandibular joint (TMJ) is common in the general population. Only about 3%-7% of the patients with pain related to TMJ seek medical attention^[1,2]. Although TMJ disorders or dysfunctions are the most common clinical conditions for imaging referrals, pathologies specific to the bone and the joints are also common. Different imaging modalities are available to image the TMJ, each with inherent strengths and weaknesses. Magnetic resonance imaging (MRI) is the most widely used and is diagnostic technique of choice. In this article, we review the imaging techniques, anatomy pathology involving the TMJ with special emphasis on MRI findings.

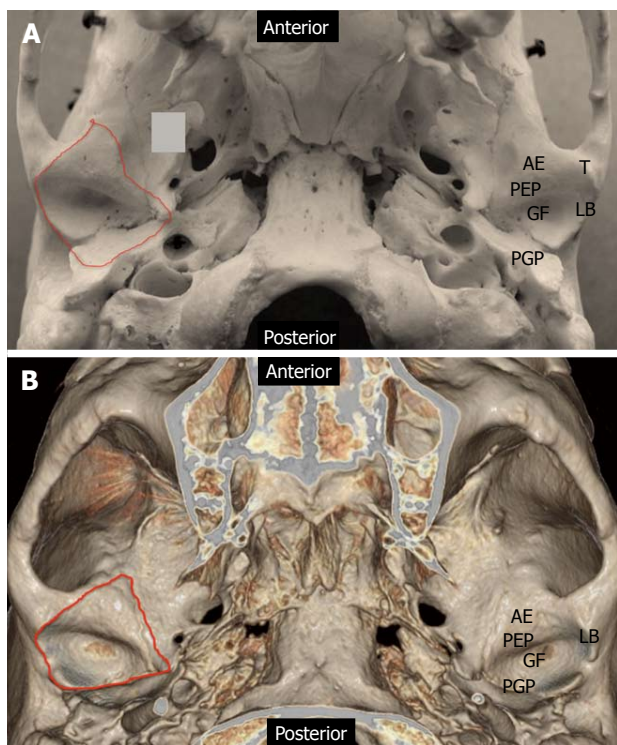


Figure 1 Anatomy of the cranial component of temporomandibular joint.
 A: Photograph of skull specimen; B: 3-D volume rendered image obtained from a temporal bone. Redline demonstrates the capsular attachment. AE: Articular eminence; GF: Glenoid fossa; LB: Lateral border; PEP: Preglenoid plane; PGP: Postglenoid plane; T: Tubercle.

Embryology and development of TMJ

The TMJ is one of the last diarthrodial joints to appear in utero and does not emerge in the craniofacial region until the 8th week of gestation. The maxilla, mandible, muscles of mastication, and biconcave disc develop embryologically from the first branchial arch through the 14th week of gestation. The TMJ is considerably underdeveloped at birth in comparison to other diarthrodial joints making it susceptible to perinatal and postnatal insults. The joint continues developing in the early childhood years as the jaw is utilized for sucking motions and eventually chewing.

ANATOMY OF TMJ

The TMJ is a ginglymoarthrodial synovial joint (Latin: ginglymus = hinge joint) that allows both backward and forward translation as well as a gliding motion^[3]. Similar to the other synovial joints in the body, the TMJ has a disk, articular surfaces, fibrous capsule, synovial fluid, synovial membrane, and ligaments. What makes this joint unique is the articular surfaces are covered by fibrocartilage instead of hyaline cartilage. The articular surfaces of the TMJ are formed inferiorly by the mandibular condyle and superiorly by the glenoid fossa (also known as mandibular fossa) and articular eminence of the temporal bone.

Articular surfaces

The mandibular component consists of the ovoid con-

dylar process that is 15-20 mm wide in the transverse dimension and 8-10 mm wide in the antero-posterior dimension^[3]. The appearance of the mandibular condyle is extremely variable between patients and in different age groups.

The cranial component of the TMJ lies below the squamous portion of the temporal bone anterior to tympanic plate. The articular fossa is formed entirely by the squamous portion of the temporal bone. The posterior part of the articular fossa is elevated to form the posterior articular ridge. In most individuals the posterior articular ridge becomes thicker on the lateral aspect and forms a cone shaped projection known as postglenoid process (PGP). The tympanosquamosal fissure lies at the posterior and lateral part of the glenoid fossa, between the squamous and tympanic portion of the petrous bone and separates the articular surface from the nonarticular surface of the glenoid fossa. Along the medial aspect of the glenoid fossa is the petrotympanic fissure anteriorly and the petrosquamous fissure posteriorly. The articular eminence (AE) forms the anterior boundary of the glenoid fossa. The AE is a transverse bony bar anterior to the glenoid fossa and medial to the posterior margin of the zygomatic process. The anterior slope of the AE is known as the preglenoid plane (PEP) and rises gently from the infratemporal surface of the squamous bone. The mandibular condyle and the articular disk travel anteriorly to the summit of the AE and onto PEP during wide mouth opening. The gentle anterior slope facilitates smooth backward movement of the condyle and disk from the anterior position back to neutral position. The articular tubercle is a small bony knob at the lateral aspect of the AE where the lateral collateral ligament attaches. The lateral border of glenoid fossa is slightly raised from the fossa joining the anterior tubercle with the PGP (Figure 1).

Articular disk

The articular disk is round or oval, biconcave, avascular fibrocartilage between the condyle and glenoid fossa. The disk is considerably thinner centrally in the intermediate zone. The triangular anterior band is approximately 2 mm in thickness and blends with the joint capsule. The posterior band is approximately 3 mm in thickness and continues as bilaminar zone (also known as retrodiscal region and posterior attachment), which consists of superior fibroelastic layer (also known as temporal lamina) that attaches to PGP and an inferior fibrous layer (also known as the inferior lamina) that attaches to the posterior condylar neck. The superior layer prevents slipping of the disk during wide mouth opening and the inferior layer prevents excessive rotation of the disk over the condyle. Both the lamina are separated by loose elastic fibers with blood vessels and nerves. These fibers attach to the posterior joint capsule and augments disk retraction during mouth closing. The bands are longer in the mediolateral dimension than in the antero-posterior dimension^[4]. The smaller anterior band attaches anteriorly to the joint

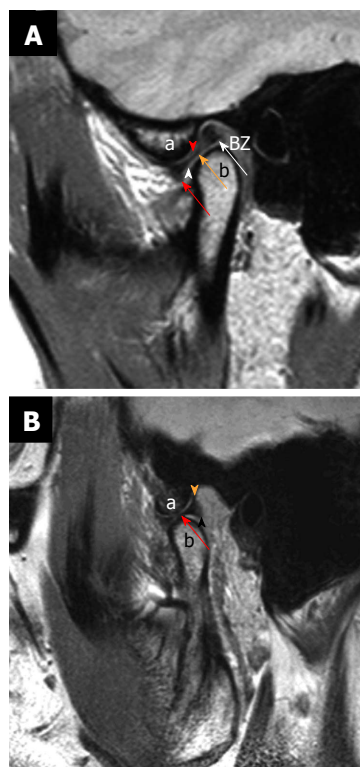


Figure 2 Normal anatomy. Sagittal proton density weighted closed mouth and open mouth view of magnetic resonance imaging. A: On the closed mouth view, the disk is located posterior to the articular eminence (the letter, a). It can be noted that the “bow-tie” shape of the disk: Thicker anterior band (red arrow) and posterior band (white arrow) with a thinner central zone (orange arrow). Bilaminar zone (BZ) is located posterior to the posterior band. It can also be noted that the inferior joint compartment (white arrowhead) between the disk and the mandibular condyle (the letter, b) and superior joint compartment (red arrowhead) between the articular eminence and the disk; B: On the open mouth view (in a different patient), the thinner intermediate zone (red arrow) of the disk is interposed between the articular eminence (the letter, a) and the condylar head (the letter, b) in a “bow-tie” fashion. Orange arrowhead demonstrates temporal lamina and black arrowhead indicate inferior lamina.

capsule, condylar head, and AE. Some patients have an additional antero-medial attachment to the superior belly of the lateral pterygoid muscle. Unlike its anterior and posterior attachments, the disk is not attached to the joint capsule medially and laterally. Instead, the disk is firmly attached to the medial and lateral poles of the mandibular condyle. This allows simultaneous movements of the disk and the condyle (Figure 2).

Muscles

The muscles of mastication (medial and lateral pterygoids, masseter, and temporalis) in addition to other accessory muscles help opening and closing of the jaw^[4,6]. The lateral pterygoid in conjunction to the stylohyoid, mylohyoid and geniohyoid muscles is used to open the jaw. The temporalis, medial pterygoid, and masseter muscles close the jaw. The lateral pterygoid, part of the masseter muscle and the medial pterygoid assist in the anterior translation of the mandible. The protrusive muscles (helping forward movement) are used alternately to move the jaw laterally from side to side. Individual muscle origins and attachments are listed below^[4,6].

Jaw-closing muscles/adductors

The masseter is the strongest muscle of mastication and has two parts that blend together anteriorly. The superficial part originates from the anterior two-thirds of the zygomatic arch and inserts on the lower one-third of the lateral surface of the mandibular ramus. The deep part originates from the entire zygomatic arch and inserts on the upper two-thirds of the ramus.

The medial pterygoid courses parallel to the masseter along the medial aspect of the mandible. The anterior part arises from the lateral surface of the palatine pyramidal process and the maxillary tuberosity. The posterior part originates from the pterygoid fossa and the medial surface of the lateral pterygoid plate. The medial pterygoid inserts on the inferomedial surface of the mandibular ramus.

The temporalis muscle originates from the temporalis fossa and inserts on the coronoid process and inner side of the mandibular ramus. The fibers also attach directly to the medial side of the coronoid process and ramus.

Jaw-opening muscles/abductors

The lateral pterygoid muscle has two bellies. The superior belly originates from the infratemporal surface of the greater wing of sphenoid. The inferior belly originates from the lateral surface of the lateral pterygoid plate. There is a wide gap between the two heads of the lateral pterygoid muscle that come together anterior to the TMJ. The fibers from the superior head primarily attach to the anteromedial surface of the mandibular neck at the pterygoid fovea. Additionally, in some patients part of the superior head directly attaches to the superomedial aspect of the joint capsule and extends to the anteromedial aspect of the articular surface. All of the fibers of the inferior head attach to the pterygoid fovea. Variability in the attachment of the lateral pterygoid muscle is reported with insertions of the muscle described only to the condyle or to the condyle, capsule, and the disk^[7,9].

The superior belly helps maintain the physiologic position of the disk in the open mouth position. This is accomplished by pulling the disk forward with a combined translation and rotation while exerting forward pressure on both the condyle and the disk thus stabilizing their relationship to each other. The inferior belly pulls the condyle forward out of the fossa. When the inferior belly alternately contracts, this produces lateral movement of the jaw.

The digastric muscle has a posterior and an anterior belly united by a conjoined tendon. The posterior belly is attached to the mastoid process of the temporal bone and extends to the hyoid bone becoming continuous with the intermediate tendon. A fibrous loop attached to the hyoid holds the tendon in place. The anterior belly extends from the tendon to the digastric fossa on the lower aspect of mandible near the symphysis. Contraction of the digastric muscles pulls the symphysis menti backwards producing the retrusive and opening movements of the mandible.

The geniohyoid, mylohyoid, stylohyoid and infra-

hyoid muscles also have supportive role in mandibular movements that are beyond the scope of this review.

Biomechanics of TMJ movements

Jaw movement involves a high level of interaction and coordination between bilateral mandibular condyles, disk, muscles, and ligaments of the joints. The functional interactions within the TMJ are complex and incompletely understood^[10,11]. A simplistic view of the complex interactions in open and closed mouth positions is described below.

In a normal joint, the thin intermediate zone of the disk is always interposed between the condyle and the temporal bone in both the closed-mouth and open-mouth positions. This is for the prevention of articular damage.

In the closed mouth position, the condyle is centered in the glenoid fossa. The disk is interposed between the condyle inferiorly and the glenoid fossa superiorly. The articular eminence is anterior to the disk (Figure 2). The normal disk is positioned such that the anterior band is in front of the condyle and the junction of the posterior band and bilaminar zone lie immediately above the condylar head near the 12 o'clock position^[1,3,4,9,12-14]. However, some controversy exists over the range of normal position of the disk^[1,3,4,14-18]. Drace *et al*^[15] suggest that the junction of the posterior band and bilaminar zone should fall within 10 degree of vertical to be within 95 percentile of normal. There is significant variation in relationship of the posterior band and bilaminar zone in normal population, resulting in inappropriate classification of anterior disk displacement^[16,18]. Rammelsberg *et al*^[17] suggest that disk positions of up to +30° from the vertical be considered normal. Many other authors have proposed that the intermediate zone be the point of reference so that in a normal joint it is interposed between the condyle and the temporal bone in all joint positions^[4,19,20]. Comparing to the different disk positions of 12, 11 and 10 o'clock, Orsini *et al*^[19] found the intermediate zone criterion for disk displacement to be more stringent. Recently Provenzano Mde *et al*^[20] have suggested similar conclusions (Figure 2).

IMAGING TECHNIQUES

A variety of modalities can be used to image the TMJ. This includes non-invasive imaging modalities such as conventional radiographs, ultrasound, Computed tomography (CT) and MRI to more invasive imaging such as arthrography. Each imaging modality has its uses.

Conventional radiographs have a limited role in evaluation of the TMJ. They can be used to evaluate only the bony elements of the TMJ. They do not give useful information when it comes to the non-bony elements such as cartilage or adjacent soft tissues. They also do not give useful information concerning joint effusions, which are commonly associated with pain and disc displacements. Another disadvantage concerning conventional radiographs is the problem of superimposition of adjacent

structures. Many different views such as the submentovertex, transmaxillary, and the transcranial are used to reduce superimposition.

Ultrasound is a less expensive and easily performed imaging modality that can be used to evaluate the TMJ. This is simple way to look for the presence of a joint effusion^[21]. Ultrasound is also used to evaluate cartilage as well as disk displacement with both open and closed mouth imaging^[21]. It is used for image-guided injections for both diagnostic and therapeutic purposes^[21]. Typically, a linear transducer of 8 MHz or higher is ideal. The patient should be lying supine with the transducer placed parallel to a line extending from the tragus of the ear to the lateral surface of the nose over the TMJ.

CT is useful to evaluate the bony elements of the TMJ as well as the adjacent soft tissues. CT is ideal for the evaluation of fractures, degenerative changes, erosions, infection, invasion by tumor, as well as congenital anomalies^[21]. A typical imaging protocol is: 120 kV, 100 mA, 1 mm collimation, 1 mm/rotation (pitch), and imaged with a closed mouth. CT also allows 3D reconstructions, which can be used for evaluating congenital anomalies and fractures^[21]. CT is predominantly done when there is suspicion of bony involvement from the MRI and if primary bony pathologies are suspected clinically. Relative advantages of CT over MRI include, exquisite bone details and 3D assessment of congenital, traumatic and postsurgical conditions.

Clinical evaluation of the TMJ can be nonspecific due to overlap of symptoms between internal derangement and myofascial pain dysfunction^[1]. MRI should be part of the standard evaluation when an internal structural joint abnormality is suspected because MRI provides high resolution and great tissue contrast. This allows for a detailed evaluation of the anatomy as well as biomechanics of the joint through open and closed mouth imaging^[1].

For optimal imaging of the TMJ, small bilateral surface coils with small field of view are used to achieve higher signal to noise ratio and simultaneous bilateral acquisition. Closed mouth coronal and axial T1 sequences are needed to evaluate the overall anatomy and bone marrow as well as the adjacent soft tissues to exclude other adjacent pathology. In our institution, axial T1 is obtained as a localizer^[14]. Bilateral closed mouth and open mouth T2, proton density (PD) and dynamic sequences are obtained in a oblique sagittal plane. In our institution, dynamic images are obtained as rapid acquisition of static images using a single shot fast spin echo (SSFSE) proton density sequence during progressive opening and closing of the mouth. These images are displayed sequentially as a cine loop. Mouth opening devices such as Burnett opening devices may be used for incremental opening of the mouth controlled by the patient. It can be argued that passive mouth opening with a Burnett device might not reproduce the physiologic conditions occurring during mouth opening given the possible role of the lateral pterygoid muscle in disc stabilization during mouth opening. Oblique imaging entails 30° medial

Table 1 Temporomandibular joint magnetic resonance imaging protocol

Plane	Sequence	Slice thickness	TR	TE	Mouth open/closed
Axial	T1	2 mm, 0 skip	500	Minimal	Closed
Coronal	T1	3 mm, 0.5 skip	500	Minimal	Closed
Bilateral Sag Oblq	T2 and PD	3 mm	3500	Min and 85	Closed and open
Bilateral Sag Oblq	T2	3 mm	1180-2000	64	Dynamic cine

PD: Proton density; TE: Echo time; TR: Repetition time.

from the true sagittal plane^[1]. Please see the table for specific MRI protocol^[1]. A total of 8 sequences will need to be performed (Table 1).

Arthrography is an invasive imaging technique to evaluate the TMJ. This imaging modality requires injection of radiopaque contrast into the TMJ under fluoroscopic guidance. Once the contrast is injected, the joint can be evaluated for adhesions, disk dysfunction, as well as disk perforation based on how contrast flows in the joint. This modality is rarely used today because MRI can be used to evaluate the TMJ without being invasive, exposing the patient to a possibility of allergic reaction from the contrast, possibility of infection, or using radiation.

IMAGING APPEARANCE OF NORMAL TMJ

MRI

On MRI, marrow fat in the condyle has a high T1 signal intensity. The cortical bone and the disk have low signal intensity on both T1 and T2 weighted images because of low proton density and short T2^[12]. Sometimes high T2 and PD signal intensity can be seen in the central portion of the disk similar to a centrally hydrated vertebral disk^[1,4]. The disk is otherwise homogeneous, hypointense and biconcave in shape. The center of the posterior band may be slightly hyperintense due to presence of loose areolar tissue (Figure 2).

The disk's posterior attachment has higher signal intensity than muscle on proton density and T1 weighted images secondary to fatty tissue. The bilaminar zone is visible as intermediate signal intensity structures.

In closed mouth position, the junction of the posterior band and posterior attachment normally lies above the condylar head near the 12 o'clock position. The posterior band and retrodiskal tissue are best depicted in the open mouth position. In open mouth position, the intermediate zone lies between the condyle and the articular eminence and the posterior band is against the posterior surface of the condyle^[1,9] (Figure 2).

The superior belly of lateral pterygoid attaches to the anterior band of the disk. The inferior belly of the lateral pterygoid attaches to the anterior surface of the condylar neck with a thin linear hypointense fibrous band. This band is seen just inferior to the position of the disk, and can sometimes be mistaken for the disk, particularly when the disk is medially or laterally displaced^[22].

In the coronal plane, the disk is crescent shaped and

its medial and lateral borders are attached to the respective aspects of the condylar head and joint capsule. The lateral and medial capsules do not demonstrate any outward bulges beyond the borders in normal condition^[1,22].

PATHOLOGIES RELATED TO ANATOMIC VARIATIONS

Anatomic variations in the TMJ can be symptomatic and/or have implications during arthroscopy and surgery. There can also be several variations in the appearance of the mandibular condyles including intra-individual variations between the two sides. The disease processes can be developmental, due to remodeling related to malocclusion, trauma or other secondary developmental abnormalities^[3].

Bifid condyle

A bi-lobed or duplicated mandibular head is an infrequently encountered incidental imaging finding. While the etiology is unknown, theories include reminiscence of congenital fibrous septum and peripartum or early childhood trauma. The duplicated heads may lie in either an antero-posterior or transverse orientation. Dennison *et al.*^[23] have suggested that the term "bifid condyle" should be reserved for describing multiple condyles in the sagittal plane only. No treatment is required for asymptomatic patients. However surgery may be performed if there is displacement of the disc or ankylosis of the joint space (Figure 3).

Foramen of Huschke

In some individuals there may be persistence of a developmental defect in the tympanic plate. The tympanic plate is present as an incomplete U-shaped cartilaginous ring at birth. Over time the ossification proceeds laterally and posteriorly leaving a defect in the floor of the external meatus, called the foramen tympanicum (foramen of Huschke). With growth of the mastoid process, this defect changes in position from inferior to anterior and usually closes by the 5th year of life. Rarely, a 3-4 mm defect persists and is found to be located at the antero-inferior aspect of the external auditory canal and posteromedial to the TMJ. These patients can present with a defect or polyp on the anterior wall of the external auditory canal (EAC) or with salivary otorrhea during mastication. TMJ tissue may also herniate into the EAC during mastication^[24,25]. During arthroscopy, there can be inadvertent



Figure 3 Bifid condyle. Coronal reformatted computed tomography image through the temporomandibular joint (TMJ) demonstrates bifid left mandibular condyle. It can be noted that one of the condyles (arrow) is smaller than the other. Advanced degenerative changes are noted in bilateral TMJ.



Figure 4 Foramen of Huschke. Sagittal reformatted computed tomography image through the temporomandibular joint demonstrates a focal defect (arrow) in the tympanic plate.

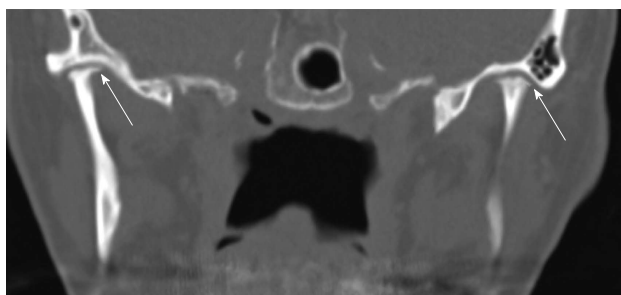


Figure 5 Idiopathic condylar resorption. Coronal reformatted computed tomography image through the temporomandibular joint of a young patient demonstrates bilateral severe condylar resorption (arrows) without any evidence of degenerative changes within the joint.

passage into the EAC resulting in otologic complications. This foramen also can act as a path of communication between the EAC and TMJ or infratemporal fossa allowing the spread of infection, inflammation or tumor^[24,25] (Figure 4).

Condylar hypoplasia

Aplasia and hypoplasia of the mandibular condyle is

secondary to non-development or underdevelopment of the condyle and can be congenital or acquired. Congenital aplasia or hypoplasia of the mandibular condyles is a rare anomaly and usually occurs as a part of more widespread 1st and 2nd branchial arch anomalies (*e.g.*, Treacher-Collins syndrome). Acquired condylar hypoplasia may be secondary to local factors (trauma, infection, radiation) or systemic factors (toxic agents, rheumatoid arthritis, mucopolysaccharoidosis)^[26]. Traumatic vaginal delivery has been implicated as a cause of hypoplasia^[27]. Hypoplasia may involve one or both of the condyles. Unilateral disease produces mandibular rotation or tilt and associated facial asymmetry. The diagnosis of bilateral condylar hypoplasia may be delayed secondary to facial symmetry. Hypoplastic condyles are frequently complicated with ankylosis^[28].

Idiopathic condylar resorption

Idiopathic condylar resorption (also known as condylitis or “cheerleader syndrome”) is primarily a disease of TMJ affecting teenage girls. There is rapidly progressive condylar erosion resulting in widening of the joint space with the chin becoming less prominent from retrognathia^[29]. Many causes have been hypothesized including estrogen influence on osteogenesis, avascular necrosis, and TMJ internal derangement. Orthognathic surgery has been implicated as a cause of the disease but also is one of the corrective approaches for idiopathic condylar resorption (Figure 5).

Condylar hyperplasia

Condylar hyperplasia is a rare disorder characterized by increased volume of the mandibular condyle, and is frequently associated with increased volume of the ramus and mandibular body^[30]. Condylar hyperplasia is usually a unilateral process. This disease presents in the second and third decades of life during brisk periods of osteogenesis suggesting a hormonal influence upon the growth disturbance. Trauma has also been implicated in asymmetric condylar hyperplasia due to hypervascularity during healing producing excessive osteogenesis. The hyperplasia produces facial asymmetry with the chin rotating away from the affected side^[30]. Resection of the hyperplastic condyle causes the abnormal growth to cease and restores facial symmetry (Figure 6).

Extensive pneumatization

Extensive pneumatization of the mastoid bone can involve the glenoid fossa and articular eminence. Knowledge of extensive pneumatization is necessary prior to surgery to prevent perforations. Complications can occur during TMJ surgery due to forceful flap retraction, dissection or with placement of screws in cases where fossa-eminence prostheses are required^[31,32]. Pneumatization can also provide a path of minimal resistance and facilitate the spread of pathological tumors, inflammation, infection or fracture into the joint. For these reasons, a CT must be performed prior to TMJ surgery when ex-



Figure 6 Condylar hyperplasia. Panoramic reformation of the source computed tomography data including both the temporomandibular joints of a young patient demonstrates hyperplasia of the left condyle (arrowhead) in comparison to the right side. Associated hypertrophy of the ramus and the neck (arrow) of the left hemi-mandible is also noted.

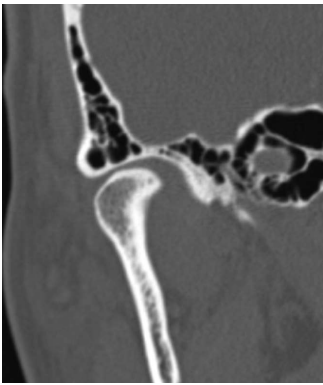


Figure 7 Extensive pneumatization. Coronal reformatted computed tomography image through the right temporomandibular joint demonstrates almost complete pneumatization of the glenoid fossa except the central part.

tensive pneumatization is detected in the panoramic radiographs^[31,32] (Figure 7).

INTERNAL DERANGEMENT OF TMJ

Internal derangement (ID) is defined as a mechanical fault of the joint that interferes with smooth joint function. This is attributed to abnormal interaction of the articular disc, condyle and articular eminence. Associated clinical features include articular pain and articular noises^[33]. Disc displacement is the most common cause of ID, though not all displaced discs are associated with derangement and not all derangements are caused by disc displacement^[34]. Additionally, it is not clear whether the displaced disc is related to onset, progression or cessation of the pain. Loose bodies and adhesions in the joint can also result in derangement. Up to 34% of asymptomatic volunteers can have anterior disc displacement and 23% of patients with derangement can have normal disc position^[18]. In most large MRI series approximately 80% of patients referred for diagnostic imaging of the TMJ demonstrate some form of disk displacement^[35-37]. MRI is the imaging modality of choice for the diagnosis of internal derangement with an accuracy of 95% in assessing the

disc position and form and 93% accuracy in assessing the osseous changes^[38].

Disc displacement

The disc displacement is categorized based on the relation of the displaced disc with mandibular condyle. The displacement can be anterior, anterolateral, anteromedial, lateral, medial and posterior^[39]. The most common pattern of disc displacement are either anterior and anterolateral accounting for more than 80% of the causes^[37]. The disc displacement can be subclassified as anterior displacement with reduction (ADR) or anterior displacement with no reduction (ADNR) based on restoration of a normal relationship between the condyle and the disc on mouth opening (Figures 8 and 9). The disc displacement can be either complete or partial^[35]. If the entire mediolateral dimension of the disc is displaced, it is referred to as complete displacement. On the other hand if only the medial or lateral portion of the disc is displaced, it is referred to as partial displacement. Partial disc displacement is commonly seen with ADR. Frequently the lateral part of the disc is displaced anteriorly while the medial part of the disc remains in normal position (rotational disk displacement)^[40].

In ADR, the anteriorly displaced disc returns to the normal position on mouth opening producing a “reciprocal click” (Figure 9). In ADNR, there is limited mouth opening and deviation of the jaw to the affected side (closed lock). Over time, stretching or perforation of the retrodiscal tissue causes deformation of the disk leading to an improvement in jaw excursion and reduced lateral deviation during mouth opening (Figure 10A). The posterior band of the disc remains anterior to the condyle even with mouth opening^[41]. There is increased association of degenerative changes in the TMJ with the ADNR. Although TMJ disorder with ADR and normal condylar cortical bone may be stable for decades, it will eventually progress to ADNR. In a study with 55 patients, de Leeuw *et al.*^[42] have demonstrated 75% of the patients with long history (approximately 30 years) of TMJ internal derangement have ADNR.

The exact mechanism for a disc displacement is unknown although trauma with injury to the posterior disc attachment is considered to be the most likely cause. Unenhanced MRI is the imaging modality of choice for evaluation of ID. During the early stage of ID the disc retains its normal shape, but over time it becomes deformed by thickening of the posterior band and thinning of the anterior band. This produces in a biconvex, teardrop shaped or a rounded disc. The disc maintains a normal biconcave shape as long as it remains on top of the condyle during mouth opening^[42]. Hence, presence of an irregular and rounded disc almost always indicates disc disease^[43]. Other MRI findings that suggest disc disease include disc flattening, decrease in the normal intermediate to high signal intensity of the disc^[44] and presence of tear or perforation in the chronic stage.

Posterior disc displacement is a rare entity and acco-

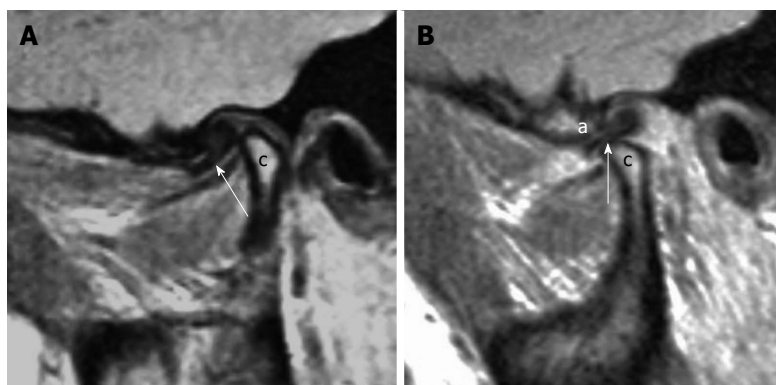


Figure 8 Anterior displacement with reduction. A: Sagittal proton density weighted magnetic resonance imaging (MRI) in the closed mouth position demonstrates anterior displacement of the disk (arrow) in front of the mandibular condyle (the letter, c); B: Sagittal proton density weighted MRI in the open mouth position demonstrates reduction of the disk (arrow) between the articular eminence (the letter, a) and the mandibular condyle (the letter, c).

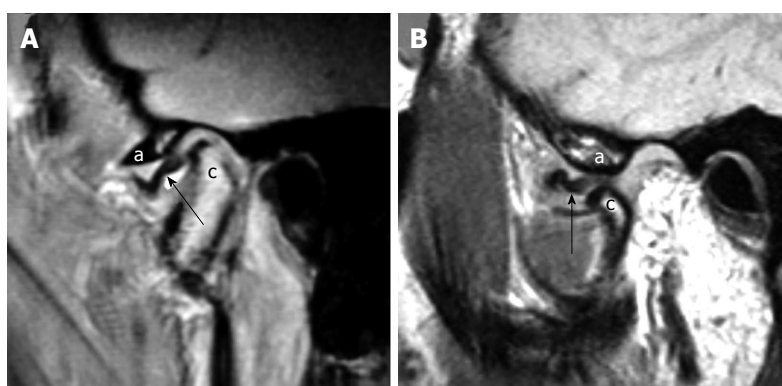


Figure 9 Anterior displacement with no reduction. A: Sagittal proton density weighted magnetic resonance imaging (MRI) in the closed mouth position demonstrates anterior displacement of the disk (arrow) related to the articular eminence (the letter, a) and anterior to the mandibular condyle (the letter, c); B: Sagittal proton density weighted MRI in the open mouth position demonstrates no reduction of the disk (arrow) between the articular eminence (the letter, a) and the mandibular condyle (the letter, c).



Figure 10 Other types of disk displacement. A: Posterior disk displacement. Sagittal proton density weighted magnetic resonance imaging (MRI) in the closed mouth position demonstrates posterior displacement of the disk (arrow) in relation to the mandibular condyle (the letter, c); B: Lateral disk displacement. Coronal proton density weighted demonstrates lateral displacement of the disk (arrow) in relation to the mandibular condyle (the letter, c); C: Pseudodisk. Sagittal proton density weighted MRI in the closed mouth position demonstrates anterior displacement of the disk (arrow) in front of the mandibular condyle (the letter, c). The thickening of the posterior attachments (arrowheads) superior to the mandibular condyle is seen as “pseudodisk”.

unts for only 0.01% to 0.001% of all disc displacements^[45]. The major clinical sign is a sudden onset of locked jaw in open position. MRI is helpful in the diagnosis by demonstrating displacement of the posterior band beyond 1° clock position^[9] (Figure 10A). Review of patient’s clinical

information is important before image interpretation as previous posterior disk plication can be mistaken for an acquired posterior disk displacement.

Anterolateral and antero-medial disk displacements are grouped under rotational displacements while the

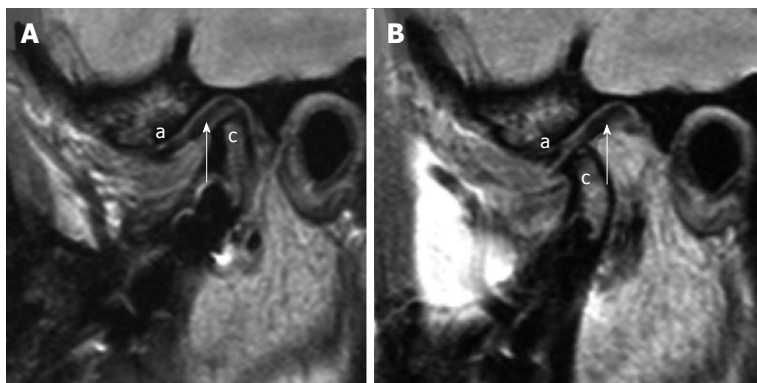


Figure 11 Stuck disk. A: Sagittal proton density weighted magnetic resonance imaging (MRI) in the closed mouth position demonstrates apparently normal position of the disk (arrow) in relation to the mandibular condyle (the letter, c). The letter “a” demonstrates the articular eminence; B: Sagittal proton density weighted MRI in the open mouth position demonstrates no anterior movement of the disk (arrow) with the mandibular condyle (the letter, c), *i.e.*, “stuck” to the glenoid fossa. The articular eminence is denoted with letter “a”.

pure lateral and medial displacements are grouped under sideways displacement^[46]. Isolated lateral displacement is rare (Figure 10B). Again these rotational and sideways displacements can be complete or partial and with or without disc reduction. Anterolateral displacement is the most common pattern^[37].

Pseudodisk

A pseudo-disk is present in some patients with an anteriorly displaced disk. This has been postulated as an adaptive reaction to anterior disk displacement within the posterior disk attachment followed by subsequent connective tissue hyalinization that^[47] appears as a band-like structure of low signal intensity replacing the normally bright signal of the posterior disk attachment^[8,9,22] (Figure 10C).

Stuck disc

The “stuck disc” is a pathologic condition characterized by an immobile disc in relation to the glenoid fossa and the articular eminence. This is present in both open and closed mouth positions^[9] and is likely related to the adhesions. It can occur with or without disc displacement and can be associated with pain and joint dysfunction due to limitation of condylar translation^[48,49]. This diagnosis can be missed unless the TMJ is imaged in both open and closed mouth positions (Figure 11). Sagittal oblique cine imaging is particularly useful in evaluation of stuck disc.

Perforated disc

Disc perforation is reported in 5% to 15% of deranged joints disc displacements^[50]. It is more common in patients with ADNR than in ADR^[51,52] and is usually seen in patients with advanced arthrosis. The prevalence of a perforated disc is higher in women than in men and prevalent in individuals over 80 years of age^[53]. MRI findings of disc perforation include disc deformity (100%), disc displacement (81%), condylar bony changes (68%), joint effusion (23%) and non-visualization of temporal posterior attachment (TPA) of the disc (65%-68%)^[54]. Conventional and MR arthrogram can be

helpful in the diagnosis of a disc perforation by demonstrating opacification of both the joint compartments from a single lower compartment injection. If the disc perforation is suspected a fat suppressed T2 weighted MRI can be obtained in sagittal and coronal plane^[55]. Absence of stretching/straightening of the posterior temporal disk attachment on mouth opening also suggests disc perforation.

Joint effusion

Joint effusion represents an abnormally large accumulation of intra-articular fluid and is commonly seen in symptomatic patients. A small amount of joint fluid can be seen in asymptomatic patients^[56]. An effusion is more prevalent in painful than in non-painful joints^[16]. Although not all patients with joint pain have effusion, patients with large effusions commonly experience pain and disc displacement^[57].

T2 weighted MR sequence is the best sequence for the assessment of joint effusion. An early joint effusion is commonly seen surrounding the anterior band but larger effusions can occupy both superior and inferior joint space. A large effusion may have diagnostic value as it outlines the disc and sometimes even the disc perforation as well as retrodiscal tissue producing “arthrographic effect”^[57]. Gadolinium enhanced T1 weighted imaging can be helpful in distinguishing a plain joint effusion from synovial proliferation. In patients with inflammatory arthropathies with associated synovial proliferation, the proliferating synovium enhances while the effusion does not^[58].

Thickening of lateral pterygoid muscle attachment (double disk sign)

The exact role of lateral pterygoid muscle (LPM) in the TMJ function is still controversial although its suggested role is in generation of side-to-side and protrusive jaw forces^[9]. There are electromyographic studies showing hyperactivity in the inferior attachment of the LPM in patients with TMJ internal derangement^[59]. Several mor-

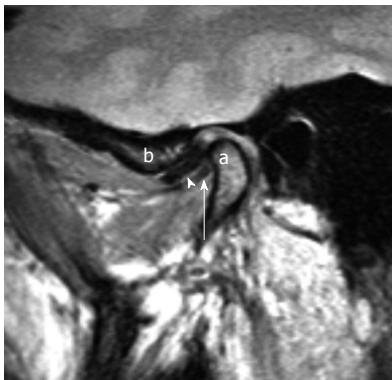


Figure 12 Double disk sign (thickening of the lateral pterygoid muscle). Sagittal closed mouth proton density image demonstrates anterior displacement of the disk (arrow head). The thickened lateral pterygoid muscle near the mandibular condylar (the letter, a) attachment appear as linear hypointense structure (white arrow) inferior to the disk in the same orientation giving the appearance of “double disk”. The articular eminence is denoted with letter “b”.

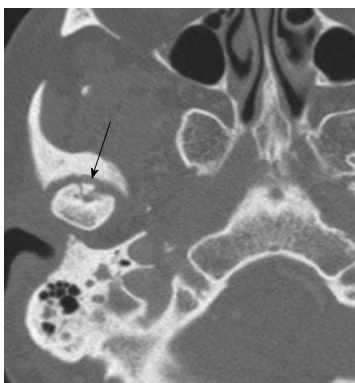


Figure 13 Osteochondritis dessicans. Axial computed tomography scan through the level of the temporomandibular joint demonstrates a tiny bone fragment (arrow) at the anterior aspect of the disk. It can be noted that there are linear lucency surrounding the bone fragment.

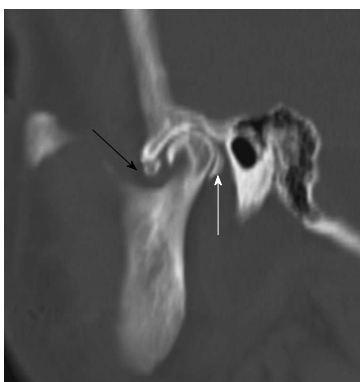


Figure 14 Loose bodies. Sagittal reformation of the axial dataset demonstrates multiple “loose bodies” in the joint cavities, anteroinferior to the articular eminence (black arrow) and immediately posterior to the mandibular condyle (white arrow).

phologic changes to the superior and inferior bellies of the LPM on MRI have been described. These include hypertrophy, atrophy and contractures in patients with

ADNR of the TMJ with these morphologic changes having a significant association with the clinical symptoms of pain or restricted jaw opening^[60]. It is suggested that there is significant association between the anterior disc displacement and attachment of the superior LPM to the disc alone and not to the condyle^[61]. The interpreting radiologist should be aware of a potential pitfall of mistaking the thickened inferior LPM to an anteriorly displaced disc (“double disc sign”)^[9] (Figure 12).

Osteochondritis dissecans and avascular necrosis

Osteochondritis dissecans (OCD) and avascular necrosis (AVN) of the mandibular condyle are similar pathologic entities likely represent a spectrum of the same pathophysiology^[62]. Common clinical features of OCD/AVN of the mandibular condyle include pain and joint disability^[63]. Pain is commonly over the joint and along the third division of the trigeminal nerve. Other symptoms include ipsilateral headache, earache and spasm of masticator muscles. These can occur with or without limitation of joint movements^[63].

MRI is the modality of choice for assessment of OCD/AVN of the mandibular condyle^[63]. There is decreased marrow signal on T1 weighted sequences in cases of AVN. T2 weighted sequences demonstrate variable signal characteristics with early AVN, healing and OCD. Early AVN consistently exhibits high signal on T2WI and acute OCD typically demonstrated a hypointense central fragment surrounded by a zone of higher signal on both T1W and T2W sequences^[63]. Although MRI is 78% sensitive and 84% specific for the diagnosis of AVN, the positive predictive value is only 54% because condylar sclerosis secondary to advanced TMJ degenerative changes have similar MRI appearances^[64]. Radiologic changes of OCD and AVN of the mandibular condyle are frequently associated with joint effusion and internal derangement of the disc^[65] (Figure 13).

Loose bodies

Loose bodies in a synovial joint can be due to primary or secondary synovial chondromatosis. The primary type is associated with spontaneous cartilaginous metaplasia in the synovium, while the secondary type is due to incorporation of osteocartilaginous loose bodies in the synovium in the setting of degenerative joint disease^[66]. Common clinical symptoms associated with loose bodies include pain, periauricular swelling, decreased range of jaw motion, crepitation and unilateral deviation of the jaw during mouth opening^[67].

Panoramic radiographs of the TMJ may or may not demonstrate loose bodies^[68]. High resolution CT^[69,70] or MRI^[70] can demonstrate small loose bodies within the TM joint space (Figure 14).

Hypermobility

Patients with a hypermobile TMJ can present with an inability to close the jaw (open lock) after wide opening of the jaw. This occurs as a result of translation of the



Figure 15 Ankylosis. Coronal reformation of the axial dataset demonstrates complete ankylosis of the right temporomandibular joint (TMJ) and near complete ankylosis of the left TMJ with subtle residual joint space at the center (black arrow).

condyle beyond the margins of the anterior attachment of the TMJ capsule. Entrapment of the condyle along the anterior slope of the articular eminence results due to various biomechanical constraints, particularly masticator muscle activity^[71].

In acute cases, there is little need for imaging studies as the open lock is clinically evident with a relevant clinical history of wide jaw opening or trauma. In chronic cases MRI can give information about the height and steepness of the articular eminences as well as the shape and position of the disc^[72].

Ankylosis

Ankylosis of the TMJ can be due to fibrous adhesions or a bony fusion resulting in the restriction of jaw motion. It can occur as a sequel of previous infection, trauma surgery^[73] and in patients with juvenile idiopathic arthritis or bifid mandibular condyles. MR arthrography is useful for the evaluation of fibrous adhesions and three-dimensional CT scan is necessary for surgical planning when bony fusion is suspected (Figure 15).

TMJ ARTHRITIS

Similar to other synovial joints in body, the TMJ is frequently involved in different inflammatory arthritides. Degenerative arthritis and arthritis secondary to crystal-line deposition disease are also common in TMJ. Arthritis secondary to infection or trauma can occur at the TMJ. Arthritis of TMJ is discussed based on the pathophysiologic mechanism.

Inflammatory arthritis

Juvenile idiopathic arthritis: Juvenile idiopathic arthritis (JIA) is the most common rheumatic disease in childhood affecting girls more frequently than boys. The disease predominantly affects synovial joints. There are two peaks of onset, first being between the ages of 1 and 3 years and the second peak between 8 and 12 years^[74]. The TMJ is involved in 17% to 87% of patients with JIA^[74].

JIA can be systemic, polyarticular and pauciarticular. The TMJ is more commonly involved in patients with polyarticular joint involvement^[75]. The typical presentation of TMJ involvement includes pain, joint tenderness, crepitation, stiffness and decreased range of motion. Bony ankylosis can develop in some patients as a late disease manifestation.

Orthopantomogram, CT, MRI and ultrasound have been used to evaluate TMJ JIA. Orthopantomogram and CT predominantly identify the bony erosions secondary to TMJ involvement. Both these techniques involve radiation exposure to young patients. MRI and ultrasound have gained popularity in evaluation of the TMJ in patients with JIA because these techniques have better soft tissue resolution allowing earlier diagnosis of TMJ involvement without any ionizing radiation. Acute TMJ arthritis typically demonstrates joint effusion and synovial thickening on T2 weighted imaging without any bony changes^[76]. Enhancement of the joint or periarticular tissue is not a specific sign of acute TMJ arthritis because abnormal joint enhancement can be present even in healthy patients^[76]. Condylar resorption can be better evaluated on non-fat suppressed T1 weighted sequence and suggests a more chronic TMJ arthritis^[76] (Figure 16).

Rheumatoid arthritis: Rheumatoid arthritis (RA) is a chronic inflammatory disorder that predominantly affects the periarticular tissue such as synovial membrane, joint capsules, tendon, tendon sheaths and ligaments. Internal joint components are secondarily involved. The prevalence of RA in the general population is approximately 2%-2.5% with female predominance. The peak onset of disease is 40-60 years and approximately 50%-75% of patients with RA have TMJ involvement^[77].

RA is a slowly progressive disease of insidious onset with progressive destruction of the articular/periarticular soft tissue and the adjacent bones resulting in joint deformity. The TMJ is involved at a later stage of disease. TMJ involvement causes deep, dull aching pain in the preauricular area, especially during chewing. Limited range of motion and morning stiffness can be present^[78]. The mandibular condyle gradually resorbs as the disease progresses.

Radiographic features of RA include loss of joint space, condylar destruction, flattening with anterior positioning of the condyle. There may be flattening of the articular eminence and erosion of the glenoid fossa. Synovial proliferation is an early process in RA and can distinguish it from other types of arthritis^[79]. Synovial proliferation is readily seen on MRI and can be seen in all patients^[79]. A joint effusion is also comparatively more common in RA.

Degenerative (osteo)arthritis

Osteoarthritis (OA) is a chronic degenerative disease that characteristically affects the articular cartilage of synovial joints and is associated with simultaneous remodeling of the underlying subchondral bone with secondary involvement of the synovium. Osteoarthritis is the most

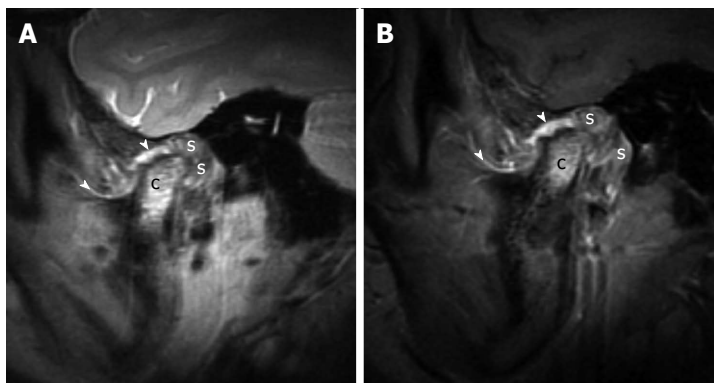


Figure 16 Juvenile idiopathic arthritis. A: Sagittal proton density weighted magnetic resonance imaging (MRI) in the closed mouth position demonstrates increased signal at the mandibular condyle (the letter, c), extensive thickening of the synovium (the letter, s) in the retrodiscal regions. It can be noted that the thickening and increased signal of the synovium at other places (arrowheads); B: Sagittal fat suppressed post contrast T1 weighted MRI in the closed mouth position demonstrates enhancement of signal at the mandibular condyle (the letter, c), enhancement and extensive thickening of the synovium (the letter, s) in the retrodiscal regions. There is thickening and enhancement of the synovium at other places (arrowheads).

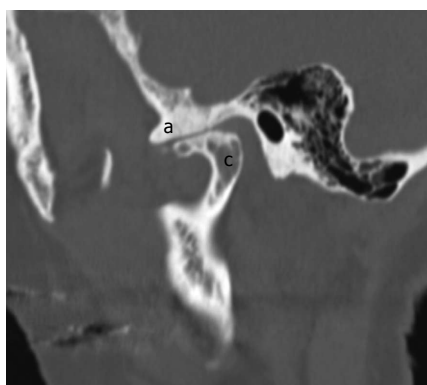


Figure 17 Degenerative changes. Sagittal reformation of the axial dataset demonstrates deformity of the mandibular condyle (the letter, c), extensive sclerosis of the articular eminence (the letter, a) and severe loss of joint space.

common joint pathology affecting the TMJ^[80]. There is a clear disparity between radiographic evidence of OA and symptoms. Population based studies demonstrate that minimal condylar flattening is present in up to 35% of asymptomatic patients while approximately 11% of patients have TMJ OA-related symptoms^[80].

The most common symptom of TMJ OA is pain during chewing. The pain usually starts in the periarticular soft tissue and the masticator muscles that are in protective reflex spasm. Fatigue of masticator muscles, trismus, decreased range of motion, difficulty opening the mouth and joint crepitations are other common symptoms.

Radiologic hallmarks of TMJ OA are articular surface cortical bone irregularity, erosion and osteophyte formation^[81]. Erosion is radiologically defined as focal area of decreased density at the cortical margin of the articular surface of the mandibular condyle and the subchondral region. Osteophyte formation typically occurs at a later stage in the disease and can stabilize and broaden the surface area of the joint in an attempt to better withstand axial loading forces. Different imaging modalities have been used with varying degree of success. There is

still no general consensus as to which imaging modality should be the gold standard^[81] (Figure 17).

Metabolic arthritis/crystalline arthropathies

Calcium pyrophosphate dehydrate deposition disease: Calcium pyrophosphate dehydrate deposition disease (CPPD) is a metabolic arthropathy caused by the deposition of calcium pyrophosphate dehydrate crystals in and around joints, especially within the articular cartilage and fibrocartilage^[82].

The spectrum of TMJ involvement ranges from asymptomatic disk calcification to a marked destruction of the joint with erosive changes in the mandibular condyle and the adjacent skull base. Common symptoms include pain and preauricular swelling with occasional hearing loss. Chewing can exacerbate the pain. Other less common symptoms include TMJ clicking, tinnitus, and malocclusion.

The radiographic appearance of CPPD is variable. Computed tomography demonstrates calcium deposition in the disk or periarticular tissue. On MRI, CPP deposits typically appear as hypointense material both on T1 and T2 weighted sequences. CT and MRI show erosions near both the condyle and fossa with adjacent CPPD deposits^[82]. The erosions may extend into the skull base and into the middle cranial fossa. Involvement of other joints with chondrocalcinosis is a clue to the diagnosis. The differential diagnosis includes synovial chondromatosis, synovial osteochondroma, and osteosarcoma (Figure 18).

Infectious arthritis

TMJ infection is usually secondary to direct extension of infection from the adjacent tissue into the joint. Systemic infections such as tuberculosis and syphilis can rarely involve the TMJ. TMJ infection is more common in the setting of immunosuppression and presence of other systematic diseases such as diabetes mellitus, rheumatoid arthritis and intravenous drug use, *etc.*

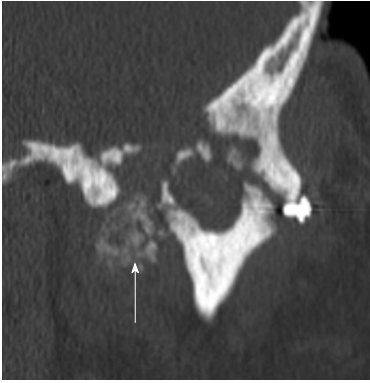


Figure 18 Calcium pyrophosphate dehydrate deposition disease. Coronal reformation of the axial dataset demonstrates destruction of the left temporomandibular joint with erosion and deformity of both the mandibular condyle and the glenoid fossa. There is extensive extensive calcium pyrophosphate dehydrate deposition disease medial to the joint space (arrow).

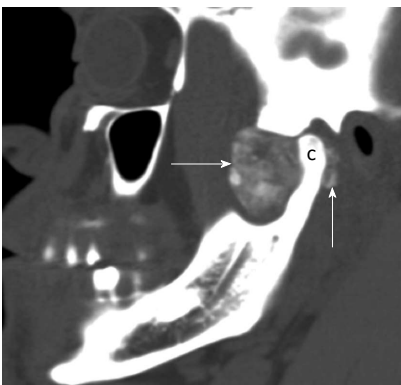


Figure 19 Synovial chondromatosis. Sagittal reformation of the axial dataset demonstrates extensive cloud-like calcification (arrows) filling and expanding the joint space anterior to the mandibular condyle (the letter, c). Calcification is also present posterior to the mandibular condyle.

TUMORS AND TUMOR-LIKE CONDITIONS OF THE TMJ

Tumors and tumor-like conditions can affect the TMJ. These conditions may have similar presentations such as pain, swelling, and limitation of motion.

Synovial chondromatosis

Synovial chondromatosis (SC) is a benign condition with chondrometaplasia of the synovial membrane and formation of cartilaginous nodules. These nodules can become detached and form loose bodies which later calcify. Synovial chondromatosis typically involves large joints, such as the knee, hip, and elbow. It is uncommon for the temporomandibular joint to be affected by SC. SC typically involves the superior compartment of TMJ while involvement of the inferior compartment is rare and secondary to perforation of the articular disc. Uncommon findings include erosion of the mandibular condylar head, temporal skull base, and intracranial extension.

Patients typically present with preauricular pain, swelling, inflammation, limitation of motion, and articular

noises. Some patients also report neurologic dysfunction, such as headache and hearing loss.

The diagnosis of TMJ synovial chondromatosis is difficult since it is a rare disease and can have similar findings to more common diseases, such as chondrocalcinosis, osteoarthritis, and chondrosarcoma. The radiologic findings of SC include calcified loose bodies, soft tissue swelling, widening of the joint space, irregularities of the joint surface, and sclerosis of the glenoid fossa and/or mandibular condyle. CT typically shows calcified nodules surrounding the mandibular condyle with degenerative changes of the condyle^[83]. MRI typically shows mixed solid and fluid signal related to the metaplasia of the synovial tissue and the fluid component of the accumulated synovial secretions. The calcified nodules are T1/T2 hypointense with a surrounding T2 hyperintense effusion and proliferative synovium, which enhances after contrast administration. MRI is preferred in evaluation of SC over CT because of the ability to detect non-calcified loose bodies, lack of radiation, and visualization of the articular disc^[84] (Figure 19).

Treatment is surgical removal of the loose bodies and excision of the metaplastic synovium. In end stage SC without synovial metaplastic activity, the treatment is often non-surgical with therapy aimed towards symptom relief.

Pigmented villonodular synovitis

Pigmented villonodular synovitis (PVNS) is a benign, non-neoplastic proliferative disorder of the synovial membranes of joints, bursae, and tendon sheaths. The disease is typically monoarticular and can involve any joint but is most often seen in the knee. Primary PVNS of the TMJ is rare. There are two forms of PVNS: nodular and diffuse. The most common nodular patterns of PVNS include giant cell tumor, xanthoma, xanthogranuloma, and myeloplaxoma, which affect a focal part of the synovium^[85]. Diffuse PVNS affects nearly the entire synovium.

The exact etiology of PVNS is unclear. It was originally postulated to be an inflammatory response to an unknown stimulus. Other theories attribute it to repetitive intra-articular hemorrhage from trauma, altered lipid metabolism, or a benign neoplastic proliferation.

PVNS commonly presents as a slowly growing and non-tender swelling of the affected joint. Patients with involvement of the TMJ, can present with a preauricular mass with swelling, pain, tenderness, clicking, otalgia, and hearing loss.

The most sensitive method for the detection of PVNS is by MRI demonstrating T1/T2 hypointensity and blooming on the GRE sequences from paramagnetic hemosiderin deposition^[86]. There may be moderate to intense inhomogeneous enhancement of the synovium. CT findings are usually nonspecific with bone erosion, subchondral cysts, and a soft tissue mass^[87]. A joint effusion may be dense from the hemosiderin. The differential diagnosis of PVNS on MRI includes synovial chondrom-

atosis, rheumatoid arthritis, synovial sarcoma, hemophilia, and synovial hemangioma.

Primary and secondary neoplasms, and other lesions

Osteochondroma is the second most common neoplastic lesion affecting the TMJ. Osteochondroma, osteoma, and condylar hyperplasia are often difficult to differentiate both clinically and on imaging. MR and CT may delineate the exact extent of the tumor and its relationship to anatomic structures within the TMJ.

Synovial cysts, ganglion cysts and simple bone cysts may also occur. Many benign primary bone neoplasms, such as chondroblastoma, osteoma, osteoid osteoma, osteoblastoma, ossifying fibroma and aneurysmal bone cyst can also involve the TMJ. Malignant primary bone neoplasms are extremely rare in TMJ but include chondrosarcoma and osteogenic sarcoma. There also can be extension of tumors from adjacent structures into the TMJ. Tumors from the external ear and parotid gland can extend into the TMJ. Less than 1% of all tumors metastasize into the maxillofacial region. Adenocarcinoma is the most common metastatic tumor of the jaw, making up about 70% of cases. Reported metastasis to TMJ includes breast, renal, lung, colon, prostate, thyroid, and testicular primary.

CONCLUSION

Imaging of TMJ should be performed on a case by case basis depending upon clinical signs and symptoms. MRI is the diagnostic study of choice for evaluation of disk position and internal derangement of the joint. CT scan for evaluation of TMJ is indicated if bony involvement is suspected and should be judiciously considered because of radiation risk. Understanding of the TMJ anatomy, biomechanics, and the imaging manifestations of diseases is important to accurately recognize and manage these various pathologies.

REFERENCES

- 1 **Aiken A**, Bouloux G, Hudgins P. MR imaging of the temporomandibular joint. *Magn Reson Imaging Clin N Am* 2012; **20**: 397-412 [PMID: 22877948 DOI: 10.1016/j.mric.2012.05.002]
- 2 **Guralnick W**, Kaban LB, Merrill RG. Temporomandibular joint afflictions. *N Engl J Med* 1978; **299**: 123-129 [PMID: 661872 DOI: 10.1056/NEJM197807202990304]
- 3 **Alomar X**, Medrano J, Cabratosa J, Clavero JA, Lorente M, Serra I, Monill JM, Salvador A. Anatomy of the temporomandibular joint. *Semin Ultrasound CT MR* 2007; **28**: 170-183 [PMID: 17571700 DOI: 10.1053/j.sult.2007.02.002]
- 4 **Sommer OJ**, Aigner F, Rudisch A, Gruber H, Fritsch H, Millesi W, Stiskal M. Cross-sectional and functional imaging of the temporomandibular joint: radiology, pathology, and basic biomechanics of the jaw. *Radiographics* 2003; **23**: e14 [PMID: 12920179 DOI: 10.1148/rg.e14]
- 5 **Sava A**, Scutariu M. Functional anatomy of the temporomandibular joint (II). *Rev Med Chir Soc Med Nat Iasi* 2012; **116**: 1213-1217 [PMID: 23700914]
- 6 **Van Eijden TM**, Korfage JA, Brugman P. Architecture of the human jaw-closing and jaw-opening muscles. *Anat Rec* 1997; **248**: 464-474 [PMID: 9214565 DOI: 10.1002/(SICI)1097-0185(199707)248:3<464::AID-AR20>3.0.CO;2-M]

- 7 **Imanimoghaddam M**, Madani AS, Hashemi EM. The evaluation of lateral pterygoid muscle pathologic changes and insertion patterns in temporomandibular joints with or without disc displacement using magnetic resonance imaging. *Int J Oral Maxillofac Surg* 2013; **42**: 1116-1120 [PMID: 23746672 DOI: 10.1016/j.ijom.2013.01.022]
- 8 **Tomas X**, Pomes J, Berenguer J, Mercader JM, Pons F, Donoso L. Temporomandibular joint soft-tissue pathology, II: Nondisc abnormalities. *Semin Ultrasound CT MR* 2007; **28**: 205-212 [PMID: 17571703 DOI: 10.1053/j.sult.2007.02.005]
- 9 **Tomas X**, Pomes J, Berenguer J, Quinto L, Nicolau C, Mercader JM, Castro V. MR imaging of temporomandibular joint dysfunction: a pictorial review. *Radiographics* 2006; **26**: 765-781 [PMID: 16702453 DOI: 10.1148/rg.263055091]
- 10 **Koolstra JH**. Dynamics of the human masticatory system. *Crit Rev Oral Biol Med* 2002; **13**: 366-376 [PMID: 12191962 DOI: 10.1177/154411130201300406]
- 11 **Lobbezoo F**, Drangsholt M, Peck C, Sato H, Kopp S, Svensson P. Topical review: new insights into the pathology and diagnosis of disorders of the temporomandibular joint. *J Orofac Pain* 2004; **18**: 181-191 [PMID: 15508997]
- 12 **Harms SE**, Wilk RM. Magnetic resonance imaging of the temporomandibular joint. *Radiographics* 1987; **7**: 521-542 [PMID: 3448646 DOI: 10.1148/radiographics.7.3.3448646]
- 13 **Katzberg RW**. Temporomandibular joint imaging. *Radiology* 1989; **170**: 297-307 [PMID: 2643133]
- 14 **Rao VM**, Bacelar MT. MR imaging of the temporomandibular joint. *Magn Reson Imaging Clin N Am* 2002; **10**: 615-630 [PMID: 12685497 DOI: 10.1016/S1064-9689(02)00011-9]
- 15 **Drace JE**, Enzmann DR. Defining the normal temporomandibular joint: closed-, partially open-, and open-mouth MR imaging of asymptomatic subjects. *Radiology* 1990; **177**: 67-71 [PMID: 2399340]
- 16 **Katzberg RW**, Westesson PL, Tallents RH, Drake CM. Anatomic disorders of the temporomandibular joint disc in asymptomatic subjects. *J Oral Maxillofac Surg* 1996; **54**: 147-153; discussion 153-155 [PMID: 8604061 DOI: 10.1016/S0278-2391(96)90435-8]
- 17 **Rammelsberg P**, Pospiech PR, Jäger L, Pho Duc JM, Böhm AO, Gernet W. Variability of disk position in asymptomatic volunteers and patients with internal derangements of the TMJ. *Oral Surg Oral Med Oral Pathol Oral Radiol Endod* 1997; **83**: 393-399 [PMID: 9084204 DOI: 10.1016/S1079-2104(97)90248-1]
- 18 **Tallents RH**, Katzberg RW, Murphy W, Proskin H. Magnetic resonance imaging findings in asymptomatic volunteers and symptomatic patients with temporomandibular disorders. *J Prosthet Dent* 1996; **75**: 529-533 [PMID: 8709019 DOI: 10.1016/S0022-3913(96)90458-8]
- 19 **Orsini MG**, Kuboki T, Terada S, Matsuka Y, Yamashita A, Clark GT. Diagnostic value of 4 criteria to interpret temporomandibular joint normal disk position on magnetic resonance images. *Oral Surg Oral Med Oral Pathol Oral Radiol Endod* 1998; **86**: 489-497 [PMID: 9798238 DOI: 10.1016/S1079-2104(98)90380-8]
- 20 **Provenzano Mde M**, Chilvarquer I, Fenyó-Pereira M. How should the articular disk position be analyzed? *J Oral Maxillofac Surg* 2012; **70**: 1534-1539 [PMID: 22079066 DOI: 10.1016/j.joms.2011.08.004]
- 21 **Vilanova JC**, Barceló J, Puig J, Remollo S, Nicolau C, Bru C. Diagnostic imaging: magnetic resonance imaging, computed tomography, and ultrasound. *Semin Ultrasound CT MR* 2007; **28**: 184-191 [PMID: 17571701 DOI: 10.1053/j.sult.2007.02.003]
- 22 **Westesson PL O-YM**, Sano T, Okano T. Anatomy, Pathology, and Imaging of the Temporomandibular Joint. In: Som PM, Curtin HD, ed. *Head and Neck Imaging-2 Volume Set, 5th Edition*. St. Louis: Mosby, 2011: 1547-613
- 23 **Dennison J**, Mahoney P, Herbison P, Dias G. The false and the true bifid condyles. *Homo* 2008; **59**: 149-159 [PMID: 99707248:3<464::AID-AR20>3.0.CO;2-M]

- 18417126 DOI: 10.1016/j.jchb.2008.02.001]
- 24 **Lacout A**, Marsot-Dupuch K, Smoker WR, Lasjaunias P. Foramen tympanicum, or foramen of Huschke: pathologic cases and anatomic CT study. *AJNR Am J Neuroradiol* 2005; **26**: 1317-1323 [PMID: 15956489]
 - 25 **Tozoglu U**, Caglayan F, Harorli A. Foramen tympanicum or foramen of Huschke: anatomical cone beam CT study. *Dentomaxillofac Radiol* 2012; **41**: 294-297 [PMID: 22517996]
 - 26 **Tank W**, Wright D, Iizuka T. Unilateral dysplasia of the mandibular condyle: report of a case. *J Oral Maxillofac Surg* 1998; **56**: 765-769 [PMID: 9632337]
 - 27 **Berger SS**, Stewart RE. Mandibular hypoplasia secondary to perinatal trauma: report of case. *J Oral Surg* 1977; **35**: 578-582 [PMID: 267174]
 - 28 **Kaneyama K**, Segami N, Hatta T. Congenital deformities and developmental abnormalities of the mandibular condyle in the temporomandibular joint. *Congenit Anom (Kyoto)* 2008; **48**: 118-125 [PMID: 18778456 DOI: 10.1111/j.1741-4520.2008.00191.x]
 - 29 **Wolford LM**. Idiopathic condylar resorption of the temporomandibular joint in teenage girls (cheerleaders syndrome). *Proc (Bayl Univ Med Cent)* 2001; **14**: 246-252 [PMID: 16369629]
 - 30 **Angiero F**, Farronato G, Benedicenti S, Vinci R, Farronato D, Magistro S, Stefani M. Mandibular condylar hyperplasia: clinical, histopathological, and treatment considerations. *Cranio* 2009; **27**: 24-32 [PMID: 19241796]
 - 31 **Ladeira DB**, Barbosa GL, Nascimento MC, Cruz AD, Freitas DQ, Almeida SM. Prevalence and characteristics of pneumatization of the temporal bone evaluated by cone beam computed tomography. *Int J Oral Maxillofac Surg* 2013; **42**: 771-775 [PMID: 23290566]
 - 32 **Miloglu O**, Yilmaz AB, Yildirim E, Akgul HM. Pneumatization of the articular eminence on cone beam computed tomography: prevalence, characteristics and a review of the literature. *Dentomaxillofac Radiol* 2011; **40**: 110-114 [PMID: 21239574]
 - 33 **Rudisch A**, Innerhofer K, Bertram S, Emschoff R. Magnetic resonance imaging findings of internal derangement and effusion in patients with unilateral temporomandibular joint pain. *Oral Surg Oral Med Oral Pathol Oral Radiol Endod* 2001; **92**: 566-571 [PMID: 11709695 DOI: 10.1067/moe.2001.116817]
 - 34 **Cholitgul W**, Nishiyama H, Sasai T, Uchiyama Y, Fuchihata H, Rohlin M. Clinical and magnetic resonance imaging findings in temporomandibular joint disc displacement. *Dentomaxillofac Radiol* 1997; **26**: 183-188 [PMID: 9442605 DOI: 10.1038/sj.dmf.4600239]
 - 35 **Larheim TA**, Westesson P, Sano T. Temporomandibular joint disc displacement: comparison in asymptomatic volunteers and patients. *Radiology* 2001; **218**: 428-432 [PMID: 11161157 DOI: 10.1148/radiology.218.2.r01fe11428]
 - 36 **Ribeiro RF**, Tallents RH, Katzberg RW, Murphy WC, Moss ME, Magalhaes AC, Tavano O. The prevalence of disc displacement in symptomatic and asymptomatic volunteers aged 6 to 25 years. *J Orofac Pain* 1997; **11**: 37-47 [PMID: 10332309]
 - 37 **Paesani D**, Westesson PL, Hatala M, Tallents RH, Kurita K. Prevalence of temporomandibular joint internal derangement in patients with craniomandibular disorders. *Am J Orthod Dentofacial Orthop* 1992; **101**: 41-47 [PMID: 1731487]
 - 38 **Tasaki MM**, Westesson PL, Raubertas RF. Observer variation in interpretation of magnetic resonance images of the temporomandibular joint. *Oral Surg Oral Med Oral Pathol* 1993; **76**: 231-234 [PMID: 8361737]
 - 39 **Tasaki MM**, Westesson PL, Isberg AM, Ren YF, Tallents RH. Classification and prevalence of temporomandibular joint disk displacement in patients and symptom-free volunteers. *Am J Orthod Dentofacial Orthop* 1996; **109**: 249-262 [PMID: 8607470]
 - 40 **Sano T**, Yamamoto M, Okano T. Temporomandibular joint: MR imaging. *Neuroimaging Clin N Am* 2003; **13**: 583-595 [PMID: 14631692]
 - 41 **Som PM**, Bergeron RT. Head and neck imaging. 2nd ed. St. Louis: Mosby Year Book, 1991
 - 42 **de Leeuw R**, Boering G, Stegenga B, de Bont LG. TMJ articular disc position and configuration 30 years after initial diagnosis of internal derangement. *J Oral Maxillofac Surg* 1995; **53**: 234-241; discussion 241-242 [PMID: 7861272]
 - 43 **Suenaga S**, Hamamoto S, Kawano K, Higashida Y, Noikura T. Dynamic MR imaging of the temporomandibular joint in patients with arthrosis: relationship between contrast enhancement of the posterior disk attachment and joint pain. *AJR Am J Roentgenol* 1996; **166**: 1475-1481 [PMID: 8633468 DOI: 10.2214/ajr.166.6.8633468]
 - 44 **Helms CA**, Kaban LB, McNeill C, Dodson T. Temporomandibular joint: morphology and signal intensity characteristics of the disk at MR imaging. *Radiology* 1989; **172**: 817-820 [PMID: 2772194]
 - 45 **Chossegras C**, Cheynet F, Guyot L, Bellot-Samson V, Blanc JL. Posterior disk displacement of the TMJ: MRI evidence in two cases. *Cranio* 2001; **19**: 289-293 [PMID: 11725853]
 - 46 **Katzberg RW**, Westesson PL, Tallents RH, Anderson R, Kurita K, Manzione JV, Totterman S. Temporomandibular joint: MR assessment of rotational and sideways disk displacements. *Radiology* 1988; **169**: 741-748 [PMID: 3186996]
 - 47 **Kontinen YT**, Ainola M, Valleala H, Ma J, Ida H, Mandelin J, Kinne RW, Santavirta S, Sorsa T, López-Otín C, Takagi M. Analysis of 16 different matrix metalloproteinases (MMP-1 to MMP-20) in the synovial membrane: different profiles in trauma and rheumatoid arthritis. *Ann Rheum Dis* 1999; **58**: 691-697 [PMID: 10531073]
 - 48 **Schellhas KP**, Wilkes CH. Temporomandibular joint inflammation: comparison of MR fast scanning with T1- and T2-weighted imaging techniques. *AJR Am J Roentgenol* 1989; **153**: 93-98 [PMID: 2735304 DOI: 10.2214/ajr.153.1.93]
 - 49 **Roberts D**, Schenck J, Joseph P, Foster T, Hart H, Pettigrew J, Kundel HL, Edelstein W, Haber B. Temporomandibular joint: magnetic resonance imaging. *Radiology* 1985; **154**: 829-830 [PMID: 3969490]
 - 50 **Katzberg RW**, Westesson P-L. Diagnosis of the temporomandibular joint, 1e. Philadelphia: W. B. Saunders Co., 1993
 - 51 **Cholitgul W**, Petersson A, Rohlin M, Akerman S. Clinical and radiological findings in temporomandibular joints with disc perforation. *Int J Oral Maxillofac Surg* 1990; **19**: 220-225 [PMID: 2120363]
 - 52 **Kondoh T**, Westesson PL, Takahashi T, Seto K. Prevalence of morphological changes in the surfaces of the temporomandibular joint disc associated with internal derangement. *J Oral Maxillofac Surg* 1998; **56**: 339-343; discussion 343-344 [PMID: 9496846]
 - 53 **Widmalm SE**, Westesson PL, Kim IK, Pereira FJ, Lundh H, Tasaki MM. Temporomandibular joint pathosis related to sex, age, and dentition in autopsy material. *Oral Surg Oral Med Oral Pathol* 1994; **78**: 416-425 [PMID: 7800370]
 - 54 **Kuribayashi A**, Okochi K, Kobayashi K, Kurabayashi T. MRI findings of temporomandibular joints with disk perforation. *Oral Surg Oral Med Oral Pathol Oral Radiol Endod* 2008; **106**: 419-425 [PMID: 18504154 DOI: 10.1016/j.tripleo.2007.11.020]
 - 55 **Yura S**, Nobata K, Shima T. Diagnostic accuracy of fat-saturated T2-weighted magnetic resonance imaging in the diagnosis of perforation of the articular disc of the temporomandibular joint. *Br J Oral Maxillofac Surg* 2012; **50**: 365-368 [PMID: 21723011 DOI: 10.1016/j.bjoms.2011.05.017]
 - 56 **Larheim TA**, Katzberg RW, Westesson PL, Tallents RH, Moss ME. MR evidence of temporomandibular joint fluid and condyle marrow alterations: occurrence in asymptomatic volunteers and symptomatic patients. *Int J Oral Maxillofac Surg* 2001; **30**: 113-117 [PMID: 11405445 DOI: 10.1054/ijom.2000.0018]
 - 57 **Westesson PL**, Brooks SL. Temporomandibular joint: rela-

- tionship between MR evidence of effusion and the presence of pain and disk displacement. *AJR Am J Roentgenol* 1992; **159**: 559-563 [PMID: 1503025 DOI: 10.2214/ajr.159.3.1503025]
- 58 **Smith HJ**, Larheim TA, Aspestrand F. Rheumatic and non-rheumatic disease in the temporomandibular joint: gadolinium-enhanced MR imaging. *Radiology* 1992; **185**: 229-234 [PMID: 1523314 DOI: 10.1148/radiology.185.1.1523314]
- 59 **Lafrenière CM**, Lamontagne M, el-Sawy R. The role of the lateral pterygoid muscles in TMJ disorders during static conditions. *Cranio* 1997; **15**: 38-52 [PMID: 9586487]
- 60 **Yang X**, Pernu H, Pyhtinen J, Tiilikainen PA, Oikarinen KS, Raustia AM. MR abnormalities of the lateral pterygoid muscle in patients with nonreducing disk displacement of the TMJ. *Cranio* 2002; **20**: 209-221 [PMID: 12150268]
- 61 **Taskaya-Yilmaz N**, Ceylan G, Incesu L, Muglali M. A possible etiology of the internal derangement of the temporomandibular joint based on the MRI observations of the lateral pterygoid muscle. *Surg Radiol Anat* 2005; **27**: 19-24 [PMID: 15750717 DOI: 10.1007/s00276-004-0267-6]
- 62 **Schellhas KP**, Wilkes CH, Fritts HM, Omlie MR, Heithoff KB, Jahn JA. Temporomandibular joint: MR imaging of internal derangements and postoperative changes. *AJR Am J Roentgenol* 1988; **150**: 381-389 [PMID: 3257330 DOI: 10.2214/ajr.150.2.381]
- 63 **Schellhas KP**, Wilkes CH, Fritts HM, Omlie MR, Lagrotteria LB. MR of osteochondritis dissecans and avascular necrosis of the mandibular condyle. *AJR Am J Roentgenol* 1989; **152**: 551-560 [PMID: 2783809 DOI: 10.2214/ajr.152.3.551]
- 64 **Larheim TA**, Westesson PL, Hicks DG, Eriksson L, Brown DA. Osteonecrosis of the temporomandibular joint: correlation of magnetic resonance imaging and histology. *J Oral Maxillofac Surg* 1999; **57**: 888-898; discussion 899 [PMID: 10437715]
- 65 **Mesgarzadeh M**, Sapega AA, Bonakdarpour A, Revesz G, Moyer RA, Maurer AH, Alburger PD. Osteochondritis dissecans: analysis of mechanical stability with radiography, scintigraphy, and MR imaging. *Radiology* 1987; **165**: 775-780 [PMID: 3685359 DOI: 10.1148/radiology.165.3.3685359]
- 66 **Xiang S**, Rebellato J, Inwards CY, Keller EE. Malocclusion associated with osteocartilaginous loose bodies of the temporomandibular joint. *J Am Dent Assoc* 2005; **136**: 484-489 [PMID: 15884318]
- 67 **Von Arx DP**, Simpson MT, Batman P. Synovial chondromatosis of the temporomandibular joint. *Br J Oral Maxillofac Surg* 1988; **26**: 297-305 [PMID: 3048377]
- 68 **Norman JE**, Stevenson AR, Painter DM, Sykes DG, Feain LA. Synovial osteochondromatosis of the temporomandibular joint. An historical review with presentation of 3 cases. *J Craniomaxillofac Surg* 1988; **16**: 212-220 [PMID: 3042809]
- 69 **Boccardi A**. CT evaluation of chondromatosis of the temporomandibular joint. *J Comput Assist Tomogr* 1991; **15**: 826-828 [PMID: 1885803]
- 70 **van Ingen JM**, de Man K, Bakri I. CT diagnosis of synovial chondromatosis of the temporomandibular joint. *Br J Oral Maxillofac Surg* 1990; **28**: 164-167 [PMID: 2135654]
- 71 **Nitzan DW**. Temporomandibular joint "open lock" versus condylar dislocation: signs and symptoms, imaging, treatment, and pathogenesis. *J Oral Maxillofac Surg* 2002; **60**: 506-11; discussion 512-3 [PMID: 11988925]
- 72 **DaSilva AF**, Shaefer J, Keith DA. The temporomandibular joint: clinical and surgical aspects. *Neuroimaging Clin N Am* 2003; **13**: 573-582 [PMID: 14631691]
- 73 **Güven O**. A clinical study on temporomandibular joint ankylosis. *Auris Nasus Larynx* 2000; **27**: 27-33 [PMID: 10648065]
- 74 **Cannizzaro E**, Schroeder S, Müller LM, Kellenberger CJ, Saurenmann RK. Temporomandibular joint involvement in children with juvenile idiopathic arthritis. *J Rheumatol* 2011; **38**: 510-515 [PMID: 21159837 DOI: 10.3899/jrheum.100325]
- 75 **Twilt M**, Moberg SM, Arends LR, ten Cate R, van Suijlekom-Smit L. Temporomandibular involvement in juvenile idiopathic arthritis. *J Rheumatol* 2004; **31**: 1418-1422 [PMID: 15229966]
- 76 **Weiss PF**, Arabshahi B, Johnson A, Bilaniuk LT, Zarnow D, Cahill AM, Feudtner C, Cron RQ. High prevalence of temporomandibular joint arthritis at disease onset in children with juvenile idiopathic arthritis, as detected by magnetic resonance imaging but not by ultrasound. *Arthritis Rheum* 2008; **58**: 1189-1196 [PMID: 18383394 DOI: 10.1002/art.23401]
- 77 **Koh ET**, Yap AU, Koh CK, Chee TS, Chan SP, Boudville IC. Temporomandibular disorders in rheumatoid arthritis. *J Rheumatol* 1999; **26**: 1918-1922 [PMID: 10493669]
- 78 **Yoshida A**, Higuchi Y, Kondo M, Tabata O, Ohishi M. Range of motion of the temporomandibular joint in rheumatoid arthritis: relationship to the severity of disease. *Cranio* 1998; **16**: 162-167 [PMID: 9852809]
- 79 **Kretapirom K**, Okochi K, Nakamura S, Tetsumura A, Ohbayashi N, Yoshino N, Kurabayashi T. MRI characteristics of rheumatoid arthritis in the temporomandibular joint. *Dentomaxillofac Radiol* 2013; **42**: 31627230 [PMID: 22842633 DOI: 10.1259/dmfr/31627230]
- 80 **Tanaka E**, Detamore MS, Mercuri LG. Degenerative disorders of the temporomandibular joint: etiology, diagnosis, and treatment. *J Dent Res* 2008; **87**: 296-307 [PMID: 18362309]
- 81 **Hussain AM**, Packota G, Major PW, Flores-Mir C. Role of different imaging modalities in assessment of temporomandibular joint erosions and osteophytes: a systematic review. *Dentomaxillofac Radiol* 2008; **37**: 63-71 [PMID: 18239033 DOI: 10.1259/dmfr/16932758]
- 82 **Matsumura Y**, Nomura J, Nakanishi K, Yanase S, Kato H, Tagawa T. Synovial chondromatosis of the temporomandibular joint with calcium pyrophosphate dihydrate crystal deposition disease (pseudogout). *Dentomaxillofac Radiol* 2012; **41**: 703-707 [PMID: 23166363 DOI: 10.1259/dmfr/24183821]
- 83 **Kahraman AS**, Kahraman B, Dogan M, Firat C, Samdanci E, Celik T. Synovial chondromatosis of the temporomandibular joint: radiologic and histopathologic findings. *J Craniomaxillofac Surg* 2012; **23**: 1211-1213 [PMID: 22801131 DOI: 10.1097/SCS.0b013e3182564a6e]
- 84 **Wang P**, Tian Z, Yang J, Yu Q. Synovial chondromatosis of the temporomandibular joint: MRI findings with pathological comparison. *Dentomaxillofac Radiol* 2012; **41**: 110-116 [PMID: 22116129 DOI: 10.1259/dmfr/36144602]
- 85 **Giannakopoulos H**, Chou JC, Quinn PD. Pigmented villonodular synovitis of the temporomandibular joint. *Ear Nose Throat J* 2013; **92**: E10-E13 [PMID: 23904309]
- 86 **Kim KW**, Han MH, Park SW, Kim SH, Lee HJ, Jae HJ, Kang JW, Chang KH. Pigmented villonodular synovitis of the temporomandibular joint: MR findings in four cases. *Eur J Radiol* 2004; **49**: 229-234 [PMID: 14962652 DOI: 10.1016/S0720-048X(03)00099-8]
- 87 **Le WJ**, Li MH, Yu Q, Shi HM. Pigmented villonodular synovitis of the temporomandibular joint: CT imaging findings. *Clin Imaging* 2014; **38**: 6-10 [PMID: 24100118 DOI: 10.1016/j.clinimag.2013.08.011]

P- Reviewer: Franco AL, Rattan V, Ramirez Aristeguieta LM
S- Editor: Ji FF **L- Editor:** A **E- Editor:** Liu SQ



Measuring consciousness in coma and related states

Carol Di Perri, Aurore Thibaut, Lizette Heine, Andrea Soddu, Athena Demertzi, Steven Laureys

Carol Di Perri, Neuroradiology, National Neurological Institute C Mondino, 27100 Pavia, Italy

Carol Di Perri, Aurore Thibaut, Lizette Heine, Athena Demertzi, Steven Laureys, Cyclotron Research Center and Neurology Department, Coma Science Group, University of Liège, 4000 Liège, Belgium

Andrea Soddu, Brain and Mind Institute, Physics and Astronomy Department, Western University, London, Ontario, N6A 3K7, Canada

Author contributions: Di Perri C designed and wrote the manuscript; Thibaut A, Heine L, Soddu A and Demertzi A were involved in designing and editing the manuscript; Laureys S supervised the manuscript design and writing; all authors were involved in literature search.

Supported by The European Commission; the James McDonnell Foundation; the European Space Agency; Mind Science Foundation; the French Speaking Community Concerted Research Action; the Belgian interuniversity attraction pole; the Public Utility Foundation “Université Européenne du Travail”; “Fondazione Europea di Ricerca Biomedica” and the University and University Hospital of Liège

Correspondence to: Carol Di Perri, MD, Cyclotron Research Center and Neurology Department, Coma Science Group, University of Liège, Allée du 6 août 8, Sart Tilman B30, 4000 Liège, Belgium. caroldiperri@hotmail.com

Telephone: +32-43-662316 Fax: +32-43-662946

Received: February 28, 2014 Revised: May 9, 2014

Accepted: June 14, 2014

Published online: March 28, 2015

patient’s cognitive abilities by providing both diagnostic and prognostic indicators.

© 2015 Baishideng Publishing Group Inc. All rights reserved.

Key words: Disorders of consciousness; Neuroimaging; Magnetic resonance imaging; Transcranial magnetic stimulation/electroencephalography; Minimally conscious state; Vegetative state/unresponsive wakefulness syndrome

Core tip: In this review we show the main ways neuroimaging techniques contribute to both understanding the neural correlates of consciousness and detecting possible consciousness residual in severely traumatic brain injured patients. In particular, we make reference to the latest research in terms of both improving the diagnosis of patients with disorder of consciousness, and understanding the brain processes underlying consciousness, such as a broad and more complex than previously thought alteration of brain connectivity architecture.

Original sources: Di Perri C, Thibaut A, Heine L, Soddu A, Demertzi A, Laureys S. Measuring consciousness in coma and related states. *World J Radiol* 2014; 6(8): 589-597 Available from: URL: <http://www.wjgnet.com/1949-8470/full/v6/i8/589.htm> DOI: <http://dx.doi.org/10.4329/wjr.v6.i8.589>

Abstract

Consciousness is a prismatic and ambiguous concept that still eludes any universal definition. Severe acquired brain injuries resulting in a disorder of consciousness (DOC) provide a model from which insights into consciousness can be drawn. A number of recent studies highlight the difficulty in making a diagnosis in patients with DOC based only on behavioral assessments. Here we aim to provide an overview of how neuroimaging techniques can help assess patients with DOC. Such techniques are expected to facilitate a more accurate understanding of brain function in states of unconsciousness and to improve the evaluation of the

INTRODUCTION

Consciousness is a multifaceted and ambiguous concept, which is often the focus of passionate multi-disciplinarian debates. Consciousness is thought to represent an emergent property of reciprocal connections between specialized areas of the grey matter within cortical and subcortical networks^[1]. To date, there is no universal definition for consciousness covering all its essential characteristics^[2], making everything particularly tricky and challenging when facing this specific topic and the related disorders.

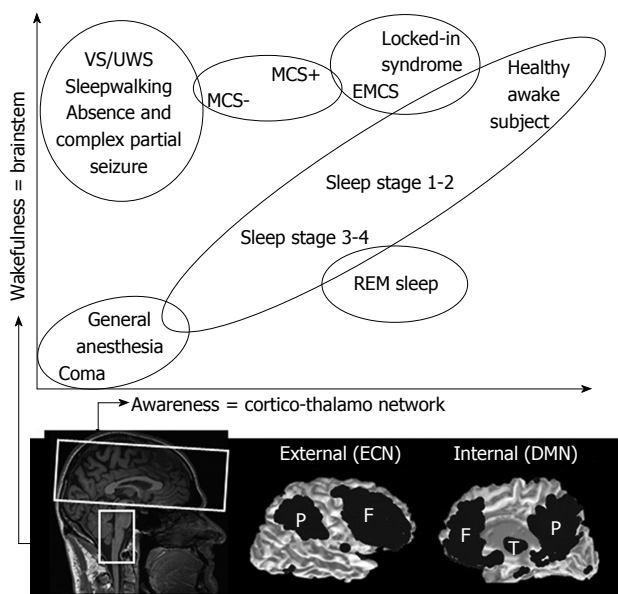


Figure 1 The two main components of consciousness: wakefulness and awareness. Correlation between wakefulness, related to the brainstem, and awareness, related to the cortico-thalamic network. In most pathological and physiological states, the two components are linearly correlated along the spectrum of consciousness. However, they are dissociated in some cases. Vegetative state/unresponsive wakefulness syndrome (VS/UWS); minimally conscious state (MCS); emergence of MCS, EMCS. Adapted from ref. [3,4]. EMCS: Emerge from minimally conscious state; ECN: Executive control network; DMN: Default mode network; REM: Rapid eyes movement.

We here adopt a perspective where consciousness is clinically defined as having two components: awareness and arousal^[3]. Arousal, also called wakefulness, refers to the level of alertness (clinically determined by eye opening), whereas awareness refers to the content of consciousness (clinically determined by command following or non-reflex motor behaviour such as eye tracking or localized responses to pain)^[3]. Arousal is anatomically related to structures in the brain and specifically in the brainstem and hypothalamus, whereas awareness has been shown to be related to a wide fronto-parietal network encompassing associative cortices and, more specifically, to the intrinsic connectivity of this network and the connectivity between the fronto-parietal associative cortices and the thalamus^[4,5]. In physiological states, there is an intimate positive correlation between arousal and awareness. Sleep is the best way to describe the relationship between these two components: the less awake we become as we move towards deep sleep, the less aware we become of our surroundings and ourselves^[3]. Based on this, subjects in pathological and pharmacological coma (*i.e.*, anesthesia) are not conscious because they cannot be awakened, even after noxious stimulation^[3]. Similarly, under sedation (a drug-dose dependent impairment of consciousness) and in hypnotic state (a suggestion-dependent alteration of conscious experience), subjects report an altered state of awareness as they move towards lower levels of arousal^[6-8]. Hence, arousal seems to be essential for awareness to emerge, *i.e.*, one needs to be awake in order to be aware. However, being awake is not sufficient in order to be aware.

There are, in fact, some exceptional cases in which these two components are dissociated. On the one hand, in the rapid eye movement stage of sleep, wakefulness is impaired while internal awareness is relatively spared. On the other hand, in vegetative state (VS), now also coined unresponsive wakefulness syndrome (UWS)^[9], in minimally conscious state (MCS) and in some more transient states such as absence seizures, complex partial seizures or somnambulism, awareness is impaired while wakefulness is spared (Figure 1)^[10-13]. The interest in understanding the neuropathology of such latter states, and in particular VS/UWS, is twofold. Firstly, VS/UWS patients offer a lesion approach to the study of human consciousness in terms of identifying the neural correlate of awareness^[3]. These patients represent cases of awareness suppression but, unlike coma patients, exhibit intact wakefulness. Secondly, VS/UWS patients represent a clinical challenge, in terms of both diagnosis, and prognosis.

We aim to review here the knowledge of (un) consciousness obtained by studying disorders of consciousness (DOC) following brain injury (coma, VS/UWS, and MCS). We will focus mainly on structural and functional neuroimaging studies and we will pinpoint how developing such techniques could improve both scientific and clinical perspectives in DOC (Table 1).

We searched the MEDLINE database for English-language reports published between 2002 and April 2014 which used the terms “disorders of consciousness”, “vegetative state”, “minimally conscious state”, “neuroimaging”, “magnetic resonance imaging (MRI)”, “positron emission tomography (PET)”, “transcranial magnetic stimulation (TMS)” and “TMS/electroencephalography (TMS/EEG)”. We reviewed the full text of all the original articles, reviews, early-release publications and associated citations retrieved, and relevant papers found in the authors’ own files.

CLINICAL ENTITIES OF DISORDERS OF CONSCIOUSNESS

Disorders of consciousness are characterized by a prolonged impaired unconsciousness following an acquired severe brain injury. These conditions are more and more frequent in the clinical setting due to progress in emergency medicine and lifesaving technologies which have led to a better survival rate after severe brain damage^[14].

Patients surviving severe brain damage may end up in a coma. This state may arise following structural or metabolic lesions to the brainstem reticular system or due to widespread bilateral cerebral damage^[1]. Patients in coma show continuous absence of eye opening and any spontaneous or stimulus induced arousal or voluntary behavioural responses. Hence, they are neither awake nor aware. Coma is a time-limited condition (it usually does not last longer than a few weeks) leading either to brain death (*i.e.*, permanent loss of brainstem functions), a VS/UWS or the recovery of consciousness. Patients in a VS/UWS have recovered wakefulness (as evinced by

Table 1 Key points of the review

<p>Novel neuroimaging techniques in patients with DOC give important key insights into both the understanding of consciousness and the differential diagnosis of clinical DOC entities, given that behavioural assessment alone can sometimes be incorrect and imprecise</p> <p>Conventional MRI and DTI investigates the structural properties of the brain and the white matter integrity. These studies showed mainly a predictive rather than diagnostic value</p> <p>PET activations show a critical role of a wide frontoparietal associative network for the emergence of consciousness</p> <p>fMRI employing active paradigm detects covert awareness in approximately 17% of unresponsive patients at bedside. However, there is a high risk of false negative. fMRI employing passive paradigm shows also a prognostic value. fMRI during resting state shows a broad alteration of brain connectivity, implying both decreased and increased connectivity in patients with DOC</p> <p>TMS-EEG shows a high diagnostic value even at single subject level</p>

DOC: Disorders of consciousness; MRI: Magnetic resonance imaging; DTI: Diffusion tensor imaging; PET: Positron emission tomography; fMRI: Functional magnetic resonance imaging; TMS-EEG: Transcranial magnetic stimulation coupled with electroencephalography.

eye opening) but their motor responses are only reflexive and, therefore, do not indicate conscious awareness^[15]. VS/UWS has been said to be permanent 12 mo after traumatic brain injury and 3 mo following non-traumatic brain damage, making chances of recovery very low^[16]. However, this has recently been challenged^[9]. It is now suggested that one substitute the term “permanent” with the association of the injury etiology (traumatic *vs* non traumatic) and the length of time since onset, as these factors appear to influence outcome. Non traumatic patients generally have the worst outcome. From VS/UWS, patients may progress into a MCS. This may either be the endpoint of their improvement or a provisional stage on the way to further recovery of consciousness^[17]. MCS is a condition of severely altered consciousness characterized by minimal, inconstant yet definite behavioural signs of awareness of self and the surroundings. Based on the level of their purposeful behavioural signs, MCS patients were recently subcategorized as MCS plus (showing command following, intelligible verbalizations or non-functional communication) and MCS minus (showing visual pursuit, localization of noxious stimulation or contingent behaviour such as appropriate smiling or crying to emotional stimuli)^[18]. Patients may emerge from MCS once they regain the ability to reliably communicate and/or use objects in a functional manner^[17]. Although there is some evidence suggesting that patients in a MCS have better chances of recovery than patients in a VS/UWS, at present, we are not in a position to refer to possible temporal boundaries of irreversible MCS^[19].

DOC must be differentiated from locked in syndrome (LIS). This is a rare state which usually follows a brain stem lesion with massive damage to the cortico-spinal and cortico-bulbar pathways, and classically results in loss of control of all voluntary muscles except for extrinsic eye muscles, making it possible for them only to communicate with small eyelid movements^[20,21].

Differential diagnosis of the above mentioned clinical DOC entities raises important ethical and medical questions such as end-of-life decision and pain treatment^[14,22,23]. Nowadays, the gold standard for assessing the level of consciousness is the clinical assessment of patients’ behavioural responsiveness. Since responsiveness is only indirect proof of consciousness (lack of responsiveness does not necessarily imply lack of con-

sciousness), reliance on these behavioural markers entails significant challenges and may lead to misdiagnoses. Clinical studies have shown that up to 40% of patients with a diagnosis of VS/UWS may in fact retain some level of awareness^[24-26], and the main causes of misdiagnosis are associated with patient’s disabilities, such as paralysis and aphasia, fluctuation in arousal level, difficulty differentiating between reflexive and involuntary movements and the non-use of standardized and sensitive clinical scales such as the Coma Recovery Scale-Revised (CRS-R)^[27]. Furthermore, conventional brain structural imaging studies have shown highly variable and heterogeneous results in patients with DOC, suggesting that a specific brain region cannot be unequivocally related to awareness^[28]. This knowledge has led to the search for other non-clinical assessment techniques which can enable us to better understand brain function in these patients and to overcome the limits of behavioural assessment in the detection of possible retained consciousness in unresponsive patients.

NEUROIMAGING STUDIES IN DOC

Functional neuroimaging methods have made it possible to objectively study cognitive processing in the absence of behavioural reports. PET measures different aspects of metabolic function according to the type of administered radioactive tracer. Structural conventional MRI and diffusion tensor imaging (DTI) reveal the structural properties of the brain and the white matter integrity respectively. Functional MRI (fMRI) quantifies brain function derived from blood-oxygen-level dependent (BOLD) changes. TMS/EEG allows us to non-invasively stimulate a subset of cortical neurons and to measure the effects of this perturbation on the rest of the brain^[29-33] (Table 2).

Below we will refer to the neuroimaging studies that have been most frequently adopted to infer covert cognitive abilities in behaviourally non responsive DOC patients.

PET

¹⁸Fluorodesoxyglucose-PET (FDG-PET) studies were the first to demonstrate massive decrease in brain metabolism in patients with DOC. Using PET in resting state conditions, it was shown that patients in VS/UWS exhibit a decrease in brain metabolism of up to 40% of the normal value^[3]. Nevertheless, recovery from the

Table 2 Main strength and limits of the different techniques

Technique	Strength	Limits
PET	Relatively direct measure of brain activity	Ionizing, radioactive tracer, low spatial and temporal resolution expensive
MRI	No use of ionizing. Permits both high resolution study of structural brain (DTI) and fMRI employing active, passive and resting state paradigms	Indirect measure of brain activity (functional) Sensitive to movement and artifacts, impractical (application precluded in patients with contraindication), expensive
TMS-EEG	Practical (no important contraindications) gives information at single subject level	Sensitive to muscle artifacts

PET: Positron emission tomography; MRI: Magnetic resonance imaging; TMS-EEG: Transcranial magnetic stimulation coupled with electroencephalography; DTI: Diffusion tensor imaging; fMRI: Functional magnetic resonance imaging.

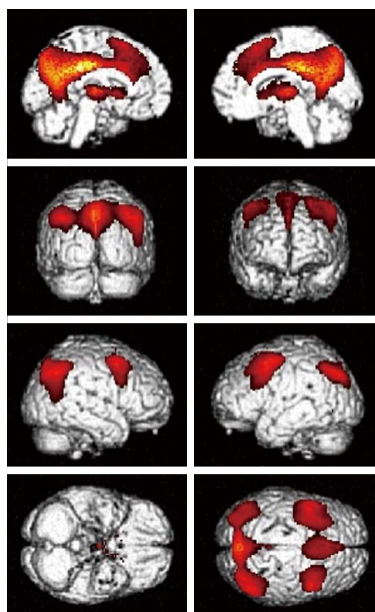


Figure 2 Brain areas where metabolism is impaired in vegetative state/unresponsive wakefulness syndrome patients compared to controls (areas in red), superimposed in a structural 3D image. $P < 0.05$, family wise error corrected.

VS/UWS does not coincide with the recovery of global metabolic levels. Instead it seems that some areas are more important to consciousness than others. In fact, patients suffering from DOC show decreased metabolism in a widespread network encompassing frontoparietal areas, such as in the lateral prefrontal and posterior parietal regions as well as midline anterior cingulate/mesiofrontal and posterior cingulate/precuneal associative cortices (Figure 2)^[34,35]. Importantly, recovery from the VS/UWS parallels connectivity restoration in these areas (cortico-cortical) and between these regions and the thalamus (thalamo-cortical)^[36].

FDG-PET cannot yet disentangle between VS/UWS and MCS at the single subject. However, it has shown to be highly sensitive in identifying patients in MCS^[37] and displaying a correlation between metabolism in the above mentioned awareness network and the CRS-R score of the patients^[38].

There is now growing evidence suggesting that this awareness network can be subdivided into two different networks: the intrinsic [default mode network (DMN)]

and the extrinsic awareness network [executive control network (ECN)]. The extrinsic awareness network encompasses the lateral fronto-parietal brain regions and is related to sensory awareness or awareness of the environment. The intrinsic awareness network (most widely known as the DMN) encompasses mainly the medial prefrontal cortex and the precuneus and bilateral posterior parietal cortices and is related to internal awareness or self-related processes, such as mind-wandering and autobiographical thinking^[39-41]. More recently, it has been demonstrated that patients in MCS retain metabolism in the lateral fronto-parietal areas whilst midline regions are highly dysfunctional^[42]. As such, this data suggests that, at group level, patients in MCS display altered self-awareness besides their abilities to, at least to a certain extent, interact (but not communicate) with their surroundings. Furthermore, patients who are considered to be in MCS minus showed impairment of the left dominant hemisphere, possibly correlated to aphasia, consistent with their command-following impairment^[18].

¹⁵H₂O-PET studies using passive auditory and noxious stimulation^[43,44], have furthermore highlighted a peculiar disconnection in VS/UWS patients between the primary sensory areas and these large-scale associative frontoparietal cortices, which are thought to be essential for conscious perception^[3]. In contrast, patients in MCS show a partial preservation of this large-scale associative frontoparietal network^[45]. Furthermore, PET studies employing nociceptive stimuli have highlighted an activation of the pain matrix in MCS patients similar to that observed in healthy controls, suggesting a possible perception of pain in this patient category. By contrast, activation in VS/UWS was limited to the primary sensory areas^[46].

Structural MRI

MRI with conventional sequences (T1-TSE, T2-TSE, FLAIR) is the method of choice to detect brain edema, contusion, hematomas, herniation, hemorrhage, hydrocephalus, or hemorrhagic shearing lesion due to diffuse axonal injuries common in post-traumatic patients (T2* sequences). Nevertheless, in an emergency setting, the computed tomography scan is preferable in some cases due to its accessibility, speed of acquisition, and sensitivity to acute hemorrhagic lesions that require a surgical approach^[38,47].

Some studies have highlighted the predictive value

of the classical conventional sequences. For example, the number of lesions detected by FLAIR and T2* sequences has been shown to be inversely correlated with the Glasgow Coma Scale (GCS) of traumatic patients in a coma. The presence of lesions in the corpus callosum and the dorsal midbrain has been shown to be correlated with lack of recovery at group level in coma patients^[47,48]. However, these methods have failed to explain why some patients in a VS/UWS and/or in a MCS have no or minimal brain lesions. This highlights the lack of specificity and sensitivity of conventional MRI in DOC, which alone cannot be considered a reliable tool for assessing this patient category.

Recently developed DTI techniques can reveal structural damage in tissue that appears normal in conventional-MRI.

These techniques have been able to predict scores on the GCS and successfully classify VS/UWS and MCS patients into their appropriate diagnostic categories with an accuracy of 95%^[49]. Furthermore, recent multicentric studies have demonstrated that DTI is better at predicting outcome for both traumatic and anoxic patients at 1 year follow up from injury than structural and clinical assessment^[50,51]. An other study evaluated the combination of DTI and MR-spectroscopy as a tool for predicting long-term outcome of traumatic patients^[52], showing that a prediction of non-recovery after 1 year could be calculated with up to 86% sensitivity and 97% specificity when taking into account both DTI and MR-spectroscopy values.

With regards to diagnostic accuracy, a recent study used DTI to assess the neuropathology of patients in VS/UWS and MCS *in vivo* and to identify measurements that could potentially distinguish the patients in these two groups^[49]. The MCS and VS/UWS patients appeared to differ significantly in subcortical white matter and thalamic regions (measured using diffusivity maps) but appeared not to differ in the brainstem. DTI results predicted scores on the GCS and successfully classified the patients into their appropriate diagnostic categories with an accuracy of 95%^[49]. Furthermore, DTI proved to be helpful for characterizing etiologic differences in patients in VS/UWS, demonstrating that DTI abnormalities in the brainstem were confined to the traumatic brain injured group^[53].

These studies suggest that DTI-MRI techniques can quantify white matter integrity and support the possible benefit of using these methods for an early classification of this patient population.

fMRI

In the last few years PET activation studies have been largely replaced by fMRI non-ionizing techniques. Activation studies using visual, auditory and somatosensory stimuli have revealed high level cortical activation encompassing the associative cortices in patients in MCS, similar to that observed in healthy controls^[54,55]. In contrast, only low level cortical activation, limited to the primary sensory areas, was detected in VS/UWS. The minority

of patients in VS/UWS with high level cortical activation often showed signs of recovery on the long term follow up^[55,56]. Besides the prognostic value of this technique, active fMRI paradigms have recently been performed to detect covert awareness in patients who are behaviourally unresponsive by investigating signs which are independent from motor command following, and in some cases even establishing yes-no communication^[57-59].

For instance, a recent fMRI study using mental imagery tasks (imagining playing tennis vs spatial navigation around one's house) showed that in a large cohort of 54 patients with DOC, 5 were able to willfully modulate their brain activity. Furthermore, one behaviourally VS/UWS patient was able to use this technique to correctly respond with yes (by imagining playing tennis) or no (by imagining visiting the rooms of his house) to autobiographical questions during the fMRI scanning^[57]. Approximately 17% of patients diagnosed as in VS/UWS following behavioural assessment seem to be able to follow commands when the commands involve a change in blood oxygenation level dependent response, rather than overt motoric behaviour. Similarly, a further study using selective auditory attention showed that 3 patients (2 in MCS and 1 in VS/UWS) were able to convey their ability to follow commands, and the one in VS/UWS was even able to correctly communicate answers to several autobiographic binary questions^[60].

Despite their potential diagnostic and prognostic value, active fMRI paradigm in terms of detecting covert awareness has remained mostly controversial. Indeed, without a comprehensive understanding of the neural correlates of awareness, the absence of cortical activation to external stimuli does not necessarily coincide with absence of awareness. Indeed, out of 31 MCS patients described in the study by Monti *et al.*^[57], only one was able to willfully modulate his brain activity. This could be due to the fact that patients may be asleep during the scan, or due to patients' disabilities, such as aphasia (patients cannot understand the task), *etc.*^[57].

In this context, the other fMRI paradigms commonly performed which partially overcome this latter limit are passive, measuring brain responses to external sensory stimulation (*e.g.*, auditory, somatosensory and visual) whilst the subject is not performing any mental task. An example is the brain activation elicited by the patient's own name spoken by a familiar voice. This is a salient auditory stimulus which has been preferred due to its attention-grabbing properties. For example, using the own-name paradigm, it was shown that 2 out of 7 patients in VS/UWS and all 4 patients in MCS not only showed activation in the primary auditory cortex, but also in higher order associative temporal areas, which are thought to be implicated in the conscious processing of the incoming stimuli^[55]. Interestingly, these 2 patients in VS/UWS subsequently recovered to MCS. The absence of higher activation did not unequivocally coincide with the absence of awareness as sensory deficits, such as deafness, could have led to a false negative.

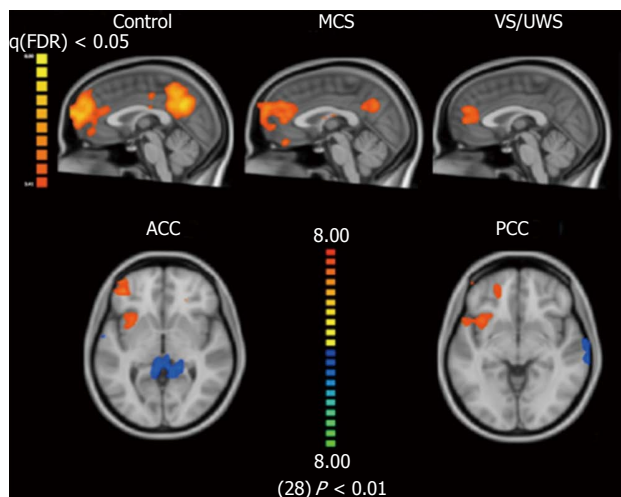


Figure 3 Default mode network in vegetative state/unresponsive wakefulness syndrome, minimally conscious state, healthy controls-sagittal view^[68]. In vegetative state/unresponsive wakefulness syndrome (VS/UWS), the anterior cingulate cortex (ACC) and posterior cingulate cortex (PCC) are hypoconnected to the default mode network (in blue) and hyperconnected to the fronto-insular cortex (in red), axial view. Correlation from random effect ($P < 0.01$) and clustered corrected ($P < 0.05$) results based on general linear model maps with seed region of interest comparing VS/UWS to healthy controls^[60]. MCS: Minimally conscious state.

Resting-state fMRI is a non invasive technique used to investigate the spontaneous temporal coherence in BOLD fluctuations related to the amount of synchronized neural activity (*i.e.*, functional connectivity) between distinct brain locations, in the absence of input or output tasks^[61]. This technique has been increasingly used in the analysis of patients with DOC, mainly because it is not invasive and it surpasses the requirement for motor output or language comprehension. Among the several functional networks that have been detected so far^[62], DMN has been the first to attract scientific attention. To date, resting state fMRI studies suggest that activity of this network is generally lower as a function of the level of consciousness. It has been demonstrated, for example, that the connectivity of this network is correlated to the level of consciousness, ranging from patients in VS/UWS (low connectivity) to patients in MCS and to healthy controls (higher connectivity)^[63] (Figure 3). In addition, DMN connectivity could not be found in a brain dead patient, which highlights the neural origin of these MRI signals^[64]. Recently, more networks at resting state have been investigated in DOC, such as the bilateral fronto-parietal or executive control networks, salience, sensorimotor, auditory, visual systems, and the cerebellar network. It was found that, besides DMN, the bilateral executive control networks and the auditory system were also significantly less identifiable (in terms of spatial and neural properties) in patients with DOC compared to healthy controls, and showed consciousness-level dependent decreases in functional connectivity across the spectrum of DOC^[65].

Interestingly, it has been found that the resting brain is characterized by a switch between the dominance of the DMN (linked to “internal” or self-awareness) and

the ECN (linked to “external” or environmental awareness^[66,67]); when one shows activation, the other does not and vice-versa. More recently, it was found that such spontaneous anticorrelated patterns are closely related to mentation and behavioral status. This means that DMN activity is linked to behavioral report of internal awareness whereas ECN activity is related to behavioural ratings for external awareness^[39]. The decrease in anticorrelated pattern in disordered consciousness supports the functional relevance of anticorrelated patterns to the phenomenological complexity of consciousness^[29].

Alongside the investigation of reduced connectivity is the presence of hyper-connectivity patterns, which might also be indicative of brain function. In fact, it has recently been demonstrated that, together with DMN hypoconnectivity, the subcortical limbic system (including the orbitofrontal cortex, insula and hypothalamus) exhibits paradoxically increased fMRI connectivity in patients with DOC when compared to healthy controls^[68] (Figure 3). This could point to a more complex scenario of brain connectivity architecture in the emergence of consciousness, where hypoconnectivity may only represent a single aspect.

TMS-EEG

Unfortunately, fMRI-based techniques are impractical. The fact that a scanner is needed limits its use to hospital settings and precludes use in patients with pace makers, metal implants or those in a critical condition in intensive care units.

In this context, EEG recording associated with TMS is a promising way to assess cerebral connectivity and it may be especially useful for assessing the level of consciousness in patients with DOC as it does not require a scanner and it does not rely on the subject’s ability to process sensory stimuli, to understand and follow instructions or to communicate. In addition, this technique permits consciousness assessment at single subject level, unlike the majority of fMRI and PET studies^[33,69].

TMS-EEG can measure brain complexity by non-invasively stimulating a subset of cortical neurons (through TMS) and can immediately measure the effects of this perturbation on the rest of the brain (through high density EEG)^[32,33].

Based on the level of consciousness, the perturbation will show either cortical interaction related to preservation or loss of information and/or integration. For example, in patients in VS/UWS, when stimulating a superficial region of the cerebral cortex, TMS either induced no response or triggered a simple, local EEG response, indicating a breakdown of effective connectivity (*i.e.*, of the influence that one brain region exerts on another^[70,71], similar to that observed in deep sleep and anesthesia^[33,72]). In contrast, for patients in MCS, TMS triggered complex EEG activations which sequentially involved distant cortical areas, similar to activations recorded in patients in LIS and healthy awake subjects. Recently, these TMS-EEG responses have been practically quantified by the

perturbational complexity index (PCI)^[32]. This index has demonstrated its potential as a unified measurement scale to grade the level of consciousness. The PCI, in fact, estimates the amount of information contained in the integrated response of the thalamo-cortical system to a direct TMS perturbation^[32]. Empirically, it showed to provide a data-driven metric that can discriminate level of consciousness in single subjects under different conditions: below 0.31 for unconsciousness, above 0.51 for healthy consciousness and in the between for MCS.

CONCLUSION

In the last decade we have witnessed the development and the validation of standardized behavioural scales, together with neuroimaging and neurophysiological techniques to better understand the variable conditions of patients with DOC. The need to objectively measure phenomena associated with consciousness has promoted an increased use of these neuroimaging and neurophysiological tools in this patient population. Here we have reviewed the basic principles of how the main neuroimaging techniques (PET, structural MRI, fMRI and TMS-EEG), provide us with important insights into brain function in DOC patients. Since every single technique gives us specific and different information, we support the integration of structural and functional neuroimaging techniques, in order to have a broader and more holistic vision of both the disease and the single patient under our care. Furthermore, we expect that in the near future, with a wider use of standardized behavioural scales and the development of multimodal neuroimaging techniques, there will be a drop in diagnosis-error. Finally, the application of these methodologies at the single subject level, as clinical reality requires, is one of the next challenges.

ACKNOWLEDGMENTS

The authors thank Ziggy Kennel for english revision.

REFERENCES

- 1 **Laureys S**, Owen AM, Schiff ND. Brain function in coma, vegetative state, and related disorders. *Lancet Neurol* 2004; **3**: 537-546 [PMID: 15324722]
- 2 **Zeman A**. Consciousness. *Brain* 2001; **124**: 1263-1289 [PMID: 11408323]
- 3 **Laureys S**. The neural correlate of (un)awareness: lessons from the vegetative state. *Trends Cogn Sci* 2005; **9**: 556-559 [PMID: 16271507 DOI: 10.1016/j.tics.2005.10.010]
- 4 **Di Perri C**, Stender J, Laureys S, Gosseries O. Functional neuroanatomy of disorders of consciousness. *Epilepsy Behav* 2014; **30**: 28-32 [PMID: 24100252]
- 5 **Laureys S**, Faymonville ME, Luxen A, Lamy M, Franck G, Maquet P. Restoration of thalamocortical connectivity after recovery from persistent vegetative state. *Lancet* 2000; **355**: 1790-1791 [PMID: 10832834 DOI: 10.1016/S0140-6736(00)02271-6]
- 6 **Faymonville ME**, Boly M, Laureys S. Functional neuroanatomy of the hypnotic state. *J Physiol Paris* 2006; **99**: 463-469 [PMID: 16750615 DOI: 10.1016/j.jphysparis.2006.03.018]
- 7 **Vanhaudenhuyse A**, Boveroux P, Boly M, Schnakers C, Bruno MA, Kirsch M, Demertzi A, Lamy M, Maquet P, Laureys S, Faymonville ME. [Hypnosis and pain perception]. *Rev Med Liege* 2008; **63**: 424-428 [PMID: 18669215]
- 8 **Boly M**, Sanders RD, Mashour GA, Laureys S. Consciousness and responsiveness: lessons from anaesthesia and the vegetative state. *Curr Opin Anaesthesiol* 2013; **26**: 444-449 [PMID: 23743554 DOI: 10.1097/ACO.0b013e3283628b5d]
- 9 **Laureys S**, Celesia GG, Cohadon F, Lavrijsen J, León-Carrión J, Sannita WG, Szabon L, Schmutzhard E, von Wild KR, Zeman A, Dolce G. Unresponsive wakefulness syndrome: a new name for the vegetative state or apallic syndrome. *BMC Med* 2010; **8**: 68 [PMID: 21040571 DOI: 10.1186/1741-7015-8-68]
- 10 **Salek-Haddadi A**, Lemieux L, Merschhemke M, Friston KJ, Duncan JS, Fish DR. Functional magnetic resonance imaging of human absence seizures. *Ann Neurol* 2003; **53**: 663-667 [PMID: 12731002 DOI: 10.1002/ana.10586]
- 11 **Blumenfeld H**. Epilepsy and the consciousness system: transient vegetative state? *Neurol Clin* 2011; **29**: 801-823 [PMID: 22032662 DOI: 10.1016/j.ncl.2011.07.014]
- 12 **Blumenfeld H**. Impaired consciousness in epilepsy. *Lancet Neurol* 2012; **11**: 814-826 [PMID: 22898735 DOI: 10.1016/S1474-4422(12)70188-6]
- 13 **Bassetti C**, Vella S, Donati F, Wielepp P, Weder B. SPECT during sleepwalking. *Lancet* 2000; **356**: 484-485 [PMID: 10981896 DOI: 10.1016/S0140-6736(00)02561-7]
- 14 **Laureys S**. Science and society: death, unconsciousness and the brain. *Nat Rev Neurosci* 2005; **6**: 899-909 [PMID: 16261182 DOI: 10.1038/nrn1789]
- 15 **Boveroux P**, Bonhomme V, Boly M, Vanhaudenhuyse A, Maquet P, Laureys S. Brain function in physiologically, pharmacologically, and pathologically altered states of consciousness. *Int Anesthesiol Clin* 2008; **46**: 131-146 [PMID: 18617821 DOI: 10.1097/AIA.0b013e318181a8b3]
- 16 Medical aspects of the persistent vegetative state (2). The Multi-Society Task Force on PVS. *N Engl J Med* 1994; **330**: 1572-1579 [PMID: 8177248 DOI: 10.1056/NEJM19940602330206]
- 17 **Giacino JT**, Ashwal S, Childs N, Cranford R, Jennett B, Katz DI, Kelly JP, Rosenberg JH, Whyte J, Zafonte RD, Zasler ND. The minimally conscious state: definition and diagnostic criteria. *Neurology* 2002; **58**: 349-353 [PMID: 11839831 DOI: 10.1212/WNL.58.3.349]
- 18 **Bruno MA**, Vanhaudenhuyse A, Thibaut A, Moonen G, Laureys S. From unresponsive wakefulness to minimally conscious PLUS and functional locked-in syndromes: recent advances in our understanding of disorders of consciousness. *J Neurol* 2011; **258**: 1373-1384 [PMID: 21674197 DOI: 10.1007/s00415-011-6114-x]
- 19 **Laureys S**, Boly M. The changing spectrum of coma. *Nat Clin Pract Neurol* 2008; **4**: 544-546 [PMID: 18762800 DOI: 10.1038/ncpneu0887]
- 20 **Laureys S**, Pellas F, Van Eeckhout P, Ghorbel S, Schnakers C, Perrin F, Berré J, Faymonville ME, Pantke KH, Damas F, Lamy M, Moonen G, Goldman S. The locked-in syndrome: what is it like to be conscious but paralyzed and voiceless? *Prog Brain Res* 2005; **150**: 495-511 [PMID: 16186044 DOI: 10.1016/S0079-6123(05)50034-7]
- 21 **Bauer G**, Gerstenbrand F, Rumpl E. Varieties of the locked-in syndrome. *J Neurol* 1979; **221**: 77-91 [PMID: 92545]
- 22 **Demertzi A**, Ledoux D, Bruno MA, Vanhaudenhuyse A, Gosseries O, Soddu A, Schnakers C, Moonen G, Laureys S. Attitudes towards end-of-life issues in disorders of consciousness: a European survey. *J Neurol* 2011; **258**: 1058-1065 [PMID: 21221625 DOI: 10.1007/s00415-010-5882-z]
- 23 **Demertzi A**, Schnakers C, Ledoux D, Chatelle C, Bruno MA, Vanhaudenhuyse A, Boly M, Moonen G, Laureys S. Different beliefs about pain perception in the vegetative and mini-

- mally conscious states: a European survey of medical and paramedical professionals. *Prog Brain Res* 2009; **177**: 329-338 [PMID: 19818911 DOI: 10.1016/S0079-6123(09)17722-1]
- 24 **Schnakers C**, Vanhaudenhuyse A, Giacino J, Ventura M, Boly M, Majerus S, Moonen G, Laureys S. Diagnostic accuracy of the vegetative and minimally conscious state: clinical consensus versus standardized neurobehavioral assessment. *BMC Neurol* 2009; **9**: 35 [PMID: 19622138 DOI: 10.1186/1471-2377-9-35]
- 25 **Andrews K**, Murphy L, Munday R, Littlewood C. Misdiagnosis of the vegetative state: retrospective study in a rehabilitation unit. *BMJ* 1996; **313**: 13-16 [PMID: 8664760 DOI: 10.1136/bmj.313.7048.13]
- 26 **Childs NL**, Mercer WN, Childs HW. Accuracy of diagnosis of persistent vegetative state. *Neurology* 1993; **43**: 1465-1467 [PMID: 8350997 DOI: 10.1212/WNL.43.8.1465]
- 27 **Giacino JT**, Kalmar K, Whyte J. The JFK Coma Recovery Scale-Revised: measurement characteristics and diagnostic utility. *Arch Phys Med Rehabil* 2004; **85**: 2020-2029 [PMID: 15605342 DOI: 10.1016/j.apmr.2004.02.033]
- 28 **Tshibanda L**, Vanhaudenhuyse A, Boly M, Soddu A, Bruno MA, Moonen G, Laureys S, Noirhomme Q. Neuroimaging after coma. *Neuroradiology* 2010; **52**: 15-24 [PMID: 19862509 DOI: 10.1007/s00234-009-0614-8]
- 29 **Heine L**, Soddu A, Gómez F, Vanhaudenhuyse A, Tshibanda L, Thonnard M, Charland-Verville V, Kirsch M, Laureys S, Demertzi A. Resting state networks and consciousness: alterations of multiple resting state network connectivity in physiological, pharmacological, and pathological consciousness States. *Front Psychol* 2012; **3**: 295 [PMID: 22969735 DOI: 10.3389/fpsyg.2012.00295]
- 30 **Tshibanda L**, Vanhaudenhuyse A, Bruno MA, Boly M, Soddu A, Laureys S, Moonen G. [MRI in coma survivors]. *Rev Med Liege* 2009; **64** Spec No: 42-48 [PMID: 20085015]
- 31 **Tshibanda L**, Vanhaudenhuyse A, Galanaud D, Boly M, Laureys S, Puybasset L. Magnetic resonance spectroscopy and diffusion tensor imaging in coma survivors: promises and pitfalls. *Prog Brain Res* 2009; **177**: 215-229 [PMID: 19818904 DOI: 10.1016/S0079-6123(09)17715-4]
- 32 **Casali AG**, Gosseries O, Rosanova M, Boly M, Sarasso S, Casali KR, Casarotto S, Bruno MA, Laureys S, Tononi G, Massimini M. A theoretically based index of consciousness independent of sensory processing and behavior. *Sci Transl Med* 2013; **5**: 198ra105 [PMID: 23946194]
- 33 **Massimini M**, Ferrarelli F, Huber R, Esser SK, Singh H, Tononi G. Breakdown of cortical effective connectivity during sleep. *Science* 2005; **309**: 2228-2232 [PMID: 16195466 DOI: 10.1126/science.1117256]
- 34 **Nakayama N**, Okumura A, Shinoda J, Nakashima T, Iwama T. Relationship between regional cerebral metabolism and consciousness disturbance in traumatic diffuse brain injury without large focal lesions: an FDG-PET study with statistical parametric mapping analysis. *J Neurol Neurosurg Psychiatry* 2006; **77**: 856-862 [PMID: 16549415 DOI: 10.1136/jnnp.2005.080523]
- 35 **Silva S**, Alacoque X, Fourcade O, Samii K, Marque P, Woods R, Mazziotta J, Chollet F, Loubinoux I. Wakefulness and loss of awareness: brain and brainstem interaction in the vegetative state. *Neurology* 2010; **74**: 313-320 [PMID: 20101037 DOI: 10.1212/WNL.0b013e3181cbcd96]
- 36 **Laureys S**, Lemaire C, Maquet P, Phillips C, Franck G. Cerebral metabolism during vegetative state and after recovery to consciousness. *J Neurol Neurosurg Psychiatry* 1999; **67**: 121 [PMID: 10454871 DOI: 10.1136/jnnp.67.1.121]
- 37 **Stender J**, Gosseries O, Bruno MA, Charland-Verville V, Vanhaudenhuyse A, Demertzi A, Chatelle C, Thonnard M, Thibaut A, Heine L, Soddu A, Boly M, Schnakers C, Gjedde A, Laureys S. Diagnostic precision of PET imaging and functional MRI in disorders of consciousness: a clinical validation study. *Lancet* 2014; **384**: 514-522 [PMID: 24746174]
- 38 **Giacino JT**, Fins JJ, Laureys S, Schiff ND. Disorders of consciousness after acquired brain injury: the state of the science. *Nat Rev Neurol* 2014; **10**: 99-114 [PMID: 24468878]
- 39 **Vanhaudenhuyse A**, Demertzi A, Schabus M, Noirhomme Q, Bredart S, Boly M, Phillips C, Soddu A, Luxen A, Moonen G, Laureys S. Two distinct neuronal networks mediate the awareness of environment and of self. *J Cogn Neurosci* 2011; **23**: 570-578 [PMID: 20515407 DOI: 10.1162/jocn.2010.21488]
- 40 **Demertzi A**, Soddu A, Laureys S. Consciousness supporting networks. *Curr Opin Neurobiol* 2013; **23**: 239-244 [PMID: 23273731 DOI: 10.1016/j.conb.2012.12.003]
- 41 **Demertzi A**, Vanhaudenhuyse A, Brédart S, Heine L, di Perri C, Laureys S. Looking for the self in pathological unconsciousness. *Front Hum Neurosci* 2013; **7**: 538 [PMID: 24027519]
- 42 **Thibaut A**, Bruno MA, Chatelle C, Gosseries O, Vanhaudenhuyse A, Demertzi A, Schnakers C, Thonnard M, Charland-Verville V, Bernard C, Bahri M, Phillips C, Boly M, Hustinx R, Laureys S. Metabolic activity in external and internal awareness networks in severely brain-damaged patients. *J Rehabil Med* 2012; **44**: 487-494 [PMID: 22366927 DOI: 10.2340/16501977-0940]
- 43 **Laureys S**, Faymonville ME, Peigneux P, Damas P, Lambermont B, Del Fiore G, Degueldre C, Aerts J, Luxen A, Franck G, Lamy M, Moonen G, Maquet P. Cortical processing of noxious somatosensory stimuli in the persistent vegetative state. *Neuroimage* 2002; **17**: 732-741 [PMID: 12377148 DOI: 10.1006/nimg.2002.1236]
- 44 **Laureys S**, Faymonville ME, Degueldre C, Fiore GD, Damas P, Lambermont B, Janssens N, Aerts J, Franck G, Luxen A, Moonen G, Lamy M, Maquet P. Auditory processing in the vegetative state. *Brain* 2000; **123** (Pt 8): 1589-1601 [PMID: 10908189]
- 45 **Laureys S**, Perrin F, Faymonville ME, Schnakers C, Boly M, Bartsch V, Majerus S, Moonen G, Maquet P. Cerebral processing in the minimally conscious state. *Neurology* 2004; **63**: 916-918 [PMID: 15365150 DOI: 10.1212/01.WNL.0000137421.30792.9B]
- 46 **Boly M**, Faymonville ME, Schnakers C, Peigneux P, Lambermont B, Phillips C, Lancellotti P, Luxen A, Lamy M, Moonen G, Maquet P, Laureys S. Perception of pain in the minimally conscious state with PET activation: an observational study. *Lancet Neurol* 2008; **7**: 1013-1020 [PMID: 18835749 DOI: 10.1016/S1474-4422(08)70219-9]
- 47 **Kampfl A**, Schmutzhard E, Franz G, Pfausler B, Haring HP, Ulmer H, Felber S, Golaszewski S, Aichner F. Prediction of recovery from post-traumatic vegetative state with cerebral magnetic-resonance imaging. *Lancet* 1998; **351**: 1763-1767 [PMID: 9635948 DOI: 10.1016/S0140-6736(97)10301-4]
- 48 **Hoelper BM**, Soldner F, Choné L, Wallenfang T. Effect of intracerebral lesions detected in early MRI on outcome after acute brain injury. *Acta Neurochir Suppl* 2000; **76**: 265-267 [PMID: 11450021]
- 49 **Fernández-Espejo D**, Bekinschtein T, Monti MM, Pickard JD, Junque C, Coleman MR, Owen AM. Diffusion weighted imaging distinguishes the vegetative state from the minimally conscious state. *Neuroimage* 2011; **54**: 103-112 [PMID: 20728553 DOI: 10.1016/j.neuroimage.2010.08.035]
- 50 **Galanaud D**, Perlberg V, Gupta R, Stevens RD, Sanchez P, Tollard E, de Champfleury NM, Dinkel J, Faivre S, Soto-Ares G, Veber B, Cottenceau V, Masson F, Tourdias T, André E, Audibert G, Schmitt E, Ibarrola D, Dailler F, Vanhaudenhuyse A, Tshibanda L, Payen JF, Le Bas JF, Krainik A, Bruder N, Girard N, Laureys S, Benali H, Puybasset L. Assessment of white matter injury and outcome in severe brain trauma: a prospective multicenter cohort. *Anesthesiology* 2012; **117**: 1300-1310 [PMID: 23135261 DOI: 10.1097/ALN.0b013e3182755558]
- 51 **Luyt CE**, Galanaud D, Perlberg V, Vanhaudenhuyse A, Stevens RD, Gupta R, Besancenot H, Krainik A, Audibert G, Combes A, Chastre J, Benali H, Laureys S, Puybasset L. Diffusion tensor imaging to predict long-term outcome after

- cardiac arrest: a bicentric pilot study. *Anesthesiology* 2012; **117**: 1311-1321 [PMID: 23135257 DOI: 10.1097/ALN.0b013e318275148c]
- 52 **Tollard E**, Galanaud D, Perlberg V, Sanchez-Pena P, Le Fur Y, Abdenmour L, Cozzone P, Lehericy S, Chiras J, Puybasset L. Experience of diffusion tensor imaging and 1H spectroscopy for outcome prediction in severe traumatic brain injury: Preliminary results. *Crit Care Med* 2009; **37**: 1448-1455 [PMID: 19242330 DOI: 10.1097/CCM.0b013e31819cf050]
- 53 **Newcombe VE**, Williams GB, Scoffings D, Cross J, Carpenter TA, Pickard JD, Menon DK. Aetiological differences in neuroanatomy of the vegetative state: insights from diffusion tensor imaging and functional implications. *J Neurol Neurosurg Psychiatry* 2010; **81**: 552-561 [PMID: 20460593 DOI: 10.1136/jnnp.2009.196246]
- 54 **Di H**, Boly M, Weng X, Ledoux D, Laureys S. Neuroimaging activation studies in the vegetative state: predictors of recovery? *Clin Med* 2008; **8**: 502-507 [PMID: 18975482 DOI: 10.7861/clinmedicine.8-5-502]
- 55 **Di HB**, Yu SM, Weng XC, Laureys S, Yu D, Li JQ, Qin PM, Zhu YH, Zhang SZ, Chen YZ. Cerebral response to patient's own name in the vegetative and minimally conscious states. *Neurology* 2007; **68**: 895-899 [PMID: 17372124 DOI: 10.1212/01.wnl.0000258544.79024.d0]
- 56 **Owen AM**, Coleman MR, Menon DK, Johnsrude IS, Rodd JM, Davis MH, Taylor K, Pickard JD. Residual auditory function in persistent vegetative state: a combined PET and fMRI study. *Neuropsychol Rehabil* 2005; **15**: 290-306 [PMID: 16350973 DOI: 10.1080/09602010443000579]
- 57 **Monti MM**, Vanhaudenhuyse A, Coleman MR, Boly M, Pickard JD, Tshibanda L, Owen AM, Laureys S. Willful modulation of brain activity in disorders of consciousness. *N Engl J Med* 2010; **362**: 579-589 [PMID: 20130250 DOI: 10.1056/NEJMoa0905370]
- 58 **Monti MM**, Coleman MR, Owen AM. Executive functions in the absence of behavior: functional imaging of the minimally conscious state. *Prog Brain Res* 2009; **177**: 249-260 [PMID: 19818906 DOI: 10.1016/S0079-6123(09)17717-8]
- 59 **Bekinschtein TA**, Manes FF, Villarreal M, Owen AM, Della-Maggiore V. Functional imaging reveals movement preparatory activity in the vegetative state. *Front Hum Neurosci* 2011; **5**: 5 [PMID: 21441977]
- 60 **Naci L**, Owen AM. Making every word count for nonresponsive patients. *JAMA Neurol* 2013; **70**: 1235-1241 [PMID: 23939634]
- 61 **Biswal BB**, Van Kylen J, Hyde JS. Simultaneous assessment of flow and BOLD signals in resting-state functional connectivity maps. *NMR Biomed* 1997; **10**: 165-170 [PMID: 9430343]
- 62 **Beckmann CF**, DeLuca M, Devlin JT, Smith SM. Investigations into resting-state connectivity using independent component analysis. *Philos Trans R Soc Lond B Biol Sci* 2005; **360**: 1001-1013 [PMID: 16087444 DOI: 10.1098/rstb.2005.1634]
- 63 **Vanhaudenhuyse A**, Noirhomme Q, Tshibanda LJ, Bruno MA, Boveroux P, Schnakers C, Soddu A, Perlberg V, Ledoux D, Brichant JF, Moonen G, Maquet P, Greicius MD, Laureys S, Boly M. Default network connectivity reflects the level of consciousness in non-communicative brain-damaged patients. *Brain* 2010; **133**: 161-171 [PMID: 20034928]
- 64 **Boly M**, Tshibanda L, Vanhaudenhuyse A, Noirhomme Q, Schnakers C, Ledoux D, Boveroux P, Garweg C, Lambertmont B, Phillips C, Luxen A, Moonen G, Bassetti C, Maquet P, Laureys S. Functional connectivity in the default network during resting state is preserved in a vegetative but not in a brain dead patient. *Hum Brain Mapp* 2009; **30**: 2393-2400 [PMID: 19350563 DOI: 10.1002/hbm.20672]
- 65 **Demertzi A**, Gómez F, Crone JS, Vanhaudenhuyse A, Tshibanda L, Noirhomme Q, Thonnard M, Charland-Verville V, Kirsch M, Laureys S, Soddu A. Multiple fMRI system-level baseline connectivity is disrupted in patients with consciousness alterations. *Cortex* 2014; **52**: 35-46 [PMID: 24480455]
- 66 **Fox MD**, Snyder AZ, Vincent JL, Corbetta M, Van Essen DC, Raichle ME. The human brain is intrinsically organized into dynamic, anticorrelated functional networks. *Proc Natl Acad Sci USA* 2005; **102**: 9673-9678 [PMID: 15976020 DOI: 10.1073/pnas.0504136102]
- 67 **Fransson P**. Spontaneous low-frequency BOLD signal fluctuations: an fMRI investigation of the resting-state default mode of brain function hypothesis. *Hum Brain Mapp* 2005; **26**: 15-29 [PMID: 15852468 DOI: 10.1002/hbm.20113]
- 68 **Di Perri C**, Bastianello S, Bartsch AJ, Pistarini C, Maggioni G, Magrassi L, Imberti R, Pichiecchio A, Vitali P, Laureys S, Di Salle F. Limbic hyperconnectivity in the vegetative state. *Neurology* 2013; **81**: 1417-1424 [PMID: 24049132 DOI: 10.1212/WNL.0b013e3182a43b78]
- 69 **Massimini M**, Ferrarelli F, Murphy M, Huber R, Riedner B, Casarotto S, Tononi G. Cortical reactivity and effective connectivity during REM sleep in humans. *Cogn Neurosci* 2010; **1**: 176-183 [PMID: 20823938]
- 70 **Ragazzoni A**, Pirulli C, Veniero D, Feurra M, Cincotta M, Giovannelli F, Chiaramonti R, Lino M, Rossi S, Miniussi C. Vegetative versus minimally conscious states: a study using TMS-EEG, sensory and event-related potentials. *PLoS One* 2013; **8**: e57069 [PMID: 23460826]
- 71 **Rosanova M**, Gosseries O, Casarotto S, Boly M, Casali AG, Bruno MA, Mariotti M, Boveroux P, Tononi G, Laureys S, Massimini M. Recovery of cortical effective connectivity and recovery of consciousness in vegetative patients. *Brain* 2012; **135**: 1308-1320 [PMID: 22226806]
- 72 **Ferrarelli F**, Massimini M, Sarasso S, Casali A, Riedner BA, Angelini G, Tononi G, Pearce RA. Breakdown in cortical effective connectivity during midazolam-induced loss of consciousness. *Proc Natl Acad Sci USA* 2010; **107**: 2681-2686 [PMID: 20133802 DOI: 10.1073/pnas.0913008107]

P- Reviewer: Boy C, Howren MB, Serafini G **S- Editor:** Ji FF
L- Editor: A **E- Editor:** Liu SQ



Echography in brain imaging in intensive care unit: State of the art

Anselmo Caricato, Sara Pitoni, Luca Montini, Maria Grazia Bocci, Pina Annetta, Massimo Antonelli

Anselmo Caricato, Sara Pitoni, Luca Montini, Maria Grazia Bocci, Pina Annetta, Massimo Antonelli, Department of Anesthesiology and Intensive Care Medicine, Catholic University of the Sacred Heart, "A. Gemelli" Teaching Hospital, Intensive Care Unit, 00168 Roma, Italy

Author contributions: Caricato A, Pitoni S and Antonelli M designed the paper; Montini L produced images; Bocci MG and Annetta P critically revised the paper; Caricato A wrote the paper. Correspondence to: Anselmo Caricato, Assistant Professor, Department of Anesthesiology and Intensive Care Medicine, Catholic University of the Sacred Heart, Largo A. Gemelli 8, 00168 Roma, Italy. anselmo.caricato@fastwebnet.it
Telephone: +39-339-3974355 Fax: +39-6-97252605
Received: January 10, 2014 Revised: March 18, 2014
Accepted: July 15, 2014
Published online: March 28, 2015

Abstract

Transcranial sonography (TCS) is an ultrasound-based imaging technique, which allows the identification of several structures within the brain parenchyma. In the past it has been applied for bedside assessment of different intracranial pathologies in children. Presently, TCS is also used on adult patients to diagnose intracranial space occupying lesions of various origins, intracranial hemorrhage, hydrocephalus, midline shift and neurodegenerative movement disorders, in both acute and chronic clinical settings. In comparison with conventional neuroimaging methods (such as computed tomography or magnetic resonance), TCS has the advantages of low costs, short investigation times, repeatability, and bedside availability. These noninvasive characteristics, together with the possibility of offering a continuous patient neuro-monitoring system, determine its applicability in the monitoring of multiple emergency and non-emergency settings. Currently, TCS is a still underestimated imaging modality that requires a wider diffusion and a qualified training process. In this review we focused on the main indications of TCS

for the assessment of acute neurologic disorders in intensive care unit.

© 2015 Baishideng Publishing Group Inc. All rights reserved.

Key words: Brain sonography; Transcranial sonography; Ultrasounds; Cerebral sonography; Brain imaging; Hydrocephalus; Cerebral hemorrhage

Core tip: Transcranial sonography (TCS) is an ultrasound-based imaging technique, which allows the identification of several structures within the brain parenchyma, not only in neonates, but also in adult patients. It can be used to diagnose intracranial space occupying lesions of various origins, intracranial hemorrhage, hydrocephalus and midline shift. In comparison with computed tomography scan, TCS has the advantages of low costs, short investigation times, repeatability, and bedside availability. These noninvasive characteristics, together with the possibility of offering a continuous patient neuro-monitoring system, determine its applicability in multiple emergency settings.

Original sources: Caricato A, Pitoni S, Montini L, Bocci MG, Annetta P, Antonelli M. Echography in brain imaging in intensive care unit: State of the art. *World J Radiol* 2014; 6(9): 636-642 Available from: URL: <http://www.wjgnet.com/1949-8470/full/v6/i9/636.htm> DOI: <http://dx.doi.org/10.4329/wjr.v6.i9.636>

INTRODUCTION

Definitions

In the last years, due to new ultrasounds technology, echographic imaging of the brain parenchyma has been obtained not only in children, but also in adults. Several authors have found a good visualization of cerebral structures using transcranial B-mode ultrasounds through a



Figure 1 Midbrain transverse scan. The butterfly-shaped mesencephalic brainstem surrounded by the echogenic basal cisterns is shown in the circle.



Figure 2 Diencephalic transverse scan. The third ventricle can be visualized as a highly echogenic double-line image (arrow head on the left). Mesencephalon is indicated by the arrow head on the right. T: Thalamus.

transtemporal approach [transcranial sonography (TCS)].

In the past, the skull was considered unsuitable for sonographic examination because of its thick structure. Aaslid *et al.*^[1] described a “temporal window”, the thinner part of the temporal bone located just above the zygomatic arch, and observed that low-frequency ultrasounds may well penetrate inside the skull in this zone. Since then, TCS has been proposed for bedside identification of many different intracranial pathologies, in both acute and chronic settings, such as intracranial space occupying lesions of various origins (intracranial hemorrhage), hydrocephalus, midline shift and neurodegenerative movement disorders. In comparison with conventional neuroimaging methods such as computed tomography (CT) and Magnetic Resonance, TCS has the advantages of low costs, short investigation times, repeatability, and bedside availability. These noninvasive characteristics, together with the possibility of offering a continuous patient neuro-monitoring system, determine its wide applicability in the monitoring of multiple emergency settings including Intensive Care Units, trauma centers and the context of emergency transportations (*i.e.*, aeromedical flights, helicopter transfers, *etc.*)^[2,3].

The main limitation of TCS is its dependence to an adequate temporal acoustic window. In fact, between 5%-18% of patients the exam is not feasible due to a particularly thick structure of the temporal bone^[4]. Higher percentage of failure rate was described in people of Asian ethnic origin^[5].

In this context, patients with skull defects, such as those who underwent decompressive craniectomy, allow a very accurate assessment of brain parenchyma by TCS^[2].

In this review, we summarize the usefulness of this technique for the assessment of acute neurological disorders in the intensive care unit, describing proposed indications, technical considerations, main advantages and limitations.

TCS technique

The patient lies in a supine position, and the examiner usually sits at the head of the examination table, firmly positioning the ultrasound probe on the temporal zone.

The location of the acoustic window may be variable. In fact, it can be either located in the anterior part of the temporal bone, close to the vertical portion of the zygomatic bone, or, more frequently, posteriorly and close to the pinna of the ear. A low-frequency probe with a 2.0-2.5 MHz phased array transducers is appropriate to insonate the brain through the intact skull. In case of decompressive craniectomy, a standard abdominal convex phased-array probe with a mean central frequency of 4 MHz and an abdominal setting can be used.

Usually, the examination starts with the identification of the mesencephalic brainstem in the axial plane parallel to the “orbitomeatal line”, so to obtain CT-like images (Midbrain transverse scan; Figures 1 and 2). The butterfly-shaped mesencephalic brainstem surrounded by the echogenic basal cisterns is the “landmark” of this scan, and can be observed in 90%-95% of the patients.

Tilting the probe about 10° upwards, a diencephalic transverse scan may be obtained. In this section, the third ventricle can be visualized as a highly echogenic double-line image, due to ipsilateral and contralateral inner layer of the hyperechogenic ependima (Figures 2-4).

Just posteriorly, *thalami* are depicted as hypoechogenic/hysoechogen structures surrounding the third ventricle (Figure 2). Anteriorly, the frontal horn of the contralateral *lateral ventricle* is visualized as hypoechogenic structure, well visible between two parallel lines corresponding to the medial and lateral layer of the ependima (Figure 4). At this plane, the largest transverse diameters of the third ventricle and of the frontal horns of the contralateral lateral ventricle may be measured^[6,7]. It may be useful to pay attention that image is generated by a sectorial probe, and the proportions are different in the central and in the lateral part of the image. Thus, lateral ventricle ipsilateral to the probe is often depicted at the same depth of the third ventricle.

The insonation planes are usually the midbrain and diencephalic transverse ones, even though the coronal orientation has been described. A free hand multiplanar approach has been observed, especially on surgically decompressed patients^[2], and attempts of standardized

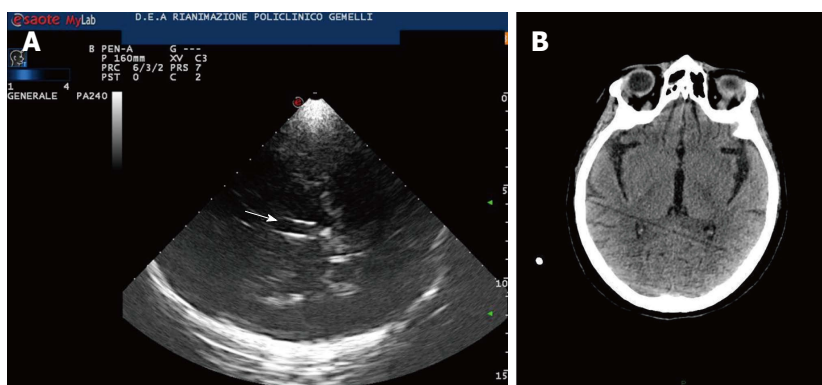


Figure 3 Third ventricle. A: Diencephalic transverse scan. A small enlargement (12 mm) of third ventricle is shown (arrow); B: Third ventricle in computed tomography (CT). CT scan correspondent of Figure 3A is shown.

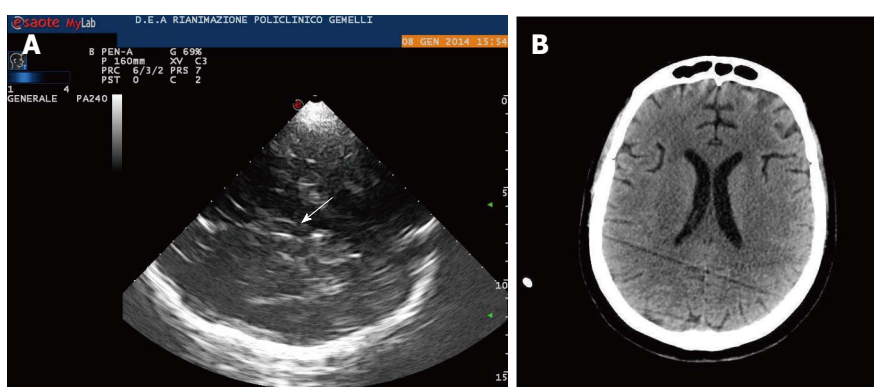


Figure 4 Lateral ventricles. A: Lateral ventricles in echography. Frontal horns of lateral ventricles are visualized as hypoechoic structure, well visible between two parallel lines corresponding to the medial and lateral layer of the ependima. The three parallel lines correspond to lateral layers of ependima and septum pellucidum. The image is generated by a sectorial probe, and lateral ventricle ipsilateral to the probe is depicted at the same depth of the third ventricle. Arrow shows third ventricle, Small arrow heads on the left show frontal horns of lateral ventricles; B: Lateral ventricles in computed tomography (CT). CT scan of lateral ventricles correspondent of Figure 4A is shown.

approaches have been reported^[8]. A standardization of insonation planes would be very useful for comparison and follow-up of sonographic findings.

With the blind technique, landmarks regularly visualized, even in moderate sonographic conditions (identification rates of > 75%) are mesencephalon, pons, third ventricle, lateral ventricles, falx, thalamus, basal ganglia, pineal gland and temporal lobe^[7]. Moreover, ultrasound (US) perfusion imaging can be enhanced by the application of echo-contrast harmonic imaging modalities^[9,10].

CLINICAL APPLICATION

Intracranial hemorrhage

In spontaneous or traumatic cerebral hemorrhage (ICH), hematoma enlargement is the most important modifiable prognostic factor; thus, monitoring of the volume of the hemorrhage is the first priority in the acute phase^[11,12].

CT's widespread acute availability makes it the primary diagnostic modality for ICH. However, in the first hours after the diagnosis, TCS may be very useful to monitor an early ICH enlargement. In fact, TCS allows the visualization of acute ICH, as an hyperechoic sharply demarcated mass within the brain parenchyma. The accuracy is limited to the first 4-6 d after the onset of the ICH, when the hematoma remains more echogenic than

the surrounding brain tissue.

Several authors studied the correlation between CT and TCS in cerebral hemorrhage. Seidel confirmed CT diagnosis by TCS in 18/23 cases (78%)^[9]. Mäurer *et al.*^[13] published a study on TCS in 151 stroke patients correctly differentiating between ischemia and hemorrhage in 95%. 12% had an insufficient temporal bone window for transcranial insonation.

Perez *et al.*^[14] prospectively studied 46 patients with supratentorial ICH evaluated within 3 h of onset. In 8 cases ICH was not observed by TCS: 5 patients showed a small-sized ICH on CT, and in 3 cases hematoma was located in brainstem or in cerebellum. In the remaining patients a very good correlation was observed for each diameter of the mass and for total hematoma volume ($r = 0.82, P < 0.001$).

TCS was also evaluated to detect hemorrhagic transformation in the early phase of ischemic stroke. Seidel *et al.*^[15] found an excellent correlation between TCS and CT on 20 patients with hemorrhagic transformation; in 2 cases small cortical hematoma was not diagnosed.

From these data, TCS seems an interesting option for ICH monitoring; actually, its accuracy appears insufficient to support therapeutic decisions in the acute setting.

Recent studies evaluated the impact of echo contrast agents on visualization of ICH by TCS. By using ultra-

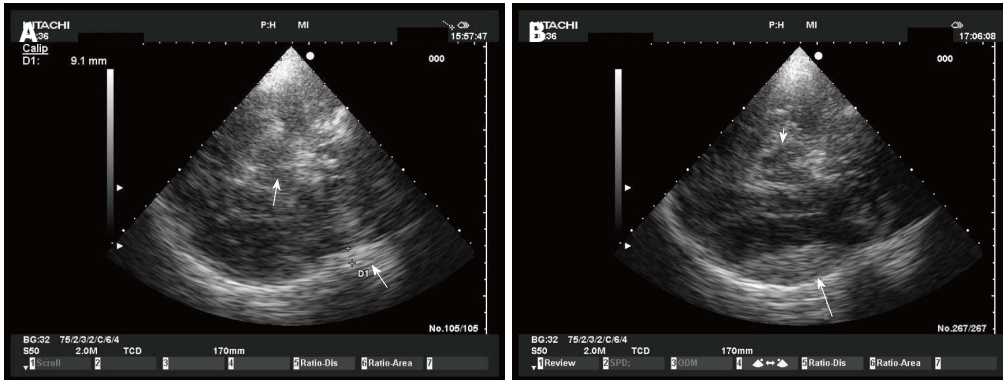


Figure 5 Epidural hematoma in echography. A: Epidural hematoma. A small epidural hematoma (arrow on the right) is shown as an hyperechogenic image just inside the skull. Arrow on the left indicates mesencephalon; B: Epidural hematoma. The same epidural hematoma of Figure A (arrow) 1 h later. White arrow indicates mesencephalon.

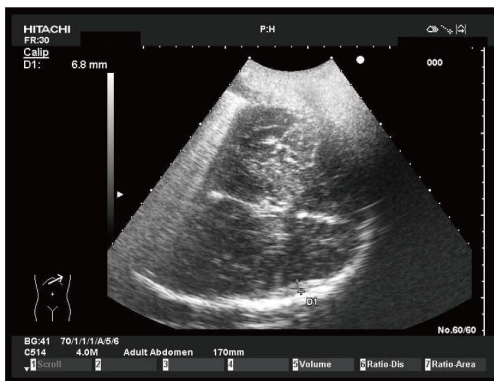


Figure 6 Epidural hematoma in decompressive craniectomy. A small acute epidural hematoma is shown as a hyperechogenic mass lesion contralateral to decompressive craniectomy.

sound perfusion imaging, Kern *et al.*^[16] observed a reduction in contrast agent arrival in the ICH core, which led to better delineation of the lesion borders from adjacent tissue. Correlation with CT was very good ($r = 0.94$, 95%CI: 0.81-0.98, $P < 0.001$). Similar results were reported by Vicenzini *et al.*^[17] and Kern *et al.*^[18].

US perfusion imaging has a wide diffusion in myocardial, renal and musculoskeletal tissue, and might be an option even for brain under difficult insonation conditions; actually, the real advantage of this technique on TCS is still unknown.

Epidural and Subdural hemorrhage

Epidural and subdural hematoma (EDH, SDH) are potentially life-threatening complications after severe, moderate and mild traumatic brain injury. If undetected and untreated, they may lead to progressive transtentorial herniation with loss of consciousness, pupillary dilation, and further neurologic deficits. In EDH-patients, the CT scan remains the diagnostic gold standard, but early bedside detection of acute EDH by TCS has been described^[19]. By using a midbrain transverse scan, contralateral skull became well visible even in absence of decompressive craniectomy, and an epidural hematoma can be observed

as an hyperechogenic image just inside the skull (Figures 5-7). Prospective data on usefulness of this technique for EDH detection are lacking and should be encouraged.

The extent of SDH has also been diagnosed and monitored by TCS^[20]. In particular, SDH has been quantified by measuring the distance between the skull and the dural border of the arachnoid, described as a highly echogenic membrane. In this context, Niesen *et al.*^[20] reliably detected SDH in 22 of the 25 patients with confirmed SDH (88%). In the remaining 3 patients, the temporal bone window was insufficient for TGS investigation. Extent of SDH measured by CT and TCS correlated linearly ($r = 0.849$)^[20].

In conclusion, TCS, when performed by a trained sonographer, may represent a possible method for noninvasively monitoring early hematoma growth at the bedside of patients with or without skull defects, with the role of complementing the CT scan diagnostic technique.

Midline shift

In the diencephalic transverse scan, midline dislocation (MLD) and hydrocephalus can be diagnosed through TCS scanning. The MLD can be observed and measured through two different methods.

According to the method described by Seidel *et al.*^[7], the third ventricle should be considered as a marker of the midline. The distance between third ventricle and external side of the temporal bone (A), needs to be measured. The same calculation can be repeated for the contralateral side (B). A MLD of the third ventricle is then estimated according to the formula $MLD = (A - B)/2$.

In that study, a reproducibility of sonographic MLD measurements corresponding to 0.3 ± 0.2 mm was reached in 10 healthy volunteers. This technique has been widely investigated by several studies in patients with acute cerebrovascular disease and after traumatic brain injury, and a very good correlation between sonographic and CT measurement of MLD are reported^[21-23].

After decompressive craniectomy this method may be difficult. Bone defects, temporal cephalhematomas, or changes in intracranial anatomy secondary to trauma

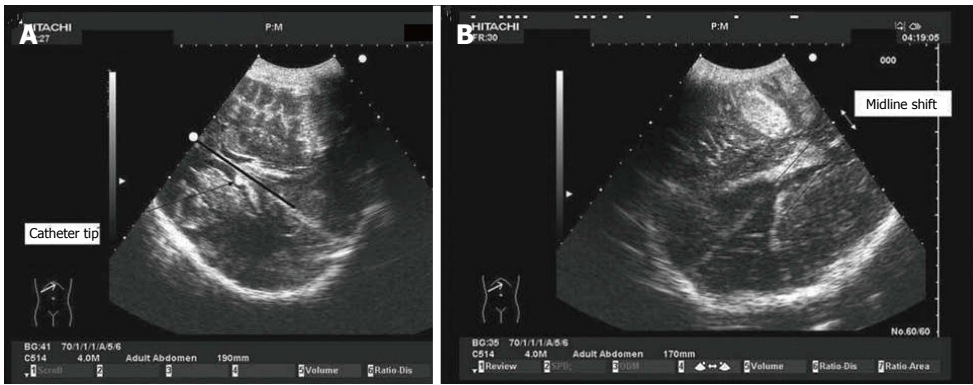


Figure 7 Midline shift in decompressive craniectomy. Images obtained through decompressive craniectomy. Midline was identified with the interventricular line. The distance between the extension of falx and the interventricular line was measured as midline shift (MLS). In the case on the left (A), the extension of the falx exactly overlaps with the interventricular line (dark line). On the right (B), MLS caused by a temporal hematoma is shown.

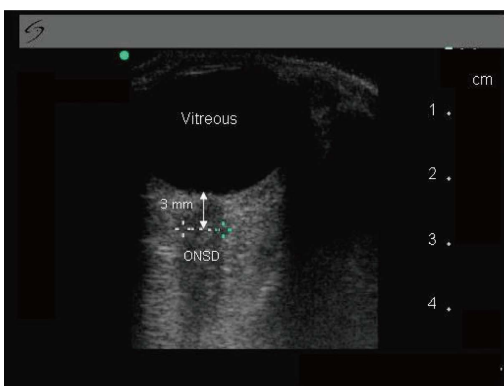


Figure 8 Optic nerve sheath diameter. Using a 7.5-MHz linear probe on the closed upper eyelid, the optic nerve was visualized as a linear hypoechoic structure with clearly defined margins posterior to the globe. Sheath diameter was measured 3 mm behind the globe. ONSD: Optic nerve sheath diameter.

may all induce bias in the measure. In such a condition, Caricato *et al*^[2] described a further method to visualize the MLD. This technique has shown an excellent agreement with CT scan measurements. In an axial plane, the midline, defined as the line between the two lateral ventricles, is measured by a convex probe with an abdominal preset. After localizing the falx cerebri, both on frontal and occipital sides, the distance between the extension of falx and the interventricular line is assessed; the present measurement is the MLD (Figure 8). The last method, which is still to be externally validated, seems rather simple and accurate because measurements are obtained on direct observation of the images and not by indirect mathematical calculations.

Hydrocephalus

Posthemorrhagic hydrocephalus is a frequent complication after subarachnoid hemorrhage or parenchymal hemorrhage; furthermore external ventricular drainage may be necessary after severe traumatic injury to control intracranial hypertension. In these conditions, direct visualization of cerebral ventricles may be required, and critical patients have to be moved to radiology for CT scan.

In this context, TCS may be an useful option. In fact, previous studies compared sonographic and CT measurements of ventricular diameters, founding a good agreement. This was observed in particular for the measurement of third ventricle, that is depicted in a plane orthogonal to the probe, and doesn't need angle correction. As we reported above, direct measurement of lateral ventricles is more difficult since its angle with the probe, and a generally moderate correlation with CT scan is reported. Actually, Kiphuth *et al*^[21] observed that TCS was a reliable technique to predict the need of cerebrospinal fluid drainage. In patients with external ventricular drainage (EVD), they estimated that a cut-off value of an increase of 5.5 mm in ventricle width after clamping had an high sensitivity (100%) and negative predictive value (100%). They suggested that an increase in ventricular width lower than the cut-off was an indication for a safe removal of EVD.

In conclusion, even if the technique still requires a wide validation, it seems to be an interesting option when repetitive CT measurement have to be performed to monitor obstructive hydrocephalus in intensive care Unit.

Evaluation of intracranial hypertension

Optic nerve sheath diameter: Measurement of optic nerve sheath diameter has been proposed as a measure of increased intracranial pressure in a variety of settings^[24-26]. In fact, the sheath around the optic nerve is a continuation of the dura; thus, a rise in ICP is transmitted to the optic nerve, eventually resulting in swelling of the optic disc and in a sheath diameter greater than the normal. The technique is easy and a quick learning curve is described. According with Cennamo *et al*^[27], patients were examined in the supine position. Using a 7.5-MHz linear probe on the closed upper eyelid, the optic nerve was visualized as a linear hypoechoic structure with clearly defined margins posterior to the globe. Sheath diameter was measured 3.00 mm behind the globe, and a value greater than 5.00 mm was considered abnormal.

The technique has been described more than 20 years ago; even if some criticism should be considered^[28], it is

proposed as screening test to rule out intracranial hypertension noninvasively at the bedside.

CONCLUSION

In neurointensive care transcranial Doppler is often used for the evaluation of the cerebral blood flow, diagnosis and monitoring of vasospasm, and autoregulation in patients with different types of brain injury. Beyond the classic indications of transcranial doppler, B-mode ultrasounds can be used as imaging technique to monitor patients in ICU, and may often reduce the indication to CT scan. In this review we summarized the main indications for TCS in intensive care unit. In our opinion, it is a still underestimated imaging modality that requires a wider diffusion. As for any other sonographic assessment, TCS is a highly user-dependent technique, and requires expertise to perform accurate evaluation. In this context, physicians working in neurologic intensive care medicine should be trained not only to apply Doppler methods for investigation of cerebral vessels but also in transcranial B-mode sonography; further studies should be encouraged for a better comprehension of usefulness and limits of this technique as option to brain CT.

REFERENCES

- 1 **Aaslid R**, Markwalder TM, Nornes H. Noninvasive transcranial Doppler ultrasound recording of flow velocity in basal cerebral arteries. *J Neurosurg* 1982; **57**: 769-774 [PMID: 7143059]
- 2 **Caricato A**, Mignani V, Bocci MG, Pennisi MA, Sandroni C, Tersali A, Antonaci A, de Waure C, Antonelli M. Usefulness of transcranial echography in patients with decompressive craniectomy: a comparison with computed tomography scan. *Crit Care Med* 2012; **40**: 1745-1752 [PMID: 22610180 DOI: 10.1097/CCM.0b013e318246b6ea]
- 3 **Libert N**, Boutonnet M, Giraud N, Tourtier JP, de Rudnicki S. Transcranial echography: an interesting tool for aeromedical evacuations. *Crit Care Med* 2012; **40**: 3331-3332; author reply 3332 [PMID: 23164789 DOI: 10.1097/CCM.0b013e3182675c60]
- 4 **Wijnhoud AD**, Franckena M, van der Lugt A, Koudstaal PJ, Dippel ED. Inadequate acoustical temporal bone window in patients with a transient ischemic attack or minor stroke: role of skull thickness and bone density. *Ultrasound Med Biol* 2008; **34**: 923-929 [PMID: 18243493 DOI: 10.1016/j.ultrasmedbio.2007.11.022]
- 5 **Yoshimura S**, Koga M, Toyoda K, Mukai T, Hyun BH, Naganuma M, Nagatsuka K, Minematsu K. Frontal bone window improves the ability of transcranial color-coded sonography to visualize the anterior cerebral artery of Asian patients with stroke. *AJNR Am J Neuroradiol* 2009; **30**: 1268-1269 [PMID: 19213827]
- 6 **Seidel G**, Kaps M, Gerriets T. Potential and limitations of transcranial color-coded sonography in stroke patients. *Stroke* 1995; **26**: 2061-2066 [PMID: 7482650 DOI: 10.1161/01.STR.26.11.2061]
- 7 **Seidel G**, Kaps M, Gerriets T, Hutzelmann A. Evaluation of the ventricular system in adults by transcranial duplex sonography. *J Neuroimaging* 1995; **5**: 105-108 [PMID: 7718936]
- 8 **Kern R**, Perren F, Kreisel S, Szabo K, Hennerici M, Meairs S. Multiplanar transcranial ultrasound imaging: standards, landmarks and correlation with magnetic resonance imaging. *Ultrasound Med Biol* 2005; **31**: 311-315 [PMID: 15749552 DOI: 10.1016/j.ultrasmedbio.2004.12.006]
- 9 **Seidel G**, Meyer-Wiethe K, Berdien G, Hollstein D, Toth D, Aach T. Ultrasound perfusion imaging in acute middle cerebral artery infarction predicts outcome. *Stroke* 2004; **35**: 1107-1111 [PMID: 15031454 DOI: 10.1161/01.STR.0000124125.19773.40]
- 10 **Bartels E**, Bittermann HJ. Transcranial contrast imaging of cerebral perfusion in patients with space-occupying intracranial lesions. *J Ultrasound Med* 2006; **25**: 499-507 [PMID: 16567439]
- 11 **Brouwers HB**, Greenberg SM. Hematoma expansion following acute intracerebral hemorrhage. *Cerebrovasc Dis* 2013; **35**: 195-201 [PMID: 23466430 DOI: 10.1159/000346599]
- 12 **Dowlatshahi D**, Demchuk AM, Flaherty ML, Ali M, Lyden PL, Smith EE. Defining hematoma expansion in intracerebral hemorrhage: relationship with patient outcomes. *Neurology* 2011; **76**: 1238-1244 [PMID: 21346218 DOI: 10.1212/WNL.0b013e3182143317]
- 13 **Mäurer M**, Shambal S, Berg D, Woydt M, Hofmann E, Georgiadis D, Lindner A, Becker G. Differentiation between intracerebral hemorrhage and ischemic stroke by transcranial color-coded duplex-sonography. *Stroke* 1998; **29**: 2563-2567 [PMID: 9836768 DOI: 10.1161/01.STR.29.12.2563]
- 14 **Pérez ES**, Delgado-Mederos R, Rubiera M, Delgado P, Ribó M, Maisterra O, Ortega G, Alvarez-Sabin J, Molina CA. Transcranial duplex sonography for monitoring hyperacute intracerebral hemorrhage. *Stroke* 2009; **40**: 987-990 [PMID: 19164795 DOI: 10.1161/STROKEAHA.108.524249]
- 15 **Seidel G**, Cangür H, Albers T, Burgemeister A, Meyer-Wiethe K. Sonographic evaluation of hemorrhagic transformation and arterial recanalization in acute hemispheric ischemic stroke. *Stroke* 2009; **40**: 119-123 [PMID: 18988915 DOI: 10.1161/STROKEAHA.108.516799]
- 16 **Kern R**, Kablau M, Sallustio F, Fatar M, Stroick M, Hennerici MG, Meairs S. Improved detection of intracerebral hemorrhage with transcranial ultrasound perfusion imaging. *Cerebrovasc Dis* 2008; **26**: 277-283 [PMID: 18648201 DOI: 10.1159/000147456]
- 17 **Vicenzini E**, Delfini R, Magri F, Puccinelli F, Altieri M, Santoro A, Giannoni MF, Bozzao L, Di Piero V, Lenzi GL. Semiquantitative human cerebral perfusion assessment with ultrasound in brain space-occupying lesions: preliminary data. *J Ultrasound Med* 2008; **27**: 685-692 [PMID: 18424642]
- 18 **Kern R**, Krogias C, Meyer-Wiethe K, Renault G, Kablau M, Sallustio F, Eyding J, Meves S, Seidel G, Meairs S. Diagnosis of acute ischemic vs. hemorrhagic stroke with transcranial ultrasound imaging – a prospective multi-center study. *Cerebrovasc Dis* 2006; **21** (suppl 4): 34
- 19 **Caricato A**, Mignani V, Sandroni C, Pietrini D. Bedside detection of acute epidural hematoma by transcranial sonography in a head-injured patient. *Intensive Care Med* 2010; **36**: 1091-1092 [PMID: 20213067 DOI: 10.1007/s00134-010-1801-0]
- 20 **Niesen WD**, Burkhardt D, Hoeltje J, Rosenkranz M, Weiller C, Sliwka U. Transcranial grey-scale sonography of subdural haematoma in adults. *Ultraschall Med* 2006; **27**: 251-255 [PMID: 16596509 DOI: 10.1055/s-2006-926544]
- 21 **Kiphuth IC**, Huttner HB, Struffert T, Schwab S, Köhrmann M. Sonographic monitoring of ventricle enlargement in posthemorrhagic hydrocephalus. *Neurology* 2011; **76**: 858-862 [PMID: 21288979 DOI: 10.1212/WNL.0b013e31820f2e0f]
- 22 **Stolz E**, Gerriets T, Fiss I, Babacan SS, Seidel G, Kaps M. Comparison of transcranial color-coded duplex sonography and cranial CT measurements for determining third ventricle midline shift in space-occupying stroke. *AJNR Am J Neuroradiol* 1999; **20**: 1567-1571 [PMID: 10512247]
- 23 **Llompert Pou JA**, Abadal Centellas JM, Palmer Sans M, Pérez Bárcena J, Casares Vivas M, Homar Ramírez J, Ibáñez Juvé J. Monitoring midline shift by transcranial color-coded sonography in traumatic brain injury. A comparison with cranial computerized tomography. *Intensive Care Med* 2004; **30**: 1672-1675 [PMID: 15197433 DOI: 10.1007/s00134-004-2348-8]

- 24 **Newman WD**, Hollman AS, Dutton GN, Carachi R. Measurement of optic nerve sheath diameter by ultrasound: a means of detecting acute raised intracranial pressure in hydrocephalus. *Br J Ophthalmol* 2002; **86**: 1109-1113 [PMID: 12234888 DOI: 10.1136/bjo.86.10.1109]
- 25 **Moretti R**, Pizzi B, Cassini F, Vivaldi N. Reliability of optic nerve ultrasound for the evaluation of patients with spontaneous intracranial hemorrhage. *Neurocrit Care* 2009; **11**: 406-410 [PMID: 19636971]
- 26 **Dubost C**, Le Gouez A, Jouffroy V, Roger-Christoph S, Benhamou D, Mercier FJ, Geeraerts T. Optic nerve sheath diameter used as ultrasonographic assessment of the incidence of raised intracranial pressure in preeclampsia: a pilot study. *Anesthesiology* 2012; **116**: 1066-1071 [PMID: 22258019 DOI: 10.1097/ALN.0b013e318246ea1a]
- 27 **Cennamo G**, Gangemi M, Stella L. The comparison between endocranial pressure and optic nerve diameter: an ultrasonographic study. *Doc Ophthalmol Proc Ser* 1987; **48**: 603-606 [DOI: 10.1007/978-94-009-3315-6_99]
- 28 **Copetti R**, Cattarossi L. Optic nerve ultrasound: artifacts and real images. *Intensive Care Med* 2009; **35**: 1488-1489; author reply 1488-1489 [PMID: 19367390 DOI: 10.1007/s00134-009-1494-4]

P- Reviewer: Brigo F, Llompart-Pou J, Zanini MA

S- Editor: Ji FF **L- Editor:** A **E- Editor:** Lu YJ



MRI in central nervous system infections: A simplified patterned approach

Krithika Rangarajan, Chandan J Das, Atin Kumar, Arun Kumar Gupta

Krithika Rangarajan, Chandan J Das, Atin Kumar, Arun Kumar Gupta, Department of Radiodiagnosis, All India Institute of Medical Sciences, Ansari Nagar East, New Delhi 110029, India
Author contributions: Rangarajan K and Das CJ wrote most of the manuscript text as well as edited the images; Kumar A and Gupta AK provided valuable inputs, edited the manuscript and approved the content.

Correspondence to: Chandan J Das, MD, Department of Radiodiagnosis, All India Institute of Medical Sciences, Ansari Nagar, Room number 60, New Delhi 110029, India. dascj@yahoo.com

Telephone: +91-11-26594868

Received: January 9, 2014 Revised: July 13, 2014

Accepted: July 27, 2014

Published online: March 28, 2015

Abstract

Recognition and characterization of central nervous system infections poses a formidable challenge to the neuro-radiologist. Imaging plays a vital role, the lesions typically being relatively inaccessible to tissue sampling. The results of an accurate diagnosis are endlessly rewarding, given the availability of excellent pharmacological regimen. The availability of numerous magnetic resonance (MR) sequences which provide functional and molecular information is a powerful tool in the hands of the radiologist. However, the plethora of sequences and the possibilities on each sequence is also intimidating, and often confusing as well as time consuming. While a large number of reviews have already described in detail the possible imaging findings in each infection, we intend to classify infections based on their imaging characteristics. In this review we describe an algorithm for first classifying the imaging findings into patterns based on basic MR sequences (T1, T2 and enhancement pattern with Gadolinium), and then sub-classify them based on more advanced molecular and functional sequences (Diffusion, Perfusion, Susceptibility imaging, MR Spectroscopy). This patterned approach

is intended as a guide to radiologists in-training and in-practice for quickly narrowing their list of differentials when faced with a clinical challenge. The entire content of the article has also been summarised in the form of flow-charts for the purpose of quick reference.

© 2015 Baishideng Publishing Group Inc. All rights reserved.

Key words: Central nervous system; Infection; Magnetic resonance imaging; Magnetic resonance spectroscopy; Perfusion weighted magnetic resonance imaging; Diffusion weighted magnetic resonance imaging

Core tip: The plethora of magnetic resonance sequences available with the radiologist today provides a wealth of information about anatomical, pathological, physiological, functional and molecular aspects of the brain. While this provides an opportunity to transform patient management, the vast number of possibilities can be bewildering, particularly for the radiologist in-training. It is often easy to get lost in the details while forgetting the larger picture. In this article we first classify the infections into broad imaging patterns, and subsequently sub-classify them based on more advanced sequences (molecular and functional imaging). The flow-charts in the article are intended as a source of quick reference to the radiologist when faced with a clinical challenge.

Original sources: Rangarajan K, Das CJ, Kumar A, Gupta AK. MRI in central nervous system infections: A simplified patterned approach. *World J Radiol* 2014; 6(9): 716-725 Available from: URL: <http://www.wjgnet.com/1949-8470/full/v6/i9/716.htm> DOI: <http://dx.doi.org/10.4329/wjr.v6.i9.716>

INTRODUCTION

Central nervous system (CNS) infections are a significant

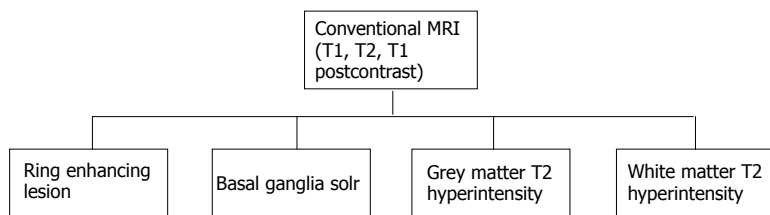


Figure 1 Classification of abnormalities on conventional magnetic resonance imaging sequences in suspected central nervous system infections.

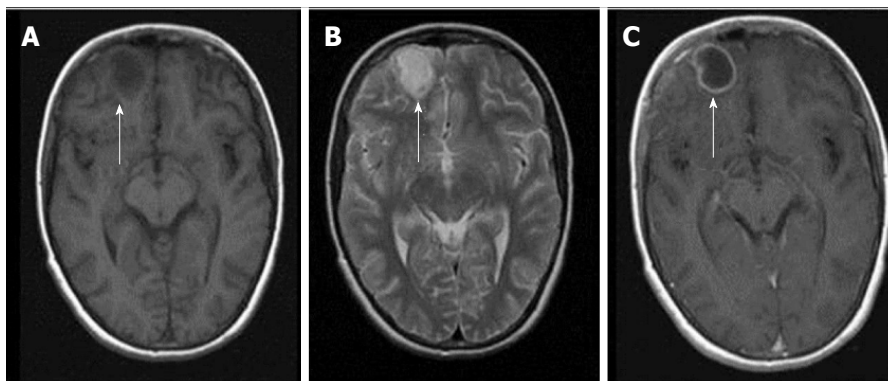


Figure 2 Ring enhancing lesions. T1 (A), T2 (B) and T1 (C) post gadolinium images from the magnetic resonance of an acutely ill child with fever. A ring enhancing lesion is seen in the right frontal lobe. This patient had a bacterial brain abscess. The differential diagnosis of this appearance would include a brain abscess of any etiology.

cause of mortality and morbidity world-wide. This is particularly true owing to its association with conditions of immunological compromise and the increasing incidence of human immunodeficiency virus (HIV) infection is further adding to the problem^[1]. Today with the availability of excellent antimicrobials, many of these disorders are potentially treatable, making early recognition imperative. Like in other disorders of the CNS, non-invasive imaging based diagnosis is the key as possibility of a tissue diagnosis by means of fine needle aspiration cytology (FNAC) or biopsy is difficult. Early diagnosis will also help to minimize long term complications related to the disease and its treatment.

The primary imaging modality, like in most CNS disorders is magnetic resonance imaging (MRI)^[2]. Coming to an exact etiological agent on the basis of conventional MRI sequences with Gadolinium enhancement is always difficult due to overlapping imaging characteristics. With the possibility of molecular and functional imaging with newer MRI techniques however, the radiologist today is better equipped to handle this dilemma. Though the use of such multiple MRI sequences adds lots of information to narrow the differential possibilities, this vast information is difficult to recall when faced with a clinical problem.

The purpose of this review is to provide a rational MRI approach to narrow the list of differentials, to quickly classify and characterize CNS infections. The flow-charts presented in this review guides the radiologist to first recognize the pattern of findings on routine MRI sequences and subsequently narrow the differential diagnosis based on the addition of other MR parameters such as diffusion weighted imaging (DWI) and MR spec-

troscopy (MRS).

CLASSIFICATION

Most infections in the CNS may be classified in one of the following categories based on their T1, T2 and contrast enhancement characteristics (Figure 1) as follows (an image demonstrating a typical lesion in each category has been provided in Figures 2-5): Ring enhancing lesions (Figure 2), Basal ganglia space occupying lesions (Figure 3), Grey matter hyperintensities (Figure 4), White matter hyperintensities (Figure 5).

RING ENHANCING LESIONS

Peripheral ring-like enhancement is a common finding in CNS imaging. Ring enhancing lesions on conventional MRI sequences have a long list of differentials ranging from infectious processes to high grade necrotic neoplasm. Glioblastoma multiforme represents the most important condition. Abscesses are usually associated with a thin smooth rim, in contrast to the nodular irregular rim seen in Glioblastoma multiforme. Satellite lesions are commonly seen in abscesses, unlike necrotic neoplasm^[1]. Recent work by some investigators has suggested a role for susceptibility weighted imaging (SWI) in this differentiation. They found that a smooth, complete rim of susceptibility is seen in abscesses in contrast to incomplete irregular rims seen in necrotic neoplasm^[3].

All mature abscesses whether bacterial, fungal or pyogenic are hypointense on T1, hyperintense on T2 and show ring enhancement following intravenous Gado-

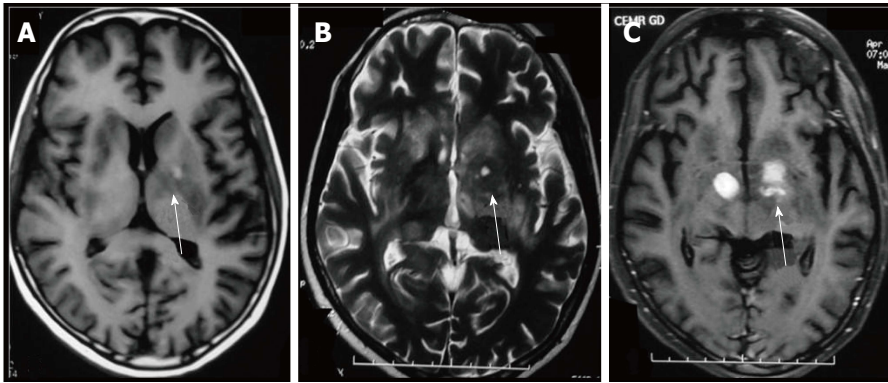


Figure 3 T1 (A), T2 (B) and Post gadolinium T1 (C) weighted images in an human immunodeficiency virus-positive patient with space occupying lesions in bilateral basal ganglia. Differentials for this appearance in such a patient would include Toxoplasmosis, Cryptococcosis as well as central nervous system (CNS) lymphoma. This patient had CNS lymphoma.



Figure 4 Fluid Attenuated Inversion Recovery Sequence in a patient with fever and altered sensorium shows hyperintensity predominantly in the grey matter of both temporal lobes and also in cerebellum. This patient was diagnosed with Japanese B Encephalitis. A similar picture may be seen in other viral encephalitis including herpes encephalitis.

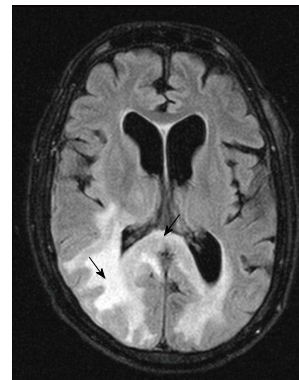


Figure 5 Fluid Attenuated Inversion Recovery Sequence image of a human immunodeficiency virus-positive patient shows hyperintensity predominantly involving the occipital white matter and splenium. The differential diagnosis for such an appearance would include human immunodeficiency virus encephalopathy, progressive multifocal leukoencephalopathy (PML) as well as other demyelinating conditions. This patient had PML.

linium injection. Further differentiation of abscesses for possible etiological cause may be made as follows.

DIFFUSION WEIGHTED IMAGING

DWI explores the molecular characteristic of diffusivity of particles within a region. It is based on the application of two gradients at a set interval of time, in such a way that only a molecule that experiences both gradients at the same position (does not exhibit motion between the two gradients) produces signal. Therefore regions of the brain that show “restricted diffusion” are hyperintense on DWI. This restricted diffusion appears as hyperintense area on DWI and needs to be corroborated with computer generated apparent diffusion coefficient (ADC) maps which show corresponding hypointense area. This corroboration rules out T2-shine through effect. Bacterial as well as tubercular abscesses show central diffusion restriction^[4,5] due to highly viscous necrotic tissue within (Figure 6). Fungal abscesses show intracavitary projections. The wall of abscess and the projections may demonstrate diffusion restriction^[5,6], though no restriction is seen in the abscess core (Figure 7).

DWI plays an important role in the differentiation of these abscesses from necrotic neoplasms, which usually demonstrate high ADC values within the core^[7].

MR SPECTROSCOPY

Spectroscopy provides information about metabolic alterations within a voxel by exploiting changes in the microenvironment produced by unique chemical characteristics of specific metabolites. Thus using this technique it is possible to infer the presence of a microorganism, based on the expected products of the microorganisms metabolism reflected in the metabolic signature.

The characteristic of the spectrum in bacterial abscesses is the presence of amino acid peak at 0.9 parts per million (ppm) [inverted peak at an time of echo (TE) 136 ms] representing valine, leucine and isoleucine (Figure 8)^[2]. The detection of succinate (2.4 ppm) and acetate (1.92 ppm) is proposed to indicate anaerobic organisms^[2].

Tuberculosis is characterised by lipid peaks at 0.9, 1.3, 2.0 and 2.8 ppm. The presence of lipids in the absence of other amino acids, lactate and succinate is strongly suggestive of tubercular abscess (Figure 9)^[5,8]. 0.9, 1.3, 2.0, 2.8, and 3.7 peaks correspond to specific chemical groups within metabolites found in these infections- 0.9 corresponds to a terminal methyl group, 1.3 to a methylene group, 2.0 and 2.8 to specific groups in fatty acyl chains and 3.7 to phosphoserine.

While lactate, acetate and succinate can all be seen

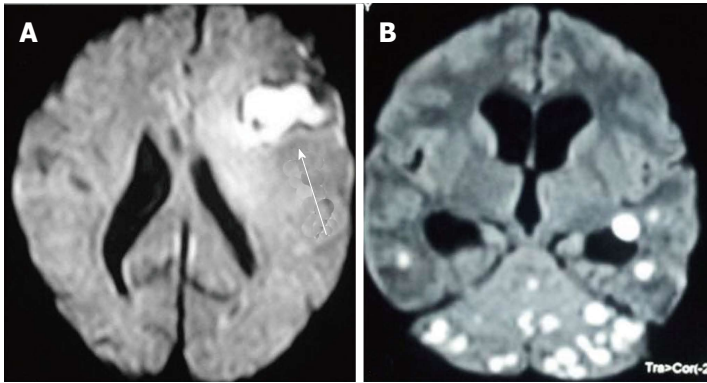


Figure 6 Diffusion weighted images show central restriction of diffusion in bacterial abscess (A) and tuberculomas (B) arrow.



Figure 7 Diffusion weighted image in a diabetic patient shows diffusion restriction in the wall and intra-cavitary projection (arrow) in the centre of a fungal abscess.

in fungal abscesses, the presence of multiple signals between 3.6 and 3.8 ppm (representing Trehalose) has been seen in some forms of fungal abscesses (Figure 10)^[5]. The absence of choline peak on MRS provides important supportive evidence for an infective etiology as compared to neoplasms which show increased choline^[7,9].

MR ANGIOGRAPHY

Tubercular vasculitis results in extensive infarction due to inflammation of vessels coursing through the basal exudates (Figure 11)^[10]. Vascular involvement with formation of aneurysms is seen in fungal infections. These aneurysms are seen as irregular dilatation of vessel wall on MRA.

SUSCEPTIBILITY WEIGHTED IMAGING

The principle underlying SWI is the alteration of local magnetic field by substances that show paramagnetic properties. This is a gradient sequence, so molecules in the vicinity of a paramagnetic substance dephase rapidly, thus do not contribute to signal production. Voxels containing molecules with different magnetic susceptibilities are imaged when they are exactly out-of-phase, such that the whole voxel appears to be of low signal intensity^[2]. This is seen as an area of “blooming”. The presence of haemorrhage is often a clue to underlying fungal cause of

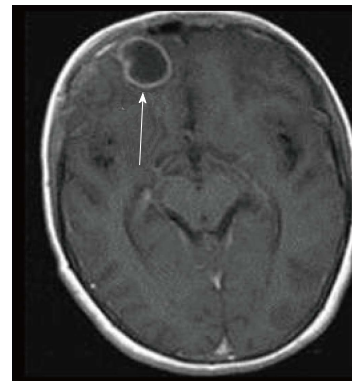
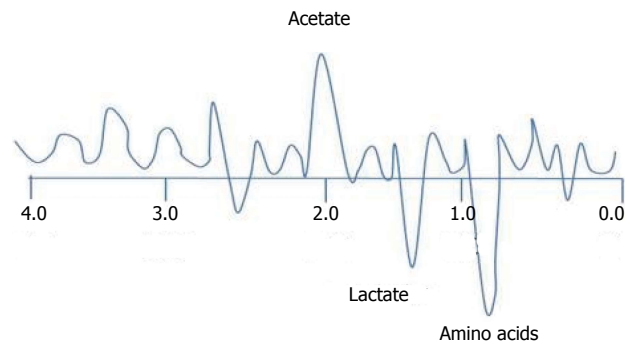


Figure 8 Representation of spectrum of metabolites in a bacterial abscess. Proton magnetic resonance spectroscopy obtained at a time of echo of 30 milliseconds shows the presence of amino acids. Succinate and acetate are seen in anaerobic abscesses.

infection (Figure 12) due to its angioinvasive nature^[11].

The presence of a complete, smooth hypointense rim on SWI favours a diagnosis of an abscess against a necrotic neoplasm. A brief summary of approach to a peripherally enhancing lesion is presented as a flowchart (Figure 13).

BASAL GANGLIA SPACE OCCUPYING LESIONS

A number of CNS lesions are seen characteristically involving the region of basal ganglia. The differential diagnosis in this category includes cryptococcosis, toxoplasmosis and primary CNS lymphoma. Cryptococcosis usually does not show enhancement after gadolinium injection. Further characterisation often requires additional

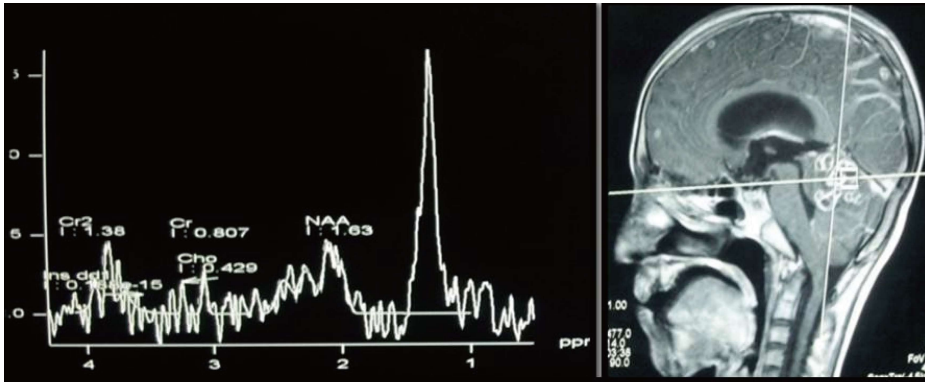


Figure 9 Proton spectroscopy at echo time of 135 ms from a tuberculoma shows a lipid peak at 1.3 ppm.

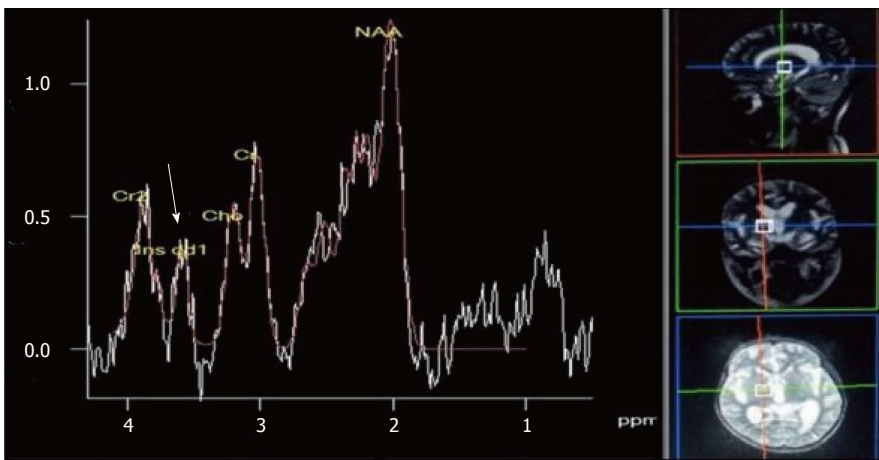


Figure 10 Proton magnetic resonance spectroscopy at time of echo of 30 ms shows multiple peaks between 3.6 and 3.8 ppm in the spectrum obtained from a cryptococcoma (fungus) representative of trehalose peak (arrow).

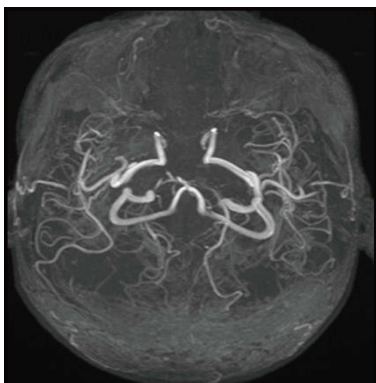


Figure 11 Time of Flight magnetic resonance angiography in a patient with tubercular meningitis. Bilateral anterior cerebral arteries are not seen whereas bilateral middle cerebral arteries are markedly attenuated suggesting vasculitis. The patient presented with extensive cerebral infarction.



Figure 12 Foci of blooming (arrow) noted within the abscess is suggestive of haemorrhage and points to a fungal cause.

sequences.

DWI

Toxoplasmosis does not usually show significant restriction of diffusion, though a wide range of ADC value have been encountered^[2,12]. A proposed explanation is

the lack of viscous contents within these lesions. Peripheral areas may show hyperintensity due to the presence of haemorrhage^[13]. Lymphoma which usually are highly cellular, shows restricted diffusion^[2,12], helping differentiation from toxoplasmosis (Figure 14). The paucity of intercellular spaces results in a decreased diffusivity of water molecules within these lesions. Cryptococcosis is also known to show restricted diffusion within the pseu-

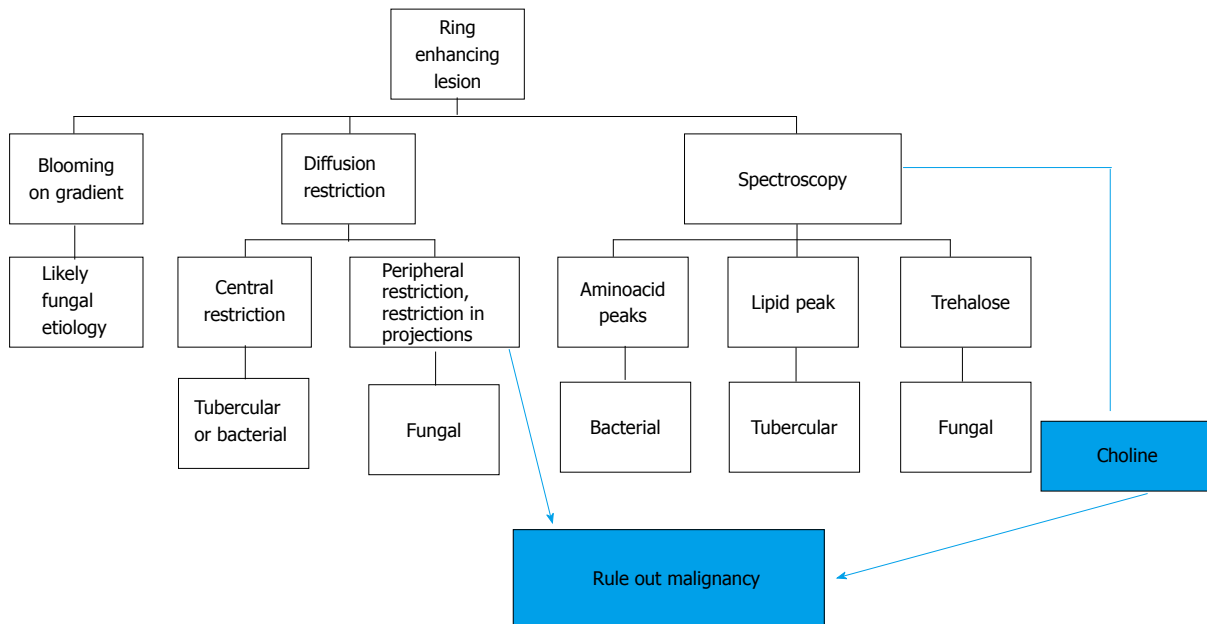


Figure 13 Approach to ring enhancing lesions.

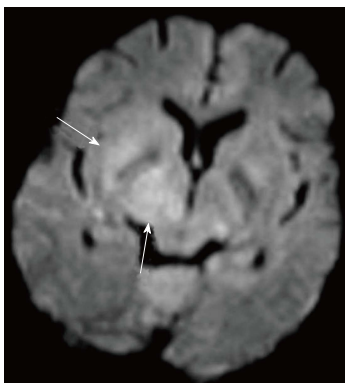


Figure 14 Diffusion weighted image from the Brain magnetic resonance imaging of an human immunodeficiency virus-positive patient with lymphoma shows restriction in the right lentiform nucleus and the thalamus (arrow).

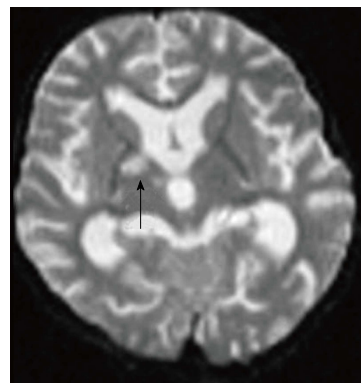


Figure 15 Apparent diffusion coefficient map showing free diffusion with in a cryptococcoma (arrow) in a human immunodeficiency virus-positive patient.

docysts^[2] owing to the viscosity of gelatinous material. Cryptococcomas have been shown to exhibit peripheral diffusion restriction akin to a necrotic brain tumour^[14], though often they may not show any restricted diffusion^[12] (Figure 15).

MRS

Presence of peak between 3.6 to 3.8 ppm (trehalose) has been observed in cryptococcosis (which is a fungus)^[5] (Figure 10). Toxoplasma lesions (Figure 16) show markedly elevated lipid and lactate with diminished levels of all other metabolites^[2]. Lymphoma (Figure 17) shows mild to moderate increase in lipid and lactate with markedly elevated choline peak^[2].

MR perfusion

Toxoplasmosis shows normal or decreased cerebral blood volume (CBV). Primary CNS lymphoma on the other

hand shows elevated CBV^[12].

SWI

Presence of hemorrhage (blooming on gradient echo sequences) points towards toxoplasmosis, as lymphoma rarely show hemorrhage before treatment^[12,15] (Figure 18). A brief summary of the approach to space occupying lesions in the basal ganglia is presented as a flowchart in Figure 19.

GREY MATTER HYPERINTENSITY

T2/ FLAIR hyperintensity involving the grey matter may be seen in encephalitis as well as infarction. This differentiation is aided by diffusion and perfusion sequences (Table 1).

Diffusion and perfusion

Reduced diffusion with increased perfusion points to an

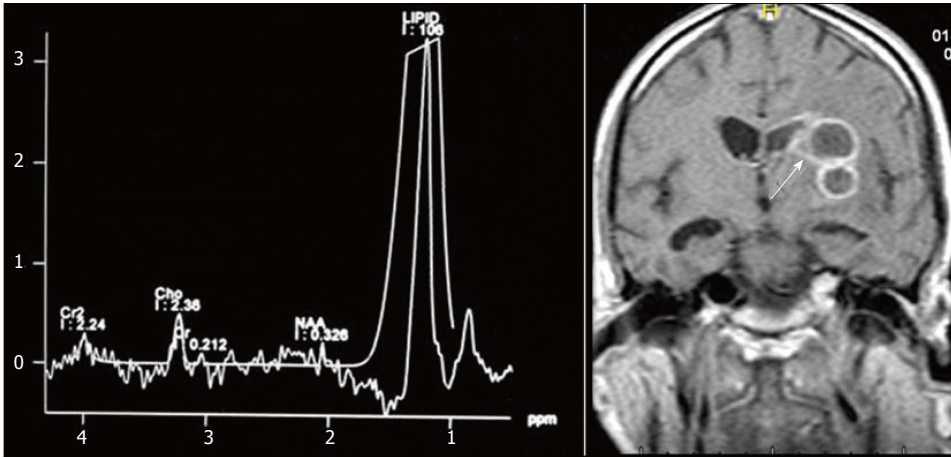


Figure 16 Proton magnetic resonance spectroscopy at echo time of 30 ms in a patient with toxoplasmosis shows a lipid lactate peak with diminished levels of all other metabolites (arrow).

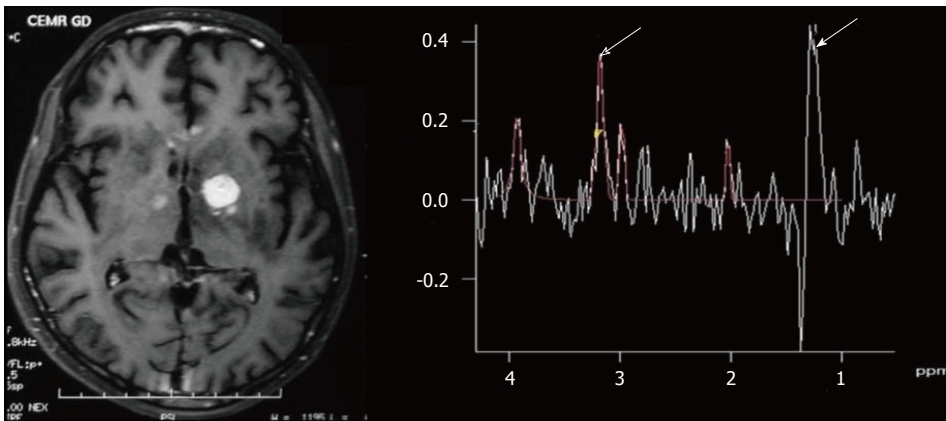


Figure 17 Proton magnetic resonance spectroscopy at echo time of 135 ms in a patient with primary central nervous system Lymphoma of basal ganglia showing elevated lipid, lactate (white arrow) and choline (open arrow).

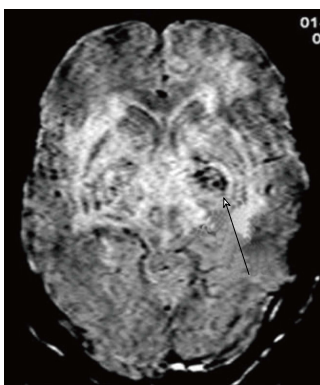


Figure 18 Gradient echo image in a patient with toxoplasmosis shows foci of blooming (arrow) suggestive of haemorrhage.

infective etiology. Reduced diffusion with decreased perfusion characterizes ischemic events. The further characterization of infection is typically based on characteristic neuro-anatomic location of the lesion on T2/FLAIR/DWI (Figure 20)^[2,16]. Prion disease can also show similar imaging manifestation. The imaging appearance of these encephalitis may be fairly non-specific. The dengue vi-

Table 1 This differentiation is aided by diffusion and perfusion sequences

	Diffusion	Perfusion
Infection	Restricted	Increased
Infarction	Restricted	Decreased

rus has been reported to show imaging features similar to Japanese encephalitis^[17] in regions where this virus is common. Cytomegalovirus can also show non-specific manifestations, though the predominant involvement of grey matter (more than white matter) is an important differentiating feature^[1]. The presence of a pencil-thin rim of enhancement in the subependymal region is considered to be a specific finding^[1]. Approach to lesions presenting with hyperintensity predominantly involving the Grey matter is presented as a flowchart in Figure 21.

WHITE MATTER HYPERINTENSITIES

The major diagnostic considerations are HIV encephalopathy (HIVE) and progressive multifocal leukoen-

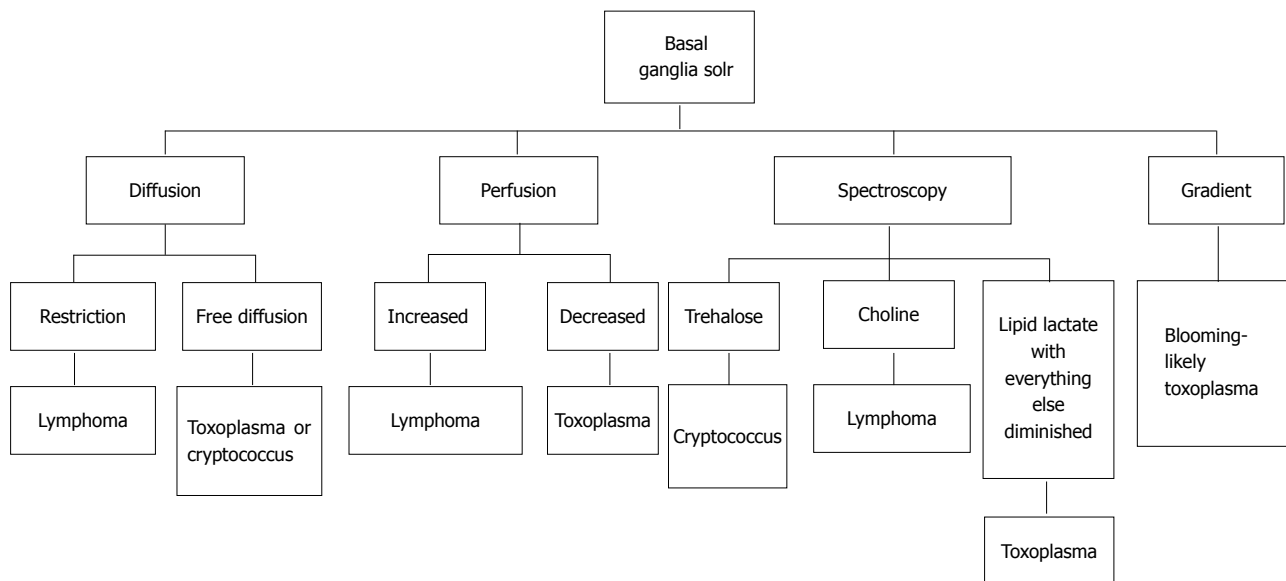


Figure 19 Approach to space occupying lesions in the basal ganglia.

Table 2 Role of additional sequences			
	T1	T2	T1 + contrast
HIV Encephalopathy	Isointense	Bilaterally symmetrical periventricular white matter hyperintensities	No enhancement
PML	Hypointense	Asymmetrical lesions involving subcortical and periventricular white matter	Faint peripheral areas of enhancement may sometimes be seen

HIV: Human immunodeficiency virus; PML: Progressive multifocal leukoencephalopathy.

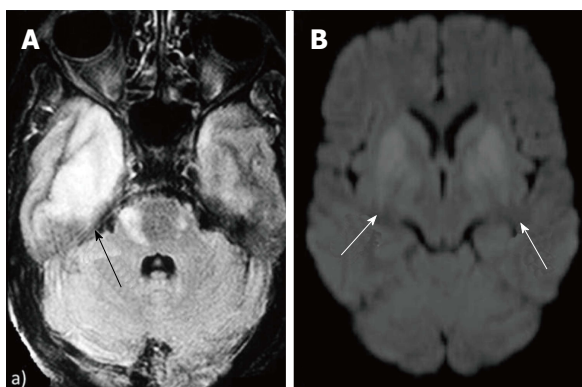


Figure 20 Fluid Attenuated Inversion Recovery Sequence hyperintensity (A) involving right temporal lobe (black arrow) in a patient with Herpes simplex virus encephalitis, diffusion weighted imaging (B) in a patient with Japanese encephalitis showing restricted diffusion in bilateral basal ganglia.

cephalopathy (PML) (Figure 22). Though both entities have characteristic imaging features on conventional MR sequences (Table 2), they may be difficult to differentiate due to overlapping features.

Magnetization transfer

Magnetization transfer (MT) reduction is seen in both PML and HIVE. In PML, it is due to demyelination whereas in HIVE it is primarily related to gliosis. Thus

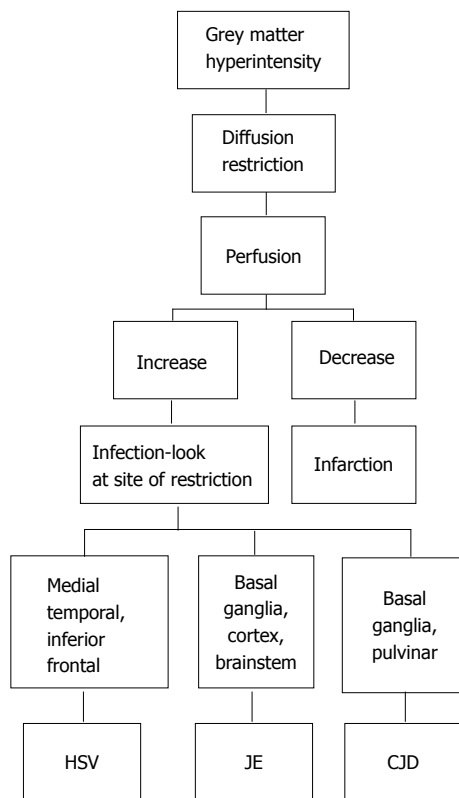


Figure 21 Approach to lesions presenting with hyperintensity predominantly involving the Grey matter.

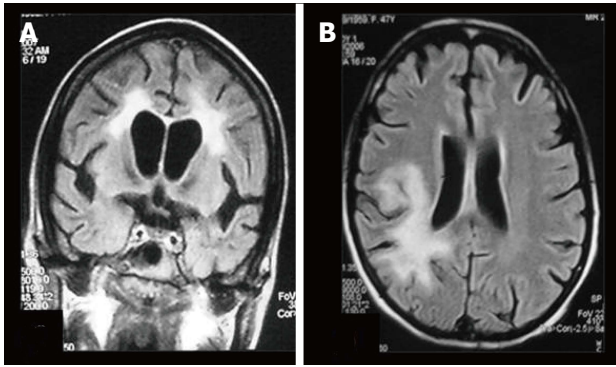


Figure 22 Fluid Attenuated Inversion Recovery Sequence image of a patient with (A) human immunodeficiency virus encephalopathy showing symmetrical periventricular white matter hyperintensity and (B) progressive multifocal leukoencephalopathy showing asymmetrical involvement of white matter, predominantly posterior subcortical white matter, with extension into the periventricular region.

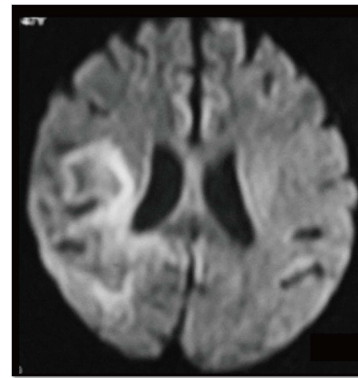


Figure 23 Diffusion weighted image in a patient with progressive multifocal leukoencephalopathy showing peripheral diffusion restriction.

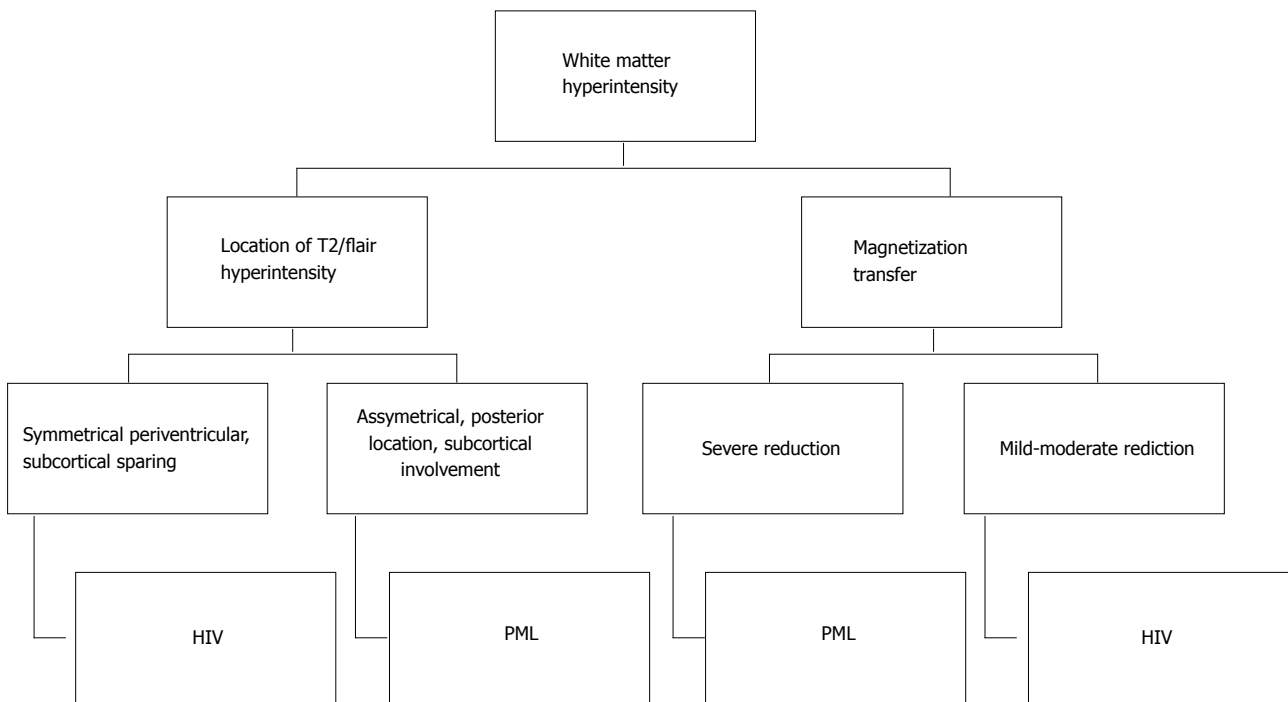


Figure 24 Approach to lesions presenting with hyperintensity predominantly involving the white matter. PML: Progressive multifocal leukoencephalopathy; HIV: Human immunodeficiency virus.

larger reduction in MT has been observed in PML as compared to HIV^[18]. The major role of MT sequence in this setting is in early detection of disease.

Diffusion and diffusion tensor imaging

Fractional anisotropy is seen to be reduced in HIV and PML before the morphologic changes in conventional sequences^[19]. Reduced diffusion is seen in the periphery and free diffusion in the centre of PML lesions^[12] (Figure 23).

MRS

Reduction of N-acetylaspartate is seen in HIV even be-

fore the onset of symptoms. Raised choline and myoinositol is also seen in the spectra. A summary of suggested approach to these white matter lesions is presented as a flowchart in Figure 24.

CONCLUSION

Imaging features of CNS infections constitute a complex myriad. Their classification based on conventional MRI sequences, may provide a quick guide to narrowing the differential diagnosis followed by further sub-differentiation into single etiology using advanced MRI sequences

and techniques.

REFERENCES

- 1 **Aiken AH**. Central nervous system infection. *Neuroimaging Clin N Am* 2010; **20**: 557-580 [PMID: 20974376 DOI: 10.1016/j.nic.2010.07.011]
- 2 **Whiteman ML**, Bowen BC, Post MJ, Bell MD. Intracranial infections. In Scott W Atlas, editor. *Magnetic Resonance Imaging of Brain and Spine*. 3rd ed. Philadelphia: Lippincott Williams and Wilkins, 2002: 1099-177
- 3 **Toh CH**, Wei KC, Chang CN, Hsu PW, Wong HF, Ng SH, Castillo M, Lin CP. Differentiation of pyogenic brain abscesses from necrotic glioblastomas with use of susceptibility-weighted imaging. *AJNR Am J Neuroradiol* 2012; **33**: 1534-1538 [PMID: 22422181 DOI: 10.3174/ajnr.A2986]
- 4 **Desprechins B**, Stadnik T, Koerts G, Shabana W, Breucq C, Osteaux M. Use of diffusion-weighted MR imaging in differential diagnosis between intracerebral necrotic tumors and cerebral abscesses. *AJNR Am J Neuroradiol* 1999; **20**: 1252-1257 [PMID: 10472982]
- 5 **Luthra G**, Parihar A, Nath K, Jaiswal S, Prasad KN, Husain N, Husain M, Singh S, Behari S, Gupta RK. Comparative evaluation of fungal, tubercular, and pyogenic brain abscesses with conventional and diffusion MR imaging and proton MR spectroscopy. *AJNR Am J Neuroradiol* 2007; **28**: 1332-1338 [PMID: 17698537 DOI: 10.3174/ajnr.A0548]
- 6 **Gaviani P**, Schwartz RB, Hedley-Whyte ET, Ligon KL, Robicsek A, Schaefer P, Henson JW. Diffusion-weighted imaging of fungal cerebral infection. *AJNR Am J Neuroradiol* 2005; **26**: 1115-1121 [PMID: 15891169]
- 7 **Lai PH**, Ho JT, Chen WL, Hsu SS, Wang JS, Pan HB, Yang CF. Brain abscess and necrotic brain tumor: discrimination with proton MR spectroscopy and diffusion-weighted imaging. *AJNR Am J Neuroradiol* 2002; **23**: 1369-1377 [PMID: 12223380]
- 8 **Gupta RK**, Roy R, Dev R, Husain M, Poptani H, Pandey R, Kishore J, Bhaduri AP. Finger printing of Mycobacterium tuberculosis in patients with intracranial tuberculomas by using in vivo, ex vivo, and in vitro magnetic resonance spectroscopy. *Magn Reson Med* 1996; **36**: 829-833 [PMID: 8946348]
- 9 **Lai PH**, Weng HH, Chen CY, Hsu SS, Ding S, Ko CW, Fu JH, Liang HL, Chen KH. In vivo differentiation of aerobic brain abscesses and necrotic glioblastomas multiforme using proton MR spectroscopic imaging. *AJNR Am J Neuroradiol* 2008; **29**: 1511-1518 [PMID: 18499784 DOI: 10.3174/ajnr.A1130]
- 10 **Trivedi R**, Saksena S, Gupta RK. Magnetic resonance imaging in central nervous system tuberculosis. *Indian J Radiol Imaging* 2009; **19**: 256-265 [PMID: 19881100 DOI: 10.4103/0971-3026.57205]
- 11 **Jain KK**, Mittal SK, Kumar S, Gupta RK. Imaging features of central nervous system fungal infections. *Neurol India* 2007; **55**: 241-250 [PMID: 17921653]
- 12 **Smith AB**, Smirniotopoulos JG, Rushing EJ. From the archives of the AFIP: central nervous system infections associated with human immunodeficiency virus infection: radiologic-pathologic correlation. *Radiographics* 2008; **28**: 2033-2058 [PMID: 19001657 DOI: 10.1148/rg.287085135]
- 13 **Lee GT**, Antelo F, Mlikotic AA. Best cases from the AFIP: cerebral toxoplasmosis. *Radiographics* 2009; **29**: 1200-1205 [PMID: 19605667 DOI: 10.1148/rg.294085205]
- 14 **Ho TL**, Lee HJ, Lee KW, Chen WL. Diffusion-weighted and conventional magnetic resonance imaging in cerebral cryptococcoma. *Acta Radiol* 2005; **46**: 411-414 [PMID: 16134319]
- 15 **Trenkwalder P**, Trenkwalder C, Feiden W, Vogl TJ, Einhäupl KM, Lydtin H. Toxoplasmosis with early intracerebral hemorrhage in a patient with the acquired immunodeficiency syndrome. *Neurology* 1992; **42**: 436-438 [PMID: 1736179]
- 16 **Ukisu R**, Kushihashi T, Tanaka E, Baba M, Usui N, Fujisawa H, Takenaka H. Diffusion-weighted MR imaging of early-stage Creutzfeldt-Jakob disease: typical and atypical manifestations. *Radiographics* 2006; **26** Suppl 1: S191-S204 [PMID: 17050516 DOI: 10.1148/rg.26si065503]
- 17 **Borawake K**, Prayag P, Wagh A, Dole S. Dengue encephalitis. *Indian J Crit Care Med* 2011; **15**: 190-193 [PMID: 22013316 DOI: 10.4103/0972-5229.84896]
- 18 **Ernst T**, Chang L, Witt M, Walot I, Aronow H, Leonido-Yee M, Singer E. Progressive multifocal leukoencephalopathy and human immunodeficiency virus-associated white matter lesions in AIDS: magnetization transfer MR imaging. *Radiology* 1999; **210**: 539-543 [PMID: 10207441]
- 19 **Pomara N**, Crandall DT, Choi SJ, Johnson G, Lim KO. White matter abnormalities in HIV-1 infection: a diffusion tensor imaging study. *Psychiatry Res* 2001; **106**: 15-24 [PMID: 11231096]

P- Reviewer: Asensi VC, Mueller WC, Radenovic L
S- Editor: Wen LL **L- Editor:** A **E- Editor:** Lu YJ



Low dose four-dimensional computerized tomography with volume rendering reconstruction for primary hyperparathyroidism: How I do it?

Timothy A Platz, Moshim Kukar, Rania Elmarzouky, William Cance, Ahmed Abdelhalim

Timothy A Platz, Moshim Kukar, William Cance, Department of Surgical Oncology, Roswell Park Cancer Institute, Buffalo, NY 14263, United States

Rania Elmarzouky, Ahmed Abdelhalim, Department of Neuroradiology, Roswell Park Cancer Institute, Buffalo, NY 14263, United States

Author contributions: All authors contributed to this paper.

Correspondence to: Moshim Kukar, MD, Department of Surgical Oncology, Roswell Park Cancer Institute, Elm and Carlton Streets, Buffalo, NY 14263,

United States. moshim.kukar@roswellpark.org

Telephone: +1-716-8458972 Fax: +1-716-8453828

Received: May 9, 2014 Revised: June 25, 2014

Accepted: July 25, 2014

Published online: March 28, 2015

and experience in the hope of improved utilization of this modality. With this technique, our results are comparable to those published in the literature for diagnostic accuracy regarding correlation to intraoperative pathology. The 3D Volume rendering reconstruction of the parathyroid pathology shown in relation to the clavicle, thyroid gland, and skin provide superior surgical guidance and an essentially "cut here" approach for directed parathyroidectomy.

Original sources: Platz TA, Kukar M, Elmarzouky R, Cance W, Abdelhalim A. Low dose four-dimensional computerized tomography with volume rendering reconstruction for primary hyperparathyroidism: How I do it? *World J Radiol* 2014; 6(9): 726-729 Available from: URL: <http://www.wjgnet.com/1949-8470/full/v6/i9/726.htm> DOI: <http://dx.doi.org/10.4329/wjr.v6.i9.726>

Abstract

Modification of 4-dimensional computed tomography (4D-CT) technique with volume rendering reconstructions and significant dose reduction is a safe and accurate method of pre-operative localization for primary hyperparathyroidism. Modified low dose 4D-CT with volume rendering reconstructions provides precise preoperative localization and is associated with a significant reduction in radiation exposure compared to classic preoperative localizing techniques. It should be considered the preoperative localization study of choice for primary hyperparathyroidism.

© 2015 Baishideng Publishing Group Inc. All rights reserved.

Key words: Radiology; Nuclear medicine; Medical imaging

Core tip: To our knowledge, this is the first paper detailing the technical aspects of a low dose 4-dimensional computed tomography with volume rendering reconstruction. It is our aim to share our institute's technique

INTRODUCTION

Improvements in imaging techniques for primary hyperparathyroidism have been critical in the ability to transition from formal cervical four-gland exploration to minimally invasive/directed parathyroidectomy. A precise anatomic localization study is the key to the success of minimally invasive parathyroidectomy. Traditionally, sestamibi single photon emission computed tomography (SPECT) and ultrasound (US) have been used with varying success rates from 29%-79%^[1-10]. With advent of 4-dimensional computed tomography (4D-CT) technology, there is improved sensitivity and a higher intraoperative correlation rate ranging from 70%-89% demonstrated by multiple institutions^[11-15]. Despite this clear advantage, the use of 4D-CT has been limited. Numerous factors including the concern of higher cost, increased radiation exposure and a lack of expertise/knowledge have been



Figure 1 Position of patient for 4-dimensional computed tomography utilizing manufacture shoulder straps.

proposed. At our institution we have modified our technique to address some of these concerns. In this manuscript, we detail our modified 4D-CT technique providing an in-depth review of technical aspects, image processing and adaptations to decrease the effective radiation exposure. The term 4D is used to describe the combination of cross-sectional imaging and basic functional analysis through perfusion information of parathyroid adenomas. The first three dimensions refer to multiplanar CT: axial acquisitions, sagittal and coronal reformatted images. The fourth dimension is the change in enhancement overtime from non-contrast images to arterial and delayed phase imaging.

RESEARCH

Workup

At our institution all patients diagnosed with primary hyperparathyroidism undergo low dose 4D-CT with volume rendering reconstructions. Additional workup includes history/physical, laboratories (serum calcium, intact parathyroid hormone level, 24-h urine calcium, vitamin D), and review of existing imaging modalities if performed (United States, sestamibi SPECT). After confirmation with localization studies, parathyroidectomy is performed *via* standard minimally invasive/directed technique or formal four-gland exploration.

TECHNIQUE DESCRIPTION

CT technique

All imaging is performed on a 64 multi-slice CT scanner (VCT 64; GE Medical Systems, Milwaukee, Wis). The patient is positioned supine in the CT scanner. The patient enters head first with the upper extremities at their side. The manufacturer-supplied head holder is used for all scans. The patient's arms are pulled caudally to minimize shoulder artifact using the manufacturer-supplied shoulder straps (Figure 1). This is very well tolerated by most patients. IV access is obtained in the right or left antecubital vein with an 18-gauge cannula and flushed with heparinized saline. The scanning protocol consists of three phases of CT imaging performed from the hard palate to the level of the carina in all phases using a 0.625 mm slice width. Scanning parameters include a voltage of

120 peak kilovolts (kVp), 200 milliamperes (mA) for the pre-contrast and delayed post-contrast phases (venous), 400 mA for the early post contrast phase (arterial), pitch of 1, and a rotation time of 0.7 s. A 64 mm × 0.625 mm detector configuration with a 10-mm beam width and a table speed of 39.37 cm per gantry rotation is utilized. Imaging is initiated with the non-contrast phase with the anticipation of the normal thyroid tissue being brighter than any parathyroid tissues due to the fact of its increased iodine concentration. The non-contrast phase is followed by intra-venous injection of 90 mL (4 mL/s) of non-ionic contrast medium (iohexol 350, 350 mg of iodine per milliliter; GE health care; Princeton, NJ). A 25 s delay is followed by repeat imaging which constitutes the arterial phase. A delay of 25 s is chosen to coincide with peak enhancement of the parathyroid adenoma as compared to enhancement of the thyroid gland and any regional lymph nodes. A higher mA (400 mA) is used in this phase to facilitate detection of small adenomas including possible multiple gland disease. Approximately 90 s after the injection, a delayed phase scan is performed. This final phase is utilized to confirm the presence of the parathyroid adenoma as it rapidly washes out the IV contrast material compared to the adjacent thyroid tissue. The duration of each phase is dependent on the distance between the hard palate and the carina as well as the table speed. Each phase takes approximately 15-17 s to complete based on the patient's body habitus.

Radiation exposure

A major dose reduction is achieved by reducing the tube current to 200 mA in precontrast and delayed phases. This allows us to detect attenuation differences in lesions adjacent to thyroid gland without compromising imaging quality while achieving significant dose reduction. The effective radiation dose administered utilizing this modification was 11-13 millisieverts (mSv). This dose was calculated from the dose-length product provided by the scanner at the end of each exam^[16]. Confirmatory CT dose index measurements using standard 16 cm head phantom and standard CT ionization chamber were also performed yielding the same numbers. Recently, our institution has implemented ASIR technology (Adaptive Statistical Iterative Reconstruction), which incorporates a new reconstructive CT algorithm with an average effec-

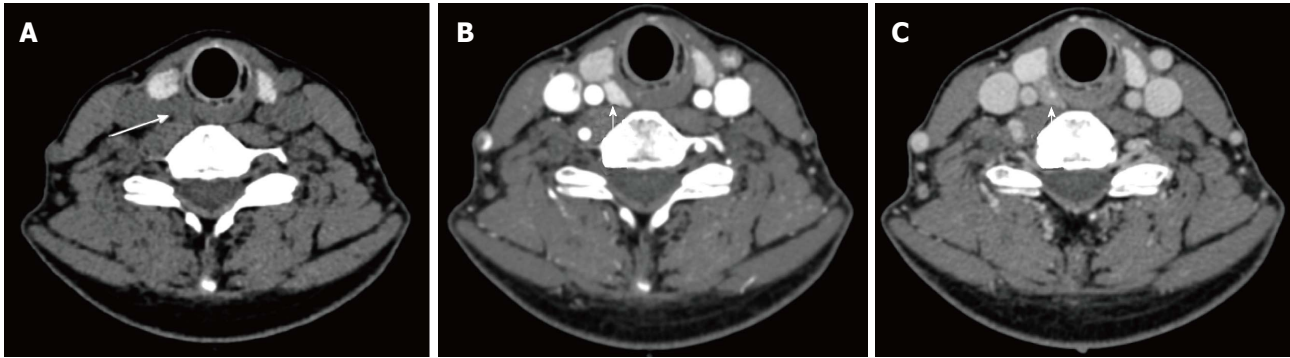


Figure 2 Four-dimensional computed tomography. Axial noncontrast (A), axial arterial phase post contrast (B) and axial delayed phase post contrast (C) images show a hypodense nodule contiguous with the right thyroid gland, which demonstrates avid early contrast enhancement and rapid washout.

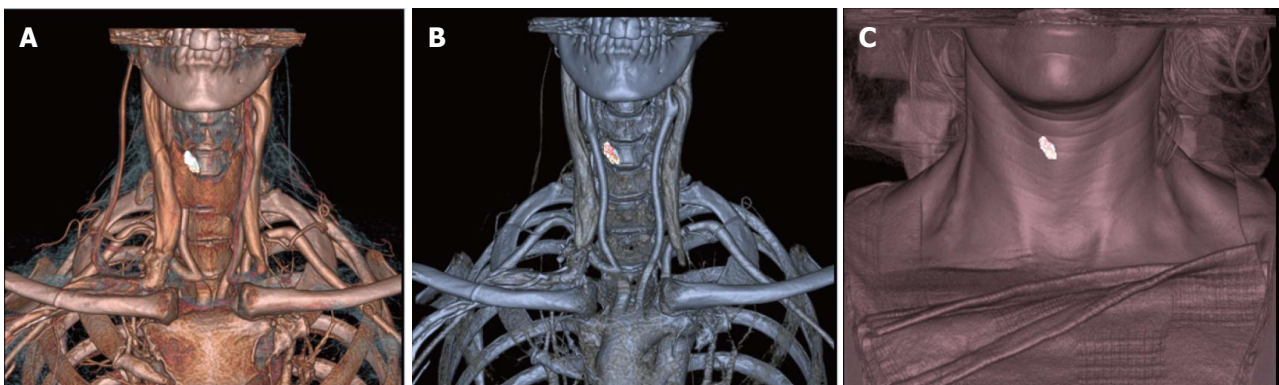


Figure 3 Three-dimensional volume rendering images in 3 different thresholds showing the presumed adenoma in relation to thyroid gland (A), bony landmarks (B) and skin (C).

tive radiation dose of 9-10 mSv.

Image processing

Standard post processing of imaging is performed by a fellowship-trained neuroradiologist on a separate workstation (Advantage Windows Workstation, version 4.5; GE Medical Systems). Two-dimensional sagittal, coronal and oblique multi-planar reformations are obtained from the arterial phase images. This is followed by 3-D reconstruction with volume rendering. The parathyroid adenoma is segmented from the axial images creating a 3-D volume of the adenoma that is merged with the original 3-D volume of the arterial phase of the study. The adenoma is assigned a different color and is shown against the original 3-D volume in three different thresholds and shown in relation to the thyroid gland, skin, and bony landmarks. Measurements are performed from the presumed parathyroid abnormality to the clavicular head and the overlying skin to aid the surgeon in operative guidance (Figures 2 and 3). Images processed on the workstation take an average of 8-10 min. The resulting images are interpreted by the attending neuroradiologist on a PACS workstation and a formal report is issued.

DISCUSSION

Multiple studies including our institute's experience have

shown excellent diagnostic accuracy of 4D-CT as a pre-operative localization study for primary hyperparathyroidism ranging from 70%-89%^[1-5,11-13]. Despite these promising results, many institutions continue to utilize sestamibi SPECT and US as the primary modalities for preoperative localization for directed parathyroidectomy. Despite superiority, 4D-CT has not gained widespread acceptance for reasons unclear to us. Plausible explanations include technical challenges, fear of increased radiation exposure and added costs.

We have utilized this technique in 150 consecutive patients undergoing parathyroidectomy for primary hyperparathyroidism. The true positive rate for modified 4D-CT with volume rendering for this cohort was 133 (89%) of 150 with a false negative (FN) of 17 (11%) of 150. In addition, utilizing our technique, the effective radiation exposure dose is 11-13 mSv. This essentially is an equivalent radiation exposure dose to that of sestamibi SPECT (9-11 mSv) but lower than that previously published for 4D-CT (27 mSv)^[17]. To put this in perspective, radiation exposure from some commonly performed procedures such as CT scan of abdomen and pelvis is 14 mSv or CT angiogram is 15 mSv. This reduced effective radiation exposure of our technique is most likely due to the fact that we utilize a lower tube current for non-contrast and delayed images. The most recent implementation of ASIR technology has further reduced the radia-

tion exposure from 4D-CT to essentially equivalent levels to that of sestamibi SPECT.

4D CT is especially useful to identify parathyroid glands in ectopic locations as the axial imaging extends from the hard palate to the level of the pulmonary artery. It is also very useful in recurrent/persistent hyperparathyroidism and improves the success rate of minimally invasive parathyroidectomy in the reoperative setting. Despite these advantages it has some limitations especially in patients with short obese necks, multinodular goiters and multiple exophytic nodules. Another limitation is the observer experience with post image processing and reconstructing 3D images.

To our knowledge, this is the first paper detailing the technical aspects of a low dose 4D-CT with volume rendering reconstruction. It is our aim to share our institute's technique and experience in the hope of improved utilization of this modality. With this technique, our results are comparable to those published in the literature for diagnostic accuracy regarding correlation to intraoperative pathology. The 3D volume rendering reconstruction of the parathyroid pathology shown in relation to the clavicle, thyroid gland, and skin provide superior surgical guidance and an essentially "cut here" approach for directed parathyroidectomy.

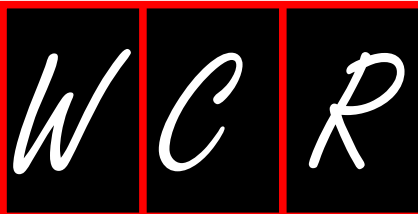
In conclusion, low dose 4D-CT with volume rendering reconstruction provides superior quality images while minimizing radiation exposure. The technique is easily reproducible and in our opinion should be the diagnostic modality of choice in patients with primary hyperparathyroidism.

REFERENCES

- 1 **Eichhorn-Wharry LI**, Carlin AM, Talpos GB. Mild hypercalcemia: an indication to select 4-dimensional computed tomography scan for preoperative localization of parathyroid adenomas. *Am J Surg* 2011; **201**: 334-338; discussion 338 [PMID: 21367374 DOI: 10.1016/j.amjsurg.2010.08.033]
- 2 **Mortenson MM**, Evans DB, Lee JE, Hunter GJ, Shellinghouth D, Vu T, Edeiken BS, Feng L, Perrier ND. Parathyroid exploration in the reoperative neck: improved preoperative localization with 4D-computed tomography. *J Am Coll Surg* 2008; **206**: 888-895; discussion 895-896 [PMID: 18471717 DOI: 10.1016/j.jamcollsurg.2007.12.044]
- 3 **Cheung K**, Wang TS, Farrokhyar F, Roman SA, Sosa JA. A meta-analysis of preoperative localization techniques for patients with primary hyperparathyroidism. *Ann Surg Oncol* 2012; **19**: 577-583 [PMID: 21710322 DOI: 10.1245/s10434-011-1870-5]
- 4 **Starker LF**, Mahajan A, Björklund P, Sze G, Udelsman R, Carling T. 4D parathyroid CT as the initial localization study for patients with de novo primary hyperparathyroidism. *Ann Surg Oncol* 2011; **18**: 1723-1728 [PMID: 21184187 DOI: 10.1245/s10434-010-1507-0]
- 5 **Rodgers SE**, Hunter GJ, Hamberg LM, Schellinghouth D, Doherty DB, Ayers GD, Shapiro SE, Edeiken BS, Truong MT, Evans DB, Lee JE, Perrier ND. Improved preoperative planning for directed parathyroidectomy with 4-dimensional computed tomography. *Surgery* 2006; **140**: 932-940; discussion 940-941 [PMID: 17188140 DOI: 10.1016/j.surg.2006.07.028]
- 6 **Glynn N**, Lynn N, Donagh C, Crowley RK, Smith D, Thompson CJ, Hill ADK, Keeling F, Agha A. The utility of 99mTc-sestamibi scintigraphy in the localisation of parathyroid adenomas in primary hyperparathyroidism. *Ir J Med Sci* 2011; **180**: 191-194 [DOI: 10.1007/s11845-010-0641-9]
- 7 **Witteveen JE**, Kievit J, Stokkel MP, Morreau H, Romijn JA, Hamdy NA. Limitations of Tc99m-MIBI-SPECT imaging scans in persistent primary hyperparathyroidism. *World J Surg* 2011; **35**: 128-139 [PMID: 20957360 DOI: 10.1007/s00268-010-0818-4]
- 8 **Gómez-Ramírez J**, Sancho-Insenser JJ, Pereira JA, Jimeno J, Munné A, Sitges-Serra A. Impact of thyroid nodular disease on 99mTc-sestamibi scintigraphy in patients with primary hyperparathyroidism. *Langenbecks Arch Surg* 2010; **395**: 929-933 [PMID: 20625763 DOI: 10.1007/s00423-010-0680-8]
- 9 **Swanson TW**, Chan SK, Jones SJ, Bugis S, Irvine R, Belzberg A, Levine D, Wiseman SM. Determinants of Tc-99m sestamibi SPECT scan sensitivity in primary hyperparathyroidism. *Am J Surg* 2010; **199**: 614-620 [PMID: 20466104 DOI: 10.1016/j.amjsurg.2010.02.001]
- 10 **Thomas DL**, Bartel T, Menda Y, Howe J, Graham MM, Juweid ME. Single photon emission computed tomography (SPECT) should be routinely performed for the detection of parathyroid abnormalities utilizing technetium-99m sestamibi parathyroid scintigraphy. *Clin Nucl Med* 2009; **34**: 651-655 [PMID: 19893394 DOI: 10.1097/RLU.0b013e3181b591c9]
- 11 **Stark DD**, Gooding GA, Moss AA, Clark OH, Ovenfors CO. Parathyroid imaging: comparison of high-resolution CT and high-resolution sonography. *AJR Am J Roentgenol* 1983; **141**: 633-638 [PMID: 6604407 DOI: 10.2214/ajr.141.4.633]
- 12 **Beland MD**, Mayo-Smith WW, Grand DJ, Machan JT, Monchik JM. Dynamic MDCT for localization of occult parathyroid adenomas in 26 patients with primary hyperparathyroidism. *AJR Am J Roentgenol* 2011; **196**: 61-65 [PMID: 21178047 DOI: 10.2214/AJR.10.4459]
- 13 **Randall GJ**, Zald PB, Cohen JI, Hamilton BE. Contrast-enhanced MDCT characteristics of parathyroid adenomas. *AJR Am J Roentgenol* 2009; **193**: W139-W143 [PMID: 19620416 DOI: 10.2214/AJR.08.2098]
- 14 **Chazen JL**, Gupta A, Dunning A, Phillips CD. Diagnostic accuracy of 4D-CT for parathyroid adenomas and hyperplasia. *AJNR Am J Neuroradiol* 2012; **33**: 429-433 [PMID: 22135127 DOI: 10.3174/ajnr.A2805]
- 15 **Gafton AR**, Glastonbury CM, Eastwood JD, Hoang JK. Parathyroid lesions: characterization with dual-phase arterial and venous enhanced CT of the neck. *AJNR Am J Neuroradiol* 2012; **33**: 949-952 [PMID: 22241395 DOI: 10.3174/ajnr.A2885]
- 16 **Huda W**, Ogden KM, Khorasani MR. Converting dose-length product to effective dose at CT. *Radiology* 2008; **248**: 995-1003 [PMID: 18710988 DOI: 10.1148/radiol.2481080042]
- 17 **Hunter GJ**, Schellinghouth D, Vu TH, Perrier ND, Hamberg LM. Accuracy of four-dimensional CT for the localization of abnormal parathyroid glands in patients with primary hyperparathyroidism. *Radiology* 2012; **264**: 789-795 [PMID: 22798226 DOI: 10.1148/radiol.12110852]

P- Reviewer: Fulop T S- Editor: Ji FF L- Editor: A
E- Editor: Lu YJ





Role of functional imaging in the development and refinement of invasive neuromodulation for psychiatric disorders

Nolan R Williams, Joseph J Taylor, Kayla Lamb, Colleen A Hanlon, E Baron Short, Mark S George

Nolan R Williams, Joseph J Taylor, Kayla Lamb, Colleen A Hanlon, E Baron Short, Mark S George, Brain Stimulation Laboratory, Medical University of South Carolina, Charleston, SC 29425, United States

Joseph J Taylor, Colleen A Hanlon, Mark S George, Ralph H Johnson VA Medical Center, Charleston, SC 29401, United States
Joseph J Taylor, Colleen A Hanlon, Mark S George, Center for Biomedical Imaging, Medical University of South Carolina, Charleston, SC 29425, United States

Author contributions: Williams NR was the primary author; Taylor JJ and Hanlon CA wrote critical sections of the imaging physics; Williams NR and Lamb K designed and created the tables; George MS and Short EB edited as senior authors.

Supported by NIDA R25

Correspondence to: Nolan R Williams, MD, Brain Stimulation Laboratory, Medical University of South Carolina, 67 President Street, Charleston, SC 29425, United States. willianr@musc.edu

Telephone: +1-843-7920333 Fax: +1-843-7923187

Received: March 3, 2014 Revised: July 4, 2014

Accepted: August 27, 2014

Published online: March 28, 2015

Abstract

Deep brain stimulation (DBS) is emerging as a powerful tool for the alleviation of targeted symptoms in treatment-resistant neuropsychiatric disorders. Despite the expanding use of neuropsychiatric DBS, the mechanisms responsible for its effects are only starting to be elucidated. Several modalities such as quantitative electroencephalography as well as intraoperative recordings have been utilized to attempt to understand the underpinnings of this new treatment modality, but functional imaging appears to offer several unique advantages. Functional imaging techniques like positron emission tomography, single photon emission computed tomography and functional magnetic resonance imaging have been used to examine the effects of focal DBS on activ-

ity in a distributed neural network. These investigations are critical for advancing the field of invasive neuromodulation in a safe and effective manner, particularly in terms of defining the neuroanatomical targets and refining the stimulation protocols. The purpose of this review is to summarize the current functional neuroimaging findings from neuropsychiatric DBS implantation for three disorders: treatment-resistant depression, obsessive-compulsive disorder, and Tourette syndrome. All of the major targets will be discussed (Nucleus accumbens, anterior limb of internal capsule, subcallosal cingulate, Subthalamic nucleus, Centromedial nucleus of the thalamus-Parafascicular complex, frontal pole, and dorsolateral prefrontal cortex). We will also address some apparent inconsistencies within this literature, and suggest potential future directions for this promising area.

© 2015 Baishideng Publishing Group Inc. All rights reserved.

Key words: Deep brain stimulation; Functional neuroimaging; Functional magnetic resonance imaging; Functional magnetic resonance imaging; Cortical stimulation; Nuclear imaging

Core tip: Deep brain stimulation (DBS) is emerging as a powerful tool for the alleviation of targeted symptoms in treatment-resistant neuropsychiatric disorders. Most recently, functional magnetic resonance imaging has been used to examine the effects of focal DBS on activity in a distributed neural network. The purpose of this review is to summarize the current functional neuroimaging findings from neuropsychiatric DBS implantation and to discuss some apparent inconsistencies within this literature, and to suggest potential future directions for this promising area.

Original sources: Williams NR, Taylor JJ, Lamb K, Hanlon CA,

Short EB, George MS. Role of functional imaging in the development and refinement of invasive neuromodulation for psychiatric disorders. *World J Radiol* 2014; 6(10): 756-778 Available from: URL: <http://www.wjgnet.com/1949-8470/full/v6/i10/756.htm> DOI: <http://dx.doi.org/10.4329/wjr.v6.i10.756>

INTRODUCTION

Deep brain stimulation (DBS) is a form of invasive neuromodulation in which electrodes are implanted into a neuroanatomical target (nucleus or fiber tract) in an effort to modulate activity throughout a neural network^[1]. Neuropsychiatric disorders can also be modulated through stimulation of cortical nodes in a neural network with similar efficacy and reduced risk^[2,3]. The cortex can be stimulated either non-invasively from outside the skull with techniques like transcranial magnetic stimulation (TMS), or by placing stimulation paddles close to the surface of the brain under the skull but outside of the dura (epidural). For the purpose of this review, these cortical stimulation studies with invasive stimulation paddles and external generators are also labeled DBS, even though the electrodes are not deep. The imaging issues with these invasive cortical stimulation methods are the same as for traditionally defined DBS. These network modulations are driven by stimulation parameters that can be optimized for maximal therapeutic benefits. DBS was first developed for movement disorders wherein high frequency electrical stimulation of the thalamus has the capacity to reduce tremors^[4]. Since that time, DBS has been investigated for treatment-resistant neuropsychiatric disorders^[5,6]. In this context, high frequency electrical stimulation of limbic system targets has the capacity to alter mood and alleviate affective symptoms. Similar to DBS for movement disorders^[7], invasive neuromodulation for neuropsychiatric disorders has similar reported open-label efficacy rates as lesion surgeries (although never directly compared) but unlike lesion surgery offers reversibility and fewer side-effects^[8,9].

Neuropsychiatric disorders are beginning to be classified based on limbic, cognitive, and motoric^[10,11] circuit dysfunction^[12]. DBS likely exerts its effects by directly modulating the target node(s) and indirectly modulating the regions connected to that node^[1,13]. Functional neuroimaging studies have attempted to capture these downstream network effects induced by DBS^[13]. While traditional nuclear medicine techniques such as positron emission tomography (PET) imaging have successfully captured gross DBS-induced changes in neural networks, functional magnetic resonance imaging (fMRI) is poised to offer more refined insights^[14]. Additionally, basic science techniques like optogenetics are now being used to explore the precise neural changes associated with DBS in animal models of disease^[15].

This review begins by describing the functional imaging techniques that have been used to examine the effects of focal DBS on activity in a distributed neural network.

Thereafter the three neuropsychiatric syndromes of interest will be introduced and their DBS targets briefly identified. The subsequent sections describe the cortical and subcortical targets for each disorder in further detail, as well as discuss their imaging results and relevance to neuropsychiatric symptoms. Table 1 summarizes advantages, disadvantages and cautions for each imaging method. Tables 2-5 and Figures 1-4 are categorized by neuropsychiatric disease and illustrate the effect each DBS target has on downstream nodes.

PET

PET can safely and effectively probe the effects of DBS without disrupting the function of the device or its electrodes. PET uses short-lived radioisotopes to create a static image of averaged neural activity over time based on changes in oxygen metabolism, glucose, blood flow or neurotransmitter receptor binding^[16,17]. PET data are static in that they are averaged over time. Thus, PET cannot yield information about the immediate (*e.g.*, second to second) time course of change induced by an experimental manipulation, although oxygen PET can image activity for one minute and can thus show changes over a few minutes.

PET is the predominant functional imaging technique in the psychiatric DBS literature, in part because it was available much earlier than modalities like fMRI, and because it is technically less difficult to combine DBS with PET^[14]. Although PET continues to make significant contributions to clinical Neuroscience, the technique has a number of limitations that are relevant to DBS research. First, PET has poor temporal and spatial resolution relative to fMRI. These resolution limitations might make it difficult to accurately assess DBS-induced changes in small subcortical nodes in limbic neural networks. Second, PET requires injections of radioactive tracers into patients who have no medical indication for such exposure. Furthermore, the cost and availability of these radiotracers can be prohibitive. Third, PET studies typically have methodological variations that make it difficult to compare data between studies. For example, a study that uses repeated injections of ¹⁵O-H₂O PET to measure cerebral blood perfusion over 60-120 s intervals^[18] cannot be contextualized with a study that uses a single injection of ¹⁸F-fluorodeoxyglucose (¹⁸F-FDG) PET to measure glucose metabolism over a 60 min interval^[19]. Fourth, PET measures of binding capacity are not specific for receptor occupancy and could reflect altered receptor density^[20,21]. This lack of clarity might make it difficult to assess the pharmacological effects of DBS. These are just a few of the considerations that should be kept in mind when considering PET DBS research.

On the other hand, there are few if any problems with performing PET studies in patients with DBS electrodes implanted, unlike with fMRI. Also, single photon emission computed tomography imaging, with perfusion tracers that capture activity summed over a minute or two, offers a less expensive and readily available op-

Table 1 Advantages and disadvantages of imaging methods

Modality	Advantages	Disadvantages
PET	Unlikely to disrupt implant placement or function Widely available Technically simple to combine with DBS (relative to fMRI)	Cost, availability and health risks of radiotracers Static data (averaged over set time interval)
MRI	Customized radiotracers to measure binding capacity Time-locked data High temporal and spatial resolution (relative to PET) Flexible data acquisition, processing and analysis Possible analysis of ON and OFF settings	Poor temporal and spatial resolution (relative to fMRI) Difficult to interpret data (receptor binding vs density) BOLD signal interpretation (temporal lag, anatomical imprecision) DBS safety considerations (lead migration, secondary lesioning) Possible deactivation of implanted impulse generators Potential DBS-related artifacts on images

PET: Positron emission tomography; DBS: Deep brain stimulation; fMRI: Functional magnetic resonance imaging; BOLD: Blood oxygen level dependent.

Table 2 Obsessive compulsive disorder deep brain stimulation targets: Activation/deactivation of cortical and subcortical targets

	STN_DBS	ALIC_DBS	VCVS_DBS
Frontal cortex		↑Nuttin ^{1a}	
Medial frontal gyrus	↓Le Jeune ^{1f}		
Inferior frontal gyrus		↓Zuo ^{1b}	
Supplementary motor area	↑Min ^{1b,5}	↓Zuo ²	
Prefrontal cortex			↑ Knight ^{1d,7}
Lateral PFC			↓Figuee ^{1b,2} , ↓ Knight
Dorsolateral PFC	↑Min ^{1b,5}		↑Sturm, ↑ Knight
Medial PFC	↓Le Jeune ²		↓Figuee ^{1a,2} , ↑ Knight
Cingulate			↑Sturm; ↑ Knight ^{1d,7}
Anterior cingulate cortex	↑Min ^{1b} ; ↓Le Jeune ^{1f}	↓Zuo ^{1b,2}	↑ Knight ^{1d} ; ↑Rauch ^{1f}
Orbitofrontal cortex	↓Le Jeune ²	↓Zuo ^{1b} ; ↓Abelson ³	↑Rauch ^{1f}
Insula	↑Min ^{1b}		↑ Figuee; ↑Knight ^{1d,6}
Striatum		↑ Nuttin ^{1a}	
Caudate	↑Min ^{1b}	↓Zuo ^{1b}	↑Figuee
Putamen	↑Min ^{1b}		↑Figuee; ↓Sturm; ↑Rauch ^{1f}
Nucleus accumbens			↑Figuee ^{1c}
Temporal cortex	↑ Min ^{1b,4}		
Superior temporal gyrus		↓Zuo ^{1b} ; ↑Nuttin ^{1a}	
Medial temporal gyrus		↑Nuttin ^{1a}	
Thalamus	↑ Min ^{1b,4}	↓Zuo ^{1b}	↑Figuee; ↓Knight ^{1d,6} ; ↑Rauch ^{1f}
Pons			↑Nuttin ^{1a}
Hippocampus/parahippocampus	↑ Min ^{1b,4}		↑ Knight ^{1d,6}
Globus pallidus			↑ Rauch ^{1f}

¹Statistically significant, ^a $P < 0.05$, ^b $P < 0.001$, ^c $P < 0.0001$, ^d $P < 0.005$, ^e $P = 0.031$ vs scans; ²Statistically correlated with treatment response; ³Decreased activity for 2 of 3 patients; ⁴Significant activation to STN vs Gpi; ⁵Significant at 2 V; ⁶As the stimulation voltage increased from 3 V to 5 V, the region of BOLD signal modulation increased; ⁷As the stimulation voltage increased from 3 V to 5 V, the region of BOLD signal modulation area decreased for $n = 2$ pigs. STN: Subthalamic nucleus; ALIC: Anterior capsulotomy of anterior limb of internal capsules; DBS: Deep brain stimulation; VCVS: Ventral (anterior internal) capsule/ventral striatum; BOLD: Blood oxygen level dependent; PFC: Prefrontal cortex.

tion^[18,22,23].

fMRI

One of the most popular ways to assess brain function is to employ fMRI. Most fMRI studies use blood oxygen level dependent (BOLD) signals that are based on magnetization differences between oxygenated and deoxygenated hemoglobin^[24]. Thus, fMRI can be used to make inferences about neural activity based on time-locked alterations in neurovascular coupling. Although BOLD fMRI is widely used, it does have limitations. The BOLD hemodynamic response takes about 1-3 s to peak, which is a lifetime in terms of neuronal firing. Also, the BOLD signal reflects general vascular changes arising from new metabolic demands, and is not precise to the actual neurons driving the signal. That is, the BOLD response is

anatomically imprecise or “smudged” with respect to the actual activated neurons, like “the garden being flooded for want of one thirsty flower”^[25]. Finally, BOLD changes occur both when a brain region is acting to excite activity, and when it is attempted to regulate or inhibit brain activity. Thus the precise interpretation of the BOLD signal direction is problematic.

In the DBS literature, fMRI is often used to examine the function of neural network(s) before and after targeted stimulation^[26,27]. Safety considerations such as MRI-induced lead migration and secondary heat lesioning have greatly slowed the utilization of this technology in patients with DBS implanted electrodes^[28]. There is also some concern that fMRI may deactivate implanted impulse generators, although this phenomenon has been linked to low battery^[29] and more recent studies have not

Table 3 Treatment-resistant depression deep brain stimulation targets: Activation/deactivation of cortical and subcortical targets

	NAC_DBS	SCG_DBS	DLFPC_EPCS
Frontal cortex			
Ventral superior frontal sulcus	↓Bewernick ^{1c}		
Dorsal superior frontal sulcus	↓Bewernick ^{1c}		
Medial frontal gyrus	↑Schlaepfer; ↓Bewernick ^{1c}		
Superior frontal gyrus	↑Schlaepfer		↓Kopell ¹²
Inferior frontal gyrus	↓Schlaepfer ^{1a}		
Prefrontal cortex (PFC)	↑Knight ^{1d,11}		
Dorsomedial PFC	↑Schlaepfer ^{1a}	↓Lozano ⁴	
Dorsolateral PFC	↑Schlaepfer ^{1a}	↑Mayberg ⁸ ; ↓Lozano ^{4,6f}	↑Kopell ^{1f} ; ↓Kopell ²
Ventral prefrontal			
Ventrolateral prefrontal	↓Schlaepfer ^{1a} ; ↑Knight	↑Lozano ^{6f}	
Ventromedial prefrontal	↓Schlaepfer ^{1a}	↑Lozano ⁴	
Medial prefrontal		↓Mayberg ⁸	
Dorsal frontal pole		↓Lozano ⁴	
Ventral frontal pole		↓Lozano ⁴	
Cingulate	↑Schlaepfer ^{1a} ; ↑Knight ^{1d,11}		
Posterior cingulate	↓Bewernick ^{1c}	↑Mayberg ^{7b} ; ↑Lozano ⁵	↓Kopell ²
Subgenual cingulate	↓Bewernick ^{1c,2}	↓Mayberg ^{7b} ; ↑Lozano ⁴	
Anterior cingulate	↓Schlaepfer ^{1a} ; ↑Knight ^{1d}	↑Mayberg ⁸ ; ↓Lozano ^{6f}	
Orbitofrontal cortex	↓Bewernick ^{1e}	↓Mayberg ^{9b}	↑Kopell ^{1f}
Lateral orbitofrontal		↑Lozano ⁴	
Medial orbitofrontal		↓Lozano ^{6f}	
Premotor cortex		↑Mayberg ^{7b} ; ↑Lozano ³	
Dorsolateral premotor		↓Lozano ³	
Striatum			
Ventral striatum	↑Schlaepfer ^{1a} ; ↑Knight		
Caudate	↓Bewernick ^{1c} ; ↑Schlaepfer ^{1c}	↑(rostral) ↓(caudal)Lozano ⁴	
Putamen	↑Schlaepfer		
Insula	↓Schlaepfer ^{1a} ; ↑Knight ^{1d}	↓Mayberg ^{7b} ; ↑Lozano ⁴	
Amygdala	↑Schlaepfer ^{1a} ; ↑Bewernick ^{1c,2}		
Pons		↓Lozano ⁵	
Thalamus	↓Bewernick ^{1c} ; ↓Schlaepfer ^{1a} ↓Knight ^{1d,10}		
Hypothalamus		↓Mayberg ^{7b}	
Hippocampus/parahippocampus	↑Schlaepfer; ↑Knight ^{1d}	↑Lozano ^{4,5}	

¹Statistically significant, ^b $P < 0.001$, ^d $P < 0.0001$, ^a $P < 0.05$, ^f $P < 0.005$, ^c $P = 0.05$, ^e $P = 0.038$ vs scans; ²Statistically correlated with change in depression scale; ³de/activation at 3 mo only; ⁴de/activation at 3 and 6 mo; ⁵de/activation at 6 mo only; ⁶significant between scans at 6 mo only; ⁷significant between scans at 3 and 6 mo; ⁸statistically correlated at 3 and 6 mo; ⁹significant between scans at 3 mo only; ¹⁰as the stimulation voltage increased from 3 V to 5 V, the region of BOLD signal modulation increased; ¹¹as the stimulation voltage increased from 3 V to 5 V, the region of BOLD signal modulation area decreased for $n = 2$ pigs; NAC: Nucleus accumbens; DBS: Deep brain stimulation; SCG: Subcallosal cingulate gyrus; DLFPC: Dorsolateral prefrontal cortex; EpCS: Epidural cortical stimulation; BOLD: Blood oxygen level dependent.

observed it^[30]. To address some of these concerns, DBS-fMRI studies have typically been conducted utilizing externalized leads connected to pulse generators that are housed in the fMRI control room. This setup may reduce the risk of hardware malfunction^[31]. This also means that most DBS fMRI studies are performed in humans immediately after surgical implantation and before connecting the DBS electrodes to the generator implanted in the chest wall. This makes longitudinal studies problematic.

Many of the original DBS-fMRI studies were performed during the roughly 2-3-wk interval between lead implantation and IPG placement. During this time, stimulator extension wires can be accessed for externalized operation and stimulation^[32]. While this approach is useful for examining the short-term effects of DBS on the limbic/cognitive networks, it cannot be used to assess long-term effects that may evolve or change over time^[33]. Furthermore, in the weeks after surgery, a “microlesion effect” may result from mechanical manipulation at the site of lead placement. Such a lesion could itself have

a unique functional imaging signature^[34] and therefore complicate predictions about the long-term effects of limbic DBS. These microlesion effects have also been shown to have unanticipated effects on adjacent neural circuits^[35,36]. IPG replacement surgery has been proposed as an optimal window of time during which the chronic effects of DBS may be explored^[37].

There are several sources of potential MRI artifacts in patients with DBS implants: 1-the skull-cap, 2- the metallic portion of the electrode contact, 3- the electrical stimulation itself, and 4-movement^[38,39]. Some of these artifacts can be reduced or eliminated. Some of these artifacts are disease specific, such as the participant having tics in the scanner^[40]. The artifact generated by the skull-cap, for example, can be addressed by replacing ferromagnetic screws with non-ferromagnetic options^[41] or by post-processing techniques normally used for sinus artifacts^[30]. Other artifacts, like those generated by the metallic portion of the lead during echoplanar acquisition^[29,42], are more difficult to address. The deep brain

Table 4 Tourette syndrome deep brain stimulation targets: Activation/deactivation of cortical and subcortical targets

	Gpi_DBS	Thalamic_DBS	Nac-ALIC_DBS	Pf_DBS	CM_DBS
Prefrontal cortex	↓Min ⁵		↑Knight ^{1d,5}	↑Kim ^{7,8b,9,10b}	↑Kim ^{7,8a,9,10a}
Dorsolateral prefrontal cortex	↑Min ^{1b}				
Cingulate					
Anterior cingulate cortex	↑Min ^{1b}				
Dorsalanterior cingulate cortex			↑Knight ⁴	↓Kim ^{7,8,10}	↓Kim ^{7a,8,9,10}
Dorsal Posterior cingulate cortex				↓Kim ^{7,8a,10}	↓Kim ^{7d,8,9,10}
Motor cortex					
Primary motor cortex	↑Min ^{1b}			↓Kim ^{7,8a,9,10a}	↓Kim ^{7,8b,9,10a}
Premotor cortex	↑Min ^{1b}			↓Kim ^{7,8a,9,10a}	↓Kim ^{7a,e,f,8ba,9a,10a}
Primary somatosensory cortex	↑Min ^{1b}			↓Kim ^{7,8a,9,10a}	↓Kim ^{7,8,9,10a}
Insula	↑Min ^{1b}		↑Knight ^{1d,4}	↓Kim ^{7,9} ↑8a,10a	↓Kim ^{7,8,9,10}
Temporal lobe					
Inferior temporal gyrus		↓Kuhn		↓Kim ^{7,8a,10}	↓Kim ^{7,9,8,10}
Striatum					
Caudate	↑Min ^{1b}	↓Kuhn ↓Vernaleken		↓Kim ^{8,10}	↑Kim ^{7,8,10}
Putamen		↑Kuhn ↑Vernaleken		↓Kim ^{8,10}	↑Kim ^{7,8,10}
Thalamus		↓Kuhn ↓Vernaleken	↓Knight ^{1d,4}		
Right thalamus		↑Kuhn ²			
Left thalamus		↓Kuhn ³			
Central thalamic nucleus					↑Kim ⁸
Hippocampus				↓Kim ^{7,8,10}	↓Kim ⁸
Parahippocampal cortex			↑Knight ^{1d,4}	↓Kim ^{7,8,10}	↓Kim ^{7,8,10}

¹Statistically significant scans; ² $P < 0.001$, ³ $P < 0.0001$, ⁴ $P < 0.05$ vs scans, ⁵Response at 130 Hz 3 V was significant vs P_t contact site at $P < 0.05$, ⁶response at 60 Hz 3 V was significant vs Pf; ⁷Patient #3, unilateral had reduction of putamen activity; ⁸Only in unilateral patient; ⁹As the stimulation voltage increased from 3 V to 5 V, the region of BOLD signal modulation increased; ¹⁰As the stimulation voltage increased from 3 V to 5 V, the region of BOLD signal modulation area decreased for $n = 2$ pigs; ¹¹Activation decreased at 2V; ¹²Response @ 130 Hz 3 V; ¹³Response @ 130 Hz 5 V; ¹⁴Response @ 60 Hz 3 V; ¹⁵Response @ 60 Hz 5 V; Gpi: Globus pallidus interna; DBS: Deep brain stimulation; Nac-ALIC: Nucleus accumbens-anterior limb of internal capsule; CM-Pf: Centromedian-parafascicular nuclei complex; BOLD: Blood oxygen level dependent.

stimulation itself can also create MR artifact in the area around the tissue-lead interface. This has been addressed by turning off the device minutes before the scan^[13]. This artifact, if present, prevents analysis of DBS-induced activity in the area surrounding the electrode. Some authors have chosen to address these issues with strict statistical thresholding in offline analysis^[43,44].

Despite its limitations, DBS-fMRI can provide unique and valuable information regarding the neurobiological effects of DBS^[45,46]. Most psychiatric DBS-fMRI studies have only utilized the device in the OFF condition^[13]. Newer protocols, however, have begun to explore the possibility that DBS-fMRI could be performed in the ON condition in patients with fully-implanted DBS hardware^[30,43]. One recent study successfully imaged Parkinson's disease (PD) patients with subthalamic nucleus (STN) DBS in the ON and OFF setting with no reported adverse effects^[43]. This protocol utilized a 1.5 Tesla MRI scanner as well as a special transmit-receive (T/R) head coil. The specific absorption ratio in the head was limited to under 0.1 W/kg for this experiment. This protocol was first performed in a phantom, demonstrating no significant heating with the sequences utilized in the human study^[30]. We encourage anyone considering such a technique to consult with a magnetic resonance physicist and take great caution as this is a risky undertaking. While this protocol appears to be safe, it is yet to be utilized in patients with DBS for psychiatric conditions.

NEUROPSYCHIATRIC DISEASE AND THEIR DBS TARGETS

This portion of the review will focus on the imaging of DBS in three neuropsychiatric syndromes: 1-obsessive-compulsive disorder (OCD), 2-major depressive disorder (MDD), and 3-Tourette syndrome (TS). The following sections will identify common DBS targets for each disorder and review relevant functional imaging data.

OCD and its DBS targets

OCD is a neuropsychiatric condition characterized by functionally impairing obsessions and compulsions. The obsessions occur as recurrent and ego-dystonic ideas, images, or impulses. By contrast, the compulsions are stereotyped, repetitive mental acts or behaviors that are performed with the intention of reducing anxiety generally related to the obsessions. OCD affects approximately 2%-3% of the population and 20%-40% of patients with OCD remain severely disabled despite conventional treatments like exposure/response prevention as well as medications such as selective serotonin reuptake inhibitors. DBS for severe, treatment-resistant OCD was recently approved through a humanitarian device exemption^[47]. Several targets have been explored for this indication, including the nucleus accumbens (NAc)^[48,49], the anterior limb of the internal capsule (ALIC)^[50], the ventral capsule/ventral striatum (VCVS)^[51-53] and the STN^[54,55].

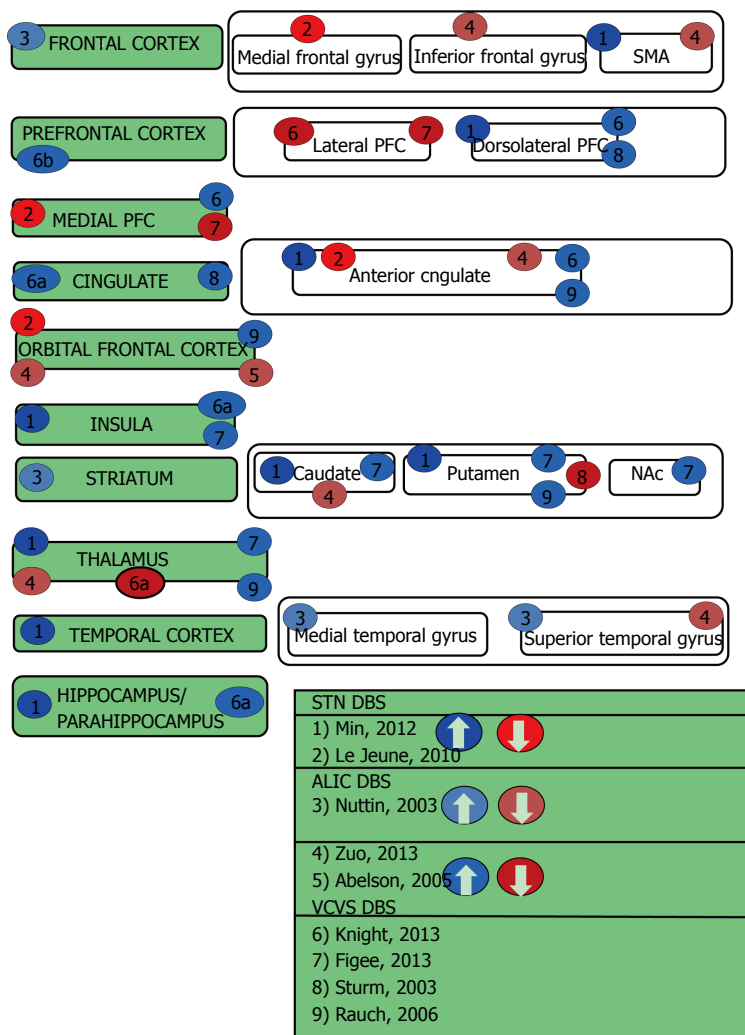


Figure 1 Obsessive compulsive disorder deep brain stimulation. ^aAs stimulation voltage increased from 3 V 130 Hz to 5 V 130 Hz, the region of BOLD signal modulation increased; ^bAs stimulation voltage increased from 3 V 130 Hz to 5 V 130 Hz, the region of BOLD signal modulation decreased for *n* = 2 pigs. SMA: Supplementary motor area; NAc: Nucleus accumbens; PFC: Prefrontal cortex; BOLD: Blood oxygen level dependent.

Four of the main OCD targets that have been imaged with PET include the ALIC^[56], VCVS^[57], STN^[58], and NAc^[50,59] (Table 2, Figure 1). Functional MRI has been performed following NAc DBS in both animals^[26] and more recently in humans with OCD^[13].

MDD and its DBS targets

Depression is a psychiatric disorder characterized by extreme sadness and/or melancholia that is of sufficient length and interferes with activities of daily living as well as socialization. One in five people will experience an episode of major depression at some point in their lifetime. The World Health Organization has indicated that major depressive disorder is one of the four most disabling illnesses worldwide^[60]. Currently, antidepressants and psychotherapy are the primary modes of treatment, although that is evolving^[61]. Minimally invasive brain stimulation methods like electroconvulsive therapy (ECT) and TMS are typically reserved for patients with treatment-resistant depression^[62]. DBS is currently being utilized in a clinical research setting for patients who do not respond to the aforementioned therapies. Three of the main depression targets that have been imaged with PET include the dorsolateral prefrontal cortex^[3], subcallosal cingulate^[63,64],

and the nucleus accumbens^[65,66] (Table 3, Figure 2). Two of the depression targets are also OCD targets have been imaged for OCD, but not depression include the anterior limb of the internal capsule^[56], ventral capsule/ventral striatum^[57]. Functional MRI has been performed in NAc in non-depressed animals^[26].

TS

TS is a neuropsychiatric movement disorder that affects approximately 1% of the world’s population, typically in childhood and/or adolescence. TS is characterized by at least two motor tics and one or more vocal tics that persist for more than a year. Approximately 90% of individuals with TS have at least one comorbid psychiatric symptom. These symptoms include attention-deficit/hyperactivity disorder, OCD, anxiety disorders, or impulse control disorders. DBS for TS has been shown to reduce the frequency and severity of motor tics as well as their associated psychiatric symptoms^[47]. Although the precise mechanism of action remains unclear, DBS for TS appears to diminish dopamine signaling in the thalamus and the striatum^[16]. Multiple targets have been introduced for TS DBS, including the thalamic centromedian nucleus and parafascicular complex (CM-pf)^[67], the globus pallidus

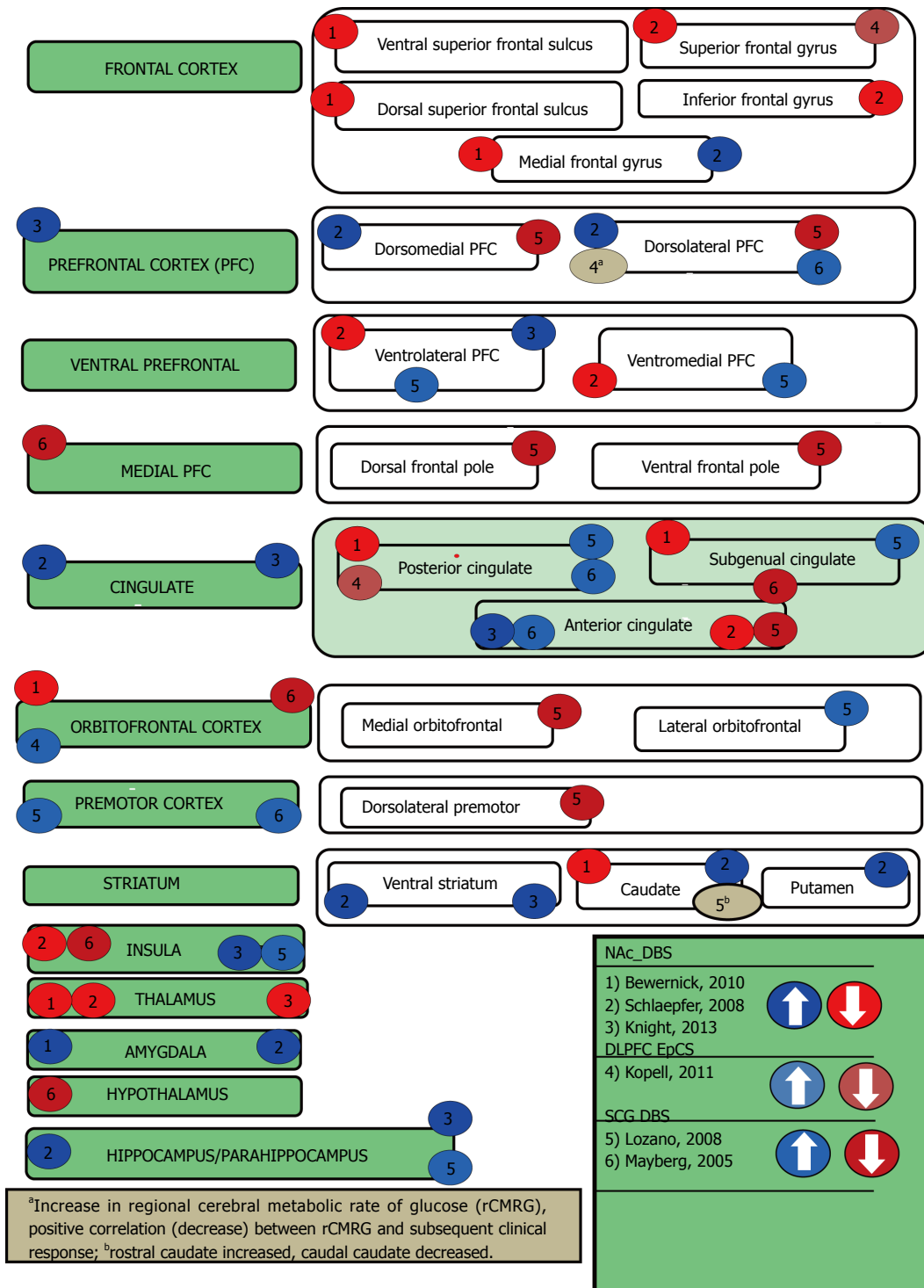


Figure 2 Treatment-resistant depression deep brain stimulation. NAc: Nucleus accumbens; DLPFC: Dorsolateral prefrontal cortex; EpCS: Epidural cortical stimulation; SCG: Subcallosal cingulate gyrus.

internus (GPI)^[68], the ALIC, and NAc^[69] (Table 4, Figure 5) While three of these targets (GPI^[70], ALIC, and NAc) have had functional neuroimaging performed in other conditions (as described above), only the medial thalamus has been imaged in the TS population^[16,17]. In a large animal model, both the CM-Pf and GPI have been imaged using fMRI^[27,71].

DBS TARGETS AND DOWNSTREAM NODES IN NEUROPSYCHIATRIC DBS

Cortical targets and nodes

Dorsolateral prefrontal cortex (BA 9 and BA 46): The dorsolateral prefrontal cortex (DLPFC) (BA 9 and 46)^[72] is a critical node in the mesocortical system, a dopami-

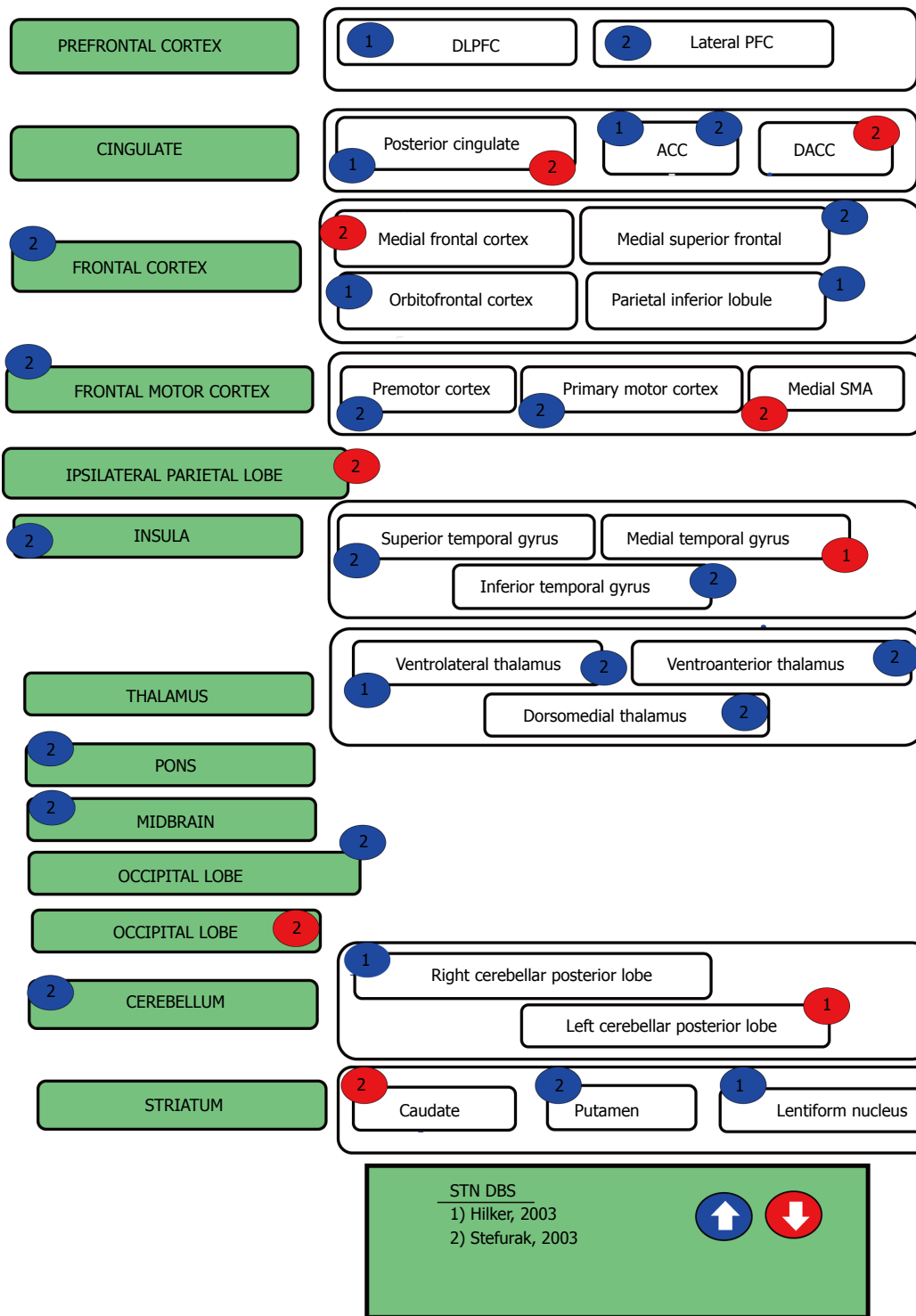


Figure 3 Parkinson's disease deep brain stimulation. DLPFC: Dorsolateral prefrontal cortex; PFC: Prefrontal cortex; ACC: Anterior cingulate cortex; DACC: Dorsal-anterior cingulate cortex; SMA: Supplementary motor area; STN: Subthalamic nucleus; DBS: Deep brain stimulation.

nergic tract that modulates anticipation, goal selection, planning monitoring, and the use of feedback in task performance^[73]. The DLPFC is critical for working memory of both spatial and non-spatial information^[74]. There has been some suggestion that direct stimulation (activation) of the DLPFC may serve to modulate parietal attentional networks involved in the automatic processing of salient environmental stimuli. For example, a recent meta-analy-

sis of 162 imaging studies revealed that co-activation of BA 9 (which spans the dorsolateral and medial prefrontal cortices) and midbrain regions like the periaqueductal gray (PAG) is essential for assigning emotional valence^[75]. These results may partially explain how the DLPFC plays such a critical role in mood regulation^[76]. In depression, the left DLPFC is hypoactive and thought to be associated with negative emotional judgment. The right

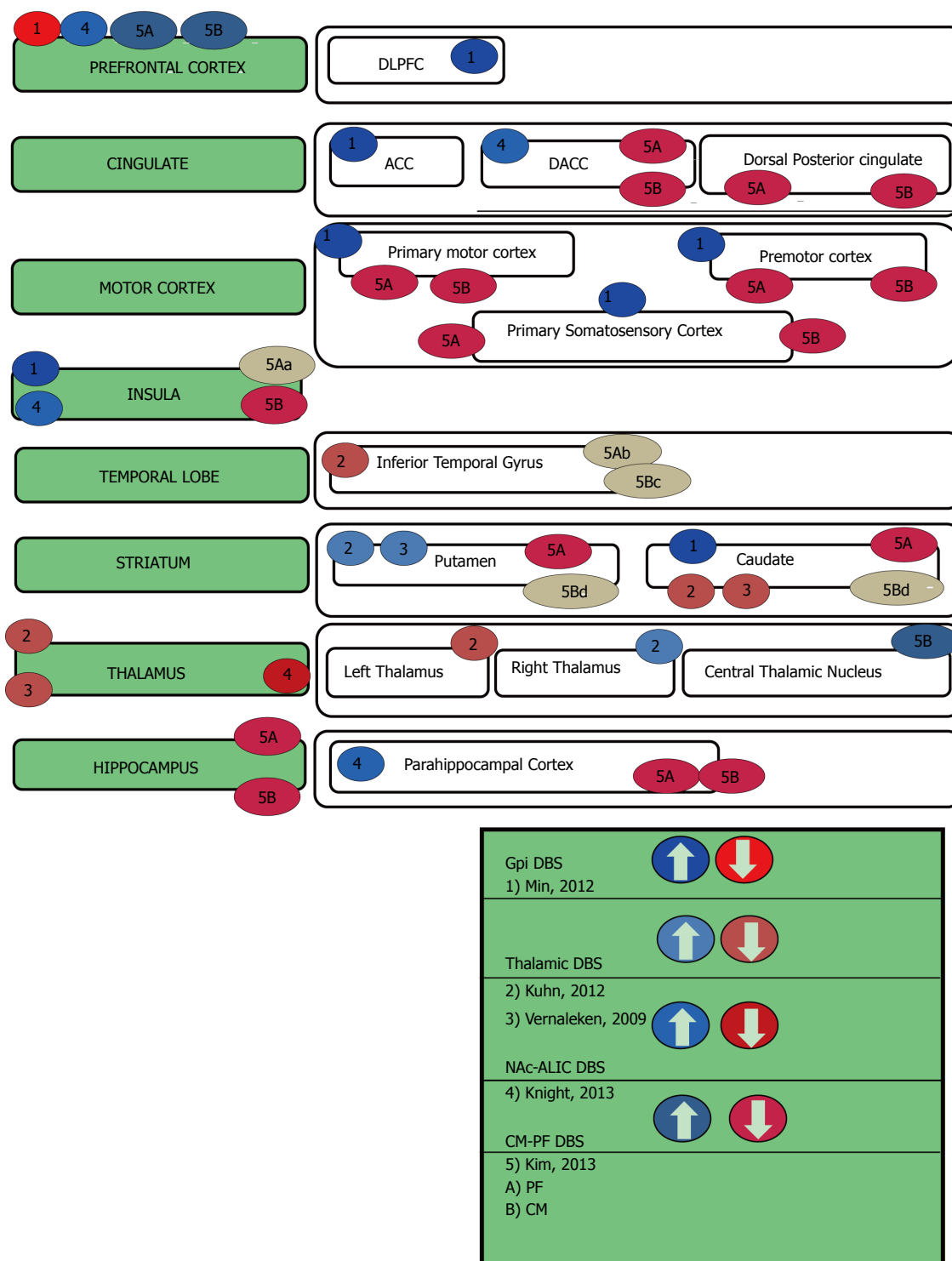


Figure 4 Tourette syndrome deep brain stimulation. ^aResponse at 130 Hz 3V AND 60 Hz 3V decreased, but increased at 130 Hz 5V and 60 Hz 5V; ^bResponse decreased at 130 Hz 3V, but increased at 130 Hz 5V and 60 Hz 5V; ^cResponse decreased at 130 Hz 3v and 60 Hz 3V, but increased at 130 Hz 5V and 60 Hz 5V; ^dResponse increased at 130 Hz 3V, but decreased at 130 Hz 5V and 60 Hz 5V. GPI: Globus pallidus internus; NAC: Nucleus Accumbens; ALIC: Anterior limb of internal capsule; CM-PF: Centromedian-parafascicular nuclei complex; DLPFC: Dorsolateral prefrontal cortex; ACC: Anterior cingulate cortex; DACC: Dorsal Anterior cingulate cortex; DBS: Deep brain stimulation.

DLPFC is hyperactive and this is linked to attentional modulation^[77]. The DLPFC has been demonstrated to have various subcortical connections, including but not limited to the mediodorsal nucleus of the thalamus^[78], the caudate^[79], hippocampus^[80], subcallosal cingulate^[81], and amygdala^[82] to name a few.

Unilateral stimulation of the DLPFC has bilateral effects^[83] as long as the corpus callosum is intact. While there have been varied downstream neural network changes in response to non-invasive magnetic stimulation of the DLPFC, it is clear that the effects of DLPFC stimulation are not isolated to a single node in the net-

Table 5 Parkinson's disease deep brain stimulation targets- limbic effects

	STN_DBS
Prefrontal	
Dorsolateral prefrontal cortex	↑Hilker ^{1b}
Lateral prefrontal cortex	↑Stefurak ^{1b}
Cingulate	
Posterior cingulate	↓Stefurak ^{1b} ; ↑Hilker ^{1b}
Anterior cingulate cortex	↑Stefurak ^{1b} ; ↑Hilker ^{1b}
Dorsal anterior cingulate cortex	↓Stefurak ^{1b}
Frontal cortex	↑Stefurak
Medial frontal cortex	↓Stefurak ^{1b}
Medial superior frontal	↑Stefurak ^{1b}
Orbitofrontal cortex	↑Hilker ^{1b}
Parietal Inferior lobule	↑Hilker ^{1b}
Frontal motor cortex	↑Stefurak ^{1b}
Premotor cortex	↑Stefurak ^{1b}
Primary motor cortex	↑Stefurak ^{1b}
Medial supplementary motor area	↓Stefurak ^{1b}
Ipsilateral parietal lobe	↓Stefurak ^{1b}
Insula	↑Stefurak ^{1b}
Superior temporal gyrus	↑Stefurak ^{1b}
Middle temporal gyrus	↓Hilker ^{1b}
Inferior temporal gyrus	↑Stefurak ^{1b}
Striatum	
Caudate	↓Stefurak ^{1b}
Putamen	↑Stefurak ^{1b}
Lentiform nucleus	↑Hilker ^{1b}
Thalamus	
Ventrolateral thalamus	↑Stefurak; ↑Hilker ^{1a}
Ventroanterior thalamus	↑Stefurak ^{1b}
Dorsomedial nuclei of Thalamus	↑Stefurak ^{1b}
Pons	↑Stefurak ^{1b}
Midbrain	↑Stefurak ^{1b}
Cerebellum	↑Stefurak ^{1b}
Right Cerebellar posterior lobe	↑Hilker ^{1a}
Left Cerebellar posterior lobe	↓Hilker ^{1b}
Parahippocampal cortex	↑Stefurak ^{1b}
Occipital lobe	↓Stefurak ^{1b}

¹Statistically significant, ^b $P < 0.001$, ^a $P = 0.002$ vs scans. STN: Subthalamic nucleus; DBS: Deep brain stimulation.

work. There is some suggestion that the antidepressant efficacy of non-invasive, repetitive transcranial magnetic stimulation of the left DLPFC sites is related to the anticorrelation of the subgenual cingulate, further supporting that the effects of DLPFC stimulation modulated deep structures in the neural network^[81]. It is also important to note that there are individual differences in DLPFC connectivity and these difference appear to affect efficacy of stimulation at this node^[84].

Left as well as bilateral epidural DLPFC stimulation has been shown to have a positive effect on depression^[2,3], and when combined with bilateral epidural frontopolar epidural cortical stimulation (EpCS) appears to be a durable therapy for treatment-resistant depression^[85]. Left DLPFC EpCS causes contralateral activation of the right DLPFC as well as superior frontal gyrus, cuneus, and posterior cingulate. In the Van Laere study, chronic, bilateral ALIC stimulation reduced right DLPFC activity on PET^[56]. Conversely, in the Sturm study, DBS of the right NAc was shown to increase the activity of the right

DLPFC in one patient on PET^[59]. Subcallosal cingulate gyrus (SCG) DBS has been demonstrated to increase metabolism in bilateral DLPFC^[63] in an earlier study, then decrease DLPFC bilaterally in a later study^[64] at essentially the same time points of 3 and 6 mo^[63,64]. An increase in activity of the DLPFC was also seen with fMRI of NAc DBS in large animals^[26]. In a functional connectivity analysis of NAc DBS, the efficacy of the stimulation was related to reduced hyperconnectivity between the lateral (and medial) prefrontal cortex and the NAc^[13].

Frontopolar cortex (BA 10): Frontopolar cortex (FPC) is the most uniquely human area in the hominid brain and is the only part of the prefrontal cortex (PFC) that has no direct inputs from the sensory cortex^[86,87]. Several studies have demonstrated the frontal pole has a significant role in self-reflection, long-term goals, past or future events, or hypothetical scenarios^[87-89]. Damage to this area impairs an individual's ability to multitask^[90]. The FPC functions to consider events beyond the present moment^[87]. Pathological patterns of rumination and self-reflection are core features of depression. The FPC is being more and more implicated in the pathogenesis of depression as well as in its recovery^[91,92]. A recent neuroimaging meta-analysis demonstrated a consistent finding of increased resting-state activity in the frontal pole (BA10) in patients with depression^[93].

Invasive neuromodulation over the FPC (along with DLPFC) bilaterally has been implanted in 5 individuals with treatment-resistant depression, termed epidural cortical stimulation^[2]. Furthermore, subgenual cingulate DBS appears to only be effective when it contacts the white matter tracts that cause downstream changes in the frontal polar cortex^[47,94,95]. The tractographic connection to the frontal pole was the invasive neuromodulation target common between the ALIC target and the SCG target^[2,96]. Chronic deep brain stimulation of NAc reduces activity in the gyri that terminate in the area of the frontal polar cortex^[65]. The therapeutic effects of NAc DBS for OCD are related to reducing functional connectivity between the NAc and the FPC^[13].

The frontal pole can be divided into a medial (ventromedial prefrontal cortex (vmPFC) part that is seen in all primates and a lateral part (the lateral frontopolar cortex (lfPFC)) that is seen only in humans^[86]. Activity of the vmPFC has been shown to be increased with NAc deep brain stimulation in an animal model, but these animals were not noted to be depressed^[26]. Furthermore, it is unclear the function of the vmPFC in non-primate mammals, although it has been consistently demonstrated to have connections with the NAc^[97]. vmPFC has been implicated in the pathogenesis of obsessive-compulsive disorder through its neural network connections to nodes involved in affective and reward processing^[13,98]. A PET study investigating the effects of STN DBS for OCD demonstrated that a decrease in Yale-Brown Obsessive Compulsive Scale (Y-BOCS) score, a 10-item scale designed to both determine severity of OCD and to monitor

tor improvement during treatment, was correlated with a decrease of metabolic activity in the vmPFC^[58].

Orbitofrontal cortex (BA 11 and BA 12/47): The orbitofrontal prefrontal cortex (OFC) includes BA 12 caudally (or more recently 47^[99] and BA 11 anteriorly^[100]. Orbitofrontal hyperactivity/hyperconnectivity has been demonstrated on numerous functional imaging studies of obsessive-compulsive disorder^[101] and Tourette^[102]. Numerous neuroimaging studies in idiopathic depression and Parkinson's-related depression have also implicated this area^[93,103]. Reduction of OFC activity is correlated with symptom improvement in medication and psychotherapy trials^[104,105]. With DBS to the inferior thalamic peduncle (connection from OFC to thalamus), it has been demonstrated to have significant reduction in OCD and depression symptoms^[106]. OFC activity has been demonstrated to be reduced in chronic NAc stimulation^[65]. In ALIC DBS for OCD, reduction in OFC activity was associated with clinical response in one study^[50] and regardless of clinical response in another^[107], as well as in larger studies of VCVS DBS^[57], ALIC DBS^[56], and capsulotomy^[108]. It is also reduced in SCG stimulation^[63,64], potentially explaining its anti-obsessional effects^[109]. A PET study investigating the effects of STN DBS for OCD revealed that the decrease in Y-BOCS score was correlated with a decrease of metabolic activity in the orbitofrontal cortex^[58]. Given that decreased orbitofrontal metabolism is associated with Parkinson's related depression, this may explain why STN is associated with increased depressive symptoms^[47], although that is likely not the whole story^[110]. Reduction in the activity of the OFC appears to be clearly linked to improvements from OCD surgery regardless of the target or methodology chosen^[57,58,108].

Cingulate cortex (BA 23, BA 24, BA 25, BA 31, BA 32): The SCG is the portion of the cingulum that lies ventral to the corpus callosum^[111,112]. The SCG has been recognized for more than two decades to be an important node in the neural networks that contribute to mood regulation. This network includes cortical structures such as the DLPFC and the FPC as well as the subcortical structures such as the limbic system, thalamus, hypothalamus, and brainstem nuclei^[111]. It has been demonstrated that activity in the SCG can reflect antidepressant efficacy, regardless of the nature of the intervention^[81,113-115]. The SCG has reciprocal connections to the orbitofrontal, FPC, anterior cingulate cortex (ACC), intralaminar thalamus, hypothalamus and amygdala. The SCG also has afferents from BA 9/46 and efferents to numerous brainstem nuclei^[111,116,117]. The SCG was the first target chosen because of functional neuroimaging data and not as the result of lesioning studies^[63]. SCG was first targeted for depression DBS (unipolar and bipolar)^[63,64,118], but has also been targeted for anorexia^[109]. The gray matter of the subgenual cingulate has reduced activity with chronic NAc DBS^[65], ALIC DBS^[56] and SCG (white matter) DBS^[63]. The white matter of the subgenual cingulate has

increased activity with SCG DBS^[63] and VCVS DBS^[57]. It appears that in order to achieve an antidepressant response, the active contact has to interface with the white matter tracts to the ventral pallidum, the mediodorsal (MD) thalamus, and to the FPC^[47,94].

The ACC has been heavily implicated in the neural circuitry of mood and anxiety regulation as well as the pathogenesis of TS^[119]. In depression, the ACC is underactive while the SCG is overactive^[120]. Conversely, the ACC is overactive in OCD during error processing^[121,122]. The ACC is involved in self-referential processing. It is an important area for determining treatment response^[120]. The higher the activity in the ACC, the higher likelihood of depression remission^[123]. Anterior cingulotomy has been demonstrated to be quite effective in the treatment of OCD and to a lesser degree depression, but with significant side effects^[9,124]. Success with anterior capsulotomy has been associated with significant reductions in dorsal anterior cingulate^[108]. DBS of the right NAc has been shown to increase the activity of the right ACC^[59] and animal studies have confirmed the laterality of these findings in a porcine model^[26]. VCVS DBS increases activity of ACC acutely^[57]. Conversely, DBS of the SCG demonstrated decreases in ACC metabolism^[63,64]. Interestingly, limbic STN DBS appears to reduce activity in the ACC^[71]. The ACC has significant connections to the posterior cingulate cortex (PCC) and the medial PFC, another target for invasive neuromodulation for depression^[2].

The PCC is a key node in the default mode network. It has been hypothesized that the posterior cingulate cortex has a role in supporting internally-directed cognition and increases in activity when individuals retrieve autobiographical memories or plan for the future^[125]. The PCC has been shown to be decreased with depression^[126] and obsessive-compulsive disorder^[127] and is associated with treatment response to multiple modalities^[128,129]. PCC activity is increased in the neural activity of the PCC is correlated with good response in DBS, but additionally in medication trials^[125]. Cingulate activity was increased with NAc DBS in a large animal model^[26] and increased in another case with OCD^[59], but appears to decrease after chronic NAc DBS^[65]. YBOCS scores for ALIC DBS were negatively correlated with PCC activity on PET^[56]. Activity of the PCC increases with SCG stimulation^[63,64]. The activity of SCG was reduced with limbic STN DBS^[58]. The PCC has been demonstrated to have reduced activity with chronic NAc stimulation for depression^[65], but this may reflect homeostatic mechanisms during chronic stimulation.

Insula: The anterior insula appears to be an important node in mood and anxiety regulation networks. A recent study demonstrated that relative hypo- or hyperactivity of the anterior insula is correlated with response to depression treatment whether cognitive behavioral therapy or medication^[130]. Disgust associated with OCD is thought to be mediated by the insula^[131]. The insula has also been

implicated in tic generation in TS^[132]. The metabolism of the insula has been demonstrated to have a significant correlation preoperative Y-BOCS score in patients undergoing capsulotomy^[108]. Anterior insular activity is reduced with ALIC DBS stimulation^[56] and NAc DBS stimulation^[66]. It is similarly reduced in SCG stimulation^[63,64] as well as in STN DBS (limbic)^[58]. Conversely, the insular signal has been demonstrated to also be decreased with a model of porcine CM-Pf DBS^[27], but increased in porcine NAc DBS^[26]. It should be noted that both porcine DBS studies utilized non-depressed animal subjects^[26,27].

Pre-supplementary motor area and supplementary motor area (BA 6): While the supplementary motor area (SMA) is an area of motor planning, the pre-SMA is an area related to response inhibition^[133]. Lesions to the SMA cause reduction of spontaneous movements and difficulty in performing voluntary motor acts^[134]. Inhibitory transcranial magnetic stimulation over the SMA and pre-SMA can reduce motor tics and OCD symptoms, respectively^[10,11]. The effects of ALIC DBS and anterior capsulotomy have been demonstrated to spread to the pre-SMA/SMA^[56,108]. SCG DBS has been shown to have effects on BA 6^[63,64].

SUBCORTICAL TARGETS

Striatum (nucleus accumbens, caudate and putamen)

The NAc is an important node in the human reward system. It can be divided into two principal parts; the core and the shell^[135]. The NAc core projects to the pallidal and nigral complexes and the NAc shell projects to the lateral hypothalamic areas, dopaminergic cell groups, and caudal mesencephalic areas^[136]. Hyperactivity of the NAc has been shown to have a negative correlation with recovery from depression^[123]. DBS has been implanted in the NAc not only for depression and OCD^[59], but also TS^[137], addiction^[138-142], eating disorders^[143], and even suggested for pain^[144].

DBS of the ALIC normalized pre-op hyperactivity of the NAc^[56]. The caudate has been shown to be involved in reward processing and hypoactive caudate responses to reward may be the functional explanation for anhedonia. The caudate has been shown to have reduced activity with chronic NAc stimulation^[65]. Furthermore, it has been implicated in the pathophysiology of OCD where specific symptom profiles can be mapped to subregions within the caudate nucleus^[145]. The caudate has been targeted for OCD DBS with apparent efficacy^[145]. VCVS has been shown to activate striatum^[57]. Right NAc inhibited the activity of the right dorsolateral rostral putamen^[59]. Recently, the white matter tract afferent from the ventral tegmental area, medial forebrain bundle, to the NAc was targeted for treatment-resistant depression with marked success^[146].

Amygdala and extended amygdalar complex

The amygdala is a brain nucleus that responds to novelty, salience and a variety of emotional stimuli. The amygdala

has been implicated as an important component of the neural network that underlies social behavior^[147]. The most commonly referenced role of the amygdala is in mediating fear and anxiety^[148]. The amygdala has been shown to be overactive in patients with both MDD and Bipolar Disorder^[149] and its activity is elevated in anticipatory anxiety in patients with generalized anxiety disorder^[150] and in contamination fear with OCD^[151]. Patients with Tourette appear to have altered functional connectivity of the amygdala^[152] as well as amygdala response to negative face pictures^[153,154]. Furthermore, the mean amygdala metabolism decreases in antidepressant treatment responders for depression, but persistence of elevated amygdala metabolism following remission is associated with a high risk for depressive relapse^[155].

DBS stimulation of the ALIC was shown to normalize baseline hyperactivity of the amygdala and trended towards significant correlation with reductions in YBOCS^[56], while this is not seen after anterior capsulotomy^[108]. Acutely (1 wk), there is an increase in amygdalar activity with NAc DBS^[66], which may explain the acute panic that has been observed^[156]. Reduction in amygdalar hyperactivity was correlated with response to chronic NAs DBS for depression and anxiety^[65]. In a functional connectivity analysis of NAc DBS, positive coupling was found with the amygdala^[13]. CM-Pf DBS in a large animal model demonstrated reductions in amygdalar signal which may explain some of the positive psychiatric improvements from CM-Pf DBS for TS^[27].

The bed nucleus of the stria terminalis (BNST) is part of the extended amygdaloid complex and a relay/integral regulator of the hypothalamic-pituitary-adrenal stress axis^[157,158]. The BNST is the major output of the basolateral (BL) amygdala and has been associated with sustained fear^[159]. Some have suggested that the bed nucleus of the stria terminalis has been responsible for the positive effects of DBS that was targeted at the VCVS^[160]. In a recent world-wide analysis, it was noted that when the "VCVS target" was shifted posterior (*i.e.*, closer to the BNST), lower voltages were required to achieve efficacy^[51].

The amygdala has been implicated in the pathogenesis of autism^[161] and its hyperarousal has been seen on fMRI^[162]. There is one case of BL amygdalar DBS, which was performed for self-injurious behavior in autism. In addition to improving self injurious behavior, DBS of the BL amygdala was found to improve the core symptoms of the autism spectrum in the emotional, social, and cognitive domains^[163].

Subthalamic nucleus

The sensorimotor STN has been demonstrated to be an efficacious target for the treatment of PD, although stimulation in this node can cause a range of neuropsychiatric symptoms^[164]. In addition to the sensorimotor region, the STN also has limbic and executive regions with segregated circuitry involved in affective and cognitive processes^[164]. Several PET studies have identified activity changes in limbic and executive regions during STN-DBS in Parkinson's patients,

including the dorsolateral prefrontal cortex and cingulate gyrus^[70,165,166]. The ventromedial or limbic STN has been demonstrated to have profound anti-OCD effects through two serendipitous findings where STN DBS treated both PD and OCD^[47].

Limbic STN DBS has been utilized successfully utilized for OCD^[54,55] and TS^[167]. Neuroimaging studies of the limbic and cognitive STN circuits have proven valuable, as these help with the STN DBS target refinement. Several of the STN DBS OCD patients underwent PET imaging^[58]. When compared to OFF stimulation, DBS ON resulted in reduction in activity of the cingulate, orbitofrontal cortex, and supplementary motor areas (BA 6). The cingulate and orbitofrontal cortex are major nodes in the emotional and executive networks and the SMA is intimately involved in OCD/TS pathophysiology as was described above. The cingulate, SMA, and orbitofrontal cortex are hyperfunctional in untreated OCD, suggesting that a possible mechanism of DBS action may be the normalization of the activity of the SMA, OFC and cingulate^[98,153,168,169].

Pallidum (globus pallidus interna, globus pallidus externa, and ventral pallidum)

The pallidal areas have been demonstrated to be immensely important in the treatment of movement disorders, such as Parkinson's disease. This target has been associated with much better neuropsychiatric side effect profiles for PD DBS than STN^[164]. The GPi has been implicated in the pathophysiology of TS^[170] and OCD^[171]. While the GPi has been implicated as a motor target, it is clear that the antero-medial portions of the GPi are limbic. In fact the ventral pallidum has been implicated to be the limbic pleasure generator^[172]. Both TS and OCD are successfully treated with GPi DBS^[68,173] and there has even been some report of mood improvement with GPi DBS^[174]. The globus pallidus externa has also been demonstrated to treat TS^[175]. Surprisingly, many of the functional imaging studies do not demonstrate changes in the pallidum with DBS^[26,50,63]. The exception is PET of patients with VCVS DBS^[57]. The efficacy of SCG DBS is optimized when the active contact interfaces with the white matter tract to the ventral pallidum^[47,94].

Thalamus

Centromedian nucleus of the thalamus and parafascicular complex: The CM-Pf nuclei complex is located in the posterior part of the intralaminar thalamus and serves as the main basal ganglia input station. Additionally, the CM-Pf controls striatal dopamine function and provides a majority of the thalamic input to the striatum^[176-178]. CM-Pf lesions have been shown to cause complex attention deficits. This has been hypothesized to be due to the role of the CM-Pf in directing attention to motivationally relevant stimuli^[179]. The CM-Pf DBS target has been utilized in TS, but has also been shown to have positive effects on mood, anxiety, and OCD^[180].

In addition to the striatum, the CM-Pf has been demonstrated to have connections with the amygdala^[181], hip-

poampus^[182], globus pallidus^[183], nucleus accumbens^[184], insular cortex, and anterior cingulate cortex^[176]. A recent large animal study looking at DBS-fMRI in the CM-Pf study was recently completed^[27]. In this study, DBS at the Pf was shown to have negative BOLD downstream effects on the hippocampus as well as the dorsal anterior cingulate cortex and posterior cingulate cortex. DBS at the CM was shown to have negative BOLD downstream effects on the sensorimotor areas and the associative area. The observed differences in structural connections of CM versus Pf in non-human primate topographical analyses were verified by this large animal CM-Pf DBS-fMRI study^[27]. The Pf has been demonstrated to innervate associative and limbic striatal areas^[185-187]. This large animal study also demonstrated a primarily limbic downstream effect with high frequency stimulation^[27]. Similarly, the CM innervates the sensorimotor striatal area^[185,188,189]. The large animal study also confirmed that the CM is has primarily sensorimotor downstream effects with high frequency stimulation^[27].

Medial dorsal thalamus

The limbic nucleus of the thalamus, the medial dorsal nucleus of the thalamus, is an important node in the limbic circuitry. Using high-resolution 7T fMRI, Metzger, et al. demonstrated general emotional arousal is localized to the mediodorsal nucleus while preceding attention and expectancy were localized to the intralaminar centromedian/parafascicular complex^[190]. A component of several of the frontal-striatal circuitry, the MD thalamus has been shown to be hyperactive in depression. In the depression associated with Parkinson's, volumetric studies have shown that the MD nucleus volume is larger than non-depressed controls, but hypoactive on the left in this population suggesting that the increase in volume is compensatory^[191]. There has been four cases where the MD was targeted for TS^[16,17]. In addition to improvement in TS symptoms, there was a hint of improvement in mood and obsessive thinking for at least one of these individuals^[16]. During chronic NAc stimulation, MD nucleus activity is reduced^[65]. This reduction in MD activity is also observed with ALIC stimulation^[56]. In large animal studies looking at porcine NAc DBS stim, similar reductions were seen^[26]. In a recent analysis of SCG DBS, tractography interfacing with the active contact was compared to presence or absence of remission and only individuals with white matter projections extending to the MD thalamus were able to achieve remission^[47]. It appears that the MD thalamus is a critical node in mood/affect regulation as well as mediating anxiety disorders.

OTHER MAGNETIC RESONANCE IMAGING TECHNIQUES

White matter tracts, tractography, and correct positioning

It is possible to non-invasively determine the anatomical connection pathways using diffusion tractography

imaging. These pathways are assumed to be consistent with known anatomy^[192,193]. This MRI technology has been utilized in determining the elements that contact and are stimulated with DBS^[194]. The benefits observed in patients with DBS appear to heavily depend on exact electrode position, which can only be truly verified with sophisticated tractography techniques^[94,95,146,194-196]. In the case of medial forebrain bundle DBS, the target can only be identified with sophisticated tractography imaging as one cannot visualize this target on conventional imaging^[146]. Slight alterations in the position of the electrode in the SCG appear to change whether this target is efficacious or not^[95]. The white matter tracts have to be completely intact for DBS to be efficacious where any alteration in the macroanatomy of the limbic white matter tracts can cause the stimulation to be ineffective^[197,198].

Conversely, verification of correct position with EpCS has been shown to only require a postoperative computed tomography (CT) scan coregistered with the presurgical MRI scan. This method will allow for all four contact electrodes on each paddle lead to be identified. In all 5 subjects of the Nahas study, contact electrodes were over the bilateral frontal pole and dorsolateral prefrontal cortex^[2]. In the Kopell study, the responders were noted to have the contacts of the electrodes placed at or anterior to the target site (DLPFC). Non-responders or partial responders had their electrodes placed posterior to the DLPFC target site^[3].

Functional connectivity analysis

Recent developments in noninvasive functional connectivity analysis demonstrate that this allows for a powerful network-level view of the neuropsychiatric disease^[199] and the effects DBS on that network^[13]. In this technique, the spontaneous fluctuations in BOLD are identified as the intrinsic marker for functional connectivity. A seed region is then identified and correlated with nodes in the connected neural network in an effort to determine areas where there is functional connectivity^[200]. The utility of this approach in DBS research comes from its ability to not only identify the aberrant functional connectivity of a particular neuropsychiatric disorder, but also normalize this aberrant functional connectivity through neuromodulation. This technique has been utilized to probe the resting state connectivity changes in patients receiving NAc DBS for OCD^[13]. In this study, the NAc DBS was shown to normalize aberrant hyperconnectivity between the NAc and lateral/medial prefrontal cortices. This reduction in connectivity correlated with the reductions in the YBOCS. While NAc is also a target for treatment-resistant depression (TRD) and TS, there have been no functional connectivity analysis studies in TRD and TS to date.

CONCLUSION

Invasive neuromodulation holds promise as a tool for treatment-resistant neuropsychiatric conditions^[47]. DBS

resides at an interface between neurophysiology, Neurosurgery, movement disorders Neurology, and interventional psychiatry^[201]. DBS has been demonstrated to be an effective therapy for essential tremor, dystonia and Parkinson's disease, and is being investigated in many other neuropsychiatric diseases^[47]. Advanced neuroimaging techniques aid in targeting, investigate the effects of, and further refine targeting of DBS all in a non-invasive manner. Although many of the functional imaging studies to date are limited to small case series and have had conflicting results, a growing trend is emerging. For most neuropsychiatric DBS imaging studies, the effects of DBS appears to have downstream effects on both cortical areas (DLPFC, FP, SCG, ACC, PCC, insula, SMA) as well as subcortical areas (thalamus, pallidum, STN, amygdala, striatum). These findings affirm that the therapeutic properties of DBS reside not only in local effects, but also downstream effects on the distributed neural network.

The effects and apparent efficacy of DBS for OCD appears to be related its downstream effects on the prefrontal cortex^[13], more specifically orbitofrontal cortex^[50,58]. This also appears to be true for invasive neuromodulation in treatment-resistant depression where the tractography and the functional imaging of depression DBS targets all converge on PFC^[13], more specifically Brodmann 10^[47,94-96]. Recent optogenetics findings have confirmed the critical role of the medial prefrontal cortex in mood regulation^[92]. While there has only been one study investigating the effects of direct BA 10 stimulation^[2], this technique appears remarkably durable^[85]. The critical role of the frontopolar cortex in mood regulation was further demonstrated when its activation was demonstrated to be associated with acute, stimulation-induced depressive symptoms in a patient with Parkinson's and a mispositioned lead^[31]. Furthermore, this cortical stimulation approach seems to avoid many of the methodological challenges seen with other techniques such as the need for advanced tractography^[95,146] and the risk of cerebral hemorrhage^[198]. The therapeutic effects of TS DBS appears to be correlated with the therapy's ability to reduce dopamine levels in various downstream targets^[17].

While the apparent efficacy of DBS for neuropsychiatric disease is promising, there are several remaining questions. Are cortical or subcortical targets better for invasive neuromodulation? Will sophisticated tractography techniques be essential to the widespread implementation of this therapy for TRD^[95,196,202]? How do symptom clusters of a given neuropsychiatric disease correlate with the pre-operative functional imaging and the DBS-induced functional activation? Will imaging eventually dictate the target with the best chance of efficacy? Will DBS move beyond its current role to affect plasticity^[203]? Will DBS confirm findings that the basal ganglia may in fact be organized in a gradient of medial to lateral where emotional/reward (most medial)-cognitive-and motor subcomponents of the nuclei are in fact highly interconnected.

As this field develops both scientifically and technically, we anticipate that larger studies will be conducted and our collective knowledge will converge. In addition to extending ongoing functional imaging studies in this area, future investigations will likely temporally pair functional MRI with information on structural integrity (including diffusion tensor imaging and voxel based morphometry) which will enable us to have a more comprehensive understanding of the effects of DBS on neural network integrity among DBS patients. Some disease specific issues to consider in future studies include inherent microstructural pathology in a given disease may influence the effect of DBS outcomes^[204,205], the role of acute vs chronic stimulation on neural network plasticity^[13], and baseline firing rates in areas downstream from the DBS target^[206]. DBS is an extremely nonselective method of stimulation and this non-specific nature may be harmful in one disorder^[207], while that same neural element being efficacious in treating another^[146]. Currently, imaging studies are unable to distinguishing between circuits of interest and those being activated unintentionally. Current steering technologies coupled with functional imaging will potentially allow for isolation of a single neural element and the ability to image that neural element^[208,209]. Such an approach when coupled with the selective circuit manipulation of optogenetics^[15] may allow for further verification of findings. It is truly an exciting time to be embarking on a journey into the interface between advanced imaging and invasive neuromodulation.

ACKNOWLEDGMENTS

We would also like to thank the Drug Abuse Research Track (DART) program at the Medical University of South Carolina with special thanks to Drs. Back and Brady, along with the grant that supports it [NIDA R25 DA020537-06 (PI's Back and Brady)].

REFERENCES

- 1 **Okun MS**, Oyama G. Mechanism of action for deep brain stimulation and electrical neuro-network modulation (ENM). *Rinsho Shinkeigaku* 2013; **53**: 691-694 [PMID: 24097315 DOI: 10.5692/clinicalneuro.53.691]
- 2 **Nahas Z**, Anderson BS, Borckardt J, Arana AB, George MS, Reeves ST, Takacs I. Bilateral epidural prefrontal cortical stimulation for treatment-resistant depression. *Biol Psychiatry* 2010; **67**: 101-109 [PMID: 19819427 DOI: 10.1016/j.biopsych.2009.08.021]
- 3 **Kopell BH**, Halverson J, Butson CR, Dickinson M, Bobholz J, Harsch H, Rainey C, Kondziolka D, Howland R, Eskandar E, Evans KC, Dougherty DD. Epidural cortical stimulation of the left dorsolateral prefrontal cortex for refractory major depressive disorder. *Neurosurgery* 2011; **69**: 1015-1029; discussion 1029 [PMID: 21709597 DOI: 10.1227/NEU.0b013e318229cfd]
- 4 **Benabid AL**, Pollak P, Louveau A, Henry S, de Rougemont J. Combined (thalamotomy and stimulation) stereotactic surgery of the VIM thalamic nucleus for bilateral Parkinson disease. *Appl Neurophysiol* 1987; **50**: 344-346 [PMID: 3329873 DOI: 10.1159/000100803]
- 5 **Nuttin B**, Cosyns P, Demeulemeester H, Gybels J, Meyerson B. Electrical stimulation in anterior limbs of internal capsules in patients with obsessive-compulsive disorder. *Lancet* 1999; **354**: 1526 [PMID: 10551504 DOI: 10.1016/S0140-6736(99)02376-4]
- 6 **Vandewalle V**, van der Linden C, Groenewegen HJ, Caemaert J. Stereotactic treatment of Gilles de la Tourette syndrome by high frequency stimulation of thalamus. *Lancet* 1999; **353**: 724 [PMID: 10073521 DOI: 10.1016/S0140-6736(98)05964-9]
- 7 **Hooper AK**, Okun MS, Foote KD, Fernandez HH, Jacobson C, Zeilman P, Romrell J, Rodriguez RL. Clinical cases where lesion therapy was chosen over deep brain stimulation. *Stereotact Funct Neurosurg* 2008; **86**: 147-152 [PMID: 18334856 DOI: 10.1159/000120426]
- 8 **Yang JC**, Ginat DT, Dougherty DD, Makris N, Eskandar EN. Lesion analysis for cingulotomy and limbic leucotomy: comparison and correlation with clinical outcomes. *J Neurosurg* 2014; **120**: 152-163 [PMID: 24236652 DOI: 10.3171/2013.9.JNS13839]
- 9 **Dougherty DD**, Baer L, Cosgrove GR, Cassem EH, Price BH, Nierenberg AA, Jenike MA, Rauch SL. Prospective long-term follow-up of 44 patients who received cingulotomy for treatment-refractory obsessive-compulsive disorder. *Am J Psychiatry* 2002; **159**: 269-275 [PMID: 11823270 DOI: 10.1176/appi.ajp.159.2.269]
- 10 **Le K**, Liu L, Sun M, Hu L, Xiao N. Transcranial magnetic stimulation at 1 Hertz improves clinical symptoms in children with Tourette syndrome for at least 6 months. *J Clin Neurosci* 2013; **20**: 257-262 [PMID: 23238046 DOI: 10.1016/j.jocn.2012.01.049]
- 11 **Berlim MT**, Neufeld NH, Van den Eynde F. Repetitive transcranial magnetic stimulation (rTMS) for obsessive-compulsive disorder (OCD): an exploratory meta-analysis of randomized and sham-controlled trials. *J Psychiatr Res* 2013; **47**: 999-1006 [PMID: 23615189 DOI: 10.1016/j.jpsy.2013.03.022]
- 12 **Ottowitz WE**, Dougherty DD, Savage CR. The neural network basis for abnormalities of attention and executive function in major depressive disorder: implications for application of the medical disease model to psychiatric disorders. *Harv Rev Psychiatry* 2002; **10**: 86-99 [PMID: 11897749 DOI: 10.1080/10673220216210]
- 13 **Figeo M**, Luigjes J, Smolders R, Valencia-Alfonso CE, van Wingen G, de Kwaastieniet B, Mantione M, Ooms P, de Koning P, Vulink N, Levar N, Droge L, van den Munckhof P, Schuurman PR, Nederveen A, van den Brink W, Mazaheri A, Vink M, Denys D. Deep brain stimulation restores frontostriatal network activity in obsessive-compulsive disorder. *Nat Neurosci* 2013; **16**: 386-387 [PMID: 23434914 DOI: 10.1038/nn.3344]
- 14 **Siebner HR**, Bergmann TO, Bestmann S, Massimini M, Johansen-Berg H, Mochizuki H, Bohning DE, Boorman ED, Groppa S, Miniussi C, Pascual-Leone A, Huber R, Taylor PC, Ilmoniemi RJ, De Gennaro L, Strafella AP, Kähkönen S, Klöppel S, Frisoni GB, George MS, Hallett M, Brandt SA, Rushworth MF, Ziemann U, Rothwell JC, Ward N, Cohen LG, Baudewig J, Paus T, Ugawa Y, Rossini PM. Consensus paper: combining transcranial stimulation with neuroimaging. *Brain Stimul* 2009; **2**: 58-80 [PMID: 20633405 DOI: 10.1016/j.brs.2008.11.002]
- 15 **Gradinaru V**, Mogri M, Thompson KR, Henderson JM, Deisseroth K. Optical deconstruction of parkinsonian neural circuitry. *Science* 2009; **324**: 354-359 [PMID: 19299587 DOI: 10.1126/science.1167093]
- 16 **Vernaleken I**, Kuhn J, Lenartz D, Raptis M, Huff W, Janouschek H, Neuner I, Schaefer WM, Gründer G, Sturm V. Bithalamic deep brain stimulation in tourette syndrome is associated with reduction in dopaminergic transmission. *Biol Psychiatry* 2009; **66**: e15-e17 [PMID: 19709645 DOI: 10.1016/j.biopsych.2009.06.025]

- 17 **Kuhn J**, Janouschek H, Raptis M, Rex S, Lenartz D, Neuner I, Mottaghy FM, Schneider F, Schaefer WM, Sturm V, Gründer G, Vernaleken I. In vivo evidence of deep brain stimulation-induced dopaminergic modulation in Tourette's syndrome. *Biol Psychiatry* 2012; **71**: e11-e13 [PMID: 22129758 DOI: 10.1016/j.biopsych.2011.09.035]
- 18 **George MS**, Ketter TA, Post RM. SPECT and PET imaging in mood disorders. *J Clin Psychiatry* 1993; **54** Suppl: 6-13 [PMID: 8270597]
- 19 **Varrone A**, Asenbaum S, Vander Borgh T, Booij J, Nobili F, Någren K, Darcourt J, Kapucu OL, Tatsch K, Bartenstein P, Van Laere K; European Association of Nuclear Medicine Neuroimaging Committee. EANM procedure guidelines for PET brain imaging using [18F]FDG, version 2. *Eur J Nucl Med Mol Imaging* 2009; **36**: 2103-2110 [PMID: 19838705 DOI: 10.1007/s00259-009-1264-0]
- 20 **Harris RE**, Clauw DJ, Scott DJ, McLean SA, Gracely RH, Zubieta JK. Decreased central mu-opioid receptor availability in fibromyalgia. *J Neurosci* 2007; **27**: 10000-10006 [PMID: 17855614 DOI: 10.1523/JNEUROSCI.2849-07.2007]
- 21 **Zubieta JK**, Smith YR, Bueller JA, Xu Y, Kilbourn MR, Jewett DM, Meyer CR, Koeppe RA, Stohler CS. Regional mu opioid receptor regulation of sensory and affective dimensions of pain. *Science* 2001; **293**: 311-315 [PMID: 11452128 DOI: 10.1126/science.1060952]
- 22 **George MS**, Ring HA, Costa DC, Ell PJ, Kouris K, Jarritt P. Neuroactivation and Neuroimaging with SPET. London: Springer-Verlag, 1991: 1-100
- 23 **Wyckhuys T**, De Geeter N, Crevecoeur G, Stroobants S, Staelens S. Quantifying the effect of repetitive transcranial magnetic stimulation in the rat brain by μ SPECT CBF scans. *Brain Stimul* 2013; **6**: 554-562 [PMID: 23127432 DOI: 10.1016/j.brs.2012.10.004]
- 24 **Ogawa S**, Lee TM, Kay AR, Tank DW. Brain magnetic resonance imaging with contrast dependent on blood oxygenation. *Proc Natl Acad Sci USA* 1990; **87**: 9868-9872 [PMID: 2124706 DOI: 10.1073/pnas.87.24.9868]
- 25 **Logothetis NK**, Pauls J, Augath M, Trinath T, Oeltermann A. Neurophysiological investigation of the basis of the fMRI signal. *Nature* 2001; **412**: 150-157 [PMID: 11449264 DOI: 10.1038/news010712-13]
- 26 **Knight EJ**, Min HK, Hwang SC, Marsh MP, Paek S, Kim I, Felmler JP, Abulseoud OA, Bennet KE, Frye MA, Lee KH. Nucleus accumbens deep brain stimulation results in insula and prefrontal activation: a large animal FMRI study. *PLoS One* 2013; **8**: e56640 [PMID: 23441210 DOI: 10.1371/journal.pone.0056640]
- 27 **Kim JP**, Min HK, Knight EJ, Duffy PS, Abulseoud OA, Marsh MP, Kelsey K, Blaha CD, Bennet KE, Frye MA, Lee KH. Centromedian-parafascicular deep brain stimulation induces differential functional inhibition of the motor, associative, and limbic circuits in large animals. *Biol Psychiatry* 2013; **74**: 917-926 [PMID: 23993641 DOI: 10.1016/j.biopsych.2013.06.024]
- 28 **Gupte AA**, Shrivastava D, Spaniol MA, Abosch A. MRI-related heating near deep brain stimulation electrodes: more data are needed. *Stereotact Funct Neurosurg* 2011; **89**: 131-140 [PMID: 21494064 DOI: 10.1159/000324906]
- 29 **Georgi JC**, Stippich C, Tronnier VM, Heiland S. Active deep brain stimulation during MRI: a feasibility study. *Magn Reson Med* 2004; **51**: 380-388 [PMID: 14755664 DOI: 10.1002/mrm.10699]
- 30 **Carmichael DW**, Pinto S, Limousin-Dowsey P, Thobois S, Allen PJ, Lemieux L, Yousry T, Thornton JS. Functional MRI with active, fully implanted, deep brain stimulation systems: safety and experimental confounds. *Neuroimage* 2007; **37**: 508-517 [PMID: 17590355 DOI: 10.1016/j.neuroimage.2007.04.058]
- 31 **Stefurak T**, Mikulis D, Mayberg H, Lang AE, Hevenor S, Pahapill P, Saint-Cyr J, Lozano A. Deep brain stimulation for Parkinson's disease dissociates mood and motor circuits: a functional MRI case study. *Mov Disord* 2003; **18**: 1508-1516 [PMID: 14673888 DOI: 10.1002/mds.10593]
- 32 **Arantes PR**, Cardoso EF, Barreiros MA, Teixeira MJ, Gonçalves MR, Barbosa ER, Sukwinder SS, Leite CC, Amaro E. Performing functional magnetic resonance imaging in patients with Parkinson's disease treated with deep brain stimulation. *Mov Disord* 2006; **21**: 1154-1162 [PMID: 16671094 DOI: 10.1002/mds.20912]
- 33 **Sestini S**, Ramat S, Formiconi AR, Ammannati F, Sorbi S, Pupi A. Brain networks underlying the clinical effects of long-term subthalamic stimulation for Parkinson's disease: a 4-year follow-up study with rCBF SPECT. *J Nucl Med* 2005; **46**: 1444-1454 [PMID: 16157526]
- 34 **Pourfar M**, Tang C, Lin T, Dhawan V, Kaplitt MG, Eidelberg D. Assessing the microlesion effect of subthalamic deep brain stimulation surgery with FDG PET. *J Neurosurg* 2009; **110**: 1278-1282 [PMID: 19301972 DOI: 10.3171/2008.12.JNS08991]
- 35 **Rozanski VE**, Lieb M, Vollmar C, Mehrkens JH, Bötzel K. Evidence of a non-motor microlesion effect following deep brain surgery: a case report. *Acta Neurochir (Wien)* 2012; **154**: 835-838 [PMID: 22281733 DOI: 10.1007/s00701-012-1281-9]
- 36 **Lefaucheur R**, Derrey S, Martinaud O, Wallon D, Chastan N, Gérardin E, Hannequin D, Maltête D. Early verbal fluency decline after STN implantation: is it a cognitive microlesion effect? *J Neurol Sci* 2012; **321**: 96-99 [PMID: 22846795 DOI: 10.1016/j.jns.2012.07.033]
- 37 **Swan BD**, Grill WM, Turner DA. Investigation of deep brain stimulation mechanisms during implantable pulse generator replacement surgery. *Neuromodulation* 2014; **17**: 419-424 [PMID: 24118257 DOI: 10.1111/ner.12123]
- 38 **Rezai AR**, Baker KB, Tkach JA, Phillips M, Hrdlicka G, Sharan AD, Nyenhuis J, Ruggieri P, Shellock FG, Henderson J. Is magnetic resonance imaging safe for patients with neurostimulation systems used for deep brain stimulation? *Neurosurgery* 2005; **57**: 1056-1062; discussion 1056-1062 [PMID: 16284576 DOI: 10.1227/01.NEU.0000186935.87971.2a]
- 39 **Rezai AR**, Phillips M, Baker KB, Sharan AD, Nyenhuis J, Tkach J, Henderson J, Shellock FG. Neurostimulation system used for deep brain stimulation (DBS): MR safety issues and implications of failing to follow safety recommendations. *Invest Radiol* 2004; **39**: 300-303 [PMID: 15087724 DOI: 10.1097/01.rli.0000124940.02340.ab]
- 40 **Wang Z**, Maia TV, Marsh R, Colibazzi T, Gerber A, Peterson BS. The neural circuits that generate tics in Tourette's syndrome. *Am J Psychiatry* 2011; **168**: 1326-1337 [PMID: 21955933 DOI: 10.1176/appi.ajp.2011.09111692]
- 41 **Giller C**, Mehta S, Yanasak N, Jenkins P. Avoidance of electrode related MRI artifact during staged deep brain stimulator implantation. *J Neurol Surg A Cent Eur Neurosurg* 2012; **73**: 320-323 [PMID: 22847067 DOI: 10.1055/s-0032-1322590]
- 42 **Rezai AR**, Lozano AM, Crawley AP, Joy ML, Davis KD, Kwan CL, Dostrovsky JO, Tasker RR, Mikulis DJ. Thalamic stimulation and functional magnetic resonance imaging: localization of cortical and subcortical activation with implanted electrodes. Technical note. *J Neurosurg* 1999; **90**: 583-590 [PMID: 10067936 DOI: 10.3171/jns.1999.90.3.0583]
- 43 **Kahan J**, Mancini L, Urner M, Friston K, Hariz M, Holl E, White M, Ruge D, Jahanshahi M, Boertien T, Yousry T, Thornton JS, Limousin P, Zrinzo L, Foltynie T. Therapeutic subthalamic nucleus deep brain stimulation reverses cortico-thalamic coupling during voluntary movements in Parkinson's disease. *PLoS One* 2012; **7**: e50270 [PMID: 23300524 DOI: 10.1371/journal.pone.0050270]
- 44 **Liu HL**, Chen HM, Wu YC, Lim SN, Huang CM, Hsu YY, Wai YY, Wu T. False-positive analysis of functional MRI during simulated deep brain stimulation: a phantom study. *J Magn Reson Imaging* 2008; **27**: 1439-1442 [PMID: 18504733 DOI: 10.1002/jmri.21222]

- 45 **Chhabra V**, Sung E, Mewes K, Bakay RA, Abosch A, Gross RE. Safety of magnetic resonance imaging of deep brain stimulator systems: a serial imaging and clinical retrospective study. *J Neurosurg* 2010; **112**: 497-502 [PMID: 19681685 DOI: 10.3171/2009.7.JNS09572]
- 46 **Jech R**, Urgosík D, Tintera J, Nebuzelský A, Krásenský J, Liscák R, Roth J, Růzicka E. Functional magnetic resonance imaging during deep brain stimulation: a pilot study in four patients with Parkinson's disease. *Mov Disord* 2001; **16**: 1126-1132 [PMID: 11748747 DOI: 10.1002/mds.1217]
- 47 **Williams NR**, Okun MS. Deep brain stimulation (DBS) at the interface of neurology and psychiatry. *J Clin Invest* 2013; **123**: 4546-4556 [PMID: 24177464 DOI: 10.1172/JCI68341]
- 48 **Huff W**, Lenartz D, Schormann M, Lee SH, Kuhn J, Koulousakis A, Mai J, Daumann J, Maarouf M, Klosterkötter J, Sturm V. Unilateral deep brain stimulation of the nucleus accumbens in patients with treatment-resistant obsessive-compulsive disorder: Outcomes after one year. *Clin Neurol Neurosurg* 2010; **112**: 137-143 [PMID: 20006424 DOI: 10.1016/j.clineuro.2009.11.006]
- 49 **Denys D**, Mantione M, Figeé M, van den Munckhof P, Koerselman F, Westenberg H, Bosch A, Schuurman R. Deep brain stimulation of the nucleus accumbens for treatment-refractory obsessive-compulsive disorder. *Arch Gen Psychiatry* 2010; **67**: 1061-1068 [PMID: 20921122 DOI: 10.1001/archgenpsychiatry.2010.122]
- 50 **Abelson JL**, Curtis GC, Sagher O, Albucher RC, Harrigan M, Taylor SF, Martis B, Giordani B. Deep brain stimulation for refractory obsessive-compulsive disorder. *Biol Psychiatry* 2005; **57**: 510-516 [PMID: 15737666 DOI: 10.1016/j.biopsych.2004.11.042]
- 51 **Greenberg BD**, Gabriels LA, Malone DA, Rezai AR, Friehs GM, Okun MS, Shapira NA, Foote KD, Cosyns PR, Kubu CS, Malloy PF, Salloway SP, Giftakis JE, Rise MT, Machado AG, Baker KB, Stypulkowski PH, Goodman WK, Rasmussen SA, Nuttin BJ. Deep brain stimulation of the ventral internal capsule/ventral striatum for obsessive-compulsive disorder: worldwide experience. *Mol Psychiatry* 2010; **15**: 64-79 [PMID: 18490925 DOI: 10.1038/mp.2008.55]
- 52 **Greenberg BD**, Malone DA, Friehs GM, Rezai AR, Kubu CS, Malloy PF, Salloway SP, Okun MS, Goodman WK, Rasmussen SA. Three-year outcomes in deep brain stimulation for highly resistant obsessive-compulsive disorder. *Neuropsychopharmacology* 2006; **31**: 2384-2393 [PMID: 16855529 DOI: 10.1038/sj.npp.1301165]
- 53 **Goodman WK**, Foote KD, Greenberg BD, Ricciuti N, Bauer R, Ward H, Shapira NA, Wu SS, Hill CL, Rasmussen SA, Okun MS. Deep brain stimulation for intractable obsessive compulsive disorder: pilot study using a blinded, staggered-onset design. *Biol Psychiatry* 2010; **67**: 535-542 [PMID: 20116047 DOI: 10.1016/j.biopsych.2009.11.028]
- 54 **Chabardès S**, Polosan M, Krack P, Bastin J, Krainik A, David O, Bougerol T, Benabid AL. Deep brain stimulation for obsessive-compulsive disorder: subthalamic nucleus target. *World Neurosurg* 2013; **80**: S31.e1-S31.e8 [PMID: 22469523 DOI: 10.1016/j.wneu.2012.03.010]
- 55 **Mallet L**, Polosan M, Jaafari N, Baup N, Welter ML, Fontaine D, du Montcel ST, Yelnik J, Chéreau I, Arbus C, Raoul S, Aouizerate B, Damier P, Chabardès S, Czernecki V, Ardouin C, Krebs MO, Bardinet E, Chaynes P, Burbaud P, Cornu P, Derost P, Bougerol T, Bataille B, Mattei V, Dormont D, Devaux B, Vérin M, Houeto JL, Pollak P, Benabid AL, Agid Y, Krack P, Millet B, Pelissolo A. Subthalamic nucleus stimulation in severe obsessive-compulsive disorder. *N Engl J Med* 2008; **359**: 2121-2134 [PMID: 19005196 DOI: 10.1056/NEJMoa0708514]
- 56 **Van Laere K**, Nuttin B, Gabriels L, Dupont P, Rasmussen S, Greenberg BD, Cosyns P. Metabolic imaging of anterior capsular stimulation in refractory obsessive-compulsive disorder: a key role for the subgenual anterior cingulate and ventral striatum. *J Nucl Med* 2006; **47**: 740-747 [PMID: 16644742]
- 57 **Rauch SL**, Dougherty DD, Malone D, Rezai A, Friehs G, Fischman AJ, Alpert NM, Haber SN, Stypulkowski PH, Rise MT, Rasmussen SA, Greenberg BD. A functional neuroimaging investigation of deep brain stimulation in patients with obsessive-compulsive disorder. *J Neurosurg* 2006; **104**: 558-565 [PMID: 16619660 DOI: 10.3171/jns.2006.104.4.558]
- 58 **Le Jeune F**, Vérin M, N'Diaye K, Drapier D, Leray E, Du Montcel ST, Baup N, Pelissolo A, Polosan M, Mallet L, Yelnik J, Devaux B, Fontaine D, Chéreau I, Bourguignon A, Peron J, Sauleau P, Raoul S, Garin E, Krebs MO, Jaafari N, Millet B. Decrease of prefrontal metabolism after subthalamic stimulation in obsessive-compulsive disorder: a positron emission tomography study. *Biol Psychiatry* 2010; **68**: 1016-1022 [PMID: 20951978 DOI: 10.1016/j.biopsych.2010.06.033]
- 59 **Sturm V**, Lenartz D, Koulousakis A, Treuer H, Herholz K, Klein JC, Klosterkötter J. The nucleus accumbens: a target for deep brain stimulation in obsessive-compulsive- and anxiety-disorders. *J Chem Neuroanat* 2003; **26**: 293-299 [PMID: 14729131 DOI: 10.1007/978-3-540-32746-2_16]
- 60 **Williams N**, Simpson AN, Simpson K, Nahas Z. Relapse rates with long-term antidepressant drug therapy: a meta-analysis. *Hum Psychopharmacol* 2009; **24**: 401-408 [PMID: 19526453 DOI: 10.1002/hup.1033]
- 61 **Brunoni AR**, Valiengo L, Baccaro A, Zanão TA, de Oliveira JF, Goulart A, Boggio PS, Lotufo PA, Benseñor IM, Fregni F. The sertraline vs. electrical current therapy for treating depression clinical study: results from a factorial, randomized, controlled trial. *JAMA Psychiatry* 2013; **70**: 383-391 [PMID: 23389323]
- 62 **Schlaepfer TE**, George MS, Mayberg H. WFSBP Guidelines on Brain Stimulation Treatments in Psychiatry. *World J Biol Psychiatry* 2010; **11**: 2-18 [PMID: 20146648 DOI: 10.3109/15622970903170835]
- 63 **Mayberg HS**, Lozano AM, Voon V, McNeely HE, Semnowicz D, Hamani C, Schwalb JM, Kennedy SH. Deep brain stimulation for treatment-resistant depression. *Neuron* 2005; **45**: 651-660 [PMID: 15748841 DOI: 10.1016/j.neuron.2005.02.014]
- 64 **Lozano AM**, Mayberg HS, Giacobbe P, Hamani C, Craddock RC, Kennedy SH. Subcallosal cingulate gyrus deep brain stimulation for treatment-resistant depression. *Biol Psychiatry* 2008; **64**: 461-467 [PMID: 18639234 DOI: 10.1016/j.biopsych.2008.05.034]
- 65 **Bewernick BH**, Hurlmann R, Matusch A, Kayser S, Grubert C, Hadrysiwicz B, Axmacher N, Lemke M, Cooper-Mahkorn D, Cohen MX, Brockmann H, Lenartz D, Sturm V, Schlaepfer TE. Nucleus accumbens deep brain stimulation decreases ratings of depression and anxiety in treatment-resistant depression. *Biol Psychiatry* 2010; **67**: 110-116 [PMID: 19914605 DOI: 10.1016/j.biopsych.2009.09.013]
- 66 **Schlaepfer TE**, Cohen MX, Frick C, Kosel M, Brodesser D, Axmacher N, Joe AY, Kreft M, Lenartz D, Sturm V. Deep brain stimulation to reward circuitry alleviates anhedonia in refractory major depression. *Neuropsychopharmacology* 2008; **33**: 368-377 [PMID: 17429407 DOI: 10.1038/sj.npp.1301408]
- 67 **Porta M**, Brambilla A, Cavanna AE, Servello D, Sassi M, Rickards H, Robertson MM. Thalamic deep brain stimulation for treatment-refractory Tourette syndrome: two-year outcome. *Neurology* 2009; **73**: 1375-1380 [PMID: 19858459 DOI: 10.1212/WNL.0b013e3181bd809b]
- 68 **Cannon E**, Silburn P, Coyne T, O'Maley K, Crawford JD, Sachdev PS. Deep brain stimulation of anteromedial globus pallidus interna for severe Tourette's syndrome. *Am J Psychiatry* 2012; **169**: 860-866 [PMID: 22772329 DOI: 10.1176/appi.ajp.2012.11101583]
- 69 **Sachdev PS**, Cannon E, Coyne TJ, Silburn P. Bilateral deep

- brain stimulation of the nucleus accumbens for comorbid obsessive compulsive disorder and Tourette's syndrome. *BMJ Case Rep* 2012; **2012**: [PMID: 22977057 DOI: 10.1136/bcr-2012-006579]
- 70 **Limousin P**, Greene J, Pollak P, Rothwell J, Benabid AL, Frackowiak R. Changes in cerebral activity pattern due to subthalamic nucleus or internal pallidum stimulation in Parkinson's disease. *Ann Neurol* 1997; **42**: 283-291 [PMID: 9307248 DOI: 10.1002/ana.410420303]
- 71 **Min HK**, Hwang SC, Marsh MP, Kim I, Knight E, Striemer B, Felmlee JP, Welker KM, Blaha CD, Chang SY, Bennet KE, Lee KH. Deep brain stimulation induces BOLD activation in motor and non-motor networks: an fMRI comparison study of STN and EN/GPi DBS in large animals. *Neuroimage* 2012; **63**: 1408-1420 [PMID: 22967832 DOI: 10.1016/j.neuroimage.2012.08.006]
- 72 **Cieslik EC**, Zilles K, Caspers S, Roski C, Kellermann TS, Jakobs O, Langner R, Laird AR, Fox PT, Eickhoff SB. Is there "one" DLPFC in cognitive action control? Evidence for heterogeneity from co-activation-based parcellation. *Cereb Cortex* 2013; **23**: 2677-2689 [PMID: 22918987 DOI: 10.1093/cercor/bhs256]
- 73 **Bonelli RM**, Cummings JL. Frontal-subcortical circuitry and behavior. *Dialogues Clin Neurosci* 2007; **9**: 141-51 [PMID: 17726913]
- 74 **Fuster JM**. The prefrontal cortex. 4th ed. Amsterdam; Boston: Academic Press/Elsevier, 2008: 293
- 75 **Kober H**, Barrett LF, Joseph J, Bliss-Moreau E, Lindquist K, Wager TD. Functional grouping and cortical-subcortical interactions in emotion: a meta-analysis of neuroimaging studies. *Neuroimage* 2008; **42**: 998-1031 [PMID: 18579414 DOI: 10.1016/j.neuroimage.2008.03.059]
- 76 **Lévesque J**, Eugène F, Joannette Y, Paquette V, Mensour B, Beaudoin G, Leroux JM, Bourgouin P, Beauregard M. Neural circuitry underlying voluntary suppression of sadness. *Biol Psychiatry* 2003; **53**: 502-510 [PMID: 12644355 DOI: 10.1016/S0002-3223(03)01817-6]
- 77 **Grimm S**, Beck J, Schuepbach D, Hell D, Boesiger P, Bermanpohl F, Niehaus L, Boeker H, Northoff G. Imbalance between left and right dorsolateral prefrontal cortex in major depression is linked to negative emotional judgment: an fMRI study in severe major depressive disorder. *Biol Psychiatry* 2008; **63**: 369-376 [PMID: 17888408 DOI: 10.1016/j.biopsych.2007.05.033]
- 78 **Klein JC**, Rushworth MF, Behrens TE, Mackay CE, de Crespigny AJ, D'Arceuil H, Johansen-Berg H. Topography of connections between human prefrontal cortex and mediodorsal thalamus studied with diffusion tractography. *Neuroimage* 2010; **51**: 555-564 [PMID: 20206702 DOI: 10.1016/j.neuroimage.2010.02.062]
- 79 **Leh SE**, Ptito A, Chakravarty MM, Strafella AP. Frontostriatal connections in the human brain: a probabilistic diffusion tractography study. *Neurosci Lett* 2007; **419**: 113-118 [PMID: 17485168 DOI: 10.1016/j.neulet.2007.04.049]
- 80 **Goldman-Rakic PS**, Selemon LD, Schwartz ML. Dual pathways connecting the dorsolateral prefrontal cortex with the hippocampal formation and parahippocampal cortex in the rhesus monkey. *Neuroscience* 1984; **12**: 719-743 [PMID: 6472617 DOI: 10.1016/0306-4522(84)90166-0]
- 81 **Fox MD**, Buckner RL, White MP, Greicius MD, Pascual-Leone A. Efficacy of transcranial magnetic stimulation targets for depression is related to intrinsic functional connectivity with the subgenual cingulate. *Biol Psychiatry* 2012; **72**: 595-603 [PMID: 22658708 DOI: 10.1016/j.biopsych.2012.04.028]
- 82 **Selemon LD**, Goldman-Rakic PS. Common cortical and subcortical targets of the dorsolateral prefrontal and posterior parietal cortices in the rhesus monkey: evidence for a distributed neural network subserving spatially guided behavior. *J Neurosci* 1988; **8**: 4049-4068 [PMID: 2846794]
- 83 **Kimbrell TA**, Little JT, Dunn RT, Frye MA, Greenberg BD, Wassermann EM, Repella JD, Danielson AL, Willis MW, Benson BE, Speer AM, Osuch E, George MS, Post RM. Frequency dependence of antidepressant response to left prefrontal repetitive transcranial magnetic stimulation (rTMS) as a function of baseline cerebral glucose metabolism. *Biol Psychiatry* 1999; **46**: 1603-1613 [PMID: 10624541 DOI: 10.1016/S0006-3223(99)00195-X]
- 84 **Fox MD**, Liu H, Pascual-Leone A. Identification of reproducible individualized targets for treatment of depression with TMS based on intrinsic connectivity. *Neuroimage* 2012; **66C**: 151-160 [PMID: 23142067 DOI: 10.1016/j.neuroimage.2012.10.082]
- 85 **Williams NR**, Short EB, Borckardt JJ, Schmidt M, Jeffery A, Korte JE, George MS, Takacs I, Nahas ZH. Five-Year Follow-up of Bilateral Epidural Prefrontal Cortical Stimulation for Treatment-Resistant Depression [Conference Poster]. *Biol Psychiatry* 2014
- 86 **Koechlin E**. Frontal pole function: what is specifically human? *Trends Cogn Sci* 2011; **15**: 241; author reply 3 [PMID: 21601507 DOI: 10.1016/j.tics.2011.04.005]
- 87 **Koechlin E**, Hyafil A. Anterior prefrontal function and the limits of human decision-making. *Science* 2007; **318**: 594-598 [PMID: 17962551 DOI: 10.1126/science.1142995]
- 88 **Johnson MK**, Raye CL, Mitchell KJ, Touryan SR, Greene EJ, Nolen-Hoeksema S. Dissociating medial frontal and posterior cingulate activity during self-reflection. *Soc Cogn Affect Neurosci* 2006; **1**: 56-64 [PMID: 18574518 DOI: 10.1093/scan/nsl004]
- 89 **Addis DR**, Wong AT, Schacter DL. Remembering the past and imagining the future: common and distinct neural substrates during event construction and elaboration. *Neuropsychologia* 2007; **45**: 1363-1377 [PMID: 17126370 DOI: 10.1016/j.neuropsychologia.2006.10.016]
- 90 **Dreher JC**, Koechlin E, Tierney M, Grafman J. Damage to the fronto-polar cortex is associated with impaired multitasking. *PLoS One* 2008; **3**: e3227 [PMID: 18795100 DOI: 10.1371/journal.pone.0003227]
- 91 **Hamani C**, Diwan M, Isabella S, Lozano AM, Nobrega JN. Effects of different stimulation parameters on the antidepressant-like response of medial prefrontal cortex deep brain stimulation in rats. *J Psychiatr Res* 2010; **44**: 683-687 [PMID: 20096858 DOI: 10.1016/j.jpsychires.2009.12.010]
- 92 **Covington HE**, Lobo MK, Maze I, Vialou V, Hyman JM, Zaman S, LaPlant Q, Mouzon E, Ghose S, Tamminga CA, Neve RL, Deisseroth K, Nestler EJ. Antidepressant effect of optogenetic stimulation of the medial prefrontal cortex. *J Neurosci* 2010; **30**: 16082-16090 [PMID: 21123555 DOI: 10.1523/JNEUROSCI.1731-10.2010]
- 93 **Fitzgerald PB**, Laird AR, Maller J, Daskalakis ZJ. A meta-analytic study of changes in brain activation in depression. *Hum Brain Mapp* 2008; **29**: 683-695 [PMID: 17598168 DOI: 10.1002/hbm.20426]
- 94 **Mayberg H**, editor Optimizing Subcallosal Cingulate DBS for Treatment Resistant Depression [Conference Poster]. Society of Biological Psychiatry; 2013 May 1, 2013; San Francisco, Ca: Biol Psychiatry
- 95 **Lujan JL**, Chaturvedi A, Choi KS, Holtzheimer PE, Gross RE, Mayberg HS, McIntyre CC. Tractography-activation models applied to subcallosal cingulate deep brain stimulation. *Brain Stimul* 2013; **6**: 737-739 [PMID: 23602025 DOI: 10.1016/j.brs.2013.03.008]
- 96 **Gutman DA**, Holtzheimer PE, Behrens TE, Johansen-Berg H, Mayberg HS. A tractography analysis of two deep brain stimulation white matter targets for depression. *Biol Psychiatry* 2009; **65**: 276-282 [PMID: 19013554 DOI: 10.1016/j.biopsych.2008.09.021]
- 97 **Sesack SR**, Grace AA. Cortico-Basal Ganglia reward net-

- 10.3171/2012.11.JNS12389]
- 125 **Leech R**, Sharp DJ. The role of the posterior cingulate cortex in cognition and disease. *Brain* 2014; **137**: 12-32 [PMID: 23869106 DOI: 10.1093/brain/awt162]
 - 126 **Mayberg HS**, Liotti M, Brannan SK, McGinnis S, Mahurin RK, Jerabek PA, Silva JA, Tekell JL, Martin CC, Lancaster JL, Fox PT. Reciprocal limbic-cortical function and negative mood: converging PET findings in depression and normal sadness. *Am J Psychiatry* 1999; **156**: 675-682 [PMID: 10327898]
 - 127 **Saxena S**, Brody AL, Maidment KM, Smith EC, Zohrabi N, Katz E, Baker SK, Baxter LR. Cerebral glucose metabolism in obsessive-compulsive hoarding. *Am J Psychiatry* 2004; **161**: 1038-1048 [PMID: 15169692 DOI: 10.1176/appi.ajp.161.6.1038]
 - 128 **Rauch SL**, Dougherty DD, Cosgrove GR, Cassem EH, Alpert NM, Price BH, Nierenberg AA, Mayberg HS, Baer L, Jenike MA, Fischman AJ. Cerebral metabolic correlates as potential predictors of response to anterior cingulotomy for obsessive compulsive disorder. *Biol Psychiatry* 2001; **50**: 659-667 [PMID: 11704072 DOI: 10.1016/S0006-3223(01)01188-X]
 - 129 **Mataix-Cols D**, Cullen S, Lange K, Zelaya F, Andrew C, Amaro E, Brammer MJ, Williams SC, Speckens A, Phillips ML. Neural correlates of anxiety associated with obsessive-compulsive symptom dimensions in normal volunteers. *Biol Psychiatry* 2003; **53**: 482-493 [PMID: 12644353]
 - 130 **McGrath CL**, Kelley ME, Holtzheimer PE, Dunlop BW, Craighead WE, Franco AR, Craddock RC, Mayberg HS. Toward a neuroimaging treatment selection biomarker for major depressive disorder. *JAMA Psychiatry* 2013; **70**: 821-829 [PMID: 23760393 DOI: 10.1001/jamapsychiatry.2013.143]
 - 131 **Stein DJ**, Arya M, Pietrini P, Rapoport JL, Swedo SE. Neurocircuitry of disgust and anxiety in obsessive-compulsive disorder: a positron emission tomography study. *Metab Brain Dis* 2006; **21**: 267-277 [PMID: 16850255 DOI: 10.1007/s11011-006-9021-6]
 - 132 **Stern E**, Silbersweig DA, Chee KY, Holmes A, Robertson MM, Trimble M, Frith CD, Frackowiak RS, Dolan RJ. A functional neuroanatomy of tics in Tourette syndrome. *Arch Gen Psychiatry* 2000; **57**: 741-748 [PMID: 10920461]
 - 133 **de Wit SJ**, de Vries FE, van der Werf YD, Cath DC, Helsenfeld DJ, Veltman EM, van Balkom AJ, Veltman DJ, van den Heuvel OA. Presupplementary motor area hyperactivity during response inhibition: a candidate endophenotype of obsessive-compulsive disorder. *Am J Psychiatry* 2012; **169**: 1100-1108 [PMID: 23032388 DOI: 10.1176/appi.ajp.2012.12010073]
 - 134 **Bannur U**, Rajshankar V. Post operative supplementary motor area syndrome: clinical features and outcome. *Br J Neurosurg* 2000; **14**: 204-210 [PMID: 10912196 DOI: 10.1080/026886900408379]
 - 135 **Groenewegen HJ**, Wright CI, Beijer AV, Voorn P. Convergence and segregation of ventral striatal inputs and outputs. *Ann N Y Acad Sci* 1999; **877**: 49-63 [PMID: 10415642 DOI: 10.1111/j.1749-6632.1999.tb09260.x]
 - 136 **Voorn P**, Vanderschuren LJ, Groenewegen HJ, Robbins TW, Pennartz CM. Putting a spin on the dorsal-ventral divide of the striatum. *Trends Neurosci* 2004; **27**: 468-474 [PMID: 15271494 DOI: 10.1016/j.tins.2004.06.006]
 - 137 **Kuhn J**, Lenartz D, Mai JK, Huff W, Lee SH, Koulousakis A, Klosterkoetter J, Sturm V. Deep brain stimulation of the nucleus accumbens and the internal capsule in therapeutically refractory Tourette-syndrome. *J Neurol* 2007; **254**: 963-965 [PMID: 17410328 DOI: 10.1007/s00415-006-0404-8]
 - 138 **Kuhn J**, Lenartz D, Huff W, Lee S, Koulousakis A, Klosterkoetter J, Sturm V. Remission of alcohol dependency following deep brain stimulation of the nucleus accumbens: valuable therapeutic implications? *J Neurol Neurosurg Psychiatry* 2007; **78**: 1152-1153 [PMID: 17878197 DOI: 10.1136/jnnp.2006.113092]
 - 139 **Müller UJ**, Voges J, Steiner J, Galazky I, Heinze HJ, Möller M, Pisapia J, Halpern C, Caplan A, Bogerts B, Kuhn J. Deep brain stimulation of the nucleus accumbens for the treatment of addiction. *Ann N Y Acad Sci* 2013; **1282**: 119-128 [PMID: 23227826 DOI: 10.1111/j.1749-6632.2012.06834.x]
 - 140 **Kuhn J**, Möller M, Treppmann JF, Bartsch C, Lenartz D, Gruendler TO, Maarouf M, Brosig A, Barnikol UB, Klosterkötter J, Sturm V. Deep brain stimulation of the nucleus accumbens and its usefulness in severe opioid addiction. *Mol Psychiatry* 2014; **19**: 145-146 [PMID: 23337942 DOI: 10.1038/mp.2012.196]
 - 141 **Heldmann M**, Berding G, Voges J, Bogerts B, Galazky I, Müller U, Baillet G, Heinze HJ, Münte TF. Deep brain stimulation of nucleus accumbens region in alcoholism affects reward processing. *PLoS One* 2012; **7**: e36572 [PMID: 22629317 DOI: 10.1371/journal.pone.0036572]
 - 142 **Voges J**, Müller U, Bogerts B, Münte T, Heinze HJ. Deep brain stimulation surgery for alcohol addiction. *World Neurosurg* 2012; **80**: S28.e21-S28.e31 [PMID: 22824557 DOI: 10.1016/j.wneu.2012.07.011]
 - 143 **Wu H**, Van Dyck-Lippens PJ, Santegoeds R, van Kuyck K, Gabriëls L, Lin G, Pan G, Li Y, Li D, Zhan S, Sun B, Nuttin B. Deep-brain stimulation for anorexia nervosa. *World Neurosurg* 2013; **80**: S29.e1-S29.10 [PMID: 22743198 DOI: 10.1016/j.wneu.2012.06.039]
 - 144 **Plow EB**, Malone DA, Machado A. Deep brain stimulation of the ventral striatum/anterior limb of the internal capsule in thalamic pain syndrome: study protocol for a pilot randomized controlled trial. *Trials* 2013; **14**: 241 [PMID: 23902631 DOI: 10.1186/1745-6215-14-241]
 - 145 **Aouizerate B**, Cuny E, Martin-Guehl C, Guehl D, Amieva H, Benazzouz A, Fabrigoule C, Allard M, Rougier A, Bioulac B, Tignol J, Burbaud P. Deep brain stimulation of the ventral caudate nucleus in the treatment of obsessive-compulsive disorder and major depression. Case report. *J Neurosurg* 2004; **101**: 682-686 [PMID: 15481726 DOI: 10.1176/appi.ajp.162.11.2192]
 - 146 **Schlaepfer TE**, Bewernick BH, Kayser S, Mädler B, Coenen VA. Rapid effects of deep brain stimulation for treatment-resistant major depression. *Biol Psychiatry* 2013; **73**: 1204-1212 [PMID: 23562618 DOI: 10.1016/j.biopsych.2013.01.034]
 - 147 **Adolphs R**. Social cognition and the human brain. *Trends Cogn Sci* 1999; **3**: 469-479 [PMID: 10562726 DOI: 10.1016/S1364-6613(99)01399-6]
 - 148 **Davis M**, Whalen PJ. The amygdala: vigilance and emotion. *Mol Psychiatry* 2001; **6**: 13-34 [PMID: 11244481 DOI: 10.1038/sj.mp.4000812]
 - 149 **Drevets WC**, Price JL, Bardgett ME, Reich T, Todd RD, Raichle ME. Glucose metabolism in the amygdala in depression: relationship to diagnostic subtype and plasma cortisol levels. *Pharmacol Biochem Behav* 2002; **71**: 431-447 [PMID: 11830178 DOI: 10.1016/S0091-3057(01)00687-6]
 - 150 **Nitschke JB**, Sarinopoulos I, Oathes DJ, Johnstone T, Whalen PJ, Davidson RJ, Kalin NH. Anticipatory activation in the amygdala and anterior cingulate in generalized anxiety disorder and prediction of treatment response. *Am J Psychiatry* 2009; **166**: 302-310 [PMID: 19122007 DOI: 10.1176/appi.ajp.2008.07101682]
 - 151 **van den Heuvel OA**, Veltman DJ, Groenewegen HJ, Dolan RJ, Cath DC, Boellaard R, Mesina CT, van Balkom AJ, van Oppen P, Witter MP, Lammertsma AA, van Dyck R. Amygdala activity in obsessive-compulsive disorder with contamination fear: a study with oxygen-15 water positron emission tomography. *Psychiatry Res* 2004; **132**: 225-237 [PMID: 15664794 DOI: 10.1016/j.psychres.2004.06.007]
 - 152 **Werner CJ**, Stöcker T, Kellermann T, Wegener HP, Schneider F, Shah NJ, Neuner I. Altered amygdala functional connectivity in adult Tourette's syndrome. *Eur Arch Psychiatry Clin Neurosci* 2010; **260** Suppl 2: S95-S99 [PMID: 20960002]

- DOI: 10.1007/s00406-010-0161-7]
- 153 **Neuner I**, Kellermann T, Stöcker T, Kircher T, Habel U, Shah JN, Schneider F. Amygdala hypersensitivity in response to emotional faces in Tourette's patients. *World J Biol Psychiatry* 2010; **11**: 858-872 [PMID: 20560820 DOI: 10.3109/15622975.2010.480984]
 - 154 **Via E**, Cardoner N, Pujol J, Alonso P, López-Solà M, Real E, Contreras-Rodríguez O, Deus J, Segalàs C, Menchón JM, Soriano-Mas C, Harrison BJ. Amygdala activation and symptom dimensions in obsessive-compulsive disorder. *Br J Psychiatry* 2014; **204**: 61-68 [PMID: 24262816 DOI: 10.1192/bjp.bp.112.123364]
 - 155 **Drevets WC**. Prefrontal cortical-amygdalar metabolism in major depression. *Ann N Y Acad Sci* 1999; **877**: 614-637 [PMID: 10415674 DOI: 10.1111/j.1749-6632.1999.tb09292.x]
 - 156 **Shapira NA**, Okun MS, Wint D, Foote KD, Byars JA, Bowers D, Springer US, Lang PJ, Greenberg BD, Haber SN, Goodman WK. Panic and fear induced by deep brain stimulation. *J Neurol Neurosurg Psychiatry* 2006; **77**: 410-412 [PMID: 16484657 DOI: 10.1136/jnnp.2005.069906]
 - 157 **Choi DC**, Furay AR, Evanson NK, Ostrander MM, Ulrich-Lai YM, Herman JP. Bed nucleus of the stria terminalis subregions differentially regulate hypothalamic-pituitary-adrenal axis activity: implications for the integration of limbic inputs. *J Neurosci* 2007; **27**: 2025-2034 [PMID: 17314298 DOI: 10.1523/JNEUROSCI.4301-06.2007]
 - 158 **Dunn JD**. Plasma corticosterone responses to electrical stimulation of the bed nucleus of the stria terminalis. *Brain Res* 1987; **407**: 327-331 [PMID: 3567648 DOI: 10.1016/0006-8993(87)91111-5]
 - 159 **Davis M**, Walker DL, Miles L, Grillon C. Phasic vs sustained fear in rats and humans: role of the extended amygdala in fear vs anxiety. *Neuropsychopharmacology* 2010; **35**: 105-135 [PMID: 19693004 DOI: 10.1038/npp.2009.109]
 - 160 **Nuttin B**, Gielen F, van Kuyck K, Wu H, Luyten L, Welkenhuysen M, Brionne TC, Gabriëls L. Targeting bed nucleus of the stria terminalis for severe obsessive-compulsive disorder: more unexpected lead placement in obsessive-compulsive disorder than in surgery for movement disorders. *World Neurosurg* 2013; **80**: S30.e11-S30.e16 [PMID: 23268197 DOI: 10.1016/j.wneu.2012.12.029]
 - 161 **Markram K**, Rinaldi T, La Mendola D, Sandi C, Markram H. Abnormal fear conditioning and amygdala processing in an animal model of autism. *Neuropsychopharmacology* 2008; **33**: 901-912 [PMID: 17507914 DOI: 10.1038/sj.npp.1301453]
 - 162 **Kleinmans NM**, Johnson LC, Richards T, Mahurin R, Greenson J, Dawson G, Aylward E. Reduced neural habituation in the amygdala and social impairments in autism spectrum disorders. *Am J Psychiatry* 2009; **166**: 467-475 [PMID: 19223437 DOI: 10.1176/appi.ajp.2008.07101681]
 - 163 **Sturm V**, Fricke O, Bührle CP, Lenartz D, Maarouf M, Treuer H, Mai JK, Lehmkuhl G. DBS in the basolateral amygdala improves symptoms of autism and related self-injurious behavior: a case report and hypothesis on the pathogenesis of the disorder. *Front Hum Neurosci* 2012; **6**: 341 [PMID: 23346052 DOI: 10.3389/fnhum.2012.00341]
 - 164 **Williams NR**, Foote KD, Okun MS. STN vs. GPi Deep Brain Stimulation: Translating the Rematch into Clinical Practice. *Mov Disord Clin Pract* 2014; **1**: 24-35 [PMID: 24779023 DOI: 10.1002/mdc3.12004]
 - 165 **Hilker R**, Voges J, Weisenbach S, Kalbe E, Burghaus L, Ghaemi M, Lehrke R, Koulousakis A, Herholz K, Sturm V, Heiss WD. Subthalamic nucleus stimulation restores glucose metabolism in associative and limbic cortices and in cerebellum: evidence from a FDG-PET study in advanced Parkinson's disease. *J Cereb Blood Flow Metab* 2004; **24**: 7-16 [PMID: 14688612 DOI: 10.1097/01.WCB.0000092831.44769.09]
 - 166 **Geday J**, Østergaard K, Johnsen E, Gjedde A. STN-stimulation in Parkinson's disease restores striatal inhibition of thalamocortical projection. *Hum Brain Mapp* 2009; **30**: 112-121 [PMID: 18041743 DOI: 10.1002/hbm.20486]
 - 167 **Martinez-Torres I**, Hariz MI, Zrinzo L, Foltynie T, Limousin P. Improvement of tics after subthalamic nucleus deep brain stimulation. *Neurology* 2009; **72**: 1787-1789 [PMID: 19451536 DOI: 10.1212/WNL.0b013e3181a60a0c]
 - 168 **Bourne SK**, Eckhardt CA, Sheth SA, Eskandar EN. Mechanisms of deep brain stimulation for obsessive compulsive disorder: effects upon cells and circuits. *Front Integr Neurosci* 2012; **6**: 29 [PMID: 22712007 DOI: 10.3389/fnint.2012.00029]
 - 169 **Evans DW**, Lewis MD, Iobst E. The role of the orbitofrontal cortex in normally developing compulsive-like behaviors and obsessive-compulsive disorder. *Brain Cogn* 2004; **55**: 220-234 [PMID: 15134855 DOI: 10.1016/S0278-2626(03)00274-4]
 - 170 **Mink JW**. Basal ganglia dysfunction in Tourette's syndrome: a new hypothesis. *Pediatr Neurol* 2001; **25**: 190-198 [PMID: 11587872 DOI: 10.1016/S0887-8994(01)00262-4]
 - 171 **Mataix-Cols D**, Wooderson S, Lawrence N, Brammer MJ, Speckens A, Phillips ML. Distinct neural correlates of washing, checking, and hoarding symptom dimensions in obsessive-compulsive disorder. *Arch Gen Psychiatry* 2004; **61**: 564-576 [PMID: 15184236 DOI: 10.1001/archpsyc.61.6.564]
 - 172 **Ho CY**. The Ventral Pallidum As a Limbic Pleasure Generator (Doctoral dissertaion). 2010. Available from: URL: <http://deepblue.lib.umich.edu/handle/2027.42/78836>
 - 173 **Nair G**, Evans A, Bear RE, Velakoulis D, Bittar RG. The anteromedial GPi as a new target for deep brain stimulation in obsessive compulsive disorder. *J Clin Neurosci* 2014; **21**: 815-821 [PMID: 24524950 DOI: 10.1016/j.jocn.2013.10.003]
 - 174 **Kosel M**, Sturm V, Frick C, Lenartz D, Zeidler G, Brodesser D, Schlaepfer TE. Mood improvement after deep brain stimulation of the internal globus pallidus for tardive dyskinesia in a patient suffering from major depression. *J Psychiatr Res* 2007; **41**: 801-803 [PMID: 16962613 DOI: 10.1016/j.jpsychires.2006.07.010]
 - 175 **Piedimonte F**, Andreani JC, Piedimonte L, Graff P, Bacaro V, Micheli F, Vilela Filho O. Behavioral and motor improvement after deep brain stimulation of the globus pallidus externus in a case of Tourette's syndrome. *Neuromodulation* 2013; **16**: 55-58; discussion 58 [PMID: 23240689 DOI: 10.1111/j.1525-1403.2012.00526.x]
 - 176 **Van der Werf YD**, Witter MP, Groenewegen HJ. The intralaminar and midline nuclei of the thalamus. Anatomical and functional evidence for participation in processes of arousal and awareness. *Brain Res Brain Res Rev* 2002; **39**: 107-140 [PMID: 12423763 DOI: 10.1016/S0165-0173(02)00181-9]
 - 177 **Smith Y**, Raju D, Nanda B, Pare JF, Galvan A, Wichmann T. The thalamostriatal systems: anatomical and functional organization in normal and parkinsonian states. *Brain Res Bull* 2009; **78**: 60-68 [PMID: 18805468 DOI: 10.1016/j.brainresbull.2008.08.015]
 - 178 **Smith Y**, Raju DV, Pare JF, Sidibe M. The thalamostriatal system: a highly specific network of the basal ganglia circuitry. *Trends Neurosci* 2004; **27**: 520-527 [PMID: 15331233 DOI: 10.1016/j.tins.2004.07.004]
 - 179 **Matsumoto N**, Minamimoto T, Graybiel AM, Kimura M. Neurons in the thalamic CM-Pf complex supply striatal neurons with information about behaviorally significant sensory events. *J Neurophysiol* 2001; **85**: 960-976 [PMID: 11160526]
 - 180 **Servello D**, Porta M, Sassi M, Brambilla A, Robertson MM. Deep brain stimulation in 18 patients with severe Gilles de la Tourette syndrome refractory to treatment: the surgery and stimulation. *J Neurol Neurosurg Psychiatry* 2008; **79**: 136-142 [PMID: 17846115 DOI: 10.1136/jnnp.2006.104067]
 - 181 **Ottersen OP**. Afferent connections to the amygdaloid complex of the rat with some observations in the cat. III. Afferents from the lower brain stem. *J Comp Neurol* 1981; **202**: 335-356 [PMID: 7298902 DOI: 10.1002/cne.902020304]
 - 182 **Cavdar S**, Onat FY, Cakmak YO, Yananli HR, Gülçebi M, Aker R. The pathways connecting the hippocampal for-

- mation, the thalamic reuniens nucleus and the thalamic reticular nucleus in the rat. *J Anat* 2008; **212**: 249-256 [PMID: 18221482 DOI: 10.1111/j.1469-7580.2008.00858.x]
- 183 **Berendse HW**, Groenewegen HJ. Restricted cortical termination fields of the midline and intralaminar thalamic nuclei in the rat. *Neuroscience* 1991; **42**: 73-102 [PMID: 1713657 DOI: 10.1016/0306-4522(91)90151-D]
- 184 **Jayaraman A**. Organization of thalamic projections in the nucleus accumbens and the caudate nucleus in cats and its relation with hippocampal and other subcortical afferents. *J Comp Neurol* 1985; **231**: 396-420 [PMID: 3968245 DOI: 10.1002/cne.902310309]
- 185 **Sadikot AF**, Rymar VV. The primate centromedian-parafascicular complex: anatomical organization with a note on neuromodulation. *Brain Res Bull* 2009; **78**: 122-130 [PMID: 18957319 DOI: 10.1016/j.brainresbull.2008.09.016]
- 186 **Sadikot AF**, Parent A, François C. Efferent connections of the centromedian and parafascicular thalamic nuclei in the squirrel monkey: a PHA-L study of subcortical projections. *J Comp Neurol* 1992; **315**: 137-159 [PMID: 1372010 DOI: 10.1002/cne.903150203]
- 187 **Parent M**, Parent A. Single-axon tracing and three-dimensional reconstruction of centre median-parafascicular thalamic neurons in primates. *J Comp Neurol* 2005; **481**: 127-144 [PMID: 15558721 DOI: 10.1002/cne.20348]
- 188 **Sidibé M**, Bevan MD, Bolam JP, Smith Y. Efferent connections of the internal globus pallidus in the squirrel monkey: I. Topography and synaptic organization of the pallidothalamic projection. *J Comp Neurol* 1997; **382**: 323-347 [PMID: 9183697 DOI: 10.1002/(SICI)1096-9861(19970609)382:33.3.CO;2-6]
- 189 **Sidibé M**, Paré JF, Smith Y. Nigral and pallidal inputs to functionally segregated thalamostriatal neurons in the centromedian/parafascicular intralaminar nuclear complex in monkey. *J Comp Neurol* 2002; **447**: 286-299 [PMID: 11984822 DOI: 10.1002/cne.10247]
- 190 **Metzger CD**, Eckert U, Steiner J, Sartorius A, Buchmann JE, Stadler J, Tempelmann C, Speck O, Bogerts B, Abler B, Walter M. High field fMRI reveals thalamocortical integration of segregated cognitive and emotional processing in mediodorsal and intralaminar thalamic nuclei. *Front Neuroanat* 2010; **4**: 138 [PMID: 21088699 DOI: 10.3389/fnana.2010.00138]
- 191 **Cardoso EF**, Maia FM, Fregni F, Myczkowski ML, Melo LM, Sato JR, Marcolin MA, Rigonatti SP, Cruz AC, Barbosa ER, Amaro E. Depression in Parkinson's disease: convergence from voxel-based morphometry and functional magnetic resonance imaging in the limbic thalamus. *Neuroimage* 2009; **47**: 467-472 [PMID: 19398020 DOI: 10.1016/j.neuroimage.2009.04.059]
- 192 **Parker GJ**, Stephan KE, Barker GJ, Rowe JB, MacManus DG, Wheeler-Kingshott CA, Ciccarelli O, Passingham RE, Spinks RL, Lemon RN, Turner R. Initial demonstration of in vivo tracing of axonal projections in the macaque brain and comparison with the human brain using diffusion tensor imaging and fast marching tractography. *Neuroimage* 2002; **15**: 797-809 [PMID: 11906221 DOI: 10.1006/nimg.2001.0994]
- 193 **Behrens TE**, Johansen-Berg H, Woolrich MW, Smith SM, Wheeler-Kingshott CA, Boulby PA, Barker GJ, Sillery EL, Sheehan K, Ciccarelli O, Thompson AJ, Brady JM, Matthews PM. Non-invasive mapping of connections between human thalamus and cortex using diffusion imaging. *Nat Neurosci* 2003; **6**: 750-757 [PMID: 12808459 DOI: 10.1038/nm1075]
- 194 **Johansen-Berg H**, Gutman DA, Behrens TE, Matthews PM, Rushworth MF, Katz E, Lozano AM, Mayberg HS. Anatomical connectivity of the subgenual cingulate region targeted with deep brain stimulation for treatment-resistant depression. *Cereb Cortex* 2008; **18**: 1374-1383 [PMID: 17928332 DOI: 10.1093/cercor/bhm167]
- 195 **Lehman JF**, Greenberg BD, McIntyre CC, Rasmussen SA, Haber SN. Rules ventral prefrontal cortical axons use to reach their targets: implications for diffusion tensor imaging tractography and deep brain stimulation for psychiatric illness. *J Neurosci* 2011; **31**: 10392-10402 [PMID: 21753016 DOI: 10.1523/JNEUROSCI.0595-11.2011]
- 196 **Coenen VA**, Panksepp J, Hurwitz TA, Urbach H, Mädler B. Human medial forebrain bundle (MFB) and anterior thalamic radiation (ATR): imaging of two major subcortical pathways and the dynamic balance of opposite affects in understanding depression. *J Neuropsychiatry Clin Neurosci* 2012; **24**: 223-236 [PMID: 22772671 DOI: 10.1176/appi.neuropsych.11080180]
- 197 **McNab JA**, Voets NL, Jenkinson N, Squier W, Miller KL, Goodwin GM, Aziz TZ. Reduced limbic connections may contraindicate subgenual cingulate deep brain stimulation for intractable depression. *J Neurosurg* 2009; **111**: 780-784 [PMID: 19284230 DOI: 10.3171/2009.2.JNS081299]
- 198 **Coenen VA**, Mädler B, Schlaepfer TE. Reply to: medial forebrain bundle stimulation-speed access to an old or entry into a new depression neurocircuit? *Biol Psychiatry* 2013; **74**: e45-e46 [PMID: 23916389 DOI: 10.1016/j.biopsych.2013.06.017]
- 199 **Lui S**, Wu Q, Qiu L, Yang X, Kuang W, Chan RC, Huang X, Kemp GJ, Mechelli A, Gong Q. Resting-state functional connectivity in treatment-resistant depression. *Am J Psychiatry* 2011; **168**: 642-648 [PMID: 21362744 DOI: 10.1176/appi.ajp.2010.10101419]
- 200 **Di Martino A**, Scheres A, Margulies DS, Kelly AM, Uddin LQ, Shehzad Z, Biswal B, Walters JR, Castellanos FX, Milham MP. Functional connectivity of human striatum: a resting state fMRI study. *Cereb Cortex* 2008; **18**: 2735-2747 [PMID: 18400794 DOI: 10.1093/cercor/bhn041]
- 201 **Williams NR**, Taylor JJ, Snipes JM, Short BE, Kantor EM, George MS. Interventional Psychiatry: How should we incorporate neuromodulation into psychiatric education? *Acad Psychiatry* 2014; **38**: 168-176 [PMID: 24554501 DOI: 10.1007/s40596-014-0050-x]
- 202 **Cho ZH**, Law M, Chi JG, Choi SH, Park SY, Kammen A, Park CW, Oh SH, Kim YB. An anatomic review of thalamo-limbic fiber tractography: ultra-high resolution direct visualization of thalamo-limbic fibers anterior thalamic radiation, superolateral and inferomedial medial forebrain bundles, and newly identified septum pellucidum tract. *World Neurosurg* 2013 Aug 22; Epub ahead of print [PMID: 23973452 DOI: 10.1016/j.wneu.2013.08.022]
- 203 **Schweder PM**, Joint C, Hansen PC, Green AL, Quaghebeur G, Aziz TZ. Chronic pedunculopontine nucleus stimulation restores functional connectivity. *Neuroreport* 2010; **21**: 1065-1068 [PMID: 20926975 DOI: 10.1097/WNR.0b013e32833ce607]
- 204 **Liu Y**, Miao W, Wang J, Gao P, Yin G, Zhang L, Lv C, Ji Z, Yu T, Sabel BA, He H, Peng Y. Structural abnormalities in early Tourette syndrome children: a combined voxel-based morphometry and tract-based spatial statistics study. *PLoS One* 2013; **8**: e76105 [PMID: 24098769 DOI: 10.1371/journal.pone.0076105]
- 205 **Neuner I**, Kupriyanova Y, Stöcker T, Huang R, Posnansky O, Schneider F, Tittgemeyer M, Shah NJ. White-matter abnormalities in Tourette syndrome extend beyond motor pathways. *Neuroimage* 2010; **51**: 1184-1193 [PMID: 20188196 DOI: 10.1016/j.neuroimage.2010.02.049]
- 206 **Shimamoto SA**, Ryapolova-Webb ES, Ostrem JL, Galifianakis NB, Miller KJ, Starr PA. Subthalamic nucleus neurons are synchronized to primary motor cortex local field potentials in Parkinson's disease. *J Neurosci* 2013; **33**: 7220-7233 [PMID: 23616531 DOI: 10.1523/JNEUROSCI.4676-12.2013]
- 207 **Coenen VA**, Honey CR, Hurwitz T, Rahman AA, McMaster J, Bürgel U, Mädler B. Medial forebrain bundle stimulation as a pathophysiological mechanism for hypomania in subthalamic nucleus deep brain stimulation for Parkinson's disease. *Neurosurgery* 2009; **64**: 1106-1114; discussion 1106-1114 [PMID: 19487890 DOI: 10.1227/01.NEU.0000345631.54446.06]
- 208 **Chaturvedi A**, Foutz TJ, McIntyre CC. Current steering to activate targeted neural pathways during deep brain stimulation of the subthalamic region. *Brain Stimul* 2012; **5**:

369-377 [PMID: 22277548 DOI: 10.1016/j.brs.2011.05.002]
209 **Arsalidou M**, Duerden EG, Taylor MJ. The centre of the brain: topographical model of motor, cognitive, affective,

and somatosensory functions of the basal ganglia. *Hum Brain Mapp* 2013; **34**: 3031-3054 [PMID: 22711692 DOI: 10.1002/hbm.22124]

P- Reviewer: Arsalidou M, Llamas EP, Sun Z, Tang GH
S- Editor: Song XX **L- Editor:** A **E- Editor:** Lu YJ



Recent advances in imaging technologies in dentistry

Naseem Shah, Nikhil Bansal, Ajay Logani

Naseem Shah, Nikhil Bansal, Ajay Logani, Department of Conservative Dentistry and Endodontics, Centre for Dental Education and Research, All India Institute of Medical Sciences, New Delhi 110029, India

Author contributions: All the authors equally contributed to this paper.

Correspondence to: Dr. Naseem Shah, Professor, Head, Department of Conservative Dentistry and Endodontics, Centre for Dental Education and Research, All India Institute of Medical Sciences, Ansari Nagar East, Gautam Nagar, New Delhi 110029, India. naseemys@gmail.com

Telephone: +91-11-26589304 Fax: +91-11-26588663

Received: December 26, 2014 Revised: July 4, 2014

Accepted: August 27, 2014

Published online: March 28, 2015

Abstract

Dentistry has witnessed tremendous advances in all its branches over the past three decades. With these advances, the need for more precise diagnostic tools, specially imaging methods, have become mandatory. From the simple intra-oral periapical X-rays, advanced imaging techniques like computed tomography, cone beam computed tomography, magnetic resonance imaging and ultrasound have also found place in modern dentistry. Changing from analogue to digital radiography has not only made the process simpler and faster but also made image storage, manipulation (brightness/contrast, image cropping, etc.) and retrieval easier. The three-dimensional imaging has made the complex cranio-facial structures more accessible for examination and early and accurate diagnosis of deep seated lesions. This paper is to review current advances in imaging technology and their uses in different disciplines of dentistry.

© 2015 Baishideng Publishing Group Inc. All rights reserved.

Key words: Dental X-rays; Intraoral X-rays; Dental cone beam computed tomography; Panoramic radiograph; Cephalogram

Core tip: Radiographs are a valuable diagnostic tool, as an adjunct to clinical examination in the diagnosis of dental diseases. Two dimensional periapical and panoramic radiographs are routinely used in dental practice. However, there are certain limitations of two-dimensional radiographs, which can be overcome by three-dimensional, imaging techniques such as cone beam computed tomography, magnetic resonance imaging and ultrasound. The purpose of this article is to review the advances made in digital dental imaging. Correct use of newer radiographic techniques, where indicated, can help early detection and appropriate and timely treatment for various dental and oral pathologies.

Original sources: Shah N, Bansal N, Logani A. Recent advances in imaging technologies in dentistry. *World J Radiol* 2014; 6(10): 794-807 Available from: URL: <http://www.wjgnet.com/1949-8470/full/v6/i10/794.htm> DOI: <http://dx.doi.org/10.4329/wjr.v6.i10.794>

INTRODUCTION

On 8 November, 1895 Wilhelm Conrad Röntgen accidentally discovered an image cast from the cathode ray generator which was projected far beyond the possible range of the cathode rays. A week after the discovery, Röntgen discovered its medical use when he made a picture of his wife's hand on a photographic plate formed due to unknown radiation, which he termed as X-rays. It clearly revealed her wedding ring and her bones. The first original dental roentgenogram from a portion of a glass imaging plate was taken by Dr. Otto Walkhoff in January 1896 in his own mouth for an exposure time of 25 min. Since then, dental imaging has seen tremendous progress and its applications in various fields of dentistry. Broadly, imaging techniques used in Dentistry can be categorized as: intraoral and extra-oral, analogue and digital, ionizing and non-ionizing im-

aging, and two-dimensional (2-D) and three-dimensional (3-D) imaging.

2-D Conventional radiographs provide excellent images for most dental radiographic needs. Their primary use is to supplement the clinical examination by providing insight into the internal structure of teeth and supporting bone to reveal caries, periodontal and periapical diseases, and other osseous conditions. A significant constraint of conventional radiography is the superimposition of overlying structures, which obscures the object of interest. Eventually it results in collapsing 3-D structural information onto a 2-D image, which leads to loss of spatial information in the third dimension.

The film-based radiography requires the presence and maintenance of darkroom, chemical handling and is associated with processing errors. All these disadvantages are overcome with the advent of digital radiography. This revolution is the result of both technologic innovation in image acquisition processes and the development of networked computing systems for image retrieval and transmission.

The very first system that was introduced in digital radiography in dentistry was Radio-visio-graphy (RVG, formerly Trex-trophy Radiology Inc., Marietta, GA) by Trophy^[1] in France in 1987. Digital radiography refers to a method of capturing a radiographic image using a solid-state technology sensor, breaking it into electronic pieces, and presenting and storing the image using a computer. There are currently three types of digital radiography systems available for use in dental imaging: (1) CCD-Charge-Coupled Device (direct system); (2) CMOS-Complementary Metal Oxide Semiconductor (direct system); and (3) PSP-photo-stimulable phosphor (indirect system). One of the most commonly cited positive features of digital radiography is the radiation dose reduction up to 80%, when compared with conventional plain film radiography^[2]. It is estimated that the dose reduction for intraoral digital imaging is in the range of 50%^[3]-60%^[4] when compared to E-speed film and for extraoral digital imaging, 50%^[5]-70%^[6], when compared to film-screen combinations. Other obvious benefits include the short processing time, *i.e.*, the ability to view the image more quickly, the elimination of the darkroom, processing chemicals and the errors associated with improper darkroom maintenance, chemical handling, solution replenishment and replacement, *etc.* It allows manipulation of the image produced such as contrast, density, sharpness and image orientation, without any additional radiation exposure to the patient or the operator.

Intraoral radiographic examination is the backbone of imaging for the general dental practitioner. It comprises of three categories: periapical, bitewing and occlusal projections.

The periapical radiograph provides detailed information about the teeth and the surrounding tissues (Figure 1A). It is mainly utilized for assessment of pulp and root canal morphology, supporting alveolar bone status in

the inter-dental region, detection of periapical pathology and crown/root fractures. It is especially useful for endodontic treatment for pre-treatment evaluation of roots and root canal morphology, calcifications, curvatures, periapical lesions, working length determination, quality and extent of root canal obturation and monitoring healing after treatment. For this purpose, a special technique of periapical radiography was developed by Gordon M. Fitzgerald, called as paralleling or long cone technique. The film is placed parallel to the long axis of the tooth to be radiographed and the central beam of X-ray is directed at right angle to the film and the teeth. The long cone of the tube increases the distance between the source and the object, resulting in decreased size of focal spot. This technique reduces the geometric distortion and also avoids overlapping of other anatomic structures, which can over shadow the teeth. For monitoring the healing of periapical lesion, the X ray image needs to be standardized to keep the same horizontal and vertical angulations at every follow-up visits. Several film holding devices are available, which allow reproducing the same angulation and getting comparable images.

An occlusal radiograph displays a large segment of a dental arch that cannot be viewed on a periapical radiograph, such as a cyst. It helps to locate supernumerary/impacted teeth and foreign bodies in the jaws and stones in the ducts of sub-mandibular glands (Figure 1B).

Bitewing or inter-proximal radiographs are taken to evaluate inter-proximal surfaces of 3-4 upper and lower teeth simultaneously (Figure 1C). The film has a flap on which the patient bites to keep the film in place against the crowns of upper and lower teeth simultaneously (hence called bite-wing X-ray). Bitewing films are particularly valuable for detecting inter-proximal caries in the early stages of development before it manifest clinically, reveal secondary caries below the restorations and evaluating the inter-proximal bone condition^[7].

The extra-oral radiographic examination used in Dentistry includes panoramic radiographs, postero-anterior and lateral skull view, Water's view and postero-anterior and lateral cephalometric examinations. Extraoral radiographs help to examine larger areas of the jaws and skull, monitor growth and development of cranio-facial skeleton, to locate impacted teeth and large pathological lesions and evaluate the temporo-mandibular joint.

Panoramic imaging has become a popular and important diagnostic tool since its introduction in the 1950s. It is a specialised tomographic technique used to produce a flat representation of the curved surfaces of the jaws. The basic imaging principle is that of curved surface tomography. It visualizes the entire maxilla, mandible, temporo-mandibular joints and associated structures on a single film, *i.e.*, gives a panoramic or bird's eye view of the jaws^[8] (Figure 1D). It is used as a preliminary screening radiograph to assess the dentition and bone support, identify impacted teeth, view the position of dental implants *etc.* It also gives a basic assessment of the osseous status of the temporo-mandibular joints and

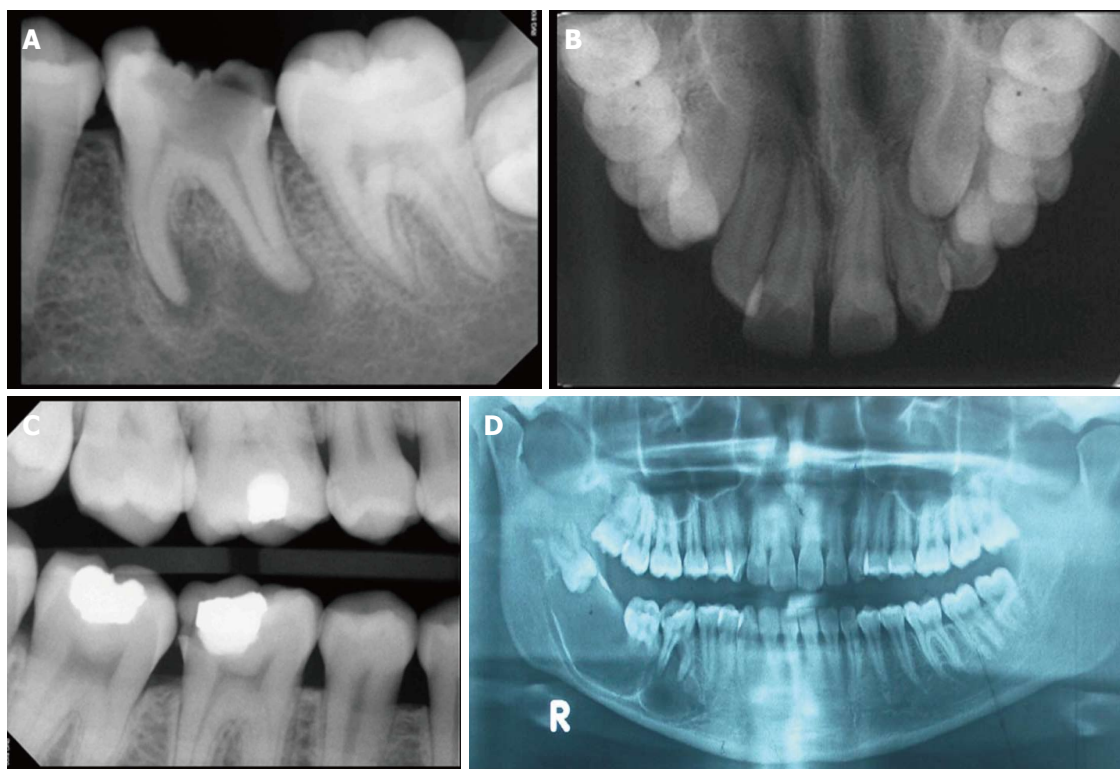


Figure 1 X-ray. A: An intraoral periapical X-ray helps to view the number and morphology of roots and root canals, periapical status and alveolar bone support interdentally. In this case, a grossly carious lower molar with diffuse radiolucency around both the root apices, denoting a chronic abscess is seen; B: An occlusal view of maxilla is useful to evaluate suture line of maxillary processes and extent of large pathological lesion such as a cyst and for location of impacted teeth. In this X-ray an impacted left maxillary canine can be seen; C: A bitewing X-ray is useful to examine a segment of upper and lower arch simultaneously to detect inter-proximal caries. In this X-ray, distal proximal surface of the lower 1st molar shows a carious defect; D: A panoramic radiograph gives a bird's-eye view of upper and lower jaws with excellent view of temporo-mandibular joint and maxillary sinuses. In this X-ray, a large, multi-locular cystic lesion, involving an impacted and inverted 3rd molar, extending up to the premolar region can be seen.

diagnoses maxillary and mandibular fractures. Panoramic radiographs are also being tested as a cost-effective tool to determine bone mineral density^[9,10].

However, it is subject to considerable and unpredictable geometric distortion and has relatively low spatial resolution compared with intra-oral radiographs. Large differences in image projection may occur in the anterior region depending on the patient positioning and individual curvature of the jaws. Also, it does not display the fine anatomic details available on intraoral periapical radiograph. But it offers a dose advantage over large numbers of intraoral radiographs^[11].

Cephalometric radiographs show the entire side of the head and help to evaluate the spatial relationships between cranial and dental structures (Figure 2). They are of value in comparing the changes in growth and development of dental and skeletal structures before, during and after orthodontic treatment, including the soft tissue profile (with lesser X-ray exposure)^[12].

Digital subtraction radiography (DSR) is a technique used to determine qualitative changes that occur between two images taken at different points in time. Subtraction method was introduced by B.G. Zeides des Plantes in the 1920s. The first image is the baseline image and the second image shows the changes that have occurred since the time the first image was taken^[13]. DSR cancels out

the complex anatomic background against which this change occurs. In order for DSR to be diagnostically useful, it is crucial that the baseline projection geometry and image intensities be reproduced. Dove *et al.*^[14] reported that angulation errors should be limited to two degrees. DSR helps to detect the alveolar bone changes of 1%-5% per unit volume and of crestal bone height change of 0.78 mm^[15,16]. Parsell *et al.*^[17] in 1998 found that digital subtraction radiography with or without enhancement improved the likelihood of a correct cancellous defect diagnosis when compared to other methods to detect oral cancellous bone lesions. However, it is only used for research purpose, as it is difficult to reproduce images with similar projection geometry every time.

Occipito-mental view, also known as Waters view, is the most favourable for visualization of maxillary sinuses, especially to compare internal radio-opacities. The frontal sinuses and ethmoid air cells can also be viewed in Waters view. When taken with open mouth position, it can help to visualize the sphenoid sinuses. The submento-vertex view is used in evaluating the lateral and posterior borders of the maxillary sinuses and the ethmoid air cells. It also visualizes the skull-base and condyles superimposed on the condylar necks and mandibular rami. It is particularly useful in diagnosis of fractures of the zygomatic arch. The Caldwell view is useful in evaluating

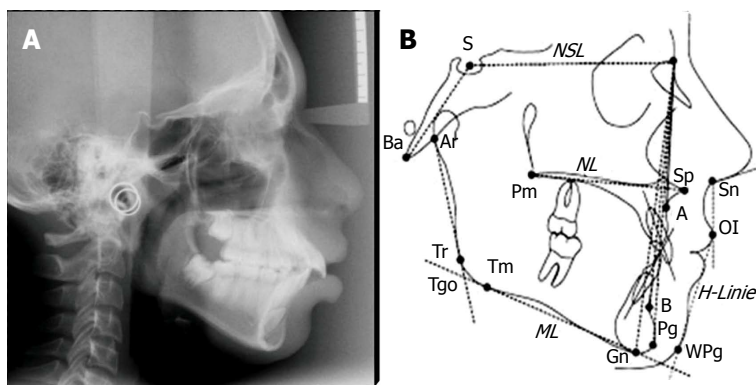


Figure 2 Cephalometric radiographs show the entire side of the head and help to evaluate the spatial relationships between cranial and dental structures. A: A lateral cephalometric X-ray is useful to determine cranio-facial structures and their relationship with position of the jaws and teeth; B: Different landmarks used to evaluate the planes and angles formed, to arrive at a diagnosis and treatment planning for orthodontic treatment/orthognathic surgery. Serial cephalograms can give the amount and direction of growth of facio-maxillary complex.

the frontal sinuses and ethmoid air cells. Reverse-towne projection is used to determine fractures of the condylar neck of the mandible.

LIMITATIONS OF 2-D IMAGES

Radiographs provide a two-dimensional image of a three-dimensional object. Relationship of the tooth to the surrounding anatomical structures cannot be assessed accurately which limits its diagnostic performance^[18]. The objects are visualized in the mesial-distal and apical-coronal plane; however the buccal-lingual plane is not possible to assess^[19]. Because of the complexity of maxillofacial skeleton, 2-D radiographic images do not accurately replicate the anatomy that is being assessed. Anatomical structures surrounding the teeth may superimpose causing anatomical or background noise, leading to difficulty in interpreting periapical radiographs. 2-D radiographs show less severe bone destruction than is actually present. Radiographs do not reveal the soft-tissue to hard-tissue relationships.

All the above listed 2-D imaging techniques provide information necessary for routine dental practice. However, in case of diagnostic dilemma and treatment planning of special cases, advanced 3-D imaging modalities, revealing additional information is desirable. Various techniques have evolved in the recent past that has revolutionized the diagnosis and treatment planning in dentistry.

COMPUTED TOMOGRAPHY

The first commercial computed tomography (CT) scanner was developed in 1972 by Sir Godfrey N. Hounsfield, an engineer at EMI, Great Britain. Since then, the introduction of clinical X-ray computed tomography has transformed medical imaging and may be described as the greatest advancement in radiology, since the discovery of X-rays. Computed tomography uses a narrow fan-shaped X-ray beam and multiple exposures around an object to reveal its internal structures which helps the clinician to view morphologic features and pathology in three-dimensions^[20]. It determines the mesio-distal as well as the bucco-lingual extent of the pathology.

CT scanner consists of a radiographic tube attached to a series of scintillation detectors or ionization cham-

bers. The patient is advanced in the circular aperture in the centre of the gantry. The tube head and reciprocal detectors within the gantry either rotate synchronously around the patient, or the detectors may form a continuous ring around the patient and the X-ray tube may move in a circle within the detector ring.

There are four generations of CTs. The Hounsfield's unit belonged to the first generation of CT scanners which used a single detector element to capture beam of X-rays. A second generation of CT systems introduced in 1975 used more than one detector and used small fan-beam, as opposed to pencil-beam scanning in the first generation. The first and second generations of CT scanners used a translate-rotate design and were used to scan only the head.

Third generation CT scanners introduced in 1976 use a large, arc-shaped detector that acquires an entire projection without the need for translation. Third generation scanners are most extensively used today. Fourth generation scanners replaced the arc-shaped detector with an entire circle of detectors. In this design, the X-ray tube rotates around the patient, while the detector stays stationary. As the fourth generation scanners were more expensive and suffer from higher levels of scatter, these are not used today. The incremental scanning approach was subject to errors relating to patient movement and limited Z-axis (vertical) image resolution resulting in loss of fracture conspicuity. The development of the power slip ring facilitated the development of spiral (or helical or volumetric) CT in the late 1980s. In spiral CT, the patient is moved continuously through the rotating gantry and image data are acquired as a "spiral" or "helix" rather than in the form of a series of slices^[21]. Compared with incremental CT scanners, spiral scanners provide improved multiplanar image reconstructions, reduced exposure time (12 s *vs* 5 min), and a reduced radiation dose (up to 75%)^[22].

Current CT scanners are called multi-slice CT scanners and have a linear array of multiple detectors (up to 64 rows) that simultaneously obtain tomographic data at different slice locations. It provides various advantages including significant reduction in scan time, reduced artifacts, and sub-millimetre resolution (up to 0.4 mm isotropic voxel)^[22]. However, these scanners are extremely

expensive and while beneficial for CT angiography and cardiac imaging, may have limited application in maxillofacial diagnosis.

CT was the first technology to allow visualization of both hard and soft tissues of the facial bones by image processing enhancement and the ability to acquire multiple, non-superimposed cross-sectional images. CT scans were used in medicine since 1973 but it became available for dental application only in 1987. CT provides high contrast resolution and allows differentiation of tissues with < 1% physical density difference compared to 10% required to be distinguished with conventional radiography^[22]. CT images have less noise (*i.e.*, they are less grainy), which results from superior collimation of the exit beam in CT machines. CT software programs can highlight pathologic lesions from normal anatomic structures using colour-enhancement features. CT images have the ability to show slices of a given tissue, with each slice thickness (1-2 mm) and location chosen by the operator^[20].

Trope *et al*^[23] in 1989 used CT scans to differentiate radicular cysts from granulomas based on marked difference in density between the content of the cyst cavity and granulomatous tissue.

CT is considered the gold standard imaging technique to assess injuries of the maxillofacial skeleton region. It is an excellent tool for detecting complex facial fractures, like those involving the frontal sinus, naso-ethmoidal region^[24], and the orbits^[25]. CT helps in defining the displacements of fractures prior to surgical reduction and fixation. It helps to diagnose undisplaced fractures of the mandible and the condyle, which are not apparent on panoramic radiographs. Markowitz *et al*^[26] found coronal CT to be the most accurate method in the diagnosis of mandibular fractures, followed by mandibular series and panoramic radiography. CT offers superb visualization of impacted teeth and its relation to nearby anatomic structures which guides the surgeon during surgical removal of impacted teeth.

Aggarwal *et al*^[27] used CT scans and ultrasound with power Doppler flowmetry in the diagnosis of large periapical lesions. They concluded that both, the CT scans and ultrasound with power Doppler flowmetry can provide an additional but more accurate diagnosis of periapical lesions with validity equivalent to histo-pathological diagnosis^[27].

CT scan is also an excellent aid in detecting vertical root fracture or split teeth which cannot be detected on periapical radiographs, since CT is not sensitive to beam orientation unlike conventional radiograph^[28].

CT helps to identify multiple extra root canals which when missed can lead to endodontic treatment failure. Chronic apical periodontitis can be seen with the CT scan in early and established stages. It is seen as an enlargement of the periodontal space, which is seen as a small osteolytic reaction around the root tips^[29]. Velvart *et al*^[30] in 2001 compared CT scans and periapical radiographs of 50 mandibular posterior teeth scheduled

for periapical surgery. They found that CT detected the presence of an apical lesion and the location of the inferior alveolar nerve in all cases, compared with 78% and 39% respectively with periapical radiographs. Robinson *et al*^[31] evaluated mandibular first premolars on 120 routine dental. CT images for variations in root/root canal morphology. They found that CT images identified a greater number of morphologic variations than did a panoramic radiograph^[31].

CT has been used as a research tool to compare the volume of root canals before and after instrumentation with different rotary nickel-titanium systems^[32] and for volumetric analysis of root filling using various obturation systems^[33].

3-D images from spiral CT helped in evaluating the close relationship between maxillary sinus disease and adjacent periodontal defects and their treatment^[34]. Rigolone *et al*^[35] obtained anatomic information using low dose CT to plan peri-radicular surgery *via* the vestibular approach. CT scan also detects resorption of adjacent roots.

CT scan can precisely distinguish between intrinsic and extrinsic salivary tumors and is used for staging these tumors^[36]. It is excellent for planning for implant placement for ear prosthesis in patients with hemifacial microsomia^[37].

The greatest disadvantage of CT imaging is the high radiation exposure. Other disadvantages of CT include high costs of the scans and scatter because of metallic objects. It has poor resolution compared to conventional radiographs. CT has limitation in the diagnosis of dental fractures (like small fissures) which are below the resolution capability of CT and may result in false-negative readings.

TUNED APERTURE COMPUTED TOMOGRAPHY

Tuned aperture computed tomography (TACT) is a relatively simple, faster method for reconstructing tomographic images, which was developed by Webber and colleagues^[38]. It is based on the concept of tomosynthesis and optical-aperture theory^[39,40]. TACT uses 2-D periapical radiographs acquired from different projection angles as base images and permits retrospective generation of longitudinal tomographic slices (TACT-S) lining up in the Z axis of the area of interest. It produces true 3-D data from any number of arbitrarily oriented 2-D projections. TACT has shown to be a promising, effective alternative to other conventional modalities for a number of clinical applications. The overall radiation dose of TACT is not greater than 1 to 2 times that of a conventional periapical X-ray film. The resolution is stated to be similar with 2-D radiographs. Artefacts associated with CT, such as starburst patterns seen with metallic restorations, do not exist with TACT.

In 1998, Nair *et al*^[41] reported TACT to be more effective imaging modality than film or individual digital

images for the detection of recurrent caries. Webber *et al*^[42] in 1999 also found TACT to be diagnostically more informative. Nance *et al* reported that with TACT 36% of extra canal [second mesio-buccal (MB 2)] were detected in maxillary molars and 80% of third (mesio-lingual) canals in mandibular molars^[43]. TACT has proved to be effective in the determination of root fractures, especially vertical fractures.

Nair *et al*^[44] found that TACT was a more effective and accurate imaging modality for non-destructive quantification of osseous changes within the healing bony defects. It was found to be better than planar images for the detectability of trauma-induced radicular fractures and mandibular fractures in *in-vitro* studies^[45]. Liang *et al*^[46] reported that TACT provides an alternative to conventional tomography for pre-surgical implant imaging. However, TACT is still at trial stage for dental applications but appears to be a promising imaging modality for the future.

Micro-computed tomography (micro-CT) is another alternative CT technique that has been used in dental imaging. However, the use of micro-CT remains a research tool limited to animal and *in vitro* studies on small samples. Because of the high radiation dose required, micro-CT cannot be employed for human imaging.

CONE BEAM COMPUTED TOMOGRAPHY

This imaging technique is based on a cone-shaped X-ray beam centered on a 2-D detector. It performs one rotation around the object and produces a series of 2-D images which are re-constructed in 3-D using a modification of the original cone-beam algorithm developed by Aboudara *et al*^[47] in 1984. Major advantage of TACT over CT is the considerably lower effective radiation dose to which patients are exposed. Radiation dose of one cone beam computed tomography (CBCT) scan may be as little as 3%-20% that of a conventional CT scan, depending on the equipment used and the area scanned^[22].

CBCT does not require an additional mechanism to move the patient during the acquisition. Cone beam technology significantly increases the X-ray utilization and requires far less electrical energy than fan-beam technology. X-ray tubes of cone-beam scanning are much less expensive than that for conventional CT. Images have isotropic voxels that can be as small as 0.125 mm. Subjective image quality is high, even compared to helical CT, for the highest resolution modalities. CBCT provides a high spatial resolution of bone and teeth which allows accurate understanding of the relationship of the adjacent structures.

CBCT has found varied application in all fields of dentistry. High resolution of CBCT has helps in detecting variety of cysts, tumors, infections, developmental anomalies and traumatic injuries involving the maxillofacial structures. It has been used extensively for evaluating dental and osseous disease in the jaws and temporo-

mandibular joints and treatment planning for dental implants.

CBCT is categorized into large, medium, and limited volume units based on the size of their field of view (FOV). The size of the FOV depicts the scan volume of CBCT machines. It depends on various factors like the size and shape of the detector, beam projection geometry and the ability to collimate the beam. Collimation of the beam limits the X-radiation exposure to the region of interest and ensures the most favorable FOV to be selected, based on disease presentation. Smaller scan volumes produce higher resolution images and lowers the effective radiation dose to the patient. Size of the field irradiated is the principal limitation of large FOV cone beam imaging^[48].

Large field of view (FOV) units encompasses those CBCTs with a FOV from 15-23 cm. These units are mainly useful in the assessment of maxillofacial trauma, orthodontic diagnosis and treatment planning, temporomandibular joint (TMJ) analysis and pathologies of the jaws. Medium FOV range from 10-15 cm and are useful for mandibulo-maxillary imaging and for pre-implant planning and pathological conditions. Small FOV units (limited FOVs) of < 10 cm with some as small as 4 cm × 4 cm in size are suitable for dento-alveolar imaging and are most advantageous for endodontic applications^[49].

APPLICATIONS OF CBCT IN VARIOUS BRANCHES OF DENTISTRY

Oral and maxillofacial surgery

CBCT is majorly used in oral and maxillofacial surgery for surgical evaluation and planning for surgery for impacted teeth, cysts and tumors, orthognathic and implant surgeries and diagnosis of fractures and inflammatory conditions of the jaws and the sinuses.

CBCT is largely used diagnostic technique in assessment of mid-face^[50] and orbital fractures^[51]. It allows easy detection of non-displaced, inter-articular fractures of the condylar head^[52]. Artefacts from metal objects are lower on CBCT images^[53], hence it provides better information in cases involving gun-shot wounds^[54]. However, in cases of trauma to the cervical vertebrae, use of CBCT is contra-indicated, as the patient is unable to be in an upright position which is required for CBCT imaging.

Detailed visualization of the inter-occlusal relationship of 3-D virtual skull model makes CBCT a valuable tool in orthognathic surgery planning. It allows for morphological analysis and spatial relationship of the neighboring structures during follow-ups to evaluate growth, development and function. It provides pre-surgical information when planning for sinus floor augmentation in preparation for implant placement^[55].

CBCT has been used for measuring the thickness of the glenoid fossa^[56]. It often reveals the possible dislocation of the disk in the joint by defining the true position of the condyle and the extent of translation of the

condyle in the fossa^[57]. It has also been used for an image guided puncture technique of the TMJ which is a treatment modality for TMJ disk adhesion^[58]. CBCT provides a dose and cost-effective alternative to helical CT for the diagnostic evaluation of osseous abnormalities of the TMJ.

Endodontics

CBCT has been extensively used in Endodontics. Numerous studies have reported its usefulness in diagnosis of periapical lesions^[59-62] (Figure 3). Estrela *et al*^[63] proposed a CBCT-based periapical index, termed as CBCT-PAI to measure and monitor periapical lesion size pre and post-endodontic treatment.

CBCT enables in the differential diagnosis of cyst from granulomas by measuring the density from the contrasted images of the periapical lesion^[64,65]. Lofthag-Hansen *et al*^[66] found that CBCT detected 62% more periapical lesions on individual roots when compared with periapical X-ray examinations. Vertical root fractures are better evaluated with CBCT images compared to periapical radiographs. CBCT can determine fractures in bucco-lingual or mesio-distal directions^[67,68].

Patel *et al*^[69] in their review of literature found CBCT to be efficacious in endodontic surgery planning and identification of root canals not seen on 2-D images. Alshehri *et al*^[70] in their review article on CBCT reported it to be useful in cases such as inflammatory external and internal resorption. CBCT not only detects the presence of resorption, but also determines its extent. They also found CBCT useful in determining root morphology; to measure the number of roots, canals, and accessory canals and to establish their working lengths, angulations and in the location of separated instrument in the canal^[70].

For most endodontic applications, limited volume CBCT is preferred over large volume CBCT for the following reasons: (1) Increased spatial resolution to improve the accuracy of endodontic-specific tasks such as the visualization of accessory canals, root fractures, apical deltas, calcifications, *etc.*; and (2) Decreased radiation exposure to the patient.

Implantology

CBCT has been used for preoperative and postoperative dental implant assessment. Preoperatively, it can accurately determine the quantity and quality of bone available for placement of implant^[71,72]. It also provides more detailed and accurate information of the adjoining vital tissues, so that these could be protected during the placement of dental implant. Heiland *et al*^[73] described a technique in which CBCT was used intra-operatively in two cases to navigate the implant insertion following microsurgical bone transfer.

Orthodontics

CBCT images have been used in orthodontic assessment and cephalometric analysis^[74]. CBCT helps to determine

root angulations, although variations are seen from the true anatomy^[75]. CBCT is valuable tool to assess the facial growth, age, airway function and disturbances in tooth eruption^[76]. CBCT can provide enhanced visualization of roots, making it a valuable tool for assessing pre and post-orthodontic root resorption.

CBCT evaluates the success of alveolar bone grafts in patients with cleft lip and palate by determining the bucco-palatal width and allowing the visualization of the 3-D morphology of the bone bridge^[77]. Kim *et al*^[78] used CBCT to construct placement guides for mini-implants between the roots of adjacent teeth in anatomically difficult sites.

Periodontics

CBCT has proved to be a practical clinical tool to detect intra-bony and furcation defects, dehiscence, fenestration, and periodontal cysts^[79]. It provides detailed morphologic description of the bone with minimal error margins. CBCT has also been used to evaluate outcome of regenerative periodontal therapy^[80].

LIMITATIONS OF CBCT

Image quality and diagnostic accuracy of CBCT is affected by the scatter and beam hardening artifacts caused by high density structures such as enamel and radiopaque materials^[81]. Scatter radiation reduces the contrast and limits the imaging of soft tissues. Hence, CBCT is principally indicated for imaging hard tissues^[82].

Because of distortion of Hounsfield Units, CBCT cannot be used for estimation of bone density. Scan times for CBCT are lengthy at 15-20 s and require the patient to stay completely still.

CONCERN FOR RADIATION EXPOSURE

Intraoral radiographic films are available as D, E and F. D is the slowest and F is the fastest speed films. Fast films require least radiation as compared to slow speed film. It is reported that switching from D to E speed film reduces radiation by 30%-40% and from D to F by 60%. However, due to cost consideration of fast speed films, majority of dentists prefer to use D speed films, though the cost difference is only marginal^[83].

Radiation exposure for panoramic radiograph is 14.2-24.3 mSv, for lateral cephalogram, it is 10.4 mSv and for a full mouth intraoral X ray series is 13-100 mSv. Digital X ray require a much lower radiation exposure, *i.e.*, 50%-75% less than equivalent film image. Digital panoramic radiation dose is 0.020 mSv and for cephalogram it is 0.007 mSv. CBCT units have radiation exposure in the range of 87-206 mSv for a full craniofacial scan. Based on these values, it is inferred that CBCT radiation exposure is equivalent to or slightly higher than traditional imaging^[84].

However, CBCT must not be used routinely for dental diagnosis or for screening purposes. The patient's

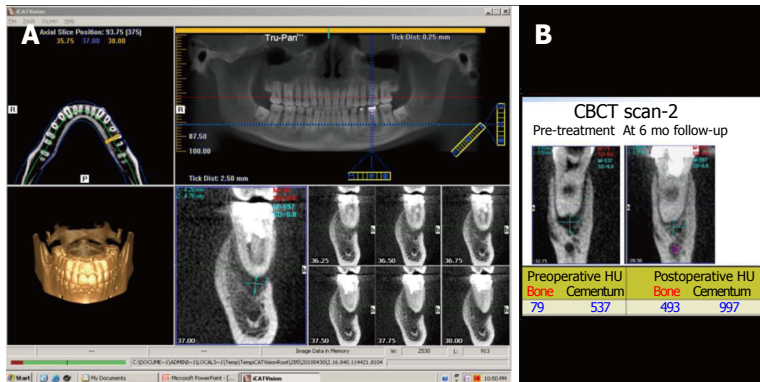


Figure 3 Cone beam computed tomography. A: A cone beam computed tomography scan gives a three-dimensional view of the area of interest. In this case, the periapical lesion is being evaluated; B: The image gives values in Hounsfield unit of cementum and alveolar bone density to measure post-treatment healing. CBCT: Cone beam computed tomography.

history and clinical examination must validate the use of CBCT by demonstrating that the benefits to the patient offset the potential risks. CBCT should only be used when lower dose conventional dental radiographs fails to provide adequate diagnostic information.

MAGNETIC RESONANCE IMAGING

Magnetic resonance imaging (MRI) is fast outpacing any other modality for *in vivo* viewing of soft tissues in the human body without the need to resort to any invasive procedures. MRI scan is a specialized imaging technique which does not use ionizing radiation. Most MRI machines are graded on the strength of the magnet, measured in Tesla units, which is the equivalent of 20000 times the magnetic field strength of Earth. MRI units for *in vivo* applications are in the range of 1.5 to 3 Tesla units.

MRI involves the behaviour of hydrogen atoms (consisting of one proton and one electron) within a strong magnetic field which is used to create the MR image. This causes the nuclei of many atoms in the body to align themselves with the magnetic field. The machine applies a radiofrequency pulse to depolarize the atoms and the energy that is released from the body is detected and used to construct the MR image by a computer. The high contrast sensitivity of MRI to soft tissue differences is the major reason MRI have replaced CT for imaging soft tissues. Hydrogen is found in abundance in soft tissue, but is lacking in most hard tissues^[85].

MRI offers the best resolution of tissues of low inherent contrast. Some cases of squamous cell carcinoma of the tongue can only be visualized with MRI. Because the region of the body imaged in MRI is controlled electronically, direct multiplanar imaging is possible without reorienting the patient.

The main dental applications of MRI to date have been the investigation of soft-tissue lesions in salivary glands, TMJ and tumour staging. Its exceptional soft-tissue contrast resolution makes it ideal for detection of internal derangement of TMJ. MRI can also detect joint effusions, synovitis, erosions and associated bone marrow oedema. Odontogenic cysts and tumors can be distinguished better on MRI than on CT. It also identifies soft tissue diseases, especially neoplasia, involving

tongue, cheek, salivary glands, neck and lymph nodes^[86].

MRI can also accurately distinguish between solid and cystic lesions on the basis of signal characteristics and enhancement patterns. Application of specific criteria for diagnosis allows accurate distinction between the keratocystic odontogenic tumour (KCOT) and other odontogenic lesions^[87]. The keratin-rich debris in a KCOT shows characteristic central drop in signal on T2-weighted images. In case of an infective lesion like a periapical abscess which expands fast in the jawbones and soft tissues, later degenerating into osteomyelitis, MRI is the diagnostic method of choice^[88]. Several studies have verified the high sensitivity of MRI in detecting cancellous marrow abnormality in acute osteomyelitis. This results in reduced T1 signal, increased T2 signal and contrast enhancement of bone and the adjacent inflamed soft tissues^[86].

A recent introduction in MRI technology is called SWEEP Imaging with Fourier Transform to visualize dental tissues. Idiyatullin *et al*^[89] reported that it can simultaneously image both hard and soft dental tissues with high resolution in short enough scanning times and hence is practical for clinical applications. An interesting observation was that it can determine the extent of carious lesions and simultaneously assess the status of pulpal tissue, whether reversible and irreversible pulpitis, which can impact clinical decision on treatment planning^[90].

MRI has been shown to be reliable in depicting sialodochitis and sialectasia, especially when globular changes are present. A study by Browne in which 50 consecutive patients presenting with facial swelling, thought clinically to be due to salivary gland disease were chosen. Prior investigation was undertaken in 29 patients, including ortho-pantomography, ultrasound and sialography; none provided additional information than MRI. Sialography was carried out in three patients after MRI and the results agreed with MRI in all cases. They concluded that MRI diagnosis of tumour was correct in all patients and that MRI appears to be an efficient first line investigation of facial swelling^[91].

Use of MRI technology has been reported to produce tooth surface digitization with an accuracy and precision sufficient for production of dental restorations^[92] and to detect root resorption^[93] in Orthodontic cases. Its use has been reported in characterization of

the inflammation and healing processes in periodontal tissues. Schara *et al*^[94] demonstrated through their *in-vivo* study that reduction of inflammation and probing depth in gingival tissues after non-surgical periodontal therapy correlated with a decrease of ratio between post- and pre-contrast signal intensity in T1 weighted MR images. They concluded that MRI could provide a new possibility to characterize the type and healing process of periodontal inflammation^[94].

The presence of a strong magnetic field can potentially cause movement of ferromagnetic metals in the vicinity of the imaging magnet. Because of this, MRI may not be safe in patients with cardiac pacemakers, implantable defibrillators, some artificial heart valves, cerebral aneurysm clips, or ferrous foreign bodies in the eye.

Artifacts caused by metallic dental restorations produced a major diagnostic problem in CT examinations of malignant tumors in the maxillofacial region. Artifacts from magnetic metals also appear on MRI^[95]. However it was found that severe artifacts that disturbed the interpretation of the images on MRI were only half that on CT^[96]. Vijay *et al*^[97] also reported that artifacts on MRI as a result of dental fillings were rather localized and did not degrade the entire image, unlike the streaking seen on CT images. Okano *et al*^[98] proposed that the MRI diagnosis of the TMJ can be performed in orthodontic patients, preferably using ceramic brackets on the anterior teeth and directly bonded tubes on the molars. However, the arch wires needed to be removed^[98].

MRI cannot always distinguish between benign and malignant tumours, which could lead to a false positive result^[99]. Some patients suffer from claustrophobia when positioned in the close confines of an MRI machine. Other drawback of MRI is the long scanning time required. Finally, MRI is expensive compared to other conventional radiographic methods.

The use of dental MRI appears to be a safe tool for 3-D imaging without ionizing radiation. However, due to high cost of MRI imaging, its use is limited to special cases where its use is specifically indicated for correct diagnosis.

ULTRASOUND

Ultrasound (US) is a non-invasive, inexpensive and painless imaging method. Unlike X-rays, it does not cause harmful ionizing radiation. US can be used for both hard and soft tissue detection. The first data of diagnostic US in dentistry was reported in 1963 by Baum *et al.* They used a 15 MHz transducer to visualize the interior structures of teeth; but the quality and clarity of the resulted RF signal was not favorable.

US is based on the reflection of sound waves (echoes) with a frequency outside the range of human hearing (1-20 kHz), at the interface of tissues which have different acoustic properties. Ultrasonic waves are created by the piezoelectric effect within a transducer (probe). US

waves transmit energy, as X-ray does, but it requires a medium for its transmission, unlike X-rays which pass readily through a vacuum. The echoes are detected by a transducer which converts them into an electrical signal and a real-time black, white and shades of grey picture is produced on a computer screen^[100].

US can be an important diagnostic tool for patients in whom MRI is contra-indicated, such as those with cardiac pacemakers, claustrophobia and metallic prostheses. Also, US can be used repeatedly as it is free of ionizing radiation.

US is used to diagnose fractures of the orbital margin and nasal bone, zygomatic arch, and the anterior wall of the frontal sinus. It has been proposed as a complementary diagnostic procedure to augment CT in the assessment of patients with mid-facial fracture. Ultrasonography is also capable in the detection of extra-capsular sub-condylar fractures. Adeyemo and Akadirri carried out a systemic review of literature to find the diagnostic value of ultrasound in detection of maxillofacial fractures. It reported sensitivity and specificity of US in detecting orbital fractures in the range of 56%-100% and 85%-100%, respectively. Studies on nasal fractures showed sensitivity and specificity in the range of 90%-100% and 98%-100%, respectively. Sensitivity or specificity of US for detecting zygomatic fractures was higher than 90% and for mandibular sub-condylar/ ramus fractures were in the range of 66%-100% and 52%-100%, respectively^[101].

US helps to differentiate solid and cystic lesions in the parotid gland. It can also detect Sialoliths in parotid, submandibular and sublingual salivary glands. These appear as echo-dense spots with a characteristic acoustic shadow^[102]. US guidance can prevent injuring the facial nerve during biopsy of the parotid gland.

US can demonstrate the internal muscle structures more clearly than CT. It can also measure the thickness of muscles which can be an important tool in diagnosis and treatment for follow-up examination of inflammatory soft tissue conditions of the head and neck region and superficial tissue disorders of the maxillofacial region^[103]. However, Serra *et al* through their review concluded that ultrasound technique generally showed lower reproducibility in relaxed than in contracted muscles.

US is a reliable diagnostic technique in determining the pathological nature (granuloma *vs* cysts) of periapical lesions^[27,104,105]. It has been used in guided fine-needle aspiration, measurement of tongue cancer thickness, and diagnosis of metastasis to cervical lymph nodes^[106]. Chandak *et al*^[107] in their study on head and neck swellings found higher accuracy and sensitivity of US imaging than the clinical diagnosis. They concluded that US would be an important diagnostic tool in association with clinical examination to detect the nature of the swelling^[107].

Rajendran *et al*^[108] conducted a study to find out the efficacy of high-resolution ultrasound and color power Doppler as a monitoring tool in the healing of periapical lesions. They found that ultrasound with color power

Doppler is an efficient tool for monitoring bone healing and would be a significant contribution to the trend toward radiation-free endodontics^[108]. Tikku *et al*^[109] also found that ultrasound and color Doppler imaging were considerably better than conventional radiography in detecting changes in the healing of periapical lesions. The authors also confirmed that only ultrasound combined with Doppler can differentiate venous from arterial flow, quantify the amount of flow, identify the anatomy of feeding vessels and offer a visual demonstration of vascularity^[109].

Yoon *et al*^[110] compared the difference in pulpal blood flow between vital and root-filled teeth by using US Doppler imaging. They found significant differences in the maximum linear velocity, average linear velocity, minimum linear velocity, pulsation index, and circulation resistance between the vital and root-filled teeth. They concluded that US Doppler imaging is an important tool to detect pulpal blood flow in vital tooth^[110].

Tagtekin *et al*^[111] while comparing DIAGNOdent (655 nm diode laser) with ultrasound for caries detection found that all measurements with US were accurate, reliable and significantly correlated between examiners. Both methods of caries detection showed high repeatability and accuracy^[111].

Even though, US have limitations in detecting the periodontal ligament, Mahmoud *et al*^[112] through their recent study found that it can be used for early diagnosis of the more severe form of periodontal disease. They used a custom-designed high-frequency (30 to 60 MHz) US imaging system to reconstruct three-dimensional surface images of periodontal defects in human^[112].

US can measure soft tissue thickness which could help practitioners to select the proper orthodontic mini-screw in clinical practice^[113]. Dental implant placement without incision and flap elevation require accurate determination of soft tissue thickness. Location of implant is difficult after healing, if the implants are deeply submerged after thick connective tissue grafts. US plays an important role in locating these submerged implants accurately for surgical exposure for subsequent prosthodontic rehabilitation^[114].

It is an alternative diagnostic method for imaging of the TMJ disorders^[115]. US showed better visualization of temporo-mandibular joint structures by using a frequency of > 12 MHz^[116].

US has limited value in diagnosing undisplaced fractures, complex maxillofacial fractures, posterior orbital floor fractures and intra-capsular mandibular condyle fractures due to overlapping of zygomatic arch^[101]. US are blocked by bone and therefore it can be used only if there is a bony defect over the lesion through which ultrasonic waves can traverse^[105].

Though placing the US in the anterior region of the mouth is easy, positioning the probe in buccal mucosa of posterior teeth is difficult.

US examination is usually applied only to the super-

ficial tissues in the maxillofacial region because the facial skeleton shields the deeper tissues. The correct interpretation of US images requires a trained radiologist, who has extensive training in the use and interpretation of US images.

CONCLUSION

Recent advances in imaging technologies have revolutionized dental diagnostics and treatment planning. Correct use of appropriate imaging technology and their correct interpretation, following the ALARA (As low as reasonably achievable) principles and cost-effectiveness, newer radiographic techniques can help to detect pathologies in very early stages, which ultimately help to reduce morbidity and mortality and improve the quality of life of the patients.

REFERENCES

- 1 **Nair MK**, Nair UP. Digital and advanced imaging in endodontics: a review. *J Endod* 2007; **33**: 1-6 [PMID: 17185117 DOI: 10.1016/j.joen.2006.08.013]
- 2 **Mouyen F**, Benz C, Sonnabend E, Lodter JP. Presentation and physical evaluation of RadioVisioGraphy. *Oral Surg Oral Med Oral Pathol* 1989; **68**: 238-242 [PMID: 2780024 DOI: 10.1016/0030-4220(89)90200-4]
- 3 **Langland OE**, Langlais RP, Preece JW. Principles of dental imaging. 2nd ed. Philadelphia: Lippincott Williams & Wilkins, 2002: 285
- 4 **Frederiksen NL**. Health Physics. In: Pharoah MJ, White SC, editors. *Oral Radiology Principles and Interpretation*. 4th ed. Mosby: St. Louis, 2000: 53
- 5 **Visser H**, Rödiger T, Hermann KP. Dose reduction by direct-digital cephalometric radiography. *Angle Orthod* 2001; **71**: 159-163 [PMID: 11407766]
- 6 **Farman AG**, Farman TT. Extraoral and panoramic systems. *Dent Clin North Am* 2000; **44**: 257-272, v-vi [PMID: 10740768]
- 7 **Kidd EA**, Pitts NB. A reappraisal of the value of the bite-wing radiograph in the diagnosis of posterior approximal caries. *Br Dent J* 1990; **169**: 195-200 [PMID: 2223291]
- 8 **Rushton VE**, Horner K, Worthington HV. Routine panoramic radiography of new adult patients in general dental practice: relevance of diagnostic yield to treatment and identification of radiographic selection criteria. *Oral Surg Oral Med Oral Pathol Oral Radiol Endod* 2002; **93**: 488-495 [PMID: 12029290 DOI: 10.1067/moe.2002.121994]
- 9 **Taguchi A**, Ohtsuka M, Nakamoto T, Naito K, Tsuda M, Kudo Y, Motoyama E, Suei Y, Tanimoto K. Identification of post-menopausal women at risk of osteoporosis by trained general dental practitioners using panoramic radiographs. *Dentomaxillofac Radiol* 2007; **36**: 149-154 [PMID: 17463099 DOI: 10.1259/dmfr/31116116]
- 10 **Bhatnagar S**, Krishnamurthy V, Pagare SS. Diagnostic efficacy of panoramic radiography in detection of osteoporosis in post-menopausal women with low bone mineral density. *J Clin Imaging Sci* 2013; **3**: 23 [PMID: 23814695 DOI: 10.4103/2156-7514.113140]
- 11 **Choi JW**. Assessment of panoramic radiography as a national oral examination tool: review of the literature. *Imaging Sci Dent* 2011; **41**: 1-6 [PMID: 21977466 DOI: 10.5624/isd.2011.41.1.1]
- 12 **Quintero JC**, Trosien A, Hatcher D, Kapila S. Craniofacial imaging in orthodontics: historical perspective, current status, and future developments. *Angle Orthod* 1999; **69**: 491-506 [PMID: 10593439]

- 13 **van der Stelt PF**. Digital radiography as a diagnostic tool. AADMRT Newsletter. Summer, 2004. Available from: URL: <http://www.aadmrt.com>
- 14 **Dove SB**, McDavid WD, Hamilton KE. Analysis of sensitivity and specificity of a new digital subtraction system: an in vitro study. *Oral Surg Oral Med Oral Pathol Oral Radiol Endod* 2000; **89**: 771-776 [PMID: 10846136]
- 15 **Gröndahl K**, Kullendorff B, Strid KG, Gröndahl HG, Henrikson CO. Detectability of artificial marginal bone lesions as a function of lesion depth. A comparison between subtraction radiography and conventional radiographic technique. *J Clin Periodontol* 1988; **15**: 156-162 [PMID: 3280612 DOI: 10.1111/j.1600-051X.1988.tb01562.x]
- 16 **Sanz M**, Newman MG. Advanced Diagnostic Techniques. In: Newman MG, Takei HH, Carranza FA. Clinical periodontology. 9th ed. Philadelphia: W.B.Saunders, 2002: 487-502
- 17 **Parsell DE**, Gatewood RS, Watts JD, Streckfus CF. Sensitivity of various radiographic methods for detection of oral cancellous bone lesions. *Oral Surg Oral Med Oral Pathol Oral Radiol Endod* 1998; **86**: 498-502 [PMID: 9798239 DOI: 10.1016/S1079-2104(98)90381-X]
- 18 **Cotti E**, Vargiu P, Dettori C, Mallarini G. Computerized tomography in the management and follow-up of extensive periapical lesion. *Endod Dent Traumatol* 1999; **15**: 186-189 [PMID: 10815569]
- 19 **Patel S**, Dawood A, Whaites E, Pitt Ford T. New dimensions in endodontic imaging: part 1. Conventional and alternative radiographic systems. *Int Endod J* 2009; **42**: 447-462 [PMID: 19298577 DOI: 10.1111/j.1365-2591.2008.01530.x]
- 20 **Brooks SL**. Computed tomography. *Dent Clin North Am* 1993; **37**: 575-590 [PMID: 8224334]
- 21 **Scarfe WC**. Imaging of maxillofacial trauma: evolutions and emerging revolutions. *Oral Surg Oral Med Oral Pathol Oral Radiol Endod* 2005; **100**: S75-S96 [PMID: 16037795 DOI: 10.1016/j.tripleo.2005.05.057]
- 22 **White S**, Pharoah M. Chapter 13. Advanced Imaging Modalities. *Oral Radiology: Principles and Interpretation*. 5th ed. Mosby: St Louis, MO, 2004: 245-264
- 23 **Trope M**, Pettigrew J, Petras J, Barnett F, Tronstad L. Differentiation of radicular cyst and granulomas using computerized tomography. *Endod Dent Traumatol* 1989; **5**: 69-72 [PMID: 2598887]
- 24 **Sargent LA**, Rogers GF. Nasoethmoid orbital fractures: diagnosis and management. *J Craniomaxillofac Trauma* 1999; **5**: 19-27 [PMID: 11951221]
- 25 **Davidson MJ**, Daly BD, Russell JL. The use of computed tomography in the management of facial trauma by British oral and maxillofacial surgeons. *Br J Oral Maxillofac Surg* 1991; **29**: 80-81 [PMID: 2049360 DOI: 10.1016/0266-4356(91)90085-J]
- 26 **Markowitz BL**, Sinow JD, Kawamoto HK, Shewmake K, Khoumeh F. Prospective comparison of axial computed tomography and standard and panoramic radiographs in the diagnosis of mandibular fractures. *Ann Plast Surg* 1999; **42**: 163-169 [PMID: 10029481]
- 27 **Aggarwal V**, Logani A, Shah N. The evaluation of computed tomography scans and ultrasounds in the differential diagnosis of periapical lesions. *J Endod* 2008; **34**: 1312-1315 [PMID: 18928838 DOI: 10.1016/j.joen.2008.08.005]
- 28 **Youssefzadeh S**, Gahleitner A, Dorffner R, Bernhart T, Kainberger FM. Dental vertical root fractures: value of CT in detection. *Radiology* 1999; **210**: 545-549 [PMID: 10207442]
- 29 **Deepak BS**, Subash TS, Narmatha VJ, Anamika T, Snehil TK, Nandini DB. Imaging techniques in endodontics: an overview. *J Clin Imaging Sci* 2012; **2**: 13 [PMID: 22530184 DOI: 10.4103/2156-7514.94227]
- 30 **Velvart P**, Hecker H, Tillinger G. Detection of the apical lesion and the mandibular canal in conventional radiography and computed tomography. *Oral Surg Oral Med Oral Pathol Oral Radiol Endod* 2001; **92**: 682-688 [PMID: 11740486]
- 31 **Robinson S**, Czerny C, Gahleitner A, Bernhart T, Kainberger FM. Dental CT evaluation of mandibular first premolar root configurations and canal variations. *Oral Surg Oral Med Oral Pathol Oral Radiol Endod* 2002; **93**: 328-332 [PMID: 11925543]
- 32 **Ozgun Uyanik M**, Cehreli ZC, Ozgen Mocan B, Tasman Dagli F. Comparative evaluation of three nickel-titanium instrumentation systems in human teeth using computed tomography. *J Endod* 2006; **32**: 668-671 [PMID: 16793477 DOI: 10.1016/j.joen.2005.12.015]
- 33 **Anbu R**, Nandini S, Velmurugan N. Volumetric analysis of root fillings using spiral computed tomography: an in vitro study. *Int Endod J* 2010; **43**: 64-68 [PMID: 19891718 DOI: 10.1111/j.1365-2591.2009.01638.x]
- 34 **Huang CH**, Brunsvold MA. Maxillary sinusitis and periapical abscess following periodontal therapy: a case report using three-dimensional evaluation. *J Periodontol* 2006; **77**: 129-134 [PMID: 16579714 DOI: 10.1902/jop.2006.77.1.129]
- 35 **Rigolone M**, Pasqualini D, Bianchi L, Berutti E, Bianchi SD. Vestibular surgical access to the palatine root of the superior first molar: "low-dose cone-beam" CT analysis of the pathway and its anatomic variations. *J Endod* 2003; **29**: 773-775 [PMID: 14651289]
- 36 **Stone DN**, Mancuso AA, Rice D, Hanafee WN. Parotid CT sialography. *Radiology* 1981; **138**: 393-397 [PMID: 7455119]
- 37 **Watson RM**, Coward TJ, Forman GH, Moss JP. Considerations in treatment planning for implant-supported auricular prostheses. *Int J Oral Maxillofac Implants* 1993; **8**: 688-694 [PMID: 8181832]
- 38 **Webber RL**, Horton RA, Tyndall DA, Ludlow JB. Tuned-aperture computed tomography (TACT). Theory and application for three-dimensional dento-alveolar imaging. *Dentomaxillofac Radiol* 1997; **26**: 53-62 [PMID: 9446991]
- 39 **Grant DG**. Tomosynthesis: a three-dimensional radiographic imaging technique. *IEEE Trans Biomed Eng* 1972; **19**: 20-28 [PMID: 5008409 DOI: 10.1109/TBME.1972.324154]
- 40 **Richards AG**. Dynamic tomography. *Oral Surg Oral Med Oral Pathol* 1976; **42**: 685-692 [PMID: 1068423 DOI: 10.1016/0304-4220(76)90219-X]
- 41 **Nair MK**, Tyndall DA, Ludlow JB, May K. Tuned aperture computed tomography and detection of recurrent caries. *Caries Res* 1998; **32**: 23-30 [PMID: 9438568 DOI: 10.1159/000016426]
- 42 **Webber RL**, Messura JK. An in vivo comparison of diagnostic information obtained from tuned-aperture computed tomography and conventional dental radiographic imaging modalities. *Oral Surg Oral Med Oral Pathol Oral Radiol Endod* 1999; **88**: 239-247 [PMID: 10468470 DOI: 10.1016/S1079-2104(99)70122-8]
- 43 **Nance R**, Tyndall D, Levin LG, Trope M. Identification of root canals in molars by tuned-aperture computed tomography. *Int Endod J* 2000; **33**: 392-396 [PMID: 11307216 DOI: 10.1046/j.1365-2591.2000.00330.x]
- 44 **Nair MK**, Seyedain A, Agarwal S, Webber RL, Nair UP, Piesco NP, Mooney MP, Gröndahl HG. Tuned aperture computed tomography to evaluate osseous healing. *J Dent Res* 2001; **80**: 1621-1624 [PMID: 11597021 DOI: 10.1177/00220345010800070501]
- 45 **Nair MK**, Nair UP, Gröndahl HG, Webber RL. Accuracy of tuned aperture computed tomography in the diagnosis of radicular fractures in non-restored maxillary anterior teeth - an in vitro study. *Dentomaxillofac Radiol* 2002; **31**: 299-304 [PMID: 12203128]
- 46 **Liang H**, Tyndall DA, Ludlow JB, Lang LA. Cross-sectional presurgical implant imaging using tuned aperture computed tomography (TACT). *Dentomaxillofac Radiol* 1999; **28**: 232-237 [PMID: 10455387]
- 47 **Aboudara CA**, Hatcher D, Nielsen IL, Miller A. A three-dimensional evaluation of the upper airway in adolescents. *Orthod Craniofac Res* 2003; **6** Suppl 1: 173-175 [PMID:

- 14606553 DOI: 10.1034/j.1600-0544.2003.253.x]
- 48 **Scarfe WC**, Levin MD, Gane D, Farman AG. Use of cone beam computed tomography in endodontics. *Int J Dent* 2009; **2009**: 634567 [PMID: 20379362 DOI: 10.1155/2009/634567]
- 49 **Tyndall DA**, Kohltfarber H. Application of cone beam volumetric tomography in endodontics. *Aust Dent J* 2012; **57** Suppl 1: 72-81 [PMID: 22376099 DOI: 10.1111/j.1834-7819.2011.01654.x]
- 50 **Blessmann M**, Pohlenz P, Blake FA, Lenard M, Schmelzle R, Heiland M. Validation of a new training tool for ultrasound as a diagnostic modality in suspected midfacial fractures. *Int J Oral Maxillofac Surg* 2007; **36**: 501-506 [PMID: 17376654 DOI: 10.1016/j.ijom.2007.01.016]
- 51 **Zizelmann C**, Gellrich NC, Metzger MC, Schoen R, Schmelzle R, Schramm A. Computer-assisted reconstruction of orbital floor based on cone beam tomography. *Br J Oral Maxillofac Surg* 2007; **45**: 79-80 [PMID: 16095777 DOI: 10.1016/j.bjoms.2005.06.031]
- 52 **Shintaku WH**, Venturin JS, Azevedo B, Noujeim M. Applications of cone-beam computed tomography in fractures of the maxillofacial complex. *Dent Traumatol* 2009; **25**: 358-366 [PMID: 19515071 DOI: 10.1111/j.1600-9657.2009.00795.x]
- 53 **Stuehmer C**, Essig H, Bormann KH, Majdani O, Gellrich NC, Rücker M. Cone beam CT imaging of airgun injuries to the craniomaxillofacial region. *Int J Oral Maxillofac Surg* 2008; **37**: 903-906 [PMID: 18768294 DOI: 10.1016/j.ijom.2008.07.007]
- 54 **Pohlenz P**, Blessmann M, Blake F, Heinrich S, Schmelzle R, Heiland M. Clinical indications and perspectives for intraoperative cone-beam computed tomography in oral and maxillofacial surgery. *Oral Surg Oral Med Oral Pathol Oral Radiol Endod* 2007; **103**: 412-417 [PMID: 17321455 DOI: 10.1016/j.tripleo.2006.05.008]
- 55 **Naitoh M**, Suenaga Y, Kondo S, Gotoh K, Ariji E. Assessment of maxillary sinus septa using cone-beam computed tomography: etiological consideration. *Clin Implant Dent Relat Res* 2009; **11** Suppl 1: e52-e58 [PMID: 19438951 DOI: 10.1111/j.1708-8208.2009.00194.x]
- 56 **Kijima N**, Honda K, Kuroki Y, Sakabe J, Ejima K, Nakajima I. Relationship between patient characteristics, mandibular head morphology and thickness of the roof of the glenoid fossa in symptomatic temporomandibular joints. *Dentomaxillofac Radiol* 2007; **36**: 277-281 [PMID: 17586854 DOI: 10.1259/dmfr/56344782]
- 57 **Tsiklakis K**, Syriopoulos K, Stamatakis HC. Radiographic examination of the temporomandibular joint using cone beam computed tomography. *Dentomaxillofac Radiol* 2004; **33**: 196-201 [PMID: 15371321 DOI: 10.1259/dmfr/27403192]
- 58 **Honda K**, Bjørnland T. Image-guided puncture technique for the superior temporomandibular joint space: value of cone beam computed tomography (CBCT). *Oral Surg Oral Med Oral Pathol Oral Radiol Endod* 2006; **102**: 281-286 [PMID: 16920534 DOI: 10.1016/j.tripleo.2005.10.042]
- 59 **Christiansen R**, Kirkevang LL, Gottfredsen E, Wenzel A. Periapical radiography and cone beam computed tomography for assessment of the periapical bone defect 1 week and 12 months after root-end resection. *Dentomaxillofac Radiol* 2009; **38**: 531-536 [PMID: 20026710 DOI: 10.1259/dmfr/63019695]
- 60 **Estrela C**, Bueno MR, Leles CR, Azevedo B, Azevedo JR. Accuracy of cone beam computed tomography and panoramic and periapical radiography for detection of apical periodontitis. *J Endod* 2008; **34**: 273-279 [PMID: 18291274 DOI: 10.1016/j.joen.2007.11.023]
- 61 **Nakata K**, Naitoh M, Izumi M, Inamoto K, Ariji E, Nakamura H. Effectiveness of dental computed tomography in diagnostic imaging of periradicular lesion of each root of a multirrooted tooth: a case report. *J Endod* 2006; **32**: 583-587 [PMID: 16728257 DOI: 10.1016/j.joen.2005.09.004]
- 62 **Patel S**. New dimensions in endodontic imaging: Part 2. Cone beam computed tomography. *Int Endod J* 2009; **42**: 463-475 [PMID: 19298576 DOI: 10.1111/j.1365-2591.2008.01531.x]
- 63 **Estrela C**, Bueno MR, Azevedo BC, Azevedo JR, Pécora JD. A new periapical index based on cone beam computed tomography. *J Endod* 2008; **34**: 1325-1331 [PMID: 18928840 DOI: 10.1016/j.joen.2008.08.013]
- 64 **Simon JH**, Enciso R, Malfaz JM, Roges R, Bailey-Perry M, Patel A. Differential diagnosis of large periapical lesions using cone-beam computed tomography measurements and biopsy. *J Endod* 2006; **32**: 833-837 [PMID: 16934625 DOI: 10.1016/j.joen.2006.03.008]
- 65 **Tyndall DA**, Rathore S. Cone-beam CT diagnostic applications: caries, periodontal bone assessment, and endodontic applications. *Dent Clin North Am* 2008; **52**: 825-841, vii [PMID: 18805231 DOI: 10.1016/j.cden.2008.05.002]
- 66 **Lofthag-Hansen S**, Huumonen S, Gröndahl K, Gröndahl HG. Limited cone-beam CT and intraoral radiography for the diagnosis of periapical pathology. *Oral Surg Oral Med Oral Pathol Oral Radiol Endod* 2007; **103**: 114-119 [PMID: 17178504]
- 67 **Wang P**, Yan XB, Lui DG, Zhang WL, Zhang Y, Ma XC. Detection of dental root fractures by using cone-beam computed tomography. *Dentomaxillofac Radiol* 2011; **40**: 290-298 [PMID: 21697154 DOI: 10.1259/dmfr/84907460]
- 68 **Hassan B**, Metska ME, Ozok AR, van der Stelt P, Wesselink PR. Comparison of five cone beam computed tomography systems for the detection of vertical root fractures. *J Endod* 2010; **36**: 126-129 [PMID: 20003950 DOI: 10.1016/j.joen.2009.09.013]
- 69 **Patel S**, Dawood A, Ford TP, Whaites E. The potential applications of cone beam computed tomography in the management of endodontic problems. *Int Endod J* 2007; **40**: 818-830 [PMID: 17697108 DOI: 10.1111/j.1365-2591.2007.01299.x]
- 70 **Alshehri MA**, Alamri H, Alshalhoub M. Applications of CBCT in Dental Practice. A Literature Review. *Dental News* 2011; **XVIII**: 26-34
- 71 **Hatcher DC**, Dial C, Mayorga C. Cone beam CT for surgical assessment of implant sites. *J Calif Dent Assoc* 2003; **31**: 825-833 [PMID: 14696834]
- 72 **Hua Y**, Nackaerts O, Duyck J, Maes F, Jacobs R. Bone quality assessment based on cone beam computed tomography imaging. *Clin Oral Implants Res* 2009; **20**: 767-771 [PMID: 19489931 DOI: 10.1111/j.1600-0501.2008.01677.x]
- 73 **Heiland M**, Pohlenz P, Blessmann M, Werle H, Fraedrich M, Schmelzle R, Blake FA. Navigated implantation after microsurgical bone transfer using intraoperatively acquired cone-beam computed tomography data sets. *Int J Oral Maxillofac Surg* 2008; **37**: 70-75 [PMID: 17822880 DOI: 10.1016/j.ijom.2007.06.011]
- 74 **Farman AG**, Scarfe WC. Development of imaging selection criteria and procedures should precede cephalometric assessment with cone-beam computed tomography. *Am J Orthod Dentofacial Orthop* 2006; **130**: 257-265 [PMID: 16905073 DOI: 10.1016/j.ajodo.2005.10.021]
- 75 **Van Elslande D**, Heo G, Flores-Mir C, Carey J, Major PW. Accuracy of mesiodistal root angulation projected by cone-beam computed tomographic panoramic-like images. *Am J Orthod Dentofacial Orthop* 2010; **137**: S94-S99 [PMID: 20381767 DOI: 10.1016/j.ajodo.2009.02.028]
- 76 **Shi H**, Scarfe WC, Farman AG. Three-dimensional reconstruction of individual cervical vertebrae from cone-beam computed-tomography images. *Am J Orthod Dentofacial Orthop* 2007; **131**: 426-432 [PMID: 17346601 DOI: 10.1016/j.ajodo.2005.12.031]
- 77 **Hamada Y**, Kondoh T, Noguchi K, Iino M, Isono H, Ishii H, Mishima A, Kobayashi K, Seto K. Application of limited cone beam computed tomography to clinical assessment of alveolar bone grafting: a preliminary report. *Cleft Palate Craniofac J* 2005; **42**: 128-137 [PMID: 15748103 DOI: 10.1597/03-035.1]
- 78 **Kim SH**, Choi YS, Hwang EH, Chung KR, Kook YA, Nel-

- son G. Surgical positioning of orthodontic mini-implants with guides fabricated on models replicated with cone-beam computed tomography. *Am J Orthod Dentofacial Orthop* 2007; **131**: S82-S89 [PMID: 17448391 DOI: 10.1016/j.ajodo.2006.01.027]
- 79 **Kasaj A**, Willershausen B. Digital volume tomography for diagnostics in periodontology. *Int J Comput Dent* 2007; **10**: 155-168 [PMID: 17899891]
- 80 **Ito K**, Yoshinuma N, Goke E, Arai Y, Shinoda K. Clinical application of a new compact computed tomography system for evaluating the outcome of regenerative therapy: a case report. *J Periodontol* 2001; **72**: 696-702 [PMID: 11394408]
- 81 **Katsumata A**, Hirukawa A, Noujeim M, Okumura S, Naitoh M, Fujishita M, Arijji E, Langlais RP. Image artifact in dental cone-beam CT. *Oral Surg Oral Med Oral Pathol Oral Radiol Endod* 2006; **101**: 652-657 [PMID: 16632279 DOI: 10.1016/j.tripleo.2005.07.027]
- 82 **Mol A**. Imaging methods in periodontology. *Periodontol* 2000 2004; **34**: 34-48 [PMID: 14717854 DOI: 10.1046/j.0906-6713.2003.003423.x]
- 83 Dental Radiography: Doses and Film Speed. U.S. Available from: URL: <http://www.fda.gov/radiationemittingproducts/radiationsafety/nationwideevaluationofxraytrend-snext/ucm116524.htm>. Accessed on 20-12-2013.
- 84 **Silva MA**, Wolf U, Heinicke F, Bumann A, Visser H, Hirsch E. Cone-beam computed tomography for routine orthodontic treatment planning: a radiation dose evaluation. *Am J Orthod Dentofacial Orthop* 2008; **133**: 640.e1-640.e5 [PMID: 18456133 DOI: 10.1016/j.ajodo.2007.11.019]
- 85 **Weishaupt D**, Köchli VD, Marincek B. How does MRI work? An introduction to the Physics and Function of Magnetic Resonance Imaging. 2nd ed. Berlin Heidelberg: Springer, 2006
- 86 **Boeddinghaus R**, Whyte A. Current concepts in maxillofacial imaging. *Eur J Radiol* 2008; **66**: 396-418 [PMID: 18082349 DOI: 10.1016/j.ejrad.2007.11.019]
- 87 **van Rensburg LJ**, Paquette M, Morkel JA, Nortjé CJ. Correlative MRI and CT imaging of the odontogenic keratocyst: a review of twenty-one cases. *Oral Maxillofac Surg Clin North Am* 2003; **15**: 363-382 [PMID: 18088689]
- 88 **DelBalso AM**. Lesions of the jaws. *Semin Ultrasound CT MR* 1995; **16**: 487-512 [PMID: 8747414 DOI: 10.1016/S0887-2171(06)80022-3]
- 89 **Idiyatullin D**, Corum C, Moeller S, Prasad HS, Garwood M, Nixdorf DR. Dental magnetic resonance imaging: making the invisible visible. *J Endod* 2011; **37**: 745-752 [PMID: 21787482 DOI: 10.1016/j.joen.2011.02.022]
- 90 **Levin LG**, Law AS, Holland GR, Abbott PV, Roda RS. Identify and define all diagnostic terms for pulpal health and disease states. *J Endod* 2009; **35**: 1645-1657 [PMID: 19932339 DOI: 10.1016/j.joen.2009.09.032]
- 91 **Browne RF**, Golding SJ, Watt-Smith SR. The role of MRI in facial swelling due to presumed salivary gland disease. *Br J Radiol* 2001; **74**: 127-133 [PMID: 11718383]
- 92 **Schmid F**, Tymofiyeva O, Rottner K, Richter E-J, Jakob PM. Dental impression using MRI. In: Proceedings of the Ninth ICMRM, Aachen, Germany, 2007: Abstract 103
- 93 **Tymofiyeva O**, Rottner K, Jakob PM, Richter EJ, Proff P. Three-dimensional localization of impacted teeth using magnetic resonance imaging. *Clin Oral Investig* 2010; **14**: 169-176 [PMID: 19399539 DOI: 10.1007/s00784-009-0277-1]
- 94 **Schara R**, Sersa I, Skaleric U. T1 relaxation time and magnetic resonance imaging of inflamed gingival tissue. *Dentomaxillofac Radiol* 2009; **38**: 216-223 [PMID: 19372109 DOI: 10.1259/dmfr/75262837]
- 95 **Hinshaw DB**, Holshouser BA, Engstrom HI, Tjan AH, Christiansen EL, Catelli WF. Dental material artifacts on MR images. *Radiology* 1988; **166**: 777-779 [PMID: 3340777]
- 96 **Schaefer SD**, Maravilla KR, Suss RA, Burns DK, Nunnally R, Merkel MA, Close LG. Magnetic resonance imaging vs computed tomography. Comparison in imaging oral cavity and pharyngeal carcinomas. *Arch Otolaryngol* 1985; **111**: 730-734 [PMID: 2996476]
- 97 **Vijay MR**, Adam EF, Barry MT. MRI and CT Atlas of Correlative Imaging in Otolaryngology. London: Martin Dunitz Ltd, 1992: 1-11
- 98 **Okano Y**, Yamashiro M, Kaneda T, Kasai K. Magnetic resonance imaging diagnosis of the temporomandibular joint in patients with orthodontic appliances. *Oral Surg Oral Med Oral Pathol Oral Radiol Endod* 2003; **95**: 255-263 [PMID: 12582369]
- 99 **Katti G**, Ara SA, Shireen A. Hypertension in response to IL-6 during pregnancy: role of AT1-receptor activation. *Int J Infeeron Cytokine Mediator Res* 2011; **2011**: 65-70 [PMID: 23002372]
- 100 **White SC**, Pharoah MJ. Chapter 13. Advanced Imaging. Oral Radiology. Principles and Interpretation. 6th ed. St Louis, MO: Mosby Elsevier, 2009: 207-224
- 101 **Adeyemo WL**, Akadir OA. A systematic review of the diagnostic role of ultrasonography in maxillofacial fractures. *Int J Oral Maxillofac Surg* 2011; **40**: 655-661 [PMID: 21377837 DOI: 10.1016/j.ijom.2011.02.001]
- 102 **White SC**, Pharoah MJ. Oral radiology, Principles and Interpretation. 6th ed. Chapter: 30 Salivary gland radiology. Mosby Elsevier, 2009: 665-666
- 103 **Arijji E**, Arijji Y, Yoshiura K, Kimura S, Horinouchi Y, Kanda S. Ultrasonographic evaluation of inflammatory changes in the masseter muscle. *Oral Surg Oral Med Oral Pathol* 1994; **78**: 797-801 [PMID: 7898913]
- 104 **Gundappa M**, Ng SY, Whaites EJ. Comparison of ultrasound, digital and conventional radiography in differentiating periapical lesions. *Dentomaxillofac Radiol* 2006; **35**: 326-333 [PMID: 16940480]
- 105 **Cotti E**, Campisi G, Ambu R, Dettori C. Ultrasound real-time imaging in the differential diagnosis of periapical lesions. *Int Endod J* 2003; **36**: 556-563 [PMID: 12887385]
- 106 **Wakasugi-Sato N**, Kodama M, Matsuo K, Yamamoto N, Oda M, Ishikawa A, Tanaka T, Seta Y, Habu M, Kokuryo S, Ichimiya H, Miyamoto I, Kito S, Matsumoto-Takeda S, Wakasugi T, Yamashita Y, Yoshioka I, Takahashi T, Tominaga K, Morimoto Y. Advanced clinical usefulness of ultrasonography for diseases in oral and maxillofacial regions. *Int J Dent* 2010; **2010**: 639382 [PMID: 20445749 DOI: 10.1155/2010/639382]
- 107 **Chandak R**, Degwekar S, Bhowte RR, Motwani M, Banode P, Chandak M, Rawlani S. An evaluation of efficacy of ultrasonography in the diagnosis of head and neck swellings. *Dentomaxillofac Radiol* 2011; **40**: 213-221 [PMID: 21493877 DOI: 10.1259/dmfr/68658286]
- 108 **Rajendran N**, Sundaresan B. Efficacy of ultrasound and color power Doppler as a monitoring tool in the healing of endodontic periapical lesions. *J Endod* 2007; **33**: 181-186 [PMID: 17258641]
- 109 **Tikku AP**, Kumar S, Loomba K, Chandra A, Verma P, Aggarwal R. Use of ultrasound, color Doppler imaging and radiography to monitor periapical healing after endodontic surgery. *J Oral Sci* 2010; **52**: 411-416 [PMID: 20881334]
- 110 **Yoon MJ**, Kim E, Lee SJ, Bae YM, Kim S, Park SH. Pulpal blood flow measurement with ultrasound Doppler imaging. *J Endod* 2010; **36**: 419-422 [PMID: 20171355 DOI: 10.1016/j.joen.2009.12.031]
- 111 **Tagtekin DA**, Ozyoney G, Baseren M, Ando M, Hayran O, Alpar R, Gokalp S, Yanikoglu FC, Stookey GK. Caries detection with DIAGNOdent and ultrasound. *Oral Surg Oral Med Oral Pathol Oral Radiol Endod* 2008; **106**: 729-735 [PMID: 18656396 DOI: 10.1016/j.tripleo.2008.05.010]
- 112 **Mahmoud AM**, Ngan P, Crout R, Mukdadi OM. High-resolution 3D ultrasound jawbone surface imaging for diagnosis of periodontal bony defects: an in vitro study. *Ann Biomed Eng* 2010; **38**: 3409-3422 [PMID: 20532630 DOI: 10.1007/s10439-010-0089-0]

- 113 **Cha BK**, Lee YH, Lee NK, Choi DS, Baek SH. Soft tissue thickness for placement of an orthodontic miniscrew using an ultrasonic device. *Angle Orthod* 2008; **78**: 403-408 [PMID: 18416626 DOI: 10.2319/051607-237.1]
- 114 **Culjat MO**, Choi M, Singh RS, Grundfest WS, Brown ER, White SN. Ultrasound detection of submerged dental implants through soft tissue in a porcine model. *J Prosthet Dent* 2008; **99**: 218-224 [PMID: 18319093 DOI: 10.1016/S0022-3913(08)60046-3]
- 115 **Manfredini D**, Guarda-Nardini L. Ultrasonography of the temporomandibular joint: a literature review. *Int J Oral Maxillofac Surg* 2009; **38**: 1229-1236 [PMID: 19700262 DOI: 10.1016/j.ijom.2009.07.014]
- 116 **Bas B**, Yılmaz N, Gökce E, Akan H. Diagnostic value of ultrasonography in temporomandibular disorders. *J Oral Maxillofac Surg* 2011; **69**: 1304-1310 [PMID: 21256654 DOI: 10.1016/j.joms.2010.07.012]

P- Reviewer: Kamburoglu K, Tomofuji T, Tsushima Y
S- Editor: Song XX **L- Editor:** A **E- Editor:** Lu YJ



Application of magnetic resonance imaging in cervical spondylotic myelopathy

Chuan Zhang, Sushant K Das, Dong-Jun Yang, Han-Feng Yang

Chuan Zhang, Sushant K Das, Dong-Jun Yang, Han-Feng Yang, Department of Radiology, Affiliated Hospital of North Sichuan Medical College, Nanchong 637000, Sichuan Province, China

Author contributions: Zhang C and Yang HF contributed equally to this work; Zhang C, Yang HF, Yang DJ and Das SK collected information about the disease; Zhang C and Yang HF designed the research; Zhang C, Yang HF, Yang DJ and Das SK collected and analyzed the literature; Zhang C and Yang HF wrote the paper.

Correspondence to: Han-Feng Yang, MD, Department of Radiology, Affiliated Hospital of North Sichuan Medical College, 63 Wenhua Road, Nanchong 637000, Sichuan Province, China. hanfengyang168@163.com

Telephone: +86-817-2262089 Fax: +86-817-2262236

Received: February 20, 2014 Revised: September 14, 2014

Accepted: September 23, 2014

Published online: March 28, 2015

nance imaging

Core tip: This article attempts to investigate the application of magnetic resonance (MR) technology to the management of cervical spondylotic myelopathy (CSM) patients and discusses recent and future advances in both conventional and novel MR techniques. The novel MR techniques, including diffusion tensor imaging, MR spectroscopy and functional MR imaging, have all played an essential role in the management of patients with CSM.

Original sources: Zhang C, Das SK, Yang DJ, Yang HF. Application of magnetic resonance imaging in cervical spondylotic myelopathy. *World J Radiol* 2014; 6(10): 826-832 Available from: URL: <http://www.wjgnet.com/1949-8470/full/v6/i10/826.htm> DOI: <http://dx.doi.org/10.4329/wjr.v6.i10.826>

Abstract

Cervical spondylotic myelopathy (CSM) is the most common cause of spinal cord dysfunction and is caused by static or dynamic repeated compression of the spinal cord resulting from degenerative arthritis of the cervical spine and some biological injuries to the cervical spine. The T2 signal change on conventional magnetic resonance imaging (MRI) is most commonly associated with neurological deficits. Diffusion tensor imaging and MR spectroscopy show altered microstructure and biochemistry that reflect patient-specific pathogenesis and can be used to predict neurological outcome and response to intervention. Functional MRI can help to assess the neurological functional recovery after decompression surgery for CSM.

© 2015 Baishideng Publishing Group Inc. All rights reserved.

Key words: Cervical spondylotic myelopathy; Magnetic resonance imaging; Diffusion tensor imaging; Magnetic resonance spectroscopy; Functional magnetic reso-

INTRODUCTION

Magnetic resonance imaging (MRI) plays an essential role in the management of patients with cervical spondylotic myelopathy (CSM). There have been many advances in MR technology over the past few years and the resolution and image quality have improved greatly. With these improvements, the application of MRI in CSM has progressed in parallel. The novel MR techniques not only offer a diagnostic modality, but also can be used to predict neurological outcome and response to intervention.

In addition to conventional MRI, recent application of novel techniques in CSM, such as diffusion tensor imaging (DTI)^[1], MR spectroscopy (MRS)^[2] and functional MR imaging (fMRI)^[3], further highlights the potential influence of MR technology on the disease process. By providing pertinent information about the spinal cord microstructure and metabolism, and assessing the neurological function after surgery, these novel techniques

provide increased sensitivity to diagnosis of spinal cord injury, especially the cellular injury that ubiquitously occurs during CSM pathogenesis^[4,5].

This article attempts to investigate the application of MR technology to the management of CSM patients and discusses recent and future advances in both conventional and novel MR techniques.

PATHOPHYSIOLOGY OF CSM

In order to be fully aware of the importance of MRI in the management of CSM, an advance in understanding of the complex CSM pathophysiology is necessary. CSM is the most common cause of spinal cord dysfunction^[6-8]. CSM is caused by static or dynamic repeated compression of the spinal cord resulting from degenerative arthritis of the cervical spine and some biological injury to the cervical spine cord. The preceding mechanism is mechanical injury, including compression, distraction and shear^[9], and direct spinal cord compression is the most frequently encountered mechanism. The biological injury in CSM is likely related to a variety of mechanisms, such as free radical-mediated cell injury, cation-mediated cell injury, glutamergic toxicity and apoptosis^[10]. Ischemia of the cervical spinal cord is considered to be a significant contributor to the pathophysiology of CSM, which includes compression of larger vessels and impaired microcirculation^[11].

CONVENTIONAL MRI

Before MR technology was well developed, computed tomography with or without myelography was commonly used for spinal structural diagnosis in CSM patients. These modalities could offer some useful anatomical information in patients with CSM, but there were some patients without myelopathy despite compression of the spinal cord and only limited information could be directly ascertained about the condition of the spinal cord. Therefore, there were some limitations in the assessment of spinal cord injury.

Through providing high-resolution imaging of soft tissue anatomy, MRI provides excellent anatomical information about the spinal cord macrostructure and gives insight into structural histopathological changes in CSM patients. In order to investigate myelomalacia, edema, gliosis and ischemic white matter changes of the spinal cord, a large number of clinical studies have examined changes in T1- and T2-weighted signals. Some authors considered that these observations were caused by irreversible spinal cord injury^[12], but others felt that these regions represented a wide spectrum of recuperative potential^[13]. Recently, several grading systems have been proposed to classify the spinal cord signaling change subtypes^[14], but the specific grading remains one of the most controversial topics in the field of degenerative spinal disease.

Assessment of the utility of MRI to predict neuro-

logical outcome following decompression surgery for CSM has attracted much attention. In 2009, the Guidelines for the Surgical Management of Cervical Degenerative Disease were published by an expert group that represents the Joint Section on Disorders of the Spine and Peripheral Nerves of the American Association of Neurological Surgeons and Congress of Neurological Surgeons^[15]. They established the relationship between spinal cord signal changes and clinical outcome in CSM patients. According to their extensive literature review, they concluded that multilevel T2 hyperintensity, T1 focal hypointensity combined with T2 focal hyperintensity, and spinal cord atrophy each indicate poor prognosis following surgical intervention. This has been confirmed by other authors. For example, Uchida *et al*^[16] reported that a T1/T2 low signal/high signal imaging pattern was associated with poor neurological recovery. On the contrary, a study has shown that the regression of high signal changes on T2 postoperatively correlates with better functional outcomes^[17]. Furthermore, some studies have suggested that if surgeons use MRI signal intensity to estimate the risk of poor outcome after surgery, they should use high signal changes in T2 in combination with other signal intensity parameters and not in isolation^[18]. Therefore, more robust and objective modalities for assessment of the condition of the spinal cord need to be developed.

DTI

Principles and parameters of DTI

DTI is a noninvasive MRI technique that measures the random motion of water molecules and provides information about the cellular integrity and pathology of anisotropic tissues^[19,20]. DTI can provide unique quantitative information on the microstructural features of white matter in the central nervous system^[21]. Diffusion properties can be evaluated using quantitative indices such as the apparent diffusion coefficient (ADC), mean diffusivity (MD) and fractional anisotropy (FA). The ADC reflects the average diffusivity of water molecules in all directions. The stronger water molecules diffuse within a tissue, the larger the ADC. In contrast, the weaker water molecules diffuse within a tissue, the lower the ADC. Therefore, tissues with high water mobility and few boundaries to water motion have high ADC values, such as cerebrospinal fluid and vasogenic edema, whereas tissues with a high degree of complexity and boundaries to diffusion have a relatively lower ADC, such as white matter fiber bundles and tumors^[22]. MD represents the degree of diffusional motion of water molecules (regardless of direction) and is measured in mm²/s. FA represents a rotationally invariant parameter, where 0 represents completely isotropic diffusion and 1 represents extremely limited diffusion in only one direction^[19].

Main features of DTI

An increasing number of studies has indicated the significance of ADC and FA and has defined the character-

istics of the two measurements within CSM patients. At the site of compression in the cervical spinal cord, FA is significantly lower and ADC significantly higher^[23]. These two measurements of DTI are more sensitive and specific than conventional MRI and can detect damage of the white matter tracts before a high signal lesion appears on T2 imaging^[23]. This theory has been demonstrated by Lee *et al.*^[24]. In that study, four patients who had no abnormal signal changes on MRI also had lower FA and higher ADC. In addition, there was another view about the effects of DTI. Some researchers consider that it may have the potential to distinguish between a symptomatic and asymptomatic group of patients. This view has also been proposed in a study by Kerkovsky *et al.*^[23] in which FA was significantly lower and ADC significantly higher in a symptomatic group than in an asymptomatic spondylotic cervical cord encroachment subgroup.

Role of ADC and FA in identification of acute and chronic compression

In addition to the above-mentioned effects, the two measurements were also commonly used in the identification of acute and chronic compression in CSM. Some studies have suggested that acute compression of spinal cord tissue may result in a focal decrease in ADC as well as a focal increase in FA. Through the establishment of diffusion MR simulations, Ford *et al.*^[25] have suggested that compression of axon fibers results in a decrease in ADC, which may lead to a slight increase in FA. Nilsson *et al.*^[26] have clearly demonstrated decreased ADC with increasing compression of spinal cord white matter. Facon *et al.*^[27] explored acute spinal cord compression in two patients and noted a slightly elevated FA at the level of compression compared to normal controls (0.80-0.83 *vs* 0.75 in healthy volunteers). Compared with the diffusion characteristics of acute compression of the spinal cord, clinical studies have clearly documented a significant increase in ADC and decrease in FA in the late stages of chronic compression of the spinal cord^[28]. Through the establishment of an animal model of chronic compression, Cheung *et al.*^[29] illustrated a characteristic increase in ADC and decrease in FA as late as 9 mo after the start of compression. Specifically, the changes in diffusion characteristics may result from chronic, repeated ischemic insults to the spinal cord, leading to downstream histopathological changes, including gliosis, loss of motor neuron function, vasogenic edema and ultimately necrosis and cavitation^[30]. All the pathological changes lead to elevation of ADC due to the increase in extracellular water and suppression of FA due to lack of directional organization within the spinal cord.

Significance of MD

Some studies have indicated that an increase in MD and decrease in FA have diagnostic utility in myelopathy and the sensitivity and specificity for prediction are higher with MD than with FA. After using the following parameters: TE: 80 ms; image matrix of 256 × 195 pixels;

nominal voxel size of 0.9 mm × 1.17 mm, three sections 5-mm thick and a gap of 1 mm, Demir *et al.*^[5] suggested approximately 80% sensitivity and 53% specificity for detecting myelopathy in patients with spinal cord compression. Furthermore, when using a single-shot fast spin-echo-based sequence with the following parameters: TE/TR, 80/6000 ms; number of excitations, 1; field of view, 240 mm²; matrix size, 160; voxel size, 1.5 mm² × 1.5 mm² in-plane; slice thickness, 3 mm; gradient directions, 15; and b values, 0 and 1000 s/mm², and from the results of receiver operating characteristic (ROC) curve analysis, when using the optimal cutoff point (an MD \bar{x} score of 1.40 at the most compressed spinal level), Uda *et al.*^[19] indicated that myelopathy could be predicted with a sensitivity of 100% and specificity of 75%. In conclusion, MD should receive more attention in the management of CSM patients.

MRS

Background to application of MRS

Although chronic spinal cord has been accepted as a major feature of CSM, the time course and evolution of cellular and microstructural damage are yet to be understood clearly. This is largely because conventional MRI, despite providing excellent macroscopic anatomical detail, provides constrained information about spinal cord cellular function and microarchitecture. Some authors postulate that there is a spectrum of cellular and microstructural changes that occur within the spinal cord as patients with cervical spondylosis progress from being asymptomatic to manifesting neurological impairment^[31]. Surgical intervention of the spinal cord in its reversible state (*i.e.*, before the onset of irreversible injury) confers better neurological outcomes. Therefore, understanding of progressive cellular alteration of the spinal cord as the patient advances to a symptomatic state would be a compelling achievement in the treatment of cervical spondylosis.

Principles and characteristics of MRS

Compared with DTI, the application of MRS to CSM has more advantages. MRS can provide metabolic information about the cellular biochemistry and function of the neural structures within the cervical spinal cord^[32]. MRS also can be used to assay a series of pertinent biochemical markers, such as N-acetyl aspartate (NAA), lactate, choline (Cho), myo-inositol (Myo-I), glutamine-glutamate complex (Glx) and creatinine (Cr), with particular sensitivity to NAA and lactate^[2]. Some studies have indicated that NAA is only found in axons and neurons and is considered an indicator of axonal integrity^[33]. Although little is known of the specific mechanism, lactate is considered to play a central role in metabolic dysfunction after central nervous system injury and may be related to ischemia and mitochondrial dysfunction.

MRS features of CSM

In recent years, spinal cord MRS has been most frequent-

ly used to investigate multiple sclerosis lesions^[33]. Many studies have demonstrated suppressed levels of NAA in multiple sclerosis patients when compared to normal volunteers and some correlation between NAA levels and clinical status^[34]. Although less studied, cervical spine MRS has recently been used in CSM. In a cohort of 21 CSM patients, Holly *et al*^[2] indicated that the NAA/Cr ratio was significantly lower in CSM patients than in normal volunteers, which suggested increased neuronal and axonal injury. Nearly one-third of CSM patients appeared to have an abnormal lactate signal and the control subjects did not, which further supports the importance of ischemia in the pathogenesis of CSM.

Early and late changes in MRS metabolites

In a study of 21 patients with cervical spondylosis and 11 healthy controls, Salamon *et al*^[31] discussed the early and late changes in MRS metabolites. In the early changes, the observation of a cervical stenosis patient without spinal cord signal changes showing slightly higher Myo-I and Glx compared to that of the control group suggested Myo-I as a potential early marker for spinal cord inflammation and early stage demyelination in cervical stenosis before neurological impairment. In the late changes, while the patient with spinal cord signal changes had a significantly higher Cho/Cr ratio than the control, the patient without spinal cord signal changes had no significant difference compared to the control. These results show that increased Cho levels appear later than the aforementioned cellular metabolic changes as cervical spondylosis progresses to a symptomatic state. In addition, they also found that higher Cho/NAA ratio was significantly associated with poorer neurological function and Cho/NAA had a significant correlation with the Modified Japanese Orthopedic Association score (mJOA), providing a potential clinically useful radiographic biomarker in the management of cervical spondylosis.

fMRI

Principle and features of fMRI

fMRI is a functional neuroimaging procedure using MRI technology that measures brain activity by detecting associated changes in blood flow^[35]. This technique relies on the coupling of cerebral blood flow and activation of neurons. When an area of the brain is active, the flow of blood in the region also increases^[36]. Discovered in 1990 by Ogawa *et al*^[37], fMRI uses blood oxygenation level dependent (BOLD) contrast. BOLD fMRI is a noninvasive and repeatable imaging modality capable of detecting changes in brain function over time. In recent years, spinal cord injury and CSM have been shown to induce changes in cortical activation during sensorimotor tasks. Although these changes have not been precisely determined, they can reflect part of the relationship between the recovery of limb motor function and the volume of cortical activation area after injury^[38]. CSM is always combined with limb motor dysfunction and pain, particularly

in the upper limbs. fMRI is being developed to assess neurological function after surgery.

Applications of fMRI to CSM

Compared with the clinical application of the aforementioned MR techniques, the current clinical application of fMRI is relatively small. Some researchers consider that spinal fMRI can reveal spinal cord function below the site of injury and may provide objective information that can be used for assessing retained function, designing rehabilitation programs, predicting the potential for recovery of function in spinal cord injury, and for assessing new experimental treatment strategies^[39]. In addition, several studies have assessed neurological function by fMRI after decompression surgery. Tam *et al*^[38] concluded that fMRI detected increased cortical activation in the primary motor cortex during finger tapping after decompression surgery in a CSM patient. These changes become more significant with the recovery of motor function. Upper and lower extremity motor subscores of the Japanese Orthopedic Association scale demonstrated a 40% and 43% improvement, respectively. According to their observation, they suggested that cortical reorganization or recruitment may be associated with the recovery of neurological function after spinal cord injury.

LIMITATIONS OF MR TECHNIQUES

In spite of these advanced imaging techniques offering novel insights into CSM, there are some limitations. The spinal cord is relatively small and has differences in magnetic susceptibility from the adjacent tissues; thus, there will be some artifacts. In the commonly used types of MRS, the minimum voxel size is only slightly smaller than the cross-sectional area of the spinal cord and a significant decrease in signal-to-noise ratio can be caused by a suboptimally placed voxel^[40]. Both MRS and DTI are sensitive in patients with CSM and the structural movement during scan acquisition. The physiological rostral-caudal movement of the spinal cord in response to cardiac pulsations and the respiratory cycle is significant and even more marked than in the brain^[38]. Furthermore, spinal fMRI encounters major technical challenges with cardiac noise being considered a major source of noise^[41]. Therefore, cardiac gating, specialized radiofrequency coils and MR signal suppression bands are more frequently used to improve the quality of MRS, DTI and fMRI in the spinal cord. In addition to the physiological noise with fMRI, there are some other limitations; the most common are the repeatability of examination and the veracity of spatial orientation^[42].

FUTURE DIRECTIONS

An increasing number of studies has suggested that DTI and MRS play a significant role in the management of CSM patients, not only to predict outcome following surgical intervention, but they also have several other po-

tential future applications. Some studies have suggested that some patients with mild CSM can be successfully treated nonoperatively. Advanced MRI techniques such as DTI or MRS have the potential to serve as noninvasive methods to monitor asymptomatic or mildly affected patients treated nonoperatively for impending neurological deterioration. However, providing an early warning is difficult because, despite the progression of cellular spinal cord injury and subsequent neurological symptoms, they present with a stable radiographic appearance in a serial standard MRI. In summary, DTI and MRS as advanced methods to assess the progression of subclinical disease are necessary.

In addition, a recently introduced extension of the DTI technique called diffusional kurtosis imaging (DKI) shows greater promise than DTI in evaluating the microstructure and pathological condition of neuronal tissue, especially gray matter^[43,44]. Hori *et al.*^[45] studied 13 consecutive patients with cervical myelopathy and concluded that the mean diffusional kurtosis (MK) in the spinal cord may reflect microstructural changes and damage of the spinal cord gray matter. Although further studies of the imaging-pathology relationship are needed, MK has the potential to provide new information beyond that provided by conventional diffusion metrics such as ADC and FA, which are based on the monoexponential model^[45].

Recently, investigation of novel molecular and biochemical therapies to treat the biological injury in cells that occurs during CSM pathogenesis has attracted more attention. These include inhibition of apoptosis with a Fas ligand-blocking antibody^[46,47], administration of neurotrophins either through genetically altered fibroblasts^[48] or adenovirus-mediated retrograde spinal cord delivery^[49], and diet therapy to repair injured plasma membranes and cellular oxidative damage^[50]. Once translated to clinical use, all the therapy methods need a noninvasive modality to ascertain cellular response to intervention. DTI, MRS and DKI could potentially serve as such a modality, which can identify subtle changes in spinal cord microarchitecture and biochemistry.

In addition, fMRI plays an important role in assessing neurological functional recovery after decompressive surgery for CSM. According to the trend of MR techniques development and the requirement to quantify neuronal function, fMRI will more frequently be used to detect functional impairment and localize regions of injury in CSM patients in the future^[4]. Furthermore, fMRI combined with DTI can establish a functional connectivity network diagram of active location. Perhaps this will be used frequently to explain the relationship between neurological structure and function in the future.

CONCLUSION

MR techniques play an indispensable role in the management of CSM patients and have evolved primarily from a diagnostic modality to a method that can potentially predict patient outcome following surgical intervention. DTI

and MRS have further enhanced our knowledge about the pathogenic mechanism in CSM by providing detailed information regarding the spinal cord microstructure and biochemistry. In addition, fMRI can help to assess the neurological functional recovery after decompression surgery in CSM. Generally speaking, these MR techniques and others may play an expanded role in the management of CSM patients in the future.

REFERENCES

- 1 **Song T**, Chen WJ, Yang B, Zhao HP, Huang JW, Cai MJ, Dong TF, Li TS. Diffusion tensor imaging in the cervical spinal cord. *Eur Spine J* 2011; **20**: 422-428 [PMID: 20938788 DOI: 10.1007/s00586-010-1587-3]
- 2 **Holly LT**, Freitas B, McArthur DL, Salamon N. Proton magnetic resonance spectroscopy to evaluate spinal cord axonal injury in cervical spondylotic myelopathy. *J Neurosurg Spine* 2009; **10**: 194-200 [PMID: 19320577 DOI: 10.3171/2008.12.SPINE08367]
- 3 **Krishnan R**, Raabe A, Hattingen E, Szelényi A, Yahya H, Hermann E, Zimmermann M, Seifert V. Functional magnetic resonance imaging-integrated neuronavigation: correlation between lesion-to-motor cortex distance and outcome. *Neurosurgery* 2004; **55**: 904-914; discussion 914-915 [PMID: 15458599]
- 4 **Smith SA**, Pekar JJ, van Zijl PC. Advanced MRI strategies for assessing spinal cord injury. *Handb Clin Neurol* 2012; **109**: 85-101 [PMID: 23098708 DOI: 10.1016/B978-0-444-52137-8]
- 5 **Demir A**, Ries M, Moonen CT, Vital JM, Dehais J, Arne P, Caillé JM, Dousset V. Diffusion-weighted MR imaging with apparent diffusion coefficient and apparent diffusion tensor maps in cervical spondylotic myelopathy. *Radiology* 2003; **229**: 37-43 [PMID: 14519868]
- 6 **Shedid D**, Benzel EC. Cervical spondylosis anatomy: pathophysiology and biomechanics. *Neurosurgery* 2007; **60**: S7-13 [PMID: 17204889]
- 7 **Baptiste DC**, Fehlings MG. Pathophysiology of cervical myelopathy. *Spine J* 2006; **6**: 190S-197S [PMID: 17097538]
- 8 **Lyu RK**, Tang LM, Chen CJ, Chen CM, Chang HS, Wu YR. The use of evoked potentials for clinical correlation and surgical outcome in cervical spondylotic myelopathy with intramedullary high signal intensity on MRI. *J Neurol Neurosurg Psychiatry* 2004; **75**: 256-261 [PMID: 14742600]
- 9 **Ellingson BM**, Salamon N, Holly LT. Advances in MR imaging for cervical spondylotic myelopathy. *Eur Spine J* 2013 [PMID: 23917647]
- 10 **Henderson FC**, Geddes JF, Vaccaro AR, Woodard E, Berry KJ, Benzel EC. Stretch-associated injury in cervical spondylotic myelopathy: new concept and review. *Neurosurgery* 2005; **56**: 1101-1113; discussion 1101-1113 [PMID: 15854260]
- 11 **Benzel EC**, Ghogawala Z. Introduction: Cervical spondylotic myelopathy. *Neurosurg Focus* 2013; **35**: Introduction [PMID: 23815255 DOI: 10.3171/2013.5.FOCUS13211]
- 12 **Wada E**, Yonenobu K, Suzuki S, Kanazawa A, Ochi T. Can intramedullary signal change on magnetic resonance imaging predict surgical outcome in cervical spondylotic myelopathy? *Spine (Phila Pa 1976)* 1999; **24**: 455-461; discussion 462 [PMID: 10084183]
- 13 **Matsuda Y**, Miyazaki K, Tada K, Yasuda A, Nakayama T, Murakami H, Matsuo M. Increased MR signal intensity due to cervical myelopathy. Analysis of 29 surgical cases. *J Neurosurg* 1991; **74**: 887-892 [PMID: 1903439]
- 14 **Yukawa Y**, Kato F, Yoshihara H, Yanase M, Ito K. MR T2 image classification in cervical compression myelopathy: predictor of surgical outcomes. *Spine (Phila Pa 1976)* 2007; **32**: 1675-1678; discussion 1679 [PMID: 17621217]

- 15 **Mummaneni PV**, Kaiser MG, Matz PG, Anderson PA, Groff M, Heary R, Holly L, Ryken T, Choudhri T, Vresilovic E, Resnick D. Preoperative patient selection with magnetic resonance imaging, computed tomography, and electroencephalography: does the test predict outcome after cervical surgery? *J Neurosurg Spine* 2009; **11**: 119-129 [PMID: 19769491 DOI: 10.3171/2009.3.SPINE08717]
- 16 **Uchida K**, Nakajima H, Sato R, Kokubo Y, Yayama T, Kobayashi S, Baba H. Multivariate analysis of the neurological outcome of surgery for cervical compressive myelopathy. *J Orthop Sci* 2005; **10**: 564-573 [PMID: 16307181]
- 17 **Vedantam A**, Rajshekhar V. Does the type of T2-weighted hyperintensity influence surgical outcome in patients with cervical spondylotic myelopathy? A review. *Eur Spine J* 2013; **22**: 96-106 [PMID: 22926434 DOI: 10.1007/s00586-012-2483-9]
- 18 **Fehlings MG**, Tetreault LA, Wilson JR, Skelly AC. Cervical spondylotic myelopathy: current state of the art and future directions. *Spine (Phila Pa 1976)* 2013; **38**: S1-S8 [PMID: 23962994 DOI: 10.1097/BRS.0b013e3182a7e9e0]
- 19 **Uda T**, Takami T, Tsuyuguchi N, Sakamoto S, Yamagata T, Ikeda H, Nagata T, Ohata K. Assessment of cervical spondylotic myelopathy using diffusion tensor magnetic resonance imaging parameter at 3.0 tesla. *Spine (Phila Pa 1976)* 2013; **38**: 407-414 [PMID: 22914703 DOI: 10.1097/BRS.0b013e31826f25a3]
- 20 **Kara B**, Celik A, Karadereler S, Ulusoy L, Ganiyusufoglu K, Onat L, Mutlu A, Ornek I, Sirvanci M, Hamzaoglu A. The role of DTI in early detection of cervical spondylotic myelopathy: a preliminary study with 3-T MRI. *Neuroradiology* 2011; **53**: 609-616 [PMID: 21344215 DOI: 10.1007/s00234-011-0844-4]
- 21 **Wang W**, Qin W, Hao N, Wang Y, Zong G. Diffusion tensor imaging in spinal cord compression. *Acta Radiol* 2012; **53**: 921-928 [PMID: 22893728 DOI: 10.1258/ar.2012.120271]
- 22 **Basser PJ**. Inferring microstructural features and the physiological state of tissues from diffusion-weighted images. *NMR Biomed* 1995; **8**: 333-344 [PMID: 8739270]
- 23 **Kerkovský M**, Bednarík J, Dušek L, Sprláková-Puková A, Urbánek I, Mechl M, Válek V, Kadanka Z. Magnetic resonance diffusion tensor imaging in patients with cervical spondylotic spinal cord compression: correlations between clinical and electrophysiological findings. *Spine (Phila Pa 1976)* 2012; **37**: 48-56 [PMID: 21228747 DOI: 10.1097/BRS.0b013e31820e6c35]
- 24 **Lee JW**, Kim JH, Park JB, Park KW, Yeom JS, Lee GY, Kang HS. Diffusion tensor imaging and fiber tractography in cervical compressive myelopathy: preliminary results. *Skeletal Radiol* 2011; **40**: 1543-1551 [PMID: 21494906 DOI: 10.1007/s00256-011-1161-z]
- 25 **Ford JC**, Hackney DB, Lavi E, Phillips M, Patel U. Dependence of apparent diffusion coefficients on axonal spacing, membrane permeability, and diffusion time in spinal cord white matter. *J Magn Reson Imaging* 1998; **8**: 775-782 [PMID: 9702877]
- 26 **Nilsson M**, Lätt J, Ståhlberg F, van Westen D, Hagslätt H. The importance of axonal undulation in diffusion MR measurements: a Monte Carlo simulation study. *NMR Biomed* 2012; **25**: 795-805 [PMID: 22020832 DOI: 10.1002/nbm.1795]
- 27 **Facon D**, Ozanne A, Fillard P, Lepeintre JF, Tournoux-Facon C, Ducreux D. MR diffusion tensor imaging and fiber tracking in spinal cord compression. *AJNR Am J Neuroradiol* 2005; **26**: 1587-1594 [PMID: 15956535]
- 28 **Mamata H**, Jolesz FA, Maier SE. Apparent diffusion coefficient and fractional anisotropy in spinal cord: age and cervical spondylosis-related changes. *J Magn Reson Imaging* 2005; **22**: 38-43 [PMID: 15971186]
- 29 **Cheung MM**, Li DT, Hui ES, Fan S, Ding AY, Hu Y, Wu EX. In vivo diffusion tensor imaging of chronic spinal cord compression in rat model. *Conf Proc IEEE Eng Med Biol Soc* 2009; **2009**: 2715-2718 [PMID: 19964039 DOI: 10.1109/IEMBS.2009.5333389]
- 30 **Harkey HL**, al-Mefty O, Marawi I, Peeler DF, Haines DE, Alexander LF. Experimental chronic compressive cervical myelopathy: effects of decompression. *J Neurosurg* 1995; **83**: 336-341 [PMID: 7616281]
- 31 **Salamon N**, Ellingson BM, Nagarajan R, Gebara N, Thomas A, Holly LT. Proton magnetic resonance spectroscopy of human cervical spondylosis at 3T. *Spinal Cord* 2013; **51**: 558-563 [PMID: 23588574 DOI: 10.1038/sc.2013.31]
- 32 **Henning A**, Schär M, Kollias SS, Boesiger P, Dydak U. Quantitative magnetic resonance spectroscopy in the entire human cervical spinal cord and beyond at 3T. *Magn Reson Med* 2008; **59**: 1250-1258 [PMID: 18421679 DOI: 10.1002/mrm.21578]
- 33 **Kendi AT**, Tan FU, Kendi M, Yilmaz S, Huvaj S, Tellioglu S. MR spectroscopy of cervical spinal cord in patients with multiple sclerosis. *Neuroradiology* 2004; **46**: 764-769 [PMID: 15258708]
- 34 **Blamire AM**, Cader S, Lee M, Palace J, Matthews PM. Axonal damage in the spinal cord of multiple sclerosis patients detected by magnetic resonance spectroscopy. *Magn Reson Med* 2007; **58**: 880-885 [PMID: 17969113]
- 35 **Binder JR**, Rao SM, Hammeke TA, Frost JA, Bandettini PA, Hyde JS. Effects of stimulus rate on signal response during functional magnetic resonance imaging of auditory cortex. *Brain Res Cogn Brain Res* 1994; **2**: 31-38 [PMID: 7812176]
- 36 **Ogawa S**, Tank DW, Menon R, Ellermann JM, Kim SG, Merkle H, Ugurbil K. Intrinsic signal changes accompanying sensory stimulation: functional brain mapping with magnetic resonance imaging. *Proc Natl Acad Sci USA* 1992; **89**: 5951-5955 [PMID: 1631079]
- 37 **Ogawa S**, Lee TM, Kay AR, Tank DW. Brain magnetic resonance imaging with contrast dependent on blood oxygenation. *Proc Natl Acad Sci USA* 1990; **87**: 9868-9872 [PMID: 2124706]
- 38 **Tam S**, Barry RL, Bartha R, Duggal N. Changes in functional magnetic resonance imaging cortical activation after decompression of cervical spondylosis: case report. *Neurosurgery* 2010; **67**: E863-E84; discussion E864 [PMID: 20657323 DOI: 10.1227/01.NEU.0000374848.86299.17]
- 39 **Leitch JK**, Figley CR, Stroman PW. Applying functional MRI to the spinal cord and brainstem. *Magn Reson Imaging* 2010; **28**: 1225-1233 [PMID: 20409662 DOI: 10.1016/j.mri.2010.03.032]
- 40 **Cooke FJ**, Blamire AM, Manners DN, Styles P, Rajagopalan B. Quantitative proton magnetic resonance spectroscopy of the cervical spinal cord. *Magn Reson Med* 2004; **51**: 1122-1128 [PMID: 15170831]
- 41 **Piché M**, Cohen-Adad J, Nejad MK, Perlberg V, Xie G, Beaudoin G, Benali H, Rainville P. Characterization of cardiac-related noise in fMRI of the cervical spinal cord. *Magn Reson Imaging* 2009; **27**: 300-310 [PMID: 18801632 DOI: 10.1016/j.mri.2008.07.019.]
- 42 **Stroman PW**. Magnetic resonance imaging of neuronal function in the spinal cord: spinal FMRI. *Clin Med Res* 2005; **3**: 146-156 [PMID: 16160069]
- 43 **Kamagata K**, Tomiyama H, Motoi Y, Kano M, Abe O, Ito K, Shimoji K, Suzuki M, Hori M, Nakanishi A, Kuwatsuru R, Sasai K, Aoki S, Hattori N. Diffusional kurtosis imaging of cingulate fibers in Parkinson disease: comparison with conventional diffusion tensor imaging. *Magn Reson Imaging* 2013; **31**: 1501-1506 [PMID: 23895870 DOI: 10.1016/j.mri.2013.06.009]
- 44 **Raz E**, Bester M, Sigmund EE, Tabesh A, Babb JS, Jaggi H, Helpert J, Mitnick RJ, Inglese M. A better characterization of spinal cord damage in multiple sclerosis: a diffusional kurtosis imaging study. *AJNR Am J Neuroradiol* 2013; **34**: 1846-1852 [PMID: 23578677 DOI: 10.3174/ajnr.A3512]
- 45 **Hori M**, Tsutsumi S, Yasumoto Y, Ito M, Suzuki M, Tanaka FS, Kyogoku S, Nakamura M, Tabuchi T, Fukunaga I, Suzuki Y, Kamagata K, Masutani Y, Aoki S. Cervical spondylosis: Evaluation of microstructural changes in spinal cord

white matter and gray matter by diffusional kurtosis imaging. *Magn Reson Imaging* 2014; **32**: 428-432 [PMID: 24602824 DOI: 10.1016/j.mri.2014.01.018]

- 46 **Yu WR**, Baptiste DC, Liu T, Odrobina E, Stanisz GJ, Fehlings MG. Molecular mechanisms of spinal cord dysfunction and cell death in the spinal hyperostotic mouse: implications for the pathophysiology of human cervical spondylotic myelopathy. *Neurobiol Dis* 2009; **33**: 149-163 [PMID: 19006686 DOI: 10.1016/j.nbd.2008.09.024]
- 47 **Yu WR**, Liu T, Kiehl TR, Fehlings MG. Human neuropathological and animal model evidence supporting a role for Fas-mediated apoptosis and inflammation in cervical spondylotic myelopathy. *Brain* 2011; **134**: 1277-1292 [PMID: 21490053]
- 48 **Tobias CA**, Han SS, Shumsky JS, Kim D, Tumolo M, Dhoot

NO, Wheatley MA, Fischer I, Tessler A, Murray M. Alginate encapsulated BDNF-producing fibroblast grafts permit recovery of function after spinal cord injury in the absence of immune suppression. *J Neurotrauma* 2005; **22**: 138-156 [PMID: 15665609]

- 49 **Xu K**, Uchida K, Nakajima H, Kobayashi S, Baba H. Targeted retrograde transfection of adenovirus vector carrying brain-derived neurotrophic factor gene prevents loss of mouse (*twy/twy*) anterior horn neurons in vivo sustaining mechanical compression. *Spine (Phila Pa 1976)* 2006; **31**: 1867-1874 [PMID: 16924202]
- 50 **Holly LT**, Blaskiewicz D, Wu A, Feng C, Ying Z, Gomez-Pinilla F. Dietary therapy to promote neuroprotection in chronic spinal cord injury. *J Neurosurg Spine* 2012; **17**: 134-140 [PMID: 22735048 DOI: 10.3171/2012.5.SPINE1216]

P- Reviewer: Algin O, Hori M, Razeq AA **S- Editor:** Song XX
L- Editor: Roemmele A **E- Editor:** Lu YJ



Partial volume effect modeling for segmentation and tissue classification of brain magnetic resonance images: A review

Jussi Tohka

Jussi Tohka, Department of Signal Processing, Tampere University of Technology, FIN-33101 Tampere, Finland
Author contributions: Tohka J designed and wrote the article.
Correspondence to: Jussi Tohka, PhD, Department of Signal Processing, Tampere University of Technology, PO Box 553, FIN-33101 Tampere, Finland. jussi.tohka@tut.fi
Telephone: +358-40-1981497 Fax: +358-3-3641352
Received: June 23, 2014 Revised: September 3, 2014
Accepted: September 23, 2014
Published online: March 28, 2015

Abstract

Quantitative analysis of magnetic resonance (MR) brain images are facilitated by the development of automated segmentation algorithms. A single image voxel may contain of several types of tissues due to the finite spatial resolution of the imaging device. This phenomenon, termed partial volume effect (PVE), complicates the segmentation process, and, due to the complexity of human brain anatomy, the PVE is an important factor for accurate brain structure quantification. Partial volume estimation refers to a generalized segmentation task where the amount of each tissue type within each voxel is solved. This review aims to provide a systematic, tutorial-like overview and categorization of methods for partial volume estimation in brain MRI. The review concentrates on the statistically based approaches for partial volume estimation and also explains differences to other, similar image segmentation approaches.

© 2015 Baishideng Publishing Group Inc. All rights reserved.

Key words: Magnetic resonance imaging; Segmentation; Tissue classification; White matter; Gray matter; Image processing; Brain imaging; Image analysis

Core tip: Each voxel in a brain magnetic resonance imaging (MRI) may contain multiple types of tissue.

Partial volume estimation refers to a generalized image segmentation task where the amount of each tissue type within each image voxel of brain MRI is solved. This is important for volume quantification and cortical thickness analysis due to the geometrical complexity of human brain structure. This review aims to provide a systematic, tutorial-like overview of methods for partial volume estimation in brain MRI.

Original sources: Tohka J. Partial volume effect modeling for segmentation and tissue classification of brain magnetic resonance images: A review. *World J Radiol* 2014; 6(11): 855-864 Available from: URL: <http://www.wjgnet.com/1949-8470/full/v6/i11/855.htm> DOI: <http://dx.doi.org/10.4329/wjr.v6.i11.855>

INTRODUCTION

Quantitative analysis of magnetic resonance (MR) brain images to gain knowledge about human brain structure is increasingly important. For example, various neuropsychiatric and neurodegenerative diseases, such as schizophrenia^[1] and Alzheimer's disease^[2], alter the brain structure. By analyzing these alterations, a better understanding of the underlying disease mechanisms could be gained and diseases could potentially be diagnosed more rapidly and accurately^[3]. This is important since brain diseases represent a major source of the overall disease burden^[4] and are often associated with heavy impact to informal caregivers.

The typical quantitative analyses to detect and quantify differences in brain structure between two or more subject groups include voxel based morphometry^[5] and cortical thickness analysis^[6]. These analyses are facilitated by the development of automated MR image (MRI) segmentation algorithms, which are standard tools in modern neuroscience. The image processing chain leading to MRI segmentation and, finally, to statistical analyses,

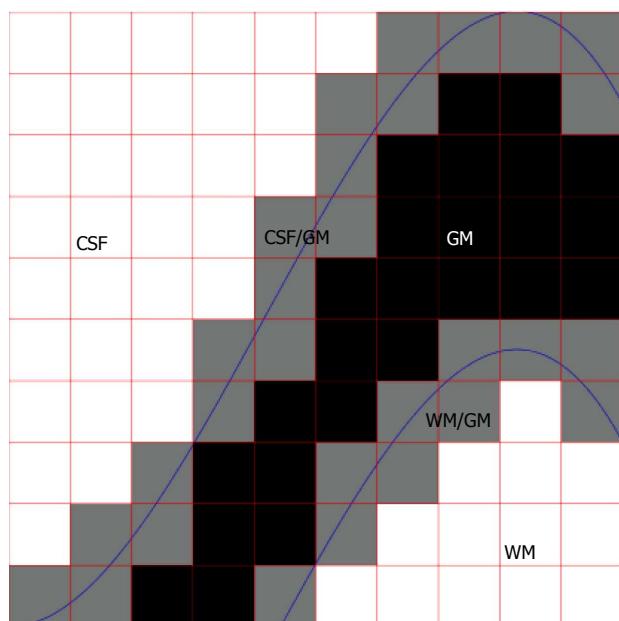


Figure 1 A schematic explanation of the partial volume effect in the context of brain magnetic resonance imaging. Voxels composed of purely gray matter (GM) are colored in black color while voxels composed of cerebro-spinal fluid (CSF) or white matter (WM) are in white color. These are termed pure tissue voxels or pure voxels. Voxels composed of multiple tissue types, termed mixed voxels, are colored in gray. In the figure, these can be either voxels containing both CSF and GM tissue types or voxels containing both WM and GM tissue types. The actual anatomical boundaries between tissue types are shown in blue and red color is used to indicate voxel boundaries.

comprises of a long pipeline of different operations including skull stripping, intensity non-uniformity correction, tissue classification, registration to the stereotactic space and cortical surfaces extraction. The point of interest in this review is the tissue classification. This refers to assigning a tissue type label to each voxel of a brain image. Typically, the three main tissue types, white matter (WM), gray matter (GM), and cerebro-spinal fluid (CSF), are considered.

A single voxel may contain of several types of tissues due to the finite spatial resolution of the imaging device. This phenomenon, termed partial volume effect (PVE), complicates the segmentation process, and, due to the complexity of human brain anatomy, the PVE is an important factor when accurate brain structure quantification is needed; see Figure 1 for a schematic explanation of the PVE in the context of brain MRI. González Ballester *et al*^[7,8] reported that ignoring the PVE can lead to volume measurement errors in the range of 20%-60%. Widely used MRI segmentation algorithms usually account for PVE, for example, by incorporating extra tissue classes^[9-11]. Ruan *et al*^[12] demonstrated that the intensity distributions of the partial volume voxels can be approximated using Gaussian distributions and an early work attributed the non-normality of the intensity distributions of the tissue classes to partial volume artefact^[13]. However, some algorithms take a step further and try to solve an extended version of the tissue classification problem, where the amount of each tissue type within

each voxel is solved. For example, hard or crisp tissue classification provides information whether a particular voxel is WM, GM, or CSF. In the extended problem, one wants to know that a voxel contains 20% GM, 80% WM and 0% of CSF and we say that the partial volume coefficients (PVCs) are 20% for GM, 80% for WM and 0% for CSF. The extended problem has various names. It has been referred to as fuzzy segmentation, partial volume segmentation, partial volume estimation, and tissue fraction estimation. It will be referred to as partial volume estimation in the remainder of this paper. In order for the partial volume estimation problem to be solvable, the intensity of a partial volume voxel has to be expressed with a model that depends on the parameters of image intensity distributions of pure tissue classes. Figure 2 exemplifies partial volume estimation as compared to hard tissue classification and also points out a specific problem of hard tissue classification particularly important to cortical thickness computations. Namely, insufficient image resolution may lead to hard tissue classification miss sulcal CSF and this may subsequently lead to incorrect cortical thickness computation if hard tissue classification is used as a preprocessing operation to the cortical thickness computation.

This review aims to provide a systematic, tutorial-like overview and categorization for different approaches for partial volume estimation in brain MRI. In addition of the author's knowledge about existing literature, the articles to be included in this review were searched on Pubmed: Search term: [(magnetic resonance [Title/Abstract] OR MRI [Title/Abstract]) AND brain [Title/Abstract] AND partial volume [Title/Abstract] AND (segmentation [Title/Abstract] OR tissue classification [Title/Abstract] OR partial volume coefficient estimation [Title/Abstract])] NOT (PET [Title/Abstract] OR emission tomography [Title/Abstract]). The search yielded 80 articles, majority of which were found relevant to this review.

IMAGE PRE-PROCESSING

The algorithms introduced in next sections require various image pre-processing steps to be performed before the partial volume estimation can take place. The pre-processing pipeline can include intensity non-uniformity correction, brain extraction (or skull stripping) and registration to a stereotactic space.

Intensity non-uniformity correction is required because MR images are known to contain low frequency spatial intensity variations often referred to as radio frequency inhomogeneity or shading artifact^[14]. All segmentation algorithms in brain MRI must account for this artifact to produce accurate segmentations. There are several ways to correct for the shading artifact^[14]. This can be assumed to be an image pre-processing step or to be performed jointly with the PV estimation, interleaving PV estimation (segmentation) and non-uniformity correction steps. In what follows, we will assume that the images have been corrected for this artifact.

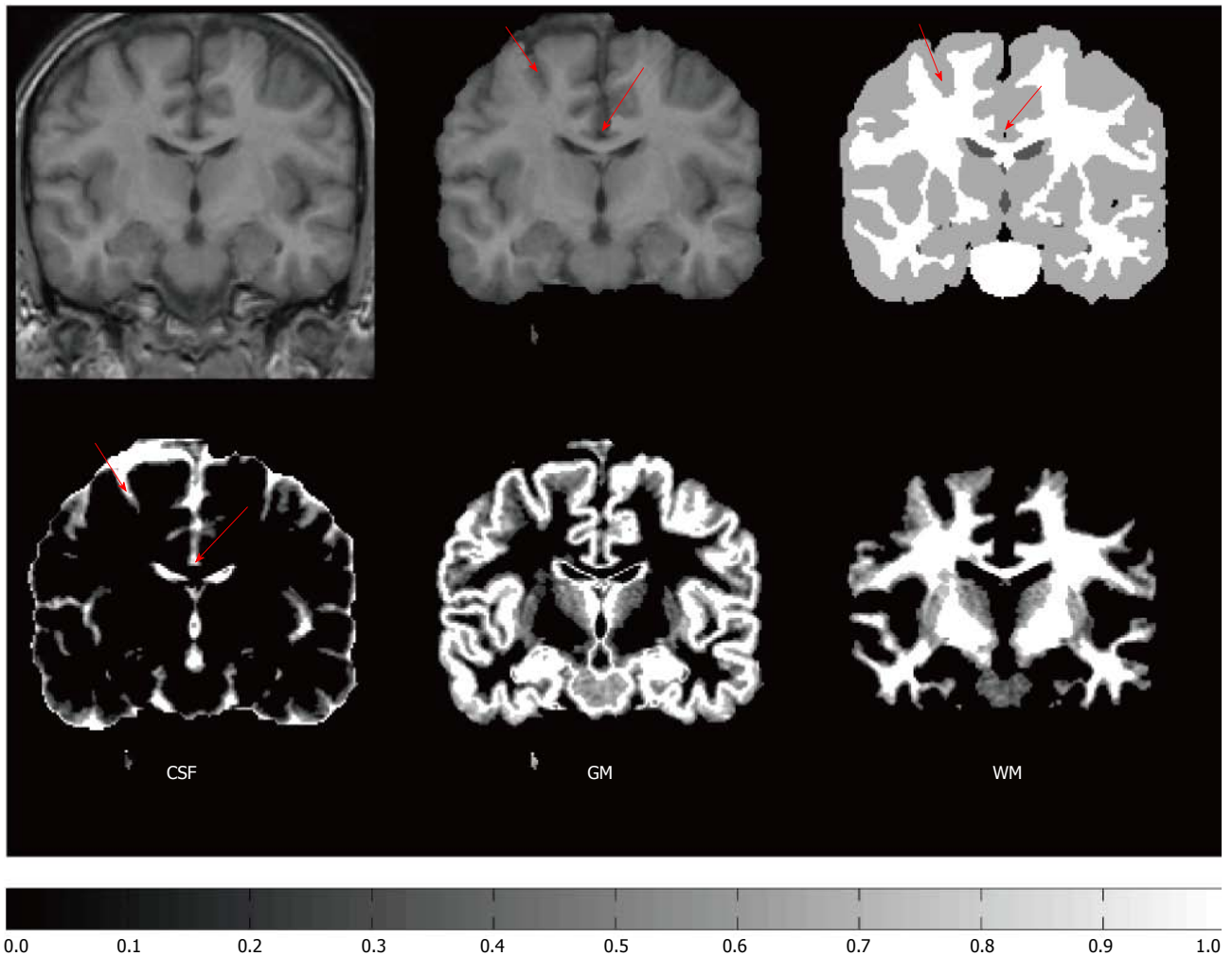


Figure 2 Example of partial volume estimation. Top row, from left: A coronal section of T1 weighted MR image; A skull stripped version of the coronal section; A manual labeling into gray matter (GM) (gray color), white matter (WM) (white color), and cerebro-spinal fluid (CSF) (dark gray color). Bottom row: Estimates of partial volume coefficients (PVCs) for CSF, GM, and WM. The color bar refers to the PVC estimates in the bottom row. The image is obtained from the IBSR2 dataset provided by the Center for Morphometric Analysis at Massachusetts General Hospital and PVCs were computed as described in the ref. [28]. Note how the manual hard labeling completely misses the CSF in the interhemispheric fissure as well as in the superior frontal sulcus pointed by red arrows. Instead PVC estimates of CSF in the bottom row capture well the sulcal CSF.

Although we are interested in segmentation of the brain tissues, brain MR images contain signal from other, extracerebral tissue types, such as skull or scalp. Because these extracerebral tissue types are often irrelevant for brain image quantification, it is useful to mask out the voxels outside the brain out before the PV estimation. This is termed skull stripping or brain extraction and the reference^[15] provides a comparison of skull stripping algorithms.

The registration to stereotactic space is usually carried out to be able to utilize information of the tissue type probability maps, which, for each voxel, give a prior probability that the voxel is of certain issue type^[16]. It should be noted that this is not as useful for partial volume estimation as it can be for hard segmentation, because tissue probability maps provide no information on tissue fractions^[17]. Moreover, if the registered images are resampled to the stereotactic space, this amplifies the partial volume effect and may not be a recommended action.

MIXEL MODEL

Definition and approximations

The most commonly used model of PVE in brain MRI is the mixel model^[18]. The mixel model assumes that each intensity value in the image is a realization of a weighted sum of random variables (RVs), each of which characterizes a pure tissue type. The original formulation^[18] requires images to be multispectral, *i.e.*, that image data from multiple pulse sequences are available (for example, T1, T2, and proton density weighted images). However, there are approaches to overcome this problem by utilizing clever approximations as we shall see in Section Solving the mixel model.

We now proceed to a more formal description of the mixel model. For this, we need to establish some notation. The observed image is $X = \{x_i : i = 1, \dots, N\}$, with the voxel intensity $x_i \in \mathbb{R}^K$, and K the number of data channels in the multispectral case. For example, if we have T1-, T2-, and proton density-weighted images, then $K = 3$.

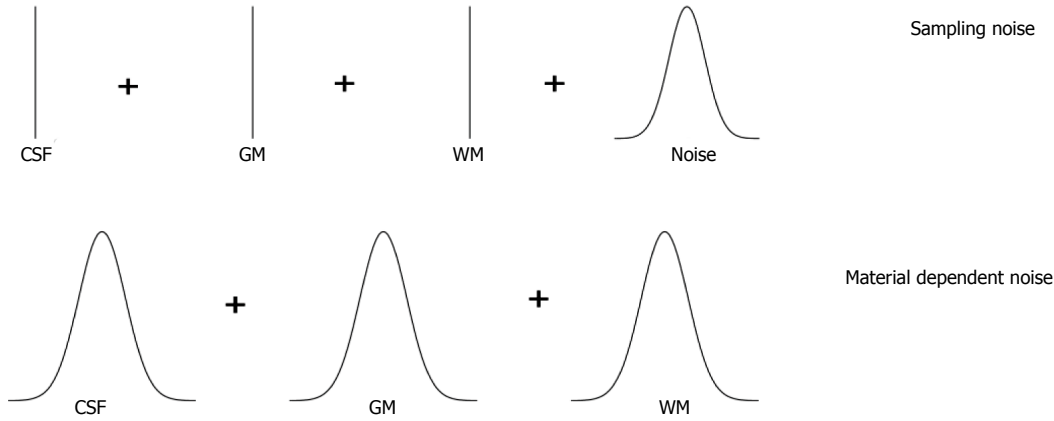


Figure 3 Sampling and material dependent noise models. Sampling noise model assumes that each tissue type is represented by a single average value and Gaussian-distributed noise is then added. Material dependent noise model assumes that the tissue types are represented by random variables. CSF: Cerebro-spinal fluid; GM: Gray matter; WM: White matter.

N denotes the number of brain voxels in the image and i is the voxel index. The voxel index has three components that correspond to the position of the voxel in the left-right, anterior-posterior, and inferior-superior axes. There are M tissue types in the image. Typically, M is equal to 3, and the tissue types are WM, GM, and CSF. The mixel model is statistically based. Thus, a voxel intensity x_i is considered to be a realization of random variable x_i . Similarly, each tissue type j is described by a random variable l_j , which is assumed to be distributed according to the multivariate normal distribution with the mean μ_j and covariance Σ_j . Random variable x_i is written as a weighted sum

$$x_i = \sum_{j=1}^M w_{ij} l_j + n, \quad (1)$$

where n represents measurement noise, typically assumed to be Gaussian (with a covariance matrix Σ) and partial volume coefficients (PVCs) $w_{ij} \in [0, 1]$ for all i, j and $\sum_{j=1}^M w_{ij} = 1$ for all i . The PVCs model the fraction of each tissue type in the voxel, for example, if w_{GM} has a value of 0.8 then the voxel contains 80% of the GM tissue type. This is similar to the fuzzy classification/segmentation problem, but in the mixel model the coefficients w_{ij} specifically model the fraction of tissue type j present in the voxel i . We will return to connections of the mixel model and the Fuzzy C-means algorithm in Section 5.

In practice, the mixel model has to be simplified because it is impossible to distinguish between measurement noise and variability within tissue types. Various simplifications have been studied by Santiago *et al*^[19,20]. They identified two possible types of simplification, namely, the sampling noise model and material dependent noise model as depicted in Figure 3. The sampling noise model assumes that all the randomness in the model is due to measurement noise. This leads to a model, where the tissue types are described by mean intensities of tissue types:

$$x_i = \sum_{j=1}^M w_{ij} \mu_j + n, \quad (2)$$

The material dependent noise model is obtained by

embedding the measurement noise into material noise components, *i.e.*, n is dropped from Eq. (1)

$$x_i = \sum_{j=1}^M w_{ij} l_j. \quad (3)$$

This model is more complex than the sampling noise model, but it is probably more realistic.

Solving the mixel model

Direct solution via penalized least squares: Assuming the sampling noise model, the PVCs can be solved directly from Eq. (2) if enough data channels are available^[18]. Denoting a matrix of all PVCs by w , the least squares criterion to minimize for solving Eq. (2) is written as

$$LS(w) = \sum_{i=1}^N \|x_i - \sum_{j=1}^M w_{ij} \mu_j\|^2 \quad (4)$$

with constraints that $\sum_{j=1}^M w_{ij} = 1$ and $0 \leq w_{ij} \leq 1$. Note that this equation can be solved individually for each voxel. In the case of single image channel and two tissue types, the solution is particularly simple:

$$w_{M1} = r\left(\frac{x_i - \mu_2}{\mu_1 - \mu_2}\right); w_{M2} = 1 - w_{M1}, \quad (5)$$

and the function r limits the solution to the interval from 0 to 1, *i.e.*, $r(y) = 0$ when $y < 0$, $r(y) = y$ when $0 \leq y \leq 1$, and $r(y) = 1$ when $y > 1$. This solution is also the maximum likelihood solution and it accounts to a simple scaling of the image intensities to the interval from 0 to 1. For this reason, the solution is also very noisy and Choi *et al*^[8] suggested to regularize it with a Markov Random Field (MRF) prior (see also Li *et al*^[21]). The idea is that PVCs of neighboring voxels should have similar values. This leads to a modified criterion to minimize, with the same constraints as above,

$$PLS(w) = \sum_{i=1}^N \|x_i - \sum_{j=1}^M w_{ij} \mu_j\|^2 + P(w) \quad (6)$$

where the term $P(w)$ penalizes differences between $w_i = [w_{i1}, \dots, w_{iM}]$ and $w_k = [w_{k1}, \dots, w_{kM}]$ if the voxels i and k are neighbours. Unfortunately, this objective cannot be

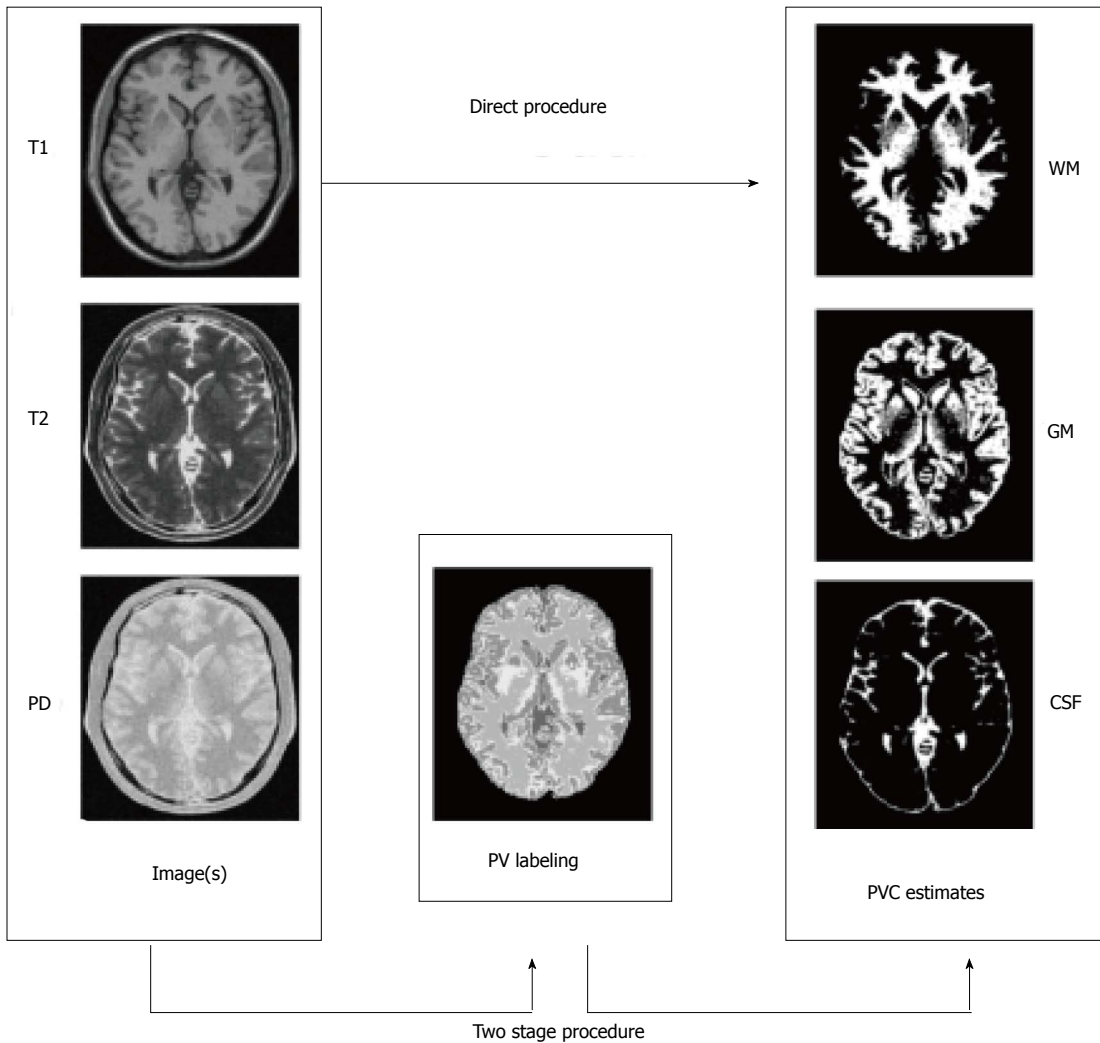


Figure 4 Direct vs two step procedure for partial volume coefficient estimation. CSF: Cerebro-spinal fluid; GM: Gray matter; WM: White matter; PVC: Partial volume coefficient.

anymore minimized separately for each voxel, but all the voxels must be taken into account. Choi *et al*^[18] used Iterative Conditional Modes algorithm^[22] to minimize the penalized least squares criterion in Eq.(6).

Two step algorithms: The simple two-class, one-channel solution above motivates a set of techniques allowing the standard PVC estimation for three tissue types even if just data from just a single image (usually T1-weighted) is available. The idea is that since the combination of more than two tissue types in a voxel is very rare, we can estimate which two tissue types are present in a voxel before the PVC estimation; Alike idea was already mentioned for multichannel data in^[18,23]. The steps of the two step algorithm can be given as follows, and they are schematically represented in Figure 4: (1) Partial volume classification: Estimate which is most likely tissue type configuration containing at most two tissue types in each voxel; and (2) PVC estimation: Solve the partial volume estimation problem limited to tissue types found in Step 1 for all the voxels.

There are at least three different approaches to solve

the task in the step 1. In the simplest approach, used for example in the reference^[24], the tissue classes are ordered based on their mean values so that $\mu_1 < \mu_2 < \dots < \mu_M$. Then, if the intensity value x_i lies in the interval $[\mu_k, \mu_{k+1}]$, it is assumed that the voxel i is a mixture of tissue types k and $k + 1$. This simple model does not account for the noise in the images and is not applicable for multichannel data because it assumes that the mean intensity values of tissue types can be ordered. The second approach is to detect most likely pure tissue types within the voxel based on the Bayes classifier^[18,23]. This is done computing the two most probable tissue types within a voxel. However, this approach, as the first one, ignores the possibility that voxels may be composed of a single tissue type. The third and preferred approach, which is we term as probabilistic partial volume classification, fixes the just mentioned problem. The probabilistic partial volume classification approach is to compute the probability of each possible tissue type mixture appearing in the voxel^[19,20,25-27]. For example, if the tissue types of interest are WM, GM, and CSF, the following 6 probabilities are computed: (1) Voxel is solely CSF; (2) Voxel is solely GM; (3) Voxel is

solely WM; (4) voxel is a mixture of background and CSF; (5) voxel is a mixture of CSF and GM; and (6) voxel is a mixture of GM and WM. (Some tissue type combinations are not considered due to their rarity in the brain.) The technical problem in the probabilistic partial volume classification approach is the construction of the probability models for mixed tissue classes; the class conditional densities for pure tissue classes are modelled by the normal density. The probability densities for the mixed tissue types can be constructed based on a marginalization technique developed originally in references^[19,20] and further applied in references^[25-28]. The idea is to integrate out the variable w_i describing the percentage of tissue type 1 in a voxel by numerical integration. Note that with current computers the numerical integration does not present computational problem and can be solved very fast^[28]. Advantages of this more complicated probabilistic approach over the two simple approaches include possibility to include spatial regularization in the form of MRFs to the step 1^[25,26] and the applicability to multispectral images^[26]. Additionally, it is often expected that the number of the pure tissue voxels should be greater than the number of mixed tissue voxels. The probabilistic partial volume classification includes automatic and elegant control for this issue that has been solved elsewhere by using Bayesian methods at the expense of introducing extra user-defined parameters^[24,29].

Once the tissue types that are probable to appear in a voxel are determined, then the PVCs can be estimated using Eq. (5) if the sampling noise model is assumed. Note that if voxel i is determined to be a voxel of pure tissue type k , then $w_{ik} = 1$ and $w_{ij} = 0$ for other tissue types $j \neq k$. One can also adopt the material dependent noise model leading to a maximum likelihood criterion. If i is a mixed voxel of tissue types j and k , the maximum-likelihood solution is

$$w_{ij}^* = \arg \max_{w \in [0,1]} \log(g(x_i | \mu(w), \Sigma(w))) \quad (7)$$

where g is the Gaussian probability density; $\mu(w) = w\mu_j + (1-w)\mu_k$; $\Sigma(w) = w^2\Sigma_j + (1-w)^2\Sigma_k$ or $\Sigma(w) = w\Sigma_j + (1-w)\Sigma_k$. Furthermore, $w_{ik}^* = 1 - w_{ij}^*$ and all the other PVCs are zero. The correct model for $\Sigma(w)$ has caused some controversy (see the references^[30,31] for details). The difference in the two models is that the first one ($\Sigma(w) = w^2\Sigma_j + (1-w)^2\Sigma_k$) results in a more regularized solution of Eq. (7) while the second one ($\Sigma(w) = w\Sigma_j + (1-w)\Sigma_k$) is conceptually more pleasing. The maximum-likelihood PVC-estimate in Eq. (7) is solved by a simple grid search. Extensions to the maximum likelihood principle of Eq. (7) include Bayesian methods^[24].

As mentioned above, the two-step algorithms can use the MRF prior to regularize the partial volume classification and this has been demonstrated to lead to more accurate partial volume estimates when the images are noisy^[25]. The use of the MRF requires the user to set a proper weighting parameter for the prior which may be considered as a disadvantage^[8]. However, often quoted

disadvantage of the added computational cost (*e.g.*, the reference^[8]) of the MRF, can be overcome by new rapid algorithms capable of performing MRF based segmentation of the typical 3-D MR images within few seconds^[28]. While the two-step algorithms often use spatial MRF prior during the partial volume classification step, they typically do not utilize spatial information during the second, PVC estimation, step. Manjón *et al*^[27] introduced an MRF for modelling of the spatial information during the PVC estimation step and compared it to the usage of prefiltering the images with a non-local means filter. The results suggested that using spatial information improved the PVC estimates and non-local means filtering performed better than the MRF-based approach.

Discretization approaches: An alternative to try to find real-valued PVC estimates is to discretize the PVC estimation problem^[32-34]. This means that instead of letting each PVC w_{ij} lie freely in the interval from zero to one, the discretization-based methods restrict the PVCs to have only a discrete set of values. For example, w_{ij} can be 0, 0.1, 0.2, ..., 1.0. The discretization-based methods then try to solve maximally probable PVCs from this discretized set resorting MRF approaches to model spatial interaction between adjacent voxels^[32-34]. While the restriction to a discrete set of PVC values is perfectly reasonable given the noisiness of the images, the discretization approaches are usually very time consuming, especially when compared to fast two step approaches^[25,28].

Parameter estimation

The necessary model parameters $\mu_{ij} = 1, \dots, M$ and Σ^* or $\Sigma_{ij} = 1, \dots, M$ must be estimated before or during the solution of the mixel model. Correct estimation of these parameters is essential for partial volume estimation^[35]. Tohka *et al*^[26] identified three potential approaches to the parameter estimation problem: (1) histogram analysis; (2) simultaneous parameter, and partial volume estimation by expectation maximization (EM)-like algorithms; and (3) the estimation based on a hard segmentation of the image.

The conceptually simplest alternative is to fit a parametric model (a mixture model of pure and mixed tissue intensity densities) to an image histogram. The objective function can be based on the maximum likelihood or least squares criterion. The disadvantage of parametric model fitting is that the formulated minimization problem is complex and non-convex rendering the standard optimization algorithms useless. Various global optimization algorithms, including genetic algorithms and tree annealing, have been used for the task^[19,36]. The EM-like algorithms start from an initial rough parameter estimates and refine the estimates jointly with the partial volume estimation^[32,34] or classification^[37] through alternating expectation and maximization steps. This can guarantee accurate parameter estimates, but the estimates depend strongly on the initial guess and the convergence of the process can be slow. The third alternative is to generate an initial rough segmentation of the image, and thereaf-

ter use outlier detection techniques based on the mathematical morphology, robust point estimates, or image gradient values to prune the set of voxels belonging to a certain tissue class^[25,26,35,38,39]. Comparisons of these three techniques have been reported in the references^[26,35]. The main result of these comparisons has been that the parameter estimation based on the hard segmentation of the image is fast and usually, but not always, works as well or better than the other two approaches.

RELATED METHODS

Fuzzy C-means

The standard Fuzzy C-means (FCM) algorithm optimizes a cost function

$$J_{\text{FCM}} = \sum_{i=1}^N \sum_{j=1}^M \mu_{ij}^q \|x_i - \mu_j\|^2,$$

where μ_{ij} are the fuzzy membership values μ_k are the class centroids, and q is the fuzzification parameter. This objective function and its modifications have been widely and successfully used for brain MRI tissue classification^[40-43]. As shown in the reference^[29], if $q = 3$, $M = 2$, and $K = 1$, optimizing the objective J_{FCM} for fixed centroids leads to the identical PVCs as PVCs derived based on Eq. (5). However, with more than two tissue types or multispectral data, fuzzy segmentations by FCM and mixel model are different.

Bayesian tissue classifiers

Often the tissue classification is casted as the Bayesian decision problem^[9,16,17,44,45]. In that, one tries to estimate the posterior probability map that the tissue type is c given the image intensities. Often approaches use prior information from tissue probability maps^[9,16] or MRFs^[44,45] or both^[17]. It should be noted that the tissue type probabilities are different from the partial volume coefficients. The exact difference of the segmentation results depends on the probability model selected, but usually these Bayesian tissue classifiers produce more crisp tissue type maps than the partial volume estimation algorithms. This issue and its ramifications are considered in a more detail by Manjón *et al.*^[27].

APPLICATIONS OF PARTIAL VOLUME ESTIMATION

Voxel based morphometry

Voxel-based morphometry (VBM) involves a voxel-wise comparison of the local concentration of gray matter between two groups of subjects. The procedure consists of segmenting the gray matter from the MR images and spatially normalizing these gray matter images from all the subjects in the study into the same stereotactic space^[5]. These gray matter images can either represent GM tissue probabilities, for example, as in the reference^[46] or GM tissue fractions resulting partial volume estimation, for

example, as in the reference^[47]. While it seems clear that the PVCs are better representations of gray matter density than gray matter probabilities, it is not clear whether this particular modelling choice has a major effect on the accuracy of the results. To author's knowledge, gray matter probability and gray matter PV-coefficient based VBM methods have not been directly compared. Tardif *et al.*^[48] examined two pipelines resulting in GM probability based VBM and PVC based VBM but the main focus of the work was on a comparison of 1.5T and 3T imaging protocols. The VBM8 software package (<http://dbm.neuro.uni-jena.de/vbm/>) offers possibility to VBM using PVCs^[49].

Cortical thickness

Cortical thickness is a quantitative measure describing the combined thickness of the layers of the cerebral cortex that can be measured using MRI either using mesh based^[16,50,51] or voxel based techniques^[52]. The thickness of the cortex, and its local variations, are of great interest in both normal development as well as a wide variety of neurodegenerative and psychiatric disorders^[6]. Cortex is a highly folded structure with an approximate average thickness of 2.5 mm^[53] and hence it is not difficult to appreciate that the partial volume effect has been an important consideration when measuring cortical thickness. Both surface mesh based^[54] and voxel based^[55-57] cortical thickness measures can be shown to be improved if the partial volume effect is taken into account. Especially, as demonstrated in Figure 2 and discussed further in the references^[26,54], hard tissue classifications may miss some of the sulcal CSF because of an insufficient image resolution. This causes incorrect reconstruction of the GM/CSF boundary, which, in turn, leads to errors in the cortical thickness computation.

Other applications

Other applications of segmentation with the PVE modeling identified during the literature review were segmentation of the brain images of the neonates^[58-61], hemisphere segmentation and related shape analysis^[62,63], EEG source localization^[64], and lesion load computations based on MRI^[65-68]. Especially, in the case of the Multiple Sclerosis (MS) lesion volumetry, the correction for the partial volume effects has a large positive effect on the reproducibility and accuracy of the analysis^[69]. In particular, it was found to be important in avoiding of misclassification of some non-lesion voxels (between CSF and brain tissue) into lesion voxels^[69].

CONCLUSION

An interesting recent development in MRI segmentation and partial volume estimation is the use of quantitative tissue type maps for the purpose^[70-72]. For example, Ahlgren *et al.*^[70] utilized the signal of a spoiled gradient-recalled echo (SPGR) sequence acquired with multiple flip angles to map T1, and subsequently to fit of a multi-

compartment model yielding parametric maps of partial volume estimates of the different compartments. West *et al*^[71] used quantitative MRI values of the longitudinal relaxation rate, the transverse relaxation rate and the proton density to define tissues (WM,GM,CSF) and constructed a lookup table for partial volume estimation. These quantitative approaches show good potential to improve the partial volume estimation accuracy. Another recent development is the use of high-field MRI to map smaller and smaller brain structures^[73], such cortical layers or hippocampal subfields^[74]. These efforts will benefit from automated segmentation. Despite of improved image resolution provided by higher field strengths the problems related to partial volume effect will remain as the structures of interest will become smaller at the same time. For example, while the improved image resolution will diminish (but not completely erase) the challenges related to partial volume effect in the cortical thickness computation, it will also possibly allow studies concerning individual cortical layers requiring a higher image resolution, where partial volume effect is again an important consideration.

REFERENCES

- 1 **Shenton ME**, Dickey CC, Frumin M, McCarley RW. A review of MRI findings in schizophrenia. *Schizophr Res* 2001; **49**: 1-52 [PMID: 11343862 DOI: 10.1016/S0920-9964(01)00163-3]
- 2 **Weiner MW**, Veitch DP, Aisen PS, Beckett LA, Cairns NJ, Green RC, Harvey D, Jack CR, Jagust W, Liu E, Morris JC, Petersen RC, Saykin AJ, Schmidt ME, Shaw L, Shen L, Siuciak JA, Soares H, Toga AW, Trojanowski JQ. The Alzheimer's Disease Neuroimaging Initiative: a review of papers published since its inception. *Alzheimers Dement* 2013; **9**: e111-e194 [PMID: 23932184 DOI: 10.1016/j.jalz.2013.05.1769]
- 3 **Frisoni GB**, Fox NC, Jack CR, Scheltens P, Thompson PM. The clinical use of structural MRI in Alzheimer disease. *Nat Rev Neurol* 2010; **6**: 67-77 [PMID: 20139996 DOI: 10.1038/nrneurol.2009.215]
- 4 **Olesen J**, Leonardi M. The burden of brain diseases in Europe. *Eur J Neurol* 2003; **10**: 471-477 [PMID: 12940825 DOI: 10.1046/j.1468-1331.2003.00682.x]
- 5 **Ashburner J**, Friston KJ. Voxel-based morphometry--the methods. *Neuroimage* 2000; **11**: 805-821 [PMID: 10860804 DOI: 10.1006/nimg.2000.0582]
- 6 **Fischl B**, Dale AM. Measuring the thickness of the human cerebral cortex from magnetic resonance images. *Proc Natl Acad Sci USA* 2000; **97**: 11050-11055 [PMID: 10984517 DOI: 10.1073/pnas.200033797]
- 7 **González Ballester MA**, Zisserman A, Brady M. Segmentation and measurement of brain structures in MRI including confidence bounds. *Med Image Anal* 2000; **4**: 189-200 [PMID: 11145308 DOI: 10.1016/S1361-8415(00)00013-X]
- 8 **González Ballester MA**, Zisserman AP, Brady M. Estimation of the partial volume effect in MRI. *Med Image Anal* 2002; **6**: 389-405 [PMID: 12494949 DOI: 10.1016/S1361-8415(02)00061-0]
- 9 **Ashburner J**, Friston KJ. Unified segmentation. *Neuroimage* 2005; **26**: 839-851 [PMID: 15955494 DOI: 10.1016/j.neuroimage.2005.02.018]
- 10 **Reddick WE**, Glass JO, Cook EN, Elkin TD, Deaton RJ. Automated segmentation and classification of multispectral magnetic resonance images of brain using artificial neural networks. *IEEE Trans Med Imaging* 1997; **16**: 911-918 [PMID: 17948730 DOI: 10.1109/42.650887]
- 11 **Cuadra MB**, Cammoun L, Butz T, Cuisenaire O, Thiran JP. Comparison and validation of tissue modelization and statistical classification methods in T1-weighted MR brain images. *IEEE Trans Med Imaging* 2005; **24**: 1548-1565 [PMID: 16350916 DOI: 10.1109/TMI.2005.857652]
- 12 **Ruan S**, Jaggi C, Xue J, Fadili J, Bloyet D. Brain tissue classification of magnetic resonance images using partial volume modeling. *IEEE Trans Med Imaging* 2000; **19**: 1179-1187 [PMID: 11212366 DOI: 10.1109/42.897810]
- 13 **Bullmore E**, Brammer M, Rouleau G, Everitt B, Simmons A, Sharma T, Frangou S, Murray R, Dunn G. Computerized brain tissue classification of magnetic resonance images: a new approach to the problem of partial volume artifact. *Neuroimage* 1995; **2**: 133-147 [PMID: 9343596 DOI: 10.1006/nimg.1995.1016]
- 14 **Vovk U**, Pernus F, Likar B. A review of methods for correction of intensity inhomogeneity in MRI. *IEEE Trans Med Imaging* 2007; **26**: 405-421 [PMID: 17354645 DOI: 10.1109/TMI.2006.891486]
- 15 **Shattuck DW**, Prasad G, Mirza M, Narr KL, Toga AW. Online resource for validation of brain segmentation methods. *Neuroimage* 2009; **45**: 431-439 [PMID: 19073267 DOI: 10.1016/j.neuroimage.2008.10.066]
- 16 **Ashburner J**, Friston K. Multimodal image coregistration and partitioning--a unified framework. *Neuroimage* 1997; **6**: 209-217 [PMID: 9344825 DOI: 10.1006/nimg.1997.0290]
- 17 **Tohka J**, Dinov ID, Shattuck DW, Toga AW. Brain MRI tissue classification based on local Markov random fields. *Magn Reson Imaging* 2010; **28**: 557-573 [PMID: 20110151 DOI: 10.1016/j.mri.2009.12.012]
- 18 **Choi HS**, Haynor DR, Kim Y. Partial volume tissue classification of multichannel magnetic resonance images-a mixel model. *IEEE Trans Med Imaging* 1991; **10**: 395-407 [PMID: 18222842 DOI: 10.1109/42.97590]
- 19 **Santago P**, Gage HD. Quantification of MR brain images by mixture density and partial volume modeling. *IEEE Trans Med Imaging* 1993; **12**: 566-574 [PMID: 18218450 DOI: 10.1109/42.241885]
- 20 **Santago P**, Gage HD. Statistical models of partial volume effect. *IEEE Trans Image Process* 1995; **4**: 1531-1540 [PMID: 18291985 DOI: 10.1109/83.469934]
- 21 **Li X**, Li L, Lu H, Liang Z. Partial volume segmentation of brain magnetic resonance images based on maximum a posteriori probability. *Med Phys* 2005; **32**: 2337-2345 [PMID: 16121590 DOI: 10.1118/1.1944912]
- 22 **Besag J**. On the statistical analysis of dirty pictures. *Journal of the Royal Statistical Society, Series B* 1986; **48**: 259-302. Available from: URL: <http://www.jstor.org/stable/2345426>
- 23 **Choi H**, Haynor D, Kim Y. Multivariate tissue classification of mri images for 3-d volume reconstruction-a statistical approach. In: Proc. SPIE vol. 1092, Medical Imaging III: Image Processing, 1989: 183-193
- 24 **Brouwer RM**, Hulshoff Pol HE, Schnack HG. Segmentation of MRI brain scans using non-uniform partial volume densities. *Neuroimage* 2010; **49**: 467-477 [PMID: 19635574 DOI: 10.1016/j.neuroimage.2009.07.041]
- 25 **Shattuck DW**, Sandor-Leahy SR, Schaper KA, Rottenberg DA, Leahy RM. Magnetic resonance image tissue classification using a partial volume model. *Neuroimage* 2001; **13**: 856-876 [PMID: 11304082 DOI: 10.1006/nimg.2000.0730]
- 26 **Tohka J**, Zijdenbos A, Evans A. Fast and robust parameter estimation for statistical partial volume models in brain MRI. *Neuroimage* 2004; **23**: 84-97 [PMID: 15325355 DOI: 10.1016/j.neuroimage.2004.05.007]
- 27 **Manjón JV**, Tohka J, Robles M. Improved estimates of partial volume coefficients from noisy brain MRI using spatial context. *Neuroimage* 2010; **53**: 480-490 [PMID: 20600978 DOI: 10.1016/j.neuroimage.2010.06.046]
- 28 **Tohka J**. FAST-PVE: Extremely fast markov random field based brain MRI tissue classification. In: Image Analysis, 18th Scandinavian Conference, SCIA 2013, Lecture notes in

- computer science vol. 7944. SCIA: Springer, 2013: 266-276 [DOI: 10.1007/978-3-642-38886-6_26]
- 29 **Pham DL**, Prince J. Partial volume estimation and the fuzzy c-means algorithm. In: Image Processing, 1998. ICIP 98. Proceedings. ICIP: 1998 International Conference on, vol. III, 1998: 819-822 [DOI: 10.1109/ICIP.1998.999071]
 - 30 **Bromiley P**, Thacker N. Multi-dimensional medical image segmentation with partial volume and gradient modelling. *Annals of the BMVA* 2008; **(2)**: 1-22. Available from: URL: <http://www.bmva.org/annals/2008/2008-0002.pdf>
 - 31 **Bromiley P**, Thacker N. Multi-dimensional medical image segmentation with partial volume and gradient modelling. Mathematical derivations and proofs. *Annals of the BMVA* 2008; **(2s1)**: 1-11. Available from: URL: <http://www.bmva.org/annals/2008/2008-0002-supplement.pdf>
 - 32 **Bricq S**, Collet Ch, Armspach JP. Unifying framework for multimodal brain MRI segmentation based on Hidden Markov Chains. *Med Image Anal* 2008; **12**: 639-652 [PMID: 18440268 DOI: 10.1016/j.media.2008.03.001]
 - 33 **Ruan S**, Moretti B, Fadili J, Bloyet D. Fuzzy markovian segmentation in application of magnetic resonance images. *Comput Vis Image Und* 2002; **85**: 54-69 [DOI: 10.1006/cviu.2002.0957]
 - 34 **Van Leemput K**, Maes F, Vandermeulen D, Suetens P. A unifying framework for partial volume segmentation of brain MR images. *IEEE Trans Med Imaging* 2003; **22**: 105-119 [PMID: 12703764 DOI: 10.1109/TMI.2002.806587]
 - 35 **Manjón JV**, Tohka J, García-Martí G, Carbonell-Caballero J, Lull JJ, Martí-Bonmatí L, Robles M. Robust MRI brain tissue parameter estimation by multistage outlier rejection. *Magn Reson Med* 2008; **59**: 866-873 [PMID: 18383286 DOI: 10.1002/mrm.21521]
 - 36 **Tohka J**, Krestyannikov E, Dinov ID, Graham AM, Shattuck DW, Ruotsalainen U, Toga AW. Genetic algorithms for finite mixture model based voxel classification in neuroimaging. *IEEE Trans Med Imaging* 2007; **26**: 696-711 [PMID: 17518064 DOI: 10.1109/TMI.2007.895453]
 - 37 **Noe A**, Gee J. Partial volume segmentation of cerebral MRI scans with mixture model clustering. In: Proc. of Information Processing in Medical Imaging. IPMI: 17th International Conference, 2001: 423-430 [DOI: 10.1007/3-540-45729-1_44]
 - 38 **Wang D**, Doddrell DM. A segmentation-based and partial-volume-compensated method for an accurate measurement of lateral ventricular volumes on T(1)-weighted magnetic resonance images. *Magn Reson Imaging* 2001; **19**: 267-273 [PMID: 11358664 DOI: 10.1016/S0730-725X(01)00235-1]
 - 39 **Wang D**, Doddrell DM. MR image-based measurement of rates of change in volumes of brain structures. Part I: method and validation. *Magn Reson Imaging* 2002; **20**: 27-40 [PMID: 11973027 DOI: 10.1016/S0730-725X(02)00466-6]
 - 40 **Suckling J**, Sigmundsson T, Greenwood K, Bullmore ET. A modified fuzzy clustering algorithm for operator independent brain tissue classification of dual echo MR images. *Magn Reson Imaging* 1999; **17**: 1065-1076 [PMID: 10463658 DOI: 10.1016/S0730-725X(99)00055-7]
 - 41 **Ortiz A**, Palacio AA, Górriz JM, Ramírez J, Salas-González D. Segmentation of brain MRI using SOM-FCM-based method and 3D statistical descriptors. *Comput Math Methods Med* 2013; **2013**: 638563 [PMID: 23762192 DOI: 10.1155/2013/638563]
 - 42 **Pham DL**, Prince JL. Adaptive fuzzy segmentation of magnetic resonance images. *IEEE Trans Med Imaging* 1999; **18**: 737-752 [PMID: 10571379 DOI: 10.1109/42.802752]
 - 43 **Yoon UC**, Kim JS, Kim JS, Kim IY, Kim SI. Adaptable fuzzy C-Means for improved classification as a preprocessing procedure of brain parcellation. *J Digit Imaging* 2001; **14**: 238-240 [PMID: 11442112 DOI: 10.1007/BF03190353]
 - 44 **Van Leemput K**, Maes F, Vandermeulen D, Suetens P. Automated model-based tissue classification of MR images of the brain. *IEEE Trans Med Imaging* 1999; **18**: 897-908 [PMID: 10628949 DOI: 10.1109/42.811270]
 - 45 **Zhang Y**, Brady M, Smith S. Segmentation of brain MR images through a hidden Markov random field model and the expectation-maximization algorithm. *IEEE Trans Med Imaging* 2001; **20**: 45-57 [PMID: 11293691 DOI: 10.1109/42.906424]
 - 46 **Good CD**, Johnsrude I, Ashburner J, Henson RN, Friston KJ, Frackowiak RS. Cerebral asymmetry and the effects of sex and handedness on brain structure: a voxel-based morphometric analysis of 465 normal adult human brains. *Neuroimage* 2001; **14**: 685-700 [PMID: 11506541 DOI: 10.1006/nimg.2001.0857]
 - 47 **Nagano-Saito A**, Washimi Y, Arahata Y, Kachi T, Lerch JP, Evans AC, Dagher A, Ito K. Cerebral atrophy and its relation to cognitive impairment in Parkinson disease. *Neurology* 2005; **64**: 224-229 [PMID: 15668417 DOI: 10.1212/01.WNL.0000149510.41793.50]
 - 48 **Tardif CL**, Collins DL, Pike GB. Regional impact of field strength on voxel-based morphometry results. *Hum Brain Mapp* 2010; **31**: 943-957 [PMID: 19862698 DOI: 10.1002/hbm.20908]
 - 49 **Gaser C**. Partial volume segmentation with adaptive maximum a posteriori (MAP) approach. *NeuroImage* 2009; **47**: S121 [DOI: 10.1016/S1053-8119(09)71151-6]
 - 50 **MacDonald D**, Kabani N, Avis D, Evans AC. Automated 3-D extraction of inner and outer surfaces of cerebral cortex from MRI. *Neuroimage* 2000; **12**: 340-356 [PMID: 10944416 DOI: 10.1006/nimg.1999.0534]
 - 51 **Lerch JP**, Evans AC. Cortical thickness analysis examined through power analysis and a population simulation. *Neuroimage* 2005; **24**: 163-173 [PMID: 15588607 DOI: 10.1016/j.neuroimage.2004.07.045]
 - 52 **Hutton C**, De Vita E, Ashburner J, Deichmann R, Turner R. Voxel-based cortical thickness measurements in MRI. *Neuroimage* 2008; **40**: 1701-1710 [PMID: 18325790 DOI: 10.1016/j.neuroimage.2008.01.027]
 - 53 **Zilles K**. Architecture of the Human Cerebral Cortex. In Paxinos G, Mai JK, The human nervous system. 2nd ed. San Diego: Elsevier, 2004: 997-1060
 - 54 **Kim JS**, Singh V, Lee JK, Lerch J, Ad-Dab'bagh Y, MacDonald D, Lee JM, Kim SI, Evans AC. Automated 3-D extraction and evaluation of the inner and outer cortical surfaces using a Laplacian map and partial volume effect classification. *Neuroimage* 2005; **27**: 210-221 [PMID: 15896981 DOI: 10.1016/j.neuroimage.2005.03.036]
 - 55 **Rueda A**, Acosta O, Couprie M, Bourgeat P, Fripp J, Dowson N, Romero E, Salvado O. Topology-corrected segmentation and local intensity estimates for improved partial volume classification of brain cortex in MRI. *J Neurosci Methods* 2010; **188**: 305-315 [PMID: 20193712 DOI: 10.1016/j.jneumeth.2010.02.020]
 - 56 **Acosta O**, Bourgeat P, Zuluaga MA, Fripp J, Salvado O, Ourselin S. Automated voxel-based 3D cortical thickness measurement in a combined Lagrangian-Eulerian PDE approach using partial volume maps. *Med Image Anal* 2009; **13**: 730-743 [PMID: 19648050 DOI: 10.1016/j.media.2009.07.003]
 - 57 **Aganj I**, Sapiro G, Parikshak N, Madsen SK, Thompson PM. Measurement of cortical thickness from MRI by minimum line integrals on soft-classified tissue. *Hum Brain Mapp* 2009; **30**: 3188-3199 [PMID: 19219850 DOI: 10.1002/hbm.20740]
 - 58 **Cardoso MJ**, Melbourne A, Kendall GS, Modat M, Haggmann CF, Robertson NJ, Marlow N, Ourselin S. Adaptive neonate brain segmentation. *Med Image Comput Comput Assist Interact* 2011; **14**: 378-386 [PMID: 22003722]
 - 59 **Leroy F**, Mangin JF, Rousseau F, Glasel H, Hertz-Pannier L, Dubois J, Dehaene-Lambertz G. Atlas-free surface reconstruction of the cortical grey-white interface in infants. *PLoS One* 2011; **6**: e27128 [PMID: 22110604 DOI: 10.1371/journal.pone.0027128]
 - 60 **Song T**, Jamshidi MM, Lee RR, Huang M. A modified probabilistic neural network for partial volume segmentation in brain MR image. *IEEE Trans Neural Netw* 2007; **18**: 1424-1432 [PMID: 18220190 DOI: 10.1109/TNN.2007.891635]

- 61 **Xue H**, Srinivasan L, Jiang S, Rutherford M, Edwards AD, Rueckert D, Hajnal JV. Automatic segmentation and reconstruction of the cortex from neonatal MRI. *Neuroimage* 2007; **38**: 461-477 [PMID: 17888685 DOI: 10.1016/j.neuroimage.2007.07.030]
- 62 **Zhao L**, Ruotsalainen U, Hirvonen J, Hietala J, Tohka J. Automatic cerebral and cerebellar hemisphere segmentation in 3D MRI: adaptive disconnection algorithm. *Med Image Anal* 2010; **14**: 360-372 [PMID: 20303318 DOI: 10.1016/j.media.2010.02.001]
- 63 **Pepe A**, Zhao L, Koikkalainen J, Hietala J, Ruotsalainen U, Tohka J. Automatic statistical shape analysis of cerebral asymmetry in 3D T1-weighted magnetic resonance images at vertex-level: application to neuroleptic-naïve schizophrenia. *Magn Reson Imaging* 2013; **31**: 676-687 [PMID: 23337078 DOI: 10.1016/j.mri.2012.10.021]
- 64 **Hyde DE**, Duffy FH, Warfield SK. Anisotropic partial volume CSF modeling for EEG source localization. *Neuroimage* 2012; **62**: 2161-2170 [PMID: 22652021 DOI: 10.1016/j.neuroimage.2012.05.055]
- 65 **Wu Y**, Warfield SK, Tan IL, Wells WM, Meier DS, van Schijndel RA, Barkhof F, Guttman CR. Automated segmentation of multiple sclerosis lesion subtypes with multichannel MRI. *Neuroimage* 2006; **32**: 1205-1215 [PMID: 16797188 DOI: 10.1016/j.neuroimage.2006.04.211]
- 66 **Li W**, Tian J, Li E, Dai J. Robust unsupervised segmentation of infarct lesion from diffusion tensor MR images using multiscale statistical classification and partial volume voxel reclassification. *Neuroimage* 2004; **23**: 1507-1518 [PMID: 15589114 DOI: 10.1016/j.neuroimage.2004.08.009]
- 67 **Meier DS**, Guttman CRG. Time-series analysis of mri intensity patterns in multiple sclerosis. *Neuroimage* 2003; **20**: 1193-1209 [DOI: 10.1016/S1053-8119(03)00354-9]
- 68 **Khademi A**, Venetsanopoulos A, Moody AR. Robust white matter lesion segmentation in FLAIR MRI. *IEEE Trans Biomed Eng* 2012; **59**: 860-871 [PMID: 22203699 DOI: 10.1109/TBME.2011.2181167]
- 69 **Wei X**, Warfield SK, Zou KH, Wu Y, Li X, Guimond A, Mugler JP, Benson RR, Wolfson L, Weiner HL, Guttman CR. Quantitative analysis of MRI signal abnormalities of brain white matter with high reproducibility and accuracy. *J Magn Reson Imaging* 2002; **15**: 203-209 [PMID: 11836778 DOI: 10.1002/jmri.10053]
- 70 **Ahlgren A**, Wirestam R, Sthlberg F, Knutsson L. Automatic brain segmentation using fractional signal modeling of a multiple flip angle, spoiled gradient-recalled echo acquisition. *MAGMA* 2014: In press [PMID: 24639095 DOI: 10.1007/s10334-014-0439-2]
- 71 **West J**, Warntjes JB, Lundberg P. Novel whole brain segmentation and volume estimation using quantitative MRI. *Eur Radiol* 2012; **22**: 998-1007 [PMID: 22113264 DOI: 10.1007/s00330-011-2336-7]
- 72 **West J**, Blystad I, Engström M, Warntjes JB, Lundberg P. Application of quantitative MRI for brain tissue segmentation at 1.5 T and 3.0 T field strengths. *PLoS One* 2013; **8**: e74795 [PMID: 24066153 DOI: 10.1371/journal.pone.0074795]
- 73 **Duyn JH**. The future of ultra-high field MRI and fMRI for study of the human brain. *Neuroimage* 2012; **62**: 1241-1248 [PMID: 22063093 DOI: 10.1016/j.neuroimage.2011.10.065]
- 74 **Van Leemput K**, Bakkour A, Benner T, Wiggins G, Wald LL, Augustinack J, Dickerson BC, Golland P, Fischl B. Automated segmentation of hippocampal subfields from ultra-high resolution in vivo MRI. *Hippocampus* 2009; **19**: 549-557 [PMID: 19405131 DOI: 10.1002/hipo.20615]

P- Reviewer: Logeswaran R, Sheehan JR, Walter M

S- Editor: Ji FF **L- Editor:** A **E- Editor:** Lu YJ



Functional topography of the corpus callosum investigated by DTI and fMRI

Mara Fabri, Chiara Pierpaoli, Paolo Barbaresi, Gabriele Polonara

Mara Fabri, Chiara Pierpaoli, Paolo Barbaresi, Dipartimento di Medicina Sperimentale e Clinica, Sezione di Neuroscienze e Biologia Cellulare, Università Politecnica delle Marche, 60020 Ancona, Italy

Gabriele Polonara, Dipartimento di Scienze Cliniche Specialistiche e Odontostomatologiche, Sezione di Scienze Radiologiche, Università Politecnica delle Marche, 60020 Ancona, Italy

Author contributions: All authors contributed to the paper.
Supported by Ministero Istruzione, Università e Ricerca (MIUR; PRIN 2007, 2009)

Correspondence to: Mara Fabri, Professor, Dipartimento di Medicina Sperimentale e Clinica, Sezione di Neuroscienze e Biologia Cellulare, Università Politecnica delle Marche, Via Tronto 10/A, 60020 Ancona, Italy. m.fabri@univpm.it

Telephone: +39-071-2206193 Fax: +39-071-2206052

Received: May 28, 2014 Revised: October 16, 2014

Accepted: October 28, 2014

Published online: March 28, 2015

Abstract

This short review examines the most recent functional studies of the topographic organization of the human corpus callosum, the main interhemispheric commissure. After a brief description of its anatomy, development, microstructure, and function, it examines and discusses the latest findings obtained using diffusion tensor imaging (DTI) and tractography (DTT) and functional magnetic resonance imaging (fMRI), three recently developed imaging techniques that have significantly expanded and refined our knowledge of the commissure. While DTI and DTT have been providing insights into its microstructure, integrity and level of myelination, fMRI has been the key technique in documenting the activation of white matter fibers, particularly in the corpus callosum. By combining DTT and fMRI it has been possible to describe the trajectory of the callosal fibers interconnecting the primary olfactory, gustatory, motor, somatic sensory, auditory and visual cortices at sites where the activation elicited by peripheral stimulation was detected

by fMRI. These studies have demonstrated the presence of callosal fiber tracts that cross the commissure at the level of the genu, body, and splenium, at sites showing fMRI activation. Altogether such findings lend further support to the notion that the corpus callosum displays a functional topographic organization that can be explored with fMRI.

© 2015 Baishideng Publishing Group Inc. All rights reserved.

Key words: Corpus callosum; Interhemispheric transfer; Functional magnetic resonance imaging and diffusion tensor imaging; Brain imaging; Topographic organization

Core tip: A combined approach using diffusion tensor imaging and tractography, two recently developed imaging techniques, and functional magnetic resonance imaging (fMRI) has enabled detection of fMRI activation evoked by specific sensory or motor tasks in the corpus callosum, and reconstruction of the trajectory of the commissural fibers interconnecting primary cortical areas activated by the same tasks. These findings confirm that the corpus callosum has a functional topographic organization and that fMRI may be used to explore it.

Original sources: Fabri M, Pierpaoli C, Barbaresi P, Polonara G. Functional topography of the corpus callosum investigated by DTI and fMRI. *World J Radiol* 2014; 6(12): 895-906 Available from: URL: <http://www.wjgnet.com/1949-8470/full/v6/i12/895.htm> DOI: <http://dx.doi.org/10.4329/wjr.v6.i12.895>

INTRODUCTION

The principal interhemispheric commissure is the corpus callosum (CC). It arises in the brain of placental mammals^[1] as an elongated midline structure composed of 200-800 million horizontal interconnecting homo-

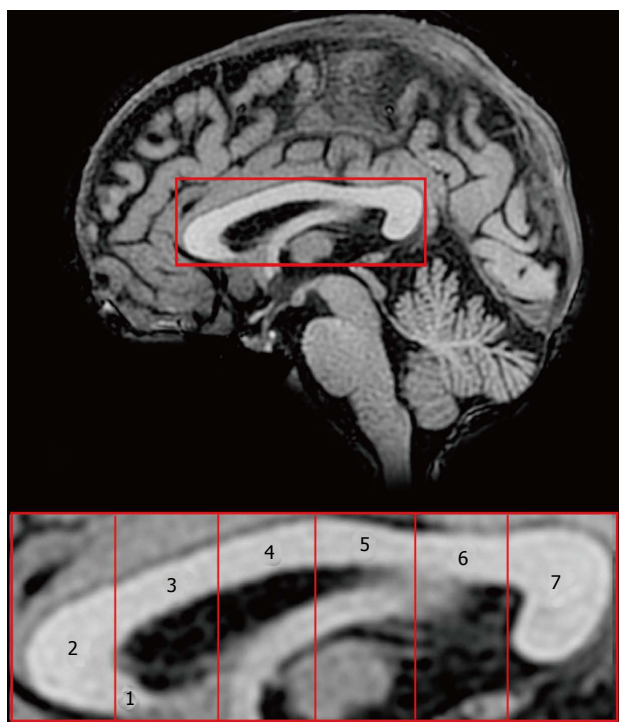


Figure 1 Subdivisions of the human corpus callosum. Midsagittal magnetic resonance image of the corpus callosum (above) and its seven anatomical regions according to Witelson^[8]. Region 1: Rostrum; 2: Genu; 3: Anterior midbody; 4: Central midbody; 5: Posterior midbody; 6: Isthmus; 7: Splenium. Both images are oriented in the Talairach space, where the origin of X, Y and Z axes coincides with the anterior commissure (coordinates 0, 0, 0).

topical and heterotopical cortical areas^[2]. The mature CC contains myelinated (70%) and unmyelinated fibers (30%), glial cells (astrocytes and oligodendrocytes), and neurons^[3-7]. The human CC has been divided into five anatomical regions, which include from front to back the genu, the rostrum, the body or trunk—often subdivided into anterior, middle and posterior body—the isthmus, and the splenium (Figure 1). Since there are no clear borders between regions, a variety of methods based principally on geometric criteria have been proposed to define subregions^[8-11]. The different callosal regions have different fiber compositions: large diameter fibers have been described in the posterior part of the splenium and in the body^[1,12], where interhemispheric sensory fibers cross the commissure and exchange information at high speed, whereas small fibers mainly connecting association cortical areas are found in the rostrum, genu and anterior body^[1,12]. Recently, different protein expression profiles have also been described in the three main CC regions, the genu, body and splenium^[13]. In particular, the expression of proteins related to glucose metabolism and antioxidant activity seems to be lower in the genu and body compared with the splenium^[13].

MORPHOLOGICAL STRUCTURE OF THE CORPUS CALLOSUM

The anterior half of the human CC (genu, rostrum and

body) contains fibers interconnecting frontal association cortical areas. The isthmus mostly contains primary motor, somatosensory, and auditory fibers. In the splenium primary visual and association temporo-occipital and parietal commissural fibers are mixed, forming a single segment with the hippocampal commissure through which parahippocampal fibers cross^[14].

Large diameter fibers (3-5 μm) are densest in the isthmus (connecting motor, somatosensory, and auditory cortices) and in the posterior splenium (connecting visual cortices), whereas small fibers (< 0.4 μm) are more numerous in the genu and anterior splenium (connecting high-order prefrontal and temporo-parietal associative areas). The largest fibers in the human CC interconnect the primary auditory cortices^[12,14].

Neurons giving rise to callosal fibers lie in cortical layers III, V and VI. The vast majority of these fibers release excitatory amino acids [glutamate (Glu) and/or aspartate] as neurotransmitters^[15], however, a small proportion of callosal neurons in cat and rat have been shown to release the inhibitory neurotransmitter GABA^[16-18].

DEVELOPMENT OF THE CORPUS CALLOSUM

The CC is a recent phylogenetic acquisition of placental mammals, developing by fusion of the interhemispheric midline fibers with specialized midline glial cells guiding callosal fibers to the contralateral side^[14]. It originates from the glial sling, above and rostral to the anterior and hippocampal commissures: it thus forms from the fusion of two separate segments. The anterior, sling-derived callosum (containing fibers connecting frontal associative and possibly primary sensory-motor areas of the two hemispheres) and the hippocampal commissure-associated splenium (containing fibers arising in the parieto-temporo-occipital cortex and directed to the opposite hemisphere) probably fuse just anterior to the hippocampal commissure^[14].

The different origin of the anterior and posterior CC portions seems to correlate with different functional properties, and the respective resection gives rise to different effects, since patients with surgical resection of the splenium show disconnection syndrome^[19] whereas those with resection of the anterior CC do not^[20].

The CC grows in size by the increase of the connectivity and the tangential growth of the cortex. In the womb and in the early postnatal period it mainly grows by fiber addition, whereas later increases are due to the development of myelin, which offsets pruning of callosal fibers; fiber myelination becomes significant at about 6 mo of postnatal life in the splenium and at about 8 mo in the genu. Myelination is believed to proceed from posterior to anterior^[21,22], reflecting the fact that myelination of primary cortical areas (somatic sensory, motor, auditory, visual) connected through the isthmus and splenium predates the myelination of the body, genu, and rostrum, which are related to the more anterior associative areas.

FUNCTION OF THE CORPUS CALLOSUM

The function of the CC has been investigated for centuries. The earliest studies date to the 16th century. Believed for many centuries to be the “seat of the soul”^[23], it took until the 18th century for Franz Joseph Gall and Johann Spurzheim, dissecting alcohol-fixed brains, to describe bundles of axons passing through the callosal white matter (WM) and connecting the two hemispheres^[24]. Its known functions include: interhemispheric exchange of information, integration of inputs reaching one or both hemispheres, facilitation of some cortical activities, and inhibition of cortical functions^[25,26]. It has recently been shown that the size of the human CC positively correlates with intelligence (Einstein’s CC was thicker than normal^[27]) and that its integrity is essential for cognitive performances; thus CC resection and microstructural or developmental alterations are often associated with cognitive decline.

The earliest hypotheses on the function of the human CC came from studies of split-brain patients, subjects whose CC was partially or completely resected to prevent the diffusion of epileptic seizures^[28]. Patients with total or partial resection involving the posterior CC suffered from disconnection syndrome^[19,29,30], whereas in those with partial anterior resection the disconnection could be evidenced only by specific tests^[20,31].

These investigations were followed and paralleled by animal studies including neuroanatomical tracing, cytological and microstructural analyses, and electrophysiological recordings. Neuropsychological and clinical studies of patients with total or partial surgical resection of the CC performed to treat drug-resistant epilepsy or remove intracallosal cysts or tumors provided further insights into its function.

TOPOGRAPHY OF THE CORPUS CALLOSUM

Ever since electrophysiological recordings demonstrated somatic sensory receptive fields in the anterior cat CC^[32,33] and visual inputs to the splenium^[34,35], the CC has been hypothesized to be topographically organized. Later electrophysiological^[36] and neuroanatomical findings^[37,38] obtained after injection of neural tracers or ablation of selected cortical areas in non-human primates; findings from post-mortem investigations^[39]; and studies of patients with surgical resection or callosal lesions^[28,40-42] provided further support for the notion. This organization appears to give rise to modality-specific regions^[43] in which anterior callosal axons transfer motor information between the frontal lobes and somatic sensory, auditory, and visual information is integrated by posterior fibers linking parietal, temporal and occipital lobes and crossing through the posterior midbody, isthmus and splenium, respectively.

Further support for the notion of a topographic organization of the CC came from the study of subjects

with callosal resection. Functional magnetic resonance imaging (fMRI) was applied by our group to investigate callosotomy patients^[44-46] and demonstrated that touch information transfer between the hemispheres may be accomplished by axons crossing at the level of the posterior CC. A more recent study of non-epileptic patients with resection of different portions of the anterior CC^[40] contributed additional evidence by showing that motor coordination transfer occurs at the level of the middle portion of the genu and somesthetic information is through the anterior CC. Examination of further sensory modalities provided evidence that transfer of visual^[47,48] and auditory information^[49,50] between the hemispheres takes place in the splenium.

The recent MRI-associated techniques, including fMRI, volumetric based morphometry, diffusion tensor imaging (DTI) and diffusion tensor tractography (DTT), are new, powerful methods to investigate the human brain *in vivo*. Data collected with DTI and fMRI are reviewed below after a brief survey of the bases of these techniques.

BRIEF OVERVIEW OF THE PRINCIPLES OF DTI

DTI is an MRI-based method enabling *in vivo* quantification of the microscopic diffusion properties of water in tissues^[51]. It allows generation of quantitative maps of diffusion indices and through them assessment of brain WM tissue structure and integrity. The underlying principle of DTI is the random motion of water molecules (Brownian motion), which can be characterized by the diffusion coefficient, *D*, and is influenced by other factors including molecular weight and viscosity. Water diffuses freely in all directions (isotropic diffusion). In gray matter (GM) water diffusion is similarly isotropic, but it is hindered by cellular structures, whereas diffusion in WM is hindered by the presence of highly ordered axonal structures. The latter conditions result in preferential diffusion parallel to WM tracts, *i.e.*, the route of least resistance, rather than perpendicular to them. This motion was noted in early experiments and designated anisotropic diffusion^[52,53]. Myelination of the axons has long been held to be the main obstruction to water diffusion in WM, and to be responsible for anisotropy; however later evidence suggested that axon membranes as well as other factors including organization of neurofilaments and microtubules also play a role^[54]. Measures of anisotropy include relative anisotropy, volume ratio and the most commonly cited fractional anisotropy (FA). These rotationally invariant indices reflect the degree of anisotropy in the diffusion tensor and are normalized to values between 0 (isotropic) and 1 (highly anisotropic).

In an extensive paper, Yap *et al.*^[55] reviewed several investigations documenting WM changes in subjects of different ages using DTI. In particular they showed that maximum FA is reached in the anterior and middle portions of the CC around 20 years of age and in the

splenium around 50 years; in older subjects FA decreases and does so more slowly in the splenium^[55,56]. FA is usually slightly lower in the anterior and middle portions of the CC (regions 1-4 described respectively as prefrontal, premotor, precentral and postcentral by Pandya and Seltzer^[38]), where it ranges from 0.5 to 0.7, and higher in the splenium (posterior parietal and temporo-occipital regions, respectively, regions 5 and 6 of Pandya and Seltzer^[38]), where it ranges from 0.6 to 0.8^[56-59].

DTI thus enables exploration of the microstructural organization of the CC by measuring FA, which has recently been shown to correlate positively with conduction velocity and may therefore be considered as an index of myelination or axon diameter^[60]. Reductions in FA have been implicated in numerous neuropsychiatric and neurological conditions including alcoholism^[61], schizophrenia^[62], traumatic brain injury^[63], multiple sclerosis^[64-66], and Wallerian degeneration^[67]. It has recently been suggested that acquisition factors such as b-value and voxel size can affect the quantification of DTI parameters (*i.e.*, FA and mean diffusivity, MD)^[68]. For this reason extreme caution is required when comparing data obtained using different acquisition factors.

Interestingly, DTI techniques also evidenced plastic changes occurring in fiber bundles in relation to development or training and resulting in an FA increase after training, thus demonstrating that the technique is not solely an anatomical tool^[69-71].

A further application of diffusion tensor data is exploration of the distribution of WM fibers in the brain, known as DTT or fiber tracking. In deterministic tractography fibers typically originate from seed points—which are entered automatically or manually to examine a specific area or the whole brain—and propagate along the direction of the principal eigenvector (e_1). Additional parameters or constraints include maximum tract curvature and a stopping criterion for the tracking, such as achievement of a minimum FA threshold^[51,72]. In probabilistic tractography a multitude of fibers, typically thousands, are generated from each seed point or voxel. Each fiber propagates in an individual manner: DTT takes into account both e_1 direction and change. Tractography is used, for example, to highlight fiber tracts in patients requiring brain surgery^[73], to investigate WM reductions related to cognitive impairment^[74], cerebellar damage^[75], specific cortical brain changes^[76], longitudinal changes^[77] and intrinsic connectivity^[78] in multiple sclerosis. DTT also evidenced increased FA in specific fiber bundles after training in given tasks^[69-71].

Over the past three decades these new imaging techniques have enabled confirmation or rejection of earlier hypotheses about the functions of the CC and provided new insights. In non-human primates and other mammals they have also allowed to verify and correlate data obtained by classic neuroanatomical techniques with DTI findings, and results of electrophysiological recordings with fMRI activation.

The callosal topography resulting from the application

of DTI and DTT techniques has thus been confirmed to be in line with the one described in previous studies. Fibers connecting prefrontal cortical areas have been seen to cross through the anterior part of the CC; those connecting premotor and motor cortical areas crossed at the level of the central callosal body^[9,25,79-81]; the fibers connecting parietal cortical areas crossed through the posterior callosal body; and those from occipital areas crossed at the level of the splenium (see also^[82,83]). Another hypothesis that has been confirmed is the topographic organization of the CC as emerging from previous neuroanatomical (axonal degeneration and tract-tracing) animal studies and human lesion and post-mortem investigations.

Slight differences have been demonstrated between human and monkey topographic organization in relation to the much greater expansion of the human frontal cortex.

FUNCTIONAL MAGNETIC RESONANCE IMAGING STUDIES

Functional MRI allows to study the intact brain non invasively. It is a functional neuroimaging approach based on MRI technology that measures brain activity by detecting associated changes in blood flow, based on the well-established notion that neuronal activation in an area of the brain is accompanied by a local increase in blood flow. The blood-oxygen-level dependent (BOLD) effect, or response, is a method based on the different ratio of oxygenated to deoxygenated hemoglobin in blood. Given that the two forms of the molecule have different magnetic behaviors, the change of their relative concentration, due to an increase in blood flow evoked by increased neural activity, generates a magnetic-electric signal that is detected by the equipment, highlighting the areas of the brain that are active at any given time.

It has long been believed that the BOLD effect is mainly due to the metabolic activity associated with synaptic rather than spiking activity, and therefore it could be evoked only in GM^[84]. However, data from the newer imaging techniques suggest that a hemodynamic response can also be evoked in WM, particularly in the CC. These findings were at first observations sporadically recorded during interhemispheric transfer tasks performed by subjects within the magnet^[85-88], or during activities not involving specific interhemispheric transfer tasks, such as voluntary swallowing^[89]. Moreover a BOLD signal was elicited in isthmus and splenium (posterior CC) by a task based on the interhemispheric transfer and integration of visuo-motor information, where crossing of the CC is needed for a behavioral response to be elicited (“crossed condition”^[88]). The above mentioned functional studies are summarized in Table 1.

A number of studies have documented that information transfer between premotor and prefrontal areas involves the anterior CC, and transfer between parietal, occipital and temporal regions involves the posterior

Table 1 Summary of studies evidencing activation of the corpus callosum in humans

Ref.	Year	Task	CC localization	Technique	Subjects
Mosier <i>et al.</i> ^[89]	2001	Swallowing	Anterior	fMRI	Healthy controls
Tettamanti <i>et al.</i> ^[85]	2003	Visuomotor	Anterior	fMRI	Healthy controls
Omura <i>et al.</i> ^[86]	2004	Visuomotor transfer	Anterior	fMRI	Healthy controls
Weber <i>et al.</i> ^[87]	2005	Visuomotor	Anterior	fMRI	Healthy controls
Mazerolle <i>et al.</i> ^[88]	2008	Visual transfer	Posterior	fMRI	Healthy controls
Mazerolle <i>et al.</i> ^[126]	2010	Visual transfer	Posterior	fMRI and DTI	Healthy controls
Fabri <i>et al.</i> ^[94]	2011	Tactile, gustatory, visual	Different regions according peripheral stimuli	fMRI	Healthy controls
Fabri <i>et al.</i> ^[99]	2013	Tactile, gustatory, visual, auditory	Different regions according peripheral stimuli	fMRI and DTI	Healthy control and Callosotomized patients
Polonara <i>et al.</i> ^[95]	2014	Tactile, gustatory, visual, auditory	Different regions according peripheral stimuli	fMRI and DTI	Callosotomized patients

A more extensive review of the studies reporting the activation in the CC can be found in Gawryluk *et al.*^[138], 2014. DTI: Diffusion tensor imaging; fMRI: Functional magnetic resonance imaging; CC: Corpus callosum.

CC^[81,90-92]. A recent systematic study by our group^[93,94] examined the BOLD effect evoked in the CC by simple sensory stimuli or by the performance of motor tasks activating the cortical areas which in healthy control subjects harbor the representation of motor activation and of gustatory, olfactory, auditory, visual and tactile sensitivity. The study was directed at establishing whether (1) a BOLD signal was able to be evoked in CC fibers; and (2) the foci related to motor tasks and sensory stimuli agreed with the notion of a topographic organization. The study did detect consistent activation foci in discrete regions of the CC: anterior (olfactory and gustatory stimulation), central (motor tasks), central-posterior (touch stimulation), isthmus (auditory stimulation) and splenium (visual stimulation) (Figure 2). It also confirmed the existence of a topographic organization of the CC from a functional point of view, demonstrating that it may be investigated using fMRI. In recent years the peripheral sensory stimulation protocols applied in the earlier studies^[94] were administered to partial callosotomy patients^[95]. The test results were assessed to determine whether the extant CC portions displayed a BOLD signal, to provide additional evidence for the concept of a functional map in the CC. In the same study DTI test data were also obtained in callosotomy and control subjects, to determine whether tracts seeded from cortical areas activated by specific sensory stimuli co-localized with CC activation (Figure 3).

CELLULAR BASIS OF THE VASCULAR RESPONSE IN THE CORPUS CALLOSUM

The neurovascular interactions inducing hemodynamic changes during increased cortical activity is the basis of functional neuroimaging with PET and fMRI^[96-98]. The BOLD signal reflects the hemodynamic responses related to neuronal activity^[98,99]. The exact mechanism underlying the BOLD effect is still debated. Hemodynamic changes have been seen to be induced by motor and visuomotor tasks and peripheral stimulation^[85-89,100] and, recently, by simple sensory tasks^[94]. Energy-dependent processes occur in the WM, too, given that ATP-dependent Na⁺-K⁺ ion pumps mediate the conduction of axonal action po-

tentials at the nodes of Ranvier, restoring ion gradients in neuron membranes^[99,101]. Actually, the block of voltage-dependent Na⁺ channels inhibits the responses to forepaw somatosensory stimulation that can be detected by fMRI^[102]. Moreover, spiking activity and fMRI activation are also correlated based on recent data^[103-105]. Various hypotheses have been advanced to explain the BOLD effect seen in WM: vessel dilation by astrocytes^[106,107] aimed at meeting the increased energy demand related to the increased neural activation; an increase in extracellular K⁺ in relation to heightened brain cell activity; or an increase in cytoplasmic Ca²⁺^[99,106,108]. Astrocytes and capillaries are both found in the CC^[109], and since the conduction of action potentials by CC axons requires energy, the mechanism is probably also active in CC fibers. According to LeBihan (2009, personal communication) the heat produced by the augmented axonal metabolism would by itself be able to induce dilation of CC microvessels.

Another hypothesis, recently advanced by Barbaresi *et al.*^[3], explains the BOLD effect seen in specific CC regions with the presence of NADPH-d+/NOS-immunopositive intracallosal neurons, whose depolarization may result in increased blood flow. The depolarization may occur in two ways: (1) through activation of specific cortical regions by peripheral stimulation, resulting in depolarization of intracallosal neurons containing nitric oxide (NO), whose dendrites reach the activated overlying cerebral cortex; NO could thus be released from neuronal processes associated with callosal vessels; this mechanism has been hypothesized to occur in the cerebral cortex, since inhibition of the NO-producing enzyme NO synthase attenuates the increase in blood flow associated with neuronal activity^[110-112]; and (2) alternatively, increased cortical activity may cause release of more Glu along callosal fibers^[113,114] belonging to glutamatergic cortical neurons^[15], possibly exciting NO-producing intracallosal neurons^[115] through NMDA receptors^[116,117]; the interaction of Glu with NMDA receptors could therefore elicit a BOLD response in the CC similar to other central nervous system regions where application of NMDA receptor antagonists attenuates blood flow responses^[118-123].

However, a concomitant role of astrocytes in neu-

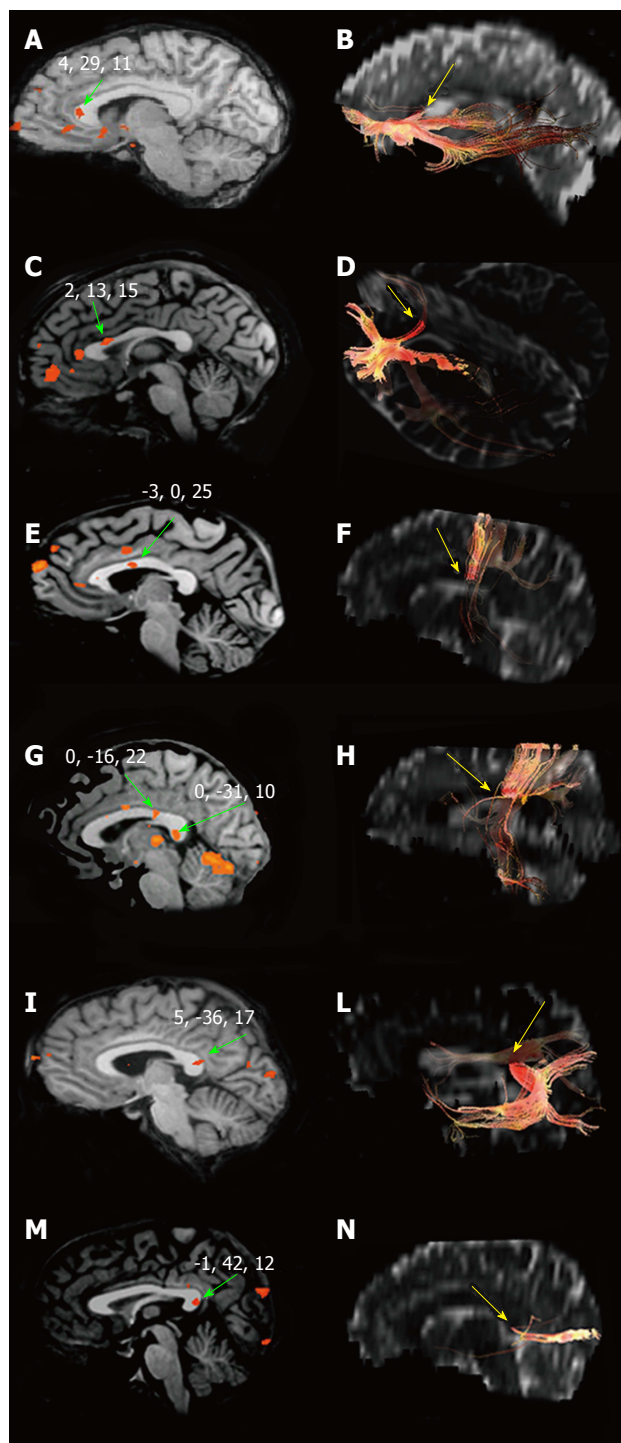


Figure 2 Blood-oxygen-level dependent effect within the corpus callosum and interhemispheric fibers. Blood-oxygen-level dependent effect evoked in the CC by different kind of peripheral sensory stimulation (left) and CC sites where fibers interconnecting the cortical areas activated cross the CC (right). A and B: Focus evoked by olfactory stimulation and callosal fibers connecting primary olfactory cortices, respectively; C and D: The same for gustatory stimuli and areas; E and F: Motor task and motor cortex; G and H: Hand tactile stimulus and somatosensory cortex; I and L: Auditory stimuli and cortex; M and N: Visual stimuli and cortex. Authors' original data. CC: Corpus callosum.

rovascular coupling^[112] in the CC cannot be ruled out. Current findings show that glial cells lack NO-producing enzymes^[3]; therefore Glu released from callosal axons

could induce release from astrocytes of vasoactive agents other than NO, such as cyclo-oxygenase (COX) products, whose inhibition significantly reduces vasodilation^[108,124].

FINAL REMARKS

As mentioned above, sensory and motor stimulation evokes activation in various areas of the CC^[94]. Two main observations have emerged from this brief review: the first is that activation foci have rarely been detected in the middle-anterior area; the second is that foci have been elicited in the posterior CC, *i.e.*, the splenium, by different sensory stimuli.

Functional activation in the middle-anterior area has sometimes been described in conditions where subjects performed interhemispheric transfer tasks involving crossed and uncrossed conditions^[85-87,125,126], which entailed a choice underpinned by a mental operation. Anterior callosal activation has been interpreted as the transfer of a premotor program leading to motor output. Results of recent behavioral and functional research suggest that activation of the anterior midbody is actually involved in the integration of cortical areas recruited in abstract mental operations. Miller *et al.*^[127] found that callosotomy patients subjected to resection of the anterior CC were unable to provide moral judgments based on a hypothetical situation; when the same patients were shown a gesture performed by a model standing in front of them and were asked to imitate it, they were unable to do so using an anatomical perspective^[128]. When during an fMRI session healthy subjects were asked to imitate mentally a series of intransitive gestures with the limb used by the model in performing them, callosal activation was detected in the anterior midbody^[129]. Altogether these data suggest that the anterior callosal midbody is involved in mental operations enabling individuals to relate themselves to other subjects, thus also allowing social interaction. The hypothesis is supported by microstructural DTI data showing that this regions has a reduced FA value in autistic and psychotic patients, indicating an impaired connectivity that in these patients is paralleled by poor or absent social competences.

As mentioned above, activation foci in the posterior region of the CC, the splenium, have sometimes been elicited in some controls and patients by taste and by touch stimulation to the hand, in addition to the specific foci seen in all subjects at more anterior sites. Since these foci do not seem to be accidental, they are likely evoked by peripheral stimulation. The foci elicited by gustatory and touch stimuli to the hand in the splenium might reflect higher-order association area activation: *e.g.*, posterior parietal cortex (touch); temporal cortex (taste and touch), since these cortical regions are interconnected by nerve fibers that cross the splenium^[10,11]. Activation of the splenium may explain the good performance in the transfer of touch information obtained by partial callosotomy patients, in whom only this callosal region is extant^[31,42,130-134]. Other findings from neuropsychological

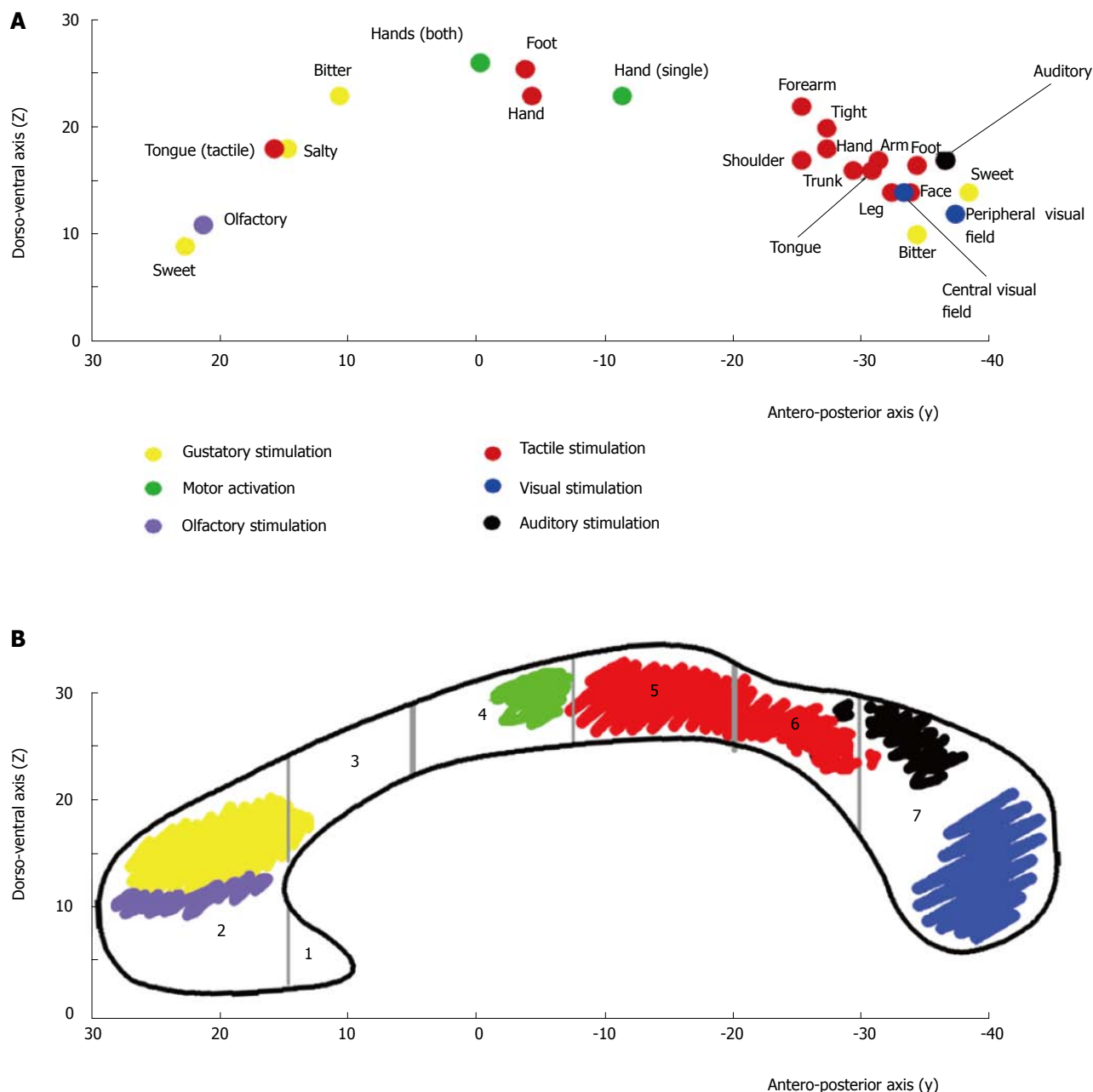


Figure 3 Callosal activation and callosal fibers topography. A: Summary diagram showing the distribution of the callosal foci evoked by different stimuli in control subjects. Each dot represents the “mean” value of the y and z Talairach coordinates (reported on the respective Cartesian axes) of the foci evoked by different stimuli. Yellow: Foci by gustatory stimuli; violet: Olfactory stimuli; green: Hand motor tasks; red: Tactile stimuli; black: Auditory stimuli; blue: Visual stimuli. See the text for a detailed description; B: Shows the crossing sites of interhemispheric fibers interconnecting the sensory and motor cortical areas activated by the specific peripheral stimuli. Vertical gray lines mark the seven CC regions according to Witelson^[8].

investigations of callosotomy patients^[134,135] point to a role for the splenium in transferring taste information. The recruitment of the splenium in the transfer of information other than visual information could be related to the large role of the visual representation of the external environment characteristic of humans, where different sensory experiences tend to be associated with a visual component. Its flexibility sets the splenium apart from more anterior callosal regions, and parallels other differences stemming from the development^[14], fiber composition^[12] and chemical specificity of this region^[136]. These morpho-functional observations are also in line with the

fact that patients where this part of the CC is extant do not exhibit disconnection syndromes^[19,28], and also suggest that the splenium might subserve most of the interhemispheric connectivity and the plasticity required for functional recovery after callosotomy or other insults.

The next step in this line of research should be the direct demonstration that functionally activated regions displaying a BOLD response correspond with the site where interhemispheric fibers interconnecting sensory or motor cortical areas involved in processing the peripheral stimuli applied cross through the commissure.

Another important issue to be addressed with the

newer techniques, like diffusion fMRI^[137], is whether the anterior and posterior portions of the CC have different roles.

CONCLUSION

This review provides a brief outline of key notions and examines recent DTI studies of the topographic organization of the CC in healthy subjects and in patients with different extents of callosal resection examined by fMRI during administration of peripheral sensory stimuli. These studies have documented a BOLD response in various portions of the commissure; they have demonstrated that it can be induced by peripheral stimuli and motor tasks; and have shown CC activation foci are found at discrete sites in relation to the sensory stimulation applied and the motor tasks performed. The resulting functional topographic map agrees with earlier findings. Additional fMRI and DTI data are clearly needed if we are to gain further insights into the callosal activation map and establish or rule out that functionally activated CC areas displaying a BOLD response correspond with sites where callosal fibers, interconnecting sensory or motor cortical areas involved in processing specific stimuli, cross through the commissure. The organization of the callosal fibers relaying information regarding different sub-modalities or areas of the sensory periphery also deserves further investigation.

ACKNOWLEDGMENTS

The researches by our group reported here have been carried out with the collaboration of the late Professor Tullio Manzoni and Professor Ugo Salvolini, who provided invaluable help and criticisms, of Doctor Giulia Mascioli, who contributed to fMRI data analysis, and of Doctors Aldo Paggi and Nicoletta Foschi, who were responsible for patient care. We gratefully acknowledge their contributions. The authors are also grateful to Dr. Silvia Modena (Word Design; www.silviamodena.com) for the language revision, and to the technical staff of the Radiology Institute for assistance in scan sessions and data transfer.

REFERENCES

- 1 **Aboitiz F**, Montiel J. One hundred million years of inter-hemispheric communication: the history of the corpus callosum. *Braz J Med Biol Res* 2003; **36**: 409-420 [PMID: 12700818 DOI: 10.1590/S0100-879X2003000400002]
- 2 **Innocenti GM**. General organization of callosal connections in the cerebral cortex. In: Jones EG, Peters A, editors. *Cerebral Cortex*. New York: Plenum Press, 1986; **5**: 291-353
- 3 **Barbaresi P**, Fabri M, Mensà E. Characterization of NO-producing neurons in the rat corpus callosum. *Brain Behav* 2014; **4**: 317-336 [PMID: 24944862 DOI: 10.1002/brb3.218]
- 4 **Rockland KS**, Nayyar N. Association of type I neurons positive for NADPH-diaphorase with blood vessels in the adult monkey corpus callosum. *Front Neural Circuits* 2012; **6**: 4 [PMID: 22363265 DOI: 10.3389/fncir.2012.00004]
- 5 **Malobabić S**, Bogdanović D, Drekić D. On the neurons with

- dendrites intermingling with the fibers of the human corpus callosum: a Golgi picture. *Gegenbaurs Morphol Jahrb* 1984; **130**: 557-564 [PMID: 6208078]
- 6 **Revishchin AV**, Okhotin VE, Korochkin LI, Pavlova GV. A new population of calretinin-positive cells, presumptively neurons, with polymorphous spines in the mouse forebrain. *Neurosci Behav Physiol* 2010; **40**: 541-552 [PMID: 20464508 DOI: 10.1007/s11055-010-9295-3]
- 7 **Riederer BM**, Berbel P, Innocenti GM. Neurons in the corpus callosum of the cat during postnatal development. *Eur J Neurosci* 2004; **19**: 2039-2046 [PMID: 15090031 DOI: 10.1111/j.1460-9568.2004.03305.x]
- 8 **Witelson SF**. Hand and sex differences in the isthmus and genu of the human corpus callosum. A postmortem morphological study. *Brain* 1989; **112** (Pt 3): 799-835 [PMID: 2731030 DOI: 10.1093/brain/112.3.799]
- 9 **Hofer S**, Frahm J. Topography of the human corpus callosum revisited--comprehensive fiber tractography using diffusion tensor magnetic resonance imaging. *Neuroimage* 2006; **32**: 989-994 [PMID: 16854598 DOI: 10.1016/j.neuroimage.2006.05.044]
- 10 **Hofer S**, Merboldt KD, Tammer R, Frahm J. Rhesus monkey and human share a similar topography of the corpus callosum as revealed by diffusion tensor MRI in vivo. *Cereb Cortex* 2008; **18**: 1079-1084 [PMID: 17709556 DOI: 10.1093/cercor/bhm141]
- 11 **Chao YP**, Cho KH, Yeh CH, Chou KH, Chen JH, Lin CP. Probabilistic topography of human corpus callosum using cytoarchitectural parcellation and high angular resolution diffusion imaging tractography. *Hum Brain Mapp* 2009; **30**: 3172-3187 [PMID: 19241418 DOI: 10.1002/hbm.20739]
- 12 **Aboitiz F**, Scheibel AB, Fisher RS, Zaidel E. Fiber composition of the human corpus callosum. *Brain Res* 1992; **598**: 143-153 [PMID: 1486477 DOI: 10.1016/0006-8993(92)90179-D]
- 13 **Kashem MA**, Sarker R, Des Etages H, Machaalani R, King N, McGregor IS, Matsumoto I. Comparative proteomics in the corpus callosal sub-regions of postmortem human brain. *Neurochem Int* 2009; **55**: 483-490 [PMID: 19433127 DOI: 10.1016/j.neuint.2009.04.017]
- 14 **Raybaud C**. The corpus callosum, the other great forebrain commissures, and the septum pellucidum: anatomy, development, and malformation. *Neuroradiology* 2010; **52**: 447-477 [PMID: 20422408 DOI: 10.1007/s00234-010-0696-3]
- 15 **Barbaresi P**, Fabri M, Conti F, Manzoni T. D-[3H]aspartate retrograde labelling of callosal and association neurones of somatosensory areas I and II of cats. *J Comp Neurol* 1987; **263**: 159-178 [PMID: 3667974 DOI: 10.1002/cne.902630202]
- 16 **Gonchar YA**, Johnson PB, Weinberg RJ. GABA-immunopositive neurons in rat neocortex with contralateral projections to S-I. *Brain Res* 1995; **697**: 27-34 [PMID: 8593589 DOI: 10.1016/0006-8993(95)00746-D]
- 17 **Fabri M**, Manzoni T. Glutamic acid decarboxylase immunoreactivity in callosal projecting neurons of cat and rat somatic sensory areas. *Neuroscience* 2004; **123**: 557-566 [PMID: 14698762]
- 18 **Higo S**, Akashi K, Sakimura K, Tamamaki N. Subtypes of GABAergic neurons project axons in the neocortex. *Front Neuroanat* 2009; **3**: 25 [PMID: 19915725 DOI: 10.3389/neuro.05.025.2009]
- 19 **Berlucchi G**. Visual interhemispheric communication and callosal connections of the occipital lobes. *Cortex* 2014; **56**: 1-13 [PMID: 23489777 DOI: 10.1016/j.cortex.2013.02.001]
- 20 **Berlucchi G**. Frontal callosal disconnection syndromes. *Cortex* 2012; **48**: 36-45 [PMID: 21663900 DOI: 10.1016/j.cortex.2011.04.008]
- 21 **Deoni SC**, Mercure E, Blasi A, Gasston D, Thomson A, Johnson M, Williams SC, Murphy DG. Mapping infant brain myelination with magnetic resonance imaging. *J Neurosci* 2011; **31**: 784-791 [PMID: 21228187 DOI: 10.1523/JNEURO-

- SCI.2106-10.2011]
- 22 **Provenzale JM**, Isaacson J, Chen S. Progression of corpus callosum diffusion-tensor imaging values during a period of signal changes consistent with myelination. *AJR Am J Roentgenol* 2012; **198**: 1403-1408 [PMID: 22623555 DOI: 10.2214/AJR.11.7849]
 - 23 **Manzoni T**. The cerebral ventricles, the animal spirits and the dawn of brain localization of function. *Arch Ital Biol* 1998; **136**: 103-152 [PMID: 9492949]
 - 24 **Manzoni T**. Fibre associative e commissurali. In *Corteccia Cerebrale e funzioni cognitive. Ventitré secoli di storia. Cap.5-5*. Roma (Italy): Carocci editore, 2011: 230-232
 - 25 **Wahl M**, Lauterbach-Soon B, Hattingen E, Jung P, Singer O, Volz S, Klein JC, Steinmetz H, Ziemann U. Human motor corpus callosum: topography, somatotopy, and link between microstructure and function. *J Neurosci* 2007; **27**: 12132-12138 [PMID: 17989279 DOI: 10.1523/JNEUROSCI.2320-07.2007]
 - 26 **Koch G**, Cercignani M, Bonni S, Giacobbe V, Bucchi G, Versace V, Caltagirone C, Bozzali M. Asymmetry of parietal interhemispheric connections in humans. *J Neurosci* 2011; **31**: 8967-8975 [PMID: 21677180 DOI: 10.1523/JNEUROSCI.6567-10.2011]
 - 27 **Men W**, Falk D, Sun T, Chen W, Li J, Yin D, Zang L, Fan M. The corpus callosum of Albert Einstein's brain: another clue to his high intelligence? *Brain* 2014; **137**: e268 [PMID: 24065724 DOI: 10.1093/brain/awt252]
 - 28 **Gazzaniga MS**. Forty-five years of split-brain research and still going strong. *Nat Rev Neurosci* 2005; **6**: 653-659 [PMID: 16062172 DOI: 10.1038/nrn1723]
 - 29 **Geschwind N**. Disconnexion syndromes in animals and man. I. *Brain* 1965; **88**: 237-294 [PMID: 5318481 DOI: 10.1093/brain/88.3.585]
 - 30 **Geschwind N**. Disconnexion syndromes in animals and man. II. *Brain* 1965; **88**: 585-644 [PMID: 5318824]
 - 31 **Gordon HW**, Bogen JE, Sperry RW. Absence of disconnection syndrome in two patients with partial section of the neocommissures. *Brain* 1971; **94**: 327-336 [PMID: 4998967 DOI: 10.1093/brain/94.2.327]
 - 32 **Innocenti GM**, Manzoni T, Spidalieri G. Cutaneous receptive fields of single fibers of the corpus callosum. *Brain Res* 1972; **40**: 507-512 [PMID: 5027175 DOI: 10.1016/0006-8993(72)90153-9]
 - 33 **Innocenti GM**, Manzoni T, Spidalieri G. Patterns of the somesthetic messages transferred through the corpus callosum. *Exp Brain Res* 1974; **19**: 447-466 [PMID: 4853559 DOI: 10.1007/BF00236110]
 - 34 **Berlucchi G**, Gazzaniga MS, Rizzolatti G. Microelectrode analysis of transfer of visual information by the corpus callosum. *Arch Ital Biol* 1967; **105**: 583-596 [PMID: 5585725]
 - 35 **Hubel DH**, Wiesel TN. Cortical and callosal connections concerned with the vertical meridian of visual fields in the cat. *J Neurophysiol* 1967; **30**: 1561-1573 [PMID: 6066454]
 - 36 **Guillemot JP**, Richer L, Prevost L, Ptito M, Lepore F. Receptive field properties of somatosensory callosal fibres in the monkey. *Brain Res* 1987; **402**: 293-302 [PMID: 3828797 DOI: 10.1016/0006-8993(87)90036-9]
 - 37 **Pandya DN**, Karol EA, Heilbronn D. The topographical distribution of interhemispheric projections in the corpus callosum of the rhesus monkey. *Brain Res* 1971; **32**: 31-43 [PMID: 5000193 DOI: 10.1016/0006-8993(71)90153-3]
 - 38 **Pandya DN**, Seltzer B. 1986. The topography of commissural fibers. In: Lepore F, Ptito M and Jasper HH, editors. *Two Hemispheres-One Brain: Functions of the Corpus Callosum*. New York: Alan Liss, 1986: 47-73
 - 39 **de Lacoste MC**, Kirkpatrick JB, Ross ED. Topography of the human corpus callosum. *J Neuropathol Exp Neurol* 1985; **44**: 578-591 [PMID: 4056827 DOI: 10.1097/00005072-198511000-00004]
 - 40 **Caillé S**, Sauerwein HC, Schiavetto A, Villemure JG, Lassonde M. Sensory and motor interhemispheric integration after section of different portions of the anterior corpus callosum in nonepileptic patients. *Neurosurgery* 2005; **57**: 50-59; discussion 50-59 [PMID: 15987540 DOI: 10.1227/01.NEU.0000163089.31657.08]
 - 41 **Berlucchi G**. Some effects of cortical and callosal damage on conscious and unconscious processing of visual information and other sensory inputs. *Prog Brain Res* 2004; **144**: 79-93 [PMID: 14650841 DOI: 10.1016/S0079-6123(03)14405-6]
 - 42 **Fabri M**, Del Pesce M, Paggi A, Polonara G, Bartolini M, Salvolini U, Manzoni T. Contribution of posterior corpus callosum to the interhemispheric transfer of tactile information. *Brain Res Cogn Brain Res* 2005; **24**: 73-80 [PMID: 15922160 DOI: 10.1016/j.cogbrainres.2004.12.003]
 - 43 **Funnell MG**, Corballis PM, Gazzaniga MS. Cortical and subcortical interhemispheric interactions following partial and complete callosotomy. *Arch Neurol* 2000; **57**: 185-189 [PMID: 10681075 DOI: 10.1001/archneur.57.2.185]
 - 44 **Fabri M**, Polonara G, Quattrini A, Salvolini U, Del Pesce M, Manzoni T. Role of the corpus callosum in the somatosensory activation of the ipsilateral cerebral cortex: an fMRI study of callosotomized patients. *Eur J Neurosci* 1999; **11**: 3983-3994 [PMID: 10583487 DOI: 10.1046/j.1460-9568.1999.00829.x]
 - 45 **Fabri M**, Polonara G, Del Pesce M, Quattrini A, Salvolini U, Manzoni T. Posterior corpus callosum and interhemispheric transfer of somatosensory information: an fMRI and neuropsychological study of a partially callosotomized patient. *J Cogn Neurosci* 2001; **13**: 1071-1079 [PMID: 11784445 DOI: 10.1162/089892901753294365]
 - 46 **Fabri M**, Polonara G, Salvolini U, Manzoni T. Bilateral cortical representation of the trunk midline in human first somatic sensory area. *Hum Brain Mapp* 2005; **25**: 287-296 [PMID: 15827999 DOI: 10.1002/hbm.20099]
 - 47 **Gazzaniga MS**, Freedman H. Observations on visual processes after posterior callosal section. *Neurology* 1973; **23**: 1126-1130 [PMID: 4795425 DOI: 10.1212/WNL.23.10.1126]
 - 48 **Clarke S**, Maeder P, Meuli R, Staub F, Bellmann A, Regli L, de Tribolet N, Assal G. Interhemispheric transfer of visual motion information after a posterior callosal lesion: a neuropsychological and fMRI study. *Exp Brain Res* 2000; **132**: 127-133 [PMID: 10836642 DOI: 10.1007/s002219900327]
 - 49 **Sugishita M**, Otomo K, Yamazaki K, Shimizu H, Yoshioka M, Shinohara A. Dichotic listening in patients with partial section of the corpus callosum. *Brain* 1995; **118** (Pt 2): 417-427 [PMID: 7735883 DOI: 10.1093/brain/118.2.417]
 - 50 **Pollmann S**, Maertens M, von Cramon DY, Lepsien J, Hugdahl K. Dichotic listening in patients with splenial and nonsplenial callosal lesions. *Neuropsychology* 2002; **16**: 56-64 [PMID: 11858226 DOI: 10.1037/0894-4105.16.1.56]
 - 51 **Basser PJ**, Mattiello J, LeBihan D. MR diffusion tensor spectroscopy and imaging. *Biophys J* 1994; **66**: 259-267 [PMID: 8130344 DOI: 10.1016/S0006-3495(94)80775-1]
 - 52 **Moseley ME**, Cohen Y, Kucharczyk J, Mintorovitch J, Asgari HS, Wendland MF, Tsuruda J, Norman D. Diffusion-weighted MR imaging of anisotropic water diffusion in cat central nervous system. *Radiology* 1990; **176**: 439-445 [PMID: 2367658 DOI: 10.1148/radiology.176.2.2367658]
 - 53 **Thomsen C**, Henriksen O, Ring P. In vivo measurement of water self diffusion in the human brain by magnetic resonance imaging. *Acta Radiol* 1987; **28**: 353-361 [PMID: 2958045 DOI: 10.3109/02841858709177362]
 - 54 **Beaulieu C**. The basis of anisotropic water diffusion in the nervous system - a technical review. *NMR Biomed* 2002; **15**: 435-455 [PMID: 12489094 DOI: 10.1002/nbm.782]
 - 55 **Yap QJ**, Teh I, Fusar-Poli P, Sum MY, Kuswanto C, Sim K. Tracking cerebral white matter changes across the lifespan: insights from diffusion tensor imaging studies. *J Neural Transm* 2013; **120**: 1369-1395 [PMID: 23328950 DOI: 10.1007/s00702-013-0971-7]
 - 56 **Sullivan EV**, Rohlfing T, Pfefferbaum A. Longitudinal

- study of callosal microstructure in the normal adult aging brain using quantitative DTI fiber tracking. *Dev Neuropsychol* 2010; **35**: 233-256 [PMID: 20446131 DOI: 10.1080/87565641003689556]
- 57 **Polonara G**, Fabri M, Mascioli G, Paggi A, Manzoni T, Salvolini U. Interhemispheric connectivity in patients with callosal resection described and quantified using diffusion tensor imaging. 32nd Eur Soc NeuroRadiol Ann Meeting. Italy: Genoa, 2007: 20-23
- 58 **Pizzini FB**, Polonara G, Mascioli G, Beltramello A, Foroni R, Paggi A, Salvolini U, Tassinari G, Fabri M. Diffusion tensor tracking of callosal fibers several years after callosotomy. *Brain Res* 2010; **1312**: 10-17 [PMID: 19931228 DOI: 10.1016/j.brainres.2009.11.030]
- 59 **Fabri M**, Polonara G. Functional topography of human corpus callosum: an fMRI mapping study. *Neural Plast* 2013; **2013**: 251308 [PMID: 23476810 DOI: 10.1155/2013/251308]
- 60 **Caminiti R**, Carducci F, Piervincenzi C, Battaglia-Mayer A, Confalone G, Visco-Comandini F, Pantano P, Innocenti GM. Diameter, length, speed, and conduction delay of callosal axons in macaque monkeys and humans: comparing data from histology and magnetic resonance imaging diffusion tractography. *J Neurosci* 2013; **33**: 14501-14511 [PMID: 24005301 DOI: 10.1523/JNEUROSCI.0761-13.2013]
- 61 **Pfefferbaum A**, Sullivan EV, Hedehus M, Lim KO, Adalsteinsson E, Moseley M. Age-related decline in brain white matter anisotropy measured with spatially corrected echoplanar diffusion tensor imaging. *Magn Reson Med* 2000; **44**: 259-268 [PMID: 10918325 DOI: 10.1002/1522-2594(200008)44:2<259::AID-MRM13>3.0.CO;2-6]
- 62 **Steel RM**, Bastin ME, McConnell S, Marshall I, Cunningham-Owens DG, Lawrie SM, Johnstone EC, Best JJ. Diffusion tensor imaging (DTI) and proton magnetic resonance spectroscopy (1H MRS) in schizophrenic subjects and normal controls. *Psychiatry Res* 2001; **106**: 161-170 [PMID: 11382538 DOI: 10.1016/S0925-4927(01)00080-4]
- 63 **Werring DJ**, Clark CA, Barker GJ, Miller DH, Parker GJ, Brammer MJ, Bullmore ET, Giampietro VP, Thompson AJ. The structural and functional mechanisms of motor recovery: complementary use of diffusion tensor and functional magnetic resonance imaging in a traumatic injury of the internal capsule. *J Neurol Neurosurg Psychiatry* 1998; **65**: 863-869 [PMID: 9854962 DOI: 10.1136/jnnp.65.6.863]
- 64 **Filippi M**, Cercignani M, Inglese M, Horsfield MA, Comi G. Diffusion tensor magnetic resonance imaging in multiple sclerosis. *Neurology* 2001; **56**: 304-311 [PMID: 11171893 DOI: 10.1212/WNL.56.3.304]
- 65 **Yu HJ**, Christodoulou C, Bhise V, Greenblatt D, Patel Y, Serafin D, Maletic-Savatic M, Krupp LB, Wagshul ME. Multiple white matter tract abnormalities underlie cognitive impairment in RRMS. *Neuroimage* 2012; **59**: 3713-3722 [PMID: 22062194 DOI: 10.1016/j.neuroimage.2011.10.053]
- 66 **Hannoun S**, Bagory M, Durand-Dubief F, Ibarrola D, Comte JC, Confavreux C, Cotton F, Sappey-Marinié D. Correlation of diffusion and metabolic alterations in different clinical forms of multiple sclerosis. *PLoS One* 2012; **7**: e32525 [PMID: 22479330 DOI: 10.1371/journal.pone.0032525]
- 67 **Igarashi H**, Katayama Y, Tsuganezawa T, Yamamuro M, Terashi A, Owan C. Three-dimensional anisotropy contrast (3DAC) magnetic resonance imaging of the human brain: application to assess Wallerian degeneration. *Intern Med* 1998; **37**: 662-668 [PMID: 9745851 DOI: 10.2169/internal-medicine.37.662]
- 68 **Papinutto ND**, Maule F, Jovicich J. Reproducibility and biases in high field brain diffusion MRI: An evaluation of acquisition and analysis variables. *Magn Reson Imaging* 2013; **31**: 827-839 [PMID: 23623031 DOI: 10.1016/j.mri.2013.03.004]
- 69 **Ditye T**, Kanai R, Bahrami B, Muggleton NG, Rees G, Walsh V. Rapid changes in brain structure predict improvements induced by perceptual learning. *Neuroimage* 2013; **81**: 205-212 [PMID: 23702411 DOI: 10.1016/j.neuroimage.2013.05.058]
- 70 **Hofstetter S**, Tavor I, Tzur Moryosef S, Assaf Y. Short-term learning induces white matter plasticity in the fornix. *J Neurosci* 2013; **33**: 12844-12850 [PMID: 23904619 DOI: 10.1523/JNEUROSCI.4520-12.2013]
- 71 **Tavor I**, Hofstetter S, Assaf Y. Micro-structural assessment of short term plasticity dynamics. *Neuroimage* 2013; **81**: 1-7 [PMID: 23702416 DOI: 10.1016/j.neuroimage.2013.05.050]
- 72 **Xue R**, van Zijl PC, Crain BJ, Solaiyappan M, Mori S. In vivo three-dimensional reconstruction of rat brain axonal projections by diffusion tensor imaging. *Magn Reson Med* 1999; **42**: 1123-1127 [PMID: 10571934 DOI: 10.1002/(SICI)1522-2594(199912)42:6<1123::AID-MRM17>3.0.CO;2-H]
- 73 **Holodny AI**, Schwartz TH, Ollenschlegler M, Liu WC, Schulder M. Tumor involvement of the corticospinal tract: diffusion magnetic resonance tractography with intraoperative correlation. *J Neurosurg* 2001; **95**: 1082 [PMID: 11765829 DOI: 10.3171/jns.2001.95.6.1082]
- 74 **Mesaros S**, Rocca MA, Kacar K, Kostic J, Copetti M, Stolic-Opincal T, Preziosa P, Sala S, Riccitelli G, Horsfield MA, Drulovic J, Comi G, Filippi M. Diffusion tensor MRI tractography and cognitive impairment in multiple sclerosis. *Neurology* 2012; **78**: 969-975 [PMID: 22377806 DOI: 10.1212/WNL.0b013e31824d5859]
- 75 **Anderson VM**, Wheeler-Kingshott CA, Abdel-Aziz K, Miller DH, Toosy A, Thompson AJ, Ciccarelli O. A comprehensive assessment of cerebellar damage in multiple sclerosis using diffusion tractography and volumetric analysis. *Mult Scler* 2011; **17**: 1079-1087 [PMID: 21511688 DOI: 10.1177/1352458511403528]
- 76 **Gorgoraptis N**, Wheeler-Kingshott CA, Jenkins TM, Altmann DR, Miller DH, Thompson AJ, Ciccarelli O. Combining tractography and cortical measures to test system-specific hypotheses in multiple sclerosis. *Mult Scler* 2010; **16**: 555-565 [PMID: 20215478 DOI: 10.1177/1352458510362440]
- 77 **Harrison DM**, Caffo BS, Shiee N, Farrell JA, Bazin PL, Farrell SK, Ratchford JN, Calabresi PA, Reich DS. Longitudinal changes in diffusion tensor-based quantitative MRI in multiple sclerosis. *Neurology* 2011; **76**: 179-186 [PMID: 21220722 DOI: 10.1212/WNL.0b013e318206ca61]
- 78 **Rocca MA**, Valsasina P, Absinta M, Riccitelli G, Rodegher ME, Misci P, Rossi P, Falini A, Comi G, Filippi M. Default-mode network dysfunction and cognitive impairment in progressive MS. *Neurology* 2010; **74**: 1252-1259 [PMID: 20404306 DOI: 10.1212/WNL.0b013e3181d9ed91]
- 79 **Abe O**, Masutani Y, Aoki S, Yamasue H, Yamada H, Kasai K, Mori H, Hayashi N, Masumoto T, Ohtomo K. Topography of the human corpus callosum using diffusion tensor tractography. *J Comput Assist Tomogr* 2004; **28**: 533-539 [PMID: 15232387 DOI: 10.1097/00004728-200407000-00016]
- 80 **Huang H**, Zhang J, Jiang H, Wakana S, Poetscher L, Miller MI, van Zijl PC, Hillis AE, Wytik R, Mori S. DTI tractography based parcellation of white matter: application to the mid-sagittal morphology of corpus callosum. *Neuroimage* 2005; **26**: 195-205 [PMID: 15862219 DOI: 10.1016/j.neuroimage.2005.01.019]
- 81 **Zarei M**, Johansen-Berg H, Smith S, Ciccarelli O, Thompson AJ, Matthews PM. Functional anatomy of interhemispheric cortical connections in the human brain. *J Anat* 2006; **209**: 311-320 [PMID: 16928200 DOI: 10.1111/j.1469-7580.2006.00615.x]
- 82 **Dougherty RF**, Ben-Shachar M, Bammer R, Brewer AA, Wandell BA. Functional organization of human occipital-callosal fiber tracts. *Proc Natl Acad Sci USA* 2005; **102**: 7350-7355 [PMID: 15883384 DOI: 10.1073/pnas.0500003102]
- 83 **Shimony JS**, Burton H, Epstein AA, McLaren DG, Sun SW, Snyder AZ. Diffusion tensor imaging reveals white matter reorganization in early blind humans. *Cereb Cortex* 2006; **16**: 1653-1661 [PMID: 16400157 DOI: 10.1093/cercor/bhj102]

- 84 **Logothetis NK**, Pauls J, Augath M, Trinath T, Oeltermann A. Neurophysiological investigation of the basis of the fMRI signal. *Nature* 2001; **412**: 150-157 [PMID: 11449264 DOI: 10.1038/35084005]
- 85 **Tettamanti M**, Paulesu E, Scifo P, Maravita A, Fazio F, Perani D, Marzi CA. Interhemispheric transmission of visuomotor information in humans: fMRI evidence. *J Neurophysiol* 2002; **88**: 1051-1058 [PMID: 12163553]
- 86 **Omura K**, Tsukamoto T, Kotani Y, Ohgami Y, Minami M, Inoue Y. Different mechanisms involved in interhemispheric transfer of visuomotor information. *Neuroreport* 2004; **15**: 2707-2711 [PMID: 15597039]
- 87 **Weber B**, Treyer V, Oberholzer N, Jaermann T, Boesiger P, Brugger P, Regard M, Buck A, Savazzi S, Marzi CA. Attention and interhemispheric transfer: a behavioral and fMRI study. *J Cogn Neurosci* 2005; **17**: 113-123 [PMID: 15701243 DOI: 10.1162/0898929052880002]
- 88 **Mazerolle EL**, D'Arcy RC, Beyea SD. Detecting functional magnetic resonance imaging activation in white matter: interhemispheric transfer across the corpus callosum. *BMC Neurosci* 2008; **9**: 84 [PMID: 18789154 DOI: 10.1186/1471-2202-9-84]
- 89 **Mosier K**, Bereznyaya I. Parallel cortical networks for volitional control of swallowing in humans. *Exp Brain Res* 2001; **140**: 280-289 [PMID: 11681303 DOI: 10.1007/s002210100813]
- 90 **Meyer BU**, Rörich S, Gräfin von Einsiedel H, Kruggel F, Weindl A. Inhibitory and excitatory interhemispheric transfers between motor cortical areas in normal humans and patients with abnormalities of the corpus callosum. *Brain* 1995; **118** (Pt 2): 429-440 [PMID: 7735884 DOI: 10.1093/brain/118.2.429]
- 91 **Stancák A**, Lücking CH, Kristeva-Feige R. Lateralization of movement-related potentials and the size of corpus callosum. *Neuroreport* 2000; **11**: 329-332 [PMID: 10674480 DOI: 10.1097/00001756-200002070-00021]
- 92 **Bonzano L**, Tacchino A, Roccatagliata L, Abbruzzese G, Mancardi GL, Bove M. Callosal contributions to simultaneous bimanual finger movements. *J Neurosci* 2008; **28**: 3227-3233 [PMID: 18354026 DOI: 10.1523/JNEUROSCI.4076-07.2008]
- 93 **Salvolini U**, Polonara G, Mascioli G, Fabri M, Manzoni T. [Functional topography of the human corpus callosum]. *Bull Acad Natl Med* 2010; **194**: 617-631; discussion 631-632 [PMID: 21171254]
- 94 **Fabri M**, Polonara G, Mascioli G, Salvolini U, Manzoni T. Topographical organization of human corpus callosum: an fMRI mapping study. *Brain Res* 2011; **1370**: 99-111 [PMID: 21081115 DOI: 10.1016/j.brainres.2010.11.039]
- 95 **Polonara G**, Mascioli G, Foschi N, Salvolini U, Pierpaoli C, Manzoni T, Fabri M, Barbaresi P. Further evidence for the topography and connectivity of the corpus callosum: An fMRI study of patients with partial callosal resection. *J Neuroimaging* 2014; **1-10** [PMID: 25039660 DOI: 10.1111/jon.12136]
- 96 **Suárez-Solá ML**, González-Delgado FJ, Pueyo-Morlans M, Medina-Bolívar OC, Hernández-Acosta NC, González-Gómez M, Meyer G. Neurons in the white matter of the adult human neocortex. *Front Neuroanat* 2009; **3**: 7 [PMID: 19543540 DOI: 10.3389]
- 97 **Iadecola C**. Intrinsic signals and functional brain mapping: caution, blood vessels at work. *Cereb Cortex* 2002; **12**: 223-224 [PMID: 11839596 DOI: 10.1093/cercor/12.3.223]
- 98 **Iadecola C**. Neurovascular regulation in the normal brain and in Alzheimer's disease. *Nat Rev Neurosci* 2004; **5**: 347-360 [PMID: 15100718 DOI: 10.1038/nrn1387]
- 99 **Lauritzen M**. Reading vascular changes in brain imaging: is dendritic calcium the key? *Nat Rev Neurosci* 2005; **6**: 77-85 [PMID: 15611729 DOI: 10.1038/nrn1589]
- 100 **D'Arcy RC**, Hamilton A, Jarmasz M, Sullivan S, Stroink G. Exploratory data analysis reveals visuovisual interhemispheric transfer in functional magnetic resonance imaging. *Magn Reson Med* 2006; **55**: 952-958 [PMID: 16506159 DOI: 10.1002/mrm.20839]
- 101 **Magistretti PJ**. Brain energy metabolism. In Zigmond MJ, Bloom FE, Landis SC, Roberts JL, Squire LR, editors. *Fundamental Neuroscience*. San Diego: Academic Press, 2003: 339-360
- 102 **Kida I**, Hyder F, Behar KL. Inhibition of voltage-dependent sodium channels suppresses the functional magnetic resonance imaging response to forepaw somatosensory activation in the rodent. *J Cereb Blood Flow Metab* 2001; **21**: 585-591 [PMID: 11333369 DOI: 10.1097/00004647-200105000-00013]
- 103 **Smith AJ**, Blumenfeld H, Behar KL, Rothman DL, Shulman RG, Hyder F. Cerebral energetics and spiking frequency: the neurophysiological basis of fMRI. *Proc Natl Acad Sci USA* 2002; **99**: 10765-10770 [PMID: 12134056 DOI: 10.1073/pnas.132272199]
- 104 **Iacoboni M**. Visuo-motor integration and control in the human posterior parietal cortex: evidence from TMS and fMRI. *Neuropsychologia* 2006; **44**: 2691-2699 [PMID: 16759673 DOI: 10.1016/j.neuropsychologia.2006.04.029]
- 105 **Nir Y**, Dinstein I, Malach R, Heeger DJ. BOLD and spiking activity. *Nat Neurosci* 2008; **11**: 523-524; author reply 524 [PMID: 18437185 DOI: 10.1038/nn0508-523]
- 106 **Rossi DJ**. Another BOLD role for astrocytes: coupling blood flow to neural activity. *Nat Neurosci* 2006; **9**: 159-161 [PMID: 16439980 DOI: 10.1038/nn0206-159]
- 107 **Jakovcevic D**, Harder DR. Role of astrocytes in matching blood flow to neuronal activity. *Curr Top Dev Biol* 2007; **79**: 75-97 [PMID: 17498548 DOI: 10.1016/S0070-2153(06)79004-4]
- 108 **Takano T**, Tian GF, Peng W, Lou N, Libionka W, Han X, Nedergaard M. Astrocyte-mediated control of cerebral blood flow. *Nat Neurosci* 2006; **9**: 260-267 [PMID: 16388306 DOI: 10.1038/nn1623]
- 109 **Rabi SJ**, Madhavi C, Antonisamy B, Koshi R. Quantitative analysis of the human corpus callosum under light microscopy. *Eur J Anat* 2007; **11**: 95-100
- 110 **Iadecola C**, Beitz AJ, Renno W, Xu X, Mayer B, Zhang F. Nitric oxide synthase-containing neural processes on large cerebral arteries and cerebral microvessels. *Brain Res* 1993; **606**: 148-155 [PMID: 7681722 DOI: 10.1016/0006-8993(93)91583-E]
- 111 **Estrada C**, DeFelipe J. Nitric oxide-producing neurons in the neocortex: morphological and functional relationship with intraparenchymal microvasculature. *Cereb Cortex* 1998; **8**: 193-203 [PMID: 9617914 DOI: 10.1093/cercor/8.3.193]
- 112 **Attwell D**, Buchan AM, Charpak S, Lauritzen M, Macvicar BA, Newman EA. Glial and neuronal control of brain blood flow. *Nature* 2010; **468**: 232-243 [PMID: 21068832 DOI: 10.1038/nature09613]
- 113 **Ziskin JL**, Nishiyama A, Rubio M, Fukaya M, Bergles DE. Vesicular release of glutamate from unmyelinated axons in white matter. *Nat Neurosci* 2007; **10**: 321-330 [PMID: 17293857 DOI: 10.1038/nn1854]
- 114 **Kukley M**, Capetillo-Zarate E, Dietrich D. Vesicular glutamate release from axons in white matter. *Nat Neurosci* 2007; **10**: 311-320 [PMID: 17293860 DOI: 10.1038/nn1850]
- 115 **Iadecola C**, Nedergaard M. Glial regulation of the cerebral microvasculature. *Nat Neurosci* 2007; **10**: 1369-1376 [PMID: 17965657 DOI: 10.1038/nn2003]
- 116 **Garthwaite J**. Glutamate, nitric oxide and cell-cell signalling in the nervous system. *Trends Neurosci* 1991; **14**: 60-67 [PMID: 1708538 DOI: 10.1016/0166-2236(91)90022-M]
- 117 **Garthwaite J**. Concepts of neural nitric oxide-mediated transmission. *Eur J Neurosci* 2008; **27**: 2783-2802 [PMID: 18588525 DOI: 10.1111/j.1460-9568.2008.06285.x]
- 118 **Tiede R**, Krautwald K, Fincke A, Angenstein F. NMDA-dependent mechanisms only affect the BOLD response in the rat dentate gyrus by modifying local signal processing. *J Cereb Blood Flow Metab* 2012; **32**: 570-584 [PMID: 22167232 DOI: 10.1038/jcbfm.2011.182]
- 119 **Gsell W**, Burke M, Wiedermann D, Bonvento G, Silva AC,

- Dauphin F, Bührle C, Hoehn M, Schwindt W. Differential effects of NMDA and AMPA glutamate receptors on functional magnetic resonance imaging signals and evoked neuronal activity during forepaw stimulation of the rat. *J Neurosci* 2006; **26**: 8409-8416 [PMID: 16914666 DOI: 10.1523/JNEUROSCI.4615-05.2006]
- 120 **Nielsen AN**, Fabricius M, Lauritzen M. Scanning laser-Doppler flowmetry of rat cerebral circulation during cortical spreading depression. *J Vasc Res* 2001; **37**: 513-522 [PMID: 11146405 DOI: 10.1111/j.1469-7793.2001.00773.x]
- 121 **Hoffmeyer HW**, Enager P, Thomsen KJ, Lauritzen MJ. Non-linear neurovascular coupling in rat sensory cortex by activation of transcallosal fibers. *J Cereb Blood Flow Metab* 2007; **27**: 575-587 [PMID: 16896350 DOI: 10.1038/sj.jcbfm.9600372]
- 122 **Iadecola C**, Li J, Xu S, Yang G. Neural mechanisms of blood flow regulation during synaptic activity in cerebellar cortex. *J Neurophysiol* 1996; **75**: 940-950 [PMID: 8714666]
- 123 **Busija DW**, Bari F, Domoki F, Louis T. Mechanisms involved in the cerebrovascular dilator effects of N-methyl-D-aspartate in cerebral cortex. *Brain Res Rev* 2007; **56**: 89-100 [PMID: 17716743 DOI: 10.1016/j.brainresrev.2007.05.011]
- 124 **Zonta M**, Angulo MC, Gobbo S, Rosengarten B, Hossmann KA, Pozzan T, Carmignoto G. Neuron-to-astrocyte signaling is central to the dynamic control of brain microcirculation. *Nat Neurosci* 2003; **6**: 43-50 [PMID: 12469126 DOI: 10.1038/nn980]
- 125 **Gawryluk JR**, Brewer KD, Beyea SD, D'Arcy RC. Optimizing the detection of white matter fMRI using asymmetric spin echo spiral. *Neuroimage* 2009; **45**: 83-88 [PMID: 19084071 DOI: 10.1016/j.neuroimage.2008.11.005]
- 126 **Mazerolle EL**, Beyea SD, Gawryluk JR, Brewer KD, Bowen CV, D'Arcy RC. Confirming white matter fMRI activation in the corpus callosum: co-localization with DTI tractography. *Neuroimage* 2010; **50**: 616-621 [PMID: 20053383 DOI: 10.1016/j.neuroimage.2009.12.102]
- 127 **Miller MB**, Sinnott-Armstrong W, Young L, King D, Paggi A, Fabri M, Polonara G, Gazzaniga MS. Abnormal moral reasoning in complete and partial callosotomy patients. *Neuropsychologia* 2010; **48**: 2215-2220 [PMID: 20188113 DOI: 10.1016/j.neuropsychologia.2010.02.021]
- 128 **Pierpaoli C**, Ferrante L, Berlucchi G, Ortenzi A, Manzoni T, Fabri M. Imitation strategies in callosotomized patients. 8th National Congress IBRO. Italy: Florence, 2011: 14-18
- 129 **Pierpaoli C**, Polonara G, Foschi N, Salvolini U, Berlucchi G, Fabri M. Cortical activation during imitative behaviour in control subjects and callosotomized patients. 9th FENS Forum of Neuroscience. Italy: Milan, 2014: 5-9
- 130 **Volpe BT**, Sidtis JJ, Holtzman JD, Wilson DH, Gazzaniga MS. Cortical mechanisms involved in praxis: observations following partial and complete section of the corpus callosum in man. *Neurology* 1982; **32**: 645-650 [PMID: 7201094 DOI: 10.1212/WNL.32.6.645]
- 131 **Bentin S**, Sahar A, Moscovitch M. Intermanual information transfer in patients with lesions in the trunk of the corpus callosum. *Neuropsychologia* 1984; **22**: 601-611 [PMID: 6504300 DOI: 10.1016/0028-3932(84)90024-1]
- 132 **Geffen G**, Nilsson J, Quinn K, Teng EL. The effect of lesions of the corpus callosum on finger localization. *Neuropsychologia* 1985; **23**: 497-514 [PMID: 4033904 DOI: 10.1016/0028-3932(85)90004-1]
- 133 **Risse GL**, Gates J, Lund G, Maxwell R, Rubens A. Inter-hemispheric transfer in patients with incomplete section of the corpus callosum. Anatomic verification with magnetic resonance imaging. *Arch Neurol* 1989; **46**: 437-443 [PMID: 2705905 DOI: 10.1001/archneur.1989.00520400097026]
- 134 **Levin HS**, Mattson AJ, Levander M, Lindquist CE, Simard JM, Guinto FC, Lilly MA, Eisenberg HM. Effects of transcallosal surgery on interhemispheric transfer of information. *Surg Neurol* 1993; **40**: 65-74 [PMID: 8322184 DOI: 10.1016/0090-3019(93)90174-Y]
- 135 **Aglioti S**, Tassinari G, Corballis MC, Berlucchi G. Incomplete gustatory lateralization as shown by analysis of taste discrimination after callosotomy. *J Cogn Neurosci* 2000; **12**: 238-245 [PMID: 10771408 DOI: 10.1162/089892900562066]
- 136 **Aglioti SM**, Tassinari G, Fabri M, Del Pesce M, Quattrini A, Manzoni T, Berlucchi G. Taste laterality in the split brain. *Eur J Neurosci* 2001; **13**: 195-200 [PMID: 11135018 DOI: 10.1046/j.0953-816X.2000.01378.x]
- 137 **Le Bihan D**. Diffusion, confusion and functional MRI. *Neuroimage* 2012; **62**: 1131-1136 [PMID: 21985905 DOI: 10.1016/j.neuroimage.2011.09.058]
- 138 **Gawryluk JR**, Mazerolle EL, D'Arcy RC. Does functional MRI detect activation in white matter? A review of emerging evidence, issues, and future directions. *Front Neurosci* 2014; **8**: 239 [PMID: 25152709 DOI: 10.3389/fnins.2014.00239]

P- Reviewer: Arsalidou M, Sijens PE S- Editor: Ji FF
L- Editor: A E- Editor: Lu YJ



Recent developments in optimal experimental designs for functional magnetic resonance imaging

Ming-Hung Kao, M'hamed Temkit, Weng Kee Wong

Ming-Hung Kao, M'hamed Temkit, School of Mathematical and Statistical Sciences, Arizona State University, Tempe, AZ 85287, United States

Weng Kee Wong, Department of Biostatistics, University of California at Los Angeles, Los Angeles, CA 90095, United States

Author contributions: Kao MH wrote the paper; Temkit M and Wong WK revised it critically for important intellectual content. **Correspondence to:** Ming-Hung Kao, Assistant Professor of Statistics, School of Mathematical and Statistical Sciences, Arizona State University, PO Box 871804, Tempe, AZ 85287, United States. mkao3@asu.edu

Telephone: +1-480-9653951 Fax: +1-480-9658119

Received: December 31, 2013 Revised: April 30, 2014

Accepted: May 28, 2014

Published online: March 28, 2015

© 2015 Baishideng Publishing Group Inc. All rights reserved.

Key words: A-optimality; Blocked designs; Design efficiencies; D-optimality; Genetic algorithms; Hadamard sequences; M-sequences

Core tip: This paper provides an overview on recent developments in the design of functional magnetic resonance imaging experiments (fMRI). We discuss both analytical results and computational approaches that are currently available for selecting high-quality fMRI designs.

Original sources: Kao MH, Temkit M, Wong WK. Recent developments in optimal experimental designs for functional magnetic resonance imaging. *World J Radiol* 2014; 6(7): 437-445 Available from: URL: <http://www.wjgnet.com/1949-8470/full/v6/i7/437.htm> DOI: <http://dx.doi.org/10.4329/wjr.v6.i7.437>

Abstract

Functional magnetic resonance imaging (fMRI) is one of the leading brain mapping technologies for studying brain activity in response to mental stimuli. For neuroimaging studies utilizing this pioneering technology, there is a great demand of high-quality experimental designs that help to collect informative data to make precise and valid inference about brain functions. This paper provides a survey on recent developments in experimental designs for fMRI studies. We briefly introduce some analytical and computational tools for obtaining good designs based on a specified design selection criterion. Research results about some commonly considered designs such as blocked designs, and m-sequences are also discussed. Moreover, we present a recently proposed new type of fMRI designs that can be constructed using a certain type of Hadamard matrices. Under certain assumptions, these designs can be shown to be statistically optimal. Some future research directions in design of fMRI experiments are also discussed.

INTRODUCTION

Recent years have seen an upsurge of functional brain imaging experiments for a better understanding of how humans learn, remember and make decisions. Such experiments are also widely conducted by researchers to help provide paths to treat/prevent some terrifying brain disorders such as Alzheimer's disease, and are thus very valuable. As in many scientific investigations, designing a high-quality experiment is an important first step for successful functional brain imaging studies. A carefully designed experiment allows experimenters to collect informative data to make precise inference on the goals/hypotheses at minimal cost. On the other extreme, data collected from a poorly designed experiment may fail to provide valid answers to the research questions of interest, resulting in a waste of resource. The importance of the use of a carefully selected experimental design (or

data collection plan) cannot be overemphasized.

This paper provides a survey on some recent developments in experimental designs for functional magnetic resonance imaging (fMRI) experiments. Functional MRI is one of the most common functional brain mapping technologies. This pioneering, noninvasive technology helps to study experimental subjects' brain activity when they are cognitively engaging with mental stimuli such as viewing pictures, tapping fingers, solving problems, recalling events, or making decisions. It is used in various research areas including psychology, economics, and cognitive neuroscience^[1], and has great clinical potentials as highlighted in a special issue on clinical applications of fMRI in *Neuropsychology Review*, Vol. 7, No. 2, 2007. However, fMRI experiments are usually expensive, and the collected data is notoriously noisy, making it difficult to draw precise statistical inference on brain functions. We thus would like a high-quality experimental design to help us make the best use of the limited resources to collect informative fMRI data.

An fMRI design is a sequence of mental stimuli to be presented to an experimental subject in an fMRI experiment. While the subject is performing the tasks determined by the selected stimulus sequence, an MRI scanner repeatedly scans his/her brain to acquire fMRI data for making statistical inference about the brain activity. The quality of the collected data depends on the selected design. However, due to the complexity of fMRI, obtaining the “best” fMRI design suited to the goal(s) of the experiment is a challenging task. We usually need to consider not only the statistical efficiency in achieving one or more (competing) study objectives, but also some unwanted psychological effects that can contaminate the data. In addition, we may want the obtained design to fulfill some practical constraints. The large diversity of the fMRI experimental settings and protocols also contributes to the difficulty of design selection. In almost all cases, we deal with a very challenging combinatorial problem.

There are some advances in the selection of fMRI designs, but much more work is needed to move this new emerging research area forward. The purpose of this article is to provide a brief overview of stochastic and deterministic computational tools for designing efficient fMRI studies as well as recent insights obtained for such studies using analytical methods. We begin in the next section with background information on fMRI studies, and introduce terminology and notation used in this article. We then present the general linear models widely used for the design and analysis of fMRI studies and popular design criteria in this area. Some recently obtained results and guidelines for selecting fMRI designs are discussed. We close the article with a summary and discussion.

BACKGROUND

Terminology and notation

In a typical fMRI experiment, a sequence of mental stimuli (*e.g.*, pictures) of one or more types interlaced with

periods of rest or, say, visual fixation is presented to each experimental subject. These stimuli give rise to neuronal activity at some brain regions that triggers an increased inflow of oxygenated blood, leading to a decrease in the concentration of deoxygenated blood. This change in the ratio of oxy- to deoxy-blood can influence the strength of the magnetic field, and results in a rise and fall in the intensity of signals collected by the MRI scanner. Specifically, the MRI scanner collects MRI measurements by repeatedly scanning each of the, say, $64 \times 64 \times 30$ brain voxels, which are volumetric image elements that cover (part of) the subject's brain. Some voxels may fall outside the brain; see also Subsection 2.1.1 of Lazar^[2]. At each voxel, MRI measurements are collected every τ_{TR} (*e.g.*, 2) seconds to form a blood oxygenation level dependent fMRI time series. The pre-specified time τ_{TR} is called the time to repetition. These time series serve as surrogate measurements of the underlying neuronal activity, and are analyzed to make inference about how the brain reacts to the stimuli; see also Lazar^[2].

The inference on brain activity is mainly based on some characteristics of the hemodynamic impulse response function (HRF). The HRF is a function of time describing the rise and fall of the noise-free MRI measurements following a brief neuronal firing that occurs at a voxel. Previous studies suggest that the HRF may increase from baseline in about two seconds after the onset of a brief stimulus, reach the peak in five to eight seconds, and possibly fall down below baseline before its complete return to baseline^[1,3]. This process may take about 30 s, counting from the onset of the brief stimulus to the HRF's complete return to baseline. If there are other neuronal firings (*e.g.*, due to the onset of other stimuli) before the cessation of the previous HRF, the evoked HRFs overlap and their heights accumulate. Since fMRI time series is typically very noisy, identifying the characteristics of the HRF by visual inspections is difficult, if not impossible. Statistical methods are thus needed to help extract useful information from the data. As an integral part of the statistical process, we would like to select a “good” fMRI design that helps to make valid inference.

An fMRI design is a sequence of mental stimuli of one or more types. When the sequence is presented to an experimental subject, each stimulus may last as brief as several milliseconds or as long as, say, a minute. Stimuli with extended presentation duration, *e.g.*, 10-60 s, are used in traditional blocked designs, which are also termed as boxcar designs. In such a design, the stimulus of the same type can appear at multiple time points during the experiment, but each long stimulus is immediately followed by a long stimulus of another type or by a period of control (*e.g.*, rest). It also is not uncommon to replace each long stimulus by a short sequence of separate but brief stimuli of the the same type. The resulting designs are still called blocked designs. For experiments with Q stimulus types, a typical blocked design may be the repetitions of $\{A_1A_2\dots A_QA_0\}$, where, for $q=1, \dots$,

Q , A_q represents a presentation of a long stimulus (or a sequence of brief stimuli) of the q^{th} type, and A_0 is a period of control. At a brain voxel responding to the q^{th} -type stimulus, neuronal firings can be expected throughout the time span of each “on-period” A_q . This leads to an accumulation of overlapping HRFs. With a long on-period of the stimulus, the MRI signal intensity increases to a high level, and may reach a plateau before dropping down to baseline following the cessation of the stimulus. The large contrast between the elevated signal intensity and baseline facilitates the detection of brain voxels (or regions) that respond to the stimulus. Blocked designs are thus often recommended for detecting brain voxels that are activated by the stimuli; see the Results on Design Selection section for a further discussion.

Moving away from blocked designs, some studies showed that an individual stimulus that is as brief as several tens of milliseconds can evoke a detectable change in the MRI measurements; see Rosen *et al.*^[3] and references therein. In addition, the heights of overlapping HRFs following multiple brief stimuli tend to be (roughly) additive when the time between stimulus onsets is not overly short (*e.g.*, at least 2 s); see also Friston *et al.*^[4]. These observations make it possible to consider event-related (ER-) fMRI designs that consist of brief stimuli whose order may be randomized. An ER-fMRI design of Q stimulus types is often written as a finite sequence of elements 0, 1, ..., Q , and may look like $d = (1012021\dots 1)$. A positive integer q in d represents an onset of a q^{th} -type stimulus, and 0 means no stimulus onset. Specifically, when the i^{th} element of d is $d_i = q (> 0)$, a q^{th} -type stimulus appears briefly at time $(i-1)\tau_{\text{ISI}}$ for a pre-determined τ_{ISI} ; time 0 may be synchronized to the first valid MRI scan. For example, when $d_3 = 1$ and $\tau_{\text{ISI}} = 4$ s, a stimulus of the first type (*e.g.*, a picture of a familiar face) will occur briefly at the $(3-1)\tau_{\text{ISI}} = 8^{\text{th}}$ second after the first valid MRI scan. With $d_4 = 2$, a stimulus of the second type (*e.g.*, a picture of an unfamiliar face) will appear at the 12^{th} second after the first valid MRI scan. When $d_i = 0$, there is no stimulus onset at time $(i-1)\tau_{\text{ISI}}$. With these 0's in the design, time between stimulus onsets may be “jittered”^[5], and thus, may not be fixed to τ_{ISI} . Typically, the control (*e.g.*, a visual fixation or rest period) fills in the time between the offset of a brief stimulus to the onset of the next stimulus. Due to its flexibility, ER-fMRI designs have gained much popularity^[6]. However, a typical design can easily contain tens or hundreds of elements, making it very challenging for selecting good designs. In this paper, we discuss some recently developed approaches for finding high-quality fMRI designs, including both blocked and ER-fMRI designs. Most of these approaches are built upon the popular general linear model framework. This framework is described below.

The general linear model framework

The fMRI time series, $\{y(t); t \geq 0\}$, of a brain voxel is typically modeled as the sum of (1) the convolution of the stimulus function and the HRF, (2) a nuisance term

allowing for a trend or drift of $y(t)$; and (3) noise^[7,8]. We consider the following continuous-time model:

$$y(t) = \sum_{q=1}^Q \int_0^t x_q(t-\tau)h_q(\tau; \beta_q)d\tau + s(t; \gamma) + e(t) \quad (1)$$

where $x_q(t)$ is the stimulus function for the stimuli of the q^{th} type, $h_q(\tau; \beta_q)$ is the HRF evoked by the q^{th} -type stimulus, β_q is an unknown parameter vector, $q = 1, \dots, Q$, $s(t; \gamma)$ is a nuisance term approximating the drift/trend of the time series, γ is the corresponding unknown parameter vector, and $e(t)$ is noise. The stimulus function $x_q(t)$ indicates the appearances of the q^{th} -type stimuli, and may be a sum of boxcar functions or a sum of (shifted) Dirac delta functions; see also Henson and Friston^[9]. Boxcar functions are often employed in experiments with blocked designs. In this case, $x_q(t)$ takes a positive value during the “on-periods” of the q^{th} -type stimulus of a block design, and is 0, otherwise. The resulting model is sometimes referred to as the epoch model^[10]. In an event-related model, the $x_q(t)$ is a sum of (shifted) Dirac delta functions that indicates the onset times of the brief stimuli of the q^{th} type.

The most commonly used fMRI data analysis method is probably the general linear model approach^[11]. Partly due to this popularity, existing studies on fMRI designs mainly focus on linear models such as models (2) and (3) that are extensions of (1), and are linear in the parameters β_q 's and γ . In the fMRI literature^[11,12], dual models are commonly considered for two popular study objectives, namely the detection of brain activations (or detection) and the estimation of the HRF (or estimation). The main difference between the two models is that they used different sets of basis functions to describe $h_q(\tau; \beta_q)$ of model (1); see also Friston *et al.*^[4].

For detection, the HRF $h_q(\tau; \beta_q)$ is typically approximated by $\theta_q h^*(\tau)$, where $h^*(\tau)$ is an assumed shape of the HRF, and θ_q is the unknown amplitude (or maximum height) of the HRF. Thus, β_q contains only one parameter θ_q that signals the strength of brain activation due to the q^{th} -type stimulus. Since the MRI measurements $y(t)$ is collected every τ_{TR} seconds, we consider the following discrete-time model:

$$y = \sum_{q=1}^Q z_q \theta_q + S\gamma + e. \quad (2)$$

Here, $\mathbf{y} = (y_1, \dots, y_T)'$ with $y_t = y((t-1)\tau_{\text{TR}})$. The vector \mathbf{z}_q is obtained by subsampling the convolution of $x_q(t)$ and $h^*(\tau)$ with a sampling rate of τ_{TR} seconds. $S\gamma$ corresponds to $s(t; \gamma)$ of (1) with S being a specified matrix. For example, the t^{th} element of $S\gamma$ might be $\gamma_0 + \gamma_1 t + \gamma_2 t^2$. The vector e in model (2) represents the noise. The focus of model (2) is typically on $C_1 \theta$ for a given matrix C_1 whose rows contain coefficients of linear combinations of $\theta_1, \dots, \theta_Q$; here, $\theta = (\theta_1, \dots, \theta_Q)'$. When $C_1 = I_Q$ is the identity matrix of order Q , the focus is on the strength of brain activation due to each stimulus type. It is also common to study $(\theta_p - \theta_q)$ for $p \neq q$. In such a case, the rows of C_1 contain the coefficients of the pairwise comparisons between the HRF amplitudes.

The estimation of the HRF is a study objective that has gained much popularity with the advent of ER-fMRI.

A widely used model for this objective is:

$$y = \sum_{q=1}^Q X_q h_q + S\gamma + e. \quad (3)$$

Here, $h_q = (h_{1q}, \dots, h_{Kq})'$ is an unknown parameter vector representing the heights of the HRF that contribute to y . Specifically, $h_{kq} = h_q((k-1)\Delta T; \beta_q)$ is the HRF height at $(k-1)\Delta T$ seconds after the onset of a q^{th} -type stimulus, where ΔT is the greatest real value making $(\tau_{\text{ISI}}/\Delta T)$ and $(\tau_{\text{TR}}/\Delta T)$ integers; $k=1, \dots, K$. The value of K is selected so that $h_q((k-1)\Delta T; \beta_q)$ becomes negligible when $\tau > (K-1)\Delta T$. For a commonly considered 32-second HRF, $K = \lceil 32/\Delta T \rceil$ with $\lceil a \rceil$ being the integer part of a . The consideration of h_q is equivalent to modeling $h_q((k-1)\Delta T; \beta_q)$ of (1) by a linear combination of K shifted Kronecker delta functions; *i.e.*, $h_q((k-1)\Delta T; \beta_q) = \sum_{k=1}^K h_{kq} \delta_k(\tau)$, where $\delta_k(\tau) = 1$ when $\tau = (k-1)\Delta T$, and $\delta_k(\tau) = 0$, otherwise; β_q thus contain all the K coefficients (HRF heights) h_{1q}, \dots, h_{Kq} . $X_q = [x_{1q}, \dots, x_{Kq}]$ in model (3) is the 0-1 design matrix of size T -by- K for the q^{th} -type stimuli. The t^{th} element of x_{kq} is 1 when h_{kq} contributes to y_t . The remaining terms in (3) are as in (2). In contrast to model (2) for detection, model (3) does not assume a known shape for the HRF. The goal is to estimate all the unknown HRF heights h_{kq} or to study some linear combinations $C_2 h$ of these heights with $h = (h_1', \dots, h_Q)'$ and a given linear combination coefficient matrix C_2 .

Design selection criteria

With models (2) and (3) respectively for detection and estimation, the main design goal is to select an fMRI design that yields the most precise parameter estimates of the parametric functions of interest. Some statistically meaningful optimality criteria have been proposed for evaluating the goodness of competing designs. Two popular criteria in the fMRI literature are A- and D-optimality criteria. For detection problems with model (2), the A-optimality criterion can be defined as the following 'larger-the-better' criterion:

$$\phi_0^A(d) = r_1 / \text{trace} \{C_1 [Z'V'(I_T - \omega\{VS\}VZ)] - C_1\} = r_1 / \text{trace} \{C_1 [M_1(d)] - C_1\} \quad (4)$$

Here, r_1 is the number of rows of C_1 , and $Z = [z_1, \dots, z_Q]$. V is a whitening matrix such that $\text{cov}(Ve) = \sigma^2 VRV' = \sigma^2 I_T$, where σ^2 is the error variance, and $R = \text{corr}(e)$ is the correlation matrix of errors. The matrix $\omega\{A\} = A(A'A)^{-1}A'$ is the orthogonal projection matrix onto the column space of A . A^{-} is a generalized inverse of A , and $M_1(d) = Z'V'(I_T - \omega\{VS\}VZ)$ is the information matrix of θ . We note that V may be obtained by, *e.g.*, the Cholesky decomposition of R^{-1} , and, depending on the assumptions made at the design stage, it may or may not contain unknown parameters; see also the Results on Design Selection section and Maus *et al.*^[13]. The criterion in (4) depends on the selected design d through the design matrix Z , and is inversely proportional to the average variance of the least-squares estimates of the parametric functions defined by $C_1\theta$. For estimating the HRF with model (3), the A-optimality criterion can be written as:

$$\phi_0^A(d) = r_2 / \text{trace} \{C_2 [X'V'(I_T - \omega\{VS\}VX)] - C_2\} = r_2 / \text{trace}$$

$$\{C_2 [M_2(d)] - C_2\} \quad (5)$$

where r_2 is the number of rows of C_2 , $X = [X_1, \dots, X_Q]$ is the design matrix depending on the selected design d , $M_2(d)$ is the information matrix for h , and all the remaining terms are as in (4).

The D-optimality criterion seeks to minimize the volume of the (asymptotic) confidence ellipsoid of $C_2 h$. For the detection of brain activation with model (2) and the estimation of the HRF with model (3), D-optimal designs are found by maximizing the following two criteria, respectively:

$$\phi_0^D(d) = \det \{C_1 [M_1(d)] - C_1\}^{-1/r_1} \quad (6)$$

$$\phi_0^D(d) = \det \{C_2 [M_2(d)] - C_2\}^{-1/r_2} \quad (7)$$

All the terms in (6) and (7) are as in (4) and (5), respectively. For the D-optimality criteria, the coefficient matrices C_1 and C_2 are required to be full row rank. The selection between the A- and D-optimality criteria depends on the need and preference of the experimenter. As indicated in Maus *et al.*^[14], while early works on fMRI designs mainly focused on the A-optimality criterion, there is no obvious reason to generally prefer one criterion over the other. In the subsequent sections, we discuss some results on fMRI design selection. Most of these results are based on the A- or D-optimality criterion.

RESULTS ON DESIGN SELECTION

Blocked designs for detecting brain activations

There is some guidance on selecting blocked designs for detecting brain activations in the literature. For example, Henson^[15] advocated the use of blocked designs having a 15-s-on-15-s-off pattern. For such a blocked design formed by $\{A_1 A_2 \dots A_Q A_0\}$, the duration of each A_q is fixed to 15 s. This suggestion is based on the Fourier transformations of the convolution in (1) by assuming that the HRF has the form of the double-gamma function:

$$g^*(\tau) = \tau^s e^{-\tau}/S! - 1/6 \times \tau^{1s} e^{-\tau}/1S! \quad (8)$$

The double-gamma function is widely used as the HRF shape, and is built in a software package, called SPM (<http://www.fil.ion.ucl.ac.uk/spm/>), for fMRI data analysis. In the frequency domain, this HRF acts as a low-pass filter that 'passes' low-frequency signals and reduces the amplitude of high-frequency signals. As demonstrated in Henson^[15], after the Fourier transformation, a large proportion of the signal energy of a 15-s-on-15-s-off blocked design is retained by the selected HRF shape. In addition, the use of an on-period A_q that is longer than 50 seconds is not recommended. This is because the signal energy of the resulting blocked designs may be lost after accounting for the low-frequency nuisance signals such as heartbeats or respirations which is modeled by $s(t; \gamma)$ in (1).

Setting the block length (or duration of A_q) to 15 s may not be optimal for an HRF shape that is different from (8). For example, Liu *et al.*^[16] considered cases with one stimulus type ($Q = 1$), and evaluated the performance of designs with the A-optimality criterion. They

observed that the blocked design with a block length of 64 s tends to have a high statistical efficiency in detection when a single gamma density function is used to model the HRF shape. This latter HRF shape is also not uncommon, especially for cases where the HRF does not fall below baseline when returning from its peak. In addition, Liu *et al.*^[16] suggested that the selection of block length also depends on $s(t; \gamma)$. In particular, they demonstrated that the blocked design with a 64-s block length can yield a smaller ϕ_0^A -value than designs with a shorter (*e.g.*, 32 s) blocked length when the statistical model also allows for a second- or third-order Legendre polynomial drift.

To provide additional information on design selection, Maus *et al.*^[14] studied blocked designs of two stimulus types ($Q = 2$) with selected block lengths (10, 15, 20, 30 or 60 s), and patterns (repetitions of $\{A_1A_2\}$, $\{A_1A_2A_0\}$, or $\{A_1A_0A_2A_0\}$). Each block A_q is formed by a sequence of 1-second stimuli of the q^{th} type; $q = 1, 2$, and the time between the onsets of consecutive stimuli in the same block is $\tau_{\text{ISI}} = 1, 2$, or 3 s. They compare the statistical efficiencies of these blocked designs in detecting brain activations *via* model (2). In their model, the nuisance term $S\gamma$ corresponds to a linear trend, and the HRF shape used to construct z_q is set to the double-gamma function of (8). The errors are assumed to have one of the three possible structures, including uncorrelated errors, first order autoregressive (AR1) process, and an AR1 process plus a measurement error (AR1+ME).

Considering both $\phi_0^A(d)$ and $\phi_0^D(d)$, Maus *et al.*^[14] suggested to keep τ_{ISI} as short as possible. In addition, they recommended to use the design pattern $\{A_1A_2A_0\}$ for studying the HRF amplitudes θ_1 and θ_2 . When the focus is on comparing the amplitudes (*i.e.*, $\theta_1 - \theta_2$), blocked designs formed by $\{A_1A_2\}$ are recommended. The results of Maus *et al.*^[14] also indicate that the selection of block length may hinge on the assumed error correlation. When the focus is on θ_1 's, a block length of 15 s is recommended for both uncorrelated and AR1 errors. As for AR1 + ME errors, a block length of 10 s is the best among the selected blocked lengths. For studying the contrast between the HRF amplitudes, the suggested block lengths are 20 s and 15 s for uncorrelated errors and correlated errors (AR1 or AR1 + ME), respectively.

These previous studies provide some guidelines on selecting blocked designs for detecting brain activations. It can also be seen that the selection of blocked designs depend on a few factors. These factors include the parametric function $C_1\theta$ of interest, the selected HRF shape, the model for capturing the drift/trend of the fMRI time series, and the error correlation structure. For cases that are not covered by these guidelines, we may obtain a good design for detection by using a computer algorithm. Some algorithms have already been proposed in the fMRI literature. Most of these computational approaches can be employed for cases considering the detection of brain activations, the estimation of the HRF, or when both detection and estimation are of interest. Some practical constraints may also be imposed when using these com-

putational tools. In what follows, we first describe some guidelines for selecting ER-fMRI designs for estimating the HRF. We then discuss computer algorithms for obtaining good fMRI designs.

ER-fMRI designs for estimating the HRF

The estimation of the HRF helps to make inference about some characteristics of the underlying neuronal activity as also described in Lindquist *et al.*^[17]. For this objective, model (3) may be considered, and the goal is to obtain a design yielding the most precise parameter estimates of C_2h for a given C_2 . By considering the A-optimality criterion of (5), Dale^[18] suggested to allow for variable time intervals between onsets of consecutive stimuli, and the average of these time intervals should be kept small. This suggestion can also be applied to the D-optimality criterion of (7). However, one should take caution that if the time between stimulus onsets is overly short (*e.g.*, < 2 s), the accumulated heights of the overlapping HRFs may saturate at a certain level. Consequently, the assumption of the additivity of the HRF heights can be violated. For such a case, the nonadditive HRF heights should be taken into account when evaluating the goodness of designs; see also, Wager *et al.*^[19] and Wager *et al.*^[20]. However, current methods for accounting for the non-additive HRF heights tend to be ad hoc, and additional investigations are needed.

While rendering useful information, Dale^[18] did not provide a systematic way for design construction. Buračas and Boynton^[21] worked on the same design issue, and advocated the use of maximum length shift-register sequences (or m-sequences). Such a design can be generated by a primitive polynomial over a Galois field $GF(Q+1)$ consisting of $Q+1$ elements, where $Q+1$ is a prime power. To construct an m-sequence, one may select a primitive polynomial $f(x) = x^r - \sum_{i=1}^{r-1} \alpha_i x^{r-i}$ from, *e.g.*, Table 3.5, 3.6 or 3.7 of Golomb and Gong^[22]. The m-sequence $d = (d_1, \dots, d_N)$ is then determined by the relation, $d_{n+r} = \sum_{i=1}^{r-1} \alpha_i d_{n+r-i} \pmod{Q+1}$ with a nonzero initial r -tuple (d_1, \dots, d_r) ; see also Lidl and Niederreiter^[24], and MacWilliams and Sloane^[24]. Such a design can also be obtained *via* an MATLAB program developed by Liu^[11]. For an m-sequence of length $N = (Q+1)^r - 1$, every nonzero r -tuple appears exactly once in the set $\{(d_1, \dots, d_r), (d_2, \dots, d_{r+1}), \dots, (d_N, d_1, \dots, d_{r-1})\}$.

Buračas *et al.*^[21] and Liu^[11] reported the high performance of m-sequences in terms of the ϕ_0^A -value when $C_2 = I_{QK}$ is the QK -by- QK identity matrix. However, when $Q > 1$, the frequency of the appearance of each stimulus type of an m-sequence can be different from the optimal stimulus frequency approximated by Liu *et al.*^[12] for A-optimality. In particular, Liu and Frank^[12] indicated that the optimal stimulus frequency of an A-optimal design for estimating the HRF h is about $1/(Q + \sqrt{Q})$ for each of the Q stimulus types. The optimal number of 0 is thus approximately $N/(1 + \sqrt{Q})$. Since the stimulus frequency of m-sequences is about $1/(Q+1)$, these designs may not be A-optimal; see also Kao *et al.*^[25]. For ϕ_0^D with $C_2 = I_{QK}$,

the optimal stimulus frequency approximated by Maus *et al.*^[13] is $1/(Q+1)$, and is close to that of m-sequences. Maus *et al.*^[13] thus suggested that the optimality of m-sequences may depend on the selected criterion.

However, attaining the (approximated) optimal stimulus frequency does not guarantee an optimal design. To derive additional insightful results, Kao^[26] also studied model (3) with the following assumption: Assumption 1. (a) The number of MRI scans T equals the length N of the design \mathbf{d} and $\tau_{\text{TR}} = \tau_{\text{ISI}}$; (b) $\mathbf{S} = \mathbf{j}_T$ is the T -by-1 vector of ones, and $\text{cov}(\mathbf{e})$ proportional \mathbf{I}_T ; and (c) the last $K - 1$ elements of design \mathbf{d} are also presented to the subject before the first valid MRI scan.

Assumptions 1(a) and 1(c) are mild, and can often be controlled by the experimenters. Assumption 1(b) is mainly for mathematical simplicity, and is also considered in some previous studies such as Liu *et al.*^[16] and Maus *et al.*^[27]. Following an argument in Kushner^[28], for the results to be discussed in the remaining of this subsection, Assumption 1(b) can be relaxed to include cases with $\text{cov}(\mathbf{e}) = \alpha \mathbf{I}_T + \lambda \mathbf{j}_T \mathbf{j}_T' + \mathbf{j}_T \lambda'$, where α is a constant and λ is a vector of constants. The results thus hold for a compound symmetric covariance matrix with $\text{cov}(\mathbf{e}) = \alpha \mathbf{I}_T + \lambda \mathbf{J}_T$, where λ is a constant, and \mathbf{J}_T is the T -by- T matrix of ones. For estimating the K -by-1 HRF parameter vector \mathbf{h}_1 with one stimulus type ($Q = 1$), Kao^[26] showed that a design of length N having $n_1 = N/2$ and $n_r^{(1)} = (n_r)^2/N$ for all $r = 1, \dots, K - 1$ is universally optimal. Here, n_q is the frequency of the q^{th} -type stimuli in the design \mathbf{d} , and $n_r^{(pq)}$ is the number of times $(\mathbf{d}_{n-r}, \mathbf{d}_n) = (\mathbf{q}, \mathbf{p})$ for $n = 1, \dots, N$; $\mathbf{d}_{n-r} = \mathbf{d}_{N+n-r}$ when $n \leq r$. We also note that an universally optimal design can be shown to be optimal in a large class of optimality criteria, including Λ - and D -optimality^[29]. For $Q > 1$, a similar sufficient condition for an ER-fMRI design to be D -optimal can also be found in Kao^[26]. In particular, if all the symbols $0, 1, \dots, Q$ appear equally often in a design \mathbf{d} of length N , and that $n_r^{(pq)} = n_p n_q / N$ for all $p, q = 1, \dots, Q$ and $r = 1, \dots, K - 1$, then the design \mathbf{d} maximizes ϕ_h^D of (7) under Assumption 1 and $C_2 = \mathbf{I}_{QK}$.

As described in Kao^[26], designs satisfying the previously mentioned sufficient conditions can be constructed by inserting an additional 0 to any $(K - 1)$ -tuple of zeros in an m-sequence of length $(Q+1)^K - 1$. The resulting design is a de Bruijn sequence^[22,30]. Aguirre *et al.*^[30] proposed to use de Bruijn sequences for estimating the HRF. The results of Kao^[26] help to establish the optimality of such designs.

Clearly, m-sequences do not satisfy the sufficient conditions provided by Kao^[26]. Additional results are thus needed for establishing the optimality of these popular designs. Kao^[31] worked on this direction, and proved that a binary m-sequence of length $N \geq 2K - 3$ is D -optimal for estimating the HRF \mathbf{h}_1 under Assumption 1 with $Q = 1$. He also proposed a new type of ER-fMRI designs for estimating the HRF. This new type of designs, which are termed as Hadamard sequences, can be constructed by a normalized Hadamard matrix, \mathbf{H} , having a circulant core. Specifically, the elements of the first row and column of

\mathbf{H} are 1 and all the other entries are +1 or -1 with $\mathbf{H}\mathbf{H}'$ proportional \mathbf{I} . After deleting the first row and column of \mathbf{H} , we have a circulant matrix called the circulant core. As described in Kao^[31], a D -optimal design can be achieved by replacing +1 and -1 in any column of the circulant core by 0 and 1, respectively. It is noteworthy that binary m-sequences can also be generated using this same method and are thus special cases of Hadamard sequences. Nevertheless, Hadamard sequences exist in many different lengths for which a binary m-sequence is unavailable. These newly proposed designs are thus much more flexible than m-sequences and the previously mentioned de Bruijn sequences in terms of design length.

Kao^[31] also conducted some case studies on the performance of Hadamard sequences when Assumptions 1(b) and 1(c) are violated. Based on empirical results, Hadamard sequences tend to remain efficient when the nuisance term $\mathbf{S}\mathbf{y}$ in model (3) corresponds to a second-order polynomial drift, the noise follows an AR1 process, and/or no stimulus is presented before the first valid MRI scan. This result is especially true when the autocorrelation coefficient of the AR1 noise is not as high as $\rho = 0.5$ or when the design is not too short (*e.g.*, $N < 100$). We also note that a violation of Assumption 1(a) can have a great impact on the performance of Hadamard sequences. For cases with $\tau_{\text{TR}} \neq \tau_{\text{ISI}}$, we may consider efficient computational methods for obtaining good designs. Some computational approaches are introduced in the next subsection. These approaches are also applicable when both estimation and detection are of interest.

Computational tools for obtaining fMRI designs

In the fMRI literature, some computer algorithms are proposed for finding an ER-fMRI design of the form $\mathbf{d} = (\mathbf{d}_1, \dots, \mathbf{d}_N)$ with \mathbf{d}_n belong to $\{0, 1, \dots, Q\}$ that optimizes a specific single- or multi-objective optimality criterion. To efficiently search over the enormous space of ER-fMRI designs for good designs, Wager and Nichols^[19] advocated the use of the genetic algorithm (GA) technique. Due to their versatility, GAs can accommodate various experimental settings to find designs suited to individual fMRI experiments. Following Wager and Nichols^[19], Kao *et al.*^[25] put forward an efficient GA that takes advantage of knowledge on the performance of some ER-fMRI designs to improve the efficiency of the GA search. Some well-known designs such as m-sequences, blocked designs, and their combinations are employed in the algorithm of Kao *et al.*^[25] to increase the diversity of the designs being explored, and to maintain a supply of good traits (or building blocks) that help to form good designs during the GA search. As demonstrated in Kao *et al.*^[25], this strategy is very effective.

With the previously mentioned GAs, one can find a (near-)optimal design for user-specified number of stimulus types Q , design length N , τ_{ISI} , τ_{TR} , and model assumptions, including the model for drift/trend of the time series, error correlation structure, and, if model (2) is considered, the HRF shape. Depending on the study

objective(s), the optimality criterion for evaluating the quality of designs may be $\phi_{\theta}^A, \phi_h^A, \phi_{\theta}^D, \phi_h^D$ or a weighted sum of some of these criteria; weights are user-selected to reflect the relative importance of detection and estimation. In a weighted sum criterion, one may also include other individual criteria to account for quantifiable constraints/requirements of the study. For example, Wager *et al.*^[19] included a counterbalancing criterion for avoiding psychological confounds such as anticipation and habituation. By optimizing this criterion, the order of the stimuli in the resulting design cannot be easily predicted by the experimental subject. Moreover, we may include an additional individual criterion to measure the departure from a target frequency of appearances of each stimulus type; see also, Kao *et al.*^[25]. Such a customized requirement on the stimulus frequency may help to increase the subject's engagement in the presented mental tasks^[32].

The GA of Kao *et al.*^[25] has been applied for studying several fMRI design issues. For example, this algorithm was used to obtain designs for cases where both individual stimulus effects (h and θ) and pairwise comparisons ($h_p - h_q$ and $\theta_p - \theta_q$ for $p \neq q$) are of interest. Maus *et al.*^[13] used the GA to work on cases where the autocorrelation coefficient ρ of the AR1 noise is uncertain. The GA is also adapted in Kao *et al.*^[33,34] for finding designs suited to experiments with multiple scanning sessions.

In addition, Maus *et al.*^[35] and Kao *et al.*^[36] utilized the GA to tackle the design problem concerning an uncertain HRF shape. The need for considering the uncertainty of the HRF shape is manifested in some previous studies^[37,38]. These studies pointed out that the HRF shape may vary across brain voxels, and that specifying a wrong HRF shape in, say, model (2) for detection may lead to an incorrect conclusion. To accommodate different HRF shapes, Kao^[39] considered at the design stage the following nonlinear model:

$$y = \sum_{q=1}^Q X_q h(u)\theta_q + sy + e \quad (9)$$

where $h(u)$ is a K -by-1 vector representing the shape of the HRF, u is an unknown parameter vector that needs to be estimated from data, and all the remaining terms are as in (2) and (3). The vector $h(u)$ may be determined by the double-gamma function of (8) with free parameters for accounting for the variability in the HRF shape; see also Wager *et al.*^[20]. In particular, the k^{th} element of $h(u)$ is $g((k-1)\Delta T; u)/\max_s g(s; u)$ with $u = (u_1, u_2)'$ and $g(\tau; u) = [(\tau - u_2)^{u_1 - 1} e^{-(\tau - u_2)}] / \Gamma(u_1) - 1/6 \times [(\tau - u_2)^{15 - 1} e^{-(\tau - u_2)}] / 15!$ ($\tau \geq u$) or 0 (otherwise) (10)

Here, u_1 is the time-to-peak parameter, which mainly determines the time for the HRF to reach the peak, counting from its onset time. The time-to-onset parameter u_2 determines the time when the HRF starts to increase from baseline, counting from the onset of a stimulus. As indicated by Wager *et al.*^[20], these two parameters are the most influential, although some additional free parameters may also be included in (10). For example, one may use a free parameter to replace the coefficient $1/6$ in the second term of the non-zero part of (10). The function $\Gamma(u) = \int_0^{\infty} t^{u-1} e^{-t} dt = (u-1)\Gamma(u-1)$ in (10) is the gamma

function. We note that the function $g^*(\tau)$ in (8) is a special case of (10) with $u = (6, 0)'$. Specifically, the HRF shape $h^*(\tau)$ in model (2) depends on $g^*(\tau)$, and is fixed. By contrast, the HRF shape in model (9) is determined by $g(\tau; u)$, and involves unknown parameters to be estimated from the data. The latter model is thus more flexible.

When making inference about θ_q for detecting brain activations, model (9) allows for an uncertain HRF shape. However, obtaining a good design for such a flexible model is quite challenging. Again, we would like a design optimizing some function (*e.g.*, the A- or D-optimality criterion) of the information matrix of θ . For model (9), this information matrix, denoted by $M(d; \theta, u)$, can be approximated by first-order Taylor approximation. In contrast to $M1(d)$ and $M2(d)$ in (4)-(7), $M(d; \theta, u)$ depends not only on the design d , but also on the unknown model parameters θ and u ; see Kao^[39] and Kao *et al.*^[36] for details. By treating θ and u as random variables, and assuming the availability of a (prior) distribution of θ and u , Kao^[39] targeted a (pseudo-)Bayesian design that maximizes $E\{\phi(M(d; \theta, u))\}$ for a larger-the-better criterion ϕ , where the expectation $E\{\cdot\}$ is taken over the (prior) distribution of the parameters.

When a prior distribution of the parameters is unavailable, it is common to consider to maximize the minimum of $\phi(M(d; \theta, u))$, where the minimum is taken over the possible values of θ and u . It also is popular to maximize the the minimum of the relative efficiency, which is defined as

$$\min(\theta \in \Theta, u \in U) \{\phi[M(d; \theta, u)] / \phi[M(d^*_{\theta, u}; \theta, u)]\}$$

Here, Θ and U contain the possible values for θ and u , respectively; and $d^*_{\theta, u}$ is a locally optimal design that maximizes $\phi(M(d; \theta, u))$ for given θ and u . Designs maximizing the former criterion are termed as maximin designs, whereas those optimizing the latter criterion are maximin-efficient designs. Both criteria are popular in the literature; see also Kao *et al.*^[36] and references therein. However, obtaining maximin-type designs is computationally very expensive. Kao *et al.*^[36] proposed an efficient shortcut. Building on some analytical results, they showed that the size of the parameter space of Θ can be greatly reduced when obtaining maximin-type designs. Specifically, when $Q=1$, we may find a very efficient maximin (or maximin-efficient) design by focusing on $\theta_1 = 1$ (or θ_1 belong to $\{0,1\}$). For $Q > 1$, instead of setting Θ to the entire Q -dimensional space, we may focus on a subspace consisting of $(1/Q)!$ of the surface of the Q -dimensional unit hemisphere centered at the origin when obtaining a maximin design; the origin needs to be included in the subspace for finding a maximin-efficient design. To further reduce computing time, Kao *et al.*^[36] focused on a restricted class, Ξ_0 , of designs when using a search algorithm to find maximin-type designs. Specifically, each design of length N in Ξ_0 is formed by a short design of length $[N/Q]$, where $[a]$ is the smallest integer greater than or equal to a . For any short design, a full-length design is constructed by cyclically permuting the labels of the Q stimulus types with 0's staying intact, and then leav-

ing out the excess elements, if any. The stimulus frequencies in the resulting design are thus (nearly) equal across stimulus types. Kao *et al.*^[36] showed that their approach is quite efficient and effective when obtaining maximin-type designs when the HRF shape is uncertain.

In addition to the GA technique, a deterministic optimization algorithm for obtaining optimal fMRI designs has recently been proposed and studied by Kao and Mittelman^[40]. Without stochastic explorations, this latter approach has been demonstrated to be efficient for some cases for which the GA requires much CPU time in finding a good design. The main idea is to combine a greedy hill-climbing algorithm with the previously mentioned cyclic permutation method for constructing designs of Ξ_0 . In particular, the algorithm first systematically perturbs a small fraction (*e.g.*, the first four elements) of a short design d_s of length $\lfloor N/Q \rfloor$ to create some neighboring short designs that are close to d_s in terms of Hamming distance. The search then moves to the neighboring short design d_s that yields the best full-length design *via* the cyclic permutation method. After this movement, the algorithm continues to work on perturbing another small fraction (*e.g.*, the fifth to eighth elements) of d_s . This process is repeated until no improvement can be achieved. Based on our experience, this approach tends to lead to very efficient designs with greatly reduced CPU time, although the obtained design might not be optimal. Kao and Mittelman^[40] demonstrated the usefulness of their algorithm by finding maximin designs that are robust to mis-specified error autocorrelation coefficients when stationary AR2 errors are assumed. For this case, the GA approach can be very challenging in terms of CPU time.

The algorithms described so far are used to optimize a single objective function. For experiments with two or more study objectives, these previous studies mainly considered weighted-sum criteria that are convex combinations of all the individual criteria of interest. However, selecting appropriate weights for such a weighted-sum criterion might be challenging for some cases, and the assigned weights may not guarantee a satisfactory design. For example, assigning equal weights does not always lead to a design with equal relative efficiency across all the study objectives of interest. To address this fMRI design issue, Kao *et al.*^[41] proposed a multi-objective optimization algorithm by modifying the nondominated sorting GA II (NSGA II) of Deb *et al.*^[42]. With a single run of the algorithm, the experimenter can obtain not one, but a class of diverse designs for approximating the Pareto frontier; a Pareto frontier is formed by the best possible solutions in a multi-objective optimization problem. A design best suited to the needs of the experiment can then be selected from the obtained design class. The algorithm can also be used to find fMRI designs when there is a constraint such as a required stimulus frequency. This algorithm is recommended when weights on the multiple study objectives are hard to determine.

CONCLUSION

Design of fMRI experiments is an exciting research area. Several analytical and computational approaches have been proposed for obtaining designs that attain high efficiencies in terms of certain practically meaningful design selection criterion. As demonstrated in Jansma *et al.*^[43], among others, fMRI designs with theoretically superior performance are often very useful in real-world experiments. The designs obtained in the previous studies are thus valuable. However, much work remains to be done in this area. As indicated by Lindquist^[1] in his recent survey on statistical methods for fMRI studies, “as research hypotheses ultimately become more complicated, the need for more advanced experimental designs will only increase further.”

One possible direction of future research is on developing designs for cases with compound stimuli, each containing two or more components; *e.g.*, each stimulus is formed by a cue followed by a task. To our knowledge, there is no systematic study on this important design issue. In addition, fMRI is also widely considered for studying the functional connectivity between brain regions. High-quality experimental designs for this type of studies are also in a great demand. Moreover, developing powerful computational approaches, and insightful analytical results for optimal fMRI designs should always be helpful. For example, the analytical results described in the Results on Design Selection section are mainly for cases where Assumption 1 holds and $C_2 = I_{QK}$. It is also useful to consider the case where C_2 is not the identity matrix when contrasts between the HRFs are of interest. Developing novel, insightful analytical results by relaxing Assumption 1 can also help to move this new research field forward.

REFERENCES

- 1 **Lindquist M.** The statistical analysis of fMRI data. *Stat Sci* 2008; **23**: 439-464 [DOI: 10.1214/09-STS282]
- 2 **Lazar N.** The Statistical Analysis of Functional MRI Data. New York: Springer, 2008 [DOI: 10.1007/978-0-387-78191-4]
- 3 **Rosen BR,** Buckner RL, Dale AM. Event-related functional MRI: past, present, and future. *Proc Natl Acad Sci USA* 1998; **95**: 773-780 [PMID: 9448240 DOI: 10.1073/pnas.95.3.773]
- 4 **Friston KJ,** Zarahn E, Josephs O, Henson RN, Dale AM. Stochastic designs in event-related fMRI. *Neuroimage* 1999; **10**: 607-619 [PMID: 10547338 DOI: 10.1006/nimg.1999.0498]
- 5 **Serences JT.** A comparison of methods for characterizing the event-related BOLD timeseries in rapid fMRI. *Neuroimage* 2004; **21**: 1690-1700 [PMID: 15050591 DOI: 10.1016/j.neuroimage.2003.12.021]
- 6 **Huettel SA.** Event-related fMRI in cognition. *Neuroimage* 2012; **62**: 1152-1156 [PMID: 21963919 DOI: 10.1016/j.neuroimage.2011.08.113]
- 7 **Martin PI,** Naeser MA, Doron KW, Bogdan A, Baker EH, Kurland J, Renshaw P, Yurgelun-Todd D. Overt naming in aphasia studied with a functional MRI hemodynamic delay design. *Neuroimage* 2005; **28**: 194-204 [PMID: 16009568 DOI: 10.1002/hbm.460010207]
- 8 **Worsley KJ,** Liao CH, Aston J, Petre V, Duncan GH, Morales F, Evans AC. A general statistical analysis for fMRI data. *Neuroimage* 2002; **15**: 1-15 [PMID: 11771969 DOI: 10.1006/nimg.2001.0933]

- 9 **Henson R**, Friston K. Convolution models for fMRI. In: Friston K, Ashburner J, Kiebel S, Nichols T, Penny W. Statistical parametric mapping: the analysis of functional brain images. London: Academic, 2007: 178-192
- 10 **Mechelli A**, Henson RN, Price CJ, Friston KJ. Comparing event-related and epoch analysis in blocked design fMRI. *Neuroimage* 2003; **18**: 806-810 [PMID: 12667857 DOI: 10.1016/S1053-8119(02)00027-7]
- 11 **Liu TT**. Efficiency, power, and entropy in event-related fMRI with multiple trial types. Part II: design of experiments. *Neuroimage* 2004; **21**: 401-413 [PMID: 14741677 DOI: 10.1016/j.neuroimage.2003.09.031]
- 12 **Liu TT**, Frank LR. Efficiency, power, and entropy in event-related fMRI with multiple trial types. Part I: theory. *Neuroimage* 2004; **21**: 387-400 [PMID: 14741676 DOI: 10.1016/j.neuroimage.2003.09.030]
- 13 **Maus B**, van Breukelen GJ, Goebel R, Berger MP. Robustness of optimal design of fMRI experiments with application of a genetic algorithm. *Neuroimage* 2010; **49**: 2433-2443 [PMID: 19833212 DOI: 10.1016/j.neuroimage.2009.10.004]
- 14 **Maus B**, van Breukelen G, Goebel R, Berger M. Optimization of blocked designs in fMRI studies. *Psychometrika* 2010; **75**: 373-390 [DOI: 10.1007/S11336-010-9159-3]
- 15 **Henson R**. Efficient experimental design for fMRI. In: Friston K, Ashburner J, Kiebel S, Nichols T, Penny W. Statistical parametric mapping: the analysis of functional brain images. London: Academic, 2007: 193-210
- 16 **Liu TT**, Frank LR, Wong EC, Buxton RB. Detection power, estimation efficiency, and predictability in event-related fMRI. *Neuroimage* 2001; **13**: 759-773 [PMID: 11305903 DOI: 10.1006/nimg.2000.0728]
- 17 **Lindquist MA**, Meng Loh J, Atlas LY, Wager TD. Modeling the hemodynamic response function in fMRI: efficiency, bias and mis-modeling. *Neuroimage* 2009; **45**: S187-S198 [PMID: 19084070 DOI: 10.1016/j.neuroimage.2008.10.065]
- 18 **Dale AM**. Optimal experimental design for event-related fMRI. *Hum Brain Mapp* 1999; **8**: 109-114 [PMID: 10524601]
- 19 **Wager TD**, Nichols TE. Optimization of experimental design in fMRI: a general framework using a genetic algorithm. *Neuroimage* 2003; **18**: 293-309 [PMID: 12595184 DOI: 10.1016/S1053-8119(02)00046-0]
- 20 **Wager TD**, Vazquez A, Hernandez L, Noll DC. Accounting for nonlinear BOLD effects in fMRI: parameter estimates and a model for prediction in rapid event-related studies. *Neuroimage* 2005; **25**: 206-218 [PMID: 15734356 DOI: 10.1016/j.neuroimage.2004.11.008]
- 21 **Buracas GT**, Boynton GM. Efficient design of event-related fMRI experiments using M-sequences. *Neuroimage* 2002; **16**: 801-813 [PMID: 12169264 DOI: 10.1006/nimg.2002.1116]
- 22 **Golomb S**, Gong G. Signal design for good correlation for wireless communication, cryptography, and radar. New York: Cambridge University Press, 2005
- 23 **Lidl R**, Niederreiter H. Introduction to finite fields and their applications. New York: Cambridge University Press, 1994
- 24 **MacWilliams F**, Sloane N. The theory of error correcting codes. Amsterdam: Elsevier/North-Holland, 1977
- 25 **Kao MH**, Mandal A, Lazar N, Stufken J. Multi-objective optimal experimental designs for event-related fMRI studies. *Neuroimage* 2009; **44**: 849-856 [PMID: 18948212 DOI: 10.1016/j.neuroimage.2008.09.025]
- 26 **Kao MH**. On the optimality of extended maximal length linear feedback shift register sequences. *Stat Probabil Lett* 2013; **83**: 1479-1483 [DOI: 10.1016/j.spl.2013.02.012]
- 27 **Maus B**, van Breukelen GJ, Goebel R, Berger MP. Optimal design of multi-subject blocked fMRI experiments. *Neuroimage* 2011; **56**: 1338-1352 [PMID: 21406234 DOI: 10.1016/j.neuroimage.2011.03.019]
- 28 **Kushner H**. Optimal repeated measurements designs: The linear optimality equations. *Ann Stat* 1997; **25**: 2328-2344 [DOI: 10.1214/aos/1030741075]
- 29 **Kiefer J**. Construction and optimality of generalized youden designs. In: Srivastava J. A survey of statistical designs and linear models. Amsterdam: North-Holland, 1975: 333-353
- 30 **Aguirre GK**, Mattar MG, Magis-Weinberg L, de Buijn cycles for neural decoding. *Neuroimage* 2011; **56**: 1293-1300 [PMID: 21315160 DOI: 10.1016/j.neuroimage.2011.02.005]
- 31 **Kao MH**. A new type of experimental designs for event-related fMRI via Hadamard matrices. *Stat Probabil Lett* 2014; **84**: 108-112 [DOI: 10.1016/j.spl.2013.09.024]
- 32 **Brendel B**, Hertrich I, Erb M, Lindner A, Riecker A, Grodd W, Ackermann H. The contribution of mesiofrontal cortex to the preparation and execution of repetitive syllable productions: an fMRI study. *Neuroimage* 2010; **50**: 1219-1230 [PMID: 20080191 DOI: 10.1016/j.neuroimage.2010.01.039]
- 33 **Kao MH**, Mandal A, Stufken J. Optimal design for event-related functional magnetic resonance imaging considering both individual stimulus effects and pairwise contrasts. *Stat Appl* 2008; **6**: 225-241
- 34 **Kao MH**, Mandal A, Stufken J. Efficient designs for event-related functional magnetic resonance imaging with multiple scanning sessions. *Commun Stat-Theory Methods* 2009; **38**: 3170-3182 [DOI: 10.1080/03610920902947626]
- 35 **Maus B**, van Breukelen GJ, Goebel R, Berger MP. Optimal design for nonlinear estimation of the hemodynamic response function. *Hum Brain Mapp* 2012; **33**: 1253-1267 [PMID: 21567658 DOI: 10.1002/hbm.21289]
- 36 **Kao MH**, Majumdar D, Mandal A, Stufken J. Maximin and maximin-efficient event-related fMRI designs under a nonlinear model. *Ann Appl Stat* 2013; **7**: 1940-1959 [DOI: 10.1214/13-AOAS658]
- 37 **Handwerker DA**, Ollinger JM, D'Esposito M. Variation of BOLD hemodynamic responses across subjects and brain regions and their effects on statistical analyses. *Neuroimage* 2004; **21**: 1639-1651 [PMID: 15050587 DOI: 10.1016/j.neuroimage.2003.11.029]
- 38 **Lindquist MA**, Wager TD. Validity and power in hemodynamic response modeling: a comparison study and a new approach. *Hum Brain Mapp* 2007; **28**: 764-784 [PMID: 17094118 DOI: 10.1002/hbm.20310]
- 39 **Kao MH**. Optimal experimental designs for event-related functional magnetic resonance imaging. PhD thesis: University of Georgia, 2009
- 40 **Kao MH**, Mittelman H. A fast algorithm for constructing efficient event-related functional magnetic resonance imaging designs. *J Stat Comput Simul* 2014; to appear [DOI: 10.1080/00949655.2013.804524]
- 41 **Kao MH**, Mandal A, Stufken J. Constrained multi-objective designs for functional MRI experiments via a modified non-dominated sorting genetic algorithm. *J Roy Stat Soc C-App* 2012; **61**: 515-534 [DOI: 10.1111/j.1467-9876.2011.01036.x]
- 42 **Deb K**, Pratap A, Agarwal S, Meyarivan T. A fast and elitist multiobjective genetic algorithm: NSGA-II. *IEEE T Evolut Comput* 2002; **6**: 182-197 [DOI: 10.1109/4235.996017]
- 43 **Jansma JM**, de Zwart JA, van Gelderen P, Duyn JH, Drevets WC, Furey ML. In vivo evaluation of the effect of stimulus distribution on FIR statistical efficiency in event-related fMRI. *J Neurosci Methods* 2013; **215**: 190-195 [PMID: 23473798 DOI: 10.1016/j.jneumeth.2013.02.017]

P- Reviewer: Bener A S- Editor: Wen LL L- Editor: A
E- Editor: Lu YJ



Neural mechanisms of mindfulness and meditation: Evidence from neuroimaging studies

William R Marchand

William R Marchand, Mental Health Service, George E Wahlen Veterans Affairs Medical Center, Salt Lake City, UT 84148, United States

William R Marchand, Department of Psychiatry, University of Utah, Salt Lake City, UT 84112, United States

Author contributions: Marchand WR reviewed the literature and wrote the manuscript.

Supported by The resources and the use of facilities at the VA Salt Lake City Health Care System

Correspondence to: William R Marchand, MD, Mental Health Service, George E Wahlen Veterans Affairs Medical Center, 500 Foothill Drive, Salt Lake City, UT 84148, United States. wmarchand@me.com

Telephone: +1-801-5578950 Fax: +1-801-9983818

Received: December 30, 2013 Revised: May 1, 2014

Accepted: May 28, 2014

Published online: March 28, 2015

Abstract

Mindfulness is the dispassionate, moment-by-moment awareness of sensations, emotions and thoughts. Mindfulness-based interventions are being increasingly used for stress, psychological well being, coping with chronic illness as well as adjunctive treatments for psychiatric disorders. However, the neural mechanisms associated with mindfulness have not been well characterized. Recent functional and structural neuroimaging studies are beginning to provide insights into neural processes associated with the practice of mindfulness. A review of this literature revealed compelling evidence that mindfulness impacts the function of the medial cortex and associated default mode network as well as insula and amygdala. Additionally, mindfulness practice appears to effect lateral frontal regions and basal ganglia, at least in some cases. Structural imaging studies are consistent with these findings and also indicate changes in the hippocampus. While many questions remain unanswered, the current literature provides evidence of brain regions and networks relevant for understanding neural processes associated with mindfulness.

© 2015 Baishideng Publishing Group Inc. All rights reserved.

Key words: Mindfulness; Meditation; Medial cortex, amygdala; Emotional control

Core tip: Mindfulness training is used for stress and as an adjunctive treatment for psychiatric disorders. Functional neuroimaging studies are beginning to provide insights into neural processes associated with the practice of mindfulness. These studies clearly indicate that the practice of mindfulness changes brain function in areas including the medial cortex, default mode network, insula, amygdala, lateral frontal regions and basal ganglia.

Original sources: Marchand WR. Neural mechanisms of mindfulness and meditation: Evidence from neuroimaging studies. *World J Radiol* 2014; 6(7): 471-479 Available from: URL: <http://www.wjgnet.com/1949-8470/full/v6/i7/471.htm> DOI: <http://dx.doi.org/10.4329/wjr.v6.i7.471>

INTRODUCTION

Mindfulness has been described as dispassionate, non-evaluative, and continuous moment-by-moment awareness of, sensations, perceptions, emotions and thoughts^[1]. A similar definition explains mindfulness as “the awareness that emerges through paying attention on purpose, in the present moment, and non-judgmentally to the unfolding of experience moment by moment^[2].”

Mindfulness training involves meditation. Mindfulness meditation practice is the framework used to develop the state, or skill, of mindfulness. The word “meditation” stems from the Latin *meditari*, which means to participate in contemplation or deliberation. Meditation includes a variety of practices aimed at focusing attention and awareness. Two general forms of meditation exist. These are focused attention and open monitoring^[3]. Initially a

practitioner will often utilize focused attention practice to enhance attentional skills^[4]. Then, it will be possible to engage in open monitoring, which involves moment-by-moment awareness of whatever occurs in one's awareness^[4].

Mindfulness originated in Buddhist spiritual practices. However, secular, group therapy approaches utilizing manuals and standardized methods have been developed for clinical use. Two of these are Mindfulness-Based Stress Reduction (MBSR) and Mindfulness-Based Cognitive Therapy (MBCT). As reviewed elsewhere^[5], there has been increased interest in mindfulness and meditation in recent years. In particular, there has been increased use of the secular mindfulness-based interventions for stress, coping with physical illness and as adjunctive treatments for psychiatric disorders^[5].

This manuscript reviews recent neuroimaging studies that enhance our understanding of the neural mechanisms of mindfulness.

SEARCH

Several PubMed searches were conducted with terms mindfulness and neuroimaging, mindfulness and fMRI, mindfulness and MRI and mindfulness and mechanisms, meditation and neuroimaging, meditation and fMRI and mediation and MRI. These initial searches resulted in the review of 248 abstracts. Those most relevant for understanding neural mechanisms of mindfulness are included herein.

STUDIES OF NEUROBIOLOGICAL MECHANISMS OF MINDFULNESS AND MEDITATION

A relatively large number of functional neuroimaging studies now enhance our understanding of the neural processes associated with mindfulness. A smaller number of structural imaging studies have been conducted as well.

FUNCTIONAL IMAGING STUDIES

The review focused on recent functional imaging studies that enhance our understanding of neural processes associated with the practice of mindfulness meditation. Results are summarized in detail in Table 1.

Many investigations studied individuals who had completed mindfulness training^[6-19]. A relatively large number studied experienced meditators^[20-33]. Additionally, some studies focused on brief mindfulness training^[34,35], state^[36] and trait^[37-39] mindfulness. One study compared expert and novice meditators^[40]. Finally some investigation focused on using mindfulness interventions for social anxiety disorder (SAD)^[8,13,15], generalized anxiety disorder (GAD)^[16] and bipolar disorder^[17].

STRUCTURAL IMAGING STUDIES

A growing body of literature indicates that mindfulness is associated with changes in brain structure. While this review focused on functional imaging a number of structural imaging studies were reviewed as well. These findings are summarized in Table 2. Studies reviewed used magnetic resonance imaging (MRI) to investigate brain morphometry^[19,41-50] as well as fractional anisotropy (FA)^[51,52] and gyrification^[53].

DISCUSSION

Though many questions remain unanswered, there is now a body of literature that provides important insights into the neural mechanisms associated with mindfulness. This evidence indicates brain regions that may be generally associated with mindfulness. More importantly, it is now possible to begin to understand neural processes that underlie the cognitive and emotional benefits of a mindfulness practice.

BRAIN REGIONS ASSOCIATED WITH MECHANISMS OF MINDFULNESS

The functional imaging studies reviewed herein indicate that mindfulness is associated with neural mechanisms involving multiple brain regions (Table 3). It is difficult to draw firm conclusions given the variability of methods utilized and diversity of the populations studied. Nonetheless, there is convincing evidence that mindfulness is associated with brain activation and/or connectivity of several regions as outlined in Table 3. Multiple studies implicate mechanisms involving frontal regions^[6,10,11,14,16-18,20,25,28,32-36,39]. A few studies implicate lateral regions^[11,16,25] including ventrolateral prefrontal cortex (VLPFC)^[16] and dorsolateral prefrontal cortex (DLPFC)^[11]. However, the strongest evidence is for medial frontal regions^[6,10,13,14,17,18,20,25,27,28,33,36] including anterior cingulate cortex (ACC)^[10,18,20,25,36]. Posterior medial regions are also involved^[13,22,29-31,33,36,37] primarily in the area of the posterior cingulate cortex (PCC) and precuneus^[13,22,30,31,33,36,37]. Thus, there is very strong evidence that anterior and posterior cortical midline structures (CMS) play a key role in the mechanisms of mindfulness^[6,10,13,14,17,18,20,25,27-33,36,37]. Since the CMS are key components of the default mode network (DMN), this circuitry is clearly implicated and a number of investigations have specifically focused on the role of the DMN^[21,24,26,30,33,37]. In addition, there is strong evidence for involvement of the insula^[6,10,14,18,23,25,32,35,38] and amygdala^[8,12,16,24,32,35,39]. A few studies also suggest involvement of the basal ganglia^[22,28] and thalamus^[10].

Structural imaging investigations (Table 2) provide strong evidence of mindfulness-related changes in the hippocampus^[19,41,45-49]. Other results are consistent with functional imaging studies and implicate CMS/DMN^[42,48,51], insula^[49,53], amygdala^[43-45], basal ganglia^[44,45,50] and thalamus^[45].

Table 1 Functional imaging studies of mindfulness and meditation

Ref.	Mindfulness intervention or condition	Result
Allen <i>et al</i> ^[11] Baerentsen <i>et al</i> ^[122]	Mindfulness Meditators	Diminished Stroop conflict and greater DLPFC responses during executive processing. At onset of meditation, activations occurred bilaterally in putamen and supplementary motor cortex with deactivations in the precuneus, the posterior cingulate cortex and the parieto-temporal area. With sustained meditation, activations were found in the caudate and deactivations were in right hemisphere white matter.
Brefczynski-Lewis <i>et al</i> ^[40]	Experienced meditators	Activation during sustained attention showed an inverted curve. Expert meditators (average 19000 h) of practice had more activation than novices but experts (average 44000 h) had less activation. In response to distracter sounds, expert meditators had less brain activation in areas associated with discursive thoughts and emotions but more activation in regions related to response inhibition and attention compared to novices.
Creswell <i>et al</i> ^[39]	Dispositional mindfulness	Dispositional mindfulness was associated with widespread prefrontal cortical activation, and decreased bilateral amygdala activity during affect labeling. Negative associations were found between prefrontal cortex and right amygdala responses in participants high in mindfulness.
Desbordes <i>et al</i> ^[12] Dickenson <i>et al</i> ^[34]	Mindfulness training Brief mindfulness induction	Decreased right amygdala activation in response to positive images. Focused breathing activated a parietal and prefrontal attention network and trait-level mindfulness correlated with parietal activation.
Farb <i>et al</i> ^[6]	MBSR	Interoceptive attention predicted greater activity in anterior insula but decreased recruitment of the DMPFC as well as altered functional connectivity between the DMPFC and the insula.
Farb <i>et al</i> ^[7]	Mindfulness training	Experiential focus resulted in reductions in cortical midline regions associated with narrative focus in novices. In trained participants, experiential focus was associated with reductions in the mPFC and increased engagement the lateral PFC, insula and somatosensory area. Analyses of functional connectivity revealed coupling between the insula and the mPFC in novices that was uncoupled in the mindfulness group.
Farb <i>et al</i> ^[14]	Mindfulness training	Participants had right-lateralized recruitment, including visceral and somatosensory areas associated with body sensation.
Gard <i>et al</i> ^[25]	Healthy meditators	Mindfulness practitioners experienced reduced unpleasantness of pain, which was associated with decreased activation in the lateral PFC and increased activation in the right insula. Anticipation of pain was associated with increased anterior cingulate cortex activation.
Garrison <i>et al</i> ^[30]	Healthy meditators	"Undistracted awareness" was associated with PCC deactivation. In contrast, "distracted awareness" corresponded with PCC activation.
Garrison <i>et al</i> ^[31] Goldin <i>et al</i> ^[8]	Healthy meditators MBSR for social anxiety disorder	Volitional decrease of the feedback graph was associated with deactivation of the PCC. MBSR yielded greater reductions in negative emotion and increased activation in attention-related parietal cortex compared to aerobic exercise.
Goldin <i>et al</i> ^[13]	MBSR for social anxiety disorder	MBSR led to increased activation in the PCC during negative self-view condition. DMPFC activation increases during negative self-view were associated with decreased disability and enhanced mindfulness.
Goldin <i>et al</i> ^[15]	MBSR for social anxiety disorder	MBSR associated with decreased anxiety and depression symptoms and improved self-esteem. Breath-focused attention task associated with decreased negative emotion and reduced amygdala activation.
Hasenkamp <i>et al</i> ^[26]	Healthy meditators	Brain activation in DMN during mind wandering, and in salience network regions during awareness of mind wandering.
Hasenkamp <i>et al</i> ^[27]	Healthy meditators	Meditation experience was associated with increased connectivity within attention networks and between regions involved with attention and medial frontal cortex.
Hölzel <i>et al</i> ^[16]	MBSR for GAD	Amygdala activation in response to neutral faces decreased, VLPFC activation increased and functional connectivity between amygdala and PFC increased. Changes in VLPFC activation and amygdala-PFC connectivity correlated with changes in Beck Anxiety Inventory scores.
Hölzel <i>et al</i> ^[20] Ives-Deliperi <i>et al</i> ^[17]	Vipassana meditators MBCT for bipolar disorder	Meditation associated with increased activation in ACC and dorsal medial prefrontal cortex. Activation increased in the medial PFC and posterior parietal lobe, in response to a mindfulness task. There was a correlation between activation changes in medial PFC and increased mindfulness.
Ives-Deliperi <i>et al</i> ^[36]	State mindfulness	Decreased activation in anterior insula, ACC, medial prefrontal cortex and bilateral precuneus during mindfulness meditation.
Kilpatrick <i>et al</i> ^[9]	MBSR	Increased functional connectivity of auditory and visual networks as well as between auditory cortex and areas associated with attention and self-referential processes. Enhanced anticorrelation between auditory and visual cortex as well as between visual cortex and attention and self-referential processing areas.
Kirk <i>et al</i> ^[23]	Experienced meditators	During the Ultimatum Game, controls recruit the anterior insula during unfair offers. In contrast, meditators display attenuated activity in high-level emotional representations of the anterior insula and increased activity in the low-level interoceptive representations of the posterior insula.
Kozasa <i>et al</i> ^[28]	Healthy meditators	Meditators had decreased activity relative to non-meditators in medial frontal, temporal, precentral, postcentral and basal ganglia regions during the incongruent conditions of the Stroop task.

Lutz <i>et al</i> ^[32]	Healthy subjects	Mindfulness increased activations in prefrontal regions during expectation of negative pictures. During perception of negative stimuli, reduced activation was found in amygdala and parahippocampal regions. Prefrontal and insular activations when expecting negative pictures correlated negatively with trait mindfulness.
Lutz <i>et al</i> ^[35]	Experienced meditators	Enhanced activity in the anterior insula and the mid-cingulate was associated with decreased pain-related unpleasantness.
Pagnoni <i>et al</i> ^[21]	Experienced meditators	vPMC activity was lower in meditators and was correlated with performance on a test for sustained attention. Functional connectivity analysis with a vPMC seed revealed attention performance was associated with the degree of temporal correlation between vPMC and the temporoparietal junction.
Pagnoni <i>et al</i> ^[29]	Zen meditators	Practitioners displayed reduced duration of the neural response linked to conceptual processing in regions of the DMN.
Paul <i>et al</i> ^[38]	Healthy subjects	Non-reactivity was inversely correlated with insula activation during inhibition to negative stimuli.
Shaurya Prakash <i>et al</i> ^[37]	Mindfulness disposition	Mindfulness disposition was associated with greater connectivity of the DMN, particularly in the PCC and the precuneus.
Taylor <i>et al</i> ^[24]	Experienced and beginning meditators	Experienced meditators had weaker functional connectivity between DMN regions.
Taylor <i>et al</i> ^[33]	Experienced and beginning meditators	Mindfulness attenuated emotional intensity. For experienced meditators, mindfulness induced a deactivation of DMN areas. For beginners, mindfulness induced a down-regulation of the left amygdala.
Wells <i>et al</i> ^[19]	MBSR	Increased functional connectivity between the PCC and medial prefrontal cortex and left hippocampus.
Baerentsen <i>et al</i> ^[22]	Mindfulness training	Reduced smoking craving associated with reduced activation of ACC. Mindful attention reduced functional connectivity between ACC and other craving-related regions.
Zeidan <i>et al</i> ^[10]	Mindfulness training	Anxiety relief associated with activation of the PFC and insula.
Zeidan <i>et al</i> ^[18]	Mindfulness training	Meditation decreased pain-associated activation of the contralateral somatosensory cortex. Reductions in pain were associated with increased activity in the ACC and insula. Decreased pain unpleasantness was associated with orbitofrontal activation and thalamic deactivation.

ACC: Anterior cingulate cortex; DMN: Default mode network; PCC: Posterior cingulate cortex; DMPFC: Dorsomedial prefrontal cortex; mPFC: Medial prefrontal cortex; vLPFC: Ventrolateral prefrontal cortex; vPMC: Ventral posterior medial cortex.

Table 2 Brain regions where structural imaging studies have demonstrated mindfulness related changes

Anterior cingulate cortex ^[42,51]
Orbitofrontal cortex ^[41]
Inferior temporal gyrus ^[49]
Insula ^[49,53]
Lingual gyrus ^[45]
Cuneus ^[45]
Sensorimotor cortex ^[42,53]
Fusiform gyrus ^[53]
Cuneus ^[53]
Corpus callosum ^[52]
Posterior cingulate cortex ^[48]
Cerebellum ^[48]
Hippocampus ^[19,41,45-49]
Amygdala ^[43-45]
Putamen ^[50]
Caudate ^[44,45]
Thalamus ^[45]

Taken together, these studies provide convincing evidence that neural mindfulness mechanisms involve the CMS/DMN, insula, hippocampus and amygdala. There is also evidence implicating lateral prefrontal regions, basal ganglia and thalamus.

NEURAL MECHANISMS OF THE COGNITIVE AND EMOTIONAL BENEFITS OF MINDFULNESS

As reviewed elsewhere^[5], the literature indicates that

mindfulness impacts attention, emotional regulation and thinking patterns. The following sections review evidence suggesting neural mechanisms underlying these effects.

ATTENTION

The development of attentional skills is the central component of mindfulness meditation practice^[3,4,54]. Training of attention skills enhances the capability to sustain non-judgmental awareness of one’s thinking patterns, emotions, and sensory perceptions^[4,55]. This awareness facilitates gain distance from thoughts and emotions such that these become less powerful and compelling. In particular, mindfulness supports the recognition of automatic thinking patterns (discussed below).

Three neural networks, the alerting, orienting and executive, are thought to play specific roles in the attention process^[56,57]. The alerting network modulates task-specific alertness and attentional engagement and involves right frontal cortex, including DLPFC and ACC, as well as right parietal cortex^[57]. The orienting network controls stimulus selection, which is the capability to select precise information from numerous sensory stimuli. This network includes the frontal eye fields, superior parietal cortex, superior colliculus and temporal parietal junction^[57]. Finally, the executive control circuitry mediates control of attention. This function includes top-down control as well as monitoring and resolution of conflict between computations involving planning or decision-making, error detection and regulation of thoughts and feelings^[57]. In regard to brain regions involve, the ACC, lateral frontal

Table 3 Brain regions involved with mindfulness mechanisms

Frontal cortex ^[6,10,11,14,16-18,20,25,28,32-36,39]
Lateral frontal cortex ^[11,16,25]
Ventrolateral prefrontal cortex ^[16]
Dorsolateral prefrontal cortex ^[11]
Medial frontal cortex ^[6,10,13,14,17,18,20,25,27,28,33,36]
Anterior cingulate cortex ^[10,18,20,25,36]
Orbitofrontal cortex ^[10]
Posterior medial cortex ^[13,22,29-31,33,36,37]
Posterior cingulate cortex/precuneus ^[13,22,30,31,33,36,37]
Ventral posteromedial cortex ^[29]
Insula ^[6,10,14,18,23,25,32,35,38]
Temporal cortex ^[28,33]
Temporoparietal junction ^[29]
Sensorimotor cortex ^[6,10,28]
Inferior parietal lobule ^[6,33]
Parahippocampal gyrus ^[35]
Amygdala ^[8,12,16,24,32,35,39]
Basal ganglia ^[22,28]
Thalamus ^[10]

cortex, and basal ganglia contribute to executive control processes^[56].

Several studies suggest neural mechanisms associated with mindfulness-related improvements in attention. An MBSR study examined the neural processes of deploying attention to control responses to negative beliefs about self in social anxiety disorder^[15]. MBSR yielded decreased negative emotion and increased activation in attention modulating parietal regions. In a study to investigate meta-awareness and regulation of mind wandering and related influence on DMN activity, investigators collected fMRI data from a group of Zen meditators and a meditation-naïve control group engaging in an attention-to-breathing task^[29]. Results indicated the incidence of states of elevated ventral posterior medial cortex (vPMC) activity was lower in meditators and was significantly correlated with performance on a test for sustained attention. Analysis of functional connectivity using the vPMC seed revealed an association between attention performance and the degree of temporal correlation between right temporoparietal junction (TPJ) and vPMC. Another study aimed to evaluate the performance of meditators and non-meditators during an fMRI adapted Stroop Task, which requires impulse and attention control^[28]. Non-meditators showed increased activity compared to meditators in the middle temporal, medial frontal, pre and postcentral gyri and basal ganglia during the incongruent conditions. The authors conclude that their results suggest that meditation improves efficiency, perhaps by enhancing the ability to sustain attention and control impulses^[28]. A study examined a model^[26] that proposes four cognitive cycle intervals relevant for meditation: mind wandering, awareness of the wandering of one’s mind, varying of attention, and prolonged attention. Fourteen meditators executed breath-focused meditation during scanning^[26]. Study participants were instructed to press a button when they realized their mind had wandered and then return their focus to the breath. Analyses of results indicated brain activity in regions associated with the

default mode during mind wandering, and in the salience network during awareness of mind wandering. Finally the executive network was active when shifting and sustaining attention.

Taken together, these investigation suggest that enhanced attention is associated with neural mechanisms involving attention-related parietal cortical regions^[15], vPMC^[29], TPJ^[29], CMS^[28], temporal cortex^[28], sensorimotor cortex^[28] and basal ganglia^[28]. Thus, mindfulness likely impacts all of the three attention networks.

In addition to training general attention processes, mindfulness facilitates the enhancement of interoceptive attention (IA) to visceral bodily sensations as they occur in the present moment. An fMRI study examined functional plasticity in accessing interoceptive representations in MBSR trained individuals^[14]. Mindfulness training predicted enhanced activity in anterior insula and diminished recruitment of dorsomedial prefrontal cortex (DMPFC) during IA, as well as changed functional connectivity between the DMPFC and insula.

In summary, mindfulness training appears to modify neural processes in the three attention networks and insula, which result in improved general and interoceptive attention respectively.

AUTOMATIC THOUGHTS AND SELF-REFERENTIAL THINKING

Cognitive neuroscience suggests two general types of mental processes, those that are controlled and those that are automatic. Automatic processes may be innately automatic or become automated as a result of learning and practice. Automated thoughts are initiated unconsciously and are not easy to interrupt or prevent^[57]. For example, when attention involuntarily drifts away from an object of conscious attention, the DMN and automatic thinking is engaged as an involuntary process^[58]. Objective awareness of automatic thoughts is understood to be a primary mechanism by which mindfulness decreases symptoms of depression, anxiety and stress^[5]. Objective awareness allows one to interpret thoughts as “just thoughts” and prevents experiencing irrational negative thinking as fact.

There is compelling evidence that mindfulness impacts DMN neural processes^[21,24,26,30,33,37]. Modification of this network likely plays a significant role in the objectification of the experience of automatic thoughts.

Most of the medial cortex acts as a functional unit known as the CMS^[59]. The CMS are part of the DMN^[60,61] and play a key role in stimulus independent thought (SIT)^[58,62]. Decreased activation of the CMS is correlated with decreased SIT^[63]. Therefore, the CMS may be the specific portion of the DMN involved with mindfulness-induced modification of automatic thinking.

As reviewed elsewhere^[5], self-referential thinking is a type of automatic cognitions particularly relevant for mood and anxiety disorders. The CMS are involved in self-referential thinking^[59,62,64]. A study of MBSR for Social anxiety disorder (SAD)^[13] used a self-referential en-

coding paradigm, which was administered at baseline and post-intervention in order to examine changes in neural and behavioral responses during fMRI. MBSR produced reductions in negative, as well as increases in positive views of self. MBSR led to increased brain responses in the PCC during the negative self-view. MBSR-related increased DMPFC activity during negative self-view was correlated with diminished social anxiety and augmented mindfulness. These findings suggest that mindfulness specifically attenuates maladaptive habitual self-views – at least in part - by impacting DMN regions and in particular the CMS.

EMOTIONAL REGULATION

A number of studies provide evidence of how mindfulness may contribute to enhanced emotional regulation. An fMRI study compared neural reactivity to provocation of sadness in participants completing 8 wk of mindfulness training (MT) and controls^[7]. Sadness caused activation of regions associated with self-referential thinking in the CMS. MT participants had a distinct activation pattern, with enhanced right hemisphere recruitment, including areas associated with body sensation. Another fMRI study examined effects of a short mindfulness intervention during the cued expectation and perception of pictures that were negative or potentially negative^[35]. The mindfulness intervention was correlated with increased activation of prefrontal cortex during the expectation of negative pictures. Perception of negative stimuli was associated with reduced activation in amygdala and parahippocampal gyrus. A study of MBCT for bipolar disorder using fMRI^[17] revealed improvements in the treatment group in measures of mindfulness, anxiety, affect regulation working memory, spatial memory and verbal fluency. Blood-oxygen level-dependent (BOLD) signal increases occurred in the medial prefrontal cortex (PFC) and parietal lobe. Analysis also revealed a correlation between signal changes in medial PFC and increased mindfulness. A study of MBSR for GAD^[16] found changes in amygdala and VLPFC activation as well as increased functional connectivity between amygdala and PFC regions comparing pre- to post-intervention. VLPFC activation and amygdala-prefrontal connectivity changes were correlated with change in Beck Anxiety Inventory scores. Another study of the longitudinal effects of meditation training on amygdala responses examined how 8 wk of meditation training impacts amygdala responses to emotional when in a non-meditative state^[12]. Adults with no prior meditation experience took part in Mindful Attention Training, Cognitively-Based Compassion Training or a control intervention. Participants underwent an fMRI experiment pre and post-intervention. In the scanner, they were presented images with positive, negative, and neutral emotional valences while remaining in a non-meditative state. Findings indicated decreased right amygdala activation in the Mindful Attention group in response to im-

ages of all valences. Another fMRI study explored the effects of mindfulness on the neural responses to emotional stimuli^[24]. Experienced and novice meditators were scanned as they viewed negative, positive, and neutral pictures in both a mindful state and non-mindful state. The mindful condition attenuated emotional intensity and imaging data indicated that this effect was achieved through distinct neural mechanisms for each group. For the experienced cohort, mindfulness produced deactivation of DMN areas but did not influence responses in brain regions involved in emotional reactivity. For beginners, mindfulness down-regulated the left amygdala during emotional processing. The authors conclude that the long-term practice of mindfulness leads to reduced emotional reactivity by promoting tolerance of emotion and enhanced present-moment awareness. A study investigated MBSR-induced changes in of emotional reactivity and regulation of negative beliefs about self in subjects with seasonal affective disorder (SAD)^[8]. Sixteen patients were scanned while reacting to negative beliefs and while regulating negative emotions. MBSR resulted in improved anxiety and depressive symptoms and self-esteem and during a breath-focused attention task. Subjects also showed diminished negative emotion and amygdala activity as well as increased activity in brain regions involved in attentional deployment.

These investigations indicate that mindfulness enhancement of emotional regulation appears involve modification of processing in lateral frontal regions^[16] CMS/DMN^[7,17,24], regions involved with IA^[7] and amygdala^[8,12,16,24,35]. Interestingly, there is evidence that these mechanisms may change based upon amount of meditation experience^[24]. The CMS are of particular interest in emotional regulation as these regions play a role in emotional processing^[65,66] including mediating the experience of sadness^[7]. Thus, these areas may represent a key link between self-referential thinking and emotional dysregulation in affective disorders.

CONCLUSION

The studies reviewed herein increase our understanding of the neural processes associated with mindfulness. A limitation of the literature is the fact that multiple methodologies have been utilized and a diverse population studied. Thus direct comparison of studies is not feasible. Nonetheless, the current literature begins to define the neural mechanisms of mindfulness and provides the groundwork for future investigations.

This review of this literature revealed compelling evidence that mindfulness impacts the function of the medial cortex and associated default mode network as well as insula and amygdala. Additionally, mindfulness practice appears to effect lateral frontal regions and basal ganglia, at least in some cases. Structural imaging studies are consistent with these findings and also indicate changes in the hippocampus.

REFERENCES

- 1 **Grossman P**, Niemann L, Schmidt S, Walach H. Mindfulness-based stress reduction and health benefits. A meta-analysis. *J Psychosom Res* 2004; **57**: 35-43 [PMID: 15256293 DOI: 10.1016/S0022-3999(03)00573-7]
- 2 **Kabat-Zinn J**, Mindfulness-based interventions in context: past, present, and future. *Clin Psychol Sci Pract* 2003; **10**: 144-156 [DOI: 10.1093/clipsy.bpg016]
- 3 **Lutz A**, Slagter HA, Dunne JD, Davidson RJ. Attention regulation and monitoring in meditation. *Trends Cogn Sci* 2008; **12**: 163-169 [PMID: 18329323 DOI: 10.1016/j.tics.2008.01.005]
- 4 **Malinowski P**. Neural mechanisms of attentional control in mindfulness meditation. *Front Neurosci* 2013; **7**: 8 [PMID: 23382709 DOI: 10.3389/fnins.2013.00008]
- 5 **Marchand WR**. Mindfulness-based stress reduction, mindfulness-based cognitive therapy, and Zen meditation for depression, anxiety, pain, and psychological distress. *J Psychiatr Pract* 2012; **18**: 233-252 [PMID: 22805898 DOI: 10.1097/01.pra.0000416014.53215.86]
- 6 **Farb NA**, Segal ZV, Mayberg H, Bean J, McKeon D, Fatima Z, Anderson AK. Attending to the present: mindfulness meditation reveals distinct neural modes of self-reference. *Soc Cogn Affect Neurosci* 2007; **2**: 313-322 [PMID: 18985137 DOI: 10.1093/scan/nsm030]
- 7 **Farb NA**, Anderson AK, Mayberg H, Bean J, McKeon D, Segal ZV. Minding one's emotions: mindfulness training alters the neural expression of sadness. *Emotion* 2010; **10**: 25-33 [PMID: 20141299 DOI: 10.1037/a0017151]
- 8 **Goldin PR**, Gross JJ. Effects of mindfulness-based stress reduction (MBSR) on emotion regulation in social anxiety disorder. *Emotion* 2010; **10**: 83-91 [PMID: 20141305 DOI: 10.1037/a0018441]
- 9 **Kilpatrick LA**, Suyenobu BY, Smith SR, Bueller JA, Goodman T, Creswell JD, Tillisch K, Mayer EA, Naliboff BD. Impact of Mindfulness-Based Stress Reduction training on intrinsic brain connectivity. *Neuroimage* 2011; **56**: 290-298 [PMID: 21334442 DOI: 10.1016/j.neuroimage.2011.02.034]
- 10 **Zeidan F**, Martucci KT, Kraft RA, Gordon NS, McHaffie JG, Coghill RC. Brain mechanisms supporting the modulation of pain by mindfulness meditation. *J Neurosci* 2011; **31**: 5540-5548 [PMID: 21471390 DOI: 10.1523/JNEUROSCI.5791-10.2011]
- 11 **Allen M**, Dietz M, Blair KS, van Beek M, Rees G, Vestergaard-Poulsen P, Lutz A, Roepstorff A. Cognitive-affective neural plasticity following active-controlled mindfulness intervention. *J Neurosci* 2012; **32**: 15601-15610 [PMID: 23115195 DOI: 10.1523/JNEUROSCI.2957-12.2012]
- 12 **Desbordes G**, Negi LT, Pace TW, Wallace BA, Raison CL, Schwartz EL. Effects of mindful-attention and compassion meditation training on amygdala response to emotional stimuli in an ordinary, non-meditative state. *Front Hum Neurosci* 2012; **6**: 292 [PMID: 23125828 DOI: 10.3389/fnhum.2012.00292]
- 13 **Goldin P**, Ziv M, Jazaieri H, Gross JJ. Randomized controlled trial of mindfulness-based stress reduction versus aerobic exercise: effects on the self-referential brain network in social anxiety disorder. *Front Hum Neurosci* 2012; **6**: 295 [PMID: 23133411 DOI: 10.3389/fnhum.2012.00295]
- 14 **Farb NA**, Segal ZV, Anderson AK. Mindfulness meditation training alters cortical representations of interoceptive attention. *Soc Cogn Affect Neurosci* 2013; **8**: 15-26 [PMID: 22689216 DOI: 10.1093/scan/nss066]
- 15 **Goldin P**, Ziv M, Jazaieri H, Hahn K, Gross JJ. MBSR vs aerobic exercise in social anxiety: fMRI of emotion regulation of negative self-beliefs. *Soc Cogn Affect Neurosci* 2013; **8**: 65-72 [PMID: 22586252 DOI: 10.1093/scan/nss054]
- 16 **Hölzel BK**, Hoge EA, Greve DN, Gard T, Creswell JD, Brown KW, Barrett LF, Schwartz C, Vaitl D, Lazar SW. Neural mechanisms of symptom improvements in generalized anxiety disorder following mindfulness training. *Neuroimage Clin* 2013; **2**: 448-458 [PMID: 24179799 DOI: 10.1016/j.nicl.2013.03.011]
- 17 **Ives-Deliperi VL**, Howells F, Stein DJ, Meintjes EM, Horn N. The effects of mindfulness-based cognitive therapy in patients with bipolar disorder: a controlled functional MRI investigation. *J Affect Disord* 2013; **150**: 1152-1157 [PMID: 23790741 DOI: 10.1016/j.jad.2013.05.074]
- 18 **Zeidan F**, Martucci KT, Kraft RA, McHaffie JG, Coghill RC. Neural correlates of mindfulness meditation-related anxiety relief. *Soc Cogn Affect Neurosci* 2014; **9**: 751-759 [PMID: 23615765 DOI: 10.1093/scan/nst041]
- 19 **Wells RE**, Yeh GY, Kerr CE, Wolkin J, Davis RB, Tan Y, Spaeth R, Wall RB, Walsh J, Kaptchuk TJ, Press D, Phillips RS, Kong J. Meditation's impact on default mode network and hippocampus in mild cognitive impairment: a pilot study. *Neurosci Lett* 2013; **556**: 15-19 [PMID: 24120430 DOI: 10.1016/j.neulet.2013.10.001]
- 20 **Hölzel BK**, Ott U, Hempel H, Hackl A, Wolf K, Stark R, Vaitl D. Differential engagement of anterior cingulate and adjacent medial frontal cortex in adept meditators and non-meditators. *Neurosci Lett* 2007; **421**: 16-21 [PMID: 17548160 DOI: 10.1016/j.neulet.2007.04.074]
- 21 **Pagnoni G**, Celic M, Guo Y. "Thinking about not-thinking": neural correlates of conceptual processing during Zen meditation. *PLoS One* 2008; **3**: e3083 [PMID: 18769538 DOI: 10.1371/journal.pone.0003083]
- 22 **Baerentsen KB**, Stødkilde-Jørgensen H, Sommerlund B, Hartmann T, Damsgaard-Madsen J, Fosnaes M, Green AC. An investigation of brain processes supporting meditation. *Cogn Process* 2010; **11**: 57-84 [PMID: 19876663 DOI: 10.1007/s10339-009-0342-3]
- 23 **Kirk U**, Downar J, Montague PR. Interoception drives increased rational decision-making in meditators playing the ultimatum game. *Front Neurosci* 2011; **5**: 49 [PMID: 21559066 DOI: 10.3389/fnins.2011.00049]
- 24 **Taylor VA**, Grant J, Daneault V, Scavone G, Breton E, Roffe-Vidal S, Courtemanche J, Lavarenne AS, Beauregard M. Impact of mindfulness on the neural responses to emotional pictures in experienced and beginner meditators. *Neuroimage* 2011; **57**: 1524-1533 [PMID: 21679770 DOI: 10.1016/j.neuroimage.2011.06.001]
- 25 **Gard T**, Hölzel BK, Sack AT, Hempel H, Lazar SW, Vaitl D, Ott U. Pain attenuation through mindfulness is associated with decreased cognitive control and increased sensory processing in the brain. *Cereb Cortex* 2012; **22**: 2692-2702 [PMID: 22172578 DOI: 10.1093/cercor/bhr352]
- 26 **Hasenkamp W**, Wilson-Mendenhall CD, Duncan E, Barsalou LW. Mind wandering and attention during focused meditation: a fine-grained temporal analysis of fluctuating cognitive states. *Neuroimage* 2012; **59**: 750-760 [PMID: 21782031 DOI: 10.1016/j.neuroimage.2011.07.008]
- 27 **Hasenkamp W**, Barsalou LW. Effects of meditation experience on functional connectivity of distributed brain networks. *Front Hum Neurosci* 2012; **6**: 38 [PMID: 22403536 DOI: 10.3389/fnhum.2012.00038]
- 28 **Kozasa EH**, Sato JR, Lacerda SS, Barreiros MA, Radvany J, Russell TA, Sanches LG, Mello LE, Amaro E. Meditation training increases brain efficiency in an attention task. *Neuroimage* 2012; **59**: 745-749 [PMID: 21763432 DOI: 10.1016/j.neuroimage.2011.06.088]
- 29 **Pagnoni G**. Dynamical properties of BOLD activity from the ventral posteromedial cortex associated with meditation and attentional skills. *J Neurosci* 2012; **32**: 5242-5249 [PMID: 22496570 DOI: 10.1523/JNEUROSCI.4135-11.2012]
- 30 **Garrison KA**, Santoyo JF, Davis JH, Thornhill TA, Kerr CE, Brewer JA. Effortless awareness: using real time neurofeedback to investigate correlates of posterior cingulate cortex activity in meditators' self-report. *Front Hum Neurosci* 2013; **7**: 440 [PMID: 23964222 DOI: 10.3389/fnhum.2013.00440]

- 31 **Garrison KA**, Scheinost D, Worhunsky PD, Elwafi HM, Thornhill TA, Thompson E, Saron C, Desbordes G, Kober H, Hampson M, Gray JR, Constable RT, Papademetris X, Brewer JA. Real-time fMRI links subjective experience with brain activity during focused attention. *Neuroimage* 2013; **81**: 110-118 [PMID: 23684866 DOI: 10.1016/j.neuroimage.2013.05.030]
- 32 **Lutz A**, McFarlin DR, Perlman DM, Salomons TV, Davidson RJ. Altered anterior insula activation during anticipation and experience of painful stimuli in expert meditators. *Neuroimage* 2013; **64**: 538-546 [PMID: 23000783 DOI: 10.1016/j.neuroimage.2012.09.030]
- 33 **Taylor VA**, Daneault V, Grant J, Scavone G, Breton E, Roffe-Vidal S, Courtemanche J, Lavarenne AS, Marrelec G, Benali H, Beauregard M. Impact of meditation training on the default mode network during a restful state. *Soc Cogn Affect Neurosci* 2013; **8**: 4-14 [PMID: 22446298 DOI: 10.1093/scan/nsr087]
- 34 **Dickenson J**, Berkman ET, Arch J, Lieberman MD. Neural correlates of focused attention during a brief mindfulness induction. *Soc Cogn Affect Neurosci* 2013; **8**: 40-47 [PMID: 22383804 DOI: 10.1093/scan/nss030]
- 35 **Lutz J**, Herwig U, Opialla S, Hittmeyer A, Jäncke L, Rufer M, Grosse Holtforth M, Brühl AB. Mindfulness and emotion regulation-an fMRI study. *Soc Cogn Affect Neurosci* 2014; **9**: 776-785 [PMID: 23563850 DOI: 10.1093/scan/nst043]
- 36 **Ives-Deliperi VL**, Solms M, Meintjes EM. The neural substrates of mindfulness: an fMRI investigation. *Soc Neurosci* 2011; **6**: 231-242 [PMID: 20835972 DOI: 10.1080/17470919.2010.513495]
- 37 **Shaurya Prakash R**, De Leon AA, Klatt M, Malarkey W, Patterson B. Mindfulness disposition and default-mode network connectivity in older adults. *Soc Cogn Affect Neurosci* 2013; **8**: 112-117 [PMID: 23051900 DOI: 10.1093/scan/nss115]
- 38 **Paul NA**, Stanton SJ, Greeson JM, Smoski MJ, Wang L. Psychological and neural mechanisms of trait mindfulness in reducing depression vulnerability. *Soc Cogn Affect Neurosci* 2013; **8**: 56-64 [PMID: 22717383 DOI: 10.1093/scan/nss070]
- 39 **Creswell JD**, Way BM, Eisenberger NI, Lieberman MD. Neural correlates of dispositional mindfulness during affect labeling. *Psychosom Med* 2007; **69**: 560-565 [PMID: 17634566 DOI: 10.1097/PSY.0b013e3180f6171f]
- 40 **Brefczynski-Lewis JA**, Lutz A, Schaefer HS, Levinson DB, Davidson RJ. Neural correlates of attentional expertise in long-term meditation practitioners. *Proc Natl Acad Sci USA* 2007; **104**: 11483-11488 [PMID: 17596341 DOI: 10.1073/pnas.0606552104]
- 41 **Luders E**, Toga AW, Lepore N, Gaser C. The underlying anatomical correlates of long-term meditation: larger hippocampal and frontal volumes of gray matter. *Neuroimage* 2009; **45**: 672-678 [PMID: 19280691 DOI: 10.1016/j.neuroimage.2008.12.061]
- 42 **Grant JA**, Courtemanche J, Duerden EG, Duncan GH, Rainville P. Cortical thickness and pain sensitivity in zen meditators. *Emotion* 2010; **10**: 43-53 [PMID: 20141301 DOI: 10.1037/a0018334]
- 43 **Hölzel BK**, Carmody J, Evans KC, Hoge EA, Dusek JA, Morgan L, Pitman RK, Lazar SW. Stress reduction correlates with structural changes in the amygdala. *Soc Cogn Affect Neurosci* 2010; **5**: 11-17 [PMID: 19776221 DOI: 10.1093/scan/nsp034]
- 44 **Taren AA**, Creswell JD, Gianaros PJ. Dispositional mindfulness co-varies with smaller amygdala and caudate volumes in community adults. *PLoS One* 2013; **8**: e64574 [PMID: 23717632 DOI: 10.1371/journal.pone.0064574]
- 45 **Pickut BA**, Van Hecke W, Kerckhofs E, Mariën P, Vanneste S, Cras P, Parizel PM. Mindfulness based intervention in Parkinson's disease leads to structural brain changes on MRI: a randomized controlled longitudinal trial. *Clin Neurol Neurosurg* 2013; **115**: 2419-2425 [PMID: 24184066 DOI: 10.1016/j.clineuro.2013.10.002]
- 46 **Luders E**, Thompson PM, Kurth F, Hong JY, Phillips OR, Wang Y, Gutman BA, Chou YY, Narr KL, Toga AW. Global and regional alterations of hippocampal anatomy in long-term meditation practitioners. *Hum Brain Mapp* 2013; **34**: 3369-3375 [PMID: 22815233 DOI: 10.1002/hbm.22153]
- 47 **Luders E**, Kurth F, Toga AW, Narr KL, Gaser C. Meditation effects within the hippocampal complex revealed by voxel-based morphometry and cytoarchitectonic probabilistic mapping. *Front Psychol* 2013; **4**: 398 [PMID: 23847572 DOI: 10.3389/fpsyg.2013.00398]
- 48 **Hölzel BK**, Carmody J, Vangel M, Congleton C, Yerramsetti SM, Gard T, Lazar SW. Mindfulness practice leads to increases in regional brain gray matter density. *Psychiatry Res* 2011; **191**: 36-43 [PMID: 21071182 DOI: 10.1016/j.psychres.2010.08.006]
- 49 **Hölzel BK**, Ott U, Gard T, Hempel H, Weygandt M, Morgen K, Vaitl D. Investigation of mindfulness meditation practitioners with voxel-based morphometry. *Soc Cogn Affect Neurosci* 2008; **3**: 55-61 [PMID: 19015095 DOI: 10.1093/scan/nsm038]
- 50 **Pagnoni G**, Cekic M. Age effects on gray matter volume and attentional performance in Zen meditation. *Neurobiol Aging* 2007; **28**: 1623-1627 [PMID: 17655980 DOI: 10.1016/j.neurobiolaging.2007.06.008]
- 51 **Tang YY**, Lu Q, Fan M, Yang Y, Posner MI. Mechanisms of white matter changes induced by meditation. *Proc Natl Acad Sci USA* 2012; **109**: 10570-10574 [PMID: 22689998 DOI: 10.1073/pnas.1207817109]
- 52 **Luders E**, Phillips OR, Clark K, Kurth F, Toga AW, Narr KL. Bridging the hemispheres in meditation: thicker callosal regions and enhanced fractional anisotropy (FA) in long-term practitioners. *Neuroimage* 2012; **61**: 181-187 [PMID: 22374478 DOI: 10.1016/j.neuroimage.2012.02.026]
- 53 **Luders E**, Kurth F, Mayer EA, Toga AW, Narr KL, Gaser C. The unique brain anatomy of meditation practitioners: alterations in cortical gyriification. *Front Hum Neurosci* 2012; **6**: 34 [PMID: 22393318 DOI: 10.3389/fnhum.2012.00034]
- 54 **Tang YY**, Posner MI. Attention training and attention state training. *Trends Cogn Sci* 2009; **13**: 222-227 [PMID: 19375975 DOI: 10.1016/j.tics.2009.01.009]
- 55 **Chiesa A**, Malinowski P. Mindfulness-based approaches: are they all the same? *J Clin Psychol* 2011; **67**: 404-424 [PMID: 21254062 DOI: 10.1002/jclp.20776]
- 56 **Posner MI**, Rothbart MK. Research on attention networks as a model for the integration of psychological science. *Annu Rev Psychol* 2007; **58**: 1-23 [PMID: 17029565 DOI: 10.1146/annurev.psych.58.110405.085516]
- 57 **Raz A**, Buhle J. Typologies of attentional networks. *Nat Rev Neurosci* 2006; **7**: 367-379 [PMID: 16760917 DOI: 10.1038/nrn1903]
- 58 **Mason MF**, Norton MI, Van Horn JD, Wegner DM, Grafton ST, Macrae CN. Wandering minds: the default network and stimulus-independent thought. *Science* 2007; **315**: 393-395 [PMID: 17234951 DOI: 10.1126/science.1131295]
- 59 **Northoff G**, Bermpohl F. Cortical midline structures and the self. *Trends Cogn Sci* 2004; **8**: 102-107 [PMID: 15301749 DOI: 10.1016/j.tics.2004.01.004]
- 60 **Raichle ME**, MacLeod AM, Snyder AZ, Powers WJ, Gusnard DA, Shulman GL. A default mode of brain function. *Proc Natl Acad Sci USA* 2001; **98**: 676-682 [PMID: 11209064 DOI: 10.1073/pnas.98.2.676]
- 61 **Gusnard DA**, Raichle ME, Raichle ME. Searching for a baseline: functional imaging and the resting human brain. *Nat Rev Neurosci* 2001; **2**: 685-694 [PMID: 11584306 DOI: 10.1038/35094500]
- 62 **McGuire PK**, Paulesu E, Frackowiak RS, Frith CD. Brain activity during stimulus independent thought. *Neuroreport* 1996; **7**: 2095-2099 [PMID: 8930966]
- 63 **McKiernan KA**, D'Angelo BR, Kaufman JN, Binder JR.

- Interrupting the „stream of consciousness“: an fMRI investigation. *Neuroimage* 2006; **29**: 1185-1191 [PMID: 16269249 DOI: 10.1016/j.neuroimage.2005.09.030]
- 64 **Northoff G**, Heinzel A, de Greck M, Bermpohl F, Dobrowolny H, Panksepp J. Self-referential processing in our brain—a meta-analysis of imaging studies on the self. *Neuroimage* 2006; **31**: 440-457 [PMID: 16466680 DOI: 10.1016/j.neuroimage.2005.12.002]
- 65 **Grimm S**, Boesiger P, Beck J, Schuepbach D, Bermpohl F, Walter M, Ernst J, Hell D, Boeker H, Northoff G. Altered negative BOLD responses in the default-mode network during emotion processing in depressed subjects. *Neuropsychopharmacology* 2009; **34**: 932-943 [PMID: 18536699 DOI: 10.1038/npp.2008.81]
- 66 **Heinzel A**, Bermpohl F, Niese R, Pfennig A, Pascual-Leone A, Schlaug G, Northoff G. How do we modulate our emotions? Parametric fMRI reveals cortical midline structures as regions specifically involved in the processing of emotional valences. *Brain Res Cogn Brain Res* 2005; **25**: 348-358 [PMID: 16081255 DOI: 10.1016/j.cogbrainres.2005.06.009]

P- Reviewer: Kim JS, Xu S, Zeng WB **S- Editor:** Wen LL
L- Editor: A **E- Editor:** Lu YJ



Impact of dose calculation algorithm on radiation therapy

Wen-Zhou Chen, Ying Xiao, Jun Li

Wen-Zhou Chen, Ying Xiao, Jun Li, Department of Radiation Oncology, Thomas Jefferson University, Philadelphia, PA 19107, United States

Author contributions: All three authors contributed to manuscript preparation

Supported by In part, under a grant with the Pennsylvania Department of Health.

Correspondence to: Jun Li, PhD, Department of Radiation Oncology, Thomas Jefferson University, 111 South 11th St., Philadelphia, PA 19107, United States. jun.li@jefferson.edu
Telephone: +1-215-9557945 Fax: +1-215-5032386

Received: May 8, 2014 Revised: August 4, 2014

Accepted: September 23, 2014

Published online: March 28, 2015

Abstract

The quality of radiation therapy depends on the ability to maximize the tumor control probability while minimize the normal tissue complication probability. Both of these two quantities are directly related to the accuracy of dose distributions calculated by treatment planning systems. The commonly used dose calculation algorithms in the treatment planning systems are reviewed in this work. The accuracy comparisons among these algorithms are illustrated by summarizing the highly cited research papers on this topic. Further, the correlation between the algorithms and tumor control probability/normal tissue complication probability values are manifested by several recent studies from different groups. All the cases demonstrate that dose calculation algorithms play a vital role in radiation therapy.

© 2015 Baishideng Publishing Group Inc. All rights reserved.

Key words: Dose calculation; Algorithm; Radiation therapy; Tumor control probability; Normal tissue complication probability

Core tip: This paper is a review of the impact of cur-

rent commercial dose calculation algorithms on radiation therapy, with a focus on discussing the impact on tumor control probability and normal tissue complication probability.

Original sources: Chen WZ, Xiao Y, Li J. Impact of dose calculation algorithm on radiation therapy. *World J Radiol* 2014; 6(11): 874-880 Available from: URL: <http://www.wjgnet.com/1949-8470/full/v6/i11/874.htm> DOI: <http://dx.doi.org/10.4329/wjr.v6.i11.874>

INTRODUCTION

The quality of radiation therapy depends on the ability to maximize the tumor control probability (TCP) while minimize the normal tissue complication probability (NTCP) at the same time. Since these two quantities are directly dependent on the absorbed dose in the targets and in the organs at risk (OARs) respectively, accurate knowledge of dose distribution within the patient are crucial in radiation therapy. International Commission on Radiation Units and Measurements (ICRU)^[1] has recommended an overall dose accuracy within 5%. Considering the uncertainties resulting from patient setup, machine calibration and dose calculation from treatment planning systems, it is necessary to have a dose calculation algorithm that can predict dose distribution within 3% accuracy.

Accurate calculation of dose distribution in an inhomogeneous medium such as human body is a complicated task, especially for tumors located in the lung. To date, only the Monte Carlo method is considered to be the most accurate algorithm for dose calculation but it requires the greatest processing time. Apart from Monte Carlo method, all other methods make different degrees of approximation and simplification which lead to much faster calculation speed but also result in less accurate dose distribution comparing with the Monte Carlo simulation.

The purpose of this study is to review the effect of dose calculation algorithms on the radiation therapy for different disease sites and special focus is given for the lung region. As mentioned in the American Association of Physicists in Medicine (AAPM) Report No. 85^[2], the level of dose differences can be detected clinically. In order to quantify the clinical effects, we review the studies on the correlation of dose calculation algorithms with computed values of tumor control probability and normal tissue complication probability. The impact of the accuracy of the algorithms is directly related to the quality of radiation therapy.

DOSE CALCULATION ALGORITHMS

The Monte Carlo dose calculation method is considered to be the most accurate algorithm and has always been used as the generation of benchmark dose distribution with which to compare the results of other less-computer-intensive dose calculation methods^[3]. The Monte Carlo method uses photon and electron transport physics to consider the trajectories of individual particles and thus the pattern of dose deposition. Each particle's history is determined by the random number generator and millions of particles' histories are traced. The dose distribution is built by summing the energy deposition in each particle's history.

Apart from the Monte Carlo simulation, all other commonly used dose calculation algorithms can be categorized into two groups^[2,4,5]: (1) Methods based on equivalent path length (EPL)^[6] scaling or equivalent tissue-air ratio (ETAR)^[7] for inhomogeneity corrections. In these methods the changes in lateral transport of electrons are not modeled; and (2) Methods based on convolution techniques, in which the inhomogeneities are handled either by an equivalent path length correction or scaled kernels and the lateral electron transport is considered in an approximate way. In this work, these two types of algorithms are referred to as type (1) and type (2) methods. In type (1) methods, the equivalent path length correction is a one-dimensional method that takes into account of electron density information along a ray path from the source to the point in question. There are two methods: ratio of tissue-air ratio (RTAR) method^[2] and power law method which is also referred as modified Batho method^[8]. These methods correctly account for the change in the attenuation of the primary dose but not in the scatter contribution, thus result in an overestimation of dose when the electron density is less than unity and an underestimation when the electron density is greater than unity. The equivalent tissue-air ratio method is a three-dimensional correction method which is based on full three-dimensional density information acquired from CT images. This method applies a ray trace to determine the change in the primary dose and calculate the scatter dose based on the three-dimensional density data. Although methods in type (1) do not perform an accurate dose distribution calculation in patients, they are still used by

some treatment planning systems for a quick dose calculation to give the planner a rough idea about the absorbed dose and by some dose verification systems to perform a second independent check to catch the gross errors.

In type (2) methods, the model-based convolution/superposition algorithms^[9-13] are widely used in commercial radiotherapy treatment planning systems (TPSs), which perform dose calculations with accuracies close to the results of Monte Carlo simulation while take much less time. All convolution algorithms have two essential components: one representing the energy imparted to the medium by the interactions of primary photons, called Terma (total energy released per unit mass) and one representing the energy deposited about a primary photon interaction site, the kernel. The kernel can be further separated into two parts: the primary kernel which calculates the primary dose and the scatter kernel which calculates the first and multiple scatter doses. The dose at any point can be calculated from the convolution of the Terma with the kernel. In order to account for tissue heterogeneities in a patient, kernel is scaled by radiological distances which are calculated from the material densities defined by CT images. Rigorously speaking, when the scaled kernel is used, the process is not a convolution any more since the kernel is not invariant in space and it is in fact a superposition of varying kernels with the Terma. The treatment planning systems that use the superposition algorithm include, for example, XiO (Elekta, Inc.). Several variations of the convolution/superposition algorithms exist today and two typical and mostly used ones are collapsed cone convolution (CCC) and pencil beam convolution (PBC) techniques^[4]. The collapsed cone convolution method uses a polyenergetic Terma and kernel, where the kernel is represented analytically and expressed in polar coordinates. There are a finite number of polar angles with respect to the primary beam. The interaction site can be considered to be at the apex of a set of radially directed lines spreading out in three dimensions. Each line is considered to be the axis of a cone. The kernel along each line is actually the energy deposited within the entire cone collapsed onto the line. The advantage of the CCC method over standard convolution is that the computation time increase with MN^3 as opposed to N^6 , where M is the number of cones and N is the number of voxels along one side of the calculation volume. The treatment planning systems that use the CCC method include, for example, Pinnacle (Philips, Inc.) and Oncentra MasterPlan (Nucletron, Inc.). In the pencil beam convolution method, the dose deposited at a point is calculated as a convolution of Terma with a pencil-shape-like kernel which is derived from the measured beam data. The pencil-beam kernel describes the dose distribution of a very narrow beam entering a water phantom along the beam's central axis. Inhomogeneity correction is performed with an equivalent path length correction for the primary dose contribution and a one-dimensional convolution along fan lines for scattered radiation^[14,15]. The anisotropic analytical algorithm (AAA)^[16,17] used by Eclipse TPS

(Varian Medical Systems) is based on the pencil beam convolution technique. The AAA uses spatially variant convolution scatter kernels which are derived from Monte Carlo simulation, and separate modeling for primary photons, scattered photons, and contaminant electrons. Inhomogeneity is handled with radiological scaling of the dose deposition functions in the beamlet direction and electron-density-based scaling of the photon scatter kernels in 16 lateral directions. The final doses are obtained by superposing the doses from the photon and electron convolutions^[18,19]. The anisotropic analytical algorithm is an attractive option for routine clinical use because of its relatively short computation time and accuracy comparing with the Monte Carlo method.

COMPARISON OF DOSE CALCULATION ALGORITHMS AND THEIR CLINICAL IMPACT

Comparisons of dose calculation algorithms for clinical treatment disease sites have been studied in many references^[4,19-21]. In this review, we first summarize the comparisons of dose calculation algorithms for four commonly treated disease sites, which demonstrate that dose calculation algorithms that can calculate dose accurately in inhomogeneous environment are essential for lung tumor treatment. Then we focus on the dose calculation algorithms for lung tumor treatment planning. Different treatment techniques are discussed. Finally we show the correlation of the algorithms with TCP/NTCP.

In Knöös *et al.*^[4]'s paper, the authors studied the performance of different dose calculation algorithms from five commercial radiotherapy treatment planning systems for four common treatment disease sites: prostate, head and neck, breast and lung. The Monte Carlo algorithm was used as a benchmark for comparison between different algorithms. Increasing the complexity from the relatively homogeneous pelvic region to the very inhomogeneous lung region resulted in less accurate dose distributions. Improvements in the accuracy of dose calculation were observed when the methods taking into account of volume scatter and changes in electron transport were used, that is, when type (2) algorithms were used. That was especially important when the extension of the irradiated volume was limited such as in the breast case and when low densities were presented such as in the lung case. In the prostate case, no significant differences were found in the results calculated with different algorithms. For instance, when 6 MV was used, the dose to 95% of the PTV was in a range of 96.2% to 100.3% for all studied systems, with an average value of 98.2%. Qualitatively, all the plans which were calculated with different methods, were very similar. The similar situation existed in the head and neck case. The average dose per monitor unit (MU) to the PTV was decreased by 1% for the low energy if more accurate methods, *i.e.*, type (2) methods, were used. This difference was not presented

for the higher energy, due to less scatter in the high energy beam. The dose to 95% of the PTV showed no significant change when moving from type (1) methods to type (2) methods for both low and high energies. The ETAR method of type (1) resulted in doses closer to that calculated with type (2) methods, due to the improved scatter integration which took into account the 3D extension of the volume more accurately. In the breast case, two equally weighted opposed tangential beams were used. The average PTV doses were decreased by 0.7% and 1.6% for low and high energies, respectively, when comparing type (1) with type (2) methods. In general, larger differences in dose calculation were found in high energy treatment due to the longer range of electrons, especially in the low density lung tissues. In the pulmonary case, for 6 MV, the average dose per MU to the PTV was decreased by 2.5% when the type (2) methods were used, compared with that calculated with type (1) methods. Changing the energy to high energies increased the difference to 3.7%. The high dose volume within the PTV was decreased by 3.4% and 4.6%, moving from type (1) methods to type (2) methods for low and high energies, respectively. This implies that accurate tumor doses are different from the doses predicted with those methods, and accurate tumor doses needs to be predicted with advanced dose calculation algorithms, *i.e.*, Monte Carlo algorithm. Thus the algorithm directly affects the local control of tumors in lung cancer. That is, less coverage for tumor is presented when more realistic and accurate methods is used. This paper and other references^[19-22] showed that the dose calculation algorithms have a significant impact on radiation therapy for lung cancer treatment.

Remarkable impact of dose calculation algorithms on radiation therapy has been observed in the treatment of lung cancer, when tissue density correction was taken into account. Differences between dose calculations with and without density corrections in the thoracic region have been reported^[23-28]. In Xiao *et al.*^[27]'s paper, a retrospective dosimetric study was carried out based on the treatment plans submitted to Radiation Therapy Oncology Group (RTOG) 0236 clinical trials of non-small-cell lung cancer (NSCLC) treatment with stereotactic body radiotherapy (SBRT). The protocol required each institution to submit two plans: one plan without heterogeneity correction and one plan with heterogeneity correction, with identical MUs. In Xiao *et al.*^[27]'s study, the authors found that the planning target volume receiving greater than 60 Gy was decreased, on average, by 10.1% when heterogeneity corrections were applied. The maximal dose to any point greater than 2 cm away from the planning target volume increased from 35.2 Gy to 38.5 Gy.

The impact of heterogeneity corrections of dose algorithms on target coverage in the SBRT lung treatment was studied in more details in Ding *et al.*^[22]'s paper. The dose calculations using four different algorithms were compared with experimental measurements. The pencil beam algorithm with no heterogeneity corrections (PB-NC) and with modified Batho heterogeneity corrections

Table 1 Calculated percent mean tumor control probability values (ranges in parentheses) for all algorithms as a function of planning target volume volume

PTV bins (cm ³)	Mean PTV volume (range, cm ³)	<i>n</i>	EPL-1D	EPL-3D	AAA	CCC	Acuros	MC
4 ≤ <i>v</i> < 10	7.8 (4.8-9.9)	15	100.0 (100-100)	99.9 (99.6-100)	93.1 (76.3-99.8)	91.3 (63.0-99.9)	91.8 (60.8-99.8)	90.5 (51.1-99.9)
10 ≤ <i>v</i> < 20	15.0 (10.4-19.8)	27	100.0 (99.8-100)	99.9 (99.5-100)	91.3 (61.7-100)	91.3 (50.4-100)	91.4 (65.4-99.9)	91.1 (53.2-100)
20 ≤ <i>v</i> < 30	24.3 (20.4-29.6)	29	98.5 (99.8-100)	98.9 (77.6-100)	92.7 (74.9-99.9)	90.5 (46.4-99.9)	90.9 (65.1-99.9)	91.1 (48.4-99.9)
30 ≤ <i>v</i> < 40	34.9 (30.2-39.8)	18	99.8 (97.4-100)	99.6 (98.2-100)	92.0 (63.4-99.9)	92.1 (69.7-99.9)	90.9 (61.6-99.8)	92.4 (56.3-99.9)
40 ≤ <i>v</i> < 60	47.3 (40.2-58.4)	17	99.5 (93.1-100)	99.1 (95.6-100)	92.6 (78.6-99.9)	91.4 (64.4-99.9)	93.6 (77.6-99.9)	92.3 (63.6-99.9)
60 ≤ <i>v</i> < 100	78.0 (60.4-95.9)	16	99.5 (95.6-100)	99.0 (95.8-100)	92.7 (70.7-99.8)	92.8 (66.2-99.9)	93.4 (70.4-99.8)	94.7 (74.6-99.9)
<i>V</i> ≥ 100	162.4 (100.5-360.2)	11	99.2 (96.1-99.9)	98.7 (95.0-100)	96.3 (89.9-100)	95.6 (91.6-99.8)	95.3 (83.0-99.9)	97.1 (88.8-99.9)

PTV: Planning target volume; EPL-1D: 1-D equivalent path-length (pencil beam-type); EPL-3D: 3-D equivalent-path-length (pencil beam-type); AAA: Anisotropic analytical algorithm; CCC: Collapsed cone convolution-superposition; Acuros: Acuros AXB; MC: Monte Carlo. (Cited from Chetty *et al*^[30] 2013).

(PB-MB), the anisotropic analytical algorithm (AAA) and Monte Carlo simulation were investigated in ten patients' treatment planning. The plans included 8-10 non-opposed photon beams and 2-4 of the beams were non-coplanar. The field sizes ranged from 3.5 cm × 3.5 cm to 6 cm × 6 cm with the mean value close to 4 cm × 4 cm. The mixed 6 and 10 MV energies were used. The authors found that the differences in calculated doses to 95% or 99% of the PTV, between calculations using the PB-NC and the AAA, were within 10% of prescribed dose. Compared to that calculated with the AAA, the minimum doses to 95% of PTV calculated using the PB-MB were overestimated by up to 40% of the prescribed dose. The calculated maximum doses were underestimated by up to 27% using the PB-NC and overestimated by 19% using the PB-MB. The dose distributions near the interface calculated with the AAA agreed with those from Monte Carlo calculations and the measurements.

The above publications demonstrated the impact of dose calculation algorithms on the lung cancer treatment. These comparisons were mainly between type (1) and type (2) methods. The direct comparisons between type (2) algorithms and Monte Carlo simulation have been done extensively. For instance, in Vanderstraeten *et al*^[20]'s study, the authors compared the accuracy between Monte Carlo, convolution/superposition, and pencil beam dose calculations for intensity modulated radiation therapy (IMRT) of lung cancer, and they found that the convolution/superposition methods showed an excellent agreement with Monte Carlo method for dose calculation within the target structures, whereas the best agreement in OAR doses was found between collapsed cone convolution model and Monte Carlo simulation. Results from pencil beam algorithm were unsatisfying for both target and OARs. In Li *et al*^[28]'s paper, the authors compared superposition algorithm with Monte Carlo method for SBRT non-small-cell lung cancer treatment and they found that the important dosimetric parameter R50 (ratio of 50% prescription isodose volume to PTV) recommended by RTOG 0813 protocol had 12% difference on average between superposition and Monte Carlo calculations.

All these research studies have demonstrated that

for dose calculation in lung region the advanced type (2) methods are necessary, and the collapsed cone convolution algorithm and anisotropic analytical algorithm are appropriate options for their relative accurate calculation results compared with the Monte Carlo method.

In the above, we have discussed that the different dose calculation algorithms could give different levels of dose distribution accuracy. Further we will discuss that this different levels of accuracy could be detected clinically, which affect the quality of radiotherapy. The American Association of Physicists in Medicine (AAPM) Report No. 85^[2] on tissue inhomogeneity corrections mentioned that a 5% change in dose may result in a significant change in tumor control probability (TCP) and normal tissue complication probabilities (NTCP). In this report, the authors mentioned two examples^[29]: A 7% difference in dose delivered to different groups of patients was discovered by a radiation oncologist; and two experiences from the Institut Gustave Roussy, which were related to tumor regression and normal tissue reactions, respectively.

Although it is still a relative new topic, the correlation between dose algorithms and local control, TCP and NTCP, has already been investigated by several groups and more research is expected to be done in the future. In Chetty *et al*^[30]'s study, 133 NSCLC patients with stereotactic ablative radiotherapy (SABR)-based treatment were chosen for the correlation study. The correction-based pencil-beam algorithm, model-based convolution/superposition algorithm, and Monte Carlo algorithm were applied for dose calculation. TCP was computed using the Marsden model^[31,32] and associations between dose and outcome were inferred. The authors found that model-based mean TCP's were approximately 8%-9%, 6%-8%, and 3%-5% lower than those of correction-based algorithms for volumes < 60, 60-100, and > 100 cm³, respectively, when the same treatment arrangement was applied. This was because that the advanced type (2) methods simulated the dose deposition physics in a more realistic way than that type (1) methods. Further, the maximum decrement in Monte Carlo-based TCP was about 50% for volumes < 30 cm³. Variation in TCP ranges among model-based algorithms is due to the differences in the

Table 2 Relative differences calculated as (without-with)/with density corrections using each algorithm

	Eclipse AAA	OTP CC	Pinnacle CC	XiO Sup	OTP PB	XiO FFT
Combined lungs						
NTCP _{Burman}	-0.29	-0.2	-0.22	-0.25	-0.36	-0.45
NTCP _{Seppenwoolde}	-0.19	-0.13	-0.12	-0.15	-0.23	-0.3
Mean dose	-0.08	-0.05	-0.05	-0.06	-0.09	-0.13
V ₂₀	-0.06	-0.06	-0.04	-0.03	-0.05	-0.07
Heart						
NTCP	-0.19	-0.15	-0.15	-0.13	-0.17	-0.21
Mean dose	-0.06	-0.05	-0.05	-0.05	-0.06	-0.09
V ₅₀	-0.11	-0.1	-0.1	-0.08	-0.08	-0.13
PTV						
Mean dose	-0.06	-0.05	-0.05	-0.05	-0.13	-0.1
D ₀₁	-0.05	-0.05	-0.04	-0.04	-0.1	-0.11
D ₉₉	-0.07	-0.04	-0.05	-0.05	-0.14	-0.09
GTV						
Mean dose	-0.07	-0.06	-0.06	-0.06	-0.08	-0.1
D ₀₁	-0.07	-0.07	-0.06	-0.06	-0.09	-0.11
D ₉₉	-0.07	-0.06	-0.06	-0.06	-0.07	-0.1

Negative results indicate lower values when no density corrections are included. Eclipse AAA: Eclipse Anisotropic Analytical Algorithm; OTP CC: Oncentra MasterPlan Collapsed Cone algorithm; Pinnacle CC: Pinnacle Collapsed Cone algorithm; XiO Sup: XiO Multigrid Superposition algorithm; OTP PB: Oncentra MasterPlan Pencil Beam algorithm; XiO FFT: XiO Fast Fourier Transform Convolution algorithm. (Cited from Nielsen *et al.*^[34] 2011).

Table 3 Clinical impact of dose calculation algorithms

Ref.	Tumor site/technique	Algorithms studied	Results/conclusion
Nielsen <i>et al.</i> ^[34] , 2011	NSCLC	Eclipse AAA OTP CC Pinnacle CC XiO Sup OTP PB XiO FFT	Differences in dose to target predicted by the different algorithms are of a magnitude. Calculated NTCP values for pneumonitis are more sensitive to the choice of algorithm than mean lung dose and V ₂₀
Chandrasekaran <i>et al.</i> ^[38] , 2011	Lung/3DCRT,SBRT	PBC, Eclipse AAA, Pinnacle CCC, Masterplan PBC and CCC	PBC yielded higher TCP in comparison with other algorithms. For small tumor, TCP was overestimated by 4%-13% by PBC; for large tumor, there was an increase of up to 6%-22%
Liu <i>et al.</i> ^[39] , 2013	Lung/SABR	EPL, MC	EPL overestimates dose by amounts that substantially decrease TCP in a large proportion. Compared with MC, prescribing based on EPL translated to a median TCP decrement of 4.3% (range, 1.2%-37%) and a > 5% decrement in 46% of tumors
Bufacchi <i>et al.</i> ^[33] , 2013	Prostate, HN, Lung, Breast /3DCRT	PBC, AAA	NTCP calculated with AAA was lower than the NTCP calculated with PBC, except for the breast treatments
Chetty <i>et al.</i> ^[30] , 2013	NSCLC/SABR	EPL-1D, EPL-3D, AAA, CCC, Acuros, MC	Average TCP decrements (5%-10%, ranging up to approximately 50%) were observed with model-based algorithms relative to the EPL-based methods

Eclipse AAA: Eclipse Anisotropic Analytical Algorithm; OTP CC: Oncentra MasterPlan Collapsed Cone algorithm; Pinnacle CC: Pinnacle Collapsed Cone algorithm; XiO Sup: XiO Multigrid Superposition algorithm; OTP PB: Oncentra MasterPlan Pencil Beam algorithm; XiO FFT: XiO Fast Fourier Transform Convolution algorithm; EPL: Equivalent path length; MC: Monte Carlo.

PTV minimum doses observed in the dose-volume histograms which were the direct products of the calculation algorithms. Though these differences did not have a significant effect on the PTV D₉₅, they had a strong impact on the TCP. The results implied that more advanced algorithms are essential to assess the quality of the treatment clinically in the more realistic way. The detailed results of the percent mean tumor control probability (TCP) values for all algorithms as a function of PTV volume are cited and listed in Table 1.

In Bufacchi *et al.*^[33]'s study, the focus was shifted to the clinical implication of algorithms on NTCP models for four tumor sites: prostate, head and neck, breast and lung. The pencil beam convolution and anisotropic analytical algorithm were used for 80 treatment plans. The authors found that when the original PBC treatment plans were

recalculated using AAA with the same number of monitor units, the NTCP became lower, except for the breast treatments. Further the authors concluded that this difference in NTCP between PBC and AAA treatment plans could be clinically significant. In Nielsen *et al.*^[34]'s paper, the study was specifically focused on the influence of dose calculation algorithms on NTCP in NSCLC patients. Six dose algorithms from four different treatment planning systems were investigated: Eclipse AAA, Oncentra MasterPlan Collapsed Cone and Pencil Beam, Pinnacle Collapsed Cone, and XiO Multigrid Superposition and Fast Fourier Transform Convolution. NTCP values for heart and lungs were calculated using the relative seriality model^[35] and the LKB model^[36,37], respectively. The authors found that the influence of density correction on the NTCP values depended on the dose calculation algo-

rithms and the NTCP model parameter set. Compared to mean lung dose (MLD) and V20, the calculated NTCP values for pneumonitis were more sensitive to the calculation algorithms. All these implied that for plan evaluation the algorithms play an extremely important role and the dosimetric parameters such as MLD and V20 might not be sensitive enough for the assessment. The differences of the quantities calculated with and without density correction using each algorithm are cited and listed in Table 2.

To summarize, we list the clinical impact of dose calculation algorithms in Table 3. Five references^[30,33,34,38,39] with their results and conclusions are summarized.

CONCLUSION

In this study we reviewed the commonly used dose calculation algorithms: correction-based type (1) methods and model-based type (2) methods. The calculation accuracy of different algorithms illustrated by several studies was summarized. Special focus was given to dose calculation comparison in the lung region. All the research studies demonstrated that for dose calculation in lung region, the advanced type (2) methods are necessary. Further, the accuracy of dose calculation algorithms was correlated to the quantities of TCP/NTCP, and the connection between the algorithms and clinical impact was established. The clinically related TCP/NTCP values are sensitive to the accuracy of dose algorithms. In conclusion, dose calculation algorithms play a vital role in radiation therapy.

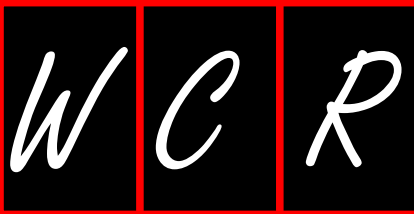
REFERENCES

- International Commission on Radiation Units and Measurements (ICRU).** Determination of absorbed dose in a patient irradiated by beams of X or gamma rays in radiotherapy procedures. ICRU Report 24. Washington (DC): ICRU, 1976: 67
- AAPM.** The American Association of Physicists in Medicine (AAPM) Report 85 Tissue inhomogeneity corrections for MV photon beams. USA: Report of Task Group No. 65 of AAPM, 2004
- Metcalfe P, Kron T, Hoban P.** The physics of radiotherapy x-rays and electrons. Madison, WI: Medical Physics Publishing, 2007
- Knöös T, Wieslander E, Cozzi L, Brink C, Fogliata A, Albers D, Nyström H, Lassen S.** Comparison of dose calculation algorithms for treatment planning in external photon beam therapy for clinical situations. *Phys Med Biol* 2006; **51**: 5785-5807 [PMID: 17068365 DOI: 10.1088/0031-9155/51/22/005]
- Fogliata A, Vanetti E, Albers D, Brink C, Clivio A, Knöös T, Nicolini G, Cozzi L.** On the dosimetric behaviour of photon dose calculation algorithms in the presence of simple geometric heterogeneities: comparison with Monte Carlo calculations. *Phys Med Biol* 2007; **52**: 1363-1385 [PMID: 17301460 DOI: 10.1088/0031-9155/52/5/011]
- Milan J, Bentley RE.** The storage and manipulation of radiation dose data in a small digital computer. *Br J Radiol* 1974; **47**: 115-121 [PMID: 4206210 DOI: 10.1259/0007-1285-47-554-115]
- Sontag MR, Cunningham JR.** The equivalent tissue-air ratio method for making absorbed dose calculations in a heterogeneous medium. *Radiology* 1978; **129**: 787-794 [PMID: 725060]
- Webb S, Fox RA.** Verification by Monte Carlo methods of a power law tissue-air ratio algorithm for inhomogeneity corrections in photon beam dose calculations. *Phys Med Biol* 1980; **25**: 225-240 [PMID: 7384209 DOI: 10.1088/0031-9155/25/2/003]
- Boyer A, Mok E.** A photon dose distribution model employing convolution calculations. *Med Phys* 1985; **12**: 169-177 [PMID: 4000072 DOI: 10.1118/1.595772]
- Mackie TR, Scrimger JW, Battista JJ.** A convolution method of calculating dose for 15-MV x rays. *Med Phys* 1985; **12**: 188-196 [PMID: 4000075 DOI: 10.1118/1.595774]
- Mohan R, Chui C, Lidofsky L.** Differential pencil beam dose computation model for photons. *Med Phys* 1986; **13**: 64-73 [PMID: 3951411 DOI: 10.1118/1.595924]
- Ahnesjö A.** Collapsed cone convolution of radiant energy for photon dose calculation in heterogeneous media. *Med Phys* 1989; **16**: 577-592 [PMID: 2770632 DOI: 10.1118/1.596360]
- Fogliata A, Nicolini G, Vanetti E, Clivio A, Cozzi L.** Dosimetric validation of the anisotropic analytical algorithm for photon dose calculation: fundamental characterization in water. *Phys Med Biol* 2006; **51**: 1421-1438 [PMID: 16510953 DOI: 10.1088/0031-9155/51/6/004]
- Ahnesjö A, Trepp A.** Acquisition of the effective lateral energy fluence distribution for photon beam dose calculations by convolution models. *Phys Med Biol* 1991; **36**: 973-985 [DOI: 10.1088/0031-9155/36/7/006]
- Ahnesjö A, Saxner M, Trepp A.** A pencil beam model for photon dose calculation. *Med Phys* 1992; **19**: 263-273 [PMID: 1584117 DOI: 10.1118/1.596856]
- Ulmer W, Kaissl W.** The inverse problem of a Gaussian convolution and its application to the finite size of the measurement chambers/detectors in photon and proton dosimetry. *Phys Med Biol* 2003; **48**: 707-727 [PMID: 12699190 DOI: 10.1088/0031-9155/48/6/302]
- Ulmer W, Pyyry J, Kaissl W.** A 3D photon superposition/convolution algorithm and its foundation on results of Monte Carlo calculations. *Phys Med Biol* 2005; **50**: 1767-1790 [PMID: 15815095 DOI: 10.1088/0031-9155/50/8/010]
- Sievinen J, Ulmer W, Kaissl W.** AAA photon dose calculation model in Eclipse. Palo Alto (CA): Varian Medical Systems, 2005
- Gagné IM, Zavgorodni S.** Evaluation of the analytical anisotropic algorithm in an extreme water-lung interface phantom using Monte Carlo dose calculations. *J Appl Clin Med Phys* 2007; **8**: 33-46 [PMID: 17592451]
- Vanderstraeten B, Reynaert N, Paelinck L, Madani I, De Wagter C, De Gersem W, De Neve W, Thierens H.** Accuracy of patient dose calculation for lung IMRT: A comparison of Monte Carlo, convolution/superposition, and pencil beam computations. *Med Phys* 2006; **33**: 3149-3158 [PMID: 17022207 DOI: 10.1118/1.2241992]
- Hasenbalg F, Neuenschwander H, Mini R, Born EJ.** Collapsed cone convolution and analytical anisotropic algorithm dose calculations compared to VMC++ Monte Carlo simulations in clinical cases. *Phys Med Biol* 2007; **52**: 3679-3691 [PMID: 17664570 DOI: 10.1088/0031-9155/52/13/002]
- Ding GX, Duggan DM, Lu B, Hallahan DE, Cmelak A, Malcolm A, Newton J, Deeley M, Coffey CW.** Impact of inhomogeneity corrections on dose coverage in the treatment of lung cancer using stereotactic body radiation therapy. *Med Phys* 2007; **34**: 2985-2994 [PMID: 17822007 DOI: 10.1118/1.2745923]
- Matsuo Y, Takayama K, Nagata Y, Kunieda E, Tateoka K, Ishizuka N, Mizowaki T, Norihisa Y, Sakamoto M, Narita Y, Ishikura S, Hiraoka M.** Interinstitutional variations in planning for stereotactic body radiation therapy for lung cancer. *Int J Radiat Oncol Biol Phys* 2007; **68**: 416-425 [PMID: 17363190 DOI: 10.1016/j.ijrobp.2006.12.012]
- Panettieri V, Wennberg B, Gagliardi G, Duch MA, Ginjume M, Lax I.** SBRT of lung tumours: Monte Carlo simulation with PENELOPE of dose distributions including respiratory

- motion and comparison with different treatment planning systems. *Phys Med Biol* 2007; **52**: 4265-4281 [PMID: 17664607 DOI: 10.1088/0031-9155/52/14/016]
- 25 **Lax I**, Panettieri V, Wennberg B, Amor Duch M, Näslund I, Baumann P, Gagliardi G. Dose distributions in SBRT of lung tumors: Comparison between two different treatment planning algorithms and Monte-Carlo simulation including breathing motions. *Acta Oncol* 2006; **45**: 978-988 [PMID: 16982567 DOI: 10.1080/02841860600900050]
- 26 **Schuring D**, Hurkmans CW. Developing and evaluating stereotactic lung RT trials: what we should know about the influence of inhomogeneity corrections on dose. *Radiat Oncol* 2008; **3**: 21 [PMID: 18662379 DOI: 10.1186/1748-717X-3-21]
- 27 **Xiao Y**, Papiez L, Paulus R, Timmerman R, Straube WL, Bosch WR, Michalski J, Galvin JM. Dosimetric evaluation of heterogeneity corrections for RTOG 0236: stereotactic body radiotherapy of inoperable stage I-II non-small-cell lung cancer. *Int J Radiat Oncol Biol Phys* 2009; **73**: 1235-1242 [PMID: 19251095 DOI: 10.1016/j.ijrobp.2008.11.019]
- 28 **Li J**, Galvin J, Harrison A, Timmerman R, Yu Y, Xiao Y. Dosimetric verification using monte carlo calculations for tissue heterogeneity-corrected conformal treatment plans following RTOG 0813 dosimetric criteria for lung cancer stereotactic body radiotherapy. *Int J Radiat Oncol Biol Phys* 2012; **84**: 508-513 [PMID: 22365630 DOI: 10.1016/j.ijrobp.2011.12.005]
- 29 **Dutreix A**. When and how can we improve precision in radiotherapy? *Radiother Oncol* 1984; **2**: 275-292 [PMID: 6522641 DOI: 10.1016/S0167-8140(84)80070-5]
- 30 **Chetty IJ**, Devpura S, Liu D, Chen D, Li H, Wen NW, Kumar S, Fraser C, Siddiqui MS, Ajlouni M, Movsas B. Correlation of dose computed using different algorithms with local control following stereotactic ablative radiotherapy (SABR)-based treatment of non-small-cell lung cancer. *Radiother Oncol* 2013; **109**: 498-504 [PMID: 24231237 DOI: 10.1016/j.radonc.2013.10.012]
- 31 **Nahum AE**, Sanchez-Nieto B. Tumour control probability modelling: basic principles and applications in treatment planning. *Phys Med* 2001; **17**: 13-23
- 32 **Webb S**, Nahum AE. A model for calculating tumour control probability in radiotherapy including the effects of inhomogeneous distributions of dose and clonogenic cell density. *Phys Med Biol* 1993; **38**: 653-666 [PMID: 8346278 DOI: 10.1088/0031-9155/38/6/001]
- 33 **Bufacchi A**, Nardiello B, Capparella R, Begnozzi L. Clinical implications in the use of the PBC algorithm versus the AAA by comparison of different NTCP models/parameters. *Radiat Oncol* 2013; **8**: 164 [PMID: 23826854 DOI: 10.1186/1748-717X-8-164]
- 34 **Nielsen TB**, Wieslander E, Fogliata A, Nielsen M, Hansen O, Brink C. Influence of dose calculation algorithms on the predicted dose distribution and NTCP values for NSCLC patients. *Med Phys* 2011; **38**: 2412-2418 [PMID: 21776775 DOI: 10.1118/1.3575418]
- 35 **Källman P**, Agren A, Brahme A. Tumour and normal tissue responses to fractionated non-uniform dose delivery. *Int J Radiat Biol* 1992; **62**: 249-262 [PMID: 1355519 DOI: 10.1080/09553009214552071]
- 36 **Lyman JT**. Complication probability as assessed from dose-volume histograms. *Radiat Res Suppl* 1985; **8**: S13-S19 [PMID: 3867079 DOI: 10.2307/3576626]
- 37 **Kutcher GJ**, Burman C. Calculation of complication probability factors for non-uniform normal tissue irradiation: the effective volume method. *Int J Radiat Oncol Biol Phys* 1989; **16**: 1623-1630 [PMID: 2722599 DOI: 10.1016/0360-3016(89)90972-3]
- 38 **Chandrasekaran M**, Panettieri V, Baker C, and Nahum AE. The clinical impact of differences in photon dose algorithms: 3DCRT and SBRT of lung tumors. *Radiother Oncol* 2011; **99**: S427-S428 [DOI: 10.1016/S0167-8140(11)71269-5]
- 39 **Liu MB**, Eclov NC, Trakul N, Murphy J, Diehn M, Le QT, Dieterich S, Maxim PG, Loo BW. Clinical impact of dose overestimation by effective path length calculation in stereotactic ablative radiation therapy of lung tumors. *Pract Radiat Oncol* 2013; **3**: 294-300 [PMID: 24674401 DOI: 10.1016/J.PRRO.2012.09.003]

P- Reviewer: Xiao Y S- Editor: Ji FF L- Editor: A
E- Editor: Lu YJ





Congenital hyperinsulinism: Role of fluorine-18L-3, 4 hydroxyphenylalanine positron emission tomography scanning

Jaya Sujatha Gopal-Kothandapani, Khalid Hussain

Jaya Sujatha Gopal-Kothandapani, Department of Paediatric Endocrinology, Royal Manchester Children's Hospital, Manchester M13 9WL, United Kingdom

Khalid Hussain, Department of Paediatric Endocrinology, Great Ormond Street Hospital for Children NHS Trust and the Institute of Child Health, University College London, London WC1N 1EH, United Kingdom

Khalid Hussain, Developmental Endocrinology Research Group, Molecular Genetics Unit, Institute of Child Health, University College London, London WC1N 1EH, United Kingdom

Author contributions: Gopal-Kothandapani JS drafted the article; and Hussain K reviewed it critically, revised and approved the final version.

Correspondence to: Dr. Khalid Hussain, Reader in Paediatric Endocrinology, Developmental Endocrinology Research Group, Molecular Genetics Unit, Institute of Child Health, University College London, 30 Guilford Street, London WC1N 1EH, United Kingdom. khalid.hussain@ucl.ac.uk

Telephone: +44-20-79052128 Fax: +44-20-74046191

Received: February 11, 2014 Revised: March 19, 2014

Accepted: May 16, 2014

Published online: March 28, 2015

Abstract

Congenital hyperinsulinism (CHI) is a rare but complex heterogeneous disorder caused by unregulated secretion of insulin from the β -cells of the pancreas leading to severe hypoglycaemia and neuroglycopenia. Swift diagnosis and institution of appropriate management is crucial to prevent or minimise adverse neurodevelopmental outcome in children with CHI. Histologically there are two major subtypes of CHI, diffuse and focal disease and the management approach will significantly differ depending on the type of the lesion. Patients with medically unresponsive diffuse disease require a near total pancreatectomy, which then leads on to the development of iatrogenic diabetes mellitus and pancreatic exocrine insufficiency. However patients with focal dis-

ease only require a limited pancreatectomy to remove only the focal lesion thus providing complete cure to the patient. Hence the preoperative differentiation of the histological subtypes of CHI becomes paramount in the management of CHI. Fluorine-18L-3, 4-hydroxyphenylalanine positron emission tomography (^{18}F -DOPA-PET) is now the gold standard for pre-operative differentiation of focal from diffuse disease and localisation of the focal lesion. The aim of this review article is to give a clinical overview of CHI, then review the role of dopamine in β -cell physiology and finally discuss the role of ^{18}F -DOPA-PET imaging in the management of CHI.

© 2015 Baishideng Publishing Group Inc. All rights reserved.

Key words: Congenital hyperinsulinism; Fluorine-18L-3, 4-hydroxyphenylalanine positron emission tomography; Focal congenital hyperinsulinism; Diffuse congenital hyperinsulinism; Ectopic congenital hyperinsulinism; Standardized uptake value

Core tip: This manuscript describes how the advent of fluorine-18L-3, 4-hydroxyphenylalanine positron emission tomography (^{18}F -DOPA-PET) scanning has revolutionised the management of patients with a very complex condition called congenital hyperinsulinism. ^{18}F -DOPA-PET scanning allows the accurate pre-operative localisation of the focal lesion in these patients which can then be surgically removed allowing complete cure from the hypoglycaemia.

Original sources: Gopal-Kothandapani JS, Hussain K. Congenital hyperinsulinism: Role of fluorine-18L-3, 4 hydroxyphenylalanine positron emission tomography scanning. *World J Radiol* 2014; 6(6): 252-260 Available from: URL: <http://www.wjgnet.com/1949-8470/full/v6/i6/252.htm> DOI: <http://dx.doi.org/10.4329/wjr.v6.i6.252>

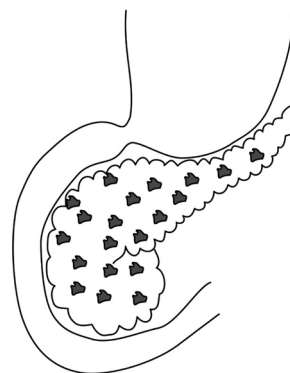
INTRODUCTION

Congenital hyperinsulinism (CHI) is a heterogeneous condition due to the dysregulated and inappropriate secretion of insulin from the β -cells of the pancreas leading to severe hypoglycaemia in infants. The incidence of CHI is 1 in 50000 in the general population and 1 in 2500 in the consanguineous cohorts^[1]. Based on the clinical presentation-CHI can be classified into two major subgroups, transient or persistent and based on histology into three forms such as focal (40%), diffuse (50%) or atypical (10%)^[2]. Transient CHI is observed in children who are born small for gestational age, those with intra-uterine growth restriction (IUGR), those subjected to birth asphyxia and those born to mothers with diabetes mellitus (pre or gestational diabetes) and can last up to a week^[3]. However it can last longer up to a few months in some children with IUGR^[4].

The insulin secreting β -cells of the pancreas consists of a potassium channel (K_{ATP} channel) which plays a crucial role in insulin secretion and glucose homeostasis^[5]. The K_{ATP} channel proteins are encoded by two genes. These are “sulphonylurea receptor subunit” (SUR1 encoded by *ABCC8*) and the “inward rectifying potassium channel subunit” (Kir6.2 encoded by *KCNJ11*) genes^[6]. Both these genes are localised to chromosome 11p15.1^[7]. Nearly 90% of medically unresponsive persistent CHI is caused by loss of function (recessive inactivating) mutations in these two subunits of the K_{ATP} channel involved in regulating insulin secretion^[8]. They are predominantly autosomal recessive (AR) and rarely autosomal dominant (AD) in inheritance.

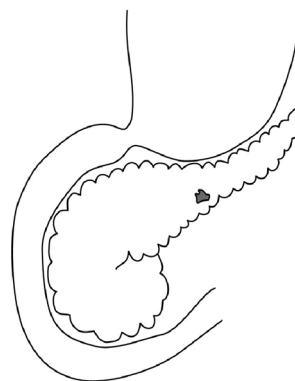
Mutations in genes encoding enzymes involved in insulin secretion are rare causes of CHI. They are (1) glutamate dehydrogenase (GDH) encoded by *GLUD1* gene (AD); (2) glucokinase (GCK) encoded by *GCK* gene (AD); (3) L-3-hydroxyacyl-coenzyme A dehydrogenase (HADH) encoded by *HADH* gene (AR); (4) hepatocyte nuclear factor 4-alpha (HNF4-a) encoded by *HNF4A* gene (AD); (5) monocarboxylate transporter (MCT1) encoded by *SLC16A1* gene (AD); and (6) uncoupling protein 2 encoded by *UCP2* gene (AD)^[9]. No genetic aetiology has been identified in about 70%-80% of patients who are responsive to medical therapy with diazoxide.

Of the three histological forms of CHI, the typical diffuse form is characterised by the abundant distribution of enlarged and hyperchromatic nuclei throughout the islets^[2]. It is predominantly caused by recessive loss of function mutations in the K_{ATP} channel (*ABCC8* and *KCNJ11* genes) and when unresponsive to medical therapy requires a near total ($\geq 95\%$) pancreatectomy^[2] (Figure 1). The focal form is characterised by an isolated cluster of abnormal insulin producing cells with ‘normal’ surrounding tissue within the pancreas (Figure 2). Histologically it involves focal adenomatous hyperplasia of the islet cells with ductuloinsular complexes and scattered giant β -cell nuclei surrounded by normal pancreatic parenchyma^[2,10,11]. Focal CHI is always sporadic in inheritance and caused by the paternal heterozygous mutation



Diffuse:
Entire pancreas affected
Associated with mutations in *ABCC8*/*KCNJ11*/*GCK*/*GLUD1*/*HNF4A*/*HADH* and *SLC16A1*

Figure 1 Diffuse lesion where the entire pancreas is affected. It is associated with recessive and dominant mutations in the *ABCC8*/*KCNJ11*/*GCK*/*GLUD1*/*HNF4A*/*HADH* and *SLC16A1*.



Focal:
Localised region of pancreas affected
Associated with a paternal mutation in *ABCC8*/*KCNJ11* and paternal UPD encompassing 11p5.1 to 11p15.5 in the focal area

Figure 2 Focal lesion affecting only a single region of the pancreas. It is associated with a paternal mutation in the *ABCC8* or *KCNJ11* and paternal uniparental disomy encompassing 11p5.1 to 11p15.5 in the focal area.

in *ABCC8*/*KCNJ11* genes along with somatic loss of maternal allele in the focal hyperplastic tissue requiring a focal lesionectomy^[12].

Nearly 10% of CHI is of atypical form, the molecular mechanism and histopathological differentiation of which is yet to be completely understood^[13]. Children with persistent CHI often require high glucose concentrations ($> 8\text{mg/kg/min}$) to maintain euglycemia. The diagnosis of CHI is primarily made by biochemical investigations demonstrating detectable levels of insulin in relation to hypoglycaemia along with reduced/absent free fatty acids and ketone bodies^[12]. Current medical management for CHI includes Diazoxide along with Chlorothiazide as the first line therapy and Octreotide as a second line drug^[12].

Children who are not responding to medical management, and in whom the genetic testing is inconclusive or in favour of a focal lesion, should undergo ¹⁸F-DOPA-PET scan to ascertain the type of lesion whether it is fo-

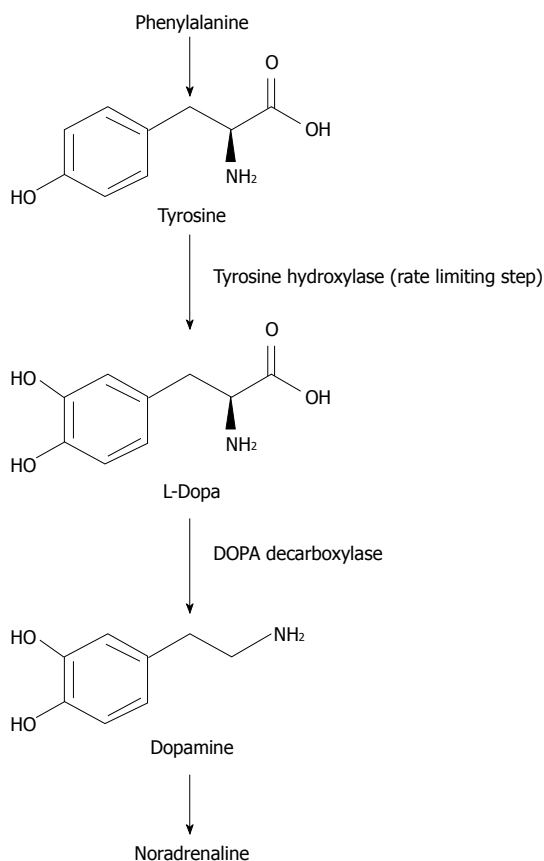


Figure 3 Dopamine biochemistry. Phenylalanine is converted into L-Tyrosine. L-Tyrosine is then converted into L-Dopa by Tyrosine Hydroxylase. L-Dopa is then converted into Dopamine by DOPA decarboxylase.

cal or diffuse and provide guidance towards surgery^[1].

Pre-operative delineation of the subtype of the lesion becomes extremely crucial as the management approach and the treatment modalities differ significantly based on the type of the lesion. Focal CHI typically does not respond to medical management and a focal lesionectomy provides a definite cure for the condition by avoiding further hypoglycaemic episodes and its neurological complications. A focal lesionectomy also minimises the risk of iatrogenic diabetes mellitus and exocrine pancreatic insufficiency. Children with diffuse CHI warrant a sub total or a near total pancreatectomy to prevent brain damage from neuroglycopenia, however the risk of developing diabetes mellitus and exocrine insufficiency in later life is quite high^[14].

DOPAMINE METABOLISM

Dopamine is synthesised from a non-essential amino acid, tyrosine which is first converted to L-dopa by tyrosine hydroxylase. This is the rate limiting step in dopamine production. Then L-Dopa is decarboxylated to dopamine by DOPA decarboxylase. Dopamine is then oxidised to nor-adrenaline (Figure 3).

Dopamine plays different roles in various internal organs. In the brain, it acts as a neurotransmitter and plays

a major role in neuropsychiatric and movement disorders such as Schizophrenia and Parkinson's disease^[15]. It also acts as a local chemical messenger in other organs such as blood vessels, kidney, gastrointestinal mucosa and including pancreas^[16].

Dopamine exerts its effects by binding to and activating receptors on the surface of cells. In humans five subtypes of dopamine receptors have been identified, labelled D1 through D5^[16]. All of them exert their effects *via* a complex second messenger system [*e.g.*, cyclic AMP]. Dopamine signalling is mediated by five cloned receptors, grouped into D1-like (D1 and D5 receptors) and D2-like (D2, D3 and D4 receptors) families. The presence of dopamine receptors from both families has been identified in human isolated islets^[16]. D2 receptor expression was confirmed by immunodetection revealing localization on insulin secretory granules of human β -cells^[16].

Studies carried out in mouse pancreatic islets have shown pancreatic islets as the site for Dopamine synthesis and storage outside the central nervous system and both Dopamine and L-Dopa exerts a negative feedback action on insulin secretion in correlation with the reduction in intracellular $[Ca^{2+}]$ influx^[17,18].

A study done recently has shown a negative feedback regulatory circuit for glucose-stimulated insulin secretion in purified human islets *in vitro*^[19]. The release of dopamine and insulin together in response to the glucose load is demonstrated by the *in-vitro* infusion of dopamine into the insulin-containing secretory granules of human β -cells. Dopamine in turn exerts an antagonistic action on the D2 receptors that are also expressed on β -cells and thus inhibiting insulin secretion^[19].

Neuroendocrine cells and pancreatic islets take up L-DOPA and convert it into Dopamine by the enzyme DOPA decarboxylase, which is expressed in β -cells of the pancreatic islets^[20-23]. Thus decarboxylation of the L-DOPA to dopamine in the β -cells of the pancreatic islets allows localization of the lesion by means of PET scanning, using radioactive isomer ¹⁸F-L-DOPA^[24]. ¹⁸F-DOPA is a radiotracer analogue of DOPA and this radioactive tracer is taken up, decarboxylated and stored in cytoplasmic secretory granules by both the endocrine and exocrine cells of the pancreas^[25,25]. This mechanism acts as the principle behind the use of this non-invasive ¹⁸F-DOPA-PET imaging technique as the diagnostic tool of choice in localising the focal lesion. Both focal and diffuse forms have high DOPA decarboxylase activity and in focal lesions there is excessive tracer uptake in the lesion when compared to the rest of the pancreas (Figure 4).

In diffuse CHI there is generalised increased tracer uptake with a relatively higher uptake in the head when compared to the rest of the pancreas^[14,26,27]. ¹⁸F-DOPA is excreted by kidneys hence normal bio-distribution is seen in kidneys, ureter and urinary bladder. An excessive uptake is also seen in gall bladder and biliary tract and a low uptake is seen in liver, heart and basal ganglia^[26].

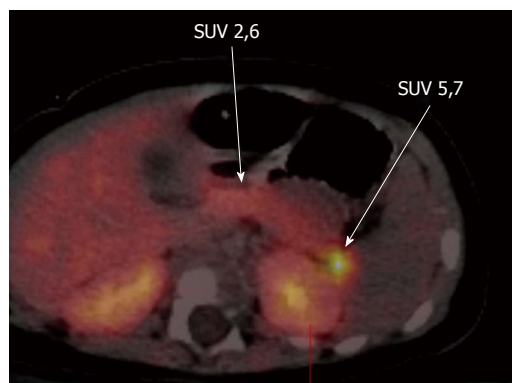


Figure 4 Fluorine-18L-3, 4-hydroxyphenylalanine positron emission tomography scan showing the focal lesion in the tail of the pancreas.

DIAGNOSTIC METHODS TO LOCALISE FOCAL LESION

Until recently the methods used to localise the focal lesion were (1) Hepatic portal venous sampling (PVS)^[28,29], (2) arterial calcium stimulation test^[30,31], and (3) tolbutamide response test^[32]. PVS is invasive, time consuming, technically challenging and is associated with risk of severe hypoglycaemia and the accuracy is only about 70%^[28,33]. Arterial calcium stimulation and tolbutamide response test are not found to be accurate in distinguishing between focal and diffuse CHI^[30,32,34,35]. Imaging modalities such as computed tomography (CT) and magnetic resonance imaging (MRI) has not been found very useful in localising the focal lesion^[14].

^{18}F -DOPA-PET/CT was first reported for the localisation of the focal lesion by Riberio *et al*^[13] in 2005 and Otonkoski *et al*^[36] in 2006. Since then several studies have shown that ^{18}F -DOPA-PET/CT provides precise differentiation between focal and diffuse forms albeit exact localisation of the lesion may not be accurately attributed by the scan technique^[13,21,37]. However, ^{18}F -DOPA-PET/CT is non-invasive, relatively simple to use and more efficient than the invasive procedures such as PVS, and arterial calcium stimulation tests in differentiating and localising the pancreatic lesions^[38]. The sensitivity and specificity of ^{18}F -DOPA-PET/CT in detecting focal lesions measuring between 2 mm and 10 mm is approximately 90% and 100% respectively^[39]. Thus the use of ^{18}F -DOPA-PET/CT has revolutionised the surgical outcome in these children with CHI.

USE OF ^{18}F -DOPA-PET/CT IN CHI

The use of ^{18}F -DOPA-PET/CT in distinguishing between focal and diffuse CHI was first reported by Riberio *et al*^[13], where the authors subjected 15 neonates to ^{18}F -DOPA-PET scan. Abnormal focal uptake was observed in 5 children and diffuse uptake in the rest. Histopathology findings of all 5 patients with focal lesion and 4 patients with diffuse uptake who underwent surgery matched with their PET scan findings.

Otonkoski *et al*^[36] used ^{18}F -DOPA-PET/CT in 14 patients (*ABCC8* mutation in 11/14 patients) and found focal uptake in 5 patients, diffuse uptake in the remaining 9 patients. ^{18}F -DOPA-PET/CT findings were confirmed by histology in all 5 patients with focal uptake and 4 out of 9 in patients with diffuse uptake. This group also measured the standardized uptake value (SUV) of ^{18}F -DOPA and found a SUV of > 50% higher uptake than the maximum SUV of the unaffected part of the pancreas in the focal group which corresponded with the histology findings. The remaining 9 patients with a diffuse uptake on the ^{18}F -DOPA-PET/CT scan had a SUV ratio of < 1.5. Histology findings confirmed diffuse disease in 4 patients and pancreatic venous sampling in 4 patients. The authors concluded by proposing ^{18}F -DOPA-PET/CT as the best modality of choice in locating a focal lesion^[36].

Riberio *et al*^[40] did a retrospective study in 2007 on forty nine children with CHI who had undergone ^{18}F -DOPA-PET/CT scanning. They identified abnormal focal pancreatic uptake of ^{18}F -DOPA in 15 children, where diffuse radio-tracer uptake was observed in the pancreatic area in the other 34 children. They also subjected 12 of the 49 children for pancreatic venous sampling (PVS) and 31 for MRI. In children who underwent both PET and PVS, the results were concordant in 11 out of 12. The authors concluded that PET scan with ^{18}F -DOPA is an accurate non-invasive technique allowing differential diagnosis between focal and diffuse forms of CHI^[40].

Arbizu Lostao *et al*^[41] reported their first patient from Spain in whom the diagnosis of focal CHI was made in a 13 month old child using combined genetic analysis [paternal heterozygous mutation (G111R) in the *ABCC8* gene] and ^{18}F -DOPA-PET/CT imaging (focal uptake in the body of the pancreas) was successfully treated by surgery. This case report reiterates the importance of performing combined investigations towards the successful management of CHI.

Barthlen *et al*^[22] in 2008 reported the correlation of ^{18}F -DOPA-PET/CT scan findings with the intra-operative findings in 9 out of 10 children. A limited resection was found to be curative in 8 out of 9 children. They also reported their follow up data on these children with no evidence of diabetes or exocrine pancreatic insufficiency^[22].

Cherubini *et al*^[42] have reported that ^{18}F -DOPA-PET/CT imaging can distinguish between focal and diffuse lesions in majority of the cases and 100% accurate in locating the focal lesion. The authors also highlighted the potentiating effects of non-invasive imaging technique using ^{18}F -DOPA-PET/CT imaging combined with laparoscopic pancreatic surgery in the prompt localisation and excision of the focal lesion, preventing iatrogenic diabetes mellitus in later life^[42].

Yorifuji *et al*^[43] reported a boy with focal CHI whose disease activity was not consistent with the uptake of ^{18}F DOPA. A diagnosis of CHI was made on day 2 of his life when he presented with hypoglycaemic seizures. A paternal heterozygous mutation c.4186G 1T (p.D1396Y)

in the *ABCC8* was identified followed by an uptake in the body of pancreas in the ^{18}F -DOPA-PET/CT scan. A diagnosis of focal CHI was made and he was managed conservatively with frequent feeding regime. He achieved spontaneous remission at 1 year and 10 mo of age and a follow up ^{18}F -DOPA-PET/CT scan revealed no difference in uptake between the two scans despite achieving clinical remission. Further to this an arterial stimulation venous sampling test was done which showed a low basal and stimulated insulin release illustrating that ^{18}F -DOPA-PET/CT uptake may not always correlate with the insulin secreting capacity of the β -cells and the spontaneous remission of hypoglycaemia can be a functional process and not due to the apoptotic death of β abnormal cells^[43].

Zani *et al*^[44] evaluated the accuracy of ^{18}F -DOPA-PET/CT imaging technique in differentiating between focal and diffuse lesions and localisation of the focal lesion. The authors reviewed the results of ^{18}F -DOPA-PET/CT scan performed in 19 patients. Five of them had diffuse uptake and the same was confirmed by histology. The remaining 14 patients showed a focal uptake which was confirmed by histology however the localisation was not accurate in 5 children leading to incorrect surgical resection. The authors concluded that ^{18}F -DOPA-PET/CT scan can distinguish between focal and diffuse CHI and the exact localisation in only 2/3 of patients with focal lesions. The authors also suggested undertaking intraoperative histological confirmation of the focal lesion prior to complete excision^[44].

Masue *et al*^[45] reported their experience of the use of ^{18}F -DOPA-PET/CT in 17 Japanese children by assessing their results either by simple inspection or by calculating the pancreas percentage and compared those results with the genetic analysis and histology. Pancreas percentage is the expression of uptake of the head, body and tail of the pancreas as the total maximum SUV of the whole pancreas. They found the localisation and histology was consistent in all 17 children. However the overall results were consistent with the molecular diagnosis and histology in only 7/17 and 6/12 patients respectively. They also reported a substantial improvement in the accuracy of PET studies by using pancreatic percentage^[45].

Ismail *et al*^[12] reported the marked variation in the clinical, genetic, radiological and histopathological features of focal CHI in 3 of their patients. All 3 of them had paternal heterozygous mutation in *ABCC8* gene (c.3992-9G \rightarrow A in the first 2 patients and c.4477G \rightarrow A in third patient). Of the 2 patients, first patient was responded to Diazoxide but not the second patient. The focal lesions in these 2 patients were accurately localised using ^{18}F -DOPA-PET/CT imaging. Both of them underwent focal lesionectomy and were completely cured. Histology confirmed the presence of focal nodules with large nuclei along with the remaining normal pancreatic tissue in the first 2 patients. The authors proposed that unknown genetic or environmental factors may influence the phenotypic variation in response to treatment and some focal

lesions can respond to medical management. The authors have also highlighted that a paternally inherited c.3992-9G \rightarrow A mutation in the *ABCC8* gene is associated with a mild focal phenotype responding to medical management in some patients of Ashkenazi Jewish origin^[12]. This finding is based on previous reports that nearly 90% of CHI in Ashkenazi Jewish population is associated with c.3992-9G \rightarrow A mutation and p.F1388del in the *ABCC8* gene^[46]. The third patient had undergone two ^{18}F -DOPA-PET/CT imaging, with an unusually large focal lesion involving the whole pancreas. The first scan showed the tracer uptake in the body and tail and the second scan performed post lesionectomy showed a tracer uptake in the head of the pancreas and the patient underwent 2 pancreatic surgeries. Macroscopically this patient had a normal looking pancreas but microscopically islet cell nodules with large nuclei were found along with some normal pancreatic tissue. Despite undergoing the second surgery this patient was reported to be dependent on continuous gastrostomy feeds to maintain euglycemia^[12].

Giurgea *et al*^[47] reported that the size of the focal lesion is determined by the timing when the somatic loss of maternal allele occurs during the gestational age^[47]. The earlier it occurs the larger the size of the focal lesion can be, as found in the 3 patient in this report. Also it has been suggested that an unknown mechanism might play a role in different rate of tracer uptake in different regions of pancreas in large focal lesions^[47].

Meintjes *et al*^[26] recently evaluated and reported the accuracy of delineating the focal and diffuse CHI using ^{18}F fluoro-L-DOPA/CT and contrast enhanced CT. They performed 22 ^{18}F fluoro-L-DOPA/CT and contrast enhanced CT studies on 18 patients and assessed those results using visual assessment followed by quantitative comparison of SUVs measured by calculating the uptake on head, body and tail of the pancreas. They derived an SUV ratio using the formula-highest SUV (max)/next highest SUV (max). The authors also proposed a time activity curve which showed the focal pancreatic islet uptake relatively constant over time suggesting performing imaging at 20 min and 50 min after the radio tracer injection. The use of intravenous contrast agents during CT provides invaluable information for the surgeons in delineating the anatomical landmarks while performing surgery.

Of the 18 patients 13 showed diffuse with an SUV ratio of < 1.3 and five showed focal uptake with an SUV ratio of > 1.5 with an SUV (max) 50% higher than that of the unaffected area of the pancreas. Out of these five patients four of them had paternal *ABCC8* mutation. All five patients were cured after limited focal resection with three of them requiring second ^{18}F -L-DOPA/CT and contrast enhanced CT and surgery. Of the 13 patients who had diffuse disease, 9 of them were negative for *ABCC8/KCNJ11* mutations and 3 had positive paternal *ABCC8* mutation. Out of 13, 2 patients underwent surgery and 11 patients remain on high dose Diazoxide treatment one of them had 3 pancreatectomies without

cure. The authors concluded by highlighting the importance of per-operative ¹⁸F-L-DOPA/CT and contrast enhanced CT studies in not only distinguishing between the focal and the diffuse disease but also the precise localisation of the anatomical landmarks^[26].

Laje *et al*^[48] did a retrospective review to determine the accuracy of ¹⁸F-DOPA-PET/CT scan in diagnosing focal CH on 105 children in whom a pre-operative ¹⁸F-DOPA-PET/CT scan was undertaken. Out of 105 patients, 53 patients had focal lesion and the remaining 52 patients had diffuse disease. Eight out of 53 patients with focal lesion were reported to have diffuse disease on their pre-operative ¹⁸F-DOPA-PET/CT scan. The location of the eight missed lesions was head (3), body (2) and tail (3) which showed a homo/heterogeneous tracer uptake throughout the pancreas. Thus the sensitivity of ¹⁸F-DOPA-PET/CT scan in diagnosing a focal lesion was 85% based on this study. Two out of 52 patients with diffuse disease were reported to have focal lesion on their pre-operative ¹⁸F-DOPA-PET/CT scan with a specificity of 96%. The positive predictive value of the study was 96% with 45 out of 47 patients having a true focal lesion. The authors concluded that the sensitivity and specificity of the ¹⁸F-DOPA-PET/CT scan varies based on the location of the lesion and the experience of the radiologists^[48].

A meta-analysis was performed and published recently by Yang J and his colleagues reviewing the diagnostic role of ¹⁸F-DOPA PET and ¹⁸F-DOPA PET/CT imaging in CHI in 10 studies involving 181 children. The pooled sensitivity and the specificity in detecting focal CHI using ¹⁸F DOPA PET and PET/CT was reported to be 88% (95%CI: 80%-94%) and 79% (95%CI: 69%-87%) respectively on a per-patient-based analysis in this systematic review. The area under the summary receiver operating characteristic curve (SROC) was estimated to be 0.92% suggesting that ¹⁸F-DOPA PET and PET/CT imaging are accurate tools for distinguishing focal diagnosing CHI, although there is a minimal risk of both false positive and false negative results. The authors concluded that ¹⁸F-DOPA PET is very helpful in differentiating between focal and diffuse lesions, and should be the first investigation of choice when the genetic test results are inconclusive and ¹⁸F-DOPA PET/CT is very helpful in localising the lesion and thereby improving the treatment outcome in focal CHI^[27].

Blomberg *et al*^[38] conducted a systematic review and meta-analysis recently to quantify the diagnostic performance of pancreatic venous sampling (PVS), selective pancreatic arterial calcium stimulation with hepatic venous sampling (ASVS) and ¹⁸F-DOPA-PET/CT in diagnosing and localising focal CH. They reported that ¹⁸F-DOPA-PET/CT is superior in distinguishing focal from diffuse CH with a summary diagnostic odds ratio (DOR) of 73.2 when compared to PVS (summary DOR 23.5) and ASVS (summary DOR, 4.3). Also the pooled accuracy for localising a focal lesion by ¹⁸F-DOPA-PET/CT is higher (0.82) when compared to PVS (0.76) and ASVS

(0.64). Thus this review concluded that ¹⁸F-DOPA-PET/CT is superior in diagnosing and localising focal CHI lesion in patients requiring surgery albeit the limitation of the review is the inclusion of small sample sizes and high probability of bias leading to the overestimation of diagnostic accuracy^[38].

ECTOPIC PANCREAS AND THE ROLE OF ¹⁸F-DOPA-PET/CT

The pancreas begins to develop from the distal end of the foregut endoderm during the fourth week when both the dorsal and ventral pancreatic buds grow into the mesogastrium^[49]. Thus the pancreatic acinar and the islet cells are derived from the endodermal cells lining the upper and duodenal region of the foregut^[50]. During the course of this development an ectopic pancreatic tissue may occur in the stomach, duodenum, jejunum, ileum and rarely in Meckel's diverticulum, appendix, biliary tract or lungs^[49].

There have been reports of ectopic pancreatic tissue causing CHI in both adults and children. We reported a child with persistent and severe hyperinsulinaemic hypoglycaemia (HH) despite undergoing three pancreatectomies with a choledochoduodenostomy and a cholecystectomy. An ¹⁸F-DOPA-PET/CT scan localised the ectopic lesion in the vicinity of the former head of pancreas. The same lesion was found to be localized near the duodenum, either in the duodenal wall or cavity on the magnetic resonance scan (MRI). He is subsequently managed medically^[33].

Peranteau *et al*^[51] in 2007 reported another patient with persistent hypoglycaemia despite undergoing a near-total pancreatectomy. A subsequent ¹⁸F-DOPA-PET/CT scan demonstrated one focus in the remnant pancreatic head and 3 in the abdomen. The lesion in the pancreatic remnant was removed completing a total pancreatectomy and further abdominal exploration revealed 4 pancreatic ectopic rests in the jejunum. The lesions were surgically removed and the histopathology confirmed focal islet cell hyperplasia in all the lesions. This patient required insulin therapy for a short term post operatively.

In both of these patients ¹⁸F-DOPA-PET/CT scan was performed post near total pancreatectomy with the persistence of hypoglycaemic symptoms. However a preoperative localisation of the focal lesions would have led to the removal of local and ectopic lesions and preservation of the rest of the pancreas. Thus the use of ¹⁸F-DOPA-PET/CT scan in the management of CHI is justified in identification of both focal lesions within the pancreas and ectopic pancreatic tissue^[51].

A standardised protocol for the use of ¹⁸F-DOPA-PET/CT was derived in 2005 and advocated to achieve maximum acquisition with minimum radiation. This guideline was derived based on the survey conducted in 2005 reviewing the experience of all the PET centres. The result of the survey showed that ¹⁸F-DOPA-PET/CT has 94% sensitivity and 100% specificity. Thus pre-

operative performance of ¹⁸F-DOPA-PET/CT has been proposed as the most accurate way of localising the focus enabling limited resection and thereby preventing the risk of iatrogenic diabetes^[14]. Studies recommended performing ¹⁸F-DOPA/CT studies only in tertiary endocrine centre equipped with necessary expertise to perform and interpret the results^[14].

CONCLUSION

We conclude that ¹⁸F-DOPA-PET/CT is a safe, non-invasive and the most preferred investigation of choice (1) to distinguish between the focal and diffuse forms of CHI; and (2) to enable accurate localisation and enucleation of the focal lesion preventing the risk of developing iatrogenic diabetes mellitus and pancreatic insufficiency. However a multi-disciplinary team (MDT) approach is essential and has to be undertaken in a tertiary centre built-in with necessary expertise for the successful interpretation and management of CHI patients.

REFERENCES

- 1 **Arnoux JB**, Verkarre V, Saint-Martin C, Montravers F, Brassier A, Valayannopoulos V, Brunelle F, Fournet JC, Robert JJ, Aigrain Y, Bellanné-Chantelot C, de Lonlay P. Congenital hyperinsulinism: current trends in diagnosis and therapy. *Orphanet J Rare Dis* 2011; **6**: 63 [PMID: 21967988 DOI: 10.1186/1750-1172-6-63]
- 2 **Rahier J**, Guiot Y, Sempoux C. Persistent hyperinsulinaemic hypoglycaemia of infancy: a heterogeneous syndrome unrelated to nesidioblastosis. *Arch Dis Child Fetal Neonatal Ed* 2000; **82**: F108-F112 [PMID: 10685982]
- 3 **Yap F**, Högl W, Vora A, Halliday R, Ambler G. Severe transient hyperinsulinaemic hypoglycaemia: two neonates without predisposing factors and a review of the literature. *Eur J Pediatr* 2004; **163**: 38-41 [PMID: 14586649 DOI: 10.1007/s00431-003-1328-2]
- 4 **Fafoula O**, Alkhayyat H, Hussain K. Prolonged hyperinsulinaemic hypoglycaemia in newborns with intrauterine growth retardation. *Arch Dis Child Fetal Neonatal Ed* 2006; **91**: F467 [PMID: 17056857 DOI: 10.1136/adc.2006.095919]
- 5 **Ashcroft FM**, Harrison DE, Ashcroft SJ. Glucose induces closure of single potassium channels in isolated rat pancreatic beta-cells. *Nature* 1984; **312**: 446-448 [PMID: 6095103]
- 6 **Thomas PM**, Cote GJ, Wohllk N, Haddad B, Mathew PM, Rabl W, Aguilar-Bryan L, Gagel RF, Bryan J. Mutations in the sulfonylurea receptor gene in familial persistent hyperinsulinemic hypoglycemia of infancy. *Science* 1995; **268**: 426-429 [PMID: 7716548 DOI: 10.1126/science.7716548]
- 7 **de Lonlay P**, Fournet JC, Rahier J, Gross-Morand MS, Poggi-Travert F, Foussier V, Bonnefont JP, Brusset MC, Brunelle F, Robert JJ, Nihoul-Fékété C, Saudubray JM, Junien C. Somatic deletion of the imprinted 11p15 region in sporadic persistent hyperinsulinemic hypoglycemia of infancy is specific of focal adenomatous hyperplasia and endorses partial pancreatectomy. *J Clin Invest* 1997; **100**: 802-807 [PMID: 9259578]
- 8 **Flanagan SE**, Clauin S, Bellanné-Chantelot C, de Lonlay P, Harries LW, Gloyn AL, Ellard S. Update of mutations in the genes encoding the pancreatic beta-cell K(ATP) channel subunits Kir6.2 (KCNJ11) and sulfonylurea receptor 1 (ABCC8) in diabetes mellitus and hyperinsulinism. *Hum Mutat* 2009; **30**: 170-180 [PMID: 18767144 DOI: 10.1002/humu.20838]
- 9 **Kapoor RR**, Flanagan SE, James C, Shield J, Ellard S, Hussain K. Hyperinsulinaemic hypoglycaemia. *Arch Dis Child* 2009; **94**: 450-457 [PMID: 19193661 DOI: 10.1136/adc.2008.148171]
- 10 **Goossens A**, Gepts W, Saudubray JM, Bonnefont JP, Nihoul-Fekete PU, Klöppel G. Diffuse and focal nesidioblastosis. A clinicopathological study of 24 patients with persistent neonatal hyperinsulinemic hypoglycemia. *Am J Surg Pathol* 1989; **13**: 766-775 [PMID: 2669541]
- 11 **Klöppel G**, Reinecke-Lüthge A, Koschoreck F. Focal and Diffuse Beta Cell Changes in Persistent Hyperinsulinemic Hypoglycemia of Infancy. *Endocr Pathol* 1999; **10**: 299-304 [PMID: 12114766]
- 12 **Ismail D**, Kapoor RR, Smith VV, Ashworth M, Blankenstein O, Pierro A, Flanagan SE, Ellard S, Hussain K. The heterogeneity of focal forms of congenital hyperinsulinism. *J Clin Endocrinol Metab* 2012; **97**: E94-E99 [PMID: 22031516 DOI: 10.1210/jc.2011-1628]
- 13 **Ribeiro MJ**, De Lonlay P, Delzescaux T, Boddaert N, Jaubert F, Bourgeois S, Dollé F, Nihoul-Fékété C, Syrota A, Brunelle F. Characterization of hyperinsulinism in infancy assessed with PET and 18F-fluoro-L-DOPA. *J Nucl Med* 2005; **46**: 560-566 [PMID: 15809476]
- 14 **Mohnike K**, Blankenstein O, Christesen HT, De Lonlay J, Hussain K, Koopmans KP, Minn H, Mohnike W, Mutair A, Otonkoski T, Rahier J, Ribeiro M, Schoenle E, Fékété CN. Proposal for a standardized protocol for 18F-DOPA-PET (PET/CT) in congenital hyperinsulinism. *Horm Res* 2006; **66**: 40-42 [PMID: 16710094 DOI: 10.1159/000093471]
- 15 **Callier S**, Snapyan M, Le Crom S, Prou D, Vincent JD, Vernier P. Evolution and cell biology of dopamine receptors in vertebrates. *Biol Cell* 2003; **95**: 489-502 [PMID: 14597267 DOI: 10.1016/S0248-4900(03)00089-3]
- 16 **Rubí B**, Ljubicic S, Pournourmohammadi S, Carobbio S, Armanet M, Bartley C, Maechler P. Dopamine D2-like receptors are expressed in pancreatic beta cells and mediate inhibition of insulin secretion. *J Biol Chem* 2005; **280**: 36824-36832 [PMID: 16129680 DOI: 10.1074/jbc.M505560200]
- 17 **Ustione A**, Piston DW. Dopamine synthesis and D3 receptor activation in pancreatic β -cells regulates insulin secretion and intracellular [Ca(2+)] oscillations. *Mol Endocrinol* 2012; **26**: 1928-1940 [PMID: 22918877 DOI: 10.1210/me.2012-1226]
- 18 **Ericson LE**, Håkanson R, Lundquist I. Accumulation of dopamine in mouse pancreatic B-cells following injection of L-DOPA. Localization to secretory granules and inhibition of insulin secretion. *Diabetologia* 1977; **13**: 117-124 [PMID: 404204 DOI: 10.1007/BF00745138]
- 19 **Simpson N**, Maffei A, Freeby M, Burroughs S, Freyberg Z, Javitch J, Leibel RL, Harris PE. Dopamine-mediated autocrine inhibitory circuit regulating human insulin secretion in vitro. *Mol Endocrinol* 2012; **26**: 1757-1772 [PMID: 22915827 DOI: 10.1210/me.2012-1101]
- 20 **Lindström P**. Aromatic-L-amino-acid decarboxylase activity in mouse pancreatic islets. *Biochim Biophys Acta* 1986; **884**: 276-281 [PMID: 3533158]
- 21 **Hardy OT**, Hernandez-Pampaloni M, Saffer JR, Suchi M, Ruchelli E, Zhuang H, Ganguly A, Freifelder R, Adzick NS, Alavi A, Stanley CA. Diagnosis and localization of focal congenital hyperinsulinism by 18F-fluorodopa PET scan. *J Pediatr* 2007; **150**: 140-145 [PMID: 17236890]
- 22 **Barthlen W**, Blankenstein O, Mau H, Koch M, Höhne C, Mohnike W, Eberhard T, Fuechtner F, Lorenz-Depiereux B, Mohnike K. Evaluation of [18F]fluoro-L-DOPA positron emission tomography-computed tomography for surgery in focal congenital hyperinsulinism. *J Clin Endocrinol Metab* 2008; **93**: 869-875 [PMID: 18073294 DOI: 10.1210/jc.2007-2036]
- 23 **de Lonlay P**, Simon-Carre A, Ribeiro MJ, Boddaert N, Giurgea I, Laborde K, Bellanné-Chantelot C, Verkarre V, Polak M, Rahier J, Syrota A, Seidenwurm D, Nihoul-Fékété C, Robert JJ, Brunelle F, Jaubert F. Congenital hyperinsulinism: pancreatic [18F]fluoro-L-dihydroxyphenylalanine (DOPA) positron emission tomography and immunohistochemistry study of DOPA decarboxylase and insulin secretion. *J Clin Endocrinol*

- Metab* 2006; **91**: 933-940 [PMID: 16403819 DOI: 10.1210/jc.2005-1713]
- 24 **Jager PL**, Chirakal R, Marriott CJ, Brouwers AH, Koopmans KP, Gulenchyn KY. 6-L-18F-fluorodihydroxyphenylalanine PET in neuroendocrine tumors: basic aspects and emerging clinical applications. *J Nucl Med* 2008; **49**: 573-586 [PMID: 18344441 DOI: 10.2967/jnumed.107.045708]
 - 25 **Koopmans KP**, Neels ON, Kema IP, Elsinga PH, Links TP, de Vries EG, Jager PL. Molecular imaging in neuroendocrine tumors: molecular uptake mechanisms and clinical results. *Crit Rev Oncol Hematol* 2009; **71**: 199-213 [PMID: 19362010 DOI: 10.1016/j.critrevonc.2009.02.009]
 - 26 **Meintjes M**, Endozo R, Dickson J, Erlandsson K, Hussain K, Townsend C, Menezes L, Bomanji J. 18F-DOPA PET and enhanced CT imaging for congenital hyperinsulinism: initial UK experience from a technologist's perspective. *Nucl Med Commun* 2013; **34**: 601-608 [PMID: 23571817 DOI: 10.1097/MNM.0b013e32836069d0]
 - 27 **Yang J**, Hao R, Zhu X. Diagnostic role of 18F-dihydroxyphenylalanine positron emission tomography in patients with congenital hyperinsulinism: a meta-analysis. *Nucl Med Commun* 2013; **34**: 347-353 [PMID: 23376859 DOI: 10.1097/MNM.0b013e32835e6ac6]
 - 28 **Brunelle F**, Negre V, Barth MO, Fekete CN, Czernichow P, Saudubray JM, Kuntz F, Tach T, Lallemand D. Pancreatic venous samplings in infants and children with primary hyperinsulinism. *Pediatr Radiol* 1989; **19**: 100-103 [PMID: 2537942 DOI: 10.1007/BF02387895]
 - 29 **Dubois J**, Brunelle F, Touati G, Sebag G, Nuttin C, Thach T, Nikoul-Fekete C, Rahier J, Saudubray JM. Hyperinsulinism in children: diagnostic value of pancreatic venous sampling correlated with clinical, pathological and surgical outcome in 25 cases. *Pediatr Radiol* 1995; **25**: 512-516 [PMID: 8545179]
 - 30 **Chigot V**, De Lonlay P, Nassogne MC, Laborde K, Delagne V, Fournet JC, Nihoul-Fékété C, Saudubray JM, Brunelle F. Pancreatic arterial calcium stimulation in the diagnosis and localisation of persistent hyperinsulinemic hypoglycaemia of infancy. *Pediatr Radiol* 2001; **31**: 650-655 [PMID: 11512008 DOI: 10.1007/s0024710310650]
 - 31 **Abernethy LJ**, Davidson DC, Lamont GL, Shepherd RM, Dunne MJ. Intra-arterial calcium stimulation test in the investigation of hyperinsulinaemic hypoglycaemia. *Arch Dis Child* 1998; **78**: 359-363 [PMID: 9623401]
 - 32 **Stanley CA**, Thornton PS, Ganguly A, MacMullen C, Underwood P, Bhatia P, Steinkrauss L, Wanner L, Kaye R, Ruchelli E, Suchi M, Adzick NS. Preoperative evaluation of infants with focal or diffuse congenital hyperinsulinism by intravenous acute insulin response tests and selective pancreatic arterial calcium stimulation. *J Clin Endocrinol Metab* 2004; **89**: 288-296 [PMID: 14715863 DOI: 10.1210/jc.2003-030965]
 - 33 **Hussain K**, Seppänen M, Näntö-Salonen K, Adzick NS, Stanley CA, Thornton P, Minn H. The diagnosis of ectopic focal hyperinsulinism of infancy with [18F]-dopa positron emission tomography. *J Clin Endocrinol Metab* 2006; **91**: 2839-2842 [PMID: 16684819 DOI: 10.1210/jc.2006-0455]
 - 34 **Huopio H**, Jääskeläinen J, Komulainen J, Miettinen R, Kärkkäinen P, Laakso M, Tapanainen P, Voutilainen R, Otonkoski T. Acute insulin response tests for the differential diagnosis of congenital hyperinsulinism. *J Clin Endocrinol Metab* 2002; **87**: 4502-4507 [PMID: 12364426 DOI: 10.1210/jc.2002-020378]
 - 35 **Giurgea I**, Laborde K, Touati G, Bellanné-Chantelot C, Nassogne MC, Sempoux C, Jaubert F, Khoa N, Chigot V, Rahier J, Brunelle F, Nihoul-Fékété C, Dunne MJ, Stanley C, Saudubray JM, Robert JJ, de Lonlay P. Acute insulin responses to calcium and tolbutamide do not differentiate focal from diffuse congenital hyperinsulinism. *J Clin Endocrinol Metab* 2004; **89**: 925-929 [PMID: 14764815 DOI: 10.1210/jc.2003-030941]
 - 36 **Otonkoski T**, Näntö-Salonen K, Seppänen M, Veijola R, Huopio H, Hussain K, Tapanainen P, Eskola O, Parkkola R, Ekström K, Guiot Y, Rahier J, Laakso M, Rintala R, Nuutila P, Minn H. Noninvasive diagnosis of focal hyperinsulinism of infancy with [18F]-DOPA positron emission tomography. *Diabetes* 2006; **55**: 13-18 [PMID: 16380471]
 - 37 **Mohnike K**, Blankenstein O, Minn H, Mohnike W, Fuchtnner F, Otonkoski T. [18F]-DOPA positron emission tomography for preoperative localization in congenital hyperinsulinism. *Horm Res* 2008; **70**: 65-72 [PMID: 18547951 DOI: 10.1159/000137655]
 - 38 **Blomberg BA**, Moghbel MC, Saboury B, Stanley CA, Alavi A. The value of radiologic interventions and (18)F-DOPA PET in diagnosing and localizing focal congenital hyperinsulinism: systematic review and meta-analysis. *Mol Imaging Biol* 2013; **15**: 97-105 [PMID: 22752652 DOI: 10.1007/s11307-012-0572-0]
 - 39 **Beheshti M**, Pöcher S, Vali R, Waldenberger P, Broinger G, Nader M, Kohlfürst S, Pirich C, Dralle H, Langsteger W. The value of 18F-DOPA PET-CT in patients with medullary thyroid carcinoma: comparison with 18F-FDG PET-CT. *Eur Radiol* 2009; **19**: 1425-1434 [PMID: 19156423 DOI: 10.1007/s00330-008-1280-7]
 - 40 **Ribeiro MJ**, Boddaert N, Bellanné-Chantelot C, Bourgeois S, Valayannopoulos V, Delzescaux T, Jaubert F, Nihoul-Fékété C, Brunelle F, De Lonlay P. The added value of [18F]fluoro-L-DOPA PET in the diagnosis of hyperinsulinism of infancy: a retrospective study involving 49 children. *Eur J Nucl Med Mol Imaging* 2007; **34**: 2120-2128 [PMID: 17661030 DOI: 10.1007/s00259-007-0498-y]
 - 41 **Arbizu Lostao J**, Fernández-Marmiesse A, Garrastachu Zumarrán P, Martino Casado E, Azcona San Julián C, Caracedo A, Richter Echevarría JA. [18F]-fluoro-L-DOPA PET-CT imaging combined with genetic analysis for optimal classification and treatment in a child with severe congenital hyperinsulinism. *An Pediatr (Barc)* 2008; **68**: 481-485 [PMID: 18447993]
 - 42 **Cherubini V**, Bagalini LS, Ianilli A, Marigliano M, Biagioni M, Carnielli V, Iasonni V, Berbellini A, Hussain K, Gabrielli O. Rapid genetic analysis, imaging with 18F-DOPA-PET/CT scan and laparoscopic surgery in congenital hyperinsulinism. *J Pediatr Endocrinol Metab* 2010; **23**: 171-177 [PMID: 20432820]
 - 43 **Yorifuji T**, Hosokawa Y, Fujimaru R, Kawakita R, Doi H, Matsumoto T, Nishibori H, Masue M. Lasting 18F-DOPA PET uptake after clinical remission of the focal form of congenital hyperinsulinism. *Horm Res Paediatr* 2011; **76**: 286-290 [PMID: 21912073 DOI: 10.1159/000328056]
 - 44 **Zani A**, Nah SA, Ron O, Totonelli G, Ismail D, Smith VV, Ashworth M, Blankenstein O, Mohnike W, De Coppi P, Eaton S, Hussain K, Pierro A. The predictive value of preoperative fluorine-18-L-3,4-dihydroxyphenylalanine positron emission tomography-computed tomography scans in children with congenital hyperinsulinism of infancy. *J Pediatr Surg* 2011; **46**: 204-208 [PMID: 21238668 DOI: 10.1016/j.jpedsurg.2010.09.093]
 - 45 **Masue M**, Nishibori H, Fukuyama S, Yoshizawa A, Okamoto S, Doi R, Uemoto S, Tokumi T, Kasai T, Yorifuji T. Diagnostic accuracy of [18F]-fluoro-L-dihydroxyphenylalanine positron emission tomography scan for persistent congenital hyperinsulinism in Japan. *Clin Endocrinol (Oxf)* 2011; **75**: 342-346 [PMID: 21521340 DOI: 10.1111/j.1365-2265.2011.04072.x]
 - 46 **Nestorowicz A**, Wilson BA, Schoor KP, Inoue H, Glaser B, Landau H, Stanley CA, Thornton PS, Clement JP, Bryan J, Aguilar-Bryan L, Permutt MA. Mutations in the sulfonylurea receptor gene are associated with familial hyperinsulinism in Ashkenazi Jews. *Hum Mol Genet* 1996; **5**: 1813-1822 [PMID: 8923011 DOI: 10.1093/hmg/5.11.1813]
 - 47 **Giurgea I**, Sempoux C, Bellanné-Chantelot C, Ribeiro M, Hubert L, Boddaert N, Saudubray JM, Robert JJ, Brunelle F, Rahier J, Jaubert F, Nihoul-Fékété C, de Lonlay P. The Knudson's two-hit model and timing of somatic mutation may account for the phenotypic diversity of focal congenital

- hyperinsulinism. *J Clin Endocrinol Metab* 2006; **91**: 4118-4123 [PMID: 16882742 DOI: 10.1210/jc.2006-0397]
- 48 **Laje P**, States LJ, Zhuang H, Becker SA, Palladino AA, Stanley CA, Adzick NS. Accuracy of PET/CT Scan in the diagnosis of the focal form of congenital hyperinsulinism. *J Pediatr Surg* 2013; **48**: 388-393 [PMID: 23414871 DOI: 10.1016/j.jpedsurg.2012.11.025]
- 49 **Cagirici U**, Ozbaran M, Veral A, Posacioglu H. Ectopic mediastinal pancreas. *Eur J Cardiothorac Surg* 2001; **19**: 514-515 [PMID: 11306324]
- 50 **Edlund H**. Developmental biology of the pancreas. *Diabetes* 2001; **50** Suppl 1: S5-S9 [PMID: 11272202]
- 51 **Peranteau WH**, Bathaai SM, Pawel B, Hardy O, Alavi A, Stanley CA, Adzick NS. Multiple ectopic lesions of focal islet adenomatosis identified by positron emission tomography scan in an infant with congenital hyperinsulinism. *J Pediatr Surg* 2007; **42**: 188-192 [PMID: 17208563 DOI: 10.1016/j.jpedsurg.2006.09.046]

P- Reviewers: Das UN, Shyng SL **S- Editor:** Wen LL
L- Editor: A **E- Editor:** Zhang DN



FDG-PET/CT response evaluation during EGFR-TKI treatment in patients with NSCLC

Matthijs H van Gool, Tjeerd S Aukema, Koen J Hartemink, Renato A Valdés Olmos, Harm van Tinteren, Houke M Klomp

Matthijs H van Gool, Koen J Hartemink, Houke M Klomp, Department of Surgical Oncology, The Netherlands Cancer Institute, Antoni van Leeuwenhoek Hospital, 1066 CX Amsterdam, The Netherlands

Tjeerd S Aukema, Renato A Valdés Olmos, Department of Nuclear Medicine, The Netherlands Cancer Institute, Antoni van Leeuwenhoek Hospital, 1066 CX Amsterdam, The Netherlands

Harm van Tinteren, Department of Biometrics, The Netherlands Cancer Institute, Antoni van Leeuwenhoek Hospital, 1066 CX Amsterdam, The Netherlands

Author contributions: All authors contributed equally on this manuscript in accordance with the standard proposed by the International Committee of Medical Journal Editors.

Correspondence to: Houke M Klomp, MD, PhD, Department of Surgical Oncology, The Netherlands Cancer Institute, Antoni van Leeuwenhoek Hospital, Plesmanlaan 121, 1066 CX Amsterdam, The Netherlands. h.klomp@nki.nl

Telephone: +31-20-5122554 Fax: +31-20-5129111

Received: January 23, 2014 Revised: April 28, 2014

Accepted: May 16, 2014

Published online: March 28, 2015

Abstract

Over recent years, [18F]-fluorodeoxyglucose positron emission tomography acquired together with low dose computed tomography (FDG-PET/CT) has proven its role as a staging modality in patients with non-small cell lung cancer (NSCLC). The purpose of this review was to present the evidence to use FDG-PET/CT for response evaluation in patients with NSCLC, treated with epidermal growth factor receptor (EGFR)-tyrosine kinase inhibitors (TKI). All published articles from 1 November 2003 to 1 November 2013 reporting on 18F-FDG-PET response evaluation during EGFR-TKI treatment in patients with NSCLC were collected. In total 7 studies, including data of 210 patients were eligible for analyses. Our report shows that FDG-PET/CT response

during EGFR-TKI therapy has potential in targeted treatment for NSCLC. FDG-PET/CT response is associated with clinical and radiologic response and with survival. Furthermore FDG-PET/CT response monitoring can be performed as early as 1-2 wk after initiation of EGFR-TKI treatment. Patients with substantial decrease of metabolic activity during EGFR-TKI treatment will probably benefit from continued treatment. If metabolic response does not occur within the first weeks of EGFR-TKI treatment, patients may be spared (further) unnecessary toxicity of ineffective treatment. Refining FDG-PET response criteria may help the clinician to decide on continuation or discontinuation of targeted treatment.

© 2015 Baishideng Publishing Group Inc. All rights reserved.

Key words: Non-small cell lung cancer; Epidermal growth factor receptor-tyrosine kinase inhibitors therapy; Positron emission tomography-computed tomography; Computed tomography; Response monitoring

Core tip: Our report shows that response monitoring using [18F]-fluorodeoxyglucose positron emission tomography (FDG-PET) acquired together with low dose computed tomography has potential in targeted treatment for non-small cell lung cancer and can be performed as early as 1-2 wk after initiation of treatment. Patients with substantial decrease of metabolic activity during epidermal growth factor receptor-tyrosine kinase inhibitors treatment will probably benefit from continued treatment. Refining FDG-PET response criteria may help the clinician to decide on continuation or discontinuation of targeted treatment.

Original sources: van Gool MH, Aukema TS, Hartemink KJ, Valdés Olmos RA, van Tinteren H, Klomp HM. FDG-PET/CT response evaluation during EGFR-TKI treatment in patients with

NSCLC. *World J Radiol* 2014; 6(7): 392-398 Available from: URL: <http://www.wjgnet.com/1949-8470/full/v6/i7/392.htm> DOI: <http://dx.doi.org/10.4329/wjr.v6.i7.392>

INTRODUCTION

Over recent years, [18F]-fluorodeoxyglucose positron emission tomography acquired together with low dose computed tomography (FDG-PET/CT) has proven its role as a staging modality in patients with non-small cell lung cancer (NSCLC)^[1-3]. In addition, *FDG-PET/CT* has been evaluated as a method to monitor tumor response to chemotherapy. Several studies demonstrated that FDG-PET/CT is able to predict response to treatment in various malignancies, *i.e.*, breast cancer^[4,5], malignant lymphoma^[6,7] and colorectal cancer^[8]. Diagnostic CT has been the clinical standard for response evaluation in NSCLC. There is an ongoing discussion on the performance of FDG-PET/CT as compared to CT^[9-11].

With advances in molecular research, molecular-targeted agents such as epidermal growth factor receptor (EGFR)-tyrosine kinase inhibitors (TKI) have emerged for the treatment of (advanced) NSCLC. EGFR-TKIs are able to induce swift responses in selected groups of NSCLC patients and TKI treatment is associated with survival benefit when given as second-line treatment in unselected patients^[12]. It blocks the tyrosine kinase domain of the EGFR, thereby inhibiting downstream signaling pathways involved in cell proliferation, angiogenesis, invasion and metastasis and prevention of apoptosis. They can be orally administered, have a relatively favorable toxicity profile, and are registered for the treatment of patients with advanced (chemotherapy-refractory) NSCLC^[13].

The probability of response to EGFR-TKIs is considerably higher in patients with EGFR-mutated tumors^[14-16]. However, prediction of response is suboptimal by mutation analysis only^[17,18]. It is known, that several patients without apparent sensitizing EGFR mutations do benefit from erlotinib therapy^[19]. This may be due to heterogeneity within the tumor or the limitations of biopsy analysis not always showing relevant mutations. On the other hand, patients who do not respond to EGFR-TKIs, despite the presence of activating mutations, could be spared unnecessary toxicity and costs. Therefore early decision making as to the effect of treatment is essential.

In this perspective, we present the evidence to use FDG-PET/CT for response evaluation in patients with NSCLC, treated with EGFR-TKI.

SEARCH

Study eligibility and identification

We performed a systematic computerized search of the of PubMed and Medline databases (last search: 01 November 2013) and the Cochrane library (Issue 10, 31 October 2013) to identify all published articles from 01

November 2003 to 01 November 2013 reporting on 18F-FDG-PET response evaluation during EGFR-TKI treatment in patients with NSCLC, using the algorithm: [(Non-Small Cell Lung Carcinoma OR NSCLC) AND (Epidermal Growth Factor Receptor OR EGFR) AND (Diagnostic Imaging) AND (18-FDG PET)]. We also hand-searched journals known to publish data relevant to our search, the reference lists of all articles we recovered and those of relevant review articles were also cross-referenced. Experts in the field were contacted to broaden our yield of potentially eligible articles. Whenever several reports pertained to overlapping groups of patients, we retained only the report with the largest number of events or largest patient population (where appropriate) to avoid duplication of information.

Inclusion and exclusion criteria

The inclusion criteria were as follows: (1) histologically proven NSCLC; (2) use of 18F-FDG as a tracer; (3) use of an 18F-FDG-PET/CT scanning apparatus in humans; (4) use of EGFR-TKI; and (5) articles reported in English.

Studies examining EGFR-targeted agents in combination with other agents were considered eligible, as were single agent anti-EGFR studies, whether they were single arm non-randomised studies, phase II or III randomised studies, prospective studies, or retrospective studies. Abstracts, meeting proceedings and case reports, defined as studies reporting on fewer than five patients, were excluded. When datasets were incomplete for required data, corresponding authors were contacted; however, no additional data were obtained by this process. Our literature search was limited to published studies.

Data extraction

The following information was manually extracted from each recovered article: first author, journal and year of publication, number of patients screened, EGFR mutational rate, stage of disease correlations with clinicopathologic and demographic data (*i.e.*, smoking status, history, gender, histologic type), and also for data to treatment outcome [*i.e.*, CR, PR CR + PR, stable disease (SD), progressive disease (PD), and nonassessable patients] with the TKIs gefitinib and erlotinib when administered as single agent, *i.e.*, monotherapy TKI. No stratification has been made according to TKI with respect to response data. Information recorded about each recovered reference is listed in Table 1. Data extraction was done independently by two of the authors (MG and TA) and discrepancies were resolved by consensus including a third author (HK).

RESEARCH

During the search period, a total of 20 articles of potential interest have been screened for 18F-FDG-PET/CT response evaluation during EGFR-TKI treatment in patients with NSCLC. Of these, 13 were excluded because

Table 1 Patient characteristics *n*(%)

Ref.	Year of publication	<i>n</i>	Age, yr	M/F	Study type	Study protocol FDG response	Stage of disease	Histology	EGFR Selection
Riely <i>et al</i> ^[20]	2007	13	56	2/11	Prospective	21 d after stopping and 21 d after restarting	IV	Adenocarcinoma 11 (85) Other (including NOS) 2 (15)	Only EGFR mutated tumors
Aukema <i>et al</i> ^[21]	2010	23	63	8/15	Prospective	After 7 d	I - III	Adenocarcinoma 17 (73) Other 6 (26)	No selection
Mileshkin <i>et al</i> ^[11]	2011	51	61	30/21	Prospective	After 14 d and 56 d	III - IV	Adenocarcinoma 37 (72) Squamous cell carcinoma 8 (16) Large-cell carcinoma 1 (2) Other (including NOS) 5 (10)	No selection
Zander <i>et al</i> ^[22]	2011	34	61	17/17	Prospective	After 7 d and 42 d	IV	Adenocarcinoma 26 (76) Squamous cell carcinoma 4 (12) Large cell carcinoma 1 (3) Bronchioalveolar carcinoma 3 (9)	No selection
Benz <i>et al</i> ^[23]	2011	22	64	6/16	Prospective	After 14 d and 78 d	III - IV	Adenocarcinoma 17 (78) Squamous cell carcinoma 3 (14) Other (including NOS) 1 (4) Large cell carcinoma 1 (4)	No selection
O'Brien <i>et al</i> ^[24]	2012	47	63	18/29	Prospective	After 42 d	III - IV	Adenocarcinoma 28 (60) Squamous cell carcinoma 6 (13) Bronchioalveolar carcinoma 7 (14) Other (including NOS) 6 (13)	No selection
Takahashi <i>et al</i> ^[25]	2012	20	69	5/15	Prospective	After 2 d and 28 d	III - IV	Adenocarcinoma 20 (100)	No selection

FDG: [18F]-fluorodeoxyglucose; EGFR: Epidermal growth factor receptor.

they did not meet the defined inclusion criteria. In total, data of 210 patients were eligible for analyses^[11,20-25]. The characteristics of eligible studies are summarised in Table 1.

FDG-PET/CT and response

The majority of studies used European Organization for Research and Treatment of Cancer (EORTC) criteria to determine response^[26] (Tables 2 and 3). Cut-off values to determine response varied from 15% to 30% change in SUVmax between baseline and response FDG-PET/CT scan. Median cut-off value was 15%. Time between initiation of EGFR-TKI therapy and response FDG-PET/CT scan varied from 2-78 d^[11,14,20-25].

FDG-PET/CT vs diagnostic CT

Four studies analysed FDG-PET and CT according to Response Evaluation Criteria in Solid Tumors (RECIST) criteria for response (Tables 2 and 3). There was a large variety in days between initiation of EGFR-TKI therapy and response FDG-PET/CT scan (2-56 d) and response CT scan (28-84 d). However all studies showed that FDG-PET response correlated with CT response. The majority of patients with response on FDG-PET/CT scan also showed response on CT-scan. In addition, zero patients with progressive disease on FDG-PET/CT scan had a response on CT-scan^[11,14,22,24,25].

FDG-PET/CT and progression free survival

Four studies reported on progression free survival (PFS)^[11,22,23,25] (Tables 2 and 3). In general, patients with metabolic response showed a prolonged progression

free survival varying from 3.0 to 8.7 mo. Mileshkin *et al*^[11] showed that response at FDG-PET/CT on day 14 was associated with improved PFS using EORTC criteria and Wahl *et al*^[27] using Response Criteria in Solid Tumors (PERCIST). In addition Zander *et al*^[22] reported the same association on day 7. Takahashi *et al*^[25] found no significant relation at 2 d using a cut-off value of 30%, however when a cutoff value of 20% was used, metabolic responders had significantly longer PFS compared with metabolic non-responders.

FDG-PET/CT and overall survival

Five studies reported on metabolic response and overall survival (OS)^[11,22-25] (Tables 2 and 3). Metabolic response was associated with improved OS. Both Mileshkin *et al*^[11] and Zander *et al*^[22] reported early FDG-PET/CT response (resp. 14 d, 7 d) to be significantly associated with longer OS. Metabolic response as shown during later FDG-PET/CT evaluation (resp. 56 d, 42 d) was also associated with longer survival, although this trend was not statistically significant. Similarly O'Brien *et al*^[24] reported that responders on FDG-PET/CT scan at 42 d lived longer than patients with metabolic stable disease. Takahashi *et al* did not find significant survival differences between metabolic responders and non-responders.

FDG-PET/CT EGFR

Forty-eight patients (23%) had an EGFR mutant tumor (Table 4). In one study patients were selected based on EGFR mutation. As shown before, patients with an EGFR mutant tumor were more likely to respond to EGFR therapy and thus to have response on FDG-

Table 2 Early [¹⁸F]-fluorodeoxyglucose positron emission tomography acquired together with low dose computed tomography response results < 21 d

Ref.	Year of publication	n	SUV	Response criteria	FDG response time	Cut-off value	FDG response n (%)	FDG response, FDG-PET/CT vs RECIST	PFS	OS
Riely <i>et al</i> ^[20]	2007	13	Max	EORTC	21 d	15%	PR 6 (46) SD 7 (54)			
Aukema <i>et al</i> ^[21]	2010	22	Max	EORTC	7 d	25%	PR 6 (26) SD 16 (70) PD 1 (4)			
Mileshkin <i>et al</i> ^[11]	2011	51	Max	EORTC	14 d	15%	PR 13 (26) SD 17 (33) PD 21 (41)	FDG PR: PR 4 SD 7 PD 2 FDG SD: PR 0 SD 12 PD 5 FDG PD: PR 0 SD 7 PD 14	R 5.5 mo NR 2.5 mo	R 11.6 mo NR 7.6 mo
Zander <i>et al</i> ^[22]	2011	34	Peak	EORTC	7 d	30%	PR 8 (24) SD/PD 26 (76)	FDG PR: PR/SD 6 PD 2 FDG SD/PD: PR/SD 5 PD 21	R 7.8 mo NR 1.5 mo	R 16.1mo NR 3.4mo
Benz <i>et al</i> ^[23]	2011	22	Max	PRECIST	14 d	30%	PR 6 (27) SD 7 (32) PD 9 (41)		R 11.1 mo NR 2.4 mo	R 16.4 mo NR 14.7 mo
Takahashi <i>et al</i> ^[25]	2012	20	Max	EORTC	2 d	25%	PR 10 (50) SD 8 (40) PD 2 (10)	FDG PR: PR 8 SD 2 PD 0 FDG SD: PR 2 SD 5 PD 1 FDG PD: PR 0 SD 1 PD 1	R 10.4 mo NR 1.7 mo	

FDG: [¹⁸F]-fluorodeoxyglucose positron emission tomography acquired together with low dose computed tomography; RECIST: Response Evaluation Criteria in Solid Tumors; PFS: Progression free survival; EORTC: European Organization for Research and Treatment of Cancer.

Table 3 Late [¹⁸F]-fluorodeoxyglucose positron emission tomography acquired together with low dose computed tomography response > 21 d

Ref.	Year of publication	n	SUV	Response criteria	Cut-off value	FDG response time	FDG Response n (%)	FDG-PET vs RECIST	PFS	OS
Mileshkin <i>et al</i> ^[11]	2011	51	Max	EORTC	15%	56 d	PR 8 (16) SD 12 (23) PD 31 (61)	FDG PR: PR 4 SD 4 PD 0 FDG SD: PR 0 SD 11 PD 1 FDG PD: PR 0 SD 11 PD 20	R 6.5 mo NR 2.7 mo	R 11.9 mo NR 7.6 mo
Zander <i>et al</i> ^[22]	2011	34	Peak	EORTC		42 d	n/a	n/a		
Benz <i>et al</i> ^[23]	2011	22	Max	PRECIST		78 d	n/a	n/a		
O'Brien <i>et al</i> ^[24]	2012	47	Max	EORTC	25%	42 d	PR 15 (32) SD 8 (17) PD 15 (32) NE 9 (19)	FDG PR: PR 11 SD 2 PD 2 FDG SD: PR 0 SD 4 PD 4 FDG PD: PR 0 SD 2 PD 7		
Takahashi <i>et al</i> ^[25]	2012	20	Max	EORTC		28 d	n/a	n/a		

FDG: [¹⁸F]-fluorodeoxyglucose positron emission tomography acquired together with low dose computed tomography; RECIST: Response Evaluation Criteria in Solid Tumors; PFS: Progression free survival; EORTC: European Organization for Research and Treatment of Cancer; n/a: Not applicable.

PET^[11,23,25].

DISCUSSION

This review summarizes the available data regarding the potential of FDG-PET/CT to predict or monitor treatment efficacy and the relation of metabolic data to clinical outcome in NSCLC patients who are treated with EGFR-TKIs. Our report shows that FDG-PET/CT response during EGFR-TKI therapy is associated with clinical and radiologic response and with survival. FDG-PET shows informative results as early as 7-14 d after initiation of treatment.

This report includes a heterogeneous group of NSCLC subtypes. Over time, it has become clear that adenocarcinomas are more likely to respond to EGFR-TKI treatment^[28]. However, histological classification of squamous-cell and adenocarcinoma is challenging^[29]. This

difficulty increases in the preoperative setting where attempts at tumor classification in small diagnostic samples are hampered by the paucity of tumor cells and the absence of tissue architecture^[30]. Although the efficacy of EGFR-TKIs is higher in patients with EGFR-mutated tumors, prediction of response is not optimal by mutation analysis only. It is known, that several patients without sensitizing EGFR mutations do benefit from EGFR-TKI therapy. This may be due to heterogeneity within the tumor and biopsies will not always show relevant mutations^[31]. Tumor response monitoring is of value since unnecessary toxicity and additional cost of administering ineffective treatment can be avoided, especially if monitoring is feasible and informative early during treatment.

For categorization of metabolic response, varying response criteria were used (EORTC, PRECIST). Different cut-off values were used between studies, resulting in suboptimal comparison. However overall, results

Table 4 Epidermal growth factor receptor

Ref.	Year of publication	n	EGFR selection	EGFR mutation (n)	Cut-off value	FDG	PFS
Riely <i>et al</i> ^[20]	2007	13	Only EGFR mutated tumors	8	n/a		
Aukema <i>et al</i> ^[21]	2010	22	No selection	4	25%		
Milishkin <i>et al</i> ^[11]	2011	51	No selection	4	> 15%	EGFR + PR 3 PD 2 SD 0 EGFR - PR SD PD	
Zander <i>et al</i> ^[22]	2011	34	No selection	4			EGFR + 6.4 mo EGFR - 1.6 mo
Benz <i>et al</i> ^[23]	2011	22	No selection	5			
O'Brien <i>et al</i> ^[24]	2012	47	No selection	11			
Takahashi <i>et al</i> ^[25]	2012	20	No selection	12		EGFR+ PR 8 SD 3 PD 1 EGFR- PR SD PD	

EGFR: Epidermal growth factor receptor; FDG: [¹⁸F]-fluorodeoxyglucose positron emission tomography acquired together with low dose computed tomography; PFS: Progression free survival; n/a: Not applicable.

suggest that any significant metabolic response on FDG-PET/CT is associated with radiologic response later on and longer survival. For example, Mileskin *et al*^[11] and Benz *et al*^[23] show similar distributions of response relations using different cut-off values 15% *vs* 30% and different response criteria. As natural variability (repeatability) of FDG-PET is also relevant for implementation of response assessment, lower cut-off values (15%-20%) may increase false positive results for identification of response^[9].

Furthermore there is no consensus regarding the optimal timing in performing FDG-PET/CT after initiation of treatment. Several authors suggest that in advanced NSCLC metabolic response on FDG-PET/CT scan as early as 1-2 wk after chemotherapy can predict progression free survival and overall survival^[17,26-29]. In this review with studies on EGFR-TKIs, Mileskin *et al*^[11] and Zander *et al*^[22] found significant associations of early response (day 14, day 7) with survival data. Other authors report the same trend. However, changing FDG-uptake on PET (early) during treatment may reflect all kinds of tissue reactions, as tumor regression (or progression) but also senescence, fibrosis formation, and inflammatory reactions as macrophage infiltration.

Several authors in this report use RECIST criteria as golden standard for response evaluation. However early diagnostic CT for response evaluation in EGFR-TKI therapy has severe limitations. EGFR-TKI therapy is expected to induce response *via* cytostasis rather than objective morphologic response^[32]. RECIST is further confounded by structural abnormalities, before and after treatment, which may not actually contain tumor^[33]. In this report all early FDG-PET-CT responses were associated with CT responses (according to RECIST), when CT was performed after a period of 28-84 d presuming that morphologic response have taken place^[11,22,24,25].

Presumably, in patients with NSCLC treated with EGFR-TKIs, the potential value of FDG-PET/CT response monitoring is best described by its possibilities of early response identification. If metabolic response does not occur within the first weeks of EGFR-TKI treatment, patients may be spared (further) unnecessary toxic-

ity of ineffective treatment. Furthermore, even disregarding EGFR mutation, metabolic response during EGFR-TKI treatment is associated with favorable (progression free) survival^[11,22-25].

Concluding, our report shows that response monitoring using FDG-PET/CT has potential in targeted treatment for NSCLC and can be performed as early as 1-2 wk after initiation of treatment. Patients with substantial decrease of metabolic activity during EGFR-TKI treatment will probably benefit from continued treatment. Refining FDG-PET response criteria may help the clinician to decide on continuation or discontinuation of targeted treatment.

REFERENCES

- Lardinois D**, Weder W, Hany TF, Kamel EM, Korom S, Seifert B, von Schulthess GK, Steinert HC. Staging of non-small-cell lung cancer with integrated positron-emission tomography and computed tomography. *N Engl J Med* 2003; **348**: 2500-2507 [PMID: 12815135 DOI: 10.1056/NEJMoa022136]
- Antoch G**, Stattaus J, Nemat AT, Marnitz S, Beyer T, Kuehl H, Bockisch A, Debatin JF, Freudenberg LS. Non-small cell lung cancer: dual-modality PET/CT in preoperative staging. *Radiology* 2003; **229**: 526-533 [PMID: 14512512 DOI: 10.1148/radiol.2292021598]
- van Tinteren H**, Smit EF, Hoekstra OS. FDG-PET in addition to conventional work-up in non-small-cell lung cancer. *J Clin Oncol* 2005; **23**: 1591; author reply 1591-1592 [PMID: 15735147 DOI: 10.1200/JCO.2005.05.201]
- Dose SJ**, Bader M, Jenicke L, Hemminger G, Janicke F, Avril N. Early prediction of response to chemotherapy in metastatic breast cancer using sequential 18F-FDG PET. *J Nucl Med* 2005; **46**: 1144-1150
- Smith IC**, Welch AE, Hutcheon AW, Miller ID, Payne S, Chilcott F, Waikar S, Whitaker T, Ah-See AK, Eremin O, Heys SD, Gilbert FJ, Sharp PF. Positron emission tomography using [¹⁸F]-fluorodeoxy-D-glucose to predict the pathologic response of breast cancer to primary chemotherapy. *J Clin Oncol* 2000; **18**: 1676-1688
- MacManus MP**, Seymour JF, Hicks RJ. Overview of early response assessment in lymphoma with FDG-PET. *Cancer Imaging* 2007; **7**: 10-18 [PMID: 17766210 DOI: 10.1102/1470-7330.2007.0004]
- Terasawa T**, Lau J, Bardet S, Couturier O, Hotta T, Hutchings M, Nishihashi T, Nagai H. Fluorine-18-fluorodeoxyglu-

- cose positron emission tomography for interim response assessment of advanced-stage Hodgkin's lymphoma and diffuse large B-cell lymphoma: a systematic review. *J Clin Oncol* 2009; **27**: 1906-1914 [PMID: 19273713 DOI: 10.1200/JCO.2008.16.0861]
- 8 **de Geus-Oei LF**, van Laarhoven HW, Visser EP, Hermesen R, van Hoorn BA, Kamm YJ, Krabbe PF, Corstens FH, Punt CJ, Oyen WJ. Chemotherapy response evaluation with FDG-PET in patients with colorectal cancer. *Ann Oncol* 2008; **19**: 348-352 [PMID: 17962202 DOI: 10.1093/annonc/mdm470]
 - 9 **Hoekstra CJ**, Stroobants SG, Smit EF, Vansteenkiste J, van TH, Postmus PE, Golding RP, Biesma B, Schramel FJ, van ZN, Lammertsma AA, Hoekstra OS. Prognostic relevance of response evaluation using [18F]-2-fluoro-2-deoxy-D-glucose positron emission tomography in patients with locally advanced non-small-cell lung cancer. *J Clin Oncol* 2005; **23**: 8362-8370
 - 10 **Tanvetyanon T**, Eikman EA, Sommers E, Robinson L, Boulware D, Bepler G. Computed tomography response, but not positron emission tomography scan response, predicts survival after neoadjuvant chemotherapy for resectable non-small-cell lung cancer. *J Clin Oncol* 2008; **26**: 4610-4616
 - 11 **Mileshkin L**, Hicks RJ, Hughes BG, Mitchell PL, Charu V, Gitlitz BJ, Macfarlane D, Solomon B, Amler LC, Yu W, Pirzkal A, Fine BM. Changes in 18F-fluorodeoxyglucose and 18F-fluorodeoxythymidine positron emission tomography imaging in patients with non-small cell lung cancer treated with erlotinib. *Clin Cancer Res* 2011; **17**: 3304-3315 [PMID: 21364032 DOI: 10.1158/1078-0432.CCR-10-2763]
 - 12 **Shepherd FA**, Rodrigues Pereira J, Ciuleanu T, Tan EH, Hirsh V, Thongprasert S, Campos D, Maoleekoonpiroj S, Smylie M, Martins R, van Kooten M, Dediu M, Findlay B, Tu D, Johnston D, Bezjak A, Clark G, Santabárbara P, Seymour L. Erlotinib in previously treated non-small-cell lung cancer. *N Engl J Med* 2005; **353**: 123-132 [PMID: 16014882 DOI: 10.1056/NEJMoa050753]
 - 13 **Johnson JR**, Cohen M, Sridhara R, Chen YF, Williams GM, Duan J, Gobburu J, Booth B, Benson K, Leighton J, Hsieh LS, Chidambaram N, Zimmerman P, Pazdur R. Approval summary for erlotinib for treatment of patients with locally advanced or metastatic non-small cell lung cancer after failure of at least one prior chemotherapy regimen. *Clin Cancer Res* 2005; **11**: 6414-6421 [PMID: 16166415 DOI: 10.1158/1078-0432.CCR-05-0790]
 - 14 **Paez JG**, Jänne PA, Lee JC, Tracy S, Greulich H, Gabriel S, Herman P, Kaye FJ, Lindeman N, Boggon TJ, Naoki K, Sasaki H, Fujii Y, Eck MJ, Sellers WR, Johnson BE, Meyerson M. EGFR mutations in lung cancer: correlation with clinical response to gefitinib therapy. *Science* 2004; **304**: 1497-1500 [PMID: 15118125 DOI: 10.1126/science.1099314]
 - 15 **Lynch TJ**, Bell DW, Sordella R, Gurubhagavatula S, Okimoto RA, Brannigan BW, Harris PL, Haserlat SM, Supko JG, Haluska FG, Louis DN, Christiani DC, Settleman J, Haber DA. Activating mutations in the epidermal growth factor receptor underlying responsiveness of non-small-cell lung cancer to gefitinib. *N Engl J Med* 2004; **350**: 2129-2139 [PMID: 15118073 DOI: 10.1056/NEJMoa040938]
 - 16 **Lara-Guerra H**, Waddell TK, Salvarrey MA, Joshua AM, Chung CT, Paul N, Boerner S, Sakurada A, Ludkovski O, Ma C, Squire J, Liu G, Shepherd FA, Tsao MS, Leigh NB. Phase II study of preoperative gefitinib in clinical stage I non-small-cell lung cancer. *J Clin Oncol* 2009; **27**: 6229-6236 [PMID: 19884551 DOI: 10.1200/JCO.2009.22.3370]
 - 17 **Yu J**, Kane S, Wu J, Benedettini E, Li D, Reeves C, Innocenti G, Wetzel R, Crosby K, Becker A, Ferrante M, Cheung WC, Hong X, Chirieac LR, Sholl LM, Haack H, Smith BL, Polakiewicz RD, Tan Y, Gu TL, Loda M, Zhou X, Comb MJ. Mutation-specific antibodies for the detection of EGFR mutations in non-small-cell lung cancer. *Clin Cancer Res* 2009; **15**: 3023-3028 [PMID: 19366827 DOI: 10.1158/1078-0432.CCR-08-2739]
 - 18 **Kawahara A**, Yamamoto C, Nakashima K, Azuma K, Hattori S, Kashiwara M, Aizawa H, Basaki Y, Kuwano M, Kage M, Mitsudomi T, Ono M. Molecular diagnosis of activating EGFR mutations in non-small cell lung cancer using mutation-specific antibodies for immunohistochemical analysis. *Clin Cancer Res* 2010; **16**: 3163-3170 [PMID: 20423982 DOI: 10.1158/1078-0432.CCR-09-3239]
 - 19 **Gridelli C**, De Marinis F, Di Maio M, Cortinovis D, Cappuzzo F, Mok T. Gefitinib as first-line treatment for patients with advanced non-small-cell lung cancer with activating Epidermal Growth Factor Receptor mutation: implications for clinical practice and open issues. *Lung Cancer* 2011; **72**: 3-8 [PMID: 21216488 DOI: 10.1016/j.lungcan.2010.12.009]
 - 20 **Riely GJ**, Kris MG, Zhao B, Akhurst T, Milton DT, Moore E, Tyson L, Pao W, Rizvi NA, Schwartz LH, Miller VA. Prospective assessment of discontinuation and reinitiation of erlotinib or gefitinib in patients with acquired resistance to erlotinib or gefitinib followed by the addition of everolimus. *Clin Cancer Res* 2007; **13**: 5150-5155 [PMID: 17785570 DOI: 10.1158/1078-0432.CCR-07-0560]
 - 21 **Aukema TS**, Kappers I, Olmos RA, Codrington HE, van Tinteren H, van Pel R, Klomp HM. Is 18F-FDG PET/CT useful for the early prediction of histopathologic response to neoadjuvant erlotinib in patients with non-small cell lung cancer? *J Nucl Med* 2010; **51**: 1344-1348 [PMID: 20720059 DOI: 10.2967/jnumed.110.076224]
 - 22 **Zander T**, Scheffler M, Nogova L, Kobe C, Engel-Riedel W, Hellmich M, Papachristou I, Toepelt K, Draube A, Heukamp L, Buettner R, Ko YD, Ullrich RT, Smit E, Boellaard R, Lammertsma AA, Hallek M, Jacobs AH, Schlesinger A, Schulte K, Quering S, Stoelben E, Neumaier B, Thomas RK, Dietlein M, Wolf J. Early prediction of nonprogression in advanced non-small-cell lung cancer treated with erlotinib by using [(18)F]fluorodeoxyglucose and [(18)F]fluorothymidine positron emission tomography. *J Clin Oncol* 2011; **29**: 1701-1708 [PMID: 21422426 DOI: 10.1200/JCO.2010.32.4939]
 - 23 **Benz MR**, Herrmann K, Walter F, Garon EB, Reckamp KL, Figlin R, Phelps ME, Weber WA, Czernin J, Allen-Auerbach MS. (18)F-FDG PET/CT for monitoring treatment responses to the epidermal growth factor receptor inhibitor erlotinib. *J Nucl Med* 2011; **52**: 1684-1689 [PMID: 22045706 DOI: 10.2967/jnumed.111.095257]
 - 24 **O'Brien ME**, Myerson JS, Coward JI, Puglisi M, Trani L, Wotherspoon A, Sharma B, Cook G, Ashley S, Gunapala R, Chua S, Popat S. A phase II study of ¹⁸F-fluorodeoxyglucose PET-CT in non-small cell lung cancer patients receiving erlotinib (Tarceva); objective and symptomatic responses at 6 and 12 weeks. *Eur J Cancer* 2012; **48**: 68-74 [PMID: 22119198]
 - 25 **Takahashi R**, Hirata H, Tachibana I, Shimosegawa E, Inoue A, Nagatomo I, Takeda Y, Kida H, Goya S, Kijima T, Yoshida M, Kumagai T, Kumanogoh A, Okumura M, Hatazawa J, Kawase I. Early [18F]fluorodeoxyglucose positron emission tomography at two days of gefitinib treatment predicts clinical outcome in patients with adenocarcinoma of the lung. *Clin Cancer Res* 2012; **18**: 220-228 [PMID: 22019513 DOI: 10.1158/1078-0432.CCR-11-0868]
 - 26 **Young H**, Baum R, Cremerius U, Herholz K, Hoekstra O, Lammertsma AA, Pruijm J, Price P. Measurement of clinical and subclinical tumour response using [18F]-fluorodeoxyglucose and positron emission tomography: review and 1999 EORTC recommendations. European Organization for Research and Treatment of Cancer (EORTC) PET Study Group. *Eur J Cancer* 1999; **35**: 1773-1782 [PMID: 10673991]
 - 27 **Wahl RL**, Jacene H, Kasamon Y, Lodge MA. From RECIST to PERCIST: Evolving Considerations for PET response criteria in solid tumors. *J Nucl Med* 2009; **50** Suppl 1: 122S-150S [PMID: 19403881 DOI: 10.2967/jnumed.108.057307]
 - 28 **Besse B**, Ropert S, Soria JC. Targeted therapies in lung cancer. *Ann Oncol* 2007; **18** Suppl 9: ix135-ix142 [PMID:

- 17631566 DOI: 10.1093/annonc/mdm308]
- 29 **Stang A**, Pohlabein H, Müller KM, Jahn I, Giersiepen K, Jöckel KH. Diagnostic agreement in the histopathological evaluation of lung cancer tissue in a population-based case-control study. *Lung Cancer* 2006; **52**: 29-36 [PMID: 16476504 DOI: 10.1016/j.lungcan.2005.11.012]
- 30 **Field RW**, Smith BJ, Platz CE, Robinson RA, Neuberger JS, Brus CP, Lynch CF. Lung cancer histologic type in the surveillance, epidemiology, and end results registry versus independent review. *J Natl Cancer Inst* 2004; **96**: 1105-1107 [PMID: 15265973 DOI: 10.1093/jnci/djh189]
- 31 **Soria JC**, Mok TS, Cappuzzo F, Jänne PA. EGFR-mutated oncogene-addicted non-small cell lung cancer: current trends and future prospects. *Cancer Treat Rev* 2012; **38**: 416-430 [PMID: 22119437 DOI: 10.1016/j.ctrv.2011.10.003]
- 32 **Tuma RS**. Sometimes size doesn't matter: reevaluating RECIST and tumor response rate endpoints. *J Natl Cancer Inst* 2006; **98**: 1272-1274 [PMID: 16985244 DOI: 10.1093/jnci/djj403]
- 33 **Vansteenkiste J**, Fischer BM, Doooms C, Mortensen J. Positron-emission tomography in prognostic and therapeutic assessment of lung cancer: systematic review. *Lancet Oncol* 2004; **5**: 531-540 [PMID: 15337482 DOI: 10.1016/S1470-2045(04)01564-5]

P- Reviewer: Rosell R **S- Editor:** Wen LL **L- Editor:** A
E- Editor: Lu YJ



Nuclear medicine and the failed joint replacement: Past, present, and future

Christopher J Palestro

Christopher J Palestro, Division of Nuclear Medicine, Molecular Imaging Long Island Jewish Medical Center, New York, NY 11040, United States

Author contributions: Palestro CJ solely contributed to this paper.

Correspondence to: Christopher J Palestro, MD, Division of Nuclear Medicine, Molecular Imaging Long Island Jewish Medical Center, 270-05 76th Avenue New Hyde Park, New York, NY 11040, United States. palestro@lij.edu

Telephone: +1-718-4707081 Fax: +1-718-8311147

Received: December 4, 2013 Revised: February 26, 2014

Accepted: May 28, 2014

Published online: March 28, 2015

Abstract

Soon after the introduction of the modern prosthetic joint, it was recognized that radionuclide imaging provides useful information about these devices. The bone scan was used extensively to identify causes of prosthetic joint failure. It became apparent, however, that although sensitive, regardless of how the images were analyzed or how it was performed, the test was not specific and could not distinguish among the causes of prosthetic failure. Advances in anatomic imaging, notably cross sectional modalities, have facilitated the diagnosis of many, if not most, causes of prosthetic failure, with the important exception of infection. This has led to a shift in the diagnostic paradigm, in which nuclear medicine investigations increasingly have focused on diagnosing infection. The recognition that bone scintigraphy could not reliably diagnose infection led to the development of combined studies, first bone/gallium and subsequently leukocyte/bone and leukocyte/marrow imaging. Labeled leukocyte imaging, combined with bone marrow imaging is the most accurate (about 90%) imaging test for diagnosing joint arthroplasty infection. Its value notwithstanding, there are significant disadvantages to this test. *In-vivo* techniques for labeling leukocytes, using antigranulocyte antibodies

have been explored, but have their own limitations and the results have been inconsistent. Fluorodeoxyglucose (FDG)-positron emission tomography (FDG-PET) has been extensively investigated for more than a decade but its role in diagnosing the infected prosthesis has yet to be established. Antimicrobial peptides bind to bacterial cell membranes and are infection specific. Data suggest that these agents may be useful for diagnosing prosthetic joint infection, but large scale studies have yet to be undertaken. Although for many years nuclear medicine has focused on diagnosing prosthetic joint infection, the advent of hybrid imaging with single-photon emission computed tomography (SPECT)/electronic computer X-ray tomography technique (CT) and the availability of fluorine-18 fluoride PET suggests that the diagnostic paradigm may be shifting again. By providing the anatomic information lacking in conventional radionuclide studies, there is renewed interest in bone scintigraphy, performed as a SPECT/CT procedure, for detecting joint instability, mechanical loosening and component malpositioning. Fluoride-PET may provide new insights into periprosthetic bone metabolism. The objective of this manuscript is to provide a comprehensive review of the evolution of nuclear medicine imaging of joint replacements.

© 2015 Baishideng Publishing Group Inc. All rights reserved.

Key words: Bone scintigraphy; Positron emission tomography; ¹⁸F-fluorodeoxyglucose; F-18; Fluoride-positron emission tomography; Gallium; Infection; Labeled leukocytes; Prosthetic joint

Core tip: Advances in anatomic imaging, notably cross sectional modalities, have facilitated the diagnosis of many, if not most, causes of prosthetic failure, with the important exception of infection. This has led to a shift in the diagnostic paradigm, in which nuclear medicine investigations increasingly have focused on diagnosing infection. This article is a comprehensive review of

the evolution of nuclear medicine imaging of joint replacements. In addition to conventional planar imaging studies such as bone, gallium, and labeled leukocyte imaging, single-photon emission computed tomography/electronic computer X-ray tomography technique and positron emission tomography imaging with ^{18}F -fluorodeoxyglucose and ^{18}F (NaI) are covered.

Original sources: Palestro CJ. Nuclear medicine and the failed joint replacement: Past, present, and future. *World J Radiol* 2014; 6(7): 446-458 Available from: URL: <http://www.wjgnet.com/1949-8470/full/v6/i7/446.htm> DOI: <http://dx.doi.org/10.4329/wjr.v6.i7.446>

INTRODUCTION

Contemporary joint arthroplasty procedures began less than 75 years ago, when the predecessor of the modern day hip replacement was introduced. A total hip arthroplasty includes both femoral and acetabular components; a hemiarthroplasty consists of only the femoral component. These prostheses are anchored to bone by various methods including polymethylmethacrylate and osseous ingrowth into the device's surface. Some devices are coated with hydroxyapatite which induces new bone formation and attaches to newly produced periprosthetic osseous tissue. The acetabular component can be forced into the acetabulum or secured by screws^[1].

The predecessor of the contemporary knee prosthesis, developed about 40 years ago, consisted of a metallic femoral component, together with plastic patellar and tibial components. Today's devices provide improved range of motion and greater durability of the components^[1].

The vast majority of lower extremity joint replacement surgeries are successful; complications like infection, fracture, dislocation, and heterotopic ossification are uncommon. At the present time the most common cause of prosthetic failure is aseptic loosening, which develops in more than a quarter of these devices and frequently results from an inflammatory reaction instigated by prosthetic components^[2,3]. The debris created by component breakdown activates and draws surrounding leukocytes, triggering secretion of cytokines and enzymes damaging osseous tissues and leading to prosthetic loosening. The cellular response is characterized by an influx of various types of leukocytes. Neutrophils, however, rarely are present^[4-6]. Most cases of aseptic loosening are treated with one surgery, the single stage exchange arthroplasty.

Infection, which occurs in up to 2% of primary implants, and up to 5% of revision implants is an uncommon complication of prosthetic joint surgery. Risk factors for infection include operative suite characteristics, surgical complexity, condition of the osseous tissue surrounding the prosthesis, and immune status of the patient.

Bacteria bind to most joint replacement components and once attached they secrete a protective biofilm^[5]. Or-

ganisms commonly encountered in infected joint replacements include *Staphylococcus epidermidis* and *Staphylococcus aureus*. *Streptococcus viridans*, *Escherichia coli*, *Enterococcus faecalis*, and group-B *Streptococcus* are occasionally identified^[4]. Early prosthetic joint infections occur by three months after implantation, while delayed infections develop within three months to one year after implantation. Late infections are defined as infections that occur more than one year after surgery. Early and delayed infections are thought to be due to organisms introduced at surgery; late infections are more likely to be due to hematogenous spread^[7].

The infected joint replacement is accompanied by an inflammatory reaction characterized by a neutrophilic response, often intense^[6]. Management of the infected joint replacement consists of removal of the device, a lengthy course (weeks to months) of antibiotic treatment, and eventually a reimplantation procedure^[8].

The correct therapeutic approach often depends on the accurate differentiation of aseptic loosening and infection. This differentiation is not always obvious. Signs and symptoms, except for pain, frequently are lacking. Laboratory tests may be suggestive, but are not diagnostic, of infection. Joint aspiration with culture, the definitive preoperative test is specific, but sensitivity is variable^[9,10]. Plain radiographs are not specific and prosthesis related artifacts limit, to some degree, cross sectional imaging studies.

Nuclear medicine procedures have, for many years, contributed useful information about the painful joint replacement. This manuscript is a comprehensive review of the evolution of nuclear medicine imaging of joint replacements.

LITERATURE SEARCH

An electronic search with no language restrictions was conducted in the bibliographic database PubMed using the terms infection, osteomyelitis, arthroplasty, joint replacement, prosthetic joint, bone scintigraphy, bone marrow scintigraphy, gallium, labeled leukocytes, besilesomab, sulesomab, sulfur colloid, antimicrobial peptides, positron emission tomography, positron emission tomography (PET), fluorodeoxyglucose (FDG), fluoride and ^{18}F . The list of articles generated was augmented by crosschecking the reference lists of the retrieved papers. This was designed as a comprehensive review, not a meta analysis, of the failed joint replacement and therefore neither specific inclusion criteria nor any evidence based quality assessment tools were used to select the included articles.

RADIONUCLIDE IMAGING

Bone scintigraphy

The first, and undoubtedly the most extensively investigated, radionuclide procedure used for imaging joint arthroplasties was bone scintigraphy. Technetium-99m ($^{99\text{m}}\text{Tc}$) labeled diphosphonates, usually methylene di-



Figure 1 Aseptically loosened right hip arthroplasty. A: X-ray reveals medial protrusion of the acetabular component of a painful 15 year old hip replacement. There is heterotopic ossification around both greater trochanters (arrows); B: On the ^{99m}Tc-methylene diphosphonate bone scan, there is focally increased radiopharmaceutical accumulation at the distal tip of the femoral component (arrow) of the right hip replacement and lateral to the femoral neck (arrowhead) corresponding to the heterotopic bone seen on the X-ray. An aseptically loosened prosthesis was revised. Focally increased radiopharmaceutical accumulation is present at the tip of the femoral component of the asymptomatic left hip arthroplasty (double arrows) which also was 15 years old.

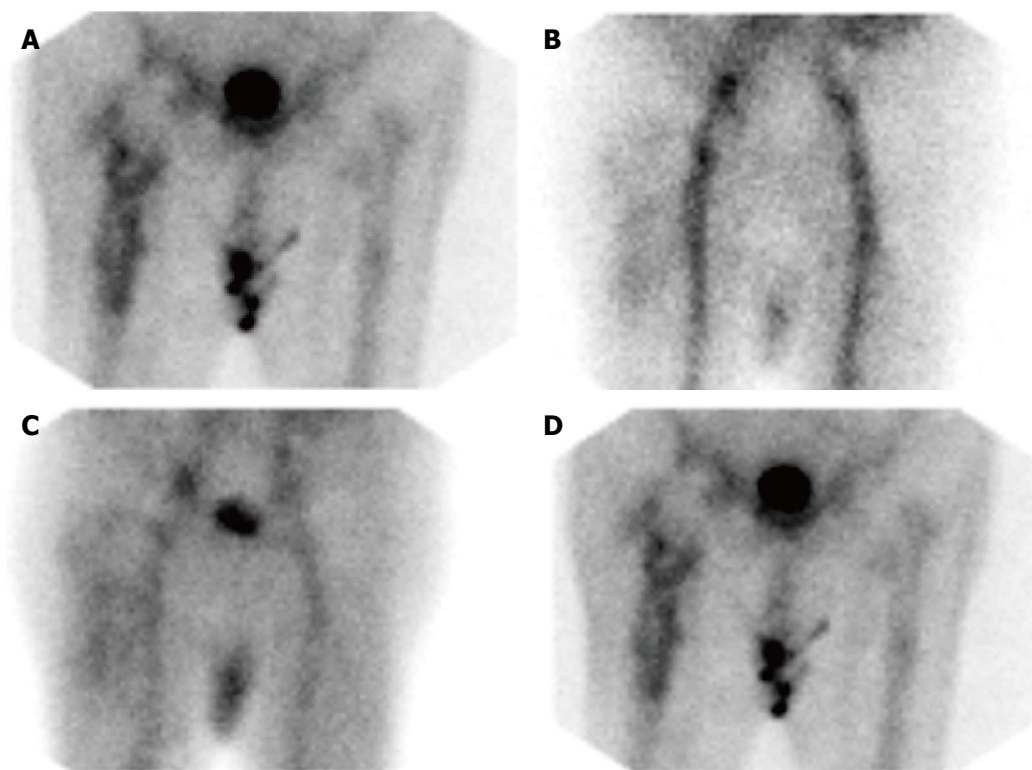


Figure 2 Infected right hip arthroplasty. A: On the ^{99m}Tc-methylene diphosphonate bone scan, there is irregularly increased radiopharmaceutical accumulation around the entire femoral component of the 2 years old cementless (revision) prosthesis, a pattern which some investigators have reported as specific for infection; B-D: On the ^{99m}Tc-MDP bone scan, there is diffuse hyperperfusion, and hyperemia around the prosthesis on the flow and blood pool images, and diffusely increased periprosthetic radiopharmaceutical on the delayed, bone image (same patient illustrated in Figure 2A); B: Flow; C: Blood pool; D: Bone.

phosphonate (MDP), are used for this study. Radiopharmaceutical incorporation into the bone depends on perfusion and rate of new bone formation. Imaging usually is performed two to four hours after injection. The procedure also can be performed as a three phase bone scan: the flow or perfusion phase, acquired immediately after radiopharmaceutical injection, followed immediately by the soft tissue or blood pool phase. The third, or bone, phase is performed between two and four hours later.

Gelman *et al*^[10] reported that bone scintigraphy was 85% accurate for prosthetic hip loosening. Weiss *et al*^[11] reported that bone scintigraphy accurately identified prostheses requiring surgical intervention. Another group of investigators, however, observed that bone scintigraphy cannot determine the cause of the failure, informa-

tion critical to patient management^[12].

In an effort to enhance its specificity, investigators have studied periprosthetic uptake patterns on bone scans. Williamson *et al*^[13] suggested that focal periprosthetic uptake indicated loosening and diffuse uptake indicated infection (Figures 1, 2A). Williams *et al*^[14] reported that diffuse periprosthetic uptake was sensitive (100%), but not specific (54%) for infection. Another group of investigators came to the opposite conclusion: diffuse periprosthetic uptake was specific, but not sensitive, for infection^[15]. Aliabadi *et al*^[16] reported that bone scintigraphy did not differentiate septic from aseptic loosening (Figure 3A).

Further confounding the analysis of periprosthetic uptake is the numerous uptake patterns present around

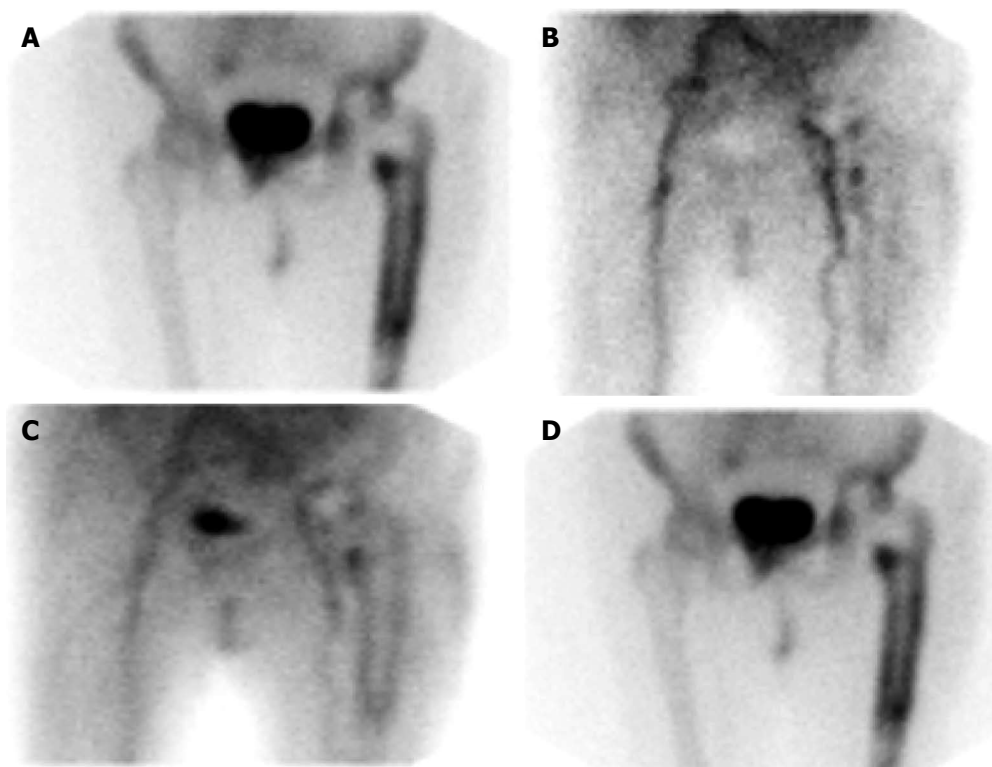


Figure 3 Aseptically loosened left hip replacement. A: On the ^{99m}Tc -MDP bone scan, there is diffusely increased radiopharmaceutical accumulation around the femoral component of the cemented 2 years old prosthesis. Compare with Figure 2A; B-D: On the ^{99m}Tc -MDP bone scan, there is diffuse hyperperfusion, and hyperemia around the prosthesis on the flow and blood pool images, and diffusely increased periprosthetic radiopharmaceutical on the delayed, bone image (same patient illustrated in Figure 3A), B: Flow; C: Blood pool; D: Delayed. The scan appearance is nearly identical to that of the infected prosthesis in Figure 2B.

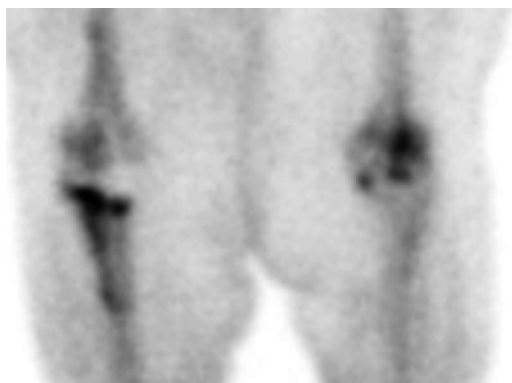


Figure 4 Asymptomatic right knee arthroplasty. On the ^{99m}Tc -MDP bone scan, there is irregular, intense radiopharmaceutical accumulation around the long stemmed tibial component of a three year old right knee replacement. The femoral component is unremarkable. The patient had a history of breast carcinoma and bone scintigraphy was performed as part of a routine evaluation for metastatic disease.

asymptomatic devices. For up to 12 m after insertion of a hip prosthesis, periprosthetic uptake is very variable; after this time ten percent of asymptomatic cemented hip prostheses still demonstrate uptake^[17]. Increased periprosthetic uptake is even more frequent in cementless devices^[18-20].

Gallo *et al*^[21] studied 27 hydroxyapatite coated hip replacements, observing that while a normal study excluded aseptic loosening with a high degree of certainty, a posi-

tive study was not reliable for diagnosing either loosening or infection. Complicating matters further is the paucity of data on radionuclide bone imaging of hybrid and bipolar prostheses.

Assessment of knee replacements also is challenging. In one investigation periprosthetic activity was seen around more than sixty percent of femoral components and nearly 90% of tibial components of asymptomatic devices for up to several years^[22] (Figure 4). In an investigation of asymptomatic knee replacements with serial bone scans periprosthetic activity generally diminished over time after implantation. There was considerable variation among patients. The authors stated, in order to determine the significance of periprosthetic activity, serial scans need to be performed^[23] (Figure 5A). Another group of investigators reported that bone scintigraphy does not accurately diagnose the infected knee arthroplasty^[24].

Performing radionuclide bone imaging as a three-phase study has been advocated to enhance its specificity^[25]. Nagoya *et al*^[26] reported that the test was 88% sensitive and 90% specific for hip replacement infection. Most other investigations, however, have reported low sensitivity, low specificity, or both^[24,27-30] (Figures 2B and 3B).

Regardless of how bone scintigraphy is performed, its accuracy for diagnosing complications of lower extremity joint prostheses is about 50%-70%. At the present time this test is used primarily for screening purposes. A nor-

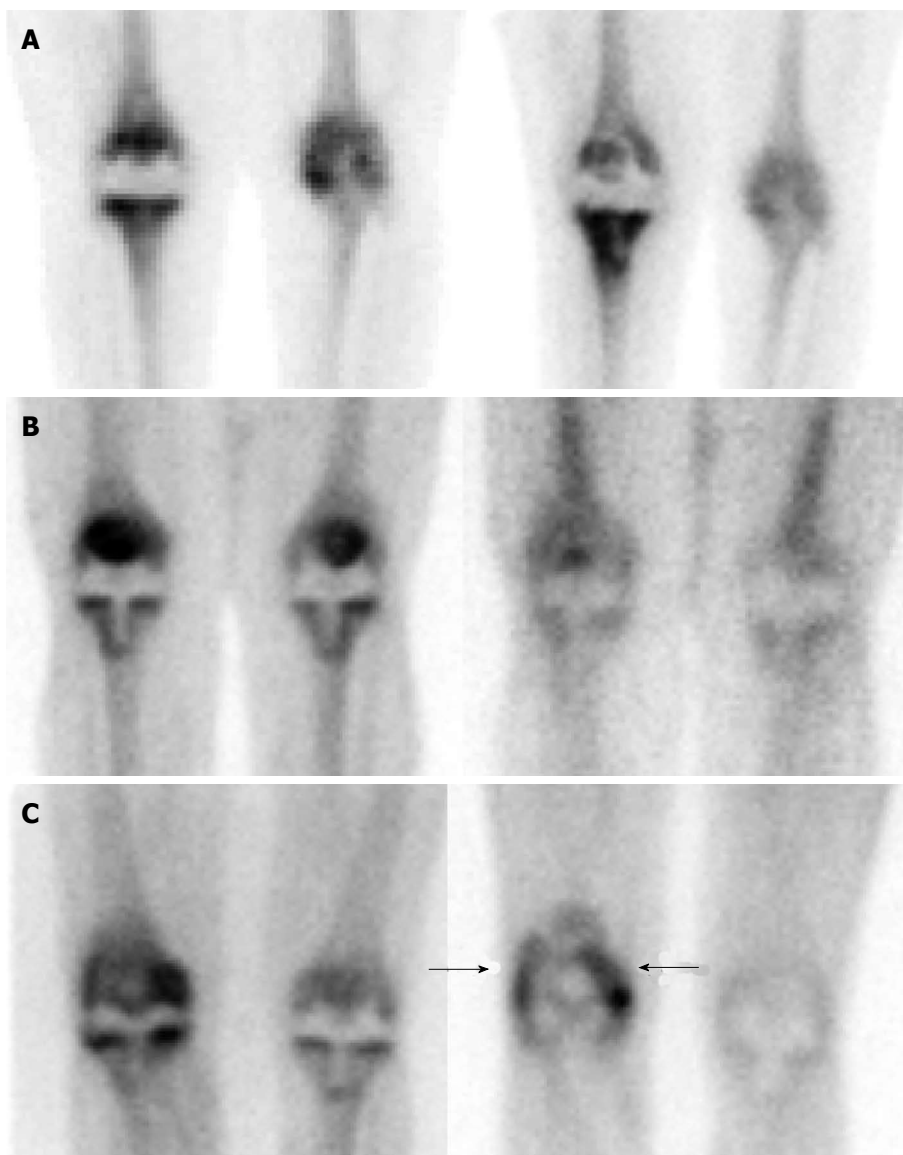


Figure 5 Aseptically loosened right knee arthroplasty. A: On the ^{99m}Tc-methylene diphosphonate (MDP) bone scan, performed about 6 mo after implantation (left), shows mildly increased radiopharmaceutical accumulation around the femoral and tibial components. On the repeat study, performed 9 mo later (15 mo after implantation), there is intensely increased radiopharmaceutical accumulation around the tibial component, while activity around the femoral component has resolved. An aseptically loosened tibial component was revised; B: On the ^{99m}Tc-MDP bone scan (left) there is increased radiopharmaceutical accumulation around the tibial component of both the symptomatic right and asymptomatic left knee prostheses. There is normal periprosthetic distribution around both prostheses on the gallium-67 image (right), and the combined study is negative for infection; C: On the ^{99m}Tc-MDP bone scan (left) there is increased radiopharmaceutical accumulation around the tibial component of the symptomatic right and faintly increased accumulation around the tibial component of the asymptomatic left knee prosthesis. On the gallium-67 image (right), in contrast to the bone scan, there is increased radiopharmaceutical accumulation around the femoral component (arrows) of the right knee replacement, while activity around the tibial component is normal. There is normal periprosthetic gallium activity around the asymptomatic left prosthesis. The distribution of activity around the right knee prosthesis on the bone and gallium studies is spatially incongruent and the combined study is (false) positive for infection. Aseptic loosening of joint replacements often is accompanied by an intense inflammatory response and gallium cannot reliably differentiate infection from inflammation.



Figure 6 Normal ^{99m}Tc-methylene diphosphonate bone scans of bilateral hip (left) and right knee (right) prostheses. A normal bone scan is defined as a scan in which periprosthetic activity is indistinguishable from adjacent, non-articular bone. The bone scan has a high negative predictive value and therefore a normal study makes it very unlikely that the patient's symptoms are related to the prosthesis.

mal study makes it very unlikely that the patient's symptoms are related to the prosthesis (Figure 6).

Gallium scintigraphy

Over the years various techniques designed to overcome the limitations inherent in bone scintigraphy have been investigated. One of the earliest was gallium-67 citrate

(gallium) imaging. Gallium uptake in infection likely is due to several factors including increased blood flow and vascular membrane permeability at inflammatory sites, lactoferrin binding and siderophore and bacterial uptake of gallium. Some gallium may be transported by leukocytes. Imaging typically is performed two to three days after injection^[31].

Reing *et al*^[32] observed that bone scintigraphy was sensitive (100%), but not specific (15%), while gallium was sensitive (95%) and specific (100%). Other investigators have reported similar results^[15,33,34]. Aliabadi *et al*^[16], in contrast, found, for the infected hip replacement, gallium scintigraphy was specific (100%) but insensitive (37%).

While some investigators have evaluated gallium imaging alone, other investigators have interpreted bone and gallium imaging together. Standardized criteria for interpretation of the combined study have been developed. The test is positive for osteomyelitis when distribution of the two tracers is different or, when their distribution is the same and the relative intensity of gallium uptake exceeds that of the bone agent. The test is equivocal for osteomyelitis when the distribution of the two radiotracers is the same, both spatially and in intensity. The test is negative for osteomyelitis when the gallium images are normal, regardless of the bone scan findings, or, when the distribution of the two tracers is the same and the relative intensity of gallium uptake is less than that of the bone agent (Figure 5B and 5C)^[11].

Tehraneh *et al*^[35] reported that bone/gallium imaging was 95% accurate for prosthetic joint infection. In most other series the test has been less successful. In 30 patients the test identified only 50% of the infected joint replacements^[14]. Gómez-Luzuriaga *et al*^[36] found that bone/gallium imaging was 80% accurate for prosthetic joint infection. Kraemer *et al*^[37] reported that the combined test was 38% sensitive, and 100% specific for hip replacement infection. Merkel *et al*^[38,39] evaluated bone/gallium imaging in an animal investigation and in patients and reported similar results.

Over the years the use of gallium for joint replacement infection has declined, and it has been replaced in most circumstances by labeled leukocyte imaging.

Labeled leukocyte scintigraphy

The accumulation of *in-vitro* labeled white cells at a site of infection depends on chemotaxis, the quantity and sorts of leukocytes labeled, and the primary cellular response in a particular situation. Neutrophils usually comprise the majority of leukocytes labeled and consequently sensitivity of WBC imaging is highest for neutrophil-mediated inflammatory processes^[40]. When indium-111 is the radiolabel, images are acquired 18-30 h after administration. When technetium-99m is the radiolabel, imaging usually is performed four to six and repeated 18 to 30 h after administration.

One would anticipate that, because neutrophils invariably are present labeled leukocyte (WBC) imaging would accurately diagnose prosthetic joint infection. Interestingly, for quite some time, the value of the test was a subject of controversy.

In a canine study, Merkel *et al*^[38] reported that WBC imaging was 94% sensitive and 86% specific for prosthetic infection. Pring *et al*^[41] found that WBC imaging was 100% sensitive and 89.5% specific for the infected prosthetic joint. In another investigation, Pring *et al*^[42]

observed that WBC activity around infected prostheses was always significant. Rand *et al*^[43] found that sensitivity and specificity for prosthetic knee infection was 83% and 85% when moderately to markedly increased periprosthetic activity was present. Magnuson *et al*^[27], in an investigation of 98 patients reported sensitivity and specificity for WBC imaging of 88% and 73% respectively, for lower extremity joint replacement infection.

In some studies, WBC imaging was specific, but not sensitive for prosthetic joint infection, while in others the test was sensitive but not specific^[15,34,44,45].

Poor sensitivity has been ascribed to the chronicity of the process; *i.e.*, presumably the neutrophilic response had ceased, or at least waned, by the time the patient underwent imaging. Neutrophils, however, almost always are present in the infected joint replacement, regardless of the duration of symptoms, so chronicity does not explain low sensitivity.

Poor specificity often has been attributed to non-specific inflammation. It was thought that false positive results were secondary to labeled leukocyte accumulation in aseptic inflammation. Although aseptic inflammation around a prosthetic joint replacement is often accompanied by an intense leukocyte response, neutrophils rarely are present. In most situations, primarily neutrophils are labeled and the sensitivity of WBC imaging is greatest for detecting infections characterized by a neutrophilic response. The test is not at all sensitive, however, for detecting inflammation that is not neutrophil mediated^[40]. Given the lack of a neutrophilic response in the aseptically inflamed prosthesis, inflammation cannot be the sole explanation for poor specificity.

What is the reason for the variable and often contradictory observations? WBC images usually are interpreted by comparing intensity of periprosthetic uptake to intensity of uptake in some predefined reference point, typically an area of presumably normal bone marrow. Studies in which intensity of labeled leukocyte activity in the area of interest exceeds intensity of activity in the reference point are classified as positive for infection; otherwise the study is negative. The likelihood of infection, however, is not related to intensity of periprosthetic activity (Figures 7A and 8A). In one investigation^[46] the accuracy of the test varied with the manner in which the studies were interpreted. The mere presence of periprosthetic activity, regardless of intensity, was 100% sensitive and 23% specific. Using periprosthetic activity exceeding activity in the contralateral extremity as the criterion for infection, sensitivity was 65%, specificity was 61%^[46].

There is another problem inherent in the interpretation of WBC images. Leukocytes, labeled or otherwise, accumulate in bone marrow, the normal distribution of which can be variable. Generalized, as well as localized, marrow expansion alter the "normal" distribution of marrow making it difficult to differentiate labeled leukocyte uptake in unusually located, but normal, marrow from uptake in infection^[47].

In a manner analogous to bone/gallium imaging, it

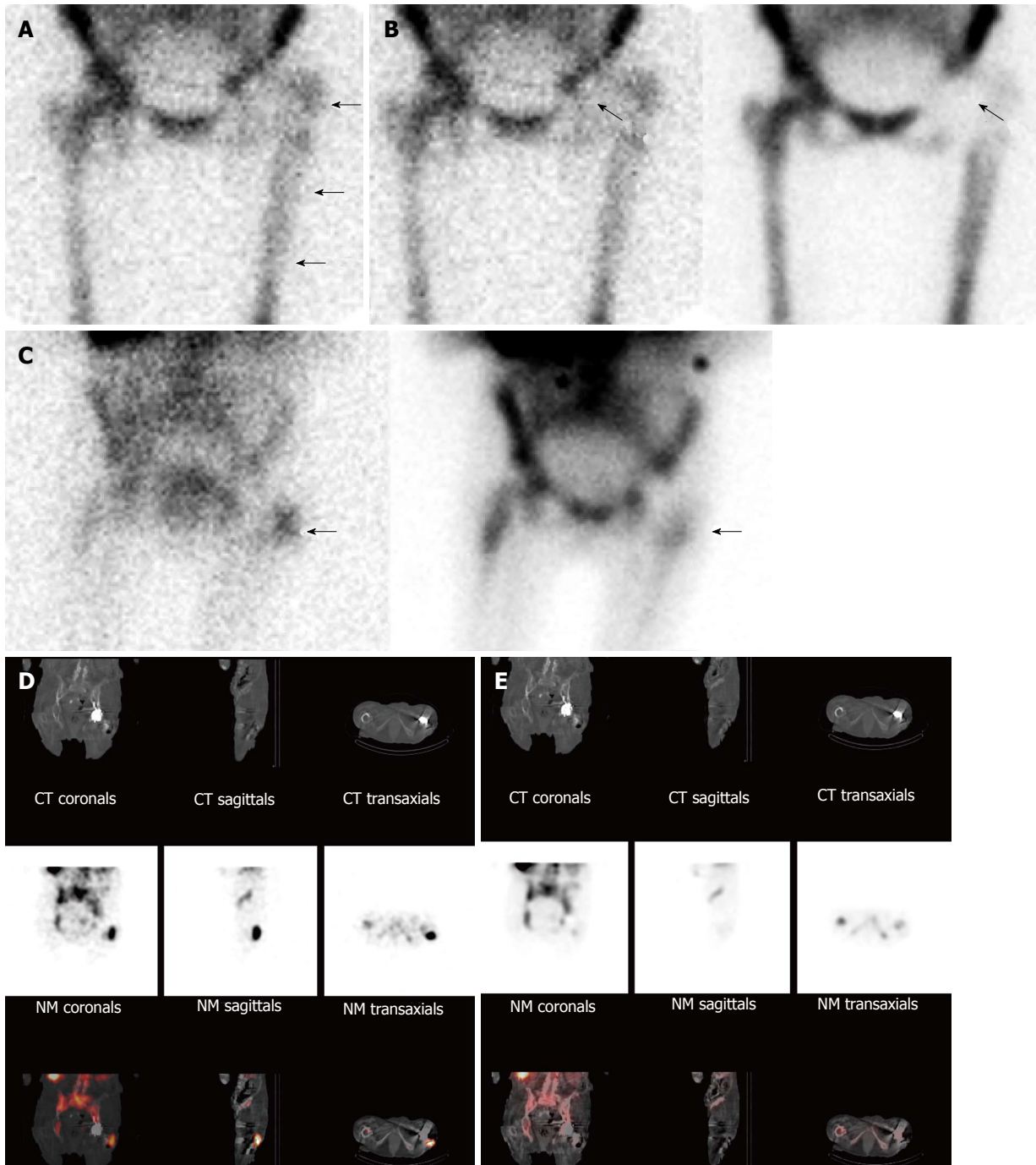


Figure 7 Infected left hip arthroplasty. A: On this anterior image from an indium-111 labeled leukocyte study, periprosthetic activity (arrows) is similar in intensity to activity in the contralateral lower extremity and less intense than pelvic activity, areas typically used as reference points when interpreting these studies. Because studies in which the intensity of labeled leukocyte activity in the region of interest does not exceed intensity of activity in the reference point, this study could be erroneously interpreted as negative for infection; B: The distribution of periprosthetic activity on the labeled leukocyte (left, ^{111}In -WBC) and sulfur colloid bone marrow (right, $^{99\text{m}}\text{Tc}$ -SC) images is spatially incongruent (arrows), *i.e.*, there is activity in the left hip joint on the labeled leukocyte image, but not on the bone marrow image. The combined study is positive for infection. (Same patient illustrated in Figure 7A); Although the planar combined indium labeled leukocyte/bone marrow study (C, left, ^{111}In -WBC; right, $^{99\text{m}}\text{Tc}$ -SC) is positive for infection (arrows), precise information about the location and extent of infection is lacking. On the fused images (bottom row) from the labeled leukocyte SPECT/CT (D) the location of the abnormal labeled leukocyte accumulation (arrows) can clearly be seen adjacent and extending to the prosthesis at the level of the greater trochanter. Note also the adjacent hypodense area in the soft tissues, consistent with abscess. Bone marrow SPECT/CT images (E) acquired simultaneously with the labeled leukocyte images in 16a confirm that the activity on the labeled leukocyte component of the examination is due to infection. Whether or not the bone marrow component of the SPECT/CT study contributes additional information beyond what planar imaging provides remains to be determined.

has been suggested that interpreting WBC images together with bone scans improves results. In one study, WBC imaging alone was 45% specific for prosthetic joint in-

fection, but improved to 85% with the addition of bone imaging^[44]. Johnson *et al*^[45] observed that the combined test was more specific and only slightly less sensitive than

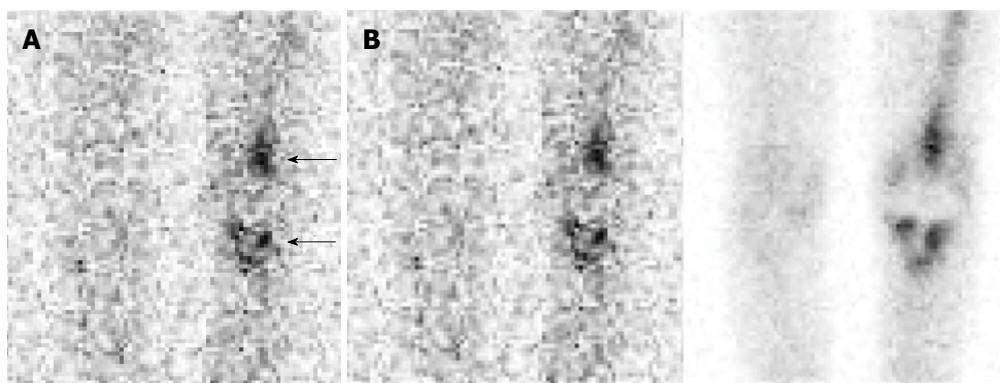


Figure 8 Aseptically loosened left knee arthroplasty. A: On this anterior image from an indium-111 labeled leukocyte study, there is intense periprosthetic activity around both the tibial and femoral components (arrows), while there is no activity around the contralateral knee. The study could be interpreted erroneously as positive for infection. Compare the intensity of activity around this prosthesis with the intensity of activity around the infected hip arthroplasty in Figure 7A. As these two cases illustrate, the intensity of labeled leukocyte activity around a prosthetic joint is not a reliable criterion for determining the presence or absence of infection; B: The distribution of periprosthetic activity on the labeled leukocyte (left, ^{111}In -WBC) and sulfur colloid bone marrow (right, $^{99\text{m}}\text{Tc}$ -SC) images is virtually identical (spatially congruent) and the combined study is negative for infection. The periprosthetic activity on the labeled leukocyte image is due to marrow, not to infection. Performing complementary bone marrow imaging eliminates the two major difficulties inherent in the interpretation of labeled leukocyte images: variable intensity of periprosthetic activity and differentiating bone marrow activity from infection. Same patient illustrated in Figure 8A.

WBC imaging for hip replacement infection.

Palestro *et al*^[24] observed that the addition of bone imaging did not increase the accuracy of WBC imaging for knee arthroplasty infection. In another investigation, the accuracy of the combined test for lower extremity joint replacement infection was only 76%^[48]. In an investigation of patients with asymptomatic cementless hip replacements, using standard interpretive criteria, WBC/bone imaging would have been classified as positive for infection 15% of the time^[18].

Another approach to WBC imaging of the prosthetic joint is to combine the test with bone marrow imaging, which usually is performed with $^{99\text{m}}\text{Tc}$ sulfur colloid. Both radiopharmaceuticals accumulate in the reticuloendothelial cells of the bone marrow. The distribution of marrow activity on WBC and bone marrow images parallel one another in most situations. The one exception is osteomyelitis, in which the distribution of these two agents differs, *i.e.*, the images are spatially incongruent (Figures 7B and 8B)^[47].

Mulamba *et al*^[49] reported 92% sensitivity and 100% specificity for prosthetic hip infection. Palestro *et al*^[24,46] reported similar results for infected hip and knee arthroplasties. Love *et al*^[50] studied 59 lower extremity joint prostheses and reported that WBC/marrow imaging was 95% accurate for infection. El Espera *et al*^[51] reported 91% accuracy for lower extremity prosthetic joint infection.

Virtually all of the investigations published to date indicate that WBC/marrow imaging is specific for joint replacement infection. In most of the investigations the test has proved to be sensitive as well. Joseph *et al*^[52] however, reported that although test was 100% specific, the test was only 66% sensitive. Pill *et al*^[53] reported similar results. It is unfortunate indeed that no illustrations of false negative studies, the salient point of these investigations, were provided in either publication.

There are some data that indicate performing WBC imaging at more than one time point could obviate the need for marrow imaging. The hypothesis is that images acquired shortly after injection represent marrow while images acquired later represent infection. Difference in uptake patterns over time is indicative of infection. The accuracy of the test improved from about 75% when images were interpreted visually, to about 95% when semi-quantitative analysis was performed^[54].

There are, unfortunately, disadvantages to WBC/marrow imaging. The leukocyte labeling procedure is demanding, not routinely available, and involves contact with blood products. Labeling enough leukocytes to produce diagnostically useful studies can be difficult in immunocompromised individuals. Image quality, especially when using indium-111, is not ideal. The need to perform marrow imaging is another disadvantage. Radiolabeled antigranulocyte antibodies and antibody fragments have been explored as alternatives.

Besilesomab is a murine monoclonal G₁ immunoglobulin that binds to Normal Cross-reactive Antigen-95 on leukocytes^[55]. Using visual image analysis the sensitivity and specificity for joint replacement infection range from 67%-91% and 57%-75%, respectively. By performing complementary bone imaging or semiquantitative analysis, sensitivity ranged from 67% to 100%; specificity ranged from 84% to 100%^[56-59].

Sulesomab is a fragment antigen binding (Fab') portion of a murine monoclonal G₁ immunoglobulin that binds to Nonspecific Cross-reactive Antigen-90 on leukocytes^[55]. Reported sensitivity and specificity for prosthetic joint infection have ranged from 75% to 93% and 65% to 86%, respectively^[60-62]. Dual time point imaging and time activity curve analysis may improve test accuracy^[63-65].

Somewhat surprisingly, even though *in-vivo* labeled leukocytes accumulate in the marrow, in much the same way that *in-vitro* labeled leukocytes do, scant attention has

been paid to combining these studies with bone marrow imaging. In one of the few investigations in which complementary bone marrow imaging was performed, Sousa *et al*^[66] reported that the specificity of ^{99m}Tc-sulesomab increased from 20% to 100%, when complementary marrow imaging was performed.

Using *in-vivo* labeled leukocytes overcomes the limitations of the *in-vitro* labeling procedure. Based on published data however, an additional study, either bone or marrow imaging probably still needs to be performed. Furthermore, besilesomab, which is a murine antibody, incites a human antimurine antibody (HAMA) response in up to 30% of patients^[57]. Patients should be screened for HAMA and a positive result is a contraindication to the procedure. Because of immunogenicity concerns, patients should not undergo repeat studies with this agent. Not surprisingly, *in-vivo* labeled WBC imaging, using anti-granulocyte antibodies, has not gained wide acceptance in the diagnostic workup of the painful joint replacement.

¹⁸F-fluorodeoxyglucose

¹⁸F-fluorodeoxyglucose (FDG) is transported into cells *via* glucose transporters and phosphorylated to ¹⁸F-2'-FDG-6 phosphate but is not metabolized. FDG uptake depends on cellular metabolic rate and the number of glucose transporters. Activated leukocytes demonstrate increased expression of these transporters with increased affinity for FDG in the presence of cytokines and growth factors. There are several advantages to FDG. The procedure is completed within two hours after injection. Target to background ratio is high. Images obtained with positron emission tomography (PET) have much higher resolution than those obtained with conventional agents^[67].

Several investigators have studied the role of FDG-PET for evaluating painful lower extremity joint prostheses. Zhuang *et al*^[68] evaluated 74 lower extremity joint prostheses and reported that increased activity along the bone prosthesis interface was 89.5% and 77.8 % for diagnosing infection of hip and knee arthroplasties, respectively. Accuracy depended on location, not intensity, of FDG uptake. Using similar criteria Chacko *et al*^[69] reported that the test was 92% sensitive and 97% specific for hip replacement infection. Infection could not be differentiated from aseptic loosening based on intensity of periprosthetic uptake.

Reinartz *et al*^[29] studied 92 hip prostheses with three phase bone scintigraphy and FDG-PET. Sensitivity, specificity and accuracy of three phase bone scintigraphy were 68%, 76% and 74% *vs* 94%, 95%, and 95%, respectively, for FDG-PET. Activity around the acetabular component and proximal aspect of the femoral component on FDG-PET images was not associated with infection. Pattern, but not intensity, of periprosthetic uptake was useful for differentiating infection from aseptic loosening. Cremerius *et al*^[70] reported that FDG was 89% accurate for hip replacement infection. Gravius *et al*^[71] reported similar results. Pill *et al*^[53] studied 92 painful hip prostheses, including 21 infected devices, and reported that FDG

was 95% sensitive and 93% specific for diagnosing infection. Fifty one of the prostheses, including ten infected devices, also were studied with WBC/marrow imaging. The sensitivity and specificity of WBC/marrow imaging in this subgroup were 50% and 95.1%, respectively.

Manthey *et al*^[72] reported that FDG was 96% accurate for prosthetic joint infection. They also reported that activity around the femoral head and neck indicated synovitis plus infection, observations that contradict those of previous investigations^[68,69].

Stumpe *et al*^[30] observed that, in patients with painful hip replacements, intense bone prosthesis interface activity was reasonably specific (81% for reader 1 and 85% for reader 2), but not sensitive (33% for reader 1, 56% for reader 2) for diagnosing infection (33% for reader 1, 56% for reader 2). The accuracy of the test, for both readers, was 69%. Bone scintigraphy was more accurate than FDG-PET (80% *vs* 69%) in this investigation.

Van Acker *et al*^[73] studied 21 patients with suspected prosthetic knee infection. FDG-PET was 100% sensitive and 73% specific. Sensitivity and specificity of WBC/bone imaging was 100% and 93%, respectively. Vanquickenborne *et al*^[74] reported similar results.

García-Barrecheuren *et al*^[75] studied 24 hip replacements. FDG-PET was neither sensitive (64%) nor specific (67%) for infection. Delank *et al*^[76] studied 27 patients with failed hip and knee replacements and concluded that FDG-PET could not reliably differentiate between infection and aseptic inflammation.

Love *et al*^[50] evaluated 59 failed lower extremity joint prostheses with FDG-PET and WBC/marrow imaging. Among the criteria used for image interpretation, bone prosthesis interface activity, with a target to background ratio greater than 3.6 for hip replacements and 3.1 for knee replacements was the most accurate (71%) for diagnosing infection. The accuracy of WBC/marrow imaging, in contrast, was 95%.

In a met analysis sensitivity and specificity of FDG-PET for prosthetic joint infection were 82% and 87% respectively^[77]. In view of the large number of inconsistent and contradictory results that have been reported to date, the place of FDG-PET in the assessment of the prosthetic joint remains to be determined.

Infection-specific tracers

Given the dramatic differences in the management of aseptic loosening and infection of prostheses, the importance of accurately differentiating between these two conditions cannot be overstated. The development of an infection specific imaging agent would be a welcome improvement over the current procedures.

The potential of radiolabeled antibiotics as “infection-specific” radiopharmaceuticals has been explored. The hypothesis is that the radiolabeled antibiotic enters, and is metabolized by, bacteria and could be used to accurately localize infection. Although the results of initial studies were encouraging, subsequent investigations raised significant doubts about the validity of this concept and

enthusiasm for radiolabeled antibiotics has faded^[78-81].

Antimicrobial peptides bind to the bacterial cell membrane. Their expression may be constant or induced on contact with microbes. They also can be transported *via* leukocytes^[82]. ^{99m}Tc-UBI 29-41, a radiolabeled synthetic fragment of the naturally occurring human antimicrobial peptide ubiquicidin, appears to be able to differentiate between infection and sterile inflammation^[83]. Recent data suggest that this agent is both sensitive and specific for prosthetic joint infection^[84,85].

FUTURE

Initial data suggest that single-photon emission computed tomography (SPECT)/electronic computer X-ray tomography technique (CT) may contribute useful information to the evaluation of the failed joint arthroplasty. For example, nuclear arthrography often is performed as a dual isotope procedure, in which the bone scan provides “anatomic detail” and another radiopharmaceutical, often an indium-111 labeled complex, is used for the arthrographic component. A potential alternative to the dual isotope technique is SPECT/CT arthrography, in which the CT component provides the anatomic landmarks necessary for radiopharmaceutical localization. In one investigation SPECT/CT was significantly better than planar imaging for the acetabular cup of hip prostheses^[86]. For knee arthroplasties, SPECT/CT offered a significant improvement over planar imaging for detecting femoral component loosening. SPECT/CT also was better than planar imaging for detecting tibial component loosening but statistical significance was not reached.

Hirschmann *et al*^[87] reported that SPECT/CT could detect mechanical loosening, joint instability, component malposition, and patellofemoral problems in patients with knee arthroplasties. In another investigation of knee arthroplasties, SPECT/CT significantly altered the working diagnosis and proposed treatment, and changed the initial intention to revise or treat the patients non-surgically. The diagnosis made with SPECT/CT was correct in all patients who underwent surgery^[88].

Graute *et al*^[89] evaluated the contribution of SPECT/CT as an adjunct to planar scintigraphy with ^{99m}Tc-besile-somab for diagnosing and localizing low-grade prosthetic joint infection. Planar imaging was 66% sensitive, and 60% specific for infection. Combining planar imaging with SPECT/CT, sensitivity and specificity improved to 89% and 73%, respectively.

The potential impact of SPECT/CT extends well beyond diagnosing infection. In patients with a positive study, for example, the examination could provide information about the extent of infection as well as other abnormalities involving the native bone and the prosthesis (Figure 7C-E); joint aspiration and culture could be performed at the same time. In patients with negative studies the CT component could provide information about other causes of prosthetic failure. In such a scenario patients would be spared the need to undergo multiple imaging

tests at different times and possibly different locations, and a diagnosis could be made more expeditiously.

Fluorine-18-fluoride-PET (fluoride-PET) bone imaging shows great promise in the evaluation of joint arthroplasties. Some investigators have used this test in a manner analogous to that of conventional bone scintigraphy. Sterner *et al*^[90] compared the results of fluoride-PET bone scans to plain radiographs in 14 patients with painful knee arthroplasties. Sensitivity, specificity, and accuracy of the fluoride PET study for detecting aseptic loosening were 100%, 56%, and 71%, respectively. Sensitivity, specificity, and accuracy of plain radiographs were 43%, 86%, and 64%, respectively.

Other investigators have explored the potential of fluoride-PET for studying bone metabolism. An important concern in patients undergoing hip resurfacing arthroplasty is the viability of the remaining femoral head, and the risk of postoperative fracture or avascular necrosis. Conventional radiographs are of limited utility, because the femoral head is obscured by the overlying metallic components of the device. Ullmark *et al*^[91] reported that fluoride PET correctly identified aseptic necrosis in three of fourteen patients with a hip resurfacing arthroplasty. Radiographs were negative in all cases. These investigators concluded that fluoride-PET is useful for evaluating bone metabolism at resurfacing arthroplasty. In another investigation, Ullmark *et al*^[92] studied bone mineralization around the femoral component of cementless hip arthroplasties. They concluded that fluoride-PET is a valuable tool for analysis of bone mineralization patterns around uncemented femoral stems and together with the modified Polar Map system could be useful to study metabolic bone responses to prosthetic implants.

There are recent data that suggest that Fluoride-PET is a valuable tool to analyse bone formation and secondary stabilization of a press-fit acetabular cup in patients undergoing total hip arthroplasty^[93].

CONCLUSION

At the moment, nuclear medicine is most valuable for determining whether or not a painful joint prosthesis is infected. WBC/marrow imaging, currently, is the best available imaging test for this purpose. Preliminary data suggest that SPECT/CT, in addition to providing information about the presence and extent of infection, may be able to provide additional information about other conditions that cause joint replacements to fail. Fluoride-PET also may provide hitherto unknown insight into periprosthetic bone metabolism.

REFERENCES

- 1 Love C, Marwin SE, Palestro CJ. Nuclear medicine and the infected joint replacement. *Semin Nucl Med* 2009; **39**: 66-78 [PMID: 19038601 DOI: 10.1053/j.semnuclmed.2008.08.007]
- 2 Wooley PH, Nasser S, Fitzgerald RH. The immune response to implant materials in humans. *Clin Orthop Relat Res* 1996; **(326)**: 63-70 [PMID: 8620660]

- 3 **Toumbis CA**, Kronick JL, Wooley PH, Nasser S. Total joint arthroplasty and the immune response. *Semin Arthritis Rheum* 1997; **27**: 44-47 [PMID: 9287389 DOI: 10.1016/S0049-0172(97)80036-4]
- 4 **Spector M**, Shortkroff S, Hsu HP, Lane N, Sledge CB, Thornhill TS. Tissue changes around loose prostheses. A canine model to investigate the effects of an antiinflammatory agent. *Clin Orthop Relat Res* 1990; (**261**): 140-152 [PMID: 2245540]
- 5 **Pandey R**, Drakoulakis E, Athanasou NA. An assessment of the histological criteria used to diagnose infection in hip revision arthroplasty tissues. *J Clin Pathol* 1999; **52**: 118-123 [PMID: 10396239 DOI: 10.1136/jcp.52.2.118]
- 6 **Del Arco A**, Bertrand ML. The diagnosis of periprosthetic infection. *Open Orthop J* 2013; **7**: 178-183 [PMID: 23898349 DOI: 10.2174/1874325001307010178]
- 7 **Hanssen AD**, Rand JA. Evaluation and treatment of infection at the site of a total hip or knee arthroplasty. *Instr Course Lect* 1999; **48**: 111-122 [PMID: 10098033]
- 8 **Palestro CJ**, Love C, Miller TT. Infection and musculoskeletal conditions: Imaging of musculoskeletal infections. *Best Pract Res Clin Rheumatol* 2006; **20**: 1197-1218 [PMID: 17127204 DOI: 10.1016/j.berh.2006.08.009]
- 9 **Tomas X**, Bori G, Garcia S, Garcia-Diez AI, Pomes J, Soriano A, Ríos J, Almela M, Mensa J, Gallart X, Martinez JC, Riba J. Accuracy of CT-guided joint aspiration in patients with suspected infection status post-total hip arthroplasty. *Skeletal Radiol* 2011; **40**: 57-64 [PMID: 20449586 DOI: 10.1007/s00256-010-0940-2]
- 10 **Gelman MI**, Coleman RE, Stevens PM, Davey BW. Radiography, radionuclide imaging, and arthrography in the evaluation of total hip and knee replacement. *Radiology* 1978; **128**: 677-682 [PMID: 674636]
- 11 **Weiss PE**, Mall JC, Hoffer PB, Murray WR, Rodrigo JJ, Genant HK. 99mTc-methylene diphosphonate bone imaging in the evaluation of total hip prostheses. *Radiology* 1979; **133**: 727-729 [PMID: 504654]
- 12 **McInerney DP**, Hyde ID. Technetium 99Tcm pyrophosphate scanning in the assessment of the painful hip prosthesis. *Clin Radiol* 1978; **29**: 513-517 [PMID: 710036 DOI: 10.1016/S0009-9260(78)80039-7]
- 13 **Williamson BR**, McLaughlin RE, Wang GW, Miller CW, Teates CD, Bray ST. Radionuclide bone imaging as a means of differentiating loosening and infection in patients with a painful total hip prosthesis. *Radiology* 1979; **133**: 723-725 [PMID: 504653]
- 14 **Williams F**, McCall IW, Park WM, O'Connor BT, Morris V. Gallium-67 scanning in the painful total hip replacement. *Clin Radiol* 1981; **32**: 431-439 [PMID: 7249522 DOI: 10.1016/S0009-9260(81)80292-9]
- 15 **Mountford PJ**, Hall FM, Wells CP, Coakley AJ. 99Tcm-MDP, 67Ga-citrate and 111In-leucocytes for detecting prosthetic hip infection. *Nucl Med Commun* 1986; **7**: 113-120 [PMID: 3459112]
- 16 **Aliabadi P**, Tumeh SS, Weissman BN, McNeil BJ. Cemented total hip prosthesis: radiographic and scintigraphic evaluation. *Radiology* 1989; **173**: 203-206 [PMID: 2675184]
- 17 **Utj JA**, Lull RJ, Galvin EG. Asymptomatic total hip prosthesis: natural history determined using Tc-99m MDP bone scans. *Radiology* 1986; **161**: 509-512 [PMID: 3763923]
- 18 **Oswald SG**, Van Nostrand D, Savory CG, Callaghan JJ. Three-phase bone scan and indium white blood cell scintigraphy following porous coated hip arthroplasty: a prospective study of the prosthetic tip. *J Nucl Med* 1989; **30**: 1321-1331 [PMID: 2502609]
- 19 **Oswald SG**, Van Nostrand D, Savory CG, Anderson JH, Callaghan JJ. The acetabulum: a prospective study of three-phase bone and indium white blood cell scintigraphy following porous-coated hip arthroplasty. *J Nucl Med* 1990; **31**: 274-280 [PMID: 2307997]
- 20 **Ashbrooke AB**, Calvert PT. Bone scan appearances after uncemented hip replacement. *J R Soc Med* 1990; **83**: 768-769 [PMID: 2269959]
- 21 **Gallo J**, Kamínek M, Myslivecek M, Zapletalová J, Spicka J. [Validity of bone scintigraphy for the diagnosis of periprosthetic complications in hydroxyapatite-coated total hip arthroplasty]. *Acta Chir Orthop Traumatol Cech* 2004; **71**: 345-351 [PMID: 15686635]
- 22 **Rosenthal L**, Lepanto L, Raymond F. Radiophosphate uptake in asymptomatic knee arthroplasty. *J Nucl Med* 1987; **28**: 1546-1549 [PMID: 3655908]
- 23 **Hofmann AA**, Wyatt RW, Daniels AU, Armstrong L, Alazraki N, Taylor A. Bone scans after total knee arthroplasty in asymptomatic patients. Cemented versus cementless. *Clin Orthop Relat Res* 1990; (**251**): 183-188 [PMID: 2295172]
- 24 **Palestro CJ**, Swyer AJ, Kim CK, Goldsmith SJ. Infected knee prosthesis: diagnosis with In-111 leukocyte, Tc-99m sulfur colloid, and Tc-99m MDP imaging. *Radiology* 1991; **179**: 645-648 [PMID: 2027967]
- 25 **Schauwecker DS**. The scintigraphic diagnosis of osteomyelitis. *AJR Am J Roentgenol* 1992; **158**: 9-18 [PMID: 1727365 DOI: 10.2214/ajr.158.1.1727365]
- 26 **Nagoya S**, Kaya M, Sasaki M, Tateda K, Yamashita T. Diagnosis of peri-prosthetic infection at the hip using triple-phase bone scintigraphy. *J Bone Joint Surg Br* 2008; **90**: 140-144 [PMID: 18256077]
- 27 **Magnuson JE**, Brown ML, Hauser MF, Berquist TH, Fitzgerald RH, Klee GG. In-111-labeled leukocyte scintigraphy in suspected orthopedic prosthesis infection: comparison with other imaging modalities. *Radiology* 1988; **168**: 235-239 [PMID: 3380966]
- 28 **Levitsky KA**, Hozack WJ, Balderston RA, Rothman RH, Gluckman SJ, Maslack MM, Booth RE. Evaluation of the painful prosthetic joint. Relative value of bone scan, sedimentation rate, and joint aspiration. *J Arthroplasty* 1991; **6**: 237-244 [PMID: 1940929 DOI: 10.1016/S0883-5403(06)80170-1]
- 29 **Reinartz P**, Mumme T, Hermanns B, Cremerius U, Wirtz DC, Schaefer WM, Niethard F-, Buell U. Radionuclide imaging of the painful hip arthroplasty: positron-emission tomography versus triple-phase bone scanning. *J Bone Joint Surg Br* 2005; **87**: 465-470 [PMID: 15795194 DOI: 10.1302/0301-620X.87B4.14954]
- 30 **Stumpe KD**, Nötzli HP, Zanetti M, Kamel EM, Hany TF, Görrer GW, von Schulthess GK, Hodler J. FDG PET for differentiation of infection and aseptic loosening in total hip replacements: comparison with conventional radiography and three-phase bone scintigraphy. *Radiology* 2004; **231**: 333-341 [PMID: 15044748 DOI: 10.1148/radiol.2312021596]
- 31 **Palestro CJ**. Scintigraphic diagnosis of inflammation and infection. In: Brant WE, Helms CA, editors. *Fundamentals of Diagnostic Radiology*. 4th ed. Philadelphia: Lippincott, Williams and Wilkins, 2012: 1339-1352
- 32 **Reing CM**, Richin PF, Kenmore PI. Differential bone-scanning in the evaluation of a painful total joint replacement. *J Bone Joint Surg Am* 1979; **61**: 933-936 [PMID: 479243]
- 33 **Rushton N**, Coakley AJ, Tudor J, Wraight EP. The value of technetium and gallium scanning in assessing pain after total hip replacement. *J Bone Joint Surg Br* 1982; **64**: 313-318 [PMID: 6212587]
- 34 **McKillop JH**, McKay I, Cuthbert GF, Fogelman I, Gray HW, Sturrock RD. Scintigraphic evaluation of the painful prosthetic joint: a comparison of gallium-67 citrate and indium-111 labelled leucocyte imaging. *Clin Radiol* 1984; **35**: 239-241 [PMID: 6425000 DOI: 10.1016/S0009-9260(84)80148-8]
- 35 **Tehranezhadeh J**, Gubernick I, Blaha D. Prospective study of sequential technetium-99m phosphate and gallium imaging in painful hip prostheses (comparison of diagnostic modalities). *Clin Nucl Med* 1988; **13**: 229-236 [PMID: 3163533]
- 36 **Gómez-Luzuriaga MA**, Galán V, Villar JM. Scintigraphy with Tc, Ga and In in painful total hip prostheses. *Int Orthop* 1988; **12**: 163-167 [PMID: 3410621 DOI: 10.1007/BF00266983]
- 37 **Kraemer WJ**, Saplys R, Waddell JP, Morton J. Bone scan,

- gallium scan, and hip aspiration in the diagnosis of infected total hip arthroplasty. *J Arthroplasty* 1993; **8**: 611-616 [PMID: 8301279 DOI: 10.1016/0883-5403(93)90008-R]
- 38 **Merkel KD**, Fitzgerald RH, Brown ML. Scintigraphic examination of total hip arthroplasty: comparison of indium with technetium-gallium in the loose and infected canine arthroplasty. *Hip* 1984; **163-192** [PMID: 6597183]
- 39 **Merkel KD**, Brown ML, Fitzgerald RH. Sequential technetium-99m HMDP-gallium-67 citrate imaging for the evaluation of infection in the painful prosthesis. *J Nucl Med* 1986; **27**: 1413-1417 [PMID: 3462352]
- 40 **Palestro CJ**, Love C, Bhargava KK. Labeled leukocyte imaging: current status and future directions. *Q J Nucl Med Mol Imaging* 2009; **53**: 105-123 [PMID: 19182734]
- 41 **Pring DJ**, Henderson RG, Keshavarzian A, Rivett AG, Krausz T, Coombs RR, Lavender JP. Indium-granulocyte scanning in the painful prosthetic joint. *AJR Am J Roentgenol* 1986; **147**: 167-172 [PMID: 3487209]
- 42 **Pring DJ**, Henderson RG, Rivett AG, Krausz T, Coombs RR, Lavender JP. Autologous granulocyte scanning of painful prosthetic joints. *J Bone Joint Surg Br* 1986; **68**: 647-652 [PMID: 3733846]
- 43 **Rand JA**, Brown ML. The value of indium 111 leukocyte scanning in the evaluation of painful or infected total knee arthroplasties. *Clin Orthop Relat Res* 1990; **(259)**: 179-182 [PMID: 2208853]
- 44 **Wukich DK**, Abreu SH, Callaghan JJ, Van Nostrand D, Savory CG, Egli DF, Garcia JE, Berrey BH. Diagnosis of infection by preoperative scintigraphy with indium-labeled white blood cells. *J Bone Joint Surg Am* 1987; **69**: 1353-1360 [PMID: 3126189]
- 45 **Johnson JA**, Christie MJ, Sandler MP, Parks PF, Homra L, Kaye JJ. Detection of occult infection following total joint arthroplasty using sequential technetium-99m HDP bone scintigraphy and indium-111 WBC imaging. *J Nucl Med* 1988; **29**: 1347-1353 [PMID: 3404252]
- 46 **Palestro CJ**, Kim CK, Swyer AJ, Capozzi JD, Solomon RW, Goldsmith SJ. Total-hip arthroplasty: periprosthetic indium-111-labeled leukocyte activity and complementary technetium-99m-sulfur colloid imaging in suspected infection. *J Nucl Med* 1990; **31**: 1950-1955 [PMID: 2266391]
- 47 **Palestro CJ**, Love C, Tronco GG, Tomas MB, Rini JN. Combined labeled leukocyte and technetium 99m sulfur colloid bone marrow imaging for diagnosing musculoskeletal infection. *Radiographics* 2006; **26**: 859-870 [PMID: 16702459 DOI: 10.1148/rg.263055139]
- 48 **Teller RE**, Christie MJ, Martin W, Nance EP, Haas DW. Sequential indium-labeled leukocyte and bone scans to diagnose prosthetic joint infection. *Clin Orthop Relat Res* 2000; **(373)**: 241-247 [PMID: 10810483]
- 49 **Mulamba L**, Ferrant A, Leners N, de Nayer P, Rombouts JJ, Vincent A. Indium-111 leucocyte scanning in the evaluation of painful hip arthroplasty. *Acta Orthop Scand* 1983; **54**: 695-697 [PMID: 6670484 DOI: 10.3109/17453678308996613]
- 50 **Love C**, Marwin SE, Tomas MB, Krauss ES, Tronco GG, Bhargava KK, Nichols KJ, Palestro CJ. Diagnosing infection in the failed joint replacement: a comparison of coincidence detection 18F-FDG and 111In-labeled leukocyte/99mTc-sulfur colloid marrow imaging. *J Nucl Med* 2004; **45**: 1864-1871 [PMID: 15534056]
- 51 **El Espera I**, Blondet C, Moullart V, Saïdi L, Havet E, Mertl P, Canarelli B, Schmit JL, Meyer ME. The usefulness of 99mTc sulfur colloid bone marrow scintigraphy combined with 111In leucocyte scintigraphy in prosthetic joint infection. *Nucl Med Commun* 2004; **25**: 171-175 [PMID: 15154708]
- 52 **Joseph TN**, Mujtaba M, Chen AL, Maurer SL, Zuckerman JD, Maldjian C, Di Cesare PE. Efficacy of combined technetium-99m sulfur colloid/indium-111 leukocyte scans to detect infected total hip and knee arthroplasties. *J Arthroplasty* 2001; **16**: 753-758 [PMID: 11547374 DOI: 10.1054/arth.2001.24446]
- 53 **Pill SG**, Parvizi J, Tang PH, Garino JP, Nelson C, Zhuang H, Alavi A. Comparison of fluorodeoxyglucose positron emission tomography and (111)indium-white blood cell imaging in the diagnosis of periprosthetic infection of the hip. *J Arthroplasty* 2006; **21**: 91-97 [PMID: 16950069 DOI: 10.1016/j.arth.2006.05.021]
- 54 **Pelosi E**, Baiocco C, Pennone M, Migliaretti G, Varetto T, Maiello A, Bellò M, Bisi G. 99mTc-HMPAO-leukocyte scintigraphy in patients with symptomatic total hip or knee arthroplasty: improved diagnostic accuracy by means of semiquantitative evaluation. *J Nucl Med* 2004; **45**: 438-444 [PMID: 15001684]
- 55 **Love C**, Palestro CJ. 99mTc-fanolesomab Palatin Technologies. *IDrugs* 2003; **6**: 1079-1085 [PMID: 14600841]
- 56 **Boubaker A**, Delaloye AB, Blanc CH, Dutoit M, Leyvraz PF, Delaloye B. Immunoscintigraphy with antigranulocyte monoclonal antibodies for the diagnosis of septic loosening of hip prostheses. *Eur J Nucl Med* 1995; **22**: 139-147 [PMID: 7758501 DOI: 10.1007/BF00838944]
- 57 **Gratz S**, Höffken H, Kaiser JW, Behr TM, Strosche H, Reize P. [Nuclear medical imaging in case of painful knee arthroplasty]. *Radiologe* 2009; **49**: 59-67 [PMID: 18597065 DOI: 10.1007/s00117-008-1703-0]
- 58 **Klett R**, Steiner D, Puille M, Khalisi A, Matter HP, Stürz H, Bauer R. [Antigranulocyte scintigraphy of septic loosening of hip endoprosthesis: effect of different methods of analysis]. *Nuklearmedizin* 2001; **40**: 75-79 [PMID: 11475076]
- 59 **Klett R**, Kordelle J, Stahl U, Khalisi A, Puille M, Steiner D, Bauer R. Immunoscintigraphy of septic loosening of knee endoprosthesis: a retrospective evaluation of the antigranulocyte antibody BW 250/183. *Eur J Nucl Med Mol Imaging* 2003; **30**: 1463-1466 [PMID: 14579084 DOI: 10.1007/s00259-003-1275-1]
- 60 **von Rothenburg T**, Schoellhammer M, Schaffstein J, Koesler O, Schmid G. Imaging of infected total arthroplasty with Tc-99m-labeled antigranulocyte antibody Fab' fragments. *Clin Nucl Med* 2004; **29**: 548-551 [PMID: 15311121]
- 61 **Iyengar KP**, Vinjamuri S. Role of 99mTc Sulesomab in the diagnosis of prosthetic joint infections. *Nucl Med Commun* 2005; **26**: 489-496 [PMID: 15891591]
- 62 **Pakos EE**, Fotopoulos AD, Stafilas KS, Gavriilidis I, Al Boukarali G, Tsiouris S, Xenakis TA. Use of (99m)Tc-sulesomab for the diagnosis of prosthesis infection after total joint arthroplasty. *J Int Med Res* 2007; **35**: 474-481 [PMID: 17697524 DOI: 10.1177/147323000703500406]
- 63 **Rubello D**, Casara D, Maran A, Avogaro A, Tiengo A, Muzzio PC. Role of anti-granulocyte Fab' fragment antibody scintigraphy (LeukoScan) in evaluating bone infection: acquisition protocol, interpretation criteria and clinical results. *Nucl Med Commun* 2004; **25**: 39-47 [PMID: 15061263]
- 64 **Rubello D**, Rampin L, Banti E, Massaro A, Cittadin S, Cattelan AM, Al-Nahhas A. Diagnosis of infected total knee arthroplasty with anti-granulocyte scintigraphy: the importance of a dual-time acquisition protocol. *Nucl Med Commun* 2008; **29**: 331-335 [PMID: 18317296]
- 65 **Gratz S**, Behr TM, Reize P, Pfestroff A, Kampen WU, Höffken H. (99m)Tc-Fab' fragments (sulesomab) for imaging septically loosened total knee arthroplasty. *J Int Med Res* 2009; **37**: 54-67 [PMID: 19215674 DOI: 10.1177/147323000903700107]
- 66 **Sousa R**, Massada M, Pereira A, Fontes F, Amorim I, Oliveira A. Diagnostic accuracy of combined 99mTc-sulesomab and 99mTc-nanocolloid bone marrow imaging in detecting prosthetic joint infection. *Nucl Med Commun* 2011; **32**: 834-839 [PMID: 21799370]
- 67 **Love C**, Tomas MB, Tronco GG, Palestro CJ. FDG PET of infection and inflammation. *Radiographics* 2005; **25**: 1357-1368 [PMID: 16160116 DOI: 10.1148/rg.255045122]
- 68 **Zhuang H**, Duarte PS, Pourdehnad M, Maes A, Van Acker F, Shnier D, Garino JP, Fitzgerald RH, Alavi A. The promising role of 18F-FDG PET in detecting infected lower limb prosthesis implants. *J Nucl Med* 2001; **42**: 44-48 [PMID: 11197979]
- 69 **Chacko TK**, Zhuang H, Stevenson K, Moussavian B, Alavi

- A. The importance of the location of fluorodeoxyglucose uptake in periprosthetic infection in painful hip prostheses. *Nucl Med Commun* 2002; **23**: 851-855 [PMID: 12195089]
- 70 **Cremerius U**, Mumme T, Reinartz P, Wirtz D, Niethard FU, Büll U. [Analysis of (18)F-FDG uptake patterns in PET for diagnosis of septic and aseptic loosening after total hip arthroplasty]. *Nuklearmedizin* 2003; **42**: 234-239 [PMID: 14668955]
- 71 **Gravius S**, Gebhard M, Ackermann D, Büll U, Hermanns-Sachweh B, Mumme T. [Analysis of 18F-FDG uptake pattern in PET for diagnosis of aseptic loosening versus prosthesis infection after total knee arthroplasty. A prospective pilot study]. *Nuklearmedizin* 2010; **49**: 115-123 [PMID: 20407734 DOI: 10.3413/nukmed-0278]
- 72 **Manthey N**, Reinhard P, Moog F, Knesewitsch P, Hahn K, Tatsch K. The use of [18 F]fluorodeoxyglucose positron emission tomography to differentiate between synovitis, loosening and infection of hip and knee prostheses. *Nucl Med Commun* 2002; **23**: 645-653 [PMID: 12089487]
- 73 **Van Acker F**, Nuyts J, Maes A, Vanquickenborne B, Stuyck J, Bellemans J, Vleugels S, Bormans G, Mortelmans L. FDG-PET, 99mTc-HMPAO white blood cell SPET and bone scintigraphy in the evaluation of painful total knee arthroplasties. *Eur J Nucl Med Mol Imaging* 2001; **28**: 1496-1504 [PMID: 11685492 DOI: 10.1007/s002590100603]
- 74 **Vanquickenborne B**, Maes A, Nuyts J, Van Acker F, Stuyck J, Mulier M, Verbruggen A, Mortelmans L. The value of (18)FDG-PET for the detection of infected hip prosthesis. *Eur J Nucl Med Mol Imaging* 2003; **30**: 705-715 [PMID: 12616322 DOI: 10.1007/s00259-002-1109-6]
- 75 **García-Barrecheguren E**, Rodríguez Fraile M, Toledo Santana G, Valentí Nin JR, Richter Echevarría JA. [FDG-PET: a new diagnostic approach in hip prosthetic replacement]. *Rev Esp Med Nucl* 2007; **26**: 208-220 [PMID: 17662187 DOI: 10.1157/13107972]
- 76 **Delank KS**, Schmidt M, Michael JW, Dietlein M, Schicha H, Eysel P. The implications of 18F-FDG PET for the diagnosis of endoprosthetic loosening and infection in hip and knee arthroplasty: results from a prospective, blinded study. *BMC Musculoskelet Disord* 2006; **7**: 20 [PMID: 16512924 DOI: 10.1186/1471-2474-7-20]
- 77 **Kwee TC**, Kwee RM, Alavi A. FDG-PET for diagnosing prosthetic joint infection: systematic review and meta-analysis. *Eur J Nucl Med Mol Imaging* 2008; **35**: 2122-2132 [PMID: 18704405 DOI: 10.1007/s00259-008-0887-x]
- 78 **Britton KE**, Wareham DW, Das SS, Solanki KK, Amaral H, Bhatnagar A, Katamihardja AH, Malamitsi J, Moustafa HM, Soroa VE, Sundram FX, Padhy AK. Imaging bacterial infection with (99m)Tc-ciprofloxacin (Infecton). *J Clin Pathol* 2002; **55**: 817-823 [PMID: 12401818 DOI: 10.1136/jcp.55.11.817]
- 79 **Sonmezoglu K**, Sonmezoglu M, Halac M, Akgün I, Türkmen C, Onsel C, Kanmaz B, Solanki K, Britton KE, Uslu I. Usefulness of 99mTc-ciprofloxacin (infecton) scan in diagnosis of chronic orthopedic infections: comparative study with 99mTc-HMPAO leukocyte scintigraphy. *J Nucl Med* 2001; **42**: 567-574 [PMID: 11337543]
- 80 **Sarda L**, Crémieux AC, Lebellec Y, Meulemans A, Lebtahi R, Hayem G, Génin R, Delahaye N, Hutten D, Le Guludec D. Inability of 99mTc-ciprofloxacin scintigraphy to discriminate between septic and sterile osteoarticular diseases. *J Nucl Med* 2003; **44**: 920-926 [PMID: 12791820]
- 81 **Siaens RH**, Rennen HJ, Boerman OC, Dierckx R, Slegers G. Synthesis and comparison of 99mTc-enrofloxacin and 99mTc-ciprofloxacin. *J Nucl Med* 2004; **45**: 2088-2094 [PMID: 15585486]
- 82 **Lupetti A**, Pauwels EK, Nibbering PH, Welling MM. 99mTc-antimicrobial peptides: promising candidates for infection imaging. *Q J Nucl Med* 2003; **47**: 238-245 [PMID: 14973416]
- 83 **Lupetti A**, Welling MM, Mazzi U, Nibbering PH, Pauwels EK. Technetium-99m labelled fluconazole and antimicrobial peptides for imaging of *Candida albicans* and *Aspergillus fumigatus* infections. *Eur J Nucl Med Mol Imaging* 2002; **29**: 674-679 [PMID: 11976807 DOI: 10.1007/s00259-001-0760-7]
- 84 **Sarda-Mantel L**, Saleh-Mghir A, Welling MM, Meulemans A, Vrigneaud JM, Raguin O, Hervatin F, Martet G, Chau F, Lebtahi R, Le Guludec D. Evaluation of 99mTc-UBI 29-41 scintigraphy for specific detection of experimental *Staphylococcus aureus* prosthetic joint infections. *Eur J Nucl Med Mol Imaging* 2007; **34**: 1302-1309 [PMID: 17334764 DOI: 10.1007/s00259-007-0368-7]
- 85 **Arteaga de Murphy C**, Gemmel F, Balter J. Clinical trial of specific imaging of infections. *Nucl Med Commun* 2010; **31**: 726-733 [PMID: 20526222]
- 86 **Chew CG**, Lewis P, Middleton F, van den Wijngaard R, Deshaies A. Radionuclide arthrogram with SPECT/CT for the evaluation of mechanical loosening of hip and knee prostheses. *Ann Nucl Med* 2010; **24**: 735-743 [PMID: 20976575 DOI: 10.1007/s12149-010-0419-1]
- 87 **Hirschmann MT**, Iranpour F, Konala P, Kerner A, Rasch H, Cobb JP, Friederich NF. A novel standardized algorithm for evaluating patients with painful total knee arthroplasty using combined single photon emission tomography and conventional computerized tomography. *Knee Surg Sports Traumatol Arthrosc* 2010; **18**: 939-944 [PMID: 20148324 DOI: 10.1007/s00167-010-1070-z]
- 88 **Hirschmann MT**, Konala P, Iranpour F, Kerner A, Rasch H, Friederich NF. Clinical value of SPECT/CT for evaluation of patients with painful knees after total knee arthroplasty - a new dimension of diagnostics? *BMC Musculoskelet Disord* 2011; **12**: 36 [PMID: 21294878 DOI: 10.1186/1471-2474-12-36]
- 89 **Graute V**, Feist M, Lehner S, Haug A, Müller PE, Bartenstein P, Hacker M. Detection of low-grade prosthetic joint infections using 99mTc-antigranulocyte SPECT/CT: initial clinical results. *Eur J Nucl Med Mol Imaging* 2010; **37**: 1751-1759 [PMID: 20309680 DOI: 10.1007/s00259-010-1431-3]
- 90 **Sternert T**, Pink R, Freudenberg L, Jentzen T, Quitmann H, Bockisch A, Lör F. The role of [18F]fluoride positron emission tomography in the early detection of aseptic loosening of total knee arthroplasty. *Int J Surg* 2007; **5**: 99-104 [PMID: 17448973 DOI: 10.1016/j.ijsu.2006.05.002]
- 91 **Ullmark G**, Sundgren K, Milbrink J, Nilsson O, Sörensen J. Osteonecrosis following resurfacing arthroplasty. *Acta Orthop* 2009; **80**: 670-674 [PMID: 19995317 DOI: 10.3109/17453670903278258]
- 92 **Ullmark G**, Nilsson O, Maripuu E, Sörensen J. Analysis of bone mineralization on uncemented femoral stems by [18F]-fluoride-PET: a randomized clinical study of 16 hips in 8 patients. *Acta Orthop* 2013; **84**: 138-144 [PMID: 23506163 DOI: 10.3109/17453674.2013.786632]
- 93 **Ullmark G**, Sörensen J, Nilsson O. Analysis of bone formation on porous and calcium phosphate-coated acetabular cups: a randomised clinical [18F]fluoride PET study. *Hip Int* 2012; **22**: 172-178 [PMID: 22547382 DOI: 10.5301/HIP.2012.9233]

P- Reviewer: Aquila I, Liu Y, Tang GH S- Editor: Ma YJ
L- Editor: A E- Editor: Lu YJ



Echographic imaging of tumoral cells through novel nanosystems for image diagnosis

Marco Di Paola, Fernanda Chiriaco, Giulia Soloperto, Francesco Conversano, Sergio Casciaro

Marco Di Paola, Fernanda Chiriaco, Giulia Soloperto, Francesco Conversano, Sergio Casciaro, Nanoimaging LAB and Bioengineering Division of the National Research Council, Institute of Clinical Physiology, 73100 Lecce, Italy
Sergio Casciaro, Consiglio Nazionale delle Ricerche, Istituto di Fisiologia Clinica (CNR-IFC) c/o Campus Ecotekne, 73100 Lecce, Italy

Author contributions: All the authors were involved in the design and writing the manuscript; Casciaro S conceived and coordinated the scientific work for the manuscript.

Supported by Bando Laboratori, DD MIUR 14.5.2005 n.602/Ric/2005 of the Italian Ministry of Instruction and Research, No. DM18604; by FESR P.O. Apulia Region 2007-2013, Action 1.2.4, No. 3Q5AX31; and by the Progetto Bandiera NANOMAX ENCODER

Correspondence to: Dr. Sergio Casciaro, Consiglio Nazionale delle Ricerche, Istituto di Fisiologia Clinica (CNR-IFC) c/o Campus Ecotekne, via per Monteroni, 73100 Lecce, Italy. sergio.casciaro@cnr.it

Telephone: +39-0832-422310 Fax: +39-0832-422341

Received: January 29, 2014 Revised: April 25, 2014

Accepted: May 16, 2014

Published online: March 28, 2015

Abstract

Since the recognition of disease molecular basis, it has become clear that the keystone moments of medical practice, namely early diagnosis, appropriate therapeutic treatment and patient follow-up, must be approached at a molecular level. These objectives will be in the near future more effectively achievable thanks to the impressive developments in nanotechnologies and their applications to the biomedical field, starting-up the nanomedicine era. The continuous advances in the development of biocompatible smart nanomaterials, in particular, will be crucial in several aspects of medicine. In fact, the possibility of manufacturing nanoparticle contrast agents that can be selectively targeted to specific pathological cells has extended molecular im-

aging applications to non-ionizing techniques and, at the same time, has made reachable the perspective of combining highly accurate diagnoses and personalized therapies in a single theranostic intervention. Main developing applications of nanosized theranostic agents include targeted molecular imaging, controlled drug release, therapeutic monitoring, guidance of radiation-based treatments and surgical interventions. Here we will review the most recent findings in nanoparticles contrast agents and their applications in the field of cancer molecular imaging employing non-ionizing techniques and disease-specific contrast agents, with special focus on recent findings on those nanomaterials particularly promising for ultrasound molecular imaging and simultaneous treatment of cancer.

© 2015 Baishideng Publishing Group Inc. All rights reserved.

Key words: Ultrasound; Molecular imaging; Nanoparticles contrast agents; Nanomedicine; Theranostics; Early diagnosis; Multimodal medical imaging; Cell targeting; Drug delivery

Core tip: The development of novel nanomaterials specifically targeting diseased cells has made possible their employment as nanosized contrast agents also for non-ionizing molecular imaging techniques namely, magnetic resonance, ultrasound and optical imaging. Among them, ultrasound imaging might represent the best choice because of its low cost, ease of use and wide availability in clinical practice. Unfortunately, their actual employment in molecular imaging is limited due to their low tissue contrast discrimination. Hence, the described development of novel ultrasound targeted contrast agent may play a crucial role for their use in clinical molecular imaging.

Original sources: Di Paola M, Chiriaco F, Soloperto G, Conversano F, Casciaro S. Echographic imaging of tumoral cells through novel

nanosystems for image diagnosis. *World J Radiol* 2014; 6(7): 459-470 Available from: URL: <http://www.wjgnet.com/1949-8470/full/v6/i7/459.htm> DOI: <http://dx.doi.org/10.4329/wjr.v6.i7.459>

INTRODUCTION

One of the hottest research topic of the last decade in the medical field is related to nanomedicine, a new open field of modern medicine relying on advanced nanotechnology applied to medicine. In fact, the latest advances in nanotechnology and their application to the biomedical environment are dramatically changing the overall disease management process, starting from first diagnosis to the evaluation of treatment effects, leading to the concept of personalized medicine, characterized by very early, even pre-symptomatic, diagnosis accompanied by highly-effective targeted therapies^[1-4]. At this regard, the introduction of novel nanotechnology-based techniques in medical imaging and drug delivery allows to define personalized diagnoses and therapies, employing minimally invasive approaches based on non-ionizing imaging techniques for early detection of diseases^[5]. From these recent advances arises the concept of molecular imaging, which is gaining an increasingly important role in both pathology understanding and specific choice of treatment^[6]. Rather than morphological or functional characteristics, molecular imaging techniques are specifically aimed at identifying the molecular causes of disease^[7], with consequent ability to detect molecular and cellular processes in living organisms and to allow an early and careful identification and differentiation between healthy and pathological tissues. The basic aspect of molecular imaging is the use of smart contrast agents able to selectively identify specific molecular targets or cellular processes, highlighting them on the corresponding images. The rationale for the development of these new methods is that many diseases have a molecular basis, whose visualization may result in a number of advantages like early diagnosis, precise staging, real-time monitoring of therapeutic treatment, and better prognostic evaluation. The quality of the final result depends on two key-factors: (1) actual ability of contrast agents to reach their specific biological target and binding to it (targeting); and (2) performance of the detection system in terms of sensitivity and contrast enhancement.

Chemical manipulation of drugs and other nanomaterials may allow a controlled modification of some of their properties and bioactivity such as solubility, blood pool retention times, controlled release, highly specific site-targeted delivery. Concerning this particular aspect, surface functionalization with synthetic polymers and/or specific ligands can target nanosized carriers to specific cells and organs within the body after intravenous or subcutaneous injection^[8-16]. These approaches may thus be used to enhance detection sensitivity in medical imaging and to improve therapeutic effectiveness with concomitant decrease of side effects. In addition, some of the

carriers can be engineered in such a way to be activated by changes in the environmental pH, chemical stimuli, by the application of a rapidly oscillating magnetic field or by the application of an external heat source^[9,17-19]. Furthermore, nanoparticles for specific diagnostic purposes can be designed to act as multifunctional agents capable, for example, to simultaneously produce signals that are detectable by more than one imaging techniques, like ultrasound (US) and magnetic resonance imaging (MRI)^[20,21].

Although different pathological conditions like atherosclerotic plaques, inflammation, angiogenesis and thrombus formation have been identified as possible targets of these innovative methodologies, the most promising applications of nanomedicine are those related to the new approaches to cancer diagnosis and therapy at cellular and molecular level^[5,22-24]. Cancer is widely considered to be one the main cause of death in modern society, characterized by a high mortality rate often due to a late diagnosis available with conventional techniques. Current therapeutic strategies for cancer treatment, which include surgery, chemotherapy and radiotherapy, are largely invasive and exhibit significant toxicities together with a variety of side effects that worsen the quality of life of patients. It is then conceivable that the specific targeting of therapeutic agents (drugs or genes) to tumor tissues may result in a great improvement of treatment effectiveness and decrease of systemic toxicity. For these reasons nanoparticle-mediated drug targeting has been widely explored in recent years, by incorporating anticancer agents into suitable nanocapsules or by attaching therapeutic molecules to nanoparticle surface, and it actually exhibits several advantages like reduced drug dosage, increased pharmaceutical effectiveness, minimal side effects, drug protection against degradation and enhanced drug stability^[10,25,26]. Anyway, one of the aspects of absolute novelty introduced by nanovector drug delivery is represented by the possibility of assessing therapy response, by directly monitoring the localization of targeted nanoparticles through non ionizing imaging techniques. Apart from these advantages, however, the possible toxicity related to nanoparticles themselves is an aspect that requires attention. The assessment of the biocompatibility of nanomaterials and their safety profile is in fact of crucial importance not only for patients treated, which can retain these materials for long period of time, but also for the production, management and disposal processes, which should be strictly regulated.

MOLECULAR IMAGING OF TUMORS

Imaging is a tool of fundamental importance in medical practice in general, and in cancer research in particular. Despite the impressive amount of imaging technologies and their applications available today, early and detailed cancer diagnosis is made possible only by using molecular imaging systems^[27]. Among these, positron emission tomography (PET) is currently the only diagnostic technique

Table 1 Nanoparticles contrast agents for molecular imaging applications

Nanomaterials	Properties	Applications	Ref.
Liposomes	Lipid spherical membranes	<i>In vivo</i> ultrasound and MRI molecular imaging	[37,38]
Emulsions	Oil-in-water-type mixtures	Ultrasound and MRI	[39-41]
Polymers	Single or multiple molecular components	Molecular imaging, drug delivery	[33]
Iron particles	Paramagnetism, superparamagnetism	MRI	[42]
Gold nanoshells	Infrared absorption	MRI, photonics imaging, <i>in vivo</i> photo-thermal therapy	[43-45]
Carbon nanotubes	Fluorescence	<i>In vitro</i> optical imaging	[46-49]
Quantum dots	Fluorescence	Optical imaging	[50-53]

MRI: Magnetic resonance imaging.

in clinical use that provides imaging of tumours at molecular level. PET systems can in fact detect abnormal cellular activity well before any anatomical change is visible and structural anomalies detectable by other macroscopic imaging techniques like ultrasound, magnetic resonance (MRI), X-rays or computed tomography (CT). Nevertheless, since the high cost and the involvement of highly ionizing radiation, with consequent risks for patients, operators and environment, PET examinations cannot be routinely used for patient follow-up or for population screening purposes.

However, the recent advances in the development of smart nanoparticle contrast agents (NPCAs) opened new perspectives for diagnostic imaging techniques, allowing on one hand the extension of molecular imaging applications to non-ionizing techniques^[28], like MRI^[29], ultrasound^[23,30] and optical imaging^[31,52], and, on the other hand, introducing the possibility of combining highly detailed diagnoses and personalized therapies in single theranostic interventions^[5].

A short overview of the most interesting properties of novel NPCAs and a summary of the most significant approaches to early molecular cancer diagnosis by employing non-ionizing techniques in combination with NPCAs will be illustrated in the next subparagraphs.

NPCAS

In recent years, many efforts have been made to synthesize new NPCAs suitable for cellular and molecular imaging through non-ionizing diagnostic techniques. To obtain an effective diagnostic imaging, NPCA must be designed to have the following basic characteristics: long circulating half-life, high vascular endothelium permeability, selective binding to the cellular/molecular target of interest, significant contrast-to-noise ratio enhancement, absence of toxicity, ease of clinical use, and compatibility with standard commercially available imaging systems^[22,33].

The very crucial point is the effective interaction of NPCAs with their molecular targets, which is strongly dependent on nanoparticle size. In normal conditions, 50 nm can be considered as the upper size threshold to cross the vascular endothelium and directly target extravascular cells, larger diameters allowing only the recognition of intravascular targets. However, since the consistent dif-

ference between normal and tumor vessels, effective targeting of cancer cells beyond the capillary endothelium can occur also with bigger NPCAs. In fact, due to the aberrant angiogenesis, tumor vasculature is more leaky than normal one and exhibits the so-called EPR (enhanced permeability and retention) effect, which results in enhanced permeability and retention of particles that are smaller than the pore diameter of tumor endothelium (typically between 380 and 780 nm)^[34-36].

One of the most common strategies to selectively target specific cellular receptors is functionalization, which is the conjugation of NPCA surface with specific ligands. Sometimes, a polymeric coating of particles may be necessary not only to improve particle stability and to modulate their intravascular half-life, but also to increase biocompatibility and to avoid immediate sequestration by the reticulo-endothelial system (RES).

Hitherto, the variety of nanomaterials synthesized that can be used as contrast agents for molecular imaging is very wide. Table 1 provides a list of different nanosized materials, with their chemical-physical properties, applications and the main literature-reported studies, their detailed description being beyond the goal of this review.

NON-IONIZING TECHNIQUES FOR MOLECULAR IMAGING

Magnetic resonance imaging

Owing to its high resolution and elevated anatomical contrast, MRI is widely and successfully adopted in clinical routine. However, while standard MRI protocols are effective in detecting global properties of a tissue (*e.g.*, relaxation times T1, T2, *etc.*), the low sensitivity of these techniques in normal conditions hampers their direct employment for molecular imaging purposes^[6].

Nevertheless, the relatively low MRI contrast might be enhanced by using novel nanotechnologies^[22]. Indeed, paramagnetic nanoparticles functionalized with several copies of Gd chelates were successfully exploited in both MRI molecular imaging and targeted therapy of atherosclerotic plaques^[22,41].

Other clinical applications of MRI molecular imaging, ranging from liver disease to several type of cancers^[27], have also been reported by using FeO nanoparticles coated with PEG (polyethylene glycol) or other polymers^[54,55].

To further improve MRI sensitivity and image contrast, alternative strategies are currently under evaluation, based mainly on the synthesis of superparamagnetic nanoparticles made of metal alloys with specific chemical and physical properties (*e.g.*, $2\text{CoFe}_2\text{O}_4$, $2\text{MnFe}_2\text{O}_4$, $2\text{NiFe}_2\text{O}_4$, FePt-FeO)^[56,57].

Other methodological approaches are aimed at synthesizing multifunctional nanoparticles, detectable by high resolution MRI as well as by less expensive techniques like ultrasound or fluorescence imaging, so taking advantages of different diagnostic techniques with a single contrast agent. At this regard, “*in vitro*” experiments with dual mode silica nanospheres covered by an outer shell of superparamagnetic nanoparticles (in order to combine MRI and ultrasonography)^[21] and with core-shell iron oxide/fluorescent silica nanoparticles (for MRI/fluorescence imaging applications)^[58] have been successfully carried out.

Ultrasound imaging

Ultrasound imaging is a cheap and widely available technique offering all the previously mentioned exciting perspectives even if some limitations do apply, which are mostly related to the physical needs for wave transmission pathway: some anatomical sites remain not easily reachable because of boundary bone structures like brain, bone marrow, pelvic organs, *etc.* Furthermore, some technological limitations for 3D and multi-planar imaging acquisitions still remain, which make echographic examinations the first level diagnostic approach and not the ideal candidate for in depth more accurate investigations.

Some of the above described limitations, however, can be overcome by employing ultrasound contrast agents, commercially available for clinical use like microbubbles, and other novel nanosized targeted contrast agents under research development.

All contrast agents approved for routinely use in clinical ultrasound imaging are in the form of aqueous solutions of shell-stabilized gas-filled microbubbles^[59]. Under an ultrasonic beam, microbubbles undergo volumetric oscillations with consequent emission of detectable ultrasound signals that can be exploited to enhance image contrast.

Upon controlled structural modifications, microbubbles can acquire targeting specificity, becoming then suitable also for molecular imaging purposes^[23]. Based on the strategy adopted^[60], microbubble targeting can be passive, in which the intrinsic properties of the shell promote cell adhesion^[61,62], or active, in which the shell is functionalized with specific ligands toward target cells or tissues^[63-66].

However, since microbubbles diameter ranges in the micrometer scale, they cannot cross endothelium wall, with consequent important limitations in their use to target extravascular cells. As a further limitation, half-lives of circulating microbubbles are in the order of just a few minutes, because of both sequestrations by reticulo-endothelial system (RES) and gas diffusion phenomena^[6].

As discussed before, mainly due to their lower size

NPCAs show significant intrinsic advantages with respect to microbubbles. In fact, nanoparticles can easily reach extravascular targets through endothelium crossing, and elude RES capturing. Moreover, the variety of specific surface modifications available for nanosized particles is particularly wide, with consequent effective targeting of a wide range of selected pathologies. In the last years most of the experimental work aimed at developing novel NPCAs for ultrasound molecular imaging has focused mainly on testing few type of nanoparticles, namely liposomes, perfluorocarbon nanoemulsions and nanobubbles^[67-69].

Recent studies have demonstrated, however, that the use of solid nanoparticles as NPCAs may be even more effective^[21,70,71]. With respect to liquid nanoparticles, solid nanomaterials exhibit in fact higher contrast enhancements, since of their higher acoustic impedance with respect to surrounding tissues, and, at the same time, are much more stable than nanobubbles, whose circulating half-life is quite limited by the aforementioned gas diffusion phenomena.

First experiments performed on solid nanoparticles as contrast agents for ultrasound imaging were carried out by using echographic probes working at very high frequencies (30-40 MHz)^[72,73], whose clinical usefulness is closely restricted to intravascular or dermatological applications. More recent studies, instead, have demonstrated that silica nanospheres can be effectively detected on conventional echographic images acquired at diagnostic frequencies (7.5-10 MHz). In addition, the coating of silica nanospheres with a shell of smaller superparamagnetic nanoparticles has made possible to obtain dual-mode NPCAs, detectable by both ultrasound and MRI^[21].

On the basis of these and other literature findings, the development of silica nanoparticles-based NPCAs for ultrasound molecular imaging seems to be particularly promising since of their well-documented biocompatibility^[74-76], ease of functionalization^[75] as well as synthesis procedures^[76], potential employment as nanovectors for controlled release of drugs^[77] or genes^[78].

Optical and optoacoustic imaging

Since of their high sensitivity and non-invasiveness, optical imaging techniques have recently attracted the interest of researchers working on the development of novel molecular imaging protocols^[6]. Optical imaging is actually mainly limited to cell biology and other non-clinical applications, due to the very low penetration of visible wavelengths into anatomical tissues. Interestingly, the use of NPCAs also in optical imaging may enhance its potential suitability in clinical applications like molecular detection of tumours. In fact, optically detectable quantum dots targeting cancer cells have been effectively visualized in both “*in vitro*” and “*in vivo*” studies^[79,80]. Gold nanoshells have been used for optical coherence tomography imaging in a mouse model of colon cancer^[81]. Detectable fluorescence has been observed in carbon nanotubes excited at visible wavelengths after uptake by breast cancer cells^[82].

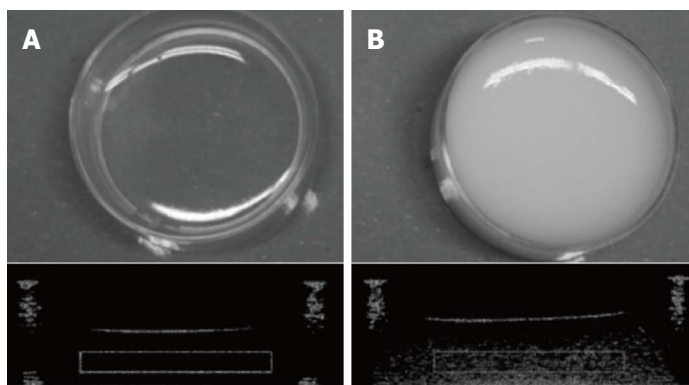


Figure 1 Echographic detection of silica nanoparticles. Sample pictures and corresponding echographic images of pure agarose gel (A) and 330 nm nanoparticle-containing gel (B).

Optoacoustic imaging is an emerging technique that combines high sensitivity and elevated contrast of optical imaging with spatial resolutions and penetration depths typical of ultrasound-based techniques^[83]. Essentially, when irradiated with near-infrared short laser pulses, tissues emit acoustic waves (photoacoustic effect) that can be detected by ultrasound probes and used for imaging purposes^[84]. As an example, the optical absorption of hemoglobin has allowed the optoacoustic visualization of breast tumor microvasculature^[85].

Many efforts are in progress to extend the optoacoustic techniques to molecular imaging applications. Particularly promising seem to be, at this regard, noble metal nanoparticles which, as a consequence of surface Plasmon resonance, strongly absorb laser energy with subsequent generation of ultrasound signals. Although several plasmonic nanoparticles have been recently tested as potential NPCAs for optoacoustic imaging^[86,87], the metal of choice seems to be gold^[86,88-90] because of its high stability, facile chemistry, easy bioconjugation and very low toxicity^[87,91-96]. Among the various type of gold nanoparticles, the most studied for molecular optoacoustic imaging applications are nanorods^[87,97-103], which are of particular interest since of their high tendency to accumulate in tumors^[24] and their potential for simultaneous photothermal therapy^[104].

LATEST DEVELOPMENTS OF NPCAs FOR ULTRASOUND MOLECULAR IMAGING

Silica nanoparticles for ultrasound imaging at clinical diagnostic frequencies

As mentioned before, solid nanoparticles exhibit both higher ultrasound signal enhancement and longer stability as compared to liquid and gaseous particles of the same size. Nevertheless, ultrasound experiments carried out so far on solid nanoparticles at very high frequencies (30-40 MHz)^[72,73] have limited clinical usefulness.

We have recently demonstrated that silica nanoparticles are effective ultrasound contrast agents already at common diagnostic frequencies, and quantified the contrast enhancement observed as a function of particle concentration and diameter, in a range of clinical usefulness for tumor targeting purposes^[70].

Diagnostic power of silica nanospheres of three different diameters (160 nm, 330 nm and 660 nm) was evaluated by measuring ultrasound backscatter in agarose phantoms containing nanoparticles at concentrations ranging from 10^{10} to 10^{13} part/mL. Imaging was performed with a digital echograph equipped with a linear transducer operating at 7.5 MHz and linked to a prototype platform for acquisition of unprocessed radiofrequency (RF) data.

Quantitative off-line analyses showed that while amplitude of nanoparticle-backscattered signals did increase as a linear function of particle concentration, image brightness did not because of saturation effects. However, when nanoparticle diameter, instead of concentration, was increased both backscatter amplitude and image brightness showed significant increments. Taking into account the previously discussed particle size characteristics for effective endothelial crossing and tumor targeting, the best combination was found to be the sample containing 330 nm silica nanospheres at a concentration of about 1 to 2×10^{11} part/mL^[70]. Figure 1 shows a typical picture, with the corresponding echographic image, of agarose sample containing 330 nm silica nanoparticles at 2×10^{11} part/mL concentration.

PEG-coating and targeting of silica nanoparticles

Among the characteristics considered basic for any NPCA to be suitable for clinical molecular imaging, their biocompatibility and effective target recognition are without doubt of major importance. In a recent paper^[105] we have evaluated the cytotoxicity of silica nanospheres of different diameters (160 nm, 240 nm and 330 nm) on two different tumor cell lines, namely MCF-7 cells (breast cancer) and HeLa cells (cervical cancer). Moreover, since sometimes polymeric coating of nanoparticle surface may affect significantly their biocompatibility as well as other parameters, we have synthesized and tested both uncoated and Methoxy (polyethyleneoxy) propyltrimethoxysilane (PEG)-coated silica nanospheres. Acoustic behavior of coated and uncoated particles was also investigated. The results obtained, summarized in Figure 2, showed that the incubation of MCF-7 cells with increasing concentration (up to 5 mg/mL) of uncoated silica nanospheres over 72 h caused a remarkable cytotoxicity,

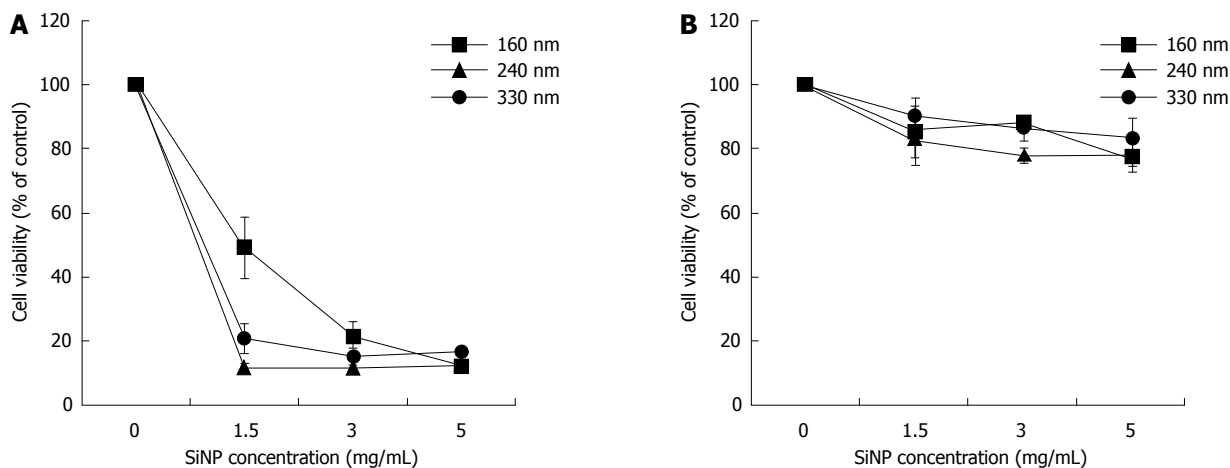


Figure 2 Effect of polyethylene glycol coating on silica nanoparticle biocompatibility. MCF-7 cells were incubated for 72 h in the presence of indicated concentrations of uncoated (A) or polyethylene glycol-coated (B) silica nanoparticles (SiNP).

which was dependent on nanoparticle diameter, concentration and incubation time, reaching percentages of cell mortality close to 80%. Conversely, in the experiments carried out using PEG-coated silica nanospheres cell viability was only slightly affected, with percentage of cell mortality lower than 30% (considered as threshold value of cytotoxicity by ISO 10993-5 international guide) at any time and at any particle concentration and diameter. Comparable results were obtained when HeLa, instead of MCF-7, cells were assayed.

Acoustic behavior of these nanoparticles was characterized exactly as described above and gave results in good agreement with those already obtained. Interestingly, at the same concentrations, 240 nm nanospheres exhibited ultrasound backscattered signals even slightly stronger than 330 nm nanoparticles, this ensuring a good contrast enhancement together with a more effective targeting potential since of their lower diameter.

Work is in progress in our laboratory aimed at functionalizing 240 nm silica nanoparticles incorporating a fluorescent probe for “*in vitro*” molecular imaging of hepatocellular carcinoma (HCC), with both ultrasound and laser-scanning confocal microscopy. HCC is the most common among all liver cancer cases (around 75%)^[106], and is characterized by the particular feature to express on its cell surface Glypican-3 protein (GPC-3) which, therefore, is a good candidate for specific targeting of HCC cells^[107]. On the basis of recent findings by Lee *et al.*^[108] demonstrating that a seven amino acid peptide exhibit high affinity in GPC-3 recognizing and binding, we have synthesized GPC-3 peptide-functionalized 240 nm fluorescent silica nanoparticles and tested them on HepG2 cells, a GPC-3 positive human hepatocarcinoma cell line. Interestingly, preliminary results show that, at concentration useful for ultrasound detection, GPC-3-targeted silica nanoparticles exhibit only negligible cytotoxic effects and seem to effectively bind to HepG2 cell plasmamembrane, as revealed by confocal microscopy and transmission electron microscopy. These results,

which however require be further substantiating by parallel experiments on GPC-3 negative cells and, more importantly, confirming also “*in vivo*”, indicate that 240 nm silica nanoparticles might be a very promising theranostic agents since of their high biocompatibility, targeting effectiveness and acoustic behavior.

SILICA-BASED NANOCOMPOSITES FOR DUAL-MODE MOLECULAR IMAGING

As mentioned in previous paragraphs, our interest in exploring the employability of silica nanoparticles as effective NPCAs was extended to the possibility of designing novel silica-based hybrid nanocomposites for dual-mode molecular imaging, combining MRI and ultrasounds. At this regard, we have developed a simple and efficient synthesis protocol for multi-component nanoparticles having a spherical silica core (160 nm, 330 nm or 660 nm in diameter) coated with an outer shell of smaller superparamagnetic nanoparticles, represented by either 15-nm FeO or 17-nm FePt-FeO nanocrystals^[21,109].

To evaluate the potential of these nanocomposites as MRI contrast agents, proton relaxivity measurements were performed at three radio frequency (RF) frequencies: 12.5, 23 and 60 MHz. Both the transversal relaxivity r_2 and the longitudinal relaxivity r_1 values were calculated for the different silica host nanospheres covered by IO or FePt-IO nanoparticles. As the ratio r_2/r_1 was greater than 2, all the synthesized systems were classified as good T2-relaxing systems. In particular, for each employed RF frequency and SiNP-core diameter, the r_2/r_1 ratios of FePt-IO coated SiNPs were higher than those of IO coated SiNPs, indicating that FePt-IO-coated SiNPs are more efficient as MRI negative contrast agents with respect to IO coated SiNPs^[110].

Ultrasound measurements were carried out on silica nanospheres dispersed in agarose gel samples, with the employment of a 10-MHz incident ultrasound frequency. As shown in Figure 3, all the nanoparticle-containing phan-

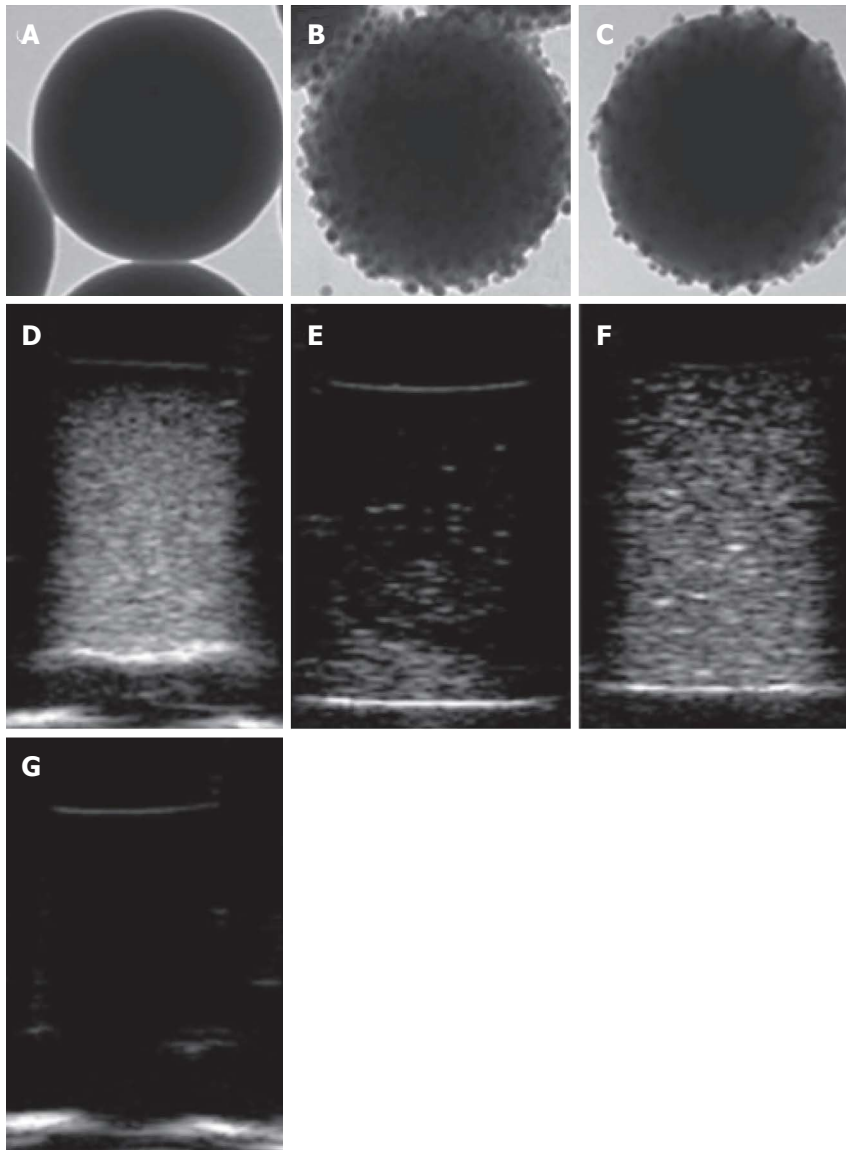


Figure 3 Morphological and echographic characterization of dual mode silica nanoparticles. A-C: Transmission electron microscopy and (D-F) corresponding ultrasound images of uncoated (A, D), IO-coated (B, E) and FePt-IO-coated (C, F) 330 nm silica nanoparticles; G: Image of pure agarose gel (negative control).

toms exhibited a clear image enhancement with respect to the pure agarose gel, that was almost completely transparent to ultrasound. Among the three nanoparticle type tested, uncoated silica nanospheres provided the highest image brightness for each considered size, as compared to IO-coated silica nanospheres, whereas FePt-IO nanocrystals showed image enhancements qualitatively analogous to those of pure silica but with a slightly less uniform brightness.

Therefore, the acoustic and magnetic characterization of coated SiNSs shows that FePt-IO, rather than IO, seems to be the best magnetic coating for realizing NPCAs suitable for dual mode molecular imaging through US and MRI techniques.

HALLOYSITE CLAY NANOTUBES FOR ECHOGRAPHIC IMAGING AT CONVENTIONAL DIAGNOSTIC FREQUENCIES

Nanostructured aluminosilicates are other new materials

of particular interest for their potential medical applications. In particular, halloysite clay is a double-layered aluminosilicate spontaneously forming empty tubular structures in the submicrometer range. They size $1 \pm 0.5 \mu\text{m}$ in length, 50 to 70 nm in external diameter and around 15 nm diameter lumen, and are capable of entrapping a wide variety of active agents in the inner lumen, followed by their retention and slow release^[111-119]. Moreover, owing to their easy surface functionalization^[120] as well as high level of biocompatibility^[121], halloysite clay nanotubes (HNTs) present an ideal profile for cell targeting and drug delivery purposes. In fact, HNTs have been recently demonstrated to be successful in intracellular delivery of antisense oligonucleotides^[122]. Furthermore, Resveratrol-loaded HNTs have been shown to effectively promote apoptotic cell death in MCF-7 breast cancer cell line^[112]. It is then conceivable that therapeutic protocols involving HNTs may take enormous advantage from the possibility of monitoring them through non-invasive imaging techniques. On the basis of these considerations, we have recently explored the feasibility of using HNTs as ultra-

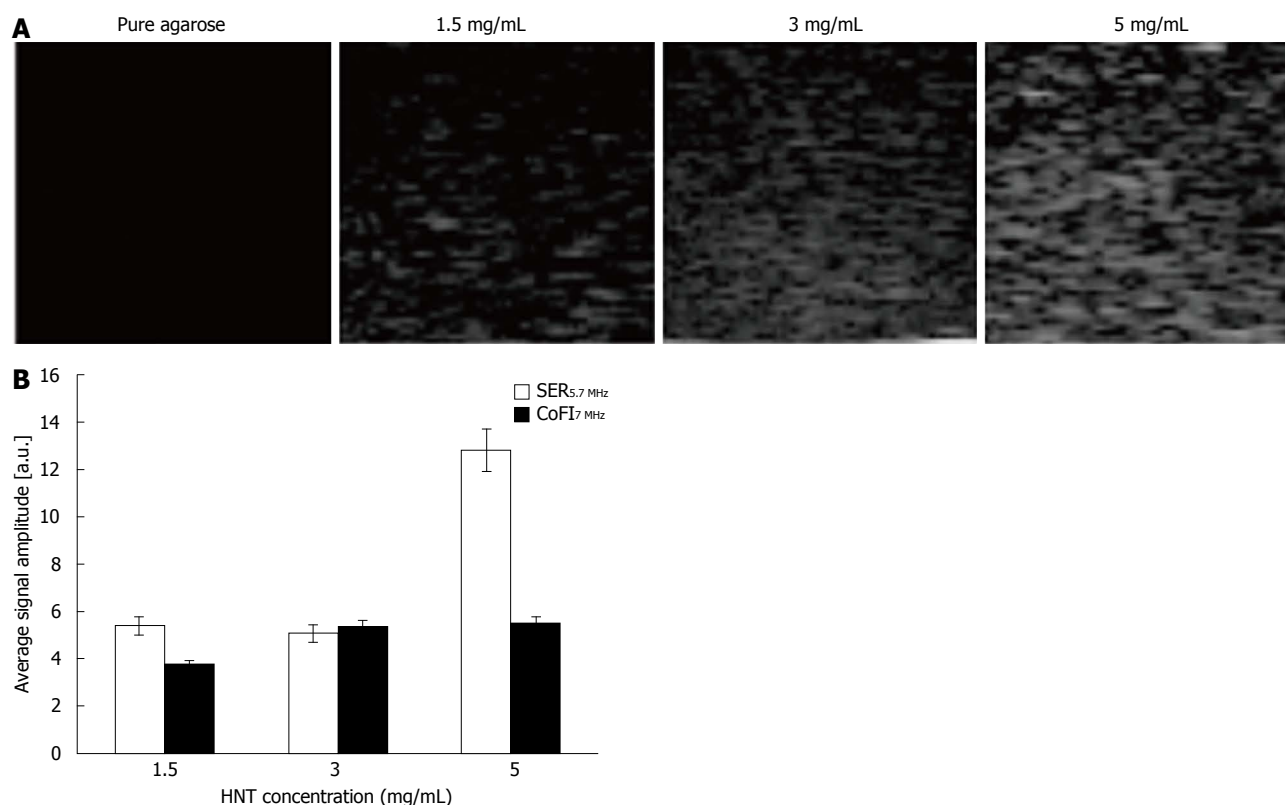


Figure 4 Ultrasound detection of halloysite clay nanotube. A: Gel sample echographic images of pure and agarose containing halloysite clay nanotube (HNT) at the indicated concentrations; B: Quantitative analysis of backscattered signal as a function of ultrasonic frequency and HNT concentration. SER: Signal enhancement ratio; CoFI: Contribution of frequency increment.

sound contrast agents for clinical echographic imaging.

HNT at different concentrations (1.5, 3 and 5 mg/mL) were dispersed in agarose gel and imaged through a commercially available echographic system, employing conventional ultrasonic frequencies (5.7-7 MHz) at an intermediate level of power (50%) of the signal emitted by clinical equipment (Figure 4A).

Acquired data were processed through a dedicated prototypal platform for ultrasonic signal amplitude extraction. The signal enhancement ratio (SER) was calculated between different values of HNT concentration at the considered echographic frequency; additionally, the contribution of frequency increment (CoFI) to the image backscatter was also quantified (Figure 4B). The average contribution of frequency increment from 5.7 to 7 MHz was found to be 4.86 ± 0.80 (corresponding to about 20%), indicating that the increasing HNT concentration determined a nonlinear increment of absolute SER. Hence, it might be useful to study a wider range of HNT concentration in order to achieve safe and effective dose optimization in future clinical application.

CONCLUSION

Recent progresses in the field of nanotechnology applied to medical diagnostic imaging are overcoming most of the constraints offered by classical clinical approaches: molecular imaging without using ionizing techniques, ear-

ly diagnosis of major social diseases, targeted tissue local therapies instead of systemic approaches, *etc.* Echography and ultrasonography provided so far, in the research arena, one of the most promising result by supporting very interesting future clinical perspectives for both diagnosis and therapies still presenting the above mentioned limitations.

Several research applications unveiled many classes of novel nanosystems as effective “theranostic” agents based on both organic and inorganic components. For ultrasound cellular applications the latter certainly offer a wide range of advantages in terms of contrast enhancement, drug loading capabilities, highly effective cell targeting even making possible gene therapy approaches at very low costs.

Nevertheless, many challenges need to be faced in order to translate in clinics those research findings, mainly related to classical difficulties faced by all new drug development steps prior to reach the human clinical trials with additional incognita for the new physical features of novel nano-materials and their eventual toxicity.

Nowadays, our society is experiencing a rapid evolution in terms of population aging, social dynamic modifications accompanied by significant cost reductions in government spending. The real challenge for modern medicine is offering higher medical standards at reduced costs: this ideal objective is not reachable relying on actual classical approaches, but that can be done only pushing

medical research toward the new frontiers made feasible by nanotheranostics and nanomedicines, whose main potentialities and challenges still remain unexpressed and unexplored.

REFERENCES

- Liu Y, Miyoshi H, Nakamura M. Nanomedicine for drug delivery and imaging: a promising avenue for cancer therapy and diagnosis using targeted functional nanoparticles. *Int J Cancer* 2007; **120**: 2527-2537 [PMID: 17390371 DOI: 10.1002/ijc.22709]
- Moghimi SM, Hunter AC, Murray JC. Nanomedicine: current status and future prospects. *FASEB J* 2005; **19**: 311-330 [PMID: 15746175 DOI: 10.1096/fj.04-2747rev]
- Gewin V. Big opportunities in a small world. *Nature* 2009; **460**: 540-541 [DOI: 10.1038/nj7254-540a]
- Caruthers SD, Wickline SA, Lanza GM. Nanotechnological applications in medicine. *Curr Opin Biotechnol* 2007; **18**: 26-30 [PMID: 17254762 DOI: 10.1016/j.copbio.2007.01.006]
- Casciaro S. Theranostic applications: Non-ionizing cellular and molecular imaging through innovative nanosystems for early diagnosis and therapy. *World J Radiol* 2011; **3**: 249-255 [PMID: 22229079 DOI: 10.4329/wjr.v3.i10.49]
- Pascali G, Conversano F, Casciaro S, Salvadori PA. [Translational perspectives in molecular imaging: methodological evolution and nanostructured materials]. *Recenti Prog Med* 2012; **103**: 142-153 [PMID: 22561993]
- Weissleder R, Mahmood U. Molecular imaging. *Radiology* 2001; **219**: 316-333 [PMID: 11323453 DOI: 10.1148/radiology.219.2.r01ma19316]
- Allen TM, Cullis PR. Drug delivery systems: entering the mainstream. *Science* 2004; **303**: 1818-1822 [PMID: 15031496 DOI: 10.1126/science.1095833]
- Moghimi SM, Hunter AC, Murray JC. Long-circulating and target-specific nanoparticles: theory to practice. *Pharmacol Rev* 2001; **53**: 283-318 [PMID: 11356986]
- Sahoo SK, Labhasetwar V. Nanotech approaches to drug delivery and imaging. *Drug Discovery Today* 2003; **8**: 1112-1120 [DOI: 10.1016/S1359-6446(03)02903-9]
- Krämer M, Stumbé JF, Grimm G, Kaufmann B, Krüger U, Weber M, Haag R. Dendritic polyamines: simple access to new materials with defined treelike structures for application in nonviral gene delivery. *ChemBiochem* 2004; **5**: 1081-1087 [PMID: 15300831 DOI: 10.1002/cbic.200300905]
- Raja KS, Wang Q, Gonzalez MJ, Manchester M, Johnson JE, Finn MG. Hybrid virus-polymer materials. 1. Synthesis and properties of PEG-decorated cowpea mosaic virus. *Biomacromolecules* 2003; **4**: 472-476 [PMID: 12741758 DOI: 10.1021/bm025740]
- Fenske DB, MacLachlan I, Cullis PR. Long-circulating vectors for the systemic delivery of genes. *Curr Opin Mol Ther* 2001; **3**: 153-158 [PMID: 11338928]
- Allen TM. Ligand-targeted therapeutics in anticancer therapy. *Nat Rev Cancer* 2002; **2**: 750-763 [PMID: 12360278 DOI: 10.1038/nrc903]
- Sudimack J, Lee RJ. Targeted drug delivery via the folate receptor. *Advanced Drug Delivery Reviews* 2000; **41**: 147-162 [DOI: 10.1016/S0169-409X(99)00062-9]
- Torchilin VP, Lukyanov AN, Gao Z, Papahadjopoulos-Sternberg B. Immunomicelles: targeted pharmaceutical carriers for poorly soluble drugs. *Proc Natl Acad Sci USA* 2003; **100**: 6039-6044 [PMID: 12716967 DOI: 10.1073/pnas.0931428100]
- Drummond DC, Zignani M, Leroux JC. Current status of pH-sensitive liposomes in drug delivery. *Progress in Lipid Research* 2000; **39**: 409-460 [DOI: 10.1016/S0163-7827(00)00011-4]
- Panyam J, Zhou WZ, Prabha S, Sahoo SK, Labhasetwar V. Rapid endo-lysosomal escape of poly(DL-lactide-co-glycolide) nanoparticles: implications for drug and gene delivery. *FASEB J* 2002; **16**: 1217-1226 [PMID: 12153989 DOI: 10.1096/fj.02-0088com]
- Clark HA, Hoyer M, Philbert MA, Kopelman R. Optical nanosensors for chemical analysis inside single living cells. 1. Fabrication, characterization, and methods for intracellular delivery of PEBBLE sensors. *Anal Chem* 1999; **71**: 4831-4836 [PMID: 10565274 DOI: 10.1021/ac990629o]
- Wickline SA, Neubauer AM, Winter P, Caruthers S, Lanza G. Applications of nanotechnology to atherosclerosis, thrombosis, and vascular biology. *Arterioscler Thromb Vasc Biol* 2006; **26**: 435-441 [PMID: 16373609 DOI: 10.1161/01.ATV.0000201069.47550.8b]
- Malvindi MA, Greco A, Conversano F, Figuerola A, Corti M, Bonora M, Lascialfari A, Doumari HA, Moscardini M, Cingolani R, Gigli G, Casciaro S, Pellegrino T, Ragusa A. Magnetic/silica nanocomposites as dual-mode contrast agents for combined magnetic resonance imaging and ultrasonography. *Advanced Functional Materials* 2011; **21**: 2548-2555 [DOI: 10.1002/adfm.201100031]
- Wickline SA, Neubauer AM, Winter PM, Caruthers SD, Lanza GM. Molecular imaging and therapy of atherosclerosis with targeted nanoparticles. *J Magn Reson Imaging* 2007; **25**: 667-680 [PMID: 17347992 DOI: 10.1002/jmri.20866]
- Conversano F, Casciaro S. Last advances in ultrasound molecular imaging. In: Casciaro S, Gersak B, editors. *New technology frontiers in minimally invasive therapies*. Lecce (Italy): Lupiensis Biomedical Publications, 2007: 161-171
- Puvanakrishnan P, Park J, Chatterjee D, Krishnan S, Tunnel JW. In vivo tumor targeting of gold nanoparticles: effect of particle type and dosing strategy. *Int J Nanomedicine* 2012; **7**: 1251-1258 [PMID: 22419872 DOI: 10.2147/IJN.S29147]
- Fahmy TM, Samstein RM, Harness CC, Mark Saltzman W. Surface modification of biodegradable polyesters with fatty acid conjugates for improved drug targeting. *Biomaterials* 2005; **26**: 5727-5736 [PMID: 15878378 DOI: 10.1016/j.biomaterials.2005.02.025]
- Couvreur P, Barratt G, Fattal E, Legrand P, Vauthier C. Nanocapsule technology: a review. *Crit Rev Ther Drug Carrier Syst* 2002; **19**: 99-134 [PMID: 12197610 DOI: 10.1615/CritRevTherDrugCarrierSyst.v19.i2.10]
- Weissleder R, Pittet MJ. Imaging in the era of molecular oncology. *Nature* 2008; **452**: 580-589 [PMID: 18385732 DOI: 10.1038/nature06917]
- Hahn MA, Singh AK, Sharma P, Brown SC, Moudgil BM. Nanoparticles as contrast agents for in-vivo bioimaging: current status and future perspectives. *Anal Bioanal Chem* 2011; **399**: 3-27 [PMID: 20924568 DOI: 10.1007/s00216-010-4207-5]
- Wickline SA, Lanza GM. Nanotechnology for molecular imaging and targeted therapy. *Circulation* 2003; **107**: 1092-1095 [PMID: 12615782 DOI: 10.1161/01.CIR.0000059651.17045.77]
- Lanza GM, Wickline SA. Targeted ultrasonic contrast agents for molecular imaging and therapy. *Curr Probl Cardiol* 2003; **28**: 625-653 [PMID: 14691443 DOI: 10.1016/j.cpcardiol.2003.11.001]
- Tsien RY. Imagining imaging's future. *Nat Rev Mol Cell Biol* 2003; **Suppl**: S16-S21 [PMID: 14587522]
- Herschman HR. Molecular imaging: looking at problems, seeing solutions. *Science* 2003; **302**: 605-608 [PMID: 14576425 DOI: 10.1126/science.1090585]
- Hawker CJ, Wooley KL. The convergence of synthetic organic and polymer chemistries. *Science* 2005; **309**: 1200-1205 [PMID: 16109874 DOI: 10.1126/science.1109778]
- Pasqualini R, Arap W, McDonald DM. Probing the structural and molecular diversity of tumor vasculature. *Trends in Molecular Medicine* 2002; **8**: 563-571 [DOI: 10.1016/S1471-4914(02)02429-2]
- Hobbs SK, Monsky WL, Yuan F, Roberts WG, Griffith L, Torchilin VP, Jain RK. Regulation of transport pathways in tumor vessels: role of tumor type and microenvironment.

- Proc Natl Acad Sci USA* 1998; **95**: 4607-4612 [PMID: 9539785 DOI: 10.1073/pnas.95.8.4607]
- 36 **Iyer AK**, Khaled G, Fang J, Maeda H. Exploiting the enhanced permeability and retention effect for tumor targeting. *Drug Discov Today* 2006; **11**: 812-818 [PMID: 16935749 DOI: 10.1016/j.drudis.2006.07.005]
- 37 **Demos SM**, Alkan-Onyuskel H, Kane BJ, Ramani K, Nagaraj A, Greene R, Klegerman M, McPherson DD. In vivo targeting of acoustically reflective liposomes for intravascular and transvascular ultrasonic enhancement. *JACC* 1999; **33**: 867-875 [DOI: 10.1016/S0735-1097(98)00607-X]
- 38 **Sipkins DA**, Cheresch DA, Kazemi MR, Nevin LM, Bednarski MD, Li KC. Detection of tumor angiogenesis in vivo by alphaVbeta3-targeted magnetic resonance imaging. *Nat Med* 1998; **4**: 623-626 [PMID: 9585240 DOI: 10.1038/nm0598-623]
- 39 **Marsh JN**, Partlow KC, Abendschein DR, Scott MJ, Lanza GM, Wickline SA. Molecular imaging with targeted perfluorocarbon nanoparticles: quantification of the concentration dependence of contrast enhancement for binding to sparse cellular epitopes. *Ultrasound Med Biol* 2007; **33**: 950-958 [PMID: 17434667 DOI: 10.1016/j.ultrasmedbio.2006.12.007]
- 40 **Lanza GM**, Winter P, Caruthers S, Schmeider A, Crowder K, Morawski A, Zhang H, Scott MJ, Wickline SA. Novel paramagnetic contrast agents for molecular imaging and targeted drug delivery. *Curr Pharm Biotechnol* 2004; **5**: 495-507 [PMID: 15579039 DOI: 10.2174/1389201043376544]
- 41 **Flacke S**, Fischer S, Scott MJ, Fuhrhop RJ, Allen JS, McLean M, Winter P, Sicard GA, Gaffney PJ, Wickline SA, Lanza GM. Novel MRI contrast agent for molecular imaging of fibrin: implications for detecting vulnerable plaques. *Circulation* 2001; **104**: 1280-1285 [DOI: 10.1161/hc3601.094303]
- 42 **Schmitz SA**, Coupland SE, Gust R, Winterhalter S, Wagner S, Kresse M, Semmler W, Wolf KJ. Superparamagnetic iron oxide-enhanced MRI of atherosclerotic plaques in Watanabe hereditary hyperlipidemic rabbits. *Invest Radiol* 2000; **35**: 460-471 [PMID: 10946973 DOI: 10.1097/00004424-200008000-00002]
- 43 **Hirsch LR**, Stafford RJ, Bankson JA, Sershen SR, Rivera B, Price RE, Hazle JD, Halas NJ, West JL. Nanoshell-mediated near-infrared thermal therapy of tumors under magnetic resonance guidance. *Proc Natl Acad Sci USA* 2003; **100**: 13549-13554 [PMID: 14597719 DOI: 10.1073/pnas.2232479100]
- 44 **Loo C**, Lin A, Hirsch L, Lee MH, Barton J, Halas N, West J, Drezek R. Nanoshell-enabled photonics-based imaging and therapy of cancer. *Technol Cancer Res Treat* 2004; **3**: 33-40 [PMID: 14750891]
- 45 **O'Neal DP**, Hirsch LR, Halas NJ, Payne JD, West JL. Photothermal tumor ablation in mice using near infrared-absorbing nanoparticles. *Cancer Lett* 2004; **209**: 171-176 [PMID: 15159019 DOI: 10.1016/j.canlet.2004.02.004]
- 46 **Cherukuri P**, Bachilo SM, Litovsky SH, Weisman RB. Near-infrared fluorescence microscopy of single-walled carbon nanotubes in phagocytic cells. *J Am Chem Soc* 2004; **126**: 15638-15639 [PMID: 15571374 DOI: 10.1021/ja0466311]
- 47 **Tsyboulski DA**, Bachilo SM, Weisman RB. Versatile visualization of individual single-walled carbon nanotubes with near-infrared fluorescence microscopy. *Nano Lett* 2005; **5**: 975-979 [PMID: 15884905 DOI: 10.1021/nl050366f]
- 48 **Barone PW**, Baik S, Heller DA, Strano MS. Near-infrared optical sensors based on single-walled carbon nanotubes. *Nat Mater* 2005; **4**: 86-92 [PMID: 15592477 DOI: 10.1038/nmat1276]
- 49 **Hertel T**, Hagen A, Talalaev V, Arnold K, Hennrich F, Kappes M, Rosenthal S, McBride J, Ulbricht H, Flahaut E. Spectroscopy of single- and double-wall carbon nanotubes in different environments. *Nano Lett* 2005; **5**: 511-514 [PMID: 15755104 DOI: 10.1021/nl050069a]
- 50 **Akerman ME**, Chan WC, Laakkonen P, Bhatia SN, Ruoslahti E. Nanocrystal targeting in vivo. *Proc Natl Acad Sci USA* 2002; **99**: 12617-12621 [PMID: 12235356 DOI: 10.1073/pnas.152463399]
- 51 **Chen L**, Zurita AJ, Ardelt PU, Giordano RJ, Arap W, Pasqualini R. Design and validation of a bifunctional ligand display system for receptor targeting. *Chem Biol* 2004; **11**: 1081-1091 [PMID: 15324809 DOI: 10.1016/j.chembiol.2004.05.019]
- 52 **Gao X**, Nie S. Quantum dot-encoded beads. *Meth Mol Biol* 2005; **303**: 61-71
- 53 **Michalet X**, Pinaud FF, Bentolila LA, Tsay JM, Doose S, Li JJ, Sundaresan G, Wu AM, Gambhir SS, Weiss S. Quantum dots for live cells, in vivo imaging, and diagnostics. *Science* 2005; **307**: 538-544 [PMID: 15681376 DOI: 10.1126/science.1104274]
- 54 **Corot C**, Robert P, Idée JM, Port M. Recent advances in iron oxide nanocrystal technology for medical imaging. *Adv Drug Deliv Rev* 2006; **58**: 1471-1504 [PMID: 17116343 DOI: 10.1016/j.addr.2006.09.013]
- 55 **Semelka RC**, Helmberger TK. Contrast agents for MR imaging of the liver. *Radiology* 2001; **218**: 27-38 [PMID: 11152776 DOI: 10.1148/radiology.218.1.r01ja2427]
- 56 **Alric C**, Taleb J, Le Duc G, Mandon C, Billotey C, Le Meur-Herland A, Brochard T, Vocanson F, Janier M, Perriat P, Roux S, Tillement O. Gadolinium chelate coated gold nanoparticles as contrast agents for both X-ray computed tomography and magnetic resonance imaging. *J Am Chem Soc* 2008; **130**: 5908-5915 [PMID: 18407638 DOI: 10.1021/ja078176p]
- 57 **Figuerola A**, Fiore A, Di Corato R, Falqui A, Giannini C, Micotti E, Lascialfari A, Corti M, Cingolani R, Pellegrino T, Cozzoli PD, Manna L. One-pot synthesis and characterization of size-controlled bimagnetic FePt-iron oxide heterodimer nanocrystals. *J Am Chem Soc* 2008; **130**: 1477-1487 [PMID: 18181628 DOI: 10.1021/ja078034v]
- 58 **Yang H**, Zhao F, Li Y, Xu M, Li L, Wu C, Miyoshi H, Liu Y. VCAM-1-targeted core/shell nanoparticles for selective adhesion and delivery to endothelial cells with lipopolysaccharide-induced inflammation under shear flow and cellular magnetic resonance imaging in vitro. *Int J Nanomedicine* 2013; **8**: 1897-1906 [PMID: 23696701]
- 59 Molecular Imaging and Contrast Agent Database (MICAD) [Internet]. Bethesda (MD): National Center for Biotechnology Information (US); 2004-2012. Available from: URL: <http://www.ncbi.nlm.nih.gov/books/NBK5330/>
- 60 **Kaufmann BA**, Lindner JR. Molecular imaging with targeted contrast ultrasound. *Curr Opin Biotechnol* 2007; **18**: 11-16 [PMID: 17241779 DOI: 10.1016/j.copbio.2007.01.004]
- 61 **Kindberg GM**, Tolleshaug H, Roos N, Skotland T. Hepatic clearance of Sonazoid perfluorobutane microbubbles by Kupffer cells does not reduce the ability of liver to phagocytose or degrade albumin microspheres. *Cell Tissue Res* 2003; **312**: 49-54 [PMID: 12712317]
- 62 **Bryant TH**, Blomley MJ, Albrecht T, Sidhu PS, Leen EL, Basilico R, Pilcher JM, Bushby LH, Hoffmann CW, Harvey CJ, Lynch M, MacQuarrie J, Paul D, Cosgrove DO. Improved characterization of liver lesions with liver-phase uptake of liver-specific microbubbles: prospective multicenter study. *Radiology* 2004; **232**: 799-809 [PMID: 15284434 DOI: 10.1148/radiol.2323030596]
- 63 **Willmann JK**, Lutz AM, Paulmurugan R, Patel MR, Chu P, Rosenberg J, Gambhir SS. Dual-targeted contrast agent for US assessment of tumor angiogenesis in vivo. *Radiology* 2008; **248**: 936-944 [PMID: 18710985]
- 64 **Palmowski M**, Huppert J, Ladewig G, Hauff P, Reinhardt M, Mueller MM, Woenne EC, Jenne JW, Maurer M, Kauffmann GW, Semmler W, Kiessling F. Molecular profiling of angiogenesis with targeted ultrasound imaging: early assessment of antiangiogenic therapy effects. *Mol Cancer Ther* 2008; **7**: 101-109 [PMID: 18202013 DOI: 10.1158/1535-7163.MCT-07-0409]
- 65 **Palmowski M**, Peschke P, Huppert J, Hauff P, Reinhardt

- M, Maurer M, Karger CP, Scholz M, Semmler W, Huber PE, Kiessling FM. Molecular ultrasound imaging of early vascular response in prostate tumors irradiated with carbon ions. *Neoplasia* 2009; **11**: 856-863 [PMID: 19724679]
- 66 **Lutz AM**, Bachawal SV, Drescher CW, Pysz MA, Willmann JK, Gambhir SS. Ultrasound molecular imaging in a human CD276 expression-modulated murine ovarian cancer model. *Clin Cancer Res* 2014; **20**: 1313-1322 [PMID: 24389327]
- 67 **Negishi Y**, Hamano N, Tsunoda Y, Oda Y, Chojiamts B, Endo-Takahashi Y, Omata D, Suzuki R, Maruyama K, Nomizu M, Emoto M, Aramaki Y. AG73-modified Bubble liposomes for targeted ultrasound imaging of tumor neovasculature. *Biomaterials* 2013; **34**: 501-507 [PMID: 23088840 DOI: 10.1016/j.biomaterials.2012.09.056]
- 68 **Díaz-López R**, Tsapis N, Fattal E. Liquid perfluorocarbons as contrast agents for ultrasonography and (19)F-MRI. *Pharm Res* 2010; **27**: 1-16 [PMID: 19902338 DOI: 10.1007/s11095-009-0001-5]
- 69 **Yin T**, Wang P, Zheng R, Zheng B, Cheng D, Zhang X, Shuai X. Nanobubbles for enhanced ultrasound imaging of tumors. *Int J Nanomedicine* 2012; **7**: 895-904 [PMID: 22393289 DOI: 10.2147/IJN.S28830]
- 70 **Casciaro S**, Conversano F, Ragusa A, Malvindi MA, Franchini R, Greco A, Pellegrino T, Gigli G. Optimal enhancement configuration of silica nanoparticles for ultrasound imaging and automatic detection at conventional diagnostic frequencies. *Invest Radiol* 2010; **45**: 715-724 [PMID: 20562708 DOI: 10.1097/RLI.0b013e3181e6f42f]
- 71 **Conversano F**, Greco A, Casciaro E, Ragusa A, Lay-Ekuakille A, Casciaro S. Harmonic ultrasound imaging of nanosized contrast agents for multimodal molecular diagnoses. *IEEE Trans Instrum Meas* 2012; **61**: 1848-1856 [DOI: 10.1109/TIM.2012.2192354]
- 72 **Liu J**, Levine AL, Mattoon JS, Yamaguchi M, Lee RJ, Pan X, Rosol TJ. Nanoparticles as image enhancing agents for ultrasonography. *Phys Med Biol* 2006; **51**: 2179-2189 [PMID: 16625034 DOI: 10.1088/0031-9155/51/9/004]
- 73 **Liu J**, Li J, Rosol TJ, Pan X, Voorhees JL. Biodegradable nanoparticles for targeted ultrasound imaging of breast cancer cells in vitro. *Phys Med Biol* 2007; **52**: 4739-4747 [PMID: 17671332 DOI: 10.1088/0031-9155/52/16/002]
- 74 **Jin Y**, Kannan S, Wu M, Zhao JX. Toxicity of luminescent silica nanoparticles to living cells. *Chem Res Toxicol* 2007; **20**: 1126-1133 [PMID: 17630705 DOI: 10.1021/tx7001959]
- 75 **Barbé C**, Bartlett J, Kong L, Finnie K, Lin HQ, Larkin M, Calleja S, Bush A, Calleja G. Silica particles: a novel drug-delivery system. *Adv Funct Mater* 2004; **16**: 1959-1966 [DOI: 10.1002/adma.200400771]
- 76 **Piao Y**, Burns A, Kim J, Wiesner U, Hyeon, T. Designed fabrication of silica-based nanostructured particle systems for nanomedicine applications. *Adv Funct Mater* 2008; **18**: 3745-3758 [DOI: 10.1002/adfm.200800731]
- 77 **Mouleri B**, Pertuit D, Pellequer Y, Lamprecht A. The targeting of surface modified silica nanoparticles to inflamed tissue in experimental colitis. *Biomaterials* 2008; **29**: 4554-4560 [PMID: 18790531 DOI: 10.1016/j.biomaterials.2008.08.009]
- 78 **Roy I**, Ohulchanskyy TY, Bharali DJ, Pudavar HE, Mistretta RA, Kaur N, Prasad PN. Optical tracking of organically modified silica nanoparticles as DNA carriers: a nonviral, nanomedicine approach for gene delivery. *Proc Natl Acad Sci USA* 2005; **102**: 279-284 [PMID: 15630089 DOI: 10.1073/pnas.0408039101]
- 79 **Liu L**, Yong KT, Roy I, Law WC, Ye L, Liu J, Liu J, Kumar R, Zhang X, Prasad PN. Bioconjugated pluronic triblock-copolymer micelle-encapsulated quantum dots for targeted imaging of cancer: in vitro and in vivo studies. *Theranostics* 2012; **2**: 705-713 [PMID: 22896772 DOI: 10.7150/thno.3456]
- 80 **Poulose AC**, Veerananarayanan S, Mohamed MS, Raveendran S, Nagaoka Y, Yoshida Y, Maekawa T, Kumar DS. PEG coated biocompatible cadmium chalcogenide quantum dots for targeted imaging of cancer cells. *J Fluoresc* 2012; **22**: 931-944 [PMID: 22227700 DOI: 10.1007/s10895-011-1032-y]
- 81 **Winkler AM**, Rice PF, Drezek RA, Barton JK. Quantitative tool for rapid disease mapping using optical coherence tomography images of azoxymethane-treated mouse colon. *J Biomed Opt* 2010; **15**: 041512 [PMID: 20799790 DOI: 10.1117/1.3446674]
- 82 **Avti PK**, Sitharaman B. Luminescent single-walled carbon nanotube-sensitized europium nanoprobe for cellular imaging. *Int J Nanomedicine* 2012; **7**: 1953-1964 [PMID: 22619533 DOI: 10.2147/IJN.S29545]
- 83 **Wang LV**. Multiscale photoacoustic microscopy and computed tomography. *Nat Photonics* 2009; **3**: 503-509 [PMID: 20161535 DOI: 10.1038/nphoton.2009.157]
- 84 **Oraevsky AA**, Karabutov AA. Optoacoustic tomography. In: Vo-Dinh T, editor. *Biomedical Photonics Handbook*. Boca Raton: CRC Press/Francis and Taylor Group, 2003
- 85 **Ermilov SA**, Khamapirad T, Conjusteau A, Leonard MH, Laceywell R, Mehta K, Miller T, Oraevsky AA. Laser optoacoustic imaging system for detection of breast cancer. *J Biomed Opt* 2009; **14**: 024007 [PMID: 19405737 DOI: 10.1117/1.3086616]
- 86 **Lu W**, Huang Q, Ku G, Wen X, Zhou M, Guzatov D, Brecht P, Su R, Oraevsky A, Wang LV, Li C. Photoacoustic imaging of living mouse brain vasculature using hollow gold nanospheres. *Biomaterials* 2010; **31**: 2617-2626 [PMID: 20036000 DOI: 10.1016/j.biomaterials.2009.12.007]
- 87 **Song KH**, Kim C, Maslov K, Wang LV. Noninvasive in vivo spectroscopic nanorod-contrast photoacoustic mapping of sentinel lymph nodes. *Eur J Radiol* 2009; **70**: 227-231 [PMID: 19269762 DOI: 10.1016/j.ejrad.2009.01.045]
- 88 **Mallidi S**, Larson T, Tam J, Joshi PP, Karpouk A, Sokolov K, Emelianov S. Multiwavelength photoacoustic imaging and plasmon resonance coupling of gold nanoparticles for selective detection of cancer. *Nano Lett* 2009; **9**: 2825-2831 [PMID: 19572747 DOI: 10.1021/nl802929u]
- 89 **Li ML**, Wang JC, Schwartz JA, Gill-Sharp KL, Stoica G, Wang LV. In-vivo photoacoustic microscopy of nanoshell extravasation from solid tumor vasculature. *J Biomed Opt* 2009; **14**: 010507 [PMID: 19256687 DOI: 10.1117/1.3081556]
- 90 **Kim C**, Cho EC, Chen J, Song KH, Au L, Favazza C, Zhang Q, Cogley CM, Gao F, Xia Y, Wang LV. In vivo molecular photoacoustic tomography of melanomas targeted by bioconjugated gold nanocages. *ACS Nano* 2010; **4**: 4559-4564 [PMID: 20731439 DOI: 10.1021/nn100736c]
- 91 **Jain PK**, El-Sayed IH, El-Sayed MA. Au nanoparticles target cancer. *Nano Today* 2007; **2**: 18-29 [DOI: 10.1016/S1748-0132(07)70016-6]
- 92 **Pan D**, Pramanik M, Senpan A, Wickline SA, Wang LV, Lanza GM. A facile synthesis of novel self-assembled gold nanorods designed for near-infrared imaging. *JNN* 2010; **10**: 8118-8123 [DOI: 10.1166/jnn.2010.3034]
- 93 **Boisselier E**, Astruc D. Gold nanoparticles in nanomedicine: preparations, imaging, diagnostics, therapies and toxicity. *Chem Soc Rev* 2009; **38**: 1759-1782 [PMID: 19587967 DOI: 10.1039/b806051g]
- 94 **Connor EE**, Mwamuka J, Gole A, Murphy CJ, Wyatt MD. Gold nanoparticles are taken up by human cells but do not cause acute cytotoxicity. *Small* 2005; **1**: 325-327 [PMID: 17193451 DOI: 10.1002/sml.200400093]
- 95 **Cai QY**, Kim SH, Choi KS, Kim SY, Byun SJ, Kim KW, Park SH, Juhng SK, Yoon KH. Colloidal gold nanoparticles as a blood-pool contrast agent for X-ray computed tomography in mice. *Invest Radiol* 2007; **42**: 797-806 [PMID: 18007151 DOI: 10.1097/RLI.0b013e31811ecdc]
- 96 **Chen YS**, Hung YC, Liao I, Huang GS. Assessment of the In Vivo Toxicity of Gold Nanoparticles. *Nanoscale Res Lett* 2009; **4**: 858-864 [PMID: 20596373 DOI: 10.1007/s11671-009-9334-6]
- 97 **Eghtedari M**, Oraevsky A, Copland JA, Kotov NA, Conjusteau A, Motamedi M. High sensitivity of in vivo detection of

- gold nanorods using a laser optoacoustic imaging system. *Nano Lett* 2007; **7**: 1914-1918 [PMID: 17570730 DOI: 10.1021/nl070557d]
- 98 **Ha S**, Carson A, Agarwal A, Kotov NA, Kim K. Detection and monitoring of the multiple inflammatory responses by photoacoustic molecular imaging using selectively targeted gold nanorods. *Biomed Opt Express* 2011; **2**: 645-657 [PMID: 21412469 DOI: 10.1364/BOE.2.000645]
- 99 **Agarwal A**, Huang SW, O'Donnell M, Day KC, Day M, Kotov N, Ashkenazi S. Targeted gold nanorod contrast agent for prostate cancer detection by photoacoustic imaging. *J Appl Phys* 2007; **102**: 064701 [DOI: 10.1063/1.2777127]
- 100 **Li PC**, Wei CW, Liao CK, Chen CD, Pao KC, Wang CRC, Wu TN, Shieh DB. Photoacoustic imaging of multiple targets using gold nanorods. *IEEE Trans Ultrason Ferroelectr Freq Control* 2007; **54**: 1642-1647 [DOI: 10.1109/TUFFC.2007.435]
- 101 **Kim K**, Huang SW, Ashkenazi S, O'Donnell M, Agarwal A, Kotov NA, Denny MF, Kaplan MJ. Photoacoustic imaging of early inflammatory response using gold nanorods. *Applied Physics Letters* 2007; **90**: 223901-223903 [DOI: 10.1063/1.2743752]
- 102 **Li PC**, Wang CR, Shieh DB, Wei CW, Liao CK, Poe C, Jhan S, Ding AA, Wu YN. In vivo photoacoustic molecular imaging with simultaneous multiple selective targeting using antibody-conjugated gold nanorods. *Opt Express* 2008; **16**: 18605-18615 [PMID: 19581946 DOI: 10.1364/OE.16.018605]
- 103 **Conversano F**, Soloperto G, Greco A, Ragusa A, Casciaro E, Chiriaco F, Demitri C, Gigli G, Maffezzoli A, Casciaro S. Echographic detectability of optoacoustic signals from low-concentration PEG-coated gold nanorods. *Int J Nanomedicine* 2012; **7**: 4373-4389 [PMID: 22927756]
- 104 **Samim M**, Prashant CK, Dinda AK, Maitra AN, Arora I. Synthesis and characterization of gold nanorods and their application for photothermal cell damage. *Int J Nanomedicine* 2011; **6**: 1825-1831 [PMID: 22114472 DOI: 10.2147/IJN.S11600]
- 105 **Chiriaco F**, Conversano F, Soloperto G, Casciaro E, Ragusa A, Sbenaglia EA, DiPaola L, Casciaro S. Epithelial cells biocompatibility of silica nanospheres for contrast-enhanced ultrasound molecular imaging. *J Nanopart Research* 2013; **15**: 1779-1792 [DOI: 10.1007/s11051-013-1779-y]
- 106 **Ahn BC**, Ronald JA, Kim YI, Katzenberg R, Singh A, Paulmurugan R, Ray S, Hofmann LV, Gambhir SS. Potent, tumor-specific gene expression in an orthotopic hepatoma rat model using a Survivin-targeted, amplifiable adenoviral vector. *Gene Ther* 2011; **18**: 606-612 [PMID: 21307888 DOI: 10.1038/gt.2011.5]
- 107 **Ho M**, Kim H. Glypican-3: a new target for cancer immunotherapy. *Eur J Cancer* 2011; **47**: 333-338 [PMID: 21112773 DOI: 10.1016/j.ejca.2010.10.024]
- 108 **Lee YL**, Ahn BC, Lee Y, Lee SW, Cho JY, Lee J. Targeting of hepatocellular carcinoma with glypican-3-targeting peptide ligand. *J Pept Sci* 2011; **17**: 763-769 [PMID: 21976137 DOI: 10.1002/psc.1400]
- 109 **Casciaro S**, Soloperto G, Greco A, Casciaro E, Franchini R, Conversano F. Effectiveness of functionalized nanospheres for multimodal molecular sensing and imaging in medicine. *IEEE Sens J* 2013; **13**: 2305-2312 [DOI: 10.1109/JSEN.2013.2252164]
- 110 **Chiriaco F**, Soloperto G, Greco A, Conversano F, Ragusa A, Menichetti L, Casciaro S. Magnetically-coated silica nanospheres for dual-mode imaging at low ultrasound frequency. *World J Radiol* 2013; **5**: 411-420 [PMID: 24349645]
- 111 **Price RR**, Gaber BP, Lvov Y. In-vitro release characteristics of tetracycline HCl, khellin and nicotinamide adenine dinucleotide from halloysite; a cylindrical mineral. *J Microencapsul* 2001; **18**: 713-722 [PMID: 11695636 DOI: 10.1080/02652040010019532]
- 112 **Vergaro V**, Lvov YM, Leporatti S. Halloysite clay nanotubes for resveratrol delivery to cancer cells. *Macromol Biosci* 2012; **12**: 1265-1271 [PMID: 22887783 DOI: 10.1002/mabi.201200121]
- 113 **Kelly HM**, Deasy PB, Ziaka E, Claffey N. Formulation and preliminary in vivo dog studies of a novel drug delivery system for the treatment of periodontitis. *Int J Pharm* 2004; **274**: 167-183 [PMID: 15072793 DOI: 10.1016/j.jipharm.2004.01.019]
- 114 **Veerabadran NG**, Price RR, Lvov YM. Clay nanotubes for encapsulation and sustained release of drugs. *Nano* 2007; **2**: 115-120 [DOI: 10.1142/S1793292007000441]
- 115 **Lvov YM**, Shchukin DG, Möhwald H, Price RR. Halloysite clay nanotubes for controlled release of protective agents. *ACS Nano* 2008; **2**: 814-820 [PMID: 19206476 DOI: 10.1021/nn800259q]
- 116 **Veerabadran NG**, Mongayt D, Torchilin V, Price RR, Lvov YM. Organized shells on clay nanotubes for controlled release of macromolecules. *Macromol Rapid Commun* 2009; **30**: 99-103 [PMID: 21706582 DOI: 10.1002/marc.200800510]
- 117 **Kommireddy D**, Ichinose I, Lvov Y, Mills D. Nanoparticle multilayer: surface modification for cell attachment and growth. *J Biomed Nanotechnol* 2005; **1**: 286-290 [DOI: 10.1166/jbn.2005.046]
- 118 **Viseras MT**, Aguzzi C, Cerezo P, Cultrone G, Viseras C. Supramolecular structure of 5-aminosalicylic acid/halloysite composites. *J Microencapsul* 2009; **26**: 279-286 [PMID: 18686141 DOI: 10.1080/02652040802312499]
- 119 **Soloperto G**, Conversano F, Greco A, Casciaro E, Ragusa A, Leporatti S, Lay-Ekuakille A, Casciaro S. Multiparametric evaluation of the acoustic behaviour of halloysite nanotubes for medical echographic image enhancement. *IEEE Trans Instrum Meas* 2014, In press
- 120 **Duartel AH**, Lourenco MP, Heine T, Guimares L. Clay mineral nanotubes: stability, structure and properties. In: *Stoichiometry, Material Sciences-When Numbers Matter*, A Innocenti, N Kamarulzaman, editors. Vukovar, Croatia: InTech, 2012
- 121 **Vergaro V**, Abdullayev E, Lvov YM, Zeitoun A, Cingolani R, Rinaldi R, Leporatti S. Cytocompatibility and uptake of halloysite clay nanotubes. *Biomacromolecules* 2010; **11**: 820-826 [PMID: 20170093 DOI: 10.1021/bm9014446]
- 122 **Shi YF**, Tian Z, Zhang Y, Shen HB, Jia NQ. Functionalized halloysite nanotube-based carrier for intracellular delivery of antisense oligonucleotides. *Nanoscale Res Lett* 2011; **6**: 608 [PMID: 22122822 DOI: 10.1186/1556-276X-6-608]

P- Reviewer: Chen K, Mani V S- Editor: Ji FF L- Editor: A
E- Editor: Lu YJ



Clinical use of bone-targeting radiopharmaceuticals with focus on alpha-emitters

Hinrich A Wieder, Michael Lassmann, Martin S Allen-Auerbach, Johannes Czernin, Ken Herrmann

Hinrich A Wieder, Department of Radiology, Zentrum für Radiologie und Nuklearmedizin, 41515 Grevenbroich, Germany
Hinrich A Wieder, Department of Nuclear Medicine, Technische Universität München, 81675 Munich, Germany

Michael Lassmann, Ken Herrmann, Department of Nuclear Medicine, University of Würzburg, 97080 Würzburg, Germany
Martin S Allen-Auerbach, Johannes Czernin, Ahmanson Translational Imaging Division, Department of Molecular and Medical Pharmacology, David Geffen School of Medicine at UCLA, Los Angeles, CA 90095, United States

Author contributions: Wieder HA, Lassmann M, Allen-Auerbach M, Czernin J and Herrmann K contributed to development of outline, and revision and approval of manuscript; Wieder HA, Czernin J and Herrmann K contributed to drafting and editing of manuscript; Lassmann M and Allen-Auerbach M contributed to figures.

Correspondence to: Hinrich A Wieder, MD, Department of Radiology, Zentrum für Radiologie und Nuklearmedizin, Zentrum für Radiologie und Nuklearmedizin, Von-Werth-Straße 5, 41515 Grevenbroich, Germany. h@wieder.de

Telephone: +49-2133-664980 Fax: +49-2133-662983

Received: November 27, 2013 Revised: March 20, 2014

Accepted: May 16, 2014

Published online: March 28, 2015

Abstract

Various single or multi-modality therapeutic options are available to treat pain of bone metastasis in patients with prostate cancer. Different radionuclides that emit β -rays such as $^{153}\text{Samarium}$ and $^{89}\text{Strontium}$ and achieve palliation are commercially available. In contrast to β -emitters, $^{223}\text{Radium}$ as a α -emitter has a short path-length. The advantage of the α -emitter is thus a highly localized biological effect that is caused by radiation induced DNA double-strand breaks and subsequent cell killing and/or limited effectiveness of cellular repair mechanisms. Due to the limited range of the α -particles the bone surface to red bone marrow dose ratio is also lower for $^{223}\text{Radium}$ which is expressed in a lower myelotoxicity. The α emitter $^{223}\text{Radium}$ dichloride is the first radiopharmaceutical that significantly prolongs

life in castrate resistant prostate cancer patients with wide-spread bone metastatic disease. In a phase III, randomized, double-blind, placebo-controlled study 921 patients with castration-resistant prostate cancer and bone metastases were randomly assigned. The analysis confirmed the $^{223}\text{Radium}$ survival benefit compared to the placebo (median, 14.9 mo vs 11.3 mo; $P < 0.001$). In addition, the treatment results in pain palliation and thus, improved quality of life and a delay of skeletal related events. At the same time the toxicity profile of $^{223}\text{Radium}$ was favourable. Since May 2013, $^{223}\text{Radium}$ dichloride (Xofigo®) is approved by the US Food and Drug Administration.

© 2015 Baishideng Publishing Group Inc. All rights reserved.

Key words: Radium; Bone targeted radiopharmaceuticals; Alpha emitters

Core tip: The incidence rate of prostate cancer worldwide is high. Ninety percent of patients dying of prostate cancer have bone metastases with varying symptoms which are significantly impairing their quality of life. $^{223}\text{Radium}$ is the first therapeutic that results in a survival benefit for patients with bone metastatic, castrate resistant prostate cancer. $^{223}\text{Radium}$ was also associated with low myelosuppression rates and fewer adverse events. This article provides an overview of the pre-clinical and clinical trials with $^{223}\text{Radium}$.

Original sources: Wieder HA, Lassmann M, Allen-Auerbach M, Czernin J, Herrmann K. Clinical use of bone-targeting radiopharmaceuticals with focus on alpha-emitters. *World J Radiol* 2014; 6(7): 480-485 Available from: URL: <http://www.wjgnet.com/1949-8470/full/v6/i7/480.htm> DOI: <http://dx.doi.org/10.4329/wjr.v6.i7.480>

INTRODUCTION

According to estimates from the International Agency

Table 1 Physical characteristics of ⁸⁹Strontium, ¹⁵³Samarium and ²²³Radium

Radionuclide	Half-life	Maximum energy (MeV)	Mean energy (MeV)	Maximum range	γ-Emission (keV)
⁸⁹ Sr	50.5 d	1.4 (β)	0.583 (β)	7 mm	None
¹⁵³ Sm	1.9 d	0.81 (β)	0.229 (β)	4 mm	103
²²³ Ra	11.4 d	5.78 (α) average	-	< 10 μm	154

for Research on Cancer (IARC, GLOBOCAN 2008), the incidence rate of prostate cancer worldwide is 13.6 per 100000 inhabitants per year, with a mortality of 6.1 per 100000 per year^[1]. The incidence rate differs quite significantly among the various regions of the world. It is lowest in Central Asia with 4.1 per 100000 and highest in Australia/New Zealand with 104 per 100000^[1]. Ninety% of patients dying of prostate cancer have bone metastases^[2]. Patients with bone metastases have varying symptoms such as pain, pathological fractures, neurological disorders, spinal cord compression, and bone marrow failure, which are significantly impairing their quality of life^[3,4].

An optimal therapy leads to pain reduction, improved quality of life, and prolonged survival. Various single or multi-modality therapeutic options are available to treat bone pain. These include analgesics, hormone therapy, chemotherapy, external beam radiation, biphosphonates, or β-emitting radionuclides.

Combined pain medication and external radiotherapy result in pain relief in up to 70% of patients with localized pain^[5]. However, external radiotherapy is only possible to a limited extent in patients with multiple bone metastases and diffuse bone pain.

Different radionuclides that emit β-rays such as ¹⁵³Samarium and ⁸⁹Strontium and achieve palliation are commercially available. ⁸⁹Strontium is a pure β-emitter with a relatively long half-life of 50.5 d. ¹⁵³Samarium has a shorter half-life of 1.9 d and emits β-rays in addition to γ-rays (Table 1). Thus, imaging of the skeletal samarium distribution post therapy is feasible. In more than half of the cases, administration of these radiopharmaceuticals results in a decrease of pain^[6-8]. Yet, an effect of this therapy on patient survival is not investigated in randomised phase III studies.

β-emitters with a low linear energy transfer (LET) and a long β-range can lead to a high radiation burden of the bone marrow and thus carry the risk of a significant myelosuppression. This bone marrow suppression may be dose limiting.

In contrast to β-emitters, α-emitters have a short path-length of less than 0.1 mm which increases the local anti-tumour effect without affecting the bone marrow. The α-emitter ²²³Radium dichloride is the first radiopharmaceutical that significantly prolongs life in castrate resistant prostate cancer patients with wide-spread bone metastatic disease. Radium-223 has been developed by the Norwegian company Algeta ASA, in a partnership with Bayer, under the trade name Xofigo[®]. ²²³Radium dichloride is approved by the US Food and Drug Admin-

istration (FDA) and by the European Commission (EC).

This article provides an overview of the pre-clinical and clinical trials with ²²³Radium.

PATIENT EXPOSURE

Lassmann *et al*^[9] provided a comprehensive dosimetry calculation of absorbed organ doses after intravenous administration of ²²³Radium chloride for 25 organs or tissues. Bone surface and red bone marrow show the highest dose coefficients followed by liver, colon, and intestines. Six cycles of ²²³Radium at 0.05 MBq/kg^[10] (corresponding to 21 MBq for a 70 kg patient), the absorbed a dose to the bone surface was calculated at around 16 Gy with a dose of approximately 1.5 Gy to the bone marrow. Patient-specific dosimetry data have not been published yet.

PHARMACOKINETICS AND PRECLINICAL STUDIES

Radium was discovered in December 1898 by the physicist Marie Curie and her husband Pierre Curie. ²²³Radium decays originates from uranium and has a natural decay balance with uranium. The α-emitter ²²³Radium is water soluble as ²²³Radium chloride. ²²³Radium can be relatively easily gained from ²²⁷Actinium through a cation exchange system. Due to the long half-life of ²²⁷Actinium (21.7 years), it could potentially be used as a long-term generator.

²²³Radium has a half-life of 11.4 d (Table 1) and decays *via* seven daughter nuclides into stable ²⁰⁷Lead-207. The half-life of the daughter nuclides ranges from seconds to minutes. During the decay of ²²³Radium, approximately four α particles and two β particles (electrons) are released. The combined energy of the particles emitted during the decay chain of ²²³Radium and its daughter nuclides is 27.5 MeV, with α-particles emitting 95.3% of the energy and β-particles emitting 3.6%. One point one percent are emitted as gamma rays.

Because of the electric charge and the relatively high mass of 4u, α-particles have a very low penetration depth in organic matter which ranges from 40 to 100 μm which approximately equals the size of micro metastases. α-particles produce high-linear energy-transfer (LET) radiation. The advantage of the α-emitter is thus a highly localized biological effect that is caused by radiation induced DNA double-strand breaks and subsequent cell killing and/or limited effectiveness of cellular repair

mechanisms.

The penetration depth into the surrounding tissue of the β -particles is higher than with $^{223}\text{Radium}$ (Table 1). Due to the limited range of the α -particles the bone surface to red bone marrow dose ratio is also lower for $^{223}\text{Radium}$ which is expressed in a lower myelotoxicity of $^{223}\text{Radium}$ as compared to the “traditional” radiopharmaceuticals.

As a calcium analogue, $^{223}\text{Radium}$ dichloride is absorbed by the bone after intravenous injection without the necessity of a carrier. Initially, approximately 25% of the injected $^{223}\text{Radium}$ dichloride is bound to the bone surface and from there quickly absorbed into the bone volume or returned into blood^[9]. Eighty percent of the activity is transferred from the exchangeable bone volume back to the bone surface at a biological half-life of 30 d. The amount of $^{223}\text{Radium}$ dichloride that the bone absorbs depends on the regional bone metabolism. The target of $^{223}\text{Radium}$ dichloride in the bone is calcium hydroxylapatite. The radiopharmaceutical accumulates in regions of osteoblast activity, therefore allowing the simultaneous treatment of multiple bone metastases. In addition to the bones $^{223}\text{Radium}$ dichloride is mainly absorbed from blood into soft tissue, including the liver. Its excretion is predominantly *via* the intestines, *i.e.*, the feces. Renal excretion is minimal. In contrast, $^{153}\text{Samarium}$ and $^{89}\text{Strontium}$ undergo predominantly renal excretion thereby increasing the probability of renal toxicity.

Because of its very limited tissue penetration the environmental risk of $^{223}\text{Radium}$ application is minimal if existent at all. Thus, $^{223}\text{Radium}$ dichloride can be administered safely in an outpatient setting.

In animal experimental studies, $^{223}\text{Radium}$ had the same bone distribution as $^{89}\text{Strontium}$ which suggested that a therapeutically relevant dose of $^{223}\text{Radium}$ could be applied to bone metastases^[11]. In addition, $^{223}\text{Radium}$ had a lower myelotoxicity than β -emitters^[11]. Rats which received chemotherapy and had biphosphonate resistant bone metastases, showed a longer survival rate when they were treated with $^{223}\text{Radium}$ ^[12]. This suggested that $^{223}\text{Radium}$ may not only be used for palliation but may in fact prolong life.

PHASE I STUDY

The pharmacokinetics, pharmacodynamics, and biodistribution were investigated in a phase I study in 10 patients with bone metastatic prostate cancer^[13]. Three patients received injections of 50 kBq/kg radium, another three received 100 kBq/kg radium, and 4 patients received 250 kBq/kg. After 6 wk, 6 of the 10 patients had another injection of 50 kBq/kg. A rapid clearance of $^{223}\text{Radium}$ from the blood was observed whereby only 0.5% of $^{223}\text{Radium}$ remained in the blood after 24 h. On average, 52% of the $^{223}\text{Radium}$ was cleared *via* the intestines, which was the main route of excretion of $^{223}\text{Radium}$. The excretion *via* the kidneys was relatively low with a mean

of 4%. No dose limiting toxicity could be verified.

In another phase I study, a total of 25 patients with bone metastatic prostate cancer ($n = 15$) and breast cancer ($n = 10$) received a single dose of 250 kBq/kg $^{223}\text{Radium}$ (46, 93, 163, 213, or 250 kBq/kg)^[14]. The goal of this dose escalation study was to investigate the safety profile and the pain response to $^{223}\text{Radium}$. The pain scale was documented before the first injection and at 1, 4, and 8 wk after the injection. In addition, in 6 patients the distribution of the daughter nuclide $^{219}\text{Radium}$ was imaged with a gamma camera and compared to the pre-therapeutic bone scintigraphy.

The patients exhibited mild and reversible myelosuppression. In one patient, a grade 1 thrombocytopenia was observed; 2 patients had a grade 3 neutropenia, and 3 patients showed a grade 3 leukopenia. Four weeks after the injection of $^{223}\text{Radium}$ a pain reduction was observed in most patients (60%). 24 h after the injection, the activity of $^{223}\text{Radium}$ rapidly decreased to below 1% (redundant). Thus, $^{223}\text{Radium}$ was well tolerated at therapeutically relevant doses. The pre- and post-therapeutic gamma camera images showed a good correlation with the $^{223}\text{Radium}$ accumulation in bone metastases.

PHASE II STUDY

In a randomized, double-blind multicentre phase II study the effect of the repeated administration of $^{223}\text{Radium}$ was investigated in patients with symptomatic hormone refractory metastatic prostate cancer. Inclusion criteria were multiple bone metastases or a painful osseous lesion with two consecutive rising PSA values^[15]. The endpoints of the study were the efficacy of $^{223}\text{Radium}$ with respect to the decrease of bone-specific alkaline phosphatase (ALP) concentration and the time to the occurrence of a skeletal event. All patients also underwent external beam radiation. Sixty-four patients were recruited of whom 33 received external beam radiation and $^{223}\text{Radium}$ while 31 received external beam radiation and placebo (saline). Patients received up to 4 injections of 50 kBq/kg $^{223}\text{Radium}$ or placebo at intervals of 4 wk. Eight patients in the $^{223}\text{Radium}$ group and 21 patients in the placebo group completed the protocol. The study demonstrated an excellent safety profile for $^{223}\text{Radium}$. There were no differences in haemotoxicity between the groups and no patient in the $^{223}\text{Radium}$ group terminated the study due to treatment related toxic effects. In the $^{223}\text{Radium}$ group, 3 patients had a grade 2/3 neutropenia, which, however, was reversible.

In addition, there was evidence of biologic effects and efficacy with $^{223}\text{Radium}$. Patients in the $^{223}\text{Radium}$ arm had a significantly greater reduction in bone-ALP (-65.6%, $P < 0.0001$) than those in the placebo group (-9.3%). The median time to skeletal related events was 124 wk in the $^{223}\text{Radium}$ group *vs* 11 wk in the placebo arm. The median time until PSA progression was 126 wk in the $^{223}\text{Radium}$ group *vs* 8 wk in the placebo group ($P = 0.048$). Four weeks after the last injection, the median

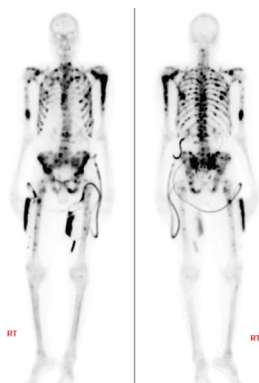


Figure 1 Sixty-one years old male with a history of high-grade Gleason 9 prostate cancer, diagnosed 8 years ago, treated with radiation treatment, prostatectomy, and androgen deprivation therapy. Patient has significant uncontrolled pain throughout the skeleton. Bone scan demonstrates wide spread metastatic disease to the skeleton.

relative change of the PSA was -23.8% in the $^{223}\text{Radium}$ arm, *vs* $+44.9\%$ in the placebo group ($P = 0.003$). Importantly, there was a trend toward improved survival in the $^{223}\text{Radium}$ group (65.3 wk) *vs* the placebo group (46.4 wk; $P = 0.066$). Thus, $^{223}\text{Radium}$ was tolerated, reduced serum ALP levels and tended to improve survival. In an additional study, the same authors published the 24 mo follow-up of the patients and confirmed the results of the previous study^[16]. They confirmed the excellent safety profile and demonstrated no increased risk for a secondary malignancy. A trend towards improved survival was again demonstrated ($P = 0.056$).

The effect of different dosages of $^{223}\text{Radium}$ on the pain reduction was investigated in another randomized and double-blinded study, involving 100 patients with castration-resistant, bone metastatic prostate cancer^[17]. More than 50% of the patients had 20 or more metastases, or a superscan. The patients received single doses of 5, 25, 50, or 100 kBq/kg $^{223}\text{Radium}$. Patients were classified as responders or non-responders using a bone pain index. Already after 2 wk, a significant pain reduction was evident ($P = 0.35$). After 8 wk, 40%, 63%, 56%, and 71% of the patients were classified as responders in the 5, 25, 50, and 100 kBq/kg groups, respectively. In the group of responders the pain was reduced by a mean of -30 , -31 , -27 , and -28 mm [according to the visual analogue scale (VAS)]. Furthermore, the favourable safety profile of $^{223}\text{Radium}$ was confirmed.

PHASE III STUDY AND FDA APPROVAL

A recently published phase III trial reported the results about Xofigo® from the Symptomatic Prostate Cancer Patients (ALSYMPCA) study^[10]. This multi-national, randomized, double-blind study started in 2008 and by February 2011 921 patients were enrolled. The goal of the study was to compare the efficacy and safety of $^{223}\text{Radium}$ *vs* placebo in patients with castration-resistant prostate cancer and bone metastases.

Patients were included in the study when they showed two or more bone metastases on skeletal scintigraphy, had no visceral metastases, and had been treated with docetaxel or if they were unable to receive docetaxel (Figure 1).

The patients were randomized in a ratio of 2:1 and received intravenous injections of $^{223}\text{Radium}$ (at a dose of 50 kBq per kilogram of body weight) or saline injections as placebo. Patient received 6 injections in 4-wk intervals. Each patient was provided with the best standard of care including local external-beam radiation therapy or treatment with glucocorticoids, antiandrogens, ketoconazole, or estrogens. Chemotherapy, hemibody external radiotherapy, and other systemic radionuclides were not permitted.

The primary end point was overall survival, defined as the time from randomization to the date of death, regardless of cause. The main secondary end points were the time to an increase in the total ALP level, a total alkaline phosphatase response, the time to the first symptomatic skeletal event, normalization of the total alkaline phosphatase level and the time to an increase in the PSA level.

The study was designed to provide a statistical power of 90% to detect a hazard ratio of 0.76 for the risk of death in the $^{223}\text{Radium}$ group *vs* the placebo group with a two-sided alpha significance level of 0.05. In total, 614 patients were enrolled in the $^{223}\text{Radium}$ group and 307 patients in the placebo group. The patients were enrolled in 136 study centres in 19 countries. The baseline patient characteristics in both groups were largely identical.

A pre-defined interim analysis was conducted after 314 deaths had occurred to assess the effect of $^{223}\text{Radium}$ on the primary end point (overall survival). On the basis of this interim analysis, which showed a survival advantage with $^{223}\text{Radium}$ and an acceptable safety profile, early discontinuation of the trial and crossover from placebo to $^{223}\text{Radium}$ was recommended. The authors report in this study the results of an updated descriptive analysis of the efficacy and safety data, performed when 528 deaths had occurred, before any crossover treatment with $^{223}\text{Radium}$ was administered.

The median overall survival was 14.9 mo in the $^{223}\text{Radium}$ group and 11.3 mo in the placebo group. The mortality risk was 30% lower in the $^{223}\text{Radium}$ group than in the placebo group ($P < 0.001$). In total 528 patients died; 333 of the 614 patients in the $^{223}\text{Radium}$ group (54%) and 195 of the 307 patients in the placebo group (64%). A secondary endpoint also confirmed the superiority of $^{223}\text{Radium}$ over the best standard of care. The time to the first symptomatic skeletal event was 15.6 mo in the $^{223}\text{Radium}$ group *vs* 9.8 mo in the placebo group ($P < 0.001$). The time to increases in the total ALP ($P < 0.001$) and PSA levels ($P < 0.001$) was significantly longer in the $^{223}\text{Radium}$ group. Finally, a significantly larger proportion of patients in the $^{223}\text{Radium}$ group showed a response of the total ALP and PSA levels ($\geq 30\%$ reduction, $P < 0.001$). Sixteen and 24 wk after initiation of $^{223}\text{Radium}$

treatment, patients had significantly less pain compared to baseline ($P < 0.001$ and $P = 0.001$, respectively).

No clear difference in the appearance of grade 3 and 4 adverse events (according to the Common Terminology Criteria for Adverse Events) was reported between the two groups. One patient in each group showed grade 3 febrile neutropenia. In the $^{223}\text{Radium}$ group one grade 5 haematologic adverse event (thrombocytopenia) occurred. Serious adverse events that occurred in $> 5\%$ of the patients in the $^{223}\text{Radium}$ or the placebo group were disease progression, bone pain, anaemia, and spinal cord compression. Overall the probability for the appearance of adverse events of all grades was lower in the $^{223}\text{Radium}$ group than in the placebo group. The quality of life (according to the Functional Assessment of Cancer Therapy-Prostate) improved significantly in the $^{223}\text{Radium}$ group.

Because of the interim analysis of the ALSYMPCA study, $^{223}\text{Radium}$ was approved by the FDA as a treatment for patients with bone metastatic castrate-resistant prostate cancer. The approval was given for patients without visceral metastases.

The suggested regimen follows that of the ALSYMPCA study and includes 50 kBq/kg at an interval of 4 wk with a maximum of 6 doses. A simultaneous administration of $^{223}\text{Radium}$ and chemotherapy is not permitted outside of clinical trials because of the unclear potential of additive effects on myelosuppression.

With its approval the FDA requested additional trials to determine the efficacy and safety of $^{223}\text{Radium}$ when given at doses > 50 kBq/kg. The FDA also requested to investigate the long term safety, the effects of $^{223}\text{Radium}$ on healthy bone marrow and the risk of the treatment for developing secondary malignancies.

CONCLUSION

$^{223}\text{Radium}$ is the first therapeutic that results in a survival benefit for patients with bone metastatic, castrate resistant prostate cancer. In addition, the treatment results in pain palliation and thus, improved quality of life and a delay of skeletal related events. At the same time the toxicity profile of $^{223}\text{Radium}$ was favourable. Thus $^{223}\text{Radium}$ may provide a new standard of care for patients with CRPC and bone metastases.

REFERENCES

- 1 GLOBOCAN 2008. Cancer Fact Sheet Prostate Cancer, 2008
- 2 Coleman R. Management of bone metastases. *Cancer Treat Rev* 1997; **23** Suppl 1: S69-S75 [PMID: 9377604 DOI: 10.1016/S0305-7372(97)90009-8]
- 3 Coleman RE. Clinical features of metastatic bone disease and risk of skeletal morbidity. *Clin Cancer Res* 2006; **12**: 6243s-6249s [PMID: 17062708 DOI: 10.1158/1078-0432.CCR-06-0931]
- 4 Lange PH, Vessella RL. Mechanisms, hypotheses and questions regarding prostate cancer micrometastases to bone. *Cancer Metastasis Rev* 1998; **17**: 331-336 [PMID: 10453276 DOI: 10.1023/A]
- 5 Wu JS, Wong R, Johnston M, Bezjak A, Whelan T. Meta-

- analysis of dose-fractionation radiotherapy trials for the palliation of painful bone metastases. *Int J Radiat Oncol Biol Phys* 2003; **55**: 594-605 [PMID: 12573746 DOI: 10.1016/S0360-3016(02)04147-0]
- 6 Robinson RG, Preston DF, Schiefelbein M, Baxter KG. Strontium 89 therapy for the palliation of pain due to osseous metastases. *JAMA* 1995; **274**: 420-424 [PMID: 7542352 DOI: 10.1001/jama.1995.03530050068035]
- 7 Sartor O. Prostate cancer and bone: a unique relationship with multiple opportunities for targeted therapy. *Clin Prostate Cancer* 2004; **3**: 71-72 [PMID: 15479486 DOI: 10.3816/CGC.2004.n.015]
- 8 Serafini AN, Houston SJ, Resche I, Quick DP, Grund FM, Eil PJ, Bertrand A, Ahmann FR, Orihuela E, Reid RH, Lerski RA, Collier BD, McKillop JH, Purnell GL, Pecking AP, Thomas FD, Harrison KA. Palliation of pain associated with metastatic bone cancer using samarium-153 lexidronam: a double-blind placebo-controlled clinical trial. *J Clin Oncol* 1998; **16**: 1574-1581 [PMID: 9552068]
- 9 Lassmann M, Nosske D. Dosimetry of ^{223}Ra -chloride: dose to normal organs and tissues. *Eur J Nucl Med Mol Imaging* 2013; **40**: 207-212 [PMID: 23053328 DOI: 10.1007/s00259-012-2265-y]
- 10 Parker C, Nilsson S, Heinrich D, Helle SI, O'Sullivan JM, Fosså SD, Chodacki A, Wiechno P, Logue J, Seke M, Widmark A, Johannessen DC, Hoskin P, Bottomley D, James ND, Solberg A, Syndikus I, Kliment J, Wedel S, Boehmer S, Dall'Oglio M, Franzén L, Coleman R, Vogelzang NJ, O'Bryan-Tear CG, Staudacher K, Garcia-Vargas J, Shan M, Bruland ØS, Sartor O. Alpha emitter radium-223 and survival in metastatic prostate cancer. *N Engl J Med* 2013; **369**: 213-223 [PMID: 23863050 DOI: 10.1056/NEJMoa1213755]
- 11 Henriksen G, Fisher DR, Roeske JC, Bruland ØS, Larsen RH. Targeting of osseous sites with alpha-emitting ^{223}Ra : comparison with the beta-emitter ^{89}Sr in mice. *J Nucl Med* 2003; **44**: 252-259 [PMID: 12571218]
- 12 Henriksen G, Breistøl K, Bruland ØS, Fodstad Ø, Larsen RH. Significant antitumor effect from bone-seeking, alpha-particle-emitting (^{223}Ra) demonstrated in an experimental skeletal metastases model. *Cancer Res* 2002; **62**: 3120-3125 [PMID: 12036923]
- 13 Carrasquillo JA, O'Donoghue JA, Pandit-Taskar N, Humm JL, Rathkopf DE, Slovin SF, Williamson MJ, Lacuna K, Aksnes AK, Larson SM, Scher HI, Morris MJ. Phase I pharmacokinetic and biodistribution study with escalating doses of ^{223}Ra -dichloride in men with castration-resistant metastatic prostate cancer. *Eur J Nucl Med Mol Imaging* 2013; **40**: 1384-1393 [PMID: 23653243 DOI: 10.1007/s00259-013-2427-6]
- 14 Nilsson S, Larsen RH, Fosså SD, Balteskard L, Borch KW, Westlin JE, Salberg G, Bruland OS. First clinical experience with alpha-emitting radium-223 in the treatment of skeletal metastases. *Clin Cancer Res* 2005; **11**: 4451-4459 [PMID: 15958630]
- 15 Nilsson S, Franzén L, Parker C, Tyrrell C, Blom R, Tennvall J, Lennernäs B, Petersson U, Johannessen DC, Sokal M, Pigott K, Yachnin J, Garkavij M, Strang P, Harmenberg J, Bolstad B, Bruland OS. Bone-targeted radium-223 in symptomatic, hormone-refractory prostate cancer: a randomised, multicentre, placebo-controlled phase II study. *Lancet Oncol* 2007; **8**: 587-594 [PMID: 17544845]
- 16 Nilsson S, Franzén L, Parker C, Tyrrell C, Blom R, Tennvall J, Lennernäs B, Petersson U, Johannessen DC, Sokal M, Pigott K, O'Bryan-Tear CG, Thuresson M, Bolstad B, Bruland ØS. Two-year survival follow-up of the randomized, double-blind, placebo-controlled phase II study of radium-223 chloride in patients with castration-resistant prostate cancer and bone metastases. *Clin Genitourin Cancer* 2013; **11**: 20-26 [PMID: 23021204 DOI: 10.1016/j.clgc.2012.07.002]
- 17 Nilsson S, Strang P, Aksnes AK, Franzén L, Olivier P, Peck-

Wieder HA *et al.* Targeted therapy with alpha-emitters

ing A, Staffurth J, Vasanthan S, Andersson C, Bruland ØS.
A randomized, dose-response, multicenter phase II study
of radium-223 chloride for the palliation of painful bone

metastases in patients with castration-resistant prostate
cancer. *Eur J Cancer* 2012; **48**: 678-686 [PMID: 22341993 DOI:
10.1016/j.ejca.2011.12.023]

P- Reviewer: Cheng Z **S- Editor:** Wen LL **L- Editor:** A
E- Editor: Lu YJ



Radiogenomic imaging-linking diagnostic imaging and molecular diagnostics

Mathias Goyen

Mathias Goyen, UKE Consult und Management GmbH, University Medical Center Hamburg-Eppendorf, 20251 Hamburg, Germany

Author contributions: Goyen M wrote and edited the entire manuscript.

Correspondence to: Mathias Goyen, MD, UKE Consult und Management GmbH, University Medical Center Hamburg-Eppendorf, Martinistrasse 52, 20251 Hamburg, Germany. mathias@goyen.de

Telephone: +49-40-741056810 Fax: +49-40-7410575

Received: December 30, 2013 Revised: June 5, 2014

Accepted: June 10, 2014

Published online: March 28, 2015

lyze the health system by creating imaging biomarkers that identify the genomics of a disease. The use of noninvasive imaging for gene expression profiling is a fast and reliable technique which has the potential to replace high-risk invasive biopsy procedures.

Original sources: Goyen M. Radiogenomic imaging-linking diagnostic imaging and molecular diagnostics. *World J Radiol* 2014; 6(8): 519-522 Available from: URL: <http://www.wjgnet.com/1949-8470/full/v6/i8/519.htm> DOI: <http://dx.doi.org/10.4329/wjr.v6.i8.519>

Abstract

Radiogenomic imaging refers to the correlation between cancer imaging features and gene expression and is one of the most promising areas within science and medicine. High-throughput biological techniques have reshaped the perspective of biomedical research allowing for fast and efficient assessment of the entire molecular topography of a cell's physiology providing new insights into human cancers. The use of non-invasive imaging tools for gene expression profiling of solid tumors could serve as a means for linking specific imaging features with specific gene expression patterns thereby allowing for more accurate diagnosis and prognosis and obviating the need for high-risk invasive biopsy procedures. This review focuses on the medical imaging part as one of the main drivers for the development of radiogenomic imaging.

© 2015 Baishideng Publishing Group Inc. All rights reserved.

Key words: Radiogenomic imaging; Personalized medicine; Diagnostic imaging

Core tip: Radiogenomic imaging has the potential to cata-

INTRODUCTION

Recent developments in high-throughput molecular techniques promise to generate biomarkers driving the future of personalized medicine^[1-3]. Gene expression profiling has the potential to gather key information regarding biology and its relationship to diagnosis, prognosis and therapy. However, a main limitation of these techniques is the need to acquire tissue for gene expression profiling through invasive biopsy thereby limiting the clinical application of this method in an everyday patient care setting. In addition, in these biopsies samples are frequently obtained from only a part of the lesion and therefore do not entirely represent the lesion's unique anatomic, functional, and physiologic properties, such as size, location, and morphology. Many of these features are obtained in routine clinical imaging exams and are very useful for diagnosis, staging, and treatment planning. Although these image features provide anatomical and morphological information, only few studies^[4-6] have generated a "radiogenomics map" integrating the genomic and image data thereby introducing the field of "radiogenomics" or "radiogenomic imaging"^[3]. Specific radiological tumor phenotypes can be used as surrogates for signatures of gene expression. If imaging can be linked to these treat-

ment-response gene-expression patterns routine clinical imaging is able to predict the likely response to specific chemotherapeutics and helps to choose the best form and duration of treatment.

DIAGNOSTIC IMAGING AS A PLATFORM FOR GENE EXPRESSION PROFILING

Radiologic imaging plays an important part in every stage of cancer treatment. Besides screening, detection and staging of disease, imaging is used to predict and evaluate individual patient's responsiveness to therapies in every stage of cancer treatment. Diagnostic imaging is a safe and accurate tool to noninvasively assess location, morphology and physiology of tissues^[3]. This crucial role for imaging biomarkers in cancer treatment is reflected by the fact that more than 90 percent of cancer patients are evaluated by imaging. However, much of the data generated by radiologic imaging remains largely unspecific at a molecular level. The integration of these noninvasive imaging tools with functional genomic assays has the power for a quick clinical translation of high-throughput technology.

IMAGING FOR MOLECULAR ASSESSMENT OF TUMOR STAGING AND DIAGNOSIS

A study by Kuo *et al*^[6] in patients with liver cancer demonstrated the relationship between imaging traits, histopathologic markers, and several predefined gene-expression programs. The study found that a liver-specific gene expression program was highly correlated with the imaging trait "tumor margin score, arterial phase". The data suggest that this radiophenotype could potentially form the basis to categorize hepatocellular carcinomas (HCCs).

Segal *et al*^[4] also demonstrated that dynamic imaging traits in computed tomography (CT) strongly correlated with the global gene expression programs of primary HCC. The authors managed to reconstruct 78% of the gene expression profiles by combining twenty-eight imaging traits, thereby showing cell proliferation, liver synthetic function, and patient outcome. Therefore, noninvasive imaging could decode genomic activity of human liver cancers, allowing for a noninvasive, frequent and quick molecular work-up on an individual level.

In patients with glioblastoma multiforme (GBM) Zinn *et al*^[7] introduced a new diagnostic imaging technique to assess molecular cancer subtypes and genomic correlates of cellular invasion using quantitative magnetic resonance imaging (MRI) volumetrics and large-scale gene- and microRNA expression profiling in GBM. Based on The Cancer Genome Atlas, discovery and validation sets with gene, microRNA, and quantitative

MRI data were created. Zinn *et al*^[7] showed that in patients with GBM the used fluid-attenuated inversion recovery sequence reliably detected main cancer genomic

components responsible for cellular migration and invasion. In addition it revealed genes and microRNAs highly associated with mesenchymal transformation and invasion. As cellular invasion is one of the main causes of treatment failure, the surgical extent of resection and adjuvant treatment planning are highly important. Thus, the authors conclude that the used method has potential therapeutic significance since successful molecular inhibition of invasion will improve therapy and patient survival in GBM.

In a recently published study in patients with GBM Jamshidi *et al*^[8] could show that MRI, messenger RNA expression and DNA copy number variation can identify MR traits which are associated with some known high-grade glioma biomarkers and associated with genomic biomarkers that have been identified for other malignancies but not GBM. Further work is needed to determine the clinical value of these findings.

IMAGING FOR MOLECULAR ASSESSMENT OF TUMOR PROGNOSIS

Radiogenomic imaging is a useful tool for molecular assessment of tumor staging and diagnosis; however, for its success in a clinical setting it is crucial that radiogenomics has the potential to also impact clinical management. Despite much recent activity in developing imaging biomarkers of disease, it is challenging to link these biomarkers to clinical outcomes as it takes years to obtain these outcomes in cohort studies^[9].

The above mentioned study by Kuo *et al*^[6] in patients with HCC showed that the tumor margin score highly correlated with a venous invasion gene expression program as well as histologically-confirmed venous invasion.

A study by Diehn *et al*^[5] sought to correlate imaging surrogates for gene-expression profiles with prognostic implications in patients with GBM. The radiogenomic maps showed a statistically significant overlap between a survival-associated gene signature and an infiltrative pattern of the edema on T2-weighted images. The hyperintense signal on the T2-weighted images allowed for a clear differentiation between edematous and infiltrative patterns reflecting the interface between a tumor and the adjacent normal brain. In a second part of the study another 110 GBMs were included; the results revealed a correlation between the infiltrative radiophenotype and a poor prognosis: a median survival of 390 d was found for those without infiltrative pattern compared to 216 for those with infiltrative pattern. The study shows a quick, easy-to-use technique to discover prognostic imaging biomarkers associated with underlying gene-expression signatures.

A study by Gevaert *et al*^[9] explored the clinical prognostic value of Radiogenomic imaging by looking at features from non-small cell lung cancer (NSCLC) CT- and positron emission tomography (PET)-cases^[10]. Gevaert *et al*^[9] study comprised 26 patients with NSCLC whose imaging features were comprehensively extracted and statistically analyzed. To obtain survival data which were

not available the authors derived prognostic conclusions by using a genomically matched NSCLC case set with known clinical outcomes from public databases^[11]. Gevaert *et al*^[9] demonstrated an imaging approach able to quickly identify prognostically relevant image biomarkers requiring only the paired acquisition of image and gene expression data as well as the existence of a large public gene expression data set where survival outcomes are available. The authors conclude that by mapping image features to gene expression data, it is possible to leverage public gene expression microarray data to determine prognosis and therapeutic response as a function of image features.

In a follow-up study Nair *et al*^[12] analyzed Nuclear factor- κ B (NF- κ B) protein expression in a group of 355 patients with NSCLC (365 tumor samples) with long-term follow-up by means of immunohistochemistry (IHC) using a Tissue Microarray.

NF- κ Bp65 as well as a positive uptake of fluorodeoxyglucose (FDG) was significantly associated with more advanced stage, tumor histology and invasion. Higher NF- κ Bp65 expression was associated with death by Kaplan Meier analysis ($P = 0.06$) while LDHA was strongly associated with recurrence ($P = 0.04$). Increased levels of combined NF- κ Bp65 and lactate dehydrogenase A (LDHA) expression were synergistic and associated with both recurrence ($P = 0.04$) and death ($P = 0.03$). The authors conclude that NF- κ B IHC was a modest biomarker of prognosis that associated with tumor glucose metabolism on FDG PET when compared to existing molecular correlates like LDHA, which was synergistic with NF- κ B for outcome.

IMAGING FOR MOLECULAR ASSESSMENT OF OPTIMAL THERAPY

By using an integrated imaging-genomic approach Kuo *et al*^[6] determined whether contrast-enhanced CT was capable to assess imaging phenotypes which are associated with a doxorubicin drug response gene expression program in patients with HCC. The authors included 30 HCCs into the study and scored them individually across six predefined imaging phenotypes. An imaging phenotype related to tumor margins on arterial phase images showed a significant correlation with the doxorubicin-response transcriptional program ($P < 0.05$, $q < 0.1$). In addition it was significantly associated with HCC venous invasion and tumor stage ($P < 0.05$, $q < 0.1$). Tumors with higher tumor margin scores were more strongly associated with the doxorubicin resistance transcriptional program and had a greater prevalence of venous invasion and worse stage. Tumors with lower tumor margin scores, however, showed a converse relationship. The authors conclude that CT has the potential to identify HCC imaging phenotypes correlating with a doxorubicin drug response gene expression program. As doxorubicin is a standard treatment in regional therapies for patients with HCC, the used imaging strategy could be used to guide

HCC therapy on a tumor-by-tumor basis on the basis of underlying tumor gene expression patterns.

The previously mentioned study by Diehn *et al*^[5] also evaluated whether in patients with GBM the expression of a therapeutic target could be predicted based on its imaging-gene-expression association. Activation of specific gene-expression programs can be inferred from imaging traits, thereby giving insights into tumor biology on a tumor-by-tumor basis. The authors could reveal potential imaging biomarkers for several classes of anti-GBM therapeutic agents, including antiangiogenesis and epidermal growth factor receptor-based therapies. In addition, the results show that intratumoral heterogeneity of several gene-expression programs can be spatially resolved by means of imaging. Furthermore, the authors identified an imaging phenotype characterized by an infiltrative appearance that was associated with aggressive clinical behavior and expression of genes involved in central nervous system development and gliogenesis. As this imaging approach is noninvasive and widely available in clinical practice it can be applied to a broad range of human disease processes.

CONCLUSION

Radiogenomic imaging has the potential to catalyze the health system by creating imaging biomarkers that identify the genomics of a disease. The use of noninvasive imaging as a surrogate for gene expression profiling is a quick and reliable tool which has the potential to replace high-risk invasive biopsy procedures. Additional studies with larger numbers of patients are necessary to confirm links between gene expression patterns and imaging features permitting fast and reliable clinical diagnosis of tumors as well as estimation of prognosis and decision for optimal therapy.

REFERENCES

- 1 **Pao W**, Kris MG, Iafrate AJ, Ladanyi M, Jänne PA, Wistuba II, Miake-Lye R, Herbst RS, Carbone DP, Johnson BE, Lynch TJ. Integration of molecular profiling into the lung cancer clinic. *Clin Cancer Res* 2009; **15**: 5317-5322 [PMID: 19706816 DOI: 10.1158/1078-0432.CCR-09-0913]
- 2 **Gevaert O**, De Moor B. Prediction of cancer outcome using DNA microarray technology: past, present and future. *Expert Opin Med Diagn* 2009; **3**: 157-165 [PMID: 23485162 DOI: 10.1517/17530050802680172]
- 3 **Rutman AM**, Kuo MD. Radiogenomics: creating a link between molecular diagnostics and diagnostic imaging. *Eur J Radiol* 2009; **70**: 232-241 [PMID: 19303233 DOI: 10.1016/j.ejrad.2009.01.050]
- 4 **Segal E**, Sirlin CB, Ooi C, Adler AS, Gollub J, Chen X, Chan BK, Matcuk GR, Barry CT, Chang HY, Kuo MD. Decoding global gene expression programs in liver cancer by non-invasive imaging. *Nat Biotechnol* 2007; **25**: 675-680 [PMID: 17515910]
- 5 **Diehn M**, Nardini C, Wang DS, McGovern S, Jayaraman M, Liang Y, Aldape K, Cha S, Kuo MD. Identification of noninvasive imaging surrogates for brain tumor gene-expression modules. *Proc Natl Acad Sci USA* 2008; **105**: 5213-5218 [PMID: 18362333 DOI: 10.1073/pnas.0801279105]
- 6 **Kuo MD**, Gollub J, Sirlin CB, Ooi C, Chen X. Radiogenomic

- analysis to identify imaging phenotypes associated with drug response gene expression programs in hepatocellular carcinoma. *J Vasc Interv Radiol* 2007; **18**: 821-831 [PMID: 17609439]
- 7 **Zinn PO**, Mahajan B, Sathyan P, Singh SK, Majumder S, Jolesz FA, Colen RR. Radiogenomic mapping of edema/cellular invasion MRI-phenotypes in glioblastoma multiforme. *PLoS One* 2011; **6**: e25451 [PMID: 21998659 DOI: 10.1371/journal.pone.0025451]
- 8 **Jamshidi N**, Diehn M, Bredel M, Kuo MD. Illuminating radiogenomic characteristics of glioblastoma multiforme through integration of MR imaging, messenger RNA expression, and DNA copy number variation. *Radiology* 2014; **270**: 1-2 [PMID: 24056404 DOI: 10.1148/radiol.13130078]
- 9 **Gevaert O**, Xu J, Hoang CD, Leung AN, Xu Y, Quon A, Rubin DL, Napel S, Plevritis SK. Non-small cell lung cancer: identifying prognostic imaging biomarkers by leveraging public gene expression microarray data--methods and preliminary results. *Radiology* 2012; **264**: 387-396 [PMID: 22723499 DOI: 10.1148/radiol.12111607]
- 10 **Jaffe CC**. Imaging and genomics: is there a synergy? *Radiology* 2012; **264**: 329-331 [PMID: 22821693 DOI: 10.1148/radiol.12120871]
- 11 **Parkinson H**, Sarkans U, Kolesnikov N, Abeygunawardena N, Burdett T, Dylag M, Emam I, Farne A, Hastings E, Holloway E, Kurbatova N, Lukk M, Malone J, Mani R, Pilicheva E, Rustici G, Sharma A, Williams E, Adamusiak T, Brandizi M, Sklyar N, Brazma A. ArrayExpress update--an archive of microarray and high-throughput sequencing-based functional genomics experiments. *Nucleic Acids Res* 2011; **39**: D1002-D1004 [PMID: 21071405 DOI: 10.1093/nar/gkq1040]
- 12 **Nair VS**, Gevaert O, Davidzon G, Plevritis SK, West R. NF- κ B protein expression associates with (18)F-FDG PET tumor uptake in non-small cell lung cancer: a radiogenomics validation study to understand tumor metabolism. *Lung Cancer* 2014; **83**: 189-196 [PMID: 24355259 DOI: 10.1016/j.lungcan.2013.11.001]

P- Reviewer: Tang GH S- Editor: Qi Y
L- Editor: A E- Editor: Liu SQ



Postoperative reactive lymphadenitis: A potential cause of false-positive FDG PET/CT

Yiyan Liu

Yiyan Liu, Nuclear Medicine Service, Department of Radiology, Rutgers University Hospital, Newark, NJ 07103, United States
Author contributions: Liu Y solely contributed this work.
Correspondence to: Yiyan Liu, MD, PhD, Nuclear Medicine Service, Department of Radiology, Rutgers University Hospital, 150 Bergen Street, H141, Newark, NJ 07103, United States. liuyl@njms.rutgers.edu
Telephone: +1-973-9726022 Fax: +1-973-9726954
Received: April 30, 2014 Revised: July 1, 2014
Accepted: October 14, 2014
Published online: March 28, 2015

Abstract

A wide variety of surgical related uptake has been reported on F18-fluoro-2-deoxy-D-glucose positron emission tomography/computed tomography (FDG PET/CT) scan, most of which can be differentiated from neoplastic process based on the pattern of FDG uptake and/or anatomic appearance on the integrated CT in image interpretation. A more potential problem we may be aware is postoperative reactive lymphadenitis, which may mimic regional nodal metastases on FDG PET/CT. This review presents five case examples demonstrating that postoperative reactive lymphadenitis could be a false-positive source for regional nodal metastasis on FDG PET/CT. Surgical oncologists and radiologists should be aware of reactive lymphadenitis in interpreting postoperative restaging FDG PET/CT scan when FDG avid lymphadenopathy is only seen in the lymphatic draining location from surgical site.

© 2015 Baishideng Publishing Group Inc. All rights reserved.

Key words: Lymphadenitis; F18-fluoro-2-deoxy-D-glucose positron emission tomography/computed tomography; False-positive; Lymphadenopathy

Core tip: On restaging F18-fluoro-2-deoxy-D-glucose (FDG) positron emission tomography/computed tomog-

raphy for oncologic patients, a potential problem we may be aware is postoperative reactive lymphadenitis, which may mimic regional nodal metastases. The size and intensity of FDG uptake of the lymph nodes cannot be reliably used for differentiation of reactive lymphadenitis from regional nodal metastasis. Surgical oncologists and radiologists should be aware of reactive lymphadenitis when FDG avid lymphadenopathy is only seen in the lymphatic draining location from surgical site.

Original sources: Liu Y. Postoperative reactive lymphadenitis: A potential cause of false-positive FDG PET/CT. *World J Radiol* 2014; 6(12): 890-894 Available from: URL: <http://www.wjgnet.com/1949-8470/full/v6/i12/890.htm> DOI: <http://dx.doi.org/10.4329/wjr.v6.i12.890>

INTRODUCTION

Today metabolic imaging positron emission tomography/computed tomography (PET/CT) with F18-fluoro-2-deoxy-D-glucose (FDG) has gained widespread clinical applications in oncology, and is accepted as a standard care in many malignancies. FDG is an analog of glucose and is used as a tracer of glycolysis. Malignant tissue and cells often demonstrate increased rate of glycolysis for rapid proliferation, due to increased number of glucose transporter protein and increased intracellular hexokinase and phosphofructokinase levels^[1,2]. FDG uptake is semi-quantitatively measured in the form of the standardized uptake value (SUV). However, FDG is not cancer-specific. Increased FDG uptake can be seen in many benign diseases or non-neoplastic conditions, most of which are inflammation or infection^[3-7].

Surgical resection of tumor is a first or best treatment in many malignancies. Postoperative PET/CT is often obtained for restaging or detection of residual/recurrent disease. Although it is generally recommended that

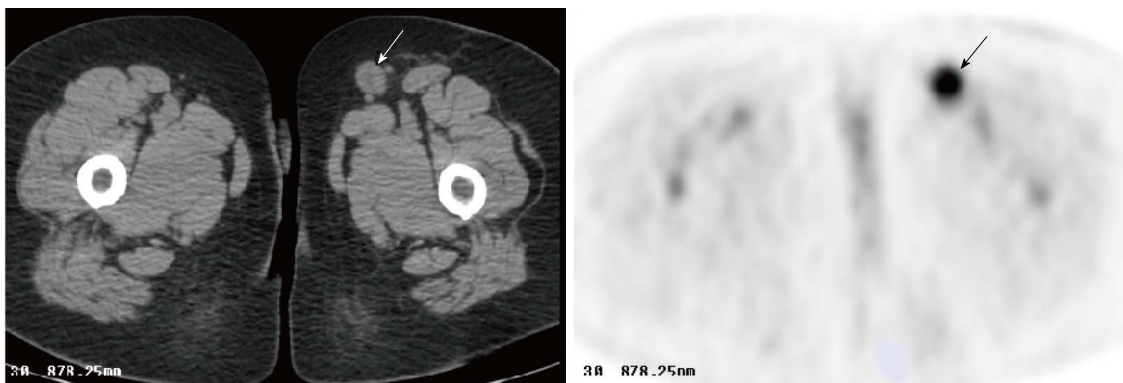


Figure 1 Axial image of F18-fluoro-2-deoxy-D-glucose positron emission tomography/computed tomography obtained 3 mo postoperatively in a 55-year-old woman with history of T2aN0Mx myxofibrosarcoma of the left ankle. Compared to preoperative image, there was a new 2.3 cm left inguinal lymph node with intense uptake (SUV 8.0, arrows), suspicious for nodal metastasis. Biopsy of the node revealed reactive lymphadenitis. SUV: Standardized uptake value.

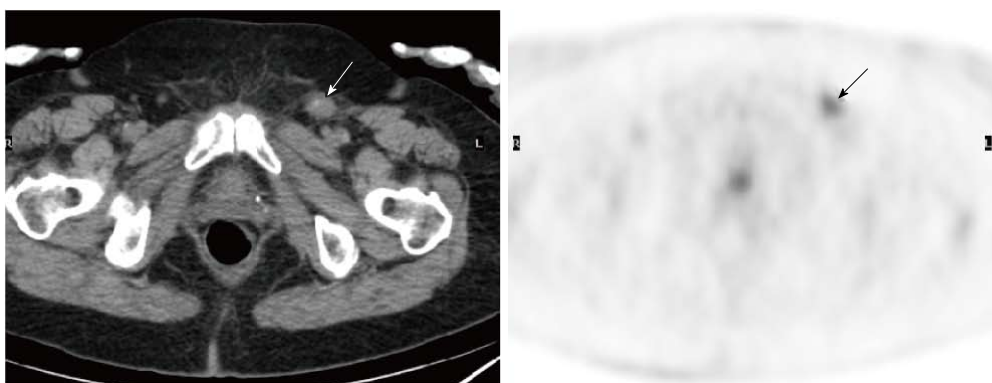


Figure 2 Axial image of F18-fluoro-2-deoxy-D-glucose positron emission tomography/computed tomography obtained 5 mo postoperatively in a 68-year-old woman with history of vulvar squamous cell carcinoma. Compared to preoperative image, there was a new 1.5 cm left inguinal lymph node with increased uptake (SUV 4.9, arrows). Incisional biopsy of the node suggested lymphadenitis. SUV: Standardized uptake value.

follow-up scan should be obtained at least 6 wk following surgery when postsurgical inflammation has subsided, a wide variety of types of surgical related uptake have been reported on FDG PET/CT scans^[8-14]. Most of them can be differentiated from neoplastic process based on the pattern of FDG uptake and/or anatomic appearance on the integrated CT, although some may cause false-positive interpretation.

A more potential postoperative false-positive FDG PET/CT finding is reactive lymphadenitis, which is encountered in clinical practice but is not well described in the literature. The followings are a few case examples of postoperative reactive lymphadenitis, which all mimic regional nodal metastases on FDG PET/CT.

CASE EXAMPLES

Case 1

A 55-year-old woman had history of T2aN0Mx sarcoma of the left ankle, status post surgical resection with free margins. A preoperative FDG PET/CT was negative for regional lymphadenopathy. Repeat FDG PET/CT 3 mo postoperatively showed a new 2.3 cm left inguinal lymph node with intense uptake, suspicious for nodal metastasis.

Biopsy of the node revealed reactive lymphadenitis (Figure 1).

Case 2

A 68-year-old woman had history of vulvar squamous cell carcinoma, status post lesion resection and left inguinal node dissection. Repeat FDG PET/CT 5 mo postoperatively showed a new 1.5 cm left inguinal lymph node with increased uptake, suspicious for nodal metastasis. Incisional biopsy of the node suggested lymphadenitis (Figure 2).

Case 3

A 16-year-old woman had alveolar soft tissue sarcoma of the left knee, status post surgical resection and chemotherapy. Preoperative image was negative for inguinal lymphadenopathy. Repeat FDG PET/CT 6 mo postoperatively showed a new 1.4 cm left inguinal lymph node with intense uptake, suspicious for nodal metastasis. Incisional biopsy indicated lymphadenitis (Figure 3).

Case 4

A 60-year-old man had history of tongue cancer, status post chemotherapy, radiation and bilateral neck dissec-

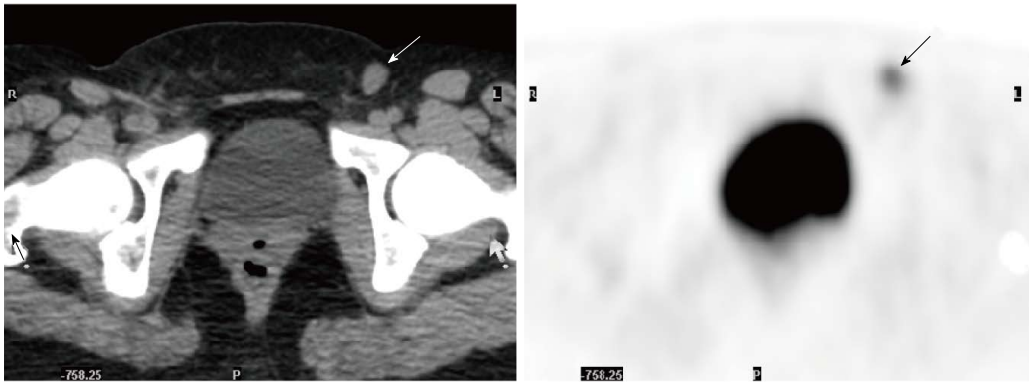


Figure 3 Axial image of F18-fluoro-2-deoxy-D-glucose positron emission tomography/computed tomography obtained 6 mo postoperatively in a 16-year-old woman with alveolar soft tissue sarcoma of the left knee. Compared to preoperative image, there was a new 1.4 cm left inguinal lymph node with intense uptake (SUV 5.2, arrows). Incisional biopsy confirmed lymphadenitis. SUV: Standardized uptake value.

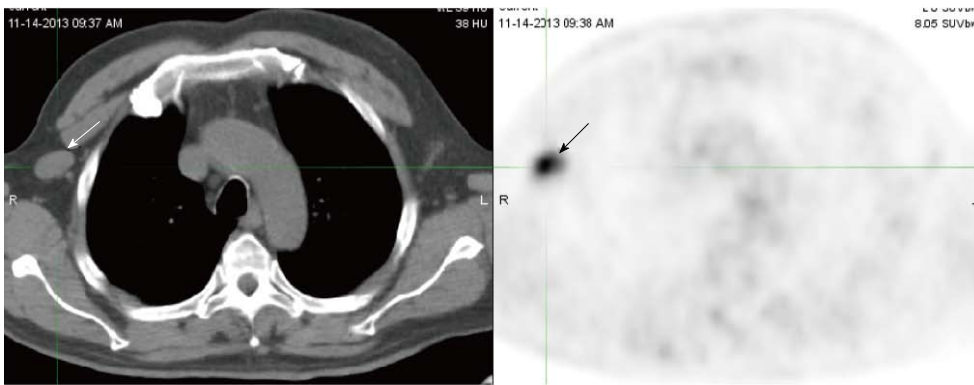


Figure 4 Axial image of F18-fluoro-2-deoxy-D-glucose positron emission tomography/computed tomography obtained 6 mo postoperatively in a 60-year-old man had history of tongue cancer. The image demonstrated a 2.6 cm x 1.5 cm right axillary lymph node with intense uptake (SUV 6.1, arrows), suspicious for metastasis. Biopsy of the node suggested chronic lymphadenitis with reactive lymphoid hyperplasia. SUV: Standardized uptake value.

tion. The patient developed osteoradionecrosis of the jaws after radiation therapy. FDG PET/CT 6 mo postoperatively demonstrated a 2.6 cm × 1.5 cm right axillary lymph node with intense uptake (SUV 6.1, arrows), suspicious for metastasis. Biopsy of the node suggested chronic lymphadenitis with reactive lymphoid hyperplasia (Figure 4).

Case 5

A 77-year-old woman had history of right breast cancer, status post lumpectomy. FDG PET/CT 3 mo postoperatively showed a few FDG avid right axillary lymph nodes, the largest 1.6 cm with SUV 5.1 (arrows), highly suspicious for regional nodal metastases. Subsequent biopsy was indicative of reactive lymphadenitis (Figure 5).

DISCUSSION

Postoperative FDG PET/CT is often obtained for restaging or detection of residual/recurrent tumor. Increased FDG uptake can be seen in the surgical site in the early postoperative period as a consequence of leukocyte infiltrate and granulation tissue involved in wound healing and absorption of necrotic debris and hematoma.

Various kinds of postoperative complications have been reported on FDG PET/CT. Makis *et al*^[14] reported 9 cases with incidental infectious or inflammatory findings on FDG PET/CT, in patients with prior surgical intervention that was part of the management of oncologic care. These included surgical wound infection, fistulas, abscess, and mesh infection. On image interpretation, most of surgery-related changes and/or inflammation can be identified without many difficulties based on the pattern of FDG uptake and CT findings.

Inflammatory/infectious lymphadenitis has been well recognized with increased FDG uptake on PET/CT, such as in the tuberculosis^[15,16], Kikuchi disease^[17,18], toxoplasmosis^[19], various viral infections including HIV^[20,21], *etc.* False-positive lymph nodes had also been reported^[22-24] on FDG PET/CT in oncologic patients. Tsukada *et al*^[22] reported a case with false-positive mediastinal lymph nodes on FDG PET/CT in rectal cancer patient. Atergin *et al*^[23] reported 3 cases of tuberculosis lymphadenitis detected on FDG PET scan in patients with concomitant cancer diagnosis. Park *et al*^[24] described false-positive tuberculous mediastinal lymphadenitis on FDG PET/CT in a melanoma patient. In all these cases, however, false-positive lymphadenitis on FDG PET/CT was not related

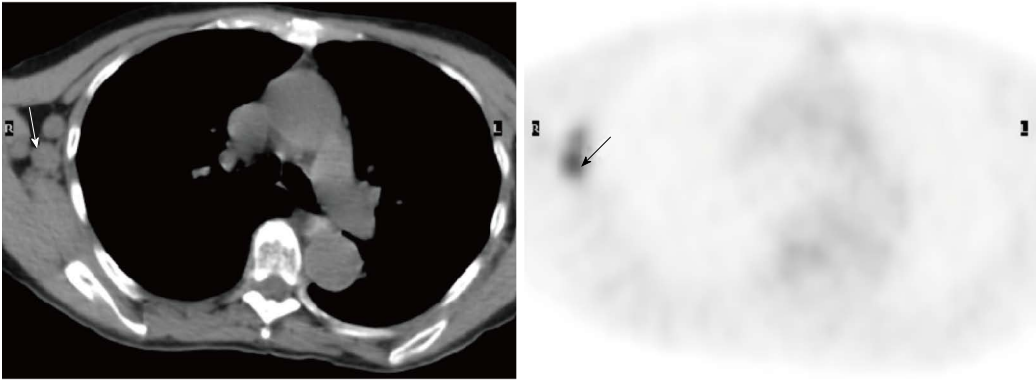


Figure 5 Axila image of F18-fluoro-2-deoxy-D-glucose positron emission tomography/computed tomography obtained 3 mo postoperatively in a 77-year-old woman had history of right breast cancer. There were a few FDG avid right axillary lymph nodes, the largest 1.6 cm with SUV 5.1 (arrows), all new compared to prior images. The findings were highly suspicious for regional nodal metastases. Subsequent biopsy was indicative of reactive lymphadenitis. SUV: Standardized uptake value.

to primary tumors in the locations, and not secondary to surgical resections of primary tumors.

Postoperative lymphadenitis is not well defined in the literatures. Regional lymphadenopathy may develop postoperatively due to an inflammatory response to the surgery, but it is typically days after the surgery and less than 1.0 cm in size^[25]. In the case examples above, FDG PET/CT was all obtained 3, 5, and 6 mo postoperatively when postoperative reaction and/or inflammation has subsided in general. The regional FDG avid lymph nodes were all located in the ipsilateral side of primary tumors and surgical procedures, and were new compared to preoperative PET/CT scans. Although FDG avid lymphadenopathy was only seen in the single location on the lymphatic draining route from the primary lesion and surgical site, CT features such as large size and solid appearance, and high FDG avidity of the lymph nodes were all suspicious for regional nodal metastases. However, surgical pathology revealed reactive lymphadenitis most likely secondary to surgical procedure. In these cases, the differentiation between regional nodal metastasis and reactive lymphadenitis was very challenging based on imaging only, and pathological diagnosis might be warranted. SUV cannot reliably discriminate between inflammation/infection and tumor.

CONCLUSION

Surgical oncologists and radiologists should be aware of reactive lymphadenitis on interpreting postoperative restaging FDG PET/CT scan when FDG avid lymphadenopathy is only seen in the lymphatic draining location from surgical site. The size and intensity of FDG uptake of the lymph nodes cannot be reliably used for differentiation of reactive lymphadenitis from regional nodal metastasis. Postoperative reactive lymphadenitis could be a potential false-positive source for regional nodal metastasis on FDG PET/CT.

REFERENCES

1 Liu Y, Ghesani NV, Zuckier LS. Physiology and pathophysiology of incidental findings detected on FDG-PET scintigraphy. *Semin Nucl Med* 2010; **40**: 294-315 [PMID: 20513451 DOI: 10.1053/j.semnuclmed.2010.02.002]

2 Chang JM, Lee HJ, Goo JM, Lee HY, Lee JJ, Chung JK, Im JG. False positive and false negative FDG-PET scans in various thoracic diseases. *Korean J Radiol* 2006; **7**: 57-69 [PMID: 16549957 DOI: 10.3348/kjr.2006.07.1.57]

3 Gorospe L, Raman S, Echeveste J, Avril N, Herrero Y, Hernandez S. Whole-body PET/CT: spectrum of physiological variants, artifacts and interpretative pitfalls in cancer patients. *Nucl Med Commun* 2005; **26**: 671-687 [PMID: 16000985 DOI: 10.1097/01.mnm.0000171779.65284.eb]

4 Asad S, Aquino SL, Piyavisetpat N, Fischman AJ. False-positive FDG positron emission tomography uptake in nonmalignant chest abnormalities. *AJR Am J Roentgenol* 2004; **182**: 983-989 [PMID: 15039176 DOI: 10.2214/ajr.182.4.1820983]

5 Metser U, Miller E, Lerman H, Even-Sapir E. Benign nonphysiologic lesions with increased 18F-FDG uptake on PET/CT: characterization and incidence. *AJR Am J Roentgenol* 2007; **189**: 1203-1210 [PMID: 17954662 DOI: 10.2214/AJR.07.2083]

6 Metser U, Even-Sapir E. Increased (18)F-fluorodeoxyglucose uptake in benign, nonphysiologic lesions found on whole-body positron emission tomography/computed tomography (PET/CT): accumulated data from four years of experience with PET/CT. *Semin Nucl Med* 2007; **37**: 206-222 [PMID: 17418153 DOI: 10.1053/j.semnuclmed.2007.01.001]

7 Wang X, Koch S. Positron emission tomography/computed tomography potential pitfalls and artifacts. *Curr Probl Diagn Radiol* 2009; **38**: 156-169 [PMID: 19464586 DOI: 10.1067/j.cpradiol.2008.01.001]

8 Dubroff JG, Alavi A, Friedberg JS, Cengel KA. Postsurgical atypical F-18 fluorodeoxyglucose positron emission tomography uptake. *Clin Nucl Med* 2009; **34**: 808-810 [PMID: 19851183 DOI: 10.1097/RLU.Ob013e3181b81e30]

9 Adejolu M, Huo L, Rohren E, Santiago L, Yang WT. False-positive lesions mimicking breast cancer on FDG PET and PET/CT. *AJR Am J Roentgenol* 2012; **198**: W304-W314 [PMID: 22358030 DOI: 10.2214/AJR.11.7130]

10 Takahara K, Kakinoki H, Ikoma S, Udo K, Tobu S, Satoh Y, Tokuda Y, Noguchi M, Aoki S, Uozumi J. Suture granuloma showing false-positive finding on FDG-PET. *Case Reports in Urol* 2013; **2013**: 472642 [PMID: 23762743 DOI: 10.1155/2013/472642]

11 Ruiz-Zafra J, Rodríguez-Fernández A, Sánchez-Palencia A, Cueto A. Surgical adhesive may cause false positives in integrated positron emission tomography and computed tomography after lung cancer resection. *Eur J Cardiothorac Surg* 2013; **43**: 1251-1253 [PMID: 23242986 DOI: 10.1093/ejcts/ezs643]

- 12 **Liu Y.** Orthopedic surgery-related benign uptake on FDG-PET: case examples and pitfalls. *Ann Nucl Med* 2009; **23**: 701-708 [PMID: 19728016 DOI: 10.1007/s12149-009-0296-7]
- 13 **Bhargava P,** Rahman S, Wendt J. Atlas of confounding factors in head and neck PET/CT imaging. *Clin Nucl Med* 2011; **36**: e20-e29 [PMID: 21467845 DOI: 10.1097/RLU.0b013e318212c872]
- 14 **Makis W,** Ciarallo A, Rush C, Hickeson M. Infectious and inflammatory complications of surgical management of cancer patients imaged with 18F-FDG PET/CT: a pictorial essay. *Clin Imaging* 2013; **37**: 669-679 [PMID: 23540832 DOI: 10.1016/j.clinimag.2013.02.003]
- 15 **Enomoto K,** Hoshida Y, Hamada K, Okada T, Kubo T, Hatazawa J. F-18 FDG PET imaging of cervical tuberculous lymphadenitis. *Clin Nucl Med* 2007; **32**: 474-475 [PMID: 17515760 DOI: 10.1097/RLU.ob013e318053764a]
- 16 **Sathekge M,** Maes A, D'Asseler Y, Vorster M, Gongxeka H, Van de Wiele C. Tuberculous lymphadenitis: FDG PET and CT findings in responsive and nonresponsive disease. *Eur J Nucl Med Mol Imaging* 2012; **39**: 1184-1190 [PMID: 22526957 DOI: 10.1007/s00259-012-2115-y]
- 17 **Kong E,** Chun K, Hong Y, Hah J, Cho I. 18F-FDG PET/CT findings in patients with Kikuchi disease. *Nuklearmedizin* 2013; **52**: 101-106 [PMID: 23681151 DOI: 10.3413/Nukmed-0513-12-06]
- 18 **Tsujikawa T,** Tsuchida T, Imamura Y, Kobayashi M, Asahi S, Shimizu K, Tsuji K, Okazawa H, Kimura H. Kikuchi-Fujimoto disease: PET/CT assessment of a rare cause of cervical lymphadenopathy. *Clin Nucl Med* 2011; **36**: 661-664 [PMID: 21716016 DOI: 10.1097/RLU.ob013e31821e2878]
- 19 **Treglia G,** Bongiovanni M, Ceriani L, Paone G, Giovanella L. Toxoplasmic Lymphadenitis Mimicking a Metastatic Thyroid Carcinoma at (18)F-FDG-PET/CT. *Nucl Med Mol Imaging* 2013; **47**: 289-290 [PMID: 24900128 DOI: 10.1007/s13139-013-0217-5]
- 20 **Sathekge M,** Maes A, Van de Wiele C. FDG-PET imaging in HIV infection and tuberculosis. *Semin Nucl Med* 2013; **43**: 349-366 [PMID: 23905617 DOI: 10.1053/j.semnuclmed.2013.04.008]
- 21 **Thomas DL,** Syrbu S, Graham MM. Epstein-Barr virus mimicking lymphoma on FDG-PET/CT. *Clin Nucl Med* 2009; **34**: 891-893 [PMID: 20139824 DOI: 10.1097/RLU.ob013e3181bed135]
- 22 **Tsukada T,** Nakano T, Matoba M, Sasaki S, Higashi K. False-Positive Mediastinal Lymphadenopathy on 18F-Fluorodeoxyglucose Positron Emission Tomography and Computed Tomography after Rectal Cancer Resection: A Case Report of Thoracoscopic Surgery in the Prone Position. *Case Rep Oncol* 2011; **4**: 569-575 [PMID: 22220152 DOI: 10.1159/000335017]
- 23 **Ataergin S,** Arslan N, Ozet A, Ozguven MA. Abnormal FDG uptake on F18-fluorodeoxyglucose positron emission tomography in patients with cancer diagnosis: case reports of tuberculosis lymphadenitis. *Inter Med* 2009; **48**: 115-119 [DOI: 10.2169/internalmedicine.48.1536]
- 24 **Park WJ,** Kim EK, Park JH. Extensive tuberculous lymphadenitis mimicking distant lymph node metastasis on F-18FDG PET/CT in a patient with a history of malignant melanoma. *Yonsei Med J* 2013; **54**: 1554-1556 [PMID: 24142667 DOI: 10.3349/ymj.2013.54.6.1554]
- 25 **Scialpi M,** Scaglione M, Volterrani L, Lupattelli L, Ragozzino A, Romano S, Rotondo A. Imaging evaluation of post pancreatic surgery. *Eur J Radiol* 2005; **53**: 417-424 [PMID: 15741015 DOI: 10.1016/j.ejrad.2004.12.013]

P- Reviewer: Li YZ, Stack BC, Treglia G **S- Editor:** Tian YL
L- Editor: A **E- Editor:** Lu YJ



Imaging of Gaucher disease

William L Simpson, George Hermann, Manisha Balwani

William L Simpson, George Hermann, Department of Radiology, Icahn School of Medicine at Mount Sinai, New York, NY 10029, United States

Manisha Balwani, Department of Genetics and Genomic Sciences, Icahn School of Medicine at Mount Sinai, New York, NY 10029, United States

Author contributions: Simpson WL, Hermann G and Balwani M contributed equally to this work; Simpson WL drafted the manuscript; Hermann G and Balwani M critically revised the manuscript; Simpson WL, Hermann G and Balwani M approved the final version.

Correspondence to: William L Simpson, Jr., MD, Associate professor of Radiology, Department of Radiology, Icahn School of Medicine at Mount Sinai, Box 1234, 1 Gustave L Levy Place, New York, NY 10029,

United States. william.simpson@mountsinai.org

Telephone: +1-212-2413832 Fax: +1-212-4278137

Received: December 28, 2013 Revised: April 9, 2014

Accepted: July 15, 2014

Published online: March 28, 2015

Abstract

Gaucher disease is the prototypical lysosomal storage disease. It results from the accumulation of undegraded glucosylceramide in the reticuloendothelial system of the bone marrow, spleen and liver due to deficiency of the enzyme glucocerebrosidase. This leads to hematologic, visceral and skeletal manifestations. Build up of glucosylceramide in the liver and spleen results in hepatosplenomegaly. The normal bone marrow is replaced by the accumulating substrate leading to many of the hematologic signs including anemia. The visceral and skeletal manifestations can be visualized with various imaging modalities including radiography, computed tomography, magnetic resonance imaging (MRI) and radionuclide scanning. Prior to the development of enzyme replacement therapy, treatment was only supportive. However, once intravenous enzyme replacement therapy became available in the 1990s it quickly became the standard of care. Enzyme replacement therapy leads to improvement in all manifestations. The

visceral and hematologic manifestations respond more quickly usually within a few months or years. The skeletal manifestations take much longer, usually several years, to show improvement. In recent years newer treatment strategies, such as substrate reduction therapy, have been under investigation. Imaging plays a key role in both initial diagnosis and routine monitoring of patient on treatment particularly volumetric MRI of the liver and spleen and MRI of the femora for evaluating bone marrow disease burden.

© 2015 Baishideng Publishing Group Inc. All rights reserved.

Key words: Gaucher disease; Lysosomal storage disease; Enzyme replacement therapy; Genetics; Medical imaging; Magnetic resonance imaging; Bone marrow

Core tip: Gaucher disease is the most common lysosomal storage disease resulting from accumulation of undegraded glucosylceramide in the reticuloendothelial system of the bone marrow, spleen and liver. Although affecting all three organs, the bone manifestations lead to the most debilitation. Visceral and bone marrow infiltration respond to enzyme replacement therapy however, the bone marrow response typically takes much longer.

Original sources: Simpson WL, Hermann G, Balwani M. Imaging of Gaucher disease. *World J Radiol* 2014; 6(9): 657-668 Available from: URL: <http://www.wjgnet.com/1949-8470/full/v6/i9/657.htm> DOI: <http://dx.doi.org/10.4329/wjrv.6.i9.657>

INTRODUCTION

Gaucher disease (GD) is the most common of the lysosomal storage diseases^[1]. It results from accumulation of undegraded glucosylceramide in lysosomes within macrophages of the reticuloendothelial cell system due to a deficiency of the enzyme glucocerebrosidase. Consequently

these macrophages, enlarged with a buildup of glycolipids, are called Gaucher cells and are most abundant in the bone marrow, spleen and liver. GD is inherited in an autosomal recessive manner^[2].

Three clinical subtypes of GD have been described^[3]. Type 1 does not have any involvement of the central nervous system and is the most common. It formerly was referred to as the “adult type”. However, this is a misnomer since type 1 can occur at any age and is currently known as the non-neuronopathic type. Although it is most common in the Ashkenazi Jewish population it can occur in all ethnic groups. Type 2 was formerly referred to as the “infantile type”. This type manifests with grave involvement of the central nervous system. It is rapidly progressive usually leading to death within 2 years. It is now known as the acute neuronopathic type. Type 3 also has central nervous system involvement but is less severe and is more indolent than type 2 leading to the current terminology, subacute neuronopathic type.

The clinical manifestations of GD are due to the accumulation of Gaucher cells in the reticuloendothelial system of the bone marrow, spleen and liver. There can be marked variability in the severity of symptoms and the course of the disease. This is particularly true for type 1 where some patients can remain asymptomatic through life. Although the visceral changes can be dramatic, the more debilitating symptoms arise from infiltration of the bone marrow and bone changes. Since type 1 is the most common and widely studied variant of Gaucher disease it will be the primary focus of this review.

GENETICS

Gaucher disease is inherited in an autosomal recessive manner. The diagnosis of GD is made by the demonstration of decreased glucocerebrosidase enzymatic activity in peripheral blood leukocytes or fibroblasts cultured from a skin biopsy. Generally there is a 70%-90% reduction in the enzyme activity when compared to normal^[4].

Molecular testing by targeted mutation analysis is used for confirmation of diagnosis and may be helpful for genotype-phenotype correlations. There are more than 300 mutations in the glucocerebrosidase gene that cause Gaucher disease^[2]. However, four common mutations - N370S, IVS2(+1), 84GG, L444P - account for approximately 96.5% of disease in Ashkenazi Jewish population in the western hemisphere and approximately 50%-60% in non-Jewish populations^[5].

Genotyping is helpful to test at risk family members, for genetic counseling as well as for prognosis. However, genotype-phenotype correlations are limited due to the clinical heterogeneity of the disease. Moreover, the majority of the work on genotype-phenotype correlation was based on a heavily Ashkenazi Jewish population which could skew the results since many affected individuals with the N370S/N370S homozygous genotype may remain asymptomatic and not come to medical attention^[2]. Never the less a few generalities can be made: (1)

the presence of at least one N370S allele precludes development of neuronopathic disease; and (2) the presence of the L444P allele is strongly (but not exclusively) associated with neuronopathic involvement. In general, those homozygous for the N370S allele tend to have less severe manifestations of disease and compound heterozygotes with one copy of N370S and a second mutation being L444P, 84GG or IVS 2 + 1 tend to have more severe disease. In fact, adults homozygous for L444P mutation (L444P/L444P genotype) typically have the type 3 neuronopathic disease. However, these rules are not hard and fast due to the limited genotype-phenotype correlation. Some patients with the N370S/N370S genotype have profound symptomatic disease whereas a type 1 patient with N370S/L444P genotype may have mild symptoms.

HEMATOLOGIC MANIFESTATIONS

Hematologic abnormalities of GD are exceedingly common. Almost all patients with symptoms present with anemia and thrombocytopenia. The etiology can be explained by depressed hematopoiesis resulting from substitution of the bone marrow by Gaucher cells. However, hypersplenism or sequestration within the spleen can be a cause as well. Symptoms that arise due to the hematologic abnormalities include fatigue, easy bruising and frequent nosebleeds. Additional blood chemistries can be elevated in GD including angiotensin converting enzyme, chitotriosidase, and tartrate resistant acid phosphatase^[6]. Changes towards normalization of the anemia, thrombocytopenia and blood chemistries can be used to monitor treatment response^[7].

VISCERAL MANIFESTATIONS

The viscera most commonly involved with accumulation of Gaucher cells are the liver and spleen. The pulmonary system can be involved as well; although it is very rare. Current recommendation for evaluating and monitoring visceral involvement is volumetric MRI (preferred due to lack of ionizing radiation) or CT every 12 to 24 mo^[6].

Gaucher cells accumulate in the Kupfer cells of the liver leading to hepatomegaly (Figure 1). Liver volumes in type 1 patients are typically approximately 2 times normal^[8]. It is notable that glycolipid does not accumulate in the hepatocytes^[8,9]. The Gaucher cells can conglomerate into nodules that can be seen with sonography or MRI. These nodules may be hypoechoic, hyperechoic, or mixed on sonography^[10,11]. On MRI the nodules typically appear isointense or low signal intensity (SI) on T1 weighted imaging (WI) and high SI on T2 WI. Focal areas of extramedullary hematopoiesis can have a similar appearance and can also be seen due the accompanying anemia. Hepatic infiltration can also lead to fibrosis and cirrhosis^[12].

Splenomegaly results from accumulation of Gaucher cells within the spleen (Figure 1). Spleen volumes in type 1 GD are typically 5-15 times normal but the spleen size can be significantly enlarged in some cases and may be

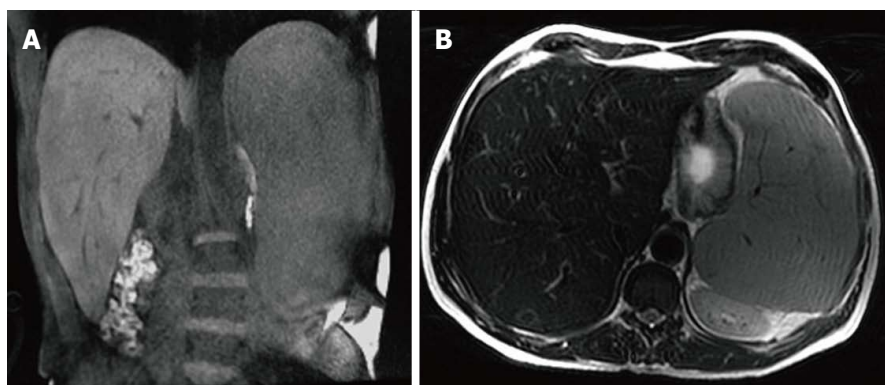


Figure 1 Hepatosplenomegaly. Coronal T1 WI (A) and axial T2 WI (B) images in a male type 1 GD patient with N370S/N370S genotype demonstrate marked hepatosplenomegaly. The liver volume measured 3235 cc. The spleen volume measured 2923 cc.

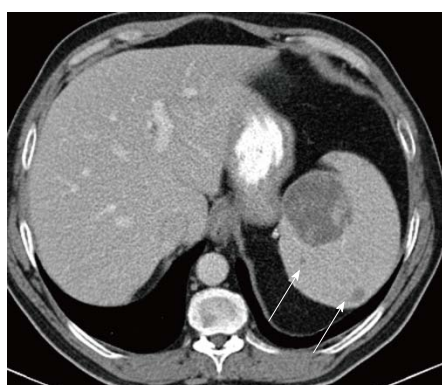


Figure 2 Splenic mass on computed tomography. Axial computed tomography image shows a large low density mass with patchy foci of soft tissue density within it in the medial aspect of the spleen. Additional smaller low density masses are present as well (arrows).

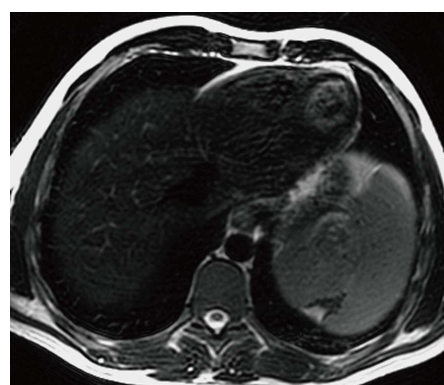


Figure 4 Splenic infarct. Axial T2 WI image demonstrates a wedge shaped defect in a subcapsular region of the spleen in its superior aspect. The defect has low signal intensity (SI) along the edges indicating fibrous tissue. In addition, high SI fat has filled the area left by the retracted capsule.

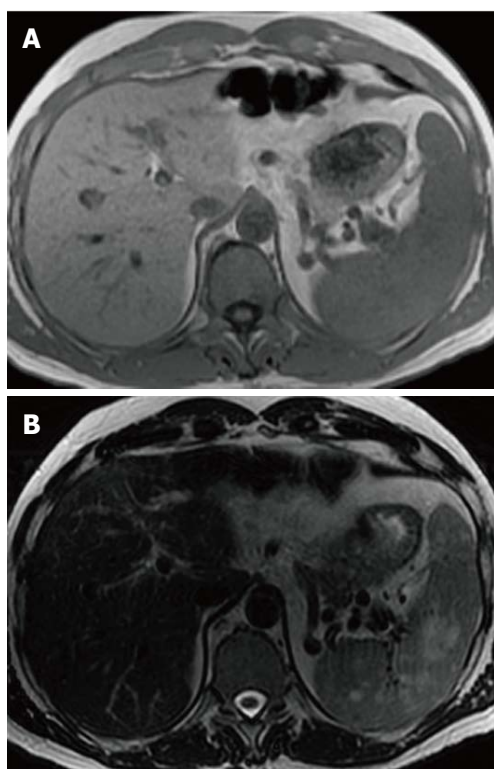


Figure 3 Splenic mass on magnetic resonance. Axial T1WI (A) image shows no apparent abnormality within the spleen consistent with isointense signal intensity (SI) masses. Axial T2WI (B) image at the same level reveals multiple masses in the spleen to be high SI.

over 50 times normal^[13]. Focal splenic masses are common and may represent clusters of Gaucher cells or extra-medullary hematopoiesis. They may be detected with sonography, CT or MRI. Similar to the liver, Gaucher masses in the spleen may be hypoechoic, hyperechoic, or mixed echogenicity^[11,14]. On CT the masses are low density^[15] and occasionally peripherally calcified (Figure 2). These masses are most commonly imaged with MRI. They typically are low SI or isointense on T1 WI and high SI on T2 WI^[16] (Figure 3). Low SI on gradient recalled echo imaging in these masses is thought to be secondary to iron contained in the Gaucher cells^[17]. Splenic infarcts can occur as well due to massive splenomegaly and can be detected with imaging as well (Figure 4).

An infrequent manifestation of GD is pulmonary involvement which is more commonly seen in type 1 patients who have undergone splenectomy and those with type 3^[18]. The lung findings are thought to be secondary to direct infiltration by Gaucher cells into the interstitial spaces, alveolar spaces and capillaries^[19] as well as indirect causes secondary to hepatopulmonary syndrome related to the liver manifestations and/or aspiration associated with neurologic manifestations. Chest radiographs generally are normal or demonstrate a reticulo-nodular pattern. The findings are best imaged by high resolution CT and include interstitial thickening (both interlobular and intralobular), ground glass opacity, consolidation and



Figure 5 Lytic lesion. Frontal radiograph of the distal right humerus demonstrates a well demarcated lytic lesion that does not show sclerotic borders, endosteal erosion or associated expansion of the humeral shaft.

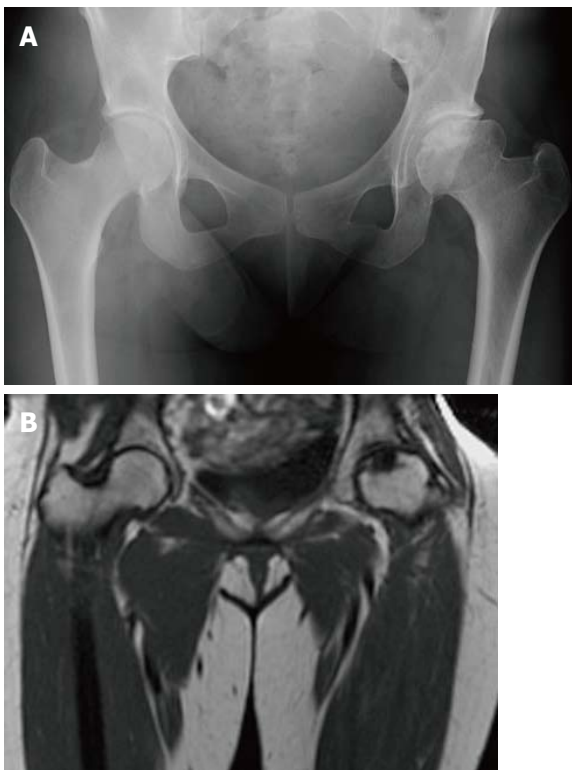


Figure 6 Osteonecrosis. Frontal radiograph of the pelvis (A) shows avascular necrosis of the left femoral head. The femoral head has a flattened contour with sclerosis in the subcapsular areas. Note that the joint space is maintained. Coronal T1 WI (B) in the same patient again demonstrated an abnormal shape of the left femoral head with flattening superiorly. In the same area there is a focus of low SI indicating the devascularized bone.

bronchial wall thickening^[20,21]. Pulmonary hypertension can be the result of lung involvement^[22-24]. Symptomatic pulmonary involvement is generally seen in patients with more striking visceral and skeletal findings.

SKELETAL MANIFESTATIONS

The skeletal manifestations of GD lead to the most debilitating complications of the disease and significant morbidity. Gaucher cells infiltrate and accumulate in the

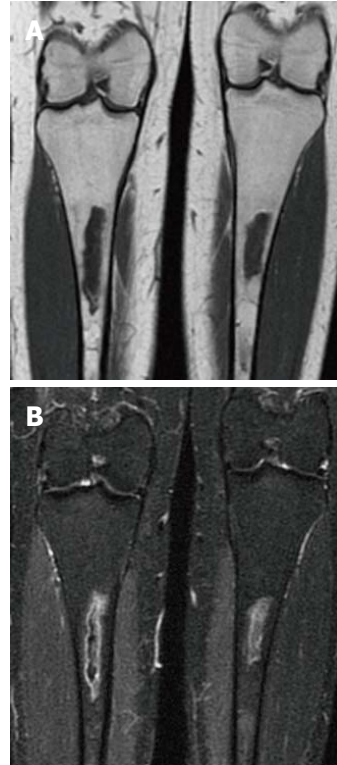


Figure 7 Medullary infarction. Coronal T1 WI (A) image shows irregularly bordered areas of low SI within the medullary cavity of both tibiae. The same areas show peripheral serpiginous high SI on the coronal short tau inversion recovery (STIR) (B) image. The appearance is typical of an infarct.

bone marrow. The pathophysiology of how the infiltration leads to the bone changes is not well understood. Proposed mechanisms include altered bone formation and resorption, as well as increased intra-osseous pressure due to the infiltration leading to vascular occlusion^[3,25].

An array of bone findings are seen in GD, including growth retardation in children, osteopenia, lytic lesions (Figure 5), pathologic fractures, bone pain, osteonecrosis (Figure 6), cortical and medullary infarcts (Figure 7) and evidence of bone crises^[3,26]. The severity of bone findings in GD depend on the extent of medullary cavity substitution. Marrow replacement with Gaucher cells can lead to expansion of the medullary cavity with thinning of the cortex and endosteal scalloping (Figure 8) and consequent diffuse osteopenia. In addition, the medullary expansion leads to a failure of remodeling in the distal femurs resulting in the so called Erlenmeyer flask deformity (Figure 9). These manifestations can be imaged using a variety of modalities including radiography, MRI, dual energy X-ray absorptiometry (DEXA) and radionuclide imaging. However, the mainstay of skeletal imaging in GD involves MRI.

Bone crises are most common in childhood and adolescence presenting as episodes of severe bone pain associated with fever and leucocytosis. The signs and symptoms are indistinguishable from osteomyelitis, however no infection exists. The terms “pseudo-osteomyelitis” and “aseptic osteomyelitis” have been historically used to

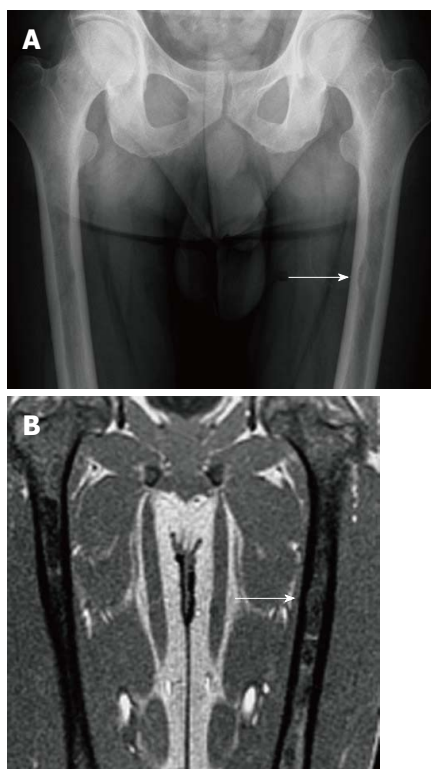


Figure 8 Endosteal scalloping. Frontal radiograph (A) of the femurs shows an area of rounded thinning of the medial cortex of the left femur (arrow). Coronal out of phase image of the femurs in the same patient (B) shows low signal intensity in that same area due to expansion of the medullary cavity due to infiltration. The thinning of the cortex is less apparent on magnetic resonance than on radiography.



Figure 9 Erlenmeyer flask deformity. Frontal radiograph of the distal femurs demonstrates flaring of the bone and thinning of the cortex due to under-tubulation of the metadiaphysis.

characterize this condition^[3,27] (Figure 10).

Osteonecrosis, otherwise known as avascular necrosis, is due to lack of blood supply and consequent bone death. It is most commonly seen in the femoral heads (Figure 6), proximal humeri and vertebral bodies. The vertebral body can “cave in” leading to the “H-shaped” vertebra, *i.e.*, Reynolds phenomenon, similar to sickle cell disease (Figure 11). While the end result is similar in both diseases the mechanism of formation is different. In GD the entire vertebral body collapses followed by peripheral regrowth while in sickle cell disease the deformity is

secondary to central growth arrest^[28]. The necrotic bone crumples and leads to malformation and/or fracture, sometimes requiring treatment with a bone prosthesis or joint replacement.

Radiography is used primarily to image cortical bone. It can detect lytic (Figure 5) or sclerotic lesions within bones. Fractures, both traumatic and pathologic, are readily detected on radiographs. In addition, endosteal scalloping (Figure 8) and the Erlenmeyer flask deformity (Figure 9) due to marrow expansion are also detected with radiography. Although changes in cortical bone secondary to marrow infiltration can be detected with this modality, the marrow space itself cannot be evaluated by radiography.

Osteopenia is near universal in GD as a representation of decreased bone mineral density. A significant decrease in bone density must occur before osteopenia is perceived on radiography leading to its poor sensitivity for detecting this abnormality. DEXA is the current modality of choice for evaluation of osteopenia and bone mineral density. However, care must be taken to avoid areas of osteonecrosis during DEXA evaluations.

The bone marrow itself is best assessed with MRI. Normal yellow (fatty) marrow is seen as high signal on T1 WI and T2 WI. The infiltration of the marrow by Gaucher cells replaces the normal yellow marrow. Marrow infiltration generally follows the distribution of cellular red marrow progressing from the axial to the peripheral skeleton and from the proximal to the distal aspects of the long bones with a tendency to spare the epiphyses^[29]. This is recognized as a change to low SI on both T1 and T2 WI^[29,30] (Figure 12). On short tau inversion recovery (STIR) images the infiltration appears slightly high SI^[31]. High SI within the marrow on T2 or STIR images suggests edema within the marrow and the presence of an “active” process such as a bone crisis or infection^[32]. Evaluation of bone marrow infiltration in children is complicated by the fact that normal red marrow which is seen in this age group manifests with low SI on both T1 and T2 WI.

Radionuclide imaging is useful for evaluating bone changes in GD. Bone scintigraphy utilizing Technetium 99m-methylene diphosphonate (^{99m}Tc-MDP) can be used to evaluate for fractures that are not readily apparent on radiography. In addition, this tracer can be used to help differentiate a bone crisis (aseptic infarction) from osteomyelitis. In a bone crisis bone scintigraphy performed within 1-3 d of the onset of pain will demonstrate decreased tracer uptake at the involved site unlike infection that shows increased uptake^[33,34]. The same agent can be used to help evaluate for complication related to joint prostheses such as loosening^[31]. Scintigraphy using leucocytes labeled with Indium-111 is commonly used to image areas of suspected infection including osteomyelitis and around joint prostheses.

Prior to the advent of MRI, radionuclide imaging was also used for evaluation of the bone marrow. Technetium 99m sulfur colloid (^{99m}Tc-SC) accumulates in normal

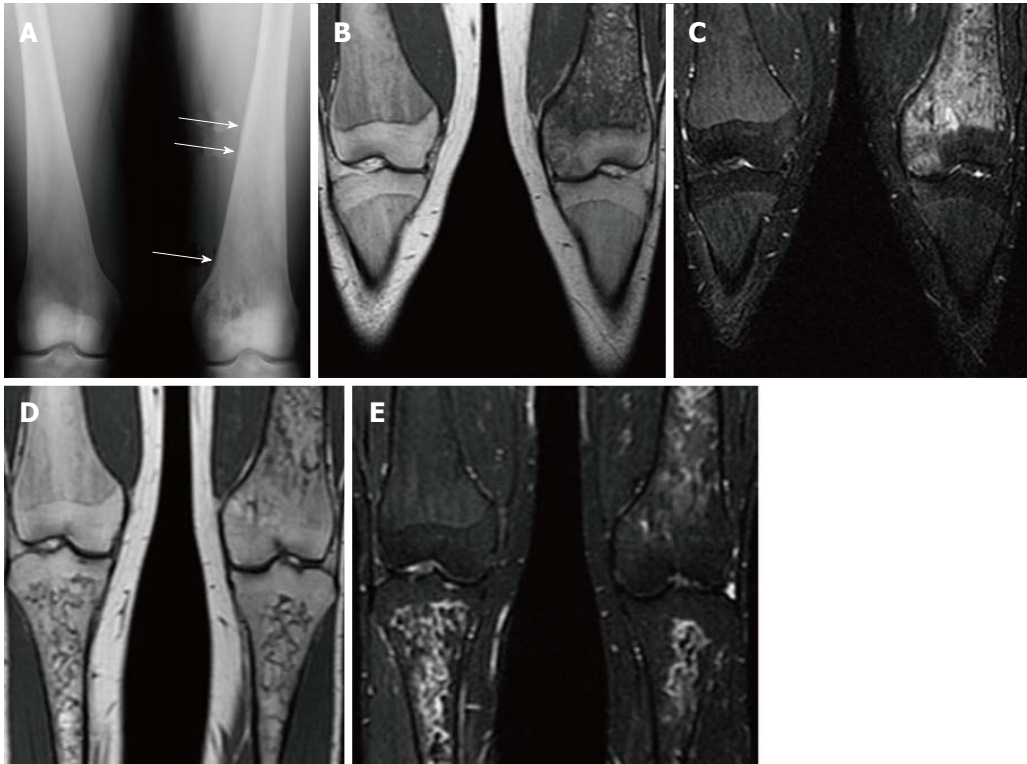


Figure 10 Pseudo-osteomyelitis. Frontal radiograph of both distal femurs in 2009 (A) demonstrates an irregular area of patchy lucency in the medial condyle of the left femur. There is periosteal reaction in this area as well as more superiorly (arrows). Coronal T1 WI (B) image at the same time in 2009 demonstrate low SI in the medial condyle of the femur extending into the medial epiphysis. There is high SI in these areas on coronal STIR (C) image which extends into the adjacent soft tissues where the periosteal reaction is seen on the radiograph. There is no joint effusion. The patient presented with left knee pain and the imaging was suspicious for osteomyelitis involving the medial distal femur. However, the patient has no fever and cultures were negative. Coronal T1 WI (D) of the same area in 2011 shows resolution of the low SI in the medial condyle and epiphysis. The corresponding high SI on the STIR image (E) has resolved as well.



Figure 11 H-shaped vertebra. Cone down frontal radiograph of the lower thoracic spine demonstrates collapse of a lower thoracic vertebral body with bi-concave upper and lower end plates giving the Reynolds phenomenon of Gaucher disease.

bone marrow. Therefore in marrow infiltrated and replaced by Gaucher cells there will be decreased uptake or an abnormal pattern of uptake compared to normal^[34]. This gives an indirect sign of infiltration. Another tracer, Technetium 99m sestamibi, has the advantage of being accumulated in areas of Gaucher cell deposition^[35,36]. Mariani *et al*^[35] imaged 74 Italian patients with Gaucher disease using technetium 99m sestamibi and showed 71 of 74 demonstrated uptake predominantly in the distal femur. An undisclosed number of these patients had MR

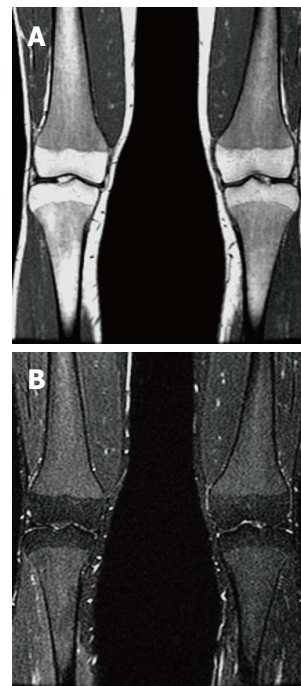


Figure 12 Bone marrow infiltration. Coronal T1 WI (A) of the distal femora and proximal tibiae in a type 1 gaucher disease patient shows low signal intensity (SI) in the bone marrow which spares the epiphyses that demonstrate the normal fatty marrow SI. Coronal short tau inversion recover (STIR) (B) image demonstrates that the low SI on T1 becomes slightly high SI on STIR.

imaging performed at the same approximate time revealing low SI in the same regions. Therefore it is a method of direct visualization of infiltration. Bone marrow sestamibi imaging can be advantageous when imaging children and trying to differentiate Gaucher infiltration from normal red marrow in children. Positron emission tomography has become widely available in recent years. Imaging with the most common radiotracer, fluoride-18 fluorodeoxyglucose, has not proven beneficial for detecting marrow involvement in GD. However, a newer tracer, fluoride-18 L-thymidine, shows promise for imaging bone marrow^[37]. Since it is not yet FDA approved its use is limited to clinical trials and its role if any in GD has not been established. Therefore, MRI remains the modality of choice for imaging bone marrow due the poor spatial resolution of scintigraphy as well as the associated radiation dose of radionuclide imaging.

An essential problem of imaging is that it only gives a qualitative assessment of bone marrow infiltration. An MRI shows decreased SI on T1 WI but there is no way to measure the “amount” of signal. A visual assessment of improvement or worsening can be made on the basis of the MR image but that is qualitative and not very useful to clinicians. One way of directly measuring bone marrow disease has been developed, Dixon’s quantitative chemical shift imaging^[38]. Chemical shift imaging leverages the difference in resonance frequencies between water and fat molecules thereby defining the amount of fat or fat fraction within bone marrow. The fat fraction of normal marrow decreases as the amount of infiltration replaces the triglyceride rich fat cells of normal marrow. Studies have shown a low marrow fat fraction as measured by quantitative chemical shift imaging to correspond to worse clinical disease and more bone complications^[39-42]. However, the technique is complex and not widely used outside academic centers. To overcome this problem several semi-quantitative methods have been developed including the Rosenthal staging system^[29], the Dusseldorf score^[43], the Terk classification^[44] and the bone marrow burden (BMB) score^[45]. All use conventional MR imaging technology and assign points based on changes in marrow signal intensity at different anatomic locations.

The BMB score is the most widely used and validated^[45,46]. The BMB score^[45] incorporates both the visual interpretation of SI and the geographic location of the disease on conventional MR images of the lumbar spine and femora. The SI of the bone marrow in the femora is compared to the subcutaneous fat on both T1 and T2 WI sequences. The SI of the bone marrow in the lumbar spine is compared to a non-diseased intervertebral disc on both T1 and T2 WI sequences. The SI is scored as hyper-intense, slightly hyper-intense, iso-intense, slightly hypo-intense, and hypo-intense. A numeric value ranging from 0-2 is assigned based on the SI. Point values are also assigned based on the location/distribution of the marrow infiltration. In the femora, sites of involvement including the diaphysis, proximal epiphysis/apophysis and distal epiphysis are evaluated. In the lumbar spine,

the distribution of infiltration is evaluated as patchy or diffuse with special attention given to absence of fat in basivertebral vein region. The score for the femora (0-8) and the lumbar spine (0-8) are added together for a total score which can range from 0 to 16. A higher score indicates more severe the bone marrow involvement. In their study of 12 patients with Gaucher disease^[45], Maas *et al*^[45] demonstrated good correlation of the BMB score with fat fraction determination by the Dixon technique. That study also showed a decrease in the BMB score in patients on enzyme replacement therapy (ERT), however, it was less sensitive for detection of marrow improvement than Dixon method.

TREATMENT

Only supportive treatment or surgical intervention including splenectomy and joint replacement was available for patients with Gaucher disease into the early 1990s. In 1991 ERT with placentally derived enzyme alglucerase (Ceredase®, Genzyme Corporation, Cambridge, Mass.) came into existence. Following this, in 1994, recombinant mannose-terminated human glucocerebrosidase (Cerezyme®, Genzyme Corporation) received FDA approval. The goal of ERT is to treat the symptoms of the disease as well as to prevent complications particularly the skeletal complications^[6].

The visceral and hematologic manifestations of GD respond relatively quickly to ERT^[47,48] (Figure 13). The anemia and thrombocytopenia can improve within 6 mo to one year of initialing ERT. The liver and spleen volumes generally can decrease by approximately 50% within the first 2 years but rarely ever return to a normal volume even with long term treatment. Although some improvement in pulmonary involvement has been reported with ERT, response is generally slow, and sometimes no improvement is seen^[23,49]. The marrow infiltration responds to ERT as well but takes much longer to be seen^[50,51] (Figures 14 and 15). Some skeletal manifestations, such as osteonecrosis, osteosclerosis and vertebral body collapse, remain irreversible. The neurologic manifestations of GD do not respond to ERT since it does not cross the blood-brain barrier^[52].

An alternative to ERT for treatment of GD is substrate reduction therapy. Whereas ERT works by replacing the deficient enzyme, substrate reduction works by decreasing the production of the substrate glucosylceramide. Since most type 1 GD patients have some residual enzyme activity, reducing the amount of substrate may allow the native enzyme to succeed. The first medication of this kind was N-butyldeoxynojirimycin (miglustat) approved by the FDA in 2003. It is an oral medication for use in mild to moderate type 1 GD patients who cannot tolerate ERT. Studies have shown improvement of anemia, platelet count, liver volume and spleen volume alone or in combination with ERT^[53-55]. One study also showed improvement of bone disease on miglustat^[56,57]. However, side effects particularly diarrhea, weight loss and tremors

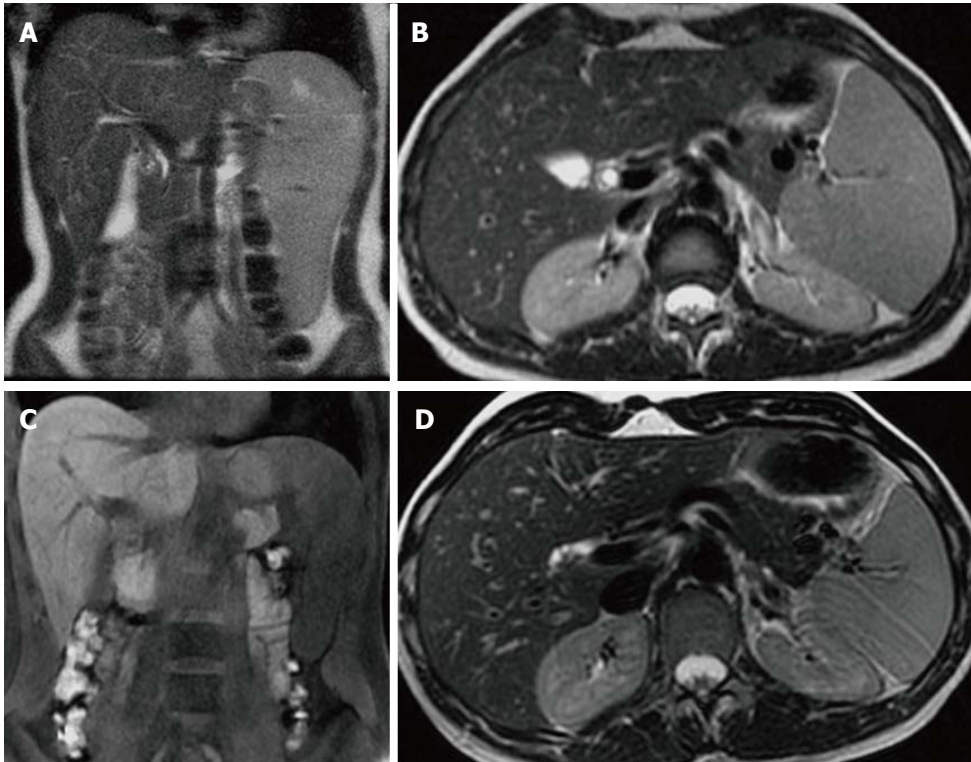


Figure 13 Visceral improvement on enzyme replacement therapy. Female type 3 Gaucher disease patient who began enzyme replacement therapy (ERT) in 2007. Initial evaluation in 2007 before starting ERT shows that the spleen extends down to the iliac crest on the T2 WI coronal image (A). On the axial T2 WI (B) the left lobe of the liver extends across the midline posterior to the lateral aspect of the left rectus abdominus muscle and anterior to the stomach. At that time the liver volume measured 1702 cc and the spleen volume measured 769 cc. After 6 years on treatment, repeat imaging in 2013 reveals the inferior edge of the spleen is now above the iliac crest on the coronal T1 WI (C) and the left lobe of the liver now extends only slightly across the midline to end posterior to the medial aspect of the rectus abdominus muscle and the stomach is now lateral to the liver on the axial T2 WI (D). In 2013, the liver volume measured 1163 cc and the spleen volume measured 368 cc.

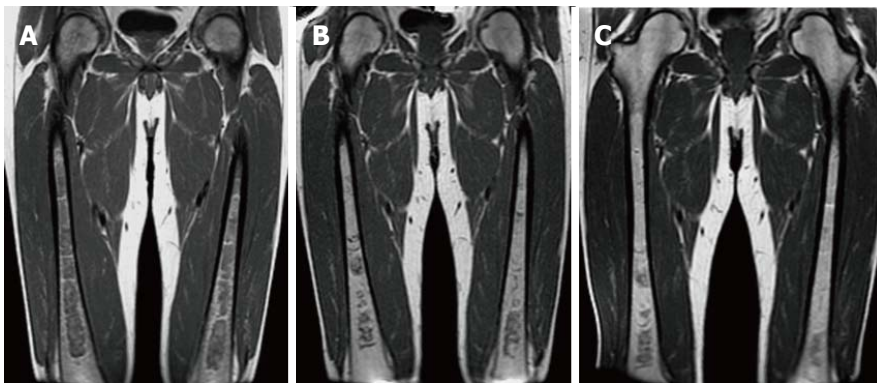


Figure 14 Bone marrow improvement on enzyme replacement therapy. Type 1 GD male patient with N370S/N370S genotype who began enzyme replacement therapy (ERT) in October of 2007 shows relatively rapid improvement of the bone marrow infiltration. Initial coronal T1 WI of the femora (A) demonstrates diffuse low SI throughout the medullary cavity consistent with marked infiltration. Coronal T1 WI in 2009 (B) after only 2 years of treatment shows significant improvement in the infiltration manifest by decreased low SI in the medullary cavity. In 2011, coronal T1 WI (C) shows continued slight decrease in the amount of low SI in the bone marrow.

were significant^[52] and its use is limited in the United States Unlike ERT miglustat can cross the blood-brain barrier^[52] and has shown promising results in treating neurologic manifestations in combination with ERT^[58,59]. A study also shows improvement of pulmonary manifestations with single drug treatment^[60]. Currently there is a newer oral substrate reduction therapy agent, eliglustat

tartrate, which has demonstrated efficacy in GD type 1 patients with a more favorable side effect profile^[61]. It is currently undergoing phase III trials.

Both ERT and substrate reduction therapy can lead to improvement in the signs and symptoms of GD. However, there is a significant cost to the treatment ranging from US\$100000 to \$250000 per year^[62]. Thus judicious

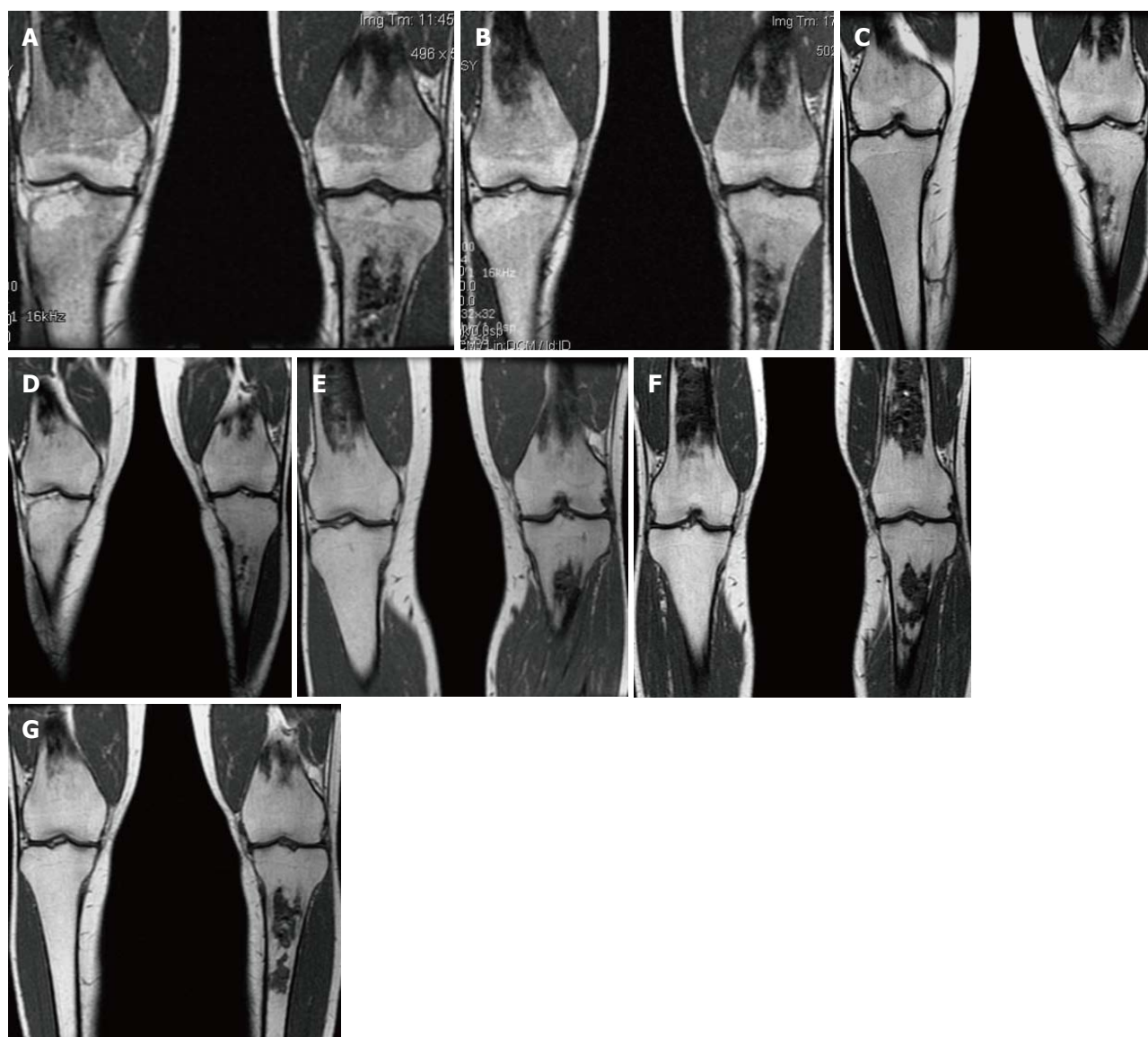


Figure 15 Bone marrow improvement. Gaucher Type 1 patient with N370S/N370S genotype who started enzyme replacement therapy (ERT) in 1997. Coronal T1 WI of the distal femora and proximal tibiae in 1998 (A), 1999 (B), 2002 (C), 2003 (D), 2006 (E), 2008 (F) and 2011 (G). Medullary infarcts are partially seen in both distal femurs and the left tibia. The low T1 SI significantly improves between 1998 and 2002 with near normal marrow signal seen in the noninfarcted areas in 2008 and years later. Although this patient has the same genotype as the patient in Figure 14, there is a longer time to improvement indicating the limited genotype/phenotype correlation.

use is warranted. Imaging plays a significant role in determining which patients need treatment and in surveillance of those on treatment. Current recommendations call for abdominal MRI for determination of liver and spleen volume, MRI of the bilateral femora, radiography of the spine and DEXA of the hips and lumbar spine in the initial assessment^[6]. For those patients not on treatment being followed and those on treatment, the same imaging protocol is recommended every 12-24 mo or at the time of a dosage change or significant clinical complication^[6].

CONCLUSION

Gaucher disease is the most common lysosomal storage disease which affects all ethnic groups. The accumulation of glycolipids in the reticuloendothelial system leads

to symptoms. Anemia, thrombocytopenia, and hepatosplenomegaly are commonly seen and respond relatively rapidly to treatment with ERT. The skeletal manifestations are due to build up of the glycolipids in the bone marrow and lead to the most debilitating aspects of GD. Treatment results in improvement of marrow infiltration however it takes much longer than the visceral and hematologic manifestations. Imaging plays a key role in both initial diagnosis and treatment monitoring. MRI of the abdomen is used to monitor liver and spleen volumes. MRI of the femora and lumbar spine is used for evaluation of bone marrow infiltration burden.

REFERENCES

- 1 Meikle PJ, Hopwood JJ, Clague AE, Carey WF. Prevalence

- of lysosomal storage disorders. *JAMA* 1999; **281**: 249-254 [PMID: 9918480 DOI: 10.1001/jama.281.3.249]
- 2 **Grabowski GA**, Petsko GA, Kolodny EH. Gaucher Disease. In: Valle D, Beaudet AL, Vogelstein B, Kinzler KW, Antonarakis SE, Ballabio A, eds. *Scriver's Online Metabolic and Molecular Bases of Inherited Disease*. Published January 2006. Accessed November 29, 2013 [DOI: 10.1036/ombid.176]
 - 3 **Wenstrup RJ**, Roca-Espiau M, Weinreb NJ, Bembi B. Skeletal aspects of Gaucher disease: a review. *Br J Radiol* 2002; **75** Suppl 1: A2-12 [PMID: 12036828 DOI: 10.1259/bjr.75.suppl_1.750002]
 - 4 **Beutler E**, Saven A. Misuse of marrow examination in the diagnosis of Gaucher disease. *Blood* 1990; **76**: 646-648 [PMID: 2116196]
 - 5 **Beutler E**, Gelbart T, Kuhl W, Zimran A, West C. Mutations in Jewish patients with Gaucher disease. *Blood* 1992; **79**: 1662-1666 [PMID: 1558964]
 - 6 **Weinreb NJ**, Aggio MC, Andersson HC, Andria G, Charrow J, Clarke JT, Erikson A, Giraldo P, Goldblatt J, Hol-lak C, Ida H, Kaplan P, Kolodny EH, Mistry P, Pastores GM, Pires R, Prakash-Cheng A, Rosenbloom BE, Scott CR, Sobreira E, Tytki-Szymańska A, Vellodi A, vom Dahl S, Wappner RS, Zimran A. Gaucher disease type 1: revised recommendations on evaluations and monitoring for adult patients. *Semin Hematol* 2004; **41**: 15-22 [PMID: 15468046 DOI: 10.1053/j.seminhematol.2004.07.010]
 - 7 **Charrow J**, Esplin JA, Gribble TJ, Kaplan P, Kolodny EH, Pastores GM, Scott CR, Wappner RS, Weinreb NJ, Wisch JS. Gaucher disease: recommendations on diagnosis, evaluation, and monitoring. *Arch Intern Med* 1998; **158**: 1754-1760 [PMID: 9738604 DOI: 10.1001/archinte.158.16.1754]
 - 8 **James SP**, Stromeyer FW, Chang C, Barranger JA. Liver abnormalities in patients with Gaucher's disease. *Gastroenterology* 1981; **80**: 126-133 [PMID: 7450398]
 - 9 **James SP**, Stromeyer FW, Stowens DW, Barranger JA. Gaucher disease: hepatic abnormalities in 25 patients. *Prog Clin Biol Res* 1982; **95**: 131-142 [PMID: 7122631]
 - 10 **Patlas M**, Hadas-Halpern I, Abrahamov A, Elstein D, Zimran A. Spectrum of abdominal sonographic findings in 103 pediatric patients with Gaucher disease. *Eur Radiol* 2002; **12**: 397-400 [PMID: 11870441 DOI: 10.1007/s003300101031]
 - 11 **Neudorfer O**, Hadas-Halpern I, Elstein D, Abrahamov A, Zimran A. Abdominal ultrasound findings mimicking hematological malignancies in a study of 218 Gaucher patients. *Am J Hematol* 1997; **55**: 28-34 [PMID: 9136914 DOI: 10.1002/(SICI)1096-8652(199705)55:1<28::AID-AJH5>3.0.CO;2-5]
 - 12 **Lee RE**. The pathology of Gaucher disease. *Prog Clin Biol Res* 1982; **95**: 177-217 [PMID: 7122634]
 - 13 **Grabowski GA**, Kolodny EH, Weinreb NJ, Rosenbloom BE, Prakash-Cheng A, Kaplan P, Charrow J, Pastores GM, Mistry PK. Gaucher disease: Phenotypic and Genetic Variation. In: Valle D, Beaudet AL, Vogelstein B, Kinzler KW, Antonarakis SE, Ballabio A, editors. *Scriver's Online Metabolic and Molecular Bases of Inherited Disease*. Published January 2006. Accessed November 29, 2013. [DOI: 10.1036/ombid.177]
 - 14 **Hill SC**, Reinig JW, Barranger JA, Fink J, Shawker TH. Gaucher disease: sonographic appearance of the spleen. *Radiology* 1986; **160**: 631-634 [PMID: 3526400]
 - 15 **Poill LW**, Koch JA, vom Dahl S, Sarbia M, Häussinger D, Mödder U. Gaucher disease of the spleen: CT and MR findings. *Abdom Imaging* 2000; **25**: 286-289 [PMID: 10823453 DOI: 10.1007/s002610000010]
 - 16 **Hill SC**, Damaska BM, Ling A, Patterson K, Di Bisceglie AM, Brady RO, Barton NW. Gaucher disease: abdominal MR imaging findings in 46 patients. *Radiology* 1992; **184**: 561-566 [PMID: 1620865]
 - 17 **Terk MR**, Esplin J, Lee K, Magre G, Colletti PM. MR imaging of patients with type 1 Gaucher's disease: relationship between bone and visceral changes. *AJR Am J Roentgenol* 1995; **165**: 599-604 [PMID: 7645477 DOI: 10.2214/ajr.165.3.7645477]
 - 18 **Hill SC**, Damaska BM, Tsokos M, Kreps C, Brady RO, Barton NW. Radiographic findings in type 3b Gaucher disease. *Pediatr Radiol* 1996; **26**: 852-860 [PMID: 8929296 DOI: 10.1007/BF03178036]
 - 19 **Amir G**, Ron N. Pulmonary pathology in Gaucher's disease. *Hum Pathol* 1999; **30**: 666-670 [PMID: 10374775 DOI: 10.1016/S0046-8177(99)90092-8]
 - 20 **McHugh K**, Olsen E ØE, Vellodi A. Gaucher disease in children: radiology of non-central nervous system manifestations. *Clin Radiol* 2004; **59**: 117-123 [PMID: 14746780 DOI: 10.1016/j.crad.2003.09.010]
 - 21 **Aydin K**, Karabulut N, Demirkazik F, Arat A. Pulmonary involvement in adult Gaucher's disease: high resolution CT appearance. *Br J Radiol* 1997; **70**: 93-95 [PMID: 9059303 DOI: 10.1259/bjr.70.829.9059303]
 - 22 **Theise ND**, Ursell PC. Pulmonary hypertension and Gaucher's disease: logical association or mere coincidence? *Am J Pediatr Hematol Oncol* 1990; **12**: 74-76 [PMID: 2309982 DOI: 10.1097/00043426-199021000-00014]
 - 23 **Mistry PK**, Sirrs S, Chan A, Pritzker MR, Duffy TP, Grace ME, Meeker DP, Goldman ME. Pulmonary hypertension in type 1 Gaucher's disease: genetic and epigenetic determinants of phenotype and response to therapy. *Mol Genet Metab* 2002; **77**: 91-98 [PMID: 12359135 DOI: 10.1016/S1096-7192(02)00122-1]
 - 24 **Pastores GM**, Miller A. Pulmonary hypertension in Gaucher's disease. *Lancet* 1998; **352**: 580 [PMID: 9716094 DOI: 10.1016/S0140-6736(05)79295-3]
 - 25 **Sims KB**, Pastores GM, Weinreb NJ, Barranger J, Rosenbloom BE, Packman S, Kaplan P, Mankin H, Xavier R, Angell J, Fitzpatrick MA, Rosenthal D. Improvement of bone disease by imiglucerase (Cerezyme) therapy in patients with skeletal manifestations of type 1 Gaucher disease: results of a 48-month longitudinal cohort study. *Clin Genet* 2008; **73**: 430-440 [PMID: 18312448 DOI: 10.1111/j.1399-0004.2008.00978.x]
 - 26 **Hermann G**, Goldblatt J, Levy RN, Goldsmith SJ, Desnick RJ, Grabowski GA. Gaucher's disease type I: assessment of bone involvement by CT and scintigraphy. *AJR Am J Roentgenol* 1986; **147**: 943-948 [PMID: 3490167 DOI: 10.2214/ajr.147.5.943]
 - 27 **Yossipovitch ZH**, Herman G, Makin M. Aseptic osteomyelitis in Gaucher's disease. *Isr J Med Sci* 1965; **1**: 531-536 [PMID: 5842267]
 - 28 **Schwartz AM**, Homer MJ, McCauley RG. „Step-off“ vertebral body: Gaucher's disease versus sickle cell hemoglobinopathy. *AJR Am J Roentgenol* 1979; **132**: 81-85 [PMID: 103410 DOI: 10.2214/ajr.132.1.81]
 - 29 **Rosenthal DI**, Scott JA, Barranger J, Mankin HJ, Saini S, Brady TJ, Osier LK, Doppelt S. Evaluation of Gaucher disease using magnetic resonance imaging. *J Bone Joint Surg Am* 1986; **68**: 802-808 [PMID: 3733771]
 - 30 **Lanir A**, Hadar H, Cohen I, Tal Y, Benmair J, Schreiber R, Clouse ME. Gaucher disease: assessment with MR imaging. *Radiology* 1986; **161**: 239-244 [PMID: 3763873]
 - 31 **Katz R**, Booth T, Hargunani R, Wylie P, Holloway B. Radiological aspects of Gaucher disease. *Skeletal Radiol* 2011; **40**: 1505-1513 [PMID: 20658285 DOI: 10.1007/s00256-010-0992-3]
 - 32 **Hermann G**, Shapiro RS, Abdelwahab IF, Grabowski G. MR imaging in adults with Gaucher disease type I: evaluation of marrow involvement and disease activity. *Skeletal Radiol* 1993; **22**: 247-251 [PMID: 8316866 DOI: 10.1007/BF00197668]
 - 33 **Katz K**, Mechlis-Frish S, Cohen IJ, Horev G, Zaizov R, Lubin E. Bone scans in the diagnosis of bone crisis in patients who

- have Gaucher disease. *J Bone Joint Surg Am* 1991; **73**: 513-517 [PMID: 2013590]
- 34 **Mikosch P**, Kohlfürst S, Gallowitsch HJ, Kresnik E, Lind P, Mehta AB, Hughes DA. Is there a role for scintigraphic imaging of bone manifestations in Gaucher disease? A review of the literature. *Nuklearmedizin* 2008; **47**: 239-247 [PMID: 19057797]
- 35 **Mariani G**, Filocamo M, Giona F, Villa G, Amendola A, Erba P, Buffoni F, Copello F, Pierini A, Minichilli F, Gatti R, Brady RO. Severity of bone marrow involvement in patients with Gaucher's disease evaluated by scintigraphy with ^{99m}Tc-sestamibi. *J Nucl Med* 2003; **44**: 1253-1262 [PMID: 12902415]
- 36 **Mariani G**, Molea N, La Civita L, Porciello G, Lazzeri E, Ferri C. Scintigraphic findings on ^{99m}Tc-MDP, ^{99m}Tc-sestamibi and ^{99m}Tc-HMPAO images in Gaucher's disease. *Eur J Nucl Med* 1996; **23**: 466-470 [PMID: 8612670 DOI: 10.1007/BF01247378]
- 37 **Agool A**, Schot BW, Jager PL, Vellenga E. 18F-FLT PET in hematologic disorders: a novel technique to analyze the bone marrow compartment. *J Nucl Med* 2006; **47**: 1592-1598 [PMID: 17015893]
- 38 **Dixon WT**. Simple proton spectroscopic imaging. *Radiology* 1984; **153**: 189-194 [PMID: 6089263]
- 39 **Maas M**, Hollak CE, Akkerman EM, Aerts JM, Stoker J, Den Heeten GJ. Quantification of skeletal involvement in adults with type I Gaucher's disease: fat fraction measured by Dixon quantitative chemical shift imaging as a valid parameter. *AJR Am J Roentgenol* 2002; **179**: 961-965 [PMID: 12239046 DOI: 10.2214/ajr.179.4.1790961]
- 40 **Johnson LA**, Hoppel BE, Gerard EL, Miller SP, Doppelt SH, Zirzow GC, Rosenthal DI, Dambrosia JM, Hill SC, Brady RO. Quantitative chemical shift imaging of vertebral bone marrow in patients with Gaucher disease. *Radiology* 1992; **182**: 451-455 [PMID: 1732964]
- 41 **Maas M**, Poll LW, Terk MR. Imaging and quantifying skeletal involvement in Gaucher disease. *Br J Radiol* 2002; **75** Suppl 1: A13-A24 [PMID: 12036829 DOI: 10.1259/bjr.75.suppl_1.750013]
- 42 **Maas M**, Akkerman EM, Venema HW, Stoker J, Den Heeten GJ. Dixon quantitative chemical shift MRI for bone marrow evaluation in the lumbar spine: a reproducibility study in healthy volunteers. *J Comput Assist Tomogr* 2001; **25**: 691-697 [PMID: 11584227 DOI: 10.1097/00004728-200109000-00005]
- 43 **Poll LW**, Koch JA, vom Dahl S, Willers R, Scherer A, Boerner D, Niederau C, Häussinger D, Mödder U. Magnetic resonance imaging of bone marrow changes in Gaucher disease during enzyme replacement therapy: first German long-term results. *Skeletal Radiol* 2001; **30**: 496-503 [PMID: 11587517 DOI: 10.1007/s002560100375]
- 44 **Terk MR**, Dardashti S, Liebman HA. Bone marrow response in treated patients with Gaucher disease: evaluation by T1-weighted magnetic resonance images and correlation with reduction in liver and spleen volume. *Skeletal Radiol* 2000; **29**: 563-571 [PMID: 11127678 DOI: 10.1007/s002560000276]
- 45 **Maas M**, van Kuijk C, Stoker J, Hollak CE, Akkerman EM, Aerts JF, den Heeten GJ. Quantification of bone involvement in Gaucher disease: MR imaging bone marrow burden score as an alternative to Dixon quantitative chemical shift MR imaging--initial experience. *Radiology* 2003; **229**: 554-561 [PMID: 14526090 DOI: 10.1148/radiol.2292020296]
- 46 **DeMayo RF**, Haims AH, McRae MC, Yang R, Mistry PK. Correlation of MRI-Based bone marrow burden score with genotype and spleen status in Gaucher's disease. *AJR Am J Roentgenol* 2008; **191**: 115-123 [PMID: 18562733 DOI: 10.2214/AJR.07.3550]
- 47 **Weinreb NJ**, Charrow J, Andersson HC, Kaplan P, Kolodny EH, Mistry P, Pastores G, Rosenbloom BE, Scott CR, Wappner RS, Zimran A. Effectiveness of enzyme replacement therapy in 1028 patients with type 1 Gaucher disease after 2 to 5 years of treatment: a report from the Gaucher Registry. *Am J Med* 2002; **113**: 112-119 [PMID: 12133749 DOI: 10.1016/S0002-9343(02)01150-6]
- 48 **Andersson H**, Kaplan P, Kacena K, Yee J. Eight-year clinical outcomes of long-term enzyme replacement therapy for 884 children with Gaucher disease type 1. *Pediatrics* 2008; **122**: 1182-1190 [PMID: 19047232 DOI: 10.1542/peds.2007-2144]
- 49 **Goitein O**, Elstein D, Abrahamov A, Hadas-Halpern I, Melzer E, Kerem E, Zimran A. Lung involvement and enzyme replacement therapy in Gaucher's disease. *QJM* 2001; **94**: 407-415 [PMID: 11493717 DOI: 10.1093/qjmed/94.8.407]
- 50 **Poll LW**, Maas M, Terk MR, Roca-Espiau M, Bembi B, Ciana G, Weinreb NJ. Response of Gaucher bone disease to enzyme replacement therapy. *Br J Radiol* 2002; **75** Suppl 1: A25-A36 [PMID: 12036830 DOI: 10.1259/bjr.75.suppl_1.750025]
- 51 **Hermann G**, Pastores GM, Abdelwahab IF, Lorberboym AM. Gaucher disease: assessment of skeletal involvement and therapeutic responses to enzyme replacement. *Skeletal Radiol* 1997; **26**: 687-696 [PMID: 9453101 DOI: 10.1007/s002560050313]
- 52 **Ficicioglu C**. Review of miglustat for clinical management in Gaucher disease type 1. *Ther Clin Risk Manag* 2008; **4**: 425-431 [PMID: 18728838]
- 53 **Cox T**, Lachmann R, Hollak C, Aerts J, van Weely S, Hrebíček M, Platt F, Butters T, Dwek R, Moyses C, Gow I, Elstein D, Zimran A. Novel oral treatment of Gaucher's disease with N-butyldeoxyojirimycin (OGT 918) to decrease substrate biosynthesis. *Lancet* 2000; **355**: 1481-1485 [PMID: 10801168 DOI: 10.1016/S0140-6736(00)02161-9]
- 54 **Elstein D**, Dweck A, Attias D, Hadas-Halpern I, Zevin S, Altarescu G, Aerts JF, van Weely S, Zimran A. Oral maintenance clinical trial with miglustat for type I Gaucher disease: switch from or combination with intravenous enzyme replacement. *Blood* 2007; **110**: 2296-2301 [PMID: 17609429 DOI: 10.1182/blood-2007-02-075960]
- 55 **Pastores GM**, Barnett NL, Kolodny EH. An open-label, non-comparative study of miglustat in type I Gaucher disease: efficacy and tolerability over 24 months of treatment. *Clin Ther* 2005; **27**: 1215-1227 [PMID: 16199246 DOI: 10.1016/j.clinthera.2005.08.004]
- 56 **Pastores GM**, Elstein D, Hrebíček M, Zimran A. Effect of miglustat on bone disease in adults with type 1 Gaucher disease: a pooled analysis of three multinational, open-label studies. *Clin Ther* 2007; **29**: 1645-1654 [PMID: 17919546 DOI: 10.1016/j.clinthera.2007.08.006]
- 57 **Mikosch P**, Reed M, Baker R, Holloway B, Berger L, Mehta AB, Hughes DA. Changes of bone metabolism in seven patients with Gaucher disease treated consecutively with imiglucerase and miglustat. *Calcif Tissue Int* 2008; **83**: 43-54 [PMID: 18553043 DOI: 10.1007/s00223-008-9143-4]
- 58 **Capablo JL**, Franco R, de Cabezón AS, Alfonso P, Poci M, Giraldo P. Neurologic improvement in a type 3 Gaucher disease patient treated with imiglucerase/miglustat combination. *Epilepsia* 2007; **48**: 1406-1408 [PMID: 17433057 DOI: 10.1111/j.1528-1167.2007.01074.x]
- 59 **Cox-Brinkman J**, van Breemen MJ, van Maldegeem BT, Bour L, Donker WE, Hollak CE, Wijburg FA, Aerts JM. Potential efficacy of enzyme replacement and substrate reduction therapy in three siblings with Gaucher disease type III. *J Inherit Metab Dis* 2008; **31**: 745-752 [PMID: 18850301 DOI: 10.1007/s10545-008-0873-2]
- 60 **Schiffmann R**, Fitzgibbon EJ, Harris C, DeVile C, Davies EH, Abel L, van Schaik IN, Benko W, Timmons M, Ries M, Vellodi A. Randomized, controlled trial of miglustat in Gaucher's disease type 3. *Ann Neurol* 2008; **64**: 514-522 [PMID: 19067373 DOI: 10.1002/ana.21491]
- 61 **Lukina E**, Watman N, Arreguin EA, Dragosky M, Iastreb-

ner M, Rosenbaum H, Phillips M, Pastores GM, Kamath RS, Rosenthal DI, Kaper M, Singh T, Puga AC, Peterschmitt MJ. Improvement in hematological, visceral, and skeletal manifestations of Gaucher disease type 1 with oral eliglustat tartrate (Genz-112638) treatment: 2-year results of a phase

2 study. *Blood* 2010; **116**: 4095-4098 [PMID: 20713962 DOI: 10.1182/blood-2010-06-293902]

62 **Grabowski GA.** Phenotype, diagnosis, and treatment of Gaucher's disease. *Lancet* 2008; **372**: 1263-1271 [PMID: 19094956 DOI: 10.1016/S0140-6736(08)61522-6]

P- Reviewer: Palumbo B **S- Editor:** Ji FF **L- Editor:** A
E- Editor: Lu YJ



2-deoxy-2-(¹⁸F)fluoro-D-glucose positron emission tomography/computed tomography imaging in paediatric oncology

John Freebody, Eva A Wegner, Monica A Rossleigh

John Freebody, Eva A Wegner, Monica A Rossleigh, Department of Nuclear Medicine and PET, The Prince of Wales and Sydney Children's Hospitals, Randwick, NSW 2031, Australia
Author contributions: All authors contributed to the writing and editing of this manuscript.

Correspondence to: John Freebody, BSc MBBS, Department of Nuclear Medicine and PET, The Prince of Wales and Sydney Children's Hospitals, Barker St, Randwick, NSW 2031, Australia. john.freebody@health.nsw.gov.au
Telephone: +61-2-93822200 Fax: +61-2-93822235
Received: December 26, 2013 Revised: March 5, 2014
Accepted: September 16, 2014
Published online: March 28, 2015

Abstract

Positron emission tomography (PET) is a minimally invasive technique which has been well validated for the diagnosis, staging, monitoring of response to therapy, and disease surveillance of adult oncology patients. Traditionally the value of PET and PET/computed tomography (CT) hybrid imaging has been less clearly defined for paediatric oncology. However recent evidence has emerged regarding the diagnostic utility of these modalities, and they are becoming increasingly important tools in the evaluation and monitoring of children with known or suspected malignant disease. Important indications for 2-deoxy-2-(¹⁸F)fluoro-D-glucose (FDG) PET in paediatric oncology include lymphoma, brain tumours, sarcoma, neuroblastoma, Langerhans cell histiocytosis, urogenital tumours and neurofibromatosis type I. This article aims to review current evidence for the use of FDG PET and PET/CT in these indications. Attention will also be given to technical and logistical issues, the description of common imaging pitfalls, and dosimetric concerns as they relate to paediatric oncology.

© 2015 Baishideng Publishing Group Inc. All rights reserved.

Key words: Positron emission tomography; Computed tomography; Fluorodeoxyglucose F18; Paediatrics; Oncology; Technical issues; Dosimetry

Core tip: Positron emission tomography/computed tomography has emerged as a powerful and important tool in the assessment of a variety of childhood cancers and can impact significantly on patient management. Further prospective studies will more clearly delineate the precise role of this modality in the assessment of individual malignancies. Accurate image interpretation requires a thorough understanding of the normal variants of uptake unique to children.

Original sources: Freebody J, Wegner EA, Rossleigh MA. 2-deoxy-2-(¹⁸F)fluoro-D-glucose positron emission tomography/computed tomography imaging in paediatric oncology. *World J Radiol* 2014; 6(10): 741-755 Available from: URL: <http://www.wjnet.com/1949-8470/full/v6/i10/741.htm> DOI: <http://dx.doi.org/10.4329/wjr.v6.i10.741>

INTRODUCTION

Although the incidence of childhood malignancy remains relatively stable, survival rates have significantly improved over the past 30 years^[1]. In addition to improved treatment strategies, survival gains have relied upon continuous improvements in the accurate detection, staging and follow-up of these cancers.

Positron emission tomography (PET) is a minimally invasive technique whereby a labelled radiopharmaceutical is injected into a patient and the resulting distribution used to generate molecular information. In practice, PET-alone scanners have largely been replaced by the hybrid modality of PET/computed tomography (CT)

which combines the functional data of PET with the morphological information of CT. There has also been ongoing interest in the utility of fusing PET with magnetic resonance imaging (PET/MR)^[2].

The use of PET and PET/CT in adult oncology is well established for the purpose of diagnosis, staging, monitoring of response to therapy, and disease surveillance^[3,4]. In contrast to this, the value of these modalities in paediatric oncology has traditionally been much less clearly defined. More recently however, evidence has emerged regarding the diagnostic utility of PET and an important role has been reported for many paediatric malignancies^[5,6]. Hybrid imaging with PET/CT has demonstrated superiority to PET alone in characterising childhood cancers, primarily by increasing diagnostic confidence and reducing equivocal findings^[7-9]. PET/CT has become a central component of paediatric oncological practice.

PET imaging has now superseded ⁶⁷Ga and ²⁰¹Tl scintigraphy for many oncological applications^[10,11]. In addition to improved accuracy and having broader clinical application, advantages of PET over ⁶⁷Ga and ²⁰¹Tl scintigraphy include lower radiation dose, reduced scanning time, same day imaging and improved anatomical localisation. Through calculation of the standardised uptake value (SUV), PET is also able to generate quantitative data on treatment response.

Although there are a number of radiopharmaceuticals available, the majority of clinical PET imaging is performed with 2-deoxy-2-(¹⁸F)fluoro-D-glucose (FDG). FDG has many characteristics that make it ideal for use in PET imaging. ¹⁸F has a relatively short half-life of 110 min, provides relatively low radiation exposures for diagnostic purposes, and is widely commercially available. FDG mimics glucose in its cellular uptake and thereby serves as a marker of glucose utilisation. FDG is therefore not a tumour-specific entity and can accumulate in a number of physiological and pathological processes. The use of dual time-point imaging, which exploits unique characteristics of malignant cells, can help improve the specificity of FDG imaging^[12].

Common indications for PET in paediatric oncology include lymphoma, sarcoma, neuroblastoma and primary brain malignancy. Other important indications include Langerhans cell histiocytosis, Wilms tumor, and neurofibromatosis type I^[13]. This article aims to review current evidence for the use of PET and PET/CT in these indications. Imaging with the radiopharmaceutical FDG will be assumed unless noted otherwise. Attention will also be given to technical and logistical issues, the description of common imaging pitfalls, and dosimetric concerns as they relate to paediatric oncology.

LYMPHOMA

Non-Hodgkin's and Hodgkin's lymphoma collectively account for between 10% and 15% of paediatric malignancies. Evaluation of lymphoma remains the most frequent

indication of PET/CT imaging in children. Its use in this context has recently been reviewed^[14].

Whilst there is a large body of evidence supporting the use of PET/CT in adults, data remains more limited in relation to paediatric lymphoma. Nevertheless, available studies in children suggest that PET/CT is both diagnostically accurate and of significant clinical importance in these children^[15-17].

In two large retrospective studies PET/CT demonstrated superiority over conventional imaging modalities [CT, ultrasound, magnetic resonance imaging (MRI) or bone scintigraphy] in the primary staging of lesions due to both Hodgkin's and non-Hodgkin's disease (Figures 1A and 2A)^[18,19]. Calculated sensitivities and specificities for initial disease staging was greater than 95% and 99% respectively^[18,19]. Furthermore, PET/CT modified staging in 27% of cases, with approximately equal instances of upstaging and down-staging^[19].

PET has been shown to demonstrate superior sensitivity in the detection of bone marrow involvement due to Hodgkin's disease when compared with bone marrow biopsy^[20,23]. Marrow involvement in Hodgkin's disease is generally unifocal or multifocal and thus can easily be missed on biopsy. PET should therefore be employed as a first-line study in the detection of marrow involvement prior to directed bone marrow biopsy. There is accumulating evidence that a negative PET may replace the need for bone marrow biopsy in patients with Hodgkin's lymphoma^[20,21].

PET/CT has also demonstrated efficacy in the evaluation of treatment response, and performs significantly better than conventional imaging modalities in the evaluation of both early and post-completion chemotherapy responses (Figures 1B and 2B)^[18]. Multiple studies have demonstrated that a complete metabolic response early in the course of chemotherapy is associated with an excellent prognosis in children with Hodgkin's disease^[24,26]. Ongoing trials are aiming to utilise this information to enable distinct treatment protocols for these patients and therefore minimise treatment-related toxicity^[14].

Finally, PET/CT may be a useful modality for the follow-up of children with lymphoma, and a negative study during routine follow-up has a high negative predictive value^[16,27,28]. PET/CT was found to be superior to conventional imaging during long-term follow-up of children with lymphoma^[19]. Therefore although conventional imaging continues to be used as part of the follow-up assessment in these patients, PET/CT may eventually replace this and come to be used as a single imaging modality for routine surveillance (Figure 1C). It should be noted that the use of PET/CT for this indication is yet to be fully elucidated in paediatric patients. Although most Hodgkin's disease recurrence is FDG-avid, surveillance PET/CT can have high false-positive rates^[29]. Furthermore, because prognosis is often favourable among children with lymphoma, radiation exposure secondary to diagnostic procedures has significant relevance in children. Current evidence for follow-up PET/CT studies

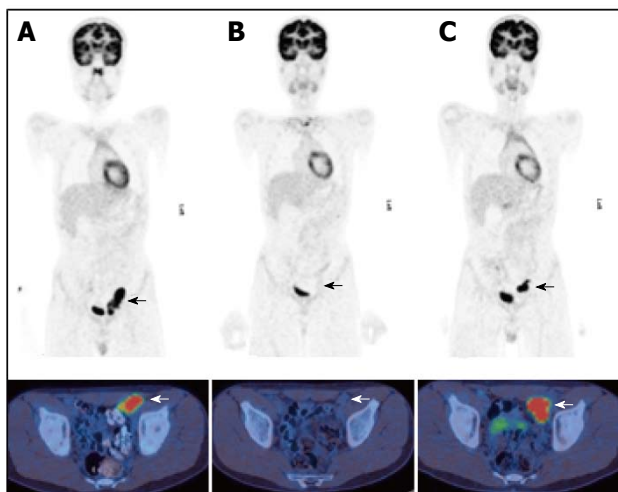


Figure 1 A 13 year-old male with nodular sclerosing Hodgkin's disease. PET/CT at staging (A) demonstrated disease in the left external iliac region. After completion of chemotherapy 4 mo later (B) there was a complete metabolic response with no activity in the residual lymph node mass. PET/CT performed 6 mo later (C) for surveillance demonstrated a recurrence at the same site. PET/CT: Positron emission tomography/computed tomography.

in paediatric lymphoma is best when relapse is clinically suspected or demonstrated by other imaging modalities.

BRAIN TUMOURS

Brain tumours represent the most common solid neoplasms in childhood and are a leading cause of cancer-related death in children^[30]. As a group they represent 25% of all childhood cancers^[31]. Common paediatric brain tumours include medulloblastoma, cerebellar astrocytoma, ependymoma and brain stem glioma^[32]. Management of these tumours is challenging and diverse, and requires extensive multidisciplinary collaboration. Survivors of childhood brain tumours often have severe neurological, neurocognitive and psychosocial sequelae^[33].

Conventional modalities for the anatomic assessment of brain tumours are CT and MRI. A major disadvantage of these modalities is that interpretation is often confounded by brain changes secondary to surgery, chemotherapy and radiotherapy. In these circumstances normal post-treatment change may be incorrectly identified as viable tumour. Functional imaging techniques are therefore of particular importance for monitoring treatment effects and recurrence.

PET has shown increasing application in paediatric neuro-oncology. Both FDG and L-methyl-(¹¹C)methionine (CMET) radiotracers have shown utility in brain tumour grading, profiling, and for detecting residual, recurrent or progressive disease in children^[34-36]. The fusion of PET data with MR images has been shown to assist with stereotactic biopsy and navigation-based resection among children in whom MR images alone were considered insufficient^[37].

FDG PET has traditionally been used to distinguish low-grade from high-grade tumours, and FDG avidity is a demonstrated predictor of outcome in adults with

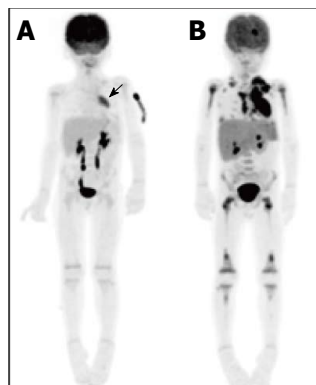


Figure 2 A 5-year-old male patient with relapsed T-cell lymphoblastic lymphoma. Restaging PET at the time of relapse 1 year after initial therapy demonstrated an FDG-avid mediastinal mass (A, arrow). Repeat PET performed following 1 cycle of FLAG-Ida chemotherapy demonstrated no response to treatment and progression of disease to stage IV with extensive bone marrow involvement (B). PET: Positron emission tomography; FDG: 2-deoxy-2-(¹⁸F)fluoro-D-glucose.

high-grade astrocytoma^[38]. Furthermore, FDG hypermetabolism has been shown to predict higher risk for disease progression among children with low-grade astrocytoma^[39]. FDG PET is an established technique for the differentiation of viable tumour and surgical change in the postoperative milieu^[40,41].

CMET is a marker of amino acid uptake and protein synthesis. It has been found useful in the differentiation of low-grade tumours (astrocytomas, oligodendrogliomas and dysembryoplastic neuroepithelial tumours), measurement of tumour boundaries, elucidation of treatment response, and prediction of patient outcome^[36,42-45].

SARCOMA

Ewing's sarcoma and osteosarcoma are the two primary bone malignancies of childhood, with osteosarcoma being more common^[46]. Rhabdomyosarcoma is the most common soft tissue malignancy of childhood^[47]. Collectively, bone and soft tissue sarcomas account for around 13% of childhood malignancies with soft tissue disease being slightly more prevalent^[46,47]. Treatment is multimodal and may involve chemotherapy, radiotherapy or surgery.

There is a growing body of literature related to the use of PET/CT in paediatric sarcoma, although standard use of the modality has not been extensively validated^[48,49]. Nevertheless, PET/CT does appear to demonstrate utility in the staging, monitoring of disease response to therapy, and detection of recurrent disease among these children (Figure 3)^[50,51]. North American consensus guidelines have recommended whole-body PET at the initial diagnosis of osteosarcoma and Ewing sarcoma in children^[52]. A previous survey has shown that PET is considered a helpful study by referrers of paediatric sarcoma patients in the vast majority of instances^[5]. The diagnostic accuracy of PET/CT has been found to be greater than either PET alone or conventional imaging in the detection of distant sarcomatous metastases in

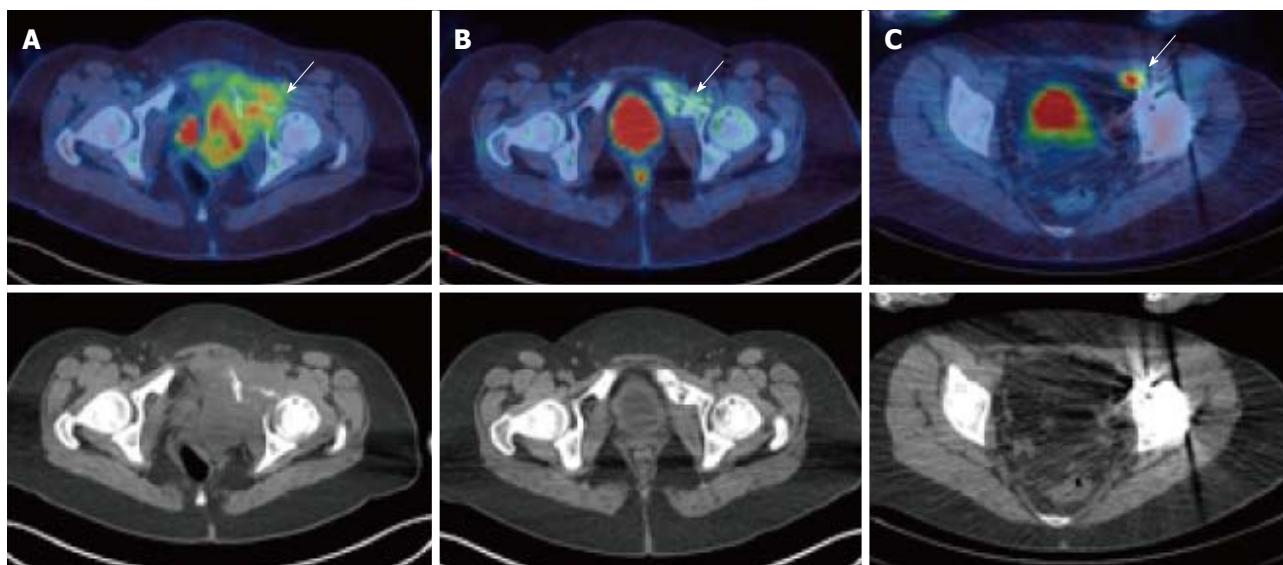


Figure 3 A 17-year-old female with Ewing's sarcoma involving the left superior pubic ramus. Staging PET/CT showed extensive disease (A, arrow) with bone destruction and a large FDG-avid pelvic mass. Following chemotherapy, at 5 mo after diagnosis, there was an excellent metabolic response with minimal residual FDG uptake (B, arrow). Patient underwent surgical resection and extracorporeal radiotherapy to the bone. Sixteen months after completion of treatment, surveillance PET/CT demonstrated recurrence in a left external iliac lymph node (C) which was not detectable on the CT or MRI due to marked metal artefact. PET/CT: Positron emission tomography/computed tomography; FDG: 2-deoxy-2-(^{18}F)fluoro-D-glucose; MRI: Magnetic resonance imaging.

children^[53].

Conventional staging of paediatric oncology patients includes bone scintigraphy, CT and MRI. PET has been found equal or superior to bone scintigraphy in the detection of osseous metastases from sarcoma^[54,55]. Such metastases are detected in Ewing sarcoma with a sensitivity ranging from 88%-100%^[54,55]. Detection of nodal metastases may also be improved with PET as compared with conventional imaging modalities^[56].

Pulmonary metastases are common among children with sarcoma, being present in up to one quarter of patients at the time of diagnosis^[50]. Prompt identification and treatment is crucial to effective management. PET alone has been proven less sensitive than diagnostic CT in the identification of sarcomatous pulmonary metastases^[56,57]. The sensitivity of PET in detecting pulmonary metastases has been reported to be as low as 24% for lesions smaller than 1 cm^[56,58]. This reduced sensitivity is multifactorial and can be attributed to technical limitations such as the finite spatial resolution of the scanner, which dictates that a lesion smaller than 3-4 mm may not be identified; as well as the partial volume effect (PVE) and respiratory movement during emission acquisition.

PVE can result in significant qualitative and quantitative changes to PET studies. In practical terms it results in the signals of small avid lesions being spread over larger volumes. It typically occurs whenever the avid lesion is smaller than 3 times the full width at half maximum, and is exacerbated when surrounding tissue uptake is particularly low (as is seen in lung tissue). PVE results in small lesions appearing larger in size but much less avid^[59].

Respiratory movements affect PET images due to the long acquisition times involved^[60]. The movement of lung lesions during respiration results in overestimated tracer-

avid volumes and reduced apparent tracer uptake^[61]. It is particularly seen in lung tissue closest to the diaphragm. Respiratory gating is a technique whereby the respiratory cycle is divided into multiple phases and the acquired events sorted into temporal bins. It aims to improve the spatial resolution of thoracic PET images at the expense of increased image noise. Respiratory gating has been shown to result in more accurate SUV and volume measurements of pulmonary nodules^[62]. It remains an ongoing area of research but may have future applications, particularly in the area of radiation therapy treatment planning^[63].

Aside from those technical limitations which affect small pulmonary metastases, PET sensitivity is reduced compared with conventional imaging even for pulmonary metastases greater than 1 cm in size, including those where the primary tumour is intensely avid. The reason for this finding is poorly understood but may relate to reduced perfusion of lesions, down-regulation of glucose receptors or altered glucose metabolism^[58].

Fused PET/CT improves detection of pulmonary metastases above PET alone^[64]. However, because PET/CT is generally undertaken with a reduced dose CT protocol, image quality may still not be sufficient to detect small pulmonary metastases. It is known that small pulmonary nodules are no more likely to be benign than larger ones among paediatric oncology patients^[65]. A diagnostic quality CT of the chest therefore remains an essential part of the staging and follow-up of paediatric sarcoma^[50].

PET has additionally been used to identify local and distant recurrence of sarcoma. Reliable follow-up however requires the use of other imaging modalities^[66]. Additionally, there has been much interest in the potential use

of PET as a prognostic tool. A correlation between the FDG SUV as measured prior to treatment, and clinically important indices such as disease progression and survival has been described^[67]. Furthermore, PET/CT demonstrates potential in the prediction of treatment response. Because tumour bulk may not significantly change in response to neoadjuvant chemotherapy, CT and MRI have limited value for such assessment. A number of studies have demonstrated that changes in FDG avidity in high-grade sarcoma following neoadjuvant therapy can identify patients at risk of relapse and therefore has potential as a non-invasive surrogate marker in the prediction of patient response^[68-70].

It should be noted that the degree of FDG avidity in sarcoma depends greatly on individual pathology and can range from low grade to markedly avid. This is particularly the case for soft tissue sarcomas including rhabdomyosarcoma, and needs to be appreciated when FDG is used for this indication^[71]. Furthermore, there may be heterogeneity of disease-related FDG uptake even within the same patient. Being able to identify the most aggressive area within a heterogenous tumour, and direct biopsy accordingly may be of clinical benefit^[71].

The use of PET and PET/CT among children with sarcoma continues to increase. As discussed above, these modalities appear to be useful in the evaluation and staging, monitoring of therapeutic response, and detection of tumour recurrence. However the exact role of this modality in the routine care of children with sarcoma remains unclear. Ongoing prospective studies are required to delineate the precise role of PET and PET/CT in their management.

NEUROFIBROMATOSIS TYPE 1

A number of studies have confirmed the utility of PET and PET/CT in the detection of malignant transformation of neurofibromatosis type 1 (NF1)^[72,73]. Patients with NF1 have an approximate 10% lifetime risk of developing malignant peripheral nerve sheath tumours (MPNST)^[74,75]. Such transformation is unreliably detected *via* conventional imaging^[76-78]. In one prospective study patients with symptomatic neurofibromas were assessed with early and delayed PET/CT imaging^[76]. This modality was found to be highly sensitive and specific in the detection of MPNSTs. In addition to there being significant differences in uptake between malignant and benign lesions, delayed imaging demonstrated a continued divergence of FDG avidity which highlights the value of dual time-point imaging for this indication.

NEUROBLASTOMA

Neuroblastoma is an embryonic tumour arising from neural crest cells of the sympathetic nervous system^[79]. It is the most common extracranial solid malignancy in children and accounts for around 8% of all childhood cancers. The clinical course is highly variable, yet the disease accounts for around 15% of all cancer deaths in

children^[80,81]. Half of all patients have distant haematogenous spread at diagnosis^[82].

The catecholamine analogue ¹²³I-metaiodobenzylguanidine (MIBG) is widely used to image neuroendocrine tumours and is well established for use in the staging and post-treatment evaluation of neuroblastoma^[83,84]. MIBG scintigraphy has a specificity of nearly 100% for neuroblastoma diagnosis and staging^[85,86]. Uptake of MIBG requires the presence of a type I catecholamine transport system^[87], which is usually but not uniformly present on neuroblastoma cells. In around 8% of patients MIBG scanning gives a false-negative result at diagnosis^[88]. False negative results may also lead to incorrect down-staging of disease. Other disadvantages of MIBG scintigraphy include limited spatial resolution, limited sensitivity in small lesions, the need for multiple and prolonged acquisition sessions and a delay between the start of examination and result.

In addition to MIBG, neuroblastoma imaging utilises the modalities of bone scintigraphy, sonography, CT and MR. There is also interest in the use of FDG and other radiopharmaceuticals for PET imaging. Because FDG PET uptake reflects glucose metabolism by cancer cells, neuroblastoma which fails to accumulate MIBG due to reduced expression of transporter proteins might be expected to be more sensitively assessed using this modality. Further potential advantages of PET over MIBG scintigraphy include improved spatial resolution, single acquisition sessions and shorter scanning times which have the potential to reduce the need for sedation^[89].

A number of studies have compared MIBG scintigraphy with PET in neuroblastoma^[90-93]. MIBG appears overall to be superior to PET in the evaluation of stage 4 neuroblastoma, primarily due to improved detection of skeletal disease. However PET appears to demonstrate superior detection in stage 1 and 2 neuroblastoma and in tumours which only weakly accumulate MIBG (Figure 4)^[90,92,93]. These results suggest that PET may be important in the context of discrepant or inconclusive findings on MIBG and morphological imaging.

To summarise, compared with PET, MIBG remains the optimal modality for the noninvasive staging of children with neuroblastoma. Overall, available evidence suggests that PET is most useful in defining the distribution of disease that either fails to concentrate MIBG or does so poorly. In particular, PET should be considered when MIBG scintigraphy reveals less disease than suggested by clinical symptoms or conventional imaging modalities. During follow-up assessment of MIBG-negative neuroblastoma, PET/CT represents the imaging modality of choice. New radiopharmaceuticals for PET imaging, including ¹⁸F-dihydroxyphenylalanine and ⁶⁸Ga-octreotate, are currently under evaluation^[94,95].

WILMS TUMOUR

Renal tumours comprise 6% of all childhood cancers. Of these, around 95% are Wilms tumours (nephroblastomas)^[96]. The molecular genetics of Wilms tumour is

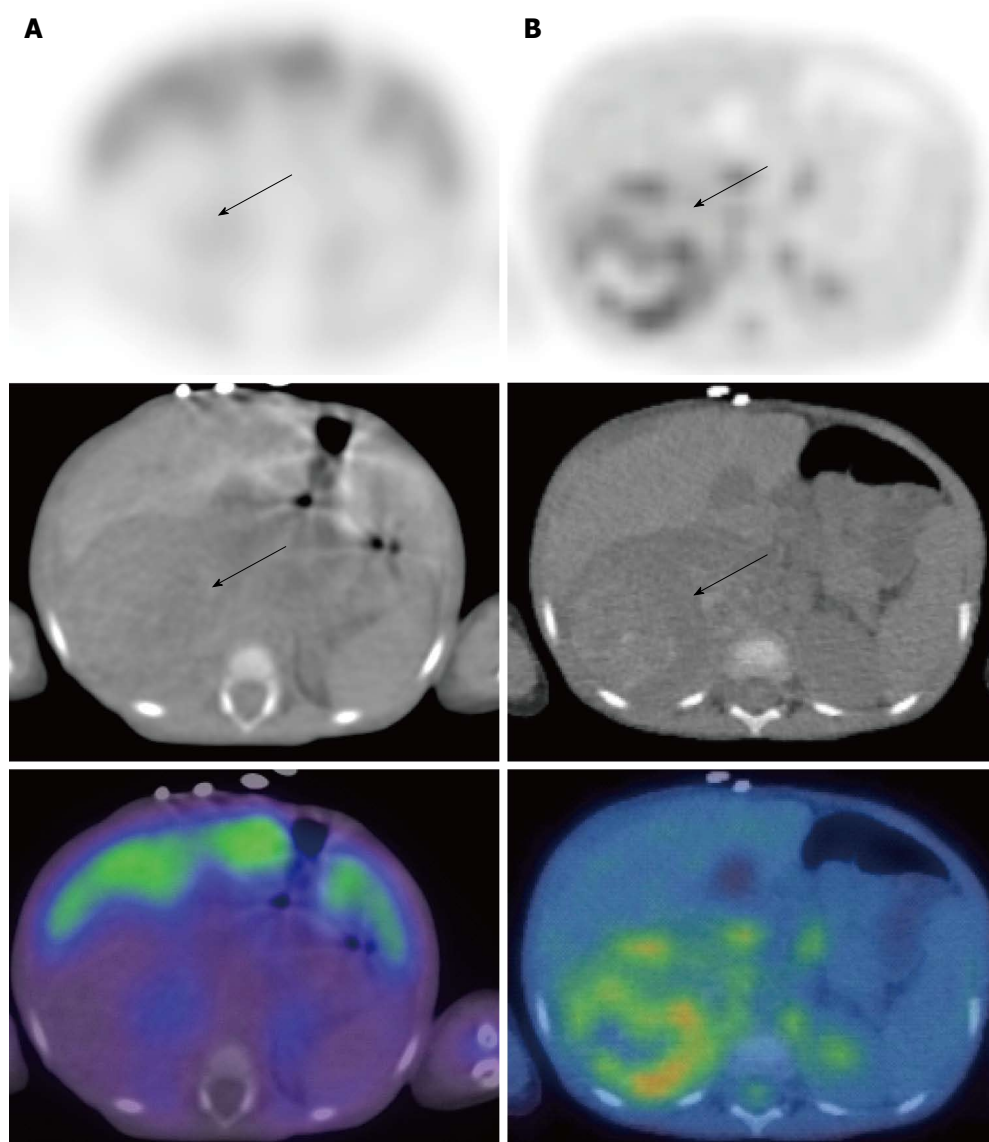


Figure 4 Neuroblastoma in a 2-year-old female. ^{123}I -metaiodobenzylguanidine (MIBG) single positron emission tomography/computed tomography (SPECT/CT) images (A) demonstrated a large right suprarenal mass displacing the organs which was not MIBG-avid (arrows). FDG PET/CT (B) showed moderate heterogeneous metabolic activity within the mass. PET/CT: Positron emission tomography/computed tomography; FDG: 2-deoxy-2-(^{18}F)fluoro-D-glucose.

complex and involves multiple loci involved with WNT signalling^[97]. Mutations in the *WT* gene are identified in 10%-15% of sporadic cases. More than 10% of children with Wilms tumour have associated abnormalities, including cryptorchidism, hypospadias, hemihypertrophy and aniridia^[98]. Synchronous bilateral Wilms tumour is present in 5% of patients^[99]. Although prognosis is generally favourable, higher stage disease carries significant mortality and treatment related morbidity.

Imaging at diagnosis typically involves ultrasound, CT and MRI. Although FDG uptake has been described in Wilms tumour^[100-102] the role of PET/CT has not been clearly established. A particular obstacle to accurate FDG PET imaging of the primary lesion is physiological excretion of tracer *via* the kidneys. Such physiological activity may generate uncertainty when attempting to distinguish pathology. The use of hybrid PET/CT scanners may be

of some benefit in this regard.

In a small series of 12 patients PET/CT was seen to be concordant with conventional imaging in primary staging and superior to conventional imaging for the detection of residual and recurrent disease^[100]. In another small series of 27 patients Wilms tumour appeared to concentrate FDG, however small pulmonary metastases were not consistently identified on PET scan^[101]. There is evidence that FDG avidity in Wilms tumour may correlate with higher histological risk^[102].

These studies demonstrate that FDG PET/CT may be a useful adjunct to conventional imaging modalities in Wilms tumour, particularly for the detection of residual and recurrent disease. Further investigation is required to confirm this. The use of functional MRI with diffusion-weighted imaging is another new technique which shows promise in the evaluation of Wilms tumour.

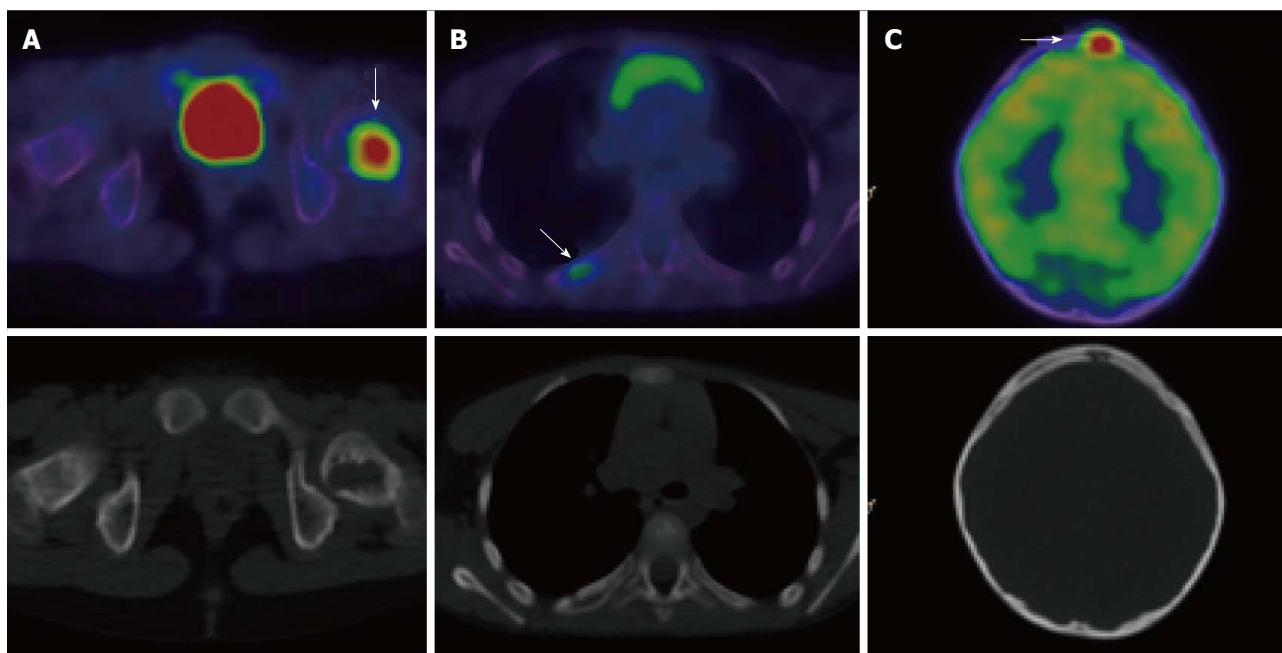


Figure 5 A 7-year-old male with Langerhans cell histiocytosis. Skeletal survey demonstrated an isolated left femoral lesion, confirmed on PET/CT (A, arrow). Additional lesions (arrows) in the right 6th rib posteriorly (B) and in the skull (C) were also identified on the PET/CT scan. Top panel: fused PET/CT images, bottom panel: low dose CT component of the scan. PET/CT: Positron emission tomography/computed tomography.

LANGERHANS CELL HISTIOCYTOSIS

Langerhans cell histiocytosis (LCH) is a rare disease which involves the clonal proliferation of activated dendrocytes and macrophages. These clonal cells form infiltrates in a variety of organs along with other inflammatory cells^[103]. LCH exists as a heterogenous and complex disease with a broad spectrum of clinical manifestations which range from spontaneous resolution to rapid progression and death^[104]. It may occur at any age but generally affects children between 1 and 15 years. Skeletal survey and bone scintigraphy are established techniques in LCH disease evaluation. In addition, CT and MRI modalities are increasingly used in the detection of skeletal and visceral disease^[105].

The use of PET and PET/CT in the assessment of patients with LCH has been reported in a number of studies and its use is now well established. PET has been shown to be superior to bone scintigraphy and skeletal survey for overall lesion detection (Figure 5)^[106-108]. Furthermore, PET has demonstrated efficacy in post-treatment lesion assessment and provides information on treatment response earlier than plain film radiography or CT^[106-110].

A recent study has compared the use of PET with MRI in paediatric patients with biopsy-proven histiocytosis^[111]. In this study PET was found to be more accurate than MRI for post-treatment evaluation due to lower false-positive rates. MRI showed a higher sensitivity and was important for primary staging and evaluation of CNS disease. Interestingly, whilst there was no clear advantage for combined PET/MRI analysis during follow-up evaluation, the combination did improve sensitivity

of primary staging through a reduced false-negative rate. These results suggest that whilst PET alone may be sufficient for post-treatment disease monitoring in LCH, the combination of PET and MRI is preferred for primary disease investigation. A potential future role therefore exists for combined PET/MRI in the primary investigation of paediatric LCH.

Taken together, these studies suggest that PET is a valuable modality in the primary assessment, therapeutic monitoring and detection of reactivation of patients with LCH.

PRACTICAL ASPECTS

PET/CT requires consideration of particular challenges that are common to paediatric nuclear medicine but uncommon to adult imaging. These include consent, fasting, intravenous access and the question of sedation^[112,113]. Patient cooperation is a significant issue. Successful imaging can be facilitated by providing a relaxed, child-oriented environment, and staff experienced in paediatric venipuncture and the management of children. Available data suggests that PET/CT artefacts due to movement, poor co-registration or non-compliance are no more frequent among paediatric patients than among adult ones^[114].

Paediatric sedation is a complex issue and requires case-by-case assessment. Often, the child's parents will be aware of previous cooperation difficulties and can assist with decision making. When sedation is required, it should be limited to the scanning phase of the study^[112]. The use of sedation in paediatrics is not without risk and has been associated with a 0.4% incidence of adverse respiratory events^[115]. Sedation protocols vary by institu-



Figure 6 An extreme case of widespread brown fat activity in a 16-year-old female with treated Hodgkin's disease.

tion, but guidelines are available^[116,117].

COMMON PITFALLS

The accuracy of PET can vary depending on tumour type, location and scan timing in relation to treatment. Furthermore, variant patterns of physiologic FDG uptake often differ in children as compared with adults and may be mistakenly interpreted as disease. A thorough understanding of normal variant FDG uptake is therefore essential for accurate image interpretation, preventing unnecessary studies or procedures and improving patient care. Image co-registration with hybrid PET/CT systems is helpful in distinguishing normal variation from pathology through the precise localisation of functional data.

Sites of physiologic FDG uptake that can differ in children as compared with adults include brown adipose tissue^[118,119], thymus^[120], brain^[121] and epiphyseal plates^[122]. Each of these potential pitfalls to image interpretation is discussed below. Other potential sites of increased FDG uptake in the paediatric patient include the pharyngeal lymphatic tissue of Waldeyer's ring, salivary glands and haematopoietic bone marrow^[123]. Additionally, paediatric patients suffer from a multitude of community acquired infections which may prompt intense reactive nodal avidity and thus mimic malignancy.

Brown adipose tissue

FDG uptake by brown adipose tissue in paediatric patients has recently been reviewed^[124]. The primary function of brown fat is non-shivering thermogenesis^[125]. This metabolic process involves expression of mitochondrial uncoupling proteins, including UCP-1, which separate oxidative phosphorylation from ATP synthesis and thereby generate energy dissipated as heat^[126].

Brown fat FDG uptake has been reported in up to 20% of children and adolescents, but is a rare occurrence among adults^[119,124]. Uptake is usually distributed symmetrically within the neck and supraclavicular regions, axillae, paraspinal regions of the posterior mediastinum, adjacent to the adrenal glands and upper abdominal wall (Figure 6). Such uptake may mimic malignancy or obscure patho-

logical lesions^[119,127]. This is particularly true for paediatric lymphoma patients, as brown fat is located adjacent to regions commonly involved in the disease.

Significant reductions in brown fat tracer uptake are made possible by controlling the environmental temperature and stress levels of the patient prior to injection and during the tracer uptake phase^[128]. Additional blankets are often employed to provide further increases in warmth. In addition, the administration of oral diazepam may reduce brown fat uptake and is recommended by several groups^[129]. Beta blockade with propranolol^[130] or intravenous fentanyl^[131] has also been advocated by some. Image co-registration with PET/CT is helpful to distinguish brown adipose tissue from pathological causes of FDG uptake^[127].

Thymus

FDG-avid thymic tissue has been demonstrated in 34% of healthy young adults on screening PET scans^[132]. Among paediatric oncology patients thymic uptake is observed in around 75% of cases irrespective of whether chemotherapy has been administered^[120]. The increased activity among paediatric oncology patients is thought to be due to reactive thymic hyperplasia secondary to stress, infection or treatment. These changes may appear late and can persist for many months following the completion of treatment.

Familiarity with normal appearances is essential to distinguish between physiologic thymic uptake and active disease in the mediastinum. This is particularly important in children with potentially curable diseases such as lymphoma, as they may often have residual non-malignant tissue in the mediastinum following treatment. The normal pattern of thymic uptake is a homogenous lambda-shaped structure in the anterior mediastinum, although multiple variants are seen (Figure 7). Very intense or heterogenous uptake raises suspicion for thymic or other anterior mediastinal disease^[133] (Figure 8).

Brain

It is important to recognise maturational changes in cerebral glucose metabolism to allow the identification of pathological alterations. A recent study describing cerebral FDG uptake in children demonstrated that all cerebral regions show increasing avidity with age, with rates of change being regionally specific^[121]. The most metabolically active areas in early childhood are the parietal and occipital lobes. By age 7 these regions have less uptake than the frontal lobes, and by age 10 they have less uptake than the thalamus. Changes in the relative pattern of cortical FDG uptake appear to continue up until at least 16 years of age.

Epiphyseal plate

Skeletally immature paediatric patients exhibit physiologic linear uptake in physes and apophyses (Figure 9)^[122]. Such uptake has the potential to obscure small skeletal lesions, or it may be mistaken for pathological activity. In addition,

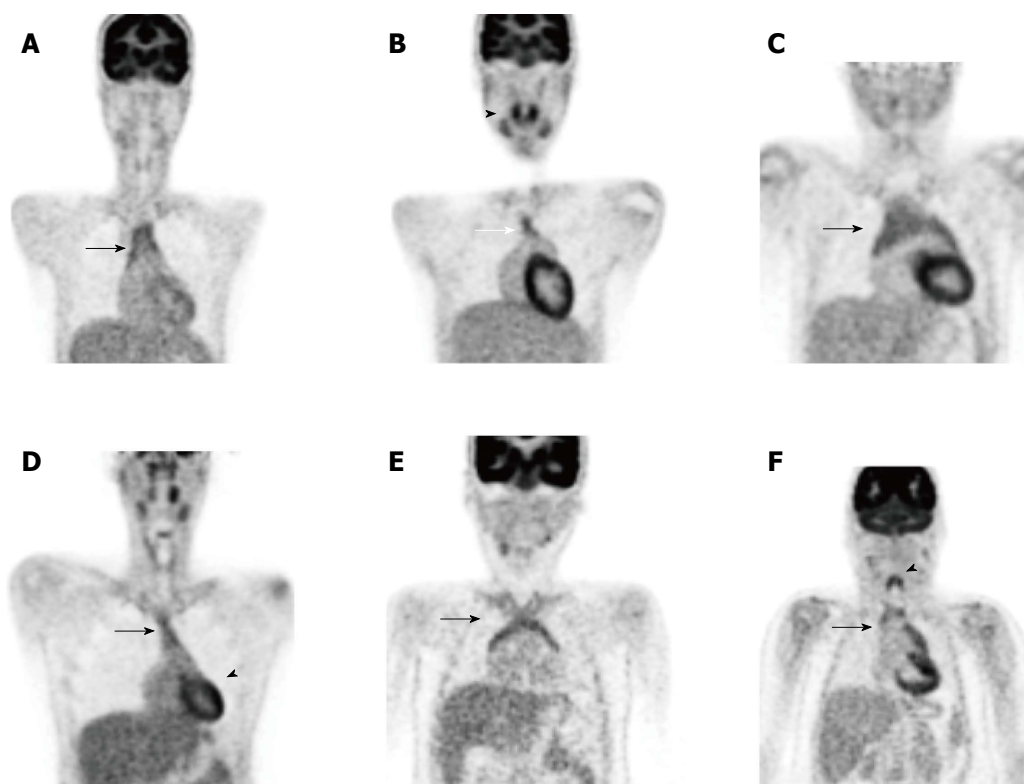


Figure 7 Normal physiological variants: various patterns of thymic uptake (A-F, arrow), tonsillar uptake (B, arrowhead), cardiac uptake (D, arrowhead) and laryngeal uptake (F, arrowhead).

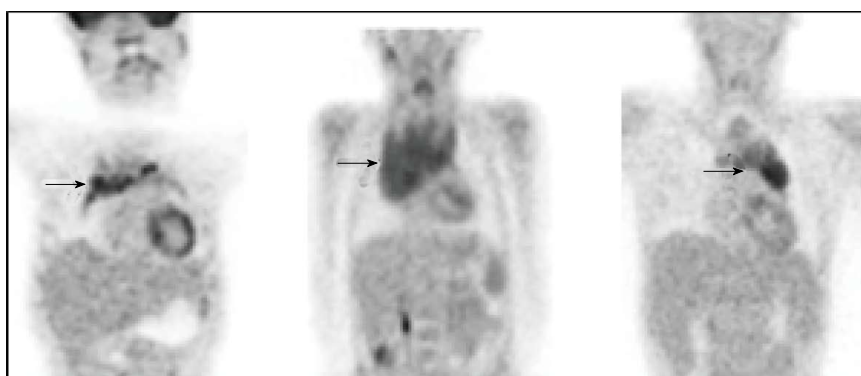


Figure 8 Examples of abnormal thymic uptake due to malignant disease (arrows).

loss of the normal sharp demarcation of uptake in the physes may reflect bone marrow infiltration or activation and should be recognised. Avid FDG uptake may occasionally occur in benign skeletal lesions (Figure 10). These include fibrous defects, which are very common in childhood^[122], and osteochondromas. An understanding that benign skeletal lesions may take up FDG, and knowledge of the typical appearances seen on the CT component of the scan will reduce false positive findings.

DOSIMETRIC CONCERNS

As with all imaging modalities that utilise ionising radiation, there are special dosimetric considerations for children undergoing PET/CT scanning. Particular atten-

tion is required to keep radiation exposure as low as is reasonably achievable (ALARA principle) in view of the increased lifetime cancer mortality risk in children compared with adults^[134]. The higher risk of radiation-induced malignancy in paediatric patients is a consequence of both the longer average post-exposure survival of children as compared with adults, and an intrinsic increase in radiosensitivity of children^[135,136].

As risk from radiation exposure is cumulative^[137], both nuclear medicine and CT components need to be considered when applying ALARA principles. In this context patient exposure may be adjusted through changes to the dose of administered radiopharmaceutical, CT protocol employed, anatomic area covered and frequency of imaging performed^[138]. Notably, the end-organ for radiotracer



Figure 9 Normal 2-deoxy-2-(¹⁸F)fluoro-D-glucose positron emission tomography scan of an 8-year-old female showing physiological growth plate uptake (arrow).

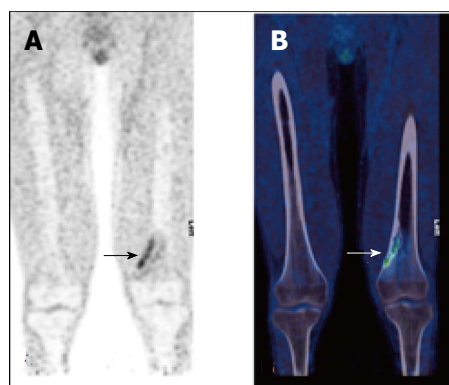


Figure 10 Non-ossifying fibroma (arrow) in the left distal femur of a 17-year-old male patient with Langerhans cell histiocytosis. FDG PET (A) showing avid uptake, CT (B) showing typical benign radiological features. PET: Positron emission tomography; CT: Computed tomography; FDG: 2-deoxy-2-(¹⁸F)fluoro-D-glucose.

administration is the bladder and therefore the bladder wall tends to receive the greatest radiation dose^[139]. This can be minimised by encouraging fluid intake and frequent voiding following scan completion.

PET and PET/CT radiopharmaceutical dosage guidelines have been established by the European Association of Nuclear Medicine (EANM) Dosimetry and Paediatrics Committees^[140,141] and the Pediatric Nuclear Medicine Dose Reduction Workgroup (North American Consensus Guidelines)^[142]. Although there are some differences between these guidelines (Figure 11) both make recommendations in line with the ALARA principles. The EANM guidelines aim for the administration of FDG as a weight independent effective dose. Doses are calculated using normalisation factors which are derived from biological behaviour and patient weight. The aim is to deliver the same effective radiopharmaceutical dose to paediatric patients regardless of body weight, provided a minimum activity is administered^[140]. The North American Consensus Guidelines recommend a standard FDG administered activity per kilogram of body weight^[142].

Effective doses to patients from CT images are dependent on tube current (mA), tube potential (kVp), rotation speed, pitch, slice thickness, patient mass and the

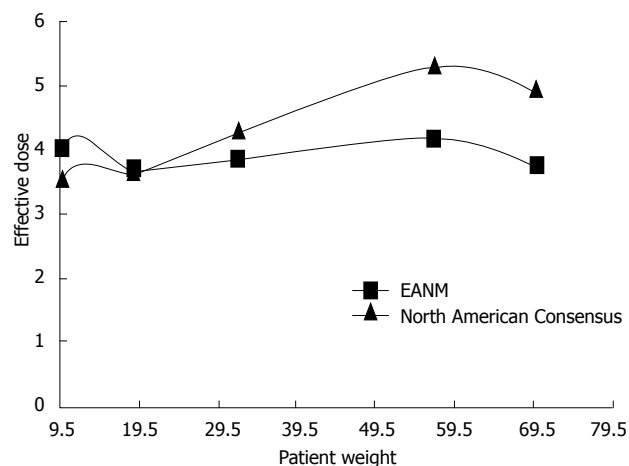


Figure 11 Effective dose vs patient weight for 2-deoxy-2-(¹⁸F)fluoro-D-glucose (European Association of Nuclear Medicine and North American Consensus Guidelines). Image courtesy of Bruce McBride, Chief Physicist, Department of Nuclear Medicine and PET, The Prince of Wales and Sydney Children's Hospitals. PET: Positron emission tomography; EANM: European Association of Nuclear Medicine.

anatomical volume included in the scan. CT exposures in hybrid PET/CT scanning may be tailored to meet the diagnostic needs of the patient. Commonly, diagnostic quality images are not required and CT exposure factors may be reduced significantly, with the production of images primarily for localisation and attenuation correction. These low dose protocols may reduce CT exposures by 50%-65% compared with typical diagnostic levels^[143].

CONCLUSION

PET and PET/CT have emerged as powerful and important imaging techniques in the assessment of a variety of childhood malignancies, with PET/CT being the preferred modality. Although a number of radiopharmaceuticals exist, FDG remains the most widely used and clinically important. PET/CT scanning should occur in the context of rational and evidence-based imaging decisions, and ongoing large prospective trials will further clarify its role in the assessment of individual malignancies. It is important that a thorough understanding of variant childhood uptake patterns is obtained for accurate image interpretation.

ACKNOWLEDGMENTS

The authors would like to acknowledge Mr. Bruce McBride, Chief Physicist, Department of Nuclear Medicine and PET, The Prince of Wales and Sydney Children's Hospitals for assistance in preparing the "Dosimetry" section of this manuscript.

REFERENCES

- 1 Gatta G, Zigon G, Capocaccia R, Coebergh JW, Desandes E, Kaatsch P, Pastore G, Peris-Bonet R, Stiller CA; EURO-CARE Working Group. Survival of European children

- and young adults with cancer diagnosed 1995-2002. *Eur J Cancer* 2009; **45**: 992-1005 [PMID: 19231160 DOI: 10.1016/j.ejca.2008.11.042]
- 2 **Ouyang J**, Li Q, El Fakhri G. Magnetic resonance-based motion correction for positron emission tomography imaging. *Semin Nucl Med* 2013; **43**: 60-67 [PMID: 23178089 DOI: 10.1053/j.semnuclmed.2012.08.007]
 - 3 **Juweid ME**, Cheson BD. Positron-emission tomography and assessment of cancer therapy. *N Engl J Med* 2006; **354**: 496-507 [PMID: 16452561 DOI: 10.1056/NEJMr050276]
 - 4 **Storto G**, Nicolai E, Salvatore M. [18F]FDG-PET-CT for early monitoring of tumor response: when and why. *Q J Nucl Med Mol Imaging* 2009; **53**: 167-180 [PMID: 19293765]
 - 5 **Wegner EA**, Barrington SF, Kingston JE, Robinson RO, Ferner RE, Taj M, Smith MA, O'Doherty MJ. The impact of PET scanning on management of paediatric oncology patients. *Eur J Nucl Med Mol Imaging* 2005; **32**: 23-30 [PMID: 15290124 DOI: 10.1007/s00259-004-1645-3]
 - 6 **Goo HW**. Regional and whole-body imaging in pediatric oncology. *Pediatr Radiol* 2011; **41** Suppl 1: S186-S194 [PMID: 21523595 DOI: 10.1007/s00247-011-2050-2]
 - 7 **Bar-Sever Z**, Keidar Z, Ben-Barak A, Bar-Shalom R, Postovsky S, Guralnik L, Ben Arush MW, Israel O. The incremental value of 18F-FDG PET/CT in paediatric malignancies. *Eur J Nucl Med Mol Imaging* 2007; **34**: 630-637 [PMID: 17048034 DOI: 10.1007/s00259-006-0253-9]
 - 8 **Yeung HW**, Schoder H, Smith A, Gonen M, Larson SM. Clinical value of combined positron emission tomography/computed tomography imaging in the interpretation of 2-deoxy-2-[F-18]fluoro-D-glucose-positron emission tomography studies in cancer patients. *Mol Imaging Biol* 2005; **7**: 229-235 [PMID: 15912427 DOI: 10.1007/s11307-005-4113-y]
 - 9 **Stauss J**, Franzius C, Pfluger T, Juergens KU, Biassoni L, Begent J, Kluge R, Amthauer H, Voelker T, Højgaard L, Barrington S, Hain S, Lynch T, Hahn K; European Association of Nuclear Medicine. Guidelines for 18F-FDG PET and PET-CT imaging in paediatric oncology. *Eur J Nucl Med Mol Imaging* 2008; **35**: 1581-1588 [PMID: 18536914 DOI: 10.1007/s00259-008-0826-x]
 - 10 **Hawkins DS**, Rajendran JG, Conrad EU, Bruckner JD, Eary JF. Evaluation of chemotherapy response in pediatric bone sarcomas by [F-18]fluorodeoxy-D-glucose positron emission tomography. *Cancer* 2002; **94**: 3277-3284 [PMID: 12115361 DOI: 10.1002/cncr.10599]
 - 11 **Bar-Shalom R**, Yefremov N, Haim N, Dann EJ, Epelbaum R, Keidar Z, Gaitini D, Frenkel A, Israel O. Camera-based FDG PET and 67Ga SPECT in evaluation of lymphoma: comparative study. *Radiology* 2003; **227**: 353-360 [PMID: 12637679 DOI: 10.1148/radiol.2272020195]
 - 12 **Costantini DL**, Vali R, Chan J, McQuattie S, Charron M. Dual-time-point FDG PET/CT for the evaluation of pediatric tumors. *AJR Am J Roentgenol* 2013; **200**: 408-413 [PMID: 23345365 DOI: 10.2214/AJR.12.8930]
 - 13 **Jadvar H**, Connolly LP, Fahey FH, Shulkin BL. PET and PET/CT in pediatric oncology. *Semin Nucl Med* 2007; **37**: 316-331 [PMID: 17707239 DOI: 10.1053/j.semnuclmed.2007.04.001]
 - 14 **Kluge R**, Kurch L, Montravers F, Mauz-Körholz C. FDG PET/CT in children and adolescents with lymphoma. *Pediatr Radiol* 2013; **43**: 406-417 [PMID: 23525767 DOI: 10.1007/s00247-012-2559-z]
 - 15 **Kabickova E**, Sumerauer D, Cumlivska E, Drahoukoupilova E, Nekolna M, Chanova M, Hladikova M, Kodet R, Belohlavek O. Comparison of 18F-FDG-PET and standard procedures for the pretreatment staging of children and adolescents with Hodgkin's disease. *Eur J Nucl Med Mol Imaging* 2006; **33**: 1025-1031 [PMID: 16565847 DOI: 10.1007/s00259-005-0019-9]
 - 16 **Hernandez-Pampaloni M**, Takalkar A, Yu JQ, Zhuang H, Alavi A. F-18 FDG-PET imaging and correlation with CT in staging and follow-up of pediatric lymphomas. *Pediatr Radiol* 2006; **36**: 524-531 [PMID: 16622665 DOI: 10.1007/s00247-006-0152-z]
 - 17 **Depas G**, De Barys C, Jerusalem G, Hoyoux C, Dresse MF, Fassotte MF, Paquet N, Foidart J, Rigo P, Hustinx R. 18F-FDG PET in children with lymphomas. *Eur J Nucl Med Mol Imaging* 2005; **32**: 31-38 [PMID: 15605288 DOI: 10.1007/s00259-004-1604-z]
 - 18 **London K**, Cross S, Onikul E, Dalla-Pozza L, Howman-Giles R. 18F-FDG PET/CT in paediatric lymphoma: comparison with conventional imaging. *Eur J Nucl Med Mol Imaging* 2011; **38**: 274-284 [PMID: 20848280 DOI: 10.1007/s00259-010-1619-6]
 - 19 **Riad R**, Omar W, Kotb M, Hafez M, Sidhom I, Zamzam M, Zaky I, Abdel-Dayem H. Role of PET/CT in malignant pediatric lymphoma. *Eur J Nucl Med Mol Imaging* 2010; **37**: 319-329 [PMID: 19756591 DOI: 10.1007/s00259-009-1276-9]
 - 20 **Purz S**, Mauz-Körholz C, Körholz D, Hasenclever D, Krause A, Sorge I, Ruschke K, Stiefel M, Amthauer H, Schober O, Kranert WT, Weber WA, Haberkorn U, Hundsdoerfer P, Ehlert K, Becker M, Rössler J, Kulozik AE, Sabri O, Kluge R. [18F]Fluorodeoxyglucose positron emission tomography for detection of bone marrow involvement in children and adolescents with Hodgkin's lymphoma. *J Clin Oncol* 2011; **29**: 3523-3528 [PMID: 21825262 DOI: 10.1200/JCO.2010.32.4996]
 - 21 **Moulin-Romsee G**, Hindié E, Cuenca X, Brice P, Decaudin D, Bénamor M, Brière J, Anitei M, Filmont JE, Sibon D, de Kerviler E, Moretti JL. (18)F-FDG PET/CT bone/bone marrow findings in Hodgkin's lymphoma may circumvent the use of bone marrow trephine biopsy at diagnosis staging. *Eur J Nucl Med Mol Imaging* 2010; **37**: 1095-1105 [PMID: 20204358 DOI: 10.1007/s00259-009-1377-5]
 - 22 **Pelosi E**, Penna D, Deandreis D, Chiappella A, Skanjeti A, Vitolo U, Bisi G. FDG-PET in the detection of bone marrow disease in Hodgkin's disease and aggressive non-Hodgkin's lymphoma and its impact on clinical management. *Q J Nucl Med Mol Imaging* 2008; **52**: 9-16 [PMID: 18235420]
 - 23 **Cheng G**, Chen W, Chamroomrat W, Torigian DA, Zhuang H, Alavi A. Biopsy versus FDG PET/CT in the initial evaluation of bone marrow involvement in pediatric lymphoma patients. *Eur J Nucl Med Mol Imaging* 2011; **38**: 1469-1476 [PMID: 21505896 DOI: 10.1007/s00259-011-1815-z]
 - 24 **Furth C**, Steffen IG, Amthauer H, Ruf J, Misch D, Schönberger S, Kobe C, Denecke T, Stöver B, Hautzel H, Henze G, Hundsdoerfer P. Early and late therapy response assessment with [18F]fluorodeoxyglucose positron emission tomography in pediatric Hodgkin's lymphoma: analysis of a prospective multicenter trial. *J Clin Oncol* 2009; **27**: 4385-4391 [PMID: 19667276 DOI: 10.1200/JCO.2008]
 - 25 **Hutchings M**, Loft A, Hansen M, Pedersen LM, Buhl T, Jurlander J, Buus S, Keiding S, D'Amore F, Boesen AM, Berthelsen AK, Specht L. FDG-PET after two cycles of chemotherapy predicts treatment failure and progression-free survival in Hodgkin lymphoma. *Blood* 2006; **107**: 52-59 [PMID: 16150944 DOI: 10.1182/blood-2005-06-2252]
 - 26 **Kostakoglu L**, Coleman M, Leonard JP, Kuji I, Zoe H, Goldsmith SJ. PET predicts prognosis after 1 cycle of chemotherapy in aggressive lymphoma and Hodgkin's disease. *J Nucl Med* 2002; **43**: 1018-1027 [PMID: 12163626]
 - 27 **Miller E**, Metser U, Avrahami G, Dvir R, Valdman D, Sira LB, Sayar D, Burstein Y, Toren A, Yaniv I, Even-Sapir E. Role of 18F-FDG PET/CT in staging and follow-up of lymphoma in pediatric and young adult patients. *J Comput Assist Tomogr* 2006; **30**: 689-694 [PMID: 16845304 DOI: 10.1097/00004728-200607000-00022]
 - 28 **Rhodes MM**, Delbeke D, Whitlock JA, Martin W, Kuttesch JF, Frangoul HA, Shankar S. Utility of FDG-PET/CT in follow-up of children treated for Hodgkin and non-Hodgkin lymphoma. *J Pediatr Hematol Oncol* 2006; **28**: 300-306 [PMID:

- 16772881 DOI: 10.1097/01.mph.0000212912.37512.b1]
- 29 **Crocchiolo R**, Fallanca F, Giovacchini G, Ferreri AJ, Assanelli A, Verona C, Pescarollo A, Bregni M, Ponzoni M, Gianolli L, Fazio F, Ciceri F. Role of 18FDG-PET/CT in detecting relapse during follow-up of patients with Hodgkin's lymphoma. *Ann Hematol* 2009; **88**: 1229-1236 [PMID: 19468730 DOI: 10.1007/s00277-009-0752-4]
 - 30 **Ramanan M**, Chaseling R. Paediatric brain tumours treated at a single, tertiary paediatric neurosurgical referral centre from 1999 to 2010 in Australia. *J Clin Neurosci* 2012; **19**: 1387-1391 [PMID: 22898201 DOI: 10.1016/j.jocn.2012.01.028]
 - 31 **Fleming AJ**, Chi SN. Brain tumors in children. *Curr Probl Pediatr Adolesc Health Care* 2012; **42**: 80-103 [PMID: 22433905 DOI: 10.1016/j.cppeds.2011.12.002]
 - 32 **Kumar R**, Shandal V, Shamim SA, Halanaik D, Malhotra A. Clinical applications of PET and PET/CT in pediatric malignancies. *Expert Rev Anticancer Ther* 2010; **10**: 755-768 [PMID: 20470007 DOI: 10.1586/era.10.12]
 - 33 **Sønderkaer S**, Schmiegelow M, Carstensen H, Nielsen LB, Müller J, Schmiegelow K. Long-term neurological outcome of childhood brain tumors treated by surgery only. *J Clin Oncol* 2003; **21**: 1347-1351 [PMID: 12663725 DOI: 10.1200/JCO.2003.08.009]
 - 34 **Herholz K**, Hölzer T, Bauer B, Schröder R, Voges J, Ernestus RI, Mendoza G, Weber-Luxemburger G, Löttgen J, Thiel A, Wienhard K, Heiss WD. 11C-methionine PET for differential diagnosis of low-grade gliomas. *Neurology* 1998; **50**: 1316-1322 [PMID: 9595980 DOI: 10.1212/WNL.50.5.1316]
 - 35 **Pirotte B**, Levivier M, Morelli D, Van Bogaert P, Detemmerman D, David P, Baleriaux D, Brotchi J, Goldman S. Positron emission tomography for the early postsurgical evaluation of pediatric brain tumors. *Childs Nerv Syst* 2005; **21**: 294-300 [PMID: 15798921 DOI: 10.1007/s00381-004-1071-7]
 - 36 **Utriainen M**, Metsähonkala L, Salmi TT, Utriainen T, Kalimo H, Pihko H, Mäkipernaa A, Harila-Saari A, Jyrkkö S, Laine J, Någren K, Minn H. Metabolic characterization of childhood brain tumors: comparison of 18F-fluorodeoxyglucose and 11C-methionine positron emission tomography. *Cancer* 2002; **95**: 1376-1386 [PMID: 12216107 DOI: 10.1002/cncr.10798]
 - 37 **Pirotte BJ**, Lubansu A, Massager N, Wikler D, Van Bogaert P, Levivier M, Brotchi J, Goldman S. Clinical impact of integrating positron emission tomography during surgery in 85 children with brain tumors. *J Neurosurg Pediatr* 2010; **5**: 486-499 [PMID: 20433263 DOI: 10.3171/2010.1.PEDS09481]
 - 38 **De Witte O**, Lefranc F, Levivier M, Salmon I, Brotchi J, Goldman S. FDG-PET as a prognostic factor in high-grade astrocytoma. *J Neurooncol* 2000; **49**: 157-163 [PMID: 11206011 DOI: 10.1023/A: 1026518002800]
 - 39 **Kruer MC**, Kaplan AM, Ettl MM, Carpentieri DF, Dickman PS, Chen K, Mathieson K, Irving A. The value of positron emission tomography and proliferation index in predicting progression in low-grade astrocytomas of childhood. *J Neurooncol* 2009; **95**: 239-245 [PMID: 19506815 DOI: 10.1007/s11060-009-9922-4]
 - 40 **Valk PE**, Budinger TF, Levin VA, Silver P, Gutin PH, Doyle WK. PET of malignant cerebral tumors after interstitial brachytherapy. Demonstration of metabolic activity and correlation with clinical outcome. *J Neurosurg* 1988; **69**: 830-838 [PMID: 2848111 DOI: 10.3171/jns.1988.69.6.0830]
 - 41 **Glantz MJ**, Hoffman JM, Coleman RE, Friedman AH, Hanson MW, Burger PC, Herndon JE, Meisler WJ, Schold SC. Identification of early recurrence of primary central nervous system tumors by [18F]fluorodeoxyglucose positron emission tomography. *Ann Neurol* 1991; **29**: 347-355 [PMID: 1929205 DOI: 10.1002/ana.410290403]
 - 42 **Kaplan AM**, Lawson MA, Spataro J, Bandy DJ, Bonstelle CT, Moss SD, Manwaring KH, Reiman EM. Positron emission tomography using [18F] fluorodeoxyglucose and [11C] l-methionine to metabolically characterize dysembryoplastic neuroepithelial tumors. *J Child Neurol* 1999; **14**: 673-677 [PMID: 10511341 DOI: 10.1177/088307389901401009]
 - 43 **Chung JK**, Kim YK, Kim SK, Lee YJ, Paek S, Yeo JS, Jeong JM, Lee DS, Jung HW, Lee MC. Usefulness of 11C-methionine PET in the evaluation of brain lesions that are hypo- or isometabolic on 18F-FDG PET. *Eur J Nucl Med Mol Imaging* 2002; **29**: 176-182 [PMID: 11926379 DOI: 10.1007/s00259-001-0690-4]
 - 44 **Galldiks N**, Kracht LW, Berthold F, Miletic H, Klein JC, Herholz K, Jacobs AH, Heiss WD. [11C]-L-methionine positron emission tomography in the management of children and young adults with brain tumors. *J Neurooncol* 2010; **96**: 231-239 [PMID: 19575148 DOI: 10.1007/s11060-009-9953-x]
 - 45 **Nariai T**, Tanaka Y, Wakimoto H, Aoyagi M, Tamaki M, Ishiwata K, Senda M, Ishii K, Hirakawa K, Ohno K. Usefulness of L-[methyl-11C] methionine-positron emission tomography as a biological monitoring tool in the treatment of glioma. *J Neurosurg* 2005; **103**: 498-507 [PMID: 16235683 DOI: 10.3171/jns.2005.103.3.0498]
 - 46 **Heare T**, Hensley MA, Dell'Orfano S. Bone tumors: osteosarcoma and Ewing's sarcoma. *Curr Opin Pediatr* 2009; **21**: 365-372 [PMID: 19421061 DOI: 10.1097/MOP.0b013e32832b1111]
 - 47 **Kumar R**, Chauhan A, Vellimana AK, Chawla M. Role of PET/PET-CT in the management of sarcomas. *Expert Rev Anticancer Ther* 2006; **6**: 1241-1250 [PMID: 16925490 DOI: 10.1586/14737140.6.8.1241]
 - 48 **Quartuccio N**, Treglia G, Salsano M, Mattoli MV, Muoio B, Piccardo A, Lopci E, Cistaro A. The role of Fluorine-18-Fluorodeoxyglucose positron emission tomography in staging and restaging of patients with osteosarcoma. *Radiol Oncol* 2013; **47**: 97-102 [PMID: 23801904 DOI: 10.2478/raon-2013-0017]
 - 49 **Treglia G**, Salsano M, Stefanelli A, Mattoli MV, Giordano A, Bonomo L. Diagnostic accuracy of ¹⁸F-FDG-PET and PET/CT in patients with Ewing sarcoma family tumours: a systematic review and a meta-analysis. *Skeletal Radiol* 2012; **41**: 249-256 [PMID: 22072239 DOI: 10.1007/s00256-001-1298-9]
 - 50 **McCarville MB**. PET-CT imaging in pediatric oncology. *Cancer Imaging* 2009; **9**: 35-43 [PMID: 19602470 DOI: 10.1102/1470-7330.2009.0008]
 - 51 **Mody RJ**, Bui C, Hutchinson RJ, Yanik GA, Castle VP, Frey KA, Shulkin BL. FDG PET imaging of childhood sarcomas. *Pediatr Blood Cancer* 2010; **54**: 222-227 [PMID: 19890901 DOI: 10.1002/pbc.22307]
 - 52 **Benz MR**, Tchekmedyan N, Eilber FC, Federman N, Czernin J, Tap WD. Utilization of positron emission tomography in the management of patients with sarcoma. *Curr Opin Oncol* 2009; **21**: 345-351 [PMID: 19412096 DOI: 10.1097/CCO.0b013e32832c95e2]
 - 53 **Tateishi U**, Hosono A, Makimoto A, Sakurada A, Terauchi T, Arai Y, Imai Y, Kim EE. Accuracy of 18F fluorodeoxyglucose positron emission tomography/computed tomography in staging of pediatric sarcomas. *J Pediatr Hematol Oncol* 2007; **29**: 608-612 [PMID: 17805034 DOI: 10.1097/MPH.0b013e318142b5ab]
 - 54 **McCarville MB**, Christie R, Daw NC, Spunt SL, Kaste SC. PET/CT in the evaluation of childhood sarcomas. *AJR Am J Roentgenol* 2005; **184**: 1293-1304 [PMID: 15788613 DOI: 10.2214/ajr.184.4.01841293]
 - 55 **Franzius C**, Sciuk J, Daldrup-Link HE, Jürgens H, Schober O. FDG-PET for detection of osseous metastases from malignant primary bone tumours: comparison with bone scintigraphy. *Eur J Nucl Med* 2000; **27**: 1305-1311 [PMID: 11007511 DOI: 10.1007/s002590000301]
 - 56 **Völker T**, Denecke T, Steffen I, Misch D, Schönberger S, Plotkin M, Ruf J, Furth C, Stöver B, Hautzel H, Henze G, Amthauer H. Positron emission tomography for staging of pediatric sarcoma patients: results of a prospective multicenter trial. *J Clin Oncol* 2007; **25**: 5435-5441 [PMID: 18048826 DOI: 10.1200/JCO.2007.12.2473]
 - 57 **Franzius C**, Daldrup-Link HE, Sciuk J, Rummeny EJ, Bielack

- S, Jürgens H, Schober O. FDG-PET for detection of pulmonary metastases from malignant primary bone tumors: comparison with spiral CT. *Ann Oncol* 2001; **12**: 479-486 [PMID: 11398879 DOI: 10.1023/A: 101111322376]
- 58 **Iagaru A**, Chawla S, Menendez L, Conti PS. 18F-FDG PET and PET/CT for detection of pulmonary metastases from musculoskeletal sarcomas. *Nucl Med Commun* 2006; **27**: 795-802 [PMID: 16969262 DOI: 10.1097/01.mnm.0000237986.31597.86]
- 59 **Soret M**, Bacharach SL, Buvat I. Partial-volume effect in PET tumor imaging. *J Nucl Med* 2007; **48**: 932-945 [PMID: 17504879 DOI: 10.2967/jnumed.106.035774]
- 60 **Allen-Auerbach M**, Yeom K, Park J, Phelps M, Czernin J. Standard PET/CT of the chest during shallow breathing is inadequate for comprehensive staging of lung cancer. *J Nucl Med* 2006; **47**: 298-301 [PMID: 16455636]
- 61 **Erdi YE**, Nehmeh SA, Pan T, Pevsner A, Rosenzweig KE, Mageras G, Yorke ED, Schoder H, Hsiao W, Squire OD, Vernon P, Ashman JB, Mostafavi H, Larson SM, Humm JL. The CT motion quantitation of lung lesions and its impact on PET-measured SUVs. *J Nucl Med* 2004; **45**: 1287-1292 [PMID: 15299050]
- 62 **Werner MK**, Parker JA, Kolodny GM, English JR, Palmer MR. Respiratory gating enhances imaging of pulmonary nodules and measurement of tracer uptake in FDG PET/CT. *AJR Am J Roentgenol* 2009; **193**: 1640-1645 [PMID: 19933659 DOI: 10.2214/AJR.09.2516]
- 63 **Biehl KJ**, Kong FM, Dehdashti F, Jin JY, Mutic S, El Naqa I, Siegel BA, Bradley JD. 18F-FDG PET definition of gross tumor volume for radiotherapy of non-small cell lung cancer: is a single standardized uptake value threshold approach appropriate? *J Nucl Med* 2006; **47**: 1808-1812 [PMID: 17079814]
- 64 **Gerth HU**, Juergens KU, Dirksen U, Gerss J, Schober O, Franzius C. Significant benefit of multimodal imaging: PET/CT compared with PET alone in staging and follow-up of patients with Ewing tumors. *J Nucl Med* 2007; **48**: 1932-1939 [PMID: 18006618 DOI: 10.2967/jnumed.107.045286]
- 65 **McCarville MB**, Lederman HM, Santana VM, Daw NC, Shochat SJ, Li CS, Kaufman RA. Distinguishing benign from malignant pulmonary nodules with helical chest CT in children with malignant solid tumors. *Radiology* 2006; **239**: 514-520 [PMID: 16641356 DOI: 10.1148/radiol.2392050631]
- 66 **Johnson GR**, Zhuang H, Khan J, Chiang SB, Alavi A. Roles of positron emission tomography with fluorine-18-deoxyglucose in the detection of local recurrent and distant metastatic sarcoma. *Clin Nucl Med* 2003; **28**: 815-820 [PMID: 14508272 DOI: 10.1097/01.rlu.0000089523.00672.2b]
- 67 **Schwarzbach MH**, Hinz U, Dimitrakopoulou-Strauss A, Willeke F, Cardona S, Mechtshheimer G, Lehnert T, Strauss LG, Herfarth C, Büchler MW. Prognostic significance of preoperative [18-F] fluorodeoxyglucose (FDG) positron emission tomography (PET) imaging in patients with resectable soft tissue sarcomas. *Ann Surg* 2005; **241**: 286-294 [PMID: 15650639 DOI: 10.1097/01.sla.0000152663.61348.6f]
- 68 **Schuetze SM**, Rubin BP, Vernon C, Hawkins DS, Bruckner JD, Conrad EU, Eary JF. Use of positron emission tomography in localized extremity soft tissue sarcoma treated with neoadjuvant chemotherapy. *Cancer* 2005; **103**: 339-348 [PMID: 15578712 DOI: 10.1002/cncr.20769]
- 69 **Hawkins DS**, Schuetze SM, Butrynski JE, Rajendran JG, Vernon CB, Conrad EU, Eary JF. [18F]Fluorodeoxyglucose positron emission tomography predicts outcome for Ewing sarcoma family of tumors. *J Clin Oncol* 2005; **23**: 8828-8834 [PMID: 16314643 DOI: 10.1200/JCO.2005.01.7079]
- 70 **Benz MR**, Czernin J, Allen-Auerbach MS, Tap WD, Dry SM, Elashoff D, Chow K, Evilevitch V, Eckardt JJ, Phelps ME, Weber WA, Eilber FC. FDG-PET/CT imaging predicts histopathologic treatment responses after the initial cycle of neoadjuvant chemotherapy in high-grade soft-tissue sarcomas. *Clin Cancer Res* 2009; **15**: 2856-2863 [PMID: 19351756 DOI: 10.1158/1078-0432.CCR-08-2537]
- 71 **Portwine C**, Marriott C, Barr RD. PET imaging for pediatric oncology: an assessment of the evidence. *Pediatr Blood Cancer* 2010; **55**: 1048-1061 [PMID: 20979168 DOI: 10.1002/pbc.22747]
- 72 **Treglia G**, Taralli S, Bertagna F, Salsano M, Muoio B, Novelis P, Vita ML, Maggi F, Giordano A. Usefulness of whole-body fluorine-18-fluorodeoxyglucose positron emission tomography in patients with neurofibromatosis type 1: a systematic review. *Radiol Res Pract* 2012; **2012**: 431029 [PMID: 22991664 DOI: 10.1155/2012/431029]
- 73 **Tsai LL**, Drubach L, Fahey F, Irons M, Voss S, Ullrich NJ. [18F]-Fluorodeoxyglucose positron emission tomography in children with neurofibromatosis type 1 and plexiform neurofibromas: correlation with malignant transformation. *J Neurooncol* 2012; **108**: 469-475 [PMID: 22407214 DOI: 10.1007/s11060-012-0840-5]
- 74 **Ferner RE**, Gutmann DH. International consensus statement on malignant peripheral nerve sheath tumors in neurofibromatosis. *Cancer Res* 2002; **62**: 1573-1577 [PMID: 11894862]
- 75 **Evans DG**, Baser ME, McLaughran J, Sharif S, Howard E, Moran A. Malignant peripheral nerve sheath tumours in neurofibromatosis 1. *J Med Genet* 2002; **39**: 311-314 [PMID: 12011145 DOI: 10.1136/jmg.39.5.311]
- 76 **Warbey VS**, Ferner RE, Dunn JT, Calonje E, O'Doherty MJ. [18F]FDG PET/CT in the diagnosis of malignant peripheral nerve sheath tumours in neurofibromatosis type-1. *Eur J Nucl Med Mol Imaging* 2009; **36**: 751-757 [PMID: 19142634 DOI: 10.1007/s00259-008-1038-0]
- 77 **Ferner RE**, Golding JF, Smith M, Calonje E, Jan W, Sanjayathnan V, O'Doherty M. [18F]2-fluoro-2-deoxy-D-glucose positron emission tomography (FDG PET) as a diagnostic tool for neurofibromatosis 1 (NF1) associated malignant peripheral nerve sheath tumours (MPNSTs): a long-term clinical study. *Ann Oncol* 2008; **19**: 390-394 [PMID: 17932395 DOI: 10.1093/annonc/mdm450]
- 78 **Brenner W**, Friedrich RE, Gawad KA, Hagel C, von Deimling A, de Wit M, Buchert R, Clausen M, Mautner VF. Prognostic relevance of FDG PET in patients with neurofibromatosis type-1 and malignant peripheral nerve sheath tumours. *Eur J Nucl Med Mol Imaging* 2006; **33**: 428-432 [PMID: 16404595 DOI: 10.1007/s00259-005-0030-1]
- 79 **Bousvaros A**, Kirks DR, Grossman H. Imaging of neuroblastoma: an overview. *Pediatr Radiol* 1986; **16**: 89-106 [PMID: 3513113 DOI: 10.1007/BF02386629]
- 80 **Spix C**, Aareleid T, Stiller C, Magnani C, Kaatsch P, Michaelis J. Survival of children with neuroblastoma. time trends and regional differences in Europe, 1978--1992. *Eur J Cancer* 2001; **37**: 722-729 [PMID: 11311646 DOI: 10.1016/S0959-8049(01)00003-X]
- 81 **Taggart D**, Dubois S, Matthay KK. Radiolabeled metaiodobenzylguanidine for imaging and therapy of neuroblastoma. *Q J Nucl Med Mol Imaging* 2008; **52**: 403-418 [PMID: 19088694]
- 82 **DuBois SG**, Matthay KK. Radiolabeled metaiodobenzylguanidine for the treatment of neuroblastoma. *Nucl Med Biol* 2008; **35** Suppl 1: S35-S48 [PMID: 18707633 DOI: 10.1016/j.nucmedbio.2008.05.002]
- 83 **Boubaker A**, Bischof Delaloye A. MIBG scintigraphy for the diagnosis and follow-up of children with neuroblastoma. *Q J Nucl Med Mol Imaging* 2008; **52**: 388-402 [PMID: 19088693]
- 84 **Claudiani F**, Stimamiglio P, Bertolazzi L, Cabria M, Conte M, Villavecchia GP, Garaventa A, Lanino E, De Bernardi B, Scopinaro G. Radioiodinated meta-iodobenzylguanidine in the diagnosis of childhood neuroblastoma. *Q J Nucl Med* 1995; **39**: 21-24 [PMID: 9002744]
- 85 **Gelfand MJ**. Meta-iodobenzylguanidine in children. *Semin Nucl Med* 1993; **23**: 231-242 [PMID: 8378796 DOI: 10.1016/S0001-2998(05)80104-7]
- 86 **Troncone L**, Rufini V, Montemaggi P, Danza FM, Lasorella

- A, Mastrangelo R. The diagnostic and therapeutic utility of radioiodinated metaiodobenzylguanidine (MIBG). 5 years of experience. *Eur J Nucl Med* 1990; **16**: 325-335 [PMID: 2351179 DOI: 10.1007/BF00842788]
- 87 **Shulkin BL**, Shapiro B. Current concepts on the diagnostic use of MIBG in children. *J Nucl Med* 1998; **39**: 679-688 [PMID: 9544682]
- 88 **Biasotti S**, Garaventa A, Villavecchia GP, Cabria M, Nantron M, De Bernardi B. False-negative metaiodobenzylguanidine scintigraphy at diagnosis of neuroblastoma. *Med Pediatr Oncol* 2000; **35**: 153-155 [PMID: 10918246 DOI: 10.1002/1096-911X(200008)35:2<153::AID-MPO18>3.0.CO;2-7]
- 89 **Mueller WP**, Coppenrath E, Pfluger T. Nuclear medicine and multimodality imaging of pediatric neuroblastoma. *Pediatr Radiol* 2013; **43**: 418-427 [PMID: 23151727 DOI: 10.1007/s00247-012-2512-1]
- 90 **Shulkin BL**, Hutchinson RJ, Castle VP, Yanik GA, Shapiro B, Sisson JC. Neuroblastoma: positron emission tomography with 2-[fluorine-18]-fluoro-2-deoxy-D-glucose compared with metaiodobenzylguanidine scintigraphy. *Radiology* 1996; **199**: 743-750 [PMID: 8637999]
- 91 **Kushner BH**, Yeung HW, Larson SM, Kramer K, Cheung NK. Extending positron emission tomography scan utility to high-risk neuroblastoma: fluorine-18 fluorodeoxyglucose positron emission tomography as sole imaging modality in follow-up of patients. *J Clin Oncol* 2001; **19**: 3397-3405 [PMID: 11454888]
- 92 **Sharp SE**, Shulkin BL, Gelfand MJ, Salisbury S, Furman WL. 123I-MIBG scintigraphy and 18F-FDG PET in neuroblastoma. *J Nucl Med* 2009; **50**: 1237-1243 [PMID: 19617326 DOI: 10.2967/jnumed.108.060467]
- 93 **Melzer HI**, Coppenrath E, Schmid I, Albert MH, von Schweinitz D, Tudball C, Bartenstein P, Pfluger T. ¹²³I-MIBG scintigraphy/SPECT versus ¹⁸F-FDG PET in paediatric neuroblastoma. *Eur J Nucl Med Mol Imaging* 2011; **38**: 1648-1658 [PMID: 21617976 DOI: 10.1007/s00259-011-1843-8]
- 94 **Piccardo A**, Lopci E, Conte M, Garaventa A, Foppiani L, Altrinetti V, Nanni C, Bianchi P, Cistaro A, Sorrentino S, Cabria M, Pession A, Puntoni M, Villavecchia G, Fanti S. Comparison of 18F-dopa PET/CT and 123I-MIBG scintigraphy in stage 3 and 4 neuroblastoma: a pilot study. *Eur J Nucl Med Mol Imaging* 2012; **39**: 57-71 [PMID: 21932116 DOI: 10.1007/s00259-011-1938-2]
- 95 **Gains JE**, Bomanji JB, Fersht NL, Sullivan T, D'Souza D, Sullivan KP, Aldridge M, Waddington W, Gaze MN. ¹⁷⁷Lu-DOTATATE molecular radiotherapy for childhood neuroblastoma. *J Nucl Med* 2011; **52**: 1041-1047 [PMID: 21680680 DOI: 10.2967/jnumed.110.085100]
- 96 **Swinson S**, McHugh K. Urogenital tumours in childhood. *Cancer Imaging* 2011; **11** Spec No A: S48-S64 [PMID: 22187115 DOI: 10.1102/1470-7330.2011.9009]
- 97 **Md Zin R**, Murch A, Charles A. Pathology, genetics and cytogenetics of Wilms' tumour. *Pathology* 2011; **43**: 302-312 [PMID: 21516053 DOI: 10.1097/PAT.0b013e3283463575]
- 98 **Geller E**, Kochan PS. Renal neoplasms of childhood. *Radiol Clin North Am* 2011; **49**: 689-709, vi [PMID: 21807169 DOI: 10.1016/j.rcl.2011.05.003]
- 99 **Buckley KS**. Pediatric genitourinary tumors. *Curr Opin Oncol* 2012; **24**: 291-296 [PMID: 22476187 DOI: 10.1097/CCO.0b013e32835265c9]
- 100 **Misch D**, Steffen IG, Schönberger S, Voelker T, Furth C, Stöver B, Hautzel H, Henze G, Amthauer H, Denecke T. Use of positron emission tomography for staging, preoperative response assessment and posttherapeutic evaluation in children with Wilms tumour. *Eur J Nucl Med Mol Imaging* 2008; **35**: 1642-1650 [PMID: 18509634 DOI: 10.1007/s00259-008-0819-9]
- 101 **Moinul Hossain AK**, Shulkin BL, Gelfand MJ, Bashir H, Daw NC, Sharp SE, Nadel HR, Dome JS. FDG positron emission tomography/computed tomography studies of Wilms' tumor. *Eur J Nucl Med Mol Imaging* 2010; **37**: 1300-1308 [PMID: 20204356 DOI: 10.1007/s00259-010-1396-2]
- 102 **Begent J**, Sebire NJ, Levitt G, Brock P, Jones KP, Ell P, Gordon I, Anderson J. Pilot study of F(18)-Fluorodeoxyglucose Positron Emission Tomography/computerised tomography in Wilms' tumour: correlation with conventional imaging, pathology and immunohistochemistry. *Eur J Cancer* 2011; **47**: 389-396 [PMID: 21074411 DOI: 10.1019/j.ejca.2010.09.039]
- 103 **Azouz EM**, Saigal G, Rodriguez MM, Podda A. Langerhans' cell histiocytosis: pathology, imaging and treatment of skeletal involvement. *Pediatr Radiol* 2005; **35**: 103-115 [PMID: 15289942 DOI: 10.1007/s00247-004-1262-0]
- 104 **Abla O**, Egeler RM, Weitzman S. Langerhans cell histiocytosis: Current concepts and treatments. *Cancer Treat Rev* 2010; **36**: 354-359 [PMID: 20188480 DOI: 10.1016/j.ctrv.2010.02.012]
- 105 **Dogan AS**, Conway JJ, Miller JH, Grier D, Bhattathiry MM, Mitchell CS. Detection of bone lesions in Langerhans cell histiocytosis: complementary roles of scintigraphy and conventional radiography. *J Pediatr Hematol Oncol* 1996; **18**: 51-58 [PMID: 8556371 DOI: 10.1097/00043426-199602000-00010]
- 106 **Phillips M**, Allen C, Gerson P, McClain K. Comparison of FDG-PET scans to conventional radiography and bone scans in management of Langerhans cell histiocytosis. *Pediatr Blood Cancer* 2009; **52**: 97-101 [PMID: 18951435 DOI: 10.1002/pbc.21782]
- 107 **Kaste SC**, Rodriguez-Galindo C, McCarville ME, Shulkin BL. PET-CT in pediatric Langerhans cell histiocytosis. *Pediatr Radiol* 2007; **37**: 615-622 [PMID: 17564738 DOI: 10.1007/s00247-007-0467-4]
- 108 **Blum R**, Seymour JF, Hicks RJ. Role of 18FDG-positron emission tomography scanning in the management of histiocytosis. *Leuk Lymphoma* 2002; **43**: 2155-2157 [PMID: 12533041 DOI: 10.1080/1042819021000032908]
- 109 **Binkovitz LA**, Olshefski RS, Adler BH. Coincidence FDG-PET in the evaluation of Langerhans' cell histiocytosis: preliminary findings. *Pediatr Radiol* 2003; **33**: 598-602 [PMID: 12879314 DOI: 10.1007/s00247-003-0943-4]
- 110 **Lee HJ**, Ahn BC, Lee SW, Lee J. The usefulness of F-18 fluorodeoxyglucose positron emission tomography/computed tomography in patients with Langerhans cell histiocytosis. *Ann Nucl Med* 2012; **26**: 730-737 [PMID: 22797842 DOI: 10.1007/s12149-012-0635-y]
- 111 **Mueller WP**, Melzer HI, Schmid I, Coppenrath E, Bartenstein P, Pfluger T. The diagnostic value of 18F-FDG PET and MRI in paediatric histiocytosis. *Eur J Nucl Med Mol Imaging* 2013; **40**: 356-363 [PMID: 23096080 DOI: 10.1007/s00259-012-2278-6]
- 112 **Kaste SC**. Issues specific to implementing PET-CT for pediatric oncology: what we have learned along the way. *Pediatr Radiol* 2004; **34**: 205-213 [PMID: 14745525 DOI: 10.1007/s00247-003-1111-6]
- 113 **Roberts EG**, Shulkin BL. Technical issues in performing PET studies in pediatric patients. *J Nucl Med Technol* 2004; **32**: 5-9; quiz 10-1 [PMID: 14990667]
- 114 **Franzius C**, Juergens KU, Schober O. Is PET/CT necessary in paediatric oncology? For. *Eur J Nucl Med Mol Imaging* 2006; **33**: 960-965 [PMID: 16830120]
- 115 **Sanborn PA**, Michna E, Zurakowski D, Burrows PE, Fontaine PJ, Connor L, Mason KP. Adverse cardiovascular and respiratory events during sedation of pediatric patients for imaging examinations. *Radiology* 2005; **237**: 288-294 [PMID: 16183936 DOI: 10.1148/radiol.2371041415]
- 116 **Weiss S**. Sedation of pediatric patients for nuclear medicine procedures. *Semin Nucl Med* 1993; **23**: 190-198 [PMID: 8378793 DOI: 10.1016/S0001-2998(05)80101-1]
- 117 **Pintelon H**, Dejonckheere M, Piepsz A. Pediatric nuclear medicine: a practical approach. *Q J Nucl Med* 1997; **41**: 263-268 [PMID: 9542417]
- 118 **Hany TF**, Gharehpapagh E, Kamel EM, Buck A, Himms-Ha-

- gen J, von Schulthess GK. Brown adipose tissue: a factor to consider in symmetrical tracer uptake in the neck and upper chest region. *Eur J Nucl Med Mol Imaging* 2002; **29**: 1393-1398 [PMID: 12271425 DOI: 10.1007/s00259-002-0902-6]
- 119 **Yeung HW**, Grewal RK, Gonen M, Schöder H, Larson SM. Patterns of (18)F-FDG uptake in adipose tissue and muscle: a potential source of false-positives for PET. *J Nucl Med* 2003; **44**: 1789-1796 [PMID: 14602861]
- 120 **Brink I**, Reinhardt MJ, Hoegerle S, Althoefer C, Moser E, Nitzsche EU. Increased metabolic activity in the thymus gland studied with 18F-FDG PET: age dependency and frequency after chemotherapy. *J Nucl Med* 2001; **42**: 591-595 [PMID: 11337547]
- 121 **London K**, Howman-Giles R. Normal cerebral FDG uptake during childhood. *Eur J Nucl Med Mol Imaging* 2014; **41**: 723-735 [PMID: 24323306 DOI: 10.1007/s00259-013-2639-9]
- 122 **Goodin GS**, Shulkin BL, Kaufman RA, McCarville MB. PET/CT characterization of fibrous defects in children: 18F-FDG uptake can mimic metastatic disease. *AJR Am J Roentgenol* 2006; **187**: 1124-1128 [PMID: 16985165 DOI: 10.2214/AJR.06.0171]
- 123 **Shammas A**, Lim R, Charron M. Pediatric FDG PET/CT: physiologic uptake, normal variants, and benign conditions. *Radiographics* 2009; **29**: 1467-1486 [PMID: 19755606 DOI: 10.1148/rg.295085247]
- 124 **Hong TS**, Shammas A, Charron M, Zukotynski KA, Drubach LA, Lim R. Brown adipose tissue 18F-FDG uptake in pediatric PET/CT imaging. *Pediatr Radiol* 2011; **41**: 759-768 [PMID: 21161205 DOI: 10.1007/s00247-010-1925-y]
- 125 **Himms-Hagen J**. Brown adipose tissue thermogenesis: interdisciplinary studies. *FASEB J* 1990; **4**: 2890-2898 [PMID: 2199286]
- 126 **Del Mar Gonzalez-Barroso M**, Ricquier D, Cassard-Doulcier AM. The human uncoupling protein-1 gene (UCP1): present status and perspectives in obesity research. *Obes Rev* 2000; **1**: 61-72 [PMID: 12119988 DOI: 10.1046/j.1467-789x.2000.00009.x]
- 127 **Truong MT**, Erasmus JJ, Munden RF, Marom EM, Sabloff BS, Gladish GW, Podoloff DA, Macapinlac HA. Focal FDG uptake in mediastinal brown fat mimicking malignancy: a potential pitfall resolved on PET/CT. *AJR Am J Roentgenol* 2004; **183**: 1127-1132 [PMID: 15385319 DOI: 10.2214/ajr.183.4.1831127]
- 128 **Garcia C**, Bandaru V, Van Nostrand D, Chennupati S, Atkins F, Acio E, Kulkarni K, Majd M. Effective reduction of brown fat FDG uptake by controlling environmental temperature prior to PET scan: an expanded case series. *Mol Imaging Biol* 2010; **12**: 652-656 [PMID: 20237858 DOI: 10.1007/s11307-010-0298-9]
- 129 **Barrington SF**, Maisey MN. Skeletal muscle uptake of fluorine-18-FDG: effect of oral diazepam. *J Nucl Med* 1996; **37**: 1127-1129 [PMID: 8965182]
- 130 **Parysow O**, Mollerach AM, Jager V, Racioppi S, San Roman J, Gerbaudo VH. Low-dose oral propranolol could reduce brown adipose tissue F-18 FDG uptake in patients undergoing PET scans. *Clin Nucl Med* 2007; **32**: 351-357 [PMID: 17452860 DOI: 10.1097/01.rlu.0000259570.69163.04]
- 131 **Gelfand MJ**, O'hara SM, Curtwright LA, Maclean JR. Pre-medication to block [(18)F]FDG uptake in the brown adipose tissue of pediatric and adolescent patients. *Pediatr Radiol* 2005; **35**: 984-990 [PMID: 15988582 DOI: 10.1007/s00247-005-1505-8]
- 132 **Nakahara T**, Fujii H, Ide M, Nishiumi N, Takahashi W, Yasuda S, Shohtsu A, Kubo A. FDG uptake in the morphologically normal thymus: comparison of FDG positron emission tomography and CT. *Br J Radiol* 2001; **74**: 821-824 [PMID: 11560830]
- 133 **Gawande RS**, Khurana A, Messing S, Zhang D, Castañeda RT, Goldsby RE, Hawkins RA, Daldrup-Link HE. Differentiation of normal thymus from anterior mediastinal lymphoma and lymphoma recurrence at pediatric PET/CT. *Radiology* 2012; **262**: 613-622 [PMID: 22157202 DOI: 10.1148/radiol.11110715]
- 134 **Brenner D**, Elliston C, Hall E, Berdon W. Estimated risks of radiation-induced fatal cancer from pediatric CT. *AJR Am J Roentgenol* 2001; **176**: 289-296 [PMID: 11159059 DOI: 10.2214/ajr.176.2.1760289]
- 135 **Pierce DA**, Shimizu Y, Preston DL, Vaeth M, Mabuchi K. Studies of the mortality of atomic bomb survivors. Report 12, Part I. Cancer: 1950-1990. *Radiat Res* 1996; **146**: 1-27 [PMID: 8677290 DOI: 10.2307/3579391]
- 136 **Brenner DJ**. Estimating cancer risks from pediatric CT: going from the qualitative to the quantitative. *Pediatr Radiol* 2002; **32**: 228-231; discussion 228-231 [PMID: 11956700 DOI: 10.1007/s00247-002-0671-1]
- 137 **Gelfand MJ**. Dose reduction in pediatric hybrid and planar imaging. *Q J Nucl Med Mol Imaging* 2010; **54**: 379-388 [PMID: 20823806]
- 138 **Kaste SC**. PET-CT in children: where is it appropriate? *Pediatr Radiol* 2011; **41** Suppl 2: 509-513 [PMID: 21847731 DOI: 10.1007/s00247-011-2096-1]
- 139 **Stabin MG**, Gelfand MJ. Dosimetry of pediatric nuclear medicine procedures. *Q J Nucl Med* 1998; **42**: 93-112 [PMID: 9695662]
- 140 **Lassmann M**, Biassoni L, Monsieurs M, Franzius C, Jacobs F, EANM Dosimetry and Paediatrics Committees. The new EANM paediatric dosage card. *Eur J Nucl Med Mol Imaging* 2007; **34**: 796-798 [PMID: 17406866 DOI: 10.1007/s00259-007-0370-0]
- 141 **Lassmann M**, Biassoni L, Monsieurs M, Franzius C, EANM Dosimetry and Paediatrics Committees. The new EANM paediatric dosage card: additional notes with respect to F-18. *Eur J Nucl Med Mol Imaging* 2008; **35**: 1666-1668 [PMID: 18574583 DOI: 10.1007/s00259-008-0799-9]
- 142 **Gelfand MJ**, Parisi MT, Treves ST; Pediatric Nuclear Medicine Dose Reduction Workgroup. Pediatric radiopharmaceutical administered doses: 2010 North American consensus guidelines. *J Nucl Med* 2011; **52**: 318-322 [PMID: 21233182 DOI: 10.2967/jnumed.110.084327]
- 143 **Gelfand MJ**, Lemen LC. PET/CT and SPECT/CT dosimetry in children: the challenge to the pediatric imager. *Semin Nucl Med* 2007; **37**: 391-398 [PMID: 17707244 DOI: 10.1053/j.semnuclmed.2007.05.002]

P- Reviewer: Brasic JR, Cheng Z, Morbelli SD, Muller HW, Storto G, Treglia G **S- Editor:** Song XX **L- Editor:** A **E- Editor:** Lu YJ



Quantitative magnetic resonance imaging of the fetal brain in utero: Methods and applications

Anat Biegon, Chen Hoffmann

Anat Biegon, Department of Neurology and Radiology, School of Medicine, Stony Brook University, Stony Brook, NY 11794-2565, United States

Chen Hoffmann, Department of Diagnostic Imaging, Sheba Health Center, Ramat Gan 52622, Israel

Author contributions: Biegon A and Hoffmann C solely contributed to this paper.

Correspondence to: Anat Biegon, PhD, Professor of Neurology and Radiology, School of Medicine, Stony Brook University, 100 Nicols Rd, Stony Brook, NY 11794-2565,

United States. anat.biegon@stonybrook.edu

Telephone: +1-631-6326228 Fax: +1-631-6326294

Received: February 9, 2014 Revised: April 24, 2014

Accepted: June 10, 2014

Published online: March 28, 2015

Abstract

Application of modern magnetic resonance imaging (MRI) techniques to the live fetus in utero is a relatively recent endeavor. The relative advantages and disadvantages of clinical MRI relative to the widely used and accepted ultrasonographic approach are the subject of a continuing debate; however the focus of this review is on the even younger field of quantitative MRI as applied to non-invasive studies of fetal brain development. The techniques covered under this header include structural MRI when followed by quantitative (*e.g.*, volumetric) analysis, as well as quantitative analyses of diffusion weighted imaging, diffusion tensor imaging, magnetic resonance spectroscopy and functional MRI. The majority of the published work reviewed here reflects information gathered from normal fetuses scanned during the 3rd trimester, with relatively smaller number of studies of pathological samples including common congenital pathologies such as ventriculomegaly and viral infection.

© 2015 Baishideng Publishing Group Inc. All rights reserved.

Key words: Fetal brain; Fetal magnetic resonance imaging;

Fetal magnetic resonance spectroscopy; Fetal apparent diffusion coefficients; Fetal functional magnetic resonance imaging; Cortical development

Core tip: This review focuses on the budding field of quantitative magnetic resonance imaging and studies of the fetal brain designed to establish normative databases relevant to regional brain growth, connectivity and function and their application to a deeper understanding of the etiology, diagnosis and prognosis of fetal brain pathologies.

Original sources: Biegon A, Hoffmann C. Quantitative magnetic resonance imaging of the fetal brain in utero: Methods and applications. *World J Radiol* 2014; 6(8): 523-529 Available from: URL: <http://www.wjgnet.com/1949-8470/full/v6/i8/523.htm> DOI: <http://dx.doi.org/10.4329/wjr.v6.i8.523>

INTRODUCTION

The history of fetal magnetic resonance imaging (MRI) in utero spans more than 3 decades, beginning with clinically driven T1 and T2 weighted studies at relatively low magnetic field published in the 1980s^[1-4]. This was followed by early echo planar imaging of fetal brains attempted in the early 1990s^[5,6]. Throughout this period, the mainstay of fetal imaging for all organ systems has been ultrasound, but the better contrast resolution of MRI relative to ultrasound made it especially attractive for studies of the central nervous system (CNS), which is relatively vulnerable to congenital anomalies. Progressive improvements in imaging hardware and software, resulting in shortened scan times and increasingly wider choice of imaging sequences, have made fetal brain MRI an increasingly valuable imaging tool in cases with uncertain diagnosis of CNS abnormalities^[7,8].

The biggest problem in acquiring reliable, reproducible and comprehensive MRI images of the fetal brain

has been motion. Early studies attempted to overcome this problem by sedation of mother and/or fetus^[9] although this approach has obviously limited the widespread use of the technique in clinical and research settings. The breakthrough came with the development of faster imaging techniques and sophisticated methods for motion correction^[10-16]. The Ultrafast sequences which have been developed, including single shot fast spin echo, fast spin echo and the half fourier single shot turbo spin echo require a second or less per slice acquisition. In these studies multiple stacks of slices are acquired at different orthogonal orientations, providing a comprehensive view of the anatomy while allowing for manual adjustment to fetal motion or gating to maternal breathing. The most recent and ongoing developments in image reconstruction and motion correction methods^[17-20] have enabled the adoption of all major MR approaches currently used in adults to in utero studies; including diffusion weighted imaging, tractography and MR spectroscopy^[21-26] consequently enabling the gathering of unprecedented amounts of information on fetal brain development in utero.

This review focuses on the budding field of quantitative MRI and studies of the fetal brain aiming at the establishment of normative databases relevant to normal regional brain growth, connectivity and function and their application to a deeper understanding of the etiology, diagnosis and prognosis of fetal brain pathologies.

QUANTITATIVE MRI IN THE STUDY OF NORMAL FETAL BRAIN DEVELOPMENT

Mapping regional and local patterns of normal fetal brain growth

An early study using the Cavalieri method to estimate whole brain volumes in a small cohort ($n = 18$) of third trimester fetuses^[27] described a linear relationship between gestational age and whole brain volume, with a growth rate averaging 2.3 mL/d. The first study to measure volume changes in brain hemispheric parenchyma, cerebellum and ventricles of 27 normal, third trimester fetal brains^[28] revealed different, non-linear growth trajectories for the three compartments, with a faster growth of cerebral hemispheres relative to cerebellum and a steady decrease in the ventricular/parenchymal volume with increasing gestational age. Subsequent work by Ghilipour *et al.*^[29] using supervised automated segmentation of brain volumes in fetuses aged 19 to 37 wk compared linear and non linear models and concluded that a quadratic model provided the best fit to the data describing the changes of fetal brain volume with gestational age. Hu *et al.*^[30] also confirmed that the growth rates of the cerebral volumes are region-dependent, with the frontal and parieto-temporal regions growing significantly faster than other regions. More recent studies have added substantial amount of detail on normal fetal brain growth, with the publication of a spatiotemporal atlas of MR intensity, tissue probability and shape of the fetal brain^[31]

and detailed descriptions of the growth of the fetal subplate and other regions^[32,33]. Corbett-Detig *et al.*^[32] examined subplate growth in relatively young (18-24 wk old) fetuses and found that the occipital pole, ventral occipito-temporal region, and planum temporale underwent the most statistically significant increases in subplate thickness, while the thickest region during this period was the developing somatosensory/motor cortex.

A more detailed study of volumetric changes in the growing fetal brain was published by Scott *et al.*^[33] examining volumes of cortical plate, subplate and intermediate zone, germinal matrix, deep gray nuclei, and ventricles from automatic segmentation of motion-corrected, 3D reconstructed MRI scans from 39 normally developing fetuses at gestational age (GA) ranging from 21 to 31. The findings again show region-specific growth trajectories, with the cortical plate having the highest growth rate (18%/wk).

The supratentorial volume, subplate and intermediate zone, germinal matrix and deep gray nuclei exhibited similar growth rates of approximately 15%/wk while the slowest growth rate was found for ventricles (9.2%/wk). Interestingly, the authors did not find sex differences or asymmetries in hemispheric volumes. This could be a group size/power issue but may also indicate that such difference only emerge later in brain development.

Quantitative studies of cortical folding

Hu *et al.*^[34] provided a regional quantification of cortical shape development from a group of normal fetuses in the gestational age range of 22-33 wk. They report faster shape changes in the occipital lobe than in other regions and conserved patterns of shape changes in gyri and sulci, whereby the gyral surface smoothens, while the sulcal surface becomes more angular, with gestational age. In addition, the authors report that smoothing of gyri is related mainly to the changes in shape of gyral crowns.

Clouchoux *et al.*^[35] examined *in vivo* fetal cortical folding patterns in healthy fetuses between 25 and 35 wk gestation, providing an explicit delineation of the sulcal pattern as well as surface area and gyrification index. The findings suggest an exuberant third trimester gyrification process and a non-linear evolution of sulcal development.

Employing a younger group (GA 20-28 wk) of fetuses, Habas *et al.*^[36] and Rajagopalan *et al.*^[37] have been able to detect early folding patterns and asymmetries in fetal brain development. Their Tensor based morphometry results show that fetal brain development exhibits a distinct spatial pattern of anisotropic growth, with the most significant changes in the directionality of growth occurring in the cortical plate at major sulci. The authors also report significant directional growth asymmetry in the peri-sylvian region and the medial frontal lobe of the fetal brain.

Studies of water diffusion in the normal developing brain

Regional differences and developmental changes in appar-

ent diffusion coefficients (ADC) have been the subject of several studies conducted and published during the last decade^[23,38-47]. All of the published studies report absolute values for ADC in a similar range and detect a trend towards a reduction in ADC with increased GA, which could be explained by progressive myelination. However, the relationship between ADC and GA appears to be region-dependent and non-linear. Thus, whether a specific study reports on significant changes of ADC with GA appears to depend on the range of developmental ages and regions included in the analysis. To illustrate, Righini *et al.*^[38] reported a mean ADC value of 1.96 ± 0.1 microm²/ms (SD) in frontal white matter, 1.95 ± 0.1 microm²/ms in occipital white matter, and 1.56 ± 0.1 microm²/ms in basal ganglia of fetuses aged 22-35 wk, with a significant negative correlation between ADC and gestational age for basal ganglia, and only a trend for frontal white matter. A subsequent study by another group involving fetuses between 31 and 37 wk gestation^[39] reported mean ADC values of 1.8 microm²/ms in the centrum semiovale, 1.2 microm²/ms in the splenium of the corpus callosum and 1.1 microm²/ms in the pyramidal tract, with mean fractional anisotropy (FA) values of 1.1%, 3.8% and 4.7%, respectively. The authors report a significant age-related decrease in ADC and an increase in FA in the pyramidal tract and corpus callosum. Manganaro *et al.*^[40] measured ADC in the grey matter, reporting mean ADC values from 1.76×10^{-3} mm²/s (at week 19) to 0.89×10^{-3} mm²/s (at week 37), whereas in the white matter, the values varied from 2.03×10^{-3} mm²/s (at week 19) to 1.25×10^{-3} mm²/s (at week 37). Cartry *et al.*^[42] reported a linear inverse correlation existed between ADC values and gestational age only in the occipital lobes of 22 normal fetuses scanned between 30 and 34 wk gestation. This theme of region-dependent developmental changes in ADC is reiterated in the largest and most recent study of this kind, where Boyer *et al.*^[43] described a study of 50 normal fetuses between 19 and 37 wk gestation. The authors report that ADC values remained constant in the basal ganglia, frontal, parietal, temporal and occipital white matter and in the centrum semiovale while significant decreases were observed in the cerebellum, pons and thalamus with advancing menstrual age.

Development of regional connectivity

Tractography presents a bigger challenge for in utero fetal imaging relative to other techniques since acquisition times are longer and therefore studies are more susceptible to motion artifacts^[21-23]. Consequently, only a few recent studies provide quantitative data from in utero studies of neuronal pathways. Kasprian *et al.*^[23] examined a group of fetuses ranging in age from 18 to 37 wk and reported that only in 40% of examined fetuses, diffusion tensor imaging measurements were robust enough to successfully calculate and visualize bilateral, craniocaudally oriented (mainly sensorimotor), and callosal trajectories in utero. However, the successful studies resulted in a wealth of quantitative information on fiber lengths, ADC, FA, and eigenvalues at different anatomically defined areas.

FA values and the axial eigenvalue [$\lambda(1)$] showed a characteristic distribution, with the highest values for the splenium, followed by the genu, the right and the left posterior limb of the internal capsule. Intriguing evidence for early asymmetry was also obtained, showing that the right-sided sensorimotor trajectories were significantly longer than on the left side, reflecting higher right-sided $\lambda(1)$ values.

A more recent publications from the same group^[44] reports on successful visualization and delineation of sensorimotor tracts and the corpus callosum as well as smaller fiber bundles, separating the internal capsule fibers into thalamocortical fibers, corticopontine and corticospinal tracts and segregating the thalamocortical fiber system to anterior, superior and posterior radiations. Association fiber tracts connecting ipsilateral cortical areas were also successfully visualized.

Development of brain chemistry using MR spectroscopy

Development of the normal fetal brain in utero using MR spectroscopy (MRS) has been studied by a number of groups. The size of the voxel necessary to acquire reliable information limits the possibility of regional measurements, so these studies mostly reflect whole brain maturation. With this caveat, levels of choline (Cho), creatine (Cr), myo-inositol (Myo-ins) and N-acetyl aspartate (NAA) have been measured in utero in fetuses in the age range of 22 to 41 wk^[26,45-48]. Kok *et al.*^[45] found no change in the absolute level of Cr using an echo time of 135 ms with 35 fetuses between 30 and 41 wk. In a later study^[46], the group reported absolute tissue levels of these metabolites resemble values measured in preterm and term babies, especially of relatively more mature brain regions, from which most of the MR spectra have been obtained. Brain maturation between 30 and 41 wk of gestation was most clearly reflected by increasing levels of the neuronal marker NAA. Subsequent studies by Girard *et al.*^[47,48] confirmed that by 34 wk the fetal brain spectrum is comparable to that of a term born neonate, with dominant resonances of Cho, Cr and NAA at a long echo time and Myo-ins, Cho, Cr and NAA dominant resonances at a short echo time. The authors further report that creatine and phosphocreatine, compounds involved in energy metabolism, both contribute to the Cr peak. In a study of 58 fetuses with a gestational age range of 22-39 wk, the authors reported that Cr levels increased in the fetal brain with increasing gestational age. However, this was only found at a short echo time (30 ms) and not at a longer echo time (135 ms).

Imaging developing brain function: Functional MRI

The feasibility of studying fetal brain activity with functional MRI was demonstrated by Hykin *et al.*^[49] just before the turn of the century, reporting on responses to maternal speech. This was followed by additional studies reporting the detection of responses to visual^[50] and various auditory^[51-54] stimuli, which were detected between 33 and 34 wk of gestation. Functional connectivity (FC)

at rest was subsequently investigated by Schöpf *et al*^[55] in fetuses from 20 to 36 gestational weeks of age. The authors report a bilateral occipital network and medial and lateral prefrontal activity pattern that involved the future Brodmann areas 9-11 and a hemispheric lateralized network that involved the superior temporal cortical regions (Brodmann areas 22 and 39). Frequency oscillations were in the range of 0.01-0.06 Hz for all networks. Thomason *et al*^[56] studied 25 healthy human fetuses in the second and third trimesters of pregnancy (24 to 38 wk of gestation) and reported the presence of bilateral fetal brain FC as well as regional and age-related variation in the strength of FC between homologous cortical brain regions, which increased with advancing gestational age. The authors also observed medial to lateral gradients in fetal functional brain connectivity. Sørensen *et al*^[57] examined the fetal blood oxygen level dependent response to maternal hyperoxia, demonstrating an increased oxygenation in a number of human fetal organs while oxygenation of the fetal brain remained constant. These studies, together with findings from other modalities like fetal electroencephalography and magnetoencephalography^[58] are truly revolutionary since unlike information on maturation of brain morphology and microstructure/chemistry which can be obtained postmortem, the development of function can only be studied *in vivo*.

QUANTITATIVE MRI IN THE STUDY OF FETAL BRAIN PATHOLOGY

Fetal ventriculomegaly/hydrocephalus

The first quantitative MRI studies in ventriculomegaly (VM) employed magnetic resonance spectroscopy^[59,60]. Kok *et al*^[59] performed ¹H MRS of the brain in 10 fetuses with ventricular dilatation and 36 normal fetuses between 28 and 37 wk and found that the inositol:Cr ratio was significantly lower in fetuses with hydrocephalus. Roelants-van Rijn *et al*^[60] examined the brain of six fetuses with ventricular dilation and were able to detect the presence of Lactate (Lac) in two of the six fetuses, two had no Lac and two spectra were un-interpretable due to contaminating lipid peaks.

The first study applying quantitative MRI to the comparison of ventricular and parenchymal volumes in cases referred because of VM and normal controls revealed that fetal VM is not associated with decreases in parenchymal volume^[28]. Using conventional T1- and T2-weighted imaging, Erdem *et al*^[61] also found that hydrocephalic fetuses had a normal signal pattern in cerebral parenchyma, but their ADC values, derived from diffusion weighted imaging, were significantly lower than those reported for fetuses with normal brain. The largest volumetric study of VM published to date^[62], which included postnatal outcomes in more than 300 fetuses, revealed that ventricular, but not parenchymal, volume was a significant predictor of live birth. The association was stronger in isolated VM relative to VM with other anomalies present. Most recently, the absence of changes

in parenchymal volume was confirmed in a cohort of mild isolated VM using motion-corrected 3D reconstruction and automatic segmentation^[63].

Congenital cytomegalo virus infection

A recently published study^[64] examined the maturation of hemispheric and temporal lobe volumes in 27 congenital cytomegalo virus (CMV) infected fetuses relative to GA-matched normal controls, all scanned during the third trimester. Temporal lobe volumes, normalized to whole brain and co-varied with gestational age; were significantly smaller in fetuses infected with CMV compared to uninfected fetuses. Furthermore, Infection during the 1st and 2nd trimester had a more pronounced effect than infection during the 3rd trimester. While Infected fetuses with no MRI findings had significantly lower temporal lobe/whole brain ratios than controls, the lowest temporal lobe/forebrain ratios were observed in fetuses with CMV as well as overt findings such as cysts or gray matter heterotopy. These findings suggest a regional vulnerability to maternal immune activation in the fetal brain, although the relationship between the results and neurological outcome still needs to be established.

Congenital heart disease

Limperopoulos *et al*^[65] compared brain volume and metabolism in 55 fetuses with Congenital heart disease (CHD) and 50 normal fetuses (gestational age range 25-37 wk) with the use of 3-dimensional volumetric MRI and proton MRS. they found progressive and significant declines in gestational age-adjusted total brain volume and intracranial cavity volume in CHD fetuses relative to controls, as well as a significantly slower increase in the NAA:Cho ratio. Predictors of lower NAA:Cho included diagnosis, absence of antegrade aortic arch flow, and evidence of cerebral lactate. In a subsequent study^[66] of 18 fetuses with hypoplastic left heart syndrome (HLHS, a severe form of congenital heart disease) and 30 control fetuses in the same age range, the authors found a progressive fall-off in cortical gray and white matter volumes as well as subcortical gray matter in fetuses with HLHS. These fetuses also showed significant delays in cortical gyrification, whereby local cortical folding delays were detected as early as 25 wk in the frontal, parietal, calcarine, temporal, and collateral regions and appeared to precede volumetric brain growth disturbances.

Intrauterine growth restriction

Quantitative studies of fetal organ growth in intrauterine growth restriction (IUGR) confirmed the expected relative sparing of the brain. Damodaram *et al*^[67] measured peripheral organs and brain volumes in 20 growth restricted and 19 normal fetuses scanned at gestational age 21-37 wk and found a significant reduction in fetal whole body volume and volume of all internal organs except the brain. A brain:liver ratio above 3.0 was associated with a 3.3 fold increase in risk of perinatal mortality. Interestingly, an MRS study^[68] detected a lactate peak in the brain of the

most severely affected IUGR fetus which was consistent with low oxygen content and high lactic acid concentration in umbilical blood obtained at delivery.

Ischemic stroke

The likelihood of detecting acute hypoxic-ischemic brain lesions by prenatal magnetic resonance imaging is small. However, a published case study^[69] reports on a fetus with a vein of Galen arteriovenous malformation in whom prenatal diffusion-weighted magnetic resonance imaging at 33 wk of gestation clearly detected cerebral acute ischemic lesions, associated with remarkable decrease of the average apparent diffusion coefficient.

Environmental toxicity

Quantitative MRI is uniquely suitable for the study of the effects of exposure of pregnant women to environmental toxins and drugs on fetal brain development. A recent study by Anblagan *et al.*^[70] reported on the effects of maternal smoking during pregnancy on fetal organ growth in 13 smokers and 13 non-smokers examined at 22-27 wk and again at 33-38 wk of gestation. Exposed fetuses showed lower brain volumes at both time points, and the effect size was larger in the 2nd visit, closer to the end of gestation.

CONCLUSION

The adaptation of quantitative MRI techniques to fetal brain imaging in utero is truly revolutionary, embodying the potential to transform this area of basic and clinical research and practice from the subjective, qualitative and arbitrarily dichotomous identification of “lesions” and “abnormalities” to the much richer and promising domain of objective, continuous measurements of salient parameters reflecting different morphological, microstructural and biochemical aspects of brain maturation. It is fair to say that if fetal MRI is in its infancy, quantitative fetal MRI is in its embryonic developmental stage, undergoing an explosive phase of methods development, fine-tuning and validation. Consequently, the majority of the published work reviewed here reflects information gathered from relatively small cohorts of normal fetuses scanned during the 3rd trimester, and the relatively smaller number of studies of pathological samples to date offer very limited or no postnatal follow-up. Further improvements in methodology and safety are needed before these studies can be extended to earlier fetal ages, affording a comprehensive view of fetal brain development in utero. The progressive accumulation of normative data bases and extended postnatal follow-up are essential prerequisite for the future use of quantitative MRI in the diagnosis, prognosis and prenatal treatment^[71] of congenital brain disorders.

REFERENCES

1 **Smith FW**, Adam AH, Phillips WD. NMR imaging in pregnancy. *Lancet* 1983; **1**: 61-62 [PMID: 6129387]

2 **Thickman D**, Mintz M, Mennuti M, Kressel HY. MR imaging of cerebral abnormalities in utero. *J Comput Assist Tomogr* 1984; **8**: 1058-1061 [PMID: 6389620]

3 **McCarthy SM**, Filly RA, Stark DD, Hricak H, Brant-Zawadzki MN, Callen PW, Higgins CB. Obstetrical magnetic resonance imaging: fetal anatomy. *Radiology* 1985; **154**: 427-432 [PMID: 3966129]

4 **Williamson RA**, Weiner CP, Yuh WT, Abu-Yousef MM. Magnetic resonance imaging of anomalous fetuses. *Obstet Gynecol* 1989; **73**: 952-956 [PMID: 2657526]

5 **Mansfield P**, Stehling MK, Ordidge RJ, Coxon R, Chapman B, Blamire A, Gibbs P, Johnson IR, Symonds EM, Worthington BS. Echo planar imaging of the human fetus in utero at 0.5 T. *Br J Radiol* 1990; **63**: 833-841 [PMID: 2252974 DOI: 10.1259/0007-1285-63-755-833]

6 **Johnson IR**, Stehling MK, Blamire AM, Coxon RJ, Howseman AM, Chapman B, Ordidge RJ, Mansfield P, Symonds EM, Worthington BS. Study of internal structure of the human fetus in utero by echo-planar magnetic resonance imaging. *Am J Obstet Gynecol* 1990; **163**: 601-607 [PMID: 2386150]

7 **De Wilde JP**, Rivers AW, Price DL. A review of the current use of magnetic resonance imaging in pregnancy and safety implications for the fetus. *Prog Biophys Mol Biol* 2005; **87**: 335-353 [PMID: 15556670]

8 **Paladini D**, Quarantelli M, Sglavo G, Pastore G, Cavallaro A, D'Armiendo, Salvatore M, Nappi C. The role of MRI in the clinical management of fetuses with central nervous system abnormalities in a tertiary referral center. *Ultrasound Obstet Gynecol* 2014; **44**: 188-196 [DOI: 10.1002/uog.13243]

9 **Daffos F**, Forestier F, Mac Aleese J, Aufrant C, Mandelbrot L, Cabanis EA, Iba-Zizen MT, Alfonso JM, Tamraz J. Fetal curarization for prenatal magnetic resonance imaging. *Prenat Diagn* 1988; **8**: 312-314 [PMID: 2969509]

10 **Haase A**, Frahm J, Matthaei D, Hänicke W, Merboldt KD. FLASH imaging: rapid NMR imaging using low flip-angle pulses. 1986. *J Magn Reson* 2011; **213**: 533-541 [PMID: 22152368 DOI: 10.1016/0022-2364(86)90433-6]

11 **Kubik-Huch RA**, Huisman TA, Wissner J, Gottstein-Aalame N, Debatin JF, Seifert B, Ladd ME, Stallmach T, Marincek B. Ultrafast MR imaging of the fetus. *AJR Am J Roentgenol* 2000; **174**: 1599-1606 [PMID: 10845491]

12 **Busse RF**, Riederer SJ, Fletcher JG, Bharucha AE, Brandt KR. Interactive fast spin-echo imaging. *Magn Reson Med* 2000; **44**: 339-348 [PMID: 10975883 DOI: 10.1002/1522-2594(200009)44:3<339::AID-MRM1>3.0.CO;2-N]

13 **Rousseau F**, Glenn OA, Iordanova B, Rodriguez-Carranza C, Vigneron DB, Barkovich JA, Studholme C. Registration-based approach for reconstruction of high-resolution in utero fetal MR brain images. *Acad Radiol* 2006; **13**: 1072-1081 [PMID: 16935719]

14 **Bonel H**, Frei KA, Raio L, Meyer-Wittkopf M, Remonda L, Wiest R. Prospective navigator-echo-based real-time triggering of fetal head movement for the reduction of artifacts. *Eur Radiol* 2008; **18**: 822-829 [PMID: 18075742]

15 **Kim K**, Hansen MF, Habas PA, Rousseau F, Glenn OA, Barkovich AJ, Studholme C. Intersection-based registration of slice stacks to form 3D images of the human fetal brain. *IEEE International Symposium on Biomedical Imaging: From Nano to Macro*, 2008: 1167-1170

16 **Jiang S**, Xue H, Counsell S, Anjari M, Allsop J, Rutherford M, Rueckert D, Hajnal JV. Diffusion tensor imaging (DTI) of the brain in moving subjects: application to in-utero fetal and ex-utero studies. *Magn Reson Med* 2009; **62**: 645-655 [PMID: 19526505 DOI: 10.1002/mrm.22032]

17 **Kim K**, Habas PA, Rousseau F, Glenn OA, Barkovich AJ, Studholme C. Intersection based motion correction of multislice MRI for 3-D in utero fetal brain image formation. *IEEE Trans Med Imaging* 2010; **29**: 146-158 [PMID: 19744911 DOI: 10.1109/TMI.2009.2030679]

18 **Kim K**, Habas PA, Rousseau F, Glenn OA, Barkovich AJ, Studholme C. Reconstruction of a geometrically correct dif-

- fusion tensor image of a moving human fetal brain. *Proceedings Medical Imaging 2010: Image Processing*, 2010: 7623 [DOI: 10.1117/12.844542]
- 19 **Malamateniou C**, Malik SJ, Counsell SJ, Allsop JM, McGuinness AK, Hayat T, Broadhouse K, Nunes RG, Ederies AM, Hajnal JV, Rutherford MA. Motion-compensation techniques in neonatal and fetal MR imaging. *AJNR Am J Neuroradiol* 2013; **34**: 1124-1136 [PMID: 22576885]
 - 20 **Griffiths PD**, Jarvis D, McQuillan H, Williams F, Paley M, Armitage P. MRI of the foetal brain using a rapid 3D steady-state sequence. *Br J Radiol* 2013; **86**: 20130168 [PMID: 24043616 DOI: 10.1259/bjr.20130168]
 - 21 **Studholme C**. Mapping fetal brain development in utero using magnetic resonance imaging: the Big Bang of brain mapping. *Annu Rev Biomed Eng* 2011; **13**: 345-368 [PMID: 21568716 DOI: 10.1146/annurev-bioeng-071910-124654]
 - 22 **Hüppi PS**, Dubois J. Diffusion tensor imaging of brain development. *Semin Fetal Neonatal Med* 2006; **11**: 489-497 [PMID: 16962837 DOI: 10.1016/j.siny.2006.07.006]
 - 23 **Kasprian G**, Brugger PC, Weber M, Krssák M, Krampl E, Herold C, Prayer D. In utero tractography of fetal white matter development. *Neuroimage* 2008; **43**: 213-224 [PMID: 18694838 DOI: 10.1016/j.neuroimage.2008.07.026]
 - 24 **Saleem SN**. Fetal magnetic resonance imaging (MRI): a tool for a better understanding of normal and abnormal brain development. *J Child Neurol* 2013; **28**: 890-908 [PMID: 23644716 DOI: 10.1177/0883073813486296]
 - 25 **Hüppi PS**. Cortical development in the fetus and the newborn: advanced MR techniques. *Top Magn Reson Imaging* 2011; **22**: 33-38 [DOI: 10.1097/RMR.0b013e3182416f78]
 - 26 **Story L**, Damodaram MS, Allsop JM, McGuinness A, Wylezinska M, Kumar S, Rutherford MA. Proton magnetic resonance spectroscopy in the fetus. *Eur J Obstet Gynecol Reprod Biol* 2011; **158**: 3-8 [PMID: 20413207 DOI: 10.1016/j.ejogrb.2010.03.003]
 - 27 **Gong QY**, Roberts N, Garden AS, Whitehouse GH. Fetal and fetal brain volume estimation in the third trimester of human pregnancy using gradient echo MR imaging. *Magn Reson Imaging* 1998; **16**: 235-240 [PMID: 9621964]
 - 28 **Grossman R**, Hoffman C, Mardor Y, Biegón A. Quantitative MRI measurements of human fetal brain development in utero. *Neuroimage* 2006; **33**: 463-470 [PMID: 16938471]
 - 29 **Gholipour A**, Estroff JA, Barnewolt CE, Connolly SA, Warfield SK. Fetal brain volumetry through MRI volumetric reconstruction and segmentation. *Int J Comput Assist Radiol Surg* 2011; **6**: 329-339 [PMID: 20625848 DOI: 10.1007/s11548-010-0512-x]
 - 30 **Hu HH**, Guo WY, Chen HY, Wang PS, Hung CI, Hsieh JC, Wu YT. Morphological regionalization using fetal magnetic resonance images of normal developing brains. *Eur J Neurosci* 2009; **29**: 1560-1567 [PMID: 19419421 DOI: 10.1111/j.1460-9568.2009.06707.x]
 - 31 **Habas PA**, Kim K, Corbett-Detig JM, Rousseau F, Glenn OA, Barkovich AJ, Studholme C. A spatiotemporal atlas of MR intensity, tissue probability and shape of the fetal brain with application to segmentation. *Neuroimage* 2010; **53**: 460-470 [PMID: 20600970 DOI: 10.1016/j.neuroimage.2010.06.054]
 - 32 **Corbett-Detig J**, Habas PA, Scott JA, Kim K, Rajagopalan V, McQuillen PS, Barkovich AJ, Glenn OA, Studholme C. 3D global and regional patterns of human fetal subplate growth determined in utero. *Brain Struct Funct* 2011; **215**: 255-263 [PMID: 21046152 DOI: 10.1007/s00429-010-0286-5]
 - 33 **Scott JA**, Habas PA, Kim K, Rajagopalan V, Hamzelou KS, Corbett-Detig JM, Barkovich AJ, Glenn OA, Studholme C. Growth trajectories of the human fetal brain tissues estimated from 3D reconstructed in utero MRI. *Int J Dev Neurosci* 2011; **29**: 529-536 [PMID: 21530634 DOI: 10.1016/j.ijdevneu.2011.04.001]
 - 34 **Hu HH**, Hung CI, Wu YT, Chen HY, Hsieh JC, Guo WY. Regional quantification of developing human cortical shape with a three-dimensional surface-based magnetic resonance imaging analysis in utero. *Eur J Neurosci* 2011; **34**: 1310-1319 [PMID: 21995768 DOI: 10.1111/j.1460-9568.2011.07855.x]
 - 35 **Clouchoux C**, Kudelski D, Gholipour A, Warfield SK, Viseur S, Bouyssi-Kobar M, Mari JL, Evans AC, du Plessis AJ, Lempereopoulos C. Quantitative in vivo MRI measurement of cortical development in the fetus. *Brain Struct Funct* 2012; **217**: 127-139 [PMID: 21562906 DOI: 10.1007/s00429-011-0325-x]
 - 36 **Habas PA**, Scott JA, Roosta A, Rajagopalan V, Kim K, Rousseau F, Barkovich AJ, Glenn OA, Studholme C. Early folding patterns and asymmetries of the normal human brain detected from in utero MRI. *Cereb Cortex* 2012; **22**: 13-25 [PMID: 21571694 DOI: 10.1093/cercor/bhr053]
 - 37 **Rajagopalan V**, Scott J, Habas PA, Kim K, Rousseau F, Glenn OA, Barkovich AJ, Studholme C. Mapping directionality specific volume changes using tensor based morphometry: an application to the study of gyrogenesis and lateralization of the human fetal brain. *Neuroimage* 2012; **63**: 947-958 [PMID: 22503938 DOI: 10.1016/j.neuroimage.2012.03.092]
 - 38 **Righini A**, Bianchini E, Parazzini C, Gementi P, Ramenghi L, Baldoli C, Nicolini U, Mosca F, Triulzi F. Apparent diffusion coefficient determination in normal fetal brain: a prenatal MR imaging study. *AJNR Am J Neuroradiol* 2003; **24**: 799-804 [PMID: 12748074]
 - 39 **Bui T**, Daire JL, Chalard F, Zaccaria I, Alberti C, Elmaleh M, Garel C, Luton D, Blanc N, Sebag G. Microstructural development of human brain assessed in utero by diffusion tensor imaging. *Pediatr Radiol* 2006; **36**: 1133-1140 [PMID: 16960686]
 - 40 **Manganaro L**, Perrone A, Savelli S, Di Maurizio M, Maggi C, Balesio L, Porfiri LM, De Felice C, Marinoni E, Marini M. Evaluation of normal brain development by prenatal MR imaging. *Radiol Med* 2007; **112**: 444-455 [PMID: 17440691]
 - 41 **Schneider JF**, Confort-Gouny S, Le Fur Y, Viout P, Bennaïthan M, Chapon F, Fogliarini C, Cozzone P, Girard N. Diffusion-weighted imaging in normal fetal brain maturation. *Eur Radiol* 2007; **17**: 2422-2429 [PMID: 17404738]
 - 42 **Cartry C**, Viallon V, Hornoy P, Adamsbaum C. [Diffusion-weighted MR imaging of the normal fetal brain: marker of fetal brain maturation]. *J Radiol* 2010; **91**: 561-566 [PMID: 20657355]
 - 43 **Boyer AC**, Gonçalves LF, Lee W, Shetty A, Holman A, Yeo L, Romero R. Magnetic resonance diffusion-weighted imaging: reproducibility of regional apparent diffusion coefficients for the normal fetal brain. *Ultrasound Obstet Gynecol* 2013; **41**: 190-197 [PMID: 22744761 DOI: 10.1002/uog.11219]
 - 44 **Mitter C**, Kasprian G, Brugger PC, Prayer D. Three-dimensional visualization of fetal white-matter pathways in utero. *Ultrasound Obstet Gynecol* 2011; **37**: 252-253 [PMID: 21264986 DOI: 10.1002/uog.8899]
 - 45 **Kok RD**, van den Berg PP, van den Bergh AJ, Nijland R, Heerschap A. Maturation of the human fetal brain as observed by 1H MR spectroscopy. *Magn Reson Med* 2002; **48**: 611-616 [PMID: 12353277 DOI: 10.1002/mrm.10264]
 - 46 **Heerschap A**, Kok RD, van den Berg PP. Antenatal proton MR spectroscopy of the human brain in vivo. *Childs Nerv Syst* 2003; **19**: 418-421 [PMID: 12811484]
 - 47 **Girard N**, Gouny SC, Viola A, Le Fur Y, Viout P, Chaumoitre K, D'Ercole C, Gire C, Figarella-Branger D, Cozzone PJ. Assessment of normal fetal brain maturation in utero by proton magnetic resonance spectroscopy. *Magn Reson Med* 2006; **56**: 768-775 [PMID: 16964617 DOI: 10.1002/mrm.21017]
 - 48 **Girard N**, Fogliarini C, Viola A, Confort-Gouny S, Fur YL, Viout P, Chapon F, Levrier O, Cozzone P. MRS of normal and impaired fetal brain development. *Eur J Radiol* 2006; **57**: 217-225 [PMID: 16387464]
 - 49 **Hykin J**, Moore R, Duncan K, Clare S, Baker P, Johnson I, Bowtell R, Mansfield P, Gowland P. Fetal brain activity demonstrated by functional magnetic resonance imaging. *Lancet* 1999; **354**: 645-646 [PMID: 10466668]
 - 50 **Fulford J**, Vadeyar SH, Dodampahala SH, Moore RJ, Young P, Baker PN, James DK, Gowland PA. Fetal brain activity

- in response to a visual stimulus. *Hum Brain Mapp* 2003; **20**: 239-245 [PMID: 14673807 DOI: 10.1002/hbm.10139]
- 51 **Fulford J**, Vadeyar SH, Dodampahala SH, Ong S, Moore RJ, Baker PN, James DK, Gowland P. Fetal brain activity and hemodynamic response to a vibroacoustic stimulus. *Hum Brain Mapp* 2004; **22**: 116-121 [PMID: 15108299 DOI: 10.1002/hbm.20019]
- 52 **Moore RJ**, Vadeyar S, Fulford J, Tyler DJ, Gribben C, Baker PN, James D, Gowland PA. Antenatal determination of fetal brain activity in response to an acoustic stimulus using functional magnetic resonance imaging. *Hum Brain Mapp* 2001; **12**: 94-99 [PMID: 11169873 DOI: 10.1002/1097-0193(200102)12:2<94::AID-HBM1006>3.0.CO;2-E]
- 53 **Jardri R**, Pins D, Houfflin-Debarge V, Chaffiotte C, Rocourt N, Pruvo JP, Steinling M, Delion P, Thomas P. Fetal cortical activation to sound at 33 weeks of gestation: a functional MRI study. *Neuroimage* 2008; **42**: 10-18 [PMID: 18539048 DOI: 10.1016/j.neuroimage.2008.04.247]
- 54 **Jardri R**, Houfflin-Debarge V, Delion P, Pruvo JP, Thomas P, Pins D. Assessing fetal response to maternal speech using a noninvasive functional brain imaging technique. *Int J Dev Neurosci* 2012; **30**: 159-161 [PMID: 22123457 DOI: 10.1016/j.ijdevneu.2011.11.002]
- 55 **Schöpf V**, Kasprian G, Brugger PC, Prayer D. Watching the fetal brain at 'rest'. *Int J Dev Neurosci* 2012; **30**: 11-17 [PMID: 22044604 DOI: 10.1016/j.ijdevneu.2011.10.006]
- 56 **Thomason ME**, Dassanayake MT, Shen S, Katkuri Y, Alexis M, Anderson AL, Yeo L, Mody S, Hernandez-Andrade E, Hassan SS, Studholme C, Jeong JW, Romero R. Cross-hemispheric functional connectivity in the human fetal brain. *Sci Transl Med* 2013; **5**: 173ra24 [PMID: 23427244 DOI: 10.1126/scitranslmed.3004978]
- 57 **Sørensen A**, Peters D, Simonsen C, Pedersen M, Stausbøl-Grøn B, Christiansen OB, Lingman G, Uldbjerg N. Changes in human fetal oxygenation during maternal hyperoxia as estimated by BOLD MRI. *Prenat Diagn* 2013; **33**: 141-145 [PMID: 23233459 DOI: 10.1002/pd.4025]
- 58 **Anderson AL**, Thomason ME. Functional plasticity before the cradle: a review of neural functional imaging in the human fetus. *Neurosci Biobehav Rev* 2013; **37**: 2220-2232 [PMID: 23542738 DOI: 10.1016/j.neubiorev.2013.03.013]
- 59 **Kok RD**, Steegers-Theunissen RP, Eskes TK, Heerschap A, van den Berg PP. Decreased relative brain tissue levels of inositol in fetal hydrocephalus. *Am J Obstet Gynecol* 2003; **188**: 978-980 [PMID: 12712096]
- 60 **Roelants-van Rijn AM**, Groenendaal F, Stoutenbeek P, van der Grond J. Lactate in the foetal brain: detection and implications. *Acta Paediatr* 2004; **93**: 937-940 [PMID: 15303809 DOI: 10.1111/j.1651-2227.2004.tb02692.x]
- 61 **Erdem G**, Celik O, Hascalik S, Karakas HM, Alkan A, Firat AK. Diffusion-weighted imaging evaluation of subtle cerebral microstructural changes in intrauterine fetal hydrocephalus. *Magn Reson Imaging* 2007; **25**: 1417-1422 [PMID: 17513078]
- 62 **Pier DB**, Levine D, Kataoka ML, Estroff JA, Werdich XQ, Ware J, Beechly M, Poussaint TY, Duplessis A, Li Y, Feldman HA. Magnetic resonance volumetric assessments of brains in fetuses with ventriculomegaly correlated to outcomes. *J Ultrasound Med* 2011; **30**: 595-603 [PMID: 21527607]
- 63 **Scott JA**, Habas PA, Rajagopalan V, Kim K, Barkovich AJ, Glenn OA, Studholme C. Volumetric and surface-based 3D MRI analyses of fetal isolated mild ventriculomegaly: brain morphometry in ventriculomegaly. *Brain Struct Funct* 2013; **218**: 645-655 [PMID: 22547094 DOI: 10.1007/s00429-012-0418-1]
- 64 **Hoffmann C**, Grossman R, Bokov I, Lipitz S, Biegon A. Effect of cytomegalovirus infection on temporal lobe development in utero: quantitative MRI studies. *Eur Neuropsychopharmacol* 2010; **20**: 848-854 [PMID: 20833515 DOI: 10.1016/j.euroneuro.2010.08.006]
- 65 **Limperopoulos C**, Tworetzky W, McElhinney DB, Newburger JW, Brown DW, Robertson RL, Guizard N, McGrath E, Geva J, Annese D, Dunbar-Masterson C, Trainor B, Laussen PC, du Plessis AJ. Brain volume and metabolism in fetuses with congenital heart disease: evaluation with quantitative magnetic resonance imaging and spectroscopy. *Circulation* 2010; **121**: 26-33 [PMID: 20026783 DOI: 10.1161/CIRCULATIONAHA.109.865568]
- 66 **Clouchoux C**, du Plessis AJ, Bouyssi-Kobar M, Tworetzky W, McElhinney DB, Brown DW, Gholipour A, Kudelski D, Warfield SK, McCarter RJ, Robertson RL, Evans AC, Newburger JW, Limperopoulos C. Delayed cortical development in fetuses with complex congenital heart disease. *Cereb Cortex* 2013; **23**: 2932-2943 [PMID: 22977063 DOI: 10.1093/cercor/bhs281]
- 67 **Damodaram MS**, Story L, Eixarch E, Patkee P, Patel A, Kumar S, Rutherford M. Foetal volumetry using magnetic resonance imaging in intrauterine growth restriction. *Early Hum Dev* 2012; **88** Suppl 1: S35-S40 [PMID: 22285415 DOI: 10.1016/j.earlhumdev.2011.12.026]
- 68 **Cetin I**, Barberis B, Brusati V, Brighina E, Mandia L, Arighi A, Radaelli T, Biondetti P, Bresolin N, Pardi G, Rango M. Lactate detection in the brain of growth-restricted fetuses with magnetic resonance spectroscopy. *Am J Obstet Gynecol* 2011; **205**: 350.e1-350.e7 [PMID: 21861968 DOI: 10.1016/j.ajog.2011.06.020]
- 69 **Baldoli C**, Righini A, Parazzini C, Scotti G, Triulzi F. Demonstration of acute ischemic lesions in the fetal brain by diffusion magnetic resonance imaging. *Ann Neurol* 2002; **52**: 243-246 [PMID: 12210800 DOI: 10.1002/ana.10255]
- 70 **Anblagan D**, Jones NW, Costigan C, Parker AJ, Allcock K, Aleong R, Coyne LH, Deshpande R, Raine-Fenning N, Bugg G, Roberts N, Pausova Z, Paus T, Gowland PA. Maternal smoking during pregnancy and fetal organ growth: a magnetic resonance imaging study. *PLoS One* 2013; **8**: e67223 [PMID: 23843995 DOI: 10.1371/journal.pone.0067223]
- 71 **Guedj F**, Bianchi DW. Noninvasive prenatal testing creates an opportunity for antenatal treatment of Down syndrome. *Prenat Diagn* 2013; **33**: 614-618 [PMID: 23595836 DOI: 10.1002/pd.4134]

P- Reviewer: Li S, Ni Y, Schopf V **S- Editor:** Song XX
L- Editor: A **E- Editor:** Liu SQ



Paediatric computed tomography radiation dose: A review of the global dilemma

Hussain Almohiy

Hussain Almohiy, Department of Radiological Sciences, College of Applied Medical Sciences, King Khalid University, Abha 61431, Saudi Arabia

Author contributions: Almohiy H solely contributed to this paper.

Correspondence to: Dr. Hussain Almohiy, Department of Radiological Sciences, College of Applied Medical Sciences, King Khalid University, P.O. Box 9060, Abha 61431, Saudi Arabia. hmohiy@kku.edu.sa

Telephone: +966-7-2419102 Fax: +966-7-2417071

Received: October 12, 2013 Revised: November 20, 2013

Accepted: December 17, 2013

Published online: March 28, 2015

Abstract

Computed tomography (CT) has earned a well-deserved role in diagnostic radiology, producing cross-sectional and three-dimensional images which permit enhanced diagnosis of many pathogenic processes. The speed, versatility, accuracy, and non-invasiveness of this procedure have resulted in a rapid increase in its use. CT imaging, however, delivers a substantially higher radiation dose than alternative imaging methodologies, particularly in children due to their smaller body dimensions. In addition, CT use in children produces an increased lifetime risk of cancer, as children's developing organs and tissues are inherently more vulnerable to cellular damage than those of adults. Though individual risks are small, the increasing use of CT scans in children make this an important public health problem. Various organizations have recommended measures to minimize unnecessary exposures to radiation through CT scanning. These include elimination of multiple or medically unnecessary scans, development of patient-specific dosing guidelines, and use of alternative radiographic methodology wherever possible. Another important factor in excessive CT exposures, however, is a documented lack of awareness among medical practitioners of the doses involved in CT usage as well as its

significant potential dangers. This review examines the effects of paediatric CT radiation, discusses the level of medical practitioner awareness of these effects, and offers recommendations on alternative diagnostic methods and practitioner education.

© 2015 Baishideng Publishing Group Inc. All rights reserved.

Key words: Computed tomography; Diagnostic imaging; Paediatric imaging; Radiation dose; Computed tomography dose

Core tip: Computed tomography (CT) delivers substantially radiation dose and risk of cancer than alternative imaging methodologies, particularly in children, and use of paediatric CT scans is increasing. Radiation exposure from CT scanning can be minimized by eliminating multiple or medically unnecessary scans, patient-specific dosing guidelines, and use of other radiographic methods where appropriate; however, medical practitioners' lack of awareness of CT dose and its potential dangers are also important. Improvements to CT protocols, referral practices and imaging professionals' education are needed to minimise unnecessary CT radiation exposure in children.

Original sources: Almohiy H. Paediatric computed tomography radiation dose: A review of the global dilemma. *World J Radiol* 2014; 6(1): 1-6 Available from: URL: <http://www.wjgnet.com/1949-8470/full/v6/i1/1.htm> DOI: <http://dx.doi.org/10.4329/wjr.v6.i1.1>

INTRODUCTION

Computed tomography (CT) is used extensively in diagnostic radiology, primarily for examination of human soft tissues. CT scans produce serial cross-sectional images of the body and generate three-dimensional views which

facilitate detailed examination of specific anatomical and pathological areas of concern. CT is used in paediatric patients as well as adults, and its use has increased rapidly since the technology's inception in the 1970s^[1]. More than 60 million CT examinations were performed in the United States in 2006, with an estimated growth rate of 10% per year; about four million of those 60 million were performed in children^[1]. Japan, the United States and Australia lead the world in number of CT scanners per head, with 64, 26 and 18 scanners per million citizens respectively^[2]. Although typical CT radiation doses have not significantly changed over the years, use of CT as a diagnostic tool has dramatically increased.

Children are being increasingly referred for CT examinations. Increased demand for CT in children is partially due to the advent of fast scanning techniques. Fast helical/multi-slice scanning can negate the need for sedation and allows the evaluation of younger or less co-operative children^[3]. The tremendous rise in the use of CT imaging is also related to the development of advanced and reliable diagnostic radiology techniques. For example, CT is now a standard diagnostic tool for paediatric cancer detection, trauma, renal calculi, appendicitis, and heart conditions^[3]. Patient-generated demand, medical insurance coverage, physicians' fear of medical malpractice lawsuits and the desire to monitor clinical progress, especially in cancer patients, have also increased the demand for CT imaging. CT has reduced the failure rate of laparotomy from 18% in 1997 to less than 5% currently, and also decreased the cost related to number of inpatient days per patient^[4]. In certain instances, it has also obviated the need for exploratory surgery^[4].

The speed, accuracy, versatility and availability of CT technology have rapidly raised the volume of CT scans performed in paediatric patients, despite the fact that CT scanning delivers a higher radiation dose to the patient than other available procedures. The radiation dose is particularly important in paediatric patients or small adults because of the increased life-time cancer risk associated with the amount of ionising radiation dose received per square meter of body surface^[5]. While the use of CT for paediatric cases has increased, often little attention is paid to adapting examination protocols developed for adult patients to suit children. The result is significantly higher doses, approximately two to six times greater than necessary, for an adequate level of image quality. As children are inherently more sensitive to the effects of ionising radiation than adults, there is a pressing need to optimize this high-dose imaging modality for these especially vulnerable patients. Numerous international organizations, including the International Commission on Radiological Protection^[5], the International Atomic Energy Agency^[6] and the European Commission^[7] have made recommendations aimed at minimizing CT doses, particularly in the paediatric population. The European Commission, to ensure optimization of performance and patient protection in CT procedures, established a set of quality criteria for adult CT examinations, published as the European

Guidelines on Quality Criteria for Computed Tomography^[8]. The US Food and Drug Administration (FDA) has similarly published a set of recommendations with the objective of keeping CT radiation doses as low as reasonably achievable, especially for children and small adults. The FDA stresses the importance of customizing CT scanner parameters for each individual's weight, size and scan region^[9].

In this article I describe CT and its advantages and review the effects of paediatric CT radiation. I examine current knowledge about the level of medical practitioner awareness of the effects of CT dose in children and offer strategies to reduce CT dose.

CT: ADVANTAGES OVER OTHER IMAGING MODALITIES

CT is an advanced imaging technology that has been in use since 1972^[10]. By rotating the X-ray beam around the patient and analysing the resulting data, the technique allows physicians to examine the body, bones, and organs one narrow "slice" at a time^[10]. Some non-ionising methodologies can obtain comparable diagnostic information, particularly ultrasound and magnetic resonance imaging (MRI). Ultrasound is very useful in paediatrics, since image quality and resolution improve with a smaller patient size. Ultrasound can also be used to image almost any area of the body, with the exception of those composed mainly of bone or air. MRI uses magnetic fields and radio waves to create a set of 2D slices of the body and thus does not expose the patient to ionising radiation. Its use in children, however, is constrained by the fact that patients need to remain absolutely still as even small amounts of motion can affect the image quality. Younger children often require sedation, necessitating specialized equipment and staff which may not be accessible in all imaging centres. Faster MRI scanning has helped to reduce blur from patient motion and coaching and distraction techniques can also help obtain a quality image^[11]. The traditional planar X-ray, developed in, only allows visual outline of bones and organs^[11]. CT differentiates overlying structures much better than planar X-ray techniques^[12] and allows greater contrast differentiation than other imaging modalities. Many medical conditions are more accurately imaged and diagnosed using CT, for example, vascular diseases with the potential to cause renal failure, stroke, or death. Thus CT is the best imaging option in many cases, and if the protocol is well optimized the value of the information obtained will offset the risks associated with the relatively large radiation dose.

ACHIEVING AN OPTIMAL RADIATION DOSE

Radiation doses from CT scanning are considerably larger than those from corresponding conventional radiography procedures. For example, a planar anterior-pos-

terior abdominal X-ray examination results in a dose to the stomach of approximately 0.25 mGy, approximately 2% of the corresponding dose from an abdominal CT scan^[13], and a CT scan of the chest delivers 100 times the radiation of a conventional chest X-ray^[10]. Although CT examinations make up 5%-11% of all radiological examinations, they contribute an estimated 40%-70% of the collective dose derived from diagnostic radiology^[11,14-16]. Moreover, many CT procedures involve multiple scans, with one study finding that 30% of CT patients were scanned three times, 7% of patients scanned five times, and 4% scanned nine times or more^[16].

The bio-effects associated with radiation exposure can be divided into two main groups: deterministic risk and stochastic effects. The deterministic risk is a function of radiation dose delivered to an organ or body region. Deterministic effects of radiation are seen above a threshold dose, with higher doses promoting more severe effects; these are rarely seen in diagnostic radiology, but may become a problem with angiographic procedures, including CT fluoroscopy^[17]. In addition, temporary hair loss has been reported in patients undergoing multi-detector row computed tomography brain perfusion studies in combination with digital subtraction angiography^[18]. Stochastic effects are dependent upon a complex series of events, including cell transformation. Stochastic effects may appear as a cancer in the patient or as genetic abnormalities in their children. The probability of seeing stochastic effects increases with the amount of radiation but the severity of the effect is independent of the dose of radiation received^[18].

Oncogenesis is a major stochastic effect of CT radiation exposure. Children's organs and tissues are highly sensitive to the oncogenic effects of radiation because they contain a large proportion of cells that are dividing and reproducing. The radiation-induced risk is also higher in paediatric patients due to wider and increased cellular distribution of red bone marrow and their greater post-exposure life expectancy^[19]. The effective radiation doses received by children are about 50% higher than those received by adults due to their smaller body size and related attenuation^[20]. At ages up to 10 years, children are more sensitive than adults by a factor of three, as their longer expected life span is combined with the higher radiation sensitivity of the developing organs^[5]. For example, the potential impact of a single 15 mSv CT examination (equivalent to 500 standard chest X-rays) on an adult is only half that of a child^[21].

The risks of paediatric CT have been assessed in several studies. Israeli researchers estimated that 9.5 lifetime deaths were associated with one year of paediatric CT scanning^[22].

Researchers from the National Cancer Institute and the Society of Paediatric Radiology in the US estimated the risk of dying from cancer to be 1 in 550 following abdominal CT and 1 in 1500 for a brain CT performed in infancy, approximately 0.35% more cancer deaths than expected in the general population^[23]. These figures were

calculated on the assumption that children were being imaged using adult CT parameters; the risk would be lower if specific paediatric CT protocols were uniformly adopted. Although the increased risk of cancer is small for each individual scanned, the impact on public health is substantial due to the increasingly large number of CT examinations being performed^[24].

ACHIEVING AN OPTIMAL CT RADIATION DOSE

As noted earlier, efforts towards dose reduction in CT have been recommended by major international organizations such as the International Commission on Radiological Protection^[24] the International Atomic Energy Agency^[25] and the European Commission^[7]. These agencies recommended the implementation of CT dose guidance levels for the most frequent examinations to promote strategies for the optimization of CT doses.

Patients undergoing CT examinations range from neonates to oversized adults. Radiation doses in CT are generally measured in cylindrical acrylic phantoms designed to simulate the head (16 cm) or body (32 cm). Because patients differ in sizes and body composition, it is often difficult to obtain reliable values of patient doses from such phantoms. If scan parameters are kept constant for all CT examinations, much larger doses will result with paediatric patients than with adults. This "one-size-fits-all" adult model underestimates the paediatric CT radiation dose displayed on the console of current CT scanners^[26]. The Alliance for Radiation Safety in Paediatric Imaging^[1], a movement of more than 500000 health care professionals, is working for an increasing awareness among radiologists and radiographers of the need for a "child size" CT scan technique. It recommends the following steps to prevent excessive dose exposure to paediatric patients: (1) Acquisition of new CT equipment should be supported by validation of the protocol to help ensure that patient doses are "As Low As Reasonably Achievable"; (2) Any increase in dose must be justified by a corresponding improvement in diagnostic information, and where possible, use iodinated contrast medium to perform CT examinations at lower kV values with no loss of diagnostic information^[1].

CT RADIATION DOSE AWARENESS AMONG PATIENTS AND HEALTHCARE PROFESSIONALS

A majority of the hospital protocols involve explanation of CT radiation risk to patient or its carer. Unfortunately, however, physicians themselves are often little more informed than their patients with regards to radiation exposure caused by CT examinations. In a 2004 paper, Lee *et al*^[27] showed that all patients and more than 70% of physicians underestimated the dose from one abdominal CT examination. Many of those questioned did not

realize that CT scans increase the lifetime risk of cancer. They also reported that radiologists are unable to provide accurate estimates of CT dose regardless of their level of experience^[27].

In addition, a 2003 questionnaire-based survey and interview of doctors of all grades, including consultant radiologists, indicated that only 2% of the participants could successfully estimate the relative doses of common diagnostic procedures^[14]. A significant proportion of the interviewees could only answer questions that involved ultrasound, which is non-ionising. The degree of knowledge was inversely proportional to seniority, with consultants scoring less than junior colleagues^[28]. It was revealed in a 2004 survey that 53% of radiologists and 91% of emergency room physicians surveyed did not believe that CT scans increased the lifetime risk of cancer^[27].

ADDRESSING THE PROBLEM

In order to protect paediatric patients from undue exposure to radiation, the FDA has established guidelines to: (1) Improve CT exposure factors in order to reduce unnecessary paediatric patient radiation dose and perform more extensive quality checks to validate the reported dose values; (2) Reduce the number of procedures requiring multiple CT scans; and (3) Utilise alternative, lower dose, radiographic exams wherever possible^[12].

Like the FDA, the “4th Framework European Programme” in paediatric radiology concentrated on developing guidelines for common paediatric CT examinations. A paediatric document was prepared based on the adult CT document, which offers general principles associated with good imaging technique, quality criteria and guidelines on radiation dose to the patient^[29].

In order to facilitate dose adjustment for paediatric patients, some equipment manufacturers have incorporated automatic exposure control (AEC) in their CT scanners. An AEC adjusts dose according to patient size and optimizes radiation dose within a single patient using dynamic tube current^[13].

While CT remains a crucial tool for paediatric diagnosis, physicians, radiographers and health authorities need to work together to reduce the radiation dose to children to as low as reasonably achievable. Semelka *et al*^[30] suggested three ways to reduce radiation. First, reduce the CT-related dose delivered to each patient (partially addressed by the AEC option on the later models of CT scanners). Their second recommendation was to use alternative imaging techniques such as ultrasound and MRI, when practical. The third and most effective way to reduce the population dose from CT is simply to decrease the number of CT studies that are prescribed^[31].

EDUCATION OF RADIOLOGY STAFF

Enhancing understanding of the factors that affect patient doses in CT should be considered the first step in optimization strategies^[16]. Basic training for radiog-

raphers/radiological technologists generally overlooks paediatric CT radiation doses. The IAEA recommends radiographers involved in paediatric CT be specifically educated and trained about paediatric radiation dose^[6]. A 1998 study found that variations of 10%-40% observed in the typical dose between individual scanners were largely due to imaging technique^[32]. A survey of health professionals in Northern Ireland on awareness of the radiation doses imparted during common diagnostic imaging procedures and their long term impact on patients demonstrated a knowledge gap which could be improved with appropriate training^[33]. A 2006 survey in New South Wales, Australia showed the need for continuing education and protocol review, particularly in paediatric CT examinations^[29]. Another study conducted in a large hospital in the United Kingdom assessed the knowledge of primary care and specialist physicians concerning radiation doses and risks. The results revealed an urgent need to improve physicians “understanding of radiation exposure”. Only 27% of doctors attained a 45% pass mark, and only 57% of radiologists and radiology-related subspecialists passed the test^[34].

The need to train radiology personnel, establish protocols, and continuously monitor the performance of CT equipment to control patient CT doses is of utmost importance. Radiologists and other imaging staff must learn that dose adjustment according to size, weight and scanning area plays an important role in radiation dose reduction in CT. Education about high radiation doses during CT examinations can reduce patient exposure and risk with no loss of image quality^[32]. However, reduced-dose protocols for common clinical indications require further investigation.

All of the studies to date suggest the need for improvements in the knowledge and training of imaging professionals about dose in CT examinations, particularly when applied to paediatric patients. To be most effective, this should involve continuing education among all staff involved in radiographic imaging, from radiographers/technologists to referring physicians. Support for this movement has been suggested not just on regional levels, but through large-scale training initiatives in which materials are translated and distributed globally^[6].

CONCLUSION

Over the past two decades CT scanning rates have increased greatly, and this has increased the average radiation dose delivered to paediatric patients. This literature review has found that medical practitioners are not adequately aware of the stochastic effects of CT, or of diagnostic alternatives to CT. Because of the stochastic effects of ionising radiation, dose reduction in CT examinations, especially for paediatric patients, must occur. Dose reduction is being implemented by CT manufacturers, but medical imaging professionals must not rely on this alone. Improvements to CT protocols, referral practices and imaging professionals’ education are needed

to minimise the amount of unnecessary CT dose that is delivered. By undertaking these changes and with continual vigilance, the benefits of CT can be obtained at low radiation dose and the minimum of harmful effects to paediatric patients.

ACKNOWLEDGMENTS

The authors would like to thank Campbell Aitken (Express Editing Writing and Research).

REFERENCES

- 1 **Goske MJ**, Applegate KE, Boylan J, Butler PF, Callahan MJ, Coley BD, Farley S, Frush DP, Hernanz-Schulman M, Jaramillo D, Johnson ND, Kaste SC, Morrison G, Strauss KJ, Tuggle N. The 'Image Gently' campaign: increasing CT radiation dose awareness through a national education and awareness program. *Pediatr Radiol* 2008; **38**: 265-269 [PMID: 18202842 DOI: 10.1007/s00247-007-0743-3]
- 2 **Hall EJ**, Brenner DJ. Cancer risks from diagnostic radiology. *Br J Radiol* 2008; **81**: 362-378 [PMID: 18440940 DOI: 10.1259/bjr/01948454]
- 3 **Donnelly LF**, Emery KH, Brody AS, Laor T, Gylys-Morin VM, Anton CG, Thomas SR, Frush DP. Minimizing radiation dose for pediatric body applications of single-detector helical CT: strategies at a large Children's Hospital. *AJR Am J Roentgenol* 2001; **176**: 303-306 [PMID: 11159061 DOI: 10.2214/ajr.176.2.1760303]
- 4 **Callahan MJ**, Rodriguez DP, Taylor GA. CT of appendicitis in children. *Radiology* 2002; **224**: 325-332 [PMID: 12147823 DOI: 10.1148/radiol.2242010998]
- 5 1990 Recommendations of the International Commission on Radiological Protection. *Ann ICRP* 1991; **21**: 1-201 [PMID: 2053748 DOI: 10.1016/0146-6453(91)90065-O]
- 6 **International Atomic Energy Agency**. International Action Plan For The Radiological Protection Of Patients. In: ConferenceBoGG, ed. Vienna: IAEA, 2002: 1-9. Available from: URL: <http://www.iaea.org/About/Policy/GC/GC46/Documents/gc46-12.pdf>
- 7 **European Communities**. European guidelines on quality criteria for computed tomography. Luxembourg: European Communities, 1999. Available from: URL: <http://www.dr.dk/guidelines/ct/quality/index.htm>
- 8 **Menzel HG**, Schibilla H, Teunen D. European guidelines on quality criteria for computed tomography. Publication no EUR 16262 EN. Luxembourg: European Commission, 2000
- 9 **Food and Drug Administration**. FDA public health notification: reducing radiation risk from computed tomography for pediatric and small adult patients. *Pediatr Radiol* 2002; **32**: 314-316 [PMID: 11956716]
- 10 **Feigal DW**. FDA public health notification: reducing radiation risk from computed tomography for pediatric and small adult patients. *Int J Trauma Nurs* 2002; **8**: 1-2 [PMID: 11793002 DOI: 10.1067/mtrn.2002.121511]
- 11 **Jessen KA**, Shrimpton PC, Geleijns J, Panzer W, Tosi G. Dosimetry for optimisation of patient protection in computed tomography. *Appl Radiat Isot* 1999; **50**: 165-172 [PMID: 10028635 DOI: 10.1016/S0969-8043(98)00024-4]
- 12 **History of CT scan**. [cited 3 April. 2009]; Available from: URL: <http://www.imaginis.com/ctscan/history.asp>
- 13 **White KS**. Invited article: helical/spiral CT scanning: a pediatric radiology perspective. *Pediatr Radiol* 1996; **26**: 5-14 [PMID: 8598996 DOI: 10.1007/BF01403695]
- 14 **Smith-Bindman R**, Miglioretti DL, Larson EB. Rising use of diagnostic medical imaging in a large integrated health system. *Health Aff (Millwood)* 2008; **27**: 1491-1502 [PMID: 18997204 DOI: 10.1377/hlthaff.27.6.1491]

- 15 **Frush DP**, Donnelly LF, Rosen NS. Computed tomography and radiation risks: what pediatric health care providers should know. *Pediatrics* 2003; **112**: 951-957 [PMID: 14523191 DOI: 10.1542/peds.112.4.951]
- 16 **Mettler FA**, Wiest PW, Locken JA, Kelsey CA. CT scanning: patterns of use and dose. *J Radiol Prot* 2000; **20**: 353-359 [PMID: 11140709 DOI: 10.1088/0952-4746/20/4/301]
- 17 **Keat N**. Real-time CT and CT fluoroscopy. *Br J Radiol* 2001; **74**: 1088-1090 [PMID: 11777764]
- 18 **Imanishi Y**, Fukui A, Niimi H, Itoh D, Nozaki K, Nakaji S, Ishizuka K, Tabata H, Furuya Y, Uzura M, Takahama H, Hashizume S, Arima S, Nakajima Y. Radiation-induced temporary hair loss as a radiation damage only occurring in patients who had the combination of MDCT and DSA. *Eur Radiol* 2005; **15**: 41-46 [PMID: 15351903 DOI: 10.1007/s00330-004-2459-1]
- 19 **Krestinina LY**, Preston DL, Ostromova EV, Degteva MO, Ron E, Vyushkova OV, Startsev NV, Kossenko MM, Akleyev AV. Protracted radiation exposure and cancer mortality in the Techa River Cohort. *Radiat Res* 2005; **164**: 602-611 [PMID: 16238437 DOI: 10.1667/RR3452.1]
- 20 **Huda W**. Dose and image quality in CT. *Pediatr Radiol* 2002; **32**: 709-713; discussion 751-754 [PMID: 12244459 DOI: 10.1007/s00247-002-0796-2]
- 21 **Brenner DJ**, Doll R, Goodhead DT, Hall EJ, Land CE, Little JB, Lubin JH, Preston DL, Preston RJ, Puskin JS, Ron E, Sachs RK, Samet JM, Setlow RB, Zaider M. Cancer risks attributable to low doses of ionizing radiation: assessing what we really know. *Proc Natl Acad Sci USA* 2003; **100**: 13761-13766 [PMID: 14610281 DOI: 10.1073/pnas.2235592100]
- 22 **Chodick G**, Ronckers CM, Shalev V, Ron E. Excess lifetime cancer mortality risk attributable to radiation exposure from computed tomography examinations in children. *Isr Med Assoc J* 2007; **9**: 584-587 [PMID: 17877063]
- 23 **Lee CI**, Forman HP. The hidden costs of CT bioeffects. *J Am Coll Radiol* 2008; **5**: 78-79 [PMID: 18242519 DOI: 10.1016/j.jacr.2007.06.013]
- 24 **National Cancer Institute**. Radiation Risks and Pediatric Computed Tomography (CT): A Guide for Health Care Providers, 2005. USA: National Cancer Institute. Available from: URL: <http://www.cancer.gov/cancertopics/causes/radiation/radiation-risks-pediatric-CT>
- 25 **International Atomic Energy Agency**. International Basic Safety Standards for Protection Against Ionizing Radiation and for the Safety of Radiation Sources. Vienna: IAEA Safety Series No. 115, 1996. Available from: URL: http://www.ilo.org/safework/info/publications/WCMS_152685/lang-en/index.htm
- 26 **Strauss KJ**, Goske MJ, Frush DP, Butler PF, Morrison G. Image Gently Vendor Summit: working together for better estimates of pediatric radiation dose from CT. *AJR Am J Roentgenol* 2009; **192**: 1169-1175 [PMID: 19380538 DOI: 10.2214/AJR.08.2172]
- 27 **Lee CI**, Haims AH, Monico EP, Brink JA, Forman HP. Diagnostic CT scans: assessment of patient, physician, and radiologist awareness of radiation dose and possible risks. *Radiology* 2004; **231**: 393-398 [PMID: 15031431 DOI: 10.1148/radiol.2312030767]
- 28 **Shiralkar S**, Rennie A, Snow M, Galland RB, Lewis MH, Gower-Thomas K. Doctors' knowledge of radiation exposure: questionnaire study. *BMJ* 2003; **327**: 371-372 [PMID: 12919987 DOI: 10.1136/bmj.327.7411.371]
- 29 **Moss M**, McLean D. Paediatric and adult computed tomography practice and patient dose in Australia. *Australas Radiol* 2006; **50**: 33-40 [PMID: 16499725 DOI: 10.1111/j.1440-1673.2005.01544.x]
- 30 **Semelka RC**, Armao DM, Elias J, Huda W. Imaging strategies to reduce the risk of radiation in CT studies, including selective substitution with MRI. *J Magn Reson Imaging* 2007; **25**: 900-909 [PMID: 17457809 DOI: 10.1002/jmri.20895]
- 31 **Frush DP**. Pediatric CT: practical approach to diminish the

- radiation dose. *Pediatr Radiol* 2002; **32**: 714-717; discussion 751-754 [PMID: 12244460 DOI: 10.1007/s00247-002-0797-1]
- 32 **Shrimpton PC**, Edyvean S. CT scanner dosimetry. *Br J Radiol* 1998; **71**: 1-3 [PMID: 9534691]
- 33 **Soye JA**, Paterson A. A survey of awareness of radiation dose among health professionals in Northern Ireland. *Br J Radiol* 2008; **81**: 725-729 [PMID: 18591196 DOI: 10.1259/bjr/94101717]
- 34 **Jacob K**, Vivian G, Steel JR. X-ray dose training: are we exposed to enough? *Clin Radiol* 2004; **59**: 928-934; discussion 926-927 [PMID: 15451354 DOI: 10.1016/j.crad.2004.04.020]

P- Reviewers: James C, Tsalafoutas IA **S- Editor:** Ma YJ
L- Editor: A **E- Editor:** Wang CH



Imaging of the small bowel: Crohn's disease in paediatric patients

Emanuele Casciani, Chiara De Vincentiis, Elisabetta Poletti, Gabriele Masselli, Giovanni Di Nardo, Fortunata Civitelli, Salvatore Cucchiara, Gian Franco Galdi

Emanuele Casciani, Elisabetta Poletti, Gabriele Masselli, Gian Franco Galdi, Department of Emergency Radiology, "La Sapienza" University-Hospital Umberto I, 00166 Rome, Italy
Chiara De Vincentiis, Department of Radiology, "La Sapienza" University-Sant'Andrea's Hospital, 00189 Rome, Italy
Giovanni Di Nardo, Fortunata Civitelli, Salvatore Cucchiara, Department of Pediatrics, Gastroenterology and Liver Unit, "La Sapienza" University-Hospital Umberto I, 00166 Rome, Italy
Author contributions: Casciani E designed the study and wrote the manuscript; De Vincentiis C helped to write the manuscript; Poletti E, Masselli G, Di Nardo G, Civitelli F, Cucchiara S and Galdi GF provided the collection of part of the material; all the authors were also involved in editing the manuscript.

Correspondence to: Dr. Emanuele Casciani, Department of Emergency Radiology, "La Sapienza" University-Hospital Umberto I, Viale del Policlinico 155, 00161 Roma, Italy. emanuelecasciani@gmail.com

Telephone: +39-06-49979465 Fax: +39-06-6630218

Received: November 27, 2013 Revised: April 14, 2014

Accepted: May 16, 2014

Published online: March 28, 2015

© 2015 Baishideng Publishing Group Inc. All rights reserved.

Key words: Barium studies; Ultrasonography; Computed tomography; Magnetic resonance; Positron emission tomography-computed tomography

Core tip: Nowadays there is a great awareness of the risks associated with the use of ionizing radiation, particularly in children. This article evaluates all the imaging methods now available for the study of Crohn's disease in pediatric patients emphasizing the magnetic resonance imaging.

Original sources: Casciani E, De Vincentiis C, Poletti E, Masselli G, Di Nardo G, Civitelli F, Cucchiara S, Galdi GF. Imaging of the small bowel: Crohn's disease in paediatric patients. *World J Radiol* 2014; 6(6): 313-328 Available from: URL: <http://www.wjgnet.com/1949-8470/full/v6/i6/313.htm> DOI: <http://dx.doi.org/10.4329/wjr.v6.i6.313>

Abstract

In more than 20% of all patients, the Crohn's disease presents before the age of 18 years. The diagnosis and management of Crohn's disease in children has changed dramatically over the last decade, mainly due to increased awareness, availability of newer diagnostic modalities such as magnetic resonance imaging (MRI) and newer, more powerful treatments such as biologics. Imaging of the small bowel is needed for diagnosis, management, follow-up and also evaluation of the disease in terms of location, extent, activity and complications. We review all the methods (barium examinations, ultrasonography, computed tomography, MR, and computed tomography- positron emission tomography) commonly used for imaging the small bowel in paediatric patients with Crohn's disease analyzing the advantages and disadvantages of each modality, with particular emphasis on MR imaging.

INTRODUCTION

Crohn's disease (CD) begins in childhood, below 20 years of age, in 20% of cases and may involve characteristically any part of the gastrointestinal (GI) tract. The Paris classification has recently revised the Montreal classification, that had several weakness points relating children's classification^[1]. Important modifications developed regarding CD include classifying age at diagnosis as A1a (0 to < 10 years), A1b (10 to < 17 years), A2 (17 to 40 years), and A3 (> 40 years), distinguishing disease above the distal ileum as L4a (proximal to ligament of Treitz) and L4b (ligament of Treitz to above distal ileum), allowing both stricturing and penetrating disease to be classified in the same patient (B2B3), and denoting, at any time, the presence of growth failure in the patient as G1 versus G0 (never growth failure)^[2].

Although the exact frequency of the small bowel (SB)

CD is unknown, most gastroenterologists believe that its prevalence has been underestimated and that it may have an increased incidence among children and young adolescents^[2]. A recent study performed in pediatric patients with magnetic resonance (MR) enterography^[3], according to previous studies^[4], confirmed that the involvement of the terminal ileum is common to more than three times compared to that of the jejunum and the rest of the ileum. Moreover, the involvement of the jejunum alone is uncommon and it is more difficult to investigate because of its tendency to stay non distended^[3].

The clinical importance of the SB CD phenotype is the impact that a diffuse SB disease is expected to have on a child's growth and development. Moreover, patients with SB CD are more likely to experience complications, including intestinal obstruction and less commonly fistulization^[4,5].

Thus, objective evaluation of the SB is essential in differentiating CD from other enteropathies and in directing the management of the patients with inflammatory bowel disease (IBD)^[6,7]. The morphological evaluation of the SB, useful in the diagnosis and management of CD, has long been made only with conventional radiology. In the last decade there has been a progressive improvement of cross-sectional imaging [ultrasonography (US), computed tomography (CT), and magnetic resonance (MR)] that has significantly changed the way to diagnose and treat the patients^[8,9]. Indeed, their accuracy in detecting mucosal alterations and transmural and perienteric inflammations, has led to a new disease staging, a detection of asymptomatic disease and a better assessment of response to therapy^[10]. For these reasons modern cross-sectional imaging have replaced the traditional fluoroscopy-based for visualization of the SB. In the "Porto criteria" small-bowel follow-through (SBFT) was the recommended imaging modality in children^[11]. However, concerns about the proven increased risk of high radiation exposure in pediatric patients mandates the use of alternative techniques when possible^[12-14]. In the European Crohn's and Colitis Organization (ECCO) guidelines^[14] it is stated that MR and CT enterography or enteroclysis are the imaging modalities with the highest diagnostic accuracy. Moreover in the pediatric section of the ECCO guidelines^[15,16] dynamic contrast-enhanced MRI is considered the best imaging to show most of the CD's lesions without exposure to ionizing radiation. In the same way the Appropriateness Criteria of the American College of Radiology^[17] point out that, in the pediatric patients, MR enterography may have sensitivity and specificity similar to CT enterography and avoids radiation risks. Ultimately the same accuracy, the choice of examination depends on several variables, such as institutional preferences and resources (US, CT, or MR scan), age and compliance of the patient, the eventually acute presentation, and finally radiologist expertise.

In this article we discuss all the methods commonly used for imaging the small bowel in paediatric patients with Crohn's disease analyzing the advantages and disad-

vantages of each modality, with particular emphasis on MR imaging.

BARIUM STUDIES

Traditionally in children with suspected CD has been studied with barium studies, enteroclysis (SBE) or SB follow-through (SBFT), considered to be the gold standard examination for the SB^[18,19]. SBE was considered the best exam for SB disease, however children poorly tolerate the required insertion of a naso-jejunal tube. SBFT has long been considered as the most common, non-invasive, inexpensive and easily accessible radiological method^[14], but, currently, it has only a secondary role in small bowel imaging. US and MR enterography are methods of choice for imaging SB diseases in pediatric populations.

Early mucosal changes, such as aphthous ulceration, can be detected by SBFT. This technique can also assess bowel motility that help to differentiate strictures from mural thickening and allows a functional evaluation of the pathological segment studying the SB transit time^[14-16].

Although SBE and SBFT can effectively depict the presence of mucosal abnormalities effectively, including fissures, cobblestone mucosa, pseudo-polyps, and skip lesions, they are imprecise for the diagnosis of transmural and extramural disease^[14,20,21], except in the overt forms (Figure 1).

A retrospective analysis of 164 children revealed a diagnostic sensitivity of only 45% for SB radiography compared with ileo-colonoscopy^[22]. Moreover, SBFT is not accurate for the detection of active CD in the SB^[20-23]. In fact, it can directly examine the mucosa demonstrating early active mucosal disease such as aphthous and linear ulcers, but it does not allow to evaluate the small bowel wall and the mesentery, except with indirect signs. Moreover, superimposed bowel loops or non-palpable bowel loops deep in the pelvis can hide active disease or its complications^[20].

Concerns regarding the risks of radiation exposure in the pediatric population has increased with the spread use of these imaging studies. Children especially are at risk because they are inherently more radiosensitive and because they have more remaining years of life during which a radiation-induced cancer could develop^[24].

A major disadvantage of barium studies, especially in children, is the radiation exposure, particularly if fluoroscopy time is not kept to a minimum^[13]. Gaca *et al*^[13] studied a total of 176 children with CD who underwent averaging 1.2 SBFTs. On average SBFT took 5.1 min with 3.3 abdominal radiographs. The effective doses (mSv) for a 5-min fluoroscopy were 0.15 for the central abdomen, 0.35 for the right lower quadrant, and 0.56 for the pelvis, yielding an average effective dose for SBFT (5-min fluoroscopy, 3.3 abdominal radiographs) of 1.8-2.2 mSv. Although 5 min of fluoroscopy time for an SBFT might seem excessive, this was calculated based on the average of 30 examinations performed by five experienced pediatric radiologists^[13]. In the young population of CD

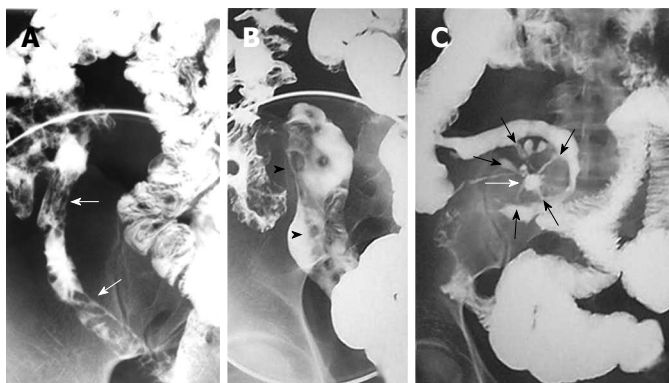


Figure 1 Barium studies in patients with Crohn's disease. Double-contrast barium enema examination (A and B) demonstrate longitudinal (arrows) and perpendicular (arrowheads) ulcerations in the terminal ileum. Small-bowel follow-through (C) demonstrates an abscess cavity (white arrow) with fistulae connecting the cavity to the adjacent small bowel (black arrows).

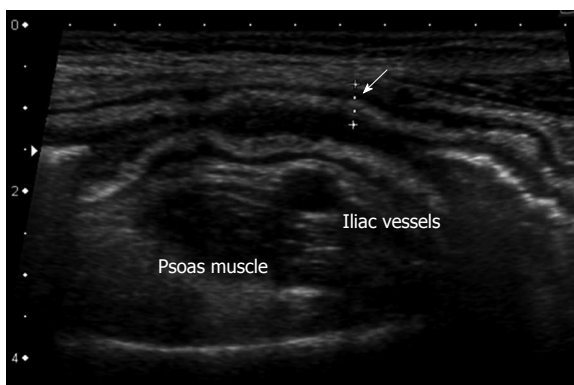


Figure 2 Thickening of the bowel wall, 5 mm, (arrow) with wall layers preserved. The hyperechoic band corresponds to thickened submucosa.

patients, the ionizing radiation required for SBE limits the use of this technique for the follow-up of the disease. Moreover, SBFT and SBE examinations can often result in incomplete studies. In fact they cause more patient discomfort compared with CT^[25] and MRI^[26], barium contrast can be poorly tolerated by children especially in severe and advanced disease and abdominal pain can limit compression preventing the adequate visualization of overlapping loops.

ULTRASONOGRAPHY

US has the distinct advantage of being widely available, inexpensive, non-invasive, radiation-free and relatively easy to perform^[7,27]. Over the past few years, improvements in US equipment such as high-frequency transducers (7-12 MHz), combined with oral and intravenous (CE-US) contrast agents^[28,29], have overcome some of the obstacles in bowel US that existed in the past, thus raising a great enthusiasm for its use in IBD children.

US can be considered a valuable tool in the preliminary diagnostic process of paediatric patients with suspected IBD, prior to further invasive tests^[30,31].

Inflamed bowel can show both mural and extramural pathological changes. Bowel wall thickness is the most important US sign of IBD (Figure 2), with different thickness values used as a threshold for a positive diagnosis in the various reports (from 1.5 mm to 3 mm in the terminal ileum and < 2 mm in the colon)^[27,32-35].

The other US signs are altered echogenicity, loss of

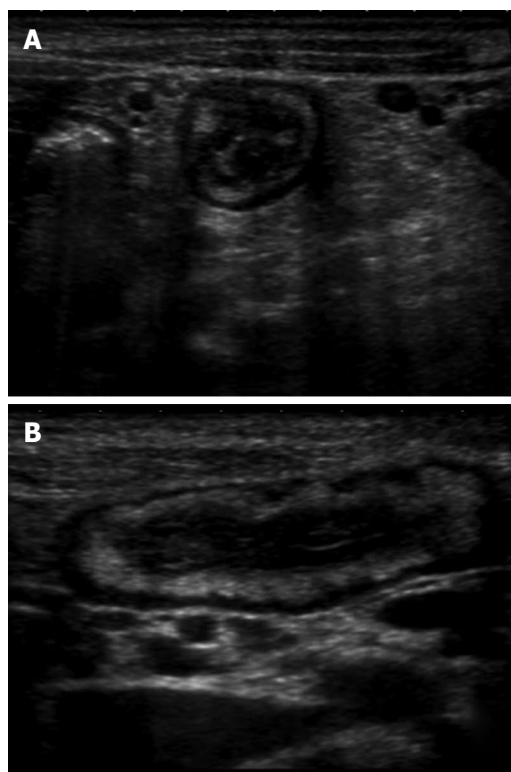


Figure 3 Transversal (A) and longitudinal (B) section of a thickened ileal loop due to Crohn's disease. The "target" sign, corresponding to remarkable bowel wall thickness, is visible as a strong echogenic centre surrounded by a hypoechoic border (A). The adjacent mesentery is thickened and hyperechoic, due to the transmural nature of inflammation in Crohn's disease (A and B).

the normally visible stratification (Figure 3), increased Colour-Doppler signal denoting hyperaemia (Figure 4) and relative decrease or lack in peristalsis signifying some degree of stiffness^[31]. Extra-mural findings include changes involving the surrounding mesentery, that appears thickened and hyperechoic and generally shows enlarged mesenteric lymph-nodes (Figure 4)^[30,36].

Bowel US and ileocolonoscopy with histology have demonstrated an overall sensitivity of 74 and 88% and a specificity of 78 and 93%, respectively, in the detection of SB CD lesions^[35,37]. The sensitivity of US in the detection of SB lesions is greater for those of the terminal ileum (approximately 90%-95%) than for those of the proximal SB (75%)^[38]. US is useful for the follow-up

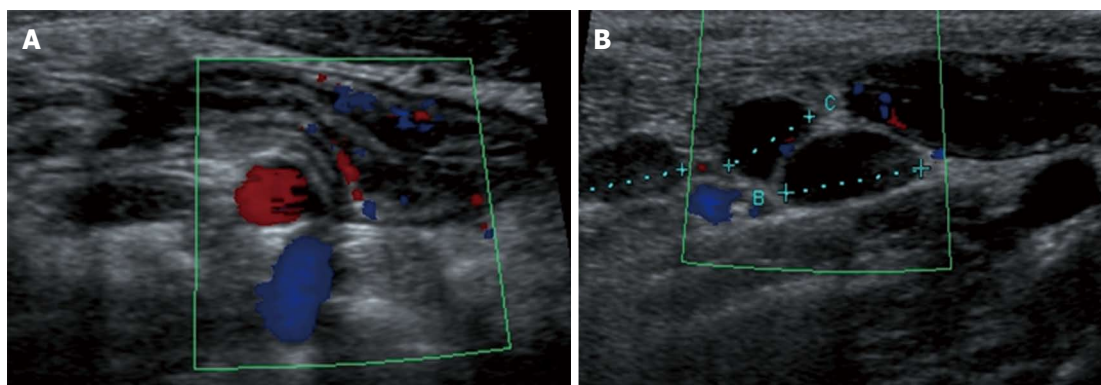


Figure 4 Longitudinal view of the terminal ileum in a 13-year-old boy with active Crohn's disease. The bowel wall is thickened and shows increase in Color Doppler signals denoting inflammatory hyperemia (A). Note in (B) the fibrofatty proliferation of the surrounding mesentery which appears hyperechoic and the enlarged mesenteric lymph-nodes.



Figure 5 Longitudinal section of a distal ileal loop showing stiffness, mural thickening (arrowhead), lumen narrowing (arrow) and mild dilatation of the pre-stenotic segment (asterisk), suggesting a fibrotic nature of the stenosis.

of patients with CD^[39,40] and in early identifying intra-abdominal complications, such as abscesses, fistulae and strictures^[41-44]. The reported sensitivity of US in detecting CD strictures approximately is 74%-80%^[41]. US can also aid differentiate between fibrotic and inflammatory strictures. An increased Colour-Doppler signal in the stenosis is suggestive of activity, while poor vascularity of the bowel wall, an adjacent loops' retraction and a pre-stenotic bowel segment distension are suggestive of fibrotic stenosis (Figure 5)^[31].

Some challenges about US still remain: US strongly relies on the operator's experience and skill more than other imaging modalities, and it requires an high resolution equipment. Moreover, even in expert hands, US may result in false positive findings^[34]: thickening of the intestinal wall is not specific for CD, also being present in infectious, neoplastic and other inflammatory conditions. US may also provide false negative results^[38,42], for example in obese patients or when CD is characterized by only superficial lesions, like isolated aphthous ulcers and mucosal erosions, or in presence of intestinal gas that make hardly visible the bowel wall, particularly the proximal ones.

Small Intestine Contrast US (SICUS). Some studies

in adults have demonstrated that the so called SICUS, enables to overcome limits of standard US. Dissociation of intestinal overlapping loops and visualization of the entire SB, from the Treitz angle to the ileo-cecal valve, are obtained by distending the SB with an oral anechoic non-absorbable contrast solution (iso-osmolar polyethylene glycol)^[36]. Briefly, US examination is performed after the ingestion of the oral contrast solution, that fill in the loops, and the administration of the intravenous (*iv*) contrast. Unfortunately the procedure is time consuming, requiring in some cases more than 2 hours. Pallotta *et al*^[28] studied 148 patients, 57 with a known diagnosis of CD, showing SICUS to be more sensitive and specific (94% and 98%, respectively) than conventional US (57% and 100% respectively) in assessing SB lesions. The use of an oral contrast agent can significantly improve US sensitivity, approximately of 90% (Figure 6) and of over 75% for a single and multiple SB stenosis, respectively^[42].

SICUS can make a dynamic evaluation of the affected segment differentiating between inflammatory and fibrotic stenosis. In fact, it can assess lumen stenosis and dilatation of the prestenotic segment, mural thickness with bowel wall stratification pattern and peristalsis of the affected segment differentiating between. SICUS is a very promising technique in children with CD, but its use in pediatric patients has still to be investigated.

CROSS SECTIONAL IMAGING

Good distension of SB loops during the CT and MRI examination is crucial for the correct evaluation of bowel wall abnormalities since collapsed SB loops are difficult to evaluate for bowel wall thickening or hyper-enhancement. Distension of the SB can be achieved by fluid administration after naso-jejunal intubation (CT/MR enteroclysis)^[45,46] or per Os (CT/MR enterography)^[47,48]. Although better distension of the loops is obtained with the MR/CT enteroclysis, there are various studies that show comparable accuracy between the two techniques^[20,45,47,48]. The placement of the nasojejunal tube, necessary for the enteroclysis, is invasive, requires the use of ionizing



Figure 6 The oral anechoic contrast solution, (polyethylene glycol), allows a better definition of lumen narrowing (arrow) and pre-stenotic dilatation (asterisk) as well as a more accurate measurement of the length of the stenosis. Small intestine contrast ultrasonography also provides a dynamic assessment of the stenotic bowel loop: poor distensibility and presence of pre-stenotic dilatation suggest fibrosis, whereas normal distensibility and preserved peristalsis are features of inflammatory stenosis.

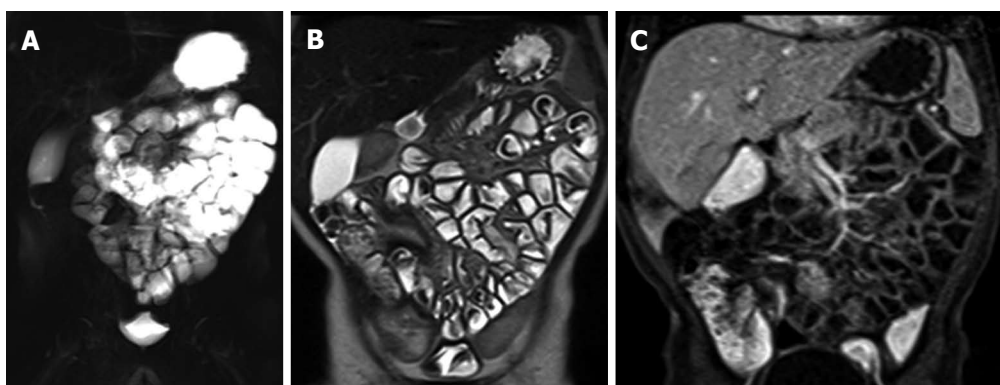


Figure 7 Magnetic resonance enteroclysis under anesthesia in one-year old male with Crohn's disease at colonoscopy. Coronal thick-slab HASTE image (A) shows good opacification of proximal and distal small bowel. The coronal T2-weighted (T2-w) image (B) and coronal fat-suppressed (FS) three-dimensional (3D) T1-weighted (T1-w) breath-hold gradient-echo (GE) image (C) are performed in free breathing.

radiations, which also entails the need for coordination between MR/CT suites and fluoroscopy units, and it can be very anxiety provoking resulting in poor patient tolerance. Moreover, the increased time and costs compared to enterography, make CT/MR enterography the preferred imaging method, respect to CT/MR enteroclysis, in pediatric patients.

An important limitation of CT/MR enterography is the need to drink an important amount of fluid in a short time, particularly uncomfortable in young patients. The assessment of mucosal abnormalities requires a correct distension of the loops obtained only with a proper timing of the study both in scanning or fluid ingestion. The collapsed bowel loops may mimic wall thickening and hyper-enhancement, leading to false-positive results.

The younger patients and the parents have to be motivated and aware of the importance of performing an adequate SB distension, which is fundamental for obtaining an optimal MR examination. The presence of a parent in the MR room is reassuring for younger children.

Most children diagnosed with IBD are of school age or adolescence. In a study from uniform data collected from a cohort of pediatric patients with IBD (1370 children), the mean age at diagnosis was 10.3 years with 47.7% diagnosed at 6 to 12 years of age and 36.9% at 13 to 17 years of age^[49]. In our experience, children of this age are generally able to undergo the exam without seda-

tion.

In the event a child refuses to drink the contrast agent, we will offer placement of a temporary nasogastric tube for contrast agent delivery. The enteric tube will be removed right after all of the contrast material is given and before the MR examination begins.

Patients under the age of 6 years, who require anesthesia do not undergo MR enterography and are usually imaged by using high-resolution bowel US or MR enteroclysis under anesthesia. The positioning of the tube takes place after the anesthesia. Children between 6 mo and 6 years of age are usually sedated with the intravenous injection of midazolam (Versed; Hoffman-La Roche, Basel, Switzerland) (0.05 mg per kilogram of body weight) or pentobarbital (Nembutal; Ovation Pharmaceuticals, Deerfield, Ill) (5 mg per kilogram of body weight). The sequences are performed in free breathing, making them as short as possible (Figure 7).

Computed Tomography

The relatively high radiation exposure is a limitation to the use of multi-detector CT (MDCT) enterography in children, and, in fact, most data regarding this method come from studies in adults^[50]. The only recent pediatric IBD population's study^[51] concluded that MDCT can be used as an alternative to barium studies for the evaluation

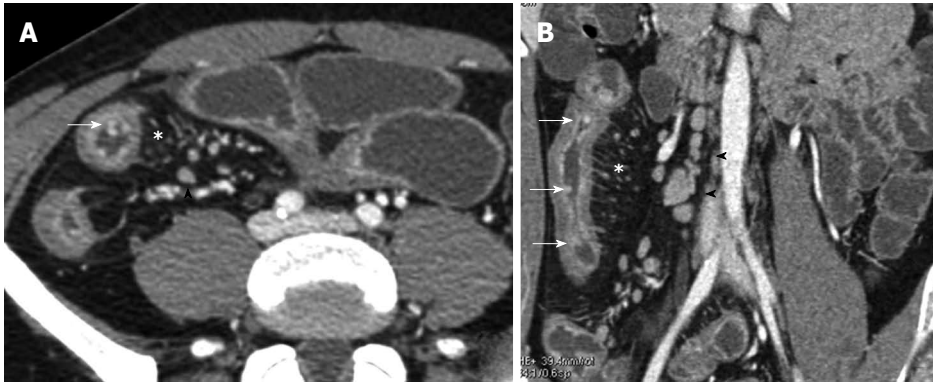


Figure 8 Transverse (A) and coronal (B) computed tomography show bowel wall thickening and mucosal hyper-enhancement with pseudo polyps (white arrows) as well as mesenteric lymph nodes, that are irregular in size and shape (black arrowhead) and increased mesenteric vascularity (asterisk). These features may be detected in case of acute exacerbation on a background of longstanding disease.

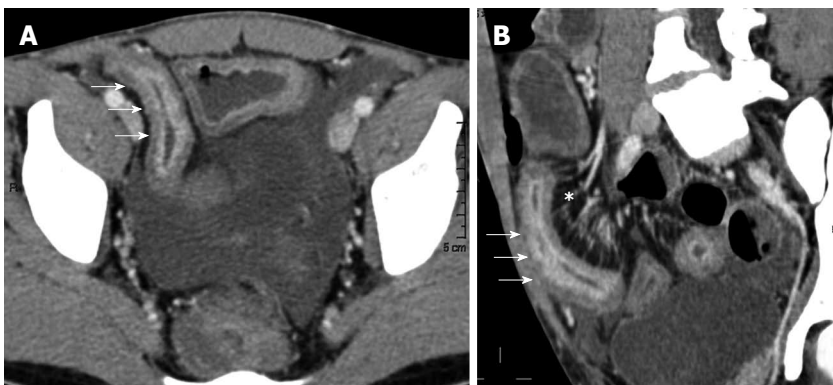


Figure 9 Transverse (A) and MRP sagittal (B) computed tomography show stratified enhancement of terminal ileum (arrows), and hyperemic mesentery with the "comb sign" (asterisk).

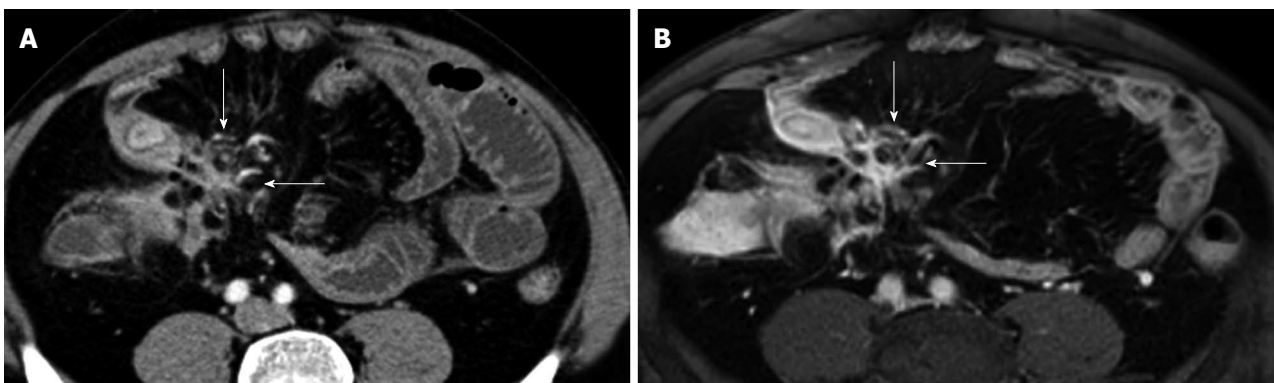


Figure 10 Transverse computed tomography (A) and post contrast T1-fat sat magnetic resonance imaging (B) images show a complex network between closely adherent small bowel loops appearing as a stellate configuration (arrows) due to entero-enteric fistulas.

of the SB and that most of the children prefer CT rather than barium studies. Several studies on adult population showed that is an excellent non-invasive tool for diagnosing CD, and for the follow-up of the disease during therapy^[19,20,52-54]. CT enterography can establish disease extension and activity on the basis of wall thickness and increased *in vivo* contrast enhancement. In recent studies bowel wall thickness is considered pathological when exceeds 3 mm^[55,56] (Figure 8). A sign of active disease is an

increased bowel wall enhancement after administration of *in vivo* contrast medium^[57,58]. The post-contrast wall pattern depends on the different enhancement of the mucosa and/or serosa and the submucosa, usually hypodense for the presence of edema, and can be seen as mural stratification or target sign (Figure 9), with two or three different layers of density respectively. In chronic CD, the affected segments may present a non-enhancement pattern after contrast medium, with the loss of mural stratifica-

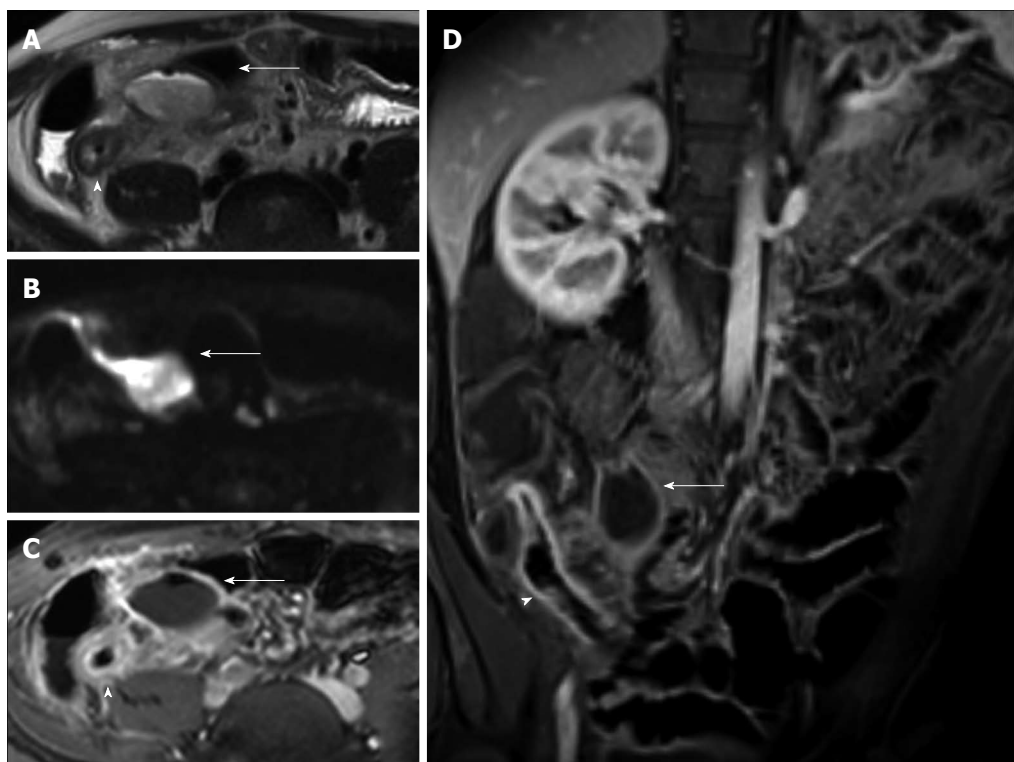


Figure 11 Eighteen-years-old female with active Crohn's disease and abscess. Transverse T2-w (A), DWI (B), transverse (C) and coronal (D) post-contrast FS-T1-w image (C) show inflamed segments of the terminal ileum (arrowhead) with pericecal fluid-collection around thickened and hyper-vascular walls (arrow), according to abscess. A small air bubble in the antideclive portion of the fluid collection is visible in the transverse T2-w (A) and transverse post-contrast FS-T1-w image (C).

tion, suggestive of fibrosis. Another typical extramural lesion in CD is the comb sign due to an increased vascularity of the mesentery seen in the images as tortuous dilated vessels associated with a wide spacing of the vasa recta (Figure 8).

The most reliable criterion to define a stricture is a localized, persistent narrowing, whose functional effects may be judged from pre-stenotic dilatation^[59]. CT, together with MRI, is the most accurate technique to detect the presence of extraluminal complications, such as abscesses, fistulae (Figure 10) and inflammatory conglomerates in CD^[20,46,53,54,60-62].

CT has a high accuracy in the imaging of CD but it is limited by the use of ionizing radiations especially in children particularly in these type of chronic diseases that require a close follow up^[13,63].

The radiation dose can be significantly reduce by the use of last generation MDCT scan with specific pediatric protocols^[64,65] which include the introduction of noise to simulate low-dose exams^[66].

Still, in pediatric patients MR must be preferred to MDCT, since it does not use ionizing radiation to which children are more vulnerable than adults for their longer life expectancy. Moreover, despite new formulations and improved safety, iodinated contrast media for CT are not without risk and the risks must be balanced against the possible benefits. However, in the hospitals without MR scan, or where it is difficult to schedule an emergent MRI, or in emergency situations, such as high-grade SB occlusion, MDCT remains the best technique in pediatric

patients, too. In fact CT has greater availability and it is less time-consuming than MR (20-30 min for MR, respect to 10 s for MDCT).

Magnetic Resonance

The main advantages of MRI are, in addition to the lack of ionizing radiations, a superior soft tissue contrast with a better assessment of trans and extramural disease, its noninvasiveness and the multiplanar capability. Additionally, some MRI sequences (diffusion, perfusion, motility) can provide functional and quantitative information of the bowel wall (diffusion, perfusion, motility) that CT cannot obtain. Especially, diffusion-weighted sequence does not significantly increase the time of the examination and may provide helpful clues for the identification of areas of active inflammation and of abscesses (Figure 11) without *in vivo* contrast agent. Moreover, the use of cine MRI in patients suffering from CD proves the association of motility changes of the SB wall and extraluminal alterations, which can help in the differential diagnosis between fibrotic and inflammatory stenosis^[67].

In relation to imaging features, CD may present as active inflammation (without strictures or fistulas), penetrating lesions, or fibrostenotic disease^[68]. Patients may present characteristics of more than one disease subtypes.

Active disease. Various MR imaging findings have been proposed as correlating with CD activity. Increased wall thickening and mural contrast enhancement (CE) on MRI were found to be sensitive and specific for active CD in pediatric population^[69]. Laghi *et al*^[69] found a strong

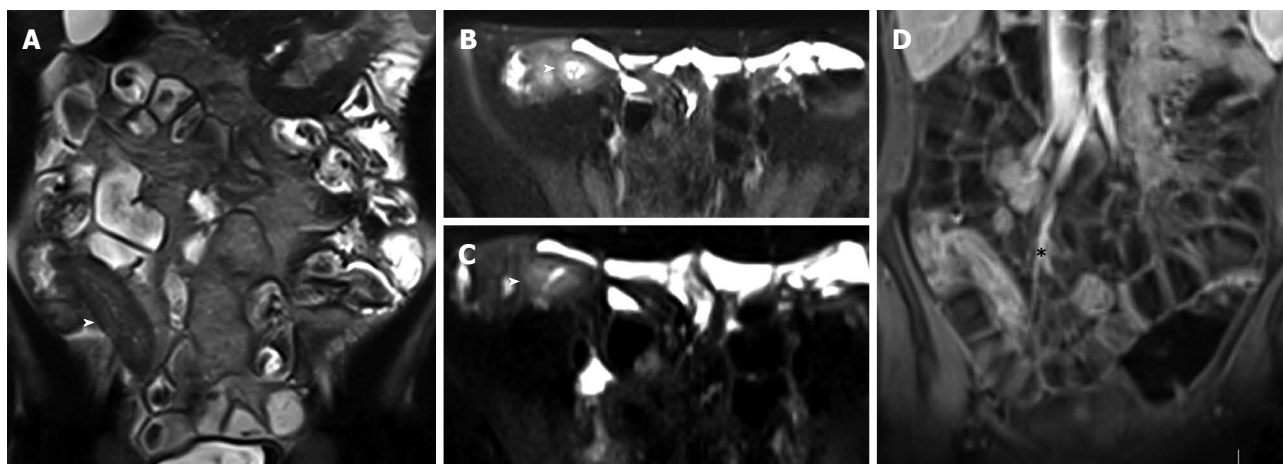


Figure 12 Thirteen years old male with active Crohn's disease. Coronal T2-weighted image (A), and transverse fat saturation T2-weighted images (B and C), show mural thickness and increased mural signal (arrowhead in B, C, and D) in the terminal ileum due to edema. Coronal post-contrast T1-weighted fat-suppressed image (D) at the same level shows mural stratification (asterisk).

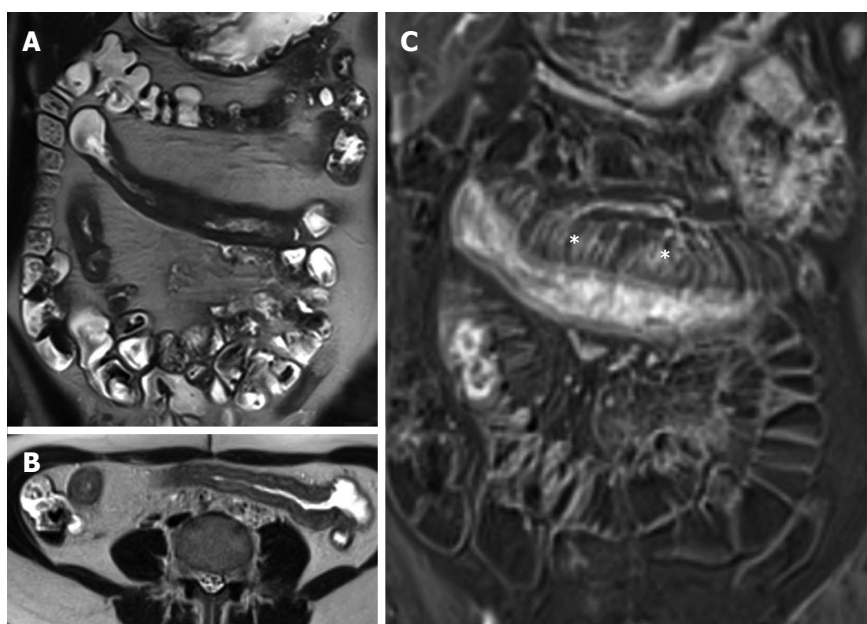


Figure 13 Thirteen years old female with active Crohn's disease. Coronal (A), transverse (B) T2-weighted images show thickened, inflamed segments of ileum and fat proliferating in the mesentery. The thin layer of high signal on T2 in b represents edema. The mass of the fat will displace adjacent small bowel. Coronal post-contrast T1-weighted fat-suppressed image (C) shows increased vascularity (asterisks), named "comb sign", adjacent to a hyper-enhancing thickened segment of ileum.

correlation between a semi-quantitative score (reflecting bowel-wall CE and thickening) and Pediatric Crohn's Disease Activity Index (PCDAI) in CD patients. In a recent study on pediatric population, Alexopoulou *et al.*^[70] showed that the MR percentage of CE (%CE) of the bowel wall do not correlate with PCDAI values. Other studies have reported similar results in the past^[71,72], while a correlation with C-reactive protein (CRP) was already demonstrated in pediatric^[70] and adult^[71] population. In children, clinical evaluation of disease activity may be even more subjective due to incomplete cooperation, and this explains the observed lack of correlation between PCDAI and %CE values, while in contrast, %CE values were correlated with CRP, which is a more objective

marker of inflammation^[70].

The wall thickening, its high mural signal intensity on T2-weighted fat-saturated (FS-T2-w) images, and the presence of mural stratification on post-contrast T1-weighted fat-saturated (FS-T1-w) images reflect histologic features of acute SB inflammation in CD^[69,71,72] (Figure 12). A purely quantitative approach would be desirable for MRI evaluation of active disease. However, in patients with CD, measurements of the bowel wall MR signal intensity are subjected to wide limits of both inter- and intra-reader agreement, which may substantially limit their utility when applied to the development of quantitative measures of inflammatory activity in the affected bowel segments^[73,74].

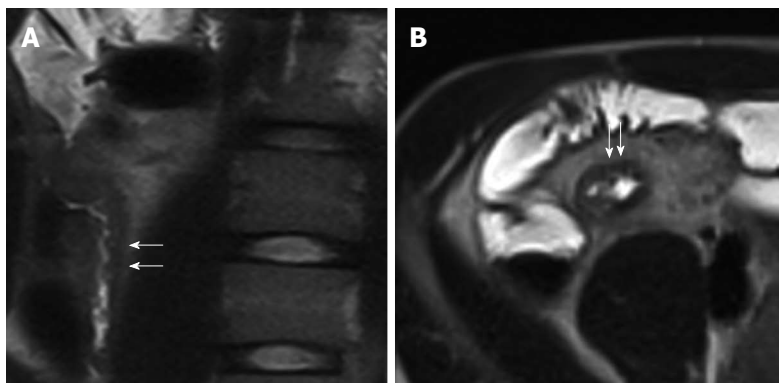


Figure 14 Coronal (A), transverse (B) T2-weighted images show thickened, inflamed segments of the terminal ileum with deep ulcers seen as high-contrast protrusions within bowel wall (arrows).

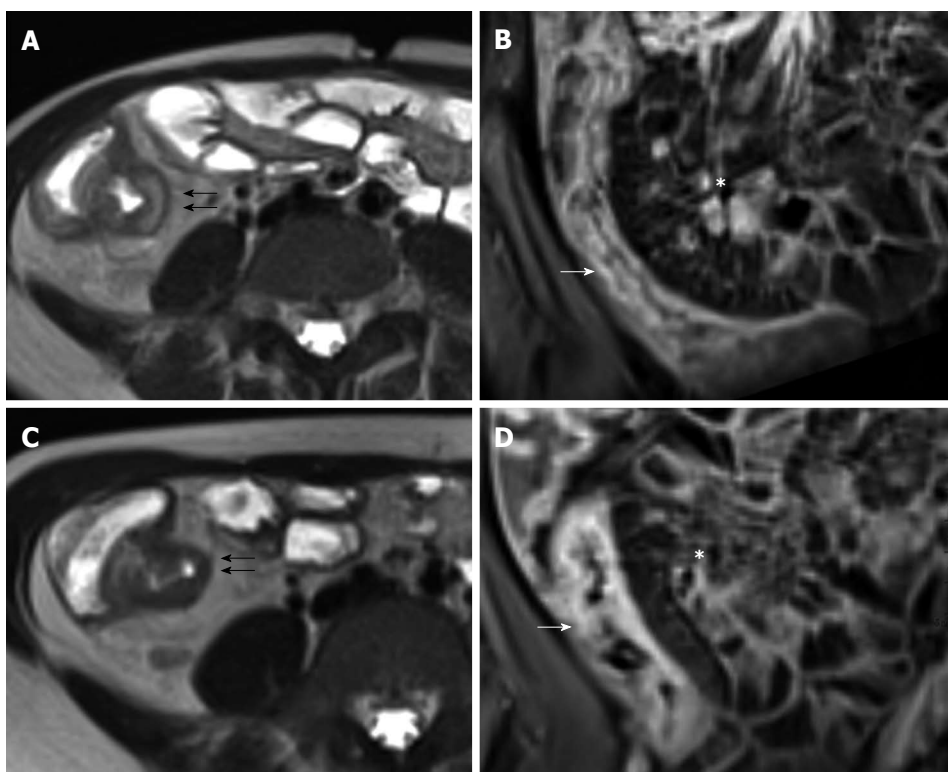


Figure 15 Twelve years old female with active disease and follow-up. Transverse T2-weighted image (A) shows mural thickening (arrows) and increased mural signal (arrow) in the terminal ileum and coronal T1-weighted image (B) shows mural stratification (arrow), increased mesenteric vascularity adjacent to the inflamed bowel loop (the comb sign), and enlargement and hyper-enhancement of lymph-nodes (asterisk). In the same patient and at the same level, six months later after therapy, transverse T2-weighted image (C) shows the loss of increased mural signal (arrow) and coronal T1-weighted image (D) shows homogeneous enhancement without mural stratification (arrow), reduction of increased mesenteric vascularity adjacent to the inflamed bowel loop, and disappearance of lymph-nodes (asterisk).

Acute inflammation can also present with the comb sign (Figure 13), due to an increased vascularity of the mesentery, ulcers (Figure 14) and enlarged and high enhancing lymph-nodes^[74-77].

A proper luminal distension is essential to assess ulcers on MRI, especially if superficial^[74]. In a systematic review of seven studies^[52], MRI showed an accuracy of 91%, 62% and 62% in correctly staging a frank, mild and in remission disease, respectively. MRI more often overstaged than understaged disease activity in CD, but in most of these patients radiological staging and disease staging by the reference standard differed one grade. However, this review has the limit of including old studies without considering the new state-of-the-art tech-

niques.

Actually radiologist use different protocols and features for grading CD, as recently showed by Ziech *et al*^[78]. The authors show that the most frequently used MR protocols include T2-w (79%) and CE FS-T1-w (83%) sequences and that the features most frequently seen as important for grading are the presence of bowel wall thickening (79% of radiologists), abscesses (75%) and CE (75%) and stratification (46%) at T1-w images.

Currently, the most important applications of MR care the confirmation of the disease and the follow-up of patients with an already established diagnosis of CD, both by monitoring the response to medical treatment by assessing disease activity (Figure 15) and by early identify-

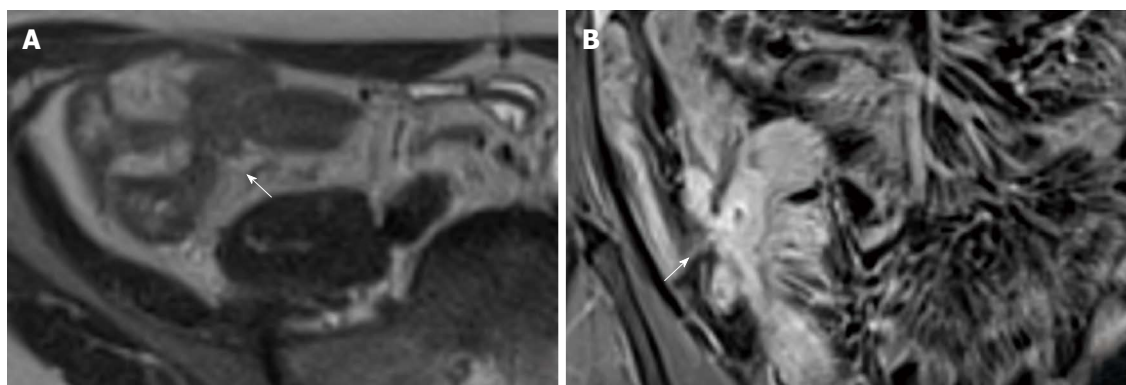


Figure 16 Transverse T2-w image (A) and coronal post-contrast FS-T1-w image (B) show cluster of bowel loops (arrow) interconnected by fistulas and adhesions.

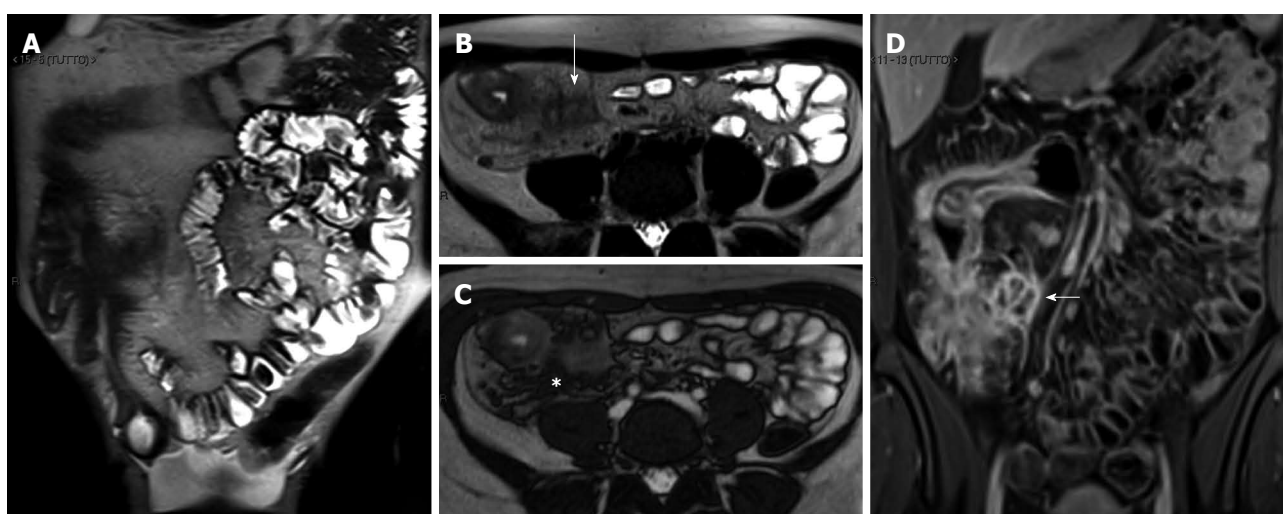


Figure 17 Coronal (A) and transverse (B and C) CE FS-T1-w 3D gradient-echo image show a small abscess close to the terminal ileum (arrows). Mural stratification and "comb sign" of the right colon flexure (black arrow), cecum (curved arrow), and appendix (white arrow) and homogeneous avid enhance of the terminal ileum (arrowhead). Enlargement and hyper-enhancement lymph-nodes (asterisk) are also visible.

ing of abscesses, fistulae and strictures.

Penetrating disease

Transmural inflammation can result from ulcers that deeply penetrate the bowel wall forming serpiginous tracts and fistulas.

MR enterography is accurate in identifying extraluminal complications of CD. In young adults MR enterography showed a diagnostic value similar to MDCT enterography at least for acute complications of CD, such as fistulas and abscesses^[79]. The abscesses can be treated by percutaneous interventions. Whereas penetrating disease may benefit from antibiotics or biologic therapies, while the use of steroids is usually avoided. Because of the exquisite sensitivity to detect fluid as well as its superior soft tissue contrast, MR easily depicts entero-entero (Figure 16), entero-vesicular, entero-cutaneous, perianal fistulae and abscesses (Figure 17). MR imaging may also detect small volumes of gas within an abscess (Figure 11). MR enterography can assess fistulizations, sinus tracts, and abscesses, especially with the use of post-contrast FS-

T1-w images (Figure 10) because of their avidly enhancing walls^[80]. Entero-enteric fistulas often form a complex network between closely adherent SB loops that may appear as a stellate configuration on CE MR images.

Fibrotensosing disease

Over the time, chronic inflammation of the bowel wall may evolve in mural fibrosis that can lead to intestinal occlusion if it causes strictures. The identification of fibrotic stenosis is fundamental for they are not responsive to medical therapy and need surgical resection. In general MR enterography has a good accuracy in assessing SB strictures that are considered significant if the dilatation of the upstream bowel exceeds 3 cm^[77] (Figure 18). When there is mural fibrosis with permanent strictures, the thickened bowel wall of the pathological segment does not show a hyperintensity on T2-w images or a stratified post-contrast pattern on T1-w images typical of acute inflammation^[74]. These items may be useful to distinguish between transient strictures supported by acute inflammation or fibrotensosing disease (Figure 19).

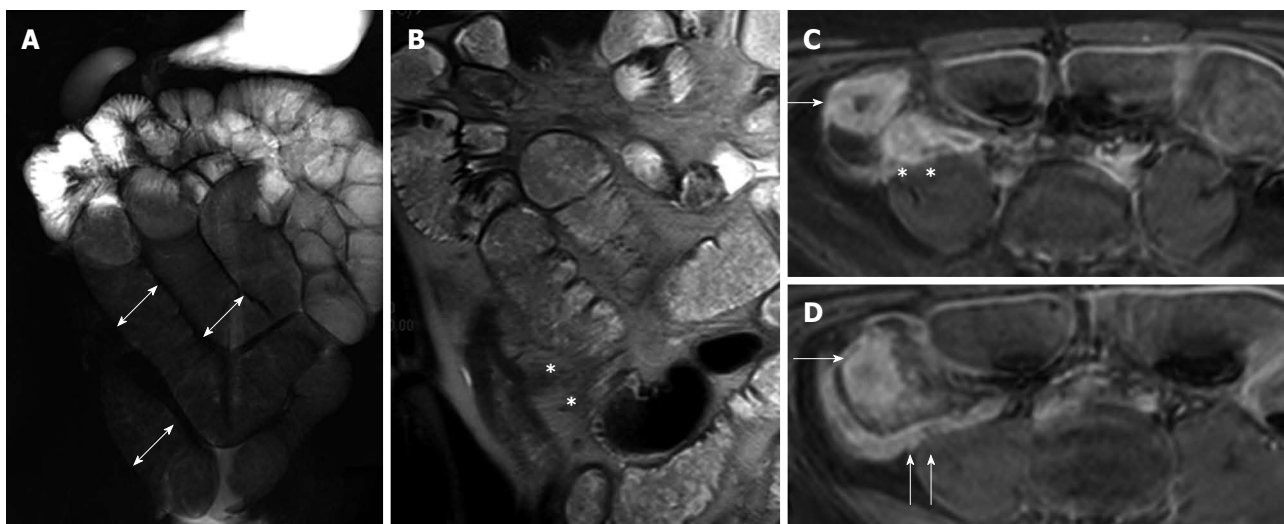


Figure 18 Fifteen years old male with small bowel obstruction caused by fibrotic stricture. Thick-slab T2-w sequence (A) shows bowel dilatation greater than 3 cm (double arrows), according to functionally significant stricture. Coronal T2-w sequence (B) shows mural thickening of the terminal ileum without increased wall signal (asterisks). Transverse (C and D) CE FS-T1-w 3D GE show a homogeneous avidly enhancing of the cecum (arrow in C and D), terminal ileum (asterisks in C) and appendix (arrows in D). These findings can be finding in the small bowel obstruction due to fibrotic stricture.

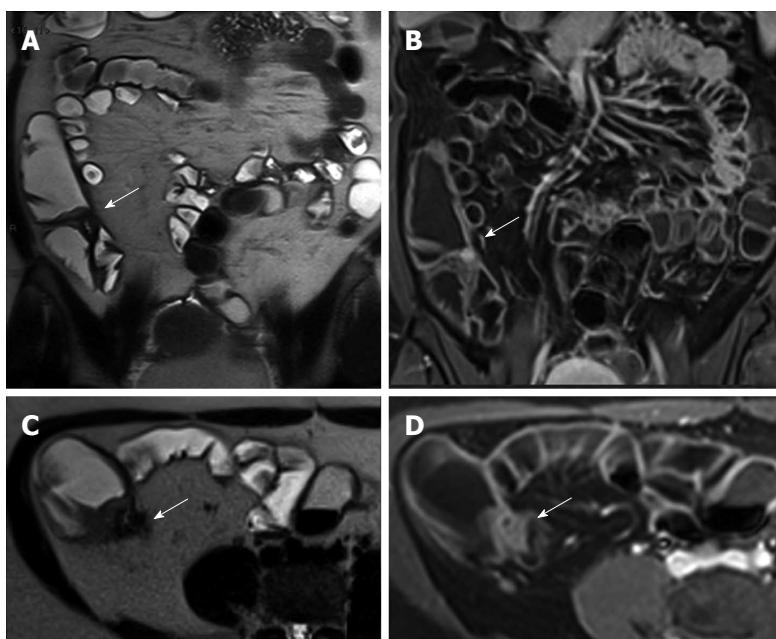


Figure 19 Eighteen-years-old female with long standing Crohn's disease. Coronal (A), transverse (B) T2-w images and coronal (C), transverse (D) post-contrast FS-T1-w images show thickening and hyper-enhancement of the ileocecal valve causing stricture.

Cine MRI sequences, allowing the evaluation of bowel motility, can further help this differential diagnosis. Inflammation along the mesenteric border often result in pseudosacculations along the antimesenteric border and can be thought of as the MR equivalent of the mesenteric border linear ulcer seen at SBF^T examination (Figure 20). In general, the affected segments are characterized by increased rigidity, loss of distensibility and diminished peristalsis.

Suspected CD: In young patients with suspected CD, MR enterography is a valid method to diagnose or ex-

clude the disease. Particularly, it can be used as the first radiological modality in pediatric patients in which the results of endoscopy examinations are normal but a high suspicion of CD is still present^[81]. However, there is much debate about the best modality to use to examine the SB, because wireless endoscopic examinations, like radiological studies, have their advantages, such as the non-invasiveness and the high diagnostic accuracy in evaluating the small intestine, especially in patients who cannot undergo MR, whose bowel loops are not optimally distended or who are uncooperative, and disadvantages, such as capsule retention due to ileal strictures and

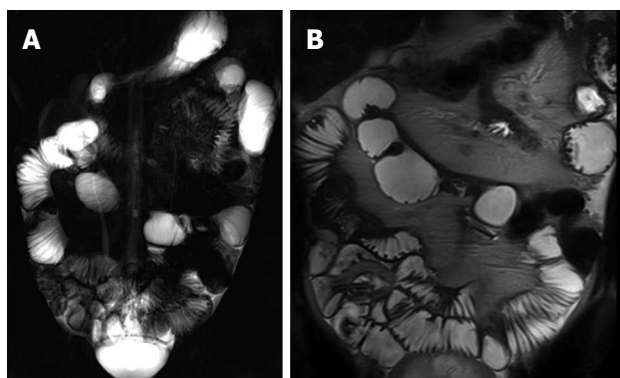


Figure 20 Coronal thick-slab HASTE (A) and coronal T2-weighted (B) images show pseudosacculations produced by asymmetric thickening of the ileal mesenteric border.

delayed capsule transit due to inflammatory lesions^[82,83]. If a bowel obstruction is suspected, MR enterography is preferred to capsule endoscopy for the risk of capsule retention^[84]. Moreover, MR enterography can help the diagnosis of terminal ileitis in symptomatic patients when endoscopy is unsuccessful.

Additional MRI findings: Extra-intestinal lesions are detected with MRI in 24%-58% of patients^[84-86]. Herfarth *et al*^[86] performed MR enteroclysis in 710 patients with a suspicion or a diagnosis of IBD finding extra-intestinal lesions in 57% of patients of which the 12% of great clinical importance. The colonic features of CD at MR enterography can reliably be diagnosed only in severe inflammation (Figure 21).

The detection of colonic mild disease can be very difficult even if the colon is well distended with the help of a rectal enema (MR colonography); moreover the main weaknesses of MR colonography is the impossibility of obtaining tissue sampling. However, Rimola *et al*^[87] demonstrated good correlations between the presence and the severity of CD lesions depicted with endoscopy and MR Colonography.

MR is an effective imaging technique for the evaluation of patients with perianal CD. During MR enterography, it is possible to perform specific pelvic sequences, such as FS-T2-w, to evaluate perianal CD, increasing only few minutes of exam time (Figure 22).

MR has an accuracy of 76%-100% compared to examination under anesthesia for fistulae and may provide additional information^[88]. This technique is an important tool because it can accurately reveal the location and extent of disease, including a clinically undetected fistula or abscess, and it can guide surgery^[89].

3T MRI: There has been little experience of the use of 3 Tesla (T) MR imaging in children with CD, but it seems to have the advantage of increasing the signal-to-noise ratio (SNR) of approximately 1.7-1.8 times compared to 1.5T MR. This increases the spatial and/or temporal resolution, improving the detection of early, superficial or subtle abnormalities. However, the 3T advantages are

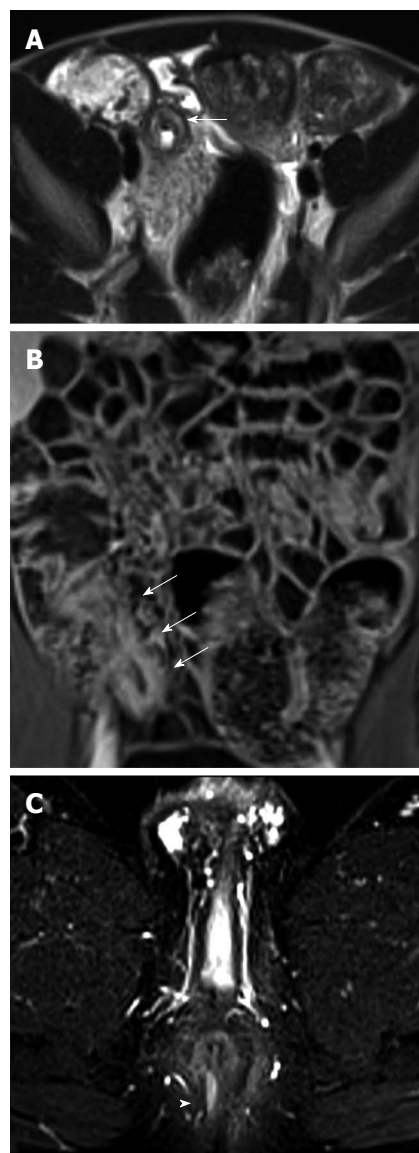


Figure 21 Colonic distention is optimized with a rectal enema. Coronal T2-w (A) and post-contrast FS-T1-w (B) images show bowel wall thickening, and mural stratification of terminal ileum (arrow) and sigma (arrows) walls.

potentially offset by other issues such as greater chemical shift, susceptibility artifact, B1 inhomogeneity and specific absorption rate^[90,91].

PET-CT ENTEROGRAPHY

Combining the morphologic patterns obtained by CT enterography with the ¹⁸F-FDG metabolic activity obtained by PET, PET-CT enterography as a single test may provide accurately fused morphologic, physiologic, and metabolic imaging, useful in the diagnosis, evaluation of activity, follow-up, and objective assessment of CD^[92]. Groshar *et al*^[93] showed a statistically significant difference in mean SUV max among the different mural patterns revealed on CT enterography: intramural edema (active inflammation), intramural soft tissue attenuation (inflammatory infiltrate), and intramural fat (chronic inflamma-

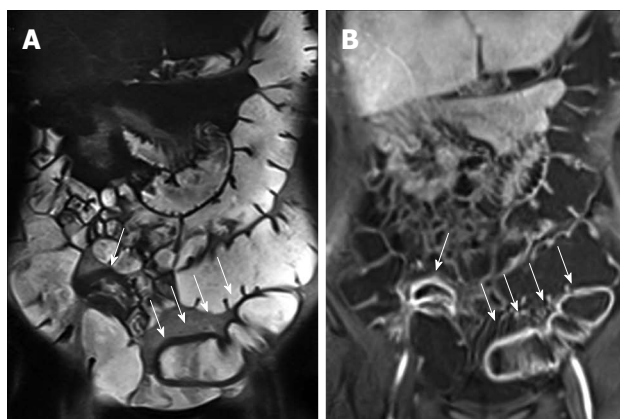


Figure 22 Twelve years old male with terminal ileum Crohn's disease and perianal fistula. Transverse T2-w (A) and post-contrast FS-T1-w (B) shows terminal ileum submucosa edema (black arrow) and mural stratification (arrows), respectively. Transverse FS-T2-w (C) image shows perianal fistula (arrowhead) in the same patient.

tion). Therefore, PET-CT data could help to distinguish between acute inflammation and fibrotic strictures. However, physiologic uptake of FDG by the intestine can lead to false positive results^[94,95]. Moreover, the effective dose from PET-CT is actually too high for pediatric patients^[92].

CONCLUSION

The diagnosis and management of CD in children has changed dramatically over the last decade, mainly due to the increased awareness of the risk of the ionizing radiations, the availability of improved diagnostic modalities, and newer, more powerful treatments such as biologics. Techniques without ionizing radiation (US and MRI) are the preferred modalities for the evaluation of the SB in pediatric patients. The goals of the proximal future studies will be the development of a MR validated score system capable of measuring intestinal damage and inflammatory disease activity in children with CD. In future, a potential new imaging technique could be the PET-MR, which combines the morphological MR images with the functional PET information. Several radiopharmaceuticals are now available for imaging CD, but new tracers could change the future of the diagnostic imaging.

REFERENCES

- 1 **Levine A**, Griffiths A, Markowitz J, Wilson DC, Turner D, Russell RK, Fell J, Ruemmele FM, Walters T, Sherlock M, Dubinsky M, Hyams JS. Pediatric modification of the Montreal classification for inflammatory bowel disease: the Paris classification. *Inflamm Bowel Dis* 2011; **17**: 1314-1321 [PMID: 21560194 DOI: 10.1002/ibd.21493]
- 2 **Cuffari C**, Dubinsky M, Darbari A, Sena L, Baldassano R. Crohn's jejunoileitis: the pediatrician's perspective on diagnosis and management. *Inflamm Bowel Dis* 2005; **11**: 696-704 [PMID: 15973125]
- 3 **Torkzad MR**, Ullberg U, Nyström N, Blomqvist L, Hellström P, Fagerberg UL. Manifestations of small bowel disease in pediatric Crohn's disease on magnetic resonance enterography. *Inflamm Bowel Dis* 2012; **18**: 520-528 [PMID: 21538711 DOI: 10.1002/ibd.21725]
- 4 **Shikhare G**, Kugathasan S. Inflammatory bowel disease in children: current trends. *J Gastroenterol* 2010; **45**: 673-682 [PMID: 20414789 DOI: 10.1007/s00535-010-0241-5]
- 5 **Chouraki V**, Savoye G, Dauchet L, Vernier-Massouille G, Dupas JL, Merle V, Laberrenne JE, Salomez JL, Lerebours E, Turck D, Cortot A, Gower-Rousseau C, Colombel JF. The changing pattern of Crohn's disease incidence in northern France: a continuing increase in the 10- to 19-year-old age bracket (1988-2007). *Aliment Pharmacol Ther* 2011; **33**: 1133-1142 [PMID: 21488915 DOI: 10.1111/j.1365-2036.2011.04628.x]
- 6 **Cuffari C**, Darbari A. Inflammatory bowel disease in the pediatric and adolescent patient. *Gastroenterol Clin North Am* 2002; **31**: 275-291 [PMID: 12122738]
- 7 **Stuart S**, Conner T, Ahmed A, Steward M, Maclachlan J, Wylie P, Beal I. The smaller bowel: imaging the small bowel in paediatric Crohn's disease. *Postgrad Med J* 2011; **87**: 288-297 [PMID: 21242573 DOI: 10.1136/pgmj.2010.106641]
- 8 **Mackalski BA**, Bernstein CN. New diagnostic imaging tools for inflammatory bowel disease. *Gut* 2006; **55**: 733-741 [PMID: 16609136]
- 9 **Fletcher JG**, Fidler JL, Bruining DH, Huprich JE. New concepts in intestinal imaging for inflammatory bowel diseases. *Gastroenterology* 2011; **140**: 1795-1806 [PMID: 21530746 DOI: 10.1053/j.gastro.2011.02.013]
- 10 **Pariente B**, Cosnes J, Danese S, Sandborn WJ, Lewin M, Fletcher JG, Chowers Y, D'Haens G, Feagan BG, Hibi T, Hommes DW, Irvine EJ, Kamm MA, Loftus EV, Louis E, Michetti P, Munkholm P, Oresland T, Panés J, Peyrin-Biroulet L, Reinisch W, Sands BE, Schoelmerich J, Schreiber S, Tilg H, Travis S, van Assche G, Vecchi M, Mary JY, Colombel JF, Lémann M. Development of the Crohn's disease digestive damage score, the Lémann score. *Inflamm Bowel Dis* 2011; **17**: 1415-1422 [PMID: 21560202 DOI: 10.1002/ibd.21506]
- 11 **IBD Working Group of the European Society for Paediatric Gastroenterology, Hepatology and Nutrition**. Inflammatory bowel disease in children and adolescents: recommendations for diagnosis—the Porto criteria. *J Pediatr Gastroenterol Nutr* 2005; **41**: 1-7 [PMID: 15990620]
- 12 **Desmond AN**, O'Regan K, Curran C, McWilliams S, Fitzgerald T, Maher MM, Shanahan F. Crohn's disease: factors associated with exposure to high levels of diagnostic radiation. *Gut* 2008; **57**: 1524-1529 [PMID: 18443021 DOI: 10.1136/gut.2008.151415]
- 13 **Gaca AM**, Jaffe TA, Delaney S, Yoshizumi T, Toncheva G, Nguyen G, Frush DP. Radiation doses from small-bowel follow-through and abdomen/pelvis MDCT in pediatric Crohn disease. *Pediatr Radiol* 2008; **38**: 285-291 [PMID: 18183380 DOI: 10.1007/s00247-007-0702-z]
- 14 **Panes J**, Bouhnik Y, Reinisch W, Stoker J, Taylor SA, Baumgart DC, Danese S, Halligan S, Marincek B, Matos C, Peyrin-Biroulet L, Rimola J, Rogler G, van Assche G, Ardizzone S, Ba-Ssalamah A, Bali MA, Bellini D, Biancone L, Castiglione F, Ehehalt R, Grassi R, Kucharzik T, Maccioni F, Maconi G, Magro F, Martín-Comín J, Morana G, Pendsé D, Sebastian S, Signore A, Tolan D, Tielbeek JA, Weishaupt D, Wiarda B, Laghi A. Imaging techniques for assessment of inflammatory bowel disease: joint ECCO and ESGAR evidence-based consensus guidelines. *J Crohns Colitis* 2013; **7**: 556-585 [PMID: 23583097 DOI: 10.1016]
- 15 **Van Assche G**, Dignass A, Panes J, Beaugerie L, Karagiannis J, Allez M, Ochsenkühn T, Orchard T, Rogler G, Louis E, Kupcinkas L, Mantzaris G, Travis S, Stange E. The second European evidence-based Consensus on the diagnosis and management of Crohn's disease: Definitions and diagnosis. *J Crohns Colitis* 2010; **4**: 7-27 [PMID: 21122488 DOI: 10.1016/j.crohns.2009.12.003]
- 16 **Van Assche G**, Dignass A, Reinisch W, van der Woude CJ, Sturm A, De Vos M, Guslandi M, Oldenburg B, Dotan I, Marteau P, Ardizzone A, Baumgart DC, D'Haens G, Gionch-

- etti P, Portela F, Vucelic B, Söderholm J, Escher J, Koletzko S, Kolho KL, Lukas M, Mottet C, Tilg H, Vermeire S, Carbonnel F, Cole A, Novacek G, Reinshagen M, Tsianos E, Herrlinger K, Oldenburg B, Bouhnik Y, Kiesslich R, Stange E, Travis S, Lindsay J. The second European evidence-based Consensus on the diagnosis and management of Crohn's disease: Special situations. *J Crohns Colitis* 2010; **4**: 63-101 [PMID: 21122490 DOI: 10.1016/j.crohns.2009.09.009]
- 17 **Huprich JE**, Rosen MP, Fidler JL, Gay SB, Grant TH, Greene FL, Lalani T, Miller FH, Rockey DC, Sudakoff GS, Gunderman R, Coley BD. ACR Appropriateness Criteria on Crohn's disease. *J Am Coll Radiol* 2010; **7**: 94-102 [PMID: 20142082 DOI: 10.1016/j.jacr.2009.10.009]
- 18 **Kurugoglu S**, Korman U, Adaletli I, Selcuk D. Enteroclysis in older children and teenagers. *Pediatr Radiol* 2007; **37**: 457-466 [PMID: 17377787]
- 19 **Brown S**, Applegate KE, Sandrasegaran K, Jennings SG, Garrett J, Skantharajah A, Maglinte DT. Fluoroscopic and CT enteroclysis in children: initial experience, technical feasibility, and utility. *Pediatr Radiol* 2008; **38**: 497-510 [PMID: 18256816 DOI: 10.1007/s00247-008-0754-8]
- 20 **Wold PB**, Fletcher JG, Johnson CD, Sandborn WJ. Assessment of small bowel Crohn disease: noninvasive peroral CT enterography compared with other imaging methods and endoscopy--feasibility study. *Radiology* 2003; **229**: 275-281 [PMID: 12944602]
- 21 **Hara AK**, Leighton JA, Heigh RI, Sharma VK, Silva AC, De Petris G, Hentz JG, Fleischer DE. Crohn disease of the small bowel: preliminary comparison among CT enterography, capsule endoscopy, small-bowel follow-through, and ileoscopy. *Radiology* 2006; **238**: 128-134 [PMID: 16373764]
- 22 **Batres LA**, Maller ES, Ruchelli E, Mahboubi S, Baldassano RN. Terminal ileum intubation in pediatric colonoscopy and diagnostic value of conventional small bowel contrast radiography in pediatric inflammatory bowel disease. *J Pediatr Gastroenterol Nutr* 2002; **35**: 320-323 [PMID: 12352520]
- 23 **Triester SL**, Leighton JA, Leontiadis GI, Gurudu SR, Fleischer DE, Hara AK, Heigh RI, Shiff AD, Sharma VK. A meta-analysis of the yield of capsule endoscopy compared to other diagnostic modalities in patients with non-stricturing small bowel Crohn's disease. *Am J Gastroenterol* 2006; **101**: 954-964 [PMID: 16696781]
- 24 **Krille L**, Zeeb H, Jahnen A, Mildenerger P, Seidenbusch M, Schneider K, Weisser G, Hammer G, Scholz P, Blettner M. Computed tomographies and cancer risk in children: a literature overview of CT practices, risk estimations and an epidemiologic cohort study proposal. *Radiat Environ Biophys* 2012; **51**: 103-111 [PMID: 22310909 DOI: 10.1007/s00411-012-0405-1]
- 25 **Hara AK**, Leighton JA, Sharma VK, Fleischer DE. Small bowel: preliminary comparison of capsule endoscopy with barium study and CT. *Radiology* 2004; **230**: 260-265 [PMID: 14617764]
- 26 **Albert JG**, Martiny F, Krummenerl A, Stock K, Lesske J, Göbel CM, Lotterer E, Nietsch HH, Behrmann C, Fleig WE. Diagnosis of small bowel Crohn's disease: a prospective comparison of capsule endoscopy with magnetic resonance imaging and fluoroscopic enteroclysis. *Gut* 2005; **54**: 1721-1727 [PMID: 16020490]
- 27 **Alison M**, Kheniche A, Azoulay R, Roche S, Sebag G, Belarbi N. Ultrasonography of Crohn disease in children. *Pediatr Radiol* 2007; **37**: 1071-1082 [PMID: 17899062]
- 28 **Pallotta N**, Tomei E, Viscido A, Calabrese E, Marcheggiano A, Caprilli R, Corazziari E. Small intestine contrast ultrasonography: an alternative to radiology in the assessment of small bowel disease. *Inflamm Bowel Dis* 2005; **11**: 146-153 [PMID: 15677908]
- 29 **Migaleddu V**, Quaia E, Scanu D, Carla S, Bertolotto M, Campisi G, Sirigu D, Virgilio G. Inflammatory activity in Crohn's disease: CE-US. *Abdom Imaging* 2011; **36**: 142-148 [PMID: 20464392 DOI: 10.1007/s00261-010-9622-8]
- 30 **Maconi G**, Radice E, Greco S, Bianchi Porro G. Bowel ultrasound in Crohn's disease. *Best Pract Res Clin Gastroenterol* 2006; **20**: 93-112 [PMID: 16473803]
- 31 **Fraquelli M**, Colli A, Casazza G, Paggi S, Colucci A, Masiroli S, Duca P, Conte D. Role of US in detection of Crohn disease: meta-analysis. *Radiology* 2005; **236**: 95-101 [PMID: 15987966]
- 32 **Darge K**, Anupindi S, Keener H, Rompel O. Ultrasound of the bowel in children: how we do it. *Pediatr Radiol* 2010; **40**: 528-536 [PMID: 20225117 DOI: 10.1007/s00247-010-1550-9]
- 33 **Haber HP**, Busch A, Ziebach R, Stern M. Bowel wall thickness measured by ultrasound as a marker of Crohn's disease activity in children. *Lancet* 2000; **355**: 1239-1240 [PMID: 10770308]
- 34 **Haber HP**, Stern M. Intestinal ultrasonography in children and young adults: bowel wall thickness is age dependent. *J Ultrasound Med* 2000; **19**: 315-321 [PMID: 10811404]
- 35 **Faure C**, Belarbi N, Mougenot JF, Besnard M, Hugot JP, Cézard JP, Hassan M, Navarro J. Ultrasonographic assessment of inflammatory bowel disease in children: comparison with ileocolonoscopy. *J Pediatr* 1997; **130**: 147-151 [PMID: 9003865]
- 36 **Maconi G**, Di Sabatino A, Ardizzone S, Greco S, Colombo E, Russo A, Cassinotti A, Casini V, Corazza GR, Bianchi Porro G. Prevalence and clinical significance of sonographic detection of enlarged regional lymph nodes in Crohn's disease. *Scand J Gastroenterol* 2005; **40**: 1328-1333 [PMID: 16243717]
- 37 **Bremner AR**, Griffiths M, Argent JD, Fairhurst JJ, Beattie RM. Sonographic evaluation of inflammatory bowel disease: a prospective, blinded, comparative study. *Pediatr Radiol* 2006; **36**: 947-953 [PMID: 16845511]
- 38 **Parente F**, Maconi G, Bollani S, Anderloni A, Sampietro G, Cristaldi M, Franceschelli N, Bianco R, Taschieri AM, Bianchi Porro G. Bowel ultrasound in assessment of Crohn's disease and detection of related small bowel strictures: a prospective comparative study versus x ray and intraoperative findings. *Gut* 2002; **50**: 490-495 [PMID: 11889068]
- 39 **Scholbach T**, Herrero I, Scholbach J. Dynamic color Doppler sonography of intestinal wall in patients with Crohn disease compared with healthy subjects. *J Pediatr Gastroenterol Nutr* 2004; **39**: 524-528 [PMID: 15572893]
- 40 **Drews BH**, Barth TF, Hänle MM, Akinli AS, Mason RA, Muehe R, Thiel R, Pauls S, Klaus J, von Boyen G, Kratzer W. Comparison of sonographically measured bowel wall vascularity, histology, and disease activity in Crohn's disease. *Eur Radiol* 2009; **19**: 1379-1386 [PMID: 19184036 DOI: 10.1007/s00330-008-1290-5]
- 41 **Maconi G**, Bollani S, Bianchi Porro G. Ultrasonographic detection of intestinal complications in Crohn's disease. *Dig Dis Sci* 1996; **41**: 1643-1648 [PMID: 8769293]
- 42 **Parente F**, Greco S, Molteni M, Anderloni A, Sampietro GM, Danelli PG, Bianco R, Gallus S, Bianchi Porro G. Oral contrast enhanced bowel ultrasonography in the assessment of small intestine Crohn's disease. A prospective comparison with conventional ultrasound, x ray studies, and ileocolonoscopy. *Gut* 2004; **53**: 1652-1657 [PMID: 15479688]
- 43 **Castiglione F**, de Sio I, Cozzolino A, Rispo A, Manguso F, Del Vecchio Blanco G, Di Girolamo E, Castellano L, Ciacci C, Mazzacca G. Bowel wall thickness at abdominal ultrasound and the one-year-risk of surgery in patients with Crohn's disease. *Am J Gastroenterol* 2004; **99**: 1977-1983 [PMID: 15447760]
- 44 **Pallotta N**, Baccini F, Corazziari E. Contrast ultrasonography of the normal small bowel. *Ultrasound Med Biol* 1999; **25**: 1335-1340 [PMID: 10626620]
- 45 **Schreyer AG**, Geissler A, Albrich H, Schölmerich J, Feuerbach S, Rogler G, Völk M, Herfarth H. Abdominal MRI after enteroclysis or with oral contrast in patients with suspected or proven Crohn's disease. *Clin Gastroenterol Hepatol* 2004; **2**:

- 491-497 [PMID: 15181618]
- 46 **Masselli G**, Casciani E, Poletti E, Lanciotti S, Bertini L, Galdi G. Assessment of Crohn's disease in the small bowel: Prospective comparison of magnetic resonance enteroclysis with conventional enteroclysis. *Eur Radiol* 2006; **16**: 2817-2827 [PMID: 16799782]
- 47 **Negaard A**, Paulsen V, Sandvik L, Berstad AE, Borthne A, Try K, Lygren I, Storaas T, Klow NE. A prospective randomized comparison between two MRI studies of the small bowel in Crohn's disease, the oral contrast method and MR enteroclysis. *Eur Radiol* 2007; **17**: 2294-2301 [PMID: 17483955]
- 48 **Masselli G**, Casciani E, Poletti E, Galdi G. Comparison of MR enteroclysis with MR enterography and conventional enteroclysis in patients with Crohn's disease. *Eur Radiol* 2008; **18**: 438-447 [PMID: 17899102]
- 49 **Heyman MB**, Kirschner BS, Gold BD, Ferry G, Baldassano R, Cohen SA, Winter HS, Fain P, King C, Smith T, El-Serag HB. Children with early-onset inflammatory bowel disease (IBD): analysis of a pediatric IBD consortium registry. *J Pediatr* 2005; **146**: 35-40 [PMID: 15644819]
- 50 **Dillman JR**, Adler J, Zimmermann EM, Strouse PJ. CT enterography of pediatric Crohn disease. *Pediatr Radiol* 2010; **40**: 97-105 [PMID: 19936733 DOI: 10.1007/s00247-009-1465-5]
- 51 **Jamieson DH**, Shipman PJ, Israel DM, Jacobson K. Comparison of multidetector CT and barium studies of the small bowel: inflammatory bowel disease in children. *AJR Am J Roentgenol* 2003; **180**: 1211-1216 [PMID: 12704025]
- 52 **Horsthuis K**, Bipat S, Bennink RJ, Stoker J. Inflammatory bowel disease diagnosed with US, MR, scintigraphy, and CT: meta-analysis of prospective studies. *Radiology* 2008; **247**: 64-79 [PMID: 18372465 DOI: 10.1148/radiol.2471070611]
- 53 **Siddiki HA**, Fidler JL, Fletcher JG, Burton SS, Huprich JE, Hough DM, Johnson CD, Bruining DH, Loftus EV, Sandborn WJ, Pardi DS, Mandrekar JN. Prospective comparison of state-of-the-art MR enterography and CT enterography in small-bowel Crohn's disease. *AJR Am J Roentgenol* 2009; **193**: 113-121 [PMID: 19542402 DOI: 10.2214/AJR.08.2027]
- 54 **Lee SS**, Kim AY, Yang SK, Chung JW, Kim SY, Park SH, Ha HK. Crohn disease of the small bowel: comparison of CT enterography, MR enterography, and small-bowel follow-through as diagnostic techniques. *Radiology* 2009; **251**: 751-761 [PMID: 19276325 DOI: 10.1148/radiol.2513081184]
- 55 **Paulsen SR**, Huprich JE, Fletcher JG, Booya F, Young BM, Fidler JL, Johnson CD, Barlow JM, Earnest F. CT enterography as a diagnostic tool in evaluating small bowel disorders: review of clinical experience with over 700 cases. *Radiographics* 2006; **26**: 641-657; discussion 657-662 [PMID: 16702444]
- 56 **Macari M**, Megibow AJ, Balthazar EJ. A pattern approach to the abnormal small bowel: observations at MDCT and CT enterography. *AJR Am J Roentgenol* 2007; **188**: 1344-1355 [PMID: 17449781]
- 57 **Booya F**, Fletcher JG, Huprich JE, Barlow JM, Johnson CD, Fidler JL, Solem CA, Sandborn WJ, Loftus EV, Harmsen WS. Active Crohn disease: CT findings and interobserver agreement for enteric phase CT enterography. *Radiology* 2006; **241**: 787-795 [PMID: 17032911]
- 58 **Bodily KD**, Fletcher JG, Solem CA, Johnson CD, Fidler JL, Barlow JM, Bruesewitz MR, McCollough CH, Sandborn WJ, Loftus EV, Harmsen WS, Crownhart BS. Crohn Disease: mural attenuation and thickness at contrast-enhanced CT Enterography--correlation with endoscopic and histologic findings of inflammation. *Radiology* 2006; **238**: 505-516 [PMID: 16436815]
- 59 **Silverberg MS**, Satsangi J, Ahmad T, Arnott ID, Bernstein CN, Brant SR, Caprilli R, Colombel JF, Gasche C, Geboes K, Jewell DP, Karban A, Loftus EV, Peña AS, Riddell RH, Sachar DB, Schreiber S, Steinhardt AH, Targan SR, Vermeire S, Warren BF. Toward an integrated clinical, molecular and serological classification of inflammatory bowel disease: report of a Working Party of the 2005 Montreal World Congress of Gastroenterology. *Can J Gastroenterol* 2005; **19** Suppl A: 5A-36A [PMID: 16151544]
- 60 **Schmidt S**, Lepori D, Meuwly JY, Duvoisin B, Meuli R, Michetti P, Felley C, Schnyder P, van Melle G, Denys A. Prospective comparison of MR enteroclysis with multidetector spiral-CT enteroclysis: interobserver agreement and sensitivity by means of "sign-by-sign" correlation. *Eur Radiol* 2003; **13**: 1303-1311 [PMID: 12764646]
- 61 **Gourtsoyiannis NC**, Grammatikakis J, Papamastorakis G, Koutroumbakis J, Prassopoulos P, Rousomoustakaki M, Papanikolaou N. Imaging of small intestinal Crohn's disease: comparison between MR enteroclysis and conventional enteroclysis. *Eur Radiol* 2006; **16**: 1915-1925 [PMID: 16673093]
- 62 **Spalinger J**, Patriquin H, Miron MC, Marx G, Herzog D, Dubois J, Dubinsky M, Seidman EG. Doppler US in patients with crohn disease: vessel density in the diseased bowel reflects disease activity. *Radiology* 2000; **217**: 787-791 [PMID: 11110944]
- 63 **Jaffe TA**, Gaca AM, Delaney S, Yoshizumi TT, Toncheva G, Nguyen G, Frush DP. Radiation doses from small-bowel follow-through and abdominopelvic MDCT in Crohn's disease. *AJR Am J Roentgenol* 2007; **189**: 1015-1022 [PMID: 17954634]
- 64 **Silva AC**, Lawder HJ, Hara A, Kujak J, Pavlicek W. Innovations in CT dose reduction strategy: application of the adaptive statistical iterative reconstruction algorithm. *AJR Am J Roentgenol* 2010; **194**: 191-199 [PMID: 20028923 DOI: 10.2214/AJR.09.2953]
- 65 **Allen BC**, Baker ME, Einstein DM, Remer EM, Herts BR, Achkar JP, Davros WJ, Novak E, Obuchowski NA. Effect of altering automatic exposure control settings and quality reference mAs on radiation dose, image quality, and diagnostic efficacy in MDCT enterography of active inflammatory Crohn's disease. *AJR Am J Roentgenol* 2010; **195**: 89-100 [PMID: 20566801 DOI: 10.2214/AJR.09.3611]
- 66 **Kambadakone AR**, Prakash P, Hahn PF, Sahani DV. Low-dose CT examinations in Crohn's disease: Impact on image quality, diagnostic performance, and radiation dose. *AJR Am J Roentgenol* 2010; **195**: 78-88 [PMID: 20566800 DOI: 10.2214/AJR.09.3420]
- 67 **Froehlich JM**, Waldherr C, Stoupis C, Erturk SM, Patak MA. MR motility imaging in Crohn's disease improves lesion detection compared with standard MR imaging. *Eur Radiol* 2010; **20**: 1945-1951 [PMID: 20379822 DOI: 10.1007/s00330-010-1759-x]
- 68 **Leyendecker JR**, Bloomfield RS, DiSantis DJ, Waters GS, Mott R, Bechtold RE. MR enterography in the management of patients with Crohn disease. *Radiographics* 2009; **29**: 1827-1846 [PMID: 19959524 DOI: 10.1148/rg.296095510]
- 69 **Laghi A**, Borrelli O, Paolantonio P, Ditto L, Buena de Mesquita M, Falconieri P, Passariello R, Cucchiara S. Contrast enhanced magnetic resonance imaging of the terminal ileum in children with Crohn's disease. *Gut* 2003; **52**: 393-397 [PMID: 12584222]
- 70 **Alexopoulou E**, Roma E, Loggitsi D, Economopoulos N, Papakonstantinou O, Panagiotou I, Pahoula I, Kelekis NL. Magnetic resonance imaging of the small bowel in children with idiopathic inflammatory bowel disease: evaluation of disease activity. *Pediatr Radiol* 2009; **39**: 791-797 [PMID: 19452148 DOI: 10.1007/s00247-009-1272-z]
- 71 **Schunk K**, Kern A, Oberholzer K, Kalden P, Mayer I, Orth T, Wanitschke R. Hydro-MRI in Crohn's disease: appraisal of disease activity. *Invest Radiol* 2000; **35**: 431-437 [PMID: 10901105]
- 72 **Durno CA**, Sherman P, Williams T, Shuckett B, Dupuis A, Griffiths AM. Magnetic resonance imaging to distinguish the type and severity of pediatric inflammatory bowel diseases. *J Pediatr Gastroenterol Nutr* 2000; **30**: 170-174 [PMID: 10697136]
- 73 **Koh DM**, Miao Y, Chinn RJ, Amin Z, Zeegen R, Westaby D, Healy JC. MR imaging evaluation of the activity of Crohn's disease. *AJR Am J Roentgenol* 2001; **177**: 1325-1332 [PMID:

- 11717076]
- 74 **Sharman A**, Zealley IA, Greenhalgh R, Bassett P, Taylor SA. MRI of small bowel Crohn's disease: determining the reproducibility of bowel wall gadolinium enhancement measurements. *Eur Radiol* 2009; **19**: 1960-1967 [PMID: 19308416 DOI: 10.1007/s00330-009-1371-0]
 - 75 **Punwani S**, Rodriguez-Justo M, Bainbridge A, Greenhalgh R, De Vita E, Bloom S, Cohen R, Windsor A, Obichere A, Hansmann A, Novelli M, Halligan S, Taylor SA. Mural inflammation in Crohn disease: location-matched histologic validation of MR imaging features. *Radiology* 2009; **252**: 712-720 [PMID: 19635832 DOI: 10.1148/radiol.2523082167]
 - 76 **Malagò R**, Manfredi R, Benini L, D'Alpaos G, Mucelli RP. Assessment of Crohn's disease activity in the small bowel with MR-enteroclysis: clinico-radiological correlations. *Abdom Imaging* 2008; **33**: 669-675 [PMID: 18228087 DOI: 10.1007/s00261-008-9368-8]
 - 77 **Tolan DJ**, Greenhalgh R, Zealley IA, Halligan S, Taylor SA. MR enterographic manifestations of small bowel Crohn disease. *Radiographics* 2010; **30**: 367-384 [PMID: 20228323 DOI: 10.1148/rg.302095028]
 - 78 **Ziech ML**, Bossuyt PM, Laghi A, Lauenstein TC, Taylor SA, Stoker J. Grading luminal Crohn's disease: which MRI features are considered as important? *Eur J Radiol* 2012; **81**: e467-e472 [PMID: 21684703 DOI: 10.1016/j.ejrad.2011.05.033]
 - 79 **Schmidt S**, Guibal A, Meuwly JY, Michetti P, Felley C, Meuli R, Schnyder P, Denys A. Acute complications of Crohn's disease: comparison of multidetector-row computed tomographic enterography with magnetic resonance enterography. *Digestion* 2010; **82**: 229-238 [PMID: 20588038 DOI: 10.1159/000288521]
 - 80 **Schmidt S**, Chevallier P, Bessoud B, Meuwly JY, Felley C, Meuli R, Schnyder P, Denys A. Diagnostic performance of MRI for detection of intestinal fistulas in patients with complicated inflammatory bowel conditions. *Eur Radiol* 2007; **17**: 2957-2963 [PMID: 17492288]
 - 81 **Gee MS**, Nimkin K, Hsu M, Israel EJ, Biller JA, Katz AJ, Mino-Kenudson M, Harisinghani MG. Prospective evaluation of MR enterography as the primary imaging modality for pediatric Crohn disease assessment. *AJR Am J Roentgenol* 2011; **197**: 224-231 [PMID: 21701034 DOI: 10.2214/AJR.10.5970]
 - 82 **Tillack C**, Seiderer J, Brand S, Göke B, Reiser MF, Schaefer C, Diepolder H, Ochsenkühn T, Herrmann KA. Correlation of magnetic resonance enteroclysis (MRE) and wireless capsule endoscopy (CE) in the diagnosis of small bowel lesions in Crohn's disease. *Inflamm Bowel Dis* 2008; **14**: 1219-1228 [PMID: 18484672 DOI: 10.1002/ibd.20466]
 - 83 **Casciani E**, Masselli G, Di Nardo G, Poletti E, Bertini L, Oliva S, Floriani I, Cucchiara S, Gualdi G. MR enterography versus capsule endoscopy in paediatric patients with suspected Crohn's disease. *Eur Radiol* 2011; **21**: 823-831 [PMID: 20922391 DOI: 10.1007/s00330-010-1976-3]
 - 84 **Cheifetz AS**, Kornbluth AA, Legnani P, Schmelkin I, Brown A, Lichtiger S, Lewis BS. The risk of retention of the capsule endoscope in patients with known or suspected Crohn's disease. *Am J Gastroenterol* 2006; **101**: 2218-2222 [PMID: 16848804]
 - 85 **Jensen MD**, Nathan T, Kjeldsen J, Rafaelsen SR. Incidental findings at MRI-enterography in patients with suspected or known Crohn's disease. *World J Gastroenterol* 2010; **16**: 76-82 [PMID: 20039452]
 - 86 **Herfarth HH**, Grunert M, Klebl F, Strauch U, Feuerbach S, Schölmerich J, Rogler G, Schreyer AG. Frequency and nature of incidental extra-enteric lesions found on magnetic resonance enterography (MR-E) in patients with inflammatory bowel diseases (IBD). *PLoS One* 2009; **4**: e4863 [PMID: 19337373 DOI: 10.1371/journal.pone.0004863]
 - 87 **Rimola J**, Rodriguez S, García-Bosch O, Ordás I, Ayala E, Aceituno M, Pellisé M, Ayuso C, Ricart E, Donoso L, Panés J. Magnetic resonance for assessment of disease activity and severity in ileocolonic Crohn's disease. *Gut* 2009; **58**: 1113-1120 [PMID: 19136510 DOI: 10.1136/gut.2008.167957]
 - 88 **Haggett PJ**, Moore NR, Shearman JD, Travis SP, Jewell DP, Mortensen NJ. Pelvic and perineal complications of Crohn's disease: assessment using magnetic resonance imaging. *Gut* 1995; **36**: 407-410 [PMID: 7698701]
 - 89 **Beets-Tan RG**, Beets GL, van der Hoop AG, Kessels AG, Vliegen RF, Baeten CG, van Engelshoven JM. Preoperative MR imaging of anal fistulas: Does it really help the surgeon? *Radiology* 2001; **218**: 75-84 [PMID: 11152782]
 - 90 **Dagia C**, Ditchfield M, Kean M, Catto-Smith T. Imaging for Crohn disease: use of 3-T MRI in a paediatric setting. *J Med Imaging Radiat Oncol* 2008; **52**: 480-488 [PMID: 19032394 DOI: 10.1111/j.1440-1673.2008.01993.x]
 - 91 **Dagia C**, Ditchfield M, Kean M, Catto-Smith A. Feasibility of 3-T MRI for the evaluation of Crohn disease in children. *Pediatr Radiol* 2010; **40**: 1615-1624 [PMID: 20689946 DOI: 10.1007/s00247-010-1781-9]
 - 92 **Shyn PB**, Morteale KJ, Britz-Cunningham SH, Friedman S, Odze RD, Burakoff R, Goldberg JE, Erturk M, Silverman SG. Low-dose 18F-FDG PET/CT enterography: improving on CT enterography assessment of patients with Crohn disease. *J Nucl Med* 2010; **51**: 1841-1848 [PMID: 21078803 DOI: 10.2967/jnumed.110.080796]
 - 93 **Groshar D**, Bernstine H, Stern D, Sosna J, Eligalashvili M, Gurbuz EG, Niv Y, Fraser G. PET/CT enterography in Crohn disease: correlation of disease activity on CT enterography with 18F-FDG uptake. *J Nucl Med* 2010; **51**: 1009-1014 [PMID: 20554741 DOI: 10.2967/jnumed.109.073130]
 - 94 **Spier BJ**, Perlman SB, Jaskowiak CJ, Reichelderfer M. PET/CT in the evaluation of inflammatory bowel disease: studies in patients before and after treatment. *Mol Imaging Biol* 2010; **12**: 85-88 [PMID: 19430844 DOI: 10.1007/s11307-009-0232-1]
 - 95 **Lemberg DA**, Issenman RM, Cawdron R, Green T, Mernagh J, Skehan SJ, Nahmias C, Jacobson K. Positron emission tomography in the investigation of pediatric inflammatory bowel disease. *Inflamm Bowel Dis* 2005; **11**: 733-738 [PMID: 16043988]

P- Reviewers: Keita AV, Maccioni F, Mayol J **S- Editor:** Wen LL
L- Editor: A **E- Editor:** Zhang DN



Role of MRI in the diagnosis and treatment of osteomyelitis in pediatric patients

Brian S Pugmire, Randheer Shailam, Michael S Gee

Brian S Pugmire, Randheer Shailam, Michael S Gee, Department of Radiology, Massachusetts General Hospital, Boston, MA 01890, United States

Author contributions: Pugmire BS and Shailam R contributed equally to the writing and editing of the manuscript; Gee MS provided editorial input and overall direction.

Correspondence to: Brian S Pugmire, MD, Department of Radiology, Massachusetts General Hospital, 55 Fruit St. FND-216, Boston, MA 01890, United States. bpgmire@partners.org
Telephone: +1-617-7244255 Fax: +1-617-7263077

Received: February 11, 2014 Revised: April 8, 2014

Accepted: July 18, 2014

Published online: March 28, 2015

Abstract

Osteomyelitis is a significant cause of morbidity in children throughout the world. Multiple imaging modalities can be used to evaluate for suspected osteomyelitis, however magnetic resonance imaging (MRI) has distinct advantages over other modalities given its ability to detect early changes related to osteomyelitis, evaluate the true extent of disease, depict extraosseous spread of infection, and help guide surgical management. MRI has assumed a greater role in the evaluation of osteomyelitis with the increase in musculoskeletal infections caused by methicillin-resistant *Staphylococcus aureus* which have unique imaging features that are well-demonstrated with MRI. This review focuses primarily on the use of MRI in the evaluation of osteomyelitis in children and will include a discussion of the clinically important and characteristic findings on MRI of acute bacterial osteomyelitis and related conditions.

© 2015 Baishideng Publishing Group Inc. All rights reserved.

Key words: Magnetic resonance imaging; Osteomyelitis; Pediatrics; Infectious diseases

Core tip: Osteomyelitis is a significant cause of morbidity

and mortality in children. Plain radiography and radionuclide bone scintigraphy, which have been the traditional imaging modalities for detecting osteomyelitis, both have significant limitations. Magnetic resonance imaging (MRI) is increasingly relied upon for detecting osteomyelitis in children, due to its superior soft tissue contrast for detecting early disease and extraosseous complication, as well as its lack of ionizing radiation exposure to patients. This article focuses on basic and advanced MRI techniques for evaluating osteomyelitis, as well as MRI imaging features of disease and their impact on clinical management.

Original sources: Pugmire BS, Shailam R, Gee MS. Role of MRI in the diagnosis and treatment of osteomyelitis in pediatric patients. *World J Radiol* 2014; 6(8): 530-537 Available from: URL: <http://www.wjgnet.com/1949-8470/full/v6/i8/530.htm> DOI: <http://dx.doi.org/10.4329/wjr.v6.i8.530>

INTRODUCTION

Musculoskeletal infection is a significant cause of morbidity and mortality in children throughout the world. This category of disease encompasses both osteomyelitis and septic arthritis, however this review will be primarily focused on the former. Osteomyelitis is typically categorized as either hematogenous or non-hematogenous. Hematogenous osteomyelitis typically occurs when circulating pathogenic organisms take up residence in the metaphyses of long bones due to sluggish circulation in these regions. Non-hematogenous osteomyelitis, on the other hand, results from direct inoculation of organisms into bone due to penetrating trauma, open fractures, etc. Acute hematogenous osteomyelitis (AHO) is the most common type of musculoskeletal infection in children with an estimated incidence of 1 case per 5000 children per year in the United States^[1]. It is primarily a disease

of young children with approximately half of all cases occurring in children 5 years of age or younger^[2]. Some recent studies have indicated that the incidence of AHO is increasing with a concurrent increase in the number of cases due to methicillin-resistant *Staphylococcus aureus* (*S. aureus*) (MRSA) infections^[3]. The signs and symptoms of AHO in children are nonspecific and as such, imaging frequently plays a significant role in the diagnosis and management of this condition.

EPIDEMIOLOGY

Infection by *S. aureus* is the most common cause of osteomyelitis. Community acquired *S. aureus* is implicated in most cases with 30% of these cases caused by community acquired MRSA (CA-MRSA)^[4,5]. Other organisms that cause osteomyelitis include *Streptococcus pneumoniae*, *Streptococcus pyogenes*, *Pseudomonas aeruginosa* and *Bartonella henselae*. *Salmonella* is an important cause of osteomyelitis in patients with Sickle cell disease. Gram-negative bacteria and group B streptococci are common causes in newborns and *Kingella Kingae* in the first two years of age^[5].

PATHOPHYSIOLOGY

Hematogenous osteomyelitis is the most common type of osteomyelitis in children^[4]. This occurs when an infection elsewhere in the body spreads to the bone *via* the bloodstream. Risk factors for development of hematogenous osteomyelitis include trauma, prematurity, urinary tract infections, vascular catheters and immunodeficiencies. The blood vessels in the metaphyses have sluggish flow and discontinuous endothelium, which predispose to infection^[4]. The most common bones to be affected are the fastest growing bones that have highly vascularized long bone metaphyses and metaphyseal equivalents. Common sites include the distal femur, proximal tibia, proximal humerus and distal radius. Most cases start with a focal infection in the metaphyseal marrow which progresses to local decalcification and bony destruction. Occasionally, multiple foci may be infected which eventually coalesce. This infection can spread within the marrow cavity and as the pressure increases within the marrow cavity, the infection can spread through Haversian canals in the cortex into the subperiosteal space, giving rise to a subperiosteal abscess. Similarly, the infection can traverse the periosteum and infect the adjacent soft tissues leading to pyomyositis. Infection may also spread across the physis into the epiphysis and joint space^[4].

The first stage of osteomyelitis occurs with vascular congestion, intravascular thrombosis and increased intraosseous pressure. Next is the suppurative stage where pus traverses the Haversian canals and forms a subperiosteal abscess. Subsequently a sequestrum may form when the periosteal and endosteal blood supply is compromised from increased pressure and vascular obstruction. This may lead to formation of an involucrum: new bone growing from the periosteum. Depending on medical or

surgical treatment at this point the infection may resolve or progress with complications.

The site of osteomyelitis varies with patient age and is related to the blood supply. In early infancy osteomyelitis occurs in epiphyses and metaphyses and epiphyseal-equivalent regions. Transphyseal vessels are present in infants younger than 18-24 mo of age, which allow easier spread of infection across the physis from the metaphysis to the epiphysis^[4,6]. This is the reason that infantile osteomyelitis frequently involves the epiphysis and joint space. It is important to note that this is not the most common cause of septic arthritis, which more often results from direct hematogenous synovial seeding^[4]. During early infancy, isolated involvement of the epiphyseal growth plate can occur. Infection of the epiphyseal growth plate during infancy can result in growth disturbance. In the 2-16 years age group, osteomyelitis is most often located in the metaphyses^[6].

IMAGING APPROACH TO OSTEOMYELITIS

Osteomyelitis in children demonstrates abnormalities on nearly all imaging modalities, including radiography, ultrasound, computed tomography, radionuclide bone scintigraphy, and magnetic resonance imaging (MRI). The conventional approach to the imaging evaluation of suspected AHO in the past has been radiography followed by bone scintigraphy if the radiographs were negative. In this algorithm, MRI was typically been reserved for cases of poor treatment response or suspected vertebral diskitis-osteomyelitis. However, due to multiple factors, including the rise of rapidly aggressive and invasive musculoskeletal infections with CA-MRSA, this approach may no longer be ideal^[7] (Figure 1).

As a first line modality radiography is useful for excluding other differential diagnoses such as trauma or tumor, however radiographs are insensitive for the detection of early osteomyelitis. Radiography may be normal in cases of osteomyelitis up to 14 d after the onset of infection and even then, only 20% of cases demonstrate radiographic abnormalities after this two-week delay^[8]. Additionally, the early radiographic findings, including soft tissue swelling, vague bony lucency, and periosteal reaction, may be subtle and may not reflect the true extent of disease.

Triple-phase bone scintigraphy using 99mTc-methylene diphosphonate (99mTc-MDP) can demonstrate evidence of infection as soon as 24 h after onset and also has the advantage of being able to depict multiple sites of infection. Osteomyelitis typically manifests as increased radiotracer uptake on all phases (angiographic, blood pool, and delayed) of the triple-phase examination. However 99mTc-MDP scintigraphy is limited by poor anatomic detail and is insensitive for the detection of abscesses and extraosseous involvement. Furthermore, the sensitivity of 99mTc-MDP scintigraphy for

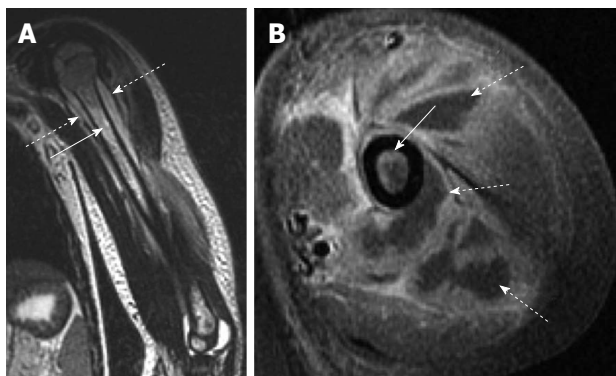


Figure 1 Acute osteomyelitis secondary to methicillin-resistant *Staphylococcus aureus* infection. A: Coronal T2-weighted image of the left humerus shows bone marrow edema (solid arrow) as well as a periosteal fluid collection (dashed arrow) consistent with periosteal abscess; B: Axial T1-weighted post-contrast image shows both enhancement of the bone marrow (solid arrow) as well as extensive periosteal and soft tissue abscess formation (dashed arrows) which is characteristic of methicillin-resistant *Staphylococcus aureus* infection.



Figure 2 Early acute osteomyelitis. A: Coronal proton-density weighted image of the right ankle of a 12-year-old male shows a subtle area of decreased intramedullary signal along the lateral aspect of the calcaneus (long arrow); B: Axial T2-weighted image with fat suppression demonstrates more conspicuous bone marrow edema (arrowhead); C: Coronal post-contrast T1-weighted image with fat suppression shows an area of enhancement corresponding to the bone marrow edema. Bone biopsy revealed bacterial osteomyelitis.

the diagnosis of osteomyelitis, which in the past has been reported to be as high as 80%^[9], may be decreasing with the increasing incidence of MRSA infections that tend to have significant soft-tissue involvement^[7]. Positron emission tomography with 18-fluorodeoxyglucose appears to be sensitive (95%) and specific (87%) for the diagnosis of osteomyelitis^[9], however it has limited availability and involves a significant amount of radiation exposure. Scintigraphic studies using white blood cells labeled with indium-111 or 99mTc hexamethylpropyleneamine oxime require relatively large volumes of blood and are not used frequently in younger children.

In contrast to the modalities listed above, MRI is both sensitive for the detection of early osteomyelitis (Figure 2) and can also accurately depict the extent of disease as well as any associated abscess or soft-tissue extension without the risks associated with radiation exposure. MRI combines high-resolution anatomic delineation of the medullary space, cortex, and periosteum with high soft tissue contrast for detection of edema and fluid. Pre-operative MRI has been shown to reduce operative time and extent of surgical exposure in cases requiring surgical debridement^[10]. MRI does have distinct disadvantages in children including long scan times and susceptibility to motion artifacts which necessitate sedation or anesthesia in young children (approximately 6 mo to 8 years of age). Additionally, MRI is contraindicated in some patients with metallic foreign bodies and certain types of implanted hardware. However, the overall superiority of MRI in evaluating osteomyelitis is reflected in recent clinical practice guidelines which indicate that MRI is the imaging modality of choice for the detection of osteomyelitis and associated infection of the extraosseous soft tissues^[11]. As such, the current best imaging approach for suspected osteomyelitis is radiography followed by MRI.

MRI TECHNIQUE

Multiple variations of MRI protocols for the evaluation

of osteomyelitis exist, however the essential sequences include both multiplanar T1 and T2-weighted fast-spin echo or turbo spin-echo (FSE/TSE) sequences and short-tau inversion recovery (STIR) or T2-weighted FSE/TSE sequences with fat-suppression (T2-FS). STIR and T2-FS sequences are particularly helpful for increasing the conspicuity of bone marrow edema and fluid collections. There is some controversy regarding when to use gadolinium in infants and children with suspected osteomyelitis. Intravenous gadolinium contrast does not appear to improve the sensitivity or specificity for the diagnosis of osteomyelitis overall. Recent studies suggest that if the fluid-sensitive images (*e.g.*, STIR, T2-FS) are normal, gadolinium enhancement provides no additional diagnostic value^[12,13]. If the fluid-sensitive images are abnormal, however, gadolinium enhancement is of value in increasing confidence in the diagnosis of an abscess (if present) and planning of the approach to abscess aspiration and drainage^[12]. Despite these recent studies that suggests that gadolinium contrast administration may not be needed for all cases, there are some specific indications for which contrast is always indicated. In cases of suspected vertebral osteomyelitis, contrast is necessary to assist in the differentiation of abscess in the epidural space or paravertebral masses from inflammatory masses^[4] (Figure 3). Additionally, epiphyseal growth plate involvement by osteomyelitis may sometimes only be seen on gadolinium enhanced T1 sequences and not seen on non-contrast T1 and fluid sensitive sequences or on radiography or bone scintigraphy. Active epiphyseal infection manifests as one or more areas of decreased or no enhancement of the epiphyseal cartilage which otherwise should enhance uniformly^[14,15]. As mentioned above, infection of the epiphyseal growth plate during infancy can result in growth disturbance and therefore gadolinium use in this age group is advised.

Because it is frequently difficult to precisely localize sites of involvement by clinical exam, especially in infants, an initial large field-of-view coronal STIR or T2-FS

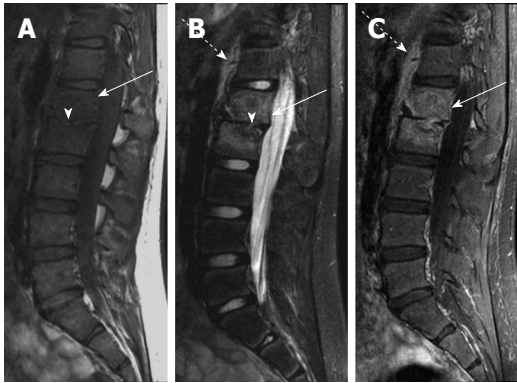


Figure 3 Chronic vertebral diskitis-osteomyelitis secondary to *S. typhi*. A: Sagittal T1-weighted image shows abnormally decreased T1 marrow signal in the L1 and L2 vertebral bodies (arrow) and loss of the L1-2 disk space (arrowhead); B: Sagittal T2-weighted image with fat suppression shows abnormally increased T2 signal in the L1 and L2 vertebral bodies (solid arrow) with loss of normal T2 intervertebral disk signal (arrowhead). T2 hyperintensity anterior to the spine (dashed arrow) likely represents adjacent soft tissue edema; C: Sagittal T1-weighted image after intravenous contrast shows intramedullary enhancement in the L1 and L2 vertebral bodies (solid arrow) with soft tissue enhancement anterior to the spine (dashed arrow).

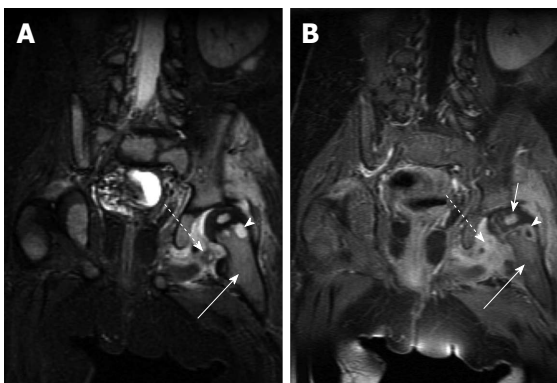


Figure 4 Acute osteomyelitis of the hip. A: Coronal fast spin echo inversion recovery image shows T2-hyperintense marrow edema in the left femoral metaphysis (solid arrow) with a small round very intense focus of T2 signal (arrowhead) which is consistent with an intraosseous abscess. Surrounding soft tissue edema (dashed arrow) is also noted; B: Coronal T1-weighted post-contrast image in the same patient shows enhancement in the metaphyseal bone marrow (solid long arrow), peripheral enhancement of the abscess (arrowhead), and surrounding soft tissue enhancement (dashed arrow). Note enhancement of the left femoral head (solid short arrow) which indicates adequate perfusion.

sequence of the general region of concern can be used to help localize the site(s) of disease followed by a tailored evaluation of the involved areas. In cases of suspected osteomyelitis affecting the lower extremities, imaging of the contralateral extremity may also be considered: abnormalities in the contralateral extremity are common, however they may not affect clinical management^[16]. Whole-body MRI (WBMRI) may be indicated in cases of suspected multifocal involvement such as in cases of severe CA-MRSA infections, which frequently involve multiple sites, or in cases of suspected chronic multifocal recurrent osteomyelitis (CRMO). WBMRI is typically performed using a series of coronal STIR acquisitions

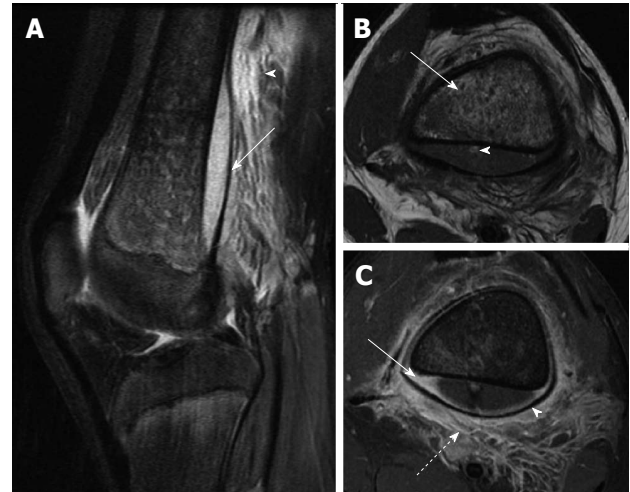


Figure 5 Osteomyelitis with subperiosteal abscess. A: Sagittal T2-weighted image with fat suppression shows a large subperiosteal abscess (solid arrow) with adjacent soft tissue edema (arrowhead); B: Axial T1-weighted image shows heterogeneous T1 hypointense marrow signal (solid arrow). Note small T1 hyperintense focus in the posterior subperiosteal fluid collection (arrowhead) indicative of a fat globule; C: Axial T1-weighted post-contrast image demonstrates peripheral enhancement of the subperiosteal abscess (solid arrow), significant periosteal elevation (arrowhead) and adjacent soft tissue inflammation (dashed arrow).

obtained in multiple anatomic stations using receiver coils spanning the entire body, with the scan table moved through the magnet between stations. The images from each station are then digitally fused at points of overlap to create a single whole body image stack.

MRI FEATURES OF ACUTE OSTEOMYELITIS

Because MRI is able to detect early marrow involvement, it is an important modality for detection of osteomyelitis in early stages. Additionally, MRI is helpful for detection of fluid collections and abscesses that may occur in the marrow, subperiosteal region or in soft tissues. Anatomical information provided by MR can be helpful for drainage and surgical treatment. T1 fat saturation gadolinium-enhanced images will show non-enhancement of fluid and pus with peripheral enhancement.

The earliest finding of osteomyelitis on MRI is bone marrow edema and T2 and STIR sequences are very important for detecting these early changes (Figures 2 and 4). MRI is also sensitive for detection of periosteal elevation and the presence of a subperiosteal fluid collection or abscess (Figure 5). Distinguishing normal hematopoietic marrow from abnormal marrow can be challenging in certain situations because of the normal hematopoietic marrow often seen in the metaphyses in children. Normal hematopoietic marrow T1 signal should be hyperintense relative to muscle. If there is marrow infiltration or edema, the T1 signal is generally isointense or hypointense to muscle (Figure 6). Normal hematopoietic marrow should appear similar in adjacent or contralateral metaphyses.



Figure 6 Early acute osteomyelitis. A: Coronal T1-weighted image of the right knee of a 4-year-old male shows ill-defined areas of low T1 signal in the bone marrow in the lateral femoral metaphysis (arrow) and lateral epiphysis (arrowhead); B: Coronal T1-weighted post-contrast image in the same patient shows associated enhancement in these areas (white arrow and arrowhead) as well as some periosteal reaction, indicated by periosteal enhancement (black arrow).



Figure 7 Osteomyelitis secondary to open fracture. A: Coronal T1-weighted image of the left distal tibia shows a displaced fracture of the distal tibial meta-diaphysis (solid arrow) with associated bone marrow edema (dashed arrow); B: Coronal T2-weighted image of the same patient shows a fluid collection adjacent to the fracture (solid arrow) with T2 hyperintense marrow edema (dashed arrow); C: Coronal T1-weighted post-contrast image shows peripheral enhancement surrounding the above-mentioned fluid collection, consistent with an abscess (solid arrows).

Imaging of the contralateral body part is often helpful for this and is more easily obtained during imaging of the pelvis and lower extremities. Since detailed small structure anatomical information is less important during evaluation of osteomyelitis (OM), imaging with a body coil should be considered if large field of view imaging would be helpful.

Pelvic osteomyelitis often occurs in metaphyseal equivalents such as the ischiopubic synchondrosis, pubic symphysis, triradiate cartilage, iliac apophyses and adjacent to the sacroiliac joint. Involvement of adjacent soft tissues, muscles and bowel is not uncommon and MRI is helpful in imaging the extent and often the source of infection.

CHRONIC OSTEOMYELITIS

Chronic infections of bone may be indolent and have minor signs, symptoms and serologic abnormalities.

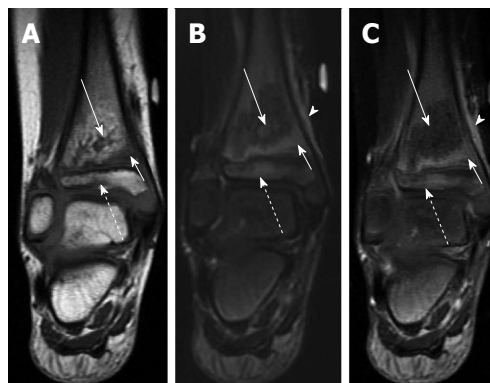


Figure 8 Transphyseal methicillin-resistant *Staphylococcus aureus* osteomyelitis with intraosseous abscess. A: Coronal T1-weighted image of the right ankle shows an area of T1 hyperintensity in the distal tibial metaphysis with central T1 hypointensity (solid long arrow) indicative of abscess formation. T1 hypointensity is seen surrounding this area in metaphysis (solid short arrow) and in the epiphysis (dashed arrow) indicative of transphyseal spread; B: Coronal T2-weighted image with fat suppression shows an area of T2 hypointensity with central T2 hyperintensity (solid long arrow) corresponding to the areas of abnormal T1 signal in A. T2 hyperintensity in the distal metaphysis (solid short arrow) and epiphysis (dashed arrow) are consistent with edema. T2 hyperintensity in periosteum and adjacent soft tissues indicating inflammation (arrowhead); C: Coronal T1-weighted image post contrast shows a lack of enhancement in the central distal metaphysis consistent with necrosis and abscess formation (solid long arrow). Enhancement is seen peripherally in the distal metaphysis and epiphysis (solid short arrow and dashed arrow). Enhancement in periosteum and adjacent soft tissues indicating inflammation (arrowhead).

However, cases of chronic osteomyelitis may be severe, incapacitating and difficult to treat. Chronic osteomyelitis may occur after the following: acute osteomyelitis, trauma (Figure 7), joint replacement, orthopedic hardware (ex. used in fracture reduction), and mycobacterium tuberculosis or syphilis infections. Chronic osteomyelitis is defined if symptoms persist after one month of appropriate antibiotic treatment or if there is persistent infection after one month of inadequate treatment.

Imaging chronic osteomyelitis is helpful to evaluate the extent of infection within bone and surrounding soft tissues, identification of an abscess, sequestrum and sinus tract (Figure 8). Sequestra of cortical bone appear as low signal on T1, T2 and STIR and do not enhance. Imaging findings of chronic osteomyelitis include Brodie abscess, thick periosteum, sequestrum/necrotic bone fragments, and cloaca/draining tract (Figure 9). Sequestra of cancellous bone also do not enhance but are relatively hyperintense to cortical sequestra on T1, T2 and STIR. Granulation tissue, soft tissue inflammation and sinus tracts are all T1 hypointense, T2 and STIR hyperintense and enhance with gadolinium.

Brodie's abscesses are usually metaphyseal and appear as a fluid filled cavity with an enhancing lining, rim of low signal sclerosis and peripheral edema (Figure 10). A "penumbra sign" has been described with Brodie abscess and results from the lining of granulation tissue around the abscess that is T1 hyperintense relative to the abscess cavity. A "double-line sign" has also been described on T2 and STIR images representing hyperintense granulation tissue surrounded by low signal sclerosis.

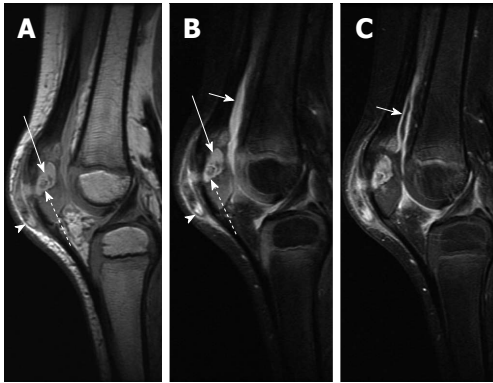


Figure 9 Chronic patellar osteomyelitis with abscess and sequestrum. A: Sagittal proton-density-weighted image of the right knee shows an abscess cavity in the patella (solid arrow) with a central low-density focus consistent with a sequestrum (dashed arrow). There is also disruption of the anterior cortex with spread of infection into the prepatellar bursa (arrowhead); B: Sagittal T2-weighted image with fat suppression again shows the intraosseous abscess (solid long arrow) with central T2 hypointense sequestrum (dashed arrow) and extension of infection into the prepatellar soft tissues (arrowhead). A knee joint effusion is more apparent on this image (solid short arrow); C: Sagittal T1-weighted post-contrast image shows enhancement of the synovium (solid short arrow) indicative synovitis, likely from intra-articular extension of infection.

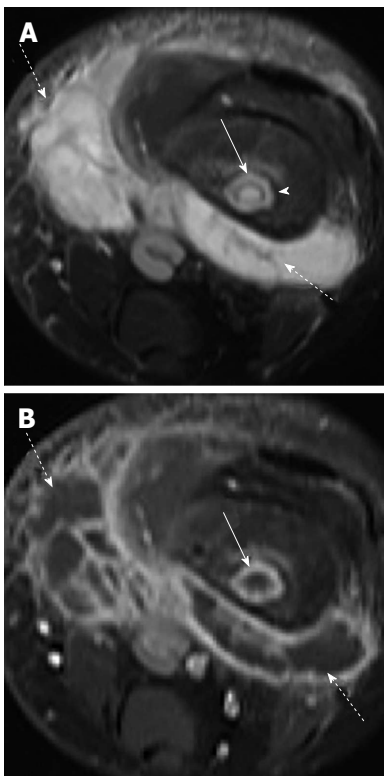


Figure 10 Osteomyelitis with intraosseous and soft tissue abscess secondary to methicillin-resistant *Staphylococcus aureus* infection. A: Axial T2-weighted fat suppressed image shows intraosseous abscess cavity (solid arrow) with rim of surrounding edema and large surrounding soft tissue fluid collection (dashed arrow). Note T2 hypointense rim (arrowhead) forming the “double-line” sign; B: Axial T1-weighted post-contrast image shows peripheral enhancement associated with the intraosseous abscess (solid arrow) and soft tissue abscesses (dashed arrows).

Sclerosing osteomyelitis of Garre is a type of chronic bone infection manifesting primarily with bony sclerosis.

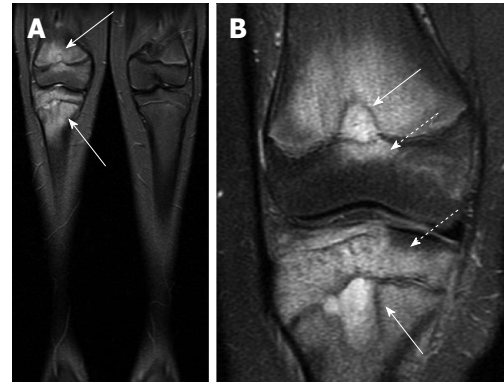


Figure 11 Chronic recurrent multifocal osteomyelitis. A: Coronal short-tau inversion recovery image from whole body magnetic resonance imaging (lower extremity station) shows areas of bone marrow edema in the distal femur and proximal tibia; B: Coronal T2-weighted fat suppressed image with smaller field of view again demonstrates the bone marrow edema as well as two areas of very hyperintense T2 signal in the femur and tibia which may represent intraosseous abscesses (solid arrows), though these are not typically found in chronic multifocal recurrent osteomyelitis. Involvement of the epiphysis is apparent at both sites (dashed arrows).

CHRONIC RECURRENT MULTIFOCAL OSTEOMYELITIS

Chronic recurrent multifocal osteomyelitis is a non-bacterial, noninfectious inflammation of bone that has been characterized as an auto-inflammatory disease. Cultures do not show an infectious source and biopsy shows non-specific inflammation. Antibiotics do not alter the course of the disease and symptoms are better treated with anti-inflammatory medications. Frequent sites of involvement include the metaphyses of the long bones, clavicles, spine and pelvis. Other sites include the mandible, scapula, ribs, sternum, hands and feet. Radiographic findings typically include lysis and sclerosis. Since this disease frequently involves multiple sites, some of which are asymptomatic, WBMRI is recommended both to help aid in the diagnosis with multifocal involvement and document the extent of disease. During the active phase, there is bone marrow edema and often periostitis and soft tissue inflammation. MRI can show transphyseal disease, which can lead to physeal bars affecting growth and angular deformities (Figure 11). Joint effusions, synovitis cartilage and subchondral bone erosions may also be seen. Larger fluid collections, abscess, sinus tracts and sequestra are not typical features of CRMO and are more often seen with bacterial osteomyelitis^[17].

DIAGNOSTIC CHALLENGES

Differentiating osteomyelitis from Ewing sarcoma can often be challenging. The fact that children often do not present with the classic signs and symptoms of an infection makes the clinical differentiation between these two diagnoses difficult. Plain film findings of both osteomyelitis and Ewing sarcoma are often similar with an aggressive intramedullary process destroying normal cancellous and cortical bone creating a moth eaten and permeative

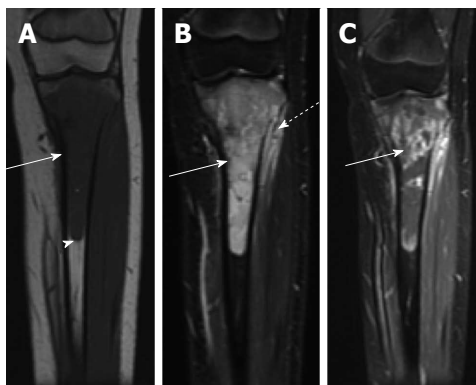


Figure 12 Ewing sarcoma. A: Coronal T1-weighted image of the left tibia shows a long segment of intramedullary T1 hypointensity (solid arrow). Note abrupt transition to normal marrow signal inferiorly (arrowhead); B: Coronal fast multi-planar inversion recovery image of the same patient shows very intense T2 signal in the marrow cavity (solid arrow) with extraosseous extension (dashed arrow); C: T1-weighted post-contrast image shows very heterogeneous intramedullary enhancement associated with this lesion (solid arrow).

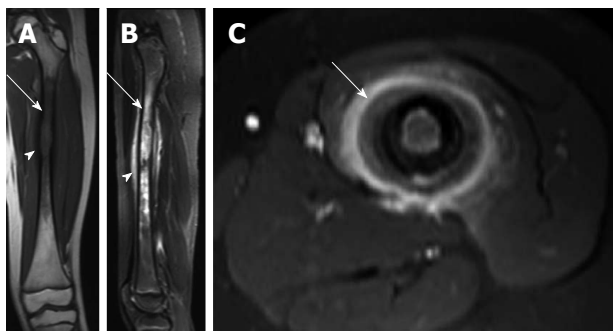


Figure 13 Langerhans cell histiocytosis. A: Coronal T1-weighted image of the left femur shows a long segment of marrow T1 hypointensity (arrow) and cortical erosion/expansion (arrowhead); B: Sagittal short-tau inversion recovery image from the same patient shows very intense T2-signal in the marrow cavity (arrow). T2 hyperintensity in the periosteum (arrowhead) is indicative of periosteal reaction; C: Axial T1-weighted image post contrast shows intense enhancement of the periosteum (arrow).

appearance. MRI can be helpful in differentiating between these two aggressive diseases. Both may produce periostitis, periosteal elevation, adjacent soft tissue mass and effacement of fat planes. Soft tissue enhancement, cystic and necrotic foci and cortical destruction are found in both diseases and are less reliable at differentiation. The presence of fat globules within the infiltrating marrow process or in a subperiosteal location is a feature of osteomyelitis more often than neoplasia^[18] (Figure 5). A recent study by Henninger *et al.*^[19] showed that all cases of Ewing sarcoma had a sharp or defined margin of the bone lesion between normal bone and edematous/affected bone on T1 which was not present in cases of osteomyelitis (Figure 12).

Langerhans cell histiocytosis often has a very similar appearance to osteomyelitis with an aggressive lytic lesion with ill-defined borders and surrounding inflammatory changes (Figure 13). A process centered in the diaphysis favors langerhans cell histiocytosis over OM. However, differentiation from Langerhans cell histiocytosis, lym-

phoma and leukemia can be challenging and biopsy is necessary for definitive diagnosis. Fractures, bone infarcts and healed osteomyelitis may pose a diagnostic challenge in differentiating between active osteomyelitis due to common features.

ADVANCED MRI TECHNIQUES

As noted above, the current protocols for MRI of suspected osteomyelitis utilize standard T1 and T2-weighted, STIR, and sometimes contrast-enhanced sequences. More advanced imaging techniques such as diffusion-weighted imaging (DWI), dynamic contrast-enhanced (DCE) MRI, and MR spectroscopy can be used as well, however their role is currently not well defined. A potential application for DWI would be characterization of fluid collections associated with osteomyelitis as abscesses characteristically demonstrate restricted diffusion on DWI. Additionally, DCE-MRI could potentially be used to identify areas of soft tissue necrosis, femoral/humeral head avascular necrosis, or possibly increase sensitivity for detection of CA-MRSA infection in non-ossified growth cartilage. Whole body MRI with digital merging of multiple anatomic stations can be helpful for assessment of multiple sites of disease as well as suspected cases of CRMO. Further research is needed to define the utility of these imaging techniques in this setting.

REFERENCES

- 1 **Steer AC, Carapetis JR.** Acute hematogenous osteomyelitis in children: recognition and management. *Paediatr Drugs* 2004; **6**: 333-346 [PMID: 15612835]
- 2 **Nelson JD.** Acute osteomyelitis in children. *Infect Dis Clin North Am* 1990; **4**: 513-522 [PMID: 2212603]
- 3 **Arnold SR, Elias D, Buckingham SC, Thomas ED, Novais E, Arkader A, Howard C.** Changing patterns of acute hematogenous osteomyelitis and septic arthritis: emergence of community-associated methicillin-resistant *Staphylococcus aureus*. *J Pediatr Orthop* 2006; **26**: 703-708 [PMID: 17065930]
- 4 **Jaramillo D.** Infection: musculoskeletal. *Pediatr Radiol* 2011; **41** Suppl 1: S127-S134 [PMID: 21523583 DOI: 10.1007/s00247-011-2001-y]
- 5 **Kalyoussef S, Tolan RW, Noel GJ.** Pediatric Osteomyelitis. 2014. Available from: URL: <http://emedicine.medscape.com/article/967095-overview>
- 6 **DiPoce J, Jbara ME, Brenner AI.** Pediatric osteomyelitis: a scintigraphic case-based review. *Radiographics* 2012; **32**: 865-878 [PMID: 22582364 DOI: 10.1148/rg.323115110]
- 7 **Browne LP, Mason EO, Kaplan SL, Cassady CI, Krishnamurthy R, Guillerman RP.** Optimal imaging strategy for community-acquired *Staphylococcus aureus* musculoskeletal infections in children. *Pediatr Radiol* 2008; **38**: 841-847 [PMID: 18560822 DOI: 10.1007/s00247-008-0888-8]
- 8 **Capitaino MA, Kirkpatrick JA.** Early roentgen observations in acute osteomyelitis. *Am J Roentgenol Radium Ther Nucl Med* 1970; **108**: 488-496 [PMID: 5415924]
- 9 **Gotthardt M, Bleeker-Rovers CP, Boerman OC, Oyen WJ.** Imaging of inflammation by PET, conventional scintigraphy, and other imaging techniques. *J Nucl Med* 2010; **51**: 1937-1949 [PMID: 21078798 DOI: 10.2967/jnumed.110.076232]
- 10 **Kan JH, Hilmes MA, Martus JE, Yu C, Hernanz-Schulman M.** Value of MRI after recent diagnostic or surgical intervention in children with suspected osteomyelitis. *AJR Am J Roentgenol* 2008; **191**: 1595-1600 [PMID: 18941107 DOI: 10.2214/

- AJR.08.1115]
- 11 **Liu C**, Bayer A, Cosgrove SE, Daum RS, Fridkin SK, Gorwitz RJ, Kaplan SL, Karchmer AW, Levine DP, Murray BE, Rybak M, Talan DA, Chambers HF. Clinical practice guidelines by the infectious diseases society of america for the treatment of methicillin-resistant *Staphylococcus aureus* infections in adults and children: executive summary. *Clin Infect Dis* 2011; **52**: 285-292 [PMID: 21217178 DOI: 10.1093/cid/cir034]
 - 12 **Averill LW**, Hernandez A, Gonzalez L, Peña AH, Jaramillo D. Diagnosis of osteomyelitis in children: utility of fat-suppressed contrast-enhanced MRI. *AJR Am J Roentgenol* 2009; **192**: 1232-1238 [PMID: 19380545 DOI: 10.2214/AJR.07.3400]
 - 13 **Kan JH**, Young RS, Yu C, Hernanz-Schulman M. Clinical impact of gadolinium in the MRI diagnosis of musculoskeletal infection in children. *Pediatr Radiol* 2010; **40**: 1197-1205 [PMID: 20180105 DOI: 10.1007/s00247-010-1557-2]
 - 14 **Browne LP**, Guillerman RP, Orth RC, Patel J, Mason EO, Kaplan SL. Community-acquired staphylococcal musculoskeletal infection in infants and young children: necessity of contrast-enhanced MRI for the diagnosis of growth cartilage involvement. *AJR Am J Roentgenol* 2012; **198**: 194-199 [PMID: 22194497 DOI: 10.2214/AJR.10.5730]
 - 15 **Guillerman RP**. Osteomyelitis and beyond. *Pediatr Radiol* 2013; **43** Suppl 1: S193-S203 [PMID: 23478935 DOI: 10.1007/s00247-012-2594-9]
 - 16 **Metwalli ZA**, Kan JH, Munjal KA, Orth RC, Zhang W, Guillerman RP. MRI of suspected lower extremity musculoskeletal infection in the pediatric patient: how useful is bilateral imaging? *AJR Am J Roentgenol* 2013; **201**: 427-432 [PMID: 23883225 DOI: 10.2214/AJR.12.9644]
 - 17 **Khanna G**, Sato TS, Ferguson P. Imaging of chronic recurrent multifocal osteomyelitis. *Radiographics* 2009; **29**: 1159-1177 [PMID: 19605663 DOI: 10.1148/rg.294085244]
 - 18 **Davies AM**, Hughes DE, Grimer RJ. Intramedullary and extramedullary fat globules on magnetic resonance imaging as a diagnostic sign for osteomyelitis. *Eur Radiol* 2005; **15**: 2194-2199 [PMID: 15864595]
 - 19 **Henninger B**, Glodny B, Rudisch A, Trieb T, Loizides A, Putzer D, Judmaier W, Schocke MF. Ewing sarcoma versus osteomyelitis: differential diagnosis with magnetic resonance imaging. *Skeletal Radiol* 2013; **42**: 1097-1104 [PMID: 23685708 DOI: 10.1007/s00256-013-1632-5]

P- Reviewer: Lichtor T **S- Editor:** Wen LL
L- Editor: A **E- Editor:** Liu SQ



Pathophysiology, clinical features and radiological findings of differentiation syndrome/all-trans-retinoic acid syndrome

Luciano Cardinale, Francesco Asteggiano, Federica Moretti, Federico Torre, Stefano Ulisciani, Carmen Fava, Giovanna Rege-Cambrin

Luciano Cardinale, Francesco Asteggiano, Federica Moretti, Federico Torre, Institute of Radiology, Department of Clinical and Biological Sciences, University of Turin, AOU S.Luigi Gonzaga, 10043 Orbassano, Torino, Italy

Stefano Ulisciani, Carmen Fava, Giovanna Rege-Cambrin, Division of Hematology and Internal Medicine, Department of Clinical and Biological Sciences of University of Turin, AOU S.Luigi Gonzaga, 10043 Orbassano, Torino, Italy

Author contributions: Cardinale L planned the research; Asteggiano F and Torre F collected the materials; Ulisciani S, Fava C, Rege-Cambrin G were involved in the collection of clinical data; Moretti F and Ulisciani S wrote the paper assisted by Fava C; Cardinale L and Rege-Cambrin G reviewed this commentary and supervised its publication; Asteggiano F, Moretti F and Torre F were involved in the language translation.

Correspondence to: Luciano Cardinale, PhD, Institute of Radiology, Department of Clinical and Biological Sciences, University of Turin, AOU S.Luigi Gonzaga, Regione Gonzole 10, 10043 Orbassano, Torino, Italy. luciano.cardinale@gmail.com
Telephone: +39-11-90261 Fax: +39-11-9026303

Received: December 28, 2013 Revised: July 9, 2014

Accepted: July 17, 2014

Published online: March 28, 2015

Abstract

In acute promyelocytic leukemia, differentiation therapy based on all-trans-retinoic acid can be complicated by the development of a differentiation syndrome (DS). DS is a life-threatening complication, characterized by respiratory distress, unexplained fever, weight gain, interstitial lung infiltrates, pleural or pericardial effusions, hypotension and acute renal failure. The diagnosis of DS is made on clinical grounds and has proven to be difficult, because none of the symptoms is pathognomonic for the syndrome without any definitive diagnostic criteria. As DS can have subtle signs and symptoms at presentation but progress rapidly, end-stage DS clinical picture resembles the acute respiratory distress syndrome with extremely poor prognosis; so it is of abso-

lute importance to be conscious of these complications and initiate therapy as soon as it was suspected. The radiologic appearance resembles the typical features of cardiogenic pulmonary edema. Diagnosis of DS remains a great skill for radiologists and haematologist but it is of an utmost importance the cooperation in suspect DS, detect the early signs of DS, examine the patients' behaviour and rapidly detect the complications.

© 2015 Baishideng Publishing Group Inc. All rights reserved.

Key words: Differentiation syndrome; All-trans-retinoic acid syndrome; Chest X-ray and computed tomography; Lungleukemic infiltrates; Acute promyelocytic leukemia; Promyelocytic leukemia/retinoic acid receptor- α

Core tip: Aim of this review is to illustrate the spectrum of chest imaging findings which lead to suspect a diagnosis of differentiation syndrome, which arise in patients suffering of Acute Promyelocytic Leukemia after treatment with all-trans-retinoic acid or other differentiating drugs, in order to facilitate the differential diagnosis with other life-threatening pulmonary complications occurring in this subset of highly immunocompromised patients.

Original sources: Cardinale L, Asteggiano F, Moretti F, Torre F, Ulisciani S, Fava C, Rege-Cambrin G. Pathophysiology, clinical features and radiological findings of differentiation syndrome/all-trans-retinoic acid syndrome. *World J Radiol* 2014; 6(8): 583-588 Available from: URL: <http://www.wjgnet.com/1949-8470/full/v6/i8/583.htm> DOI: <http://dx.doi.org/10.4329/wjr.v6.i8.583>

LEARNING OBJECTIVES

The treatment of acute promyelocytic leukemia with agents capable of inducing the differentiation of leu-

kemic cells can be complicated by a peculiar syndrome, named differentiation syndrome (DS); this was previously classified as retinoic acid syndrome, as all-trans-retinoic acid (ATRA) was the first agent to be involved in this complication. DS is a syndrome of cardiac and respiratory distress which represents a life-threatening complication, and is associated with severe morbidity and mortality; so early diagnosis and immediate therapeutic intervention are essential in reducing the risk of death^[1].

In this work we illustrate the imaging findings on chest X-ray, and in standard or high-resolution computed tomography (CT) useful to suggest this uncommon diagnosis. The aim of this work is to underline the importance of an early diagnosis of DS, to show how radiologists can confirm the diagnosis of DS, to stimulate the cooperation and communication between radiologists and clinicians.

BACKGROUND

Acute promyelocytic leukemia (APL), identified as acute myeloid leukaemia (AML) M3 by the French-American-English classification, is an acute myeloid disorder due to a maturative block of myeloid precursor at the promyelocytic stage, leading to peculiar clinical manifestations, and characterized by a reciprocal balanced translocation between chromosome 15 and 17 $t(15, 17)$ ^[2]. APL represents about 10% of all AML in United States and Europe and is more frequent in adults; median age at diagnosis is 40^[3,4].

The finding of a translocation $t(15, 17)$, with a consequent transcriptional fusion between promyelocytic leukaemia (*PML*) gene and retinoic acid receptor- α (*RAR α*) gene, responsible of the maturative and differentiative stop, offered the basis to develop a specific target therapy with retinoic acid. *PML-RAR α* rearrangement is detectable in approximately 95% of APL cases^[2,3].

APL is usually a primitive disorder, but there are also cases of APL arising following a previous exposure to chemotherapy or radiotherapy^[5,6].

On the clinical side APL represents a hematologic emergency because of its typical presentation with pancytopenia and a life-threatening disseminated intravascular coagulation, that enforces a quick start of treatment, even before a cytogenetic and molecular diagnosis. Diagnosis of APL is usually based on peripheral blood and bone marrow morphology, supported by typical laboratory and clinical picture. Confirmation then comes from the molecular finding of *PML-RAR α* rearrangement. Treatment of APL is based on the association of ATRA with conventional chemotherapy (usually anthracyclines), or with arsenic trioxide (ATO). Since the introduction of ATRA in the treatment, the complete remission rate raised up to 90% and the 5-year disease free survival to 74%^[7-9].

Induction treatment with ATRA and ATO, either as a single agent or in combination with cytotoxic drugs, can induce the DS^[10] in 2% to 31% of APL patients^[10,11], while the association with chemotherapy compared with

Table 1 Signs and symptoms

Differentiation syndrome: Sign and symptoms	
Elevated white blood cell count	Weight gain > 5 kg
Dyspnea	Bone pain
Respiratory distress	Headache
Fever	Hypotension
Pulmonary edema	Congestive heart failure
Pulmonary infiltrates	Acute renal failure
Pleural and pericardial effusion	Hepatotoxicity

ATRA as single-agent lead to a reduction risk of DS (9% vs 18%-25%)^[12,13]. Mortality due to DS has declined from 30% to 2%-10% because of the early recognition and clinical intervention^[10]. Notably, DS is rarely seen during consolidation and maintenance phases^[12,14,15].

The pathophysiology of DS is not completely understood. Both ATRA and ATO exert their action by degradation of the *PML-RAR α* fusion product. As a consequence, malignant leukemic cells undergo differentiation and final maturation^[16,17].

Exposition to ATRA and ATO cause continued generation of inflammatory cytokines and adhesion molecules, with the consequent extravasation into the tissues from the blood. Increased in cytokine and adhesion molecules level also occurs in liver, heart and spleen^[11,18].

DS is typically diagnosed during the first induction treatment, more often 10 to 12 d after therapy start, with a range of 2 to 46 d^[10,11,18-20]. Main symptoms at presentation are fever, respiratory failure and fluid retention with weight increase, occurring in around 80% of the cases^[10,18]. Additional common findings are lung infiltrates (50%), pericardial and pleural effusions (30%) and acute renal failure (10% of the cases)^[18]. DS has to be distinguished from other clinical conditions which may occur in the setting of acute leukaemia, including pulmonary infection, leukostasis, and heart failure. Diagnosis of DS is made when three or more of the symptoms and signs listed in Table 1 are present. Clinical management and outcome are greatly influenced by early pharmacological treatment. Dexamethasone must be used at a dosage of 10 mg twice daily *iv* as soon as DS is suspected. Steroid treatment should continue until DS resolves, and then the dosage can be gradually tapered in the following weeks^[21,22]. Hemodynamic and ventilatory support is also indicated in severe cases, which may require admission at the intensive care unit. In Table 2, modified from^[1], the measures to be taken at suspicion of DS are reported. Discontinuation of treatment with ATRA (or ATO) is mandatory in severe DS cases^[4]. Corticosteroid are commonly used as DS prophylaxis, although there is no evidence that such treatment may ameliorate the morbidity and mortality of DS. However, in patients with leukocytosis at diagnosis (white blood cells > 5 × 10⁹/L), preemptive steroids administration has been shown useful in reducing incidence and severity of DS. No definite risk factors for developing DS were found, but a close monitoring of patients presenting with hyperleukocytosis

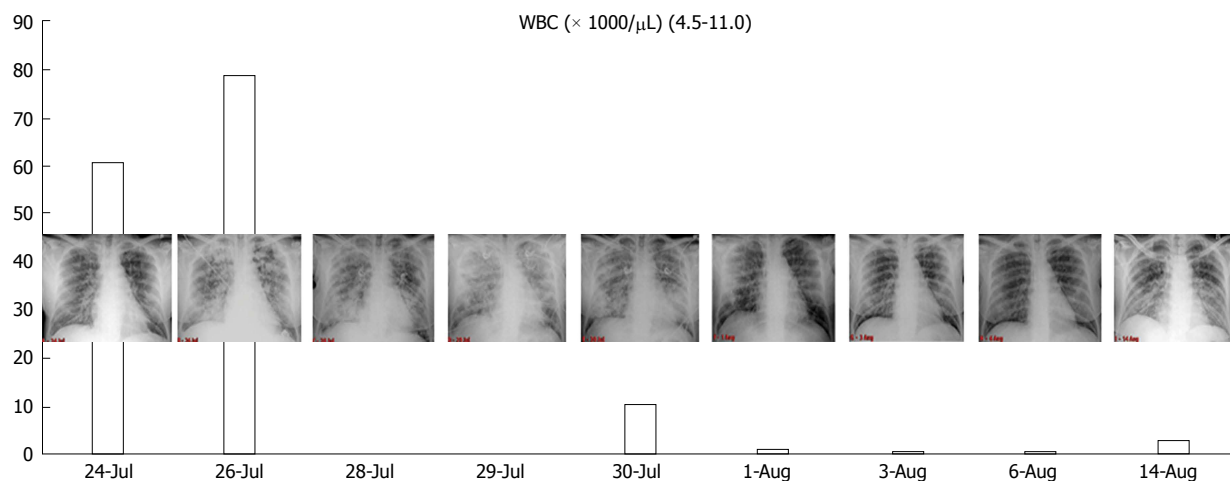


Figure 1 Correlation between white blood cell count and chest X-ray. Note that the worsening of chest X-ray is directly linked with the fall of white blood cell due to the massive differentiation during the onset of differentiation syndrome. References: Institute of Radiology, Department of Clinical and Biological Sciences of University of Turin, AOU S. Luigi Gonzaga, Regione Gonzole 10, 10043 Orbassano, Torino, Italy. WBC: White blood cells.

Table 2 Measures at suspicion of differentiation syndrome

Measures at suspicion of DS
Chest X-ray, renal function (creatinine and urea), hepatic function (amino transferases and bilirubin), blood cell counts, coagulation test, oxygen saturation
Weight monitoring
Ventilatory support/O ₂ supplementation
Blood pressure maintenance measures
Fluid restriction (renal failure)
Steroid administration at first suspicion: dexamethasone 10 mg twice daily until clinical resolution, then tapered dose for a few days
Suspend ATRA or ATO in severe cases, which can be restarted after clinical improvement. If DS recurs after restart, ATRA must be definitively discontinued during induction

Some patients have DS that is refractory to corticosteroids. There are yet no widely accepted alternatives to it. It seems reasonable to employ, in the future, agents that block migration, adhesion or transmigration of APL cells. References: Institute of Radiology, Department of Clinical and Biological Sciences of University of Turin, AOU S.Luigi Gonzaga, Regione Gonzole 10, 10043 Orbassano, Torino, Italy. DS: Differentiation syndrome; ATRA: All-trans-retinoic acid; ATO: Arsenic-trioxide.

is recommended^[22,23].

A better knowledge and early identification of DS, with rapid initiation of treatment, allowed to obtain a decrease in mortality associated with APL in the recent years.

IMAGING FINDINGS

As stated before, there are no clinical signs or laboratory tests to diagnose DS, nor is there a radiological finding pathognomonic for DS.

Radiologic features may be explained by the proposed hypotheses of pathophysiology of the DS^[24]. Most of the patients with DS showed cardiomegaly, widening of the vascular pedicle width, increased pulmonary blood volume, peribronchial cuff, ground-glass opacity, septal lines, and pleural effusion: these findings are similar to those of congestive heart failure with pulmonary edema,

but they could also probably be produced by leukemic lung infiltration and endothelial leakage^[24].

If the disease progresses, acute respiratory distress syndrome develops. Diffuse alveolar damage and massive intra-alveolar hemorrhage were found in a necropsy patient study by Frankel *et al*^[25]. Endothelial cell damage, including intra-alveolar oedema, intra-alveolar hemorrhage, and fibrinous exudate, were found by Tallman *et al*^[26] and by Nicolls *et al*^[27]. Others histological analysis of lungs reported extensive interstitial and alveolar lung infiltration by maturing myeloid cells, endothelial cells damage, oedema, hemorrhage, and fibrinous exudates that correspond in poorly defined centrolobular nodules and ground-glass opacity with or without interlobular septal thickening.

To our knowledge only a few cases are reported describing the CT aspect in DS: Davis *et al*^[28] reported CT findings in three patients with DS. CT findings were peripheral nodules reticular and ground-glass opacity and pleural effusions. They also reported the case of a patient with DS who developed pneumothorax^[28].

In mild DS, lesions are prevalent in the lower lobes, while in severe DS, lesions are ubiquitous, with no difference within peripheral or central regions^[6,9].

In Figure 1, we present the correlation with radiological findings and white blood cells (WBC). The pathogenesis of DS suggest that this syndrome is due to a massive lung interstitial invasion by leukemic cells. The finding of a negative peak of WBC nearly contemporary to the massive lung oedema seems to confirm this theory.

Patients with PML and DS have an highly compromised immune system; therefore, it is not a rare event to find other concurrent pathologic conditions as pneumonia or fungine infections which can confound the radiological picture of DS/ATRA syndrome.

CT findings of ATRA syndrome are nonspecific (Figure 2).

All findings have differential diagnoses: leukemic infiltrates, drug toxicity, pulmonary edema, hemorrhage, can all have similar appearances.

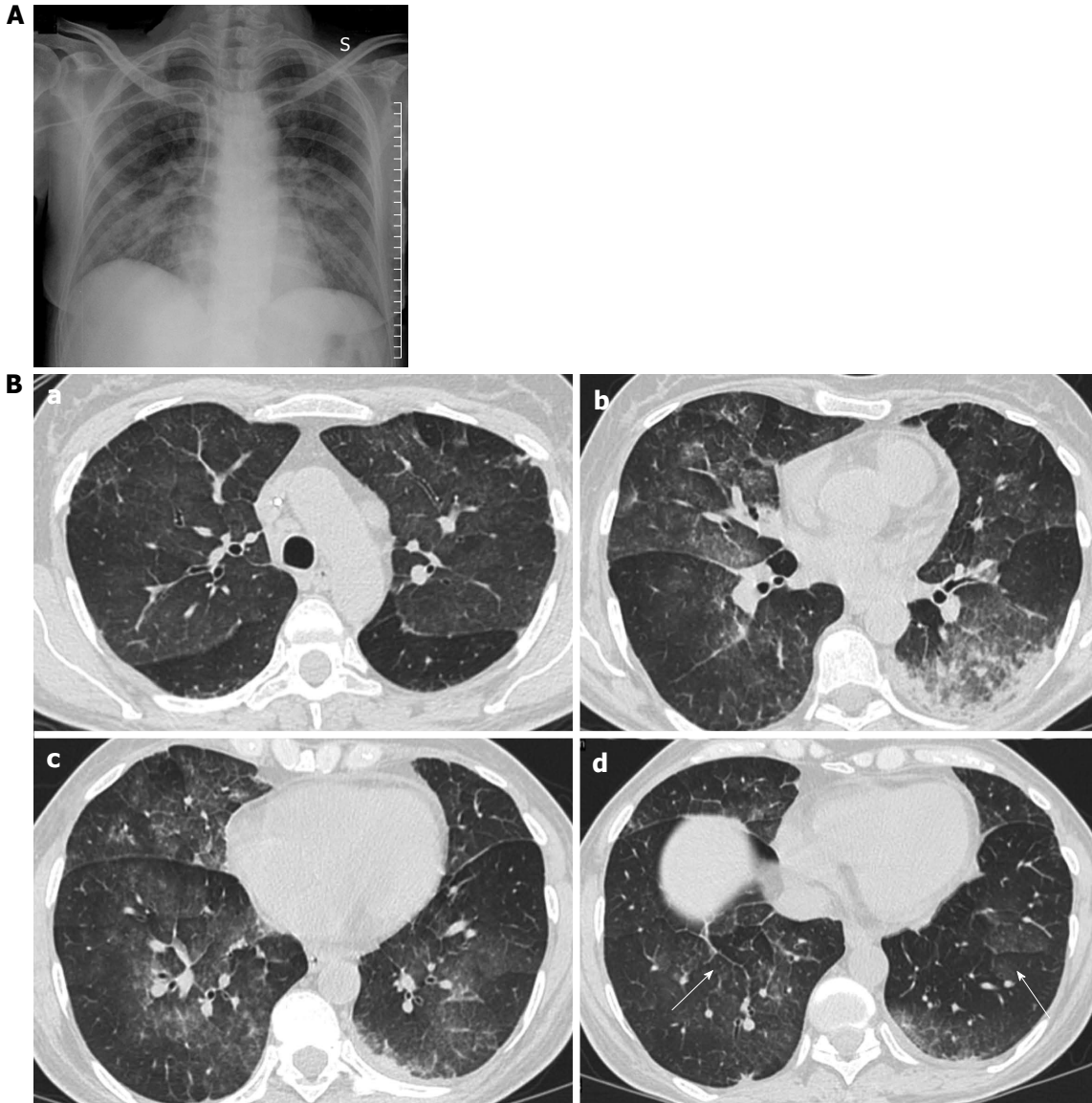


Figure 2 Photograph. A: Chest X-ray shows subtle patchy ground glass opacities of the middle inferior lung fields; B: Computed tomography scans of the same patient as Figure 4 shows patchy ground glass opacities (a, b and c) with interlobar septal thickening (arrows in d). References: Institute of Radiology, Department of Clinical and Biological Sciences of University of Turin, AOU S.Luigi Gonzaga, Regione Gonzole 10, 10043 Orbassano, Torino, Italy.

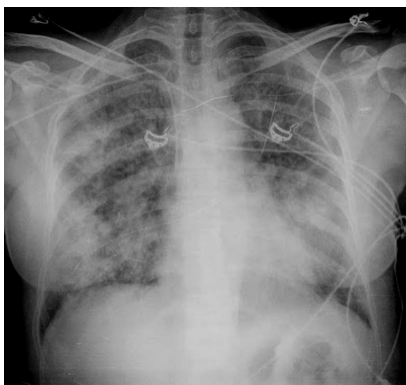


Figure 3 Supine Chest X-ray showing bilateral, asymmetrical patchy consolidation. Septal lines and pleural effusions are absent. Based on the only radiologic features, it would be difficult to differentiate one from acute respiratory distress syndrome or hemorrhage on these findings. References: Institute of Radiology, Department of Clinical and Biological Sciences of University of Turin, AOU S.Luigi Gonzaga, Regione Gonzole 10, 10043 Orbassano, Torino, Italy.

Although the imaging features are not characteristic, in combination with the clinical picture, they may contribute to the early identification of DS and consequently to its fast resolution (Figures 3 and 4).

CONCLUSION

Diagnosis of DS requires a great skill for radiologists and hematologists, and cooperation and treatment is of utmost importance when DS is confirmed.

Chest X-ray still remains the first imaging step, but often, in mild cases, it is not sufficient.

In summary chest X-ray features include increased cardiothoracic ratio and vascular pedicle width, interstitial edema with peribronchial cuffing and Kerley lines.

The chest CT is useful to evaluate the lung parenchyma and also to discover other signs of severity, as pericardial and pleural effusions, and sometimes to find



Figure 4 Chest X-ray in patient with differentiation syndrome showed mild cardiomegaly and increased pulmonary vascular marking in both lungs with thickening of small fissure and minimal pleural effusion on the right side seen as obliteration of right costo-phrenic angle: These findings are similar to those of congestive heart failure with pulmonary edema. In contrast with congestive heart failure the time for the complete healing is long, and is similar to that of interstitial pneumonia or acute respiratory distress syndrome. References: Institute of Radiology, Department of Clinical and Biological Sciences of University of Turin, AOU S.Luigi Gonzaga, Regione Gonzole 10, 10043 Orbassano, Torino, Italy.

others concurrent lung infections.

Take home message: (1) Suspect DS in patient with acute APL under treatment with ATRA and/or arsenic trioxide; (2) Detect the early signs of DS to confirm the clinical diagnosis; (3) Examine the patient's behaviour; and (4) Rapidly detect and treat the complications.

REFERENCES

- 1 **Rego EM**, De Santis GC. Differentiation syndrome in promyelocytic leukemia: clinical presentation, pathogenesis and treatment. *Mediterr J Hematol Infect Dis* 2011; **3**: e2011048 [PMID: 22110898 DOI: 10.4084/MJHID.2011.048]
- 2 **Melnick A**, Licht JD. Deconstructing a disease: RARalpha, its fusion partners, and their roles in the pathogenesis of acute promyelocytic leukemia. *Blood* 1999; **93**: 3167-3215 [PMID: 10233871]
- 3 **Rogers JE**, Yang D. Differentiation syndrome in patients with acute promyelocytic leukemia. *J Oncol Pharm Pract* 2012; **18**: 109-114 [PMID: 21364078 DOI: 10.1177/1078155211399163]
- 4 **Sanz MA**, Grimwade D, Tallman MS, Lowenberg B, Fenaux P, Estey EH, Naoe T, Lengfelder E, Büchner T, Döhner H, Burnett AK, Lo-Coco F. Management of acute promyelocytic leukemia: recommendations from an expert panel on behalf of the European LeukemiaNet. *Blood* 2009; **113**: 1875-1891 [PMID: 18812465 DOI: 10.1182/blood-2008-04-150250]
- 5 **Pulsoni A**, Pagano L, Lo Coco F, Avvisati G, Mele L, Di Bona E, Invernizzi R, Leoni F, Marmont F, Mele A, Melillo L, Nosari AM, Pogliani EM, Vignetti M, Visani G, Zagonel V, Leone G, Mandelli F. Clinicobiological features and outcome of acute promyelocytic leukemia occurring as a second tumor: the GIMEMA experience. *Blood* 2002; **100**: 1972-1976 [PMID: 12200354]
- 6 **Mistry AR**, Felix CA, Whitmarsh RJ, Mason A, Reiter A, Cassinat B, Parry A, Walz C, Wiemels JL, Segal MR, Adès L, Blair IA, Osheroff N, Peniket AJ, Lafage-Pochitaloff M, Cross NC, Chomienne C, Solomon E, Fenaux P, Grimwade D. DNA topoisomerase II in therapy-related acute promyelocytic leukemia. *N Engl J Med* 2005; **352**: 1529-1538 [PMID: 15829534]
- 7 **Wang ZY**, Chen Z. Acute promyelocytic leukemia: from highly fatal to highly curable. *Blood* 2008; **111**: 2505-2515 [PMID: 18299451 DOI: 10.1182/blood-2007-07-102798]
- 8 **Bennett JM**, Catovsky D, Daniel MT, Flandrin G, Galton DA, Gralnick HR, Willman CL. Hypergranular promyelocytic leukemia: correlation between morphology and chromosomal translocations including t(15; 17) and t(11; 17). *Leukemia* 2000; **14**: 1197-1200 [PMID: 10914542]
- 9 **de la Serna J**, Montesinos P, Vellenga E, Rayón C, Parody R, León A, Esteve J, Bergua JM, Milone G, Debén G, Rivas C, González M, Tormo M, Díaz-Mediavilla J, González JD, Negri S, Amutio E, Brunet S, Lowenberg B, Sanz MA. Causes and prognostic factors of remission induction failure in patients with acute promyelocytic leukemia treated with all-trans retinoic acid and idarubicin. *Blood* 2008; **111**: 3395-3402 [PMID: 18195095]
- 10 **Patatanian E**, Thompson DF. Retinoic acid syndrome: a review. *J Clin Pharm Ther* 2008; **33**: 331-338 [PMID: 18613850]
- 11 **Luesink M**, Pennings JL, Wissink WM, Linszen PC, Muus P, Pfundt R, de Witte TJ, van der Reijden BA, Jansen JH. Chemokine induction by all-trans retinoic acid and arsenic trioxide in acute promyelocytic leukemia: triggering the differentiation syndrome. *Blood* 2009; **114**: 5512-5521 [PMID: 19828696 DOI: 10.1182/blood-2009-02-204834]
- 12 **De Botton S**, Dombret H, Sanz M, Miguel JS, Caillot D, Zittoun R, Gardembas M, Stamatoulas A, Condé E, Guerci A, Gardin C, Geiser K, Makhoul DC, Reman O, de la Serna J, Lefrere F, Chomienne C, Chastang C, Degos L, Fenaux P. Incidence, clinical features, and outcome of all trans-retinoic acid syndrome in 413 cases of newly diagnosed acute promyelocytic leukemia. The European APL Group. *Blood* 1998; **92**: 2712-2718 [PMID: 9763554]
- 13 **de Botton S**, Chevret S, Coiteux V, Dombret H, Sanz M, San Miguel J, Caillot D, Vekhoff A, Gardembas M, Stamatoulas A, Conde E, Guerci A, Gardin C, Fey M, Cony Makhoul D, Reman O, de la Serna J, Lefrere F, Chomienne C, Degos L, Fenaux P. Early onset of chemotherapy can reduce the incidence of ATRA syndrome in newly diagnosed acute promyelocytic leukemia (APL) with low white blood cell counts: results from APL 93 trial. *Leukemia* 2003; **17**: 339-342 [PMID: 12592333]
- 14 **Rust DM**, Soignet SL. Risk/benefit profile of arsenic trioxide. *Oncologist* 2001; **6** Suppl 2: 29-32 [PMID: 11331438]
- 15 **Gupta V**, Yi QL, Brandwein J, Lipton JH, Messner HA, Schuh AC, Wells RA, Minden MD. Role of all-trans-retinoic acid (ATRA) in the consolidation therapy of acute promyelocytic leukaemia (APL). *Leuk Res* 2005; **29**: 113-114 [PMID: 15541484]
- 16 **Roche Laboratories, Inc.** Vesanoid (tretinoin) package insert. Nutley, NJ, 2004. Available from: URL: http://www.accessdata.fda.gov/drugsatfda_docs/label/2004/20438s004lbl.pdf
- 17 **Nasr R**, Lallemand-Breitenbach V, Zhu J, Guillemain MC, de Thé H. Therapy-induced PML/RARA proteolysis and acute promyelocytic leukemia cure. *Clin Cancer Res* 2009; **15**: 6321-6326 [PMID: 19808868 DOI: 10.1158/1078-0432.CCR-09-0209]
- 18 **Larson RS**, Tallman MS. Retinoic acid syndrome: manifestations, pathogenesis, and treatment. *Best Pract Res Clin Haematol* 2003; **16**: 453-461 [PMID: 12935962]
- 19 **Luesink M**, Jansen JH. Advances in understanding the pulmonary infiltration in acute promyelocytic leukaemia. *Br J Haematol* 2010; **151**: 209-220 [PMID: 20735400 DOI: 10.1111/j.1365-2141.2010.08325.x]
- 20 **Montesinos P**, Bergua JM, Vellenga E, Rayón C, Parody R, de la Serna J, León A, Esteve J, Milone G, Debén G, Rivas C, González M, Tormo M, Díaz-Mediavilla J, González JD, Negri S, Amutio E, Brunet S, Lowenberg B, Sanz MA. Differentiation syndrome in patients with acute promyelocytic leukemia treated with all-trans retinoic acid and anthracy-

- cline chemotherapy: characteristics, outcome, and prognostic factors. *Blood* 2009; **113**: 775-783 [PMID: 18945964 DOI: 10.1182/blood-2008-07-168617]
- 21 Acute Myeloid Leukemia NCCN Clinical Practice Guidelines in Oncology (Version 2.2014)
- 22 **Wiley JS**, Firkin FC. Reduction of pulmonary toxicity by prednisolone prophylaxis during all-trans retinoic acid treatment of acute promyelocytic leukemia. Australian Leukaemia Study Group. *Leukemia* 1995; **9**: 774-778 [PMID: 07769839]
- 23 **Sanz MA**, Martín G, González M, León A, Rayón C, Rivas C, Colomer D, Amutio E, Capote FJ, Milone GA, De La Serna J, Román J, Barragán E, Bergua J, Escoda L, Parody R, Negri S, Calasanz MJ, Bolufer P. Risk-adapted treatment of acute promyelocytic leukemia with all-trans-retinoic acid and anthracycline monochemotherapy: a multicenter study by the PETHEMA group. *Blood* 2004; **103**: 1237-1243 [PMID: 14576047]
- 24 **Jung JI**, Choi JE, Hahn ST, Min CK, Kim CC, Park SH. Radiologic features of all-trans-retinoic acid syndrome. *AJR Am J Roentgenol* 2002; **178**: 475-480 [PMID: 11804921]
- 25 **Frankel SR**, Eardley A, Lauwers G, Weiss M, Warrell RP. The "retinoic acid syndrome" in acute promyelocytic leukemia. *Ann Intern Med* 1992; **117**: 292-296 [PMID: 1637024]
- 26 **Tallman MS**, Andersen JW, Schiffer CA, Appelbaum FR, Feusner JH, Ogden A, Shepherd L, Rowe JM, François C, Larson RS, Wiernik PH. Clinical description of 44 patients with acute promyelocytic leukemia who developed the retinoic acid syndrome. *Blood* 2000; **95**: 90-95 [PMID: 10607690]
- 27 **Nicolls MR**, Terada LS, Tuder RM, Prindiville SA, Schwarz MI. Diffuse alveolar hemorrhage with underlying pulmonary capillaritis in the retinoic acid syndrome. *Am J Respir Crit Care Med* 1998; **158**: 1302-1305 [PMID: 9769296]
- 28 **Davis BA**, Cervi P, Amin Z, Moshi G, Shaw P, Porter J. Retinoic acid syndrome: pulmonary computed tomography (CT) findings. *Leuk Lymphoma* 1996; **23**: 113-117 [PMID: 9021693]

P- Reviewer: Agarwal R, Sureka B **S- Editor:** Wen LL
L- Editor: A **E- Editor:** Liu SQ



Vascular anomalies: A pictorial review of nomenclature, diagnosis and treatment

John L Noshier, Philip G Murillo, Mark Liszewski, Vyacheslav Gendel, Christopher E Gribbin

John L Noshier, Philip G Murillo, Mark Liszewski, Vyacheslav Gendel, Christopher E Gribbin, Department of Radiology, Rutgers Medical School, Robert Wood Johnson University Hospital, New Brunswick, NJ 08901, United States

Author contributions: All authors contributed textual and illustrative material to this paper.

Correspondence to: John L Noshier, MD, Department of Radiology, Rutgers Medical School, Robert Wood Johnson University Hospital, 1 Robert Wood Johnson Place, MEB404, New Brunswick, NJ 08901, United States. vgendel@gmail.com

Telephone: +1-732-8283000

Received: January 25, 2014 Revised: July 13, 2014

Accepted: July 25, 2014

Published online: March 28, 2015

Abstract

Vascular anomalies, including vascular malformations and tumors, are frequently straightforward to detect; however, accurate diagnosis and appropriate treatment are often challenging. Misdiagnosis of these lesions can lead clinicians in the wrong direction when treating these patients, which can have unfavorable results. This review presents an overview of the classification systems that have been developed for the diagnosis of vascular lesions with a focus on the imaging characteristics. Pictorial examples of each lesion on physical examination, as well as non-invasive and minimally invasive imaging are presented. An overview of the endovascular treatment of these lesions is also given. In some cases, vascular anomalies may be associated with an underlying syndrome and several of the most commonly encountered syndromes are discussed. Understanding of the classification systems, familiarity with the treatment options and knowledge of the associated syndromes are essential for all physicians working with this patient population. The approach to the described entities necessitates an organized multi-disciplinary team effort, with diagnostic imaging playing an increasingly important role in the proper diagnosis and a com-

bined interventional radiologic and surgical treatment method showing promising results.

© 2015 Baishideng Publishing Group Inc. All rights reserved.

Key words: Vascular malformation; Lymphatic malformation; Overgrowth syndromes; Arteriovenous malformation; Hemangioma

Core tip: Accurate diagnosis and appropriate treatment of vascular anomalies are challenging endeavors. This review presents a summary of the classification systems for vascular anomalies, a review of endovascular treatment options, and a brief look at several associated syndromes. Understanding of the diagnosis and treatment of these lesions is essential for all physicians working with this patient population.

Original sources: Noshier JL, Murillo PG, Liszewski M, Gendel V, Gribbin CE. Vascular anomalies: A pictorial review of nomenclature, diagnosis and treatment. *World J Radiol* 2014; 6(9): 677-692 Available from: URL: <http://www.wjgnet.com/1949-8470/full/v6/i9/677.htm> DOI: <http://dx.doi.org/10.4329/wjr.v6.i9.677>

INTRODUCTION

Anatomist and obstetrician William Hunter first described vascular anomalies in the mid-18th century in the context of iatrogenic creation of arteriovenous fistulas by phlebotomists^[1]. Over the next century, description of these and more complex vascular lesions was furthered by the work of Dupuytren, Virchow, and others but the lack of a cohesive system of classification led to confusion, hampering further understanding of these entities. Since that time, categorization of these lesions has advanced from primitive descriptions and disorganized nomenclatures to a more a structured catalogue of classification. Mulliken

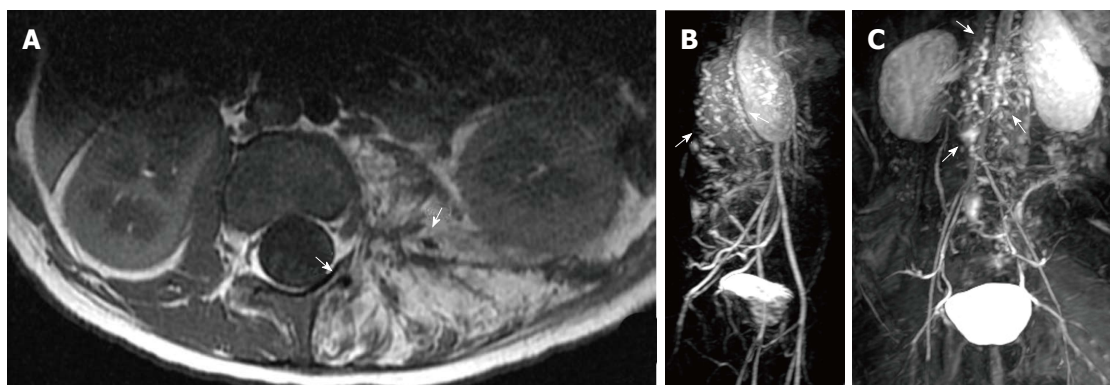


Figure 1 Kaposiform hemangioendothelioma. A: Magnetic resonance (MR) of the retroperitoneum demonstrating infiltrative tumor with fat and interspersed signal void (arrows) consistent with high flow arterial signal; B, C: MR angiogram demonstrating arteriovenous shunting within the tumor (arrows).

and Glowacki pioneered this transformation^[2], while the Hamburg classification system further refined it^[3].

Early attempts at classification were based on the pathological appearance of the lesions without consideration for underlying biologic behavior. Terms such as “erectile tumors,” “naevus maternus,” and “stigma metrocelsis” were applied without clear delineation^[2]. It wasn’t until 1982, when Mulliken and Glowacki introduced a classification system rooted in the pathophysiology of these lesions that much of the confusion surrounding these lesions was clarified^[2]. This system divided vascular anomalies into two categories: vascular tumors (hemangiomas) and vascular malformations. This standard was adopted by the International Society for the Study of Vascular Anomalies (ISSVA)^[3,4] and continues to be embraced by many clinicians in current practice. Subsequent modifications to this classification system have included the addition of other rare vascular tumors distinct from hemangiomas, including tufted angioma, Kaposiform hemangioendothelioma, angiosarcoma and others. With these additions, vascular anomalies continue to be divided into two categories: vascular tumors, which include hemangiomas, and vascular malformations. Several years later, the Hamburg classification system adopted an embryologic perspective to further aid in the classification of vascular malformations^[3]. Lesions are identified first based on the prevailing vascular structure involved- arterial, venous, lymphatic, or capillary, also considering arteriovenous shunting and combined vascular defects^[3]. The embryological background of the lesion is then considered for additional delineation^[5]. Extratruncular lesions result from developmental arrest in the early reticular embryonic stage, prior to the development of vascular trunks. Extratruncular malformations may be infiltrating and diffuse or limited and localized. Truncular lesions result from a defect occurring during the stage of fetal development following the reticular stage, as the vascular trunks are developing. Truncular forms develop from stenosis or obstruction of vascular trunks, with resulting hypoplasia, or dilatation of vascular trunks, which in turn may be localized or diffuse^[6].

VASCULAR TUMORS

In their seminal paper, Mulliken and Glowacki^[2], reported vascular tumors - then referred to as hemangiomas - to demonstrate specific mitotic activity and eventual involution, setting them apart from vascular malformations. Much has been discovered about vascular tumors, and while beyond the scope of this discussion, this information encompasses a variety of different entities. These include but are not limited to infantile hemangiomas and rapidly involuting and noninvoluting congenital hemangiomas, as well as more aggressive tumors, such as tufted angiomas, Kaposiform hemangioendotheliomas, and angiosarcomas.

Infantile hemangiomas are the most common tumor of infancy and childhood affecting up to 12% of children with a female preponderance^[7,8]. Histologically, these lesions stain positively for glucose transporter-1 protein (GLUT-1). Tumors typically appear between 2 wk and 2 mo of life and follow a proliferating phase, an involuting phase, and a state of complete involution^[9,10].

Congenital hemangiomas are tumors that demonstrate intrauterine development with growth completed at birth^[11]. These lesions more commonly affect the extremities, close to the joint, or on the head and neck, close to the ear^[12]. In contrast to infantile hemangiomas, these lesions stain negative for GLUT-1^[11,12]. Lesions are divided into two categories based on biologic activity: rapidly involuting congenital hemangiomas (RICHs) and noninvoluting congenital hemangiomas (NICHs). RICHs typically regress within 6-14 mo while NICHs do not regress and have a tendency for progression, usually leading to surgical excision^[12].

Kaposiform hemangioendothelioma (Figure 1) is a rare vascular neoplasm, which usually arises in the skin and infiltrates into the deeper tissues over time. Most cases are associated with consumptive coagulopathy or Kasabach-Merritt Syndrome, as well as lymphangiomatosis^[13].

VASCULAR MALFORMATIONS

Vascular malformations are structural lesions resulting



Figure 2 Low flow extratruncular venous malformation. Radiograph of the right lower leg (A) demonstrates phleboliths within the soft tissues (arrows). T2-weighted magnetic resonance images in the coronal (B), sagittal (C), and axial (D) planes demonstrate hyperintense signal within the gastrocnemius muscle due to infiltrative low flow extratruncular venous malformation.

from errors of vascular morphogenesis^[2]. Differentiation of vascular malformations into high flow, low flow or mixed lesions is critical in developing treatment strategies. The distinction of truncal from extratruncal may provide insight in predicting response to treatment.

IMAGING OF VASCULAR ANOMALIES

Several noninvasive imaging modalities are useful in characterizing vascular anomalies, contributing information about lesion size, flow characteristics and relationship to adjacent structures^[14]. Conventional radiography plays a minor role, though may be valuable in defining bone and joint involvement and presence of phleboliths^[14] (Figure 2A). Contrast enhanced computed tomography (CT) and CT angiograph are useful in evaluating osseous involvement and phleboliths, but also provides information about enhancement, thrombosis, calcification, vascular anatomy and involvement of adjacent structures^[14]. The use of ionizing radiation and relatively limited ability to provide information about flow dynamics decreases its usefulness. For these reasons ultrasonography (US) and magnetic resonance imaging (MRI) are the primary noninvasive imaging modalities used in the evaluation of vascular anomalies^[15].

US is indispensable in the evaluation of superficial vascular lesions given its low cost, ease of use, high temporal and spatial resolution, and ability to evaluate flow dynamics^[14,16]. With US, hemangiomas are reliably differentiated from vascular malformations based on depiction of a well-circumscribed solid mass^[16]. Hemangiomas and high-flow vascular malformations, including arteriovenous malformations (AVMs) and arteriovenous fistulae (AVFs), demonstrate arterial and venous waveforms on pulsed Doppler US, but are differentiated based on a lack of associated mass in AVMs and AVFs^[15,16]. AVMs and AVFs will contain multiple enlarged subcutaneous arteries and veins on grey scale and color Doppler US with associated low-resistance arterial and venous waveforms on pulsed Doppler US^[15,16]. Low-flow vascular malformations, including venous and lymphatic malformations, can be differentiated from high flow lesions based on

Doppler analysis. Venous malformations contain enlarged subcutaneous vessels without an associated mass, are compressible and demonstrate venous flow on color and pulsed Doppler US^[16]. Lymphatic malformations are characterized by macrocystic or microcystic spaces with or without debris separated by septae. On color and pulsed Doppler US these cysts will contain no flow, however the septa may contain small arteries and veins^[16]. US is limited in its ability to evaluate deep lesions and lesions that involve bone^[14].

MRI is the most valuable modality for imaging vascular anomalies due to its superior contrast resolution, ability to characterize flow dynamics, depiction of deep and adjacent structures and lack of ionizing radiation^[14]. Most information needed to characterize a vascular anomaly can be obtained from T1-weighted, fat saturated T2-weighted and gradient echo MR sequences^[15]. Basic MR imaging protocols should include each of these sequences in the axial plane along with fast spin echo T2-weighted images in the coronal and sagittal planes^[15,17]. Dynamic contrast-enhanced MRI can provide supporting information about flow dynamics^[18] and may also be employed. On MRI, hemangiomas will appear as a mass^[15,19] with flow voids and intermediate signal on T1-weighted images, flow voids and high signal on T2-weighted images, high signal within vessels on gradient echo sequences and arterial enhancement on contrast enhanced images^[15,19]. High-flow vascular malformations including AVMs and AVFs will also demonstrate flow voids and intermediate signal on T1-weighted images, flow voids and high signal on T2-weighted images, high signal within vessels on gradient echo sequences and arterial enhancement on contrast enhanced images, but no associated soft tissue mass^[14,19]. Low flow lesions including venous malformations and lymphatic malformations can also be differentiated based on MRI. Venous malformations will appear as multiple serpentine tubular structures or amorphous dilated channels containing intermediate signal on T1 weighted images, high signal on T2 weighted images, intermediate signal on gradient echo sequences and delayed enhancement on dynamic contrast enhanced MRI^[14,19]. Flow voids are not seen within venous malformations

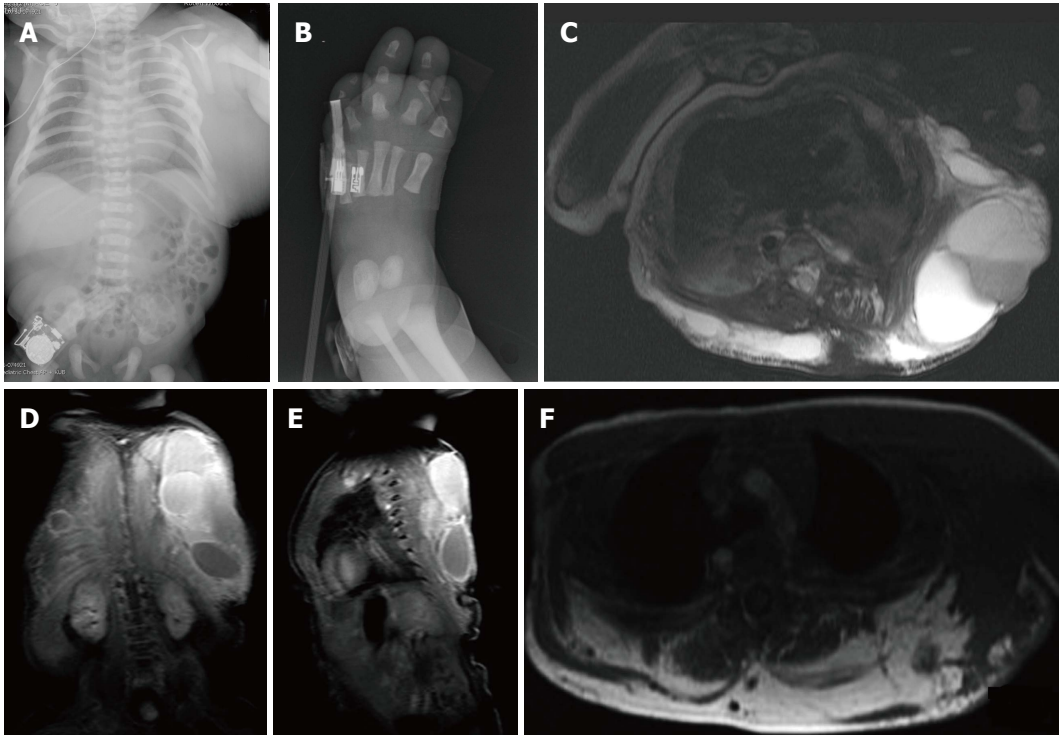


Figure 3 Three-month-old child with CLOVES syndrome. Radiograph of the chest and abdomen (A) demonstrates large soft tissue mass within the left chest and upper abdominal wall. Radiograph of the foot (B) demonstrates overgrowth of the third and fourth digits. Fat suppressed T2 weighted magnetic resonance (MR) images in axial (C), coronal (D) and sagittal (E) planes show the large soft tissue mass within the chest wall contains several loculations, some of which demonstrate hypointense fluid-fluid levels due to hemorrhage. T1 weighted MR image in the axial plane (F) confirms lipomatous overgrowth admixed with muscle.

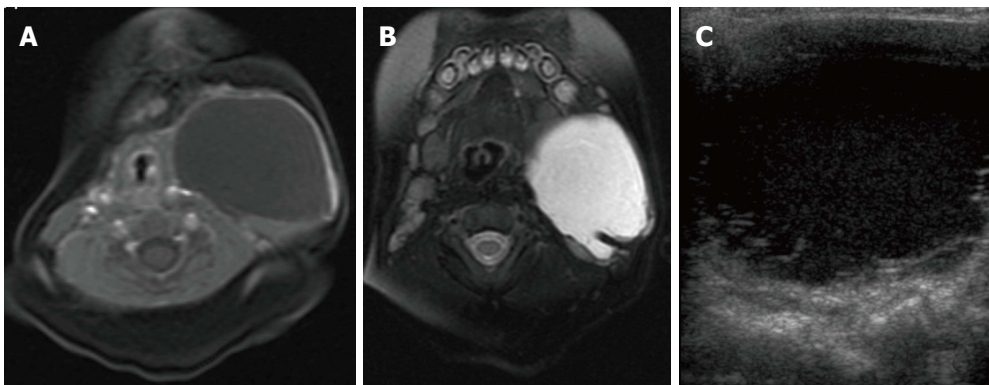


Figure 4 Cervicothoracic macrocystic lymphatic malformation. T1- (A) and T2-weighted (B) fat suppressed magnetic resonance images (MRI) demonstrate a macrocyst within the left neck that is predominantly hypointense on T1-weighted image and hyperintense on T2-weighted image. Trace blood products layering within the posterior aspect of the cyst are hyperintense on the T1 weighted image and hypointense on the T2 weighted image. Transverse ultrasound (C) demonstrates a predominantly anechoic macrocyst with layering low-level echoes, corresponding to blood products seen on MRI.

due to a lack of fast-flowing blood. Lymphatic malformations are characterized by micro- or macrocystic spaces that often contain fluid-fluid levels due to hemorrhage or proteinaceous material within the cysts^[15] (Figures 3-5). Cysts will often be hyperintense on T2-weighted images, hypointense on T1 weighted images (though may be iso- to hyperintense depending on proteinaceous contents), and will not enhance^[15,19]. When microcystic, the cystic spaces may not be visible with the fibrovascular stroma seen as regions of intermediate signal on T1-weighted images and high signal on T2-weighted images with associated enhancement on post-contrast images (Figure 2).

LOW-FLOW VASCULAR MALFORMATIONS

Capillary malformations present as flat pink or red macules that do not involute. These lesions result from abnormal morphogenesis of superficial dermal blood vessels, which lead to ectatic papillary dermal capillaries and postcapillary venules^[20]. Histologically, these lesions stain positive for fibronectin, von Willebrand factor, and collagenous basement membrane proteins^[21]. Particularly, in port wine stains, there is increased expression of vascular endothelial growth factor VEGF-A as well as its most

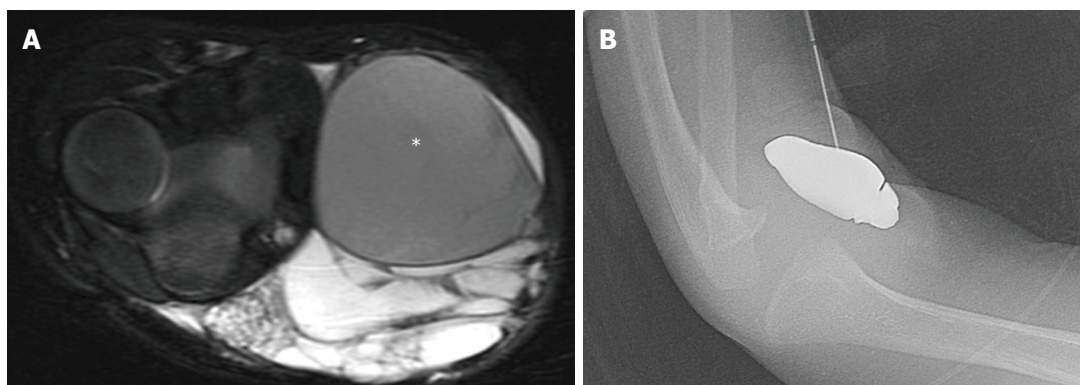


Figure 5 Macrocystic lymphatic malformation with hemorrhage. Axial fat suppressed T2 weighted magnetic resonance image of the elbow (A) demonstrates a predominantly hyperintense malformation with hypointense hemorrhage in a loculation (asterisk). Direct access to the malformation is obtained with a 22-gauge needle for sclerosis (B), subsequently performed with doxycycline.

Table 1 Commonly used sclerosants and liquid embolic agents	
Sclerosants and liquid embolic agents	Comments
Sodium tetradecyl sulfate (STS)	Combined with non-ionic contrast for final concentration of 1.5%; foamed according to Tessari's method ^[39]
Doxycycline	10 mg/mL, maximum dose 1000 mg
Ethanol	95% concentration; Risk of systemic toxicity increases with doses > 1 mL/kg or total volume > 60 mL
Bleomycin	0.3-0.5 mg/kg
OK-432/Picibanil	1-3 intralesional injections of 0.2 mL each dose at 0.01 mg/kg
Polidocanol	0.5-1.0% concentration; Inject 0.1-0.3 mL for a total administered dose of 10 mL
n-BCA glue	Combined with Ethiodol for polymerization
Onyx	Dissolved with DMSO and tantalum; three different concentrations (6%, 6.5%, 8%)

STS: Sotradecol; n-BCA: n-butyl cyanoacrylate.

active receptor VEGF-R2, which is suggestive of an underlying mechanism for pathogenesis^[22]. These lesions occur in 0.3% of newborns without preponderance for gender^[23]. Detection typically occurs at birth, although acquired capillary malformations are rarely identified. Capillary malformations can be seen with several different syndromes as described later.

LYMPHATIC MALFORMATIONS

Lymphatic malformations arise from abnormal development of the lymphatic system during the early phases of angiogenesis and may be diffuse, often described as lymphedema, or localized, commonly described as a lymphangioma^[20]. These malformations are typically large, spongy masses that are non-tender. These lesions can affect any area of the body, but there is a propensity for the head and neck, where they are often referred to as cystic hygromas^[20]. Sixty five to 75% of lesions present at birth whereas the remainder of cases appear within 2 years of age^[24]. While most lesions are sporadic, some are occur as part of syndromes, such as CLOVES (Figure 3). Complications of these lesions may include bleeding or infection for superficial lesions and encroachment on other anatomic structures such as airways or abdominal viscera for deep lesions.

Lymphatic malformations may be macrocystic (Figures 4, 5), consisting of lymphatic spaces arbitrarily de-

finied as greater than two centimeters in diameter, microcystic, or a combination of macrocystic and microcystic. As these lesions are commonly encountered in infants and children ultrasound plays an important role in the diagnosis, staging, and treatment of lymphatic malformations. MR is useful in determining the type and anatomic relationships of lesions but often requires sedation or general anesthesia in children.

Treatment

Sclerotherapy is the primary form of treatment of macrocystic lymphatic malformations. Lesions are punctured under ultrasound guidance and accessed with 3 to 8. French multiholed drainage catheters. The entire contents of the cysts are aspirated and then 25% to 50% of the volume replaced with a sclerosant. The sclerosant is instilled for several hours and then aspirated. Some remove the catheters at this time and re-access the malformation as required, while others leave the catheters in place for serial sclerosis over 24-48 h. Many sclerosants have been described (Table 1), including doxycycline, sodium tetradecyl sulfate (Sotradecol, STS), ethanol, bleomycin, and OK-432 (picibanil). Using bleomycin as a sclerotherapy agent in macrocystic lymphatic malformations has been reported as successful in up to 72% of patients^[25,26]. Using OK-432 (picibanil) has shown success in up to 66.5% of patients, while using doxycycline (Figures 5, 6) has demonstrated success in up to 93% of patients^[27].

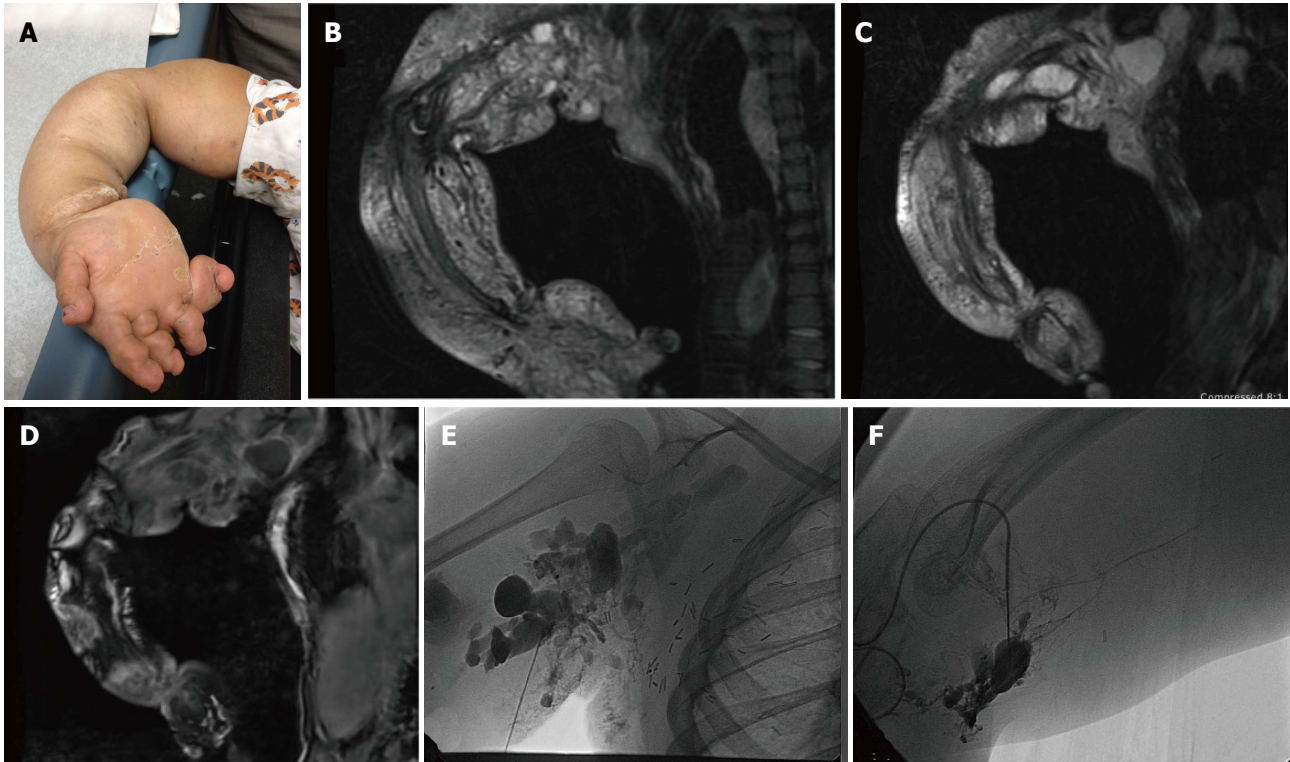


Figure 6 Ten-year-old girl with CLOVES syndrome. Photograph (A) demonstrates right upper extremity overgrowth. Pre-treatment coronal MR images of the right upper extremity (B, C, D) demonstrate a large, combined macro/microcystic lymphatic malformation with venous lakes in the axilla and evidence of lipomatous overgrowth. Angiographic images (E, F) demonstrate direct puncture of the malformation followed by sclerosis with doxycycline.

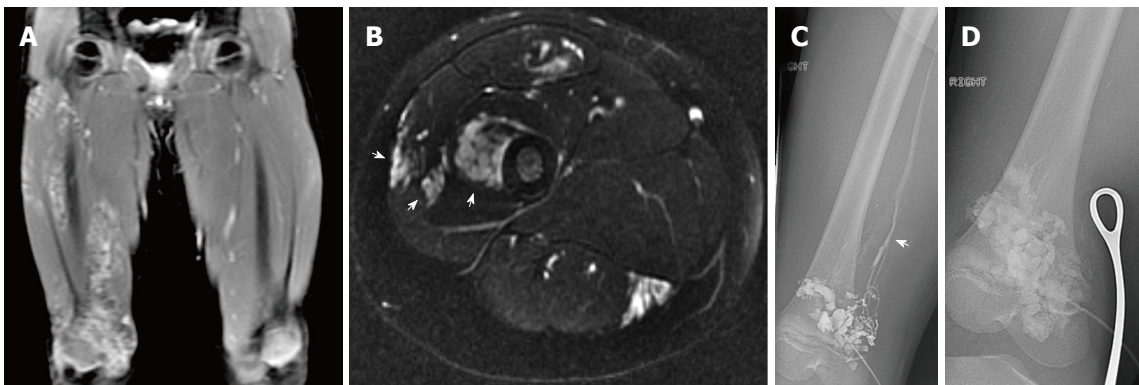


Figure 7 Infiltrative extratruncular low flow vascular malformation of the right leg. Coronal (A) and axial (B) T2-weighted magnetic resonance images demonstrate a high signal intensity infiltrative lesion (arrows). Venography (C) demonstrates filling of the malformation with outflow communication to the femoral vein (arrow). Sclerosis was subsequently performed utilizing 3% STS opacified with contrast (D) with compression of the outflow vein using metal forceps.

LOW-FLOW VENOUS MALFORMATIONS

Venous malformations result from abnormal sprouting or branching during embryonic development. Venous malformations may be focal, multifocal or diffuse and infiltrative. These dysmorphic vascular channels are lined with flattened endothelium^[2,20] and defective smooth muscle, leading to progressive expansion under hydrostatic pressure. Stasis promotes *in-situ* thrombosis and lysis. Patients present most often with swelling and pain, worse as the day progresses and exacerbated in the standing position. On physical examination there may be an associated dermal capillary malformation. Clinically, these lesions appear

as a soft, compressible, blue mass typically within the cutaneous tissues of the face, trunk, and limbs, although involvement of the viscera and bones has also been described^[28,29] (Figure 7). It should be noted that two thirds of all vascular malformations are venous predominant^[30]. Although it is felt that there is no gender predisposition, one series did find a female preponderance^[29,31].

Treatment

Low flow venous malformations may be treated by compression, surgical excision or sclerosis. Treatment should be reserved for symptomatic or cosmetically disfiguring malformations (Figure 8). Sclerosing agents,



Figure 8 Superficial low flow venous malformation. This soft compressible mass with nodular purple skin discoloration in the buttock is typical of a superficial low flow venous malformation.

which comprise the main form of treatment, include STS, polidocanol, and absolute alcohol. Overall, good to excellent results with sclerotherapy have been reported in 53%-100% patients, depending on the size and definition of the treated lesion^[14,32-36]. Technical success rates using absolute alcohol have been reported in up to 95% with no evidence of recurrence^[32]. Studies looking at STS have reported moderate to excellent clinical results in 68%-86% of patients^[33,37,38]. Polidocanol has shown a treatment benefit in 78%-100% of patients^[33,39,40].

Access to the venous vascular malformation is generally achieved by direct puncture, utilizing ultrasound guidance. A butterfly needle is frequently utilized for more superficial malformations. Venography is then performed, and the volume of contrast administered to fill the malformation is noted. The appearance of any outflow into the deep venous structures is also noted. The malformation is emptied of as much blood as possible to increase contact of the sclerosant with the vein wall. Compression of previously visualized outflow veins is applied with tourniquets or direct pressure (Figure 9). Sclerosant is then injected, generally at a volume of 50%-60% of that which was noted to fill the malformation with contrast. Foam sclerotherapy is ideal for treatment of low flow venous vascular malformations (Figure 10). The sclerosant 3% STS is combined on a one-to-one basis with non-ionic contrast, for a final concentration of 1.5%, and is then foamed according to Tessari's method^[41] with 4 parts of air, or an O₂/CO₂ mixture, with one part sclerosant. Foaming the sclerosant increases the surface contact of the foam micelles with the endothelium of the malformation (Figure 9). Depending upon the size of the malformation, additional access is obtained and the process is repeated. Large truncular malformations may require coil embolization or balloon occlusion of larger outflow veins, in addition to sclerotherapy.

HIGH FLOW VASCULAR MALFORMATIONS

High flow vascular malformations exhibit variable pre-

sentation dependent on location (Figures 11, 12). Superficial lesions may present as a warm painless mass with palpable bruit and associated dilated veins. Skin erosion and bleeding is possible (Figure 12). Deeper lesions may present with steal phenomena as the malformation deprives blood flow from downstream structures. Staging of these lesions can be accomplished by scoring according to the Schobinger clinical staging system^[20,42]. Within this system, stage I describes a phase of quiescence where there is a cutaneous blush and skin warmth. In stage II, there is expansion with a darkening blush, lesion pulsation, as well as a bruit or palpable thrill. Stage III is defined by destruction, namely pain, dystrophic skin changes, ulceration, distal ischemia, and steal. Finally, stage IV is marked by decompensation or high output cardiac failure.

High flow vascular malformations include macrofistulas, or truncular malformations, that consist of single or multiple arteries directly communicating with outflow veins without an interposed high resistance capillary system. In contrast, arteriovenous malformations, which are often extratruncular, consist of a low resistance nidus recruiting blood supply from numerous regional inflow arteries and draining by multiple outflow veins.

Treatment

Macrofistulous malformations are treated by coil occlusion of the fistula at the distal arterial end of the communication. Accurate oversizing of the coils is essential to eliminate systemic embolization of the coil. The use of detachable coils, released only when satisfactory placement is achieved, may increase the safety of the procedure (Figure 13). In addition to coils, occlusion devices such as the Amplatzer occluder device (St. Jude Medical, Plymouth, MN, United States) may be considered.

The goal in the treatment of high flow arteriovenous vascular malformations is eradication of the nidus. This is best accomplished with a liquid embolic agent, which will penetrate the feeding vessels into the nidus. A coaxial guiding and microcatheter system is advanced toward the nidus and repeat angiography is performed to determine the volume of embolic agent required to penetrate and fill the nidus.

Particulate agents, such as polyvinyl alcohol (PVA)^[43,44] may be used independently or in conjunction with liquid embolic agents. Particulate agents do not generally provide complete occlusion, and recanalization may occur (Figure 14).

A commonly employed embolic agent is n-butyl cyanoacrylate (n-BCA), commonly referred to as "glue." n-BCA is a non-adherent liquid in a nonionic environment that rapidly polymerizes in an ionic environment. Polymerization rate is decreased by mixing with increasing volumes of Ethiodol, permitting progressively distal penetration. Selecting the ideal ratio of n-BCA/ethiodol permits polymerization to occur within the nidus of the AVM rather than the feeding artery (Figure 15).

An alternative to n-BCA as a liquid embolic agent is Onyx (ev3 Endovascular, Inc., Plymouth, MN, United States)^[45-47]. Distal microcatheter placement is essential.

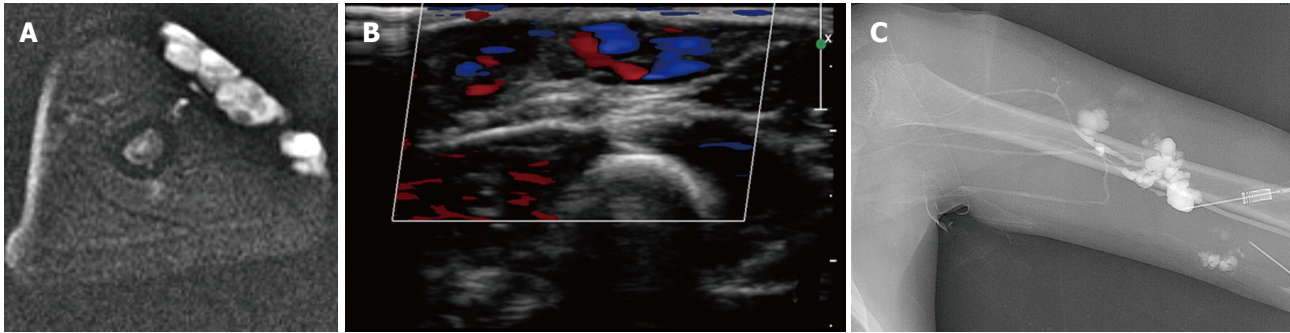


Figure 9 Foaming the sclerosant increases the surface contact of the foam micelles with the endothelium of the malformation. Axial T2 magnetic resonance demonstrating high signal intensity subcutaneous low flow venous malformation of the left upper arm (A). The lower signal small round structure likely represents a phlebolith. Color Doppler ultrasound demonstrates low flow signal in the venous malformation (B). Venography prior to sclerotherapy with tourniquet in place on upper arm demonstrates the venous malformation with no filling of normal deep venous drainage (C). A few faint radio-opaque phleboliths are seen in the venographic image.

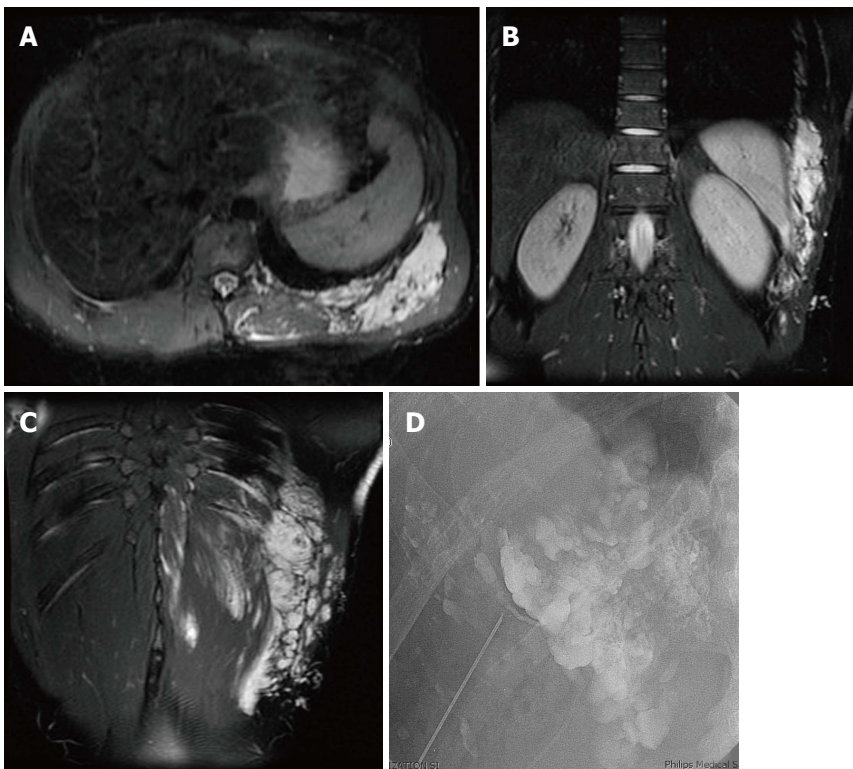


Figure 10 Foam sclerotherapy is ideal for treatment of low flow venous vascular malformations. Axial and coronal T2 weighted magnetic resonance images demonstrate a low flow venous malformation of the chest and upper abdominal wall (A, B, C). Direct access venography with a 22-gauge needle shows foamed STS opacified with contrast filling the malformation (D).

The technique of delivery of Onyx differs from glue in that a “plug” of Onyx is first formed around the tip of the microcatheter, preventing retrograde flow after the agent is forced in the direction of the nidus (Figure 15).

Absolute alcohol is an extremely effective alternative liquid agent, which causes protein denaturation and endothelial cell destruction (Figure 16). The treatment success rate of using ethanol in arteriovenous malformations has been reported up to 68% in certain small series^[48]. Its efficacy decreases with decreasing concentration, making it difficult to mix with contrast agents and still achieve the same result. It has a greater tendency for peripheral penetration and a higher incidence of non-target injury such as skin necrosis, nerve injury and related complications (Figure 12). Using a balloon

occlusion catheter during ethanol delivery may decrease the incidence of complications. Acute pulmonary hypertension, right heart strain, and sudden death during the administration of alcohol have been reported, urging careful monitoring of pulmonary arterial pressures during procedures involving alcohol sclerosis^[49-51].

SYNDROMES ASSOCIATED WITH VASCULAR MALFORMATIONS

While most vascular malformations occur sporadically, some are associated with known syndromes. In some syndromes, the vascular malformation is the predominant source of morbidity, while in the majority of syndromes, the vascular malformation is present in association with

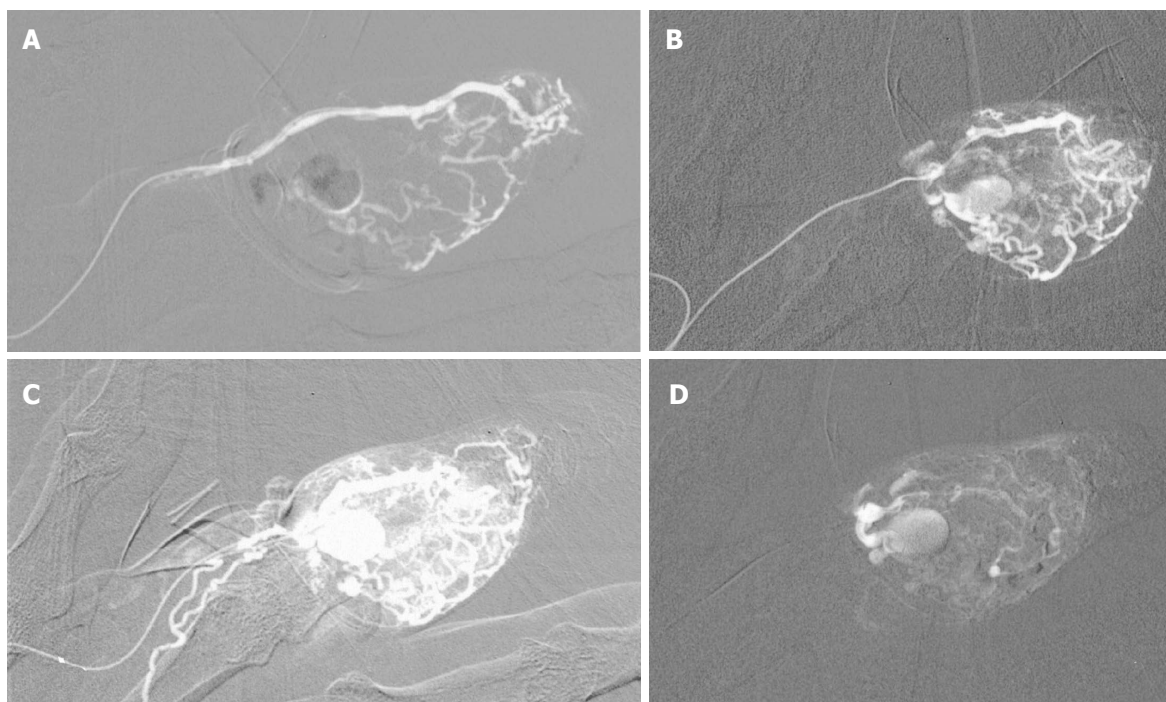


Figure 11 High flow arteriovenous malformation of second digit. This patient scheduled for amputation due to intractable pain under went alcohol embolization as a last resort prior to surgery. Digital arteriography with a microcatheter in the lateral digital artery with the tip at the level of the middle phalanx demonstrating filling of the nidus of the malformation (A, B, C). Following embolization, there is stasis of flow in the malformation (D). The medial digital artery remained patent with preservation of arterial flow to the digit.

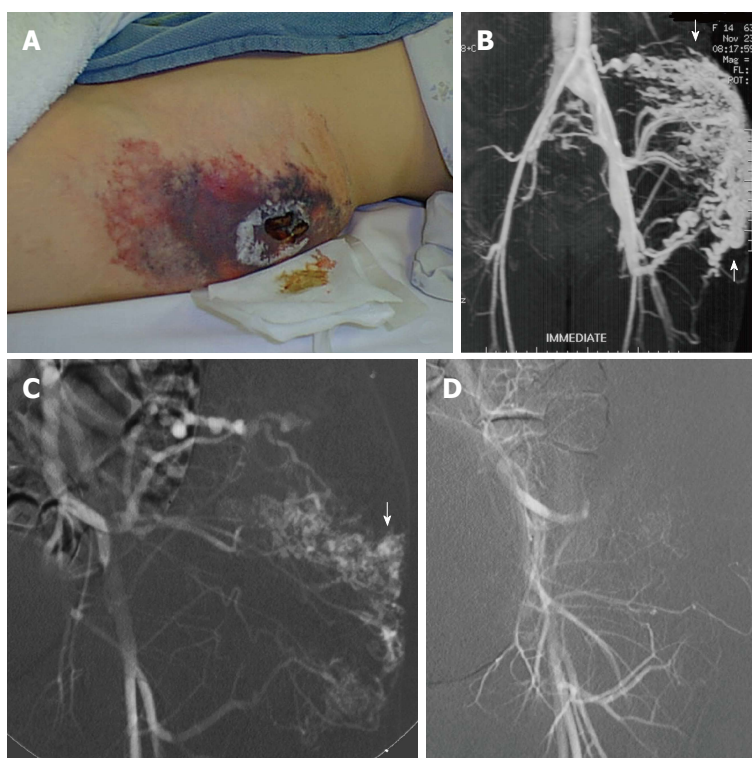


Figure 12 Superficial lesions may present as a warm painless mass with palpable bruit and associated dilated veins. High flow arteriovenous malformation with extensive skin breakdown in the region of this superficial malformation (A). Magnetic resonance angiogram demonstrates a high flow arteriovenous malformation with arteriovenous shunting (arrow) (B). Left internal iliac arteriogram demonstrating filling of the nidus of the malformation (arrow) (C). Arteriography following alcohol embolization shows eradication of the nidus of the malformation (D). As the malformation was located in subcutaneous fat, it was resected en block and skin grafts were created to bridge the area of skin breakdown.

other components, which produce the more significant pathology. When considered from the point of view of the vascular malformation, syndromes associated with vascular malformations may be classified according to

their flow characteristics. Syndromes involving predominantly the head and neck or characterized by capillary malformations only are well described within the literature and are not included in this review.

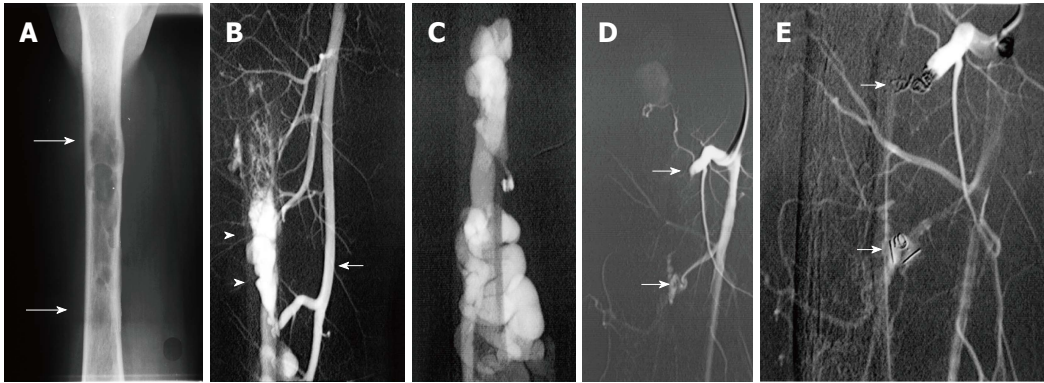


Figure 13 Use of detachable coils, released only when satisfactory placement is achieved, may increase the safety of the procedure. Radiograph of the mid-diaphysis of the femur demonstrates a region of endosteal erosion (arrows) (A). Arteriography demonstrates a multifistulous malformation with arterial supply from two muscular branches of the superficial femoral artery (arrow) with early filling of intraosseous venous drainage (arrowheads) (B, C). Occlusion of the feeding arteries was accomplished with large coils (arrow) eliminating the fistulous communications (D, E).

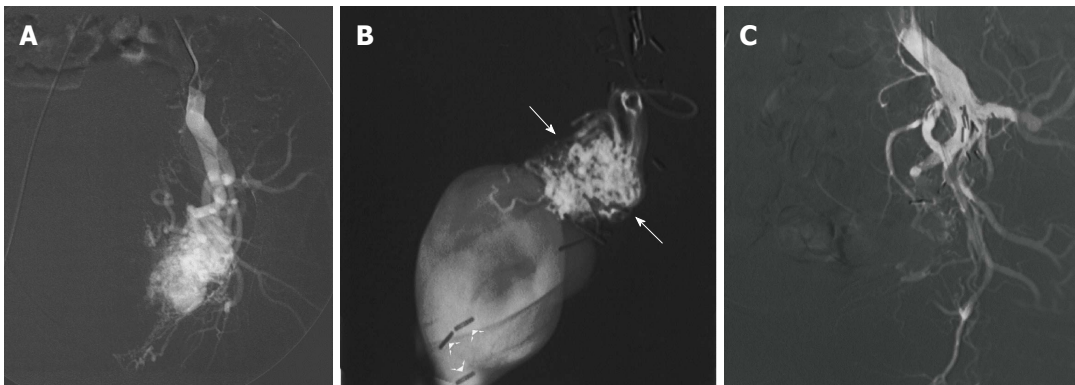


Figure 14 Particulate agents do not generally provide complete occlusion, and recanalization may occur. High flow arteriovenous malformation with nidus and venous aneurysm originating from branches of the left internal iliac artery (A). Following superselective catheterization of the feeding branch of the inferior gluteal artery there is demonstration of the nidus and venous aneurysm (arrow) (B). Following particulate embolization with PVA, there is occlusion of the nidus. Surgical clips are seen overlying internal iliac artery branches from previous unsuccessful attempts at surgical treatment (C).

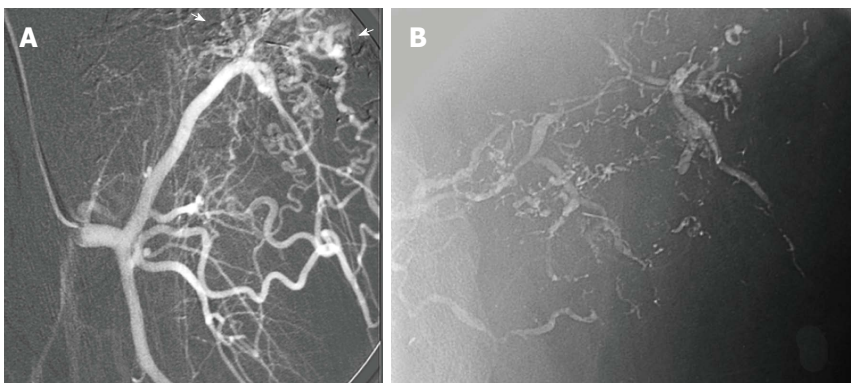


Figure 15 Arteriogram of high flow arteriovenous malformation. A: Arteriogram demonstrates nidus (arrows) of a high flow arteriovenous malformation of the abdominal wall, supplied in part by a muscular branch of the circumflex femoral artery; B: The lesion was treated twice, initially with Onyx, then with n-BCA glue, seen within the arterial feeders of the malformation on post-embolization imaging.

SYNDROMES ASSOCIATED WITH HIGH FLOW AND MIXED VASCULAR MALFORMATIONS

Hereditary hemorrhagic telangiectasia S

Hereditary hemorrhagic telangiectasia (HHT) is an autosomal dominant disorder involving mutations in the transforming growth factor-beta signaling pathway result-

ing in irregular cytoskeletal architecture and abnormal vascular tubule formation characterized by telangiectasias and fistulous malformations. Incidence is estimated to be between 1 in 5000 to 8000 with males and females affected equally^[52,53]. Onset of symptoms most commonly occurs within the second and third decades of life. Telangiectasias are seen on mucosal surfaces and associated with epistaxis and gastrointestinal bleeding. Arteriovenous fistulas, particularly in the lung, liver, brain and

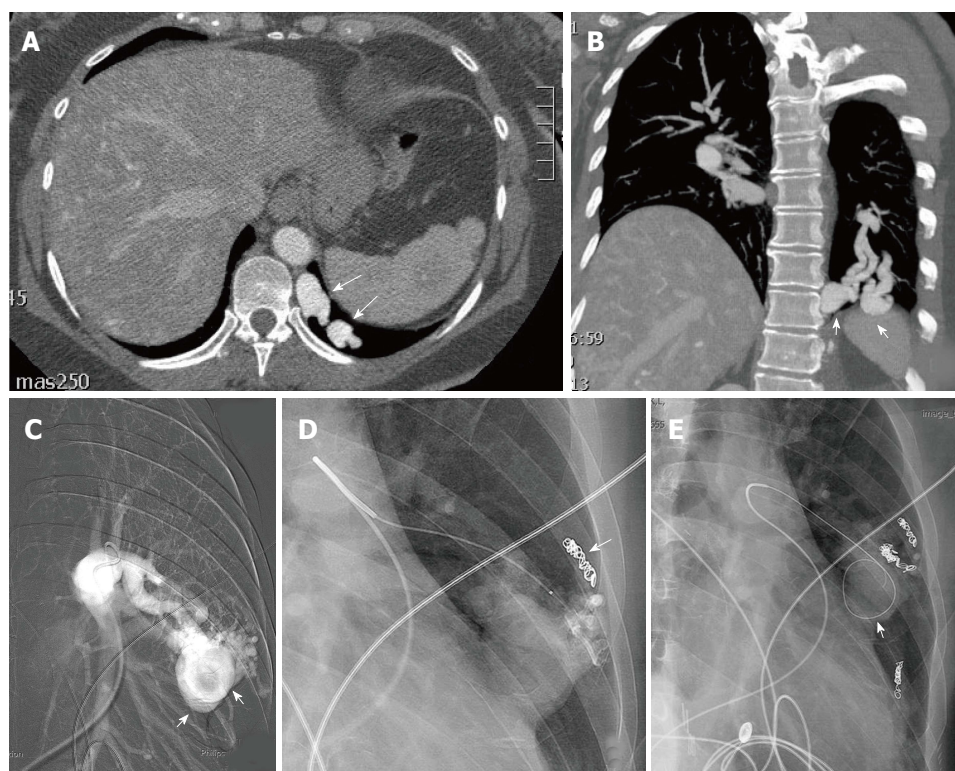


Figure 16 This patient with hereditary hemorrhagic telangiectasia presented with an abnormal chest radiograph. A computed tomography angiogram was performed for further evaluation. Axial CTA demonstrates a left lower lobe high flow vascular malformation (arrows) (A). Coronal reconstruction demonstrates several branches of the left lower lobe pulmonary artery feeding the malformation (arrows) (B). Sequential coil embolization of pulmonary arterial branches feeding the malformation was performed (arrow) (C). A framing coil was then placed in the venous aneurysm (D) followed by coil occlusion of the venous aneurysm and each of the remaining pulmonary arterial feeding branches (arrow) (E).

gastrointestinal tract are a major source of morbidity and mortality.

While 30% of patients with HHT have pulmonary arteriovenous fistulas, 80% of pulmonary arteriovenous fistulas occur in patients with HHT. As these fistulas act as right to left shunts, patients can present with hypoxia, stroke or brain abscess and less frequently hemoptysis or hemothorax. Lesions may be single or multiple. Simple lesions consist of fistulas between a single segmental branch of the pulmonary artery and the pulmonary vein, or complex with multiple segmental pulmonary artery branches supplying the fistula. Fistulas with arterial supply greater than 3 mm in diameter are considered at greatest risk of complication.

Surgical resection of pulmonary arteriovenous fistulas has currently been replaced by transcatheter occlusion. Superselective catheterization of the feeding pulmonary arterial branch close to the site of arteriovenous communication is required for placement of coils. Coil size selection, usually 20% larger than the target artery, is critical to avoid systemic coil embolization. Complete occlusion of each feeding artery is critical. Occasionally, occlusion of the aneurysmal draining vein can precede arterial occlusion in order to prevent systemic coil loss (Figure 17). Success of coil embolization approaches 80% but recanalization of the occluded artery or recruitment of additional feeding arterial supply results in recurrence of

the fistula in up to 25% of patients, necessitating retreatment^[54]. Careful follow-up of patients, therefore, is essential. Detachable coils or use of the Amplatzer occluder device may increase the safety of the procedure in select cases.

Parkes Weber syndrome

Parkes Weber Syndrome is an OSCVA syndrome^[55] (Overgrowth Syndrome with Complex Vascular Anomalies), characterized by extremity overgrowth and vascular anomaly. In contrast to the Klippel Trenaunay syndrome, venous abnormalities are associated with high flow arteriovenous malformations within the hypertrophied extremity. A third component of the syndrome is a cutaneous capillary malformation. Arteriovenous fistulas may form around the time of puberty, and exacerbation of the vascular abnormalities is associated with trauma (Figure 17).

PTEN Hamartoma Syndrome

PTEN mutations promote stimulation of angiogenesis by the Akt/mTOR pathway^[56]. PTEN Hamartoma Syndrome (PHTS) usually involves cutaneous lesions, capillary or capillary venous malformations, typically small deep tissue vascular malformations, and multiple high flow AVMs, associated with hamartomatous lesions^[55]. Occasionally, lymphatic and venous malformations may

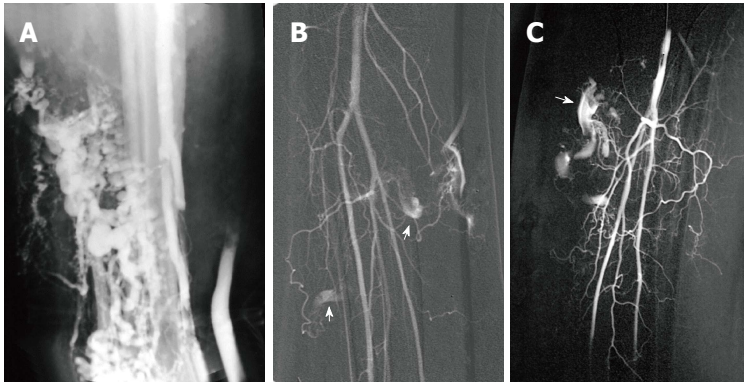


Figure 17 Venogram of low flow venous malformation in Parkes Weber Syndrome. Right lower extremity venogram demonstrates extensive low flow venous malformation in a patient with the Parkes Weber syndrome (A). Right lower extremity arteriogram demonstrating tibial artery shunting to the venous malformation (arrows) (B, C).

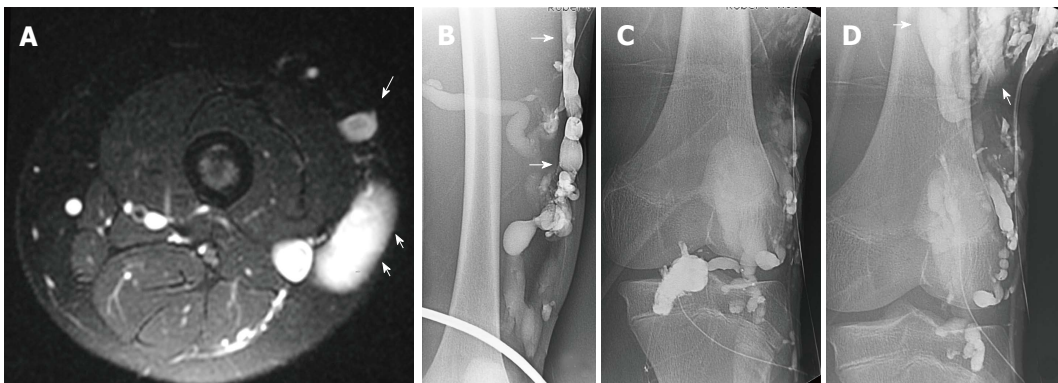


Figure 18 Klippel Trenaunay Syndrome. Axial T2 weighted fat suppressed magnetic resonance image of the thigh (A) in a patient with Klippel Trenaunay syndrome demonstrates a lateral embryonic vein (arrows) and venous malformation (short arrows). Lower extremity venogram demonstrates the lateral embryonic vein (arrows) (B). Direct puncture venography prior to alcohol sclerotherapy demonstrates progressive filling of the low flow truncular venous malformation (arrows) (C, D).

be present. High flow AVMs may be present in the limbs, paraspinal region and dura. They are frequently intramuscular and associated with ectopic fat. The hamartomatous lesion, comprised of vascular clusters, fibrous tissue, large veins and fat, has been termed PTEN hamartoma of soft tissue. Cowden syndrome, Bannayan-Riley-Ruvalcaba syndrome (BRRS) and some instances of Proteus syndrome are classified together with PHTS. More extensive high flow AVMs are occasionally seen in the BRRS.

SYNDROMES ASSOCIATED WITH LOW FLOW VASCULAR MALFORMATIONS

Klippel trenaunay syndrome

Klippel trenaunay syndrome (KTS) is another OSCVA syndrome with extremity overgrowth, associated with a superficial vascular stain, venous malformations, and usually partial aplasia of the deep venous system. The syndrome may also involve lymphatic anomalies. The vascular venous vascular malformations in KTS are characterized as truncal malformations, and may be related to persistence of the embryonic dorsal vein system in the lateral aspect of the extremity (lateral marginal vein in the lower extremity). Large varicosities may result in venous thrombosis and pulmonary embolism. Coagulopathy and gram-negative sepsis are also complications. Limb gigantism is especially prominent when there is an associated lymphatic malformation. MRI is the mainstay of imag-

ing in KTS, with sonography reserved for guiding interventions and for distinguishing venous from lymphatic components of malformations (Figures 18, 19). Catheter based venography is occasionally needed to determine the presence, absence or partial aplasia of the deep venous system, when this is not obvious on other imaging modalities.

CLOVES Syndrome

The congenital lipomatous overgrowth, vascular malformations, epidermal nevi, and scoliosis and other skeletal deformities (CLOVES) syndrome consists of truncal lipomatosis, vascular malformations, and acral/musculoskeletal anomalies. The lipomatous lesions are often infiltrative and tend to recur following resection. Skeletal overgrowth and malformation are common in the extremities, as is scoliosis. Vascular lesions include capillary, lymphatic, venous and arteriovenous malformations (Figures 3, 19). In contrast to the Proteus and BRRS syndrome there is no mental impairment. Treatment includes sclerotherapy of lymphatic and venous malformations and resection of lipomatous lesions^[55].

Blue rubber bleb nevus syndrome

This syndrome consists of venous malformations of the skin and those within the gastrointestinal tract. The skin lesions are comprised of a compressible blue subcutaneous nodule, representing a cutaneous venous malforma-

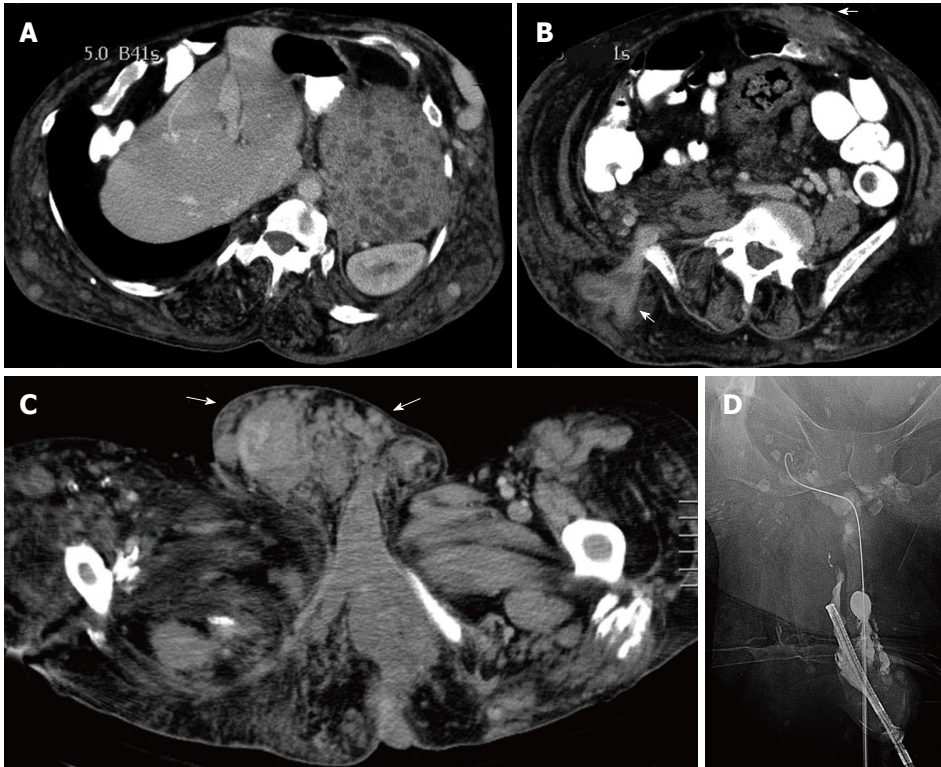


Figure 19 Klippel Trenaunay Syndrome. CT scan of the abdomen in a patient with the Klippel Trenaunay syndrome demonstrating extensive venous malformation in the abdominal wall (arrows) as well as venous malformations in the spleen (asterisk) (A, B). CT scan of the pelvis demonstrating extensive venous malformation in the inguinal canal and scrotum (arrows) (C). Sclerotherapy was performed through the dorsal vein of the penis to treat intractable urethral hemorrhage (D).

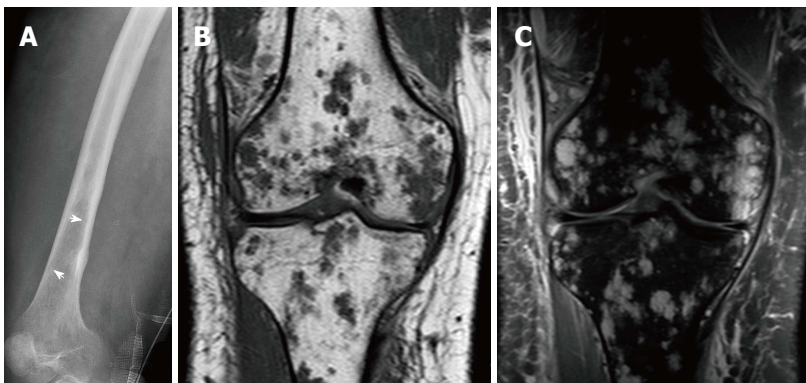


Figure 20 21-year-old man, who presented with pain and swelling of his leg. Radiograph of the femur demonstrates cortical erosion of the distal femur (arrows) (A). T1 weighted coronal magnetic resonance (MR) of the knee demonstrates innumerable focal lesions in the tibia and femur (B). These lesions are high signal intensity on T2 weighted coronal MR (C), however no contrast enhancement was seen within the lesions. Biopsy of the femur demonstrated a lymphatic microcystic lymphatic malformation.

tion. Clinical consequences generally result from gastrointestinal venous malformations, which may lead to occult or frank gastrointestinal bleeding.

Maffucci syndrome

In this syndrome, enchondromas are found in coexistence with venous malformations. There is a high frequency of malignant transformation of the enchondromas into chondrosarcomas.

Generalized Lymphatic Anomaly and Gorham-Stout disease

Generalized Lymphatic Anomaly (GLA) and Gorham-Stout Disease are two different disorders of the lymphatic system with overlapping features^[57]. GLA is synonymous with “generalized cystic lymphangiomas”,

“cystic angiomas” and “lymphangiomas,” though the term GLA is preferred based on the ISSVA classification system. GLA is a multisystem disorder characterized by dilated lymphatic vessels^[58,59]. Features of GLA may include splenic cysts, hepatic cysts, pleural effusions, and macrocystic lymphatic malformations, which may involve several organ systems, including bone^[57-59]. On imaging, osseous lesions in GLA are seen as lucent lesions within the medullary cavity on radiography and display hyperintensity on T2-weighted MR imaging, but do not demonstrate cortical destruction^[57,60]. Numerous bones are typically affected in GLA, and the axial and appendicular skeleton are both affected with similar frequency^[57]. In cases of osseous involvement, patients may present with pain and pathologic fracture (Figure 20).

Gorham-Stout disease, which has been called “vanish-

ing bone disease,” is also a vascular anomaly of the lymphatics characterized by proliferation of lymphatic vessels within bone, resulting in progressive bony destruction^[61]. Though the skeletal system is the primary site of disease in GSD, extra-osseous findings are also seen in GSD and include pleural effusions, splenic cysts, hepatic cysts, and infiltrating soft tissue abnormalities, which may extend from the bone into the adjacent soft tissues^[57]. On imaging, osseous lesions are lytic, as in GLA, but are characterized by progressive osseous resorption and cortical destruction. On MRI, osseous lesions in GSD are most frequently accompanied by infiltrating soft tissue signal that is iso-to hypointense to muscle on T1-weighted images, hyperintense and heterogeneous on T2 weighted images, and enhances with contrast^[57,62]. Infiltrative soft tissue is less common in GLA, which is seen in a minority of cases^[57]. Unlike GLA, which affects the appendicular and axial skeleton with similar frequency, the axial skeleton is more commonly affected in GSD, with appendicular involvement seen in a minority of cases^[57]. Macrocytic lymphatic malformations are infrequently seen in GSD^[57]. As in GLA, patients with GSD may present with pain and pathologic fracture.

CONCLUSION

Accurate diagnosis of vascular malformations and their associated syndromes is often challenging but crucial in the formulation of appropriate treatment. The approach to the described entities requires an organized multidisciplinary team effort, with diagnostic imaging playing an increasingly important role in the proper diagnosis and a combined interventional radiologic and surgical treatment method showing promising results.

REFERENCES

- 1 **Yaşargil MG.** *Microneurosurgery: AVM of the Brain, History, Embryology, Pathological Considerations, Hemodynamics, Diagnostic Studies, Microsurgical Anatomy.* Vol. IIIA: Thieme, 1987
- 2 **Mulliken JB, Glowacki J.** Hemangiomas and vascular malformations in infants and children: a classification based on endothelial characteristics. *Plast Reconstr Surg* 1982; **69**: 412-422 [PMID: 7063565 DOI: 10.1097/00006534-198203000-00002]
- 3 **Belov S.** Anatomopathological classification of congenital vascular defects. *Semin Vasc Surg* 1993; **6**: 219-224 [PMID: 8305976]
- 4 **Enjolras O, Wassef M, Chapot R.** *Color atlas of vascular tumors and vascular malformations.* New York: Cambridge University Press, 2007: 1-11
- 5 **Lee BB, Laredo J, Lee TS, Huh S, Neville R.** Terminology and classification of congenital vascular malformations. *Phlebology* 2007; **22**: 249-252 [PMID: 18274331 DOI: 10.1258/026835507782655236]
- 6 **Lee BB, Lardeo J, Neville R.** Arterio-venous malformation: how much do we know? *Phlebology* 2009; **24**: 193-200 [PMID: 19767485 DOI: 10.1258/phleb.2009.009032]
- 7 **Bree AF, Siegfried E, Sotelo-Avila C, Nahass G.** Infantile hemangiomas: speculation on placental trophoblastic origin. *Arch Dermatol* 2001; **137**: 573-577 [PMID: 11346335 DOI: 10-1001/pubs.Arch]
- 8 **Chiller KG, Passaro D, Frieden IJ.** Hemangiomas of infancy: clinical characteristics, morphologic subtypes, and their relationship to race, ethnicity, and sex. *Arch Dermatol* 2002; **138**: 1567-1576 [PMID: 12472344 DOI: 10.1001/archderm.138.12.1567]
- 9 **Moore CW, Lowe LH.** *Caffey's Pediatric Diagnostic Imaging.* Philadelphia, PA: Mosby Elsevier, 2008: 1929-1948
- 10 **Haggstrom AN, Drolet BA, Baselga E, Chamlin SL, Garzon MC, Horii KA, Lucky AW, Mancini AJ, Metry DW, Newell B, Nopper AJ, Frieden IJ.** Prospective study of infantile hemangiomas: clinical characteristics predicting complications and treatment. *Pediatrics* 2006; **118**: 882-887 [PMID: 16950977 DOI: 10.1542/peds.2006-0413]
- 11 **Krol A, MacArthur CJ.** Congenital hemangiomas: rapidly involuting and noninvoluting congenital hemangiomas. *Arch Facial Plast Surg* 2005; **7**: 307-311 [PMID: 16172338 DOI: 10.1001/archfaci.7.5.307]
- 12 **Mulliken JB, Enjolras O.** Congenital hemangiomas and infantile hemangioma: missing links. *J Am Acad Dermatol* 2004; **50**: 875-882 [PMID: 15153887 DOI: 10.1016/j.jaad.2003.10.670]
- 13 **Fernández Y, Bernabeu-Wittel M, García-Morillo JS.** Kaposiform hemangioendothelioma. *Eur J Intern Med* 2009; **20**: 106-113 [PMID: 19327597 DOI: 10.1016/j.ejim.2008.06.008]
- 14 **Hyodoh H, Hori M, Akiba H, Tamakawa M, Hyodoh K, Hareyama M.** Peripheral vascular malformations: imaging, treatment approaches, and therapeutic issues. *Radiographics* 2005; **25** Suppl 1: S159-S171 [PMID: 16227489 DOI: 10.1148/rg.25si055509]
- 15 **Donnelly LF, Adams DM, Bisset GS.** Vascular malformations and hemangiomas: a practical approach in a multidisciplinary clinic. *AJR Am J Roentgenol* 2000; **174**: 597-608 [PMID: 10701595 DOI: 10.2214/ajr.174.3.1740597]
- 16 **Paltiel HJ, Burrows PE, Kozakewich HP, Zurakowski D, Mulliken JB.** Soft-tissue vascular anomalies: utility of US for diagnosis. *Radiology* 2000; **214**: 747-754 [PMID: 10715041 DOI: 10.1148/radiology.214.3.r00mr21747]
- 17 **Rak KM, Yakes WF, Ray RL, Dreisbach JN, Parker SH, Luethke JM, Stavros AT, Slater DD, Burke BJ.** MR imaging of symptomatic peripheral vascular malformations. *AJR Am J Roentgenol* 1992; **159**: 107-112 [PMID: 1609682 DOI: 10.2214/ajr.159.1.1609682]
- 18 **van Rijswijk CS, van der Linden E, van der Woude HJ, van Baalen JM, Bloem JL.** Value of dynamic contrast-enhanced MR imaging in diagnosing and classifying peripheral vascular malformations. *AJR Am J Roentgenol* 2002; **178**: 1181-1187 [PMID: 11959728 DOI: 10.2214/ajr.178.5.1781181]
- 19 **Meyer JS, Hoffer FA, Barnes PD, Mulliken JB.** Biological classification of soft-tissue vascular anomalies: MR correlation. *AJR Am J Roentgenol* 1991; **157**: 559-564 [PMID: 1872245 DOI: 10.2214/ajr.157.3.1872245]
- 20 **Garzon MC, Huang JT, Enjolras O, Frieden IJ.** Vascular malformations: Part I. *J Am Acad Dermatol* 2007; **56**: 353-370; quiz 371-374 [PMID: 17317485 DOI: 10.1016/j.jaad.2006.05.069]
- 21 **Finley JL, Clark RA, Colvin RB, Blackman R, Noe J, Rosen S.** Immunofluorescent staining with antibodies to factor VIII, fibronectin, and collagenous basement membrane protein in normal human skin and port wine stains. *Arch Dermatol* 1982; **118**: 971-975 [PMID: 6816146 DOI: 10.1001/archderm.1982.01650240015012]
- 22 **Vural E, Ramakrishnan J, Cetin N, Buckmiller L, Suen JY, Fan CY.** The expression of vascular endothelial growth factor and its receptors in port-wine stains. *Otolaryngol Head Neck Surg* 2008; **139**: 560-564 [PMID: 18922344 DOI: 10.1016/j.otohns.2008.07.015]
- 23 **Kanada KN, Merin MR, Munden A, Friedlander SF.** A prospective study of cutaneous findings in newborns in the United States: correlation with race, ethnicity, and gestational status using updated classification and nomenclature. *J Pediatr* 2012; **161**: 240-245 [PMID: 22497908 DOI: 10.1016/

- j.peds.2012.02.052]
- 24 **Redondo P.** [Classification of vascular anomalies (tumours and malformations). Clinical characteristics and natural history]. *An Sist Sanit Navar* 2004; **27** Suppl 1: 9-25 [PMID: 15148508]
 - 25 **Sainsbury DC,** Kessell G, Fall AJ, Hampton FJ, Guhan A, Muir T. Intralesional bleomycin injection treatment for vascular birthmarks: a 5-year experience at a single United Kingdom unit. *Plast Reconstr Surg* 2011; **127**: 2031-2044 [PMID: 21532430 DOI: 10.1097/PRS.0b013e31820e923c]
 - 26 **Acevedo JL,** Shah RK, Brietzke SE. Nonsurgical therapies for lymphangiomas: a systematic review. *Otolaryngol Head Neck Surg* 2008; **138**: 418-424 [PMID: 18359347 DOI: 10.1016/j.otohns.2007.11.018]
 - 27 **Nehra D,** Jacobson L, Barnes P, Mallory B, Albanese CT, Sylvester KG. Doxycycline sclerotherapy as primary treatment of head and neck lymphatic malformations in children. *J Pediatr Surg* 2008; **43**: 451-460 [PMID: 18358281 DOI: 10.1016/j.jpedsurg.2007.10.009]
 - 28 **Dubois J,** Soulez G, Oliva VL, Berthiaume MJ, Lapierre C, Therasse E. Soft-tissue venous malformations in adult patients: imaging and therapeutic issues. *Radiographics* 2001; **21**: 1519-1531 [PMID: 11706222 DOI: 10.1148/radiographics.21.6.g01nv031519]
 - 29 **Mazoyer E,** Enjolras O, Bisdorff A, Perdu J, Wassef M, Drouet L. Coagulation disorders in patients with venous malformation of the limbs and trunk: a case series of 118 patients. *Arch Dermatol* 2008; **144**: 861-867 [PMID: 18645137 DOI: 10.1001/archderm.144.7.861]
 - 30 **Eifert S,** Villavicencio JL, Kao TC, Taute BM, Rich NM. Prevalence of deep venous anomalies in congenital vascular malformations of venous predominance. *J Vasc Surg* 2000; **31**: 462-471 [PMID: 10709058 DOI: 10.1067/mva.2000.101464]
 - 31 **Boon LM,** Mulliken JB, Enjolras O, Vikkula M. Glomuvenous malformation (glomangioma) and venous malformation: distinct clinicopathologic and genetic entities. *Arch Dermatol* 2004; **140**: 971-976 [PMID: 15313813 DOI: 10.1001/archderm.140.8.971]
 - 32 **Lee BB,** Do YS, Byun HS, Choo IW, Kim DI, Huh SH. Advanced management of venous malformation with ethanol sclerotherapy: mid-term results. *J Vasc Surg* 2003; **37**: 533-538 [PMID: 12618688 DOI: 10.1067/mva.2003.91]
 - 33 **Legiehn GM,** Heran MK. Venous malformations: classification, development, diagnosis, and interventional radiologic management. *Radiol Clin North Am* 2008; **46**: 545-597, vi [PMID: 18707962 DOI: 10.1016/j.rcl.2008.02.008]
 - 34 **Goyal M,** Causer PA, Armstrong D. Venous vascular malformations in pediatric patients: comparison of results of alcohol sclerotherapy with proposed MR imaging classification. *Radiology* 2002; **223**: 639-644 [PMID: 12034929 DOI: 10.1148/radiol.2233010025]
 - 35 **Rautio R,** Saarinen J, Laranne J, Salenius JP, Keski-Nisula L. Endovascular treatment of venous malformations in extremities: results of sclerotherapy and the quality of life after treatment. *Acta Radiol* 2004; **45**: 397-403 [PMID: 15323391 DOI: 10.1080/02841850410004913]
 - 36 **Rimon U,** Garniek A, Galili Y, Golan G, Bensaid P, Morag B. Ethanol sclerotherapy of peripheral venous malformations. *Eur J Radiol* 2004; **52**: 283-287 [PMID: 15544907 DOI: 10.1016/j.ejrad.2003.09.010]
 - 37 **Tan KT,** Kirby J, Rajan DK, Hayeems E, Beecroft JR, Simons ME. Percutaneous sodium tetradecyl sulfate sclerotherapy for peripheral venous vascular malformations: a single-center experience. *J Vasc Interv Radiol* 2007; **18**: 343-351 [PMID: 17377179 DOI: 10.1016/j.jvir.2006.12.735]
 - 38 **O'Donovan JC,** Donaldson JS, Morello FP, Pensler JM, Vogelzang RL, Bauer B. Symptomatic hemangiomas and venous malformations in infants, children, and young adults: treatment with percutaneous injection of sodium tetradecyl sulfate. *AJR Am J Roentgenol* 1997; **169**: 723-729 [PMID: 9275886 DOI: 10.2214/ajr.169.3.9275886]
 - 39 **Pascarella L,** Bergan JJ, Yamada C, Mekenas L. Venous angiomas: treatment with sclerosant foam. *Ann Vasc Surg* 2005; **19**: 457-464 [PMID: 15981122 DOI: 10.1007/s10016-005-4656-z]
 - 40 **Jain R,** Bandhu S, Sawhney S, Mittal R. Sonographically guided percutaneous sclerosis using 1% polidocanol in the treatment of vascular malformations. *J Clin Ultrasound* 2002; **30**: 416-423 [PMID: 12210459 DOI: 10.1002/jcu.10091]
 - 41 **Tessari L,** Cavezzi A, Frullini A. Preliminary experience with a new sclerosing foam in the treatment of varicose veins. *Dermatol Surg* 2001; **27**: 58-60 [PMID: 11231246 DOI: 10.1111/j.1524-4725.2001.00192.x]
 - 42 **Kohout MP,** Hansen M, Pribaz JJ, Mulliken JB. Arteriovenous malformations of the head and neck: natural history and management. *Plast Reconstr Surg* 1998; **102**: 643-654 [PMID: 9727427]
 - 43 **Simons ME.** Peripheral vascular malformations: diagnosis and percutaneous management. *Can Assoc Radiol J* 2001; **52**: 242-251 [PMID: 11512297]
 - 44 **Patel AA,** Solomon JA, Soulen MC. Pharmaceuticals for Intra-arterial Therapy. *Semin Intervent Radiol* 2005; **22**: 130-138 [PMID: 21326683 DOI: 10.1055/s-2005-871868]
 - 45 **Vanninen RL,** Manninen I. Onyx, a new liquid embolic material for peripheral interventions: preliminary experience in aneurysm, pseudoaneurysm, and pulmonary arteriovenous malformation embolization. *Cardiovasc Intervent Radiol* 2007; **30**: 196-200 [PMID: 17205359 DOI: 10.1007/s00270-006-0071-2]
 - 46 **Castaneda F,** Goodwin SC, Swischuk JL, Wong GC, Bonilla SM, Wang MJ, Abdel-Sayed PS. Treatment of pelvic arteriovenous malformations with ethylene vinyl alcohol copolymer (Onyx). *J Vasc Interv Radiol* 2002; **13**: 513-516 [PMID: 11997360 DOI: 10.1016/S1051-0443(07)61532-2]
 - 47 **Rautio R,** Haapanen A. Transcatheter embolization of a renal artery aneurysm using ethylene vinyl alcohol copolymer. *Cardiovasc Intervent Radiol* 2007; **30**: 300-303 [PMID: 17206392 DOI: 10.1007/s00270-005-0238-2]
 - 48 **Do YS,** Yakes WF, Shin SW, Lee BB, Kim DI, Liu WC, Shin BS, Kim DK, Choo SW, Choo IW. Ethanol embolization of arteriovenous malformations: interim results. *Radiology* 2005; **235**: 674-682 [PMID: 15858106 DOI: 10.1148/radiol.2352040449]
 - 49 **Shin BS,** Do YS, Lee BB, Kim DI, Chung IS, Cho HS, Kim MH, Kim GS, Kim CS, Byun HS, Shin SW, Park KB. Multistage ethanol sclerotherapy of soft-tissue arteriovenous malformations: effect on pulmonary arterial pressure. *Radiology* 2005; **235**: 1072-1077 [PMID: 15833991 DOI: 10.1148/radiol.2353040903]
 - 50 **Ko JS,** Kim JA, Do YS, Kwon MA, Choi SJ, Gwak MS, Lee JJ, Yang M. Prediction of the effect of injected ethanol on pulmonary arterial pressure during sclerotherapy of arteriovenous malformations: relationship with dose of ethanol. *J Vasc Interv Radiol* 2009; **20**: 39-45; quiz 45 [PMID: 19028113 DOI: 10.1016/j.jvir.2008.10.012]
 - 51 **Chapot R,** Laurent A, Enjolras O, Payen D, Houdart E. Fatal cardiovascular collapse during ethanol sclerotherapy of a venous malformation. *Interv Neuroradiol* 2002; **8**: 321-324 [PMID: 20594492]
 - 52 **Dakeishi M,** Shioya T, Wada Y, Shindo T, Otaka K, Manabe M, Nozaki J, Inoue S, Koizumi A. Genetic epidemiology of hereditary hemorrhagic telangiectasia in a local community in the northern part of Japan. *Hum Mutat* 2002; **19**: 140-148 [PMID: 11793473 DOI: 10.1002/humu.10026]
 - 53 **Schoen FJ.** Cotran RS, Vinay K, Collins T. Robbins Pathologic Basis of Disease. 5th ed. WB Saunders, 1994: 509
 - 54 **Woodward CS,** Pyeritz RE, Chittams JL, Trerotola SO. Treated pulmonary arteriovenous malformations: patterns of persistence and associated retreatment success. *Radiology* 2013; **269**: 919-926 [PMID: 23912618 DOI: 10.1148/ra-

- diol.13122153]
- 55 **Alomari AI.** Characterization of a distinct syndrome that associates complex truncal overgrowth, vascular, and acral anomalies: a descriptive study of 18 cases of CLOVES syndrome. *Clin Dysmorphol* 2009; **18**: 1-7 [PMID: 19011570 DOI: 10.1097/MCD.0b013e328317a716]
- 56 **Iacobas I, Burrows, P.** PTEN: Structure, mechanisms-of-action, role in cell signaling and regulation. Nova Science, 2013: 215-217
- 57 **Lala S, Mulliken JB, Alomari AI, Fishman SJ, Kozakewich HP, Chaudry G.** Gorham-Stout disease and generalized lymphatic anomaly--clinical, radiologic, and histologic differentiation. *Skeletal Radiol* 2013; **42**: 917-924 [PMID: 23371338 DOI: 10.1007/s00256-012-1565-4]
- 58 **Wunderbaldinger P, Paya K, Partik B, Turetschek K, Hörmann M, Horcher E, Bankier AA.** CT and MR imaging of generalized cystic lymphangiomatosis in pediatric patients. *AJR Am J Roentgenol* 2000; **174**: 827-832 [PMID: 10701634 DOI: 10.2214/ajr.174.3.1740827]
- 59 **Rasalkar DD, Chu WC.** Generalized cystic lymphangiomatosis. *Pediatr Radiol* 2010; **40** Suppl 1: S47 [PMID: 20574655 DOI: 10.1007/s00247-010-1694-7]
- 60 **Boyle WJ.** Cystic angiomatosis of bone. A report of three cases and review of the literature. *J Bone Joint Surg Br* 1972; **54**: 626-636 [PMID: 4639439]
- 61 **Mavrogenis AF, Zambirinis CP, Dimitriadis PA, Tsakanikas A, Papagelopoulos PJ.** Gorham-Stout disease. *J Surg Orthop Adv* 2010; **19**: 85-90 [PMID: 20727303]
- 62 **Ozbayrak M, Yilmaz MH, Kantarci F, Ozer H, Harmanci K, Babacan M, Dervisoglu S.** A case of an idiopathic massive osteolysis with skip lesions. *Korean J Radiol* 2013; **14**: 946-950 [PMID: 24265571 DOI: 10.3348/kjr.2013.14.6.946]

P- Reviewer: Behr GG S- Editor: Wen LL L- Editor: A
E- Editor: Lu YJ



Use of stereotactic radiosurgery in the treatment of gynecologic malignancies: A review

Beverly Long, Ramez N Eskander, Krishnansu S Tewari

Beverly Long, Department of Obstetrics and Gynecology, University of California, Irvine Medical Center, Orange, CA 92868, United States

Ramez N Eskander, Krishnansu S Tewari, Division of Gynecologic Oncology, Department of Obstetrics and Gynecology, University of California, Irvine Medical Center, Orange, CA 92868, United States

Author contributions: Long B and Eskander RN performed the literature review and wrote the manuscript; Tewari KS provided expert opinion and final review and final edits.

Correspondence to: Ramez N Eskander, MD, Division of Gynecologic Oncology, Department of Obstetrics and Gynecology, University of California, Irvine Medical Center, 101 The City Drive, Building 56, Room 260, Orange, CA 92868, United States. eskander@uci.edu

Telephone: +1-714-4566026 Fax: +1-714-4567754

Received: December 29, 2013 Revised: April 1, 2014

Accepted: April 17, 2014

Published online: March 28, 2015

Abstract

Recent retrospective studies have reported the use of stereotactic radiosurgery (SRS) in the treatment of gynecologic cancers. SRS uses real-time imaging and high dose radiation beams attached to precise robotic arms to target malignant lesions while sparing normal tissue. The purpose of this review is to examine the indications for SRS in gynecologic oncology, review the current literature regarding the use of SRS in gynecologic cancers, and identify future directions for research in this area. Literature on stereotactic radiosurgery was reviewed using the PubMed search engine. Articles written in English from 1993-2013 were reviewed, and 20 case series and clinical trials were included. The safety and efficacy SRS has been demonstrated in all gynecologic disease sites including cervical, endometrial, vulvar, vaginal, and ovarian cancers. Indications for its use include non-central pelvic recurrences in previously irradiated patients, complex or non-resectable disease recurrence, and solitary brain metastases. Toxicities

are usually mild, though grade 3-4 toxicities have been reported. SRS is a promising second line treatment modality for patients with primary or recurrent disease who cannot undergo standard surgical or radiation therapy. Further research is required to determine optimal dosing and fractionation schedules, delineate appropriate patient populations, and assess longterm morbidity and survival.

© 2015 Baishideng Publishing Group Inc. All rights reserved.

Key words: Stereotactic radiosurgery; Stereotactic body radiotherapy; Gynecologic oncology

Core tip: Stereotactic radiosurgery is a novel treatment modality in gynecologic oncology. Its use has been reported for inoperable primary tumors, recurrent tumors in or near irradiated fields, and isolated pelvic nodal metastases. Associated toxicities are usually mild. Though further research is needed to establish the role of SRS in gynecologic oncology, it represents an important second line therapy in appropriately selected patients.

Original sources: Long B, Eskander RN, Tewari KS. Use of stereotactic radiosurgery in the treatment of gynecologic malignancies: A review. *World J Radiol* 2014; 6(6): 366-373 Available from: URL: <http://www.wjgnet.com/1949-8470/full/v6/i6/366.htm> DOI: <http://dx.doi.org/10.4329/wjr.v6.i6.366>

INTRODUCTION

Stereotactic radiosurgery (SRS) is an emerging technology in the treatment of gynecologic cancers. It targets malignant lesions using real-time imaging in combination with high dose radiation beams attached to precise robotic arms. First used in the treatment of intracranial lesions, technological advancements in radiation and

image-guidance have allowed for its use in a variety of extracranial locations. Because SRS can focus on targets with sub-millimeter accuracy, it has been used for inoperable primary tumors near radiosensitive tissues, recurrent tumors in or near irradiated fields, and isolated pelvic nodal metastases. Its precise beams spare normal tissues and result in decreased toxicity when compared to conventional radiotherapy.

SRS is of particular interest in women with gynecologic malignancies, since many of these patients will recur in or near previously irradiated tissues, inoperable anatomic regions, or sites inaccessible to traditional radiation therapy^[1]. Recent retrospective studies have reported on the safety and efficacy of SRS in the treatment of gynecologic cancers. The purpose of this review is to examine the indications for SRS in gynecologic oncology, review the current literature regarding the use of SRS in gynecologic cancers, and identify future directions for research in this area.

STEREOTACTIC RADIOSURGERY

Stereotactic radiosurgery combines the complex dose distributions of intensity modulated radiation therapy (IMRT), the accuracy, reproducibility, and high doses of radiosurgery, and the fractionation of external beam radiation therapy to build a technique capable of treating complex abdominal-pelvic tumors. In this method, linear accelerators generate multiple X-ray beams, which can precisely target malignant tissues using advanced treatment planning, real-time imaging, and/or fiducial marker localization. The precision of these X-ray beams allows delivery of high doses to the tumor while sparing normal tissues. Doses are usually divided into 1-5 fractions given over 1-2 wk. Body immobilizers may be used to maintain spatial relationships during treatment sessions. Real-time image guidance ensures accurate tumor location, as abdominal and pelvic structures can exhibit substantial inter- and intra-fraction movement.

SRS has been utilized for lung, liver, pancreatic, renal, prostate, spinal, and pelvic tumors. It was first described for use in liver and lung lesions in the 1980s and has been used for gynecologic cancers since 2006. Twelve, small retrospective case series and one phase II clinical trial have described single institution experiences with SRS in the treatment of uterine, cervical, vaginal, vulvar, and ovarian cancers (Table 1). These series include a combined 291 patients who have undergone SRS for distant, local, lateral pelvic, or isolated pelvic node recurrences or as a substitute for brachytherapy in primary disease. One study specifically reported hematologic toxicities associated with SRS. Populations in these studies were heterogeneous, and varying doses and fractionation schedules have been described. Differences in reporting these results make it difficult to calculate a composite rate of survival, loco-regional control, or disease response.

The largest population was described by Kunos *et al.*^[1], in a phase II clinical trial evaluating the safety and

efficacy of SRS in 50 patients with recurrent cervical, endometrial, ovarian, and vulvar cancer. SRS was used to deliver 24 Gy in 3 fractions to a clinical target volume (CTV) that included the gross tumor volume (GTV) as well as surrounding fluorodeoxyglucose (FDG)-avid areas. The positron emission tomography (PET) images were overlaid and co-registered with computed tomography (CT) scans in order to accurately target the entire tumor site. One patient had a complete response, and the overall response rate (defined as complete response, partial response, or stable disease without progression) was 96%. Sixty-two percent of patients showed clinical benefit at 6 mo. Most toxicity was mild, though one patient did experience grade 4 hyperbilirubinemia and another developed an enterovaginal fistula. The study authors concluded that SRS was safe and efficacious for patients with recurrent gynecologic malignancies^[1]. All other data are derived from case series, and no controlled trials have been published. While studies mostly describe patients with endometrial or cervical primaries, SRS has been utilized for all gynecologic disease sites.

CERVICAL CANCER

Since radiation therapy is commonly used in cervical cancer, SRS is an attractive option for inoperable patients with primary or recurrent disease. Overall, 76 cases describing the use of SRS in cervical cancer have been published in 9 series. Four papers describe its use in the primary setting (usually as a substitute for brachytherapy), while others report its use for loco-regional, para-aortic node, or pelvic side-wall recurrences. All series included only patients who were unsuitable or unwilling to undergo other treatment modalities such as brachytherapy or surgical resection.

The largest series of patients treated with SRS for primary disease was published by Hsieh *et al.*^[2] in 2013. They described 9 patients with locally advanced cervical cancer who were treated with SRS (*via* helical tomotherapy) as a replacement for brachytherapy boost after the standard dose of EBRT and concurrent cisplatin. These patients were unable to undergo the recommended brachytherapy due to anatomic factors or medical comorbidities. Though three-year actuarial loco-regional control was 77.8%, three-year disease free survival was only 28.6%. Distant metastases were the most common pattern of failure, suggesting efficacy of SRS in controlling central pelvic disease^[2]. Mollà *et al.*^[3] reported similar results when treating primary disease. Their population included seven cervical cancer patients who underwent EBRT with SRS boost due to high-risk disease after initial surgical management. Only one patient recurred within the 12-month follow up period; however, actuarial values were not calculated. Toxicities were low in both series, consisting mostly of grade 1 or 2 sexual and GI symptoms. However, one patient did have grade 3 diarrhea, and another had grade 3 thrombocytopenia. One patient with stage 4A disease developed a rectovaginal fistula. Four patients

Table 1 Summary of case series of stereotactic radiosurgery

Ref.	n	Cancer types	Disease setting	Dose	Response/control rate	Survival	Grade 3/4 toxicities	Patterns of failure
Molla <i>et al</i> ^[3]	16	Cervical (7) Uterine (9)	Primary (stage 1-3) and recurrence	EBRT 45 GyT SRS 14-20 Gy/2-5 fractions +/- para-aortic boost (2 pts)	15 pts NED at 12.6 mo (1 recurrence)	Not reported	Rectal bleeding (1)	Not reported
Deodato <i>et al</i> ^[13]	11	Ovarian (4) Cervical (4) Uterine (3)	Recurrence	SRS 20-30 Gy/4-6 fractions	83.3% overall response rate 63% recurrence at 19 mo	Not reported	None	Systemic/distant progression (n = 4) Local progression (n = 1) Local and systemic progression (n = 1)
Guckenburger <i>et al</i> ^[7]	19	Cervical (12) Uterine (7)	Recurrence	EBRT 50 Gy SRS 15 Gy/3 fractions +/- vaginal BT (3 pts)	3 yr local control rate 81%	Median OS 25 mo, PFS 16 mo	Intestino-vaginal fistula (2) Small bowel ileus (1)	Systemic progression (n = 7) Local tumor progression (n = 1) Comorbid illness (n = 1) Unknown (n = 1)
Choi <i>et al</i> ^[10]	30	Cervical (28) Uterine (2)	Recurrence	EBRT 27-45 Gy SRS 13-45 Gy/1-3 fractions	4 yr local control rate 67.4%	Median PFS 32 mo	Various (5)	Locoregional failure (13.8%) Distant mets (10.3%) Local and distant failure (6.9%)
Dewas <i>et al</i> ^[9]	16	Cervical (4) Uterine (1) Rectal (4) Anal (6) Bladder (1)	Recurrence	EBRT 36-66 Gy (3 pts) SRS 36 Gy/6 fractions	1 yr local control rate 51.4%	Median OS 11.5 mo (DFS 8.3 mo)	None	Not reported
Haas <i>et al</i> ^[6]	6	Cervical (6)	Primary (stage 3B-4)	EBRT 45 Gy SRS 19.5-20 Gy/3-5 fractions +/- 50.4-61.2 Gy IMRT boost (5 pts)	100% local control at 14 mo	100% at 14 mo	None	Not reported
Hsieh <i>et al</i> ^[2]	9	Cervical (9)	Primary (stage 3B-4A)	EBRT 50.4 Gy SRS 15-27 Gy/5-9 fractions	3 yr local control rate 77.8%	Median OS 13 mo	Diarrhea (1) Thrombocytopenia (1) Rectal bleeding (3) Rectovaginal fistula (1)	Distant metastases (44%)
Hsieh <i>et al</i> ^[2]	31	Uterine (31)	Primary (stage 1B-3C)	IMRT or SRS <i>via</i> HT 45-50.4 Gy/25-28 fractions ICBT 4.5-5 Gy x 2-6 fractions	Not reported	Median OS 21 mo	None	Distant metastases
Kubicek <i>et al</i> ^[19]	11	Cervical (7) Uterine (2) Vaginal (2)	Primary (stage 2-3C) and recurrence	EBRT or IMRT 45-50.4 Gy SRS 5-27.5 Gy/1-5 fractions	Not reported	73% overall survival at follow-up	Rectal bleeding (1)	Not reported
Kunos <i>et al</i> ^[20]	3	Vulvar (3)	Recurrence	SRS 24 Gy/3 fractions	Not reported	1-3 mo PFS	None	Out of field recurrence
Kunos <i>et al</i> ^[15]	5	Endometrial (1) Ovarian (3) Cervical (1)	Recurrence	SRS 5-8 Gy x 3-5 fractions	Not reported	Not reported	Fatigue (1)	Distant metastases
Kunos <i>et al</i> ^[1] Phase II trial	50	Cervix (9) Endometrial (14) Ovarian (25) Vulvar (2)	Recurrence	SRS 24 Gy/3 fractions	6 mo clinical benefit 68%	Median OS 20.2 mo	Hyperbilirubinemia (1) Enterovaginal fistula (1)	Out of field recurrence (62%)

EBRT: External beam radiation therapy; SRS: Stereotactic radiosurgery; NED: No evidence of disease; BT: Brachytherapy; OS: Overall survival; HT: Helical tomotherapy; IMRT: Intensity modulated radiation therapy; PFS: Progression free survival.

had rectal bleeding following treatment^[3]. Two other papers by Hsieh *et al*^[4,5] report similar findings in this patient population, and Haas *et al*^[6] described 100% disease free survival at 14 mo in a series of six patients treated with SRS boost for primary disease.

These rates of local control exceed that of brachytherapy in many studies; however, the small sample sizes,

short duration of follow-up, and lack of a brachytherapy control group make it impossible to compare the two treatments. Still, the authors of these papers suggest that SRS could be considered as an alternative to brachytherapy boost, especially in patients unsuited for brachytherapy.

SRS has been more frequently described for recur-



Figure 1 CyberKnife (left) and GammaKnife (right). The CyberKnife device employs a mobile frame to radiate tumors in complex locations. The GammaKnife provides head immobilization for more accurate radiation delivery.

rent disease. Guckenberger *et al*^[7] describe its use in 12 patients with local recurrences of cervical cancer. Six patients in this study (which included patients with endometrial and cervical cancer) had undergone previous radiation, though most had received only vaginal brachytherapy. The majority of patients had been surgically treated for their primary disease. Those who had not had previous EBRT underwent standard external radiation at a dose of 45 Gy followed by a SRS boost using 14-20 Gy in 3 fractions. Patients previously treated with external beam radiation underwent only SRS. Loco-regional control was again excellent, with 81% loco-regional control at 3 years. Overall 3-year survival was 34%, and systemic disease progression remained the most common pattern of failure^[7]. This survival rate is similar to that of patients who undergo brachytherapy boost after EBRT for recurrent disease.

Interestingly, while pelvic sidewall recurrences carry a poor prognosis in patients treated with brachytherapy boost, location was not found to be a prognostic factor for patients treated with SRS^[8]. Dewas *et al*^[9] included four cervical cancer patients in their series describing SRS for lateral pelvic recurrences of cervical, uterine, anal, rectal, and bladder cancers. In this study, previously irradiated patients were treated with CyberKnife SRS (36 Gy in 6 fractions) for lateral pelvic masses (Figure 1). While disease free survival remained relatively low (8.3 mo), the authors argued that this treatment delayed local progression, as these recurrences would usually progress much more rapidly, improving quality of life. No grade 3 or higher toxicities were noted, and self-reported pain scores were improved after treatment. However, results should be interpreted with caution, as none of these patients exhibited unequivocal response. Favorable response was reported based on decreased uptake of contrast material on follow up PET studies^[9]. Further research is needed to determine whether SRS is superior to alternate radiation modalities in patients with lateral pelvic recurrences.

Another clinical challenge in recurrent cervical cancer occurs in patients with isolated, unresectable, para-aortic nodal recurrence. Though this type of recurrence is rare, it is associated with a poor prognosis and high post-treatment morbidity due to the radiosensitivity of surrounding organs, particularly the small bowel. Because of the precision of its radiation beams, SRS could be an excellent treatment modality for this type of recurrence. Choi *et al*^[10] described their experience in 28 patients with cervical cancer recurrence confined to para-aortic nodes. These patients received EBRT followed by SRS boost with 33-45 Gy in 3 daily fractions. Twenty-five patients received cisplatin before, during, or immediately after their radiation courses. Four year overall survival was 50.1%, and 96.5% of patients had at least partial response. Median time to disease progression was 32 mo. Though this population is small, SRS appears to be associated with improved overall survival, fewer toxicities, and shorter treatment times when compared for EBRT for nodal para-aortic recurrence^[11,12].

In combination, these reports indicate that SRS may be a promising therapeutic modality for primary and recurrent cervical cancer, especially in patients who have undergone previous radiation and/or are not candidates for surgical resection. Further studies are needed to clarify patient populations most likely to benefit from SRS. The role of concurrent chemotherapy with SRS is also an important area of research, as distant metastases are the most common sites of failure.

ENDOMETRIAL CANCER

SRS has been similarly studied in endometrial cancer. Seventy cases of SRS use for primary or recurrent endometrial cancer have been described in nine unique series. However, dosing regimens are not uniform, and study populations are heterogeneous. SRS has been used as a substitute for both EBRT and brachytherapy boost after

surgical therapy for high-risk disease, as well as in the treatment of recurrent endometrial cancer. It has also been used as a substitute for IMRT, due to its improved accuracy and ability to target higher doses of radiation to precise areas of tissue.

The largest series of SRS in the primary setting was published by Hsieh *et al*^[2]. They reported 31 cases of FIGO stage I B to III C uterine cancer, in which either SRS or IMRT was used as a substitute for EBRT after surgical staging for primary disease. IMRT or SRS was followed by vaginal brachytherapy in all patients. Two patients received concurrent cisplatin. This study is unique in that it is the only study that has compared SRS to another treatment modality. However, the study was not powered to detect statistical differences between the groups. While the study found no differences in overall survival or toxicity in SRS when compared to IMRT, SRS did provide significantly better critical organ sparing for the rectum, bladder, femoral heads, and intestines when compared to IMRT using dose-volume histograms. One cervical stump failure occurred in each group, and no grade 3 or 4 toxicities were noted^[2].

SRS has also been studied as a substitute for brachytherapy in patients with primary endometrial cancer. Mollà *et al*^[3] included nine patients with FIGO stage I - III uterine cancer in their series describing SRS boost after primary or post-operative EBRT. As described above, patients received 45 Gy EBRT or IMRT followed by 14-20 Gy SRS, usually following surgical treatment for either endometrial or cervical cancer. While most subjects had primary disease, two patients were enrolled due to local relapse. Patients underwent therapy at varying doses and fractionations. At 12-month median follow up, no recurrences were reported for the endometrial cancer group. Mostly grade 1 or 2 toxicities were noted, though one of the patients with recurrent endometrial cancer experienced persistent (grade 3) rectal bleeding 18 mo after re-irradiation at the vaginal vault^[3].

SRS is more commonly used in the setting of recurrent endometrial cancer, especially in previously irradiated patients. Both Guckenberger *et al*^[7] and Deodato *et al*^[13] have published separate series describing the use of SRS for distant or local recurrences of endometrial and cervical cancers. Favorable rates of local control were demonstrated, though statistics for cervical vs. uterine cancers were not separately reported. Both series were small, including only seven and three endometrial cancer patients, respectively^[7,13]. Two patients with isolated para-aortic nodal recurrences of endometrial cancer were also included in the above-mentioned study by Choi *et al*^[10] with results as described above. While it is likely that results from cervical cancer patients could be extrapolated to those with endometrial cancers, it is difficult to draw conclusions with these small patient populations. Study authors have suggested that SRS could benefit patients with pelvic or para-aortic node recurrences who are not candidates for exenteration or salvage radiotherapy; however, further studies are needed to confirm these results

and delineate optimal SRS dosing and fractionation.

OVARIAN CANCER

While the use of radiation therapy is much more common in endometrial and cervical cancers, SRS has also been used in the treatment of recurrent or non-operative ovarian cancers. Higginson *et al*^[14] describe the use of SRS for patients with isolated lung metastasis, para-aortic nodes, or vaginal cuff recurrences after primary surgery and adjuvant therapy.

Kunos *et al*^[15] included three cases of ovarian cancer in a 2009 report of their single-institution experience with SRS. These cases involved patients with multiple local and distant recurrences treated with multiple courses of chemotherapy, prior radiation, and/or surgeries. One patient with FIGO stage III C papillary serous cancer received primary surgery followed by two differing chemotherapy courses, as well as a repeat operation with intra-operative radiation before opting for SRS in the place of pelvic exenteration for a third relapse of her cancer. Stable disease remained after radiotherapy and the patient was without evidence of progression for 9 mo, treated with concurrent bevacizumab and cyclophosphamide. Another patient was free of disease at 10 mo after SRS was used to treat a persistent vaginal lesion following primary debulking, several chemotherapy courses, and external pelvic radiation. A third patient who underwent SRS after multiple surgeries, one dose of intra-operative radiation, and 3 mo of single-agent chemotherapy had stable disease at six month follow up with no more than grade 2 acute toxicities^[15].

Deodato *et al*^[13] described four other cases of SRS use in ovarian cancer. Three patients were without evidence of disease at 37, 31, and 19 mo after undergoing SRS to presacral lymph nodes, hepatic lesions, and supraclavicular nodes, respectively. One patient was alive with disease at 18 mo after SRS dosing to anterior mediastinal and left internal mammary nodes^[13]. Further studies are needed to define the appropriate patient population for SRS use in ovarian cancer. Currently, SRS is only used as a palliative measure for patients with localized, recurrent disease.

TOXICITIES

Most toxicities associated with SRS are mild and self-limiting. They include grade 1-2 fatigue, diarrhea, dysuria, nausea, and sexual side effects. However, rare grade 3 toxicities have been reported in almost every series. Rectal bleeding was reported in 4 patients in two different series of patients receiving EBRT followed by SRS boost. One of these events occurred in a patient with a history of prior radiation; however, the other patients with rectal bleeding had not undergone previous radiation therapy. Four patients in three series reported enterovaginal fistulas; all of these occurred in the recurrent setting^[1,2,7].

The largest study of toxicities associated with SRS was published by Kunos *et al*^[16] in 2012. This retrospec-

tive series analyzed hematologic toxicity in 61 women treated with SRS for stage 4 gynecologic malignancies. Ninety-three percent of these patients had received chemotherapy prior to SRS. Twenty-five percent had grade 2 fatigue, but the incidence of grade 3 fatigue was only 3%. All symptoms resolved by 30 d post-radiation. No neutropenia was reported; however, 5% of women had grade 1 anemia (Hb < 10.0 g/dL), and there were single incidences of grade 1, 2, and 3 thrombocytopenia. Further studies are required to better estimate the rates of non-hematologic toxicities, though it is difficult to isolate SRS as the cause of morbidity, since many patients receive surgery, chemotherapy, and other methods of radiation prior to receiving SRS^[16].

SRS IN GYNECOLOGIC CANCER

For now, the indications for SRS in gynecologic oncology remain undefined. Our review found three clinical scenarios for which SRS could provide benefit. These include non-central pelvic recurrences in previously irradiated patients, complex or unresectable disease recurrence, and solitary brain metastases (Table 2). This is an especially promising area of research, as few treatment options are available for these patients.

RECURRENT CERVICAL CANCER

Patients with locally advanced primary cervical cancer are usually treated with curative chemoradiation. Others may undergo primary surgery but require adjuvant chemoradiation due to high-risk pathologic features, positive margins, positive parametria or positive pelvic lymph nodes. In this population, utilization of traditional radiotherapy in a previously irradiated field is associated with prohibitive toxicity, and thus, SRS may represent a suitable alternative. While central pelvic recurrences can be treated with surgical exenteration, many patients have non-central recurrences or comorbid conditions that make them unsuitable for aggressive surgical resection with significant quality of life implications. Currently, the majority of these patients are treated with systemic chemotherapy using cisplatin, paclitaxel, and bevacizumab (following presentation of GOG 240)^[17] or are enrolled in clinical trials. Cyberknife SRS represents another therapeutic alternative and has decreased morbidity compared to exenteration. Series by Guckenberger, Dewas, and Deodata report mostly grade 1-2 toxicity, even in previously irradiated patients^[7,9,13]. In one series, two out of the three patients with grade 3-4 toxicities had received prior radiation; however, most previously irradiated patients did not suffer significant morbidity^[7].

COMPLEX OLIGOMETASTASES

Although the location of gynecologic cancer recurrence is unpredictable, patients with cervical and endometrial cancer commonly recur in the pelvis. A proportion, how-

Table 2 Indications for SRS in recurrent and metastatic gynecologic malignancy

Recurrent cervical cancer	Recurrence in a previously radiated fields Recurrence in patients who are not candidates for pelvic exenteration
Complex oligometastases	Unresectable oligometastases Oligometastases in abdominal retroperitoneum
Central nervous system and brain metastases	Intracranial lesions not accessible to Gamma Knife

ever, will have distant disease recurrence in complex locations involving the abdominal retro-peritoneum. Clinical options in this setting are limited, as access for adequate surgical resection is difficult to achieve. Treatment using chemotherapeutics or biologic agents is encouraged, and a combined approach utilizing systemic chemotherapy in conjunction with SRS is promising. Research regarding the above is limited, and given the unmet clinical need, warrants further investigation. There are well-defined selection criteria for utilization of SRS in the treatment of oligometastases for other primary disease sites such as lung, prostate and liver, and this data can may be extrapolated to gynecologic cancer patients.

CENTRAL NERVOUS SYSTEM AND BRAIN METASTASES

Central nervous system (CNS) and brain metastases are rare in gynecologic malignancies. Between 0.4%-1.2% of cervical cancers involve intracranial metastases, and percentages are similar for other pelvic disease sites. These lesions are usually treated with whole brain radiation or Gamma Knife stereotactic radiosurgery (Figure 1). A series by Menedez *et al.*^[18] included 14 patients with brain metastases from primary endometrial, ovarian, or cervical cancer. Patients received 16-20 Gy and experienced median survival of 5-13 mo. While the CyberKnife system is not well studied in gynecologic malignancies, its use is described for brain metastases in primary lung, breast, colon, and other cancers. CyberKnife eliminates the need for target fixation and allows for expanded treatment freedom for large or complex lesions.

The preference for Gamma Knife in the treatment of brain and spinal cord metastasis stems from the theoretical improvement in accuracy, 0.5 mm or less, over CyberKnife (1 mm or less), although these measurements have been disputed (Figure 1). Additionally, the smaller size of the Gamma Knife collimators reduce the potential injury to neighboring normal brain tissue, improving long term morbidity. The Gamma Knife also improves precision using a rigid immobilization device to prevent head movement during treatment. Conversely, utilization of CyberKnife SRS, allows for improved therapeutic versatility given the dynamic nature of the robotic arms, compensating for target organ motion, and allowing access to portions of the CNS that are difficult to treat using

Gamma Knife therapy.

FUTURE RESEARCH

While SRS is a promising treatment modality for inoperable or recurrent gynecologic cancers, many aspects of treatment remain uncertain. The available series describing SRS use heterogeneous dosing and fractionation schedules, and the optimal regimen has not been delineated. Controlled trials comparing SRS to brachytherapy or IMRT are also needed. Studies of SRS use for adjuvant therapy in high risk disease could further define the role of SRS in gynecologic malignancies. Today, SRS remains a second line treatment, reserved for patients with primary disease who are unsuitable for standard surgical or radiation therapy or for recurrent disease in a previously irradiated field.

Because most patients in the above-mentioned series suffered disease recurrence or progression outside the treatment area, many researchers have proposed concurrent chemotherapy with SRS to prevent progression of occult disease. Twenty five patients reported in the literature have received concurrent cisplatin during SRS, and four patients have received other chemotherapy regimens within 4 mo of SRS^[1,2,3,7,10]. However, this patient population is too small for any comparisons to be made regarding the benefits of concurrent chemotherapy. A phase I clinical trial of palliative SRS with gemcitabine and carboplatin is currently enrolling patients with recurrent or persistent cervical, endometrial, ovarian, vulvar, and vaginal cancers (NCT01652794).

CONCLUSION

SRS is an emerging area of radiation oncology, which has been successfully used in high risk gynecologic malignancies. Because of its unique ability to precisely target malignant lesions while sparing surrounding normal tissues, SRS can safely radiate tumors that may be difficult or impossible to treat with surgery or conventional radiotherapy. SRS has been described for all gynecologic malignancies and appears to have an excellent safety profile. Further research is necessary to determine optimal dosing and fractionation schedules, delineate appropriate patient populations, and evaluate long term survival and morbidity.

REFERENCES

- 1 **Kunos CA**, Brindle J, Waggoner S, Zanutti K, Resnick K, Fusco N, Adams R, Debernardo R. Phase II Clinical Trial of Robotic Stereotactic Body Radiosurgery for Metastatic Gynecologic Malignancies. *Front Oncol* 2012; **2**: 181 [PMID: 23227452 DOI: 10.3389/fonc.2012.00181]
- 2 **Hsieh CH**, Shueng PW, Hsiao SM, Wei MC, Wu WY, Sun HD, Tien HJ, Wang LY, Hsieh YP. Helical tomotherapy provides efficacy similar to that of intensity-modulated radiation therapy with dosimetric benefits for endometrial carcinoma. *Onco Targets Ther* 2012; **5**: 245-253 [PMID: 23055750 DOI: 10.2147/OTT.S35958]
- 3 **Mollà M**, Escude L, Nouet P, Popowski Y, Hidalgo A, Rouzaud M, Linero D, Miralbell R. Fractionated stereotactic radiotherapy boost for gynecologic tumors: an alternative to brachytherapy? *Int J Radiat Oncol Biol Phys* 2005; **62**: 118-124 [PMID: 15850911 DOI: 10.1016/j.ijrobp.2004.09.028]
- 4 **Hsieh CH**, Wei MC, Hsu YP, Chong NS, Chen YJ, Hsiao SM, Hsieh YP, Wang LY, Shueng PW. Should helical tomotherapy replace brachytherapy for cervical cancer? Case report. *BMC Cancer* 2010; **10**: 637 [PMID: 21092235 DOI: 10.1186/1471-2407-10-637.]
- 5 **Hsieh CH**, Wei MC, Lee HY, Hsiao SM, Chen CA, Wang LY, Hsieh YP, Tsai TH, Chen YJ, Shueng PW. Whole pelvic helical tomotherapy for locally advanced cervical cancer: technical implementation of IMRT with helical tomotherapy. *Radiat Oncol* 2009; **4**: 62 [PMID: 20003321 DOI: 10.1186/1748-717X-4-62]
- 6 **Haas JA**, Witten MR, Clancey O, Episcopia K, Accordino D, Chalas E. CyberKnife Boost for Patients with Cervical Cancer Unable to Undergo Brachytherapy. *Front Oncol* 2012; **2**: 25 [PMID: 22655266 DOI: 10.3389/fonc.2012.00025]
- 7 **Guckenberger M**, Bachmann J, Wulf J, Mueller G, Krieger T, Baier K, Richter A, Wilbert J, Flentje M. Stereotactic body radiotherapy for local boost irradiation in unfavourable locally recurrent gynaecological cancer. *Radiother Oncol* 2010; **94**: 53-59 [PMID: 20079550 DOI: 10.1016/j.radonc.2009.12.004]
- 8 **Jain P**, Hunter RD, Livsey JE, Coyle C, Swindell R, Davidson SE. Salvaging locoregional recurrence with radiotherapy after surgery in early cervical cancer. *Clin Oncol (R Coll Radiol)* 2007; **19**: 763-768 [PMID: 17931845 DOI: 10.1016/j.clon.2007.08.015]
- 9 **Dewas S**, Bibault JE, Mirabel X, Nickers P, Castelain B, Lacornerie T, Jarraya H, Lartigau E. Robotic image-guided reirradiation of lateral pelvic recurrences: preliminary results. *Radiat Oncol* 2011; **6**: 77 [PMID: 21699690 DOI: 10.1186/1748-717X-6-77]
- 10 **Choi CW**, Cho CK, Yoo SY, Kim MS, Yang KM, Yoo HJ, Seo YS, Kang JK, Lee DH, Lee KH, Lee ED, Rhu SY, Choi SC, Kim MH, Kim BJ. Image-guided stereotactic body radiation therapy in patients with isolated para-aortic lymph node metastases from uterine cervical and corpus cancer. *Int J Radiat Oncol Biol Phys* 2009; **74**: 147-153 [PMID: 18990511 DOI: 10.1016/j.ijrobp.2008.07.020]
- 11 **Grigsby PW**, Vest ML, Perez CA. Recurrent carcinoma of the cervix exclusively in the paraaortic nodes following radiation therapy. *Int J Radiat Oncol Biol Phys* 1994; **28**: 451-455 [PMID: 8276660 DOI: 10.1016/0360-3016(94)90070-1]
- 12 **Hong JH**, Tsai CS, Lai CH, Chang TC, Wang CC, Chou HH, Lee SP, Hsueh S. Recurrent squamous cell carcinoma of cervix after definitive radiotherapy. *Int J Radiat Oncol Biol Phys* 2004; **60**: 249-257 [PMID: 15337563 DOI: 10.1016/j.ijrobp.2004.02.044]
- 13 **Deodato F**, Macchia G, Grimaldi L, Ferrandina G, Lorusso D, Salutari V, Cilla S, Valentini V, Cellini N, Piermattei A, Scambia G, Morganti AG. Stereotactic radiotherapy in recurrent gynecological cancer: a case series. *Oncol Rep* 2009; **22**: 415-419 [PMID: 19578785 DOI: 10.3892/or_00000453]
- 14 **Higginson DS**, Morris DE, Jones EL, Clarke-Pearson D, Varia MA. Stereotactic body radiotherapy (SBRT): Technological innovation and application in gynecologic oncology. *Gynecol Oncol* 2011; **120**: 404-412 [PMID: 21194733 DOI: 10.1016/j.jgyno.2010.11.042]
- 15 **Kunos C**, Chen W, DeBernardo R, Waggoner S, Brindle J, Zhang Y, Williams J, Einstein D. Stereotactic body radiosurgery for pelvic relapse of gynecologic malignancies. *Technol Cancer Res Treat* 2009; **8**: 393-400 [PMID: 19754216]
- 16 **Kunos CA**, Debernardo R, Radivoyevitch T, Fabien J, Dobbins DC, Zhang Y, Brindle J. Hematological toxicity after robotic stereotactic body radiosurgery for treatment of metastatic gynecologic malignancies. *Int J Radiat Oncol Biol Phys* 2012; **84**: e35-e41 [PMID: 22543208 DOI: 10.1016/j.ijrobp.2012.02.027]

- 17 **Tewari KS**, Sill MW, Long HJ, Penson RT, Huang H, Ramondetta LM, Landrum LM, Oaknin A, Reid TJ, Leitao MM, Michael HE, Monk BJ. Improved survival with bevacizumab in advanced cervical cancer. *N Engl J Med* 2014; **370**: 734-743 [PMID: 24552320 DOI: 10.1056/NEJMoa1309748]
- 18 **Menendez JY**, Bauer DF, Shannon CN, Fiveash J, Markert JM. Stereotactic radiosurgical treatment of brain metastasis of primary tumors that rarely metastasize to the central nervous system. *J Neurooncol* 2012; **109**: 513-519 [PMID: 22870850 DOI: 10.1007/s11060-012-0916-2]
- 19 **Kubicek GJ**, Xue J, Xu Q, Asbell SO, Hughes L, Kramer N, Youssef A, Chen Y, Aikens J, Saul H, Pahlajani N, LaCouture T. Stereotactic body radiotherapy as an alternative to brachytherapy in gynecologic cancer. *Biomed Res Int* 2013; **2013**: 898953 [PMID: 24000329 DOI: 10.1155/2013/898953]
- 20 **Kunos C**, von Gruenigen V, Waggoner S, Brindle J, Zhang Y, Myers B, Funkhouser G, Wessels B, Einstein D. Cyberknife radiosurgery for squamous cell carcinoma of vulva after prior pelvic radiation therapy. *Technol Cancer Res Treat* 2008; **7**: 375-380 [PMID: 18783287]

P- Reviewers: Baglaj MS, Sharma DN, Tsili AC
S- Editor: Wen LL **L- Editor:** A **E- Editor:** Zhang DN





Published by **Baishideng Publishing Group Inc**

8226 Regency Drive, Pleasanton, CA 94588, USA

Telephone: +1-925-223-8242

Fax: +1-925-223-8243

E-mail: bpgoffice@wjgnet.com

Help Desk: <http://www.wjgnet.com/esps/helpdesk.aspx>

<http://www.wjgnet.com>

